IHTEC 2025

www.ihtec2025.org

info@ihtec2025.org

9th International HYDROGEN TECHNOLOGIES Congress

25-28 May 2025

Dokuz Eylül University, İzmir, Türkiye

EDITORS

Can Özgür Çolpan
Azize Ayol
Mehmet Akif Ezan
Mustafa Umut Karaoğlan

ISBN: 978-625-95734-1-0

PROCEEDINGS

International Association for Hydrogen Energy

International Journal of Hydrogen Energy

Cooperating Institutions

TENMAK
TURKISH ENERGY, NUCLEAR AND MINERAL RESEARCH AGENCY

YTÜ
CLEAN ENERGY TECHNOLOGIES INSTITUTE

International Association for Hydrogen Energy

International Journal of Hydrogen Energy

ENSIA
ENERGY INDUSTRIALISTS & BUSINESS ASSOCIATION

PROCEEDINGS

EDITORS

Can Özgür Çolpan
Azize Ayol
Mehmet Akif Ezan
Mustafa Umut Karaoğlan

ISBN: 978-625-95734-1-0

INDEX

Forewords	4
Committees	6
Scientific Program	8
Proceedings	30

FOREWORDS

MESSAGE FROM THE PRESIDENT

The Hydrogen Technologies Association has continued its mission of promoting research, development, and innovation in the field of hydrogen energy, while fostering collaboration between academia, industry, and government at both national and international levels. Over the years, the Association has organized numerous scientific and technical events, creating valuable opportunities for knowledge exchange and partnership building. These efforts have strengthened Turkey's role in the global hydrogen community and contributed to advancing sustainable energy solutions.

The 9th International Hydrogen Technologies Congress (IHTEC-2025) was successfully held in İzmir, Türkiye, from May 25 to 28, 2025, under the joint organization of Dokuz Eylül University and the Hydrogen Technologies Association. This year's congress brought together more than 500 participants from 25 countries and numerous companies with their latest products and technologies, providing a dynamic platform for presenting the latest scientific findings and technological developments in hydrogen production, storage, and utilization, and their applications in various sectors. The program featured a rich combination of thematic sessions, special sessions, panel discussions, and a dedicated workshop, contributing to productive conversations and new collaborations. The successful realization of IHTEC-2025 was made possible by the dedication and efforts of the Rector of Dokuz Eylül University and Honorary Chair, Prof. Dr. Bayram Yılmaz, and the Congress Co-Chairs, Prof. Dr. Can Özgür Çolpan and Prof. Dr. Azize Ayol. I also sincerely thank the organizing and executive committees, technical chairs, session chairs, speakers, authors, and volunteers for their valuable contributions. I would like to thank our sponsors for their generous support.

I believe that the networks established and the knowledge shared during IHTEC-2025 will continue to inspire progress towards a cleaner, more sustainable, and innovative hydrogen energy future. I look forward to welcoming our community to IHTEC-2026 in the Istinye University in Istanbul, where we will strengthen international cooperation and further contribute to the global advancement of hydrogen technologies.

Prof. Dr. İbrahim Dinçer
President, National Hydrogen Association

FOREWORDS

MESSAGE FROM THE CHAIRS

We are delighted to present the proceedings of the 9th International Hydrogen Technologies Congress (IHTEC-2025), held in İzmir, Türkiye, from May 25 to 28, 2025, under the joint organization of Dokuz Eylül University and the Hydrogen Technologies Association.

IHTEC-2025 brought together over 400 participants from 25 countries, creating a dynamic international platform for the exchange of scientific and technological knowledge in hydrogen energy. The scientific program featured 269 oral and 73 poster presentations across 36 thematic sessions, along with 2 special sessions, 2 panel discussions, and 1 dedicated workshop, covering key topics ranging from hydrogen production and storage to its applications in industry and defense.

The congress officially opened with addresses by Prof. Dr. Can Özgür Çolpan and Prof. Dr. Azize Ayol (Congress Co-Chairs), Prof. Dr. Bayram Yılmaz (Rector of Dokuz Eylül University and Honorary Chair), and Dr. Süleyman Elban (Governor of İzmir), whose participation and support we gratefully acknowledge. The plenary session continued with an insightful overview by Prof. Dr. İbrahim Dinçer (President of the Hydrogen Technologies Association), followed by a special talk by Dr. Abdullah Buğrahan Karaveli (President of TENMAK), both of whom provided valuable perspectives on hydrogen's strategic importance.

We were honored by the contributions of distinguished keynote and invited speakers, including Prof. Luigi Crema (President of Hydrogen Europe Research / Fondazione Bruno Kessler, Italy), Prof. Adélio Mendes (University of Porto, Portugal), Prof. John Irvine (University of St Andrews, UK), Prof. Eileen Yu (University of Southampton, UK), Prof. Feridun Hamdullahpur (University of Waterloo, Canada), Prof. Saim Özkar (Middle East Technical University, Türkiye), and Dr. Tareq Al-Ansari (Qatar Environment and Energy Research Institute, Qatar), who greatly enriched the scientific program.

Two high-level panel sessions enriched the IHTEC-2025 program. The pre-congress panel, titled "Innovative Hydrogen Policies in Combating Climate Change," was moderated by Prof. Dr. Adnan Midilli (ITU Energy Institute), featuring Prof. Dr. Arif Hepbaşlı (Yaşar University), Osman Arda Göçmen (Ford Otosan), Elis Şaşmaz (Topkapı Industry), and Yusuf Can Uz (Filament Technology). The second panel, "Hydrogen Technologies in the Defense Industry," was coordinated by Prof. Dr. Can Özgür Çolpan and Prof. Dr. Hüseyin Turan Arat (Sinop University) and moderated by Prof. Dr. Selmiye Alkan Gürsel (Sabancı University). This panel included key experts from the national defense sector: Deniz Demirci (Presidency of Defense Industries - SSB), Hüseyin Devrim (TEKSİS), Uğur Kayasal (Roketsan Missiles Inc.), Devrim Köseoğlu (TUSAŞ), and İbrahim Pamuk (LENTATEK). We sincerely thank all moderators and panelists for their valuable insights into the policy and strategic dimensions of hydrogen technologies.

A dedicated workshop on "Innovations on Hydrogen-based Processes & Technologies" was organized by Dr. Adolfo Iulianelli (CNR-ITM, Italy) and Dr. Canan Acar (University of Twente, Netherlands). The workshop provided a focused environment for discussions on membrane processes, hydrogen production systems, and fuel cell innovations. In addition, a special session on "Membrane Technologies in Hydrogen Production, Separation and Utilization" was coordinated by Prof. Dr. Can Özgür Çolpan and Dr. Adolfo Iulianelli. The session covered a broad range of timely topics including membrane engineering in the hydrogen economy, renewable sources and catalytic systems for hydrogen generation, hydrogen separation/purification and utilization by membrane technologies, hybrid industrial plant solutions for decarbonized hydrogen generation, and hydrogen and fuel cells. We extend our sincere thanks to all speakers who contributed their expertise and insights to this special session.

The successful realization of IHTEC-2025 was made possible through the commitment and collaboration of many individuals and institutions. We extend our sincere gratitude to Prof. Dr. Bayram Yılmaz, Rector of Dokuz Eylül University, for his unwavering support, and to Prof. Dr. İbrahim Dinçer, President of the Hydrogen Technologies Association and General Chair of the congress, for his visionary leadership. We would also like to thank Prof. Dr. Mehmet Akif Ezan and Assoc. Prof. Dr. Mustafa Umut Karaoğlan, the Technical Co-Chairs, for their outstanding efforts in shaping the scientific program, as well as the organizing and executive committees, the international scientific board, the reviewers, and the volunteers.

We are deeply grateful to our sponsors, whose generous support ensured the successful execution of the event. These include TENMAK, ARMELSAN Enerji, HABAŞ, Anton Paar, Hydrogenix, International Association for Hydrogen Energy (IAHE), BPlas, Doğu İklimlendirme, Koç University Hydrogen Technologies Center, TÜBİTAK, Consapp Engineering, Truva Bakır, Kurukahveci Mehmet Efendi, BREW MOOD COFFEE TEA, KFC Gıda, Dimes A.Ş., and Eker.

We believe that the knowledge shared and the collaborations formed during IHTEC-2025 will contribute meaningfully to the advancement of hydrogen-based solutions for a more sustainable future. Serving as Co-Chairs of this international event has been a great honor and a reflection of our shared commitment to progress in hydrogen technologies.

We thank all participants for their valuable contributions and hope to see continued collaboration and innovation in future editions of IHTEC.

Kind regards,

Prof. Dr. Can Özgür Çolpan & Prof. Dr. Azize Ayol
Congress Co-Chairs, IHTEC-2025

COMMITTEES

Honorary Chairs

Turhan Nejat Veziroğlu, *Founder, International Association for Hydrogen Energy (IAHE), International Journal of Hydrogen Energy (IJHE), USA*
Bayram Yılmaz, *Rector, Dokuz Eylül University, Türkiye*

General Chair

Ibrahim Dincer, *National Hydrogen Association, Türkiye*

Congress Chairs

Can Özgür Çolpan, *Dokuz Eylül University, Türkiye*
Azize Ayol, *Dokuz Eylül University, Türkiye*

Technical Chairs

Mehmet Akif Ezan, *Dokuz Eylül University, Türkiye*
Mustafa Umut Karaoğlan, *Dokuz Eylül University, Türkiye*

Organizing Committee

Canan Acar, *University of Twente, Netherlands*
Huseyin Turan Arat, *Sinop University, Türkiye*
İstemi Berk, *Dokuz Eylül University, Türkiye*
Anıl Erdoğan, *Vestel, Türkiye*
Alper Can İnce, *University of Connecticut, USA*
Adolfo Iulianelli, *CNR-ITM, Italy*
Olgun Konur, *Dokuz Eylül University, Türkiye*
Aykut Korkmaz, *Dokuz Eylül University, Türkiye*
Ankica Kovac, *University of Zagreb, Croatia*
Yağmur Nalbant Atak, *Atılım University, Türkiye*
Özgün Tezer, *Dokuz Eylül University, Türkiye*
Ömer Faruk Tunçbilek, *TENMAK, Türkiye*

Executive Committee

Can Özgür Çolpan, *Dokuz Eylül University, Türkiye*
İbrahim Dinçer, *National Hydrogen Association, Türkiye*
İnci Eroğlu, *Middle East Technical University, Türkiye*
Aysel Kantürk Figen, *Yıldız Technical University, Türkiye*
Mehmet Karakılçık, *Çukurova University, Türkiye*
Filiz Karaosmanoğlu, *İstanbul Technical University, Türkiye*
Adnan Midilli, *İstanbul Technical University, Türkiye*
Bestami Özkaya, *Istinye University, Türkiye*
Mahmut Temel Özdemir, *Fırat University, Türkiye*
Ramazan Solmaz, *Bingöl University, Türkiye*

COMMITTEES

International Scientific Board

Veziroglu, T.N., *USA*
Amani, Y., *USA*
Avaca, L.A., *Brazil*
Azbar, N., *Türkiye*
Baker, R., *UK*
Barbir, F., *USA*
Baykara, S., *Türkiye*
Bolcich, J.C., *Argentina*
Chen, W.H., *Taiwan*
Devrim, Y., *Türkiye*
Dincer, I., *Canada*
Eroglu, I., *Türkiye*
Goltsov, V.A., *Ukraine*
Hamdullahpur, F., *Canada*
Hepbasli, A., *Türkiye*
Hirohisa, U., *Japan*
Kakac, S., *Türkiye*
Karakoc, H., *Türkiye*
Karaosmanoglu, F., *Türkiye*
Kargı, F., *Türkiye*
Kendall, K., *UK*
Koca, A., *Türkiye*
Kumbur, E.C., *USA*
Li, X., *Canada*
Mench, M.M., *USA*
Midilli, A., *Türkiye*
Min, Z., *China*
Miranda, P.E., *Brazil*
Mohammadi, A.H., *South Africa*
Muradov, N., *USA*
Naterer, G.F, *Canada*
Ozkar, S., *Türkiye*
Ozturk, T., *Türkiye*
Ramenskiy, A.Y., *Russia*
Rosen, M.A., *Canada*
Sahin, O., *Türkiye*
Sahin, S., *Türkiye*
Sattler, C., *Germany*
Sheffield, J.W., *USA*
Spazzafumo, G., *Italy*
Stanislaw, S., *Poland*
Stolten, D., *Germany*
Vasudevan, S., *India*
Veziroglu, E.A., *USA*
Veziroglu, A., *USA*

SCIENTIFIC PROGRAM

SCIENTIFIC PROGRAM

Sunday – May 25, 2025

12:00 18:00	**CONFERENCE REGISTRATION**
16:30 18:00	**Pre-Congress Panel (Online / Onsite in Turkish) (HALL B)** **Innovative Hydrogen Policies in Combating Climate Change** **Moderator** **Adnan Midilli**, *ITU Energy Institute, Türkiye* **Panelists** **Arif Hepbaşlı**, *Yaşar University, Türkiye* **Hatice Eser Okten**, *IZTECH, Türkiye* **Osman Arda Göçmen**, *Ford Otosan, Türkiye* **Elis Şaşmaz**, *Topkapı Industry, Türkiye* **Yusuf Can Uz**, *Filament Technology, Türkiye*

Monday – May 26, 2025

07:30 09:00	**CONFERENCE REGISTRATION**	
09:00 09:30	**OPENING CEREMONY (HALL A)** **Can Ozgur Colpan**, *Congress Co-Chair* **Azize Ayol**, *Congress Co-Chair & Dean of Faculty of Engineering, Dokuz Eylul University* **Bayram Yılmaz**, *Honorary Chair & Rector of Dokuz Eylul University* **Süleyman Elban,** *Governor of Izmir*	
09:30 09.50	**OVERVIEW TALK (HALL A)** **Ibrahim Dincer**, *National Hydrogen Association President* **National Hydrogen Association and Critical Advantages of Hydrogen**	
09.50 10:20	**SPECIAL TALK (HALL A)** **Abdullah Bugrahan Karaveli**, *TENMAK President* **Türkiye's Long-Term Energy Strategy and the Role of Hydrogen**	
10:20 10:30	**Sponsor Recognition Ceremony (HALL A)**	
10:30 10:50	**Coffee Break**	
	KEYNOTE SESSION 1 (HALL A) **Session Chair: Adolfo Iulianelli**	**EXHIBITION**
10:50 11:30	**Luigi Crema**, *President, Hydrogen Europe Research / Fondazione Bruno Kessler* **Overview on the European Research and Innovation in the Hydrogen Sector: Best Practices and Priorities**	
11:30 12:10	**Adélio Mendes**, *University of Porto, Faculty of Engineering* **Given a North to the Energy Decarbonization**	
12:10 12:20	**Family Photo (In front of Rectorate Building)**	
12:20 14:00	**LUNCH (Lokal Çatı Restaurant, Dokuz Eylul University Rectorate)**	

SCIENTIFIC PROGRAM

Monday – May 26, 2025

PARALLEL SESSIONS – 1		
	HALL A	**HALL B**
	Session 1. Strategic Stakeholder Presentations **Session Chairs: Adnan Midilli & Arif Hepbaşlı**	**Session 2. Fuel Cells and Applications – I** **Session Chair: Bora Timurkutluk**
14:00 16:00	**Emre Yıldırım** *TENMAK, Türkiye* Strategic R&D Initiatives in Hydrogen Technologies at TENMAK	**#146** "Development of Hydrogen Powered Ejection System for Air Platforms" *T. Kalay, H. Özcan, S. Çelik* **#262** "Parametric Estimation and Performance Analysis of Direct Ethanol Fuel Cells and Lithium Batteries for Hybrid Energy Systems" *M. Yavuz Çelikdemir* **#263** "An Innovative Approach to Determine Effective Variables on Fault Detection of PEMFCs" *M. Yavuz Çelikdemir, S. Çelikdemir* **#282** "Synergistic Effects of Temperature, Gas Flow, and Clamping Force on Fuel Cell Performance" *B. Yılgın, F. G. B. San, C. Celik* **#110** "Experimental Study on Regenerative Fuel Cell Performance: Electrolyzer and Fuel Cell Mode Analysis" *M.A. Kesercioğlu, F.G. Boyacı San, N. Sözbir, Y. Çay* **#111** "Performance Optimization and Design Advancements of Proton Exchange Membrane Fuel Cells for Portable Energy Applications" *A. Algherbawi, S. Ekici*
	Hilal Gümüşlü *TENMAK, Türkiye* Policy Framework on Hydrogen Technology and Calls	
	Ali Rıza Arslan *Hydrogenix* Evaluations about Hydrogen and BESS Vehicles	
	Ornov Maulik *Anton Paar* Characterizing Metal Hydrides and their Hydrogen Storage Capacity	
	Nurettin Tekin *Kawasaki* Hydrogen Road of Kawasaki Heavy Industries	
	#238 "Innovative Blue Hydrogen Production from Gas Hydrate – Methane" *S. S. Çelebi, G. Çifçi, S. Obut, E Ercek* **#309** "Studies Conducted on On-Board/On-Site Catalytic Hydrogen Production and Carbon Capture and Utilization (CCU) in the SNG & Hyd Tec Lab at Boğaziçi University" *A. E. Aksoylu, B. S. Çağlayan*	
16:00 16:30	**Coffee Break (with Poster Session-1)**	

SCIENTIFIC PROGRAM

Monday – May 26, 2025

PARALLEL SESSIONS – 1

HALL C	HALL D	HALL E	
Session 3. Sustainable Hydrogen Technologies – I **Session Chair: Hüseyin Turan Arat**	**Session 4. Hydrogen Carriers – I** **Session Chair: Pedro J. Megía**	**Session 5. Modeling, Simulation, and Optimization – I** **Session Chair: Thomas Fend**	
#224 "Enhancement of Ionic Conductivity in Anion Exchange Membranes: Effect of Modified MOF Structures in PBI Membranes" *H. Altınışık, Y. Devrim* **#287** "Applications of MWCNTs in HHO Dry Cell Technology" *M. K. Baltacıoğlu, O. Bulut, Ç. Conker* **#288** "Enhancing HHO Dry Cell Efficiency with Graphene-Supported Electrolytes" *M. K. Baltacıoğlu, O. Bulut* **#289** "Metaheuristic Optimization of PID Controllers for Temperature Regulation in HHO Dry Cells" *C. Conker, M. K. Baltacıoğlu* **#290** "Development of Dopamine Modified Graphene Oxide Doped Composite Anion Exchange Membranes" *N. G. Önel, Y. Devrim* **#275** "Preparation of Pyridine Polybenzimidazole / Amine Functionalized Boron Nitride Composite Membrane" *R. Akay, A. H. Ali, H. N. Arkalı, G. Aktaş, Z. Pekdemir, E. Erünal* **#268** "Theoretical Insights into ZIF-71: Adsorption Potential for H_2 and H_2S as well as Its Response to External Electric Field" *O. S. Sarisoy, Y. Gürdal* **#272** "H_2 Sorption Potential of ZIFs Revealed Through Grand Canonical Monte Carlo Simulations" *G. Tunç, Y. Gürdal*	**#134** "NH_3 Synthesis with Ca_2NH Supported Ru Catalyst Under Mild Conditions" *T. A. Boynueğri, J.T.S. Irvine, G. Irvine, S. Jowitt, O. Magdysyuk, H. Ünsal, A. Long* **#165** "A Study on Fe-Zr/Al_2O_3 Catalyst for Hydrogen Production via Sodium Borohydride Methanolysis" *E. Ertun, Ö. Şahin* **#196** "Various Metal Oxide Catalysts Supported on Al_2O_3 for Hydrogen Generation from Alkaline $NaBH_4$ Solution" *S. Salt, H. Erdoğan, H. E. Figen, M. K. Elibol* **#216** "Investigation of the Activity of Composite Nanofiber Catalysts Synthesized by Electrospinning Technique for Hydrogen Production from Boron Fuels" *B. E. Ülgen, B. C. Filiz, A. K. Figen* **#223** "Borohydrides for Highly Selective Catalytic Methanol Production: Inside into Perovskite-Type Catalyst" *G. Özdemir, B. C. Filiz, F. N. Tekeli, A. K. Figen* **#329** "Modification of MOF-235 with Graphene Oxide for Enhanced Hydrogen Production from Sodium Borohydride Hydrolysis" *R. Ozdemir, D. Unlu* **#247** "Hydrogen Production via Methanolysis of Sodium Borohydride Using La_2O_3 and $La_2O_2CO_3$ Nanowire Catalysts" *E. Engintepe, S. Duman, A. N. Akın* **#252** "Synthesis and Characterization of Nanostructured La_2O_3-Based Catalysts for Hydrogen Production via $NaBH_4$ Methanolysis" *E. Engintepe, S. Duman, A. N. Akın*	**#241** "Machine Learning-Based Modeling and Performance Analysis of Solid Oxide Electrolysis Cells (SOECs)" *M. T. Durmaz, M. S. Akkuş* **#267** "Design and Performance Analysis of Hybrid Renewable Energy System with Hydrogen Storage: A Case Study In İzmir" *Y. A. Yıldız, Ş. E. Hayber* **#270** "Fuzzy Logic-Controlled Load Management in a Hybrid Microgrid with Fuel Cell, Wave, Solar, and Wind Power Integration" *Ş. Ataç, M. Güçyetmez* **#278** "Feature and LSTM-Based Capacity Prediction for Lithium-Ion Batteries: Application of Linear Regression and LSTM Models, with Future Expansion to Fuel Cell Datasets and Optimization" *S. Akkaya, M. Uyar* **#284** "A Data-Driven DA-LSTM Approach for Predicting PEMFC Degradation Trends in Dynamic Load Conditions" *N. K. Ekmekçi, M. Uyar* **#184** "Simulation and Analysis of Methane Thermal Decomposition in an Aerosol Flow Reactor" *İ. Ekmekci, İ. Karabay* **#218** "Development and Assessment of a Solar Energy-Based Multigeneration Plant Integrated with a Hydrogen Generation Unit for Clean Products" *F. Yılmaz, Y. E. Yuksel, M. Ozturk* **#217** "Design and Analysis of a Biomass-Based Integrated Plant for Green Hydrogen Generation and Beneficial Commodities" *F. Yılmaz, M. Ozturk, R. Selbas*	**EXHIBITION**
Coffee Break (with Poster Session-1)			

SCIENTIFIC PROGRAM

Monday – May 26, 2025

PARALLEL SESSIONS – 2		
	HALL A	**HALL B**
	Session 6. Catalysts for Hydrogen Applications – I **Session Chair: Ramazan Solmaz**	**Session 7. Hydrogen Vehicles and Mobility – I (Sponsored by HABAŞ)** **Session Chair: Canan Acar**
16:30 18:45	Invited Speaker **Saim Özkar** *Middle East Technical University, Türkiye* **Recent Advances in Catalyzing the Hydrolytic Dehydrogenation of Ammonia Borane** **#190** "The Synthesis of Ni-Co-B Catalyst for Ammonia Borane Dehydrogenation" *I. Nas, R. Kiziltas, A. Koç, E. Yildirim* **#191** "Development of Rhodium-Based Catalyst for Ammonia Borane Dehydrogenation" *A. Koç, R. Kiziltas, I. Nas, E. Yildirim* **#81** "The Effect of Different Types of Metal Phthalocyanine on the Electrodecomposition of H_2S to H_2 and Polysulfides" *F. Nazari, A. Sarioglan, M.S. Yazici* **#84** "Nickel-Lanthanum Catalysts Supported on Silicon Carbide to Produce CO_x-free Hydrogen and Valuable Carbons Under Microwave Energy" *H.P. Köse, D. Varışlı* **#85** "Development of Silicon Carbide Supported Nickel-iron Bimetallic Catalysts for Microwave-assisted Catalytic Methane Decomposition" *C. Acar, D. Varışlı* **#86** "Cu-BTC Synthesis via Solvothermal andMicrowave-assisted Methods: Characterization and Adsorbent Applications" *D. Dumlu, N. Ayas* **#124** "Enhanced Alcohol Oxidation in Acidic and Alkaline MEADIA Using Pt-Modified Nickel Layered Double Hydroxide Supported on Multiwall Carbon Nanotubes and Carbon Black Surfaces" *S. Saipanya, J. Jakmunee, L. Fang*	**#10** "Assessment of Metaheuristic Algorithms of Fuel Cell Vehicles: A Short Review" *O. Yasar, M.U. Karaoglan, C.O. Colpan* **#34** "Environmental Assessment of a Hybrid Ship Electrification System Integrating Molten Carbonate Fuel Cells, Battery, and Waste Heat Recovery" *O. Yuksel, E.Blanco-Davis, V. Shagar, A. Spiteri, D.Hitchmough, M.C. Di Piazza, M. Pucci, N.Tsoulakos, J. Wang* **#68** "Simulation of Wheeled and Tracked Fuel Cell Vehicles: A Comparative Study Using Proposed a New Tool Called PADSIP" *B. Açık, M.U. Karaoğlan, Z.S. İşleyen* **#72** "A Dual-Layered Control Strategy for Ultracapacitor/ PEMFC Hybrid Systems in Micro-FCEVs" *A. Yılmaz, N. Aksoy, G. Bayrak* **#315** "Assessment of Hydrogen and Methanol as Alternative Fuels in the Shipping Industry" *S. A. Korkmaz, E. T. Livanos, S. Afshan* **#260** "Determining the Hydrogen Pipeline Route in Türkiye for Sustainable Energy Transition Between Asia and Europe Using Hybrid Optimization" *M. T. Özdemir, S. Çelikdemir* **#36** "Effect of Hydrogen Addition on the Energy and Environmental Performance of a Compression Ignition Dual Biofuel Engine" *A. Rimkus* **#105** "An Optimization Model for Heavy-Duty Fleet Transition using Hydrogen Fuel-cell Vehicles" *F. Eser, Ş.I. Satoğlu*
19:00 20:30	**Welcoming Reception** *(Foyer)*	

SCIENTIFIC PROGRAM

Monday – May 26, 2025

PARALLEL SESSIONS – 2

HALL C	HALL D	HALL E	
Session 8. Combustion of Hydrogen and Fuel Mixtures – I **Session Chair: Alberto Figoli**	**Session 9. Photocatalysis and Water Splitting** **Session Chair: Giuseppe Barbieri**	**Session 10. Green Hydrogen Technologies** **Session Chair: Bilge Coşkuner Filiz**	
#113 "Numerical Simulations of Reacting Flows in Hydrogen Enriched Methane Blends and Pure Hydrogen Combustion" *H. Monteiro, L. Marcon, F. Oliveira, L. Vaz* **#136** "Effects of Hydrogen Enrichment and Gravity on Soot Formation in n-dodecane Laminar Diffusion Flames: A CFD Study" *A. Korucu* **#176** "Non-Premixed Hydrogen Combustion for an Industrial Ceramic Furnace: A Numerical Analysis" *S. Yılmaz, T. Bayramoğlu, K. Bayramoğlu, A. Özarslan, B. Kılıç, A. Akbay* **#319** "Predictive Modelling for Enhanced Petrol Engine Reliability with Petroleum and Hydrogen Fuels Mixture" *J. Matijošius, T. Žvirblis, A. Rimkus, U. Kale, A. Kilikevičius* **#344** "Bayesian Optimization Framework for Hosting Capacity Evaluation in Hydrogen-Electricity Integrated Networks" *S. Shahzad, H. Kilic* **#59** "Numerical Investigation of Exhaust Emissions of Hydrogen-Diesel Dual Fueled Medium-Speed Marine Diesel Engine under Different Fumigated Hydrogen Mass Fractions" *E.F. Pehlivan* **#31** "The Synergistic Effect of HHO Gas and Gasoline-Bioethanol Blends on Spark Ignition Engine Efficiency and Emissions" *A. Rimkus, E. Kozłowski, J. Matijošius, M. Zimakowska-Laskowska* **#54** "Effects of Hydrogen Addition on Methane Fuel Reactivity in High-temperature $CO_2/O_2/N_2$ Coflow in a Non-premixed Lab-scale Tube Burner" *M.K. Büyükakın*	**#17** "Solid Solution Oxide Catalysts for Enhanced Visible-light-driven Hydrogen Evolution by Water Splitting" *T.P. Perng* **#205** "$LaNiO_3$-Perovskite Type Photoelectrode Synthesis and Photoelectrochemical (PEC) Performance for Hydrogen Production" *B. Yıldırım, M. İ. Aydın, A. K. Figen* **#209** "Ga-Doped ZnO Coated Stainless Steel Electrodes for Photoelectrochemical Hydrogen Production" *S. Ayca, I. Dincer* **#303** "Design of a New Photonically Enhanced Electrolyser with ZnS Photocatalyst" *M. Gursoy, I. Dincer* **#350** "Development of Stability and Efficiency of $CsPbBr_3$ Perovskite Solar Cells" *Ş. Tüzüner, O. Mahmood, Ş. Ela, A. Vomiero* **#39** "Machine Learning Analysis of Photocatalytic Hydrogen Production over Halide Perovskites" *B. Yılmaz, R. Yıldırım* **#276** "Understanding the Kinetic Mechanism of WO_3 Photoanodes for PEC Applications" *E. I. Haznedar, F. Uçar, E. Ardalı, E. Altuntaş, S. Kaya* **#193** "Performance Assessment of Low-Cost Transition Metal-Based Electrode and Catalyst for Photoelectrochemical and Photocatalytic Hydrogen Generation" *M. Ayoub, I. Dincer* **#75** "Comparison of Performances of Imidazole-based Polymeric Catalysts for Hydrogen Production" *M. Zurnacı, K. Gökkuş, M. Gür*	**#67** "Sustainable Energy Solutions: 3D Printed PLA-NiMo@Ag for Green Hydrogen Production" *B. Doğru Mert, H. Nazlıgül, G. Aksaray, M.E. Mert, M. Seyedzavvar, G. Kardaş* **#70** "Application of Response Surface Methodology in Hybrid Green Hydrogen System Design and Optimization" *M. Gül, E. Akyüz* **#71** "Spatial Multicriteria Decision-making for Green Hydrogen Production: A Case Study of Southern Marmara, Türkiye" *M. Gül, E. Akyüz* **#145** "Determination of Green Hydrogen Production Capacity by Wave Energy Prediction: Model Development with an Adaptive Hybrid Method" *M. Tan* **#149** "Solar Driven Green Hydrogen Production: TiO_2@ MOS_2 Nanocomposite Synthesis and Performance" *M. Yurdakul, B. Yıldırım, A.K. Figen* **#266** "MLP Hyperparameter Optimization and Price Prediction Models on Fuel-cell Stock Data: Stability and Performance Analysis" *S. Akkaya, Ş. E. Hayber* **#273** "Evaluation of Green Hydrogen Production Using Weibull and Gamma Distributions: Technical, Economic, and Environmental Perspectives" *Y. A. Yıldız, M. Güçyetmez* **#340** "Boosting the Performance of Layered Titanate in Photocatalytic Water Splitting" *E. Doustkhah* **#135** "Green Hydrogen Production in Energy Islands" *N. Yabar, C. Haydaroğlu, A.N. Akpolat, H. Kılıç*	**EXHIBITION**

SCIENTIFIC PROGRAM

Tuesday – May 27, 2025

PARALLEL SESSIONS – 3		
08:30 09:00	**Conference Registration**	
09:00 10:30	**HALL A**	**HALL B**
	SPECIAL SESSION **Membrane Technologies in H_2 Production, Separation, and Utilization - I** **Session Chairs: A. Iulianelli & C.O. Colpan**	**Session 11. Catalysts for Hydrogen Applications – II** **Session Chair: Alessandra Beretta**
	Adele Brunetti *National Research Council – Institute on Membrane Technology, Italy* **Lecture 1: Sustainable E-fuel Production: Catalytic and Photocatalytic Membrane Innovations**	**#231** "Electrodeposition of Highly-Efficient Iron-Ruthenium Alloy Cathodes for Hydrogen Evolution Reaction in Alkaline Solutions" *D. Kutyła* **#237** "Electrodeposition of Nanocone-Shaped Ni–Pt Alloys for Enhanced Electrocatalytic Activity in Alkaline Solutions" *D. Kutyła* **#244** "Cobalt Doped Platinum-Cellulose-Carbon Aerogel Prepared by Supercritical Deposition as Electrocatalyst for Hydrogen Evolution Reaction" *A. Alsuhile, P. S. Pein, B. Schroeter, I. Smirnova, C. Erkey* **#254** "Investigation of the Effect of Tween Surfactant on Catalytic Performance and Structural Properties in the Electrochemical Deposition of Platinum" *J. H. Özdemir, A. K. Figen, O. K. Özdemir* **#277** "H_2 Evolution Reaction Pathways of Cobalt Based Molecular Catalysts Investigated by AB-initio Simulations" *Y. Gurdal* **#98** "Next-Gen Energy Catalysis: MXENE-Based Composites for High-Impact Hydrogen Evolution Reaction" *D. Onaylı, D.Ö. Özgür*
	Ivana Perović *Vinca Institute of Nuclear Sciences, Serbian National Institute, Serbia* **Lecture 2: Advances in Electrochemical Catalysts for Enhanced Hydrogen Production in Membrane Reactors**	
	Antonio Vita *National Research Council – Institute of Advanced Technologies for Energy, Italy* **Lecture 3: 3D-printed Ni-alloy based Structured Catalysts with Locally Tuned Porosity and Shape for Process Intensification of Ammonia Synthesis and Decomposition**	
	David Alique *Rey Juan Carlos University of Madrid, Spain* **Lecture 4: Towards the Industrialization of Pd-based Membranes Synthesis for Hydrogen Applications: Continuous Flowing Electroless Pore-Plating**	
10:30 10:50	**Coffee Break (with Poster Session-2)**	
	KEYNOTE SESSION 2 (HALL A) **Session Chair: Azzam Abu Rayash**	
10:50 11:30	**John T. S. Irvine**, *University of St. Andrews* **Interfacial Engineering in Solid Oxide Cells**	
11:30 12:10	**Eileen Yu**, *University of Southampton* **An Electrolysis and Microbial Electrochemical Hybrid System for Hydrogen Production and Wastewater Treatment**	
12:10 14:00	**LUNCH** *(Lokal Çatı Restaurant, Dokuz Eylul University Rectorate)*	

SCIENTIFIC PROGRAM

Tuesday – May 27, 2025

PARALLEL SESSIONS – 3			
Conference Registration			
HALL C	**HALL D**	**HALL E**	**EXHIBITION**
Session 12. Combustion of Hydrogen and Fuel Mixtures – I **Session Chair: Selda Ozkan**	**Session 13. Hydrogen in Smart Grids and Microgrids** **Session Chair: Damla Eroğlu Pala**	**Session 14. Hydrogen Safety** **Session Chair: Nader Javani**	
#177 "Numerical Investigation of the Effect of the Co-Combustion of Hydrogen and Natural Gas on Temperature and Carbon Emissions in Ceramic Furnace" *B. Kılıç, K. Bayramoğlu, S. Yılmaz, T. Bayramoğlu, A. Özarslan, A. Akbay* **#185** "Investigation of NO_x Reduction by NH_3-SCR in Aftertreatment System for H_2 Internal Combustion Engine" *T. B. Sarı, S. E. Bozbağ, D. Ş. Yıldız, C. Erkey* **#207** "Probative Assessment of Hydrogen Enriched Methane Induction in Gasoline Direct Injection Engine for Homogeneous Stoichiometric Lean Mixture Formation" *E. G. Varuvel, J. Stanley, L. J. Martin* **#302** "An Alternative Fuel for Afterburner: Energy and Economic Comparison for NH_3/H_2 and JP-8" *E. Oğur, A. Koç, H. Yağlı, Ö. Köse, Y. Koç* **#311** "CFD-Based Thermal and Emission Analysis of a 2D Hydrogen-Fueled Combustor Using Real Engine Data at Cruise Altitude" *Y. F. Görgülü, S. Ekici, T. H. Karakoc* **#312** "Combustion and Emission Behavior of a Hybrid Ammonia–Jet-A Blend Under Real Jet Engine Operating Conditions" *Y. F. Görgülü, S. Ekici, T. H. Karakoc*	**#40** "Use of Conventional and Renewable Energy in Türkiye's Hydrogen Supply Chain: A Grid-based Risk Assessment" *H. Kırış, M.G. Güler, Ö.N. Bilişik* **#213** "Type-2 Fuzzy MPPT Control of Fuel Cells Using a Hybrid Genetic-Grey Wolf Optimizer" *Ö. F. Özcan* **#214** "Hybrid Optimized Takagi Sugeno Type 2 Fuzzy-Based Voltage–Frequency Controller for Fuel Cell Integrated Isolated Microgrid" *Ö. F. Özcan, H. Kılıç, Ö. F. Özgüven* **#228** "Enhancing Longevity of Hydrogen-Powered Electric Vehicles, an Adaptive Neuro Fuzzy Control-Based High-Gain, Low-Stress Power Converter" *M. Özden, D. Ertekin, K. Baltacı* **#229** "Design and Implementation of Pseudo Levenberg-Marquardt Learning Artificial Neural Network Controller for Power Conversion in Fuel Cell to Battery Charging Systems, Improving Power Efficiency and Reliability" *M. Özden, D. Ertekin, K. Baltacı* **#261** "Sustainable Energy Based on Optimizing Load Frequency Control in Military Microgrid" *M. T. Özdemir, S. Çelikdemir, B. Yıldırım*	**#44** "Hydrogen Detection and Electrical Properties of Perovskite $BaTiO_3$ Schottky Diode" *L.B. Tasyurek, H. Karakurt, N. Kilinc* **#52** "Evaluation of Deformation via in situ SEM and EBSD on Hydrogen Embrittlement" *S.H. Nahm, H.S. Yun* **#127** "HAZOP and Fault Tree Analysis of Ammonia Leakage in a Ship's Ammonia Fuel System" *B. Zincir, B.A. Zincir* **#291** "Systematic Risk Analysis for Hydrogen Fuel Cell Vehicles and Safety Management in Fuel Cells" *N. Özaslan, B. Tanç* **#271** "SIC Schottky Diodes: Electrical Characterization and Gas Sensor Applications" *L. U. Kendirli, L. B. Taşyürek, N. Kılınç*	
Coffee Break (with Poster Session-2)			
LUNCH *(Lokal Çatı Restaurant, Dokuz Eylul University Rectorate)*			

SCIENTIFIC PROGRAM

Tuesday – May 27, 2025

PARALLEL SESSIONS – 4		
	HALL A	**HALL B**
14.00 16:00	**SPECIAL SESSION** **Membrane Technologies in H_2 Production, Separation, and Utilization - II** **Session Chairs: A. Iulianelli & C.O. Colpan**	**Session 15. Fuel Cells and Applications – II** **Session Chair: İnci Eroğlu**
	Giuseppe Barbieri *National Research Council – Institute on Membrane Technology, Italy* **Lecture 5: Revolutionizing Syngas and Biogas Valorization: Advanced Membrane Gas Separation for CO_2 and H_2 Recovery**	**Sarp Kaya** *Koç University* **Koç University Hydrogen Technologies Center (KUHyTech): Pioneering Sustainable Innovation for the Future**
	Simona Liguori *Clarkson University, United States* **Lecture 6: Engineering a Paradigm Shift in How We Think About Reactors: Metallic Membranes for Highly Intensified Hydrogen Production**	**#12** "Development of Operation Strategies for Improving Polymer Electrolyte Membrane Fuel Cell System Water Management and Hydrogen Circulation" *J. Bae, H. Park, I.J. Son, S. M. Park* **#24** "A-site Deficient $La_{0.4}Ca_{0.4}Ti_{0.995}Pt_{0.005}O_3$ with Low Pt Substitution as an Oxygen Reduction Electrocatalyst for Fuel Cell Applications" *S. Ozkan, S.Kim, J.T.S. Irvine* **#32** "Analysis of $MgCr_{2-x}Mn_xO_4$ (X=0.1/0.5/1) Spinel and LSM Composite Coatings as a Protective Layer for SOFC Interconnect" *H. Unsal, C.D. Savaniu, J.T.S. Irvine* **#102** "Experimental Analysis of Reversible Solid Oxide Cells Performance Degradation from Varying Power Ratios and Switching Frequencies in Operation" *N. Ali, G. Loreti, D. Pumiglia, Y.De Pra, L.D. Seta, V. Cigolotti, G. Monteleone, D. Borello* **#109** "Investigation of LSC-Based Composite SOFC Cathode Layers by ESD Coating Method" *E. Erğen, S. Akkurt* **#233** "Investigation of Carbon Felt Fabric as a Gas Diffusion Layer in PEM Fuel Cells: Stability and Coating Capability" *A. Şirin, J. H. Özdemir, O. K. Özdemir, N. Alp, M. Alp, E. Akarsu* **#234** "Investigation of Fuel Cell Performances by Recycling Used Membranes" *B. Aktaş, O. K. Özdemir, J. H. Özdemir*
	Simona Liguori *Clarkson University, United States* **Lecture 6: Engineering a Paradigm Shift in How We Think About Reactors: Metallic Membranes for Highly Intensified Hydrogen Production**	
	Kamran Ghasemzadeh *University of Edinburgh, United Kingdom* **Lecture 7: In situ Hydrogen Production, Utilisation and CO_2 Valorisation for Fuel Production by Membrane Reactor Technology**	
	Gabriel Bernardo *University of Porto, Portugal* **Lecture 8: Carbon Molecular Sieve Membranes for the Purification of Hydrogen**	
	#63 "Synthesis, Characterization of MOFs, and Evaluation as Adsorbents in Hydrogen Purification" *Z. Bilgin, D. Dumlu, N. Ayas* **#4** "Optimization of Green Hydrogen Electrolyser Plant Efficiency and Required Power Quality Solution" *T. Aydın, H. Bezerra* **#11** "The Potential of Offshore Wind Farms as Hydrogen Fuel Station: A Case Study of Marmara Sea" *V. Dixit, C. Acar*	
16:00 16:30	**Coffee Break (with Poster Session-3)**	

SCIENTIFIC PROGRAM

Tuesday – May 27, 2025

PARALLEL SESSIONS – 4			
HALL C	**HALL D**	**HALL E**	
Session 16. Catalysts for Hydrogen Applications – III **Session Chair: Tsong-pyng Perng**	**Session 17. Hydrogen Economy, Infrastructure, and Policy – I** **Session Chair: Emrah Erginer**	**Session 18. Gasification and Reforming Technologies** **Session Chair: Eileen Yu**	**EXHIBITION**
#163 "NASICON ($Na_3NiCo_2(PO_4)(SO_4)_2$) Doped Polyaniline as a New Candidate Electrocatalyst in Hydrogen Evaluation Reaction" *S. M. Yılmaz, A. K. Figen* **#181** "Development of Ce-Promoted Ni-Based Methanation Catalysts for Enhanced CH_4 Production" *B. Acar, B. S. Çağlayan, A. E. Aksoylu* **#182** "A Mechanistic Drifts-MS Investigation and Active Intermediate Determination of DRM at Low Temperature over Ru-La/ZrO_2 Catalyst" *O. Ordulu, A. Uzun, C. Öztepe, B. M. Eropak, B. S. Çağlayan, A. E. Aksoylu* **#183** "Operando Drifts Investigation of Active Intermediates in CO_2 Methanation over Ni-La/γ-Al_2O_3 Catalysts Under Low H_2/CO_2 Feed Ratios" *C. Öztepe, O. Ordulu, A. Uzun, B. M. Eropak, B. S. Çağlayan, A. E. Aksoylu* **#74** "Shaped Ni/Mesoporous CeO_2 as Active Catalysts in Hydrogen Production from Acetic Acid Oxidative Steam Reforming" *Á.M. de la Calle, A.J. Vizcaíno, A. Carrero, J.A. Calles, P.J. Megía* **#154** "Preparation of Zinc and Cobalt with Boron Doped Nickel Electrodes for Alkaline Electro-catalytic Hydrogen Production Activities" *A.D. Tümer, C. Demir, B. C. Filiz* **#226** "High-Entropy $NiCoCuFeMoMnO_x$ Oxide Thin Films Deposited via Open-Air Pulsed Laser for Efficient Electrocatalytic Oxygen Evolution Reaction" *H. Mahdavi, A. A. Alamdari, U. Ünal, H. Jahangari*	**#83** "Hydrogen Fuel Viability in EU Maritime Transport with Emissions and Policy Implications" *B.A. Zincir, B. Zincir* **#97** "Planning And Managing Renewable Gas Integration in the Portuguese Natural Gas Network" *F. Machado, L. Fernandes, L. Marcon* **#155** "Design of a Future Hydrogen Supply Chain Under Carbon Emission Constraints: The Case Study of Central Anatolia" *T. Ulusoy, A. Döyen, M.G. Güler* **#173** "Impact of Transportation Constraints on Hydrogen Supply Chain Performance of Türkiye" *B. Türkali-Özbek, A. Erdoğan, M. G. Güler* **#227** "The Role of Hydrogen Energy in Net Zero City Strategies" *M. T. Balta, M. Ö. Balta* **#256** "A Comparison of Systemic Performance: The Framework Models of Hydrogen Strategies in (Inter)National Energy Policies for Clean Energy Transition" *E. Gürler, A. Gürler Akdeniz, Y. Ateş, A. R. Boynueğri* **#356** "A Novel Framework of Synergistic Hydrogen City Design for Urban Decarbonization and Net-Zero Energy Autonomy" *A. Abu-Rayash*	**#73** "Hydrogen from Bio-oil: Thermodynamic Insights on Steam Reforming Technologies" *P.J. Megía, C. Rocha, A.J. Vizcaíno, A. Carrero, J.A. Calles, L.M. Madeira, M.A. Soria* **#87** "Steam Reforming of Sugar Beet Pulp with Dolomite-Based Ni-La Catalyst" *S. Karadeniz, .K. Kanatlı, N. Pourmoghadam, Ş. Genç, S.M.A. Aljafreh, N. Ayas* **#195** "In Situ Characterization of Pt-Re-Na/CeO_2 System and Operando Analysis of WGS Mechanism on its Sites by FTIR-DRIFTS-MS" *B. M. Eropak, A. Uzun, B. S. Çağlayan, A. E. Aksoylu* **#215** "Transfer Learning from Steam and Dry Reforming of Methane to Tri-Reforming of Biogas for Syngas Production" *R. Yıldırım, A. Coşgun, M. E. Günay* **#248** "A Simulation Study for Hydrogen Production from Low Rank Turkish Lignite Through Gasification in Trijen Pilot Plant in Soma" *Ö. O. Er, G. Kavas, M. Ünsal, A. S. Kartay, N. Ünlü, E. Muşdu, Ö. Ataç* **#259** "Thermal Modelling of Autothermal, Steam, and Partial Oxidation Solid Oxide Fuel Cell Reformers" *M. T. Çoban, H. Genceli, M. Asker, O. E. Turgut, M. S. Turgut* **#294** "Experimental and Theoretical Study of an Active Ni Nanocatalyst for the Hydrolysis of Sodium Borhydride and Dimethylamine Borane" *E. Karabulut, M. S. İzgi, E. Onat, S. Faal, F. A. Çelik, Ö. Şahin* **#347** "Sewage Sludge and MSW Gasification for Hydrogen Production: Integrating Renewable Energy with Desalination and Agriculture" *O. Tezer, A. Ayol*	
Coffee Break (with Poster Session-3)			

SCIENTIFIC PROGRAM

Tuesday – May 27, 2025

PARALLEL SESSIONS – 5		
	HALL A	**HALL B**
16:30 18:30	**WORKSHOP** **Innovations on Hydrogen-based Processes & Technologies** **Session Chair: Adolfo Iulianelli & Canan Acar**	**Session 19. Electrolysis and Electrolyzer Technologies – I** **(Sponsored by ARMELSAN Energy)** **Session Chair: Mustafa Kaan Baltacıoğlu**
	Alberto Figoli *National Research Council – Institute on Membrane Technology, Italy* **Operational Plan for Hydrogen Research, POR H_2 – EU/ NextGeneration EU – Program Agreement MASE/ENEA PNRR**	**#78** "Dynamic Modeling of an Anion Exchange Membrane Electrolyser" *S. Obut* **#305** "Electrolysis-Based Hydrogen Production Using Coaxial Cylindrical Electrodes with a Scrubber-Wire Cathode" *D. Erdemir, A. Y. G. Kara, I. Dincer* **#144** "Enhanced PEM Water Electrolysis with Low Equivalent Weight Aquivion® Membranes" *F. Giacobello, S. Siracusano, M.A. Mancuso, V. Cicciò, A. Muscolino, A.S. Aricò* **#90** "Green Hydrogen Production through AEM Electrolysis Technology" *V. Cicciò, S. Siracusano, S.C. Zignani, M. Pascale, A.S. Aricò* **#91** "MOS_2-Based Catalyst for Hydrogen Production in PEM Electrolysis" *M.A. Mancuso, S. Siracusano, F. Giacobello, V. Cicciò, A. Muscolino, A.S. Aricò* **#100** "Rapid and Scalable Synthesis of 3D Gas Diffusion Electrodes for AEM Water Electrolysers" *F. Lisi, R. Viscardi, I. Gualandi, E. Scavetta, F. Mariani, A. Fasolini, F. Basile* **#120** "Text-mining and Bibliometric Analyses for Proton Exchange Membrane Electrolyzers" *A. Fırtın, A. Yılmaz, İ. Eroğlu, R. Yıldırım, D. Eroğlu* **#130** "Synthesis of New Polystyrene Based Anion Exchange Membrane for Alkaline Electrolyzer" *L. Başat, M. Farsa, G. Kardaş*
	Selmiye Alkan Gürsel *University of Sabanci, Türkiye* **The Hydrogen Valley Project of Türkiye: HYSouthMarmara Hydrogen Shore**	
	Jan Veres *Technical University of Ostrava, Czech Republic* **Research Excellence for Region Sustainability and High-Tech Industries, REFRESH – International Project**	
	Antonio Agresta *National Agency for New Technologies, Energy and Sustainable Economic Development, Italy* **Driving Innovation Towards Future Aviation with Cutting-Edge Refuelling Technologies and Processes ALRIGH2T – EU Project**	
	Krzysztof Kapusta *Clean Coal Technology Centre – Centre for Climate and Renewable Energy Research, Poland* **Development of H_2 Oriented Municipal Waste Refinery Based on a Novel Borehole Gasification Process Combined with Advanced Gas Separation Techniques, HYDROMINE – EU Project**	
	Alessandra Beretta *Politecnico di Milano, Italy* **EMERALD – A Novel Electrified Reactor with Radial Current and Flow for the Intensification of Endothermic Catalytic Processes** **Research Project Funded by Air Liquide**	
19:00 21:00	**Banquet** *(Lokal Çatı Restaurant, Dokuz Eylul University Rectorate)*	

SCIENTIFIC PROGRAM

Tuesday – May 27, 2025

PARALLEL SESSIONS – 5			
HALL C	**HALL D**	**HALL E**	
Session 20. Hydrogen Storage Systems – I **Session Chair: Tugba Akkas Boynuegri**	**Session 21. Renewable Hydrogen Technologies and Integration** **Session Chair: Anıl Erdoğan**	**Session 22. Hydrogen Use in Industrial Applications** **Session Chair: Ismail Ekmekci**	
#6 "Numerical Study of Novel Thermal Management Methods for Hydrogen Storage in a Metal Hydride Reactor" *F. Selimefendigil, G.Şenol, H.F. Öztop* **#16** "FEM Based Numerical Study of Hybrid Nanofluid Enhanced Hydrogen Absorption in a Metal Hydride Reactor" *F. Selimefendigil, G. Şenol, H.F.* Öztop **#35** "Statistical Analysis of Hydrogen Storage on Boron Materials via Machine Learning" *A. Stif, E.C.Özcan* **#116** "Influence of the Technology for Obtaining IMC of the Mg-7%Ni-3%Ce System on the Evolution of Phase Transformations" *N. Ukhamedova, A. Miniyazov, Z. Ospanova, A. Sabyrtaeva, K. Shaikieva* **#118** "Integrating Metal Hydride-based Hydrogen Storage Tank with a PEM Fuel Cell Stack for Enhanced Energy Efficiency in Underwater Applications" *B. Sezgin, T.Öztürk, İ. Eroğlu* **#122** "Role of Hydrogen Adsorption and Desorption in Underground Storage within Coal Seams" *Ö. İmir, Ş. Merey, A. Fişne* **#158** "Optimization of Assembly Torque and Lubrication Amount for Hydrogen Tank Valves" *O. Özkan* **#322** "Production and Characterization Sulfonated Polyphenyl Sulfone PEM Membrane for Vanadium Redox Battery" *E. Çolak, S. Kahraman, B. Çetin, D. Ünlü, F. Ugur Nigiz*	**#8** "Solar Thermochemical Hydrogen Generation with a 250-kW Structured Reactor: Experiences from Tests at the Jülich Solar Tower" *T. Fend, V.K.Thanda, J. Lampe, S.Menz, S.Schmitz, G.Piesche, S.Berger* **#50** "Securing Geothermal Energy Projects: Hydrogen Production and Underground Storage as a Solution for Electricity Market Fluctuations" *H. Aydın, S. Merey* **#77** "AI-Based Optimization of a PV-Battery-Electrolyzer System for Green Hydrogen Production" *A. Yılmaz, N. Aksoy, G. Bayrak* **#236** "The Evaluation of Renewable Energy Alternatives in Hydrogen Supply Chain in Türkiye Using Hybrid Fermatean Fuzzy AHP-WPM Approach" *H. Kırış, Ö. N. Bilişik* **#202** "Thermodynamic Evaluation of Hybrid Thermochemical Process for Lignin to Hydrogen and Methane Conversion" *S. Yadav, F. Khalid* **#201** "Thermodynamics Assessment of a New Three-Step Cycle for Methane to Methanol and Hydrogen Production" *V. Yadav, I. Khan, F. Khalid* **#306** "An Experimental Investigation for Improved Hydrogen Production from Magnesium-Seawater Reaction" *Y. Hafez, I. Dincer* **#307** "Application of Synthesized Ammonium Formate as an Electrolyte in Stainless Steel-Stainless Steel Electrode H-Cell Configuration" *C. G. Turk, I. Dincer*	**#133** "Optimizing Energy Investments for Growing Demand of Türkiye: Hydrogen-Based Batteries and Renewable Integration" *A.O. Kabil, M.G. Güler* **#232** "Designing a Multiple Production System Based on CO_2 Capture and Utilization in Glass Industry" *I. Akgun, I. Dincer* **#281** "Theoretical Investigation of Using of Hydrogen and Natural Gas Blending in Slab Tundish Heating Systems for Green Steel Revolution" *H. T. Arat, M. K. Baltacıoğlu, S. M. Has* **#358** "Solar-based Green Hydrogen Production for Decarbonizing Natural Gas: An Emissions Perspective" *Habip Şahin* **#206** "Utilization of a Boron Co-Doped Activated Carbon/Starch Based Metal-Free Biocathode for Hydrogen Production" *A. T. Goren, I. Dincer* **#199** "Activated Charcoal for Sustainable Solid State Hydrogen Storage by Physical Adsorption" *A. Capoglu, I. Dincer*	**EXHIBITION**
Banquet *(Lokal Çatı Restaurant, Dokuz Eylul University Rectorate)*			

SCIENTIFIC PROGRAM

Wednesday – May 28, 2025

PARALLEL SESSIONS – 6		
08:30 08:45	**Conference Registration**	
	HALL A	**HALL B**
	Session 23. Hydrogen Economy, Infrastructure and Policy – II **(Sponsored by ARMELSAN Energy)** **Session Chair: Jan Veres**	**Session 24. Hydrogen Vehicles and Mobility – II** **Session Chair: Antonio Vita**
08:45 10:45	**Invited Speaker** **Tareq Al-Ansari** *Qatar Environment and Energy Research Institute* **Role of Hydrogen in the Energy, Water and Food Nexus** **#359** "A Policy on H_2/SAF Valley in Türkiye" *A. Midilli* **#255** "Hydrogen Value Chains in Positive Energy Districts: A Multi-Level Analysis on the Dynamics between Energy Transition Plans and Integrated Spatial Planning" *A. Gürler Akdeniz, E. Gürler, Y. Ateş, A. R. Boynueğri* **#253** "Critical Path Analysis for a Future Hydrogen Supply Chain: A Case Study for Central Anatolia" *M.G. Güler, T. Ulusoy, A. Döyen, F. Kosanoğlu* **#265** "Optimizing Hydrogen Refueling Infrastructure in Qatar: A Maximum Coverage Location Model Approach" *C. Méndez, R. Baldacci, M. Contestabile, Y. Bicer* **#310** "Techno-Economic Analysis of Green Hydrogen Production: Investigating Hybridization Potential in İzmir" *E. D. Gülay, C. O. Colpan, M. A. Ezan*	**#188** "Comparative Life Cycle Carbon Emissions Assessment of Utilizing Diesel Oil and Hydrogen Fuel on a Ferry" *O. Konur, M. E. Aydın, M. S. Aydın* **#204** "High Voltage Gain LLC Resonant Converter Design for Energy Transfer from Fuel Cell Electric Vehicle to Electric Vehicle" *M. Akkuş, E. Akboy, A. R. Boynueğri* **#211** "Investigation of T-Class Fuel Cell Hybrid Electric Off-Road Vehicle" *Z. S. İşleyen, M. U. Karaoğlan* **#221** "Performance Analysis of a Small Hybrid Vehicle on Inclined Roads Under WLTP Class 2 Drive Cycle" *B. Yılmaz, C. O. Colpan* **#225** "Uninterrupted Communication with PEMFC-Enhanced UAVs in Disaster Scenarios" *M. Kayaoğlu, S. Unal, B. Calisir* **#251** "Design of a Standalone Electric Vehicle DC Fast Charging Station Based on a Hybrid Energy System with Fuel Cell and PV for a Tourist Resort" *M. Yıldırım, S. Unal* **#314** "Numerical and Experimental Investigation of Electric and Fuel Cell Hybrid Mini UAV" *İ. Sağlam, Z. İşleyen, M. Karaoğlan, Ş. Yavuz* **#174** "Mathematical Modeling and Ground Tests of a Fuel Cell Hybrid Unmanned Aerial Vehicle in Cruise Phase" *M. Azer, M. U. Karaoğlan, C. O. Colpan, T. H. Karakoc*
10:45 11:05	**Coffee Break (with Poster Session-4)**	

SCIENTIFIC PROGRAM

Wednesday – May 28, 2025

PARALLEL SESSIONS – 6			
Conference Registration			
HALL C	**HALL D**	**HALL E**	**EXHIBITION**
Session 25. Fuel Cells and Applications – III **Session Chair: Adele Brunetti**	**Session 26. Thermodynamics of Hydrogen Energy Systems** **Session Chair: Aysel Kantürk Figen**	**Session 27. Sustainable Hydrogen Technologies – II** **Session Chair: Ivana Perović**	
#125 "Development of Flat-Tubular Solid Oxide Fuel Cells via Mold Casting" *K. Bilgil, Ç. Timurkutluk, S. Onbilgin, B. Timurkutluk* **#129** "Microtubular Solid Oxide Fuel Cells with Ytterbium Doped Zirconia Electrolytes" Ç. Timurkutluk, E. Yıldız, *G. Germen Tutaş, S. Onbilgin, B. Timurkutluk* **#132** "Lightweight and Optimized End Plates for PEM Fuel Cells: A Comparative Structural Analysis" *F. Çetiner, A.E. Kılıç, S. Çelik, S. Toros, R.E. Ece* **#142** "Developing and Designing Different Channel Types for Micro Direct Methanol Fuel Cells Based on Mitochondria Cell Structure" *M. Menteş, A.E. Kılıç, S. Çelik, F.D. Güzel, M.K. Birhanu* **#157** "Scale up Techniques for PEMFC: Fluid Mechanics Approach" *G. Tol, A.C. Türkmen, C. Çelik, F.G. Boyacı San* **#212** "Impact of Current Density on Temperature and Water Content Distribution in a PEM Fuel Cell using a Coupled Heat and Mass Transfer Model" *M. Jahanbakhsh, E. Aydın, C. Erkey*	**#5** "Efficiency and Performance Analysis of IT-SOFC Integrated with S-CO_2 Brayton Cycles: A Comprehensive Study on Waste Heat Utilization" *S. Beygül, Y. Kalıncı* **#197** "Thermodynamic Analysis of Synthetic Fuel Production from Carbon Dioxide Obtained from Carbon Capture Facility in Oil Refinery by Combination of Hydrogen Production and Power Conversion" *S. B. Sungur, E. Kayabasi, E. Alp* **#198** "Analysis of Synthetic Fuel Production Utilizing the Waste Heat from Blast Furnace Hot Stoves by Combination of Thermal Energy Storage and Power Cycle" *S. B. Sungur, E. Alp, E. Kayabasi* **#192** "Performance Assessment of Hydrogen Production from Geothermal-Solar Based ORC System" *Y. N. Atak* **#208** "Thermodynamic Modeling of an Innovative Integrated Polygeneration System Using Sustainable Energy Resources" *M. A. Sabbaghi, C. O. Colpan, H. Genceli* **#330** "Green Hydrogen Production Station: Applying Exergetic Sustainability Parameters to a 1 MW PEM Electrolyzer" *A. E. Aluç, A. Midilli* **#308** "Mathematical Modeling and Simulation of an Anion Exchange Membrane Water Electrolyzer Using COMSOL Multiphysics" *A. Demirtaş, C. O. Colpan, Y. Devrim, Y. N. Atak* **#141** "Thermodynamic and Electrochemical Modeling of Direct Methanol Fuel Cell System for Portable Applications" *E. Kalkan, M. Alobeid, S. Çelik, H. Özcan*	**#333** "An Efficient and Sustainable Approach to Green Hydrogen Production Using PV Systems" *H. Topcan, A. Akpolat, U. Aydemir* **#343** "Hybrid Hydrogen Systems for Mitigating Sub Synchronous Oscillations in Weak Power Grids" *S. Shahzad, H. Kilic* **#313** "Boosting Photocatalytic Hydrogen Production through Ni_2P/g-C_3N_4/Ti_3C_2 Quantum Dots" *D. Akyüz, B. Güven, E. Demirbaş* **#338** "Metal-organic Frameworks for Hydrogen Storage" *S. Demir* **#283** "Manta Ray Foraging Optimization for Accurate Parameter Estimation of Proton Exchange Membrane (PEM) Fuel Cell Model" *D. Yağcı, H. Genceli, O. E. Turgut* **#89** "Plasma-catalytic Method of Methane Conversion in Microwave Discharge" *M. Skakov, A. Miniyazov, T. Tulenbergenov, I. Sokolov, A. Agatanova* **#151** "Speed Control of a Synchronized Induction Motor Powered by Hydrogen Fuel Cell" *H. Erdoğan*	
Coffee Break (with Poster Session-4)			

SCIENTIFIC PROGRAM

Wednesday – May 28, 2025

PARALLEL SESSIONS – 7		
	HALL A	**HALL B**
	PANEL **Hydrogen Technologies in the Defense Industry**	**Session 28. Electrolysis and Electrolyzer Technologies – II** **Session Chair: Gülfeza Kardaş**
11:05 12:50	**Moderator** **Selmiye Alkan Gürsel** *Sabancı University, Türkiye* **PANELISTS** **Deniz Demirci** *Secretariat of Defense Industries (SSB), Türkiye* **Hüseyin Devrim** *TEKSIS, Türkiye* **Uğur Kayasal** *Roketsan Missiles Inc., Türkiye* **Devrim Köseoğlu** *Turkish Aerospace Industries (TUSAŞ), Türkiye* **İbrahim Pamuk** *LENTATEK, Türkiye* *This panel aims to provide insights into how hydrogen can revolutionize military propulsion systems, enhance energy resilience, and support sustainable logistics.*	**#138** "Synthesis of NiFeMo HER Catalyst on Nickel Foam for AEM Electrolyser" *Y.S. Adam, M. Farsak, G. Kardaş* **#166** "Simulation-Based Performance and Cost Optimization of Alkaline Electrolysers" *S. Ş. Demirezen, H. Özcan, S. Çelik* **#168** "Comparison of IrO_2-FeVS and IrO_2-FeVS-Co Catalysts in PEM Electrolysis at Different Temperatures" *M. Çokyaşa, A. Ekinci, Ö. Şahin, O. Baytar* **#243** "Experimental Analysis of Proton Exchange Membranes for Water Electrolyzers Across a Range of Operating Parameters" *A. Albadwi, S. B. Selçuklu, M. F. Kaya* **#48** "Optimization of Boron-doped Nickel Electrodes for Enhanced Hydrogen Production via Alkaline Electrolysis" *C. Demir, K.A. Uğurlu, D. Türkyılmaz, A.D. Tümer, B.C. Filiz* **#139** "Investigation of Long-term Degradation Effects in PEM Electrolyzers" *A. Çankaya, S. Çelik, B. Sevinç, K. Dağıdır, H. Özcan* **#148** "Design of Single Porous Transport Layer with Strut-based Lattice Structures for PEM Electrolyzers" *K. Dağıdır, A. Çankaya, S. Çelik*
12:50 13:30	**LIGHT LUNCH** *(Foyer)*	
KEYNOTE SESSION 3 (HALL A) **Session Chair: Azize Ayol**		
13:30 14:10	**Feridun Hamdullahpur**, *University of Waterloo* **Green Ammonia: A Pragmatic Pathway for Early Green Hydrogen Commercialization**	

SCIENTIFIC PROGRAM

Wednesday – May 28, 2025

PARALLEL SESSIONS – 7			
HALL C	**HALL D**	**HALL E**	
Session 29. Hydrogen Storage Systems – II **Session Chair: S. Aykut Korkmaz**	**Session 30. Sustainable and Renewable Hydrogen Technologies** **Session Chair: David Alique**	**Session 31. Biohydrogen and Waste-to-Hydrogen** **Session Chair: Krzysztof Kapusta**	**EXHIBITION**
#126 "Geological Hydrogen Storage for Long-duration Energy Resilience" *A. Özmumcu, A. Baba* **#180** "Performance Assessment of a Hybrid Compressed Air Energy Storage System Fed by Hydrogen from RES" *V. Tola, R. Caria* **#239** "Fly Ash-Derived Supported Iron Catalysts for Efficient Ammonia Decomposition: A Sustainable Approach for CO_x-free Hydrogen Storage" *B. Sekizkardeş, S. F. Kurtoğlu-Öztulum* **#361** "Intelligent Health monitoring of Hydrogen Storage and Transport Systems" *S. Sikdar*	**#298** "Sustainable Hydrogen Production Through Hybrid Nanofluid Integrated Evacuated Tube Solar Collectors with Organic Rankine Cycle" *S. G. Güngör* **#346** "From Agricultural Waste to Renewable Energy: Integration of Soil-based Microbial Fuel Cells in Biobed Systems for Sustainable Treatment of Olive Oil Mill Wastewater" *S. Gunes, A. Ayol* **#316** "Producing Hydrogen and Heat from Solar Towers: A Path toward Energy-Independent Cities" *E. Kocaman, H. Yağlı, H. Tutumlu, E. Oğur, R. Yumrutaş* **#106** "Investigation of the Conditions for the Use of New Generation Hydrogen Generator in Geothermal Power Plants: Kizildere Geothermal Field Case Study" *R. Ş. Çetin, F.G.Boyacı San, F. S. T. Haklıdır* **#334** "Hydrogen Production from NaCl, $CaCl_2$ and $MgCl_2$ Salts using Carbon Rods Extracted from Waste Batteries" *S. Damarseckin, M. Erden, A. Atiz, H. Karakilcik, M. Karakilcik* **#366** "Development and Analyses of a Nuclear-Driven Polygeneration System with Helium Brayton Cycle, Hydrogen and Ammonia Production, Ejector Cooling, and Desalination" *O. Kizilkan, G. Soytürk*	**#42** "Comparative Analysis of Biohydrogen Production Studies in Türkiye Using Evidence Synthesis Methodology" *K.K. Yiğit, T. Keskin-Gündoğdu* **#43** "Evaluating the Performance of Boosting Regressors for Predicting Biohydrogen Production under Variable Experimental Conditions" *M.A. Ergün, T. Keskin-Gündoğdu, B.E. Köktürk- Güzel* **#99** "Evaluation of Hydrogen Production Efficiency by Dark Fermentation Process of Various Airport-derived Wastes" *F. Altay, N. Semerci, A. Öngen, Ş. Duran, M.C. Altay, N. Yeşilova* **#219** "Challenges and Limitations of Dark Fermentative Hydrogen Production" *Ş. Arıcı, G. Koçar* **#220** "Integration of Dark Fermentation and Microbial Electrolysis Cells for Hydrogen Production from Wheat Straw" *Y. D. Yilmazel, İ. Konar, R. Kunayeva, İ. Bulat, R. Harb* **#345** "Comparative Assessment of Bioelectricity Generation from Various Industrial Wastewaters and High-strength Organic Wastes Using Microbial Fuel Cell Technology" *I. Biryol, A. Ayol* **#79** "Enhanced Catalytic Performance of Titanium Dioxide-supported CuCo Bimetallic Catalyst for Hydrolysis of Ammonia Borane" *M. Kılıç, E. Özdemir*	
LIGHT LUNCH *(Foyer)*		**Optional Social Tour (starts at 12:30)**	

SCIENTIFIC PROGRAM

Wednesday – May 28, 2025

14:10 14:30	**NHA AWARDS CEREMONY & REMARKS (HALL A)**	
PARALLEL SESSIONS – 7		
	HALL A	**HALL B**
	Session 32. Catalysts for Hydrogen Applications – IV **Session Chair: Hadi Genceli**	**Session 33. Sustainable Hydrogen Technologies – III** **Session Chair: Canan Acar**
14:30 16:30	**#23** "Development of Fe-C Microwave Catalysts for Conversion of H_2S into CO_x-free H_2" *Y. Ataseven, M.Y.Doğan, S.Yaşyerli, H.Arbağ, H.M.Taşdemir, N.Yaşyerli* **#29** "Ultrasonic Spray Synthesis of Coal Layered Double Hydroxide: A Novel and Scalable Approach to Oxygen Reduction Catalysis" *K. Büyükkanber, Ö. Şahin* **#66** "Synthesis of Ru/C and PtRu/C Catalysts by Microwave-Assisted Polyol Method at High Temperature and Pressure" *S. Karadeniz, N. Ayas* **#69** "Microwave Assisted Methane Decomposition Reaction Using Nickel-palladium Catalysts Supported on Different Carbon Supports" *R.C. Seyfeli, D. Varisli* **#119** "Preparation of Pd/Ni Foam Catalyst and Its Catalytic Performance for Hydrogen Production by Hydrolysis of Ethylenediamine Bisborane Solution" *O.S. Angı, G. Özkan, G. Özkan* **#274** "Understanding of the Activity of NiFe Oxide Based OER Catalysts Toward Mesoporous NiFe Oxide Thin Films" *A. E. Başaran, C. Karakaya, N. Solati, S. Kaya* **#370** "Development of Innovative Catalysts for AEM Electrolyzers Through Various Electrodepotions Techniques" *E.S. Akyüz, Ö. Aydın, B. Hüner, E. Telli, M. Farsak*	**#46** "Trends and Insights in Hydrogen Energy: A Bibliometric Approach" *N. Ersoy, İ. Ekmekci* **#189** "Hydrogen Production from Wastewater of Domestic Heat Pump Based Tumble Dryers: An Innovative Approach for Sustainable Energy" *A. Erdogan, A. Basdemir* **#28** "Modeling the Economic Viability of Integrated Hydrogen Fuel Cell / Heat Pump CHP Systems for Residential Applications" *F. van der Laan, C. Acar, W Rohlfs* **#167** "Effect of Temperature and Cathode Flow Rate on Performance of Hydrogen-Bromine Redox Flow Battery" *A. C. Turkmen, C. Celik, F. G. B. San* **#194** "Development of Membranes for Hydrogen Bromide Redox Flow Batteries" *K. C. Ata, A. C. Türkmen, F. G. B. San, C. Çelik* **#360** "The Effect of Earthquakes on Underground Hydrogen Storage Caverns" *H. Karakilcik* **#164** "Green Synthesis of MnVS and Co-Doped MnVS Nanoparticles: Applications in Photocatalysis and Hydrogen Production via Methanolysis" *M. Çokyaşa, Ö. Şahin, A. Ekinci, O. Baytar*
16:30 16:45	**CLOSING REMARKS (HALL A)**	

SCIENTIFIC PROGRAM

Wednesday – May 28, 2025

NHA AWARDS CEREMONY & REMARKS (HALL A)

PARALLEL SESSIONS – 7

HALL C	HALL D	HALL E
Session 34. Hydrogen Carriers – II **Session Chair: Özgün Tezer**	**Session 35. Modeling, Simulation, and Optimization – II** **Session Chair: Yağmur Nalbant Atak**	**Session 36. Electrolysis and Electrolyzer Technologies – III** **Session Chair: Olgun Konur**
#25 "Investigating the Superior Effect of g-C_3N_4 on Co-B Catalysts for Efficient Hydrogen Generation via $NaBH_4$ Hydrolysis" *B.C. Çelik, H.Elçiçek* **#47** "Cobalt-copper-boron Doped Graphitic Carbon Nitride as a Promising Catalyst for Hydrogen Production Via Sodium Borohydride Hydrolysis" *Ö. Şahin, F.E.G. Güner, M.E. Kenar* **#348** "Hydrogen-rich Syngas for Cold Chain Logistics: A Life Cycle Assessment of Biomass Gasification Integration" *M. U. Ozturk, A. Ayol* **#104** "Catalytic Potential of g-C_3N_4 in $NaBH_4$ Hydrolysis: A Scientometric Study on Hydrogen Production" *B. Yılmaz, B.C. Çelik, H. Elçiçek, A.S. Karakurt* **#117** "Maximizing the Degree of Dehydrogenation of Perhydro-dibenzyl Toluene via in-line Distillation for Continuous Hydrogen Release" *M. Naseem, M. Luqman, Y. Biçer* **#301** "Advancements and Challenges in Liquid Hydrogen Storage Tank Design for Maritime Applications: A Comprehensive Review" *S. A. Çetinkaya, S. A. Korkmaz, N. Bimbo, S. Afshan* **#332** "Effect of Thermal Conditions on a PV-AEMWE System Integrated with Metal Hydride Storage Tanks" *C. Celebi, M. Ezan, C. Colpan, Y. Devrim*	**#9** "Techno-economic Evaluation of Hydrogen's Role in Dutch Heating Networks: A Dynamic Modeling Approach" *A. Kaabinejadian, A.Pozarlik, C.Acar* **#94** "Simulation Tool for Techno-Economic Analysis of Renewable Hydrogen Production Plants" *F. Machado, H. Monteiro, L. Fernandes, L. Marcon* **#321** "Design and Analysis of a Wind-powered Hydrogen Production System for a Maritime Autonomous Surface Vessel" *S. A. Korkmaz, S. Balakrishnan, P. Manias, S. Turnock* **#337** "Numerical Simulation of High-Temperature Proton Exchange Membrane Fuel Cell Performance Using 3-D COMSOL Model" *M. Buyuk, Y. Nalbant Atak, Y. Devrim* **#367** "Design and Evaluation of Dual-Fluid Geothermal Cycles with tRC Topping and ORC Bottoming for Electricity, Hydrogen, and HDH unit" *O. Kizilkan, G. Soytürk*	**#324** "Solar Syngas Production via a ZnO/Zn Based Carbothermal Reduction and Water Splitting Cycle" *R. Bhosale* **#279** "Investigation on Performance of Anion Exchange Membrane Electrolyzer with Different Flow Field Configurations" *U. Ergin, A. B. A. Ibrahim, S. Tumse, G. M. Ozkan, G. Kardas, H. Akilli* **#172** "Techno-Economic Analysis of MoS_2/Carbon Composites as Sustainable Platinum Alternatives in PEM Electrolyzer Cathodes" *H. Sarıaltın* **#352** "A Comparative Study on the Hydrogen Production Efficiency of Various Membranes in a Chlor-alkali Electrolyzer" *S. Damarseckin, E. Durar, M. Karakılçık, A. Atiz, H. Karakılçık* **#128** "Fluid Flow of Alkaline Water Electrolysis Hydrogen Cell: Design and Experimental Investigation" *M.A. Farahat, M. Abdelmordy, H.H. Eldeeb, A.M. Abdelsalam, W. A. El-Askary, I.M. Sakr* **#304** "Novel Cylindrical Electrolysis System with Copper-Coated Electrodes for Enhanced Hydrogen Production" *E. K. Oguz, I. Dincer* **#178** "Structural and Catalytic Insights into Sr-Modified $LaNi_{0.5}Mg_{0.5}O_3$ Perovskites" *P. Ebrahimi, A. Kumar, M. Al-Marr*

EXHIBITION

CLOSING REMARKS (HALL A)

SCIENTIFIC PROGRAM

Poster Session

Poster Sessions Chair: Olgun Konur

Poster Session – 1 (Monday – May 26, 2025 | 16:00 – 16:30)

#13 "Eco-friendly Leaching Strategies for Recycling Electronic Waste CPUs to Enhance Hydrogen and Oxygen Evolution" *S. Mitrović, S. Brković, M. Seović, M. Pijović Radovanović, P. Laušević, N. Zdolšek, I. Perović*

#14 "Electrochemical Surface Modification and Effects on the Catalytic Activity of Nickel-based Electrodes for Hydrogen Evolution" *S. Mitrović, S. Brković, M. Seović, P. Laušević, N. Zdolšek, Đ. Katnić, I. Perović*

#15 "Non-stoichiometric Tungsten-oxides as the Anode Catalyst Supports for PEM Fuel Cells" *S. Brković, I. Perović, M. Seović, S. Mitrović, P. Laušević, V. Nikolić, M.M. Kaninski*

#18 "Dual-doped Iron-copper Carbon Electrocatalyst for Enhanced Water Splitting Performance in Alkaline Media" *J. Georgijević, I. Perović, S. Brković, M. Seović, N. Zdolšek, J. Milikić, B.Šljukić*

#19 "Synthesizing Cost-effective, Dual-function Catalysts from Recycled CPUs and Lemon Peel for Water Splitting" *M. Seović, S. Brković, I. Perović, D. Jugović, J.M. Vukajlović, P.Laušević, S.Mitrović*

#21 "Life Cycle Assessment of Green Hydrogen Production via Electrolysis" *H. Camur, A. Isler-Kaya, F. Karaosmanoglu*

#22 "Development of Iron-Sulfide Catalysts for Green H_2 Production from H_2S" *N. Demirhan, H.Akansu, Y. Ataseven, M.Y.Doğan, S.Yaşyerli, H.Arbağ, H.M.Taşdemir, N.Yaşyerli*

#56 "Gasification of Agricultural Residual Biomass, Vector in the Production of Green H_2" *G.C. Lăzăroiu, L. Mihăescu, I. Pîșă, R.M. Grigoriu, D. Stoica, I. Simion*

#58 "Cost-effective Porous NiO/Ni@NF Nanosheet Catalysts for Hydrogen Production via Electrocatalytic Ethylene Glycol (EG) Oxidation" *S.A. Aladeemy, T.R.Al-Rijraji, M.S.Amer, P. Arunachalam, A.M. Al-Mayouf*

#60 "Results of Combustion Tests of H_2 – CH_4 Mixture with High H_2 Content" *L. Mihăescu Lucian, G. Lăzăroiu, A. Niculescu, D. Stoica, R.M. Grigoriu, M.G. Osman*

#61 "Ionic Liquid-enhanced Multifunctional Electrolytes for Hydrogen Evolution Reaction and Zn-based Batteries" *N. Zdolšek, A. Dimitrijević, I. Perović, S. Brković, M. Seović, P. Laušević, M.K. Roković*

#62 "Enhanced Electrochemical Performance of V_2O_5 Electrode with 1-butyl-3-methylimidazolium Salicylate Electrolyte for Hydrogen Evolution, Oxygen Evolution and Oxygen Reduction Reactions" *N. Zdolšek, A. Dimitrijević, I. Perović, S. Brković, M. Seović, M.K. Roković, M. Božiković*

#64 "Performance Analysis of Stand-alone Solar Systems in Coastal Environments: A Case Study" *M.G. Osman, G. Lazaroiu, C.V. Strejoiu, C. Panait, D. Stoica*

#65 "Increasing the Energy Efficiency and Economic Viability of a Photovoltaic Park in Craiova" *M.G. Osman, G. Lazaroiu, C.V. Strejoiu, C. Panait, D. Stoica*

Poster Session – 2 (Tuesday – May 27, 2025 | 10:30 – 10:50)

#80 "Synthesis and Characterization of Semiconductor Oxides CuO and ZnO for the Production of Green H_2 by Photo Catalysis under UV-visible Light" *N. Djamel, A. Samira, S. Farouk, F. Djawad, H.H. Aya*

#82 "Hydrogen Gas Production onto Fe_2O_3 and Clay/ Fe_2O_3 by Photo Chemical Conversion under UV-visible Light" *N. Djamel, A. Samira, S. Farouk, F. Djawad, H.H. Aya*

#88 "High-Value Carbon Production through Thermal Plasma Dry Reforming for E-fuel Viability" *A.R.C. Labanca, A.G. Cunha, R.P. Ribeiro, C.G. Zucolotto, M.B. Cevolani, M.A. Schettino Jr., F.G. Emmerich*

#92 "Innovative Electrolysis Using Non-Critical Raw Materials and Circular Economy Techniques to Improve Green Hydrogen Production" *A. Muscolino, A.S. Aricò*

#93 "A PEM Electrolyser with Low Precious Metal Loading" *V. Cicciò, S. Siracusano, A.S. Aricò*

#121 "Dehydrogenation of Dimethylamine Borane in the Presence of Ru^0/TiO_2 Catalyst" *A. Al-Areedheea, S. Karaboğa, İ.A. Morkana, S. Özkar*

#123 "Electrodeposition of Platinum on Electropolymerized ABA on Reduced Graphene Oxides as a Catalyst for Propanol Oxidation in Alkaline Solution" *P. Waenkaew, S. Sriwichai, S. Themsirimongkon*

#137 "Development of $NiCo(OH)_2$ Based OER Catalysis for Alkaline Water Electrolysis" *Y.S. Adam, G. Aksaray, E. Faki, M. Farsak, G. Kardaş*

#140 "Performance Analysis of Plant-Inspired Bipolar Plate Flow Channels for PEM Electrolysers using 3D Modelling" *M. Alobeid, S. Çelik*

#143 "Hydrogen Economy: Key Developments in China, Europe, and the USA" *D. Üngüder, A.C. Krutoff, M. Wappler*

#150 "The Role of Ammonia in Renewable Energy and Emergency Power Supply: A Feasibility Study" *H. B. Perçin, A. Çalışkan*

#152 "Exploring Hydrogen Mobility: A Feasibility Study on Sustainable Campus Transportation" *H. B. Perçin, A. Çalışkan*

#156 "Synthesis and Characterization of (Gd,Nd) – Doped $CeO_2/SrTiO_3$ Heterostructures for Lt-SOFC" *N. Kırkgeçit Aksoy, D. Kara, S. Kerli, M. Şaşmaz Güldal, O. Türkoğlu, H. Özlü Toru*

#159 "Seawater Electrolysis for an Advanced H_2 Production" *F. Giacobello, S. Siracusano, A. Muscolino, V. Cicciò, M. A. Mancuso, V. Antonucci*

#171 "Contribution of SM-Doped CeO_2 Nanoparticles to Hydrogen Production" *A. Kırkgeçit, H. Ö. Torun, N. K. Aksoy, M. Kisti, G. Özkırar, M. F. Kaya*

#175 "Development of Alkaline Electrolysis Catalyst Using Waste Zinc-Carbon Batteries" *H. Hançer, M. Farsak*

#200 "High-Efficiency Hydrogen Storage via Porous Germanene Nanostructures" *A. Miranda, G. González, B. J. Cid, M. Calvino, J. E. Santana, F. Salazar*

#222 "Energy Management in a Hybrid System Integrating PV Panels, PEM Fuel Cells, and Batteries" *B. Yılmaz, C. O. Colpan*

#235 "Electrooxidation of Methanol and Sodium Borohydride on Nano-Silver Electrode for Alkaline Fuel Cells" *A. Aytaç, F. Ö. Gökmen*

SCIENTIFIC PROGRAM

Poster Session

Poster Session – 3 (Tuesday – May 27, 2025 | 16:00 – 16:30)

#240 "Development of a New Generation Hybrid System for the Electric Vehicle" *A. Aytaç, O. Yılmaz*

#242 "Optimal Design of a New Photovoltaic-Electrolyser-Fuel Cell-Battery Hybrid System" *A. Aytaç, O. Yılmaz*

#246 "Impact of Operational Stoppages on the Stability of Anion Exchange Membrane Electrolysis" *M. Mizanur Rahman, A.H.M Monteverde, M. Santarelli*

#257(1) "Green Synthesis of Fuel Bioadditive Solketal Levulinate by Functional Catalytic Membrane" *N. Y. Yüzer, G. Hasırcı, A. O. Hoşöz, E. E. Çakırca, E. Alptekin, O. İlgen, M. Çanakçı, N. Hilmioğlu*

#257(2) "Development of Environmentally Friendly the Catalytic Membrane as a Catalyst for Synthesis of the Green Fuel Bioadditive Glycerin Carbonate" *G. Hasırcı, N. Y. Yüzer, A. O. Hoşöz, E. E. Çakırca, E. Alptekin, O. İlgen, M. Çanakçı, N. Hilmioğlu*

#258 "Integration and Storage of Hydrogen-Based Fuel Cells for Unmanned Aerial Vehicles" *M. F. Özbek, R. Ak, E. Telci, E. Çelik, H. Settaşı, S. Sezer, V. Alizada, E. C. Duğan, S. A. Angin, R. G. Akay, C. Çelik*

#264 "Sc- and Ti-Functionalized Doped SnC Nanosheets for Hydrogen Storage" *D. Romero, A. R. Montoya-García, L. G. Arellano, M. I. Iturrios, L. A. Pérez, M. Cruz-Irisson*

#269 "Kinetic Modelling on Transient Photocurrent Responses of WO_3 Photoanodes" *E. Ayral, F. Uçar, E. Haznedar, E. Altuntaş, S. Kaya*

#280 "Understanding the Kinetic Mechanism of WO_3 Photoanodes for PEC Applications" *E. İ. Haznedar, F. Uçar, E. Ardalı, E. Altuntaş, S. Kaya*

#295 "Performance Assessment of a Hydrogen Liquefaction Cycle Utilizing Liquefied Natural Gas Regasification and Photovoltaic Panel-Based Power Generation Unit" *M. Taghavi, C. O. Colpan*

#297 "Hydrogen and Volatile Fatty Acid Production from Posidonia Oceanica Seagrass by Dark Fermentation" *D. Kurtdemir, E. Taylan, Ş. Arıcı*

#300 "Thermodynamic Analysis of Claude Cycle for Hydrogen Liquefaction" *Y. Kumlutaş, C. O. Colpan*

#317 "Effect of MoP/g-C_3N_4/Ti_3C_2 Quantum Dots on Photocatalytic Hydrogen Production" *E. S. Şahin, D. Akyüz, E. Demirbaş*

#362 "Assessing Electrolyte Effects in Fuel Cell Systems" *E. Durar, B. Memişoğlu Güzelgün, S. Damarseckin, A. Atız, M. Karakılçık*

#363 "High-Pressure Hydrogen Direct Injection in Optical Combustion Research" *Y. Rousseeuw*

#369 "Scalable Electrode Design Using MPt (M: Cu, Co, Ni) Alloy Nanoparticles for Efficient and Durable Hydrogen Evolution in Seawater Electrolysis" *M.Z. Nezhad, O. Metin*

Poster Session – 4 (Wednesday – May 28, 2025 | 10:45 – 11:05)

#318 "Enhancement of Photocatalytic Hydrogen Production with CoP/g-C_3N_4/Ti_3C_2 Quantum Dots" *B. Camgöz, D. Akyüz, E. Demirbaş*

#320 "Development of a Novel Catalytic Membrane by Loading Silico Molybdic Acid to Polyvinyl Alcohol and its Use as a Catalyst for Fuel Additive Solketal Synthesis" *N. Yenihan Yüzer, N. Hilmioğlu*

#323 "Electrospun Copper-doped Recycled PVDF Membranes for Microbial Fuel Cell Applications" *A. Katırcı, Ö. Ipsalali, S. Kahraman, F. Ugur Nigiz*

#325 "Solar Energy Storage via H_2 Production Using a Thermochemical MnSO4/MnO Water Splitting Cycle" *R.R. Bhosale, A. Arnold, M. Ball, K. Collins, K. Hamilton, N. Heath, J. Hobbs, C. Howell, W. Johnson, C. Kouvarakis, V. Kyslytsya, C. Latham, G. Prater, M. Sanchez, R. Self, A. Sellers, M. Serven*

#335 "Evaluation of the Social Dimensions of Integrating Natural Gas and Hydrogen in Energy Consumption: The Case of Turkiye" *B. Yenihan, K. Çolak, O. Özcan*

#336 "Clean Energy Demand: Evaluating the Use of Hydrogen in Electricity Generation from a Corporate Cost Perspective" *K. Çolak, B. Yenihan, O. Özcan*

#339 "Hydrogen Storage Properties of a Zirconium Metal-organic Framework" *S. Demir, N. Bilgin*

#341 "Enhanced Photoelectrochemical Performance of CeO_2/TiO_2 Heterostructure for Hydrogen and Oxygen Evolution Reactions" *M. Behroozi, E. Doustkhah*

#342 "Integration of Metal–organic Frameworks with Titanium Dioxide for Enhanced Photoelectrochemical Performance in Sustainable Hydrogen Production" *S. Sadighi, E. Doustkhah*

#349 "Enhancing Electric Vehicle Performance with Fuel Cell Integration: Driving Range Optimisation" *V. Tekin, K. Unustu, O. Ozel, C. Colpan, M. Karaoglan*

#351 "Development of Stability and Efficiency of $FAPbI_3$ Perovskite Solar Cells for Hydrogen Evolution" *Ş. Tüzüner, O. Mahmood, Ş. Ela, P. Reiss*

#353 "An Experimental Study of Jet-wall and Jet-jet Interactions of Directly Injected Hydrogen and Methane in a Wave-piston Geometry" *M. Gong, M. Lundgren, J. Eismark, M. Andersson*

#354 "Modernization of a Semi-empirical PEM Fuel Cell Model for Heavy-duty Applications" *B. Dursun, M. Johansson, Ö. Andersson, P. Tunestål*

#357 "Process Simulation of Hydrogen Generation from Biomass Using Aspen Plus" *A. Ataş, N. Javani, Ö. Yücel*

#364 "Effect of Convective Heat Transfer Coefficient on the Metal Hydride Tank During the Absorption Process" *S.C. Bozkır, M.A. Ezan, C.O. Colpan*

#368 "Hydrogen Fuel Cell-Powered UAV Systems: Thermal Management for Extended Flight Missions" *T.M. Tavman, C.Ö. Colpan, M.U. Karaoğlan*

#372 "Development and Verification of 700 Bar Type IV Composite Tank", *A. Gürlek, Ç. Tüfekçi, A.F. Yılmaz, F. Kandeger, F. Keleşoğlu*

PROCEEDINGS

CRITICAL ADVANTAGES OF HYDROGEN

Ibrahim Dincer
Clean Energy Research Laboratory (CERL), Faculty of Engineering and Applied Science, Ontario Tech. University, 2000 Simcoe Street North, Oshawa, Ontario L1G 0C5, Canada

E-mail: ibrahim.dincer@ontariotechu.ca

ABSTRACT
Energy has always been one of the most important needs of humanity throughout centuries, and its role has really been a critical asset for civilizations and their developments. It has closely affected humanity's basic needs, such as water, air and food, and it is as a crucial resource that has shaped the past, continues to shape the present and is expected to shape the future. The importance and need for clean energy in the process we are entering is a fact known by everyone. On the other hand, with the increasing use of fossil fuels (coal, oil and natural gas) used to meet energy needs, many problems related to air, water and food have emerged in the world and these problems have significantly affected human health and life. An unavoidable effect of fossil-based energy sources used in the process after the industrial revolution has made an energy change necessary with the intense carbon dioxide emissions that have emerged and the climate changes and global warming results on both regional and global scales. In a way, this has strengthened our transition from the carbon age to the hydrogen age as of 2020. This article evaluates historical transformations in energy options, highlights the role of hydrogen and answers the questions of what we should do in the hydrogen age.

Keywords: Clean water, clean air, clean food, clean energy, clean hydrogen, hydrogen age, sustainability

1. INTRODUCTION

Today, we are in an era where everything is designed to be smarter and better, and in this regard, new energy solutions are expected to be more efficient and effective. Of course, when we look around us, it is based on many things in daily life; smart materials, smart devices, smart phones, smart grid, smart measurement, etc. We need to make energy diversity and, in relation to this, the technologically improved processes under smart energy solutions. With advanced technologies and artificial intelligence applications, humanity can easily address the entire energy spectrum in five categories, as energy basics and concepts, energy materials, energy production, energy conversion and energy management, and this clearly shows that we need to change the roadmap, in short, our energy diet, regarding these issues. When we consider the energy dimensions and examine the historical processes, we see that energy affects many areas from technical dimensions to economic dimensions, from economic dimensions to environmental dimensions, from environmental dimensions to social dimensions and even the most important of these, political dimensions. In fact, historically, humanity's desire to own energy and energy sources in its energy journey has caused many clashes and wars. This article brings numerous dimensions to examine the needs for humanity in a general perspective and link all to clean energy where clean hydrogen becomes a crucial commodity and its role becomes critical for societal development and sustainable future.

2. BASIC NEEDS OF HUMANITY

It is apparent that there are four basic needs which are essential for human beings to live. These are: clean water, clean air, clean food and clean energy, as illustrated in Figure 1. One should note that if energy is not clean enough, the rest of the needs of humanity is greatly affected. This is exactly what has happened since industrial revolution.

Fig. 1. Four essential needs required for a sustainable future of humanity.

Looking into history, in terms of energy, humanity has used wood as the first source of energy for many of its daily tasks, and this period has evolved over the centuries into the coal era (which technically mobilized the industrial revolution through steam engines), the oil era (primarily after the first world war) and the natural gas era (increasingly after the 1980s). There is noticeably a final destination in this energy journey towards hydrogen as a carbon-free fuel and energy carrier. Throughout this journey, carbon/hydrogen (C/H) ratio has been decreasing, obviously over the centuries and is expected to bring us into a carbon free society where hydrogen economy is clearly expected to flourish. The humanity's journey is a clear indication of a shift towards a carbon-free economy or a carbon-free society.

3. A CLEAR TRANSITION FROM CARBON AGE TO HYDROGEN AGE

Historically, we all remember the metal ages, the copper age, then the bronze age and then the iron age. These have historically ended, of course, the end of these ages was not due to the end of copper, bronze or iron. This transformation was entirely due to the development of humanity and the increase in its technical capabilities and the efficient use of resources and the needs in life. In regards to energy, the beginning of the carbon-based age is the primary and intensive use of coal that started with the industrial revolution, followed by the intensive use of oil and then natural gas, which made this process intensively carbon-based and in parallel with this, the very rapid increase in carbon dioxide emissions and the negative environmental effects that came with it, regional and global climate changes and irregularities, global warming, etc. It is an inevitable result of its harmful effects. Now we are calling for hydrogen and this process has technically accelerated with the pandemic effect caused by the COVID-19 virus that broke out in the world in 2020 [1]. Therefore, the COVID-19 coronavirus pandemic, which directly or indirectly affects every person, has particularly affected the elderly, those with weak immune systems and those who suffer from various respiratory and cardiovascular diseases. This is clearly a turning point where we cannot continue the carbon age and can no longer leave ourselves vulnerable to such pandemics. This turning point is a decisive moment for the opening of a new era with hydrogen and the closing of the carbon age. As indicated in Dincer [1], the carbon age, which continued with hydrocarbon fuels until the coronavirus outbreak in 2020, will be replaced by the hydrogen age, where the use of hydrocarbon fuels (fossil fuels) will decrease exponentially and the use of hydrogen energy will increase. In this hydrogen age, the following benefits are expected to be provided: better environment, better ecosystem, better efficiency, better economy and economic development, better synchronization of use with renewable energy options, better health and healthier societies, and better sustainability development countable.

Furthermore, it is necessary to carefully consider the economic development periods and their roles historically. In this regard, Figure 6 is given to show the economic periods after the 1950s, basically after the second world war, and how such economic periods have impacted the humanity, societies and societal developments. The period between 1950 and 1970 was a labor-intensive era where industrial development depended heavily upon the human labor. This was followed by a skill-intensive period between 1970-1980 where societies started developing further to better train people and make them skilful for industrial development. Following this, there was a capital-intensive era, referring to a period where businesses or industrial enterprises required some significant capital investments and physical assets and infrastructure development with a goal to produce goods or services. By 1990 the technology era started while the innovation era began by the year 2000 which was followed by the digital intensive period by the year 2010, and obviously, more recently the hydrogen era has come to reality by the year 2020. We are now in hydrogen era, which is introduced by Dincer [2] as hydrogen age (*Hydrogen 1:0*). The current hydrogen age also requires all three periods of technology, innovation and digitalization combined with a common goal of humanity to achieve a sustainable future.

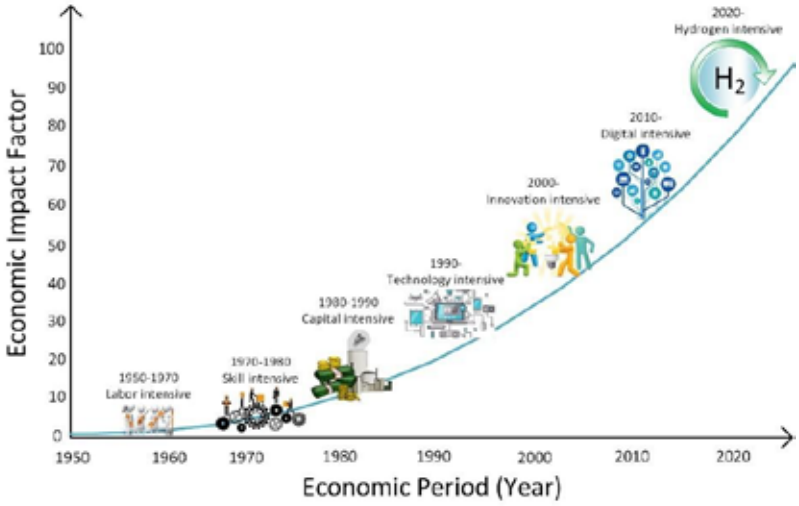

Fig. 2. An illustration of economic periods and their impacts historically after the second world war (Dincer [2]).

4. CLOSURE

The world has incredibly experienced rapid change and transformation processes throughout the history. These have actually been in every dimension of life and affected the way that humanity has covered their needs, including energy. Intensive local and global challenges have required clean energy solutions by addressing the need of carbon free solutions with a unique address towards clean hydrogen and its clean derivatives which will help achieve cleaner and more sustainable future.

Acknowledgment

This publication was made possible by the NPRP grant (NPRP12S-0123-190011) from the Qatar National Research Fund (a member of Qatar Foundation). The findings achieved herein are solely the responsibility of the authors.

REFERENCES

1) I. Dincer (2020). COVID-19 coronavirus: closing the carbon era but opening the hydrogen era. International Energy Research Journal 44(8), 6093-6097.
2) I. Dincer (2023). Hydrogen 1.0: a new era. International Hydrogen Energy Journal 48, 16143-16147.

EFFICIENCY AND PERFORMANCE ANALYSIS OF IT-SOFC INTEGRATED WITH S-CO_2 BRAYTON CYCLES: A COMPREHENSIVE STUDY ON WASTE HEAT UTILIZATION

[1*]*Semanur Beygul*, [2]*Yildiz Kalinci*
[1] Dokuz Eylul University, Engineering Faculty, Department of Mechanical Engineering, Tınaztepe Campus, Izmir, 35390, Turkiye
[2] Dokuz Eylül University, Izmir Vocational School, Education Campus, Izmir, 35380, Turkiye

*Corresponding author e-mail: semadadk@gmail.com

ABSTRACT

This study investigates the performance of various hybrid systems, coupling intermediate temperature solid oxide fuel cell (IT-SOFC) with different supercritical carbon dioxide (S-CO_2) Brayton cycle configurations. The investigation aims to efficiently harness waste heat from IT-SOFC, converting it into useful work. At the standard operating conditions of the IT-SOFC (600°C, 0.3 A/cm^2), the efficiency of the isolated solid oxide fuel cell (SOFC) stack is 34.75%. The efficiencies of the novel hybrid systems are as follows: the SOFC/S-CO_2 Basic Brayton cycle (SBBC) hybrid system at 43.93%, the S-CO_2 Recompression Brayton cycle (SRCBC) at 49.8%, and the SOFC/S-CO_2 Regenerative Brayton cycle (SRBC) hybrid system achieving the highest at 54.66%. Different cycles favor different temperature ranges, with SRCBC being efficient at lower temperatures (<600°C) and SRBC thriving at medium-high temperatures (>600°C) due to the temperature sensitivity in the recuperator. The SOFC/SRBC hybrid system demonstrates superior efficiency with reduced complexity, making it a promising solution for effective waste heat utilization.
Keywords: Supercritical CO_2 Brayton cycle, Intermediate temperature solid oxide fuel cell, Waste heat, Hybrid system

1. INTRODUCTION

The global shift to eco-friendly energy highlights SOFCs and SOFC/gas turbine (GT) hybrid systems as efficient, flexible solutions to combat climate challenges. SOFCs directly convert the free energy of a chemical reactant to electrical energy and heat without the efficiency limitations typical of thermodynamic cycles. SOFC systems operate at temperatures of 500-1000°C, but high temperatures increase material costs and reduce lifespan. To address these challenges, IT-SOFCs have been developed to operate efficiently at 600-800°C [1]. The S-CO_2 Brayton cycle is an appropriate option for bottoming cycle due to the advantages of high efficiency and compact equipment sizes in the moderate temperature range (450-750˚C) [2]. With critical conditions of 30.98˚C and 7.38 MPa, CO_2 behaves like an incompressible fluid, reducing compression work. The S-CO_2 Brayton cycle has gained attention as an alternative for waste heat recovery, outperforming air cycles in intermediate-temperature applications [3]. Limited studies have analyzed fuel cell/S-CO_2 Brayton cycle hybrid systems. To summarize the studies on SOFC/S-CO_2 hybrid systems in the literature: Hybrid systems which integrate MCFC with a S-CO_2 Brayton cycle were investigated and compared with other hybrid systems based on SOFC/S-CO_2 [2,3]. Liu et al. [4] analyzed the novel hybrid system based on the SOFC/GT/CO_2 cycle. The energy efficiency of the system and the power generation efficiency of the SOFC reached about 79.81% and 50.96%, respectively. Schöffer et al. [5] compared several configurations of SOFC/S-CO_2 Brayton cycle hybrid system. It was found that recirculating cathodic air increases the efficiency of the system and decreases the size of the heat exchangers but increases the complexity of the system. Sadeghi et al. [6] investigated two S-CO_2 Brayton cycles for waste heat recovery in a SOFC-based system. Findings indicated that, at the optimized condition, the capability of a simple S-CO_2 cycle for recovering heat from the SOFC is 30.86% higher than a recompression S-CO_2 layout. Liu et al. [7] proposed an efficient energy system combining SOFC, S-CO_2 Brayton cycle, and CO_2 capture. Results showed 60.96% net electrical efficiency and 0.342 kg/kWh CO_2 reduction. Guo et al. [8] optimized a hybrid SOFC/S-CO_2 Brayton cycle, achieving improved power output and ecological performance over standalone SOFCs. Chen et al. [9] analyzed a hybrid system with SOFC, gas turbine, and recompression S-CO_2 Brayton cycle, finding the optimum point at 68% exergy efficiency and 0.0575 kWh^{-1} electricity cost. Integrating fuel cell technologies with S-CO_2 Brayton cycles is critical for enhancing efficiency and promoting sustainability. However, research on SOFC/S-CO_2 hybrid systems remains limited, leaving a significant gap in understanding their performance and optimization potential. This study addresses this gap by analyzing the performance and efficiency of IT-SOFC/S-CO_2 hybrid systems across various configurations. The key innovation lies in leveraging the waste heat from an intermediate-temperature commercial SOFC in different S-CO_2 cycle designs, providing valuable insights into intermediate-temperature waste heat utilization and system optimization.

2. MATERIALS AND METHODS

The study examines three different configurations: the integration of SOFC with SBBC, the combination of SOFC with SRBC, and the integration of SOFC with SRCBC. The hybrid system considered in this study is configured with main compressor (MC), low temperature recuperator (LTR), re-compressor (RC), high-temperature recuperator (HTR), heat exchanger (HEX), turbine, cooler, and SOFC stack the schematic diagram of which is shown in Fig. 1. The analysis implemented the metal-supported IT-SOFC cell developed by Ceres Power, which is suitable for integration into stacks

and larger systems [10]. The examined IT-SOFC functions under typical parameters of a temperature of 873 K and a current density of 0.3 A/cm^2 [10]. Inlet parameters of Brayton cycles were determined from an S-CO_2 Brayton cycle power system which has been operated by Sandia National Laboratories [11].

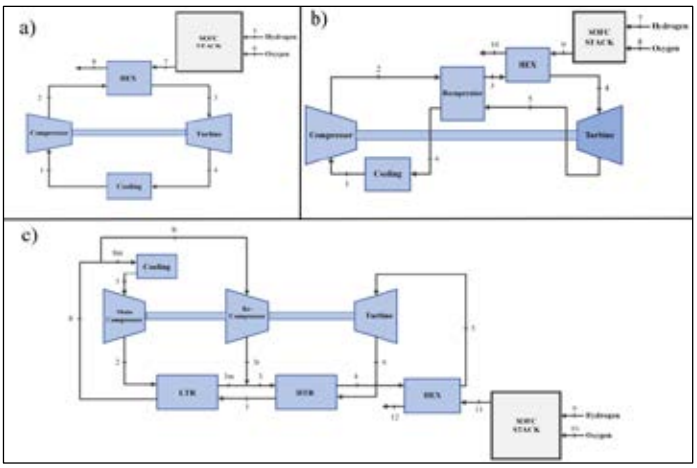

Fig. 1.SOFC/S-CO_2 hybrid systems; a) SOFC/SBBC hybrid system, b) SOFC/SRBC hybrid system (modified from [12]) c) SOFC/SRCBC hybrid system (modified from [13])

From thermodynamics of systems in equilibrium, Nernst Voltage and SOFC voltage:

$$V_n = V_{max} + \frac{\bar{R}\cdot T}{n\cdot F} ln\left(\frac{a_A^{v_A}\cdot a_B^{v_B}}{a_C^{v_C}\cdot a_D^{v_D}}\right) \quad (1)$$

$$V_{cell} = V_n - V_{act} - V_{ohm} - V_{con} \quad (2)$$

where the v's are the stoichiometric coefficients of the balanced electrochemical reaction, the a's are the thermodynamic activity coefficients for the reacting species, F is Faraday constant, n is the number of moles of the electrons transferred, where V_{act} is the activation, V_{ohm} ohmic and V_{con} concentration polarization. The power produced by the SOFC stack, which is calculated as follow:

$$\dot{W}_{SOFC} = N_{cell} \cdot A_{cell} \cdot i_{cell} \cdot V_{cell} \quad (3)$$

Where N_{cell} is the number of cells, A_{cell} is cell active area, and i_{cell} is the current density. The energy balance of the system is calculated based on the first law of thermodynamics. Brayton cycles efficiency is calculated as follow:

$$\eta_{cycle} = \frac{\dot{W}_{net}}{\dot{Q}_{in}} \quad (4)$$

Where $\dot{Q}$, $\dot{W}$, and $\dot{m}$, means heat rate, work rate and mass flow rate, respectively. The hybrid system's net power and efficiency is written as:

$$\dot{W}_{net,hybrid} = \dot{W}_{net} + \dot{W}_{SOFC} \quad (5)$$

$$\eta_{hybrid} = \frac{\dot{W}_{net}+\dot{W}_{SOFC}}{\dot{m}_{H_2,in}\times LHV} \quad (6)$$

3. RESULTS AND DISCUSSION

This study aims to evaluate the performance and efficiency of different configurations to identify optimal integration strategies. A 50 K temperature difference between TIT and SOFC operating temperature was maintained to prevent pinch point issues within the examined current density range (0.05–0.8 A/cm^2). Three intermediate temperatures (550°C, 600°C, and 650°C) were selected, and the Brayton cycle's mass flow rate was determined based on the SOFC's capacity and operating conditions. Fig. 2a. illustrates the efficiencies of the SBBC and SOFC/SBBC hybrid systems at different temperatures, considering varying current densities. The SBBC achieves efficiencies of 0.1510 at 823 K, 0.1514 at 873 K, and 0.1513 at 923 K, with the highest efficiency observed at 873 K, though the differences are minimal. This trend aligns with previous studies [14] and can be attributed to notable changes in the specific heat of S-CO_2 near its critical point. The efficiency of the SOFC/SBBC hybrid system varies with current density, primarily influenced by the SOFC performance, which impacts overall system efficiency. Higher current densities reduce efficiency due to increased polarization losses [15]. The highest efficiency is achieved at 923 K, as higher temperatures reduce irreversibility in the SOFC. Utilizing SOFC waste heat and integrating SBBC raises the hybrid system's efficiency to 43.93%. Fig. 2b. shows the efficiency of the SRBC and SOFC/SRBC hybrid system at different temperatures and SOFC current densities. At 0.3

A/cm^2 and 873 K, SRBC efficiency reaches 47.4%. Adding a recuperator to the SBBC improves Brayton cycle efficiency by 32.26%, with its impact increasing at higher temperatures. In the SRBC, the SOFC operating temperature plays a more critical role than in the SBBC. Incorporating SOFC waste heat into the SRBC raises the hybrid system's efficiency to 54.66%. Fig. 2c. reveals that, unlike the first two cycles, SRCBC efficiency decreases with rising SOFC operating temperature, dropping from 0.3654 at 823 K to 0.3612 at 923 K. Notably, the SRCBC achieves its peak efficiency at 823 K, highlighting its suitability for mid-low SOFC operating temperatures (<873 K). Higher SOFC temperatures increase turbine inlet temperature (TIT), raising the RC inlet temperature and reducing overall efficiency. The efficiency gap between SRCBC and SRBC is likely due to the additional compressor in SRCBC and the need for optimization of parameters such as temperature, split ratio, and heat exchanger effectiveness. The SOFC/SRCBC hybrid system achieves 49.8% efficiency at 0.3 A/cm^2 and 873 K. Fig. 2d. shows the power distribution between the SOFC and Brayton cycle at 873 K across varying current densities. As current density increases, the SOFC's power share decreases due to higher energy levels in the SOFC's output and increased irreversibility, while the Brayton cycle's share rises. At 0.3 A/cm^2, the SOFC power share is 79.1% in the SOFC/SBBC, 63.57% in the SOFC/SRBC, and 69.78% in the SOFC/SRCBC hybrid systems. The SOFC/SRBC stands out for its superior waste heat utilization and reduced complexity, making it the most efficient option.

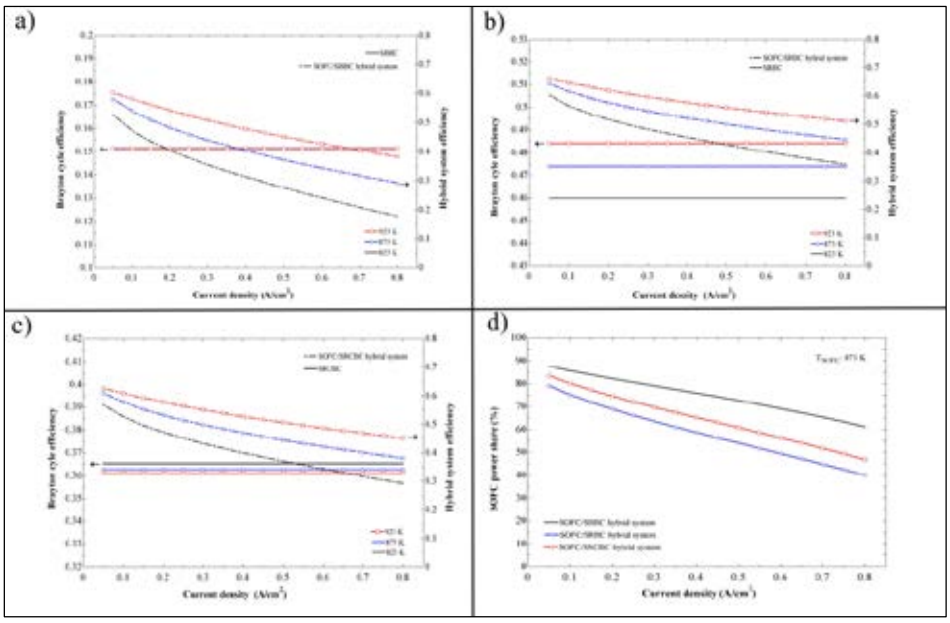

Fig. 2. a) The efficiency of SBBC and SOFC/SBBC hybrid system, b) the Efficiency of SRBC and SOFC/SRBC cycle hybrid system, c) Efficiency of SRCBC and SOFC/SRCBC hybrid system and d) The percentile of SOFC power in different hybrid systems according to current density change

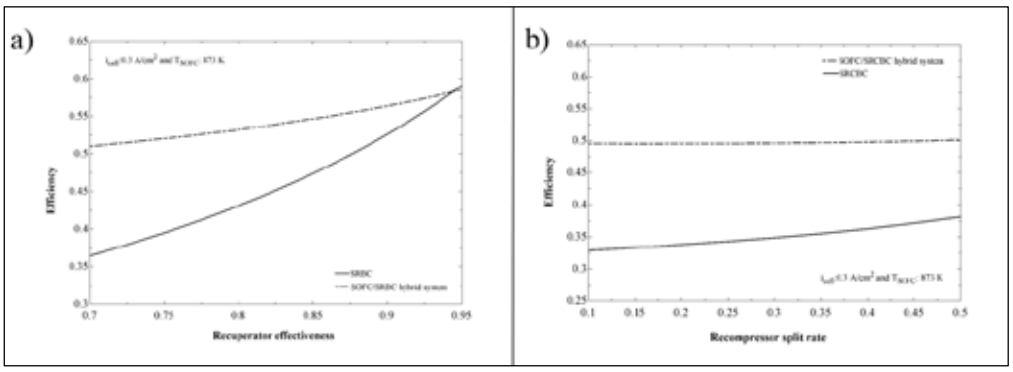

Fig. 3. a) Variation of the efficiency of SRBC and SOFC/SRBC hybrid system according to the change of recuperator effectiveness, b) Variation of SRCBC and SOFC/SRCBC hybrid system efficiency according to RC split rate change

In the SRBC, the recuperator significantly influences performance, with higher exergy destruction in heat exchangers than in turbomachinery [16]. In Fig. 3a, increasing the recuperator effectiveness from 0.7 to 0.95 boosts SRBC efficiency from 0.3646 to 0.5913—a 29.29% improvement. Similarly, in the SOFC/SRBC hybrid system, this rise in effectiveness enhances efficiency by 7.54%. The recuperator's sensitivity to temperature changes makes the SRBC more efficient at medium-high SOFC operating temperatures (>873 K). Fig. 3b. examines the effect of RC split rate on efficiency. As the

split rate increases, cycle efficiency improves, rising from 0.329 at 0.1 to 0.3814 at 0.5 [17]. Higher split rates reduce heat extraction by directing more fluid from the LTR to the RC, increasing heat retention and lowering Q_{in}. In the SOFC/SRCBC hybrid system, altering the split rate from 0.1 to 0.5 results in a modest efficiency increase, from 49.55% to 50.13%.

4. CONCLUSIONS

This study thoroughly examined the integration of IT-SOFC with different configurations of the Brayton cycle to optimize energy utilization. The analytical framework employed a metal-supported IT-SOFC cell developed by Ceres Power, which is compatible with the integration of stack and system. The tool chosen for this comprehensive analysis was EES.

- The efficiency of the SRBC, notably impacted by the recuperator, experiences a substantial enhancement with increased recuperator effectiveness.
- An intriguing observation was made regarding temperature preferences for different cycles. SRCBC exhibited optimal efficiency at lower temperatures (<600°C), while SRBC thrived at medium-high temperatures (>600°C), a trend attributed to the sensitivity of the recuperator to temperature changes.
- The power distribution of Brayton efficiencies in the total hybrid system power highlights the superiority of SOFC/SRBC in converting waste heat into useful work compared to SBBC and SRCBC.
- At the standard operating conditions of the IT-SOFC (873 K, 0.3 A/cm^2), the efficiencies stand at 43.93% for the SOFC/SBBC hybrid system, 54.66% for the SOFC/SRBC hybrid system, and 49.8% for the SOFC/SRCBC hybrid system. The SOFC/SRBC hybrid system arises as the most favorable option for harnessing the waste heat potential of IT-SOFC due to its notable increase in efficiency and simplified design, thereby making it a practical solution.

REFERENCES

1. Shao Z and Tadé MO. 2016. Intermediate-Temperature Solid Oxide Fuel Cells. Berlin, Springer.
2. Mehrpooya M, Bahramian P, Pourfayaz F and Rosen MA. 2016. Introducing and analysis of a hybrid molten carbonate fuel cell-supercritical carbon dioxide Brayton cycle system. Sustainable Energy Technologies and Assessments 18:100-6.
3. Sánchez D, Chacartegui R, Jiménez-Espadafor F and Sánchez T. 2009. A New Concept for High Temperature Fuel Cell Hybrid Systems Using Supercritical Carbon Dioxide. J Fuel Cell Sci Technol 6(2):021306.
4. Liu Y, Han J, You H. 2019. Performance analysis of a CCHP system based on SOFC/GT/CO_2 cycle and ORC with LNG cold energy utilization. International Journal of Hydrogen Energy 44:29700-10.
5. Schöffer SI, Klein SA, Aravind PV and Pecnik R. 2021. A solid oxide fuel cell- supercritical carbon dioxide Brayton cycle hybrid system. Applied Energy 283:115748.
6. Sadeghi M, Seyed Mahmoudi SM and Rosen MA. 2022. Thermoeconomic analysis of two solid oxide fuel cell based cogeneration plants integrated with simple or modified supercritical CO_2 Brayton cycles: A comparative study. Energy 259:125038.
7. Liu Z, Wang Y, Xie M, He X, Zhang W, Xie S and Zhao, Y. 2023. Off-design performance analysis for an integrated system of solid oxide fuel cell and supercritical carbon dioxide Brayton cycle with CO_2 capture. Energy Conversion and Management 292:117406.
8. Guo Y, Guo X, Wang J, Guan Z, Wang Z, Zhang Y, et al. 2023. Performance analysis and multi-objective optimization for a hybrid system based on solid oxide fuel cell and supercritical CO_2 Brayton cycle with energetic and ecological objective approaches. Applied Thermal Engineering 221:119871.
9. Chen Y, Wang M, Liso V, Samsatli S, Samsatli NJ, Jing R, et al. 2019. Parametric analysis and optimization for exergoeconomic performance of a combined system based on solid oxide fuel cell-gas turbine and supercritical carbon dioxide Brayton cycle. Energy Conversion and Management 186:66-8.
10. Leah RT, Brandon NP and Aguiar P. 2005. Modelling of cells, stacks and systems based around metal-supported planar IT-SOFC cells with CGO electrolytes operating at 500–600°C. Journal of Power Sources 145:336-52.
11. Pasch J, Conboy T, Fleming D and Rochau G. 2012. Supercritical CO_2 Recompression Brayton Cycle: Completed Assembly Description.
12. Jin Q, Xia S, Li P and Xie T. 2022. Multi-objective performance optimization of regenerative S-CO_2 Brayton cycle based on neural network prediction. Energy Conversion and Management 14:100203.
13. Zhang F, Liao G, E J, Chen J and Leng E. 2021. Comparative study on the thermodynamic and economic performance of novel absorption power cycles driven by the waste heat from a supercritical CO_2 cycle. Energy Convers Manag 228:113671.
14. Beygul S and Kalinci Y. 2024. Thermodynamic analysis of a supercritical CO_2 Brayton cycle integrated with solid oxide fuel cell. International Journal of Hydrogen Energy 67:933-941.
15. Tarroja B, Mueller F, Maclay J, and Brouwer J. 2008. Parametric thermodynamic analysis of a solid oxide fuel cell gas turbine system design space. In Turbo Expo: Power for Land, Sea, and Air 43123:829-841.
16. Sharma OP, Kaushik SC and Manjunath K. 2017. Thermodynamic analysis and optimization of a supercritical CO_2 regenerative recompression Brayton cycle coupled with a marine gas turbine for shipboard waste heat recovery. Thermal Science and Engineering Progress 3:62-74.
17. Dyreby J. Klein S. Nellis G. and Reindl D. 2014. Design considerations for supercritical carbon dioxide Brayton cycles with recompression. Journal of Engineering for Gas Turbines and Power 136:101701.

NUMERICAL STUDY OF NOVEL THERMAL MANAGEMENT METHODS FOR HYDROGEN STORAGE IN A METAL HYDRIDE REACTOR

Fatih Selimefendigil, Gürel Şenol, Hakan F. Öztop
Department of Mechanical Engineering, Manisa Celal Bayar University, Manisa 45140, Turkey
Vocational School of Technical Sciences, Manisa Celal Bayar University, Manisa 45140, Turkey
Department of Mechanical Engineering, Technology Faculty, Fırat University, Elazığ 23119, Turkey

Corresponding author e-mail:gurel.senol@hotmail.com, fatih.selimefendigil@cbu.edu.tr

ABSTRACT

This study focuses on the effectiveness of different thermal management methods for hydrogen absorption of a metal hydride reactor. The metal hydride bed is selected as ammonia borane (NH_3BH_3). The numerical study consists of three different cases. FEM based solution method is utilized. In Case 1, the hydrogen absorption was examined in the reactor with a corrugated cooling channel. In Case 2, the absorption was examined with baffles on the corrugated cooling channel. In Case 3, the absorption was examined with a baffle combined with U-tubes. In Case 2, baffles and in Case 3, baffle were placed on the inner surface of the cooling channel in the metal hydride bed for a better cooling. The absorbed hydrogen fraction (wt. %) and the average temperature distributions in the metal hydride bed were obtained. In Case 2 and Case 3, the hydrogen absorption increased by 9.4% and 10.5%, respectively. The average bed temperature in Case 2 and Case 3 decreased by 18% and 35%, respectively.

Keywords: Metal hydride, Hydrogen storage, Reactor, FEM, Thermal Management.

1. INTRODUCTION

The ever-increasing demand for energy coupled with decreasing fossil fuel resources make the establishment of a clean and sustainable energy system an impellent need [1]. Hydrogen has a crucial place in terms of energy. Considering the historical development of the energy carriers towards more hydrogen-rich fuels and the necessity to decrease carbon dioxide emissions, hydrogen should be the energy carrier of the future [2]. The energy gain per electron is very high. The chemical energy per mass of hydrogen (39.4 $kWh \cdot kg^{-1}$) is three times larger than that of other chemical fuels, e.g. liquid hydrocarbons (13.1 $kWh \cdot kg^{-1}$). In other words, the energy content of 0.33 kg of hydrogen corresponds to the energy content of 1 kg of oil. [3]. For decades hydrogen storage has had an important place in research of most technologically progressive nations of the world. The motivation behind the move is the trust given to the fact that hydrogen can help to tackle the growing demand for energy and hold up global climate change [4-8].

A storage technology with potential for different kinds of applications is hydrogen storage through absorption in metal hydrides. This technology offers high volumetric energy densities and increased safety due to hydrogen chemically bound at lower pressures. In addition, based on the thermodynamic properties of metal hydrides, this class of materials gives the chance to improve a new hydrogen compression technology. They allow the direct conversion from thermal energy into the compression of hydrogen gas with no need of any moving parts [9]. Thermal management is an important issue in systems which consist of heat transfer phenomena. Since hydrogen absorption is an exothermic process, it's significant to control the temperature factor in the system. One of the studies related to this issue belongs to Disli et al [10]. Tong et al [11], conducted a numerical study based on complete and reduced models to examine the thermal effects on the system. Tong et al [12], performed a study with phase change material to examine the thermal effects of a metal hydride storage system. Zhu et al [13], conducted a study based on proton exchange membrane fuel cell and metal hydride hydrogen storage tank for active thermal management. Askri et al [14], performed a study for the optimization of hydrogen storage in metal hydride tanks. Nguyen et al [15], performed a study for the thermal management of metal hydride hydrogen storage using phase change materials for standalone solar hydrogen systems.

This study focuses on the development of new thermal management techniques in hydrogen storage in metal hydrides. Effect of baffle(s) on the hydrogen absorption is examined. The baffles and the baffle used in Case 2 and Case 3, respectively are placed on the inner surface of the cooling channel in the metal hydride bed for a better cooling. Thus, better hydrogen absorption process is expected. These special structures attached to the cooling channel may be promising for a better hydrogen storage in a metal hydride bed.

2. MODELLING

Each model for Case 1, Case 2 and Case 3 is shown on Fig. 1 (a), Fig. 1(b) and Fig. 1(c). For each case, the cooling channel of the metal hydride reactor has a corrugated structure based on half circle profiles. The corrugated structure is used to increase the local velocity of the coolant. For a better cooling process and a faster absorption, baffles are placed on the inner surface of the cooling channel to be present in the metal hydride bed in Case 2. The baffles are placed in equal spacing (number of baffles is 10) in contact with the metal hydride bed. The same attempt is performed in Case 3 with a different profile of the baffle. Instead of using more than one baffle, a single baffle which has a structure of a

combination of U-tubes is considered. The U-turning movements of the coolant through the baffle creates a flow profile for a faster cooling process for better hydrogen sorption.

Fig 1. Models (a) Case 1, b) Case 2, c) Case 3)

Mass conservation for hydrogen is given as [10]

$$\varepsilon \frac{\partial \rho_g}{\partial t} = -\dot{m} \tag{1}$$

The mass conservation of metal hydride bed is [10]

$$(1-\varepsilon)\frac{\partial \rho_{mhb}}{\partial t} = \dot{m} \tag{2}$$

where $m^{\cdot}$ is the volumetric mass flow rate of the hydrogen during the sorption process. It's evaluated from the common kinetics equation [11],

$$\dot{m} = Ca\, exp\left[-{}^{E_a}/_{R\,T}\right]\ln\left({}^{P_g}/_{P_{eq}}\right) = [\rho_{st} - \rho_s] \tag{3}$$

where Ca and E_a are reaction constant and activation energy respectively. P_g is the hydrogen supply pressure, ρ_{st} is the density of saturated metal hydride, ρ_s is the density of metal hydride at a particular time during sorption.

Energy conservation equation is given by [11]

$$\left(\rho C_p\right)_{eff}\left(\frac{\partial T}{\partial t}\right) + \left(\rho C_p\right)_g(\vec{u}\,\nabla \mathrm{T}) = k_{eff}\nabla^2 T + Q \tag{4}$$

$\left(\rho C_p\right)_{eff}$ and k_{eff} stand for effective heat capacity and thermal conductivity for solid and gaseous phases. These expressions are given as

$$\left(\rho C_p\right)_{eff} = (1-\varepsilon)\left(\rho C_p\right)_s + \varepsilon\left(\rho C_p\right)_g \tag{5}$$

$$k_{eff} = (1-\varepsilon)k_s + \varepsilon k_g \tag{6}$$

The momentum conservation equation is given by [16]

$$\frac{\rho}{\varepsilon}\frac{\partial \vec{v}_s}{\partial t} + \left(\frac{\mu}{K} + \frac{S_0}{\varepsilon^2}\right)\vec{v}_s = -\nabla P + \nabla.\left[\frac{\mu}{\varepsilon}\left(\nabla\vec{v}_s + \nabla\vec{v}_s{}^T\right)\right] - \nabla.\left[\left(\frac{2\mu}{3} - \eta_d\right)\left(\frac{1}{\varepsilon}\right)(\nabla.\vec{v}_s)I\right] \tag{7}$$

At the beginning of the sorption process, metal hydride bed, fins and coolant in the channel are in ambient conditions. The density of metal hydride bed is uniform.

$$P = P_{\mathrm{i}} = 10\ atm \tag{8}$$

$$T = T_0 = 288.15\ K \tag{9}$$

$$\rho_{MH} = \rho_i = 780\ {}^{kg}/_{m^3} \tag{10}$$

$$\dot{Q} = 0.5\ {}^{m^3}/_{h} \tag{11}$$

The outer wall of the reactor is considered adiabatic.

$$\left(-k\frac{\partial T}{\partial r}\right)_{r=r_w} = 0 \tag{12}$$

Finite element method (FEM) is used for the solution of the governing equations. Lagrange FEMs of different orders are used for the approximation of field variables in different domains of thermal management system coupled with hydrogen

storage. Number of tetrahedra elements used is 578111. Minimum element quality is 0.00379. COMSOL Multiphysics 6.2 is utilized for the simulation of the coupled system.

3. RESULTS AND DISCUSSION

Fig. 2 shows the hydrogen absorption fraction (wt. %) for three cases. Based on the results, the absorption process in Case 2 and Case 3 (cases in which ten baffles and one baffle in the structure of U-tubes, respectively) is improved by 9.4% and 10.5%, respectively. The best result was obtained with the usage of baffle combined with U-tubes. Models in Case 2 and Case 3 improved the sorption process with significant difference compared to the model in Case 1 as it's seen in Fig. 2.

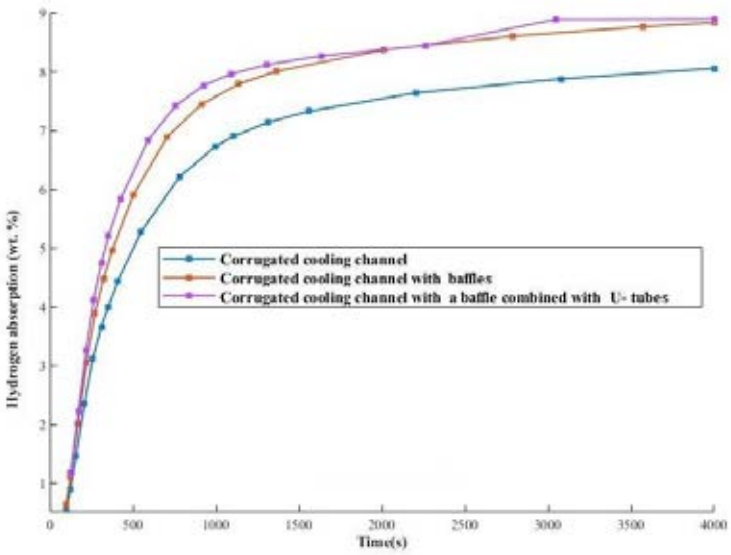

Fig 2. Hydrogen absorption (wt. %) for Case 1, Case 2 and Case 3

Fig. 3 demonstrates the average bed temperature values for three cases. The improvement in the average bed temperature in the metal hydride bed of the reactor is clearly seen in Fig. 3. The average bed temperature in Case 2 and Case 3 decreased by 18% and 35%, respectively. The best performance was shown by the model in Case 3 with an improvement of 17% compared to the model in Case 2. The wavy flow the baffle created during the cooling process caused this improvement. Fig. 4 shows the average bed temperature at 2000 s and 4000 s for each case. The wavy flow of the coolant due to the U-turns of the baffle created a remarkable acceleration in the coolant velocity. This enhancement of the coolant caused a faster absorption process for the reactor and a much better average temperature distribution in the metal hydride bed. The favorable properties of the ammonia borane metal hydride are a remarkable contribution to sorption due to its high volumetric and gravimetric capacity of hydrogen absorption. The corrugated structure of the cooling channel also improved the hydrogen sorption process in all three cases.

According to the results, it may be promising to use baffle(s) on the cooling channel surface in contact with the metal hydride bed for a faster absorption and average temperature distribution in a reactor in terms of thermal management.

4. CONCLUSIONS

Novel thermal management methods for hydrogen storage in metal hydride is developed. FEM based simulation method is utilized. Based on the data obtained from the study,

1) The best result is obtained in Case 3 (in which the cooling channel had a baffle with a structure of several U-tubes). The absorption process is improved by 10.5% compared to the model in Case 1(which had a corrugated structured cooling channel with no baffle(s) on)

2) The average bed temperature in the metal hydride in the hydrogen reactor is reduced by 35%.

3) The baffle used in Case 3 has the biggest effect on the enhancement of the hydrogen storage system.

4) The corrugated structure and the metal hydride ammonia borane are two factors which contributed to the hydrogen storage system.

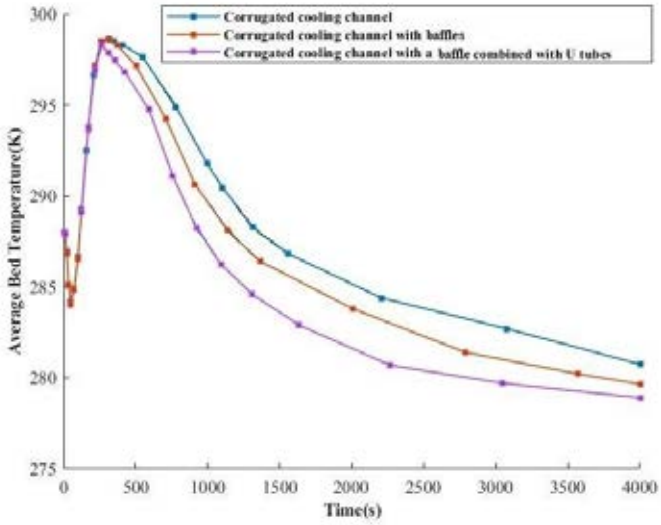

Fig 3. Average bed temperature values for Case 1, Case 2 and Case 3

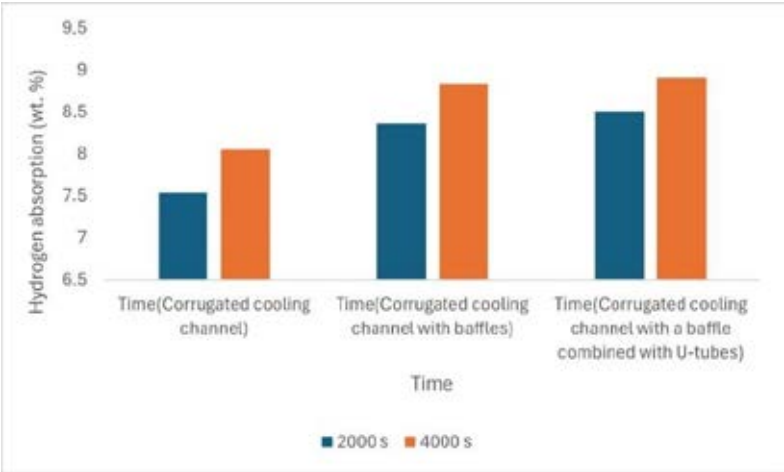

Fig. 4. Average bed temperature values at 2000 s and 4000 s for Case 1, Case 2 and Case 3

REFERENCES

1. Dresselhaus, M., Crabtree, G., Buchanan, M., & Mallouk, T. (2003). *Basic research needs for the hydrogen economy*. Technical report, Argonne National Laboratory, Basic Energy Sciences, US DOE, http://www. sc. doe. gov/bes/hydrogen. pdf.
2. Züttel, A. (2004). Hydrogen storage methods. Naturwissenschaften, 91, 157-172.
3. Weast RC (ed) (1976) Handbook of chemistry and physics, 57th edn. CRC, Boca Raton
4. Sahaym U, Norton MG. Advances in the application of nanotechnology in enabling a 'hydrogen economy'. J Mater Sci 2008; 43:5395e429.
5. Jia Y, et al. Combination of nanosizing and interfacial effect: future perspective for designing Mg-based nanomaterials for hydrogen storage. Renew Sustain Energy Rev 2015; 44:289e303
6.Balema V. Hydrogen storage materials. Mater Matters 2007;2(2):2
7. Sakintuna B, Lamari-Darkrim F, Hirscher M. Metal hydride materials for solid hydrogen storage: a review. Int J Hydrogen Energy 2007; 32:1121e40
8. Yang Z, Weil KS, Michael PB. Materials in clean power systems: applications, status and challenges. Int J Hydrogen Energy 2007; 32:3609.
9. Von Colbe, J. B., Ares, J. R., Barale, J., Baricco, M., Buckley, C., Capurso, G., ... & Dornheim, M. (2019). Application of hydrides in hydrogen storage and compression: Achievements, outlook and perspectives. *international journal of hydrogen energy*, *44*(15), 7780-7808.
10. Disli, T., Çetinkaya, S. A., Ezan, M. A., & Colpan, C. O. (2024). Numerical investigations on the absorption of a metal hydride hydrogen storage tank based on various thermal management strategies. *International Journal of Hydrogen Energy*, *51*, 504-522.

11.Tong, L., Xiao, J., Yang, T., Bénard, P., & Chahine, R. (2019). Complete and reduced models for metal hydride reactor with coiled-tube heat exchanger. *International Journal of Hydrogen Energy*, *44*(30), 15907-15916.
12.Tong, L., Xiao, J., Bénard, P., & Chahine, R. (2019). Thermal management of metal hydride hydrogen storage reservoir using phase change materials. International Journal of Hydrogen Energy, 44(38), 21055-21066.
13.Zhu, D., Ait-Amirat, Y., N'Diaye, A., & Djerdir, A. (2019). Active thermal management between proton exchange membrane fuel cell and metal hydride hydrogen storage tank considering long-term operation. Energy Conversion and Management, 202, 112187.
14. Askri, F., Salah, M. B., Jemni, A., & Nasrallah, S. B. (2009). Optimization of hydrogen storage in metal-hydride tanks. *International journal of hydrogen Energy*, *34*(2), 897-905.
15. Nguyen, H. Q., & Shabani, B. (2022). Thermal management of metal hydride hydrogen storage using phase change materials for standalone solar hydrogen systems: An energy/exergy investigation. *International Journal of Hydrogen Energy*, *47*(3), 1735-1751.
16. Hardy, B., Corgnale, C., Chahine, R., Richard, M. A., Garrison, S., Tamburello, D., ... & Anton, D. (2012). Modeling of adsorbent based hydrogen storage systems. *International Journal of Hydrogen Energy*, *37*(7), 5691-5705.

SOLAR THERMOCHEMICAL HYDROGEN GENERATION WITH A 250-KW STRUCTURED REACTOR: EXPERIENCES FROM TESTS AT THE JÜLICH SOLAR TOWER

Thomas Fend[1], Vamshi K. Thanda[1], Jörg Lampe[2], Steffen Menz[2], Stefan Schmitz[3], Gregor Piesche[4], Stefan Berger[4]*
[1]Institute of Future Fuels, German Aerospace Center (DLR), 51147 Cologne, Germany
[2]Department of Energy Technology, University of Applied Science Cologne (RH), 50825 Cologne, Germany
[3]Institute of Solar Research, German Aerospace Center (DLR), 52428 Jülich, Germany[c]
[4]Stausberg & Vosding GmbH, Reichsweg 30, 52068 Aachen, Germany

*Corresponding author e-mail: thomas.fend@dlr.de

ABSTRACT

Thermochemical water splitting using two-stage REDOX processes and concentrated solar radiation as an energy source has been the focus of process engineering research for more than two decades. It is considered as a promising technology for producing green hydrogen and liquid green fuels at competitive prices in the medium term. In this process concentrated solar radiation is directly converted into storable chemical energy. The present article reports the results of an experimental campaign, which has been carried out at the research level of the Solar Tower Jülich to further demonstrate the feasibility of this technology. Based on the experience from prior tests at a large-scale solar simulator a combined receiver/reactor has been re-designed and built up. The reactor was operated at temperatures between 1200 °C and 1000 °C using radiative power of up to 780 kW generated by part of the heliostat field of the Solar Tower. As redox material ceria has been used which has been coated on a framework of a zirconia foam due to stability reasons. It could be shown that the production of hydrogen in a medium scale structured reactor is possible. The tests also revealed which improvements concerning structure, optical and thermal management as well as operational parameters are necessary to achieve satisfying efficiencies.

Keywords: thermochemical cycle, green hydrogen, redox reaction, ceria, solar hydrogen reactor

1. INTRODUCTION

Solar thermochemical water splitting has been investigated at the Institute for Future Fuels and its predecessor since 2002. Together with national and international partners such as the major research organisations CERTH (Greece) and CIEMAT (Spain) as well as industrial partners such as HELPE (Greece), ABENGOA (Spain) and ENGICER (Switzerland), this technology has been advanced to a great extent. It has high theoretical solar-to-fuel efficiency potential of up to 50% [1, 2] and provides a way to generate hydrogen directly from the sun without prior generation of electricity. A two-stage redox process is used in which a metal oxide is alternately reduced and oxidised, releasing hydrogen in the process (Fig. 1). As part of the NRW projects ASTOR and ASTOR-ST, which have been realized in co-operation with RH Cologne, Stausberg & Vosding and AWS-Technik, this technology has been demonstrated with a 250-kW solar reactor in a large-scale solar simulator [3].

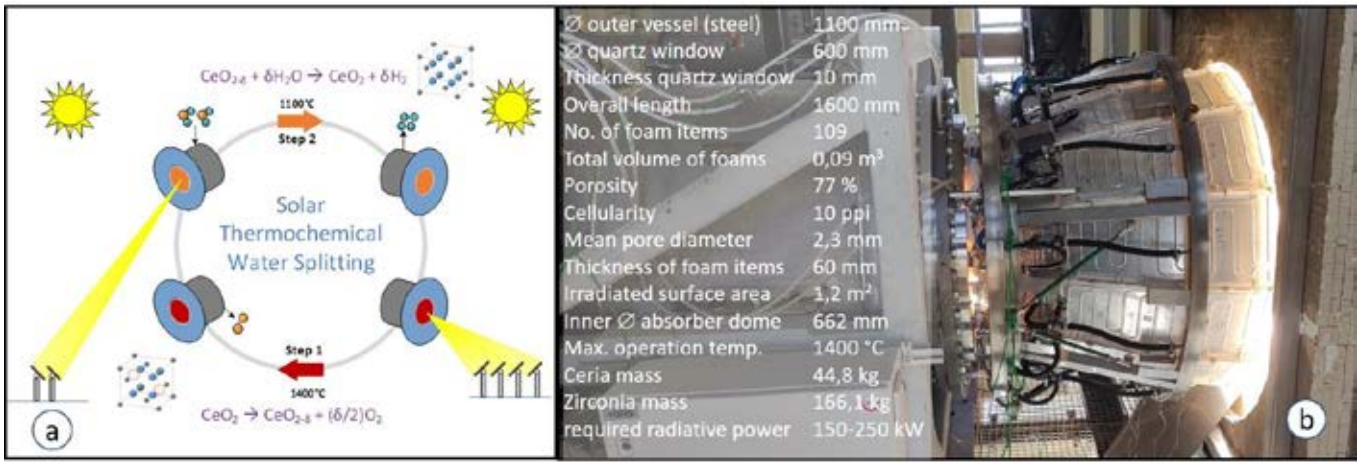

Fig. 1. The two-stage redox-process with ceria as a functional material (a). The reaction takes place to a certain extent described by the non-stoichiometry parameter δ depending on oxygen partial pressure and temperature in the reactor. (b) Reactor and secondary concentrator in operation on the research level of the Solar Tower Jülich along with some technical data of the receiver.

2. MATERIALS AND METHODS

2.1. Redox material

The redox material used was pure ceria, which appeared as a coating on a zirconia framework consisting of an RPC 10ppi foam produced by EngiCER using the classical Schwarzwalder process. A total of 44.8 kg of ceria and 166 kg of zirconia was used. 109 blocks of slightly different geometry were manufactured, which were then assembled to form the reactor dome shown in Fig. 2d. After the tests in the solar simulator, which totalled 52 operating hours, the entire redox material was replaced with the objective of improving the absorption properties of the reactor. A two-stage porosity was created in each block, in a way that the porosity was higher on the irradiated side to allow deeper penetration of solar radiation (Fig. 2c). Model calculations by RH Cologne have shown that this equalises the temperature in the receiver and thus enables higher efficiency levels.

Some of the material used in the first test campaign exhibited severe traces of degradation, which were particularly evident in strut fractures and detachment of the cerium oxide layer (Fig 2 a and b). The blue colouration at the interface between zirconia and ceria oxide was also conspicuous. X-ray analysis suggests that this is the solid solution ZrCeO2 (Fig 4a), which has been proposed in other studies to improve the reduction properties of the material [4].

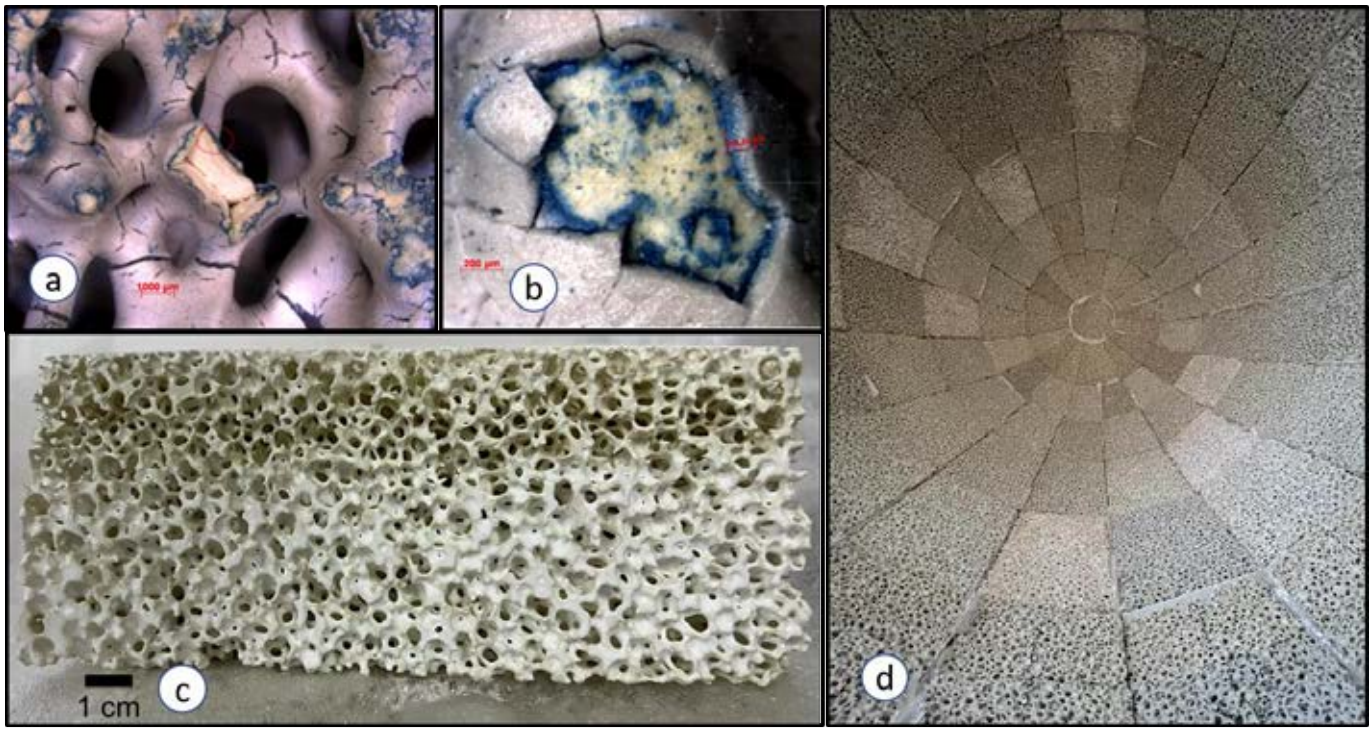

Fig. 2. 10ppi ceria coated zirconia foam used for the reactor. (a) Micrograph of the material after approx. 52 operation hours. (b) Parts of the approx. 135 µm thick ceria-layer detached from the zirconia substrate during tests of the 1st campaign. (c) One of the 109 as received modules of the reactor-dome for the 2nd campaign with two-stage porosity. (d) Front view of the reactor as a whole.

2.2. Experimental set-up

As part of the ASTOR-ST project, we developed a 250-kW reactor, the centrepiece of which was the REDOX dome described in the last section. It can be seen as a further development of the reactors built for the solar gas turbine as part of the EMPOLI and REFOS projects [5], which were also used in a modified form for the solar methane reformation demonstrated in the SOLREF project [6]. The outer vessels of these reactors as well as secondary concentrators with an optical efficiency of up to 80% have been reused, which caused some constraints concerning size and aperture geometry. The reactor is shown schematically in Fig. 3a. An inner vessel separates the incoming and outgoing fluids, which pass the wall of the redox dome from left to right before they finally leave the reactor through the gas outlet. The solar radiation enters the reactor through a flat fused silica window, which replaces the formally used dome shaped version, because the experiment was operated under close to ambient pressure conditions, thus fixing the flat window was easier and the operation safer. Fig. 3b shows a simplified map of the entire set-up. Stausberg & Vosding developed the system control. It consisted of a LabVIEW-controlled PLC that enabled real-time operation and measurement as well as automatic mode and multi reactor operation. During the reduction step the reactor is heated up and flooded with nitrogen 5.0, creating an oxygen partial pressure of 10^{-5} bar provided that the reactor is completely filled up. Only the valves v301, v400 and v500 are open and an O2-meter monitors the O2 content of N2/O2 mixture leaving the reactor.

Hereafter, v401 is opened and steam enters the reactor to introduce the oxidation step. In the same time v500 is closed, v600 is opened enabling the N2/H2 mixture to leave the system and to be analyzed by a mass spectrometer. The reactor temperature was measured from the rear using thermocouples at a depth of 1.5-3 cm. The whole set-up was put onto the research level of the Solar Tower. In the inserted photograph in Fig. 4c the irradiated reactor can be seen in the middle of the left tower from the outside. The radiative power from the Heliostat-field on the outer aperture of the secondary concentrator was estimated by creating a second similar focus on a white screen equipped with a standard high-flux radiometer.

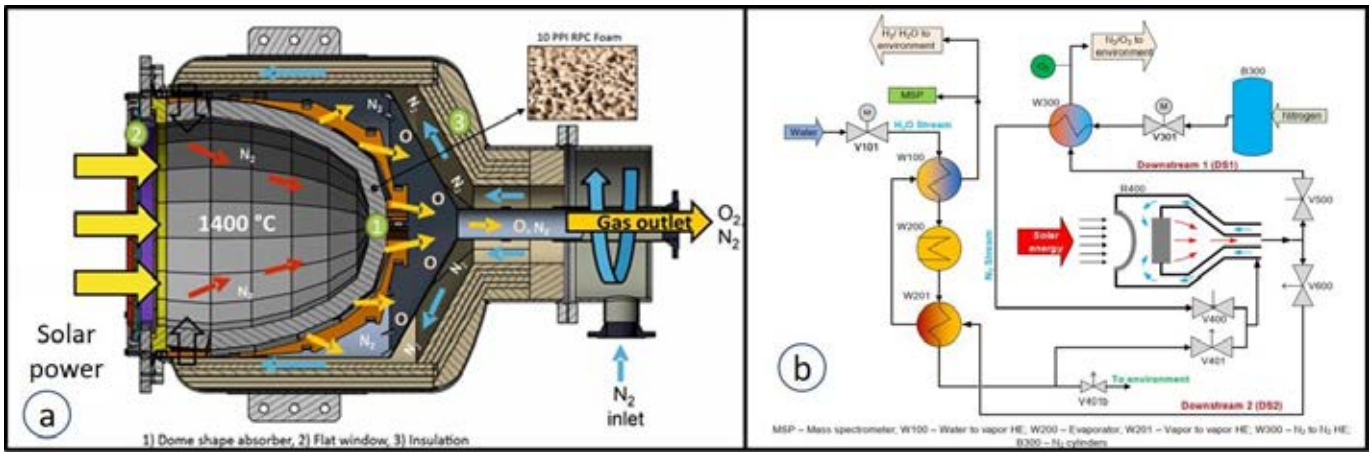

Fig. 3. Schematic representation of the reactor (a) and simplified diagram of the piping and instrumentation for the supply of the reactor with steam and nitrogen as well as the treatment of the outlet gases including three heat exchangers for heat recovery (b).

3. RESULTS AND DISCUSSION

Fig. 4 b and c show the course of an experiment on the research level of the Solar Tower Jülich. On this day, conditions were almost clear sky and up to 285 heliostats each with an aperture area of about 8 m² could be used for the experiment. The blue curve represents the power on the aperture of the secondary concentrator. Due to larger optical losses compared to the mentioned gas-turbine application, only a smaller fraction of this power reached the surface of the reactor. These additional optical losses were caused by a relatively low position of the focus, a horizontal alignment of the reactor and the use of a flat window showing less transmittance due to higher incident angles. The concentration ration was approx. 350. Additionally, reactor average and maximum temperature as well as the steam mass flow is displayed. By successively increasing the radiative power to 690 kW, the reactor was heated up to 979 °C maximum temperature at the backside. At this point a first oxidation phase was introduced resulting in a hydrogen production rate of 0.6 g/h. Once the rate of hydrogen production had fallen to almost zero, a second reduction phase was initiated. Now the maximum available power (780 kW) was put on the experiment. Consequently, the reactor temperature increased and in the subsequent second oxidation phase the hydrogen yield was correspondingly greater and a hydrogen mass flow 1.2 g/h was achieved. However, the reactor temperature did not exceed 1000 °C on the rear. We know from the previous measurement campaign in the solar simulator that the temperature on the irradiated side is significantly higher [3] but the redox foam used during this campaign had a slightly different porosity. From model calculations this effect could be estimated [7, 8] so that we assume that the temperature at the front side was approx. up to 1200 °C. Integration of the hydrogen curve from Fig. 4b provides the absolute values of hydrogen produced during the two cycles carried out. These were 0.2 g and 0.57 g respectively. This is much less then expected but simply be explained by the fact that within this experiment the lay-out temperature of 1400 °C could not be reached by far, because overheating problems with the secondary concentrator and the window flange occurred, which could not be solved in the remaining time of the project. However, the stoichiometry of the reduction equation (Fig. 1a) predicts these amounts for temperatures of 1000 °C and 1080 °C along with a ceria mass of 44.8 kg and an oxygen partial pressure of 10^{-5} bar [9]. Thus, in principle, the reactor is able to generate hydrogen according to predictions based on theoretical calculations and lab scale experimental experiences.

4. CONCLUSIONS

It has been shown that solar thermochemical hydrogen production on a medium scale is possible with the reactor concept developed. The amount of produced hydrogen per mass of redox material used, as predicted by theory, was largely achieved. However, the efficiency of the process in these first tests was relatively low. The main reasons for this are the large aperture to reactor surface area relationship and the associated low concentration ratio. Moreover, the optical efficiency of the secondary concentrator was low. Further work on the optical design of the reactor and the secondary concentrator is planned with the aim of significantly increasing the concentration ratio and thus the overall efficiency.

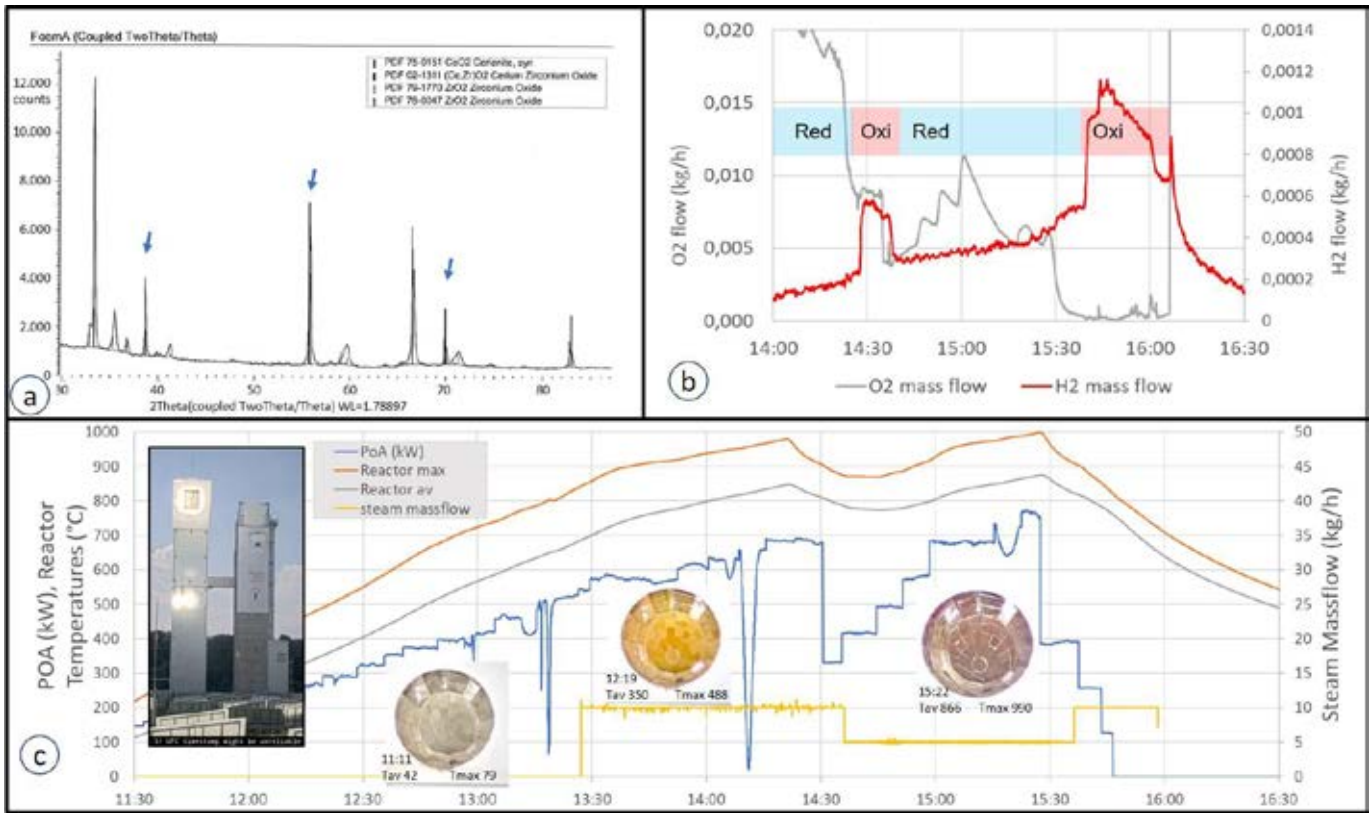

Fig. 4. An X-ray analysis (a) of the degraded material (see Fig. 2) shows the formation of a solid solution (CeZrO2, blue arrows) in the transition region between cerium oxide and zirconium oxide. (b) Oxygen and hydrogen mass flow during the reduction and oxidation phase of the experiment. (c) Related reactor temperatures, radiative power from the heliostat field and steam mass flow. Note that steam was only inserted into the reactor during the oxidation phase by opening valve V401and closing the by-pass V401-b

ACKNOWLEDGEMENT

The study has been carried out in the frame of project ASTOR-ST (EFRE-0801815). The funding of the EFRE fund and the NRW Ministry of Economic Affairs, Innovation, Digitalisation and Energy is gratefully acknowledged

REFERENCES

1. Steinfeld A and Palumbo R. 2001. Solar Thermochemical Process Technology. In Encyclopedia of physical science & technology*, 2001, Edited by* Meyers RA, Academic Press, 15, 237-256.
2. Call F. 2014. Investigation of Ceria based redox materials for thermo-chemical solar fuel production. 2014. PhD thesis. Aachen RWTH.
3. Thanda VK, Fend T, Laaber D, Lidor A, von Storch H, Saeck JP, Hertel J, Lampe J, Menz S, Piesche G, Berger S, Lorentzou S, Syrigou M, Denk T, Gonzales-Pardo A, Vidal A, Roeb M and Sattler C. 2022. Experimental Investigation of the Applicability of a 250 kW Ceria Receiver/Reactor for Solar Thermochemical Hydrogen Generation. Renewable Energy.198:389-398.
4. Bulfin B, Call F, Vieten J, Roeb M, Sattler C and Shvets IV. 2016. Oxidation and Reduction Reaction Kinetics of Mixed Cerium Zirconium Oxides. J. of Physical Chemistry.120:2027-2035.
5. Buck R, Bräuning T, Denk T, Pfänder M, Schwarzbözl P and Tellez F. 2002. Solar-Hybrid Gas Turbine-based Power Tower Systems (REFOS). Journal of Solar Energy Engineering (ASME). 124(1): 2-9.
6. Agrafiotis C, von Storch H, Roeb M and Sattler C. 2014. Solar thermal reforming of methane feedstocks for hydrogen and syngas production - A review. Renewable and Sustainable Energy Reviews. 29:656-682.
7. Menz S, Lampe J, Krause J, Seeger T and Fend T. 2022. Holistic energy flow analysis of a solar driven thermo-chemical reactor set-up for sustainable hydrogen production. J of Renewable Energy. 189:1358-1374.
8. Lampe J, Henke S, Menz S and Fend T. 2024. Solar-driven thermochemical water splitting: 3D energy flow analysis of a volumetric fixed-bed reactor design. Int. Journal of Hydrogen energy, in press
9. Bulfin B, Lowe AJ, Keogh KA, Murphy BE, Lübben O, Krasnikov SA and Shvets IV. 2013. Analytical Model of CeO2 Oxidation and Reduction. The Journal of Physical Chemistry. 117(46):24129–24137.

TECHNO-ECONOMIC EVALUATION OF HYDROGEN'S ROLE IN DUTCH HEATING NETWORKS: A DYNAMIC MODELING APPROACH

[1*]*Amirreza Kaabinejadian*, [1]*Artur Pozarlik*, [1,2]*Canan Acar*
[1] University of Twente, Faculty of Engineering Technology, Department of Thermal Engineering, Drienerlolaan 5, 7522 NB Enschede, The Netherlands
[2] Bahcesehir University, Faculty of Engineering and Natural Sciences, Ciragan Cad. No:4-6 34353, Istanbul, Turkey

*Corresponding author e-mail: a.kaabinejadian@utwente.nl

ABSTRACT

Expanding the penetration of renewable energy sources to address the greenhouse gas emissions from residential heating systems is imperative. However, renewable energy sources, such as solar and wind have an intermittency issue. Hydrogen emerges as a potential energy vector to be used as a storage medium or to be directly processed for generating the required heat and power. Therefore, this study outlines a hydrogen-based heating system to decarbonize residential heating while meeting thermal demands. Furthermore, the present investigation focuses on district heating networks as they deal with central energy production plants and hold significant potential to deploy large-scale zero-emission units to decarbonize the built environment. The proposed system uses hybrid solar and wind sources as the prime movers of the system and combination of a proton exchange (PEM) electrolyzer, a stacked PEM fuel cell, and an air-source heat pump to generate the required thermal demand. In addition, a series of electrical, hydrogen, and thermal storage options exist to manage the load shifting. Two detached houses with different floor areas have been selected in Almere City, located in Flevoland province to meet their demands through the proposed system. Based on anticipated results, using hydrogen for bigger homes is more cost-effective.

Keywords: Hydrogen, Decarbonization, Residential buildings, Dynamic modeling, District heating

1. INTRODUCTION

Currently, most residential heating systems across Europe rely on non-renewable sources, including natural gas. For instance, around 85% of the required residential thermal demands are provided using natural gas boilers in houses in the Netherlands [1]. Therefore, evaluating the feasibility of sustainable heating solutions is of great importance to decarbonizing residential heating systems. Electrification, through using heat pumps is a favorable choice for Dutch stakeholders to use in newly built houses to reduce the CO_2 emissions [2]. However, electrifying all residential buildings could lead to grid congestion in the absence of sufficient grid capacity, endangering the balance between supply and demand. This underscores the need for stakeholders to adopt a mix of sustainable solutions to decarbonize buildings while maintaining grid resiliency. Therefore, hydrogen is introduced as a versatile energy vector, capable of being used directly as a fuel to generate heat or indirectly as a storage medium to mitigate the fluctuations of renewable energy sources such as wind and solar [3]. Decentralizing energy production helps decarbonize buildings, but costly microgrids remain a challenge. Using existing heating networks is a practical solution to meet thermal needs and support the energy transition. District heating networks (DHN) are connected to centralized plants to produce the required thermal energy, which is then delivered to homes through insulated pipes in the form of hot water. These heating networks hold a significant potential to boost energy efficiency within communities and mitigate greenhouse gas emissions [3].

Few studies have focused on hydrogen's potential role in heating networks in the Netherlands. Thus, this study aims to introduce a hydrogen-based heating system and perform a techno-economic analysis to assess its technical and financial characteristics using the dynamic modeling approach.

2. METHODOLOGY

The designed hydrogen-driven heating system along with the selected methodology is introduced in this section.

2.1. System description

According to Fig.1, the designed system is equipped with hybrid solar/wind sources to produce clean electricity. A lithium iron phosphate ($LiFePO_4$) battery package stores excess electricity to ensure the electrolyzer demand is met later. In this study, a proton exchange membrane electrolyzer (PEME) generates hydrogen. In fact, this electrical storage system is designed to shave the peak demand of the PEME as it leads to its longevity and decreases its wear and tear. Fig. 2 depicts the flowchart of the battery system to manage the generated power. The excess amount of produced hydrogen is then stored in a gaseous form for storage purposes. The stacked proton exchange membrane (PEM) fuel cell is used

to produce the required heat and power. The generated power by the stacked PEM is sent to an air-source heat pump to produce complimentary thermal energy. In this study, a portion of produced heat in the PEM fuel cell is used to pre-heat the heat pump to increase its coefficient of performance (COP) and consequently total energy efficiency of the system. In the end, after storing excess heat in phase change material (PCM) tanks, heating networks transfer the required thermal energy of studied houses in the form of hot water at 60°C

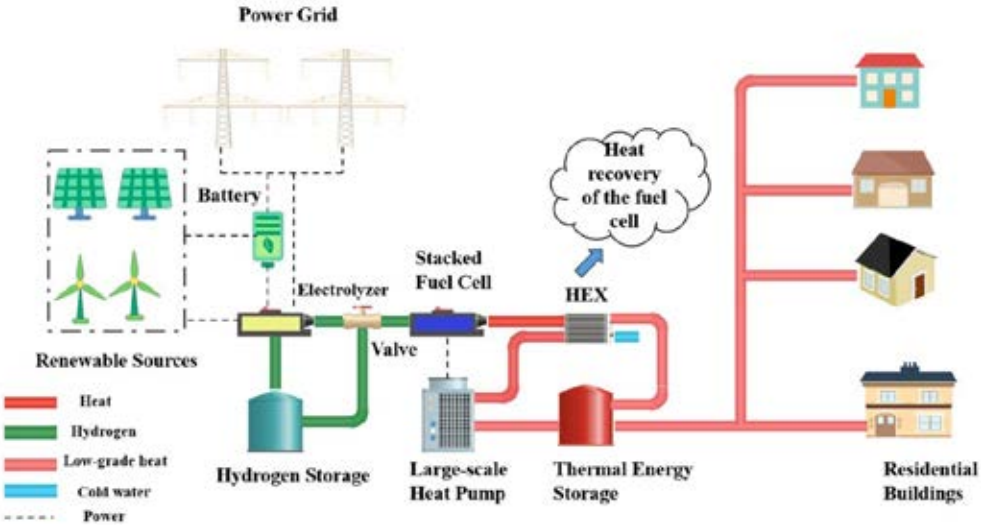

Fig. 1. Hydrogen-driven heating system

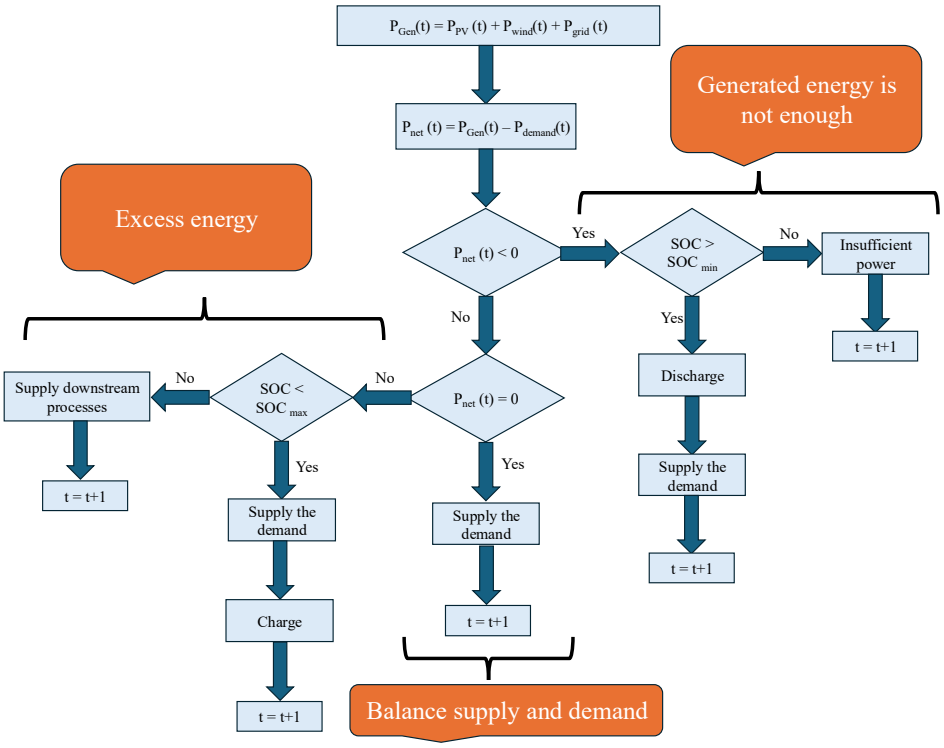

Fig. 2. Flowchart of the used electrical energy storage system

2.2. Selecting the case study location

As was mentioned earlier, around 85 % of residential houses in the Netherlands are equipped with natural gas boilers to meet their space heating and hot water demands. However, heating networks are leveraged in different locations to diversify utilized heating systems and reduce greenhouse gas emissions. As shown in Fig. 3, District heating without gas consumption accounts for 32% of the heating methods in the Flevoland province of the Netherlands in recent years which is recognized as the highest among other regions [4]. This highlights the availability of the necessary facilities from both the energy providers' and consumers' perspectives. Therefore, Almere City, located in this province, has been selected

to evaluate the incorporation of hydrogen heating technologies in their heating networks.

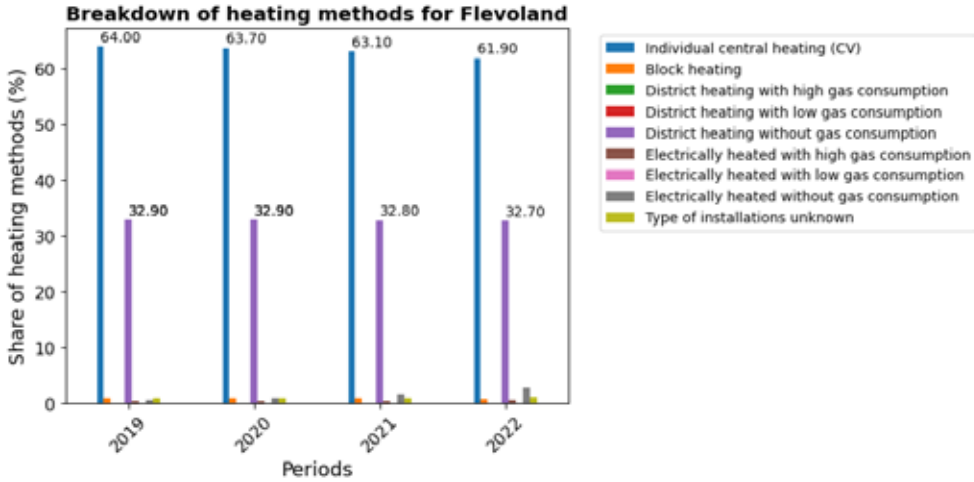

Fig. 3. Breakdown of available heating methods in Flevoland province across different years

2.3. Mathematical modeling approach

The following equations are employed to conduct dynamic system-level modeling and determine the technical and economic characteristics of the designed system [5].

$$\frac{dE}{dt} = \dot{E}_{in} - \dot{E}_{out} \tag{1}$$

$$\frac{dm}{dt} = \dot{m}_{in} - \dot{m}_{out} \tag{2}$$

$$\frac{dEx}{dt} = \dot{Ex}_{in} - \dot{Ex}_{out} - \dot{Ex}_{dest} \tag{3}$$

$$\dot{C}_{total} = \dot{C}_{fuel} + \dot{Z}_{total} \tag{4}$$

3. RESULTS AND DISCUSSION

The first step in conducting system integration is to ensure the validity of the used mathematical model for each component by comparing the results of the simulation with the prior experimental endeavors. As shown in Fig. 4, polarization curves of employed PEME and PEM fuel cells are in good agreement with experimental results [6,7]. Through polarization curves, key parameters such as operating voltage, overpotential losses, and critical characteristics of studied PEM fuel cell or electrolyzer, which are rooted in electrochemical processes can be obtained. This highlights the accuracy of the current simulation and shows that the simulation results validate the system model.

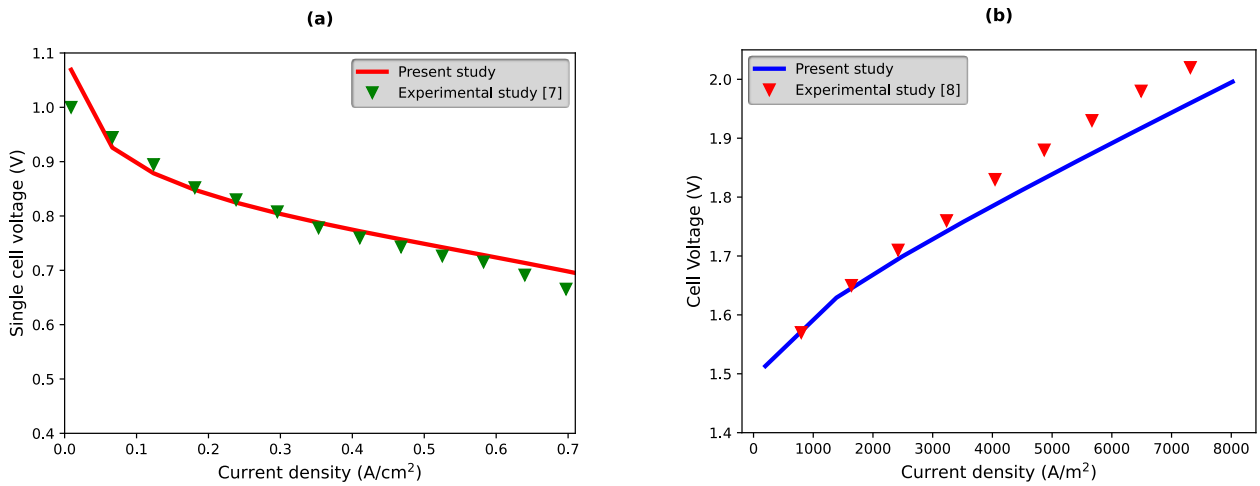

Fig. 4. Validation results for a) PEM fuel cell and for b) PEME

After carrying out the system integration, the capacity of all components is determined based on the heating demand profiles of the studied houses. In fact, their heating demand is reported as consumed natural gas in cubic meters (m^3). Afterward, considering the difference between calorific values of hydrogen and natural gas, it can be converted to demand of hydrogen which leads to calculating the appropriate sizing of components. It is expected to completely decarbonize the residential heating systems in the studied region in the Netherlands by utilizing the proposed hydrogen-driven heating option. Furthermore, grid congestion is expected to be addressed by introducing hybrid hydrogen/electricity-based heating system which enables stakeholders to manage the distribution of thermal energy. From the economic perspective, it is anticipated that hydrogen would be more cost-effective in houses with larger surface areas owing to the economy of scale notion.

4. CONCLUSIONS

The present study aims to decarbonize the residential heating systems in the Netherlands by using hydrogen in district heating systems. The proposed plan consists of a combination of photovoltaic panels and horizontal-axis wind turbines to generate clean electricity. The generated electricity is used to drive a PEME for hydrogen production which will later be used for thermal energy production through a stacked PEM fuel cell. The generated power in the fuel cell is used to drive an air-source heat pump for the generation of complimentary thermal energy. This produced heat flow is used to provide space heating and hot water for two detached houses in Almere City, located in Flevoland province. Key findings of this study show that the proposed system leads to decarbonization of the residential heating systems in the studied region. Furthermore, this enables energy providers to manage hydrogen, and electricity flows to prevent grid congestion. For future studies, it is recommended to consider a semi-decentralized system, partially decentralizing certain aspects of energy production. This approach could help evaluate its effect on improving the manageability of thermal demand distribution and achieving a better balance between production and transmission costs.

REFERENCES

[1] Gross R, Hanna R. Path dependency in provision of domestic heating. Nat Energy 2019;4:358–64. https://doi.org/10.1038/s41560-019-0383-5.

[2] Sahoo S, van Stralen JNP, Zuidema C, Sijm J, Yamu C, Faaij A. Regionalization of a national integrated energy system model: A case study of the northern Netherlands. Appl Energy 2022;306:118035. https://doi.org/10.1016/j.apenergy.2021.118035.

[3] Kaabinejadian A, Pozarlik A, Acar C. A systematic review of predictive, optimization, and smart control strategies for hydrogen-based building heating systems. Appl Energy 2025;379:124994. https://doi.org/10.1016/j.apenergy.2024.124994.

[4] StatLine - Energy consumption private dwellings; type of dwelling and regions n.d. https://opendata.cbs.nl/#/CBS/en/dataset/81528ENG/table (accessed December 11, 2024).

[5] Dincer I, Rosen MA, Ahmadi P. Optimization of Energy Systems. John Wiley & Sons; 2017.

[6] Ferreira RB, Falcão DS, Oliveira VB, Pinto AMFR. 1D + 3D two-phase flow numerical model of a proton exchange membrane fuel cell. Appl Energy 2017;203:474–95. https://doi.org/10.1016/j.apenergy.2017.06.048.

[7] Abdin Z, Webb CJ, Gray EMacA. Modelling and simulation of a proton exchange membrane (PEM) electrolyser cell. Int J Hydrog Energy 2015;40:13243–57. https://doi.org/10.1016/j.ijhydene.2015.07.129.

ASSESSMENT OF METAHEURISTIC ALGORITHMS OF FUEL CELL VEHICLES: A SHORT REVIEW

[1*]*Onur Yasar*, [2]*Mustafa Umut Karaoglan*, [2]*C. Ozgur Colpan*
[1] Balıkesir University, Faculty of Engineering, Mechanical Engineering Department, Balıkesir, 10145, Turkiye
[2] Dokuz Eylul University, Faculty of Engineering, Mechanical Engineering Department, Tinaztepe, Buca, Izmir, 35397, Turkiye

*Corresponding author e-mail: onur.yasar@balikesir.edu.tr

ABSTRACT

Fuel cell vehicles are studied by researchers due to their zero emission and performance. In researches of fuel cells, cost, size and hydrogen consumption can be problematic. Some methods and algorithms are required to optimize cost, size and hydrogen consumption. Metaheuristic algorithms are the algorithms that can provide the fastest response and provide the most optimum solutions on the subject. Hence, a wide variety of metaheuristic algorithms are derived. This study mainly deals with metaheuristic algorithms for fuel cell vehicles. Various studies of open literature are assessed in accordance with metaheuristic algorithms. In addition to algorithm types, input and output parameters, objectives, results, iteration and standard deviations are also discussed. According to the results, fuel cell powered locomotives are involved with metaheuristic algorithms. Particle swarm optimization is used more than other metaheuristic algorithms.

Keywords: Fuel cell, metaheuristic, algorithm, review, vehicle

1. INTRODUCTION

Metaheuristic algorithms are methods used for problem solving and optimization based on the acts of animals [1]. The term of ''metaheuristic'' is beyond concept of simple heuristics in engineering. The algorithms are stochastic based algorithms provide effective modeling and solutions [2]. Many complex and difficult engineering problems can be solved by using metaheuristic algorithms in short time [3]. Algorithms present an acceptable error in engineering problems with satisfactory results [4]. Considering that there are many animals in nature, it is inevitable that metaheuristic algorithms are quite different than each other [5]. Owl search algorithm, eagle strategy, genetic algorithm, artificial bee colony, monkey algorithm, dolphin echolocation, particle swarm optimization are some nature-inspired metaheuristic algorithms [6]. In addition to these algorithms, artificial fish swarm algorithm, bat algorithm, emperor penguin optimizer, jaguar algorithm, puma optimizer, whale optimization algorithm and grey wolf optimizer are other metaheuristic algorithms [7]. Thus, metaheuristic algorithms are also named ''animal algorithms'' [8].
Metaheuristic algorithms are widely used for fuel cells or hydrogen systems. Fuel cell vehicles are one of the most useful areas for metaheuristic algorithms. In open literature, various studies are conducted. Li et al., [9] suggested converged barnacles mating optimizer (CBMO) algorithm for fuel cell/battery vehicles. With the use of CBMO algorithm, fuel consumption, fuel cell stack lifetime and battery or stack sizes are investigated. The results exhibit that decrement in stack size causes higher fuel consumption. On the other hand, stack lifetime is affected adversely by smaller battery size. In recent studies, bald eagle search (BAS), multi-objective particle swarm optimization (CMOPSO) and genetic algorithm (GA) are preferred. Savran et al., [10] examined fuel cell electric vehicles from the viewpoint of hydrogen consumption and battery cycles. Hydrogen consumption and battery cycles of fuel cell electric vehicles are studied via BAS algorithm to optimize. It is asserted that BAS algorithm enables less hydrogen consumption about 60% in hybrid driving conditions. Liu et al., [11] employed CMOPSO algorithm to fuel cell hybrid vehicles. By using the metaheuristic algorithm, capacity investigation, vehicle durability, energy management and durability are searched. According to the results, CMOPSO presents satisfactory capacity configuration results. Furthermore, safe and efficient operation can be done with 22 kW rated power, 7 batteries in parallel and 100 batteries in series. Mazouzi et al., [12] applied GA to fuel-cell hybrid electric vehicles for energy management purposes. Fuzzy logic-based energy management system is implemented and simulations are performed via Matlab/Simulink. Proposed system with genetic algorithm is found successful in respect to fuel utilization and efficiency operation. Fuel utilization and efficiency operation increase about 30% and 14% respectively.
In this paper, studies of fuel cell vehicles are shortly reviewed in respect to metaheuristic algorithms. Studies are listed from the past to present in tables. Besides metaheuristic algorithms, parameters, error rates, objective functions and iterations are examined and results and conclusion are clarified.

2. APPLICATION OF METAHEURISTIC ALGORITHMS ON FUEL CELL VEHICLES

Applications of metaheuristic algorithms for fuel cell vehicles are challenging. Metaheuristic algorithms are used to reveal dynamic performance, predict stack lifetime, meet power demand or supply, optimize size and reduce total cost.

Additionally, decrement in hydrogen consumption and optimize speed trajectory are other purposes. Dynamic performances of fuel cell vehicles are related to operating conditions. Load conditions, air flow and pressure are significant performance parameters. Dynamic performance of fuel cell vehicles is crucial to investigate and operate [13]. Besides, dynamic performance, stack lifetime is investigated by researchers. Sudden load changes reduce stack lifetime in fuel cell vehicles. Load cycling process can't be neglected in terms of stack lifetime [14]. Power demand and supply are other factors. Power demand can be short-term or long-term. In fuel cell vehicles, it is expected to provide the necessary power at any time. Size optimization and cost reduction are important evaluation parameters. An optimal design of fuel cell vehicles includes battery, fuel cell or hydrogen tank [15].
While optimizing size, it is important to reduce total cost and hydrogen consumption as much as possible. Dynamic performance, drivability and degradation are considerably affected by fuel cell or battery size [16]. Speed planning or trajectory is compulsory for energy or power management of fuel cell vehicles. Vehicle's energy consumption is related to speed trajectory. Revealing speed trajectory is useful to reduce energy consumption of fuel cell vehicles. Therefore, speed trajectory is searched in open literature [17].
Studies of metaheuristic algorithms for fuel cell vehicles are explained. Metaheuristic algorithms for fuel cell vehicles with input, output parameters are listed and given. In addition to input and output parameters, main objective of metaheuristic algorithms are presented in Table 1.

Table 1. Metaheuristic algorithms for fuel cell vehicles

No	Citation	Metaheuristic Algorithm	Input Parameters	Output Parameters	Main Objective
1	Li et al. [13]	Effective Informed Adaptive Particle Swarm Optimization (EIA-PSO)	air flow, stack temperature, hydrogen pressure and fuel cell current	dynamic performance of locomotive	to predict the dynamic performance of locomotive
2	Macauley et al. [14]	Genetic Algorithm (GA)	humidity level, temperature, platinum, oxygen concentration, cell voltage, humidity cycling	stack lifetime	predict stack lifetime
3	Sarma and Ganguly [15]	Particle Swarm Optimization (PSO)	drive cycle, total driving time, distance, maximum speed, average speed, number of stops, maximum acceleration, average acceleration, maximum deceleration, average deceleration	size and dynamics of fuel cell with battery including fuel consumption and total cost	to conduct energy management of system in terms of power demand and supply
4	Zhang et al. [16]	Lion Optimization (LO), Modified Student Psychology Optimization (MSPO), Elephant Herd Optimization (EHO) and Student Based Psychology Optimization (SBPO)	distance, average speed, total driving time, acceleration, average speed, deceleration, state-of-charge (SOC), acceleration force, friction force, force needed for climbing slopes and force of air resistance, total power demand	sizes of fuel cell and battery, overall cost	to achieve optimum size and reduce overall cost as possible
5	Ajayan and Immanuel Selvakumar [17]	Differential Evolution (DE), Teaching Learning Based Optimization (TLBO), Particle Swarm Optimization (PSO), Firefly Algorithm (FA), Artificial Bee Colony (ABC) and Invasive Weed Optimization (IWO)	slope, number of fuel cell replacements, work-life of battery, panel unit cost, number of battery replacements, battery unit cost, motor constant cost, work-life of fuel cell, drive cycle, battery constant cost, motor unit cost, rate of interest, panel constant cost and fuel cell unit cost	cost	to minimize cost and fuel consumption

According to Table 1, metaheuristic algorithms are generally used to decrease cost and increase performance. Additionally, size optimization is other purpose. It can be seen that metaheuristic algorithms are particularly employed to fuel cell powered locomotives. PSO is applied more than other metaheuristic algorithms.

3. RESULTS AND DISCUSSION

Main results of studies are explained in Table 2. In Table 2, standard deviation, population size, iteration, run number and significant results are highlighted. Flowchart of metaheuristic algorithm for fuel cell vehicles is given in Fig. 1.

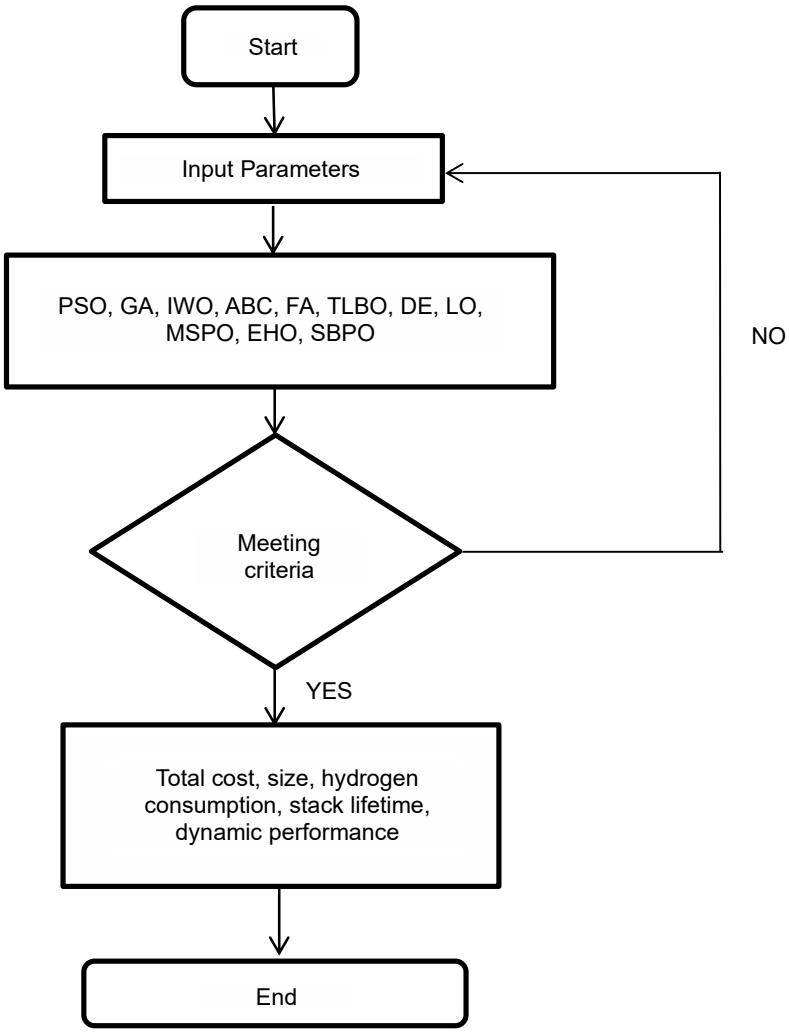

Fig. 1. Flowchart of metaheuristic algorithm for fuel cell vehicles

Table 2. Main results

No	Citation	Metaheuristic Algorithm	Standard Deviation	Population Size	Iteration	Run Number	Main results
1	Li et al. [13]	EIA-PSO	0.028	25	30 (maximum)	5	EIA-PSO exhibits optimum solutions for locomotives in respect to dynamic response
2	Macauley et al. [14]	GA	Not Available	Not Available	Not Available	Not Available	In accordance with operating time, GA is used to leak initiation and found useful to reveal membrane lifetime within 20%.
3	Sarma and Ganguly [15]	PSO	Not Available	200 (for the best results)	100 (maximum)	Not Available	PSO provides 3.93 x 10^6 $ total cost in accordance with 2% of slope.
4	Zhang et al. [16]	LO, SPO, EHO and SBPO	Not Available	Not Available	Not Available	Not Available	MSPO can be recommended in terms of minimization of total cost.
5	Ajayan and Immanuel Selvakumar [17]	DE, TLBO, PSO, FA, ABC and IWO	Not Available	50 (population of students)	Not Available	144 different case	TLBO presents better results than DE, PSO, ABC, IWO and FA.

According to Table 2 the least amount of standard deviation is noticed in EIA-PSO. Population size is also crucial for algorithms. In examined studies, general population size is taken as 25, 50 and 200. Minimum and maximum population sizes are used in EIA-PSO and PSO respectively. Besides population size, number of iterations is significant. With the use of 30 and 100 iterations, optimum solutions via PSO are obtained. Minimum and maximum number of iterations is belonged to EIA-PSO and PSO respectively.

4. CONCLUSIONS

This paper is an initial attempt to evaluate studies of fuel cell vehicles in respect to metaheuristic algorithms. Little amount of studies are reviewed based on metaheuristic algorithms. The algorithms are mainly used to minimize fuel consumption with overall cost. Additionally, metaheuristic algorithms are employed for size optimization. The findings indicate that PSO algorithm is effectively used for locomotives. PSO algorithm is expressed as useful to decrease maximum iteration number, population size, standard deviation and run number. The algorithm is practical to reveal system dynamic response. GA is utilized to predict membrane lifetime. MSPO gives satisfactory results from the viewpoint of minimization of total cost. DE, TLBO, PSO, FA, ABC and IWO enable different cases. This paper also exhibits how effectively metaheuristic algorithms can be used to fuel cell vehicles.

REFERENCES

1. Metaheuristic Applications in Structures and Infrastructures. Elsevier; 2013.
2. Gandomi AH, Yang X-S, Talatahari S, Alavi AH. Metaheuristic Algorithms in Modeling and Optimization. In: Metaheuristic Applications in Structures and Infrastructures. Elsevier; 2013, p. 1–24.
3. Nanda SJ, Panda G. A survey on nature inspired metaheuristic algorithms for partitional clustering. Swarm and Evolutionary Computation 2014;16(2):1–18. https://doi.org/10.1016/j.swevo.2013.11.003.
4. Agrawal P, Abutarboush HF, Ganesh T, Mohamed AW. Metaheuristic Algorithms on Feature Selection: A Survey of One Decade of Research (2009-2019). IEEE Access 2021;9:26766–91. https://doi.org/10.1109/ACCESS.2021.3056407.
5. Osaba E, Villar-Rodriguez E, Del Ser J, Nebro AJ, Molina D, LaTorre A et al. A Tutorial On the design, experimentation and application of metaheuristic algorithms to real-World optimization problems. Swarm and Evolutionary Computation 2021;64(4):100888. https://doi.org/10.1016/j.swevo.2021.100888.
6. Yang X-S (ed.). Recent Advances in Swarm Intelligence and Evolutionary Computation. Cham: Springer International Publishing; 2015.
7. Yang X-S, Karamanoglu M. Swarm Intelligence and Bio-Inspired Computation. In: Swarm Intelligence and Bio-Inspired Computation. Elsevier; 2013, p. 3–23.
8. Pan J-S, Hu P, Snášel V, Chu S-C. A survey on binary metaheuristic algorithms and their engineering applications. Artif Intell Rev 2023;56(7):6101–67. https://doi.org/10.1007/s10462-022-10328-9.
9. Li H, Guo H, Yousefi N. A hybrid fuel cell/battery vehicle by considering economy considerations optimized by Converged Barnacles Mating Optimizer (CBMO) algorithm. Energy Reports 2020;6(1):2441–9. https://doi.org/10.1016/j.egyr.2020.09.005.
10. Savran E, Karpat E, Karpat F. Fuel Cell Electric Vehicle Hydrogen Consumption and Battery Cycle Optimization Using Bald Eagle Search Algorithm. Applied Sciences 2024;14(17):7744. https://doi.org/10.3390/app14177744.
11. Liu Y, Sun Z, Wang Y, Li M, Chen Z. Capacity configuration of fuel cell hybrid vehicles using enhanced multi-objective particle swarm optimization with competitive mechanism. Energy Conversion and Management 2024;321(3):119039. https://doi.org/10.1016/j.enconman.2024.119039.
12. Mazouzi A, Hadroug N, Alayed W, Hafaifa A, Iratni A, Kouzou A. Comprehensive optimization of fuzzy logic-based energy management system for fuel-cell hybrid electric vehicle using genetic algorithm. International Journal of Hydrogen Energy 2024;81(9):889–905. https://doi.org/10.1016/j.ijhydene.2024.07.237.
13. Li Q, Chen W, Liu Z, Guo A, Huang J. Nonlinear multivariable modeling of locomotive proton exchange membrane fuel cell system. International Journal of Hydrogen Energy 2014;39(25):13777–86. https://doi.org/10.1016/j.ijhydene.2013.12.211.
14. Macauley N, Watson M, Lauritzen M, Knights S, Wang GG, Kjeang E. Empirical membrane lifetime model for heavy duty fuel cell systems. Journal of Power Sources 2016;336:240–50. https://doi.org/10.1016/j.jpowsour.2016.10.068.
15. Sarma U, Ganguly S. Determination of the component sizing for the PEM fuel cell-battery hybrid energy system for locomotive application using particle swarm optimization. Journal of Energy Storage 2018;19(2):247–59. https://doi.org/10.1016/j.est.2018.08.008.
16. Zhang G, Li H, Xiao C, Jermsittiparsert K. Optimal size selection for fuel cell and battery in a hybrid power system of the intercity locomotives. Journal of Cleaner Production 2021;317(5):128498. https://doi.org/10.1016/j.jclepro.2021.128498.
17. Ajayan S, Immanuel Selvakumar A. Metaheuristic optimization techniques to design solar-fuel cell-battery energy system for locomotives. International Journal of Hydrogen Energy 2022;47(3):1845–62. https://doi.org/10.1016/j.ijhydene.2021.10.130.

THE POTENTIAL OF OFFSHORE WIND FARMS AS HYDROGEN FUEL STATION: A CASE STUDY OF MARMARA SEA

[1*]*Viney Dixit*, [2]*Canan Acar*
[1]University of Twente, Faculty of Engineering Technology, Department of Thermal Engineering, 7522 NB Enschede, The Netherlands
*Corresponding author e-mail: v.dixit28@gmail.com

ABSTRACT

This article explores the concept of using offshore wind farms as hydrogen fuel stations for maritime applications. It covers site assessment and traffic analysis to estimate fuel requirements at a specific location, as well as the amount of hydrogen production needed to meet the fuel demand. The Marmara Sea has been chosen as the study area due to its strategic importance, as a significant number of ships travel between Europe and Asia through this region. The integration of a hydrogen fuel station with an offshore wind farm presents a potential solution for long-distance vessels, as it eliminates the need for ships to return to nearby ports for refuelling. This study provides a sustainable solution for the maritime industry, addressing the environmental impact of fuel emissions from cargo ships and vessels and contributing to pollution reduction efforts. The approach outlined in this research offers a promising pathway for reducing the carbon footprint of maritime transportation while promoting the use of hydrogen.

Keywords: Offshore wind farm**,** Hydrogen production**,** Offshore fuel station, Marmara Sea

1. INTRODUCTION

The maritime shipping industry is the backbone of global trade, as it handles the majority of the worldwide cargo transport [1]. However, it is responsible for approximately 3% of global greenhouse gas emissions [2]. To control global warming, it is essential to reduce these emissions and adopt more sustainable practices. Agreements like the Paris Agreement and the Glasgow Climate Pact, along with recent climate reports, are pushing the shipping industry to quickly switch to cleaner, low- or zero-carbon technologies for powering ships [2]. Cargo ships running on heavy oil fuel cause serious air and water pollution [1]. These ships also release nitrogen oxides (NOx), which can cause harmful algal blooms in coastal waters. According to the report by the Pacific Northwest National Laboratory [1], large cargo ships transport $4 trillion worth of goods annually, handling 80% of global trade by volume. These ships emit over one billion tonnes of greenhouse gases [1]. If no action is taken, these emissions are expected to increase in the coming decades. However, switching to cleaner fuels such as hydrogen can significantly reduce these pollutants, helping to protect both the air and oceans [1]. However, lack of infrastructure for their large-scale production, storage, and distribution poses a significant barrier. Despite these challenges, hydrogen presents a potential solution, offering a pathway to zero-carbon shipping if these obstacles can be addressed. This study focuses on the potential of offshore wind farms for hydrogen fuel production and their role as fuelling stations for ships. However, extensive research has already been conducted on offshore wind infrastructure, covering key aspects of hydrogen production such as site selection, wind turbines and foundations, wind electrolysis integration, desalination units, hydrogen storage, and transportation [3]. In addition, three primary models of wind electrolysis integration have also been explored: onshore (centralised), offshore (centralised), and in-turbine (decentralised) [3]. Unlike previous research, this research article aims not only to highlight hydrogen as a viable solution to maritime pollution but also to explore the use of offshore wind farms as direct fuelling stations for ships. By enabling ships to refuel directly at the wind farm, the need to transport hydrogen from offshore to port can be eliminated which can reduce the transportation costs. Additionally, this approach would allow ships to bypass ports for refuelling, thereby helping to alleviate port congestion. The Marmara Sea has been selected as the site for deploying an offshore wind farm as a fuel station. This region experiences high shipping traffic due to its strategic connectivity with sea routes linking Asia and Europe [4]. It serves as a global trade hub and supports a diverse local shipping network, making it an ideal location to study the impact of hydrogen-propelled ships on both short and long hauls. Additionally, previously available data further supports the suitability of the Marmara Sea for this type of study [4].

2. PROPOSED MODEL

2.1 Site selection for offshore wind farm

The site assessment of the Marmara Sea has been extensively explored in numerous research articles, which has proven to be beneficial for the current investigation [4]. A key consideration in this study is the shipping routes, as wind farms cannot be deployed in busy areas. To gain insights into these routes, a live map from the Marine Vessel Traffic website was utilised, as shown in Fig. 1(b) [5]. By examining areas with high traffic density, a less congested region was selected for this study, which is highlighted by the black square in the figure. The area of the selected region (526 Km^2) was then

calculated using Google Earth. Additionally, using the EMODnet Map Viewer, the average depth of the Marmara Sea at various locations was estimated [6]. As shown in Fig. 1(b), the average depth of the selected region is approximately 50 meters, and it has been reported that the wind speed in this area is around 8 m/s at 100 m elevation [4]. Further factors influencing site selection will also be assessed using Quantum Geographic Information System (QGIS) software. Based on the depth, area, and wind speed of the selected site, the appropriate wind turbine foundation will be determined, and the electricity generation will be optimised. All this analysis is under process.

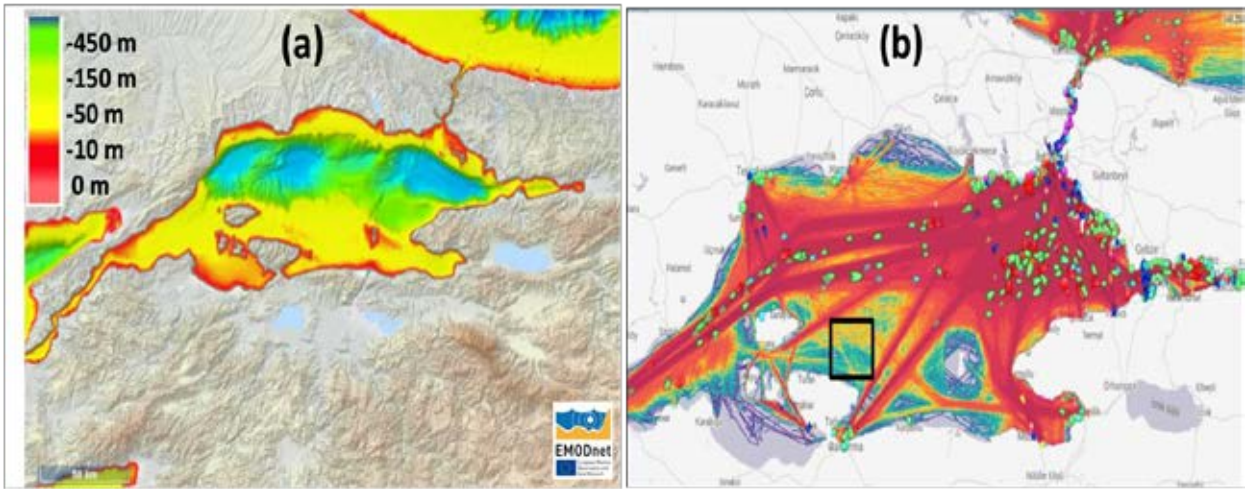

Fig. 1. AIS data and shipping routes traffic in Marmara Sea [5, 6]

2.2. Assessing the suitability of offshore wind farms as fuel stations

Figures 2 and 3 illustrate the schematic diagram and the strategic flowchart of an offshore wind farm integrated hydrogen fuel station. The flowchart provides a clear and systematic overview of the approach required for integrating a fuel station with an offshore wind farm

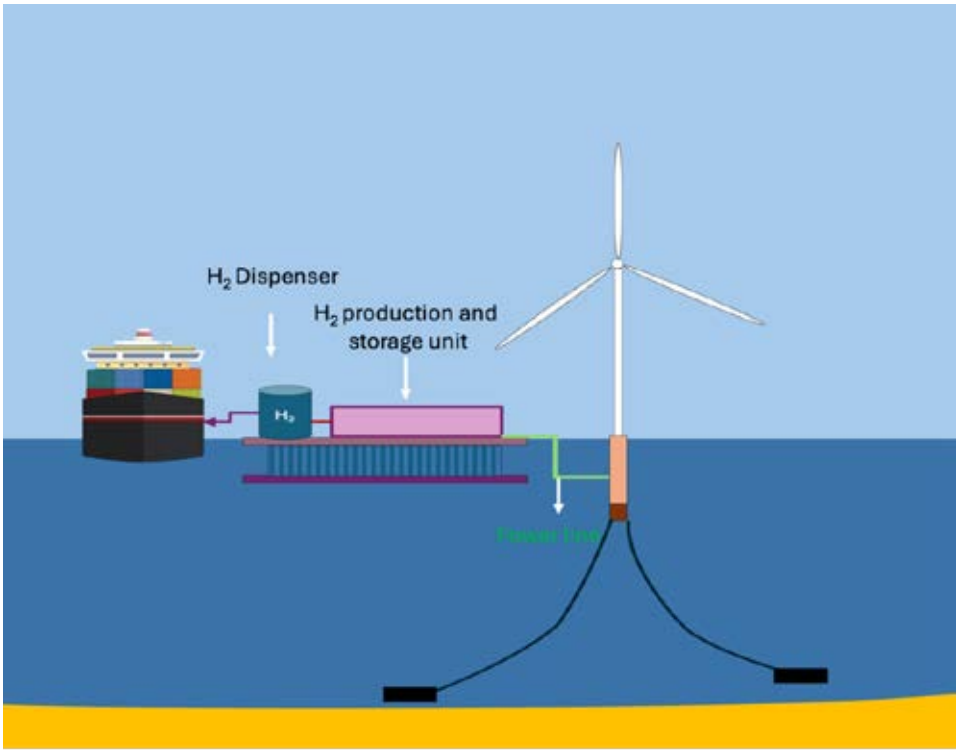

Fig. 2. Schematic diagram of an offshore hydrogen fuel station powered by an offshore wind turbine system.

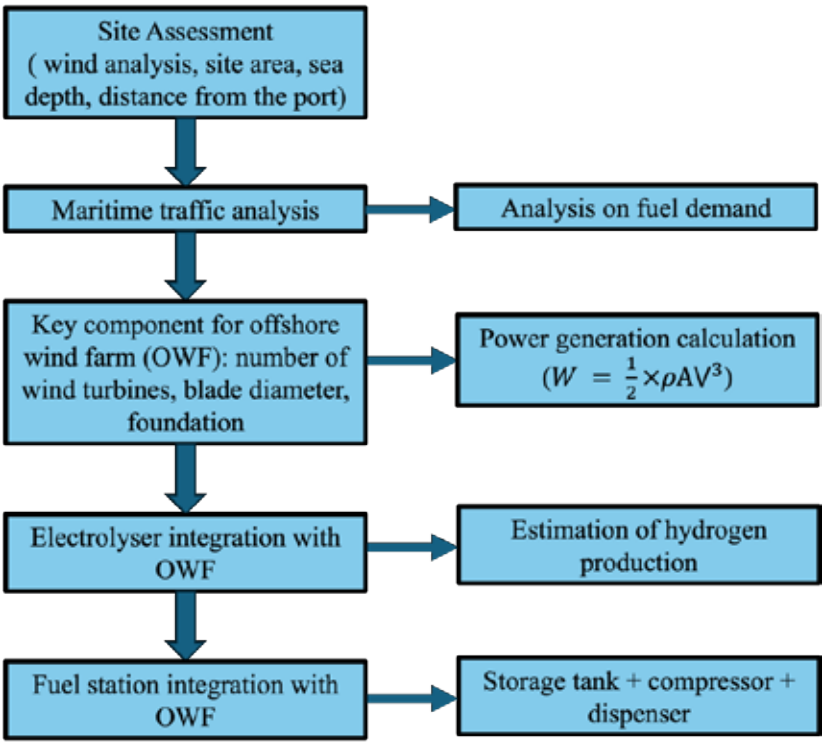

Figure 3: Flowchart of an offshore hydrogen fuel station powered by an offshore wind

In this section, an estimation of the wind farm's capacity to consistently produce sufficient electricity for hydrogen production will be conducted, ensuring that the location is suitable for ship and vessels for refuelling.
The analysis of ships, ferries, cargo vessels, or tankers passing through or near the location will help to determine the demand for fuelling services and identify peak operational periods. An assessment of energy fuel requirements help in determining whether the projected farm's capacity can meet this need and, if not, what other elements need to be changed. This data will also aid in determining whether the chosen location is appropriate for integrating a fuel station and wind farm. All the key components, such as the electrolyser, desalination unit, storage, and dispenser techniques, since we wish to combine a hydrogen fuel station with a wind farm, will be discussed.

3. CONCLUSION

This study emphasises the utilisation of offshore wind farms as hydrogen fuel stations. It provides a systematic overview, from site selection to the use of hydrogen as a fuel for maritime applications. The site assessment process includes key factors such as marine traffic, wind speed, and water depth, which are crucial for optimising the location for offshore wind farm installation. Additionally, this work highlights the role of marine traffic analysis in optimising fuel demand calculations. By doing so, it is possible to determine the number of turbines required to generate the electricity needed for hydrogen production, which can then be directly used by ships and vessels. An advantage of this study is that, by utilising offshore wind farms for hydrogen production, the need to transport hydrogen to onshore fuel stations is eliminated. Furthermore, ships can directly charge at sea without the need to return to port, thus improving efficiency and reducing operational costs. To the best of our knowledge, no existing literature has explored this type of study, making this research unique in its approach.

NOMENCLATURE

W	Power, watts
A	Cross-section area of the wind, m^2
V	Wind velocity, m/s

Greek Letters

ρ	Air density, Kg/m^3

REFERENCES

[1] https://www.pnnl.gov/explainer-articles/maritime-decarbonization. Accessed: 2024- 12-18.
[2] Hanna B and Teis H. 2023. Imo off course for decarbonisation of shipping? three challenges for stricter policy. Marine Policy, 147:105379.
[3] Shanmugam R, Mostafa D, Caillean C, Daniel N, Mohanraj V, and Mohamed M. 2024. Offshore green hydrogen production from wind energy: Critical review and perspective. Renewable and Sustainable Energy Reviews, 195:114320.
[4] Fatih K. 2020. Importance of offshore wind farms Marmara Sea for turkey's renewable energy targets: a case study Marmara Sea. Technium.
[5] https://www.marinevesseltraffic.com/SEA-OF-MARMARA/ship-traffic-tracker. Accessed: 2024-12-18.
[6] https://emodnet.ec.europa.eu/geoviewer/ .Accessed: 2024- 12-18.
[7] https://www.mjrpower.com/news/parkwind-installs-vessels-charging-system-at-noblewind-offshore-wind-farm. Accessed: 2024- 12-18.

DEVELOPMENT OF OPERATION STRATGIES FOR IMPROVING POLYMER ELECTROLYTE MEMBRANE FUEL CELL SYSTEM WATER MANAGEMENT AND HYDROGEN CIRCULATION

[1]*Jaekwan Bae*, [1]*Haewook Park*, [1]*Ik Jae Son,* [1]*Seung Man Park*
[1] Hyundai Motor Company, Fuel Cell System Test Team, Mabuk-ro 240beon-gil 17-5, Yongin-si, 16891, Republic of Korea

ABSTRACT

In this study, we discussed methods of increasing anode water discharge and enhancing hydrogen circulation during polymer electrolyte membrane fuel cell (PEMFC) operation. Constant current measurement was performed by changing the operating conditions in three major ways: increasing the pressure difference between the inlet of hydrogen and air, increasing air stoichiometry ratio (SR), and oscillating the hydrogen pressure. As a result, it was possible to distinguish the correlation between anode water discharge rate and performance degradation. In particular, it was confirmed that hydrogen pressure oscillation using step peak pressure circulation (SPPC) control boosts anode water discharge and reduces performance degradation at low current range due to hydrogen distribution improvement in the PEMFC stacks. Ultimately, we demonstrated that the commercialization of PEMFCs can be accelerated by developing a PEMFC operation strategy with improved durability and performance.

Keywords: PEMFC System, Operation Strategy, Anode Water Discharge, Fuel Cell Performance, Performance Degradation, Hydrogen Circulation

1. INTRODUCTION

Recently, as carbon neutrality is emerging to prevent global warming, energy sources that do not emit carbon dioxide or greenhouse gases are receiving attention. Among them, hydrogen fuel cells have attracted interest as a next-generation energy source because they produce electricity through the electrochemical reaction of hydrogen and oxygen and only emit pure water. In particular, PEMFCs can be applied not only to various mobility such as vehicles, ships, railways, etc., based on their high-power density [1, 2]. However, they have problems with the physical and chemical deterioration of composition materials including electrodes, electrolyte membranes, and gas diffusion layers (GDLs) as the operating time increases [3].

One of the main causes of this degradation is related to water management within the system. In the dry-out state, ion conductivity decreases due to insufficient hydration of the membrane, which reduces the channels for proton (H^+) movement. Furthermore, sulfonic acid groups with a small amount of moisture form radicals ($OH\cdot$) to destroy the membrane, which raises the quantity of fluorine released, and creates pinholes and cracks in the membrane [4]. On the other hand, if the generated water is not expelled smoothly, the transfer of reactants to the triple phase boundary (TPB) where the electrochemical reaction occurs is obstructed, leading to issues like a decline of fuel cell performance and hydrogen utilization efficiency in the short term, as well as a diminishment in the anticipated operational lifespan due to irreversible damage in the long term [5]. Since excessive hydrogen supply is impossible, there is a limit for discharging the back-diffused water to the anode. Therefore, it is essential to develop an operating strategy that can secure PEMFC performance and durability by preventing fuel electrode flooding and ensuring hydrogen circulation.

2. EXPERIMENTAL

2.1. Fuel Cell System Test Condition

All experiments were conducted in a 100 kW system unit with balance of plants (BOP) attached to a pair of PEMFC stacks positioned one on top of the other, and the hydrogen supply was controlled by following the target pressure based on a sensor located at the inlet side. Since a recirculation system using an ejector was adopted, there is a limit to improving water discharge through excessive fuel provision in the low current section. In order to compare the degree of stack deterioration according to the operating conditions, constant current operation for more than 1 hour was performed as a test protocol. Stack temperature was maintained at 60 ℃, and the system was dried based on 20 purge cycles after the examination to minimize the influence of the previous operating conditions. In the case of exhausted anode water, the droplets within the fuel processing system (FPS) were captured and the amount was measured.

2.2. Increase hydrogen/air inlet differential pressure

This method improves the anode water discharge by increasing the base pressure of the hydrogen supply and inducing more electro-osmotic drag. It does not require large power consumption except for controlling the pressure. While maintaining the air pressure constantly, the fuel was pressurized at 0.8 A/cm^2 operation so that the inlet pressure difference satisfies 10 to 40 kPa.

2.3. Increase the amount of air supply

It is possible to prevent flooding issues on the fuel electrode by diminishing back-diffusion rate within the system in the manner of enhancing the SR of the air. As holding the air pressure at 0.8 A/cm^2 equally, air flow rates corresponding to 1.5, 1.6, and 1.8 SR were applied sequentially.

2.3. Repeated cycles of hydrogen pressure up and down

The instantaneous pressure change of the supplied hydrogen was utilized to strengthen the hydrogen flow rate in the FPS. Three control methods were proposed in this experiment, and they were named One Peak Pressure Circulation (OPPC) control, Step Peak Pressure Circulation (SPPC) control, and Slew Rate Pressure Circulation (SRPC) control, respectively. Although the management logic is different depending on the circulation method, all of them maintained the same 150 kPa during the purge. The average pressure of hydrogen was 150 kPa, and operated under a low current density condition of 0.18 A/cm^2 (small amount of hydrogen supply) so that the effect of the improvement could be confirmed clearly. OPPC had the disadvantage of generating flow noise in the FPS due to the sudden rise with a single pressure increase. To prevent this, SPPC was also applicated, which divides the same pressure enhancement into steps and maintains one step about 610 ms. Lastly, we conducted additional comparisons of the SRPC method, which allows the gradient to vary with pressure change.

3. RESULTS AND DISCUSSION

3.1. Increase hydrogen/air inlet differential pressure

The results of increasing the hydrogen pressure during constant current operation of 0.8 A/cm^2 are summarized in Fig. 1. When the hydrogen/air inlet differential pressure (ΔP) is 40 kPa, it can be confirmed that the anode water discharge amount decreases from 2.78 g/s (10 kPa) to 2.57 g/s due to the effect of reduced water back-diffusion following larger prsessure difference between electrodes. In addition, it shows that the cell performance deterioration is improved from -3.499 mV/h to -1.884 mV/h at ΔP 30 kPa. However, it demonstrates that the oversupply makes hydrogen crosse-over to the cathode, which affects the catalyst and binder leading to a negative impact on the performance as -2.084 mV/h (40 kPa). So, it is possible to minimize the fuel electrode flooding by optimizing ΔP while preventing cell degradation.

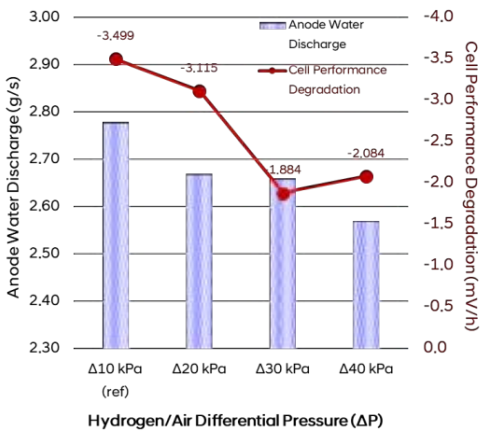

Fig. 1. Anode water discharge during 3-hour constant current operation and cell performance degradationof the last 2 hours according to the supply hydrogen/air differential pressure (0.8 A/cm^2, temperature 60 ℃)

3.2. Increase the amount of air supply

The effects of the air SR increase are analyzed in Fig. 2. In the case of operating SR at the existing ΔP 10 kPa are increased to (1.6 → 1.8), the system discharge decreases to 2.47 g/s due to the diminished amount of water back-diffusion. Furthermore, we can also find that cell voltage degradation is also evoluted from -3.499 mV/h to -2.172 mV/h. Despite the expelled water amount decreases significantly, the performance improvement is smaller than the effect of the increase in ΔP. Then, we also check the influence of the air SR change based on ΔP 30 kPa, which was the optimal condition among the ΔP control. The total amount of discharged water slightly increases (2.66 → 2.75 g/s) at SR 1.5 because of the weakness in the water discharge capacity of the cathode. It affects the deterioration of cell performance (-1.884 → -1.996 mV/h) adversely. On the contrary, the increase in air SR plays a sufficient role in removing the residual water in the stack making the anode water discharge significantly decrease (2.68 → 2.35 g/s). However, the air oversupply (1.6 → 1.8) has the potential to form a dry-out state in the system, accelerating the deterioration of cell

performance (-1.884 → -2.589 mV/h). The larger energy is consumed by the air compressor in this situation, which negatively impacts both the system efficiency and stack durability. According to these results, we can realize that the air SR not only affects the anode water removal but also is an invaluable element related to maintaining PEMFC performance.

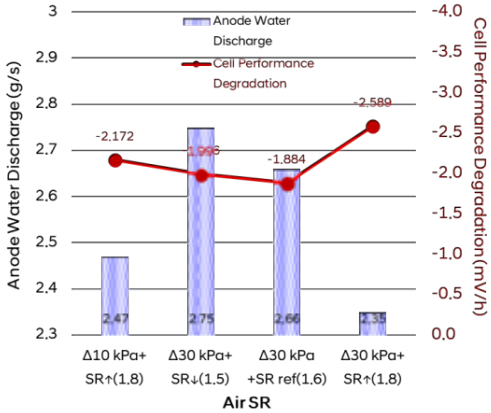

Fig. 2. Anode water discharge during 3-hour constant current operation and cell performance degradationof the last 2 hours according to the air SR (0.8 A/cm^2, temperature 60 ℃)

3.3. Repeated cycles of hydrogen pressure up and down

It is demonstrated that the repetitive hydrogen pressure oscillation cycle can effectively improve the exhaust of generated water accumulated in materials such as bipolar plates and GDLs (Fig. 3).

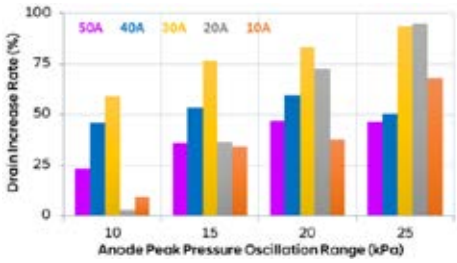

Fig. 3. Anode water discharge increase rate according to the hydrogen pressure oscillation range (0.18 A/cm^2, temperature 60 ℃ / 5 kPa reference)

Stack performance decrease change under the constant current operation according to SPPC on/off is shown in Fig. 4. It is confirmed that the performance improvement rate is 21.2% at 40 ℃ with SPPC on, and 3.5% enhancement at the temperature 60 ℃. In other words, it indicates that the irreversible deterioration caused by anode flooding is shrinked by early discharge of the generated water through SPPC control.

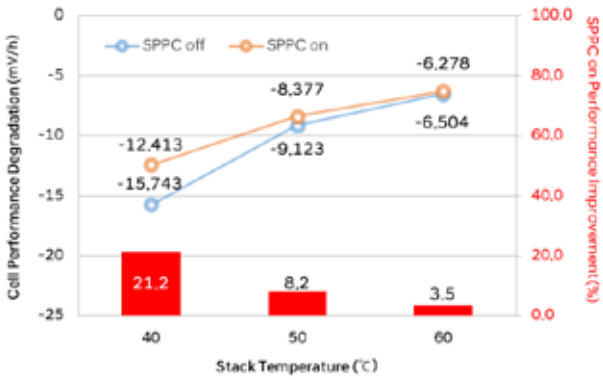

Fig. 4. Cell performance degradation data based on SPPC on/off according to stack temperature (0.18 A/cm^2)

4. CONCLUSIONS

In this study, we showed a novel approach for securing durability by increasing the anode water discharge and hydrogen circulation of the PEMFC system.

- Enhanced ability for expelling anode water and maintaining cell performance was confirmed through hydrogen/air pressure difference optimization.
- Although the discharge of generated water was improved by the air overprovision, there is a concern that the deterioration can be serious due to drying out. Furthermore, this method has a constraint because of the higher energy usage of the air compressor.
- Controlling the fuel supply pressure with appropriate steps and peaks had a positive effect on anode water exile and reducing the hydrogen concentration deviation.

According to these results, durability improvement of the fuel cell system is expected by preventing stagnation of the generated water based on the step and peak pressure control modeling. Moreover, if the water droplets inside the stack induce the irreversible deterioration of the electrode materials, an upgraded driving technique can solve this real-time dry out & flooding issue in the near future.

REFERENCES

1. Kamyar Maleki Bagherabadi et al. 2022. System-level modeling of marine power plant with PEMFC system and battery. International Journal of Naval Architecture and Ocean Engineering 14:100487.
2. D.Guida et al. 2017. Design methodology for a PEM fuel cell power system in a more electrical aircraft. Applied Energy 192:446-456.
3. Jian Zhao et al. 2019. A review of polymer electrolyte membrane fuel cell durability for vehicular applications: Degradation modes and experimental techniques. Energy Conversion and Management 199:112022.
4. Chikara Takei et al. 2016. Load cycle durability of a graphitized carbon black-supported platinum catalyst in polymer electrolyte fuel cell cathodes. Journal of Power Sources 324:729-737.
5. Jian Shan et al. 2018. EIS and local resolved current density distribution analysis on effects of MPL on PEMFC performance at varied humidification. International Journal of Heat and Mass Transfer 127:1076-1083.

ECO-FRIENDLY LEACHING STRATEGIES FOR RECYCLING ELECTRONIC WASTE CPUS TO ENHANCE HYDROGEN AND OXYGEN EVOLUTION

[1*]Stefan Mitrović, [1]Snežana Brković, [1]Mina Seović, [1]Milena Pijović Radovanović, [1]Petar Laušević, [1]Nikola Zdolšek, [1]Ivana Perović

[1]University of Belgrade, Vinča Institute of Nuclear Sciences, National Institute of the Republic of Serbia, Mike Petrovića Alasa 12-14, 11351 Vinča, Serbia

*Corresponding author e-mail: stefan.mitrovic@vin.bg.ac.rs

ABSTRACT

This study explores the potential of recycling electronic waste, particularly CPUs, for hydrogen and oxygen evolution reactions as a step towards sustainable energy generation and resource recovery. A multi-step, eco-friendly leaching protocol was developed to extract valuable metals such as gold, silver, and copper from discarded CPUs. The extracted metals were incorporated into an electrolyte, which was then subjected to electrochemical evaluation in a three-electrode setup.

Cyclic voltammetry and Tafel analysis provided insights into the electrochemical behavior of the recycled metals. The results revealed a preferential enhancement of hydrogen evolution over oxygen evolution, attributed to the lower activation energy barrier and favorable kinetics of hydrogen production. Despite the promising electrocatalytic activity for hydrogen evolution, further optimization is necessary to improve oxygen evolution efficiency.

This research underscores the dual benefits of e-waste recycling: mitigating environmental hazards and advancing renewable energy technologies. By demonstrating the feasibility of repurposing e-waste for sustainable applications, this study contributes to the development of circular economy models and supports the global transition toward greener energy solutions.

Keywords: e-waste recycling, hydrogen evolution reaction, oxygen evolution reaction, CPU recycling, sustainable energy

1. INTRODUCTION

The exponential growth of electronic waste (e-waste), driven by rapid technological advancements and increasing consumer demand, has become a critical environmental challenge. Among various e-waste components, central processing units (CPUs) represent a significant proportion due to their widespread use and short lifecycle. Effective recycling strategies for CPUs are essential not only to mitigate environmental hazards but also to recover valuable embedded resources such as gold, silver, and copper [1].

Traditional recycling methods often rely on aggressive chemical treatments, posing significant environmental risks. This study aims to address these challenges by introducing an eco-friendly multi-step leaching process for metal recovery from discarded CPUs. By utilizing the recovered metals to produce electrolytes for electrochemical hydrogen and oxygen evolution reactions, the study explores a sustainable pathway for renewable energy generation.

The production of hydrogen and oxygen through electrolysis holds immense potential as a clean energy source, contributing to global efforts to reduce carbon emissions. This research bridges the gap between resource recovery and renewable energy, demonstrating the feasibility of integrating e-waste recycling into sustainable energy applications.

2. MATERIALS AND METHODS

2.1. Sample collection and preparation

All discarded CPUs used in this study were sourced from the same brand and generation. The computers and motherboards were disassembled, and the processors were carefully removed from their sockets. A thorough cleaning process was then employed to remove contaminants such as dirt, plastic residues, and thermal paste, ensuring uniformity across all samples.

After cleaning, the CPUs were mechanically shredded and milled using an electrical mill. The resulting powder exhibited some variability in particle size, which was subsequently assessed using a lab sieve [2].

2.2. Leaching procedure

To achieve optimal leaching results, a multi-step procedure was employed to effectively separate the various metals present in the CPU powder.

The first step involved dissolving the powder in 1 M HCl at ambient temperature under an inert gas atmosphere for 5 hours. This step aimed to dissolve and segregate iron (Fe) and nickel (Ni) from the other metals present in the powder.

After dissolution, the solution was filtered, and the sediment was separated, washed, and dried until completely dry. The dry powder was then immersed in a solution consisting of $NH_3/(NH_4)_2SO_4 + H_2O_2$ at room temperature for 2 hours. This

step facilitated the dissolution and removal of copper (Cu) and silver (Ag) from the sample.
Following this leaching step, the powder underwent another round of filtration, washing, and complete drying. The final leaching step consisted of dissolution in a mixture of 4-PSH + DMF + H_2O_2 at 60 °C for 25 minutes. In this step, the metallic gold (Au) dissolved from the powder and formed a complex with 4-PSH. Finally, the solution underwent one last filtration and the relutling solution was reseved for subsequent testing [3].

2.3. Electrochemical evaluation

Electrochemical testing was conducted using a three-electrode glass cell setup. The working electrode was a pure metallic nickel electrode with a surface area of 1 cm², while high-surface-area nickel foam served as the counter electrode. An Ag/AgCl electrode was used as the reference electrode.
Electrochemical characterization involved recording and analyzing polarization curves to determine the kinetics of hydrogen and oxygen evolution reactions within the electrolyte, which was prepared from the leached powder.

3. RESULTS AND DISCUSSION

The main focus of this investigation was to explore the feasibility of employing recycled metals sourced from electronic waste, particularly CPUs, in hydrogen and oxygen evolution reactions.
Upon the examination of cyclovoltamogram (Fig 1), the peak of nickel oxidation, at approximately 0.5 V vs Ag/AgCl can be observed, but the absence of a corresponding reduction peak, expected around 0.1 V vs Ag/AgCl indicates the involvement of additional processes at the electrode surface [4].

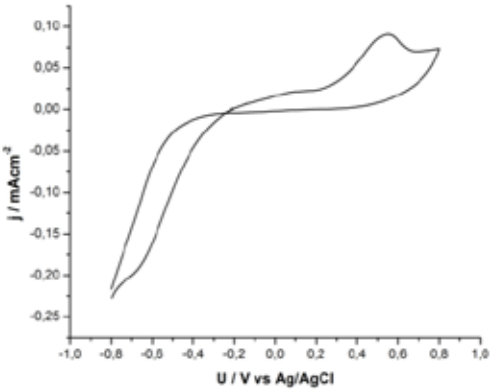

Fig. 1. Cyclic voltammogram of a pure nickel electrode in prepared solution

The next step in the activity evaluation was the recording of linear sweep polarization curves for hydrogen and oxygen evolution reactions (Fig. 2). The results presented below indicate that the metal complex, likely the Au-PSH complex, demonstrated relatively favorable electrochemical activity for the hydrogen evolution reaction. However, its performance in oxygen evolution was comparatively less effective.

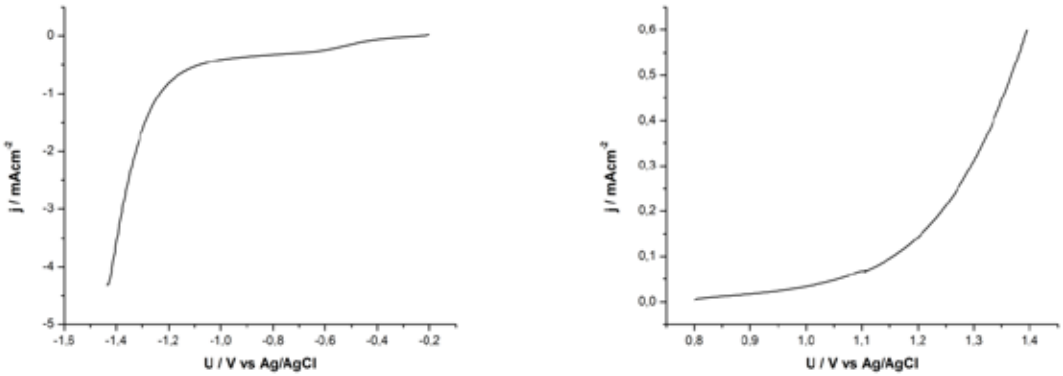

Fig. 2. Polarization curves for hydrogen (left) and oxygen (right) evolution reactions

A subsequent Tafel analysis was performed on the recorded polarization curves, with the resulting plots shown in Fig. 3. The Tafel plot reveals a linear relationship between the logarithm of the current density and the overpotential. The slope of these curves, known as the Tafel slope, offers critical insights into the reaction mechanism and activation energy.

Based on the Tafel slope values, the reactions can be classified into three primary mechanisms: activation-controlled, diffusion-controlled, or mixed-controlled.

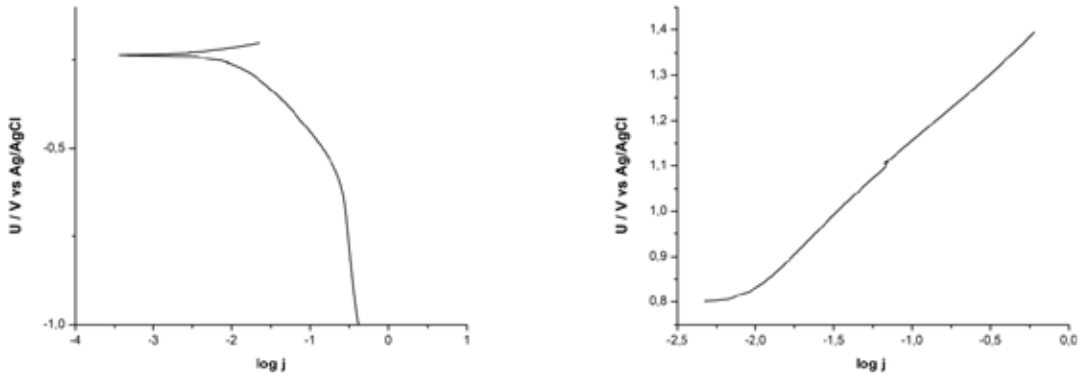

Fig. 3. Tafel plots for hydrogen (left) and oxygen (right) evolution reaction

The Tafel slope values derived from the analysis support the initial hypothesis, showing that the electrolyte prepared using this protocol demonstrates superior electrocatalytic activity for hydrogen evolution compared to oxygen evolution. This disparity in electrocatalytic performance between the two reactions highlights the complex behavior of the electrolyte and emphasizes its preferential enhancement of hydrogen evolution.

Table 1. Kinetick parameters for Ni electrode in prepared solution

Reaction	Tafel slope (mV dec^{-1})
HER	-266.8
OER	318.8

The observed variation in Tafel slope values between the hydrogen and oxygen evolution reactions suggests a lower activation energy barrier for hydrogen production, resulting in a more efficient electrochemical process. Conversely, the higher activation energy barrier for oxygen evolution signifies slower reaction kinetics, which hinder the overall rate of oxygen generation [5].

4. CONCLUSIONS

The recycling of electronic waste, particularly CPUs, for hydrogen and oxygen evolution reactions represents a complex yet impactful approach to promoting sustainability and clean energy generation. The increasing volume of e-waste emphasizes the need for effective recycling strategies, and this study highlights the potential of environmentally friendly leaching techniques for extracting valuable metals from discarded electronic components.

The multi-step leaching protocol developed in this research offers a promising pathway for recovering metals from e-waste CPUs, with the extracted solution functioning directly as an electrolyte for electrochemical evaluation. Cyclic voltammetry and Tafel analysis have provided critical insights into the electrochemical behavior of the recycled metals, demonstrating a notable preference for enhancing hydrogen evolution over oxygen evolution.

The relationship between electrolyte composition and electrochemical performance underscores the importance of tailored strategies when utilizing recycled materials for sustainable energy applications. While the electrolyte exhibits strong electrocatalytic activity for hydrogen production, further optimization may be required to improve its effectiveness for oxygen evolution reactions.

This study highlights the dual benefits of e-waste recycling: resource recovery and renewable energy generation. By advancing eco-friendly leaching methods and elucidating the electrochemical mechanisms involved, this work contributes to the development of a circular economy and supports the global transition towards sustainable energy solutions.

ACKNOWLEDGEMENT

The authors would like to thank Ministry of Science, Technological Development and Innovation of the Republic of Serbia for financial support (grant number: 451-03-66/2024-03/200017).

REFERENCES

1. Robinson BH. 2009. E-waste: An assessment of global production and environmental impacts. *Science of the Total Environment* 408(2):183–191.
2. Mitrović S, et al. 2023. From e-waste to hydrogen evolution: Harnessing recycled precious metals for catalytic efficiency in hydrogen evolution reactions. *Materials* 16(20):6795.
3. Räisänen M, et al. 2018. Pyridinethiol-assisted dissolution of elemental gold in organic solutions. *Angewandte Chemie International Edition* 57(52):17104–17109.
4. Ghosh S, Bagchi D, Mondal I, Sontheimer T, Jagadeesh RV, and Menezes PW. 2024. Deciphering the role of nickel in electrochemical organic oxidation reactions. *Advanced Energy Materials* 24:00696.
5. Shinagawa T, Garcia-Esparza AT, and Takanabe K. 2015. Insight on Tafel slopes from a microkinetic analysis of aqueous electrocatalysis for energy conversion. *Scientific Reports* 5(1):1–21.

ELECTROCHEMICAL SURFACE MODIFICATION AND EFFECTS ON THE CATALYTIC ACTIVITY OF NICKEL-BASED ELECTRODES FOR HYDROGEN EVOLUTION

[1*]Stefan Mitrović, [1]Snežana Brković, [1]Mina Seović, [1]Petar Laušević, [1]Nikola Zdolšek, [1]Đurica Katnić, [1]Ivana Perović

[1]University of Belgrade, Vinča Institute of Nuclear Sciences, National Institute of the Republic of Serbia, Mike Petrovića Alasa 12-14, 11351 Vinča, Serbia

*Corresponding author e-mail: stefan.mitrovic@vin.bg.ac.rs

ABSTRACT

This study explores the impact of electrochemical surface preparation on the catalytic activity of nickel-based electrodes for the hydrogen evolution reaction (HER) in alkaline media. Two distinct forms of nickel hydroxides, α-$Ni(OH)_2$ and β-$Ni(OH)_2$, were synthesized through potential cycling within specific voltage ranges and subsequently evaluated for their catalytic performance. Carbon-based materials doped with nickel nanoparticles were used as catalytic substrates, and their suspensions were applied to glassy carbon electrode surfaces to create working electrodes. Electrochemical characterization, including polarization curve analysis and Tafel slope evaluation, was conducted to assess the catalytic efficiency and reaction kinetics.

The results indicate that both hydroxide forms exhibit comparable catalytic activity, with β-$Ni(OH)_2$ showing slightly superior performance due to lower overpotential and a more favorable Tafel slope. The kinetic analysis confirmed a diffusion-controlled reaction mechanism for both forms, with β-$Ni(OH)_2$ demonstrating subtly enhanced reaction kinetics. These findings underline the significance of surface modification in optimizing nickel-based catalysts for HER and provide insights into the role of nickel oxidation states in catalytic processes.

Keywords: hydrogen evolution reaction, nickel hydroxides, electrochemical surface modification, catalytic efficiency

1. INTRODUCTION

The growing global demand for energy, fueled by rapid industrial and technological advancements, necessitates the exploration of alternative energy sources. While fossil fuels remain the dominant energy resource, the adoption of renewable energy technologies has been steadily increasing. However, the limited efficiency of these sustainable solutions prevents a complete transition to renewable energy. Among the most promising alternatives is hydrogen energy, which offers an environmentally sustainable pathway for converting chemical energy into electricity. [1].

Despite its immense potential, the large-scale implementation of hydrogen energy systems hinges on continual advancements, particularly in the development of catalytic materials [2]. Efficient and cost-effective catalysts are crucial to enhancing hydrogen production processes. Currently, the most widely used catalysts for hydrogen evolution rely on precious metals from the platinum group, valued for their high efficiency but limited by availability and cost. Thus, identifying alternative catalytic materials that deliver comparable performance at a lower cost is an essential research priority.

Nickel has emerged as a promising candidate for catalytic applications due to its versatile properties. A silver-white metal belonging to group VIIIb of the periodic table, exhibits high thermal and electrical conductivity, ferromagnetic properties, and notable resistance to corrosion by air, water, and alkalis [3], [4]. It dissolves efficiently in diluted oxidizing acids, while the solubility of its salts varies depending on the nature of the acid.

For nickel to function effectively as a catalytic material, it must be supported on a suitable substrate. This study examines carbon-based materials doped with nickel nanoparticles as catalytic substrates. Suspensions containing a specific concentration of nickel will be prepared and applied to electrode surfaces to create working electrodes. These electrodes will undergo comprehensive electrochemical evaluations to determine their catalytic properties. Additionally, this study provides insights into the various oxidation states and forms of nickel, evaluating their potential as catalytic materials for the hydrogen evolution reaction.

2. MATERIALS AND METHODS

The catalytic material utilized in this study was commercially available 1% Nickel supported on Vulcan XC-72 (Fuel Cell Store). The ink for electrode preparation was formulated using deionized water and 1 mg/ml of catalyst, subsequently sonicated for 30 minutes. Following sonication, the ink was drop-casted onto a pre-polished glassy carbon electrode surface and left to dry for 24 hours. After the surface was completely dry, and prior to the electrochemical teasting, the 5 µl of a Isopropyl alcohol and Nafion (50:1) mixture solution was added to the surface.

Electrochemical evaluation of prepared electrodes was perfomed in a three-electrode glass cell. The working electrode was a rotating disk electrode (RDE) consisted of a glassy carbon with drop casted catalytic material. The surface area of a RDE glassy carbon electrode was 0.196 cm^2. The counter electrode was high-surface area Pt mesh, while the

reference electrode was a saturated calomel electrode (SCE). Presented potential values were converted to fit Reversible Hydrogen Electrode (RHE) scale. The conversion was perfomed using the Equation 1. Electrochemical measurements were carried out using Gamry Interface 1000 Potentiostat/Galvanostat/ZRA. The electrolyte used in this study was an analytical-grade 1 M KOH from Merck, with a pH value of 13.2. Prior to the measurements, electrolyte was purged with N_2 for 20 minutes, and the RDE was continually rotated at a rate of 1600 rpm.

$$E_{RHE} = E_{SCE} + 0.244\,V + 0.059 \cdot pH \quad (1)$$

The first part, prior to the electrochemical evaluation of activity, the electrochemical surface modification was conducted. Cycling in a specific potential range the electrode surface can oxidyze and produce different oxides and hydroxides (Fig 1). In this study, surface was modified to produce alpha and beta $Ni(OH)_2$.

Fig. 1. Representation of potential values for oxidation and reduction of NiO

Emideatly after surface modification, the linear sweep was used to determin the HER activity. Potenial was measured between 0 V and 0.65 V vs RHE.

3. RESULTS AND DISCUSSION

In order to investigate the influence of produced nickle hydroxide form on the electrode surface, two different types were produced based on the potential rage presented in Fig 1. The first produced was α – $Ni(OH)_2$ by cycling in adequant potential range (Fig 2. a). Analysis of the polarization curves for the formation of α-$Ni(OH)_2$ indicates that this hydroxide exhibits significant reduction potential, as nearly all the formed oxide can be reduced, returning the electrode surface to its original state.

a) b)

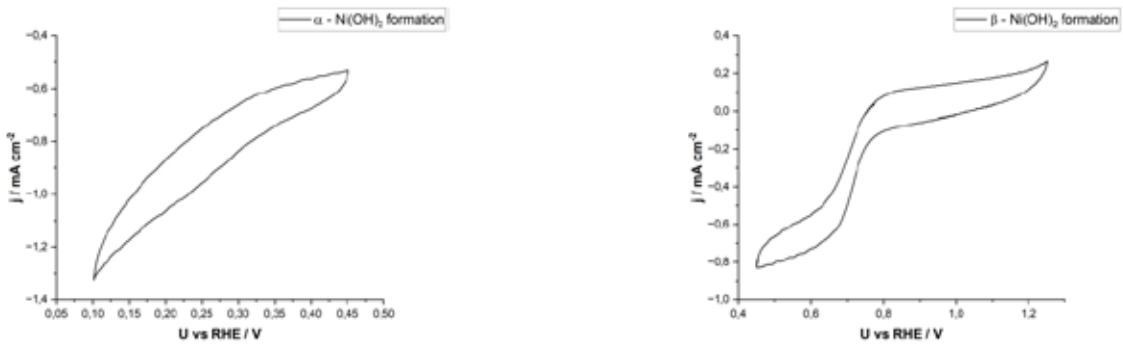

Fig. 2. Cyclovoltamograms of α (left) and β (right) $Ni(OH)_2$ oxidation

The next aspect investigated was the formation of β-$Ni(OH)_2$ and its influence on the hydrogen evolution reactions. This hydroxide form was created through potential cycling in the range of 0.45 to 1.25 V, with the polarization curve of the modified material shown in Fig. 2. b).
It was observed that, although both oxide forms are considered reducible, only alpha nickel hydroxide actively undergoes reduction under the working conditions of the hydrogen evolution reaction. After completing the experimental protocol, the electrode coated with the formed alpha hydroxide fully returned to its original state, with no traces of alpha oxide present on the surface. In contrast, the electrode with beta oxides formed on its surface retained its oxide features and formes [5].

Analysis of the polarization curve reveals that the presence of β-$Ni(OH)_2$ on the electrode surface increases the activity for the hydrogen evolution reaction, compared to the α – $Ni(OH)_2$ activitie (Fig. 4.). Several explanations for this enhanced activity have been proposed. One possibility is that the oxidation of nickel and the formation of β-$Ni(OH)_2$ result in improved development of the active surface area, directly contributing to higher catalytic performance. Additionally, the formation of this hydroxide may increase the material's electrical conductivity, further boosting its activity.

a) b)

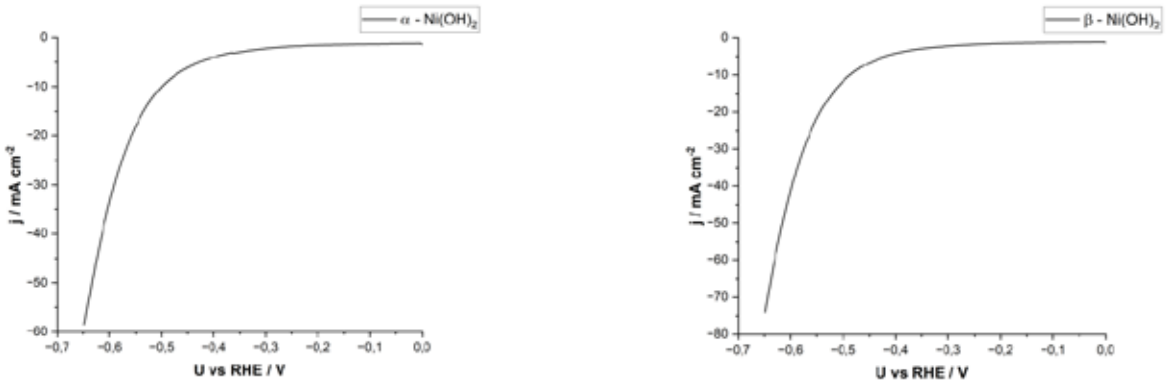

Fig. 3. Polaryzation curves for HER on α – $Ni(OH)_2$ (left) and β – $Ni(OH)_2$ (right) electrode surface

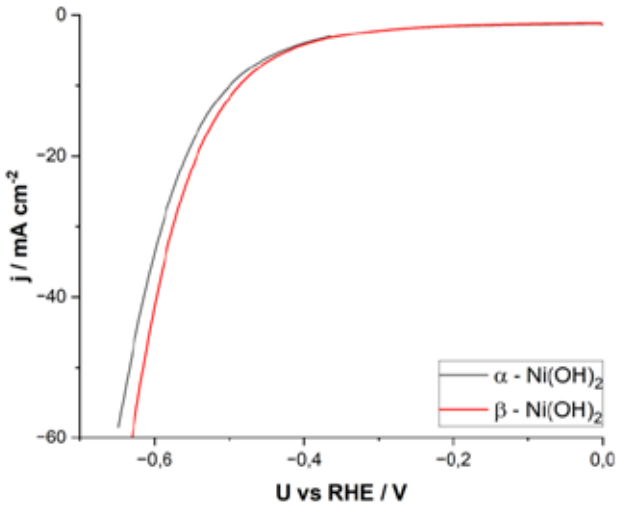

Fig. 4. Comparison of catalytic activity for hydrogen prodyction of α – $Ni(OH)_2$ and β – $Ni(OH)_2$

Based on the obtained polarization curves, the Tafel analysis was condycted to get insights on hydrogen evolution reaction mechanisms and kinetics. In the Tafel plot, a linear relationship emerges between the logarithm of the current desity and the overpotential. The curve's slope. Known as the Tafel slope, provides insight into the reactio's activation energy, implying a diminished reaction rate [6]. Broadly, three mechanisms can be categorized based on the Tafel slope value: activation – controlled, diffusion – controlled and mixed – controlled reaction mechanism [7].
The Tafel slope values are presented in Table 1. For both α – $Ni(OH)_2$ and β – $Ni(OH)_2$ slope values were between -180 and -210 mV dec^{-1}, correlating with a diffusion - controlled reaction mechanism.

Table 1. Overpotential and Tafel slope values for evaluated electrodes

	Overpotential at 10 mA cm^{-2} [mV]	**Tafel slope [mV dec^{-1}]**
α – $Ni(OH)_2$	-502	-205
β – $Ni(OH)_2$	-487	-187

4. CONCLUSIONS

This study highlights the influence of electrochemical surface preparation on the catalytic performance of nickel-based electrodes for the hydrogen evolution reaction (HER) in alkaline media. Two distinct nickel hydroxide forms, α-$Ni(OH)_2$ and β-$Ni(OH)_2$, were synthesized through potential cycling and evaluated for their catalytic properties. While both forms exhibited similar polarization curve profiles and catalytic activities, β-$Ni(OH)_2$ demonstrated slightly better performance, reflected in its lower overpotential and improved Tafel slope values.
The enhanced catalytic activity of β-$Ni(OH)_2$ is attributed to its ability to develop a more active surface area and potentially increased electrical conductivity during formation. Kinetic analysis confirmed that both hydroxides follow a

diffusion-controlled reaction mechanism, with β-$Ni(OH)_2$ exhibiting a lower Tafel slope, indicating improved reaction kinetics.
These findings emphasize the role of nickel oxidation states and structural modifications in improving catalytic efficiency for HER, offering valuable insights for designing cost-effective and high-performance nickel-based catalysts for hydrogen production in alkaline media.

ACKNOWLEDGEMENT

The authors would like to thank Ministry of Science, Technological Development and Innovation of the Republic of Serbia for financial support (grant number: 451-03-66/2024-03/200017).

REFERENCES

1. Ursúa A, Gandía LM, and Sanchis P. 2012. Hydrogen production from water electrolysis: Current status and future trends. *Proceedings of the IEEE* 100(2):410-426.
2. Atilhan S, Park S, El-Halwagi MM, Atilhan M, Moore M, and Nielsen RB. 2021. Green hydrogen as an alternative fuel for the shipping industry. *Current Opinion in Chemical Engineering* 31:100668.
3. Kong D, Cha JJ, Wang H, Lee HR, and Cui Y. 2013. First-row transition metal dichalcogenide catalysts for hydrogen evolution reaction. *Energy & Environmental Science* 6(12):3553-3558.
4. Barceloux DG and Barceloux DD. 1999. Nickel: Environmental and health effects. *Clinical Toxicology* 37(2):239-258.
5. Ferreira EB and Jerkiewicz G. 2021. On the electrochemical reduction of β-Ni(OH)2 to metallic nickel. *Electrocatalysis* 12(2):199-209.
6. Shinagawa T, Garcia-Esparza AT, and Takanabe K. 2015. Insight on Tafel slopes from a microkinetic analysis of aqueous electrocatalysis for energy conversion. *Scientific Reports* 5(1):13801.
7. Fang YH and Liu ZP. 2014. Tafel kinetics of electrocatalytic reactions: From experiment to first-principles. *ACS Catalysis* 4(12):4364-4376.

NON-STOICHIOMETRIC TUNGSTEN-OXIDES AS THE ANODE CATALYST SUPPORTS FOR PEM FUEL CELLS

[1*]Snežana Brković, [1] Ivana Perović, [1]Mina Seović, [1]Stefan Mitrović, [1]Petar Laušević, [2]Vladimir Nikolić, [2]Milica Marčeta Kaninski

[1] University of Belgrade, Vinča Institute of Nuclear Sciences, National Institute of the Republic of Serbia, Mike Petrovića Alasa 12-14, 11351 Vinča, Serbia
[2] Institute of General and Physical Chemistry, Studentski trg 12/V, 11158, Belgrade, Serbia

*snezana.miulovic@vin.bg.ac.rs

ABSTRACT

The mass production and use of fuel cells are limited by the cost of components, primarily the price of catalysts. Fuel impurities lead to the degradation and poisoning of catalysts. Therefore, there is an intensive development of cheaper and more durable catalysts and their interactive supports. In this study, we synthesized non-stoichiometric tungsten oxides as supports for PtRu-based catalysts for Proton Exchange Membrane (PEM) fuel cells. The performance of obtained PtRu/WO_x+C catalysts was investigated using cyclic voltammetry and linear sweep voltammetry. Limiting diffusion currents of hydrogen oxidation reactions are reached very quickly and maintain constant values over a wide range of potentials corresponding to anodic potentials of an active PEM fuel cell. The synthesized catalysts show greater catalytic activity and CO tolerance compared to commercial catalysts. The 30% PtRu/WO_x+C catalyst, as the catalyst with the highest catalytic activity and tolerance to CO poisoning, could be a good candidate for commercial application.

Keywords: Anode catalyst, Tungsten-oxide, CO tolerance, PEM fuel cells

1. INTRODUCTION

By developing and utilizing technologies that use renewable energy sources, the emission of carbon dioxide and other harmful gases into the atmosphere will be reduced, while also increasing energy sustainability and the security of energy supply. A significant number of studies are focused on the development of smaller energy supply devices, known as fuel cell stacks, which would be located near or at the point of energy consumption [1]. Fuel cell stacks, as the name implies, are composed of a series of individual fuel cells. Each individual fuel cell represents a system that converts the chemical energy of fuel into electrical energy and heat [2]. For widespread use, the most practical option is Proton Exchange Membrane (PEM) fuel cells, which produce clean electrical energy, heat, and water while operating at low temperatures. The commercialization of PEM fuel cells faces significant challenges due to two key factors: durability and cost. Agglomeration of catalyst particles and oxidation of the catalyst support, along with high sensitivity to impurities in the fuel and oxidant, directly affect the cost-efficiency, durability, and reliability of fuel cells [3]. The high cost primarily stems from the expensive catalysts required. The platinum-group metals, though highly active as electrocatalysts for hydrogen and oxygen electrode reactions in PEM fuel cells and electrolyzer, are prohibitively expensive. Additionally, platinum-based catalysts face challenges with poisoning: impurities in the hydrogen fuel, such as small amounts of CO, can significantly degrade performance and shorten the lifespan of the PEM fuel cell [4]. Therefore, significant efforts are being made to develop longer-lasting and more affordable catalysts, as well as their interactive supports.
The research goal of this study is to develop new, efficient non-stoichiometric tungsten oxides as supports for anode catalysts for use in fuel cells with a proton-conducting membrane. The advantage of tungsten oxide as a catalyst support is primarily improved tolerance to CO poisoning. This material serves as the support for PtRu nanoparticles. The loading of PtRu on this support is varied, and the electrochemical performance of the catalysts is evaluated. Thin-film electrodes combined with (rotating disc electrode) voltammetry, are employed to examine the catalysts' activity and CO tolerance.

2. MATERIALS AND METHODS

2.1. Catalyst preparation

In the present work, tungsten oxide was synthesized by first suspending 1g of tungsten (powder, Sigma-Aldrich) in 25 cm³ of deionized water. To this suspension, 25 cm³ of 30% (by weight) hydrogen peroxide (Sigma-Aldrich) was added, and after 15 minutes, an additional 20 cm³ of 30% H_2O_2 was introduced. The suspension was then left to allow excess liquid to evaporate, followed by drying at 110ºC. A powdery sample, lemon yellow in color, was obtained and labeled as WO_x (non-stoichiometric tungsten oxide).
Anode catalysts were prepared by adding small amounts of commercial hexachloroplatinic acid (H_2PtCl_6, Merck) and ruthenium chloride ($RuCl_3$, Merck) to a 35 ml solution of 0.005 mol dm^{-3} perchloric acid ($HClO_4$, Sigma-Aldrich) with synthesized WO_x support, followed by 30 minutes of ultrasonication and magnetic stirring each. Next, 5 ml of 0.1 mol dm^{-3} sodium borohydride solution was added dropwise while stirring, continued for another 30 minutes before mixing in Vulcan XC72R carbon black. After a final 30 minutes of stirring, the mixture was left to settle, filtered, washed with

deionized water, and dried at 50ºC for 24 hours, producing PtRu/WO_x+C samples at 10%, 20%, and 30% concentrations.

2.2. Cyclic voltammetry and kinetics of HOR

After confirming the composition of all prepared catalysts, electrochemical tests were conducted using a thin film of the catalyst suspension applied to a gold rotating disk electrode (RDE) with a consistent platinum loading of 40 µg cm^{-2}. The catalysts, compared against a commercial 30% PtRu/C catalyst, were tested in a PEM fuel cell application scenario. Electrochemical measurements started with cyclic voltammetry after nitrogen purging the 0.5 mol dm^{-3} $HClO_4$ electrolyte for 30 minutes at room temperature, cycling the potential between 0.03 V and 1.2 V vs. RHE at 100 mV s^{-1}. Hydrogen oxidation reaction (HOR) kinetics were assessed by recording linear sweep voltammetry (LSV) curves at various electrode speeds (1000, 1500, 2000, and 2500 rpm) within 0 to 0.3 V vs. RHE, with calculations for kinetic and mass activity based on the Koutecky-Levich ($\frac{1}{i} = \frac{1}{i_k} + \frac{1}{i_l}$) and a specific activity equation ($i_m = \frac{i_k}{L}$) [5]. Lastly, the catalysts' carbon monoxide tolerance was tested by adsorbing CO for 2000 seconds at 50 mV vs. RHE, followed by a potential scan up to 0.9 V and cycling between 0 V and 1.2 V vs. RHE to facilitate CO oxidation.

3. RESULTS AND DISCUSSION

The elemental composition of all prepared catalysts (Table 1) was determined by EDS analysis using a JEOL JSM-6610LV microscope. This method confirmed the desired composition of the catalyst with smaller deviations from the target mass percentage for Pt and Ru.

Table 1. The elemental composition of catalysts based on Pt and Ru on WO_x supports.

Catalysts	Pt (weight %)	Ru (weight %)	W (weight %)	O (weight %)	C (weight %)
10% PtRu/WO_x-C	7,0	3,5	15,9	11,8	61,8
20% PtRu/WO_x-C	14,0	7,4	15,1	10,4	53,1
30% PtRu/WO_x-C	20,7	10,1	14,7	9,3	45,2

Figure 1 (a) shows the cycle voltammogram for a commercial PtRu/C and 30% PtRu/WO_x+C catalyst. It can be seen that in the typical hydrogen adsorption/desorption region (0.03 V < E < 0.35 V vs. RHE) the PtRu/C catalyst exhibits certain symmetrical anodic and cathodic features attributable to hydrogen adsorption/desorption.

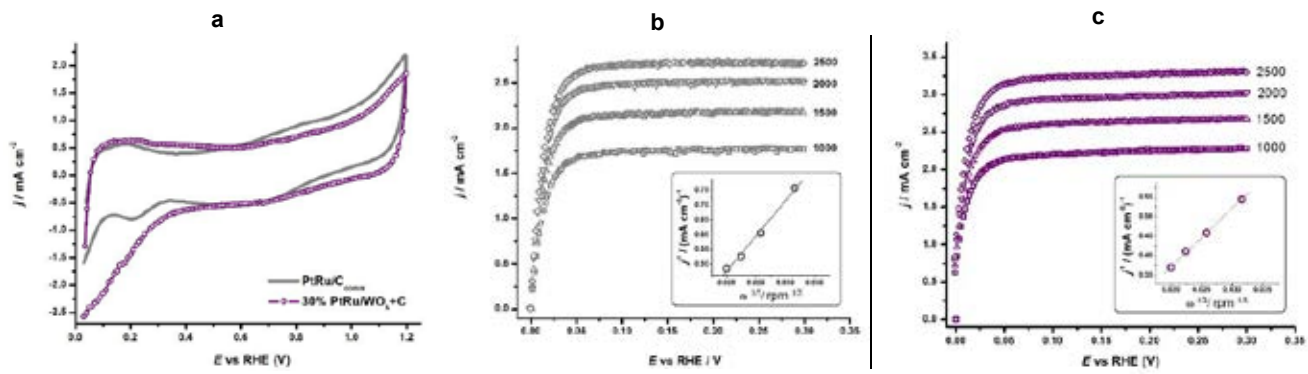

Fig. 1. Comparison of the cyclovoltammograms of the commercial and 30% PtRu/WO_x+C catalysts (a); LSV curves of H_2 oxidation at different rotation speeds with the fitted Koutecky-Levich line at 0.02 V vs. RHE for 30% PtRu/C (b) and 30% PtRu/WO_x+C (c)

H_2 oxidation curves at different rotation speeds are shown in Fig. 1 for a commercial 30% PtRu/C catalyst (b) and 30% PtRu/WO_x+C catalyst (c). For all catalyst, it can be noted that the limiting diffusion current density is reached very quickly (at an overvoltage of about 60 mV) with good definition and stability in a wide potential area (anode potential area of an active PEM fuel cell).

Table 2. Kinetic current densities and mass activities for HOR

Catalysts	j_k / mA cm^{-2}	j_m / A mg_{Pt}^{-1}	$j_{m,CO}$ / A mg_{Pt}^{-1}
30% PtRu/C	7,86	0,197	0,028
10% PtRu/WO_x-C	10,51	0,263	0,050
20% PtRu/WO_x-C	11,40	0,285	0,060
30% PtRu/WO_x-C	12,97	0,324	0,121

From the HOR curves, at different rotation speeds, the current densities are read and from them the Koutecki-Levich line is obtained (insets of Fig. 1. for 30% PtRu/C (b) and 30% PtRu/WO_x+C (c)). The kinetic current density at an overvoltage

of 20 mV (j_k) was calculated and the mass activity (j_m) for all catalysts (Table 2.) As can be seen from Table 2, all of the prepared catalysts have a higher activity for hydrogen oxidation compared to commercial catalysts (30% PtRu/C). Also, it can be seen that the most active is the 30% PtRu/WO_x+C catalyst with a kinetic activity of 12.97 mA cm^{-2} and a mass activity of 0.324 $\mathrm{A\ mg_{Pt}^{-1}}$.

Given that the prepared catalysts are synthesized for use in PEM fuel cells, it is very important that they have the highest possible tolerance to carbon monoxide poisoning. For this reason, all prepared catalysts were analyzed in a hydrogen atmosphere with a proportion of carbon monoxide (98% H_2 + 2% CO) simulating reformate which is used in real systems as fuel for PEM fuel cells. By recording and analyzing the electrooxidation curves of adsorbed CO and the HOR curves in the presence of carbon monoxide, the tolerance of the catalyst to CO poisoning can be assessed.

The first cycle of the cycle voltammogram (CO stripping) represents the CO_{ads} oxidation curve with a pronounced CO oxidation peak, and the second cycle (basic cycle voltammogram) is a curve that should match the cycle voltammogram recorded in a pure hydrogen atmosphere. From recorded cyclovoltammograms and HOR curves in the presence of CO, the following values were determined: active surfaces for COads oxidation (ESA_{CO} /cm^2) and mass activities for hydrogen oxidation ($j_{m,CO}$ /$\mathrm{A\ mg_{Pt}^{-1}}$) in a mixture (98% H_2 + 2% CO) of gases.

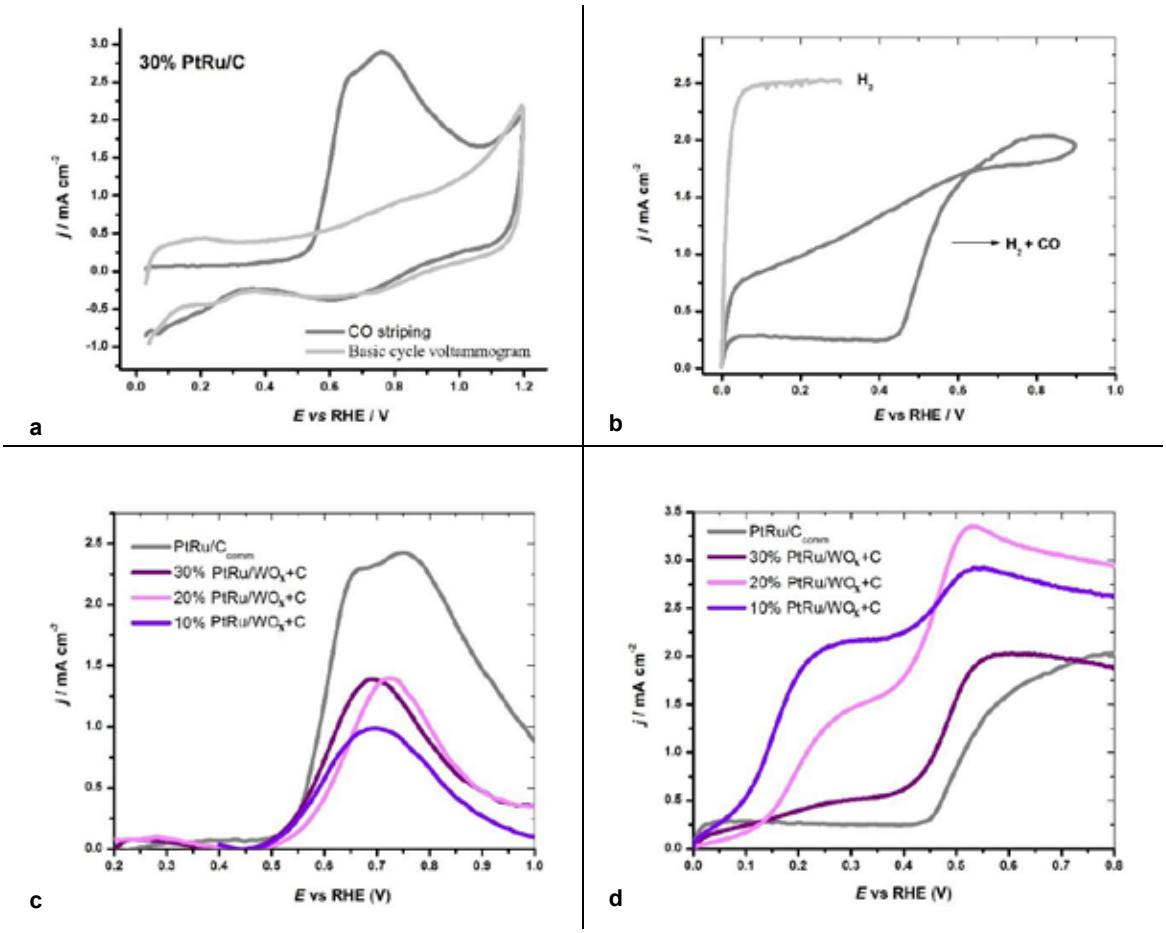

Fig. 2. Cyclovoltammogram of CO ads desorption for commercial 30% PtRu/C catalyst (a); HOR curves for commercial 30% PtRu/C catalyst recorded in pure H_2 and mixture (H_2 +2%CO) gases, at 2000 rpm (b); Cyclovoltammogram of CO_{ads} desorption - comparison of CO_{ads} oxidation peaks of commercial, 10%, 20% and 30% PtRu/WO_x+C catalyst (c) and HOR curves in H_2 + 2%CO mixture at 2000 rpm - Comparison of anode branches of commercial and PtRu/WO_x+C catalyst (d)

Figure 2.(a) shows the CO_{ads} desorption cycle voltammogram (CO stripping voltammogram) of the commercial 30% PtRu/C catalyst. The curve marked as CO stripping is the first cycle of the cyclovoltammogram and shows a pronounced, broad peak corresponding to the amount of adsorbed CO on the catalyst surface. The second cycle (basic cyclovoltammogram) was cleaned of adsorbed CO and corresponds to the cyclovoltamogram recorded in a nitrogen atmosphere. Based on the size of the CO peak area (Q in mC), ESA_{CO} was calculated according to equation $ESA=Q/q$: 0.605 cm^2. Figure 2 (b) shows HOR curves recorded in pure hydrogen and gas mixture with RDE rotation of 2000 rpm and polarization rate of 5 mV s^{-1}. From the HOR curve recorded in the gas mixture, the oxidation potential of adsorbed carbon monoxide, i.e. desorption of CO_{ads} from platinum nanoparticles (E_{onset}): 0.460 V vs. RHE. Figure 2 (b) shows that

the current recorded in the anodic direction, in a mixture of gases, is smaller than the anodic current recorded in pure hydrogen. The potential was scanned down to 0.9 V vs. RHE, during which the surface is not completely cleaned of CO_{ads}, but partially, and back to 0 V vs. RHE. In the reverse current branch (cathodic direction of current), higher current values are recorded compared to anode currents. From this part, the current at an overvoltage of 20 mV was read and the mass activity $j_{m,CO}$ was calculated: 0.028 $\mathrm{A\ mg_{Pt}^{-1}}$.
Figure 2 (c) shows the high-potential parts of the cyclovoltammogram, i.e. the CO_{ads} oxidation peaks of all prepared catalysts. By recording the cyclovoltammogram of CO_{ads} desorption for a series of PtRu/WO_x+C catalysts, differences are observed compared to the cyclovoltammogram recorded for a commercial PtRu/C catalyst, in the entire potential range. In the region of low potentials (E < 0.5 V vs. RHE), these deviations are attributed to the existence of OH species in the interfacial space that joins/separates the phases of the WO_x carrier and PtRu nanoparticles (PtRu|WO_x) [6,7].
In the region of high potentials (E > 0.5 V vs. RHE) all catalysts are rapidly cleaned of CO_{ads}. With the commercial PtRu/C catalyst, the appearance of a broad, double peak with the main peak at 0.760 V vs. RHE, while only one CO_{ads} oxidation peak occurs with the PtRu/WO_x+C series catalyst. Also, one can see a shift of these peaks by 40 to 70 mV towards more negative potentials compared to the CO_{ads} oxidation peak of the commercial catalyst. In this potential area, CO_{ads} are dominantly removed at the expense of OH species from the oxidized metal phases (Pt-OH_{ads} and Ru-OH_{ads}) in both the synthesized catalysts and the commercial catalyst. Since there is a difference in the amount of oxidized CO_{ads} species between PtRu/WO_x+C and the commercial catalyst, there is another effect that accelerates the removal of adsorbed CO from the catalyst surface. The improved CO_{ads} removal is attributed to the electronic carrier effect affecting the chemisorption properties of PtRu in PtRu/WO_x+C catalysts. This effect can also explain the less complex peaks of these catalysts compared to commercial ones. ESA_{CO} were calculated from the areas of CO_{ads} peaks of PtRu/WO_x+C catalysts. It was found that PtRu/WO_x+C catalysts have a significantly smaller ESA_{CO} surface area (from 0.204 cm^2, 270 cm^2 and 0.290 cm^2) compared to the commercial catalyst (0.604 cm^2). Mass activity $j_{m,CO}$ ($\mathrm{A\ mg_{Pt}^{-1}}$) in a mixture (98% H_2 + 2% CO) of gases of all analyzed catalysts was also determined and the obtained values are shown in Table 2.

4. CONCLUSIONS

Pt and Ru-based catalysts were prepared on a synthesized WO_x support. The performance of the obtained catalysts was investigated by cyclic voltammetry and voltammetry on a rotating disk electrode. Special attention was paid to the examination of carbon monoxide poisoning, in order to evaluate the contribution of the prepared catalysts to CO tolerance. The obtained results show significantly lower values of mass activities for HOR in the mixture (98% H_2 + 2% CO) of gases compared to the mass activities obtained for HOR in pure hydrogen. The commercial 30% PtRu/C catalyst has the lowest mass activity, while the obtained catalysts based on PtRu have significantly higher mass activities. Higher activities are explained by the formation of the interphase space PtRu|carrier, but also by the formation of Ru-CO_{ads} species, which frees Pt centers for HOR reactions. Most of the synthesized catalysts show a shift of the CO_{ads} desorption peak towards more negative potentials. This confirms that they are more tolerant to CO poisoning compared to commercial catalysts. Based on the presented conclusions, it can be said that the 30% PtRu/WO_x catalyst could be a good candidate for commercial application.

ACKNOWLEDGEMENT

This work was supported by the ministry of education, science and technological development of the republic of serbia (grant no 451-03-66/2024-03/200017)

REFERENCES

[1] Cigolotti V, Genovese M and Fragiacomo P. 2021. Comprehensive Review on Fuel Cell Technology for Stationary Applications as Sustainable and Efficient Poly-Generation Energy Systems. Energies 14:4963.
[2] Hirschenhofer JH, Stauffer DB, Engleman RR at al. 1998. Fuel cell handbook. fourth edi. Morgantown, West Virginia: U.S. Department of Energy Office of Fossil Energy National Energy Technology Laboratory.
[3] Shabani B, Hafttananian M, Khamani S, at al. 2019. Poisoning of proton exchange membrane fuel cells by contaminants and impurities: Review of mechanisms, effects, and mitigation strategies. Journal of Power Sources 427:21–48.
[4] Postole G and Auroux A. 2011. The poisoning level of Pt/C catalysts used in PEM fuel cells by the hydrogen feed gas impurities: The bonding strength. International Journal of Hydrogen Energy 36:6817–25.
[5] Arenz M and Markovic NM. 2010. Half-Cell Investigations of Cathode Catalysts for PEM Fuel Cells: From Model Systems to High-Surface-Area Catalysts. In: Fuel Cell Sci. Theory, Fundam. Biocatal., New Jersey: John Wiley & Sons, Inc.
[6] Micoud F, Maillard F, Bonnefont A, at al. 2010. The role of the support in COads monolayer electrooxidation on Pt nanoparticles: Pt/WOx vs. Pt/C. Physical Chemistry Chemical Physics 12:1182–93.
[7] Brković SM, Nikolić VM, Marčeta Kaninski MP, at al. 2019. Pt/C catalyst impregnated with tungsten-oxide – Hydrogen oxidation reaction vs. CO tolerance. International Journal of Hydrogen Energy 44:13364–72.

FEM BASED NUMERICAL STUDY OF HYBRID NANOFLUID ENHANCED HYDROGEN ABSORPTION IN A METAL HYDRIDE REACTOR

Fatih Selimefendigil, Gürel Şenol, Hakan F. Öztop
Vocational School of Technical Sciences, Manisa Celal Bayar University, Manisa 45140, Turkey
Department of Mechanical Engineering, Manisa Celal Bayar University, Manisa 45140, Turkey
Department of Mechanical Engineering, Technology Faculty, Fırat University, Elazığ 23119, Turkey
Corresponding author e-mail:gurel.senol@hotmail.com, fatih.selimefendigil@cbu.edu.tr

ABSTRACT

This study focuses on the hydrogen absorption of a metal hydride reactor with different cooling methods. The metal hydride bed was selected as magnesium hydride (MgH_2). The numerical study was based on four different cases by using FEM based solver. In case 1, the metal hydride reactor had a simple structured cooling channel with water as the coolant. In case 2, the coolant used in the system was pure water, but the cooling channel had a baffle with a structure of combined U-tubes. Case 3 had one difference when it was compared to Case 2. The coolant used in the metal hydride reactor was a ternary nanofluid (tnf) of Al_2O_3 nanoparticles, MWCNT cylindrical nanoparticles and platelet graphene nanoparticles in water. Case 4 was based on Case 3. Effects of different mass rates of the ternary nanofluid on the hydrogen storage were examined. For each case, the absorbed hydrogen (wt.%), average bed temperature results were obtained and comparative results were provided. According to the results, in Case 2 and Case 3, the hydrogen absorption increased by 15% and %18, respectively. The average bed temperature decreased by 8% and 10%, respectively. In Case 4 the hydrogen absorption increased by 15% when the flow rate was taken as two times of the original one and the average bed temperature decreased by 8%.

Keywords: Hydrogen storage, Ternary Nanofluid, CFD, Metal Hydride

1.INTRODUCTION

Hydrogen storage in metal hydrides has gained a significant place in hydrogen storage methods, since metal hydrides show a good performance during the sorption process due to their storage capacities. Also, they are more reliable unlike many other hydrogen storage techniques. As it's known, the vital parameters which affect the sorption process performance are hydrogen supply pressure, the coolant temperature and the porosity of the metal hydride used in the system. Despite this fact, the need for a better hydrogen sorption must be considered. One of the enhancement methods for the hydrogen storage is improving the thermophysical properties of the coolant. Nanofluids can't be ignored when this issue is considered.

In a basic way, a nanofluid is a new type of fluid based on using extremely small particles (smaller than micro-structures) and adding them into a kind of base fluid; in other words, it involves creating a suspension using nano-sized particles and a specific base fluid. The term used for this special suspension was first used by Choi et al. [1]. Depending on their nature, the researchers have focused on the improvement of nanofluids' macro-scale and mega-scale properties by controlling micro-scale features of them [2,3]. Nanofluids can be prepared by using more than one nano material. They are called as hybrid nanofluids. Ternary nanofluids are the ones which consist of three different nano material particles in the base fluid [4-8]. Researchers have performed studies which emphasize the contribution of nanofluids for hydrogen storage in metal hydrides in terms of thermal management [9-12]

This study focuses on the effect of a ternary nanofluid of Al_2O_3 nanoparticles, multiwall carbon nanotubes (MWCNT) cylindrical nanoparticles and platelet graphene nanoparticles with water considering the contribution of a baffle with a structure of combined U-tubes on the hydrogen absorption process. The baffle used in cases except for Case 1, is placed on the inner surface of the cooling channel in the metal hydride bed. Within the contribution of the ternary nanofluid used as the coolant in the system a better performance has been obtained.

2. MATHEMATICAL MODELLING

Each basic model for Case 1 (a) and Case 2 (b) are shown on Fig. 1. For Case 1, the cooling channel of the metal hydride reactor had a simple structure with no baffle. For other cases, the cooling channel had a baffle with a structure of combined U-tubes. Water was used as the coolant in Case 1 and Case 2. For Case 3 and Case 4, ternary nanofluid was used for a better sorption process. Case 4 was aimed for the effect of flow rate($\dot{Q}$) of the coolant (ternary nanofluid). Different flow rates as $0.5\dot{Q}$, $\dot{Q}$, $1.5\dot{Q}$ and $2\dot{Q}$ were taken. The ternary nanofluid had Al_2O_3 nanoparticles, MWCNT cylindrical nanoparticles and platelet graphene nanoparticles in water [13].

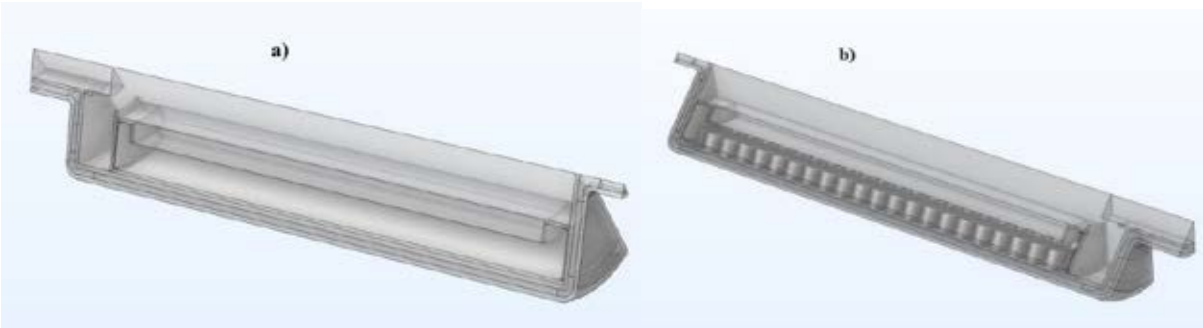

Fig. 1. Models (a) Case 1, b) Case 2

Finite element method (FEM) was used for the solution of the governing equations. Lagrange FEMs of different orders were used for the approximation of field variables in different domains of thermal management system within hydrogen storage. Number of elements and tetrahedral elements used are 987314 and 690904, respectively. Minimum element quality is 0.01008. As CFD program, COMSOL Multiphysics 6.2 is used for the simulation of the coupled system.

2.1 Governing Equations

Mass conservation for hydrogen is given as [14]:

$$\varepsilon \frac{\partial \rho_g}{\partial t} = -\acute{m} \tag{1}$$

The mass conservation of metal hydride bed is [14]:

$$(1-\varepsilon)\frac{\partial \rho_{mhb}}{\partial t} = \acute{m} \tag{2}$$

where $\acute{m}$ is the volumetric mass flow rate of the hydrogen during the sorption process. It's evaluated from the common kinetics equation [15],

$$\acute{m} = Ca\ exp\left[-{E_a}/{R\ T}\right]\ln\left({P_g}/{P_{eq}}\right) = [\rho_{st} - \rho_s] \tag{3}$$

where Ca and E_a are reaction constant and activation energy respectively. P_g is the hydrogen supply pressure, ρ_{st} is the density of saturated metal hydride, ρ_s is the density of metal hydride at a particular time during sorption.

The momentum conservation equation is given by [15, 16]:

$$\frac{\rho}{\varepsilon}\frac{\partial \vec{v}_s}{\partial t} + \left(\frac{\mu}{K} + \frac{S_0}{\varepsilon^2}\right)\vec{v}_s = -\nabla P + \nabla.\left[\frac{\mu}{\varepsilon}\left(\nabla\vec{v}_s + \nabla\vec{v}_s{}^T\right)\right] - \nabla.\left[\left(\frac{2\mu}{3} - \eta_d\right)\left(\frac{1}{\varepsilon}\right)(\nabla.\vec{v}_s)I\right] \tag{4}$$

Energy conservation equation is given by [15, 16]:

$$\left(\rho C_p\right)_{eff}\left(\frac{\partial T}{\partial t}\right) + \left(\rho C_p\right)_g(\vec{u}\,\nabla \mathrm{T}) = k_{eff}\nabla^2 T + Q \tag{5}$$

At the beginning of the sorption process, at t=0 s metal hydride bed, and the coolant in the channel were in ambient conditions. The density of metal hydride bed is uniform.

$$P = P_{\mathrm{i}} = 10\ atm \tag{6}$$

$$T = T_0 = 288.15\ K \tag{7}$$

$$\rho_{MH} = \rho_i = 1450\ {kg}/{m^3} \tag{8}$$

$$\dot{Q} = 0.4\ {m^3}/{h} \tag{9}$$

The outer wall of the reactor is considered adiabatic.

$$\left(-k\frac{\partial T}{\partial r}\right)_{r=r_w} = 0 \tag{10}$$

Equations of ternary nanofluid thermophysical properties.

The density of the composite ternary nanofluid material is [13]:

$$\rho_{tnf} = \varphi_1\rho_1 + \varphi_2\rho_2 + \varphi_3\rho_3 + (1 - \varphi_1 - \varphi_2 - \varphi_3)\rho_{bf} \quad (11)$$

where ρ_1, ρ_2, ρ_3 are the density of several nanomaterials and φ_1, φ_2, φ_3 represent volume ratio of nano particles for Al_2O_3, MWCNT and graphene nano particles, respectively. $\varphi = \varphi_1 + \varphi_2 + \varphi_3$ denotes the total number of volume ratios of the nanofluids of ternary composition. Here, ρ_{bf} is the density of the basic fluid (water).

The dynamic viscosity of the ternary composite nanofluid is [13]:

$$\mu_{tnf} = \frac{\varphi_1\mu_{nf1}+\varphi_2\mu_{nf2}+\varphi_3\varphi_{nf3}}{\varphi} \quad (12)$$

here $\mu_{nf1} = \mu_{bf}$ (1 + $2.5\,\varphi + \varphi^2$) (Al_2O_3, spherical form), $\mu_{nf2} = \mu_{bf}$ (1 + $13.5\,\varphi + 904.4\,\varphi^2$) (MWCNT, cylindrical form), and φ_{nf3}= = μ_{bf} ($1 + 37.1\,\varphi + 612.6\,\varphi^2$) (graphene, platelet form). = $\mu_{bf}$is the dynamic viscosity of the basic fluid.

The specific heat capacity of ternary composite nanofluid is [13]:

$$(\rho C_p)_{tnf} = \varphi_1(\rho C_p)_1 + \varphi_2(\rho C_p)_2 + \varphi_3(\rho C_p)_3 + (1 - \varphi_1 - \varphi_2 - \varphi_3)(\rho C_p)_{bf} \quad (13)$$

where$(\rho C_p)_1$, $(\rho C_p)_2$, $(\rho C_p)_3$ represent the specific thermal capacity and $(C_p)_1$, $(C_p)_2$, $(C_p)_3$are particular temperatures of (Al2O3) nano particles (spherical), (MWCNT) nanoparticles (cylindrical), and graphene nanoparticles (platelet) and $(\rho C_p)_{bf}$is the specific ther mal capacity of the basic fluid.

3. RESULTS AND DISCUSSION

Fig. 2 presents the hydrogen absorption fraction (wt. %) for Case 1, Case 2 and Case 3. Dynamics of absorbed hydrogen storage were found to be influenced by different thermal management methods. Fig. 3. demonstrates the average bed temperature values for Case 1, Case 2 and Case 3. Based on the results, in Case 2 and Case 3, the hydrogen sorption increased by 15% and 18%, respectively. When nanofluids are used, enhanced thermal transport features due to favorable properties of nanoparticles results in better cooling. The average bed temperature decreased by 8% and 10%, respectively. Fig. 4. shows the hydrogen absorption fraction (wt. %) for Case 4 based on different flow rates. Fig. 5 demonstrates the average bed temperature values for Case 4 based on different flow rates. Higher flow rates and nanofluid results in better cooling while lower bed temperatures were achieved. In Case 4 the hydrogen absorption increased by 15% most when the flow rate was taken as two times of the original one and the average bed temperature decreased by 8%.

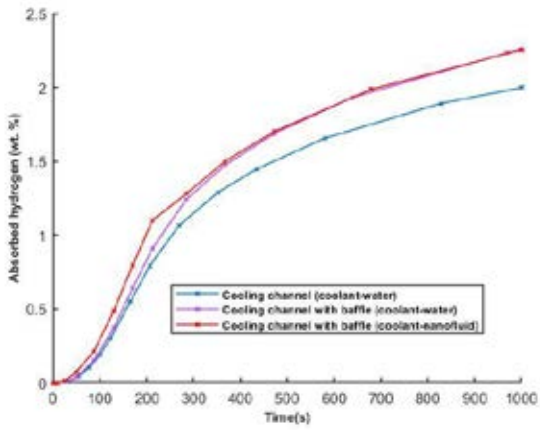

Fig. 2. Hydrogen absorption (wt. %) for Case 1, Case 2 and Case 3

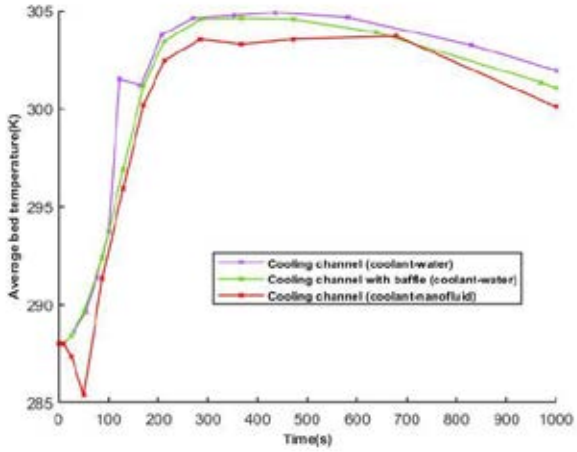

Fig. 3. Average bed temperature values for Case 1, Case 2 and Case 3

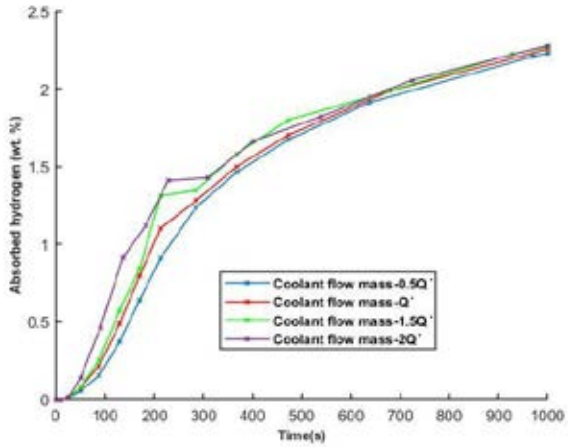

Fig. 4. The hydrogen absorption fraction (wt. %) for different flow rates

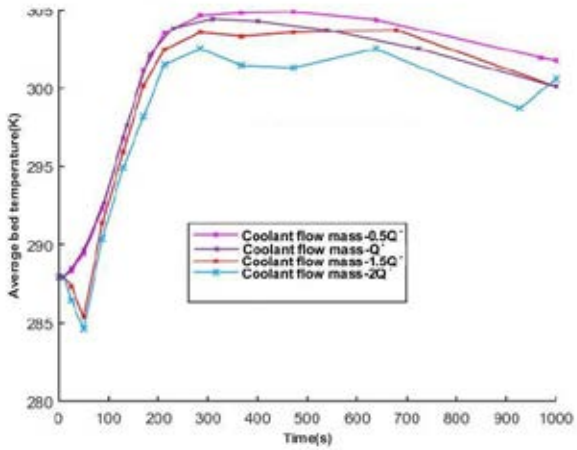

Fig. 5. Average temperature values for different flow rates

4. CONCLUSIONS

Current study proposes different thermal management methods by using ternary nanofluid for hydrogen storage in a metal hydride reactor. The best result was obtained in Case 3 (in which the cooling channel had a baffle with a structure of several U-tubes and the coolant was ternary nanofluid.). The absorption process was improved by 18% compared to the model in Case 1(which had a plain cooling channel with no baffle(s) on, with the usage of water as the coolant. The average bed temperature in the metal hydride of the hydrogen reactor was improved by 10%.The ternary nanofluid used in Case 3 had the most impact on the enhancement of the hydrogen storage system. Also, it was seen that increasing the flow rate of the ternary nanofluid in Case 4 had an extra positive effect on the metal hydride reactor, causing an improvement in sorption and average bed temperature by %15 and %8, respectively compared to the one with the reference flow rate ($\dot{Q}$).

REFERENCES

1. Choi, S.U.; Eastman, J.A. Enhancing Thermal Conductivity of Fluids with Nanoparticles; No. ANL/MSD/CP-84938; CONF-951135-29; Argonne National Lab. (ANL): Argonne, IL, USA, 1995.
2. Wang, L.Q.; Xu, M.; Wei, X. 4 Multiscale Theorems. Adv. Chem. Eng. 2008, 34, 175.
3. Wang, L.Q. Flows through porous media: A theoretical development at macroscale. Trans. Porous Media 2000, 39, 1.
4. Yang, X., Boroomandpour, A., Wen, S., Toghraie, D., Soltani, F., 2021. Applying Artificial Neural Networks (ANNs) for prediction of the thermal characteristics of water/ ethylene glycol-based mono, binary and ternary nanofluids containing MWCNTs, titania, and zinc oxide. Powder Technol. 388, 418–424
5. Dezfulizadeh, A., Aghaei, A., Joshaghani, A.H., Najafizadeh, M.M., 2021. An experimental study on dynamic viscosity and thermal conductivity of water-CuSiO2-MWCNT ternary hybrid nanofluid and the development of practical correlations. Powder Technol. 389, 215–234
6. Adun, H., Kavaz, D., Wole-osho, I., Dagbasi, M., 2021a. Synthesis of Fe 3 O 4 -Al 2 O 3 -ZnO/water ternary hybrid nanofluid: investigating the effects of temperature, volume concentration and mixture ratio on Specific heat capacity, and development of Hybrid machine learning for prediction. J. Energy Storage 41 (April), 102947
7. Cakmak, N.K., Said, Z., Sundar, L.S., Ali, Z.M., Tiwari, A.K., 2020. Preparation, characterization, stability, and thermal conductivity of rGO-Fe3O4-TiO2 hybrid nanofluid: an experimental study. Powder Technol. 372, 235–245
8. Mousavi, S.M., Esmaeilzadeh, F., Wang, X.P., 2019b. Effects of temperature and particles volume concentration on the thermophysical properties and the rheological behavior of CuO/MgO/TiO2 aqueous ternary hybrid nanofluid: experimental investigation. J. Therm. Anal. Calorim. 137 (3), 879–901.
9. Kumar Kanti Praveen, Parmanand Shrivastav Ankush, Sharma Prabhakar, Maiya MP. Thermal performance enhancement of metal hydride reactor for hydrogen storage with graphene oxide nanofluid: model prediction with machine learning. Int J Hydrogen Energy 2024; 52:470–84
10. Urunkar Rahul U, Patil Sharad D. Performance analysis of sodium alanate hydride reactor with different nanofluids. Int J Hydrogen Energy 2023;48(96):37944–53.
11. Elarem Raja, Alqahtani Talal, Mellouli Sofiene, Edacherian Abhilash, Askri Faouzi, Jemni Abdelmajid. Numerical analysis of a built-in thermal storage system of metal hydride and nanoparticles enhanced phase change material and nanofluid. Int J Energy Res 2021;45(4):5881–93.
12. Urunkar Rahul U, Patil Sharad D. Enhancement of heat and mass transfer characteristics of metal hydride reactor for hydrogen storage using various nanofluids. Int J Hydrogen Energy 2021;46(37):19486–97.
13. Ahmed, S. E., Raizah, Z., Arafa, A. A., & Hussein, S. A. (2023). FEM treatments for MHD highly mixed convection flow within partially heated double-lid driven odd-shaped enclosures using ternary composition nanofluids. *International Communications in Heat and Mass Transfer*, *145*, 106854.
14. Disli, T., Çetinkaya, S. A., Ezan, M. A., & Colpan, C. O. (2024). Numerical investigations on the absorption of a metal hydride hydrogen storage tank based on various thermal management strategies. *International Journal of Hydrogen Energy*, *51*, 504-522.
15. Tong, L., Xiao, J., Yang, T., Bénard, P., & Chahine, R. (2019). Complete and reduced models for metal hydride reactor with coiled-tube heat exchanger. *International Journal of Hydrogen Energy*, *44*(30), 15907-15916.
16. Hardy, B., Corgnale, C., Chahine, R., Richard, M. A., Garrison, S., Tamburello, D., ... & Anton, D. (2012). Modeling of adsorbent based hydrogen storage systems. *International Journal of Hydrogen Energy*, *37*(7), 5691-5705.

SOLID SOLUTION OXIDE CATALYSTS FOR ENHANCED VISIBLE-LIGHT-DRIVEN HYDROGEN EVOLUTION BY WATER SPLITTING

Tsong-Pyng Perng
National Tsing Hua University, Department of Materials Science and Engineering, 101 Sec.2, Kuang-Fu Road, Hsinchu, 30013, Taiwan

tpperng@mx.nthu.edu.tw

ABSTRACT
Atomic layer deposition (ALD) was employed to fabricate Zn-doped TiO_2 nanotubes via nanolaminated stacks of binary layers of TiO_2 and ZnO. The bilayers were alternately deposited on the polycarbonate (PC) membrane template by ALD with various cyclic sequences. With a doping ratio of 0.01, the hydrogen production rate from water splitting was 6 times higher than that of commercial P25 TiO_2. Nanolamination of GaN and ZnO layers by ALD was also employed to fabricate GaN-ZnO homogeneous solid solution thin films. By varying the ALD cycle ratios of GaN:ZnO from 5:10 to 10:5, the $(GaN)_{1-x}(ZnO)_x$ films with $0.39 \leqq x \leqq 0.79$ were obtained. The density function theory (DFT) calculations are performed to understand the difference of density of states (DOS) and evaluate the bandgaps for various atomic configurations in the solid solution films. Visible-light-driven photocatalytic hydrogen evolution was conducted to confirm the applicability of the solid solution films.

Keywords: ZnO, TiO_2, GaN, Atomic layer deposition, Hydrogen evolution.

1. INTRODUCTION

Atomic layer deposition offers advantages such as atomically smooth surface, precise control of film thickness in atomic scale, and good conformality [1]. Therefore, it is widely employed as a thin film deposition technology. Moreover, ALD of two different materials layer by layer may create nanolaminates that enable formation of solid solution of the two materials, offering new physical properties. Herein, we report two examples of ALD nanolamination, i.e., ZnO/TiO_2 and GaN/ZnO, to form solid solutions which enable enhanced visible-light driven water splitting to generate hydrogen.
TiO_2 and ZnO have different crystal structures and lattice parameters. Because of their high energy gap (3.2 eV for both), they can only utilize UV light for photocatalytic reaction. Based on the phase diagram [2], there is no mutual solubility in this binary system. However, ALD nanolamination is able to dope a substantial amount of ZnO into TiO_2. On the contrary, GaN and ZnO have the same crystal structure and similar lattice parameters, but GaN has an even larger bandgap, 3.4 eV. By varying the ALD cycle ratios of GaN:ZnO, from 5:10 to 10:5, complete solid solutions of $(GaN)_{1-x}(ZnO)_x$ can be formed.

2. EXPERIMENTAL

Homogeneous Zn-doped TiO_2 nanotubes were fabricated by ALD via nanolaminated stacks of alternate layers TiO_2 and ZnO on the polycarbonate (PC) membrane template with various cyclic sequences [3,4]. The precursors for Zn and Ti were diethyl zinc ($Zn(C_2H_5)_2$) and titanium tetrachloride ($tiCl_4$), respectively. A total of 400 ALD cycles were conducted. The Zn-doped TiO_2 nanotubes in a length of 20 μm and a diameter of 220 nm were obtained after removal of the PC membrane by annealing at 450 °C. The schematic fabrication process is shown in Fig. 1 [3].
Nanolamination of GaN and ZnO layers on a Si substrate with various ratios was conducted using TMG ($Ga(CH_3)_3$) and DEZ ($Zn(C_2H_5)_2$) as the Ga and Zn precursors, respectively [5]. The substrate temperature was set at 200 °C. For the growth of GaN, an NH_3 plasma was employed to form the nitride in a direct plasma reactor by a RF generator. The solid solution films were obtained by alternating the deposition of GaN and ZnO layers with different repeated cycles. The total number of ALD cycles was fixed at 300 cycles.
The photocatalytic hydrogen generation efficiency was measured by a gas chromatograph. A 20% methanol solution was used as the sacrificial reagent, and a 150 W high-pressure Xe lamp or a 300-W Xe lamp equipped with a filter (λ≥420 nm) was employed as the visible light source [5,6].

3. RESULTS AND DISCUSSION

3.1 Zn-doped TiO_2 (ZnO/TiO_2) nanotubes

The SEM image of Zn-doped TiO_2 nanotubes is also shown in Fig. 1. The doping amount of Zn in TiO_2 could be tuned by varying the fraction of cycle number of ZnO. From the depth profiles measured by second ion mass spectrometry, Zn was uniformly distributed across the thickness, which was also supported by the analyses of X-ray diffraction, X-ray photoelectron spectroscopy (XPS), and Raman spectroscopy. Although there is no mutual solubility of these two oxides from the phase diagram, a uniform bulk solubility of ~8 at% (determined by inductively coupled plasma-mass spectroscopy (ICP-MS)) was achieved with the cycle ratio of ZnO:TiO_2 at 0.04, and the surface concentration of Zn (determined by XPS) was even higher, ~16 at%, as shown in Fig. 2. With a total of 400 cycles of ALD, the tube thickness

was measured to be ~28 nm.
The effects of doping composition on the photocatalytic and photoelectrochemical (PEC) activities were investigated. There was an optimal range of Zn doping to get enhanced photocatalytic activity and higher PEC efficiency. As shown in Fig.3 (a), with a doping ratio of 0.01, the hydrogen production rate from water splitting is 6 times higher than that of commercial P25 TiO_2 [6]..

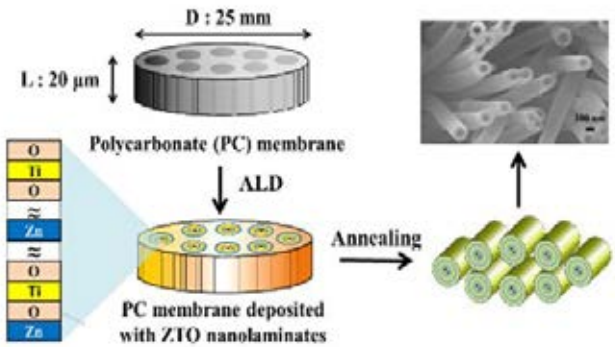

Fig. 1. Schematic illustration for fabricating Zn-doped TiO_2 nanotubes using PC membrane as a template and SEM image of free standing nanotubes.

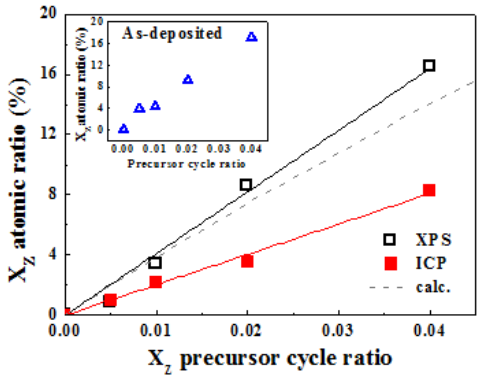

Fig. 2. Atomic ratio of Zn measured by XPS and ICP-MS in annealed Zn-doped TiO_2 nanotubes versus precursor cycle ratio. The dashed line represents theoretical values calculated by the rule of mixtures formula. The inset shows the atomic ratio of as-deposited surface layer of the samples measured by XPS.

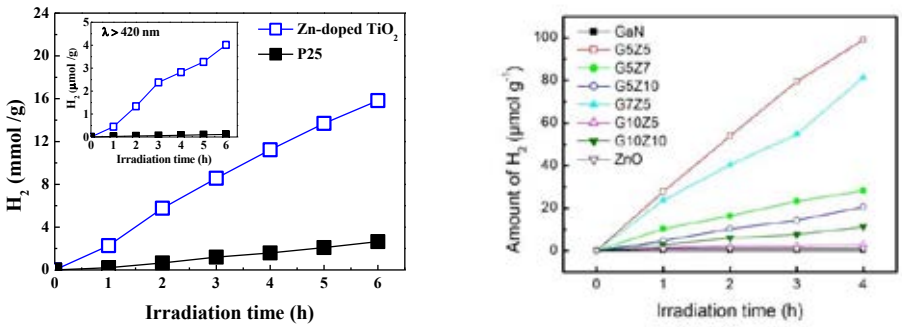

Fig. 3. (a) Hydrogen evolution from water splitting by Zn-doped TiO_2 (X_Z=0.01) nanotubes and P25 irradiated with a 150 W Xe lamp without filter. The inset shows hydrogen evolution under visible light irradiation. (b) Comparison of visible-light-driven hydrogen evolution efficiencies of GaN, ZnO, and all solid solution films under 300-W Xe lamp irradiation with a cut-off filter of 420 nm.

3.2 GaN/ZnO solid solution films

Nanolamination of GaN and ZnO layers was conducted by varying the ALD cycle ratios of GaN:ZnO from 5:10 to 10:5. The $(GaN)_{1-x}(ZnO)_x$ solid solution films with $0.39 \leqq x \leqq 0.79$ were obtained. Figure 4 shows a cross-sectional high resolution transmission electron microscopic (HRTEM) image of the G5Z5 thin film. It clearly reveals that the film with a homogeneous polycrystalline microstructure is deposited on the Si substrate. The lattice spacing of 0.279 nm observed in Figure 4(b) is attributed to the formation of a solid solution of GaN and ZnO.

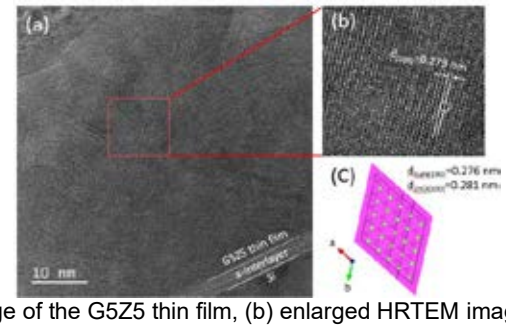

Fig. 4. (a) Cross-sectional HRTEM image of the G5Z5 thin film, (b) enlarged HRTEM image, and (c) schematic hexagonal wurtzite atomic arrangement on the (001) facet.

The DFT calculations were performed to understand the difference of DOS and evaluate the bandgaps for various atomic configurations. Figure 5(a) shows the summary of Fermi levels and positions of conduction band and valence band of GaN, ZnO, and $(GaN)_{1-x}(ZnO)_x$ solid solution films with various values of *x*. It reveals that all of the valence band positions are located at more positive potentials than that of bare ZnO. On the other hand, all of the conduction band positions of $(GaN)_{1-x}(ZnO)_x$ are very close to that of bare ZnO. Consequently, the bandgap reduction of $(GaN)_{1-x}(ZnO)_x$ is mainly attributed to the positive shift of the VBM caused by GaN. In addition, it is worthy of observing the relative band positions in the DFT calculations, as shown in Figure 5(b). The calculated values of DOS show that the positions of CBM and VBM tend to decrease systematically with increasing *x*.

The photocatalytic hydrogen evolution efficiencies of GaN, ZnO, and GaN-ZnO solid solution films under visible light irradiation are shown in Fig. 3(b). The bare GaN and ZnO exhibit nearly zero hydrogen evolution even after 4 h irradiation due to their large bandgaps. Further, G10Z5 and G10Z10 exhibit very low efficiencies, which may be attributed to their poor crystallinity. By contrast, the other GaN-ZnO solid solution films reveal significantly improved photocatalytic hydrogen evolution efficiencies. The highest value of 99.1 μmol/g for 4 h was achieved by the G5Z5 sample (*x*=0.66), and the second highest efficiency was obtained by G7Z5 (*x*=0.52) [5].

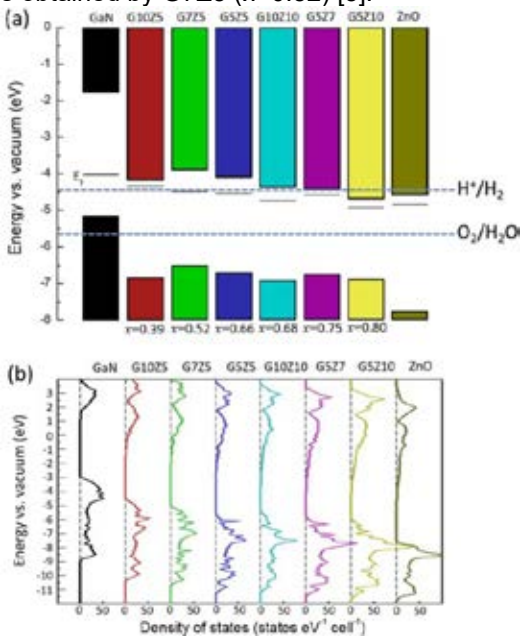

Fig. 5. Summary of (a) energies of Fermi level, conduction band, and valence band of GaN, ZnO, and $(GaN)_{1-x}(ZnO)_x$ solid solution films with various values of *x* and (b) corresponding calculated values of DOS from DFT calculations. The reduction potential of H^+/H_2 and oxidation potential of O_2/H_2O are also plotted in (a).

4. CONCLUSIONS

(1) Uniform doping of Zn ions into TiO_2 nanotubes with a bulk solubility of ~8 at% (~16 at% on the surface) was achieved by nanolamination of ALD. Compared with P25 powder, TiO_2 nanotubes with X_Z=0.01 show 6 times higher hydrogen production rate under irradiation with a 150 W Xe lamp.

(2) Nanolamination of GaN and ZnO layers with cycle ratios of GaN:ZnO from 5:10 to 10:5, the $(GaN)_{1-x}(ZnO)_x$ films with $0.39 \leqq x \leqq 0.79$ were obtained. The DFT calculations were performed. Reduction of the bandgaps to 2.19-2.67 eV was obtained from the calculations. A significant evolution of 99.1 μmol/g for 4 h was achieved by G5Z5.

ACKNOWLEDGEMENTS
This work was supported by the National Science and Technology Council of Taiwan under the Contract Nos. NSC 99-2221-E-007-066-MY3, 102-2120-M-007-007, and MOST 107-2221-E-007-006-MY2, 109-2221-E-007-060-MY3.

REFERENCES
1. Wang CC, Kei CC, Yu YW, and Perng TP. 2007. Organic nanowire-templated fabrication of alumina nanotubes by atomic layer deposition. Nano Letters 7:1566-1569.
2. Dulin FH and Rase DE. 1960. Phase Equilibria in the system ZnO-TiO_2.. Journal of American Ceramic Society 43:125-131.
3. Su CY, Wang CC, Hsueh YC, Gurylev V, Kei CC, and Perng TP. 2015. Enabling high solubility of ZnO in TiO_2 by nanolamination of atomic layer deposition. Nanoscale 7:19222-19230.
4. Su CY, Hsueh YC, Gurylev V, Kei CC, and Perng TP. 2017. Fabrication of highly homogeneous Al-doped TiO_2 nanotubes by nanolamination of atomic layer deposition. Journal of American Ceramic Society 100:4988-4993.
5. Liao MY, Jeng HT, and Perng TP. 2022. Formation mechanism and bandgap reduction of GaN-ZnO solid solution thin films fabricated by nanolamination of atomic layer deposition. Advanced Materials 35:2207849.
6. Su CY, Wan LC, Li WS, Wang CC, and Perng TP. 2018. Photocatalysis and hydrogen evolution of Al- and Zn-doped TiO_2 nanotubes fabricated by atomic layer deposition. ACS Applied Material Interfaces 10:33287-33295.

DUAL-DOPED IRON-COPPER CARBON ELECTROCATALYST FOR ENHANCED WATER SPLITTING PERFORMANCE IN ALKALINE MEDIA

[1]Jelena Georgijević, [1*]Ivana Perović, [1]Snežana Brković, [1]Mina Seović, Nikola Zdolšek[1], [2]Jadranka Milikić, [2,3]Biljana Šljukić

[1]University of Belgrade, Vinča Institute of Nuclear Sciences, National Institute of the Republic of Serbia, Mike Petrovića Alasa 12-14, 11351 Vinča, Serbia

[2]University of Belgrade, Faculty of Physical Chemistry, Studentski trg 12-16, Belgrade, Serbia,

[3]Center of Physics and Engineering of Advanced Materials, Laboratory for Physics of Materials and Emerging Technologies, Chemical Engineering Department, Instituto Superior Técnico, Universidade de Lisboa, 1049-001 Lisbon, Portigal

*Corresponding author e-mail: ivanaperovic@vin.bg.ac.rs

ABSTRACT

This study introduces a novel electrocatalyst, iron and copper co-doped carbon (FeCu-C), derived from the carbonization of specific ionic liquids. The material's catalytic efficiency was evaluated for both the oxygen evolution reaction (OER) and the hydrogen evolution reaction (HER) in an alkaline environment. The FeCu-C demonstrated superior performance in OER with a low onset potential of -1.485 V and a peak current density of 160 mA cm^{-2} at 2 V versus RHE. In contrast, HER displayed lesser efficacy with a maximum current density of approximately 4 mA cm^{-2} at -0.4 V versus RHE. A lower charge-transfer resistance during OER, determined via electrochemical impedance spectroscopy, confirms its higher catalytic activity in comparison to HER conditions.

Keywords: HER, OER, Ionic liquid, electrocatalyst, *d* metals

1. INTRODUCTION

The growing global energy demand and the shift toward sustainable energy systems have intensified the search for efficient methods of hydrogen production. Water electrolysis has emerged as a promising solution, offering a clean route for generating hydrogen and oxygen. Central to this process are the hydrogen evolution reaction (HER) and oxygen evolution reaction (OER), which require efficient electrocatalysts to overcome high energy barriers and achieve practical performance. Platinum and iridium/ruthenium oxides are benchmark catalysts for HER and OER, respectively, but their high cost and scarcity pose significant challenges to scalability and widespread adoption [1,2].

In recent years, earth-abundant transition metals, such as iron and copper, have gained attention for their potential as cost-effective and efficient alternatives. Research has demonstrated that combining multiple transition metals can synergistically enhance catalytic activity and durability [3,4]. The incorporation of ionic liquids as precursors for catalyst synthesis has opened new possibilities, leveraging their unique chemical and physical properties to produce high-performance carbon-based materials [5].

This study focuses on developing a dual-doped iron-copper carbon material (FeCu-C) using a simple and scalable method of ionic liquid carbonization. Unlike previous studies that primarily explore single-metal doping or more complex synthesis routes, this work investigates the synergistic effects of iron and copper in a carbon matrix for improving OER and HER performance. The specific objectives are to evaluate the electrocatalytic activity of FeCu-C in alkaline media, analyze the kinetic parameters, and identify factors influencing its performance under anodic and cathodic conditions. This approach provides valuable insights into designing cost-effective electrocatalysts for sustainable hydrogen production.

2. MATERIALS AND METHODS

In this study, a FeCu-dual doped carbon material was synthesized through the direct carbonization of two ionic liquids, $[Bmim]_2[CuCl_4]$ and $[Bmim]_2[FeCl_4]$, at 800 °C in a nitrogen atmosphere for one hour, followed by cooling to room temperature. For electrochemical evaluation, a working electrode was fabricated by evenly spreading a catalytic ink—composed of FeCu-C electrocatalyst powder mixed with polyvinylidene fluoride binder in N-methyl-2-pyrrolidone—onto a glassy carbon electrode. Electrochemical properties were assessed using an Ivium V01107 potentiostat/galvanostat in a 40 cm^3 glass cell equipped with a three-electrode system, where a saturated calomel electrode and a graphite rod served as the reference and counter electrodes, respectively. Measurements relative to the reversible hydrogen electrode (RHE) were conducted in 8 M KOH at 25 °C, using linear cyclic voltammetry with scan rates of 2 mV s^{-1} for the hydrogen evolution reaction (HER) and 5 mV s^{-1} for the oxygen evolution reaction (OER), and electrochemical impedance spectroscopy across the frequency range of 100 kHz to 0.1 Hz.

3. RESULTS AND DISCUSSION

The electrocatalytic properties of FeCu-C were initially assessed for the oxygen evolution reaction (OER) in an alkaline medium, given the critical role of OER in determining the rate and efficiency of electrolytic water splitting. The activity was measured in 8 M KOH, mirroring the electrolyte concentration predominant in industrial alkaline electrolyzers. Linear sweep voltammetry (LSV) was performed from the open circuit potential (OCP) to 2 V at a scan rate of 5 mV s^{-1}, as depicted in Figure 1. The onset potential for OER, defined as the potential at which a current density of 1 mA cm^{-2} is achieved, was recorded at a notably low 1.485 V. The material exhibited robust activity, reaching current densities around 160 mA cm^{-2} at 2 V during OER polarization. Subsequent Tafel analysis utilized the polarization curve to construct a Tafel plot, analyzed via the relationship $\eta = a + b \times \log j$, where '*a*' represents the intercept correlating to the exchange current density j_0 and '*b*' the Tafel slope. This slope was calculated to be 134 mV dec^{-1}, indicating the kinetic favorability of the reaction under study.

Furthermore, the activity of FeCu-C for the hydrogen evolution reaction (HER) was evaluated under similar conditions. As shown in Fig. 1, voltammograms recorded from OCP to -0.4 V at a scan rate of 2 mV s^{-1} revealed HER activity with a current density reaching - 4.2 mA cm^{-2} at -0.4 V. The onset potential for HER was observed at -0.335 V, and the Tafel slope was measured at -151 mV dec^{-1}, suggesting that the HER process on FeCu-C likely follows the Volmer-Heyrovsky mechanism. This mechanism encompasses electrochemical hydrogen adsorption on the electrode surface (MH_{ads}) as the initial step (Volmer reaction, (1)), followed by either electrochemical desorption (Heyrovsky reaction, (2)) or catalytic recombination (Tafel reaction, (3)), with the equations:

$$M + H_2O + e^- \leftrightarrow MH_{ads} + OH^- \quad \text{(Volmer reaction)} \quad (1)$$
$$MH_{ads} + H_2O + e^- \leftrightarrow H_2 + M + OH^- \quad \text{(Heyrovsky reaction)} \quad (2)$$
$$MH_{ads} + MH_{ads} \leftrightarrow H_2 + 2M \quad \text{(Tafel reaction)} \quad (3)$$

These reactions collectively facilitate hydrogen evolution through two potential pathways: Volmer-Heyrovsky or Volmer-Tafel, with Tafel slopes typically observed at 120, 40, or 30 mV dec^-1 at 25 °C, depending on the rate-determining step.

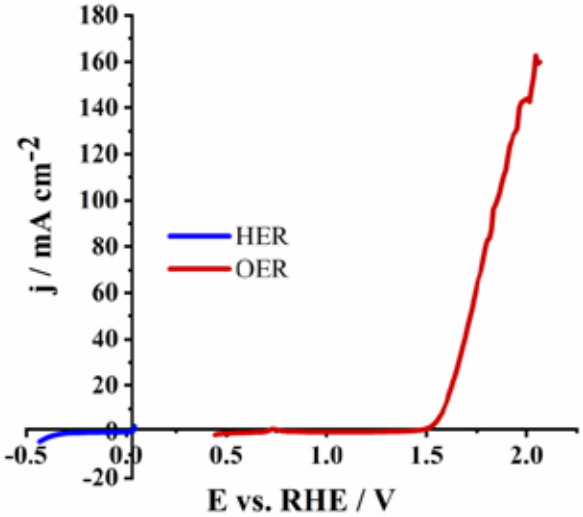

Fig. 1. Linear Sweep Voltammetry Profiles of FeCu-C in 8 M KOH for Hydrogen and Oxygen Evolution Reactions at 25 °C.

Table 1 presents the kinetic parameters obtained for the HER and OER activities of FeCu-C in 8 M KOH at 25 °C. The current density (j_{400}) measured at an overpotential of 400 mV was significantly higher for OER compared to HER, highlighting the superior activity of FeCu-C under anodic polarization. Similarly, the exchange current density (j_0), an indicator of the material's intrinsic catalytic activity and efficiency in charge transfer, was greater for OER than HER, further demonstrating the material's enhanced performance in oxygen evolution.

Electrochemical impedance spectroscopy (EIS) measurements provided additional insights into the charge-transfer resistance (R_{ct}) of FeCu-C under both HER and OER conditions. Nyquist plots (Fig. 2) revealed that R_{ct} during OER at 0.6 V was approximately 35 Ω, while under HER conditions at -1.4 V, it was higher at around 50 Ω. The lower R_{ct} observed during OER correlates with the higher current densities and greater catalytic activity for oxygen evolution, emphasizing the material's suitability for anodic processes in water splitting applications.

Table 1. Summary of HER and OER Kinetic Parameters for FeCu-C in 8 M KOH at 25 °C.

Reaction	E_{onset} / V	j_{400} / mAcm^{-2}	b /mV dec^{-1}	j_0 /10^{-2} mA cm^{-2}
HER	-0.335	2.73	-151	1.42
OER	1.485	24.78	134	2.50

**E_{onset}: Onset potential; j_{400}: Current density at an overpotential of 400 mV; b: Tafel slope; j_0: Exchange current density.*

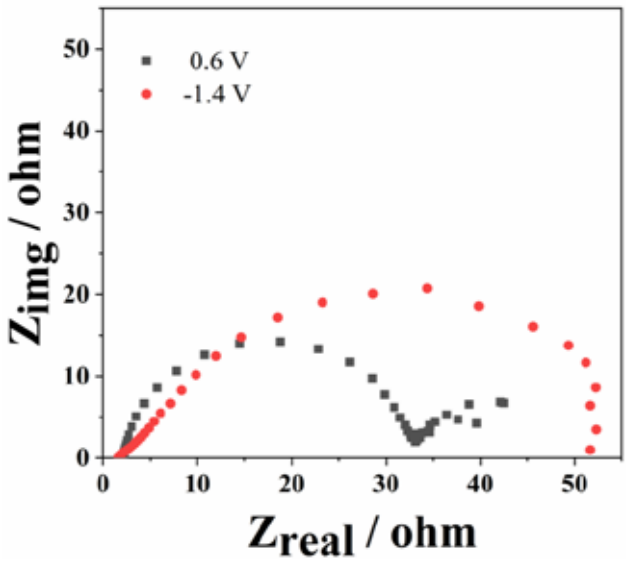

Fig. 2 Nyquist plots at potential of -1.4 V and at potential of 0.6 V at temperature of 25 °C

4. CONCLUSIONS

This study highlights the successful synthesis and characterization of FeCu-dual doped carbon (FeCu-C) as an electrocatalyst for water splitting in alkaline media. The synthesized FeCu-C material, through the innovative approach of ionic liquid carbonization, displays excellent catalytic properties for OER and moderate performance for HER. This differential activity could be partially attributed to the variances in charge-transfer resistance observed under different polarization conditions. These findings position FeCu-C as a promising non-precious metal catalyst for water electrolysis, particularly for applications emphasizing oxygen evolution. Future work may focus on optimizing the material's structure and composition to enhance HER performance, as well as long-term stability testing to assess its practical viability in industrial electrolyzers.

ACKNOWLEDGEMENT

The authors would like to thank Ministry of Science, Technological Development and Innovation of the Republic of Serbia for financial support (grant number: 451-03-66/2024-03/200017).

REFERENCES

1. Sun H, Kim H, Song S, et al. 2022. Transition metal-based catalysts for sustainable energy conversion. *Materials Reports: Energy* 2(2):100092.
2. Chakraborty B, Beltrán-Suito R, Hausmann JN, et al. 2020. Synergistic effects in multimetallic electrocatalysts for water splitting. *Advanced Energy Materials* 10(30):2001377.
3. Zdolšek N, Vujković M, Metin Ö, et al. 2022. Performance of transition metal-doped catalysts in hydrogen evolution reactions. *International Journal of Hydrogen Energy* 47(33):14847-14858.
4. Santos DMF, Amaral L, Šljukić B, et al. 2014. Electrochemical performance of ionic liquid-derived electrocatalysts. *Journal of Electrochemical Society* 161(4):F386.
5. Chiappe C and Pieraccini D. 2005. Ionic liquids: solvent properties and organic reactivity. *Journal of Physical Organic Chemistry* 18(4):275-297.

SYNTHESIZING COST-EFFECTIVE, DUAL-FUNCTION CATALYSTS FROM RECYCLED CPUs AND LEMON PEEL FOR WATER SPLITTING

[1]Mina Seović, [1]Snežana Brković, [1]Ivana Perović, [2]Dragana Jugović, [1]Jadranka Miletić Vukajlović, [1]Petar Laušević, [1]Stefan Mitrović*
[1] University of Belgrade, Vinča Institute of Nuclear Sciences, National Institute of the Republic of Serbia, Mike Alasa 12-14, 11351, Vinča, Serbia
[2] Institute of Technical Sciences of SASA, Knez Mihailova 35/IV, 11000 Belgrade, Serbia

*Corresponding author e-mail: mina050@vin.bg.ac.rs

ABSTRACT

The pressing need for sustainable and cost-effective energy solutions drives the exploration of innovative materials for clean energy technologies. This study introduces a novel approach to synthesizing electrocatalysts from waste materials, specifically recycled central processing units (CPUs) and carbonized lemon peel. By repurposing these abundant waste sources, we developed a dual-function catalyst that facilitates both the hydrogen evolution reaction (HER) and oxygen evolution reaction (OER) in water splitting. Our catalyst showcases promising electrochemical properties, including low overpotential and decent catalytic activity, particularly for HER. Additionally, the synthesized material exhibits potential for use in supercapacitors, demonstrating significant charge storage capabilities. This research not only presents a viable strategy for reducing reliance on rare and expensive metals but also contributes to waste reduction and resource recovery
Keywords: e-waste, activated carbon, electrocatalyst, HER, alkaline electrolysis.

1. INTRODUCTION

Clean energy technologies, such as water splitting via electrolysis, are more important than ever because our energy consumption relies on sources that cause serious environmental pollution.HER and OER are essential reactions in the electrocatalysis of water splitting and play a leading role in clean energy technologies [1]. However, the widely adoption of these technologies is hindered by the high cost and scarcity of effective catalysts, typically made from precious metals such as platinum and iridium. Addressing this challenge, our research explores the potential of synthesizing electrocatalysts from recycled materials, thus not only mitigating the issue of waste but also reducing reliance on expensive, rare metals. Discarded electronic components such as computer processors, are an abundant source of valuable metals that can be repurposed into catalytic materials. Simultaneously, organic waste, like lemon peel, offers a carbon-rich matrix that can be utilized for catalyst support. By integrating these two forms of waste, we aim to create a novel, cost-effective catalyst for HER and OER [2]. Our goal in this study is to connect two kinds of waste and use it instead of expensive metals and coatings. We investigated the efficacy of carbon-based materials doped with metals extracted from computer processing units (CPUs). Dried lemon peels were immersed in aqua regia, enriched with dissolved metals from CPUs, facilitating the formation of a metal-doped carbon matrix upon subsequent carbonization. The resulting composite is then applied to electrode surfaces, forming a working electrode that undergoes extensive electrochemical testing to evaluate its catalytic properties and potential applications in clean energy technologies.

2. MATERIALS AND METHODS

2.1. Material preparation

Lemon peel was collected and dried in sunlight for 24 hours. After that, it was shredded into small pieces and used in the next step. For the recycling of the e-waste, specifically the CPUs, aqua regia was used to dissolve it [3].
Finally, the dried lemon peel was immersed into this solution for 24 hours, then washed with deionized water and dried at room temperature. The carbonization was conducted at 600°C in an inert nitrogen atmosphere. The heating rate for the carbonization was 5°C per minute, and the furnace was held at the final temperature for 1 hour. After carbonization, the sample was powdered and used for following phases.
The ink was prepared in this manner: 1 mg/mL of catalys, 20 µL of 5 wt% Nafion, deionized water and sonication for 30 minutes. The following step was ink drop-casting onto a pre-polished glassy carbon electrode surface, which was dried for 1 hour.

2.2. Electrochemical testing

The electrochemical properties of the catalyst we made were evaluated using cyclic voltammetry (CV) and linear sweep voltammetry (LSV) in 6 M KOH at room temperature using the three-electrode method. Electrochemical evaluation of the prepared electrodes was performed in a three electrode glass cell. The working electrode was a rotating disk electrode

(RDE) with the surface area of 0.196 cm². The counter electrode was a carbon rod, while the reference electrode was a saturated calomel electrode (SCE). The presented potential values were converted to the Reversible Hydrogen Electrode (RHE) scale.
Electrochemical measurements were carried out using a Gamry Interface 1000 Potentiostat/Galvanostat/ZRA. The electrolyte used in this study was analytical-grade 6 M KOH from Merck. Prior to the measurements, the electrolyte was purged with N_2 for 20 minutes, and the RDE was continually rotated at a rate of 1600 rpm.

3. RESULTS AND DISCUSSION

Prior to electrochemical characterization, the synthesized material was analyzed using X-ray diffraction (XRD) to investigate its crystal structure and phase composition. This versatile, non-destructive analytical technique provided insights into the material's structural properties.
The newly synthesized material, produced by combining recycled CPU waste with carbonized lemon peel, was then electrochemically evaluated for various potential applications, including hydrogen and oxygen evolution reactions as well as supercapacitor functionality.

3.1. Material characterization

The X-ray diffraction pattern of sample is shown in Figure A. The pattern is characterized by one broad diffraction peak and several crystalline peaks. The broad peak can be assigned to (002) plane of graphite-2H (PDF# 41-1487), while the crystalline peaks are assigned to Cu (PDF# 2-1225) and Cu_2O (PDF# 5-667) crystal phases. When we refer to Cu here, since the diffractogram reflects the structure, it is possible that, in addition to Cu atoms, there are other atoms present in the crystal lattice, like nickel and chromium. This means that the possibility of an alloy with nickel or chromium cannot be excluded; however, structurally, they are equivalent and cannot be distinguished.

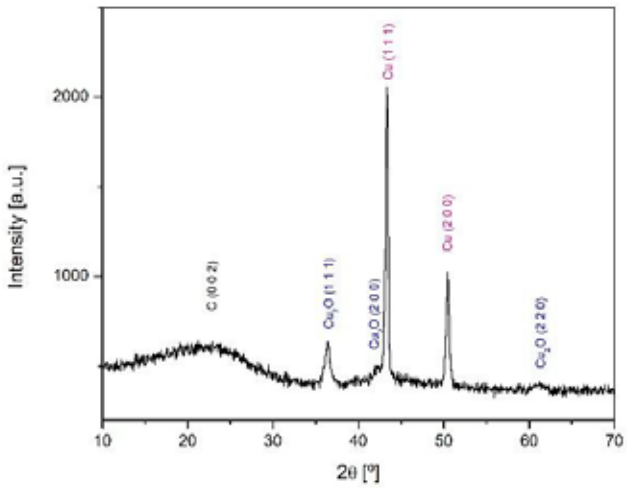

Fig. 1. XRD spectra of synthesized material with corresponding peak deconvolution

3.2. Electrochemical characterization

The initial phase of the electrochemical investigation focused on evaluating the material's activity for hydrogen and oxygen production. The prepared material was tested in a three-electrode cell for separate electrolytic reactions.
Before recording the polarization curves, the material underwent comprehensive evaluation by potential cycling over a broad range. This process provided valuable insights into the various structures and oxidation/reduction processes occurring on the electrode surface (Fig. 2).
The polarization curve exhibits a distinct structure, characterized by three oxidation peaks. The seddle-like peaks at approximately 0.5 V and 0.8 V vs. RHE correspond to the oxidation of $Cu(OH)_2^{2-}$ & $Cu(OH)_2$ and $Cu(OH)_2$ & CuO consequatlivy [4]. The third peak, in terms of both its intensity and position, correlate to the oxidation peak of nickel hydroxide ($Ni(OH)_2$) converting into nickel oxyhydroxide (NiOOH) [5].

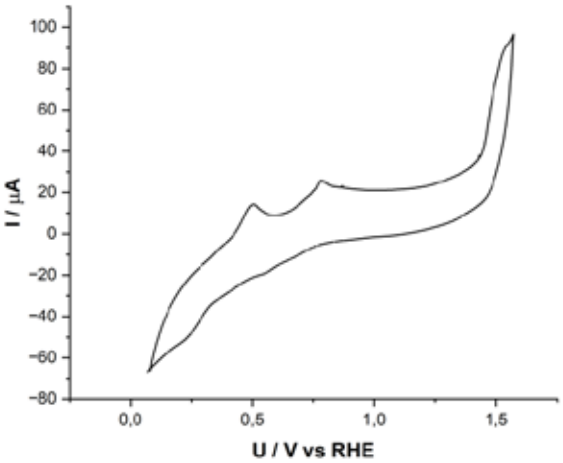

Fig. 2. Cyclic voltammogram of prepared material

The next step in the electrochemical investigation involved evaluating the material's catalytic activity for HER and OER. Polarization curves were recorded and are presented in Fig. 3.

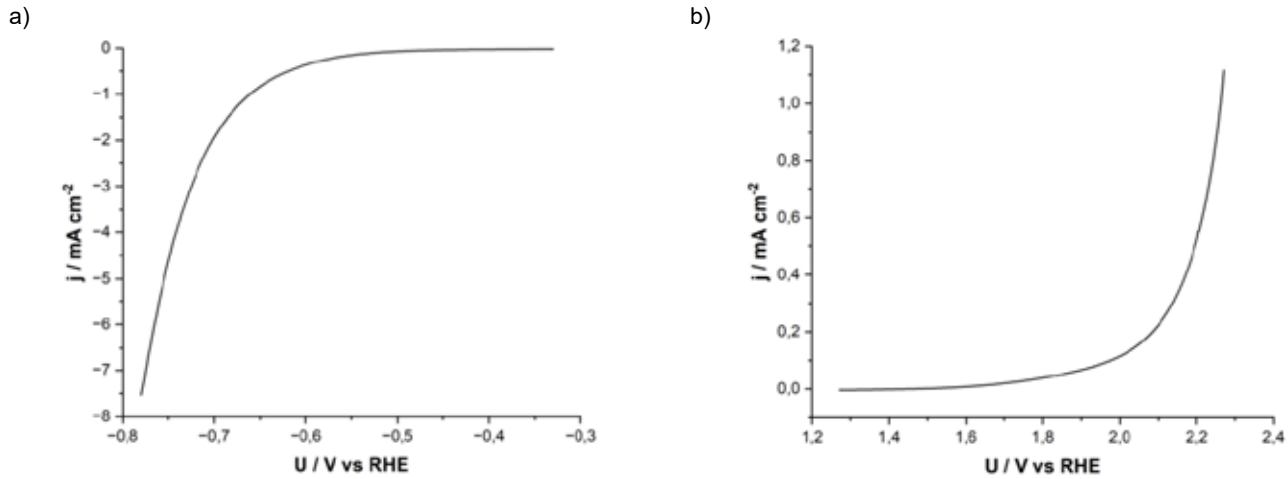

Fig. 3. Polaryzation curves for HER (a) and OER (b)

Additionally, Tafel analysis was conducted to gain insights into the reaction mechanisms and kinetics. Reaction mechanisms can be categorized into three types based on the Tafel slope: activation-controlled, diffusion-controlled, and mixed-controlled.

The synthesized material demonstrated higher activity for hydrogen evolution, exhibiting a lower overpotential and Tafel slope value (Table 1). For oxygen evolution, the overall activity was relatively low, characterized by a high overpotential and Tafel slope. This suggests that the kinetics of the oxygen evolution reaction (OER) are diffusion-controlled. In contrast, the hydrogen evolution reaction (HER), with a Tafel slope value of 137 mV dec $^{-1}$, follows mixed-controlled kinetics [6].

Table 1. Summary of IHTEC2025 formatting details

Reaction	Overpotential at 1 mA cm^{-2} [V]	Tafel slope values [mV dec^{-1}]
HER	-0.661	137
OER	2.264	405

The next phase of the electrochemical characterization focused on evaluating the synthesized material's capacitance and its potential application in energy storage devices such as supercapacitors. Supercapacitors, known for their high power density and excellent charge-discharge cycling stability, require materials with superior charge storage capabilities. To assess the material's charge storage behavior, cyclic voltammetry was performed within an appropriate potential

range (Fig. 4). The analysis revealed that the material demonstrated its highest specific capacitance of 99.767 F g^{-1} at a scan rate of 20 mV s^{-1}.

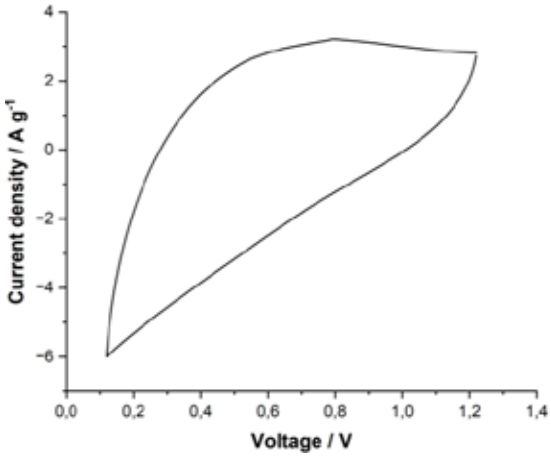

Fig. 4. Cyclic voltammogram of synthesized material for capacitance analysis

4. CONCLUSIONS

The main conclusions can be defined as follows:
Demonstration of the potential of utilizing recycled CPUs and carbonated lemon peel which present new electrocatalytic materials made of different waste.
The synthetized material exhibited promising catalytic activity, particulary for HER, with good Tafel slope values, and mixed controlled reaction mechanism. Also, electrochemical testing for OER showed lower materials performance with higher Tafel slope and overpotential, and diffusion-controlled reaction mechanism.
The XRD analysis confirmed the presence of crystalline phases which oxidation was also noticed in cyclic voltammogram. Beyond electrolytical investigation, the material demonstrated potential in energy storage applications. Cyclic voltammetry revealed a high specific capacitance of 99.767 F $g^{-1.}$
By developing eco-friendly synthesis methods and utilizing waste derived material, this research contributes to sustainable resource utilization and advances the transition toward renewable energy solution.

ACKNOWLEDGEMENT

The authors would like to thank Ministry of Science, Technological Development and Innovation of the Republic of Serbia for financial support (grant number: 451-03-66/2024-03/200017).

REFERENCES

[1] Abdullah A. A., Dincer I, 2017. Thermodynamic and electrochemical analyses of a solid oxide electrolyzer for hydrogen production, International Journal of Hydrogen Energy 33: 21404-21413
[2] Verma, J., Goel, S. 2022. Cost-effective electrocatalysts for Hydrogen Evolution Reactions (HER): Challenges and Prospects. International Journal of Hydrogen Energy: 47: 38964-38982.
[3] Mitrović, S., Brković, S., Živković, S., Zdolšek, N., Seović, M., Georgijević, J., Perović, I. 2023. From E-Waste to Hydrogen Evolution: Harnessing Recycled Precious Metals for Catalytic Efficiency in Hydrogen Evolution Reactions. Materials 16(20):6795.
[4] Giri, S., Sarkar, A. 2016. Electrochemical Study of Bulk and Monolayer Copper in Alkaline Solution. Journal of The Electrochemical Society 163: 252-259.
[5] D. S. Hall, D. J. Lockwood, C. Bock, B. R. MacDougall, 2015. Nickel hydroxides and related materials: a review of their structures, synthesis and properties, Proceedings of the Royal Society A 471: 2174.
[6] T. Shinagawa, A. T. Garcia-Esparza, K. Takanabe, 2015. Insight on Tafel slopes from a microkinetic analysis of aqueous electrocatalysis for energy conversion. Sci. Reports 2015 5:1–21.

LIFE CYCLE ASSESSMENT OF GREEN HYDROGEN PRODUCTION VIA ELECTROLYSIS

[1*]*Hakan Camur*, [2]*Asli Isler-Kaya*, [1]*Filiz Karaosmanoglu*
[1] Istanbul Technical University, Chemical Engineering Department, Maslak, Istanbul, 34469, Turkey
[2] Turkish-German University, Faculty of Science, Energy Science and Technology, Beykoz, Istanbul, 34820, Turkey

*Corresponding author e-mail: camur23@itu.edu.tr

ABSTRACT

The increasing global energy demand necessitates a transition to sustainable and low-carbon energy systems. Hydrogen, as a versatile energy carrier, holds a significant promise for communities to achieve carbon neutrality goals. Among various hydrogen production methods, green hydrogen production through water electrolysis from renewable electricity by minimizing carbon emissions stands out as an environmentally friendly and sustainable method. However, challenges such as efficiency, cost and production capacity prevent its widespread adoption.
This paper performs a life cycle assessment (LCA) of green hydrogen production by evaluating greenhouse gas emissions, energy consumption and resource utilization under different renewable and non-renewable energy scenarios. The results highlight the importance of renewable energy integration and electrolyser efficiency in minimising environmental impacts. Green hydrogen achieves up to 90% lower greenhouse gas emissions compared to conventional methods, highlighting its potential as a sustainable energy solution.

Keywords: Green hydrogen, Electrolysis, Life Cycle Assessment, Sustainability, Hydrogen Production

1. INTRODUCTION

Energy has been one of the key determinants of social welfare and development throughout history. The discovery and utilisation of fossil fuels during the Industrial Revolution enabled rapid economic growth and improved living standards. However, concerns such as increasing energy demand and climate change have necessitated a transition to sustainable energy systems. In this regard, hydrogen has emerged as a promising energy carrier for the future due to its versatility and potential to enable a clean economy.
Hydrogen, which is abundant in nature as compounds, is not a natural primary energy source because it does not exist in free form. Therefore, hydrogen is an energy carrier produced from other energy sources. Hydrogen has great potential as a clean and renewable energy carrier depending on the method of production. However, today hydrogen is mainly used in the refining and chemical sectors and is produced using fossil fuels such as coal and natural gas and is therefore responsible for significant annual greenhouse gas emissions [1]. Therefore, for green hydrogen to be widely adopted, it needs to overcome challenges such as high production costs, efficiency limitations and the need for infrastructure development.
This study aims to perform a life cycle assessment of green hydrogen production through water electrolysis. The paper describes the importance of renewable energy integration and optimisation strategies to minimise the environmental footprint of hydrogen production systems.

2. THEORETICAL STUDY AND METHODOLOGY

In this section, theoretical study results for hydrogen are presented in general terms under the following headings:

- Hydrogen Production
- Hydrogen Colouring
- Life Cycle Assessment (LCA) Methodology

2.1. Hydrogen Production

Hydrogen can be produced using various methods, broadly categorized into fossil fuel based and renewable source based.

- **Fossil Fuels Based Methods:** The most widely used fossil fuel-based methods are steam methane reforming (SMR), partial oxidation (POX) and coal gasification (CG). SMR produces grey hydrogen, causing significant CO_2 emissions, but can produce blue hydrogen when combined with carbon capture and storage (CCS). POX involves reacting hydrocarbons with limited oxygen to produce hydrogen and CO, often used in combination with other processes. CG converts coal into syngas, a mixture of hydrogen and CO, but needs CCS to address high carbon emissions. In addition, other methods such as autothermal reforming (ATR), dry reforming (DR) and chemical loop reforming (CLR) are being developed to increase efficiency and minimise environmental impact [2], [3], [4].

- **Renewable Sources Based Methods:** Renewable-based hydrogen production includes water splitting, biological, and thermochemical process methods. The most common renewable-based method is water electrolysis, the water splitting method. Powered by solar or wind energy, water electrolysis produces green hydrogen with virtually no greenhouse gas emissions. On the other hand, biological processes and thermochemical processes offer a sustainable way to utilize hydrogen by converting organic matter into hydrogen. These renewable methods are important for the future, with ongoing research focussed on improving efficiency and scalability [2], [3].

2.2. Hydrogen Colouring

The environmental impacts of hydrogen production vary depending on the methods used. These methods are usually expressed with colours. These colours represent the environmental footprints of production processes, not the visible properties of hydrogen. In general, technical articles can be separated into those that discuss various hydrogen production methods (colours) and specific technological elements. Of course, hydrogen itself is colourless. Still, there is no universal agreement on the colour coding for hydrogen. A summary of the colours defined below [5]:

- Black/Brown Hydrogen: It is produced through coal gasification. It refers to bituminous coal (black) and lignite (brown) types of coal.
- Grey Hydrogen: It is produced from natural gas through SMR.
- Blue Hydrogen: It is produced similarly to grey hydrogen, but CO_2 emissions are captured using CCS technology.
- Turquoise Hydrogen: It is produced from natural gas using methane pyrolysis, with solid carbon as a byproduct and no CO_2 emissions.
- Green Hydrogen: It is produced by the electrolysis of water using renewable energy, resulting in nearly zero emissions.
- Yellow Hydrogen: It is produced through the electrolysis of water like green hydrogen but uses grid electricity as the power source.
- Pink Hydrogen: It is obtained from the electrolysis of water using nuclear energy.
- White Hydrogen: It refers to hydrogen found naturally in its elemental form.

2.3. Life Cycle Assessment (LCA) Methodology

The LCA methodology was employed to evaluate the environmental impacts of green hydrogen production. The study followed the ISO 14040 standard, encompassing four phases [6]: goal and scope definition, life cycle inventory analysis (LCI), life cycle impact assessment (LCIA), and life cycle interpretation. The life cycle boundaries of this study adopted a cradle-to-grave approach, considering all stages from raw material extraction to hydrogen utilisation and disposal. Key performance indicators such as greenhouse gas emissions, energy consumption and resource utilisation were quantified using specialised LCA software. In addition, sensitivity analysis was performed to assess the impact of variables such as electrolyser efficiency and electricity sources on the results.
A review of existing LCA studies on hydrogen production was conducted to contextualise and evaluate the findings. Table 1 summarises the key parameters from the literature, including life cycle boundaries, LCA programmes and main impact categories.

Table 1. Literature Review on LCA of Hydrogen Production

Study	Life Cycle Boundary	Main LCA Program	Main LCIA method	Functional unit	Main Impact Category (midpoint - endpoint)	Ref no
Bhandari et al. (2014)	Cradle to gate	Not specified	CML 2001, Eco-indicator 95	1 kg of hydrogen	GWP, AP	7
Rinawati et al. (2022)	Cradle to gate/grave	SimaPro, GaBi	ReCiPe, CML	1 kWh/MWh of electricity	GWP, AP, EP, POCP, HTP, SS	8
Valente et al. (2016)	Cradle to gate/grave	GREET	CML, VDI, IPCC	Multifunctional system	GWP, AP, EP, ADP, POCP, ODP, HTP, CED	9
Spath and Mann (2004)	Cradle to grave	Not specified	Not specified	1 kg of hydrogen	GWP, SW, AE	10
Shaya and Glöser-Chahoud (2024)	Cradle to gate/grave	Not specified	CML 2001, ReCiPe, ILCD 2011	1 kg of hydrogen	GWP, AP, EP	11
Iyer et al. (2024)	Cradle to gate	GREET	Not specified	1 kg of hydrogen	GWP, CF, EU	12
Gerhardt-Mörsdorf et al. (2024)	Cradle to grave	GaBi	CML 2001	1 kg of hydrogen	GWP, AP, EP, ADP, HTP	13

Ajeeb et al. (2024)	Not specified	SimaPro	ILCD 2011	1 kg of hydrogen	GWP, AP, EP, ODP, PM, HTP, POCP	14
Khan et al. (2005)	Cradle to grave	Not specified	IPCC	1 kWh of electricity	GWP	15
Cetinkaya et al. (2012)	Not specified	Not specified	Not specified	1 kg of hydrogen	GWP, SW, AE	16
Patel et al. (2024)	Cradle to gate	GaBi	IPCC	1 kg of hydrogen	GWP, AP	17
Koroneos et al. (2004)	Not specified	GEMIS	Eco-indicator 95	1 MJ of energy	GWP, AP, EP, WS	18
Mehmeti et al. (2018)	Cradle to grave	SimaPro	ReCiPe, AWARE	1 kg of hydrogen	GWP, AP, EP, POCP, ODP, ETP, WCP	19
Maniscalco et al. (2024)	Cradle to gate	SimaPro	CML 2001, ReCiPe	1 kg of hydrogen	GWP, AP, ADP, HTP	20
Weidner et al. (2023)	Not specified	Activity Browser (brightway2)	PB-LCIA, ReCiPe,	500 Mt/yr hydrogen	GWP, HTP, ETP, POCP, PM	21

Global Warming Potential (GWP), Acidification Potential (AP), Eutrophication Potential (EP), Photochemical Ozone Creation Potential (POCP), Human Toxicity Potential (HTP), Single Score (SS), Abiotic Depletion Potential (ADP), Ozone Layer Depletion Potential (ODP), Cumulative Energy Demand (CED), Solid Waste (SW), Air Emissions (AE), Capacity Factor (CF), Energy Use (EU), Particulate Matter (PM), Winter Smog (WS), Ecotoxicity Potential (ETP), Water Consumption Potential (WCP)

3. RESULTS AND DISCUSSION

Three renewable energy integration scenarios were analysed to assess the environmental performance of hydrogen production through electrolysis:

1. Full renewable energy supply
2. Grid electricity dominated by fossil fuels.
3. Partial renewable and grid electricity mix.

3.1. Global Warming Potential (GWP) Performance

- **Renewable Energy Systems**: Electrolysis powered by wind and hydroelectric energy emerged as the most environmentally friendly options, achieving the lowest GWP values (e.g., 0.97–4.45 kg CO_2-e/kg H_2 for wind). Solar energy (PV and thermal) and biomass-based systems exhibited moderately higher GWP values compared to wind and hydroelectric systems.
- **Grid Electricity**: Electrolysis relying on grid electricity showed the highest GWP values due to the predominant use of fossil fuels in electricity generation. For instance, a PEM water electrolyser (PEMWE) using the German grid mix emitted 34 kg CO_2-e/kg H_2, which could be reduced by 89% to 3.45 kg CO_2-e/kg H_2 with a fully decarbonized energy system.
- **Partial Renewable and Grid Electricity**: Electrolysis operated with a combination of renewable energy and grid electricity resulted in intermediate GWP values reflecting the proportional contribution of renewable energy. The results indicate that increasing the share of renewable energy in the mix significantly reduces the environmental impact. A more detailed analysis of this scenario will be conducted in future studies.

3.2. Acidification Potential (AP) Performance

Nuclear based systems exhibited the best AP performance, followed by wind energy. However, there are significant environmental and social concerns related to nuclear waste disposal and safety, which should be included in a more comprehensive LCA. On the other hand, biomass and PV-based electrolysis showed the worst performances in this category.

3.3. Comparison of Electrolysis Technologies

- **Alkaline Electrolysis (AEL)**: It is an old technology with low cost and long life. However, it exhibited high environmental impacts due to the use of materials such as nickel and steel.
- **Proton Exchange Membrane (PEM)**: It produces hydrogen efficiently and with high purity, is suitable for renewable energy integration and has been the recommended electrolyser method in many studies. However, its cost is high due to expensive catalysts.
- **Solid Oxide Electrolysis Cell (SOEC)**: It has high efficiency and showed lower and more consistent GWP values in the long term. However, it has short lived components and high emissions during installation.
- **Anion Exchange Membrane (AEM)**: More efficient than AEL, but with lower performance compared to PEM. As it is a new technology, it needs extensive analyses and has limited capacity.

4. CONCLUSIONS

Green hydrogen production through electrolysis represents a sustainable solution to global energy needs, with renewable energy integration and advancements in electrolyser efficiency playing pivotal roles in reducing environmental impacts. Wind-based systems achieved the lowest GWP (0.97–4.45 kg CO_2-e/kg H_2) but require infrastructure scaling to overcome production limitations. Balancing environmental performance with cost, scalability and operational challenges is key to optimising hydrogen production pathways.
Policymakers and industry should invest in renewable energy and innovative technologies to accelerate the hydrogen transition, while future research should address economic viability and integration with existing energy systems to unlock its full potential for a low-carbon future.

REFERENCES

1. https://www.iea.org/energy-system/low-emission-fuels/hydrogen#tracking. Accessed on August 11, 2024.
2. Qazi UY. 2022. Future of hydrogen as an alternative fuel for next-generation industrial applications; challenges and expected opportunities. Energies 15(13):1-15.
3. Singh H, Li C, Cheng P, Wang X, and Liu Q. 2022. A critical review of technologies, costs, and projects for production of carbon-neutral liquid e-fuels from hydrogen and captured CO2. Royal Society of Chemistry 2022:1-10.
4. Salahshoor S and Afzal S. 2022. Subsurface technologies for hydrogen production from fossil fuel resources: A review and techno-economic analysis. International Journal of Hydrogen Energy 2022:1-20.
5. Ajanovic A, Sayer M, and Haas R. 2022. The economics and the environmental benignity of different colors of hydrogen. International Journal of Hydrogen Energy 47(57):24136-24154.
6. ISO 14040:2006 Environmental management — Life cycle assessment — Principles and framework
7. Bhandari R, Trudewind CA, and Zapp P. 2014. Life cycle assessment of hydrogen production via electrolysis – A review. Journal of Cleaner Production 85:151–163.
8. Rinawati DI, Keeley AR, Takeda S, and Managi S. 2022. Life-cycle assessment of hydrogen utilization in power generation: A systematic review of technological and methodological choices. Frontiers in Sustainability 3.
9. Valente A, Iribarren D, and Dufour J. 2016. Life cycle assessment of hydrogen energy systems: A review of methodological choices. The International Journal of Life Cycle Assessment 22(3):346–363.
10. Mann M and Spath P. 2004. Life cycle assessment of renewable hydrogen production via wind/electrolysis: Milestone completion report.
11. Shaya N and Glöser-Chahoud S. 2024. A review of life cycle assessment (LCA) studies for hydrogen production technologies through water electrolysis: Recent advances. Energies 17(16):3968.
12. Iyer RK, Prosser JH, Kelly JC, James BD, and Elgowainy A. 2024. Life-cycle analysis of hydrogen production from water electrolyzers. International Journal of Hydrogen Energy 81:1467–1478.
13. Gerhardt-Mörsdorf J, Peterssen F, Burfeind P, Benecke M, Bensmann B, Hanke-Rauschenbach R, and Minke C. 2024. Life cycle assessment of a 5 MW polymer exchange membrane water electrolysis plant. Advanced Energy and Sustainability Research 5(4).
14. Ajeeb W, Baptista P, and Neto RC. 2024. Life cycle analysis of hydrogen production by different alkaline electrolyser technologies sourced with renewable energy. Energy Conversion and Management 316:118840.
15. Khan FI, Hawboldt K, and Iqbal MT. 2005. Life cycle analysis of wind–fuel cell integrated system. Renewable Energy 30(2):157–177.
16. Cetinkaya E, Dincer I, and Naterer GF. 2012. Life cycle assessment of various hydrogen production methods. International Journal of Hydrogen Energy 37(3):2071–2080.
17. Patel GH, Havukainen J, Horttanainen M, Soukka R, and Tuomaala M. 2024. Climate change performance of hydrogen production based on life cycle assessment. Green Chemistry 26(2):992–1006.
18. Koroneos C, Dompros A, Roumbas G, and Moussiopoulos N. 2004. Life cycle assessment of hydrogen fuel production processes. International Journal of Hydrogen Energy 29(14):1443–1450.
19. Mehmeti A, Angelis-Dimakis A, Arampatzis G, McPhail S, and Ulgiati S. 2018. Life cycle assessment and water footprint of hydrogen production methods: From conventional to emerging technologies. Environments 5(2):24.
20. Maniscalco MP, Longo S, Cellura M, Miccichè G, and Ferraro M. 2024. Critical review of life cycle assessment of hydrogen production pathways. Environments 11(6):108.
21. Weidner T, Tulus V, and Guillén-Gosálbez G. 2023. Environmental sustainability assessment of large-scale hydrogen production using prospective life cycle analysis. International Journal of Hydrogen Energy 48(22):8310–8327.

DEVELOPMENT OF IRON-SULFIDE CATALYSTS FOR GREEN H_2 PRODUCTION FROM H_2S

[1]*Neslihan Demirhan*, [1]*Hale Akansu,* [1,2*]*Yaren Ataseven*, [1]*Mert Yekta Doğan*, [1]*Sena Yaşyerli,* [1]*Hüseyin Arbağ,* [1]*Hacı Mehmet Taşdemir,* [1]*Nail Yaşyerli*
[1]Gazi University, Faculty of Engineering, Chemical Engineering Department, Ankara, 06570, Türkiye
[2]Gazi University, Graduate School of Natural and Applied Sciences, Chemical Engineering Department, Ankara, 06570, Türkiye

*Corresponding author e-mail: 23830901022@gazi.edu.tr

ABSTRACT

In this study, unsupported (Fe-S) and activated carbon supported (Fe-S@AC) iron-sulfide catalysts were prepared and tested green H_2 production via H_2S decomposition. Activated carbon (AC) was prepared using a one-step method with sawdust as a starting material. The unsupported iron-sulfide catalyst was prepared using the solvothermal method and added into the support by the wet-impregnation. H_2S decomposition catalytic activity tests were performed in a conventionally heated packed-bed reactor system at 800°C using 1% H_2S-N_2 gas mixture. The catalysts were characterized using XRD, SEM-EDS and N_2-physisorption techniques. The results of the activity tests showed H_2S conversion values of 12% and 18% over the Fe-S and the Fe-S@AC catalysts, respectively. The activity test results, conducted over 60 minutes, indicated that Fe-S@AC exhibited higher activity in hydrogen production through H_2S decomposition. Synthesis, characterization and activity test studies are ongoing as part of this research.

Keywords: Hydrogen, H_2S decomposition, iron-sulfide, activated carbon.

1. INTRODUCTION

Globally, oil refineries and natural gas plants produce more than 40 million tons of hydrogen sulfide (H_2S) each year, and this amount is expected to increase in the future. Nowadays, H_2S is converted to elemental sulfur and water vapor by commercial Claus process, resulting in a large loss of hydrogen. The increasing demand for green hydrogen requires the evaluation of low-cost hydrogen sources other than hydrocarbon steam reforming. Hydrogen production from H_2S is an attractive issue because it can significantly reduce CO_2 emissions [1,2].

Hydrogen sulfide decomposes into hydrogen and sulfur vapor at high temperatures (≥600°C). At temperatures between 200-1000°C, sulfur vapor may includes different type of sulfur species from S_2 to S_8. Therefore, the reaction mixture may contain different species of sulfur (such as S_2-S_4) together with H_2. In the literature, equilibrium mixture estimation have been made using free energy minimization and the results have been confirmed experimentally. In general, since the decomposition reaction requires high temperatures to obtain significant conversion, the sulfur will be produced as diatomic. Therefore, the thermal decomposition reaction can be considered the following (R1; [3]):

$$2H_2S_{(g)} \leftrightarrow 2H_{2(g)} + S_{2(g)} \qquad (R1)$$

Several mechanisms have been proposed in the literature to understand the behaviour of metal-sulfide catalysts in H_2S decomposition. The interaction of hydrogen sulfide with metal-sulfide leads to the formation of hydrogen and “higher” sulfide (R2). This 'higher' sulfide then decomposes to form elemental sulfur and “lower” sulfide (M_xS_y) (R3) [4,5].

$$M_xS_y + zH_2S \rightarrow M_xS_{y+z} + zH_2 \qquad (R2)$$

$$M_xS_{y+z} \rightarrow M_xS_y + zS^0 \qquad (R3)$$

The H_2S decomposition reaction requires high energy due to its highly endothermic nature. To overcome this problem, various approaches have been adopted including use of catalysts to achieve higher conversions at relatively low temperatures, separation of products from reactor effluent gas stream [6]. Development of highly active catalyst is key to reducing the reaction temperature by lowering the apparent activation energy of H_2S decomposition. Transition metal-oxides and their sulfides (Mo, Cr, Fe, Co, Cu, Ni, V, and W) have been studied as catalysts for H_2S decomposition. Sulfides appear to be more active and more stable than their oxide counterparts [1,7]. For this purpose, unsupported iron-sulfide and activated carbon supported iron-sulfide catalysts were prepared and tested in a conventional heated reactor system for the thermal and catalytic decomposition reaction of H_2S to produce COx-free H_2.

2. EXPERIMENTAL

2.1. Synthesis of Unsupported Iron-Sulfide

In this study, unsupported iron-sulfide particles were prepared by solvothermal method. In this method, iron (III) chloride and thiourea were weighed in such a way that the Fe/S molar ratio is ¼, dissolved in deionized water and stirred for 15 minutes at ambient temperature under vigorous stirring. At the end of the stirring process, the solution was taken into a Teflon coated stainless steel autoclave and kept in an oven at 160°C for 10 hours and solvothermal treatment was carried out. Then, the autoclave was cooled to room temperature and the suspension was filtered and washed with deionized water for 4-times. The catalyst obtained after washing was dried in an oven at 60°C for 24-hours. The dried catalyst was calcined in a tube furnace under He gas flow at 800°C for 6-hours.

2.2. Synthesis of Activated Carbon Support Material

Activated carbon with mesoporous properties was prepared in a single step using sawdust as a precursor material and phosphoric acid (H_3PO_4) as an activating agent [8]. Initially, the raw material was sieved to obtain particles approximately 3 mm in size and treated with a 10% H_2SO_4 solution for 24-hour to remove impurities. Afterwards, it was washed with deionized water until the pH reached 6–7, filtered, and dried at 120°C until a constant weight was achieved. The dried material mixed with a 15% H_3PO_4 solution at a phosphoric acid to raw material weight ratio of 1.25 and stirred at room temperature for 24-hour. The suspension was filtered, and the residue was dried at 120°C to achieve a stable weight. Carbonization was carried out under a high-purity helium atmosphere, at 800°C for 45 minutes with a heating rate of 10°C/min. The resulting material was washed with 0.1 M HCl and hot distilled water until the pH stabilized between 6 and 7, followed by drying at 120°C to achieve a constant weight.

2.3. Synthesis of Supported Iron-Sulfide Catalysts

The support material and deionized water were mixed in a beaker with a magnetic stirrer until the temperature reached to 40°C. Iron-sulfide particles were weighted and dissolved in some deionized water. The solution containing iron-sulfide particles was added dropwise to the suspension of the support material mixed at 40°C. The suspension is allowed to dry under these conditions until the water is evaporated. The dried supported catalysts were calcined in a tube furnace under He gas flow at 800°C for 6 hours.

2.4. Evaluation of Catalytic Performances of Catalysts

In this study, supported and unsupported iron-sulfide catalysts were tested in a conventionally heated packed-bed flow reactor using a gas mixture containing 1% H_2S (with N_2 balance) with a total flow rate of 100 mL/min at 800°C and atmospheric pressure for thermal and catalytic decomposition of H_2S reaction. The product gas mixture obtained as a result of catalytic activity test studies was analysed with SRI-8610C gas chromatography equipment with Chromosil-310 column, thermal conductivity detector and N_2 gas as carrier.

2.5. Characterization Studies

QuantaChrome Autosorb 1C/MS instrument was used to perform N_2-physisorption analysis to measure the BET surface area of the spent catalysts. The X-ray diffraction (XRD) analysis was carried out using Rigaku MiniFlex X-ray diffractometer with Cu Kα radiation source to identify the crystal structures of the fresh and spent catalysts. For SEM-EDS analysis, by using a QUANTA 400F Field Emission microscope, morphological structure and elemental composition of the catalysts were determined.

3. RESULTS AND DISCUSSION

H_2S gas is a by-product released in large quantities in coal gasification, natural gas refining plants and oil refineries. Since it is a corrosive and toxic gas, it must be safely removed from the processes. The unwanted H_2S gas can be converted into green H_2, a valuable product, by thermal and catalytic decomposition reaction. In this study, the catalytic activities of new Fe-sulfide catalysts were investigated for the production of green H_2 from H_2S. Within the scope of the study, activated carbon prepared from sawdust was used as catalyst support.

In order to identify the structural/physical properties of fresh and spent catalysts, XRD, SEM-EDS and N_2-physisorption studies were performed. XRD patterns of fresh and spent unsupported Fe-S and activated carbon supported Fe-S@AC catalysts were presented in Figure 1. In the XRD pattern of the unsupported fresh Fe-S catalyst prepared by solvothermal method, only the FeS (troilite, Card No.: 01-089-1950) characteristic diffraction peaks were observed. However, fresh Fe-S@AC catalyst has more complex structure. In the XRD pattern of fresh Fe-S@AC showed that different crystalline structures such as Fe-P ($Fe_2(P_2O_7)$ (iron diphosphate, Card No.: 04-009-1838), Fe_2P (barringerite, Card No.: 01-078-6747), $Fe_3(PO_4)_2$ (graftonite, Card No.: 00-049-1087)) and Fe-S (FeS (troilite, Card No.: 01-089-1950)). The presence of P-containing species in the catalyst structure is probably due to the use of phosphoric acid as an activation agent during the preparation of activated carbon.

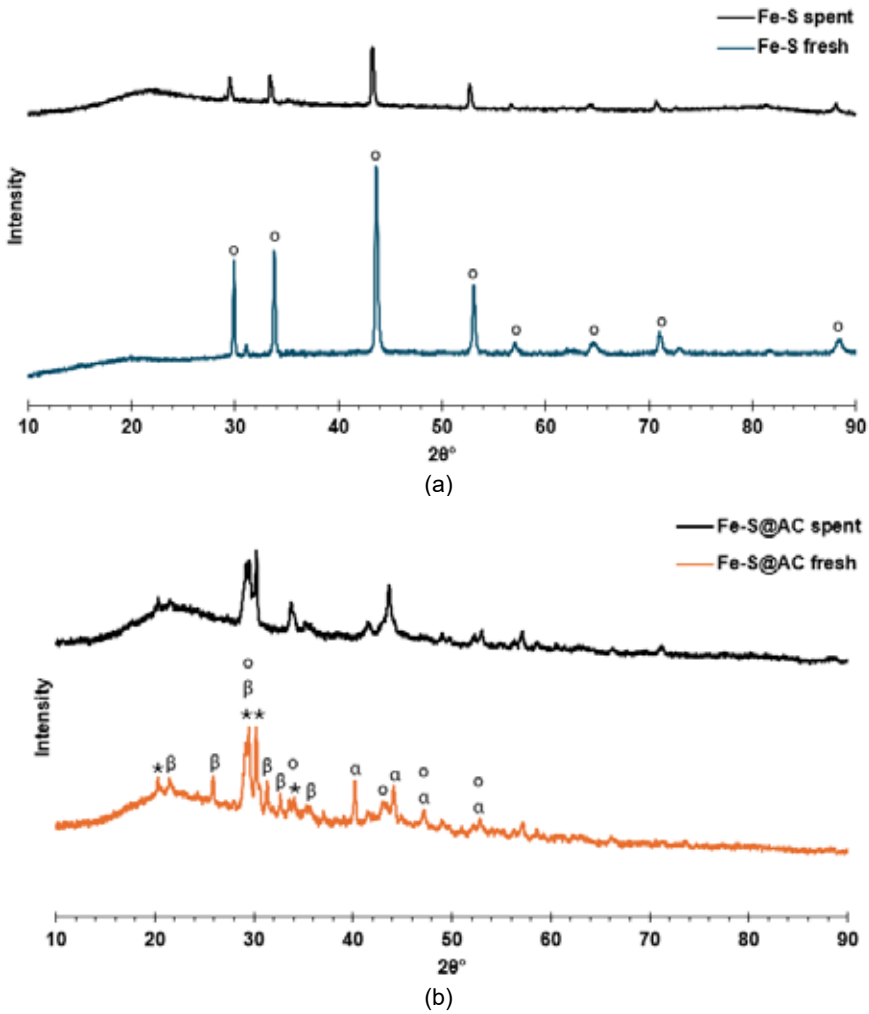

Fig. 1. XRD patterns of fresh and spent (a) Fe-S and (b) Fe-S@AC catalysts (o: FeS, *: $Fe_2(P_2O_7)$, α: Fe_2P, β: $Fe_3(PO_4)_2$)

The activity test results of the catalysts obtained in conventional heated reactor system are given in Fig. 2. Fe-S catalyst prepared by solvothermal method as unsupported bulk phase showed the lowest activity. The average H_2S conversion obtained in the 60 min test was 12% and the catalyst showed a relatively stable behaviour. Approximately 18% H_2S conversion was obtained with activated carbon supported Fe catalyst. The H_2S conversion estimated by "Gaseq Chemical Equilibrium" software under catalytic activity test conditions (1% H_2S with N_2 balance and 800°C) was 28%. Among the catalysts prepared from the study, 65% of the equilibrium conversion value was approached using the activated carbon supported Fe catalyst (Fe-S@AC).

In order to see structural change of both catalyts, XRD patterns of spent catalyts were also presented in Fig. 1. Fe-S catalyst retained its FeS structure after activity test. However, there was a structural change in the case of Fe-S@AC catalyst. The XRD peaks belonging to Fe_2P and $Fe_3(PO_4)_2$ structures disappeared while FeS and $Fe_2(P_2O_7)$ phases were still present in the Fe-S@AC catalyst. The surface area of spent Fe-S@AC (892 m^2/g) was considerably higher than the surface area of spent Fe-S catalyst (6 m^2/g) as expected. It is thought that there might be two possible reasons for the high activity of Fe-S@AC catalyst in this reaction: Fe-P structures showing activity in addition to FeS and/or the high surface area due to presence of activated carbon support material. The results obtained in this study indicate that the activated carbon supported Fe-S catalyst is worth further investigation for the production of green H_2 by H_2S decomposition.

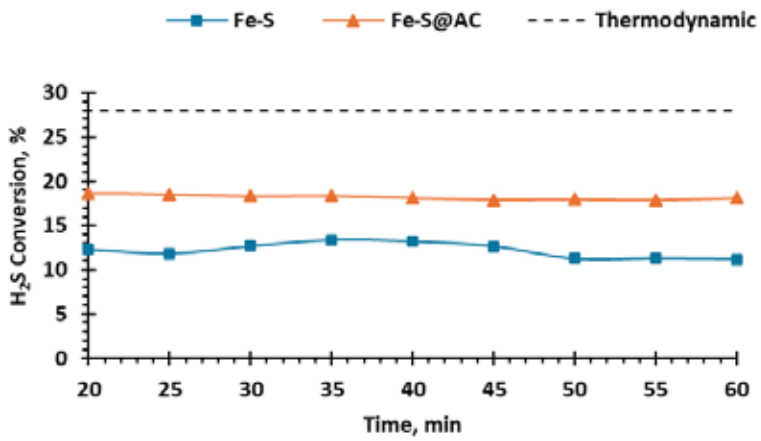

Fig. 2. H_2S conversions over iron-sulfide catalysts (800°C, 1%H_2S with N_2 balance)

4. CONCLUSIONS

In this study, unsupported Fe-S and activated carbon supported Fe-S@AC catalysts were synthesized and tested in a conventionally heated reactor system to produce green-H_2 via H_2S decomposition. The activity test results showed that the activated carbon supported catalyst showed higher activity than the unsupported catalyst and is a promising catalyst for this reaction. A conversion close to 65% of the equilibrium conversion of H_2S was achieved with the Fe-S@AC catalyst. This study investigates the utilization/conversion of wastes such as H_2S and sawdust into valuable products. As part of this research, catalyst preparation, characterization, and activity test studies are still being conducted.

ACKNOWLEDGEMENT

The valuable contributions of Prof. Dr. Gülşen DOĞU of Gazi University are gratefully acknowledged. This study was supported by the Scientific and Technological Research Council of Türkiye (TUBITAK) under Grant Number 122M400 and 2247-C Intern Researcher Scholarship (STAR) programme. The authors would like to thank TUBITAK for their support.

REFERENCES

1. Xu J, Tang S, Zhong S, Song L, Wu P, Jiang W, Wu K, Hu Q, Liu C, Yue H, Liang B and Yang Y. 2023. Solution combustion synthesis of CoSx, MoSx, CoSx-MoSx and their catalytic activity in H_2 production from H_2S decomposition. International Journal of Hydrogen Energy 48(24):8807-8818.
2. Kraia T, Kaklidis N, Konsolakis M and Marnellos GE. 2019. Hydrogen production by H_2S decomposition over ceria supported transition metal (Co, Ni, Fe and Cu) catalysts. International Journal of Hydrogen Energy 44(20): 9753-9762.
3. Zaman J and Chakma A. 1995. Production of hydrogen and sulfur from hydrogen sulfide. Fuel processing technology 41(2):159-198.
4. Al Blooshi A, Al-Ali K, AlHajaj A, Palmisano G. 2024. Chemical kinetics of two-step thermochemical decomposition of hydrogen sulfide over nickel sulfide. International Journal of Hydrogen Energy 52: 433-446.
5. Reshetenko TV, Khairulun SR, Ismagilov ZR and Kuznetsov VV. 2002. Study of the reaction of high-temperature H_2S decomposition on metal oxides (γ-Al_2O_3, α-Fe_2O_3, V_2O_5). International journal of Hydrogen Energy 27:387-394.
6. Guldal NO, Figen HE and Baykara SZ. 2015. New catalysts for hydrogen production from H_2S: preliminary results. International Journal of Hydrogen Energy 40(24): 7452-7458.
7. Sukhanova EV, Baidyshev VS, Manakhov AM, Al-Qasim AS and Popov ZI. 2023. Hydrogen production from H_2S on metal-doped FeS Mackinawite monolayer via DFT calculations. Applied Surface Science 609: 155322.
8. Dogan MY, Tasdemir HM, Arbag H, Yasyerli N, Yasyerli, S. 2024. H_2 production via H_2S decomposition over activated carbon supported Fe-and W-catalysts. International Journal of Hydrogen Energy 75: 483-495.

DEVELOPMENT OF Fe-C MICROWAVE CATALYSTS FOR CONVERSION OF H_2S INTO CO_X-FREE H_2

[1**] Yaren Ataseven, [1*] Mert Yekta Doğan, [1*] Sena Yaşyerli, [1*] Hüseyin Arbağ, [1*] H. Mehmet Taşdemir, [1*] Nail Yaşyerli
[1**]Graduate School of Natural and Applied Sciences, Gazi University Central Campus Faculty of Technology, Chemical Engineering Department, 06500, Ankara, Türkiye.
[1*] Gazi University, Engineering Faculty, Chemical Engineering Department, Ankara, 06570, Türkiye

[1**]e-mail: 23830901022@gazi.edu.tr

ABSTRACT

In this study, activated carbon (DAC) supported iron (Fe@DAC & Fe-C@DAC) and unsupported iron carbide (Fe-C) catalysts were prepared to determine their activities in the decomposition reaction of H_2S. Support material activated carbon was synthesized from sawdust using a two-step synthesis method. While the Fe@DAC catalyst was prepared using the wet impregnation method, the Fe-C@DAC catalyst was obtained by applying the carburization process to Fe@DAC catalyst. BET, XRD, and TGA/DTA techniques were used to determine the physical and structural properties of the catalysts. While the XRD analysis of DAC showed amorphous graphitic carbon in the structure, it was determined that the supported catalysts had metallic Fe, Fe_3C, and graphitic carbon structures. Catalytic activity tests were performed in a continuous-flow packed-bed reactor system with %1H_2S-N_2 gas mixture, using a microwave-heated reactor at an average temperature of 600°C and as well as in conventional heated reactor at 800°C. In the microwave heated reactor system, it was observed that the thermodynamic equilibrium conversion was exceeded. Fe-C@DAC catalyst exhibited the best activity with 32% H_2S conversion. The catalysts have shown promising results in H_2S decomposition reaction in both microwave and conventionally heated reactor systems. This study is ongoing, presented the primary results obtained in the microwave heated reactor system.

Keywords: Microwave Heated, Activated Carbon, Iron, H_2 Production, H_2S Decomposition

1. INTRODUCTION

Hydrogen, as a clean energy carrier, has the potential to meet future energy demands while reducing COx emissions. It plays a critical role in technologies like hydrogen-powered vehicles and fuel cells, paving the way for a sustainable, low-carbon energy future. Hydrogen sulfide (H_2S), a toxic by-product of industries like oil refining, is a promising alternative for hydrogen production. While the Claus process efficiently removes H_2S, it fails to recover hydrogen. Conventional methods like reforming rely on fossil fuels and emit CO_2, highlighting the need for cleaner alternatives. The direct decomposition of H_2S into hydrogen and sulfur (R1) is a more efficient and sustainable solution.

$$H_2S(g) \leftrightarrow H_2(g) + 1/n\ S_n(g) \qquad \Delta H^o_{298} = 21\ kJ/mol;\ \Delta G^o_{298} = 33\ kJ/mol \qquad (R1)$$

However, achieving highly effective direct decomposition of H_2S into CO_x-free hydrogen and sulfur remains a significant challenge due to the equilibrium limitations [1, 2, 3]. For this reaction to be an effective hydrogen production method, it is essential to develop active and stable catalysts. Biomass-derived activated carbons are promising materials for improving H_2S decomposition due to their low cost, high surface area, and reversible kinetic properties [4]. Their catalytic reactions and adsorption efficiency can be enhanced through surface functionalization or metal impregnation, making them ideal for hydrogen production [5].

In this study, sawdust-based activated carbon (DAC) and activated carbon-supported catalysts (Fe, Fe-C) were prepared. The use of microwave heated reactors is being investigated to increase the production of COx-free H_2 from H_2S and to do so with less energy requirement. In order to compare, catalytic activity tests were conducted using both a conventionally heated reactor system and a microwave-heated reactor system.

2. MATERIALS AND METHOD

Preparation of Activated Carbon (DAC): Activated carbon was prepared using a two-step method with sawdust as the starting material. The starting material is sieved to obtain particles approximately 3 mm in size. The sieved material is mixed with 10% H_2SO_4 for 24 hours and then washed with deionized water until the pH reaches 6-7. After filtration, the material is dried at 120°C until a constant weight is achieved. The carbonization process is carried out at 500°C for 120 minutes under a helium flow of 100 mL/min, producing semi-coke. In the activation step, NaOH is mixed with semi-coke at 1:1 NaOH/semi-coke mass ratios using 30 mL of water and left to rest for 24 hours. The NaOH/semi-coke mixture is

then filtered, and the obtained material is dried at 120°C until a constant weight is reached. A second carbonization is performed at a heating rate of 10°C/min, reaching 800°C, and maintained for 45 minutes. The material is then stirred with 0.1 M HCl for 20 minutes and washed with warm distilled water until the pH reaches 6-7. Finally, the resulting activated carbon is dried at 120°C until a constant weight is obtained.

Preparation of Activated Carbon Supported Iron (Fe@DAC) Catalyst: Fe@DAC catalyst containing 10% iron by mass was prepared using the wet impregnation method. Iron (III) nitrate nanohydrate ($Fe(NO_3)_3 \cdot 9H_2O$) is used as the iron source. A suspension is prepared using activated carbon and deionized water, and its temperature is kept at 40°C. A certain amount of metal salt is weighed and dissolved in a small amount of deionized water. This solution is added drop by drop into the suspension. The final solution is then left to dry under these conditions. The dried supported catalyst is calcined in a tube furnace under He gas flow at 800°C for 5 hours.

Preparation of Activated Carbon Supported Iron Carbide (Fe-C@DAC) Catalyst: Carburization process was used to obtain Fe-C@DAC catalyst. In this process, the activated carbon-supported iron catalyst (Fe@DAC) obtained using the wet impregnation method is exposed to a He gas flow to remove impurities at 500°C for 30 minutes in a tube furnace. Then, the catalyst undergoes carburization in a gas mixture, including H_2 and CH_4 gases (CH_4:H_2 = 1:4) with a total volumetric flow rate of 50 mL/min at 900°C for 2 hours.

Preparation of Iron Carbide (Fe-C) Catalyst: Fe-C catalyst was prepared using Fe-O catalyst synthesized using the complexation method. In the complexation method, Iron (III) nitrate nanohydrate ($Fe(NO_3)_3 \cdot 9H_2O$) is used as the iron source and ethanol (99.9%) as the solvent. Metal salt and citric acid solutions are mixed in an equimolar ratio at 60°C, forming organo-metallic complexes. The solution is allowed to become viscous, poured into thin layers, and dried at 80°C to form solid foams. These foams are crushed, ground, and calcined at 800°C for 6 hours in a muffle furnace to obtain the metal oxide catalyst. The Fe-O catalysts are carburized under a gas mixture comprising 80% CH_4 and 20% H_2 with a controlled gas flow rate of 50 mL/min at 900°C for 6 hours.

Catalyst Characterization: N_2 adsorption–desorption (Quantachrome Autosorb1), XRD (Rigaku D/MAX 2200), SEM-EDS (QUANTA 400F Field Emission SEM), and TGA-DTA (Netzsch/STA 449 F3 Jupiter) analysis were performed for the characterization of the samples.

Catalytic Activity Test Studies: Catalytic activity test was performed in a conventional continuous flow-packed bed reactor system at 800°C and in a microwave-heated reactor system at average temperature of 600°C. Details of the experimental work was reported in [4].

3. RESULT AND DISCUSSION

The study aims to prepare highly active and stable iron-based catalysts to produce CO_x-free H_2 from thermal catalytic H_2S decomposition. The H_2S decomposition reaction is highly endothermic, requiring significant energy to achieve high conversions. Compared to conventional heated reactors, microwave heated reactors can accelerate reaction kinetics by enabling inside-out heating of particles, enhancing catalytic activity through localized hot spots and selective heating effects. Additionally, the potential of microwave heating to reduce energy consumption and shorten reaction times has attracted significant attention from researchers. Due to carbon's strong microwave energy absorption, catalysts containing activated carbon and metal carbides were prepared, and their activities in this reaction were investigated. N_2-adsorption-desorption analysis was performed to determine the surface areas and pore distribution of the catalysts. The BET surface area values to be found as 409 m^2/g, 606 m^2/g and 347 m^2/g for DAC, Fe@DAC and Fe-C@DAC, respectively. Using X-ray diffraction (XRD) analysis, the crystal structures of the materials were examined.

Fig. 1(a) displays the XRD patterns of activated carbons made from waste sawdust (DAC). The diffraction patterns of amorphous graphitic carbon were represented by two broad peaks that were centered at $2\theta \approx 23^o$ and 44° [6].Structures belonging to metallic Fe ($2\theta=43.58^o$, $2\theta=50.8^o$, $2\theta=64.94^o$, $2\theta=74.72^o$), Fe_3C($2\theta=37.67^o$, $2\theta=43.58^o$, $2\theta=44,6^o$, $2\theta=45^o$, $2\theta=82.26^o$), and graphitic carbon($2\theta=26.08^o$) were observed in the XRD patterns of Fe@DAC and Fe-C@DAC catalysts [7, 8]. Interestingly, a slight increase was observed in the characteristic XRD peaks belonging to metallic iron as well as the Fe-C structures attempted to be formed by the carburization process.

To observe thermal stability, structural changes, and carbon type of DAC under heat flow, TGA-DTA analysis was conducted in a dry air atmosphere within a temperature range of 25–950 °C (not shown here). 94 % weight loss was determined as a result of TGA. DTA analysis gives information about carbon species. It was reported that amorphous carbon up to 600 °C can be removed under dry air flow. The DAC sample exhibited the highest intensity at approximately 600 °C, suggesting the formation of amorphous carbon during the preparation [4]. The time-dependent variations in H_2S conversion values obtained with the synthesized catalysts at a reaction temperature of 800°C in the conventional system are presented in Fig. 2a, while the H_2S conversion at 600°C in the microwave reactor system is shown in Fig. 2(b). 26%, 17%, 25%, and 23% H_2S conversion values were obtained over the DAC, Fe-C, Fe@DAC, and Fe-C@DAC catalysts, respectively in the conventional heating system. In the microwave heated reactor system, the Fe-C@DAC catalyst exhibited the best activity with 32% H_2S conversion. The literature reported thermodynamic equilibrium values as %8 at

600°C and %28 at 800 °C [1, 9, 10]. In the conventional heated system, H_2S conversions very close to the equilibrium conversion were obtained with other catalysts except the Fe-C catalyst. The situation is quite different in the microwave heated reactor system. The highest conversion was obtained with the Fe-C@DAC catalyst and the thermodynamic conversion was exceeded, as expected. In the microwave heated reactor system, the catalytic activity order is Fe-C@DAC>Fe-C>Fe@DAC>DAC. Possible explanations for achieving high H_2S conversion are; the formation of hot spots during microwave irradiations and the polar property of H_2S (selective catalytic effect) in the microwave-heated reactor system [3].

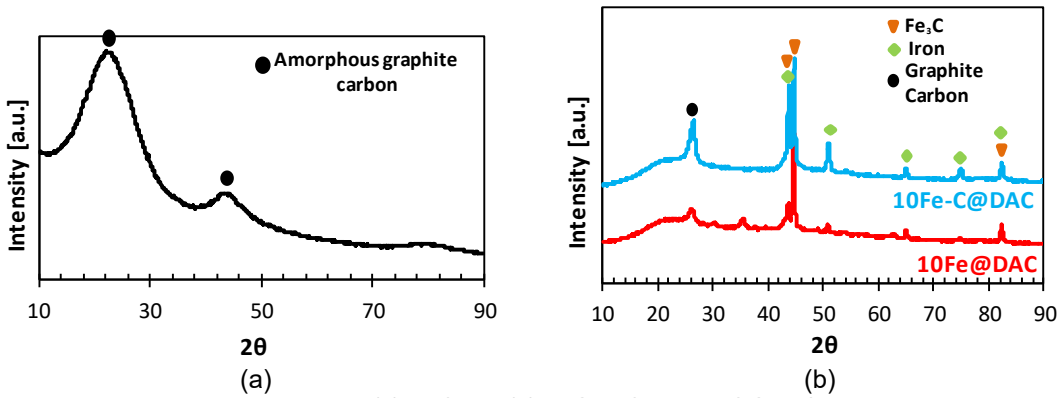

Fig. 1. XRD patterns (a) DAC and (b) Fe@DAC and Fe-C@DAC catalysts

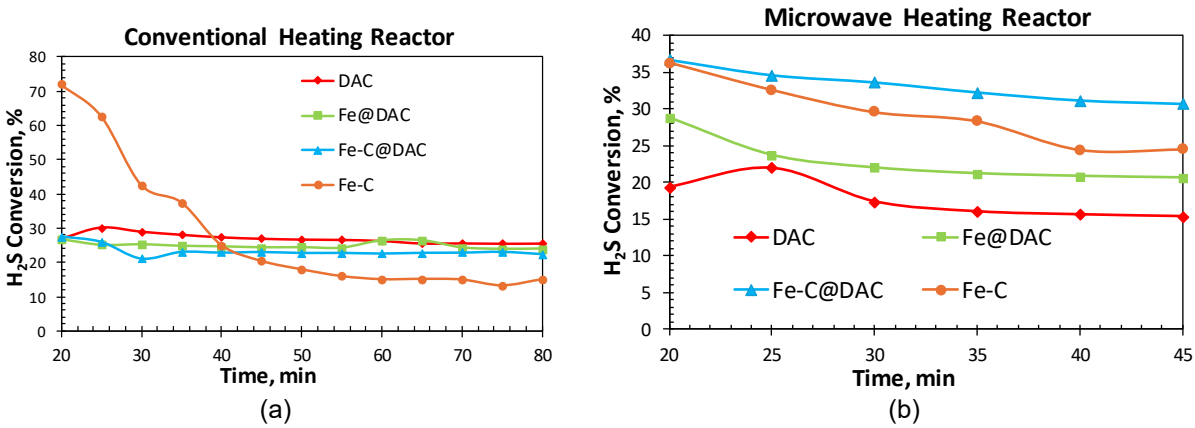

Fig. 2. (a) Catalytic Activities in a) Conventional Heating Reactor (800°C) b) Microwave Heating Reactor (~600°C) (%1H_2S-N_2, Catalyst: 0.1 g; Total gas flow rate: 100 mL/min)

4. CONCLUSION

The catalytic thermal decomposition of H_2S plays a crucial role in the producing CO_x-free hydrogen and might be a key process for sustainable energy applications. In this study, activated carbon (DAC), activated carbon-supported iron (Fe@DAC and Fe-C@DAC) catalysts, and unsupported Fe-C catalysts were successfully synthesized and tested in microwave and conventional heated reactor systems. While characteristic peaks belonging to amorphous graphitic carbon were observed in the XRD patterns of the DAC material, peaks belonging to metallic iron, Fe_3C, and graphitic carbon were observed in the XRD patterns of the Fe@DAC and Fe-C@DAC catalysts. As a result of the activity test carried out at approximately 600°C in the microwave reactor system with the Fe-C@DAC catalyst, the highest H_2S conversion value (32%) was obtained among other catalysts. This conversion value exceeds the thermodynamic equilibrium conversion (7%) at 600 °C. The results show that the Fe-C@DAC catalyst is quite promising for the microwave heated reactor system.

ACKNOWLEDGEMENT

The valuable contributions of Prof. Dr. Gülsen DOGU of Gazi University are gratefully acknowledged. This study was supported by the Scientific and Technological Research Council of Türkiye (TUBITAK) under Grant Number 122M400. The authors would like to thank TUBITAK for their support.

REFERENCES

1. Barin İ., 1989. Thermochemical Data of Pure Substances, VCH Verlagsgesellschaft, Weinheim, Germany.
2. Guldal, N.O., Figen, H.E., Baykara, S.Z. 2018. Perovskite catalysts for hydrogen production from hydrogen sulfide, International Journal of Hydrogen Energy, 43, 1038-1046.
3. Chen, J., Xu, W., Zhu, J., Wang, X., Wang X., Zhou J. 2019. Highly Effective Microwave Catalytic Direct Decomposition of H_2S Over Carbon Encapsulated Mo_2C-CoC@SiC Composite, International Journal of Hydrogen Energy, 44, 25680-25634.
4. Dogan, M.Y., Tasdemir, H.M., Arbag, H.M., Yasyerli, N., Yasyerli, S. 2024. H_2 Production via H_2S Decomposition over Activated Carbon Supported Fe- and W- Catalysts, International Journal of Hydrogen Energy, 75, 483-495.
5. Pavlenko, V., Khosravi S., Zoltowska S., Haruna A.B., Zahid M., Mansurov Z., Supiyeva Z., Galal A., Ozoemena K.I., Abbas Q., Jesionowski T. 2022. A comprehensive review of template-assisted porous carbons: Modern preparation methods and advanced applications, Materials Science & Engineering R, 149, 100682.
6. Zhang, Y., Liu, L., Zhang, P., Wang, J., Xu, M., Deng, Q. 2019. Ultra-high surface area and nitrogen-rich porous carbons prepared by a low-temperature activation method with superior gas selective adsorption and outstanding supercapacitance performance, Chemical Engineering Journal, 355, 309-19.
7. Tan, Y., Zhu, K., Li, D., Bai, F., Wei, Y., Zhang, P. 2014. N-doped graphene/Fe–Fe_3C nano-composite synthesized by a Fe-based metal organic framework and its anode performance in lithium-ion batteries, Chemical Engineering Journal, 285, 93-100.
8. Ning, L., Xiaohong, W., Honghao, Y., Chengjiao, Z., Haito, W. 2010. Synthesis and characterization of carbon-encapsulated iron/iron carbide nanoparticles by a detonation method, Carbon, 48, 3858-3863.
9. Zaman, J., Chakma, A. 1995. Production of hydrogen and sulfur from hydrogen sulfide, Fuel Processing Technology, 41, 159-198.
10. Xu, W., Hu, X., Xiang, M., Luo, M., Peng, R., Lan, L., Zhou, J. 2017. Highly effective direct decomposition of H_2S into H_2 and S by microwave catalysis over CoS-MoS_2/γ-Al_2O_3 microwave catalysts, Chemical Engineering Journal, 326, 1020-1029.

A-SITE DEFICIENT $La_{0.4}Ca_{0.4}Ti_{0.995}Pt_{0.005}O_3$ WITH LOW Pt SUBSTITUTION AS AN OXYGEN REDUCTION ELECTROCATALYST FOR FUEL CELL APPLICATIONS

*Selda Ozkan, SeoJin Kim, John T.S. Irvine
University of St Andrews, School of Chemistry, St Andrews, KY16 9ST, United Kingdom

*Corresponding author e-mail: so53@st-andrews.ac.uk

ABSTRACT

An electrocatalyst with good stability and superior activity for oxygen reduction reaction (ORR) is the essential criterion for fuel cell application. Intensive research has been dedicated to minimizing the Pt loading while boosting the dispersion and utilization of nanoparticles and overcome the sluggish reaction kinetic of ORR. In the present report, we prepared A-site deficient $La_{0.4}Ca_{0.4}Ti_{0.995}Pt_{0.005}O_3$ based perovskite oxides with minimal Pt substitution synthesized using solid-state and sol-gel methods and assessed ORR activity of electrocatalyst in alkaline electrolyte. The experimental findings show that Pt exsolved $La_{0.4}Ca_{0.4}Ti_{0.995}Pt_{0.005}O_{3-x}$ perovskite oxides delivered superior mass activity of 3.6 mA/μg_{Pt} and good stability in alkaline electrolyte.

Keywords: Perovskite oxide, Pt nanoparticles, electrocatalyst, oxygen reduction reaction

1. INTRODUCTION

The main challenge with the oxygen reduction reaction (ORR) in fuel cells is slow reaction kinetics, low product yield towards water formation and poor catalyst stability due to poor catalyst-support interaction. The interaction between Pt and carbon is weak compared to the interaction between Pt and oxide supports [1], which deteriorates the longevity of the catalyst by inducing dissolution, detachment, and agglomeration of Pt nanoparticles during fuel cell operation. Besides, the oxidation of the carbon support during electrocatalytic tests introduces oxygen-containing groups on the support surface, which further weakens the support-particle interaction and increases the resistance [2].
In the current research work, we used perovskite oxide as catalyst support and employ exsolution method [3] for the decoration of catalytically active nanoparticles (in this work Pt nanoparticles). The exsolution process—first incorporating catalytically active component into B-site of the ABO_3 perovskite lattice in oxidizing conditions and then releasing it under reducing atmosphere—provides highly dispersed, chemically stable, and catalytically active nanoparticles anchored onto the oxide support [4,5]. Once, B-site ions are reduced to metallic state, the nature of the bond is physical-mechanical, and they are embedded into the oxide up to 30%. These provide a larger area to interact with the support, facilitate three-phase junction/contact, enhance the adhesion, inhibits the agglomeration and growth of nanoparticles during fuel cell operation, all of which contribute to the catalytic activity and stability [6,7]. Besides the reduction process improves the electronic properties and electrocatalytic activity of perovskite oxide by forming oxygen vacancies, Ti^{3+} ions, and crystal defects in $LaTiO_3$ [8,9].
In the current research work, we compared electrocatalytic activity of Pt-substituted $La_{0.4}Ca_{0.4}Ti_{0.995}Pt_{0.005}O_3$ (LCPTO) and $La_{0.4}Ca_{0.3925}Ba_{0.0075}Ti_{0.995}Pt_{0.005}O_3$ (LCBPTO) perovskite oxides prepared using two different methods, sol-gel (pechini) and solid-state reaction methods. We evaluated electrocatalytic oxygen reduction reaction (ORR) activity of perovskite oxides in alkaline (0.1 M KOH) electrolyte.

2. MATERIALS AND METHODS

The following chemicals were used to synthesise perovskite oxide by using sol-gel method $Ca(NO_3)_2.4H_20$, $La(NO_3)_3.6H_2O$, titanium(IV) bis(ammonium lactato) dihydroxide solution, $H_2[Pt(NO_3)_6]$, citric acid ($C_6H_8O_7$), ethylene glycol ($C_2H_6O_2$). To prepare perovskite oxide by using solid-state reaction, we used high purity La_2O_3, TiO_2, $CaCO_3$, PtO_2 and $BaCO_3$ supplied from Sigma Aldrich, Alfa Aesar.
The perovskite oxide was prepared by solid-state reaction method reported previously in the following manuscript.[10] As a Pt precursor, house developed $Ba_3Pt_2O_7$ perovskite oxide prepared by solid-state reaction was used. The reason of using $Ba_3Pt_2O_7$ instead PtO_2 is that PtO_2 tends to volatilize or to be reduced to metallic form, due to poor phase stability of the compound at high temperatures [11]. The as-prepared perovskite oxide ground for an hour and fired under pure oxygen atmosphere (100 ml/min) as a pellet at 1200 °C for 12 h. The prepared pellet was fractured and reduced in 5% H_2/N_2 between 700 to 900 °C for 12 h. $La_{0.4}Ca_{0.4}TiO_3$ and $La_{0.4}Ca_{0.4}Ti_{0.95}Pt_{0.05}O_3$ were prepared using solgel technique. First, citric acid and EG with the ratio of 2:1 dissolved in 200 ml water under continuous stirring. After the dissolution of the substances, other chemicals (analytic grade titanium (IV) bis (ammonium lactato) dihydroxide solution (50 wt. % in H_2O), calcium nitrate, platinum nitrate and lanthanum nitrate, respectively, were added. When the transparent solution was obtained, the temperature was increased to 80-100 °C to evaporate water and form a gel. The gel formation was followed by a combustion at 300-400 °C resulting in black powder. The black powder was ground prior to calcination at 800 °C for 6 h with a heating/cooling rate of 4 °C/min and then reduced in 5% H_2/N_2. Perovskite oxide powders reduced

at 700°C for 12h to exsolve Pt nanoparticles.
To confirm the phase purity and crystallinity, oxidized and reduced samples were analysed by using a PANalytical Empyrean X-ray diffractometer (XRD) operated in reflection mode. The collected XRD data was further analysed using WinXPOW software. The morphology of the perovskite oxides was investigated using JSM-IT800 Schottky Field Emission Scanning Electron Microscope (SEM). The electrochemical activity of the perovskite oxide samples was probed using rotating ring disc electrode (RRDE) assembly manufactured by Pine Research.

3. RESULTS AND DISCUSSION

Fig. 1 a-f illustrates SEM images of oxidized (as-prepared) and reduced perovskite oxides prepared using solid-state reaction and sol-gel pechini methods. The sample prepared using solid-state method has large grains (~1 µm) with low porosity. The particles exsolved from reduced $La_{0.4}Ca_{0.3925}Ba_{0.0075}Ti_{0.995}Pt_{0.005}O_{3-x}$ at 700°C in H_2/N_2 are around 4-6 nm and finely dispersed on perovskite oxide as demonstrated in Figure 1b-c.

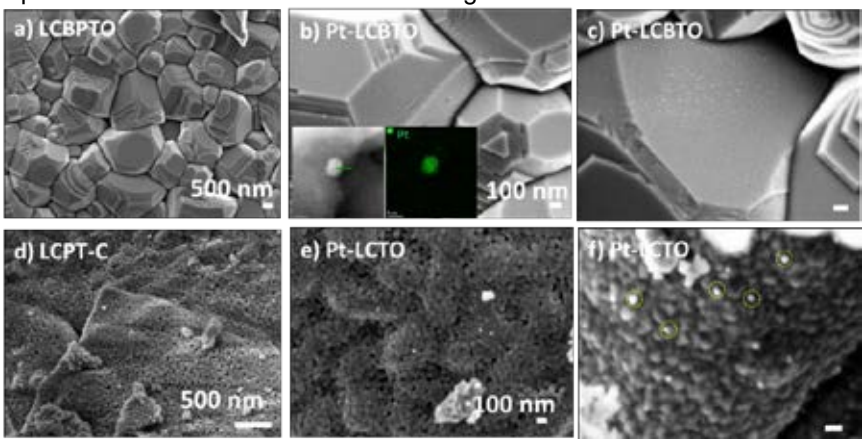

Fig. 1. a-b illustrate SEM images of perovskite oxides before and after reduction heat treatment. a) As-prepared $La_{0.4}Ca_{0.3925}Ba_{0.0075}Ti_{0.995}Pt_{0.005}O_3$-ref doped with 0.5% Pt, b-c) reduced $La_{0.4}Ca_{0.3925}Ba_{0.0075}Ti_{0.995}Pt_{0.005}O_{3-x}$ (reduced at 700 °C, inset image shows the exsolved Pt nanoparticle). c) As-prepared $La_{0.4}Ca_{0.4}Ti_{0.995}Pt_{0.005}O_3$- ref doped with 0.5% Pt, d-f) reduced $La_{0.4}Ca_{0.4}Ti_{0.995}Pt_{0.005}O_{3-x}$ (at 700 °C).

For comparison, we prepared 0.5 % Pt substituted $La_{0.4}Ca_{0.4}Ti_{0.995}Pt_{0.005}O_3$ by sol-gel method, see Figure 1d-f. The solgel-derived Pt doped LCPTO powders with ~50 nm grain size exhibit mesoporous morphology with the BET surface area of 19 m^2/g, approximately eighteen times larger surface area than solid-state derived sample. Reduction heat treatment in H_2/N_2 results in Pt exsolution on $La_{0.4}Ca_{0.4}Ti_{0.995}O_{3-x}$, as indicated with yellow circles in Figure 1f.

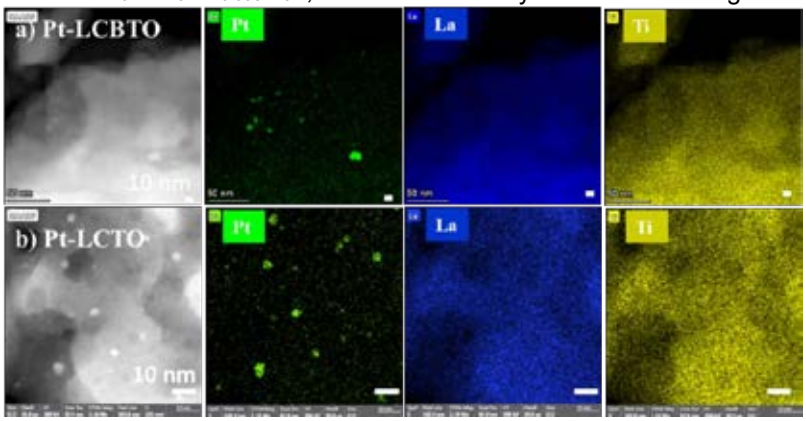

Fig. 2. HRTEM of exsolved nanoparticles on reduced $La_{0.4}Ca_{0.3925}Ba_{0.0075}Ti_{0.995}Pt_{0.005}O_{3-x}$, $La_{0.4}Ca_{0.4}Ti_{0.995}Pt_{0.005}O_{3-x}$ and elemental mapping. HRTEM image and EDX mapping of (Ti, La, Pt) reduced a) $La_{0.4}Ca_{0.3925}Ba_{0.0075}Ti_{0.995}Pt_{0.005}O_{3-x}$ and b) $La_{0.4}Ca_{0.4}Ti_{0.995}Pt_{0.005}O_{3-x}$.

We investigated the microstructure and chemical composition of exsolved nanoparticles using HRTEM as shown in Figure 2. HRTEM images show the exsolved Pt nanoparticles with the size of 16±4 nm on $La_{0.4}Ca_{0.4}Ti_{0.995}Pt_{0.005}O_{3-x}$.and 4.5±2 nm on $La_{0.4}Ca_{0.3925}Ba_{0.0075}Ti_{0.995}Pt_{0.005}O_{3-x}$. The elemental distribution of Pt, O provides evidence of exsolution of metallic Pt. In all cases, we detected unreacted Pt chunks in the bulk structure of perovskite oxide. The presence of unreacted Pt/PtO_2 in (only) calcined on $La_{0.4}Ca_{0.4}Ti_{0.995}Pt_{0.005}O_3$ can be explained by two probabilities *i)* PtO_2 is not fully

decomposed in $LaTiO_3$-based perovskite oxide, *ii)* PtO_2 displays poor stability at elevated temperatures, and is reduced to metallic Pt at earlier steps of synthesis. The formation of Pt chunks was also observed by other researchers in $CaTiO_3$- and $LaTiO_3$-based perovskite oxides [12,13].

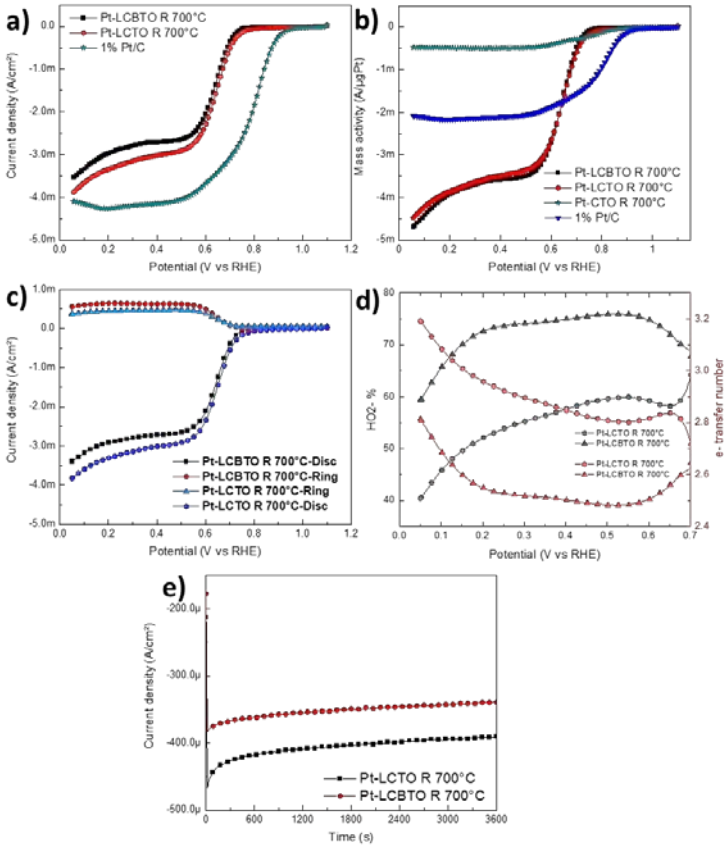

Fig. 3. Electrocatalytic activity of reduced $La_{0.4}Ca_{0.3925}Ba_{0.0075}Ti_{0.995}Pt_{0.005}O_{3-x}$ and $La_{0.4}Ca_{0.4}Ti_{0.995}Pt_{0.005}O_{3-x}$ in 0.1 M KOH. a) Comparisons of specific activity and b) the mass activity of samples in oxygen reduction region. c) RRDV profile showing the ring and disc voltammetry. d) Graph showing the $HO2^-$ yield and electron transfer number at different voltages. e) Chronoamperometric measurement of samples at 0.7 V vs RHE.

We assessed Pt exsolved perovskite oxides as ORR electrocatalysts in 0.1 M KOH. The onset potentials and diffusion limiting current densities are 0.82, 0.92 V and 2.7, 3.05 mA/cm^2 for reduced $La_{0.4}Ca_{0.3925}Ba_{0.0075}Ti_{0.995}Pt_{0.005}O_{3-x}$ and $La_{0.4}Ca_{0.4}Ti_{0.995}Pt_{0.005}O_{3-x}$, respectively. (For the commercial reference material, 1wt% Pt on C, onset potential and limiting current density values are 1.034 V, 4.14 mA/cm^2, respectively.) When the plot was converted to mass activity, the onset potential and limiting current density values are 3.48 and 3.6 mA/cm^2 for reduced $La_{0.4}Ca_{0.3925}Ba_{0.0075}Ti_{0.995}Pt_{0.005}O_{3-x}$ and $La_{0.4}Ca_{0.4}Ti_{0.995}Pt_{0.005}O_{3-x}$, respectively. We observe comparable electrocatalytic activity for perovskite oxide with Pt/C reference electrode. It is worth mentioning that the exsolution behaviour of reduced $La_{0.4}Ca_{0.3925}Ba_{0.0075}Ti_{0.995}Pt_{0.005}O_{3-x}$ is not uniform, not all Pt exsolved and the hidden Pt in the agglomerated Pt chunks (observed under TEM, data not shown) is not active for catalytic reactions and considered as an inactive catalyst. This finding indicates the importance of the uniform dispersion of fine (1-6 nm) Pt nanoparticles for effective utilization of the active material, as we previously reported [5].

The RRDE profiles of perovskite oxides are recorded in 0.1 M KOH electrolyte to understand the reaction mechanism, we estimated the HO^-_2 % yield and electron transfer numbers (n) for each sample, see Figure 5c-d. The highest HO_2^- % yield (60 %) and lowest electron transfer number (app. 2.6) within the voltage range of interest were observed for reduced $La_{0.4}Ca_{0.3925}Ba_{0.0075}Ti_{0.995}Pt_{0.005}O_{3-x}$. Overall, the perovskite oxide was prepared by solid-state reaction is more active for a sluggish two-electron reaction pathway in two steps to complete the reduction of O_2 molecules to OH^- ions. The superior activity of solid-state derived sample for two-electron reactions in alkaline media can be explained by the surface termination-segregation, structure, and poor catalytic activity towards four-electron reactions. The surface termination of the perovskite oxide might affect the binding sites of ions, OH^-, H^+, and O_2, and facilitate two-electron reactions.

We assessed the stability of reduced $La_{0.4}Ca_{0.3925}Ba_{0.0075}Ti_{0.995}Pt_{0.005}O_{3-x}$ and $La_{0.4}Ca_{0.4}Ti_{0.995}Pt_{0.005}O_{3-x}$ for 4 h by polarizing at 0.7 V vs RHE. We monitored 27 % and 9 % decay in performance for reduced $La_{0.4}Ca_{0.3925}Ba_{0.0075}Ti_{0.995}Pt_{0.005}O_{3-x}$ and $La_{0.4}Ca_{0.4}Ti_{0.995}Pt_{0.005}O_{3-x}$, respectively.

4. CONCLUSIONS

Overall, reduced $La_{0.4}Ca_{0.4}Ti_{0.995}Pt_{0.005}O_{3-x}$ prepared by sol-gel technique exhibits good electrocatalytic stability and superior mass ORR activity. Superior electrocatalytic activity of solgel derived sample is attributed to the better exsolution behaviour of Pt nanoparticles, higher surface area and better accessibility of electrocatalytically active sites compared to perovskite oxides synthesised by solid-state reaction method.

ACKNOWLEDGEMENT

The authors acknowledge support from the Engineering and Physical Sciences Research Council (EPSRC) for Critical Mass Grant EP/R023522/1, Light element Analysis Facility Grant EP/T019298/1 and the Strategic Equipment Resource Grant EP/R023751/1.

REFERENCES

[1] Tripković V, Abild-Pedersen F, Studt F, Cerri I, Nagami T, Bligaard T, et al. Metal Oxide-Supported Platinum Overlayers as Proton-Exchange Membrane Fuel Cell Cathodes. ChemCatChem 2012;4:228–35. https://doi.org/10.1002/cctc.201100308.
[2] Zhao L, Zhu J, Zheng Y, Xiao M, Gao R, Zhang Z, et al. Materials Engineering toward Durable Electrocatalysts for Proton Exchange Membrane Fuel Cells. Adv Energy Mater 2022;12:2102665. https://doi.org/10.1002/aenm.202102665.
[3] Tsekouras G, Neagu D, Irvine JTS. Step-change in high temperature steam electrolysis performance of perovskite oxide cathodes with exsolution of B-site dopants. Energy Environ Sci 2013;6:256–66. https://doi.org/10.1039/C2EE22547F.
[4] Neagu D, Tsekouras G, Miller DN, Ménard H, Irvine JTS. In situ growth of nanoparticles through control of non-stoichiometry. Nat Chem 2013;5:916–23. https://doi.org/10.1038/nchem.1773.
[5] Ozkan S, Kim SJ, Miller DN, Irvine JTS. A New Approach to Fuel Cell Electrodes: Lanthanum Aluminate Yielding Fine Pt Nanoparticle Exsolution for Oxygen Reduction Reaction. Adv Energy Mater 2024;14. https://doi.org/10.1002/aenm.202303025.
[6] Neagu D, Oh T-S, Miller DN, Ménard H, Bukhari SM, Gamble SR, et al. Nano-socketed nickel particles with enhanced coking resistance grown in situ by redox exsolution. Nat Commun 2015;6:8120. https://doi.org/10.1038/ncomms9120.
[7] van Deelen TW, Hernández Mejía C, de Jong KP. Control of metal-support interactions in heterogeneous catalysts to enhance activity and selectivity. Nat Catal 2019;2:955–70. https://doi.org/10.1038/s41929-019-0364-x.
[8] Neagu D, Irvine JTS. Enhancing Electronic Conductivity in Strontium Titanates through Correlated A and B-Site Doping. Chem Mater 2011;23:1607–17. https://doi.org/10.1021/cm103489r.
[9] Bradha M, Hussain S, Chakravarty S, Amarendra G, Ashok A. Synthesis, structure and total conductivity of A-site doped LaTiO3-δ perovskites. J Alloys Compd 2015;626:245–51. https://doi.org/10.1016/j.jallcom.2014.12.033.
[10] Kothari M, Jeon Y, Miller DN, Pascui AE, Kilmartin J, Wails D, et al. Platinum incorporation into titanate perovskites to deliver emergent active and stable platinum nanoparticles. Nat Chem 2021;13:677–82. https://doi.org/10.1038/s41557-021-00696-0.
[11] Chaston JC. Reactions of Oxygen with the Platinum Metals; II-OXIDATION OF RUTHENIUM, RHODIUM, IRIDIUM AND OSMIUM. Platin Met Rev 1965;9:51–6.
[12] Katz MB, Zhang S, Duan Y, Wang H, Fang M, Zhang K, et al. Reversible precipitation/dissolution of precious-metal clusters in perovskite-based catalyst materials: Bulk versus surface re-dispersion. J Catal 2012;293:145–8. https://doi.org/10.1016/j.jcat.2012.06.017.
[13] Dai S, Zhang S, Katz MB, Graham GW, Pan X. In Situ Observation of Rh-CaTiO 3 Catalysts during Reduction and Oxidation Treatments by Transmission Electron Microscopy. ACS Catal 2017;7:1579–82. https://doi.org/10.1021/acscatal.6b03604.

INVESTIGATING THE SUPERIOR EFFECT OF g-C_3N_4 ON Co-B CATALYSTS FOR EFFICIENT HYDROGEN GENERATION VIA $NaBH_4$ HYDROLYSIS

[1*]*Burak Can ÇELİK*, [1]*Hüseyin ELÇİÇEK*
[1] Yildiz Technical University, Marine Engineering, Istanbul, Türkiye

*Corresponding author e-mail: can.celik@yildiz.edu.tr

ABSTRACT

Hydrogen has gained considerable attention as a zero-emission fuel due to its potential to significantly reduce the environmental impacts of fossil fuel usage and contribute to decarbonization efforts. However, the development of safe, efficient, and environmentally friendly hydrogen storage technologies remains a significant challenge to its widespread adoption. Sodium borohydride has emerged as a key material for hydrogen storage and production due to its high hydrogen content and controllable release properties. This study investigates the potential of graphitic carbon nitride (g-C3N4) as a support material for enhancing the performance of Co-B catalysts in NaBH4 hydrolysis. The catalysts were synthesised using a chemical reduction method, and the effect of different g-C3N4 concentrations was thoroughly analysed. Experimental results demonstrated that the optimal addition of g-C3N4 to the Co-B catalyst increased the hydrogen generation rate by approximately 2.6 times compared to the Co-B catalyst. Additionally, the activation energy of the hydrolysis reaction was found to be 72.07 $kJ \cdot mol^{-1}$. These findings underscore the necessity for precise catalyst composition to optimize performance and underscore the value of further research into reaction kinetics and structural optimization. These findings highlight the potential of g-C3N4 as an effective material in NaBH4 hydrolysis, offering a pathway to more efficient and sustainable hydrogen production.

Keywords: Hydrogen storage, Sodium borohydride, g-C3N4, Co-B catalysts

1. INTRODUCTION

The global energy crisis has given rise to a significant increase in interest in clean, economic and sustainable energy alternatives [1]. Hydrogen stands out as a promising energy source due to its high calorific value, which makes it an efficient fuel, and its environmentally friendly combustion products, which contribute to reducing pollution and greenhouse gas emissions. Additionally, hydrogen is considered a sustainable energy carrier, as it can be produced from renewable resources, making it an attractive alternative to fossil fuels. However, despite these advantages, several challenges remain in the widespread adoption of hydrogen as a mainstream energy source. The safe production, storage, and transportation of hydrogen are critical issues that hinder its large-scale deployment. In this context, sodium boron hydride (NaBH4) is an attractive candidate for hydrogen storage and production due to its impressive hydrogen storage capacity, which reaches up to 10.8% [2]. The hydrolysis of $NaBH_4$ under ambient conditions proceeds slowly, with a low conversion rate. Catalysts play a crucial role in enhancing the conversion rates, accelerating the reaction kinetics, and facilitating the reaction under these conditions. Catalysts used in the hydrolysis reaction face significant challenges, primarily due to deactivation caused by the formation of polyborates. These polyborates can form on the catalyst surface, leading to a reduction in catalytic efficiency. To address this issue, it is crucial to design and develop effective support materials that can not only prevent the agglomeration of metal particles but also enhance the overall surface area of the catalyst [3]. The utilisation of support materials has been shown to enhance catalytic performance and stability by increasing the surface area of the catalyst and improving the dispersion of nanoparticles. Materials such as carbon-based supports, metal oxides and zeolites play a critical role in hydrogen production processes by providing structural stability and optimising mass transfer [4]. In this context, graphitic carbon nitride (g-C3N4) is a particularly noteworthy support material due to its high chemical stability, non-toxicity and low cost [5,6]. Its planar structure facilitates electron conduction, ensuring effective performance in catalytic processes. It also increases catalytic efficiency and provides long-term stability through complexation with pyridine-like nitrogen atoms and metal ions [7]. The catalytic potential of g-C3N4 is being explored through various modification strategies, including the incorporation of different elemental dopants to form composite catalysts. The incorporation of non-metallic elements, including N, O, S, B, and P, into g-C3N4 has been identified as a highly effective modification strategy [8–10]. The superior properties of Co-B catalysts in $NaBH_4$ hydrolysis have been emphasized by numerous researchers [11–13]. The present study aims to explore the hydrogen production efficiency derived from the hydrolysis of $NaBH_4$ by investigating the superior properties of Co-B and g-C3N4 components. In this context, the effect of adding varying amounts of g-C3N4 to the Co-B catalyst will be experimentally investigated. By systematically varying the composition of the g-C3N4 content on the Co-B catalyst, the study seeks to evaluate the impact of this modification on the overall catalytic performance.

2. MATERIALS AND METHODS

In this section, details of catalyst preparation and hydrogen releasing processes have been summarized. All the chemicals used in this study were of analytical grade and employed directly without any additional purification steps.

2.1. Catalyst Preparation

In this study, pure Co-B and g-C3N4 supported Co-B-g-C3N4 catalysts were synthesised by chemical reduction method. A specific amount of g-C3N4 was added to an ethanol solution and placed in an ultrasonic bath for 1 hour to ensure a homogeneous mixture. Subsequently, a 0.02 M CoCl2 solution was prepared and added to the mixture, which was then stirred continuously using a magnetic stirrer. The initial pH value of the solution was recorded using a WTW Multi 3420 pH meter. The final pH of the solution was adjusted to 4 using NaOH and HCl. Subsequently, the solution was cooled to 6°C in a circulating water bath, and the reduction process was achieved by the dropwise addition of 10 mL of aqueous sodium borohydride solution under vigorous stirring. The obtained black precipitate exhibited magnetic properties, allowing it to be separated magnetically. The resulting black precipitate was washed with distillate water and ethanol to remove residual ions. The precipitate were then dried in an oven at 105°C for a minimum of 8 hours and then pulverised in a mortar and pestle to yield a fine powder.

2.2. Hydrogen Releasing Tests

An important parameter for evaluating the performance of catalysts in the sodium borohydride hydrolysis process is the hydrogen generation rate (HGR). This parameter is expressed as the volume of hydrogen generated (in milliliters) per minute per gram of catalyst. The amount of hydrogen was quantified using a water displacement method in a temperature-controlled reactor, which maintained a constant temperature within an accuracy of ±0.5 ℃. The HGR tests were conducted using the experimental setup schematically depicted in Fig. 1.

The experimental procedure involved the amalgamation of sodium borohydride, sodium hydroxide pellets, and distilled water within a small beaker. This mixture was then placed in a heater, with the temperature set to 65°C. The precise mass of the catalyst, near 6 mg, was measured using an analytical balance. The heated fuel was then transferred to a volumetric flask. The mouth of the flask was sealed with a flexible hose connected to a bubbler and a gas burette to direct the gas outlet. It is imperative to note that the reaction temperature was maintained at a constant level throughout the duration of the experiment.

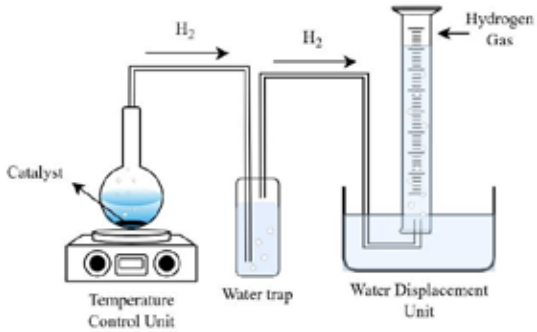

Fig. 1. Schematic representation of the experimental setup.

Total released hydrogen per gram catalyst and minute ($Lg^{-1}min^{-1}$) is defined as hydrogen generation rate:

$$HGR = L_H2/(g_cat * min) \quad (1)$$

3. RESULTS AND DISCUSSION

The performance of pure Co-B and modified Co-B with g-C3N4 catalysts was systematically evaluated based on their hydrogen generation rates (HGR). The proportion of the g-C3N4 precursor in the synthesized catalyst was optimized to maximize hydrogen production. Fig. 2 shows that incorporating different quantities of g-C3N4 into the Co-B catalyst, ranging from 1 to 30 mg, notably influences the hydrogen production rate. It has been observed that increasing the loading of g-C3N4 beyond 10 mg leads to a decline in catalytic activity. As a result, the optimal amount of g-C3N4 precursor in the Co-B catalyst composition has been identified as 10 mg. This result is clearly supported by the HGR results presented in Fig. 2b. The addition of g-C3N4 has led to achieving a maximum hydrogen production rate of 37.26 $L \cdot g_{cat}^{-1} \cdot min^{-1}$, which signifies an impressive enhancement compared to the Co-B (14.01 $L \cdot g_{cat}^{-1} \cdot min^{-1}$) catalyst. This substantial increase in activity indicates the considerable potential of g-C3N4 in enhancing catalytic activity, likely attributable to its capacity to provide a high surface area, enhanced dispersion of active sites, and improved interaction with the Co-B alloy. The observed decrease following the addition of a certain amount of g-C3N4 can likely be attributed to the excessive loading of g-C3N4, which may result in several issues. These include steric hindrance, which can

obstruct the interaction between the catalyst and the reactants, and the saturation of active sites, reducing the availability of catalytic sites for the reaction. Furthermore, the excessive amount of g-C3N4 might cause increased particle aggregation, which in turn can hinder the efficiency of mass transfer. This reduced mass transfer efficiency, coupled with the other factors, ultimately limits the overall performance.

Under the optimum reaction conditions, the hydrogen production rate of the identified catalyst was determined at different temperatures. The temperature range was controlled and tested between 65°C and 45°C with a 5°C temperature gradient. This study was also conducted to determine the activation energy associated with the hydrogen production process. The experimental results demonstrate that high temperatures have a significant impact on the catalytic hydrogen production performance of the catalyst, in line with expectations. To investigate the reaction kinetics of the catalyst, the apparent activation energy of the catalyst, which catalyzes the reaction of sodium borohydride, was determined based on experimental data collected at various temperatures. The activation energy (Ea) of the catalyst was calculated using the Arrhenius equation as follows.

$$lnk = lnk_0 - \frac{E_a}{R}\left(\frac{1}{T}\right) \quad (2)$$

The equation represents the rate of hydrogen production (k) in terms of several key parameters: k_0, the frequency factor; E_a, the activation energy (measured in kJ·mol^{-1}); R, the ideal gas constant (8.314 kJ·mol^{-1}·K^{-1}); and T, the temperature of the reaction (in Kelvin).

The activation energy of the catalyst reaction, calculated from the slope of the ln(k) versus 1/T curve presented in Fig. 3, was found to be 72.07 kJ·mol^{-1}. This value is lower than the activation energy of 75 kJ·mol^{-1} reported by Kaufman and Sen [14] for cobalt-based catalysts. The reaction was completed within four minutes and forty-four seconds at the 65°C temperature, producing a total of 1000 ml. However, at a lower temperature of 300 K, the same reaction took approximately 20 minutes to reach completion.

a) b)

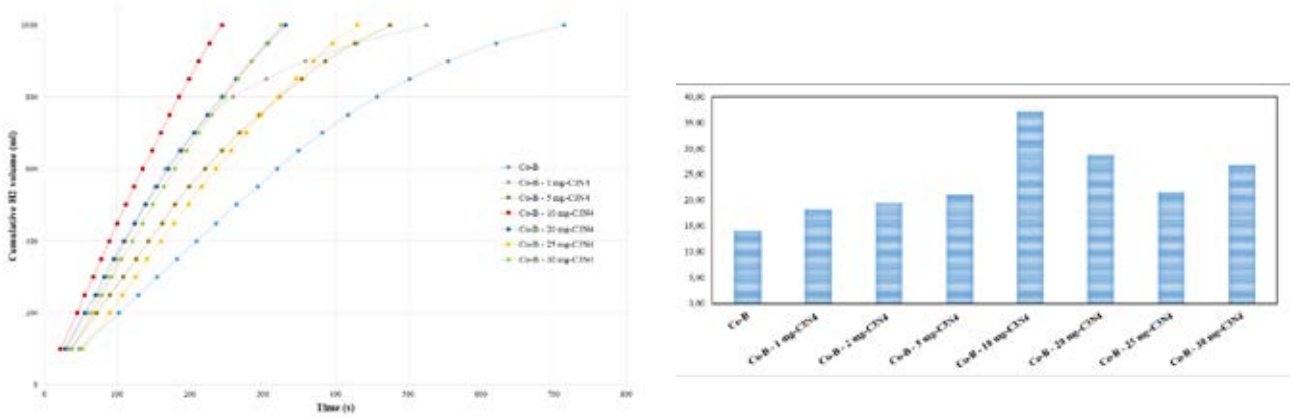

Fig. 2. a) Cumulative hydrogen volume as a function of time for different g-C3N4 amounts and b) their HGR values.

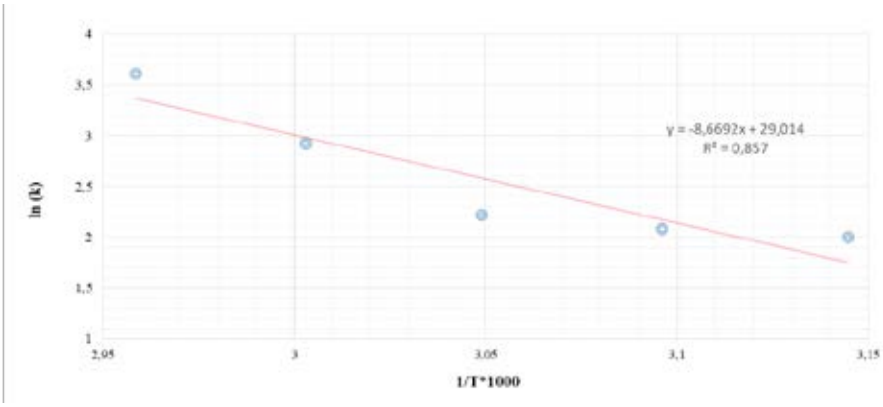

Fig. 3. Kinetic curves of hydrogen production at different temperatures.

4. CONCLUSIONS

In present study, the addition of various g-C3N4 to the Co-B catalyst under the given experimental conditions has demonstrated a significant improvement in hydrogen production rate. The results show that the incorporation of g-C3N4 leads to a maximum hydrogen production rate of 37.26 $L \cdot g_{cat}^{-1} \cdot min^{-1}$, which is notably higher than the rate observed for the Co-B catalyst (14.01 $L \cdot g_{cat}^{-1} \cdot min^{-1}$). Furthermore, the activation energy of the catalytic reaction, calculated to be 72.07 $kJ \cdot mol^{-1}$, suggests that the modified catalyst exhibits favorable catalytic efficiency. These findings indicate that g-C3N4 is a promising material for enhancing the performance of Co-B catalysts in $NaBH_4$ hydrolysis, providing a pathway for more efficient and sustainable hydrogen production systems.

ACKNOWLEDGEMENT

This study has been supported by Yildiz Technical University Scientific Research Projects Coordination Unit under project number FCD-2024-6486

REFERENCES

1. York R, Bell SE (2019) Energy transitions or additions?: Why a transition from fossil fuels requires more than the growth of renewable energy. *Energy Research & Social Science* 51: 40–43.
2. Elçiçek H (2023) Determination of critical catalyst preparation factors (cCPF) influencing hydrogen evolution. *International Journal of Hydrogen Energy* 48: 3824–3837.
3. Ren J, Ma J, Xu F, et al. (2024) Hydrogen generation from hydrolysis of NaBH4 solution with efficient g-C3N4/Co–Mo–B/Ni foam catalyst. *International Journal of Hydrogen Energy* 50: 1213–1222.
4. Saka C (2024) Facile fabrication of N-doped heterostructured hybrid particles based on montmorillonite incorporated with g-C3N4 for enhanced hydrogen production by NaBH4 in methanol. *Diamond and Related Materials* 142: 110740.
5. Wang Y, Wang H, Li X, et al. (2023) Oxygen vacancy-mediated direct solid phase integration of interfacial chemical bond reinforced LaNiO3/RGO/g-C3N4 heterojunction for improving hydrogen production. *Applied Surface Science* 616: 156501.
6. Zhang B, Li J, Song Q, et al. (2022) g-C3N4-modulated bifunctional SnO2@g-C3N4@SnS2 hollow nanospheres for efficient electrochemical overall water splitting. *Applied Surface Science* 589: 153016.
7. Cong H, Wei Y, Han Y, et al. (2024) Hydrogen generation from catalytic hydrolysis of ammonia borane with Co-Cu-B/g-C3N4/NF catalyst. *Applied Catalysis O: Open* 194: 206995.
8. Yi F, Gan H, Jin H, et al. (2020) Sulfur- and chlorine-co-doped g-C3N4 nanosheets with enhanced active species generation for boosting visible-light photodegradation activity. *Separation and Purification Technology* 233: 115997.
9. Saka C (2022) Surface modification with oxygen doping of g-C3N4 nanoparticles by carbon vacancy for efficient dehydrogenation of sodium borohydride in methanol. *Fuel* 310: 122444.
10. Arumugam M, Tahir M, Praserthdam P (2022) Effect of nonmetals (B, O, P, and S) doped with porous g-C3N4 for improved electron transfer towards photocatalytic CO2 reduction with water into CH4. *Chemosphere* 286: 131765.
11. Kaya C, Özdemir JH, Elçiçek H, et al. (2024) Enhancing the efficiency of sodium borohydride hydrolysis with a novel CoB-Triton catalyst. *International Journal of Hydrogen Energy* 51: 489–503.
12. Sağır K, Elçiçek H, Özdemir OK (2021) Optimization of catalyst preparation conditions for hydrogen generation in the presence of Co–B using taguchi method. *International Journal of Hydrogen Energy* 46: 5689–5698.
13. Patel N, Fernandes R, Miotello A (2010) Promoting effect of transition metal-doped Co–B alloy catalysts for hydrogen production by hydrolysis of alkaline NaBH4 solution. *Journal of Catalysis* 271: 315–324.
14. Kaufman CM, Sen B (1985) Hydrogen generation by hydrolysis of sodium tetrahydroborate: effects of acids and transition metals and their salts. *J Chem Soc, Dalton Trans* 307–313.

MODELING THE ECONOMIC VIABILITY OF INTEGRATED HYDROGEN FUEL CELL / HEAT PUMP CHP SYSTEMS FOR RESIDENTIAL APPLICATIONS

[1*]*T.H.M. van der Laan,* [1]*C. Acar,* [1]*W. Rohlfs*
[1] University of Twente, Faculty of Engineering Technology, Thermal and Fluid Engineering,
Drienerlolaan 5, Enschede, 7522 NB, the Netherlands

*Corresponding author e-mail: t.h.m.vanderlaan@utwente.nl

ABSTRACT

Domestic heating contributes to 10% of the total Dutch CO_2 emissions. Heat pumps are a sustainable way to produce heat efficiently. However, in winter, their performance reduces, renewable energy supply is low, and heat demand is high, resulting in high electricity prices. Adding a fuel cell to the system enables the utilization of waste heat produced during the conversion of hydrogen to electricity. The integration improves both the overall system efficiency and fuel cell's heat utilization. We assess the economic viability through system simulation of different energy system configurations with a zero-dimensional model controlled by a model predictive controller as an energy management system. Under current market conditions, adding a heat pump-fuel cell system has a low marginal gain compared to a stand-alone heat pump or solar panels. However, the fuel cell dynamics mitigate the heat pump shortcomings during periods of high heat demand and/or price peaks, making it an interesting solution for certain applications.

Keywords: low temperature proton exchange membrane fuel cell, air-source heat pump, model predictive control, combined heating and power system, techno-economic analysis

1. INTRODUCTION

Currently, domestic heating contributes to approximately 10% of the total CO_2 emissions in the Netherlands [1], and more than 85% of the family houses rely on the combustion of natural gas to produce heat [2]. A new generation of energy systems is required to reduce this dependency on fossil fuels, which achieve better or comparable efficiencies and comfort levels as conventional methods. Air-source heat pumps (HP) are gaining interest due to their operation on low-emissions electricity [3]. They extract energy from their surroundings to transfer heat inside a building [4], and they produce multiple times more heat per unit of electricity input than conventional heaters, making them very efficient heating devices [5]. However, in winter, their performance reduces, renewable energy supply is low, and heat demand is high, resulting in high electricity prices. These periods are called dark doldrums. Here, Fuel Cells (FC) come into the picture.

Integrated systems of hydrogen fuel cells and heat pumps simultaneous generate power and heat. This system potentially reduces grid dependency and greenhouse gas emissions [3]. FCs produce a substantial quantity of heat in addition to electricity. This heat improves the total system efficiency to 76%-90% (HHV) [6]. Furthermore, FC systems with solar power are already comparable in price to fossil fuel alternatives for remote off-grid applications [7]. Despite the low quality of the heat recovered from an FC, the heat in the coolant stream is sufficient to be captured and utilized for a wide range of heating applications [8]. Heat recovery from proton exchange membrane FCs has multiple advantages, although it is not always cost-effective. Therefore, there is a need to investigate the combination of a hydrogen fuel cell and heat pump to cover heat demand [9].

This study evaluates the performance of the fuel cell-heat pump system in a typical residential family building in the Netherlands to determine the economic viability and required system dimensions. Since many buildings have already installed solar panels [2] and the presence of lithium-ion battery energy storage is increasing, adding more energy systems will change the marginal payback time of the overall system. Which conditions have a positive business case for utilizing an integrated fuel cell-heat pump system for domestic applications?

This short paper is structured as follows: Section 2 describes the model and energy management system to simulate the system behavior and costs. Section 3 presents the results and discussion of the simulations. Finally, Section 4 concludes the paper.

2. MODELING

In this section, the model inputs, energy systems, energy management system and various system configurations are explained together with their assumptions to evaluate the energy consumption and system behavior.

2.1 Energy demand

We consider the energy demand of a residential building to assess the marginal gain of a heat pump-fuel cell system. The energy demand consists of electricity, space heating, and hot water consumption, which fluctuate throughout the

day and year. Furthermore, building size and occupancy also influence the energy demand. Heating demand profiles are retrieved from Staffel et al., which utilize weather data and the heat capacity of a building to determine the heat demand [10]. The hot water consumption profiles are retrieved from the European energy labeling standard [11]. Waiting times for hot water are neglected because of the presence of the buffer tank. The heat demand is highly seasonal, while hot water consumption remains constant throughout the year. The yearly heat demand is equivalent to 1722 m^3 of natural gas. The annual electricity demand is set equivalent to 3650 kWh. The daily and seasonal patterns in electricity consumption are implemented, using the variation factors described by Melo et al. [12].

2.2 Energy systems

Energy systems are present in domestic buildings to satisfy their heat and power demand, schematically represented in Figure 1. The system is evaluated as a zero-dimensional model, describing the energy flows through the system. The FC and solar panels (PV) produce electricity to meet the demand. In case of an electricity deficit or surplus, electricity is exchanged with the electricity grid or stored in a battery energy storage system (BESS). The water circulation through the heat pump and the cooling circuit of the fuel cell provides heat to the buffer tank. The hot water is then distributed to the heating system and hot water consumers, after which the cooled-down water flows back to the buffer tank. A connected gas pipeline supplies the fuel to the fuel cell.

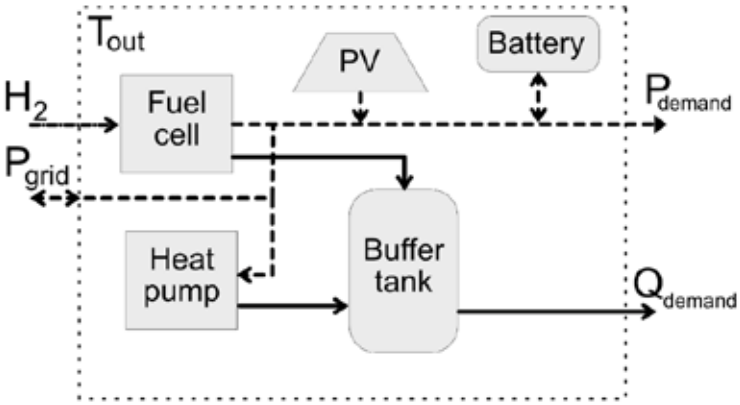

Fig. 1. Schematic representation of the energy systems

2.2.1 Fuel cell

The fuel cell produces both power and heat as the conversion from hydrogen to electricity is not fully reversible. This is described in equation 1. The fuel cell is assumed to operate with a constant efficiency.

$$\begin{bmatrix} P_{FC}[k] \\ Q_{FC}[k] \end{bmatrix} = \begin{bmatrix} \eta_{FC} t_s h_{HHV} \dot{m}_{H_2}[k] \\ (1-\eta_{FC}) t_s h_{HHV} \dot{m}_{H_2}[k] \end{bmatrix} = \begin{bmatrix} \eta_{FC} u_{FC}[k] \\ (1-\eta_{FC}) u_{FC}[k] \end{bmatrix} \quad (1)$$

2.2.2 Heat pump

The HP's heat output is a function of the input power and the coefficient of performance (COP), shown in equation 2.

$$Q_{\mathrm{hp}}[k] = \mathrm{COP}[\Delta T[k]] * P_{\mathrm{hp}}[k] \quad (2)$$

The COP is temperature dependent. The larger the difference between the source and the sink, the lower the COP. defines a relation for the COP in equation 3 between the difference in sink and source temperature $\Delta T = T_{\mathrm{tank}} - T_{\mathrm{out}}$ [13].

$$\mathrm{COP}(\Delta T) = 6.08 - 0.0941\Delta T + 0.000464\Delta T^2 \quad (3)$$

2.2.3 Other systems

The state of charge describes the energy content in the battery. Electricity cannot be stored in its original form and must be converted into other forms of energy. Batteries, consisting of chemical cell arrays, store the electrical energy in chemical bonds. However, the charging and discharging processes are irreversible, resulting in energy losses.
The solar panels are sized according to the yearly power demand of the home appliances. The power output of the photovoltaic panels was determined with the model of [10]. This model combines the geographic location, solar radiation,

panel efficiency, outside temperature, angle with the sky, and peak power to determine the output power.
We model the buffer tank as a large tank filled with water. Its state describes its average temperature. Over time, the tank loses energy to its surroundings. The fuel cell and heat pump heated the water inside the buffer tank, and the heating and hot water utilized this water. The temperature range is between 50°C and 70°C.

2.2.4 Grid inputs

Hydrogen pipelines and a low-voltage electric power grid connect the residential building to power and hydrogen utilities. The electricity grid is regarded as an inexhaustible energy source that provides and receives power. Domestic buildings buy and sell energy from this grid. Electricity prices are considered dynamic and change on an hourly basis. The fluctuation is based on current market conditions, described by the day-ahead prices. Another price component is the grid fees and taxes for charging energy from the grid. The hydrogen price is assumed to be equal to natural gas prices.

2.3 Energy management system

An energy management system determines which energy systems are addressed to meet the energy demand. Since there is no trivial solution to decide on the control action, we implement a Model Predictive Controller (MPC) to determine the most appropriate control action at each time step. This type of control uses a dynamic model to predict future system behavior for a specific control horizon. The advantage of MPC is its usability for a large variety of problems and guarantee of optimum [14]. The dynamic of the house's energy systems are combined in a linear time-varying model, shown in equation 4.

$$\begin{bmatrix} E_{\mathrm{BESS}}[k+1] \\ P_{\mathrm{grid}}[k+1] \\ T_{\mathrm{BT}}[k+1] \end{bmatrix} = \begin{bmatrix} \eta_{\mathrm{selfdis}} & 0 & 0 \\ 0 & 0 & 0 \\ 0 & 0 & \eta_{\mathrm{loss}} \end{bmatrix} \begin{bmatrix} E_{\mathrm{BESS}}[k] \\ P_{\mathrm{grid}}[k] \\ T_{\mathrm{BT}}[k] \end{bmatrix} + \begin{bmatrix} 0 & 0 & -1 \\ -\eta_{\mathrm{FC}} & 1 & -1 \\ c_p * \eta_{\mathrm{FC}} & c_p * \mathrm{COP}[\Delta T] & 0 \end{bmatrix} \begin{bmatrix} u_{\mathrm{FC}} \\ P_{\mathrm{HP}} \\ P_{\mathrm{BESS}} \end{bmatrix} + \begin{bmatrix} 0 & 0 & 0 \\ -1 & 0 & 1 \\ 0 & -c_p & 0 \end{bmatrix} \begin{bmatrix} P_{\mathrm{PV}}[k] \\ Q_{\mathrm{demand}}[k] \\ P_{\mathrm{demand}}[k] \end{bmatrix} \quad (4)$$

2.4 Optimal control

The MPC finds the optimal control action to match the current heat and power demand, minimizing the operation cost and penalizing excessive output switching of the fuel cell and heat pump. This optimization problem is quantified in a linear cost function, shown in Equation 5. The stage cost has a control horizon of N=12 hours. The MPC calculates the optimal control action for the entire control horizon in each time step. However, we only implement the control action for the next time step, and then the optimal control horizon is calculated again in the next iteration. Since most physical systems are bounded, a set of constraints defines the feasibility domain of the cost function. The energy systems' power outputs are unbounded to estimate maximum system sizes.

$$J[k] = \sum_{j=0}^{N-1} C_{\mathrm{grid}}[k+j] P_{\mathrm{grid}}[k+j] + \sum_{j=0}^{N-1} C_{\mathrm{H_2}} P_{\mathrm{FC}}[k+j] + W_{\mathrm{FC}} \sum_{j=0}^{N} |P_{\mathrm{FC}}[j] - P_{\mathrm{FC}}[j-1]| + W_{\mathrm{HP}} \sum_{j=0}^{N} |P_{\mathrm{HP}}[j] - P_{\mathrm{HP}}[j-1]| \quad (5)$$

2.5 System configurations

To assess the added value of an integrated heat pump-fuel cell system, we analyzed various energy system configurations to determine the impact of additional energy systems on the marginal gain and payback time. The considered configurations are the following:

1. Electric heater
2. HP
3. PV + HP
4. PV + HP + FC
5. PV + BESS + HP + FC

In the first scenario, only an electric heater was considered because it is a simple and cheap method for heat production. Despite its electric efficiency being 100%, heat pumps exhibit significantly higher efficiencies. Therefore, in the second scenario, a heat pump replaced the electric heater. Thereafter, an additional energy system is added in each scenario.

We simulate the various configurations for an entire year to evaluate the system's behavior and determine the energy consumption. The Total Cost of Ownership (TCO) quantifies the overall system costs by combining the initial capital expenditures and the yearly operation costs. The initial capital expenditures depend on the energy systems' size. The marginal gain is calculated by determining the reduction in operation costs compared to the additional investment costs.

3. RESULTS AND DISCUSSION

Simulating the various configurations shows that heat pumps and solar panels cover a significant portion of the annual energy demand. The fuel cell operates during the morning and evening price peaks when electricity is more expensive than natural gas, typically in winter due to low renewable energy inflow, low outdoor temperatures, and high demand. In

those hours, operating the heat pump is less effective. In certain cold periods with high heat demand, the EMS operates the fuel cell continuously. In those periods, the fuel cell provided enough electricity that the building was not required to import electricity from the grid. The EMS minimizes power export by prioritizing the more economically advantageous options of using the energy, charging the battery, or buffer tank. In summer, the low electricity price results from a substantial inflow of renewable energy, making fuel cell operations less cost-effective. Also, adding batteries to the energy system reduces the fuel cell operation hours. The battery cycles daily, charging during periods with low electricity prices and discharging in the evening hours.

The economic results of the various configurations are shown in Table 1. Heat pumps and solar panels in scenarios 2 and 3 are the most cost-effective measures to reduce the energy bill with a reasonable payback time compared to the electric heaters in scenario 1. Adding a fuel cell to the system in scenario 4 had no significant effect on the operation costs. They were even higher due to losses caused by the unused buffer tank during fuel cell operations. Furthermore, this configuration required high initial capital. However, this configuration required a smaller heat pump. The addition of a battery system in scenario 5 had a minor effect on the operation cost, but the high initial cost resulted in a long payback time.

Table 1. Energy system operation costs, additional investment costs and payback time for the different scenarios

Scenario	Yearly cost electricity	Yearly cost H_2	Sum yearly operation cost	Cost index (Scen.1=100)	P_{pv} [kW]	$P_{hp,max}$ [kW]	$P_{fc,max}$ [kW]	E_{bess} [kWh]	Additional investment [15]	Payback time [years]
1	€ 2,937.00	€ -	€ 2,937.00	100	0.00	11.20	0.00	0.00		
2	€ 1,202.00	€ -	€ 1,202.00	41	0.00	4.22	0.00	0.00	€ 5,013.50	2.9
3	€ 982.00	€ -	€ 982.00	33	3.60	4.22	0.00	0.00	€ 3,556.80	16.2
4	€ 671.00	€363.00	€ 1,034.00	35	3.60	3.65	6.00	0.00	€ 16,287.75	313.2
5	€ 738.00	€271.00	€ 1,009.00	34	3.60	3.65	6.00	10.00	€ 4,750.00	190.0

4. CONCLUSIONS

The fuel cell dynamics mitigate the heat pump shortcomings during periods of high heat demand and/or price peaks, making it an interesting solution for certain applications. However, the economic viability of a heat pump-fuel cell system for domestic applications is largely dependent on the development of the prices on hydrogen and fuel cell systems. In the current market, utilizing electricity from the grid and producing heat with just a heat pump, even in conditions with reduced COP, is more cost effectively to fulfill household's energy demand.

Future investigations will evaluate scenarios involving CO_2 emissions pricing, rush hour-based grid fees and electric car charging. These evaluations could provoke a favor for utilizing hydrogen in an integrated fuel cell - heat pump system. This is because green hydrogen has a significant lower CO_2 emission, the grid fees increase price of utilizing the electricity grid, making local production favorable and electric car charging has a large impact on the electricity grid demand as well.

An interesting application arises in the context of a centralized heat pump-fuel cell system. If small scale decentralized fuel cells are not economically viable, a centralized fuel cell could supply heat to a district heating network during winter. Centralized heating network benefit from their economy of scale. Therefore, there is a potential business case for the co-generation of power and heat with centralized heat pump-fuel cell systems.

ACKNOWLEDGEMENT

This project is funded by De Nederlandse Organisatie voor Wetenschappelijk Onderzoek (NWO) and Der Projektträger Jülich (PtJ), titled *HX-electrode: System integration of fuel cell and heat pump*, under grant number *KICH2.V4P.DUI21.002*.

NOMENCLATURE

C	Price [euro/kWh]
c	Specific heat [kJ/(kg*K)]
E	Energy content [kWh]
h	specific enthalpy [kJ/kg]
J	Stage cost
$\dot{m}$	Mass flow rate [kg/s]
P	Power [kW]
Q	Heat [kW]

T	Temperature [C]
t	Time [s]
u	Operation setpoint [-]
W	Weight [-]

Greek Letters

η	Efficiency [-]
Δ	Delta [-]

Subscripts

BESS	Battery energy storage system
BT	Buffer tank
demand	Demand
FC	Fuel cell
grid	Electricity import and export from the grid
HHV	Higher heating value
HP	Heat pump
loss	Losses
out	Outside
p	constant pressure
PV	Photovoltaic cells
selfdis	Battery self-discharge

REFERENCES

[1] Emissies van broeikasgassen berekend volgens IPCC-voorschriften. CBS Statline. (2024). Retrieved December 17, 2024 from https://opendata.cbs.nl/#/CBS/nl/dataset/85669NED/table?ts=1697028832754.

[2] Klimaatverandering en energietransitie: opvattingen en gedrag van Nederlanders in 2020. Kloosterman. (2021). Retrieved December 17, 2024 from https://www.cbs.nl/nl-nl/longread/rapportages/2021/klimaatverandering-en-energietransitie-opvattingen-en-gedrag-van-nederlanders-in-2020/4-duurzaam-wonen.

[3] Ren, H., & Gao, W. (2010). Economic and environmental evaluation of micro CHP systems with different operating modes for residential buildings in Japan. In Energy and Buildings (Vol. 42, Issue 6, pp. 853–861). Elsevier BV.

[4] Hepbasli, A., & Kalinci, Y. (2009). A review of heat pump water heating systems. In Renewable and Sustainable Energy Reviews (Vol. 13, Issues 6–7, pp. 1211–1229). Elsevier BV.

[5] Kim, J., Han, C., Lee, S., Lee, D., & Kim, Y. (2024). Performance analysis of PEMFC-assisted renewable energy source heat pumps as a novel active system for plus energy buildings. In Energy and Buildings (Vol. 319, p. 114477). Elsevier BV.

[6] Arsalis, A., Kær, S. K., & Nielsen, M. P. (2015). Modeling and optimization of a heat-pump-assisted high temperature proton exchange membrane fuel cell micro-combined-heat-and-power system for residential applications. In Applied Energy (Vol. 147, pp. 569–581)

[7] Assaf, J., & Shabani, B. (2019). A novel hybrid renewable solar energy solution for continuous heat and power supply to standalone-alone applications with ultimate reliability and cost effectiveness. In Renewable Energy (Vol. 138, pp. 509–520). Elsevier BV.

[8] Nguyen, H. Q., & Shabani, B. (2020). Proton exchange membrane fuel cells heat recovery opportunities for combined heating/cooling and power applications. In Energy Conversion and Management (Vol. 204, p. 112328). Elsevier BV.

[9] Wilberforce, T., Olabi, A. G., Muhammad, I., Alaswad, A., Sayed, E. T., Abo-Khalil, A. G., Maghrabie, H. M., Elsaid, K., & Abdelkareem, M. A. (2024). Recovery of waste heat from proton exchange membrane fuel cells – A review. In International Journal of Hydrogen Energy (Vol. 52, pp. 933–972). Elsevier BV

[10] Staffell, I., Pfenninger, S., & Johnson, N. (2023). A global model of hourly space heating and cooling demand at multiple spatial scales. In Nature Energy (Vol. 8, Issue 12, pp. 1328–1344). Springer Science and Business Media LLC.

[11] Bonk, S. (2012). Methodology for the Assessment of the Hot Water Comfort of Factory Made Systems and Custom Built Systems (IEE/08/593/SI2.529236). University of Stuttgart.

[12] Melo, F. C., Carrilho da Graça, G., & Oliveira Panão, M. J. N. (2023). A review of annual, monthly, and hourly electricity use in buildings. In Energy and Buildings (Vol. 293, p. 113201). Elsevier BV

[13] Gao, H., Cai, L., Fang, Y., Ma, Z., & Wang, H. (2023). Performance evaluation of proton exchange membrane fuel cell and air source heat pump system with energy storage for residential application. *International Journal of Green Energy*, 1–15.

[14] Rawlings, J. B., Mayne, D. Q., & Diehl, M. M. (2017). *Model predictive control theory, computation, and design*. Madison, Wisconsin Nob Hill Publishing.

[15] He, Y., Guo, S., Zhou, J., Wu, F., Huang, J., & Pei, H. (2021). The quantitative techno-economic comparisons and multi-objective capacity optimization of wind-photovoltaic hybrid power system considering different energy storage technologies. *Energy Conversion and Management*, *229*, 113779–113779.

ULTRASONIC SPRAY SYNTHESIS OF COAL LAYERED DOUBLE HYDROXIDE: A NOVEL AND SCALABLE APPROACH TO OXYGEN REDUCTION CATALYSIS

[1]*Kaan Büyükkanber*, [2*]*Ömer Şahin*
[1,2] Istanbul Technical University, Chemical & Metallurgical Engineering Faculty, Chemical Engineering Department, 34469, Maslak, Istanbul, Turkey

*Corresponding author e-mail: omersahin@itu.edu.tr

ABSTRACT

This study investigates the synthesis and electrochemical performance of CoAl layered double hydroxide (LDH) catalysts prepared via two distinct methods: a conventional approach and a novel ultrasonic spray synthesis. The ultrasonic spray synthesis, employing a vapor-liquid interface reaction, is introduced for the first time as a scalable and innovative method for CoAl LDH preparation. Comparative analyses were conducted using scanning electron microscopy (SEM), energy-dispersive X-ray analysis (EDAX), Fourier Transform Infrared Spectroscopy (FT-IR), and cyclic voltammetry (CV). Morphological characterization revealed significant differences in particle size and surface texture between the two synthesis methods, with the ultrasonic spray approach producing more uniform and porous structures. Elemental composition analysis confirmed the successful incorporation of Co and Al in both catalysts. Electrochemical performance demonstrated improved catalytic stability and enhanced charge transfer properties for the catalyst synthesized via ultrasonic spray. These findings highlight the potential of ultrasonic spray synthesis as a cost-effective and efficient method for developing advanced LDH-based catalysts for electrochemical applications.

Keywords: Ultrasonic spray synthesis, CoAl LDH, electrochemical performance

1. INTRODUCTION

Hydrogen energy is increasingly recognized as a critical component of sustainable energy strategies [1]. In the pursuit of efficient ways to store and convert hydrogen energy, materials like Layered Double Hydroxides (LDHs) come to the forefront due to their versatility in catalytic, electrochemical, and environmental applications [2]. LDHs, consisting of positively charged brucite-like layers and charge-balancing interlayer anions, offer unique properties such as high surface area, tunable composition, and excellent stability, making them promising candidates for energy conversion and storage technologies, including oxygen reduction reactions (ORR) [3, 4]. In this study, we present a novel synthesis route for LDH materials using an ultrasonic spray method. Ultrasonic spray offers advantages such as rapid production, uniform particle size distribution, the creation of crystalline structures, and scalability [5, 6]. To the best of our knowledge, this is the first report on LDH synthesis using ultrasonic spray technology. The synthesized materials were characterized using FT-IR, SEM, and EDAX to investigate structural and morphological differences. Furthermore, electrochemical performance was evaluated through CV to assess their potential in ORR applications. A detailed comparison of the properties and performance between the ultrasonic spray-synthesized LDH and conventionally prepared LDH materials highlights the novelty and efficacy of the new synthesis approach.

2. EXPERIMENTAL

2.1. CoAl LDH Synthesis via Co-precipitation Method

Using a conventional co-precipitation technique, referenced from established literature [7] , we synthesized CoAl-LDH nanosheets, hereafter referred to as “CON-CoAl”. Initially, solutions were prepared by dissolving 2 mmol of cobalt nitrate hexahydrate and 1 mmol of aluminum nitrate nonahydrate into 20 mL of deionized water (Solution A), stirred for 15 minutes. Concurrently, 6 mmol of sodium hydroxide and 5 mmol of anhydrous sodium carbonate were dissolved in an equal volume of deionized water to form Solution B. Solution A was then incrementally introduced into Solution B with continuous stirring. After mixing, the blend was enclosed in a 50 mL Teflon-lined autoclave and subjected to a temperature of 110 °C for a duration of nine hours. Once the process was complete, the resultant solid was isolated through filtration, extensively rinsed with deionized water, and subsequently dried under vacuum conditions at 60 °C.

2.2. CoAl LDH Synthesis via Ultrasonic Spray Method

The ultrasonic spray synthesis method is similar to the conventional co-precipitation method but includes a key variation: Solution A, containing cobalt nitrate hexahydrate and aluminum nitrate nonahydrate in 20 mL deionized water, was atomized into fine droplets using nitrogen gas in an ultrasonic spray atomizer. These droplets were continuously introduced into Solution B, which held dissolved sodium hydroxide and anhydrous sodium carbonate in an equivalent volume of water, under constant stirring. The subsequent steps of autoclave heating, filtration, washing, and drying mirrored the conventional method. The material produced is termed 'US-CoAl', with the setup detailed in Fig. 1.

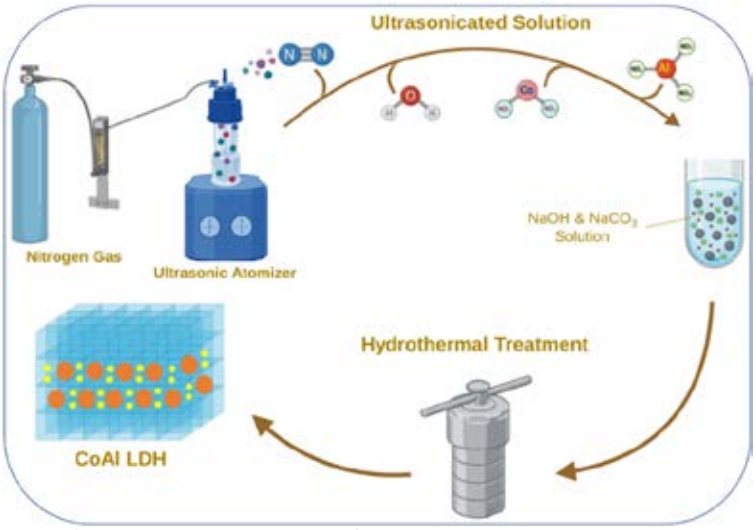

Fig. 1. Schematic representation of the ultrasonic spray synthesis method.

2.3. Material Characterization and Electrochemical Measurements

Analyses involving SEM and EDAX were carried out using a Zeiss EVO LS 10 microscope. FT-IR was employed to characterize the samples in transmission mode under normal conditions, spanning a spectral range from 4000 to 400 cm^{-1}. These measurements were conducted at room temperature using a Thermo Scientific Nicolet 380 spectrometer. Electrochemical characterization, including cyclic voltammetry, was performed with an Ivium Vertex.One potentiostat. A three-electrode system was used, consisting of a platinum wire as the counter electrode, an Ag/AgCl reference electrode, and a glassy carbon electrode (GCE) with a diameter of 3 mm serving as the working electrode. A volume of 5 µL from a 10 mg/mL catalyst suspension was applied onto the surface of the GCE. All electrochemical tests were carried out in 0.1 M KOH solution saturated with oxygen gas (O_2), with the CV scans conducted at a rate of 10 and 100 mV/s.

3. RESULTS AND DISCUSSION

The FT-IR spectra of both US-CoAl and CON-CoAl LDH samples demonstrated in Fig. 2 align with literature values for layered double hydroxides (LDHs) [8]. A broad band near 3434 cm^{-1} corresponds to O–H stretching of water molecules or hydroxyl groups in the brucite-like layers [9]. The absence of peaks in the 2931–2864 cm^{-1} range indicates a lack of organic C–H groups. A strong band around 1176 cm^{-1}, present in both samples, corresponds to carbonate ion (CO_3^{2-}) asymmetric stretching, as commonly observed near 1360 cm^{-1} [10]. In the 400–800 cm^{-1} range, peaks at 497 cm^{-1} and 576 cm^{-1} for US-CoAl, and at 418 cm^{-1} for CON-CoAl, align with M–O and M–OH vibrations characteristic of LDHs [11]. These findings confirm the structural integrity and functional features of CoAl-LDHs.

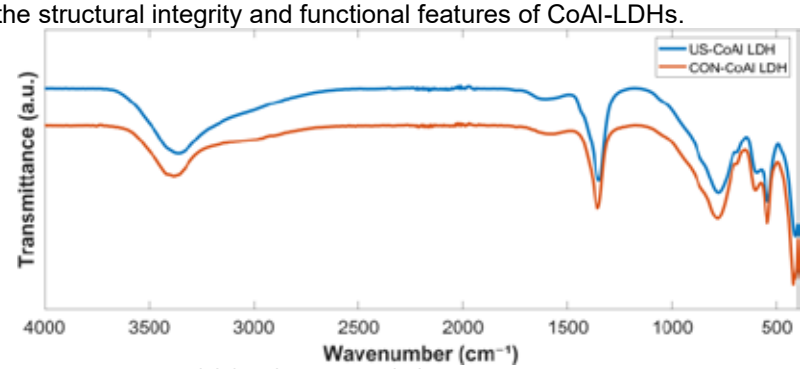

Fig. 2. Analysis of CON-CoAl and US-CoAl LDHs using FT-IR spectroscopy.

SEM analysis revealed distinct morphological differences between the CoAl LDH catalysts synthesized using the conventional method (Fig. 3a, b) and the ultrasonic spray synthesis approach (Fig. 3c, d). Hydrothermal treatment has been reported to improve CoAl LDH materials by forming compact nanosheets [12], which is evident in the conventional synthesis. However, the material produced through this method exhibited larger, aggregated particles with irregular shapes and dense packing, indicating a lower surface area and limited accessibility of active sites, potentially restricting catalytic efficiency. In contrast, the ultrasonic spray-synthesized CoAl LDH displayed a uniform and porous structure, characterized by well-dispersed nanosheets or smaller particles. This morphology results in a higher surface area and improved accessibility of active sites, enhancing catalytic activity. Additionally, the increased porosity observed with the ultrasonic spray method facilitates better mass transport, a critical factor for electrochemical reactions.

EDAX confirmed the successful incorporation of cobalt and aluminum in both catalysts. Figs. 3e and 3f demonstrate the elemental mapping of the conventional method and ultrasonic spray-synthesized CoAl LDH material, respectively. It is evident that both methods achieved the intended stoichiometry, as shown in Figs. 3g and 3h. Additionally, the uniform distribution of elements in both catalysts is clearly visible. This homogeneity ensures the effective utilization of active sites during electrocatalytic reactions.

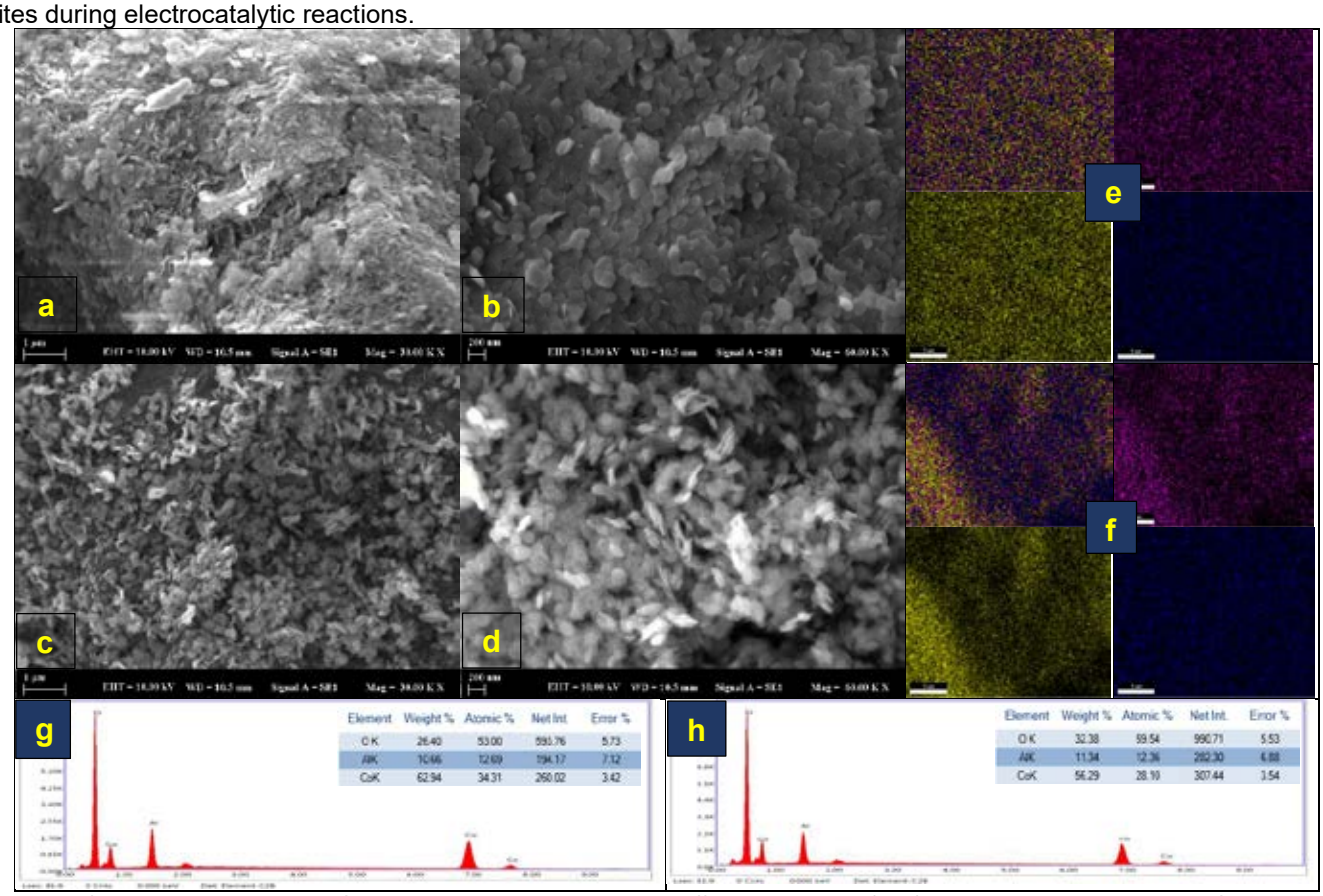

Fig. 3. SEM images comparing CoAl LDH catalysts prepared by different methods: (a, b) conventionally synthesized CoAl LDH, showing larger, aggregated particles with irregular morphology; (c, d) ultrasonic spray-synthesized CoAl LDH, exhibiting a uniform, porous structure with well-dispersed nanosheets. EDAX elemental mapping of (e) conventionally synthesized and (f) ultrasonic spray-synthesized catalysts. Stoichiometry validation for (g) conventional and (h) ultrasonic spray methods.

Both LDH materials exhibit the same peak current at a scan rate of 10 mV/s, which aligns with the literature [13], as shown in Fig. 4a, indicating similar levels of maximum ORR activity. However, the peak potential differs slightly, with US-CoAl LDH displaying a more negative peak potential. A more negative peak potential can indicate slightly better catalytic activity, as it suggests that the catalyst can reduce oxygen at a lower overpotential. These results suggest that the LDH produced via ultrasonic synthesis might be slightly more effective or efficient at catalyzing the ORR under the given experimental conditions.

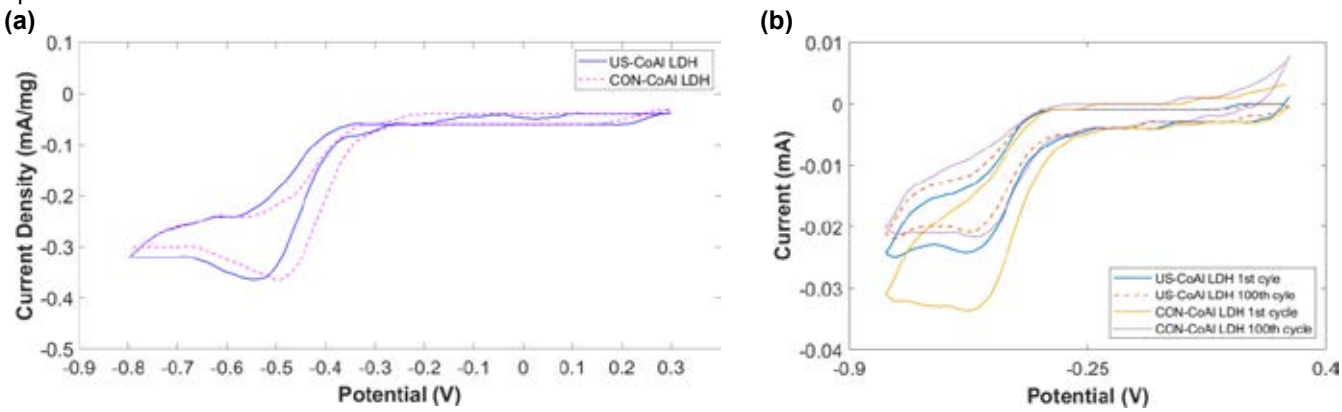

Fig. 4. Cyclic voltammetry analysis of CON-CoAl and US-CoAl LDHs: (a) at a scan rate of 10 mV/s and (b) at 100 mV/s over 100 cycles.

The electrochemical stability of CON-CoAl LDH and US-CoAl LDH catalysts was evaluated over 100 cycles using CV at 100 mV/s scan rate. The stability assessment focused on the changes in peak current between the first and last cycles. For CON-CoAl LDH, the peak current decreased from 0.034 mA in the first cycle to 0.022 mA in the 100th cycle, as shown in Fig. 4b. This corresponds to a 35.3% degradation in activity, indicating a significant decline in performance. In contrast, for the US-CoAl LDH catalyst, the peak current decreased from 0.025 mA in the first cycle to 0.022 mA in the 100th cycle, as shown in Fig. 4b. This corresponds to a 12.0% degradation, suggesting a relatively better retention of activity compared to CON-CoAl LDH. The data indicate that US-CoAl LDH exhibits superior electrochemical stability under identical conditions, with a significantly lower percentage degradation of peak current. In contrast, CON-CoAl LDH shows a higher degradation rate, suggesting a more pronounced loss of catalytic activity over time.

4. CONCLUSIONS

This study highlights the synthesis and electrochemical performance of CoAl LDH catalysts prepared via conventional and ultrasonic spray methods. Both catalysts demonstrated similar maximum oxygen reduction reaction (ORR) activity at a scan rate of 10 mV/s, with comparable peak currents. However, US-CoAl LDH exhibited a more negative peak potential, indicating slightly better catalytic activity due to its ability to reduce oxygen at a lower overpotential. Stability testing over 100 cycles at 100 mV/s revealed that US-CoAl LDH retained 88% of its initial activity, compared to 64.7% for CON-CoAl LDH, confirming the superior durability of the ultrasonic spray-synthesized material.
The improved electrochemical durability and heightened catalytic performance of US-CoAl LDH indicate its viability for use in systems that convert energy, such as in fuel cells and metal-air batteries, where robust stability and effective oxygen reduction reaction (ORR) catalysis are essential. To further improve its performance, integrating other materials, such as conductive carbon supports, graphene derivatives, or doping with noble metals, could boost charge transfer properties and overall activity. These findings underscore the viability of ultrasonic spray synthesis for producing advanced, scalable, and cost-effective catalysts tailored for next-generation energy systems.

ACKNOWLEGMENTS

The authors would like to acknowledge the support of the TÜBİTAK 2224-B – Support Program for Participation in National Scientific Activities.

REFERENCES

1. Kenar ME, Kutluay S, Şahin Ö, Genceli Güner FE (2024) Cobalt-boron-fluoride decorated graphitic carbon nitride composite as a promising candidate catalyst for highly efficient hydrogen production via NaBH4 hydrolysis process. Int J Hydrogen Energy 90:732–746. https://doi.org/10.1016/J.IJHYDENE.2024.09.445
2. Han C, Zhao Y, Yuan Y, et al (2024) Transition metal-based layered double hydroxides and their derivatives for efficient oxygen evolution reaction. Int J Hydrogen Energy 63:918–936. https://doi.org/10.1016/J.IJHYDENE.2024.03.150
3. Esmaeili MS, Mehrpooya M, Ganjali MR (2025) Three-dimensional nanocomposites derived from combined metal organic frameworks doped with Ce, La, and Cu as a bifunctional electrocatalyst for supercapacitors and oxygen reduction reaction. Int J Hydrogen Energy 97:483–500. https://doi.org/10.1016/J.IJHYDENE.2024.11.450
4. Sherryna A, Tahir M, Nabgan W (2022) Recent advancements of layered double hydroxide heterojunction composites with engineering approach towards photocatalytic hydrogen production: A review. Int J Hydrogen Energy 47:862–901. https://doi.org/10.1016/J.IJHYDENE.2021.10.099
5. Büyükkanber K, Ekinci A, Şahin Ö (2024) High catalytic activity of cobalt nanoparticles synthesized by ultrasonic spray method in sodium borohydride hydrolysis. Int J Hydrogen Energy 79:335–345. https://doi.org/10.1016/J.IJHYDENE.2024.06.372
6. Ekinci A, Büyükkanber K, Akdag A, Şahin Ö (2024) Improved catalytic activity in PdCo nanocatalysts synthesized via ultrasonic spray method for PEMFC applications. Int J Hydrogen Energy 92:810–820. https://doi.org/10.1016/J.IJHYDENE.2024.10.293
7. Wang K, Zhang L, Su Y, et al (2018) Photoreduction of carbon dioxide of atmospheric concentration to methane with water over CoAl-layered double hydroxide nanosheets. J Mater Chem A Mater 6:8366–8373. https://doi.org/10.1039/c8ta01309h
8. Guoxiang P, Xinhui X, Jingshan L, et al (2014) Preparation of CoAl layered double hydroxide nanoflake arrays and their high supercapacitance performance. Appl Clay Sci 102:28–32. https://doi.org/10.1016/j.clay.2014.10.003
9. Guo H, Wang Y, Li C, Zhou K (2018) Construction of sandwich-structured CoAl-layered double hydroxide@zeolitic imidazolate framework-67 (CoAl-LDH@ZIF-67) hybrids: Towards enhancing the fire safety of epoxy resins. RSC Adv 8:36114–36122. https://doi.org/10.1039/c8ra06355a
10. Tanaka T, Kameshima Y, Nishimoto S, Miyake M (2012) Determination of carbonate ion contents in layered double hydroxides by FTIR spectrometry. Analytical Methods 4:3925–3927. https://doi.org/10.1039/c2ay25850a
11. Estrada-Moreno JC, Jiménez-Núñez ML, Zavala-Arce RE, et al (2021) X-ray diffraction and FTIR analysis on effect of time and temperature layered double hydroxides synthesis. MRS Adv 6:980–984. https://doi.org/10.1557/s43580-021-00157-3
12. Fui H, Gao S, Ma X, Huang Y (2023) Facile fabrication of CoAl-LDH nanosheets for efficient rhodamine B degradation via peroxymonosulfate activation. RSC Adv 13:29695–29705. https://doi.org/10.1039/d3ra04575g
13. Wang Y, Wang Z, Wu X, et al (2016) Synergistic effect between strongly coupled CoAl layered double hydroxides and graphene for the electrocatalytic reduction of oxygen. Electrochim Acta 192:196–204. https://doi.org/10.1016/j.electacta.2016.01.201

THE SYNERGISTIC EFFECT OF HHO GAS AND GASOLINE-BIOETHANOL BLENDS ON SPARK IGNITION ENGINE EFFICIENCY AND EMISSIONS

[1,2]*Alfredas Rimkus*, [3] *Edward Kozłowski*, [1,4*]*Jonas Matijošius,* [5] *Magdalena Zimakowska-Laskowska*
[1] Vilniaus Kolegija Higher Education Institution, Technical Faculty, Department Transport Engineering, Saltoniškių g. 58 - 1, 08105, Vilnius, Lithuania
[2] Vilnius Gediminas Technical University – Vilnius Tech, Transport Engineering Faculty, Department Automobile Transport, Saulėtekio al. 11, LT-10223 Vilnius
[3] Faculty of Management, Lublin University of Technology, Nadbystrzycka 38, 20-618 Lublin, Poland
[4] Vilnius Gediminas Technical University – Vilnius Tech, Mechanical Science Institute, Saulėtekio al. 11, LT-10223 Vilnius
[5] Environment Protection Centre, Motor Transport Institute, 03-301 Warsaw, Poland

*Corresponding author e-mail: jonas.matijosius@vilniustech.lt

ABSTRACT

The several fuel mixtures, including gasoline-bioethanol combinations (E10 and E70), this work explores the effects of hydrogen and oxygen (HHO) gas on the ecological and energy efficiency characteristics of a spark ignition (SI) engine, were used. Under several air excess ratios (λ), experimental investigation was carried out to assess the effects of HHO gas on brake thermal efficiency (BTE), fuel economy, and emissions. Especially in lean mixtures, results demonstrate that adding HHO gas greatly increases BTE and lowers hazardous emissions including nitrogen oxides (NOx), hydrocarbons (HC), and carbon monoxide (CO). E70 gasoline combined with HHO gas showed the best BTE and lowest emissions, so verifying its possible use as a sustainable solution for maximising engine performance and reducing environmental effect. Programmable control systems and real-time emission analysis were part of advanced experimental settings that guaranteed exact and consistent results, thereby helping to clarify HHO gas as a useful and environmentally benign additive for internal combustion engines.

Keywords: HHO gas, brake thermal efficiency, emissions reduction, bioethanol-gasoline blends.

1. INTRODUCTION

As the use of HHO gas as a fuel additive in internal combustion engines reduces emissions and fuel consumption, it is becoming increasingly important as a sustainable way to improve the environmental friendliness and energy efficiency of gasoline engines. Studies show that HHO gas burns more efficiently overall, reduces fuel consumption in a certain range, and increases the brake thermal efficiency. Including HHO gas increases the indicated mean effective pressure (IMEP) and reduces the burning time. The lean of the combination will determine the outcomes, though [1,2].
Furthermore highly significant are HHO gas cuts in NOx, HC, and CO. Adding relatively little amounts of HHO gas when the engine was idle reduced CO emissions by up to 98% according one study [3]. Burning a mixture of gasoline and bioethanol (E70) with HHO gas reduced CO and HC emissions per another study. When the fuel was not burning completely, the best effects were observed. Further lowering emissions, HO gas accelerates and increases the temperature of burning, hence lowering emissions [4].
One more great advantage is the several applications for HHO gas. Studies have indicated that HHO technologies are more energy efficient since they can be readily included to already in use engine systems. Using HHO gas in power generators and dual-fuel vehicles, for example, improved the thermal efficiency from 28% to 35% and, depending on the load, lowered CO and HC emissions by 7–11% [5]. New technologies such as thermoelectric generators and fast DC power systems are increasingly being used to produce HHO gas [6].
To fully understand the long-term effects of HHO technology on humans, additional research is needed to fully assess engine performance factors such as torque, power, and economy, as well as to determine the technological limits of engine operation [7].
The scientific novelty of this work is confirming under lean mixture conditions the synergistic effects of HHO gas and bioethanol-blended fuels (E70) on lowering emissions (CO, HC, and NOx) and enhancing combustion efficiency. This work also presents cutting-edge experimental methods to assess the practical relevance of HHO gas as a sustainable addition improving gasoline engine ecological and energy efficiency.

2. MATERIALS AND METHODS

The impact of HHO gas on the environmental and energy efficiency of a spark ignition (SI) engine was studied using different fuel mixtures in this study. In the study, E70 fuel (30% gasoline and 70% ethanol) was switched out for E10 fuel (90% gasoline and 10% ethanol) with an extra supply of HHO gas addative. The experiment was carried out using a Nissan Qashqai HR 16DE engine (four cylinders in one cylinder with a four-valve mechanism). It was controlled by a programmable MoTeC M800 electronic control unit (ECU); an AMX 200/100 load bench generated the engine load to

ensure accurate measurement conditions for the study.
Fuel consumption was calculated using an AMX 212F electronic fuel meter; air intake was measured using a BOSCH HFM 5 mass flow meter. The AVL DiCom 4000 analyzer was used to analyze the exhaust gas composition and obtain accurate, consistent emission data. The fuel mixtures were prepared by blending pure gasoline and bioethanol, and their properties were assessed in terms of density, carbon-to-hydrogen (C/H) ratio, and lower heating value. Additionally, a constant flow of 3.8 l/min HHO gas was introduced into the engine's intake manifold to evaluate its effects on combustion processes. Driven by an external energy source, an electrolysis machine created hho gas. With a 700 W power consumption during gas generation, the system's efficiency was at 0.65%. A flashback arrestor was included to the system to protect the HHO generator from any backfire, therefore guaranteeing safety. The throttle was set at 15% and the experimental trials ran at a 2000 rpm constant engine speed. Considering changes in fuel mixture composition and air excess ratio (λ= 1.0, 1.1, 1.2, 1.3, 1.4) the ignition duration was varied over a broad range. This experimental system replicated real-world engine operating circumstances, allowing for a thorough examination of the impacts of fuel mixes and HHO gas delivery under various operating regimes. The study collected data on engine torque, fuel consumption, and BTE. In addition, ecological indicators such as CO, HC, NOx, and CO_2 emissions were measured to thoroughly assess the impact of fuel composition and HHO gas on the engine's performance and emissions.
The findings of this study provide insights into the influence of fuel composition and HHO gas on engine performance and emissions. They also highlight the potential of such fuels and technologies for practical applications in real-world operating conditions.

2.1. Mathematical aparatus

Let $\{(x_i, y_i)\}_{1\le i\le n}$ the set of realisations of features X and Y. Below we analyse the dependence betwen these features as follows (1):

$$y = Ce^{\beta_1 x + \cdots + \beta_k x^k} \tag{1}$$

To estimate the unknown parameters we transform the model (2) to auxiliary form

$$\tilde{y} = \beta_0 + \beta_1 x + \cdots + \beta_k x^k + \varepsilon e^{\beta_1 x + \cdots + \beta_k x^k}, \tag{2}$$

where $\tilde{y} = \log(y)$, $\beta_0 = \log(C)$ and ε is a random variable with $N(0, \sigma^2)$ normal distribution.

The coefficient of determination presents (3) proportion of the variation in the dependent variable that explained by the model and is calculated as follows

$$R^2 = 1 - \frac{\sum_{j=1}^{n} \varepsilon_j^2}{\sum_{j=1}^{n} (\bar{y}_i - \bar{y})^2}, \tag{3}$$

where $\bar{y} = \frac{1}{n}\sum_{j=1}^{n} \tilde{y}_i$.

To assess the quality of the model (1) in explaining the dependent variable (the statistical significance of the model as a whole) at significant level $0 < \alpha < 0$ we define the null hypothesis:
H_0: $R = 0$ (the coefficient of multiple correlation is equal zero or insignificantly differ from zero)
and alternative hypothesis
H_1: $R \neq 0$ (the coefficient of multiple correlation significantly differ from zero).
The test statistic

$$f = \frac{R^2}{1-R^2}\frac{n-k}{k-1}, \tag{4}$$

has Fisher–Snedecor distribution with $(k-1, n-k)$ degrees of freedom.

3. RESULTS AND DISCUSSION

For each fuel type and λ we analyse the influence IT into BTE as follows (5):

$$\log\big(BTE(IT)\big) \overset{def}{=} \log(BTE) = \beta_0^{BTE} + \beta_1^{BTE} IT + \beta_2^{BTE} IT^2 + \varepsilon_{BTE} \tag{5}$$

and the impact of IT on the pollution rate to BTE (6-9):

$$\log\left(\frac{CO}{BTE}(IT)\right) \overset{def}{=} \log\left(\frac{CO}{BTE}\right) = \beta_0^{CO} + \beta_1^{CO} IT + \beta_2^{CO} IT^2 + \varepsilon_{CO,} \quad (6)$$

$$\log\left(\frac{CO_2}{BTE}(IT)\right) \overset{def}{=} \log\left(\frac{CO_2}{BTE}\right) = \beta_0^{CO_2} + \beta_1^{CO_2} IT + \beta_2^{CO_2} IT^2 + \varepsilon_{CO_2,} \quad (7)$$

$$\log\left(\frac{HC}{BTE}(IT)\right) \overset{def}{=} \log\left(\frac{HC}{BTE}\right) = \beta_0^{HC} + \beta_1^{HC} IT + \beta_2^{HC} IT^2 + \varepsilon_{HC}, \quad (8)$$

$$\mathrm{llog}\left(\frac{NOx}{BTE}(IT)\right) \overset{def}{=} \log\left(\frac{NOx}{BTE}\right) = \beta_0^{NOx} + \beta_1^{NOx} IT + \beta_2^{NOx} IT^2 + \varepsilon_{NOx.} \quad (9)$$

For each model the parameters, standard deviation of residuals, determination coefficient and test probability have been estimated.
Additionally the optimal IT has been determined (10-14):

$$IT_{BTE} = \arg_{\max_{IT_{min} \le IT \le IT_{max}}} BTE(IT), \quad (10)$$

$$IT_{CO} = \arg_{\min_{IT_{min} \le IT \le IT_{max}}} \frac{CO}{BTE}(IT), \quad (11)$$

$$IT_{CO_2} = \arg_{\min_{IT_{min} \le IT \le IT_{max}}} \frac{CO_2}{BTE}(IT), \quad (12)$$

$$IT_{HC} = \arg_{\min_{IT_{min} \le IT \le IT_{max}}} \frac{NC}{BTE}(IT), \quad (13)$$

$$IT_{NOx} = \arg_{\min_{IT_{min} \le IT \le IT_{max}}} \frac{NOx}{BTE}(IT). \quad (14)$$

The findings (Table 1) indicate that the incorporation of HHO gas consistently enhances BTE across all evaluated fuel combinations, especially under lean air-fuel situations (elevated λ values). Furthermore, the amalgamation of E70 fuel with HHO gas attains elevated determination coefficients (R^2), signifying a more significant effect on enhancing engine performance and diminishing residual standard deviation in comparison to E10 fuel mixtures.

Table 1. Summary Parameters of model (5), optimal IT, standard deviation of residuals and determination coefficient

Fuel	λ	β_0^{BTE}	β_1^{BTE}	β_2^{BTE}	IT_{BTE}	σ	R^2	p.val
E10	1.0	-1.2538	0.0185	-0.000385	24.04	0.00523	0.7264	$< 2.2 * 10^{-16}$
10+HHO	1.0	-1.2549	0.0187	-0.000403	23.18	0.00326	0.8465	$< 2.2 * 10^{-16}$
E70	1.0	-1.1177	0.0085	-0.000194	22.06	0.00373	0.5405	$3 * 10^{-8}$
E70+HHO	1.0	-1.1489	0.0112	-0.000260	21.48	0.00299	0.8099	$< 2.2 * 10^{-16}$
E10	1.1	-1.2348	0.0180	-0.000353	25.53	0.00426	0.8531	$< 2.2 * 10^{-16}$
E10+HHO	1.1	-1.2043	0.0156	-0.000317	24.70	0.00400	0.7995	$< 2.2 * 10^{-16}$
E70	1.1	-1.1902	0.0132	-0.000247	26.74	0.00303	0.9149	$< 2.2 * 10^{-16}$
E70+HHO	1.1	-1.1914	0.0138	-0.000275	24.98	0.00287	0.8645	$< 2.2 * 10^{-16}$
E10	1.2	-1.3921	0.0274	-0.000480	28.48	0.00562	0.9488	$< 2.2 * 10^{-16}$
E10+HHO	1.2	-1.3204	0.0221	-0.000393	28.05	0.00752	0.8563	$< 2.2 * 10^{-16}$
E70	1.2	-1.3443	0.0238	-0.000424	28.08	0.00451	0.9511	$< 2.2 * 10^{-16}$
E70+HHO	1.2	-1.3009	0.0203	-0.000365	27.78	0.00414	0.9383	$< 2.2 * 10^{-16}$
E10	1.3	-1.6093	0.0343	-0.000520	33.04	0.00575	0.9370	$< 2.2 * 10^{-16}$
E10+HHO	1.3	-1.6104	0.0357	-0.000564	31.67	0.00582	0.9033	$< 2.2 * 10^{-16}$
E70	1.3	-1.4010	0.0223	-0.000321	34.76	0.00441	0.9462	$< 2.2 * 10^{-16}$
E70+HHO	1.3	-1.3083	0.0173	-0.000261	33.14	0.00770	0.6843	$< 2.2 * 10^{-16}$
E10	1.4	-1.6552	0.0291	-0.000360	40.35	0.00690	0.9726	$< 2.2 * 10^{-16}$
E10+HHO	1.4	-1.6786	0.0327	-0.000431	37.86	0.00521	0.9798	$< 2.2 * 10^{-16}$
E70	1.4	-1.6966	0.0351	-0.000456	38.48	0.00563	0.9821	$< 2.2 * 10^{-16}$
E70+HHO	1.4	-1.5671	0.0291	-0.000386	37.67	0.00592	0.9660	$< 2.2 * 10^{-16}$

The determination coefficient is high. At significant level 0.05 for each fuels and λ for model null hypothesis H_0 should be rejected in favour of the alternative hypothesis, thus the coefficient of multiple correlation significantly differ from zero. From Table 1 we can conclude, that as parameter λ the optimal IT also increases.

The BTE of all fuel blends is considerably enhanced by the addition of HHO gas, with the E70+HHO combination obtaining the highest BTE values. Additionally, the combination of bioethanol-rich fuels with HHO gas significantly reduces CO, HC, except NOx emissions, thereby demonstrating its efficacy in improving combustion efficiency and minimizing environmental impact.

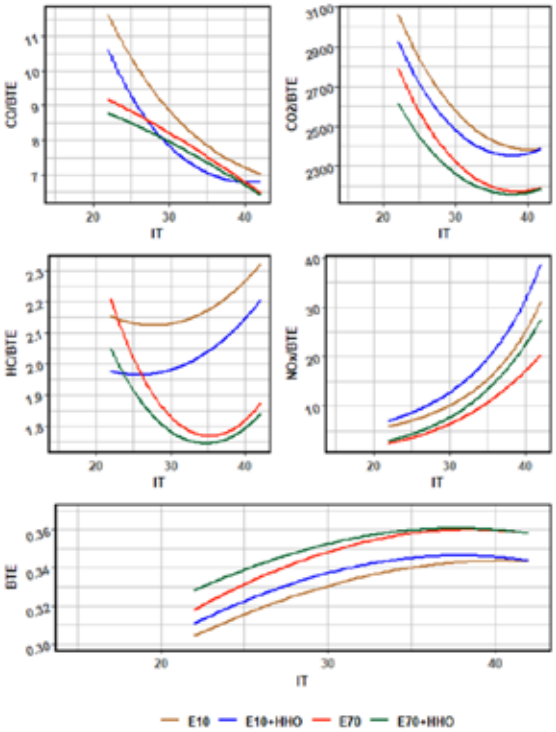

Fig. 1. BTE and pollutant ratios to BTE due to fuel type for λ =1.4

4. CONCLUSIONS

1. The introduction of HHO gas, particularly under lean mixture conditions, significantly improves the combustion efficiency of gasoline-bioethanol combinations in spark ignition engines.
2. With the best environmental benefits seen in E70 fuel blends, HHO gas fundamentally reduces harmful emissions such as CO, HC, and NOx.
3. The best BTE comes from combining HHO gas with bioethanol-rich fuel mixes like E70, therefore proving their ability to raise engine performance.
4. The findings validate the feasibility of including HHO gas as a sustainable additive in current internal combustion engines, so offering a route towards more environmentally friendly and effectively run vehicles.

REFERENCES

1. Zhao Z, Huang Y, Yu X, Guo Z, Li M, Wang T. 2022. Effect of brown gas (HHO) addition on combustion and emission in gasoline engine with exhaust gas recirculation (EGR) and gasoline direct injection. Journal of Cleaner Production 360:132078. https://doi.org/10.1016/j.jclepro.2022.132078.
2. Arjun TB, Atul KP, Muraleedharan AP, Walton PA, Bijinraj PB, Raj AA. 2019. A review on analysis of HHO gas in IC engines. Materials Today: Proceedings 11:1117–29. https://doi.org/10.1016/j.matpr.2018.12.046.
3. Salek F, Zamen M, Hosseini SV, Babaie M. 2020. Novel hybrid system of pulsed HHO generator/TEG waste heat recovery for CO reduction of a gasoline engine. International Journal of Hydrogen Energy 45:23576–86. https://doi.org/10.1016/j.ijhydene.2020.06.075.
4. Rimkus A, Mejeras G, Matijošius J. 2023. The influence of hydrogen and oxygen (HHO) gas on engine characteristics under the effect of the lean mixtures of gasoline and bioethanol. International Journal of Hydrogen Energy 48:39612–24. https://doi.org/10.1016/j.ijhydene.2023.07.167.
5. Shajahan MI, Sambandam P, Michael JJ, Abdelmoneam Hussein HM. 2024. Environmental impact of oxyhydrogen addition on high-speed gasoline engine characteristics. Energy Sources, Part A: Recovery, Utilization, and Environmental Effects 46:15632–45. https://doi.org/10.1080/15567036.2020.1812768.
6. Gutarevych Y, Shuba Y, Matijošius J, Karev S, Sokolovskij E, Rimkus A. 2018. Intensification of the combustion process in a gasoline engine by adding a hydrogen-containing gas. International Journal of Hydrogen Energy 43:16334–43. https://doi.org/10.1016/j.ijhydene.2018.06.124.
7. Ayissi MZ, Newen IA, Alloune R, Bitondo D. 2022. Effects of Gasoline and Hydrogen Blends on Exhaust Gas Emissions and Fuel Consumption from Gasoline Internal Combustion Engines. Journal of Combustion 2022:5526205. https://doi.org/10.1155/2022/5526205.

ANALYSIS OF $MgCr_{2-x}Mn_xO_4$ (x=0.1/0.5/1) SPINEL AND LSM COMPOSITE COATINGS AS A PROTECTIVE LAYER FOR SOFC INTERCONNECT

[1]*Huseyin Unsal, [1]Cristian D. Savaniu, [1]John T.S. Irvine
[1] University of St Andrews, School of Chemistry, Fife, KY16 9ST, Scotland, UK

*Corresponding author e-mail: hu1@st-andrews.ac.uk

ABSTRACT

In this study $MgCr_{2-x}Mn_xO_4$ (x=0.1/0.5/1) spinel and LSM composite layers were deposited on 430 stainless steel. The coated steels were exposed to 500 hour oxidation at 800 °C. The growing Cr_2O_3 layer has been investigated, which is cause of chromium poisoning and a critical parameter for the electrical conductivity of SOFC interconnects. Interface analysis was carried out using scanning electron microscopy. Results demonstrated that for the spinel protection increasing chromium content in the B-site decreased forming oxide layers. After oxidation, $MgCr_{1.9}Mn_{0.1}O_4$ and LSM composite coating offered high stability and the growing Cr_2O_3 layer stopped at 2 microns.

Keywords: SOFC, Interconnect, Chromium Poisoning, Spinel Coating

1. INTRODUCTION

Solid oxide fuel cells are energy-converting devices that convert chemical energy to electrical energy. SOFC has a large fuel selection from hydrogen to hydrocarbons [1]. After the chemical energy conversion, SOFC usually produces only water as a waste product. For this reason, these devices are classified as environmentally friendly energy. However, they operate at high temperatures and this negatively affects cell components. One of the most affected components is the interconnect due to its metallic structure, which has low oxidation resistance. Stainless steel contains 10-25% chromium in its composition and can form easily Cr_2O_3 layer in high temperatures 600-800 oC. Forming a Cr_2O_3 layer increases area specific resistance, and can cause delamination problems and chromium poisoning throughout the cathode layer with the diffusion of chromium volatiles[2]. To address this issue, there are two methods which are new alloy design via doping elements and coating with protective layers[3]. The coating approach is a more common method because of cost-effective manufacturing [4].

2. EXPERIMENTAL

In this study, as an interconnect substrate AISI 430 stainless steel was selected. They were cut into 2x10x10mm dimensions. Square steel pieces were sanded with silicon carbide P240 and P600. In the next step the stells were kept in ultrasonic acetone bath to clean the remaining particles after polishing. For the spinel protective layer, three different spinel powders $MgCr_{2-x}Mn_xO_4$ (x=0.1/0.5/1) were prepared with sol-gel combustion method. For the second layer coating commercial LSM ($(La_{0.65}Sr_{0.35})_{0.95}MnO_3$, Praxair, 99.9%) powder was used. In the ink preparation period, appropriate amounts of terpineol, DBP (dibutyl phthalate), PEG 300 (polyethylene glycol), PVB (polyvinyl butyral) was mixed with spinel and LSM powders. It is obtained high adhesion inks for screen printing and then deposited on the steel surface. After coating the substrates were exposed drying and sintering process in order room temperature, 80 ^{0}C in air, 800 ^{0}C in 5%H2/Ar, and 800 ^{0}C in air furnaces. After obtaining coated steels, they were oxidized at 800 ^{0}C 500 hour in air. Firstly, X-ray diffraction patterns were collected on a PANalytical X-ray diffractometer operating with CuKα radiation (λ = 1.5406 Å). The range of 2θ is 5-90˚ for the spinel powders. Secondly, the Scanning Electron Microscope (SEM) was used to observe cross-section interfaces of coated steels. Finally, area specific resistance (ASR) test was carried out by using two probes four-point DC method.

3. RESULTS AND DISCUSSION

X-ray diffraction (XRD) patterns of spinel powders are illustrated in Fig.1 with different amounts of manganese doping. All spinels have a single-phase cubic structure without any secondary phase formations. Diffracted peak positions were matched with collected magnesium chromite spinel data. Obtained spinels were deposited on the steel surface as first layer and secondary layer LSM were applied. Spinel and perovskite bilayer coating was studied by Ludwig et. al [5], they used $NiFe_2O_4$ and $La_{0.6}Sr_{0.4}CoO_3$ for coating on the steel surface and observed dual layer coating increase oxidation resistance. In Fig.2, bilayer coated steel SEM cross-section analysis is demonstrated together EDS (Energy-dispersive X-ray spectroscopy) elemental line analysis after 500-hour oxidation. According to the results, all samples showed stability against chromium poisoning. The growing Cr_2O_3 oxide layer is a critical parameter in decreasing electrical conductivity. Here, it is detected that chromium content in the spinel composition effects chromium outward diffusion from steel. After heat treatment $MgCr_{1.9}Mn_{0.1}O_4$ and LSM coated steel showed best performance with the growing Cr_2O_3 oxide layer stayed at 2 microns thickness.

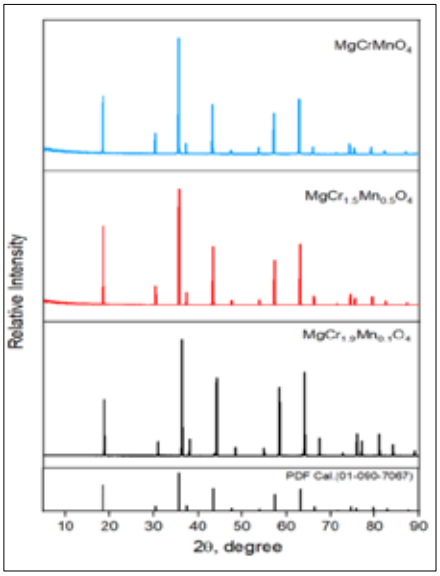

Fig.1. XRD patterns of spinel powders

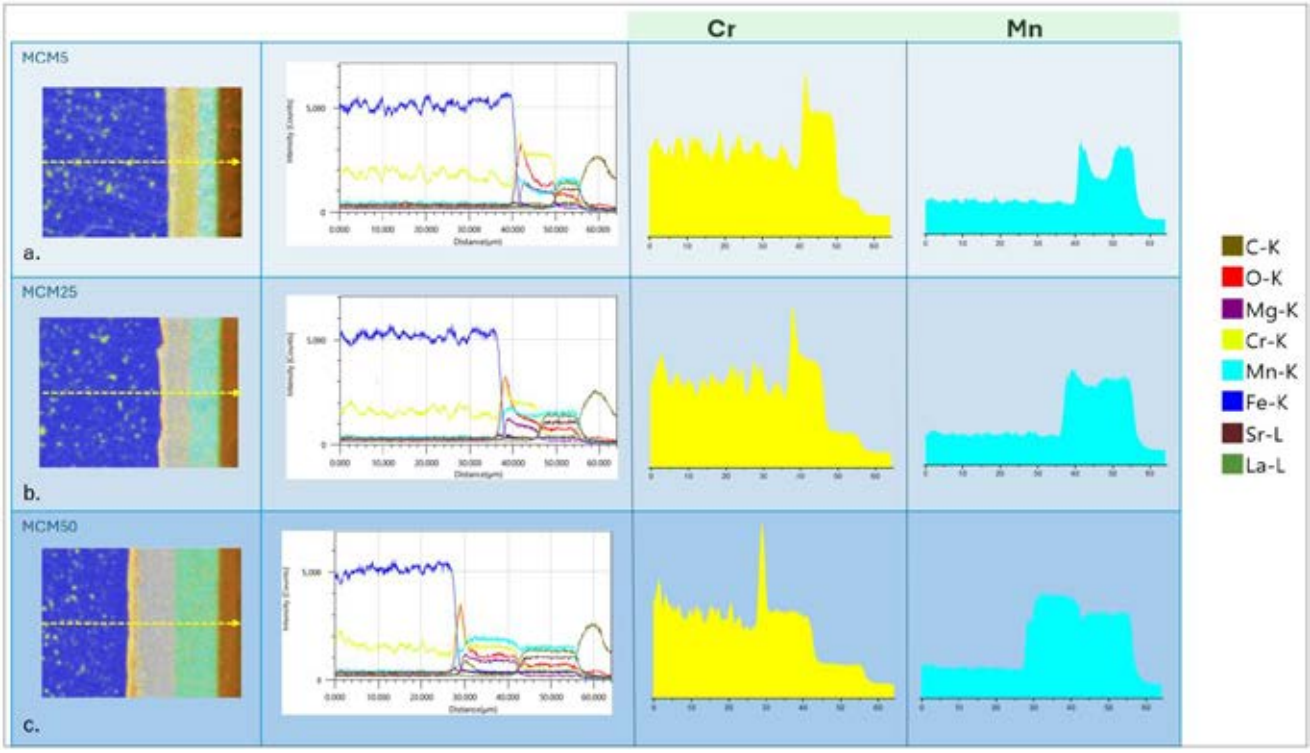

Fig. 2. SEM Cross-Section analysis of coated 430 stainless steel after 500-hour oxidation at 800 ºC a.MCM5: $MgCr_{1.9}Mn_{0.1}O_4$ and LSM b.MCM25: $MgCr_{1.5}Mn_{0.5}O_4$ and LSM c.MCM50: $MgCrMnO_4$ and LSM

Electrical tests were measured before and after 500-hour oxidation at 800 °C of coated steels (Fig. 3). Significant increase in ASR values was noticed for $MgCrMnO_4$ and LSM coated steel with a rise from 50 to 94 mΩ.cm^2. However, $MgCr_{1.9}Mn_{0.1}O_4$ and $MgCr_{1.5}Mn_{0.5}O_4$ dual-coated steel samples showed stability before-after oxidation tests.

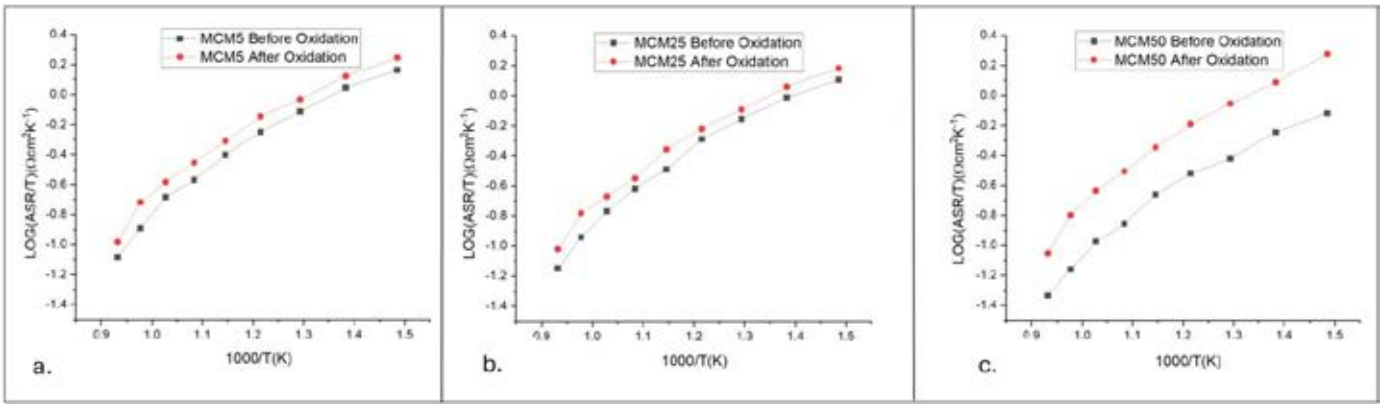

Fig. 3. ASR results with temperature plots before and after 500-hour oxidation at 800 °C. a.MCM5: $MgCr_{1.9}Mn_{0.1}O_4$ and LSM b.MCM25: $MgCr_{1.5}Mn_{0.5}O_4$ and LSM c.MCM50: $MgCrMnO_4$ and LSM

4. CONCLUSIONS

After the oxidation test, it is observed that spinel composition has critical importance against oxidation. The results showed that manganese-doped Mg chromite spinel coating on steel surfaces has high oxidation resistance. However, increasing manganese in spinel content enables to grove Cr_2O_3 layer, which can cause spallation and delamination problems in long-term operating conditions. Composite $MgCr_{1.9}Mn_{0.1}O_4$ spinel coating with LSM dramatically reduced the growing Cr_2O_3 oxide layer and showed stable ASR results after-before oxidation. Dual-layer coating with magnesium-based chromium-rich spinel and LSM coating is promising for SOFC interconnect materials.

REFERENCES

[1] Zamfirescu C, and Dincer I. 2008. Thermodynamic performance analysis and optimization of a SOFC-H+ system. Thermochim Acta,486:32–40.
[2] Pan Y, Liu Y, Shi D, Wang J, Xie Y, Wang R, and Xu Z. 2024. Fabrication and Oxidation Behavior of the Cu−Fe Spinel Coating for SOFC Steel Interconnect Applications. ACS Appl. Energy Mater, 7:4950−4959
[3] Mao J, Wang E, Wang H, Ouyang M, Chen Y, Hu H, Lu L, Ren D, and Liu Y. 2023. Progress in metal corrosion mechanism and protective coating technology for interconnect and metal support of solid oxide cells. Renewable and Sustainable Energy Reviews,185:113597.
[4] Zhou L, Mason JH, Li W, and Liu X. 2020. Comprehensive review of chromium deposition and poisoning of solid oxide fuel cells (SOFCs) cathode materials. Renewable and Sustainable Energy Reviews, 134:110320.
[5] Ludwig GA, Korb MA, Lima DAS, Macías MA, Gauthier GH, and Malfatti CF. 2015. Protective coatings for AISI 430 stainless steel at high temperatures using perovskite oxides La0.6Sr0.4CoO3 on spinel type oxide NiFe2O4. Ceramics International, 41:14561–73.

ENVIRONMENTAL ASSESSMENT OF A HYBRID SHIP ELECTRIFICATION SYSTEM INTEGRATING MOLTEN CARBONATE FUEL CELLS, BATTERY, AND WASTE HEAT RECOVERY

Onur Yuksel[1,2*], *Eduardo Blanco-Davis*[1], *Viknash Shagar*[1], *Andrew Spiteri*[1], *David Hitchmough*[1], *Maria Carmela Di Piazza*[3], *Marcello Pucci*[3], *Nikolaos Tsoulakos*[4], *Jin Wang*[1]

[1] Liverpool Logistics Offshore and Marine Research Institute (LOOM), School of Engineering, Liverpool John Moores University, Byrom Street, Liverpool, L3 3AF, UK.

[2] Zonguldak Bülent Ecevit University, Marine Engineering Department, Maritime Faculty, Kepez District, Hacı Eyüp Street, No:1 67300, Kdz. Ereğli/Zonguldak, Türkiye.

[3] National Research Council of Italy (CNR), Institute of Marine Engineering (INM), via Ugo La Malfa 153, 90146 Palermo, Italy.

[4]Laskaridis Shipping Co. LTD. address is 5 Xenias Str. & Ch. Trikoupi, Kifissia, 14562, Athens, Greece.

*Corresponding author e-mail: O.Yuksel@ljmu.ac.uk

ABSTRACT

This study aims to analyse the integration of a hybrid system, including a Molten Carbonate Fuel Cell (MCFC), battery and an organic Rankine cycle-based waste heat recovery system (WHRS) into marine power distribution through numerical simulations and environmental assessments using sensory data. It contributes to the literature by evaluating the environmental viability of a liquefied natural gas-powered MCFC system as an investment for maritime decarbonisation goals. The data collection was undertaken on a Kamsarmax bulk carrier. The environmental assessment examines the plant's upstream (well-to-tank) and operational (tank-to-wake) emissions. Results indicate that implementing LNG tanks and MCFC has required design modifications to accommodate additional volume and weight. The hybrid MCFC/Battery/WHRS configuration has significantly reduced the marine power distribution plant's equivalent carbon dioxide (CO_2-Eq). Although methane (CH_4) emissions have increased due to LNG usage, non-greenhouse gas emissions have decreased considerably. A rise in combined CH_4 emissions from propulsion and electrification plants has been found. However, the hybrid system has achieved a considerable reduction in CO_2-Eq.

Keywords: Hybrid power system, fuel cell, maritime decarbonization, emissions, ship electrification

1. INTRODUCTION

Maritime transportation has been responsible for a great deal of air pollution due to the increasing usage of fossil fuels and its utilisation share in transportation [1, 2]. Marine diesel engines (MDE) in shipping have produced 3 % of global greenhouses (GHGs) that increase the risk of global warming while also yielding other health hazards [3-5]. To decrease the environmental damage due to shipping activities, the International Maritime Organization (IMO) has entered emission reduction objectives into force and revised them in July 2023 [6]. The updated decarbonisation targets aim to reduce emissions by 20% before 2030 and 70% by 2040 relative to 2008. Finally, there is an intention to achieve net-zero emissions by 2050 [7]. Energy efficiency improvements can be achieved through conventional measures such as engine power limitation, alternative energy sources or speed optimization [8, 9].

Molten Carbonate Fuel Cells (MCFC) have been investigated as an option in hybrid or stand-alone applications for marine propulsion and power distribution units focusing on large commercial vessels. Dimopoulos et al. [10] conducted an exergy analysis on MCFC and WHRS while optimising the configurations. Optimising the simple MCFC system has improved exergy efficiency. In the combined cycle MCFC, heat recovery boosted power by 40%and achieved a 45% relative increase in efficiency. İnal and Deniz [11]presented a case study reducing emissions based on MCFC usage on a chemical tanker's propulsion unit., Baccioli et al. [12] created an MCFC-MDE hybrid model to gauge the efficiency. Compared to the sole MDE-utilised conventional scenario, efficiency improvement was obtained. Korkmaz et al. [13] performed a benchmarking of different FC types and found that a MCFC/battery combination led to a 49.75% operational CO_2 reduction. Yuksel and Bayraktar [14] built an analysis considering MCFC plants in propulsion and auxiliary systems and obtained a 51.7% CO_2 decrease.

This study's motive is to provide an analysis of hybrid MCFC/Battery/WHRS integration to the marine power distribution plant through numerical simulation, and environmental performance assessments using sensory data for more precise data analysis.

2. MATERIALS AND METHODS

This section explains the framework and mathematical background of the methodology used while highlighting the specifications of the case study elements. Data collection included power output, engine speed, fuel consumption of main and auxiliary engines and vessel-specific parameters such as speed, draft, and deadweight over 1.96 years. The study's industry partner provided the ADLM-sourced data and noon reports from the Kamsarmax bulk carrier, Laskaridis Shipping Co. Ltd. The data was analysed and an MCFC/Battery/WHRS hybrid system was designed to meet the vessel's power demand. A numerical model was developed to estimate the LNG consumption of the MCFC and benchmark its

emission reduction against conventional diesel engines. The algorithm calculates exhaust flow and temperature based on engine power, followed by power generation from the WHRS. It then evaluates the main and auxiliary engines' utilization times, fuel consumption, and emissions. Subsequently, LNG consumption and emissions from the MCFC system are computed. Results are logged, converted into data frames, and exported to spreadsheets for analysis.

2.1. Case Study

The vessel selected for the case study is a Kamsarmax bulk carrier, the M/V KASTOR. Constructed in 2020, the ship has a deadweight (DWT) of 80,996 tons and a length overall (LOA) of 229 meters. Its propulsion system comprises of a HYUNDAI 6S60ME-C8.5 engine, capable of delivering a maximum power output of 9,930 kW. Additionally, the vessel is equipped with an electrification plant consisting of three YANMAR 6EY22LW diesel generators (DGs), each providing a terminal power capacity of 720 kW. Figure 1 indicates a simplified schematic of the proposed hybrid marine power distribution system, which integrates an MCFC, battery, and WHRS. The diagram also includes the LNG cracking process based on water-gas shift reactions.

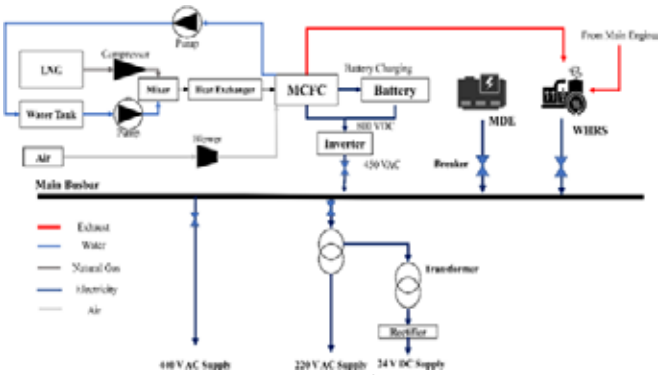

Fig. 1. The schematic of the hybrid plant

The conventional power plant consists of three equivalent DGs with a total output of 2,160 kW. In contrast, the hybrid plant features a single MCFC unit with a power output of 1,400 kW and a battery with a capacity of 40 kWh to accommodate instantaneous increases in power demand. The WHRS can generate up to 200 kW of electrical power, primarily utilising waste heat from the main engine's exhaust, with supplemental heat from the MCFC when necessary. The MCFC unit has an LNG reforming system for hydrogen production. One DG is maintained to ensure emergency reserve. The battery cell for assembling the stack utilized in the hybrid configuration to support the SureSource 1500 MCFC system is the Panasonic NCR18650GA, featuring a capacity of 3.45 Ah and a nominal voltage of 3.6V. The specifications of the MCFC unit employed in the system are presented in Table 1. LNG consumption and emissions of MCFC system have been computed from the coefficients given in Table 1 depending on the energy generated.

Table 1. MCFC specifications[15].

Parameter	Value	Unit
Electric Power Output	1400	kW
Electrical Efficiency	47%±2%	-
LNG Consumption	615.12	m³/h
NO_x	0.0045	kg/MWh
CO_2	444.5	kg/MWh
PM	9.07*106	kg/MWh
SOx	0.000045	kg/MWh
Weight	48.53	t
Length/Width/Diameter	16.98/3.88/6.09	m

2.2. Modelling Background

The WHRS utilises an Organic Rankine Cycle (ORC) to generate electricity from the exhaust waste heat. The exhaust flow rates and temperatures of the main engine after the turbine exit data have been gathered from the main engine (ME) manufacturer's datasheet [16]. The ORC model is based on the models developed by Konur et al. [17]. Equation 1 indicates the calculation of WHRS power generation $\dot{W}_{WHRS}$) in kW [18].

$$\dot{W}_{WHRS}\ (kW) = \dot{m}_{ex} \times \left(T_{in,\,ex} - T_{out,\,ex}\right) \times C_{p,\,ex} \times \eta_{ORC}. \quad (1)$$

where $\dot{m}_{ex}$ represents the exhaust mass flow rate in kg/s, $T_{in,\,ex}$ denotes the inlet temperature of the exhaust (after the

exhaust boiler), and $T_{out,\,ex}$ is the outlet temperature from the ORC, which is set at 100°C. The specific heat capacity at constant pressure, $C_{p,\,ex}$, is the amount of thermal energy the exhaust gas emits or absorbs when its temperature changes, assuming constant pressure, and is taken to be 1.089 kJ/kg [19]. The efficiency of ORC (η_{ORC}) is 13.2% [17].

The algorithm calculates the required engine power and the number of active generators for each time interval (t = 1 minute). In the simulation, the load and power of each generator were determined, and their specific fuel consumption was obtained by interpolating the curve provided by the manufacturer. The load distribution has been established using the model presented by Yuksel and Koseoglu [4]. The operational emissions (OE) in g of the MCFC and MDEs have been calculated employing the operational emission factors (OEF) given in Table 1 (for MCFC) and Table 2 (for heavy fuel oil (HFO)) [14]. The OEF and upstream emission factors (UEF)for HFO and the UEF for LNG are presented in Table 2.

Table 2. Emissions of the main propulsion plant [20-22].

Emission Factor	CO_2	N_2O (g/kWh)	CH_4 (g/kWh)	NO_x	SO_x	PM	VOC
LNG - UEF	0.131	0.004	1.718	0.007	0.158	0	0
HFO - UEF	0.147	0.004	0.879	0.010	0.102	0.022	0
HFO – OEF	3.114	0.00015	0.00006	0.903	0.025	0.00278	0.004

The LNG – UEF SOx coefficients, nitrous oxide (N_2O), and methane (CH_4) units are in g/kWh, while others are in g-UE/g-OE. Equation 2 indicates the calculation of upstream emissions (UE) depending on the unit of the UEF [1].

$$UE(g)= \sum P\ (kW) \times\ t(h) \times UEF\ (\frac{g}{kWh})\ \text{or}\ UE(g)= UEF\ \left(\frac{g\text{-}UE}{g\text{-}OE}\right) \times OE\ (g) \quad (2)$$

The power output of the electrification plant, in general, is depicted as P in Equation 2. The equivalent CO_2 (CO_2-Eq) considering the global warming potential for 100 years has been calculated using the IMO Life Cycle Assessment Guideline for alternative fuels [23]. The CH_4 slip in MCFCs has been insignificant, unlike dual-fuel engines, and can be prevented by smart engineering applications [24].

3. FINDINGS

The analysis spans 17,167 operating hours (1.96 years), covering the entire operation period. Fuel consumption was measured at 8,851.62 t for the ME and 1,823.15 t for the DGs, while the MCFC LC required 3,491.13 t to meet the same power demand. Accordingly, the LNG capacity of the hybrid plant was set at 655.95 m³, with a reduced HFO capacity for the MDEs calculated at 2,425.52 m3. The marine power distribution plant delivered 6,749.27 MWh over 1.96 years, averaging 3,443.93 MWh annually. Table 3 summarises emissions from the main propulsion plant during this period.

Table 3. Emissions of the main propulsion plant

Pollutant	OE	UE	Total
CO_2	27,563.96	4,051.90	31,615.86
N_2O	1.33	0.19	1.52
CH_4	0.53	41.97	42.50
CO_2-Eq	27,930.68	5,277.62	33,208.30
NO_x	7,993.02	79.93	8,072.95
SO_x	221.29	22.57	243.86
PM	24.61	0.54	25.15
VOC	27.26	0.00	27.26

The propulsion plant has emitted 33,208.3 tons of CO_2-eq over 1.96 years, resulting in an average annual emission of 16,943 tons of CO_2-eq. NOx emissions have been the second highest, averaging 4,118.85 tons (t) annually. Fig. 2 illustrates the operational and upstream emissions for conventional and hybrid marine power distribution plants. Fig. 2 shows that the conventional plant emitted much more CO_2 overall than the hybrid plant. Notably, the hybrid plant eliminated operational N_2O emissions, but the upstream component remains the same. Likewise, the hybrid plant eliminated operational CH_4 emissions.

Figure 3 indicates the non-GHG emissions from the hybrid and conventional plants. The hybrid plant is shown to eradicate overall NOx emissions. Operational SOx emissions were effectively eliminated. LNG usage has been proven to reduce SOx upstream emissions substantially.

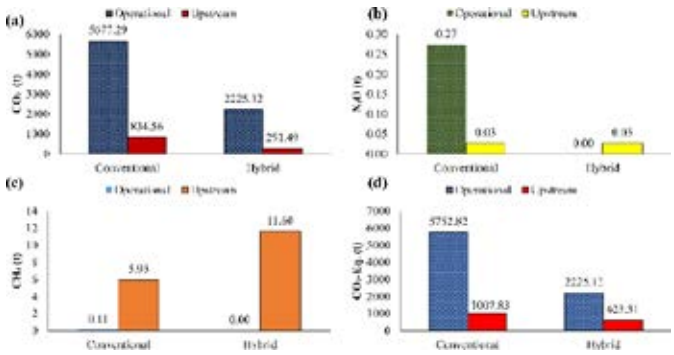

Fig. 2. GHG emissions of the ship electrification plants: (a) CO_2, (b) N_2O, (c) CH_4, and (d) CO_2-Eq.

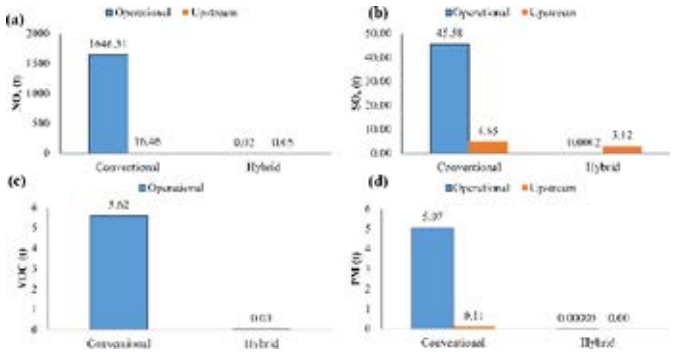

Fig. 3. Other emissions of the ship electrification plants: (a) NOx, (b) SOx, (c) VOC, and (d) PM.

LNG avoids upstream PM emissions from HFO. Additionally, the hybrid unit heavily reduces operational PM and operational VOC emissions.

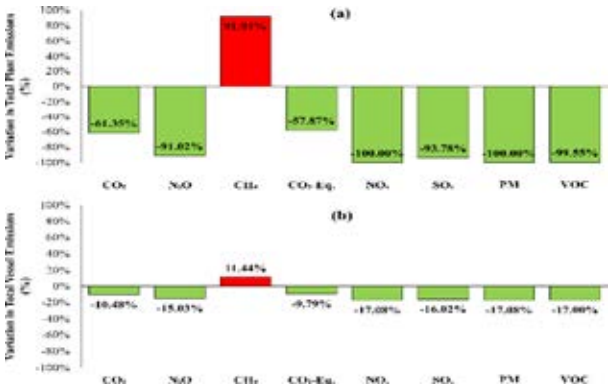

Fig. 4. Emission variations of the hybrid system in (a) sole electrification plant and (b) overall vessel emissions including propulsion unit in comparison with that using the conventional system.

Figure 4 summarizes total emissions from the electrification plant and combined emissions from the power and propulsion units, highlighting significant reductions in NOx, SOx, PM, and VOC emissions achieved through the hybrid configuration. The total emissions of the ship's electricity generation plant have been reduced, except for CH_4, which increased significantly, as shown in Figure 4 (a). The overall CO_2 reduction of the plant is considerable, yielding a slight decrease in the overall emissions of the propulsion and electrification plants. Despite the small CH_4 increment in combined emissions, the hybrid plant achieved a CO_2-Eq decrease while other emissions have been reduced drastically.

4. CONCLUSIONS

This study evaluated the integration of an MCFC/Battery/WHRS hybrid system into a marine electrification plant using a mathematical model supported by sensor-based data from a Kamsarmax bulk carrier recorded over a period of nearly two years. Environmental performance was assessed, including a future cost projection scenario, to examine the viability of an LNG-powered MCFC system as an alternative solution to decarbonize the maritime sector. The analysis incorporated upstream and operational emissions. Key findings include:

- The MCFC/Battery/WHRS hybrid system reduced CO_2-Eq emissions from the marine power distribution plant by 57.87%.
- CH_4 emissions increased due to LNG usage, but non-GHG emissions were significantly reduced.
- Despite an 11.44% rise in combined CH_4 emissions from propulsion and electrification plants, the hybrid system achieved a 9.79% reduction in overall CO_2-Eq emissions.

REFERENCES

1. Yuksel, O., O. Konur, M. Pamik, and M. Bayraktar, *The economic and environmental assessment of alternative marine fuels and nuclear energy utilization on a floating power plant.* Environ Sci Pollut Res Int, 2024.
2. Ammar, N.R. and I.S. Seddiek, *Hybrid/dual fuel propulsion systems towards decarbonization: Case study container ship.* Ocean Engineering, 2023. **281**: p. 114962.
3. Styhre, L., H. Winnes, J. Black, J. Lee, and H. Le-Griffin, *Greenhouse gas emissions from ships in ports – Case studies in four continents.* Transportation Research Part D: Transport and Environment, 2017. **54**: p. 212-224.
4. Yuksel, O. and B. Koseoglu, *Numerical simulation of the hybrid ship power distribution system and an analysis of its emission reduction potential.* Ships and Offshore Structures, 2023. **18**(1): p. 78-94.
5. Yüksel, O. and B. Köseoğlu, *Regression Modelling Estimation of Marine Diesel Generator Fuel Consumption and Emissions.* Transactions on Maritime Science, 2022. **11**(1): p. 79-94.
6. Tu, H., Z. Liu, and Y. Zhang, *Study on Cost-Effective Performance of Alternative Fuels and Energy Efficiency Measures for Shipping Decarbonization.* Journal of Marine Science and Engineering, 2024. **12**(5).
7. Ejder, E., S. Dinçer, and Y. Arslanoglu, *Decarbonization strategies in the maritime industry: An analysis of dual-fuel engine performance and the carbon intensity indicator.* Renewable and Sustainable Energy Reviews, 2024. **200**: p. 114587.
8. Bayraktar, M. and O. Yuksel, *A scenario-based assessment of the energy efficiency existing ship index (EEXI) and carbon intensity indicator (CII) regulations.* Ocean Engineering, 2023. **278**.
9. Konur, O., O. Yuksel, S. Aykut Korkmaz, C. Ozgur Colpan, O.Y. Saatcioglu, and B. Koseoglu, *Operation-dependent exergetic sustainability assessment and environmental analysis on a large tanker ship utilizing Organic Rankine cycle system.* Energy, 2023. **262**.
10. Dimopoulos, G.G., I.C. Stefanatos, and N.M.P. Kakalis, *Exergy analysis and optimisation of a marine molten carbonate fuel cell system in simple and combined cycle configuration.* Energy Conversion and Management, 2016. **107**: p. 10-21.
11. İnal, Ö.B. and C. Deniz, *Emission Analysis of LNG Fuelled Molten Carbonate Fuel Cell System for a Chemical Tanker Ship: A Case Study.* Marine Science and Technology Bulletin, 2021. **10**(2): p. 118-133.
12. Baccioli, A., A. Liponi, J. Milewski, A. Szczęśniak, and U. Desideri, *Hybridization of an internal combustion engine with a molten carbonate fuel cell for marine applications.* Applied Energy, 2021. **298**: p. 117192-117192.
13. Korkmaz, S.A., K.E. Erginer, O. Yuksel, O. Konur, and C.O. Colpan, *Environmental and economic analyses of fuel cell and battery-based hybrid systems utilized as auxiliary power units on a chemical tanker vessel.* International Journal of Hydrogen Energy, 2023. **48**(60): p. 23279-23295.
14. Yuksel, O. and M. Bayraktar, *THE ASSESSMENT OF MOLTEN CARBONATE FUEL CELL USAGE AS THE MAIN AND AUXILIARY ENGINES ON A TANKER SHIP*, in *2nd International İzmir Congress on Life, Engineering, and Applied Sciences*. 2023: Izmir.
15. FuelCellEnergy. *SureSource 1500' 1.4 MEGAWATTS*. 2019 [cited 2024 01/05/2024]; Available from: https://d3pcsg2wjq9izr.cloudfront.net/files/download/457994/55.pdf.
16. MAN. *CEAS engine calculations*. 2024 [cited 2024 17/09/2024]; Available from: https://www.man-es.com/marine/products/planning-tools-and-downloads/ceas-engine-calculations.
17. Konur, O., O. Yuksel, S.A. Korkmaz, C.O. Colpan, O.Y. Saatcioglu, and I. Muslu, *Thermal design and analysis of an organic rankine cycle system utilizing the main engine and cargo oil pump turbine based waste heats in a large tanker ship.* Journal of Cleaner Production, 2022. **368**.
18. Konur, O., O.Y. Saatcioglu, S.A. Korkmaz, A. Erdogan, and C.O. Colpan, *Heat exchanger network design of an organic Rankine cycle integrated waste heat recovery system of a marine vessel using pinch point analysis.* International Journal of Energy Research, 2020. **44**(15): p. 12312-12328.
19. Lyu, L., A. Kan, W. Chen, Y. Zhang, and B. Fu, *Energy, Exergy and Environmental Analysis of ORC Waste Heat Recovery from Container Ship Exhaust Gases Based on Voyage Cycle.* Journal of Marine Science and Engineering, 2023. **11**(10).
20. Gilbert, P., C. Walsh, M. Traut, U. Kesieme, K. Pazouki, and A. Murphy, *Assessment of full life-cycle air emissions of alternative shipping fuels.* Journal of Cleaner Production, 2018. **172**: p. 855-866.
21. Pavlenko, N., Comer B., Y. Zhou, and N. Clark, *The climate implications of using LNG as a marine fuel*. 2020, INTERNATIONAL COUNCIL ON CLEAN TRANSPORTATION.
22. Kuzu, S.L., L. Bilgili, and A. Kiliç, *Estimation and dispersion analysis of shipping emissions in Bandirma Port, Turkey.* Environment, Development and Sustainability, 2021. **23**(7): p. 10288-10308.
23. IMO. *GUIDELINES ON LIFE CYCLE GHG INTENSITY OF MARINE FUELS TY OF MARINE FUELS (LCA GUIDELINES)*. 2023 [cited 2024 23/05/2024]; Available from: https://wwwcdn.imo.org/localresources/en/OurWork/Environment/Documents/annex/MEPC%2080/Annex%2014.pdf.
24. Barckholtz, T.A., K.M. Taylor, S. Narayanan, S. Jolly, and H. Ghezel-Ayagh, *Molten carbonate fuel cells for simultaneous CO2 capture, power generation, and H2 generation.* Applied Energy, 2022. **313**: p. 118553.

STATISTICAL ANALYSIS OF HYDROGEN STORAGE ON BORON MATERIALS VIA MACHINE LEARNING

*Ayah STIF, Elif CAN ÖZCAN
[1] Ondokuz Mayıs University, Engineering Faculty, Department of Chemical Engineering, Samsun, 55270, Turkey

* E-mail: elif.can@omu.edu.tr & eng.ayastif@gmail.com

ABSTRACT
This study analyzed a database of 37 articles (1300 instances) published between 2000 and 2023 on hydrogen storage in boron materials using machine learning techniques. The database was created with 35 descriptors, including preparation methods, post-preparation processes, and physical properties of boron materials. A descriptive analysis was first conducted using basic statistical tools to identify trends in variables and hydrogen adsorption. Association rule mining was then applied to identify the most impactful variables on hydrogen adsorption. The random forest (RF) technique was used to test the predictability of key output variables. RF and decision tree algorithms also helped develop simple heuristics for identifying optimal conditions or avoiding conditions that lead to low hydrogen adsorption. The best decision tree model achieved 56% accuracy, with temperature, pressure, and preparation method identified as critical variables. These variables also had a significant impact in the RF analysis. While temperature and pressure are clearly important, the preparation method is emphasized because many studies fail to measure or report factors like pore characteristics which are the actual key variables. Therefore, the preparation method, indirectly influencing these factors, is found to be effective. This study underscores the need for a standardized measurement and reporting approach in hydrogen adsorption research to ensure accurate comparisons.
Keywords: Hydrogen Storage, Machine Learning, Association Rule Mining, Random Forest, Decision Tree

1. INTRODUCTION

The high hydrogen content, attractive thermodynamic properties, and low atomic weight of boron-containing materials make them highly appealing as solid-state hydrogen storage media [1]. Material properties play a crucial role in determining hydrogen storage capacity and kinetics. Among these materials, boron-based compounds, particularly borohydrides, have been recognized as suitable candidates for high-density hydrogen storage at low pressures [2]. To optimize their performance as hydrogen storage media, guidelines are needed for the rational design of these materials. Machine learning techniques, applied to large and diverse experimental datasets, can reveal powerful trends and interrelationships [3]. This study focuses on developing a database containing experimental data on hydrogen storage in boron-containing materials. Machine learning is used to establish correlations between material characteristics and hydrogen storage capacity. The database, created specifically for this research, stores experimental data on hydrogen storage in boron-based materials. We apply machine learning techniques to develop strategies for predicting hydrogen storage capacity based on material properties. This work generates a machine learning model trained on experimental data to identify correlations between various material properties and hydrogen storage capacity [4]. Multiple machine learning algorithms, including decision trees, random forests, and neural networks, are used to predict the optimal conditions for hydrogen storage, providing guidelines for the design of next-generation materials. Insights into how machine learning can be applied to material configuration will guide efforts to advance hydrogen storage systems along the technology roadmap

2. MATERIALS AND METHODS

A comprehensive database was constructed by scanning hundreds of scientific papers on hydrogen storage in boron materials published between 2000 and 2023 at 13 different online sources. After a detailed review (top hits in relevance sorting), 1300 experiments from 37 experimental articles were included in the database. The materials used for the storage and their preparation processes, as well as the factors related to hydrogen storage (such as temperature and pressure) were chosen as input variables (descriptors), while hydrogen adsorption (%wt) of the working hydrogen storage volume (%wt) and hydrogen desorption (%wt) were defined as the output variables. An important aspect discussed here is converting continuous hydrogen adsorption data into categorical form. In many studies, adsorption results are given as a function of pressure, which increases with adsorption. To avoid bias, a new term was introduced for each experiment. The logarithm of pressure values was taken, linearizing the adsorption graph, and its slope was used as a single evaluation criterion. Finally, hydrogen storage volume data were categorized into three classes: high (Class A), medium (Class B), and low (Class C).
The "arules" package in R was utilized to apply association rule mining to the dataset. The results from ARM are also visualized using the " arulesviz" package. The random forest algorithm was applied for the prediction of hydrogen storage performance parameters based on the identified effective input variables. The “randomForest” package of R was used for the RF application. During the prediction process, 5-fold cross-validation (5-fold CV) was used, and instances with unknown hydrogen storage values were excluded. The optimal model, identified through the 5-fold CV results, was then

tested using unseen data, comprising 25% of the total dataset. The evaluation criteria for RF algorithm were selected as the mean absolute error, root mean squared error (RMSE), and R^2. A wide range of the parameters of ntree (number of trees in the forest) and node size (number of instances in a terminal node of a tree) were scanned and the results were evaluated to find the model with minimum complexity and highest prediction accuracy. In the last step, decision tree (DT) analysis extracts heuristic rules that can help identify which input variables are crucial for classifying hydrogen storage and pinpointing high-performance materials and methods. This analysis was performed using rpart and rattle packages for modeling and visualization, respectively. The complexity parameter was chosen as the optimization criterion in the DT algorithm, and again 5-fold CV was applied to obtain the optimum tree model. All models created using R were developed in RStudio.

3. RESULTS AND DISCUSSION

3.1 Effective Variables

In this study, an extensive literature review was conducted, and useful information and generalizations were presented using simple descriptive analyses. This approach was applied to each variable in the dataset. For example, the relationship between surface area and hydrogen storage is thoroughly explained in Fig. 1. The y-axis represents the SSA in m²/g, while the x-axis shows the different types of materials. The size of the spheres indicates the hydrogen storage capacity (wt% H_2) for each sample; larger spheres represent higher storage capacity. The spheres represent BC (boron-carbon compounds), blue spheres represent BN (boron nitride-based compounds), red spheres represent lithium borohydrides, and yellow spheres represent MgNi/BG-based compounds. Our preliminary statistical analysis of experimental articles in the literature revealed that while specific surface area positively influences hydrogen storage, it is not a dominant or sufficient variable on its own. Fig. 1 shows examples from our database where materials with high surface area have low storage capacities, while high-capacity materials tend to have lower surface areas. Additionally, consistent with the literature, lithium borohydride compounds are more likely to exhibit higher adsorption capacities

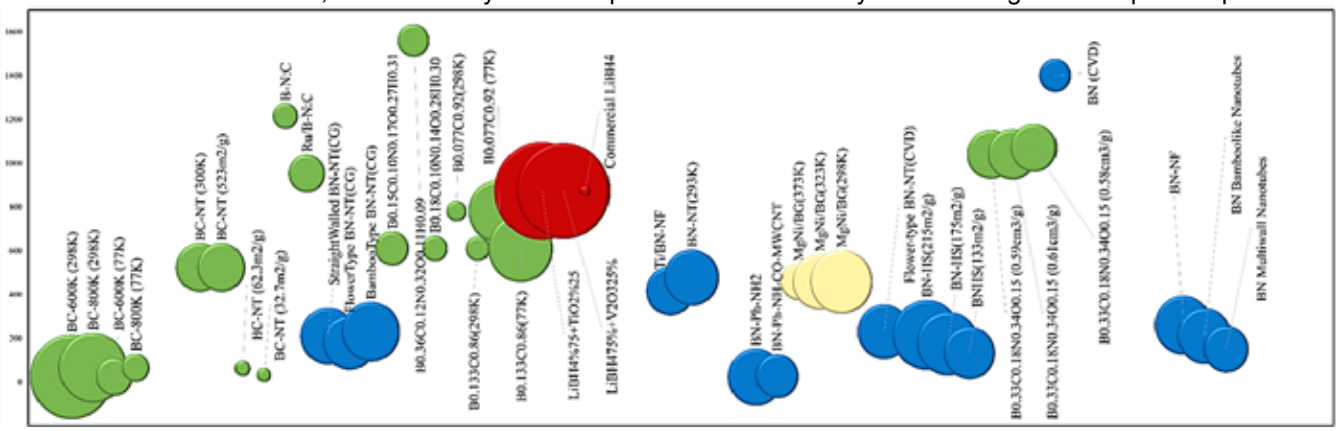

Fig. 1. The relation graph between surface area and hydrogen adsorption obtained from the dataset developed

3.2 Association Rule Mining

Association Rule Mining (ARM) was used to identify relationships among variables that provide the highest efficiency for hydrogen storage. This technique analyzes relationships between different variables to determine the most effective combinations. In Table 1, data with "slope=low" indicates low hydrogen storage capacity and inefficient adsorption. The "SurfaceArea=3" term represents materials with a surface area between 500 and 1600, showing that while hydrogen storage reaches a certain level, it is not sufficient for high-efficiency adsorption. Only relationships with a lift value greater than 1.0 were considered, indicating that these relationships are stronger than expected, suggesting they are significant and warrant further investigation. A lift value of 1.76 demonstrates a strong positive relationship between these factors, revealing that materials with a surface area in this range tend to have lower hydrogen adsorption capacity. This relationship, observed in 12 instances, highlights the need to avoid materials in this surface area range for improving hydrogen adsorption efficiency. The other rules in the table can be interpreted using a similar approach.

Table 1. Association rules affecting hydrogen storage capacity

Lhs	Rhs	Support	Confidence	Coverage	Lift	Count
{slope=high}	{Env=N2}	0.159	0.466	0.340	2.281	14
{slope=medium}	{SurfaceArea=0}	0.102	0.321	0.318	2.571	9
{slope=low}	{PrepMeth=CVD}	0.102	0.3	0.340	2.030	9
{slope=low}	{Env=Ar}	0.204	0.6	0.340	2.030	18
{slope=medium}	{PrepMeth=Others}	0.102	0.321	0.318	2.020	9
{slope=low}	{SurfaceArea=3}	0.136	0.4	0.340	1.76	12

3.3 Decision tree

In this study, hydrogen adsorption data were evaluated using the "slope," representing the rate of change in adsorption for each experiment. Factors like temperature, pressure, surface area, pore volume, preparation method, and conditions were defined as input variables. The decision tree model below (Fig. 2) was developed to classify and identify conditions for high-performance hydrogen adsorption.

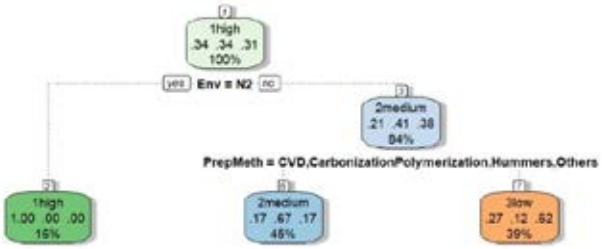

Fig. 2. Decision tree mode for hydrogen adsorption

Fig. 2 shows the results of the decision tree for hydrogen storage classification, where the optimal cp value is set to 0.04. The decision tree (DT) should be read through the branches to the leaf node; data meeting the condition specified in the node are directed to the left branch, while the remaining data go to the right branch. In the decision tree shown in Fig. 2, the first node (1high) was selected as the hydrogen storage class since it contains 34% of 1high class examples. The class distribution at this node is 34% (1high), 34% (2medium), and 31% (3low), covering 100% of the total samples. The first rule is based on the "Env = reactions under N_2 gas" environmental condition. If this condition is met, the tree moves left; otherwise, it moves right. The decision tree should be interpreted like this through the last node (leaf node).

The model's normal test accuracy is calculated as 54.54%, and the balanced test accuracy is 55.62%. While the normal test accuracy does not take into account the number of samples in each group, the balanced test accuracy adjusts the accuracy values based on the number of elements in the predicted dataset. The small difference between these values indicates that the distribution of samples across the classes is well balanced. The model predicted the examples in the 1high, 2medium, and 3low classes with accuracies of 50%, 45.5%, and 71.4%, respectively. More detailed information about the accuracies is provided in Table 2.

Table 2. Confusion matrix created with decision tree algorithm results

		Predicted Class				
		1high	2medium	3low	#Total number	Class Accuracy (Recall) %
Real Class	1high	2	0	2	4	50
	2medium	1	5	5	11	45.5
	3low	2	0	5	7	71.4
	Accuracy	0.40	1	0.417		

The confusion matrix given in Table 2 shows the performance of the classification model for hydrogen data. Accuracy rates were calculated by comparing the actual results (rows) with the predicted results (columns). For the "1high" class, the model correctly predicted 2 out of 4 data points, resulting in an accuracy of 50%. For the "2medium" class, the model correctly predicted 5 out of 11 data points, achieving 45.5% accuracy. In the "3low" class, 5 out of 7 data points were correctly predicted, resulting in 71.4% accuracy. Precision values were calculated as 0.40, 1, and 0.417 for the respective classes. These results indicate that the model performs better in the "3low" class but shows lower performance in the other classes.

3.4 Random Forest

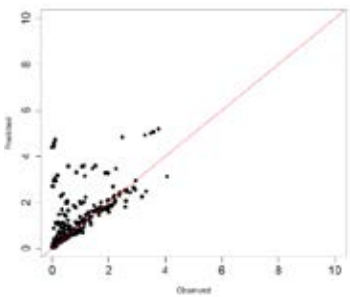

Fig. 3. Actual vs predicted values by random forest algorithm

As mentioned earlier, the modeling process using the Random Forest (RF) algorithm was validated and tested using the five-fold cross-validation method. In this process, each round labeled 648 samples for training, 162 samples for validation, and 270 samples for testing. The parameters for the best model were determined as ntree=22 and nodesize=10. This model was then applied to the test set. Fig. 3 shows the hydrogen adsorption data predicted by the model on the test data. The x-axis represents the actual values, while the y-axis represents the predicted values. Therefore, the more data points are located along the diagonal line (y=x) drawn in red, the higher the prediction accuracy. The test error for the model, reflecting its performance, was measured as 0.5831 RMSE, 1.16 MAE, and -0.79 R^2.

The random forest algorithm generates importance analysis by including and excluding each variable in the dataset, measuring its contribution to improving the model's performance. According to the analysis results, pressure, preparation method, temperature, and material used are the most influential variables in predicting hydrogen storage in boron-based compounds. However, the lack of expected importance of factors such as pore volume, pore size, and surface area may be due to the incomplete reporting of these data in the literature.

4. CONCLUSIONS

This study analyzed hydrogen storage in boron-based materials using machine learning techniques, focusing on a database of 37 articles (1300 instances) from 2000 to 2023. The database incorporated 35 descriptors, such as preparation methods, physical properties, and post-preparation processes of boron materials. Descriptive analysis and association rule mining (ARM) were employed to identify key variables affecting hydrogen adsorption. A random forest (RF) algorithm was used for prediction, revealing the critical influence of temperature, pressure, and preparation methods on hydrogen storage performance. The best decision tree model achieved 56% accuracy, highlighting that preparation methods, indirectly influencing factors like pore characteristics, are vital. The study also stressed the importance of consistent reporting of pore characteristics, as many studies overlook these details. ARM identified the most efficient combinations of variables for hydrogen storage, finding that surface area between 500 and 1600 tends to lower hydrogen adsorption capacity. The decision tree model, optimized with a complexity parameter of 0.04, classified conditions for high-performance adsorption. The model's test accuracy was 54.54%, with a balanced accuracy of 55.62%, indicating well-distributed sample classes. A confusion matrix showed that the model predicted the "high," "medium," and "low" classes with accuracies of 50%, 45.5%, and 71.4%, respectively. The RF model achieved significant predictive performance with a test error of 0.5831 RMSE, 1.16 MAE, and -0.79 R^2. Random forest also evaluated variable importance by assessing their impact on model performance. The findings revealed that pressure, temperature, preparation methods, and material used were the most significant factors, while factors like pore volume and surface area were less influential, potentially due to inconsistent reporting in the literature. This study underscores the need for standardized measurement and reporting practices in hydrogen adsorption research.

REFERENCES

[1] Yang, X., Kong, J., Lu, X., Su, J., Hou, Q., & Li, W. (2024). Hydrogen storage properties of metal borohydrides and their improvements: Research progress and trends. *International Journal of Hydrogen Energy*, *60*, 308–323. https://doi.org/10.1016/j.ijhydene.2024.02.097

[2] Varin, R. A., Czujko, T., & Wronski, Z. S. (2009). *Nanomaterials for Solid State Hydrogen Storage*. Springer US. https://doi.org/10.1007/978-0-387-77712-2

[3] Ramprasad, R., Batra, R., Pilania, G., Mannodi-Kanakkithodi, A., & Kim, C. (2017). Machine learning in materials informatics: Recent applications and prospects. *Npj Computational Materials*, *3*(1), 1–13. https://doi.org/10.1038/s41524-017-0056-5

[4] Pilania, G., Gubernatis, J. E., & Lookman, T. (2017). Multi-fidelity machine learning models for accurate bandgap predictions of solids. *Computational Materials Science*, *129*, 156–163. https://doi.org/10.1016/j.commatsci.2016.12.004.

[5] CRAN, arules: Mining Association Rules and Frequent Itemsets, https://cran.r-project.org/web/packages/arules/index.html,CRAN, rpart: Recursive Partitioning and Regression Trees, https://cran.r-project.org/web/packages/rpart/rpart.pdf, (accessed Decmber 2024).

EFFECT OF HYDROGEN ADDITION ON THE ENERGY AND ENVIRONMENTAL PERFORMANCE OF A COMPRESSION IGNITION DUAL BIOFUEL ENGINE

[1*]*Alfredas Rimkus*
[1] Vilnius Gediminas Technical University, Faculty of Transport Engineering, Department of Automobile Engineering, Saulėtekio al. 11, Vilnius, LT-10223, Lithuanian

*Corresponding author e-mail: alfredas.rimkus@vilniustech.lt

ABSTRACT

The use of renewable fuels in energy and transport is a priority to effectively reduce the use of depleting fossil resources and greenhouse gas emissions. This paper presents a study of the performance of a compression ignition engine over a wide range of engine loads, by replacing fossil diesel with dual biofuels. Diesel has been replaced by hydrotreated vegetable oil and biogas, with gas energy shares of 40%, 60% and 80%. Biogas is one of the cheapest renewable energy sources suitable for the internal combustion engine. In order to improve the combustion and energy efficiency of biogas, different concentrations of hydrogen additives were used in the experimental study. The paper presents the engine performance with different fuel cases: fossil diesel; hydrotreated vegetable oil and natural gas; hydrotreated vegetable oil and biogas; hydrotreated vegetable oil and biogas-hydrogen gas mixtures. It has been shown that under certain conditions, an engine running on dual hydrogen-added biofuels can maintain high energy performance and reduce environmental pollution such as NO_x and CO_2 emissions and smokiness.

Keywords: Dual biofuel, Hydrotreated vegetable oil, Biogas; Engine thermal efficiency, Environmental pollution

1. INTRODUCTION

Greenhouse gas (GHG) emissions are one of the most pressing issues of our time, affecting many aspects of our environmental sustainability [1]. Gases such as methane (CH_4), carbon dioxide (CO_2), nitrous oxide (N_2O) and ammonia (NH_3) are the main factors in the greenhouse effect [2]. One of the main ways of reducing the greenhouse effect is through the use of renewable energy sources and increasing energy efficiency [3]. The extensive use of internal combustion engines in transport, power generation, which emit greenhouse gases, necessitates the increased use of renewable fuels [4]. Compression ignition (CI) engines have higher energy efficiency due to higher compression ratio [5], and it is rational to use this advantage. Various renewable fuels can be used in CI engine, among which hydrotreated vegetable oil (HVO) is one of the most promising, which has higher energy density, lower NO_x emissions and better storage properties compared to biodiesel [6]. One of the cheapest biofuels is biogas (BG), which has a high raw material potential and less complex production technology [7]. In dual-fuel (D-F) engines, gas and diesel can be used in different proportions, with diesel used for the pilot ignition of the gas [8]. However, in D-F engines, the CO_2 suppression effect of biogas slows down the combustion process, reduces the thermal efficiency of the engine, and increases CO, HC and smoke emissions [9]. Studies show that the addition of hydrogen to biogas increases the intensity and quality of combustion of the gas mixture [8]. However, there are limited studies and no reliable information on the excess air ratio (λ) at which different concentrations of biogas in the engine cylinder reach the flammability limit and achieve high energy efficiency, and how the addition of hydrogen affects combustion at different levels of λ. The aim of this study is to determine the influence of a hydrogen additive on the combustion process, energy and environmental performance of a CI engine fuelled with dual biofuels at different excess air ratios.

2. MATERIALS AND METHODS

The four-cylinder turbocharged CI engine Audi-Wolkswagen 1.9 TDI (1z) was used for the experimental tests. Engine displacement 1869 cm^3, compression ratio 19.5, direct fuel injection, maximum torque 180 Nm (2000–2500 rpm), maximum power 66 kW (4000 rpm). A schematic of the experimental equipment is shown in Fig. 1, and the main details of the equipment are given in Table 1. For more information on the equipment, see the article [10].
During testing, the CI engine was run on a wide variety of fuels and fuel blends. The first case used pure diesel (D100) and the second case used pure hydrotreated vegetable oil (HVO100). In swcond cases, different dual fuels are used: gas was supplied to the intake manifold and the gas energy fractions (GES) are 40%, 60% and 80%. The third case used D-F, hydrotreated vegetable oil – natural gas (HVO_NG). The fourth case uses dual biofuel: hydrotreated vegetable oil – biogas (HVO_BG). Biogas was simulated using a mixture of NG (96.8% CH_4) and CO_2 with a 60/40 volume ratio of NG to CO_2. For the fifth, sixth and seventh cases, HVO_BG fuels were used, with hydrogen added to the gas, with H_2 at 10%, 20% and 30% of NG volume (HVO_BG+H10, HVO_BG+H20 and HVO_BG+H30). The main characteristics of the fuel are described in article [10]. The tests were carried out with the engine running at n = 2000 rpm (maximum torque mode), using brake torques of 30 Nm, 60 Nm, 90 Nm, 120 Nm (corresponding to brake mean effective pressures (BMEP) of 0.2 MPa, 0.4 MPa, 0.6 MPa and 0.8 MPa). In order to better evaluate the changes in combustion, the fixed start of

injection time was set to -4 CAD, -5 CAD, -6 CAD and -7 CAD respectively for each load.

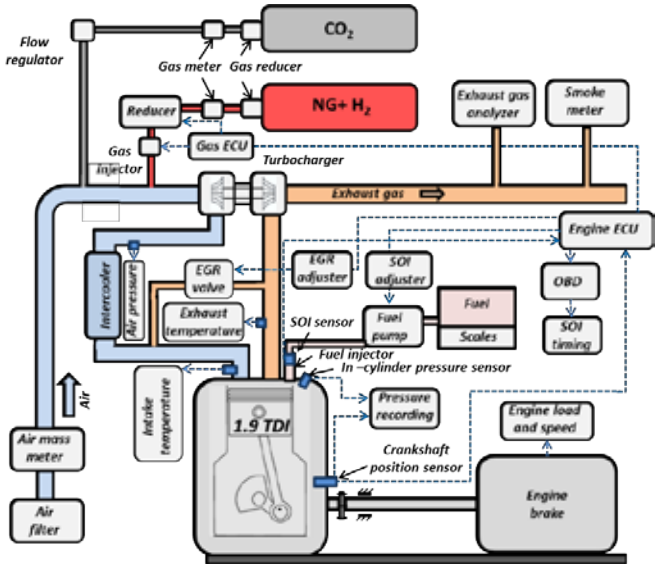

Fig. 1. Schematic of the experimental test equipment

Table 1. Basic data on the experimental test equipment

Equipment		Measurement ranges, accuracy
КИ-5543, engine load bench		0–440 Nm, ±1.2 Nm
RHM 015, gas mass flow meter		0.09–36 kg/h, ±0.1%
BOSCH HFM 5, air mass flow meter		8–370 kg/h, ±2%
SK-5000, fuel scales		0–5.0 kg, ±1.0 g
AVL GH13P, in cylinder pressure sensor		0–250 bar, ±0.3 %
A58M-F, crankshaft position sensor		0–360 CAD, 0.176 CAD
Delta OHM HD, pressure meter		0–10 bar, ±0.25%
K-type thermocouple, temperature sensor		0–1200, ±1.5° C
AVL DiCom 4000, exhaust emissions tester	CO_2 CO HC NO_x Smoke (K-Val.)	0–20% vol., 0.1% v. 0–10% vol., 0.01% v. 0–20000 ppm v., 1 ppm 0–5000 ppm vol., 1 ppm 0–99.99 m^{-1}, 0.01 m^{-1}

The rate of heat release (ROHR), temperature rise, cylinder pressure rise and other combustion parameters in the cylinder were determined using the BURN subprogram of the AVL BOOST programme. Cylinder pressure, fuel and air flow rates, and other experimental data were used. The energy efficiency of the engine was evaluated by calculating the brake thermal efficiency (BTE) using Eq. (1), where the fuel properties of the individual fuels were considered:

$$BTE = (P_B \cdot 3.6)/\sum_i (B_{f_i} \cdot LHV_i) \quad (1)$$

where P_B – brake pover (kW); B_{f_i} – hourly fuel consumption (kg/h); LHV_i – lower heating value (MJ/kg).
The environmental performance is evaluated by calculating the specific emissions, in the case of CO_2 using Eq. (2):

$$SCO_2 = (CO_2 \cdot M_{CO2} \cdot m_{ex} \cdot 10)/(M_{ex} \cdot P_B) \quad (2)$$

where CO_2 – CO_2 concentration in exhaust gases (% vol.); M_{CO2} – molecular mass of the components (g/mol); m_{ex} – exhaust mass flow (kg/h); M_{CO2} – molecular mass of the exhaust gases (g/mol).

3. RESULTS AND DISCUSSION

3.1. Combustion characteristics

The combustion process in a CI engine is strongly affected by the excess air ratio. With a D-F fuel system and an increase in GES, λ decreases (Fig. 2) as the gas occupies the volume in the cylinder and less volume is left for fresh air. λ also decreases with the increase in engine load due to the increase in fuel supply. The composition of the gas also has an impact, with the largest reduction in λ occurring with BG due to its low calorific value. Increasing the H_2 concentration in the biogas increased λ by increasing the LHV of the fuel mixture, and in the case of HVO_BG+H30, λ increased by 6–10% compared to HVO_BG. However, at high excess air ratios, the gas does not reach the flammability limit. For NG and BG to burn, λ must not exceed 1.8 and 1.9, respectively, and hydrogen extends these limits. This limit is only achievable when the engine is running at an medium load of 90 Nm (BMEP = 0.6 MPa) and above and GES reaches 80%. Rate of heat realase diagrams at medium load (BMEP = 0.6 MPa) show that HVO100 has a lower ROHR in the pre-combustion phase due to higher cetane number and shorter ignition delay phase (Figure 3), but the maximum ROHR is similar. Increasing the GES to 80% resulted in a significant slowing of the combustion process, and in the case of HVO_BG, the maximum ROHR decreased by 22% with a delay of 3 CAD compared to HVO100. In the case of HVO_BG+H30, the ROHR drops by 17%, indicating that H_2 partially compensates for the slower initial combustion of biogas and reduces the ROHR in the later combustion phase. The ROHR graph confirms that in all D-F cases, if the gas does not reach the flammability limit, combustion is delayed, which increases the exhaust temperature and reduces the thermal efficiency of the engine.

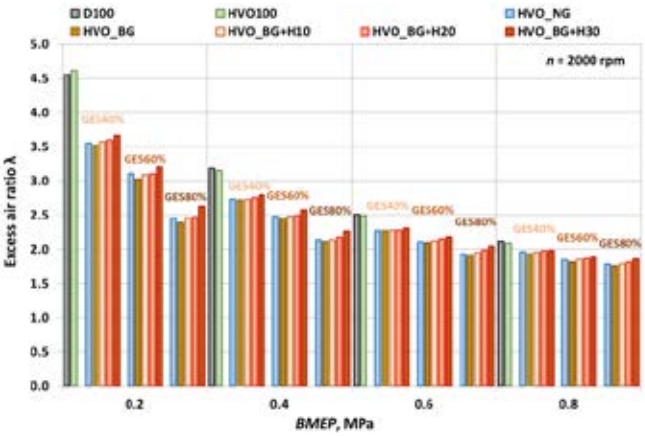

Fig. 2. λ at different fuel compositions and engine loads

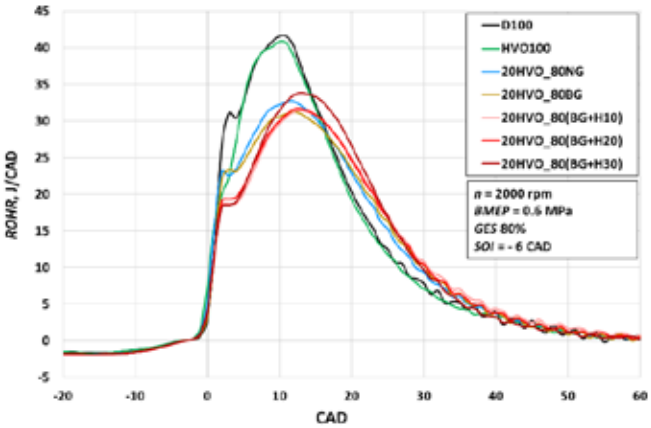

Fig. 3. ROHR at different fuel compositions

3.2. Energy characteristics

Over the entire engine load range, HVO biofuel achieved the highest thermal efficiency as it was easier to ignite due to its higher cetane number and had better combustion quality due to the higher H2 concentration in the fuel compared to D100 (Fig. 4). For HVO100, the lowest BTE (0.255) was achieved at low load (BMEP = 0.2 MPa). In the case of D-F engine BTE was significantly dependent on load, GES and gas composition. The largest reduction in BTE (46%) was observed at low load using BD, at GES 80%, as the excess air ratio exceeded 2.4 and the gas combusted late, inefficiently and incompletely. For HVO_BG+H30, the reduction in BTE was slightly lower (41%), as too high a λ could not ensure high-quality combustion. This is confirmed by the significant increase in specific emissions of incomplete combustion products (CO, HC). The highest BTE = 0.375 was achieved for HVO100 at BMEP = 0.8 MPa. At this load, the flammability limit of the gas is reached throughout the GES range, and the BTE reaches 0.36 for HVO_NG and slightly lower at 0.355 for HVO_BG due to the effect of CO2 combustion suppression. When HVO_BG+H30 was used, the BTE increased to 0.374 for 80% GES and equalled HVO100.

3.3. Environmental pollution

Specific CO_2 emissions were significantly influenced by fuel composition, engine load and BTE. At BMEP = 0.2 MPa, SCO_2 was the highest, reaching 895 g/kWh for HVO100. Using D-F at 80% GES, SCO_2 increased by 20% when switching from HVO100 to HVO_BG (Fig. 5), but SCO_2 decreased by 6% for HVO_BG+H30 and by 24% for HVO_NG due to the lower carbon content of the fuel. At the highest BTE, at BMEP = 0.8, SCO2 decreased to 667 g/kWh for both fuels (HVO100 and D100), but it is more sustainable to use HVO as it is a renewable fuel. With HVO_BG_H30, SCO_2 was reduced by an additional 10%, as combustion was efficient, with the lowest fuel consumption, and hydrogen reduced the carbon content of the fuel. In this case, renewable fuel was also used, which means an additional 70% reduction in CO_2 emissions over the life cycle. At low BTE, specific emissions of products of incomplete combustion (CO and CH) increased significantly with D-F, but at higher BTE, emissions decreased several times, especially with hydrogen addition. For HVO_BG+H30, NO_x emissions were reduced by about 30% and smoke abaut 5 time compared to HVO due to less intensive combustion in the initial combustion phases and lower carbon content in the fuel.

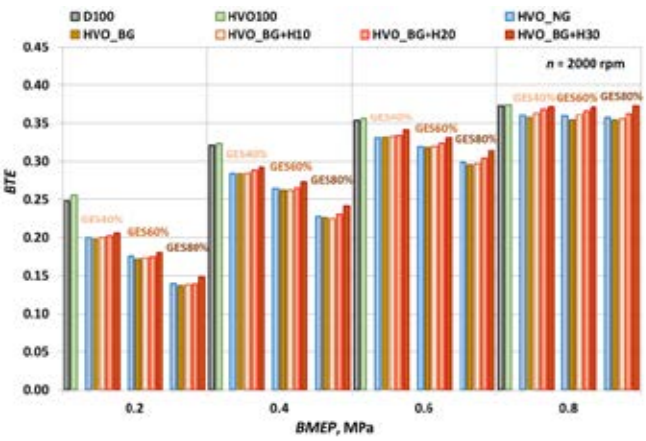

Fig. 4. BTE at different fuel compositions and engine loads

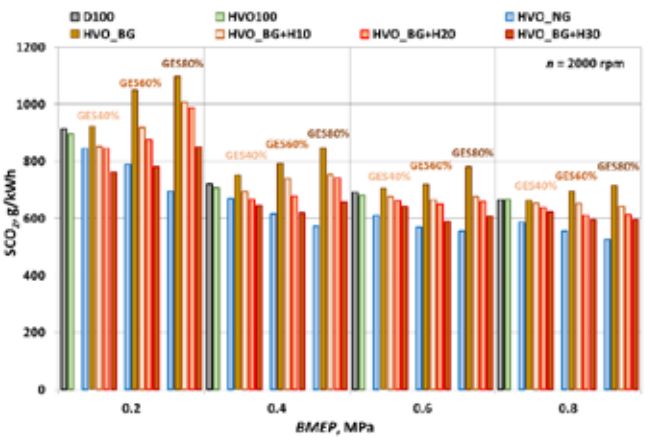

Fig. 5. CO_2 emissions at different fuel compositions

4. CONCLUSIONS

The change from D100 to HVO100 due to higher cetane number resulted in shorter ignition delay phase and lower ROHR during the pre-combustion phase, resulting in lower NO_x emissions. Due to the lower carbon and higher hydrogen content and the intensive combustion in the diffusion combustion phase, HVO reduced CO, HC specific emissions and smoke emissions compared to D100. When HVO100 was used for pilot ignition of gas in D-F engines, these fuel characteristics had a positive effect on the energy and environmental performance of the engine. Using dual biofuels consisting of HVO and simulated biogas (consisting of 60% vol. NG and 40% vol. CO_2), the engine performance was significantly dependent on the GES and the exces air ratio. At low engine loads, when λ was well above the flammability limit, the energy and environmental performance of the D-F engine deteriorated compared to pure HVO, and the addition of H2 did not significantly improve these parameters. By increasing the engine load to BMEP = 0.8 MPa and the GES to 60–80%, when λ was reduced to the biogas flammability limit (1.8), the addition of hydrogen (20–30% of vol. NG) had a significant effect in reducing CO, HC and smoke emissions. For HVO_BG+H30, the smoke emission reduction is about 5 times, NO_x emission reduction is about 30% and CO_2 emission reduction is about 10% compared to HVO100, which in most cases is better than for HVO_NG fuel. When analysing GHG emissions, it should be taken into account that HVO, BG and H2 are renewable fuels and can further reduce CO2 emissions by about 70% over their life cycle, while biogas combustion avoids methane emissions to the atmosphere.

NOMENCLATURE

BG	Biogas
BMEP	Brake mean effective pressures
BTE	Brake thermal efficiency
CI	Compression ignition
D100	Pure diesel fuel
D-F	Dual-fuel
GHG	Greenhouse gas
H_2	Hydrogen
HVO100	Pure hydrotreated vegetable oil
LHV	Lower heating value
NG	Natural gas
ROHR	Rate of heat release
SCO_2	Specific CO_2 emissions
λ	Excess air ratio

REFERENCES

1 Tripathi S, Kolodziej CP, Lu Z, De Castro Gomez D, He X, Bouchard J, et al. 2024. Life cycle greenhouse gas emissions and cost of energy transport from Saudi Arabia with conventional fuels and liquefied natural gas. Energy Conversion and Management 24:100747. https://doi.org/10.1016/j.ecmx.2024.100747.

2 Naqvi A. 2021. Decoupling trends of emissions across EU regions and the role of environmental policies. Journal of Cleaner Production 323:129130. https://doi.org/10.1016/j.jclepro.2021.129130.

3 Filonchyk M, Peterson MP, Yan H, Gusev A, Zhang L, He Y, et al. 2024. Greenhouse gas emissions and reduction strategies for the world's largest greenhouse gas emitters. Science of The Total Environment 944:173895. https://doi.org/10.1016/j.scitotenv.2024.173895.

4 Li J, Ye L, Gong S, Deng X, Wang S, Liu R, et al. 2024. Review on the combustion progress and engine application of tailor-made fuels from biomass. Renewable and Sustainable Energy Reviews 192:114242. https://doi.org/10.1016/j.rser.2023.114242.

5 Rosha P, Kumar S, Senthil Kumar P, Kowthaman CN, Kumar Mohapatra S, Dhir A. Impact of compression ratio on combustion behavior of hydrogen enriched biogas-diesel operated CI engine. Fuel 2022;310:122321. https://doi.org/10.1016/j.fuel.2021.122321.

6 da Costa RBR, Roque LFA, de Souza TAZ, Coronado CJR, Pinto GM, Cintra AJA, et al. 2022. Experimental assessment of renewable diesel fuels (HVO/Farnesane) and bioethanol on dual-fuel mode. Energy Conversion and Management 258:115554. https://doi.org/10.1016/j.enconman.2022.115554.

7 Tjutju NAS, Ammenberg J, Lindfors A. 2024. Biogas potential studies: A review of their scope, approach, and relevance. Renewable and Sustainable Energy Reviews 201:114631. https://doi.org/10.1016/j.rser.2024.114631.

8 Nguyen VN, Nayak SK, Le HS, Kowalski J, Deepanraj B, Duong XQ, et al. 2023. Performance and emission characteristics of diesel engines running on gaseous fuels in dual-fuel mode. International Journal of Hydrogen Energy 46: https://doi.org/10.1016/j.ijhydene.2023.09.130

9 Rosha P, Dhir A, Mohapatra SK. Influence of gaseous fuel induction on the various engine characteristics of a dual fuel compression ignition engine: A review. 2018. Renewable and Sustainable Energy Reviews 82:3333–49. https://doi.org/10.1016/j.rser.2017.10.055.

10 Rimkus A, Stravinskas S, Matijošius J, Hunicz J. 2024. Effects of different gas energy shares on combustion and emission characteristics of compression ignition engine fueled with dual-fossil fuel and dual-biofuel. Energy 312:133443. https://doi.org/10.1016/j.energy.2024.133443.

MACHINE LEARNING ANALYSIS OF PHOTOCATALYTIC HYDROGEN PRODUCTION OVER HALIDE PEROVSKITES

Beyza Yılmaz, **Ramazan Yıldırım*
[1]Boğaziçi University, Faculty of Engineering, Department of Chemical Engineering, Bebek, Istanbul, 34342, Türkiye

*Corresponding author e-mail: yildirra@bogazici.edu.tr

ABSTRACT

In this study, a dataset that contains 498 data points gathered from 67 published articles on photocatalytic H2 evolution over halide perovskites was constructed and analyzed by machine learning techniques. Random forest (RF) algorithms were employed to predict bandgap of halide perovskite photocatalysts and H_2 production rates. The predictive model for bandgap was quite successful with RMSE of 0.12 (R2=0.95) and 0.19 (R2=0.86) for training and testing, utilized to estimate missing bandgap values within the dataset. The other RF model was developed to predict H_2 production rates by means of 19 descriptors such as perovskite properties, synthesis methods, cocatalysts, and reaction conditions; RMSE of training and testing were 0.35 (R2=0.91) and 0.62 (R2=0.71) respectively.

Keywords: Photocatalysis, hydrogen evolution reaction, halide perovskites, machine learning

1. INTRODUCTION

Hydrogen is a promising and environmentally friendly energy carrier, which can be used as a fuel or reactant in various chemical processes[1,2]. Despite of its abundance, hydrogen is not present as molecules in nature and mostly produced from fossil fuels causing greenhouse gas emissions[3]. Hence, novel clean hydrogen generation strategies have been extensively studied nowadays.

One alternative approach is the conversion of solar energy into hydrogen by means of photocatalytic processes [4,5]. So, there was a need for an efficient photocatalyst, hence, numerous semiconductors have been used to facilitate H_2 production reactions[6]. Among them, halide perovskites appeared to be a favorable photocatalyst owing to their adjustable bandgap, excellent light absorption, and convenient charge mobility[6,7].

Halide perovskites are compounds that exhibit ABX_3 chemical structure, where A-site and B-site is a cation and X-site is a halide anion[8]. Since the properties of halide perovskites can be easily tuned by change in composition or synthesis method, various experimental studies have been conducted to explore the most efficient photocatalyst under optimal reaction conditions[9–11]. The recent popularity of halide perovskite photocatalysts resulted in accumulation of experimental data in literature, which can be extracted and investigated further applying machine learning techniques to discover the way leads to excellent photocatalysis.

The aim of this work is to get valuable information on photocatalytic H_2 production rate over halide perovskites from literature, to create a dataset using experimental data, and to examine by machine learning. Key trends on the data distribution were analyzed and influential factors were determined to build predictive models for bandgap of halide perovskites and H_2 production rates.

2. COMPUTATIONAL DETAILS

Literature on photocatalytic H_2 evolution over halide perovskites was investigated for years between 2016 and 2024. A search was conducted on Web of Science using keywords *"photocatalytic H_2 evolution" "or" "photocatalytic H_2 production" "and" "halide perovskite"* to get a list of relevant articles. Then, experimental data was extracted manually by reading the selected 67 articles in detail. A dataset with 498 data points was formed by recording 21 descriptors which cover the halide perovskite properties including dimension, bandgap, elemental compositions, and synthesis methods, cocatalysts, cocatalyst deposition techniques, reaction conditions, photocatalyst stability, and H_2 production rate.

Some publications did not provide bandgap values for halide perovskites; hence, there were 246 data points without bandgap information. Due to the fact that bandgap is a key property for photocatalysts, deficiency of this data was undesirable. Therefore, a random forest model was developed to calculate unknown bandgap values with the help of known properties such as perovskite synthesis method and temperature, A-site, B-site and X-sites of perovskites, their dimensions and cocatalysts. Then, the dataset was completed with predicted bandgap values.

The target variable was determined to be H_2 evolution rate, which exhibited a skewed data distribution since the data was gathered at the lower values as seen in Fig. 1a. In order for a better understanding of data, logarithmic transformation

was applied on H_2 evolution rate providing normal data distribution as in Fig. 1b.

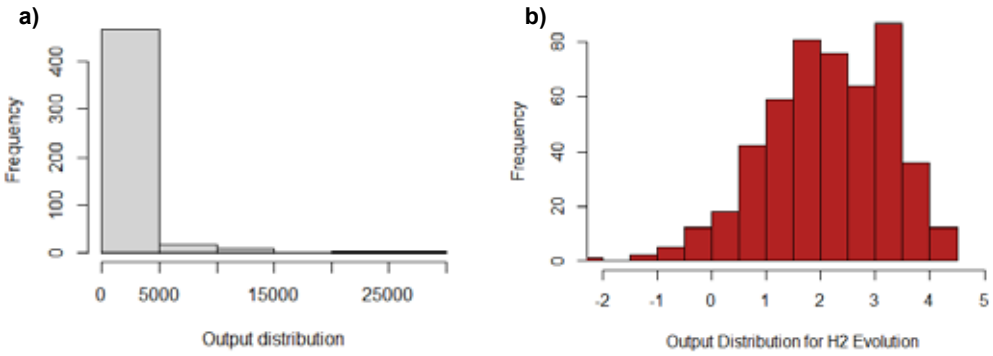

Fig. 1. Distribution of H_2 evolution rate data points before (a) and after (b) application of logarithmic transform.

A predictive RF model for H_2 production rate was developed as a function of 19 descriptors from the dataset. First, the dataset was divided into training (75%) and testing (25%) subsets. Training data was processed further applying 5-fold cross validation procedure to optimize hyperparameters of the model. Iterations were performed for nodesize (from 5 to 50), ntree (from 5 to 300) and mtry (from 3 to 9) for each fold to determine the hyperparameter values with minimum root mean square error (RMSE). Once the optimum hyperparameters were decided to be nodesize of 6, ntree of 43, and mtry of 3, test set was used to assess the predictive accuracy of the model.

3. RESULTS AND DISCUSSION

The performance of a photocatalyst largely depends on its optoelectric properties, mainly the bandgap. On the other hand, there were 246 data points without bandgap information. RF regression was employed to calculate the unknown bandgap values in order not to lose valuable data in further analysis. Original versus predicted bandgap values for train and test sets were shown in Fig. 2a and Fig. 2b and their RMSE values were 0.12 (R2=0.95) and 0.19 (R2=0.86), respectively. The significance of descriptors was represented via MSE and Node Purity methods in Fig. 2c. The most influential parameters were related to perovskite structure: the materials that were used to form perovskite, namely A, B, X-site elements, followed by perovskite synthesis methods and dimensions. The importance analysis showed that bandgap was essentially dependent on the perovskites' constitutional properties.

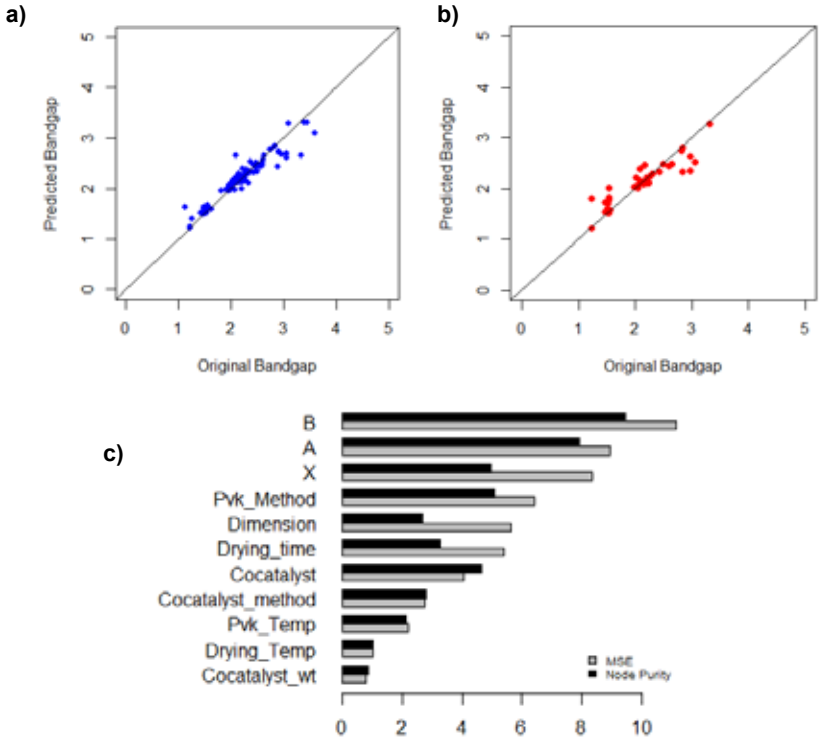

Fig. 2. Bandgap prediction results for (a) training, (b) testing and (c) descriptor importance

RF algorithm was applied on the dataset where the output variable H2 production rate was transformed into logarithmic scale to normalize the data distribution (the missing bandgap values were filled with the predictions by the model mentioned above). The original versus predicted H2 production rate for training and testing are shown in Fig. 3a and Fig. 3b with RMSE values of 0.35 (R2=0.91) and 0.62 (R2=0.71), respectively. As seen in Fig. 3a, RF model showed an excellent performance on training set, with predictions almost matching the original data points; the predictions for the test set, which is not seen by the model before, were also quite accurate. The model had a slight inclination to underestimate lower values and overestimate higher values of hydrogen production; this is more apperent in testing dataset, and it is probably stemmed from a missing information that I not represented by the current descriptors. However, the RF model can be still considered as successful for predicting the hydrogen producyion rate.

In contrast to bandgap prediction, the significant variables were not only related to perovskite structure but also reaction environments and cocatalysts (Fig. 3c). The liquids used as reaction medium also exhibited a strong effect on H2 evolution, since the medium is the source of hydrogen itself. The cocatalyst deposited on perovskite was found to be significant because it provided improved stability against reaction conditions, enhanced charge mobility, and tuned bandgap.

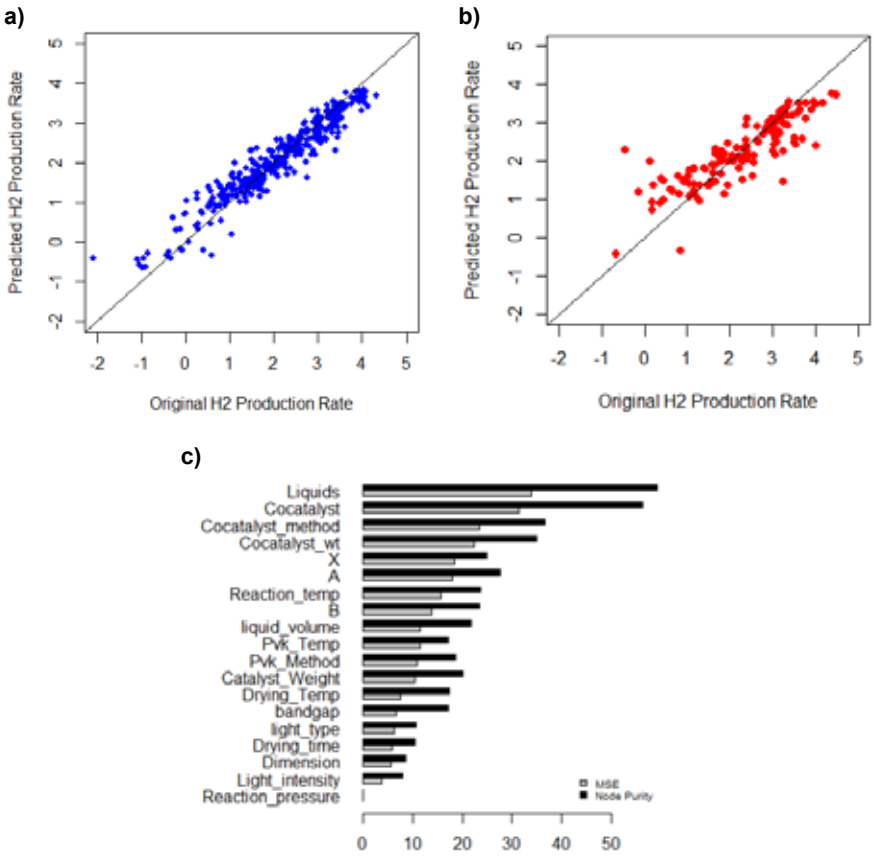

Fig. 3. H_2 production rate prediction results for (a) training, (b) testing and (c) descriptor importance

4. CONCLUSIONS

In summary, a detailed dataset was established using the data collected from articles on photocatalytic H2 evolution over halide perovskites and analyzed using machine learning tools. The variable importance analysis revealed that bandgap was primarily influenced by the structural components of perovskites which were mainly B-site cations, A-site cations, halogens as well as the synthesis methods and dimensions. The random forest model for bandgap prediction exhibited a good performance with RMSE of 0.12 (R2=0.95) and 0.19 (R2=0.86) for train and test set, respectively. Additionally, RF regression successfully predicted H2 production rate in training with RMSE values of 0.35 (R2=0.91). On the test set, predictions were reliable with RMSE of 0.62 (R2=0.71) despite minor overestimations for lower end of the data. Besides perovskite structure, reaction environment and cocatalysts were identified as critical descriptors influencing photocatalytic activity.

ACKNOWLEDGEMENT

This work was financially supported by Boğaziçi University Research Fund through Project No: 19950

REFERENCES

1. Can E and Yildirim R. 2019. Data mining in photocatalytic water splitting over perovskites literature for higher hydrogen production. Applied Catalalysis B: Environmental 242:267–83.
2. Saadetnejad D, Oral B, Can E, Yıldırım R. 2022. Machine learning analysis of gas phase photocatalytic CO2 reduction for hydrogen production. International Journal of Hydrogen Energy 47:19655–68.
3. Yılmaz B, Oral B, Yıldırım R. 2023. Machine learning analysis of catalytic CO2 methanation. International Journal of Hydrogen Energy 48:24904–14.
4. Xue Y, Xu T, Qi S, Zhang H, Wang H, Bai M, et al. 2024. Nickel Phosphide-Coupled Methylammonium Lead Halide as an Efficient and Stable Photocatalyst for Photocatalytic H2 Evolution from HI Splitting. Catalysis Letters 154:3346–56.
5. Pancielejko A, Miodyńska M, Głowienke H, Gołąbiewska A, Gontarek-Castro E, Klimczuk T, et al. 2024. Rational designing of TiO2-X@Cs3Bi2X9 nanocomposite for boosted hydrogen evolution. Catalysis Today 432.
6. Ali SA and Ahmad T. 2023. Treasure trove for efficient hydrogen evolution through water splitting using diverse perovskite photocatalysts. Materials Today Chemistry 29:101387.
7. Temerov F, Baghdadi Y, Rattner E, Eslava S. 2022. A Review on Halide Perovskite-Based Photocatalysts: Key Factors and Challenges. ACS Applied Energy Materials 5:14605–37.
8. Fu X, Ren T, Jiao S, Tian Z, Yang J, Li Q. 2023. Development strategies and improved photocatalytic CO2 reduction performance of metal halide perovskite nanocrystals. Journal of Energy Chemistry 83:397–422.
9. Zhang H, Ji X, Xu H, Zhang R, Zhang H. 2023. Design and modification of perovskite materials for photocatalytic performance improvement. Journal of Environmental Chemical Engineering 11:109056.
10. Miodyńska M, Klimczuk T, Lisowski W, Zaleska-Medynska A. 2023. Bi-based halide perovskites: Stability and opportunities in the photocatalytic approach for hydrogen evolution. Catalysis Communications 177.
11. Bienkowski K, Solarska R, Trinh L, Widera-Kalinowska J, Al-Anesi B, Liu M, et al. 2024. Halide Perovskites for Photoelectrochemical Water Splitting and CO 2 Reduction: Challenges and Opportunities. ACS Catalysis 14:6603–22.

USE OF CONVENTIONAL AND RENEWABLE ENERGY IN TURKEY'S HYDROGEN SUPPLY CHAIN: A GRID-BASED RISK ASSESSMENT

[1*]*Hande KIRIŞ*, [2]*Mehmet Güray GÜLER*, [3]*Özge Nalan BİLİŞİK*
[1] Yıldız Technical University, Faculty of Mechanical Engineering, Department of Industrial Engineering, Istanbul, 34353, Türkiye
[2] Istanbul Technical University, Faculty of Management, Department of Industrial Engineering, Istanbul, 34367, Türkiye
[3] Yıldız Technical University, Faculty of Mechanical Engineering, Department of Industrial Engineering, Istanbul, 34353, Türkiye

*Corresponding author e-mail: hande.kiris@std.yildiz.edu.tr

ABSTRACT

Hydrogen is one of the cleaner alternative energy sources for hydrogen fuel cell electric vehicles (HFCVs) in the transportation sector. The infrastructure for the production, storage, distribution and use of hydrogen needs to be well planned. Various traditional and renewable energy sources are used in hydrogen production. This study aims to find grid-based risks for the designed Hydrogen Supply Chain (HSC) when hydrogen is obtained from traditional and renewable energy sources. In grid-based risk calculation, the model is associated with capacities, unlike existing studies in literature. Risks arising from production, transportation and storage are redefined. In addition, the Fermatean Fuzzy Weighted Product Method (FF-WPM) method, one of the Multi-Criteria Decision Making (MCDM) techniques, is used to determine optimal renewable alternative energy source for grids. The results show that as the penetration rate increases, the risks of grids can be distributed more equally and the risks can be reduced thanks to the established renewable energy facilities. This study presents a methodology that aims to integrate optimal renewable energy sources determined for grids into hydrogen supply chains connected to traditional energy sources. It also aims to contribute to the assessment of risks in the design of a sustainable HSC for Türkiye.

Keywords: Hydrogen supply chain, Risk analysis, Renewable Energy, Mixed integer programming, Multi-Criteria Decision Making

1. INTRODUCTION

With population growth, increased consumption of fossil fuels leads to environmental problems. Environmental pollution, especially in the transportation sector, has reached a remarkable point. At this point, HFCVs seem to be a good alternative. While designing HSC for widespread adoption of HFCVs, production facilities, raw material supply and delivery of hydrogen to the consumer are points to be considered. Conventional and renewable alternative energy sources can be used in hydrogen production. Güler et al. [1] designed a multi-period HSC for Turkey and then transformed it into a single-period, multi-purpose HSC [2]. Although one of the main objectives in the HSC designed by Erdogan et al. [2] is to minimize the risk, renewable alternative energy sources are not considered within the scope of the study. Azadnia et al. used an integrated approach of the Delphi method and Best-worst method (BWM) to determine and analyze the risk factors of the green hydrogen supply chain in Europe [3]. They aimed to develop a framework for sustainable supply chain risk management (SSCRM) assessment [4]. For this purpose, an integrated fuzzy MCDM approach based on the technique of preference order according to similarity to the ideal solution (TOPSIS) and correlation between criteria (CRITIC) methods was proposed [4]. The best renewable energy options in the sustainable development of the country in Turkey were analyzed using the IF-TOPSIS method [5]. Gatzert and Kosub [6] presented the current risks and risk management solutions of renewable energy projects in a comprehensive manner. In this study, a single-objective model is first proposed to find grid-based risks when an HSC is designed considering traditional energy sources for Turkey. Green hydrogen production potential, which has recently been one of the most important factors in HSC design, will also be addressed in this study. The optimal renewable alternative energy sources for grids will be determined with the MCDM method.

2. MATERIALS AND METHODS

Erdogan et al. [2] propose HSC design in Turkey until 2050. Their model is a multi-purpose model that minimizes cost, CO2 emissions and risk by considering traditional energy sources. The aim of this study is to first present a grid-based model to minimize the risk in HSC based on traditional energy sources and then to determine optimal alternative renewable energy sources for grids in Turkey with the MCDM method and add them to the model to address the risk factors that will occur in the sustainable HSC network. First, it is seen that the studies in the literature have disproportionate risk levels according to the capacities of the components of the supply chain. A model is proposed that normalizes according to their capacities while calculating the risk. With this model, the risks of grids based on traditional production HSC are calculated. Then, renewable energy sources will be integrated into the model for a sustainable HSC. For this purpose, the most suitable alternative energy sources for grids will be determined with the FF-WPM, one of the MCDM methods. In this context, a determination is made among six renewable energy sources such as Wind (WI), Solar

(SO), Geothermal (GE), Biomass (BI), Wave (WA) and Hydraulic (HC) according to the expert evaluations of three academicians. There are 21 sub-criteria, including five main criteria in the selection of renewable energy types. In addition, the FF-WPM method is used to rank one or more alternatives among possible alternatives according to more than one criteria. There are two important points that distinguish this study from other models. The first of these is to calculate the grid-based risk in Turkey by normalizing it with capacities. The second is to include optimal alternative renewable energy sources for inputs in the model.

2.1. Redefining the risk measures

Risk in the supply chain process occurs in production, storage, and transportation processes. The total risk of production facilities *(TPR)* is related to the number of facilities opened, the hazard level of the facility opened and the population weight factor of the facility opened. The total risk of storage facilities *(TSR)* is calculated by multiplying the number of storage facilities, the risk level of the storage facility and the population weight factor of the facility. The risks arising from transportation *(TTR)* are related to the number of vehicles, the road used and the type of transportation. In this study, some changes are made to the risk definition used in [2,7]. *TPRs* are remodeled to be associated with production capacities. For this purpose, *TPR* is normalized with production capacities by dividing $(pCap_{plarge}^{max})$ by the largest capacity and multiplying $(pCap_{pj}^{max})$ by the associated capacity. According to the new normalized risk calculation, the risk of a small electrolysis production facility established in Istanbul is now 0.21 units, and the risk of a large electrolysis production facility established in Istanbul is 21 units. Similarly, *TSR* and *TTR* are normalized with storage and transportation capacities.

$$TPR = \left(\sum_{p,i,g} (((NP_{pjg} * PR_p * PW_g) * pCap_{pj}^{max}) \,/\, pCap_{plarge}^{max}) \right) \tag{1}$$

$$TSR = \sum_{s,g} (((NS_{sg} * SR_s * PW_g) * sCap_s^{max}) \,/\, pCap_{plarge}^{max}) \tag{2}$$

$$TTR = \sum_{g,g'} (((NTU_{gg'} * DR_{gg'l} * TR_l) * tCap_l) \,/\, pCap_{plarge}^{max}) \tag{3}$$

$$TDR = TPR + TSR + TTR \tag{4}$$

TPR is obtained by multiplying the number of hydrogen production facilities installed in the grid *(NPpig),* the hazard level of the production facility *(PRp)* and the risk level of these production facilities by the population weighting factor *(PWg)*. *TSR* is obtained by multiplying the number of hydrogen storage facilities (NS_{sg}), SR_s by the risk level of storage facilities and *(PWg). TTR* is $(NTU_{gg'})$ where *g* is the number of transportations between grids *g and g'*, TR_l, is the risk level of transportation model *t*, $DR_{gg'l}$, represents the risk level of the path between grids for transportation mode t for hydrogen distribution. *TDR* is equal to the sum of all risk levels associated with production, transportation and storage.

2.2. FF-WPM

For an MCDM problem specified in the Fermatean fuzzy environment, suppose that there are m alternatives, S_i $(i = 1,2,\dots,m)$ and *n* criteria C_j $(j = 1,2,\dots,n)$ and the criterion weight vector is $w = (w_1, w_2, \dots, w_n)^T$ and $0 \le W_j \le 1$, $j = 1,2,\dots,n$ and $\sum_{j=1}^{n} W_j = 1$.

Step 1: Fermatean fuzzy decision matrix is created.

$$R = (X_{ij})_{mxn} = \begin{pmatrix} u_{11}, v_{11} & u_{12}, v_{12} & \dots & u_{1n}, v_{1n} \\ u_{21}, v_{21} & u_{22}, v_{22} & \dots & u_{2n}, v_{2n} \\ \vdots & \vdots & \ddots & \vdots \\ u_{m1}, v_{m1} & u_{m2}, v_{m2} & \dots & u_{mn}, v_{mn} \end{pmatrix} \tag{5}$$

Here each of the elements $X_{ij} = u_{ij}, v_{ij}$ is an FFN, which means that if the alternative S_i satisfies the attributes C_j the degree will be the value u_{ij} and if the alternative S_i does not satisfy the attributes C_j the degree will be the value v_{ij}.

Step 2: It is to normalize the matrix $\mathrm{R} = (X_{ij})_{mxn}$ by a linear method. The decision matrix R, normalize matris is

transformed into the normalized matrix $\bar{R}$. The criteria are classified into a subset of benefit criteria, B and a subset of cost criteria, C. The linear normalization for any $j \in \boldsymbol{B}$ and the linear normalization for any $j \in \boldsymbol{C}$ are defined as follows, respectively:

$$\bar{X}_{ij} = \frac{X_{ij}}{max_i X_{ij}}, \tag{6}$$

$$\bar{X}_{ij} = \frac{min_i X_{ij}}{X_{ij}}, \tag{7}$$

Step 3: The total relative importance of alternative *i* according to WPM is denoted as Q_i and is defined as:

$$\bar{Q}_i = \prod_{J=1}^{n} X_{ij}{}^{w_j} \tag{8}$$

Step 4: In the last step, the score functions (SF) for $\bar{Q}_i$ $(i = 1,2, \dots, m)$ are calculated and the final rankings of the alternatives are determined according to the decreasing order of $\bar{Q}_i$ $(i = 1,2, \dots, m)$.

$$SF = \left(\mu_T^3 - \mathrm{v}_T^3\right) \tag{9}$$

3. RESULTS AND DISCUSSION

The calculation results of grid-based risks normalized by capacities produce optimal solution as shown in Table 1. With the proposed solution method, the risks of the three grids are reduced by 13.8% in G1 (Istanbul), 17.2% in G2 (Ankara) and 37.6% in G3 (Izmir), respectively. Despite the decrease in risk values in densely populated areas, the overall risk is increased by only 4.1%.

Table 1. Total risk values for G1 and G2 and G3

G1(İstanbul) Risk (unit)	G2(Ankara) Risk (unit)	G3(İzmir) Risk (unit)	Total Risk (unit)
103	26	9	286,67

Finally, FF-WPM calculations are made for all alternatives to determine optimal renewable energy source for their grids. The results are shown in Table 2. The rankings of the alternatives in Table 2 were obtained by calculating the score function of FF-WPM.

Table 2. Numerical results obtained by FF-WPM

Alternatives/Grids	**FF-WPM**						**Score**			**Rank**		
	G1		**G2**		**G3**		**G1**	**G2**	**G3**	**G1**	**G2**	**G3**
S_1	0.734	0.761	0.744	0.725	0.753	0.729	-0.045	0.031	0.039	3	3	2
S_2	0.742	0.760	0.760	0.722	0.763	0.728	-0.031	0.062	0.060	2	**1**	**1**
S_3	0.707	0.767	0.752	0.724	0.743	0.733	-0.098	0.046	0.017	6	2	4
S_4	0.729	0.762	0.703	0.743	0.685	0.753	-0.055	-0.063	-0.104	4	5	6
S_5	0.732	0.772	0.542	0.890	0.751	0.729	-0.068	-0.546	0.037	5	6	3
S_6	0.745	0.758	0.710	0.730	0.740	0.733	-0.023	-0.032	0.011	**1**	4	5

According to the results, it is seen that the alternative renewable energy source type is suitable for the renewable energy potential in the grids. When the alternatives are ranked with FF-WPM, optimal alternative energy source for G1 is S6 (Hydropower), and optimal alternative energy source for G2 and G3 is S2 (Solar). In the ranking obtained with the FF-WPM method, it is seen that the values for G1 are very close to each other. This situation can be considered as Istanbul is suitable for various alternative energy sources.

4. CONCLUSIONS

This study aims to find optimal alternative renewable energy sources for grids designed to minimize the HSC network risk for the transportation sector in Turkey in 2050. The FF-WPM methodology, one of the MCDM techniques, is fused in the selection of renewable energy resources because it can take into account many criteria that change over time, such as renewable energy types and priorities, and six renewable energy sources were evaluated for grids with five main criteria and 21 sub-criteria. According to the results, the alternative energy source in the grids is compatible with the renewable energy sources of that grid.

REFERENCES

1. Güler, M. G., Geçici, E., & Erdogan, A. 2021. Design of a future hydrogen supply chain: A multi period model for Turkey.International Journal of Hydrogen Energy 46(30):16279-16298.
2. Erdogan, A., Geçici, E., & Güler, M. G. 2023. Design of a future hydrogen supply chain: A multi-objective model for Turkey. International Journal of Hydrogen Energy 48(31):11775-11789
3. Azadnia, A. H., McDaid, C., Andwari, A. M., & Hosseini, S. E. 2023. Green hydrogen supply chain risk analysis: A european hard-to-abate sectors perspective. Renewable & Sustainable Energy Reviews 182.
4. Rostamzadeh, R., Keshavarz Ghorabaee, M., Govindan, K., Esmaeili, A., & Nobar, H. B. K. 2018. Evaluation of sustainable supply chain risk management using an integrated fuzzy TOPSIS- CRITIC approach. Journal of Cleaner Production 175:651-669.
5. Bilgili, F., Zarali, F., Ilgün, M. F., Dumrul, C., & Dumrul, Y. 2022. The evaluation of renewable energy alternatives for sustainable development in Turkey using intuitionistic fuzzy-TOPSIS method. Renewable Energy 189.
6. Gatzert, N., and Kosub, T.2016. Risks and risk management of renewable energy projects: The case of onshore and offshore wind parks. Renewable & Sustainable Energy Reviews 60:982-998.
7. Bique, A. O., Maia, L. K. K., La Mantia, F., Manca, D., & Zondervan, E. 2019. Balancing costs, safety and CO2 emissions in the design of hydrogen supply chains. Computers & Chemical Engineering 129.

COMPARATIVE ANALYSIS OF BIOHYDROGEN PRODUCTION STUDIES IN TÜRKİYE USING EVIDENCE SYNTHESIS METHODOLOGY

Kadir Kazım Yiğit[1] Tuğba Keskin-Gündoğdu[1,2],
[1] Izmir Demokrasi University, Graduate School of Natural and Applied Sci., Dept. of Operations Research, 35140, Izmir, Türkiye
[2] Izmir Demokrasi University, Faculty of Engineering, Dept of Industrial Engineering, 35140, Izmir, Türkiye

*Corresponding author e-mail: tugba.keskingundogdu@idu.edu.tr

ABSTRACT

Evidence synthesis is a method that systematically collate and synthesize existing research evidence to provide a comprehensice summary of available knowledge on a particular topic. Based on the evidence synthesis approach, this study presents a comprehensive analysis of the research conducted on biohydrogen production in Turkey. In this context, the methods of photofermentation, dark fermentation, and biophotolysis have been evaluated using systematic literature review and meta-analysis methods. The research aimed to compare the hydrogen efficiency performance of these methods, bringing together the evidence from the existing literature and providing a holistic perspective. Based on evidence synthesis, the strengths and limitations of biological methods have been identified, and it has been discussed how these limitations can be overcome with innovative approaches. The results of the study provide a detailed perspective on the research in Turkey, while also highlighting areas that are lacking and need improvement. This study aims to make a significant contribution to the knowledge base on sustainable hydrogen production and offers recommendations that will guide future research in this field.

Keywords: Evidence Synthesis, Biohydrogen Production, Dark Fermentation, Photofermentation, Biophotolysis

1. INTRODUCTION

The evidence synthesis method is an effective approach for methodically presenting critical and summarized information to decision-makers. The evidence synthesis approach offers a framework for the methodical integration, combination, and interpretation of research findings, thereby providing an in-depth overview of the current information relevant to a certain issue. The evidence synthesis technique enables the clear identification of system gaps, strengths, and weaknesses, offering a robust reference for decision-makers and policymakers. Evidence Synthesis (ES) are currently being utilized in fields such as international development and environmental decision-making [1-2].ES offers numerous advantages in academia, similar to its role in decision-making and policy development. It fosters transparency and impartiality, reduces bias, and improves the dependability of results. This fosters stakeholder confidence in the conclusions derived from the evidence, resulting in more efficient and dependable decision-making processes. Furthermore, it assists in recognizing deficiencies in knowledge and research. Through the systematic examination of existing literature, researchers may identify regions with limited or conflicting evidence. This promotes the development of new evidence and can inform future research objectives.

Due to the increasing global demand for energy and the growing problems caused by the environmental impacts of fossil fuels on human life, the need for sustainable energy sources is increasing. Hydrogen is a promising resource that stands out among sustainable energy sources. Biohydrogen is one of the most sustainable hydrogen production methods due to the advantages of organic waste conversion potential and low energy need of operation[3]. Moreover compared to fossil fuels, biohydrogen is the type of fuel with the highest energy potential per unit mass. One kilogram of hydrogen is equivalent to the energy contained in 2.8 kilograms of petroleum or 2.1 kilograms of natural gas [4]. Biohydrogen can be produced by recycling organic materials such as sugarcane bagasse, corn cobs, fruit pulps, wheat bran, and grass residues [5]. This method offers significant contributions to both environmental and economic sustainability. In this study, academic studies on biohydrogen production in Turkey over the past 10 years will be systematically examined, and the biological methods used in biohydrogen production will be comprehensively analyzed in accordance with efficiency criteria. In addition to the advantages of biological methods, their current limitations will also be evaluated, and suggestions on how to overcome these limitations will be discussed. In this context, it is aimed to provide a holistic perspective on the potential and limitations of biological methods in energy production processes by examining the existing literature through the evidence synthesis method.

Biohydrogen production can be carried out using different methods. The common feature of these methods is that they do not require high pressure and high temperature conditions. These projects, which have low energy requirements, can be carried out in accordance with the principles of zero waste and zero emissions. The biohydrogen production methods are [6];

-Dark fermentation: Dark fermentation occurs using carbohydrates by spore-forming anaerobic and anoxic bacteria. Regardless of day or night, the process can be carried out without the need for any light source. In the dark fermentation process, different organic materials can be used as sources for hydrogen production. In hydrogen production through Dark Fermentation, agricultural wastes containing starch and cellulose, wastewater rich in carbohydrates from the food industry, and sewage sludge can be considered as raw materials [7].

-Photofermentation: The photofermentation method is an innovative biotechnological approach that stands out in biohydrogen production. This method is a biotechnological process that enables the production of hydrogen gas from organic waste using light energy. During this process, organic materials are used as an energy source by bacteria. The efficiency of this process can vary depending on the organic matter used, light intensity, and other environmental factors.

-Biophotolysis: In direct biophotolysis, solar energy directly separates water molecules into hydrogen ions and oxygen through photosynthetic reactions. The hydrogen ions released from this reaction are converted into hydrogen gas using the hydrogenase enzyme. This hydrogenase enzyme is provided by green algae and blue-green algae. Indirect biophotolysis is used to avoid the problems caused by O_2 accumulation in the direct biophotolysis method. Indirect biophotolysis is a method that involves the biomass production capability of photosynthetic microorganisms and the use of this biomass for hydrogen production [6].

-Hybrid processes are the combination of at least two biohydrogen method to improve the hydrogen production yields and process efficiencies[6].

2. METHODOLOGY

Meta-analysis is a method in which various analyses are conducted to summarize the results of quantitative research on a topic. To facilitate comparison between studies, quantitative meta-analysis uses a statistic called effect size, which defines the strength and magnitude of an effect [4]. The purpose of this method is to evaluate the results of quantitative studies conducted on the same topic in a brief and detailed manner. Meta-analysis studies are generally grouped into six stages.

i. Determining the Objectives and Goals of the Research
ii. Literature Review
iii. Coding of Studies
iv. Effect Size Index
v. Statistical Analysis
vi. Results and Comments

As in all research, it is important in meta-analysis to fully understand the quality of the data, the rigor applied during the coding and analysis phases, and the statistical assumptions made [8].
Research Approach
This study aims to conduct a comparative analysis of the biological methods used in biohydrogen production in terms of efficiency criteria. For this purpose, the existing literature has been systematically examined using the "evidence synthesis" method. This method allows for a comprehensive evaluation by bringing together information obtained from different studies.

Data collection
In the study conducted by Melitos et al [9], it is observed that there has been an increasing trend in biohydrogen production over the past 10 years. As in the rest of the world, it is observed that the number of academic studies on hydrogen production has increased in our country as well, and with the guidance of government incentives and national policies, there have been advancements in academic studies in this field. Within the scope of this study, academic works in Turkey have been examined. Therefore, academic studies in Turkey have been examined both in terms of articles and completed theses. With the results of this study, the current state of the biohydrogen topic is presented, aiming to prepare a resource for decision-makers to create a roadmap.

Literature Review Method
The literature review was conducted using the following databases and keywords:
• Databases: YÖK-Tez, GoogleScholar (for Turkish journals), DergiPark

Keywords are “Biyohidrojen Üretimi”, “Biyofotoliz”, “Direkt Biyofotoliz”, “İndirekt Biyofotoliz”, “Karanlık Fermentasyon”, “Fotofermentasyon”, “Biohydrogen Production”, “Biophotolysis”, “Direct Biophotolysis”, “Indirect Biophotolysis”, “Dark Fermentation”, “Photofermentation”.

Initial screening
In the initial screening, articles were evaluated based on their titles and abstracts. Duplicate articles in different databases and articles not directly related to the research question were removed from the list, and the remaining articles were included for the next step.

Inclusion and Exclusion Criteria

The inclusion and exclusion criteria for the study have been established in accordance with specific standards. Among the inclusion criteria are that the studies were published between 2014-2024, written in Turkish, addressed the production of biohydrogen using biological methods, and reported hydrogen efficiency metrics. On the other hand, the exclusion criteria include publications that are not directly related to biological methods, studies that do not contain sufficient technical details, and sources whose full text is not accessible. Search results will primarily be evaluated through title and abstract screening; studies that pass this stage will then be included in the detailed full-text analysis process.

Full Text Review
At this stage, the articles that pass the initial screening and criteria review are examined in detail. At this stage, the scientific approach, quality, and accuracy of the article, as well as the relevance and comparability of the results, are examined.

Data Source and Selection
Initially, YOKTEZ system, DergiPark and google scholar was screened. This selection process was carried out according to the PRISMA (Preferred Reporting Items for Systematic Reviews and Meta-Analyses) guidelines.

3. RESULTS AND DISCUSSION

In the initial screening conducted within the scope of this study, 62 studies were found in the YÖKTEZ system, 14 studies in Turkish sources on Google Scholar, and a total of 54 studies in the DergiPark database. When systematic elimination is performed according to the specified criteria, a total of 26 studies are found. When these studies are examined, it is observed that biohydrogen research has gained importance in our country academically. Using the evidence synthesis method, the stages to be detailed in these studies will include the type of process used, the amounts of organic waste, hydrogen production yields, and efficiency values. With the results obtained, the current status of biohydrogen studies in our country will be presented to decision-makers. Studies on biohydrogen are of significant strategic importance in achieving zero waste and zero emissions within the framework of a circular economy. Therefore, the results of this study will serve as a guide for increasing the number of studies on biohydrogen, diversifying the incentives provided, and advancing academically in this field [Fig.1]. In the analysis based on the evidence synthesis method, it is observed that various academic studies have been conducted on all processes of biohydrogen production in Turkey. Based on the diversity of organic waste in our country, dark fermentation studies have been conducted using different types of waste as substrates [10]. As a country that receives sunlight for a long period of the year, both photofermentation and biophotolysis studies have been carried out. In photofermentation studies, pilot-scale outdoor systems are noteworthy[11]. The ability to produce biohydrogen at an industrial level is crucial for achieving higher yields from academic studies and for collaboration with industry. Collaboration with industry and the determination of production capacities at an industrial scale should be established, and roadmaps to achieve these capacities should be drawn. With this study, it is aimed to create one of the starting points of this roadmap.

4. CONCLUSION

In conclusion, our synthesis of biohydrogen studies in Türkiye reveals a dynamic and rapidly evolving field with significant potential for sustainable energy solutions. The evidence highlights the importance of continued research and development to overcome current limitations and harness biohydrogen's full potential. Future studies should focus on optimizing production methods, exploring new biomass sources, and enhancing the scalability of biohydrogen technologies. This evidence synthesis reveals that biohydrogen research in Turkey has shown promising advancements. Fostering collaboration among academic, industrial, and governmental stakeholders could accelerate innovation and commercialization. Future studies should prioritize biohydrogen production to align with global trends and Turkey’s strategic energy objectives. Biohydrogen holds the potential to significantly contribute to a sustainable and circular economy, positioning Turkey as a leader in renewable energy technologies. By addressing these challenges, this study aims to be a brief report for researchers and for policy makers.

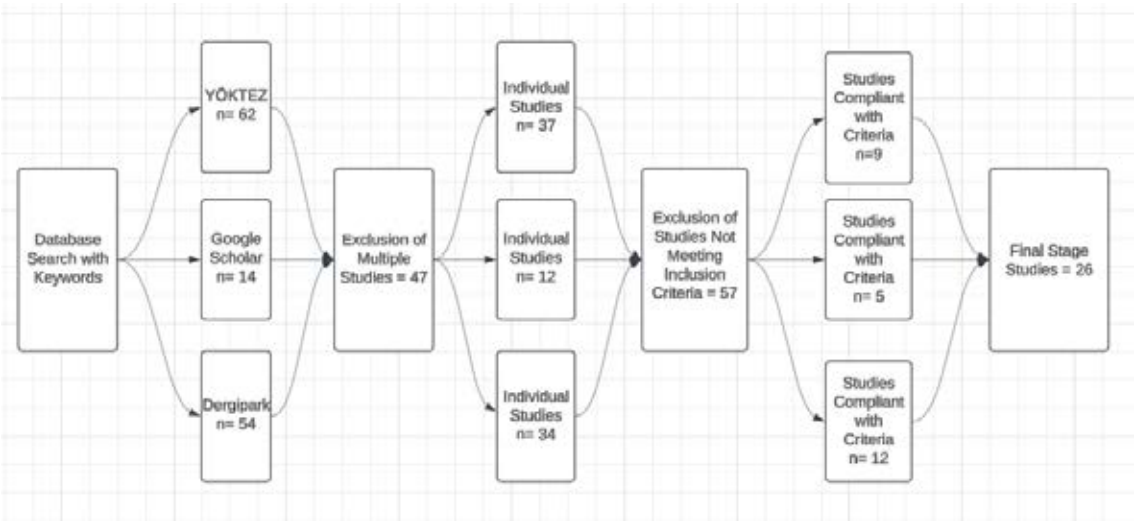

Fig. 1. Prisma diagram

REFERENCES

[1] Bilotta GS, Milner AM and Boyd I. 2014. On the use of systematic reviews to inform environmental policies. Environmental Science & Policy 42: 67-77.

[2] White H and Waddington H. 2012. Why do we care about evidence synthesis? An introduction to the special issue on systematic reviews. Journal of Development Effectiveness 4(3): 351-358.

[3]Govea, LC, Nayak S, Kumar PS, Vinayagam R, Selvaraj R, & Rangasamy G. 2024. Recent advances in fermentative biohydrogen production. International Journal of Hydrogen Energy 54: 200-217.

[4] Dursun N ve Gülşen H. 2019. “Biyohidrojen Üretim Yöntemleri ve Biyohidrojen Üretiminde Biyoreaktörlerin Kullanımı”, Iğdır Üniv. Fen Bil Enst. Der. 9(1) 66–75.

[5] Guo XM, Trably E, Latrille C, Carrere H & Steyer JP. 2010.. Hydrogen production from agricultural waste by dark fermentation: a review. International Journal of Hydrogen Energy. 35 (19):10660–10673.

[6] Genç N. 2019. "Biyolojik hidrojen üretim prosesleri," Balıkesir Üniversitesi Fen Bilimleri Enstitüsü Dergisi, 11(2) 17-36.

[7] Onaran G. 2016. "Atık kağıt havludan karanlık fermantasyon ile hidrojen gazı üretimi," Yüksek Lisans Tezi, Çevre Mühendisliği Ana Bilim Dalı, Fen Bilimleri Enstitüsü, Pamukkale Üniversitesi, Denizli, Türkiye

[8] Toker A., 2022. Bir araştırma metodolojisi olarak sistematik literatür incelemesi: Meta-sentez yöntemi. Anadolu Üniversitesi Sosyal Bilimler Dergisi 22(2):313-340.

[9] Melitos G, Voulkopoulos X, & Zabaniotou A. 2021. Waste to sustainable biohydrogen production via photo-fermentation and biophotolysis− A systematic review. Renewable Energy and Environmental Sustainability. 6: 45-54.

[10] Keskin T, Nalakath Abubackar H, Arslan K, Azbar N. 2019. Biohydrogen Production From Solid Wastes In Bıohydrogen, 321-346, Elsevier

[11] Genç Ş, & Koku H. 2024. A preliminary techno-economic analysis of photofermentative hydrogen production. International Journal of Hydrogen Energy. 52: 212-222.

EVALUATING THE PERFORMANCE OF BOOSTING REGRESSORS FOR PREDICTING BIOHYDROGEN PRODUCTION UNDER VARIABLE EXPERIMENTAL CONDITIONS

Merve Aslı Ergün[1] Tuğba Keskin Gündoğdu[1,2], Başak Esin Köktürk Güzel[3]*
[1] Izmir Demokrasi University, Graduate School of Natural and Applied Sci., Dept. of Operations Research, 35140, Izmir, Türkiye
[2] Izmir Demokrasi University, Faculty of Engineering, Dept of Industrial Engineering, 35140, Izmir, Türkiye
[3] Izmir Demokrasi University, Faculty of Engineering, Dept. of Electical-Electronical Engineering, 35140, Izmir, Türkiye

*Corresponding author e-mail: basak.guzel@idu.edu.tr

ABSTRACT

Biohydrogen production is a promising sustainable energy source, requiring accurate yield predictions to optimize processes and scale industrial applications. This study evaluates advanced boosting regression algorithms—Gradient Boosting Regressor (GBR), Extreme Gradient Boosting (XGBoost), Adaptive Boosting (AdaBoost),—for modeling biohydrogen production. Experimental data, including inoculum, glucose and oxygen concentrations were used to train and test the models. Key evaluation metrics—mean absolute error (MAE), root mean square error (RMSE), and coefficient of determination (R^2)—highlight the effectiveness of boosting algorithms in capturing complex, nonlinear relationships in biohydrogen production. Among the models, XGBoost demonstrated superior accuracy. This study emphasizes the potential of boosting regressors as robust tools for biohydrogen process optimization. It also offers guidance on algorithm selection and parameter tuning, contributing to predictive framework development for biohydrogen research and industrial applications.

Keywords: Biohydrogen Production, Boosting Regressors, Gradient Boosting Regressor (GBR), Extreme Gradient Boosting (XGBoost) and Adaptive Boosting (AdaBoost) Algorithms

1. INTRODUCTION

Sustainability, one of the most important concepts of recent years, has environmental, social and economic dimensions. For a sustainable world, these three concepts should proceed in harmony with each other like the gears of a machine. However, the emphasis on economic growth to meet the demands of the growing world population has left environmental and social growth behind. At this point, it is necessary to turn to clean technologies and clean energy sources to achieve a rebalance. Biotechnological approaches play a major role in clean technologies. Renewable energy sources and especially the use of biofuels meet many of the United Nations Sustainable Development Goals[1]. Hydrogen is one of the most important resources because it can be used both as a fuel, in electricity generation and in the production of valuable chemicals. Hydrogen energy has the potential to meet 80% of the world's energy needs[2]. Among renewable energy sources, biohydrogen is one of the best alternative fuels because, among hydrogen production technologies, biohydrogen production is the most sustainable as it occurs at ambient temperature and therefore requires only a low energy input [3-6]. In addition, since different organic wastes can be used, an important evaluation is made on waste recycling. The biggest indicator that biohydrogen production is a clean technology is that only water is produced as a by-product of combustion or conversion to electricity [7]. Among different hydrogen production methods, biohydrogen production is the most environmentally friendly method because of the advantages of operating at mild conditions, possibility of organic waste transformation and less energy input [8]. The main disadvantages of biohydrogen production are low production yields and high process costs. Therefore, many studies are focused on cost reduction and process optimization. The optimization of the parameters such as carbon/nitrogen ratios, pH levels, temperature, and light wavelength and intensity, among other characteristics could be done by using experimental design methodologies. In recent years, machine learning algorithms have been increasingly applied to model and optimize biohydrogen production. These methods have shown promising results in capturing complex and nonlinear relationships between process parameters. However, studies utilizing machine learning techniques for biohydrogen production remain limited in the literature. In this study, we focus specifically on boosting methods and evaluate the performance of Gradient Boosting Regressor (GBR) [9], Extreme Gradient Boosting (XGBoost) [10] and Adaptive Boosting (AdaBoost) algorithms[11]. The potential of these algorithms to model and predict biohydrogen yields under varying experimental conditions was investigated. The results demonstrate that boosting-based models offer high accuracy and low error rates, making them powerful tools for process optimization. This study highlights the applicability of machine learning methods to improve the efficiency and scalability of biohydrogen production systems.

2. MATERIALS AND METHODS

Experimental data were collected from a study on optimization of sequential microaerobic dark-and photo-fermentation biohydrogen production by photo fermentative biohydrogen production [12]. The key optimization parameters - inoculum amount, glucose and oxygen concentrations, were systematically varied to capture a wide range of production scenarios using Box-Behnken experimental design and the regression analysis performed to predict biohydrogen production.

Boosting algorithms are ensemble techniques designed to transform weak base learners into strong predictive models. These algorithms improve performance by iteratively focusing on samples that are difficult to predict, reducing bias and variance in the process. At each iteration, a weak learning model is applied to the data, giving more emphasis to samples that were misclassified in previous steps. This iterative approach ensures that the model continuously refines its predictions, becoming increasingly accurate over time. The boosting process typically follows a series of steps. First, the model is initialized by assigning equal weights to all data samples. Next, a weak learner is trained, and prediction errors are calculated. Weights of misclassified samples are then increased to emphasize harder-to-predict instances. This process is repeated until a predefined accuracy level or maximum number of iterations is reached. Finally, the predictions from all weak learners are combined to form a strong final output. The general block diagram of boosting algorithms is illustrated in Figure 1, highlighting the sequential training and integration process that defines these methods.

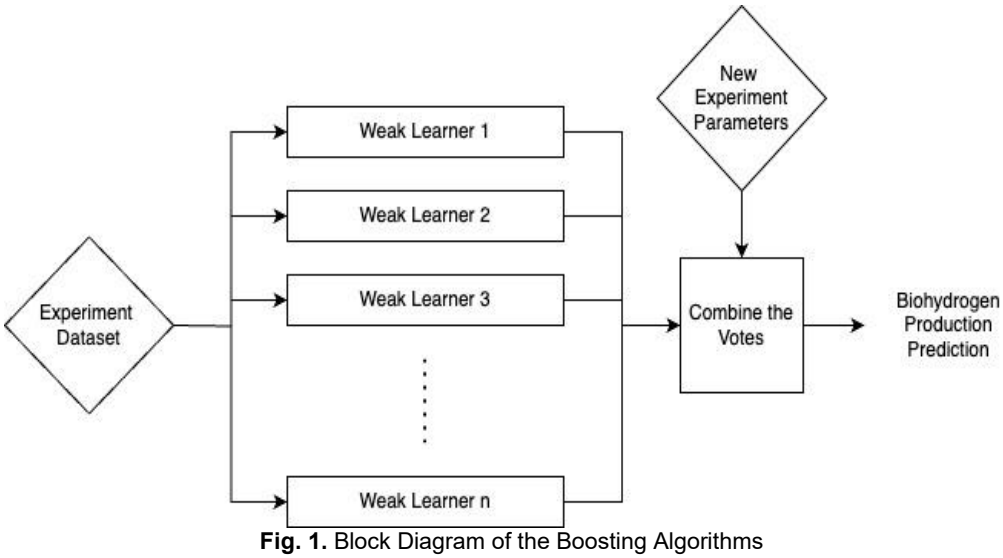

Fig. 1. Block Diagram of the Boosting Algorithms

In the literature, three boosting algorithms are commonly discussed: AdaBoost [11], Gradient Boosting [9], and Extreme Gradient Boosting (XGBoost) [10]. AdaBoost applies weak learners sequentially, updating weights to emphasize misclassified samples. Each iteration seeks to improve upon errors made by previous iterations. It is simple and effective for smaller datasets, with tunable hyperparameters like learning rate and number of estimators. GBR minimizes prediction errors by fitting new models to the residuals of prior models. Each step improves upon previous errors by calculating gradients and minimizing loss using gradient descent. It is highly customizable, offering hyperparameters such as learning rate, number of estimators, and maximum tree depth. XGBoost builds on gradient boosting by introducing regularization terms to prevent overfitting. It uses advanced techniques such as column subsampling and parallel computing for faster training. It also handles missing values and prunes trees effectively, making it one of the most efficient boosting algorithms. Since the objective was to predict H_2 production values, model performance was evaluated using root mean square error (RMSE) and coefficient of determination (R^2). These metrics were selected to assess the precision, reliability, and generalization ability of the models. RMSE emphasizes larger errors, and R^2 indicates the proportion of variance explained by the model, providing a comprehensive evaluation of predictive performance.

3. RESULTS

The dataset consists of the following columns based on the raw file inspection: Inoculum concentration, which represents the concentration of the inoculum used in the experiment and is likely measured in units such as g/L or mg/L; oxygen concentration, which denotes the concentration of oxygen in the experimental setup and potentially influences anaerobic conditions necessary for biohydrogen production; and glucose concentration, which refers to the glucose concentration in the medium, acting as a carbon source for microbial activity and measured in specific units (e.g., g/L). These variables

serve as key predictors in determining hydrogen yield. Data preprocessing and analysis were conducted in Python 3.8. Libraries such as Pandas and NumPy facilitated data handling, while Matplotlib and Seaborn supported data visualization. Model development leveraged Scikit-learn and XGBoost frameworks for training and evaluation.

Table 1.Experiment Values and Hydrogen Production Predictions

	İnoculum Concentration	Oxygen Concentration	Glucose Concentration	H2 Yield (Y),mol/mol	Hydrogen Production, mmol	Predictions_AdaBoost	Predictions_GradientBoosting	Predictions_XGBoost	Is_Test
0	62.500	1.000	2	6.500	0.200	0.170	0.108	0.162	TRUE
1	25.000	1.000	6	1.250	0.140	0.500	0.395	0.291	TRUE
2	100.000	4.500	2	5.500	0.170	0.170	0.170	0.170	FALSE
3	62.500	4.500	6	6.720	0.720	0.770	0.750	0.749	FALSE
4	62.500	4.500	6	7.450	0.750	0.770	0.750	0.749	FALSE
5	62.500	8.000	10	1.370	0.220	0.240	0.188	0.203	TRUE
6	25.000	4.500	2	2.660	0.080	0.110	0.080	0.081	FALSE
7	100.000	4.500	10	4.000	0.620	0.620	0.620	0.620	FALSE
8	25.000	8.000	6	0.880	0.090	0.090	0.090	0.091	FALSE
9	100.000	1.000	6	5.710	0.600	0.600	0.600	0.600	FALSE
10	62.500	8.000	2	3.500	0.110	0.110	0.110	0.111	FALSE
11	25.000	4.500	10	1.960	0.300	0.300	0.300	0.300	FALSE
12	62.500	1.000	10	2.940	0.500	0.550	0.500	0.501	FALSE
13	62.500	4.500	6	6.980	0.710	0.770	0.750	0.749	FALSE
14	100.000	8.000	6	2.300	0.240	0.240	0.240	0.240	FALSE
15	62.500	4.500	6	7.630	0.840	0.770	0.750	0.749	TRUE
16	62.500	4.500	6	7.800	0.820	0.770	0.750	0.749	FALSE

Table 2.Mean squared error and R2 measures for the regression algorithms on BBD data.

Model	RMSE	R^2
Gradient Boosting	0.0206	0.7452
Adaboost	0.0339	0.5803
XGBoost	0.0081	0.8988

4. CONCLUSION

The results of this study demonstrate that boosting regression algorithms are effective in predicting biohydrogen production under varying experimental conditions. These methods can reduce experimental costs by enabling accurate predictions of hydrogen yield, thereby minimizing the need for extensive physical experiments. Furthermore, in experiments involving multiple variables, each material or parameter can be treated as a feature. Feature importance can be calculated to determine the most influential factors affecting biohydrogen production. This insight can guide future experiments and process optimizations. Future work will extend this study by applying these regression techniques to different biohydrogen production processes and exploring their performance with more complex datasets. This expanded approach aims to further enhance the predictive modeling of biohydrogen yields, contributing to improved efficiency and scalability in biohydrogen production systems.

REFERENCES

[1] Melitos G, Voulkopoulos X, & Zabaniotou A. 2021. Waste to sustainable biohydrogen production via photo-fermentation and biophotolysis− A systematic review. Renewable Energy and Environmental Sustainability. 6: 45-54.
[2] Rezania S, Din MFD, Taib SM, Sohaili J.,Chelliapan S, Kamyab H, Saha BB. 2017. Review on fermentative biohydrogen production from water hyacinth, wheat straw and rice straw with focus on recent perspectives, International Journal of Hydrogen Energy. 42: 20955–20969.
[3] Das D, Veziroglu TN. 2001. Hydrogen production by biological processes: A survey of literature. International Journal of Hydrogen Energy, 26: 13-28.
[4] Adessi A, Philippis RD. 2014. Photobioreactor design and illumination systems for H_2 production with anoxygenic photosynthetic bacteria: A review. International Journal of Hydrogen Energy, 39: 3127-3141.

[5] Keskin T, Hallenbeck PC. 2012. Hydrogen production from sugar industry wastes using single-stage photofermentation. Bioresource Technology, 112: 131-136.
[6] Dursun N, Gülşen H. 2019. Biyohidrojen üretim yöntemleri ve biyohidrojen üretiminde biyoreaktörlerin kullanımı. Journal of the Institute of Science and Technology. 9(1):66-75.
[7] Tenca A, Schievano A, Perazzolo F, Adani F, Oberti R. 2011. Biohydrogen from thermophilic co-fermentation of swine manure with fruit and vegetable waste: maximizing stable production without pH control. Bioresource Technology.102:8582-8588.
[8] Srivastava RK, Shetti NP, Reddy KR, & Aminabhavi TM. 2020. Biofuels, biodiesel and biohydrogen production using bioprocesses. A review. Environmental Chemistry Letters. 18:1049-1072.
[9] Friedman JH. Greedy function approximation: a gradient boosting machine. 2001. Annals of statistics, 1189–1232.
[10] Chen T and He T. Xgboost: extreme gradient boosting. 2015. R package version 0.4-2.
[11] Freund Y and Schapire RE.1995. A decision-theoretic generalization of on-line learning and an application to boosting. In European conference on computational learning theory, 23–37. Springer.
[12] Sağır E., Yucel M, & Hallenbeck PC. 2018. Demonstration and optimization of sequential microaerobic dark-and photo-fermentation biohydrogen production by immobilized *Rhodobacter capsulatus* JP91. Bioresource Technology. *250*: 43-52.

HYDROGEN DETECTION AND ELECTRICAL PROPERTIES OF PEROVSKITE $BaTiO_3$ SCHOTTKY DIODE

[1,2*]*Lutfi Bilal Tasyurek*, [3]*Huseyin Karakurt*, [4]*Necmettin Kilinc*
[1]Depertment of Opticians, Malatya Turgut Ozal University, 44700 Malatya, Türkiye
[2]Department of Physics, Faculty of Science, Ataturk University, 25240, Erzurum, Türkiye
[3]Department of Chemical Engineering, Faculty of Engineering, Inonu University, 44280, Malatya, Türkiye
[4]Department of Physics, Faculty of Science & Arts, Inonu University, 44280, Malatya, Türkiye
* bilaltasyurek@gmail.com

ABSTRACT
Hydrogen (H_2), a clean, efficient and renewable energy source, is considered as an ideal energy source in the near future. Today, H_2 is used in many industrial areas such as chemistry, food, semiconductor, transport. There is a need for sensors that can measure hydrogen quickly and accurately in a wide concentration range. These sensors are used in security, determination of H_2 purity in hydrogen production plants and leakage control in H_2 storage areas. In this research, perovskite $BaTiO_3$ based H_2 sensors will be investigated. H_2 sensor applications of perovskites, which are a very large family, easily available and low cost, are very limited.

Keywords: $BaTiO_3$, perovskite, hydrogen sensors, electrical characterization

1.INTRODUCTION
As a sustainable, renewable and clean fuel, hydrogen (H_2) can be used as a kind of green fuel due to its advantages (Hübert et al., 2011; Zhang et al., 2013), such as low density, significant combustion heat and no pollution emission (Mirzaei et al., 2019). In recent years, there has been a lot of research and investment in the world to obtain clean energy. These studies are especially focused on hydrogen. In addition, the importance of hydrogen sensors is increasing due to the development of hydrogen gas as an energy carrier and chemical reactant and the expansion of its usage area. As a colourless, odourless and tasteless flammable gas, hydrogen cannot be detected by human senses and therefore other methods are required to detect its presence and measure the concentration (Esfandiar et al., 2014; Seekaew et al., 2019). Fast and accurate hydrogen gas concentration measurement is crucial to herald the formation of potentially explosive mixtures with air and help prevent the risk of explosion. As the diffusion coefficient in air is large (0.6 cm^2/s), they are highly likely to cause a sudden explosion (Hübert et al., 2011). However, hydrogen has many disadvantages in terms of safety. The very low minimum energy required for ignition in air at atmospheric pressure causes it to ignite easily olur (Kabcum et al., 2016; Korotcenkov et al., 2009). When mixed with air, the explosive concentration range is quite wide between 4-75 % by volume (Korotcenkov et al., 2009; Y. Liu et al., 2014). Due to its ultra-small molecular size, it can easily leak out of containers (Nakate et al., 2018). Therefore, it is very important to develop H_2 sensors to precisely monitor H_2 concentration. H_2 sensors have different uses such as safety, leakage, quality and biomarker.
The perovskite oxide structure, formula ABO_3, consists of a wide variety of oxides with transport properties ranging from predominantly ionic conduction to electronic conduction. Perovskite oxides are particularly attractive for high-temperature applications because they often have high melting and/or decomposition temperatures, as well as providing microstructural and morphological stability to improve reliability and long-term sensor performance. In addition, the perovskite structure has two different sized cations, making it amenable to a variety of dopants. This doping flexibility allows control of transport and catalytic properties to optimize sensor performance in specific applications (Fergus, 2007). Perovskite oxides have been used in many gas sensor applications such as oxygen (Shimizu et al., 1985), CO (Malavasi et al., 2005), CO_2 (Wang et al., 2013), NO_2 (Ueda et al., 2009), acetone (X. Liu et al., 2008), ethanol/methanol (Doroftei et al., 2013), hydrocarbon (Sahner et al., 2005) and H_2 (Huang et al., 2019).
The detection of H_2 gas, which is difficult to be detected by human senses because it is colorless and odorless, requires the development of highly sensitive, selective and low-cost portable sensors (Sisman et al., 2024). One of the most promising sensors developed for this purpose is semiconductor metal oxide (SMO)-based chemoresistive gas sensors with high sensitivity, low fabrication cost and compatibility with standard semiconductor technologies (Dey, 2018). In the semiconductor-based Schottky diode H_2 sensors shown in Figure 1, gas molecules are decomposed on the metal surface through a catalytic reaction (Kilinc et al., 2024). The reaction products and intermediates can be polarized and absorbed on the metal surface or spilled onto the exposed parts of the oxide surface. Hydrogen atoms formed by the decomposition reactions of hydrogen or hydrogen-containing species diffuse through the catalytic metal and form dipoles at the metal-insulator interface (Tobias et al., 1997). The resulting dipole layer alters the electric field distribution within the sensors, causing a shift in current-voltage (I-V), capacitance-voltage (C-V) or conductance-voltage (G-V) characteristics.

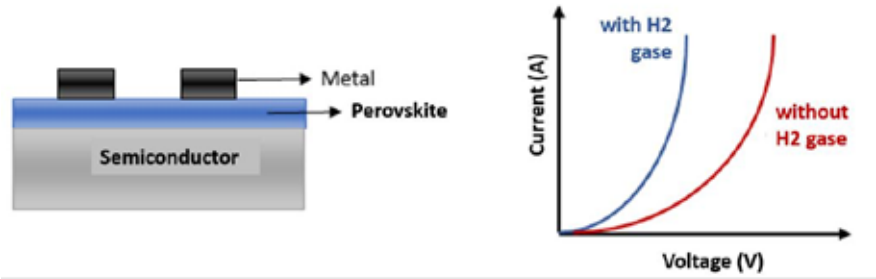

(a) **(b)**

Figure 1. (a) Cross-sectional representation of semiconductor-based gas sensors and **(b)** I-V variations under the influence of H_2 gas (Trinchi et al., 2008).

SMO-based gas sensors, especially small-sized SMO-based gas sensors, have become increasingly important as they enable the development of portable sensors (Gu et al., 2012; Sahoo & Kale, 2021). However, there are some problems with SMO-based gas sensors such as high operating temperature, poor stability, sensitivity and selectivity (Korotcenkov & Cho, 2017). To solve these problems, research has been conducted on various perovskite oxides (Fergus, 2007). Because perovskite oxides generally have a stable structure, they have attracted particular attention to improve long-term sensor performance. Perovskite-based sensors have proven to provide high sensitivity and good selectivity in addition to their stable structure (Toàn et al., 2003).
In the research conducted on $BaTiO_3$ based CO sensors, an increase in gas detection sensitivity was observed due to the increase in porous structure at high temperature (400 ^{0}C) (Park & Seo, 2004). $BaTiO_3$ thin films have been used in many gas sensors such as CO_2 (Mandayo et al., 2006), NO_2 and NH_3 (Patil et al., 2019). Metal oxide doped $BaTiO_3$ has been proposed as a thin film for the detection of LPG gas and has shown high sensitivity and selectivity for gases such as H_2, H_2S, CO (Chaudhari et al., 2006). In addition, $BaTiO_3$ nanotubes have shown efficient results as humidity sensors (Soderznik et al., 2019). The advantages that make $BaTiO_3$ material attractive for industrial applications include high response, low operating temperature and fast response-recovery times. Therefore, investigating the H_2 sensor parameters of $BaTiO_3$ material will make an important contribution to the literature.

2. MATERIALS AND METHODS

2.1. Experimental Set-up and Procedure

For the fabrication of n-Si/$BaTiO_3$/Pt devices, commercially available n-Si wafer RCA1 cleaning procedure was applied (Taşyürek 2022). The matte surface of the cleaned n-Si wafer was coated with 100 nm aluminum (Al) metal by DC sputter method as a back contact. $BaTiO_3$ was coated on the glossy surface of the n-Si wafer by drip-coating method as an interface. Finally, platinum (Pt) point contacts for electrical measurements were coated by DC sputtering. I-V and AC measurements of the fabricated n-Si/$BaTiO_3$/Pt devices were performed at room temperature and temperature dependent. Keysight B2901BL Precission Source/Measure Unit was used for I-V measurements and Hioki IM3536 LCR Meter was used for AC measurements.

2.2. Analysis

The I-V characteristic of the Schottky type contact and the corresponding voltage at forward bias can be explained by the Thermionic Emission (TE) theory (Tung, 2001);

$$I = I_0 \left[exp\left(\frac{(qV)}{nkT}\right) - 1 \right] \quad (1)$$

$$I_0 = AA^*T^2\, exp\left(\frac{q\Phi_B}{kT} - 1\right) \quad (2)$$

where A* is the Richardson constant, A is the current diode area, Φ_B is the barrier height, T is the temperature, k is the constant of Boltzmann, V is the voltage, q is the electric charge, I_0 is the saturation current, and n is the ideality factor. The following formulae are used to calculate n and Φ_B using the TE method;

$$n = \frac{q}{kT}\frac{dV}{d(ln\, I)} \quad (3)$$

$$q\Phi_B = kT\, ln\left(\frac{AA^*T^2}{I_0}\right) \quad (4)$$

3. RESULTS AND DISCUSSION

Figure 2 shows the I-V characteristics of the n-Si/$BaTiO_3$/Pt device measured in the range 293-433 K in 20 K steps. As can be seen from the graphs, the n-Si/$BaTiO_3$/Pt device exhibited Schottky behavior at low temperatures near room temperature. However, it exhibited ohmic behavior as the temperature increased. This can be attributed to the inhomogeneities in the contact area and the series resistance effect. Figure 3 shows the H_2 sensor tests of the n-Si/$BaTiO_3$/Pt device. The normal and semi-logaritmic I-V variations of the device at room temperature in dry air and 1% H_2 flow are given. As can be seen from the figure, the n-Si/$BaTiO_3$/Pt device showed sensitivity to H_2 gas. Sensor response $(I_{H2}-I_{air})/I_{air}$ value was calculated 6.99.

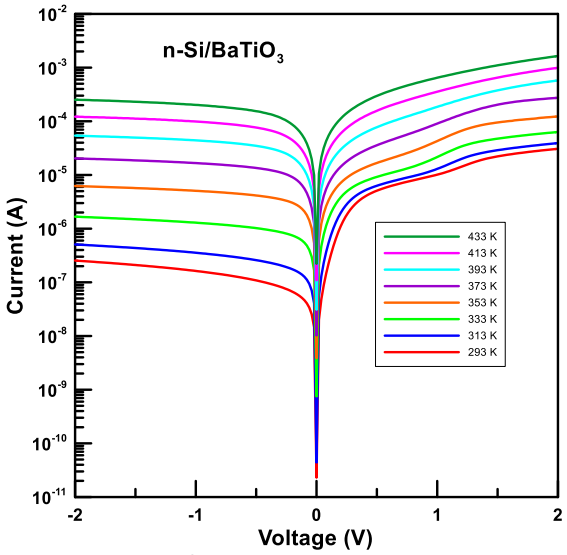

Figure 2. Temperature dependent changes of semi-logaritmic I-V graphs with 20 K steps between 293-433 K

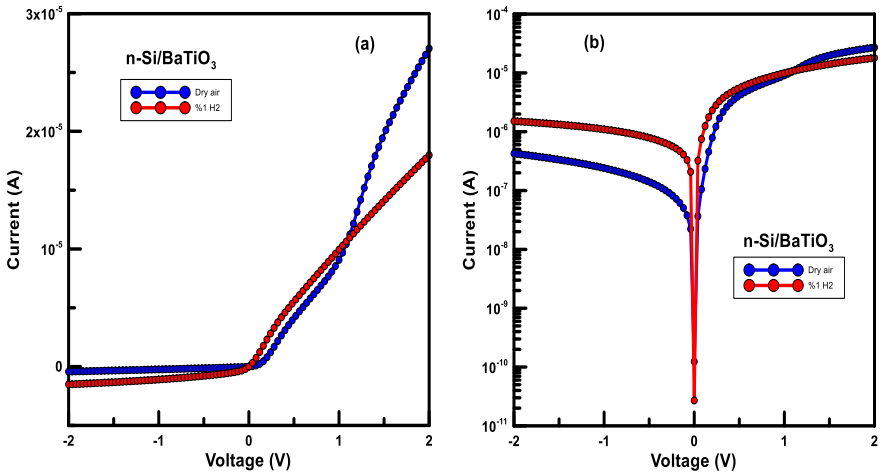

Figure 3. Variation of **(a)** I-V and **(b)** semi-logaritmic I-V graphs at room temperature, dry air and 1% H_2 flow

4. CONCLUSIONS

DC magnetron sputtering and drip-coating methods were used to fabricate n-Si/$BaTiO_3$/Pt devices. I-V measurements showed Schottky behavior at low temperatures and ohmic behavior as the temperature increased. In gas measurements at room temperature, measurements were made in dry air and 1% H_2 flow. According to the gas tests, the device showed sensitivity to H_2 gas.

ACKNOWLEDGEMENTS

This study was funded by The Scientific and Technological Research Council of Türkiye (TUBİTAK), Project Number: 121C433 and Malatya Turgut Ozal University BAP, Project Number: 2022/07.

REFERENCES

Chaudhari, G. N., Bambole, D. R., & Bodade, A. B. (2006). Structural and gas sensing behavior of nanocrystalline BaTiO3 based liquid petroleum gas sensors. *Vacuum*, *81*(3), 251–256.

Dey, A. (2018). Semiconductor metal oxide gas sensors: A review. *Materials Science and Engineering: B*, *229*, 206–217.

Doroftei, C., Popa, P. D., & Iacomi, F. (2013). Selectivity between methanol and ethanol gas of La–Pb–Fe–O perovskite synthesized by novel method. *Sensors and Actuators A: Physical*, *190*, 176–180. https://doi.org/https://doi.org/10.1016/j.sna.2012.11.018

Esfandiar, A., Irajizad, A., Akhavan, O., Ghasemi, S., & Gholami, M. R. (2014). Pd–WO3/reduced graphene oxide hierarchical nanostructures as efficient hydrogen gas sensors. *International Journal of Hydrogen Energy*, *39*(15), 8169–8179.

Fergus, J. W. (2007). Perovskite oxides for semiconductor-based gas sensors. *Sensors and Actuators B: Chemical*, *123*(2), 1169–1179.

Gu, H., Wang, Z., & Hu, Y. (2012). Hydrogen gas sensors based on semiconductor oxide nanostructures. *Sensors*, *12*(5), 5517–5550.

Huang, W., Li, Y., Ding, Y., & Li, H. (2019). Preparation and conductive properties of double perovskite Ba3Sr1+xTa2−xO9−δ and

application for hydrogen sensor. *Journal of Alloys and Compounds*, *792*, 759–769. https://doi.org/https://doi.org/10.1016/j.jallcom.2019.04.089

Hübert, T., Boon-Brett, L., Black, G., & Banach, U. (2011). Hydrogen sensors–a review. *Sensors and Actuators B: Chemical*, *157*(2), 329–352.

Kabcum, S., Channei, D., Tuantranont, A., Wisitsoraat, A., Liewhiran, C., & Phanichphant, S. (2016). Ultra-responsive hydrogen gas sensors based on PdO nanoparticle-decorated WO3 nanorods synthesized by precipitation and impregnation methods. *Sensors and Actuators B: Chemical*, *226*, 76–89.

Kilinc, N., Sisman, O., Tasaltin, C., & Gurol, I. (2024). Room temperature gas and VOCs sensors based on metal oxide composites. In *Complex and Composite Metal Oxides for Gas, VOC and Humidity Sensors, Volume 2* (pp. 465–500). Elsevier.

Korotcenkov, G., & Cho, B. K. (2017). Metal oxide composites in conductometric gas sensors: Achievements and challenges. *Sensors and Actuators B: Chemical*, *244*, 182–210.

Korotcenkov, G., Han, S. Do, & Stetter, J. R. (2009). Review of electrochemical hydrogen sensors. *Chemical Reviews*, *109*(3), 1402–1433.

Liu, X., Hu, J., Cheng, B., Qin, H., & Jiang, M. (2008). Acetone gas sensing properties of SmFe1− xMgxO3 perovskite oxides. *Sensors and Actuators B: Chemical*, *134*(2), 483–487.

Liu, Y., Yu, J., & Lai, P. T. (2014). Investigation of WO3/ZnO thin-film heterojunction-based Schottky diodes for H2 gas sensing. *International Journal of Hydrogen Energy*, *39*(19), 10313–10319.

Malavasi, L., Tealdi, C., Flor, G., Chiodelli, G., Cervetto, V., Montenero, A., & Borella, M. (2005). NdCoO3 perovskite as possible candidate for CO-sensors: thin films synthesis and sensing properties. *Sensors and Actuators B: Chemical*, *105*(2), 407–411.

Mandayo, G. G., González, F., Rivas, I., Ayerdi, I., & Herrán, J. (2006). BaTiO3–CuO sputtered thin film for carbon dioxide detection. *Sensors and Actuators B: Chemical*, *118*(1–2), 305–310.

Mirzaei, A., Yousefi, H. R., Falsafi, F., Bonyani, M., Lee, J.-H., Kim, J.-H., Kim, H. W., & Kim, S. S. (2019). An overview on how Pd on resistive-based nanomaterial gas sensors can enhance response toward hydrogen gas. *International Journal of Hydrogen Energy*, *44*(36), 20552–20571.

Nakate, U. T., Lee, G. H., Ahmad, R., Patil, P., Hahn, Y.-B., Yu, Y. T., & Suh, E. (2018). Nano-bitter gourd like structured CuO for enhanced hydrogen gas sensor application. *International Journal of Hydrogen Energy*, *43*(50), 22705–22714.

Park, K., & Seo, D. J. (2004). Gas sensing characteristics of BaTiO3-based ceramics. *Materials Chemistry and Physics*, *85*(1), 47–51.

Patil, R. P., Hiragond, C., Jain, G. H., Khanna, P. K., Gaikwad, V. B., & More, P. V. (2019). La doped BaTiO3 nanostructures for room temperature sensing of NO2/NH3: focus on La concentration and sensing mechanism. *Vacuum*, *166*, 37–44.

Sahner, K., Moos, R., Matam, M., Tunney, J. J., & Post, M. (2005). Hydrocarbon sensing with thick and thin film p-type conducting perovskite materials. *Sensors and Actuators B: Chemical*, *108*(1–2), 102–112.

Sahoo, T., & Kale, P. (2021). Work function-based metal–oxide–semiconductor hydrogen sensor and its functionality: A review. *Advanced Materials Interfaces*, *8*(23), 2100649.

Seekaew, Y., Wisitsoraat, A., Phokharatkul, D., & Wongchoosuk, C. (2019). Room temperature toluene gas sensor based on TiO2 nanoparticles decorated 3D graphene-carbon nanotube nanostructures. *Sensors and Actuators B: Chemical*, *279*, 69–78.

Shimizu, Y., Fukuyama, Y., Narikiyo, T., Arai, H., & Seiyama, T. (1985). Perovskite-type oxides having semiconductivity as oxygen sensors. *Chemistry Letters*, *14*(3), 377–380.

Sisman, O., Erkovan, M., & Kilinc, N. (2024). *Chapter 5.1 - Hydrogen sensors for safety applications* (D. Jaiswal-Nagar, V. Dixit, & S. B. T.-T. H. I. Devasahayam, Eds.; pp. 275–314). Elsevier. https://doi.org/https://doi.org/10.1016/B978-0-323-95553-9.00061-3

Soderznik, K. Z., Fabrega, C., Hernandez-Ramirez, F., Prades, J. D., & Čeh, M. (2019). BaTiO3 Based Nanostructures for Humidity Sensing Applications. *Multidisciplinary Digital Publishing Institute Proceedings*, *15*(1), 9.

Toàn, N. N., Saukko, S., & Lantto, V. (2003). Gas sensing with semiconducting perovskite oxide LaFeO3. *Physica B: Condensed Matter*, *327*(2–4), 279–282.

Tobias, P., Baranzahi, A., Spetz, A. L., Kordina, O., Janzén, E., & Lundstrom, I. (1997). Fast chemical sensing with metal-insulator silicon carbide structures. *IEEE Electron Device Letters*, *18*(6), 287–289.

Trinchi, A., Kandasamy, S., & Wlodarski, W. (2008). High temperature field effect hydrogen and hydrocarbon gas sensors based on SiC MOS devices. *Sensors and Actuators B: Chemical*, *133*(2), 705–716. https://doi.org/https://doi.org/10.1016/j.snb.2008.03.011

Tung, R. T. (2001). Recent advances in Schottky barrier concepts. *Materials Science and Engineering: R: Reports*, *35*(1–3), 1–138.

Ueda, T., Nagano, T., Okawa, H., & Takahashi, S. (2009). Zirconia-based amperometric sensor using La–Sr-based perovskite-type oxide sensing electrode for detection of NO2. *Electrochemistry Communications*, *11*(8), 1654–1656.

Wang, X., Qin, H., Sun, L., & Hu, J. (2013). CO2 sensing properties and mechanism of nanocrystalline LaFeO3 sensor. *Sensors and Actuators B: Chemical*, *188*, 965–971. https://doi.org/https://doi.org/10.1016/j.snb.2013.07.100

Zhang, C., Kanta, A.-F., Yin, H., Boudiba, A., D'Haen, J., Olivier, M.-G., & Debliquy, M. (2013). H2 sensors based on WO3 thin films activated by platinum nanoparticles synthesized by electroless process. *International Journal of Hydrogen Energy*, *38*(6), 2929–2935.

TRENDS AND INSIGHTS IN HYDROGEN ENERGY: A BIBLIOMETRIC APPROACH

[1]Nagihan Ersoy, [2]İsmail Ekmekci
[1]Manisa Celal Bayar University, Soma Vocational School, 45500 Manisa, Türkiye
[2]İstanbul Ticaret University, Eng. Faculty, 34840, İstanbul, Türkiye

*Corresponding author e-mail: iekmekci@ticaret.edu.tr

ABSTRACT

In this study, articles on hydrogen energy were examined with the bibliometric analysis technique and the first 100 most cited articles were analyzed. Bibliometric analysis allows planning research, determining trends in the field and focusing on important studies in the field. In this context, it is aimed to contribute to the literature by analyzing hydrogen energy studies with the bibliometric approach. Bibliometric analysis is an important tool for measuring the scientific impact and popularity of authors, keywords, journals, institutions and countries in the field of research, as well as being used to determine potential directions for future studies in the field of research. The most fundamental determinant of bibliometric research is the quality of the data representing the relevant literature. It is important to choose the relevant database correctly and determine the search criteria. There are many databases that provide data sets for bibliometric research. Web of Science (WoS) is the oldest and most widely used database in the world. For this purpose, 83500 articles were found in the search made on hydrogen energy in the Web of Science database. The first 100 most cited articles were selected and this data set was analyzed with the VOSviewer Program for bibliometric analysis, and comments were presented along with suggestions.

Keywords: Citation analysis, Bibliometric analysis, hydrogen, hydrogen energy

1. INTRODUCTION

Hydrogen is not a natural fuel, but there are various ways to produce hydrogen by utilizing primary energy sources, extracting it from fossil fuels, or by greener and more sustainable methods such as electrochemical methods, thermochemical cycles, photonic methods, biological methods, etc. In addition, biomass utilization using thermochemical processes is a promising way to produce hydrogen while treating waste. Pyrolysis is a thermal process that breaks down biomass into liquid biofuel, solid coal, and synthesis gas, which can be further processed to obtain hydrogen [1]. The most important feature that distinguishes hydrogen from other alternative energy sources is that it can be transported and stored. With the development of hydrogen production over approximately thirty years, there is a hydrogen economy that is dependent on the chemical and petroleum industry worldwide and is growing. For this reason, hydrogen is pointed out as the only alternative to petroleum, coal and natural gas that can become widespread in the future [2]. Bibliometric analysis serves as a tool used to map the latest status in a field related to given scientific knowledge. For this reason, the bibliometric method is used to analyze the scientific performance of authors, articles, journals, institutions, countries, keywords, and citation counts [3]. Although the number of bibliometric analyses in our country has increased, it is seen that the studies conducted in the field of bibliometrics in our country have not reached a sufficient level when compared to the international literature. Scientific knowledge is increasing exponentially today. Researchers need to look at more research and studies than in the past. It is not easy for researchers to follow developments with traditional literature reviews. In this sense, bibliometric analysis is of critical importance for researchers to follow all developments in the field of research. Bibliometric analysis allows the researcher to reach the data required at the beginning of the research in a short time with minimal effort [4]. Bibliometric analysis is an analysis method that is used to obtain qualitative and quantitative data on current developments in the field of hydrogen energy and provides information by visualizing what has been done before us. Citation analysis is a method that examines how often an academic study is cited by other studies. With citation analysis, the most influential studies, authors, journals, institutions and countries in the field of hydrogen energy can be quickly determined before reading and researching. If more than one author is listed as a co-author for the same publication, it is clear that these authors collaborated [5]. In these studies, a network is created based on author and citation relationships. When these networks are examined, clusters are seen with different densities and high interactions between clusters are seen with the same colors. The size of the clusters is directly proportional to the number of cited articles. As the size of the clusters increases, the number of citations and interactions increases. In bibliometric research, network analysis and network maps are made available [6]. VOSviewer is a software tool used to create and visualize bibliometric networks. Visualization is done through VOSviewer. The first visualization shows the clusters in a clustering solution and the citation relationships between these clusters. Bibliometric studies are valuable tools that allow us to understand the performance, change, interaction of literature in a scientific field to a certain extent, with its structure affected by different disciplines, and are increasingly used every day. The first 100 most cited articles in the field of hydrogen

energy were selected and this data set was analyzed with the VOSviewer Program for bibliometric analysis, and comments were presented with suggestions.

2.1. Results Regarding Co-Author Analysis

In the co-author analysis, authors who collaborated in the dataset and the collaboration networks between authors were presented. In our study, authors with at least 4 articles were included.

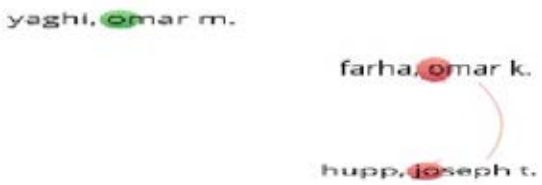

Fig.1. Co-author analysis relationship network map and country relationship network map

2.2. Results Related to Common Keyword Analysis

Common keyword analysis shows the frequency of words in the titles, keywords, and abstracts of studies on hydrogen energy and the relationship network between them. Common keyword analysis is done based on bibliographic data, on the keywords of the studies. It is very important to choose the keywords in the article well and use them in their proper place [7]. Keywords used at least 2, 3 and 6 times were included and determined.

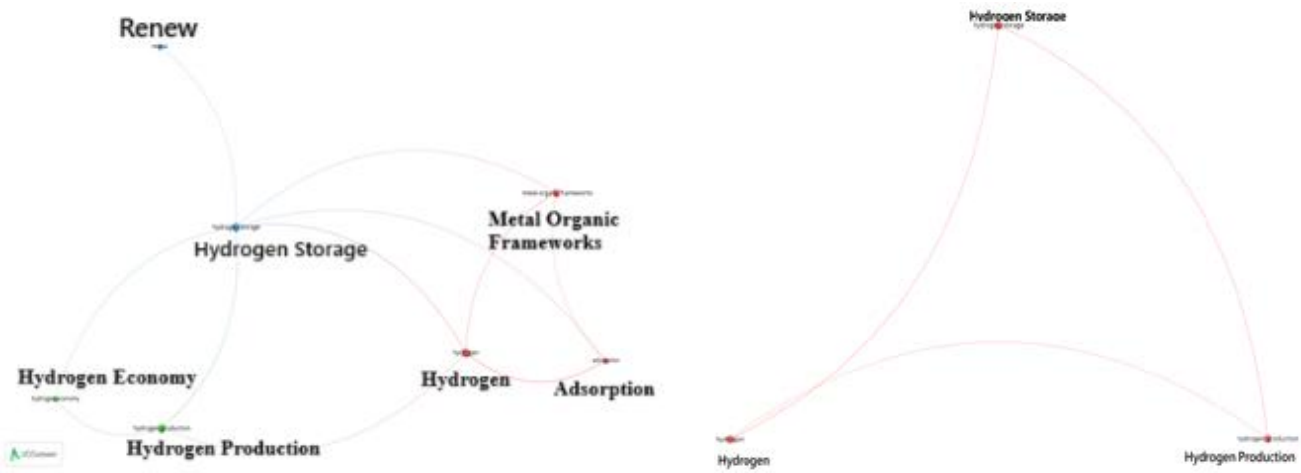

Fig. 2. Common three-times-repeated keywords network map and six-times-repeated keywords network maps

2.3. Results Regarding Citation Analysis

Citation analysis is related to the impact of studies and how often other researchers are cited as sources. It is known that citation analysis is used in the literature for two purposes:

- Citation analysis of studies downloaded as data
- Citation analysis of bibliographies of studies downloaded as data

VOSviewer performs citation analysis on studies in the dataset. It offers an approach where the performance of each element is measured based on the number of studies and citations. However, citation information only shows the number of citations made to the articles in the downloaded dataset by articles published in the Web of Science. The citation counts of articles are an important indicator in measuring their impact. In order to reach the citation count, the publication of the article and its scientific recognition and citations require a long-term process. As a scientific article attracts attention, the number of citations increases. The number of citations is one of the most important measurements used to measure the impact of the article [6]. Fig.4 shows that out of a total of 14649 studies, only 111 studies were cited 6 or more times by the studies in the dataset.

3. RESULTS AND EVALUATION

In this study, articles on hydrogen energy were examined with the bibliometric analysis technique and the first 100 most cited articles were analyzed. Bibliometric analysis is a modern type of analysis and detailed information is obtained by analyzing the co-author, common keyword, citation counts, and reference match of important studies

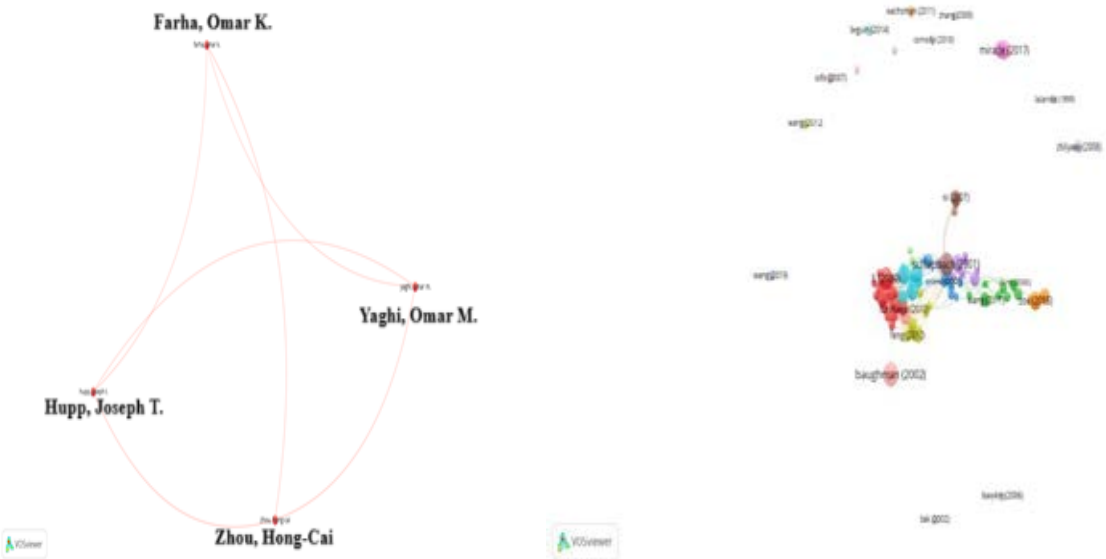

Fig. 3. Network map of the most influential authors analysis and authors with at least 100 citations

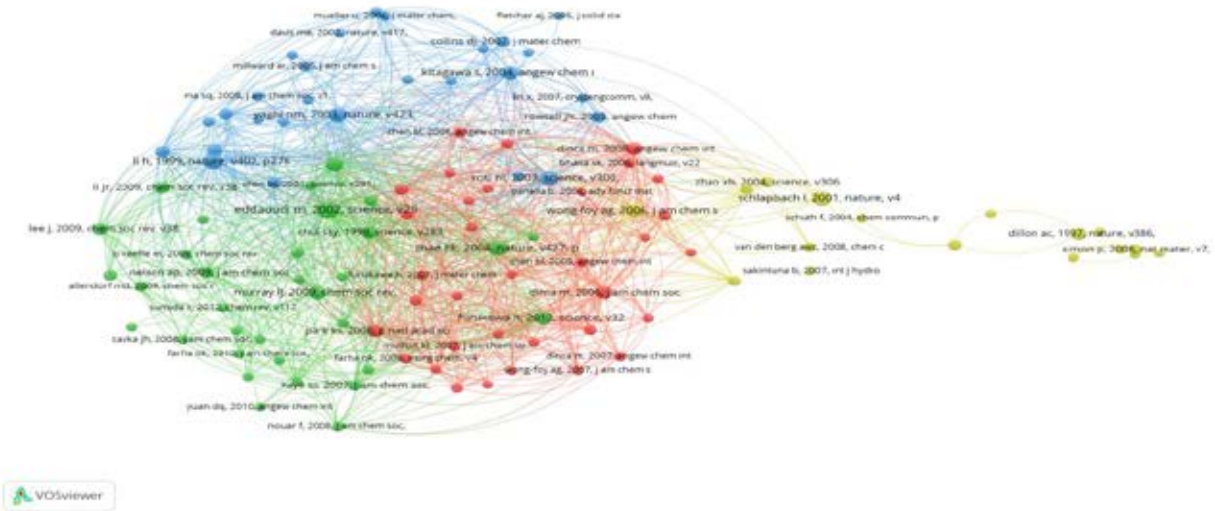

Fig. 4. Co-citation analysis network map in the context of cited studies

on hydrogen energy. In this context, bibliometric analysis allows researchers to quickly and easily access qualified studies on hydrogen energy. Bibliometric analysis used in the study is a modern type of analysis and has contributed to the development of researchers' perspective as a method that can quickly and easily access qualified studies on hydrogen energy. The main purpose is to examine the trend in the field of hydrogen energy and to provide researchers with quick and easy access. In this context, a comprehensive bibliometric analysis guiding the literature on hydrogen energy and visualizing the most cited scientific studies in the Web of Science (WOS) database was applied. The most cited 100 studies were analyzed under co-author analysis, keyword analysis, co-citation analysis and reference matching in terms of the most influential study, author, country, institution and journals, etc. and their relationship with various aspects. When the common keyword was repeated at least 2 times, it was seen that hydrogen storage, hydrogen, hydrogen production, metal organic frameworks, adsorption, carbon dioxide, zeolites, catalysis, porous

materials, water electrolysis, hydrogen economy, microporous materials, high-entropy alloys, hydrogen evolution, renewable energy, energy storage, review. The author who has done the most studies was determined as Yaghi, Omar M. with 5 articles and 14181 citations. When the 100 most cited articles on hydrogen energy were examined, it was seen that the classification of the citations to the articles according to their subjects was Chemical Society Reviews. Although the bibliometric analysis method has gained great popularity recently, it is one of the first bibliometric analysis studies conducted directly in the field of hydrogen energy. Bibliometric analyzes on hydrogen energy can determine serious contributions to research conducted over the years and highlight scientific developments in many studies. It is thought that it will provide convenience to researchers who want to research the literature on hydrogen energy.

REFERENCES

1. Dincer, I., & Aydin, M. I. (2023), New paradigms in sustainable energy systems with hydrogen, *Energy Conversion and Management*, *283*, 116950.
2. Kılıç, Nurel (2009), Geleceğin Enerjisi Olarak Adlandırılan Hidrojen Enerjisi, Izmir Ticaret Odası, Arge Bülten, Ekim, Izmir. Ponomariov, B., & Boardman, C. 2016. What is co-authorship? *Scientometrics*, *109*, 1939-1963.
3. Sengupta, I. N. (1992), Bibliometrics, Informetrics, Scientometrics and Librametrics: An Overview. Libri: International Journal of Libraries and Information Studies, 42(2), 75–98.
4. Block, J. H., & Fisch, C. 2020, Eight tips and questions for your bibliographic study in business and management research. Management Review Quarterly, 70, 307-312.
5. Ponomariov, B., & Boardman, C. (2016). What is co-authorship? , *Scientometrics*, *109*, 1939-1963.
6. Ersoy, N., & Ekmekçi, İ. 2023. Bibliyometrik Yaklaşımla Kömürlü Termik Santraller Konusunun Analizi. *Dünya Multidisipliner Araştırmalar Dergisi*, *6*(2), 136-151.
7. Zhang, J., Yu, Q., Zheng, F., Long, C., Lu, Z., & Duan, Z. 2016. Comparing keywords plus of WOS and author keywords: A case study of patient adherence research. Journal of the association for information science and technology, 67(4), 967-972.

COBALT-COPPER-BORON DOPED GRAPHITIC CARBON NITRIDE AS A PROMISING CATALYST FOR HYDROGEN PRODUCTION VIA SODIUM BOROHYDRIDE HYDROLYSIS

[1]*Ömer Şahin,* [2]*Fatma Elif Genceli Güner,* [3*]*Mehmet Emre Kenar*
[1,2,3*] Istanbul Technical University, Faculty of Chemical and Metallurgical Engineering,
Department of Chemical Engineering, Maslak, Istanbul, 34469, Turkey
*Corresponding author e-mail: kenarme@itu.edu.tr

ABSTRACT

Hydrogen (H_2) is a clean and sustainable energy source, and it has an important role for the future and environment. Catalysts are essential for H_2 production by catalytic hydrolysis of sodium borohydride ($NaBH_4$). Here, effective cobalt-copper-boron doped graphitic carbon nitride (g-C_3N_4@Co-Cu-B) catalyst was fabricated by reduction method. Then, this new synthesized catalyst showed a high catalytic activity on the hydrolysis of $NaBH_4$. The structural characteristics of this catalyst were verified by X-ray diffraction (XRD), Scanning Electron Microscopy (SEM), and Energy Dispersive X-ray (EDX) methods. The performance of the catalyst was investigated via carried experiments based on metal Co-Cu-B/(g-C_3N_4+Co-Cu-B) ratio, wt%NaOH concentration, temperature, and reusability parameters. As a result, the best metal ratio and wt% NaOH were found as 40% and 7% respectively. Besides, g-C_3N_4@Co-Cu-B catalyst was viewed as reusable, and about 100% reaction conversion was observed at each cycle in reusability tests. In the studies, H_2 generation rate (HGR) was calculated as 6598 $mlH_2\ min^{-1}\ g_{cat}^{-1}$ at 30 °C. According to all obtained results, it was deduced that using of g-C_3N_4@Co-Cu-B is suitable for $NaBH_4$ hydrolysis.

Keywords: Borohydride, Catalyst, Hydrogen, Hydrolysis

1. INTRODUCTION

In recent years, hydrogen is a prominent alternative energy source against common unrenewable fossil fuels leading to environmental pollution. Hydrogen can be stored in the form of solid metal hydrides, liquid form, and as compressed gas. Borohydrides, outstanding lately are a part of metal hydrides. Borohydrides such as sodium borohydride ($NaBH_4$), potassium borohydride (KBH_4), lithium borohydride ($LiBH_4$) and ammonium borohydride (NH_4BH_4) are effective hydrogen storage sources. Besides, when the borohydrides were used, half of the hydrogen obtained in the production of hydrogen by hydrolysis of borohydrides in aqueous environment came from water. Thus, they can be used for hydrogen production. The most preferred borohydride used in the studies is sodium borohydride ($NaBH_4$) due to its good stability, practicality, and easy workability. $NaBH_4$ has 10.8% hydrogen storage capacity. $NaBH_4$ solutions are very stable, non-flammable, and non-toxic. Various substances such as metal catalysts (Ru, Co, Cu, Ni), complex hydrides and supported catalysts are used to facilitate the degradation of $NaBH_4$ and accelerate the release of H_2 by reducing the required activation energy [1-8].

Hydrogen production reaction via catalytic hydrolysis of $NaBH_4$ is shown in Eq.(1) [2]:

$$\mathrm{NaBH_4 + 4H_2O \xrightarrow{catalyst} NaBO_2 + 4H_2} \quad (1)$$

Supporting materials provide a structural framework, providing a stable environment for catalyst activities. The metal catalysts can be loaded to the supporting materials such as alumina (Al_2O_3), active carbon (C), multiwalled carbon nano tubes (MWCNT), carbon nitride nanotubes (CNNT), zeolite, graphitic carbon nitride (g-C_3N_4), titanium dioxide (TiO_2), cobalt oxide (CoO and Co_3O_4), which are common-used for $NaBH_4$ based catalysts. The choice of supporting material is important to optimize catalyst performance since it can affect the chemical stability, dispersion, and overall effectiveness of the catalyst by providing high surface area. [2, 9-13].

g-C_3N_4 is an interesting supporting material used primarily with $NaBH_4$-based catalyst. Its chemical stability, photocatalyst activity, electronic structure, high surface area, interaction with catalyst, synergistic effects and environmental friendliness effect the overall strength of the combined catalyst system performance positively [14].

In general perspective, it is well-known that cobalt and copper catalysts are highly efficient in sodium borohydride hydrolysis [5, 15-17]. Thus, in this study, boron bounded cobalt-copper bimetallic catalyst was prepared with g-C_3N_4 supporting material. As a result, g-C_3N_4@Co-Cu-B catalyst was synthesized first time at the end of adsobtion of g-C_3N_4 and reduction with $NaBH_4$ processes, then the suitability and performance of this new catalyst on sodium borohydride hydrolysis were investigated.

2. MATERIALS AND METHODS

2.1. Problem Description and Materials

In this study, as a solution to the hydrogen storage and safety problems, sodium borohydride which has high hydrogen storage capacity was preferred. However, the hydrolysis reaction of sodium borohydride is a slow process. As a solution to this, g-C3N4@Co-Cu-B catalyst was developed to accelerate the reaction.

Throughout the study, cobalt (II) chloride hexahydrate ($CoCl_2.6H_2O$, ≥99% purity, SRL), copper (II) nitrate trihydrate ($Cu(NO_3)_2.3H_2O$, 99.5% purity, SRL), sodium borohydride ($NaBH_4$, ≥98% purity, Sigma-Aldrich), sodium hydroxide (NaOH, ≥97% purity, Merck), ethanol (C_2H_5OH, 96% purity, Merck), nitrogen gas, distilled water, and dicyandiamide ($C_2H_4N_4$, 99% purity, Sigma-Aldrich) were used as materials.

2.2. Methods and System Description

Firstly, during the g-C_3N_4 supporting material synthesis step, 6 g dicyandiamide ($C_2H_4N_4$) was placed in a closed-crucible to a muffle furnace with a 3 ˚C/min heating rate. When the temperature was 550 ˚C, it was kept for 4 hours under this temperature. After the sample was cooled and crushed, it was then placed in the open-crucible to the muffle furnace with a 5 ˚C/min heating rate -starting from room temperature- as the second step. After the furnace temperature reached 500 ˚C, the sample was kept for 2 hours there. Finally, it was waited for cooling.

In the experiments carried out in order to find the best metal ratio, five aqueous solutions containing $CoCl_2.6H_2O$ - $Cu(NO_3)_2.3H_2O$ salts and g-C_3N_4 were prepared so that Co-Cu-B/(g-C_3N_4+Co-Cu-B) ratios were 10, 20, 30, 40, and 50%. Here, the ratio of mole of Co/Cu was adjusted as 3. After g-C_3N_4 adsorbtion to the salts in the solutions for about 4 hours at 400 rpm at room temperature, $NaBH_4$ solution was added drop by drop to the solutions to reduce Co^{+2} and Cu^{+2} ions. The solutions were kept at 0 ˚C during this reduction step to bind boron easily. Then, the solid parts in the solutions were filtered. They were washed with distilled water and ethanol a lot of times to remove the unwanted impurities. Finally, the solid catalysts were dried in the oven at about 90 ˚C under inert N_2 gas for about 4 hours. As a result, five new g-C_3N_4@Co-Cu-B catalysts containing different amounts of metals were obtained. The best metal ratio and the best wt% NaOH ratio were tried to be determined by testing these catalysts. Then, temperature effect and reusability experiments were conducted by using the before-founded best ratios as reaction conditions. In the experiments, 50 mg catalyst and 1.5 wt% $NaBH_4$ in 10 ml solutions were used.

The g-C_3N_4@Co-Cu-B catalyst synthesis and hydrolysis reaction -in which this catalyst is used- processes were shown in Figure 1. These processes were similar to the system in our previous research, where g-C_3N_4@Co-B-F catalyst was synthesized [2].

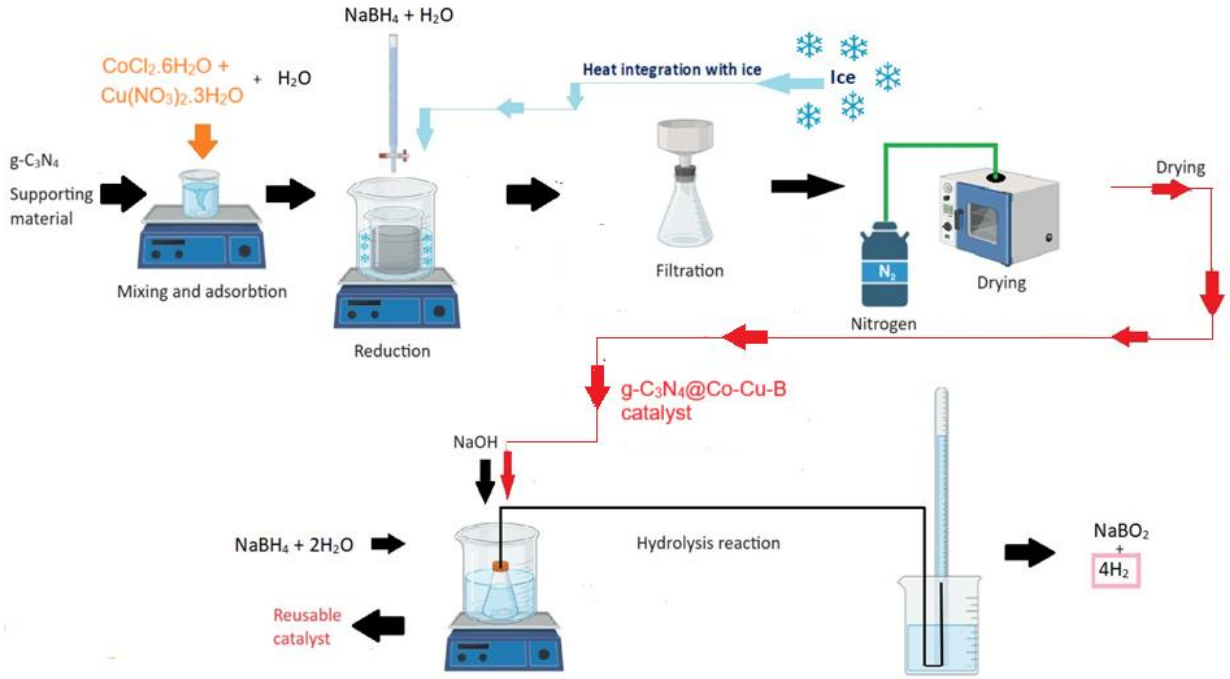

Fig. 1. The synthesis of g-C_3N_4@Co-Cu-B catalyst and the using of this catalyst in $NaBH_4$ hydrolysis processes

3. RESULTS AND DISCUSSION

3.1. The Effect of Metal Ratio, NaOH Concentration, Temperature on Hydrolysis of Sodium Borohydride In the Presence of g-C_3N_4@Co-Cu-B Catalyst and Reusability Tests of This Catalyst

The results of the experiments to determine the best conditions of hydrolysis reactions, temperature effect, and reusability were shown in Fig. 2.

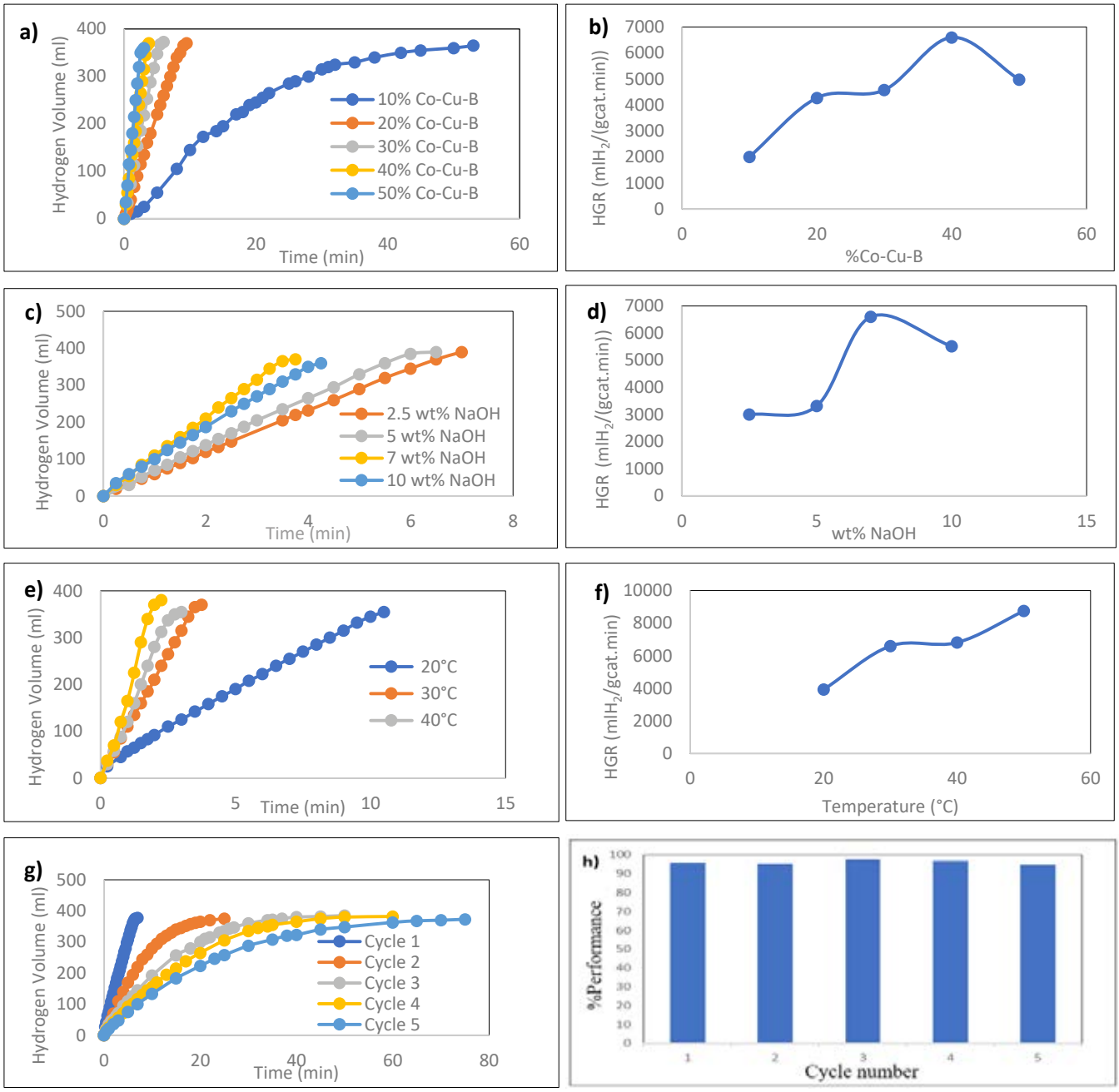

Fig. 2. When g-C_3N_4@Co-Cu-B catalyst was used in hydrolysis of $NaBH_4$, a-b) The effect of metal ratio in the catalyst - a) H_2 production, b) HGR values (NaOH = 7 wt%, T = 30 °C) ; c-d) The effect of NaOH concentration - c) H_2 production, d) HGR values (metal ratio = 40 wt%, T = 30 °C) ; e-f) The effect of temperature - e) H_2 production, f) HGR values (metal ratio = 40 wt%, NaOH = 7 wt%) ; g-h) The reusability tests - g) H_2 production, h) %Performance (metal ratio = 40 wt%, NaOH = 7 wt, T = 30 °C)

Hydrogen volumes as a result of $NaBH_4$ hydrolysis for each metal ratio were seen in Fig. 2a. Then, hydrogen generation rate (HGR) values were calculated for each metal ratio, and they were given in Fig. 2b. According to that, the best ratio of Co-Cu-B/(g-C_3N_4+Co-Cu-B) was determined as 40% which gives high HGR value. Next experiments were continued with the catalyst having this 40% ratio. According to Fig. 2c and 2d, 7 wt% NaOH was determined as the best NaOH concentration for hydrolysis of $NaBH_4$ in the presence of g-C_3N_4@Co-Cu-B catalyst. Then, according to Figs. 2e and 2f, an increase in HGR values was observed from 3925.35 to 8747.5 $mlH_2/g_{cat}.min$ at from 20 °C to 50 °C as expected. The reason for this is that the hydrolysis reaction is faster in high temperatures. Finally, as seen in Figs. 2g and 2h, the expected teoric H_2 gas volume was almost obtained even if five cycles of experiments were completed. Thus, the catalyst performance was said to be close to 100% even if the reactions were slower at each cycle.

3.2. Characterization Results

SEM, EDX and XRD characterization results of g-C_3N_4@Co-Cu-B catalyst were shown in Fig. 3.

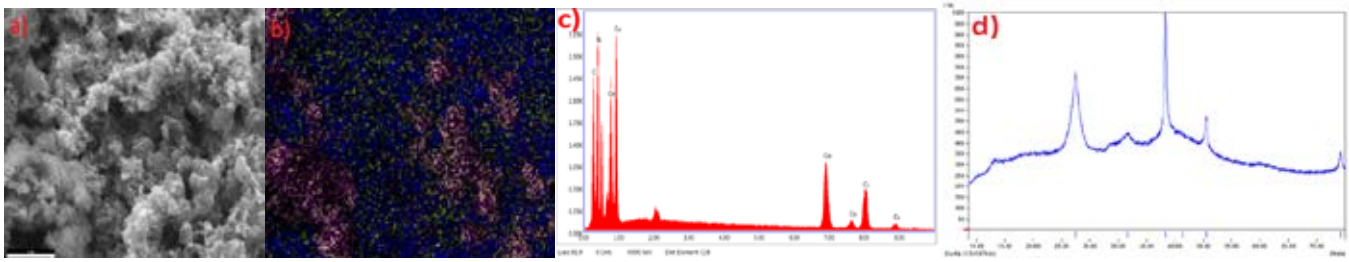

Fig. 3. g-C_3N_4@Co-Cu-B catalyst's a) SEM image (15 kV, 10000x); b) overlapped EDX image (purple:carbon, white:nitrogen, blue:cobalt, yellow-green:copper); c) EDX spectra; d) XRD spectra (Cu-Ka)

As seen in Fig. 3, the SEM image of the catalyst showed that Co-Cu-B particles were dispersed on g-C_3N_4 particles. With the help of the EDX mapping, the presence of each element (C,N,Co,Cu) was verified in the structure of the catalyst. In XRD spectra, as 2theta is about 30-40, Co and Cu peaks were observed as expected.

4. CONCLUSIONS

According to the results obtained from the experiments and characterization, it was concluded that g-C_3N_4@Co-Cu-B catalyst was successfully fabricated, and this catalyst showed a good performance with its reusability and high HGR values like 6598 mlH_2 min^{-1} g_{cat}^{-1}. Thus, g-C_3N_4@Co-Cu-B was acceptable as an appropriate catalyst for $NaBH_4$ hydrolysis in industrial applications.

ACKNOWLEDGMENTS

The authors would like to acknowledge the support of the TÜBİTAK 2224-B - Support Program for Participation in National Scientific Activities.

REFERENCES

1. https://fchea.org/learning-center/hydrogen-storage-and-distribution/. Accessed on December 29, 2024.
2. Kenar ME, Kutluay S, Şahin Ö, Güner FEG. 2024. Cobalt-boron-fluoride decorated graphitic carbon nitride composite as a promising candidate catalyst for highly efficient hydrogen production via $NaBH_4$ hydrolysis process. Int. J. of Hydrogen Energy 90:732-746.
3. Liu BH, Li, ZP. 2009. A review: hydrogen generation from borohydride hydrolysis reaction. J. of Power Sources 187(2):527-534.
4. Kılınç D, Şahin Ö, Saka C. 2017. Investigation on salisylaldimine-Ni complex catalyst as an alternative to increasing the performance of catalytic hydrolysis of sodium borohydride. Int. J. of Hydrogen Energy 42(32):20625-20637.
5. Ekinci A, Genli N, Şahin Ö, Baytar O. 2024. Facile "Green" synthesis of a novel Co–W–B catalyst from Rheum ribes shell extract and its effect on sodium borohydride hydrolysis: Kinetic mechanism. Int. J. of Hydrogen Energy 51:796-808.
6. Büyükkanber K, Ekinci A, Şahin Ö. 2024. High catalytic activity of cobalt nanoparticles synthesized by ultrasonic spray method in sodium borohydride hydrolysis. Int. J. of Hydrogen Energy 79:335-345.
7. Retnamma R, Novais AQ, Rangel C. 2011. Kinetics of hydrolysis of sodium borohydride for hydrogen production in fuel cell applications: A review. Int. J. of Hydrogen Energy 36(16):9772-9790.
8. Wang C, Ye S, Cheng L, Yan P. 2023. Electronic transfer enhanced coral-like CoxP loaded Ru nanoclusters as efficient catalyst for hydrogen generation via $NaBH_4$ hydrolysis. Int. J. of Hydrogen Energy 48(4):1440-1449.
9. Yang F, Xiang C, Fang S, Xu F, Sun L, Shen CY, Zou Y. 2023. Synthesis and catalytic performance of nanoflower-like Ru@ CoAl-LDH composite catalyst for $NaBH_4$ hydrolysis. Journal of Alloys and Compounds 945:169280.
10. Yuan ZZ, Chen JM, Lu Y, Chen XD. 2008. Preparation and magnetic properties of amorphous Co–Zr–B alloy nano-powders. Journal of Alloys and Compounds 450(1-2):245-251.
11. Loghmani MH, Shojaei AF. 2015. Reduction of cobalt ion improved by lanthanum and zirconium as a triphenylphosphine stabilized nano catalyst for hydrolysis of sodium borohydride. Int. J. of Hydrogen Energy 40(20):6573-6581.
12. Wang T, Xi J, Sheng H, Zhao Y. 2024. Mechanism of catalytic performance enhancement for hydrolysis of sodium borohydride by modification of cobalt boride with metals: A review. Int. J. of Hydrogen Energy *85*:120-134.
13. Xu F, Ren J, Ma J, Wang Y, Zhang K, Cao Z, Sun Q, Wu S, Li G, Bai S. 2023. A review of hydrogen production kinetics from the hydrolysis of $NaBH_4$ solution catalyzed by Co-based catalysts. Int. J. of Hydrogen Energy
14. Krishnan A, Yoosuf M, Archana K, Arsha A, Viswam A. 2023. Metal derivative (MD)/g-C3N4 association in hydrogen production: A study on the fascinating chemistry behind, current trend and future direction. Journal of Energy Chemistry 80:562-583.
15. Wang Y, Zou K, Zhang D, Cao Z, Zhang K, Xie Y, …, Bai S. 2020. Cobalt–copper–boron nanoparticles as catalysts for the efficient hydrolysis of alkaline sodium borohydride solution. Int. J. of Hydrogen Energy 45(16):9845-9853.
16. Baytar O, Izgi MS, Horoz S, Sahin O, Nar S. 2019. Al2O3 supported Co-Cu-B (Co-Cu-B/Al2O3) catalyst for hydrogen generation by hydrolysis of aqueous sodium borohydride ($NaBH_4$) solutions. Dig J Nanomater Biostruct 14(3):673-681.
17. Yuan W, Yang X, Liu C, Xue L, Niu W, Yan Q, …, Zhang B. 2024. High-Surface-Area Co-Cu-B Monolithic Self-Supported Catalyst for Efficient Sodium Borohydride Hydrolysis. Processes *12*(7):1384.

OPTIMIZATION OF BORON-DOPED NICKEL ELECTRODES FOR ENHANCED HYDROGEN PRODUCTION VIA ALKALINE ELECTROLYSIS

[1]Ceyda DEMİR,[1] Kadir Arda UĞURLU, [1] Deniz TÜRKYILMAZ [1]Aysu Doğa TÜMER, [1,2] Bilge COŞKUNER FİLİZ*
[1] Yıldız Technical University, Metallurgical and Materials Engineering Department, Istanbul, Turkey
[2] Yıldız Technical University, Clean Energy Technology Institute, Istanbul, Turkey

e-mail: ceydademir0920@outlook.com

ABSTRACT

This study focuses on the preparation of boron-doped nickel electrodes and the evaluation of their hydrogen production activity under alkaline conditions. Electrodes were fabricated using electroplating, optimizing the electrolyte composition with nickel salts (Nickel Chloride ($NiCl_2 \cdot H_2O$), Nickel Sulfate ($NiSO_4 \cdot H_2O$)) and boric acid (H_3BO_3, 2–6 wt.%). The influence of key experimental parameters, including H_3BO_3 concentration (2–4 wt.%), applied voltage (4–5 V), and bath temperature (20–60°C), was investigated for electrode preparation. The coating efficiency and hydrogen production performance of the electrodes under alkaline conditions were analyzed. Results indicated that B-doped Ni electrodes electroplated with 20 g/L H_3BO_3 at 4.5 V and 60°C exhibited optimal activity. Additionally, the impact of electrolyte composition was examined by varying the sodium hydroxide to potassium hydroxide (NaOH:KOH) ratio as 1:0, 2:1, 1:1, 1:2, and 0:1. Hydrogen production studies demonstrated that electrodes achieved enhanced performance %630 in the presence of pure KOH as the electrolyte.
Keywords: Boron-doped Nickel Electrodes; Electroplating Optimization; Hydrogen Production; Alkaline Electrolysis; Electrolyte Composition

1. INTRODUCTION

Energy is crucial for enhancing the quality of life and sustaining modern society. As the global population grows, energy demand rises. While traditional sources like oil, coal, and natural gas have dominated electricity generation, environmental concerns and fossil fuel depletion are driving a shift toward renewables [1]. Hydrogen energy offers a promising alternative as a clean, abundant, and efficient energy carrier. Although not a primary energy source, hydrogen can be produced through methods such as water electrolysis and hydrocarbon processing [2]. Water electrolysis, particularly when powered by renewable energy, is an attractive option [3]. This process, occurring in electrolyzers with electrodes, an electrolyte, and a power supply, involves splitting water into hydrogen and oxygen through the following reactions:

Anode Reaction: $2OH^-_{(aq)} \rightarrow H_2O_{(l)} + \frac{1}{2}O_{2(g)} + 2e^-$ (1)

Cathode Reaction: $2H_2O_{(l)} + 2e^- \rightarrow H_{2(g)} + 2OH^-_{(aq)}$ (2)

Alkaline electrolyzers are widely used due to their efficiency, low operating temperatures, and scalability. These systems typically use potassium hydroxide (KOH) or sodium hydroxide (NaOH) as the electrolyte, making them cost-effective for industrial hydrogen production [4]. Graphite electrodes are preferred for anodes due to their chemical resistance, conductivity, and affordability, though they may degrade over time, requiring maintenance. For cathodes, materials such as stainless steel, platinum, and nickel are commonly used. Stainless steel is favored for its durability, corrosion resistance, and electrochemical stability in alkaline environments. The formation of a chromium oxide (Cr_2O_3) layer further enhances its longevity. Nickel plating is often applied to stainless steel cathodes to improve corrosion resistance and electrocatalytic performance [5].
Nickel electroplating is a widely used industrial process that enhances durability, corrosion resistance, and conductivity. It requires an electrolyte containing nickel precursors and often boric acid (H_3BO_3), which stabilizes pH, enhances conductivity, and is environmentally friendly [6]. The electrolysis process begins by preparing the electrolyte solution and positioning the electrodes. A power supply is then connected, with the cathode linked to the negative terminal and the anode to the positive terminal.
Hydrogen serves as an energy carrier, efficiently storing and transporting energy, making it essential for future energy systems. It is classified into gray, blue, turquoise, and green hydrogen based on production methods. Green hydrogen, produced through electrolysis powered by renewable energy, is the most sustainable option. Alkaline water electrolysis remains the most widely used method for large-scale hydrogen production due to its high efficiency and ability to generate high-purity hydrogen.

This study explores hydrogen production via alkaline electrolysis using a boric acid-added electrolyte, a nickel-plated stainless steel cathode, a graphite anode, and a power supply. Boric acid was selected as a pH stabilizer, while nickel plating improved the corrosion resistance and efficiency of the stainless steel cathode. Various experimental conditions, including boric acid concentration, temperature, and voltage, were examined to assess their impact on electrode performance. The electrodes were weighed before and after coating, and their surface characteristics analyzed via optical microscopy. Additionally, pH variations in the nickel bath were monitored. The goal was to determine optimal conditions for efficient plating and hydrogen production. Alkaline electrolysis presents a sustainable approach to future energy needs. Optimizing the electrolytic process and electrode materials enhances hydrogen production efficiency, supporting the transition to renewable energy. The combination of graphite and nickel-plated stainless steel electrodes with boric acid-added electrolytes is crucial for improving electrolysis performance, ensuring durability and cost-effective hydrogen generation.

2. MATERIALS AND METHODS

Electrodes were fabricated using electroplating, optimizing the electrolyte composition with Nickel Chloride ($NiCl_2 \cdot H_2O$), Nickel Sulfate ($NiSO_4 \cdot H_2O$), and Boric Acid (H_3BO_3) within a concentration range of 2–6 wt.%. The influence of key experimental parameters, including H_3BO_3 concentration (2–4 wt.%), applied voltage (4–5 V), and bath temperature (20–60°C), was systematically investigated to optimize electrode preparation. For electrode deposition, 316L stainless steel plates were used as the substrate, while 99% pure nickel strips served as the cathode during electroplating. Prior to coating, the substrates were pretreated with hydrochloric acid in an ultrasonic bath to ensure surface cleanliness. Electroplating was performed at an optimized voltage of 4–5 V under controlled conditions. The coating efficiency and hydrogen production performance of the electrodes under alkaline conditions were analyzed by weight change and optic microscope. Table 1 presented the experimental conditions of sample electrodes. Ni-plated electrodes were tested with 30% wt. KOH solution at room temperature with 2.3V. Additionally, the impact of alkaline electrolyte composition on hydrogen generation was examined by varying the NaOH:KOH ratio at 1:0, 2:1, 1:1, 1:2, and 0:1 at room temperature with 2.3V.

Table 1. Electroplating experiment parameters

Experiment/ Electrode	Temperature, °C	Voltage, V	H_3BO_3, g/L
1	20	4	20
2	20	4.5	30
3	20	5	40
4	40	4	30
5	40	4.5	40
6	40	5	20
7	60	4	40
8	60	4.5	20
9	60	5	30

3. RESULTS AND DISCUSSION

This study investigates the use of boron additives in electrode preparation and their impact on hydrogen production activity in alkaline electrolyzers. It examines the relationship between electrode performance and the composition of alkaline electrolytes, focusing on the effects of different concentrations and ratios of NaOH and KOH on hydrogen production efficiency. The research aims to answer two key questions: how boron doping during electrode preparation influences activity in alkaline electrolysis and how varying alkaline agent concentrations affect hydrogen production performance. It is hypothesized that boron-doped electrodes enhance hydrogen electrolysis efficiency and that the concentration and ratio of alkaline agents play a significant role in optimizing hydrogen production. Fig.1 showed the electrode preperation conditions and its electroplating efficiency and hydrogen production activity. As it could be clearly seen from the Fig.1a, electrode prepared under conditions 60 °C, 4.5 V and 20 g/L H_3BO_3 showed the highest efficiency value. Research has shown that boron content positively influences the process up to a certain level, specifically between 30-40 g/L. However, it can hinder efficiency beyond this range, particularly at lower temperatures, as observed with the 5th and 7th electrodes. This limitation may stem from the impact of boron additives on the conductivity of the electrolyte. To determine the optimal conditions, it would be beneficial to further analyze the interactions between temperature, voltage, and boron content.

Subsequently, all electrodes were subjected to the alkaline electrolysis process. A 2.3 V direct current was applied to an electrolyte solution containing 30% potassium hydroxide (KOH) to investigate hydrogen production efficiency. Figure 1c illustrates the relationship between gas produ5ction and time, demonstrating that the optimized coatings positively influenced the hydrogen production rate

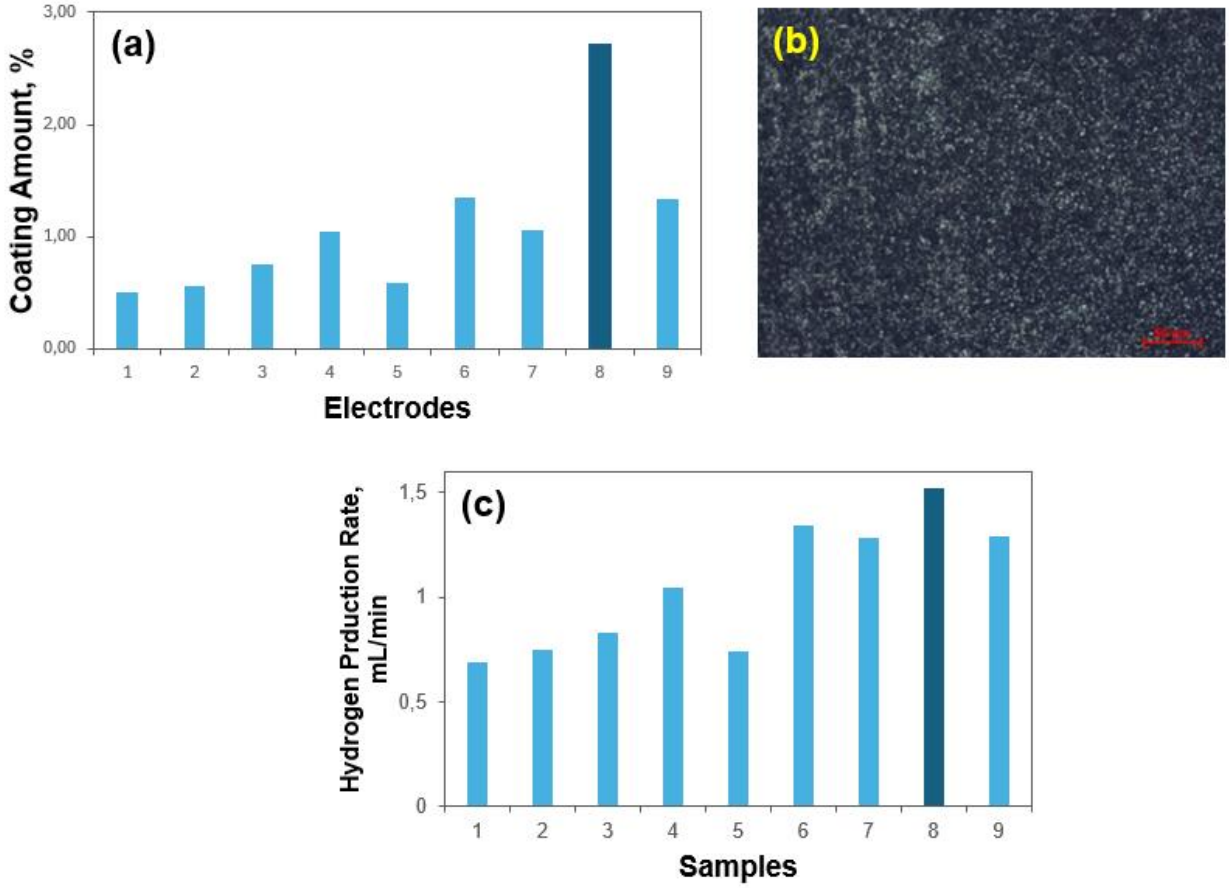

Fig. 1. Experimental results: (a) Electro-plating efficiency, (b) optic microscope image of 8th sample and (c) hydrogen production activity

The electrode prepared under optimized conditions (Electrode No. 8) was also tested to evaluate the effect of the alkaline electrolyte content. To further analyze variations in hydrogen production rates, experiments were conducted using sodium hydroxide (NaOH) solutions in combination with KOH. Five different electrolyte compositions were prepared: 30% KOH, 20% KOH-10% NaOH, 15% KOH-15% NaOH, 10% KOH-20% NaOH, and 30% NaOH. During these experiments, hydrogen production was measured to assess the effect of electrolyte composition. According to Figure 3, solely KOH exhibits superior ionization properties compared to NaOH. As the reaction progresses, the number of available electrons decreases, leading to a slowdown in the reaction rate due to the consumption of water molecules. Additionally, as the hydroxide concentration increased, the performance of KOH remained consistently high. The fourth and fifth electrolyte samples produced similar results, indicating that increasing the NaOH ratio had a limited effect on hydrogen production performance.

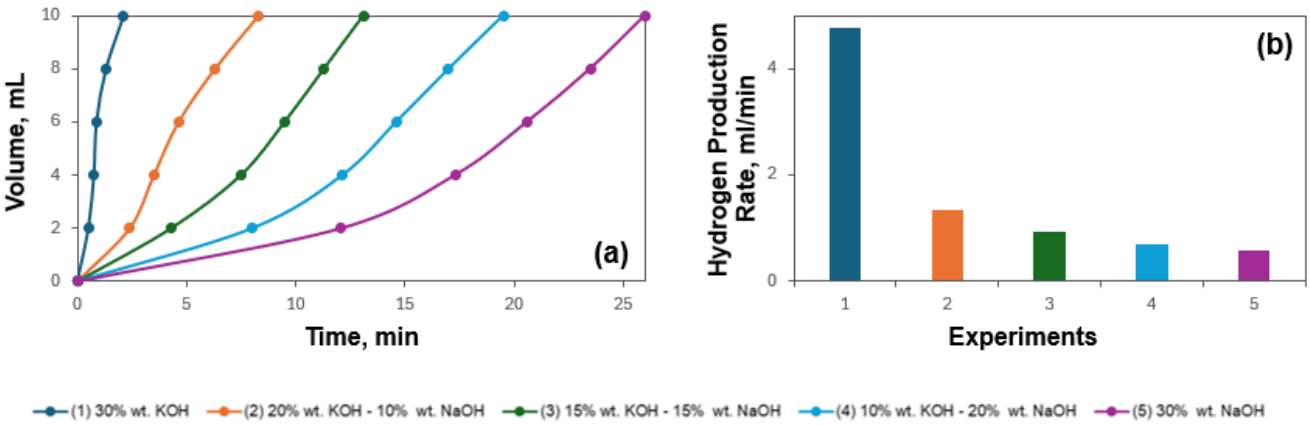

Fig. 2. (a) Comparison of various alkaline electrolyte performances (b) Hydrogen production activity

4. CONCLUSIONS

Alkaline water electrolysis powered by renewable energy sources like solar and wind presents a viable alternative to fossil fuel-based hydrogen production. This study focused on optimizing boron-doped nickel (Ni-B) electrodes for enhanced hydrogen generation efficiency in alkaline electrolyzers. The results demonstrated that boron doping, electrolyte composition, and electroplating conditions significantly impact electrode performance.. Optimal electroplating was achieved using 20 g/L H_3BO_3 at 4.5 V and 60°C, where excessive H_3BO_3 concentrations beyond 30 g/L led to reduced coating thickness. Additionally, KOH showed superior ionization properties compared to sodium hydroxide (NaOH), although NaOH remains a more economical and accessible alternative. By balancing voltage, H_3BO_3 concentration, and electrolyte composition, the efficiency and longevity of nickel-based electrodes can be enhanced, making hydrogen production more sustainable and cost-effective. Future research will explore advanced Ni-based electrode materials, such as Ni-Co Ni-Fe and Ni-Ru alloys, to improve long-term stability in flow-type electrolyzers. Additionally, integrating microbial electrolysis with alkaline electrolysis offers a dual benefit of hydrogen generation and wastewater recycling, further reducing costs and environmental impact.

ACKNOWLEDGEMENTS

The authors express their gratitude to the TÜBİTAK 2209 program for its support in the realization of this study.

REFERENCES

1. Demirbas, A., Sahin-Demirbas, A., & Demirbas, A. H. (2004). Global energy sources, energy usage, and future developments. *Energy Sources*, *26*(3), 191–204. https://doi.org/10.1080/00908310490256518
2. Hassan, Q., Algburi, S., Sameen, A. Z., Jaszczur, M., & Salman, H. M. (2024). Hydrogen as an energy carrier: properties, storage methods, challenges, and future implications. Environment Systems and Decisions, 44(2), https://doi.org/10.1007/s10669-023-09932-z
3. Zou, C., Li, J., Zhang, X., Jin, X., Xiong, B., Yu, H., ... & Pan, S. (2022). Industrial status, technological progress, challenges, and prospects of hydrogen energy. Natural Gas Industry B, 9(5), 427-447. https://doi.org/10.1016/j.ngib.2022.04.006
4. Naqvi, S. A. H., Taner, T., Ozkaymak, M., & Ali, H. M. (2023). Hydrogen production through alkaline electrolyzers: A techno-economic and enviro-economic analysis. Chemical Engineering & Technology, 46(3), 474-481. https://doi.org/10.1002/ceat.202200234
5. Zayat, B., Mitra, D., & Narayanan, S. R. (2020). Inexpensive and Efficient Alkaline Water Electrolyzer with Robust Steel-Based Electrodes. *Journal of the Electrochemical Society*, *167*(11), 114513. https://doi.org/10.1149/1945-7111/aba792
6. Sadananda, K., Yang, J. H., Iyyer, N., Phan, N., & Rahman, A. (2021). Sacrificial Zn–Ni coatings by electroplating and hydrogen embrittlement of high-strength steels. Corrosion reviews, 39(6), 487-517. https://doi.org/10.1515/corrrev-2021-0038
7. Wu, J., Li, B., & Lu, J. (2021). Life cycle assessment on boron production: is boric acid extraction from salt-lake brine environmentally friendly?. Clean Technologies and Environmental Policy. https://doi.org/10.1007/s10098-021-02092-1

SECURING GEOTHERMAL ENERGY PROJECTS: HYDROGEN PRODUCTION AND UNDERGROUND STORAGE AS A SOLUTION FOR ELECTRICITY MARKET FLUCTUATIONS

[1*]*Hakki AYDIN*, [2]*Sukru MEREY*
[1] Zorlu Enerji, Manisa, 45600, Turkiye
[2] Batman University, , Department of Petroleum and Natural Gas Engineering, Batman, 72100, Turkiye
*Corresponding author e-mail: hakki.aydin@zorlu.com

ABSTRACT
Geothermal energy provides base-load power to the grid and serves as a critical renewable and clean energy source. To encourage investment in these risky, long-term projects, governments often offer feed-in tariff mechanisms and special incentives. However, these tariffs are typically available for only 10 to 15 years, after which electricity prices are determined by open market rates. To address revenue challenges from low market prices, energy storage emerges as a solution, allowing electricity to be stored during low-price periods and sold during peak demand. This study explores energy storage for geothermal electricity through hydrogen (H_2) production, underground storage, and re-electrification. A case study of the Alaşehir geothermal field is presented, featuring a conceptual model that generates geothermal power from basement metamorphic rocks and uses sandstone formations for hydrogen storage. A stochastic Monte Carlo simulation accounts for uncertainties such as reservoir storage potential, costs, and re-electrification efficiency. Results show that storing energy via hydrogen during low-demand periods and re-electrifying it during peak demand nearly doubles revenue, leveraging fluctuations in open-market electricity prices.
Keywords: electricity, geothermal, hydrogen, prices, underground storage

1. INTRODUCTION
Geothermal energy is considered a renewable, environmentally friendly, and sustainable energy resource, providing base-load power, meaning it operates 24/7 throughout the year. Renewable Energy Promotion Mechanism (YEKDEM) that was introduced in September 2005 (No: 5346, Issued Date: May 10, 2005) and it was run until September 2020 provided by Turkish government. This legislation provides incentives for the use of renewables in power generation such as feed-in tariffs, purchase guarantees, connection priorities, lowered license fees, license exemptions in exceptional circumstances and various practical conveniences in project preparation and land acquisition [1]. The guaranteed prices were 105 USD per MW, with an additional incentive of 0.7 USD per MW for the use of domestic equipment, applicable for ten years after the commissioning of the power plant. Recently, the government announced an extension of the tariff purchase period for geothermal energy to 15 years, with a floor price of 100 USD and a ceiling price of 120 USD per MW. Over the last two decades, installed geothermal capacity of Turkiye has increased from 15 MW to 1,726.8 MW, driven by these incentives and feed-in tariff mechanisms. However, after the guaranteed period, selling prices are determined by open market rates. Electricity open market prices in Turkiye fluctuate over the years due to factors such as global war risks, economic crises, and pandemic outbreaks. Open market prices fluctuate hourly, ranging from 30 to 57 USD over the past three years, making energy storage during low prices and selling at peak times a viable strategy to secure long-term cash flow.
This study investigates using geothermal reservoirs for hydrogen production and storage in Turkiye's Alaşehir geothermal field. By storing hydrogen in sandstone formations and supporting the grid during peak demand, it mitigates electricity price fluctuations and stabilizes cash flow in long-term projects. A probabilistic Monte Carlo simulation assesses impacts of uncertain factors, including reservoir temperature, power plant technology, hydrogen recovery, and market prices.

2. MATERIALS AND METHODS
The study begins with an evaluation of the hydrogen production and storage capacity of the Alaşehir geothermal field. Subsequently, the re-electrification of hydrogen to meet peak demand is examined. Storage capacity of Alaşehir field in Manisa, Turkiye can be assessed using Eq. (1).

$$\mathrm{H_{mass}} = \emptyset \times \mathrm{S_g} \times \mathrm{A} \times \mathrm{h} \times \frac{P}{Z \times R \times T} \times M_{H_2} \quad (1)$$

The source of parameters in Eq. (1) are from well testing data and drilling operations in the field. Z-factor is calculated from equations of state (e.g., Peng-Robinson). Eq. (1) employs a deterministic approach, but due to the heterogeneity and anisotropy of tectonically active geological formations, a stochastic approach is necessary. Monte Carlo simulation, implemented in Excel, addresses parameter uncertainties. The triangular distribution, often used with limited data, defines the probability density function using minimum, maximum, and most likely values.
In the Alaşehir field, the Menderes Metamorphic Unit serves as the reservoir rock for the geothermal system. It consists of marble, schist, and quartzite. The geothermal potential of the field is initially assessed using the heat-in-place method. As shown in Fig. 1, the Menderes Metamorphic Unit forms the basement of the field and represents a productive section for geothermal applications. It is overlain by the Çaltılık and Hamamdere Formations, which are composed of sandstone and conglomerates, making them suitable candidates for hydrogen storage. Therefore, in this conceptual model, the metamorphic rocks are utilized for geothermal power generation, while the produced hydrogen is stored in the Çaltılık

and Hamamdere Formations.

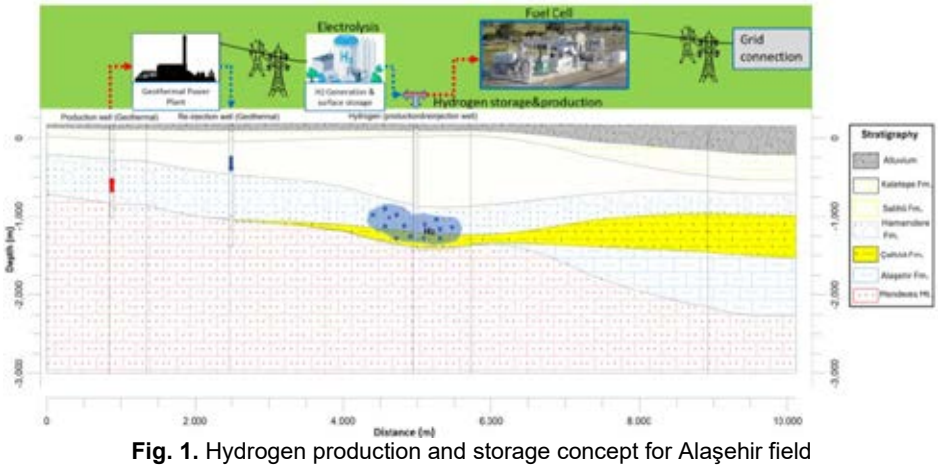

Fig. 1. Hydrogen production and storage concept for Alaşehir field

Fig. 2. A double flash combined geothermal power plant in Alaşehir field

We use Eq. (2) to calculate the mass of hydrogen produced annually from geothermal-sourced electricity. Eq. (3) calculates the cost of hydrogen production and storage, while Eq. (4) calculates the re-electrification from the fuel cell.

$$M_{hm} = Power\ Generation(\frac{kW}{hr}) \times \frac{1825\ hr}{365\ day} \times \frac{365\ day}{year} \div \frac{kW}{H_2(kg)} \quad (2)$$

$$\sum C_{hp} \times M_{hm} + \sum C_{hs} \times M_{hm} \quad (3)$$

$$\sum \eta_{FC} \times M_{hm} \times P_{electricity} \quad (4)$$

The electricity output (E_{elec}) from the fuel cell is given by Eq. (5):

$$E_{elec} = \frac{H_{mass} \times E_H \times \eta_{FC}}{3600} \times 1000 \quad (5)$$

Hydrogen generation and liquefaction utilize energy input and heat supply from geothermal power plants, such as binary (ORC units) and combined (flash and binary) geothermal power plants. Fig. 2 presents the operational scheme of a combined geothermal power plant in Alaşehir field.

3. RESULTS AND DISCUSSION

The Alaşehir field's electricity production capacity, based on Akın [2], is estimated at 103 MW (minimum), 183 MW (most likely), and 335 MW (maximum) per hour for 30 years. Using 2024 market prices, the lowest-priced hours (03:00–07:00 AM) and highest-priced hours (17:00–21:00 PM) were selected for daily hydrogen production and re-electrification, totaling 1,825 hours annually. H_2 is produced during low-price periods and sold at peak demand, with price differences of 30 USD (maximum), 25 USD (most likely), and 20 USD (minimum) per MWh used to estimate profits. H_2 production and storage costs were reviewed. Studies report production costs ranging from 0.979 to 2.615 USD/kg H_2 [3]. Operating

costs for geothermal-assisted electrolysis are about 2.04 USD/kg H_2 [4]. Considering Alaşehir's geothermal resource, production costs of 3 USD (maximum), 2.3 USD (most likely), and 1.6 USD (minimum) per kg H_2 were used. Geological storage costs were set at 5% (maximum), 3.5% (most likely), and 2.5% (minimum) of total hydrogen costs [5]. Energy consumption for hydrogen production was reported between 50–60 kW/kg H_2 [6-7].

Table 1. Costs for hydrogen production and underground storage

Parameters	Minimum	Mean	Maximum	Distribution
Power generation potential of Alaşehir field, MW/hr	103	183	335	Triangular
Power consumption for hydrogen production, kW/kg H_2	50	55	60	Triangular
Hydrogen production costs, USD/kg	1.6	2.3	3	Triangular
Underground storage costs, USD/kg	0.07	0.11	0.16	Triangular
Additional price during Peak demand of electricity, USD/MW	20	25	30	Triangular
Hydrogen production time in a year, hr	1825	1825	1825	Uniform
Re-electrification efficiency, %	40	50	60	Triangular

Table 2. Parameters for underground hydrogen storage

Parameters	Minimum	Mean	Maximum	Distribution
Area, km^2	20	30	40	Triangular
Thickness, m	500	1000	1500	Triangular
Porosity, fraction	0.15	0.20	0.35	Triangular
Reservoir Temperature, K	373.15	398.15	423.15	Triangular
Reservoir Pressure, MPa	10	15	20	Triangular
Gas saturation, fraction	0.15	0.20	0.3	Triangular
Z factor of Hydrogen	1.0300	1.0462	1.062	Triangular
R-Universal gas constant, J/(mol\K)	8.314	8.314	8.314	uniform
MH2 is hydrogen molecular weight, g/mol	2.016	2.016	2.016	uniform

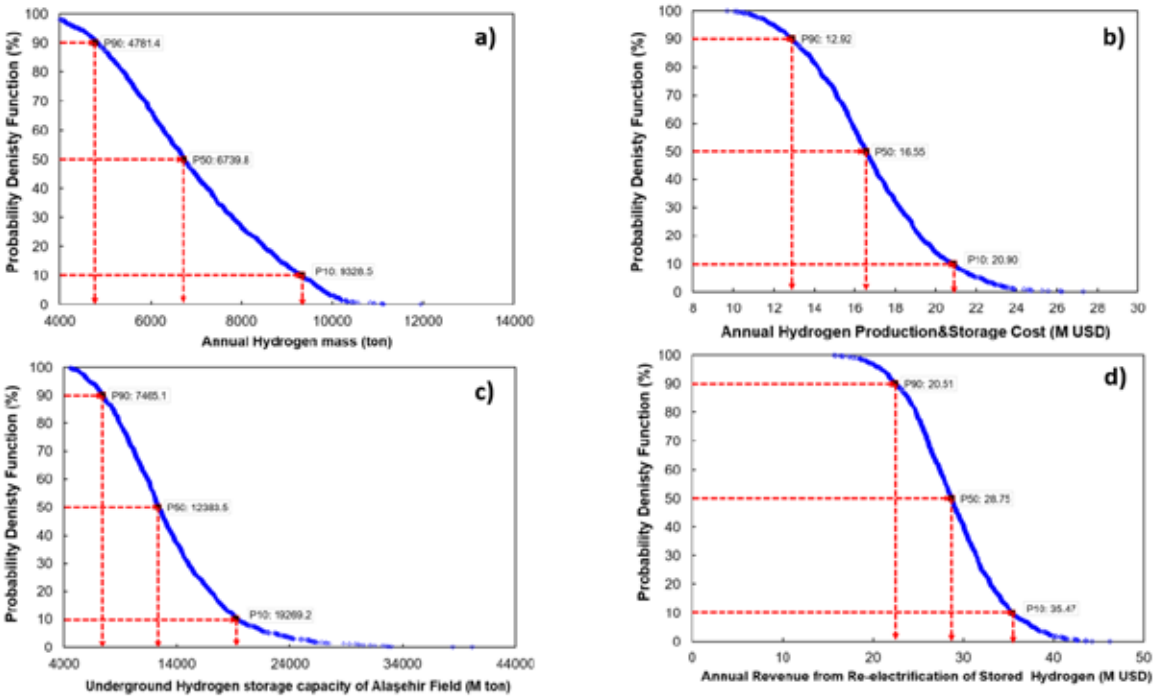

Fig. 3. a) Monte Carlo Simulation results of annual H_2 production capacity **b)** Monte Carlo simulation results for cost of annual production and underground storage **c)** Monte Carlo simulation results of underground H_2 storage capacity **d)** Monte Carlo simulation results for annual revenue from re-electrification of stored H_2 in Alaşehir field

A Monte Carlo simulation of Eq. (2) used a triangular distribution for most variables and a uniform distribution for production time (see Fig. 3). Fig.3-a shows results: proven capacity (90% certainty) is 4,781.4 tons, probable capacity (50%) is 6,739.8 tons, and possible capacity (10%) is 9,328.5 tons of H_2. Using Eq. (3), hydrogen production potential (Fig. 3-a), and data from Table 1, a Monte Carlo simulation assessed the costs of hydrogen production and underground storage in the Alaşehir field. Results (Fig.3-b) show annual costs of 12.92 million USD (90% certainty), 16.55 million USD

(50%), and 20.90 million USD (10%). The study evaluated the Alaşehir field's underground hydrogen storage capacity to determine its suitability for storing produced hydrogen. Using well test data, stratigraphy, and geological formations, parameters influencing pore volume were selected (Table 2). Based on findings by Dehury et al. [8], gas saturation values after brine displacement were set at 0.15 (minimum), 0.2 (most likely), and 0.3 (maximum). The Z factor interval was calculated using the Newton-Raphson method in Python. A Monte Carlo simulation (Eq. 1) with a triangular distribution for uncertain parameters yielded a proven storage capacity of 7,465.1 million tons, sufficient for all hydrogen production (Fig. 3-b). H_2 produced in the Alaşehir field can be stored in sandstone and conglomerate formations above the geothermal reservoir. Re-electrification is feasible using gas turbines or fuel cells, with fuel cells offering higher efficiency (60–80%) compared to gas turbines (30–40%). Waste heat recovery from fuel cells can boost efficiency to 80–90%. Among fuel cells, PEMFCs are favored for their low operating temperature and 40–60% efficiency, while SOFCs provide higher efficiency but face maintenance challenges due to high operating temperatures. Using Eq. (5) in a Monte Carlo simulation (Table 1), annual re-electrification revenue is estimated at 20.51 million USD (90% certainty), nearly double the 12.92 million USD cost of hydrogen production and storage (Fig. 3-b). This demonstrates the cost-effectiveness of hydrogen-based energy storage during low-demand periods and re-electrification during peak demand. Further analysis should evaluate capital investments in infrastructure and well completion for full feasibility.

4. CONCLUSIONS

This study investigated hydrogen production, storage, and re-electrification in the Alaşehir geothermal field, demonstrating that energy storage through hydrogen production and underground storage, followed by re-electrification via fuel cells, can mitigate price fluctuations and enhance project feasibility. The Monte Carlo simulation showed that the field has hydrogen production capacities of 4,781.4 tons (90% certainty), 6,739.8 tons (50%), and 9,328.5 tons (10%), with annual re-electrification revenue of 20.51 million USD at 90% certainty, significantly improving revenue due to market price fluctuations.

NOMENCLATURE

A	Reservoir area, m^2
C_{hp}	Cost of hydrogen production
C_{hs}	Cost of hydrogen storage
E_{elec}	Electricity generation from 1 kg of hydrogen kW per hour
E_H	Energy content from 1 kg of hydrogen equals to 119.96 MJ
H	Reservoir thickness, m
H_{mass}	Total hydrogen mass to be stored, kg
η_{FC}	Fuel cell efficiency ranging between 40 and 60 %
M_{H2}	Hydrogen molecular weight, 2.016 g/mol
M_{hm}	Mass of hydrogen, kg/year
P	Reservoir pressure, Pa
$P_{electricity}$	Open market electricity prices
$Ø$	Effective porosity, fraction
R	Universal gas constant, 8.314 J/(mol·K)
S_g	Gas saturation, fraction
T	Reservoir temperature, K
Z	Compressibility factor, dimensionless

REFERENCES

1. Aydin, H., Akin, S., and Senturk, E. 2020. Evaluation of production capacity of geothermal power plants in Turkey. GRC Transactions 40: 163-174.
2. Akin, S. 2017. Geothermal Resource Assessment of Alaşehir Geothermal Field. 42nd Workshop on Geothermal Reservoir Engineering Stanford University, Stanford, California, February 13-15, 2017.
3. Yilmaz, C., Kanoglu, M., Bolatturk, A., and Gadalla, M. 2012. Economics of hydrogen production and liquefaction by geothermal energy. International Journal of Hydrogen Energy 37(2): 2058-2069.
4. Kanoglu, M., Ayanoglu, A., and Abusoglu, A. 2011. Exergoeconomic assessment of a geothermal assisted high temperature steam electrolysis system. Energy 36(7): 4422-4433.
5. Le Duigou, A., Bader, A. G., Lanoix, J. C., and Nadau, L. 2017. Relevance and costs of large-scale underground hydrogen storage in France. International Journal of Hydrogen Energy 42(36): 22987-23003.
6. Buttler, A., and Spliethoff, H. 2018. Current status of water electrolysis for energy storage, grid balancing and sector coupling via power-to-gas and power-to-liquids: A review. Renewable and Sustainable Energy Reviews 82: 2440-2454.
7. Burton, N. A., Padilla, R. V., Rose, A., and Habibullah, H. 2021. Increasing the efficiency of hydrogen production from solar powered water electrolysis. Renewable and Sustainable Energy Reviews 135: 110255.
8. Dehury, R., Chowdhury, S., and Sangwai, J. S. 2024. Dynamics of hydrogen storage in subsurface saline aquifers: A computational and experimental pore-scale displacement study. International Journal of Hydrogen Energy 69: 817-836.

EVALUATION OF DEFORMATION VIA *in situ* SEM AND EBSD ON HYDROGEN EMBRITTLEMENT

[1*] *Seung Hoon Nahm*, [1,2] *Hee Soo Yun*
[1] Hydrogen Energy Group, Strategic Technology Research Institute,
Korea Research Institute of Standards and Science, Daejeon, 34113, Republic of Korea
[2] Department of Materials Science and Engineering, Yonsei University, Seoul, 03722, Republic of Korea

*Corresponding author e-mail: shnahm@kriss.re.kr

ABSTRACT
Hydrogen, recognized as an energy carrier, can compromise the structural integrity of metals by contributing to hydrogen embrittlement, which reduces their mechanical strength. Examining only fracture behavior is insufficient to comprehend hydrogen embrittlement, prompting this research to focus on deformation processes. To investigate this, slow strain rate testing (SSRT) was conducted on both hydrogen-charged and uncharged specimens, accompanied by *in situ* scanning electron microscopy (SEM) and electron backscatter diffraction (EBSD) to monitor real-time deformation. When hydrogen penetrated the austenitic stainless steel (ASS) 304 at lower strain levels than the uncharged specimen, it activated the formation of strain-induced martensite (SIM). The hydrogen precharged specimens exhibited a more significant degree of SIM even at equivalent strain levels. These SIM, linked to dislocation activity, were further studied using single crystal (SX) superalloys, which almost deform only dislocation slip. It was found that hydrogen induced secondary slip at lower strains, which led to dislocation pinning and an increase of dislocation density, thereby facilitating the formation of stacking faults earlier in the deformation process. As with interstitial elements, hydrogen modifies dislocation motion, promotes stacking fault at lower strains, and activates fracture initiation. The hydrogen effects on the deformation process was directly related to the hydrogen amount absorbed by the ASS 304. By examining the deformation process, predictive models were established to quantify the loss of tensile properties based on hydrogen embrittlement mechanism. This research offers critical insights into understanding and mitigating the reduction of mechanical properties in metals exposed to hydrogen.

Keywords: Hydrogen embrittlement, *in situ* EBSD, deformation behavior, predicted mechanical properties, stacking fault

1. INTRODUCTION
Hydrogen is increasingly regarded as a sustainable energy carrier due to its non-carbon emissions during use. However, the phenomenon of hydrogen embrittlement remains a significant challenge for hydrogen application to metallic materials, as it degrades their mechanical properties. This degradation of strength and ductility is primarily due to hydrogen permeation into the metal. Several models, including hydrogen enhanced decohesion (HEDE), hydrogen enhanced localized plasticity (HELP), and nanovoid coalescence, have been proposed to explain these phenomena [1].

While much of the focus has traditionally been on fracture-based studies, recently, research has shifted to understanding the influence of hydrogen on the deformation process. In face-centered cubic (FCC) metals, the effects of hydrogen have been explored in relation to dislocation mobility [4], deformation via stacking faults [5], and the occurrence of SIM [6]. For example, Barnoush et al. [7] noted that hydrogen reduces the energy required for dislocation initiation during deformation, as demonstrated by nanoindentation experiments. Similarly, Yamada et al. [8] and Pontini [9] observed that hydrogen increases deformation via stacking fault (SFE) in FCC structures. San Marchi [10] examined the role of hydrogen in either enhancing or inhibiting phase transitions in metals. Additionally, Chen et al. [11] documented an increase in dislocation density in pure Pd after hydrogen precharging. Multiple interpretations have been suggested for when hydrogen embrittlement occurrs. In this study, the aim was to investigate the various factors that govern hydrogen embrittlement during the deformation process. To assess how hydrogen influences the mechanical properties of FCC materials, the study evaluated the hydrogen embrittlement and deformation process of two kinds of FCC metals (ASS and Ni-based superalloy).

2. EXPERIMENTAL PROCEDURE
2.1 Materials
To assess how hydrogen affects fracture and the deformation process, two distinct materials were selected: a commercial grade of ASS (STS 304) and a Ni-based single crystal superalloy. The superalloy composition is as follows: 7.0Cr-6.2Al-7.5Co-1.5Mo-0.15Hf-6.5Ta-3.0Re-5.0W, with nickel being the primary component. The orientation of the Ni-based superalloy was aligned along the <101> crystallographic direction, which encourages the development of Lüders bands, offering a clearer view of hydrogen influence on the dislocation motion during unidirectional slip.

2.2 Hydrogen Precharging Techniques

Two techniques for hydrogen precharging were employed: electrochemical hydrogen absorption and thermal hydrogen exposure. In the electrochemical method, the specimens were immersed in a 3% NaCl electrolyte at 70°C with a current density of 100 mA/cm² for a period of three days, followed by tensile testing performed within 10 minutes. For the thermal method, specimens were exposed to hydrogen gas at a temperature of 250°C under various pressures for a duration of 4 days, then stored at -80°C to prevent any hydrogen release before testing. Hydrogen content was quantified using thermal desorption spectroscopy (TDS, HTDS-003, R-DEC), and the tensile tests were conducted at a cross-head speed of 2 µm/s, in compliance with ASTM G142, using a tensile testing module (DDS 003, Kammrath & Weiss, Fig. 1a).

2.3 *in Situ* SEM/EBSD and Microstructural Observations

To examine the hydrogen effects on the deformation process, *in situ* SEM (Fig. 1b, c) and EBSD (Fig. 1d) were utilized. During tensile testing, microstructural changes were recorded at set intervals within the SEM. For enhanced electron backscatter intensity in the EBSD system, the specimens were positioned on a 40° pre-tilt stage, with the testing specimen holder inclined at 30°. This setup resulted in an overall tilt angle of 70°, ideal for observing the deformation process. Additionally, crystallographic variations were analyzed using EBSD (Nordlynano, Oxford Instruments). Fracture morphology was further investigated on the broken specimens using SEM, X-ray diffraction, and EBSD to provide a comprehensive understanding of the fracture mechanisms.

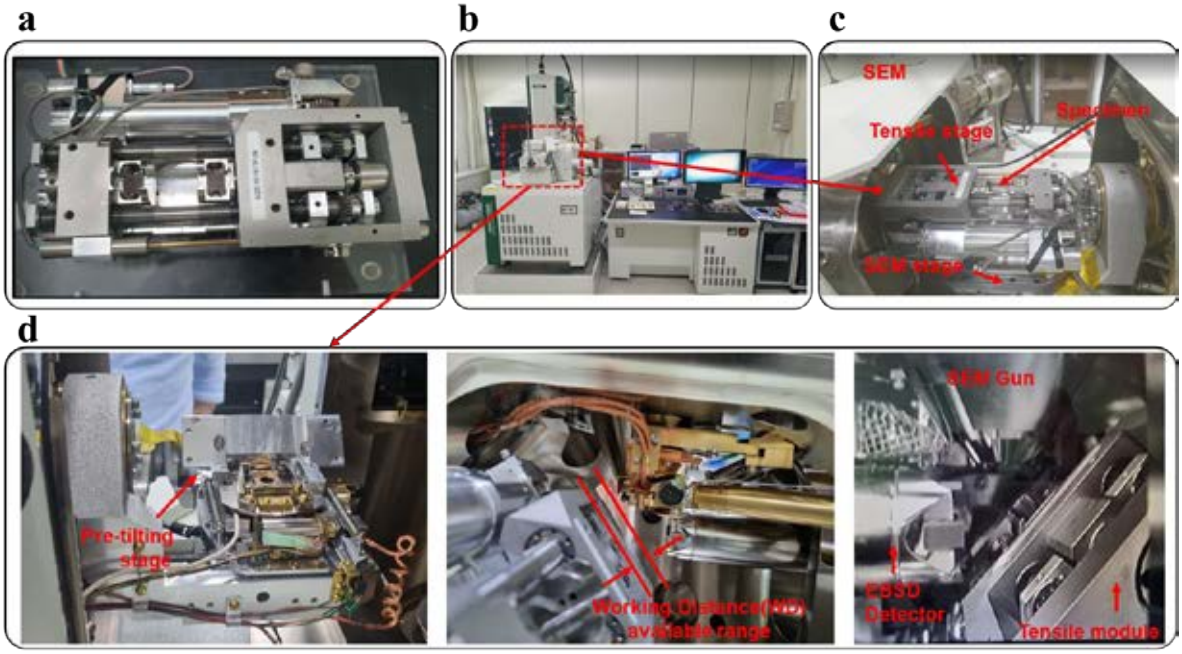

Fig. 1 Evaluation of hydrogen embrittlement system, mechanical deformation module(a), scanning electron microscopy (SEM)(b), *in situ* SEM system(c), and *in situ* EBSD system(d)

3. RESULTS AND DISCUSSION

3.1 Alternation of fracture and deformation via hydrogen on STS 304.

In STS 304, although both hydrogen charging methods produced similar fracture microstructures, notable differences were verified in the deformation. As shown in Fig. 2a, the mechanical properties of hydrogen precharged specimens were reduced. In the case of electrochemical hydrogen precharging (304-E, Fig. 2b), grain boundaries were accumulation sites, while in the case of gaseous hydrogen exposure (304-G, Fig. 2c), hydrogen was mainly trapped within the grains (lattice). Despite these differences in deformation process, the similar fracture mechanisms were verified in both hydrogen precharging methods (Fig. 2d). SIM induced fracture was started at twin boundary due to the prepared site in both methods. The deformation process was influenced by where the hydrogen was trapped, particularly in the low-angle boundaries (Fig. 2e). In the electrochemical method (304-E), where hydrogen gathered at the grain boundaries, the deformation until 700 µm closely resembled that of the uncharged specimen (304-N). However, for the gaseous method (304-G), where hydrogen was accumulated at lattices, the early deformation until 700 µm was distinctly altered. Additionally, SIM observed after fracture highlighted the hydrogen-induced stacking fault process during SSRT (Fig. 2f). In the 304-E specimens, where hydrogen diffusion was restricted, a noticeable difference in SIM fraction between the edge and center were observed. Thus, this study confirms that hydrogen precharging induces significant changes in both fracture and deformation process in STS 304.

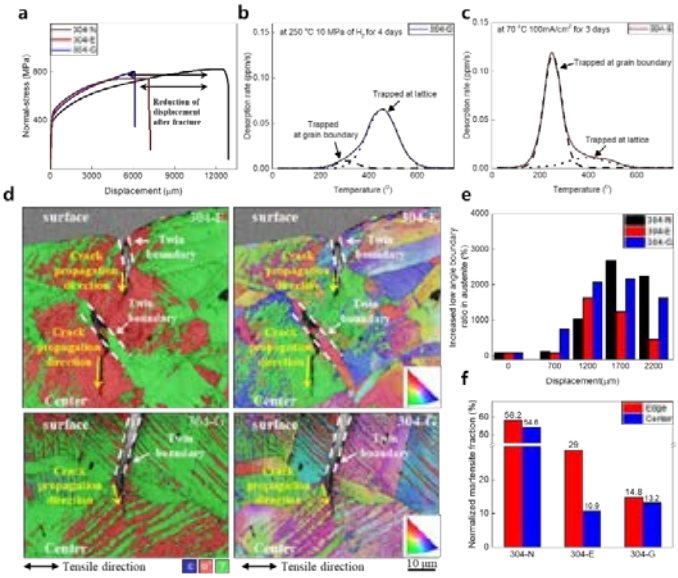

Fig. 2 Effects of hydrogen on deformation and fracture. (a) displacement-stress curve, (b) desorption behavior for 304-E, (c) desorption behavior for 304-G, (d) microstructural fracture mechanism, changes of low angle boundary(e) and SIM (f) of deformation behavior via *in situ* EBSD [].

3.2 Changes of slip Systems via hydrogen

Previous studies have demonstrated that hydrogen affects deformation by increasing low-angle boundary formation and SIM, which correlates with a rise in dislocation density. To investigate this further, the effects of hydrogen on the deformation process were studied using a Ni-based SX superalloy, which has a unidirectional slip system. After exposure to a 10 MPa hydrogen environment for 4 days, the hydrogen content was measured at 173 ppm. The reduction in ductility was found to correlate directly with the hydrogen content (Fig. 3a). The deformation progression for hydrogen precharged specimens is illustrated in Figs. 3b and c. Initially, microstructure deformed with unidirectional dislocation slip (b-1), followed by secondary slip (b-2). As strain increased, the secondary slip was more marked (b-3), leading to fracture at the cross site of the two kinds of slip (b-4). In the hydrogen-precharged specimens (Fig. 3c), both dislocation slips (primary and secondary) were activated at 4.9% (c-1). As strain increased, the secondary slips intensified (c-2, c-3), and fracture similarly occurred (c-4).This confirms that hydrogen promotes the activation of cross slip, resulting in an increase of dislocation density in FCC metallic material.

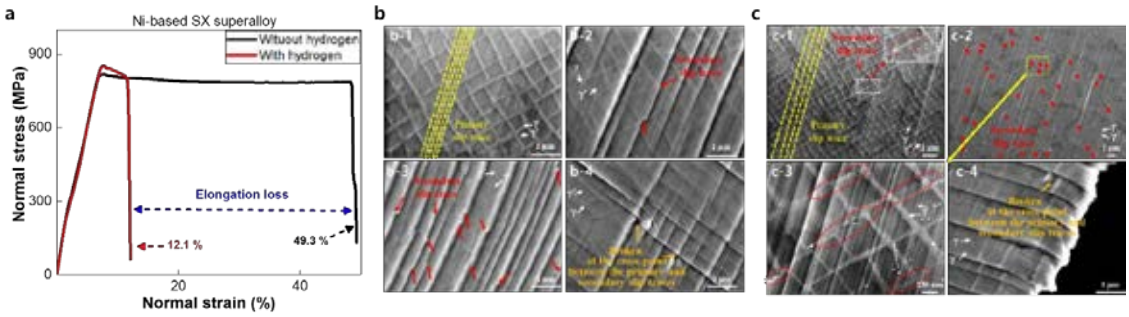

Fig 3. Hydrogen induced dislocation slip in Ni-based single crystal superalloy. (a) reduction of fracture strain by hydrogen embrittlement, (b) evaluation of deformed microstructure of specimens without hydrogen at 4.9%(b-1), 19.7%(b-2), 39.4%(b-3), 49.3%(b-4), and (c) evaluation of deformed microstructure of specimens with hydrogen at 4.9%(c-1), 9.3%(c-2,3), 12.8%(c-4).

3.3 Predictive tensile properties on hydrogen embrittlement in STS 304

The main contributors to hydrogen embrittlement in STS 304, as identified in this study, are SIM formation and the increase of dislocation density due to hydrogen. To examine these effects, tensile properties of specimens with different hydrogen contents were evaluated. As the hydrogen content increased, the fracture elongation reduced (Fig. 4a). Two trends were observed in the phase fraction (Fig. 4b). Additionally, once the phase fraction saturated, an increase in grain orientation spread (GOS) was noted (Fig 4c). This rise of GOS value also indicated a higher dislocation density. This nature was clearly evident during the deformation process, as predicted by the Olson-Cohen model (Fig. 4d). In specimens with low hydrogen content (Region 1), the SIM observed after fracture was matched in the Olson-Cohen model (similar to the uncharged state), whereas, in Region 2, the SIM fraction remained constant, but the activation of

cross slip due to hydrogen led to SIM appearing through lower strain levels, resulting in elongation loss. Based on these observations, a model was developed to predict fracture elongation as a function of hydrogen content (Fig. 4e).

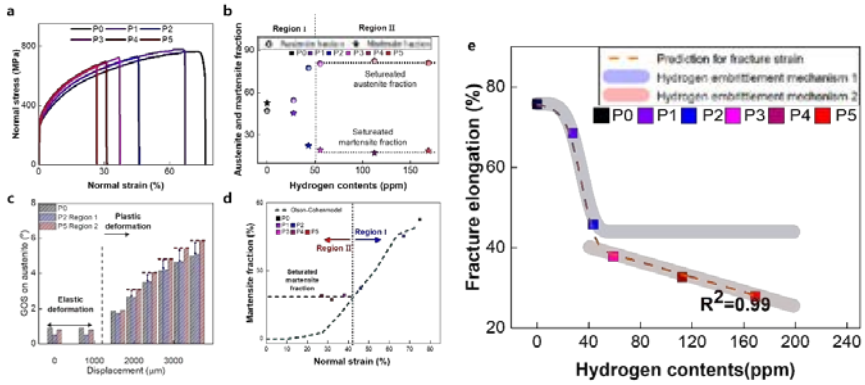

Fig. 4 Predictied various hydrogen embrittlement in STS 304 according to hydrogen contents. (a) evaluation of SSRT, (b) phase fraction after fracture, (d) changes of GOS during the deformation (e) matching various hydrogen precharged specimens in Olson-cohen model, and (f) prediction of fracture elongation on hydrogen embrittlement.

4. CONCLUSIONS

This study investigated the hydrogen embrittlement mechanism of FCC metal, with the following key findings:

1) The fracture behavior of STS 304, resulting from hydrogen embrittlement, was primarily driven by decohesion, which occurred due to differences in hydrogen solubility and was linked to SIM formation.
2) In FCC metals, the increase in dislocation density by hydrogen was attributed to the activation of secondary slip.
3) The model for prediction of tensile properties was developed to predict fracture elongation as a function of hydrogen content, based on the identified mechanisms for the two types of hydrogen embrittlement.

5. ACKNOWLEDGMENT

This research was supported by Development of Reliability Measurement Technology for Hydrogen Refueling Station funded by Korea Research Institute of Standards and Science (KRISS – 2024 – GP2024-0010).

6. REFERENCE

[1] S.K. Dwivedi, M. Vishwakarma, 2018, Hydrogen embrittlement in different materials: A review, International Journal of Hydrogen Energy. 43:21603–21616.
[2] W.S. Walston et al., 1992, The effect of internal hydrogen on a single-crystal nickel-base superalloy, Metallurgical Transactions A. 23:1313–1322.
[3] J.-H. Han et al., 2003, Orientation rotation behavior during in situ tensile deformation of polycrystalline 1050 aluminum alloy, International Journal of Mechanical Sciences. 45:1613–1623.
[4] S. Asano, R. Otsuka, 1976, The lattice hardening due to dissolved hydrogen in iron and steel, Scripta Metallurgica. 10:1015–1020.
[5] E. Norouzi et al., 2023, Effect of hydrogen on the deformation mechanisms of metastable 304 ASS, Materials Letters. 338:134021.
[6] C.-S. Yoo et al., 2008, Effect of grain size on transformation-induced plasticity in an ultrafine-grained metastable austenitic steel, Scripta Materialia. 59
[7] A. Barnoush, H. Vehoff, 2010, Recent developments in the study of hydrogen embrittlement: Hydrogen effect on dislocation nucleation, Acta Materialia. 58:5274–5285. https://doi.org/10.1016/j.actamat.2010.05.057.
[8] K. Yamada et al., 2015, Positive and negative effects of hydrogen on tensile behavior in polycrystalline Fe–30Mn–(6− x) Si–xAl austenitic alloys, Scripta Materialia. 105:54–57.
[9] A.E. Pontini, J.D. Hermida, 1997, X-ray diffraction measurement of the stacking fault energy reduction induced by hydrogen in an AISI 304 steel, Scripta Materialia. 37:1831–1837.
[10] C. San Marchi et al., 2021, Effect of microstructural and environmental variables on ductility of ASSs, International Journal of Hydrogen Energy. 46:12338–12347.
[11] Y.Z. Chen et al., 2013, Increase in dislocation density in cold-deformed Pd using H as a temporary alloying addition, Scripta Materialia. 68:743–746.
[12] Yun, H. S et al., 2024, Effect of precharging methods on the hydrogen embrittlement of 304 stainless steel. International Journal of Hydrogen Energy, 50, 175-188.
[13] Yun, H. S et al., 2024, Hydrogen induced activation of cross slip in Ni-based single crystal superalloy. Materials Science and Engineering: A, 913, 147082.
[14] Yun, H. S et al., 2025, Characterizing microstructural changes due to hydrogen embrittlement: Predicting mechanical properties according to hydrogen amount, Materials characterization 219, 114574

EFFECTS OF HYDROGEN ADDITION ON METHANE FUEL REACTIVITY IN HIGH-TEMPERATURE $CO_2/O_2/N_2$ COFLOW IN A NON-PREMIXED LAB-SCALE TUBE BURNER

[1*]*Mustafa Kemalettin Büyükakın*
[1] Trakya University, Engineering Faculty, Mechanical Engineering Department, Edirne, 22030, Türkiye

*Corresponding author e-mail: mkbuyukakin@trakya.edu.tr

ABSTRACT

The effects of hydrogen addition to methane fuel on the flame parameters and methane reactivity were numerically studied in this paper. A lab-scale tube burner forming a central fuel jet in the coflow oxidizer mixture was employed. The hydrogen addition to methane fuel was adjusted in such a way that the hydrogen ratio varied from 10% to 40% on molar base. The inlet temperature and composition of the high-temperature coflow oxidizer mixture were kept constant in order to evaluate the pure effects of hydrogen addition. The results show that the maximum flame temperature slightly increases from 1670K for the pure methane case to 1738K for the 40% hydrogen addition case, due to mild combustion behavior occurring from the high-temperature diluted oxidizer. However, hydrogen addition makes methane fuel more reactive by getting it reacted in a shorter axial distance and eliminates the temperature jump, which is formed for the pure methane case. Hydrogen addition increases the OH radical concentration in the flame and enchances the mixing rate of the reactants due to the increased axial momentum of the central fuel jet, which shifts the combustion flame upstream of the burner and makes it more stable.

Keywords: Hydrogen addition, Methane fuel, Mild combustion

1. INTRODUCTION

The population of our world is increasing every year and the energy demand from all of the sectors is also increasing accordingly. The energy industry still relies heavily on fossil fuels in our day. Hydrocarbon fuel shortage is likely to be the main problem to be faced in the near future. Therefore, the utilization of alternative fuels and efficiency optimization studies on the current energy systems are intensely conducted to remedy the possible energy shortage. One of the methods to increase thermal efficiency of combustion systems is the application of mild combustion regime. Mild combustion can be defined as a slow reaction process of a fuel under diluted hot oxidizer conditions. With this combustion regime, an increased flame volume with uniform temperature distribution can be formed and the overall heat transfer rate from the combustion flame to the surroundings can be enhanced. However, combustion stability issues can occur under mild conditions, since the chemical time scale is comparable with turbulence or the mixing time scale. Some of the research studies related to mild and diluted combustion are reviewed. Tu et al. [1] conducted CFD studies to investigate the mild combustion behavior of hydrogen and methane fuel mixtures. Their results indicated that CO_2 diluent was a better option to obtain mild conditions than H_2O diluent. Erete et al. [2] performed some experimental studies to reveal the effects of CO_2 dilution of methane fuel on the flame parameters such as flame length and lift-off height. Fordoei et.al [3] numerically studied on the effects of hydrogen addition to methane on the flame parameters under CO_2 dilution conditions of the oxidizer mixture. EDC combustion model was used in their study. The obtained results reported a reduction in the ignition delay time of fuel with the increasing hydrogen addition ratio. Fordoei et. al [4] conducted some series of numerical studies for the CO_2 diluted oxidizer-methane combustion cases. They analysed CH_2O species distribution in the flame to measure its mild behavior. Schluckner et.al [5] compared the results obtained from the flamelet models, EDC model and EDM for the oxy-fuel combustion case in a natural gas combustor. Their results reported that the partially premixed flamelet model showed the best performance for NO_X emission predictions. In this paper, the effects of hydrogen addition to methane fuel, under the CO_2 diluted coflow hot oxidizer conditions in a tube burner, on the central methane fuel reactivity and flame parameters are numerically investigated using non-premixed combustion model with the steady flamelet approach. The physical and chemical effects of hydrogen addition on the flame parameters are revealed. The improvement in the combustion stability of methane fuel with the increasing hydrogen addition ratio is evaluated.

2. COMPUTATIONAL DETAILS

In this paper, a combustion tube from the study of Brokes and Moss [6] was utilised as the combustion volume. Fluent code was used as the computational tool. This burner originally measures 1m in length and 0.155m in diameter. However, the tube length was extended to 2m in this paper for the purpose of the diluted combustion flame analysis. The burner has a central fuel injector, which measures 4.07mm in diameter, and a coflow oxidizer annulus inlet with the same size of the burner diameter. The tube burner is modelled as a 2D non-premixed type and axisymmetric one, and presented in Fig.1. It should be noted that the gravity is applied towards the reactants inlet.

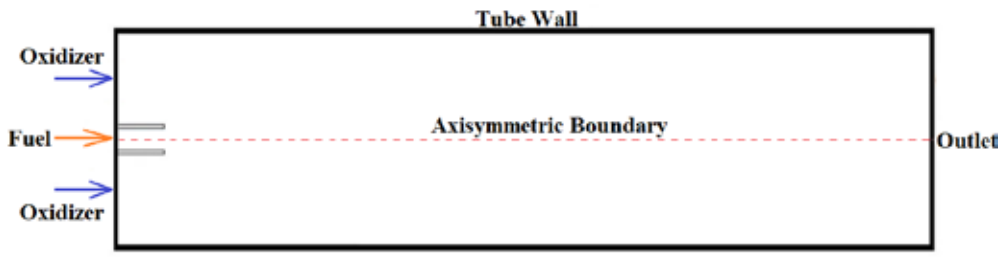

Fig. 1. 2D Modelling of Tube Burner

In this numerical study, the methane fuel inlet rate was taken as 0.000172 kg/s, which corresponded to 8.6 kW thermal load. The oxidizer inlet rate was adjusted to have an excess coefficient ratio of 4 for methane fuel. The fuel inlet temperature and oxidizer inlet temperature were kept constant as 290K and 1000K, respectively. In addition, the oxidizer was adjusted to have a composition of 12% O_2, 20% CO_2 and 68% N_2 on molar base in order to sustain diluted or mild combustion conditions. Five different cases were studied in this paper by changing the hydrogen addition ratio to methane from 0% to 40% on molar base by 10% step, while keeping the methane flow rate constant. For the simulations in the combustion tube, the governing equations related to mass, momentum and energy conservation were solved and they are given in Eq. (1), Eq. (2) and Eq. (3) respectively [7].

$$\frac{\partial \rho}{\partial t} + \nabla.(\rho \mathbf{v}) = 0 \tag{1}$$

$$\frac{\partial (\rho \mathbf{v})}{\partial t} + \nabla.\rho \mathbf{v}\mathbf{v} = -\nabla.P + \rho \sum_{i=1}^{N} Y_i f_i \tag{2}$$

$$\frac{\partial (\rho h)}{\partial t} + \nabla.(\rho \mathbf{v} h) = \nabla.[\frac{k_t}{c_p} \nabla h] + S_h \tag{3}$$

Here in these equations, ρ is density (kg/m^3), **v** is velocity vector (m/), P is stress tensor (N/m^2), h is enthalpy (kJ/kgK), Y_i is mass fraction of i_{th} species, f_i is force acting on i_{th} species (kJ/kg), k_t is thermal conductivity (kW/mK), c_p is specific heat (kJ/kgK), t is time (s) and S_h represents the source term for radiation . The radiation intensity equation was also solved to take into account the radiation heat transfer mechanism in the combustion flame and to the surroundings from the flame [8]. The equations were solved by Reynolds averaging. Therefore, standart k-ϵ turbulence modelling [8] was chosen to close the equation system. For the chemical modelling of the simulations, the non-premixed combustion model with the steady flamelet approach was used. For this purpose, the averaged mixture fraction conservation equation [8] was solved and it is given as;

$$\frac{\partial (\rho \bar{f})}{\partial t} + \nabla.(\rho \mathbf{v} \bar{f}) = \nabla.(\frac{\mu_t}{\sigma_t} \nabla \bar{f}) \tag{4}$$

In this equation, $\bar{f}$ is the averaged mixture fraction, μ_t is turbulent viscosity (kg/ms) and σ_t is a constant. The mean scaler variables such as density, temperature and species mass fractions are calculated taking into account of turbulence-chemistry interaction by Eq. (5) [8] and tabulated prior to the numerical simulations.

$$\bar{\emptyset} = \int \emptyset(f, \bar{H}) P(f)\, df \tag{5}$$

In Eq. (5), P(f) is the β type probability density function, which is a function of $\bar{f}$ and the averaged mixture fraction variance ($\overline{f'^2}$). Therefore, a conservation equation for $\overline{f'^2}$ [8] was also solved together with the averaged mixture fraction formulation. The scaler variable $\emptyset$ is a function of f and this function is set with the use of flamelet equations. GRI-Mech 3.0 reaction mechanism [9] was used in the flamelet equation calculations. All of the equations were discretized and numerically solved using Fluent code. The steady state assumption was made for all the cases. Coupled method was chosen for pressure-velocity coupling. Second order scheme and second order upwind scheme were used for pressure and equation discretization, respectively. Discrete Ordinates was utilised for the radiation modelling and wsggm-domain based was used for the absorption coefficient [8]. The adiabatic wall condition was assigned for the burner walls. Around 600000 meshing elements were used for the flow volume, since further increment in the meshing elements did not give any significant change in the central axial temperature values. The mathematical modelling and numerical parameters were validated with the experimental data of Brokes and Moss [6] for the methane-air case. However, it could not be presented in this paper.

3. RESULTS AND DISCUSSION

The obtained results from the simulations as the temperature variations in the combustion tube are presented in Fig.2.

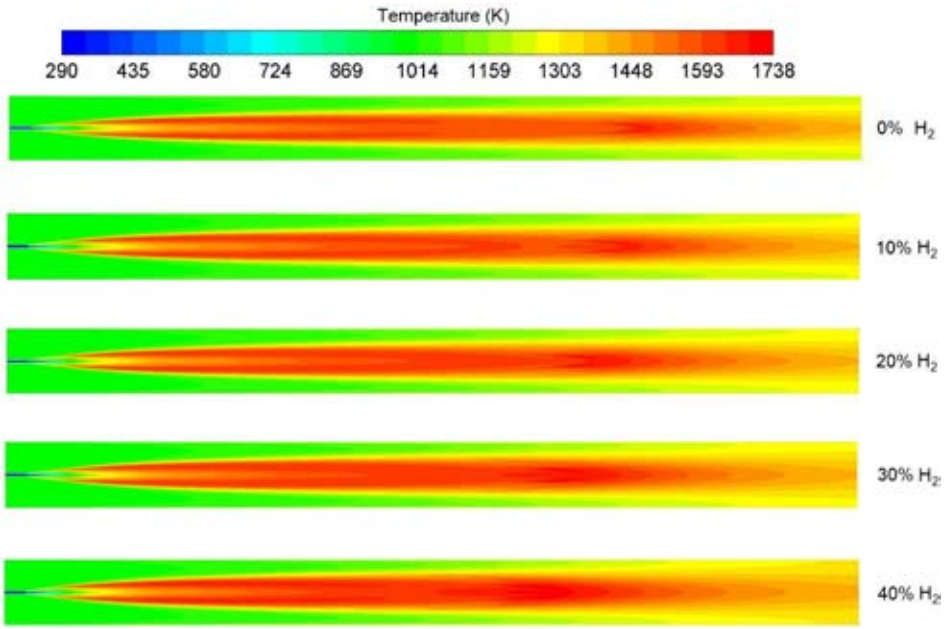

Fig. 2. Temperature Variations in Tube Burner

The axial variations in the centre of the tube burner related to the temperature, excess oxidizer coefficient (EOC) for methane fuel and OH radical mole fraction are plotted in Fig.3 for some of the cases. The total flow rate variations of the unreacted methane fuel in the tube burner according to the different axial positions are also outlined in Fig.3.

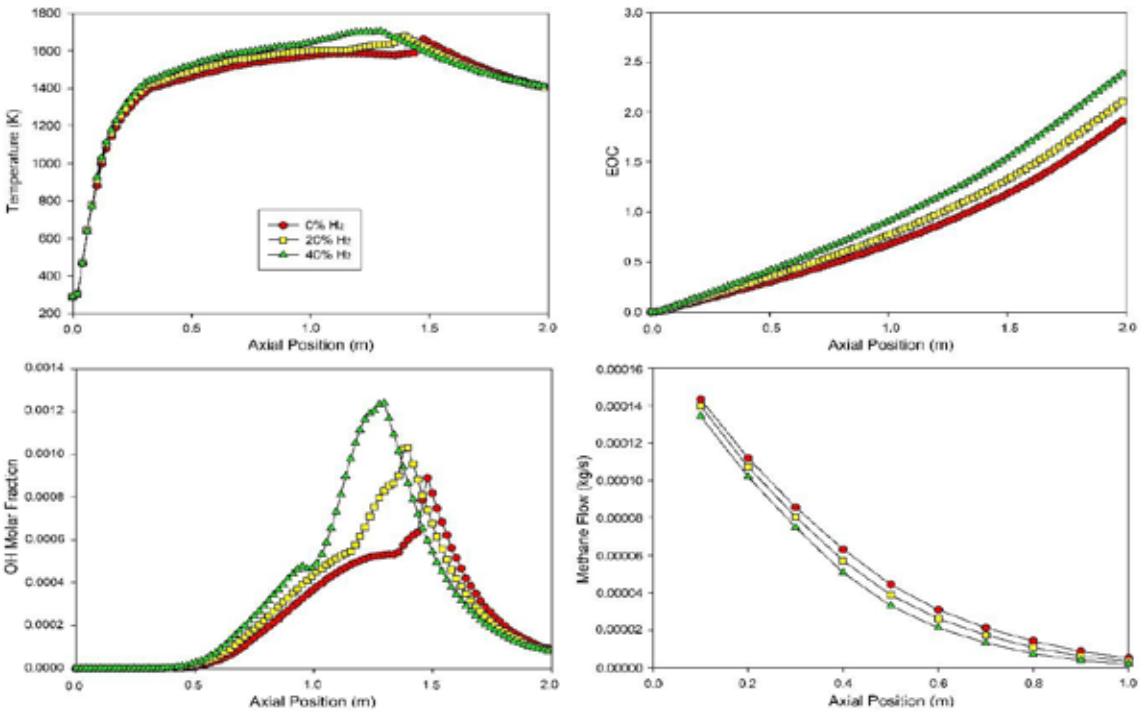

Fig. 3. Variations in Flame Parameters for Different Hydrogen Addition Ratios

The results show that hydrogen addition enhances the mixing rate of the reactants. EOC parameter for methane fuel shows an increasing trend at any axial position with the increasing hydrogen addition ratio. This occurs due to the

increasing axial momentum of central fuel jet with hydrogen addition. This can be classified in the physical effects of hydrogen addition to methane. The hydrogen addition also increases the molar fraction of OH radical, which is the most effective on decomposition of CH_4 molecule. This increment in OH radical is both due to the better mixing of the reactants and the chemical effects of hydrogen molecule, which form OH and H radicals, as hydrogen molecule is reacted with O radicals. Fig.2 and Fig.3 show that the flame uniformity is improved with the hydrogen addition. The maximum flame temperature point is shifted towards the reactants inlet and therefore the temperature jump formation for the pure methane case is eliminated. The temperature jump is formed due to the poor mixing of the reactants in more than half length of the burner for the pure methane case under diluted oxidizer conditions. The poor mixing of the reactants causes scarcity in the necessary radicals for decomposition of methane fuel, up to some point close to the outlet section. The enhanced mixing rate of the reactants and formation of OH, H and O radicals by hydrogen addition contribute to the acceleration of the methane reaction rate and the temperature jump formation is eliminated accordingly. Therefore, in general, the reactivity of methane fuel is determined to be enhanced with hydrogen addition. Fig.3 proves that the flow rate of methane fuel in the tube at the different axial points is reduced, which indicates that methane fuel is reacted in shorter axial distance with the hydrogen addition. The maximum flame temperature does not significantly increase with the hydrogen addition, due to the diluted oxidizer and mild combustion behaviour of the flame. It increases from 1670K for the 0% hydrogen addition case to 1738K for the 40% hydrogen adition case, which will not contribute significantly on the NO_X formation rate in the flame. It is determined that hydrogen addition to methane can offer solutions to stability issues under diluted or mild combustion conditions, while the flame temperature increase by hydrogen addition can be limited to prevent the NO_X emission formation.

4. CONCLUSION

The following conclusions can be achieved from this study;

- Hydrogen addition to methane slightly increases the maximum flame temperature due to diluted or mild combustion conditions. The maximum flame temperature increases from 1670K for the case without hydrogen addition to 1738K for the case with 40% hydrogen addition ratio.
- Hydrogen addition to methane improves the mixing rate of the reactans for the central fuel jet burners.
- The flame uniformity and stability are improved with hydrogen addition to methane fuel. The temperature jump formation for the pure methane combustion case under diluted oxidizer conditions is diminished with hydrogen addition. This is an indication of the increased reactivity of methane fuel under diluted oxidizer conditions.
- Hydrogen fuel contributes to the methane fuel reactivity by changing both physical and chemical properties of the combustion flame.

REFERENCES

1. Tu Y, Liu H, Yang W. 2017. Flame characteristics of CH_4/H_2 on a jet-in-hot-coflow burner diluted by N_2, CO_2, and H_2O. Energy&Fuels. 31: 3270−3280
2. Erete JI, Hughes KJ, Ma L, Fairweather M, Pourkashanian M, Williams A. 2017. Effect of CO_2 dilution on the structure and emissions from turbulent, non-premixed methane-air jet flames. Journal of the Energy Institute. 90: 191-200
3. Fordoei EE, Mazaheri K, Mohammadpour A. 2021. Effects of hydrogen addition to methane on the thermal and ignition delay characteristics of fuelair, oxygen-enriched and oxy-fuel MILD combustion. International Journal of Hydrogen Energy. 46: 34002-34017
4. Fordoei EE, Mazaheri K, Mohammadpour A. 2021. Numerical study on the heat transfer characteristics, flame structure, and pollutants emission in the MILD methane-air, oxygen-enriched and oxy-methane combustion. Energy. 218: 119524
5. Schluckner C, Gaber C, Landfahrer M, Demuth M, Hochenauer C. 2020. Fast and accurate CFD-model for NOx emission prediction during oxy-fuel combustion of natural gas using detailed chemical kinetics. Fuel. 264; 116841
6. Brookes SJ, Moss JB. 1999. Measurements of soot production and thermal radiation from confined turbulent jet diffusion flames of methane. Combustion and Flame. 116: 49–61
7. Law C.K. 2006. Combustion Physics, Cambridge University Press, New York
8. ANSYS Fluent theory guide. 2021. https://dl.cfdexperts.net/cfd_resources/Ansys_Documentation/Fluent/Ansys_Fluent_Theory_Guide.pdf. Accessed 30 June 2024
9. Smith GP, Golden DM, Frenklach M, Moriarty NW, Eiteneer B, Goldenberg M, Bowman CT, Hanson RK, Song S, Gardiner WC, Jr, Lissianski VV, Qin Z. http://www.me.berkeley.edu/gri_mech/. Accessed 30 June 2024

GASIFICATION OF AGRICULTURAL RESIDUAL BIOMASS, VECTOR IN THE PRODUCTION OF GREEN H_2

[1]*Lăzăroiu George Cristian*, [2]*Mihăescu Lucian*, [2]*Pîșă Ionel*, [1]*Grigoriu Rodica –Manuela*, [3*]*Stoica Dorel*, [1]*Simion Iulia*
[1]National University of Science and Technology POLITEHNICA Bucharest, Faculty of Energy, Splaiul Independenței 313, Bucharest, 060042, Romania
[2] POLITEHNICA Bucharest, Faculty of Mechanical and Mechatronics Engineering
[3] POLITEHNICA Bucharest, Faculty of Biotechnical Systems Engineering
*Corresponding author e-mail: dorel.stoica@upb.ro

ABSTRACT
Europe, like other agricultural regions in the world, through waste resulting from agriculture and energy potential. In fact, achieving a circular economy will require agriculture to use various forms of valorization of important energy waste, remaining one of the most important. The use of pyrolysis technologies and especially gasification allows obtaining H_2 in high proportions. If for wood mass the results of gasification are significant, both in terms of flow rates and quality of synthesis gas, with electrical power achievements of the order of MW, for agricultural biomass they are for now only achievements, at the pilot stage level. The paper presents the current study of the performance of gasification of agricultural residual biomass, highlighting the possibilities of obtaining green H_2. To this end, experimental tests are also presented for the characteristics of residential agricultural biomass in the European Union (EU). The paper also contains a simulation of the green H_2 country through the gasification of agriculture in the EU, with which it also refers to the costs associated with production.

Keywords: Gasification, Agricultural Biomass, Green Hydrogen, Energy

1. INTRODUCTION

The achievement of a society without CO_2 emissions will also have to include the agricultural sector, where agricultural waste could constitute an important energy potential, with a final reflection in the achievement of a circular economy. Despite all the technological advances in recent times, including the use of fermentation, agriculture still delivers an enormous amount of waste, possibly to be recovered as energy. Current ecological requirements no longer allow their direct combustion, generating CO_2 [1], [2], [3].

EU agriculture, represented by France, Germany, Italy, Romania, Poland, Spain, Hungary and England, mainly produces cereals, maize and sunflower, but also vines and fruit trees, all of which can be used as primary fuel for gasification. For the period 2016 – 2021, these 8 countries produced an annual average of 109.63 million tonnes of wheat grains, 50.39 million tonnes of maize grains and 56.70 million tonnes of sunflower seeds [1], [2]

For the first 15 EU countries, the cultivated areas included: wheat: $21.6 \cdot 10^6 ha$; maize: $7.14 \cdot 10^6 ha$; sunflower: $3.91 \cdot 10^6 ha$. For these crops, the waste of the countries, [2], [3], [4]: wheat straw: $3.2 - 4.0\ t/ha$; maize stalks: $5.8\ t/ha$; corn cobs: $0.7\ t/ha$; sunflower stalks: $1.8\ t/ha$; vine tails and orchard branches: $0.25 - 0.38\ t/ha$.

Comparing this waste to the cultivated area in the EU results in considerable quantities, of which about 40% have internal use, the remaining 60% can be used for energy production [2], [4]. To define the energy characteristics of plant biomass, the easiest analysis can be used, the technical one, which includes in gravimetric percentages the moisture content, W; the volatile content V; the fixed carbon content, C_f and the ash content, *A*.

$$W + V + C_f + A = 100\% \quad (1)$$

The gasifier gas consists of the components H_2, CO, CO_2, CH_4 and N_2 (in air gasification, nitrogen is dominant, reaching around 50%), has a calorific value corresponding to the proportion of the respective gases. This gas, through combustion, from the components CO, CO_2 and CH_4 forms CO_2, so the respective installations will have to be coupled to a CO_2 capture installation (see subchapter 5).

2. TECHNOLOGICAL CHARACTERISTICS OF FUEL GAS PRODUCTION THROUGH GASIFICATION

Gasification is a source of thermochemical processes that leads to the transformation of a primary solid fuel into a synthesis gas (gasogen). The heat required to carry out thermochemical processes comes from an internal source (combustion of the primary fuel), from an external source, or from a combination of these. Gasogens in the first category are called autonomous and are exclusively applicable to plant biomass. The combustion agent can be air, oxygen-enriched air, less often oxygen, but also steam (in which case the heat introduced by the steam represents an external heating source).

Gasification includes the following characteristic steps:

- removal of water (W) from the primary fuel (drying). The process ends at a temperature in the range of $105 - 200^0C$;
- pyrolysis, obtained by heating the fuel in the absence of an oxidizing agent, characterized by the removal of volatiles (V), the process ends in the range of $450 - 700^0C$;

- combustion of carbon with the formation of a high-temperature reactive zone;
- realization of the conversion equations, with the formation of synthesis gas (gasogen).

In the pyrolysis zone, the first part of the synthesis gas composition is formed from the fuel, consisting of: H_2, CO, CO_2, CH_4, N_2. Combustion includes the reactions, [1]:

$C + O_2 = CO_2$ (exothermic reaction) (2)

$C + H_2O = CO_2 + H_2$ (endothermic reaction) (3)

The main reduction reaction (endothermic):

$CO_2 + C = 2CO$ (4)

Hydrogenation reactions (exothermic):

$C + 2H_2 = CH_4$ (5)

$H_2O + CO = CO_2 + H_2$ (6)

Methanation reactions (exothermic):

$C + 3H_2 = CH_4 + H_2O$ (7)

$CO_2 + 4H_2 = CH_4 + 2H_2O$ (8)

The combustion Eq. (1) represents the main heat source and the temperature level is ensured by the amount of air (excess air) admitted. The hydrogenation Eq. (6) and Eq. (7) form the amount of H_2 gas, along with that formed in the pyrolysis process from the composition of the synthesis gas. The hydrogenation reactions highlight the importance of water vapor (H_2O). A classification of gasification plants is shown in Fig. 1.

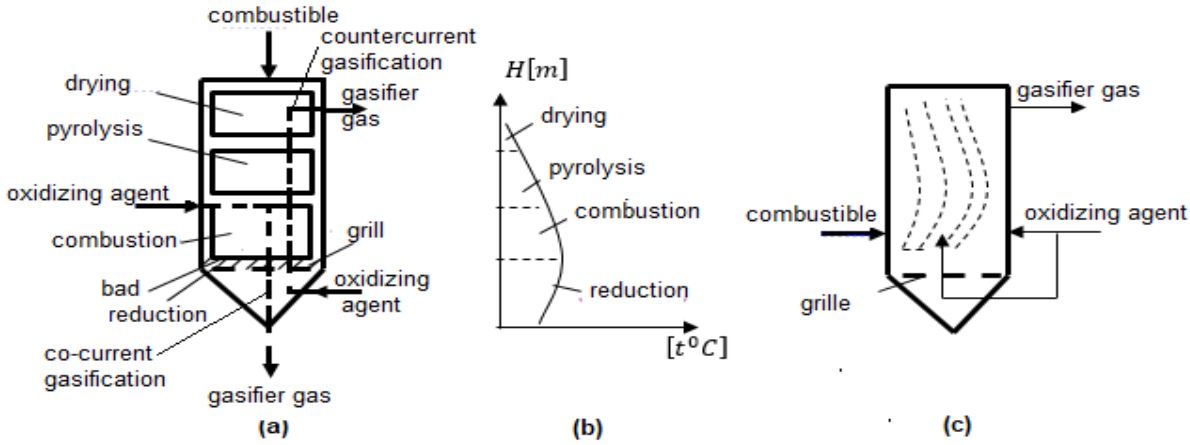

Fig. 1. Construction and functional principles for gasification plants
a – fixed bed gasifier (in co-current or downcurrent and countercurrent, respectively); b – temperature evolution in the gasifier body; c – gasifier with fluidized state and flow in the stream

Fluidized bed or flow-through gasification plants provide higher flow rates and therefore higher thermal power than fixed bed plants, but these plants are currently only applicable to primary fuels made from woody biomass.

Synthesis gas (gasifier gas), in air gasification, includes the following components:

$H_2 + CO + CO_2 + CH_4 + N_2 = 100$ (9)

The gaseous component CO_2 is strongly reduced with the increase in the state temperature, at temperatures above 950^0C, having subunit values ($CO_2 < 1\%$), so that the gasifier gas will contain the combustible components (H_2, CO, CH_4) in a proportion of about $44 - 49\%$.

3. STATUS OF ACHIEVEMENTS OF VEGETABLE BIOMASS GASIFICATION FACILITIES

Achievements in the field of agricultural biomass gasification are currently at the level of low powers, usually below 1MW, but with the advantage of a synthesis gas with a sufficiently high calorific value. Agricultural biomass gasification requires air as an oxidizing agent, provided that it is gradually distributed in the combustion zone, because the temperature in the layer must not exceed $850 - 900^0C$, especially in the case of cereal straw, to avoid the grill clogging [1], [2], [3], [5].

The best results for agricultural biomass - as a primary fuel are presented by gasifiers with a fixed bed and downward circulation – Fig. 1, both due to the control of the reduction reactions that lead to the formation of H_2 and CH_4, and because they thermally destroy the tar formed in the pyrolysis operation, which is forced to travel through the fixed bed. Good results were also obtained with a hybrid gasifier, between those with downward and upward circulation, namely the cross-circuit gasifier, Fig. 2, in which the biomass has a downward flow, and the gas a lateral (transverse) one.

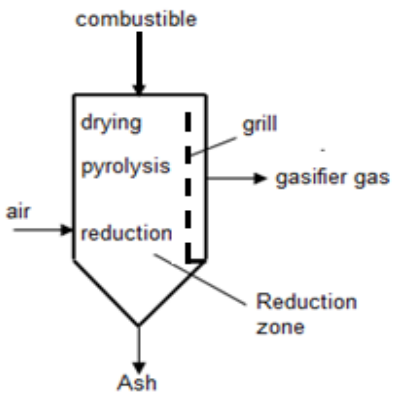

Fig. 2. Cross-circuit gasifier diagram

From the data in the paper [6], regarding the gasification of vegetable biomass, it results the presence of carbon in minute quantities in the discharged ash, below 1%, as well as for hydrogen sulfide and hydrochloric acid. Regarding tar, it can be included in the category of bituminous oil. Regarding the dimensions of vegetable biomass, the advantage of pelletization was found (the dimensions obtained are for a diameter of 5-6 mm and a length of 20 - 25 mm), even compared to briquettes. Special attention is also paid to the use of vegetable biomass in the form of chips (average diameter 2 - 5 mm), for a humidity controlled at 10-12 %. Regarding the efficiency of the vegetable biomass gasification process, it was in the range of 61-73 %, above that achieved with municipal waste, [7], [8].

The amount of gasifier gas, characterized by the ratio of its gaseous components, demonstrates: $CO/CO_2 = 1.3 - 1.5$, and $H_2/CO = 0.45 - 0.75$. These data are especially for Asian plant biomass (Thailand, Malaysia, India), in Europe research is still in its infancy, [9], [10].

4. EXPERIMENTAL TESTS OF GASIFICATION OF EUROPEAN VEGETABLE BIOMASS

These tests were carried out at the POLITEHNICA Bucharest, with a 4KW pilot gasifier, for dominant vegetable biomass in EU agriculture. The tests aimed to achieve a high H_2 content in the synthesis gas. For this purpose, the following was achieved: fixed bed gasification with descending circulation; gradual air distribution (on 0.35 of the gasifier height); an increased constructive height/thickness ratio; humidity control in the range of 10-20%; fixed bed temperature control; biomass size control. Agricultural biomass was represented by the dominant waste, namely: cereal straw (in the form of chopped or pellets), corn stalks (in the form of chopped), vine ropes, walnut shells [5]. The pilot gasifier has the characteristic dimensions [1], [3], [4]: internal diameter, $\Phi = 88mm$, height $400\,mm$, primary fuel flow $1kg/h$. Fig. 3 shows a picture of the complex gasification installation.

Fig. 3. Appearance of the 4 KW pilot gasifier.

The gasification of a wide range of plant biomass is presented in Table 1.

Table 1. Experimental test results

Biomass	Technical analysis, %				t_r^* [°C]	R_{H_2}
	W	V	C_f	A		
Cereal straw	9.8	72.0	12.6	5.6	850	0.62
Cereal straw pellets	8.7	70.0	15.9	5.4	850	0.49
Chopped corn stalks, **	13.3	67.5	13.1	6.1	870	0.61
Chopped vine strings, **	8.7	67.5	17.9	5.9	900	0.44
chopped fruit tree branches, **	14.2	66.2	13.1	6.5	885	0.59
Walnut shells, **	9.1	66.0	18.8	6.1	900	0.42

*) with t_r the steady state temperature was noted; **) particle size within the limits of 3 – 5 mm.

The H_2/CO ratio in the gasifier gas was denoted by R_{H_2}. The gasification installation includes air supply systems (Einhell TC $\frac{190}{2418.165}$ $l/_{min}$). The fixed layer temperature measurement and control system (thermocouple type "S" PtRh 10% - Pt, Φ 6, l = 500 mm, vertically immersed from the outside of the plant into the fixed layer, indicator device type SREN 61326 – 1:2013. The average calorific value of the gasifier gas was between $5.4\ and\ 7.6\ MJ/m_N^3$. Experimental tests with agricultural waste in the EU have demonstrated the production of a gasifier gas with a high H_2 content, on average about 13 – 31% (for air gasification).

5. CAPACITY TO PRODUCE AND USE H2 PRODUCED BY GASIFICATION OF AGRICULTURAL BIOMASS

For a first estimate of the annual potential of agricultural biomass that can be gasified in the EU, only cereal, corn and sunflower crops were considered, resulting in the following quantities of waste (see subchapter 1):

- wheat: $21.6 \cdot 10^6 ha \cdot 3.6\ t/ha = 77.76 \cdot 10^6\ t/year$;
- maize: $7.14 \cdot 10^6 ha \cdot 5.8\ t/ha = 41.41 \cdot 10^6\ t/year$;
- sunflower: $3.91 \cdot 10^6 ha \cdot 1.8\ t/ha = 7.04 \cdot 10^6\ t/year$.

This results in a total of $126.21 \cdot 10^6\ t/\text{year}$ of agricultural vegetation waste, of which 40% is considered to be internal consumption, resulting in an amount of $75.72 \cdot 10^6\ t/\text{year}$ for energy. The gasification test data demonstrated a gasifier gas production of $2 - 2.8\ m_N^3/kg$ biomass, so that the total annual potential becomes: $(151.4 - 212.0) \cdot 10^9\ m_N^3/\text{year}$. This gasifier gas can be considered impure hydrogen, being similar to the current energy stage of transition to a decarbonized economy with the use of mixing, H_2 in CH_4. This gasifier gas can be used by direct combustion either in an internal combustion engine or in an electrical and/or thermal energy generator. For an average content of 16% green H_2 in the gasifier gas, a productive potential of $(24.1 - 33.9) \cdot 10^9 m_N^3/\text{year}$ results, in mass units approximately $(2.4 - 3.3) \cdot 10^5 t/\text{year}$. The cost of green hydrogen produced by gasification is lower than that produced by photosynthesis based on wind energy $(3.40 - 11.04\ EUR/kg)$, or solar energy $(3.50 - 10.04\ EUR/kg)$, having the value $(1.84 - 6.44\ EUR/kg)$, on average it can be considered $(4.14\ EUR/kg)$ [9].

6. CONCLUSIONS

The paper presents the economic and ecological importance of using agricultural waste for the production of green hydrogen through gasification. For the current stage of transition to a neutral economy in terms of CO_2 emissions, gasifier gas represents a comparative solution to the one expected for the use of the $H_2 - CH_4$ mixture in proportions of up to 10-15%. Current analytical and experimental data indicate a high potential for green hydrogen, with a lower price than that obtained through electrolysis based on renewable energy. The paper also mentions the need to continue research into the gasification of agricultural residual biomass, for the construction of higher power plants.

ACKNOWLEDGEMENT

This work was supported by a grant of the Ministry of Research, Innovation and Digitalization, project number PNRR-C9-I8-760090/23.05.2023, COD CF 30/14.11.2022 and PNRR-C9-I8-760089/23.05.2023, COD CF 31/14.11.2022.

REFERENCES

1. Lazaroiu G and Mihaescu L. 2021. Innovative Renewable Waste Conversion Technologies. ISBN 978– 3–030–81430–4. Springer.
2. Lazaroiu G, Mihaescu L, et.al. 2018. Holistica impactului surselor regenerabile de energie asupra mediului si climei. Vol 2. Biomasa solidă sursă de energie curată. Politehnica Press. ISBN 978-606-515-838-2.
3. Lazaroiu CG, Roscia M and Vasile Dancu VS. Published: 13.11.2024. Energy Transition Holistic Impact Challenge (ETHIC): A New Environmental and Climatic Era. 978-3-031-55447-6. Springer.
4. Lazaroiu G, Mihaescu L, et.al. 2018. Holistica impactului surselor regenerabile de energie asupra mediului si climei. Vol 3. Spre o energetică circulară. Politehnica Press. ISBN 978-606-515-838–2.
5. Simion I, Lăzăroiu G and Grigoriu RM. 2023. The hydrogen – carbon dioxide binominal, a possible new energy vector. University POLITEHNICA of Bucharest Scientific Bulletin, Series B Chemistry and Materials Science, ISSN: 1454-2331, Vol. 85 (3).
6. Moiseev Y, Afxentiou N, Fokaides P. 2021. The State of the Art Overview of the Biomass Gasification Technology. Current Sustainable/Renewable Energy Reports 8(1). DOI: 10.1007/s40518-021-00196-2.
7. Chawdhurya MA, Mahkamovb K. 2011. Development of a Small Downdraft Biomass Gasifier for Developing Countries. Journal of Scientific Research 3 (1), 51-64.
8. Homdoung N, Dussadee N, Sasujit K, Kiatsiriroat T and Tippayawong N. Performance investigation of a gasifier and gas engine system operated on municipal solid waste briquettes. International Journal of Renewable Energy Development (ISSN:2252-4940)
9. Sasujit K., Dussadee N, Homdoung N, Ramaraj R and Kiatsiriroat T. 2017. Waste-to-Energy: Producer Gas Production from Fuel Briquette of Energy Crop in Thailand/International Energy Journal 17.
10. Frieden F and Leker J.2024. Future costs of hydrogen: a quantitative review. Issue 9. Sustainable Energy & Fuels.

NUMERICAL INVESTIGATION OF EXHAUST EMISSIONS OF HYDROGEN-DIESEL DUAL FUELED MEDIUM-SPEED MARINE DIESEL ENGINE UNDER DIFFERENT FUMIGATED HYDROGEN MASS FRACTIONS

[1*]*Enes Fatih PEHLİVAN*
[1]Ordu University, Fatsa Faculty of Marine Sciences, Department of Naval Architecture and Marine Engineering, Evkaf Street, No. 239/C, Fatsa, Ordu, 52400, Turkey

*Corresponding author e-mail: enespehlivan@odu.edu.tr

ABSTRACT

This study conducts a numerical investigation into the exhaust emissions of a hydrogen-diesel dual-fueled medium-speed marine diesel engine, focusing on the impact of varying fumigated hydrogen mass fractions while keeping diesel injection mass constant. Employing advanced computational models, including the RNG k-ε turbulence model and the SAGE combustion model, the analysis examines the combustion process and the exhaust emissions, including nitrogen oxides (NO_x), carbon monoxide (CO), carbon dioxide (CO_2) and unburned hydrocarbons (UHC). The findings reveal that NO_X and CO_2 emissions enhances increasing fumigated hydrogen mass fractions, whereas UHC emissions exhibit a comparatively stable behavior and CO emissions first decreased then increased. The lowest values of maximum NO_X, UHC, CO and CO_2 emissions are 810, 1392, 4433 and 49683 ppm, respectively. The optimum fumigated hydrogen mass fraction is chosen as 0.0001 according to lowest NO_X, UHC and CO_2 emission values and 0.0002 according to lowest CO emission value. This research not only enhances the understanding of dual-fuel combustion processes but also provides valuable insights for the development of sustainable marine engine solutions in alignment with global emissions regulations.

Keywords: Numerical investigation, Medium-speed marine diesel engine, Exhaust emissions, Fumigated hydrogen mass fractions

1. INTRODUCTION

The maritime transportation sector plays a pivotal role in the global economy, with over 80% of international trade reliant on ships for the movement of goods across vast distances [1]. This heavy reliance on shipping logistics is mainly backed by the use of internal combustion engines (ICE), which are essential for about 98% of the entire merchant fleet, allowing these ships to effectively move goods to different places worldwide [2]. This sector contributes approximately 10% of the total emissions produced by the transportation sector and accounts for 2.9% of overall emissions [3], thus rendering it crucial to identify alternatives that ensure maritime transportation is both economically and environmentally sustainable. Indeed, the maritime sector predominantly relies on fossil fuels, exhibiting a 20% escalation in greenhouse gas emissions over the preceding decade [1]. In this sense, international merchant ships must obey the emission regulations defined by the International Maritime Organization (IMO) [4], which have become stricter over the years [5]. While multiple strategies may be contemplated for realizing a near zero-carbon future, it is anticipated that ICEs will persist in their predominance within maritime applications for an extended period, owing to their superior torque, efficiency, and weight characteristics, which align with the operational requirements and structural design of vessels [6]. One of these strategies is the usage of alternative fuels, such as hydrogen or ammonia, in diesel engines, which offer promising potential for reducing greenhouse gas emissions while maintaining the performance standards required in marine operations [7].
Recent advancements in hydrogen/diesel dual-fuel engines have garnered significant attention for their potential to reduce emissions while improving fuel efficiency in the maritime sector. By adopting hydrogen as a complementary fuel, these engines realize a decrease of nearly 50% in CO_2 emissions alongside traditional diesel systems [8]. Nonetheless, obstacles remain, particularly with respect to ignition properties and combustion stability across varying hydrogen mass fractions. Also, the transition towards dual-fuel technology entails significant infrastructure investment and modifications to current vessels, raising issues about its economic practicality and enduring feasibility in fulfilling strict International Maritime Organization (IMO) regulations [9]. As the sector navigates these challenges, ongoing scholarly inquiry seeks to optimize dual-fuel technologies to effectively reconcile performance with ecological obligations.
This research aims to examine numerically exhaust emissions in medium-speed marine diesel engine with a constant diesel injection mass and five different fumigated hydrogen mass fractions in-cylinder. By developing a comprehensive numerical model for simulating hydrogen combustion, this study seeks to identify optimal hydrogen mass fractions that minimize exhaust emissions without compromising engine performance, thereby offering valuable insights for engine manufacturers and ship operators in the pursuit of more sustainable maritime operations.

2. MODEL SETUP

In various R&D fields, CFD softwares are widely used for simulations. This study developed a numerical model of the

MAN Diesel L32-40 medium-speed marine diesel engine using CONVERGE Studio v3.2. To reduce analysis time and operational volume, a sector geometry representing the full engine was utilized. The sector geometry is shown in Fig. 1, and the engine's specifications under full load are listed in Table 1.

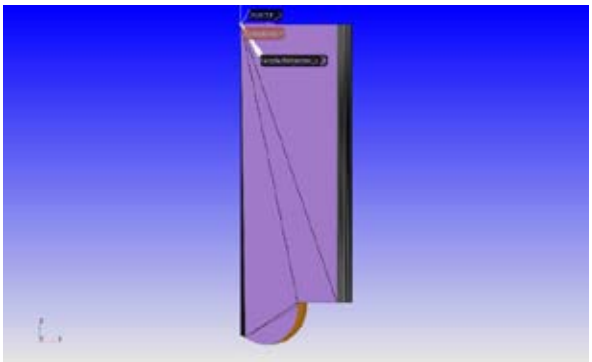

Fig. 1. MAN 32/40 medium speed marine diesel engine sector geometry

Table 1. MAN 32/40 engine specifications

Parameters	Value
Compression ratio	22.0
Engine speed (rpm)	750
Bore (mm)	320
Stroke (mm)	400
Connecting rod length (mm)	533
Diesel nozzle hole diameter (mm)	0.259
Diesel injection temperature (K)	341
Number of diesel injector	1
Number parcels of per nozzle	5000

The primary computational models utilized in this simulation include the RNG k-ε turbulence model [10], which is widely adopted in engineering, and the modified KH-RT model [11] for spray breakup. The Frossling Correlation model [12] is employed for evaporation simulation, while the SAGE model [13] is used for combustion, integrating a chemical reaction kinetic mechanism with a solver to address the combustion of the computational fuel. This study combines ammonia and n-heptane mechanisms, substituting n-heptane for diesel due to their comparable combustion properties. The chemical reaction mechanism, based on Xu et al. [14], consists of 69 species and 389 reactions, yielding satisfactory predictions for the skeletal mechanism.

3. RESULTS AND DISCUSSION

3.1. Model validation

All computational analyses were conducted using CONVERGE Studio v3.2, utilizing cell counts of 50,000, 75,000, and 100,000, derived from base grid dimensions of 4.82413 mm, 4.214267 mm, and 3.82892 mm, respectively. The Mean Absolute Percentage Errors (MAPE) were calculated for each scenario based on experimental data, yielding values of 18.62%, 17.25%, and 17.48% for the respective cell counts. Consequently, Case-2 (75000 cell count) was determined to be the most favorable solution based on MAPE results.

3.2. Exhaust emission characteristics

A study was conducted to analyze the fluctuations NO_X, UHC, CO and CO_2 emissions in relation to crank angle, utilizing five various fumigated hydrogen mass fractions (0.0001, 0.0002, 0.0003, 0.0004, 0.0005). The fluctuation of NO_X emissions in relation to the crank angle is illustrated in Figure 2(a). As the fumigated hydrogen mass fraction increases, NO_X emissions also rise due to changes in combustion characteristics and reaction pathways. Hydrogen's rapid flame velocity and broad flammability spectrum alter the combustion environment, promoting NO_X generation [15]. The maximum NO_X emission recorded is 903 ppm at a 0.0005 fumigated hydrogen mass fraction, with end-of-cycle values of approximately 810 ppm, 821 ppm, 852 ppm, 874 ppm, and 903 ppm for mass fractions ranging from 0.0001 to 0.0005. The variation of unburned hydrocarbon (UHC) emission with respect to the crank angle is shown in Figure 2(b). As the fumigated hydrogen mass fractions increase, UHC emissions remain relatively constant due to the complex interactions of hydrogen's combustion properties with other fuels and combustion conditions [16,17]. The maximum UHC emission recorded is about 1392 ppm at full fumigated hydrogen mass fractions, with end-of-cycle HC emission values ranging

from 1.1142 ppm to 1.1601 ppm for fumigated hydrogen mass fractions between 0.0001 and 0.0005.

Figure 2(c) exhibits how carbon monoxide (CO) emissions vary with the crank angle. As the fumigated hydrogen mass fractions increase, CO emissions first decreased due to improving combustion efficiency and increasing flame temperatures, which aids in converting CO to CO_2 [18] and after a certain threshold, additional hydrogen may result in incomplete combustion, causing CO emissions to increase again [19]. The maximum CO emission values range from 4433 ppm to 4547 ppm for fumigated hydrogen mass fractions between 0.0001 and 0.0005. Additionally, the end-of-cycle HC emission values vary from 4.6534 ppm to 7.9344 ppm within the same range of hydrogen mass fractions.

Figure 2(d) exhibits how carbon dioxide (CO_2) emissions vary with the crank angle. As the mass fractions of fumigated hydrogen rise, there is a corresponding increase in CO_2 emissions due to improving combustion efficiency by increasing flame temperature and leading to a more complete combustion of the carbon-based components [20]. Both the maximum CO_2 emission and the end-of-cycle HC emission values range from 49683 ppm to 49819 ppm for fumigated hydrogen mass fractions between 0.0001 and 0.0005.

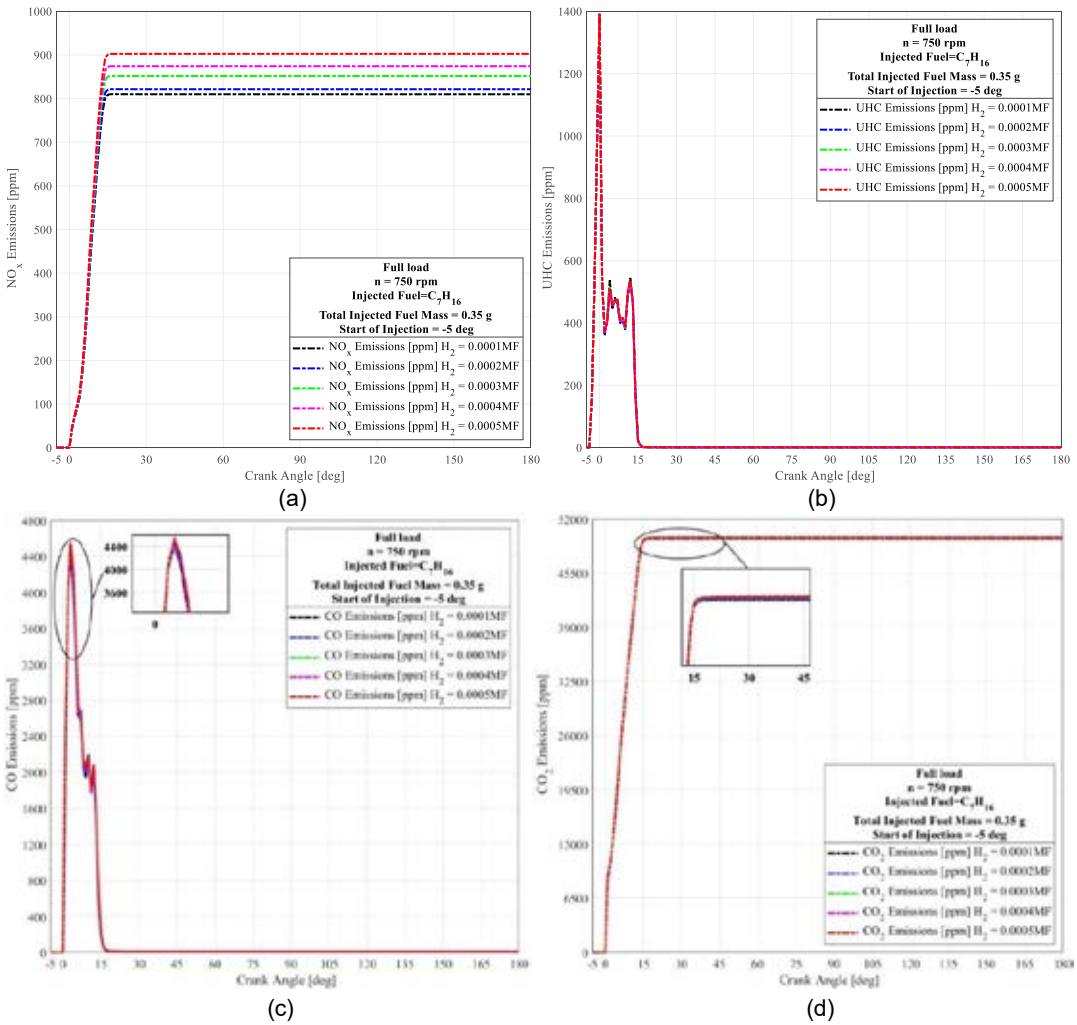

Fig. 2. The variation of exhaust emissions on crank angle degree (a) NO_X (b) UHC (c) CO (d) CO_2

4. CONCLUSIONS

The study conducted on the fluctuations of NO_X, UHC, CO, and CO_2 emissions in relation to crank angle, influenced by various fumigated hydrogen mass fractions, yielded the following main findings:

- All analyses were performed using CONVERGE Studio v3.2, with cell counts of 50,000, 75,000, and 100,000, determining Case-2 (75,000 cell count) to be the most favorable based on Mean Absolute Percentage Errors (MAPE) of 17.25%.
- A direct correlation was observed between the increase in fumigated hydrogen mass fractions and NO_X emissions, with a maximum emission recorded at 903 ppm for a mass fraction of 0.0005.
- UHC emissions remained relatively constant across varying hydrogen mass fractions, with a maximum emission of

approximately 1392 ppm noted at full fumigation.

- CO emissions initially decreased with increasing hydrogen mass fractions due to enhanced combustion efficiency, but later increased beyond a certain threshold, with maximum values ranging from 4433 ppm to 4547 ppm.
- CO_2 emissions increased alongside the fumigated hydrogen mass fractions, reflecting improved combustion efficiency, with maximum values ranging from 49683 ppm to 49819 ppm.

These findings highlight the complex interactions between hydrogen fumigation and combustion emissions, emphasizing the importance of optimizing hydrogen mass fractions for improved emission control.

REFERENCES

1. https://unctad.org/rmt2022. Accessed on January 17, 2025.
2. Bilousov I, Bulgakov M and Savchuk, V. 2020. Modern Marine Internal Combustion Engines-A Technical and Historical Overview (First Edition). Springer Cham. https://doi.org/10.1007/978-3-030-49749-1
3. Sæther SR and Moe E. 2021. A green maritime shift: Lessons from the electrification of ferries in Norway. Energy Research & Social Science 81(102282). https://doi.org/10.1016/j.erss.2021.102282.
4. Eyring V, Isaksen ISA, Berntsen T, Collins WJ, Corbett JJ, Endresen O, Grainger RG, Moldanova J, Schlager H and Stevenson DS. 2010. Transport impacts on atmosphere and climate: Shipping. Atmospheric Environment 44(37):4735–4771. https://doi.org/10.1016/j.atmosenv.2009.04.059
5. Godet A, Nurup J, Saber J, Panagakos G. and Barfod, MB. 2023. Operational cycles for maritime transportation: A benchmarking tool for ship energy efficiency. Transportation Research Part D: Transport and Environment 121(103840). https://doi.org/10.1016/j.trd.2023.103840
6. Cameretti MC, De Robbio R and Palomba M. 2023. Numerical Analysis of Dual Fuel Combustion in a Medium Speed Marine Engine Supplied with Methane/Hydrogen Blends. Energies 16(18): 6651. https://doi.org/10.3390/en16186651
7. Qu W, Fang Y, Song M, Wang Z, Xia Y, Lu Y and Feng L. 2024. Hydrogen injection optimization of a low-speed two-stroke marine hydrogen diesel engine. Fuel 366(131352):1–14. https://doi.org/10.1016/j.fuel.2024.131352
8. Cameretti M, De Robbio R, Mancaruso E and Palomba M. 2022. CFD Study of Dual Fuel Combustion in a Research Diesel Engine Fueled by Hydrogen. Energies 15(5521):1–21. https://doi.org/10.3390/en15155521
9. Karvounis P, Tsoumpris C, Boulougouris E and Theotokatos G. 2022. Recent advances in sustainable and safe marine engine operation with alternative fuels. Frontiers in Mechanical Engineering 8(994942):1-20. https://doi.org/10.3389/fmech.2022.994942
10. Han Z and Reitz RD. 1995. Turbulence Modeling of Internal Combustion Engines Using RNG k-ε Models, Combustion Science and Technology 106(4-6):267-295.
11. Reitz RD and Bracco FV. 1986. Mechanisms of Breakup of Round Liquid Jets, Encyclopedia of Fluid Mechanics, Gulf Publishing Company.
12. Amsden AA, O'Rourke PJ and Butler TD. 1989. KIVA-II: A Computer Program for Chemically Reactive Flows with Sprays," Los Alamos National Laboratory, Technical Report No. LA-11560-MS.
13. Senecal PK, Pomraning E. and Richards KJ. 2003. Multi-Dimensional Modeling of Direct-Injection Diesel Spray Liquid Length and Flame Lift-off Length using CFD and Parallel Detailed Chemistry, SAE Technical Paper 2003-01-1043.
14. Xu L, Chang Y, Treacy M, Zhou Y, Jia M and Bai XS. 2023. A skeletal chemical kinetic mechanism for ammonia/n-heptane combustion. Fuel 331(125830):1-13.
15. Luo QH, Hu JB, Sun B, Liu F, Wang X, Li C and Bao LZ. 2019. Experimental investigation of combustion characteristics and NOx emission of a turbocharged hydrogen internal combustion engine. International Journal of Hydrogen Energy 44(11):5573-5584. https://doi.org/10.1016/J.IJHYDENE.2018.08.184
16. Marin WE, Wiese DP and Erickson PA. 2011. An Experimental Investigation of Hydrogen Fumigation in a Small Direct-Injection Diesel Engine During Part-Load Operation. ASME 2011 Internal Combustion Engine Division Fall Technical Conference, Morgantown, West Virginia, USA, October 2–5, pp. 339-348.
17. Nemitallah MA, Abdelhalim A, Abdelhafez A and Habib MA. 2024. Experimental and numerical study on flow/flame interactions and pollutant emissions of premixed methane-air flames with enhanced lean blowout hydrogen injection. International Journal of Hydrogen Energy 65:14-32. https://doi.org/10.1016/j.ijhydene.2024.03.329
18. Sriwardani N, Okamoto Y, Seo T and Mikami M. 2014. The Influence of Hydrogen Addition to Diesel Fuel Spray Combustion for Different Atomization Conditions. Applied Mechanics and Materials 493:33–38. https://doi.org/10.4028/WWW.SCIENTIFIC.NET/AMM.493.33
19. Hu ZQ and Zhang X. 2011. Effect of Hydrogen Addition on Combustion Characteristics of a Spark Ignition Engine Fueled With Low Heat Value Gas. Advanced Materials Research 688–691. https://doi.org/10.4028/WWW.SCIENTIFIC.NET/AMR.197-198.688
20. Nosek R, Zvada B, Ďurčanský P, Čajová Kantová N and Mičko P. 2024. Numerical Analysis of Hydrogen-Enriched Natural Gas on Combustion and Emission Characteristics. Arabian Journal for Science and Engineering 1-10. https://doi.org/10.1007/s13369-024-09484-7

RESULTS OF COMBUSTION TESTS OF H_2 – CH_4 MIXTURE WITH HIGH H_2 CONTENT

[1]*Mihăescu Lucian*, [2]*Lăzăroiu Gheorghe*, [3]*Niculescu Alina*, [4*]*Stoica Dorel*, [3]*Grigoriu Rodica –Manuela*, [2]*Mohammed Gmal Osman*
[1]National University of Science and Technology POLITEHNICA Bucharest, Faculty of Mechanical and Mechatronics Engineering, Splaiul Independenței 313, Bucharest, 060042, Romania
[2]Maritime University of Constanța, Energy Engineering, Mircea cel Bătrân Street 104, 900663, Romania
[3]POLITEHNICA Bucharest, Faculty of Energy
[4*]POLITEHNICA Bucharest, Faculty of Biotechnical Systems Engineering

*Corresponding author e-mail: dorel.stoica@upb.ro

ABSTRACT
The work addressed the combustion technology of the $H_2 - CH_4$ mixture for high values of up to 40% for H_2. The work developed previous theoretical and experimental studies. Starting from these, a diffusion burner was developed, with five nozzles for gas intake, each surrounded by coaxial air intake. The burner was mounted on a stand, built for this purpose, which achieved a controlled and stable mixing for CH_4 and H_2 components. The flame developed in free space. During the tests, a proportion of 17.25% and 40% for H_2 was used. The flames obtained were very stable, without vibrations and pulsations, with the first dominant part of H_2 combustion. The results obtained will represent a basis for future research and experimental testing.

Keywords: Methane, Hydrogen, Mixture, Diffusive Combustion, Cylindrical Flame

1. INTRODUCTION

The increase in the percentage of H_2 in CH_4 will have to be studied sequentially, each step raising the issue of the transition from the dominance of the combustion characteristic by CH_4 to the dominance of the H_2 component. Up to a mixing ratio of 10% for H_2, even 15%, as practice has shown, the flame is practically CH_4. As a result, for the proportion of the mixture below 15%, the combustion of premixes with air can be used, even with the full preservation of methane burners. In addition, a very simple technology can be used, represented by burners with self-aspiration of air. The main problems for the combustion process are represented by [1], [2], [3]:
- flame return for the technology of combustion of the gas-air premix;
- the correlation between the flame entry velocity for gas and air in the case of their separate admission, also called diffusive flame.

The combustion velocity of hydrogen amplifies these aspects, which is about 8 times higher than that of methane. The combustion velocity is perpendicular to the flame front and in the opposite direction to the flow. A stable flame is characterized by the equality of the flow velocity with the air velocity. In addition, other essential parameters intervene, such as temperature, turbulence, excess air (the ratio between the real air in the jets and the stoichiometric one). The main problem is the stability of combustion, represented by the correlation between the flow velocity in the jet that defines the flame and the combustion velocity.
Figure 1 presents a synthetic sketch of the constructive - functional variants of burners for the $CH_4 - H_2$ mixture, [4].

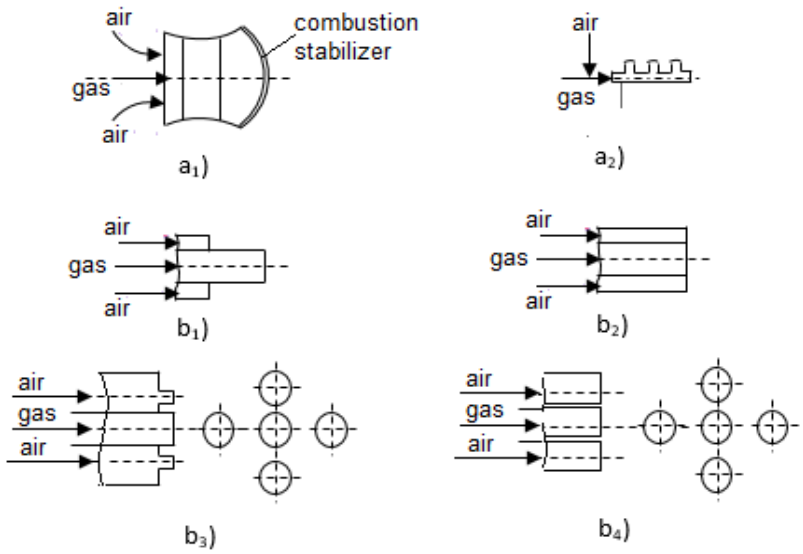

Fig.1. Construction variants for $CH_4 - H_2$ mixture burners.
a - with air premix: a_1 – with self-aspiration, a_2 – forced premix;
b – diffusion burners with separate gas-air jets: b_1 and b_2 – with coaxial jets, b_3 and b_4 – with separate jets.

2. COMBUSTION STABILITY CONTROL

The premix burners shown in Fig. 1. have domestic applications (heating, cooking, apartment heating systems). The presented diffusive burner variants (see figure 1) allow for combustion without flame return and thermal powers represented by fuel flows, significantly higher than those with premix do, and their modular construction allows for the achievement of high thermal powers [4].
The combustion of the gas-air premix depends on the kinetic characteristics of the gaseous fuel, which is why it is also called kinetic combustion, with “kinetic burners”, respectively [5], [6]. Diffusive combustion, existing in separate gas-air jets, depends on the diffusive transport of air to the fuel and has a much greater dependence on the gas dynamics of the gas-air mixture than on the energetic (kinetic) characteristics of the gaseous fuel. This gas-dynamic dependence of the gas-air ensemble is even more pronounced for hydrogen, due to the increased air velocity [7], [8], [9].
The very high laminar combustion velocity causes the main gasdynamic problem, of $3.1\,m/s$ for hydrogen, compared to $0.4\,m/s$ for methane. As a result, a mixture between them will have to solve this gap through the gas dynamics of the flame. This aspect is positive, so that at the base of the flame (at the burner exit), there will be hydrogen combustion, and at the periphery methane combustion [4].
Theoretically and experimentally for the diffusive flame it is found that the length "L" is little influenced by the exit velocity of the jets from the burner. The diffusion equation of the fuel concentration "C" for the coordinates in Fig. 2, for a symmetrical cylindrical flame is in the form (with D $[m/s]$ the fuel-air diffusion coefficient was noted):

$$\frac{\delta C}{\delta t} = \frac{D}{u}\left(\frac{\delta^2 C}{\delta y^2} + \frac{1}{y}\frac{\delta C}{\delta y}\right) \quad (1)$$

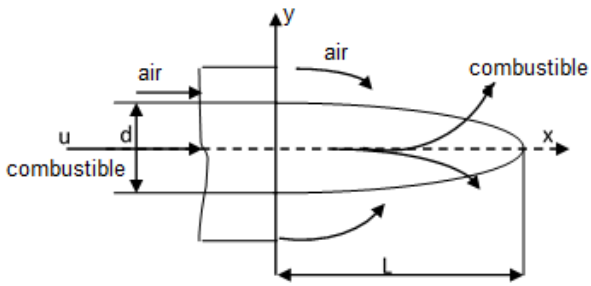

Fig. 2. Diffusion for a cylindrical flame.

A difference appears for the two gaseous components in the mixture $CH_4 - H_2$, where for $H_2 - air$ $D_0 = 6.11 \cdot 10^{-5} m^2/s$ and $CH_4 - air$ where $D_0 = 1.96 \cdot 10^{-5} m^2/s$ (both at 273 K), the diffusion coefficient in air being about 3 times higher for hydrogen than for air. This difference, as well as that of the momentum difference, leads to the combustion of hydrogen in the initial part of the flame, with the combustion of methane pushed towards the axial extremity of the flame.
For turbulent diffusion, governed by the turbulent diffusion coefficient ε, a coefficient proportional to the length of the turbulence ladder and to the turbulence intensity which is proportional to the velocity u, the dependence of the flame length proportional to the nozzle diameter d results.

$$L \sim d\ [m] \quad (2)$$

For a stable flame, the equality between the flow velocity $u\,[m/s]$ and the combustion velocity S_L $[m/s]$ for laminar regime, respectively S_T $[m/s]$ for turbulent regime, must be achieved. For both situations the combustion velocity depends on the fuel concentration C in air expressed in m^3/m^3, Fig.3, where C_{st} is the stoichiometric concentration.

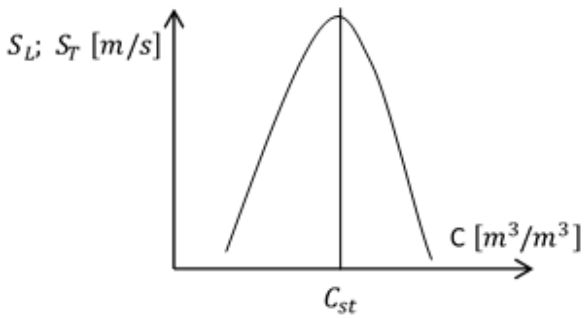

Fig 3. Variation of burning rate with fuel – air concentration.

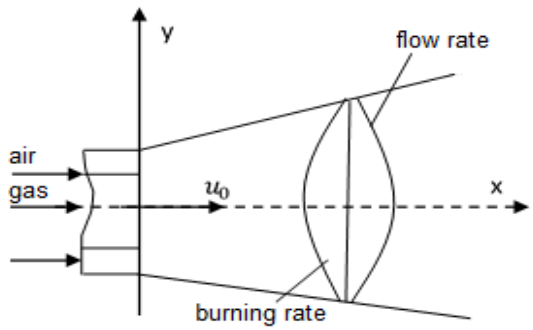

Fig. 4. The stability condition presented globally, as equality between the flow velocity and the combustion velocity which is in the opposite direction.

Finally, for the burning velocity in a jet, a parabolic distribution appears, Fig.4.

Along the axial flow "x" axis, the flow velocity exhibits a hyperbolic decrease $u = \sim\frac{1}{x}$, so the velocity u_0 at the exit of the fuel nozzle must ensure the stability condition $u = S_L$, respectively $u = S_T$. For this condition, the velocity u_0 must comply with condition (3).

$u \geq 10S_T$, respectively $u \geq 10S_L$ (3)

3. METHODOLOGY AND RESULTS OF TESTING THE COMBUSTION OF CH4-H2 FUEL, WITH HIGH H2 CONTENT

Experimental research included the creation of a stand for mixing the two gaseous fuels and a burner that allows combustion with a concentration of H_2 up to 60% in a mixture with CH_4. The burner presented conceptually in Fig. 5 comprises 5 fuel intake modules axially framed by air, and Fig. 6 shows an image of the burner, where $d_1 = 3mm,\ d_2 = 7mm,\ d_3 = 10mm$.

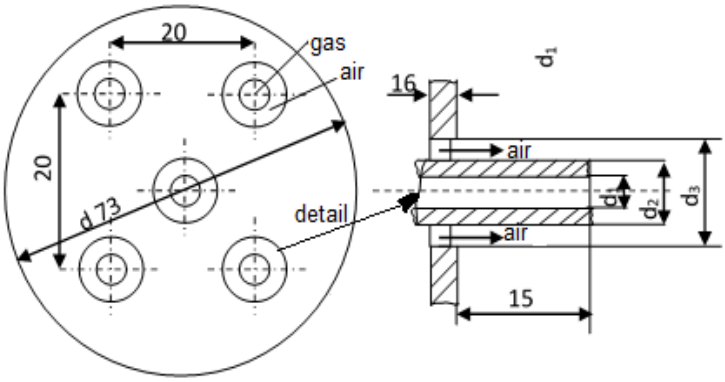

Fig. 5. Burner design.

Fig.6. Image of the burner.

Figure 7 shows a schematic of the stand designed to test the combustion of the $CH_4 - H_2$ mixture with a high H_2 content.

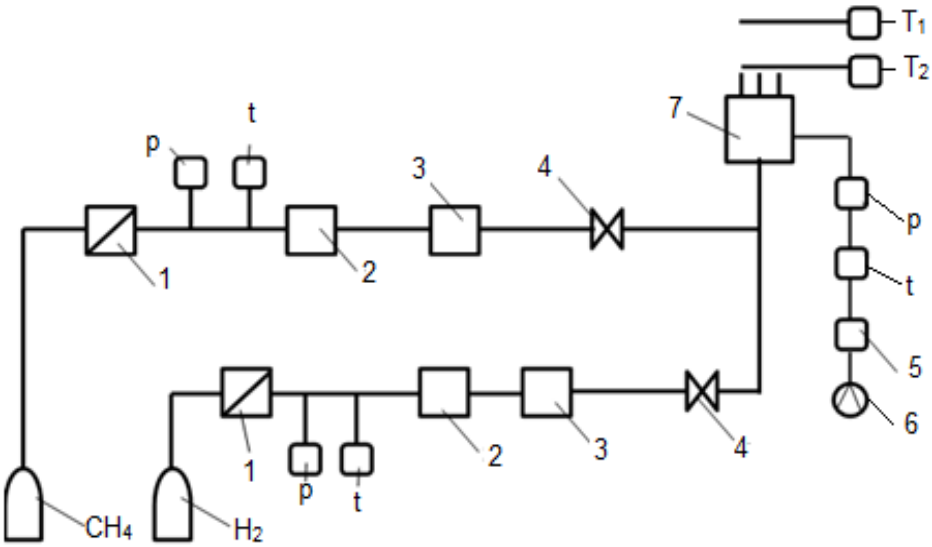

Fig.7. Experimental stand.
1- pressure reducing valve; 2 – flow programmer type Bronkhorst Flow; 3 – combustion process control type EMKOESM 4430; 4 – one-way valve; 5 – flow controller; 6 – air compressor, 7 – burner,
p, t – pressure and temperature measurement; T_1 and T_2 – thermocouples.

An image of the experimental stand is show in Fig. 8. It is worth noting the placement of two thermocouples for measuring the temperature in the flame, type $P_tR_h10\% - P_t(s),\ \Phi\ 6,\ L = 500\ mm, t_{max} = 1400^0C$, with the placement at a distance of 50 mm and 100 mm respectively from the fuel outlet section.

Fig.8. General view of the stand.

Fig. 9. Flame appearance 17% H2.

Fig. 10. Flame appearance 25% H2.

Fig. 11. Flame appearance 40% H2.

Table 1. Synthetic data of the experiments

No.	CH_4 flow (m^3)	H_2 flow (m^3)	H_2 / CH_4 (%)	Air flow (m^3)	t_1^* (°C)	t_2^* (°C)	CO_2^{**} (%)
1	1.0	0.2	17	10.5	768	907	9.2
2	1.5	0.5	25	16.4	-	928	6.4
3	1.5	1.0	40	17.8	-	986	5.2

*) temperatures at thermocouples T_1 and T_2, (Fig. 7); **) measurements at thermocouple T_2; they are for $O_2 = 3\%$.

Figures 9, 10, 11 show the appearance of the flames for the three situations specified by the data in Table 1, respectively the H_2/CH_4 ratios of 17% (Fig. 9), 25% (fFig. 10) and 40% (Fig. 11), respectively. The analysis of the images identifies by color, the combustion of hydrogen in the immediate area from the exit of the gas nozzles (flame with high transparency), and the combustion of methane for the rest of the flame length (reddish blue flame). During the testing period, no deviations from the combustion present in these figures were noted, this being without vibrations and shocks.

4. CONCLUSIONS

The paper presented the results of experimental tests of methane combustion mixed with hydrogen in proportions of 17%, 25% and 40%. To carry out these tests, it was necessary to create a stand that would allow the desired mixing, a stand equipped with a diffusive combustion burner, which included five gas jets, each framed by a concentric jet of accompanying air. The combustion tests showed perfect combustion, validating the developed burner concept, recommending the diffusive combustion technology as a safe and efficient one. The results obtained will be used to extend research for the combustion of the H_2/CH_4_4 mixture at values for H_2 above the 40% limit reached.

ACKNOWLEDGEMENT

This work was supported by a grant of the Ministry of Research, Innovation and Digitalization, project number PNRR-C9-I8-760089/23.05.2023, COD CF 31/14.11.2022, and PNRR-C9-I8-760111/23.05.2023, code CF 48/14.11.2022.

REFERENCES

1. Bouras F, Khaldi F. 2020. Optimization of Combustion Efficiency Using a Fuel Composition Based on CH4 and/or H2. Russ J Appl Chem 93, 1954–1959. https://doi.org/10.1134/S1070427220120198
2. Qiangqiang H, Zhenmin L, Tao W, Chao X, Siqi Z, Mingshu B, Jun D, 2021, The flammability limits and explosion behaviours of hydrogen-enriched methane-air mixtures, Experimental Thermal and Fluid Science, Volume 126, https://doi.org/10.1016/j.expthermflusci.2021.110395
3. Bouras F, Attia M, Khaldi F, Si-Ameur M, 2017, Control of methane flame properties by hydrogen fuel addition: Application to power plant combustion chamber, International Journal of Hydrogen Energy, Volume 42, Issue 13, Pages 8932-8939, https://doi.org/10.1016/j.ijhydene.2016.11.146
4. Schoonman J, Krol R, Nanostructured materials for solar Hydrogen production, 2011, U.P.B. Sci. Bull., Series B, Vol. 73, Iss. 4, ISSN 1454-2331
5. Vance FV, Shoshin Y, Goey P, Oijen J, 2021, Flame Stabilization and Blow-Off of Ultra-Lean H2-Air Premixed Flames, Energies, 14(7), 1977; https://doi.org/10.3390/en14071977
6. Schlup J, Blanquart G, 2018, A reduced thermal diffusion model for H and H_2, Combustion and Flame, Volume 191, Pages 1-8, https://doi.org/10.1016/j.combustflame.2017.12.022
7. Wawrzak A, Tyliszczak A, 2021, Numerical Study of Hydrogen Auto-Ignition Process in an Isotropic and Anisotropic Turbulent Field., Energies, 14(7), 1869; https://doi.org/10.3390/en14071869
8. Haworth DC, 2010, Progress in probability density function methods for turbulent reacting flows, Progress in Energy and Combustion Science, Volume 36, Issue 2, Pages 168-259, https://doi.org/10.1016/j.pecs.2009.09.003
9. Jones WP, Navarro-Martinez S, 2007, Large eddy simulation of autoignition with a subgrid probability density function method, Combustion and Flame, Volume 150, Issue 3, Pages 170-187, https://doi.org/10.1016/j.combustflame.2007.04.003

IONIC LIQUID-ENHANCED MULTIFUNCTIONAL ELECTROLYTES FOR HYDROGEN EVOLUTION REACTION AND Zn-BASED BATTERIES

[1,2*]*Nikola Zdolšek*, [1]*Aleksandra Dimitrijević*, [1]*Ivana Perović*, [1]*Snežana Brković*, [1]*Mina Seović*, [1]*Petar Laušević* and [2]*Marijana Kraljić Roković*
[1]University of Belgrade, "Vinca" Institute of Nuclear Sciences – National Institute of the Republic of Serbia, Departamanet of Physical Chemistry, Mike Petrovica Alasa 12-14, Belgrade, Serbia
[2]University of Zagreb, Faculty of Chemical Engineering and Technology, Trg Marka Marulica 19, Zagreb, Beograd

*Corresponding author e-mail: zdolsek@vin.bg.ac.rs

ABSTRACT
The growing demand for efficient energy storage and conversion systems has driven the exploration of advanced electrolytes, including ionic liquids (ILs), for improving hydrogen evolution reaction (HER) and performance of Zn-based batteries. In this study, we investigated the effects of five ILs - four newly synthesized choline-based ILs ([Ch][Sal], [Ch][Sac], [Ch][Ace], [Ch][Lac]) and one commercial IL ([Bmim][BF4]) - as additives to enhance electrolyte performance for both HER and Zn-ion batteries. Electrochemical measurements were conducted to evaluate their impact on HER efficiency and inhibition of Zn dendrite growth in Zn-ion batteries. The addition of ILs significantly shifted the HER onset potential to more positive values, increased the current density and influenced the Tafel´s slopes. In Zn-ion batteries, [Ch][Sac] demonstrated superior performance by stabilizing voltage and inhibiting dendrite growth, while [Ch][Sal] accelerated dendrite formation, leading to faster short-circuiting. These findings highlight the potential of specific ILs to optimize electrochemical processes and open up new possibilities for their application in advanced energy technologies.
Keywords: Ionic liquids, HER, Zn-ion batteries

1. INTRODUCTION

The growing global demand for sustainable and efficient energy solutions has encouraged significant research into the development of advanced materials and systems for energy storage and conversion. Among them, hydrogen evolution reaction (HER) and zinc-based batteries (zinc-air, zinc-ion batteries) have gained considerable attention due to their potential for renewable energy technologies. HER plays an important role in electrochemical water splitting, a key process for clean hydrogen production [1]. Zinc-based batteries are emerging as promising alternatives to lithium-ion batteries, offering safety, cost-efficiency and environmental benefits [2]. However, both systems face challenges that limit their widespread application.

The HER efficiency is often hindered by sluggish reaction kinetics, electrode degradation and limited stability under harsh operating conditions [1]. Similarly, all zinc-based batteries suffer from issues such as dendrite formation, side reactions and insufficient cycling stability, primarily due to the limitations of conventional aqueous electrolytes. The main problem with zinc-based batteries is the formation and growth of dendrites at the anode, which leads to short circuits and battery failure [2]. Addressing these challenges requires innovative approaches in the development of electrolytes that can simultaneously enhance the performance, stability and safety of these systems.

In this sense, ionic liquids (ILs) are pomising electrolyte additives for the activation of HER and the inhibition of dendrite growth in zinc-based batteries. With their unique physicochemical properties such as high ionic conductivity, wide electrochemical stability windows and tunable viscosity, ILs have proven to be promising candidates for advanced electrolyte formulations. The application of ILs as electrolyte additives for HER and zinc batteries is still at an early stage of investigation. 1-butyl-3-ethylimidazolium bromide ([Beim][Br]) and 1,3-diethylimidazolium bromide ([Eeim][Br]) were first investigated as electrolyte additives for HER [3]. In this study, the addition of 2 vol% [Beim][Br] in 8M KOH electrolyte enganced HER, increased the current density and improved the efficiency of alkaline electrolysis compared to the pure 8M KOH electrolyte without the addition of ILs. In another research, HER was investigated in an 8M KOH electrolyte containing small amounts of three salicylate-based ILs: 1-butyl-3-methylimidazolium salicylate ([Bmim][Sal]), 1-(3-hydroxylpropyl)-3-methylimidazolium salicylate ([C3OHmim][Sal]), and imidazolium salicylate ([Im][Sal]) [4]. The addition of salicylate-based ILs resulted in higher current densities and enhanced HER. Furthermore, 1-butyl-3-methylimidazolium tetrafluoroborate ([Bmim][BF4]) and 1-butyl-3-methylimidazolium hexafluorophosphate ([Bmim][PF6]) have been studied as electrolytes for water electrolysis on various electrode materials [5,6]. (Optimal hydrogen production rates were achieved with solutions containing 10 vol% of these ILs, which was attributed to the enhanced ionic conductivity of the electrolyte.

The different ILs were used as electrolyte additives to suppress dendrite growth in zinc-based batteries. For example, [BMIm][OTF] with a very low melting point was used as an electrolyte additive in ZIBs, which in this case operate at a low temperature of -30°C [7]. The mixture of [EMIm][BF4] and Zn(BF4)2 has also been used as an electrolyte for effective dendrite inhibition [8]. It should be emphasised that the application of ILs as electrolyte additives for differente

electrochemical devices is still at an early stage of investigation.

In this work, we investigated for the first time the application of five ILs as electrolyte additives for HERs and ZIBs; two commercially available ILs (1-butyl-3-methylimidazolium tetrafluoroborate [Bmim][BF4] and choline acetate [Ch][Ace]) and three newly synthesised ones: choline-based iLs (choline salicylate [Ch][Sal], choline saccharinate [Ch][Sac] and choline lactate [Ch][Lac]).

2. MATERIALS AND METHODS

2.1. Synthesis of ILs and electrolyte preparation

The syntheses of ILs were performed according the procedure described in references: [9,10,11]. These ILs are:

- 1-butyl-3-methylimidazolium tetrafluoroborate [Bmim][BF4] (commertial, Acros Organics),
- choline salicylate [Ch][Sal],
- choline saccharinate [Ch][Sac],
- choline acetate [Ch][Ace] (commertial, Acros Organics) and
- choline lactate [Ch][Lac].

1M Na_2SO_4 for HER and 1M $ZnSO_4$ for Zn-ion batteries were used as the base electrolytes. To study the impact of various ionic liquids, each was dissolved in 1M Na_2SO_4 or in 1M $ZnSO_4$ solution at a concentration of 5 g L^{-1}. The resulting electrolyte solutions were labeled with abbreviations representing the respective ionic liquids to facilitate identification and comparison during the analyses.

2.2. Electrochemical measurements

All electrochemical measurements were performed in three- and two-electrode configurations. For all measurements BioLogic SP-150 potentiostat was used and all measurements were conducted at room temperature.

HER was examined in neutral 1M Na_2SO_4 electrolyte, without and with addition of ILs. Measurements was perfomed in three-celectrode configuration with Pt as counter electrode, Ag/AgCl as reference electrode and Au as working electrode (diameter of Au electrode was 0.16 cm). Linear sweep voltammetry (LSV) was performed in potential range from -0.5 V to -2 V vs. Ag/AgCl, with scan rate of 20 mV s^{-1}.

ZIB and dendrite formation was investigated in 1M $ZnSO_4$ electrolyte without and with addition of ILs. For this investigation measurements was performed in two-electrode configuration. The setup included two parallel Zn plates, each with a surface area of 0.25 cm^2, separated by a 1 mm gap to ensure a uniform distance. The prepared electrodes were immersed in glass vials containing 100 µL of electrolyte. The plating and stripping processes (i.e. dendrite growth) were investigated using the Galvanostatic Cycling with Potential Limitation (GCPL) technique.

3. RESULTS AND DISCUSSION

In the first step of this inevstigation, HER was analysed at an Au electrode in pH-neutral 1M Na_2SO_4 electrolyte, without and with the addition of ILs. As shown in Fig. 1, the hydrogen evolution reaction was influenced by the ILs and all electrochemical parameters are listed in Table 1.

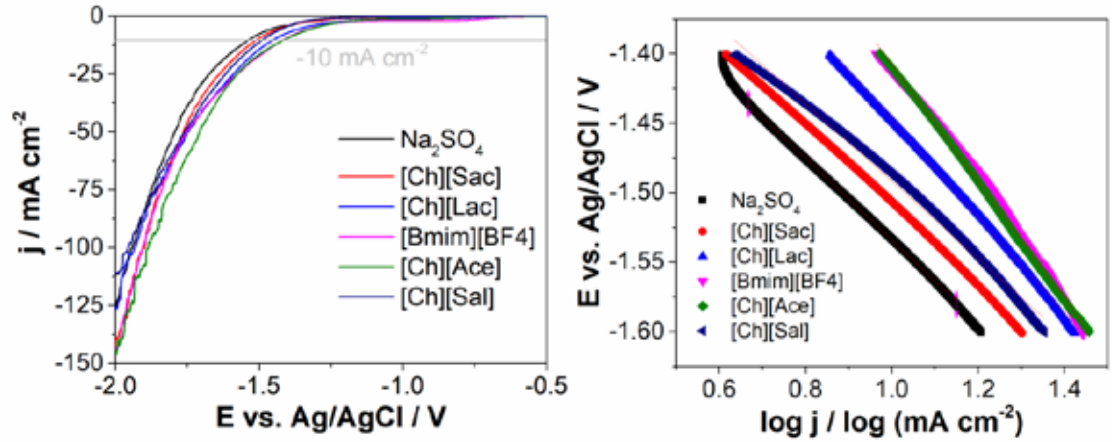

Fig. 1. LSV curves (left) and Tafels plots (right) obtained in all investigated electrolytes

.

The addition of ILs to the Na_2SO_4 electrolyte shifts the onset potential of hydrogen evolution to more positive values compared to the onset potential obtained in pure 1M Na_2SO_4. The onset potentials were evaluated at -10 mA cm^{-2}. The onset potential obtained in 1M Na_2SO_4 electrolyte showed the most negative value (-1.54 V vs. Ag/AgCl). On the other

side, in Na_2SO_4 electrolyte with addition of ILs, the onset potential moves to positive values and follows the order: [Ch][Sac] (-1.51 V), [Ch][Sal] (-1.49 V), [Ch][Lac] (-1.46 V), [Ch][Ace] and [Bmim][BF4] showed almost the same value of -1.42 V.

Table 1. Electrochemical parameters evaluated for HER.

Electrolyte	E_{onset} @ -10 mA cm-2 / V	j@-2 V / mA cm^{-2}	Tafel's slope / mV dec^{-1}
1M Na_2SO_4	-1.54	-122	-294
[Ch][Sac]	-1.51	-140	-298
[Ch][Sal]	-1.49	-112	-278
[Ch][Lac]	-1.46	-126	-347
[Ch][Ace]	-1.42	-146	-422
[Bmim][BF4]	-1.42	-143	-418

Furthermore, the addition of ILs additives showed a significant influence on the current density (j). The j value (at -2 V vs Ag/AgCl) value was lowest for [Ch][Sal], followed by Na_2SO_4 electrolyte without addition of ILs (Table 1). On the other side, the j values increase with the addition of ILs to the electrolyte. Additionally, to the HER investigation, a Tafel analysis was performed. As can be seen from Table 1 and Figure 1, the Tafel jumps vary between the electrolytes. A higher value of the Tafel´s slope was evaluated for the electrolyte [Ch][Ace], while the lowest value was determined for the electrolyte [Ch][Sal].

These values demonstrate the beneficial impact of the addition of ILs to the electrolyte on HER efficiency. We assume that the addition of ILs changes the conductivity of the electrolyte, which may be favourable for HER.

In addition to this research, a 1M $ZnSO_4$ solution with added ILs was investigated as a potential electrolyte for Zn-ion batteries. The study aimed to address the main issue of zinc dendrite growth, which is a major problem in all types of Zn batteries. The plating/stripping processes and dendrite formation were investigated using the Galvanostatic Cycling with Potential Limitation (GCPL) technique at a current density of 10 mA cm^{-2}, 2.5 mAh cm^{-2}, Figure 2.

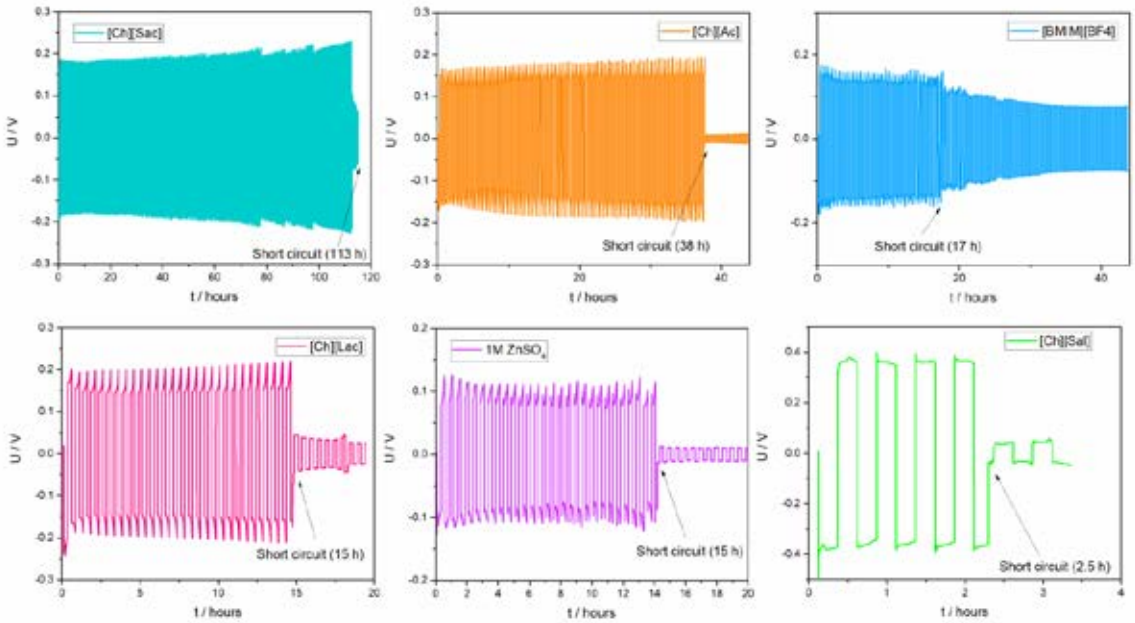

Fig. 2. Zn plating/stripping performances at 10 mA cm^{-2}, 2.5 mAh cm^{-2}.

The stability of the overpotential (Fig. 2) was highest for the [Ch][Sac]-based electrolyte. In contrast, the other IL-based electrolytes exhibited deviations of the overpotential from their initial values over time. As the number of cycles increased, the overpotential gradually fade, which may be attributed to rapid growth of the Zn dendrites on the electrode surface. Figure 2 also shows that the short circuit between the two Zn electrodes occurred faster in the $ZnSO_4$ electrolyte containing [Ch][Sal]. This suggests that the [Ch][Sal]-based electrolyte accelerates dendrite growth, while [Ch][Sac] inhibits dendrite growth.

A notable difference between the electrolytes was observed in short-circuiting behaviour (i.e. dendrite growth): [Ch][Sac] effectively inhibited dendrite formation, while [Ch][Sal] significantly accelerated dendrite growth. In the case of the ionic liquids [Ch][Sac], the [Sac] anion acts as a traffic aid for Zn^{2+} and as a passive layer on the electrode surface and therefore inhibits dendrite formation [12].

4. CONCLUSIONS

This study demonstrated the dual functionality of ILs in enhancing HER and inhibiting the growth of zinc dendrites in Zn-based batteries. The addition of ILs to the electrolyte shifted the initial HER onset potential to more positive values, improved the current density and affected the Tafel slopes, confirming their ability to enhance HER efficiency. Among the investigated ILs, [Ch][Sac] exhibited superior performance for Zn-ion batteries by effectively stabilizing the overpotential and suppressing dendrite growth due to its unique interaction with Zn ions. In contrast, [Ch][Sal] promoted rapid dendrite formation, highlighting the critical role of IL composition in determining electrolyte behaviour. These results underline the potential of tailored ILs as versatile additives to improve both the HER efficiency and stability of Zn-based batteries. Further research of IL-electrolyte interactions is essential to optimize these systems for practical applications in sustainable energy technologies.

ACKNOWLEDGEMENT

We are grateful for the support from the NATO SPS programme, which funded this research under project number SPS G5910; to the Ministry of Science, Education and Youth of the Republic of Croatia for the funding under the framework “Ciljana znanstvena istrazivanja”, under the number NPOO.C3.2.R3-I1.04.0187 and to the Ministry of Science, Technological Development and Innovation of the Republic of Serbia (contract number 451-03-66/2024-03/200017). N.Z. would like to thank the Croatian Science Foundation for financial support through the NextGenerationEU, MOBDOL-2023-12 program (Financira Europska unija – NextGenerationEU).

NOMENCLATURE

j	current density, mA cm^{-2}
E	potential, V
E_{onset}	onset potential, V

REFERENCES

1. Quan L, Jiang H, Mei G, Sun Y and You B. 2024. Bifunctional Electrocatalysts for Overall and Hybrid Water Splitting. Chemical Reviews 124(7): 3694-3812.
2. Yang SJ, Zhao LL, Li ZX, Wang P, Liu ZL, Shu J and Yi TF. 2024. Achieving stable Zn anode via artificial interfacial layers protection strategies toward aqueous Zn-ion batteries. Coordination Chemistry Reviews 517: 216044.
3. Amaral L, Minkiewicz J, Šljukić B, Santos DM, Sequeira CA, Vraneš M and Gadžurić S. 2019. Custom-made bromide-based ionic liquids as electrolyte additives for enhancing hydrogen evolution in alkaline water electrolysis. Journal of The Electrochemical Society 166(16): F1314.
4. Amaral L, Minkiewic J, Šljukić B, Santos DM, Sequeira CA, Vraneš M and Gadžurić S. 2018. Toward tailoring of electrolyte additives for efficient alkaline water electrolysis: salicylate-based ionic liquids. ACS Applied Energy Materials 1(9): 4731-4742.
5. De Souza RF, Padilha JC, Gonçalves RS, De Souza MO and Rault-Berthelot J. 2007. Electrochemical hydrogen production from water electrolysis using ionic liquid as electrolytes: towards the best device. Journal of Power Sources 164(2): 792-798.
6. De Souza RF, Loget G, Padilha JC, Martini EM and De Souza MO. 2008. Molybdenum electrodes for hydrogen production by water electrolysis using ionic liquid electrolytes. Electrochemistry Communications 10(11): 1673-1675.
7. Chen J, Zhou W, Quan Y, Liu B, Yang M, Chen M and Shi S. 2022. Ionic liquid additive enabling anti-freezing aqueous electrolyte and dendrite-free Zn metal electrode with organic/inorganic hybrid solid electrolyte interphase layer. Energy Storage Materials 53: 629-637.
8. Ma L, Chen S, L, N, Liu Z, Tang Z, Zapien JA and Zhi C. 2020. Hydrogen‐free and dendrite‐free all‐solid‐state Zn‐ion batteries. Advanced Materials 32(14): 1908121.
9. Tanzi L, Nardone M, Benassi P, Ramondo F, Caminiti R and Gontrani L. 2016. Choline salicylate ionic liquid by X-ray scattering, vibrational spectroscopy and molecular dynamics. Journal of Molecular Liquids 218: 39-49.
10. Vraneš M, Panić J, Tot A, Popsavin M, Jocić A and Gadžurić S. 2019. Physicochemical characterization of choline based ionic liquids with chelating anions. The Journal of Chemical Thermodynamics 131: 80-87.
11. Nockemann P, Thijs B, Driesen K, Janssen CR, Van Hecke K, Van Meervelt L and Binnemans K. 2007. Choline saccharinate and choline acesulfamate: ionic liquids with low toxicities. The Journal of Physical Chemistry B 111(19): 5254-5263.
12. Xi M, Liu Z, Ding J, Cheng W, Jia D and Lin H. 2021. Saccharin anion acts as a “traffic assistant” of Zn2+ to achieve a long-life and dendritic-free zinc plate anode. ACS Applied Materials & Interfaces 13(25): 29631-29640.

ENHANCED ELECTROCHEMICAL PERFORMANCE OF V_2O_5 ELECTRODE WITH 1-BUTYL-3-METHYLIMIDAZOLIUM SALICYLATE ELECTROLYTE FOR HYDROGEN EVOLUTION, OXYGEN EVOLUTION AND OXYGEN REDUCTION REACTIONS

[1,2*]*Nikola Zdolšek*, [2]*Mia Božiković*, [1]*Aleksandra Dimitrijević*, [1]*Snežana Brković*, [1]*Mina Seović*, [1]*Ivana Perović* and [2]*Marijana Kraljić Roković*
[1]University of Belgrade, "Vinča" Institute of Nuclear Sciences – National Institute of the Republic of Serbia, Department of Physical Chemistry, Mike Petrovića Alasa 12-14, Belgrade, Serbia
[2]University of Zagreb Faculty of Chemical Engineering and Technology, Trg Marka Marulica 19, Zagreb, Beograd

*Corresponding author e-mail: zdolsek@vin.bg.ac.rs

ABSTRACT
The hydrogen evolution reaction (HER), the oxygen evolution reaction (OER) and the oxygen reduction reaction (ORR) are essential for renewable energy applications like water splitting, fuel cells and metal-air batteries. This study explores the synergistic effects of combining V_2O_5 electrode material with 1-butyl-3-methylimidazolium salicylate ([Bmim][Sal]) as an additive to an ionic liquid electrolyte. Electrochemical measurements in 0.1 M KOH, with and without [Bmim][Sal], reveal enhanced performance for HER and OER. The addition of [Bmim][Sal] shifts HER and OER onset potentials to more favourable values, indicating improved catalytic activity. Furthermore, ORR studies demonstrate an increased current density and a transition to a direct four-electron pathway in the presence of [Bmim][Sal]. These findings highlight the potential of [Bmim][Sal] as a promising electrolyte additive to optimize the electrochemical performance of V_2O_5 electrodes for sustainable energy technologies.
Keywords: HER, OER, ORR, V_2O_5, ionic liquids.

1. INTRODUCTION

The hydrogen evolution reaction (HER), the oxygen evolution reaction (OER) and the oxygen reduction reaction (ORR) are critical electrochemical processes in renewable energy technologies such as water splitting, fuel cells and metal-air batteries [1]. HER facilitates hydrogen production and provides a clean and sustainable energy carrier, while OER is essential for the production of oxygen in water splitting, which is often hindered by slow kinetics and high overpotential. Similarly, ORR plays an important role in energy conversion in fuel cells and requires efficient and durable catalysts to ensure high performance. ORR and OER are crucial electrochemical processes in rechargeable metal-air batteries (such as Zn-air, Al-air, etc.). However, all these reactions are very slow, which significantly limits the application of electrochemical devices. As a result, current research is focussed on the development of new materials (electrocatalysts) and advanced electrolytes that can improve the efficiency and kinetics of these reactions.

Carbon materials occupy a significant place in the field of catalysis. It can be used as a support, but also it will show good catalytic properties by doping, functionalization or introduction of defracts [2]. Materials such as graphene, carbon nanotubes and porous carbon structures have been extensively studied for their ability to enhance catalytic performance when doped with heteroatoms (e.g. N, S or P) or functionalized with transition metal nanoparticles. Furthermore, various metal oxides have gained significant attention as electrocatalysts for these reactions due to their unique electronic structures, high stability and tunable catalytic properties. In the last years, the use of V_2O_5 for applications in electrocatalysis for HER, OER and ORR has gained considerable importance. V_2O_5 materials exhibit high OER performance due to the multivalent states of V and the abundant V=O groups, which enhance the active intermediates (OOH*) by modulating the V valence electron structure and stabilizing the oxygen sites [3]. On the other side, their intrinsic HER performance remains limited due to the weak H* adsorption at the V centre, hindering the rate-determining step at the electrode–electrolyte interface [4]. Beside, HER and OER, V_2O_5 was also used for ORR. In this context, ORR on V_2O_5 electrode materials predominantly follows a two-electron pathway leading to the generation of hydrogen peroxide [5].

Besides the development of new electrode materials, the design of novel electrolytes is another approach to improving electrochemical performance. The most popular approach is application of ionic liquids (ILs) as new, versatile electrolytes [6]. ILs are organic salts that remain in a liquid state at room temperature and consist of large organic cations and inorganic or organic anions. They are used as electrolytes in electrochemistry due to their high ionic conductivity, their wide electrochemical potential window and their stability and are therefore suitable for various applications. However, application of ILs as electrolytes or electrolyte additives is still at an early stage of research.

In this paper, we combined V_2O_5 electrode material with 1-butyl-3-methylimidazolium salycilate ([Bmim][Sal]) as an electrolyte additive to improve HER, OER and ORR.

2. MATERIALS AND METHODS

2.1. 1-butyl-3-methylimidazolium salycilate synthesis and electrolyte preparation

1-butyl-3-methylimidazolium salycilate (abbrev. [Bmim][Sal]) was prepared according the procedure described in reference [7]. 0.1M KOH was used as electrolyte, without and with addition of [Bmim][Sal] in concentration of 1%. 0.1M KOH with addition of IL was noted as 0.1M KOH+ [Bmim][Sal].

2.2. Electrode preparation and electrochemical measurements

The working electrode was prepared by mixing V_2O_5 (purity 99.6%, Sigma Aldrich) with carbon black (Vulcan, Cabot Corporation) in a mass ratio of 1:0.5. The resulting mixture was dispersed in a binder solution and sonicated for 2 hours at room temperature. The binder solution was consised of 0.2% chitosan in 1% aqueous acetic acid solution [8]. The reason for using this binder solution instead of the most commonly used Nafion is the negligible toxicity of chitosan. A 5 µL aliquot of the dispersed solution was applied to a rotating disc electrode made of glassy carbon (surface area: 0.07 cm^2) and dried under an IR lamp.

All electrochemical measurements were performed using a BioLogic SP-150 instrument at room temperature. The electrochemical cell consisted of a platinum counter electrode, an SCE reference electrode and a modified glassy carbon rotating disc electrode as the working electrode (as described above). All potentials were related to the reversible hydrogen electrode (RHE) using the formula $E_{RHE}=E_{SCE}+0.242+0.059pH$. For HER and OER studies, linear sweep voltammetry (LSV) was recorded at a scan rate of 50 mV s^{-1}. For ORR, cyclic voltammetry (in N_2- and O_2-saturated electrolytes) was recorded at a scan rate of 50 mV s^{-1} within the potential range of 1.1 to 0.27 V versus RHE. LSV was performed at different rotation speeds (from 500 to 2000 rpm) with a scan rate of 50 mV s^{-1} within the potential range of 1 to 0.27 V vs. RHE.

3. RESULTS AND DISCUSSION

The electrocatalytic properties of V_2O_5 in a 0.1 M KOH solution with the addition of [Bmim][Sal] for HER and OER were first explored. Fig. 1 represents LSV curves for HER (left) and OER (right) in 0.1M KOH without and with addition of [Bmim][Sal] ionic liquid.

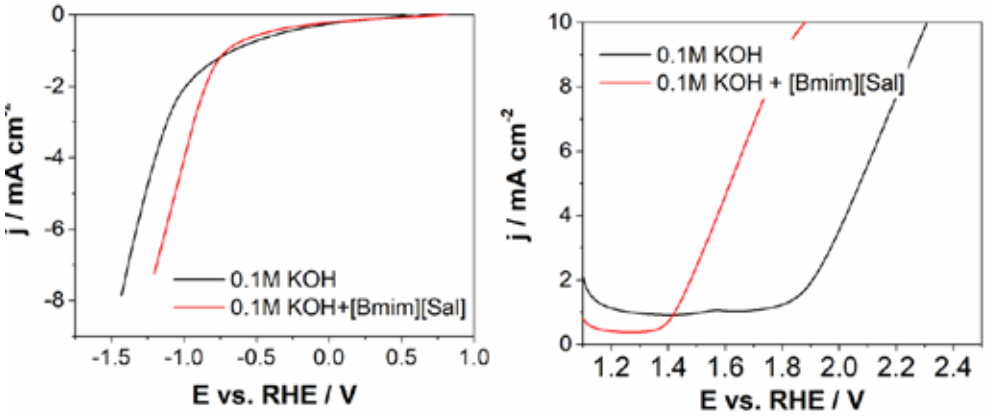

Fig. 1. LSV curves of V_2O_5 in pure 0.1M KOH and 0.1M KOH with addition of [Bmim][Sal] for HER (left) and OER (right).

As can be seen form Figure 1, HER and OER in pure 0.1M KOH (without addition) started at -1.1 V and 1.9 V, respectively. These results showed that V_2O_5 electrode material is active for HER and OER. In comparison with literature data, for example for cobalt-doped carbon OER starts at around 1.6 V vs. RHE [9] implying that V_2O_5 in pure 0.1M KOH electrolyte has suitable electrocatalytical activity towards OER. On the other side, electrocatalytical activity towards HER is slighty lower when compare to carbon-based materias (where HER starts arund -0.5 V vs. RHE depending on electrolyte concentration and material properties).

On the other side, addition of ionic liquid [Bmim][Sal] showed positive impact on both HER and OER. The onset potential of HER move to positive values (-0.8 V), while OER potential moves from 1.9 V to 1.4 V vs. RHE.

ORR was investigated by CV and LSV in N_2 and O_2 saturated electrolyte, without and with addition of [Bmim][Sal]. As can be seen in Figure 2, the V_2O_5 electrode material showed no oxido-reduction peaks in N_2-saturated electrolytes. On the other side, in electrolytes saturated with O_2, oxygen reduction peaks occur in both electrolytes. These results clearly show that the V_2O_5 electrode material is active for oxygen reduction.

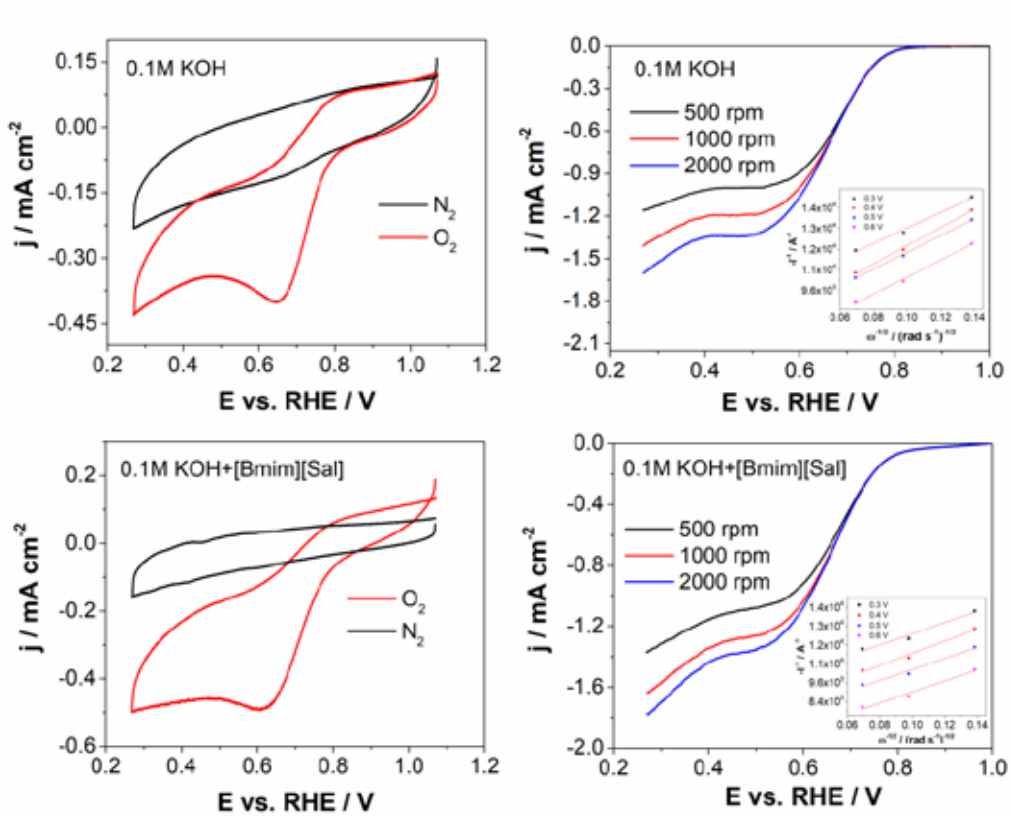

Fig. 2. CVs and LSVs with inserted Kouteky-Levich plots for V_2O_5 electrocatalysts in 0.1M KOH and 0.1M KOH electrolyte with addition of [Bmim][Sal].

No significant differences were found between the two electrolytes with regard to the initial and peak potential of oxygen reduction. The oxygen reduction starts in both cases begins at 0.85 V vs. RHE, with the reduction peak occurring around 0.75 V vs. RHE. However, the current density of the reduction peak is higher in the electrolyte containing [Bmim][Sal]. This increase could be attributed to the increased conductivity of the electrolyte and increased solubility of O_2 in the electrolyte with the addition of [Bmim][Sal].

In order to get insight into the kinetics of oxygen reduction at V_2O_5 electrodes in two investigated electrolytes. The Koutecky-Levich plots are represented in Figure 2 (inset diagrams). Details of the Koutecky-Levich analysis can be found in reference [9]. The number of exchange electrons during the ORR can be determined from the slope of the Koutecky-Levich plot. It is known that the ORR can occur via two pathways: the direct four-electron pathway (which is favourable in electrochemical devices) and the indirect two-step two-electron electro pathway (which is unfavourable in electrochemical devices). In the case of a pure 0.1 M electrolyte, the ORR at the V_2O_5 electrode occurred via the two-step two-electron pathway, which is in agreement with the literature. The average number of exchange electrons in the potential range of 0.6 to 0.3 V vs. RHE was calculated to be 2.4. In contrast, the Koutecky-Levich analysis for the electrolyte with [Bmim][Sal] showed that the average number of exchange electrons in the same potential range is 3.7, which corresponds to the direct four-electron pathway. It can be concluded that the addition of IL (i.e. [Bmim][Sal]) has no influence on the electrochemical parameters, such as the onset ponetial, but this addition has an influence on the oxygen reduction pathway.

4. CONCLUSIONS

The integration of [Bmim][Sal] with V_2O_5 electrodes significantly improves their electrochemical performance for her, oer and orr. the ionic liquid reduces the overpotentials of her and oer and promotes the favourable four-electron pathway in ORR, demonstrating its ability to improve efficiency and kinetics. This approach underlines the potential of ionic liquid additives to revolutionize energy conversion processes and open a pathway to more efficient and sustainable renewable energy technologies. Further studies on optimization and long-term stability are recommended to advance practical applications.

ACKNOWLEDGEMENT
We are grateful for the support from the NATO SPS programme, which funded this research under project number SPS G5910; to the Ministry of Science, Education and Youth of the Republic of Croatia for the funding under the framework "Ciljana znanstvena istrazivanja", under the number NPOO.C3.2.R3-I1.04.0187 and to the Ministry of Science, Technological Development and Innovation of the Republic of Serbia (contract number 451-03-66/2024-03/200017). N.Z. would like to thank the Croatian Science Foundation for financial support through the NextGenerationEU, MOBDOL-2023-12 program (Financira Europska unija – NextGenerationEU).

NOMENCLATURE

E	Potential, V
j	Current density, mA cm^{-2}
I	Current, A
ω	Rotation speed, rad s^{-1}

REFERENCES

1. Qin DD, Tang Y, Ma G, Qin L, Tao CL, Zhang X and Tang Z. 2021. Molecular metal nanoclusters for ORR, HER and OER: Achievements, opportunities and challenges. International Journal of Hydrogen Energy 46(51): 25771-25781.
2. Wang J, Kong H, Zhang J, Hao Y, Shao Z and Ciucci F. 2021. Carbon-based electrocatalysts for sustainable energy applications. Progress in Materials Science 116: 100717.
3. Zhang J, Zhang H, Liu M, Xu Q, Jiang H and Li C. 2020. Cobalt-stabilized oxygen vacancy of V2O5 nanosheet arrays with delocalized valence electron for alkaline water splitting. Chemical Engineering Science 227: 115915.
4. Meena A, Ha M, Chandrasekaran SS, Sultan S, Thangavel P, Harzandi AM, Singh B, Tiwari JN and Kim KS. 2019. Pt-like hydrogen evolution on a V 2 O 5/Ni (OH) 2 Electrocatalyst. Journal of Materials Chemistry A 7(26): 15794-15800.
5. Zhang S, Feng G, Bao Z, Peng X, Jiang C, Shao Y, Wang S and Wang J. (2023). Oxygen Vacancy Boosts the V2O5 Performance for the Electrochemical H2O2 Product. Industrial & Engineering Chemistry Research, 62(15), 6113-6120.
6. Ghandi K. 2014. A review of ionic liquids, their limits and applications. Green and sustainable chemistry, 2014.
7. Amaral L, Minkiewic J, Šljukić B, Santos DM, Sequeira CA, Vraneš M and Gadžurić S. 2018. Toward tailoring of electrolyte additives for efficient alkaline water electrolysis: salicylate-based ionic liquids. ACS Applied Energy Materials 1(9): 4731-4742.
8. Salleh NA, Kheawhom S and Mohamad AA. 2021. Chitosan as biopolymer binder for graphene in supercapacitor electrode. Results in Physics 25: 104244.
9. Zdolšek N, Vujković M, Metin Ö, Brković S, Jocić A, Dimitrijević A, Trtić-Petrović T and Šljukić B. 2022. Boosting electrocatalysis of oxygen reduction and evolution reactions with cost-effective cobalt and nitrogen-doped carbons prepared by simple carbonization of ionic liquids. International Journal of Hydrogen Energy 47(33): 14847-14858.

SYNTHESIS, CHARACTERIZATION OF MOFS, AND EVALUATION AS ADSORBENTS IN HYDROGEN PURIFICATION

[1]Zeynep BİLGİN, [1]Damla DUMLU,[1]*Nezihe AYAS,
[1]Eskişehir Technical University, Engineering Faculty, Chemical Engineering, İki Eylül Campus, Eskişehir, 26555, Türkiye

*Corresponding author e-mail: nazcan@eskisehir.edu.tr

ABSTRACT

With the advancement of industry and technology, addressing and solving the increasing energy demand has become one of the most critical challenges for humanity. To meet this demand, current chemical process technologies have shifted their focus toward hydrogen-based energy systems where hydrogen serves as an energy carrier, transferring energy from various sources to practical applications. This study involves the synthesis of metal-organic frameworks (MOFs) to be used as adsorbents for hydrogen purification applications. Among the thousands of MOF varieties, MOF-74 was selected for this project due to its high surface area, pore volume, and thermal stability. MOF-74 was synthesized in various forms by modifying temperature and duration parameters using the solvothermal method, followed by purification processes. Characterization was conducted using XRD, FT-IR, and SEM analyses. The results from XRD and SEM analyses confirmed the formation of the Zn-MOF-74 structure. Furthermore, the carbondioxide (CO_2) adsorption capacities of the MOFs were examined, with the highest CO_2 adsorption capacity observed at 120°C.

Keywords: MOF, Solvothermal Method, Adsorption

1. INTRODUCTION

The increasing industrialization and technological advancements have made the rising energy demand a significant issue. To address this demand and reduce greenhouse gas emissions, chemical process technologies have shifted their focus towards hydrogen energy. Despite being the most abundant element in the universe, hydrogen gas is produced from hydrogen-containing raw materials such as hydrocarbons, biomass, and water. For industrial applications, hydrogen needs to be purified. This purification process eliminates impurities such as carbon dioxide in hydrogen gas, enabling the production of high-purity hydrogen required for applications like fuel cells [1,2].

Commercial hydrogen purification methods include pressure swing adsorption (PSA) [1,2]. Traditional adsorbents include organic materials like activated carbon and inorganic materials like zeolites. While activated carbon exhibits high adsorption capacity, it has an irregular structure. On the other hand, zeolites have a regular structure but are limited in terms of stability and diversity [3,4]. Metal-organic frameworks (MOFs) are emerging porous materials composed of metal ions or metal clusters coordinated with organic linkers. MOFs stand out for their applications in adsorption, catalysis, sensing, drug delivery, and renewable energy. They offer advantages such as high surface area, tunable porosity, good selectivity, chemical stability, and flexible structures, allowing performance customization. These materials have significant potential in adsorption processes [4,5].

In this study, Zn-MOF-74 was synthesised by the solvothermal method at different temperatures (100, 110 and 120 °C) to investigate the effect of synthesis temperture and characterized with XRD, FTIR and SEM. CO_2 adsorption tests were carried out at 25 °C in a fixed bed reactor to determine the CO_2 adsorption capacity.

2. MATERIALS AND METHODS

2.1. Synthesis MOF-74

In this study, the synthesis process was carried out using the solvothermal method. 1.065 g of zinc nitrate hexahydrate (Carlo Erba Regents) and 0.234 g of 2,5-dihydroxyterephthalic acid (Abcr, 97%) were dissolved in 22.5 ml of dimethylformamide (DMF, Carlo Erba Regents, 99.9%). The mixture was subjected to sonication for 30 minutes. The mixture was then placed in a Teflon-lined autoclave reactor and heated in an oven for 24 hours. The obtained sample was washed with DMF and methanol (Sigma Aldrich, 99.7%) using vacuum filtration. Afterward, the sample was washed twice with methanol by centrifuging at 6000 rpm for 45 minutes at 24-hour intervals. Following the washing steps, it was dried in an oven at 105°C for 24 hours. Synthesized MOF labeld as Zn-T-24 where T represents the synthesis temperature.

2.2. Characterization

X-ray diffraction (XRD) analysis of the crystal structure was performed using a Rigaku XRD MiniFlex 600 device operating with Cu-Kα, at a scanning angle of 0.02°, a scan rate of 4°/min, and in the 2θ range of 5°–45°. The Fourier Transform

Infrared Spectroscopy (FTIR) analysis was conducted using a Thermo Scientific Nicolet IS10 FTIR in the scanning range of 525–4000 cm^{-1}, with a scanning speed of 64 and a resolution of 4 cm^{-1}. Surface morphology was analyzed using a ZEISS-SUPRA 50 VP scanning electron microscope (SEM). Energy Dispersive X-ray Spectroscopy (EDS) analysis was carried out to determine the elemental composition of Zn-MOF-74.

2.3. Carbon Dioxide Adsorption

The adsorption process was conducted using a stainless-steel tubular continuous-flow reactor with a length of 45 cm, an inner diameter of 0.8 mm, and an outer diameter of 1.2 mm. Zn-MOF-74 was fixed in place with two layers of glass wool, forming a fixed bed. For activity studies conducted using the continuous-flow tubular reactor, pure carbon dioxide was used at a flow rate of 0.2 L/min for 40 minutes per experiment. Before each experiment, Zn-MOF-74 was activated in an oven at 100°C for 1 hour. The adsorption capacity of the adsorbent can be calculated using the following equation:

$$CO_2\ Adsorption\ capacity\ \left(\frac{mmol}{g}\right) = \left(\frac{W_{before\ CO_2\ adsorption} - W_{after\ CO_2\ adsroption}}{W_{adsorbent}\ x\ MW_{CO_2}}\right) x\ 1000 \quad (1)$$

3. RESULTS AND DISCUSSION

Experiments were conducted at three different temperatures, maintaining a constant synthesis duration of 24 hours. SEM images of the synthesized structures are presented in Fig. 1. (a) synthesis at 100°C, (b) 110°C, and (c) to 120°C. Examination of the SEM images revealed that, although the Zn-MOF-74 structure formed at 100°C and 110°C, the temperatures were below the appropriate synthesis temperature, leading to the presence of structures that had not yet fully formed. In contrast, the morphological structure observed in the SEM images of Fig. 1., corresponding to synthesis at 120°C, aligns with the Zn-MOF-74 structure reported in the literature**.**

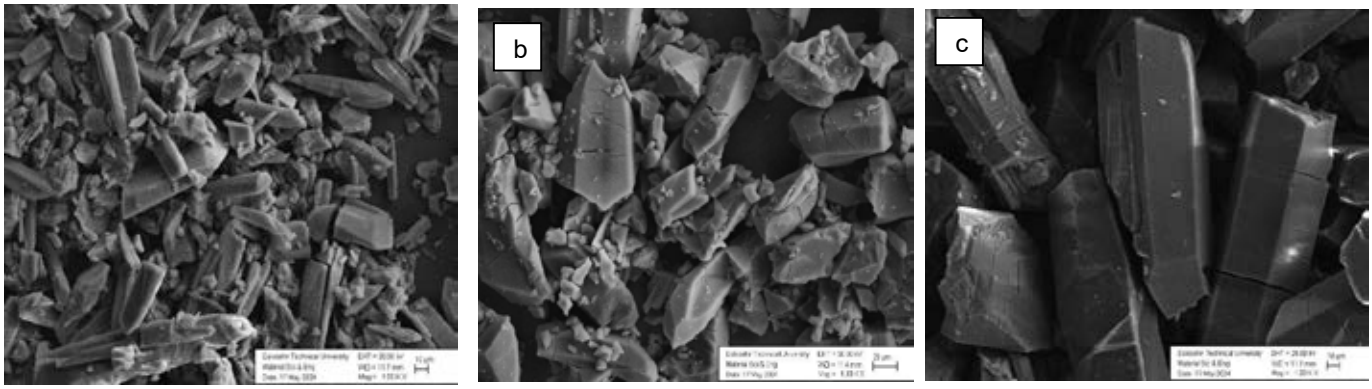

Fig. 1. SEM images for MOF-74 synthesized at different temperature, (a) 100°C (b) 110°C (c) 120°C

FTIR spectras of synthesized MOFs are given on Fig. 2. Examination of these spectra reveals that the region between 3000 cm^{-1} and 3500 cm^{-1} corresponds to the stretching and vibration region of RNH_2 groups. The peak observed around 1500 cm^{-1} corresponds to the stretching and vibration of CH_2 groups. These spectra indicate that DMF has not been completely removed.

Fig. 3. presents the XRD patterns of three different syntheses of Zn-MOF-74 conducted at 120°C, 110°C, and 100°C, each with a synthesis duration of 24 hours. Peaks marked with a ★ symbol indicate the presence of Zn-MOF-74. The small peaks observed in the Zn-120-24 pattern confirm the existence of MOFs. These peaks are not observed in the Zn-100-24 and Zn-110-24 patterns. The synthesis conducted at 120°C yielded a pattern most consistent with the literature.

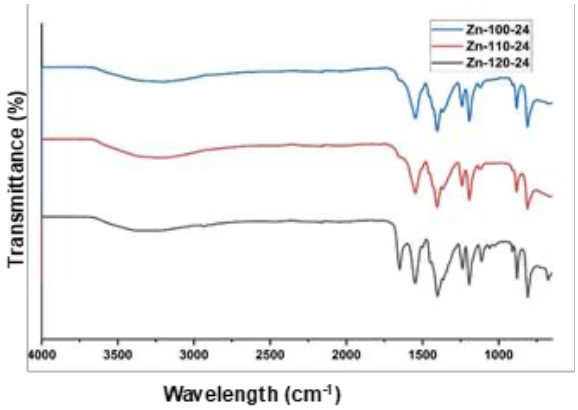

Fig. 2. FTIR spectras of MOF-74

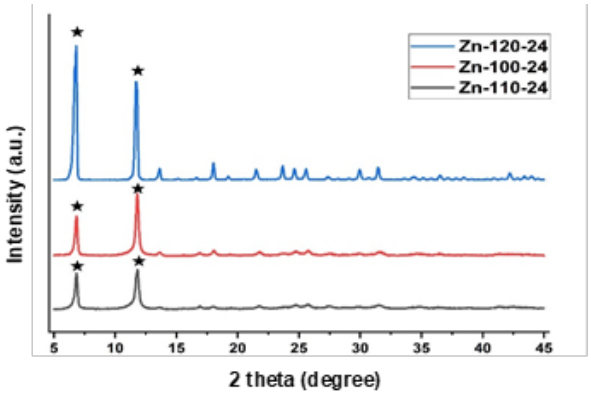

Fig. 3. XRD patterns of MOF-74

CO_2 adsorption capacities of Zn-MOF-74 structures with synthesized different temperatures were determined. The calculated values are presented in Table 1. As a result of incremental temperature increases of 10°C, it was found that the adsorption capacity increased by 0.19 mmol/g when the synthesis temperature was raised from 100°C to 110°C, and by 0.81 mmol/g when comparing 110°C to 120°C. The highest CO_2 adsorption capacity obtained with Zn-120-24 as 2.33 mmol/g and these result inlined with literature data [5,6]

Table 1. The adsorption capacities of Zn-MOF-74 synthesized at different temperatures for 24 hours

Synthesis Temperature (°C)	CO_2 adsorption capacities (mmol/g)
100	1.33
110	1.52
120	2.33

4. CONCLUSIONS

In this study, the effect of synthesis temperature on the structural and adsorption properties of Zn-MOF-74 was systematically investigated. Three different temperatures (100°C, 110°C, and 120°C) were evaluated while maintaining a constant synthesis duration of 24 hours. SEM analysis revealed that although the Zn-MOF-74 structure began to form at 100°C and 110°C, the structures were not fully developed at these temperatures. In contrast, the morphology observed at 120°C corresponded well with the Zn-MOF-74 structure reported in the literature, indicating optimal synthesis conditions. XRD analysis indicated that the characteristic peaks of Zn-MOF-74 were more clearly observed at 120°C, aligning well with literature data. In comparison, smaller and less distinct peaks were observed at 100°C and 110°C. CO_2 adsorption measurements highlighted the effect of synthesis temperature on adsorption capacity. At 120°C, the maximum adsorption capacity was determined to be 2.33 mmol/g. As observed in other characterizations, the highest

CO_2 adsorption capacity was also achieved at 120°C. In future studies, Brunauer-Emmett-Teller (BET) analysis will be conducted to further investigate the surface area and porosity characteristics of the material.

ACKNOWLEDGEMENT

This study is supported by the TUBITAK 2209-B research projects support program for university students aimed at industry (project no: 1139B412302017) and the scientific research projects commission of Eskişehir Technical University (project no: 24LÖP073).

REFERENCES

[1] Mao, D., Griffin, J. M., Dawson, R., Fairhurst, A., & Bimbo, N. (2021). Metal organic frameworks for hydrogen purification. International Journal of Hydrogen Energy, 46(45), 23380-23405.
[2] Saha, D., Wei, Z., & Deng, S. (2009). Hydrogen adsorption equilibrium and kinetics in metal–organic framework (MOF-5) synthesized with DEF approach. Separation and Purification Technology, 64(3), 280-287.
[3] Yay, B., & Gizli, N. (2019). A review on silica aerogels for CO2 capture applications. Pamukkale
[4] Rouquerol, J., Rouquerol, F., Llewellyn, P., Maurin, G., & Sing, K. S. W. (2013). *Adsorption by Powders and Porous Solids: Principles, Methodology, and Applications* (2nd ed.). Academic Press.
[5] Ma, S., Min, J., Yang, C., Liao, C., Zhu, Y., Zhao, X., ... & Shih, K. (2024). Developing a low-carbon, scalable strategy for the conversion of spent batteries into metal-organic framework-74 for CO2 capture. *Resources, Conservation and Recycling*, *209*, 107707.
[6] Zhu, W., Wang, L., Liang, W., Guo, R., & Li, Z. (2024). Bimetallic MOF-74-based mixed matrix membrane for efficient CO2 separation. *Microporous and Mesoporous Materials*, *379*, 113288.

PERFORMANCE ANALYSIS OF STAND-ALONE SOLAR SYSTEMS IN COASTAL ENVIRONMENTS: A CASE STUDY

[1*]*Mohammed Gmal Osman*, [1]*Gheorghe Lazaroiu*, [1]*Cristian-Valentin Strejoiu*, [1]*Cornel Panait,* [2]*Dorel Stoica*
University MARITIMA of Constanta, Strada Mircea cel Batran, 104, 900663, Constanta, Romania
[2] POLITEHNICA Bucharest, Faculty of Mechanical and Mechatronics Engineering

*Corresponding author's e-mail: mohagamal123@gmail.com,

ABSTRACT
This paper provides a detailed analysis of a stand-alone photovoltaic (PV) system implemented in Constanta, Romania, designed to deliver sustainable energy for residential use. Utilizing PVsyst software, the system's design and performance were evaluated over one year. The system comprises a 5.75 kWp PV array, 48 lead-acid batteries (12V, 1200 Ah total), and an MPPT-equipped inverter. The simulation results show an annual energy production of 8.13 MWh and a specific yield of 1414 kWh/kWp/year. Key performance metrics include a performance ratio (PR) of 40.71% and a solar fraction (SF) of 98.46%, indicating a high level of solar energy utilization.
The study highlights that significant energy losses are attributed to storage inefficiencies and environmental factors. Economic analysis demonstrates the potential for long-term cost savings and energy independence, despite high initial investment costs. Findings suggest that optimizing storage capacity and reducing system losses are critical to enhancing overall efficiency and reliability.
This research contributes to the understanding of deploying solar technologies in high-insolation regions and underscores the need for customized energy solutions tailored to regional characteristics. Future work will focus on integrating advanced storage technologies and intelligent energy management systems to maximize performance and economic benefits. The results provide valuable insights for policymakers and stakeholders aiming to advance renewable energy adoption and reduce reliance on conventional power sources in similar geographic settings.

Keywords: Stand-alone photovoltaic system, Solar energy, Renewable energy, Energy storage, Performance ratio.

1. INTRODUCTION

The global demand for sustainable and renewable energy solutions has been on a significant rise, driven by the urgent need to mitigate climate change, reduce greenhouse gas emissions, and enhance energy security. Among the various renewable energy sources, solar power stands out as a particularly attractive option due to its abundance, sustainability, and decreasing cost of technology [1]. The sun provides an inexhaustible source of energy, making solar power a critical component in the transition towards greener energy systems. As countries worldwide strive to reduce their carbon footprints, the deployment of solar photovoltaic (PV) systems has become increasingly widespread [2].
In this context, regions with substantial sunlight exposure are ideally positioned to harness solar energy efficiently. Constanta, a city located on the Black Sea coast in Romania, is one such region that benefits from a high solar irradiance, making it an excellent location for implementing solar power systems [3]. This geographic advantage provides a unique opportunity to explore the effectiveness and viability of stand-alone solar power systems in meeting local energy demands.
This study focuses on evaluating the performance of a stand-alone solar power system installed in Constanta to cater to the energy needs of a residential setup. By examining key metrics such as system performance, energy savings, cost-effectiveness, and reliability, this research aims to provide comprehensive insights into the operational viability of solar installations in similar geographic locations. The findings from this study not only contribute to the understanding of solar energy's potential in residential applications but also offer valuable data for future projects aiming to optimize the integration of solar technologies in urban and semi-urban environments [4].
Furthermore, the study addresses the technical challenges and economic considerations associated with stand-alone solar systems, including storage solutions, load management, and system sizing. Understanding these factors is crucial for developing efficient solar installations that can operate independently of the grid while maximizing energy output and minimizing costs. As the world moves towards a more sustainable energy future, the results of this study could play a vital role in shaping energy policies and investment strategies in solar technologies for regions with similar solar potential to Constanta [5].

2. SYSTEM CONFIGURATION

The stand-alone solar system in Constanta was designed with the following specifications: Location: Constanta, Romania (Latitude 44.22° N, Longitude 28.63° E, Altitude 5 m). PV Array: Consists of 23 PV modules, model 8.250MSGB, with a total nominal power of 5.75 kWp. The modules are mounted with a tilt of 30° and azimuth of 0° to optimize solar exposure. Battery Storage: Comprises 48 units of lead-acid batteries (12V, 100 Ah each) configured to provide a total storage capacity of 48 V / 1200 Ah. Controller and Converter: Utilizes a Universal controller with MPPT (Maximum Power Point Tracking) technology, ensuring high conversion efficiencies (97% maximum and 95% European

efficiency). Fig. 1. Illustrates the flow of energy in a PV system, showing the connections between the PV array, backup generator, batteries, and the user load, with a regulator managing the energy distribution and battery charging/discharging processes.

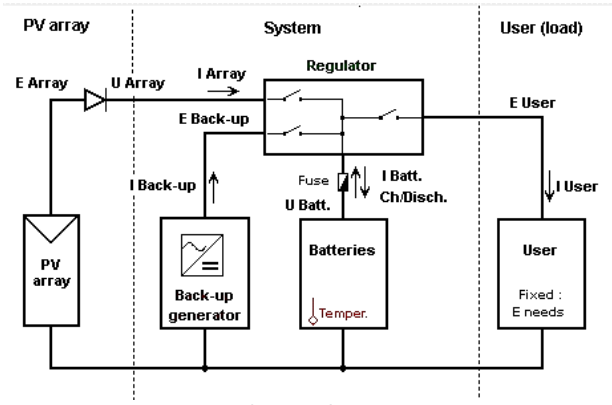

Fig. 1. Overall System Diagram

3. SIMULATION PARAMETERS AND METHODS

The PVsyst software was used to simulate the system's performance over a year, accounting for local meteorological data and specific load requirements. Key parameters such as global horizontal irradiation, module temperature, and load profiles were integrated into the simulation to derive accurate energy production and consumption metrics [6].

Table 1. presents monthly data on global and diffuse irradiance, temperature, and wind velocity, showing seasonal variations with peak solar irradiance and temperatures in the summer months, while wind velocity remains relatively consistent throughout the year [7].

Table 1. Metrological data

Month	Global Irradiance (kWh/m²/month)	Diffuse Irradiance (kWh/m²/month)	Temperature (°C)
January	43.2	19.3	-1.0
February	69.6	35.1	1.5
March	110.0	51.3	6.7
April	142.5	58.1	11.8
May	181.5	75.2	17.9
June	195.9	81.8	21.8
July	203.8	82.7	23.7
August	178.3	69.4	23.1
September	125.1	57.2	17.1
October	85.0	37.5	11.9
November	45.9	24.9	5.6
December	34.7	20.1	0.4
Year	**1415.5**	**610.6**	**11.7**

Table 2. Summarizes household energy consumption by detailing the power usage, daily operational hours, and daily energy consumption of various appliances, including lighting, electronics, domestic appliances, refrigeration, washers, ventilation, and standby devices.

Table 2. House hold load

Appliance	Power (W)	Daily Use (h/day)	Daily Energy (Wh/day)	Notes
Lamps (LED)	10	6.0	600	10 lamps using 10W each, used for 6 hours daily.
TV / PC / Mobile	100	6.0	1200	2 devices using 100W each, used for 6 hours daily.
Domestic appliances	500	6.0	3000	1 appliance using 500W, used for 6 hours daily.
Fridge / Deep-freeze	0.80	24.0	1598	2 units using 0.80 kWh daily, continuously running.
Dish & Cloth-washers	1000	2.0	2000	1 unit using 1000W, used for 2 hours daily.
Ventilation	1000	24.0	2400	1 unit using 1000W, continuously running.
Stand-by consumers	6	24.0	144	Standby consumption, continuous use.

4. RESULTS AND DISCUSSIONS

Fig. 2. Shows the relationship between the installed PV power and the probability of loss of load (PLOL) for different battery capacities, illustrating how increased battery capacity reduces the required PV power to achieve a specific PLOL. Fig. 3. Shows the average daily state of charge (SOC) of a battery throughout the year, indicating higher charge levels from January to October and significantly lower levels from November to December.

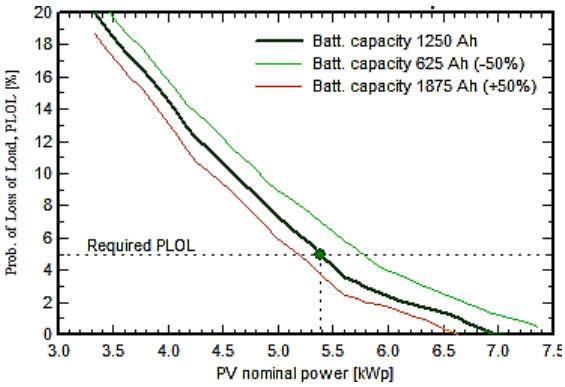

Fig. 2. PLOL as function of the installed PV

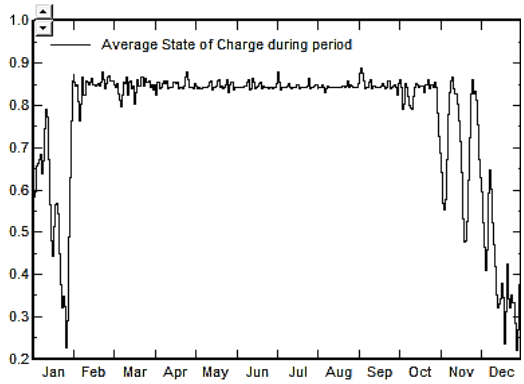

Fig. 3. State of charge daily Distribution

Fig. 4 shows the distribution of effective power output from a solar array throughout the year, with most frequent outputs occurring between 1.5 and 4 kW. Fig. 5. Shows the daily array output energy over the year, indicating fluctuations in effective energy production from the solar array with varying daily outputs.

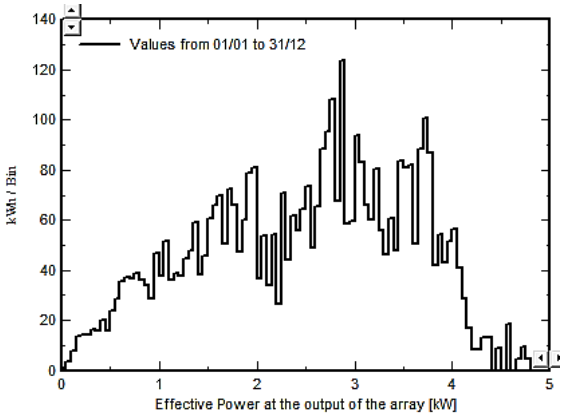

Fig. 4. Array power distribution

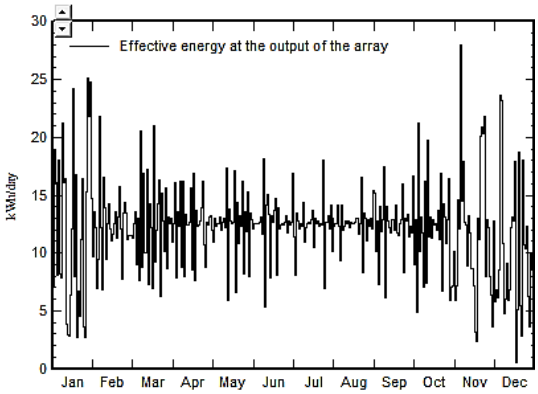

Fig. 5. Daily output energy

Fig. 6. Compares the Performance Ratio (PR) and Solar Fraction (SF) for each month of the year, showing variations in solar energy system efficiency and the proportion of energy load met by solar power. Fig. 7. Illustrates the normalized production and loss factors for a 5.75 kWp solar system across each month, highlighting the distribution of unused energy, collection losses, system losses, and energy supplied to the user.

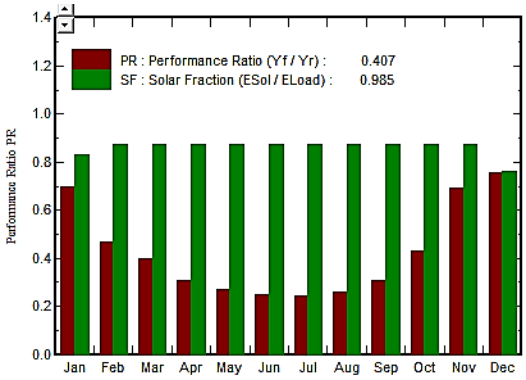

Fig. 6. Performance Ratio and solar fraction

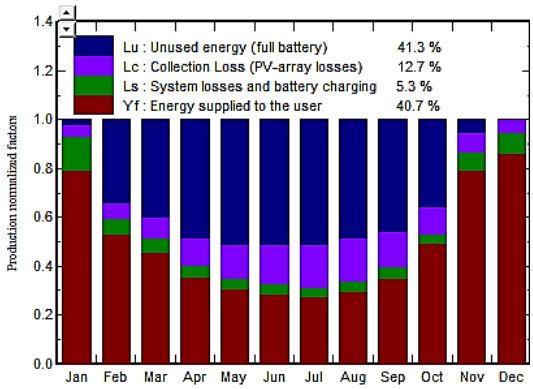

Fig. 7. Normalized production and loss factors

Fig. 8. Displays the normalized daily energy production per installed kWp for a 5.75 kWp solar system, breaking down the energy supplied to the user, unused energy, collection losses, and system losses throughout the year. Fig. 9. Shows the reference incident energy on the collector plane for each month, with the highest energy levels observed in the summer months, peaking in July. The system's performance was evaluated based on several key metrics: Energy Production: The system produced an annual available energy of 8.13 MWh, with a specific production rate of 1414 kWh/kWp/year. Energy Usage and Losses: Of the total energy produced, 3.93 MWh was used to meet the household's energy needs, while 3.99 MWh remained unused due to battery storage limitations. The performance ratio (PR) was calculated at 40.71%, and the solar fraction (SF) was 98.46%, indicating a high level of solar energy utilization.

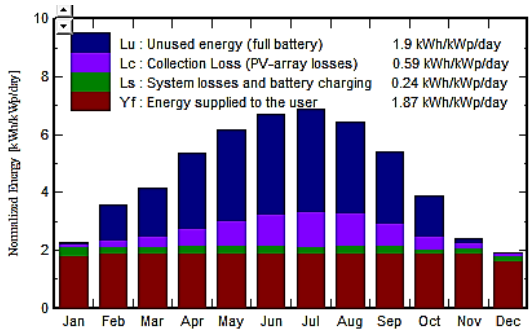

Fig. 8. Normalized productions

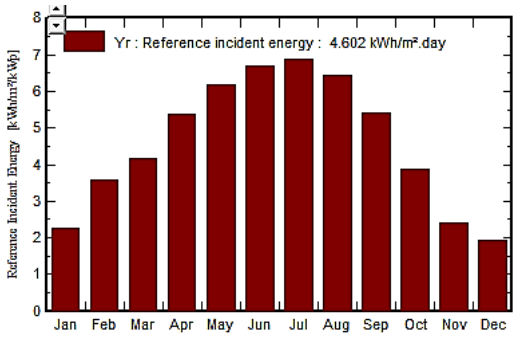

Fig. 9. Reference incident energy

System Losses: Major losses were attributed to unused energy due to full battery conditions (47.3%), followed by PV losses due to irradiance levels (0.7%), temperature effects (6.8%), and wiring losses (2.5%). The results indicate that the stand-alone solar system is capable of meeting the energy demands of a residential setup in Constanta, with minimal reliance on external power sources. However, the high percentage of unused energy suggests the need for optimizing battery capacity or incorporating additional energy storage solutions. The performance ratio indicates potential areas for improvement, such as reducing wiring losses and enhancing battery efficiency.

6. CONCLUSIONS

This study has demonstrated the potential and effectiveness of a stand-alone solar power system in Constanta, Romania, highlighting its viability as a sustainable energy solution for residential setups. The findings reveal that such systems can significantly contribute to meeting energy demands while providing substantial cost savings over time. With Constanta's favorable geographic conditions and high solar irradiance, the solar installation achieved impressive performance metrics, underscoring the region's suitability for solar energy adoption.

The research also underscores the importance of optimizing solar technology integration, particularly in regions with high solar potential. The study's insights into energy savings, system reliability, and cost-effectiveness provide valuable information for stakeholders, including policymakers, investors, and homeowners, interested in transitioning to renewable energy sources. Additionally, the consideration of technical challenges, such as storage solutions and load management, emphasizes the need for a comprehensive approach to the design and implementation of solar power systems.

The successful deployment and performance of the stand-alone solar power system in Constanta confirm the economic and environmental benefits of solar energy in similar geographic contexts. As the world seeks sustainable alternatives to traditional energy sources, this research contributes to the growing body of evidence supporting the adoption of solar power as a key component of future energy strategies.

ACKNOWLEDGEMENT

This work was supported by a grant of the Ministry of Research, Innovation and Digital ization, project number PNRR-C9-I8-760089/23.05.2023, COD CF31/14.11.2022, and PNRR-C9-I8 760111/23.05.2023, code CF 48/14.11.2022.

REFERENCES

1. M. G. Osman, D. -A. Ciupagenau, G. Lazaroiu and I. Pisa, "Increasing Renewable Energy Participation in Sudan," 2022 11th International Conference on Renewable Energy Research and Application (ICRERA), Istanbul, Turkey, 2022, pp. 169-173,
2. Akkaya, R. and Kulaksiz, A.A., 2004. A microcontroller-based stand-alone photovoltaic power system for residential appliances. Applied Energy, 78(4), pp.419-431.
3. Osman, M.G., Strejoiu, C.V., Panait, C., Lazaroiu, G. and Lazaroiu, A.C., 2023. Renewable energy integration, climate analysis, and efficiency optimization for greener transportation-case study in dobrogea. International Multidisciplinary Scientific GeoConference: SGEM, 23(6.2), pp.675-687.

4. Fragaki, A. and Markvart, T., 2008. Stand-alone PV system design: results using a new sizing approach. Renewable Energy, 33(1), pp.162-167.
5. Iqbal, A. and Iqbal, M.T., 2019. Design and Analysis of a Stand‐Alone PV System for a Rural House in Pakistan. International Journal of Photoenergy, 2019(1), p.4967148.
6. Ingale, G.B., Padhee, S. and Pati, U.C., 2016, April. Design of stand-alone PV system for DC-micro grid. In 2016 International Conference on Energy Efficient Technologies for Sustainability (ICEETS) (pp. 775-780). IEEE.
7. Dorel S, Gmal Osman M, Strejoiu C-V, Lazaroiu G. Exploring Optimal Charging Strategies for Off-Grid Solar Photovoltaic Systems: A Comparative Study on Battery Storage Techniques. Batteries. 2023; 9(9):470.
8. M. G. Osman, C. -V. Strejoiu, C. Panait, A. C. Lazaroiu and G. Lazaroiu, "Microgrid Model for Evaluating the Operational Dynamics of Solar-Powered Hydrogen Production," 2024 9th International Conference on Energy Efficiency and Agricultural Engineering (EE&AE), Ruse, Bulgaria, 2024, pp. 1-6,

INCREASING THE ENERGY EFFICIENCY AND ECONOMIC VIABILITY OF A PHOTOVOLTAIC PARK IN CRAIOVA

[1]*Gheorghe Lazaroiu*, [1*]*Cristian-Valentin Strejoiu*, [1]*Mohammed Gmal Osman*, [1] *Cornel Panait*, [2*]*Dorel Stoica*
[1]University MARITIMA of Constanta, Strada Mircea cel Batran, 104, 900663, Constanta, Romania
2 POLITEHNICA Bucharest, Faculty of Mechanical and Mechatronics Engineering

*Corresponding author e-mail: dorel.stoica@upb.ro

ABSTRACT
This paper provides an efficient generation of electricity from solar energy, which is crucial in the global transition to renewable sources. A key factor in this process is the optimal positioning of photovoltaic (PV) panels, which capture sunlight and convert it into electrical power. Two primary geometric parameters—tilt (inclination) and azimuth angles—significantly influence conversion efficiency.
This study analyzes the photovoltaic park in Craiova to evaluate how these geometric factors impact energy efficiency. The inclination angle determines the panel's tilt relative to the horizontal plane and is essential for maximizing energy capture throughout the year. Similarly, the azimuth angle, which defines orientation along the north-south axis, plays a vital role in maintaining consistent sunlight exposure and ensuring reliable electricity generation.
Craiova's unique climatic conditions, with seasonal variations and cloudy periods, highlight the need for optimal panel alignment. This study assesses the park's current configurations against optimal theoretical values to provide recommendations for improved efficiency. The zenith angle, which measures the sun's position relative to the vertical, is also introduced to further refine energy capture strategies.
The PVsyst application is used to simulate and analyze various tilt and azimuth scenarios, evaluating their impact on energy output and economic viability. It also includes financial analysis features to estimate amortization costs, considering initial capital expenditures, operational expenses, and projected revenue from energy production. Additionally, integrating a hydrogen system enables surplus solar energy to be converted into green hydrogen, enhancing economic value. This analysis helps determine the payback period and overall return on investment, offering key insights into the feasibility of different configurations.

Keywords: photovoltaic system, solar power, tilt angle, PVsyst, hydrogen system, green hydrogen, optimization.

1. INTRODUCTION

Solar energy plays a crucial role in sustainable electricity generation, with solar cells offering a pollution-free solution. Technological advances have improved efficiency and reduced costs, making photovoltaic (PV) systems more accessible and vital to the transition to renewable energy.
Craiova, with its favorable climate, flat terrain, and extensive agricultural land, presents significant opportunities for solar energy deployment. The region benefits from abundant sunlight, enabling high energy output and offering dual land use for both solar installations and agriculture. This integration can boost productivity and economic gains for local farmers. The availability of large tracts of unused land provides the flexibility to install large-scale solar farms without disrupting existing agricultural activities. Additionally, the region's proximity to infrastructure, such as roads and power distribution networks, facilitates the efficient transmission of generated electricity to the grid [1].
Despite the vast potential of solar energy, it remains underutilized. Strategic planning and optimization of PV systems are essential to fully harness this resource and reduce dependence on fossil fuels. In Craiova, factors such as geographic positioning, climate variations, and system design influence PV efficiency. Seasonal variations in solar radiation levels require adaptive system configurations to ensure consistent performance year-round. Proper installation and maintenance are critical to achieving optimal performance. Regular inspections and cleaning schedules can help maintain panel efficiency by preventing dust accumulation and shading effects, which can reduce energy output [2].
A thorough analysis of PV system configurations, including azimuth and inclination angles, is necessary to maximize energy capture and conversion. The azimuth angle, which determines the orientation of the panels relative to the sun's position, plays a crucial role in maintaining consistent energy generation throughout the day. Similarly, the inclination angle, which sets the tilt of the panels, is essential for optimizing the amount of solar radiation absorbed. Adjusting these angles based on seasonal variations and latitude-specific conditions can significantly enhance energy production. Collaboration with experts ensures the effective implementation of sustainable energy solutions and promotes long-term energy security in Craiova. The energy from the photovoltaic park will be used for hydrogen production via electrolysis, converting water into green hydrogen for storage and various applications, improving energy flexibility and grid stability [3].
The economic viability of solar energy projects in Craiova is influenced by several factors, including initial investment costs, operational expenses, and the potential revenue generated from energy sales. Financial incentives such as government subsidies and tax credits can further improve the return on investment for solar projects. Additionally, partnerships with local stakeholders and investors can help secure the necessary funding to develop large-scale

installations [4].[5].

2. DETERMINING THE ORIENTATION AND TILT ANGLES OF PHOTOVOLTAIC PANELS

The efficiency of photovoltaic (PV) panels in converting solar energy into electricity is largely influenced by their positioning relative to the sun and Earth's surface. Two key factors affecting energy capture are the tilt angle, which determines the panel's inclination to the horizontal plane, and the azimuth angle, which defines orientation concerning the north-south axis.

A comprehensive approach combining mathematical and empirical methods is critical to optimizing energy capture and ensuring the economic viability of solar power systems. Fig. 1 illustrates these key angles and their relationship to the sun's position [7].

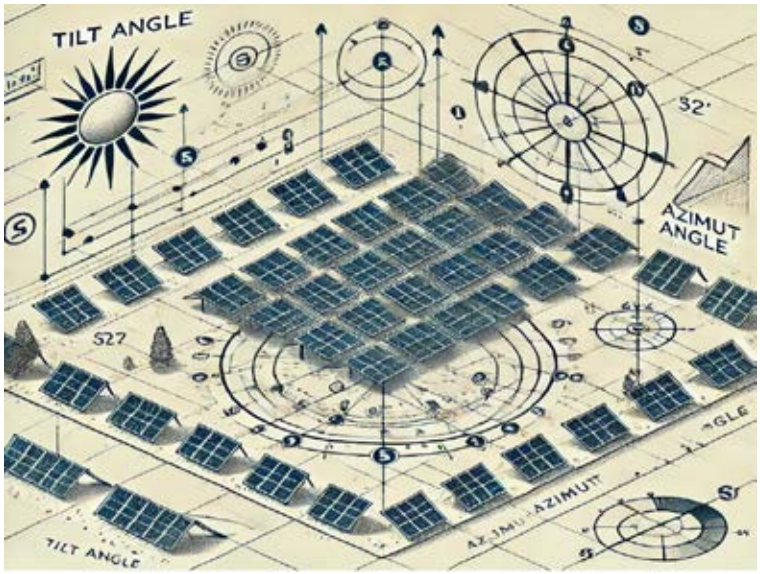

Fig. 1. Angle Diagram for Photovoltaic Panels

Fig. 1 shows the key angles for positioning photovoltaic panels to maximize solar energy capture. It illustrates the tilt angle, which is the panel's inclination to the horizontal plane, and the azimuth angle, which defines its orientation relative to the north-south axis. These angles are essential for optimizing solar exposure and energy efficiency.

3. SYSTEM CONFIGURATION

The photovoltaic park is located in the Craiova area, Olt County, Romania. This facility, with an installed capacity of approximately 3000 kWp, is relatively smaller compared to other solar power plants in the region. It is integrated into the local power grid via a 20 kV distribution line and occupies an area of approximately 12,000 square meters dedicated to photovoltaic panels.

The park comprises 5263 TSP-720-XYZ polycrystalline silicon photovoltaic modules, which are arranged into 10 parallel strings per inverter, with each string consisting of approximately 526 modules. These strings are connected to 10 SUN3000-400KTL-H2 inverters, which are securely mounted on a robust supporting structure.

The inverters enable connection to the national grid through a 0.4/20 kV transformer and an electricity meter, ensuring optimal power transmission efficiency. The entire photovoltaic installation is supported by a corrosion-resistant galvanized steel structure [8]. Surplus energy can be used in a hydrogen production system through electrolysis.

4. SIMULATION PARAMETERS AND METHODS

The simulation study will consider three different scenarios based on different tilt and azimuth angles of the system. In the first scenario, the system will be analyzed with a tilt angle of 30 degrees and an azimuth angle of 70 degrees. The second case will investigate the performance at a tilt angle of 70 degrees with the same azimuth angle. Finally, the third case will use optimized tilt and azimuth angles, specifically tailored for the selected location to maximize efficiency. Following the simulations, the results obtained will be analyzed in detail to assess the impact of these angle variations on the system performance [9].

In this simulation study, PVsyst software was used to determine the optimal tilt and azimuth angles for the photovoltaic system. The values obtained from PVsyst were subsequently verified using the PVGIS application to ensure accuracy. All collected data were then imported into MATLAB, where further calculations were performed to analyze the financial aspects of the project, specifically focusing on determining the investment payback period.

Table 1. Cases analyzed

Case 1:	Case 2:	Case 3: Optimized angles
Tilt angle: 30° Azimuth Angle: 70°	Tilt angle: 70° Azimuth Angle: 70°	Tilt angle: 36° Azimuth Angle: 2°

5. RESULTS AND DISCUTIONS

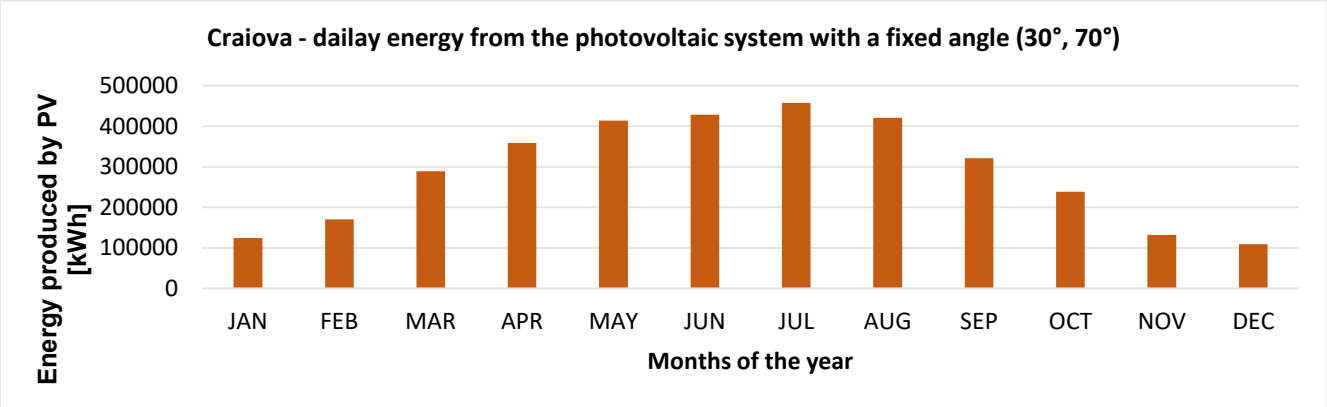

Fig. 2. Craiova - Lunar energy from the photovoltaic system with a fixed angle (30°, 70°)

Fig. 2 provides an overview of the total annual energy production of the system. The photovoltaic system, with an installed panel capacity of 3000 kWp, is capable of generating an annual energy production of 3463062.77 kWh. This production capacity is for the analyzed case 1 which highlights the efficiency of the system in harnessing solar energy to meet the energy demands over a year.

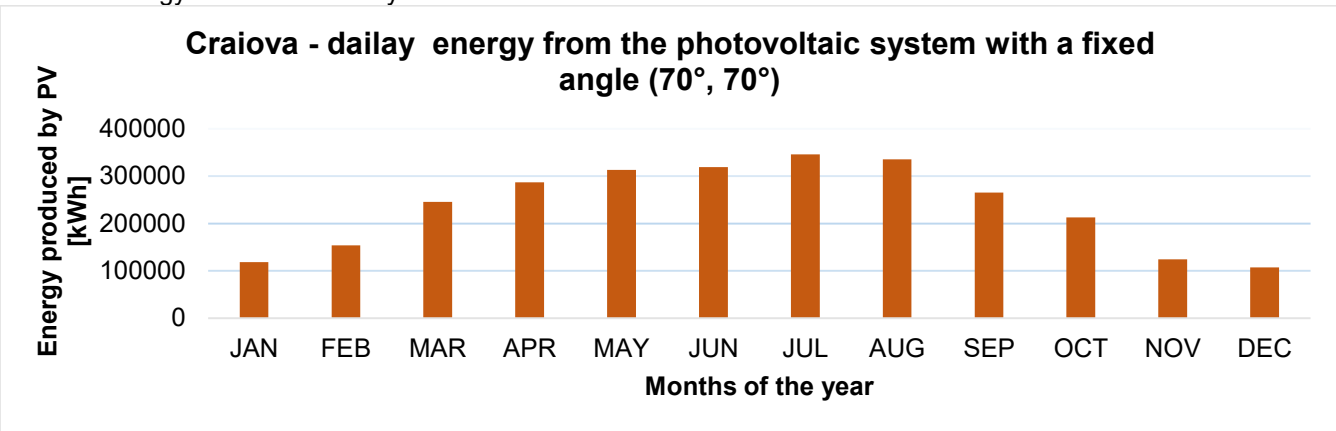

Fig. 3. Craiova - Lunar energy from the photovoltaic system with a fixed angle (70°, 70°)

Fig. 3 presents a summary of the system's total yearly energy output. With an installed panel capacity of 3000 kWp, the photovoltaic system is designed to produce approximately 2830477.79 kWh of energy annually.

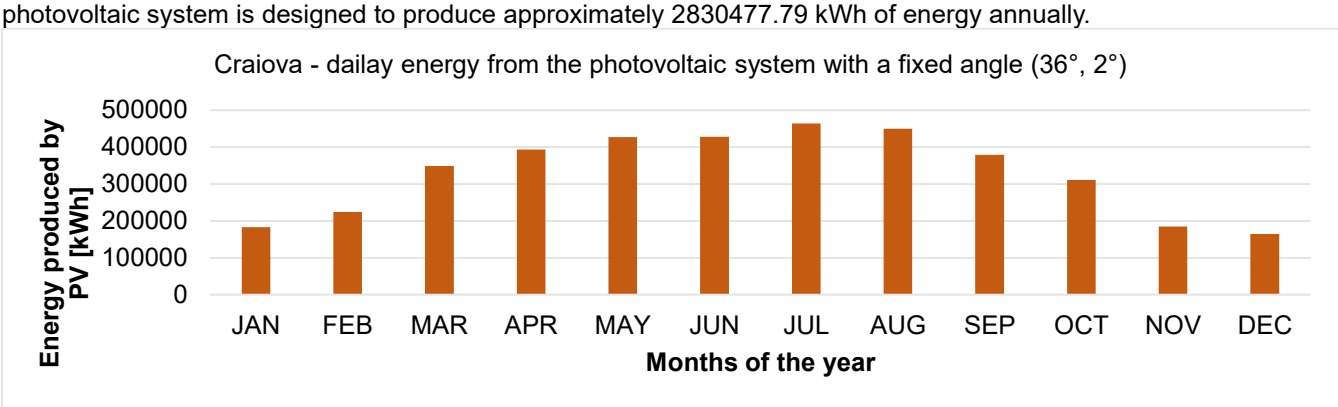

Fig. 4. Craiova - Lunar energy from the photovoltaic system with optimized angles (36°, 2°)

Fig. 4 presents an overview of the system's total annual energy production. The photovoltaic system, with an installed

capacity of 3000 kWp, is expected to generate around 3955381.39 kWh per year. This energy output corresponds to the conditions evaluated in case 3, which represents the optimal scenario, highlighting the system's effectiveness in utilizing solar energy to satisfy annual energy demands.

Table 2. Centralization of total annual energy

Analysis of Craiova:	Case 1: 30°, 70°	Case 2: 70°, 70°	Case 3: Optimized angles
Total annual energy produced [kWh]	3463062.77	2830477.79	3955381.39

Table 2 provides a detailed comparison of the energy production values for each analyzed case. A significant variation can be observed among the three scenarios. In the first case, the system generates 3,463,062.77 kWh annually, while in the second case, the energy production drops to 2,830,477.79 kWh. The third case, representing the optimal configuration, achieves the highest energy output of 3,955,381.39 kWh per year. These differences emphasize the impact of system orientation and optimization on overall performance.
Table 3 provides a summary of all the data obtained and calculated using MATLAB, including the total investment costs and the payback period for each analyzed case.

Table 3. Economic calculation

	Case 1: (30°, 70°)	Case 2: (70°, 70°)	Case 3: Optimized angles
The total power produced by the photovoltaic panels [kW]	3000	3000	3000
Total annual energy produced [kWh]	3463062.77	2830477.79	3955381.39
Total Cost [€]	3455000	3455000	3455000
Amount obtained for injection into the network	346300	283000	395500
Investment recovery:	10 years	12 years	9 years

In the optimized case, the investment payback period was the shortest compared to the other two scenarios, emphasizing the effectiveness of optimizing system parameters. This outcome highlights the importance of carefully selecting the tilt and azimuth angles to maximize energy production and financial returns. Additionally, integrating a hydrogen production system further enhances profitability by converting excess solar energy into green hydrogen, creating additional revenue streams and increasing energy flexibility. A shorter payback period makes the project more attractive to investors, ensuring a faster return on investment and greater long-term sustainability [10].

6. CONCLUSIONS

Optimizing the tilt and azimuth angles significantly enhances the photovoltaic system's performance by maximizing energy capture. The optimized configuration achieved the highest annual energy output, demonstrating the importance of site-specific adjustments for improved efficiency.
The financial analysis revealed that the optimized case resulted in the shortest investment payback period, making the project more economically attractive. Faster returns on investment highlight the benefits of proper system design in ensuring long-term profitability and sustainability. Additionally, integrating a hydrogen production system enhances economic viability by utilizing surplus solar energy to generate green hydrogen, creating new revenue streams and increasing energy resilience.
Optimized configurations significantly improved energy production, while non-optimized setups led to lower outputs and longer payback periods, highlighting the importance of accurate simulations for maximizing performance.
The optimized system enhances sustainability by maximizing solar energy use and reducing dependence on conventional power, supporting clean energy goals.

ACKNOWLEDGEMENT

This work was supported by a grant of the Ministry of Research, Innovation and Digitalization, project number PNRR-C9-I8-760089/23.05.2023, COD CF 31/14.11.2022, and PNRR-C9-I8-760111/23.05.2023, code CF 48/14.11.2022.

REFERENCES

[1] R. Xu, K. Ni, Y. Hu, J. Si, H. Wen, and D. Yu, “Analysis of the optimum tilt angle for a soiled PV panel,” Energy Convers Manag, vol. 148, pp. 100–109, 2017.
[2] C.-V. Strejoiu, M. G. Osman, D. STOICA, C. Panait, and L. Gheorghe, “Evaluation of Energy Distribution in a Photovoltaic Park

Located in Tulcea County, Romania," 2024.
[3] Y. S. Khoo et al., "Optimal orientation and tilt angle for maximizing in-plane solar irradiation for PV applications in Singapore," IEEE J Photovolt, vol. 4, no. 2, pp. 647–653, 2013.
[4] C.-V. Strejoiu, M. G. Osman, G. Lăzăroiu, D. Stoica, and C. Panait, "Efficiency Evaluation and Performance Analysis of a Photovoltaic Park Connected to a 20 kV Distribution Network in Galati County, Romania," in 2024 9th International Conference on Energy Efficiency and Agricultural Engineering (EE&AE), IEEE, 2024, pp. 1–5.
[5] S. Yadav, S. K. Panda, and C. Hachem-Vermette, "Optimum azimuth and inclination angle of BIPV panel owing to different factors influencing the shadow of adjacent building," Renew Energy, vol. 162, pp. 381–396, 2020.
[6] S. Dorel, M. Lucian, L. Gheorghe, and L. G. Cristian, "Green Hydrogen, a Solution for Replacing Fossil Fuels to Reduce CO2 Emissions," Processes, vol. 12, no. 8, p. 1651, 2024.
[7] A. Savin, O. Svensson, and M. Leijon, "Azimuth-inclination angles and snatch load on a tight mooring system," Ocean engineering, vol. 40, pp. 40–49, 2012.
[8] A. Z. Hafez, A. Soliman, K. A. El-Metwally, and I. M. Ismail, "Tilt and azimuth angles in solar energy applications–A review," Renewable and sustainable energy reviews, vol. 77, pp. 147–168, 2017.

SYNTHESIS OF Ru/C AND PtRu/C CATALYSTS BY MICROWAVE-ASSISTED POLYOL METHOD AT HIGH TEMPERATURE AND PRESSURE

[1]Serkan KARADENİZ, [1*]Nezihe AYAS
[1]Eskisehir Technical University, Faculty of Engineering, Department of Chemical Engineering, Eskisehir, 26555, TURKEY
*Corresponding author e-mail: nazcan@eskisehir.edu.tr

ABSTRACT
In search of sustainable solutions to the worldwide energy crisis, PEM fuel cells (PEMFCs) are attracting attention as an environmentally friendly energy production system. Within the scope of this study, an alternative microwave-assisted polyol method has been developed by modifying the polyol method for the synthesis of Ru/C and PtRu/C catalysts. This method allowed catalyst synthesis at high temperatures and pressures, without being constrained by the boiling point of the mixture typically used in polyol synthesis. Catalysts were synthesized at 200 °C. Characterization studies were carried out using XRD and SEM-EDS. The anode activity of the catalyst at different temperatures (60, 70 and 80 °C) was determined in a single-cell test system. PtRu/C catalyst synthesized at high temperatures demonstrated anode side activity of 171.2 mW/cm^2 @ 70 °C, which was comparable to commercial Pt/C.

Keywords: Fuel cell, PEM, Polyol, Microwave heating, PtRu

1. INTRODUCTION

The worldwide energy crisis has become increasingly important in recent years due to the demand for energy and the limitations of current energy production methods. The energy demand is primarily met by fossil fuels, such as coal, oil, and natural gas. However, concerns regarding the sustainability of these energy production methods have emerged due to the limited nature of these resources, their rapid depletion, and their negative environmental impacts. As a result, the focus is shifting towards renewable energy sources. Among renewable energy sources, hydrogen has emerged as a critical component. As the most abundant element in the universe, hydrogen is a clean and versatile energy carrier [1], [2]. Hydrogen can be produced using different methods and when produced using renewable energy sources, it is classified as a zero-emission fuel.

With respect to the utilization of hydrogen, there is an ever-increasing focus on fuel cells. In its most fundamental form, a fuel cell is an electrochemical system that directly converts the chemical energy of a fuel into electrical energy. Among the various types of fuel cells, PEM fuel cells are distinct in their capacity to directly utilize hydrogen, resulting in the production of water and heat as by-products through electrochemical reactions within the cell. The primary factor hindering the commercialization of these PEMFC is the high cost of the catalyst. Platinum (Pt) metal is the most commonly used electrocatalyst in PEMFC due to its stability and activity [3]. The main challenge of catalyst development lies in improving the cost-effectiveness of platinum. To address this challenge, various approaches have been adopted to enhance the utilization of Pt by addition of metals like Ru. One of these approaches involves reducing the particle size of the active metal and enhancing its dispersion on the support material.

Microwave-assisted polyol synthesis is an important method due to its simplicity and efficiency in controlling the synthesis of metal nanoparticles. This approach involves the reduction of metal ions to form colloids. The main advantages of this method is enhanced reaction kinetics, the formation of particles with uniform size distribution, the generation of new phases, and a significant reduction in energy consumption.

In this study, an alternative method that has already been developed for the synthesis of Pt/C [1] was adapted for synthesis of Ru/C and PtRu/C catalysts under pressure by microwave assisted polyol method. This study aims to fill the knowledge and method gap between synthesis at atmospheric pressure and synthesis under supercritical conditions. In this context, the synthesis of the catalysts was carried out under pressure, at a temperature of 200 °C, which is above the boiling point of the polyol mixture. The catalysts were characterized by X-Ray Diffraction (XRD) and Scanning Electron Microscopy-Energy Dispersive X-Ray Spectroscopy (SEM-EDS). Fuel cell tests were performed in a single-cell test station to determine the activity of the PtRu/C catalyst.

2. MATERIALS AND METHODS

Dihydrogen hexachloroplatinate(IV) hexahydrate (ACS, Premion™), Ruthenium(III) chloride trihydrate (Sigma-Aldrich) ethylene glycol (Sigma-Aldrich), sodium hydroxide (VWR Chemicals), hydrochloric acid, sulfuric acid, and isopropyl alcohol from Riedel-de Haën were used as received. Vulcan carbon (Cabot) was used as the carbon support and 20 wt% Nafion™ solution (Ion Power) was used in Membrane Electrode Assembly (MEA) preparation.

The Ru/C catalysts were synthesized by using the modified polyol method described in a previous study [1]. In summary, a Teflon reactor (HPR-1000/10S) and the Milestone Start S system was utilized. The reaction temperature was 200 °C, and the reaction was carried out for 35 minutes. To further improve the previously developed method, the synthesis of the PtRu/C catalyst was carried out in a single step, in which the synthesized metal nanoparticles are directly deposited on the carbon support.

For the characterization of the catalysts, XRD analysis was carried out using Rigaku XRD MiniFlex 600 (5°/min scanning

speed, step size of 0.02°, in the range of 5°<2θ<85°) and SEM-EDS analysis were carried out using Zeiss Supra 50 VP where prior to imaging, the samples were subjected to Au-Pd coating to ensure electron conductivity. Catalyst ink for the MEA was made by ultrasonically mixing calculated amounts of catalyst, Nafion solution, deionized water, and isopropyl alcohol for 1 hour. After that, the ink was spray coated onto the carbon paper via a spray gun. Cathode electrode was prepared by the same methodology, where the commercial 20% Pt/C was used as the catalyst. MEA was manufactured by hot pressing the electrodes and membrane at 130 °C, under 400 psi pressure for 3 minutes. To condition the cell (5 cm^2 active area) and stabilize its performance, the cell voltage was kept constant at 0.5 V and power is drawn from the cell with an electronic load until the change in power stabilized. The activity tests were carried out at 100% relative humidity at different cell temperatures of 60, 70, and 80 °C, using hydrogen feed rate of 0.25 L/min and dry air feed rate of 1.0 L/min.

3. RESULTS AND DISCUSSION

The crystal structure of Vulcan carbon support and the Pt and Ru metals in the catalysts are determined by XRD analysis, as illustrated in Figure 1.

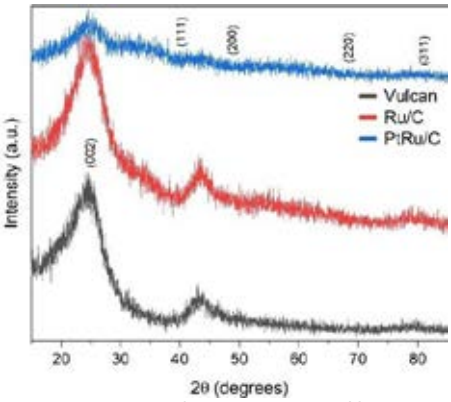

Fig. 1. XRD patterns of the Vulcan, Ru/C, and PtRu/C

The peak observed in the range of 15°<2θ<30° corresponds to the hexagonal structure of Vulcan carbon [4]. The Ru peak at about 43° corresponds to the (101) plane [5]. The diffraction peaks attributed to RuO_2 at 28.1° and 40.1° were not observed due to the extremely small size of the Ru [6]. In the diffraction patterns of all Ru/C catalysts, extremely broad peaks are observed [7], indicating that the crystallinity of Ru/C catalysts is very low. The absence of diffraction peaks at approximately 35° (101) and 55° (211) further confirms the amorphous structure. During the formation and growth of Ru nanoparticles, it has been reported that this process occurs selectively on the carbon support, with carbon support acting as the core center for the growth of Ru nanoparticles. The method used in this study successfully synthesizes Ru catalysts with small particle sizes and homogeneous distribution. For the PtRu/C catalyst, the barely visible peaks at approximately 46.5°, and 69.5° in the diffraction patterns represent diffractions of Pt-Ru alloy. The absence of diffractions from monometallic Pt, Ru, or RuO_2 compounds may serve as evidence that the metals in the catalyst PtRu/C mostly in the form of Pt-Ru alloy [8]. The mean crystallite size of Pt and Ru nanoparticles is expected to be less than 1.5 nanometers. However, due to the extreme peak broadening precise calculations were not possible.
The results obtained from the SEM-EDS analysis of the Ru/C and PtRu/C catalysts are presented in Figure 2.

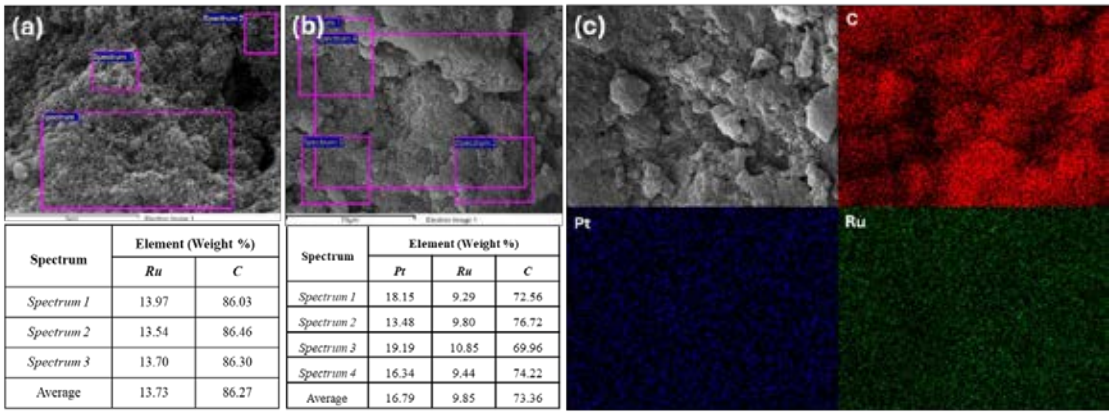

Spectrum	Element (Weight %)	
	Ru	*C*
Spectrum 1	13.97	86.03
Spectrum 2	13.54	86.46
Spectrum 3	13.70	86.30
Average	13.73	86.27

Spectrum	Element (Weight %)		
	Pt	*Ru*	*C*
Spectrum 1	18.15	9.29	72.56
Spectrum 2	13.48	9.80	76.72
Spectrum 3	19.19	10.85	69.96
Spectrum 4	16.34	9.44	74.22
Average	16.79	9.85	73.36

Fig. 2. SEM image and respective elemental composition for (a)Ru/C, (b)PtRu/C, and (c)EDS mapping of PtRu/C

As illustrated in Fig. 2(a), the characteristic structure of the carbon support remains unchanged during catalyst synthesis. Analysis of the SEM image shows that there is no Ru clustering, indicating that Ru metal is distributed homogeneously on the carbon support. The results obtained from different EDS regions are similar, further supporting that Ru metal is homogeneously distributed on the carbon support.
In Fig. 2(b), the weight percentages of Pt, Ru, C on the surface of the catalyst varies. On average, Pt's weight percentage is 16.8%, and Ru's weight percentage is 9.85%. Furthermore, the Pt:Ru ratio is close to the ratio of atomic 1:1, and this ratio is reported to be a suitable ratio for bimetallic catalysts [4], [9].
Upon examination of the EDS maps provided in Fig. 2(c), it can be seen that the PtRu/C catalyst has homogenous Pt and Ru distribution on the surface. This result shows that the method presented in this study is suitable for synthesizing bimetallic catalysts, as high temperature and pressure conditions used in this work enhance the catalyst synthesis. The polarization curves of the PtRu/C catalyst at temperatures of 60, 70, and 80 °C are given in Figure 3. The hydrogen and air feed rates were 0.25 L/min and 1.00 L/min, respectively.

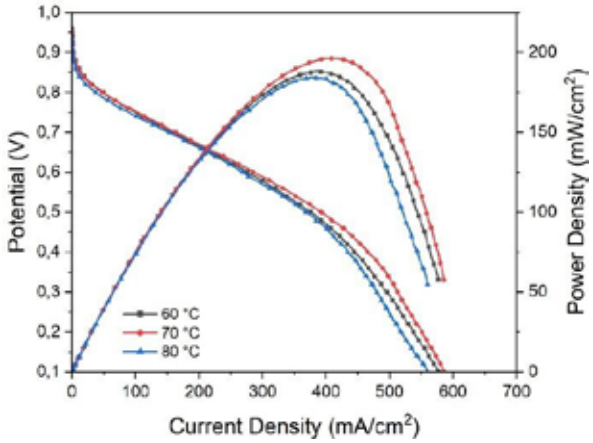

Fig. 3. The polarization curves of the PtRu/C catalyst at different temperatures

For the PtRu/C bimetallic catalyst, the highest cell performance was obtained at 70 °C. The performance loss at 80°C indicates that the degradation of membrane takes place at high temperatures [10]. The highest power density value was obtained at 70 °C cell temperature, while the decrease in power density at 80 °C is attributable to the reduction in proton conductivity of the Nafion membrane [3]. Activation polarization, ohmic losses, and mass transfer losses are discernible in the current density curves at all temperatures. At high current densities, mostly the mass transfer losses contribute to the cell performance degradation. But, at low and medium current densities, the performance decline is attributed to activation losses and ohmic losses.The temperature effect becomes more pronounced as the current density increases. This can be attributed to that the activation energy required for electrochemical reactions at low currents being lower than the energy required at high current [11].

4. CONCLUSIONS

In this study, Ru/C and PtRu/C catalysts were synthesized under high-temperature and pressure conditions by microwave-assisted polyol method. To address the knowledge gap in literature, the polyol method was modified. XRD analysis showed that synthesized PtRu/C catalyst had ultra-small crystallite sizes (<1.5 nm). SEM-EDS analysis showed that no metal clustering was present on the surface of the catalysts and Pt and Ru metal were distributed homogeneously over the carbon support. The activity of the PtRu/C catalyst was investigated in a single-cell test system and the highest activity of (171.2 mW/cm^2) was obtained at 70 °C. The loss of performance at 80 °C was attributed due to the degradation of the Nafion membrane. Addition of Ru also positively influenced the cost of the catalyst. The metal nanoparticles and catalysts that are synthesized in this work have the potential to be used in many different areas.

ACKNOWLEDGEMENT

This research was supported by the Eskisehir Technical University (ESTU) Scientific Research Projects Commission under grant number 21DRP140. The authors are grateful to ESTU Materials Science and Engineering Department for their equipment support for XRD and SEM analyses.

REFERENCES

[1] S. Karadeniz and N. Ayas, "Microwave-assisted synthesis of Pt/C catalyst at high temperatures for PEM fuel cells," *Int. J. Hydrog. Energy*, vol. 52, pp. 1564–1576, Jan. 2024, doi: 10.1016/j.ijhydene.2023.09.147.
[2] N. Pourmoghaddam and N. Ayas, "Synthesis, structure characterization, and electrochemical hydrogen storage of reduced graphene oxide and graphene," *Int. J. Hydrog. Energy*, vol. 82, pp. 1422–1434, Sep. 2024, doi: 10.1016/j.ijhydene.2024.08.053.
[3] F. Donmez Dayi and N. Ayas, "Potential of kaolin as filler in Nafion composite membranes for PEM fuel cells," *Renew. Energy*, p.

121754, Oct. 2024, doi: 10.1016/j.renene.2024.121754.
[4] J. Guo *et al.*, “Polyol-synthesized PtRu/C and PtRu black for direct methanol fuel cells,” *J. Power Sources*, vol. 168, no. 2, pp. 299–306, Jun. 2007, doi: 10.1016/j.jpowsour.2007.02.085.
[5] M. Wei, C. Hsu, and F. Liu, “One-pot Synthesis of Mixed-phase Pd-Ru/C as Efficient Catalysts for Electro-oxidation of Formic Acid,” *Int. J. Electrochem. Sci.*, vol. 11, no. 3, pp. 2185–2196, Jan. 2016, doi: 10.1016/S1452-3981(23)16093-7.
[6] M. Montiel *et al.*, “Relevance of the synthesis route of Se-modified Ru/C as methanol tolerant electrocatalysts for the oxygen reduction reaction,” *J. Power Sources*, vol. 195, no. 9, pp. 2478–2487, May 2010, doi: 10.1016/j.jpowsour.2009.11.080.
[7] Y. Ren, S. Zhang, and X. Wei, “Ru effect on the catalytic performance of Pd@Ru/C catalysts for methanol electro-oxidation,” *J. Energy Chem.*, vol. 24, no. 2, pp. 232–238, Mar. 2015, doi: 10.1016/S2095-4956(15)60306-0.
[8] Y.-C. Wei, C.-W. Liu, W.-J. Chang, and K.-W. Wang, “Promotion of Pt–Ru/C catalysts driven by heat treated induced surface segregation for methanol oxidation reaction,” *J. Alloys Compd.*, vol. 509, no. 2, pp. 535–541, Jan. 2011, doi: 10.1016/j.jallcom.2010.09.096.
[9] D. Lee, S. Hwang, and I. Lee, “One-step preparation and characterization of PtRu (1:1)/C electrocatalysts by polyol method for polymer electrolyte fuel cells,” *J. Power Sources*, vol. 160, no. 1, pp. 155–160, Sep. 2006, doi: 10.1016/j.jpowsour.2006.01.069.
[10] D. N. Ozen, B. Timurkutluk, and K. Altinisik, “Effects of operation temperature and reactant gas humidity levels on performance of PEM fuel cells,” *Renew. Sustain. Energy Rev.*, vol. 59, pp. 1298–1306, Jun. 2016, doi: 10.1016/j.rser.2016.01.040.
[11] N. Solehati, J. Bae, and A. P. Sasmito, “Optimization of operating parameters for liquid-cooled PEM fuel cell stacks using Taguchi method,” *J. Ind. Eng. Chem.*, vol. 18, no. 3, pp. 1039–1050, May 2012, doi: 10.1016/j.jiec.2011.12.003.

SUSTAINABLE ENERGY SOLUTIONS: 3D PRINTED PLA-NiMo@Ag FOR GREEN HYDROGEN PRODUCTION

[1*]Başak DOĞRU MERT, [1]Hüseyin NAZLIGÜL, [2]Goncagül AKSARAY, [3]Mehmet Erman MERT, [4]Mirsadegh SEYEDZAVVAR, [2*]Gülfeza KARDAŞ
[1]Adana Alparslan Türkeş Science and Technology University, Engineering Faculty, Energy Systems Engineering Dep., Adana,01250, Türkiye
[2]Çukurova University, Science and Letters Faculty, Chemistry Dep., Adana, 01330, Türkiye
[3]Adana Alparslan Türkeş Science and Technology University, Advanced Technology Research and Application Center, Adana, 01250, Türkiye
[4]Adana Alparslan Türkeş Science and Technology University, Engineering Faculty, Mechanical Engineering Dep., Adana, 01250, Türkiye

* E-mail: bdogrumert@atu.edu.tr, gulfeza@gmail.com

Abstract
The climate crisis necessitates inclusive, climate-resilient solutions, with renewable energy and hydrogen gas as key components. This study aimed to produce electrodes for PV-supported electrolyzer systems using 3D printing technology, ensuring scalable, repeatable, and cost-effective production. Electrodes with enhanced electrical conductivity and electrocatalytic efficiency were developed via FDM-based filament production. For this purpose, NiMo@Ag additive made using green chemistry methods was combined with commercial polymer resins that contain graphene and polylactic acid (PLA). The mixture was extruded to create filaments that can be used in 3D printers. Electrode geometry in honeycomb form was constructed with the aid of the software application. The cathode was connected to the PV panel on our university campus, enabling the production of "green hydrogen". The characterization of catalyst (NiMo@Ag) was achieved by XRD, FESEM-EDX and TEM. The electrochemical behaviour was investigated by LSV and EIS.
Keywords: Green Hydrogen, Fused Deposition Modeling (FDM), Electrolysis Systems, Sustainable Manufacturing.

I. INTRODUCTION

The use of sustainable energy sources is very important in combating climate change; however, the intermittency of solar and wind energy presents a significant drawback. Hydrogen gas serves as a solution to this issue by acting as an energy carrier, with green hydrogen production via water electrolysis from renewable sources emerging as a key focus. While there are deficiencies in industrial-scale, cost-effective, and high-performance electrocatalyst production in Türkiye, 3D printing technology offers scalability and reproducibility advantages in electrode manufacturing [1,2]. In this study, NiMo@Ag was prepared via green chemistry method. The active compound in the extract used for electrocatalyst modification is curcumin, a polyphenol with strong chelating properties. It binds to metal ions (Mo^{5+} and Ni^{2+}) through various functional groups:

(a) Complexation with Mo^{5+}:

- Two curcumin molecules can form complexes with Mo^{5+} through keto-enol tautomers:
  $$\text{Curcumin-enol} + Mo^{5+} \rightleftharpoons [\text{Curcumin-Mo(V)}]^{2+} + H^+ \quad (1)$$
- Alternatively, a single curcumin molecule can bind to Mo^{5+} via bidentate coordination through a phenolic oxygen and a β-diketone carbonyl group:
  $$\text{Curcumin} + Mo^{5+} \rightleftharpoons [\text{Curcumin-O,O′-Mo(V)}]^{1+} + H^+ \quad (2)$$

(b) Complexation with Ni^{2+}:

- One or two curcumin molecules can coordinate with Ni^{2+} through their phenolic oxygen atoms:
  $$\text{Curcumin} + Ni^{2+} \rightleftharpoons [\text{Curcumin-O-Ni(II)}]^{+} + H^+ \quad (3)$$
  $$2\ \text{Curcumin} + Ni^{2+} \rightleftharpoons [\text{Curcumin-O,O′-Ni(II)}] + 2H^+ \quad (4)$$

The extract contains various reducing agents, such as phenolic compounds, that donate electrons to the metal-curcumin complexes:

$$[\text{Curcumin-Mo(V)}]^{2+} + e^- \rightarrow [\text{Curcumin-Mo(IV)}] + H^+ \quad (5)$$
$$[\text{Curcumin-Ni(II)}]^{+/2+} + e^- \rightarrow [\text{Curcumin-Ni(I)}]^{0/1+} + H^+ \quad (6)$$
$$Mo^{4+} + Ag \rightarrow MoO_x@Ag \quad (7)$$
$$Ni^{1+/0} + Ag \rightarrow NiO_x@Ag \quad (8)$$

Further addition of metal ions and their reaction with the extract promotes the growth of a core-shell structure:

$$Mo^{4+} + [\text{Curcumin-Mo(IV)}] \rightarrow Mo@MoO_x@Ag \quad (9)$$
$$Ni^{1+/0} + [\text{Curcumin-Ni(I)}]^{0/1+} \rightarrow Ni@NiO_x@Ag \quad (10)$$

Curcumin stabilizes the core-shell structure through chemisorption onto the newly formed metal oxide surface.

In summary, the complexation of curcumin with metal ions enhances their solubility and prepares them for reduction. The reduction of these ions by the reducing agents in the extract forms nucleation centers for nanoparticle growth.

After the sythnesis of NiMo@Ag characterization was achieved and then PLA- NiMo@Ag was produced via FDM method, the prepared electrocatalyst was tested in 1 M KOH solution for HER.

2. MATERIALS AND METHODS

Ammonium molybdate (0.5 mmol, analytical grade) was dissolved in 20 mL of deionized water using an ultrasonic bath operating at 40 kHz and 100 W for 15 minutes at room temperature. Separately, a solution of nickel nitrate hexahydrate (0.5 mmol) was prepared in 20 mL of deionized water and added dropwise to the ammonium molybdate solution at a controlled rate of 1 drop per second, under continuous magnetic stirring at 500 rpm for 30 minutes. Subsequently, 10 mL of the prepared Curcuma longa (C. longa) ethanol extract (5.72 mg/mL) was introduced into the mixture dropwise over 10 minutes while maintaining stirring at 400 rpm, followed by an additional 30 minutes of stirring to ensure uniform incorporation. Ag suspension (0.5 mmol) was prepared by dispersing Ag in 20 mL of ethanol using an ultrasonic bath (40 kHz, 120 W) at 60 °C for 15 minutes. This suspension was then added dropwise to the reaction mixture while stirring continuously at 500 rpm. The mixture was stirred at 400 rpm for a further 10 minutes to ensure homogeneity. The reaction mixture was then transferred to a 50 mL Teflon-lined autoclave, sealed, and subjected to hydrothermal treatment at 121 °C for 1.5 hours under autogenous pressure (~1.5 bar), ensuring uniform heating throughout. After cooling the autoclave to room temperature, the product was collected by centrifugation at 5000 rpm for 10 minutes using a bench-top centrifuge. The resulting precipitate was thoroughly washed three times with 20 mL each of ethanol and deionized water to remove any residual impurities. Finally, the purified product was dried in a vacuum oven at 60 °C for 24 hours to obtain the MoNi@Ag nanoparticles. X-ray diffraction (XRD) analysis was performed on Pan Analytical Philips. The surface morphology, and elemental compositions of the nanocatalyst were examined using SEM and energy dispersive X-ray (EDX) spectroscopy on a Czech FEI SEM-type instrument at an accelerating voltage of 25 kV. The HR-TEM analysis (Thermoscientific, Talos F200i) was used to characterize the size, morphology, aggregation, and crystallization of the nanoparticles. As the first step in producing filaments with NiMo@Ag particles, a conductive PLA/NiMo@Ag polymer matrix (Protopasta) was fabricated using mechanical mixing and melt blending. Specifically, 1.5% NiMo@Ag was incorporated into PLA via mechanical mixing, followed by extrusion in a twin-screw extruder and pelletization to obtain PLA/NiMo@Ag nanocomposite granules. These granules were subsequently processed through a single-screw extruder and a winding mechanism to produce nanocomposite filaments with a standard 1.75 mm diameter. During extrusion, the barrel temperatures of the twin-screw and single-screw extruders were set to 160°C, 160°C, and 170°C for the three heating zones from the nozzle to the hopper. Then the obtained flament was used during the 3D printing procedure via 3D printer (Raise3D Pro3). The obtained form was 1*1*0.1 cm honeycomb shaped electrode. Electrochemical measurements were performed using a CHI 660B electrochemical analyzer at room temperature. A conventional three-electrode electrochemical cell was employed. The LSV was obtained at 100 mV s^{-1} scan rate. The EIS was performed at - 1.5 V, in the frequency range with 100 kHz and 10^{-2} Hz with the 5 mV amplitude. The energy harvesting experimental setup consisted of an 80 W photovoltaic (PV) panel installed on the roof of Adana Alparslan Türkeş Science and Technology University building to evaluate Adana's hydrogen production potential throughout 2024. The system was integrated with an HMI interface and a PLC control unit, enabling real-time monitoring and control of the setup. Data from solar radiation, wind speed, and temperature sensors were collected and processed through the PLC system. This comprehensive monitoring system ensured accurate data acquisition under varying environmental conditions. The aim was to analyze the energy generation performance of the PV panel and identify the most suitable periods for maximizing hydrogen production. This advanced setup provides a robust framework for evaluating renewable energy potential in real-world applications.

3. RESULTS AND DISCUSSION

In Fig. 1, diffraction peaks were detected at angles of 9.3599°, 12.4303°, 13.8173°, 14.9532°, 17.0897°, 19.1665°, 22.0755°, 24.0724°, 24.9882°, 25.8552°, 26.5454°, 27.1364°, 28.2495°, 30.6494°, 32.2314°, 33.1564°, 38.2176°, 40.1133°, 42.5428°, 44.9120°, 47.5648°, 54.3999°, 61.9902°, 64.5393°, 74.4323°, and 77.5770° in the XRD pattern. Notably, the strong peak at 27.1364° (d = 3.28614 Å, 100% relative intensity) matches the JCPDS card 00-038-0449, indicating the presence of a Ni-Mo alloy phase in the sample. This phase suggests an intermetallic structure formed by the strong interaction between Ni and Mo atoms. Additionally, the peaks at 38.2176° (d = 2.35499 Å, 41.12% relative intensity), 64.5393° (d = 1.44396 Å, 14.14% relative intensity), and 77.5770° (d = 1.22963 Å, 6.50% relative intensity) match the JCPDS cards 01-087-0718 and 00-038-0449, demonstrating that the Ni-Mo intermetallic phase is stabilized by Ag coating. Examination of the peak widths (FWHM) reveals that the narrow band at 14.9532° (0.0984°) indicates high crystallinity of the material, while the broad band at 28.2495° (0.7085°) suggests that some crystal regions may be in the nanometer scale. In conclusion, the detected peaks and their matching with JCPDS cards confirm the successful synthesis of the Ni-Mo intermetallic phase and its stabilization through Ag coating. These findings verify that the NiMo@Ag nanocomposite has achieved the intended structure and ensured phase stability. The morphology of the nanoparticles is formed by the aggregation of spherical structures exhibiting size diversity. Most nanoparticles are characterized by a lighter-colored shell surrounding a darker core. This structure indicates that the core consists of a NiMo alloy, while the shell is composed of silver, which can be attributed to either Ag(OH) or Ag_2O. The FESEM-EDX results further corroborated this finding.

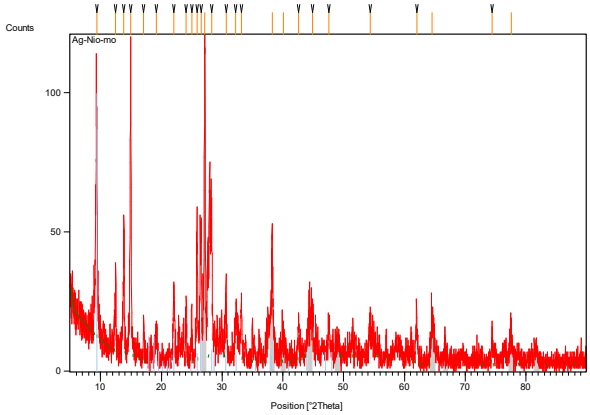

Fig. 1. The XRD of MoNi@Ag

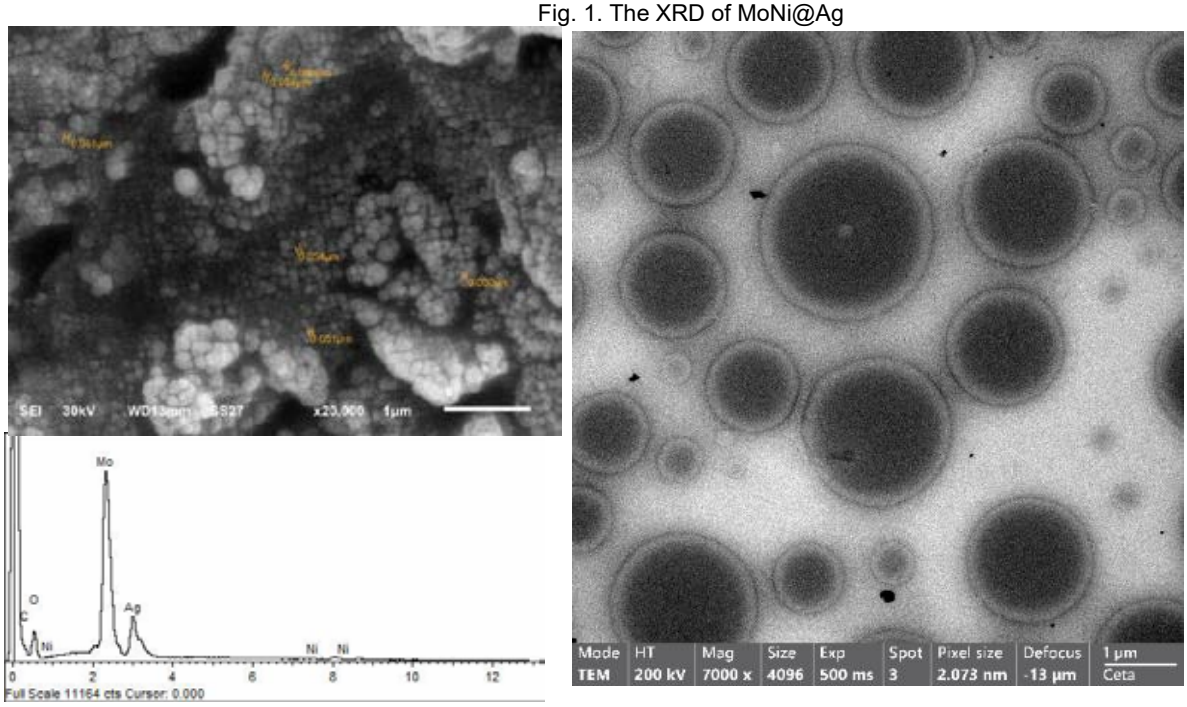

Fig. 2. FESEM (a)-EDX (b) and TEM (c) analysis of MoNi@Ag

The LSV curve presented in Fig. 3a demonstrated the enhanced HER activity of the 3D printed PLA-MoNi@Ag electrode in KOH electrolyte compared to the bare 3D electrode. The significantly lower onset potential and higher current density of the 3D PLA-MoNi@Ag electrode indicated its higher catalytic efficiency for HER vs bare electrode. This can be attributed to the synergistic effect of MoNi and Ag, which enhances electron transfer kinetics and provides more active sites for HER. The corresponding Nyquist plot (Fig. 3b) further supported this observation, revealing a lower charge transfer resistance for PLA-MoNi@Ag, suggesting faster charge transfer and improved electrocatalytic performance. This study also evaluated the monthly maximum power output performance of an 80 W photovoltaic (PV) panel using solar radiation and temperature data from Adana for the year 2024. The findings indicate that the power generation capacity of the panel is directly influenced by solar radiation levels, with temperature also playing a significant role in overall efficiency.

Table 1. Monthly maximum power output values for the 80 W PV panel in Adana during 2024

Month	Max Power Output (W)	Radiation (W/m^2)	Temperature (°C)
August	71.3	950.6	35.0
September	71.3	950.8	32.3
October	63.9	852.5	26.5
November	55.8	744.7	19.8
December	46.7	623.1	15.0

In August, the maximum power output of 71.3 W was observed at a solar radiation level of 950.6 W/m² and a temperature of 35.0°C, representing the highest performance recorded throughout the year. Similarly, in September, the panel achieved the same maximum power output of 71.3 W with slightly higher radiation (950.8 W/m²) and a lower temperature of 32.3°C, highlighting the continued high solar potential during late summer. In October, the maximum power output decreased to 63.9 W at a radiation level of 852.5 W/m² and a temperature of 26.5°C, reflecting the seasonal decline in solar radiation. November showed a further reduction, with a maximum output of 55.8 W at 744.7 W/m² radiation and 19.8°C temperature. Finally, in December, the lowest maximum power output of 46.7 W was recorded at a radiation level of 623.1 W/m² and a temperature of 15.0°C, corresponding to the reduced solar intensity during winter.

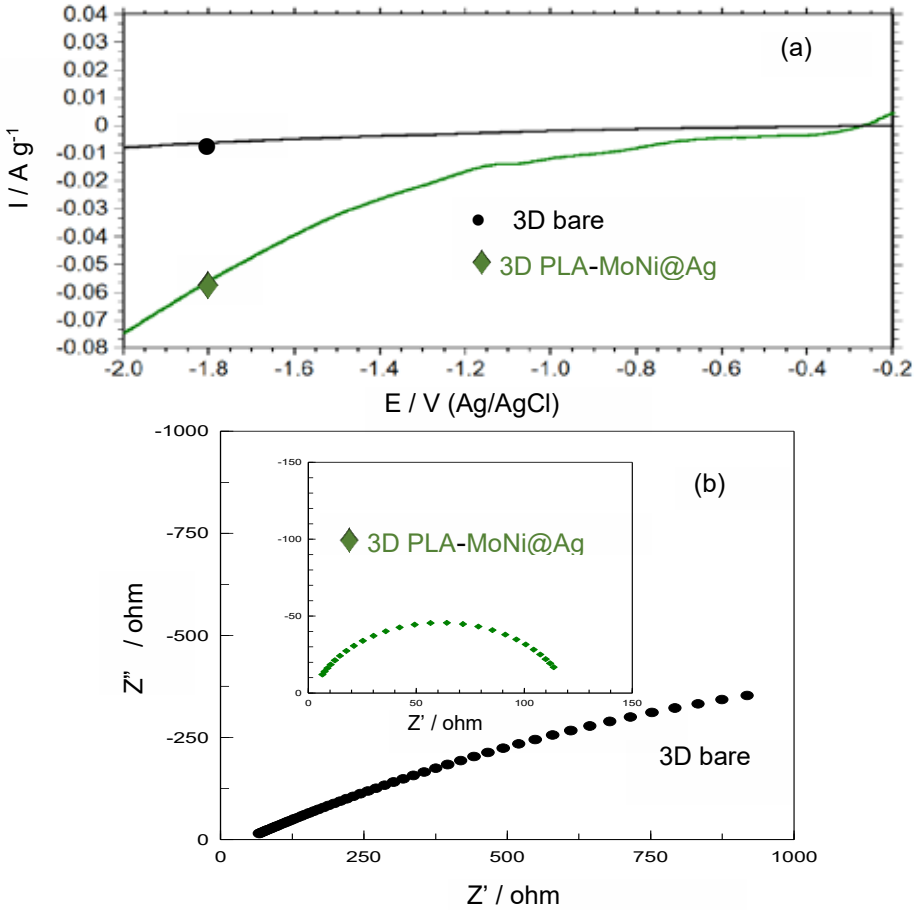

Fig. 3. The LSV curves (a) and Nyquist plots (b) of electrodes in 1M KOH

4. CONCLUSIONS

The structural, morphological and electrochemical analyses confirmed the formation of the MoNi@Ag structure. FESEM-EDX and TEM analyses further corroborated this core-shell configuration, demonstrating the uniform encapsulation. Electrochemical characterization revealed high HER catalytic activity of the 3D PLA-MoNi@Ag, as evidenced by its lower onset potential, higher current density, and reduced charge transfer resistance compared to the bare electrode. It can be attributed to the synergistic effect of MoNi and Ag, which enhances electron transfer kinetics and increases the density of active sites. PV results demonstrated that the power generation capacity of panels is primarily driven by solar radiation levels, while temperature has a secondary effect. Higher temperatures may reduce efficiency, but the impact is less significant during periods of high solar radiation, such as summer months. Conversely, the reduced solar radiation in winter months significantly limits power output. Therefore, in regions like Adana, which receive high solar radiation, PV panels operate more efficiently during summer and early autumn, while seasonal variations significantly affect their performance.

ACKNOWLEDGEMENTS

This study was supported by Scientific and Technological Research Council of Türkiye (TUBITAK) under Grant Number 223M523.The authors thank TUBITAK for their support.

REFERENCES

1. Khalil M and Dinçer İ. 2024. Experimental investigation of newly designed 3D-printed electrodes for hydrogen evolution reaction in alkaline media. Energy 304:909-132017.
2. Dinçer İ, Iberia Aydin M. 2023. New paradigms in sustainable energy systems with hydrogen. Energy Convers Manag 283:116950.

SIMULATION OF WHEELED AND TRACKED FUEL CELL VEHICLES: A COMPARATIVE STUDY USING PROPOSED A NEW TOOL CALLED PADSIP

[1*]*Berkay Açık*, [1,2]*Mustafa Umut Karaoğlan*, [1]*Zeynep Sude İşleyen*
[1]Dokuz Eylul University, Faculty of Engineering, Department of Mechanical Engineering, Tinaztepe, Buca, Izmir, 35397, Turkey
[2]Dokuz Eylul University, Energy Application and Research Center, Tinaztepe, Buca, Izmir, 35397, Turkey

*Corresponding author e-mail: acik.berkay@ogr.deu.edu.tr

ABSTRACT
Increasing energy demand and environmental concerns cause efficient and clean transportation solutions. Therefore, hydrogen fuel cell electric vehicles (FCEVs) emerge as an effective alternative to reduce dependence on fossil fuels. This study presents a new simulation tool named Performance Analysis and Driving Simulation Program (PADSIP) to determine performance results and powertrain simulations of the FCEVs and compare them for wheeled and tracked vehicle configurations. The vehicle dynamics and powertrain component models are designed in the Matlab-Simulink environment and simulated using the Worldwide Harmonized Light Vehicles Test Cycle (WLTC). The main results indicate that the tracked vehicle provides better traction on rough terrains, but it causes higher energy and hydrogen consumption compared to the wheeled vehicle. Finally, it can be seen that PADSIP enables simulation and optimization of the FCEVs in their design and development process with its user-friendly interface.
Keywords: fuel cell vehicle, powertrain simulation, wheeled vehicle, tracked vehicle

1. INTRODUCTION

The transportation sector is undergoing a significant transformation toward alternative energy sources to address environmental concerns and reduce dependence on fossil fuels. Among these alternatives, hydrogen fuel cell electric vehicles have gained considerable attention due to their high energy efficiency, zero greenhouse gas emissions, and fast refueling capabilities [1]. FCEVs offer a sustainable solution for a wide range of applications, from urban mobility to heavy-duty operations. However, their performance and energy management depend heavily on the drivetrain configuration. Wheeled and tracked systems provide unique advantages tailored to specific operational needs. While wheeled vehicles are widely used for on-road transportation due to their efficiency and maneuverability, tracked vehicles perform better in off-road and rugged terrains because of their superior traction and stability [2]. Understanding the differences in energy consumption and dynamic behavior between these systems is critical for optimizing their design and application.

Research on FCEV energy management and performance optimization has predominantly focused on wheeled configurations. However, studies comparing wheeled and tracked FCEVs within the same simulation environment remain limited, as existing research often focuses on one configuration, overlooking the unique challenges and opportunities of the other. Additionally, there is a lack of studies integrating user-friendly interfaces to facilitate parameter adjustments and configuration selection, which are essential for practical applications. This study aims to address these gaps by directly comparing the energy consumption, dynamic performance, and operational efficiency of both configurations under the same conditions of wheeled and tracked vehicles using a new proposed simulation tool named PADSIP. The primary objective is to develop a comprehensive simulation model to evaluate and optimize energy management strategies for these systems. By analyzing their dynamic behavior and energy consumption, this research not only distinguishes itself from existing literature but also provides a practical tool for engineers and researchers to enhance FCEV designs. The findings are expected to contribute significantly to the advancement of FCEV technology, offering valuable insights for improving energy efficiency and performance across various applications.

2. MODELING AND SIMULATION

In this study, two separate heavy-duty vehicle models (wheeled and tracked FCEVs) were developed in the Matlab-Simulink environment to compare their performance and optimize energy management strategies (Fig. 1). Both models include essential subsystems, such as vehicle dynamics, powertrain components, battery, fuel cell, and control strategies, while also considering design-specific dynamics and resistance forces. The system icludes an electric motor for traction, a battery for energy storage, and a fuel cell as a complementary power source. Both the battery and the fuel cell supply power to the electric motor, which also operates as a generator during regenerative braking, recovering energy to recharge the battery. The simulation uses the Worldwide Harmonized Light Vehicles Test Cycle (WLTC) Class 1 speed and acceleration profiles, following global standards to evaluate performance and energy efficiency. This section details the structure of the models, their mathematical foundations, the simulation methodology, and the parameter management system integrated with a user-friendly Graphical User Interface (GUI).

2.1. Vehicle models

The power required for traction in heavy-duty FCEVs (wheeled or tracked) is determined by calculating resistance forces

acting on the wheels or tracks, using a 1,022-second driving cycle (Fig. 3), that incorporates low-to-medium speeds, with a maximum vehicle speed of 64.44 km/h. For wheeled vehicles, key resistances include rolling resistance (F_R, [N]), Eq. (1), aerodynamic drag resistance (F_L, [N]), Eq. (2), and acceleration resistance (F_a, [N]), Eq. (3), while tracked vehicles include for internal resistance (R_{in}, [N]), Eq. (4), and movement resistance (R_c, [N]), Eq. (5). These forces are computed using longitudinal motion equations and suitable parameters for heavy-duty vehicles to simulate energy consumption under dynamic conditions. The methodology integrates empirical coefficients and soil mechanics models, e.g., sinkage depth (z_0, [m]), track width (b, [m]), to ensure accurate power demand predictions for both vehicle types [3].

The rolling resistance is calculated using the vehicle mass (m, [kg]), gravitational acceleration (g, [m/s^2]), and rolling resistance coefficient (f_r, [-]), while the aerodynamic drag force is determined by considering air density (ρ, [kg/m^3]), vehicle frontal area (A, [m^2]), aerodynamic drag coefficient (C_W, [-]), and vehicle speed (V, [m/s]). The acceleration resistance is computed using the rotational inertia factor (λ, [-]), vehicle mass and vehicle acceleration (a, [m/s^2]). Additionally, while b represents the track width [m], n [-], k_c [kN/m$^{(n+1)}$] and k_ϕ [kN/m$^{(n+1)}$] are variables that depend on the type of terrain [3].

$$F_R = m \,.\, g \,.\, f_r \tag{1}$$

$$F_L = \frac{1}{2} \,.\, \rho \,.\, A \,.\, C_W \,.\, V^2 \tag{2}$$

$$F_a = \lambda \,.\, m \,.\, a \tag{3}$$

$$R_{in} = m \,.\, g \,(222 + 3 \,.\, V) \tag{4}$$

$$R_c = 2 \,.\, b \left(\frac{k_c}{b} + k_\phi\right)\left(\frac{{z_0}^{n+1}}{n+1}\right) \tag{5}$$

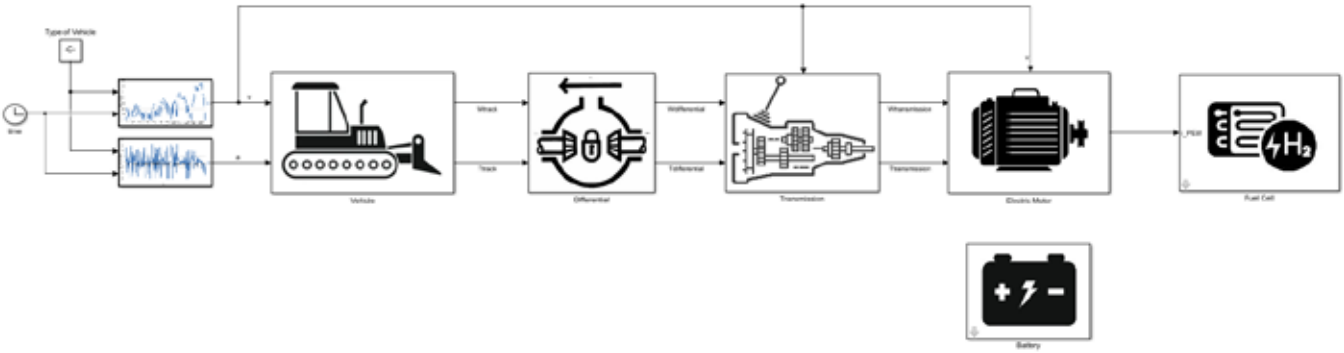

Fig. 1. Matlab/Simulink model for fuel cell electric tracked vehicle

2.2. Mathematical modeling of powertrain systems with energy conversion and storage

The power output of the electric motor (P_{EM}, [W]) can be calculated by dividing the total time-dependent resistance forces by the product of drivetrain efficiency (η_d, [-]) and transmission efficiency (η_t, [-]), then multiplying by the vehicle speed. For wheeled vehicles in Eq. (6), the power depends on the rolling resistance force, aerodynamic drag force and acceleration force:

$${P_{EM}}^w = \frac{(F_R + F_L + F_a)}{\eta_d \cdot \eta_t} \,.\, V \tag{6}$$

For tracked vehicles in Eq. (7), additional resistances are included: internal resistance and movement resistance, alongside F_L and (F_a) [1].

$${P_{EM}}^t = \frac{(R_{in} + R_c + F_L + F_a)}{\eta_d \cdot \eta_t} \,.\, V \tag{7}$$

The battery model estimates the state of charge (SOC, [%]) of the battery in FCEVs during simulation. The battery is represented as an energy source using the R_{int} model, which simplifies internal resistance and open-circuit voltage dynamics. The SOC, calculated based on the battery current (I_B, [A]) and battery capacity [A.h] for both wheeled and tracked vehicles, is formulated in Eq. (8). Here, $SOC(t)$ represents the instantaneous state of charge, while SOC_i represents the initial state of charge. The model integrates these parameters to simulate energy storage behavior under

varying operational demands [4].

$$SOC(t) = SOC_i - \frac{1}{Q_B}\int_0^t I_B \,.\, dt \tag{8}$$

The fuel cell model dynamically estimates the voltage output (V_{cell}, [V]), hydrogen consumption rate [g/s], and power output (P_{cell}, [kW]) in fuel cell electric vehicles. The cell voltage is derived from the Nernst potential (E_{Nernst}, [V]) and calculated for voltage losses: activation loss ($\eta_{activation}$, [V]) due to electrode reaction kinetics, ohmic loss (η_{ohmic}, [V]), from electrolyte and component resistance, and concentration loss ($\eta_{concentration}$, [V]) caused by mass transport limitations, as shown in Eq. (9). Hydrogen consumption depends on electrochemical reactions and current demand. The motor's power requirement, converted to current (I_{motor}, [A]), is fed into the fuel cell model per the energy management strategy, ensuring accurate dynamic response modeling under varying conditions [5].

$$V_{cell} = E_{Nernst} - \eta_{activation} - \eta_{ohmic} - \eta_{concentration} \tag{9}$$

2.3. Tracked and wheeled fuel cell vehicle simulator - PADSIP

A GUI designed for performance analysis and driving cycle simulations of tracked and wheeled FCEVs is illustrated in Fig. 2. Users can input parameters such as vehicle type, vehicle dynamic properties, battery configurations, powertrain, electric motor and fuel cell parameters, and energy management system limits to initiate simulations. Critical parameters such as terrain properties (e.g., moisture content [%], specific weight [kN/m^3], etc.) for tracked vehicles was particularly considered. Defined data via the "Confirm Parameters" option is processed through the "Run" command to generate results including vehicle performance, energy consumption, and system efficiency. This GUI provides a user-friendly interface for academic and industrial modeling studies, enabling detailed analysis of fuel cell vehicle dynamics under diverse operational and environmental conditions.

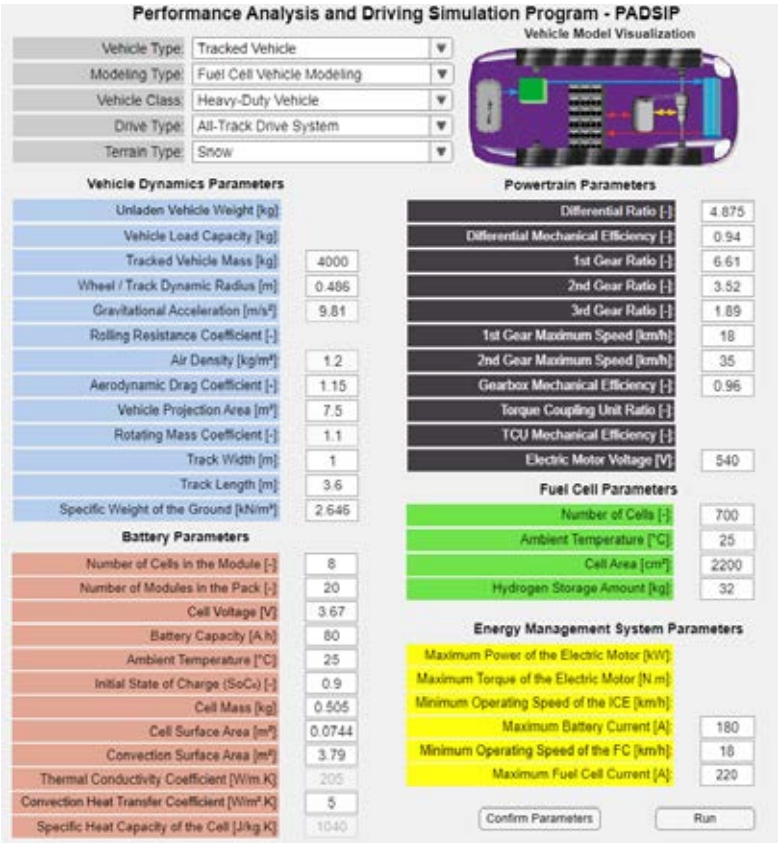

Fig. 2. Input parameters for performance analysis and driving simulation

3. RESULTS AND DISCUSSION

In the simulation study conducted under the WLTC Class 1 driving cycle, the performance of tracked and wheeled heavy-duty FCEVs was compared (Fig. 3). Although both vehicle types shared identical acceleration and speed profiles, the tracked vehicle exhibited 115-120% higher electric motor output power due to elevated terrain interaction resistances (e.g., internal and movement resistances). Additionally, the dominance of motion resistance over acceleration resistance in tracked systems significantly limited negative torque generation during regenerative braking, reducing energy recovery

efficiency. Both vehicle configurations utilized a battery system capable of delivering up to 180 A, which effectively met motor power requirements at *SOC* below 90%. As a result, their *SOC* levels and battery power profiles remained almost close. However, the tracked vehicle's higher energy demand was offset by its fuel cell, which operated at significantly higher power levels. This resulted in hydrogen consumption increasing by roughly 11 times compared to the other configuration.

It can be clearly stated that tracked vehicles demonstrate superior performance in challenging terrain conditions (e.g., rough paths, steep slopes, etc.), whereas they exhibit weaker range performance compared to wheeled vehicles, particularly when hydrogen consumption is considered [6]. To further explore this comparison and achieve more comprehensive results, future studies should integrate factors such as drive cycles, battery capacities, road condition parameters, and steering dynamics into simulation models.

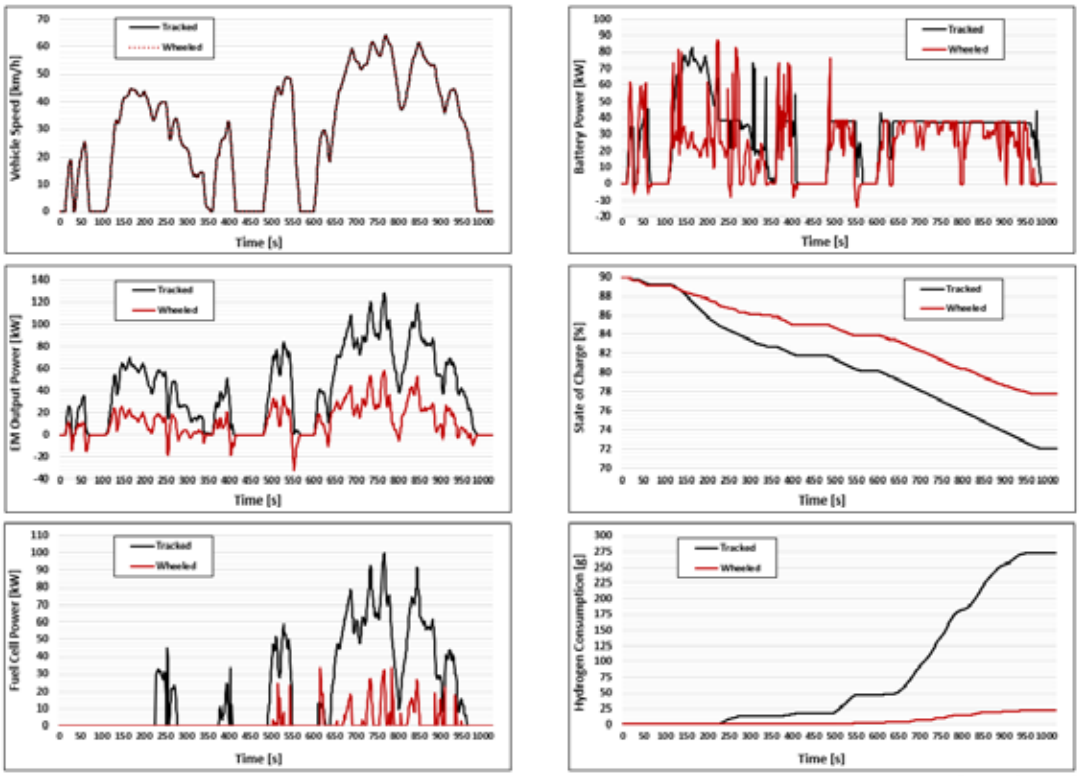

Fig. 3. Comparative analysis of speed, battery power, electric motor output power, state of charge, fuel cell power, and hydrogen consumption over time

4. CONCLUSIONS

This study has pointed the significant differences between wheeled and tracked hydrogen fuel cell electric vehicles in terms of energy consumption, performance, and hydrogen efficiency under the same operating conditions. Tracked vehicles demonstrated better performance in challenging and rough terrain conditions but faced considerably higher energy demand, particularly in terms of hydrogen consumption. The developed simulation tool, PADSIP, has proven to be an effective and reliable resource, enabling users to easily explore and optimize various configurations for detailed performance analyses. Future studies should aim to further enhance simulation models and expand their applicability to real-world conditions by incorporating different driving cycles, extended environmental parameters, and steering dynamics.

REFERENCES

1. Ehsani M, Gao Y and Emadi A. 2010. Modern electric, hybrid electric, and fuel cell vehicles. Boca Raton, CRC Press.
2. Guzzella L and Sciarretta A. 2005. Vehicle propulsion systems. Berlin, Springer.
3. Alpaslan E, Karaoglan MU and Colpan CO. 2021. Drive cycle simulations of wheeled and tracked heavy-duty electric vehicle powertrains. DEUFMD 23(69), 913-921.
4. Mallon KR, Assadian F and Fu B. 2017. Analysis of on-board photovoltaics for a battery electric bus and their impact on battery lifespan. Energies 10:943.
5. Larminie J and Dicks A. 2003. Fuel cell systems explained. Chichester, John Wiley & Sons.
6. Wong JY. 2001. Theory of ground vehicles. Chichester, John Wiley & Sons.

MICROWAVE ASSISTED METHANE DECOMPOSITION REACTION USING NICKEL-PALLADIUM CATALYSTS SUPPORTED ON DIFFERENT CARBON SUPPORTS

[1,2*]*Rukan Can Seyfeli*, [2]*Dilek Varisli*,
[1] Ondokuz Mayis University, Faculty of Engineering, Chemical Engineering Department, Atakum, Samsun, 55139, Turkey
[2] Gazi University, Faculty of Engineering, Chemical Engineering Department, Maltepe, Ankara, 06500, Turkey

*Corresponding author e-mail: dilekvarisli@gazi.edu.tr

ABSTRACT

Methane decomposition is a promising pathway for hydrogen production that avoids CO_2 emissions while yielding valuable carbon nanomaterials. This study examines the catalytic performance of carbon supported nickel (Ni) activated catalyst with and without promoter in a microwave-assisted system. Two different carbon materials, namely mesoporous carbon (MC) and silicon carbide (SiC) were used as a support and palladium (Pd) is selected as a promoter. Different characterization techniques, including Raman spectroscopy, SEM/EDS, and TEM, revealed that Pd addition significantly improves the structural and catalytic properties of Ni-based catalysts. Pd enhances nickel dispersion, reduces particle agglomeration, and facilitates the formation of uniform carbon nanostructures. Activity tests demonstrated that while 40Ni@SiC achieved the highest methane conversion (80%) among SiC-supported catalysts, and 10Ni@MC exhibited the highest initial activity (89%) with rapid deactivation, Pd-modified catalysts like 50Ni1Pd@MC stood out for their exceptional stability, maintaining high activity for over 400 minutes. This underscores Pd's critical role in enhancing catalyst durability and enabling precise control over carbon morphology. By integrating Pd-promoted catalysts with microwave-assisted technology, this approach provides an efficient and sustainable method for methane decomposition, advancing clean hydrogen production and the synthesis of high-value carbon nanomaterials.

Keywords: Methane decomposition, microwave reactor, palladium, carbon nanomaterials.

1. INTRODUCTION

Fossil fuels play a critical role in meeting global energy demands but pose significant challenges, such as greenhouse gas emissions and resource depletion. These issues have driven the search for cleaner, sustainable alternatives, with hydrogen emerging as a particularly promising energy carrier. Hydrogen boasts high energy density, generates three times more energy than conventional fuels, and is efficiently utilized in fuel cells for heat and electricity production [1,2]. One innovative approach to clean hydrogen production is the catalytic decomposition of methane, a process that not only avoids greenhouse gas emissions but also produces valuable carbon nanomaterials. While catalysts like nickel (Ni), cobalt (Co), and iron (Fe) have been widely studied, Ni is preferred for its superior activity at moderate temperatures (500–700°C) [3]. However, methane decomposition faces challenges such as high reaction temperatures (above 750°C) and catalyst deactivation due to carbon deposition and metal sintering. To overcome these hurdles, microwave reactor technology has emerged as a game-changer, enabling rapid and volumetric heating, enhancing reaction rates, catalyst stability, and product selectivity. Studies have shown that microwave systems achieve superior conversion rates at lower temperatures compared to conventional heating, making them a sustainable and efficient alternative [4].However, application of MW technology on methane decomposition reaction is limited and it is still to open research. Palladium (Pd) has garnered significant attention as an effective promoter in catalytic systems, particularly for methane decomposition. Incorporating Pd into Ni-based catalysts significantly enhances both catalytic activity and stability. [5,6]. The integration of Pd into catalyst design, combined with the advantages of microwave-assisted technology, represents a significant breakthrough in methane decomposition. These advancements address the limitations of conventional systems, paving the way for efficient, sustainable hydrogen production while enabling the simultaneous synthesis of high-value carbon nanomaterials. The study conducted a detailed analysis of mesoporous carbon (MC) and silicon carbide (SiC)-supported nickel-based catalysts, highlighting the transformative effect of palladium (Pd) on their structural and physical properties and showing the effects of microwave on the catalysts acitivity.

2. EXPERIMENTAL

2.1. Catalyst Preparation

Mesoporous carbon and silicon carbide supported catalysts were prepared using the impregnation method, with improvements to ensure homogeneous metal distribution and minimize agglomeration, especially for high metal loadings (up to 50 wt%). Mesoporous carbon (99.95% purity, Sigma Aldrich) and silicon carbide (99.9% purity, Nanografi) were used as supports. Nickel(II) nitrate hexahydrate ($Ni(NO_3)_2 \cdot 6H_2O$, 97% purity, Sigma Aldrich) was used for nickel loading, while palladium(II) nitrate hydrate ($Pd(NO_3)_2 \cdot H_2O$, Sigma Aldrich) served as the promoter. The catalysts were labeled as XMP@S, where X represents the metal loading percentage (10–50%), M is the metal type (Ni), P is the promoter (Pd),

and S is the support material. Samples were calcined at 700°C for 5 hours under a nitrogen flow (10°C/min heating rate) and reduced at 400°C for 3 hours under a hydrogen flow.

2.2. Catalyst Characterization

The physical and structural properties of the synthesized catalysts were characterized using various techniques, such as Inductively Coupled Plasma (ICP) analysis, Nitrogen physisorption, X-ray diffraction (XRD), Scanning electron microscopy (SEM) and energy-dispersive spectroscopy (EDS), Raman spectroscopy, Transmission electron microscopy (TEM).

2.3. Catalytic Activity Studies

The catalytic activities of the synthesized catalysts were evaluated under continuous flow conditions using a microwave generator provided by SAIREM. The system operates at a frequency of 2.45 GHz with a maximum power capacity of 2 kW. Temperature control during reactions was achieved by adjusting the power level of the microwave generator, and temperature measurements were conducted using an infrared pyrometer (Raytek M13).

3. RESULTS AND DISCUSSION

3.1. Characterization of synthesized catalysts

X-ray diffraction analyses confirmed successful reduction, showing distinct peaks for amorphous carbon and metallic nickel phases in MC-supported catalysts (10%–50% metal loadings) and metallic nickel alongside SiC structures in SiC-supported catalysts. Notably, SiC-supported catalysts exhibited larger crystal sizes compared to their MC counterparts. SEM and EDS provided further insights into surface morphology and elemental distribution. While the 50Ni@SiC catalyst displayed nickel agglomeration at high metal loadings despite good dispersion, the 50Ni@MC catalyst suffered from significant agglomeration and uneven particle distribution. The addition of Pd (50Ni1Pd@MC) substantially improved these characteristics, achieving greater particle homogeneity, reducing agglomeration, and enhancing nickel dispersion. These findings underscore the pivotal role of Pd in tailoring catalyst structure and morphology. By improving nickel dispersion and reducing agglomeration, Pd enhances the performance potential of nickel-based catalysts, demonstrating its critical importance in the design of advanced catalytic systems for methane decomposition and other applications.

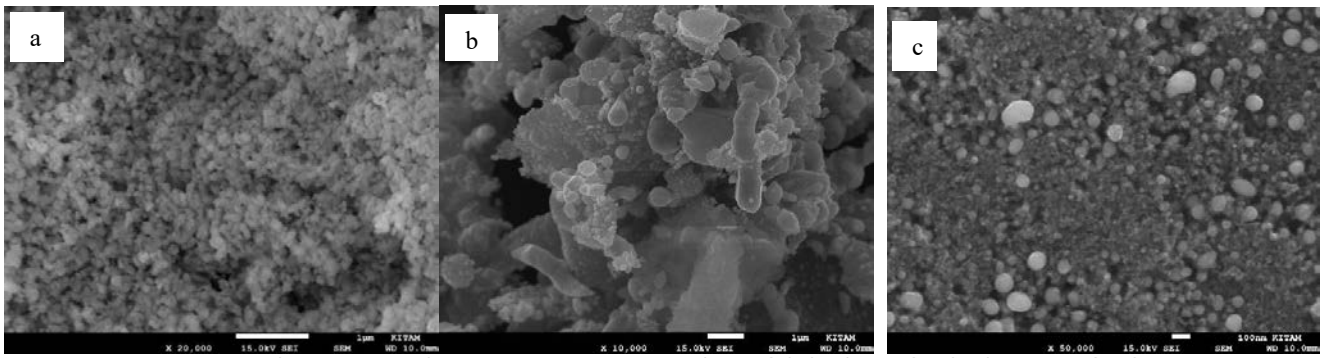

Fig.1. SEM images of the synthesized catalyst a)50Ni@SiC, b)50Ni@MC, c)50Ni1Pd@MC

3.2. Catalytic Activity Results

The catalytic activity of synthesized catalysts was evaluated in a microwave-heated reactor under methane flow at 500°C. Among the Ni@SiC catalysts, 50Ni@SiC achieved the higher activity and stability than the lowest Ni loaded 10Ni@SiC catalyst (Fig.2a), whereas, for Ni@MC catalysts, the 10Ni@MC catalyst exhibited the highest initial activity (89%) but suffered from rapid deactivation (Fig.2b). Higher metal loadings resulted in more prolonged, albeit less active, catalytic behavior due to changes in crystal size and surface area. The addition of Pd as a promoter significantly improved catalyst stability and activity. Pd-modified catalysts such as 50Ni1Pd@MC, 30Ni1Pd@MC, and 50Ni15Pd@MC exhibited enhanced durability, with 50Ni15Pd@MC maintaining high activity for 400 minutes under reaction conditions (Fig.2c). Pd facilitated better nickel dispersion, reduced agglomeration, and enhanced methane conversion efficiency. The addition of Pd as a promoter significantly enhanced catalyst performance and stability. These results highlight the critical role of Pd in enhancing the stability and efficiency of nickel-based catalysts, emphasizing its importance in optimizing catalyst design for effective methane conversion in microwave-assisted systems.

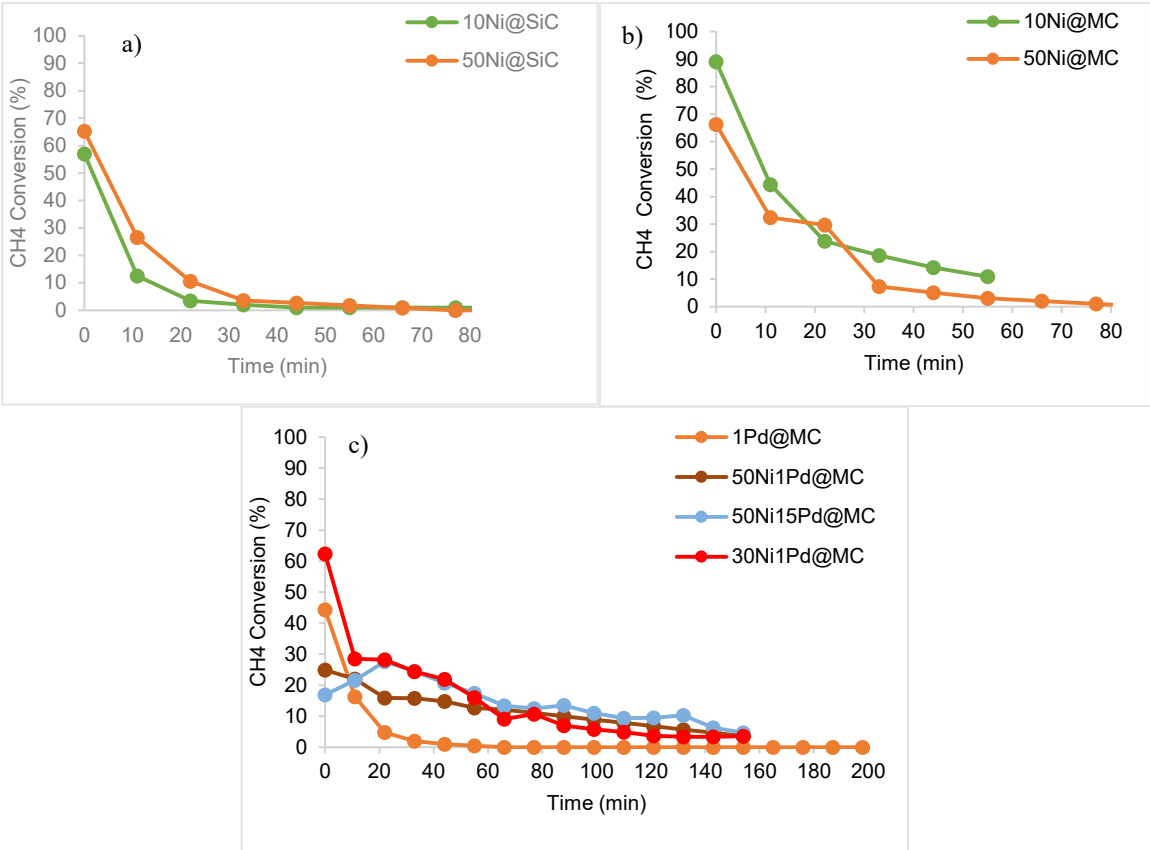

Fig.2. Catalytic activity results of microwave heated system a) MC support, b) SiC support, c) Palladium promoted catalysts

3.3 Characterization of post-reaction catalysts

The post-reaction properties of nickel (Ni) and palladium (Pd) catalysts were analyzed using Raman spectroscopy, SEM/EDS, and TEM, highlighting the significant impact of Pd incorporation. Raman spectroscopy revealed differences in graphitization and defect density among the catalysts, while SEM/EDS demonstrated that carbon morphology—ranging from filamentary to bamboo-shaped and nanotube-like structures—was influenced by metal loading, reaction conditions, and catalyst composition (Fig.3). Notably, the addition of Pd promoted the formation of uniform carbon structures and significantly enhanced catalytic stability. TEM analysis further confirmed the presence of carbon nanostructures on Pd-modified catalysts, showing that filament dimensions were closely linked to Ni particle sizes. These results underscore the critical role of Pd in improving carbon uniformity, stabilizing the catalyst, and optimizing catalytic performance, offering valuable insights into the structural evolution of catalysts for advanced methane decomposition applications.

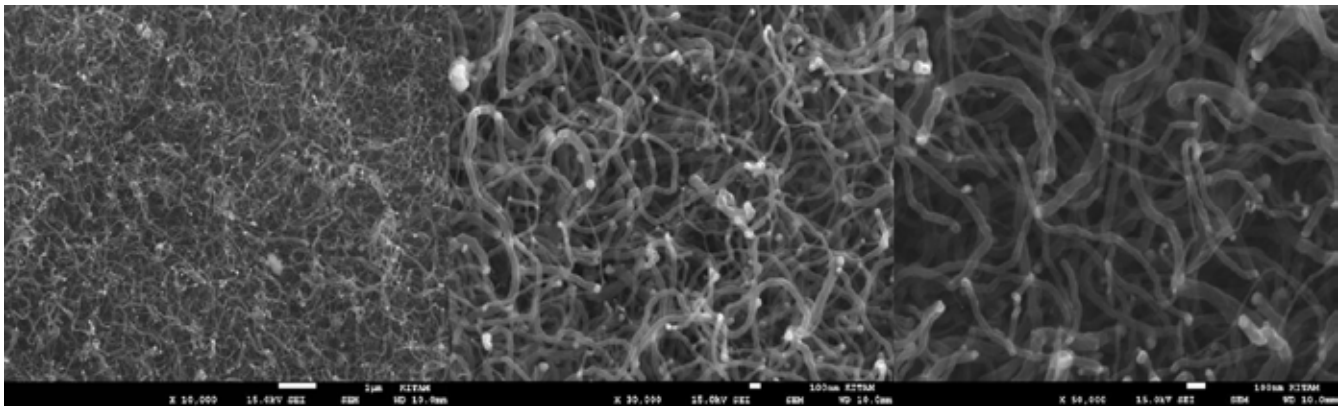

Fig 3. SEM Images of spent form of 50Ni1Pd@MC in different magnification

4. CONCLUSIONS

This study focuses on the synthesis and performance evaluation of mesoporous carbon (MC) and silicon carbide (SiC)-supported nickel (Ni) and palladium (Pd) catalysts for methane decomposition in microwave-assisted systems, with a particular emphasis on the pivotal role of Pd. Catalytic activity results revealed that Pd addition significantly enhanced both activity and stability. Pd-promoted catalysts, such as 50Ni1Pd@MC, sustained higher activity over extended reaction durations compared to non-promoted counterparts. Among the catalysts, 40Ni@SiC achieved the highest methane conversion (80%) within the Ni@SiC group, though its stability declined rapidly over time. For MC-supported catalysts, 10Ni@MC exhibited the highest initial activity (89%) but experienced rapid deactivation. In contrast, Pd-modified catalysts demonstrated superior performance, with 50Ni1Pd@MC retaining activity for up to 400 minutes under reaction conditions. Pd's ability to promote the growth of uniform carbon nanostructures, mitigate carbon agglomeration, and prevent sintering greatly enhanced catalytic efficiency. These findings highlight Pd's critical role in driving sustainable hydrogen production while simultaneously enabling the efficient synthesis of valuable carbon nanomaterials in energy-efficient catalytic systems.

ACKNOWLEDGEMENT

This work was supported by the The Scientific and Technological Research Council of Turkiye (TUBITAK, project code:123M056).

REFERENCES

1. Khalifeh, O., Mosallanejad, A., Taghvaei, H., Rahimpour, M.R., Shariati, A. 2016. 'Decomposition of methane to hydrogen using nanosecond pulsed plasma reactor with different active volumes, voltages and frequencies', Applied Energy, 169, 585–96.
2. Rastegarpanah, A., Rezaei, M., Meshkani, F., Zhang, K., Zhao, X., Pei,W., Liu,Y., Deng, J., Arandiyan, H., Dai, H. 2019. 'Mesoporous Ni/MeOx (Me = Al, Mg, Ti, and Si): Highly efficient catalysts in T the decomposition of methane for hydrogen production', Applied Surface Science, 478, 581–93.
3. Hasnan, N.S.N., Timmiati, S.N., Lim, K.L., Yaakob, Z., Kamaruddin, N.H.N., Teh, L.P. 2020. 'Recent developments in methane decomposition over heterogeneous catalysts: an Li Y, Zhang B, Xie X, Liu J, Xu Y, Shen W. Novel Ni catalysts for methane decomposition to hydrogen and carbon nanofibers. J Catal 2006; 238:412e24.
4. Bai, X., Muley, P.D., Musho, T., Abdelsayed, V., Robinson, B., Caiola, A., Shekhawat, D., Jiang, C., Hu, J. 2022. 'A combined experimental and modeling study of Microwave-assisted methane dehydroaromatization process', Chemical Engineering Journal, 433,134445
5. Pudukudy, M., Yaakob, Z., Akmal, Z.S. 2015c. 'Direct decomposition of methane over Pd promoted Ni/SBA-15 catalysts', Applied Surface Science Volume 353, 127-36.
6. Bayat, N., Rezaei, M., Meshkani, F. 2016b. 'Hydrogen and carbon nanofibers synthesis by methane decomposition over Ni–Pd/Al2O3 catalyst', Int J Hydrogen Energy; 41:5494–503.

APPLICATION OF RESPONSE SURFACE METHODOLOGY IN HYBRID GREEN HYDROGEN SYSTEM DESIGN AND OPTIMIZATION

[1,3]Metin Gul, [2,3]*Ersin Akyuz*,
[1] Balikesir University, Department of Vocational School, Balikesir, 10145, Türkiye
[2] Balikesir University, Department of Electrical and Electronics Engineering, Balikesir, 10145, Türkiye
[3]Renewable Energy Research and Application Center, Balıkesir University

*Corresponding author e-mail: metingul@balikesir.edu.tr

ABSTRACT

This study performed a comprehensive technical, economic, and environmental evaluation of a hybrid green hydrogen production plant integrating photovoltaic (PV) panels and wind turbines. The analysis focused on comparing various hybrid configurations both with one another. The optimization of the hybrid systems was conducted using Simulink and the Response Surface Methodology (RSM), aiming to determine the most cost-effective configuration for achieving an optimal levelized cost of hydrogen (LCOH). The findings revealed that the optimal hybrid system configuration consists of a 1 MW PV, 2,82 of WT and 1 MW electrolyzer system. This configuration demonstrated the optimal energy cost, with an LCOH of 4,99 $/kgH2. Sensitivity analyses were also carried out to evaluate the influence of critical parameters, interest rates, and system efficiency. These analyses provided valuable insights into the robustness and adaptability of the system under varying conditions, highlighting the potential for further optimization and scalability in real-world applications.

Keywords: Levelised cost of hydrogen, optimization, response surface methodology, optimization

1. INTRODUCTION

The integration of hybrid renewable energy systems with hydrogen production represents a significant advancement in the pursuit of sustainable energy solutions. This approach enhances the reliability and efficiency of energy systems while addressing the intermittency challenges associated with renewable energy sources such as solar and wind. By coupling hydrogen production with hybrid systems, it is possible to create a versatile energy storage solution that can buffer against fluctuations in energy supply and demand, thereby facilitating a more stable energy grid [1].

One of the primary advantages of integrating hydrogen production into hybrid renewable systems is the ability to utilize excess energy generated during peak production times. For instance, when solar or wind resources are abundant, the surplus energy can be directed towards electrolysis to produce hydrogen. This hydrogen can then be stored and used later when energy demand exceeds supply, effectively acting as a long-term energy storage solution [2],[3]. Such integration maximizes the utilization of renewable resources and mitigates issues of energy waste that can occur when production exceeds immediate consumption needs [4].

Moreover, the hybridization of renewable energy systems with hydrogen production can significantly enhance the economic viability of these systems. Recent advancements in electrolyzer and fuel cell technologies have reduced costs and improved efficiencies, making hydrogen production more competitive with traditional energy sources [5],[6]. For example, studies have shown that hybrid systems combining solar, wind, and hydrogen production can achieve lower levelized costs of energy and hydrogen compared to systems relying solely on conventional energy sources [7],[8].

The operational flexibility offered by hybrid renewable systems with hydrogen production is another critical advantage. These systems can be designed to operate in various configurations, allowing for tailored solutions that meet specific energy demands and resource availability [9]. For instance, in off-grid applications, hybrid systems can provide continuous power supply to remote locations by integrating hydrogen storage with battery systems, thereby ensuring reliability even in the absence of direct renewable energy generation [10].

Recent studies emphasize that one of the most critical cost determinants in green hydrogen production is the cost of renewable energy. For instance, it has been observed that the production cost of green hydrogen varies significantly depending on the type of renewable energy source utilized. The integration of high-capacity renewable energy sources, such as wind and solar power, facilitates the efficient operation of electrolyzers, thereby substantially reducing the levelized cost of hydrogen [11],[12].

A comprehensive review of the literature on hybrid renewable energy systems integrated into hydrogen production plants reveals that optimization studies are often conducted using oversimplified methodologies and basic formulas. Such approaches may limit the depth of analysis and the potential for accurately capturing the complexities of these systems. Additionally, research focusing specifically on hybrid configurations involving PV and wind energy systems is relatively scarce, highlighting a gap in the existing body of knowledge.

In this study, a detailed and comprehensive approach was adopted to address these limitations. A hybrid system comprising PV panels, wind turbines, and an electrolyzer was modeled extensively within the Simulink environment. The

model incorporated technical, economic, and operational parameters to ensure a realistic representation of the system. System sizing and configuration optimization were performed using the Response Surface Methodology (RSM), a technique less frequently employed in the literature but capable of capturing complex interactions between system variables and delivering robust optimization results.
Furthermore, sensitivity analyses were conducted to evaluate the effects of various critical variables, such as efficiency, capacity factors, economic parameters, and operational conditions, on the system's performance. These analyses provided valuable insights into the resilience and adaptability of the hybrid system under different scenarios. By integrating detailed modeling with advanced optimization techniques, this study offers a significant contribution to literature and demonstrates a novel approach to designing and optimizing hybrid renewable energy systems for hydrogen production.

2. MATERIALS AND METHODS

In this study, a comprehensive mathematical modeling of a off-grid system comprising PV panels, wind turbines, a PEM electrolyzer, and a compressor was developed and implemented in the Matlab-Simulink environment, as illustrated in Figure 1. Unlike most models in literature, which often rely on simplified equations, our approach employs detailed mathematical models to enhance accuracy and reliability. An economic model was integrated with the mathematical framework to calculate the Levelized Cost of Hydrogen, and based on system variables, an optimization model was developed using Response Surface Methodology to determine the most suitable system size. Finally, a sensitivity analysis was conducted to examine the influence of key variables on the system's performance and economic viability.

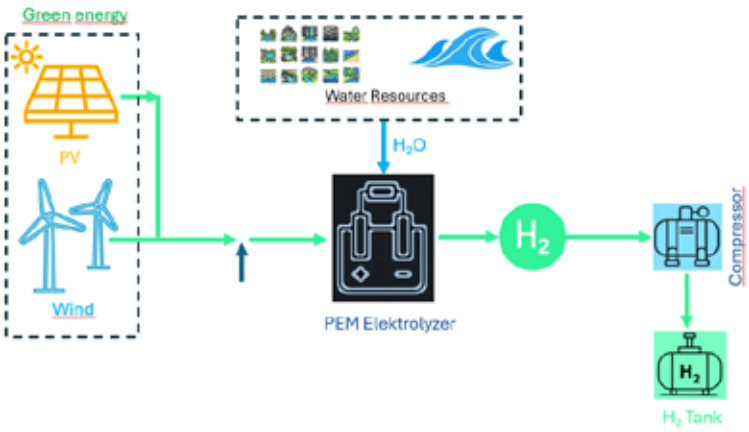

Fig. 1. The diagram of the modelled system

2.1. Mathematical Modelling

The electrical characteristics of the PV module and the equivalent circuit of a PV cell with a single diode, on which the mathematical model is based, are presented in Figure 2.

Spesifications	Value	Unit
Open Circuit Voltage (Voc)	32.8	V
Short Circuit Current (Isc)	8.1	A
Number of Cells	54	Adet
Module Area	1.222	m²
Maximum Power Current (Imp)	7.7	A
Maximum Power Voltage (Vmp)	26	V

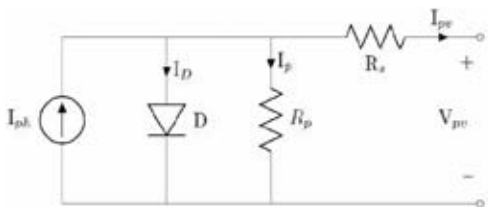

Fig. 2. Spesifications and single-diode model of the modelled PV

All the equations for pv modelling are given below:

Photon Current

$$I_{ph} = [I_{sc} + K_i(T - T_n)]x\left(\frac{G}{Gn}\right)$$

Reverse Sat. Cur.

$$I_{rs} = \frac{I_{sc}}{e^{\left(\frac{qV_{oc}}{nN_sKT}\right)} - 1}$$

Saturation Cur.

$$I_0 = I_{rs}\left[\frac{T}{Tn}\right]^3 e^{\left[\frac{qE_{go}\left(\frac{1}{T_n}-\frac{1}{T}\right)}{nK}\right]}$$

I shunt

$$I_{sh} = \frac{V + IR_s}{R_{sh}}$$

I output

$$I = I_{ph} - I_0\left[e^{\frac{q(V+IR_s)}{nKNT}} - 1\right] - I_{sh}$$

The specifications of the turbine used in the study are presented in Table 2.

Table 1. Spesifications of the modelled WT

Manufacturer	LEITWIND AG / SPA (Italy)	**Number of Blades**	3
Model	LTW77	**Maximum Rotor Speed**	18 U/min
Cut-in Wind Speed	3 m/s	**Hub Height**	80 m
Cut-out Wind Speed	25 m/s	**Power Output**	1000 kW
Rotor Area	4.608 m²	**Blade Pitch Angle (β)**	0
Rotor Diameter	76,6 m		

All the equations for wind turbine modelling are given below:

Electrical Output

$$P_m = \frac{1}{2} Cp(\lambda_i)\rho A V^3$$

Performance Coefficent

$$Cp = C_1 e^{(C_2\lambda_i)} + C_3 e^{(C_4\lambda_i)}$$

Speed Rate

$$\frac{1}{\lambda_i} = \frac{1}{\lambda + 0.08\beta} - \frac{0.035}{1+\beta^3}$$

Speed Constant

$$\lambda = \frac{w_r R}{V}$$

Figure 3 illustrates the equivalent circuit structure of a single PEM electrolyzer cell. This circuit model enables the analysis of current-voltage relationships among the components representing the internal dynamics of the PEM electrolyzer [13].

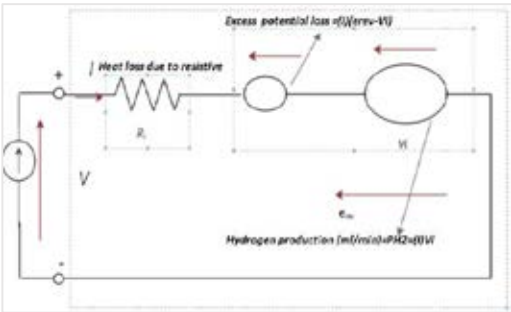

Fig. 3. The modelled PEM electrolyzer model

All the equations for PEM electrolyzer modelling are given below:

Current-Voltage

$$V(T,P) = E_{rev}(T,P) - E_{rev}(T,P)e^{\frac{5I}{0.02}} + I.R_i(T,P)$$

Reversible Voltage

$$E_{rev}(T,P) = E_{rev_0} + \frac{R(273+T)}{2F} ln\left(\frac{P}{P_0}\right)$$

H2 Rate

$$v_H = \frac{60000 v_m I}{2F}$$

$$V(T,P) = \begin{bmatrix} 0 & V \le E_{rev}(T,P) \\ \frac{1}{R_i(T,P)}V - E_{rev}(T,P) & V \ge E_{rev}(T,P) \end{bmatrix}$$

İdeal Voltage

$$V_i = \frac{\Delta G}{2F}$$

Molar volume

$$v_m = \frac{R(273+T)}{P}$$

Electrolyzer resistant

$$R_i(T,P) = R_{i_0} + k ln\left(\frac{P}{P_0}\right) + dR_T(T - T_0)$$

$$\Delta G = 285.84 - 163.2(273+T)$$

The specifications of the electrolyzer used in the study are presented in Table 3.

Table 2. Spesifications of the modelled WT

Property	Value	**Property**	Value
Nominal Current Density	1-2 A cm⁻²	**Voltage Efficiency (LHV)**	50 - 68 %
Voltage Range	1.4-2.5 V	**Size**	1 MW
Cell Pressure	<30 bar	**Electrode Area**	1500 cm²

The equations used for calculating the LCOH are provided below:

Annualized Cost

$$ACS(\$) = \sum_{i=1}^{n} N_i \times [(CAPEX_i + RC_i \times F_i(rdr, L_i, y_i)) \times CRF(rdr, R) + OPEX_i]$$

Capital Recovery Cost

$$CRF = \frac{r_{dr}\,(1+r_{dr})^R}{(1+r_{dr})^R - 1}$$

LCOH

$$\mathrm{LCoH}\left(\frac{\$}{\mathrm{kg}}\right) = \frac{\mathrm{ACS}}{\mathrm{AP}_{\mathrm{H_2}}}$$

NPV

$$F = \sum_{n=1}^{Q_i} \frac{1}{[1+ir]^{L_i \times n}}$$

3. RESULTS AND DISCUSSION

The Response Surface Methodology (RSM) was utilized to analyze the interactions among 5 parameters: PV and wind turbine sizes, electrolyzer temperature, pressure, and current density, in relation to the cost of hydrogen production. A Box-Behnken design was employed, and the lower and upper limits of the parameters are provided in Table 3.

Table 3. Design parameters of the Response surface methodology

	Pv Size (MW)	WT Size (MW)	Pressure (Bar)	Temperature (^{0}C)	Current Density (A/cm2)
Lower Limit	1	1	5	50	1000
Upper Limit	5	5	30	80	3500

The Pareto chart given in Figure 4 highlights that current density (E) is the most influential factor affecting the LCOH, with a standardized effect value far exceeding those of other parameters. Additionally, interaction terms involving current density (EE) and wind turbine size (BB) also demonstrate significant impacts. This underlines the critical role of optimizing these variables to achieve cost reductions.

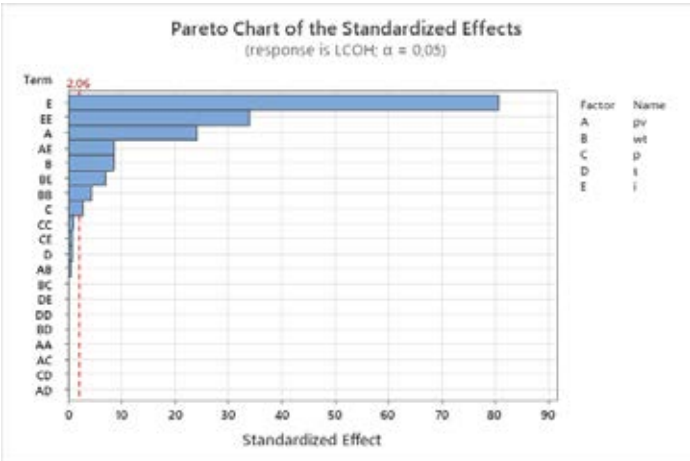

Fig. 4. Pareto Analysis of Factor Effects on LCOH

The regression analysis further emphasizes the importance of specific parameters. Among the linear terms, PV size, wind turbine size, and current density are statistically significant (P-value < 0.05), with current density having the most pronounced effect. Quadratic terms also reveal that the square of current density is highly significant, indicating a nonlinear relationship with LCOH. Furthermore, interaction terms such as those between PV size and current density, and wind turbine size and current density, are shown to be statistically meaningful.

The regression equation for LCOH is:

LCOH = 19.60 + 1.792 * PV + 0.510 * WT - 0.0516 * P + 0.0040 * T - 0.010191 * I + 0.0019 * PV² + 0.0952 * WT² + 0.000503 * P² - 0.000047 * T² + 0.000002 * I² - 0.0197 * PV * WT + 0.00019 * PV * P + 0.00002 * PV * T - 0.000437 * PV * I + 0.00090 * WT * P + 0.00046 * WT * T - 0.000354 * WT * I + 0.000008 * P * T + 0.000007 * P * I - 0.000001 * T * I

Where, PV and WT are the size of pv and WT, T is temperature, P is pressure, and I is current density of electrolyzer.

The optimization results indicate that the minimum LCOH achieved is 4.99, with optimal parameter settings of PV size at 1 MW, wind turbine size at 2.82 MW, pressure at 26.46 bar, temperature at 80°C, and current density at 3070.71 A/cm². The model shows a high desirability of 1.00, confirming the optimal solution's reliability. The predicted LCOH has a standard error of 0.269, with a 95% confidence interval of (4.44; 5.54) and a 95% prediction interval of (4.23; 5.75), demonstrating strong model accuracy and prediction capability.
Using the optimized parameters obtained from the design process, the LCOH was calculated in Simulink for varying discount rates. Figure 5. illustrates the relationship between the discount rate and LCOH. As the discount rate increases from 4% to 12%, the LCOH shows a consistent upward trend, starting at \$3.87/kgH_2 at a 4% discount rate and rising to \$6.82/kgH_2 at a 12% discount rate.

Fig. 5. The LCOH variation with changing discount rate

With advancements in technology, the costs of renewable energy components are continuously decreasing. In line with this trend, an analysis was conducted in Simulink to evaluate the impact of reduced initial expenditures on the LCOH. The results show that as the initial expenditure rate decreases from 1 to 0.8, the LCOH significantly drops from \$5.22/kgH_2 to \$4.18/kgH_2. This highlights the direct correlation between technological advancements, reduced costs, and the economic feasibility of hydrogen production systems.

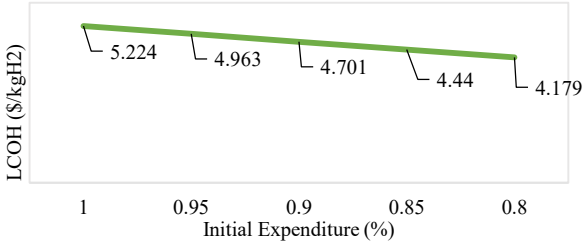

Fig. 6. The LCOH variation with changing initial expenditure

4. CONCLUSIONS

The size optimization was performed using the RSM for a system comprising PV and WT units, as well as an electrolyzer. The optimization considered key parameters such as PV and WT capacities, electrolyzer pressure, temperature, and current density. The results indicate that the optimal configuration includes a 1 MW PV, 2.88 MW WT, an electrolyzer pressure of 26.46 bar, a temperature of 80°C, and a current density of 3070.71 A/cm², achieving an LCOH of \$4.99. The analysis was conducted using Simulink, which allowed for a detailed and dynamic modeling approach.
Unlike many studies in the literature that rely on simplified formulas, our approach incorporated detailed and comprehensive equations to enhance the accuracy of the results. Furthermore, sensitivity analyses were conducted to evaluate the impact of various parameters on system performance.
For future work, integrating biogas into the system to develop a triple-hybrid configuration could be a promising direction. Additionally, optimizing the production of other power-to-X gases, such as e-methane and e-methanol, could further expand the scope and applications of such systems.

REFERENCES

[1] M. Sharifzadeh, A. Sikinioti-Lock, and N. Shah, Renewable and Sustainable Energy Reviews **108**, 513 (2019).
[2] E. Grant, K. Brunik, J. King, and C.E. Clark, J Phys Conf Ser **2767**, 082019 (2024).
[3] T. Shi, L. Gu, Z. Xu, and J. Sheng, Processes **12**, 541 (2024).
[4] D. Scamman, M. Newborough, and H. Bustamante, Int J Hydrogen Energy **40**, 13876 (2015).
[5] A.I. Atteya, D. Ali, and N. Sellami, Energies (Basel) **16**, 5449 (2023).
[6] N. Wang, Z. Feng, and X. Guo, Int J Energy Res **46**, 24158 (2022).
[7] S.J. Mirazimi and M. Fathi, 917 (2011).
[8] Y. Lin and L. Fu, Ieee Access **10**, 85355 (2022).
[9] S. Zhang, X. Wang, B. Li, J. Dai, and J. Zheng, 412 (2024).

[10] D. Scamman, M. Newborough, and H. Bustamante, Int J Hydrogen Energy **40**, 13876 (2015).
[11] Q. Hassan, Proceedings of the Institution of Mechanical Engineers Part a Journal of Power and Energy **238**, 569 (2023).
[12] A. Acharya, J Sustain Dev **16**, 106 (2023).
[13] A. Beainy, N. Karami, and N. Moubayed, in *International Conference on Renewable Energies for Developing Countries 2014* (IEEE, 2014), pp. 145–149.

SPATIAL MULTICRITERIA DECISION-MAKING FOR GREEN HYDROGEN PRODUCTION: A CASE STUDY OF SOUTHERN MARMARA, TURKEY

[*1,3]*Metin Gul*, [2,3]*Ersin Akyuz*,
[1] Balikesir University, Department of Vocational School, Balikesir, 10145, Türkiye
[2] Balikesir University, Department of Electrical and Electronics Engineering, Balikesir, 10145, Türkiye
[3]Renewable Energy Research and Application Center, Balıkesir University

*Corresponding author e-mail: metingul@balikesir.edu.tr

ABSTRACT
This study integrates Geographic Information System (GIS), Analytical Hierarchy Process (AHP), and the TOPSIS method within the Multicriteria Decision-Making (MCDM) framework to assess the potential for green hydrogen production in the Southern Marmara region of Turkey. By evaluating technical, economic, and environmental criteria across 12 sub-criteria, suitable sites for solar and wind-based green hydrogen production were identified. Results reveal that 44636 ha of the study area, particularly in western and northern Balıkesir, is highly suitable for constructing solar-wind powered green hydrogen plants. These identified locations hold significant potential for fostering the green hydrogen industry in the region. Furthermore, the applied methodology can be adapted for assessing green hydrogen production potential in other regions, contributing to national and global green hydrogen roadmaps. This approach underscores the importance of combining advanced spatial analysis with decision-making techniques to support sustainable energy strategies.
Keywords: Hydrogen, Site selection, TOPSIS, AHP

1. INTRODUCTION

The selection of optimal locations for renewable energy projects, particularly in wind and solar energy, plays a crucial role in advancing sustainable energy systems. Multi-Criteria Decision Making (MCDM) methods are widely utilized for site selection, allowing experts to evaluate and balance various conflicting factors while prioritizing alternatives across multiple dimensions. Among these, AHP is particularly notable for its ability to decompose complex problems into a hierarchical structure, facilitating the evaluation of criteria and sub-criteria through systematic pairwise comparisons. [1],[2]. This approach has been particularly effective in renewable energy site selection, as demonstrated by research on wind energy projects [3],[4]. AHP's strength lies in determining the relative importance of various criteria, which is critical for prioritizing locations based on their suitability for energy production. However, AHP has limitations, such as the potential for inconsistency in pairwise comparisons and subjective biases in weight assignments [5].

TOPSIS, in contrast, mitigates some of these challenges by ranking alternatives based on their geometric proximity to an ideal solution—defined as the most favorable outcome across all criteria. This method not only offers a clear range of options but also enhances decision-making by incorporating relative proximity to the ideal scenario [6]. One advantage of TOPSIS over AHP is its ability to handle a larger number of criteria without requiring extensive pairwise comparisons, making it suitable for complex scenarios involving numerous factors such as environmental impact, cost-effectiveness, and social acceptability [7].

On the other hand, site selection for hydrogen production facilities involves additional challenges due to the complexity of factors involved. While AHP and TOPSIS are commonly used, many studies rely on a narrow set of criteria, potentially neglecting key environmental, social, and economic considerations critical to the sustainability of hydrogen production sites [8]. This limitation can lead to suboptimal decisions that fail to align with broader sustainability goals or community needs. Furthermore, inadequate integration of geographical and spatial data in MCDM analyses remains a significant gap. Geographic Information Systems (GIS) are essential for improving site selection methodologies, yet many studies continue to use conventional AHP and TOPSIS approaches without fully leveraging GIS capabilities. As a result, geographical factors such as proximity to renewable energy sources, infrastructure availability, and environmental constraints are often underrepresented in the analysis [9]. Combining GIS with MCDM techniques like AHP and TOPSIS can provide a more comprehensive understanding of site suitability and enhance decision-making outcomes.

Building on these considerations, Messaoudi et al. (2019) integrated AHP with GIS for selecting sites for wind-powered hydrogen refueling stations, showcasing the potential of combining spatial analysis with MCDM methods. Despite these advancements, the application of such methods specifically for green hydrogen production remains limited. Future research should focus on refining these methodologies to incorporate broader sustainability metrics, stakeholder engagement, and geographic analysis for identifying optimal locations for hydrogen facilities [10]. Additionally, studies such as Jozaghi et al. (2018) demonstrate the effectiveness of MCDM techniques in site selection for dams, emphasizing the potential for analogous applications in hydrogen production. However, criteria unique to hydrogen, including renewable energy accessibility, infrastructure readiness, and environmental considerations, warrant further investigation

to address existing gaps and strengthen site selection frameworks in this emerging field [11].

A significant body of literature has examined the costs associated with PV-wind-driven hydrogen production, both under current conditions and in future projections. These studies often focus on regions with optimal meteorological conditions, such as high solar radiation or wind potential, to showcase the feasibility of hydrogen production. By addressing the existing gaps in the literature, this study aims to serve as a valuable resource for policymakers involved in planning and decision-making processes regarding green hydrogen production facilities in Turkey. Given the global emphasis on reducing dependence on hydrocarbons, our research highlights the potential of blending hydrogen with natural gas pipelines as a promising strategy. Turkey's strategic geographical location, acting as a critical bridge between energy-producing and energy-consuming regions, further strengthens its role as a prospective energy hub. Capitalizing on its abundant renewable energy resources for hydrogen production and integrating this hydrogen into natural gas networks could provide substantial benefits. This transition holds considerable importance not only for Turkey but also for Europe's broader efforts toward a sustainable and renewable energy future. In this context, Balıkesir was selected as the focus area for this study due to the ongoing development of a hydrogen production facility project in the region. By exploring this potential, our research aims to contribute significantly to the strategic planning of green hydrogen infrastructure and its integration into existing energy systems.

2. MATERIALS AND METHODS

In this study, the criteria weights were first determined using the Analytical Hierarchy Process (AHP) method. Subsequently, the criteria were rated and evaluated within ArcMap, and unsuitable locations were excluded from the analysis. Based on these evaluations, a Weighted Overlay Analysis was conducted to identify suitable areas along with their respective suitability levels. The coordinate data, originally in point format, were then converted to polygons. Polygons larger than 10 hectares were selected and exported to Excel for further processing. A TOPSIS analysis was then applied to these polygons to identify the most suitable ones. Finally, the selected polygons were re-mapped in ArcMap and visualized on Google Earth to provide a comprehensive spatial representation.

2.1. Multi-Criteria Analysis

The Multi-Criteria Analysis (MCA) was conducted using the first AHP, which is widely applied to assign weights to various criteria.
The AHP methodology follows these steps:

The decision problem is defined, and the goal is clearly identified. A hierarchical structure is created, encompassing the goal, criteria, and sub-criteria. Saaty's 9-point scale [12] is performed for comparison matrix. A pairwise comparison matrix is constructed using Saaty's scale (Eq. 1),

$$A(n_i x n_j) = \begin{bmatrix} a_{11} & a_{12} & \cdots & a_{1n} \\ a_{21} & a_{22} & \cdots & a_{2n} \\ \cdots & \cdots & \cdots & \cdots \\ a_{n1} & a_{n2} & \cdots & a_{nn} \end{bmatrix} \quad (1)$$

The pairwise comparison matrix is normalized using Eq. 2:

$$N_{ij} = \frac{a_{ij}}{\sum_{i=1}^{n} a_{ij}} \quad (2)$$

where i,j=1,2,…,n, The row averages of the normalized matrix form the priority vector.

Consistency is checked by multiplying the pairwise comparison matrix with the priority vector to obtain the weighted sum matrix. Each element of the weighted sum matrix is divided by its corresponding priority vector to calculate consistency values. The average of these values provides λi. The Consistency Index (CI) is calculated using Eq. 3, and the Consistency Ratio (CR) is determined using Eq. 4. A CR value below 0.1 indicates acceptable consistency.

$$Concistency\ Index\ (CI) = \frac{\lambda_{max} - n}{n - 1} \quad (3)$$

$$Concistency\ Ratio\ (CR) = \frac{CI}{RI} \quad (4)$$

Table 1. Random inconsistency index (RI) values

n	1	2	3	4	5	6	7	8	9	10
RI	0	0	0.58	0.9	1.12	1.24	1.32	1.41	1.45	1.49

TOPSIS Methodology:
The goal, alternatives, and criteria are defined. A decision matrix is constructed, where the features of alternatives based on the criteria are represented.

Alternatives	Features
a1	y11 y12 ... y1k
a2	y21 y22 ... y2k
a3	yn1 yn2 ... ynk

The normalized decision matrix is calculated using Equation (5):

$$\boldsymbol{Z_{ij}} = \frac{\boldsymbol{y_{ij}}}{\sqrt{\sum_{i=1}^{n} \boldsymbol{y_{ij}^2}}} \quad \boldsymbol{i = 1, \dots, n; j = 1, \dots, k} \tag{5}$$

The weighted normalized decision matrix is determined using Equation (6), where wij represents the weight of the jth criterion

$$\boldsymbol{X_{ij}} = \boldsymbol{w_{ij}\ x\ Z_{ij}} \quad \text{i=1, …, n;j=1, …, k} \tag{6}$$

The maximum and minimum values for each column are identified:

$$\begin{aligned} \mathbf{A}^* &= \{\mathbf{x_1^*}, \mathbf{x_2^*}, \dots, \mathbf{x_k^*}\} \ (\textbf{max values}) \\ \mathbf{A}^- &= \{\mathbf{x_1^-}, \mathbf{x_2^-}, \dots, \mathbf{x_k^-}\} \ (\textbf{min values}) \end{aligned} \tag{7}$$

The distance from the positive ideal solution (PIS) is calculated using Equation (8):

$$\boldsymbol{S_i^*} = \sqrt{\sum_{i=1}^{k} \left(\boldsymbol{x_{ij} - x_j^*}\right)^2} \quad \boldsymbol{i = 1, \dots, n} \tag{8}$$

The distance from the negative ideal solution (NIS) is calculated using Equation (9):

$$\boldsymbol{S_i^-} = \sqrt{\sum_{j=1}^{k} \left(\boldsymbol{x_{ij} - x_j^-}\right)^2} \quad \boldsymbol{i = 1, \dots, n} \tag{9}$$

The relative closeness to the ideal solution is determined using Equation (10):

$$\boldsymbol{C_i^*} = \frac{\boldsymbol{S_i^-}}{\boldsymbol{S_i^- + S_i^*}} \quad \boldsymbol{0 \le C_i^* \le 1,\ \ i = 1, \dots, n} \tag{10}$$

Alternatives are ranked based on C_i^* values, where the alternative closest to the ideal solution has the highest priority.

3. RESULTS AND DISCUSSION

Figure 3 illustrates the maps generated for each criterion using Euclidean Distance in ArcMap. These maps facilitate the identification of spatial patterns and relationships within the analyzed data, enabling more informed and data-driven decision-making processes.

The land suitability map in Fig. 2. identifies the most optimal location for establishing a solar-wind-based hydrogen production plant within the Balıkesir region. The total suitable area is calculated to be 44636 hectares. This map was created using ArcMap's Weighted Overlay Analysis, which integrates criteria weighted through the AHP. The map is color-coded based on the degree of suitability, providing a visual representation of varying levels of appropriateness across the region. It is observed that the western and northern parts of Balıkesir exhibit higher suitability, making these areas particularly favorable for the proposed plant's development.

The TOPSIS analysis was utilized alongside the AHP-based weighted criteria to identify the most suitable site for a wind-solar-based hydrogen production plant in the Balıkesir region. TOPSIS enabled the ranking of potential sites by calculating the relative closeness of each site to the ideal solution.

The analysis revealed that Site X emerged as the most suitable location, achieving the highest TOPSIS score of 0.867115. This site demonstrated the closest proximity to the ideal solution, indicating its superior alignment with the weighted 12 criteria. Additionally, the analysis identified the top 25 most suitable locations, as presented in Figure 3, providing a comprehensive ranking for site selection. This highlights the effectiveness of the integrated AHP-TOPSIS approach in systematically evaluating site suitability for the proposed hydrogen production plant.

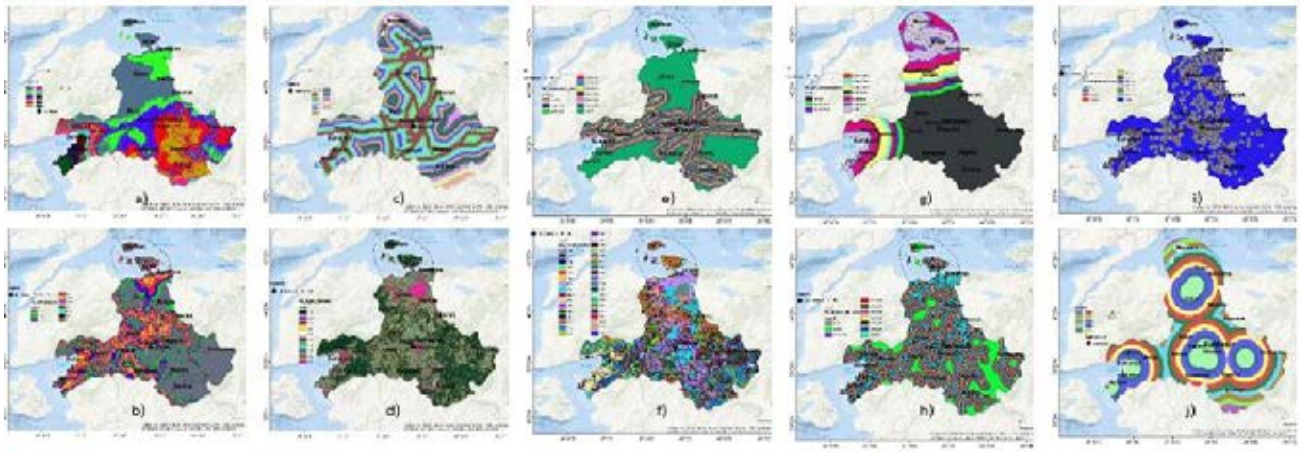

Fig. 1. Euclidean distance analyses of selection criteria for Balıkesir in ArcMap: The criteria include a) solar radiation, b) wind potential, c) distance to electrical power lines, d) slope, e) distance to fault lines, f) land use, g) distance to the sea, h) distance to rivers, i) distance to settlements, and j) distance to industrial zones

Fig. 2. Weighted overlay analysis for site selection in Balıkesir using AHP

Fig. 3. Top 25 most suitable locations identified through TOPSIS analysis

To further illustrate the findings, the top 25 most suitable locations identified through the analysis were visualized using Google Earth (Figure 4). This graphical representation provides a geospatial perspective, enabling a clear understanding of the spatial distribution of the most optimal sites across the Balıkesir region.

Fig. 4. Visualization of the top 25 most suitable locations using Google Earth.

4. CONCLUSIONS

This study utilized an integrated approach combining AHP and TOPSIS methods to determine the most suitable location for the installation of a solar-wind-powered hydrogen production plant. The AHP method was employed to calculate the criteria weights, while TOPSIS facilitated the ranking of alternatives based on their alignment with these weighted criteria. The results can support the adoption of sustainable energy in Turkey, by guiding stakeholders, investors, and policymakers in making informed decisions on solar-wind-based hydrogen plant construction.

Site selection is a critical step in renewable energy projects, as it significantly influences their feasibility and efficiency. By addressing this stage systematically, this study provides a foundation for future research, including detailed optimization, energy performance assessments, and comprehensive economic analyses. These subsequent steps will further enhance the decision-making process, ensuring both technical and economic viability for hydrogen production initiatives.

REFERENCES

[1] P.K. Choudhuri, Journal of the Institution of Engineers (India) Series E **95**, 63 (2014).
[2] M. Haddad, D. Sanders, N. Bausch, G. Tewkesbury, A. Gegov, and M. Hassan, 1303 (2018).
[3] O. Artun, European Journal of Science and Technology (2020).
[4] M. Maklad, H. Tawfeek, and G. El-Fiky, The Egyptian International Journal of Engineering Sciences and Technology **40**, 53 (2022).
[5] A. Yazdani-Chamzini, M.M. Fouladgar, E.K. Zavadskas, and S.H.H. Moini, Journal of Business Economics and Management **14**, 957 (2013).
[6] M. Shao, Z. Han, J. Sun, C. Xiao, S. Zhang, and Y. Zhao, Renew Energy **157**, 377 (2020).
[7] M.P. de Souza, L.C. Bernardo Moura, C.A. Nunes Cosenza, S. de Macedo Amaral, R.P. Cunha Telles, M.O. Lemos Alexandre, S. Barbosa, B. de Sousa Elia, M.F. Zelaya Correia, A.C. de Lemos Oliveira, R.V. da Silva, and T.R. Pinheiro, Pertanika J Sci Technol **32**, 551 (2024).
[8] M. Marzouk and M. Sabbah, Cleaner Environmental Systems **2**, 100034 (2021).
[9] G.R. Faqe Ibrahim, K. Wali Mahmood, and M.M. Mahmud, (2020).
[10] D. Messaoudi, N. Settou, B. Negrou, S. Rahmouni, B. Settou, and I. Mayou, Energy Procedia **162**, 67 (2019).
[11] A. Jozaghi, B. Alizadeh, M. Hatami, I. Flood, M. Khorrami, N. Khodaei, and E. Ghasemi Tousi, (2018).
[12] R.W. Saaty, Mathematical Modelling **9**, 161 (1987).

A DUAL-LAYERED CONTROL STRATEGY FOR ULTRACAPACITOR/PEMFC HYBRID SYSTEMS IN MICRO-FCEVS

[1,2]*Alper Yılmaz*, [1]*Necati Aksoy*, [1,2*]*Gökay Bayrak*
[1] Bursa Technical University, Renewable Energy Systems and Smart Grids Laboratory, Department of Electrical and Electronics Engineering, 16300, Bursa, Turkey
[2] Bursa Technical University, Electric Vehichles Application and Research Center, 16300, Bursa, Turkey

* E-mail: gokay.bayrak@btu.edu.tr

ABSTRACT
This study presents a novel dual-layered control strategy for a 1 kW micro-mobility vehicle powered by a proton exchange membrane fuel cell (PEMFC) and ultracapacitor hybrid system. The proposed approach consists of two main components: motor drive control, which regulates the speed and operation of the electric motor, and an energy management system utilizing a DC/DC converter to optimize power flow between the fuel cell, ultracapacitor, and load. This hybrid configuration leverages the complementary characteristics of PEMFCs and ultracapacitors, enabling efficient handling of transient and steady-state power demands. Simulation results demonstrate the effectiveness of the control strategy, achieving rapid dynamic response, improved energy efficiency, and enhanced system stability. The ultracapacitor supplies transient power demands, while the PEMFC handles steady-state operation, minimizing fuel cell degradation and extending its operational lifespan. This approach shows significant potential for sustainable and efficient micro-mobility solutions, paving the way for future advancements in hybrid energy systems.

Keywords: Hydrogen energy, Micro-mobility applications, Proton Exchange Membrane Fuel Cell (PEMFC), Ultracapacitor hybrid systems, Energy management strategies.

1. INTRODUCTION

The increasing need for sustainable and efficient transportation solutions has driven significant advancements in the field of electric mobility [1]. Among the alternatives to conventional internal combustion engines, proton exchange membrane fuel cells (PEMFCs) have emerged as a promising power source due to their high efficiency, environmental benefits, and zero-emission characteristics [2]. However, the inherent limitations of PEMFCs, such as their slow dynamic response and inability to handle transient power demands, necessitate the integration of complementary energy storage systems. Ultracapacitors, with their rapid charge-discharge capabilities and high power density, present an ideal solution for balancing these limitations in hybrid systems.

Hybridization of PEMFCs with ultracapacitors has gained significant attention in recent years due to its potential to address the limitations of standalone fuel cell systems. PEMFCs, while offering high energy density and zero emissions, are inherently limited by their slow dynamic response and challenges in meeting transient power demands. Ultracapacitors, on the other hand, are characterized by their high power density, rapid charge-discharge capabilities, and excellent cycle life, making them an ideal complement to fuel cells in hybrid configurations [3].

Various hybridization topologies have been explored in the literature, including fully active, semi-active, and passive configurations, each differing in the number and role of DC/DC converters. Fully active systems, as discussed in studies [4,5], provide maximum control over power distribution but come at the cost of increased system complexity, weight, and energy losses. Semi-active configurations, which reduce the number of converters, have been shown to improve efficiency while maintaining some degree of control over energy management. Passive configurations, where ultracapacitors and fuel cells are directly connected, leverage the inherent characteristics of each component to achieve a natural power split. For instance, ultracapacitors handle transient loads, while fuel cells provide steady-state power. Studies such as [6] and [7] demonstrate the feasibility of this approach in automotive applications, emphasizing its ability to reduce fuel cell stack size, minimize hydrogen consumption, and enhance overall system efficiency.

Recent advancements in control strategies have also been pivotal in optimizing the performance of PEMFC/ultracapacitor hybrid systems. Model predictive control techniques have been employed to minimize fuel cell degradation and hydrogen consumption, as highlighted in [8]. Additionally, adaptive droop control methods have been proposed for dynamic power distribution, ensuring stable operation under varying load conditions. While significant progress has been made, challenges remain in ensuring robust control, optimizing component sizing, and improving the overall energy efficiency of these systems. Future research is likely to focus on the integration of machine learning-based energy management strategies and the development of lightweight and cost-effective hybrid configurations tailored for specific applications, such as micro-mobility and unmanned vehicles.

In light of these considerations, this study proposes a dual-layered control strategy for a 1 kW micro-mobility vehicle powered by a PEMFC and ultracapacitor hybrid system. The control framework is divided into two key components: the motor drive control, which ensures precise operation and speed regulation, and the energy management system, which utilizes a DC/DC converter to optimize power distribution between the fuel cell, ultracapacitor, and the load. This paper

focuses on the design, implementation, and evaluation of this novel control strategy, highlighting its potential to improve the performance of small-scale electric mobility solutions.

2. PEMFC-ULTRACAPACITOR HYBRIDIZATION MODEL

Fig.1 illustrates the hybrid power system architecture integrating a PEMFC and an ultracapacitor to drive an electric motor [9]. The hydrogen tank supplies fuel to the PEMFC, which generates electrical energy. This power is then conditioned by Converter-I before being supplied to the inverter, which drives the electric motor. In parallel, the ultracapacitor, managed through DC/DC converter-II, provides transient power support to enhance system dynamics and efficiency [10]. This dual energy source approach ensures stable power delivery while optimizing energy efficiency and component longevity. The detailed electrical characteristics and specifications of the PEMFC and ultracapacitor are provided in Table 1.

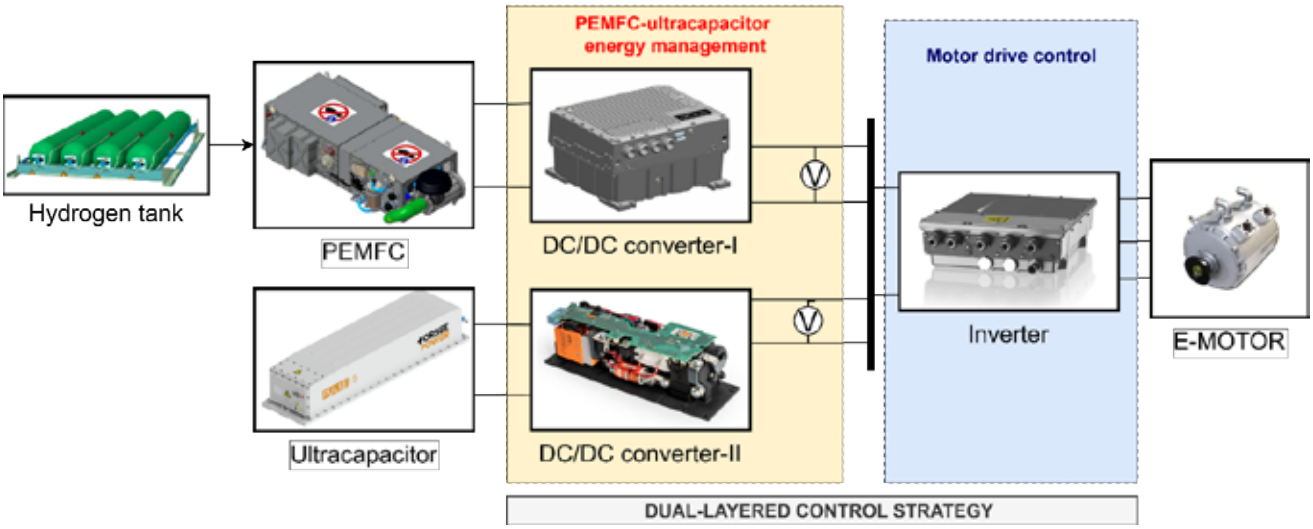

Fig. 1. PEMFC-Ultracapacitor Hybridization Model

Table 1. Parameters in Fuel cell-ultracapacitor system model [9,10]

PEMCF Parameters	Value	Ultracapacitor Parameters	Value
Rated power (kW)	1	Rate discharge capacitance (F)	1.25 F
Operating Temperature (℃)	55	C tolerance (%)	-10 to +20
Nerst voltage of one cell (V)	1.115	Operating Temperature (℃)	-40 to +70
Number of Cells	42	Nominal voltage (V)	50
Nominal stack efficiency (%)	*46*	Nominal current (A)	5
Nominal air flow rate (lpm)	*2400*	Maximum voltage (V)	56
Nominal fuel flow rate (lpm)	*12.2*	Maximum peak current (A)	15
Fuel supply pressure (bar)	*1.5*	Equivalent series resistance	mΩ at 1000Hz
Air supply pressure (bar)	*1*		
Nominal composition (H2) (%)	*99.95*	-	-
Nominal composition (O2) (%)	*21*	-	-

3. DUAL-LAYERED CONTROL STRATEGY APPROACH

The control strategy is implemented in two main parts: the motor drive, which governs the operation and speed of the electric motor, and the fuel cell-ultracapacitor energy management system, which utilizes a DC/DC converter to efficiently regulate the power flow between the fuel cell, ultracapacitor, and the load. This dual-layered approach ensures optimal performance, balancing dynamic response and energy efficiency.

(i) Fuel cell-ultracapacitor energy management: In systems integrating a fuel cell and ultracapacitor, DC/DC control plays a critical role in managing the power flow between energy sources, ensuring seamless operation by balancing the slow dynamic response of the fuel cell with the rapid energy delivery capability of the ultracapacitor. The hybrid topology presented in Fig. 1 integrates a proton exchange membrane fuel cell (PEMFC) and an ultracapacitor through a DC/DC converter to manage power flow efficiently. This configuration balances the slow dynamic response of the PEMFC with the rapid transient power delivery capability of the ultracapacitor. As observed in Fig. 2, the fuel cell provides a stable base power, ensuring continuous energy supply, while the ultracapacitor effectively handles transient loads by supplying or absorbing power instantaneously. The fuel cell further supports the system by compensating for medium-term variations in power demand. The numerical results demonstrate that the system

efficiently distributes power, with the ultracapacitor initially supplying up to 1000 W and then stabilizing, while the fuel cell fluctuates between 300 W and 800 W, adapting dynamically to system needs. This coordination reduces fuel cell stress, minimizes voltage fluctuations, and enhances overall efficiency. The ability to maintain DC bus voltage stability within ±2V despite varying loads further validates the robustness of the control strategy. These findings confirm that the proposed hybrid system effectively improves energy efficiency, extends fuel cell lifespan, and ensures reliable power delivery for micro-mobility applications.

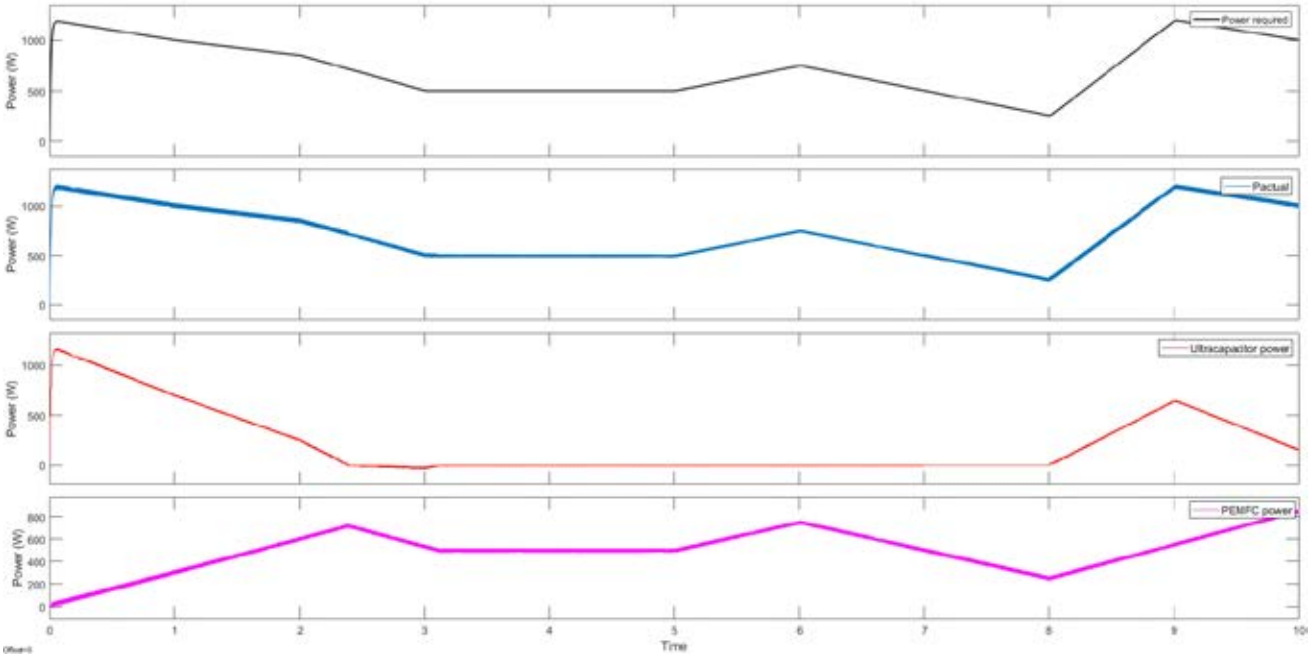

Fig. 2. Power distribution in a PEMFC-Ultracapacitor hybrid system

(ii) Motor drive control: The analyzed system incorporates a PEMFC connected to an electric motor through an inverter (Fig.3). The inverter operates using a hysteresis-based switching technique, which dynamically regulates the direct-axis current to manage the active power supplied to the motor. This control strategy enables efficient and reliable power transfer from the PEMFC to the electric motor, ensuring smooth operation across varying load conditions.

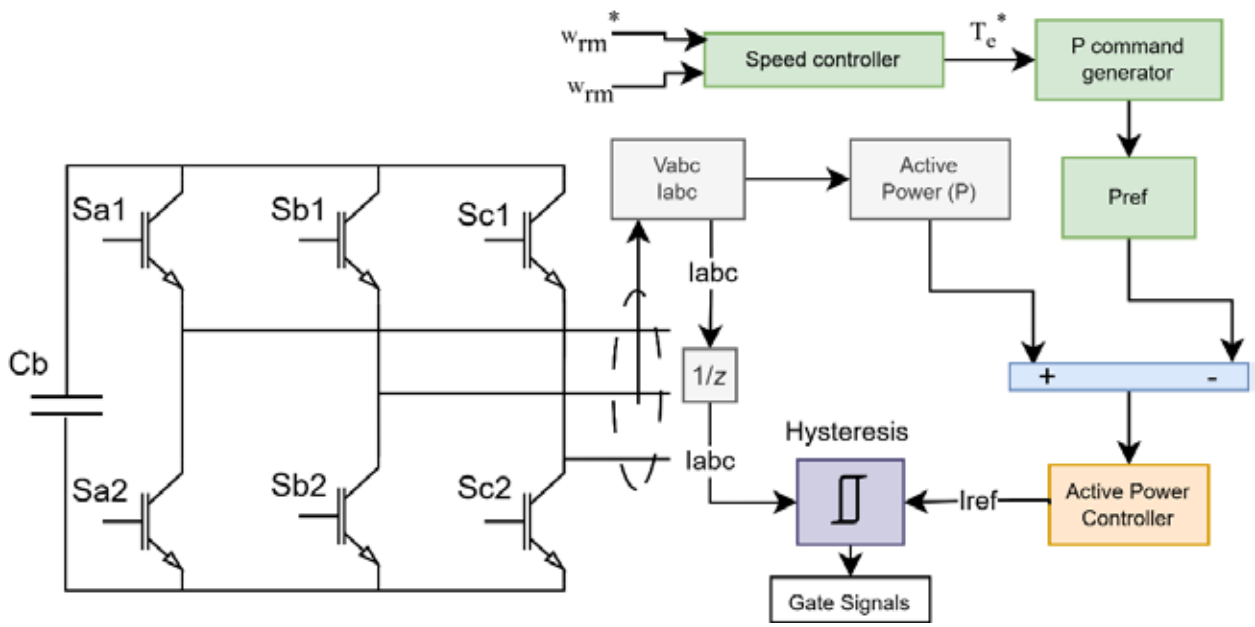

Fig. 3. Active power-based control strategy

As illustrated in Fig. 4, the motor's active power demand initially started at 1 p.u. and was successfully reached within

0.1 seconds, demonstrating the system's rapid response and effective control strategy. At 1 second, the demand sharply increased to 1.2 p.u. representing a significant load change. Despite this abrupt increase, the system smoothly transitioned to meet the higher demand, as shown by the red curve (Pactual) which tracks the reference power (pref) with minimal delay. This seamless adaptation highlights the critical role of the supercapacitor, which provides instantaneous power support during transient conditions. The supercapacitor compensates for the PEMFC's inherently slower dynamic response, ensuring uninterrupted power delivery and stability during load changes. The control strategy, implemented through the inverter, efficiently managed the power flow by adjusting the direct-axis current to match the new load while maintaining system efficiency and stability. This configuration demonstrates the synergy between the PEMFC, inverter, and supercapacitor, showcasing their ability to work together for reliable, energy-efficient, and fast power delivery in electric motor drive systems under varying load conditions.

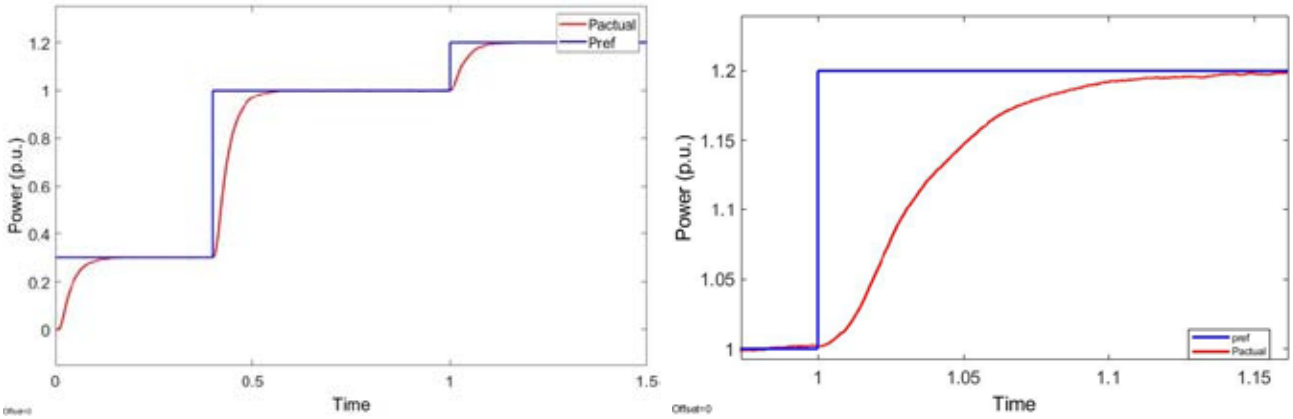

Fig. 4. Dynamic interaction between motor power demand and ultracapacitor support

4. CONCLUSIONS

This study demonstrates a dual-layered control strategy for a 1 kW micro-mobility vehicle powered by a PEMFC-ultracapacitor hybrid system. The proposed approach effectively balances power distribution, ensuring that the ultracapacitor handles transient demands, while the PEMFC provides steady-state power, improving efficiency and system stability. The dual-layered approach integrates motor drive control for precise speed regulation and an energy management system that optimizes power distribution between the PEMFC and ultracapacitor, ensuring efficient, stable, and responsive operation in dynamic load conditions. Simulation results confirm the robustness of the control strategy, maintaining DC bus voltage stability and enabling fast dynamic response to load variations. The findings highlight the feasibility of PEMFC-ultracapacitor integration for micro-mobility applications, offering a reliable and energy-efficient solution. Future work will focus on optimizing energy management and real-world validation.

REFERENCES

1. Munsi M S and Joshi R P. 2024. Comprehensive Analysis of Fuel Cell Electric Vehicles: Challenges, Powertrain Configurations, and Energy Management Systems. IEEE Access.
2. Doğan S, Haydaroğlu C, Gümüş B and Mohammadzadeh A. 2024. Innovative fuzzy logic type 3 controller for transient and maximum power point tracking in hydrogen fuel cells. International Journal of Hydrogen Energy.
3. Vural B, Boynuegri A R, Nakir I, Erdinc O, Balikci A, Uzunoglu M ... and Dusmez S. 2010. Fuel cell and ultra-capacitor hybridization: A prototype test bench based analysis of different energy management strategies for vehicular applications. . International Journal of Hydrogen Energy 35(20), 11161-11171.
4. Xun Q and Liu Y. 2019. Evaluation of fluctuating voltage topology with fuel cells and supercapacitors for automotive applications. International Journal of Energy Research 43(9), 4807-4819.
5. Xun, Q., Lundberg, S., & Liu, Y. (2021). Design and experimental verification of a fuel cell/supercapacitor passive configuration for a light vehicle. Journal of Energy Storage, 33, 102110.
6. Wu B, Parkes M A, Yufit V, De Benedetti L, Veismann S, Wirsching C, ... and Brandon N. P. 2014. Design and testing of a 9.5 kWe proton exchange membrane fuel cell–supercapacitor passive hybrid system. International Journal of Hydrogen Energy 39(15), 7885-7896.
7. Arora D, Bonnet C, Mukherjee M, Rael S and Lapicque F. 2019. Direct hybridization of PEMFC and supercapacitors: Effect of excess hydrogen on a single cell fuel cell durability and its feasibility on fuel cell stack. Electrochimica Acta 310, 213-220.
8. Pramuanjaroenkij A and Kakaç, S. 2023. The fuel cell electric vehicles: The highlight review. International Journal of Hydrogen Energy 48(25), 9401-9425.
9. Souleman N M, Tremblay O and Dessaint L A 2009. A generic fuel cell model for the simulation of fuel cell power systems. In 2009 IEEE Power & Energy Society General Meeting (pp. 1-8).
10. Do T C, Truong H V A, Dao H V, Ho C M, To X D, Dang T D and Ahn K K. 2019. Energy management strategy of a PEM fuel cell excavator with a supercapacitor/battery hybrid power source. Energies 12(22), 4362.

HYDROGEN FROM BIO-OIL: THERMODYNAMIC INSIGHTS ON STEAM REFORMING TECHNOLOGIES

[1*]Pedro J. Megía, [2,3]Claudio Rocha, [1]Arturo J. Vizcaíno, [1,4]Alicia Carrero, [1,4]José A. Calles, [2,3]Luis M. Madeira, [2,3]Miguel A. Soria
[1] Chemical and Environmental Engineering Group, Rey Juan Carlos University, c/Tulipán s/n, Móstoles 28933, Spain
[2] LEPABE – Laboratory for Process Engineering, Environment, Biotechnology and Energy, Faculty of Engineering, University of Porto, Rua Dr. Roberto Frias, 4200-465 Porto, Portugal
[3] ALiCE – Associate Laboratory in Chemical Engineering, Faculty of Engineering, University of Porto, Rua Dr Roberto Frias, 4200-465 Porto, Portugal
[4] Institute of Sustainable Technologies. Rey Juan Carlos University, c/Tulipán s/n, Móstoles 28933, Spain

*Corresponding author e-mail: pedro.megia@urjc.es

ABSTRACT
This study compares from a thermodynamic perspective different bio-oil steam reforming technologies: conventional steam reforming, autothermal reforming, and sorption-enhanced steam reforming. The effect of temperature, pressure, and steam-to-carbon ratio was evaluated on the energy requirements and hydrogen yield using Aspen Plus® V12.1. Conventional steam reforming achieves high hydrogen production but demands significant external energy due to its endothermic nature. Autothermal reforming integrates endothermic steam reforming with exothermic partial oxidation, enabling thermal neutrality and lowering energy requirements at the expense of reducing the hydrogen yield. Conversely, sorption-enhanced steam reforming by using sorbents for in-situ CO_2 capture, shifts the equilibrium toward hydrogen production, achieving purities above 98 mol%. Additionally, the exothermic CO_2 capture reactions reduce energy consumption or even generate excess energy that can serve as a heat source. Across all configurations, sorption-enhanced steam reforming achieves superior hydrogen production efficiency and lower energy demands, making it a promising option for sustainable hydrogen generation from bio-oil. The composition of bio-oil shows minimal impact on hydrogen yield, indicating broad applicability to different bio-oils.

Keywords: thermodynamic analysis, hydrogen, steam reforming, sorbents, autothermal

1. INTRODUCTION
Energy, being fundamental for society can transition from fossil fuels – which dominate energy generation and drive climate change [1] – to other renewable options like biomass-to-energy processes [2]. Biomass can be converted into bio-oil with higher energy density through thermochemical processes. This bio-oil can be further revalorized to produce renewable hydrogen via steam reforming, although this process is highly energy-intensive and susceptible to catalyst-deactivating side reactions that produce coke [3]. To address these challenges, advanced reforming techniques such as autothermal reforming where oxygen is added to balance energy needs, and sorption-enhanced reforming where CO_2 is captured – improving both energy and hydrogen efficiency – have been developed [4,5]. In this regard, thermodynamics studies can provide valuable insights for evaluating different process strategies to optimize hydrogen production assessing the theoretical feasibility of different steam reforming technologies. These results can also provide preliminary findings and recommendations for future research on this topic. Sugarcane with global production exceeding 1.5 billion tonnes annually, generates large quantities of fibrous residues named sugarcane bagasse [6]. In this study, a thermodynamic analysis was carried out using Aspen Plus® V12.1 to assess various reforming scenarios for bio-oil produced from sugarcane bagasse torrefaction. The bio-oil composition used in the analysis was based on data reported by Chang et al [7]. Additionally, this work examines how variations in bio-oil compositions – obtained from torrefaction or pyrolysis of different biomass feedstocks – affect hydrogen production in reforming processes.

Based on the above, the main goal of this research is to provide a thermodynamic comparison of three different bio-oil reforming technologies: conventional steam reforming (SR), autothermal reforming (ATR), and sorption-enhanced steam reforming (SESR). For that purpose, the influence of the operating conditions – pressure, temperature, and the steam-to-carbon ratio – on the reaction performance to maximize hydrogen production while minimizing coke formation was analyzed. Next, the energy requirements of conventional steam reforming were assessed, focusing on the minimum oxygen required to achieve neutral-thermal conditions in autothermal reforming. Then, the performance of autothermal reforming was compared to that of conventional reforming under the same conditions. Lastly, the sorption-enhanced steam reforming configuration which uses CO_2-selective sorbents was evaluated as an alternative to autothermal reforming. In this process, the CO_2 is captured not only by providing heat – due to the exothermic nature of the adsorption reaction – for driving forward the endothermic steam reforming reactions but also by shifting the water-gas shift reaction toward hydrogen production.

2. MATERIALS AND METHODS
Simulations were carried out using Aspen Plus V12.1® software, utilizing a non-stoichiometric approach that focuses on

minimizing Gibbs free energy through the RGIBBS block. To calculate the equilibrium composition at the reactor outlet the Peng-Robinson thermodynamic model was used. The general simulation flowsheet is illustrated in Fig. 1. It includes four separate feed streams: “BIO-OIL” for bio-oil on a dry basis, “WATER” for water to provide the steam required for the reaction, “O2” for oxygen to support the autothermal reaction, and “SORBENT” for calcium oxide (CaO), which acts as a CO_2-selective sorbent in the sorption-enhanced steam reforming process. A sensitivity analysis was conducted at different temperatures (400–800 ºC), pressures (1–20 bar), steam-to-carbon molar ratios (S/C = 0.5–5), oxygen-to-carbon molar ratios (O_2/C = 0–0.4), and sorbent-to-carbon molar ratios (CaO/C = 0–4).

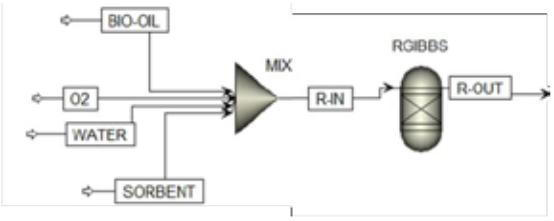

Fig. 1. Steam reforming flowsheet.

Reaction performance was evaluated based on product yields, calculated as the ratio of the molar flow rate of each component at the reactor outlet to the maximum molar flow rate of hydrogen (for hydrogen yields) or the molar flow rate of carbon in the bio-oil feed (for carbon co-product yields). It was assumed complete conversion, as the molar flow rate of oxygenated hydrocarbons in the outlet stream was almost zero. The bio-oil used in this work ($C_{1.00}H_{1.91}O_{0.85}$ is a blend of oxygenated hydrocarbons derived from the torrefaction of sugarcane bagasse. Table 1 provides a summary of its composition in molar fractions on a dry basis.

Table 1. Bio-oil composition on a dry basis [7]

Compound	Mole fraction on a dry basis (%)
Acetic acid	73.48
Acetol	1.41
Propionic acid	12.27
Methanol	4.79
Furfural	4.18
Furfuryl alcohol	2.34
Phenol	0.42
Guaiacol	0.38
Eugenol	0.56
Vanillin	0.17

3. RESULTS AND DISCUSSION

3.1. Conventional steam reforming

Figure 2 shows the effect of pressure, temperature, and S/C ratios on hydrogen yields. Despite industrial processes generally working at pressures of 15–30 bar to optimize reaction rates, efficiency, and process stability; hydrogen yield decreases as pressure increases due to Le Chatelier’s principle, which shifts the equilibrium away from hydrogen production. In contrast, hydrogen yield improves with temperature due to the endothermic nature of bio-oil steam reforming reactions, which are more favorable at higher temperatures. For lower S/C ratios (0.5-1), hydrogen yields gradually increase with temperature regardless of pressure, as the steam is below the stoichiometric level required for bio-oil reforming. In contrast, higher S/C ratios (2-5) achieve the highest yields (78-91%) within the 600-700ºC range. Further increase in temperature decreases the hydrogen yield given that the reverse water-gas shift reaction is favored thus consuming some of the hydrogen produced. While higher S/C ratios improve hydrogen yields, they also require larger equipment and more energy for steam generation. Therefore, an optimal balance between yield, cost, and energy efficiency is essential. The outlet stream contains other gaseous products alongside hydrogen, including CO, CO_2, and CH_4. Although CO and CO_2 do not directly interfere with hydrogen production, CH_4 does thus, to maximize the hydrogen production during bio-oil steam reforming effective control of these species and the reactions they participate in is essential. The obtained results demonstrate that atmospheric pressure is better for increasing hydrogen yield, as it favors reactions that produce fewer gaseous moles. A temperature range of 500–700 ºC enhances the reaction performance, but temperatures above 700ºC may lead not only to a decrease in hydrogen production but also to CO formation.

Maintaining an S/C ratio above the stoichiometric value helps reduce secondary products like CO, CH_4, and coke, particularly for ratios over 2. However, higher ratios require more energy to produce steam. Based on these factors, atmospheric pressure, temperatures between 500-700ºC, and an S/C ratio of 2 and 3 will be used in further analyses.

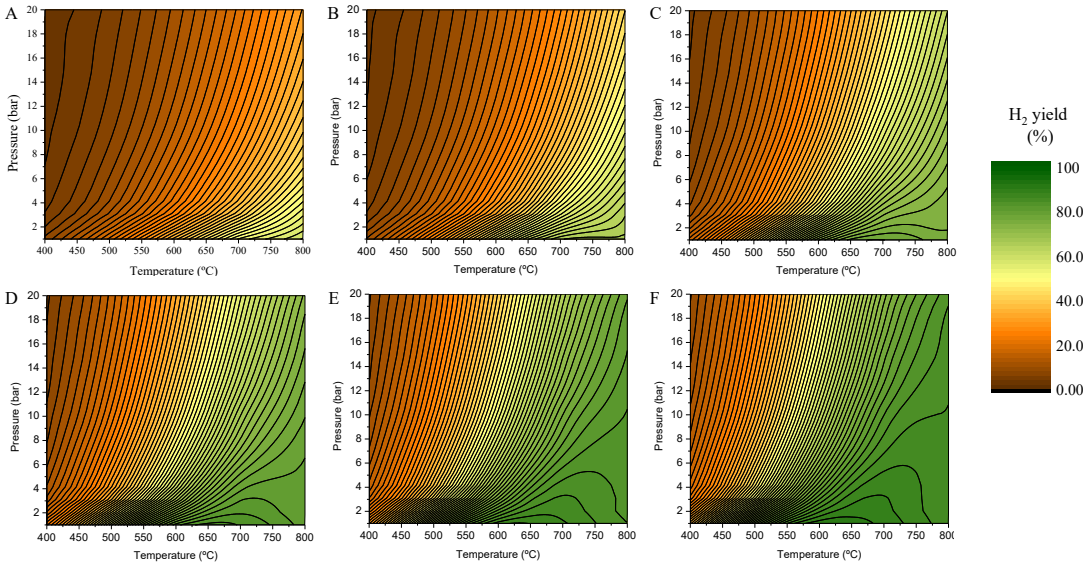

Fig. 2. Effect of pressure and temperature on H_2 yield for varying S/C molar ratios: (A) 0.5, (B) 1, (C) 2, (D) 3, (E) 4, and (F) 5.

3.2. Autothermal steam reforming

Conventional steam reforming requires significant energy due to its endothermic reactions, but co-feeding oxygen can overcome this by promoting exothermic partial oxidation reactions. These reactions release heat, which can meet some or all of the energy demand for steam reforming, leading to thermal neutrality. This approach also helps control the reaction environment, reducing undesirable byproducts like coke and carbon monoxide. The amount of oxygen needed for thermal neutrality depends on the temperature and S/C ratio. Higher temperatures and S/C ratios require more oxygen to balance the energy demand, as higher steam levels increase thermal energy needs. This strategy improves the energy efficiency of hydrogen production but, under thermal neutral conditions, hydrogen yields were significantly lower compared to conventional steam reforming, especially at higher temperatures due to its consumption in the oxidation reactions. CO yields were also lower than in steam reforming due to the partial oxidation reactions that convert CO to CO_2. Similarly, methane yields were decreased because the combined partial oxidation and reforming reactions reduce methane concentrations by converting it to hydrogen and CO_2.

3.2. Sorption-enhanced steam reforming

Autothermal steam reforming offers advantages like improved energy efficiency and reduced CO and CH_4 production but results in lower hydrogen yields compared to traditional methods, posing a challenge for hydrogen-centric applications. To address this, sorption-enhanced steam reforming has gained attention. This process uses CO_2 sorbents like CaO to capture CO_2 in situ, shifting the thermodynamic equilibrium towards hydrogen production. The presence of CaO in the feed stream, significantly improves hydrogen yield, especially at lower temperatures, stabilizing at CaO/Cfeed ratios above 1. This technology minimizes byproduct formation and produces higher-purity hydrogen compared to conventional steam reforming. Optimizing the CaO/C_{feed} ratio, temperature, and S/C ratio improves hydrogen yield, energy efficiency, and carbon capture while reducing emissions. Excess heat from the process can lower operating costs by serving other uses like electricity generation.

Table 2 displays the ideal conditions for the reforming technologies studied – SR, ATR, and SESR – using S/C molar ratios of 2 and 3. It also includes the energy needed to drive the reactions under these conditions. This information is crucial for assessing the trade-off between energy use and hydrogen yield/purity, providing a solid foundation for optimizing the reforming process. These parameters provide valuable insights for optimizing hydrogen production while considering the reactor's energy efficiency, opening the way for future economic and environmental analyses. Finally, the effect of the bio-oil composition was evaluated on the hydrogen yield. Higher H content enhances hydrogen production, while higher O content can create byproducts that reduce efficiency. Using an S/C ratio of 2, hydrogen yields ranging from 81-95% were obtained following the same trend for 5 different bio-oil compositions obtained from: sugarcane bagasse, maple, oak, spruce wood, and maize stalk; in agreement with other results reported in the literature.

Given no significant changes were obtained, the insights of this study are broadly applicable to various bio-oil compositions, independent of the biomass source.

Table 2. Maximum hydrogen yield and energy requirements for different reforming technologies under atmospheric pressure

Reactor configuration	S/C	Temperature (ºC)	O_2/C	CaO/C	Y H_2 (%)	H_2 molar fraction (on a dry basis)	Energy requirements (kJ/kg_{feed})
SR	2	700	-	-	78.0	0.622	5762.55
ATR	2	600	0.28	-	58.2	0.551	-
SESR	2	550	-	1	95.8	0.987	-1102.58
SR	3	650	-	-	84.5	0.641	6037.58
ATR	3	600	0.32	-	60.6	0.561	-
SESR	3	550	-	1	99.1	0.996	-468.78

4. CONCLUSIONS

This study evaluates traditional, autothermal and sorption-enhanced steam reforming of bio-oil, with an emphasis on hydrogen production, energy efficiency and byproduct generation. While conventional steam reforming allows high hydrogen yields, particularly at raised temperatures, its endothermic characteristics make this process energy-intensive. Autothermal steam reforming balances energy needs through exothermic partial oxidation, reducing energy demand but lowering hydrogen yield by about 25% compared to traditional methods. Conversely, sorption-enhanced steam reforming reached better results than the other technologies by capturing CO_2 in situ with CaO to shift equilibrium toward hydrogen production. This configuration achieves hydrogen yields exceeding 95% of the theoretical maximum, reduces CO_2 emissions, minimizes byproducts, and improves energy efficiency by leveraging exothermic CO_2 capture reactions. This study also shows that hydrogen yields vary slightly with the H and O balance in bio-oil composition, making the findings applicable across a wide range of bio-oils. These findings offer key insights for optimizing reforming processes in industrial settings, incorporating renewable energy and investigating advanced materials to enhance CO_2 capture and catalyst efficiency.

REFERENCES

1. https://www.iea.org/reports/world-energy-outlook-2023. IWorld Energy Outlook 2023, International Energy Agency. Accessed on January 24, 2025.
2. Megía PJ, Vizcaíno AJ, Calles JA and Carrero A. 2021. Hydrogen Production Technologies: From Fossil Fuels toward Renewable Sources. A Mini Review. Energy and Fuels 35:16403–16415.
3. Megía PJ, Rocha C, Vizcaíno AJ, Carrero A, Calles JA, Madeira LM and Soria MA. 2025. Thermodynamic Comparison between Conventional, Autothermal, and Sorption-Enhanced Bio-oil Steam Reforming. Energy and Fuels 39:1652–1667.
4. Moreira R, Bimbela F, Gandía LM, Ferreira A, Sánchez JL and Portugal A. 2021. Oxidative steam reforming of glycerol. A review. Renewable and Sustainable Energy Reviews 148:111299.
5. Cerqueira P, Soria MA and Madeira LM. 2021. Hydrogen production through chemical looping and sorption-enhanced reforming of olive mill wastewater: Thermodynamic and energy efficiency analysis, Energy Conversion and Management 238:114146.
6. Singh Rawat S and Sharma A. 2023. Sugarcane bagasse ash—The future composite material: A literature review. Materials Today Proceedings (*in press* https://doi.org/10.1016/J.MATPR.2023.07.272).
7. Chang S, Zhao Z, Zheng A, He F, Huang Z and Li H. 2012. Characterization of Products from Torrefaction of Sprucewood and Bagasse in an Auger Reactor. Energy and Fuels 26:7009–7017.

SHAPED Ni/MESOPOROUS CeO_2 AS ACTIVE CATALYSTS IN HYDROGEN PRODUCTION FROM ACETIC ACID OXIDATIVE STEAM REFORMING

[1,*]Álvaro Moreno de la Calle, [1]Arturo J. Vizcaíno, [1,2]Alicia Carrero, [1,2]José A. Calles and [1]Pedro J. Megía
[1] Chemical and Environmental Engineering Group, Rey Juan Carlos University, Tulipán Street s/n., 28933 Mostoles, Madrid, Spain
[2] Institute of Sustainable Technologies, Rey Juan Carlos University, Tulipán Street s/n., 28933 Mostoles, Madrid, Spain

*Corresponding author e-mail: alvaro.moreno@urjc.es

ABSTRACT
In this study, agglomerated catalysts were synthesized by combining powdered Ni catalysts supported on mesostructured ceria with different clays (kaolinite, sepiolite, attapulgite and bentonite) to get suitable extrudates for large-scale use in the oxidative steam reforming of acetic acid. Extrudates prepared with bentonite and attapulgite and then calcined at a heating rate of 1 ºC/min showed higher mechanical strength. Despite having slightly lower mechanical resistance, better catalytic results in terms of acetic acid conversion and hydrogen yield were achieved over Ni/m-CeO_2 using attapulgite as a binder. External and internal resistance to mass transfer were evaluated for shaped catalysts, disregarding the presence of reactant concentration gradients neither around the catalyst particle's external surface nor through the particle porosity, in this sense, there are no limitations for internal diffusion since the calculated Weisz-Prater modulus was below 1.
Finally, the reusability of the Ni/m-CeO_2-A extrudates was assessed to have information about its suitability for industrial-scale reformers. Thus, its catalytic performance was tested over multiple cycles. Reactions were performed for 6 hours at 550 ºC at a high space velocity to ensure fast deactivation (WHSV of 41.8 h^{-1}). Between cycles, the catalyst was regenerated in situ by introducing an air stream to remove coke deposits, followed by a hydrogen stream to reduce the active phase again before the next cycle. The results revealed good stability, maintaining complete conversion and just 10% lower hydrogen yield compared to the first run after six reaction cycles.

Keywords: extrusion, nickel, mesoporous ceria, hydrogen, regeneration

1. INTRODUCTION
As the global population grows and energy demand rises, greenhouse gas emissions from fossil fuels continue to increase, highlighting the need for alternative energy sources [1]. In this context, hydrogen is receiving attention as an interesting option to replace fossil fuels. It is primarily produced from methane reforming, but researchers are increasingly focused on its production from renewable sources to avoid fossil fuel use [2]. Acetic acid is emerging as a promising alternative renewable feedstock for hydrogen production, with its market projected to grow significantly, reaching $319.6 million by 2030 [3]. Unlike other hydrogen production sources like methanol or ethanol, acetic acid is non-flammable and non-toxic, making it safer and more convenient to store and transport [4]. Moreover, it can be produced through fermentative processes using different sources including carbohydrates, as well as agricultural and forestry lignocellulose, shells, and microalgae.
To obtain hydrogen from acetic acid, steam reforming is widely reported [5]. Steam reforming is constrained by some limitations including high operating temperatures and coke formation. To address these challenges, including oxygen in the feed stream resulting in oxidative reforming has emerged. This configuration decreases the energy requirements given the exothermicity of the partial oxidation reactions and reduces coke formation [6]. In this regard, catalyst formulation plays a crucial role in maximizing hydrogen production while limiting activity loss. As an active phase, noble metal catalysts are commonly used for reforming purposes, however, their high cost has driven interest toward transition metals, such as nickel or cobalt since they have demonstrated excellent performance on the cleavage of C-C and C-H bonds [7]. As catalyst support, cerium oxide (CeO_2) has gained widespread use in oxidative reforming reactions due to its high oxygen mobility which reduces coke deposition on the catalyst apart from being active in the water-gas shift reaction. Most of the catalysts reported in the literature are prepared in powder resulting in high-pressure drops in large-scale reactors hindering their implementation in the industry. For this reason, it is necessary to prepare pelletized catalysts by adding different binders to improve mechanical strength, water, and an organic additive, such as methylcellulose to get plasticity in the paste during the extrusion process [8].
Based on the above, this work investigates the effect of the inorganic binder – bentonite, attapulgite, kaolinite, and sepiolite – in the mechanical strength and the physicochemical properties of extrudates obtained in Ni/m-CeO_2 agglomeration. Additionally, to study the possibility of overcoming catalyst deactivation by coke deposition, regeneration cycles between two catalytic tests were performed.

2. MATERIALS AND METHODS
The synthesis of the mesostructured CeO_2 was carried out by nanocasting using SBA-15 as a template as described elsewhere [9]. The incorporation of Ni as the active phase was done through the wet impregnation method to get a 7 wt.% of Ni loading. Extruded materials were synthesized by mixing 70 wt.% of powder catalyst with 30 wt.% of clay

(bentonite, attapulgite, sepiolite, or kaolinite). Additionally, methylcellulose was added as a plasticizer to enhance the viscosity of the paste formed as a result of adding deionized water. To facilitate the extrusion the paste was left overnight in a humid atmosphere. The pellets were obtained using a circular homemade extruder and subjected to calcination, first to select which clays have the highest mechanical resistance a heating rate of 0.1 ºC/min up to 110 ºC and then 0.5 ºC/min up to 650 ºC was used according to previous work [8]. Then, with the selected clays, the influence of the calcination ramp on the mechanical strength was evaluated. The synthesized pellets were characterized and those samples with high mechanical strength were tested in the oxidative steam reforming of acetic acid under regeneration cycles, which were done by initially introducing a stream of air to eliminate the coke formed with a ramp of 10 ºC/min up to 600 ºC and, subsequently, a stream of H_2 was added to reduce the active phase for another hour.

3. RESULTS AND DISCUSSION

3.1. Catalysts characterization

Using commercial ceria, the mechanical resistance of pellets synthesized with different clays was evaluated as summarized in Table 1. It can be discerned that the samples prepared using attapulgite and bentonite showed the highest mechanical resistance using a calcination rate of 0.1 ºC/min up to 110 ºC and then 0.5 ºC/min up to 650 ºC.

To prepare extrudates with high resistance, both clays were selected to evaluate the influence of the heating rate during calcination, as can be seen in Table 1. The highest mechanical resistance was achieved for both samples with a calcination ramp of 1ºC/min, being the mechanical resistance 11.8 N and 13.1 for the pellets prepared with attapulgite and bentonite, respectively. Consequently, this ramp was selected to evaluate the catalytic activity in the oxidative steam reforming of acetic acid.

Table 1. Mechanical resistance of pellets prepared with 4 different clays using commercial CeO_2.

Clay	Calcination rate (ºC/min)	Mechanical resistance (N)
Kaolinite	0.1ºC/min up to 110ºC, 0.5ºC/min up to 650ºC	2.4
Sepiolite	0.1ºC/min up to 110ºC, 0.5ºC/min up to 650ºC	4.1
Attapulgite	0.1ºC/min up to 110ºC, 0.5ºC/min up to 650ºC	8.1
	0.5ºC/min up to 650ºC	8.9
	1ºC/min up to 650ºC	11.8
	2.5ºC/min up to 650ºC	7.9
	5ºC/min up to 650ºC	5.8
Bentonite	0.1ºC/min up to 110ºC, 0.5ºC/min up to 650ºC	11.1
	0.5ºC/min up to 650ºC	12.8
	1ºC/min up to 650ºC	13.1
	2.5ºC/min up to 650ºC	10.2
	5ºC/min up to 650ºC	9.1

Once selected the clays and the heating rate; new pellets were prepared with powder Ni catalysts supported on mesostructured ceria synthesized by nanocasting. Samples were named as Ni/mCeO_2-X where X indicates the clay used (A for attapulgite and B for bentonite). The mechanical strength, BET surface area, pore volume, and Ni content estimated from ICP analysis are shown in Table 2. As a consequence of the mixing of the catalyst and the clay during pellet preparation, both samples have Ni content of around 5 wt.%. It is noteworthy that the mechanical resistance of the extruded catalysts is lower than that achieved with commercial ceria, ascribed to the higher porosity of the mesostructured ceria compared to the non-porous commercial ceria. Additionally, textural properties revealed higher BET surface area and pore volume for Ni/mCeO_2-A because of higher values of these parameters in attapulgite than in bentonite.

Table 2. Characterization of the catalysts.

Clay	Mechanical resistance (N)	S_{BET} (m^2/g)	V_p (cm^3/g)	Ni (wt. %)
Ni/mCeO_2-A	5.5	80.8	0.253	5.2
Ni/mCeO_2-B	7.6	59.3	0.179	5.4

3.2. Catalytic tests

The selected materials – Ni/mCeO_2-A and Ni/mCeO_2-B – were tested in the oxidative steam reforming of acetic acid. The catalytic results in terms of acetic acid conversion and hydrogen yield, are presented in Table 4. From these results, it is possible to observe that the conversion and the hydrogen yield are significantly lower with Ni/mCeO_2-B, being the

hydrogen yield three times lower than that achieved with Ni/mCeO_2-A. This difference can be attributed to the lower BET surface area obtained when using bentonite, which may limit the active phase dispersion thus resulting in a lower number of active sites necessary to catalyze the reaction effectively.

Table 4. Conversion in the oxidative steam reforming of acetic acid and hydrogen yield using Ni/mCeO_2-A and Ni/mCeO_2-B catalysts with time-on-stream (T=550 ºC; WHSV = 21.4 h^{-1}; steam/C/O_2 molar ratio =2/1/0,0375, P= 1 atm).

Time on stream (h)	Ni/mCeO_2-A		Ni/mCeO_2-B	
	Acetic acid conversion (%)	Yield to H_2 (%)	Acetic acid conversion (%)	Yield to H_2 (%)
1 h	79.9	37.0	82.9	12.3
2 h	55.7	34.8	58.1	11.8
3 h	51.2	33.4	32.5	11.3
4 h	51.1	32.3	25.6	12.6
5 h	49.3	31.5	25.0	13.2

Given that Ni/mCeO_2-A reached better catalytic performance, this sample was selected to evaluate the influence of diffusion resistance to mass transfer. To study external concentration gradients new tests were carried out keeping a WHSV of 21.4 h^{-1} but varying the amount of catalyst and the feed flow rate, whose results are summarized in Table 5. It is evident that as the flow rate increases, the conversion and the hydrogen yield values also rise, reaching a maximum at a liquid feed flow rate of 0.094 ml/min. This is a consequence of higher turbulence within the reactor which improves the mass transfer coefficient thus decreasing the acetic acid concentration gradient around the external catalyst particle surface. Beyond this flow rate, no significant changes are detected in either hydrogen yield or conversion, suggesting that external mass transfer limitations are negligible under these conditions. Moreover, the internal diffusion was evaluated following the Weisz-Prater criterion.

$$C_{WP}=\frac{(-r_A)\cdot\rho_c\cdot R^2}{D_e\cdot C_{AA}} \quad (1)$$

Where $(-r_A)$ refers to the reaction rate, ρ_c is the catalyst density, R is the catalyst radius, D_e is the effective diffusivity of gas and C_{AA} is the concentration of gas. If C_{WP} <1 there is no internal diffusion. In this case C_{WP} =$9\cdot10^{-2}$, so it was confirmed no internal diffusion.

Table 5. Experimental conditions used to analyze the external diffusion effect.

$m_{catalyst}$ (g)	Q_{feed} (ml/min)	Gas flow (ml/min)	Acetic acid conversion (%)	Yield to H_2 (%)
0.32	0.057	45	72.6	35.4
0.43	0.075	60	79.9	37.0
0.48	0.084	65	82.6	43.6
0.54	0.094	75	99.4	61.3
0.64	0.113	90	99.9	60.3

To evaluate the reusability of the catalyst, reaction-regeneration cycles were performed with Ni/m-CeO_2-A. For that purpose, 6-hour reaction tests were conducted at a WHSV=41.8 h^{-1} to ensure significant catalyst deactivation, enabling a more detailed analysis of the regeneration process. During regeneration, an air stream was added with a ramp rate of 10 ºC/min up to 600 ºC to eliminate the coke formed over the catalyst and subsequently, a hydrogen stream was passed during an hour through the catalytic bed to reduce again the active phase. The obtained results are displayed in Fig. 1. In all the cycles it is possible to observe both a conversion and hydrogen yield drop with time, ascribed to the formation of carbonaceous species which are deactivating the catalysts. After successive regeneration cycles, the activity is completely recovered given that the conversion follows a stationary trend. In contrast, hydrogen yield increases after each cycle but the value during the first hour slightly decreases until reaching values near 40% in the 6th cycle, around 10% lower than the value obtained during the first cycle. This fact suggests that although the conversion is being recovered, the selectivity towards hydrogen is affected during the catalyst regeneration increasing the formation of other compounds like CH_4.

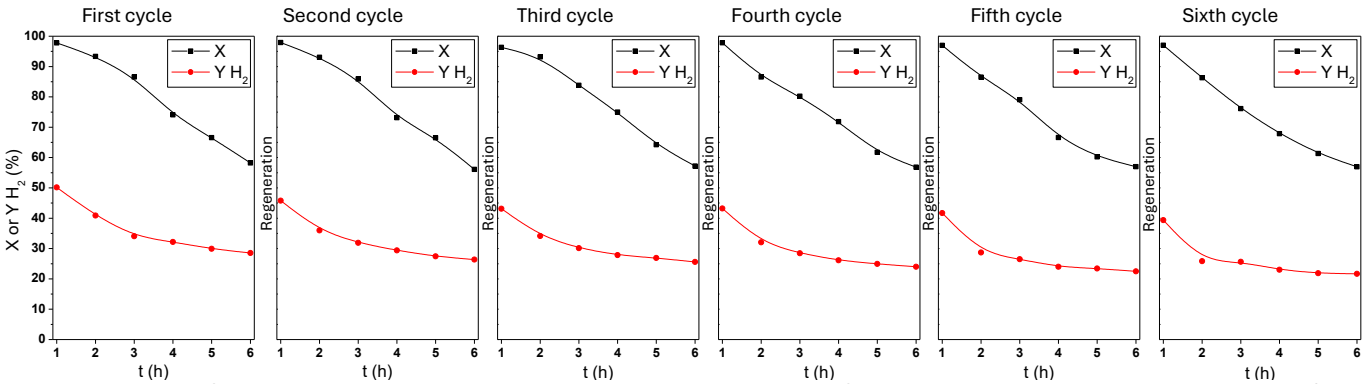

Fig. 1. Evolution of the acetic acid conversion and hydrogen yield in oxidative reforming reaction-regeneration cycles using Ni/m-CeO_2-A. Reaction conditions (T=550 ºC; WHSV = 41.8 h^{-1}; steam/C/O_2 molar ratio =2/1/0.0375, P= 1 atm)

4. CONCLUSIONS

This study focused on the influence of clay type during the agglomeration of Ni-based catalysts supported over mesostructured ceria in the oxidative steam reforming of acetic acid. Among the clays tested, attapulgite and bentonite demonstrated superior mechanical resistance in the prepared extrudates, maximizing their resistance when a calcination rate of 1 ºC/min was used. Despite attapulgite exhibiting slightly lower mechanical resistance compared to bentonite, it reached better catalytic performance in terms of acetic acid conversion and hydrogen yield.

To assess mass transfer limitations, both external and internal resistances were evaluated for shaped catalysts. In this context, the calculated Weisz-Prater modulus remained below 1, indicating that internal diffusion constraints were not significant, and the point at which the external diffusion limitations disappeared was experimentally determined.

The reusability of the Ni/mCeO_2-A extrudates was further analyzed to assess their industrial feasibility. Therefore, the catalytic performance was tested over multiple reaction cycles at 550 ºC using a WHSV of 41.8 h^{-1} to ensure rapid deactivation. Between cycles, the regeneration process involved in situ coke removal followed by reduction of the active phase. The results showed good stability, with full recovery conversion and only a 10% drop in hydrogen yield after six reaction cycles compared to the first run. These findings underscore that Ni/mCeO_2-A extrudates are suitable catalysts for the oxidative steam reforming of acetic acid, with promising application for future industrial-scale up.

ACKNOWLEDGEMENT

The authors acknowledge the Community of Madrid for its financial support through the framework of the Multiannual Agreement with the Rey Juan Carlos University in line of action 1, “Encouragement of Young Ph.D. students’ investigation” Project Ref. M2743 with the acronym HYDROGREFOX. Additional support from the Spanish Ministry for Science and Innovation through projects PID2020-117273RB-I00 and TED2021-131499B-I00 is also gratefully acknowledged.

REFERENCES

1. Yang Y, Wu Z, Yao J, Guo T, Yang F, Zhang Z, Ren J, Jiang L and Li B. 2024. An overview of application-oriented multifunctional large-scale stationary battery and hydrogen hybrid energy storage system. Energy Reviews 3:100068.
2. Worku AK, Ayele DW, Deepak DB, Gebreyohannes AY, Agegnehu SD, and Kolhe ML. 2024. Recent Advances and Challenges of Hydrogen Production Technologies via Renewable Energy Sources. Advanced Energy and Sustainability Research 5: 2300273.
3. Chen Y, Yang Y, Liu S, Shi X, Wang C, Zhoong H and Jin F. 2023. Sustainable production of formic acid and acetic acid from biomass. Molecular Catalysis 545:113199.
4. Chen G, Tao J, Liu C, Yan B, Li W and Li X. 2017. Hydrogen production via acetic acid steam reforming : A critical review on catalysts. Renewable and Sustainable Energy Reviews 79:1091-1098.
5. Nguyen A, Hoong Ng K, Kumar PS, Pham TT, Setiabudi HD, Yusuf M, Pham LKH, Show PL, Hussain I and Vo DN. 2024. Sustainable hydrogen production and CO_2 mitigation from acetic acid dry reforming over Ni/Al_2O_3 catalyst. International Journal of Hydrogen Energy 67:1044-1055.
6. Chen WH, Biswas PP, Ong HC, Hoang AT, Nguyen TB and Dong CD. 2023. A critical and systematic review of sustainable hydrogen production from ethanol/bioethanol: Steam reforming, partial oxidation, and autothermal reforming. Fuel 333:126526.
7. Megía PJ, Morales A, Vizcaíno AJ, Calles JA and Carrero A. 2022. Hydrogen production through oxidative steam reforming of acetic acid over Ni catalysts supported on Ceria-based materials. Catalysts 12:1526.
8. Calles JA, Carrero A, Vizcaíno AJ and Megía PJ. 2020. Agglomerated Co-Cr/SBA-15 catalysts for hydrogen production through acetic acid steam reforming. International Journal of Hydrogen Energy 45:15941-15950.
9. Moreno de la Calle A, Vizcaíno AJ, Carrero A, Calles JA and Megía PJ. 2024. Study of Mesostructured CeO_2 Synthesis via Nanocasting Using SBA-15 as a Template: Influence of the Cerium Precursor. International Journal of Molecular Sciences 25:13016

AI-BASED OPTIMIZATION OF A PV-BATTERY-ELECTROLYZER SYSTEM FOR GREEN HYDROGEN PRODUCTION

[1,2]Alper Yılmaz, [1]Necati Aksoy, [1,2*]Gökay Bayrak
[1] Bursa Technical University, Renewable Energy Systems and Smart Grids Laboratory, Department of Electrical and Electronics Engineering, 16300, Bursa, Turkey
[2] Bursa Technical University, Electric Vehichles Application and Research Center, 16300, Bursa, Turkey

* E-mail: gokay.bayrak@btu.edu.tr

ABSTRACT
This study presents the development and simulation of an AI-optimized photovoltaic (PV)-battery-electrolyzer system for green hydrogen production. A MATLAB Simulink model was created to evaluate system performance over a one-day period, focusing on energy management and hydrogen generation under varying solar irradiance conditions. The AI-based optimization strategy dynamically adjusted power distribution to maximize efficiency while ensuring stable operation. The results demonstrated that the PV system reached a peak power of 250 kW, with the electrolyzer consuming up to 200 kW, effectively utilizing solar energy. The battery played a stabilizing role, discharging ~500 kW to support the electrolyzer when solar generation declined, while its charge decreased from 100% to ~95%. Hydrogen production reached ~25 kg, with a nearly constant specific energy consumption of ~65 kWh/kg H_2, confirming the system's efficiency and reliability. These findings highlight the potential of AI-driven optimization in enhancing renewable-powered hydrogen production, providing insights for future large-scale applications.

Keywords: Green hydrogen production, Proton Exchange Membrane (PEM) Electrolyzer, AI-based optimization, Renewable energy integration, Hydrogen production efficiency

1. INTRODUCTION
Hydrogen has emerged as a key energy carrier in the transition to sustainable energy systems, particularly when integrated with renewable energy sources. In recent years, photovoltaic (PV)-battery-electrolyzer systems have gained significant attention due to their potential to enhance energy flexibility and facilitate green hydrogen production [1]. The combination of solar energy, energy storage, and water electrolysis offers a promising pathway to utilize intermittent renewable power efficiently. However, optimizing hydrogen production under varying solar irradiance conditions remains a critical challenge. To address this, standardized performance evaluation methods and optimization strategies are essential to ensure reliable and cost-effective hydrogen generation [2]. Furthermore, analyzing production trends under different irradiance levels will contribute to the development of more efficient system designs and operational strategies. Several studies have explored PV- and wind-based hydrogen production systems, focusing on their design, operation, and performance evaluation [2]. In this context, a comprehensive system model was developed to assess the efficiency of green hydrogen production by integrating a proton exchange membrane (PEM) electrolyzer with a vertical axis wind turbine (VAWT), utilizing MATLAB, Simulink, and Simscape for system optimization under varying operational conditions [3].To further enhance the integration of renewable energy sources, Tatar et al. proposed a multi-period Mixed-Integer Linear Programming (MILP) model for the optimal design and operation of microgrids. Their model accounts for the uncertainties of renewable energy sources while incorporating green hydrogen and synthetic methanation technologies [4]. Similarly, Hüner et al. developed a mathematical model for a photovoltaic (PV)-assisted PEM water electrolyzer system, evaluating the effects of operating temperature and membrane thickness on hydrogen generation efficiency [5]. In addition to system performance optimization, Criollo et al. introduced a simulation model to enhance the technical and economic aspects of green hydrogen production by integrating PV and energy storage technologies. Their study demonstrated that replacing high-fidelity electrolyzer models with reduced-order models could significantly improve computational efficiency while maintaining accuracy [6]. Building on these approaches, a techno-economic assessment was conducted to evaluate off-grid PV-based hydrogen production, optimizing electrolyzer sizing and analyzing production efficiency under varying solar irradiance conditions [7]. These studies highlight the importance of transient electrolyzer behavior, battery degradation, and grid stability in integrated hydrogen production systems. However, a systematic approach to standardizing the comparison of different renewable hydrogen production configurations is still lacking. This research aims to contribute to the field by establishing a PV-battery-electrolyzer system, evaluating its hydrogen production performance under varying irradiance conditions, and proposing optimal strategies for maximizing hydrogen yield.
In this study, a MATLAB Simulink model was developed to simulate an AI-based optimization strategy for a photovoltaic (PV) system integrated with a battery and an electrolyzer for green hydrogen production. The model represents a DC islanded microgrid that optimally manages power distribution to the electrolyzer using a solar array and an energy storage system. The simulation evaluates hydrogen production over a one-day period, incorporating electrical, thermal liquid, and thermal gas domains.

2. GREEN HYDROGEN PRODUCTION SYSTEM

In this study, a MATLAB Simulink model was developed to simulate and optimize a photovoltaic (PV)-battery-electrolyzer system for green hydrogen production (Fig. 1). The system operates as a DC islanded microgrid, where energy from a solar array and an energy storage unit is utilized to power a proton exchange membrane (PEM) electrolyzer. The AI-based optimization strategy dynamically adjusts energy distribution to maximize hydrogen production efficiency while considering real-time solar irradiance and battery state of charge. The model includes electrical, thermal liquid, and thermal gas domains to provide a comprehensive evaluation of the system's performance.

Key system parameters were defined to ensure an accurate simulation. The PV system operates with a maximum power output (Pw_max) that is dynamically regulated by a maximum power point tracking (MPPT) controller. The electrolyzer consists of 100 cells with an efficiency range between 55% and 90%, a membrane thickness of 2 cm, and a resistance of 0.25 Ohm. The hydrogen storage tank has a volume of 100 cm³ and operates at a temperature of 273.15 K. The energy storage unit consists of a battery with a nominal capacity of 50,000 As, an internal resistance of 0.2 Ohm, and a nominal voltage of 240V. The battery is managed by a DC-DC converter, which ensures efficient power distribution with an efficiency of up to 99%. Control parameters, such as the sampling time (Ts = 10s), were carefully selected to enhance the model's responsiveness and accuracy in optimizing hydrogen production.

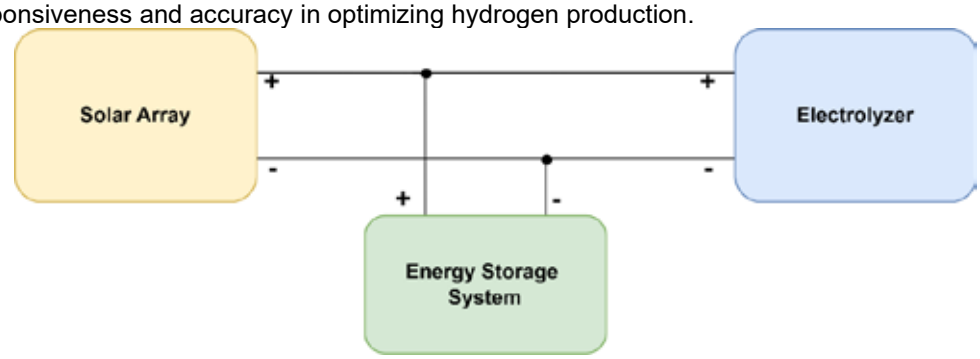

(a)

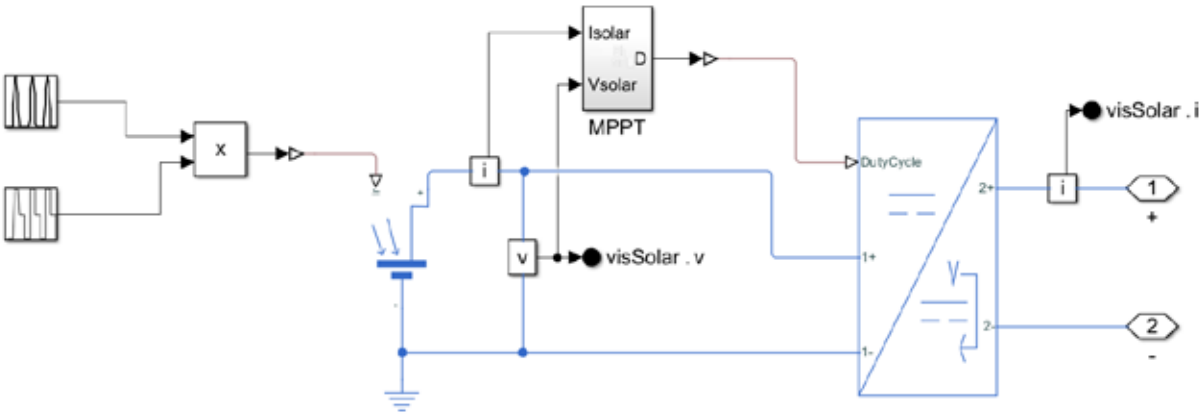

(b)

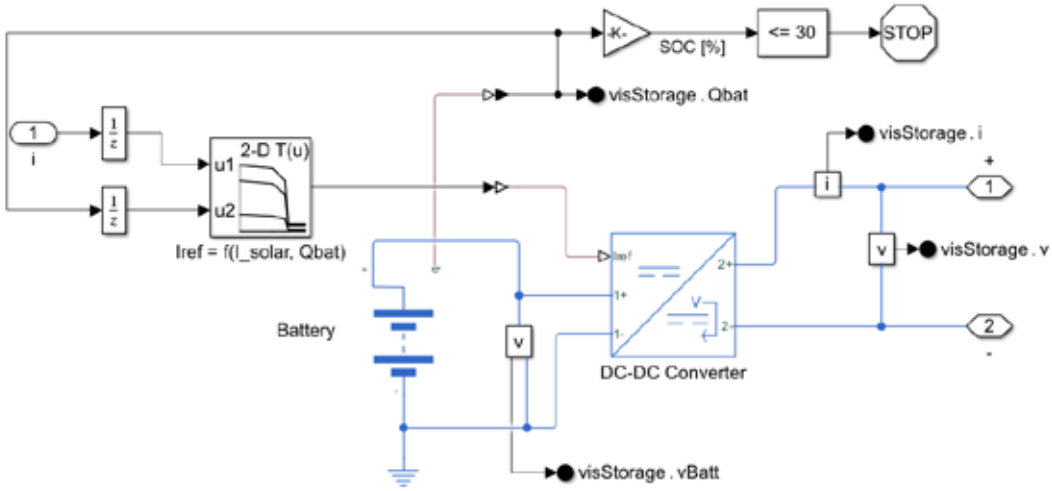

(c)

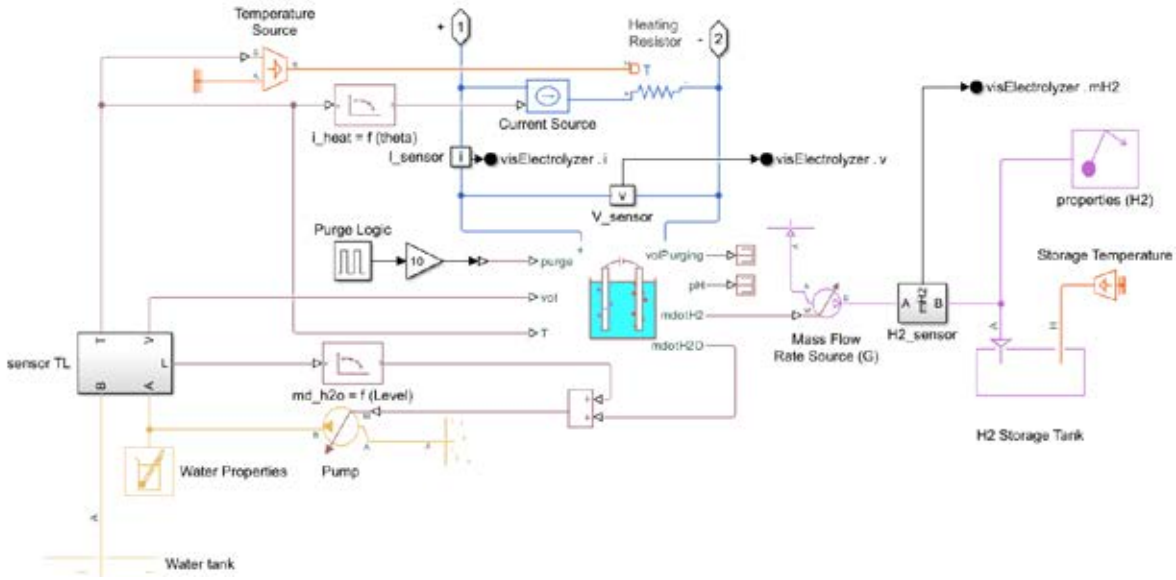

(d)

Fig. 1. (**a**) Green Hydrogen Microgrid, **(b)** PV system model, **(c)** battery model, and **(d)** electrolyzer model

3. RESULTS

The simulation results demonstrate the power distribution and utilization of the AI-optimized PV-battery-electrolyzer system over a one-day period. As observed in the upper plot, the PV system follows a typical solar generation curve, with peak power production occurring around midday. The electrolyzer's power consumption closely follows the PV output, indicating efficient energy utilization for hydrogen production. The energy storage system plays a stabilizing role by compensating for energy fluctuations, charging during peak solar hours, and discharging when PV generation declines. The simulation results show that the PV system reaches a peak power of approximately 250 kW around midday, while the electrolyzer operates at a maximum consumption of 200 kW, efficiently utilizing solar energy for hydrogen production (Fig. 2). The energy storage system absorbs excess power early in the day, reaching a charge of ~500 kW, and later discharges ~-500 kW to support the electrolyzer when solar generation declines. Over the one-day period, the electrolyzer maintains a stable hydrogen production rate, demonstrating the effectiveness of AI-based energy management in balancing power flow and ensuring optimal system performance.

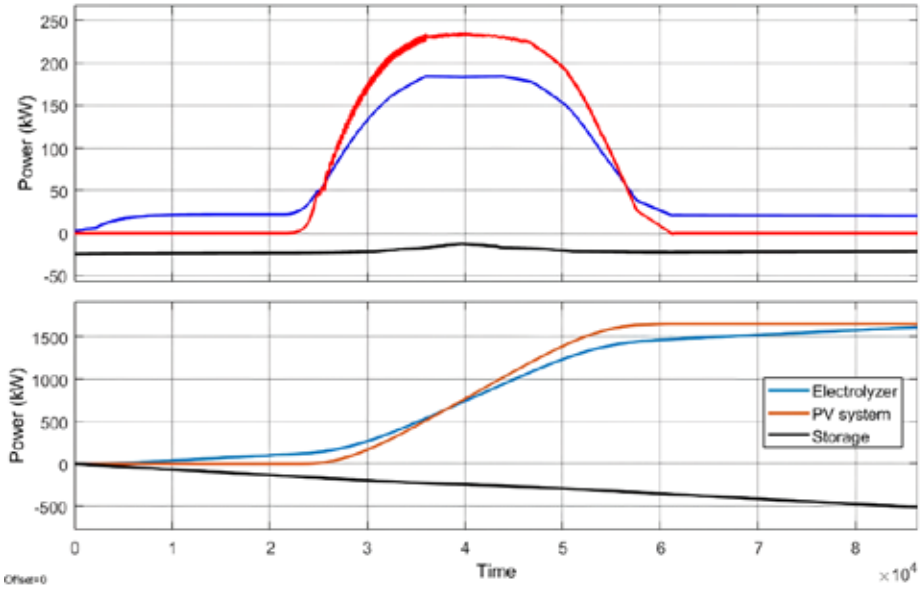

Fig. 2. Utilization in the AI-optimized PV-Battery-Electrolyzer System over a one-day period

The simulation results, as shown in Fig. 3, illustrate the system's performance over a one-day period. The electrolyzer reaches a peak current of ~750 A, following the PV system's peak generation, while the energy storage system provides a steady current of ~100 A throughout the day. Hydrogen production gradually increases, reaching ~25 kg by the end of the day. The battery charge declines from 100% to ~95%, indicating its role in stabilizing the power supply. The specific energy consumption remains nearly constant at ~65 kWh/kg H_2, demonstrating the efficiency and stability of the AI-based energy management strategy.

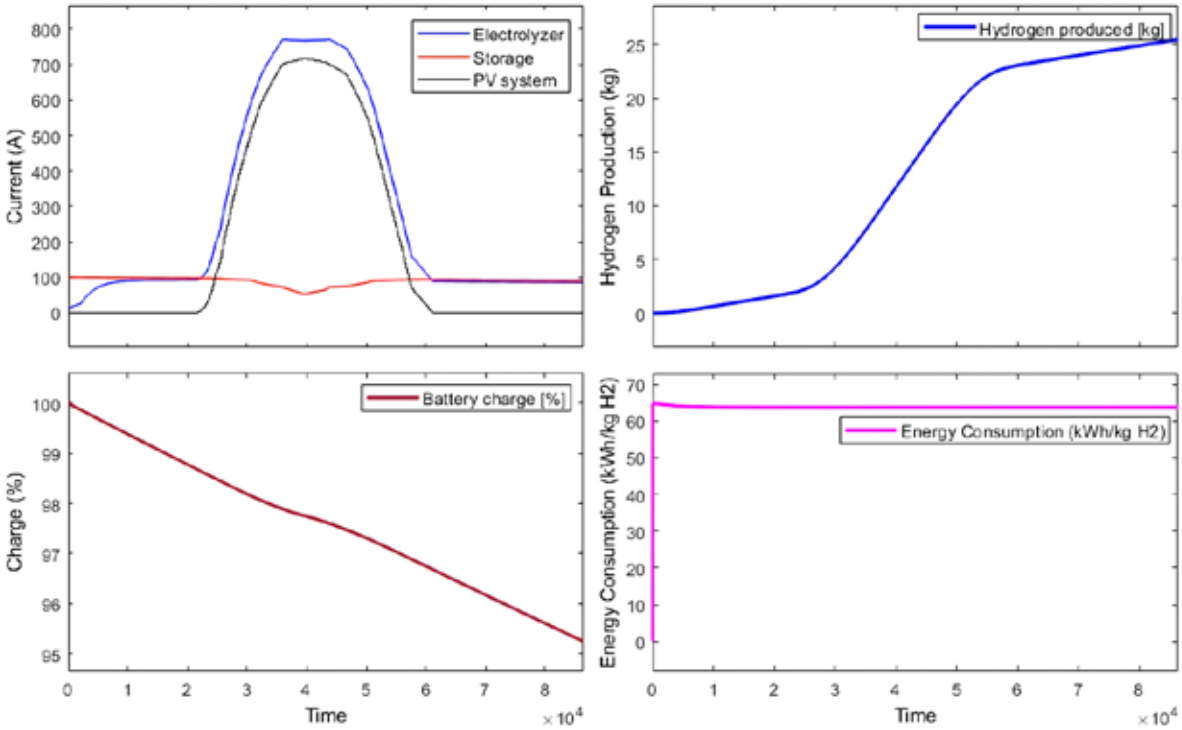

Fig. 3. System performance over a one-day period

4. CONCLUSIONS

This study successfully developed and simulated an AI-optimized PV-battery-electrolyzer system for green hydrogen production. The results demonstrate that the integration of an AI-based energy management strategy enables efficient power distribution, ensuring optimal hydrogen generation under varying solar irradiance conditions. The system's

performance over a one-day period showed that the PV system reached a peak power of 250 kW, while the electrolyzer operated at a maximum consumption of 200 kW, effectively utilizing available solar energy. The battery storage system played a critical role in stabilizing power flow, with its charge decreasing from 100% to ~95% while supporting the electrolyzer during periods of low solar generation. Additionally, hydrogen production steadily increased throughout the day, reaching ~25 kg, while the specific energy consumption remained nearly constant at ~65 kWh/kg H_2, highlighting the efficiency and stability of the proposed system. These findings confirm that AI-driven optimization can enhance the reliability and economic feasibility of renewable-powered hydrogen production. Future work could explore the integration of predictive forecasting models to further improve system efficiency and scalability for larger energy applications.

REFERENCES

1. Dincer, I., & Joshi, A. S. (2013). Solar based hydrogen production systems (Vol. 553). New York: Springer.
2. Herdem M S, Mazzeo D, Matera N, Baglivo C, Khan N, Congedo P M and De Giorgi M G. 2024. A brief overview of solar and wind-based green hydrogen production systems: Trends and standardization. International Journal of Hydrogen Energy 51 340-353.
3. Wilberforce T, Olabi A G, Imran M, Sayed E T and Abdelkareem M A. 2023. System modelling and performance assessment of green hydrogen production by integrating proton exchange membrane electrolyser with wind turbine. International Journal of Hydrogen Energy 48(32) 12089-12111.
4. Tatar S M, Akulker H, Sildir H and Aydin E. 2022. Optimal design and operation of integrated microgrids under intermittent renewable energy sources coupled with green hydrogen and demand scenarios. International Journal of Hydrogen Energy 47(65) 27848-27865.
5. Hüner B. 2024. Mathematical modeling of an integrated photovoltaic-assisted PEM water electrolyzer system for hydrogen production. International Journal of Hydrogen Energy 79 594-608.
6. Criollo A, Michala-Ávila L I, Benavides D, Ochoa-Correa D, Tostado-Véliz M, Meteab W K, and Jurado F 2024. Green Hydrogen Production—Fidelity in Simulation Models for Technical–Economic Analysis. Applied Sciences 14:10720.
7. Ismail T M, Ramzy K, Elnaghi B E, Abelwhab M N and Abd El-Salam M. 2019. Using MATLAB to model and simulate a photovoltaic system to produce hydrogen. Energy Conversion and Management, 185, 101-129.

DYNAMIC MODELING OF AN ANION EXCHANGE MEMBRANE ELECTROLYSER

[1*]*Salih Obut*
[1] ARMELSAN Enerji A.Ş., Sanayi Mah. Teknopark Bul. Teknopark 4A No:1/4A/408, İstanbul, 34906, Türkiye
*Corresponding author e-mail: salih.obut@armelsanenerji.com

ABSTRACT
Anion Exchange Membrane (AEM) electrolysers (AEMWEs) have gained attention as a promising technology for green hydrogen production, primarily due to their potential to reduce material costs and their ability to operate efficiently in low-concentration alkaline environments. Unlike Proton Exchange Membrane (PEM) electrolysers (PEMWEs), which rely on expensive precious metals as catalyst raw materials, AEMWEs do not require precious metals for the electrodes, offering a more cost-effective solution and greater scalability for industrial large-scale applications. To fully understand the behavior of AEMWEs and optimize their operation, it is essential to develop dynamic models that capture both steady-state and transient characteristics. In this context, this study extends previously developed steady-state AEMWE model to a dynamic one to examine the impact of lye solution (KOH solution) circulation rate and temperature on the start-up dynamics. The findings indicate that a higher circulation rate and higher inlet temperature speed up thermal equilibrium. Additionally, a higher lye circulation rate minimizes the temperature difference between the stack's inlet and outlet.

Keywords: Anion exchange membrane, dynamic modeling, electrolyser, hydrogen, thermal model.

1. INTRODUCTION

AEMWEs are emerging as promising technology for high purity hydrogen production due to their potential for lower material costs and the ability to operate in low-concentration alkaline environments. Unlike PEMWEs, AEMWEs do not require precious metals for electrodes, which can reduce material costs and enhance scalability for large-scale applications. While PEMWEs are widely used in industry, AEMWEs have started to appear as an increasingly prominent alternative, particularly in the context of lower installation cost. The development of dynamic models and transient analysis of AEMWEs will help us to understand their dynamic behavior and contribute to the broader adoption of these electrolysers.

Several studies have proposed steady-state models for AEM electrolysers to understand their static performance characteristics, such as voltage-current relationships and gas production rates [1-5]. However, accurate dynamic modeling is essential for optimizing their operation, as transient behaviors during start-up, load changes, and thermal effects play a key role in the performance and energy efficiency. Dynamic models are necessary to investigate the temporal changes in temperature and voltage, which impact the overall efficiency and lifespan of the electrolyser system. Therefore, this study extends a previously developed steady-state model [1] to a dynamic one to better understand the dynamics of the AEMWE. The model is implemented in MATLAB/Simulink environment and is used to investigate the effect of lye solution circulation rate and temperature on the start-up behavior of a kW scale AEMWE.

2. MODELING

AEMWEs involve electrochemical reactions as well as heat transfer and mass transport processes. In this study, a dynamic model is developed by extending a previously established steady-state model [1]. The steady-state model developed in the previous work focused on the electrochemical behavior of the AEM electrolyser and its steady-state performance characteristics. It utilized a simplified approach based on electrochemical kinetics to describe the current-voltage relationship, considering the overpotentials at both the anode and cathode. The model incorporated Faraday's law to estimate the hydrogen and oxygen gas production rates based on the applied current.

The core of the present study is the unsteady-state energy balance. The thermal model includes key parameters such as internal heat generation within the cells and heat losses to the surroundings. The energy balance equation accounts for these thermal effects, ensuring that both the electrochemical performance and the temperature evolution of the stack are modeled dynamically. Heat generation is linked to the current density, while heat dissipation is modeled through convective heat transfer mechanisms. Additionally, the model considers the influence of solution circulation on the thermal dynamics, as it impacts the rate of heat transfer and temperature uniformity across the stack. This extension to the steady-state model allows for a more accurate simulation of the AEM electrolyser's behavior, particularly under transient conditions such as during start-up or load changes, where thermal effects are significant for system stability and performance.

The thermal model of the system requires thermal inertia of the system, i.e. the thermal capacity of the AEMWE stack. In this work, lumped thermal capacity assumption is considered so that stack temperature is homogeneous and volume

average of the specific heat of stack components are used to calculate lumped thermal capacitance, C_t, of the stack [6-10].

$$C_t = \sum_j \rho_j V_j c_j \quad (1)$$

where; c_j, ρ_j, and V_j and are the specific heat, density and volume, respectively, of each of the electrolyzer parts denoted by j. Due to the limited availability of the stack component dimensions and material information and by considering the significant contribution of the thermal capacitance of the bipolar plates and end plates, the thermal capacitance of the stack is estimated using bipolar plate and end plate information.

The stack energy balance can be written as follows

$$C_t \frac{dT}{dt} = W - Q + \sum_j^{inlet} \dot{m}_j h_j - \sum_j^{outlet} \dot{m}_j h_j \quad (2)$$

where; T is the stack temperature, W electrical work, i.e. power supplied to stack, Q is the heat loss to the surroundings, $\dot{m}_j$ is the mass flow rate of species j and h_j is the enthalpy of the species j. Heat transfer from AEMWE stack to the environment is calculated by

$$Q = h_t A (T - T_a) \quad (3)$$

where; h_t is the total heat transfer coefficient, which is approximated as 19 W/(m^2.K) [11], A is the external surface area of the stack, and T_a is the ambient temperature.

3. RESULTS AND DISCUSSION

In this study, a 46-cell AEMWE stack with a 50 cm^2 active area was considered as a case study. The AEMWE stack has nominal power of 5 kW at a current density of 1 A/cm^2 and the estimated thermal capacitance is 4.6 kJ/K. AEMWE stack cell parameters are used as given in previous study [1]. The developed model was initially used to analyze the AEMWE stack temperature response for various inlet temperature profiles. Constant inlet temperature and ramp input temperature profiles are applied, and the stack temperature response is recorded for different lye flow rates. Fig. 1 shows the stack temperature response for a constant inlet temperature at four different lye flow rates at 1 A/cm^2 current density. According to the results, as the lye flow rate increases, the stack temperature reaches the steady-state temperature more quickly. Additionally, the inlet and outlet lye solution temperature difference decreased to approximately 11°C. It has been determined that to maintain a temperature difference of less than 10°C at a stack power of 5 kW, the lye flow rate must be kept above 2.5 mL/(min.cm^2). For constant inlet temperature the stack reaches thermal equilibrium within 3 minutes.

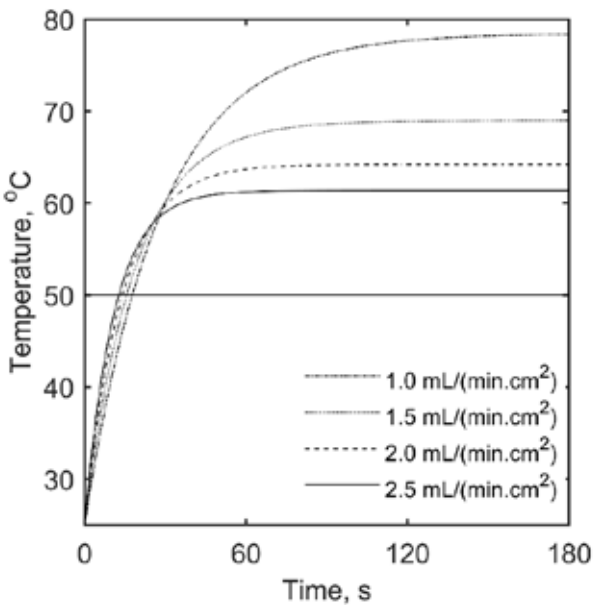

Fig. 1. Stack temperature response for a constant inlet temperature at four different lye flow rates and at 1A/cm^2

The developed model is then utilized to investigate the effect of the ramp inlet temperature profile. For this purpose, the dynamics of stack temperature is analyzed for two different rates of inlet temperature increase, with the inlet temperature rising from 25°C ambient temperature to 50°C at 1 A/cm^2. Fig. 2 illustrates the thermal behavior of the stack for different lye solution inlet temperature heating rates. The results show that as the heating rate increases, the stack temperature stabilizes more rapidly. Moreover, it has been observed that the ramp increase of the inlet temperature, compared to a constant inlet temperature, significantly prolongs the time required for the stack to reach thermal equilibrium. This suggests that a ramped inlet temperature profile can delay the startup time of AEMWE stack, which must be considered for optimal operation of AEMWE.

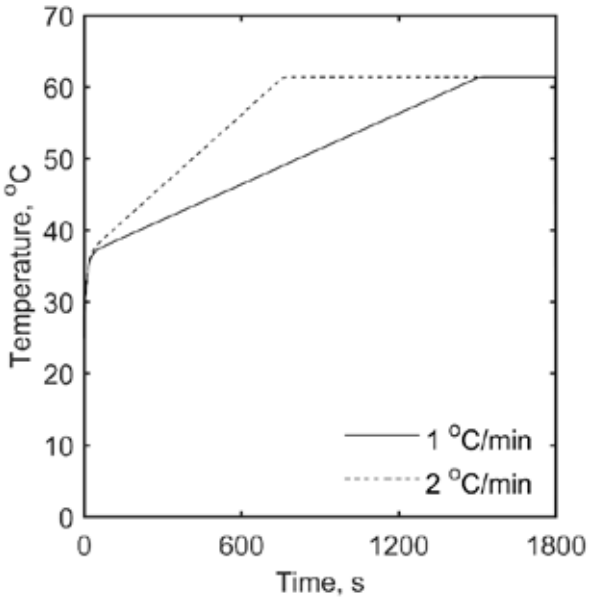

Fig. 2. Stack temperature evolution at a constant lye flow rate, 2.5 mL/(min.cm^2) for two different inlet temperature increase rates.

While the focus of this study is solely on the stack, it is important to recognize that the stack typically operates as part of a closed-loop lye circulation system in an electrolyzer system. Considering the complete electrolyzer system, it has been evaluated that using a pre-heater in the lye circulation circuit, prior to the stack, to maintain a constant inlet temperature would be more effective in shortening the stack's startup time than heating the lye solution with the heat produced by the stack and feeding it back into the stack. In the former approach, it is also recommended to consider the potential thermal stress that could be caused by the rapid stack temperature increase. Additionally, the energy consumption of the pre-heater should also be considered, as it could increase the overall energy demand of the system, potentially offsetting some of the benefits gained from reduced startup time.

4. CONCLUSIONS

In this study, a dynamic model was developed and utilized to investigate the thermal behavior and startup characteristics of a 46-cell AEMWE stack under various lye solution flow rates and inlet temperature profiles. The results demonstrated that increasing the lye solution flow rate accelerates the stack's stabilization, reducing the lye solution inlet and outlet temperature difference to approximately 11°C, with a required flow rate of 2.5 mL/(min.cm^2) to maintain this temperature difference. Additionally, the effect of different inlet temperature profiles was examined, showing that a ramped inlet temperature significantly delays the stack's startup time compared to a constant inlet temperature profile. Based on this comparison of stack thermal responses, it is suggested that the use of a pre-heater in an electrolyzer system containing an AEMWE stack would be more effective. The results obtained in this study also highlight the importance of predicting the thermal behavior of the stack in AEMWE systems using a model for optimizing the stack startup processes.

REFERENCES

1. Obut S. 2024. Mathematical modelling and performance analysis of an AEM electrolyzer. Journal of Scientific Reports-A 58:27-39.
2. Vidales AG, Millan NC, Bock C. 2023. Modeling of anion exchange membrane water electrolyzers: The influence of operating parameters. Chemical Engineering Research and Design 194:636-48.
3. Nafchi FM, Afshari E, Baniasadi E. 2024. Anion exchange membrane water electrolysis: Numerical modeling and electrochemical

performance analysis. International Journal of Hydrogen Energy 52:306-21.
4. Kim M, Lee D, Qi M, Kim J. 2024. Techno-economic analysis of anion exchange membrane electrolysis process for green hydrogen production under uncertainty. Energy Conversion and Management 302:118134.
5. Lawand K, Sampathkumar SN, Mury Z, Van Herle J. 2024. Membrane electrode assembly simulation of anion exchange membrane water electrolysis. Journal of Power Sources 595:234047.
6. Olivier P, Bourasseau C, Bouamama PB. 2017. Low-temperature electrolysis system modelling: A review. Renewable and Sustainable Energy Reviews 78:280-300.
7. Diéguez PM, Ursúa A, Sanchis P, Sopena C, Guelbenzu E, Gandía LM. 2008. Thermal performance of a commercial alkaline water electrolyzer: Experimental study and mathematical modeling. International Journal of Hydrogen Energy 33(24):7338-54.
8. Lebbal ME, Lecœuche S. 2009. Identification and monitoring of a PEM electrolyser based on dynamical modelling. International Journal of Hydrogen Energy 34(14):5992-9.
9. Hammoudi M, Henao C, Agbossou K, Dubé Y, Doumbia ML. 2012. New multi-physics approach for modelling and design of alkaline electrolyzers. International Journal of Hydrogen Energy 37(19):13895-913.
10. García-Valverde R, Espinosa N, Urbina A. 2012. Simple PEM water electrolyser model and experimental validation. International Journal of Hydrogen Energy 37(2):1927-38.
11. Tiktak WJ. 2019. Heat management of PEM electrolysis. Delft University of Technology: CD Delft, The Netherlands.

ENHANCED CATALYTIC PERFORMANCE OF TITANIUM DIOXIDE-SUPPORTED CuCo BIMETALLIC CATALYST FOR HYDROLYSIS OF AMMONIA BORANE

[1,2*]*Merve Kılıç*, [1]*Ercan Özdemir*
[1] Gebze Technical University, Chemical Engineering Department, Hydrogen Technologies Research Lab., Kocaeli, 41400, Türkiye
[2] ARMELSAN Enerji A.Ş., Sanayi Mah. Teknopark Bul. Teknopark 4A No:1/4A İç Kapı No:408 Pendik, İstanbul, 34906, Türkiye

*Corresponding author e-mail: merve.kilic2018@gtu.edu.tr

ABSTRACT
Material-based hydrogen storage systems stand out for their reliability and ease of use. Studies on ammonia borane (AB), having hydrogen storage capacity of 19.6%, have gained significant attention. Although noble metal-based catalysts (such as Pt, Ru, etc.) show the best results in AB dehydrogenation, their high cost has shifted focus toward transition metal-based alternatives. In this study, copper and cobalt, as transition metals, were supported on titanium dioxide and their performances were investigated under various parameters, including different stoichiometric ratios, AB amount, temperatures and sodium hydroxide concentrations. At 30°C, the $CuCo/TiO_2$ catalyst demonstrated a maximum catalytic activity of 218 min^{-1} and an apparent activation energy of 41.8 kJ/mol. This result represents promising performance among transition metal-based catalysts, highlighting the synergistic effect of Cu-Co compared to monometallic copper or cobalt catalysts.

Keywords: Ammonia borane, Hydrolysis, Material-based hydrogen storage, Bimetallic catalyst, Synergistic effect.

1. INTRODUCTION
The world's energy demand is increasing along with the population. Unfortunately, a significant amount of today's energy needs is still met from fossil resources. However, due to stringent regulatory frameworks and protocols aimed at reducing carbon emissions, such as the Carbon Border Adjustment Mechanism (CBAM) and The European Green Deal, countries are compelled to develop clean energy solutions. Hydrogen, with its high energy density, is notable as a promising clean and alternative energy source. The challenges of storing hydrogen in conventional gaseous and liquid forms, such as high pressure and energy costs, highlight the importance of solid hydrogen storage technologies. Among these, ammonia borane stands out as a promising material due to its stability in air and water at room temperature, low molecular weight, high hydrogen content by weight (19.6%), and non-toxicity. Compared to highly flammable and toxic compounds like $LiBH_4$ and $NaBH_4$, ammonia borane provides a safer and more efficient alternative with its superior gravimetric hydrogen storage capacity [1].
There are three ways to produce hydrogen from ammonia borane. These include (1) thermolysis, which releases 6.5% hydrogen by mass when heat is applied; (2) hydrolysis, which releases 3 moles of H_2 per 1 mole of AB at room temperature but requires appropriate catalysts because of the strong N-B bonds in ammonia borane; and (3) methanolysis, uses methanol, which is highly soluble in ammonia borane (23% at 23°C), in place of water in hydrolysis. Catalysts required for the dehydrogenation of AB can include transition metals, noble metals etc. While catalysts containing 4d and 5d metals (such as Ru, Pt, etc.) exhibit high activity, their scarcity results in high costs. In contrast, those incorporating 3d transition metals (such as Ni, Fe, Co etc.) present a cost-effective alternative with the potential for efficient hydrolysis [2].
In particular, bimetallic and trimetallic catalysts formed by combining different metals have been observed to be more active and efficient than their monometallic versions due to the synergistic effect between the elements. CuCo, CuNi, NiCo and FeNi are examples of active catalyst candidates [3]. However, it has been reported that unsupported metal alloy nanoparticles tend to agglomerate quickly while the reaction progress. Therefore, the use of support materials to prevent agglomeration by cost effectively has come to the fore. With using support materials, the active sites of the catalyst are dispersed over the support. Popular support materials include metal oxides (e.g., TiO_2, SiO_2, CeO_2, Al_2O_3), activated carbon, graphene species, and carbon nanotubes [4-5].
Copper and cobalt as a versatile non-precious metal catalyst is a good catalyst candidate with its abundant availability (i.e. low cost) and catalytic activity in the hydrolysis of amine boranes. In addition, the synergistic effect between Cu-Co has been emphasized in many studies. In this work, bimetallic, TiO_2 supported catalysts containing copper and cobalt from transition metals developed using impregnation reduction method for ammonia borane hydrolysis. The reason for the use of support material is to increase the surface area by preventing agglomeration.

2. MATERIALS AND METHODS

2.1 Materials
Reagents (analytical grade), including Copper(II)nitrate hemipentahydrate (Alfa Aesar, $Cu(NO_3)_2 \cdot 2.5H_2O$, 98%), Cobalt(II)nitrate hexahydrate (Alfa Aesar, $Co(NO_3)_2 \cdot 6H_2O$, 98%), Titanium dioxide (Alfa Aesar, TiO_2, 99,9%) and sodium

borohydride (Alfa Aesar, $NaBH_4$, 98.0%) were used in catalyst synthesis and sodium hydroxide (VWR, NaOH, 99.9%) were utilized during the hydrolysis reaction. All experiments employed high-resistivity ultrapure water (18.2 MΩ·cm⁻¹) to ensure consistency and purity. The synthesis of ammonia borane followed the procedure outlined by Ramachandran and Gagare (2007) [6].

2.2 Catalyst Synthesis

The catalysts were prepared using the impregnation-reduction process, a straightforward, useful, one-pot synthesis technique. To synthesize $Cu_{40}Co_{60}/TiO_2$ catalyst, copper (II) nitrate hemipentahydrate (2.51 mg Cu) and cobalt (II) nitrate hexahydrate (3.49 mg Co) were dissolved in 25 mL deionized water. The support material (144 mg TiO_2) was added to the solution and then stirred for 1-1.5 h to facilitate impregnation of metal ions onto the support surface. $NaBH_4$ reducing solution was then prepared in six-fold molar excess and added dropwise to the mixture to provide the amount required for complete reduction of the metal ions. Following the reduction process, the catalyst was seperated via vacuum filtration, washed thoroughly with ultrapure water, and allowed to dry overnight at 80°C in a vacuum oven.

2.3. Measurement of Catalytic Activity

The catalytic activity measurements of the bimetallic CuCo catalysts were carried out in a 4-necked jacketed reactor (20 mL) connected to a gas collection tube in a sealed manner. Temperature adjustment was provided by circulation from the reactor jacket with cryostat (Lauda RP870). Ammonia borane was dissolved in NaOH solution and injected into the reactor. The water displacement method was used to determine the volume of hydrogen generated.

2.4. Characterization

The elemental analyses and surface morphology of Cu/TiO_2, Co/TiO_2, and $Cu_{40}Co_{60}/TiO_2$ catalysts were performed using scanning electron microscopy (SEM-Philips XL30 SFEG) and energy-dispersive X-ray spectroscopy (EDS-Bruker). The crystal structures of the samples were examined using an X-ray diffractometer (XRD-Rigaku D/Max - 2200/PC) with Cu-Kα radiation at 40 kV and 40 mA. XRD patterns were recorded in the 2θ range of 5°–90° and at 3°/min scanning speed.

3. RESULTS AND DISCUSSION

In Fig. 1a – Fig. 1c SEM images of the Co/TiO_2, Cu/TiO_2 and $Cu_{40}Co_{60}/TiO_2$ catalysts are shown, respectively. According to SEM images of the catalysts, irregular structures were observed and particle diameters ranged from 1-2 µm. Analysis of the EDS results in Fig. 2 shows a peak at 2.4 keV binding energy in all spectra, corresponding to the Au coating used during sample preparation. Additionally, peaks for Copper (Cu), Cobalt (Co), Titanium (Ti), Boron (B), and Oxygen (O) were identified at their characteristic binding energies. The elemental composition analysis indicates that Cu/TiO_2 contains 5.49 wt% Cu, Co/TiO_2 contains 3.56 wt% Co and $Cu_{40}Co_{60}TiO_2$ contains 2.06% and 2.44 wt% Cu and Co, respectively. These values are consistent with the metal loading rate of the catalysts of 4 wt%. XRD analysis was performed to investigate the crystal structures of Co/TiO_2, Cu/TiO_2 and $Cu_{40}Co_{60}/TiO_2$ catalysts.

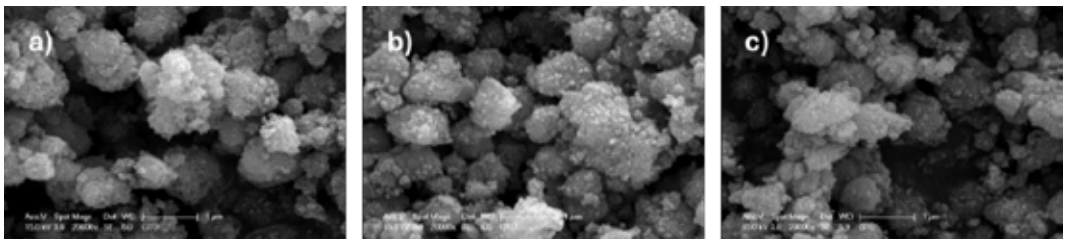

Fig. 1. The SEM images of catalysts at a scale of 1 µm, a) Co/TiO_2, b) Cu/TiO_2 and c) $Cu_{40}Co_{60}/TiO_2$

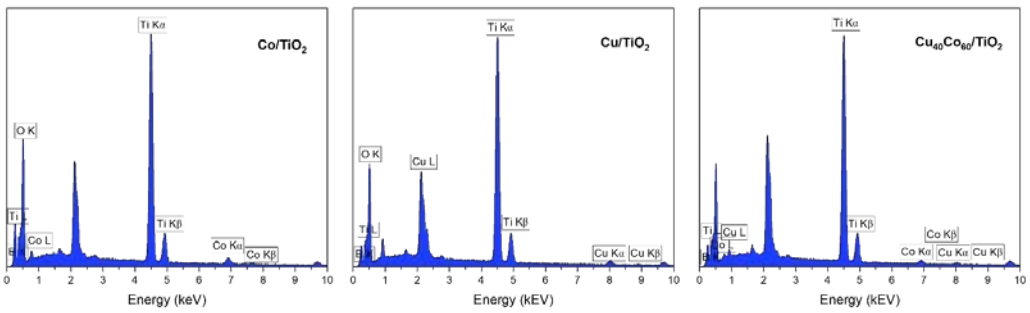

Fig. 2. EDS spectrum of Co/TiO_2, Cu/TiO_2 and $Cu_{40}Co_{60}/TiO_2$

The results of the analysis are shown in Fig.3. Peaks of TiO_2 anathase phase were sharply detected in each of the catalysts. The copper and cobalt structures were not visible in the XRD spectra as they are amorphous and only constitute a small fraction of the catalyst content (4%wt.).

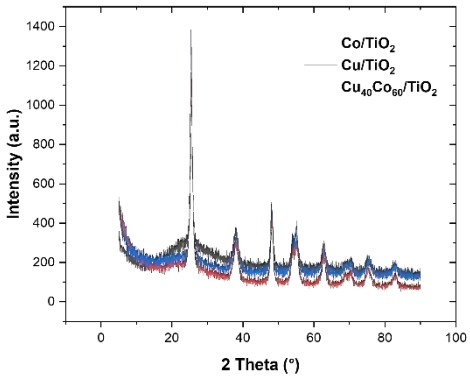

Fig. 3. XRD patterns of Co/TiO_2, Cu/TiO_2 and $Cu_{40}Co_{60}/TiO_2$

In the first part of the study, copper and cobalt catalysts were synthesized as monometallic (Cu/TiO_2 and Co/TiO_2) and bimetallic in different stoichiometric ratios ($Cu_{20}Co_{80}/TiO_2$, $Cu_{40}Co_{60}/TiO_2$, $Cu_{50}Co_{50}/TiO_2$, $Cu_{60}Co_{40}/TiO_2$ and $Cu_{80}Cu_{20}/TiO_2$). The performance test results are shown in Fig.4 a) (initial test parameters: 1mmol AB, 4%wt. Catalyst metal loading, 1 mg metal, 0.1M NaOH, 25°C).

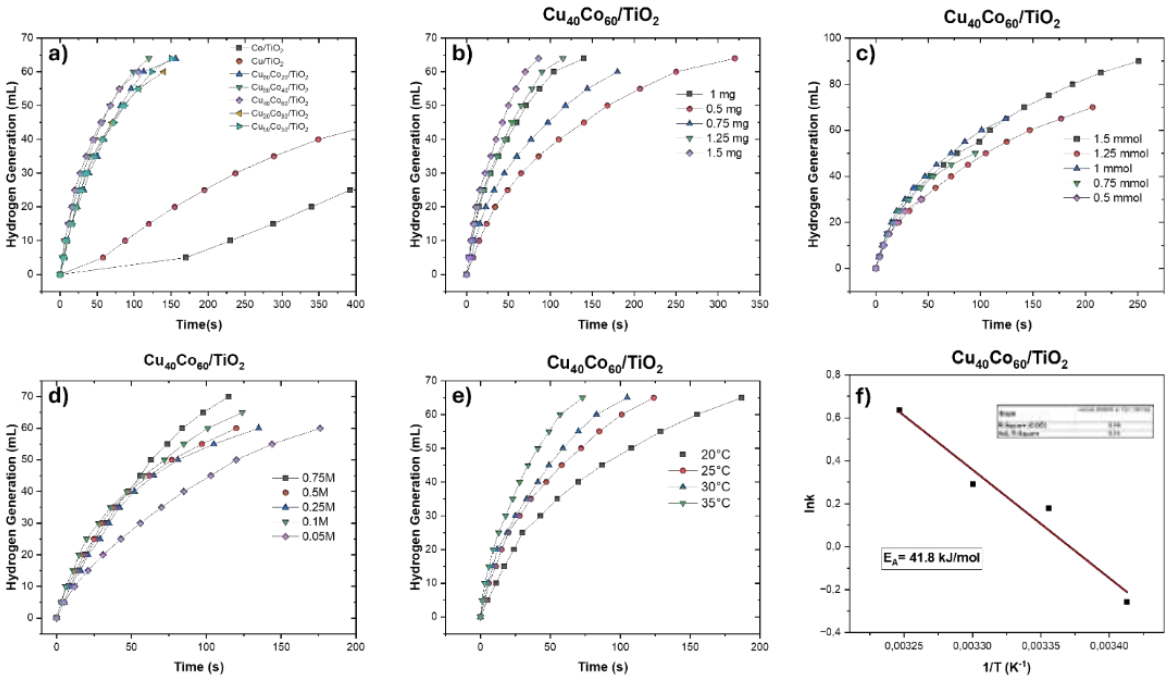

Fig. 4. Catalyst performans tests a) testing of catalysts in different stoichiometric ratios, b) The metal amount effect on $Cu_{40}Co_{60}/TiO_2$ catalyst, c) The AB mmol effect on the $Cu_{40}Co_{60}/TiO_2$ catalyst, d) The NaOH concentration effect on the $Cu_{40}Co_{60}/TiO_2$ catalyst, e) The temperature effect on the $Cu_{40}Co_{60}/TiO_2$ catalyst, f) Using Arrhenius plot for the determination of the $Cu_{40}Co_{60}/TiO_2$ catalyst

It is evident that the monometallic Cu/TiO_2 and Co/TiO_2 catalysts exhibited a lower performance than the bimetallic catalysts. $Cu_{40}Co_{60}/TiO_2$ was selected as the most active. Subsequently, as shown in Fig. 4b, tests were conducted with the $Cu_{40}Co_{60}/TiO_2$ catalyst to examine the impact of the catalyst metal amount on activity. The tests were carried out using total Cu and Co metal amounts in the range of 0.5 - 1.5 mg, with the optimum metal amount determined to be 1 mg. Further tests were conducted with varying AB fuel amounts in the range of 0.5 - 1.5 mmol AB to evaluate its impact, with the optimal AB amount determined as 1 mmol (33 mg), as shown in Fig. 4c. To examine the effect of sodium hydroxide on the reaction, experiments were performed with NaOH concentrations in the range of 0.05 - 0.75 M. The highest activity was achieved in a 0.1 M NaOH solution (Fig. 4d). Finally, tests were performed at 20°C, 25°C, 30°C, and 35°C, revealing that the reaction rate increased with rising temperature. Based on the findings from all tests, the optimum

reaction conditions for the most active catalyst, $Cu_{40}Co_{60}/TiO_2$, were determined as follows: 4 wt.% catalyst loading, 1 mg total metal content, 1 mmol AB (33 mg), 0.1 M NaOH solution, and 30°C. Under these conditions, the catalyst exhibited a turnover frequency (TOF) of 218 min^{-1} and an activation energy of 41.38 kJ/mol. Catalysts developed for ammonia borane hydrolysis are summarized in Table 1, along with their activation energies and TOF values. The $Cu_{40}Co_{60}/TiO_2$ catalyst demonstrates superior performance compared to many other catalysts reported in the literature, achieving higher catalytic activity while reducing activation energy.

Table 1. Comparison of catalyst for ammonia borane hydrolysis

	TOF (min^{-1})	**Ea (kJ/mol)**	**Ref.**
$Ni_{0.6}Cu_{0.4}O/NC$	26.20	56.8	[7]
CoCu-NC-5	8.12	34.25	[8]
$Co_{0.52}Cu_{0.48}$	3.40	33.7	[9]
$Ni_{0.19}Cu_{0.81}$	2.70	33.3	[9]
$Ni_{0.3}Co_{0.3}Cu_{0.4}/TiO_2$	10	61.4	[10]
$Co_{0.8}Cu_{0.2}/CNC$	23.37	50.79	[11]
$Cu_{40}Co_{60}/TiO_2$	218	41.8	This work

4. CONCLUSIONS

One of the safe and practical methods for hydrogen storage is ammonia borane, which has been gaining increasing importance. Particularly in scenarios requiring rapid and convenient hydrogen production, such as critical and emergency situations, ammonia borane plays a vital role. For the hydrolysis of AB, cost-effective catalysts based on non-noble transition metals are essential. This study focuses on copper and cobalt catalysts with synergistic effects, revealing that at 30°C, the $Cu_{40}Co_{60}/TiO_2$ catalyst achieves a TOF value of 218 min^{-1} and an activation energy of 41.8 kJ/mol. These values stand out in the literature for their high activity and low activation energy among non-noble metal-based catalysts.

REFERENCES

[1] Ishaq, H., Dincer, I., & Crawford, C. (2022). A review on hydrogen production and utilization: Challenges and opportunities. *International Journal of Hydrogen Energy*, *47*(62), 26238-26264.

[2] Figen, A. K. (2013). Dehydrogenation characteristics of ammonia borane via boron-based catalysts (Co–B, Ni–B, Cu–B) under different hydrolysis conditions. *International Journal of Hydrogen Energy*, *38*(22), 9186-9197.

[3] Zhou, J., Feng, X., Zhao, Y., Cui, R., Wang, D., & Zhang, B. (2022). Noble-metal-free CuNi/Co3O4 hybrid nanosheets as efficient and magnetically recyclable catalysts for hydrolysis of ammonia borane. *Journal of Alloys and Compounds*, *923*, 166345.

[4] Alpaydın, C. Y., Gülbay, S. K., & Colpan, C. O. (2020). A review on the catalysts used for hydrogen production from ammonia borane. *International Journal of Hydrogen Energy*, *45*(5), 3414-3434.

[5] Feng, Y., Chen, X., Wang, H., Li, X., Huang, H., Liu, Y., & Li, H. (2021). Durable and high performing Ti supported Ni0. 4Cu0. 6Co2O4 nanoleaf-like array catalysts for hydrogen production. *Renewable Energy*, *169*, 660-669.

[6] Ramachandran, P. V., & Gagare, P. D. (2007). Preparation of ammonia borane in high yield and purity, methanolysis, and regeneration. *Inorganic Chemistry*, *46*(19), 7810-7817.

[7] Li R., Zuo Y., Hua J., Hao S., Xu L., Ye M., Wan C. (2024). Preparation of $Ni_{0.6}Cu_{0.4}O/NC$ catalyst and its catalytic performance for hydrogen production from hydrolysis of ammonia borane. *International Journal of Hydrogen Energy*, 52(8), 1184−1192

[8] Song, Y., Gao, C., Liu, J., & Liu, Z. (2023). Fabrication of multiatomic structure of Cu-CoO/Co interface for efficient hydrogen generation from ammonia borane hydrolysis. *International Journal of Hydrogen Energy*, *48*(67), 26162-26172.

[9] Sang, W., Wang, C., Zhang, X., Yu, X., Yu, C., Zhao, J., ... & Li, L. (2017). Dendritic Co0. 52Cu0. 48 and Ni0. 19Cu0. 81 alloys as hydrogen generation catalysts via hydrolysis of ammonia borane. *international journal of hydrogen energy*, *42*(52), 30691-30703.

[10] Yang, X. J., Wang, C. Y., Gao, R. Y., Lu, Z. M., Zhang, X. H., Yu, X. F., & Li, L. L. (2018). Non-noble metallic nanoparticles supported on titania spheres as catalysts for hydrogen generation from hydrolysis of ammonia borane under ultraviolet light irradiation. *International Journal of Hydrogen Energy*, *43*(34), 16556-16565.

[11] Rong, L. I., Youhua, Z. U. O., Licheng, X. U., Junfeng, H. U. A., Jiajia, F. E. N. G., Lixin, X. U., ... & Chao, W. A. N. (2024). The effects of calcination temperature and dispersants on the catalytic performance of Co0. 8Cu0. 2/CNC for the hydrolysis of ammonia borane to hydrogen. *Journal of Fuel Chemistry and Technology*, *52*(11), 1736-1744.

SYNTHESIS AND CHARACTERIZATION OF SEMICONDUCTOR OXIDES CuO AND ZnO FOR THE PRODUCTION OF GREEN H_2 BY PHOTO CATALYSIS UNDER UV-VISIBLE LIGHT

Nibou Djamel, Amokrane Samira, Sebati Farouk, Ferhat Djawad and Hammoudi Hadda Aya
Laboratory of Materials Technology, University Science and Technology Houari Boumediene 32, Bab-Ezzouar, Algiers, Algeria.

*Corresponding author e-mail: djamelnibou@gmail.com

ABSTRACT
The study deals with the synthesis and characterization of semiconductor oxides CuO and ZnO for the production of green H_2 gas by photo catalysis reaction under UV-visible light. The oxides were hydrothermally synthesised from reactive reagents with a thermally treatment at 450-500°C during 6 h for several anneals. The oxides were identified and observed by X-ray diffraction (XRD) and scanning electron microscopy (SEM) respectively. The chemical composition of oxides was determined by energy dispersive spectroscopy (EDS) analysis. The results showed that CuO and ZnO oxides as semiconductor phases were obtained successfully. The gas production by photo catalysis was carried out in a double-walled pyrex glass photo reactor, equipped with a thermostat. It is connected to a U-shaped water pressure gauge that allows the volume of gas released to be measured directly. The photo catalytic tests are carried out in various media. The oxides have shown promising results in terms of improving the catalytic activity of semiconductors in a neutral environment, showing to be effective in hydrogen gas production.

Keywords: Hydrogen, Oxides, CuO, ZnO, Photo catalysis, Neutral and basic medium

1. INTRODUCTION

The 21st century is marked by unprecedented energy challenges, where the search for renewable and sustainable energy sources has become a global priority. In the face of the climate crisis and the depletion of fossil resources, technological innovation plays a crucial role in the transition to a green economy [1-2]. Among the many emerging solutions, the production of biohydrogen stands out for its potential to provide clean and abundant energy, without greenhouse gas emissions. Hydrogen, as an energy carrier, offers considerable advantages [2]. It can be used in various applications, ranging from fuel cells for electric vehicles to energy storage systems, as well as for the production of heat and electricity [2-3].
However, the method of producing this hydrogen is crucial for its environmental impact. Traditional methods, often based on hydrocarbons, are energy-intensive and generate a significant amount of CO_2. Therefore, the production of biohydrogen, exploiting renewable sources and ecological processes, has become a particularly promising avenue of research [4-6]. Hydrogen is not a primary energy like coal, oil or natural gas; it is an energy vector that must be produced before being used. Hydrogen production represents a major advance in the search for renewable and sustainable energy. Unlike conventional hydrogen, which is often produced from fossil fuels, hydrogen is a process that is produced by electrolysis of water and uses electricity from renewable sources such as wind and solar [4-5]. Since this process does not emit CO_2, it has become an ecological and promising alternative to reducing greenhouse gas emissions. Hydrogen can also be produced from chemical reactions and photo catalysis [5-6]. Hydrogen has the potential to play an important role in the global energy transformation.
In this context, our work focuses on the synthesis and characterization of oxides CuO and ZnO as semiconductors for the production of hydrogen gas.

2. MATERIALS AND METHODS

The oxides were prepared by hydrothermal method using $Cu(NO_3)_2.3H_2O$) and $Zn(NO_3)_2.6H_2O$) nitrate salts from Merk with a purity of 99%. The mixtures are stirred at room temperature and heated to 100 °C to remove water and then to 300 °C to denitrify them. After grinding, the homogenized powder is heated in the oven at a temperature of 450 to 500°C for 6 h under several anneals to obtain the semiconductor phases of CuO and ZnO.
The H_2 production by photo catalysis was carried out in a double-walled glass reactor in neutral and basic media as reported in previously work [6]. The reactor (125 cm^3) is irradiated by tungsten lamps with a total power of 600 W. The photo activity was measured by the gas volume produced in these media solutions. All reactions are carried out at 50°C under stirring of about 300 rpm. The bubble of solutions is used with He gas in the presence or without catalysts during 15 and 30 respectively.
The oxides were identified by XRD using a Philips diffractometer type PW 1710. The morphology of the samples was observed by SEM using an equipment type XL20. The chemical composition of the oxides was determined by EDS analysis coupled in the same SEM equipment.

3. RESULTS AND DISCUSSION

3.1. Characterization of samples

The Fig.1 shows XRD patterns of prepared CuO and ZnO oxides. All XRD peaks are indexed as Muller (hkl) in the range 2θ of 5 to 120° and identified as belong to the pure phases of CuO and ZnO oxides according to the standard files JCPDS 01-080-0076 and JCPDS 01-089-7102 respectively. These results are in agreement with those of Belaissa and al.[7].
The morphology of the oxides is highlighted by SEM micrographs shown in Fig.2. One can observe irregular forms of CuO and ZnO grains with average size between 0.5 and 1 µm. These fine particles offer are necessary to diffuse into the interface of CuO and ZnO oxides to improve the photo catalysis reaction for the H_2 gas production.
The Table 1 shows the results of EDS analysis of prepared oxides, confirming the presence of the main elements Cu and Zn in their structures. The carbon element is detected by EDS because it was used on the surface of the samples to make them conductive and facilitate the analysis.

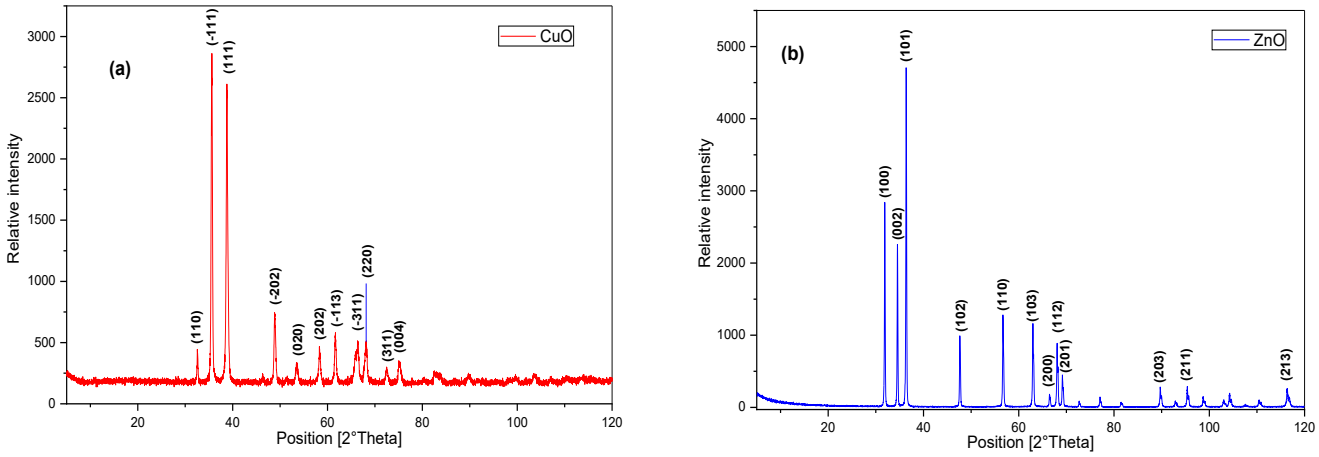

Fig.1. XRD patterns of CuO (a) and ZnO (b)

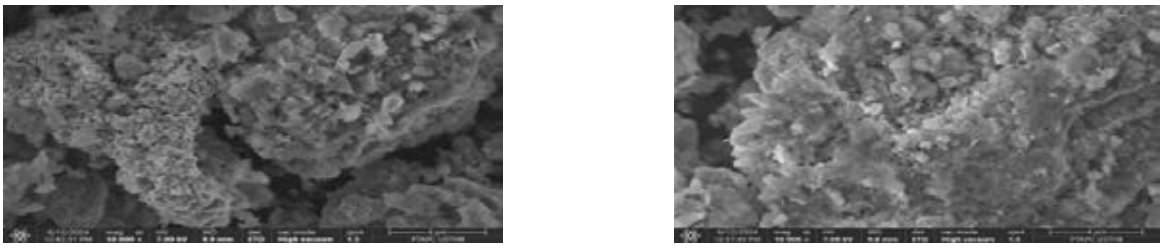

Fig.2. Micrographs by SEM of CuO (a) and ZnO (b)

Table 1. Chemical composition by EDS analysis of CuO and ZnO oxides

	C	O	Cu	Zn
CuO				
At. %	12.0	52.0	35.4	-
Wt. %	6.2	35.5	57.3	-
ZnO				
At. %	14.4	58.0	-	27.5
Wt. %	9.0	48.64	-	41.1

3.2. Hydrogen production by photo catalysis

The H_2 production by photo catalysis was carried out firstly in neutral medium using sodium sulfate Na_2SO_4 dissolved in water. We start with a blank test (nb) using a bubble of the He gas to eliminate all the gases dissolved in the solution. After closing the He, the reactor is placed under visible light in order to produce H_2 gas. One gas production has stopped, the lamps are closed and 0.1 g of CuO is introduced into the reactor. A bubble is also carried out and after the

production of H_2 is obtained in the presence of CuO oxide or semi conductor (nsc). When equilibrium is reached, the lamps are turned off again and a quantity of 0.19 g of hole sensor (Na_2SO_3) is added to the previous solution. We then measure the quantity of H_2 gas produced in the presence of the holes in the solution (nct).
Fig.3 shows the evolution in time of the mole number of hydrogen produced in this media for CuO and ZnO oxide catalyst respectively. According to the Figures, it seems that the behavior of the two catalysts is different. In the case of CuO catalyst (Fig.3(a)), the mole number of H_2 gas increases rapidly during the 5 minutes of the reaction to reach a maximum in the case of (nct) and (nsc) modes of 4 10^{-7} and 2.25 10^{-7} mole respectively. After these times, a decrease of the production of H_2 is observed until 40 min of reaction. The test of blank mode highlights a maximum of H_2 quantity of 3 10^{-7} mole reached at 10 min with a visible plateau between 6 and 12 min, indicating an equilibrium. In the other hand, Fig.3(b) shows another behavior of ZnO catalyst toward the evolution of mole number of H_2 in different modes. The test under (nsc) condition performs well and reaches a maximum of H_2 gas production (4 10^{-7} mole) during 12 min. It is followed then by (nb) and (nct) modes with 3 10^{-7} and 2.5 10^{-7} mole respectively. In the three modes, an equilibrium plateau is observed at 9-14 min (nsc), 6-14 min (nb) and 5-11 min (nct), revealing that great quantity of H_2 can be produced during these equilibriums. From these results, the performance of ZnO catalyst in (nsc) mode is best to that CuO and reached a double quantity of H_2 produced. However, the performances of CuO and ZnO in the (nb) mode still stable.

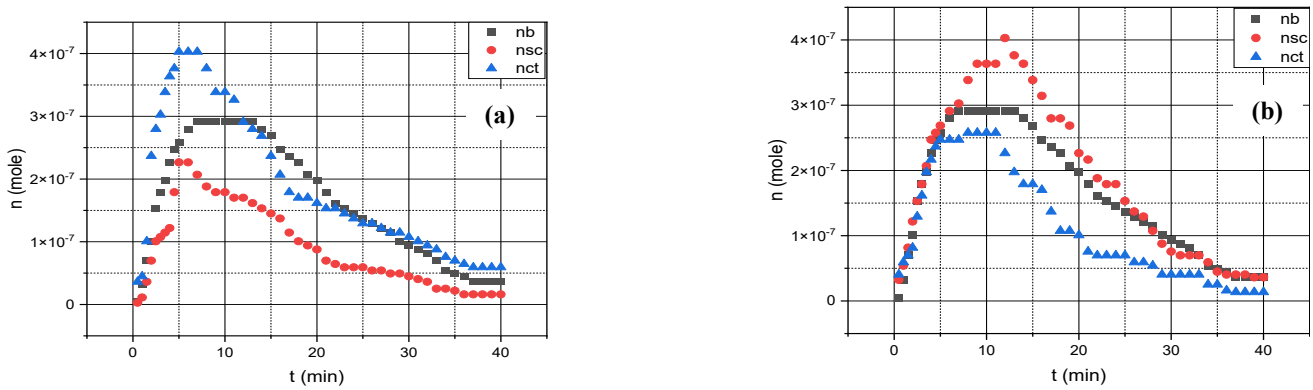

Fig.3. Evolution of mole number of H_2 in time under neutral medium using CuO (a) and ZnO(b) oxide catalysts at different modes (nb, nsc and nct)

Fig.4 shows the evolution in time of the mole number of H_2 gas produced in basic medium for CuO and ZnO oxide catalysts using KOH dissolved in water. All tests are carried out as used in the same way as those in neutral environment. From these results, the best tests for the production of H_2 are obtained in (nb) mode onto the CuO catalyst (2.6 10^{-7} mole) with a equilibrium plateau between 10-17 min. ZnO catalyst records a 3.25 10^{-8} mole of H_2 gas less than CuO. Comparing the obtained results Fig.3 and Fig.4, it is clearly that the two catalysts perform best in neutral media. These results are in agreement with those reported in the literature [6].
In this regard, the CuO and ZnO oxides are optically active semi conductors because of their chemical stability. They generate electron/hole (e−/h+) pairs according to the radicals OH• and/or O_2 • through valence (VB) and conduction (CB) bands with high oxidative aptitude to cause a destructive oxidation reaction. ZnO is known with its wide band gap (2.98 eV) requires an excitation in the UV region and CuO is a p type oxide with a thin band gap of 1.2 eV [7]. The production of H_2 gas can be achieved via a photo catalytic reaction onto p CuO and n ZnO according to the following mechanism:

$$CuO + h\,v \rightarrow (h^{+}_{VB})\ CuO + (e^{-}_{CB}) \quad \text{and} \quad ZnO + h\,v \rightarrow (h^{+}_{VB})\ ZnO + (e^{-}_{CB}) \qquad (1)$$

$$2SO_3^{2-} + (h^{+}_{VB}) \rightarrow S_2O_6^{2-} \qquad (2)$$

$$H_2O + 2(e^{-}_{CB}) \rightarrow H_2 + OH^{-} \qquad (3)$$

Due to the elevated energetic location of CuO and ZnO valence bands, the oxygen molecules do not compete with the water oxidation and it is necessary to reduce the photo holes which are scavenged by SO_2^{3-} (Eq.(2)). This reaction has a potential (E°) of about -0.2 V compared to that of the couple SO_4^{2-}/SO_3^{2-} of -1.2 V. This last potential is very negative and doesn't contribute in the oxidation reaction which explains the observed equilibrium plateau in Fig.3 and Fig.4. The phenomenon is due to the saturation of competitive reduction at the end product $S_2O_6^{2-}$.

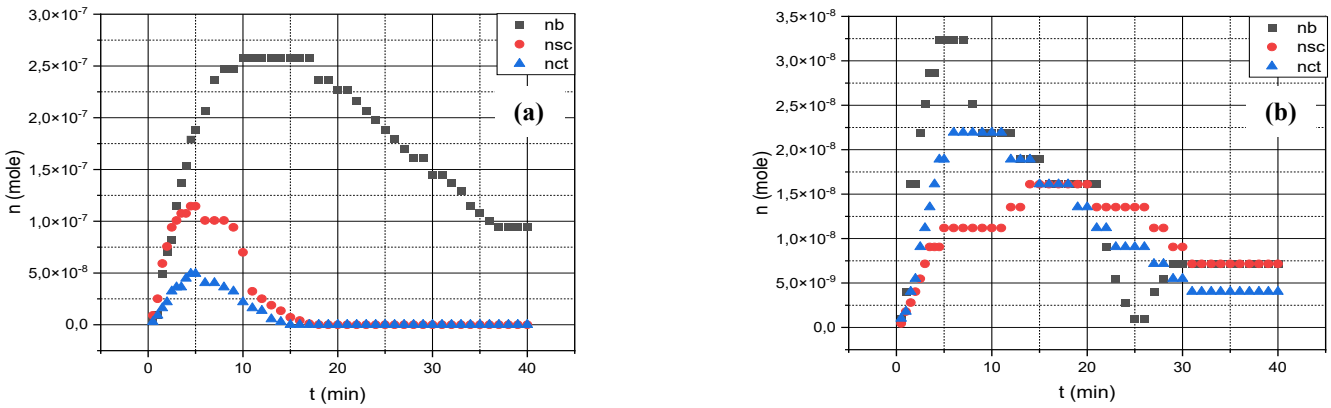

Fig.4. Evolution of mole number of H_2 in time under neutral medium using CuO (a) and ZnO (b) oxide catalyst at different modes (nb, nsc and nct)

4. CONCLUSIONS

CuO and ZnO catalysts have been prepared successfully in the production of H_2 gas by photo catalytic reaction. They have identified by XRD and the structural properties have highlighted by SEM and EDS analysis. Their optical gaps and stability allow them to be very interesting in the photo catalysis conversion reaction. The CuO and ZnO catalysts showed good performances in neutral media recording a maximum quantity of hydrogen of 4 10^{-7} mole. The hydrogen was produced in presence of SO_2^{3-} under UV-visible light and a mechanism process was proposed. The CuO and ZnO oxides are low cost and non toxic and can be attractive as photo catalysts for the production of green H_2 gas.

REFERENCES

1. https://www.moncourtierenergie.com/hydrogene-vert-une-solution-davenir/ Accessed on August 4, 2023
2. Bjrklund A, Melaina M, Keoleian GA. 2001.Hydrogen as a transportation fuel produced from thermal gasification of municipal solid waste: an examination of two integrated technologies, International Journal of Hydrogen Energy 26:1209-1221.
3.https://www.dashdoc.com/fr/blog/le-vehicule-hydrogene-la-course-pour-un-trm-plus-vert. Accessed on May 8, 2022
4.Maeda K, Kazunari D. 2010. Photocatalytic Water Splitting: Recent Progress and Future Challenges, Journal Physics and Chemistry Letters, 1 (18): 2655-2661.
5.Jing, D., Guo, L., Zhao, L., Zhang, X., Liu, H., Li, M., Shen, S., Liu, G., Hu, X., Zhang, X., Zhang, K., Ma, L. Guo, P., 2010. Efficient solar hydrogen production by photocatalytic water splitting: From fundamental study to pilot demonstration, International Journal of Hydrogen Energy 35:7087-7097.
6.Mekatel, E., Trari, M., Nibou, D., Sebai, I., Amorkrane, S. 2019. Preparation and characterization of α-Fe_2O_3 supported clay as a novel photocatalyst for hydrogen evolution. International Journal of Hydrogen Energy, 44(21):10309-10315.
7. Belaissa Y, Nibou D, Assadi AA, Bellal B, Trari M, 2016. A new hetero-junction p-CuO/n-ZnO for the removal of amoxicillin by photocatalysis under solar irradiation, Journal of the Taiwan Institute of Chemical Engineers, 68:254-265

THE EFFECT OF DIFFERENT TYPES OF METAL PHTHALOCYANINE ON THE ELECTRODECOMPOSITION OF H_2S TO H_2 AND POLYSULFIDES

[1]*Faezeh Nazari*, [1]*Alper Sarioglan*, [2*]*Mehmet Suha Yazici*
[1] Istanbul Technical University, Chemical Engineering, 34467 Maslak-Istanbul, Turkey
[2]Istanbul Technical University, Energy, ITU Energy Institute, 34467 Maslak-Istanbul, Turkey

*Corresponding author e-mail: syazici@itu.edu.tr

ABSTRACT

The effect of phthalocyanine with different central metals like cobalt and nickel in hydrogen evolution from hydrogen sulfide (H2S) is investigated. Impact of using different gas diffusion layers, i.e. nickel (Ni), titanum (Ti), and stainless steel (SS), as the support of metal phthalocyanines (MPc's) in the three-electrodes system are studied. The linear sweep voltametry (LSV) and electrochemical impedance spectroscopy (EIS) are measured to understand the behavior of the catalysts and supports. The cobalt phthalocyanine (CoPc) on nickel (Ni) gave the best electrochemical response in compare to other catalysts and supports. Long term performance aspect needs to be investigated.

Keywords: Hydrogen Sulfide, Hydrogen, Electrolysis, Phthalocyanine

1. INTRODUCTION

The predominant sources of hydrogen sulfide include the hydrogen desulfurization (HDS) process utilized for oil purification, as well as its occurrence in natural gas wells, jeothermal sources and during steel manufacturing (Hensen et al., 2001).
One of the common methods is the convertion of H2S by thermal methods like Claus. In Claus process H_2S is converted to sulfur and at a tempeature more than 1000°C:

$H_2S + 3/2O_2 \rightarrow SO_2 + H_2O$, and $2H_2S + SO_2 \rightarrow 2H_2O + 3S\downarrow$

The other product of this reaction is water. This method does not provide any hydrogen, but also consumes a huge amount of energy. On the other hand, the electrochemical technique remains the best option due to its unrivaled advantages such as quick response, cost effectiveness, environmental friendliness, and ease of operation. Therefore, H_2S electrolysis is a "killing two birds with one stone" technique that delivers a new cost-effective H_2 source while also removing the pollutant H_2S from the atmosphere(Dan et al., 2017). H_2S electrolysis involves cathodic H_2 and anodic sulfur oxidation reactions (SOR) at a low cell voltage of 0.14 V (Hakim et al., 2023). Replacing the oxygen evolution reaction (OER) with the sulfur oxidation reactions (SOR) reduces the electrolysis potential from 1,23 V (H_2O electrolysis) to 0,14 V (H_2S electrolysis), resulting in significant energy savings for pure H_2 generation (Kumar and Nagaiah, 2022). In the alkali solution H_2S is desolved in the solution(Yang et al., 2019):

$H_2S + OH^- \rightarrow H_2O + HS^-$

And then in the electrolysis reaction:

Anode: $2HS^- \rightarrow S + H_2S + 2e^-$, and $HS^- + OH^- \rightarrow S + H_2O + 2e^-$

Cathode: $2H_2O + 2e^- \rightarrow H_2 + 2OH^-$

and then, sulfur rapidly dissolves in the alkaline media forming polysulfides:

$S + HS^- + OH^- \rightarrow S_2^{-2} + H_2O$

Phthalocyanine with different central metals has distinctive benefits as a catalyst such as, the ease of large-scale production, distinctive redox behavior, high efficiency, ease of separation, and recyclability (Yang et al., 2021). An ideal system for conducting redox reactions is produced by MPcs with a metal cation in the middle of the macrocycle and long conjugated π-bonds (Osmanbas et al., 2008). Since the catalytic reaction has been driven in two different processes, including the metal-based and ligand-based reductions, the central metal plays a critical role in MPc performance (Koca et al., 2011). Therefore, by building complexes with redox active metal cations, Pcs' redox activity can be raised. If the

π-system is extended by substituting groups with conjugated double bonds, the redox behavior of MPc can be further enhanced (Özçeşmeci et al., 2013). The type of metal center, substitution, support, and aggregation of Pcs are some of the critical parameters that determine the total H_2 production rate for the photo- and electrocatalytic H_2 formation processes of Pc-based catalysts(Keshipour and Asghari, 2022). For a thorough understanding of the role of the central metal atom in a three-electrode cell electrolysis of H_2S for hydrogen production, cobalt, and nickel phthalocyanines were selected for this study.

2. MATERIALS AND METHODS

2.1. Materials

$Na_2S{\cdot}9H_2O$ was utilized as the source of H_2S. The original pH values of the Na_2S aqueous solution were adjusted with sodium hydroxide (from Riedel-DeHaen and LabKim). Cobalt phthalocyanine (CoPc) 96%, and nickel phthalocyanine (NiPc) 98% were bought from BLD Pharmatech GmbH. Tetrahydrofuran (THF, 99.9%) used as solvent. Support materials were 300 micron stainless steel fiber, 150 micron %56 porosity titanium fiber, and 200 micron %83 porosity nickel fiber from Bekaert.

2.2. Electrode Preparation

In order to prepare electrode ink, 10 mg of MPc's, 20 mg of 5% Nafion, 0,1 ml distilled water, and 140 mg THF were added in a container, and mixed in an ultrasonic bath. Then, surface of the electrode supports (porous nickel, titanium, and stainless steel) were either painted or spray-coated. The dyed materials were kept at 130°C for 10 minutes, then they were allowed to cool and weighed. Loading of cobalt phthalocyanine (CoPc), and nickel phthalocyanine (NiPc) on the surface of electrode's supports were measured and provided in Table 1.

Table 1. The amount of catalyst loaded on the surface of different types of porous supports

Support/Material	CoPc	NiPc
Stainless Steel (SS)	1.3631 mg/cm²	2.0248 mg/cm²
Titanium (Ti)	1.0179 mg/cm²	1.3913 mg/cm²
Nickel (Ni)	1.8882 mg/cm²	1.7205 mg/cm²

2.3. Electrochemical measurement

All electrochemical measurements have done by potentiostat Gamry 5000. A conventional three-electrode cell, wherein MPc (1cm^2) on diffusion support acts as a working electrode (WE), and a platinum wire as counter and 3.5M KCl Ag/AgCl as reference electrodes. The electrolyte solution was 0.1M Na_2S, and 0.1M NaOH. The SOR activity of the catalysts was illustrated by performing linear sweep voltammetry (LSV) over a potential range of -0,4 to 0,1 V vs. SHE at scan rate 50 mV/s. The electrochemical impedance spectroscopy (EIS) measurements were performed in a frequency range of 100 kHz to 200 mHz at open circuit potential (OCP) and 0.1 V vs. SHE.

3. RESULTS AND DISCUSSION

The electrocatalytic performance is done by LSV at 50 mV/s scan rate. The sulfide oxidation reaction (SOR) shows the different catalyst performance including NiPc on Ni and CoPc on Ni in compare to the porous Ni, Ti, and SS without catalyst and also platinum in 0.1 M Na_2S and 0.1 M NaOH electrolyte solution. As it is shown in **Figure 1a**, CoPc on Ni and NiPc on Ni have the lowest OCP around −380 mV vs. SHE. At 10 mA/cm² current density, the potential of CoPc on Ni, NiPc on Ni, and Ni are −32, −2, and +131 mV vs. SHE, respectively. As it is clear, CoPc on Ni has the minimum polarization. Besides, Pt with the maximum 2.21 mA/cm² current density at 200 mV is not a desirable electrode for H_2S, while the CoPc on Ni with maximum current density 20 mA/cm² at 173 mV seems to be a better choice.

By changing the support to Ti, the SOR behavior of the catalysts is almost similar to the Ni support; however, Ti without a catalyst shows a lower potential at 8 mA/cm² current density than NiPc on Ti and CoPc on Ti (Fig. 1b). The negligible current densities up to 350 mV vs. SHE in the LSV graph of Fig. 1c reveal that SS cannot be a desirable support for the H_2S system.

The electrochemical impedance spectroscopy (EIS) was performed at the beginning of the experiments at open-circuit potential (OCP) and 0.1 V vs. SHE to understand which electrode has lower impedance among Ni, Ni-coated catalysts, and platinum (Pt) as a reference for comparison. As shown in Fig. 2a, coated Ni electrodes (NiPc and CoPc) have lower charge transfer resistance (R_ct) compared to Ni and Pt. By fitting these results to the LSV data, one may conclude that

lower charge transfer resistance causes faster electron transfer on the surface of the electrodes. Platinum exhibits the highest resistance compared to other catalysts, possibly due to sulfur poisoning.

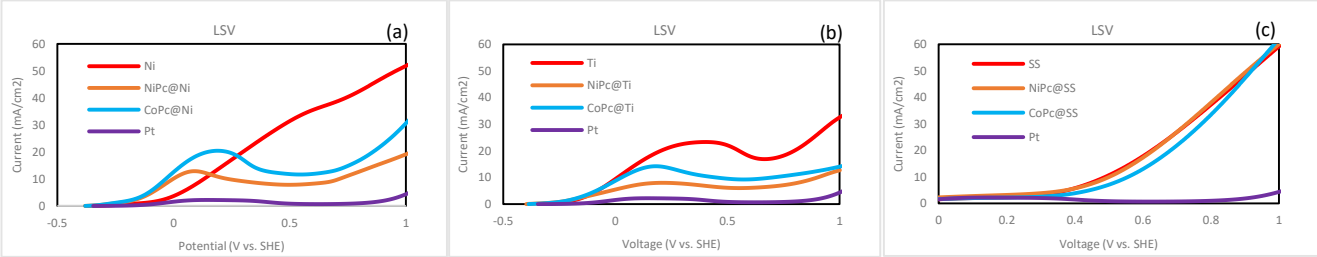

Figure 1. LSV measurements for CoPc and NiPc on a) Ni support, b) Ti support, and C) SS support (scan rate 50 mV/s, and the electrolyte solution 0.1MNa_2S+0.1NaOH)

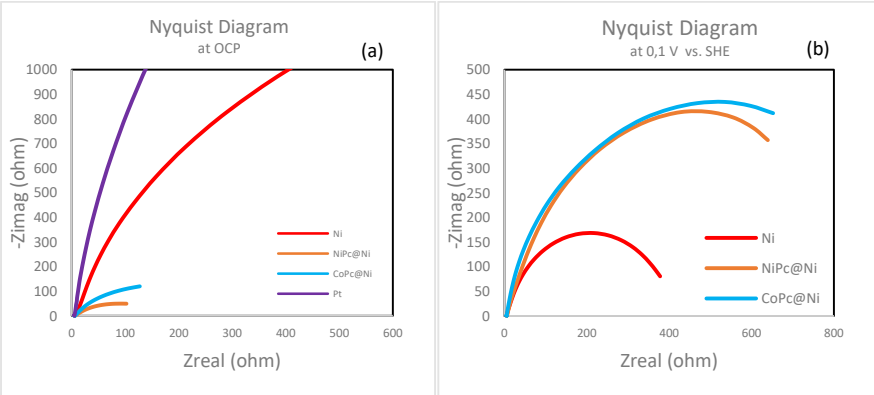

Fig. 2 EIS measurements for CoPc and NiPc at a) open circuit potential (OCP), b) 0.1 V vs. SHE (in the electrolyte solution 0.1MNa_2S+0.1MNaOH)

By comparing the LSV results of different types of supports (Fig. 3a and 3b), it is clear that the porous Ni is a better support for NiPc, while Ti has a better response when CoPc is coated on it.

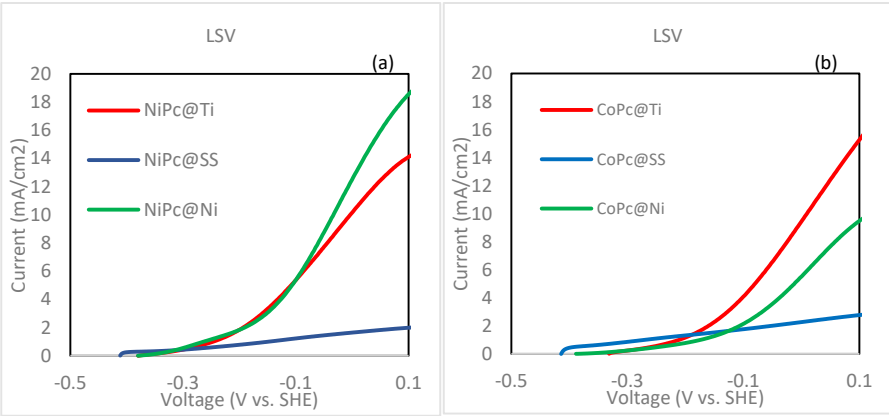

Fig. 3 Linear Sweep Potential measurements for a) NiPc, b) CoPc on Ti, Ni, SS. (electrolyte solution 0.1MNa_2S+0.1MNaOH)

4. CONCLUSIONS

The influence of phthalocyanine with different central metals including cobalt, and nickel in hydrogen evolution electrolysers from hydrogen sulfide is explored. Nickel (Ni), titanum (Ti), and stainless steel (SS) diffusion supports for metal phthalocyanines (MPc's) are compared in three-electrodes system. The linear sweep potential (LSV) and electrochemical impedance spectroscopy (EIS) are measured to understand the behavior of the catalysts and supports. The Cobalt phthalocyanine (CoPc) on nickel (Ni) exhibits the best reaction in relation to other catalysts and supports. In addition nickel and titanium are considered as effective supports for MPc's. Polarization potentials are lowered in the presence of H_2S.

Acknowledgment
This study was financially supported by Turkish Scientific and Technological Research Council (TUBITAK) under 2502–Research Projects-BAS Bilateral Collaboration program with Grant #123N020.

REFERENCES

1. Dan, M., Zhang, Q., Yu, S., Prakash, A., Lin, Y., Zhou, Y., 2017. Noble-metal-free MnS/In2S3 composite as highly efficient visible light driven photocatalyst for H2 production from H2S. Appl. Catal. B Environ. 217, 530–539. https://doi.org/10.1016/j.apcatb.2017.06.019
2. Hakim, L., Sari, R., Fadli, Fajar, Safrizal, Selvy, Emma, 2023. Hydrogen production from seawater using H2SO4 catalyst by photovoltaic-electrolysis method. Mater. Today Proc. 87, 315–320. https://doi.org/10.1016/j.matpr.2023.03.289
3. Hensen, E.J.M., Kooyman, P.J., Van Der Meer, Y., Van Der Kraan, A.M., De Beer, V.H.J., Van Veen, J.A.R., Van Santen, R.A., 2001. The Relation between Morphology and Hydrotreating Activity for Supported MoS2 Particles. J. Catal. 199, 224–235. https://doi.org/10.1006/jcat.2000.3158
4. International Symposium on the Scientific Bases for the Preparation of Heterogeneous Catalysts (Ed.), 1995. Preparation of catalysts VI: scientific bases for the preparation of heterogeneous catalysts proceedings of the Sixth International Symposium, Louvain-la-Neuve, September 5-8, 1994, Studies in surface science and catalysis. Elsevier, Amsterdam New York.
5. Keshipour, S., Asghari, A., 2022. A review on hydrogen generation by phthalocyanines. Int. J. Hydrog. Energy 47, 12865–12881. https://doi.org/10.1016/j.ijhydene.2022.02.058
6. Koca, A., Kalkan, A., Bayır, Z.A., 2011. Electrocatalytic oxygen reduction and hydrogen evolution reactions on phthalocyanine modified electrodes: Electrochemical, in situ spectroelectrochemical, and in situ electrocolorimetric monitoring. Electrochimica Acta 56, 5513–5525. https://doi.org/10.1016/j.electacta.2011.03.068
7. Kumar, M., Nagaiah, T.C., 2022. Pure hydrogen and sulfur production from H_2 S by an electrochemical approach using a NiCu–MoS_2 catalyst. J. Mater. Chem. A 10, 13031–13041. https://doi.org/10.1039/D2TA02751H
8. Osmanbas, O., Koca, A., Kandaz, M., Karaca, F., 2008. Electrocatalytic activity of phthalocyanines bearing thiophenes for hydrogen production from water. Int. J. Hydrog. Energy 33, 3281–3288. https://doi.org/10.1016/j.ijhydene.2008.04.018
9. Özçeşmeci, İ., Burat, A.K., İpek, Y., Koca, A., Bayır, Z.A., 2013. Synthesis, electrochemical and spectroelectrochemical properties of phthalocyanines having extended π-electrons conjugation. Electrochimica Acta 89, 270–277. https://doi.org/10.1016/j.electacta.2012.11.015
10. Yang, J., Smulders, V., Smits, J.J.T., Mei, B.T., Mul, G., 2019. Electrochemical oxidation of H2S on polycrystalline Ni electrodes. J. Appl. Electrochem. 49, 929–936. https://doi.org/10.1007/s10800-019-01334-x
11. Yang, S., Yu, Y., Gao, X., Zhang, Z., Wang, F., 2021. Recent advances in electrocatalysis with phthalocyanines. Chem. Soc. Rev. 50, 12985–13011. https://doi.org/10.1039/D0CS01605E

HYDROGEN GAS PRODUCTION ONTO Fe_2O_3 AND Clay/ Fe_2O_3 BY PHOTO CHEMICAL CONVERSION UNDER UV-VISIBLE LIGHT

Amokrane Samira, Nibou Djamel, Sebati Farouk, Ferhat Djawad and Hammoudi Hadda Aya
Laboratory of Materials Technology, University Science and Technology Houari Boumediene 32, Bab-Ezzouar, Algiers, Algeria.

*Corresponding author e-mail: samiraamokrane@gmail.com

ABSTRACT

In the present study, Fe_2O_3 and Clay/Fe_2O_3 were prepared by hydrothermal method for the hydrogen gas production. The Fe_2O_3 oxide was obtained from reactive reagents with a thermally treatment at 450°C during 6 h and during various anneals. Algerian clay was used as support to prepare Clay/Fe_2O_3 by dispersing method. All obtained samples were characterized by X-ray diffraction (XRD), scanning electron microscopy (SEM) and energy dispersive spectroscopy (EDS) for highlighted their textural properties. The results showed that the hematite α-Fe_2O_3 semiconductor phase was obtained successfully. Neutral and basic media were tested for the production of Hydrogen by photo chemical conversion under UV-visible irradiation in presence of Na_2SO_3 as hole sensor. These experiments showed promote results in gas H_2 production using the synthesised composite Clay/Fe_2O_3, semiconductors α-Fe_2O_3, CuO and ZnO in neutral medium.

Keywords: Hydrogen, Oxides, Fe_2O_3, Clay/Fe_2O_3, Photo conversion, Neutral and basic medium

1. INTRODUCTION

Actually, the explore of innovative energetic sources is an significant world subject due to the reduction of fossils energy [1-2]. The use of other clean energies as solar or UV-visible light can be attractive [3-4]. In this context, the hydrogen production is an environmentally friendly gas [5] and is produced from the methane (90%) which is responsible to liberate a great quantity of CO_2 pollution and changing the climate [6]. Several alternatives as thermal, photo conversion and photochemistry are like inexpensive and attractive means for water electrolysis. The gases separation from these processes makes them more difficult. In the opposite, the water photo electrolysis is an interesting way using oxides as semi conductors or composites prepared by oxides doping [7]. Nevertheless, the main obstruction limiting their uses is the wide band gap which limits the solar absorption to UV light since the small energy of the valence band made up of O_2:2p orbital (6.5 eV). Thus, the use of oxides as Fe_2O_3 can decrease the optical gap because it is reported to be active in photo catalysis [8-9] and its two electronic bands are joined together. This oxide is low cost and it is known
having a fine band semi conductor which can translate about 40% of the solar radiation [10] with n or p types. To improve the photo conversion, a new approach is used to apply composites [11-12]. The natural clays are used as support with different metals or oxides and revealed interesting activities in the electrochemical reduction [13]. The aim of the present work is the doping of the Algerian clay by hematite α-Fe_2O_3 which supposed to increase radiance to energy conversion and improve hydrogen production onto composite material by water reduction upon UV-visible light.

2. MATERIALS AND METHODS

The Fe_2O_3 oxide was prepared by hydrothermal method using $Fe(NO_3)_3.9H_2O$) nitrate salt from Merk with a purity of 99%. The mixture is stirred at room temperature and heated to 100 °C to remove water and then to 300 °C to denitrify it. After grinding, the homogenized powder is heated in the oven at a temperature of 450 °C for 6 h under several anneals to obtain the semiconductor hematite phase (α-Fe_2O_3). After, we prepared a heterogeneous composite by mixing clay and α-Fe_2O_3 by a hydrothermal process. The mixture is stirred for 2 h at room temperature and heated to 100 °C to remove water.
The H_2 production by photo catalysis was carried out in a double-walled glass reactor in neutral and basic media as reported in previously work [7] (Fig.1). The reactor (125 cm^3) is irradiated by tungsten lamps with a total power of 600 W. The photo activity was measured by the gas volume produced in these media solutions. All tests are carried out at 50°C under stirring of about 300 rpm. The bubble of solutions is used with He gas in the presence or without catalysts during 15 and 30 respectively.
The oxide and composite were identified by XRD using a Philips diffractometer type PW 1710. The morphology of the samples was observed by SEM using an equipment type XL20. The chemical composition of the samples was determined by EDS analysis coupled in the same SEM equipment.

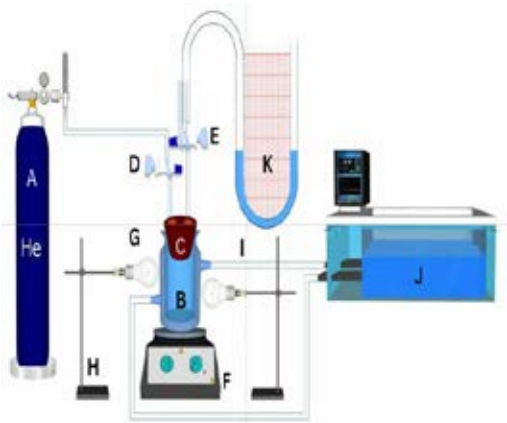

Fig.1. Experimental setup. A: Helium bottle; B: Reactor; C: Plug; D: Two-way valve; E: Three-way valve; F: Magnetic stirrer; G: Tungsten lamps; H: stands; I: Water circulation and K: U-shaped tube

3. RESULTS AND DISCUSSION

3.1. Characterization of samples

The Fig.2 shows XRD patterns of prepared Fe_2O_3 and Clay/Fe_2O_3. The XRD peaks in the range 2θ of 5 to 90° and identified as belong to the pure phases of hematite (α-Fe_2O_3) and clay according to the previously works [7, 9]. Fig.2(a) shows the XRD peaks of Fe_2O_3 at 2θ: 24°, 33°, 35°, 44°, 49°, 55°, 62° and 64° and Fig.2(b) illustrates the peaks of Clay/Fe_2O_3 at 9°, 19°, 21°, 22°, 24°, 27°, 29°, 33°, 35°, 42°, 50°, 55°, 62°, 64° and 73°. The results confirm that all peaks of hematite are present in the structure of clay and the decrease of their intensities is attributed to its good dispersion in the structure of final composite. These results are in agreement with those of Mekatel et al.[7].

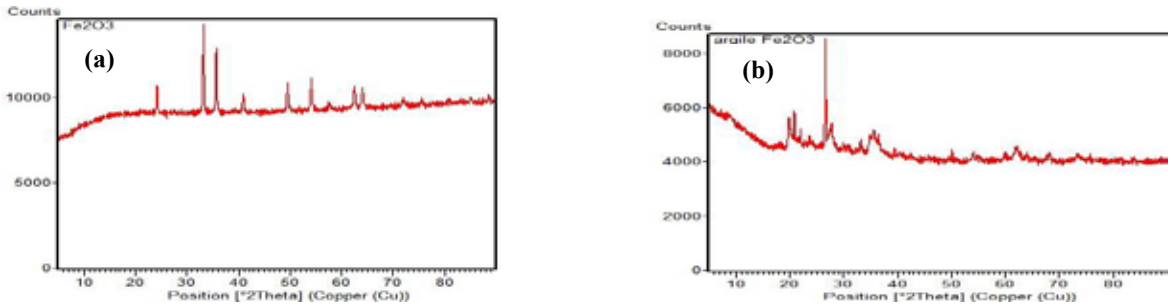

Fig.2. XRD patterns of Fe_2O_3 (a) Clay/Fe_2O_3 (b)

The morphology of the samples is observed by SEM micrographs as shown in Fig.3. From Fig.3(a), it can observe a fine particles of Fe_2O_3 with an average size of 0.1 to 0.2 µm and agglomerates of irregular forms of grains. However, Fig. 3(b) reveals a sheet forms of clay with a dispersed fine Fe_2O_3 particles on its surface, highlighted also by EDS analysis. The Table 1 shows the results of EDS analysis of prepared Clay/Fe_2O_3, confirming the presence of the main elements of clay matrix as Si, Al, Na, Mg, K and Ca and specially Fe incorporated in its structure. The carbon was used during EDS analysis as coating to make the sample conductive.

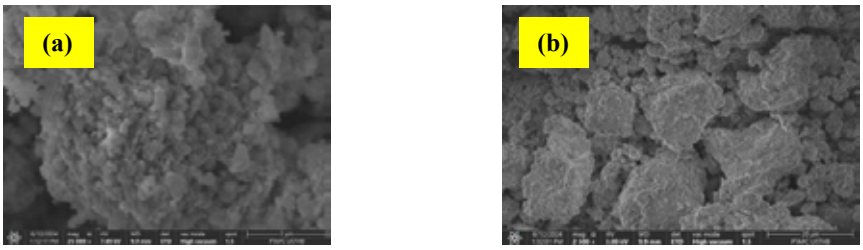

Fig.3. Micrographs by SEM of Fe_2O_3 (a) Clay/Fe_2O_3 (b)

Table 1. Chemical composition by EDS analysis of Fe_2O_3 and Clay/Fe_2O_3

	C	O	Na	Mg	Al	Si	K	Ca	Fe
Fe_2O_3									
At. %	13.2	48.7	-	-	-	-	-	-	38.7
Wt. %	5.1	24.9	-	-	-	-	-	-	70.0
Clay/Fe_2O_3									
At. %	13.4	59.0	2.4	1.3	4.9	12.1	0.6	0.3	6.0
Wt. %	7.9	46.6	2.7	1.6	6.5	16.7	1.1	0.5	16.4

3.2. Hydrogen production by photo catalysis

The H_2 production reaction by photo conversion was carried out in three steps. The first one called blank test is used in neutral medium via an aqueous solution containing Na_2SO_4. In this case, a He gas bubbling was used to eliminate the dissolved gases in the solution. In the second step, we close the He flow and the glass reactor is placed under UV-visible light for produce H_2 gas. After saturation of gas production, the lamps are closed and 0.1 g of Fe_2O_3 is added in the solution with bubbling it during 15 min. Then, the production of H_2 is obtained in the presence of Fe_2O_3 or semi conductor (nsc). In the last step, the equilibrium is reached after a time, the lamps are turned off again and a quantity of 0.2 g of hole sensor (Na_2SO_3) is added to the previous solution (nct).

Fig. 4 shows the evolution in time of the mole number of hydrogen produced in this media for Fe_2O_3. According to the Fig. 4, it seems that the behavior of the two samples is different. In the case of Fe_2O_3 (Fig. 4(a)), the mole number of H_2 gas increases during the 10 minutes of the reaction to reach a maximum in the case of (nct) and (nsc) modes of 6 10^{-7} and 3.5 10^{-7} mole respectively. After this time, clear plateaus were observed during 10-14 and 8-12 min respectively and a decrease of the production of H_2 is observed until 40 min of reaction. The test of blank mode reveals a maximum of H_2 quantity of 1.75 10^{-7} mole reached at 11 min with a long plateau between 11 to 20 min, indicating an equilibrium step and a continuous production of H_2 gas. Moreover, Fig. 4(b) shows the behavior of Clay/Fe_2O_3 composite toward the evolution of the mole number of H_2 in different modes.

The test under (nsc) condition performs well compared to others where the evolution of the number mole of H_2 increases gradually to reach a maximum of 7 10^{-6} mole during 30 min. After, an equilibrium plateau is observed during 30 to 40 min. The tests modes (nct) and (nb) have also recorded 4 10^{-6} and 3.1 10^{-6} mole respectively with also a long plateaus between 10 to 40 min. These best performances can be explained by the use of semi conductor Fe_2O_3 with fine particles of 0.1 µm which allow a high surface and more photo electrochemical sites necessary to enhance the production of H_2 gas. These results are in good agreement with those reported in the literature [1-2].

In the other hand, the results of Fig.5 illustrates the evolution in time of the mole number of H_2 gas produced in basic medium for Fe_2O_3 and Clay/Fe_2O_3 using a aqueous solution of KOH. All tests are carried out as used in the same way as those in neutral medium. According the Fig.5(a), the production of H_2 gas started after 5 min and increased rapidly to reach a quantity value of 5.5 10^{-7} mole in (nct) mode and finally stopped suddenly at 14 min. There is no H_2 gas in (nsc) mode but in (nb) an equilibrium plateau is formed between 10 to 20 min in which the mole number of H_2 reach a quantity of 1.75 10^{-7} mole. It seems that the basic medium has a negative effect on the behavior of Fe_2O_3 towards the production of hydrogen. This can be due probably to the potential of H_2O/H_2 couple changes with pH (Eq.(3)), either to the valence and conduction bands of Fe_2O_3 which are pH insensitive or the optimal band bending at the junction Fe_2O_3 /solution as reported in [7].

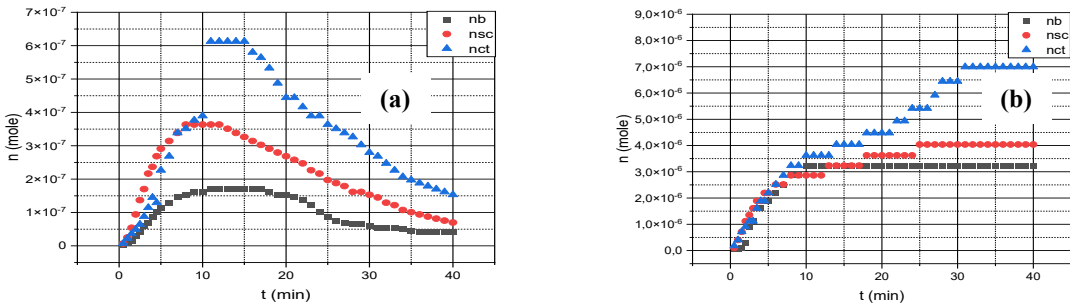

Fig.4. Evolution of mole number of H_2 in time under neutral medium using Fe_2O_3 (a) and Clay/Fe_2O_3 (b) at different modes (nb, nsc and nct)

The Fig. 5(b) shows also low performances in the production of H_2 gas using Clay/ Fe_2O_3 composite in the three modes recording a little amounts 1.5 10^{-7} mole (nsc), 1.0 10^{-7} mole (nct) and 3 10^{-8} mole (nb). This time, the test in (nsc) mode using Clay/ Fe_2O_3 was performed compared to that of Fe_2O_3. In this regard, the Clay/ Fe_2O_3 became optically active and bring more stability to the composite. According to the literature [1-2], Fe_2O_3 generate electron/hole (e−/h+) pairs according to the radicals OH• and/or O_2• through valence (VB) and conduction (CB) bands with high oxidative aptitude to cause a destructive oxidation reaction. The production of H_2 gas can be achieved via a photo catalytic reaction

conversion onto Fe_2O_3 according to the following mechanism:

$$Fe_2O_3 + h\,v \rightarrow (h^+_{VB})\ Fe_2O_3 + (e^-_{CB}) \quad (1)$$

$$2SO_3^{2-} + (h^+_{VB}) \rightarrow S_2O_6^{2-} \quad (2)$$

$$H_2O + 2(e^-_{CB}) \rightarrow H_2 + OH^- \quad (3)$$

Due to the elevated energetic location of Fe_2O_3 valence bands, the oxygen molecules do not compete with the water oxidation and it is necessary to reduce the photo holes which are scavenged by SO_2^{3-} (Eq.(2)). This reaction has a potential (E°) of about -0.2 V compared to that of the couple SO_4^{2-}/SO_3^{2-} of -1.2 V. This last potential is very negative and doesn't contribute in the oxidation reaction which explains the observed equilibrium plateau in Fig.4 and Fig.5. The phenomenon is due to the saturation of competitive reduction at the end product $S_2O_6^{2-}$.

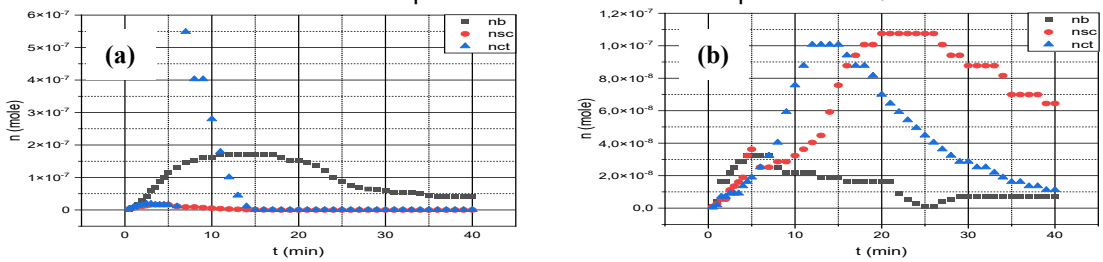

Fig.5. Evolution of mole number of H_2 in time under neutral medium using Fe_2O_3 (a) and Clay/Fe_2O_3 (b) at different modes (nb, nsc and nct)

4. CONCLUSIONS

Fe_2O_3 and Clay/Fe_2O_3 composite have been synthesized successfully in the production of H_2 gas by photo conversion reaction. They structural properties have highlighted by XRD, SEM and EDS analysis. The good dispersion of Fe_2O_3 particles in the surface clay allows an optical gap and a stability to use in the photo catalysis conversion reaction. The Clay/Fe_2O_3 composite showed best performances in neutral media recording a maximum quantity of hydrogen of 7 10^{-6} mole. The hydrogen was produced in presence of SO_2^{3-} under UV-visible light and a mechanism process was proposed. The Clay/Fe_2O_3 composite are low cost and non toxic and can be attractive as photo catalysts for the production of green H_2 gas.

REFERENCES

1. Boudjemaa A, Bachari K, Trari M. 2013. Photo-electrochemical characterization of porous material Fe-FSM-16. Application for hydrogen production. Mater Sci Semicond Process;16:838e44.
2. Abdi A, Denoyelle A, Commenges-Bernole N, Trari M. 2013. Photocatalytic hydrogen evolution on new mesoporous material Bi2S3/Y-zeolite. Int J Hydrogen Energy;38:2070e8.
3. Yang Y, SunY,Jiang Y. 2006. Structure and photocatalytic property of perovskite and perovskite-related compounds. Mater Chem Phys;96:234e9.
4. Li Z, Wang Y, Liu J, Chen G, Li Y, Zhou C. 2009. Photocatalytic hydrogen production from aqueous methanol solutions under visible light over Na (BixTa1-x)O3, solid-solution. Int J Hydrogen Energy;34:147e52.
5. Semiconductors: data handbook. Berlin: Otfried Madelung; 2004.
6. Caravaca A, Ferreira VJ, de Lucas-Consuegra A, Figueiredo JL, Faria JL, Valverde JL, Dorado F. 2013. Simultaneous production of H2 and C2 hydrocarbons by using a novel configuration solidel-ectrolyte þ fixed bed reactor. Int J Hydrogen Energy;38:3111e22.
7. Mekatel, E., Trari, M., Nibou, D., Sebai, I., Amorkrane, S. 2019. Preparation and characterization of α-Fe_2O_3 supported clay as a novel photocatalyst for hydrogen evolution. International Journal of Hydrogen Energy, 44(21):10309-10315.
8. Satsangia VR, Kumaria S, Singha AP, Shrivastavb R, Dass S. 2008. Nanostructured hematite for photoelectrochemical generation of hydrogen. Int J Hydrogen Energy;33:312e8.
9. Mekatel H, Amokrane S, Bellal B, Trari M, Nibou D. 2012. Photocatalytic reduction of Cr(VI) on nanosized Fe2O3 supported on natural Algerian clay: characteristics, kinetic and thermodynamic study. Chem Eng J. 200:611e8.
10. Boumaza S, Boudjemaa A, Omeiri S, Bouarab R, Bouguelia A, Trari M. 2010. Physical and photoelectrochemical characterizations of hematite a-Fe2O3: application to photocatalytic oxygen evolution. Sol Energy;84:715e21.
11. Gherbi R, Nasrallah N, Amrane A, Maachi R, Trari M. 2011. Photocatalytic reduction of Cr(VI) on the new hetero-system CuAl2O4/TiO2. J Hazard Mater;186:1124e30.
12. Vignesh K, Priyanka R, Rajarajan M, Suganthi A. 2013. Photoreduction of Cr(VI) in water using Bi2O3eZrO2 nanocomposite under visible light irradiation. Mater Sci Eng B;178:149e57.
13. Fatimah I, Wang S, Wulandari D. 2011. ZnO/montmorillonite for photocatalytic and photochemical degradation of methylene blue. Appl Clay Sci;53:553e60.

HYDROGEN FUEL VIABILITY IN EU MARITIME TRANSPORT WITH EMISSIONS AND POLICY IMPLICATIONS

[1*]*Bugra Arda Zincir*, [2]*Burak Zincir*
[1] Maritime Vocational School, Galatasaray University, Besiktas, Istanbul, 34349, Türkiye
[2] Maritime Faculty, Istanbul Technical University, Tuzla, Istanbul, 34940, Türkiye

*Corresponding author e-mail: bazincir@gsu.edu.tr

ABSTRACT
The maritime industry is under increasing pressure to reduce greenhouse gas (GHG) emissions in line with EU regulations such as FuelEU and the EU Emissions Trading System (ETS). This study evaluates the environmental and economic impacts of using gray, blue, and green hydrogen as alternative marine fuels compared to marine diesel oil (MDO). Well-to-wake (WTW) emissions and associated regulatory costs were analyzed using data from the THETIS database and emission calculation models. The results show that while hydrogen-based fuels significantly lower tank-to-wake (TTW) emissions, gray and blue hydrogen still contribute to high WTW emissions due to upstream production processes. Consequently, gray hydrogen incurs the highest penalties, followed by blue hydrogen, making them less viable long-term solutions. Green hydrogen, however, demonstrates the lowest emissions and regulatory costs, emerging as the most sustainable option for decarbonizing maritime transport. The study highlights the need for policy incentives and technological advancements to enhance green hydrogen adoption.
Keywords: Decarbonization, EU ETS, FuelEU, Hydrogen fuel, Maritime emissions

1. INTRODUCTION

The maritime industry is a significant contributor to global greenhouse gas (GHG) emissions, prompting stringent regulations to reduce its environmental impact. The European Union (EU) has implemented policies such as FuelEU and the Emissions Trading System (ETS) to encourage the adoption of low-carbon fuels in shipping. As a result, alternative energy sources like hydrogen are gaining attention for their potential to decarbonize the sector. However, the environmental benefits of hydrogen vary depending on its production method. While green hydrogen, produced using renewable energy, offers the lowest emissions, gray and blue hydrogen, derived from fossil fuels, still contribute to carbon footprints. Understanding the emissions and regulatory implications of these hydrogen fuel options is crucial for assessing their viability in maritime transport.
This study assesses the well-to-wake (WTW) emissions and economic implications of hydrogen-based fuels in EU maritime transport compared to marine diesel oil (MDO). Using data from the THETIS database, the analysis explores the impact of hydrogen on tank-to-wake (TTW) emissions while accounting for upstream production emissions and regulatory costs. By evaluating policy-driven penalties and emissions performance, the research provides insights into the feasibility of hydrogen adoption in the maritime sector.

2. METHODOLOGY

In this section, gray, blue, and green hydrogen fuels are investigated regarding the GHG emissions they produce and their impacts on recent regulations in the EU region. During the analysis, data obtained from the THETIS database under the European Maritime Safety Agency (EMSA) [1] are presented in Table 1. It shows the ships involved in trading activities at EU ports in 2023. A total of 12,182 vessels arrived at or departed from EU ports in 2023, while 40,142,214 tons of fuel were combusted. Although the types of combusted fuel are not specified, it is assumed during the analysis that all the ships combusted MDO, since currently, there are 715 LNG-powered, 150 LPG-powered, and 62 methanol-powered ships [2] out of 109,000 ships [3].

Table 1. Retrieved data from the THETIS Platform

Ship types	Number of ships	Fuel consumption (mtons)	CO_2 emissions at sea (mtons)	CO_2 emissions from voyages to ports under MS jurisdiction (mtons)	CO_2 emissions from voyages to ports under a MS jurisdiction (mtons)	CO_2 emissions at ports (mtons)
Bulk carrier	3545	4,464,219	1,354,171	5,412,741	6,535,307	696,531
Chemical tanker	1304	2,445,271	2,298,620	2,083,528	2,474,135	800,205
Combination carrier	7	12,269	4,528	15,266	16,492	1,659
Container ship	1865	11,343,724	8,835,257	12,394,910	12,681,004	1,476,651

Container/ro-ro cargo ship	57	327,451	325,899	297,274	352,389	48,387
Gas carrier	330	818,207	327,530	1,029,243	1,008,145	158,722
General cargo ship	1121	1,516,878	1.326,824	1,584,990	1,599,460	261,015
LNG carrier	359	3,377,706	479,440	4,252,929	4,399,828	413,557
Oil tanker	1841	5,181,798	2,089,401	5,795,521	6,777,898	1,580,109
Other ships	343	702,907	561,915	754,448	771,614	111,704
Passenger ship	205	2,336,208	4,069,381	1,050,016	1,073,751	1,093,170
Cruise passenger ship	9	33,653	55,344	16,562	15,876	17,747
Refrigerated cargo ship	136	338,524	116,034	395,607	510,124	37,742
Ro-pax ship	391	4,214,439	9.968,419	1,153,783	1,129,187	910,712
Ro-ro ship	213	1.,700,121	2.525,124	1,289,693	1,259,570	228,942
Vehicle carrier	456	1,328,839	707,967	1,511,077	1,706,638	172,710

For hydrogen cases, hydrogen is combusted in an internal combustion engine with 85% hydrogen and 15% pilot diesel fuel developed by BeHydro [4]. Another important aspect is that, according to FuelEU and EU ETS regulations, if a ship departs from an EU port and arrives at a non-EU port, or vice versa, 50% of the emitted CO_2eq needs to be included. Once the assumptions and boundaries are defined, WTW emissions can be calculated using Equation 1.

$$WTWCO_2eq = WTTCO_2eq + TTWCO_2eq \quad (1)$$

In the equation WTT is well-to-tank and TTW is tank-to-wake. To determine WTTCO_2eq, equation 2 is used.

$$TTWCO_2eq = TTWCO_2 + TTWCH_4 \times CFCH_4 + TTWN_2O \times CFN_2O \quad (2)$$

In equation 2, the coefficient factor (CF) for CH_4 is 28, while 265 for N_2O [5]. TTW emissions for MDO are specified in FuelEU Regulation [5], but for hydrogen, it is obtained from GREET Model 2023 [6]. Additionally, WTTCO_2eq is calculated by equation 3.

$$WTTCO_2eq = (FC \times WTTCO_2eq \times LCV)_{Pilot\ fuel} + (FC \times WTTCO_2eq \times LCV)_{Primary\ fuel} \quad (3)$$

In the equation, FC represents fuel consumption and LCV is a lower calorific value. Also, during the WTT calculations, MDO and gray hydrogen are given in the FuelEU Regulation, yet for blue and green hydrogen it is gathered from GREET Model 2023. All the variables considered in the study are presented in Table 2.

Table 2. Parameters that are used in the study

Variables	**MDO**		**Gray hydrogen**		**Blue hydrogen**		**Green hydrogen**	
	WTT	TTW	WTT	TTW	WTT	TTW	WTT	TTW
$CFCO_2$	N/S	3.206	N/S	0	0.00006	0	0.000002	0
$CFCH_4$	N/S	0.00005	N/S	0	0.0000004	0	0.000000003	0
CFN_2O	N/S	0.00018	N/S	0.001037	0.000000003	0.001037	0.00000000002	0.001037
CO_2eq	14.4	3.2551	132	0.2747	75.6	0.0275	1.8	0.2747
LCV (MJ/g)	0.0427		0.12		0.12		0.12	

The WTW emissions are presented in Fig. 1, and the results show that container shipping is the highest contributor, with a 28% share. Therefore, in this paper, the calculations are made based on container ships transversing in EU regions.

After WTW emissions are determined, GHG intensity and FuelEU penalty cost can be calculated using equations 4 and 5 [5].

$$GHG_{intensity} = \frac{WTWCO_2eq}{(FC \times LHV)_{Primary\ fuel} + (FC \times LHV)_{Pilot\ fuel}} \quad (4)$$

$$Penalty\ cost = \frac{(GHG_{intensity} - TargetGHG_{intensity}) \times (FC \times LHV)_{Primary\ fuel} + (FC \times LHV)_{Pilot\ fuel}}{GHG_{intensity} \times Euro/MJ} \quad (5)$$

In Equation 5, the target GHG intensity represents the limit determined by the FuelEU regulation. Moreover, the EU ETS quota cost is calculated three times: in 2025, 40% of the CO_2eq will be reported; in 2026, 70% of the CO_2eq will be reported; and in 2027 and beyond, 100% of the CO_2eq will be reported [7]. Therefore, Equations 6–8 are utilized to determine the impact for each year.

$$EU\ ETS\ cost = 0.4 \times TTWCO_2 \times Quota\ cost \quad (6)$$

$$EU\ ETS\ cost = 0.7 \times TTWCO_2eq \times Quota\ cost \quad (7)$$

$$EU\ ETS\ cost = TTW\,CO_2eq \times Quota\ cost \quad (8)$$

During the calculations, quota costs are estimated at $90 as was the case in 2023 [8].

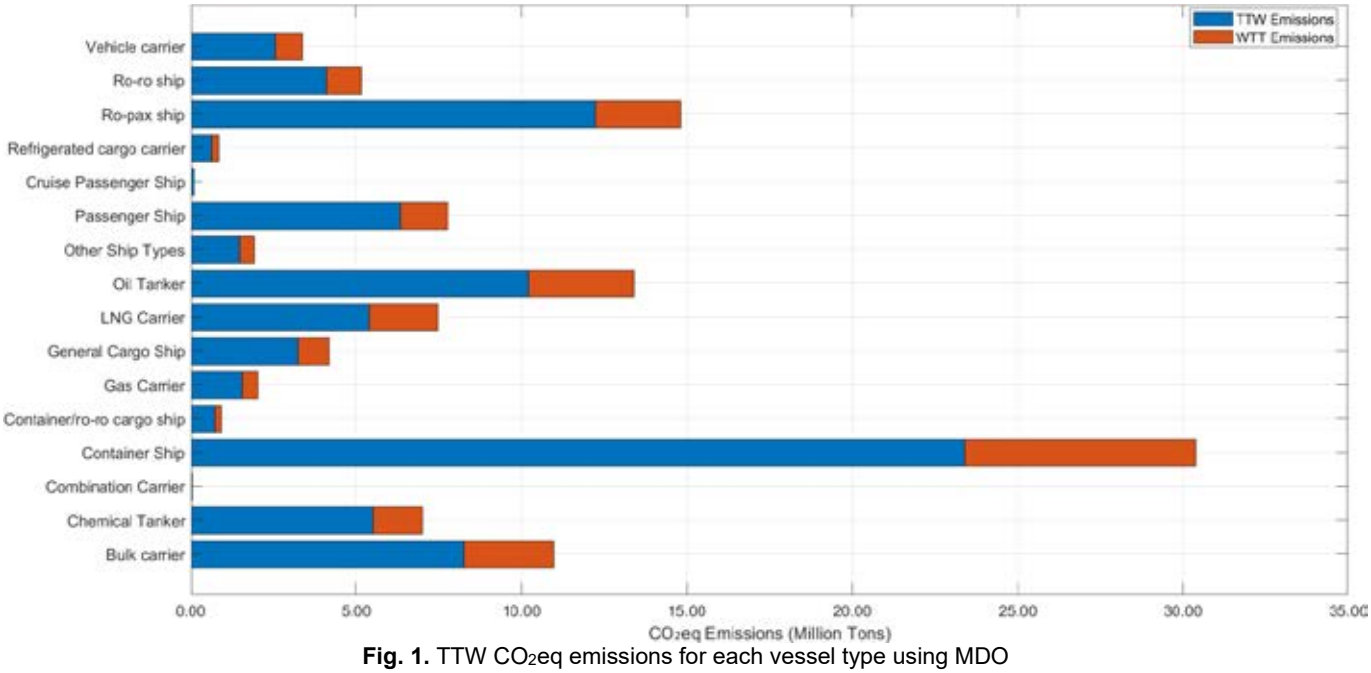

Fig. 1. TTW CO_2eq emissions for each vessel type using MDO

3. RESULTS AND DISCUSSION

Fig. 2 shows the FuelEU penalty costs for each fuel selection. The findings highlight that gray hydrogen has the highest GHG impact, resulting in higher penalties, followed by blue hydrogen and MDO, while no additional expenses arise from utilizing green hydrogen. Despite the TTW CO_2eq for hydrogen options being almost one-fourth of MDO's—23,406,842 tons for MDO and 6,481,237 tons for hydrogen derivatives—the WTT CO_2eq of gray hydrogen is 694% higher and that of blue hydrogen is 361% higher than the MDO option. On the other hand, green hydrogen WTT CO_2eq is 74% lower compared to MDO's. The cumulative outcomes indicate that by using gray hydrogen, penalties will begin in 2025, for blue hydrogen in 2035, and for continued use of MDO, penalties will start after 2040.

In Fig. 3, EU ETS quota prices are illustrated for each case. According to the results, MDO incurs the highest expense, while the others have the same outcome since the EU ETS considers TTW emissions rather than WTW emissions. Consequently, the outcome does not change because each case utilizes a fuel blend of 15% pilot diesel and 85% hydrogen. However, in 2025, only CO_2 emissions are considered; thus, MDO has 319% higher costs, while in subsequent years, the cost difference decreases to 261% as N_2O and CH_4 emissions are also included.

In Table 3, costs are listed for all fuel options. FuelEU and EU ETS costs are annual costs, and penalties will be paid each year. The findings reveal that compared to FuelEU costs, EU ETS costs are much lower; therefore, gray hydrogen does not provide the desired benefits. Additionally, blue hydrogen is only attractive in the period between 2035 and 2040, as the EU ETS benefit outweighs the harms from FuelEU penalties. However, green hydrogen is a prominent choice across all years.

Table 3. Fuel EU penalty and EU ETS quota costs for each fuel choice

Fuel types	FuelEU 2025	FuelEU 2030	FuelEU 2035	FuelEU 2040	Fuel EU 2045	FuelEU 2050	EU ETS 2025	EU ETS 2026	EU ETS 2027
MDO	-	-	-	-	$12,686M	$20,099M	$822M	$1,474M	$2,106M
Gray Hydrogen	$8,518M	$9,327M	$11,046M	$14,383M	$20,651M	$24,291M	$196M	$408M	$583M
Blue hydrogen	-	-	$650M	$5,992M	$16,031M	$21,859M	$196M	$408M	$583M
Green hydrogen	-	-	-	-	-	-	$196M	$408M	$583M

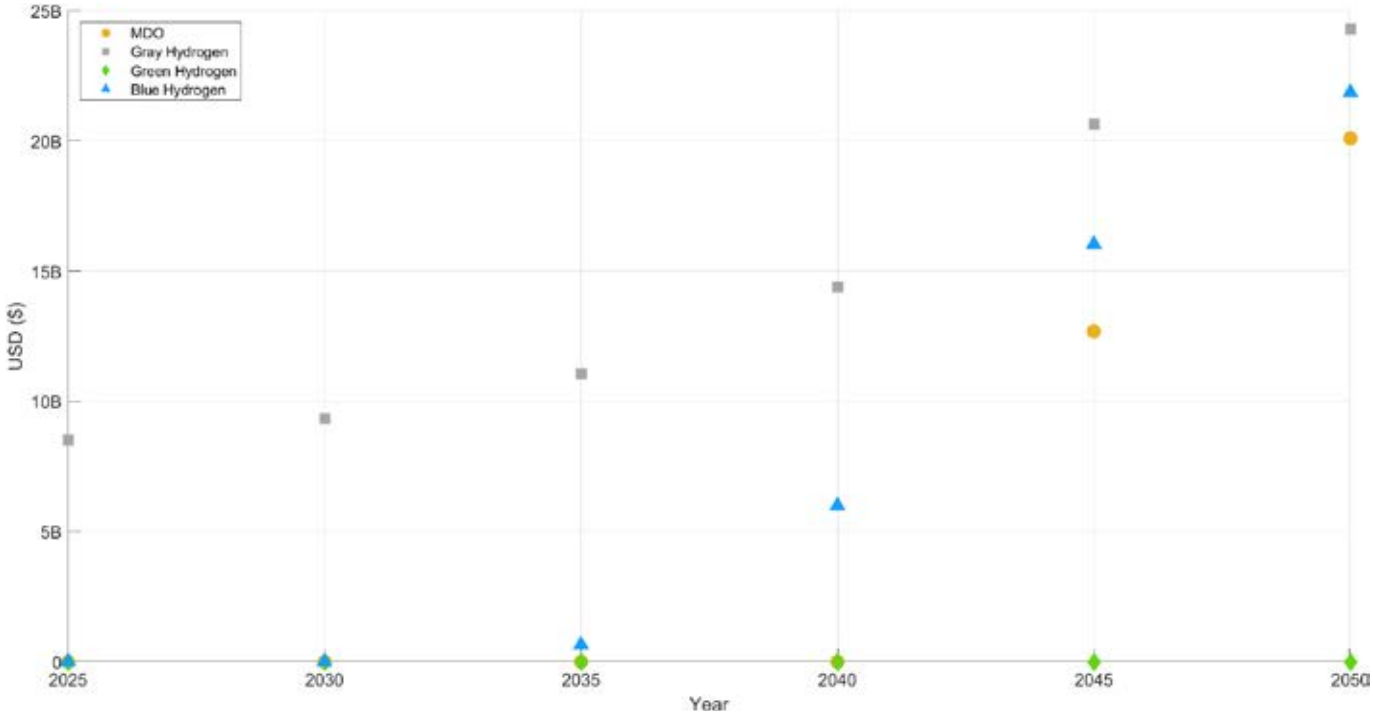

Fig. 2. FuelEU penalty costs across five-year intervals

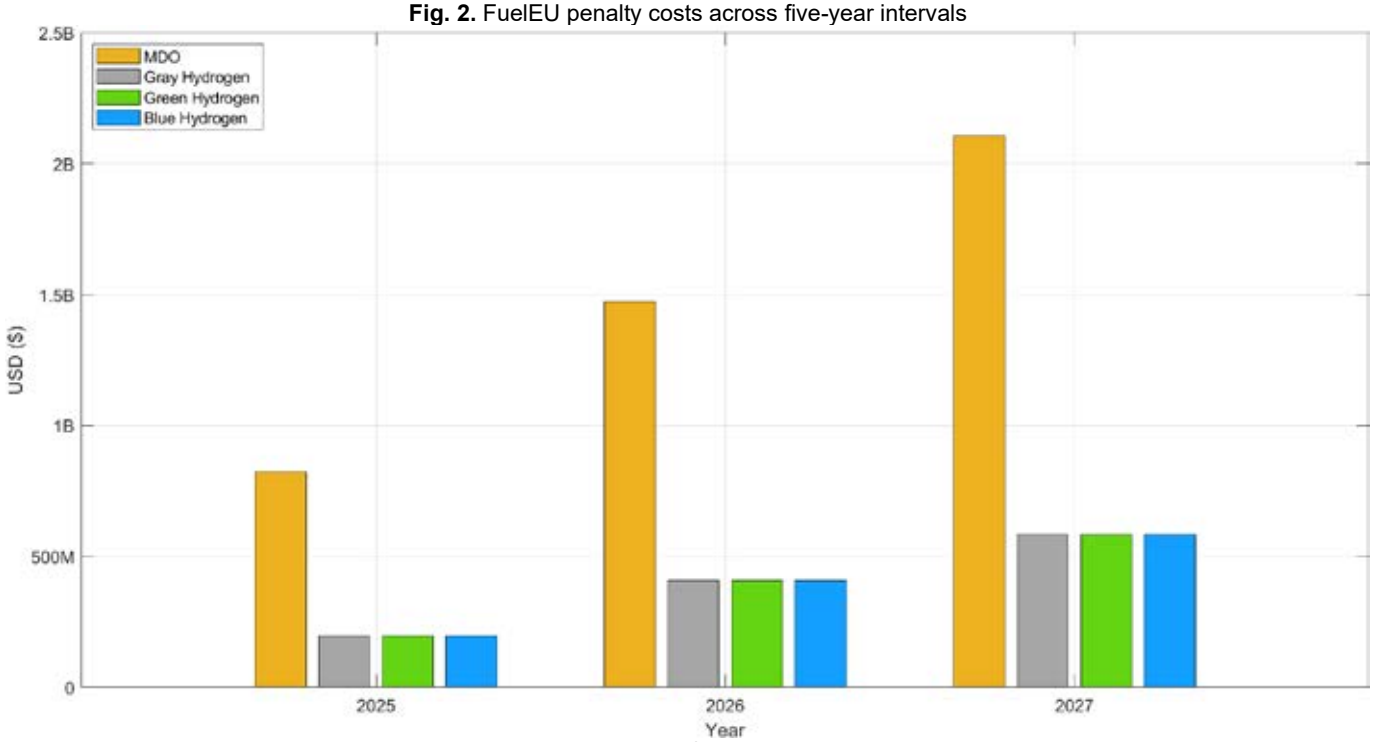

Fig. 3. EU ETS quota costs

4. CONCLUSIONS

This study evaluated the GHG emissions and regulatory impacts of using gray, blue, and green hydrogen fuels in maritime transport within the EU. The findings indicate that while hydrogen-based fuels significantly reduce TTW emissions compared to MDO, their WTW emissions and associated costs vary substantially. Gray hydrogen has the highest GHG intensity and incurs the highest penalties under FuelEU and EU ETS regulations, making it an unfavorable option. Blue hydrogen offers moderate benefits, particularly between 2035 and 2040, but its long-term viability remains limited due to rising penalties. In contrast, green hydrogen emerges as the most sustainable alternative, with the lowest emissions and regulatory costs, making it a viable solution for decarbonizing the maritime sector. In future research, various ammonia production pathways will be considered to evaluate the environmental impact of ammonia as a fuel. Additionally, an economic analysis will be conducted, encompassing both capital and operational expenditures.

Furthermore, while this study focuses solely on container ships, future studies will expand the analysis to include all types of vessels to determine whether the outcomes differ across ship types.

REFERENCES

1. https://portal.emsa.europa.eu/web/thetis/home. Accessed on October 11, 2024.
2. Det Norske Veritas (DNV). 2024. Energy Transition Outlook 2024.
3. United Nations Conference on Trade and Development (UNCTAD). 2024. Review of maritime transport.
4. https://www.abc-engines.com/en/news/launch-behydro-si-hydrogen-engine. Accessed on November 7, 2024.
5. European Union (EU). 2023. Regulation (EU) 2023/1805 of the European Parliament and of the Council on the use of renewable and low-carbon fuels in maritime transport, and amending Directive 2009/16/EC.
6. https://greet.anl.gov/. Accessed on November 8, 2024.
7. European Union (EU). 2023. Commission Implementing Regulation (EU) 2023/2449 laying down rules for the application of Regulation (EU) 2015/757 of the European Parliament and of the Council as regards templates for monitoring plans, emissions reports, partial emissions reports, documents of compliance, and reports at company level, and repealing Commission Implementing Regulation (EU) 2016/1927.
8. https://icapcarbonaction.com/en/ets/eu-emissions-trading-system-eu-ets. Accessed on December 2, 2024.

NICKEL-LANTHANUM CATALYSTS SUPPORTED ON SILICON CARBIDE TO PRODUCE CO_X-FREE HYDROGEN AND VALUABLE CARBONS UNDER MICROWAVE ENERGY

[1]*Hazal Pınar KÖSE,* [2*]*Dilek VARIŞLI*
[1]Gazi University, Graduate School of Natural and Applied Sciences, Central Campus Faculty of Technology, B-Block, 2nd Floor 06500, Teknikokullar, ANKARA
[2] Gazi University, Faculty of Engineering, Chemical Engineering Department, Maltepe, Ankara, 06500, Turkey

e-mail: [1] hpinar.kose@gazi.edu.tr, [2*] dilekvarisli@gazi.edu.tr (*Corresponding author)

ABSTRACT
Hydrogen energy is a clean and alternative solution to global warming which is enhanced by using fossil fuels. Catalytic decomposition of methane produces hydrogen and valuable carbon product. This study examines microwave assisted catalytic decomposition of methane using SiC supported Ni/La catalysts at different temperatures. Effects of nickel loading as well as lanthanum loading were investigated and it was found that reaching to total initial conversion was seen at 700°C. Lanthanum addition amount and the reaction temperature was found to be the key to conversion and stability of the catalysts. With increasing temperature, the conversion values increased generally, however some catalysts showed a decrease in activity due to thermal sintering of metals and high metal doping amounts.

Keywords: Catalytic methane decomposition, microwave reactor, Lanthanum promoter, SiliconCarbide

1. INTRODUCTION

Fossil fuels play a significant role in energy production. However, the utilization of fossil fuels causes major source for greenhouse gas emissions, contributing to global warming. Hydrogen energy is an alternative and promising way to replace fossil fuels, as hydrogen only produces water when burned, and has a calorific value of 39.4 $kWh.kg^{-1}$, which is higher than liquid hydrocarbons [1]. Methane has a high H/C ratio which makes it an abundant reserve for hydrogen. Catalytic decomposition of methane is a green way to produce hydrogen without the need for separation from other products, since this reaction only results in hydrogen and high-quality carbon [2]. One of the advantages of this process is that the produced carbon can be used for various application, increasing the feasibility of this reaction. Despite the positive aspects, the reaction can only take place at temperatures above 1200°C owing to methane's thermodynamic stability necessitating catalyst utilization [3]. Nickel-based catalysts are frequently employed for their high activity in the catalytic decomposition of methane however, at high temperatures they are prone to sintering and deactivation [4]. Lanthanum addition to nickel-based catalysts improved both the activity and stability of the catalyst by enhancing nickel dispersion, attributed to lanthanum's unique 4f electron structure, which inhibits graphite layer formation [5]. Microwave heating is a novel heating method because of its unique heating characteristics like volumetric and fast heating, heating without contact and formation of hot spots, however, its application on the catalytic methane decomposition reaction is limited. There are still challenging points to be discussed. It is necessary to employ materials that absorb microwave energy and silicon carbide (SiC) is indicated as one of the most promising microwave absorbers due to its excellent dielectric properties, high thermal conductivity, and thermal stability [6]. In the present study, investigations were carried out on the microwave assisted methane decomposition reaction using SiC supported Ni catalysts with La promoter.

2. MATERIALS AND METHODS

2.1. Synthesis and Characterization of Catalysts

SiC supported lanthanum promoted nickel-based catalysts were synthesized using wet impregnation method. Lanthanumnitratehexahydrate ($La(NO_3)_3{\cdot}6H_2O$), and nickelnitratehexahydrate ($Ni(NO_3)_2{\cdot}6H_2O$), salts were utilized and catalysts were synthesized keeping the nickel loading at a high (50%), and low value (10%), and changing the Ni/La mol ratio as 0.45/0.1, 2/0.25, 2/0.1, and 2/0.002. The metal solution was prepared by putting the Ni and La metal precursors into a beaker simultaneously and adding 20 ml of distilled water. This metal solution is added drop by drop to a solution of SiC and 20 ml of ethanol. The resulting solution was left on the magnetic stirrer at 60°C, 200 rpm until it dried. Then, the catalysts were dried in an oven for 18h before it is calcined and reduced. Calcination and reduction conditions were 700°C-5h and 600°C- 4h respectively. The synthesized catalysts were subjected to different characterization studies such as ICP-OES, XRD analysis and N_2 adsorption-desorption analysis. The conversion of methane was calculated using the data obtained from the effluent gas.

2.2. Reaction Studies

The reaction studies were carried out using 0.7/0.3 nitrogen/methane gas with a flow rate of 20 ml/min in the microwave reactor system with a microwave generator (SAIREM). In each experiment 0.1 g of reduced catalysts were inserted into the quartz reactor and reaction temperature were changes in the range of 500 and 700°C by adjusting the microwave power. The products were analysed using Gas Chromatography equipped with Carboxen column and TCD detector. The

conversion of methane was calculated using the data obtained from the effluent gas.

3. RESULTS AND DISCUSSION

Activity results for catalysts prepared at high nickel loading (50wt%) with different La loading at 500 and 700°C are presented in Fig.1a and 1b, respectively. The Ni/La raito in these catalysts was kept as (0.45/0.1) and (0.2/0.02). At 500°C, 50Ni-La(0.45/0.1)@SiC catalyst, showed the highest activity, when the temperature was raised to 700°C, the initial methane conversion increased to 75%. However, a very fact deactivation was recogined at 700°C over this catalyst, implying that 21wt% the lanthanide additives causing thermal sintering at higher temperatures [5]. The 50Ni-La(2/0.002)@SiC catalyst, containing 0.17 wt% lanthanum as per ICP-OES results, showed an initial activity of 43% at 500°C but deactivated rapidly. At 600°C, while its initial conversion remained similar at 38%, its stability improved significantly. Interestingly, at 700°C, both its activity and stability increased, suggesting that this lanthanum loading, although insufficient to enhance activity at lower temperatures, helps prevent pore blockage, nickel sintering, and coke deposition, contributing to improved performance at higher temperatures.

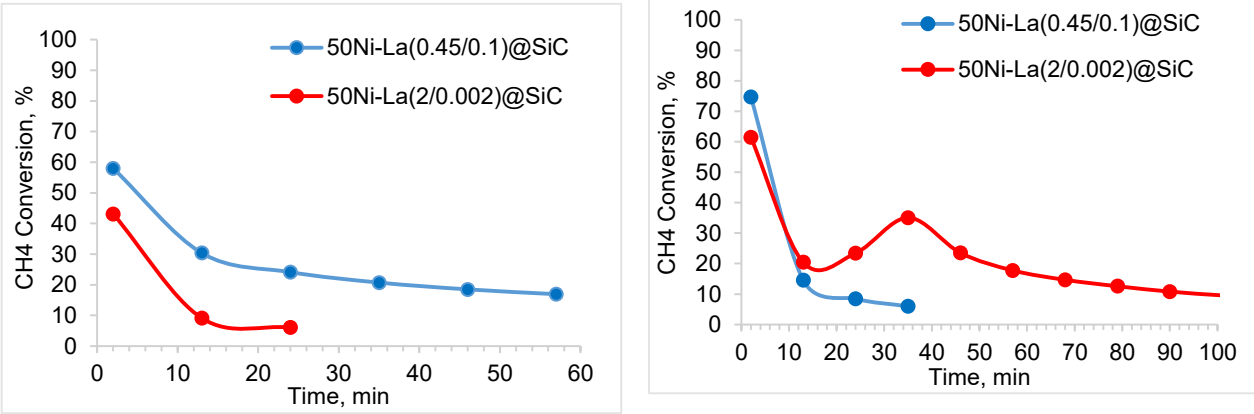

Fig. 1. Activity of catalysts with high nickel loading with different La loading, at a)500°C, b)700°C

When compared to 50% wt nickel loaded catalysts, 10% wt nickel loaded catalysts showed no obvious superiority in the long term, and initial conversion values when the reaction was carried out at 500°C and 700°C (Fig.2). Using higher amount of La may be effective when the catalysts were run at higher temperatures. In literature, catalytic methane decomposition is mostly studied in conventional reactors. Ying et al. [7] reported a 25% conversion at 500°C using Ni-La-Si (0.45:0.45:0.1 mol ratio), while Anjaneyulu et al.[8] achieved 36% conversion at 600°C with Ni-La-SiO2 (2:0.1:0.9 mol ratio). In our study, higher conversion values at comparable temperatures highlight the potential of microwave energy for more efficient methane decomposition. Characterization of spent catalysts will reveal the impact of microwave energy on carbon product.

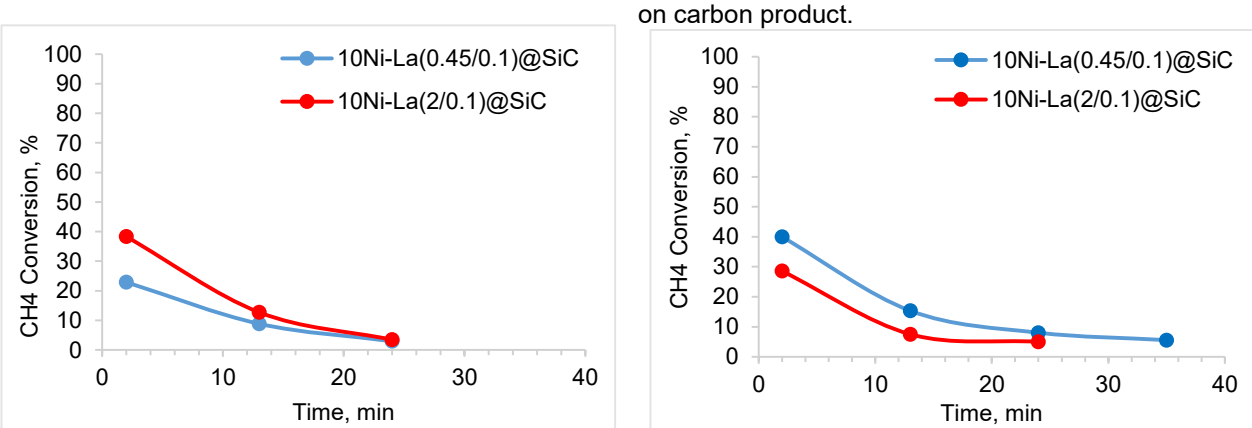

Fig. 2. Activity of catalysts with low nickel loading with different La loading, at a)500°C, b)700°C

SEM images of the 50Ni-La(0.45/0.1)@SiC and 50Ni-La(2/0.002)@SiC catalysts which were used in the reaction at 500oC were presented in Fig.3. The carbon nanotube structures (shown by red arrow) were observed besides the encapsulated carbon structres (shown by yellow arrow) for 50Ni-La(0.45/0.1)@SiC. Whereas encapsulated carbon was seen for 50Ni-La(2/0.002)@SiC catalyst as an indication of lower activity.

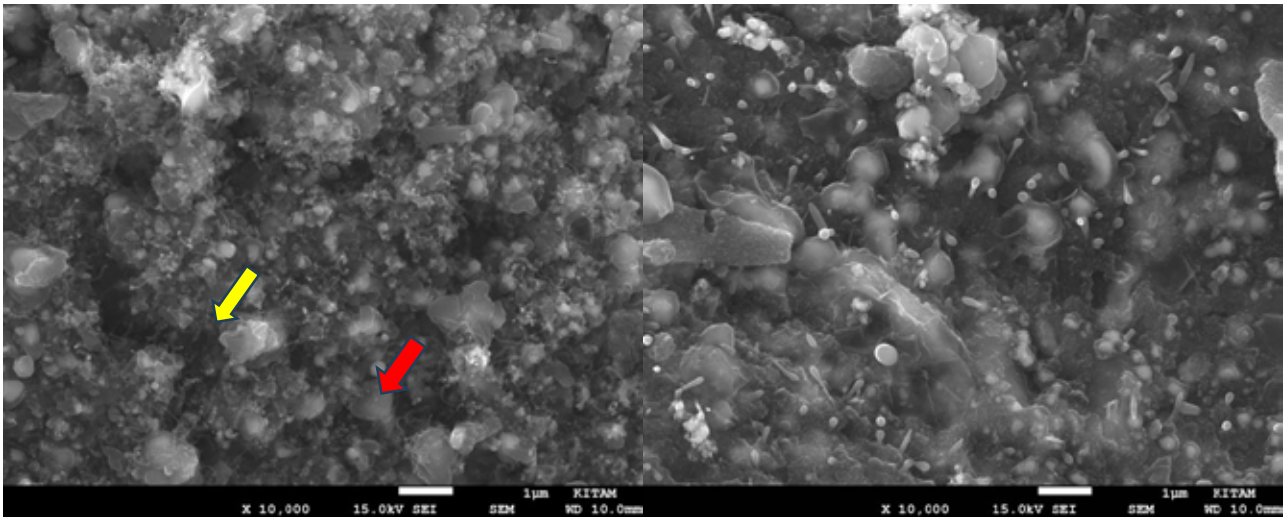

Fig. 3. SEM images of 50Ni-La(0.45/0.1)@SiC (left), 50Ni-La(2/0.002)@SiC(right) catalysts used at 500°C

4. CONCLUSIONS

In this study SiC supported Ni/La catalysts were tested in the reaction of catalytic methane decomposition, which is an alternative way for producing clean hydrogen without carbon emissions. Results obtained under microwave reactor show the effect of metal (Ni and La) loadings as well as the temperature had a great effect on the performance of the catalysts.. Among the catalysts 50Ni-La(0.45/0.1)@SiC gave the better performance at 500°C, even though higher reaction temperature favored the reaction, it caused faster deactivation. Indeed, at higher reaction temperatures such as 700°C, using significantly low amount of lanthanum, containing 0.17 wt% lanthanum as per ICP-OES results, enhanced the activity of the catalyst with 50 wt% Ni loading (50Ni-La(2/0.002)@SiC). Characterization of fresh and spent catalysts will give some insight of the performance of the catalysts under microwave exposure.

ACKNOWLEDGEMENTS

This work was supported by the The Scientific and Technological Research Council of Turkiye (TUBITAK, project code:123M056) and Gazi University Research Fund with th Project Code: FYL-2024-9614

REFERENCES

[1] Fan, Z., Weng, W., Zhou, J., Gu, D., & Xiao, W. (2021). Catalytic decomposition of methane to produce hydrogen: A review. *Journal of Energy Chemistry*, *58*, 415-430.

[2] Tamura, K., Kokuryo, S., Kitamura, H., Hernandez Gaitan, J. A., Tsubota, S., Miyake, K., ... & Nishiyama, N. (2024). Cr-promoted Ni Catalyst on Dealuminated Zeolite for Producing Hydrogen via Catalytic Decomposition of Methane. *Industrial & Engineering Chemistry Research*.

[3] Seong, I. H., Kang, S. C., Lee, J. D., & Im, J. S. (2024). Effect of active metals and process factors on the catalytic decomposition of methane for hydrogen production. *Research on Chemical Intermediates*, 1-18.

[4] Hantoko, D., Khan, W. U., Osman, A. I., Nasr, M., Rashwan, A. K., Gambo, Y., ... & Hossain, M. M. (2024). Carbon–neutral hydrogen production by catalytic methane decomposition: a review. *Environmental Chemistry Letters*, 1-41.

[5] Karimi, S., Bibak, F., Meshkani, F., Rastegarpanah, A., Deng, J., Liu, Y., Dai, H. (2021). 'Promotional roles of second metals in catalyzing methane decomposition over the Ni-based catalysts for hydrogen production: A critical review', Int. J. Hydrogen Energy, 46, 20435-20480.

[6] Ke, C., Liu, T., Zhang, Y., & Xiong, Q. (2022). Energy absorption performances of silicon carbide particles during microwave heating process. *Chemical Engineering and Processing-Process Intensification*, *172*, 108796.

[7] Ying, Y. U., Meisheng, C. U. I., Minglai, L. I., Na, Z. H. A. O., Zhiqi, L. O. N. G., & Yongxi, S. H. I. (2014). Rare earth modified Ni-Si catalysts for hydrogen production from methane decomposition. *Journal of Rare Earths*, *32*(8), 709-714.

[8] Anjaneyulu, C., Kumar, V. V., Bhargava, S. K., & Venugopal, A. (2013). Characteristics of La-modified Ni-Al2O3 and Ni-SiO2 catalysts for COx-free hydrogen production by catalytic decomposition of methane. *Journal of energy chemistry*, *22*(6), 853-860.

DEVELOPMENT OF SILICON CARBIDE SUPPORTED NICKEL-IRON BIMETALLIC CATALYSTS FOR MICROWAVE-ASSISTED CATALYTIC METHANE DECOMPOSITION

[1]*Ceren Acar*, [2*]*Dilek Varışlı*
[1] Gazi University, Graduate School of Natural and Applied Sciences, Gazi University Central Campus Faculty of Technology, B-Block, 2nd Floor, Ankara, 06500, Turkiye
[2] Gazi University, Faculty of Engineering, Department of Chemical Engineering, Ankara, 06500, Turkiye

E-mail: [1] ceren.acar@gazi.edu.tr, [2*] dilekvarisli@gazi.edu.tr (*Corresponding author)

ABSTRACT

In this study catalytic methane decomposition is carried out using carbon supported Ni-Fe bimetallic catalysts in the microwave reactor system. Silicon carbide was selected as the supporting material due to their high microwave absorptive properties. The catalyst synthesis was carried out by impregnation process. Before the catalytic tests calcination and reduction process were done. In the activity studies, microwave energy was used as the heating system. Activity studies conducted at 500°C, 600°C and 700℃ revealed that the catalysts exhibited greater stability at 600°C. High methane conversions were observed at 700 degrees, but the catalysts were deactivated in a short time.

Keywords: Methane decomposition, microwave energy, hydrogen, catalyst, silicon carbide

1. INTRODUCTION

As a clean fuel, hydrogen is gaining popularity as a desirable product for renewable energy sources. In addition, hydrogen has drawn a lot of interest due to its significance in fuel cell technology. The catalytic decomposition of methane (CDM) ($CH_4 \rightarrow C + H_2O$, $\Delta H°_{298}$ = 74.8 kJ mol^{-1}), primarily on Fe, Co, Ni, has gained popularity recently as a promising method for creating hydrogen and carbon products. Moreover, the catalytic decomposition of methane eliminates the need for laborious procedures for purifying reaction products, which greatly streamlines the process and could lower the cost of producing hydrogen in comparison to the steam reforming method. CDM is an endothermic process that occurs at high temperatures, such as around 1200℃, can be carried out at lower temperatures in the presence of a catalyst. As catalyst, nickel is the most active catalyst for the CDM process. At high temperatures, however, nickel-based catalysts are readily deactivated. Adding additional metals creates an intriguing path to boost the CDM reaction's stability and carbon output at higher temperatures [1]. Due to its high stability at elevated temperatures, iron is a promising candidate for incorporation alongside nickel metal [2]. Conventional heating is extensively utilized in literature as a heating method, however, microwave-based heating has been found to boost catalytic reaction rates and selectivity [3]. Additionally, compared to conventional heating for chemical reactions, microwave heating offers several advantages, such as high heating power, volumetric and quick heating, contactless heating, easy drying or heating control, and smaller equipment sizes [2]. In this study, microwave assisted methane decomposition reaction was investigated by using SiC supported Ni-Fe bimetallic catalysts.

2. MATERIALS AND METHODS

In the synthesis process, impregnation procedure was followed, and silicon carbide (SiC) were used as support material. Bimetallic catalysts have been prepared using nickel nitrate hexahydrate and iron nitrate nonahydrate salts. Calcination and reduction conditions for nickel-iron catalyst supported by silicon carbide were 750°C for 5h and 450°C for 3h. Catalysts were called as (A)Ni-(B)Fe@SiC where A refers to nickel metal loading (10wt % and 50 wt%) and B refers to iron metal loading (6-15 wt%). The fresh form of the synthesized catalysts was characterized via XRD, SEM/EDS analyses. XRD and RAMAN analyses were performed as after reaction characterization. A microwave reactor was used for utilizing catalytic performance under atmospheric pressure using 0.1g of catalyst with the gaseous feedstock (0.7/0.3 nitrogen/methane mixture gas) at a flow rate of 20 mL/min. Microwave generator was adjusted to reach the necessary reaction temperature. Reactant and products were analyzed with a gas chromatography device equipped with Thermal Conductivity Detector (TCD) and Carboxen column. Methane conversions were calculated using Eq. (1). Characterization investigations are ongoing because the research is continuously under progress.

$$X = \frac{F^0_{CH_4} - F_{CH_4}}{F^0_{CH_4}} \times 100\% \quad (1)$$

3. RESULTS AND DISCUSSION

Results of XRD analysis, the characteristic peaks of nickel, iron and SiC were observed. Fe_3C structures were formed after the reaction [4]. It was observed in the SEM images before the reaction that the loaded metals adhered to the

surface due to its 8.5 m^2/g surface area. In the catalytic tests, 50% nickel loaded catalysts with 15% iron loaded catalyst exhibited the highest initial conversion at 500℃ reaching to 70% shown in Fig1a. The other two catalysts provided approximately 30% conversion. However, it has been observed that they quickly had a loss of activity, with conversion levels dropping below 10%. In catalysts with 10% nickel loading, the 10% iron-loaded catalyst achieved the highest conversion at 500°C, reaching 60%. Reaction was stopped at 25 min due to faster deactivation of catalysts (Fig.1b). When the temperature was increased to 600°C, it is expected to see better activity over the catalysts. However, it is observed that much lower methane conversion was seen with 50Ni-15Fe@SiC, impliying sintering at higher at this temperature may cause this results (Fig.2a). For longer period of time, up to 100min, catalysts were still active and show the same conversion values regardless of their metal loading. For the low nickel loaded catalysts, it was seen that the stability of these catalysts was greater at 600°C compared to 500°C, maintaining a stable conversion rate of 10% across all three catalysts for up to 100 minutes (Fig.2b). However, all three catalysts experienced deactivation within approximately 30 minutes. Catalysts were also run for 700 ℃ and all of these studies indicated that 600℃ was seen to be the optimum temperature and 50Ni-6Fe and 50Ni-10Fe catalysts gave the best results. Charahterization studies which will be carried out over the spent catalysts will give insights to the microwave assisted methane decomposition reaction.

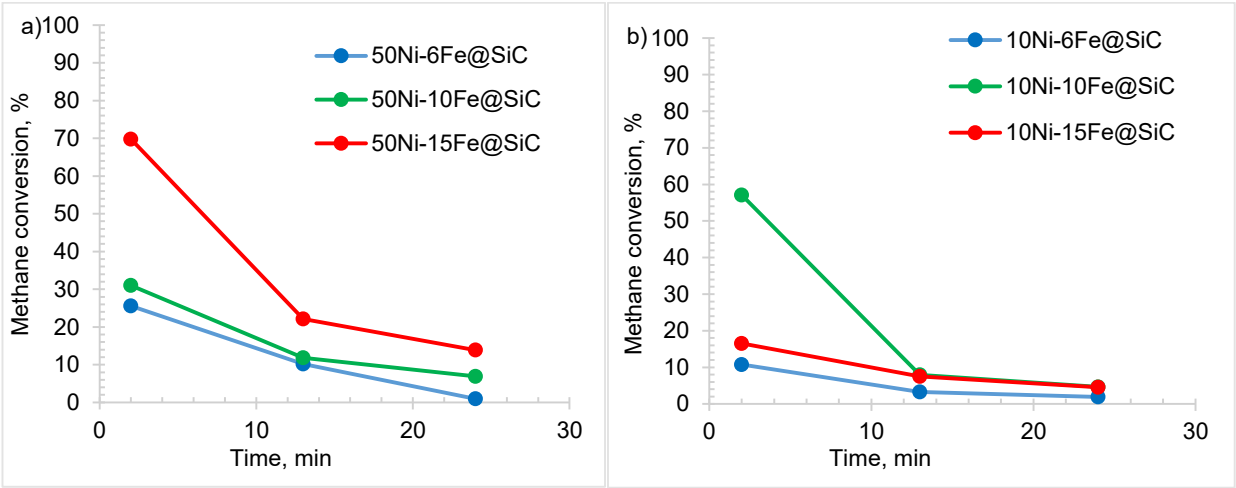

Fig. 1. Methane conversion values for 50 wt% Ni (a) and 10 wt% (b) Ni loaded catalysts at different Fe loadings at 500℃

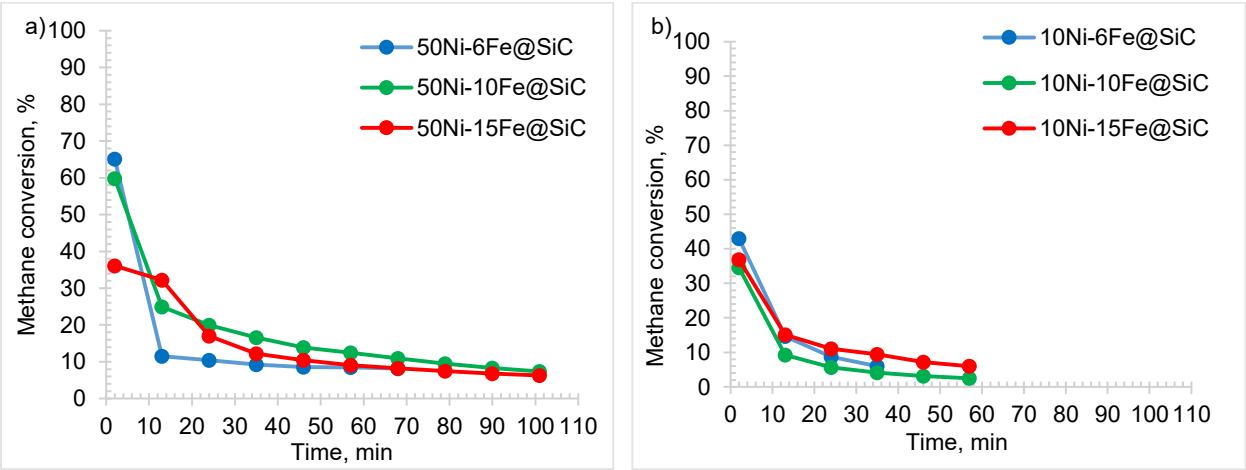

Fig. 2. Methane conversion values for 50 wt% Ni (a) and 10 wt% Ni (b) loaded catalysts at different Fe loadings at 600℃

4. CONCLUSIONS

In this work, catalysts synthesis, characterization and activity studies of SiC supported catalysts for catalytic decomposition of methane using microwave reactor system were conducted. At 500°C, methane conversions were observed to be high; however, the catalysts experienced rapid deactivation. At 600°C, while a slight reduction in methane conversion was noted, the catalysts demonstrated enhanced stability. For 700℃, even if high methane conversions were

seen, stability could not be achieved. The optimal temperature for the reaction was determined to be 600°C, at which both the 50Ni-6Fe and 50Ni-10Fe catalysts demonstrated favorable performance in terms of stability and methane conversion. Characterization studies, which are continued over spent form of the catalysts, will provide information about the carbon structures.

ACKNOWLEDGEMENT

This work was supported by the The Scientific and Technological Research Council of Turkiye (TUBITAK, project code:123M056) and Gazi University Research Fund (project code: FYL-2024-9603).

REFERENCES

1. Bayat, N., Rezaei, M., & Meshkani, F. 2016. Methane decomposition over Ni–Fe/Al_2O_3 catalysts for production of COx-free hydrogen and carbon nanofiber. International journal of hydrogen energy, 41(3), 1574-1584.
2. Chen, W. H., Liou, H. J., & Hung, C. I. 2013. A numerical approach of interaction of methane thermocatalytic decomposition and microwave irradiation. International journal of hydrogen energy, 38(30), 13260-13271.
3. Xu, W., Zhou, J., Su, Z., Ou, Y., & You, Z. 2016. Microwave catalytic effect: a new exact reason for microwave-driven heterogeneous gas-phase catalytic reactions. Catalysis Science & Technology, 6(3), 698-702.
4. Zhang, F., Song, Z., Zhu, J., Liu, L., Sun, J., Zhao, X., ... & Wang, W. 2018. Process of CH4-CO2 reforming over Fe/SiC catalyst under microwave irradiation. *Science of The Total Environment*, *639*, 1148-1155

Cu-BTC SYNTHESIS VIA SOLVOTHERMAL AND MICROWAVE-ASSISTED METHODS: CHARACTERIZATION AND ADSORBENT APPLICATIONS

[1]*Damla DUMLU and* [1*]*Nezihe AYAS*
[1] Eskisehir Technical University, Faculty of Engineering, Chemical Engineering, Eskisehir, 26555, Turkey

*Corresponding author e-mail: nazcan@eskisehir.edu.tr

ABSTRACT

Metal-organic frameworks (MOFs) have attracted considerable attention in recent years due to their high specific surface area and highly porous structures. These materials find applications in a variety of fields with particular significance as adsorbents. Solvothermal method is the most extensively used synthesis technique, due to its effectiveness in producing high-quality crystalline structures. However, its practical application is often constrained by prolonged reaction durations and significant energy demands, prompting the exploration of more efficient synthesis alternatives. In this context, microwave-assisted synthesis emerges as a promising alternative, offering substantial reductions in reaction time. This study investigates the synthesis of MOFs via both solvothermal and microwave-assisted methods for potential use as adsorbents in the purification of hydrogen. Synthesized MOFs were characterised using X-ray diffraction (XRD). The findings reveal that the microwave method offers a promising alternative to the solvothermal method.

Keywords: Cu-BTC, MOF, Microwave assisted method, Adsorbent, Hydrogen purification

1. INTRODUCTION

MOFs are a class of porous materials composed of metal ions or clusters connected by organic ligands, forming a highly structured and tunable network. Lattice topologies and pore structures of MOFs can be designed using different metal centres and ligands [1]. MOFs have several applications, including adsorption, catalysis and gas storage. They have gained importance as adsorbents due to their higher surface area, thermal stability and gas selectivity compared to other adsorbents such as activated carbon and zeolites.

MOFs can be synthesized through various methods, with the solvothermal method being the most traditional and widely used. It is simple but time-consuming and energy intensive. Alternative techniques, such as microwave-assisted and sonochemical methods, offer faster reaction times, lower energy consumption, and influence MOF properties by affecting pore morphology and particle size, which are crucial for separation and gas storage applications [2,3].

The microwave-assisted synthesis of MOFs utilizes microwave radiation to heat a solution of metal salts, ligands, and solvent within the temperature. This method enables reactions to occur within a short time frame, usually between 4 minutes and 4 hours, significantly faster than traditional solvothermal techniques [2,4]. In this study, Cu-BTC synthesized using two distinct methods: the solvothermal method and the microwave-assisted method. The synthesized MOFs were characterized using X-ray Diffraction (XRD). This study aims to investigate the potential of microwave-assisted synthesis as an alternative to solvothermal method for the development of MOFs.

2. MATERIALS AND METHODS

2.1. MOF Synthesis

Cu-BTC (copper benzene-1,3,5-tricarboxylic acid) was synthesized by two different methods based on previously reported procedures [5,6]. For the solvothermal method, 1,3,5-benzenetricarboxylic acid and ($Cu(NO_3)_2 \cdot 3H_2O$) were dissolved in ethanol and deionized water, then mixed and stirred. The mixture was subjected to thermal treatment in a sealed reactor. In the microwave-assisted method, the same precursors were used, and the procedure was similarly followed, except that the reaction was carried out using microwave irradiation. In both cases, the resulting blue solid was washed with a water–ethanol mixture, centrifuged, and dried under vacuum. The final products were labeled as Cu-BTC-S and Cu-BTC-M, respectively.

2.2. Characterization

Crystallinity of Cu-BTC were determined with XRD analysis on a Rigaku Miniflex 600 using Cu-Kα radiation at 40kV and 30 mA. A scanning speed of 0.02° and a scan speed of 2°/min with a scan angle of 5-45°.

3. RESULTS AND DISCUSSION

3.1. Characterization of MOF

XRD patterns of Cu-BTC samples synthesized with different synthesis method given in Figure 1. The characteristic peaks at 2θ=6.8°, 9.6°, 11.7°, 13.5° belong to Cu-BTC [7] and can be observed in the MOF synthesized by both solvothermal and microwave-assisted methods. No peaks corresponding to CuO and Cu_2O were detected in either of the MOFs, which suggests that pure MOF was successfully synthesized.

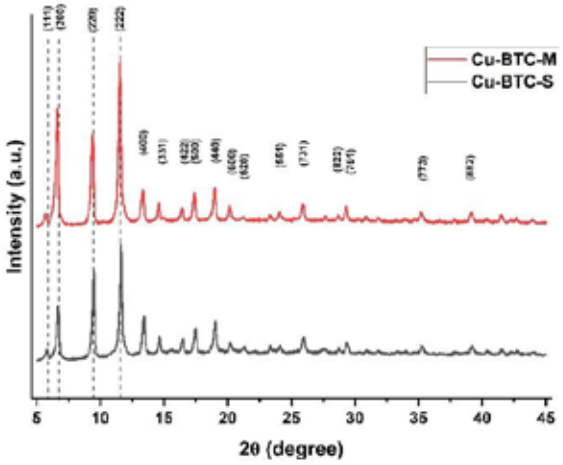

Fig. 1. XRD patterns of Cu-BTC with solvothermal and microwave assisted method

4. CONCLUSIONS

In this study, Cu-BTC was synthesised via solvothermal and microwave-assisted synthesis methods to investigate the influence of synthesis techniques on the structural properties of the resulting MOFs. The synthesized materials were subsequently characterized through X-ray Diffraction (XRD). It was seen that both methods successfully yielded crystalline Cu-BTC structures. The microwave-assisted synthesis significantly reduced the reaction time, making it a more efficient and practical approach for MOF production. Future studies will involve detailed micropore structure analysis and surface characterization using BET.

ACKNOWLEDGEMENT

This research was supported by the Scientific and Technological Research Council of Turkey (TÜBİTAK), project number 22AG034 – “Environmentally Compatible Sustainable Advanced Vehicle Technologies” and the Eskisehir Technical University (ESTU) Scientific Research Commission under grant number 24LÖT219. The authors are grateful to ESTU Materials Science and Engineering Department for their equipment support for XRD.

NOMENCLATURE

Cu-BTC	Copper benzene-1,3,5-tricarboxylate
MOF	Metal-organic framework
XRD	X-ray diffractometry

REFERENCES

[1] Tao YR, Xu HJ. A critical review on potential applications of Metal-Organic frameworks (MOFs) in adsorptive carbon capture technologies. Applied Thermal Engineering 2024;236:121504. https://doi.org/10.1016/j.applthermaleng.2023.121504.
[2] Ghanbari T, Abnisa F, Wan Daud WMA. A review on production of metal organic frameworks (MOF) for CO2 adsorption. Science of The Total Environment 2020;707:135090. https://doi.org/10.1016/j.scitotenv.2019.135090.
[3] Safaei M, Foroughi MM, Ebrahimpoor N, Jahani S, Omidi A, Khatami M. A review on metal-organic frameworks: Synthesis and applications. TrAC Trends in Analytical Chemistry 2019;118:401–25. https://doi.org/10.1016/j.trac.2019.06.007.
[4] Newton Augustus E, Nimibofa A, Azibaola Kesiye I, Donbebe W. Metal-organic Frameworks as Novel Adsorbents: A Preview. ENV 2017;5:61–7. https://doi.org/10.12691/env-5-2-5.
[5] Liu Y, Ghimire P, Jaroniec M. Copper benzene-1,3,5-tricarboxylate (Cu-BTC) metal-organic framework (MOF) and porous carbon composites as efficient carbon dioxide adsorbents. Journal of Colloid and Interface Science 2019;535:122–32.

https://doi.org/10.1016/j.jcis.2018.09.086.
[6] Seo Y-K, Hundal G, Jang IT, Hwang YK, Jun C-H, Chang J-S. Microwave synthesis of hybrid inorganic–organic materials including porous Cu3(BTC)2 from Cu(II)-trimesate mixture. Microporous and Mesoporous Materials 2009;119:331–7. https://doi.org/10.1016/j.micromeso.2008.10.035.
[7] Jeyaprakash JS, Rajamani M, Bianchi CL, Ashokkumar M, Neppolian B. Highly efficient ultrasound-driven Cu-MOF/ZnWO4 heterostructure: An efficient visible-light photocatalyst with robust stability for complete degradation of tetracycline. Ultrasonics Sonochemistry 2023;100:106624. https://doi.org/10.1016/j.ultsonch.2023.106624.

STEAM REFORMING OF SUGAR BEET PULP WITH DOLOMITE-BASED Ni-La CATALYST

[1]Serkan KARADENİZ, [1]Tolga Kaan KANATLI, [1]Nasrin POURMOGHADAM, [1]Şehnaz GENÇ, [1]Salahaldeen M. A. ALJAFREH, [1*]Nezihe AYAS
[1]Eskisehir Technical University, Faculty of Engineering, Department of Chemical Engineering, Eskisehir, 26555, TURKEY

*Corresponding author e-mail: nazcan@eskisehir.edu.tr

ABSTRACT

In this study, hydrogen-rich gas synthesis through the gasification and steam reforming of sugar beet pulp was investigated using Ni-La/Dolomite catalyst. The catalyst was synthesized using the impregnation method and were characterized by FT-IR and SEM-EDX. Gasification experiments examined the effect Ni-La on the resulting gas composition. Gasification studies were conducted in a 316 stainless steel updraft tubular reactor (900 mm length, 10 mm inner diameter) equipped with a peristaltic pump. The highest hydrogen concentration was 50.3% by mole, and the calorific value was 6,268 kJ/m^3. The experimental results demonstrate that the Ni-La/Dolomite catalyst employed in this study efficiently converts sugar beet pulp into hydrogen-rich syngas. Additionally, the findings indicate that sugar beet pulp has significant potential for biomass utilization and bioenergy production.

Keywords: Sugar Beet Pulp, Steam Reforming, Catalyst, Ni-La, Dolomite

1. INTRODUCTION

The rapid increase in global energy demand driven by population growth, industrialization, economic development, and climate change, coupled with the environmental hazards of fossil fuels like petroleum, coal, and natural gas, has started a transition toward renewable and cleaner energy sources such as biomass and hydrogen. Hydrogen is the most abundant element in the universe, and it is a clean energy carrier with the highest energy content per unit mass, that offers significant advantages such as releasing only water vapor upon combustion and presenting a sustainable alternative to mitigation of carbon emissions [1], [2], [3], [4]. Hydrogen can be sustainably produced from biomass via thermochemical conversion processes like gasification, pyrolysis, and catalytic steam reforming, therefore providing a renewable and environmentally friendly alternative to fossil fuels [5].

Steam reforming can be an alternative to gasification when higher hydrogen yield and concentration in the resulting syngas are the main objective. The use of various catalysts like Ni can enhance reaction rates and selectivity toward hydrogen. Coke formation can be reduced by incorporating rare earth metals like La which improves catalyst stability and prevents metal sintering. Additionally, La promotes the water-gas shift reaction and reacts with CO and CO_2 to also reduce coke deposition [6], [7]. The catalytic process also facilitates the water-gas shift reaction, maximizing hydrogen output while reducing the concentration of impurities, therefore making the catalytic steam reforming process a preferred method for hydrogen production from biomass.

Among the sources of biomass, sugar beet is a vital crop in Turkey, due to its economic significance as a key material for sugar production [8], [9]. Sugar beet is also emerging as a promising energy crop within the European Union (EU) with its pulp serving as a valuable co-product of the sugar refining industry [10]. Rich in hemicellulose, cellulose, and pectin, sugar beet pulp offers potential as lignocellulosic biomass for producing hydrogen-rich gas [11], although it is mainly used as an animal feedstock in Turkey.

Therefore, this study aims to investigate the potential of sugar beet pulp obtained as a sugar factory by-product for hydrogen-rich syngas production by hydrothermal gasification. Within the scope of this study, dolomite-supported bimetallic Ni-La catalyst was synthesized by the wet impregnation method. Activity of this catalyst was tested in a tubular updraft gasification reactor at a steam-to-biomass ratio of 3:1 and a gasification temperature of 700 °C and then compared to the uncatalyzed condition.

2. MATERIALS AND METHODS

2.1. Synthesis and characterization of the catalysts

Synthesis of the Ni-La/Dolomite catalyst by the wet impregnation method was described in detail in a previous work [12]. For the characterization of the catalyst, Zeiss Supra 50 VP was used for the SEM imaging, Thermo Fisher Scientific Nicolet IS10 spectrometer in ATR mode was used for recording the FTIR spectra.

2.2. Steam reforming of the sugar beet pulp

Steam reforming studies were conducted in an updraft 316 stainless steel tubular reactor. Steam was generated using a peristaltic pump to feed water through a 1.5 m heated line maintained at 150 °C. Steam-to-biomass ratio was 3:1 by mass. Each experiment utilized 2 g of sugar beet pulp mixed with 0.4 g of catalyst (20 wt% catalyst-to-biomass) and was

carried out over a reaction duration of 15 minutes. The resulting product gas was collected and analyzed using a µ-GC.

3. RESULTS AND DISCUSSION

Fig. 1 shows the FTIR spectra of the 10-5% Ni-La/Dolomite catalyst.

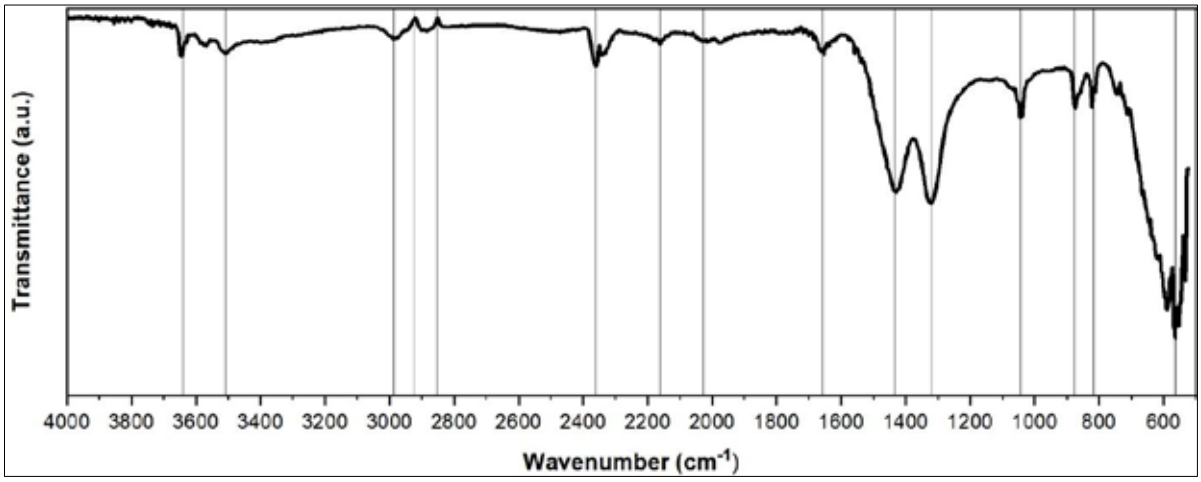

Fig. 1. FTIR spectra of 10-5% Ni-La/Dolomite

O-H groups on the Ni-La/Dolomite surface exhibit a peak at about 3570 cm^{-1} originating from CaO and MgO. Metal oxide vibrations appear in the range 600-750 cm^{-1} reflecting the presence of La and Ni metals. In addition, the peaks observed at 1300-1715 cm^{-1} indicate the stretching vibration of carbonate groups formed on the catalyst surface because of the interaction between CO_2 and CaO, MgO [13].
The SEM images and the Energy Dispersive X-ray Spectroscopy (EDS) results of the %10-5 Ni-La/Dolomite catalyst are given in Fig. 2.

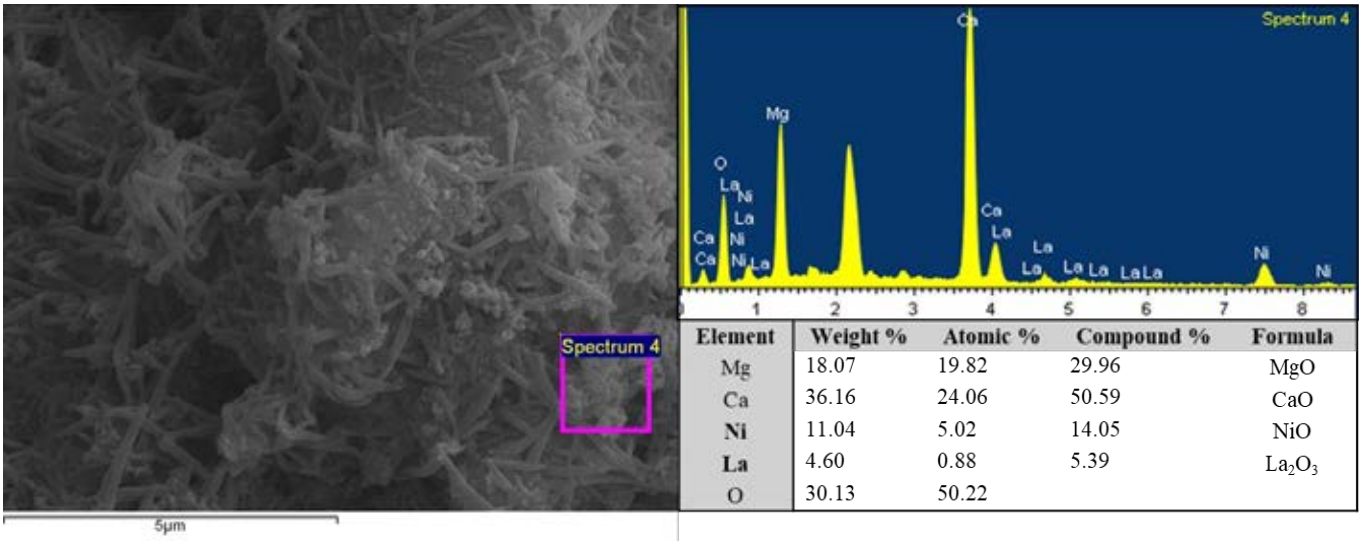

Element	Weight %	Atomic %	Compound %	Formula
Mg	18.07	19.82	29.96	MgO
Ca	36.16	24.06	50.59	CaO
Ni	11.04	5.02	14.05	NiO
La	4.60	0.88	5.39	La_2O_3
O	30.13	50.22		

Fig. 2. SEM-EDS analysis results of %10-5 Ni-La/Dolomite catalyst

The SEM image shows a rough and aggregated surface morphology consisting of interconnected, randomly oriented needle-shaped structures, along with dispersed particulate clusters. Furthermore, specific elements such as NiO, LaO, CaO, and MgO that have been confirmed through XRF analysis are also evidenced by SEM-EDS. Fig. 3 illustrates the influence of this catalyst on the syngas yield.

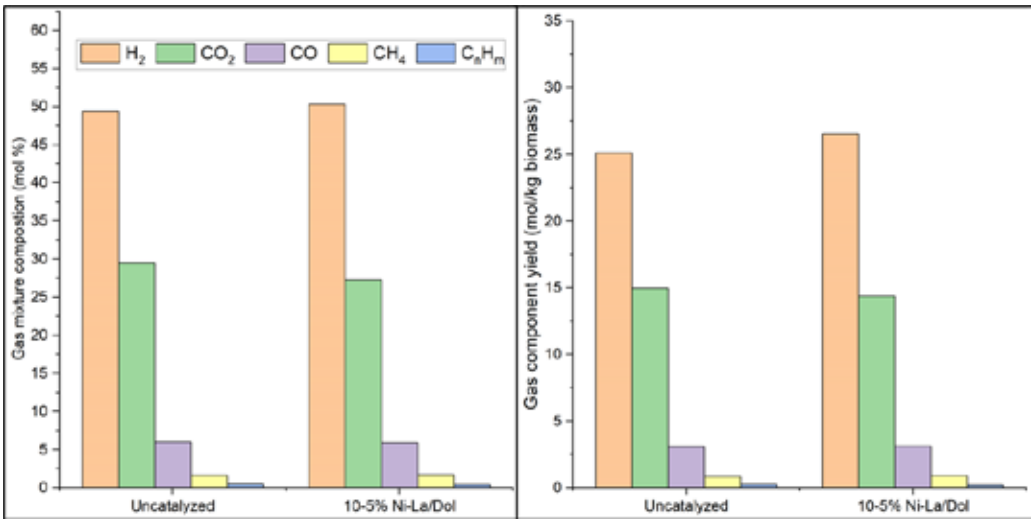

Fig. 3. The effect of 10-5% Ni-La/Dolomite catalyst on gas concentrations and gas product yields obtained during the steam reforming process (15 minutes, 700 °C, 3:1 S:B ratio).

The effectiveness of the 10-5% Ni-La/Dolomite catalyst in sugar beet pulp gasification can be seen on the figure given above. While the catalyst did not significantly alter the gas composition percentages, it notably enhanced the overall gas yield per kilogram of biomass, particularly increasing the hydrogen (H_2) yield. The results align with the findings in the literature [14]. This suggests that the catalyst promotes gasification efficiency, resulting in higher hydrogen production, thus improving the suitability of sugar beet pulp for hydrogen-rich syngas generation. One of the reasons for the higher yields obtained in experiments using catalysts is the use of dolomite as the catalyst support material. Dolomite is known to enhance the conversion of tar produced during the reaction at high temperatures [15], [16]. It was observed that the CO and CO_2 yields were approximately at similar levels. This enhancement is due to the breakdown of C-H, Caryl-C, and aromatic C=C bonds in tar molecules on the basic sites of the dolomite material, forming active carbon. This process involves water dissociation, which generates OH* and H* free radicals, with OH* radicals reacting with active carbon to form formates and other oxygenate intermediates, ultimately converting into gas products [17].
The concentrations of the components forming the gas mixture obtained from the experiments and their yields per unit of biomass are presented in Table 1.

Table 1. The effect of catalyst on gas concentrations, gas volumes, and yields obtained during the steam reforming process

Catalyst	Gas Volume (mL)	Gas Component Concentration (% mol)							Gas Component Yield (mol component/kg pulp)				
		H_2	CH_4	CO	CO_2	C_nH_m	O_2	N_2	H_2	CH_4	CO	CO_2	C_nH_m
Uncatalyzed	2525	49.4	1.6	6.0	29.4	0.5	1.6	4.5	25.1	0.8	3.1	15.0	0.2
10-5% Ni-La/Dolomite	2625	50.3	1.7	5.9	27.3	0.4	2.1	8.2	26.5	0.9	3.1	14.4	0.2

It was observed that in experiment conducted without a catalyst, the primary component of the gas mixture was hydrogen (49.4% mol). One of the critical parameters in gasification processes is the calorific value of the resulting gas product. The most critical determinant of the gas mixture's calorific value was hydrogen. Additionally, the concentration of carbon dioxide in the gas mixture was sufficiently high (~15 mol/kg) to significantly influence the calorific value. Therefore, the calorific value was 6,268 kJ/m^3 for the catalytic gasification experiment.

4. CONCLUSIONS

Improvements in the hydrogen yield obtained from the steam reforming of sugar beet pulp were achieved using bimetallic Ni-La/Dolomite catalyst. Using 10-5% Ni-La/Dolomite catalyst resulted in a syngas with the calorific value of 6,268 kJ/m^3 and hydrogen concentration of 50.3%. The findings of this study reveal that sugar beet pulp is an effective biomass for hydrogen-rich gas production via steam reforming, with Ni-La/Dolomite catalyst presenting a viable alternative to conventional catalysts.

ACKNOWLEDGEMENT

This research was supported by the Scientific and Technological Research Council of Turkey (TÜBİTAK), project number 22AG018 – “Environmentally Compatible Sustainable Advanced Vehicle Technologies”

REFERENCES

[1] S. Karadeniz and N. Ayas, "Microwave-assisted synthesis of Pt/C catalyst at high temperatures for PEM fuel cells," *Int. J. Hydrog. Energy*, vol. 52, pp. 1564–1576, Jan. 2024, doi: 10.1016/j.ijhydene.2023.09.147.

[2] D. Dumlu, S. Karadeniz, T. K. Kanatlı, E. Ceylan, M. Bayrakdar, and N. Ayas, "Synthesis of bentonite-supported Ni, La, and Ca catalysts for hydrogen production through steam reforming of acetic acid," *Int. J. Hydrog. Energy*, vol. 85, pp. 976–996, Oct. 2024, doi: 10.1016/j.ijhydene.2024.08.299.

[3] T. K. Kanatlı and N. Ayas, "Simulating the steam reforming of sunflower meal in Aspen Plus," *Hydrog. ENERGY Syst.*, vol. 46, no. 57, pp. 29076–29087, Aug. 2021, doi: 10.1016/j.ijhydene.2020.12.195.

[4] N. Pourmoghaddam and N. Ayas, "Synthesis, structure characterization, and electrochemical hydrogen storage of reduced graphene oxide and graphene," *Int. J. Hydrog. Energy*, vol. 82, pp. 1422–1434, Sep. 2024, doi: 10.1016/j.ijhydene.2024.08.053.

[5] E. E. Çağlı and N. Ayas, "H2 rich gas production from agricultural waste mixture over Ni/kaolin and Ni/bentonite catalyst by gasification," *Int. J. Hydrog. Energy*, vol. 52, pp. 909–922, Jan. 2024, doi: 10.1016/j.ijhydene.2022.05.170.

[6] M. Wang, F. Zhang, and S. Wang, "Effect of La 2 O 3 replacement on γ-Al 2 O 3 supported nickel catalysts for acetic acid steam reforming," *Int. J. Hydrog. Energy*, vol. 42, no. 32, pp. 20540–20548, Aug. 2017, doi: 10.1016/j.ijhydene.2017.06.147.

[7] A. Kumar and A. S. K. Sinha, "Hydrogen production from acetic acid steam reforming over nickel-based catalyst synthesized via MOF process," *Int. J. Hydrog. Energy*, vol. 45, no. 46, pp. 24397–24411, Sep. 2020, doi: 10.1016/j.ijhydene.2020.06.040.

[8] G. Erdal, K. Esengün, H. Erdal, and O. Gündüz, "Energy use and economical analysis of sugar beet production in Tokat province of Turkey," *Energy*, vol. 32, no. 1, pp. 35–41, Jan. 2007, doi: 10.1016/j.energy.2006.01.007.

[9] S. Kiymaz and A. Ertek, "Yield and quality of sugar beet (Beta vulgaris L.) at different water and nitrogen levels under the climatic conditions of Kırsehir, Turkey," *Agric. Water Manag.*, vol. 158, pp. 156–165, Aug. 2015, doi: 10.1016/j.agwat.2015.05.004.

[10] J. A. Panagiotopoulos, R. R. Bakker, T. de Vrije, K. Urbaniec, E. G. Koukios, and P. A. M. Claassen, "Prospects of utilization of sugar beet carbohydrates for biological hydrogen production in the EU," *Sustain. Hydrog. Biomass*, vol. 18, pp. S9–S14, Dec. 2010, doi: 10.1016/j.jclepro.2010.02.025.

[11] M. A. Babatabar, M. Manouchehri, H. Abbasi, and A. Tavasoli, "Supercritical water Co-gasification of biomass and plastic wastes for hydrogen-rich gas production using Ni-Cu/AC-CaO catalyst," *J. Energy Inst.*, vol. 108, p. 101251, Jun. 2023, doi: 10.1016/j.joei.2023.101251.

[12] T. K. Kanatlı, N. Pourmoghaddam, S. Karadeniz, and N. Ayas, "Steam Reforming of Sugar Beet Pulp in the Presence of Ni/Dolomite Catalyst for the Synthesis of Hydrogen-Rich Gas," presented at the 8th International Hydrogen Technologies Congress, Diyarbakır, May 2024.

[13] B. Kiren and N. Ayas, "Nickel modified dolomite in the hydrogen generation from sodium borohydride hydrolysis," *Int. J. Hydrog. Energy*, vol. 47, no. 45, pp. 19702–19717, May 2022, doi: 10.1016/j.ijhydene.2021.11.159.

[14] R. S. Tan, T. A. Tuan Abdullah, S. A. Mahmud, R. Md Zin, and K. Md Isa, "Catalytic steam reforming of complex gasified biomass tar model toward hydrogen over dolomite promoted nickel catalysts," *Int. J. Hydrog. Energy*, vol. 44, no. 39, pp. 21303–21314, Aug. 2019, doi: 10.1016/j.ijhydene.2019.06.125.

[15] B. Zhang, L. Zhang, Z. Yang, and Z. He, "An experiment study of biomass steam gasification over NiO/Dolomite for hydrogen-rich gas production," *Int. J. Hydrog. Energy*, vol. 42, no. 1, pp. 76–85, Jan. 2017, doi: 10.1016/j.ijhydene.2016.10.044.

[16] A. C.-C. Chang, L.-S. Chang, C.-Y. Tsai, and Y.-C. Chan, "Steam reforming of gasification-derived tar for syngas production," *Int. J. Hydrog. Energy*, vol. 39, no. 33, pp. 19376–19381, Nov. 2014, doi: 10.1016/j.ijhydene.2014.07.133.

[17] B. Li, C. F. Magoua Mbeugang, Y. Huang, D. Liu, Q. Wang, and S. Zhang, "A review of CaO based catalysts for tar removal during biomass gasification," *Energy*, vol. 244, p. 123172, Apr. 2022, doi: 10.1016/j.energy.2022.123172.

HIGH-VALUE CARBON PRODUCTION THROUGH THERMAL PLASMA DRY REFORMING FOR E-FUEL VIABILITY

[1*]*Aurelio R.C. Labanca*, [2]*Alfredo G. Cunha*, [2]*R.P. Ribeiro*, [2]*C.G. Zucolotto*, [2]*M.B. Cevolani*, [2]*M.A. Schettino Jr.*, [2]*F.G. Emmerich*
[1] Cenpes/Petrobras, Avenida Horácio Macedo, 950, Cidade Universitária, Rio de Janeiro, 21941-915, Brazil
[2] LPT/Universidade Federal do Espírito Santo, Avenida Fernando Ferrari, 514, Vitória, Espírito Santo, 29075-910, Brazil

*Corresponding author e-mail: aurelio.labanca@petrobras.com.br

ABSTRACT
The use of electrified reactors appears promising for reducing CO_2 emissions in industries. The potential emission reduction can reach close to 100%, depending on the H_2 production process, as in the case of natural gas (NG) plasma pyrolysis, which sequesters carbon in a solid state as a valuable by-product. Employing renewable feedstocks, such as biogas, is another strategy for achieving nearly emission-free industrial processes. This work presents results of NG dry reforming using a plasma reactor, which produces syngas with reduced emissions compared to conventional fired reactors. Furthermore, the dry reforming produces hydrogen and carbon monoxide without the consumption of water, as occurs in the methane steam reforming process, which is the most used hydrogen production process worldwide. The technology primarily utilizes methane and CO_2, key components of biogas, making it suitable for CO_2-neutral e-fuel production pathways. Additionally, it offers the potential for co-producing high-quality syngas and reduced graphene oxide, demonstrating its capability for generating valuable products.

Keywords: Plasma Reactor, Dry Reforming, Synthesis Gas, E-fuel, Nanostructured Carbon

1. INTRODUCTION
Dry reforming can utilize biogas as a feedstock and holds significant interest to produce e-fuels, such as diesel, Sustainable Aviation Fuel, and methanol. However, a major drawback of catalytic dry reforming is coke formation [1] and has hampered its full development. Plasma reactors, powered by clean electrical energy, offer a substantial reduction in emissions compared to conventional fired reactors. This article presents results from an electrified reactor that produces high-quality syngas through non-catalytic CH_4 dry reforming with CO_2 thermal plasma, eliminating the issue of carbon formation. Additionally, the reactor has the flexibility to produce reduced graphene oxide, potentially enhancing its economic viability. Carbon materials formation occurs when the molar ratio “n” of CH_4 to CO_2 slightly exceeds unity, as shown in Equation (1).

$$nCH_4 + CO_2 + \text{Electricity} \rightarrow 2nH_2 + 2CO + (n-1).C \quad (1)$$

The reaction described may not form carbon materials when the molar ratio n equals 1. For values of n greater than 1, both graphene oxide (GO) and thermally reduced graphene oxide (rGO) can be produced [2].

2. EXPERIMENTAL
The CO_2 plasma torch used in this study is schematically shown in Fig. 1a. It has two natural gas (NG) injections to allow for a wider range of NG volumes to be introduced into the electric arc. A schematic diagram of the experimental setup is presented in Fig. 1b. The produced gases are cooled and then combusted in a flare, as described in the previous article [2]. CO_2 and NG (~90% CH_4) were used, yielding the following products: H_2, CO, C, and C_2H_2. Product yields also depend on plasma power.

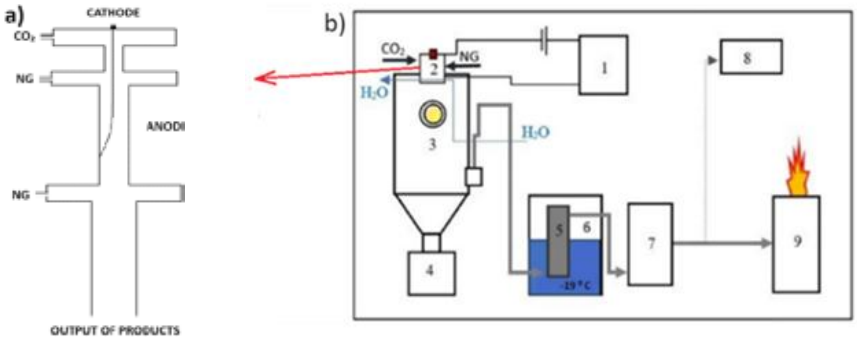

Fig. 1. Diagrams of (a) plasma torch and (b) experimental setup

3. RESULTS AND DISCUSSION

Fig. 2a shows the molar fraction of each product (C, H_2, CO, and C_2H_2) for four different NG flow rates (VNG) with a fixed CO_2 flow rate (VCO_2) of 151 mol/h. Fig. 2b presents the mass spectrum for an NG flow rate of 566 mol/h.

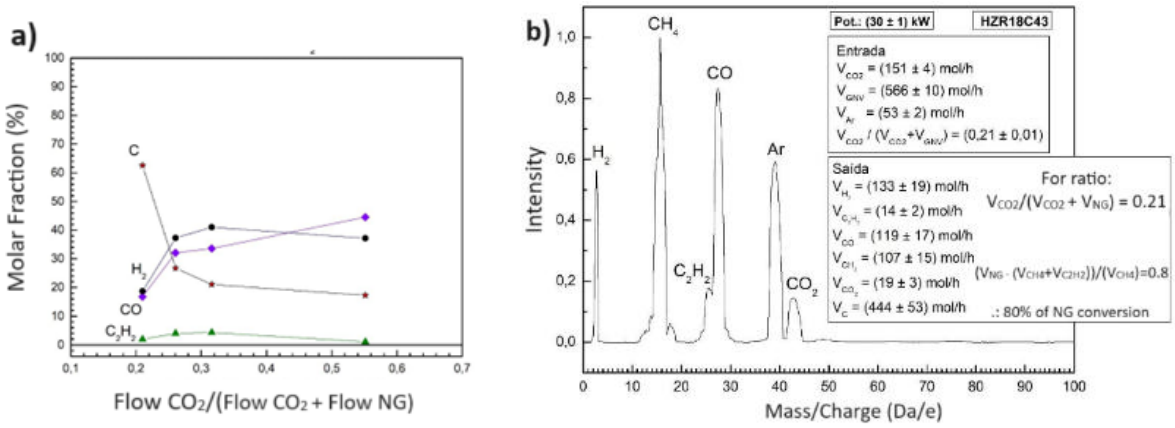

Fig. 2. (a) Molar fraction of products; (b) Mass spectrum at VNG/VCO2~ 3.7

Figure 3 presents transmission electron micrographs (TEM) of two samples of carbon materials, revealing the presence of graphene derivatives as semi-transparent thin films. The images display edges, folds, and pores within the structure.

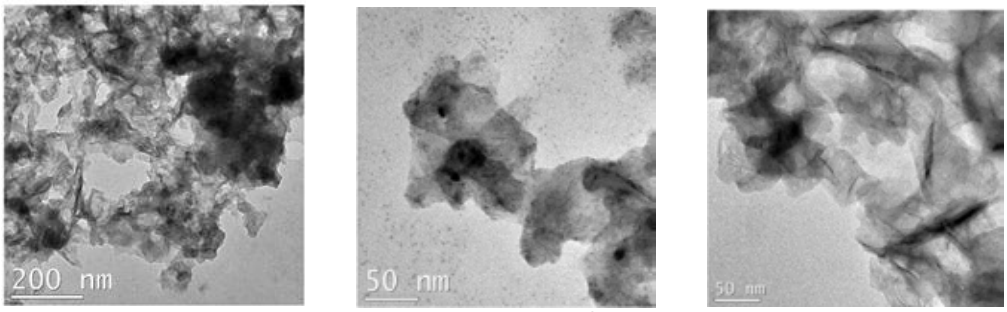

Fig.3. TEM images of samples

Figure 4 shows Raman spectra for two samples of carbon materials. They spectra exhibit three dominant bands (G, D, and 2D). The G band at ~1574 cm^{-1} arises from carbon atoms with sp^2 hybridization, indicating the presence of graphenic material. The D band at ~1337 cm^{-1} suggests disorder in the crystalline structure, likely caused by oxygen. The D band also indicates other imperfections, such as edge defects. The 2D band, along with the G band, confirms the presence of graphene. The ratio IG/I2D is typically used to estimate the number of layers in a graphene derivative sample [3]. The observed Raman spectra are consistent with literature reports for rGO and/or GO.

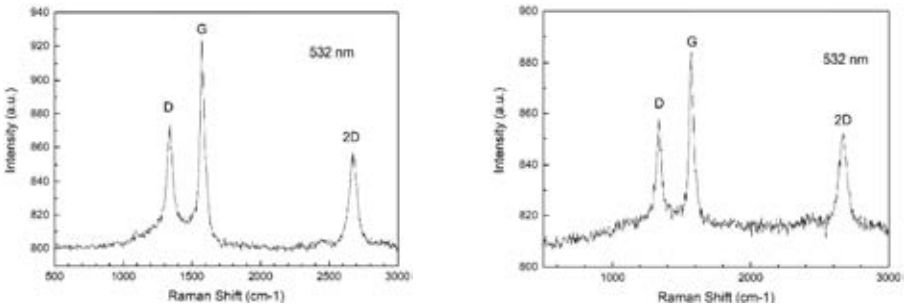

Fig.4: Raman spectra of two samples

4. CONCLUSIONS

This plasma torch demonstrated the ability to produce carbon materials with molar fractions ranging from 15% to 62%. The highest yield (62%) was achieved at a molar ratio of [NG]/[CO_2] ~ 3.7 with 80% NG conversion, generating high-quality syngas. Oxygen atoms from CO_2 bonded with NG carbon, forming CO gas and solid-phase graphene oxide. Reduced graphene oxide was also detected in both current and previous experiments, suggesting thermal reduction due to high process temperatures. This technology demonstrates successful production of high-quality syngas without the use of catalysts or fuel combustion and can therefore be effectively used in the production of synthetic fuels with reduced CO2 emissions and without water consumption. Additionally, it has the potential to synthesize larger quantities of valuable graphene derivatives compared to top-down synthesis processes. Graphene oxide and reduced graphene oxide are versatile materials with applications in sensors [3], energy storage, water treatment, and desalination. These experiments highlight the capability to produce carbon nanomaterials and syngas using clean electricity. Its potential to utilize biogas (CH_4 and CO_2) as feedstock enables the production of green syngas, facilitating the creation of green synthetic liquid fuels. Furthermore, the commercialization of produced carbon nanomaterials could enhance the economic viability of e-fuels.

REFERENCES

1.Song Y, Ozdemir E, Ramesh S et al. 2020. Dry reforming of methane by stable Ni–Mo nanocatalysts on single-crystalline MgO. Science, Vol 367, Issue 6479: 777-781

2. Labanca ARC, Cunha AG, Ribeiro RP, Zucolotto CG, Cevolani MB and Schettino MA. 2022. Technological solution for distributing vehicular hydrogen using dry plasma reforming of natural gas and biogas. Renewable Energy, Vol. 201, Part 2:11-21.

3. Silva, JJA. 2013.Microscopia de força elétrica em amostra de óxido de grafeno. PhD Thesis. Universidade Federal do Ceará, Brazil.

PLASMA-CATALYTIC METHOD OF METHANE CONVERSION IN MICROWAVE DISCHARGE

[1]*Mazhyn Skakov*, [2,3]Arman Miniyazov, [2,3]*Timur Tulenbergenov,* [2,3]*Igor Sokolov,* [2,3]**Alina Agatanova*
[1] RSE "National Nuclear Center of the Republic of Kazakhstan", Kurchatov, 071100, Kazakhstan
[2] "Institute of Atomic Energy" Branch RSE NNC RK, Kurchatov, 071100, Kazakhstan
[3] JSC "Shakarim University of Semey", Semey, 071412, Kazakhstan

*Corresponding author e-mail: agatanova@nnc.kz

ABSTRACT
Hydrogen is increasingly recognized as a crucial element in the decarbonized global energy framework. Serving both as a fuel and as an energy storage medium, the interest in hydrogen is growing steadily. As a result, the development of hydrogen production methods with minimal environmental impact has emerged as a critical area of research [1-3]. The objective of the present study is to examine hydrogen generation through methane conversion utilizing a catalyst in an ultra-high-frequency discharge, while ensuring the elimination of CO_2 emissions. This investigation focuses on the use of ultra-high-frequency discharge in conjunction with a catalyst for methane pyrolysis, a combination that facilitates the achievement of optimal conditions for efficient methane decomposition. This methodology significantly reduces the reaction time and improves the yield of the desired products.

Keywords: Hydrogen energy, Hydrogen, Methane conversion, Microwave discharge, Catalyst

1. INTRODUCTION

One of the main threats to global climate change is the combustion of fossil fuels. For this reason, hydrogen is considered a promising alternative fuel. Many developed countries are actively developing and implementing national hydrogen energy strategies to meet the growing global demand for clean energy [4,5]. In 2024, the Minister of Energy of the Republic of Kazakhstan approved Order No. 342, which outlines the Concept for the Development of Hydrogen Energy until 2030 [6]. The primary objective of this concept is to promote hydrogen energy in Kazakhstan to reduce carbon emissions and stimulate economic growth. As part of the implementation plan, it is proposed to establish hydrogen clusters, scientific and technological infrastructure, and launch pilot projects. The plan also envisions the integration of low-carbon hydrogen into industry and transport, the development of infrastructure for hydrogen transportation, and local energy systems. An essential aspect of the plan is government support for research, investment, and production, as well as the creation of mechanisms for regulating carbon dioxide emissions and subsidizing hydrogen projects, which will enhance the competitiveness of hydrogen.

However, the primary challenge lies in the fact that hydrogen is rarely found in its pure form on Earth, as it tends to form covalent bonds with other elements. This necessitates the development of environmentally safe and economically viable methods for hydrogen production. There are many widely used methods for hydrogen production, such as coal gasification, water electrolysis, steam methane reforming, and others. Currently, numerous studies are being conducted to optimize hydrogen production with minimal atmospheric emissions. One such method is plasma-catalytic methane conversion, which is an environmentally clean and efficient way to produce hydrogen [7-9], provided renewable energy sources are utilized.

This work examines the application of ultra-high-frequency discharge and a catalyst to achieve the necessary conditions for efficient methane decomposition. This method significantly reduces reaction time and increases the yield of target products [10-13]. It is known that the methane decomposition process is complex and follows the Kassel scheme [14, 15]. One of the key factors influencing catalyst efficiency is the increase in their temperature, as it improves gas-catalyst contact, thereby accelerating the methane decomposition process. Among the most effective catalysts, nickel and iron stand out for their high activity in methane decomposition [16-19].

The National Nuclear Center of the Republic of Kazakhstan (RSE NNC RK) is implementing a scientific program focused on the development of hydrogen energy. The research cycle includes the development of methods for hydrogen production, storage, and its application for electricity generation. At the Center for Technological Competencies in Hydrogen Energy of RSE NNC RK, the process of hydrogen production through methane pyrolysis is being studied. For this purpose, the PM-6 experimental setup has been developed [20].

The aim of this study is to analyze the effect of a catalyst with varying nickel content on its surface on the methane pyrolysis process and its interaction with ultra-high-frequency discharge technologies.

2. MATERIALS AND METHODS

The experiments were conducted on the PM-6 installation for applied research. The main components of the setup include a microwave generator with a power output of up to 6 kW and a frequency of 2450 MHz. The reaction chamber is a quartz tube with a diameter of 30 mm, which intersects a rectangular waveguide perpendicularly. The working gas (mixture) is introduced into the center of the quartz tube from above, where a plasma discharge is initiated. The operating principle of the installation and its external appearance have been described in previously published works [20-23].

The catalyst used was a steel cylinder with a length of 20 mm and a diameter of 25.5 mm, with an elemental composition of 30 at.% carbon, 26 at.% iron, 22 at.% oxygen, 8 at.% chromium, 5 at.% aluminum, and 8 at.% nickel. The flow rates of the working gases (methane and argon) were determined by the maximum conversion efficiency during the experiments. The magnetron power was 0.6 kW. The temperature of the gas mixture flow during methane decomposition ranged from 580°C to 720°C. Argon was used to generate the plasma, into which methane was gradually introduced. The analysis of the methane decomposition products was performed using a mass spectrometer, and the results are shown in Figure 1.

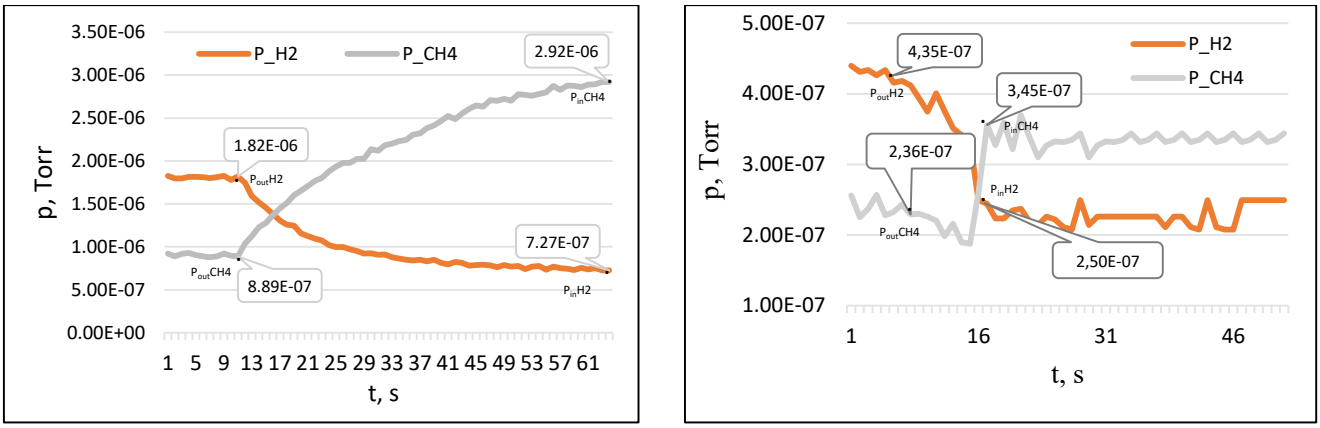

a) with the use of a catalyst b) without the use of a catalyst

Fig. 1. Diagrams of partial pressures of gases resulting from methane decomposition

3. RESULTS AND DISCUSSION

Using the data from the mass spectrometric analysis presented in Fig. 1, both qualitative and quantitative assessments of methane decomposition and hydrogen formation selectivity were carried out. The conversion degree was calculated using the following equation:

$$K_{CH_4} = \frac{P_{CH_4}(in) - P_{CH_4}(out)}{P_{CH_4}(in)} \cdot 100\% \quad (1)$$

The qualitative evaluation, which determines the fraction of methane from the chemical reaction that goes to the formation of the target product, i.e., hydrogen, is called hydrogen selectivity. It was calculated using the equation:

$$S_{H_2} = \frac{1}{2} \cdot \frac{P_{H_2}(out) - P_{H_2}(in)}{P_{CH_4}(in) - P_{CH_4}(out)} \cdot 100\% \quad (2)$$

The results of the study showed that in experiments without the use of a catalyst, the conversion degree was 82% and hydrogen selectivity was 15%. Under conditions where a catalyst was used, the methane conversion degree and hydrogen selectivity reached 32% and 85%, respectively. The use of a catalyst also significantly reduces gas consumption, which directly impacts the energy efficiency of the methane conversion process.

4. CONCLUSIONS

During the experiments, the maximum degrees of methane decomposition and hydrogen selectivity in the super high-frequency discharge on the PM-6 installation were determined, depending on the use of a catalyst. The results showed that the use of a steel catalyst is effective in increasing hydrogen selectivity. The integration of methane pyrolysis with super high-frequency discharge and the use of metallic catalysts could lead to the creation of closed cycles, ensuring cleaner and more sustainable hydrogen production. The experimental results presented in this paper demonstrate the effectiveness of plasma-catalytic methane decomposition in super high-frequency discharge.

ACKNOWLEDGEMENT

This research has been/was/is funded by the Committee of Science of the Ministry of Science and Higher Education of the Republic of Kazakhstan (Grant No. BR21882200).

REFERENCES

1. Jin R, Hou P, Qi Y, Huang Z, Wu T, Cai X. 2025. Hydrogen production efficiency: A critical factor in integrated planning of distribution and transmission system for large-scale centralized offshore wind-hydrogen system. Energy Conversion and Management: X 25:100840.

2. Bhuiyan MMH, Siddique Z. 2025. Hydrogen as an alternative fuel: A comprehensive review of challenges and opportunities in production, storage, and transportation. International Journal of Hydrogen Energy. 102:1026-1044.
3. Lu H, Xi D, Cheng YF. 2025. Hydrogen production in integration with CCUS: A realistic strategy towards net zero. Energy 315:134398.
4. Kuku M, Arishi M. 2025. Advanced materials for sustainable fabrication, desalination, hydrogen production, and CO2 reduction. Alexandria Engineering Journal 115:411-422.
5. Gaudernack B, Lynum S. 1998. Hydrogen from natural gas without release of CO2 to the atmosphere. International Journal of Hydrogen Energy 23(12):1087-1093.
6. Приказ об утверждении Концепции развития водородной энергетики в Республике Казахстан до 2030 года (№342 от 27.09.2024) https://www.gov.kz/memleket/entities/energo/documents/details/733801?lang=ru. Accessed in January 30, 2024.
7. Navarro RM, Peña MA, Fierro JLG. 2007. Hydrogen production reactions from carbon feedstocks: Fossil fuels and biomass. Chemical Reviews 107(10):3952-3991.
8. Rusu I, Cormier J, Khacef A. Hydrogen production from simple compounds via plasma reactors. Social Science Research Network, Science Direct Working Paper No S1574-0331(04)70527-5.
9. Ravasio S, Cavallotti C. 2012. Analysis of reactivity and energy efficiency of methane conversion through non-thermal plasmas. Chemical Engineering Science 84:580–590.
10. Ashik UPM, Wan Daud WMA, Abbas HF. 2015. Production of greenhouse gas free hydrogen by thermocatalytic decomposition of methane – A review. Renewable and Sustainable Energy Reviews 44:221–256.
11. Galanov SI, Zherlitsyn AG, Medvedev YV, Sidorova OI, Shiyan VP. 2011. Production of a highly dispersed carbon material and hydrogen from natural gas in a microwave reactor with metallic catalysts. Russian Journal of Applied Chemistry 84(6):997–1002.
12. Cunha AF, Órfão JJ, Figueiredo JL. 2009. Methane decomposition on Ni–Cu alloyed Raney-type catalysts. International Journal of Hydrogen Energy 34(11):4763–4772.
13. Lestinsky P, Zikmund Z, Grycova B, Ryczkowski R, Grams J, Inayat A. 2020. Production of hydrogen over Ni/carbonaceous catalyst. Fuel 278:118398–118406.
14. Kassel LS. 1935. The role of methyl and methylene radicals in the decomposition of methane. Journal of the American Chemical Society 57(5):833–834.
15. Kassel LS. 1932. The thermal decomposition of methane. Journal of the American Chemical Society 54(10):3949–3961.
16. Villacampa JI, Royo C, Romeo E, Montoya JA, del Angel P, Monzón A. 2003. Catalytic decomposition of methane over Ni–Al2O3 coprecipitated catalysts: reaction and regeneration studies. Applied Catalysis A: General 252:363–383.
17. Qian W, Liu T, Wei F, Wang Z, Li Y. 2004. Applied Catalysis A: General 258:121–124.
18. Li Y, Chen J, Qin Y, Chang L. 2000. Energy Fuels 14:1188–1194.
19. Serrano DP, Botas JA, Fierro JLG, Guil-López R, Pizarro P, Gómez G. 2010. Hydrogen production by methane decomposition: Origin of the catalytic activity of carbon materials. Fuel 89(6):1241–1248.
20. Скаков МК, Миниязов АЖ, Бакланов ВВ, Коянбаев ЕТ, Туленбергенов ТР, Соколов ИА, Жанболатова ҒҚ, Бейсенов ЕС. 2024. Устройство для получения водорода и твердого углерода на основе плазменного пиролиза метана в СВЧ-разряде. Патент на изобретение №36605 Республики Казахстан, №2022/0518.1; заявл. 25.08.2022; опубл. 16.02.2024.
21. Skakov M, Miniyazov A, Tulenbergenov T, Sokolov I, Zhanbolatova G, Kaiyrbekova A, Agatanova A. 2024. Hydrogen production by methane pyrolysis in the microwave discharge plasma. AIMS Energy 12(3):548–560.
22. Скаков МК, Туленбергенов ТР, Соколов ИА, Миниязов АЖ, Агатанова АА. 2024. Экспериментальное исследование конверсии метана в сверхвысокочастотном разряде. Вестник НЯЦ РК 3:123–128.
23. Skakov MK, Miniyazov AZh, Sokolov IA, Agatanova AA, Tulenbergenov TR, Gradoboev AV. 2024. Hydrogen from Methane: Application of Microwave Discharge and Catalyst. Bulletin of the Karaganda University. “Physics” Series 29(4):175–182.

GREEN HYDROGEN PRODUCTION THROUGH AEM ELETROLYSIS TECHNOLOGY

[1]*Veronica Cicciò*, Stefania Siracusano, Sabrina Campagna Zignani, Mariarosaria Pascale, Antonino Salvatore Aricò*
CNR-ITAE, Salita Santa Lucia sopra Contesse, 5, 98126, Messina

*Corresponding author e-mail: veronica.ciccio@itae.cnr.it

ABSTRACT
Green hydrogen production is being advanced through Anion Exchange Membrane (AEM) technology, which is highly compatible with renewable energy sources. The research investigates the use of NiMo-based catalysts at the cathode and NiFe-oxide-hydroxide (LDH) catalysts at the anode in AEM water electrolysis. These catalysts are coated on carbon-based supports, with Ni felt used for diffusion. The catalysts are synthesized using co-precipitation and gas reduction methods, and their physico-chemical and electrochemical properties are analyzed with various techniques. Membrane electrode assemblies (MEAs) are developed by spray-coating the catalysts onto Ni foam and carbon paper supports. Electrochemical tests, including polarization curves, impedance spectroscopy and galvanostatic durability tests, are performed to assess the MEA performance and degradation. The optimal configuration for AEM electrolysis was found to involve NiFe-LDH at the anode, unsupported NiMo at the cathode, a 10% ionomer included in the electrodes, and specific membrane.

Keywords: Water electrolysis, Hydrogen, anion exchange membrane, NiFe catalyst, NiMo catalyst.

1. INTRODUCTION

In recent decades, due to global warming, alternative and renewable methods have been sought to avoid the use of fossil fuels. The most common renewable energy sources are solar, hydroelectric and wind energy. Even Hydrogen's function as an energy vector is increasly looking like a wise decision. Most hydrogen production comes from fossil fuels. There are four different technologies for the production of Hydrogen green which are based on the splitting of water through electrolysis: polymer electrolyte membrane-based (PEM); liquid electrolyte alkaline-based (AEL); anion exchange membrane-based (AEM); solid oxide-based at high temperature (SOEC).
The Anion Exchange Membrane (AEM) technology is ideal for linking up with renewable energy sources because have some advantages: low cost of components, low quality of water used as feed, use of non-critical raw materials and non-fluorinated membranes, high pressure and purity of hydrogen. [1]
It is relevant to optimise and further develop base components that have demonstrated suitable properties in the AEMWE environment. With regard to the catalyst development the approach addresses the use of NiMo-based catalyst at the cathode and NiFe-oxide-hydroxide (Layered Double Hydroxide, LDH) catalyst at the anode coated on carbonaceous structures and Ni felt as diffusion media for the hydrogen evolution reaction (HER) and oxygen evolution reaction (OER), respectively. [2]

2. MATERIALS AND METHODS

The synthesis of NiFe-LDH and NiMo electrocatalysts are based on co-precipitation method. A gas reduction was adopted in the case of the cathode catalysts.
To study the physico-chemical and morphological properties of the electrocatalysts, different characterization techniques were used: x-ray diffraction (XRD), x-ray fluorescence (XRF), transmission electron microscopy (TEM), Brunauer–Emmett–Teller (BET), thermogravimetric analysis (TGA), Temperature-programmed reduction (TPR).
Membrane electrode assemblies (MEAs) were produced by spray-coating catalyst onto the anode and cathode supports (Ni foam from Bekaert and Carbon paper from Sigracet, respectively). These assemblies were then electrochemically tested in a 5 cm² square single cell. Galvanostatic polarization curves and electrochemical impedance spectroscopy (EIS) measurements were carried out at 1.5V, 1.8V, and 2V at 50°C, by a galvanostatic durability test at 1 A/cm², to evaluate both the performance and degradation behaviour of the MEAs.

3. RESULTS AND DISCUSSION

To optimize and analyse AEM technology, an assessment of ionomer percentage on the anode in the MEA preparation was carried out by electrochemical measurements; for the cathode, a comparison was made between supported and unsupported NiMo. The most promising configuration involves NiFe-LDH at the anode, unsupported NiMo at the cathode, 10% ionomer configuration, Piperion membrane, densified Ni felt at the anode and Sigracet diffusion layer at the cathode.

4. CONCLUSIONS

In conclusion, the development of green hydrogen production technologies, particularly through AEM electrolysis, represents a promising avenue for reducing dependence on fossil fuels and combating global warming. Continued optimization of the key components, such as catalysts and ionomer, is essential for improving efficiency and performance. The results of this study, particularly the promising combination of NiFe-LDH and unsupported NiMo catalysts, suggest

that AEM technology holds great potential for large-scale, sustainable hydrogen production, making it a vital part of the clean energy transition.

ACKNOWLEDGEMENT
The author acknowledges the financial support from the HERAQCLES. The project is supported by the Clean Hydrogen Partnership and its members under grant agreement No 101111784 fund-ed by the European Union. Views and opinions expressed are however those of the author(s) only and do not necessarily reflect those of the European Union. Neither the European Union nor the granting authority can be held responsible for them.

REFERENCES
[1] S. Campagna Zignani, M. Lo Faro, A. Carbone, C. Italiano, S. Trocino, G. Monforte, A.S. Aricò. 2022. performance and stability of a critical raw materials-free anion exchange membrane electrolysis cell, Electrochimica Acta 413, 140078
[2] M. Gong, Y. Li, H. Wang, Y. Liang, J. Z. Wu, J. Zhou, J. Wang, T. Regier, F. Wei, H. Dai. 2013. an advanced Ni-Fe Layered Double Hydroxide Electrocatalyst for water oxidation, Journal of the American Chemical Society, 135, 8452-8455

MoS_2-BASED CATALYST FOR HYDROGEN PRODUCTION IN PEM ELECTROLYSIS

[1*]*Maria Aurora Mancuso*, *Stefania Siracusano*, *Fausta Giacobello, Veronica Cicciò, Alessandra Muscolino, Antonino Salvatore Aricò*
[1] CNR-ITAE, Salita Santa Lucia Sopra Contesse, 5, 98126, Messina

*Corresponding author e-mail: maria.mancuso@itae.cnr.it

ABSTRACT
Developing low-cost electrocatalysts is key to improving proton exchange membrane (PEM) water electrolysis for sustainable hydrogen production. In the research for alternative catalyst materials, molybdenum disulfide (MoS_2) has shown great potential for the hydrogen evolution reaction (HER). This study investigates MoS_2-based catalysts synthesized via a hydrothermal method, including an unsupported variant and two supported on Ketjenblack EC carbon (KB). Physico-chemical characterization was conducted using different techinques, while electrochemical performance was evaluated in a PEM single cell through polarization, electrochemical impedance spectroscopy (EIS) , and durability tests. The supported MoS_2 catalyst, incorporating KB during synthesis, exhibited superior performance with higher current densities, lower polarization resistance and higher durability, demonstrating its potential as a viable alternative to noble metal-based cathodes.

Keywords: PEM electrolyzer, non-Noble catalysts, MoS_2, Hydrogen, Proton Exchange Membrane

1. INTRODUCTION

The increasing global energy demand and the environmental impact of CO_2 emissions from fossil fuel combustion make the research for sustainable alternative energies crucial. Hydrogen is considered one of the most promising options, offering a more sustainable solution with a lower environmental impact in the context of modern energy consumption, and its combustion results exclusively in water [1]. Among the available technologies, proton exchange membrane (PEM) water electrolysis is distinguished by its efficiency and reliability, though the reliance on noble metal catalysts such as platinum and iridium limit its economic sustainability. In the context of today's scientific efforts to advance hydrogen production, there is a growing focus on developing non-precious catalysts to make water electrolysis more accessible and cost-effective [2].
Molybdenum disulfide (MoS_2) has emerged as a promising alternative due to its abundance and favorable catalytic properties, offering a viable pathway for sustainable hydrogen production.

2. MATERIALS AND METHODS

2.1. Catalyst preparation

Three MoS_2 catalysts were synthesized for cathode applications using a suitable and low-cost hydrothermal method: one unsupported and two supported on Ketjenblack EC carbon (KB). The difference between the two supported catalysts lies in the preparation: one was mechanically mixed with KB (supported-1), while in the other, KB was incorporated with the precursors (supported-2) to enhance catalytic efficiency while reducing the metal catalyst loading.

2.2. Physico-chemical characterization

To investigate the physico-chemical properties of the synthesized electrocatalysts, various characterization techniques were employed. X-ray Diffraction (XRD) was used to analyze the crystal structure and to evaluate crystallite size, while X-ray Fluorescence (XRF) was performed to determine the elemental composition of the catalysts. Transmission Electron Microscopy coupled with Energy-Dispersive X-ray Spectroscopy (TEM-EDX) allowed to know the powders morphology, structure, and elemental distribution. Additionally, Thermogravimetric Analysis (TGA) was conducted to monitor mass variations as a function of temperature under controlled atmospheric conditions.

2.3. PEM electrolyser setup

The electrochemical performances of the synthesized MoS_2 and MoS_2/C catalysts were investigated in a single PEM cell with a 5 cm² active area by polarization corves and electrochemical impedance spectroscopy (EIS) in a range of temperature between ambient to 90°C; galvanostatic durability tests were performed at an operating temperature of 80°C. The cells were assembled using a commercial IrO_2 as the anode and the three synthesized MoS_2 catalysts as the cathodes. A NAFION 212 membrane was placed between the electrodes to complete the PEM-based MEA assembly.

3. RESULTS AND DISCUSSION

The comparative analysis of the three catalysts revealed that the supported-2 MoS_2 catalyst exhibited superior electrochemical performance. In polarization measurements, it achieved higher current densities at lower voltages compared to both the unsupported and supported-1. Electrochemical impedance spectroscopy (EIS) further confirmed lower polarization resistance at different voltage values, which suggests enhanced charge transfer efficiency; additionally,

galvanostatic durability showed greater stability.
These findings confirmed the supported-2 MoS_2 as the most operative cathode catalyst for hydrogen evolution reaction in PEM electrolisis.

4. CONCLUSIONS

In this work is reported a screening of catalysts based on MoS_2 and MoS_2/C for hydrogen evolution reaction (HER) in acid environment. Non-CRM (non critical raw material) catalysts were synthetized by hydrothermal processes and characterized by physico chemical analyses, as XRD, XRF, TGA and TEM. The electrochemical characterization was carried out in terms of polarization curve, EIS at different potential value and galvanostatic durability test. The electrochemical evaluation of MoS_2 and MoS_2/C as cathodes in a PEM single cell revealed improved performance and stability for the supported MoS_2 catalysts, particularly for the one incorporating Ketjenblack EC carbon in the initial step with precursors.

ACKNOWLEDGEMENT

The project is supported by the Clean Hydrogen Partnership and its members. Co-funded by the European Union under Grant Agreement No 101137893. Views and opinions expressed are however those of the author(s) only and do not necessarily reflect those of the European Union or the Clean Hydrogen Partnership. Neither the European Union nor the granting authority can be held responsible for them.

REFERENCES

1. J. Mo, S. Wu, T.H.M. Lau, R. Kato, K. Suenaga, T.-S. Wu, Y.-L. Soo, J.S. Foord, S.C.E. Tsang. 2020. Transition metal atomedoped monolayer MoS 2 in a proton-exchange membrane electrolyzer. Material Today Advances 6:100020
2. Tachmajal Corrales-Sànchez, Jordi Ampurdanés, Atsushi Urakawa. 2014. MoS2 -based materials as alternative cathode catalyst for PEM electrolysis. International Journal of Hydrogen Energy 39:20837-20843

INNOVATIVE ELECTROLYSIS USING NON-CRITICAL RAW MATERIALS AND CIRCULAR ECONOMY TECHNIQUES TO IMPROVE GREEN HYDROGEN PRODUCTION

[1*]*Alessandra Muscolino*, [2]*Antonino Salvatore Aricò*
CNR-ITAE, Salita Santa Lucia sopra Contesse, 5, 98126, Messina

* E-mail: alessandra.muscolino@itae.cnr.it

ABSTRACT
The constraints of existing electrolysis techniques, which depend on crucial raw materials (CRMs) like Ir, Pt, and Ru, are brought to light by the rising need for green hydrogen. The endurance and scalability of proton exchange membrane (PEM) electrolysis are hampered by these expensive materials. An alternative method that uses non-CRM materials is anion exchange membrane electrolysis (AEMEL), which presents a viable solution. This strategy supports a circular economy by concentrating on materials like Ni, Fe, Mo, and Cu that may be obtained from waste products. In order to achieve high efficiency, low cell voltage, and little degradation, the novel electrocatalysts were tested throughout a range of temperatures and their performance was assessed. The comprehension of membrane and electrode contributions to overall system performance is further improved by the application of impedance analysis.

Keywords: green hydrogen, non-critical raw materials, nanocatalysts, sustainable energy supply

1. INTRODUCTION
Due to the limited performances and durability of critical raw materials (CRMs), state-of-the-art electrolysis methods are unable to effectively meet the significant increase in demand for green hydrogen. In this context it takes on particular importance the use of a technology based on non-critical raw materials.
High loading of precious metal electro-catalysts, such as Ir, Pt, and Ru, as well as expensive titanium bipolar plates and Ti/Pt-based porous transfer layers, are actually necessary for high throughput water electrolyzers based on proton exchange membrane (PEM) technology. An alternative technique, the anion exchange membrane electrolysis (AEMEL), has the potential to be created with diffusion layers, stack plates and catalysts that are not based on CRMs. [1,2]
The novel electrolysis prototypes utilize materials free of CRM based on Ni [3], Fe, Mo, and Cu and offer pathways for recycling and upscaling in a circular approach using secondary raw materials as starting sources. [4] It's important to highlight that utilizing waste as raw material for nanomaterial synthesis is the key to supporting the concept of a circular economy, which views waste as a valuable resource. Transforming conventional waste into nanomaterials could help reduce the need for primary resource extraction and prevent future shortages of raw materials.

2. MATERIALS AND METHODS
2.1. Catalysts and electrodes preparation
Nanocatalysts synthesis were carried out using environmentally friendly techniques, such as chemical bath deposition (CBD), electroless deposition (ELD) and the hydrothermal (HT) method. The synthesized catalysts were used to prepare electrodes, focusing on optimizing their electrochemical activity for hydrogen evolution reaction (HER) and oxygen evolution reaction (OER). Membrane-electrode assemblies (MEAs) were prepared by spray deposition of the cathodic catalyst on sigracet and the anodic catalyst on Ni felt as supports and combined with a commercial membrane, Fumatech FAA-3.

2.3. Physico-chemical and electrochemical characterization
Different techniques were used to study structure, morphology and composition of the novel catalysts. Physical-chemical properties were studied by Scanning Electron Microscope (SEM), Transmission Electron Microscopy (TEM), X-ray Diffraction Spectroscopy (XRD), X-ray Fluorescence Spectroscopy (XRF) and X-ray Photoelectron Spectroscopy (XPS). Electrochemical tests were performed in single cells (5 cm^2) using polarization curves, alternating current (AC) impedance spectroscopy and galvanostatic durability tests to evaluate performances and stability of electrocatalysts.

3. RESULTS AND DISCUSSION
The new electrocatalysts were tested in a AEM single cell of 5 cm^2 in a temperature range from ambient to 60°C; the cells were supplied with diluted KOH (0.1-1 M) or pure water.
By using polarization curve a current density of 1 A/cm^2 at a cell voltage below 2V was obtained and a degradation rate under 10 μV/cell, during a durability test, was observed. The goal was also to separate the contributions of the membrane and electrodes to the overall performance using AC impedance analysis across a wide frequency range.

4. CONCLUSIONS
In summary, the electrochemical performance of electrodes for hydrogen and oxygen evolution processes (HER and OER) has been successfully improved by the ecologically friendly production of new nanocatalysts. The promising

structural and compositional characteristics of these catalysts were validated by characterisation using a variety of physico-chemical techniques. Their durability and performance in membrane-electrode assemblies (MEAs) were further demonstrated by electrochemical testing, which emphasized obtaining a high current density at low cell voltage and minimizing degradation rates. These discoveries open the door to electrochemical energy conversion systems that are more sustainable and effective.

ACKNOWLEDGEMENT
This work was funded by the Ministry of University and Research (Italy) (MUR), PRIN 2022 PNRR, within the project “Innovative non-critical raw materials-based electrocatalysts for electrolytic green hydrogen generation-IMAGE", Nr. P2022KACL7.

REFERENCES

1. Campagna Zignani S., Faro M.L., Carbone A., Italiano C., Trocino S., Monforte, G., Arico' A.S. 2022. Performance and stability of a critical raw materials-free anion exchange membrane electrolysis cell. ELECTROCHIMICA ACTA, Vol. 413, 140078.
2. Zignani S.C., Lo Faro M., Trocino S., ARICO' A.S. 2020. Investigation of NiFe-based catalysts for oxygen evolution in anion-exchange membrane electrolysis. ENERGIES, Vol. 13, en13071720.
3. Zhongliao Wang, Jiajie Fan, Bei Cheng, Jiaguo Yu, Jingsan Xu. 2020. Nickel-based cocatalysts for photocatalysis: Hydrogen evolution, overall water splitting and CO2 reduction. Materials Today Physics. Vol. 15.
4. Acerbi, F.; Sassanelli, C.; Terzi, S.; Taisch, M. 2021. A Systematic Literature Review on Data and Information Required for Circular Manufacturing Strategies Adoption. Sustainability 13, 2047.

A PEM ELECTROLYSER WITH LOW PRECIOUS METAL LOADING

[1]*Veronica Cicciò*, Stefani*
a Siracusano. A. S. Aricò
CNR-ITAE, Salita Santa Lucia sopra Contesse, 5, 98126, Messina

*Corresponding author e-mail: veronica.ciccio@itae.cnr.it

ABSTRACT
The aim of this work was to develop electrocatalysts with high catalytic activity for oxygen evolution reaction (OER) consisting of low noble metal loading, such as Pt and Ir. IrRuOx-based anodic catalyst with a core-shell structure having Ru in the core and a high amount of Ir on the surface was developed through modified Adams synthesis [1].
This catalyst was in the form of dispersed nanocrystals (≤ 9 nm) and with a high surface area (155 m²/g) such as to allow a reduced loading in the membrane electrode assembly (MEA) while maintaining high activity and stability for operation at high current density. A recombination catalyst based on Pt-Co alloys through sulphite synthesis route was also developed. This catalyst was integrated with the anode catalyst in order to reduce the crossover of hydrogen permeated through the membrane [2].

Keywords: Renewable Energies, Hydrogen production, Proton exchange membrane

1. INTRODUCTION
Proton Exchange Membrane (PEM) water electrolysis is a very promising alternative to the more conventional liquid electrolyte alkaline water electrolysis for the production of “green” hydrogen. The membranes used for this type of technology are based on sulfonated perfluoropolymers (PFSA), which allow the crossing of proton charges from cathode to the anode side, leading to the formation of oxygen and hydrogen gases.

2. MATERIALS AND METHODS
Physical-chemical properties of anode and recombination catalysts developed were studied by Xray-diffraction (XRD), Xray-fluorescence (XRF), scanning and transmission electron microscopy (SEM/TEM). After a structural, compositional, superficial and morphological characterization of the catalysts, MEAs were prepared by spray deposition, using an automatic system. Electrochemical tests were performed in single cell (5 cm^2) using the protocols of harmonization developed by JRC (European Commission).

3. RESULTS AND DISCUSSION
To evaluate performance different electrochemical techniques were used such as polarization, spectroscopy impedance and durability tests over a temperature range of 30 to 90 °C. A Pt/C-based catalyst was used at the cathode while the anode was based on IrRuOx (Ir:Ru=70:30). The quantities of catalyst used were 0.3 $mg_{Pt}cm^{-2}$ and 0.37 $mg_{IrRu}cm^{-2}$ + 0.2 $mg_{PtCo}cm^{-2}$ at the cathode and anode, respectively.

4. CONCLUSIONS
Polarization, impedance spectroscopy and stability measurements were conducted to evaluate materials developed for hydrogen generation under specific operating conditions in the PEM electrolysis system. A "steady state" durability test at 90 °C, with an initial conditioning phase at 1 $A{\cdot}cm^{-2}$ for approximately 250 h and subsequently at 4 A cm^{-2} demonstrates good stability after more than 1400 hours of testing.The next step will be to reach new goals in terms of crossover (H_2 conc. in O_2 stream) by using the recombination catalyst-based MEAs.

ACKNOWLEDGEMENT
This research was funded by the European Union – NextGeneration EU from the Italian Ministry of Environment and Energy Security POR H2 AdP MMES/ENEA with involvement of CNR and RSE, PNRR - Mission 2, Component 2, Investment 3.5 “Ricerca e sviluppo sull’idrogeno”, CUP: B93C22000630006

REFERENCES
[1] Stefania Siracusano, Nejc Hodnik, Primoz Jovanovic, Francisco Ruiz-Zepeda, Martin Šala, Vincenzo Baglio, Antonino Salvatore Aricò. New insights into the stability of a high performance nanostructured catalyst for sustainable water electrolysis. Nano Energy 40 (2017) 618-632.
[2] N. Briguglio, F. Pantò, S. Siracusano, A.S. Aricò. Enhanced performance of a PtCo recombination catalyst for reducing the H2 concentration in the O2 stream of a PEM electrolysis cell in the presence of a thin membrane and a high differential pressure. Electrochimica Acta 344 (2020) 136153.

SIMULATION TOOL FOR TECHNO-ECONOMIC ANALYSIS OF RENEWABLE HYDROGEN PRODUCTION PLANTS

[1*]*Francisco Machado*, [1]*Henrique Monteiro*, [1]*Leonardo Fernandes,* [1]*Lucas Marcon*
[1] INEGI, Porto, 4200-465, Portugal

*Corresponding author e-mail: fmachado@inegi.up.pt

ABSTRACT
This paper presents a modular, object-oriented simulation tool to analyze the technical and economic performance of renewable hydrogen production plants. Users define key components (PV plant, electrolyzer, compressor, battery storage, grid connection, hydrogen storage, and demand), and the tool simulates their interactions on an hourly basis over a 20-year horizon. By modeling energy flows, hydrogen production, storage utilization, and grid exchanges, it supports plant promoters in optimizing design and operation. The tool also conducts an economic analysis, calculating the levelized cost of hydrogen, CAPEX, and OPEX. Results highlight the trade-offs between off-grid and grid-connected scenarios: while off-grid operation achieves a lower LCOH (5.95 €/kg vs. 6.05 €/kg), the grid-connected setup enables higher hydrogen production (240,020 tons vs. 95,593 tons) but with increased OPEX. These findings emphasize how system configuration influences costs and production capacity. The modular approach ensures flexibility, allowing integration of new technologies and scalability of existing systems. This tool bridges the gap between technical feasibility and economic viability, facilitating the development of sustainable hydrogen production plants aligned with global decarbonization goals.

Keywords: Hydrogen Production Simulation, Renewable Energy Integration, Plant Design Decision Support

1. INTRODUCTION

The transition to renewable hydrogen production is critical for decarbonizing hard-to-abate sectors, yet scaling these plants requires significant upfront investment. Given the financial risks and technical complexity of such projects, rigorous techno-economic analysis across multiple phases – from design to long-term operation – is essential to ensure viability and attract stakeholders. Existing tools aimed at supporting decision-making often lack the granularity to model interactions between critical components (e.g., electrolyzers, PV plants, storage systems) or rely on oversimplified assumptions, limiting their utility for real-world project planning.

A review of current simulation frameworks reveals three key shortcomings: (1) insufficient modularity to adapt to diverse plant configurations, (2) simplified temporal resolution that overlooks hourly variability in renewable energy supply and hydrogen demand, and (3) insufficient integration of equipment-specific performance dynamics. These gaps hinder promoters' ability to assess operational trade-offs, such as balancing battery buffering against grid reliance or optimizing electrolyzer sizing to match intermittent solar generation.

To address these challenges, this work introduces a modular, object-oriented simulation tool designed for high-resolution, long-term analysis of renewable hydrogen plants. By □ulfil□nc hourly interactions between all core components – PV arrays, electrolyzers, compressors, storage systems, and grid connections – over a 20-year timeframe, the tool provides actionable insights into energy flows, hydrogen output, and storage utilization. It further integrates economic metrics (e.g., LCOH, CAPEX/OPEX) to quantify the impact of design choices on financial viability. This approach empowers decision-makers to test scenarios, identify bottlenecks, and optimize plant configurations with robust technical and economic data, ultimately de-risking investments in the emerging hydrogen economy.

2. MATERIALS AND METHODS

The user begins by creating each module (e.g., PV plant, electrolyzer, compressor, hydrogen storage) and specifying its characteristics, such as capacity, efficiency, and operational constraints.

Once the components are defined, the user establishes the connections between them, determining how energy and hydrogen flow throughout the system. Additionally, a priority hierarchy is set, which dictates the order in which each component □ulfil□ the requirements of its successors. This priority system ensures that energy distribution and hydrogen supply are managed efficiently, optimizing the overall plant operation.

With this modular approach, the tool provides flexibility in configuring different plant layouts while maintaining a structured simulation process.

2.1. Tool Architecture and Modular Design

The simulation tool is developed using an object-oriented programming (OOP) approach in Python, enabling modular representation of plant components (e.g., PV, electrolyzer, hydrogen storage). Each component is □ulfil□n as a class with defined attributes (e.g., efficiency, capacity) and methods to calculate hourly performance (e.g., energy output, degradation). Interactions between components are managed through a central controller that synchronizes energy flows, storage levels, and grid exchanges. This modularity allows users to add, remove, or scale components without

restructuring the entire framework, aligning with best practices for energy system □ulfil□nc. The operation of the entire plant is dependent on hydrogen demand (demand itself and storage requirements). At each simulated hour, the demand dictates the operation of each component, with each system responding to the specific needs of the plant. Components work in a request-response manner, where each piece functions in response to the existing hydrogen demand, ensuring the plant operates efficiently and meets the required hydrogen supply.

2.2. Component modelling

The renewable energy supply can be modelled by 3 different manners: Photovoltaic plant, PPA contract or grid connection.

PV Plant: Users input an hourly electricity production profile via an Excel file. Current simulations utilize simulated data generated by a software, which provides location-specific solar irradiance and temperature profiles. This enables site-specific □ulfil□nc of PV output variability.

Grid connection: The grid is □ulfil□n as an unlimited backup source to meet unmet demand. Users assign electricity prices (€/MWh) to evaluate the grid's influence on the levelized cost of hydrogen (LCOH).

Electrolyzer system: The electrolyser model is implemented with a variable efficiency dependent on its load factor following the work developed by Koponen et al. [1]. Additionally, electrolyser's degradation is considered at a fixed rate of 0.25% per 1,000 operating hours [2]. The entire efficiency curve decreases over time according to this factor, ensuring that long-term performance degradation is accounted for in the simulation.

Compressor: The compressor is □ulfil□n using theoretical thermodynamic equations. Since different compressor models exhibit varying behaviors, a generic approach based on fundamental thermodynamic principles was chosen First, the number of compression stages (N) is calculated using [3]:

$$N = \frac{\log(P_{out}/P_{in})}{\log(x)} \quad (1)$$

Where P_{in} and P_{out} are the outlet and inlet pressures, respectively, and x is the compression ratio per stage.

The energy required for compressing hydrogen is calculated assuming an insenthropic compression with an □ulfil□ncy of 80%. Finally, the power required by the compression system (P) to □ulfil the plant's hydrogen needs is given by [3]:

$$P = N\left(\frac{k}{k-1}\right)\left(\frac{z}{\eta}\right)T_{in}\,Q\,R\left[\left(\frac{P_{out}}{P_{in}}\right)^{\left(\frac{k-1}{Nk}\right)} - 1\right] \quad (2)$$

Where z is the compressibility factor, k is the ratio of specific heat under constant pressure to to specific heat under constant volume, T_{in} is the inlet temperature [K], Q is the molar flow rate [mol/s], η is the efficiency and R the universal gas constant [J/(K.mol)].

Importantly, the compressor does not act as a bottleneck in hydrogen supply, as its capacity is determined only after the simulation, based on the peak power demand observed during the simulation period.

Hydrogen Storage: Hydrogen storage is modeled based on user inputs, including the maximum storage pressure and the maximum hydrogen mass capacity.

Demand: Hydrogen demand is modeled based on user input. It can be set as a fixed value or as a variable profile, in which case it is defined through an Excel file provided by the user.

2.3. Graphical interface

The tool's graphical interface was developed using Streamlit, an open-source Python framework, to ensure user-friendliness and efficient analysis of simulation outputs. The GUI simplifies input parameterization (e.g., component specifications) and enables interactive visualization of results, such as hourly hydrogen production, energy flows, and cost breakdowns. Key design principles include: (1) Modular Workflow: Input forms are structured to mirror the plant's physical components, aligning with the tool's object-oriented architecture. (2) Dynamic Visualization: Outputs are displayed as interactive time-series plots and summary tables, allowing users to toggle between technical and economic metrics. (3) Data Export: Results can be exported in standardized formats for further analysis or reporting.

3. RESULTS AND DISCUSSION

The tool's performance was validated through two case studies analyzing a solar-driven hydrogen production plant under distinct configurations: Scenario 1 (off-grid, renewable-only) and Scenario 2 (hybrid, grid-connected). Key parameters for both scenarios are summarized in Table 1, while Fig. 1 illustrates the plant layout and component interactions.

Table 1. Case study scenarios summary table

Item	Off-grid scenario	Grid-connected scenario
Photovoltaic Plant [MW]	300	
Photovoltaic Plant Location	Sines, Portugal	
Grid connection	x	✓
Electrolyser [MW]	100	

Low pressure hydrogen storage [kg]	10000
High pressure hydrogen storage tank [kg]	15000
Low pressure hydrogen demand [kg/hour]	750
High pressure hydrogen demand [kg/hour]	375

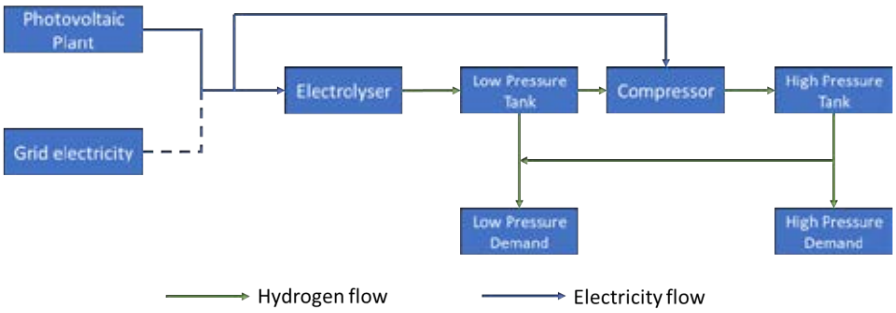

Fig. 1. Layout for simulated case study

Lastly, for the simulated case studies, it is considered that the remaneiscence electricity produced by the photovoltaic plant is sold for a quarter of the price it is bought to the grid.

3.1. Tool results

The case study outcomes (Table 2) demonstrate how operational strategies – specifically grid integration – impact hydrogen production volumes and cost structures. Despite identical initial capital expenditures (CAPEX), the two scenarios diverge significantly in LCOH due to differences in output and operational expenses (OPEX).

Table 2. Case study scenarios results summary table

Item	Off-grid scenario	Grid-connected scenario
Plant CAPEX [M€]	333	333
Electrolyser CAPEX [M€]	108	108
Total OPEX [M€]	235	861
Total Hydrogen produced [ton]	95,593	197,121
CAPEX percentage on LCOH [%]	58.7	27.9
OPEX percentage on LCOH [%]	41.3	72.1
LCOH [€/kg]	5.95	6.06

The comparative analysis of two hydrogen production plant configurations – off-grid scenario and grid-connected scenario reveals critical insights into the trade-offs between renewable autonomy and grid dependency. Despite identical initial capital expenditures (CAPEX) for the whole plant which €108 million was for the electrolyzer, the operational strategies yield stark differences in hydrogen output and cost structures.
Off-grid scenario, reliant solely on a 300 MW photovoltaic plant, produced 95,593 tons of hydrogen over the 20-year simulation. While its LCOH is marginally lower at €5.95/kg, the system's dependence on intermittent solar energy led to significant downtime, limiting production volume as represented in the photovoltaic plant alocations in determined timeframe – Fig 2. The LCOH is dominated by CAPEX (58.7%), reflecting underutilization of infrastructure due to renewable variability.

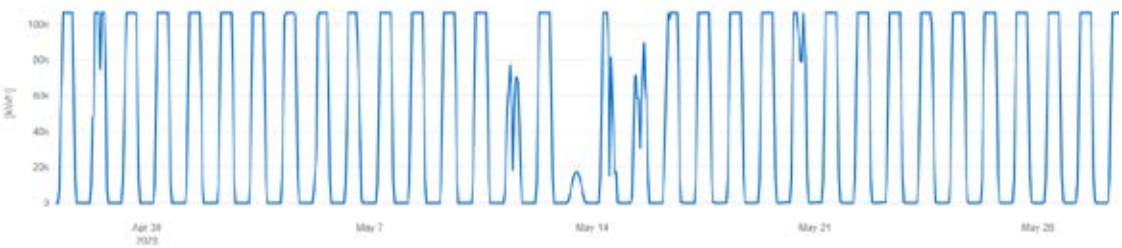

Fig 2. Photovoltaic alocations in a determined timeframe

In contrast, grid-connected scenario leveraged grid connectivity to achieve 240,000 tons of hydrogen - 2.5 times more

than the first one. The grid stabilized production by ensuring near-continuous electrolyzer operation (Fig. 3), but this came at a cost: higher reliance on grid electricity inflated operational expenditures (OPEX), which account for 72.1% of the LCOH. Consequently, while the larger output diluted the CAPEX impact (27.9% of LCOH), the total LCOH rose to €6.06/kg.

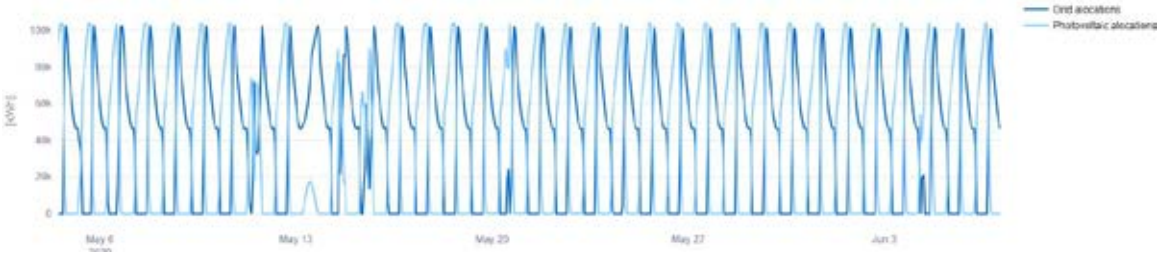

Fig 3. Photovoltaic and grid alocations in a determined timeframe

This paradox - higher production but higher costs in grid-connected scenario - stems from the grid's dual role. While it enables consistent operation and maximizes electrolyzer utilization, electricity costs also burden OPEX.
However, off-grid scenario's lower LCOH masks operational risks. Its CAPEX - heavy structure leaves investors vulnerable to prolonged low-irradiance periods, which could further reduce output and extend payback periods. Grid-connected scenario's higher output, meanwhile, aligns better with industrial-scale hydrogen demand, suggesting it may be preferable for markets prioritizing volume over marginal cost savings.
Ultimately, the choice between these configurations hinges on regional energy prices, policy incentives and demand profiles. Hybrid models - combining limited grid use with battery storage - could balance cost and reliability, though further analysis is needed to optimize such systems.

4. CONCLUSIONS

The developed tool equips hydrogen plant promoters with valuable techno-economic insights, enabling more informed decision-making by improving the quality and granularity of available information. By modeling interactions between key components and simulating their performance over a long-term horizon, the tool helps assess the feasibility of different plant configurations.
The case study demonstrates that grid connection significantly enhances production stability, making it a more reliable option for industrial-scale hydrogen supply. However, this stability comes at the cost of higher operational expenditures, resulting in a higher LCOH. This trade-off highlights the challenge of balancing cost efficiency with production reliability, which is crucial for ensuring hydrogen's competitiveness in the energy market. It is also important to acknowledge that the economic assumptions in this study are based on literature values, which may introduce some uncertainty in the final results.
To refine the accuracy of the analysis, future work will focus on incorporating real-world business case data, enabling a more precise economic evaluation. Additionally, a comprehensive sensitivity analysis will be conducted to assess the impact of variations in component costs, efficiency degradation, and market fluctuations, further strengthening the tool's applicability in decision-making processes.

ACKNOWLEDGEMENT

Project co-financed by the PRR - Recovery and Resilience Plan by the European Union, in particular, the Mobilizing Agenda "Moving2Neutrality" (Project no. 32, with reference no. C644927397-00000038).

REFERENCES

1. Koponen J, Kosonen A, Huoman K, Ahola J, Ahonen T, and Ruuskanen R. 2016. "Specific energy consumption of PEM water electrolysers in atmospheric and pressurised conditions". 18th European Conference on Power Electronics and Applications. doi: 10.1109/EPE.2016.7695576.
2. https://www.energy.gov/eere/fuelcells/technical-targets-proton-exchange-membrane-electrolysis. Accessed on January 29, 2024.
3. Khan MA, Young C, and MacKinnon C and Layzell D 2021. The Techno-Economics of Hydrogen Compression. Transition Accelerator Technical Briefs Vol. 1, Issue 1, Pg. 1-36. ISSN 2564-1379

PLANNING AND MANAGING RENEWABLE GAS INTEGRATION IN THE PORTUGUESE NATURAL GAS NETWORK

[1*]*Leonardo Fernandes*, [1]*Lucas Marcon*, [1]*Francisco Machado*
[1] INEGI, Energy department, Rua Dr. Roberto Frias 400, Porto, 4200-465, Portugal

*Corresponding author e-mail: lfernandes@inegi.up.pt

ABSTRACT
Renewable gases can become an important piece in the decarbonization wave occurring in the energy sector. Renewable gases can be injected in the gas network and contribute as a gradual replacement of natural gas. The mixing of renewable gases and natural gas can be somehow complex from a technical standpoint to ensure that all the infractructure from a macro point of view can continue to be manageable and from a local point of view does not endanger the transport of gas or be a possible hazard. It is also important to know where are the major natural gas consumption points and the relevant points of the network to plan the quantities of renewable gases demanded and necessary resources to produce them. A tool to aid in the planning and management of renewable gases injections in the the Portuguese natural gas network was developed. The information on the natural gas consumption and renewable gases requirements were aggregated and the results are displayed in a map with all the important references.
Keywords: Renewable gases, Gas network, Power2Gas

1. INTRODUCTION

The introduction of renewable gases into the energy mix is something that has been discussed in recent years and follows on from the impossibility of completely electrifying the energy mix as a measure to decarbonize the economy. The gradual integration of renewable gases into the Portuguese gas network has been part of the country's plans since 2020, with the advent of the National Hydrogen Strategy [1] and later, in 2024, with the release of National Action Plan for Biomethane [2]. The idea has already been tested, with the Green Pipeline Project [3], since 2021, allowing a mixture of natural gas and hydrogen to circulate in the gas network and be made available to 80 consumers of different types. The injection of renewable gases into the network will allow a reduction in emissions from the sector equivalent to the reduction in natural gas consumption achieved. Renewable hydrogen is known to be carbon neutral as long as it is produced using renewable electricity. Biomethane is considered a low-carbon gas and its carbon intensity necessarily depends on the origin and life cycle of the organic waste from which it is produced. It is currently known that the current infrastructure is capable of receiving up to 20% of hydrogen (by volume) into the network and that there are no known restrictions on the physical limit of biomethane that can be integrated into the network, since it is interchangeable with natural gas.

The diversification of energy sources makes it possible to create a system that is resilient to uncertainty and to adapt the most appropriate energy sources to the most suitable means and purposes. Fossil fuels are highly energy-dense substances and therefore make it possible to produce a reliable and uninterrupted flow of high energy with relatively simple and affordable technology. This makes them attractive and useful for high-temperature, energy-intensive processes. Natural gas is known to be probably the least polluting of all known fossil fuels. Furthermore, of all the fossil fuels, it is the one that has maintained the most constant consumption in recent years (despite the slight drop since 2020). This is an indication that there is a substantial dependence on natural gas consumption in Portugal and in other countries, and that this is therefore a difficult energy vector to decarbonize. It's not just the easy accessibility of the current gas transportation and distribution network, it's the reliability of the fuel and the maturity of the technological processes that feed into it. It is against this backdrop that renewable gases are positioning themselves to take on a possible decarbonization role in the natural gas sector.

As far as legislation is concerned, the Portuguese Order No. 806-B/2022 already refers to the introduction of renewable gases into the network, already allowing the network to operate with up to 100% renewable or low-carbon gases. The order also refers to the need to ensure the interoperability of gas infrastructures and to comply with ISO 13686 or other technically applicable standards. The portuguese quality-of-service regulation (RQS) for the gas network also refers to the parameters for regulating the quality of service in the gas sector, with specific reference to the characteristics of the gas, namely, ranges of admissible values for properties of the gas circulating in the gas network, as well as values for compounds or contaminants.

2. ANALYSIS OF THE TOOL

General planning for the injection of renewable gases into the grid has become a necessity. It is imperative to know the distribution of natural gas consumption in the country, to understand which municipalities consume more natural gas, where the gas transmission network and its points of interest are located, where the renewable gas producers already registered with Directorate-General for Energy and Geology (DGEG) are located, and where the autonomous gas units (AGU) are located.

2.1. Data and Structure of the tool

The data was collected from several sources. The national gas grid and the location of its relevant points were collected from REN (the national transmission system operator (TSO) [4]. The information regarding the location of the renewable gases producers pre-registered was collected from DGEG [5]. The consumption of natural gas per municipality in the year of 2023 was collected also from DGEG [6]. To perform the calculation, some assumptions were made. The calculation of the demand of hydrogen upon definition of a value of integration of hydrogen, in volume, was made assuming the energy flow should be exactly the same. The same was made with the integration of biomethane. The calculus of the new volume of the mixture will be like:

$$V_{mixture} = \frac{LHV_{NG} * \dot{V}_{i_{GN}}}{(LHV_{NG} * X_{NG} + LHV_{H_2} * X_{H_2} + LHV_{Biomethane} * X_{Biomethane})} \quad (1)$$

The demand of water regarding the demand of hydrogen is calculated like the following way, considering that the water need to produce 1 kg of hydrogen is of 9 kg of water:

$$Water\ demand\ [10^3\ m^3] = H_2\ demand\ [10^3\ m^3] * \rho_{H_2} \left[\frac{kg}{m^3}\right] * 9 \left[\frac{kg_{H_2O}}{kg_{H_2}}\right] \quad (2)$$

The required electrical renewable energy to produce the hydrogen demanded, assuming that the need of electric energy is of 55 kWh per kg of hydrogen, is calculated like:

$$Renewable\ energy\ [MWh] = H_2\ demand\ [10^3\ m^3] * \rho_{H_2} \left[\frac{kg}{m^3}\right] * 55\ \left[\frac{kWh}{kg_{H_2}}\right] \quad (3)$$

The demand of urban solid biorresidues (UBR), considering there are 73 m3 of biomethane being produced per ton of bio municipal solid waste, is calculated according to:

$$UBR\ [ton] = Biomethane\ demand\ [10^3\ m^3]\ /73\ [\frac{m^3 biomethane}{ton\ RBU}] \quad (4)$$

A parameter to evaluate if there is necessary urban solid biorresidues per municipality to meet the necessary biorresidues to produce the demanded biomethane was created. If this parameter is superior to 1, it means there are not sufficient urban solid biorresidues to meet the requirement, if it is inferior to 1, there are more urban solid biorresidues than the required. The parameter is calculated like this:

$$R = \frac{biorresidues\ required}{biorresidues\ needed} \quad (5)$$

3. RESULTS AND DISCUSSION

Figure 1 shows the compilation of data on natural gas consumption per municipality, the gas network, the relevant points of the natural gas network, renewable gas producers and autonomous gas units. This figure is part of the tool which was developed in Power BI to hold a complete database with relevant data to the process and hold this interface, of this map, which was developed in ArcGIS PRO.

According to figure 1, some interesting conclusions can be drawn about the current layout of the plan. The areas with the highest consumption of natural gas are generally located close to the gas transmission network. Reference should also be made to the northern region of the country, which has considerable consumption and is fairly evenly distributed in terms of area, despite not being completely covered by the gas transmission network. Renewable gas producers are registered in regions with a high demand for natural gas and in the vicinity of the gas network, with the exception of the Chaves area, there will be renewable gas production, but there is no access to the transmission network, it should be noted, however, that gas consumption in the region is ensured by autonomous gas units. It can be seen that there are still plenty of areas and regions in the country with potential for renewable gas production, given the large number of areas with high gas demand.

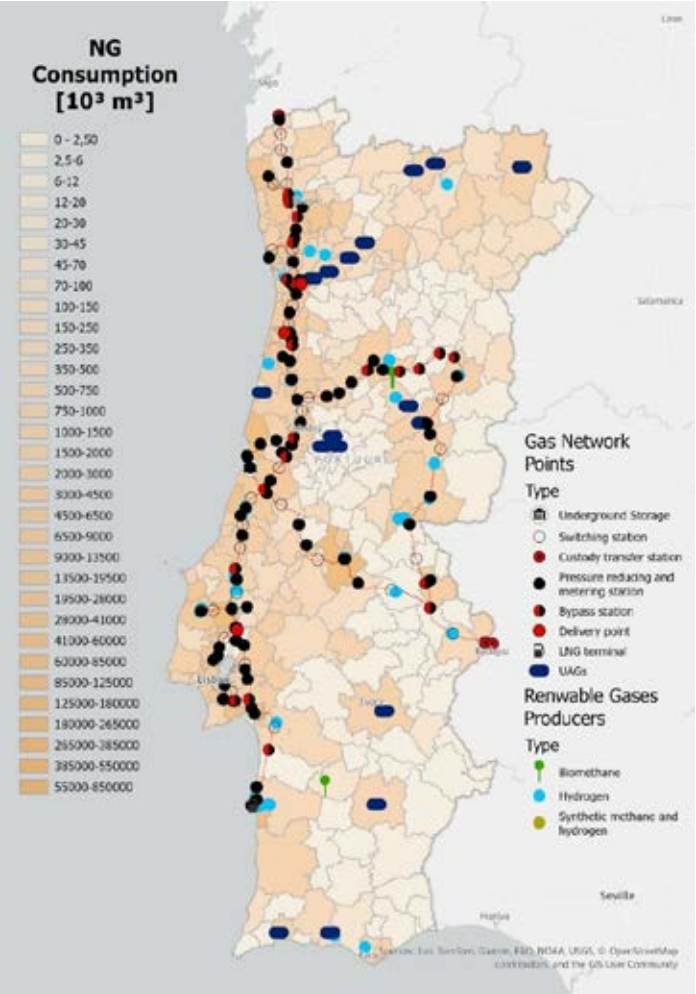

Fig. 1. Portugal Map with the gas network and points of interest localization, consumption of natural gas per municipality, location of renewable gas producers and autonomous gas units.

Assuming the 20% introduction of hydrogen into the gas network as a limit scenario, some data was gathered on the demand for renewable gases and the resources needed to produce them.

The demand for hydrogen will be closely linked to the demand for natural gas by region, so regions with a higher consumption of natural gas will necessarily represent a higher demand for hydrogen. The tool developed for the effect was used and some results were generated on how much water would be needed to produce this annual hydrogen demand, as well as renewable electricity. In order to meet the target of 20% hydrogen in the gas network by volume, while maintaining the energy flow supplied, it would be necessary, just to get a perspective in numbers, to install around 2.8 GW of photovoltaic power, taking into account the average Portuguese capacity factor of 19% [7]. As for water availability, the total amount of water needed to produce hydrogen demand at national level is negligible, way below 1%, when compared to the amount of water captured annually, according to the national institute of statistics (INE) data [8].

Assuming a biomethane integration scenario of between 10% and 50%, considering it to be an interchangeable gas and therefore with no physical limit to its integration into the network, calculations were made of the demand created for biomethane, the amount of municipal bio solid waste needed to be collected and also a fraction ratio between the amount of municipal solid waste needed and the municipal solid waste available, by municipality. Values of this ratio of less than 1 mean that the municipality in question generates enough biodegradable municipal solid waste to produce the biomethane needed to meet the target. To calculate this ratio, based on data published in the Portuguese Environment Agency's Annual Report on Municipal Waste 2023 [9], it was assumed that, on average, each inhabitant produced 505 kg of municipal waste in 2023, 38% of which was bio-waste. Assuming this average value per inhabitant and knowing the population of each municipality, an estimate was made of the amount of bio-waste produced per municipality. In figure 2, it can be seen that, for a value of 10% biomethane integration into the network, there are a fairly large number of municipalities that manage to generate enough bio-waste to meet the local need for biomethane production. However, it is important to note that of these, 31 municipalities do not account for any natural gas consumption and others account for very low natural gas consumption. The municipality with the highest natural gas consumption does not generate enough bio-waste to meet the need created by 10% biomethane in the gas network, proof of which is that the

municipalities with a ratio of less than 1 only account for around 25% of national gas consumption. Even so, it is interesting to note that the generation of solid urban biowaste in Portugal in 2023 would be enough to supply 82% of the need for biowaste to produce the biomethane needed to reach the target of 10% biomethane injected into the grid. Important to note that this analysis is only theoretical as it does not account for the total logistics associated. Also, this analysis only takes into account municipal solid biowaste and that many other types of waste could be used to produce biomethane.

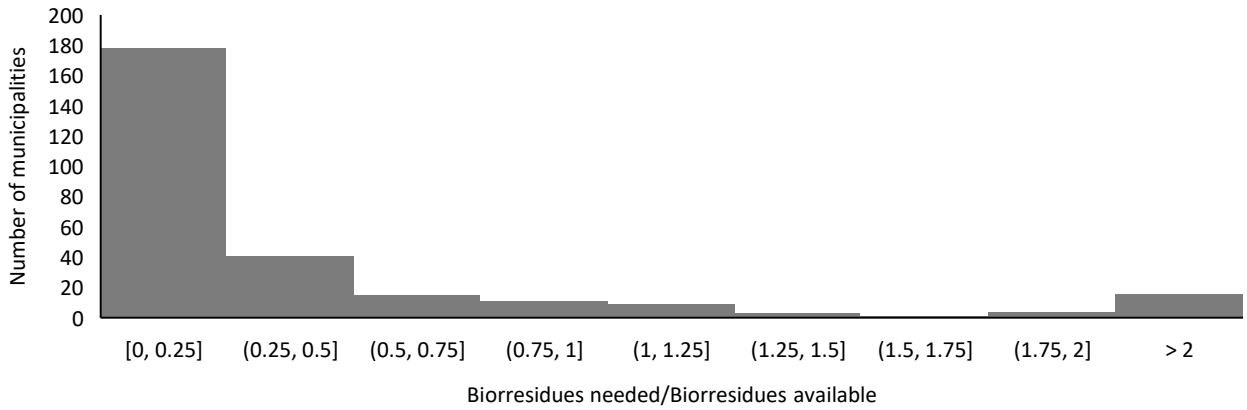

Fig. 2. Histogram of reason demand UBR vs availability UBR per municipality, for 10% biomethane integration in the gas grid.

If we consider an injection of 50% biomethane by volume into the network, the data shows that the municipal solid biowaste currently generated over the course of a year would represent a very small amount of biomethane production potential within the demand created for biomethane. Therefore, municipalities with a biomethane demand vs biomethane availability ratio greater than 1 would correspond to 99% of the country's natural gas consumption. And looking at the generation of solid urban biowaste at national level, this would be enough to ensure 14% of the national demand created to supply 50% of the gas network, by volume, with biomethane.

4. CONCLUSIONS

The development of this tool to support the management of operation of renewable gases injection in the Portuguese national gas grid allowed the aggregation of some relevant data and the elaboration of some interesting conclusions:

- Relevant locations to install renewable gases producers and inject renewable gases into the gas grid.
- Renewable gases demand to meet the expectations and requirements defined in the national plans.
- Requirements to meet the production of the desired renewable gases. For example, the water needs, the renewable energy needs and the residues needed to produce the required biomethane.

ACKNOWLEDGEMENT

Project co-financed by the PRR - Recovery and Resilience Plan by the European Union, in particular, the Mobilizing Agenda "Aliança para a transicão energética" (Project no. 56, with reference no. 02/C05-i01.02/2022.PC644914747-00000023).

REFERENCES

1. https://www.dgeg.gov.pt/pt/areas-transversais/relacoes-internacionais/politica-energetica/plano-de-acao-para-o-biometano-2024-2040-pab/, Accessed on January 29, 2025
2. https://www.dgeg.gov.pt/pt/areas-transversais/relacoes-internacionais/politica-energetica/estrategia-nacional-para-o-hidrogenio-en-h2/, Accessed on January 29, 2025
3. https://floene.pt/en/green-pipeline-project/, Accessed on January 29, 2025
4. https://datahub.ren.pt/pt/redes/rede-gas/, Accessed on January 28, 2025
5. https://www.dgeg.gov.pt/media/e0gmtvag/337-24.pdf, Accessed on January 28, 2025
6. https://www.dgeg.gov.pt/pt/estatistica/energia/gas-natural/consumos/, Accessed on January 28, 2025
7. https://www.irena.org/-/media/Files/IRENA/Agency/Statistics/Statistical_Profiles/Europe/Portugal_Europe_RE_SP.pdf, Accessed on January 27, 2025
8. https://www.ine.pt/xportal/xmain?xpid=INE&xpgid=ine_indicadores&indOcorrCod=0009598&contexto=bd&selTab=tab2&xlang=pt, Accessed on January 27, 2025
9. https://apambiente.pt/sites/default/files/_Residuos/Producao_Gest%C3%A3o_Residuos/Dados%20RU/2023/raru_2023.pdf, Accessed on January 27, 2025

NEXT-GEN ENERGY CATALYSIS: MXENE-BASED COMPOSITES FOR HIGH-IMPACT HYDROGEN EVOLUTION REACTION

[1*]*Deniz Onaylı*, [2*]*Derya Öncel Özgür*
[1] Gazi University, Institute of Science, Technology Faculty, Ankara, 06500, Turkey
[2] Gazi University, Engineering Faculty, Chemical Engineering Department, Ankara, 06570, Turkey

*E-mail: onaylideniz@gmail.com

ABSTRACT
Electrochemical hydrogen production has recently become a focal point of research because of the increasing global energy demand, impending depletion of fossil resources, and the associated environmental impacts. Although precious metals such as platinum provide the highest catalytic efficiency for hydrogen evolution reactions (HER), their limited availability and high cost have driven the search for alternative catalysts that are both abundant and economically viable. Two-dimensional materials, particularly reduced graphene oxide (rGO) and $Ti_3C_2T_x$ MXenes, are promising candidates because to their unique intrinsic properties. rGO has been widely investigated for HER applications; however, achieving the desired catalytic efficiency using rGO alone remains a challenge. MXenes, a recently discovered family of materials, offer superior properties for HER and have emerged as promising alternatives. The combination of rGO and MXene is expected to create a synergistic effect that enhances HER performance. MXenes were synthesized from the MAX phase precursor (Ti_3AlC_2) through an in-situ hydrofluoric acid etching process, whereas rGO was synthesized using Hummers' method. Post-synthesis X-ray diffraction (XRD) and X-ray photoelectron spectroscopy (XPS) confirmed the successful formation of the desired structures. These results validated the successful synthesis and characterization of the hybrid materials, and electrochemical measurements confirmed their potential applicability in electrochemical hydrogen production.

Keywords: MXene, Hydrogen Evolution Reaction (HER), Catalyst, Graphene

1. INTRODUCTION

Hydrogen energy has emerged as a key focus in both global energy strategies and scientific research because of its potential as a clean, renewable energy source, which aligns with the global sustainability goals. The growing demand for energy, depletion of fossil fuel reserves, and urgent need to address environmental concerns have positioned hydrogen as not only an environmentally advantageous energy carrier but also a strategic element in ensuring energy security and fostering economic development. Among the various methods available for hydrogen production, electrocatalytic water splitting has gained significant attention, as it offers a promising route for generating ‘green hydrogen’ while minimizing harmful environmental impacts and ensuring both economic and technological sustainability. Although platinum-based catalysts have long been considered the most efficient for HERs, their high cost, limited availability, and scarcity of other precious metals have created significant obstacles for large-scale applications. This has accelerated the need to identify alternative catalysts that are both cost-effective and readily available [1,2,3,4].

Recent research has identified two-dimensional materials, particularly rGO and MXenes, as promising candidates for enhancing the HER performance. These materials offer a range of advantages, such as high surface area, good electrical conductivity, and potential for modification to further improve their catalytic properties. However, when used independently, each material has its own limitations that can hinder its overall efficiency. The development of hybrid materials has emerged as a particularly attractive strategy to overcome these challenges. By combining the complementary properties of rGO and MXenes, this approach enhances catalytic activity by improving charge transfer efficiency, increasing active site density, and ensuring greater structural stability, ultimately leading to superior HER performance [2,3,5,6].

In this study, a hybrid material was developed by combining $Ti_3C_2T_x$ MXenes with rGO. This hybrid structure is expected to significantly improve the HER efficiency by leveraging the complementary properties of both materials. The combination of MXenes and rGO creates a synergistic effect, which not only enhances the adsorption of hydrogen ions, but also accelerates the reaction kinetics. This synergy allows the hybrid material to overcome the individual limitations of MXenes and rGO, leading to an overall improvement in long-term stability and catalytic performance. As a result, the hybrid material holds considerable promise as a cost-effective and high-performance electrocatalyst for sustainable hydrogen production with strong potential for future commercial applications.

2. MATERIALS AND METHODS

2.1. Synthesis of MXene ($Ti_3C_2T_x$) via In-Situ HF Etching Method

To synthesize $Ti_3C_2T_x$, 2 mg of LiF was gradually added to 20 mL of 12 M HCl with constant stirring. The mixture was then vigorously stirred for 40 min. Next, 500 mg of Ti_3AlC_2 (MAX) was added to the solution and stirred continuously for

one week at 45 °C. After the reaction, the product was washed with deionized water to increase the pH above 6 and then allowed to dry under ambient conditions. The final product was $Ti_3C_2T_x$ powder form [3].

2.2. Synthesis of Graphene Oxide (GO)

To obtain graphene oxide (GO), 1 g of graphite powder was added to 25 mL of cooled H_2SO_4. Subsequently, 0.5g $NaNO_3$ and 3 g of $KMnO_4$ was added to the mixture and stirred for 30 min both in an ice bath and at the room temperature. Afterwards, 45 mL of deionized water was slowly added, and the mixture was stirred for an additional 30 min. To complete the process, 150 mL of deionized water and 8.5 mL of a 30% H_2O_2 solution were added. The mixture was then washed five times with 5% HCl solution to remove metal ions. The final product was washed with deionized water until the pH became neutral. The mixture was dried in an oven at 60 °C, and then in a vacuum oven at 60 °C for 24 h. The final product, GO, was obtained [7].

2.3. Synthesis of Reduced Graphene Oxide (rGO)

A reduction process was applied to the obtained graphene to produce reduced graphene oxide (rGO). Deionized water (900 mL) was added to 3 g of powdered GO and the mixture was stirred at 35 °C for 24 h. The mixture was then ultrasonicated for 2 h. Hydrazine hydrate (90 mL, H_6N_2O) was then added to the mixture and stirred at 95 °C for 24 h. The mixture was then placed in an oil bath which is connected to a reflux system. After cooling to room temperature, the mixture was washed with acetone, followed by washing with deionized water, and filtered. The resulting material was dried in an oven at 40 °C for 24 h to yield rGO in powder form [8].

2.4. rGO@MXene Hybrid Structure

To form the 2D/2D $Ti_3C_2T_x$@Graphene heterojunctions, 0.5 g of MXene ($Ti_3C_2T_x$) and 0.5 g of rGO were dissolved in 70 mL of ultrapure DI water. Ethylene glycol (10 mL) was added to this solution, and the mixture was stirred to form a homogeneous solution. The mixture was then placed in a Teflon-coated container and allowed to react at 150 °C for 14 h. The resulting suspension was washed with deionized water and dried in a vacuum oven at 80 °C [9,10].

2.5. Electrocatalytic Performance of Materials

Electrocatalytic performance analysis was performed using a Gamry Reference 3000 potentiostat/galvanostat/ZRA device. Three glassy carbon working electrodes were used in the experiments, with each electrode loaded with 3 µL of the catalyst ink. The catalyst ink was prepared by dispersing 5 mg of the solid catalyst in 250 µL water, 750 µL alcohol, and 50 µL nafion. Ag/AgCl electrode was used as the reference electrode, and a graphite electrode served as the counter electrode. A 0.1 M H_2SO_4 solution was used as the electrolyte. The structural and chemical properties of the catalysts were characterized using X-ray diffraction (XRD) and X-ray photoelectron spectroscopy (XPS).

3. RESULTS AND DISCUSSION

3.1. Characterization Results

The synthesized GO, rGO, and MXene samples were characterized using XRD (5º–90º, Cu Kα) and XPS techniques. The XRD patterns for GO and rGO are presented in Fig. 1, while those for $Ti_3C_2T_x$, synthesized via in-situ etching from Ti_3AlC_2, are shown in Fig. 2. These results align with those of previous studies, and further investigations are ongoing to explore the structural and surface characteristics of these materials [11-17].

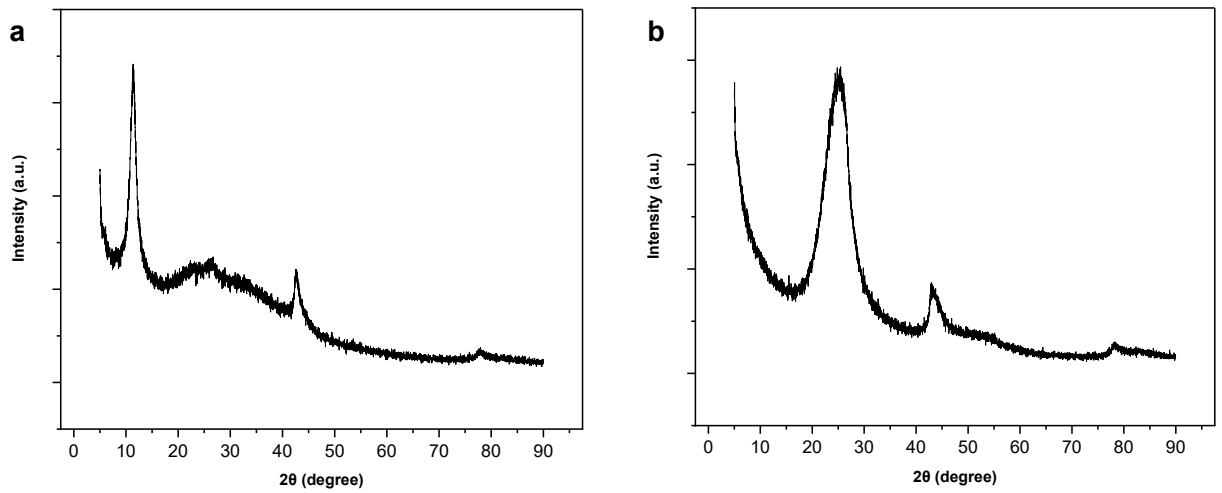

Fig. 1. XRD Analysis of (a) Graphene Oxide (GO) and (b) Reduced Graphene Oxide (rGO)

Figure 1a presents the XRD pattern of GO. The prominent peak at 2θ = 11.35° corresponds to the characteristic reflection of GO, which arises from the oxidation of the graphene. This oxidation resulted in an increase in the interlayer spacing, allowing for the incorporation of oxygenated functional groups and water molecules within the carbon structure. The smaller peaks observed at 2θ = 23.2° and 2θ = 26.4° suggest that the oxygen groups were not fully bonded, indicating some degree of incomplete oxidation in the GO structure [11]. The peak at 2θ = 42.56° reflects the short-range ordering in the stacked graphene layers, corresponding to the turbostratic arrangement [12,14].
Figure 1b presents the XRD pattern of rGO, revealing its structural characteristics. The pronounced peak at 2θ = 25.24° indicates rGO, which was synthesized by the removal of oxygen-containing functional groups from GO. This peak suggests that a significant portion of the conjugated π bonds was restored during the reduction [13,14]. Additionally, the peak at 2θ = 43.08° reflects short-range ordering in the graphene layers, a feature that is also observed in GO, further confirming the existence of disordered stacking [12,14].

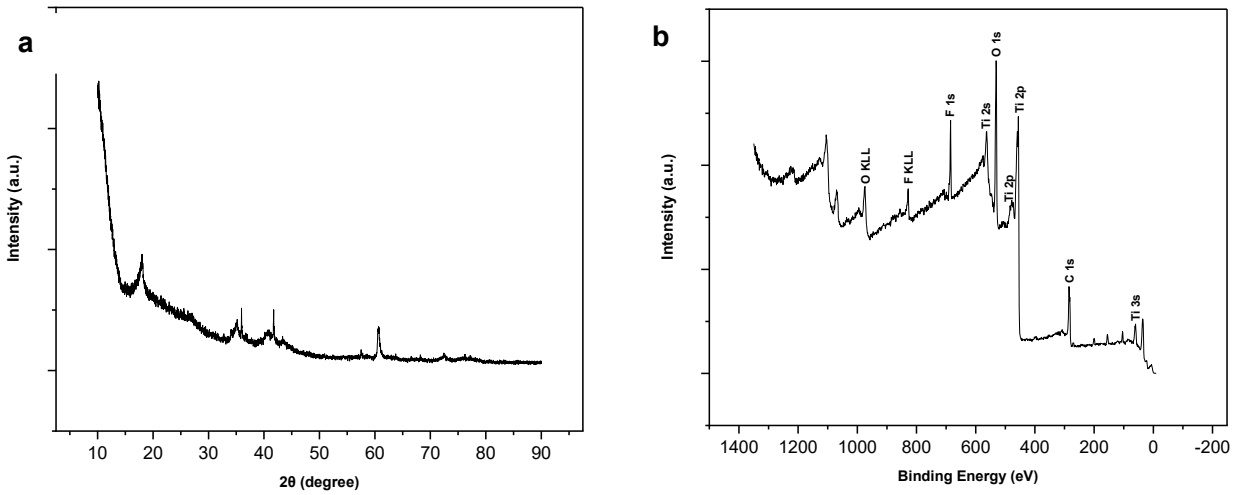

Fig. 2. Ti_3C_2 Characterization: (a) XRD Pattern and (b) XPS Spectrum

Figure 2-a a presents the XRD pattern of the synthesized MXene. The absence of the characteristic peaks corresponding to Ti_3AlC_2 MAX (2θ = 10°, 39°) and the observed shifts and intensity reductions in the remaining peaks (2θ = 19.1°, 34.0°, 41.8°, 48.4°, 56.4°, and 60.2°) provide strong evidence that the Ti_3C_2 structure of MXene was successfully obtained, indicating the complete removal of Al from the MAX phase. Figure 3b shows the XPS spectrum of the same sample. Upon examination, the absence of any peaks corresponding to Al or associated bonding states further supports the XRD findings, confirming the successful synthesis of the $Ti_3C_2T_x$ MXene structure, free from Al contamination [15,16,17].

3.2. Electrochemical performance of $Ti_3C_2T_x$ MXene@rGO *hybrids*

The polarization curves for $Ti_3C_2T_x$ MXene, rGO, and their $Ti_3C_2T_x$ MXene@rGO hybrid structures were evaluated for the HER reactions. MXene exhibited a lower overpotential compared to rGO, and the hybrid structure showed improved performance in both overpotential and Tafel slope. These results suggest that the combination of MXene and rGO can enhance the electrocatalytic performance for HER.

4. CONCLUSIONS

In this study, $Ti_3C_2T_x$ from the MXene family and rGO were successfully synthesized. GO was prepared using the Hummers method, followed by its reduction to rGO. Both materials were characterized using X-ray diffraction (XRD), and the results confirmed the successful synthesis of the intended structures. $Ti_3C_2T_x$ MXene was synthesized via the in-situ HF etching method. XPS and XRD characterization revealed the successful removal of the Al layer from the Ti_3AlC_2 MAX precursor, confirming the formation of the desired MXene structure. Finally, the $Ti_3C_2T_x$ MXene@rGO hybrid structure demonstrated promising Tafel slopes and low overpotential values for the HER. These results highlight the potential of the hybrid structure to enhance electrocatalytic efficiency.

ACKNOWLEDGEMENT

The authors gratefully acknowledge the support provided by the Gazi University through the ADEP Project (No: FGA-2024-9097).

REFERENCES

1. Aghamohammadi P, Hüner B, Altıncı OC, Akgül, ET, Teymur B, Şimşek UB and Demir M. 2024. Recent advances in the electrocatalytic applications (HER, OER, ORR, water splitting) of transition metal borides (MBenes) materials. International Journal of Hydrogen Energy 87:179-198.
2. Pamungkas A, Rahmani FN, Fariz I, Mardiana S and Kadja GTM. 2024. MXene-based nanocomposite for electrochemical hydrogen evolution. FlatChem, 46:100692.
3. Shen B, Huang H, Liu H, Jiang Q, He H and Shen BH. 2021. Bottom-up construction of three-dimensional. International Journal of Hydrogen Energy 46:29984-29993.
4. Qadeer MA, Zhang X, Farid MA, Tanveer M, Yan Y, Du S, Huang ZF, Tahir M and Zou, JJ. 2024. A review on fundamentals for designing hydrogen evolution electrocatalyst. Journal of Power Sources 613:234856.
5. Li XY, Feng YS, Li XL, Yin X, Cao andFF, Ye H. 2024. Green synthesis and applications of MXene for lithium–sulfur batteries. Energy Storage Materials, 67:103257.
6. Iravani S, Zarepour A, Zare EN, Makvandi P, Khosravi A and Zarrabi A. 2024. Synergistic advancements: Exploring MXene/graphene oxide and MXene/reduced graphene oxide composites for next-generation applications. FlatChem 48:100759.
7. Hummers WS and Offeman RE. 1958. Preparation of Graphitic Oxide. Journal of the American Chemical Society 80:1339.
8. Chen H, Ding L, Zhang K, Chen Z, Lei Y, Zhou Z and Hou R. 2020. Preparation of chemically reduced graphene using hydrazine hydrate as the reduction agent and its NO2 sensitivity at room temperature. International Journal of Electrochemical Science. 15: 10231-10242.
9. Jin W, Jiang L, Lv Y, Li K, Liu H, Cao W, Chen C, Chen Z and Li W. 2024. Experimental study on preparation and heat transfer efficiency of ethylene glycol/water-based hybrid nanofluids enhanced by graphene oxide/MXene nanoparticles. Journal of Molecular Liquids 405:12503.
10. Zhu C, Pei C, Park HS and Yu X. 2023. Design of 2D/2D heterostructure by coupling cobalt hydroxides with Mxene on nickel foam for high energy density supercapacitors. Journal of Alloys and Compounds. 948:169809.
11. Siburian R, Sihotang H, Raja S. L, M. Supeno and Simanjuntak C. 2018. New Route to Synthesize of Graphene Nano Sheets. Oriental Journal Of Chemistry, 34:182-187.
12. Stobinski L, Lesiak B, Malolepszy A, Mazurkiewicz M, Mierzwa B, Zemek J, Jiricek P and Bieloshapka I. 2014. Graphene oxide and reduced graphene oxide studied by the XRD, TEM and electron spectroscopy methods. Journal of Electron Spectroscopy and Related Phenomena 195:145-154.
13. Gonçalves AHA, Siciliano PHC, Alves OC, Cesar DV, Henriques CA and Gaspar AB. 2020. Synthesis of a Magnetic Fe3O4/RGO Composite for the Rapid Photo-Fenton Discoloration of Indigo Carmine Dye. Topics in Catalysis 63:1017–1029.
14. Said NHM, Liu WW, Lai CW, Zulkepli NN, Khe CS, Hashim U and Lee HC. 2017. Comparison on graphite, graphene oxide and reduced graphene oxide: Synthesis and characterization. AIP Conference Proceedings 1892:150002.
15. Huang JHR, Tseng SW and Chen IWP. 2025. In-situ electrochemical XRD and raman probing of ion transport dynamics in ionic liquid-etched $Ti_3C_2T_x$ MXene for energy storage applications. Chemical Engineering Journal 503:158232.
16. Fatima S, Hakim MW, Khan S, Ning Y, Liu J and Li H. 2025. Enhanced thermal stability and switching performance of transition and alkali metal functionalized MXene films for high-temperature memristor applications. Applied Surface Science 687:162253
17. Luo G, Zhang Z and Wang J. 2023. High-Performance Ultraviolet Photodetectors Enabled by van der Waals Schottky Junction Based on TiO2 Nanorod Arrays/Au-Modulated Ti3C2Tx MXene. Advanced Functional Materials 33:2211610.

EVALUATION OF HYDROGEN PRODUCTION EFFICIENCY BY DARK FERMENTATION PROCESS OF VARIOUS AIRPORT-DERIVED WASTES

[1,2*]*Fatih Altay*, [2]*Neslihan Semerci*, [3]*Atakan Öngen,* [1]*Şahin Duran,* [4]*Melek Cumbul Altay,* [1]*Nazlıcan Yeşilova*
[1] İGA Istanbul Airport Operation Inc., Environment and Landscape Directorate, Environment and Water Management Senior Management
[2] Marmara University Faculty of Engineering Department of Environmental Engineering
[3] Istanbul University-Cerrahpasa Faculty of Engineering, Department of Environmental Engineering
[4] Istanbul University-Cerrahpaşa Faculty of Engineering, Department of Metallurgy and Materials Engineering

*Corresponding author e-mail: fatih.altay@igairport.aero

ABSTRACT
An increasing number of airport operators around the world are realizing their responsibilities in protecting the environment and are changing their perspectives towards the natural environment. In this context, it is seen that environmental awareness is being established in operators with the efficient use of resources, reduction of waste and recycling, and reductions in costs. Among various biomass-to-hydrogen conversion technologies, dark fermentation has attracted great attention due to its high energy efficiency potential and ability to use a wide range of waste substrates. This study focuses on evaluating the efficiency of the dark fermentation process for hydrogen production using various wastes originating from airports. Various wastes from airports have been found to be rich in organic matter and are potentially suitable raw materials for hydrogen production through the dark fermentation process. As a result of the analysis, it was determined that approximately 1800-2000 ml of gas was formed in the studies and that 25% to 40% of the gas formed contained hydrogen. As a result, a feasible model for our country is presented that is compatible with the zero waste and circular economy approach in terms of energy and raw material recovery from alternative sources, environmental technologies and renewable energy.
Keywords: Airport-Derived Wastes, Dark Fermentation, Hydrogen Energy, Waste to Energy

1. INTRODUCTION

The European Green Deal aims to make Europe a climate-neutral continent by 2050; to achieve zero greenhouse gas emissions, to switch to a circular economy model; and to achieve the goals of clean, reliable energy use. The implementation of waste-to-energy processes supports the overarching goals of the circular economy by converting waste into useful energy carriers. Hydrogen is an important energy carrier that can be used in sustainable energy systems due to the high efficiency in the production, conversion and use of hydrogen energy systems. Hydrogen has emerged as a promising alternative because it can be produced from a wide range of renewable sources, including biomass [1,2]. It is predicted that hydrogen production will increase with a growth of approximately 10% by 2050 and the balances in the hydrogen market will change [3]. Hydrogen energy is the cleanest among alternative energy sources and has "zero emissions" since it produces water as the only combustion product [4,5,6]. Among hydrogen production technologies, biohydrogen production is the most sustainable method as it occurs at ambient temperature and therefore requires only a low energy input. Among various biomass-to-hydrogen conversion technologies, dark fermentation has attracted great attention due to its high energy efficiency potential and ability to use a wide range of waste substrates [2]. The production and use of bioenergy with a sustainable management helps support energy security and price stability, while also providing social and economic benefits that support the achievement of the United Nations Sustainable Development Goals, including the promotion of rural economic activities.
An increasing number of airport operators around the world are realizing their responsibilities in protecting the environment and are changing their perspectives towards the natural environment. In this context, it is seen that environmental awareness is being established in the operators with the efficient use of resources, reduction of waste and recycling, and reductions in costs. In terms of environmental awareness, recycling/recovery of waste and management according to sustainable waste management principles are important. This study focuses on evaluating the efficiency of the dark fermentation process for hydrogen production using various wastes originating from airports. With this study, an alternative that will make a positive contribution to both the clean and circular economy and sustainability goals aimed at the "zero emission for 2053" target in the 12th Development Plan prepared in line with our country's 2053 vision and the "Net Zero CO_2 Emission" commitment declared by Istanbul Airport by 2050 will be obtained.

2. MATERIALS AND METHODS

2.1. Design and Commissioning of the Experimental Setup

In order to evaluate the efficiency in hydrogen production by the dark fermentation method, the experimental setup where the studies will be carried out was designed. The designed experimental setup consists of a reactor, gas pipe, isolation

valve and Tedlar bag. The schematic of the experimental setup and laboratory scale experimental setup given in Figure 1. Due to the nature of the anaerobic process, mixing must be provided. As seen in Figure 1, 500 ml (and later 1000 ml) volume reactors are positioned on a variable speed shaker. The shaker is a FOURE's Scientific Brand (Figure 2). The minimum and maximum shaking speeds are 30 and 500 rpm, respectively. The shaker speed will be fixed at 140 rpm and the experiments will be started. The experiments will be carried out in a Miprolab Brand MSI Model 250 lt capacity incubator (Figure 3). The incubator temperature can be adjusted between -10 and +80 ^{o}C. In the first stage, a constant temperature of 35 ^{O}C will be applied. The gas formed in the 500 ml volume PE reactors will be transmitted to the 2 lt volume tedlar bags (higher volume tedlar bags (gas collection bags) are planned to be used later) via PE 5 mm diameter pipes. 2 valves will be installed between the reactor and the tedlar bag. In case the tedlar bags need to be separated from the reactor for gas measurement or if the tedlar bag needs to be renewed while production is continuing, gas leakage will be prevented in this way. Gas measurements will be made in the ABB brand Continuous Gas Measurement Device located in the Istanbul University Cerrahpaşa Environmental Engineering Department Laboratory (Figure 4). CO, CH4, H2, O2, CO2 gases will be measured in this device. The measurement values detected by the gas analyzer will be transferred to the computer via a data transfer cable and will be recorded with the “Alp Teknik- BACA” software loaded onto the computer. The photograph of the experimental setup is given in Figure 5.

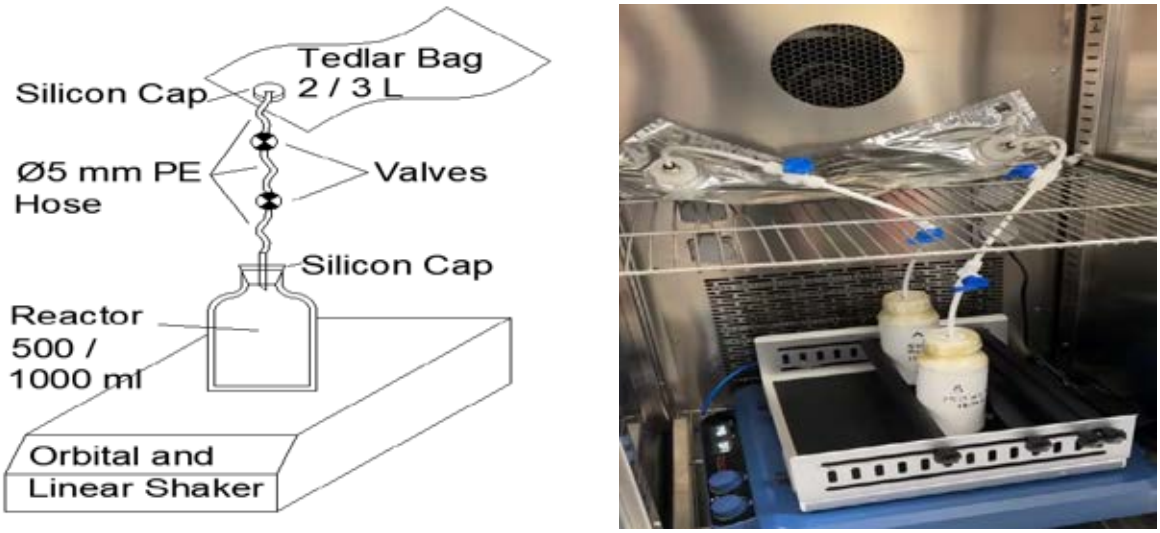

Figure 1. The schematic of the experimental setup and laboratory scale experimental setup

Figure 2. Orbital and linear shaker

Figure 3. Incubator

Figure 4. ABB AO2020 model gas analyzer

In the experimental set, the efficiency of hydrogen production through dark fermentation of various wastes generated as a result of airport activities will be determined.

2.2. Waste Characterization

Wastes originating from airports were separated into four different types: organic wastes originating from places such as cafeterias and restaurants, wastes resulting from de-icing and anti-icing applications, wastes originating directly from aircraft, and biological wastewater treatment plant return sludge. Visuals of the wastes used for analysis are provided in Figures 6, 7, 8, and 9.

Figure 6. Wastewater from Aircraft (WWA)

Figure 7. De/Anti Icing Wastewater (DAIW)

Figure 8. Food Waste (FW)

Figure 9. Recirculated Sludge (RCS)

It was determined that these various waste streams are rich in biodegradable organic matter and are potentially suitable raw materials for hydrogen production via dark fermentation process. Hach brand DR1900 model spectrometer device was used to evaluate the composition and properties of the waste streams generated from airports for hydrogen production via dark fermentation process. After waste characterization, hydrogen production studies were carried out by laboratory scale dark fermentation. In the studies carried out in batches, hydrogen production potentials of different wastes under different conditions were evaluated.

3. RESULTS AND DISCUSSION

The results of the analyses yielded the following average values for WWA: COD 11685 mg/lt, Ammonia 2604 mg/lt, TSS 1350 mg/lt, VSS 1200 mg/lt, Alkalinity 8281 mg/lt, pH 9.2, Conductivity 19994 μS/cm, Total Phosphorus 302 mg/lt. The results of the analyses yielded the following average values for the DAIW: COD 1039 mg/lt, Ammonia 1.1 mg/lt, TSS 42.8 mg/lt, VSS 36.8 mg/lt, Alkalinity 300 mg/lt, pH 7.2, Conductivity 520 μS/cm, Total Phosphorus 2.3 mg/lt. The results of the analyses yielded an average COD value of 463 mg/g for FW. As a result of these analyses, the average analytical results of RCS were calculated as COD 18960 mg/lt, Ammonia 123 mg/lt, TSS 12290 mg/lt, VSS 9123 mg/lt, Alkalinity 650 mg/lt, pH 6.9, Conductivity 1616 μS/cm, Total Phosphorus 336 mg/lt. In laboratory-scale dark fermentation hydrogen production studies, experiments were carried out with different conditions and wastes. As a result of the experiments, gas formation was observed and gas analysis was performed. As a result of the analysis, it was determined that approximately 1800-2000 ml of gas was formed in the studies and that 25% to 40% of the gas formed contained hydrogen.

4. CONCLUSIONS

The aim of study focuses on evaluating the efficiency of the dark fermentation process for hydrogen production using various wastes originating from airports. For this purpose, the potential of various wastes from the airport for hydrogen production by dark fermentation method was investigated. The results of the study are given below.

- Various wastes from airports have been found to be rich in organic matter and are potentially suitable raw materials for hydrogen production through the dark fermentation process.
- As a result of the analysis, it was determined that approximately 1800-2000 ml of gas was formed in the studies and that 25% to 40% of the gas formed contained hydrogen.
- As a result, a feasible model for our country is presented that is compatible with the zero waste and circular economy approach in terms of energy and raw material recovery from alternative sources, environmental technologies and renewable energy.
- It is possible to evaluate the outputs of this study for full-scale applications. It is essential to conduct studies on the pilot-scale system to facilitate full-scale applications.

Acknowledgments

This study was partially based on a Ph.D. thesis pursued by H.F. Altay.

REFERENCES

1. Dincer, I., & Zamfirescu, C. (2012). Sustainable hydrogen production options and the role of IAHE. International Journal of Hydrogen Energy, 37(21), 16266–16286. https://doi.org/10.1016/j.ijhydene.2012.02.133.
2. Lepage, T., Kammoun, M., Schmetz, Q., & Richel, A. (2020). Biomass-to-hydrogen: A review of main routes production, processes evaluation and techno-economical assessment. Biomass and Bioenergy, 144, 105920. https://doi.org/10.1016/j.biombioe.2020.105920.
3. Lepage T, Kammoun M, Schmetz Q, Richel A (2021) Biomass-to-hydrogen: a review of main routes production, processes evaluation and techno-economical assessment. Biomass Bioenerg 144:105920.
4. Li MH, Xu JP, Xie HP, Wang YH (2018) Transport biofuels technological paradigm based conversion approaches towards a bio electric energy framework. Energy Convers Manag 172:554–566.
5. Yiin CL, Yusup S, Quitain AT, Uemura Y, Sasaki M, Kida T (2018) Thermogravimetric analysis and kinetic modeling of low-transition-temperature mixtures pretreated oil palm empty fruit bunch for possible maximum yield of pyrolysis oil. Biores Technol 255:189–197.
6.Dursun, N., & Gülşen, H. (2019). Methods of biohydrogen production and usage of bioreactors for biohydrogen production. Journal of the Institute of Science and Technology, 9(1), 66-75.

RAPID AND SCALABLE SYNTHESIS OF 3D GAS DIFFUSION ELECTRODES FOR AEM WATER ELECTROLYSERS

[1*]*F. Lisi*, [2]*R. Viscardi*, [1]*I. Gualandi*, [1]*E. Scavetta*, [1]*F. Mariani*, [1]*A. Fasolini*, [1]*F. Basile*
[1] University of Bologna Alma Mater Studiorum, Industrial Chemistry Department "Toso Montanari", Navile District, Via Pietro Gobetti 85, Bologna, 40129, Italy
[2] ENEA, Department of Energy Technologies and Renewable Sources, Casaccia research center, Via Anguillarese 301, 00123 Rome, Italy

*fabrizio.lisi2@unibo.it

ABSTRACT

Anion Exchange Membrane (AEM) water electrolysis represents a cost-effective and sustainable alternative for hydrogen production, due to its ability to operate with non-precious metal catalysts. Leveraging a rapid and scalable electrodeposition procedure, the research addresses the industrial need for efficient and economically viable fabrication techniques. The study focuses on the synthesis and optimization of Ni-based layered double hydroxides (LDHs) as electrocatalysts for AEM electrolysers. The tailored electrocatalysts exhibit excellent overpotential and reaction kinetics, optimizing the energy efficiency of the process. Surface modifications and doping strategies are investigated to enhance the catalytic activity and durability under operating conditions. Metallic foams outperform carbon paper as gas diffusion layers (GDLs), achieving high current densities due to superior conductivity and capillary effects. This work provides a pathway for industrial-scale production of high-performance electrodes, advancing the development of AEM technology.

Keywords: hydrogen, water electrolysis, anion exchange membrane, layered double hydroxides.

1. INTRODUCTION

In the last decade, AEM water electrolysis has emerged as promising technology for sustainable hydrogen production, combining the advantages of traditional systems such as alkaline and proton exchange membrane (PEM) electrolysers. By operating under alkaline conditions, AEM electrolysers enable the use of non-precious metals as electrocatalysts, significantly reducing material costs. Critical bottleneck in the process is the Oxygen evolution reaction (OER), as a multistep, four-electron transfer reaction that requires significant overpotential. Developing efficient and cost-effective catalysts for OER is thus a key challenge for improving the performance and viability of AEM water electrolysers.

1.1. Layered double hydroxides as promising OER electrocatalysts

Layered double hydroxides (LDHs) are lamellar compounds consisting of positively charged metal hydroxide layers intercalated with charge-balancing anions and water molecules [1]. Also known as hydrotalcite-like compounds, LDHs are characterized by high surface area and tunable composition. By incorporating various metal cations into the hydroxide layers, LDHs offer excellent opportunities for tailoring their electronic and catalytic properties. When electroactive metals are inserted in the structure, these compounds are redox active systems that can be used as electrocatalysts. Regarding OER performance, LDHs containing Ni, Co, and Fe showed low onset potential values and fast kinetics, therefore a huge appeal for electrocatalytic applications (Fig. 1) [2].

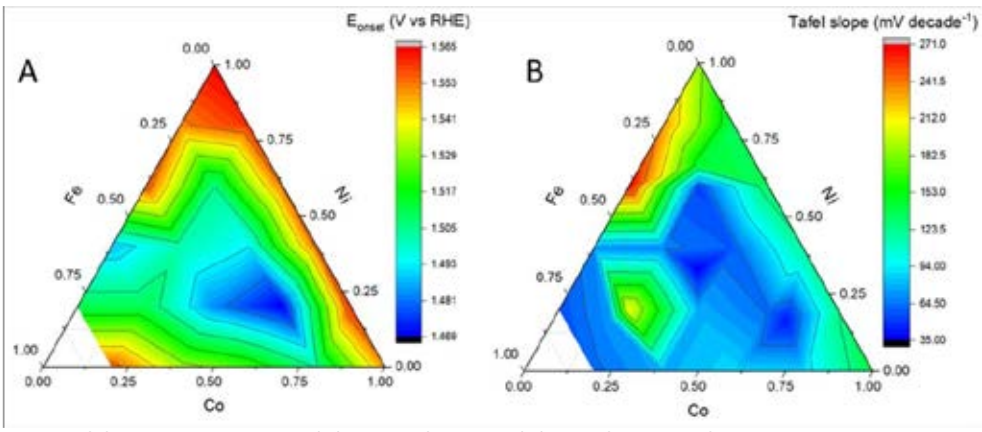

Fig. 1. Ternary diagram of OER onset potential (A) and Tafel slope (B) as a function of the electrosynthesis bath composition [2]. Data are obtained from LSV recorded in 1.0 M KOH.

2. MATERIALS AND METHODS

Electrodes fabrication occurred via potentiodynamic electrodeposition of LDHs on gas diffusion layers as carbon paper and Nickel foams [3]. Bare supports (geometric area: 6.25 cm²) were immersed in an electrolytic bath containing catalysts precursors in form of nitrates, and two cycles of cyclic voltammetry (CV) were performed at cathodic potentials between 0 and -1.3 V vs SCE. The induced electrochemical reduction of nitrates generates an increase of the local pH at the electrode surface, leading to catalyst precipitation as LDHs (Fig. 2). Nickel nitrate (>99%), cobalt nitrate (>98%), iron nitrate (>99%), and sodium hydroxide were purchased from Sigma–Aldrich (Germany). The deposition was carried out in a single compartment three-electrode cell (Amel, Italy), connected to a potentiostat Multi Autolab/M204 (Metrohm Italiana Srl, Italy).

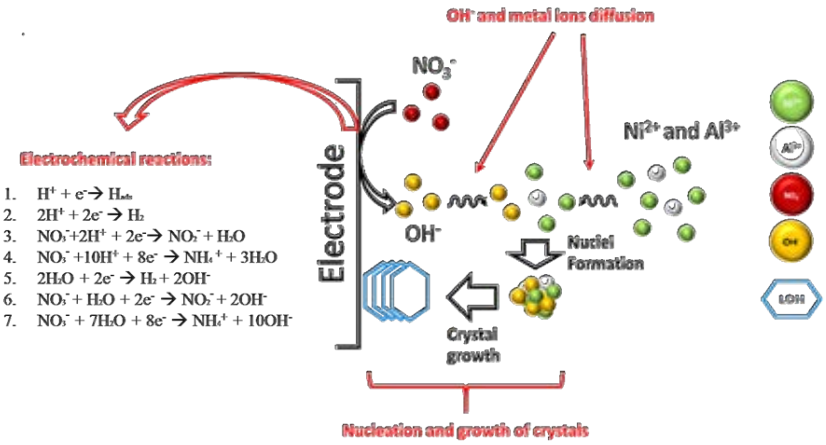

Fig. 2. Main steps involved in the potentiodynamic electrodeposition of LDH catalysts [3].

Characterization techniques such as X-ray diffraction (XRD), scanning electron microscopy (SEM), and electrochemical impedance spectroscopy (EIS) provided insights into the material properties and their correlation with electrochemical performance. The catalytic performance was evaluated in AEM flow cell operation (X-Cell, RedoxFlow), with key metrics including overpotential, current density, and long-term stability (Fig.3). Gas production was analysed with gas chromatography (Focus Series, Thermo Fisher Scientific) and high-performance liquid chromatography (1260 Infinity, Agilent Technologies) was used to quantify the liquid fraction. The presence of metals in the electrolyte solution was assessed via inductively coupled plasma mass spectroscopy (4210-MP-AES, Agilent Technologies).

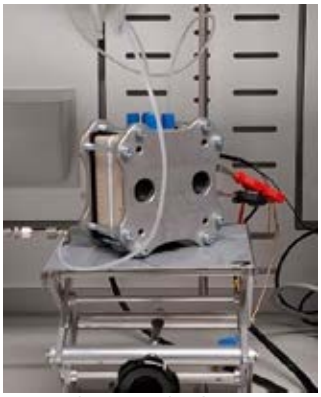

Fig. 3. AEM flow cell (X-Cell, RedoxFlow).

3. RESULTS AND DISCUSSION

3.1. Electrosynthesis of LDHs

The study provided an efficient and scalable solution for producing industrially viable electrodes for green hydrogen application. The physic-chemical characterization of the GDEs confirmed the accuracy of the synthetic method, providing stable and homogeneous catalyst deposition (Fig. 4). No catalyst leaching was observed after stress tests in both potentiostatic and potentiodynamic conditions. Catalyst composition was easily controlled by changing metals

concentration in the deposition solution, and a wide range of transition metals was successfully placed in the LDH structure to optimize the structural and electronic properties. A quantitative SEM-EDS analysis on carbon paper electrodes confirmed the metals ratio of the precursors' solution, indicating excellent tunability of the synthesis (Table 1).

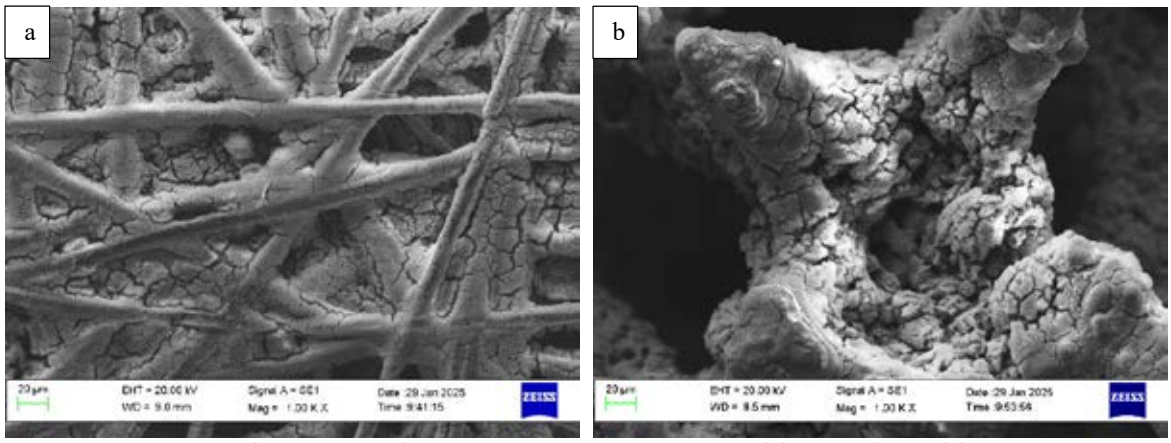

Fig. 4. SEM images of LDHs deposited on carbon paper (a) and Ni foams (b).

Table 1. Catalyst composition obtained via SEM-EDS analysis.

Catalyst	Ni atomic ratio (%Ni)
Ni75Fe25	75 ± 2
Ni75Al25	78 ± 3
Ni67Al33	68 ± 2

3.2. Optimization of electrodes performance

The tailored electrocatalysts achieved excellent performance in terms of overpotential and reaction kinetics, minimizing the energy consumption of the process. Ni foams GDEs achieved current densities up to ten times higher than carbon paper electrodes, due to higher conductivity and capillary effect of the support, which led to a higher electrochemically active surface area (ECSA). The catalyst Ni75Fe25 LDH exhibited high OER activity, with an onset potential of 0.335 V vs SCE and Tafel slope of 70 mV dec^{-1} (Fig. 5). Among the dopants, Co resulted in enhancing the electrocatalytic performance. The presence of Co in Ni/Fe LDH structure lowered the OER onset potential, due to synergistic effects between Co and Fe that increased the electrical conductivity of the material.

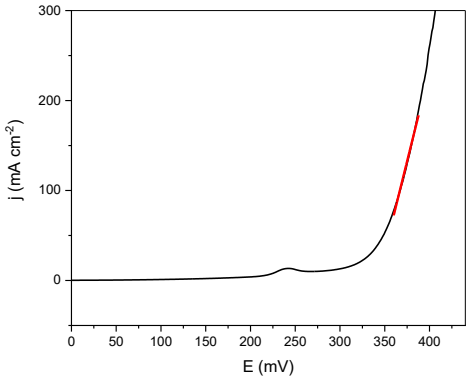

Fig. 5. Linear sweep voltammetry (LSV) of Ni75Fe25 LDH on Ni foam recorded in 1.0 M NaOH.

4. CONCLUSIONS

The research provided an industrially viable solution for producing GDEs for AEM water electrolysers. The synthetic protocol adopted allowed stable, homogeneous, and controlled deposition of Ni-based LDHs on both carbon paper electrodes and Ni foams. In particular, Co-doped Ni/Fe LDHs supported on Ni foams turned out to be the most performing OER catalysts, showing low cell overpotential, good reaction kinetics, and long-term stability.

ACKNOWLEDGEMENTS

F.L. would like to acknowledge the NextGeneration EU from the Italian Ministry of Environment and Energy Security POR H2 AdP MMES/ENEA with involvement of CNR and RSE, PNRR – Mission 2, Component 2, Investment 3.5 “Ricerca e sviluppo sull’idrogeno” under the ENEA – UNIBO agreement (Procedure 1.1.3 PNRR POR H_2).

REFERENCES

1. Gualandi I, Monti M, Scavetta E, Tonelli D, Prevot V, and Mousty C. 2015. Electrodeposition of Layered Double Hydroxides on platinum: Insights into the reactions sequence. Electrochimica Acta 152:75-83.
2. Gualandi I, Musella E, Costa G, Gazzano M, Scavetta E, Zappoli S, and Tonelli D. 2025. On the Quest for Oxygen Evolution Reaction Catalysts Based on Layered Double Hydroxides: An Electrochemical and Chemometric Combined Approach. Adv. Energy Sustainability Res. 6:2400233.
3. Gualandi I, Vlamidis Y, Mazzei L, Musella E, Giorgietti M, Christian M, Morandi V, Scavetta E, and Tonelli D. 2019. Ni/Al Layered Double Hydroxide and Carbon Nanomaterial Composites for Glucose Sensing. ACS Applied Nano Materials 2:143-155.

EXPERIMENTAL ANALYSIS OF REVERSIBLE SOLID OXIDE CELLS PERFORMANCE DEGRADATION FROM VARYING POWER RATIOS AND SWITCHING FREQUENCIES IN OPERATION

[1,2]*Navaid Ali*, [2*]*Gabriele Loreti*, [2]*Davide Pumiglia*, [2]*Yuri De Pra,* [2]*Livia Della Seta,* [2]*Viviana Cigolotti,* [2]*Giulia Monteleone,* [1]*Domenico Borello,*
[1] Department of Astronautical, Electrical and Energy Engineering, Sapienza University of Rome, 00184, Rome, Italy
[2]Department of Energy Technologies and Renewable Sources (TERIN), ENEA C.R. Casaccia, Rome/Italy

*Corresponding author e-mail: gabriele.loreti@enea.it

ABSTRACT
Reversible Solid Oxide Fuel Cells (R-SOFCs) are a promising green energy technology, efficiently operates in fuel cell and electrolysis modes. Dual functionality reduces operational complexity and system integration costs while enhancing affordability. However, degradation issues may hinder the lifetime and durability of such systems. This makes an in-depth scientific evaluation of their complex performance crucial for future advancements. In literature, there is limited work that methodically investigates main degradation parameters: operating in Solid Oxide Electrolysis Cell mode SOEC/duration in Solid Oxide Fuell Cell mode SOFC; daily switches; power in SOEC/power in SOFC. This study evaluates the performance of two cells (each 10 cm²) of Ni-YSZ|YSZ|LSM, effective area of 9x9 cm² (81 cm²) operated periodically at 750 °C in reversing mode at 0.3 A/cm². The first cell operates for 15 h in SOFC (2 h measurements), while cell 2 operates 15 h in SOEC and 7 h in SOFC. We investigate optimal switching frequency and power levels that could help predict failure modes and improve operational strategies to minimize degradation. The cell behavior was analyzed using electrochemical impedance spectroscopy (EIS) and IV curve measurements under load to determine polarization resistance. Result shows how operating conditions significantly impact cell performance, power ratios, efficiency, stability, and performance.

Keywords: Reversible solid oxide fuel cells, degradation, durability, EIS, performance

1. INTRODUCTION

Fuel cell technology is a clean and effective way to produce energy, by electrochemical means using hydrogen and oxygen, byproducts producing only water and electricity. It reduces fossil fuel reliance, helps to combat climate change, [1] and advances towards reducing greenhouse gas emissions. Fuel cells operate using an electrochemical system within a conductive electrolyte that directly converts the chemical energy of fuels into electricity without intermediate conversions [2]. Fuel cells are essential for the global shift toward green energy and reducing carbon emissions as the world moves toward renewable energy. Solid Oxide Cells (SOC) are the most efficient electrochemical technology for power generation. SOCs can operate in dual mode - fuel cell mode and electrolysis mode, which enables high utilization of fuels and promising energy management. SOCs are the prominent electrochemical energy conversion and storage devices that are used at a high-temperature range (600 – 1000 °C). When a Solid Oxide cell is operated in Electrolysis Mode (SOEC), then electrical energy is converted into a chemical form of hydrogen (H_2) and syngas (CO + H_2) with high-temperature steam and CO_2 co-electrolysis. Produced H_2 and syngas could be reused and stored for further processing. Whereas the SOFC mode is used to regenerate electricity by the use of stored fuels. This technology is reversible and can work in a switching operational mode, known as reversible solid oxide cells (R-SOC). SOC typically requires two separate devices for both modes, however, RSOCs eliminate these distinct two units by a single cell combining within a facilitating SOFC and SOEC functions.
R-SOCs is an advanced technology that can operate in dual modes, making promising applications in a versatile energy storage solution [4]. Reversible operations give stability to cells and decrease electrode degradation alternating between SOFC and SOEC modes [5]. This helps to reduce the time spent under high-stress conditions, redistribute thermal and electrochemical stresses across both electrodes, preventing localized degradation and enhancing material longevity.
This versatility enhances renewable energy integration and storage, stabilizing cells and reducing electrode degradation. However, degradation due to sintering and poisoning still remains a significant challenge, impacting performance, lifespan, and cost of a cell. [6].
Reversible solid oxide fuel cells (RSOFCs) are classified based on electrolyte material, cell geometry, mechanical support, operating temperature, and fuel flexibility [7]. Electrolyte materials include phosphoric acid, yttria-stabilized zirconia, and gadolinium-doped ceria. The cell designs include planar and tubular, while support types encompass electrolyte, cathode, anode, and substrate-supported cells. RSOFCs operate at low (400-600°C), intermediate (600-800°C), and high temperatures (800-1000°C) and can utilize various fuels. Current-Voltage (I–V) curves are obtained using a potentiostat/galvanostatic system. Electrochemical impedance spectroscopy is used to determine irreversible degradation, measuring the internal resistance, and allowing the estimation of potential degradation through polarization resistance analysis across operating cycles. EIS distinguishes ohmic, activation, and concentration losses that assess cell's performance[8]. At the end of each operational cycle, EIS is performed across SOFC and SOEC. The I-V curve

shows cell's voltage output at specific current densities, collected using a potentiostat. Accurate measurements are required for steady-state conditions [9], with one curve recorded each day for fuel cell and electrolysis operations in each test. From the analyzed literature that gap is left, and we try to fill it.

2. Experimental Procedures

2.1 Materials and methods

This was performed using a test bench developed by the Korean Institute of Science and Technology (KIST). The setup includes flow meters, a gas-tight furnace, and humidification for anodic gases. CHINO Corporation supplied the SOC cell housing, featuring ceramic compartments, type K thermocouples, and current collectors made of nickel and silver, respectively, along with sensors and high-temperature seals. The experiment on two SolydEra's Ni-YSZ|YSZ|LSM anode-supported cells, with dimensions of (10x10 cm² sides, 81 cm² active area), operated at 750 °C are performed.
The electronic load utilizes a reversible power supply, ITECH IT-M3902C-32-80. The Zahner ZENIUM X potentiostat conducts EIS by linking its terminals to the fuel and air electrodes of the test cell. EIS occurs twice daily for two experimental campaigns, with measurements taken after SOFC (15 hours) and SOEC (7 hours) operations at specified intervals, ensuring a thorough analysis of each operational cycle. The ceramic housing can tolerate current increases of 0.3 A/min. The anode uses a 50% H2 and 50% steam mix, while air flows at 2000 ml/min for 80% utilization.

2.2 Chemical characterization

For the first and second experimental campaigns, cell degradation and performance were characterized through in-situ electrochemical testing using I-V polarization curves during operation. During data acquisition for the polarization curves, the current increased allowing at a rate of 0.27 A/min from zero to -0.3 A/cm². Then, the current dropped to zero. The ramp-up phase of the current was considered for the analysis of polarization curves in both fuel cell and electrolysis modes. Data acquisition occurred at 1 Hz, generating 5401 points for the fuel cell polarization curve. In electrolysis mode, the current ramped down from zero to -0.3 A/cm².
Two experimental campaigns, the first cell lasting in 10 days, produced 10 (I-V) polarization curves for SOFC and SOEC modes while second cell data operated for 7 days. EIS was conducted in galvanostatic mode, maintaining a constant current while measuring voltage across frequencies from 10 mHz to 100 kHz. After configuring parameters for the Nyquist diagram, a stepped current input was applied, distinguishing between measurements after fuel cell and electrolysis operations. The amplitude was set to 1, and the measured periods were set to 1. After setting parameters, input a stepped current. Distinguish between EIS after fuel cell and electrolysis mode cycles.

- In the first case, the system is supplied with a positive stepped current input, where each step is 0.1 A, starting at 0 and increasing to a maximum of 1 A.
- In the second case, the system is supplied with a negative stepped current input, starting at 0 and decreasing to -1 A, with each step equal to -0.1 A.

Table 1 summarizes the parameters used in the two experimental campaigns:

Table 1. Description of the experimental campaign

Test No.	Current density SOFC [A/cm2]	Current density SOEC [A/cm2]	SOFC time [h]	SOEC time [h]	Intraday cycles	Duration per cycle [h]	Cycles	Campaign duration [h]	Campaign duration [days]
1	0.3	0.3	15	7	1	24	10	240	10
2	0.3	0.3	7	15	1	24	10	240	10

3. RESULTS AND DISCUSSION

First test cell operates approximately twice as long in SOFC, whereas in the second campaign, the opposite is true. I-V polarization curves and EIS, graphing voltage over time to reveal detailed trends for both cells. Fig. 1 I-V curves for both fuel cell mode and electrolysis mode operation. Polarization curves reveal cell degradation through contrasting voltage trends over time indicating that the cell is undergoing degradation. To quantitatively assess degradation, calculate the percentage difference in maximum voltage during electrolysis at the first cycle, midpoint (fifth cycle), and final work cycles, also applying this to minimum voltage in fuel cell operation.

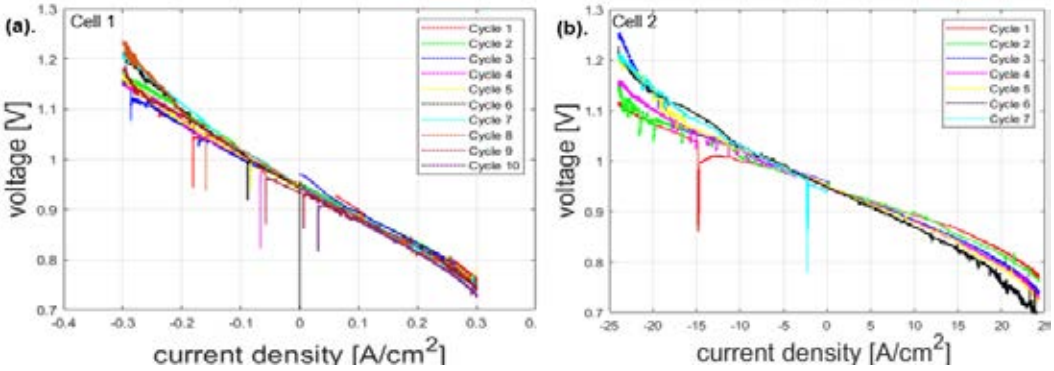

Fig. 1. I-V polarization curves (a) Cell 1 (b) Cell 2

Table 2 shows the percentage difference in voltage for both operating modes across the different work cycles.

Table 2. Percentage variation in cell voltage as the cycles increase (Cell 1 & Cell 2)

	Cell 1		**Cell 2**	
	%cycle1-cycle5	**%cycle1-cycle9**	**%cycle1-cycle4**	**%cycle1-cycle7**
V_{min}FC	-1,2%	-4,9%	-5,4%	-10,7%
V_{max}EL	0,8%	7,7%	4,1%	9,8%

The table indicates significant voltage variation for SOFC and SOEC with increased operating hours, with cell 1 & Cell 2 showing greater variation compared to cell 1 during the second campaign. Fig. 2 displays the trend of the imaginary part of the impedance as a function of the real part for the work cycles for Cell 1 & Cell 2 underwent during the campaign.

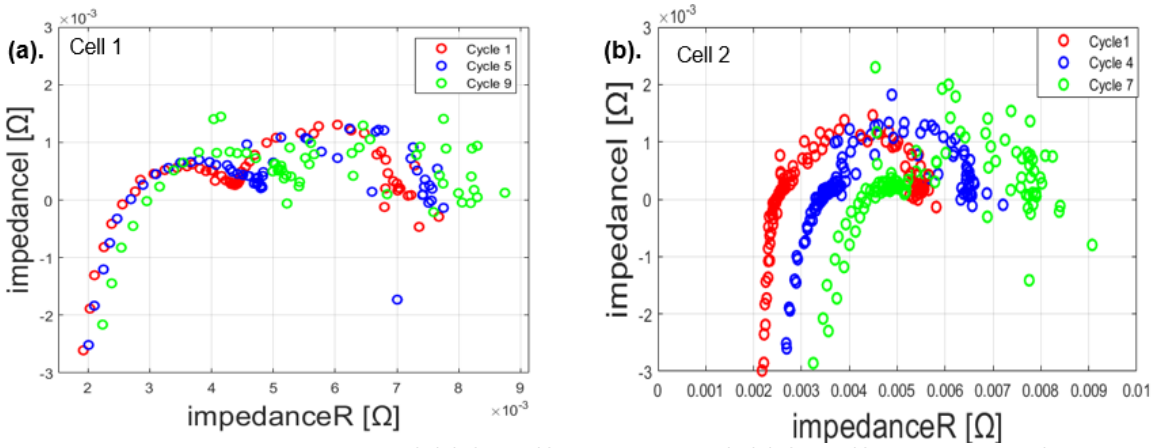

Fig. 2. Impedance spectra EIS (a) Cell 1 (Cycles 1, 5, and 9), (b) Cell 2 (Cycles 1, 4, and 7)

To improve data interpretation, the impedance spectrum is analyzed for Cell 1 (Cycles 1, 5, and 9), and Cell 2 (Cycles 1, 4, and 7), facilitating comprehension and studying impedance trends throughout the campaign. Removing data points enhances graph interpretation; impedance spectra shift with more cycles, indicating increased internal resistance and semicircle diameter growth.

Comparing the EIS graphs of cells 1 and 2 reveals that cell 2 exhibits a more uniform trend. As operating cycles and working hours increase, cell 2's internal resistance steadily rises, evident in its clear graph. In contrast, cell 1 shows fluctuations in resistance, especially in early cycles, leading to a less coherent EIS graph, where increased cycles do not consistently correlate with resistance increase. Both cells undergo electrochemical impedance spectroscopy for performance evaluation.

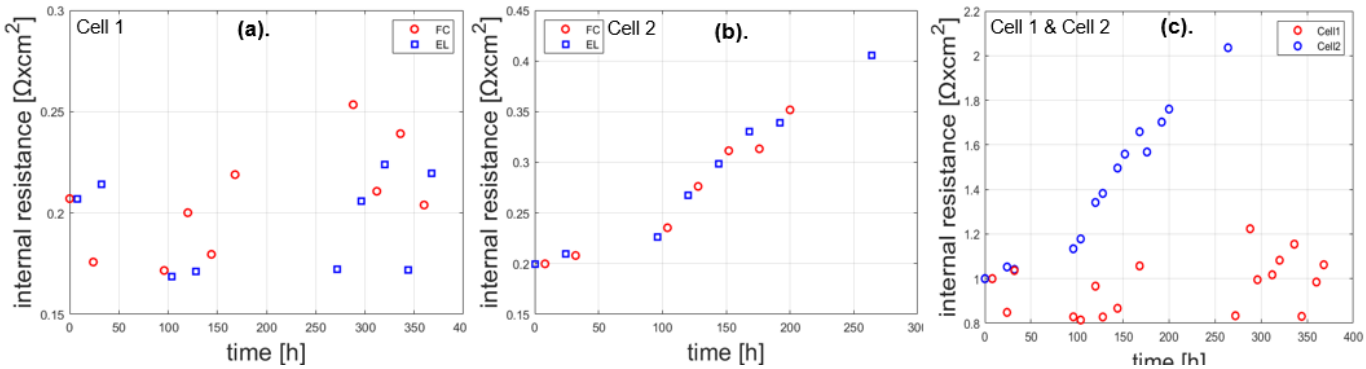

Fig. 4. (a) Internal resistance of Cell1 (b) Internal resistance of Cell 2 (c). Internal resistance of Cell1& Cell 2

In Fig. 4 (a), the value of internal resistance is calculated using the Nyquist plot. In the impedance curve at low frequency region, the real part of the impedance is defined by internal resistance of the cell. Cell 1 shows a rise during electrolysis while recovery in fuel cell mode, and potential degradation with increased operational hours over time. (b) In Cell 2 the resistance graph indicates degradation with increased resistance during electrolysis, while the SOFC exhibits variable lower resistance, that's confirming greater degradation in SOEC compared to SOFC mode. (c) This graph summarizes the earlier observations regarding the resistance fluctuations for Cell 1 throughout the campaign, with final values slightly above initial measurements. In contrast, Cell 2 shows consistent growth, culminating in significantly higher resistance. The distinct outcomes stem from different operating times, underscoring the literature's emphasis on usage duration as crucial for SOC performance. As mentioned for Cell 1, the goal is to quantify the increase in internal resistance during the second experimental campaign. To achieve this, the table presents the percentage differences between the initial resistance value and two resistance values at the end of two intermediate cycles (cycle 4 and cycle 6) and finally, between the initial value and the value of one of the final cycles (cycle 8).

Table 3. Percentage variation of internal resistance values for Cell 1 & Cell 2

Cell 1	**IR Min value[Ω/cm^2]**	**IR max value[Ω/cm^2]**	**IR Final value[Ω/cm^2]**
IR First Value [Ω/cm^2]	-18.4 %	23.3 %	5.9 %
Cell 2	**IR Cycle 4[Ω/cm^2]**	**IR Cycle 6[Ω/cm^2]**	**IR Cycle [Ω/cm^2]**
IR Cycle 1 Value [Ω/cm^2]	34.1 %	22.3 %	103.6 %

This table clearly summarizes what was mentioned earlier; it is evident how, for cell 1, the resistance values fluctuate throughout the entire campaign, with both increases and decreases in values compared to the corresponding value measured in the previous cycle. Moreover, the final cycle value is only slightly higher than the initial cycle value. For cell 2, the trend between cycles shows continuous growth, reaching the final cycle with a resistance value significantly higher than the value at cycle 1.

4. CONCLUSIONS

R-SOC is a very useful technology in the future, but it still needs technological advancement in terms of stability, modularity, and durability. These findings allowed for evaluating voltage values during SOFC and SOEC operations to ascertain which cell exhibited greater degradation. These plots reveal cell degradation over time, showing recovery or at least experiencing a lower amount of degradation after fuel cell mode compared to electrolysis. It can therefore be observed that prolonged use of the SOC in electrolysis mode, as in the second campaign, leads to significantly greater degradation of the cell compared to prolonged use in SOFC, as with cell 1. In particular, it must be stated that more extensive use of SOEC not only leads to greater degradation but can even result in irreversible cell degradation. It needs systematic study towards analysing various degradation parameters improving the reliability and lifetime of RSOCs.

ACKNOWLEDGEMENT

This research was funded by the European Union - NextGenerationEU from the Italian Ministry of Environment and Energy Security, POR H2 AdP MEES/ENEA with involvement of CNR and RSE, PNRR - Mission 2, Component 2, Investment 3.5 "Ricerca e sviluppo sull'idrogeno", CUP: I83C22001170006.

REFERENCES

1. W. E. M. (2020). The Energy Transition: A Handbook - Discusses the environmental damage caused by fossil fuel use and the need for cleaner technologies like fuel cells.
2. Al-Zaidi, Muthana & Qussay, Rand & Al-Zubaidi, Dhuha & Mahmood, Mohanad. (2021). A Review: Fuel Cell Types and their Applications. 7. 375-390.
3. Anjaneyulu, K. S. R., & Bhaskar, T. M. G. (2020). Fuel Cells: From Fundamentals to Applications. Wiley.
4. Mench, M. M., & Wang, Y. (2015). Reversible Solid Oxide Cells: Energy Conversion and Storage. Elsevier.
5. Gauthier, M., & Baud, C. (2020). Degradation and Durability of Solid Oxide Fuel Cells. Springer.
6. Wang, W., & Zhou, X. (2017). Electrode Materials for Fuel Cells: Fundamentals, Degradation Mechanisms, and Solutions. Wiley.
7. Vlachos, D. G., & Mavrikakis, M. (2018). Electrochemical Impedance Spectroscopy: Fundamentals and Applications. Springer.
8. Giner, J., & Zhou, H. (2018). Electrochemical Characterization of Fuel Cells. Springer.
9. Koutroulakis, G., et al. (2020). "Degradation of Solid Oxide Fuel Cells: Monitoring Techniques and Performance Analysis." Journal of Power Sources, 448, 227-242.

CATALYTIC POTENTIAL OF g-C_3N_4 IN $NaBH_4$ HYDROLYSIS: A SCIENTOMETRIC STUDY ON HYDROGEN PRODUCTION

[1*]*Bedirhan YILMAZ*, [2]*Burak Can ÇELİK*, [2]*Hüseyin ELÇİÇEK*, [1]*Asım Sinan KARAKURT*
[1] Naval Architecture and Marine Engineering Department, Yildiz Technical University, Istanbul, Türkiye
[2] Yildiz Technical University, Marine Engineering, Istanbul, Türkiye

*Corresponding author e-mail: bedirhan.yilmaz@yildiz.edu.tr

ABSTRACT

The efficient storage and utilization of hydrogen energy are crucial for the advancement of clean energy technologies. Sodium borohydride ($NaBH_4$), a promising hydrogen carrier, has gained attention for its potential in hydrogen generation through hydrolysis. This study provides a comprehensive overview of the research landscape concerning g-C_3N_4-based catalysts for hydrogen production, focusing on trends and developments from 2009 to December 2024. Through the systematic evaluation of publication volumes, thematic shifts, and the evolution of key keywords, the study offers valuable insights into the field's emerging priorities. Additionally, the analysis identifies leading countries and institutions driving global research efforts, highlighting significant contributions to g-C_3N_4 catalyst development. The study also uncovers a notable research gap related to the application of $NaBH_4$ in hydrogen production, with only 47 publications published on this topic up to December 2024. This finding emphasises the necessity for additional exploration and research in this field to bridge the existing gap and optimise hydrogen production technologies.

Keywords: g-C3N4 Catalyst, NaBH4 Hydrolysis, Hydrogen, Bibliometric Analysis

1. INTRODUCTION

In today's world, the energy crisis has become a significant global problem caused by various factors such as rapid population growth, rising living standards, depletion of limited energy and water resources, and the emission of greenhouse gases [1]. This crisis has led to an increasing interest in clean, affordable, and sustainable alternative energy sources. The limited reserves of fossil fuels and their adverse environmental impacts indicate the necessity for the development and widespread adoption of sustainable alternative energy sources. In this context, the urgent global imperative is for the development and deployment of new energy sources that are abundant, environmentally compatible, and efficient. Hydrogen energy is recognized as one of the most promising alternatives due to its high calorific value, non-polluting combustion products, and renewability [2]. In recent years, various high-capacity hydrogen storage materials, such as sodium borohydride ($NaBH_4$), lithium borohydride ($LiBH_4$), and ammonium borane (NH_3BH_3), have attracted the attention of researchers. Among these, $NaBH_4$ stands out for its safe structure and high hydrogen storage capacity. It can store hydrogen at a weight percentage of 10.8% and efficiently releases large amounts of pure hydrogen through hydrolysis in an alkaline solution [3]. To enhance the hydrolysis process, researchers have focused on developing efficient and durable catalysts using both noble metals (e.g., Ru, Pt, Pd,) and non-noble metals (e.g., Co, Ni). Although noble metals have superior performance, their high cost and limited availability limit their widespread industrial use. In contrast, non-noble metal catalysts attract attention due to their low cost and abundance. The limitations of noble metals have encouraged the search for alternative options, leading to the widespread use of non-noble metals in catalysts [4]. While single-component non-noble metals often lack sufficient performance and durability, doping them with other elements to form binary, ternary, or multicomponent alloys (e.g., Co-B, Ni-B, Co-Ni-B) significantly enhances their effectiveness and stability. However, these catalysts face challenges, such as deactivation due to polyborate formation during the hydrolysis reaction [5]. Addressing this issue requires the use of suitable catalyst supports that facilitate polyborate desorption, prevent metal agglomeration, and increase surface area. To optimize metal catalysts further, reducing metals to nanoparticle sizes maximizes the surface-to-volume ratio. However, the high surface energy associated with nanoparticles often leads to aggregation, which reduces catalytic activity. Support materials, such as oxides, carbon-based materials, mesoporous materials, zeolites, and nickel foam, help prevent aggregation, enhance surface area, and improve catalytic activity by optimizing the distribution of active sites and reaction kinetics. Recently, among the support materials, multilayer graphite carbon nitride (g-C_3N_4) has become an important research topic in applications such as catalysts and energy storage due to its unique electronic structure, superior chemical properties and high thermal stability [6]. g-C3N4 acts as an electron transporter for metal ions due to the free electron pairs on the nitrogen atoms in its structure. It has become a popular catalyst in recent years because it is inexpensive to produce and can be easily synthesized in a single step using affordable materials like cyanamide, urea, thiourea, and melamine [7]. The present study systematically conducts a bibliometric analysis with a view to highlighting the significance of g-C_3N_4 as a support material in enhancing the activity of catalysts for hydrogen production via $NaBH_4$ hydrolysis. Furthermore, the study provides a comprehensive overview of the current state of research in the hydrogen production, offering valuable insights derived from statistical data and analyses. In addition to providing a thorough review of existing trends in research, it also identifies potential future directions for research and development.

2. MATERIALS AND METHODS

Bibliometrics, first defined by Pritchard in 1969 as “the application of mathematical and statistical approaches to books and other forms of communication,” has since become a cornerstone of research evaluation [8]. Bibliometric analysis is a highly effective tool that can be used to identify critical insights from a highly extensive body of literature. It enables researchers to explore the evolution, emerging trends, research boundaries, and current topics of interest within a chosen field. Moreover, it allows the examination of many relationships such as articles, citations, productivity of authors and emerging trends in keywords. These assessments often allow the identification of research gaps in the field through the visualization of network structure analysis [9]. This method has been widely applied across various disciplines, demonstrating its effectiveness in systematically mapping scientific knowledge and providing a data-driven foundation for strategic research planning [10–13].

2.2. Data Collection and Analysis

This study aims to systematically analyze the articles on renewable energy and hydrogen production in the Scopus database until December 2024. Scopus is the most comprehensive abstract and citation database in the peer-reviewed literature for information retrieval processes and approximately 3 million new articles are published each year [14]. The methodology employed in this study plays a crucial role in systematically identifying and analyzing relevant literature on hydrogen production using g-C_3N_4-based catalysts. The use of the TITLE-ABS-KEY search strategy, with carefully selected keywords such as "hydrogen evolution," "hydrogen generation," and "hydrogen production," AND “g-c3n4”, “g c3n4” and “graphitic carbon nitride”, ensures that only the most relevant and high-impact studies are included. After the title-based search, the document type was limited as “article” and the search results were filtered on the condition that the language of the article was English. The data extracted from the Scopus database in CSV format were meticulously analyzed using the Biblioshiny package in R software [15], a recognized tool in bibliometric research. This approach, covering documents from 2009 to December 2024, enables a systematic exploration of citation patterns, trends, and key scholarly contributions within the field.

3. RESULTS AND DISCUSSION

According to data from the Scopus database for the period 2009- December 2024, the productivity and collaboration dynamics of academic publications were analyzed. In this period, with a remarkable average annual growth rate of 45.63%, a total of 3,696 articles were sourced from 332 different publications. On average, each article received 62.09 citations, reflecting the significant impact of this body of work. Moreover, a total of 150,376 references were cited across these articles, demonstrating the extensive literature coverage within the field. In terms of author collaborations, 6081 authors contributed during this period and only 9 authors produced single-authored articles. An average of 6.5 co-authors collaborated per document and the international co-authorship rate in this period was 23.38%. The analysis of the distribution of publications shown in Fig. 1a shows that China leads in scientific output with a significantly higher number of published articles compared to other countries. This data demonstrates the significant impact of Chinese research on the global scientific environment. Especially Asian countries have an important place in this ranking. Countries such as China, India and South Korea stand out in terms of the number of scientific research and publications, while European countries and the USA are ranked further behind. Fig. 1b clearly shows that Asian institutions, especially universities in China, have made the largest contribution in this field. Jiangsu University stands out as the largest contributor with 833 publications. It is followed by Xi'an Jiaotong University, University of Science and Technology of China and Zhengzhou University.

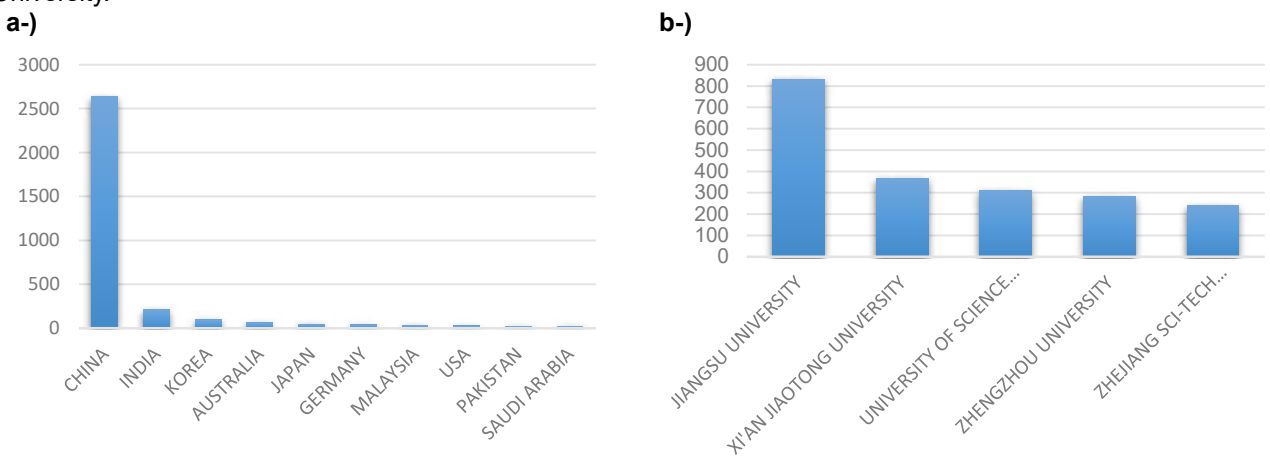

Fig. 1. (a) Distribution of Publications by Country. (b) Academic Publication Performance by University

Fig. 2a visualizes the interactions between authors, keywords and sources in scientific research areas. The diagram provides a data-guided overview of the relationships between authors, keywords and journals. This visual representation allows us to analyze research trends, identify developing areas and understand the larger context of scientific publications. Zhang Y, Wang Y, Wang X, Li Y, Liu Y, are the most frequently cited authors in the diagram. These authors have generally worked on key topics in the field of renewable energy, photocatalysis, hydrogen production and water separation. These keywords reveal that sustainable energy technologies are at the center of the studies and important scientific contributions have been made, especially for hydrogen production. The majority of the articles published by these authors appear in prestigious scientific journals. The main journals featured in the diagram include International Journal of Hydrogen Energy, Applied Catalysis B: Environmental, Journal of Colloid and Interface Science, Chemical Engineering Journal and ACS Applied Materials and Interfaces. These journals present important work on interdisciplinary and application-oriented topics such as hydrogen energy and photocatalysis. The variation of keywords preferred by authors reveals the main scientific focus in this research area and offers a view of the potential for future research. The network analysis, as shown in Fig. 2b, presented visually represents key words and the relationships between them in scientific research areas such as hydrogen production and photocatalytic activity. The different colored groups in the diagram show the connections around specific research topics. The red group concentrates on critical research areas like hydrogen production and photocatalytic activity, particularly in the areas of light absorption and photocatalytic hydrogen evolution. These topics are central to the development of hydrogen production. The green group is investigating the use of carbon nitrides in light-based reactions and highlighting their potential for photocatalytic processes. This research highlights the importance of carbon-based materials in hydrogen production. Lastly, the blue group covers more specific topics such as photocatalysis and electron microscopy, which are crucial in the development of hydrogen production. Overall, these groups represent key areas of research in the field of hydrogen production solutions.

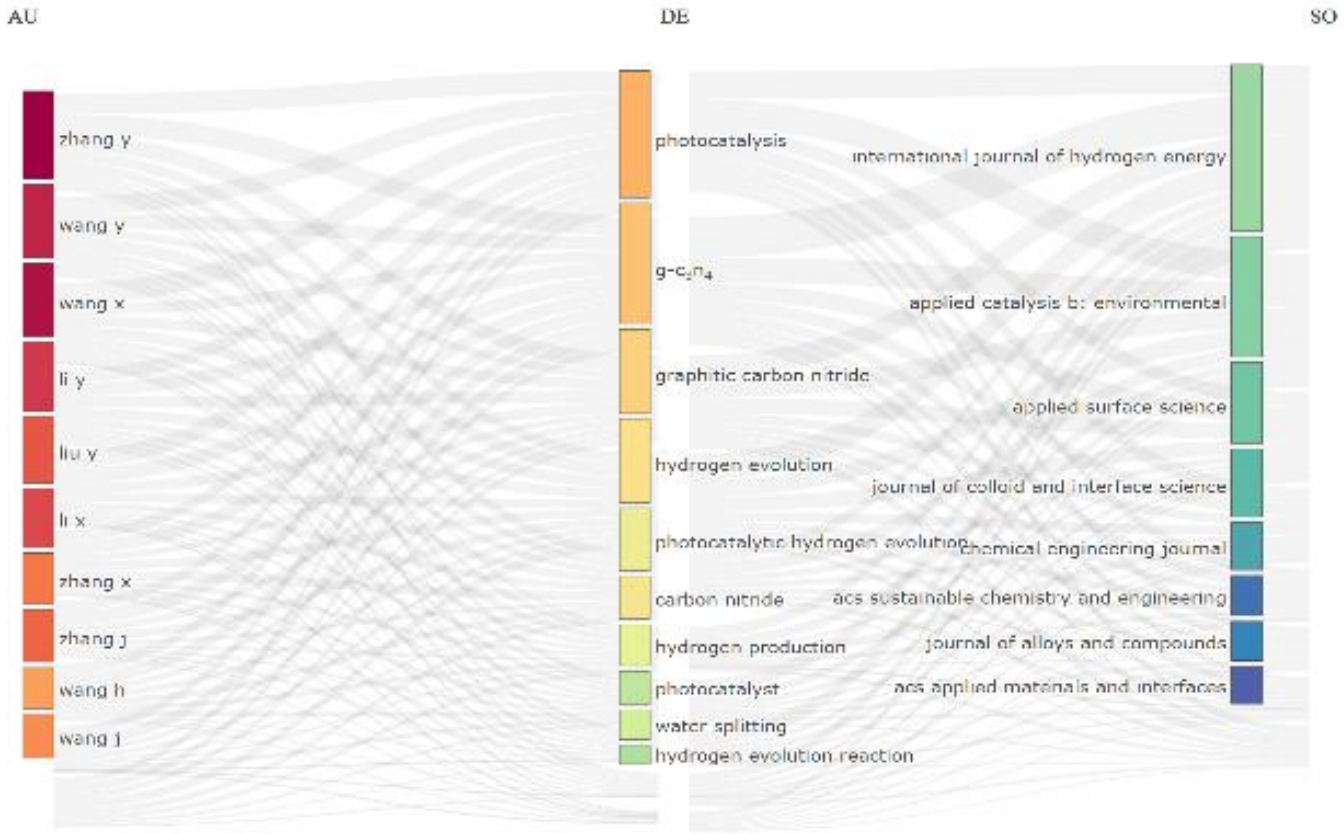

(a)

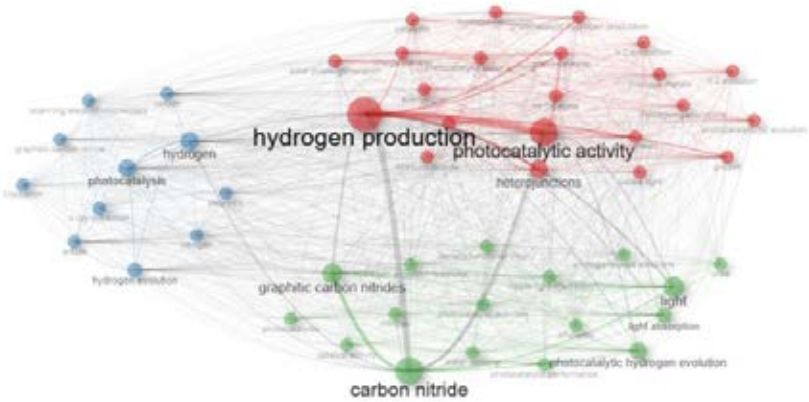

Fig. 2. (a) Sankey diagram and (b) Network Analysis

The thematic analysis presented in the graph is divided into four main categories based on the degree of development (intensity) and centrality (importance) of keywords in scientific research areas such as hydrogen production and photocatalysis. In this graph, the area in the upper right part of the graph means that it is both at the center of the relevant issue and will play an active role in future studies. In the lower right corner, it is again at the center of the related issue, but the expressions here have completed their development and no further innovations can be made in these areas. In the upper left corner are meanings that are not at the center of the related topic but are likely to be developed in future studies. The expressions in the lower left corner indicate either that they have completed their development in that field and will not be at the center of the subject in future studies, or that the relevant subject is developing but has not yet been included in the studies in large numbers. Thematic diagrams are used to help identify areas that have been studied in the past and are potentially to be studied in the future.

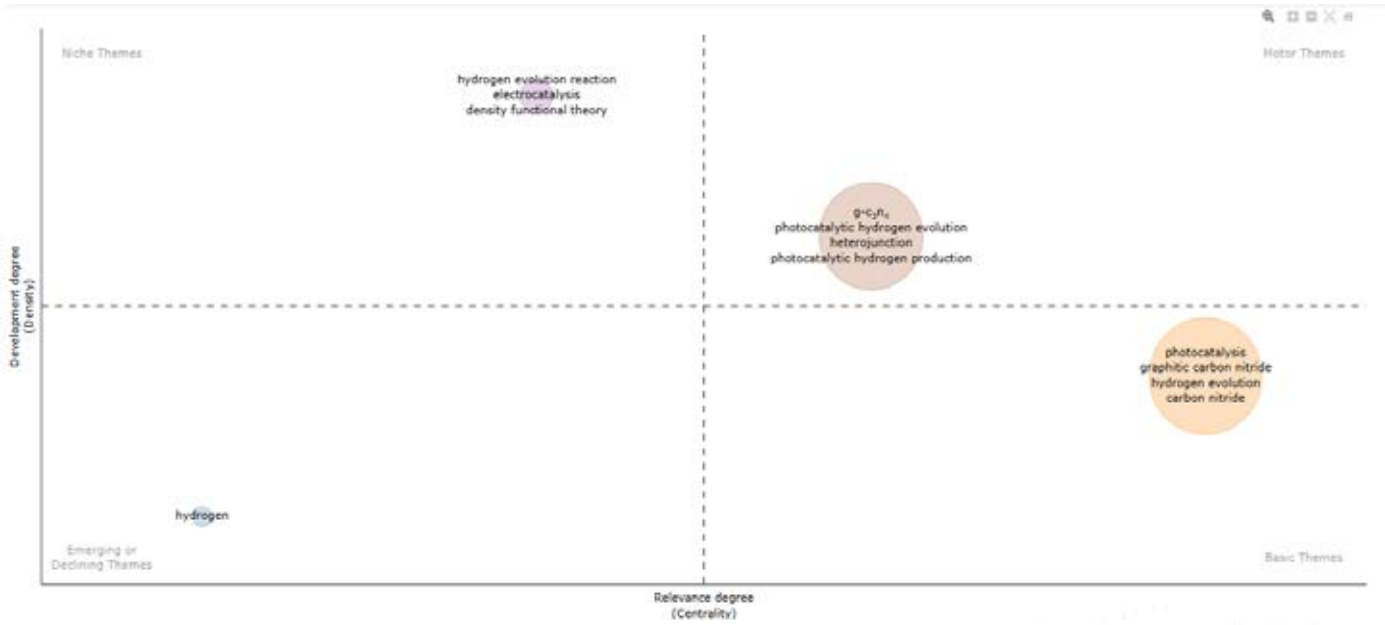

Fig. 3. Thematic Analysis

4. CONCLUSIONS

This bibliometric analysis provides a comprehensive overview of the current research landscape use of g-C_3N_4 based catalysts in hydrogen production, highlighting key trends and developments from 2009 to December 2024. By systematically analyzing publication volumes, thematic shifts, and the evolution of top keywords, this study offers valuable insights into the emerging focal points within the field. Furthermore, it identifies leading countries and prominent institutions that are shaping the direction of research, underscoring the global efforts in advancing g-C_3N_4 based catalysts developments. The study reveals a notable gap in research concerning the application of $NaBH_4$ in hydrogen production, with only 47 publications to date, emphasizing the need for further investigation in this critical area. This insight underscores the importance of expanding research efforts to bridge this gap, ultimately contributing to the continued

progress and optimization of hydrogen production technologies.

REFERENCES

1. Zhou B, Gao R, Zou J-J, et al. (2022) Surface Design Strategy of Catalysts for Water Electrolysis. *Small* 18: 2202336.
2. Habib MA, Abdulrahman GAQ, Alquaity ABS, et al. (2024) Hydrogen combustion, production, and applications: A review. *Alexandria Engineering Journal* 100: 182–207.
3. Pham SH, Phan TS, Nguyen HN, et al. (2024) Hydrogen generation from an alkaline solution of NaBH4 using a NiB catalyst supported on hydroxyapatite. *Journal of Energy Storage* 96: 112545.
4. Kaya C, Özdemir JH, Elçiçek H, et al. (2024) Enhancing the efficiency of sodium borohydride hydrolysis with a novel CoB-Triton catalyst. *International Journal of Hydrogen Energy* 51: 489–503.
5. Elçiçek H (2023) Determination of critical catalyst preparation factors (cCPF) influencing hydrogen evolution. *International Journal of Hydrogen Energy* 48: 3824–3837.
6. He Q, Wang L, Xiao F, et al. (2024) Cauliflower-like Co–B–P ternary catalyst loaded on graphitic carbon nitride nanosheets with synergistically enhanced electrocatalytic activity for hydrogen evolution reaction. *International Journal of Hydrogen Energy* 58: 149–157.
7. Zhang B, Li J, Song Q, et al. (2022) g-C3N4-modulated bifunctional SnO2@g-C3N4@SnS2 hollow nanospheres for efficient electrochemical overall water splitting. *Applied Surface Science* 589: 153016.
8. Pritchard A (1969) Statistical bibliography or bibliometrics. *Journal of documentation* 25: 348.
9. Green consumer research: Trends and way forward based on bibliometric analysis - ScienceDirect Available from: https://www.sciencedirect.com/science/article/pii/S2666784322000432#bib10.
10. Karakurt AS, Özsarı İ, Başhan V, et al. (2021) Evolution of steam turbines: A bibliometric approach. *Journal of Thermal Engineering* 8: 681–690.
11. Geng Y, Zhu R, Maimaituerxun M (2022) Bibliometric review of carbon neutrality with CiteSpace: evolution, trends, and framework. *Environmental Science and Pollution Research* 29: 76668–76686.
12. Elçiçek H (2024) Bibliometric analysis on hydrogen and ammonia: a comparative evaluation for achieving IMO's decarbonization targets. *International Journal of Environmental Science and Technology* 1–22.
13. Hu H, Xue W, Jiang P, et al. (2022) Bibliometric analysis for ocean renewable energy: An comprehensive review for hotspots, frontiers, and emerging trends. *Renewable and Sustainable Energy Reviews* 167: 112739.
14. Baas J, Schotten M, Plume A, et al. (2020) Scopus as a curated, high-quality bibliometric data source for academic research in quantitative science studies. *Quantitative Science Studies* 1: 377–386.
15. Aria M, Cuccurullo C (2017) bibliometrix: An R-tool for comprehensive science mapping analysis. *Journal of informetrics* 11: 959–975.

AN OPTIMIZATION MODEL FOR HEAVY-DUTY FLEET TRANSITION USING HYDROGEN FUEL-CELL VEHICLES

[1]*Fidan Eser*, [1*]*Sule Itir Satoglu*
[1] Istanbul Technical University Management Faculty, Industrial Engineering Department, ITU Isletme Fakultesi Macka, 34369 Istanbul, TURKIYE
*Corresponding author e-mail: onbaslis@itu.edu.tr

ABSTRACT
Alternative fuels are proposed as a solution to reduce carbon emissions in the transportation sector. Hydrogen is an attractive alternative for heavy-duty transportation due to its quick refueling time and longer range compared to electric vehicles when used in fuel cells. However, no single method has been proposed for hydrogen production, storage, and transportation decisions simultaneously. Therefore, in this study, an optimization model is proposed to decide the number, sizes, and technologies of the hydrogen production facilities as well as the number and sizes of the storage facilities, over a planning horizon. Hence, the hydrogen demand of the grids is intended to be satisfied. The objective of the model is to minimize total investment costs of the facilities. As the hydrogen production and storage facilities are built, the fuel-cell vehicles of heavy-duty transport can be started to be used. Hence, decarbonization of the logistics activities can be achieved. The model was illustrated with a synthetic example.

Keywords: Fleet transition, heavy-duty fleet, fuel-cell, hydrogen supply chain

1. INTRODUCTION

The increasing global population has raised the demand for energy, and the dominant role of fossil fuels in energy supply has led to serious environmental problems. Industrialization, population growth, and human activities have significantly increased greenhouse gases in the atmosphere. Among the greenhouse gases responsible for climate change, CO_2 holds the largest share at 80%. The primary source of CO_2 emissions is fossil fuels. On a global scale, the energy sector is the largest emitter of greenhouse gases, highlighting the crucial role of energy policies in reducing emissions. The two sectors with the largest shares in energy-related emissions are industry (24.2%) and transportation (16.2%), with road transportation being the dominant mode within the transportation sector.

Electric vehicles have emerged as a prominent alternative to reduce greenhouse gas emissions. However, over time, it has become clear that relying solely on electric vehicles is not sufficient and introduces new challenges. The fact that the materials used in electric vehicle batteries are not readily available in every country, along with the logistical and economic challenges of their supply, has become an obstacle to the widespread adoption of this technology. Additionally, the environmental waste caused by used batteries is another significant issue. Therefore, instead of focusing on a single alternative fuel technology, evaluating a variety of energy solutions together seems to be a more sustainable and long-term strategy.

Alternative fuels are proposed as a solution to reduce carbon emissions in the transportation sector. In particular, hydrogen is an attractive alternative for heavy-duty transportation due to its quick refueling time and longer range compared to electric vehicles when used in fuel cells. However, no single method has been established for hydrogen production, storage, and transportation. The management of these processes and the identification of the most environmentally and economically viable options remain ongoing research topics.

The lack of a single method for hydrogen production, storage, and transportation has made it an important research question to determine which of the available alternatives is the most environmentally friendly and economically viable [1]. Analyses have evaluated 11 different hydrogen production technologies and 4 different storage and transport alternatives, considering their environmental impacts from multiple perspectives. The findings provide valuable insights for developing a sustainable hydrogen supply chain. Kotze et al. [2] analyzed the impact of green hydrogen usage in heavy-duty vehicles on investments in New Zealand using system dynamics modeling. Çabukoğlu et al. [3] examined the feasibility of hydrogen as an alternative in heavy-duty transportation in Switzerland and demonstrated that hydrogen is technically viable. Similarly, Erdoğan et al. [4] proposed the design of a hydrogen supply chain network for Turkey, which minimizes cost, security risks, and carbon emissions.

Additionally, facility location models are explored to balance the construction of refueling infrastructure with the widespread use of alternative fuel vehicles. The placement of refueling stations is a critical factor in the effective distribution of hydrogen. Kuby and Lim [5] used the Flow-Refueling Location Model (FRLM) to determine the optimal locations for hydrogen refueling stations. Furthermore, the planning and management of the hydrogen supply chain will not be limited to technical and economic factors alone; it will also encompass regulatory frameworks, incentive mechanisms, and carbon pricing strategies. Regulations and government support will be decisive in the development of hydrogen infrastructure. Many countries in Europe and Asia have developed policies to promote the hydrogen economy, and Turkey must also develop similar strategies.

Although there is a significant amount of research on hydrogen, studies that illustrate the step-by-step transformation to hydrogen are limited and insufficient. This gap in the literature hinders the development of strategies and policies to

support the transition to hydrogen-based solutions. This study aims to address this gap by focusing on a systematic and phased approach to hydrogen transition, providing a comprehensive framework that can guide future implementations and facilitate a more effective shift toward a sustainable hydrogen economy. Specifically, this study will focus on the mathematical modeling and design of a hydrogen supply chain for heavy-duty transportation. By considering hydrogen production technologies, transportation methods, storage alternatives, and the process of delivering hydrogen to the end-user, the aim will be to minimize costs and reduce environmental impacts. The design of the hydrogen supply chain is a critical component of the transition to sustainable energy, and optimizing this supply chain will play a key role in accelerating the green transformation of the energy sector.

2. MATERIALS AND METHODS

This study presents a model-based decision support system for the transition of heavy-duty vehicle fleets to hydrogen fuel-cell vehicles. The formulation builds on Almansoori and Shah's multi-period hydrogen supply chain model [6] and is tailored to our scope with a few targeted revisions. The model considers various hydrogen production technologies and the associated processes. Specifically, the region is divided into grids, with the assumption that each grid has a specific demand. Grid-level demand is determined based on the number of registered heavy-duty vehicles and their forecasted counts. The model focuses on critical decisions regarding whether to establish hydrogen production and storage facilities, and if so, where and at what capacity they should be located, in order to meet the demand in each grid. Additionally, the system determines the most suitable method for storing the produced hydrogen. The solution to the model is obtained using the Gurobi optimization software. The goal of this research is to implement the developed mathematical model on a micro scale within a real-world heavy-duty transportation company, providing a practical solution for the transition to hydrogen-powered vehicle fleets.

2.1. The Optimization Model

In this sub-section, we present our optimization model. The indices of the model are as follows: *g*: grid, *t*: period, *i*: physical form of hydrogen (liquid, gas), *j*: facility size, *p*: production technology (1: Steam methane reforming, 2: Coal gasification, 3: Biomass gasification, 4: Water electrolysis), *l*: transportation mode (tanker, railway), *s*: storage facility type (liquid, gas), *e*: energy source (natural gas, coal, biomass, renewable energy, nuclear energy). The parameters of the problem are summarized in Table 1. The parameters pertain to the demand of the grids in each year, the minimum and maximum capacity of each production facility type of each size to produce each hydrogen product type, the minimum and maximum product inventory holding capacity of the storage facilities, and the cost and capacity parameters related to the transport modes and flow rates.

Table 1. The parameters of the mathematical model.

Parameters
D_{gti}: Total demand for product i of grid g in period t
$PCap_{pji}^{min}$: Minimum production capacity of production facility p in size j to produce product i
$PCap_{pji}^{max}$: Maximum production capacity of production facility p in size j to produce product i
$SCap_{sji}^{min}$: Minimum product holding capacity of storage facility *s* of size j for product i
$SCap_{sji}^{max}$: Maximum product holding capacity of storage facility *s* of size j for product *i*
Q_{il}^{min}: Minimum flow rate of product i by transportation mode *l*
Q_{il}^{max}: Maximum flow rate of product i by transportation mode *l*
β: Storage factor (to take into account uncertainties in supply and demand, facility outages)
$AD_{gg'}$: Average distance between grids g and g'
SP_l: Average speed of transportation mode *l*
LUT_{il}: Hydrogen loading and unloading time in transportation mode *l* for product *i*
TMA_{il}: Availability of transportation mode *l* for product *i*
$TCap_{il}$: Capacity of transportation mode *l* for product *i*
IE_{ge}: Amount of energy *e* available in grid *g* (for t=1)
EP_{egt}: Amount of energy *e* produced in grid *g* in period *t*
γ_{epji}: Consumption of energy source *e* by production facility *p* with size j to produce product i
HCC_{pijt}: Investment cost of production facility p in size j to produce product i in period t
SCC_{sijt}: Investment cost of storage facility *s* of size j for product i in period t

The optimization model is presented below. The objective function minimizes the total hydrogen supply chain costs including the total hydrogen production and storage facilities initial investment and hydrogen fuel transportation costs through all years. The constraints pertain to the demand satisfaction constraints of the grids, production plants' construction constraints to satisfy the demand of the grids, the transportation constraints to satisfy the demand of the grids by transporting the required hydrogen fuel among the grids, and storage constraints for the hydrogen storage facilities to be built beside the production facilities. Besides, the constraints of the production and storage units force them to be kept open after construction, and the energy constraints that stipulates satisfaction of the grids' hydrogen energy demand.

Objective function

$$\text{Minimize } TAC$$

Subject to:

$$TAC = \sum_{t} \frac{TAC_t}{(1+r)^t} \tag{1}$$

$$HFCC_t = \sum_{p,i,j,g} HCC_{pijt} IP_{pijgt} \ ; \forall t \tag{2}$$

$$SFCC_t = \sum_{s,i,j,g} SCC_{pijt} IS_{sijgt} \quad ; \forall t \tag{3}$$

$$TAC_t = HFCC_t + SFCC_t \quad ; \quad \forall t \tag{4}$$

Demand Constraints

$$D^L_{gti} + D^I_{gti} = D_{gti} \quad \forall i, g, t \tag{5}$$

$$HP^T_{gti} \geq D^L_{gti} \quad \forall i, g, t \tag{6}$$

$$D^I_{gti} = \sum_{l} Q_{ilg'gt} \quad \forall i, g, t; g \neq g' \tag{7}$$

Production plants' constraints

$$PCap^{min}_{pij} NHP_{pijgt} \leq HPR_{pijgt} \leq PCap^{max}_{pij} NHP_{pijgt} \quad \forall p, i, j, g, t \tag{8}$$

$$PCap^{min}_{pij} NHP_{pijgt} \leq HPR_{pijgt} \leq PCap^{max}_{pij} NHP_{pijgt} \quad \forall p, i, j, g, t \tag{9}$$

$$HP^T_{gti} = D_{gti} + \sum_{l,g'} (Q_{ilgg't} - Q_{ilg'gt}) \quad \forall\, i, g, t; g \neq g' \tag{10}$$

$$HP^T_{gti} = \sum_{p,j} HPR_{pijgt} \quad \forall\, i, g, t \tag{11}$$

Transportation constraints

$$Q^{min}_{il} X_{ilgg't} \leq Q_{ilgg't} \leq Q^{max}_{il} X_{ilgg't} \quad \forall\, i, l, g, t; g \neq g' \tag{12}$$

$$Y_{igt} \geq X_{ilgg't} \quad \forall\, i, l, g, t; g \neq g' \tag{13}$$

$$Z_{igt} \geq X_{ilg'gt} \quad \forall\, i, l, g, t; g \neq g' \tag{14}$$

$$Y_{igt} + Z_{igt} \leq 1 \quad \forall\, i, g, t \tag{15}$$

Storage

$$HS^T_{gti} = \beta D_{gti} \quad \forall\, i, g, t \tag{16}$$

$$HS^T_{gti} = \textstyle\sum_{s,j} HS_{sijgt} \quad \forall\, i, g, t \tag{17}$$

$$\sum_{s,j} SCap^{min}_{sij} NHS_{sijgt} \leq HS^T_{gti} \leq \sum_{s,j} SCap^{max}_{sij} NHS_{sijgt} \quad \forall\, i, g, t \tag{18}$$

$$SCap^{min}_{sij} NHS_{sijgt} \leq HS_{sijgt} \leq SCap^{max}_{sij} NHS_{sijgt} \quad \forall\, s, i, j, g, t \tag{19}$$

Number of production and storage units

$$NHP_{pijgt} = IP_{pijgt} \quad \forall\, p, i, j, g, t; t = 1 \tag{20}$$

$$NHP_{pijgt} = NHP_{pijg(t-1)} + IP_{pijgt} \quad \forall\, p, i, j, g, t; t = 1 \tag{21}$$

$$NHS_{sijgt} = IS_{sijgt} \quad \forall\, s, i, j, g, t; t = 1 \tag{22}$$

$$NHS_{sijgt} = NHS_{sijg(t-1)} + IS_{sijgt} \quad \forall\, s, i, j, g, t; t = 1 \tag{23}$$

$$NTU_{ilgg't} = \left(\frac{2AD_{gg'}}{SP_l} + LUT_{il}\right) \frac{Q_{ilgg't}}{TMA_{il} * TCap_{il}} + V_{ilgg't} \quad \forall\, i, l, g, t; g \neq g' \tag{24}$$

$$V_{ilgg't} \geq 0 \quad \forall\, i, l, g, t; g \neq g' \tag{25}$$

$$V_{ilgg't} \leq X_{ilgg't} \quad \forall\, i, l, g, t; g \neq g' \tag{26}$$

Energy constraints

$$EA_{egt} = IE_{ge} - \sum_{p,j,i} \gamma_{epj}\ HPR_{pijgt} \quad \forall\, e,g,t; t = 1 \tag{27}$$

$$EA_{egt} = EA_{eg(t-1)} - \sum_{p,j,i} \gamma_{epj}\ HPR_{pijgt} \quad \forall\, e,g,t; t \neq 1 \tag{28}$$

3. APPLICATION RESULTS AND DISCUSSION

The model is solved for a synthetic dataset with five grids, five periods, two product forms (*gas and liquid*), three facility sizes, four production technologies (*1: Steam methane reforming, 2: Coal gasification, 3: Biomass gasification, 4: Water electrolysis*), two transportation modes (*1: tanker, 2: railway*), two storage modes (*1: gas, 2: liquid*), and four energy resources (*1: natural gas, 2: coal, 3: biogas, 4: renewable energy*).

The model determines the number and sizes of production and storage facilities to be built in each year and in each grid. Since the results have several details, a representative set of results for the Grid-1 for the five years is presented in Fig. 1. For the five-year period, the numbers of production and storage facilities built in each year and their types are presented here. For year-1, four production facilities were decided to be built, such that one of them will employ steam methane reforming technology (*p=1*) to produce liquid hydrogen, other two facilities will employ coal gasification (*p=2*) to produce liquid (*i=1*) and gas (*i=2*) hydrogen, and the other facility will empoy water electrolysis (*p=4*) to produce liquid hydrogen (*i=1*). Besides, in the first year, in Grid-1, two storage facilities will be built to store liquid (*i*=1) and gaseous hydrogen (*i=2*). In the following years, as the hydrogen demand of the Grid-1 is expected to increase, more production and storage facilities are planned to be built. In Fig. 1, only the number of the facilities to be built in years 3-5 is shown. Similar results were obtained for the other four grids, for the five-year planning horizon.

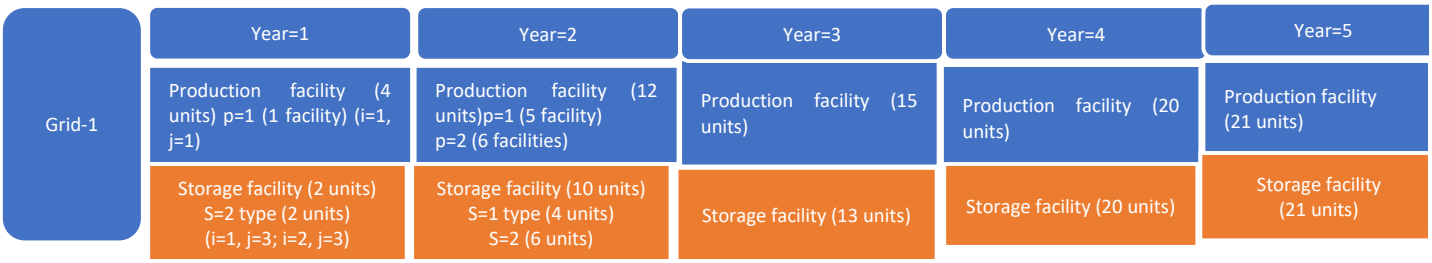

Fig. 1. Results of the model for Grid-1 for all years.

4. CONCLUSIONS

In this study, a mathematical model is proposed to decide the number, sizes, and technologies of the hydrogen production facilities, as well as the number and sizes of the satorage facilities, over a planning horizon. Hence, the hydrogen demand is intended to be satisfied. The objective of the model is to minimize total investment and operational costs of the facilities and material handling costs. As the hydrogen production and storage facilities are built, the fuel-cell vehicles of heavy-duty transport can be started to be used. Hence, decarbonization of the logistics activities can be achieved.

The model is illustrated with a synthetic example. In future studies, it will be solved for a real case example of an industrial zone located in Turkiye, where heavy-duty transportation is dense. As another potential future study, industrial use of the hydrogen in industrial zones based on the established hydrogen supply chain can be planned, and the saved carbon dioxide emissions can be computed.

REFERENCES

1. Hren R., Vujanovi A., Fan Y.V., Kleme˘ J.J., Krajnc D., and Cucek L., 2023. Hydrogen production, storage and transport for renewable energy and chemicals: An environmental footprint assessment, *Renewable and Sustainable Energy Reviews*, 173:113113.
2. Kotze A. C., Brent, J., Musango I. Kock, and Malczynski L. A., 2021. Investigating the Investments Required to Transition New Zealand's Heavy-Duty Vehicles to Hydrogen, *Energies,* 14(6), 1646.
3. Çabukoglu E., Georges G., Güng, L., Pareschi G., and Boulouchos K, 2019. Fuel cell electric vehicles: An option to decarbonize heavy-duty transport? Results from a Swiss case-study, *Transportation Research Part D: Transport and Environment,* 70:35-48.
4. Erdoğan A., Geçici E., and Gürler M.G., 2023. Design of a future hydrogen supply chain: A multi-objective model for Turkey, *International Journal of Hydrogen Energy*, 48(31): 11775-11789.
5. M. Kuby and S. Lim, 2005. The flow-refueling location problem for alternative-fuel vehicles, *Socio-Economic Planning Sciences,* 39(2):125-145.
6. Almansoori A. and Shah N., 2009. Design and operation of a future hydrogen supply chain: multi-period model, *International Journal of Hydrogen Energy*, 34(17):7883-7897.

INVESTIGATION OF THE CONDITIONS FOR THE USE OF NEW GENERATION HYDROGEN GENERATOR IN GEOTHERMAL POWER PLANTS: KIZILDERE GEOTHERMAL FIELD CASE STUDY

[1*]*Raziye Şengün Çetin*, [2]*SFatma Gül Boyacı San,* [1*]*Füsun Servin Tut Haklıdır*
[1] Zorlu Enerji Elektrik Üretimi A.Ş. Levent 199 Şişli, İstanbul, Türkiye
[2] Biasis Enerji Ltd.Şti. Mutlukent Mah.No:21, Çankaya, Ankara, Türkiye

raziye.sengun@zorlu.com; fgb@biasis.tr

ABSTRACT
Geothermal energy, which is one of the important renewable energy sources of energy conversion, is an energy production method that provides continuity with circular heat transfer by separating the hot fluid obtained from geothermal reservoirs into liquid and steam phases and re-injecting the waste liquid phase underground. Depending on the temperature of the fluid, energy production is carried out worldwide with different technologies (flash, binary ORC cycle or integrated systems).
Geothermal wells, which are drilled from deep in the earth's crust to reach the surface conditions, are generally distributed in the geothermal field due to geological and structural factors and are located at long distances from the geothermal power plant. Inhibitor dosing pump systems, which are critical equipment for uninterrupted flow production in geothermal wells and providing remote control and communication between the power plant power control center and different locations throughout the field, and, require energy as long as the power plant is operating. In case of short-term power outages, diesel generators are used to meet the energy load, which requires additional equipment and fuel.
This study aims to examine the use of sodium borohydride-based fuel cell systems, a clean alternative to wellhead generators that produce energy from fossil fuels during failure conditions, and to reveal their contribution to energy conversion. Fuel cells are off-grid systems that convert the chemical energy of the fuel directly into electrical energy with high efficiency. Polymer electrolyte membrane fuel cells (PEMFC) are a type of fuel cell that has the potential to be used in a wide power range. In this study, the use of high-purity hydrogen, required for a 10kW PEMFC during a 1–3-day failure condition, will be investigated by producing it from sodium borohydride. Issues such as the safe and long-term storage of sodium borohydride in solid form, its suitability for hydrogen production when needed, the controllability of the reaction, the environmental impact of by-products, and the potential use of Turkey's boron resources—which account for more than 70% of global reserves—in high-value-added applications will be evaluated.

Keywords: Geothermal, Sodium borohydride, Remote Area, PEMFC

1. INTRODUCTION

Kizildere geothermal field is a multifunctional integrated production site located on the border of Denizli and Aydın with a total electricity generation capacity of 260 MWe, providing resources for city heating, high-volume greenhouse heating, thermal tourism, and pure liquid CO2 production. The first power plant was established as single flash cycle in 1984 and the capacity expeanding studies continued between 2008-2018 with thriple flash and combined binary cycle in the field [1].
In order to produce geothermal energy, the hot geothermal fluid deep in the earth's crust is usually pumped to the surface by geothermal wells located scattered in the geothermal field due to geological and structural factors (e.g., Fig. 1). Power plant communication between different locations throughout the field, inhibitor dosing pump systems, which are critical equipment for uninterrupted flow production in geothermal wells, require energy as long as the power plant is operating. During planned maintenance at the power plant and in case of failure at the power plant, the energy supplied to the well areas is cut off. In case of short-term power outages, diesel generators are used to meet the energy load, which creates additional equipment and fuel needs.
In this study, the use of PEMFC is proposed to meet the emergency energy needs in remote areas far from power plant facilities. In comparison to fossil fuels, sodium borohydride fuel cells are a cleaner source of energy and it is intended to use the boron mineral, 70% of the world reserves of which are located in Turkey, in energy needs.

2. MATERIALS AND METHODS

In cases where geothermal power plants are connected to the grid, they meet all their internal consumption including well zones. In case of emergency in the geothermal power plant, power outages occur and the systems in the power plant stop working. This does not apply to the wells that produce artesian production and the wells continue to produce

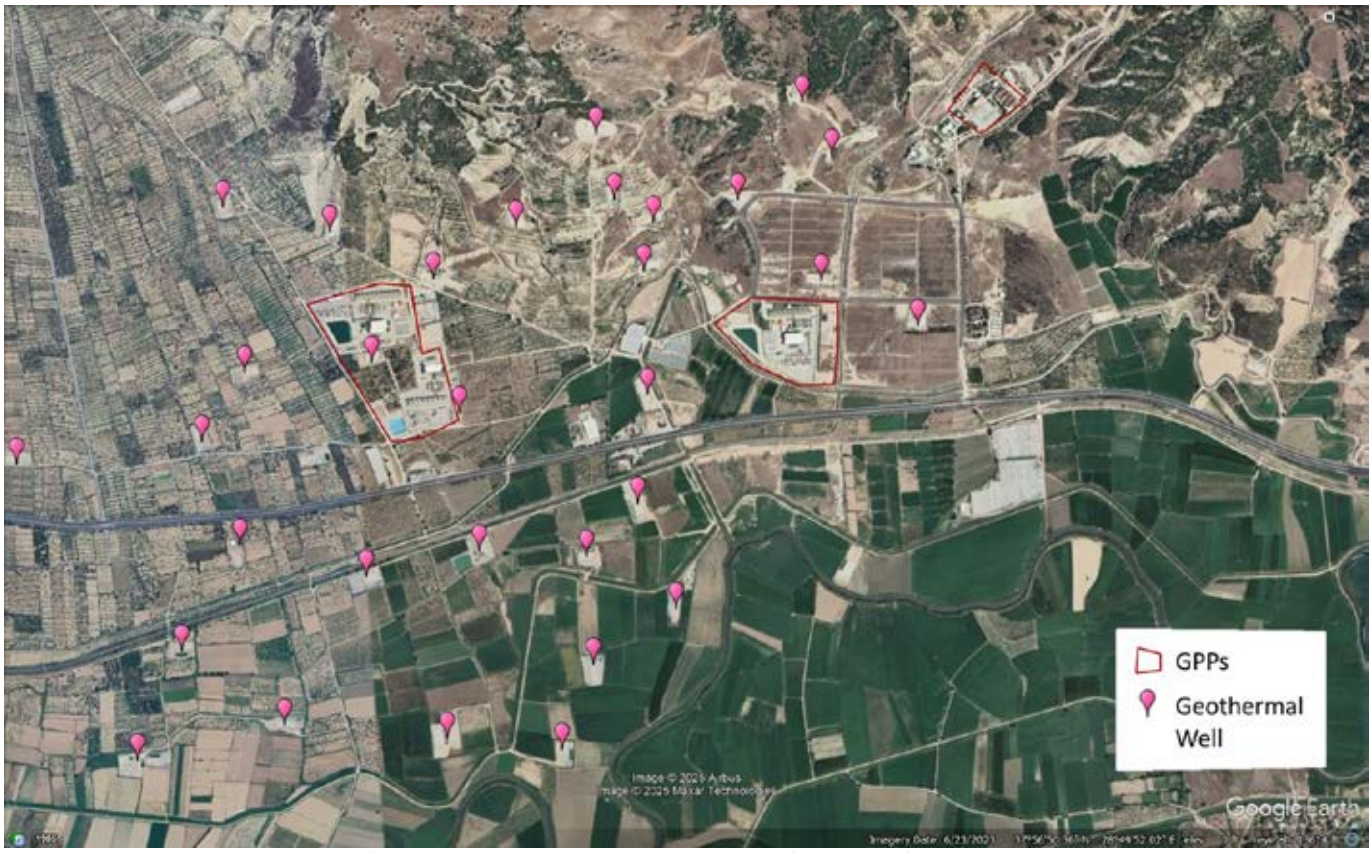

Fig. 1. GPPs and the production well locations of Kızıldere Geothermal Field.

fluid. Considering parameters such as well depth, fluid temperature and reservoir pressure, geothermal production wells, which are very difficult to be reactivated when shut down, are required to continue production even when the power plant is not in operation. these wells discharge their fluids into emergency pools. In order to control the geothermal wells, the communication between the control room and the wells and therefore the energy should not be interrupted. Inhibitor dosing systems are another system affected by power failure in the well area. Inhibitor dosing systems are the risk of precipitation in the well as a result of physicochemical reactions of geothermal fluid containing dissolved minerals. In order to prevent precipitation, capillary tubings reaching kilometres in length are lowered into the wells and inhibitors are injected into the well through them. In the event of a power failure, if the inhibitor dosing system stops, the inhibitors in the capillary tubing burn and disable the tubing, resulting in precipitation in the well. This leads to costly operational requirements at the well site and in order to prevent this situation from developing, generators are located at the well sites.

It is common use to utilise generators in emergency power outages in industry and residences. At Kızıldere geothermal field well sites, diesel generators are also preferred. A total of 7A current is drawn in the well area. Each well needs a 5 kW 3-phase generator in case of emergency. 16 kW diesel generators are activated in emergency conditions at the well sites. Considering that each litre of diesel fuels creates 2.68 kg of CO_2 emissions each time it burns, therefore each generator has the capacity to create 107.2 kg of emissions. Only the number of production wells in Kizildere Geothermal Field is more than 50. For this reason, diesel generators produce a considerable amount of emissions in case of power outages. In order to prevent carbon emission, it is purposed to use $NaBH_4$ PEMFC, which is sustainable and relatively cleaner, instead of fossil fuelled generators.

$NaBH_4$ (Sodium borohydride) has been investigated as a potential hydrogen source for PEMFCs due to its high hydrogen content and ability to release hydrogen when reacting with water by various researchers [2],[3],[4]. $NaBH_4$ can release hydrogen gas through hydrolysis. $NaBH_4$ stored in solid state does not release hydrogen directly at room temperature. Controlled hydrolysis of $NaBH_4$, with the reaction rate and efficiency increased by catalysts, is a common method to supply hydrogen to PEMFC's anode side. The reaction can be controlled to release hydrogen at a rate suitable for the demand of the fuel cell. The general hydrolysis reaction is:

$$NaBH_4 + 2H_2O \rightarrow NaBO_2 + 4H_2$$

Generated hydrogen from $NaBH_4$, is sent to the anode part of the PEM fuel cell, creating an electrochemical reaction. At

the anode, hydrogen molecules are split into protons and electrons with a catalyst. On the other hand, at the cathode, oxygen molecules combine with the protons and electrons transferred from the anode to form water.

$2H_2 \rightarrow 4H^+ + 4e^-$ anode

$O_2+4H^++4e^- \rightarrow 2H_2O$ cathode

$2H_2 + O_2 \rightarrow 2H_2O$ total

Once the $NaBH_4$ has been consumed, it will be necessary to refill the fuel compartment with fresh $NaBH_4$ and remove the $NaBO_2$ produced by the reaction.

3. RESULTS AND DISCUSSION

If the energy requirement is considered as 10 kW for a well, it is calculated that 80 kg of solid $NaBH_4$ can meet the daily energy requirement of a well in Kızıldere geothermal field.

$NaBH_4$ is a source with adjustable reaction conditions and a high volumetric energy density that can be stored and transported more easily than hydrogen gas, which requires high-pressure tanks. These properties make it a potential option for portable or mobile fuel cell applications, but the by-products generated during hydrogen production present some challenges such as efficiency, cost and scalability. In any case $NaBH_4$ based PEMFC, which are still open to improvement, can be an alternative that can be used in emergencies with the development of cost, fast start-up and efficiency.

4. CONCLUSIONS

The Kizildere geothermal field wells have an average energy requirement of 10 kW, so 16 kW diesel generators are activated in emergency conditions at the well sites. Considering that each litre of diesel fuels creates 2.68 kg of CO_2 emissions each time it burns, therefore each generator has the capacity to create 107.2 kg of emissions. Only the number of production wells in Kizildere Geothermal Field is more than 50. For this reason, diesel generators produce a considerable amount of emissions in case of power outages. In order to prevent carbon emission, it is recommended to use $NaBH_4$ PEMFC, which is sustainable and relatively safer, instead of fossil fuelled generators.

REFERENCES

1. Haklıdır, F. S. T., Şengün, R., & Aydın, H. (2021). Characterization and Comparison of geothermal fluids geochemistry within the Kızıldere Geothermal Field in Turkey: New findings with power capacity expanding studies. Geothermics, 94, 102110.
2. Kim, H., Oh, T. H., & Kwon, S. (2016). Simple catalyst bed sizing of a NaBH4 hydrogen generator with fast startup for small unmanned aerial vehicles. *International Journal of Hydrogen Energy*, *41*(2), 1018-1026.
3. San, F. G. B., Okur, O., Karadağ, Ç. İ., Isik-Gulsac, I., & Okumuş, E. (2014). Evaluation of operating conditions on DBFC (direct borohydride fuel cell) performance with PtRu anode catalyst by response surface method. Energy, 71, 160-169.
4. San, F. G. B., Karadağ, Ç. İ., Okur, O., & Okumuş, E. (2016). Optimization of the catalyst loading for the direct borohydride fuel cell. Energy, 114, 214-224.

INVESTIGATION OF LSC-BASED COMPOSITE SOFC CATHODE LAYERS BY ESD COATING METHOD

Emre Erğen[1,], Sedat Akkurt[1]*
[1]Izmir Institute of Technology, Department of Materials Science and Engineering, 35430 Urla, Izmir, Turkey

*Corresponding author e-mail: emreergen@iyte.edu.tr

ABSTRACT

Recent research on intermediate temperature solid oxide fuel cells (IT-SOFC) address on issues about developing more efficient cathode structures. The purpose is to relay ionic conduction through the cathode as fast as possible. Materials based on LSC (La, Sr, Co oxides) with both $(La,Sr)CoO_3$ (LSC113) and $(La,Sr)_2CoO_4$ (LSC214) stoichiometry are chosen in this study. In the literature, several coating and fabrication processes were used to combine these materials to form composite cathode structures. In this study, electrospray deposition (ESD) method is used to coat polymeric precursor solutions prepared with these material compositions onto gadolinia-doped cerium oxide (GDC) electrolyte material. Layered coating approach were tested to form composite coating structures and compared different compositions. The approach involved coating thin LSC113 and LSC214 layers one on top of the other. Electrochemical Impedance Spectroscopy (EIS) measurements were done with the symmetrically coated samples. Promising EIS measurements were taken and the work is ongoing.

Keywords: Electrospray deposition, solid oxide fuel cell, LSC113, LSC214, cathode layer

1. INTRODUCTION

Fuel cells, are environmentally friendly energy production technologies that are named according to the type of the electrolyte material used. Solid Oxide Fuel Cells (SOFC) can convert chemical energy into electrical energy silently and efficiently. Only heat and water are formed as by-products. However, high operating temperatures (>800°C) lead to problems such as corrosion, reduced durability, long start-up times and high maintenance costs. To overcome these problems, operating temperatures need to be reduced to the intermediate-temperature range (500-700°C), but this causes a decrease in ionic and electronic conductivities and thus a decrease in energy production efficiency. The selection of materials is very important to increase efficiency in the intermediate temperature range. The ionic conductivity of the electrode layers, especially the cathode layer, is increased by using Mixed Ionic-Electronic Conductor (MIEC) materials. LaSrCo-based perovskite oxides have been shown to have promising electrochemical properties among MIEC materials for IT-SOFCs.

Cathode layers are coated on the electrolyte layer with various methods such as PLD, screen printing, solid-state reaction, etc [1–4]. In this study, the Electrospray Deposition (ESD) method, which is a low-cost and faster method compared to other techniques, was used. In the literature, the ESD method has not yet been used for LaSrCo-based compounds. ESD allows the atomization of liquids with the help of electrical forces. The liquid used is a solution containing the components of the cathode layer such as La, Sr and Co in stoichiometric ratios. Upon impact with the targeted heated electrolyte pellet the solution is rapidly vaporized and metal ions form an amorphous oxide attached to the surface. Coatings with the desired composition and structures can be created by controlling the ESD parameters. In this way, different coating structures such as reticular, dense, etc. structures can be obtained on the electrolyte surface by optimizing the ESD parameters for different experimental plans [5–7]. Recently, Tayfur Ozturk et al. have studied the coating of LSC-based cathode materials onto the electrolyte by the sputtering coating method [8]. In these studies, LSC113 was combined with LSC214 in certain proportions and used to form composite cathode layers.

In this study, LaSrCo oxide solutions were prepared in specific A-site stoichiometries such as $(La_{0.5}Sr_{0.5})CoO_3$, $(La_{0.8}Sr_{0.2})CoO_3$, $(La_{0.5}Sr_{0.5})_2CoO_4$ and $(La_{0.8}Sr_{0.2})_2CoO_4$ and were symmetrically coated onto gadolinia doped ceria (GDC) pellets used as electrolyte. Electrochemical impedance spectroscopy (EIS) measurements were performed with symmetrically coated samples.

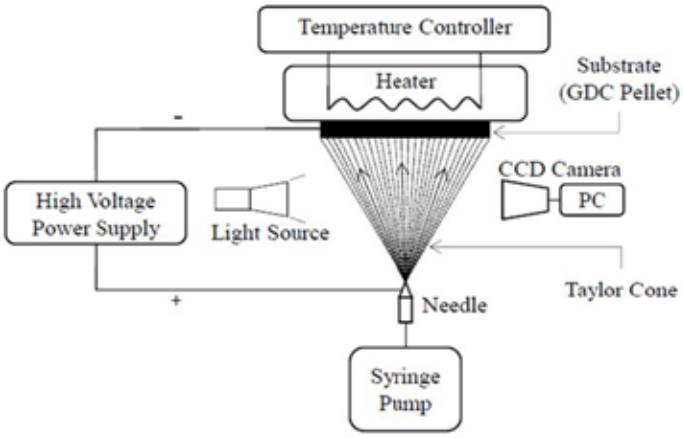

Fig. 1. Schematic of electrospray deposition (ESD) method [7]

2. MATERIALS AND METHODS

$(La_{0.5}Sr_{0.5})CoO_3$, $(La_{0.8}Sr_{0.2})CoO_3$, $(La_{0.5}Sr_{0.5})_2CoO_4$ and $(La_{0.8}Sr_{0.2})_2CoO_4$ solutions were prepared from precursor solutions in the stoichiometric proportions which were selected based on the literature in order to make electrochemical performance comparisons of the resulting cathode layers. For these solutions, Lanthanum (III) nitrate hexahydrate (ALFA-AESAR >99.99%), cobalt (II) nitrate hexahydrate (ALFA-AESAR >97.7%) and strontium chloride hexahydrate (ALFA-AESAR >99%) precursor salts were used to prepare the solutions to be coated on dense GDC pellets by Electrospray Deposition (ESD) method. The composite cathode layers were formed by ESD with layered coating structure approach. This approach is explicable by coating different solutions one by one on GDC pellet. The electrolyte pellets were made from commercial GDC powder by pressing in a uniaxial hydraulic press at 180 MPa pressure followed by sintering to >95% density. Experimental ESD parameters were flow rate (2 ml/h), voltage (13 kV), solution concentration (0.02M), working distance (27 mm), temperature (350 °C) and coating duration (10 minutes). Finally, XRD analysis was used for determining phase compositions, SEM was used for microstructural analysis and EIS for electrochemical performance analysis. An in-house silver (Ag) paste and Ag wires were employed to facilitate efficient current collection. The wires were secured using a high-temperature ceramic adhesive (Ceramabond). Electrochemical impedance spectroscopy (EIS) measurements were conducted with an Autolab (Metrohm, Switzerland) instrument over a temperature range of 500–700 °C in stagnant air (Protherm Tube Furnace). The EIS analyses utilized an excitation voltage of 15 mV and covered a frequency range of 10^{-2} to 10^{5} Hz.

3. RESULTS AND DISCUSSION

Cathode layers with $(La_{0.5}Sr_{0.5})CoO_3$, $(La_{0.8}Sr_{0.2})CoO_3$, $(La_{0.5}Sr_{0.5})_2CoO_4$ and $(La_{0.8}Sr_{0.2})_2CoO_4$ compositions were deposited onto the electrolyte using ESD. It was crucial to evaluate the chemical and phase compositions of the cathode layers after deposition. Precursor solutions were individually heated in a glass beaker at 250 °C to evaporate the solvents, simulating the final cathode composition. Energy-dispersive X-ray spectroscopy (EDX) were performed on these powder samples to determine the elemental composition of the cathode layers after coating process. The results closely matched the intended stoichiometric ratios as listed in Table 1 below. This was done so because coatings sraped off from the pellet surface were too-rich in GDC and XRD analysis peaks for LSC were overshadowed by GDC peaks.

Table 1. Stoichiometric ratios of precursor solutions

Sample	Stoichiometric Ratios	
	Intended	Calculated
1	$(La_{0.5}Sr_{0.5})CoO_3$	$(La_{0.49}Sr_{0.51})CoO_3$
2	$(La_{0.8}Sr_{0.2})CoO_3$	$(La_{0.77}Sr_{0.23})CoO_3$
3	$(La_{0.5}Sr_{0.5})_2CoO_4$	$(La_{0.51}Sr_{0.49})_2CoO_4$
4	$(La_{0.8}Sr_{0.2})_2CoO_4$	$(La_{0.79}Sr_{0.21})_2CoO_4$

Cross-sectional SEM image obtained from the fracture of coatings made using layered-structured coating approach by ESD method with $(La_{0.5}Sr_{0.5})CoO_3$ ve $(La_{0.5}Sr_{0.5})_2CoO_4$ is shown in Fig. 2. This sample shows partially dense coating structure. Nevertheless, the approach showed the availability for formation of desired reticular structures.

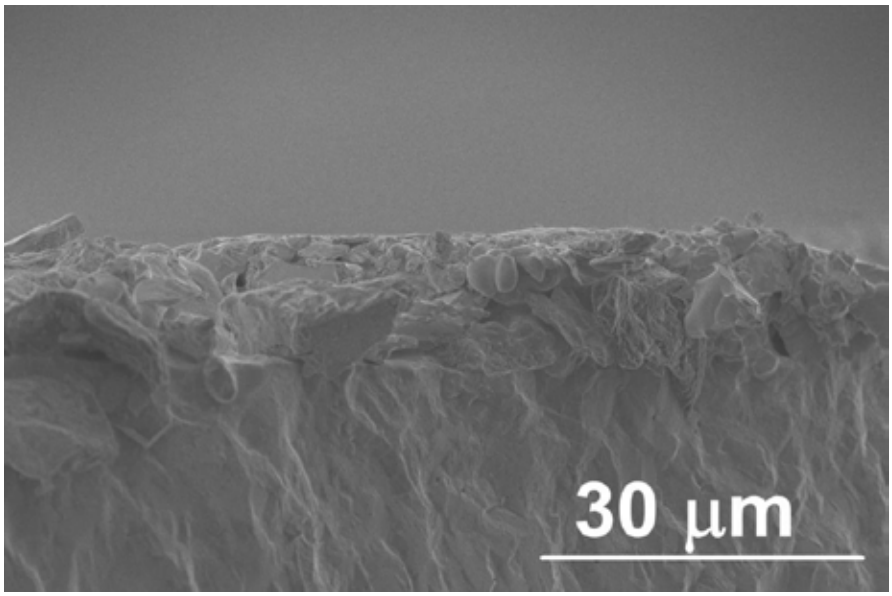

Fig. 2. SEM image of coating made using the layered-structure approach by ESD method with $(La_{0.5}Sr_{0.5})CoO_3$ and $(La_{0.5}Sr_{0.5})_2CoO_4$ solution.

4. CONCLUSIONS

The prepared precursor solutions were successfully coated on dense GDC electrolyte pellets. EDX analysis performed to check intended stoichiometric ratios. SEM observations revealed partially dense and desired reticular structures according to the composite constituents and coating conditions. Thus, the effects of layered-structured composite coatings were observed. Electrochemical impedance spectroscopy (EIS) measurements confirmed the effectiveness of ESD method on coatings on GDC electrolyte. Area specific resistance (ASR) measurements at 700°C showed better values than the benchmark of 0.15 Ω·cm² for IT-SOFC cathodes.

5. REFERENCES

[1] E.J. Crumlin, E. Mutoro, S.-J. Ahn, G.J. la O', D.N. Leonard, A. Borisevich, M.D. Biegalski, H.M. Christen, Y. Shao-Horn, Oxygen Reduction Kinetics Enhancement on a Heterostructured Oxide Surface for Solid Oxide Fuel Cells, J. Phys. Chem. Lett. 1 (2010) 3149–3155. https://doi.org/10.1021/jz101217d.

[2] J. Hayd, L. Dieterle, U. Guntow, D. Gerthsen, E. Ivers-Tiffée, Nanoscaled La0.6Sr0.4CoO3−δ as intermediate temperature solid oxide fuel cell cathode: Microstructure and electrochemical performance, J. Power Sources 196 (2011) 7263–7270. https://doi.org/10.1016/j.jpowsour.2010.11.147.

[3] Y.-C. Wu, P.-Y. Huang, G. Xu, Properties and microstructural analysis of La1−xSrxCoO3−δ (x=0–0.6) cathode materials, Ceram. Int. 43 (2017) 2460–2470. https://doi.org/10.1016/j.ceramint.2016.11.041.

[4] H.E. Aysal, F. Kılıç, G. Çakmak, T. Öztürk, Thermal plasma synthesis of (La,Sr)CoO3-(La,Sr)2CoO4 composite cathodes for intermediate temperature solid oxide fuel cells (IT-SOFC), Int. J. Hydrogen Energy 51 (2024) 1477–1486. https://doi.org/10.1016/j.ijhydene.2023.07.031.

[5] C. Sındıraç, S. Akkurt, Formation of La1−xSrxCo1−yFeyO3−δ cathode materials from precursor salts by heating in contact with CGO electrolyte, Int. J. Hydrogen Energy 41 (2016) 18157–18165. https://doi.org/10.1016/j.ijhydene.2016.07.143.

[6] C. Sındıraç, S. Akkurt, Microstructural investigation of the effect of electrospraying parameters on LSCF films, Int. J. Hydrogen Energy 45 (2020) 35139–35148. https://doi.org/10.1016/j.ijhydene.2020.02.194.

[7] S. Akkurt, C. Sındıraç, T.Ö. Egesoy, G. Atıcı, E. Erişman, E. Erğen, A. Büyükaksoy, Effects of electrospraying parameters on deposition of La 0.3 Sr 0.7 Fe 0.7 Cr 0.3 O 3− δ cathode layer on GDC, Int. J. Appl. Ceram. Technol. 20 (2023) 1512–1525. https://doi.org/10.1111/ijac.14303.

[8] D. Sari, F. Piskin, Z.C. Torunoglu, B. Yasar, Y.E. Kalay, T. Ozturk, Combinatorial development of nanocrystalline/amorphous (La,Sr)CoO3-(La,Sr)2CoO4 composite cathodes for IT-SOFCs, Solid State Ionics 326 (2018) 124–130. https://doi.org/10.1016/j.ssi.2018.10.003.

EXPERIMENTAL STUDY ON REGENERATIVE FUEL CELL PERFORMANCE: ELECTROLYZER AND FUEL CELL MODE ANALYSIS

[1*]*Muhammed Asım Kesercioğlu* [2]*Fatma Gül Boyacı San*, [3]Nedim Sözbir, [1]*Yusuf Çay*
[1] Sakarya University of Applied Science, Faculty of Technology, Department of Mechanical Engineering, Sakarya, 54000, Turkey
[2]BIASIS Energy Limited Company, Mutlukent No:21, Ankara, 06800, Turkey
[3] Sakarya University, Faculty of Engineering, Department of Mechanical Engineering, Sakarya, 54000, Turkey

* mkesercioglu@subu.edu.tr

ABSTRACT
In this study, the performance of a regenerative fuel cell with a 9 cm² active area was experimentally investigated in both electrolyzer and fuel cell modes. The MEA consisted of 75% Platinum Black and 25% Iridium Black on the anode side, while Platinum Carbon was used on the cathode side. In the bipolar plate design, serpentine flow channels were used on the cathode side, whereas a titanium mesh structure was employed on the anode side.
The experiments were conducted using the L9 orthogonal array Taguchi experimental design. In electrolyzer mode; compression torque (5-7-10 N.m), temperature (40-60-80°C) and water flow rate (10-20-30 ml/min) were varied, and current density were measured. In fuel cell mode, compression torque and temperature were selected the same as in electrolyzer mode, while hydrogen flow rate (1.296, 1.62, 1.944 ml/min.) was varied, current density and power density were measured. The findings reveal the effects of compression torque, temperature, and flow rate variations on the performance of the regenerative fuel cell.
Keywords: Regenerative Fuel Cell, Hydrogen

1. INTRODUCTION

In recent years, energy production and storage technologies have been rapidly advancing with a focus on sustainability and environmental impact [1]. In this context, regenerative fuel cells (RFCs) have gained attention as innovative systems capable of both hydrogen production and electrical energy conversion [2]. RFCs operate in electrolyzer mode by splitting water into hydrogen and oxygen for energy storage, and in fuel cell mode, they utilize these gases to generate electricity, with water as the only byproduct [3]. This bidirectional working principle offers high efficiency and an environmentally friendly approach to energy storage and recovery.
Regenerative fuel cells are categorized into separated and unified systems. In separated systems, the electrolyzer and fuel cell are designed as independent modules, operating with an external hydrogen storage unit. The hydrogen produced in the electrolyzer is stored separately and later used by the fuel cell. In contrast, unified systems integrate both functionalities within a single cell, allowing it to operate in both electrolyzer and fuel cell modes[4]. Unified systems provide advantages in energy storage applications due to their compact design and lower costs. However, for efficient operation in both modes, it is essential to optimize the membrane, catalyst, and flow field design[5]. There are two design strategies for unified regenerative fuel cells: fixed electrode and fixed gas configurations. In a traditional fixed gas setup, the URFC consists of a hydrogen electrode (HOR/HER) and an oxygen electrode (ORR/OER). The primary advantage of this configuration is preventing hydrogen and oxygen mixing while also enabling rapid switching between electrolyzer (EL) and fuel cell (FC) modes. However, a major limitation of this design is that both kinetically and thermodynamically controlled OER and ORR reactions occur on the same side of the device, leading to efficiency losses [6]. In contrast, the fixed electrode approach operates with a continuous gas exchange mechanism, where HER/ORR occurs at the cathode and OER/HOR at the anode. This configuration enhances energy conversion efficiency, improves oxygen transport and ORR kinetics, and allows for lower material loading while enhancing OER kinetics. Additionally, operating with a single electrode in a continuous mode enables more efficient coordination of gas diffusion layers. However, the main drawback is that the wide potential range experienced by the electrodes increases material degradation, leading to a shorter lifespan compared to the fixed gas configuration.[7].
Although various studies in the literature have focused on different design approaches for regenerative fuel cells, the majority emphasize material innovations. In the study by Kim et al.[8] bifunctional Pt-Ir catalysts were synthesized via spray pyrolysis and optimized through thermal treatment for RFC applications. The physical structure of the catalysts was analyzed, and their electrochemical performance was evaluated. Results indicated that heat-treated Pt-Ir/rGO catalysts exhibited high ORR and OER activity along with enhanced stability, demonstrating the potential of Pt-Ir alloys as an efficient alternative for RFCs.
In another study by Regmi et al., a low-temperature unified regenerative fuel cell (URFC) design achieved 60% round-trip efficiency and 10,000 cycle durability. The fixed electrode (CE) and fixed gas (CG) configurations were compared, revealing that the CE configuration provided higher current density and efficiency. In the CE setup, HOR and OER occurred at the anode, while ORR and HER took place at the cathode. Accelerated stress tests confirmed that stable performance was maintained over 10,000 cycles.
Park at al.[9], focused on optimizing the membrane electrode assembly (MEA) for URFCs. The study investigated gas diffusion layers, ionomer content, ORR/OER catalysts, and catalyst loading on oxygen electrodes. Results indicated that

MEA parameters had the most significant impact on RFC performance in both fuel cell (FC) and water electrolysis (WE) modes. An optimized design achieved 49% round-trip efficiency at 500 mA/cm², comparable to values reported in the literature.
Yim et al. [10] optimized bifunctional electrocatalysts for PEM-based unified RFCs. The study synthesized and evaluated various Pt-based catalysts for oxygen electrodes. Cell temperature, catalyst loading, and electrode stability were analyzed to determine the optimal operating conditions. The findings demonstrated that Pt-Ir catalysts provided the highest efficiency and stability in both FC and EL modes, confirming their effectiveness as oxygen electrode materials for URFC systems.
In this study, a novel RFC design was introduced by replacing the conventional bipolar plate with a titanium mesh structure on the anode side. While traditional designs typically use bipolar plates on both the anode and cathode, this study aims to investigate the impact of using a titanium mesh on RFC performance in both electrolyzer and fuel cell modes. This approach has been minimally explored in the literature, and the influence of mesh structures on gas transfer at the membrane-electrode interface and bidirectional cell operation remains insufficiently studied. Therefore, this study aims to contribute to the field by analyzing the effects of replacing bipolar plates with a titanium mesh on RFC performance.
Additionally, to achieve systematic optimization, the study employs the L9 orthogonal array Taguchi experimental design. The effects of compression torque, temperature, and flow rate on cell performance were examined to determine optimal operating conditions. Experimental investigations were conducted by first testing the system in electrolyzer mode, followed by fuel cell mode, and repeating the same procedures for each compression torque value. The findings highlight the significant impact of using a titanium mesh instead of a bipolar plate on RFC performance, offering valuable insights for future studies in this area.

2. MATERIALS AND METHODS

2.1. Design of the Regenerative Fuel Cell

The active area of the regenerative fuel cell used in the experiments was set to 9 cm². The cell operates in a fixed electrode mode. The Membrane Electrode Assembly (MEA) consists of 75 wt.% Platinum Black and 25 wt.% Iridium Black on the anode side, while the cathode side contains Platinum-Carbon catalyst. In terms of bipolar plate design, a serpentine flow channel structure is utilized on the cathode side, whereas a titanium mesh structure is implemented on the anode side.

2.2. Experimental Design and Parameters

In this study, the L9 orthogonal array Taguchi experimental design was employed to investigate the effects of three key variables at three different levels:
Electrolyzer Mode Parameters:

- Compression Torque: 5, 7, 10 N.m
- Temperature: 40, 60, 80°C
- Water Flow Rate: 10, 20, 30 ml/min.

Fuel Cell Mode Parameters:

- Compression Torque: 5, 7, 10 N.m
- Temperature: 40, 60, 80°C
- Hydrogen Flow Rate: 1.296, 1.62, 1.944 ml/min.

The impact of each parameter on performance was analyzed based on the output data of the fuel cell.

Table 1. Electrolyzer Mode Taguchi Experimental Design

Experiment No	Torque (N.m)	Temperature (°C)	Water Flow Rate (ml/min.)
1	5	40	10
2	5	40	20
3	5	40	30
4	7	60	20
5	7	60	30
6	7	60	10
7	10	80	30
8	10	80	10
9	10	80	20

Table 2. Fuel Cell Mode Taguchi Experimental Design

Experiment No	Torque (N.m)	Temperature (°C)	H_2 Flow Rate (ml/min.)
1	5	40	1.296
2	5	40	1.62
3	5	40	1.944
4	7	60	1.944
5	7	60	1.296
6	7	60	1.62
7	10	80	1.62
8	10	80	1.944
9	10	80	1.296

3. RESULTS AND DISCUSSION

3.1. Performance in Electrolyzer Mode

As the temperature increased, a significant rise in current density was observed, as higher temperatures accelerate electrochemical reaction kinetics and enhance ion mobility within the membrane. At elevated temperatures, the activation energy required for electrode surface reactions decreases, reducing the overall internal resistance of the cell and leading to a more efficient current flow.

Additionally, an increase in compression torque contributed to a more stable current density by reducing the contact resistance between the electrodes. Higher compression torque levels improved the contact interface between the electrode and membrane, enhancing electrical conductivity and minimizing resistance losses at the contact points. As a result, at higher compression torque values, the cell performance and current density remained more stable and consistent.

On the other hand, a slight decrease in current density was observed with increasing water flow rate. While a higher water flow rate facilitates the removal of gas bubbles from the electrode surface, it can also lead to water accumulation on the electrode, restricting gas diffusion in reaction sites. This limitation can hinder the optimal progression of the reaction mechanism, causing a minor reduction in cell performance. However, this decrease remains relatively small and does not pose a significant obstacle to the overall system efficiency.

3.2. Performance in Fuel Cell Mode

As the temperature increased, both current density and power density showed a significant improvement. This enhancement can be attributed to the acceleration of electrochemical reaction kinetics at higher temperatures, which reduces the activation energy required for electrode reactions. Additionally, increased temperature enhances ion mobility within the membrane, leading to a reduction in internal resistance and improved proton conductivity. These factors collectively result in a more efficient electron transfer process, allowing the cell to operate at higher performance levels. Furthermore, the improved gas diffusion at elevated temperatures enhances mass transport, ensuring a more effective utilization of the reactant gases at the electrode surfaces, thereby maximizing the overall energy conversion efficiency.

Conversely, as the compression torque increased, both current density and power density exhibited a decline. Higher compression torque, while beneficial up to a certain limit by improving contact between the membrane and electrodes, can also lead to excessive mechanical stress on the cell components. This excessive pressure can compress the gas diffusion layers (GDLs), reducing their porosity and impeding effective gas transport. Consequently, the limited gas supply to the catalyst sites results in mass transport losses, negatively impacting the overall reaction rates. Furthermore, excessive torque can introduce structural deformations in the membrane-electrode assembly (MEA), potentially increasing internal ohmic resistance, leading to reduced current and power output.

Although hydrogen flow rate had a less significant impact compared to temperature and compression torque, the highest performance was achieved at a hydrogen flow rate of 1.296 ml/min. Maintaining an optimal hydrogen flow rate is crucial for ensuring sufficient reactant supply to the catalyst sites, enabling efficient electrochemical reactions. Insufficient hydrogen flow can lead to reactant starvation, causing mass transport limitations and reduced reaction rates. Conversely, excessively high hydrogen flow may result in unreacted hydrogen bypassing the catalyst layer, leading to inefficient gas utilization and lower energy conversion efficiency. The optimal performance observed at 1.296 ml/min suggests that this specific hydrogen flow rate provides the best balance between reactant availability and reaction efficiency, ultimately enhancing the overall performance of the fuel cell.

4. CONCLUSIONS

In this study, the performance of a regenerative fuel cell was experimentally investigated under different parameters in both electrolyzer and fuel cell modes. The optimum performance, affecting both electrolyzer and fuel cell operations, was

achieved at 7 Nm compression torque and 80°C temperature. Additionally, in electrolyzer mode, the best performance was observed at the lowest water flow rate of 10 ml/min, while in fuel cell mode, the highest performance was recorded at the lowest hydrogen flow rate of 1.296 ml/min.

Experimental results indicate that temperature is the most influential parameter on the performance of the regenerative fuel cell. An increase in temperature enhances electrochemical reaction kinetics, significantly improving efficiency in both electrolyzer and fuel cell modes. Compression torque is also a critical factor in determining cell performance; however, its impact is more limited compared to temperature. Increasing torque up to a certain level improves electrode contact by reducing contact resistance, thus enhancing conductivity. However, excessive compression torque negatively affects gas diffusion, leading to performance losses.

In contrast, the effects of water and hydrogen flow rates were significantly lower compared to temperature and torque. In electrolyzer mode, decreasing the water flow rate resulted in higher performance, with the best efficiency observed at the lowest water flow rate of 10 ml/min. In fuel cell mode, the highest performance was achieved at the lowest hydrogen flow rate of 1.296 ml/min. Excessive hydrogen supply led to unreacted hydrogen exiting the system, reducing overall efficiency.

Overall, temperature was identified as the most influential parameter on the performance of the regenerative fuel cell, while compression torque had a moderate effect, and water and hydrogen flow rates had the least impact compared to the other parameters.

To further improve the performance of regenerative fuel cells, several key aspects should be explored in future studies. Testing different catalyst combinations can help enhance the efficiency and durability of cell components by optimizing electrocatalytic activity and stability. Additionally, conducting long-term durability tests is essential to assess the system's stability over extended operational periods, ensuring reliable performance under varying conditions. Furthermore, performing comparative analyses of different flow field designs can provide valuable insights into optimizing mass transport and gas distribution within the cell, ultimately improving overall efficiency. These factors will be crucial for future research aimed at enhancing the performance and longevity of regenerative fuel cells.

In conclusion, the efficiency of regenerative fuel cells can be enhanced by selecting the right operating parameters, making these systems promising solutions for sustainable energy applications.

REFERENCES

[1] Q. Hassan, A. Z. Sameen, H. M. Salman, M. Jaszczur, ve A. K. Al-Jiboory, “RETRACTED: Hydrogen energy future: Advancements in storage technologies and implications for sustainability”, *J. Energy Storage*, c. 72, s. 108404, Kas. 2023, doi: 10.1016/j.est.2023.108404.

[2] J. Garche, T. Smolinka, M. A. Navarra, S. Panero, ve B. Scrosati, “Regenerative fuel cells”, ss. 365-406, 2022, doi: 10.1016/B978-0-12-819424-9.00007-0.

[3] V. N. Nguyen ve L. Blum, “Reversible fuel cells”, Elsevier, 2016, ss. 115-145. doi: 10.1016/B978-1-78242-363-8.00005-0.

[4] J. Andrews ve A. K. Doddathimmaiah, “Regenerative fuel cells”, Elsevier, 2008, ss. 344-385. doi: 10.1533/9781845694838.344.

[5] F. Mitlitsky, B. Myers, ve A. H. Weisberg, “Lightweight pressure vessels and unitized regenerative fuel cells”, Ara. 1996, s. CONF-961107--Absts., 460339. doi: 10.2172/460339.

[6] Y. N. Regmi *vd.*, “A low temperature unitized regenerative fuel cell realizing 60% round trip efficiency and 10 000 cycles of durability for energy storage applications”, *Energy Environ. Sci.*, c. 13, sy 7, ss. 2096-2105, 2020, doi: 10.1039/c9ee03626a.

[7] Z. Pu *vd.*, “Regenerative fuel cells: Recent progress, challenges, perspectives and their applications for space energy system”, *Appl. Energy*, c. 283, s. 116376, Şub. 2021, doi: 10.1016/j.apenergy.2020.116376.

[8] I. G. Kim, I. W. Nah, I.-H. Oh, ve S. Park, “Crumpled rGO-supported Pt-Ir bifunctional catalyst prepared by spray pyrolysis for unitized regenerative fuel cells”, *J. Power Sources*, c. 364, ss. 215-225, Eki. 2017, doi: 10.1016/j.jpowsour.2017.08.015.

[9] J. E. Park, M. Karuppannan, O. J. Kwon, Y.-H. Cho, ve Y.-E. Sung, “Development of high-performance membrane-electrode assembly in unitized regenerative fuel cells”, *J. Ind. Eng. Chem.*, c. 80, ss. 527-534, Ara. 2019, doi: 10.1016/j.jiec.2019.08.029.

[10] S.-D. Yim *vd.*, “Optimization of bifunctional electrocatalyst for PEM unitized regenerative fuel cell”, *Electrochimica Acta*, c. 50, sy 2, ss. 713-718, Kas. 2004, doi: 10.1016/j.electacta.2004.02.068.

PERFORMANCE OPTIMIZATION AND DESIGN ADVANCEMENTS OF PROTON EXCHANGE MEMBRANE FUEL CELLS FOR PORTABLE ENERGY APPLICATIONS

[1]*Ahmed Algherbawi and* [1*]*Sami Ekici*
[1] Firat University, Faculty of Technology, Department of Energy Systems Engineering, Elazig, 23200, Turkiye

*Corresponding author e-mail: sekici@firat.edu.tr

ABSTRACT
The study is centered on the design and development of a cost-effective 3-cell Proton Exchange Membrane Fuel Cell (PEMFC) prototype, delivering a power output of 150 W. The focus is on optimizing the fuel cell design by using Nafion 212 membranes, platinum-based catalysts, and serpentine flow channels to enhance efficiency and durability. On the analysis, attention was paid to key performance factors such as temperature, pressure and reactant flow. Simulations and experimental evaluations conducted using MATLAB and SolidWorks verified the system's reliability. The obtained results demonstrate the potential of PEMFCs for handling energy shortages as well as reducing greenhouse gas emissions, with further enhancements thought to support scalability for higher power applications.

Keywords: Hydrogen energy, Proton exchange membrane fuel cells, Emission reduction, Renewable energy.

1. INTRODUCTION

Proton Exchange Membrane Fuel Cells (PEMFCs) are increasingly recognized as a key clean energy technology with broad applications in portable power systems and transportation [1]. Monitoring and optimizing the performance of PEMFCs is critical for their reliable and efficient operation, particularly under varying conditions [2]. Unlike conventional systems, this project introduces a customized 3-cell PEMFC stack design with serpentine flow channels and optimized Nafion 212 membranes to address energy efficiency, durability, and portability challenges [3]. Aspects such as balancing efficiency, stability and scalability, can often represent limitations on traditional PEMFC designs, specially concerning real-world applications [4,5]. This study offers a novel approach by integrating advanced modeling techniques and experimental validation to enhance the performance and practicality of PEMFC systems. By focusing on reactant flow optimization, system thermal stability, and precise voltage-current response analysis, this study sets a benchmark for portable PEMFC systems in remote or energy-deficient areas. As part of the methodology, simulation tools such as MATLAB and SolidWorks were employed with experimental analysis to validate the system's efficiency. Key innovations include the use of advanced platinum catalysts for minimizing activation losses and a tailored design to improve reactant distribution and water management [6]. These improvements contribute to the practical application of PEMFCs by reducing material costs, extending operational stability, and ensuring compatibility with real-world energy demands. This study draws attention to the potential of PEMFCs and their capacity to face global energy challenges while providing an efficient, cost-effective, and scalable solution for portable energy applications. Furthermore, the aim is to contribute to the vast adoption of hydrogen-based clean energy technologies by advancing the performance standards of PEMFC systems.

2. PERFORMANCE AND DESIGN ADVANCEMENTS OF THE PEMFC PROTOTYPE

The performance and design process of a 3-cell Proton Exchange Membrane Fuel Cell (PEMFC) prototype, tailored for portable energy applications, reached significant upgrading through this study. By integrating Nafion 212 membranes, platinum-based catalysts, and serpentine flow channels, the system demonstrated a stable power output of 150 W and an efficiency of approximately 50%, outperforming previous designs. Advanced simulations using MATLAB and SolidWorks optimized the reactant distribution and water management, while experimental validation under real-world conditions confirmed the system’s reliability and durability. Improvements on power output, efficiency and operational stability are featured on Table 1.

Table 1. Comparative analysis of PEMFC performance metrics

Parameters	Previous Studies	This Study
Power Output	100–120 W	150 W
Efficiency	40–45%	~50%
Operating Temperature	50–70°C	60–80°C
Flow Channel Design	Parallel/single-path	Serpentine
Stability Duration	6–8 hours	10 hours

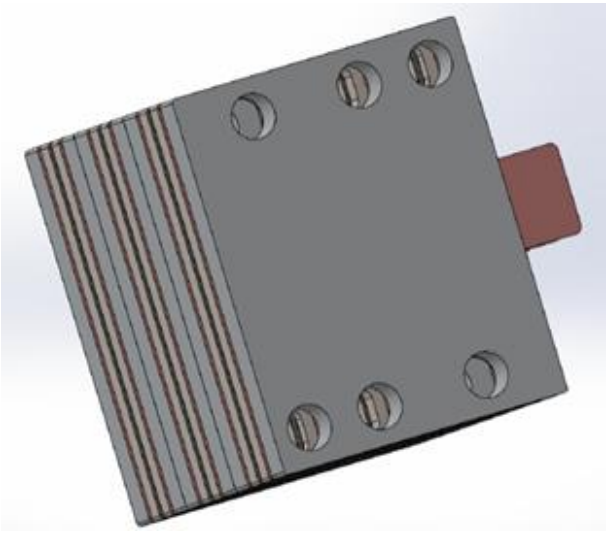

Fig. 1. 3D design of fuel cell stack

The 3D design of the PEMFC stack was developed using SolidWorks to ensure precise optimization of the system's geometry and flow dynamics. To enhance reactant distribution and water management, serpentine flow channels were specifically designed, minimizing concentration losses and ensuring uniform current density through the active area. This detailed design plays a crucial role in achieving the system's high efficiency and stability, making it suitable for real-world applications in portable energy solutions [7]. The visual representation provides an overview of the stack structure and flow channel configuration.

3. PERFORMANCE OPTIMIZATION OF PEMFC

Advanced optimization techniques and MATLAB modeling was applied in this study to enhance the performance of Proton Exchange Membrane Fuel Cells (PEMFCs). Key improvements included minimizing polarization losses and identifying optimal parameters under different operating conditions. The Multi-Verse Optimizer (MVO) algorithm was implemented and compared against other methods like SSA, PSO, SCA, and MFO [8,9], showing superior performance with reduced error and convergence time. Matlab simulink model of fuel cell is depicted in Fig.2.

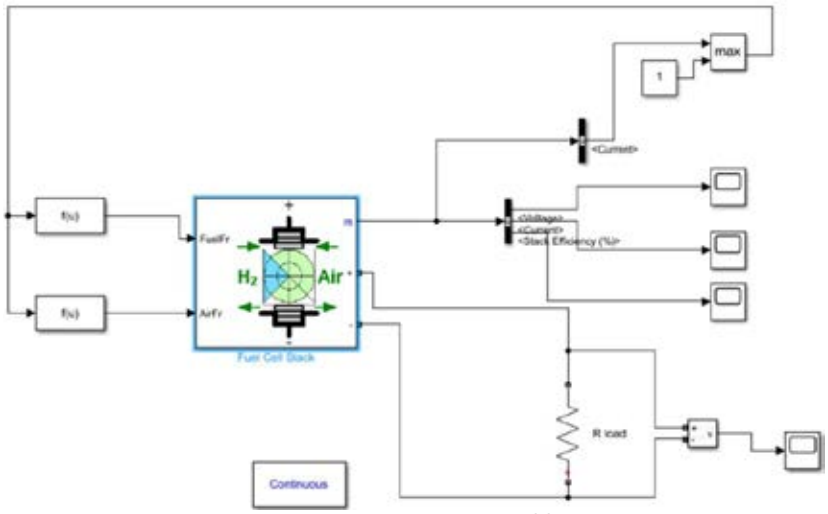

Fig. 2. Matlab simulink model of fuel cell

The attached figures and tables provide a consistent and detailed representation of the performance optimization process for PEMFCs. The result is a logical flow of evidence supporting the effectiveness of the Multi-Verse Optimizer (MVO) [10]. Fig. 3 (a) and (b) highlight the comparative performance of various optimization algorithms under two distinct operating conditions. Fig. 3. (a) focuses on SSA, SCA, MFO, PSO, and MVO under the first condition, showcasing how MVO minimizes polarization losses and stabilizes voltage more effectively than other methods. In contrast Fig. 3. (b) compares HABC (Hybrid Artificial Bee Colony) [11], HADE (Hybrid Adaptive Differential Evolution) algorithms [12], and MVO under the second condition, further validating MVO's consistent superiority in enhancing PEMFC performance.

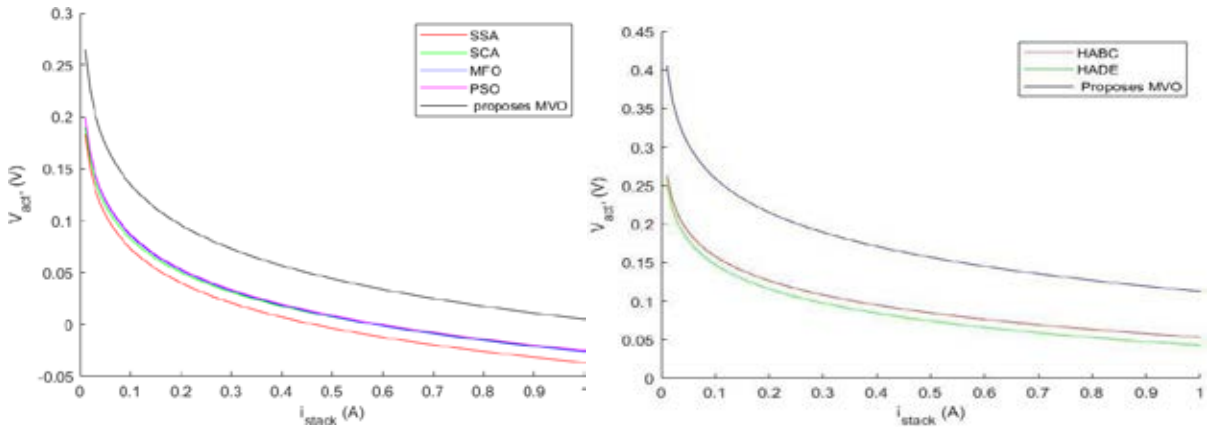

(a) (b)

Fig. 3. Polarization curves obtained via some different algorithms (a) conditions #1, (b) conditions #2

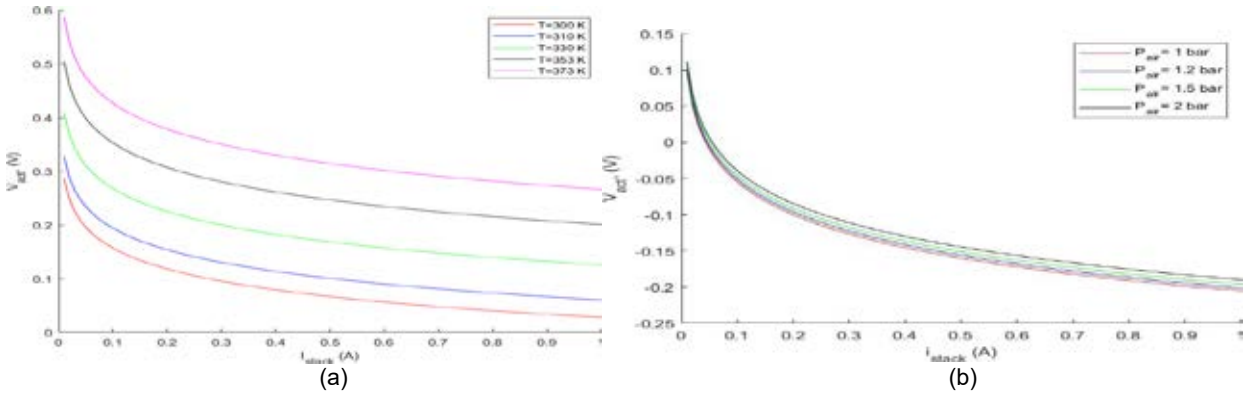

(a) (b)

Fig. 4. PEM fuel cells' polarization curves for (a) different temprature conditions, (b) different pressure conditions

To furtherly examine the operational parameters, Fig. 4 (a) presents V-I polarization curves under five different temperature conditions, demonstrating the critical role of temperature in improving reactant distribution and reducing concentration losses. These enhancements lead to better system efficiency and highlight the importance of precise thermal management. Complementing this, Fig. 4 (b) examines the effect of varying pressure, with V-I polarization curves under four pressure conditions. The results reveal that increasing pressure significantly reduces ohmic and concentration losses, thus boosting overall system performance. Tables 2 and 3 provide the technical foundation and experimental setup for these findings. Table 2 summarizes the PEMFC stack's specifications, such as the number of cells, active cell area, Nafion membrane thickness, and rated power. These parameters form the backbone for accurate modeling and optimization efforts. Table 3 details the operating conditions, including pressure, temperature, relative humidity, voltage, and reactants, ensuring consistent and reliable testing protocols. The figures and tables provided can illustrate a clear narrative of how MVO outperforms traditional optimization methods like PSO and SCA. This is achieved through an effective reduction of losses, an enhanced reactant distribution and by stabilizing system efficiency, proving the MVO to be a powerful tool in advancing PEMFC performance. These visual and tabular results not only validate the study's approach but also underscore the practical potential of PEMFCs as a scalable and sustainable solution for clean energy applications.

Table 2. Technical data

Stack parameter	Value
Number of cells in a stack, cells	42
Active cell area (c m ^{2})	27
Nafion membrane thickness 1	127μm
Maximum current density Jmax (A c m$_{-2}$)	0.86
Rated power(W)	250

Table 3. Operating conditions

Parameters	Value
Pa (bar)	1-3
Pc (bar)	1-5
Stack temperature T (K)	343,15 - 353,15
Relative humidity in anode RHa	1
Relative humidity in cathode RHc	1
Voltage (V)	24
Maximum Current (A)	100
Reactants	H2 and Air

4. CONCLUSIONS

In this study, a 3-cell Proton Exchange Membrane Fuel Cell (PEMFC) prototype tailored for portable energy applications was successfully developed. By leveraging optimized Nafion 212 membranes and platinum-based catalysts, the system achieved a stable power output of 150 W under standard conditions. The system's efficiency and durability were enhanced through the measurement of key performance parameters, including pressure, temperature, and reactant flow, were carefully analyzed to enhance the system's efficiency and durability. The integration of advanced modeling tools, including MATLAB and SolidWorks, allowed for precise optimization of the PEMFC design. Notably, the serpentine flow channel configuration improved reactant distribution and water management, minimizing losses and ensuring stable operation over extended periods. The system demonstrated an electrical efficiency of approximately 50%, highlighting its potential for portable and remote energy solutions. Future research can focus on scaling the PEMFC design to accommodate higher power requirements, further reducing material costs, and exploring alternative catalyst compositions to enhance overall performance. These advancements would position PEMFCs as a practical and sustainable energy solution capable of addressing global energy challenges and reducing greenhouse gas emissions. This study draws attention to the critical role of innovation in the development of reliable, efficient, and scalable clean energy technologies.

REFERENCES

[1] Han I-S, Jeong J, Shin HK. PEM fuel-cell stack design for improved fuel utilization. Int J Hydrogen Energy 2013;38:11996–2006. https://doi.org/10.1016/j.ijhydene.2013.06.136.
[2] Devrim Y, Devrim H, Eroglu I. Development of 500 W PEM fuel cell stack for portable power generators. Int J Hydrogen Energy 2015;40:7707–19. https://doi.org/10.1016/j.ijhydene.2015.02.005.
[3] Eker Kahveci E, Taymaz I. Performance Analysis of a PEM Fuel Cell Stack Having 150 cm 2 Active Layer by Using Design of Experiments (DOE). E3S Web of Conferences 2020;162:01004. https://doi.org/10.1051/e3sconf/202016201004.
[4] Ahmed M, Shusheng X. Comprehensive review of serpentine flow fields for effective thermal management of proton exchange membrane fuel cell. Heliyon 2024;10:e39793. https://doi.org/10.1016/j.heliyon.2024.e39793.
[5] Yakubu AU, Zhao J, Jiang Q, Ye X, Liu J, Yu Q, et al. A comprehensive review of primary cooling techniques and thermal management strategies for polymer electrolyte membrane fuel cells PEMFC. Heliyon 2024;10:e38556. https://doi.org/10.1016/j.heliyon.2024.e38556.
[6] Qureshi A, Wahab MA, Badreldin A, Abdel-Wahab A, Castaneda H, Abdala A. Advances in photothermal catalysts for solar-driven hydrogen production. Int J Hydrogen Energy 2024;96:160–81. https://doi.org/10.1016/j.ijhydene.2024.11.124.
[7] Park J-T, Xu X-R, Wang J, Zhu X-J. A small-scale and portable 50 W PEMFC system that automatically generates hydrogen from a mixture of Al, CaO, NaOH and sodium CMC in water without external power supply. Int J Hydrogen Energy 2013;38:10511–8. https://doi.org/10.1016/j.ijhydene.2013.05.177.
[8] Amiri MH, Mehrabi Hashjin N, Montazeri M, Mirjalili S, Khodadadi N. Hippopotamus optimization algorithm: a novel nature-inspired optimization algorithm. Sci Rep 2024;14:5032. https://doi.org/10.1038/s41598-024-54910-3.
[9] Abaza A, El-Sehiemy RA, Mahmoud K, Lehtonen M, Darwish MMF. Optimal Estimation of Proton Exchange Membrane Fuel Cells Parameter Based on Coyote Optimization Algorithm. Applied Sciences 2021;11:2052. https://doi.org/10.3390/app11052052.
[10] Fathy A, Rezk H. Multi-verse optimizer for identifying the optimal parameters of PEMFC model. Energy 2018;143:634–44. https://doi.org/10.1016/j.energy.2017.11.014.
[11] Hachana O, El-Fergany AA. Efficient PEM fuel cells parameters identification using hybrid artificial bee colony differential evolution optimizer. Energy 2022;250:123830. https://doi.org/10.1016/j.energy.2022.123830.
[12] Sun Z, Wang N, Bi Y, Srinivasan D. Parameter identification of PEMFC model based on hybrid adaptive differential evolution algorithm. Energy 2015;90:1334–41. https://doi.org/10.1016/j.energy.2015.06.081.

NUMERICAL SIMULATIONS OF REACTING FLOWS IN HYDROGEN ENRICHED METHANE BLENDS AND PURE HYDROGEN COMBUSTION

[1*]*Henrique Monteiro*, [1]*Lucas Marcon,* [2]*Filipa Oliveira,* [2]*Luís Vaz*
[1] INEGI, Energy department, Rua Dr. Roberto Frias 400, Porto, 4200-465, Portugal
[2] COLEP PK, R. Comentador Arlindo Soares de Pinho 1977, 3730-423, Vale de Cambra, Portugal

*Corresponding author e-mail: hmonteiro@inegi.up.pt

ABSTRACT
This study presents a methodology for steady-state CFD simulations to analyze key combustion parameters, including flame temperature, velocity fields, and pollutant formation (CO_2, CO, and NO_x). The proposed approach provides researchers and engineers with an accessible framework for simulating complex fuel systems, facilitating improved system design and optimization. To assess its accuracy and practical applicability, the methodology is currently being tested in a real case study with unique characteristics. The simulation provides a comprehensive analysis of multiple combustion parameters. As examples, results show that blending hydrogen with methane increases the adiabatic flame temperature by 0.2% and 0.5% for hydrogen blends of 10% and 20% (by volume), respectively, and by 8.9% for pure hydrogen. The maximum CO_2 molar fraction decreases by 2.6% and 6.1% for 10% and 20% hydrogen blends, respectively, and is entirely eliminated with 100% hydrogen combustion. Additionally, temperature and pollutant concentrations were analyzed at the combustion chamber outlet. While some trends observed in the flame zone were confirmed, others exhibited different behaviors due to mixing, heat loss, and chemical kinetics along the flow path. These findings highlight the potential of hydrogen-enriched combustion for reducing pollutant emissions while emphasizing the importance of detailed spatial analysis in combustion studies.

Keywords: Computational Fluid Dynamics, Combustion, Methane-Hydrogen Blending.

1. INTRODUCTION

The ongoing global transition toward sustainable energy sources necessitates a deep understanding of alternative fuel systems to mitigate environmental concerns and promote cleaner energy solutions. Among these alternatives, hydrogen combustion stands out as a promising candidate due to its lower carbon footprint and potential as a renewable energy source. However, transitioning entirely to hydrogen presents several challenges, including infrastructure limitations, safety concerns, and economic viability. A practical intermediate solution is the use of hydrogen-enriched natural gas blends, which can reduce greenhouse gas emissions while ensuring compatibility with existing energy systems. By integrating hydrogen into the current natural gas network, this approach enables a gradual transition toward hydrogen-based energy without requiring immediate large-scale infrastructure changes.

Blending hydrogen with natural gas influences combustion characteristics, affecting flame stability, temperature distribution, pollutant formation, and overall system efficiency. While hydrogen-enriched combustion reduces CO_2 emissions due to the absence of carbon in hydrogen fuel, it can also impact NO_x emissions and alter flame behavior. Understanding these effects is critical for optimizing combustion performance and ensuring safe, efficient operation in industrial and power generation applications.

Computational Fluid Dynamics (CFD) simulations provide a powerful tool for analyzing the complex fluid dynamics and combustion behavior of hydrogen-natural gas blends. CFD allows researchers and engineers to model key parameters such as temperature distribution, velocity fields, and pollutant formation, offering valuable insights that can inform the design and optimization of combustion systems. Previous studies have demonstrated the effectiveness of CFD in predicting combustion performance, but further research is needed to validate simulation methodologies and assess their accuracy in real-world applications.

2. SYSTEM DESCRIPTION AND METHODOLOGY

2.1. Case Study Overview

This study focuses on an industrial drying process installed in a Portuguese industry, which utilizes a vertical drying oven with a recirculating combustion system. The system is designed to provide controlled heat for the drying process, optimizing energy efficiency while ensuring effective moisture removal from the processed materials. The drying oven is equipped with a burner coupled to a combustion chamber, where fuel is burned to generate heat. A portion of the combustion gases is reinjected into the chamber to improve thermal efficiency and reduce overall emissions.

At the combustion chamber outlet, a fan plays a crucial role in extracting air and combustion products, distributing the hot gases through ducts that supply heat to the drying process. This fan also facilitates the recirculation of air from within the drying oven back into the combustion chamber, further enhancing heat utilization. Any remaining air and exhaust gases are released through the system's chimney. This process is illustrated in Figure 1.

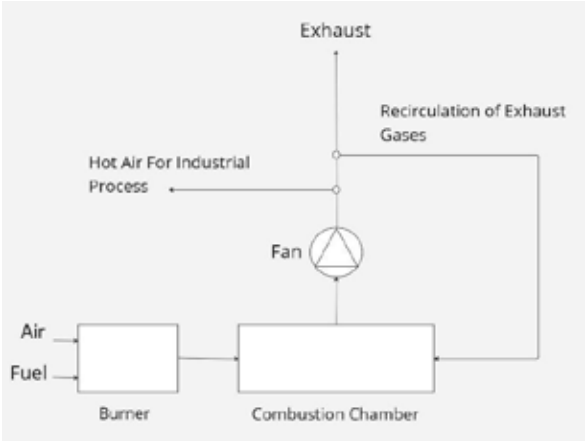

Fig. 1. System working principle

The numerical simulations carried out aim to determine the combustion characteristics inside the combustion chamber, whose geometry is presented in Figure 2, while also considering the burner's injection system. For this purpose, it was necessary to study each component of this system.

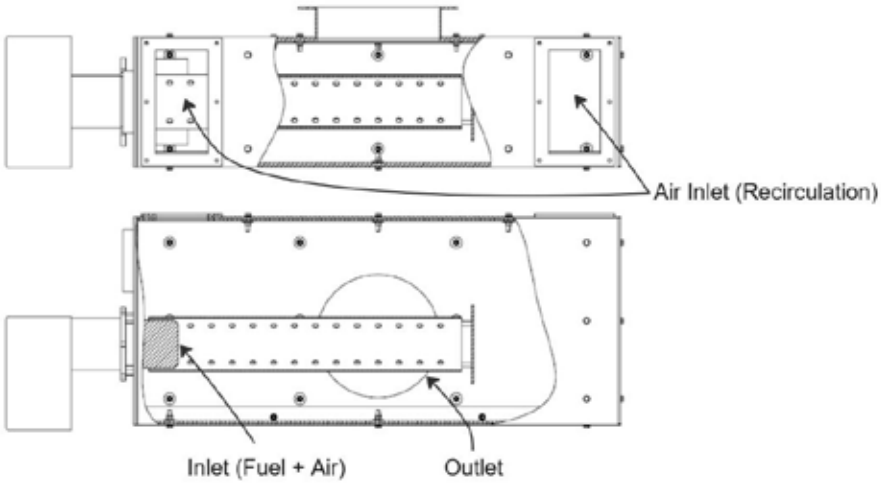

Fig. 2. Geometry of the combustion chamber

One of the key components to be studied is the burner's injection system, which consists of 8 injectors, hereafter referred to as primary injectors, that supply gas in the direction of the flow, and 6 injectors that supply gas in directions perpendicular to the flow, hereafter referred to as secondary injectors (see Figure 3). On one of the faces, there are also 4 openings for the passage of air into the zone where the fuel is injected perpendicular to the flow. This injection system also includes a turbulator, aimed at promoting the homogenization of the air-fuel mixture before it reaches the ignition electrode.

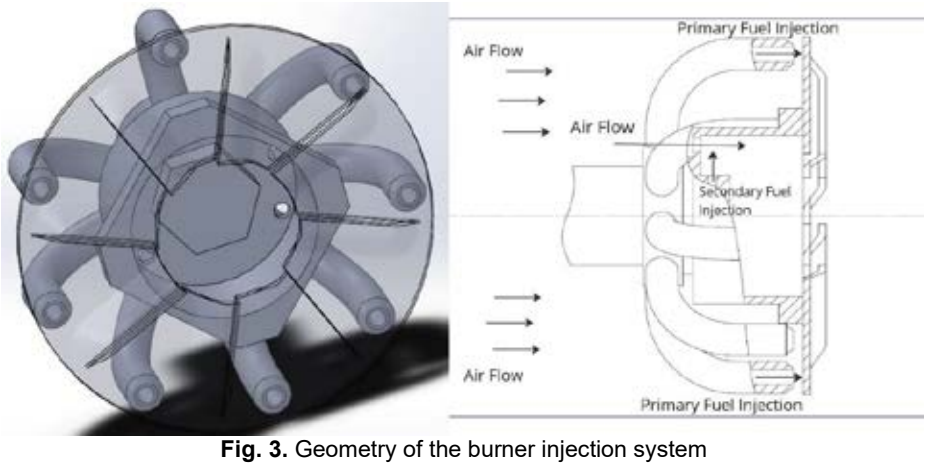

Fig. 3. Geometry of the burner injection system

2.2. Methodology

To support the CFD analysis of combustion in the chamber, a tool was developed to calculate the total fuel and air flow rates in the burner based on its operating power, the molar composition of the fuel, and the excess air percentage. Additionally, preliminary CFD simulations were conducted to examine the fuel flow within this specific injection system, aiming to determine the flow distribution at each injector outlet.

All CFD models in this study were developed using ANSYS Fluent [1]. For conducting combustion CFD simulations in this case study, the species transport model was employed. This model enables the simulation of mixing and chemical species transport by solving conservation equations that describe convection, diffusion, and reaction sources for each species involved in the process [2].

The combustion reactions were modeled using the Finite-Rate/Eddy Dissipation model, which is widely used in CFD combustion simulations as it accounts for both finite-rate chemical kinetics and turbulence effects. By combining finite-rate chemical reactions with turbulent mixing effects, this approach provides an accurate representation of combustion in turbulent flows.

Chemical modeling increases computational complexity as the number of species and reactions involved grows. To reduce the computational effort in numerical modeling, a reduced mechanism was proposed in [3] to describe the combustion of CH_4 and H_2, considering a significantly lower number of chemical species and reactions compared to the two previously identified detailed mechanisms. This kinetic mechanism is also capable of predicting NO_x (NO and NO_2) formation.

3. RESULTS AND DISCUSSION

In this section, a selection of results obtained from the simulations is presented, focusing on key parameters such as combustion characteristics, temperature distributions, and pollutant formation. Figure 4 illustrates an example of a temperature contour for the base scenario (combustion of 100% CH_4), generated using the ParaView postprocessing tool [4]. Although the temperature distribution in the flame region changes with fuel composition, the overall pattern remains quite similar across all scenarios.

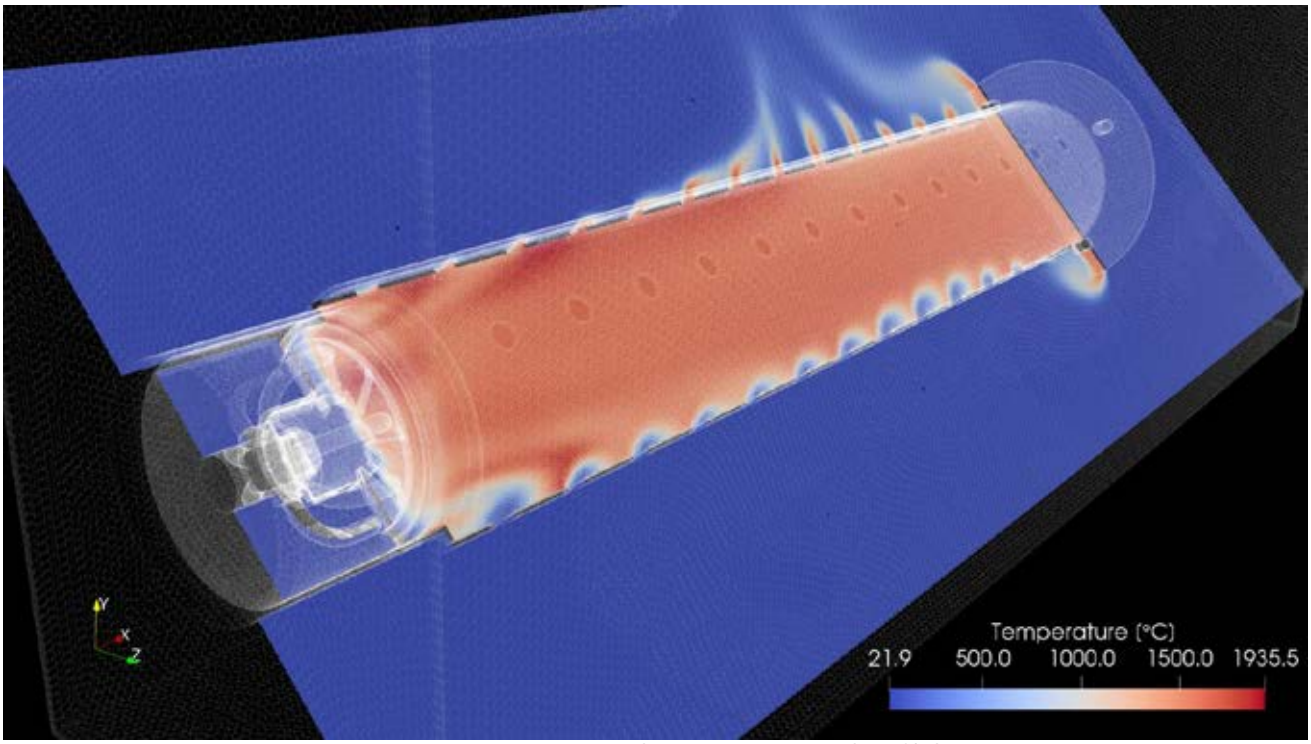

Fig. 4. Temperature contour for the combustion of 100% CH_4

To analyze the detailed temperature, pollutant, and H_2O formation values, selected maximum values obtained in the flame region are presented in Figure 5.

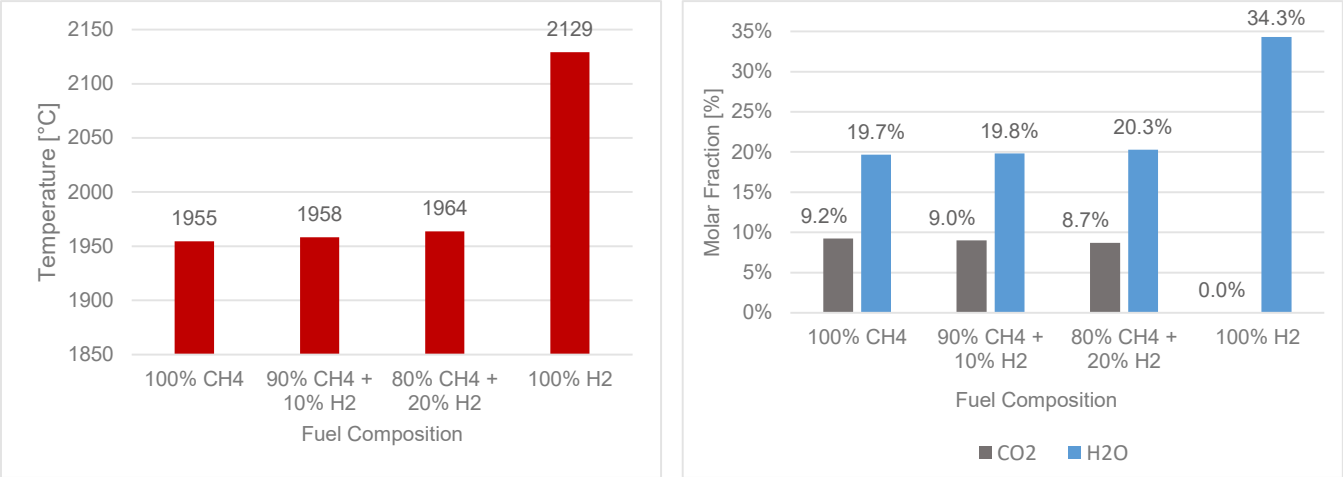

Fig. 5. Maximum temperature, CO_2 and H_2O mole fractions in the flame region

According to the results shown, the maximum flame temperature, increases with the higher percentage of H_2 in the fuel. For the air excess in this study (30%) and assuming excellent fuel-air mixture uniformity, lower maximum temperature values were expected. However, due to the non-uniform fuel distribution before the reaction zone, there are regions where the fuel-air mixture is richer (near stoichiometry), leading to higher combustion temperatures in those regions. The maximum increase in this parameter, compared to 100% CH_4, is approximately 9%.
The maximum CO_2 value in the flame decreases with the increasing percentage of hydrogen in the fuel, reaching zero for 100% H_2 combustion, as expected. Additionally, the maximum H_2O value increases with the higher percentage of hydrogen, showing a maximum increase of about 74% compared to 100% CH_4.
The results presented represent only a small portion of the study. This research includes a detailed analysis of the temperature field, velocity field, pollutant mole fraction fields, and water mole fraction fields. The maximum values obtained for each fuel composition were analyzed, along with the study of these quantities at the chamber outlet and for three different recirculation flow rates. The impact of pollutant mass fractions at the outlet enabled a decarbonization analysis. Additionally, profiles of these quantities along the flame region were plotted.

4. CONCLUSIONS

According to all the results obtained from the CFD study for this case, it can be concluded that blending up to 20% hydrogen with CH_4 can reduce CO_2 formation by up to 7.5%. The addition of hydrogen to the fuel increases the flame temperature, but the outlet temperature remains unchanged. Even in the case of 100% hydrogen combustion, the outlet temperature can be similar to that obtained with 100% CH_4 combustion or even slightly lower. Possible reasons for this behavior may be related to the thermal capacity and composition of the combustion gases. It was also observed that hydrogen blending increases NO_x formation in the flame region, although the values at the outlet remain similar.
To further validate the numerical modeling methodology, experimental studies will be conducted. Additionally, the development of auxiliary tools to provide accurate inputs for the CFD model was crucial in ensuring reliable simulations and meaningful conclusions.

ACKNOWLEDGEMENT

This work has been supported by the European Union under the Next Generation EU, through a grant of the Portuguese Republic's Recovery and Resilience Plan (RRP) Partnership Agreement, within the scope of the project PRODUTECH R3 – "Agenda Mobilizadora da Fileira das Tecnologias de Produção para a Reindustrialização".

REFERENCES

1. https://www.ansys.com/products/fluids/ansys-fluent. Accessed on January 30, 2025.
2. https://www.afs.enea.it/project/neptunius/docs/fluent/html/th/node126.htm. Accessed on January 30, 2025.
3. Azevedo P, Cabrita I and Pinho C. 2014. Reduced Mechanism for Combustion of Hydrogen and Methane with Nitrogen Chemistry. Computational Thermal Sciences Vol. 6, nº 6, p. 541-551.
4. https://www.paraview.org/. Acessed on January 30, 2025

INFLUENCE OF THE TECHNOLOGY FOR OBTAINING IMC OF THE Mg-7%Ni-3%CE SYSTEM ON THE EVOLUTION OF PHASE TRANSFORMATIONS

[1,2*]*Mukhamedova Nuriya*, [1]*Miniyazov Arman*, [1,3*]*Ospanova Zhanna*, [1]*Sabyrtaeva Aisara*, [1]*Shaikieva Karina*
[1]Institute of Atomic Energy Branch of the National Nuclear Center of the Republic of Kazakhstan, 10 Beybit Atom str., Kurchatov, 071100, Kazakhstan
[2]Shakarim University, 20 Glinki st., Semey, 071412, Kazakhstan
[3] D. Serikbayev East Kazakhstan technical university, D. Serikbayev STR., 19, Ust-Kamenogorsk, 070004, Kazakhstan

*Corresponding author e-mail: ospanova@nnc.kz, bakayeva@nnc.kz

ABSTRACT

The paper presents the results of studies on the evolution of phase transformations in the Mg-7%Ni-3%Ce system under successive exposure to mechanical fusion (MF) and spark plasma sintering (SPS), with a focus on structural changes after the SPS stage. During the MS stage, the gradual formation of phases from the initial components to the intermetallic compounds Mg_2Ni and $CeMg_3$ was observed, accompanied by the transformation of the magnesium crystal lattice and an increase in structural defects. Notably, the SPS process played a key role in stabilizing the material structure. During sintering, phase transformations were completed, leading to the formation of a dense, multicomponent microstructure with a uniform distribution of intermetallic compounds. SPS facilitated grain growth and densification, as well as the elimination of defects accumulated during the MF stage. The average crystallite size after sintering ranged from 20 to 70 nm, depending on the processing conditions. Thus, the combined application of MF and SPS allows for controlled management of the phase composition and microstructure of the material, ensuring the development of stable hydrogen-absorbing alloys with improved properties.

Keywords: mechanical fusion, spark plasma sintering, phase transformations, intermetallic compounds.

1. INTRODUCTION

Magnesium-based (Mg) metal hydride materials have attracted significant attention due to their high hydrogen storage capacity (up to 7.6 wt.%), availability, and environmental safety [1-4]. However, their practical application is limited by the high thermodynamic stability of the hydride phase, which requires elevated temperatures for effective sorption kinetics, as well as low resistance to atmospheric contaminants, leading to the degradation of sorption properties [5-9]. Methods for improving the hydrogen sorption kinetics of Mg-based materials include alloying with transition metals [10], nanostructuring of Mg via mechanical synthesis in ball mills [11–13], and severe plastic deformation [14-16]. The incorporation of transition metals (e.g., Ni) and rare earth elements (RE) promotes the formation of intermetallic phases such as Mg_2Ni, $Mg_{12}Ni_6$, and CeNi, which exhibit enhanced hydrogen sorption and desorption kinetics [17]. Additionally, RE elements stabilize the fine-grained structure and reduce the hydrogen desorption temperature through the formation of new intermetallic phases, such as $REH_{2.73}$ [18-20]. The combination of mechanical fusion (MF) and spark plasma sintering (SPS) offers promising opportunities for alloy consolidation. However, research in this field remains insufficient, necessitating a deeper investigation into the effects of MF and SPS on the structure, phase state, and properties of these alloys.

During SPS, structure stabilization, defect elimination, material densification, and uniform distribution of intermetallic compounds occur. A key advantage of SPS is its ability to prevent excessive oxidation, which may be observed at high ball-to-powder mass ratios (BPR) during MF. Furthermore, SPS facilitates the formation of a dense microstructure with low porosity and minimal residual stresses, which positively affects the mechanical and functional properties of the material [21]. The novelty of this study lies in the investigation of the phase transformation evolution in the Mg-7%Ni-3%Ce system under successive application of MF and SPS, with an emphasis on structural changes after SPS. For the first time, the influence of sintering conditions on the formation of the CeNi phase, which was absent after MF but appeared as a result of SPS at 500–560 °C, has been studied. The obtained results demonstrate the possibility of targeted control over phase evolution and improvement of hydrogen-absorbing properties through the combined application of MS and SPS.

2. MATERIALS AND METHODS

As the starting materials, high-purity metal powders were used: magnesium powder (GOST 6001-79, grade MPF-3, purity 99%, particle size 120–180 μm), metallic cerium (purity 99.99%, particle size 70 μm), and nickel carbonyl powder (grade PNK-UT3, purity 99.99%, particle size 20 μm) (supplier: Suoyi, China).

Based on the analysis of technical literature, the Mg-7%Ni-3%Ce composition was mixed in optimally predetermined proportions and then successively processed in a Retsch PM100 planetary mill under the parameters specified in Table 1.

Table 1.

Sample composition	Ball-to-powder ratio (BPR)	Milling time (h)	Rotation speed (rpm)
Mg-7%Ni-3%Ce	10:1,20:1,30:1	5 and 10	350 and 450

SPS was carried out at 500–560 °C under a pressure of 1 MPa for 5 minutes. Phase composition analysis was performed using X-ray diffraction (XRD) on an EMPYREAN (Panalytical) diffractometer with Cu-Kα radiation in the range of 20–90° 2θ (step size 0.013° 2θ). The experimental parameters were as follows: 45 kV, 40 mA, divergence slit 1°, incident beam mask 15, and exposure time 30.6 s. Data processing was conducted using the HighScore software with the Crystallography PDF-4 AXIOM database.

To complement the XRD data and calculate crystallite sizes, scanning electron microscopy (SEM) was performed using a Hitachi TM4000plus. The studies included topographic and compositional contrast, energy-dispersive spectroscopy (EDS), and particle size measurements. Morphological and elemental analysis was conducted on four randomly selected areas of each sample.

3. RESULTS AND DISCUSSION

XRD analysis confirmed that MF induces significant phase changes in the Mg-Ni-Ce system. At a BPR of 30:1 and a milling duration of 10 hours, a significant decrease in the intensity of Mg peaks was observed in Fig. 1a, indicating an increase in structural defects. After SPS (Fig. 1c), the high degree of crystallinity of these phases was confirmed by the presence of sharp and well-defined peaks in the diffraction patterns. Structural changes related to the percentage content of alloying elements in the samples are also evident.

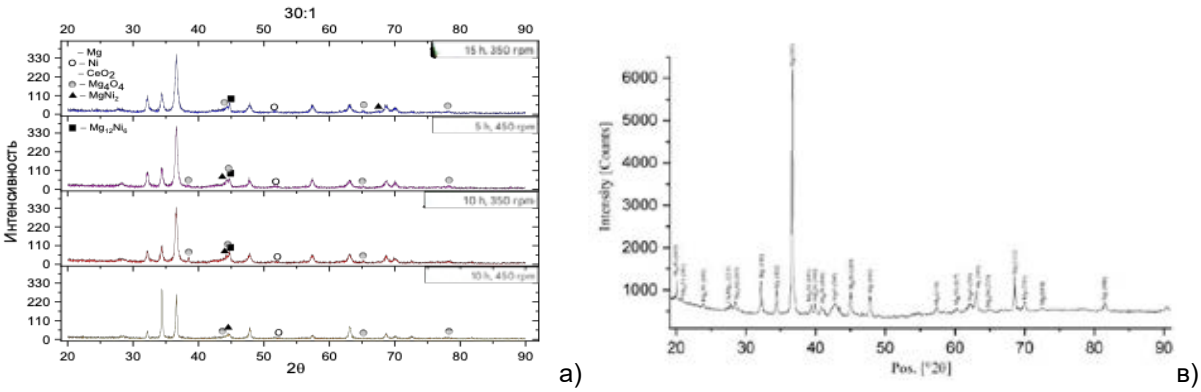

Fig. 1. a) Diffraction patterns of the studied PS of the Mg-7%Ni-3%Ce system after MS, grinding ball ratio – 30:1 c) Diffraction pattern of the Mg-7%Ni-3%Ce sample after SPS.

After IPS, the CeNi phase appeared, which was absent after MF. At a temperature of 500-560 °C, a uniform distribution of components occurred, which prevented the formation of large oxide phases.

4. CONCLUSIONS

Thus, the study of phase transformations in the Mg-7%Ni-3%Ce system during mechanical fusion (MF) and spark plasma sintering (SPS) showed that their sequential application allows for effective control of the phase composition and structure of the material. X-ray phase analysis and scanning electron microscopy confirmed that an increase in the ball-to-powder mass ratio, mechanical treatment duration, and rotation speed accelerates the formation of intermetallic compounds Mg_2Ni and CeNi, which catalyze hydrogen sorption processes. Further work on dispersion and sorption/desorption is planned.

ACKNOWLEDGEMENT

This research has been/was/is funded by the Committee of Science of the Ministry of Science and Higher Education of the Republic of Kazakhstan (AP19574566 "Development of hydrogen storage materials based on Mg-Ni-Ce").

REFERENCES

1. Ding, Z.M., Fu, Y.K., Wang, Y., Bi, J., Zhang, L., Peng, D.D., Li, Y., & Han, S.M. (2019). International Journal of Hydrogen Energy, 44(3), 8347–8356.
2. Sakintuna, B., Lamari-Darkrim, F., & Hirscher, M. (2007). Metal hydride materials for solid hydrogen storage: a review. International Journal of Hydrogen Energy, 32(9), 1121–1140. https://doi.org/10.1016/j.ijhydene.2006.11.022
3. Barthelemy, H., Weber, M., & Barbier, F. (2017). Hydrogen storage: recent improvements and industrial perspectives. International Journal of Hydrogen Energy, 42(11), 7254–7262. https://doi.org/10.1016/j.ijhydene.2016.03.178
4. Wang, H., Lin, H.J., Cai, W.T., Ouyang, L.Z., & Zhu, M. (2016). Tuning kinetics and thermodynamics of hydrogen storage in light metal element based systems – A review of recent progress. Journal of Alloys and Compounds, 658, 280-300. https://doi.org/10.1016/j.jallcom.2015.10.090
5. Lin, H.J., Cai, W.T., Ouyang, L.Z., & Zhu, M. (2016). Tuning kinetics and thermodynamics of hydrogen storage in light metal element-based systems. Materials Research Express. https://doi.org/10.1016/j.matre.2024.100252 *(Note: DOI indicates Materials Research Express, but year suggests a possible error. Please double-check)*
6. Ding, Z., Li, Y., Lu, Y., et al. (2022). Tailoring MgH_2 for hydrogen storage through nanoengineering and catalysis. Journal of Magnesium and Alloys.
7. Li, Q., Luo, Q., Yang, X., & Tan, J. (2021). Thermodynamics and kinetics of hydriding and dehydriding reactions in Mg-based hydrogen storage materials. Journal of Magnesium and Alloys. https://doi.org/10.1016/j.jma.2021.10.002
8. Pluengphon, P., & Bovornratanaraks, T. (2019). High-pressure phases induce H-vacancy diffusion kinetics in TM-doped MgH_2. International Journal of Hydrogen Energy. http://dx.doi.org/10.1016/j.ijhydene.2019.06.066
9. Stuart, A., Adams, M., Grant, D.M., & Walker, G.S. (2019). Modeling the kinetic deviation of magnesium hydrogenation reaction under near-equilibrium conditions. International Journal of Hydrogen Energy. https://doi.org/10.1016/j.ijhydene.2019.04.036
10. Shang, Y., Pistidda, C., & Klassen, T. (2021). Mg-based materials for hydrogen storage. Journal of Magnesium and Alloys. https://doi.org/10.1016/j.jma.2021.06.007
11. Cermak, J., & David, B. (2011). Catalytic effect of Ni, Mg2Ni and Mg2NiH4 upon hydrogen desorption from MgH2. International Journal of Hydrogen Energy, 36(21), 13614–13620. https://doi.org/10.1016/j.ijhydene.2011.07.133
12. Kozhakhmetov, Y.A., Skakov, M.K., Kurbanbekov, S.R., Mukhamedov, N.M., & Mukhamedov, N.Ye. (2021). Powder composition structurization of the Ti-25Al-25Nb (At.%) system upon mechanical activation and subsequent spark plasma sintering. Eurasian Chemico-Technological Journal, 23(1), 37-44.
13. Kozhakhmetov, Y., Skakov, M., Wieleba, W., Sherzod, K., & Mukhamedova, N. (2020). Evolution of intermetallic compounds in Ti-Al-Nb system by the action of mechanoactivation and spark plasma sintering. AIMS Materials Science, 7(2), 182-191.
14. Floriano, R., et al. (2013). Cold rolling of MgH2 powders containing different additives. International Journal of Hydrogen Energy, 38(36), 16193–16198. https://doi.org/10.1016/j.ijhydene.2013.10.029
15. Peng, C., Li, Y., & Zhang, Q. (2022). Enhanced hydrogen desorption properties of MgH2 by highly dispersed Ni: The role of in-situ hydrogenolysis of nickelocene in ball milling process. Journal of Alloys and Compounds, 900, 163547. https://doi.org/10.1016/j.jallcom.2021.163547
16. Leiva, D.R., Jorge, A.M., Jr., Ishikawa, T.T., & Botta, W.J. (2019). Hydrogen Storage in Mg and Mg-Based Alloys and Composites Processed by Severe Plastic Deformation. Materials Transactions, 60, 1561-1570.
17. Yartys, V.A., et al. (2019). Magnesium based materials for hydrogen based energy storage: Past, present and future. International Journal of Hydrogen Energy, 44, 7809-7859. https://doi.org/10.1016/j.ijhydene.2018.12.212
18. Zou, J., Zeng, X., Ying, Y., Chen, X., Guo, H., Zhou, S., & Ding, W. (2013). Study on the hydrogen storage properties of core–shell structured Mg–RE (RE = Nd, Gd, Er) nano-composites synthesized through arc plasma method. International Journal of Hydrogen Energy, 38, 2337-2346. https://doi.org/10.1016/j.ijhydene.2012.11.145
19. Shang, C.X., & Guo, Z.X. (2007). Structural and desorption characterizations of milled powder mixtures for hydrogen storage. International Journal of Hydrogen Energy, 32(14), 2920-2925. https://doi.org/10.1016/j.ijhydene.2006.11.035
20. Huot, J., Ravnsbæk, D.B., Zhang, J., Cuevas, F., Latroche, M., & Jensen, T.R. (2013). Mechanochemical synthesis of hydrogen storage materials.Progress in Materials Science, 58(1), 30–75. https://doi.org/10.1016/j.pmatsci.2012.07.001
21. Aoyagi, H., Aoki, K., & Masumoto, T. (1995). Effect of ball milling on hydrogen absorption properties of FeTi, Mg2Ni and LaNi5. Journal of Alloys and Compounds, 231(1-2), 804–809. https://doi.org/10.1016/0925-8388(95)01721-6

MAXIMIZING THE DEGREE OF DEHYDROGENATION OF PERHYDRO-DIBENZYL TOLUENE VIA IN-LINE DISTILLATION FOR CONTINUOUS HYDROGEN RELEASE

[1]*Mujahid Naseem*, [1,2*]*Muhammad Luqman*, [3]*Yusuf Bicer*
[1] King Fahad University of Petroleum and Minerals, Interdisciplinary Research Center for Sustainable Energy Systems, Dhahran, 31261, Saudia Arabia
[2] King Fahad University of Petroleum and Minerals, Department of Architectural Engineering and Construction Management, Dhahran, 31261, Saudia Arabia
[3] Hamad Bin Khalifa University, Division of Sustainable Development, College of Science and Engineering, Doha, Qatar

*Corresponding author e-mail: Muhammad.luqman@kfupm.edu.sa

ABSTRACT
Dibenzyl toluene is an organic compound that can store hydrogen via chemical bonding of hydrogen having a storage capacity of 9 mol_{H2}/mol_{DBT} to form perhydro-dibenzyl toluene. When required, the stored hydrogen can be retrieved by supplying thermal energy, however, for a continuous hydrogen supply as required by fuel cell applications, the degree of dehydrogenation can go well below 30% making the process highly inefficient as well as uneconomic. This study introduces the use of in-line distillation within the dehydrogenation process to enhance the degree of dehydrogenation to a minimum of 80%. This will highly increase the process efficiency while reducing the cost incurred for hydrogen release.

Keywords: LOHC, perhydro-dibenzyl toluene, degree of dehydrogenation, hydrogen, fractional distillation

1. INTRODUCTION

High-temperature heat waves are striking across the globe and one of the fundamental reasons is the global warming [1], [2]. To overcome this issue, the highest priority is being given to renewable energy resources. However, the renewable energy resources have high fluctuations with seasonal variations and other weather conditions. The fluctuations in the energy from these renewable energies can be stored as hydrogen gas. This concept of storing seasonal fluctuation energy in the form of hydrogen in form of chemical hydrides and using it for transportation purposes dates back to early 1980's [3], [4], [5], [6]. However, its realization at that time was not aggressively pursued due to economic issues. The price of renewable energy is considerably higher than the conventional energy generation via fossil fuel [3]. As a result of these techno-economic issues at that era, the concept of hydrogen storage from renewable energies was not a pressing issue. Research continued in this area but at a sluggish rate. One such published work during this time is done by S. Yolcular and Ö. Olgun where the hydrogen storage is classified as chemical hydrides [7]. Recently, due to the visible outcome of global warming, energy production from renewable energy resources became the focal issue throughout the globe with renewable energy production growth increasing exponentially since 2009 with 12.2% increase recorded for the year 2018 [8]. Due to this, the concept hydrogen storage was re-introduced in 2011 by D. Teichmann, W. Arlt, P. Wasserscheid, and R. Freymann classified as Liquid Organic Hydrogen Carrier (LOHC) [9]. Their research group have made significant commendable advances in this topic with a few notable ones given in [9], [10], [11], [12].
Various methods can be used for the storage of hydrogen including compression, liquefaction, adsorption, chemical/metal hydrides. Compression of hydrogen requires a high pressure of 100-400 bar and exhibits a low volumetric and gravimetric storage density [9], [13], [14]. Liquefaction of hydrogen is a well-established industrialized process. However, it is an energy-intensive process due to an extremely low boiling point of -253 °C at 1 bar pressure and moreover, it does not cool down during the throttling process [13]. Hydrogen can also be stored via adsorption on an adsorbent surface, but it is only implemented lab-scale and is highly expensive with very less hydrogen storage capacity [13]. Hydrogen is also stored in the form of metal hydrides by forming chemical bonds with the metal which results in a high energy density but results in a high energy demand for dehydrogenation with very sluggish kinetics [13]. Another way of hydrogen storage is by chemically bonding the hydrogen with light elements to form chemical hydrides which are generally liquid at ambient conditions. However, most of the suggested chemical hydrides for hydrogen storage including methanol, ammonia, and formic acid are synthesized via methane gas [13].
LOHC materials are similar to chemical hydrides with an additional quality to endure a fully cyclic hydrogenation and dehydrogenation and retain their original structure [10], [13]. Due to this definition, methanol and formic acid are not considered to be LOHC material despite being organic and liquid at ambient conditions [13]. Bourane et al. have considered LOHC materials to be a subset of chemical hydrides [14]. LOHC materials store hydrogen by chemically bonding the hydrogen atoms to either of the double-bonds between carbon atoms of aromatic compounds. Dehydrogenation of LOHC+ materials results in pure hydrogen at the output which is highly suitable for fuel-cell applications.
One of the methods to obtain hydrogen gas is to produce it via surplus energy from various fluctuating renewable energy resources. The hydrogen produced can be stored and/or transported as chemical energy in the form of hydrogenated Liquid Organic Hydrogen Carrier (LOHC) [11], [15]. The hydrogenated LOHC referred to as LOHC+ can be stored,

transported, and it is economically more viable over long-distance transportation [16]. The dehydrogenation of LOHC+ is an endothermic process requiring 53~65 kJ/mol_{H_2} depending on the LOHC material used.

Brückner et al. proposed the use of heat transfer fluids; Marlotherm(s); as LOHC materials. They tested the dehydrogenation of H12-MLH at 270 °C and H18-DBT at 290~310 °C in presence of platinum on alumina catalyst and culminated these LOHC materials to be better than the previously reported materials discussed as NEC, TOL, and NPT [17]. Their mixtures appear to be more attractive LOHC material for hydrogen storage [18]. Among al the different LOHC materials, dibenzyl toluene (DBT) is an optimal selection due to high storage capacity, availability and finally its recovery after dehydrogenation [19]. The dehydrogenation reaction kinetics is very slow and keeps declining as the degree of dehydrogenation increases. For a small-scale plug flow reactor, the reaction kinetics obtained experimentally by S. Park et al. is given in Eq. (1) [20].

$$r = 5.4 \times 10^{11} e^{\frac{-171.72}{RT}} C_{H18-DBT}^{2.395 \pm 0.045} \quad (1)$$

With this reactor the only 30% degree of dehydrogenation (DoD) was achieved with an elapse of almost 5 hours. The reactor kinetics are highly improved using a rotating bed reactor studied by J. Lee et al. [21]. Despite the signification improvement in reaction kinetics, almost double that of previous study, the maximum DoD achieved was 50%. In this study, a new process design to maximize the degree of dehydrogenation by increasing the H18-DBT concentration at the reactor inlet via distillation column is proposed. The distillation column will be utilized to separate the two miscible hydrogenated and dehydrogenated forms of DBT according to the boiling points. It is further improvised to utilize dual distillation columns to investigate the possibility of further improvements.

2. MATERIALS AND METHODS

2.1. Material Properties

Three materials have been defined, hydrogen, H18-DBT, and H0-DBT. Due to the complexity of the problem, the reaction intermediate, H12-DBT and H6-DBT, are not considered in this study. The properties of DBT are evaluated using the thermodynamic data engine (TDE) and is validated as given in [19]. The LOHC materials have varying properties when hydrogenated which also serves to measure the degree of hydrogenation/dehydrogenation. For this analysis the most important property is the binary mixture liquid/vapor transition temperature at different mole ratio of H18/H0-DBT and is shown in Fig. 1.a.

2.2. Process Design and Simulation

Three different processes are modeled to simulate the dehydrogenation process as shown in Fig. 1. The first process is the conventional process where the flow passes through the dehydrogenation reactor and hydrogen is obtained. The second is the proposed process utilizing the distillation column to keep highest concentration of H18-DBT at the reactor as the H0-DBT is continuously removed from the product mixtures via the distillation column. The third process serves as an extension to the proposed concept in which two distillation columns are used in series to highly enhance the concentration of the dehydrogenated DBT at the outlet increasing the H18-DBT concentration at the reactor. The corresponding parameters for the simulation are compiled in Table I.

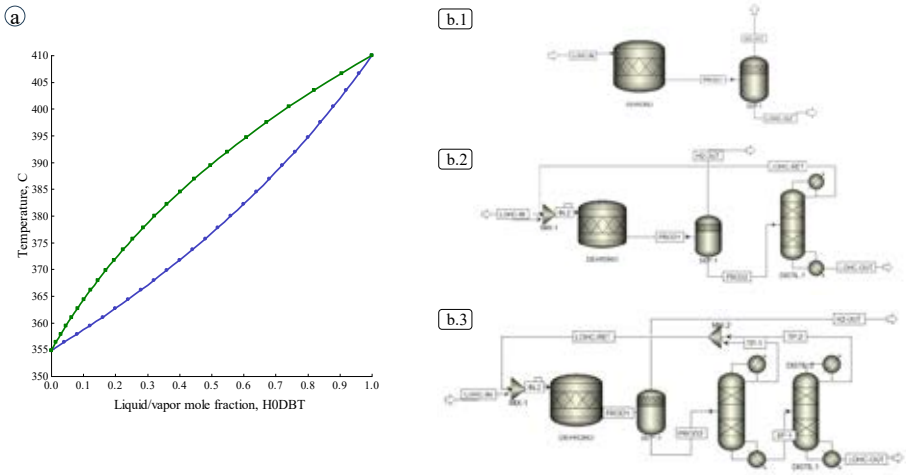

Fig. 1 a. Liquid/Vapor transition temperatures between mixtures of H18/H0-DBT for varying mole fractions of H0–DBT, b. Process Layout used for simulation of different systems, a. conventional, b. with single distillation column, and c. with dual distillation column.

Table 1. Simulation Parameters used for analysis

Variable	Value	Units
Dehydrogenation Reactor		
Temperature	290	°C
Pressure	1	bar
Reaction Yield	30	%
Single Distillation Column		
No. of stages	20	
Feed stage	12	
Feflux ratio	1	
Distillate-feed ratio	0.8	
Condenser pressure	1	bar
Reboiler Pressure	1.1	bar
Dual Distillation Column		
No. of stages	12	
Feed stage	2	
Feflux ratio	1	
Distillate-feed ratio	0.9	
Condenser pressure	1	bar
Reboiler Pressure	1.1	bar

3. RESULTS AND DISCUSSION

The different configurations are simulated and compared with the conventional system for hydrogen release rate when supplied with a continuous LOHC supply at a rate of 10 mol/hr. The hydrogen release obtained is shown in Fig. 2.

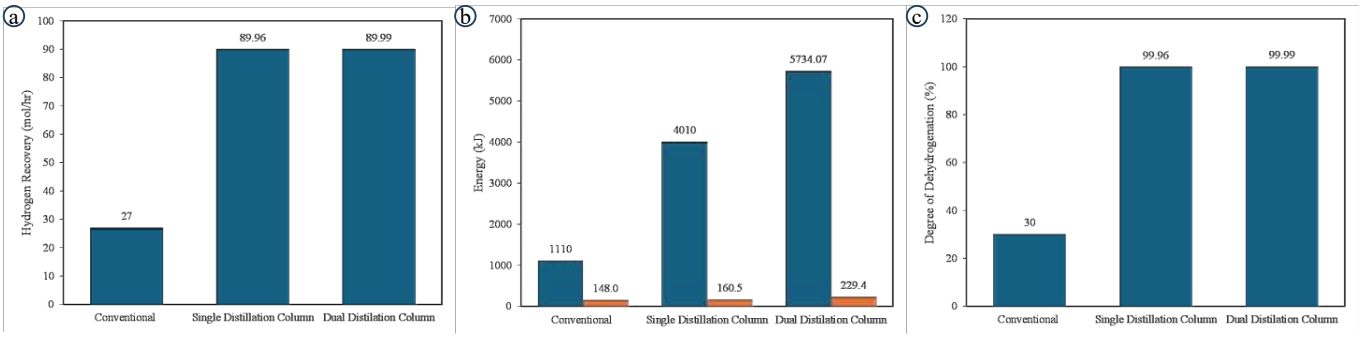

Figure 2. a. Hydrogen recovery achieved via dehydrogenation of DBT for the different process, b. Total energy and the specific energy required for different process to release hydrogen, c. Degree of dehydrogenation achieved for different process layouts using a constant reactor yield of 30%.

By adding distillation process in-line with the dehydrogenation reactor highly enhances the maximum hydrogen release rate from 27 mol/hr to 89.96 mol/hr. However, an insignificant increase is obtained using a dual distillation column. Likewise, the energy requirement also increase as the heat of reaction is the same but the total amount of hydrogen produced increases. Moreover, the distillation column also requires energy for the reboiler making this process more energy intensive increasing the energy required per unit mole of hydrogen from 148 kJ/mol to 160.5 kJ/mol as shown in Fig. 6. Following the trend, the dual distillation increases the energy requirement even higher up to 229.4 kJ/mol.

The degree of dehydrogenation increases tremendously by employing a distillation column as shown in Fig.7. using the conventional method, that is, a batch type system, a maximum of 30% dehydrogenation occurs since the reaction yield is set at 30% however, by employing a distillation column, the degree of dehydrogenation goes beyond 99%. This is probably due to the recirculation of H18-DBT back to the dehydrogenation reactor.

4. CONCLUSIONS

A new process to employ in-line distillation column with the dehydrogenation reactor is proposed. Employing a single distillation column highly enhances the hydrogen produced as well as the degree of dehydrogenation with a cost of an increased energy demand of 20 kJ/mol. Using a dual distillation column gives more adverse effects and hence is not viable.

This study is continued further with the following improvements:

- Reaction intermediates will be considered.

- Investigate the various parameters of the distillation column for optimal hydrogen recovery.
- Process optimization to achieve maximum degree of dehydrogenation for minimum energy consumption.
- The reaction kinetics be incorporated to accommodate the changes in input concentration.

REFERENCES

[1] J. W. Baldwin, J. B. Dessy, G. A. Vecchi, and M. Oppenheimer, "Temporally Compound Heat Wave Events and Global Warming: An Emerging Hazard," *Earths Future*, vol. 7, no. 4, pp. 411–427, 2019, doi: 10.1029/2018EF000989.
[2] G. Ouzeau, J. M. Soubeyroux, M. Schneider, R. Vautard, and S. Planton, "Heat waves analysis over France in present and future climate: Application of a new method on the EURO-CORDEX ensemble," *Clim Serv*, vol. 4, pp. 1–12, 2016, doi: 10.1016/j.cliser.2016.09.002.
[3] N. F. Grünenfelder and T. H. Schucan, "Seasonal storage of hydrogen in liquid organic hydrides: description of the second prototype vehicle," *Int J Hydrogen Energy*, vol. 14, no. 8, pp. 579–586, 1989, doi: 10.1016/0360-3199(89)90117-1.
[4] M. Taube and P. Taube, "A liquid organic carrier of hydrogen as a fuel for automobiles.," in *Advances in Hydrogen Energy*, 1981, pp. 1077–1085.
[5] M. Taube, D. W. Rippin, D. L. Cresswell, and W. Knecht, "A system of h y d r o g e n - p o w e r e d vehicles with liquid organic hydrides," *Int J Hydrogen Energy*, vol. 8, no. 3, pp. 213–225, 1983.
[6] A. Touzani, D. Klvana, and G. BÉLanger, "A mathematical model for the dehydrogenation of methylcyclohexane in a packed bed reactor," *Can J Chem Eng*, vol. 65, no. 1, pp. 56–63, 1987, doi: 10.1002/cjce.5450650110.
[7] S. Yolcular and Ö. Olgun, "Hydrogen storage in the form of methylcyclohexane," *Energy Sources, Part A: Recovery, Utilization and Environmental Effects*, vol. 30, no. 2, pp. 149–156, 2008, doi: 10.1080/00908310600712315.
[8] B. Looney, "Statistical Review of World Energy, 2020 | 69th Edition," *Bp*, vol. 69, p. 66, 2020.
[9] D. Teichmann, W. Arlt, P. Wasserscheid, and R. Freymann, "A future energy supply based on Liquid Organic Hydrogen Carriers (LOHC)," *Energy Environ Sci*, vol. 4, no. 8, pp. 2767–2773, 2011, doi: 10.1039/c1ee01454d.
[10] P. Preuster, C. Papp, and P. Wasserscheid, "Liquid organic hydrogen carriers (LOHCs): Toward a hydrogen-free hydrogen economy," *Acc Chem Res*, vol. 50, no. 1, pp. 74–85, 2017, doi: 10.1021/acs.accounts.6b00474.
[11] D. Geburtig, P. Preuster, A. Bösmann, K. Müller, and P. Wasserscheid, "Chemical utilization of hydrogen from fluctuating energy sources - Catalytic transfer hydrogenation from charged Liquid Organic Hydrogen Carrier systems," *Int J Hydrogen Energy*, vol. 41, no. 2, pp. 1010–1017, 2016, doi: 10.1016/j.ijhydene.2015.10.013.
[12] M. Reuß, T. Grube, M. Robinius, P. Preuster, P. Wasserscheid, and D. Stolten, "Seasonal storage and alternative carriers: A flexible hydrogen supply chain model," *Appl Energy*, vol. 200, pp. 290–302, 2017, doi: 10.1016/j.apenergy.2017.05.050.
[13] J. Andersson and S. Grönkvist, "Large-scale storage of hydrogen," *Int J Hydrogen Energy*, vol. 44, no. 23, pp. 11901–11919, 2019, doi: 10.1016/j.ijhydene.2019.03.063.
[14] A. Bourane, M. Elanany, T. V. Pham, and S. P. Katikaneni, "An overview of organic liquid phase hydrogen carriers," *Int J Hydrogen Energy*, vol. 41, no. 48, pp. 23075–23091, 2016, doi: 10.1016/j.ijhydene.2016.07.167.
[15] L. Shi, S. Qi, J. Qu, T. Che, C. Yi, and B. Yang, "Integration of hydrogenation and dehydrogenation based on dibenzyltoluene as liquid organic hydrogen energy carrier," *Int J Hydrogen Energy*, 2019, doi: 10.1016/j.ijhydene.2018.09.083.
[16] M. Hurskainen and J. Ihonen, "Techno-economic feasibility of road transport of hydrogen using liquid organic hydrogen carriers," *Int J Hydrogen Energy*, no. xxxx, 2020, doi: 10.1016/j.ijhydene.2020.08.186.
[17] N. Brückner *et al.*, "Evaluation of industrially applied heat-transfer fluids as liquid organic hydrogen carrier systems," *ChemSusChem*, vol. 7, no. 1, pp. 229–235, 2014, doi: 10.1002/cssc.201300426.
[18] H. Jorschick, M. Geißelbrecht, M. Eßl, P. Preuster, A. Bösmann, and P. Wasserscheid, "Benzyltoluene/dibenzyltoluene-based mixtures as suitable liquid organic hydrogen carrier systems for low temperature applications," *Int J Hydrogen Energy*, vol. 45, no. 29, pp. 14897–14906, 2020, doi: 10.1016/j.ijhydene.2020.03.210.
[19] M. Naseem, M. Usman, and S. Lee, "A parametric study of dehydrogenation of various Liquid Organic Hydrogen Carrier (LOHC) materials and its application to methanation process," *Int J Hydrogen Energy*, vol. 46, no. 5, pp. 4100–4115, 2021, doi: 10.1016/j.ijhydene.2020.10.188.
[20] S. Park, M. Naseem, and S. Lee, "Experimental Assessment of Perhydro-Dibenzyltoluene Dehydrogenation Reaction Kinetics in a Continuous Flow System for Stable Hydrogen Supply," *Materials*, vol. 14, no. 24, p. 7613, Dec. 2021, doi: 10.3390/ma14247613.
[21] J. Lee, M. Usman, S. Park, S. Lee, and M. H. Song, "Development of Dehydrogenation System for Liquid Organic Hydrogen Carrier with Enhanced Reaction Rate," *Applied Sciences (Switzerland)*, vol. 14, no. 13, Jul. 2024, doi: 10.3390/app14135803.

INTEGRATING METAL HYDRIDE-BASED HYDROGEN STORAGE TANK WITH A PEM FUEL CELL STACK FOR ENHANCED ENERGY EFFICIENCY IN UNDERWATER APPLICATIONS

[1*]*Berna Sezgin*, [1]*Tayfur Ozturk*, [2]*Inci Eroglu*
[1] Middle East Technical University, Metallurgical and Materials Engineering Dept., Çankaya, Ankara, 06800, Turkey
[2] Middle East Technical University, Chemical Engineering Dept., Çankaya, Ankara, 06800, Turkey

*Corresponding author e-mail: berna.sezgin@metu.edu.tr

ABSTRACT
Integrating metal hydride-based hydrogen storage tanks with PEM fuel cells offers a transformative solution for sustainable energy applications, particularly in underwater environments. Metal hydrides are recognized for their high volumetric hydrogen storage capacity, safety, and structural stability under varying pressure conditions. This study aims to integrate and optimize such systems by addressing critical challenges in hydrogen desorption processes, particularly in the endothermic desorption phase. The hydrogen storage system is integrated with PEM fuel cells to ensure a continuous energy supply in underwater conditions. A system architecture showing a flow diagram, visualizing energy and mass flows while incorporating thermal and water management strategies to maximize system reliability and efficiency.
Keywords: Metal hydride; Hydrogen storage; PEM fuel cell; Underwater hydrogen energy system

1. INTRODUCTION

A central challenge in hydrogen-based energy systems is hydrogen storage, which is crucial in enabling efficient and safe utilization. Among various storage methods—such as compressed gas, cryogenic liquid, and solid-state storage—metal hydrides have gained significant attention due to their high volumetric hydrogen density, reversibility, and ability to operate at relatively moderate pressures and temperatures. For underwater hydrogen energy systems applications [1], metal hydride-based storage systems offer significant advantages, such as safety, structural stability under pressure, and integration with thermal management systems. While metal hydrides provide an effective storage medium, optimizing their thermodynamic and reaction kinetics performance is essential to ensure efficient hydrogen desorption and a reliable supply to PEM fuel cells at operational temperatures.

Integrating metal hydride storage tanks with PEM fuel cells presents a promising approach to address these challenges. PEM fuel cells are known for their high efficiency, rapid response time, and ability to generate clean electricity, making them ideal power sources for underwater systems. However, the endothermic nature of the hydrogen desorption process necessitates effective thermal management to sustain continuous operation.

It is known that numerous studies have been conducted on hydrogen storage in metal hydride-based hydrogen storage systems, with the majority concentrating on hydrogen absorption reactions [2]. However, numerical investigations focusing on the hydrogen desorption process remain comparatively scarce. Therefore, the primary goal is to optimize thermodynamics, desorption kinetics, and thermal management of metal hydride-based hydrogen storage systems. This study focuses on integrating and optimizing a metal hydride-based hydrogen storage system with a PEM fuel cell to enhance system performance in underwater environments. A key aspect of this research is addressing thermal and water management strategies to ensure a stable and efficient hydrogen supply. To illustrate the system design and functionality, a flow diagram is presented, mapping energy and mass flows within the integrated system.

2. DESORPTION CALCULATIONS OF METAL HYDRIDE-BASED HYDROGEN STORAGE SYSTEMS

Hydrogen storage in metal hydrides (such as $LaNi_5$) is governed by the reversible absorption and desorption of hydrogen molecules. The fundamental reaction is shown by Eq. (1):

$$M + \frac{x}{2} H_2 \leftrightarrows MH_x \tag{1}$$

Hydrogen absorption and desorption in metal hydrides is a reversible process that allows for efficient hydrogen storage and release. The absorption reaction occurs when a metal or metal alloy reacts with hydrogen to form a metal hydride, releasing heat in an exothermic process.

The hydrogen desorption rate is estimated using the following equation Eq. (2) [3]:

$$n_d = C_d exp\left(\frac{-E_d}{RT_{MH}}\right)\left(\frac{P_g - P_{eq}}{P_{eq}}\right)(\rho^s - \rho^0) \tag{2}$$

where n_d is the rate of H_2 desorption in kg/m^3.s, C_d is desorption rate constant in 1/s, E_d is activation energy for desorption reaction in J/mol, R is the universal gas constant in J/mol.K, T_{MH} is the temperature of the metal hydride tank in °C or K, P_g is the pressure of the metal hydride tank in bar, P_{eq} is the equilibrium pressure at temperature T, ρ^s is the density of saturated metal hydride material in kg/m^3 and ρ^0 is the initial density of metal hydride material in kg/m^3.

The equilibrium pressure, P_{eq}, is related to the changes in enthalpy ΔH and entropy ΔS, which are functions of temperature and can be estimated by the van't Hoff equation, i.e., Eq. (3):

$$ln(P_{eq}) = \frac{\Delta H}{RT} - \frac{\Delta S}{R} \quad (3)$$

Once the rate of desorption is found, the heat required during the endothermic reaction of hydrogen desorption is calculated by Eq. (4) [4]:

$$Q_{des} = \dot{m}_{H_2}\Delta H_{des} + m_{MH}c_{P_{MH}}\frac{dT_{MH}}{dt} + m_{H_2}c_{P_{H2}}\frac{dT_{H_2}}{dt} \quad (4)$$

where Q_{des} is the required heat for desorption in W, $\dot{m}_{H_2}$ is the mass flow rate of hydrogen released from a metal hydride tank in g/s, m_{MH} is the mass of metal hydride material in g or kg, $c_{P_{MH}}$ is the heat capacity of metal hydride material in J/kg.K, T_{MH} is the temperature of the metal hydride tank in °C or K, m_{H_2} is the mass of hydrogen in g or kg, $c_{P_{H2}}$ is the heat capacity of hydrogen in J/kg.K and T_{H_2} is the temperature of hydrogen in °C or K.

2.1. Design Considerations and Hydrogen Consumption Analysis of a PEM Fuel Cell Stack

Before performing these calculations, the mass flow rate of hydrogen released from the metal hydride-based storage system must be determined. This requires selecting a PEM fuel cell system's power output, design parameters, and operating conditions to estimate hydrogen demand. A PEM fuel cell stack with a power output of 60 kW is chosen for an underwater application. It is selected that the system will operate for 10 hours. The design parameters and results of different cases of the PEMFC stack are listed in Table 1.

Table 1. Design Parameters and Results of Different Cases

Parameters	CASE 1	CASE 2	CASE 3	CASE 4	CASE 5
Net Power Output of a PEMFC Stack (kW)	60	60	60	60	60
Voltage Output of a PEMFC Stack (V)	100	125	150	100	100
Current Output of a PEMFC Stack (A)	600	480	400	600	600
Cell Voltage (V/cell)	0.60	0.60	0.60	0.55	0.50
Current Density (A/cm^2)	1.5	1.2	1	1.5	1.5
Stoichiometry of Hydrogen	1.05	1.05	1.05	1.05	1.05
Stoichiometry of Oxygen	1.2	1.2	1.2	1.2	1.2
Operation Duration (hr)	10	10	10	10	10
Stack Temperature (°C)	70	70	70	70	70
Ambient Temperature (°C)	25	25	25	25	25
Results	**CASE 1**	**CASE 2**	**CASE 3**	**CASE 4**	**CASE 5**
Heat duty of desorption (kW)	123.8	123.9	123.8	125.6	127.28
Number of cells	167	209	250	182	200
The mass flowrate of hydrogen (g/s)	1.06	1.06	1.06	1.16	1.27
The heat generated in Fuel Cell (kW)	84.7	84.9	84.4	97.7	113.4

Considering these design bases, one can calculate the amount of hydrogen required by the PEM fuel cell stack using Eq. (4):

$$\dot{m}_{H_2} = S_{H_2} \times \frac{I_{stack}N_{cell}}{2F} \times MW_{H_2} \quad (4)$$

Where $\dot{m}_{H_2}$ is the flowrate of hydrogen supplied to the PEMFC stack in g/s, S_{H_2} is the stoichiometry of hydrogen, I_{stack} is the current of PEMFC stacks in A, N_{cell} is the number of cells of PEMFC stacks, F is the Faraday constant in C, MW_{H_2} is the molecular weight of hydrogen in g/mol.

Moreover, the number of cells in each stack is calculated using Eq. (5):

$$N_{cell} = \frac{Total\ voltage\ output}{Cell\ voltage} \quad (5)$$

Case 1 is chosen as the primary case for evaluation. As a result, the fuel cell stack is calculated to contain 167 cells. Using Eq. (4), the hydrogen mass flow rate required for the stack is determined to be 1.06 g/s. The other cases were designed while keeping the active area of the fuel cell at 400 cm^2 because of the electrode manufacturing technology [5].

3. SYSTEM ARCHITECTURE OF THE INTEGRATED METAL HYDRIDE AND PEM FUEL CELL STACK

Fig. 1 presents a flow diagram of the proposed system architecture to provide a clear understanding. This illustration offers an in-depth view of the interaction between the metal hydride-based hydrogen storage tank and the PEM fuel cell stack.

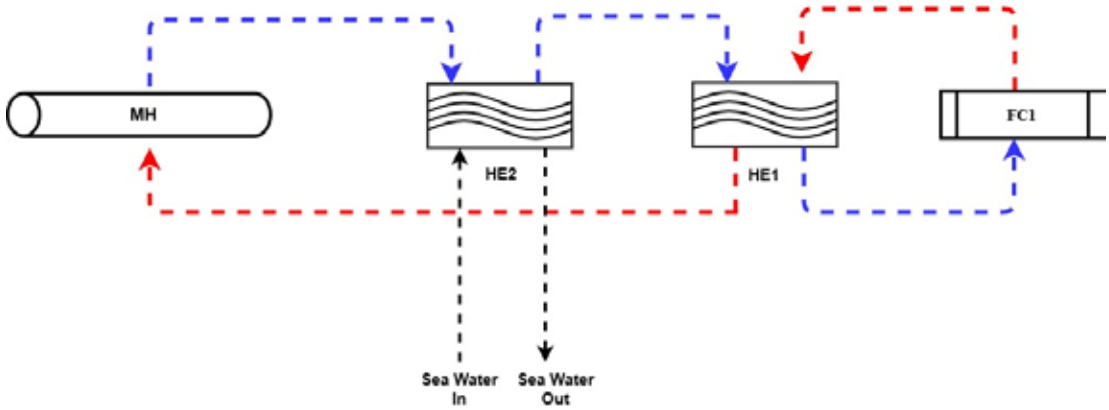

Fig. 1. System architecture of PEM fuel cell stack with metal hydride

The heat management system in this system is designed to maintain thermal balance during hydrogen desorption and fuel cell operation. The system includes a metal hydride tank (MH) for storing and supplying hydrogen. A PEM fuel cell stack (FC), delivering 60 kW, generates electricity by electrochemical reaction. Heat is required to release hydrogen from the metal hydride tank during hydrogen desorption. This heat is provided by a hot water circulation system, depicted by the red dashed lines in the diagram. Hot water flows through the MH tank, transferring thermal energy to the hydride material to facilitate hydrogen release. After absorbing heat from the MH tank, the water cools down and is recirculated back to HE2. The system integrates seawater cooling to manage waste heat effectively. Seawater flows through HE2, which uses the seawater to cool or heat the water circulating in the system. This closed-loop circulation ensures a continuous heat supply to the MH tank during desorption. Proper heat management in the MH tank is critical for maintaining the efficiency of hydrogen release and preventing thermal stress on the system components.

Once desorbed, the hydrogen flows to the PEM fuel cell stack (FC), generating electricity. The fuel cell produces waste heat as a byproduct of the electrochemical reaction. This heat is managed by the same hot water loop, which removes excess heat from the fuel cell stack to prevent overheating. The heated water from the fuel cell stack is directed to heat exchanger HE1, which is cooled before recirculating.

4. CONCLUSIONS

The hydrogen desorption process in a metal hydride-based storage system is criticalin enabling efficient hydrogen utilization for power generation, particularly when integrated with PEM fuel cells The desorption process is inherently endothermic, requiring a carefully designed heat management system to provide the necessary thermal energy while maintaining optimal operational conditions across all system components. The discussion so far has encompassed the system's architecture, thermodynamic calculations for desorption, and the role of the heat management infrastructure.
Moreover, the hydrogen desorption system architecture integrates thermodynamic principles, advanced material properties, and efficient heat management to facilitate the reliable delivery of hydrogen to PEM fuel cells. The design demonstrates a sustainable and scalable solution for hydrogen-based energy systems, with the potential for further optimization to meet varying operational demands and environmental conditions. The foundation is laid for improving hydrogen energy systems' overall efficiency, sustainability, and practicality through the combined understanding of system architecture and desorption calculations.

NOMENCLATURE

FC	Fuel Cell
HE	Heat Exchanger
MH	Metal Hydride

REFERENCES

1. Sezgin B. et al. 2022. Hydrogen energy systems for underwater applications. International Journal of Hydrogen Energy 47:19780-96.
2. Sezgin B. et al. 2025. Modeling and design for metal hydride-based hydrogen storage systems in underwater PEMFC applications. Materials Research Bulletin 182:113139.
3. Cavo M. et al. 2021. Dynamic analysis of PEM fuel cells and metal hydrides on a zero-emission ship: A model-based approach. International Journal of Hydrogen Energy 46:32630-44.
4. Tong L. et al. 2023. Thermal management of metal hydride hydrogen storage tank coupled with proton exchange membrane fuel cells. Case Studies in Thermal Engineering 43:102812.
5. Erkan S. and Eroglu I. 2015. Ultrasonic Spray Coating Technique for High-Performance PEM Fuel Cell Electrode Manufacturing. "Progress in Clean Energy", Chapter 34, p.481-492. Springer, Cham, Volume 2, 481-492.

PREPARATION OF Pd/Ni FOAM CATALYST AND ITS CATALYTIC PERFORMANCE FOR HYDROGEN PRODUCTION BY HYDROLYSIS OF ETHYLENEDIAMINE BISBORANE SOLUTION

[1*]*Okay Serkan Angı*, [2]*Gülay Özkan*, [3]*Göksel Özkan*
[1] Gazi University, Chemical Engineering Department, Ankara, 06570, Turkey
[2] Ankara University, Chemical Engineering Department, Ankara, 06100, Turkey
[3] Gazi University, Chemical Engineering Department, Ankara, 06570, Turkey

*Corresponding author e-mail: gozkan@gazi.edu.tr

ABSTRACT
Ethylenediamine bisborane (EDAB) possesses a relatively high hydrogen storage capacity, and the hydrogen can be liberated via hydrolysis using a suitable catalyst. In this work, Palladium (Pd) was deposited on nickel foam (Pd/Ni foam) for EDAB hydrolysis to produce hydrogen. For hydrolysis of EDAB solution approximately 5-6 equivalent moles of hydrogen is generated and lower apparent activation energy of 30.88 kJ·mol-1 were achieved. Moreover, 79.3 % HGR was still maintained for Pd/foam Ni after five cycles, which disclosed the good cycle stability. The enhanced catalytic performance might be due to the smaller particle size, supplying more active sites.

Keywords: EDAB, Catalytic hydrolysis,nickel foam

1. INTRODUCTION

Today, energy consumption has increased with the development of technology and the human population. Most of the energy needs are met from fossil fuels. Considering the environmental effects of fossil fuels, it is necessary to turn to renewable energy sources. Hydrogen, the most abundant chemical element in the universe, is one of the renewable energy sources and has the potential to meet global energy needs in an environmentally friendly way. Hydrogen (H_2,) which is not found in pure form in nature, is abundant in water, natural fuels containing carbon,hydrogen,nitrogen (C-H-N) (such as coal, natural gas, etc.), and many chemical raw materials. In addition to hydrogen production, it must be stored in materials that can release hydrogen safely and efficiently when needed to adapt it to our daily life. In addition, suitable storage materials must be used for hydrogen energy in fuel cell systems, which are considered to be the future technology. Today, H_2, which is produced for energy production, is stored by two methods: physical and chemical storage. Compressed form storage, a commonly used type of physical storage, contains significant risks, especially in the transportation and portable device sectors, due to security. For this reason, chemical storage materials that contain 7% and above H_2 by mass and can quickly release H_2 under suitable conditions have recently come to the fore. In particular, amine and alkyl amine boranes such as metal borohydride (such as Hydrazine borane, $NaBH_4$, $LiBH_4$, $Ca(BH_4)_2$), ammonia borane (NH_3BH_3) and ethylenediamine bisborane ($C2H_4(NH_2)_2(BH_3)_2$), which are boron-containing storage materials, have high mass [1,2]. They are very popular research areas with their hydrogen storage capacities.
Conventional catalysts include homogeneous catalysts such as acid and metal-based homogeneous catalysts; heterogeneous catalysts such as noble metals, transition metals, metal-free catalysts, metal-organic frameworks (MOFs), and so on[3]. At present, metal Ni-based catalysts are attracting attention due to their relatively low price and intense activity [4]. The hydrogen production reaction of EDAB hydrolysis is shown in Equation (1)

$$BH_3NH_2CH_2CH_2NH_2BH_3(aq) + 4H_2O \rightarrow BO_2NH_3CH_2CH_2NH_3BO_2(aq) + 5H_2(g) \text{ or } 6H_2(g) \quad (1)$$

The combination of the non-precious metal Ni with Pd can greatly improve the catalytic activity of cobalt, so more researchers have devoted their attention to the preparation and research of Ni-based catalysts. Okay et al. and Büşra et al. [5,6] prepared a novel noble metal Pd /TiO2, catalyst for catalytic hydrolysis of EDAB and its hydrogen production was found as 5 equivalent mole of hydrogen at 313 K. Murathan et al. [7,8] reported a range of Pd-Ni-Zr-B-O with different contents, including (40%Ni, 60% Zr by mass) and Pd-Ni-Zr-B-O (5% Pd, 38% Ni and 57% Zr by mass). All of these nickel series exhibit excellent hydrogen evolution reactivity. Karataş (2024) et al. [9] prepared Pd/GO-SO4 catalyst by chemical deposition. The concentration, deposition time and temperature EDAB had obvious effects on the catalytic activity. The hydrogen production was found as 6 equivalent mole of hydrogen. Therefore, it can be indicated that the development of highly active Pd /Ni catalysts has important research and practical value. To date, a large number of supported Pd-Ni catalysts in powder form have been prepared. However, powdered catalysts have some drawbacks such as being difficult to separate and easy to reunite. In the past few years, in order to solve the disadvantages of powdered catalysts, a lot of studies have been conducted to exploit the bulk supported catalysts. In this study, the chemical deposition route was adopted to manufacture Pd-Ni catalysts using nickel foam as a support (Pd/foam Ni). In the experiment, the depositional pH value was investigated for obtaining the optimal conditions. Different characterization methods were used to characterize the catalyst. The hydrolysis reaction kinetics, apparent activation energy and durability of the catalyst were also tested. The result showed that the Pd/foam Ni was an effective catalyst toward EDAB

hydrolysis.
This study aims to conduct dehydrogenation by catalytic vapor phase and low-temperature hydrolysis of ethylenediamine bisborane (EDAB), a compound in which hydrogen is chemically stored. The catalytic vapor phase experiments were carried out in a tubular-packed reactor. Nickel foam is used as catalyst support, and nickel/carbon foam electrochemical precipitation/coating is used. Low-temperature experiments will be carried out in a batch reactor with the same catalysts. As a result of experimental studies in which temperature, concentration, and amount of catalysis were chosen as experimental parameters, 5 equivalent mol of H_2 was produced at 80°C, where the hydrolysis reaction followed Langmuir-Hinshelwood kinetics, and the activation energy was 33.61 $kJ.mol^{-1}$. In addition, it was concluded that 7 equivalent moles of H_2 were produced at 300°C and 9.5 equivalent moles at 450°C in vapor phase dehydrogenation experiments.

2. EXPERIMENTAL

2.1. Synthesis of Nickel/Carbon Foam (Ni/C-Foam)

In the experimental studies, the carbon powder used to prepare nickel foam, which was determined as the support material, was supplied commercially. Nickel foam was synthesized under laboratory conditions by creating an electrochemical experimental system.
Polyurethane sponge/foam was selected as the first support layer where Nickel would be electrochemically deposited. Polyurethane foam was first kept in dilute 0.1 M HNO3. Then, it was cleaned by passing through pure water. The cleaned foam was made conductive so that the coating process could be carried out. A carbon-based conductive solid-liquid suspension mixture was prepared to provide conductivity[10]. This mixture was prepared with graphite powder and organic solvent. The cleaned polyurethane foams were dipped into the prepared mixture and kept for one day. Afterward, it was removed from the mixture and allowed to dry at room temperature, and the polyurethane foam was coated with a black graphite layer, thus providing conductivity.
A nickel-containing electrolyte solution was prepared so that Nickel could be electrochemically coated onto the conductive foam. This solution was prepared in accordance with the literature and 200 ml of electrolyte solution was prepared as nickel sulfate hexahydrate, nickel chloride hexahydrate, and boric acid in the ratio of 5:1:0.5 [11]. A nickel plate (30x20x50 mm in size) was connected to the anode (+) end of the power supply, and the conductive polyurethane foam to be coated was connected to the cathode (-) end and immersed in the prepared electrolytic solution. A voltage of 1.5 volts was applied with the power supply, and the coating process was completed. The light gray polyurethane and nickel foam formed by coating on carbon surfaces were removed from the bath, washed with pure water at least three times, and then dried. The dried Ni/C-foam raw structure was placed in a quartz tube reactor and calcined at 500°C in an N_2 gas environment to ensure carbonization of the polyurethane in the structure.

2.2. Synthesis of Pd/C-Ni Foam Catalyst

Palladium coating on Ni/C-foam was carried out using two different methods: impregnation-reduction and electrochemical deposition of Palladium.

2.2.1 Coating of Palladium onto nickel surface by impregnation-reduction method

Palladium coating of Ni/C-foam was carried out by the wet impregnation method. 0.1M Na2PdCl4 solution was prepared for wet impregnation. Ni/C-foam was added to the prepared solution separately to impregnate 2% and 4% Pd by mass. It was decided that the impregnation process progressed with the lightening of the solution color and that it was completely covered based on the completely clear color of the solution.

2.2.2 Coating of Palladium onto nickel surface by electrochemical deposition method

A solution containing 1 mmol/L PdCl2 and 3 mmol/L NaCl was prepared for electrochemical plating of Palladium. The electrochemical precipitation of Palladium was carried out in a similar manner to the nickel foam preparation method. The plating system was created by connecting the nickel foams to the power supply's negative (-) cathode end and the platinized titanium, which is not dissolved in the solution, to the positive (+) anode end. Mechanical mixing was applied throughout the plating process. The plating process continued for 35 minutes, and the lightening of the solution color was evaluated as a physical indicator that the palladium concentration in the solution had decreased and accumulated on the nickel foams.

2.3. Catalytic Activity Test

Catalytic hydrolysis experiments were carried out in two different reactor systems. First, the batch reactor experimental system given in Figure 1. Pd/C-Ni foam catalyst experiments were carried out in two different amounts, 0.06g and 0.012g, and at 3 different temperatures (40, 60, 80°C).

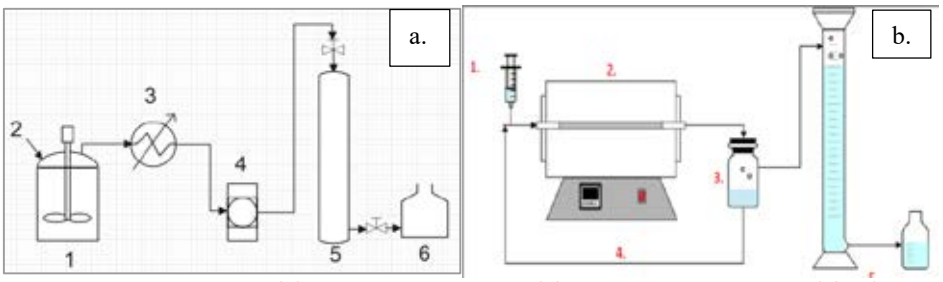

Fig. 1. a) Batch reactor experimental setup, (1) hot plate and reactor, (2) EDAB solution injector, (3) reflux condenser, (4) wash bottle, (5) gas burette, (6) reservoir b) Injector (1) Oven (2) Washing Bottle (3) reflux (4) wash bottle (5) gas burette,

The second stage experiments were carried out under continuous conditions, and vapor phase dehydrogenation experiments were carried out by placing a Pd/C-Ni foam catalyst in a 60 cm long Pyrex glass reactor with an inner diameter of 0.8 cm. In the experiment, 0.015 g EDAB was used in a 3 ml de-ionized water solution. This prepared solution was taken into the injector and fed to the packed reactor at the specified temperatures (300-450 ^{o}C). The feeding was completed in approximately 3-4 minutes.

3. RESULTS AND DISCUSSION

3.1. Pd/Ni Foam Characterization

SEM Analysis

In Figure 2(a) SEM images of the commercial Nickel foam used in the literature and (b) SEM images of the Ni-foam support materials prepared by electrochemical deposition method in a laboratory environment are given.

When the images in Figure 2(a) and (b) are viewed from a wide angle, it is seen that the porous foam structure is obtained with the synthesis (b) carried out in the laboratory environment. When examined at a larger magnification, it is seen that the surface morphology of the commercial Ni-foam is quite flat and smooth. Three different methods generally prepare commercial nickel foam. These are sputtering, electrochemical coating/deposition, and chemical vapor deposition (CVD).[12]. In commercially prepared nickel foams, high temperatures are reached (600-850°C) for sintering or reduction-sintering processes. For this reason, nickel metal lumps are welded together and form a tight, non-porous and flat layer (Figure 2(a). On the other hand, various nickel lump bumps and a more porous structure and possible carbon particles in between are seen on the surface of the Ni-foam synthesized by the electrochemical deposition method in the laboratory environment, which darkens the color of the foam obtained (Figure 2(b).

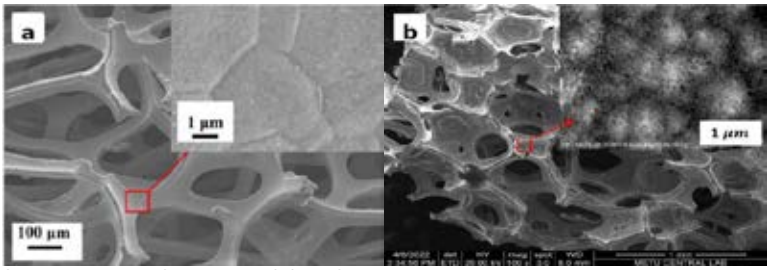

Fig. 2. (a) Commercial Ni-foam [13], (b) Ni-foam prepared by electrochemical deposition method

The EDS spectrum of nickel foam is given in Figure 3. According to this analysis, 10-12% carbon was found in the structure of the prepared nickel foam. It is thought that this carbon may have come from the carbon solution used during the nickel foam preparation process or from the polyurethane after the calcination process.

BET Analysis

The nitrogen adsorption-desorption isotherm curve of the prepared Pd/C-Ni foam catalyst is given in Figure 3.2. The prepared catalyst showed Type III isotherm behavior according to the IUPAC classification. The hysteresis interval started and ended at approximately P/P_0 = 0.05. The starting point of hysteresis indicates the starting point of capillary condensation[13]. Unlike the Pd/TiO_2 catalyst, the hysteresis onset P/P_0 value of the Pd/C-Ni foam catalyst is much lower. The surface area of the prepared catalyst was found to be 19 and 18 m^2/g according to the multi-point BET and BJH methods, respectively.

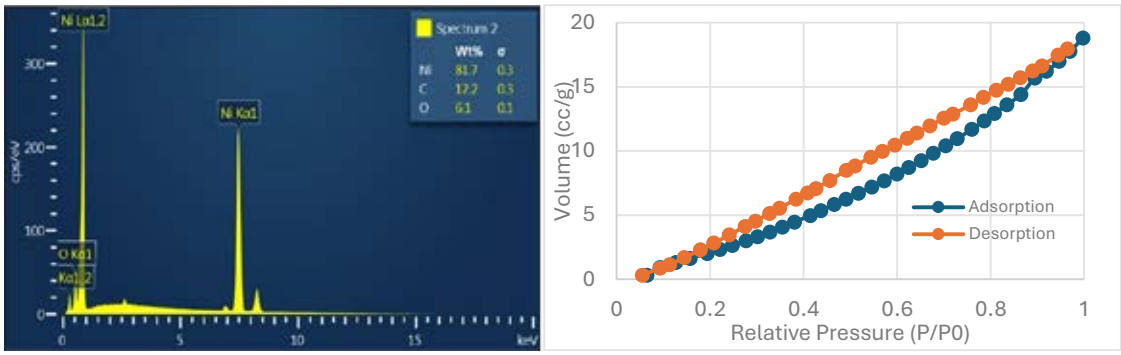

Fig. 3. Nickel foam EDS spectrum and N_2 (nitrogen) adsorption-desorption isotherm of Pd/C-Ni foam (electrochemical) catalysts

4. CONCLUSIONS

In summary, the Pd/C-Ni foam was successfully prepared via a simple electrochemical deposition method. Approximately 6 equivalent moles of hydrogen were produced in the EDAB hydrolysis with the Pd/C-Ni foam catalyst, and the E_a value was 30.88 kJ·mol^{-1}. The reason might be the relatively small particle size of the catalyst under this condition, which supplied a higher surface area for hydrogen transfer on the catalyst surface. In addition, the produced mole equivalent hydrogen amount for the hydrolysis of EDAB was still about 79.3% of the initial value after five cycles, indicating that the Pd/C-Ni foam catalyst had good cycling stability. The SEM and EDX analysis manifested that the increase in particle size and decrease in the amount of Pd after 5 cycles might be the main reason for the attenuation of catalytic activity.

ACKNOWLEDGEMENT

We are thankful to Gazi ADEP-BAP, Turkey, for the financial support of this work (ID:8167 Code: FGA-2023-8167).

REFERENCES

[1] Bayram Ö, Begüm Murathan H, Serkan Angı O, Özkan G, Özkan G.2024.Innovation in the synthesis of hydrazine borane by mechanochemical method and hydrolysis of hydrazine borane with Pd/TiO2 catalyst. Mater Chem Phys
[2] Özgür DÖ, Şimşek T, Özkan G, Akkuş MS, Özkan G. 2018.The Hydroloysis of ammonia borane by using Amberlyst-15 supported catalysts for hydrogen generation. Int J Hydrogen Energy
[3] Yang K, Yang K, Zhang S, Luo Y, Yao Q, Lu ZH.2018. Complete dehydrogenation of hydrazine borane and hydrazine catalyzed by MIL-101 supported NiFePd nanoparticles. J Alloys Compd
[4] Lim D, Özkan G, Özkan G. 2021. Ni–B and Zr–Ni–B in-situ catalytic performance for hydrogen generation from sodium borohydride, ammonia borane and their mixtures. Int J Hydrogen Energy
[5] Dülger B, Özkan G, Angı OS, Özkan G. 2024.Green synthesis of TiO2 nanoparticles using Aloe Vera extract as catalyst support material and studies of their catalytic activity in dehydrogenation of Ethylenediamine Bisborane. Int J Hydrogen Energy
[6] Angı OS, Murathan HB, Özkan G, Özkan G.2022.Non-linear kinetic analysis of catalytic hydrolysis of ethylenediamine bisborane with nano-structured Pd/TiO2 catalyst. Int J Hydrogen Energy
[7] Murathan HB, Özkan G, Özkan G. 2023.Hydrogen generation from the hydrolysis of ethylenediamine bisborane using Ni/NixBy-Zr and Pd-Ni/NixBy-Zr as highly active catalysts. Environ Prog Sustain Energy
[8] Murathan HB, Özkan G, Özkan G. 2024.Catalytic dehydrogenation of ethylene diamine bisborane in ethylene diamine media. Int J Hydrogen Energy
[9] Karataş Y, Gülcan M. 2024.Enhancing the catalytic activity of Pd nanoparticles in the hydrolysis of ethylenediamine-bisborane through sulfonation of graphene oxide as a solid support. Int J Hydrogen Energy
[10] Liu PS, Liang KM.2000. Preparation and corresponding structure of nickel foam. Mater Sci Technol
[11] Islam T, Sharif A. 2014.Nickel Plating Handbook. Harsh Environ Electron Interconnect Mater Perform Assess
[12] Poserin V, Marcuson S, Shu J, Wilkinson DS. 2004.CVD technique for Inco nickel foam production. Adv Eng Mater.
[13] Shen Y, Lu S, Xu W, Lv A, Wang Z, Wang H. 2021. Fabrication of Composite Material with Pd Nanoparticles and Graphene on Nickel Foam for Its Excellent Electrocatalytic Performance. Electrocatalysis

TEXT-MINING AND BIBLIOMETRIC ANALYSES FOR PROTON EXCHANGE MEMBRANE ELECTROLYZERS

[1]Ayca Firtin, [1]Ayca Yilmaz, [2*]Inci Eroglu, [1*]Ramazan Yildirim, [1*]Damla Eroglu
[1] Bogazici University, Department of Chemical Engineering, Istanbul, 34342, Turkey
[2] Middle East Technical University, Department of Chemical Engineering, Ankara, 06800, Turkey

*Corresponding author e-mail: eroglud@boun.edu.tr (D. Eroglu), yildirra@boun.edu.tr (R. Yildirim), ieroglu@metu.edu.tr (I. Eroglu)

ABSTRACT

In this study, bibliometric and text-mining analyses are conducted for the PEM electrolyzer to understand the general trends and provide insight into future works. First, the data was gathered from the Scopus webpage using 'PEM electrolyzer*' and its alternative combinations in January 2024, and 1631 articles were obtained. *Tidytext* and *stringr* libraries and Biblioshing environment were used in R Studio Language for the bibliometric analysis. In contrast, Colaboratory environment and *nltk, pandas,* and *numpy* libraries in Python programming language were used to conduct the text mining analysis. This study proves that the attention paid to PEM electrolyzers has increased dramatically, especially in the last decades. In addition, the research topics on which researchers focused changed during those years. At the beginning of the given period, 'polymeric membrane' was a popular research topic for eight years. Afterward, researchers focused on various research topics such as organic Rankine cycle, optimization, energy management, cathodes, etc. It is seen that besides cost and optimization analysis, the number of studies on the integration of PEM electrolyzers with other energy systems has increased recently.

Keywords: Hydrogen Production**,** PEM Electrolyzer, Text-Mining, Bibliometric analysis, Machine Learning

1. INTRODUCTION

Due to the changing lifestyle as a result of technological development, energy consumption is increasing continuously. Correspondingly, the increase of emissions and depletion of fossil fuels led researchers to seek alternative green energy sources. Hydrogen is one of the most promising green and sustainable energy sources when produced from renewable sources [1,2]. Water electrolysis, splitting water into oxygen and pure hydrogen, is one of the most promising hydrogen production methods. Among the various types of electrolyzers, such as Alkaline Water Electrolyzers (AWE), Solid Oxide Electrolysis Cells (SOEC), and Anion Exchange Membrane Water Electrolyzers (AEMWE), Proton Exchange Membrane (PEM) Electrolyzer is the most favorable method for the production of hydrogen with high purity because of its high efficiency and compact design [3,4]. In addition to high current density and minor carbon footprint due to oxygen production as a byproduct, PEM electrolyzers operate at low temperatures and high pressure, enabling quick response and easy storage of the byproducts [2,5–7]. The PEM electrolyzer enables water to oxidize by using electricity. In this way, the Oxygen Evolution Reaction (OER) occurs at the anode side, producing oxygen and protons. Produced oxygen is removed from the electrolyzer while protons pass through the membrane and electrons flow through an external circuit. At the cathode side, electrons reduce the protons to produce hydrogen and complete the Hydrogen Evolution Reaction (HER) [2,5,8]. Despite the advantages, operation under harsh conditions, such as high potential and acidic environments, requires the use of highly resistant catalytic materials such as noble metals, and these materials are limited and expensive, giving rise to high maintenance costs [4,8–10].

In order to be able to operate at high efficiency in the long term, alternative catalysts with low or no noble metal loadings are studied in the literature. In other words, the design of the electrode materials that operate efficiently under low over-potential and pH and high current densities in the long term is studied. In this regard, Machine Learning (ML) plays a significant role in the design of more effective materials and the improvement of design parameters [11]. Gunay et al. used varying statistical and machine-learning approaches, such as classification and a regression tree, to identify high-performance pathways and risks, and estimated the performance of the PEM electrolyzer. They concluded that polarization patterns can be forecasted without experiments with the aid of current information in the literature [11]. In addition to their previous study, Günay and Tapan used three different machine-learning techniques, local interpretable model-agnostic explanation (LIME), neutral network pattern recognition, and association rule mining (ARM), for the data of two different electrolyzers that are PEM and AEM. They observed that the LIME technique reveals the rules or pathways giving rise to high current densities and low polarization and power density. Also, key factors leading to high current density were identified by the ARM method, and the importance of catalytic material on the current density was revealed successfully with the neural network pattern [12]. In another study in the literature, Arsad et al. used bibliometric analysis to predict future trends and apply hydrogen electrolysis with the help of the most cited academic papers in the Scopus database [13]. In this study, we conducted detailed bibliometric and text-mining analyses for the PEM electrolyzers to project the research trends and the most important future research directions considered to have a high

impact on the development of the technology.

2. METHODS

This study aims to conduct a comprehensive examination of trend topics in PEM electrolyzers in the open literature by using bibliometric analysis and text mining. First, data analysis was done by searching keywords in the Scopus database (January 2024) using the term "PEM electrolyzer*" and 1631 published articles were obtained from 1998 to 2024. The title, keyword, and abstract of the articles were used, and the output was classified for its relevance with the PEM electrolyzers. The resources were documented following the articles' Authors, Author full names, Author IDs, Title, Year, Source Title, Volume, DOI number, Scopus website link for the article, Abstract, Author Keywords, Document type, and Source Name, after revision of each document meticulously, and all the information of the results gathered were exported as CVS document. In the text mining study, the information used for data visualization majorly consisted of author keywords, abstract, and DOI numbers. R studio environment was used to demonstrate various graphs in bibliometric analysis. Basic algorithms and libraries such as '*tidytext*' and '*stringer*' were used to clean repeated words from the text. '*Biblioshiny'* environment was used for the visualization of trends corresponding to research on PEM electrolyzers from 1998 onward. The Collaboratory environment, which provided tokenizing and filtering large amounts of data in Python programming language, was used to conduct detailed text-mining analysis for the abstract of the articles. Also, large datasets were tokenized and filtered using relevant Python libraries such as '*nltk', 'pandas'*, and '*numpy'.*

3. RESULTS AND DISCUSSION

The timeline/trend graph (Fig.1), constructed by the R programming language and 'Biblioshiny' environment, gives information about the frequency of occurrence of specific terms or keywords studied in the literature over a period of time. In the graph, the length of the line for each term represents the period along which the terms are studied or discussed in the literature, while the dots illustrate the most frequently appeared year, and the size of the dots represents the frequency of the term in a certain year.

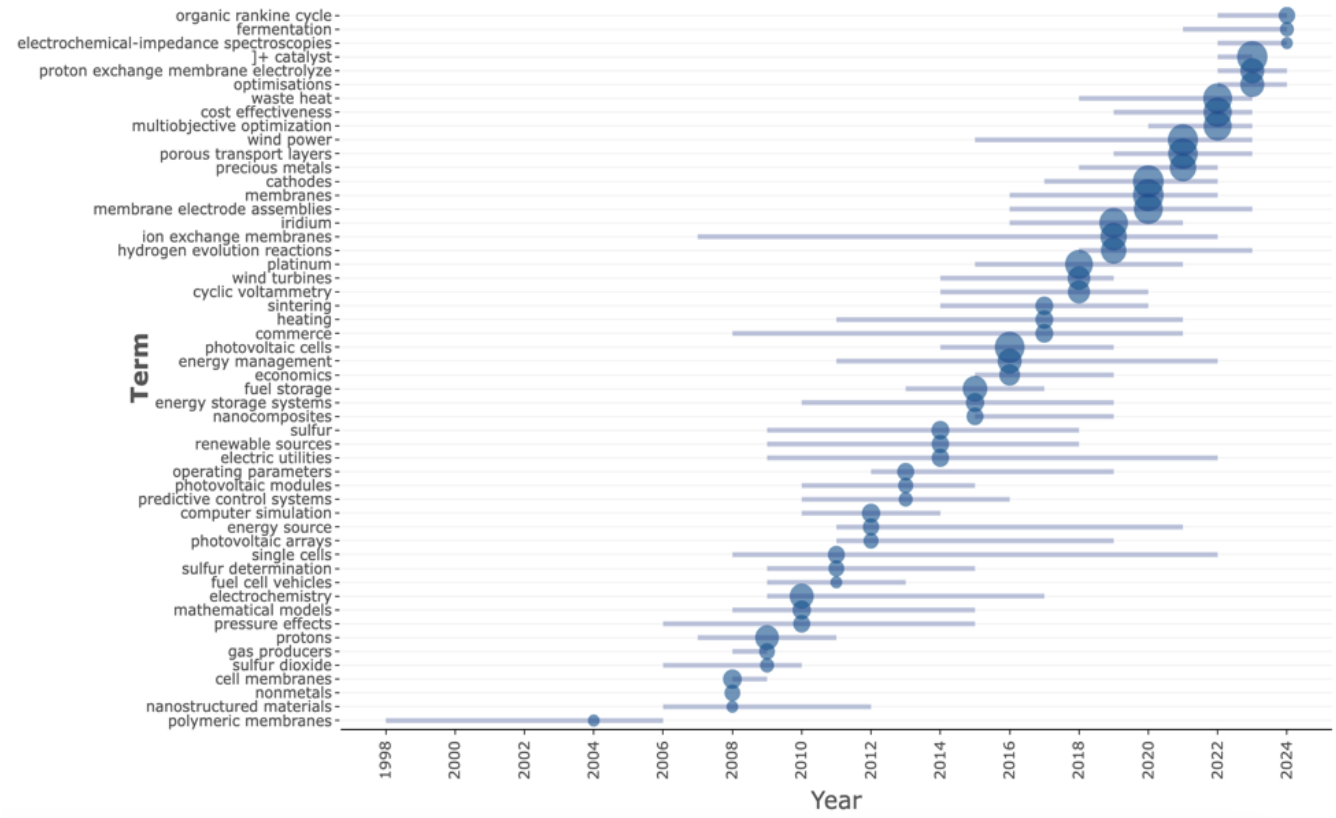

Fig. 1. Trend topics based on abstracts of scientific publications between 1998 and 2024.

In this regard, at the beginning of the period, between 1998 and 2006, polymeric membranes were the top research topic of PEM electrolyzers. On the other hand, for the last two years, "organic Rankine cycle," "fermentation," "electrochemical impedance spectroscopies," "catalyst," "proton exchange membrane electrolyzers," and "optimizations" were the most

commonly mentioned topics in literature. It is seen from this result that PEM electrolyzers can be integrated with different power systems. In the study conducted by Onwuemezie et al., renewable energy sources such as wind and solar energy with the PEM electrolyzer were used together with biohydrogen production [14]. Also, it is clear that the keyword “catalyst” had the highest frequency; in other words, “catalyst” was the most significant research topic among these keywords during those years. This is because one of the challenges of the PEM electrolyzer is the use of noble metals such as Pt, Ir, and Ru in the electrolyzer. These noble metals can operate efficiently under harsh conditions, but they are limited, which makes them more expensive [15,16]. Therefore, to use the PEM electrolyzers widely, researchers focused on decreasing the use of precious metals or designing alternative catalysts for noble metals with a longer lifetime [4,17,18]. The terms “single cell,” “ion exchange membrane,” and “energy management” were discussed over the longest period, while “nonmetals” occurred only in 2008.

Fig. 2. illustrates the most frequent 50 keywords mentioned in abstracts of publications about PEM electrolyzers from 1998 to 2024. It is seen that the most frequently aforementioned words are “cathodes,” “membranes,” ”catalyst,” “wind power,” “photovoltaic cell,” “porous transport layers,” “membrane electrode assemblies,” “waste heat,” and “iridium” with the 74, 73, 71, 69, 67, 65, 61, 61 and 59 absolute frequency respectively and 3% of entire data.

Fig. 2. Word frequency treemap of the word phrases in the specified domain.

4. CONCLUSIONS

This study conducted bibliometric and text-mining analyses for the PEM electrolyzer to demonstrate the trend topics and commonly discussed words about this field between 1998 and 2024. First, by using a keyword search, 1631 documents were extracted from the Scopus database. Then, the R Studio environment, Python programming language, and relevant libraries were used for the analysis. It was obtained from this analysis that the PEM electrolyzer has become a more popular research field in recent years, while the research topics have changed over the years. Topics of ‘ion exchange membrane’, ‘single cell’, and ‘energy management’ were discussed for the longest period in literature, while ‘nonmetals’ was mentioned only in 2008. Overall, this analysis can provide insight into the knowledge of PEM electrolyzers and guidance for future research areas.

ACKNOWLEDGMENT

This study was funded by the Bogazici University Research Fund, Grant No: BAP-20121

REFERENCES

1. Islam J, Yoon BS, Thien PT, Ko CH, Kim S-K. 2024. Enhancing oxygen evolution reaction performance in PEM water electrolyzers through support pore structure optimization. Catal Today 425:114349.
2. Shiva Kumar S, Himabindu V. 2019. Hydrogen production by PEM water electrolysis – A review. Mater Sci Energy Technol 2:442–54.
3. Azam. AMIN, Li. NK, Zulkefli NN, Masdar MS. 2024. Parametric Study and Electrocatalyst of Polymer Electrolyte Membrane (PEM) Electrolysis Performance. Polymers 15:560.
4. Torrero J, Morawietz T, Sanchez DG. 2023. High Performance and Durable Anode with 10-Fold Reduction of Iridium Loading for Proton Exchange Membrane Water Electrolysis. Advanced Energy Materials - Wiley Online Library 13:2204169.
5. Banti A, Papazisi KM, Balomenou S, Tsiplakides D. 2023. Effect of Calcination Temperature on the Activity of Unsupported IrO2 Electrocatalysts for the Oxygen Evolution Reaction in Polymer Electrolyte Membrane Water Electrolyzers. Molecules 28:5827.
6. Ahn S, Rudolph M. 2024. Development of Fine Particle Mechanical Separation Processes with Representative Catalyst Materials for Recycling PEM Water Electrolyzers Exploiting their Wetting Characteristics. ChemCatChem 16:e202300931.
7. Lee H-O, Yesuraj J, Kim K. 2022. Parametric study to optimize proton exchange membrane electrolyzer cells. Appl Energy 314:118928.
8. Falcão DS, Pinto AMFR. 2020. A review on PEM electrolyzer modelling: Guidelines for beginners. J Clean Prod 261:121184.
9. Carmo M, Fritz DL, Mergel J, Stolten D. 2013. A comprehensive review on PEM water electrolysis. Int J Hydrog Energy 38:4901–34.
10. Metawea ORM, Nara M, Murakami T, Wada S, Fujii K, Ito Y, et al. 2023. Highly Efficient Electrocatalytic Hydrogen Production over Carbon Nanotubes Loaded with Platinum Nanoparticles Using Solution Processing. Adv Mater Interfaces 10:2300094.
11. Günay ME, Tapan NA, Akkoç G. 2022. Analysis and modeling of high-performance polymer electrolyte membrane electrolyzers by machine learning. Int J Hydrog Energy 47:2134–51.
12. Günay ME, Tapan NA. 2023. Analysis of PEM and AEM electrolysis by neural network pattern recognition, association rule mining, and LIME. Energy AI 13:100254.
13. Arsad AZ, Hannan MA, Al-Shetwi AQ, Hossain MJ, Begum RA, Ker PJ, et al. 2023. Hydrogen electrolyser for sustainable energy production: A bibliometric analysis and future directions. Int J Hydrog Energy 48:4960–83.
14. Onwuemezie L, Gohari Darabkhani H. 2024. Biohydrogen production from solar and wind assisted AF-MEC coupled with MFC, PEM electrolysis of H2O and H2 fuel cell for small-scale applications. Renew Energy 224:120160.
15. Wu Y, Yao R, Zhao Q, Li J, Liu G. 2023. RuO2 nanoparticles anchored on g-C3N4 as an efficient bifunctional electrocatalyst for water splitting in acidic media. Dalton Trans 10515–21.
16. Wang Y, Wen Y, Cheng Y, Chen X, Zhuansun M, Wang T, et al. 2024. Enriched electrophilic oxygen species facilitate acidic oxygen evolution on Ru-Mo binary oxide catalysts. Nano Res 17:1165–72.
17. Huang H, Chen T, Fang D, Cao L, Wang G, Hao J, et al. 2024. Modulation in the electronic structure of Ir-rich shell on AuIr solid solution as OER electrocatalyst for PEM electrolyzer. J Appl Electrochem 54:2269–79.
18. Feng M, Huang J, Peng Y, Huang C, Yue X, Huang S. 2022. Tuning Electronic Structures of Transition Metal Carbides to Boost Oxygen Evolution Reactions in Acidic Medium. ACS Nano 16:13834-13844.

ROLE OF HYDROGEN ADSORPTION AND DESORPTION IN UNDERGROUND STORAGE WITHIN COAL SEAMS

[1*]*Omer IMIR*, [2]*Sukru MEREY*, [1]*Abdullah FISNE*
[1] Istanbul Technical University, Department of Mining Engineering, Istanbul, 34467, Turkiye
[2] Batman University, Department of Petroleum and Natural Gas Engineering, Batman, 72100, Turkiye

*Corresponding author e-mail: imir@itu.edu.tr

ABSTRACT
This study examines adsorption and desorption values, which are among the most critical factors indicating the storability of hydrogen (H_2) in coal seams. Our work emphasizes the increasing prominence of hydrogen as a clean and sustainable energy source in response to global warming and rising energy demands. The reliable storage of hydrogen is considered one of the cornerstones of future energy systems. The research highlights that the micro and nano-pore structures of coal seams offer favorable properties for hydrogen storage. Notably, the high adsorption capacity of these pore structures enables the safe and efficient storage of hydrogen. Findings from literature reviews reveal the detailed effects of factors such as pressure and temperature on hydrogen storage capacity. Additionally, the comparison of hydrogen's adsorption/desorption behavior with other gases constitutes a significant dimension of this study. Investigating the hydrogen storage potential of coal seams is considered a crucial step toward energy security and sustainable energy management.
Keywords: adsorption, coal seams, desorption, hydrogen, underground storage

1. INTRODUCTION

The increase in the global population and rising living standards have led to higher energy demand, resulting in carbon dioxide (CO_2) emissions and global warming. In this context, zero-emission hydrogen energy has emerged as a significant alternative for addressing environmental issues [1]. The growing utilization of renewable energy sources has created the need for large-scale energy storage [2]. Hydrogen, as a clean energy source, has the potential to transform energy systems. However, developing effective and large-scale storage methods is essential for establishing a sustainable hydrogen economy. The high energy density and storability of hydrogen provide a flexible solution for ensuring energy security [3].

Underground gas storage methods have gained attention due to their low costs and minimal environmental impacts. Among these methods, geological formations such as salt caverns, depleted natural gas reservoirs, and coal seams hold significant potential for long-term hydrogen storage [4, 5, 6]. In particular, the micro- and nano-scale pore structures of coal seams are considered a viable option for hydrogen storage [7,8]. However, the mechanisms of hydrogen adsorption and desorption in coal seams are not yet fully understood. Investigating these mechanisms in detail is critical for accurately evaluating the storage potential of hydrogen.

In this study, adsorption/desorption, one of the most important factors for assessing hydrogen storage in coal seams, was examined based on findings from the literature.

2. MATERIALS AND METHODS

In literature, anthracite, bituminous and sub-bituminous coal samples were used in H_2 adsorption experiments. The micro/nanopore structures of these samples were analyzed. Adsorption and desorption processes were analyzed using the Langmuir isotherm model, with measurements conducted at a pressure range of 0.1–14.32 MPa and a temperature range of 303–318 K. BET and FTIR techniques were utilized for surface analysis.

Langmuir Model for Representing Experimental Hydrogen Adsorption Capacity in Coal: Adsorption models, including the linear Henry's law [9], the Freundlich model [10], the Langmuir model [11], the Brunauer-Emmett-Teller (BET) model [12], the Dubinin-Radushkevich (D-R) model [13], and the Dubinin-Astakhov (D-A) model, have been extensively studied to theoretically estimate the adsorption capacity of coal. Among these, the Langmuir model, which assumes that the amount adsorbed is limited by a threshold capacity at typical gas pressures [11], is widely used.

$$V = \frac{V_L p}{p + p_L} \tag{1}$$

Where p: pressure, V: the amount of gas adsorbed at typical gas pressure, V_L: the maximum adsorption capacity, p_L:the equilibrium pressure of the gas corresponding to half of V_L.

Eq. (1) describes adsorption by assuming that the adsorbate behaves as an ideal gas under isothermal conditions and exhibits monolayer coverage behavior on the solid adsorbent. Additionally, the surface coverage ratio can be represented as follows:

$$\theta = \frac{p}{p + p_L} \tag{2}$$

Where θ: represents the surface coverage ratio. Based on the equations, Eq. (1) and Eq. (2), the sorption behavior of

hydrogen on coal has been evaluated.

3. RESULTS AND DISCUSSION

Studies on hydrogen adsorption, a critical parameter for underground hydrogen storage systems in coal seams, and the influencing factors are relatively scarce worldwide. The findings from these studies are explained below.

Iglauer et al. [7] measured H_2 adsorption on a typical bituminous coal sample and demonstrated that significant amounts of H_2 could be stored even at moderate pressures using this approach. They observed that H_2 adsorption increased significantly with increasing pressure (Fig. 1). Initially, this increase was rapid, but the adsorption curve plateaued at approximately 4 MPa. At low pressure (0.1 MPa), only a small amount of H_2 was adsorbed (0.005 mol/kg coal). At 3.38 MPa, 0.23709 mol H_2/kg coal was adsorbed (both measured at 303 K). Hydrogen adsorption increased by a factor of 47.418 as the pressure rose from 0.1 MPa to 3.38 MPa. At 11.74 MPa (303 K), 0.54686 mol H_2/kg was adsorbed, while at 14.3207 MPa (318 K), this value reached 0.60183 mol H_2/kg. Compared to the initial condition (0.1 MPa), the amount of adsorbed H_2 increased by a factor of 120 at 14.3207 MPa. Additionally, changes in temperature (from 303 K to 333 K) had only a slight effect on the adsorption profile (slightly smaller amounts of H_2 were recorded at higher temperatures). They concluded that significant amounts of H_2 could be stored in deep coal seams dominated by high pressures and temperatures (Fig. 1). However, at the same temperature, the amount of CO_2 adsorbed was approximately 10 times that of H_2 (e.g., 2.64 mol CO_2/kg coal at 3.302 MPa vs. 0.23709 mol H_2/kg coal at 3.382 MPa, both measured at 303 K). Iglauer et al. [7], also investigated the effects of pressure and temperature on H_2 and CO_2 adsorption rates through experiments on sub-bituminous coal. At moderate pressure and temperature (303 K, 3.3 MPa), 0.23709 mol H_2/kg coal could be adsorbed, whereas at higher pressures (14.3 MPa, 318 K), this value reached 0.60183 mol H_2/kg coal. Their study presented data supporting hydrogen storage in deep coal seams and the establishment of a large-scale hydrogen supply chain.

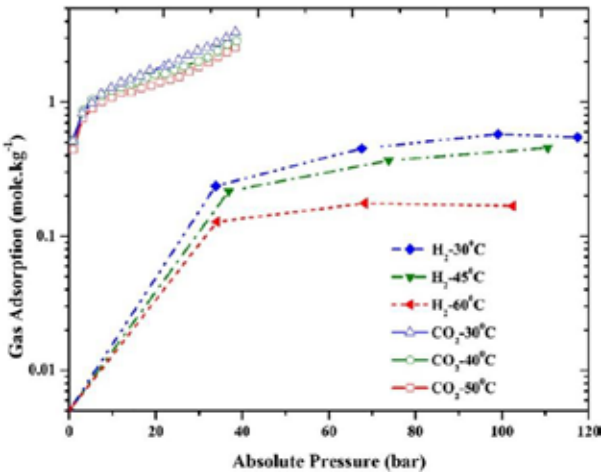

Fig. 1. Monte Hydrogen adsorption on sub-bituminous coal as a function of pressure and temperature. (CO_2 data included for comparison purposes.) [14]

Arif et al. [15] conducted hydrogen adsorption measurements on three coal samples of varying ranks at high pressures (0 to 102 bar) and high temperatures (303 K to 333 K) to evaluate their hydrogen storage potentials (Fig. 2). They observed that adsorption capacity increased with increasing pressure but decreased with rising temperature, regardless of coal rank. The highest recorded hydrogen adsorption was 0.721 mol/kg for anthracite coal at 303 K and 102 bar. Higher adsorption was observed in high-rank coal. All samples predominantly exhibited type I adsorption behavior across the entire pressure range. To investigate the microstructure and surface chemistry associated with these adsorption tendencies, micro-pore analysis, and Fourier transform infrared spectroscopy measurements were conducted. The micro-pore content of the three samples followed this order: anthracite > sub-bituminous > bituminous, while the H_2 adsorption tendency followed this order: anthracite > bituminous > sub-bituminous. In other words, they observed that there was no direct correlation between the micro-pore content of the coal and its H_2 adsorption capacity. This situation could potentially be attributed to the high clay content in bituminous coal, which reduces its micro-pore content. Furthermore, while bituminous and sub-bituminous samples exhibit a significant number of oxygen-containing functional groups, anthracite coal shows notable aromatic content; this reveals that the H_2 adsorption capacity is a complex function of both the coal's surface chemistry and micro-pore content [15]. Overall, high-rank coal seams at high pressure and temperature showed the highest hydrogen adsorption, similar to CO_2 adsorption potential, albeit at lower absolute values. Thus, these results provide preliminary data regarding the hydrogen storage potential of coal seams and the mechanisms behind hydrogen adsorption, contributing to the relevant scientific understanding.

The rankings of eight coals from significant coal fields in the United States, based on fixed carbon content, vitrinite reflectance, vitrinite content, O/C ratio, and H/C ratio, were measured and analyzed for their adsorption and diffusion

behaviors by Liu & Liu [4]. Adsorption data showed that all eight coals had considerable adsorption capacities. Among them, LvB coal has a maximum adsorption capacity of approximately 1.17 mol/kg, followed by coal with a maximum hydrogen adsorption capacity of ~0.95 mol/kg, and SemiAn coal with ~0.82 mol/kg [4]. The fixed carbon content and typically the O/C ratio are related to the maximum hydrogen adsorption capacity in coals, which can be attributed to oxygen-containing functional groups. Hydrogen has superior diffusivity and is characterized by its effective propagation.

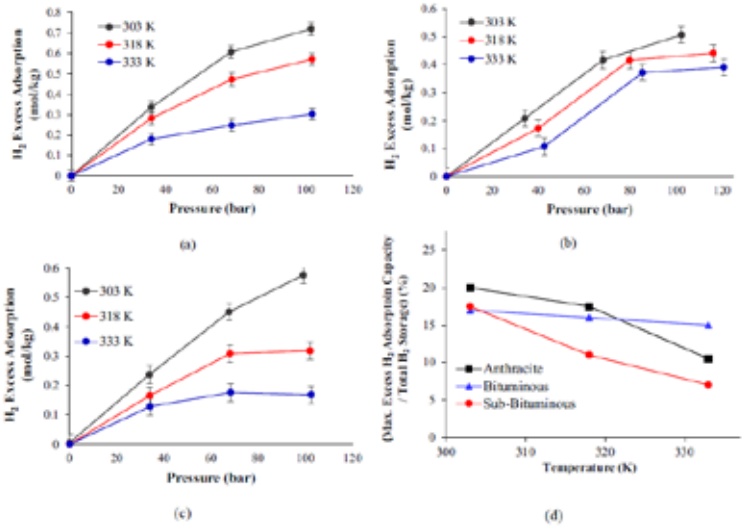

Fig. 2. Monte Hydrogen adsorption on coal samples as a function of pressure at different temperatures; a) anthracite, b) bituminous, c) sub-bituminous, d) Excess H_2 Adsorption/Total H_2 Storage (%) (at 102 bar) [15]

In the SemiAn coal, the effective diffusion of hydrogen decreases from ~0.00156 to ~9.26×10^{-4} 1/s with an increase in pressure from ~2.45 MPa to ~10.07 MPa; among these, the lowest diffusion at ~10.07 MPa is four times higher than that of CH_4 at the equivalent pressure [4]. This indicates that coal seams with maximum injectability are a promising area for hydrogen storage. The results suggest that the adsorption and diffusion behaviors of hydrogen in coals with different ranks, moving toward methane formation in depleted coal beds with injected hydrogen, could function as a geological "H_2-Battery."

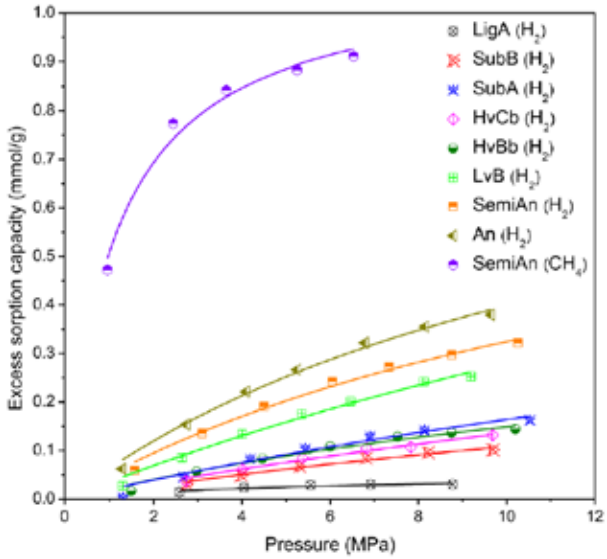

Fig. 3. Modeling of the hydrogen adsorption isotherm using the Langmuir adsorption model (Eq. 3) [4]

Wang and Chen [16] examined the hydrogen (H_2) adsorption behavior in dry and moist coals (moisture content 0-10% by weight) under different temperature (293.15 K - 333.15 K) and pressure (1.3 MPa - 15 MPa) conditions using large canonical molecular dynamics simulations. The effects of temperature, pressure, coal rank, and moisture on H_2 storage capacity were analyzed. The study showed that H_2 adsorption capacity is positively correlated with coal rank, linking it to the effects of surface chemical properties and pore structure. It was noted that as pore size decreases, the isosteric heat of adsorption increases, and in moist coal, the adsorption capacity of H_2 decreases due to the competitive adsorption

of water. It was concluded that anthracite coal seams, containing abundant micro-pores and few hydrophilic groups, have a high potential for H_2 storage. As pressure increased, the adsorption capacity also increased. Adsorption at 0.1 MPa was 0.005 mol/kg, while at 14.32 MPa, it reached 0.60183 mol/kg. An increase in temperature reduces the adsorption, which is attributed to the exothermic nature of adsorption. The adsorption capacity of CO_2 is approximately 10 times higher than that of H_2. This difference is due to CO_2's stronger interaction with the surface. Anthracite coal, with its high micro-pore content, has the highest adsorption capacity among the coal types [16].
Determining the H_2 adsorption capacity of the underground hydrogen storage (UHS) reservoir and its boundaries is crucial for assessing both storage capacity and well integrity [17]. The adsorption ranges of CO_2 and CH_4 in Turkish coals vary depending on coal type and regional conditions. However, they generally fall within the range of 1–10 m³/ton for CH_4 and 5–20 m³/ton for CO_2 [18]. These values are crucial for assessing the gas storage potential of coal seams. However, the H_2 adsorption capacity of Turkish coals remains unknown due to the lack of studies on this subject. In our future research, we plan to conduct these experiments by using the coal samples in Turkiye, as they are essential for evaluating their UHS potential..

4. CONCLUSIONS

This study has highlighted the hydrogen storage potential of coal seams. The hydrogen adsorption capacity can be optimized based on variations in pressure and temperature. High-rank coal types stand out with higher adsorption capacities. From a practical application perspective, the use of coal seams as geological hydrogen storage reservoirs offers a low-cost and sustainable energy storage solution. However, technical challenges such as improving competitive gas adsorption and desorption kinetics should be the focus of future research. The results are significant for energy security and sustainable energy management.

REFERENCES

[1] Muthukumar, P., Kumar, A., Afzal, M., Bhogilla, S., Sharma, P., Parida, A., Jana, S., Kumar, E.A., & Jain, I. P. (2023). Review on large-scale hydrogen storage systems for better sustainability. International Journal of Hydrogen Energy.
[2] Ma, N., Zhao, W., Wang, W., Li, X., & Zhou, H. (2023). Large scale of green hydrogen storage: Opportunities and challenges. International Journal of Hydrogen Energy.
[3] Seifi, H., & Masoum, S. (2017). Electrochemical hydrogen storage performance of carbon nanosheets synthesized from bituminous coal. International Journal of Hydrogen Energy, 42(51), 30145-30155.
[4] Liu, A., & Liu, S. (2023). Hydrogen sorption and diffusion in coals: Implications for hydrogen geo-storage. Applied Energy, 334, 120746.
[5] Tarkowski, R., & Czapowski, G. (2018). Salt domes in Poland–Potential sites for hydrogen storage in caverns. International Journal of Hydrogen Energy, 43(46), 21414-21427.
[6] Pan, B., Yin, X., & Iglauer, S. (2021). Underground hydrogen storage: Influencing parameters and future outlook. Advances in Colloid and Interface Science, 294, 102473. https://doi.org/10.1016/j.cis.2021.102473
[7] Iglauer, S., Abid, H., Al-Yaseri, A., & Keshavarz, A. (2021). Hydrogen adsorption on sub-bituminous coal: Implications for hydrogen geo-storage. Geophysical Research Letters, 48(10), e2021GL092976.
[8] Keshavarz, A., Abid, H., Ali, M., & Iglauer, S. (2022). Hydrogen diffusion in coal: Implications for hydrogen geo-storage. Journal of Colloid and Interface Science, 608, 1457-1462.
[9] King, G. R. (1990, September). Material balance techniques for coal seam and Devonian shale gas reservoirs. In SPE Annual Technical Conference and Exhibition? (pp. SPE-20730). SPE.
[10] Freundlich, H. (1907). Über die Adsorption in Lösungen. Z Für Phys Chem 57U: 385–470.
[11] Langmuir, I. (1918). The adsorption of gases on plane surfaces of glass, mica and platinum. J. Am. Chem. Soc. 40, 1361–1403.
[12] Brunauer, S., Emmett, P.H., Teller, E. (1938). Adsorption of gases in multimolecular layers. J. Am. Chem. Soc.60, 309-319.
[13] Dubinin, M. M. (1969). The potential theory of adsorption of gas. Chemical Reviews, 60(13), 235–241.
[14] Alfadlil, B. R., Knowles, G. P., Parsa, M. R., Subagyono, R. D., & Chaffee, A. L. (2019, July). Carbon monolith from Victorian brown coal for hydrogen storage. In Journal of Physics: Conference Series (Vol. 1277, No. 1, p. 012024). IOP Publishing.)
[15] Arif, M., Abid, H. R., Keshavarz, A., Jones, F., & Iglauer, S. (2022). Hydrogen storage potential of coals as a function of pressure, temperature, and rank. Journal of colloid and interface science, 620, 86-93.
[16] Wang, G., & Chen, W. (2024). Molecular simulations of hydrogen adsorption on coal with different ranks: Implications for hydrogen geo-storage. International Journal of Hydrogen Energy, 51, 10-20.
[17] Merey, S., & Aydin, H. (2025). Simulating Hydrogen Adsorption-Driven Thermal Variations for Improved Well Integrity Monitoring in Underground Hydrogen Storage. International Journal of Hydrogen Energy,
Doi: 10.1016/j.ijhydene.2025.01.252
[18] Rend, A. R., Özer, S. C., Esen, O., Soylu, A., Bozdoğan, S., & Fişne, A. (2023). Developing basin-specific emission factors for accurate methane inventory and emission reduction strategies in Zonguldak Coal Basin, Turkey: Implications for enhancing safety and sustainability. *Journal of Cleaner Production*, *426*, 139177.

ELECTRODEPOSITION OF PLATINUM ON ELECTROPOLYMERIZED ABA ON REDUCED GRAPHENE OXIDES AS A CATALYST FOR PROPANOL OXIDATION IN ALKALINE SOLUTION

[1*]Paralee Waenkaew, [1]Saengrawee Sriwichai, [1,2]Suwaphid Themsirimongkon
[1] Chiang Mai University, Faculty of Science, Department of Chemistry, 239 Huay Kaew Rd., Suthep, Chiang Mai, 50200, Thailand
[2] Chiang Mai University, Office of Research Administration, 239 Huay Kaew Rd., Suthep, Chiang Mai, 50200, Thailand

*Corresponding author e-mail: paralee.w@gmail.com

ABSTRACT
In this study, the electro-oxidation of 1-propanol and 2-propanol on Pt/PABA/GO and Pt/GO catalysts was investigated, highlighting the significant influence of alcohol molecular structure on electrochemical reactivity. The electrodeposition of Pt nanoparticles on PABA/GO resulted in smaller Pt particles compared to Pt on GO. 1-Propanol exhibited higher oxidation currents across a broader potential range than 2-propanol, indicating its more favorable electro-oxidation behavior. The Pt/PABA/GO composite demonstrated superior catalytic activity and a lower onset potential compared to Pt/GO, emphasizing the importance of structural conditions in optimizing propanol oxidation mechanisms. Furthermore, Pt/PABA/GO exhibited enhanced stability during oxidation, outperforming Pt/GO in terms of long-term catalytic activity. The improved performance of Pt/PABA/GO is attributed to the unique PABA-GO hybrid support, which prevents Pt nanoparticle agglomeration and promotes a uniform distribution. The interactions between PABA, carbon supports, and Pt nanoparticles not only reduce overpotentials but also significantly enhance catalytic efficiency, positioning the Pt/PABA/GO composite as a promising catalyst for alcohol oxidation reactions.

Keywords: Platinum, Conducting Polymer, Alkaline media, Propanol, Electrocatalyst

1. INTRODUCTION

In the expedition for sustainable and efficient energy sources, alcohols, particularly in direct alcohol fuel cells (DAFCs), have harvested significant attention due to their high energy density, ease of storage, and refueling capabilities compared to gaseous hydrogen [1, 2]. These attributes make alcohols ideal candidates for low-power demand applications, such as laptops and mobile phones. However, despite their potential, real commercial breakthroughs have been hindered by the high cost of fuel cell components, especially the use of noble metal catalysts [1, 3]. To lower the cost of these catalysts, it is essential to reduce the amount of noble metal required while maintaining high performance.

One promising approach to achieve this goal is the use of alkaline media, which enhances the reaction kinetics compared to acidic media. In alkaline solutions, the same current density can be achieved with lower catalyst loadings, offering a way to optimize the use of precious metals [1, 4]. The re-emergence of interest in alkaline media for DAFCs has been fueled by the development of new anion exchange membranes, which enable better performance in these environments. Among the various catalysts, platinum (Pt) is widely considered the most effective monometallic catalyst for the electro-oxidation of small organic molecules, such as alcohols, due to its ability to break carbon-hydrogen bonds and oxidize carbon monoxide at relatively low overpotentials [2 - 4].

Although much attention has been given to the electrochemical oxidation of shorter-chain alcohols, such as methanol and ethanol, the oxidation of C3 alcohols, like 1-propanol and 2-propanol, has been less explored [5, 6]. Electrochemical oxidation of C3 alcohols in DAFCs has the potential to generate significant electrical energy through dehydrogenation reactions and C–C bond cleavage [1, 5, 6]. However, the performance of C3 alcohols in DAFCs is generally inferior to that of methanol and ethanol, making it crucial to study the oxidation reactions of these alcohols to better understand the influence of their molecular structure on reaction behavior[2, 4 - 6]. 2-Propanol, in particular, stands out as an attractive fuel for DAFCs due to its relatively low toxicity, high boiling point, and low permeability through electrolyte membranes compared to methanol [1, 4 - 6]. Several studies have focused on the electrochemical oxidation of 2-propanol on platinum in acidic media, but further research in alkaline conditions is necessary to fully assess its potential for DAFC applications.

Graphene oxide (GO) and its reduced form (rGO) have gained significant attention as catalyst supports in electrochemical applications due to their high surface area, which provides abundant active sites for catalyst dispersion, thereby enhancing catalytic activity [1, 5, 6]. The oxygen-containing functional groups on GO facilitate metal nanoparticle anchoring, improving both stability and performance [7]. Moreover, rGO exhibits excellent electrical conductivity, which is essential for efficient electron transfer during electrochemical reactions. Graphene derivatives also offer strong mechanical properties, chemical stability, and durability, making them suitable for harsh electrochemical environments [7, 8]. Their cost-effectiveness and lightweight nature further enhance their attractiveness as catalyst supports in fuel cells and other electrochemical devices.

The modification of carbon materials with conducting polymers presents another promising approach to stabilize metal nanoparticles and enhance their performance. Conducting polymers, such as polypyrrole, polyaniline, and polythiophene, have been widely studied for their unique electronic properties, including electrical conductivity, low energy optical transitions, and high electron affinity [7, 8]. Among these conducting polymers, poly(aminobenzoic acid) (PABA), a derivative of polyaniline, is of particular interest. PABA's electron-rich nitrogen atom and high electron density of the

carbonyl group make it highly suitable for electropolymerization, providing a stable matrix for the deposition of metal catalysts and facilitating interactions with fuel molecules like propanol [9].
In this study, thin films of PABA/rGO composites were fabricated through electropolymerization of 3-aminobenzoic acid (ABA) onto electrodes. Pt was electrodeposited onto these composite films using cyclic voltammetry (CV). The electrochemical performance of the resulting Pt/PABA/GO catalysts was primary evaluated for propanol oxidation in alkaline solution, using both cyclic voltammetry (CV) and chronoamperometry (CA) to assess their activity and stability.

2. MATERIALS AND METHODS

Graphene oxide (GO) was made from graphite (powder < 20 um; Sigma-Aldrich) according to a previously published procedure [7, 8]. 2 mg GO was mixed in 1 mL of mixed solution (5 wt% Nafion/ethanol/DI water = 6.25:20:73.75) in an ultrasonic bath for 30 min. 5 μL of the suspension was drop-casted onto the GCE and dried under a lamp. 3-Aminobenzoic acid (ABA) was electropolymerized on the surface of the working electrode (GCE) by repetitive cyclic potential scan for 2 cycles between −0.2 and + 1.0 V at 50 mV s^{-1} in 14 mL of 0.5 M H_2SO_4 (Merck) containing ABA (1 mM). The electrode obtained was labeled as ABA-rGO. The monometallic catalysts were consequently electrodeposited in an electrolytic solution containing 1 mM $H_2PtCl_6 \cdot 6H_2O$ solution by two scanning cycles between −0.4 and 1.0 V. The metal loaded on the GO-modified GCE with and without ABA loading were denoted as M/ABA-rGO and M/GO (M = Pt), respectively. The electrochemical characterization of the catalyst electrodes was investigated in N_2-saturated 0.5 M KOH solution in the potential region from −0.85 to 0.2 V at a scan rate of 50 mV s^{-1}. In addition, the activities of the prepared catalyst electrodes for oxidation were measured in N_2-saturated 0.5 M 1-propanol and 0.5 M 2-propanol in 0.5 M KOH as a supporting electrolyte in the potential region from -0.85 to 0.2 V. The morphologies and chemical compositions of the prepared catalysts were determined by a JEOL transmission electron microscope connected to an energy dispersive X-ray spectroscope.

3. RESULTS AND DISCUSSION

After the electropolymerization of PABA on the GO surface, resulting in the PABA-GO support, Pt was electrodeposited onto the PABA-GO support to produce the Pt/PABA-GO catalyst. The surface morphology of the resulting Pt/PABA-GO and Pt/GO electrocatalysts was analyzed using TEM, with the images presented in Fig. 1 (a and b). The TEM images reveal that the surface structure of GO was notably influenced by the incorporation of Pt and PABA microparticles. Specifically, small Pt nanoparticles were observed to be deposited and agglomerated on the GO surface. In contrast, Pt nanoparticles on the PABA/GO support exhibited a more homogeneous distribution with fewer signs of agglomeration, and the particles appeared smaller.
The elemental compositions of the catalysts were further characterized using energy-dispersive X-ray (EDX) spectroscopy, as shown in Fig. 1(c and d). The EDX spectra revealed distinct peaks corresponding to platinum (Pt), nitrogen (N), oxygen (O), and carbon (C), which confirmed the presence of Pt nanoparticles. The high levels of carbon, nitrogen and oxygen observed in the spectra indicated the significant contribution of PABA and GO to the surface composition of the catalyst, highlighting the successful functionalization of GO with PABA and subsequent deposition of Pt nanoparticles.

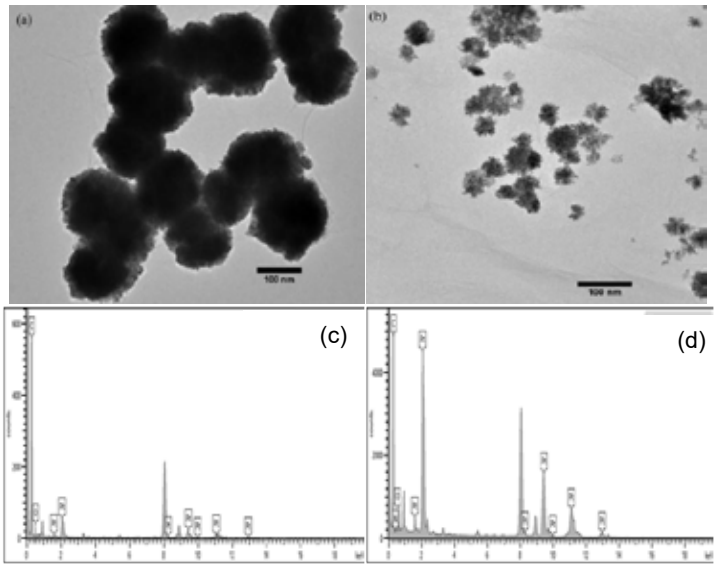

Fig. 1. TEM-EDX images of (a and c) Pt/GO and (b and d) Pt/PABA-rGO catalysts.

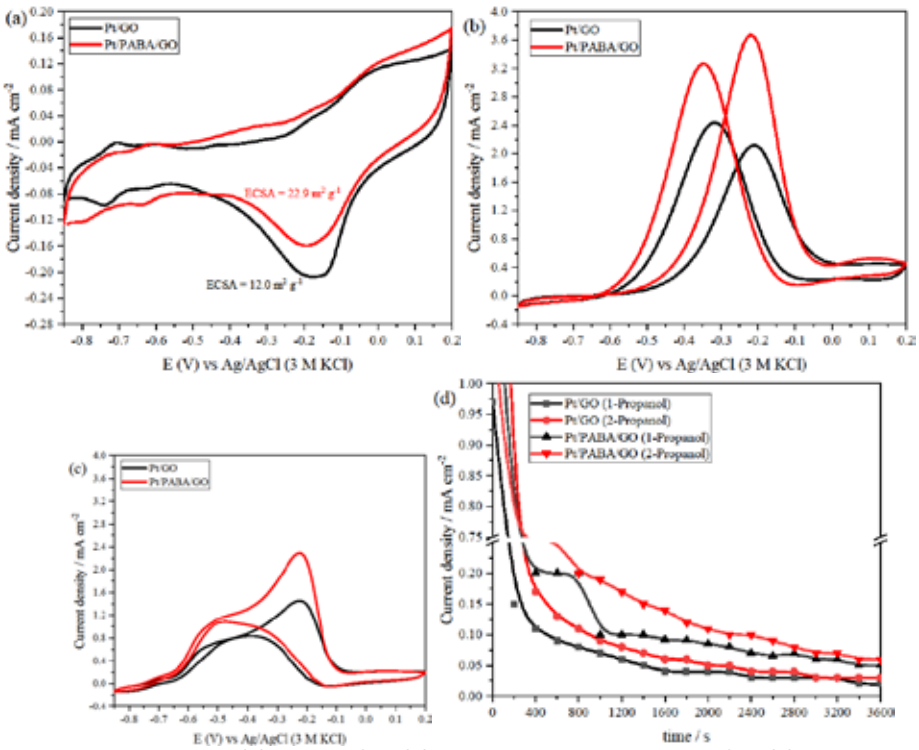

Fig. 2. CVs of the as-prepared catalysts in (a) 0.5 M KOH, (b) 0.5 M 1-propanol + 0.5 M KOH, (c) 0.5 M 2-propanol + 0.5 M KOH and (d) CA of Pt/GO (black line) and Pt/PABA-rGO (red line) in 1- and 2-propanol.

The electrochemical behavior of the obtained deposits was investigated in a 0.5 M KOH solution at a scan rate of 0.05 mV s^{-1}. As depicted in Fig. 2 (a), the voltammetric profiles of the Pt/PABA/GO and Pt/GO electrocatalysts exhibit similar features to those observed for electrodeposited Pt nanoparticles. Specifically, both catalysts show typical hydrogen and oxygen adsorption/desorption regions, along with the presence of a distinct double-layer region, which is characteristic of platinum-based electrocatalysts.

However, a notable difference is observed in the Pt/PABA/GO electrocatalyst, where the adsorption of oxygen species during the anodic scan (after -0.1 V) appears broader compared to the Pt/GO catalyst. This suggests an enhanced interaction between the oxygen species and the Pt/PABA/GO surface. Consequently, the peak current density associated with the reduction of Pt oxide is significantly enhanced on the Pt/PABA/GO catalyst. This improvement can be attributed to the unique structural and compositional properties of the Pt/PABA/GO catalyst, which facilitate more efficient oxygen adsorption and subsequent electrochemical processes.

Fig. 2 (b and c) presents the cyclic voltammograms for the oxidation of 1-propanol and 2-propanol in a 0.5 M KOH solution containing 0.5 M alcohol on a Pt electrode. The potential sweep was conducted at a rate of 0.05 V s^{-1} within the range of -0.85 V to 0.2 V. When compared to the cyclic voltammogram obtained in the absence of alcohol, a distinct alcohol oxidation peak is clearly visible. The oxidation of alcohol on the Pt electrode is characterized by two well-defined current peaks in both the forward and reverse scans.

In the forward scan, the oxidation peak, observed at E = -0.2 V, corresponds to the oxidation of freshly chemisorbed species resulting from alcohol adsorption. The reverse scan peak, observed at E = -0.4 V, is primarily associated with the removal of carbonaceous species that were not completely oxidized during the forward scan. The onset potentials for both 1-propanol and 2-propanol oxidation on the Pt/PABA/GO catalyst are lower than those observed on the Pt/GO catalyst, suggesting that the Pt/PABA/GO catalyst offers a lower energy barrier for oxidation, indicating it is more easily oxidized.

The magnitude of the peak current in the forward scan provides insight into the electrocatalytic activity of the electrocatalysts for alcohol oxidation in an alkaline medium. Notably, the current densities for the oxidation of 1-propanol at the corresponding potentials are higher than those for 2-propanol oxidation on both Pt/PABA/GO and Pt/GO electrodes. Furthermore, the Pt/PABA/GO catalyst demonstrates a higher current density compared to Pt/GO, signifying superior catalytic activity. This highlights that the activity order for alcohol oxidation on Pt electrodes is 1-propanol > 2-propanol, with the Pt/PABA/GO catalyst exhibiting enhanced electrocatalytic performance.

The stability of 1-propanol and 2-propanol oxidation on the Pt electrode in a 0.5 M KOH + 0.5 M alcohol solution was evaluated using chronoamperometry at a constant potential of -0.2 V. The results, shown in **Fig. 2(d)**, reveal a rapid decay in current, indicating the poisoning of the Pt electrode during the oxidation process. Despite this, it is noteworthy that at the conclusion of the test, the oxidation current for 2-propanol is higher than that for 1-propanol on the Pt electrode.

Furthermore, the current intensities measured after 3600 s for the Pt/PABA/GO catalyst are higher than those for the Pt/GO catalyst for both 1-propanol and 2-propanol. This indicates that the Pt/PABA/GO catalyst exhibits better stability, maintaining higher catalytic activity over time compared to Pt/GO, and is less prone to deactivation during the alcohol oxidation process.

Based on previous reports, the primary electrochemical reaction for 2-propanol oxidation is generally considered to be dehydrogenation, where 2-propanol is converted to acetone, accompanied by a charge-transfer reaction of hydrogen [1, 4, 10]. In addition to this main reaction, an alternative electrochemical pathway proceeds in parallel, involving an intermediate species, where 2-propanol is oxidized to an intermediate and then further oxidized to CO_2. While the exact molecular structure of this intermediate has not been definitively identified, it is likely to be an acetone species or acetone itself adsorbed on the Pt surface. Taking into account these possible reactions, a simple reaction model for 2-propanol electro-oxidation can be proposed. This model involves parallel reaction pathways, with the dehydrogenation of 2-propanol to acetone as the dominant process, while a secondary reaction pathway leads to the formation of CO_2 through the oxidation of an intermediate. The proposed pathway model highlights the complexity of the electrochemical oxidation of 2-propanol on the Pt electrode [10].

$$CH_3CHOHCH_3 + 2OH^- \rightarrow CH_3COCH_3 + 2H_2O + 2e^- \quad \text{Eq. (1.)}$$

$$CH_3COCH_3 + 16OH^- \rightarrow 3CO_2 + 11H^+ + 16e^- \quad \text{Eq. (2.)}$$

These two reactions highlight the distinct but interconnected pathways involved in the electro-oxidation of propanol on the electrode surface, with each contributing to the overall catalytic performance.

4. CONCLUSIONS

In conclusion, the Pt/PABA/GO composite catalyst demonstrates significantly improved electrochemical performance for the oxidation of 1-propanol and 2-propanol compared to the Pt/GO catalyst. The smaller Pt nanoparticles and their uniform distribution on the PABA/GO support contribute to enhanced catalytic activity and stability. The results show that 1-propanol exhibits more favorable oxidation behavior than 2-propanol, as evidenced by higher oxidation currents over a broader potential range. Additionally, the Pt/PABA/GO catalyst exhibits a lower onset potential and greater stability during oxidation reactions, indicating its superior performance in alcohol oxidation processes. The unique PABA-GO hybrid support plays a crucial role in preventing Pt nanoparticle agglomeration, reducing overpotentials, and improving the overall catalytic efficiency. This study highlights the potential of the Pt/PABA/GO composite as a promising catalyst for alcohol oxidation reactions, with implications for various electrochemical applications.

ACKNOWLEDGEMENT

This research project was supported by Chiang Mai University, Fundamental Fund, Chiang Mai University, the Center of Excellence for Innovation in Chemistry (PERCH-CIC), Office of the Higher Education Commission, Ministry of Education (OHEC), Chiang Mai University Thailand.

REFERENCES

1. Berretti E, Osmieri L, Baglio V., et al. 2023. Direct Alcohol Fuel Cells: A Comparative Review of Acidic and Alkaline Systems. Electrochemical Energy Reviews 6:30.
2. Shaari N, Kamarudin S K, Bahru R, Osman S H, Md Ishak N, 2021. Progress and challenges: Review for direct liquid fuel cell. International Journal of Energy Research. 45:6644–6688.
3. Huang C, Wang F, Chen X, Li J, Shao M, Wei Z. 2025. Innovative strategies for designing and constructing efficient fuel cell electrocatalysts. Chemical Communications.61:2658-83.
4. Themsirimongkon S, Waenkaew P, Fang L, Jakmunee J, Kuntalue B, Kuimalee S, et al. 2024, Development of a Pd-xCNT-Ni-yCB composite catalyst to enhance the oxidation of various alcohols in alkali mediums. Biomass and Bioenergy. 181:107032.
5. Darabi R, Karimi F, Bayat R, et al. 2024. Carbon Nanofibre Modified Platinum Nanomaterials: Synthesis, Characterization and Their Applications toward C1 to C3 Alcohols for Direct Alcohol Fuel Cells. Topics in Catalysis. 67:650–660.
6. Bayat R, El Attar A, Akin M, Bekmezci M, El Rhazi M, Sen F. 2024. Copper nanoparticle modified chain-like platinum nanocomposites for electro-oxidation of C1-, C2-, and C3- type alcohols. International Journal of Hydrogen Energy. 51:1577-86.
7. Waenkaew P, Saipanya S, Maturost S, Themsirimongkon S, Somsunan R, Promsawan N. 2022. Enhanced catalytic efficiency of bimetallic Pt-Pd on PAMPs-modified graphene oxide for formic acid oxidation. International Journal of Hydrogen Energy, 47:16189-200.
8. Themsirimongkon S, Ounnunkad K, Saipanya S. 2018. Electrocatalytic enhancement of platinum and palladium metal on polydopamine reduced graphene oxide support for alcohol oxidation. Journal of Colloid and Interface Science. 530:98-112.
9. Sriwichai S, Baba A, Phanichphant S, Shinbo K, Kato K, Kaneko F. 2010. Electrochemically controlled surface plasmon resonance immunosensor for the detection of human immunoglobulin G on poly(3-aminobenzoic acid) ultrathin films. Sensors and Actuators B: Chemical. 147:322-9.
10. Ye J, Liu J, Xu C, Jiang SP, Tong Y. 2007. Electrooxidation of 2-propanol on Pt, Pd and Au in alkaline medium. Electrochemistry Communications. 9:2760-3.

ENHANCED ALCOHOL OXIDATION IN ACIDIC AND ALKALINE MEADIA USING Pt-MODIFIED NICKEL LAYERED DOUBLE HYDROXIDE SUPPORTED ON MULTIWALL CARBON NANOTUBES AND CARBON BLACK SURFACES

[1*]*Surin Saipanya*, [2]*Jaroon Jakmunee*, [3]*Li Fang*
[1] Chiang Mai University, Faculty of Science, Department of Chemistry, Laboratory of Vantage Electromaterials (LOVEs), 239 Huay Kaew Rd., Suthep, Chiang Mai, 50200, Thailand
[2] Chiang Mai University, Faculty of Science, Department of Chemistry, Research Laboratory for Analytical Instrument and Electrochemistry Innovation, 239 Huay Kaew Rd., Suthep, Chiang Mai, 50200, Thailand
[3] Shanxi University, Faculty, School of Chemistry and Chemical Engineering, Taiyau, Shanxi, 030006, China

*Corresponding author e-mail: surin_saipanya@hotmail.co.uk

ABSTRACT
Pt catalysts supported on multi-walled carbon nanotubes (MWCNTs)-nickel (Ni)-carbon black (CB) composites were synthesized as anode catalysts for high-performance alcohol electrooxidation (methanol, ethanol, and propanol) in direct alcohol fuel cells (DAFCs). A simple method utilizing ethylene glycol as a reducing agent was employed to synthesize the metal electrocatalysts. The morphology and structure of the as-synthesized catalysts were characterized using Transmission Electron Microscopy (TEM), which revealed small Pt nanoparticles uniformly dispersed on the surfaces of xMWCNTs-Ni-yCB. The electrocatalytic performance of the catalysts was evaluated through various electrochemical techniques, including Cyclic Voltammetry (CV) and Chronoamperometry (CA). The Pt/xMWCNTs-Ni-yCB catalysts with different carbon ratios (x:y = 1:1, 1:2, and 2:1) exhibited significantly enhanced catalytic activity and stability compared to other catalysts and commercial PtRu/C towards alcohol oxidation. The design of the hybrid MWCNTs and CB carbon structure imparted remarkable structural and functional properties, contributing to improved electrochemical activation and catalytic performance of Pt nanoparticles. The synergistic effect between these components enhances the overall catalytic efficiency, demonstrating a promising strategy for advanced alcohol oxidation in fuel cell applications.

Keywords: Platinum, multiwalled carbon nanotubes, nickel, carbon black, alcohol oxidation

1. INTRODUCTION
Direct alcohol fuel cells (DAFCs) have gained significant attention as promising green energy generators, capable of converting renewable fuels directly into electrical energy with thermodynamic high efficiencies, as energy is converted without the limitations imposed by Carnot's theorem [1, 2]. These fuel cells are capable of selectively producing high-value products while generating electric power, which makes them attractive for both energy production and value-added byproducts [3, 4]. Among various alcohol fuels, methanol has long been the primary focus due to its high energy density, ease of decomposition, and ability to deliver high energy per unit volume of CO_2 produced during oxidation [2 - 4]. However, the primary challenge in using methanol in DAFCs lies in its toxicity to the catalyst caused by intermediate products formed during the oxidation process [3, 4]. This issue has prompted research into other alcohols, including C2-alcohols such as ethanol and isopropanol, which offer higher energy densities and can undergo complete oxidation, though they too introduce challenges related to catalyst stability due to the production of intermediates like CO or oxalic acid [3, 4].

Pt-based electrocatalysts are widely regarded as the most effective catalysts for alcohol oxidation reactions, particularly at low temperatures [5, 6]. However, due to the high cost and limited availability of platinum, there is a growing need to enhance its catalytic activity and utilization. Strategies to improve Pt-based catalysts include the dispersion of Pt nanoparticles onto carbon supports with high surface areas and good electrical conductivity, such as carbon black (CB) and carbon nanotubes (CNTs), as well as the development of Pt-alloy catalysts like Pt-Au [5, 6], Pt-Ni [7], and Pt-Pd [5, 6]. These materials are designed to improve catalytic performance while reducing the amount of Pt required.

Despite extensive research on the electrocatalytic oxidation of methanol and other alcohols in DAFCs, there remains a lack of comprehensive comparisons of the key factors that influence their performance, such as catalysts, fuels, and electrolytes, especially across different pH environments. This study aims to fill this gap by investigating the electro-oxidation behavior of methanol, ethanol, and isopropanol on various electrodes, including commercial Pt, Pd, and Au electrodes, as well as self-synthesized Pt/MWCNTs-Ni-CB electrodes. CV and CA are employed to evaluate the catalytic performance of these electrodes, offering new insights into the influence of different fuels, catalysts, and electrolytes on the electro-oxidation reactions, with the ultimate goal of optimizing DAFC performance.

2. MATERIALS AND METHODS

Catalyst synthesis were prepared as follows. The Pt/1MWCNTs-Ni-1CB catalyst was synthesized as follows: 50 mg Carbon Black - Vulcan XC 72 (Fuel cell Store) and 10 mL., nickel (II) chloride hexahydrate ($NiCl_2.6H_2O$ (1 mg/ mL; QReC) solution were dissolved in deionized water (30 mL) and sonicated for 20 min and 100 mL of ethylene glycol solution (70:30 (EG:DI-water), Ajax Finechem Pty Ltd) were mixed in the solutions with sonicated for 20 min. 50 mg of multiwalled carbon nanotubes (MWCNTs, Merck KGaA) was mixed in the solution and sonicated for 20 min. Then, 10 mL of hexachloroplatinic acid hexahydrate ($H_2PtCl_6.6H_2O.6H_2O$ (1 mg/mL); Sigma-Aldrich Merck) solution was added to the resulting mixture above in a flask under ultrasonication for 20 min. Then, the mixture was adjusted to pH ≈ 11.0 with 0.1 M NaOH (Merck KGaA), heated to 120 °C to perform a refluxed reaction for 2 h, centrifuged, washed with deionized water numerous times until neutral pH and dried at 60 °C overnight to obtain Pt/1MCNTs-Ni-1CB electrocatalysts. The Pt/1MWCNTs-Ni-2CB, Pt/2MWCNTs-Ni-1CB, Pt/1MWCNTs-1CB, Pt/MWCNTs and Pt/CB catalysts were synthesized with a similar process using different weight ratios of each carbons. For all catalysts synthesized, the Pt and Ni content in all the above electrocatalysts was controlled at 10.0 wt.%.

Electrochemical performance data were collected using the PalmSens4 electrochemical workstation in a standard three-electrode configuration. The working electrode was a glassy carbon electrode (GCE), while a Pt wire served as the counter electrode, and a silver/silver chloride electrode (Ag/AgCl) was used as the reference electrode. To prepare the GCE for testing, 5 µL of catalyst ink was drop-cast onto the electrode surface and allowed to dry naturally before electrochemical measurements. Cyclic voltammetry (CV) was performed to investigate the alcohol oxidation behaviors of methanol, ethanol, and iso-propanol in both acidic (0.5 M H_2SO_4) and alkaline (0.5 M KOH) solutions. Additionally, chronoamperometry (CA) was conducted at a constant potential of 0.1 V for 3600 seconds to assess the long-term stability and catalytic activity of the electrodes.

3. RESULTS AND DISCUSSION

TEM images of the catalyst regime and corresponding particle size distribution histograms are shown in Fig.1. As illustrated in Fig. 1(a)., spherical Pt nanoparticles are uniformly distributed on xMWCNTs-Ni-yCB. The average diameter of the prepared catalysts is approximately ca. 2.1-2.4 nm and selected Pt/1MWCNTs-Ni-1CB and Pt/1MWCNTs-1CB catalysts nanoparticles is shown. An EDX analysis of the prepared Pt/1MWCNTs-Ni-1CB revealed distinct peaks for Pt and Ni, indicating that Pt with Ni nanoparticles were successfully attached to the surface of MWCNTs-CB. Additionally, the atomic percentages of Pt and Ni were found to be 9.5 and 8.0, respectively, which closely align with the theoretical composition of 1:1.

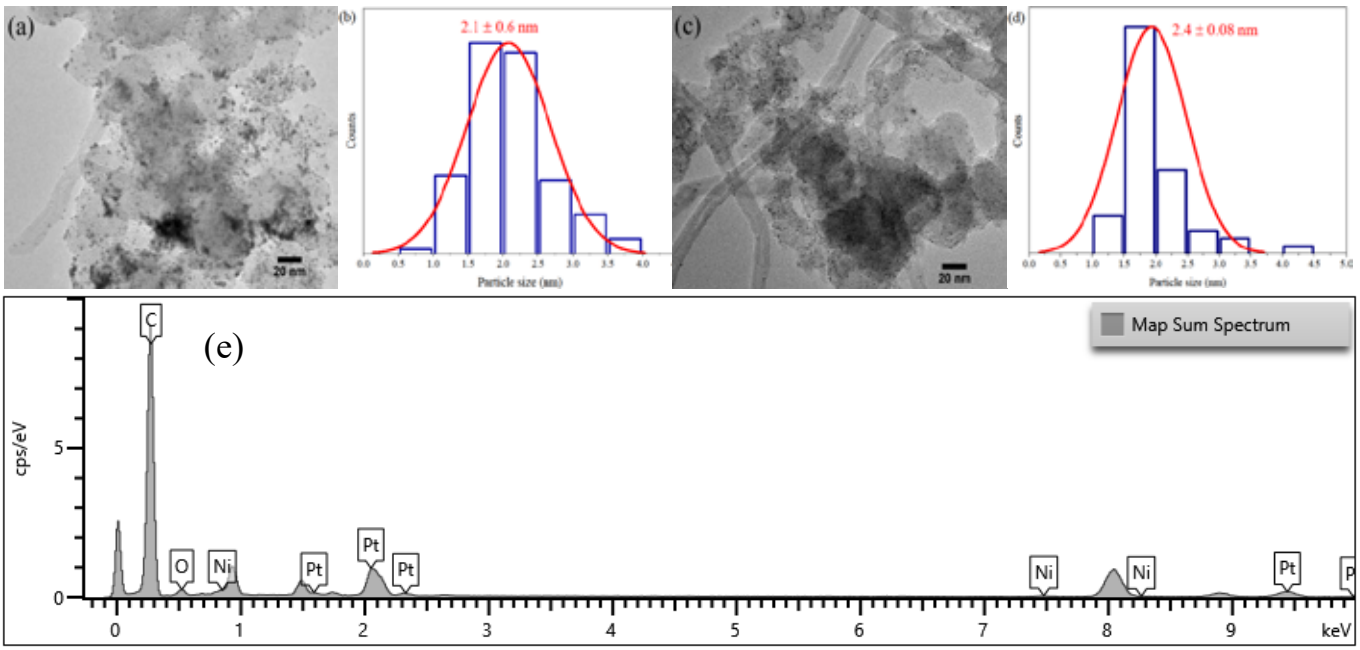

Fig. 1. TEM images and particle size distribution of Pt nanoparticles in (a, b) Pt/1MWCNTs-Ni-1CB, (c, d) Pt/1MWCNTs-1CB, and (e) EDX analysis of Pt/1MWCNTs-Ni-1CB catalysts.

The electro-oxidation behaviors of methanol, ethanol, and isopropanol were systematically investigated using cyclic voltammetry (CV) on Pt/xMWCNTs-Ni-yCB electrodes in both acidic and alkaline media. The results demonstrated that

the acid-base property of the electrolyte media plays a crucial role in influencing the catalytic activity of the electrodes. In alkaline media, oxidation peaks were observed in the expected potential range for all electrodes, indicating effective alcohol oxidation.

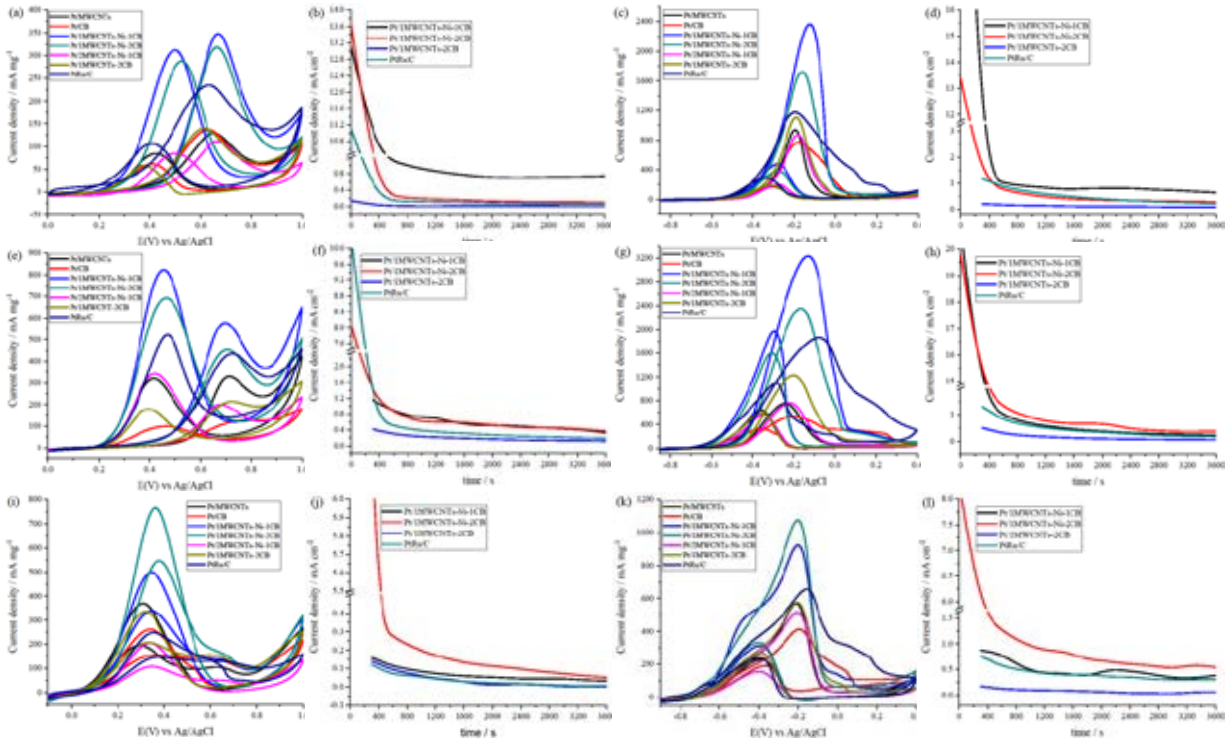

Fig. 2. CV and CA responses of the as-prepared catalysts for the electro-oxidation of methanol, ethanol, and isopropanol in (a, e, i and b, f, j) acidic and (c, g, k and d, h, l) alkaline solutions, respectively.

The comparison of the CV curves revealed that the lowest onset potential and the highest current density were generally observed in alkaline media, suggesting that alkaline media is optimal for the electro-oxidation of alcohols. This is consistent with the understanding that alkaline conditions facilitate easier dehydrogenation and oxidation reactions [5 - 7], which are essential for efficient alcohol oxidation. Additionally, the onset potential, which represents the energy barrier for the oxidation reaction, and the peak current density, which corresponds to the maximum reaction rate, were used to quantitatively assess the catalytic performance. The lowest onset potential and highest current density were mostly observed with the Pt/1MWCNTs-Ni-1CB electrodes, except in the oxidation of isopropanol. The comparison of the onset potentials for methanol (-0.51 V), ethanol (-0.73 V), and isopropanol (-0.80 V) revealed that alcohols with longer carbon chains required lower negative potentials for oxidation, indicating that the oxidation of larger alcohol molecules induces a lower energy barrier resulting from the increased complexity of the oxidation process as the chain length of the alcohol increases. The Pt/1MWCNTs-Ni-1CB electrodes exhibit the best catalytic activity while the Pt/1MWCNTs-Ni-2CB electrodes show highest stability for the oxidation of most alcohols, particularly in alkaline media. The findings emphasize the importance of optimizing both the catalyst composition and electrolyte medium to maximize the efficiency of alcohol oxidation in DAFCs. These results provide valuable understandings for the development of more effective catalysts for renewable energy applications.

4. CONCLUSIONS

This study investigated the electro-oxidation behavior of various alcohols over Pt/xMWCNTs-Ni-yCB electrodes in both acidic and alkaline media, revealing several key trends. The acid-base nature of the electrolyte significantly influences catalytic activity, with alkaline media demonstrating superior performance over acidic media. Specifically, the onset potentials for oxidation in alkaline media were approximately 0.6 V lower than in acidic media. This difference highlights the enhanced catalytic activity in alkaline conditions, which is likely attributed to the increased availability of hydroxide ions that aid in the oxidation process. Among the catalysts tested, Pt/1MWCNTs-Ni-1CB exhibited the best activity for methanol and ethanol oxidation in all media, while Pt/1MWCNTs-Ni-2CB showed exceptional activity for isopropanol oxidation in alkaline media. Both catalysts also demonstrated high stability in CA tests across media. Notably, Pt/1MWCNTs-Ni-2CB exhibited excellent stability for the oxidation of most alcohols. While the underlying reasons for these trends are still under investigation, the findings offer valuable insights for the development of DAFCs in the future.

ACKNOWLEDGEMENTS
This research project was supported by Chiang Mai University, Fundamental Fund, Chiang Mai University, the Center of Excellence for Innovation in Chemistry (PERCH-CIC), Office of the Higher Education Commission, Ministry of Education (OHEC), Chiang Mai University Thailand.

REFERENCES
1. Lutz A. E., Larson R. S. , Keller J. O. 2002. Thermodynamic comparison of fuel cells to the Carnot cycle. International Journal of Hydrogen Energy. 27:1103-1111.
2. Lamy C., Coutanceau C., Leger J-M., 2009. Catalysis for Sustainable Energy Production. WILEY-VCH Verlag GmbH & Co. KGaA, Weinheim.
3. Matthews T., Mbokazi S. P., Dolla T. H., et al. 2024. Electrocatalyst Performances in Direct Alcohol Fuel Cells: Defect Engineering Protocols, Electrocatalytic Pathways, Key Parameters for Improvement, and Breakthroughs on the Horizon. Small Science., 4: 2300057.
4. Berretti E., Osmieri L., Baglio V. *et al.* 2023. Direct Alcohol Fuel Cells: A Comparative Review of Acidic and Alkaline Systems. Electrochemical Energy Reviews. 6:30.
5. Miao L., Cheng Y., Liu Y., Li X., Zhang L., Wang W., 2024. Developing high-effective Pt-based high-entropy-alloy electrocatalyst for direct ethylene glycol fuel cells. Journal of Alloys and Compounds. 984:173951.
6. Themsirimongkon S., Sarakonsri T., Lapanantnoppakhun S., Jakmunee J., Saipanya S. 2019. Carbon nanotube-supported Pt-Alloyed metal anode catalysts for methanol and ethanol oxidation. International Journal of Hydrogen Energy 44:30719-30731.
7. Themsirimongkon S., Pongpichayakul N., Fang L., Jakmunee J., Saipanya S. 2020. New catalytic designs of Pt on carbon nanotube-nickel-carbon black for enhancement of methanol and formic acid oxidation. Journal of Electroanalytical Chemistry. 876:114518.

DEVELOPMENT OF FLAT-TUBULAR SOLID OXIDE FUEL CELLS VIA MOLD CASTING

[1,2*]*Keremhan Bilgil*, [2,3]*Cigdem Timurkutluk*, [1,2]*Sezer Onbilgin,* [1,2]*Bora Timurkutluk*
[1] Nigde Omer Halisdemir University, Prof. Dr. T. Nejat Veziroglu Clean Energy Research Center, Nigde, 51240, Türkiye
[2] Nigde Omer Halisdemir University, Mechanical Engineering Department, Nigde, 51240, Türkiye
[3] Nigde Omer Halisdemir University, Department of Energy Science and Technologies, Nigde, 51240, Türkiye

*Corresponding author e-mail: keremhanbilgil@gmail.com

ABSTRACT
Solid oxide fuel cells (SOFCs) are promising energy conversion devices due to their high efficiency and ability to operate at high temperatures. Among the various geometrical designs of SOFCs, flat-tubular cells combine the advantages of planar and tubular configurations, offering both enhanced thermal stability and improved performance. This study presents an innovative fabrication method for producing flat-tubular anode supports using a 3D-printed mold, which serves as a cost-effective alternative to traditional extrusion techniques. A detailed experimental procedure is outlined, including the design of the mold, fabrication of the anode support, and cell assembly. The electrochemical performance of the fabricated flat-tubular SOFC is evaluated, revealing a peak power density of 223 mW/cm^2 at 800°C. These results demonstrate the potential of the proposed approach for producing flat-tubular anode supports for SOFCs.

Keywords: Solid oxide fuel cell, Flat-tubular, Mold casting, Electrochemical performance

1. INTRODUCTION
SOFCs are high-temperature electrochemical devices that directly convert chemical energy into electrical energy with high efficiency. Therefore, SOFCs are regarded as a promising technology for sustainable energy production, driving ongoing research in materials science, manufacturing techniques, and system integration. Due to their ceramic-based solid-state structure, SOFCs can be fabricated in various geometries; however, planar and tubular configurations remain the most widely utilized designs. Planar SOFCs consist of flat, layered electrode-electrolyte structures that enable high power density and cost-effective manufacturing [1]. However, they are more vulnerable to thermal stress and necessitate effective sealing, making them more prone to gas leakage [2]. In contrast, tubular SOFCs, characterized by their cylindrical geometry, offer enhanced thermal stability while reducing gas leakage concerns [3]. Nevertheless, their design typically results in higher internal resistance due to longer current collection paths, leading to lower power density compared to the planar configuration [4]. Among other SOFC geometrical designs, which are primarily based on modifications of planar and/or tubular structures, the flat-tubular SOFC was developed as a hybrid structure that combines the thermal stability benefits of tubular geometry with the high-performance advantages of planar geometry [5]. Therefore, both numerical and experimental studies have been undertaken in the literature to investigate this design [6-9].

Similar to other SOFC geometries, flat-tubular cells are typically fabricated with an anode-supported structure to enhance cell performance by minimizing the thickness of the electrolyte layer. In this regard, the extrusion method is commonly employed to fabricate flat-tubular anode supports [10-13]. This established mass production method provides a cost-effective and versatile approach for fabricating both ductile and brittle materials with intricate cross-sectional shapes. However, besides high initial cost, maintaining the structural integrity, preventing warping or twisting, and avoiding defects in thin walls can be challenging during the fabrication process [14-16]. Therefore, this study seeks to investigate a more efficient and cost-effective approach for producing the anode support for flat-tubular SOFCs by utilizing a mold fabricated with a conventional 3D printer, as an alternative to the traditional extrusion method. Furthermore, a flat-tubular cell is fabricated, and its electrochemical performance is subsequently evaluated.

2. EXPERIMENTAL
2.1. Mold Design
The technical drawings of the mold designed for producing anode supports with flat-tube geometry are presented in Fig. 1. This mold is composed of six components: a bottom support, four sides, and a top cover. Following the design, the mold elements were produced using Creality Ender 3 S1 3D printer. Discharge channels were incorporated into the two side components to facilitate the easy removal of excess material, while holes were created in the other two side components to form the tube gaps in the flat-tube design. Additionally, holes were drilled into the components to allow for the placement of bolts, thereby enabling the assembly of the mold parts. Metal bars were then placed through these gaps during production of the anode support flat-tubes.

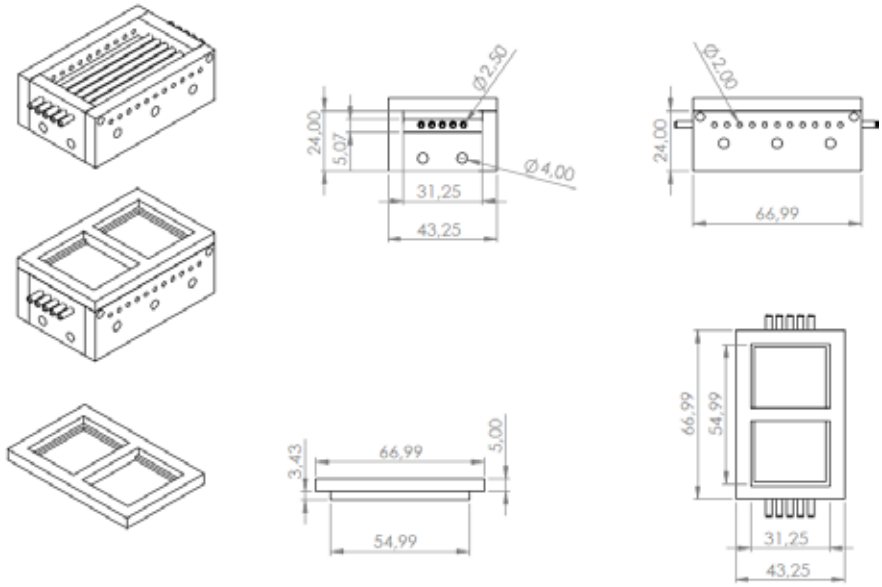

Fig. 1. Technical drawing of 3D printed mold

2.2. Flat-tubular Anode Support Fabrication

To prepare the paste for anode support fabrication, commercial NiO (NiO-A, Novamet, USA) and YSZ (yttria stabilized zirconia, YSZ8-TC, Nexceris, USA) powders were weighed in a ratio of 66% to 34% by weight. Appropriate proportions of dispersant (fish oil, Sigma-Aldrich, Germany) and solvent (a mixture of ethanol and methyl ethyl ketone, Sigma-Aldrich) were then added, and the mixture was subjected to 24 hours of ball milling. Subsequently, specific amounts of binder (Butvar, Sigma-Aldrich) and plasticizer (PEG, Sigma-Aldrich) were incorporated into the solution. The mixture was homogenized by mixing at 100°C with appropriate proportions of high-temperature paraffin and stearic acid using a mechanical mixer until the desired viscosity was achieved. The prepared paste was then placed into the mold fabricated by the 3D printer. After metal bars were positioned in the designated areas to create the tube spaces and the structure was pressed at 5 MPa using a uniaxial press. Next, it was transferred to an isostatic press for the final forming process, which was performed at 15 MPa for 1 min. The mold was dissembled after 24 h drying step and the flat-tubular anode support was obtained. The final shape was achieved using a laser cutter and the support was pre-sintered at 1150 ºC for 2 h. The support surface was dip-coated with YSZ electrolyte, leaving the areas at the edges reserved for current collection uncoated. The structure was then fired at 1400°C for 4 h. Similarly, LSM (LSM20-HP, Nexceris, USA)-YSZ (wt. %: 50-50) cathode functional and LSM (LSM20-P, Nexceris)-YSZ (wt. %: 90-10) cathode current collection layers were screen printed on the flat surfaces. The cathode layers were sintered at 1050 ºC for 2 h. The flat-tubular cell had a total cathode active area of ~10 cm^2.

2.3. Cell Fabrication and Testing

The components of the test setup are given in Fig. 2. After assembling cell, current collection meshes, sealants and endplates, the test apparatus was placed in an oven. Once the testing temperature of 800°C was reached, the anode side was reduced by applying a hydrogen flow of 1 NL/min for an hour. After 2 NL/min air was also supplied to the cathode and the cell performance was measured with a fuel cell test station (Arbin Instruments, FCTS, ABD).

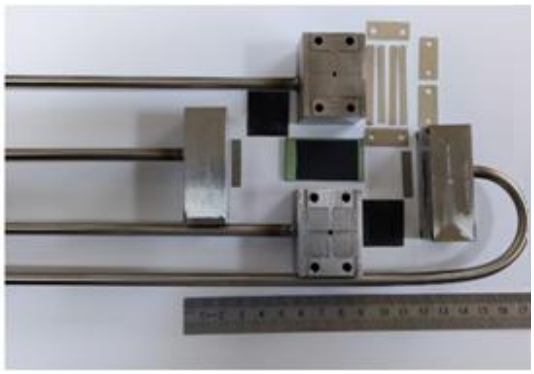

Fig. 2. Components of flat-tubular SOFC test setup

3. RESULTS AND DISCUSSION

The photo of the flat-tubular SOFC developed in this study is presented in Fig. 3, while the electrochemical performance of the cell is depicted in Fig. 4. No cracks or delamination are visible in the cell. Furthermore, the measured open circuit potential, which closely aligns with theoretical value, indicates that the electrolyte structure is free of cracks or pinholes. The cell exhibits a peak power density of 223 mW/cm^2 under 1NL/min hydrogen and 2 NL/min air flow at an operating temperature of 800 ºC. Although no optimization study was conducted, the obtained performances are found to be comparable to those reported in the literature [11, 12]. Therefore, the proposed method is regarded as a promising approach for the fabrication of anode support flat-tubes for SOFCs.

Fig. 3. Final flat-tubular cell

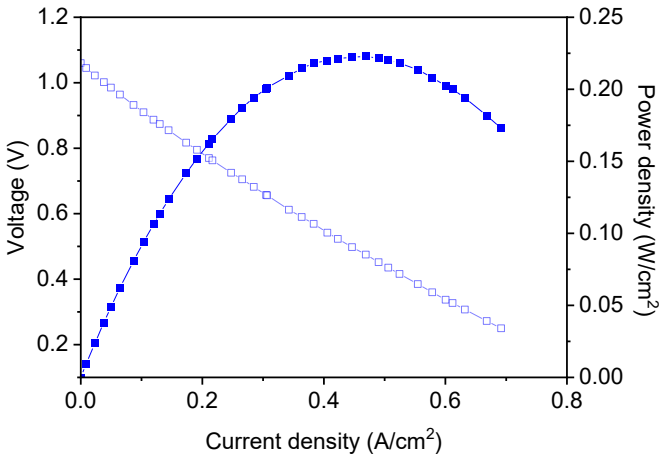

Fig. 4. Cell performance at 800 ºC

4. CONCLUSIONS

The results of this study indicate that using a 3D-printed mold for fabricating anode support flat-tubes is an efficient and promising alternative to the traditional extrusion method. The electrochemical performance of the flat-tubular SOFC fabricated in this study is comparable to those reported in the literature, with a peak power density of 223 mW/cm^2 at 800°C. The absence of cracks or delamination in the cell structure further supports the viability of this approach. This method offers significant advantages in terms of cost, production flexibility, and the potential for manufacturing of flat-tubular SOFC supports. Future work could focus on optimizing the fabrication process and further enhancing cell performance.

REFERENCES

1. Corigliano O, Pagnotta L and Fragiacomo P. 2022. On the technology of solid oxide fuel cell (SOFC) energy systems for stationary power generation: A review. Sustainability 14:15276.
2. Deepi AS, Priya SD, Nesdaraj AS and Selvakumar AI. 2022. Component fabrication techniques for solid oxide fuel cell (SOFC) – A comprehensive review and future prospects. International Journal of Green Energy 19: 1600-1612.
3. Chen R, Gao Y, Gao J, Zhang H, Motola M, Hanif MB and Li C. 2024. From concept to commercialization: A review of tubular solid oxide fuel cell technology. Journal of Energy Chemistry 97:79-109.
4. Zhang X, Jin Y, Li D and Xiong Y. 2021. A review on recent advances in micro-tubular solid oxide fuel cells. Journal of Power Sources 506:230135.
5. Khan MZ, Iltaf A, Ishfaq HA, Khan FN, Tanveer WH, Song R, Mehran MT, Saleem M, Hussain A and Masaud Z. 2021. Journal of Asian Ceramic Societies 9:745-770.

6. Lim T, Park J, Lee S, Park S, Song R and Shin D. 2010. Fabrication and operation of a 1 kW class anode-supported flat tubular SOFC stack. International Journal of Hydrogen Energy 35: 9687-9692.
7. Cimen FM, Kumuk B and Ilbas M. 2022. Simulation of hydrogen and coal gas fueled flat-tubular solid oxide fuel cell (FT-SOFC). International Journal of Hydrogen Energy 47: 3429-3436.
8. Ilbas M, Alemu MA and Cimen FM. 2022. Comparative performance analysis of a direct ammonia-fuelled anode supported flat tubular solid oxide fuel cell: A 3D numerical study. International Journal of Hydrogen Energy 47: 3416-3428.
9. Kim D, Yun U, Lee J, Lim T, Lee S, Park S, Song R and Kim G. 2014. Fabrication and operating characteristics of a flat tubular segmented-in-series solid oxide fuel cell unit bundle. Energy 72: 215-221.
10. Park S, Sammes NM, Song K, Kim T and Chung J. 2017. Monolithic flat tubular types of solid oxide fuel cells with integrated electrode and gas channels. International Journal of Hydrogen Energy 42: 1154-1160.
11. Kim J, Song R, Song K, Hyun S, Shin D and Yokokawa H. 2003. Fabrication and characteristics of anode-supported flat-tube solid oxide fuel cell. Journal of Power Sources 122: 138-143.
12. Hosseini NR, Sammes NM and Chung JS. 2014. Manganese-doped lanthanum calcium titanate as an interconnect for flat-tubular solid oxide fuel cells. Journal of Power Sources 245: 599-60.
13. Park B, Lee J, Lee S, Lim T, Park S, Song R, Im WB and Shin D. 2012. La-doped SrTiO3 interconnect materials for anode-supported flat-tubular solid oxide fuel cells. International Journal of Hydrogen Energy 37: 4319-4327.
14. Chen C, Liu M, Yang L and Liu M. 2011. Anode-supported micro-tubular SOFCs fabricated by a phase-inversion and dip-coating process. International Journal of Hydrogen Energy 36:5604-5610.
15. Jamil SM, Othman MHD, Rahman MA, Jaafar J, Ismail AF and Li K. 2015. Recent fabrication techniques for micro-tubular solid oxide fuel cell support: A review. Journal of the European Ceramic Society 35:1-22.
16. Lawlor V. 2013. Review of the micro-tubular solid oxide fuel cell (Part II: Cell design issues and research activities). Journal of Power Sources 240: 521-441.

GEOLOGICAL HYDROGEN STORAGE FOR LONG-DURATION ENERGY RESILIENCE

*Alper Özmumcu** and *Alper Baba*
Izmir Institute of Technology, Department of Civil Engineering, 35430 Urla, Izmir/Türkiye

*Corresponding author e-mail: alperozmumcu@iyte.edu.tr

ABSTRACT

Electricity is expected to have a much larger share in future energy systems due to the electrification trends in buildings, industry, and transport sectors while most net-zero projections assume a very high penetration of variable renewables in their grid mix. These trends will be accompanied by further divestment from fossil fuels that normally balance the energy system variability. Therefore, there will be a need for long-duration energy storage in order to build resilience against the disruptive effects of intermittency and counter-correlation. The storage of gaseous hydrogen in salt caverns is proposed here as a viable energy storage option, based on wide geological availability. To that end, the existing plans for hydrogen blending are refuted and the synergies between hydrogen storage and enhanced geothermal systems are postulated.

Keywords: Variable Renewable Energy, Long-Duration Hydrogen Storage, Enhanced Geothermal Systems

1. INTRODUCTION

While national climate pledges proliferate, the global challenge for decarbonisation lies in the energy trilemma between sustainability, affordability, and security. Recently, there has been an exponential growth of wind and solar power plant installations as their costs continue to fall due to experience curve effects and the investments continue to flow into clean energy transition [1]. Nevertheless, electricity still accounts for just over 20% of the final energy consumption in most of the major economies. Going forward, the path towards decarbonisation is through the electrification of heat (buildings and low-temperature industrial processes) and mobility (road passenger and rail transport), both of which tend to have low load factors. Therefore, as illustrated in **Fig. 1** for the case of Türkiye, all of these tasks will require investment in grid infrastructure at unprecedented scales, prompting strategic decisions such as improving energy storage capacity [2].

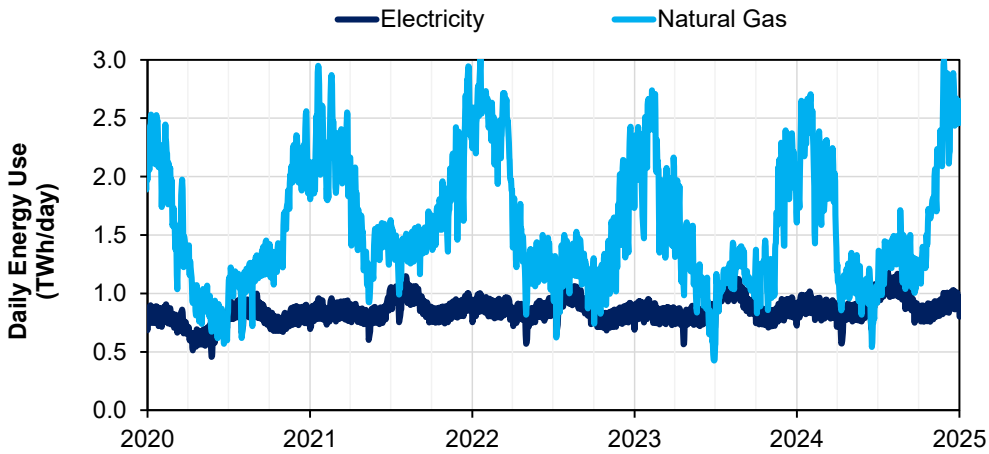

Fig. 1. Türkiye's daily energy use in the forms of electricity and natural gas, based on data from EXIST [3]

On the other hand, as the future energy systems become more electrified, they will also be inherently more efficient, owing to the fact that typically two-thirds of the primary energy supply is currently being lost as waste heat. This fact counteracts the fallacy that electricity from renewables must replace an equivalent amount of primary energy from fossil fuels (coal, oil, and gas) when it will actually reduce the total demand for primary energy. Yet the selective imposition of externalities upon the prices of electricity and fossil fuels remains as the main barrier against this drive towards efficiency. If these are all priced in, then fossil fuels can gradually be phased out. However, this will also imply the loss of fossil fuel buffers that normally balance the variability in energy systems. For resilience concerns, energy stocks are just as important as energy flows; and how to replicate their storage functions in a net-zero world is still an unresolved issue.

2. ANALYSIS AND MODELLING

There has been an emerging quest to mitigate the disruptive effects of intermittency and counter-correlation. Different combinations of demand side response, interconnections, and overcapacity have been proposed as potential solutions

[4]. Yet there is still a need to bridge the extended periods of dark lulls. While well suited for this type of operation, nuclear power plants and pumped hydro projects are often over budget and over schedule. Hydrogen storage can be a viable option but most of the industrial strategies were influenced by post-pandemic hype cycles and hydrogen, despite its low heat value, was misallocated into blending with natural gas [5]. As illustrated in **Fig. 2**, this brings minimal reduction to the carbon intensity of natural gas while causing its energy cost to rise significantly. Besides, no practical benefit is being offered to avoid the curtailment of wind and solar output. As the large funding gap for the required interventions becomes evident, there will be calls for a hydrogen reset, this time with a clear focus on the merit order of hydrogen use cases [6].

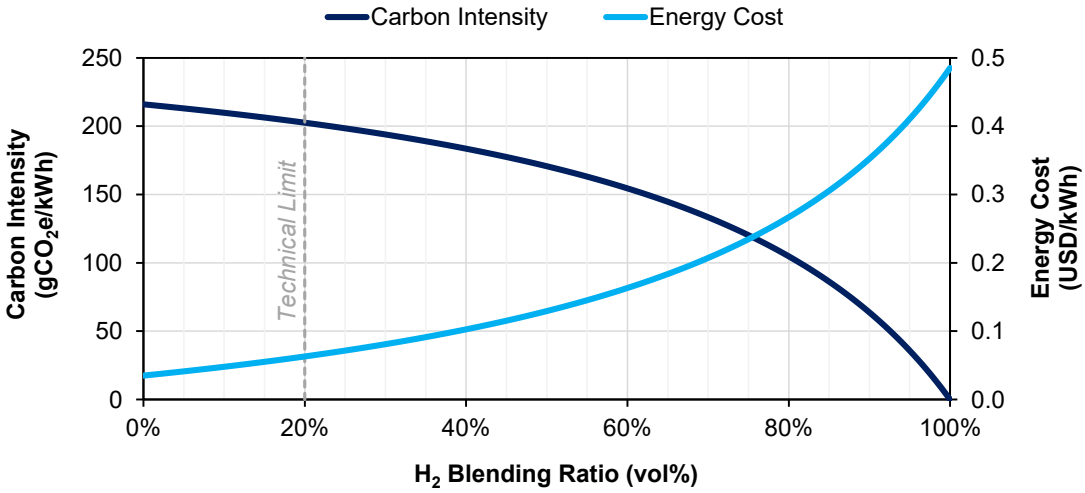

Fig. 2. The impact of hydrogen blending on the carbon intensity and energy cost of natural gas

Gaseous hydrogen stored in salt caverns or depleted reservoirs can deliver the capacity needed for long-duration energy storage [7]. Hydrogen is a suitable energy storage medium because it has a very high energy density by mass and salt caverns are widely available geological formations that can store large volumes with relatively low maintenance [8]. These storage facilities can be operated centrally and infrequently as an expensive but strategic reserve which can be procured through a resilience levy. As illustrated in **Fig. 3**, resilience of the variable renewable energy (VRE) resources, such as wind and solar, can be quantified as the share of their capacity that is being firmed by hydrogen storage over periods of dark lulls which can last for multiple days. There is a trade-off between the duration and proportion of firming which can be partly offset by requiring larger volumes of hydrogen storage per unit capacity of VRE. The breakeven conditions for arbitrage in the power markets will depend on the roundtrip efficiency and leakage losses of storage.

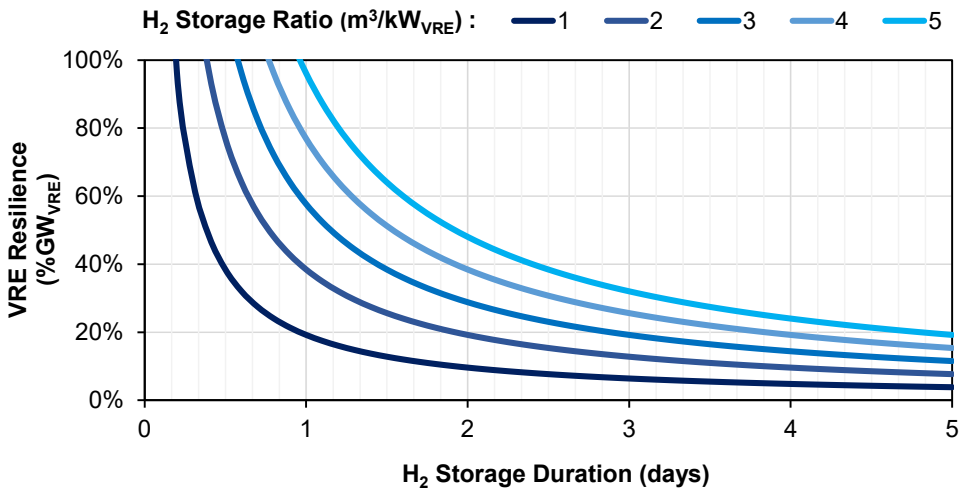

Fig. 3. Resilience of the variable renewable energy resources, firmed by long-duration hydrogen storage

3. RESULTS AND DISCUSSION

Storing hydrogen in salt caverns can prove to be a cost-effective resilience strategy for countries like Türkiye with abundant renewable energy resources and favourable geological formations. Türkiye targets to reach 120 GW of wind

and solar capacity by 2035 [9]. In that case, more than half of the country's installed capacity will be in the form of VRE, posing a resilience risk to the power system. According to Fig. 3, firming 20% of this VRE capacity for 5 days would require a hydrogen storage volume of 0.6 bcm. This would fill half of the capacity currently available at the underground natural gas storage facilities near Lake Tuz, located in Central Anatolia Region. These salt caverns, which are engineered by solution mining, will quadruple in storage capacity once the construction is complete. As the country's natural gas consumption is expected to peak and decline, instead of stranding these assets, vast quantities of gaseous hydrogen can be injected into them. The roundtrip efficiency and leakage losses of storage can be verified in advance through pilot projects and model simulations that will be able to characterise the geological conditions with some degree of uncertainty.

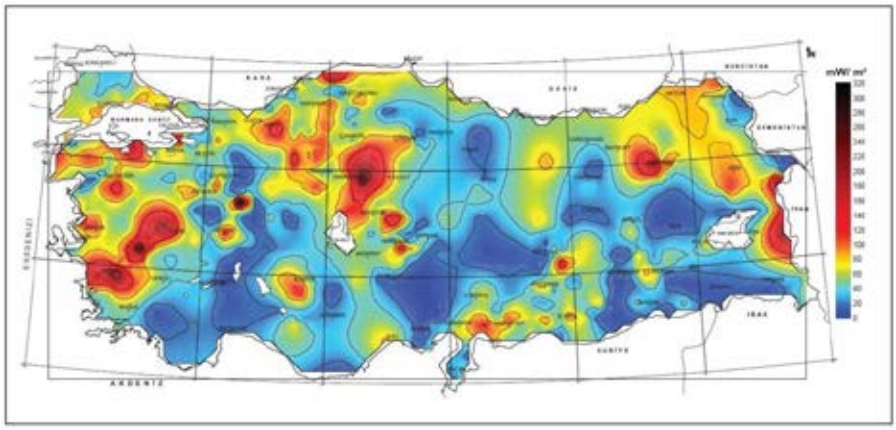

Fig. 4. Geothermal heat flow map of Türkiye [10]

Geothermal energy is particularly well suited to be coupled with long-duration hydrogen storage as it can reduce the levelised cost of storage due to its low marginal cost and high capacity factor [11]. Türkiye has a high geothermal potential because of its tectonic and volcanic features, and utilises this resource both directly and indirectly in many areas [12]. As illustrated in the geothermal heat flow map of Türkiye (**Fig. 4**), Central Anatolia Region is home to the country's largest untapped geothermal fields. Reaching temperatures well above 300°C [13], these fields may be suitable for deploying enhanced geothermal systems (EGS) which can power the electrolysers and compressors for the production and storage of hydrogen at the nearby Lake Tuz facilities. As the technology readiness levels improve with recent breakthroughs, EGS can expand the technical potential of geothermal energy in such fields that have high temperatures but low fluid volumes and low reservoir permeability. Furthermore, the techniques of horizontal drilling and hydraulic fracturing apply similarly to the development of EGS and salt caverns; thus synergies can be explored through regional planning.

4. CONCLUSIONS

Achieving decarbonisation through clean energy transition is a complex task in growth economies like Türkiye. Therefore, maximising efficiency in terms of both energy and exergy needs to be the main objective of all conversions between heat, electricity, and fuels. In buildings, industry, and transport sectors, the process of electrification will follow as the corollary of this objective. It also follows that, if not hindered by incumbents such as the proponents of hydrogen blending, the process of degasification will lead to the decommissioning and repurposing of many stranded assets. Most net-zero projections assume a very high penetration of variable renewables in their grid mix. At that point, the concept of "reserve margin" will replace the current practice of "baseload" as the underlying mechanism of resilience in the power system architecture. Under these new circumstances, long-duration hydrogen storage is proposed here as a critical component of that reserve margin. As a next step, the techno-economic prospects for developing geological hydrogen storage in Türkiye can be further investigated through detailed feasibility studies.

REFERENCES

1. Lazard (2024). *Levelized Cost of Energy+.* Lazard, New York. https://www.lazard.com/research-insights/levelized-cost-of-energyplus/
2. NIC (2023). *National Infrastructure Assessment*. NIC, London.https://nic.org.uk/studies-reports/national-infrastructure-assessment/
3. EXIST (accessed on January 1, 2025). *Transparency Platform.* EXIST, Istanbul. https://seffaflik.epias.com.tr/home
4. MIT (2022). *The Future of Energy Storage.* MIT, Cambridge. https://energy.mit.edu/research/future-of-energy-storage/
5. IRENA (2024). *Green Hydrogen Strategy: A Guide to Design*. IRENA, Abu Dhabi. https://www.irena.org/Publications/2024/Jul/Green-hydrogen-strategy-A-guide-to-design

6. BNEF (2024). *Hydrogen Supply Outlook: A Reality Check*. BNEF, London. https://about.bnef.com/blog/hydrogen-supply-outlook-2024-a-reality-check/
7. The Royal Society (2023). *Large-Scale Electricity Storage*. The Royal Society, London. https://royalsociety.org/news-resources/projects/low-carbon-energy-programme/large-scale-electricity-storage/
8. Arup (2024). *Assessing the Regional Demand for Geological Hydrogen Storage*. Arup, London. https://www.arup.com/insights/assessing-the-regional-demand-for-geological-hydrogen-storage/
9. MENR (2024). *Energy Transition: Renewable Energy 2035*. MENR, Ankara. https://enerji.gov.tr/announcements-detail?id=30482
10. MTA (2006). *Geothermal Heat Flow Map of Türkiye.* MTA, Ankara. https://www.mta.gov.tr/v3.0/hizmetler/jeofizik-haritalari
11. IEA (2024). *The Future of Geothermal Energy*. IEA, Paris. https://www.iea.org/reports/the-future-of-geothermal-energy
12. EGEC (2024). *Geothermal Market Report.* EGEC, Brussels. https://www.egec.org/media-publications/egec-releases-the-2023-geothermal-market-report/
13. Baba, A. and Chandrasekharam, D. (2022). Geothermal Resources for Sustainable Development: A Case Study, *Int J Energy Res.*1-18. doi: 10.1002/er.7778

HAZOP AND FAULT TREE ANALYSIS OF AMMONIA LEAKAGE IN A SHIP'S AMMONIA FUEL SYSTEM

[1,2]*Burak Zincir*, [3*]*Buğra Arda Zincir*
[1] Maritime Faculty, Istanbul Technical University, Tuzla, Istanbul, 34940, Türkiye
[2] Maritime Clean Energy Research Laboratory (MarCERLab), Tuzla, Istanbul, 34940, Türkiye
[3] Maritime Vocational School, Galatasaray University, Besiktas, Istanbul, 34349, Türkiye

*Corresponding author e-mail: bazincir@gsu.edu.tr

ABSTRACT
Ammonia is considered as the future alternative fuel to overcome emissions from low-quality fuel. Despite ammonia being a promising alternative fuel, its toxic and corrosive properties are the main drawbacks and increase risks on a ship. This study aims to determine the events and failures that lead to ammonia leakage from the high-pressure ammonia fuel system of a ship. Five experts from the maritime industry and academy prepared the basics of the study by doing HAZOP. After this step, an FTA diagram was formed to show which basic and intermediate events result in ammonia leakage.

Keywords: Ammonia, Fault tree analysis, Fuel system, HAZOP, Maritime transport

1. INTRODUCTION

Maritime transportation is the most important transportation mode worldwide. There were 108,789 merchant ships of 100 gross tons and above in January 2024, and the ship number increased by 3.4% from 2023 to 2024 [1]. Since 98% of these ships use low-quality fossil fuels [2], maritime transportation accounts for 9.84% of global sulfur oxide (SO_X) emissions, 14.74% of nitrogen oxides (NO_X) emissions, 6.75% of particulate matter 2.5 (PM2.5) emissions, 3.56% of particulate matter 10 (PM10) emissions, 0.61% of carbon monoxide (CO) emissions [3], and 2.89% of global carbon dioxide (CO_2) emissions [4]. To overcome these emissions, using alternative fuels on ships is the most promising and attractive solution due to a higher emission reduction potential [5]. There are various alternative fuels, such as liquefied natural gas (LNG), methanol, ammonia, and hydrogen. But ammonia is considered as the future alternative fuel for maritime transportation. Despite ammonia being a promising alternative fuel, its toxic and corrosive properties are the main drawbacks and increase risks on a ship.
In this study, an ammonia leakage event at a high-pressure ammonia fuel system is investigated. Possible events and failures that lead to ammonia leakage are determined by hazard and operability analysis and a fault tree diagram of the events and failures is formed.

2. PROPERTIES OF AMMONIA

Ammonia consists of one nitrogen atom and three hydrogen atoms, and it does not contain carbon or sulfur atoms. Therefore, its combustion is free of carbon dioxide, carbonaceous emissions, sulfur oxides, and particulate matter. On the other hand, ammonia combustion results in water, nitrogen, NO_X, nitrous oxide (N_2O), and a small amount of ammonia slip [6]. Ammonia is a low-reactivity fuel with a low heating value (LHV) of 18.5 MJ/kg. The auto-ignition temperature of ammonia is 651 ˚C and the flammability limits in the air are between 16 -25% by volume. The low burning velocity of ammonia at 14 cm/s affects the combustion reactivity of this fuel [7]. Although it has low reactivity, ammonia is suitable for large marine diesel engines thanks to their large cylinder displacement volume, low engine speeds, and constant high engine loads [8]. The storage options for ammonia as a fuel are either at -33 ˚C at 1 bar or at room temperature at 10 bars [9]. Thus, ammonia-fueled ships require 2.4 times larger tank volume than the conventional-fueled ships [10]. Using ammonia as a fuel brings some risks that are associated with its properties. Ammonia is a toxic chemical that has a toxicity level of more than three times higher than other marine fuels, marine diesel oil, and methanol [11], [12]. The toxicity of ammonia causes dehydration, caustic burning, and freezing when human contact [9]. The toxicity of ammonia to aquatic life is an issue. Ammonia spilling into the sea can cause extreme risk to aquatic life. Corrosiveness is another risk of ammonia. Ammonia is incompatible with aluminum, brass, copper, magnesium, and zinc alloys [8]. Moreover, ammonia can cause stress corrosion in tanks and fuel supply lines. The last risk of ammonia is fire and explosion risk. Due to its low combustion reactivity, the risk of fire and explosion is lower than the other alternative fuels, such as LNG, LPG, methanol, etc. But ammonia has a high reaction speed with halogens and oxidizers that may lead to explosions [6].

3. METHODOLOGY

This study uses a combination of hazard and operability analysis (HAZOP) and fault tree analysis (FTA). The opinions of the specified experts in Table 1 are taken at a brainstorming session to apply the methodology.

2.1. Hazard and Operability Analysis (HAZOP)

HAZOP is an analysis that is developed to identify the operational problems and potential hazards of a system [13]. The

analysis was formed to find the possible defects and deviations that result in explosions, fires, and toxic releases [14]. HAZOP analysis is done according to the opinions of the experts related to the specific field of the study.

2.2. Fault Tree Analysis (FTA)

The FTA is a top-down approach that starts by identifying the top event. The next steps are the formation of a fault tree diagram, qualitative evaluation, and quantitative evaluation [15]. The fault tree is drawn by using symbols in Table 2. This study focuses on only one top event, and the fault tree diagram of this top event with its intermediate events, basic events, and their logic gates is formed.

Table 1. The specifications of the experts

Expert	Position / Experience / Education	Information
1	Oceangoing Chief Engineer / 11 years / BSc.	The expert has a good knowledge on fuel systems and their risks.
2	Oceangoing Chief Engineer / 2 years / MSc.	The expert has worked on chemical tankers and has a good knowledge on ammonia.
3	Oceangoing Chief Engineer – Academician / 10 years – 19 years / PhD.	The expert had worked on chemical tankers and has academic studies on alternative fuels.
4	Academician / 10 years / PhD.	The expert has academic studies on alternative fuels and their risks.
5	Academician / 4 years / PhD.	The expert has academic studies on alternative fuels and their risks.

Table 2. Fault tree analysis symbols and descriptions [16]

Symbol	Meaning	Description
	AND gate	The output event commences if all input events arise
	OR gate	The output event commences if any of the input events arise
	Basic event	The basic cause of a failure or intermediate event
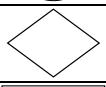	Undeveloped event	Undeveloped primary cause due to lack of knowledge
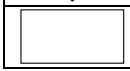	Intermediate event	An event that commences due to one or more sub-events

4. RESULTS AND DISCUSSION

4.1. Ammonia-fueled Ship Fuel System Components

In this study, it is assumed that the ammonia fuel system is a high-pressure fuel system. Thus, the components of the system are a bunkering station, fuel storage area, fuel preparation, supply and recirculation unit (FPSR), fuel valve train (FVT), double-walled piping, the main engine components, ammonia catch system, and vent mast [17]. The FTA diagram is formed by considering these components.

4.2. FTA Diagram

The FTA diagram of ammonia leakage (TE) from the ammonia-fueled ship fuel system is constituted by brainstorming with the experts. Fig. 1, the FTA diagram, contains 23 intermediate events (IE) and 39 basic events (BE). All events are shown in Table 3. The TE mainly depends on the IEs from 1 to 6. IE-1 is associated with IE-7 to IE-10; IE-2 is associated with IE-11 and IE-12; IE-3 depends on IE-13 to IE-16; IE-4 depends on IE-17 and IE18; IE-5 is associated with IE-19 and IE-20; and IE-6 is associated with IE-21 to IE-23. All IEs are connected to OR gates which means any of the input events arise for the output event to commence. The IEs depend on 39 BEs as the basic events that have to happen to constitute intermediate events. The IEs result in TE, ammonia leakage from the fuel system.

Table 3. Definition of the events in FTA diagram

Event	Description	Event	Description
TE	Ammonia fuel leakage	BE-9	Ammonia-induced stress corrosion cracking
IE-1	Storage tank leakage	BE-10	External environmental exposure
IE-2	Piping and valve leakage	BE-11	Leaking flanges or couplings
IE-3	Transfer system leakage	BE-12	Improper assembly
IE-4	Control system failure	BE-13	Faulty valve seals or internal wear
IE-5	External factors	BE-14	Material fatigue from repeated temperature fluctuations
IE-6	Human factor	BE-15	Wear and tear over time
IE-7	Corrosion	BE-16	Poor material compatibility
IE-8	Structural failure	BE-17	Pressure build-up causing weak points to fail
IE-9	Seal failure	BE-18	Frozen ammonia leading to rupture
IE-10	Overpressure	BE-19	Improper closing or wear
IE-11	Corrosion of piping	BE-20	Actuator failure
IE-12	Joint failures	BE-21	Cracks or wear in flexible parts
IE-13	Pump seal failure	BE-22	Misalignment or improper installation
IE-14	Pipeline blockage	BE-23	Failure to detect pressure or temperature abnormalities
IE-15	Valve malfunction	BE-24	Late detection of leaks
IE-16	Hose or flexible connection failure	BE-25	Incorrect valve actuation
IE-17	Sensor failure	BE-26	Inability to trigger safety shutoff systems
IE-18	Control unit malfunction	BE-27	Alarm system failure
IE-19	Operational errors	BE-28	Faulty software leading to incorrect actions
IE-20	Third-party damage	BE-29	Extreme weather conditions causing material degradation
IE-21	Improper operation	BE-30	Mishandling of equipment
IE-22	Maintenance errors	BE-31	Inadequate maintenance or inspections
IE-23	Insufficient training	BE-32	Accidental impact during loading/unloading
BE-1	Material degradation due to exposure to ammonia	BE-33	Fire or explosion near storage or piping
BE-2	Poor maintenance or protective coatings	BE-34	Incorrect valve or pump operation
BE-3	Cracks caused by pressure fluctuations	BE-35	Lack of adherence to procedures
BE-4	Physical damage during operations	BE-36	Failure to detect wear or damage
BE-5	Degraded gaskets or seals	BE-37	Use of incompatible materials during repair
BE-6	Improper assembly	BE-38	Lack of knowledge about system operation
BE-7	Faulty pressure relief valves	BE-39	Failure to recognize early signs of leakage
BE-8	Temperature variations causing pressure build-up		

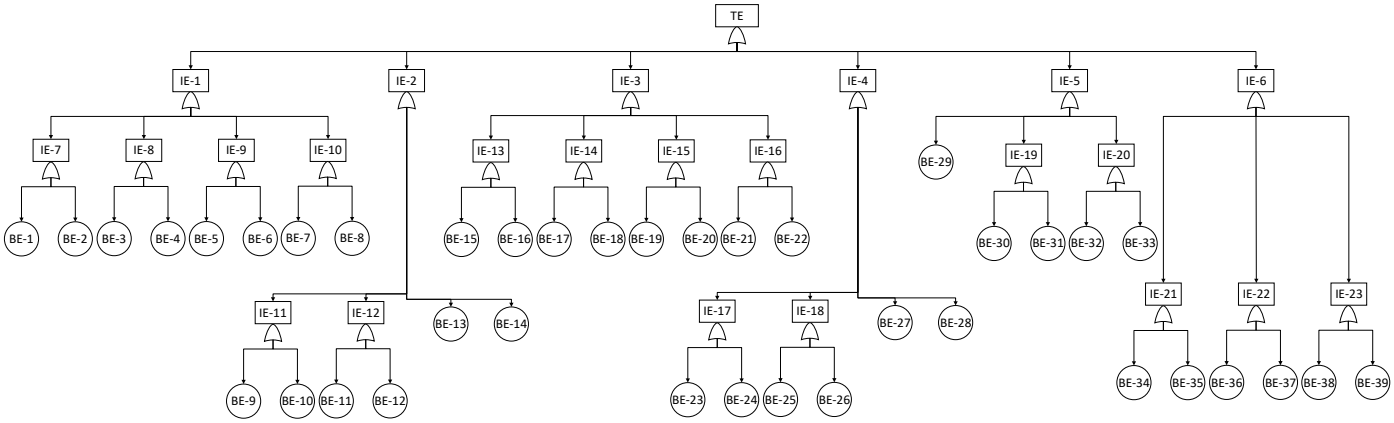

Fig. 1. Ammonia leakage FTA diagram

5. CONCLUSION

This study aims to determine the events and failures that lead to ammonia leakage from the high-pressure ammonia fuel system of a ship. Five experts from the maritime industry and academy prepared the basics of the study by doing HAZOP. After this step, an FTA diagram was formed to show which BEs and IEs result in ammonia leakage (TE). IE-1 Storage tank leakage, IE-2 Piping and valve leakage, IE-3 Transfer system leakage, IE-4 Control system failure, IE-5 External factors, and IE-6 Human factor are the related IEs to TE. The next study will be an extended version that contains quantitative analysis of the ammonia leakage FTA diagram. Furthermore, other TEs will be analyzed by the same expert team to further enlarge the safety analysis of the ammonia fuel system of a ship.

ACKNOWLEDGEMENT

This work was supported by the Research Fund of Istanbul Technical University (Project ID: 45857).

REFERENCES

1. United Nations Conference on Trade and Development (UNCTAD). 2024. Review of maritime transport 2024.
2. DNV. 2024. Energy transition outlook 2024, Maritime forecast 2050.
3. European Energy Agency (EEA). 2025. Emissions of air pollutants from transport. https://www.eea.europa.eu/data-and-maps/indicators/transport-emissions-of-air-pollutants-8/transport-emissions-of-air-pollutants-8. Accessed on January 6, 2025
4. International Maritime Organization (IMO). 2024. Fourth IMO greenhouse gas study.
5. Zincir BA, Arslanoglu Y. 2024. Comparative life cycle assessment of alternative marine fuels, Fuel 358:129995, 2024.
6. Zincir B. 2022. Ammonia for decarbonized maritime transportation. Clean Fuels for Mobility, Energy, Environment and Sustainability, Springer, Singapore.
7. Zincir B. 2019. An alternative fuel assessment model for ships and experiments on the effect of methanol on diesel engines. Dissertation thesis. Department of Maritime Transportation Engineering, Istanbul Technical University.
8. Klüssmann JN, Ekknud LR, Ivarsson A, Schramm J. 2020. Ammonia application in CI engines, special report, a report from the advanced motor fuels technology collaboration programme.
9. Ayvalı T, Tsang SCE, Van Vrijaldenhoven T. 2021 The position in decarbonizing maritime industry: an overview and perspective: part II, costs, safety and environmental performance and the future prospects for ammonia in shipping. Johnson Matthey Technol Rev 65(2):291-300.
10. American Bureau of Shipping (ABS). 2020. Ammonia as marine fuel, Sustainability Whitepaper, 2020.
11. Aziz M, Wijayanta AT, Nandiyanto ABD. 2020. Ammonia as effective hydrogen storage: a review on production, storage and utilization. Energies 13:3062.
12. McKinlay CJ, Turnock SR, Hudson DA. 2020. A comparison of hydrogen and ammonia for future long distance shipping fuels. LNG/LPG and Alternative Fuels, The Royal Institution of Naval Architects, London.
13. Ay C, Güler T, Bal Beşikçi E. 2022. Implementation of ARAMIS methodology in the risk assessment of chemical tankers: the case of loading operatio. Ocean Engineering 261.
14. Solukloei HRJ, Nematifard S, Hesami A, Mohammadi H, Kamalinia M. 2022. A fuzzy-HAZOP/ant colony system methodology to identify combined fire, explosion, and toxic release risk in the process industries. Expert Syst. Appl. 192.
15. Fuentes-Bargues JL, Gonzalez-Cruz MC, Gonzalez-Gaya C, Baixauli-Perez MP. 2017. Risk analysis of a fuel storage terminal using HAZOP and FTA. Int. J. Environ. Res. Publ. Health 14(7).
16. Durukan O, Akyuz E, Destanoğlu O, Arslanoğlu Y, Sezer SI. 2024. Quantitative HAZOP and D-S evidence theory-fault tree analysis approach to predict fire and explosion risk in inert gas system on-board tanker ship. Ocean Engineering 308:118274.
17. MAN. 2024. MAN B&W ammonia engine development. https://netl.doe.gov/sites/default/files/netl-file/ACT_0324_Wilche.pdf.

FLUID FLOW OF ALKALINE WATER ELECTROLYSIS HYDROGEN CELL: DESIGN AND EXPERIMENTAL INVESTIGATION

[1,2] *Mohamed A. Farahat,*[1] *M. Abdelmordy,* [1] *H.H. Eldeeb,* [1*] *Ali M. Abdelsalam,*
[1,3] *W. A. El-Askary,*[1,4] *I. M. Sakr*
[1] Mechanical Power Engineering Dept., Faculty of Engineering, Menoufia University, 32511, Egypt
[2] Faculty of Technological Industry and Energy, Delta Technological University (DTU), Quwaysna 32631, Egypt
[3] Alexandria Higher Institute of Engineering & Technology (AIET), Alexandria, Egypt
[4] Pyramids Higher Institute of Engineering and Technology (PHI), Cairo, Egypt

*Corresponding author: alimabdelsalam@gmail.com

ABSTRACT

This study investigates the performance of Hydrogen Single Cell (HSC) for production of HHO gases using two methods. First, Solar Cell and DC-DC controller. Second, Institiute's AC and AC-DC converter. The study focuses on the fluid flow of electrolyte and stagnant electrolyte at specific concentration 30 w.t % which is using the latter method.Then, the evolution process of hydrogen,specially,is photographed at different current and specific inlet velocity of 0.03 m/s.The results show that the maximum Gain Output Ratio (GR) in stagnant fluid around 2.6 Volt is 75% better than all inlet velocities of 0.03,0.06 and 0.09 m/s.The findings of photographing indicate that there is a positive relationship between the hydrogen evolution rate and input current.As a result of these investigations, suggestions are identified for future research that will be an extension for different concentrations besides photographing of each case to more explanation of fluid flow behaviour
Keywords: Hydrogen Production; Fluid Flow; Hydrogen Cell Design

1. INTRODUCTION

The global reliance on fossil fuels leads to pressing challenges such as pollution, climate change, and resource depletion. Consequently, a shift toward renewable energy sources like solar and wind is underway, although their intermittent nature heightens the need for efficient energy storage. Hydrogen fulfills this requirement, with global demand expected to rise from 87 million tons in 2020 to as high as 680 million tons by 2050 [1]. Hydrogen's combustion produces only water, making it a crucial clean energy vector [2]. Water electrolysis, especially alkaline water electrolysis (AWE), is widely recognized for its simple operation and lack of harmful emissions [3]. Despite these advantages, AWE's relatively low efficiency and current density necessitate further research [4]. Numerous studies have addressed bubble behavior, including bubble-induced and forced convection within electrolyzers [5-6]. Cao et al. [7] highlighted that the hydrogen bubble curtain width scales with electrolyte inlet velocity, significantly affecting overpotential. Meanwhile, Sakr et al. [8] reported higher hydrogen production rates using polymeric membranes and narrower electrode gaps.
The present study experimentally assesses a Hydrogen Single Cell (HSC) powered by a solar panel under varying electrolyte velocities, documenting gas evolution at different currents to better understand and optimize performance. It aims to provide insights into critical operational parameters that influence hydrogen generation efficiency.

2. MATERIALS AND METHODS

The Hydrogen Single Cell (HSC) was designed to accommodate both flowing and stagnant electrolytes. As shown schematically in Figure [1], it comprises two outer Teflon covers chosen for their nonconductive, anticorrosive properties and ability to withstand mechanical stress. Each cover houses a square stainless steel (SS316L) electrode (10 cm × 10 cm), separated by a transparent acrylic spacer (1.5 cm gap) that facilitates direct observation of gas evolution within the cell. Although literature suggests that nickel electrodes can offer superior performance, SS316L was selected as a cost-effective alternative. Rubber gaskets are placed between the Teflon covers and the acrylic spacer to prevent electrolyte or gas leakage, and the assembly is secured using bolts, washers, and nuts.
To ensure adequate electrical conductivity, potassium hydroxide (KOH) is dissolved in water instead of relying on pure water. The specific KOH concentration strongly influences both current conduction and hydrogen evolution rate, as described by Equation (1):

$$v_{H_2} = \frac{i}{FZ} \tag{1}$$

Here, v_{H_2} is the volumetric flow rate of hydrogen, i is the current, F is Faraday's constant, and Z is the number of electrons transferred per molecule. KOH was selected over sodium hydroxide (NaOH) based on evidence indicating superior conductivity at equivalent concentrations and temperatures [9].

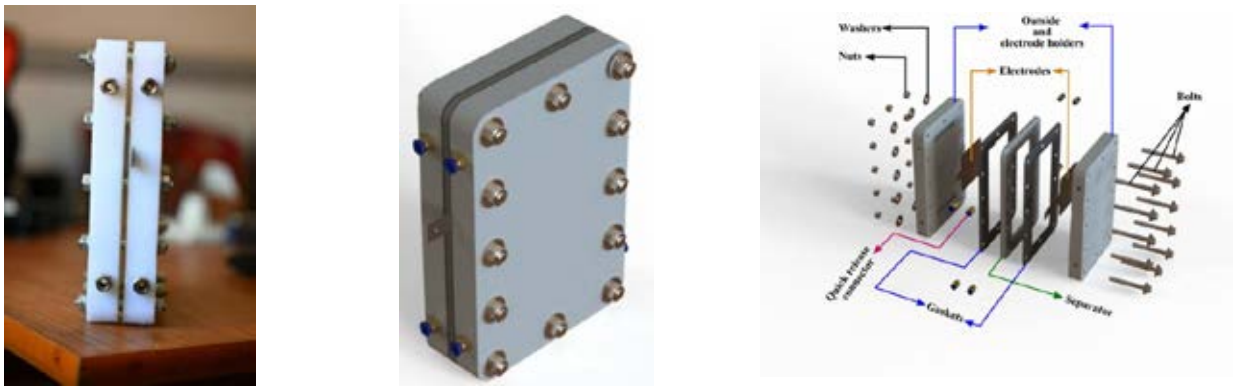

Fig. 1. Real photo and CAD model of Hydrogen Cell

When fluid flow is needed, a centrifugal pump and ball valves control the electrolyte's inlet flow rate. The Hydrogen Single Cell (HSC) has four quick-release fittings, two inlets and two outlets, so it can switch easily between flowing and stagnant modes. Valves and a bubbler help separate gases from the circulating electrolyte.Two main power sources are used to cover a wide range of currents. First, a solar panel (see Table [1]) supplies direct current (DC) for electrolysis, managed by a DC–DC controller (see Table [2]). This setup allows for multiple measurements and fine-tuning of power input, enabling high-quality photographs to be taken under carefully controlled conditions.

Table 1. Characteristics of the PV module

Parameter	Specs.	Parameter	Specs.
Model	JAM72S30 -550/MR/1500V.	I_{mp}	13.11 A
Dimension	2279 x 1134 mm	V_{Oc}	49.9 V
P_m	550 W	I_{SC}	14 A
V_{mp}	41.96 V	STC	1000 W/m^2 at 25 C and 1.5 Am

Table 2. Charachteristics of Riden DC-DC converter

Parameter	Specs	Parameter	Specs
Output voltage	0-60.00V	**Output voltage accuracy**	±0.3%
Output current	0-18.000A	**Output current accuracy**	±0.5%
Output power	0-1080W		

For currents higher than 18 A (the limit of the DC–DC controller), an AC–DC converter (see Table [3]) is used. This setup allows the higher current levels needed to study greater hydrogen production rates under more demanding conditions.A Nikon Z8 camera with an AF 85 mm f/1.8 Z lens (see Table [4]) captures the gas evolution between the electrodes. Photos are captured at different current settings, showing how hydrogen and oxygen bubbles form and spread in the 1.5 cm gap, offering clear insights into electrochemical reactions.

Table 3. Charachteristics of BK-Precision 1900B AC-DC converter

Parameter	Variable Output Voltage	Variable Output Current	Maximum Output Power
Specs	1-16 V	0-60A	0-960W

Table 4. Technical specifications of Nikon Z8

Parameter	Specs	Parameter	Specs
Max resolution	8256 x 5504	**Boosted ISO (maximum)**	102400
Sensor size	Full frame (35.9 x 23.9 mm)	**Minimum shutter speed**	900 sec
Boosted ISO (minimum)	32	**Maximum shutter speed**	1/32000 sec

The Hydrogen Single Cell (HSC) is built with Teflon covers, SS316L electrodes, and a clear acrylic spacer, sealed by rubber gaskets. It can run with either flowing or stagnant electrolyte made by dissolving KOH in deionized water. A solar panel and DC–DC controller handle low-to-medium currents, while an AC–DC converter handles higher currents beyond 18 A. During testing, electrolyte flow rate, KOH concentration, and current are systematically changed, and measurements of current, voltage, and hydrogen output are registered. A Nikon Z8 camera captures images of bubble formation to show how different conditions affect hydrogen production and overall cell performance.

3. RESULTS AND DISCUSSION

The system performance is evaluated by analyzing the variation of current, hydrogen production rate, and gain output ratio with voltage under natural conditions and at flow velocities of 0.03 m/s, 0.06 m/s, and 0.09 m/s.
Figure [2] illustrates the relationship between current and voltage for natural generation and different velocities. Generally, the current increases proportionally with voltage in all cases. Notably, the current variation under natural conditions

closely aligns with that at a velocity of 0.09 m/s, albeit with slightly lower values. for instance, in natural case a current lower value could be observed at voltage lower than 2.55 volt. This is because in the natural case, where there is no forced flow, ion transport relies primarily on diffusion. This results in slower reaction rates and a lower current compared to cases with forced flow. Conversely, for a given voltage, the current decreases at 0.06 m/s but increases again at 0.09 m/s, exceeding the values observed at 0.03 m/s. The current values for 0.03, 0.06 and 0.09 m/s at 3.25 volt are equal 35, 24 and 45 amperes, respectively.

Figure [3]. illustrates the variation of the gain output ratio with voltage under natural generation and different velocities. A consistent trend is observed, where the gain output ratio initially increases slightly with voltage before decreasing. The highest gain output ratio is achieved in the natural generation case. For forced flow, at constant voltage, the gain output ratio rises from velocity 0.03 to 0.06 m/s and then declines at velocity 0.09 m/s. The recorded values of grain output ratio at 3.5 volt are 48%, 50%, and 43% for velocities of 0.03, 0.06, and 0.09 m/s, respectively.

Figure [4]. illustrates the variation of the gain output ratio with voltage under natural generation and different velocities. A consistent trend is observed, where the gain output ratio initially increases slightly with voltage before decreasing. The highest gain output ratio is achieved in the natural generation case. For forced flow, at constant voltage, the gain output ratio rises from velocity 0.03 to 0.06 m/s and then declines at velocity 0.09 m/s. The recorded values of gain output ratio at 3.5 volt are 48%, 50%, and 43% for velocities of 0.03, 0.06, and 0.09 m/s, respectively.

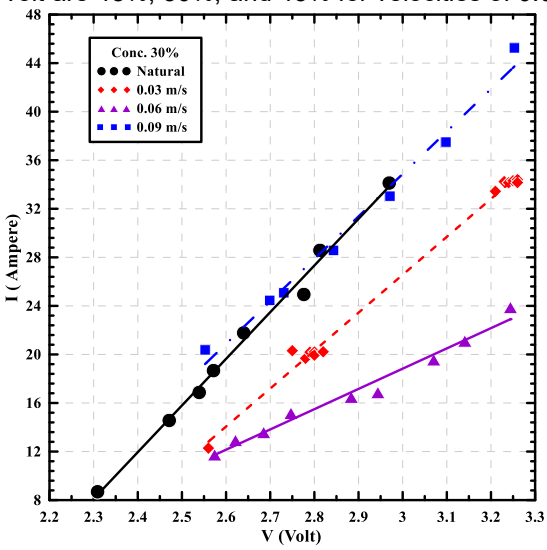

Fig. 2. The variation of the current with the voltage at natural and different velocities

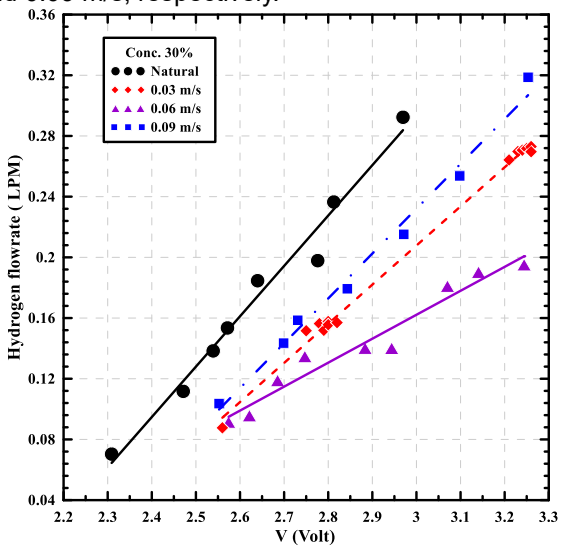

Fig. 3. The variation of the hydrogen production rate with the voltage at natural generation and different velocities

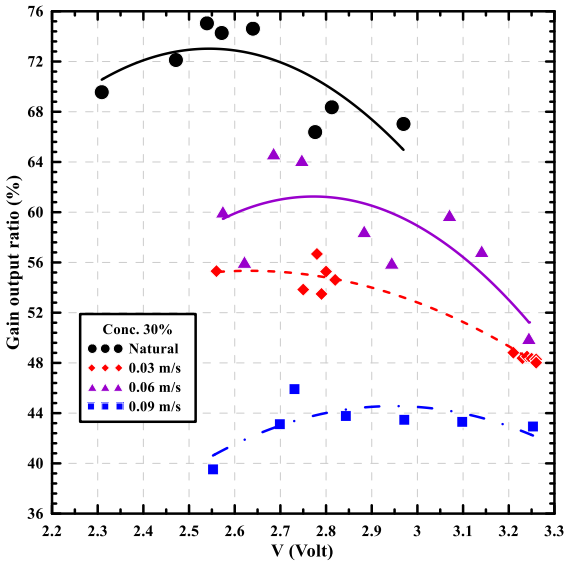

Fig. 4. The variation of the gain output ratio with the voltage at natural generation and different velocities

Figure [5] shows the developing hydrogen layer over the electrode. The images are presented with different applied

currents between the electrodes. The gap distance between the two electrodes is 16 mm. The area of the electrodes is 10cm x 10 cm. The concentration of the electrolyte is 10%. The flow rate of the electrolyte is 3.5 L/m (velocity equals 0.03 m/s). Regarding the presented images, it is clearly observed that hydrogen production increases with the increase in the applied current.

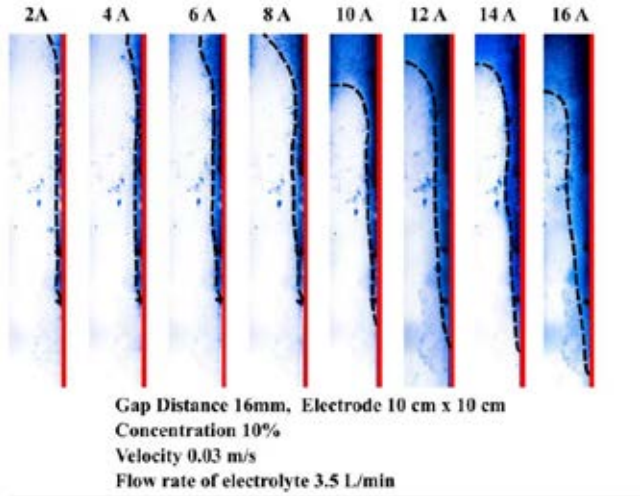

Fig. 5. Photograph of hydrogen gas layer at different currents

4. CONCLUSIONS

This study investigated the fluid flow and stagnant fluid at 30 w.t% concentration influencing hydrogen production in AWEs with a square electrode 10 cm x 10 cm. Our findings revealed that stagnant fluid and 0.09 m/s inlet velocity consumes much current at the same voltage and the consumption decreases from 0.03 m/s to 0.06 m/s then increases at 0.09 m/s. where stagnant fluid gains maximum flow rate larger than 0.09m/s at the same power consumed. This makes GR is maximum trend for AWEs for stagnant fluid which is 75% at around 2.6 Volt. In addition to photographing, we deduced the current is vital in hydrogen production rate wich increases by increasing the current. The aim is to enhance the GR of the hydrogen production process in AWE by testing different operational mehods.

5. ACKNOWLEDGEMENT

This paper is based upon work supported by science technology & Innovation Funding Authority (STDF) under grant number 47247**.**

6. REFERENCES

1. Srinivasan S, Wilson JF, Srinivasan SS, Moore BM, Henderson L, Iii SE, et al. Hydrogen production using solar energy. 2014.
2. Xu X, Zhou Q, Yu D. The future of hydrogen energy: bio-hydrogen production technology. Int J Hydrog Energy 2022;47:33677–98. https://doi.org/10.1016/j.ijhydene.2022.07.261
3. Dincer I, Acar C. Review and evaluation of hydrogen production methods for better sustainability. Int J Hydrog Energy 2015; 40:11094–111. https://doi.org/10.1016/j.ijhydene.2014.12.035.
4. Ulleberge, O., "Modeling of advanced alkaline electrolyzers: a system Approach"; J of hydrogen energy, 28, pp. 21-23, 2003.
5. Hreiz R, Abdelouahed L, Fuenfschilling D, Lapicque F. Electrogenerated bubbles induced convection in narrow vertical cells: PIV measurements and EulereLagrange CFD simulation. Chem Eng Sci 2015; 134:138e52.
6. El-Askary WA, Sakr IM, Ibrahim KA, Balabel A. Hydrodynamics characteristics of hydrogen evolution process through electrolysis: numerical and experimental studies. Energy 2015; 90:722e37
7. Cao, X., Zhao, N., Zhang, S., Zhou, L., Hu, Y., & Yun, J. (Year). Investigation of the hydrogen bubble effect on the overpotential in an alkaline water electrolyzer.
8. Sakr, I. M., Abdelsalam, A. M., & El-Askary, W. A. (2017). Effect of electrodes separator-type on hydrogen production using solar energy. *Energy, Volume* (Issue), Pages. https://doi.org/10.1016/j.energy.2017.09.019
9. Gambou, F., Guilbert, D., Zasadzinski, M., & Rafaralahy, H. (2022). *A Comprehensive Survey of Alkaline Electrolyzer Modeling: Electrical Domain and Specific Electrolyte Conductivity.* Energies, 15(9), 3452.

MICROTUBULAR SOLID OXIDE FUEL CELLS WITH YTTERBIUM DOPED ZIRCONIA ELECTROLYTES

[1,2]Cigdem Timurkutluk, [3]Esra Yildiz, [4,5*]Gulsah Germen Tutas, [1,5]Semiha Onbilgin and [1,5]Bora Timurkutluk
[1] Nigde Omer Halisdemir University, Prof. Dr. T. Nejat Veziroglu Clean Energy Research Center, Nigde, 51240, Türkiye
[2] Nigde Omer Halisdemir University, Department of Energy Science and Technologies, Nigde, 51240, Türkiye
[3] Yozgat Bozok University, Hemp Research Institute, Department of Basic Sciences and Health, Yozgat, 66900, Türkiye
[4] Nigde Omer Halisdemir University, Center of Application and Research for Industrial Raw Materials and Building Materials, Nigde, 51240, Türkiye
[5] Nigde Omer Halisdemir University, Mechanical Engineering Department, Nigde, 51240, Türkiye

*Corresponding author e-mail: gulsahgermentutas@ohu.edu.tr

ABSTRACT
$(Yb_2O_3)_x(ZrO_2)_{1-x}$ powders are synthesized by a modified sol-gel method for $0.08 \leq x \leq 0.12$ and tested as an electrolyte material for microtubular solid oxide fuel cells (SOFCs). XRD measurements reveal that stabilization of face-centered cubic (fcc) zirconia (ZrO_2) is observed at all doping ratios studied, resulting in ytterbium(III)-stabilized zirconia (YbSZ). Electrochemical performance tests show that the Yb content of 10 mol% gives the best results. This is attributed to the ionic conductivity and grain size of the corresponding YbSZ powders. Therefore, zirconia stabilized with 10 mol% Yb_2O_3 (10YbSZ) is considered as a promising alternative to conventional yttria-stabilized zirconia (YSZ) electrolytes in SOFCs and a peak power density of 0.357 W/cm^2 is obtained at 800 ^oC.

Keywords: Ytterbium stabilized zirconia; Synthesis; Solid oxide fuel cells; Microtubular; Electrolyte.

1. INTRODUCTION
SOFCs consist of three basic components: anode, electrolyte and cathode. The electrolyte component is the heart of the SOFC systems. Although proton conducting electrolytes have recently been investigated for future low temperature applications, oxygen ion conducting electrolytes are more common in SOFCs. In addition to conducting oxygen ions, electrolyte materials also act as a barrier to prevent direct contact between hydrogen and oxygen. The most common electrolyte material is zirconium oxide stabilized with yttrium oxide (YSZ). However, YSZ exhibits the desired ionic conductivity values at very high temperatures. In this context, some electrolyte materials such as doped cerium oxides or zirconium oxide stabilized with scandium oxide have been developed (Fergus, 2006). However, they exhibit structural problems and performance degradation due to short circuiting (Zheng et al., 2009). Therefore, new research has focused on ZrO_2 systems with different dopants. It has been shown in the literature that doping ZrO_2 with Sc, Yb, Y, Sm can increase ionic conductivity in the order Sc > Yb > Y > Sm (Feng, Ren, Wang, Zhou, & Pan, 2012). Due to the high price of Sc_2O_3, Yb_2O_3 (YbSZ) doped ZrO_2 material is an excellent candidate material for SOFCs as an electrolyte. The ionic radius of $Yb3^+$ is also closer to Zr^{4+}. Therefore, Yb_2O_3 co-doping can be adopted as an approach to enhance the stability of the cubic phase and improve the conductivity of scandia-stabilized zirconia electrolytes. The nanocrystalline structure of the powders has also been shown to improve the electrical properties of solid oxide electrolytes (Vijaya Lakshmi & Bauri, 2011). In a planar electrolyte-supported SOFC cell, a maximum power density of 0.56 W/cm^2 at 830 ^oC was achieved using 5YbSZ electrolyte material (Xue et al., 2015). Yamaji et al. (Yamaji, Koshikawa, Araki, & Adachi, 2008) successfully stabilized the cubic phase and obtained a maximum conductivity of 0.30 S/cm and a maximum power density of 210 mW/cm^2 at 1000 °C from 1Yb8ScSZ by co-doping Sc_2O_3 and Yb_2O_3 into ZrO_2. However, their research was limited to a specific range of Yb_2O_3 doping from %1 mol to %2 mol.

The literature on Yb_2O_3-doped zirconia materials mainly focuses on synthesis characterization and planar SOFCs. There is less emphasis on practical SOFC applications with regular electrode materials, especially for microtubular SOFCs, which have attracted great interest due to their high tolerance to thermal cycling, fast start-up capabilities, high power density per unit volume, and robust portability (Sahu, Panthi, Soliman, Feng, & Du, 2022). Therefore, in this study, $(Yb_2O_3)_x(ZrO_2)_{1-x}$ (x= 0.08, 0.09, 0.10, 0.11 and 0.12) is tested as an electrolyte material for microtubular SOFCs with conventional anode (NiO-YSZ) and cathode (LSM (lanthanum strontium manganite)-YSZ) materials. For this purpose, NiO-YSZ anode support microtubes are fabricated by conventional extrusion method. The NiO-YSZ anode functional layer was then coated by dip coating technique. Ytterbium-doped zirconia materials are synthesized using the sol-gel method, which is a very common method (Wang, Dommati, & Hsieh, 2019). After characterization of the obtained powders, a corresponding dip coating slurry is prepared and applied onto the anode functional layer acting as electrolyte. The cathode layers are similarly coated, and electrochemical measurements are performed on the resulting microtubular cells.

2. EXPERIMENTAL

2.1. Materials synthesis

$(Yb_2O_3)_x(ZrO_2)_{1-x}$ (x= 0.08, 0.09, 0.10, 0.11 and 0.12) binary systems were synthesized using a modified sol-gel technique. First, commercially available pure $ZrCl_4$ (99.9% purity) and $Yb(NO_3)_3.5H_2O$ (99.99% purity) were dissolved in stoichiometric amounts in pure water at room temperature. Citric acid ($C_6H_8O_7$) was then slowly added while stirring on a magnetic stirrer. Ethylene glycol ($C_2H_6O_2$) was added to the solution and completely dissolved (citric acid and ethylene glycol in a molar ratio of 1:4). The colorless solution was stirred and then heated on a hot plate at 80 ºC until it formed a viscous gel. Afterwards, the gel was transferred to alumina crucibles of appropriate size and dried in an oven at 120 ºC for 18 hours. Next, the gel was subjected to pre-heat treatment at 900 ºC for 12 hours to decompose the organic components. The final heat treatment was carried out at three different temperatures (1000 ºC, 1100 ºC and 1200 ºC) to decide the calcination temperature for the desired crystal structure. The obtained powders were milled in ethanol for 10 hours at 400 rpm with a planetary ball milling machine (PM100, Retsch, Germany).

2.2. Microtubular anode support fabrication

Commercial NiO (NiO-A, Novamet, USA) and YSZ (YSZ8-TC, Nexceris, USA) powders were mixed in a 1:1 mass ratio to formulate an extrusion slurry for the fabrication of anode support microtubes. Appropriate amounts of dispersant (fish oil, Sigma-Aldrich, Germany) and solvent (mixture of ethanol and methyl ethyl ketone, Sigma-Aldrich) were added to the mixture and then subjected to a 24-hour mixing process using a ball mill. The binder (Butvar, Sigma-Aldrich) and plasticizer (PEG, Sigma-Aldrich) were then added to the solution in the specified proportions. After a second 24-hour ball milling, the mixture was transferred to a magnetic stirrer and stirred for another 2 hours. The solution was then combined with paraffin and stearic acid in appropriate proportions and homogenized using a mechanical mixer until the desired viscosity was reached. The prepared extrusion slurry was extruded through a die with an inner diameter of 4 mm and an outer diameter of 5 mm using a laboratory-scale vertical extruder. After drying at room conditions for 24 hours, the microtubular anode supports were cut into 80 mm lengths and then pre-sintered at 1100 °C for 2 hours. After the micro-tube fabrication process, a solution was prepared by mixing the anode functional layer (50:50 wt%) NiO/YSZ powders and HVS 085 resin (Heraeus, Germany), thinner and alcohol in certain proportions. The mixture was then mixed in a ball mill with zirconium balls for 24 hours. The bilayer structure coated with AFL using the dip coating method on micro-tubes was co-sintered at 1150 °C. Different YbSZ powders (8-12YbSZ) and standard YSZ electrolyte solution were prepared similarly to the AFL solution. Then, AFL-coated anodes were coated with various electrolytes by dip coating method. The prepared ternary structures were then subjected to sintering at 1450 ºC. Similar to electrolyte coating, LSM-YSZ (40:60 wt%) cathode functional layer (CFL) and LSM-YSZ (90:10 wt%) cathode current collector layer (CCL) were coated on the electrolytes by dip coating technique, respectively. After both cathode layers were sintered together at 1050 °C, the anode supported microtubular cells were ready for testing and characterizations (Table 1). The outer diameter, length and cathode length of the final microtubular SOFCs were measured as ~4.5 mm, ~6.5 mm and ~3 mm, respectively. The cells are named according to the electrolyte materials as YbSZ 8-12 and RC (reference cell with a YSZ electrolyte).

Table 1. Details of the cell layers

Cell layer	Material(s)	Composition (wt. %)	Sintering conditions
AFL	NiO (NiO-F, Novamet)-YSZ	50:50	1150 ºC for 2 h
Electrolyte	8-12 mol % Yb-doped zirconia /YSZ	-	1450 ºC for 5 h
CFL	LSM (LSM20-HP, Nexceris)-YSZ	40:60	1050 ºC for 2 h
CCL	LSM (LSM20-P, Nexceris)-YSZ	90:10	1050 ºC for 2 h

2.3. Cell Fabrication and Testing

The electrochemical performance of the cells at 800 ºC was measured via a fuel cell test station (Arbin Instruments, FCTS, USA). The anode side was fed by 0.3 NL/min hydrogen for an hour through a pipe welded to the corresponding manifold. Performance tests were performed without additional air supply (i.e., stagnant air inside the test furnace as oxidant), maintaining hydrogen flow at 0.3 NL/min. Cell resistances under open circuit potential were determined immediately after the performance measurements by an impedance analyzer (Parstat 2273, Princeton Applied Research, USA) for the frequency range 0.1 Hz-250 kHz. Three cells were fabricated for each case and the highest electrochemical performances are reported in this study.

3. RESULTS AND DISCUSSION

Images of microtubular SOFCs prepared with different YbSZ electrolyte materials are given in Fig. 1, while electrochemical performance comparison is depicted in Fig. 2. The cells with YbSZ electrolytes exhibit performances compared to that with a YSZ electrolyte. In this context, the best peak performance is obtained with 10YbSZ electrolyte, although ionic conductivity is found to decrease with Yb_2O_3 content. Moreover, open circuit potentials also vary depending on the electrolyte material and some of them are found to be lower than the theoretical one, indicating incomplete electrolyte sintering as shown in Fig. 3. These findings reveal that sinterability and resultant grain size are also significant

for the performance of YbSZ electrolytes.

Fig. 1. Microtubular cells with %12-8 YbSZ and YSZ electrolyte (from top to bottom)

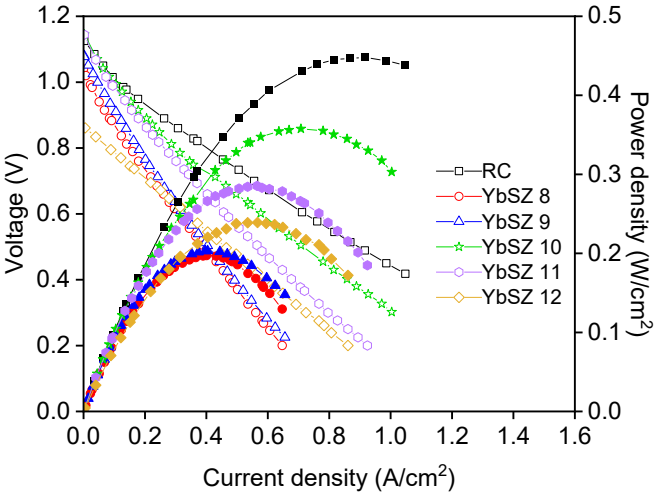

Fig. 2. Cell performances at 800 ºC

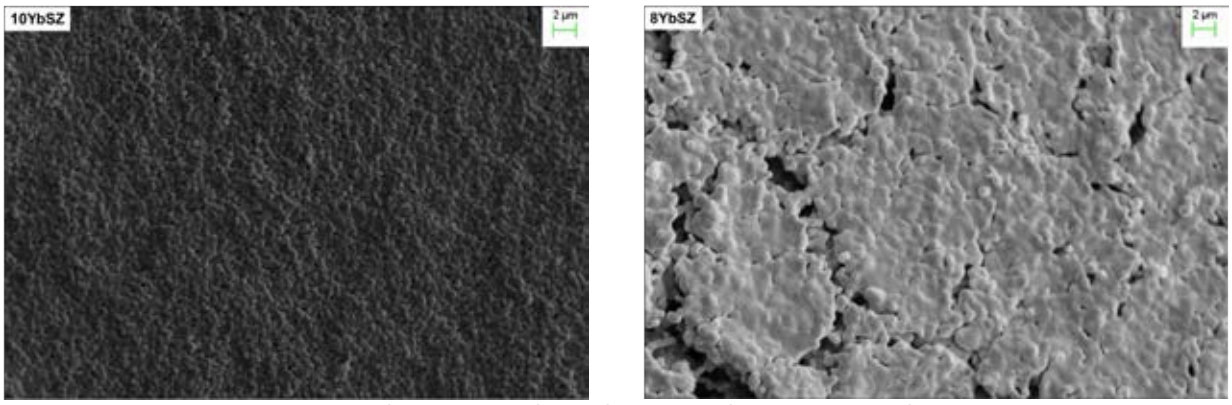

Fig. 3. SEM images of 10YbSZ and 8YbSZ electrolyte surface

4. CONCLUSIONS

The results of this study show that YbSZ can be an alternative to YSZ in microtubular SOFCs as an electrolyte material. In this context, a peak power density of 0.357 W/cm² is achieved with 10YbSZ, while the reference cell with a YSZ electrolyte shows 0.448 W/cm² maximum power density under the same conditions. However, electrochemical performance tests and microstructural analyses indicate incomplete sintering of YbSZ electrolytes. Therefore, sintering

conditions and/or coating solution formulation need to be studied and optimized for high performance. Moreover, long-term performance and phase stability of the YbSZ electrolyte should be investigated in detail.

REFERENCES

1. Feng, J., Ren, X., Wang, X., Zhou, R., & Pan, W. 2012. Thermal conductivity of ytterbia-stabilized zirconia. Scripta Materialia, 66, 41–44.
2. Fergus, J. W. 2006. Electrolytes for solid oxide fuel cells. Journal of Power Sources, 162, 30–40.
3. Sahu, S. K., Panthi, D., Soliman, I., Feng, H., & Du, Y. 2022. Fabrication and Performance of Micro-Tubular Solid Oxide Cells. Energies, 15, 1–17.
4. Vijaya Lakshmi, V., & Bauri, R. 2011. Phase formation and ionic conductivity studies on ytterbia co-doped scandia stabilized zirconia (0.9ZrO2-0.09Sc2O3-0. 01Yb2O3) electrolyte for SOFCs. Solid State Sciences, 13, 1520–1525.
5. Wang, J. C., Dommati, H., & Hsieh, S. J. 2019. Review of additive manufacturing methods for high-performance ceramic materials. International Journal of Advanced Manufacturing Technology, 103, 2627–2647.
6. Xue, Y. J., Miao, H., He, C. R., Wang, J. X., Liu, M., Sun, S. S., … Wang, W. G. 2015. Electrolyte supported solid oxide fuel cells with the super large size and thin ytterbia stabilized zirconia substrate. Journal of Power Sources, 279, 610–619.
7. Yamaji, A., Koshikawa, T., Araki, W., & Adachi, T. 2008. Stabilization of a Zirconia System and Evaluation of Its Electrolyte Characteristics for a Fuel Cell: Based on Electrical and Mechanical Considerations. Journal of Engineering Materials and Technology, 131, 11010.
8. Zheng, Y., Wu, L., Gu, H., Gao, L., Chen, H., & Guo, L. 2009. The effect of Sr on the properties of Y-doped ceria electrolyte for IT-SOFCs. Journal of Alloys and Compounds, 486, 586–589.

SYNTHESIS OF NEW POLYSTYRENE BASED ANION EXCHANGE MEMBRANE FOR ALKALINE ELECTROLYZER

[1]*Leyla BASAT, [2,3] Murat FARSAK, [1]*Gülfeza KARDAŞ
[1] Cukurova University, Faculty of Arts and Sciences, Chemistry Department, Adana, 01330, Türkiye
[2] Osmaniye Korkut Ata University, Department of Battery Systems and Hydrogen Technologies, Osmaniye, Türkiye
[3] Osmaniye Korkut Ata University, Department of Hybrid and Electric Vehicles Technology, Osmaniye, Türkiye

* leylabasat@gmail.com, gulfeza@gmail.com

ABSTRACT

In this study, the high thermal and chemical stability PMMA-b-PS anion exchange membrane was obtained by blending poly(methyl methacrylate) (PMMA) and polystyrene (PS) through the film casting method.PS was synthesized via the radical polymerization method and subsequently chloromethylated. Chloromethylated polystyrene was quaternized by adding trimethylamine (TMA) to the PS ring. Characterization and electrochemical tests (Electrochemical Impedance Spectroscopy (EIS)) were carried out from 10^{-1} Hz to 10^{5} Hz. The synthesis, chloromethylation, and quaternization of polystyrene were characterized by FTIR analysis. According to the TGA results, the first thermal degradation began at approximately 200°C, which indicates that the membranes maintained their thermal stability at high temperatures. Thermal measurements determined that the membranes exhibited backbone degradation at 450°C. The solution resistance was measured in 1 M KOH using EIS measurements. The PMMA-b-PS membrane exhibited a resistance of 75 Ω at room temperature. At 80°C, its resistance decreased to 66 Ω.

Keywords: Anion Exchange Membrane, Green Hydrogen, Polymer

1. INTRODUCTION

Nowadays, AEMs have become a highly active research area in electrochemical systems, including electrolyzers, fuel cells, and membranes. All electrochemical devices for energy storage and conversion (such as redox flow batteries, fuel cells, and electrolyzers) require selective ion transport under various conditions, including temperature, pH, and electrochemical voltage [1]. Anion exchange membranes are used in applications requiring hydroxide transport because they contain cationic groups in their polymer chains. AEMs should have high ionic conductivity, dimensional stability, film-forming ability, and long-term alkali resistance stability [2].

One of the biggest challenges in the application of AEMs is their stability. Stability tests are conducted. Most of the research focuses on developing high OH^- conductivity. Zhang et al. synthesized a poly(ether ether ketone) (PEEK) membrane and achieved an extremely high OH^- conductivity of 155 mS/cm at 60°C [3]. Shang et al. obtained conductivities of 49.6 and 30.9 mS/cm at 80 °C with the PEEK membrane they synthesized [4]. Tuli et al. developed a polystyrene-based cross-linked AEM and achieved a high conductivity of 156 mS/cm in their tests [5]. Yang et al. synthesized a polystyrene-co-4-vinyl pyridine copolymer, and its conductivity reached 74.29 mS/cm [6].In previous studies, Zhang et al. synthesized a PEEK membrane and determined a 56% water uptake and a 15% low swelling ratio at 60°C [3]. Xu et al. synthesized imidazolium- and zinc/graphene oxide-doped PEEK in their study and obtained 35.45% water uptake and an 18.87% swelling ratio [7]. Ren et al. (2022) obtained an 8.3% swelling ratio and 24.3% water uptake at 80°C in their study [2]. It has been determined in several studies that alkyl chain length increases water uptake and swelling ratio [8]. An increase in the swelling ratio may extend the life cycle of the membrane, but excessive swelling negatively affects the mechanical properties [9].

In this study aims to synthesize and make commercially available original, high-performance and durable membranes that exhibit high conductivity and strength. Methyl groups attached to the polymer chain structure of AEMs play a crucial role in stability and ionic conductivity. It has been determined that the methyl groups in the PS chain provide an advantage in terms of increasing the ionic conductivity of the membrane. Additionally, the phenyl rings in the PS chain restrict the rotation of the chains around the carbon-carbon bonds and contribute to the polymer's significant hardness. PMMA, which contains methyl groups, was selected as polymer.

2. MATERIALS AND METHODS

2.1. Synthesis of PMMA-b-PS Membrane

The required styrene, trimethylamine, benzoyl peroxide, and methanol were all obtained from Sigma Aldrich. Toluene (99.5%) and ethanol (99.9%) were acquired from ACS. Methyl methacrylate polymer (PMMA) was purchased from TCI and chloroform was purchased from Merck.

In the first stage of membrane production; after preparing the styrene/toluene solution, the benzoyl peroxide initiator is added, and the polymerization reaction is started at 70 °C. It is precipitated in methanol, which becomes viscous. The

polymer solution was filtered, and poured into a glass petri dish and dried at room temperature for 24 h. The filtered polymer is dried in a vacuum oven at 40 °C for 12 hours.The chloromethylation reaction was carried out in a three-necked flask of 100 mL equipped with a mechanical stirrer and a thermometer. Polystyrene was dissolved in toluene and added to the flask. $AlCl_3$ was slowly added to the flask at 60 °C and stirred for 6 h. After 6 h polymer solution precipitated in methanol and was filtered and poured into a glass petri dish and drying at room temperature for 24 h.The membrane was peeled from the petri dish and immersed in deionized water to wash away residual solvent. The membranes were then soaked in a TMA solution at 60 °C for 48 h. The membranes were soaked in a 1 M NaOH (aq) solution. The membrane was then washed with distilled water.In the second stage of membrane preparation, PMMA-b-PS polymeric blend with different compositions were prepared by the solution casting method. Membranes were dried in a vacuum at 60 °C, for 24 h in order to ensure the removal of the solvent.

2.2. Characterization Tests

FT-IR measurements of the membranes were performed using a Thermo Infrared Spectrometer. The measurements were conducted within a wavenumber range of 4000–500 cm^{-1}. The thermal stability of the membranes was evaluated using a Perkin Elmer thermogravimetric analyzer. The samples were heated from 15°C to 700°C at a heating rate of 20°C/min.The Tg values of the polymers were obtained by analyzing of their DSC curves in the temperature range of 100°C to 300°C, with a heating and cooling rate of 10°C/min.

Water uptake (WU) and swelling ratio (SR)

WU and SR were defined as the percentage change in mass and size of the membranes after water absorption, respectively. The membrane was dried in an oven at 60°C for 1 day, and its weight and average thickness were measured and recorded. The dried membrane was then soaked in deionized water at fixed temperatures for 24 hours. Afterward, the hydrated membrane was removed, surface water was wiped off, and its weight and thickness were measured and recorded. The WU and SR values of the AEMs were calculated using the following equations.

$$\%\mathrm{WU} = \frac{\mathrm{Wwet-Wdry}}{\mathrm{Wdry}}\ \mathrm{x}100 \quad (1)$$

$$\%SR = \frac{\mathrm{Lwet-Ldry}}{\mathrm{Ldry}}x100 \quad (2)$$

2.3. Electrochemical Measurements

The solution resistance of the membranes was measured using Electrochemical Impedance Spectroscopy (EIS) with a three-electrode method. The EIS measurement was performed in a 1M KOH solution using Pt electrodes over a frequency range of 10^{-1} to 10^{-5} Hz. The membrane and non-membrane solution resistances were measured using the glass cell shown in Figure 1.

Fig. 1. The glass cell used in the EIS measurement

3. RESULTS AND DISCUSSION

FT-IR spectra were used to confirm the chemical structure of anion exchange membranes. As shown in Fig. 2.a., 1216 cm^{-1} chloromethyl rocking vibration and 695 cm^{-1} C-Cl stretching vibration emerged, this results demonstrated the success of PS chloromethylation (KPS) [10]. The absorption band at 1600 cm^{-1} and 1422 cm^{-1} correspond to the stretching vibrations to the ammonium group [11]. The appearance of new characteristic peaks at 1651 and 3377 cm^{-1} assignable to the C-N and O-H stretching vibration indicates the successful quaternization reaction (QPS) [12].

The thermal stability of AEMs was measured using a TGA and DSC. As shown in Fig. 2.b., the membranes exhibited similar curves for weight loss. The first weight loss in PMMA-b-PS was observed at around 200, which corresponded to

the degradation of the ammonium group as a conducting head group. Secondly, in all two polymer membranes, backbone degradation was observed at a similar temperature of around 450 °C. In Fig 2.c. the DSC curve shows that Tg of the PS membrane is observed at 105 °C. while in Fig 2.d., Tg of the PMMA-b-PS membrane is 129 °C. PMMA-b-PS membrane exhibits the thermal properties of PMMA and PS.

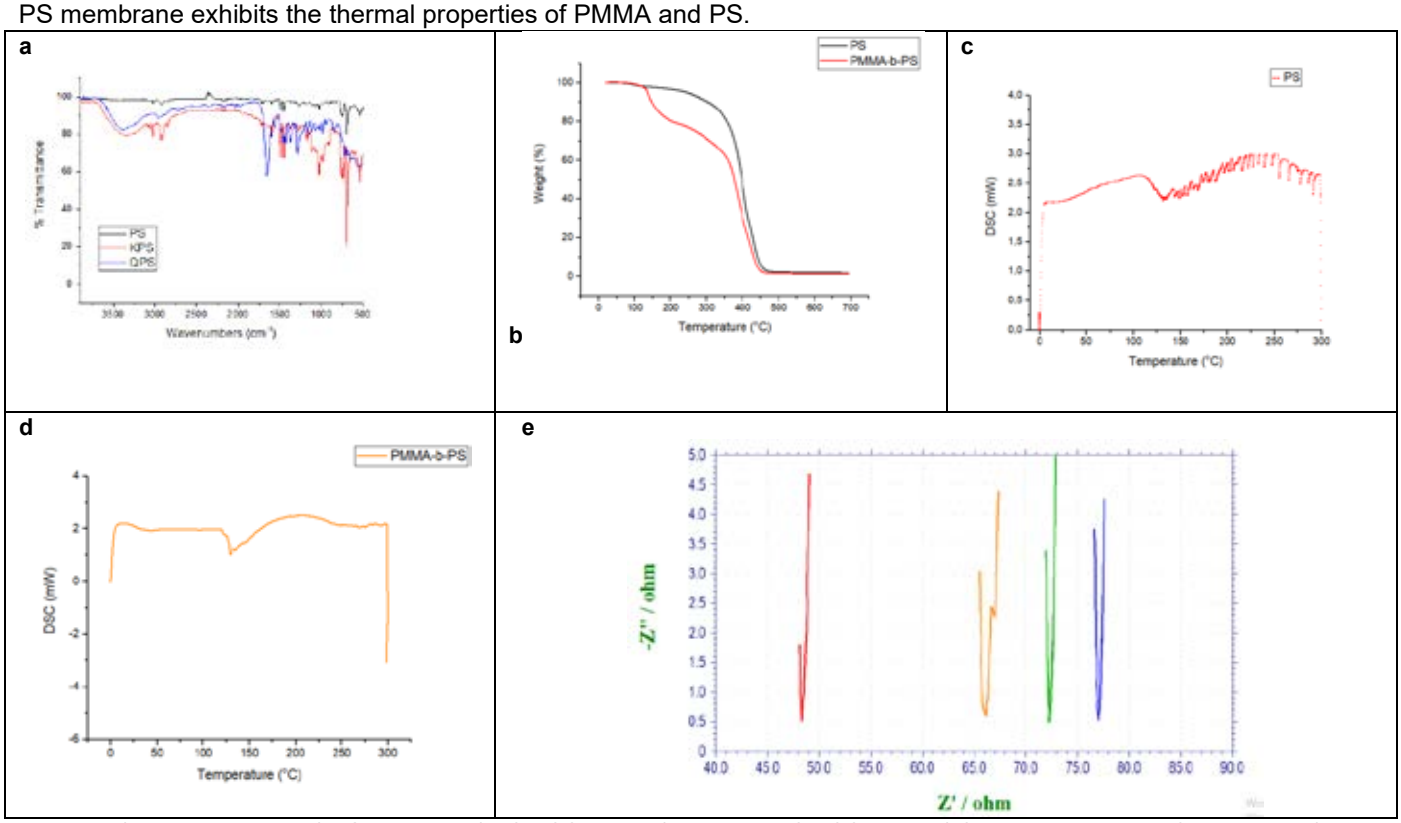

Fig. 2. a) FTIR spectrum b) TGA curves c) PS DSC curve d) PMMA-b-PS DSC curve e) Solution resistance of membranes(non-membrane-red, PMMA-b-PS in 80°C-orange, PMMA-b-PS in 30°C-green, PMMA-b-PS in 20°C-blue)

The resistance of membranes was measured in 1 M KOH. According to the obtained results, the resistance decreases with rising temperature (Table 1). According to Fig. 2.e., the solution resistances of the membranes are higher than the non-membrane solution resistance. The difference between the measurements shows the transfer of hydroxide ions in the solution.

Table 1. The resistance of membranes

Membrane	Temperature (°C)	Resistance (Ω)
Non-membrane	20	**48**
Fumasep-FAAM-20	20	**360**
Fumasep-FAAM-20	30	**270**
Fumasep-FAAM-20	80	**90**
PMMA-b-PS	20	**75**
PMMA-b-PS	30	**71**
PMMA-b-PS	80	**66**

4. CONCLUSIONS

In this study, quaternary ammonium polymer blends based on polystyrene were synthesized. FTIR results demonstrated the successful quaternization of PS. When compared to the commercial Fumasep-FAAM-20 membrane, the obtained membranes exhibited low resistance. Upon examining the %WU and %SR ratios of the membranes, the PMMA-b-PS membrane exhibited %18 WU and %11 SR. The swelling and water uptake ratios indicate that the membranes maintain their stability. Considering the TGA results, no significant thermal degradation is observed in either membrane up to approximately 200°C. The membranes exhibit thermal stability at high temperatures.

ACKNOWLEDGEMENT
This work was supported by a grant from TÜBİTAK 2211-C National PhD Scholarship Programs (1649B032401440). This work was also supported by Cukurova University BAP (Scientific Research Projects Coordination Unit) (FDK-2023-16117).

REFERENCES

1. Treichel, M., Gaitor, J. C., Birch, C., Vinskus, J. L., and Noonan, K. J. 2022. Anion-exchange membranes derived from main group and metal-based cations. Polymer, 124811.
2. Ren, J., Xu, J., Ju, M., Chen, X., Zhao, P., Meng, L. and Wang, Z. 2022. Long-term durable anion exchange membranes based on imidazole-functionalized poly (ether ether ketone) incorporating cationic metal− organic framework. Advanced Powder Materials, 1(2), 100017.
3. Zhang, Z., Xiao, X., Yan, X., Liang, X., and Wu, L. (2019). Highly conductive anion exchange membranes based on one-step benzylation modification of poly (ether ether ketone). Journal of Membrane Science, 574, 205-211.
4. Shang, L., Yao, D., Pang, B., and Zhao, C. (2021). Anion exchange membranes based on poly (ether ether ketone) containing N-spirocyclic quaternary ammonium cations in phenyl side chain. International Journal of Hydrogen Energy, 46(36), 19116-19128.
5. Tuli, S. K., Roy, A. L., Elgammal, R. A., Zawodzinski, T. A., and Fujiwara, T. (2018). Polystyrene-based anion exchange membranes via click chemistry: improved properties and AEM performance. Polymer International, 67(9), 1302-1312.
6. Yang, Z., Zhang, M., Zhao, Z., Lan, W., Zhang, X., and Fan, M. (2022). Highly alkaline stable fully-interpenetrating network poly (styrene-co-4-vinyl pyridine)/polyquaternium-10 anion exchange membrane without aryl ether linkages. International Journal of Hydrogen Energy, 47(37), 16580-16596.
7. Xu, J., Ju, M., Chen, X., Meng, L., Ren, J., Lei, J., and Wang, Z. (2022). High alkaline stability and long-term durability of imidazole functionalized poly (ether ether ketone) by incorporating graphene oxide/metal-organic framework complex. International Journal of Hydrogen Energy, 47(61), 25755-25768.
8. Yan, X., Zhao, B., Liu, J., Zhang, X., and He, G. (2018). Tailoring the nanophase-separated morphology of anion exchange membrane by embedding aliphatic chains of different lengths into aromatic main chains. Journal of membrane science, 564, 436-443.
9. Banerjee, A., Calay, R. K., and Eregno, F. E. (2022). Role and important properties of a membrane with its recent advancement in a microbial fuel cell. Energies, 15(2), 444.
10. Liu, R., Nie, Y., Chen, J., Shen, C.,and Gao, S. (2023). Anion exchange membranes based on poly (styrene-b-(ethylene-co-butylene)-b-styrene) grafted poly (2, 6-dimethyl-1, 4-phenylene oxide). Journal of Applied Polymer Science, 140(10), e53579.
11. Xu, Y., Zhao, C., Huang, S., Gan, Y., Xiong, L., Zhou, J., and Liang, H. (2022). Bis-pyridinium crosslinked poly (ether ether ketone) anion exchange membranes with enhancement of hydroxide conductivity and alkaline stability. International Journal of Hydrogen Energy, 47(9), 6097-6110.
12. Lin, C. X., Wang, X. Q., Hu, E. N., Yang, Q., Zhang, Q. G., Zhu, A. M., & Liu, Q. L. (2017). Quaternized triblock polymer anion exchange membranes with enhanced alkaline stability. Journal of Membrane Science, 541, 358-366.

LIGHTWEIGHT AND OPTIMIZED END PLATES FOR PEM FUEL CELLS: A COMPARATIVE STRUCTURAL ANALYSIS

[1, 2*]*Furkan Cetiner*, [1, 2]*Ahmed Emin Kilic*, [1, 2]*Selahattin Celik,* [3]*Serkan Toros,* [4]*Remzi Ecmel Ece*
[1] Ankara Yıldırım Beyazıt University, Faculty of Engineering and Natural Sciences, Department of Mechanical Engineering, Ankara, 06010, Türkiye
[2] Hydrogen Technologies and Energy Research Center (H2 TEAM), Ankara Yıldırım Beyazıt University, Ankara, 06010, Türkiye
[3] Nigde Omer Halisdemir University, Faculty of Engineering, Department of Mechanical Engineering, Nigde, 51245, Türkiye
[4] Turkish Aerospace Industry Inc, Additive Manufacturing Department, Ankara, 06980, Türkiye

*Corresponding author e-mail: furkan_cetiner@hotmail.com

ABSTRACT
This study investigates the structural optimization of end plates in proton exchange membrane fuel cells (PEMFCs) to enhance mechanical integrity while reducing weight. End plates are critical for maintaining uniform pressure distribution, minimizing contact resistance, and preventing fuel leakage. Various configurations, including bolted and steel belt connections, were analyzed using finite element analysis (FEA) and validated through experimental pressure distribution tests with Fujifilm Prescale films. The bolted end plate model exhibited the best pressure distribution, with a uniformity improvement of approximately 30% compared to steel belt configurations. However, it also resulted in a 66% increase in weight. A manually optimized bolted design reduced mass by up to 50%, while maintaining a von Mises stress profile close to the bulk model. Topology optimization further contributed to a 39% reduction in material usage without compromising structural integrity. Although steel belt connections provided improved pressure homogeneity, localized pressure concentration led to efficiency limitations. These findings emphasize the need for optimized end plate designs to enhance PEMFC performance, especially in weight-sensitive applications like aerospace and portable energy systems.
Keywords: PEM fuel cells, end plates, pressure distribution, structural optimization, finite element analysis, topology optimization, lightweight design, metal additive manufacturing

1. INTRODUCTION

Proton Exchange Membrane Fuel Cells (PEMFC) stand out as an important innovative technology due to their potential to provide environmentally friendly energy production. PEM fuel cells offer a zero-emission power source by directly converting chemical energy into electrical energy. Thanks to their advantages such as low operating temperature, high power density, and fast start-up, they are attracting attention in many areas such as automotive, portable energy, and stationary power generation systems. PEMFCs, which use hydrogen as a feedstock and produce only water as a by-product, play a critical role in the transition to sustainable energy technologies. However, the efficient operation of these systems depends on the mechanical, electrical, and chemical compatibility of their components, especially the membrane-electrode assembly (MEA), gas diffusion layer (GDL), and bipolar plates [1,2,3]. In PEM fuel cells, end plates have critical functions such as ensuring the assembly of cell stacks as well as maintaining the mechanical integrity and appropriate contact pressure distribution of the system. These plates hold the cell components together, prevent fuel leakage, and minimize electrical contact resistance by optimizing the contact pressure on the membrane electrode assembly (MEA). Inappropriate contact pressure can negatively affect cell performance and lead to excessive hot spots and component damage. The design of the end plates has a direct impact on performance, depending on the connection method used (bolt, steel belt, reinforcement plate, etc.), material properties (low density, high mechanical strength, corrosion resistance), and geometric structure. Several innovative connection methods and designs are being investigated to increase fuel cell efficiency and optimize the mass-to-power ratio [4,5,6].

In this study, the connection methods used in the end plates of PEM fuel cells were discussed and a comparative analysis of different designs was performed. In addition to the bolt-nut connection, a novel connection method compressed with steel tapes was examined in detail within the scope of the study. Stack models were created and optimized for both connection methods using computer-aided design (CAD) software. These models were designed to analyze the effects of different connection methods on mechanical and electrical performance by keeping the dimensions constant (rectangular end plates with dimensions of 58.9 x 175 mm). As a result of parametric analyses, the effects of the connection methods on performance criteria such as contact pressure distribution, sealing, corrosion resistance, and mechanical strength were evaluated. In addition, the weight optimization of the end plates was also performed; this offers a significant advantage, especially in applications where weight is critical such as unmanned aerial vehicles and in cost optimization. The study revealed that the steel tape connection method provides a more homogeneous pressure distribution compared to the bolt-nut connection in some cases, but requires careful optimization in terms of design and assembly.

2. MATERIALS AND METHODS

This study focuses on the design and optimization of the end plates of PEM fuel cell stacks, and the performances of

these structures are analyzed by comparing bolt and steel belt connection methods. In the stack designs, critical features of the end plates such as mechanical strength, low weight, and corrosion resistance are provided for the efficient operation of the PEM fuel cell. First, in the bolted end plate design, a rectangular model with dimensions of 58.9 x 175 mm and a thickness of 8 mm is created, and a total of 10 bolt holes are placed, five on each long edge. Hydrogen and air inlets and outlets are placed on the short edges of the plates. In the steel belt connection design, 3 curved surfaces are added and the steel belts are passed through these surfaces and tightened with worm screws.

In the design and analysis stages, the geometric structures of the end plates are optimized by applying topology optimization for both models. In this process, material usage is reduced and mechanical strength is preserved. Topology optimization is performed using the FEA (Finite Element Analysis) program which is ANSYS; Aluminum 7075 T6 was preferred due to its high strength, low density, and suitable elastic modulus. The Young modulus of this material was determined as 71.7 GPa, density as 2.88 g/cm³, and Poison ratio as 0.33. In the topology optimization, the mass reduction in the bolted model was performed manually for different parameters, and then verifications were made with FEA. In the steel belt model, the optimization for mass reduction was applied in a similar way, but the compressive pressure was increased by removing the inclined surfaces. As a result, structural analyses for both models were performed with the structural analysis module of the FEA program. In the bolted model, 2.5 MPa pressure was applied to the bolt areas, while 13,500 N force was applied to the belt section in the steel belt model.

3. RESULTS AND DISCUSSION

The obtained results include the comparison of the mechanical performance and pressure distribution of bolted and steel belt-connected end plate designs. In the bolted design, 2.5 MPa pressure resistance and a homogeneous pressure distribution were achieved, but it was observed that irregularities that may occur during the placement of the bolts may affect the pressure homogeneity. In contrast, in the steel belt-connected design, the pressure was distributed more evenly between the plates thanks to the compression with three curved surfaces and worm screws. However, it was also determined that this method may cause deformation in applications requiring high compression pressure. The topology optimization results provided significant improvements in terms of mass reduction and mechanical strength in both models. In the bolted model, the risks of strength loss were determined in the manual optimizations, whereas the compression pressure was increased by removing the curved surfaces in the steel belt model. In the fifth model, a mass reduction of up to 50% was achieved in line with the optimization results obtained with the FEA program, which offered advantages in terms of both cost and efficiency. Table 1 shows the comparison of different end plates (rod and belt types) and Table 2 shows the ANSYS structural analysis results of them.

Table 1. Comparison of end plate models with different parameters as; bolt bulk (a), belt bulk (b), bolt manual optimized (c), belt manual optimized (d), and belt topology optimized (e)

#	Model	Mass (g)	Maximum Total Deformation (mm)	Maximum Directional Deformation (mm)	Equivalent Stress (MPa)
a		332.8	0.000209	0.000115	3.60
b		366.5	0.000114	0.000124	1.32
c		113.2	0.000328	0.000246	2.92
d		137.9	0.000445	0.000445	3.48
e	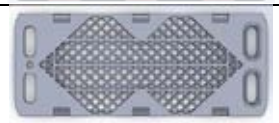	201.1	0.000290	N/A	2.79

Table 1. ANSYS structural analysis results for bolt bulk (a), belt bulk (b), bolt manual optimized (c), belt manual optimized (d), and belt topology optimized (e)

#	Model	ANSYS Structural Analysis
a		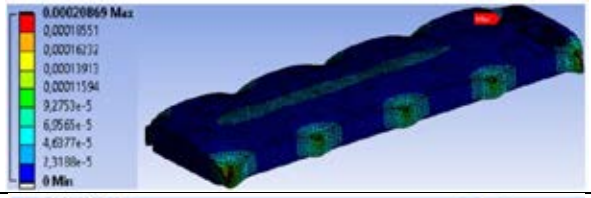
b		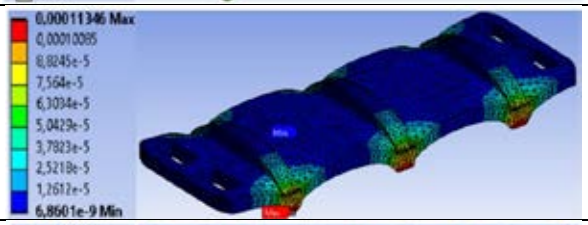
c		
d	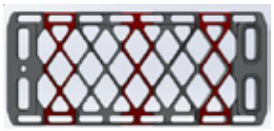	
e	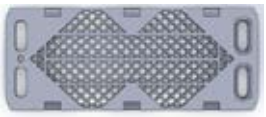	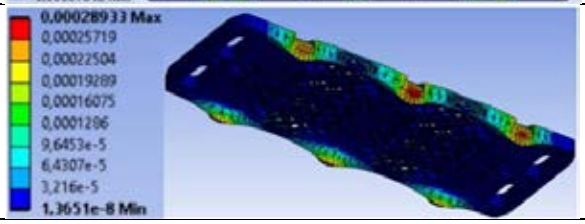

The experimental results were verified with Fujifilm Prescale films used to observe the pressure distribution, and it was determined that a homogeneous pressure distribution has a critical effect, especially on fuel cell performance. While the pressure distribution was controlled by the cross-tightening technique in the bolted model, homogeneity was achieved by precisely adjusting the torque value of the worm screws in the steel belt model. The use of AISI 430 quality steel as the steel belt material contributed to the durability of the design, but this connection method required additional cost and labor during the production and assembly process. As a result, the advantages and disadvantages of both connection methods were determined, and it was seen that the steel belt-connected design was superior in terms of homogeneous pressure distribution, but it needed improvement in factors such as manufacturing complexity and cost. Figure 1 shows the comparison of pressure distribution for all end plate designs.

Fig. 1. Comparison of pressure distribution of bolt bulk (a), belt bulk (b), bolt manual optimized (c), belt manual optimized (d), and belt topology optimized (e), respectively from left to right

4. CONCLUSIONS

The results of this study demonstrate that structural optimization of PEMFC end plates significantly impacts both weight and mechanical performance. The bolted end plate model achieved the best pressure distribution, with a 30% improvement compared to steel belt designs, but was found to be 66% heavier. The manually optimized bolted model emerged as the most effective alternative, reducing mass by 50% while maintaining an equivalent von Mises stress level. Topology optimization further decreased material usage by 39%, enhancing efficiency without compromising strength. While the steel belt connection improved pressure uniformity, it led to localized pressure concentrations that reduced efficiency. Future studies should explore advanced materials and hybrid connection techniques to optimize both weight and structural stability for PEMFC applications.

REFERENCES

[1] O'hayre, R., Cha, S. W., Colella, W., & Prinz, F. B. 2016. *Fuel cell fundamentals*. John Wiley & Sons.
[2] Dey, T., Deshpande, J., Singdeo, D., & Ghosh, P. C. 2019. Study of PEM fuel cell end plate design by structural analysis based on contact pressure. Journal of Energy, 2019(1), 3821082.
[3] Wang, Y., Yuan, H., Martinez, A., Hong, P., Xu, H., & Bockmiller, F. R. 2021. Polymer electrolyte membrane fuel cell and hydrogen station networks for automobiles: Status, technology, and perspectives. Advances in Applied Energy, 2, 100011.
[4] Habibnia, M., Shirkhani, M., & Tamami, P. G. 2020. Optimization of proton exchange membrane fuel cell's end plates. SN Applied Sciences, *2*, 1-8.
[5] Zhang, Z., Zhang, J., & Zhang, T. 2022. Endplate Design and Topology Optimization of Fuel Cell Stack Clamped with Bolts. Sustainability, 14(8), 4730.
[6] Asghari, S., Shahsamandi, M. H., & Khorasani, M. A. 2010. Design and manufacturing of end plates of a 5 kW PEM fuel cell. International journal of hydrogen energy, *35*(17), 9291-9297.

OPTIMIZING ENERGY INVESTMENTS FOR GROWING DEMAND OF TÜRKİYE: HYDROGEN-BASED BATTERIES AND RENEWABLE INTEGRATION

[1]*Ali Osman Kabil,* [2*]*Mehmet Güray Güler*
[1] Yıldız Technical University, Faculty of Mechanical Engineering, Department of Industrial Engineering, İstanbul, 34349, Türkiye
[2] Istanbul Technical University, Faculty of Management, Department of Data Science and Analytics, İstanbul, 34367, Türkiye

*Corresponding author e-mail: mguler@itu.edu.tr

ABSTRACT
Meeting Turkey's growing electricity demand requires a balanced approach to ensure reliable generation and consumption at all times. The study focuses on addressing the variability introduced by renewable energy sources, such as solar and wind, through the integration of energy storage systems. An optimization model is developed to determine the optimal storage locations, types, and capacities, with a particular emphasis on hydrogen-based batteries. The approach aims to minimize total costs while enhancing grid stability and supporting renewable energy integration. By using Turkey as a case study, the findings provide valuable insights for sustainable energy planning and storage technology deployment.
Keywords: Energy system optimization, Renewable energy integration, Hydrogen-based energy storage, Cost minimization, Turkey energy planning

1. INTRODUCTION
Global energy systems are undergoing a profound transformation as nations strive to meet growing electricity demand while transitioning to sustainable energy sources. Turkey, as one of the fastest-growing economies, faces significant challenges in balancing demand and supply. Between 2000 and 2019, Turkey's electricity demand increased from 128 TWh to 303.3 TWh, driven by industrial expansion, urbanization, and population growth. Meeting this increasing demand necessitates expanding generation capacity and addressing critical issues such as supply reliability, grid stability, and cost efficiency. The integration of renewable energy sources like solar and wind, which have become a significant part of Turkey's energy system, has increased the challenges of balancing electricity supply. These sources produce energy intermittently, depending on weather conditions and time of day, leading to daily and seasonal fluctuations in generation that can threaten the stability of the grid [1].

Unlike lithium-ion or flow batteries, hydrogen batteries can store energy for extended periods, aligning with global decarbonization goals by utilizing surplus renewable energy for hydrogen production through electrolysis. This capability positions hydrogen-based systems as a crucial component in modernizing energy infrastructures and achieving sustainability targets [3]. This study develops an optimization model tailored to Turkey's energy landscape to identify optimal locations, types, and capacities for storage facilities, particularly focusing on hydrogen-based solutions, to minimize system costs while enhancing grid reliability and supporting the clean energy transition [2].

2. MATERIALS AND METHODS
This study develops an optimization model to address the challenges of balancing Türkiye's growing electricity demand and integrating renewable energy sources. The model focuses on determining the optimal locations and sizes of battery storage systems, including hydrogen-based, lithium-ion, and flow batteries. It aims to minimize total system costs while ensuring grid reliability and accommodating the variability in both electricity demand and renewable generation. By considering factors such as system stability, economic feasibility, and Türkiye's energy transition goals, the model provides a comprehensive framework for strategic investment in energy storage technologies. To model the problem effectively, a representative day was selected from a 365-day dataset obtained from EPİAŞ to capture the load profile of Türkiye, considering daily variations in electricity demand across the country.

2.1. Problem Definition
The optimization model addresses the critical challenge of designing a cost-effective and reliable energy system for Turkey, capable of balancing the increasing electricity demand and integrating renewable energy sources while adhering to carbon emission reduction targets. This problem arises from the intricate dynamics of energy systems, where electricity supply and demand fluctuate across different times of the day and regions. These fluctuations are influenced by factors such as industrial activity, residential energy use, and seasonal variations in consumption patterns. Additionally, the integration of renewable energy sources like solar and wind further complicates the system due to their inherent intermittency, as their generation is highly dependent on weather conditions and time of day, leading to unpredictable and variable energy outputs.

The model seeks to determine the optimal investment strategies in ESS, particularly hydrogen-based batteries, alongside the optimal expansion of power generation capacities. It considers multiple objectives, including minimizing total system

costs, maintaining grid stability, and meeting strict emission targets. To achieve these goals, the model incorporates detailed constraints such as hourly demand satisfaction, production capacities, energy storage dynamics, and emission limits. By evaluating trade-offs between economic and operational factors, the model provides actionable insights for decision-makers to ensure a resilient and sustainable energy future for Turkey.

2.2. Model Formulation

The optimization problem is structured to minimize the total cost of meeting energy demand while considering investments, operational costs, and carbon emission constraints. The objective function is defined as follows:

$$\min Z = \sum_{t=0}^{T}\Big(\sum_{e\in E} c_e \cdot I_{e,t} + \sum_{e\in E}\frac{o_e}{100}\cdot c_e \cdot \big(C_e + \sum_{\tau=0}^{t} I_{e,\tau}\big) + \sum_{e\in E}\sum_{g\in G}\sum_{h\in H} w_g \cdot 365 \cdot p_e \cdot P_{e,t,g,h} + \sum_{g\in G}\sum_{h\in H} u \cdot U_{t,g,h} + \sum_{b\in B}\Big(c_b \cdot B_{b,t} + \frac{o_b}{100}\cdot B_{b,t}\Big)\Big) \quad (1)$$

$$\sum_{e\in E} P_{e,t,g,h} + \sum_{b\in B} BD_{b,t,g,h} + U_{t,g,h} = d_{g,h}\cdot(1 + r\cdot t) + \sum_{b\in B} BC_{b,t,g,h}, \quad \forall t \in \{0,1,\dots,T\}, \forall g \in G, \forall h \in H \quad (2)$$

$$P_{e,t,g,h} \le \big(C_e + \sum_{\tau=0}^{t} I_{e,\tau}\big)\cdot CF_{e,h}, \quad \forall t \in \{0,1,\dots,T\}, \forall g \in G, \forall h \in H, \forall e \in E \quad (3)$$

$$S_{b,t,g,h} = S_{b,t,g,h-1}\cdot(1 - SDR_b) + BC_{b,t,g,h-1}\cdot \eta_b - BD_{b,t,g,h-1}\cdot \eta_b, \quad \forall t \in \{0,1,\dots,T\}, \forall g \in G, \forall b \in B, \forall h \in \{1,2,\dots,H\} \quad (4)$$

$$S_{b,t,g,0} = 0, \quad \forall t \in \{0,1,\dots,T\}, \forall g \in G, \forall b \in B \quad (5)$$

$$BC_{b,t,g,h} \le MCR_b \cdot \big(\sum_{t'=0}^{t} B_{b,t}\big), \quad \forall t \in \{0,1,\dots,T\}, \forall g \in G, \forall h \in H, \forall b \in B \quad (6)$$

$$BD_{b,t,g,h} \le S_{b,t,g,h}, \quad \forall t \in \{0,1,\dots,T\}, \forall g \in G, \forall h \in H, \forall b \in B \quad (7)$$

$$S_{b,t,g,h} \le \big(\sum_{t'=0}^{t} B_{b,t}\big), \quad \forall t \in \{0,1,\dots,T\}, \forall g \in G, \forall h \in H, \forall b \in B \quad (8)$$

$$\sum_{e\in E}\sum_{g\in G}\sum_{h\in H} P_{e,t,g,h}\cdot EF_e \cdot 365 \cdot w_g \le ET_t \quad (9)$$

$$I_{e,t}, P_{e,t,g,h}, U_{t,g,h}, S_{b,t,g,h}, BC_{b,t,g,h}, BD_{b,t,g,h}, B_{b,t} \ge 0 \quad (10)$$

$$\sum_{b\in B} BC_{b,t,g,h} \le IsC_{t,g,h}\cdot M, \quad \forall t \in \{0,1,\dots,T\}, \forall g \in G, \forall h \in H \quad (11)$$

$$\sum_{b\in B} BD_{b,t,g,h} \le \big(1 - IsC_{t,g,h}\big)\cdot M, \quad \forall t \in \{0,1,\dots,T\}, \forall g \in G, \forall h \in H \quad (12)$$

where;

- c_e : Investment cost for energy type e ($/MW)
- $I_{e,t}$: Investment amount for energy type e in year t (MW)
- o_e: Operation and maintenance cost percentage for energy type e (% of CAPEX per year)
- C_e: Initial installed capacity for energy type e (MW)
- w_g: Weight of representative day g
- p_e: Production cost for energy type e ($/MWh)
- $P_{e,t,g,h}$: Production amount for energy type e in year t, day g and hour h (MWh)
- u: Cost of unmet demand ($/MWh)
- $U_{t,g,h}$: Unmet demand in year t, day g and hour h (MWh)
- c_b: Investment cost for battery type b ($/MW)
- $B_{b,t}$: Investment amount for battery type b in year t
- o_b: Operation and maintenance cost percentage for battery type b (% of CAPEX per year)
- $BD_{b,t,g,h}$: Discharging amount for battery type b in year t, day g and hour h (MWh)
- $d_{g,h}$: Hourly demand at day g and hour h (MWh)
- r: Annual demand growth rate
- $BC_{b,t,g,h}$: Charging amount for battery type b in year t, day g and hour h (MWh)
- $CF_{e,h}$: Capacity factor for energy type e at hour h (reflects seasonal and hourly variations)
- $S_{b,t,g,h}$: State of charge for battery type b in year t, day g and hour h (MWh)
- SDR_b : Self-discharge rate for battery type b
- η_b : Charge/discharge efficiency for battery type b
- MCR_b: Maximum charging rate for battery type b (MW)
- $IsC_{t,g,h}$: Binary variable indicating charging 1 or discharging 0
- M : Large positive constant (Big-M)

The objective function, as presented in Eq. (1), minimizes the total cost, encompassing investment costs for energy and battery systems, operation and maintenance expenses, production costs, unmet demand penalties, and battery-related costs. Eq. (2) ensures that the total energy supply, including production, battery discharge, and unmet demand, meets or exceeds the growing hourly energy demand while considering battery charging requirements. Eq. (3) limits energy production to the available capacity, factoring in capacity expansion investments and capacity factors specific to each energy type and hour. Eq. (4) tracks battery state dynamics, balancing self-discharge, charging, and discharging activities

across hours, starting from $h = 1$. Eq. (5) resets the battery state to zero at the beginning of each day. Eq. (6) enforces limits on battery charging rates relative to their installed capacities. Eq. (7) ensures that battery discharging does not exceed the stored energy in the battery, while Eq. (8) ensures that the battery state does not exceed the total installed capacity of the battery system. Eq. (9) imposes annual carbon emission limits, aligning with predefined reduction targets. Eq. (10) mandates non-negativity for all decision variables, ensuring practical feasibility. Finally, Eqs. (11) and (12) enforce logical constraints to prevent simultaneous charging and discharging of batteries by using a binary variable $IsC_{t,g,h}$ and a large constant M.

3. RESULTS AND DISCUSSION

To evaluate the economic impact of integrating battery storage into Türkiye's energy system, the optimization model was executed under six different scenarios. BatteryLevel0 represents a case with no additional battery capacity, while BatteryLevel1 to BatteryLevel5 correspond to increasing storage capacities of 1, 2, 4, 8, and 10 GWh for each battery type, respectively. These battery technologies were chosen for their complementary characteristics, with hydrogen-based batteries offering long-term storage, lithium-ion batteries providing high energy density and rapid response, and flow batteries delivering scalability and durability for large-scale applications. The aim was to determine how the presence of battery systems could influence total production costs compared to a scenario without battery storage. Fig. 1 shows that increasing battery capacities leads to a reduction in production costs. In the BatteryLevel0 scenario, where no batteries are installed, the total production cost was approximately 27.85 billion USD, reflecting a high reliance on conventional energy sources and higher operational expenses. As battery capacities increased, production costs steadily declined. For instance, in the BatteryLevel1 scenario, where 1 GWh of each battery type was added, the cost decreased to 27.79 billion USD. By the BatteryLevel5 scenario, with 10 GWh of capacity for each battery type, the cost further dropped to 27.72 billion USD. This highlights the role of batteries in optimizing energy production by enhancing supply flexibility and reducing reliance on expensive conventional generation.

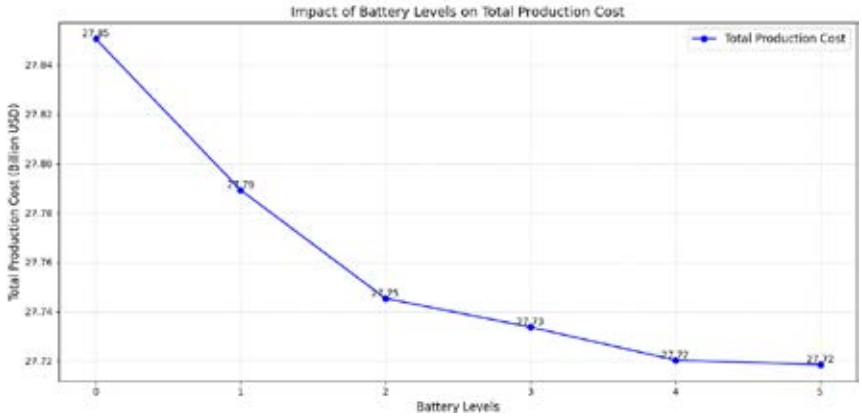

Fig. 1. Impact of battery capacities on total system cost

The impact of battery storage on total carbon emissions was also analyzed. As seen in Fig. 2, increasing battery capacities leads to a steady decline in total emissions. In the BatteryLevel0 scenario, where no batteries were installed, total carbon emissions reached approximately 141.91 million tons. However, as battery capacities increased, emissions gradually decreased. By the BatteryLevel5 scenario, where each battery type had a capacity of 10 GWh, total emissions dropped to 140.80 million tons. This trend highlights the role of battery storage in reducing reliance on fossil fuel-based generation, thereby lowering carbon emissions and supporting a more sustainable energy system.

Fig.3 illustrates the hourly usage of battery storage across different capacity levels on a representative day. As the battery capacity increases, its utilization becomes more prominent, particularly during periods of high demand. For example, scenarios with higher battery levels (BatteryLevel4 and BatteryLevel5) exhibit greater flexibility in storing and discharging energy throughout the day, especially during peak hours. This demonstrates how increased battery capacity provides the system with enhanced flexibility to optimize energy production and consumption patterns.

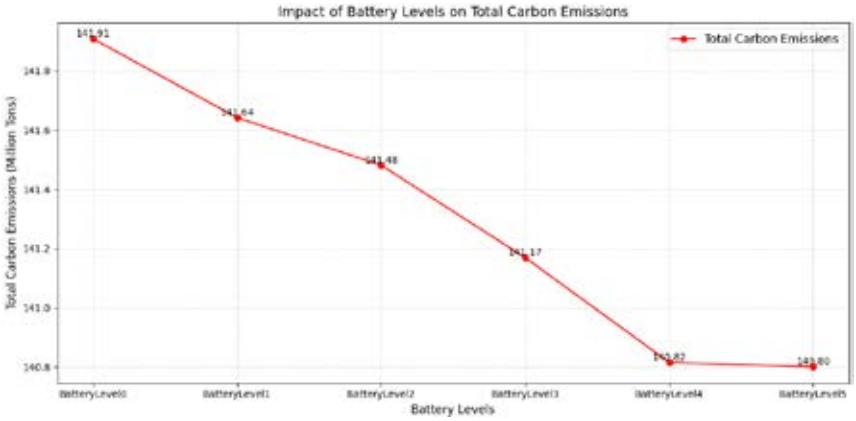

Fig. 2. Impact of battery capacities on total carbon emissions

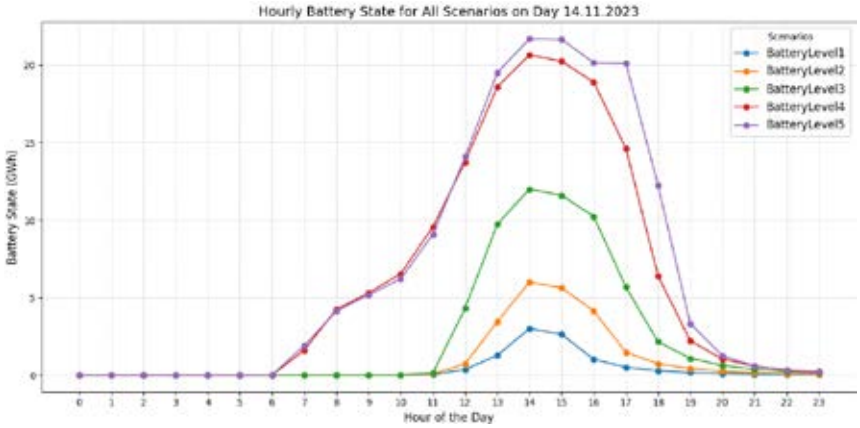

Fig. 3. Hourly battery state for different capacity scenarios on two representative days

4. CONCLUSIONS

Integrating battery storage into the energy system enhances flexibility, reduces production costs, and minimizes unmet demand penalties by storing surplus energy during low-demand periods and discharging it during peak hours. This improves the integration of renewables like wind and solar, stabilizing the grid and reducing reliance on conventional generation. Higher battery capacities help balance supply and demand, cutting the need for costly on-demand generation and minimizing energy wastage. Additionally, increased battery storage lowers total carbon emissions by reducing fossil fuel dependency, supporting both economic efficiency and environmental sustainability.

ACKNOWLEDGEMENT

The authors would like to acknowledge that this paper is submitted in partial fulfilment of the requirements for PhD degree at Yıldız Technical University.

REFERENCES

[1] H. Gözde and M. C. Taplamacioğlu, 'Integration of renewable energy sources into Turkey electric energy network-General problems and solution proposals', 2018 5th International Conference on Electrical and Electronics Engineering, ICEEE 2018, pp. 289–292, Jun. 2018, doi: 10.1109/ICEEE2.2018.8391348.

[2] H. Caliskan, I. Dincer, and A. Hepbasli, 'Energy, exergy and sustainability analyses of hybrid renewable energy based hydrogen and electricity production and storage systems: Modeling and case study', Appl Therm Eng, vol. 61, no. 2, pp. 784–798, 2013, doi: https://doi.org/10.1016/j.applthermaleng.2012.04.026.

[3] R. Bhandari and N. Adhikari, 'A comprehensive review on the role of hydrogen in renewable energy systems', Int J Hydrogen Energy, vol. 82, pp. 923–951, Sep. 2024, doi: 10.1016/J.IJHYDENE.2024.08.004.

NH_3 SYNTHESIS with Ca_2NH SUPPORTED Ru CATALYST UNDER MILD CONDITIONS

[1*]*Tugba Akkas Boynuegri*, [1]*John T.S. Irvine*, [1]*Gavin Irvine,* [1]*Samuel Jowitt,* [1]*Oxana Magdysyuk,* [1]*Huseyin Unsal, and* [2]*Annabel Long*
[1]University of St Andrews, School of Chemistry, North Haugh, St Andrews, KY16 9ST, UK
[2]University of St Andrews, School of Earth and Environmental Science, Bute Building, Queen's Terrace, St AndrewsKY16 9TS, UK

*Corresponding author e-mail: tab9@st-andrews.ac.uk

ABSTRACT
Recently, there has been an intense focus on the development of mild condition ammonia synthesis (MCAS) to overcome the scalability issues associated with the Haber Bosch process. In this study, the main interest was to clarify the impact of the precursors for Ca_2NH synthesis on Ru-Ca_2NH catalyst activity for ammonia synthesis. For this reason, β-Ca_2NH was synthesized using CaH_2 and N_2, which is different from reported in the literature. The structure of the synthesized material was thoroughly analyzed and confirmed via X-ray diffraction (XRD). Subsequently, Ru-Ca_2NH catalysts were prepared at varying percentages, ranging from 1% to 18%, to determine the optimum amount of Ru. After that, these samples underwent XRD and scanning electron microscopy (SEM) analysis. Finally, the performance of these catalysts was investigated in ammonia synthesis reaction conducted under continuous gas flow (80 ml/min, H_2: N_2=3: 1) in a quartz-tube reactor at 340°C and 0.1MPa. The outlet gas was monitored via mass spectrometer, and showed 5% Ru-Ca_2NH had the best activity. Additionally, UV-Vis spectrometry was carried out to determine total ammonia production rate, and was calculated as 1.6 mmol/g cat. h. This production rate was higher than the performance of most of the reported Ru-based catalysts.

Keywords: Ammonia, heterogeneous catalyst, energy, hydrogen storage.

1. INTRODUCTION

The global impact of the COVID-19 pandemic and Russia's war on Ukraine on the energy sector highlighted the significant importance of the need for greater energy diversification and reliance on local, renewable energy sources. Additionally, how vital of the energy storage and its use when needed has been revealed explicitly. NH_3 is seen as one potential energy storage medium due to having several advantageous properties listed below. Also, the well-developed procedures make ammonia such an attractive hydrogen carrier material and an environmentally friendly fuel [1, 2]. The expectation is to boost hydrogen powered system via essential chemical buy 2050 [3].

- ✓ It has a significant weight fraction of hydrogen, 17.65%.
- ✓ It can be liquefied under mild conditions (25°C and 0.99MPa).
- ✓ Its volumetric hydrogen density is higher than that of liquid hydrogen.
- ✓ It can be stored in a pressure vessel having a reasonable cost, like propane.
- ✓ It can be burned directly in an internal combustion engine (ICE) with no carbon emission.
- ✓ Globally well-established infrastructures for its production, storage, transport and utilization.

The current and major production method of NH_3 depends on steam reforming of methane via the Haber-Bosch process which requires high pressure (150-300 bar) and temperature (350-500°C) in the presence of Fe-based catalyst. Steam reforming of methane results in 500 million tonnes of CO_2 release into the atmosphere each year [4]. The industrialization of NH_3 synthesis dates back a hundred years. However, an ideal catalyst preparation has always been non-stop work to set up mild synthesis conditions [5].

$$N_2(g) + 3H_2(g) \xrightarrow{\text{Catalyst}} 2NH_3(g) \quad (1)$$

NH_3 is utilised in industrial, agricultural and domestic products and processes, but its main use is as fertilizer (70%) with a stabile production of about 150 million metric tonnes each year [6,7]. It is predicted novel applications of the chemical such as energy storage and power generation will result in a three fold rise in production by 2050 [8]. As a result of climate change policy, the production of NH_3 will have to shift away from carbon intensive methods. However, cost will still play an important role in the production method of ammonia. To achieve these goals, replacement of conventional iron (Fe) catalyst that show better activity at lower temperatures (around 300°C) are required. Second generation heterogeneous ruthenium (Ru) catalysts have shown promise for MCAS [9].
As for catalyst development, heterogeneous, homogeneous, and natural types of catalysts have been studied to activate N_2 molecules for NH_3 formation [10].Beyond this, research has focused on developing electronically and ionically active support materials. Previously research has shown the undeniable influence these catalyst/support materials have on the catalytic performance of the system. So far, carbon materials, nitrides, zeolites, oxides, and ceria nanocrystals have been well-developed and achieved competitive ammonia synthesis [11]. Especially, using Ru-based heterogeneous catalysts

were accepted as promising solution to reach desired production rates. The complex compounds such as $Ru_3(CO)_{12}$ and Ru $(NO)(NO_3)_3$ have been prevalently reported as Ru source for more than two decades [12-14].
The more detailed search pointed out that when nitrogen-hydrogen based alkali and alkaline earth metal compounds such as Li-N-H, CaNH, Ca_2NH, Ba-$Ca(NH_2)_2$, Sr_2NH etc. supported the catalyst, a satisfactory NH_3 production rate was achieved under mild conditions. Specifically, Ca_2NH-supported Ru catalyst showed superior performance in MCAS even in long-term tests [14-16]. The outstanding performance of the Ca_2NH was attributed to its better ionic conductivity than that of CaNH [17]. In particular, the crucial role of β-Ca_2NH, a fast H- ionic conductor, for promoting ammonia synthesis in Ru-based catalyst was emphasized in the literature [18]. Different Ca_2NH synthesis routes resulted in different ionic conductivities [14-18]. However, how the selection of starting materials for the synthesis of Ca_2NH affects the performance of Ru-Ca_2NH catalyst in the ammonia synthesis has not been clarified so far.
In this study, our motivation is to solve this puzzle and enlighten the relation between catalyst (Ru-Ca_2NH) activity and support material (Ca_2NH) synthesis route. With this aim, first, Ca_2NH was synthesized using CaH_2 and N_2. Next, catalysts involving Ru in different ratios were prepared to compare their performance for making a decision about optimum amount of Ru. After determination of the ideal catalyst composition, its long-term activity was investigated for NH_3 production. Finally, the performance of the catalyst was evaluated by making comparison with some other Ru-based catalysts.

2. EXPERIMENTAL.

2.1. Ca_2NH synthesis

Ca_2NH was synthesized via CaH_2 (Merck, Cas number: 7789-78-8) and N_2 using dosing and continuous flow reactions in a sealed reactor. Basically, CaH_2 reacted with N_2 in the sealed reactor to synthesize β-Ca_2NH. The reactor temperature was ramped up 5 °C/min to 600 °C inside a furnace (EUROTERM) and dwelled for 6 hours under N_2 flow. It was then cooled to room temperature and purged with argon [19].

2.2. Ru-Ca_2NH catalyst preparation

Ru-loading was carried out by heating a mixture of Ca_2NH powder and $Ru_3(CO)_{12}$ (Sigma Aldrich, Cas number: 15243-33-1) in the sealed reactor under continuous argon gas flow. The temperature program had five steps: 2 C/min up to 40 C, held for 1 h; 0.5 °C/ min up to 70°C, held for 1 hour; 0.9 °C/min up to 120°C, held for 1 hour; 0.9 °C/min up to 230-250 °C, held for 2 hours by using a furnace (EUROTERM) and then cooled to ambient temperature. Five different percentages (w/w) of Ru from 1% to 18% were selected to load the Ca_2NH samples in accordance with previous studies [14,20]. For comparison, 5%Ru-Ca_2NH* (Ca(m) + N_2+ H_2 → Ca_2NH*), 5%Ru-Ca_2NH +BaH_2 and 5%Ru-Al_2O_3 catalysts prepared with the same heat treatment.

2.3. Catalytic reaction for ammonia synthesis

The performance of the prepared catalysts were investigated in a NH_3 synthesis reaction. A quartz-tube reactor involving the prepared Ru-Ca_2NH catalyst powder (0.1g) was used for ammonia synthesis by applying 80 ml flow of the inlet stream with the ratio, H_2:N_2=3:1 at 340°C and 0.1MPa. The composition of the outlet stream was analysed instantaneously via the mass spectrometer (CIRRUS – MKS Spectra Products).

2.4 UV spectroscopy analysis to measure ammonium (NH_4^+)

The total amounts of synthesized ammonium were determined via a UV-Vis spectrophotometer (Thermo-Scientific, Evolution 220). All analyses were carried out by using a 640 nm wavelength.1 ml standard/sample-filled UV cuvettes were prepared for detection by following the procedures given in the literature [21,22]. Principally, 10 µl of the sample was diluted to 1 ml by adding 0.99 ml of water. 0.5 ml of alcoholic phenol, 0.5 ml of sodium nitroprusside, and 1 ml of oxidizing solution were added to all samples. The final reaction mixture was incubated at room temperature for 1 h, and the resulting coloured-sample was measured at 640 nm.

2.5 X-Ray Diffraction (XRD) Characterization Analysis

XRD patterns of the samples were collected to clarify their structure via STOE STADI P diffractometer using Mo radiation (λ Mo Kα1 = 0.70932 Å) and MYTHEN position-sensitive detector (DECTRIS) at the room temperature in reflection mode. All samples were prepared inside the glovebox and transferred within a sealed capillary (0.7mm) tube. Data were collected between 30 and 45 min per scan with two-theta range of 2° to 50°. The XRD patterns of Ca_2NH samples (before and after the reaction) were evaluated to identify their purity. First, the material identification database search program, File-4(PDF-4), helped to clarify the sample structure by taking data from the International Centre for Diffraction Data (ICDD). After all the peaks in the sample matched were matched with ICDD data, the amounts of the different phases were quantified via refinement using JANA2006.

2.5 Scanning Electron Microscope (SEM) Analysis

SEM analysis was conducted to investigate the microstructure of Ru nanoparticles on the catalysts' surface using JSM-IT800 scanning electron microscope with a JEOL energy dispersive X-ray spectrometer (EDS). Air-sensitive samples were prepared inside the glovebox and transferred in a closed transfer vessel to JSM-IT800.

3. RESULTS AND DISCUSSION

Calcium nitride-hydride (β-Ca_2NH) was successfully synthesized from CaH_2 and N_2 precursors and proved via XRD analysis sketched using OriginPro9 software, as seen in Figure-1. Here, the sample pattern was compared with the Inorganic Crystal Structure Database (ICSD) data [23].

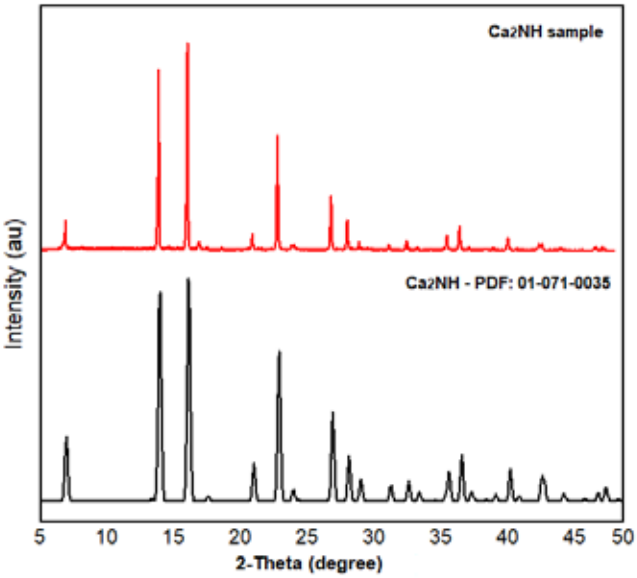

Fig. 1. XRD pattern of Ca_2NH sample and literature data [23]

The XRD pattern of the main component belonged to Ca_2NH. However, the sample also contained CaO as an impurity resulting from oxygen or air exposure in the synthesis procedure (3 %). The prepared of β-Ca_2NH was then used as a support material for adding the metal source to prepare a final form of catalyst involving 1, 2, 5, 10, and 18 % Ru. The heat treatment was applied, 1-10% and 18% Ru-loaded samples up to 240°C and 250 °C, respectively. Briefly, the samples' crystal structures were mainly in conformity with the Ca_2NH structure. When its Ru content exceeded 2%, it could be detectable via XRD. In addition to structure characterization of these catalyst, their surfaces were analysed to clarify distribution of Ru particles on Ca_2NH support materials. Ru particle distribution on the surface was more homogeneous and smaller at the 5°C/min heating rate as seen in Figure-2 (3kV, WD:3.9-4.00mm, 130k).

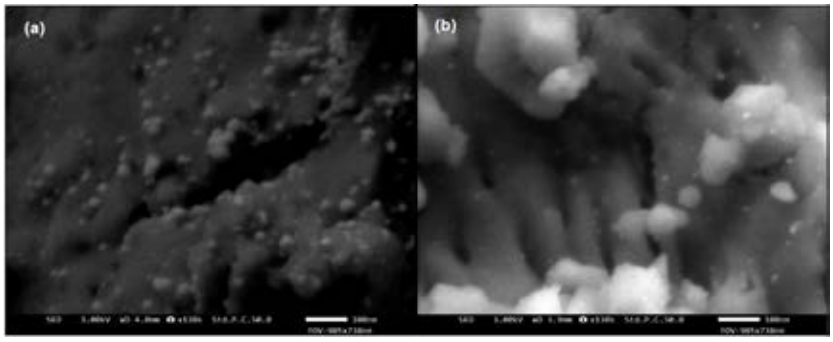

Fig. 2. SEM images of 5%Ru-Ca_2NH (a) 5°C/min (b) 10°C/min

The samples were tested for ammonia synthesis at the mentioned conditions in the experimental part. The synthesized ammonia was captured in a distilled water trap during the reactions, and then the phenol-hypochlorite method was applied to quantify the amount of ammonia present [21,22]. UV results indicated that 2 % and 5 % Ru-load Ca_2NH samples had similar performance. NH_3 production rate for 5% Ru-loaded Ca_2NH catalyst was calculated as 1.6 mmol/ g cat. h. This amount was smaller compared to the given amount in the literature (~3.5 mmol/g cat. h) for 2% Ru-loaded Ca_2NH [14]. This difference could be caused by using different types of reactors and applying higher flow rates. Despite this difference, there was no doubt that its performance was much better than that of other Ru-based catalysts producing up to 1 mmol/g cat. h reported in the literature [14]. Also, the long-term activity of 5%Ru-Ca_2NH was examined to illuminate its stability characteristics. The result of this test demonstrated that its performance decreased sharply at the 20th hours of the reaction. Consequently, its ammonia production rate was compared with Al_2O_3, Ca_2NH* and Ca_2NH +BaH_2 supported Ru catalysts.

4. CONCLUSIONS

In this study, Ca_2NH was synthesized successfully starting from CaH_2 and N_2 as following procedure given in the literature [19]. This recently promising support material was utilized to prepare Ru-based catalyst for mild condition NH_3 synthesis. The results indicated that ammonia synthesis rate, 1.6 mmol/ g cat. h., was pretty satisfactory at the beginning of the reaction when compared to literature [14]. According to UV results, ammonium synthesis rate row for these support materials was Ca_2NH > Al_2O_3 > Ca_2NH^* > Ca_2NH +BaH_2, but changed to Ca_2NH +BaH_2 > Ca_2NH^* > Ca_2NH > Al_2O_3 at the end of the monitored period. All these catalysts were deactivated in the long-term. However, the cumulative ammonium amount rose significantly when %5Ru-Ca_2NH +BaH_2 was used for the reaction. Hence, BaH_2 could be a solution to reach higher and more stable NH_3 production.

ACKNOWLEDGEMENT

This work was performed at the University St Andrews under the grant of TUBITAK 2219-International Postdoctoral Research. The authors are grateful for support of all JTSI group members.

REFERENCES

1 Thomas G and Parks G. 2006.Potential roles of ammonia in a hydrogen economy: a study of issues related to the use of ammonia for on-board vehicular hydrogen storage, US Department of Energy.
2 Aziz M, Wijayanta AT and Nandiyanto ABD. 2020. Ammonia as effective hydrogen storage: A review on production, storage and utilization, Energies, 13, 3062.
3 Erdemir D and Dincer I.2020 A perspective on the use of ammonia as a clean fuel: Challenges and solutions, International Journal of Energy Research, 1-8.
4 https://royalsociety.org/-/media/policy/projects/green-ammonia/green-ammonia-policy-briefing.pdf. Accessed in February 2024.
5 Liu H. 2014. Ammonia synthesis catalyst 100 years: Practice, enlightenment and challenge, Chinese Journal of Catalysis, 35, 1619-40.
6 Ishaq H and Crawford C. 2024. Review and evaluation of sustainable ammonia production, storage and utilization, Energy Conversion and Management, 300, 117869.
7 https://www.statista.com/statistics/1266378/global-ammonia-production/#:~:text=Ammonia%20production%20has%20remained%20fairly,some%20150%20million%20metric%20tons , Accessed in February 2024.
8 https://www.statista.com/statistics/1345797/forecast-global-ammonia-demand-by-application/. Accessed in February 2024.
9 Brown DE, Edmonds T, Joyner RW, McCarroll JJ, Tennison SR. 2014. The Genesis and Development of the Commercial BP Doubly Promoted Catalyst for Ammonia Synthesis, Catalysis Letters,144, 545-52.
10 Chen J, Chen Y, Wang H and Hu P. 2023. Correlation between the structural features and intrinsic activity trend of Fe surfaces for ammonia synthesis, Catalysis Science and Technology, 13, 5237-47.
11 Ma Z, Zhao S, Pei X, Xiong X and Hu B. 2017. New insights into the support morphology-dependent ammonia synthesis activity of Ru/CeO_2 catalysts, Catalysis Science and Technology, 7, 191-99.
12 Kobayashi K, Manaka Y and Nanba T. 2024. Effects of low crystallinity cerium oxide on ammonia synthesis activity for cerium oxide supported ruthenium catalyst, European Journal of Inorganic Chemistry, e2023006.
13 Rosowski F, Hornung A, Hinrichsen O, Herein D, Muhler M and Ertl G. 1997. Ruthenium catalysts for ammonia synthesis at high pressures: Preparation, characterization, and power-law kinetics, Applied Catalysis A: General, 151, 443-60.
14 Kitano M, Yamagata K and Hosono H. 2021. Why Ca_2NH works as an efcient and stable support of Ru catalyst in ammonia synthesis, Research on Chemical Intermediates, 47:235-48.
15 Kitano M, Inoue Y, Ishikawa H, Yamagata K, Nakao T, Tada T, Matsuishi S, Yokoyama T, Hara M and Hosono H. 2016. Essential role of hydride ion in ruthenium-based ammonia synthesis catalysts, Chemical Science, 7:4036-43.
16 Hattori M, Mori T, Arai T, Inoue Y, Sasase M., Tada T, Kitano M, Yokoyama T, Hara M, Hosono H. 2018. Enhanced catalytic ammonia synthesis with transformed BaO, ACS Catalysis, 8(12), 10978-84,
17 Irvine GJ and Irvine JTS. 2023. Ionic conductivity and disorder in calcium and barium nitrogen hydrogen phase, Royal Society of Chemistry, Faraday Discussions, 243, 38–54.
18 Irvine GJ, Smith RI, Jones MO and Irvine JTS. 2023., Order-disorder and ionic conductivity in calcium nitride-hydride, Nature Communications, 4:4389.
19 Irvine GJ. 2021. PhD Thesis: Studies of hydride ion conductors using combined spectroscopy techniques, School of Chemistry, University of St Andrews.
20 Kitano M, Inoue Y, Yamazaki Y, Hayashi F, Kanbara S, Matsuishi S, Yokoyama T, Kim S-W, Hara M and Hosono H.2012. Ammonia synthesis using a stable electride as an electron donor and reversible hydrogen store, Nature Chemistry, 4, 934-40.
21 Solorzano L. 1969. Determination of ammonia in natural waters by the phenol hypochlorite method, Limnololgy Oceanography,14(5), 799–801.
22 Cleaves HJ, Chalmers JH, Lazcano A, Miller SL and Bada JL. 2008. A reassessment of prebiotic organic synthesis in neutral planetary atmospheres, Prebiotic Chemistry, 38: 105-15.
23 Brice JF , Motte JP, Courtois A, Protas J , Aubry J. 1976. Etude structurale de Ca_2NH par diffraction des rayons x, diffraction des neutrons et resonance magnetique nucleaire du proton dans le solide, Journal of Solid State Chemistry, 17, 135-42.

GREEN HYDROGEN PRODUCTION IN ENERGY ISLANDS

[1*]Nermin Yabar, [1]Cem Haydaroğlu, [2]Alper Nabi Akpolat, [3]Heybet Kılıç
[1] Dicle University, Engineering Faculty, Department of Electrical and Electronics Engineering, Sur, Diyarbakır, 21280, Turkey
[2] Marmara University, Technology Faculty, Department of Electrical and Electronics Engineering, Maltepe, İstanbul, 34854, Türkiye
[3] Dicle University, Department of Electric Power and Energy System Department, Sur, Diyarbakır, 21280, Türkiye

*E-mail: 248051013@ogr.dicle.edu.tr

ABSTRACT
The rapid increase in global demand for clean energy has highlighted green hydrogen production as a sustainable solution. This study examines the role of energy islands (EAs) in hydrogen production based on renewable energy sources through Power-to-X (P2X) systems. Energy islands, which integrate distributed energy resources (DER) such as photovoltaic (PV) panels and wind turbines (WT), enable local and independent energy production, allowing for the efficient and stable production of green hydrogen. To enhance the effectiveness of these systems, the performance of power electronic converters (PEC) has been optimized using machine learning (ML)-based control techniques. Machine learning is utilized to ensure system stability and improve production efficiency. Furthermore, this study emphasizes that energy islands can play a significant role in the transition to sustainable energy. The paper comprehensively discusses the components of energy islands, the technical and economic challenges faced, strategies that could contribute to the energy transition, and perspectives for future development.

Keywords: Energy islands, Green hydrogen production, Power electronic converters, Machine learning, Power-to-X

1. INTRODUCTION

Traditional fossil fuels continue to dominate global energy consumption. The decreasing lifespan of currently used fossil fuels, along with their negative impacts on the environment and human health, is leading countries to turn towards renewable energy sources. Renewable energy sources such as solar, geothermal, wind, biomass, and wave energy have become preferred alternative energy sources in recent times [1]. However, the production levels of renewable sources like wind and solar fluctuate instantaneously depending on meteorological and environmental conditions [2]. This situation increases the need for innovative solutions and technologies that support the integration of renewable energy sources, enabling energy systems to operate more efficiently and continuously. Turkey is rapidly increasing its dependence on solar and wind energy in line with ambitious renewable energy targets. The global energy transition from fossil fuels to zero-carbon emission clean technologies is progressing rapidly with a sense of urgency [3]. Green hydrogen production (GHP) from renewable sources is emerging as a viable solution for energy storage and carbon reduction, particularly in energy islands (EAs). However, ensuring the stability and reliability of hydrogen production in these systems requires advanced control methodologies such as ML-based optimization. Machine learning is highly capable in tasks such as data classification, regression, and other related tasks. Artificial intelligence and machine learning can efficiently manage energy storage in the energy grid by shaving peak points or using stored energy when these resources are unavailable [4].

2. RENEWABLE ENERGY SOURCES FOR GREEN HYDROGEN PRODUCTION

Green hydrogen production emerges as an important option in the search for solutions to the global clean energy demand. Green hydrogen is produced through electrolysis using renewable energy sources such as solar and wind energy.

In this study, the role of energy islands (EAs) in hydrogen production from renewable energy sources (RES) using Power-to-X (P2X) systems is discussed. As seen in Figure 1, energy islands equipped with distributed energy sources such as photovoltaic (PV) panels and wind turbines (WT) ensure a stable and efficient production process, improving the system's efficiency and reliability. The proper management of power electronic converters (PEC) is crucial for efficiently distributing renewable energy to the load side. In this process, artificial intelligence (AI) and machine learning (ML)-based control techniques offer solutions that improve system performance and predict failures in advance. ML algorithms are increasingly preferred for solving control problems in distributed generation systems. Additionally, the management of PECs in energy islands has been optimized with ML-based methodologies. The study discusses strategies that could contribute to Turkey's renewable energy goals and presents solutions that enable high penetration of solar and wind energy. The aim of the study is to demonstrate how ML-based methods contribute to the creation of reliable and efficient energy islands.

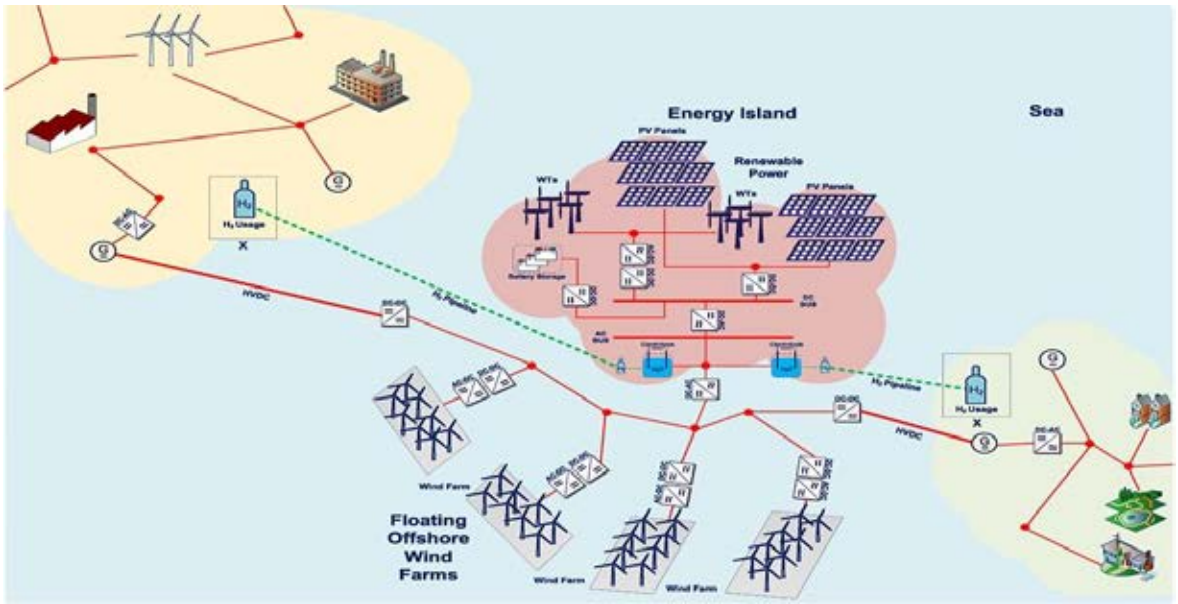

Fig. 1. The P2X systems can also be located onshore or offshore. For an EI with large-scale offshore WTs and PVs, a P2X station on the island, and a power connection to the shore, this connection can be made both electrically with high voltage DC (HVDC) and with a gas (hydrogen-H2) pipeline. [5].

3. CASE STUDY

Green hydrogen production is a process that involves renewable energy sources and is free from carbon emissions. In this process, hydrogen is produced using electrolysers powered by electricity obtained from sources such as solar, wind, biomass, and hydroelectric energy. Electrolysers work by splitting water into hydrogen and oxygen gases using electricity. The efficiency of solar energy varies depending on environmental factors, so it is optimized using energy storage and Maximum Power Point Tracking (MPPT) techniques. PEM electrolyzers play a significant role in hydrogen production and provide advantages in terms of efficiency. The potential for hydrogen production from solar energy can be examined according to local irradiation and temperature conditions. Offshore wind energy holds great potential among renewable energy sources, but technical analyses are required for successful projects. Small-scale wind turbines can operate efficiently even at low wind speeds. Microgrids and Distributed Energy Resources (DERs) play an important role in energy transmission. In these systems, Power Electronic Converters (PECs) are critical for ensuring energy transfer and efficiency. Additionally, the integration of energy storage systems enables the efficient operation of energy systems. Energy Island (EI) structures aim to reduce fossil fuel dependency and decrease carbon dioxide emissions by establishing local energy production and sustainable energy systems. Artificial intelligence and deep learning techniques can be applied in areas such as energy management and load forecasting, ensuring the efficient operation of systems. The integration of these technologies can make energy transitions more efficient.

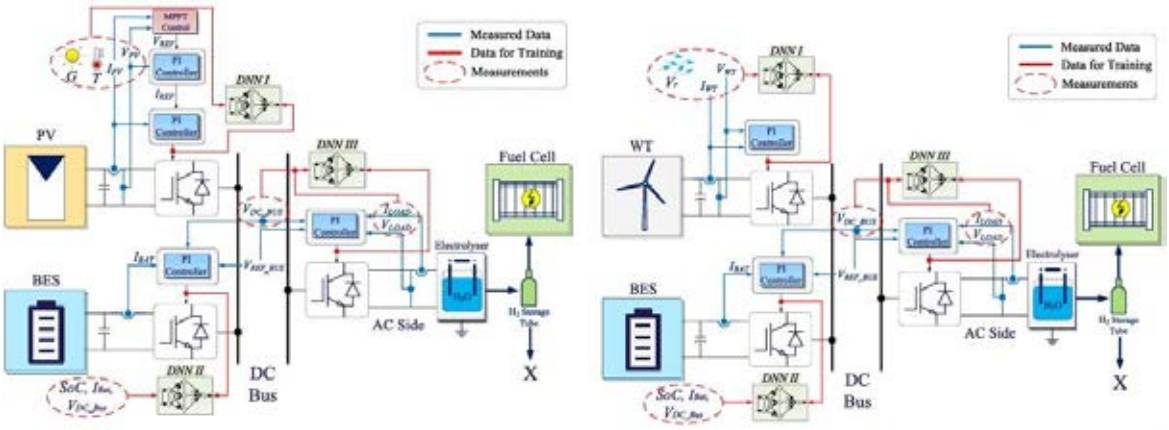

Fig. 2. Operational overview of the structure and control scheme of a photovoltaic (PV) and wind turbine (WT)-based green hydrogen production (GHP) system [6].

This study was simulated in the MATLAB/Simulink environment. The general system model is shown in Figure 2. The DC bus voltage was maintained at 48V and remained stable between 50-55V despite variable input-output conditions. Voltage fluctuations in the DC bus were reduced by 3.47%. The system exhibited a response time that was 6.6 ms faster compared to traditional methods. Hydrogen production efficiency, determined by Faraday efficiency (ηF), ranged from 67% to 82%. The operating temperature for the PEM electrolyzer was set between 50 - 80°C, the pressure was kept below 50 bar, and the lifetime was determined to be between 60,000 and 90,000 hours. High-accuracy predictions with a 39.6% error (MSE = 0.0396) were made in the system using deep learning (DNN)-based control strategies. The training time was 89.69 seconds, and the model was optimized with the best parameters. The proposed design demonstrated satisfactory results by reducing voltage oscillation, providing a faster rise rate, and delivering an early response.

4. CONCLUSIONS

Green hydrogen production in energy islands represents a transformative step towards achieving global renewable energy targets. This study proposes the use of machine learning (ML)-based techniques to enhance the continuity, stability, and reliability of energy islands (EAs). Power electronic converters (PECs) play a critical role as the backbone of renewable energy transfer. In this context, it is crucial to maintain the inputs and outputs of the converters as stable as possible. This study presents modern engineering solutions for the integration and optimization of renewable energy systems, addressing sustainable energy production, storage, and utilization.

REFERENCES

[1] Ürün, E., & Soyu, E. (2016). Türkiye' Nin Enerji Üretiminde Yenilenebilir Enerji Kaynaklari Üzerine Bir Değerlendirme. Dumlupınar Üniversitesi Sosyal Bilimler Dergisi31-45.

[2] M.-H. Khooban, T. Niknam, M. Shasadeghi, T. Dragicevic, and F. Blaabjerg, "Load Frequency Control in Microgrids Based on a Stochastic Noninteger Controller," IEEE Transactions on Sustainable Energy, vol. 9, no. 2, pp. 853–861, Apr. 2018.

[3] SHURA Energy Transition Center. (2021). *Turkey's green hydrogen production and export potential*. SHURA. https://shura.org.tr/wp-content/uploads/2021/12/SHURA-2021-12-Turkiyenin-Yesil-Hidrojen-Uretim-ve-Ihracat-Potansiyelinin.pdf

[4] Flores Sanchez, S., Flores Segovia, M. A., & Rodríguez López, L. C. (2020). Estimating a national energy security index in Mexico: A quantitative approach and public policy implications. *Energy Reports, 6*, 1067-1077. https://doi.org/10.1016/j.egyr.2020.07.017

[5] Blaabjerg, F., Yang, Y., Kim, K. A., & Rodriguez, J. (2023). Power Electronics Technology for Large-Scale Renewable Energy Generation. Proceedings of the IEEE, 111(4), 335 - 355. Article 10070105. https://doi.org/10.1109/JPROC.2023.3253165

[6] Akpolat, A. N., (2025). Enhancing operational reliability for high penetration of green hydrogen production in energy islands: A power-to-X case study. International Journal of Hydrogen Energy .

EFFECTS OF H_2 ENRICHMENT AND GRAVITY ON SOOT FORMATION IN N-DODECANE LAMINAR DIFFUSION FLAMES: A CFD STUDY

Ayse Korucu
Izmir Institute of Technology, School of Engineering, Mechanical Engineering, Izmir Institute of Technology, Urla, 35433, Turkiye
Corresponding author e-mail: aysekorucu@iyte.edu.tr

ABSTRACT
This study investigates the effects of H_2 enrichment and gravitional forces on soot formation in laminar n-dodecane ($C_{12}H_{26}$) diffusion flames using Computational Fluid Dynamics (CFD) simulations in ANSYS Fluent 24 R1. A stretched quadrilateral mesh with 10,500 elements and for an axisymmetric domain is employed to reduce computational cost. The SIMPLEC solver is implemented with a pseudo-time Courant number of 0.001 for transient solution stability, and radiative heat transfer is modeled using the P1 radiation model. Combustion is simulated with a skeletal $C_{12}H_{26}$ mechanism (54 species, 269 reactions) validated against multiple combustion configurations. Soot formation is predicted using the Method of Moments soot model, with acetylene (C_2H_2) as the primary precursor. Four cases were analyzed, varying H_2concentrations (0%, 10%, and 50%) and gravity conditions. The results show that H_2 enrichment significantly reduces the soot volume fraction (fvmax) by approximately 50%. For instance, the 10% H_2case exhibits a soot volume fraction of about 80 ppm, compared to the 169 ppm in the pure $C_{12}H_{26}$ case. Gravity's effect on soot formation is minimal, as the soot volume fraction for the 10% H_2 cases (both gravity off and on) remains nearly identical. These findings suggest that while H_2 enrichment is effective in reducing soot formation, gravity has a minor role in altering soot levels in the tested cases. The results provide valuable insights for optimizing combustion strategies to reduce soot emissions in energy and aerospace applications.
Keywords: N-dodecane, H_2, Soot, Laminar Diffusion Flames

1. INTRODUCTION
Hydrocarbon combustion in engines and gas turbines is a major energy source but contributes significantly to environmental pollution, particularly through soot and polycyclic aromatic hydrocarbons (PAHs). Soot formation occurs via the nucleation and growth of PAHs, leading to particulate emissions that pose environmental and health concerns. Weakening soot emissions is essential as global energy demand increases. One approach is H_2 enrichment, which, as a zero-carbon fuel, modifies the chemical pathways leading to PAH and soot formation [1].
Recent studies have demonstrated that H_2enrichment reduces soot precursor formation. Akram et al. [2] found that H_2 addition suppresses key soot precursors such as acetylene (C_2H_2) and benzene, leading to a lower soot volume fraction. Wang et al. [3] highlighted how fuel composition affects soot and aromatic species distributions, emphasizing the role of non-premixed diffusion flames in soot formation. Additionally, Das et al. [4] showed that fuel molecular structure, particularly aromatic content, influences soot production, reinforcing H_2's role in reducing soot. Beyond its effect on soot precursors, $C_{12}H_{26}$ decomposition plays a crucial role in flame behavior. Smolke et al. [5] found that $C_{12}H_{26}$ decomposes into smaller hydrocarbons such as ethylene (C_2H_4) and H_2, which affect flame propagation and extinction. Furthermore, Qiu et al. [6] reported that H_2 blending reduces soot formation by modifying reaction pathways, increasing OH radical concentrations, and enhancing oxidation mechanisms.
Building on these findings, this study investigates the impact of H_2 enrichment and gravity on soot formation in $C_{12}H_{26}$ laminar diffusion flames using CFD simulations in ANSYS Fluent. The results provide insights into how H_2 enrichment and gravity influence soot dynamics, advancing the development of cleaner combustion technologies.

2. MATERIALS AND METHODS
The data presented in Table 1 summarizes four cases with varying compositions of H_2 and $C_{12}H_{26}$, gravity conditions, temperature (T), inner radius (r_i), outer radius (r_o), and flow velocity (v_f). Cases 1 and 2 both have 10% H_2 and 90% $C_{12}H_{26}$, but Case 1 has gravity turned OFF, while Case 2 has gravity ON. Cases 3 and 4 explore different fuel volumetric compositions, with Case 3 volumetricly having a 50% H_2 and 50% $C_{12}H_{26}$ mixture, and Case 4 using 100% $C_{12}H_{26}$. All cases are conducted at 700 K, with identical inner and outer radii (5 mm and 80 mm, respectively) and a flow velocity of 0.1 m/s. This study employs CFD simulations in ANSYS Fluent 24 R1 [7] to examine the effects of H_2 enrichment and gravity on soot formation in $C_{12}H_{26}$ laminar diffusion flames.
Fig. 1 (a) illustrates a stretched quadrilateral mesh with 10,500 elements ensures the computational efficiency in the simulations. The computational domain used for the axisymmetric simulations, representing half of the full geometry. The fuel jet (i.e. fuel inlet) has a radius of 5 mm, the air flows (i.e. air inlet) in a coflow arrangement through an annulus with a radius of 80 mm, with the velocity set to 0.1 m/s (Fig. 1(b)) while height of the domain is 150 mm. The SIMPLEC solver is used for numerical stability, with a pseudo-time Courant number of 0.001 for proper transient solution control. Additionally, the P1 radiation model is implemented to account for radiative heat transfer effects, ensuring a comprehensive analysis of the combustion dynamics under varying conditions.
Combustion is modeled using a skeletal chemical mechanism with 54 species and 269 reactions, developed to predict

$C_{12}H_{26}$ pyrolysis and oxidation under both high-temperature (high-T) and low-temperature (low-T) conditions [8].

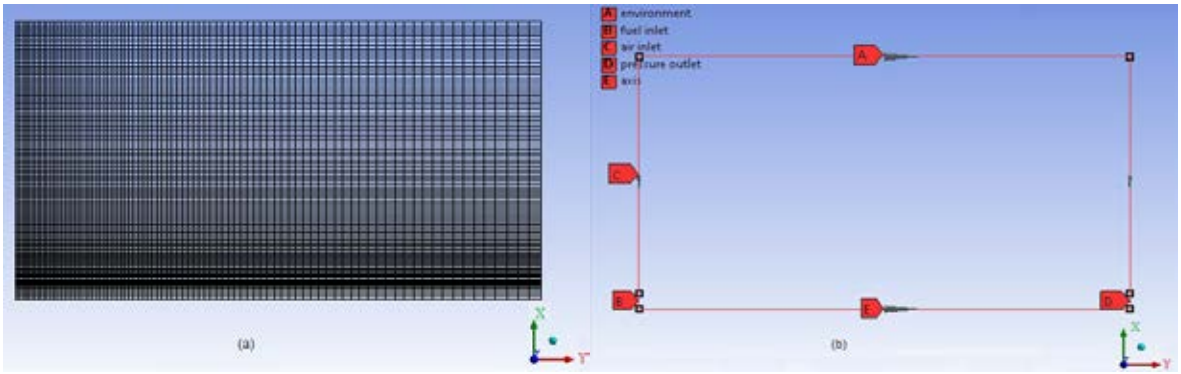

Fig. 1. Computational Domain (a) Stretched Quadrilateral Mesh, (b) Boundary Types Set

This mechanism was derived from a semi-detailed mechanism developed at the University of Southern California (USC) and reduced using reaction flow analysis (RFA) and isomer lumping [8]. The mechanism was validated across auto-ignition, perfectly stirred reactors (PSR), flow reactors, and laminar premixed flames and was previously used to model turbulent spray flames under compression ignition engine conditions [8]. Soot formation is modeled using the method of moments soot model, with acetylene (C_2H_2) as the primary soot precursor, considering soot agglomeration and soot-radiation interactions.

Table 1. Summary of the cases

Case	H_2	$C_{12}H_{26}$	Gravity	T (K)	r_i (mm)	r_o (mm)	v_f (m/s)
1	10	90%	OFF	700	5	80	0.1
2	10%	90%	ON	700	5	80	0.1
3	50%	50%	ON	700	5	80	0.1
4	0%	100%	ON	700	5	80	0.1

3. RESULTS AND DISCUSSION

Table 2 summarizes the peak values of key combustion parameters for four cases with different H_2 contents and gravity conditions. A nuanced analysis reveals several trends and interactions between H_2 enrichment, gravity, and soot formation.

Table 2. Peak values for the considered cases

	Case 1	Case 2	Case 3	Case 4
T_{max} (K)	1941.5	1941.3	1949.8	1947.4
f_{vmax} (ppm)	80.1	80.0	81.7	169.0
x_{C2H2}	0.0092	0.0092	0.0092	0.0103
x_{CO}	0.0466	0.0464	0.0438	0.0483
x_{CO2}	0.1339	0.1362	0.1316	0.1352
x_{OH}	0.0031	0.0031	0.0032	0.0030

3.1 Soot Formation Trends with Hydrogen Addition

The simulations show a significant reduction in soot volume fraction (fv) when hydrogen is added to n-dodecane, particularly between the pure hydrocarbon case (Case 4) and the hydrogen-enriched cases (Cases 1–3). The maximum soot volume fraction decreases from 169 ppm in Case 4 (0% H_2) to approximately 80 ppm in the 10% H_2 cases (Cases 1 and 2), corresponding to a reduction of over 50%. This sharp decrease suggests that even low levels of hydrogen significantly alter the flame structure and suppress soot formation. However, increasing hydrogen to 50% (Case 3) does not lead to further soot reduction. Instead, fvmax slightly increases to 81.7 ppm.

3.2 Temperature and Transport Effects

Interestingly, the peak flame temperatures remain relatively constant across all cases, ranging narrowly from 1941 K to

1950 K. This suggests that hydrogen enrichment, despite increasing reactivity and reducing soot formation, does not significantly raise flame temperature. A key reason is the low mass fraction of hydrogen, which corresponds to only about 1.16% by mass at 50% hydrogen volume (approximately 0.13% by mass for 10% hydrogen). Hydrogen's high diffusivity and low molecular weight allow it to rapidly move toward hot regions via thermal diffusion, altering flame shape and combustion intensity. This results in a more spatially distributed heat release, rather than an overall temperature increase. Additionally, since hydrogen-rich flames tend to produce less soot, radiative heat losses are reduced, contributing to the stabilization of the temperature across all cases.

3.3 Gravity's Limited Influence

When comparing Case 1 (gravity off) and Case 2 (gravity on), both with 10% H_2, the fvmax values are nearly identical (80.1 vs. 80.0 ppm), and Tmax is unchanged. This suggests that, under these laminar and symmetric conditions, gravity has a minimal effect on soot suppression. The weak buoyancy-driven flows in these small, low-speed diffusion flames do not significantly alter the mixing or oxidation processes of soot. In Case 3 (50% H_2 with gravity), a slight increase in soot is observed compared to the 10% H_2 cases, indicating that while gravity enhances upward convection of heat and reactive species, it is not enough to counteract the broader flame structure and intensified burning induced by the high hydrogen content.

3.4 Speculations on Species Stability and Soot Reduction

Despite significant changes in soot volume fraction (f_v), the volume fractions of key species such as C_2H_2, OH, CO, and CO_2 remain relatively stable across all cases, including the 10% H_2 and 50% H_2 cases. C_2H_2, a known soot precursor, and OH, a primary oxidizer, exhibit minimal fluctuations even with hydrogen addition. This stability suggests that hydrogen enrichment does not drastically alter the reaction pathways for soot formation and oxidation. The rate constants for key reactions, such as $C_2H_2 + O \rightleftharpoons CH_2 + CO$ and $CO + OH \rightleftharpoons CO_2 + H$, are temperature-dependent, and with the peak flame temperature remaining stable across cases, these reactions do not experience significant shifts in equilibrium. As a result, the concentrations of C_2H_2, OH, CO, and CO_2 remain relatively constant despite the changes in soot formation.

The slight reduction in soot volume fraction with hydrogen addition is largely attributed to enhanced oxidation due to the presence of hydrogen, which improves oxygen availability. However, hydrogen's primary role seems to be in modifying the flame's diffusivity and structure rather than directly affecting the fundamental fuel chemistry or precursor species. As hydrogen is introduced into the flame, it shifts the flame geometry, potentially allowing soot particles to persist longer in hotter regions, which might explain the minimal change in the intermediate species levels. At higher hydrogen concentrations, the dilution effect on the carbon content suppresses soot formation, but the stability of C_2H_2 and OH levels suggests that hydrogen's effect is more on soot oxidation efficiency rather than altering the core reaction dynamics of soot precursors.

4. CONCLUSIONS

The addition of H_2 to $C_{12}H_{26}$ flames results in a significant reduction in soot volume fraction, particularly at low to moderate hydrogen concentrations (10% H_2), where a sharp decrease from 169 ppm to around 80 ppm is observed. However, when hydrogen is increased to 50%, the soot volume fraction stabilizes at approximately 81.7 ppm. This non-linear trend can be attributed to changes in flame structure, where the enhanced thermal diffusivity of hydrogen shifts the combustion zone, increasing the residence time of soot particles in hotter regions, partially counteracting the soot reduction benefits.

Despite the reduction in soot volume fraction, the volume fractions of key species such as C_2H_2, OH, CO, and CO_2 remain largely unchanged across all cases, even with varying hydrogen concentrations. This suggests that hydrogen's role is more focused on altering the flame's diffusivity rather than directly influencing the chemical pathways for soot formation and oxidation. The stable temperature profile across all cases (ranging from 1941 K to 1950 K) further supports this, as temperature-dependent reaction dynamics for species like C_2H_2 and OH are not significantly altered. Overall, H_2 enrichment effectively suppresses soot at moderate concentrations, with higher hydrogen levels introducing competing effects that may offset the benefits of soot reduction, primarily due to changes in flame morphology and soot residence time in hot regions.

Future studies could explore the effects of varying flame velocities on soot formation and species concentration in H_2-enriched $C_{12}H_{26}$ flames. Flame velocity significantly influences flame structure, mixing, and the residence time of soot particles, which could provide insights into the interplay between velocity, thermal diffusion, and soot suppression at different hydrogen concentrations. Additionally, examining a broader range of volumetric hydrogen enrichment (beyond 50%) would help to further understand the non-linear behavior observed at higher hydrogen concentrations, potentially revealing new dynamics related to soot formation, flame shape, and thermal transport.

Investigating the combined effects of different velocities and hydrogen enrichment levels could also enhance the understanding of H_2's role in modifying flame characteristics under realistic combustion conditions. This would contribute to more robust models for soot formation in practical applications such as combstion engines or industrial burners, where variable operational conditions are common.

REFERENCES

1. Tang, C., Zhang, Y., & Huang, Z. (2014). Progress in combustion investigations of hydrogen-enriched hydrocarbons. Renewable and Sustainable Energy Reviews, 30, 195–216.
2. Akram, M. Z., Ma, F., & Akram, M. W. (2022). A numerical approach to elucidate the combustion and emission characteristics of n-dodecane under hydrogen enrichment. Energy Conversion and Management, 255, 115294.
3. Wang, Y., Makwana, A., Iyer, S., Linevsky, M., Santoro, R. J., Litzinger, T. A., & O'Connor, J. (2018). Effect of fuel composition on soot and aromatic species distributions in laminar, co-flow flames. Part 1. Non-premixed fuel. Combustion and Flame, 189, 443–455.
4. Das, D. D., McEnally, C. S., Kwan, T. A., Zimmerman, J. B., Cannella, W. J., Mueller, C. J., & Pfefferle, L. D. (2017). Sooting tendencies of diesel fuels, jet fuels, and their surrogates in diffusion flames. Fuel, 197, 445–458.
5. Smolke, J., Carbone, F., Egolfopoulos, F. N., & Wang, H. (2018). Effect of n-dodecane decomposition on its fundamental flame properties. Combustion and Flame, 190, 65–73.
6. Qiu, L., Hua, Y., Zhuang, Y., Wei, J., Qian, Y., & Cheng, X. (2020). Numerical investigation into the decoupling effects of hydrogen blending on flame structure and soot formation in a laminar ethylene diffusion flame. International Journal of Hydrogen Energy, 45, 15672-15682.
7.ANSYS fluent release 24.0, theory guide. 2024. https://www.ansys.com/products/fluids/ansys-fluent
8.Yao, T., Pei, Y., Zhong, B.-J., Som, S., Lu, T., & Luo, K. H. (2017). A compact skeletal mechanism for n-dodecane with optimized semi-global low-temperature chemistry for diesel engine simulations. Fuel, 191, 339–349.

DEVELOPMENT OF $NiCo(OH)_2$ BASED OER CATALYSIS FOR ALKALINE WATER ELECTROLYSIS

[1*]Yakubu Sawadogo ADAM,[1]Goncagül AKSARAY, [1]Ender FAKI, [2,3]Murat FARSAK [1*]Gülfeza KARDAŞ
[1]Çukurova University, Faculty of Arts and Sciences, Chemistry Department, Adana, 01330, Türkiye
[2]Osmaniye Korkut Ata University, Department of Battery Systems and Hydrogen Technologies, Osmaniye, Türkiye
[3]Osmaniye Korkut Ata University, Department of Hybrid and Electric Vehicles Technology, Osmaniye, Türkiye

* E-mail: yakubuadam24@yahoo.com, gulfeza@cu.edu.tr, gulfeza@gmail.com

ABSTRACT
This study aim at preparing a highly efficient binary hydroxide electrocatalyst ($NiCo(OH)_2$) with Nickel Carbonyl on stainless steel (304) as an anode for alkaline water electrolysers. In order to increase the efficiency, Iridium (Ir) and Rutheniun (Ru) were doped as well as Silver (Ag) precipitation. Electrochemical techniques, such as Electrochemical Impedance Spectroscopy (EIS) and Linear Sweep Voltammetry (LSV) were applied in 1 M KOH while Scanning Electron Microscopy (SEM) and Energy Dispersive X-ray spectroscopy (EDX) analysis were used for characterisation and surface morphology. Considering the charge transfer resistances of the electrodes determined from the EIS results obtained at 0.8 V, the OER efficiency of ruthenium doping was over 90%. Considering the increase in current density, it was determined that silver precipitation upon ruthenium and iridium doping increased the OER efficiency.

Keywords: Electrocatalysts, OER, water splitting, binary hydroxide

1. INTRODUCTION
Highly effeicient, environmentally friednly and sustainable energy sources have been the current interest in research in order to counter fort he increased in demand of energy alternatively. Hydrogen energy received great attention in this perspective. From research water electrolysis tend to be the best form for hydrogen production. In the process of producing hydrogen on one side (cathode) tends to come with oxygen on the other side (anode) and thats fort he importance of water electrolysers. Water electrolysis consists of two half-cell reactions, the formation of H_2 (HER) at the cathode and O_2 (OER) at the anode. While the rapid production of the purest hydrogen is achieved through the electrolysis of water, the release of oxygen also causes the reaction, which is theoretically expected at 1.23V, to appear at overpotentials and not occur at this voltage [1,2]. Electrocatalysis for the oxygen evolution reaction (OER) plays an important role in this sense. It is known that metal oxide materials form the basis of the OER mechanism, and non-oxide materials exhibit very promising performance for general water splitting. Synthesizing electrocatalysis for OER is at least as important as the electrocatalysis synthesized for the cathode in obtaining hydrogen by electrolysis of water [3]. Research has attempted to design low-cost and effective catalysts. Nitride, sulfur, carbide and phosphide compounds of transition metals are widely used in the preparation of catalysts for HER in acid or alkaline solution [4-8].
The OER performance of the catalyst produced by ruthenium and iridium doping then silver precipitation of a binary hydroxide produced by hydroxidation and direct immersion was assessed in this work. Energy dispersive X-ray spectroscopy (EDX) analysis and scanning electron microscopy (SEM) were used to accomplish the characterisation. In a 1 M KOH solution, electrochemical behavior was investigated using linear sweep voltammetry (LSV) and electrochemical impedance spectroscopy (EIS).

2. EXPERIMENTAL
Synthesis of Catalysts; $NiCo(OH)_2$ coated on nickel plated steel by direct dipping method. Coating was carried out by dipping and hydroxidation. For this, 1.0 M $NiNO_3$ solution, 30% KOH solution and 1.0 M $CoNO_3$ solutions were used. The electrode was immersed first in $NiNO_3$ solution, then in KOH solution, then in $CoNO_3$ solution and again in KOH solution. In order to obtain oxyhydroxide forms, a potential of 0.8 V was applied to the electrode in 1.0 M KOH solution for 60 minutes using the three-electrode technique. In this process, 2 cm^2 Pt mesh was used as the counter electrode and Ag/AgCl (3 M KCl) was used as the reference electrode. Then, a solution was prepared with 0.005 M $IrCl_3.H_2O$ boric acid to pH 3.5, and iridium was doped on the $NiCo(OH)_2$ structure by applying a -1.5 V potential for 30 seconds using the chronoamperometry technique [9]. Silver precipitation was performed on the iridium-doped electrode surface by dissolving 1.0 M $AgNO_3$ solution in 0.1 M HNO_3 acid and applying it for 30 s at a current density of 1 mA cm^{-2}. Additionally, 0.1 M $RuCl_3.H_2O$ solution was prepared to dope ruthenium onto the $NiCo(OH)_2$ double hydroxide structure. For chemical doping in the prepared ruthenium solution, the $NiCo(OH)_2$ double hydroxide electrode was kept in the ruthenium solution for 30 minutes, then ruthenium doping was done in 10 cycles using the cyclic voltammetry technique in the range of -0.2 - 1 V [10]. Silver precipitation on ruthenium was carried out using the same method as on iridium.
All electrochemical experiments were performed using a Gamry Interface 1000 potentiostat/galvanostat. The Ag/AgCl (3M KCl) electrode was utilized as the reference electrode, and a 2 cm^2 Pt sheet was employed as the counter electrode. Using a Gamry Interface 1000 electrochemical workstation at room temperature in an open atmosphere, the electrochemical experiments were performed in a 1 M KOH solution. Electrochemical Impedance Spectroscopy (EIS)

measurements were taken with an amplitude of 5 mV and a frequency range of 10^5 -0.01 Hz at 0.8 V. To determine the OER efficiency of the electrodes, current potential curves in the anodic direction were obtained in 1.0 M KOH solution at a scan rate of 1 mV s^{-1} in the range of 1.0 V with the open circuit potential.

3. RESULTS AND DISCUSSION

In Fig. 1, the SEM images of $NiCo(OH)_2Ir$ doped (a), $NiCo(OH)_2IrAg$ precipitation (b), $NiCo(OH)_2Ru$ doped (c) and $NiCo(OH)_2RuAg$ precipitation (d) electrodes are presented to demonstrate their surface characteristics. These SEM images provide valuable insights into the surface characteristics of these electrodes.

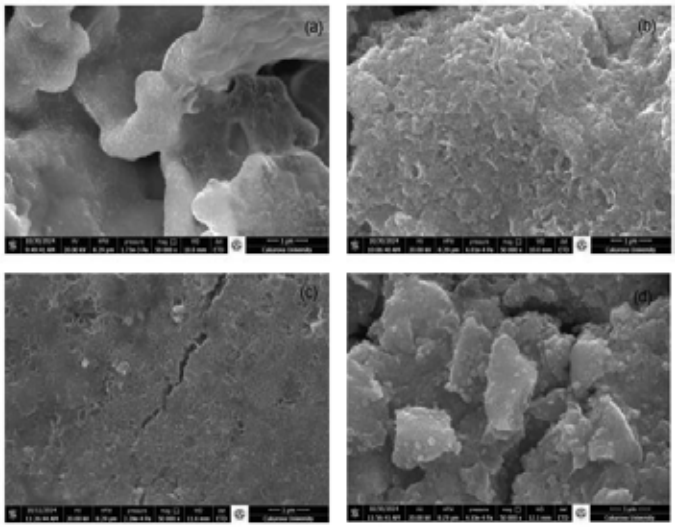

Fig. 1. SEM images (X50000) of $NiCo(OH)_2Ir$ doped (a), $NiCo(OH)_2IrAg$ precipitation (b), $NiCo(OH)_2Ru$ doped (c) and $NiCo(OH)_2RuAg$ precipitation (d) electrodes

$NiCo(OH)_2Ir$ doped electrode (Fig.1.a), seems to have a uniform distribution of nanoscale structures and the presences of well-defined agglomerates could mean favourable sites for OER, possibility of enhanced conductivity and catalytic activity could also be due to dense coating. In Fig.1.b, $NiCo(OH)_2IrAg$ precipitation electrode, addition of Ag may influence the surface roughness and particle distribution. A more heterogeneous morphology compared to the Ir doped electrode, which could enhance catalytic efficiency by providing additional active sites. Incorporation of Ru resulted in a relatively smoother morphology with densely packed features and better electrocatalytic performance facilitated by electron transfer could have been improved by the uniform dispersion of Ru in Fig.1.c. Ru and Ag combinations introduced complex surface structure with fine and coarse agglomerates which might have lead to enhanced surface area and catalytic efficiency through synergistic effect as seen in Fig.1.d, $NiCo(OH)_2RuAg$ coated electrode. Overall, the SEM analysis provides insights into the surface texture, particle distribution and potential active site density, all of which are crucial for optimizing OER performance.

Table 1. EDX analysis of the $NiCo(OH)_2Ir$, $NiCo(OH)_2IrAg$, $NiCo(OH)_2Ru$ and $NiCo(OH)_2RuAg$ electrodes

Elements	$NiCo(OH)_2Ir$ electrode (%wt)	$NiCo(OH)_2IrAg$ electrode (%wt)	$NiCo(OH)_2Ru$ electrode (%wt)	$NiCo(OH)_2RuAg$ electrode (%wt)
C	2.68	1.62	1.91	2.26
O	9.54	21	25.86	17.44
Ag	-	12.07	-	11.64
K	1.17	2.60	3.60	1.72
Co	1.02	24.49	45.16	0.5
Ni	83.78	37.51	20.33	59.05
Ir	0.58	0.71	-	-
Ru	-	-	0.45	0.13
Fe	1.23	-	2.66	7.37

EDX analysis results show the presence of iridium, ruthenium doped and silver precipitation on the nickel cobalt hydroxide surface (Table 1).

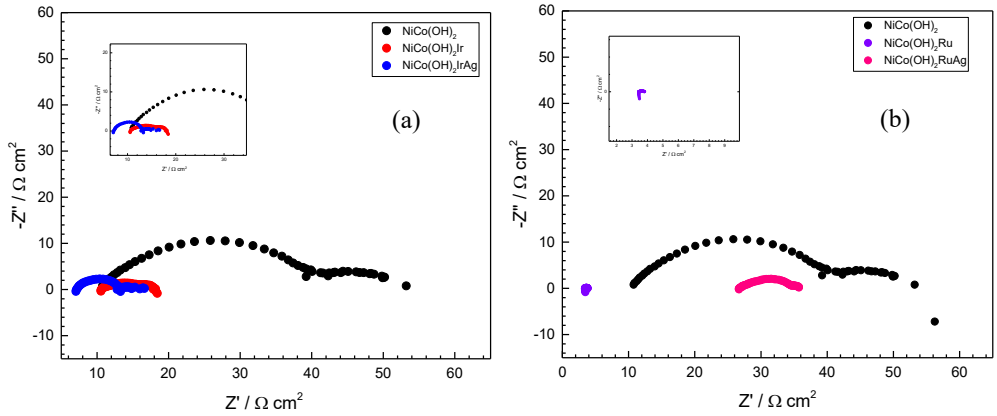

Fig. 2. Nyquist diagrams of $NiCo(OH)_2$, $NiCo(OH)_2Ir$ and $NiCo(OH)_2IrAg$ (a), $NiCo(OH)_2$, $NiCo(OH)_2Ru$ and $NiCo(OH)_2RuAg$ (b)

Nyquist curves of $NiCo(OH)_2$, $NiCo(OH)_2Ir$ and $NiCo(OH)_2IrAg$ electrodes obtained at 0.8 V are given in Fig.2(a). It is seen from the Nyquist curves that the charge transfer resistances (Rct) decreased significantly as a result of iridium doping and silver precipitation. The charge transfer resistance of the electrode was determined as ~43.48 Ω cm^2, ~10.32 Ω cm^2, ~9.06 Ω cm^2 for $NiCo(OH)_2$, $NiCo(OH)_2Ir$ and $NiCo(OH)_2IrAg$ electrodes respectively. A lower charge transfer resistance, which is a good factor for OER efficiency study was observed for $NiCo(OH)_2IrAg$ electrode compared to the others. This may be attributed to the presence of the Iridium and Silver. Nyquist curves of $NiCo(OH)_2$, $NiCo(OH)_2Ru$ and $NiCo(OH)_2RuAg$ electrodes obtained at 0.8V are given in Fig.2(b). It can be interpretated from Figure 2.b. that doping ruthenium significantly reduces the charge transfer resistance. The charge transfer resistance of the $NiCo(OH)_2$ electrode was determined as ~43.48 Ω cm^2, ~0.69 Ω cm^2 for $NiCo(OH)_2Ru$ and that of $NiCo(OH)_2RuAg$ as ~10.09 Ω cm^2. The charge transfer resistance of $NiCo(OH)_2Ru$ electrode was lower compared to the other electrodes. Therefore, it was determined that the electrode formed as a result of ruthenium doping on the binary hydroxide structure significantly increased the OER efficiency.
The charge transfer resistances of the prepared electrodes determined from the Nyquist curves obtained at 0.8 V potential are given in Table 2. Percentage efficiencies from load transfer resistors were calculated according to Eq. (1).

$$\%\eta = \frac{R_{ct,double\ hydroxide} - R_{ct,metal\ coated}}{R_{ct,double\ hydroxide}} x100 \quad (1)$$

Table 2. Charge transfer resistances (Rct) of the electrodes determined from the EIS results obtained at 0.8 V.

Electrode	Rct	Efficiency (η%)
$NiCo(OH)_2$	43.48	-
$NiCo(OH)_2Ir$	10.32	76.26
$NiCo(OH)_2Ru$	0.69	98.41
$NiCo(OH)_2IrAg$	9.06	79.16
$NiCo(OH)_2RuAg$	10.09	76.80

As seen in Table 2, the OER efficiency of ruthenium doping is over 90%. As a result of silver precipitation, OER efficiencies in iridium silver and ruthenium silver were determined to be over 70%.

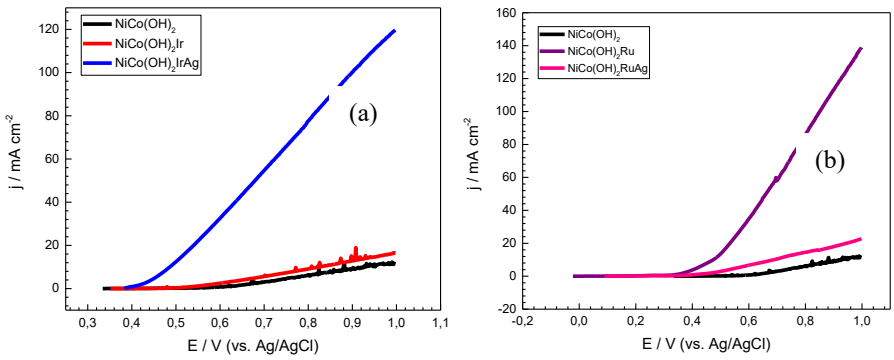

Fig. 3. Anodic current-potential curves of $NiCo(OH)_2$, $NiCo(OH)_2Ir$ and $NiCo(OH)_2IrAg$ (a), $NiCo(OH)_2$, $NiCo(OH)_2Ru$ and $NiCo(OH)_2RuAg$ (b) electrodes in 1.0 M KOH

In Fig. 3(a)., to determine the OER activities of $NiCo(OH)_2$, $NiCo(OH)_2Ir$ and $NiCo(OH)_2IrAg$ electrodes, anodic tests were performed in 1.0 M KOH solution at a scan rate of 1 mV s^{-1}. From these curves, the oxygen evolution efficiency of the electrodes were determined. The potential at which oxygen evolution begins was determined as 0.57 V, 0.55 V and 0.47 V for $NiCo(OH)_2$, $NiCo(OH)_2Ir$ and $NiCo(OH)_2IrAg$, respectively. It is observed that iridium doped and silver precipitation on the oxyhydroxide structure reduces the OER overvoltage. When OER efficiencies are compared, high current and low overvoltages are seen in the $NiCo(OH)_2IrAg$ electrode. In Fig. 3(b)., to determine the OER activities of $NiCo(OH)_2$, $NiCo(OH)_2Ru$ and $NiCo(OH)_2RuAg$ electrodes. The potential at which oxygen evolves for $NiCo(OH)_2$, $NiCo(OH)_2Ru$ and $NiCo(OH)_2RuAg$ was observed at 0.57 V, 0.39 V and 0.48 V, respectively. Examination of the curves indicated $NiCo(OH)_2Ru$ electrode had the lowest OER overvoltage potential. Although the OER efficiency of the electrode $NiCo(OH)_2RuAg$ is lower than that $NiCo(OH)_2Ru$, it is higher than that of the $NiCo(OH)_2$ electrode.

In Table 3, the oxygen release potential determined from the anodic current potential curves of the electrodes and the current densities obtained at 0.8 V are given.

Table 3. Electrochemical parameters of the electrodes determined from the current potential curves

Electrode	OER potential (V)	Current density at 0.8 V (mA cm^{-2})	Current Increase (%)
$NiCo(OH)_2$	0.57	6.35	-
$NiCo(OH)_2Ir$	0.55	9.17	44.41
$NiCo(OH)_2Ru$	0.39	87.68	>100
$NiCo(OH)_2IrAg$	0.43	76.88	>100
$NiCo(OH)_2RuAg$	0.48	14.61	>100

The catalytic activities of Ru and Ir, which have high OER efficiency, increased with silver (Table 3). In doping, conductivity, bond energies and structural features of the catalysts cause the number of active centers to increase and therefore the OER efficiency to be high.

4. CONCLUSIONS

Hydrogen is an interesting energy source due to its lack of waste, carbon neutrality and high energy density. In the electrolysis of water, which is the most used and most suitable method for hydrogen production, the anode material is as important as the cathode material. According to the experimental results of the study, the surface of the prepared electrode is an effective electrocatalytic surface for OER. According to EIS result OER efficiency of ruthenium doping was 98.41%. Considering the current values, it was found that ruthenium and iridium doping and silver precipitation on the surface increased the OER efficiency.

ACKNOWLEDGEMENTS

We acknowledge support from Turkey's Scientific and Technological Research Council (TUBITAK-Grant Number: 121C260) within the “2247 – A National Outstanding Researchers Program” program

REFERENCES

[1] Ananthara S, Kundu S, & Noda S. 2021. “The Fe Effect”: A review unveiling the critical roles of Fe in enhancing OER activity of Ni and Co based catalysts. Nano Energy, 80, 105514.
[2] Yaqoob L, Noor T, Iqbal N, Nasir H, Zaman N, & Talha K. 2021. Electrochemical synergies of Fe–Ni bimetallic MOF CNTs catalyst for OER in water splitting. Journal of Alloys and Compounds, 850, 156583.
[3] Zeng F, Mebrahtu C, Liao L, Beine AK, & Palkovits R. 2022. Stability and deactivation of OER electrocatalysts: A review. Journal of Energy Chemistry, 69, 301-329.
[4] Wu A, Xie Y, Ma H, Tian C, Gu Y, Yan H, & Fu H. 2018.Integrating the active OER and HER components as the heterostructures for the efficient overall water splitting. Nano Energy, 44, 353-363.
[5] Liu Y, Liu J, Li Z, Fan X, Li Y, Zhang F, & Wang S. 2018. Exfoliated MoS_2 with porous graphene nanosheets for enhanced electrochemical hydrogen evolution. International Journal of Hydrogen Energy, 43(30), 13946-13952.
[6] Zhang X, Wu A, Wang D, Jiao Y, Yan H, Ji, C, & Tian C. 2023. Fine-tune the electronic structure in Co-Mo based catalysts to give easily coupled HER and OER catalysts for effective water splitting. Applied Catalysis B: Environmental, 328, 122474.
[7] Wan C, Jin J, Wei X, Chen S, Zhang Y, Zhu T, & Qu H. 2022. Inducing the SnO2-based electron transport layer into NiFe LDH/NF as efficient catalyst for OER and methanol oxidation reaction. Journal of Materials Science & Technology, 124, 102-108.
[8] Dutta S, Indra A, Feng Y, Han H, & Song T. 2019. Promoting electrocatalytic overall water splitting with nanohybrid of transition metal nitride-oxynitride. Applied Catalysis B: Environmental, 241, 521-527.
[9] Pourbaix M, 1974. Atlas of Electrochemical Equilibria in Aqueous Solutions, NACE Pub., Houston.
[10]Tezcan F, Düdükcü MK. 2023. Fotoelektrokimyasal Yolla Hidrojen Gazı Üretiminde Kullanılan $BiVO_4/Cr_2O_3$ Fotoelektrodunun RuO_2 İle Katalitik Etkinliğinin Artırılması.Osmaniye Korkut Ata Üniversitesi Dergisi, 6(3), 2183-220.

SYNTHESIS OF NiFeMo HER CATALYST ON NICKEL FOAM FOR AEM ELECTROLYSER

[1*]Yakubu Sawadogo ADAM, [2,3]Murat FARSAK [1*]Gülfeza KARDAŞ
[1]Çukurova University, Faculty of Arts and Sciences, Chemistry Department, Adana, 01330, Türkiye
[2]Osmaniye Korkut Ata University, Department of Battery Systems and Hydrogen Technologies, Osmaniye, Türkiye
[3]Osmaniye Korkut Ata University, Department of Hybrid and Electric Vehicles Technology, Osmaniye, Türkiye

* E-mail: yakubuadam24@yahoo.com, gulfeza@cu.edu.tr; gulfeza@gmail.com

ABSTRACT
The work focuses on the research of three metal based electrocatalyst on a nickel coated nickel foam for its high HER efficiency and catalytic activity to be used as a cathode material in an anion exchange membrane (AEM) water electrolyzer. The developed ternary catalyst composed of nickel-iron-molybdenum (NiFeMo). Linear sweep voltammetry (LSV) and Electrochemical Impedance Spectroscopy (EIS) techniques were used in electrode efficiency examinations, while Scanning Electroscopy Measurement and Energy Dispersive Spectroscopy for the characterization and surface morphology. Significant increase in current density was obtained as seen from the LSV curve. Increased current density values for foam, nickel coated foam(#Ni) and NiFeMo#Ni were -14.89 mA cm^{-2}, -26.09 mA cm^{-2}, and -33.21 mA cm^{-2}, respectively calculated at -1.3 V for HER catalysis.

Keywords: HER, electrocatalyst, AEM water electrolyzer, ternary catalyst

1. INTRODUCTION
The focus to divert energy usage from fossil fuel sources to sources that are environmentally friendly and green is gaining much attention due to much concern over the sharp rise in environmental pollution and global warming. These concerns may also be attributed to the hike in energy usage especially considering the factor with which electric cars and other electric devices production has doubled. Instead of carbon based fuels, hydrogen studies have got much attention and consideration due to its properties. Natural availability of hydrogen helps with its studies and utilization in several methods [1]. Water electrolysis is considered the method for about 2-4% of the world's H_2 production [2]. In water electrolysis there is the necessity to develop more cost effective and naturally available electrocatalyst in place of platinum. In this case the reduction of overpotential must be considered. Nickel foam is considered a positive exchange in AEM studies with much consideration of thermodynamic stability and passivation ability [3]. Expansion of contact area between electrode and nanostructure catalytic layer which is to decrease in ohmic resistance is one factor considered for the development of our NiFeMo#Ni electrode. Therefore, a tenary NiFeMo alloy bifunctional electrocatalysts development is vital, being scientifically important and easily applicable [4].
The HER performance of the catalyst produced by electrodeposition was studied in this work. Energy dispersive X-ray spectroscopy (EDX) analysis and scanning electron microscopy (SEM) were used to accomplish the characterization. In a 1 M KOH solution, electrochemical behaviour was examined using linear sweep voltammetry (LSV) and electrochemical impedance spectroscopy (EIS).

2. EXPERIMENTAL
Synthesis of Catalysts; The electrodes to be studied were prepared from W300 x L1000mm Ni foam and cut to approximately 1 x1 cm. The nickel foam was cleaned in an ultrasonic bath for half an hour in acetone. The nickel mesh electrodes were left in the ultrasonic bath for 1 h in 3.0M HCl to make them electrically conductive. The foam was electrochemically coated with nickel at 10mA cm^{-2} for 60s, dried and later proceeded with the coating of NiFeMo at 50mA cm^{-2} for 30s using the bath compositions in Table 1.

Table 1. Coatings bath composition

	Bath composition	Conditions
Ni Coating	30% $NiSO_4.7H_2O$ 1.25% H_3BO_3 1.0 % $NiCl_2.6H_2O$ pH=3.5	60s, 10mA cm^{-2}, 25^0C
NiFeMo Coating	$NiSO_4.6H_2O$ = 6.4g $FeSO_4 \cdot 7H_2O$ = 1.6g $Na_2MoO_4.2H_2O$ = 0.96g $Na_3C_6H_5O_7 \cdot 2H_2O$ = 5.28g pH = 9.8	30s, 50mA cm^{-2}, 25°C

Gamry Interface 1000 potentiostat/galvanostat was used in performing the electrochemical experiments. A three electrode system with Ag/AgCl (3M KCl) as a reference electrode, 1 cm² Pt sheet as a counter electrode and 1 cm² nickel foam as a working electrode. Electrochemical measurements were done in 1 M KOH solution at room temperature. EIS

was taken in the frequency range of 10^5 -0.01 Hz, 5 mV and at -1.3 V. HER efficiency of electrodes was determined by LSV in the cathodic direction from open circuit potential to -1.5 V at 1 mV s^{-1} scan rate.

3. RESULTS AND DISCUSSION

Figure 1 is a representation of surface characteristics of foam (a), #Ni (b) and NiFeMo#Ni (c). In (a) fine roughness of struts were observed in the foam, indication of increased surface area which is an important tool for electrochemical performance. Image (b) displays a characteristic rough and porous structure which is common to foam substrates therefore, the increase in surface area for HER studies. Deposition quality is also observed from the uniformity that's the evenness. In Fig.1(c), co-deposition of NiFeMo on #Ni may have resulted in the significant roughness observed.

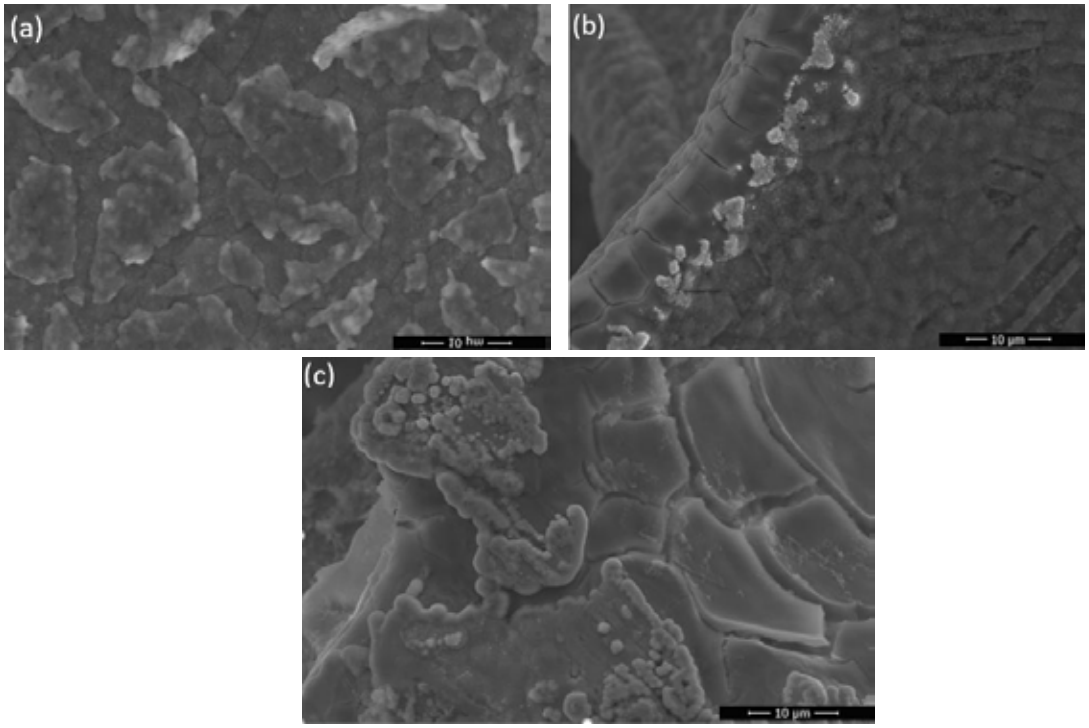

Fig.1. SEM images (scale bar: 10 µm) of foam (a), #Ni (b), and NiFeMo#Ni deposited (c) electrodes (Mag: x5000)

There may be good ion transport due to the highly porous and interconnected network observed. This roughness is enhanced by the active surface area. It's highly possible that the co-depositiion of NiFeMo caused the small granular formations seen and these lead to an increase in active surface area vital for electrochemical reactions, HER studies for example. The deposition created by the multi-metal layer deposition improved the ion transport and gas release in the HER process.

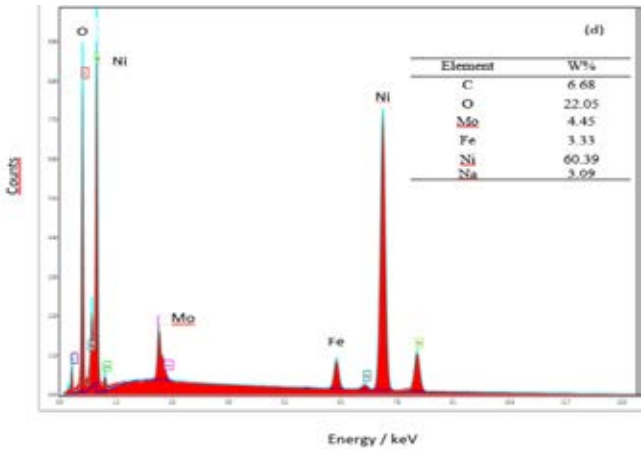

Fig. 2. EDX analysis representation of NiFeMo#Ni electrode (inset: Table shows % elemental composition of Ni, Mo, Fe, O, Na and C).

Compositional observation necessary for HER studies were seen in the NiFeMo#Ni electrode's EDX results with the most abundant being nickel. Nickel providing high electrical conductivity important for HER catalysis serves as a basic substrate. Creation of synergistic effects with nickel and molybdenum to improve catalytic performance and stability by iron (Fe) was also present at 3.33 wt%. Molybdenum (Mo) also contributing to active sites that improves HER kinetics, particularly in alkaline media, by facilitating electron transfer and reducing hydrogen evolution overpotential was found to be 4.45 wt%. surface oxides formed during deposition or sample exposure, which can influence catalytic activity by modifying electronic properties possibly contributed to oxygen at 22.05 wt%. Environmental contaminations or bath solution residuals count contribute the detection of lower concentrations of carbon(C) and sodium (Na) at 6.68 wt% and 3.09 wt%, respectively.

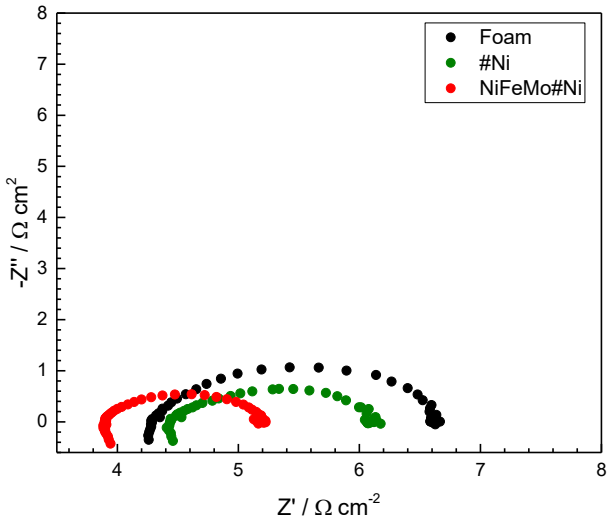

Fig. 3. Nyquist diagrams of foam(black), #Ni (green) and NiFeMo#Ni (red) electrode at -1.3 V 1 M KOH.

The EIS measurements at -1.3 V of the different electrodes for HER studies as seen im fig.2 gives key observations about their charge transfer properties and catalytic performances. The foam is seen to have the largest semi-circle signifying the highest charge transfer resistance and least efficient among the three due to poor conductivity and sluggish electron transfer. However, the coating of nickel on foam (NiF) tend to have decrease the semi-circle indicating a lower charge transfer resistance and thereby increasing its HER activity compared to the foam. NiFeMo#Ni exhibited the lowest charge transfer resistance meaning it was the best with a catalytic effect for HER studies amongst the three as seen with it having the smallest semi-circle. The shift in solution resistances may be attributed to the readiness of the surface at the applied potential. We could therefore conclude that NiFeMo increased the active surface area, reduced the charge transfer resistance and thereby increasing the catalytic activity for the HER stuies.

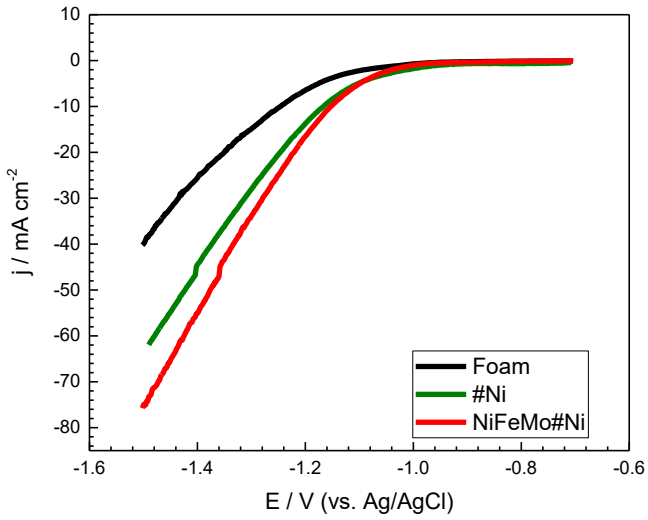

Fig. 4. Cathodic current-potential curves of foam (black), #Ni (green) and NiFeMo#Ni (red) deposited electrodes in 1.0 M KOH.

The cathodic current measurements were taken from the open circuit potential to -1.5 V at 1mV s^{-1} scan rate in 1.0 M KOH solution. with specific focus on a nickel-iron-molybdenum (NiFeMo) composition electrodeposited on nickel-coated nickel foam (#Ni), the performances of different electrode materials for the (HER) were compared in Fig. 4 above. Compared to #Ni and bare foam, the NiFeMo#Ni exhibited significant increase in current density as well as a decrease in the onset potential. A more negative potential (E) is required for the foam and #Ni to achieve equivalent current densities as NiFeMo#Ni, indicating higher overpotentials for HER. electrocatalytic efficiency was enhanced by lowering the energy barrier for hydrogen evolution. This property of our material as in the increase in current density and the lowering of onset overpotential could be attributed to the synergistic effect of our multi-metal (NiFeMo) layer coating, which likely optimize the adsorption and desorption steps in the HER mechanism. This is another factor of evidence that the incorporation of NiFeMo in our HER cathodic material studies, enhances catalytic activity and increases efficiency. Moreover, NiFeMo composition on Ni@F showed a unique morphology and inherent conductivity that improves electron transfer and catalytic site availability.

4. CONCLUSIONS

As a better alternative source of energy with the great advantages, it is important to focus on the best way to increase the production of hydrogen. The preparation of an ideal electrocatalyst to boost up the cathodic reactions in AEM water elecytrolyzer is vital. Our experimental results showed the electrocatalytic efficiency and activity of the prepared NiFeMo#Ni on hydrogen evolution reaction in 1 M KOH. Increased in current density and the decrease in charge transfer resistance as proof due to our synergistic NiFeMo#Ni electrode were observed in our LSV and EIS measurements respectively.

ACKNOWLEDGEMENTS

We acknowledge support from Çukurova University, Scientific Research Projects (BAP – Project Number: FDK-2023-16118.

REFERENCES

[1] Laszczyńska, A., & Szczygieł, I. (2020). Electrocatalytic activity for the hydrogen evolution of the electrodeposited Co–Ni–Mo, Co–Ni and Co–Mo alloy coatings. International Journal of Hydrogen Energy, 45(1), 508-520.

[2] Bartoli, F., Capozzoli, L., Peruzzolo, T., Marelli, M., Evangelisti, C., Bouzek, K., ... & Vizza, F. (2023). Probing the activity and stability of MoO 2 surface nanorod arrays for hydrogen evolution in an anion exchange membrane multi-cell water electrolysis stack. Journal of Materials Chemistry A, 11(11), 5789-5800.

[3] Pushkareva, I. V. Pushkarev, A. S. Solovyev, M. A. Butrim, S. I., Kuleshov, V. N., Kurochkin, S. V., ... & Fateev, V. N. (2023). Application of Nickel Foam as a Porous Transport Layer in an Anion Exchange Membrane Water Electrolyzer. Nanobiotechnology Reports, 18(Suppl 2), S389-S397.

[4] Hsieh, C. T. Huang, C. L. Chen, Y. A. & Lu, S. Y. (2020). NiFeMo alloy inverse-opals on Ni foam as outstanding bifunctional catalysts for electrolytic water splitting of ultra-low cell voltages at high current densities. Applied Catalysis B: Environmental, 267, 118376.

INVESTIGATION OF LONG-TERM DEGRADATION EFFECTS IN PEM ELECTROLYZERS

[1*,2]*Alperen Çankaya*, [1,2]*Selahattin Çelik,* [1,2]*Büşra Sevinç,* [2,3]*Kayhan Dağıdır,* [1,2]*Hasan Özcan*
[1] Ankara Yıldırım Beyazıt University, Engineering and Natural Science Faculty, Mechanical Engineering Department, Keçiören, Ankara, 06010, Türkiye
[2] Ankara Yıldırım Beyazıt University, Hydrogen Technologies and Energy Research Center (H2 TEAM), Keçiören, Ankara, 06010, Türkiye
[3] Tarsus University, Engineering Faculty, Mechanical Engineering Department, Tarsus, Mersin, 33400, Türkiye

*Corresponding author e-mail: alperencankaya@aybu.edu.tr

ABSTRACT
The increasing global energy demand and efforts to reduce environmental impact have accelerated the search for sustainable energy solutions. Hydrogen energy has emerged as a key player in achieving net-zero greenhouse gas emissions, with Proton Exchange Membrane (PEM) electrolyzers being a promising technology for clean hydrogen production. However, their long-term durability remains a critical challenge, especially after extended periods of inactivity. This study investigates the degradation effects in a PEM electrolyzer that was initially operational but remained idle for approximately 15 years. Experimental analyses were conducted to evaluate key performance parameters, including voltage loss and current density variations. The results indicate a significant increase in overpotential, suggesting membrane degradation, catalyst sintering, and increased internal resistance over time. A 15% efficiency loss was observed, highlighting the need for advanced materials and maintenance strategies to extend the operational lifespan of PEM electrolyzers.
The findings provide valuable insights into the long-term reliability and degradation mechanisms of PEM electrolyzers, contributing to their future development and commercialization.

Keywords: PEM electrolyzer, degradation, hydrogen production, long-term performance, electrolysis.

1. INTRODUCTION

In recent years, global energy consumption has been steadily rising due to factors such as population growth and improved living standards. This increase has led to a greater dependence on fossil fuels, contributing significantly to environmental pollution, intensifying global warming, and causing a range of other crises. Furthermore, the sharp rise in fossil fuel costs over the past few years has brought renewable energy solutions, particularly green hydrogen production through electrolysis [1-3]. Among the various electrolysis technologies, PEM water electrolysis is one of the most used method, along with alkaline electrolysis. Although alkaline electrolysis is a mature and reliable technology with lifespans of over 30 years, PEM electrolysis is also a commercially viable technology that boasts a high readiness level. One of its primary advantages is its quick and dynamic response, making it ideal for integration with fluctuating energy sources [4].

The efficiency and performance of PEM electrolyzers are directly influenced by the seamless integration of several advanced components. The Proton Exchange Membrane plays a crucial role in ensuring proton conductivity while preventing gas crossover. The anode, composed of iridium oxide, is responsible for oxygen evolution, whereas the platinum-based cathode acts as an efficient hydrogen production catalyst. Additionally, electrodes with large surface areas facilitate gas diffusion, improving overall efficiency. Bipolar plates contribute to electron conductivity and enhance the mechanical durability of the system. Meanwhile, seals and gasket materials play a critical role in preventing gas leakage and ensuring operational safety, all of which are essential for optimizing performance [5-6].

Despite these advantages, the long-term durability of PEM electrolyzers remains a significant challenge, especially after extended periods of inactivity. Over time, various degradation mechanisms can impact system efficiency and reliability. This study investigates the degradation effects observed in a PEM electrolyzer following nearly a decade of idle operation. Through experimental analysis, key performance parameters such as voltage and current density are evaluated. The findings will provide valuable insights into the long-term reliability, maintenance strategies, and potential improvements necessary for the future development and commercialization of PEM electrolyzers.

2. MATERIALS AND METHODS

This study investigates the long-term degradation effects in PEM electrolyzers by employing a structured experimental approach. The methodology encompasses material selection, experimental setup configuration, and data collection techniques to ensure accurate and reproducibility. The experimental framework is designed to assess key degradation parameters by analyzing performance changes over time. The system was equipped with thermocouples placed at the anode, cathode, and water outlet to monitor temperature variations. A digital data logger recorded real-time voltage and current density variations during operation.

In the PEM electrolyzer system, fine titanium meshes and sintered porous titanium serve as current collectors and diffusion media, while stainless steel is used for the end plates. A single cell utilizes a 100 cm² circular-shaped MEA supplied by Giner Inc. This MEA incorporates a Nafion 110 membrane and features catalyst loadings of 2 mg/cm² Pt and 2 mg/cm² Ir on the anode side, whereas the cathode side contains 4 mg/cm² Pt. The experimental conditions and assessment techniques are structured to provide insights into the durability and performance of PEM electrolyzers over extended periods of inactivity.

2.1. Experimental Setup

A schematic representation of the test setup is shown in Figure 1. In the setup, an adjustable peristaltic pump (12V) is used to supply water. Portable thermocouples (Ordel) and a data logger (Elimko 680) are used to control both water and stack temperatures. To provide the stack with the energy needed to split the water into hydrogen and oxygen, a 3 kW (30V-100 A) power supply (AlphaWorld) is used. All of the data have been recorded on a computer to analysis.

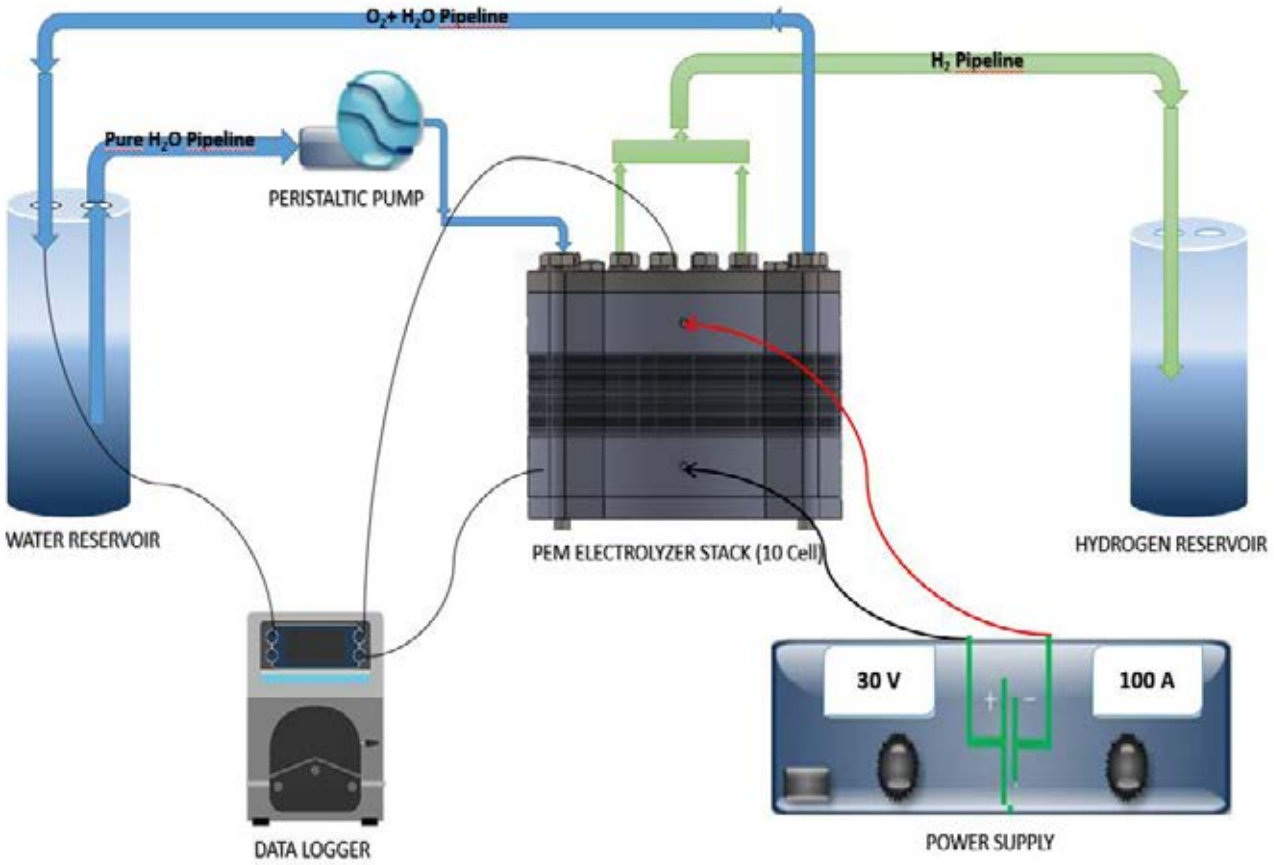

Fig. 1. Schematic representation of the experimental setup

When testing the performance of the stack, it is crucial to measure the temperature correctly. Temperature data were recorded using three thermocouples, each connected to a data logger. Two thermocouples were placed at the top of the stack and at the bottom of the end plates, while another thermocouple was placed at the water and oxygen outlets. Therefore, temperature changes in the system were checked with measurements at various points simultaneously.

2.2. Performance Measurement

Voltage losses, polarization curves, and electrochemical surface area (ECSA) measurements were conducted to assess performance degradation. The degradation rate was quantified using the following equation**:**

$$\text{Degradation rate}(\%) = \frac{V_{initial}_V_{final}}{V_{initial}}\ x\ 100 \quad (1)$$

where represents the initial stack voltage, and is the voltage measured after long-term inactivity.

3. RESULTS AND DISCUSSION

Voltage loss and polarization curve measurements were performed to assess performance degradation. The data taken from the same PEM electrolyzer at the initial condition and at the final condition are shown in Figure 2. The initial condition represents the performance of the electrolyzer 15 years ago, while the final condition reflects its performance after being operated intermittently and then idle for approximately 10 years prior to testing. Each graph shows the tests performed separately at 30, 40, 50 and 60 degrees, respectively.

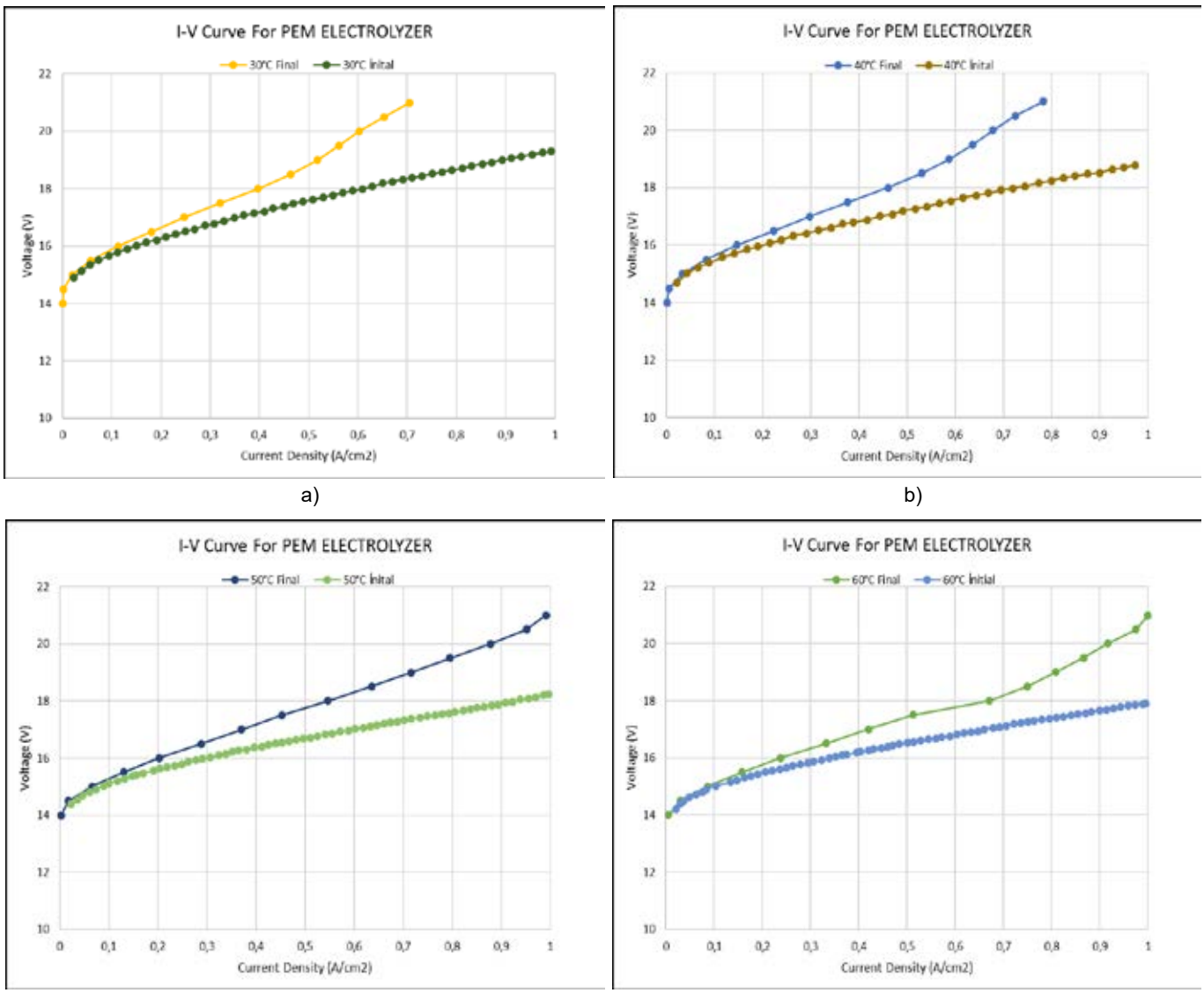

Fig. 2. Graphical representation of the degradation of the pem electrolyzer after 15 years at different temperatures a) 30°C b) 40°C c) 50°C d) 60°C

In all graphs, the final I-V curves show significantly higher voltage values at the same current densities compared to the initial curves, indicating increased overpotential and that the system requires more energy to achieve the same hydrogen production rate. This suggests membrane degradation, catalyst layer degradation, or increased internal resistance due to aging effects such as electrode delamination, membrane thinning, or catalyst sintering.

The experimental results revealed a notable increase in voltage losses and a decline in current density over time. A 15% decrease in overall efficiency was observed after ten years of inactivity. The performance measurements indicated an increase in membrane resistance, suggesting ionic conductivity deterioration. Figure 2 presents the polarization curve shifts, highlighting performance decline. Material degradation, particularly catalyst sintering and membrane thinning,

contributed to efficiency losses. The findings align with previous studies on PEM electrolyzer aging mechanisms [7,8]. The polarization curves demonstrated a significant shift towards higher voltage requirements at equivalent current densities. This shift is indicative of increased overpotential, which can be attributed to both catalyst deactivation and membrane resistance increase. The initial operational voltage at 1 A/cm² was recorded at approximately 1.8 V, whereas after ten years, it rose to nearly 2.1 V, marking a 16.7% increase in voltage loss. This trend is consistent with previous findings in literature, where long-term exposure to fluctuating operational conditions accelerates catalyst sintering and ionomer degradation [9].

4. CONCLUSIONS

This study investigates the long-term degradation effects in a PEM electrolyzer that remained idle for approximately 15 years while being continuously exposed to a water-filled environment. The prolonged exposure to moisture contributed to additional degradation mechanisms, including membrane hydrolysis, electrode delamination, and catalyst layer deterioration. These effects were reflected in the significant performance losses observed during testing.

The experimental results revealed a notable increase in voltage losses and a decline in current density over time. A 15% decrease in overall efficiency was observed, with the operational voltage at 1 A/cm² increasing from approximately 1.8 V to nearly 2.1 V, marking a 16.7% increase in voltage loss. The polarization curves demonstrated a significant shift toward higher voltage requirements, indicative of increased overpotential, which can be attributed to catalyst deactivation and increased ohmic losses due to aging effects such as electrode delamination, membrane thinning, and catalyst sintering.

While higher operating temperatures enhance efficiency by improving reaction kinetics and ion conductivity, they also accelerate degradative processes such as membrane degradation and catalyst deactivation. The findings emphasize the necessity for periodic maintenance, proper storage conditions, and refurbishment strategies to extend the operational lifespan of PEM electrolyzers.

To further understand the observed degradation, future studies will focus on advanced material characterization techniques such as X-ray diffraction (XRD) and scanning electron microscopy (SEM). These analyses will be conducted on both electrode materials and porous flow plates to investigate structural and chemical changes, including catalyst degredation, membrane thinning, and porosity alterations. Additionally, alternative electrode materials, improved membrane compositions, and enhanced flow plate designs will be explored to mitigate performance losses. The insights gained from this study will contribute to the development of more durable and commercially viable PEM electrolyzers with extended operational lifetimes exceeding 50,000 hours.

ACKNOWLEDGEMENT

This work was supported by the Turkish Energy, Nuclear, and Mineral Research Agency (TENMAK) under project Grant No:1311.

REFERENCES

1. Makhsoos, A., Kandidayeni, M., Pollet, B. G., & Boulon, L. (2023). A perspective on increasing the efficiency of proton exchange membrane water electrolyzers–a review. International Journal of Hydrogen Energy, 48(41), 15341-15370.
2. Hernández-Gómez, Á., Ramirez, V., Guilbert, D., & Saldivar, B. (2020). Development of an adaptive static-dynamic electrical model based on input electrical energy for PEM water electrolysis. International Journal of Hydrogen Energy, 45(38), 18817-18830.
3. Barbir, F. (2005). PEM electrolysis for production of hydrogen from renewable energy sources. Solar energy, 78(5), 661-669.
4. Wallnöfer-Ogris, E., Grimmer, I., Ranz, M., Höglinger, M., Kartusch, S., Rauh, J., ... & Trattner, A. (2024). A review on understanding and identifying degradation mechanisms in PEM water electrolysis cells: Insights for stack application, development, and research. International Journal of Hydrogen Energy, 65, 381-397.
5. Carmo, M., Fritz, D. L., Mergel, J., & Stolten, D. (2013). A comprehensive review on PEM water electrolysis. International journal of hydrogen energy, 38(12), 4901-4934.
6. Kumar, S. S., & Himabindu, V. (2019). Hydrogen production by PEM water electrolysis–A review. Materials Science for Energy Technologies, 2(3), 442-454.
7. Millet, P., Ngameni, R., Grigoriev, S. A., & Fateev, V. (2019). Durability of PEM water electrolysis cells: Mechanisms and mitigation strategies. *Electrochimica Acta, 317*, 710-721.
8. Vincent, I., & Bessarabov, D. (2018). Low-cost hydrogen production by PEM electrolysis: A review. *International Journal of Hydrogen Energy, 43*(48), 22701-22715.
9. S. B. D. S. Gunawardhana, M. A. Rahman, "Proton Exchange Membrane Fuel Cell Catalyst Layer Degradation Mechanisms: A Succinct Review," *Materials*, vol. 15, no. 1, pp. 97, 2022. https://doi.org/10.3390/materials15010097

PERFORMANCE ANALYSIS OF PLANT-INSPIRED BIPOLAR PLATE FLOW CHANNELS FOR PEM ELECTROLYSERS USING 3D MODELLING

[1,2*]*Mohammad Alobeid*, [1,2]*Selahattin Çelik*
[1]Ankara Yıldırım Beyazit University, Faculty of Engineering and Natural Sciences, Ankara 06010, Türkiye
[2]Ankara Yıldırım Beyazit University, Hydrogen Technologies and Energy Research Center (H2 TEAM), Ankara 06010, Türkiye

*Corresponding author e-mail: mohammed.alobed@gmail.com

ABSTRACT
Polymer Electrolyte Membrane Water Electrolysers (PEMWEs) efficiently produce high-purity, compressed hydrogen, with bipolar plate design playing a key role in performance. This study proposes a novel flow channel inspired by vine leaf patterns from various plant species. The design, featuring a 13.85 cm² circular cross-section, is analyzed using COMSOL Multiphysics, integrating key physical and fabrication factors. Results show improved velocity uniformity, lower pressure drop, and enhanced mixture homogeneity compared to conventional serpentine models.

Keywords: bio-inspired, plant leaves, bipolar plates, PEM water electrolysis, flow channel design.

1. INTRODUCTION
The global shift toward clean energy has made hydrogen a key solution for decarbonization. Proton Exchange Membrane Water Electrolysis (PEMWE) is a promising technology for producing high-purity hydrogen due to its efficiency and compact design. However, high costs, especially for bipolar plates (BPPs), limit its widespread adoption [1,2].

This study introduces a novel bio-inspired flow-field design for BPPs, inspired by natural structures like leaf veins. These designs aim to improve fluid distribution, reduce pressure drops, and enhance water management. Preliminary results show significant improvements in performance compared to traditional flow fields, such as serpentine and parallel channels, paving the way for more efficient and cost-effective PEMWE systems [3,4].

2. METHODOLOGY
A 3D computational model of a PEMWE half-cell was developed in COMSOL Multiphysics shown in Fig.1. The model solved conservation equations across seven regions, including catalyst layers, gas diffusion layers, and membranes. Five bio-inspired and three traditional flow-field designs were analyzed. Assumptions included steady-state laminar flow, isothermal conditions, and negligible contact resistance. A mesh independence study ensured accuracy, and the model was validated against experimental polarization curve data [5].

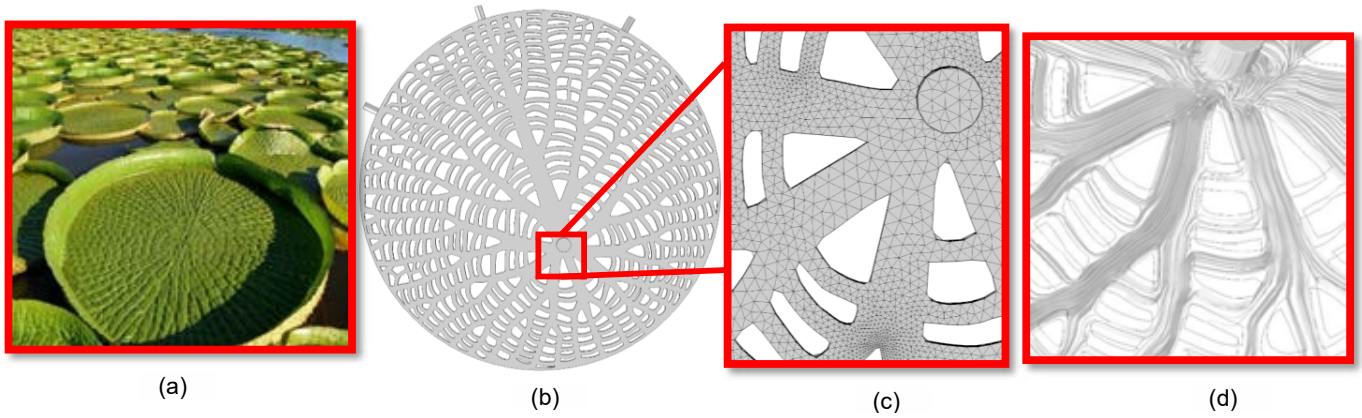

Fig. 1. Model process Victoria Amazonica Water Lily (L2V): (a) The real leaf selection (b) Design and extract the exact vein geometry (c) Mesh the model (d) Flow streamlines.

3. RESULTS AND DISCUSSION
The Victoria Amazonica Water Lily (L2V) model demonstrated superior performance compared to the serpentine model (SR8) across multiple metrics:

- Polarization Curve: The L2V model achieved lower voltages (1.9751–2.5173 V) at current densities ranging from 200 to 15,000 A/m², outperforming SR8.
- Pressure Drop: L2V exhibited a significantly lower pressure drop (8.05 Pa) compared to SR8, ensuring more efficient water management and uniform reactant distribution.
- Mixture Distribution: L2V showed better oxygen concentration and water mole fraction uniformity,

reducing reactant density inconsistencies and enhancing current density stability.

- Velocity Distribution: L2V achieved a more uniform velocity profile, improving water removal and reactant delivery compared to SR8.

These results highlight the L2V model's potential to optimize PEMWE performance, surpassing traditional serpentine designs like SR8 shown in Fig.2.

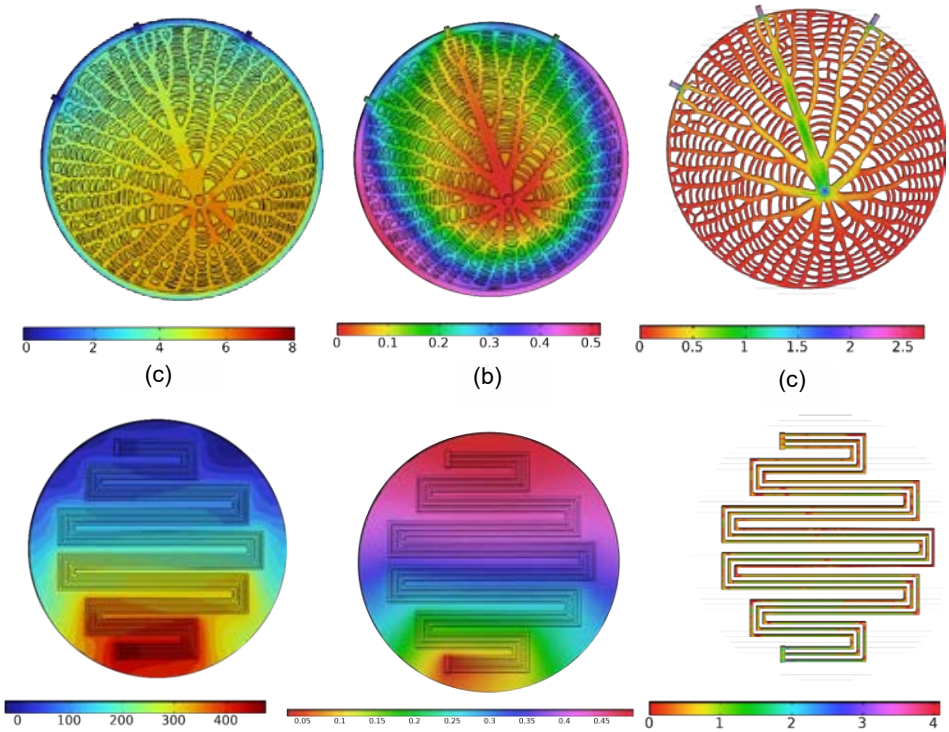

Fig. 2. Results Comparison Between the Victoria Amazonica Water Lily (L2V) and the Serpentine Model (SR8): (a) Pressure distribution (Pa) (b) Oxygen Mole Fraction distribution (c) Water Channels Velocity distribution (m/s)

4. CONCLUSION

This study demonstrates the remarkable advantages of bio-inspired designs in PEMWE performance, with the L2V Victoria Amazonica Water Lily model emerging as the most efficient design. At a current density of 15,000 A/m², L2V achieved up to 5%, 4.1%, and 4% lower voltage than parallel, serpentine, and point flow channels, respectively. It also exhibited the lowest pressure drop (8.05 Pa), outperforming traditional models by 97.9%, 98.6%, and 79.3%.
Additionally, L2V provided the most uniform water and velocity distributions, with homogeneity improvements of 40.8%, 40.1%, and 33.6% compared to parallel, serpentine, and point flow channels. Optimization studies revealed that increased exchange current density and active specific surface area, along with lower operating temperatures, enhanced polarization curve performance without significantly impacting pressure drop or velocity.
These results underline the superiority of bio-inspired designs, particularly L2V, in achieving efficient, durable, and sustainable PEMWE systems.

REFERENCES

[1] Sebbahi, S., Nabil, N., Alaoui-Belghiti, A., Laasri, S., Rachidi, S., & Hajjaji, A. Assessment of the three most developed water electrolysis technologies: Alkaline water electrolysis, proton exchange membrane and solid-oxide electrolysis. Materials Today: Proceedings, *(66)*, 140-145. 2022

[2] Teuku, H., Alshami, I., Goh, J., Masdar, M. S., & Loh, K. S. Review on bipolar plates for low-temperature polymer electrolyte membrane water electrolyzer. International Journal of Energy Research, *(15)*, (45) 20583-20600. 2021

[3] Li, W., Zhang, Q., Wang, C., Yan, X., Shen, S., Xia, G., ... & Zhang, J. Experimental and numerical analysis of a three-dimensional flow field for PEMFCs. Applied Energy, *(195)*, 278-288. 2017

[4] Asadzade, M., & Shamloo, A. Design and simulation of a novel bipolar plate based on lung-shaped bio-inspired flow pattern for PEM fuel cell. International Journal of Energy Research, *(41)*, (12) 1730-1739. 2017

[5] Upadhyay, M., Kim, A., Paramanantham, S. S., Kim, H., Lim, D., Lee, S., ... & Lim, H. Three-dimensional CFD simulation of proton exchange membrane water electrolyser: Performance assessment under different condition. Applied Energy, *(306)*, 118016. 2022

THERMODYNAMIC AND ELECTROCHEMICAL MODELING OF DIRECT METHANOL FUEL CELL SYSTEM FOR PORTABLE APPLICATIONS

[1]*Erva Kalkan*, [1, 2*]*Mohammed Alobeid*, [1, 2]*Selahattin Celik*, [1, 2]*Hasan Ozcan*
[1] Ankara Yıldırım Beyazıt University, Faculty of Engineering and Natural Sciences, Department of Mechanical Engineering, Keçiören/Ankara, 06010, Türkiye
[2] Hydrogen Technologies and Energy Research Center (H2 TEAM), Ankara Yıldırım Beyazit University, Ankara 06010, Türkiye

*Corresponding author e-mail: mohammed.alobed@gmail.com

ABSTRACT
Zero-dimensional modeling is a practical approach for analyzing the internal processes of Direct Methanol Fuel Cells (DMFC). Mathematical models play a crucial role in efficiently assessing fuel cell system performance. In this study, the Engineering Equation Solver (EES) was utilized to evaluate key performance parameters, including flow rate, voltage, and current density, based on the semi-empirical equations developed by Meyers and Newman. The results indicate that under ideal conditions, the maximum power density is approximately 0.166 W/cm², achieved at a voltage of 0.44 V and a current density of 0.38 A/cm². The effect of varying current density on system efficiency was examined, and the methanol flow rate was determined as 0.753 mL/min, calculated using both the higher heating value (HHV) of methanol and Faraday's law. The findings suggest that optimizing operating conditions and design parameters can significantly enhance the efficiency and performance of DMFC systems.
Keywords: Direct methanol fuel cell, semi-empirical modeling, mathematical analysis, power density, methanol flow rate.

1. INTRODUCTION
Direct Methanol Fuel Cells (DMFC) have attracted significant interest in recent years as a promising technology for various small-scale energy system applications, such as portable electronic devices, with their design combining small size and high efficiency. Particularly, the ease of transportability of methanol fuel in liquid form contributes to wider application areas. The performance of Direct Methanol Fuel Cells is affected by certain electrochemical events and various processes occurring within the cell. To better understand and improve this situation, simplified modeling approaches, such as zero-dimensional semi-empirical formulas, serve as important tools. By using these models, the need for extensive experimental data or computationally intensive simulations is reduced. In this study, the zero-dimensional modeling of a direct methanol fuel cell system was performed using the EES (Engineering Equation Solver) program. This modeling approach is a significant method used to estimate the performance and losses of fuel cells. During the modeling process, the semi-empirical equations developed by Meyers and Newman [1] were utilized. These formulas are simplified equations validated with experimental data and aligned with electrochemical principles. With this approach, dimensional details within the cell are neglected. By using semi-empirical formulas instead of complex computational methods, fast and practical analysis results are obtained. This reduces the need for costly and time-consuming experimental studies. In this context, existing studies on the zero-dimensional modeling of DMFC systems have been reviewed. Ince et al. (2019) developed a thermodynamic model for the system components of an active direct methanol fuel cell system. The modeling equations were implemented using the Engineering Equation Solver (EES) program. This model provides the heat and work transfer between the system components and their surroundings, as well as the electrical efficiency of the system. They investigated the effects of methanol concentration (between 0.5 to 1.25 M) and air flow rate (between 20 to 30 mL cm−2 min−1) on the net power output, electrical efficiency, and condenser outlet temperature of the system. As a result of their findings, they identified the maximum value for the system's electrical efficiency [2]. Chiu et al. (2011) stated that theoretical approaches in a direct methanol fuel cell (DMFC) are complex and less practical, while experimental processes are time-consuming. As a result, they proposed a semi-empirical model incorporating many parameters to evaluate DMFC performance. In the proposed model, the power density and efficiency of the DMFC were studied in relation to parameters such as operating temperature, fuel concentration, and current density. Performance indices and operating variables were presented in a diagram. They concluded that a semi-empirical model is generally necessary for practical scenarios [3]. Yang et al. (2011) modeled the relationships between operating parameters and performance measurements for a single-stack direct methanol fuel cell (DMFC). To consider both modeling accuracy and simplicity, a semi-empirical model was developed in this study by integrating theoretical and approximate models. As a result of error analyses, they concluded that the semi-empirical model is effective for predicting the performance of DMFC. Furthermore, the potential applications of the semi-empirical model in the optimal control of fuel cell systems were discussed [4].

2. MATERIALS AND METHODS
This section elaborates on the steps involved in the zero-dimensional modeling of the DMFC system in detail. The semi-empirical models used provide a foundation for analyzing the system's behavior under different conditions. Computational methods for the anode, cathode, and overall cell structure of the DMFC system, as well as the relationships between current density, voltage, and power, and flow rate calculations, are presented below.

2.1. Anode and Cathode Modeling

The anode and cathode behaviors in the DMFC system were modeled using Meyers and Newman's semi-empirical equations. In this context, the equations defining the current-voltage (I-V) characteristics through theoretical modeling are provided below.

Anode:

The current density (i) is calculated as:

$$i = \frac{i_* C_M \, a \exp\,(2.303\eta/b)}{C_M + K \, a \exp\,(2.303\eta/b)} \tag{1}$$

The anode overpotential (η_{an}) is expressed as:

$$\eta_{an} = f_1 + f_2 \ln(i) + \, f_3 \exp\left(\frac{f_4}{C_M}\right) \tag{2}$$

Cathode:

$$i_{perm} = m_1 + m_2 \tag{3}$$

$$m_1 = 4.65 \, x \, 10^{-2} \frac{d}{d_{ref}} \frac{c}{1M} \exp\big(0.01329\,(T - 273.15K)\big) \frac{A}{cm^2} \tag{4}$$

$$m_2 = -0.4 + 0.27 \frac{n_{drag}}{n_{drag}^{ref}} \frac{c}{c_{ref}} \tag{5}$$

The cathode overpotential (η_C) is given by:

$$\eta_C = \frac{RT}{aF} \ln\left[\frac{i}{l_{cat} i_*}\left(\frac{c_{O2,ref}{}^{\gamma}}{c_{o2}{}^{\gamma}}\right)\right] + k(i) i_{perm} \tag{6}$$

Cell potential:

The total cell voltage, E_0 (open circuit voltage), is calculated using Eq. (7) and Eq. (8):

$$E = E_0 - \eta_C - \eta_{ohm} \tag{7}$$

Ohmic losses (η_{ohm}) are defined as:

$$\eta_{ohm} = \frac{l_{mem}}{\sigma_{mem}} \, i \tag{8}$$

Using these equations with the EES application, fundamental parameters such as flow rate, voltage, and current density were calculated to analyze the performance of the direct methanol fuel cell system.

2.2. Current Density and Voltage Relationship

Graphs showing the relationship between current density (A/cm²) and voltage (V) for different operating temperatures were created using EES. These are shown in Figure 1. It can be observed that as the current density increases, there is a change in the cell voltage. Thus, as current density increases, the effect of polarization losses in the system can be discussed.

2.3. Power Output

In the power density graphs, the maximum power density and the current density at which this value is obtained were determined. These are shown in Figure 2. This value represents the optimal performance point of the system. Beyond this point, a decrease in power density was observed due to potential losses on the electrodes and reactant limitations.

2.4. Current Density, Voltage, and Power Relationship

The I-V (current-voltage) and P (power density) curves of the DMFC are key parameters in understanding the overall performance of the system. The intersection point of the I-V and P curves determines the maximum power point. This is shown in Figure 3. This point represents the optimal performance of the DMFC in terms of efficiency and energy output. It is the point at which the balance between reactant consumption, energy production, and losses is best achieved.

2.5. Flow Rate Calculation

2.5.1. Methanol Flow Rate Calculation with Faraday's Law

Methanol flow is calculated by taking Faraday's law into consideration:

Basic Parameters:

- Current density: $0.38\ A/cm^2$
- Active area: Approx. $50\ cm^2$
- Number of cells: 10

As a result of the calculations, the methanol flow rate for the 3% methanol mixture was found to be 0.796 mL/min. Considering the 97% water fraction and a 1.5 stoichiometric safety factor, the total flow rate was calculated to be 39.782 mL/min. Yücel et al. (2015) developed a direct methanol fuel cell charger unit for 40W military wireless. The methanol flow rate for the developed fuel cell charger unit was calculated to be 40 mL/min [5].

2.5.2. Methanol Flow Rate Calculation with Power Balance and Efficiency

In this method, methanol flow is calculated by taking into account the total power and energy efficiency of the fuel cell.

Basic Parameters:

- Power per cell: $P = i\,V$ (i: current density, V: cell voltage)
- Total power: $\dot{W}_{for\ 10cell}$ (for 10 cells)
- Energy efficiency (η): %42
- High heating value of methanol: $HHV_{\text{methanol}} = 5540\ Wh/kg$
- Density of methanol: $0.792\ g/mL$

As a result of the calculation through EES, the methanol flow rate was found to be 0.753 mL/min. The lack of significant differences between the results from the two methods indicates that the calculations are generally consistent.

3. RESULTS AND DISCUSSION

The performance of the Direct Methanol Fuel Cell (DMFC) system was analyzed using a zero-dimensional modeling approach. The Engineering Equation Solver (EES) was employed to evaluate the relationships between current density, voltage, and power density under varying operating conditions.

Current Density and Voltage Relationship

The relationship between current density and cell voltage was examined for different operating temperatures, as illustrated in Fig. 1. The results indicate that voltage decreases non-linearly as current density increases, which is a typical behavior in fuel cells due to polarization losses. Higher operating temperatures generally improve reaction kinetics and reduce activation losses, leading to an increase in cell voltage. However, excessive temperatures may result in performance degradation due to membrane dehydration and increased methanol crossover. This trade-off highlights the importance of determining an optimal temperature range to ensure efficient fuel cell operation.

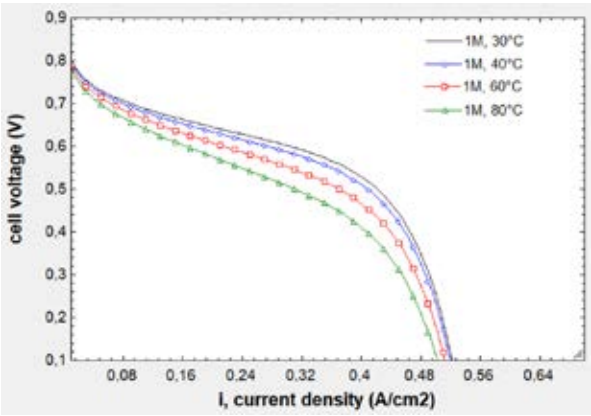

Fig. 1. Current density (A/cm^2) and voltage (V) graph for different operating temperatures

Power Density and Maximum Power Point

The power density curve, shown in Fig. 2, was analyzed to determine the maximum power output conditions. The findings reveal that the maximum power density of 0.166 W/cm² is achieved at a current density of 0.38 A/cm². Beyond this point, power density decreases due to increased ohmic and mass transport losses, which limit the effective utilization of reactants.

The intersection of the I-V and power density (P) curves represents the **maximum power point**, which is crucial for optimizing DMFC performance. Operating the fuel cell at or near this point ensures a balanced trade-off between power output and efficiency. These results underscore the necessity of precise control over fuel cell operating parameters to maximize energy efficiency while minimizing performance losses.

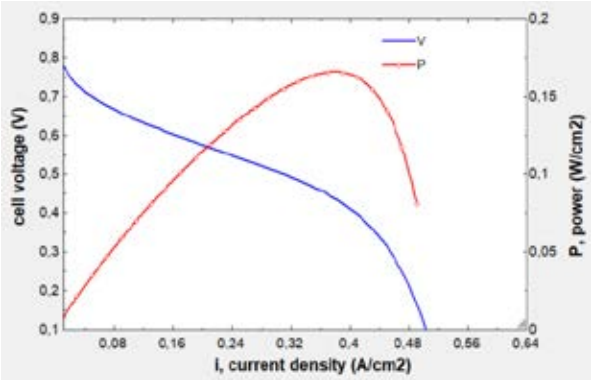

Fig. 2. Current density (A/cm²), voltage (V), and power density (W/cm²) graph

The study demonstrates that semi-empirical modeling is a reliable method for evaluating the performance of DMFCs. The observed trends in Fig. 1 and Fig. 2 confirm that optimizing key parameters such as current density, methanol concentration, and operating temperature is essential for enhancing overall system efficiency.
Future research can focus on refining these models to incorporate additional electrochemical and thermal effects. Additionally, integrating real-time monitoring and control strategies could further enhance the stability and operational longevity of DMFCs, making them more viable for portable energy applications.

4. CONCLUSIONS

This study presents a performance analysis of Direct Methanol Fuel Cells (DMFC) using a zero-dimensional modeling approach based on Meyers and Newman's semi-empirical equations. The results demonstrate that the system reaches its optimal power density of 0.166 W/cm² at a current density of 0.38 A/cm². The analysis of I-V and power density curves indicates that this operating point provides the best balance between energy output and efficiency, with an overall system efficiency of approximately 42%. The methanol flow rate was calculated as 0.796 mL/min using Faraday's law and 0.753 mL/min through energy balance equations, showing consistency between different estimation methods. These findings highlight the effectiveness of zero-dimensional modeling in evaluating DMFC performance, providing valuable insights for optimizing fuel cell operation in portable applications.

REFERENCES

[1] Oliveira V.B., Falcão D.S., Rangel C.M., Pinto A.M.F.R. 2007. A comparative study of approaches to direct methanol fuel cells modelling. International Journal of Hydrogen Energy 32 (3), 415-424.
[2] Ince A.C., Karaoglan M.U., Glüsen A., Colpan C.O., Müller M., Stolten D. 2019. Semiempirical thermodynamic modeling of a direct methanol fuel cell system. International Journal of Energy Research 43 (7), 1-15.
[3] Chiu Y.J., Yu T.L., Chung Y.C. 2011. A semi-empirical model for efficiency evaluation of a direct methanol fuel cell. Journal of Power Sources 196 (11), 5053-5063.
[4] Yang Q., T.L., Kianimanesh A., Freiheit T., Park S.S., Xue D. 2011. A semi-empirical model considering the influence of operating parameters on performance for a direct methanol fuel cell. Journal of Power Sources 196 (24), 10640-10651.
[5] Yücel F., Koç S., Er M., Çelik S. 2015. Askeri Telsizler İçin Doğrudan Metanol Yakıt Pili Şarj Ünitesi Geliştirilmesi 1.Savunma Sanayi Sempozyumu, Turkey.

DEVELOPING AND DESIGNING DIFFERENT CHANNEL TYPES FOR MICRO DIRECT METHANOL FUEL CELLS BASED ON MITOCHONDRIA CELL STRUCTURE

[1,2]*Merve Menteş*, [1,2*]*Ahmed Emin Kılıç*, [1,2]*Selahattin Çelik*, [1,3]*Fatma Doğan Güzel*, [1,2]*Mulatu Kassie Birhanu*
[1] Ankara Yıldırım Beyazıt University, Engineering and Natural Science Faculty, Mechanical Engineering Department, Keçiören, Ankara, 06010, Türkiye
[2] Ankara Yıldırım Beyazıt University, Hydrogen Technologies and Energy Research Center (H2 TEAM), Keçiören, Ankara, 06010, Türkiye
[3] Ankara Yıldırım Beyazıt University, Faculty of Engineering and Natural Sciences, Department of Mechanical Engineering and Biomedical Engineering, 06010, Ankara, TÜRKIYE.
*Corresponding author e-mails: aekilic@aybu.edu.tr

ABSTRACT

This study aims to develop, simulate, and validate different microchannel designs for a micro-sized direct methanol fuel cell (μ-DMFC). Inspired by the structure of mitochondria, novel membrane channels were designed for fuel cell applications. Mitochondria are organelles responsible for energy production within the cell and their structure is curved to increase surface area. The primary goal is to examine how variations in microchannel geometry influence the efficiency and performance of μ-DMFCs. Five different models were developed and simulated to analyze flow behavior and performance characteristics. After the design and simulation phase, microchannels were fabricated using the polydimethylsiloxane (PDMS) method, a widely used technique for microscale applications. Validation is crucial to ensure the reliability of the simulation tools and the accuracy of the predicted results. The outcomes of this study provide significant insights into the impact of microchannel design on μ-DMFC performance. This research highlights the role of advanced manufacturing techniques and optimized channel designs in enhancing micro fuel cell technology. In the simulations, it was observed that the 4th design, inspired by mitochondria, created a 42.76% better power density compared to the classical serpentine design. Considering that this structure provides efficient material transport, a similar principle was adopted in the micro channel design of the micro fuel cell in the study. The aim is to increase cell performance by optimizing fuel and oxidant flows.

Keywords: Micro Direct Methanol Fuel Cell (μ-DMFC), mitochondria-inspired design, microchannel optimization, polydimethylsiloxane (PDMS) fabrication, portable energy systems

1. INTRODUCTION

Among the many green energy sources, fuel cells are one of the most essential technologies that need to be developed worldwide. Fuel cells and hydrogen energy are low-cost carbon-free energy sources. A fuel cell is an electrochemical system that uses two redox processes to transform the chemical energy of an oxidizing agent (usually oxygen) and fuel (usually hydrogen) into electrical energy. In contrast to most batteries, which typically derive their chemical energy from materials already present, fuel cells require a constant supply of fuel and oxygen, typically air, to maintain the chemical reaction. When fuel and oxygen are available, fuel cells constantly generate power. Fuel cells are renewable energy sources with low carbon emissions that do not require a specific place or location for production. The development of direct methanol fuel cells (DMFC) is crucial for the production of green energy resources. DMFC is a type of polymer electrolyte membrane fuel cell that can operate at room temperature. High energy conversion efficiency, low weight, safe fuel storage, and easy refueling are only a few advantages of DMFC. Methanol has additional benefits over hydrogen, including easy handling, storage, and transportation methods, similar to gasoline. In the development of future sustainable energy conversion devices, DMFC has demonstrated superior performance in comparison to traditional internal combustion engines and batteries [1-3]. Fuel-cell technologies are used globally in various applications. Stationary power systems, transportation, space exploration, military applications, radar, communications, portable devices, submarines, fuel cars, and other fields are applications of hydrogen technology and fuel cells [4-7]. Various fuel-cell studies have been performed by different researchers. Ke *et al*. investigated recent developments in noncarbon support materials for advanced and direct methanol fuel cell development [5]. These materials are notable because of their synergistic mechanisms that can prevent Pt poisoning during the reaction process. The use of non-carbon material supports has advantages, such as increased chemical stability, corrosion resistance, and enhanced electrical conductivity. Massing *et al*. developed a novel heating system to accelerate the start-up timing in microfluidic direct methanol fuel cells [6]. The indium tin oxide heating layer helps the cell reach the desired temperature within 25 s, which is an important development of fuel cells in this work. Shen *et al*. developed a monolithic microfluidic proton exchange membrane (PEM) fuel cell by integrating a narrow strip of Nafion into the polydimethyl siloxane (PDMS) structure [2]. The PDMS/Nafion assembly was sandwiched between a glass chip and catalyst-coated Au electrodes to achieve rapid prototyping and sealed fuel cells. The effectiveness of various oxidant solutions and methanol fuel was studied, and the effect of the flow rate on the cell performance was analyzed. This work makes a significant contribution to research on the design and performance of microfluidic PEM fuel cells.

However, most studies did not consider and address the significant impacts and limitations of the technology arising from the design and models of different types of fuel cells. Therefore, in this study, we focused on the design and simulation of different cell models for a micro-sized direct methanol fuel cell (μ-DMFC), each containing different microchannel configurations. Our model was developed based on an impressive mitochondrial cell structure. Mitochondria have different shapes, sizes, and dynamics according to the cell type, energy status, and environment. Several mitochondrial functions are linked to their morphology, which is maintained by fission and fusion. Mitochondria are central to cellular metabolism [7, 8]. For this work, we chose a general structure of mitochondrial organelles. The primary objective is to investigate how changes in the microchannel geometry affect the performance and efficiency of μ-DMFCs. To increase the fuel delivery and cell efficiency, five unique cell models were initially developed, focusing on microchannel layout optimization. Numerical simulations were conducted to predict the flow behavior and performance features of each design. Following the design and simulation stage, the polydimethylsiloxane (PDMS) method, which is a technique known for its sensitivity and adaptability for microscale applications, is used to create microchannels. The fabricated microchannels were then integrated into μ-DMFCs, and a series of performance tests were performed to measure key parameters, such as power output, fuel usage efficiency, and overall cell stability. To verify the models and identify any differences, the simulation data and experimental results were compared. To ensure the accuracy of the anticipated results and reliability of the simulation tools, this verification process is essential. The results of this study provide important information on how microchannel design improves μ-DMFC performance. This study emphasizes the contributions of creative manufacturing techniques and optimized cell channel designs to the field of MFC technology. Ultimately, this effort seeks to advance the development of more effective and efficient μ-DMFCs, while opening the way for their wider use in small-scale and portable generation systems.

2. MODEL DEVELOPMENT

The aim of this model development is to identify the effects of channel design and shape on fuel cell activity with different numbers of inlets and outlets of the fuel cell system. We are inspired by the nature of mitochondrial organelles, and we plan to design a μ-DMFC channel based on the structure of mitochondria (Fig. 1A). A direct methanol fuel cell performs an electrochemical reaction with a mixture of methanol and water fed directly by the anode and oxygen fed by the cathode. The working principle of the electrochemical system based on our model is shown in Fig. 1B. It is known that the membrane structure of mitochondrial organelles provides the energy needs of the cell. Single-, double-, and multiple-channel designs can be created to develop a channel structure that is similar to that of the mitochondrial membrane. Considering the function of the mitochondria, we designed a model based on the structure of this organelle. The general membrane structure was drawn as a channel structure for application in solid works. Therefore, we developed five different designs in two categories (one inlet/outlet, two inlets/outlets, and four inlet/outlet channels). A schematic illustration of the different designs for the two categories is shown in Fig. 2. Design 2, 3, and 4 have two inlets and outlets, whereas Design-5 has four inlets and outlets.

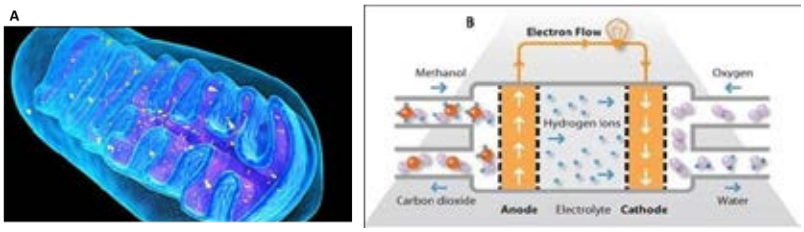

Fig. 1. General view of mitochondria cell structure (A) Credit: science photo library. Working principle of DMFC (B).

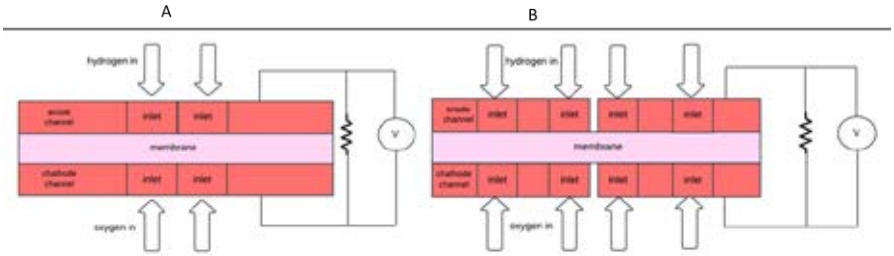

Fig. 2. Schematic illustration for different designs. A. The schematic represents the designs with two inlets (Design 2, 3 & 4). B. The schematic represents the designs with two inlets (Design 5).

3. RESULT AND DISCUSSION

The fuel cell channel designs were developed on a 5 mm × 5 mm square plate, resulting in a total working area of 25 mm^2. The first design includes a commonly used serpentine channel design. The purpose of designing a serpentine channel is to observe the efficiency of new designs compared with a classic design with the same active area of a fuel cell, such as Nafion. The channel bend numbers and bend lines differ from each other. In the designs, the maximum channel length that can fit into the same active area of the fuel cell is the priority of this study. The fuel cells were established based on each design. All schematic channel designs are shown in Fig. 3A. We have showed the demonstration of fuel cells for all designs. However, in this paper, we only showed for design 5 as shown in Fig. 3B.

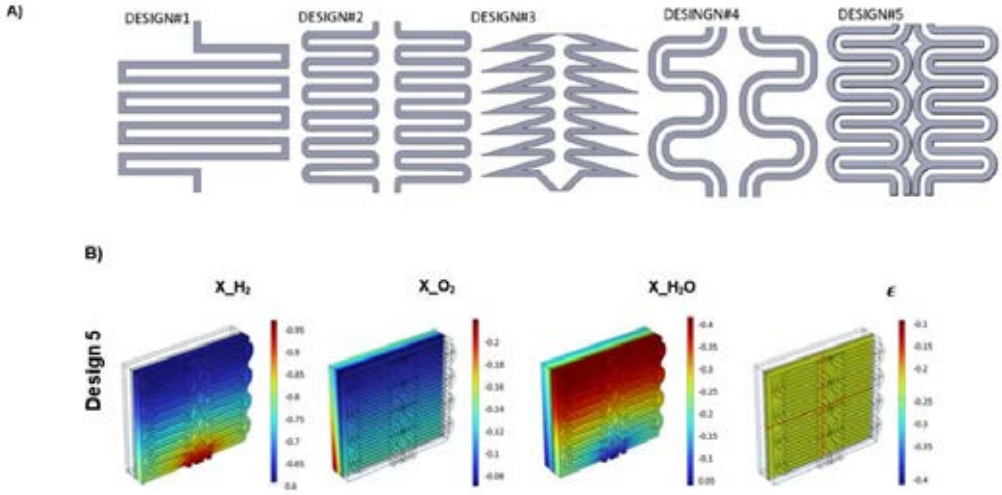

Fig. 3. A) Schematic showing the individual designs (Design 1, 2, 3, 4 & 5) B) Demonstrations of the fuel cell for Design-2 with mole fractions of H_2, O_2 & H_2O, respectively including the electric potential needed (ϵ).

Following the designed channel, it is possible to establish the fuel cell system using each five type channels by incorporating other component such as gas/sample inlet and outlet, power supply, reaction chambers and other constituents of the fuel cell set up. The thicknesses of the gas diffusion layers and reaction layers have set by considering and refereeing various studies and literatures. Each design channel has its specific area and perimeter as shown in Table 1.

Table 1. Perimeter and area dimensions of channel designs

Parameter	Channel				
	Design 1	Design 2	Design 3	Design 4	Design 5
Area (mm^2)	8.69	11.14	12.10	8.20	9.64
Perimeter (mm)	86.58	115.04	123.14	83.48	96.44

Our model development is carried out based on COMSOL 6.1 simulation program. It is known that the COMSOL software is used worldwide as an indispensable tool for various computer simulations for research and development and for multiple types of learning related to model and design development. It is a general-purpose simulation software package for modeling designs, devices, and processes in all fields of engineering, manufacturing, and scientific research. This study uses a hydrogen fuel cell (methanol oxidation) module and free and porous media to analyze the performance of fuel cells with different channel designs. For the design, channels and layers we have done as best as possible in a way suitable for simulation. The fuel cell designs will be simulated in two different types i.e. PEM and DMFC. The designed model channel setup includes H_2, O_2, H_2O mole fractions and electric potential analysis. This model is planned to observe the distribution of H_2, O_2, and H_2O in the cell and the electric potential distribution. The module created in the COMSOL simulation program was run and simulation results were obtained for the 5 fuel cell designs indicated in Fig. C and D. Results are recorded in the context of the values of the applied potential, mole fractions of H_2, O_2 and water. When the analyses are examined, channel designs must have a certain channel area to produce voltage. Although there is 0.96 mm^2 between Design-2 and Design-3, the power density in Design-3 is 19.91% higher than the power density in Design-2. Although the area of Design-2's channel is higher than the area of Design-4 and Design-5, high current is generated using Design-4 and Design-5 fuel cells. Design-3 has the highest channel area in which it generates the highest electricity. However, increasing the channel area does not necessarily increase the energy produced. Using each design, the simulation of voltage versus current density, power versus current density and power versus voltage is shown in Fig.4. When the simulation analysis is carried out, channel designs must have a certain channel area in order to produce

voltage. Although Design-1 has 0.49 mm^2 more area than Design-4, the fuel cell using Design-4 produced a power density of 17.62 mW/m^2 more than the fuel cell using Design-1. Although the channel area of Design-2 is more than the channel area of Design-4 and Design-5, the fuel cell used in Design-4 and Design-5 produced more electricity. The graph shows that the amount of electricity produced by the fuel cell depends on the channel design and shape.

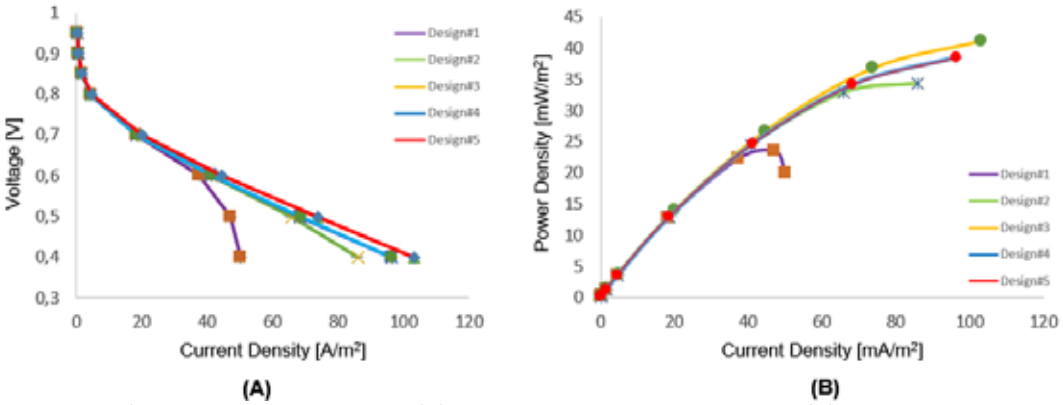

Fig. 4. Simulation results of voltage vs. current density (A), power density vs. current density (B) and power density vs. voltage using each design channel (Desing-1 to Design-5).

4. CONCLUSION

The development of single and multiple inlet/outlet channel designs demonstrated a significant impact on micro fuel cell performance. Among the channels of five designs 1, 2, 3, 4, and 5 were obtained to be suitable for fuel cell applications, with channel of Design-3 yielding the best power. To enhance manufacturability and ensure ease of assembly, modifications were made for the inlet and outlet configurations of channel of Design-1. Additionally, the complexity of channel of Design-5's structure was simplified to improve production feasibility. Future studies will focus on analyzing DMFCs with different channel designs and comparing their performance with PEM fuel cells. Inspired by the natural structure of mitochondria, this research contributes to the development of new μ-DMFC models with improved efficiency. These advancements aim to optimize fuel cell performance for portable and small-scale energy applications, paving the way for more practical and effective designs in the future. In the simulations, current density and power density values for five different designs are measured at eight different voltage levels: 0.95V, 0.90V, 0.85V, 0.80V, 0.70V, 0.60V, 0.50V and 0.40V. The highest current density for Design-1 was determined as 50.03 mA/m² at 0.4V, while 85.94 mA/m², 103.05 mA/m² and 96.28 mA/m² values were obtained for Design-3, Design-4 and Design-5 at the same voltage, respectively. The highest current density of Design-2 was measured as 96.31 mA/m² at 0.4V. In terms of power density, the highest value of Design-1 was recorded as 34.38 mW/m² at 0.5V; while for Design-2, Design-3, Design-4 and Design-5, the values were found as 41.22 mW/m², 38.51 mW/m², 38.52 mW/m² and 38.51 mW/m² at 0.4V, respectively. According to the simulation results, the best performance in terms of both current density and power density was obtained in Design-3.

ACKNOWLEDGEMENT

This research was funded by TÜBİTAK under the 2209-A Program (Project No: 1919B012323797). The authors sincerely thank TÜBİTAK for its support.

REFERENCES

[1] Alobeid M, Çelik S, Ozcan H and Amini Horri B. 2024. Flow Configurations of Membraneless Microfluidic Fuel Cells: A Review. Energies 14:3381.
[2] Yagiz M and Çelik S. 2025. Experimental investigation of bio-inspired flow field designs for direct methanol fuel cell. Fuel 381:133624.
[3] Tanveer M and Kim KY. 2021. Flow Configurations of Membraneless Microfluidic Fuel Cells: A Review. Energies 14:3381.
[4] Sun MH, Casquillas GV, Guo SS, Shi J, Ji H, Ouyang Q and Chen Y. 2007. Characterization of microfluidic fuel cell based on multiple laminar flow. Microelectronic Engineering 84:1182–1185.
[5] Ke Y, Zhang B, Bai Y, Yuan W, Li J, Liu Z, Su X, Zhang S, Ding X, Wan Z, Tang Y and Zhou F. 2023. Bubble-derived contour regeneration of flow channel by in situ tracking for direct methanol fuel cells. Energy 264:126167.
[6] Massing J, van der Schoot N, Kahler CJ and Cierpka C. 2019. A fast start up system for microfluidic direct methanol fuel cells. International journal of hydrogen energy 44:26517-26529.
[7] Yang Z, Wang L, Yang C, Pu S, Guo Z, Wu Q, Zhou Z and Zhao H. 2022. Mitochondrial Membrane Remodeling. Frontiers in Bioengineering and Biotechnology 9:786806.
[8] Alan L and Scorrano L. 2022. Shaping fuel utilization by mitochondria. Current Biology 32:589–683.

HYDROGEN ECONOMY: KEY DEVELOPMENTS IN CHINA, EUROPE, AND THE USA

[1*]*Dilek Unguder*, [1]*Anne-Charlotte Krutoff*, [1]*Mona Wappler*
[1] Rhein-Waal University of Applied Sciences, Faculty of Communication and Environment, Friedrich-Heinrich-Allee 25
47475 Kamp-Lintfort, North Rhine-Westphalia, Germany
*Corresponding author e-mail: dilek.uengueder@hochschule-rhein-waal.de

ABSTRACT
Hydrogen can be a key player in the global transition to cleaner energy, offering a sustainable and versatile solution to reduce carbon emissions across various sectors such as transportation, industry, and power generation. However, the development of the hydrogen market differs widely across countries and regions, shaped by the energy structure, resources, and goals of the countires. This study aims to compare the hydrogen market developments in China, Europe, and the USA by exploring the differences in national targets, regulatory frameworks and support mechanisms, and project pipelines. The findings of the study suggest that in Europe, hydrogen market development is slow but steady, with firm steps taken to ensure long-term growth and sustainability. In contrast, in China developments occur at a rapid pace, positioning the country as a frontrunner in the hydrogen market. Meanwhile, in the USA, the Inflation Reduction Act was initially seen as a game changer, and expected to have a significant positive impact on hydrogen market development. However, following the recent elections and the transition to a new administration, the outlook for hydrogen market development in the USA has become uncertain since the implementation of key acts lingers in a state of ambiguity.

Keywords: Clean hydrogen market, Regional analysis, China, Europe, the USA

1. INTRODUCTION

Clean hydrogen is seen as a key element in achieving the energy system transition. As countries all over the world have formulated emission reduction targets to mitigate climate change, viable and cost-effective decarbonization pathways are needed to support these strategies. Produced via zero or low carbon methods, clean hydrogen offers cross-sectoral opportunities to cut the carbon footprint. With more than 99% of current hydrogen production based on high emission production methods, a transition to clean hydrogen has the potential to decarbonize both existing applications, e.g. in industry and refineries, as well as new applications such as aviation, shipping or energy generation and storage [1].
While still an emerging market, the clean hydrogen industry is gaining traction. Based on project announcements, clean hydrogen production can reach 48 Mt p.a. by 2030. As of 2024, USD 75 billion have been invested in clean hydrogen projects in committed stages, the amount having almost doubled within a year [2]. However, several obstacles are hindering faster market development. To close the cost gap, stimulate demand and production, and reduce regulatory uncertainty, action is necessary. Against this background, hydrogen roadmaps have been formulated worldwide, highlighting different goals and strategies and providing insights into intended market-building efforts. Additionally, several countries and regions have started implementing policies and support mechanisms tailored to their individual hydrogen strategies. Thus, the clean hydrogen industry is currently characterized by high dynamics and regional disparities, and therefore warrants careful analysis.This paper provides an overview of recent developments in three frontrunners of the industry, China, Europa and the USA. By reviewing hydrogen strategies, implemented regulations, support mechanisms, and project pipelines, it offers an in-depth understanding of the hydrogen market status and outlook in these regions.

2. MATERIALS AND METHODS

This study provides an analysis of the hydrogen markets in China, the USA, and Europe by examining multiple sources to highlight the status of the key developments in these regions. First, national roadmaps and strategy documents from each region are reviewed to identify their main targets and strategic goals related to hydrogen market development. Next, the analysis explores the regulations and policies enacted by each region to support hydrogen market growth, focusing on the legal frameworks and incentives designed to meet their hydrogen targets. Additionally, news articles and media coverage are included to gather general insights into public reactions and industry sentiment surrounding the regulations and market developments.Finally, the study incorporates recent reports from the International Energy Agency (IEA) and the Hydrogen Council to assess the progress of hydrogen project pipelines in each region. This multi-source approach enables a comprehensive understanding of the evolving hydrogen landscape in China, the USA, and Europe.

3. REGIONAL ANALYSIS

The national hydrogen roadmaps and strategies for hydrogen market development differ significantly across countries and regions, primarily due to differences in their energy structures, resource availability, and future energy needs. As a result, each region sets distinct goals for hydrogen adoption, targeting various sectors and transition strategies. To meet these strategic goals, regulations and policies focus on different priorities, such as creating demand, mitigating investment risks, supporting domestic manufacturing of hydrogen technologies, and encouraging innovation and research. Additionally, the support mechanisms utilized, such as grants, competitive bidding schemes, contracts for difference, and tax incentives, can vary significantly from one region to another [1]. These differences make direct

comparisons between regions challenging, but this study aims to provide a concise overview of the national strategies and regulatory frameworks in China, Europe, and the USA. Morevover, the examination of the hydrogen project pipeline in each region might offer insights into how these varying strategies and support mechanisms may influence the development of the market. The following sub-sections will explore each region's hydrogen market in more detail, focusing on national strategies, key regulatory drivers, and developments in the project pipeline.

3.1. China

The Medium- and Long-term Plan for the Development of the Hydrogen Energy Industry (2021-2035), published by China's National Development and Reform Commission in March 2022, outlines the strategic direction for the country's hydrogen energy sector through 2035. The document sets specific targets for 2025, including the deployment of 50,000 fuel cell electric vehicles (FCEVs) and the production of 0.1 to 0.2 million tons of green hydrogen annually. The supply strategy emphasizes not only green hydrogen but also the use of industrial by-product hydrogen, particularly in the short term, given its wider availability. However, the plan does not address the role of Carbon Capture, Utilization, and Storage (CCUS) technologies, leaving them out of the hydrogen development strategy [3]. Although the central government's targets may seem modest, the primary driving force in China comes from regional strategies. A range of provincial hydrogen development frameworks, each designed to align with local resources, capabilities, and specific requirements, supports the national plan. In some provinces, hydrogen development plans can be more ambitious than the national plan. For instance, Inner Mongolia alone plans to produce nearly 0.5 million tons of green hydrogen per year by 2025, a target that greatly exceeds the national goal of 0.1 to 0.2 million tons [4]. When the production goals of other provinces are summed up, the total hydrogen production target reaches up to 1.2 million tons annually, demonstrating the crucial role of regional initiatives in propelling China's hydrogen market development [1].

China's approach to foster the hydrogen market demonstrates collaborative characteristics between central and regional governments. The central government sets the main framework and serves as a role model by promoting technological advancements, research activities, strategic initiatives, and pilot projects. Additionally, it provides financial rewards to regional governments that achieve their targets. For example, USD 109 million was awarded for the first phase of FCEV pilot programs to provinces that met their goals [1]. Meanwhile, regional governments handle the implementation and management of specific targets, offering financial incentives and support mechanisms that are specifically tailored to the needs of the region, to drive local hydrogen market development. As an example, Inner Mongolia is a favorable location for green hydrogen production due to its abundant renewable energy sources, and the region provides subsidies to support production. In Ordos City, which is located in the province, green hydrogen production is supported with subsidies ranging from USD 0.28 to 0.57 per kilogram of hydrogen based on sales volume from 2022 to 2025. In Hebei province, where FCEVs are prioritized, both CAPEX subsidies of up to USD 280,000 for hydrogen refueling stations and OPEX subsidies of USD 2.8 per kilogram of hydrogen for stations selling hydrogen below USD 4.2 per kilogram are offered. In the Ningdong region, to boost the demand, companies utilizing green hydrogen receive subsidies of approximately USD 0.79 per kilogram of hydrogen over a three-year period [1],[4].

The division of responsibilities between regional and central governments in China appears to be effective, as the rapid pace of developments in the hydrogen market is unparalleled anywhere else in the world. Hydrogen production projects in China which have passed final investment decision (FID) and are expected to be operational by 2030, have reached 1.4 Mt p.a., accounting for 30% of the committed global capacity of 4.6 Mt p.a.. More than 95% of this production capacity is dedicated to renewable hydrogen. Moreover, China is leading in terms of installed electrolyzer capacity. As of May 2024, installed electroylzer capacity in China has reached 1150 MW, which accounts for 65% of the installed capacity worldwide. Additionally, the scale of projects in China is larger than in the rest of the world. For instance, the Ningxia Solar Hydrogen Project, with a 150 MW electrolyzer installation, and Sinopec's Kuqa plant, with a 260 MW installed electrolyzer capacity, set records for the largest hydrogen plants in 2021 and 2023, respectively [2]. These achievements position China as the frontrunner in the global hydrogen economy.

3.2. Europe

In July 2020, the European Commission published the hydrogen strategy for the European Union. The strategy's main focus was on green hydrogen, which is produced through water electrolysis powered by renewable energy sources. The strategy set an initial target of installing 6 GW of electrolyzer capacity in the EU by 2024 to produce 1 million tonnes (Mt) of green hydrogen. The next step in the strategy is to increase the installed electrolyzer capacity to 40 GW by 2030, with the goal of securing the production of 10 Mt of green hydrogen. Moreover, the strategy aims to support the installation of an additional 40 GW of electrolyzer capacity in the neighboring regions of the EU, showcasing the EU's ambition to lead the global hydrogen economy beyond its own borders [5]. EU member states also published their own hydrogen roadmaps in alignment with the EU strategy, further strengthening the coordinated efforts toward developing a hydrogen market in Europe.

In June 2023, to bring regulatory clarity to what counts as green hydrogen, the European Commission adopted two delegated acts. These acts introduced the term renewable fuel of non-biological origin (RFNBO), which refers to fuels produced from renewable electricity. The main objective of these acts was to define renewable hydrogen based on the calculation of life-cycle greenhouse gas emissions, and categorize it under the term RFNBO [6]. Following this, in October 2023, the European Union increased the share of renewable energy target to 42.5% by 2030 with Renewable Energy Directive III (RED III). To reach this target, the directive defines separate sub-targets for the use of RFNBOs in the

transport, industry, and building sectors. As an example, for the industry sector, the directive mandates that 42% of hydrogen used should come from RFNBOs by 2030 and 60% by 2035, excluding by-product hydrogen. There is a possibility to discount the contribution of RFNBOs in industry use by 20% if the expected overall contribution of the member state is realized and the share of hydrogen from fossil fuels does not exceed 23% in 2030 and 20% in 2035. Furthermore, the directive addresses the slow permitting process for renewable energy solutions (RES) projects. Member states should determine renewables acceleration areas that allow for simplified and faster processing of permits. According to the directive, the maximum allowed permit-granting time for RES projects should not exceed 12 months, with an exception for offshore wind projects, which can take two years due to their higher complexity [7]. In addition to regulations, several hydrogen projects receive subsidies as Important Projects of Common European Interest (IPCEIs) and benefit from investment aids. For example, the IPCEI projects Hy2Tech and Hy2Use, funded with a total of EUR 10.6 billion, include the development of electrolyzer and hydrogen infrastructure technologies, as well as the advancement of technologies for various end-use applications [8], [9].

Considering these regulations and subsidies, it can be stated that the European Union addresses both the production and consumption side of the hydrogen market with concrete targets and with very detailed specifications. However, this level of detail might be hindering project realisations. In terms of number of announced hydrogen projects and total investments, Europe leads the world with 617 projects and USD 199 billion, respectively. However, the actualization of projects has been relatively slow. As of May 2024, the installed electrolyzer capacity in Europe is only 250 MW, which falls significantly short of the 6 GW target set for 2024. When considering the hydrogen production target for 2030, the announced 13 Mt p.a. production capacity has exceeded the 10 Mt target. However, only 0.3 Mt p.a. is currently committed, with around 2.9 Mt p.a. at the Front-End Engineering Design (FEED) stage. This means that the majority of the projects are still in the announcement phase or undergoing feasibility studies [2]. Under these circumstances, it is still in question whether Europe will manage to speed up the development of the hydrogen market in the upcoming years. The answer to this might lie in how member states implement the binding consumption targets and the faster processing of permits defined by the RED III directive.

3.3. USA

The official U.S. National Clean Hydrogen Strategy and Roadmap came into force in June 2023. According to the roadmap, the USA aims to achieve a clean hydrogen demand of 10 Mt by 2030, 20 Mt by 2040, and eventually 50 Mt by 2050. Additionally, the strategy specified cost reduction targets for clean hydrogen production. The USA aims to reduce the production cost of hydrogen via electrolysis to USD 2/kg H_2 by 2026, and USD 1/kg H_2 before 2035 [10].

In the USA, two key support mechanisms target the development of the clean hydrogen market: the Bipartisan Infrastructure Law, and the Inflation Reduction Act (IRA). As part of the Bipartisan Infrastructure Law, USD 8 billion has been allocated to establish hydrogen hubs in various regions across the country. These hubs differ in production methods, end-use applications, and funding levels. For example, the California Hydrogen Hub and the Pacific Northwest Hydrogen Hub focus on producing hydrogen solely from renewable energy sources. In contrast, the Appalachian Hydrogen Hub leverages the extensive natural gas resources in the West Virginia, Ohio, and Pennsylvania region. The Heartland Hydrogen Hub aims to decarbonize the agricultural sector by using clean hydrogen in fertilizer production, while the Midwest Hydrogen Hub targets supplying clean hydrogen to steel and glass producers. Additionally, USD 1 billion of the allocated funding is designated for end-users to boost demand for clean hydrogen within these selected hubs [11]. With the Inflation Reduction Act (IRA), introduced in August 2022, nearly USD 400 billion was allocated to clean energy investments through tax incentives, grants, and loan guarantees by the Biden administration. The IRA positively impacted hydrogen projects in the USA by providing incentives for solar and wind power facilities, clean fuel production, and tax credits for hydrogen production and CCUS deployment. Following the introduction of the IRA, both green and clean hydrogen production projects gained momentum in the USA, as the act's technology-neutral approach ensures that tax credits for hydrogen production are based on emission levels. For example, green hydrogen, with emissions lower than 0.45 tons of CO_2 per ton of hydrogen qualifies for the full tax credit of USD 3.00/kg H_2. In contrast, hydrogen with emissions of 4 tons of CO_2 per ton, the maximum eligible threshold set by the Department of Energy (DOE), receives a reduced tax credit of USD 0.60/kg H_2 [12].

The availability of vast natural gas and renewable energy resources, combined with these powerful acts, makes the USA a favorable location for a hydrogen economy. However, as of May 2024, only 110 MW of electrolyzer capacity has been installed in the USA. The share of blue hydrogen projects is higher than that of renewable hydrogen projects in the country. Blue hydrogen, produced from natural gas with CCUS, is more prevalent in the region due to the availability of natural gas resources and the relative easiness of converting existing SMR plants, while renewable hydrogen projects usually require the new installation of solar or wind infrastructure. This also increases the share of projects that have reached the maturity stages in the USA compared to Europe and China. Based on projects that have passed the FID stage, around 1.6 Mt of clean hydrogen production is committed in the USA by 2030, with approximately 85% being blue hydrogen [2], [12]. Yet the future of the project pipeline remains uncertain under the newly elected administration, as the disbursement of funds from the IRA and bipartisan infrastructure law has been paused in January 2025. [13].

4. CONCLUSION

The clean hydrogen industry is evolving rapidly, driven by distinct strategies and regulatory frameworks across different

regions. Table 1 compares the main factors discussed above for China, Europe, and the USA. In China, the collaborative efforts between central and regional governments have led to swift advancements in the hydrogen market. This positions the country as a frontrunner in the clean hydrogen market. In Europe the pace of market development remains slow. How member states will implement the robust but very specific regulations will impact the future of the market growth. Yet it can be stated that increased synergy between the EU-level directives and country-level implementations is essential for achieving cohesive progress. In the USA, with its abundant resources and the momentum gained from announced policies, the market was on track to become a clean hydrogen industry leader. However, recent political developments have put a brake on this progress by creating uncertainty regarding the implementation of the announced acts.

Table 1. Summary of Key Hydrogen Market Findings by Region

	China	Europe	USA
Main Roadmap Target	0.1 -0.2 Mt p.a. clean H_2 production capacity and deployment of 50 000 FCEVs by 2025 [3]	40 GW installed electrolyzer capacity by 2030 to produce 10 Mt green H_2 [5]	10 Mt clean H_2 demand by 2030 and reduction of cost of hydrogen with electrolysis to USD 2/kg H_2 by 2026 [10]
Key Regulatory Drivers & Funding Opportunities [1]	Provincial hydrogen targets and subsidy policies	Renewable Energy Directive (RED) III Important Projects of Common European Interest (IPCEIs)	Bipartisan Infrastructure Law Inflation Reduction Act (IRA)
Clean H_2 production capacity past FID until 2030 as of May 2024 [2]	≈ 1.4 Mt p.a (>95% renewable)	≈ 0.30 Mt p.a (≈ 60% renewable)	≈ 1.6 Mt p.a (≈ 15% renewable)
Installed Electrolyzer Capacity as of May 2024 [2]	1150 MW	250 MW	110 MW

ACKNOWLEDGEMENT
The research was funded by the German Federal Ministry of Education and Research under the grant no. 03HY102.

REFERENCES
[1] IEA, “Global Hydrogen Review 2024,” IEA, Paris, Oct. 2024. Accessed: Feb. 21, 2025. [Online]. Available: https://www.iea.org/reports/global-hydrogen-review-2024
[2] Hydrogen Council, “Hydrogen Insights 2024,” Sep. 2024. [Online]. Available: https://hydrogencouncil.com/en/hydrogen-insights-2024/
[3] National Development and Reform Commission, “氢能产业发展中长期规划（2021-2035 年）.” Mar. 23, 2022. Accessed: Feb. 21, 2025. [Online]. Available: https://www.gov.cn/xinwen/2022-03/24/5680975/files/6b388f7c324a4b1db0b30dc6f52b7e02.pdf
[4] Y. Lou and A.-S. Corbeau, “China’s Hydrogen Strategy: National vs. Regional Plans,” Center on Global Energy Policy at Columbia University SIPA | CGEP. Accessed: Feb. 21, 2025. [Online]. Available: https://www.energypolicy.columbia.edu/publications/chinas-hydrogen-strategy-national-vs-regional-plans/
[5] European Commission, “A Hydrogen Strategy for a Climate-Neutral Europe.” Jul. 08, 2020. Accessed: Feb. 21, 2025. [Online]. Available: https://eur-lex.europa.eu/legal-content/EN/TXT/?uri=CELEX:52020DC0301
[6] “Renewable hydrogen - European Commission.” Accessed: Feb. 25, 2025. [Online]. Available: https://energy.ec.europa.eu/topics/eus-energy-system/hydrogen/renewable-hydrogen_en
[7] Directive (EU) 2023/2413 of the European Parliament and of the Council of 18 October 2023 amending Directive (EU) 2018/2001, Regulation (EU) 2018/1999 and Directive 98/70/EC as regards the promotion of energy from renewable sources, and repealing Council Directive (EU) 2015/652. 2023. Accessed: Feb. 25, 2025. [Online]. Available: http://data.europa.eu/eli/dir/2023/2413/oj/eng
[8] “Remarks by Executive Vice-President Vestager,” European Commission - European Commission. Accessed: Feb. 25, 2024. [Online]. Available: https://ec.europa.eu/commission/presscorner/detail/en/SPEECH_22_4549
[9] “State Aid,” European Commission - European Commission. Accessed: Feb. 25, 2025. [Online]. Available: https://ec.europa.eu/commission/presscorner/detail/en/ip_22_5676
[10] The U.S. Department of Energy, “U.S. National Clean Hydrogen Strategy and Roadmap.” Jun. 2023. Accessed: Feb. 21, 2025. [Online]. Available: https://www.hydrogen.energy.gov/library/roadmaps-vision/clean-hydrogen-strategy-roadmap
[11] T. W. House, “Biden-Harris Administration Announces Regional Clean Hydrogen Hubs to Drive Clean Manufacturing and Jobs,” The White House. Accessed: Feb. 24, 2025. [Online]. Available: https://bidenwhitehouse.archives.gov/briefing-room/statements-releases/2023/10/13/biden-harris-administration-announces-regional-clean-hydrogen-hubs-to-drive-clean-manufacturing-and-jobs/
[12] Hydrogen Council and McKinsey & Company, “Hydrogen Insights 2023: An update on the state of the global hydrogen economy, with a deep dive into North America,” May 2023. Accessed: Sep. 06, 2023. [Online]. Available: https://hydrogencouncil.com/en/hydrogen-insights-2023/
[13] H. Siri, “Trump puts clean hydrogen hopefuls back on defense after tax credit debate,” S&P Global Commodity Insights. Accessed: Feb. 25, 2025. [Online]. Available: https://www.spglobal.com/commodity-insights/en/news-research/latest-news/electric-power/013125-trump-puts-clean-hydrogen-hopefuls-back-on-defense-after-tax-credit-debate

ENHANCED PEM WATER ELECTROLYSIS WITH LOW EQUIVALENT WEIGHT AQUIVION® MEMBRANES

[1*]*Fausta Giacobello*, [1]*Stefania Siracusano*, [1]*Maria Aurora Mancuso,* [1]*Veronica Cicciò*[1], [1]*AlessandraMuscolino,* [1]*Antonino S. Aricò*
[1] CNR – ITAE, Institute of Advanced Energy Technologies, National Research Council, Via Salita S. Lucia sopra Contesse 5, 98126 Messina, Italy
*Corresponding author e-mail: fausta.giacobello@itae.cnr.it

ABSTRACT
This study evaluates the performance and durability of various Aquivion® membranes for PEM electrolysis, focusing on different configurations: bare cast polymers, polymers with radical scavengers and reinforced ones. Membrane-electrode assemblies (MEAs) were produced and tested for hydrogen production by means of polarization curves, electrochemical impedance spectroscopy (EIS) and long-term durability tests. Microscopic and physico-chermical analyses (TEM, SEM, optical microscopy, XRD, XRF,) were used to understand the membrane and ionomer structure and its impact on performance. The goal was to identify optimal membrane strategies for enhancing PEM water electrolysis efficiency and stability in green hydrogen production.

Keywords: Water electrolysis, Hydrogen, proton exchange membrane

1. INTRODUCTION

The transition to clean energy is crucial for sustainable growth and climate change mitigation. However, challenges exist in developing efficient energy vectors and integrating them with renewable energy sources and existing infrastructure. Water electrolysis, using surplus renewable electricity to produce green hydrogen, presents a promising solution. [1]

Green hydrogen from electrolysis offers advantages in energy storage, transportation, and diverse applications across energy and industrial sectors. Proton exchange membrane (PEM) electrolysis is particularly attractive due to its high efficiency, purity, rapid response times, compact design, and direct high-pressure hydrogen production, reducing downstream compression costs. [2, 3] These factors support the development of hydrogen market, given hydrogen's transportability and broad applicability in fuel cells, chemical synthesis, and industrial processes.

Nevertheless, large-scale PEM electrolysis implementation requires advancements in membrane technology. PEM membranes must provide high proton conductivity while maintaining chemical and mechanical stability under demanding operational conditions. [4, 5] Membrane degradation negatively impacts system lifespan, maintenance, and production costs. Developing robust and efficient PEM membranes is therefore vital for widespread adoption of PEM electrolysis. High-performance, stable ionomers are critical for efficient PEM water electrolysis. This study compares three membrane types a bare cast membrane, a membrane incorporating a radical scavenger (RSP-50) and a reinforced membrane to assess their performance and stability. Membrane-electrode assemblies (MEAs) were subjected to polarization tests, electrochemical impedance spectroscopy (EIS), and long-term (2000 hour) stability testing. Microscopic and physico-chermical analyses analyses (XRD, XRF, TEM, SEM, optical microscopy) were employed to correlate membrane properties with MEA performance. The findings aim to identify strategies for optimizing membrane characteristics to enhance PEM water electrolysis.

2. EXPERIMENTAL

2.1. Membrane-electrode assemblies (MEAs) - preparation

Four distinct Aquivion® membranes composed of the same polymer, Aquivion® perfluorosulfonic acid (PFSA), with an equivalent weight of 720 g/eq, were examined for the single cell characterizations: reinforced membrane R720, reinforced membrane NR720, cast membrane C720, and cast membrane with radical scavenger C720-RSP-50.

Two distinct grades of expanded PTFE fibers were used as support to create reinforced Aquivion® membranes. The primary distinction between the two e-PTFE grades is based on the characteristics of ePTFE in NR720, which exhibit greater thickness and mechanical qualities in comparison to grade ePTFE in R720.

Membrane-electrode assemblies were made using the catalyst-coated technique, in which the ionomer ink of the catalyst was sprayed directly onto the membrane. With the help of an automated equipment (Sono-Tek, model Exacta Coat), which has an ultrasonic nozzle (AccuMist, 128 kHz) that enables the nebulization of the ink based on the catalyst, the catalyst coated membranes (CCMs) were produced using a spray coating approach.

2.2. Electrochemical characterization

To assess the electrolysis performance at various temperatures (30 to 90 °C), electrochemical studies were conducted in a single cell with an active area of 5 cm^2. More in detail, polarization curves (voltage vs. current density) and electrochemical impedance spectroscopy (EIS) were carried out obtaining, the series resistance, Rs, by using the Nyquist plot as the high-frequency point where a curve intersection occurs on the real axis. Conversely, the difference between the low and high frequency intercepts on the real axis was used to infer the polarization resistance, or Rp.

3. RESULTS AND DISCUSSION

Both reinforced and radical scavenger-based membranes achieved excellent electrolysis performance, 1.87 V at 5 A cm^{-2}, and 79% voltage efficiency at 90°C. High voltage efficiency minimizes renewable energy consumption and green hydrogen cost, while high current density reduces capital costs due to increased production rates, this is essential for reducing the use of critical raw materials (CRMs).

Both CeO_2 (radical scavenger) and PTFE (reinforcement) fillers slightly improved proton conductivity, likely by altering membrane morphology and ionic pathways. Both reinforced and radical scavenger membranes exhibited similar stability over 2000 hours, with initial degradation attributed to increased series resistance (Rs) possibly due to initial impurity release. The test was carried out at 1 A cm^{-2} for 100 h at the beginning and there after a switch to 5 A cm^{-2} was carried out. The voltage loss was 39 μV/h and 46 μV/h for the R720 and CAST-RSP-50-based MEAs, respectively over 2000 h at 5 A cm^{-2}.

Polarization resistance (Rp), primarily related to the catalytic layers, increased slowly, minimally affecting initial degradation.

Post-mortem analysis (XRD, TEM and SEM) revealed negligible changes in the catalytic layers and minimal membrane thinning, suggesting excellent long-term durability. The reinforced membrane showed the lowest temperature dependence of Rs, and Rp was the dominant factor influencing performance at high current densities.

4. CONCLUSIONS

Due to their improved crystallinity, stronger protonic conductivities, and higher glass transition temperature compared to traditional Nafion® equivalents, Aquivion® membranes and associated ionomer dispersions are achieving popularity in PEM electrolysis. These increased characteristics allow them to function in a broad temperature range and provide better performance in PEM electrolysis. The possibility of modifying these membranes by adding reinforcing fillers or radical scavengers can provide further insights into improved chemical stability and mechanical tolerance against peroxide radical threat. These characteristics are crucial for electrolysers that offer a longer lifetime than traditional Nafion® electrolyte-based electrolysis systems.

ACKNOWLEDGEMENT

The authors acknowledge the financial support from the ADVANCEPEM project. This project has received funding from the European Union's Horizon Europe research and innovation programme under grant agreement No 101101318.

REFERENCES

1. A.S. Aricò, S. Siracusano, N. Briguglio, V. Baglio, A. Di Blasi, V. Antonucci. 2013. Polymer electrolyte membrane water electrolysis: status of technologies and potential applications in combination with renewable power sources, Journal of Applied Electrochemistry, 43:107-118.
2. A.A. Kebede, T. Kalogiannis, J. Van Mierlo, M. Berecibar 2022. A comprehensive review of stationary energy storage devices for large scale renewable energy sources grid integration, Renewable and Sustainable Energy Reviews, 159:112213.
3. T. Freire-Barceló, F. Martín-Martínez, Á. Sánchez-Miralles. 2022. A literature review of Explicit Demand Flexibility providing energy services, Electric Power Systems Research, 209:107953.
4. M. Canavar, Y. Kaplan. 2015. Effects of mesh and interconnector design on solid oxide fuel cell performance, International Journal of Hydrogen Energy, 40:7829-7834.
5. M. Carmo, D.L. Fritz, J. Mergel, D. Stolten. 2013. A comprehensive review on PEM water electrolysis, International Journal of Hydrogen Energy, 38:4901-4934.

DETERMINATION OF GREEN HYDROGEN PRODUCTION CAPACITY BY WAVE ENERGY PREDICTION: MODEL DEVELOPMENT WITH AN ADAPTIVE HYBRID METHOD

Mustafa Tan[1]
[1]Department of Electric-Electronic Engineering, Faculty of Engineering and Architecture, Tokat Gaziosmanpasa University, 60150, Tokat, Turkey

* Correspondence: mustan79@gmail.com

ABSTRACT: In today's world of ever-increasing energy dependency, fossil fuels are still the primary source of energy. However, the environmental pollution and global warming caused by these resources have led countries to look for new sources. For this reason, the use of hybrid renewable energy is increasing day by day in many developing countries. Wave, wind, solar, hydro and similar sources are the most preferred renewable energy sources. In addition, hydrogen fuel, which is gaining popularity today, is another storable, clean renewable energy source that can be easily produced by electrolysis of water. This study aims to estimate the amount of emission-free hydrogen that can be produced by an electrolysis process using wave energy. An innovative adaptive model using data parsing and deep learning architectures is proposed. The prediction results show that high regression and low error values are obtained.

Keywords: Hydrogen production, Wave energy, Electrolysis, Renewable energy

1. INTRODUCTION

Since the last quarter of the twentieth century, the reduction of developing technologies to individual use and the increase in their diversity, and the accompanying increase in urbanization and population have made the need for energy important. However, a significant portion of energy is still obtained from fossil resources. The more important problem than the scarcity of these resources is that they cause climate change with their carbon emissions [1]. For this reason, many studies have been carried out to regulate the use of renewable energy sources found in nature for the utilization of energy resources. Renewable energy sources include wave energy, wind energy, solar energy, biomass energy, hydrogen energy, hydroelectric energy, tidal energy and geothermal energy. Wave energy is a renewable energy source that aims to generate electricity using the kinetic and potential energy of waves moving on the surface of oceans and seas. This energy is a clean and sustainable alternative with the potential to reduce dependence on fossil fuels [2]. Therefore, with the increasing demand for wave energy, different fields of study have emerged in the literature. Considering the stochastic nature of waves, it is important to accurately predict the wave height for efficient energy production [3]. At the same time, the many advantages of hydrogen fuel as an alternative to energy sources increase the interest in the product. Hydrogen fuel is considered an energy carrier and is an excellent energy source that can be used to replace traditional fuels [4]. An important feature that makes hydrogen fuel unique is that it can be stored. Therefore, it can be used as an energy provider anytime, anywhere [5]. This advantage is very useful in renewable energy sources where it increases system efficiency during periods when electricity generation is intermittent as a result of the demand-supply balance in the grid [6]. Therefore, excess electricity generated from renewable energy sources can be used to produce hydrogen as a clean fuel and stored for later supply during peak times when demand is high [7].

In this study, an adaptive innovative model (Iterated Frequency Decomposition (IF) - Multiple Fractional Generalized Fluctuation Analysis (NF-DFA) - Bidirectional Long Short-Term Memory Network (BI-LSTM)) is proposed for hydrogen quantity forecasting. For this purpose, firstly, the wave height, which is the most important input of the wave energy system, was estimated. Using the obtained results, the electrical power required for the catalyst process was calculated. Finally, the amount of hydrogen likely to be obtained through the necessary conversions was determined.

2. METHODOLOGY

In this section, the definition of the study area and obtaining the wave height data, decomposition of the wave height data, construction of the wave height prediction model, calculations required for the electrolysis process according to the wave energy power, and estimation of the amount of hydrogen likely to be produced are presented in detail.
In this study, the province of Samsun, Turkey was selected as the reference for the case study to show the potential wave energy on the southern coast of the Black Sea. The data set used was obtained from the SAMSUN Offshore Buoy (E:41.4375 W:36.475834) of the General Directorate of Meteorology. The data set consists of 35040 hours of standard meteorological data. The dataset includes the parameters Significant Wave Height (SWH), Dominant Wave Period (DPD), Average Period (APD), Mean Wave Direction (MWD), Water Temperature (WTMP). These data were used for the analysis. Missing data were filled using a linear interpolation method that gives greater weight to the nearest available value. From these data, a dataset of 35040 units was created using data from 2020-2023. Iterated Frequency Decomposition (IF) was used to decompose this data set. IF is a decomposition technique that provides a complete reconstruction of the original signal and a better spectral separation of the intrinsic mode functions (IMFs) [8].
The obtained IMFs were combined according to their dominant fractal properties with the MF-DFA method and a new

data was obtained. This method is used to analyze multiple fractal properties of time series. **MF-DFA** is especially preferred for analyzing data with intrinsic scaling properties in fields such as finance, biology, climate sciences and engineering [9]. The Bidirectional Long Short-Term Memory Network (BI-LSTM) deep network model was used in the prediction process. LSTM is a type of **recurrent neural network (RNN)** model that can learn long-term dependencies. However, the standard LSTM only processes data from the past to the future. The **BI-LSTM, on the other hand, processes data both from the past to the future and from the future to the past**, thus learning **contextual information better. When BI-LSTN is analyzed, it has been reported that it provides better accuracy in applications such as speech recognition, text processing, time series prediction, and can learn long-term dependencies** more effectively than standard LSTM [10]. The power of the wave energy was determined by using the parameters in the data set, especially the wave height and period. Depending on the determined wave power, the necessary calculations used in the hydrogen production stages were made and the amount of hydrogen expected to be produced according to the estimated wave height was determined.

3. RESULTS AND DISCUSSIONS

The graph of the wave height change measured by the buoy off Samsun between 2020-2023 is shown in Fig. 1. Of these, 24528 data were used as training data, 8760 data as test data and 1752 data as validation data for the prediction process.

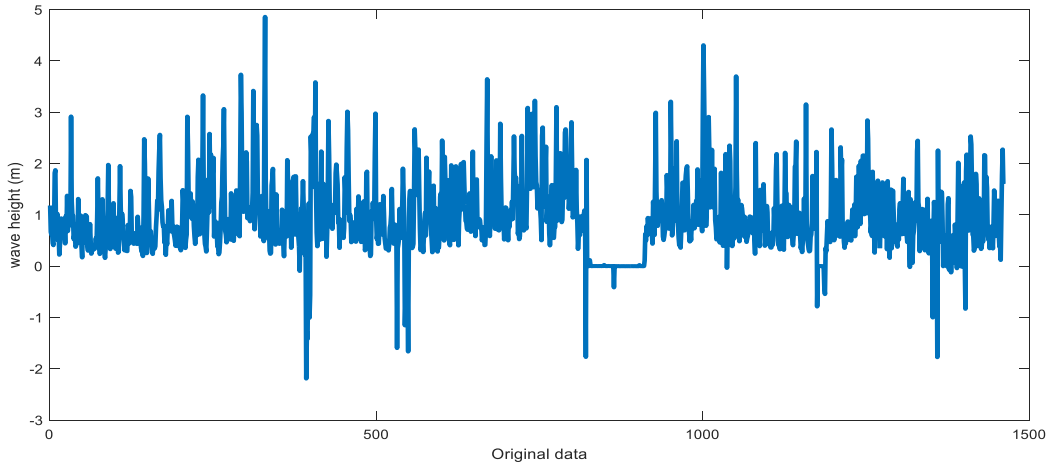

Fig. 1. Wave height variation

The data set used was subjected to decomposition by the IF method and 7 internal mode functions were obtained. The variations of the obtained internal mode functions are shown in Fig. 2.

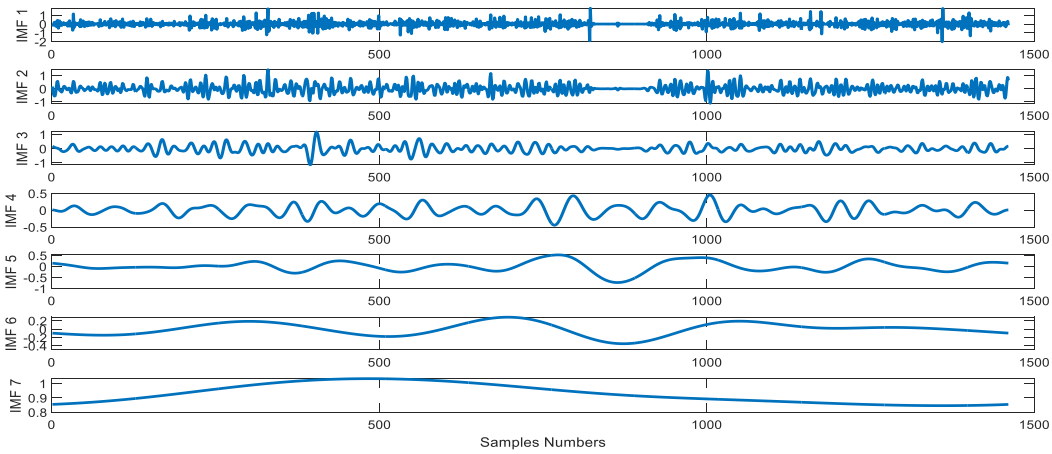

Fig. 2. Internal Mode Functions (IMF1-IMF7)

Each of the IMFs was analyzed by MF-DFA, and the IMF series showing dominant fractal characteristics (IMF2-IMF3-IMF5) were collected and a new data was generated and shown in Fig. 3.

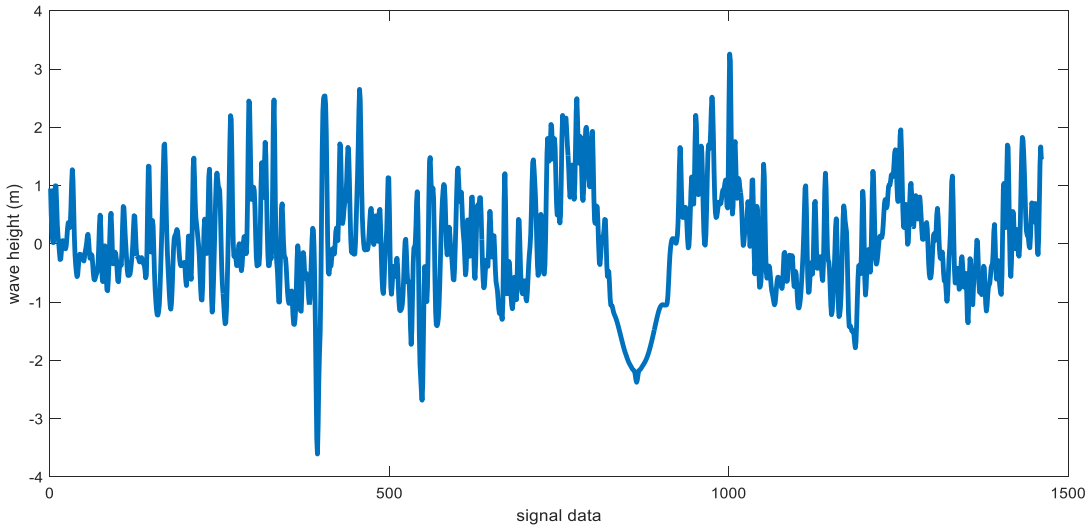

Fig. 3. Data graph obtained as a result of MF-DFA analysis

According to the prediction model, the proposed adaptive model (IF - MF-DFA - BI-LSTM) performed more accurately and reliably than the other methods compared in Table 1.

Table 1. Performance Metrics

Models	MAPE	R^2	RMSE
IF - MF-DFA - CLSTM	1.650	0.930	1.447
IF - MF-DFA – LSTM	46.482	0.079	1.400
IF - MF-DFA - BI-LSTM	1.313	0.953	0.859
IF - MF-DFA - CGRU	2.171	0.896	1.475
IF - MF-DFA – GRU	101.138	0.012	4.265
IF - MF-DFA - CRNN	1.373	0.869	1.404
IF - MF-DFA – RNN	70.383	0.018	2.198

On the basis of the obtained estimation results, the necessary calculations for the electrolysis process using wave energy in the region selected for the case study were performed and the daily amount of hydrogen production for one year was estimated for the proposed and other models. The difference between the calculated amount of hydrogen that can be produced and the estimated amount of hydrogen that can be produced is shown in Fig. 4. In addition, the total estimated amount of hydrogen energy for one year is shown in Table 2.

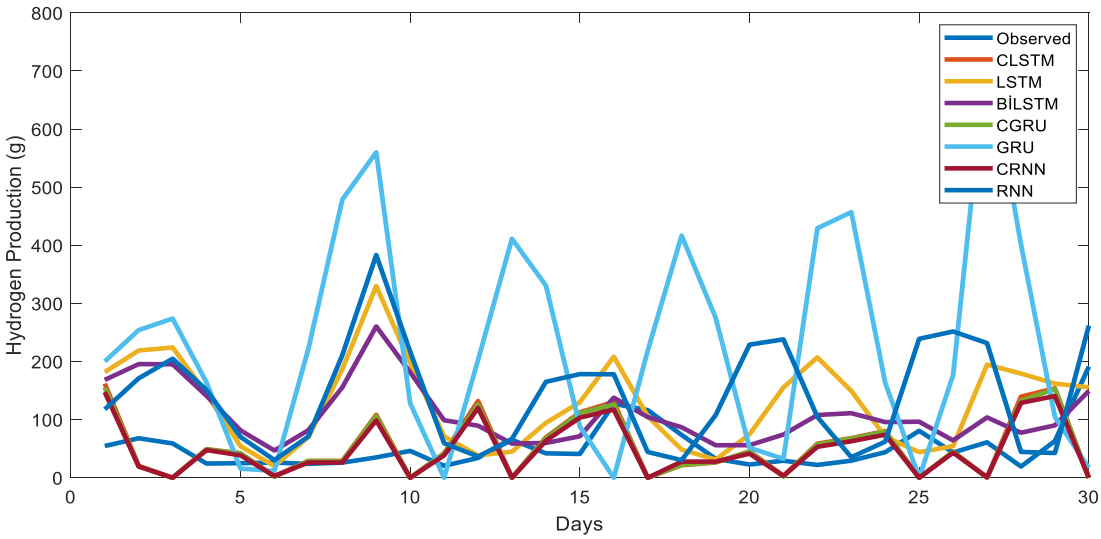

Fig. 4. Determined hydrogen production for all models in 30 days

Table 2. Hydrogen production

Models	The Amount of hydrogen produced per day (Gr)	The amount of hydrogen produced per year (kg)
TEST DATA SET	60.337	21.84
IF - MF-DFA - CLSTM	65.412	23.68
IF - MF-DFA – LSTM	129.769	46.98
IF - MF-DFA - BI-LSTM	62.044	22.46
IF - MF-DFA - CGRU	64.428	23.32
IF - MF-DFA – GRU	278.677	100.88
IF - MF-DFA - CRNN	64.281	23.27
IF - MF-DFA – RNN	172.713	62.52

4. CONCLUSIONS

In this study, 1-year hydrogen production is estimated. Wave energy is used as the source for hydrogen production. Wave height, which is the most important input of wave energy, is estimated using the proposed innovative adaptive model. Thus, using the system parameters, the actual amount of hydrogen energy to be produced by the proposed model was estimated with an accuracy of 97.32%.

REFERENCES

[1] Das H.S., Tan C.W., Yatim A.H.M., Lau K.Y., Feasibility analysis of hybrid photovoltaic/ battery/fuel cell energy system for an indigenous residence in East Malaysia, Renew Sustain Energy Rev, 76, 1332–47, (2017).
[2] Akpınar, A. Ve Kömürcü, M.I., 2012. Wave energy potential along the south-east coasts of the Black Sea, Energy 42 (1) (Jun. 2012) 289–302
[3] Paduano B, Parrinello L, Niosi F, Dell'Edera O, Sirigu SA, Faedo N, et al. To-wards standardised design of wave energy converters: A high-fidelity modelling approach. Renew Energy 2024;224:120141
[4] Sun H., Ebadi A.G., Toughani M., Nowdeh S.A., Naderipour A., Abdullah A., Designing framework of hybrid photovoltaic-biowaste energy system with hydrogen storage considering economic and technical indices using whale optimization algorithm, Energy, 238, 121555, (2022).
[5] Wakui T., Akai K., Yokoyama R., Shrinking and receding horizon approaches for long-term operational planning of energy storage and supply systems, Energy, 239, 122066, (2021).
[6] Kovac A, Marcius D, Budin L. Solar hydrogen production via alkaline water electrolysis. International Journal of Hydrogen Energy 2019;44:9841-9848.
[7] Pelaez-Pelaez S., Colmenar-Santos A., Perez-Molina C., Rosales A.E., Rosales-Asensio E., Techno-economic analysis of a heat and power combination system based on hybrid photovoltaic-fuel cell systems using hydrogen as an energy vector, Energy, 224, 120110, (2021).
[8] Guermoui, M., Bouchouicha, K., Bailek, N., & Boland, J. W. (2021). Forecasting intra-hour variance of photovoltaic power using a new integrated model. Energy Conversion and Management, 245, 114569.
[9] J.W. Kantelhardt, S.A. Zschiegner, E. Koscielny-Bunde, S. Havlin, A. Bunde, H.E. Stanley, Multifractal detrended fluctuation analysis of nonstationary time series, Physica A (2002) 28.
[10] Jaseena, K. U., & Kovoor, B. C. (2021). Decomposition-based hybrid wind speed forecasting model using deep bidirectional LSTM networks. Energy Conversion and Management, 234, 113944.

DEVELOPMENT OF HYDROGEN POWERED EJECTION SYSTEM FOR AIR PLATFORMS

[1*]*Talha KALAY*, [1,2]*Hasan ÖZCAN*, [1,2]*Selahattin Çelik*
[1] Ankara Yıldırım Beyazıt University, Faculty of Engineering and Natural Sciences, Mechanical Engineering Department, Institute Address, Ankara, 06010, Türkiye
[2] Hydrogen Technologies and Energy Research Centre (H2 TEAM), Ankara Yıldırım Beyazit University, Ankara 06010, Türkiye

*Corresponding author e-mail: talha.kalay@tubitak.gov.tr

ABSTRACT
Hydrogen is a potential alternative solution for ejection systems that separate stores from air platforms. In this study, Hydrogen powered ejection system is developed instead of conventional ejection systems. This system contains hydrogen production and storage equipment. Ignition of the mixture of gases which contains onboard produced Hydrogen in the combustion chamber. In-cylinder pressure reaches to 350 bar and pistons push to eject the external stores from air platform.
In this study, the ejection system performance characteristics were examined using the laws of thermodynamics and ideal gas equations. For this purpose, previously tested conventional ejection system performance data are collected for a wide range of stores. Aircraft compatibility issues are considered to determine the usage concept of a hydrogen-powered ejection system. Then, sizing and rating calculations are carried out on these configurations. Engineering Equation Solver and Comsol Multiphysics software are used to compute performance predictions of the system and compare them to previous system data. The design of the electrolyzer and storage equipment depends on the calculated amount of hydrogen required.
It has been found that hydrogen is a very suitable and clean alternative for ejection systems, and the practical costs of maintenance are very low compared to other systems.
Keywords: Store Separation, Hydrogen, Bomb Rack Unit, Ejection System, Aircraft

1. INTRODUCTION
Bomb Rack Units are used to launch external stores from aircraft. The most widely used ejection systems use electrically ignited impulse cartridges or a compressed air vessel. The unit's ejection pistons are touching to store and always ready-to-launch. In this study, MAU-12 ejector rack's ejection system will be replaced with hydrogen powered ejection system. Hydrogen is less corrosive for bomb rack units rather than cartridge explosive system since it only emits water vapor when it burns. Air platform and maintenance personnel are also at risk when carrying the compressed air vessel on board.

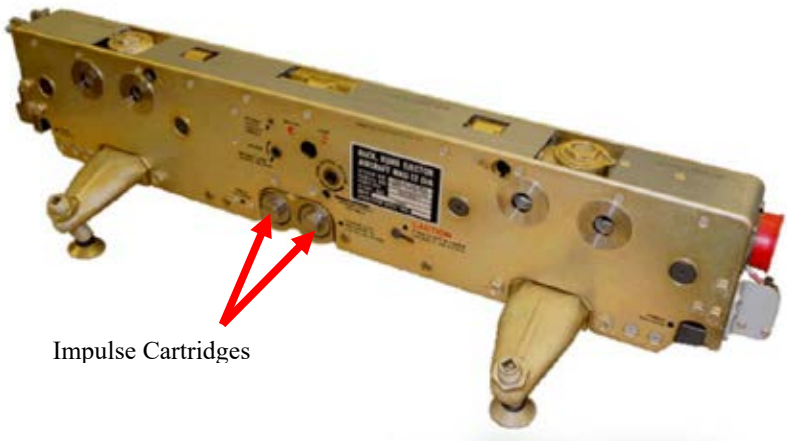

Fig. 1. Bomb Rack Unit (MAU-12)

Researchers are studying ejection systems for air platforms; however, they haven't looked into hydrogen-powered ejection systems yet. This system has never been integrated on an air platform and has no current applications. For this reason, conventional ejection systems are being studied. Hydraulic, Pneumatic, Thermal Controlled and Cold Gas systems are also developed for ejection in the literature.
This study is driven by the belief that using Hydrogen as an alternative to other systems in ejection on the air platform will prevent maintenance costs from increasing and degradetion of ejection system. System development is carried out and the ejection system performance is calculated. Zero dimensional simulations are run for verification of calculations.

2. SYSTEM MODELING
System model is developed based on conceptual usage of F-16 aircraft which is considered as air platform. Hydrogen is produced onboard by a water electrolyser. All water splitting technologies are examined and PEM water electrolyser is

selected to produce Hydrogen from water. Usable volume in the bomb rack unit is constraining the dimensions of PEM electrolyser and water tank dimensions. Unit is examined for external dimensions of electrolyser is maximum 50x50x80 mm. Bomb rack unit's explosive cartridge slots are used as combustion chamber in this system. Produced Hydrogen can be storaged in metal hydrides in the Unit or directly filled in the combustion chamber and ignited by the pilot's signal.

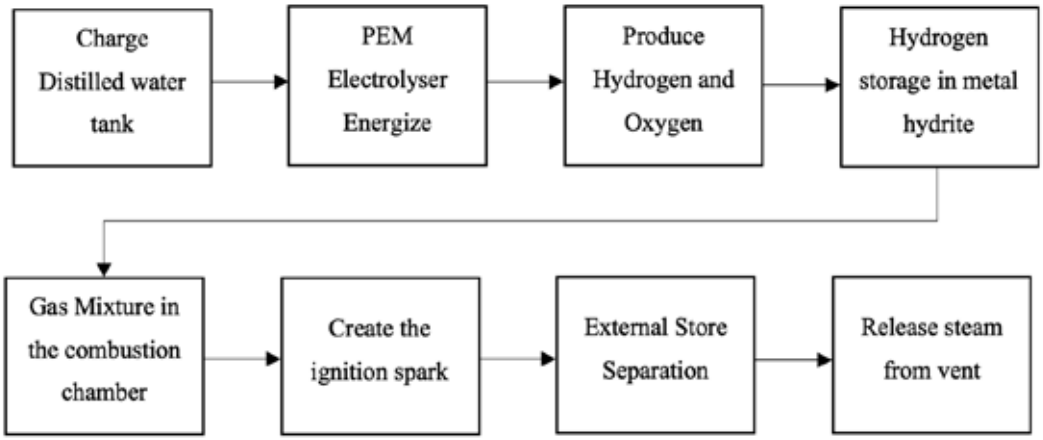

Fig. 2. System Functional Flow

Electrical power for Hydrogen production could be supply from the aircrafts power distribution system or an external battery. There is a usable volume in the aircraft's pylon for battery placement.

2.1. PEM Water Electrolysis

Proton exchange membrane (PEM) water electrolysis has emerged as a major technique for the creation of hydrogen, because of its great efficiency and small size [1]. PEM electrolysers are superior to traditional alkaline electrolysers in that they can run at pressures greater than 100 bars and reach higher current densities, which increases both the overall efficiency of the system and the purity of the hydrogen produced[2].

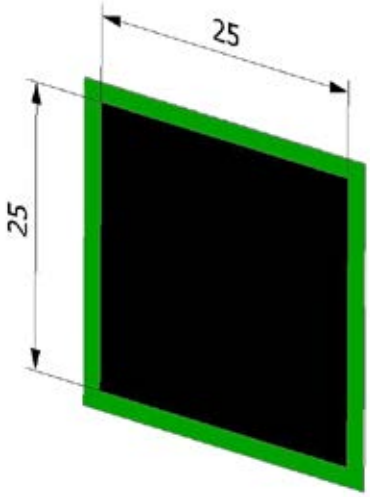

Fig. 3. Proton Exchange Membrane Dimensions

The solid polymer electrolyte membrane is the fundamental part of PEM electrolysers. It blocks gases such as hydrogen and oxygen and only permits protons to pass through. As shown in **Error! Reference source not found.**, gas crossing is avoided and high-purity hydrogen output is guaranteed by this feature[3].
Designed electrolyser contains 12 cells and each cell has 25x25 mm Proton Exchange Membrane surface.

2.1. Required Piston Force

The ejector performance requirement can be figured out by applying ground tests to MAU-12 ejector with different weights of the external stores under investigation. Test data obtained regarding the performance of the MAU-12 ejector with explosive cartridges were added to the literature by Carter . As shown in **Error! Reference source not found.**4, experimental data regarding the single piston forces in lbf obtained using different weights are shown. The unit of piston forces is lbf. Required piston forces and in-cylinder pressure values for each weight of external store given in Table 1.

Table 1. Required piston force and in-cylinder pressure values

Heaviest External Store [lb]	Piston Force [N]	In-Cylinder Pressure [bar]
4800	34500	358,6

MAU-12 ejector has pistons to eject external store. Given performance datas is for aft and forward single pistons applied force. The thrust-generating mechanism in the pistons is separated into four states as shown in Fig.5, for the purpose of simplifying design calculations. Assumptions for each state are done and mathematical models set in the Engineering Equation Solver program. The calculations are based on these assumptions.

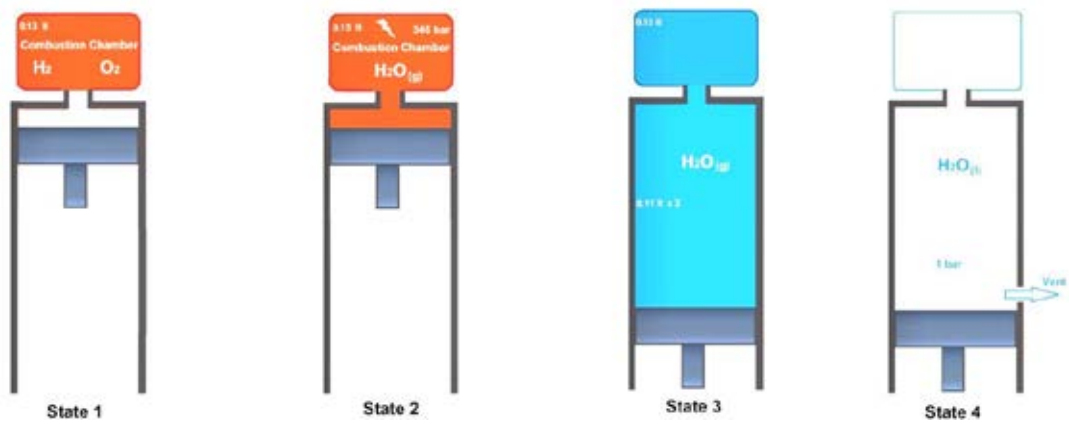

Fig. 4. Four States of Ejection

In the first state, required Hydrogen mass which was produced in PEM electrolyser and stored in metal hydrite is sent to combustion chamber. Gas mixture is ready to ignite in chamber. In this state, the temperature of the gas mixture assumed is 27° [C]. In the second state, an ignition spark is created when the pilot of the air platform pushes the pickle button. The gas mixture is burned immediately and in-cylinder pressure increases. There is no displacement of the pistons in this state, so volume is assumed to be constant. This process is assumed to be adiabatic because burning is completed in miliseconds[4]. The third state is the expansion of the aft and forward pistons affected by in-cylinder pressure. External store reaches the end of stroke velocity after expansion. When stroke is completed in fourth state, a ventilation line is opened, and in-cylinder pressurized steam is vented to the atmosphere.

2.2. Required Hydrogen Mass

In this study, required Hydrogen mass calculations are carried out for combustion with pure oxygen and dry air. Stoichiometric combustion reaction equations are calculated and solved in Engineering Equation Solver. Adiabatic flame temperature of Hydrogen when combusted with dry air is 2400 [K][5]. P[1] is the initial pressure in the first state and P[2] is the in-cylinder pressure. Required Hyrdogen amount providing P[2] value 350 bar is approximately obtained.

$$H_2\,(g) + 0{,}5\,O_2(g) + 1{,}881 N_2\,(g) \rightarrow H_2O\,(g) + 1{,}881\,N_2\,(g) \quad (1)$$

Using pure oxygen as oxidizer increases the adiabatic flame temperature to 4920 [K][6]. As shown in Fig.6, approximately obtained Hydrogen amount combusted with pure oxygen is providing P[2] value 350 bar.

$$H_2\,(g) + 0{,}5\,O_2(g) \rightarrow H_2O\,(g) \quad (2),$$

3. RESULTS AND DISCUSSIONS

Comsol Multiphysics software is used to simulate zero-dimensional combustion reactions to obtain and verify in-cylinder pressure values as shown in Fig .5.

Designed PEM electrolyser placement in Bomb Rack Unit is shown in Fig. 6. Development and design process are in progress. Hydrogen production rate of electrolyser will be obtained and system ready to ejection times for each weight of store will be calculated. All component designs and technical drawings will be completed in the end of study.

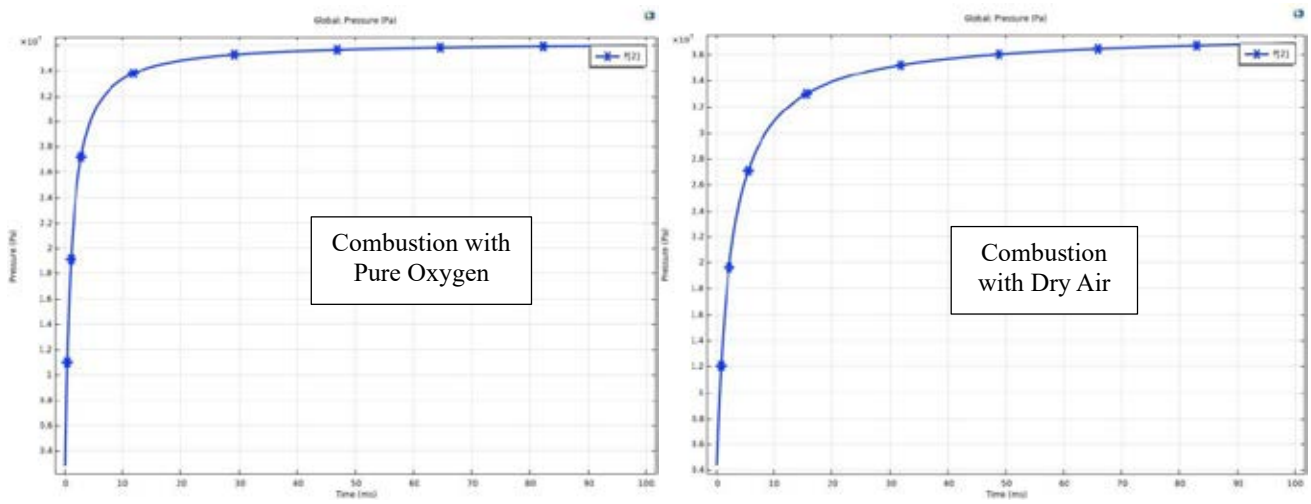

Figure 5. In-cylinder Pressure During Combustion

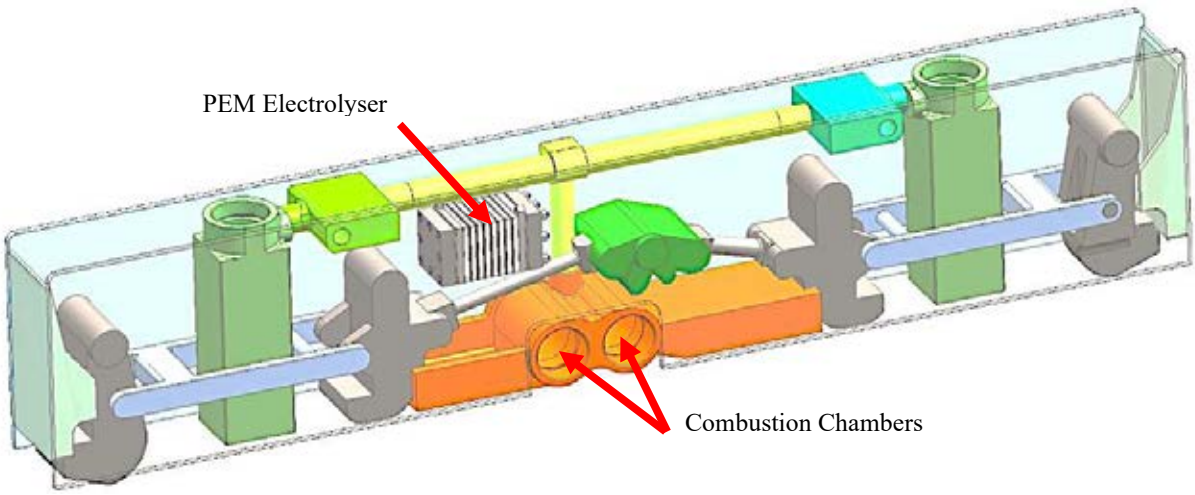

Fig. 6. PEM Electrolyser Placement in the Bomb Rack Unit

4. CONCLUSIONS

This study demonstrates the potential of Hydrogen as an alternative for conventional ejection systems. The PEM electrolyzer is designed and mounted in the bomb rack unit. The results of the calculations and analysis are provided. In order to evaluate the design, studies have been conducted based on conceptual alternatives. Moreover, this system can be designed for different air platforms for ejection of the external stores.

REFERENCES

1. Carmo M, Fritz DL, Mergel J and Stolten D. 2013. A comprehensive review on PEM water electrolysis. Int J Hydrogen Energy. 38(12):4901-4934915.
2. Slade S, Campbell SA, Ralph TR and Walsh FC. 2002. Ionic Conductivity of an Extruded Nafion 1100 EW Series of Membranes. J Electrochem Soc. 149(12):A1556.
3. Millet P. 2015. PEM Water Electrolysis. In: Hydrogen Production. 63-116.
4. Kozak MT, Yildiz EN, Yazicioglu Y and Cigeroglu E. 2013. Effects of Aircraft Aeroelastic Deformations on External Store Separation Dynamics.
5. Sforza PM. Combustion Chambers for Air-Breathing Engines. In: Theory of Aerospace Propulsion. Elsevier.

DESIGN OF SINGLE POROUS TRANSPORT LAYER WITH STRUT-BASED LATTICE STRUCTURES FOR PEM ELECTROLYZERS

[1,2*]*Kayhan Dağıdır*, [2,3]*Alperen Çankaya*, [2,3]*Selahattin Çelik*
[1] Tarsus University, Faculty of Engineering, Department of Mechanical Engineering, 33400 Mersin, Turkiye
[2] Hydrogen Technologies and Energy Research Center (H2 TEAM), Ankara Yıldırım Beyazıt University, 06010 Ankara, Turkiye
[3] Ankara Yıldırım Beyazıt University, Faculty of Engineering and Natural Sciences, Department of Mechanical Engineering, 06010 Ankara, Turkiye
*Corresponding author e-mail: kayhandagidir@tarsus.edu.tr

ABSTRACT
This study presents the geometric design of single-layer porous transport layers (PTLs) with strut-based lattice structures for proton exchange membrane (PEM) electrolyzers, aiming to enhance mass transport, electron conductivity, and gas removal efficiency. Conventional PTLs often suffer from high interfacial resistance and suboptimal water management, limiting overall electrolyzer performance. To address these challenges, this work explores novel lattice geometries with tunable porosity and superior fluid dynamics characteristics. Additive manufacturing is highlighted as a key fabrication technique, enabling precise control over structural parameters and scalability in production. Preliminary findings indicate that optimized lattice designs can effectively minimize mass transport losses and improve water utilization. This study establishes a foundation for further experimental validation and optimization, contributing to the advancement of high-efficiency and cost-effective PEM electrolyzers for sustainable hydrogen production.

Keywords: PEM electrolyser, lattice structure, porous transport layer, additive manufacturing, hydrogen production.

1. INTRODUCTION
Proton exchange membrane (PEM) electrolyzers are a key technology for green hydrogen production and experts emphasise that water electrolysis is the most effective zero-emission hydrogen production technology when a renewable energy source such as solar energy is used as an electricity source [1]. In the electrolysis of water, Proton Exchange Membrane (PEM) electrolysers are widely used to produce high purity hydrogen at high efficiency. PEM electrolysers, which are already commercially available, have a similar operating principle to fuel cells and can produce hydrogen with approximately 99.9% purity [2]. Although PEM electrolysers provide the advantage of high purity green hydrogen production, they also bring disadvantages such as high material cost, cross-permeability phenomena that increase with pressure, and the presence of water vapour that requires dehumidification with the produced hydrogen [3]. On the one hand, the possibility of high purity green hydrogen production increases the interest in PEM electrolyzers, and on the other hand, studies on the development of the system are continuing [4]. Web of Science [5] data, it is seen that the number of research on PEM electrolysers is quite low compared to fuel cells. This has generally been the case in the past, and studies on fuel cells have been at higher levels compared to electrolyzers [6].

The performance and durability of these systems are strongly influenced by the design and material properties of their internal components, particularly the porous transport layer (PTL). The PTL plays a crucial role in facilitating water distribution, gas removal, and electron transport while minimizing interfacial resistance and mass transport losses. The aim of this study is to increase the electrochemical reaction efficiency in the system by improving the fluid distribution with flow fields designed as a single piece using lattice structured porous material for PEM electrolysers.

Recent advancements in additive manufacturing have enabled the development of tailored PTL structures with enhanced transport properties. Strut-based lattice structures, in particular, offer a highly tunable architecture with optimized porosity, permeability, and mechanical stability. Unlike conventional sintered or fibrous PTLs, lattice-based designs can improve fluid dynamics, reduce pressure drop, and enhance water management within the electrolyzer. Additionally, additive manufacturing allows for precise control over geometric features, enabling the fabrication of complex PTLs with high reproducibility and scalability [7-9].

By integrating advanced lattice structures into PEM electrolyzers, the efficiency and cost-effectiveness of green hydrogen production can be significantly improved. This study explores the potential of single-layer PTLs with strut-based lattice geometries, laying the foundation for future experimental validation and optimization. Lesmana and Aziz [10] utilised porous material with lattice structure in a cell type called gyroid to increase heat transfer efficiency and consequently hydrogen storage capacity. As a result of the study, it was reported that the use of cage structured porous material with a wall thickness of 1 mm gave very good results in terms of volumetric capacity, material weight and thermal efficiency. Peng et al. [11] placed a high thermal conductivity lattice-structured porous material in the adsorbent bed to improve the system performance in an adsorption-based hydrogen storage system. As a result of the study, it was reported that the use of lattice-structured porous material allows lower average bed temperature, higher hydrogen fraction and larger adsorption amount compared to finned structures. However, studies on the use of lattice-structured porous materials in

hydrogen technologies are very limited in the current literature. At the same time, there are currently no studies on the use of these materials in PEM electrolyser flow fields. In this context, the use of cage structured porous materials as a single piece in porous flow fields consisting of multiple layers to improve electrochemical performance in PEM electrolysers is seen as a promising application.

2. MATERIALS AND METHODS

In this study, the effects of innovative flow field designs containing porous material with lattice structure on system performance will be investigated to increase electrochemical efficiency in PEM electrolyser. PEM electrolysers consist of a compression plate, bipolar plates, gas diffusion layer and membrane electrode assembly. The main components of a PEM electrolyser are shown in Fig. 1a and detailed views of the components are shown in Fig. 1b.

The compression plates are used to fix the PEM electrolyser cell and are manufactured from aluminium alloy. Bipolar plates are used to evenly distribute the voltage supplied by the power supply by connecting multiple electrolysis cells in series. These separator plates contain various flow field channels and are manufactured from materials with properties such as high thermal conductivity, high mechanical strength, high chemical stability and low resistivity to enhance the heat transfer mechanism. Titanium is generally considered to be the most suitable material to meet these properties and is widely used. The gas diffusion layer ensures efficient mass transfer by electrical conductivity and fluid flow between the membrane and the bipolar plate. At the anode, purified liquid water is transported from the bipolar plate through the current collector to the catalyst layer on the membrane, where it decomposes into oxygen and protons. The released oxygen diffuses in the direction opposite to the flow direction from the current collector. At the cathode, liquid water and hydrogen are transported from the membrane through the current collector to the bipolar plate gates. Electrons start from the catalyst layer on the anode side, pass through the current collector and bipolar plate and reach the cathode side. The membrane is the most basic component of the electrolyser process in which water is separated into hydrogen and oxygen by exposure to electric current. It is a material that conducts protons coated with porous flow areas on the anode and cathode sides. At the anode, water is split into oxygen and protons. Protons pass to the cathode, while electrons pass to the cathode through the external circuit. At the cathode, protons gain electrons to form hydrogen gas. This study focuses on the PTL obtained by stacking titanium meshes on the left and right sides of the membrane shown in Fig. 2. On both the anode and cathode side, the titanium meshes will be designed as a single piece of porous materials with a lattice structure. Thus, the additional resistances occurring at the interfaces of the stacked grid structures will be eliminated and the amount of material will be reduced. Thus, it is aimed to increase the system performance with the design of the flow field containing porous materials with lattice structure.

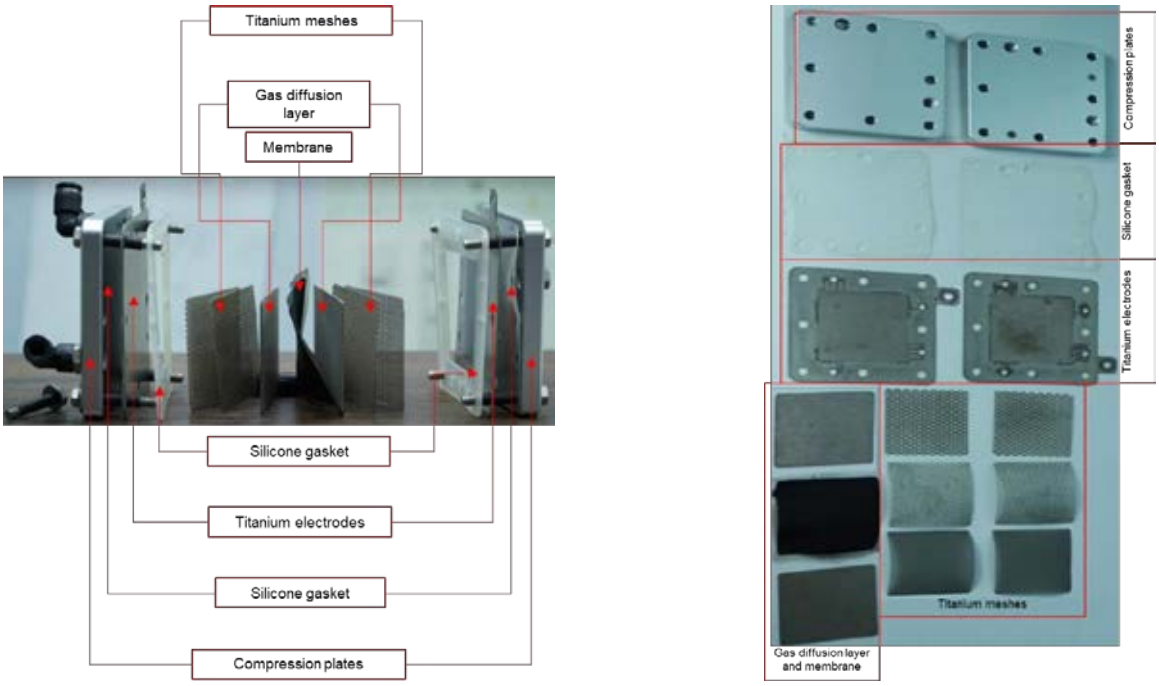

(a) (b)

Fig. 1. PEM electrolysers a) general and b) detailed views of the components (adapted from reference [12]).

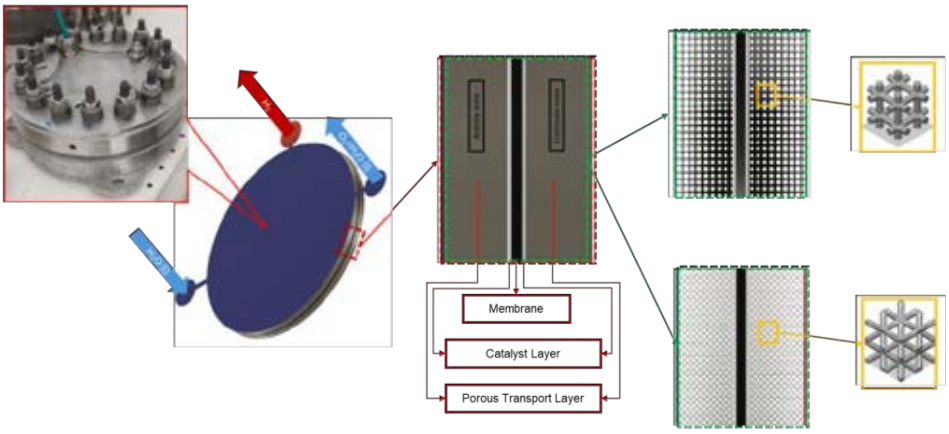

Fig. 2. PTLs containing strut-based lattice structured titanium material

Within the scope of this study, the results will be evaluated by comparing the performance parameters of the traditional structured PTL and the innovative lattice structured PTL containing porous material. In the hydrogen production process in PEM electrolysers, the chemical reactions that take place at the anode and cathode side are as follows.

Anode side:

$$2H_2O \rightarrow O_2 + 4H^+ + 4e^- \quad (1)$$

Cathode side:

$$4H^+ + 4e^- \rightarrow 2H_2 \quad (2)$$

Total reaction:

$$H_2O + electricity + heat \rightarrow H_2 + \frac{1}{2}O_2 \quad (3)$$

In the electrolysis reaction, the cell efficiency (thermodynamic efficiency) of the PEM electrolyser, in other words the voltage efficiency, is calculated as in Eq. (4).

$$\eta = \frac{V_{\text{neutral}}}{V_{cell}} \quad (4)$$

Where V_{neutral} is the smallest potential difference value at which neutral electrolysis can occur, V_{cell} is the potential difference of the electrolyser cell. For each innovative design, the cell efficiency will be calculated and the effects of porous materials with lattice structure on the system performance will be determined.

3. RESULTS AND DISCUSSION

As illustrated in Fig. 3, the PTL structure of the PEM electrolyser investigated in this study consists of low, medium and high titanium mesh layers produced by conventional methods. A review of the PTL structure reveals that overlapping meshes can cause additional resistances and adversely affect the electrochemical activity. The random stacking of titanium mesh layers on top of each other creates an unpredictable complex structure in the PTL. To address the challenges posed by this irregular PTL structure, the proposed strut-based lattice PTL designs are outlined in Fig. 4. The advent of additive manufacturing techniques has facilitated the fabrication of complex porous structures. The single PTL, as illustrated in Fig. 5, can be produced from SLA resin through the utilisation of additive manufacturing techniques. It has been demonstrated that a wide range of porosity, spanning from 20% to 80%, can be achieved by employing a singular layer PTL configuration. As a result, it has been demonstrated that single layer titanium PTLs in PEM electrolysers can be produced by additive manufacturing technique. It is considered that single layer PTLs, which have many advantages such as eliminating additional resistances between layers, can be evaluated as a new research field.

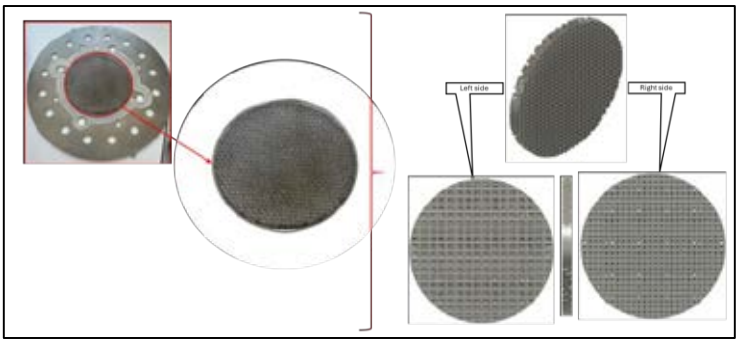

Fig. 3. PTLs composed of multilayer titanium mesh material.

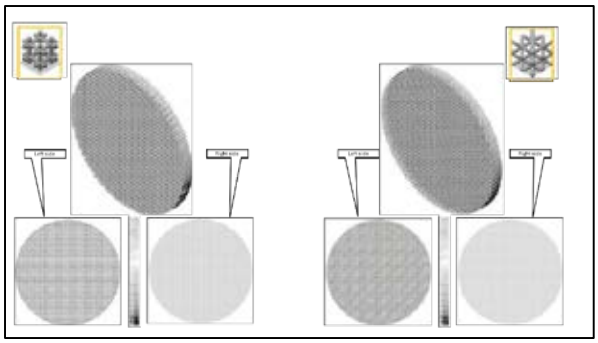

Fig. 4. PTLs containing strut-based lattice structured.

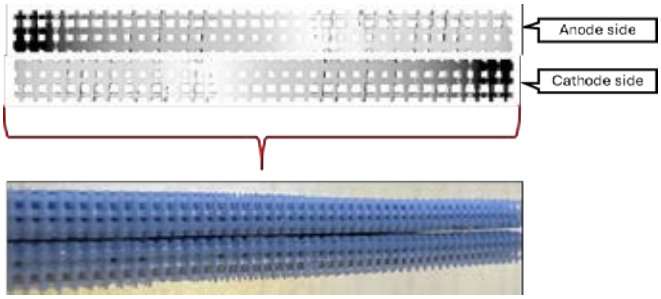

Fig. 5. Fabrication of a PTL designed using a strut-based lattice structure with SLA resin.

4. CONCLUSIONS

This study investigates the design and potential benefits of strut-based lattice porous transport layers (PTLs) in PEM electrolyzers. By integrating advanced lattice structures, it is possible to enhance mass transport, electron conduction, and water management while reducing interfacial resistance. The application of additive manufacturing enables precise fabrication of complex PTL geometries, offering improved structural integrity and performance. The preliminary results suggest that optimized lattice structures can contribute to increased electrolyzer efficiency and durability. Future studies will focus on experimental validation and further optimization to assess the practical viability of these designs in real-world applications.

ACKNOWLEDGMENT

This study was supported by the Scientific and Technological Research Council of Türkiye (TÜBİTAK) under the 2218 – National Postdoctoral Research Fellowship Program (Project No: 124C134). The authors gratefully acknowledge this support.

REFERENCES

1. El-Shafie M. 2023. Hydrogen production by water electrolysis technologies: A review. Results in Engineering, 101426.
2. Kumar S.S. and Himabindu V. 2019. Hydrogen production by PEM water electrolysis–A review. Materials Science for Energy Technologies, 2(3), 442-454.
3. Carmo M., Fritz D.L., Mergel J. and Stolten D. 2013. A comprehensive review on PEM water electrolysis. International journal of hydrogen energy, 38(12), 4901-4934.
4. Kumar S.S. and Lim H. 2022. An overview of water electrolysis technologies for green hydrogen production. Energy reports, 8, 13793-13813.
5. https://www.webofknowledge.com/. Accessed on January 15, 2025.
6. Falcao D.S. and Pinto A.M.F.R. 2020. A review on PEM electrolyzer modelling: Guidelines for beginners. Journal of cleaner production, 261, 121184.
7. Gado M.G., Al-Ketan O., Aziz M., Al-Rub R.A. and Ookawara S. 2024. Triply Periodic Minimal Surface Structures: Design, Fabrication, 3D Printing Techniques, State - of - the - Art Studies, and Prospective Thermal Applications for Efficient Energy Utilization. Energy Technology, 12(5), 2301287.
8. Hamidi E., Ganesan P.B., Sharma R.K. and Yong K.W. 2023. Computational study of heat transfer enhancement using porous foams with phase change materials: A comparative review. Renewable and Sustainable Energy Reviews, 176, 113196.
9. Al-Ketan O., Lee D.W., Rowshan R. and Al-Rub R. K.A. 2020. Functionally graded and multi-morphology sheet TPMS lattices: Design, manufacturing, and mechanical properties. Journal of the mechanical behavior of biomedical materials, 102, 103520.
10. Lesmana L.A. and Aziz M. 2023. Adoption of triply periodic minimal surface structure for effective metal hydride-based hydrogen storage. Energy, 262, 125399.
11. Peng C., Long R., Liu Z. and Liu W. 2024. Improving adsorption hydrogen storage performance via triply periodic minimal surface structures with uniform and gradient porosities. International Journal of Hydrogen Energy, 53, 422-433.
12. https://senzahydrogen.com/blog/. Accessed on January 15, 2025.

SOLAR DRIVEN GREEN HYDROGEN PRODUCTION: TiO_2@MoS_2 NANOCOMPOSITE SYNTHESIS AND PERFORMANCE

[1]*Meltem Yurdakul*, [2]*Beyza Yıldırım*, [1,2*]*Aysel Kantürk Figen*
[1] Yıldız Technical University, Institute of Clean Energy Technologies, İstanbul, 34220, Türkiye
[2] Yıldız Technical University, Faculty of Chemistry and Metallurgy, Department of Chemical Engineering, Davutpaşa-Esenler, İstanbul, 34220, Türkiye

*Corresponding author e-mail: akanturk@yildiz.edu.tr

ABSTRACT

The hydrogen economy has rapidly become a vital energy carrier, feedstock, and fuel in long-term climate action strategies, contributing to the achievement of affordable and clean energy goals and playing a critical role in decarbonization efforts for a net-zero economy. With this content, green hydrogen plays a critical role in achieving net zero in decarbonization of hard-to-abate sectors. Solar green hydrogen production is a promising approach to utilizing solar energy in hydrogen economy. However, further development of catalysts is still needed to achieve economic viability and high efficiency. In this study for solar-driven green hydrogen production, TiO_2@MoS_2 nanocomposites were synthesized via the sol-gel method owing to its ability to manipulate the nanostructure, and of high homogeneity. The effect of varying molybdenum disulfide (MoS_2) ratios in composites was investigated to determine its impact on hydrogen production yield. The crystal structure and morphology of the composites were confirmed using X-ray diffraction (XRD) and field emission scanning electron microscopy (FESEM) techniques. Hydrogen production performance was evaluated using a solar simulator, and hydrogen production profiles were analyzed. XRD analysis revealed that titanium dioxide (TiO_2) exhibited an anatase phase with a tetragonal crystal structure, while MoS_2 displayed a hexagonal crystal structure. FESEM images confirmed that the MoS_2 nanosheets were coated with agglomerated TiO_2 nanoparticles, leading to the absence of the MoS_2 c-plane. Based on the photocatalytic performance driven by solar energy, the TM1 (TiO_2@MoS_2 nanocomposite with 1% MoS_2 ratio) was identified as the most effective, outperforming the other catalysts (TM3, MoS_2, and TiO_2).

Keywords: Green Hydrogen, Solar Driven, TiO_2, MoS_2

1. INTRODUCTION

A result of the global energy crisis, the Paris Agreement established the importance of depleting the effect of climate change by reducing carbon emissions globally [1]. Furthermore, hydrogen stands out as a critical energy carrier, feed stock, and fuel due to its high energy density and low environmental impact in global energy demand and zero emission industry. Investments in hydrogen technologies are expected to grow significantly in the coming years, aligning with global sustainability goals and the vision of a net-zero carbon economy by 2053 due to Türkiye's Hydrogen Strategy and Roadmap [2]. One of the impeccable solutions to hydrogen production is photocatalytic water splitting since the most excessive, clean, and renewable energy resources on earth are solar energy and water [3]. Photocatalytic hydrogen production occurs in three steps which are photon absorption, transport of electron-hole pairs to active sites, and hydrogen and oxygen production in those sites, respectively [4]. Hence, it could prevent the side reactions causing instability in the materials and decomposition of photocatalysts [5].

One of the vital and most utilized semiconductor-driven photocatalysts in hydrogen production is titanium dioxide (TiO_2) due to its suitable conduction and valence positions, high stability, non-toxicity, and low cost. Improving the efficiency of TiO_2 has been studied via semiconductor heterostructure formation, doping, noble metal deposition, etc. Since the construction of semiconductor heterostructures effectively improves the separation and transfer of photogenerated electron-hole pairs while enhancing visible light absorption, it is a widely preferred method [6]. Having a 2D layered structure, good ion transport capacity, large surface area, layered structure held via weak Wan der Waals interactions, and ability to control the recombination of electron-hole pairs on TiO_2 surface makes molybdenum disulfide (MoS_2) a favorable choice for semiconductor heterostructure formation [7].

Several photocatalyst synthesis methods have been studied such as chemical reduction, hydrothermal synthesis, sol-gel method, chemical vapor deposition, etc. In studies on MoS_2 and TiO_2 composite photocatalysts used for hydrogen production, it has been observed that the hydrothermal synthesis method is the most employed. However, in this study, the sol-gel method was chosen to synthesize the TiO_2@MoS_2 photocatalyst for photocatalytic water-splitting hydrogen production. This method was preferred due to its ability to control the microstructure of the product, operate at low temperatures to save energy, ensure high homogeneity, avoid the need for complex systems, and produce catalysts with the desired properties [8].

2. MATERIALS AND METHODS

2.1. Nanocomposite Synthesis and Characterization

In terms of hydrogen production, TiO_2@MoS_2 composites were synthesized with 1% and 3% MoS_2 ratios by sol-gel method. For the synthesis method [9], molybdenum disulfide (MoS_2, Alfa Aesar, 99%, metals basis) at different amounts was added to distillate water (DW) – ethanol (EtOH, Honeywell) solution in order to prepare MoS_2 suspension. The solution was mixed for 30 minutes in an ultrasonic bath. While ethanol was mixed, tetrabutyl titanate ($Ti(O(CH_2)_3)_4$, Alfa Aeser, 99+%) was added. Then, 0.75 ml hydrochloric acid (Tekkim, 37%) was added to tertbutyl titanate-ethanol solution. Finally, MoS_2 suspension was poured into the solution. The final solution was stirred until gel formation was obtained. The gel was heated in the oven which's temperature was set to 180°C for 4 hours. The sample, which got dust formation, was then washed until its supernatant part did not contain any impurity. As a final step of photocatalyst synthesis, to dry the samples, they were kept in the oven at the temperature of 40°C for 12 hours (Fig. 1). The composites were named TM1 and TM3 concerning their MoS_2 ratios. The characterization of the composite photocatalyst was made by X-ray diffraction (XRD, Philips Panalytical X'Pert-Pro) with CuKα tube at 45 kV and 40 mA and Field Emission Scanning Electron Microscopy (FESEM, Thermo Scientific Apreo 2 S LoVac) analysis.

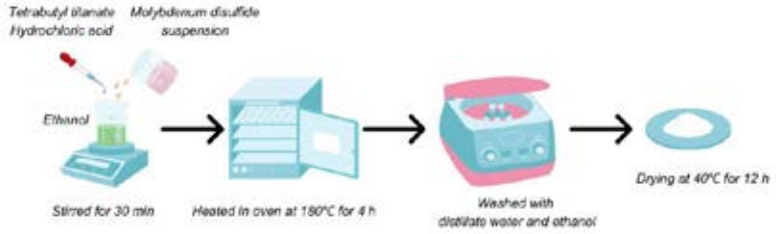

Fig. 1. TiO_2@MoS_2 Nanocomposite Synthesis with Sol-Gel Method

2.2. Solar-Driven Hydrogen Production Performance

Solar-driven hydrogen production (based on water splitting) was carried out in a batch type reactor set in solar simulator with a wavelength range between 400 and 1000 nm (FYTRONIX). In order to figure out the catalytic performance of composites under solar irradiation, hydrogen production was carried out using commercially available TiO_2 (Aeroxide, Fumed Metal Oxide), and MoS_2 as a catalyst. In a typical process, 200 mg of TiO_2, MoS_2, or TiO_2@MoS_2 was introduced to 120 ml water (25% methanol aqua solution) in hydrogen production. Methanol (Honeywell) was chosen as a sacrificial agent due to its capacity of limiting the formation of electron-hole pairs in the semiconductor via consuming valence band holes, hence increasing the H2 production efficiency of photocatalysts [10]. The photocatalytic performance was tested for 96 minutes, and hydrogen generation profile was plotted using evolved gas measured against to time.

3. RESULTS AND DISCUSSION

3.1. Characterization

The crystal structure of TiO_2@MoS_2 nanocomposites with different composition were determined by XRD analysis. XRD patterns are illustrated in Fig. 2. The peaks observed at 25.13°, 37.52°, 47.72°, and 54.27° are associated with (101), (004), (200), and (105) which are correlated to TiO_2's anatase phase and crystal plane of tetragonal, respectively (JCPDS card 04-014-0246) while corresponding peaks of MoS_2 are found at 14.39°, 39.58°, and 43.75° representing (003), (104), and (009) lattice planes. According to lattice planes, MoS_2 has a hexagonal crystal structure (JCPDS card 04-007-3026). The slight peak at 14.39° for TM3 and the absence of this peak in TM1 indicates the c-plane of MoS_2, which proves the successful formation of the layered S-Mo-S structure. The reason behind this might be due to the few layers and thinness of the MoS_2 nanosheets which makes it challenging to detect [11].

Additionally, the morphology of MoS_2, commercial TiO_2, and TM1 nanocomposite was evaluated by FESEM analysis (Figure 2). MoS_2 has nanosheet morphology (Figure 2b). When looking at similar FESEM results in the literature, it was observed that TiO_2 nanoparticles tend to agglomerate. Tang et al. (2022) noted that close interaction occurs between TiO_2 and MoS_2 nanoparticles due to TiO_2 agglomerations on the surfaces [9]. Furthermore, the study of Ciesielczyk et al. (2020) indicates that MoS_2 structures are covered by TiO_2 nanospheres owing to TiO_2's agglomeration affinity [12]. Considering these facts, Fig. 2.d demonstrates that agglomerated TiO_2 nanoparticles cover MoS_2 nanosheets.

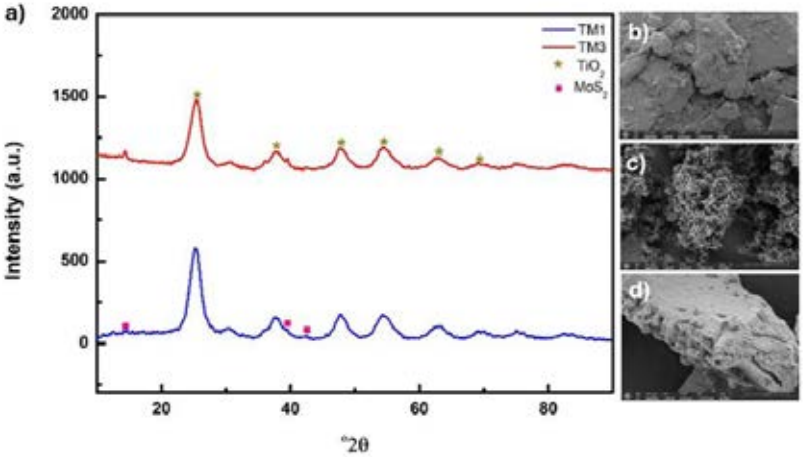

Fig. 2. a) XRD Patterns of TM1 and TM3, FESEM Images of b) Pure MoS_2, c) Pure TiO_2, and d) TiO_2@MoS_2 (TM1)

3.2. Solar-Driven Hydrogen Production Performance

The hydrogen production performance was evaluated under solar simulated irridation over 1.6 hours. The amounts of hydrogen produced in DW catalysize with MoS_2, TiO_2 and TM1 and TM3 coded TiO_2@MoS_2 composite photocatalysts are presented in μmol/$g_{catalyst}$ in Fig. 3.

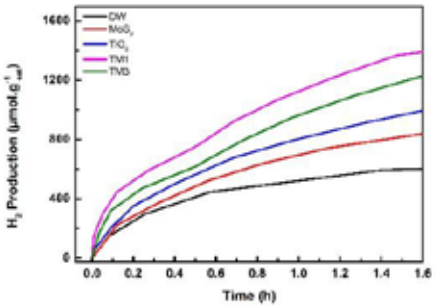

Fig. 3. Effect of MoS_2 Loading on Photocatalytic Hydrogen Production

According to Fig. 3, although the performance of the MoS_2 nanosheet is lower than that of TiO_2, its electrical, physicochemical, and mechanical properties have enhanced the rate of the water-splitting reaction when combined with TiO_2 in a composite form, resulting in hydrogen production that is 1.5 to 2 times greater in a shorter period. The highest hydrogen production (~1450 μmol.g^{-1}) was performed by TM1. While still, TM3 illustrated better hydrogen production (~1200 μmol.g^{-1}) than TiO_2 and MoS_2 which implies the importance of the inclusion of MoS_2.
To maximize hydrogen production, optimizing MoS_2 content in the composite has a substantial role. Depletion in hydrogen production efficiency may be due to excessive loading of MoS_2 in TM3 which could be as a result of aggregation or decreased light absorption. The hydrogen production profiles show a stable performance without major deactivation, suggesting good catalyst stability. On the whole, TiO_2@MoS_2 composites have been found to outperform the pure components, with the TM1 sample proving to be the most effective, emphasizing the potential of composite materials for efficient hydrogen production by water splitting.

4. CONCLUSIONS

In the study, TiO_2@MoS_2 nanocomposites at varying MoS_2 ratios (1% and 3%) were synthesized by the sol-gel method to generate green hydrogen via the photocatalytic water splitting method. Crystal structure, composite morphology, and hydrogen production performances were evaluated via XRD, FESEM, and solar simulator system. In accordance with XRD results TiO_2 particles showed an anatase phase with a tetragonal crystal phase while MoS_2 was revealed to be a hexagonal crystal phase. FESEM images illustrated that MoS_2 nanosheets were covered with agglomerated TiO_2 nanoparticles which was supported by the absence of a c plane of MoS_2. Finally, the most active catalyst was determined as TM1 due to the superb performance in the solar simulated irradiation in comparison to other catalysts.

ACKNOWLEDGEMENT
This work was supported by the Yıldız Technical University Scientific Research Projects Coordinator with identification number FYL-2025-6962. The authors also express their gratitude for the financial support of the solar simulator system (Yildiz Technical University Research Foundation, Project No: FBA-2023-5648).

REFERENCES

1. U. Nations, “The Paris Agreement,” *Nature*, vol. 127, no. 3207, pp. 600–601, 1931, doi: 10.1038/127600a0.
2. T. C. E. ve T. K. Bakanlığı, “Hidrojen Stratejisi ve Yol Haritası,” pp. 1–23, 2016.
3. H. Ahmad, S. K. Kamarudin, L. J. Minggu, and M. Kassim, “Hydrogen from photo-catalytic water splitting process: A review,” *Renew. Sustain. Energy Rev.*, vol. 43, pp. 599–610, 2015, doi: 10.1016/j.rser.2014.10.101.
4. A. Killi and M. İ. Ocakoğlu, “Fotokatalitik hidrojen üretimi için subftalosiyanin temelli fotokatalizörler,” 2023.
5. Y. Qu and X. Duan, “Progress, challenge and perspective of heterogeneous photocatalysts,” *Chem. Soc. Rev.*, vol. 42, no. 7, pp. 2568–2580, 2013, doi: 10.1039/c2cs35355e.
6. B. Anandha Priya, T. Sivakumar, and P. Venkateswari, “Construction of MoS2 nanoparticles incorporated TiO2 nanosheets heterojunction photocatalyst for enhanced visible light driven hydrogen production,” *Inorg. Chem. Commun.*, vol. 136, no. November 2021, p. 109118, 2022, doi: 10.1016/j.inoche.2021.109118.
7. S. V Kite *et al.*, “Nanostructured TiO 2 Sensitized with MoS 2 Nano fl owers for Enhanced Photodegradation E ffi ciency toward Methyl Orange,” 2021, doi: 10.1021/acsomega.1c02194.
8. A. Kubiak and T. Jesionowski, “Titania-Based Hybrid Materials with ZnO, ZrO2 and MoS2: A Review,” 2018, doi: 10.3390/ma11112295.
9. Z. Tang, L. Xu, K. Shu, J. Yang, and H. Tang, “Fabrication of TiO2 @MoS2 heterostructures with improved visible light photocatalytic activity,” *Colloids Surfaces A Physicochem. Eng. Asp.*, vol. 642, no. December 2021, 2022, doi: 10.1016/j.colsurfa.2022.128686.
10. W. T. Chen, Y. Dong, P. Yadav, R. D. Aughterson, D. Sun-Waterhouse, and G. I. N. Waterhouse, “Effect of alcohol sacrificial agent on the performance of Cu/TiO2 photocatalysts for UV-driven hydrogen production,” *Appl. Catal. A Gen.*, vol. 602, p. 117703, 2020, doi: 10.1016/j.apcata.2020.117703.
11. W. Zhou *et al.*, “Synthesis of few-layer MoS2 nanosheet-coated TiO2 nanobelt heterostructures for enhanced photocatalytic activities,” *Small*, vol. 9, no. 1, pp. 140–147, 2013, doi: 10.1002/smll.201201161.
12. K. Siwińska-Ciesielczyk *et al.*, “Crystallization of TiO2-MoS2 hybrid material under hydrothermal treatment and its electrochemical performance,” *Materials (Basel).*, vol. 13, no. 12, pp. 1–21, 2020, doi: 10.3390/ma13122706.

THE ROLE OF AMMONIA IN RENEWABLE ENERGY AND EMERGENCY POWER SUPPLY: A FEASIBILITY STUDY

[1*]*Hasan Bektas Percin*, [2]*Abuzer Caliskan*
[1] Firat University, Elazig, 23119, Türkiye
[2] Firat University, Faculty of Engineering, Department of Electrical and Electronics Engineering, Elazig, 23119, Türkiye

*Corresponding author e-mail: hbpercin@firat.edu.tr

ABSTRACT
Ammonia is increasingly being acknowledged as a versatile energy carrier, offering substantial promise for applications in low-carbon energy storage, transport, and electricity production. As a carbon-free fuel, ammonia offers several key advantages, making it a strong alternative for integrating renewable energy sources into existing energy infrastructures. The proposed methodology takes advantage of excess power generated during periods of high solar radiation or strong wind conditions to synthesize and store ammonia, which can then be used for power generation when energy availability is low. This approach enhances the flexibility and reliability of renewable energy systems by addressing the intermittency challenges associated with solar and wind power. A feasibility analysis was conducted based on the available energy sources, evaluating both the feasibility and cost-effectiveness of utilizing ammonia as a renewable energy storage and power generation solution. By leveraging its characteristics, ammonia can play a crucial role in enabling efficient long-term renewable energy storage, supporting grid stability, and facilitating a sustainable energy transition toward a low-carbon future. where ensuring a stable and secure, particularly during natural disasters and other emergency situations.

Keywords: Ammonia, Green hydrogen, Renewable, Feasibility

1. INTRODUCTION

The inevitable consequences of fossil energy sources have led to considerable damage to human health, well-being, and the environment. This situation has heightened the urgency for environmentally friendly and sustainable energy alternatives. According to the International Energy Agency (IEA), renewable energy sources are projected to account for 50% of the global primary energy supply by 2050, aligning with international efforts to mitigate these problems [1].Recent studies highlight the potential of hydrogen-based sources, which is widely regarded as an ideal synthetic source due to its clean combustion properties and versatility across various applications [2]. The most challenging problem to overcome in the adoption of hydrogen are storage and transportation requirements. Additionally, Hydrogen's high volatility, wide flammability range, and elevated explosion risk make it essential to implement rigorous safety protocols and advanced containment technologies [2]. As a result, over time, several alternatives have been proposed to serve as hydrogen carriers. Among these options, ammonia stands out as a promising candidate due to its high hydrogen content, ease of liquefaction, and existing global infrastructure. Its ability to store and transport large quantities of hydrogen in a stable form makes ammonia an attractive solution for addressing the challenges associated with hydrogen storage and distribution [1,3]. Projections indicate that over the next 10 years, the global ammonia market is expected to expand by approximately 3%, positioning ammonia as a viable alternative to conventional fuels [4]. Beyond its safety benefits, ammonia plays a crucial role in optimizing renewable energy utilization, particularly for intermittent sources like wind and solar power. By storing renewable energy in the form of chemical fuels, ammonia enables efficient long-term energy storage and facilitates transportation over extended distances, thereby supporting the development of a more sustainable energy infrastructure [3]. In the context of ammonia production, it is important to note that existing ammonia synthesis technologies are fully mature and widely deployed on an industrial scale. However, under current production pathways, ammonia cannot be classified as green, as the majority of its production still relies on fossil fuel-based hydrogen generation, primarily through steam methane reforming (SMR) [5].

Green ammonia is synthesized via the Haber-Bosch process, in which hydrogen, derived from electrolysis, is combined with nitrogen extracted from the air. Unlike conventional ammonia production, the entire process is powered by renewable energy sources, making it a carbon-free and sustainable alternative. This approach significantly reduces greenhouse gas emissions and aligns with global efforts toward achieving a net-zero carbon economy [6].

Numerous researchers have conducted techno-economic assessments to evaluate the viability of green ammonia production, analyzing its economic feasibility, energy efficiency, and potential role in the global shift towards sustainable energy systems [7–10]. These studies focus on various production pathways, cost factors, and integration strategies to determine how green ammonia can be scaled efficiently and competitively [11–13]

Some other studies explore the potential development as a fuel source by examining multiple fuel production plants, utilizing aggregated data, and modeling the entire energy system at a regional or national level. These studies aim to assess the feasibility, scalability, and impact of integrating synthetic fuels into existing energy and transportation infrastructures [14–16].

The decarbonization of the power and transportation sectors through green ammonia will require the development of strategic transition pathways that ensure its practical and economically viable implementation in real-world applications.

Successfully integrating green ammonia into the energy system involves overcoming several key barriers, which can be categorized into economic, technical, and political challenges [1]. Addressing these challenges through technological advancements, policy support, and economic incentives will be essential for unlocking the full potential of green ammonia in achieving a low-carbon energy future.
In regions susceptible to severe earthquakes, maintaining a reliable and resilient energy supply is crucial for emergency response and recovery efforts. In this study, green ammonia, as an energy carrier, serves as an effective hydrogen energy carrier in such disaster-prone areas due to its storage efficiency, transportability, and safety advantages over conventional hydrogen storage methods. When assessing the most efficient pathway for green ammonia production, it is essential to consider key factors that influence its economic viability and sustainability. By carefully evaluating these factors, the most cost-effective and scalable strategies for integrating green ammonia into the global energy transition can be provided [3]. The renewable power generation technologies analyzed in this study include onshore wind turbines and fixed-axis solar panels. By integrating location-dependent energy profiles into the analysis, this study provides a realistic assessment of how different renewable sources can be optimized for green ammonia production, ensuring cost-effective and reliable energy supply for large-scale applications [17].

2. MATERIALS AND METHODS

Ammonia is predominantly utilized in the agriculture sector as a fertilizer, playing a crucial role in crop production. Additionally, it is widely employed as a refrigerant due to its efficient cooling properties. Beyond these traditional uses, ammonia has gained attention as a potential fuel source, particularly in engines and fuel cells, where it is being explored for its feasibility in sustainable energy systems[4]. Ongoing research continues to investigate its viability as a carbon-free alternative for power generation and transportation applications. At present, hydrogen production for ammonia synthesis is predominantly achieved through the natural gas reforming process, which presents significant challenges due to its high costs and negative environmental impacts, primarily linked to fossil fuel dependency. One of the main drivers for innovation in this field is the effort to replace fossil fuels with renewable energy (RE)-based hydrogen production, enabling the creation of clean ammonia. Figure 1 highlights the various green ammonia production pathways powered by renewable energy sources [17].

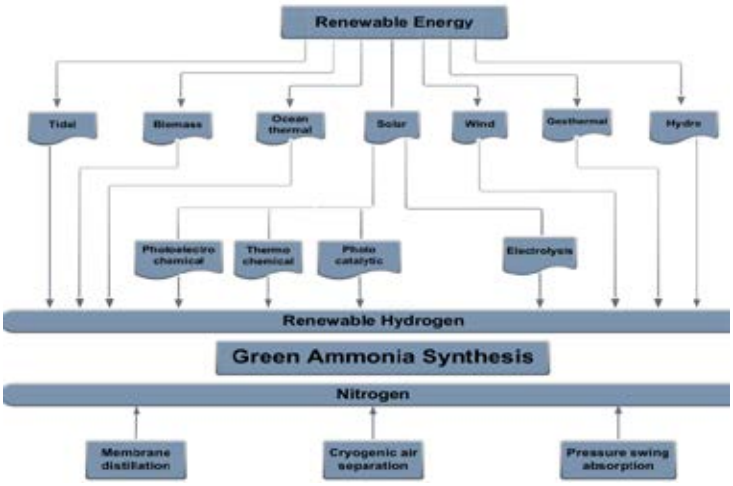

Fig. 1. Green ammonia production pathways [3]

In recent years, global ammonia production has experienced significant growth. Among the various techniques used in ammonia synthesis, the cryogenic air separation process is the most widely industrialized, allowing for bulk production of ammonia at a lower cost and higher efficiency. Another method called as Haber-Bosch process can be utilized method for large-scale ammonia production due to its well-established infrastructure and widespread adoption in the industry. However, ongoing advancements in cryogenic separation and alternative ammonia synthesis technologies continue to improve efficiency and sustainability in the sector [4]. The synthesis of ammonia follows an exothermic reaction between nitrogen (N_2) and hydrogen (H_2), which is represented by Eq. (1).

$$N_2 + 3H_2 \rightarrow 2NH_3 \quad (1)$$

Ammonia is classified as "green" when its production process is entirely carbon-free and relies 100% on renewable energy sources (excluding emissions from embodied systems). This method forms the basis of the Haber-Bosch process, which remains the primary method for industrial ammonia production. Ongoing researches focuses on identifying more sustainable alternatives to reduce carbon emissions and energy consumption in the process [18]. Haber-Bosch (H–B)

method differs in that the energy required for hydrogen production is derived from renewable energy sources (RES) rather than fossil fuels, as used in conventional centralized H–B technology. This transition significantly reduces carbon emissions, making ammonia production more sustainable and environmentally friendly. Additionally, the nitrogen (N_2) supply in this process is obtained using proven air separation technologies, such as cryogenic distillation or pressure swing adsorption (PSA), ensuring a reliable and efficient nitrogen source for ammonia synthesis. This approach supports the shift toward green ammonia production, aligning with global efforts to decarbonize industrial processes and promote sustainable energy solutions [19]. The general application framework of this method is illustrated in Figure 2.

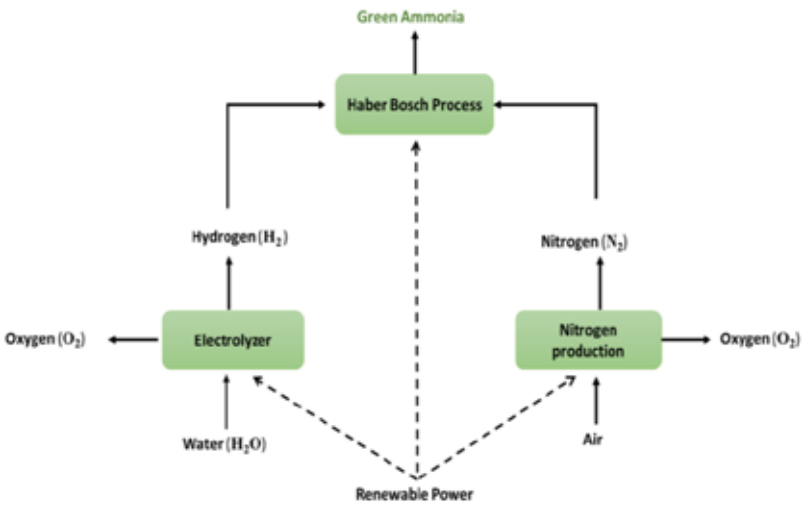

Fig. 2. The general application framework of green ammonia production [3]

3. RESULTS AND DISCUSSION

The technical and economic feasibility of green ammonia production depends on several key factors that influence its cost-effectiveness and long-term viability. One of the primary considerations is the production method selected, as different technological approaches impact both capital investment and operational efficiency. The initial costs of establishing green ammonia production facilities, including electrolyzers, renewable energy infrastructure, and synthesis units, play a significant role in determining financial feasibility. While green ammonia requires a high initial investment, particularly for infrastructure and technology deployment, it offers lower daily operational costs compared to conventional fossil fuel-based ammonia production methods. This is largely due to the absence of fuel costs associated with natural gas reforming and the potential for low-cost renewable electricity to power the process. When evaluating the most efficient pathway for green ammonia production, it is crucial to account for key factors that influence its economic feasibility and sustainability. Key factors factors encompass the accessibility of renewable energy sources, the development of infrastructure for ammonia storage and distribution, and the economic viability of hydrogen production via electrolysis. This study focuses on Elazığ, a city located in the Eastern Anatolia Region of Turkey, as a strategic location for the production and storage of green ammonia as an alternative energy source. Elazığ's geographical and seismic characteristics, along with its exposure to natural disasters, make it an ideal candidate for developing resilient energy solutions that can support disaster preparedness and emergency response efforts. The geographical location of the selected region, along with the system configuration for ammonia production, is illustrated in Figure 3.

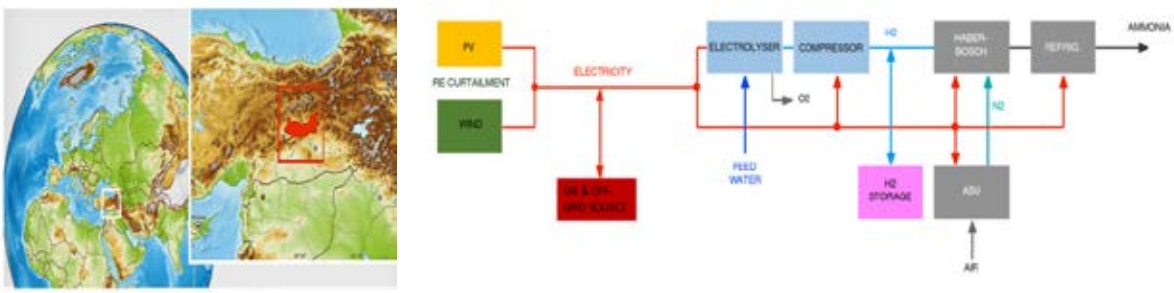

Fig. 3. The general application framework of green ammonia production

The figure provides a visual representation of how Elazig's regional characteristics align with the technical setup required for green ammonia production and storage**.** The selected location was chosen based on its potential for renewable energy integration, particularly from solar and wind resources, which are essential for powering the electrolysis process and

Haber-Bosch process. The economic viability of green ammonia production is influenced by several key factors, including initial capital investment, daily operational expenses, and long-term cost savings. Despite the high capital expenditure (CAPEX), the daily operational costs (OPEX) of green ammonia production are generally lower compared to traditional fossil fuel-based ammonia production. This is due to the elimination of natural gas dependence, as renewable energy sources (solar, wind, or hydropower) can be utilized to generate hydrogen through electrolysis. Additionally, maintenance costs for renewable-powered ammonia plants are expected to be lower than fossil fuel-based alternatives, contributing to overall cost efficiency in the long run.

4. CONCLUSIONS

The decarbonization of the transportation and power generation sectors and the reduction of fossil fuel dependency can be achieved by developing alternative green fuels derived from clean energy sources. Among these alternatives, green ammonia has recently emerged as a promising hydrogen energy carrier, offering a carbon-free solution for energy storage and utilization. While hydrogen is a promising clean fuel, its storage, transport, and distribution present significant technical and economic challenges. Ammonia, as a hydrogen carrier, offers key benefits that enhance the feasibility of hydrogen-based energy systems at both domestic and global scales. As advancements in production, storage, and transportation technologies continue, expected to play a significant role in energy transition initiatives, particularly in power generation, industrial applications, and the transportation sector. This study focuses on the production of ammonia as a key milestone in the transition to a hydrogen economy, analyzing its technical and economic feasibility across selected regions. The findings will contribute to the development of resilient cost-effective energy infrastructure in Türkiye and neighboring regions, where ensuring a stable and secure energy supply is essential, particularly during natural disasters and other emergency situations. Future research should focus on the cost analysis and feasibility of ammonia transportation and distribution via pipelines across different regions.

REFERENCES

1. Kurien C, Mittal M. 2022 Review on the production and utilization of green ammonia as an alternate fuel in dual-fuel compression ignition engines. Energy Convers Manag 2022;251:114990.
2. Zamfirescu C, Dincer I. 2009 Ammonia as a green fuel and hydrogen source for vehicular applications. Fuel Process Technol 2009;90:729–37.
3. Jafar U, Nuhu U, Khan WU, Hossain MM. 2024. A review on green ammonia as a potential CO2 free fuel. Int J Hydrog Energy 71:857–76.
4. Yapicioglu A, Dincer I. 2019. A review on clean ammonia as a potential fuel for power generators. Renew Sustain Energy Rev 103:96–108.
5. Chorowski M, Lepszy M, Machaj K, Malecha Z, Porwisiak D, Porwisiak P, et al. 2023. Challenges of Application of Green Ammonia as Fuel in Onshore Transportation. Energies 16:4898.
6. Kojima Y, Yamaguchi M. Ammonia as a hydrogen energy carrier. 2022 Int J Hydrog Energy 47:22832–9.
7. Sousa J, Waiblinger W, Friedrich KA. 2022. Techno-economic Study of an Electrolysis-Based Green Ammonia Production Plant. Ind Eng Chem Res 61:14515–30.
8. Ikäheimo J, Kiviluoma J, Weiss R, Holttinen H. 2018. Power-to-ammonia in future North European 100 % renewable power and heat system. Int J Hydrog Energy 43:17295–308.
9. Nayak-Luke RM, Bañares-Alcántara R. 2020. Techno-economic viability of islanded green ammonia as a carbon-free energy vector and as a substitute for conventional production. Energy Environ Sci 13:2957–66.
10. Campion N, Nami H, Swisher PR, Vang Hendriksen P, Münster M. 2023. Techno-economic assessment of green ammonia production with different wind and solar potentials. Renew Sustain Energy Rev 2023;173:113057.
11. Arnaiz del Pozo C, Cloete S. 2022. Techno-economic assessment of blue and green ammonia as energy carriers in a low-carbon future. Energy Convers Manag 255:115312.
12. Herbinet O, Bartocci P, Grinberg Dana A. 2022. On the use of ammonia as a fuel – A perspective. Fuel Commun 11:100064.
13. Wang C, Walsh SDC, Longden T, Palmer G, Lutalo I, Dargaville R. 2023. Optimising renewable generation configurations of off-grid green ammonia production systems considering Haber-Bosch flexibility. Energy Convers Manag 280:116790.
14. Grahn M, Malmgren E, Korberg AD, Taljegard M, Anderson JE, Brynolf S, et al. 2022. Review of electrofuel feasibility—cost and environmental impact. Prog Energy 4:032010.
15. Brynolf S, Taljegard M, Grahn M, Hansson J. 2018. Electrofuels for the transport sector: A review of production costs. Renew Sustain Energy Rev 81:1887–905.
16. Miura D, Tezuka T. 2014. A comparative study of ammonia energy systems as a future energy carrier, with particular reference to vehicle use in Japan. Energy 68:428–36.
17. Ishaq H, Crawford C. 2024. Review of ammonia production and utilization: Enabling clean energy transition and net-zero climate targets. Energy Convers Manag 300:117869.
18. Olabi AG, Abdelkareem MA, Al-Murisi M, Shehata N, Alami AH, Radwan A, et al. 2023. Recent progress in Green Ammonia: Production, applications, assessment; barriers, and its role in achieving the sustainable development goals. Energy Convers Manag 277:116594.
19. Bora N, Kumar Singh A, Pal P, Kumar Sahoo U, Seth D, Rathore D, et al. 2024. Green ammonia production: Process technologies and challenges. Fuel 369:131808.

SPEED CONTROL OF A SYNCHRONIZED INDUCTION MOTOR POWERED BY HYDROGEN FUEL CELL

[1*]*Hüseyin Erdoğan*
[1] Turkish Airlines Inc., Sales Directorate, Diyarbakir New Airport, Diyarbakir, 21090, Türkiye
*Corresponding author e-mail: huseyinerdogan@thy.com

ABSTRACT
Induction machines are widely employed in industry due to their low cost, high starting torque, and minimal maintenance requirements. In contrast, synchronous machines, designed to operate either as motors or generators, offer advantages such as constant-speed operation and the relatively straightforward implementation of vector control methods, despite their higher expense and maintenance demands. Hydrogen energy, unlike other renewable sources, provides uninterrupted power generation independent of environmental conditions. In applications that demand both high starting torque and constant speed, particularly in remote installations with limited grid connectivity, the combined benefits of induction and synchronous motors become crucial. This paper investigates the conditions under which an induction motor can operate in synchronous mode, implements a hydrogen fuel cell model to power the system, and applies a vector control strategy. A simulation model incorporating both the detailed PEM fuel cell dynamics and the three-phase induction motor's phase-variable model is developed and analyzed.
Keywords: Hydrogen Fuel Cell, Synchronized Induction Motor, Vector Control, Phase Variable Modeling

1. INTRODUCTION

Induction motors are favored in industrial applications primarily due to their economical design and low maintenance requirements. However, these machines inherently operate below synchronous speed, which limits their performance in applications requiring strict speed constancy. In contrast, synchronous machines, although costlier and demanding continuous maintenance, provide stable rotational speeds and simplify the implementation of advanced control methods such as vector control.

Originally, the concept of synchronizing a wound-rotor induction motor was proposed by Danielson in 1901 [1] to improve power factor, and subsequent work in England led to the term "British Machine" [2]. Recent studies have focused on high-conductivity synchronized induction motors and self-excited variants [3]–[5]. Moreover, integrating hydrogen fuel cells—a renewable energy source capable of delivering continuous power regardless of ambient conditions—further enhances the applicability of such motor drives in isolated installations.

2. METHODOLOGY AND SYSTEM MODELING

This paper presents an in-depth analysis of the synchronization techniques for induction motors, with a particular emphasis on the Danielson rotor connection. It also details the development of a phase-variable model for the motor, the integration of a detailed PEM fuel cell model, and the implementation of a vector control strategy to regulate speed.

2.1 Phase Variable Modeling of the Induction Motor

A critical initial step in engineering analysis is the formulation of a mathematical model that closely represents the physical system. The phase-variable approach offers significant advantages since the variables directly correspond to measurable physical quantities (currents, voltages, and torque), thereby enabling the direct analysis of transient responses without the need for coordinate transformations [3].

In this study, the dynamic behavior of a three-phase wound-rotor induction motor is modeled using phase variables. The voltage equations for the stator and rotor can be expressed as:

$$[V_{s,r}] = [R_{s,r} I_{s,r}] + [L_{s,r}]\left[\frac{di_{s,r}}{dt}\right] + \left[\frac{dL_{s,r}}{d\theta}\right][i_{s,r}]\left[\frac{d\theta}{dt}\right] \quad (1)$$

Here, $[L_{s,r}]$ denotes the inductance matrix defined via flux linkages, while $[R_{s,r}]$ is the diagonal resistance matrix of the windings. Under the assumption of sinusoidal winding distribution, the effects of slot harmonics and air-gap variations are neglected.

The mechanical dynamics of the motor are given by:

$$\frac{d\omega_m}{dt} = \frac{1}{j}\left(T_d - T_y\right) \quad (2)$$

Furthermore, the rotor's angular position is defined by:

$$\omega = \frac{d\theta}{dt} \quad (3)$$

and the induced torque is calculated as:

$$T_d = -\frac{P}{2} M_{sr} \left((i_{ra} i_{sa} + i_{rb} i_{sb} + i_{rc} i_{sc}) \sin\theta + (i_{ra} i_{sb} + i_{rb} i_{sc} + i_{rc} i_{sa}) \sin\left(\theta - \frac{2\pi}{3}\right) + (i_{ra} i_{sc} + i_{rb} i_{sa} + i_{rc} i_{sb}) \sin\left(\theta + \frac{2\pi}{3}\right) \right) \tag{4}$$

Table 1 below summarizes the motor parameters used in the simulation [3]:

Table 1. Summary of IHTEC2025 formatting details

P_g = 150 W	U = 220 V	f = 50 Hz	p = 4
R_r = 211 Ω	R_s = 109.399 Ω	L_{ls} = 0.158 H	L_{lr} = 0.158 H
L_m = 1.579 H	J = 1.521e-3 kg.m/s^2	B = 0	

2.2. The Danielson Synchronization Technique

One effective method to achieve synchronous operation without modifying the motor's physical structure is the Danielson connection. In this technique, multiple rotor winding connection schemes are available; some require specific design modifications while others can be retrofitted to existing wound-rotor motors.

During startup, the rotor windings are connected through external resistors (referred to as "starting resistors") to provide a high starting torque. Once the rotor speed approaches the synchronous speed (typically around t=2t = 2t=2 s in simulations), the starting resistors are bypassed, and the appropriate excitation voltage is applied to the rotor windings following the Danielson connection scheme. This transition enables the motor to operate at synchronous speed while maintaining the high-torque characteristics of an induction motor [1],[3], [6-8].

A schematic of the rotor winding connection in the Danielson method is illustrated in Fig. 1.

a) **b)**

Fig. 1. Rotor winding connection in the Danielson method

a) Starting b) Synchronous Operation

3. MODELING THE HYDROGEN FUEL CELL

Hydrogen fuel cells convert the chemical energy stored in hydrogen directly into electrical energy through electrochemical reactions. In a Polymer Electrolyte Membrane (PEM) fuel cell, hydrogen is split at the anode into protons and electrons; the protons traverse a semi-permeable membrane, while the electrons generate current via an external circuit. At the cathode, oxygen reacts with protons and electrons to form water and heat.

3.1 Fundamental Equations

The overall reaction can be summarized as:

$$H_2 + \frac{1}{2} O_2 \rightarrow H_2O + heat \tag{5}$$

Subsequently, the Nernst voltage (E) is calculated by:

$$E = \begin{cases} K_c N \left(1.229 + K_z \frac{RT}{zF} \ln\left(p_{H_2} p_{O_2}^{\frac{1}{2}} \right) \right) - E_{\text{Tafel}} - E_{\text{conc}}, T < 373.15\text{K} \\ K_c N \left(1.229 + K_z \frac{RT}{zF} \ln\left(\frac{p_{H_2} p_{O_2}^2}{p_{H_2O}} \right) \right) - E_{\text{Tafel}} - E_{\text{conc}}, T \geq 373.15\text{K} \end{cases} \tag{6}$$

Here, the parameters defined based on nominal conditions of operation [9-12].

4. VECTOR CONTROL OF THE SYNCHRONIZED INDUCTION MOTOR

4.1 System Overview

For locations with limited grid access and where maintenance activities are severely restricted, powering motor drives with hydrogen fuel cells is an attractive solution. Such a configuration eliminates dependency on external energy sources while leveraging the maintenance-free operation of induction motors. Once synchronized, the motor benefits from the constant speed characteristics of synchronous machines, making it ideal for applications that require both high starting torque and precise speed regulation.

4.2 Implementation of Vector Control

A vector control method is directly applied to the phase-variable model to regulate motor speed. By comparing a reference speed with the measured rotor speed, an error signal is generated and used to compute the required reference currents. These currents are then transformed into three-phase (abc) signals via an inverse Park transformation to drive the inverter. The result is a synthesized stator voltage that enables rapid and precise speed tracking even under varying load conditions.

5. SIMULATION RESULTS

The motor, initially loaded with 0.1 Nm, undergoes a transition to synchronous operation at approximately 2 s when the Danielson method is activated. At 4 s, a load increase to 0.2 Nm is introduced, and at 6 s the vector control system adjusts the speed to a target of 120 rad/s. The simulation confirms that the hydrogen fuel cell supplies the expected electrical outputs, that the motor reliably achieves synchronous operation, and that the vector control ensures smooth torque and current responses.

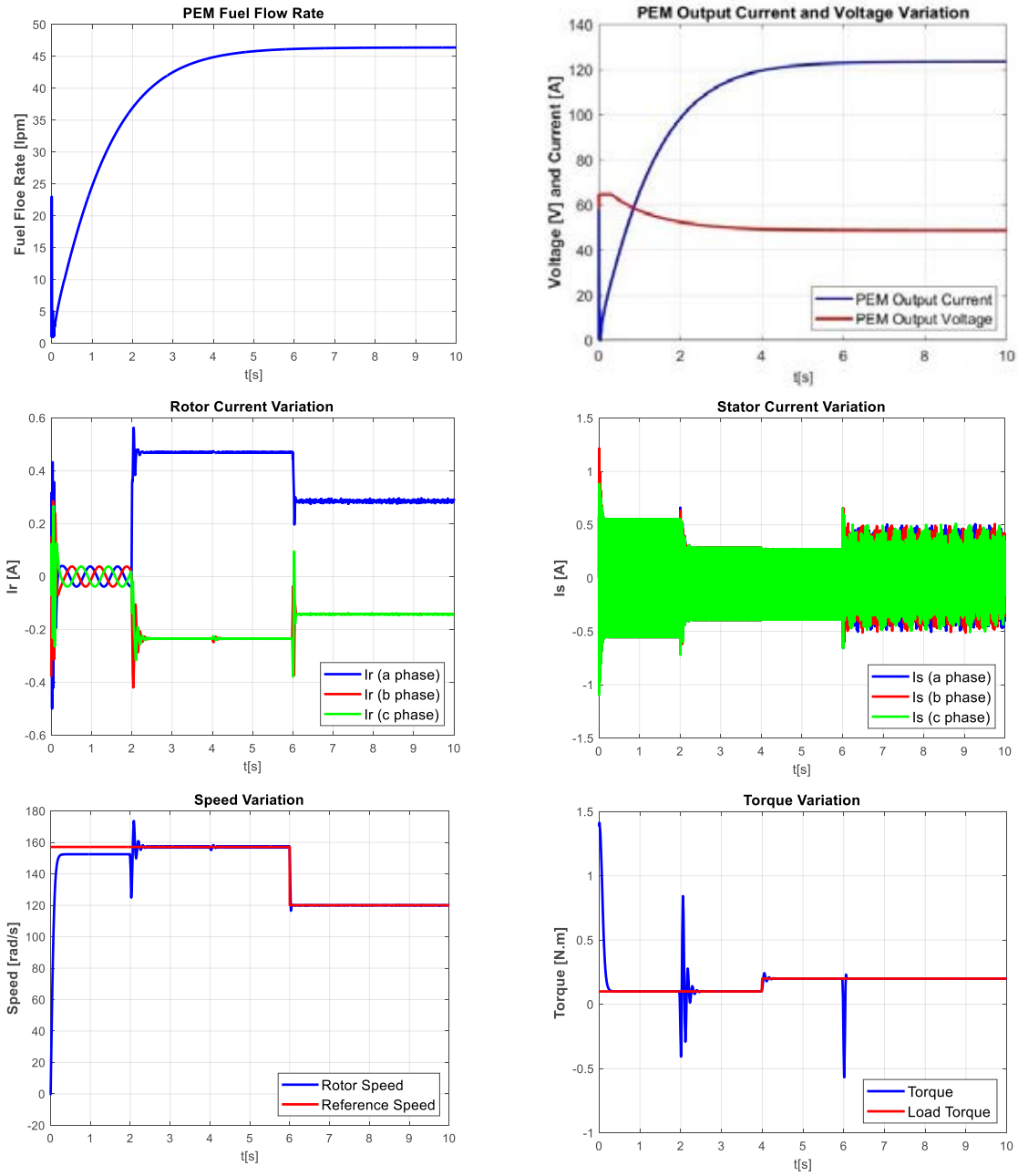

Fig. 4 Simulation results of the proposed model

6. CONCLUSION AND RECOMMENDATIONS

The study demonstrates that converting an induction motor to synchronous operation using the Danielson rotor connection is both feasible and effective. Coupling the motor with a hydrogen fuel cell offers a robust solution for off-grid applications, while the direct implementation of vector control on the phase-variable model guarantees accurate speed regulation. This integrated system is recommended for industrial applications requiring both high starting torque and precise, constant-speed performance in remote locations.

REFERENCES

1. Danielson E. 1901. The induction motor as a synchronous motor, Elektrotechnische Zeitschrift, vol. 22, pp. 1065–1066, 1901.
2. Rawcliffe G. H. 1940. Secondary Circuits of Synchronous Induction Motors, Journal of the Institution of Electrical Engineers, vol. 87, pp. 282–298, 1940.
3. Erdoğan H and Özdemir M. 2017. Vector Control of Synchronized Induction Motor, Middle East Journal of Technic, vol. 2, no. 1, pp. 37–44, 2017.
4. Özdemir M and Önbilgin G. 2003. Computer Simulation of a Series Excited Synchronous Motor, Electric Power Components and Systems, vol. 31, no. 6, pp. 565–578, 2003.
5. Tubbs S. P. 1990. Superconducting Synchronous Induction Motor Performance, IEE Proceedings B: Electric Power Applications, vol. 137, no. 2, p. 120, 1990.
6. Cotton H. 1925. The pulling into step of a synchronous induction motor, Journal of the Institution of Electrical Engineers, vol. 63, no. 338, pp. 211–230, 1925.
7. Williamson A. C. and Chalmers B. J. 1977. New form of inverter-fed synchronous motor with induced excitation, Proceedings of the Institution of Electrical Engineers, vol. 124, no. 3, p. 213, 1977.
8. Williamson A. C. et al. 1980. A new connection for synchronous motor excitation, Proceedings of the Institution of Electrical Engineers, vol. 127, no. 3, pp. 169–173, 1980.
9. Do T. C. et al. 2019. Energy Management Strategy of a PEM Fuel Cell Excavator with a Supercapacitor/Battery Hybrid Power Source, Energies, vol. 12, no. 22, 2019.
10. Motapon S. N., Tremblay O., and Dessaint L. 2009. A Generic Fuel Cell Model for the Simulation of Fuel Cell Vehicles, Proceedings of the IEEE Vehicle Power and Propulsion Conference, Dearborn, MI, pp. 1722–1729, 2009.
11. Hirschenhofer J. H. et al. 1988. Fuel Cell Handbook, 4th ed., U.S. Department of Energy, 1988.
12. Larminie J. and Dicks A. 2003. Fuel Cell Systems Explained, John Wiley & Sons, Ltd., West Sussex, England, 2003.

EXPLORING HYDROGEN MOBILITY: A FEASIBILITY STUDY ON SUSTAINABLE CAMPUS TRANSPORTATION

[1*] *Hasan Bektas Percin*, [2] *Abuzer Caliskan*
[1] Firat University, Elazig, 23119, Türkiye
[2] Firat University, Faculty of Engineering, Department of Electrical and Electronics Engineering, Elazig, 23119, Türkiye
*Corresponding author e-mail: hbpercin@firat.edu.tr

ABSTRACT
The negative environmental impact of transportation remains a critical challenge for urban areas, requiring a shift toward sustainable mobility solutions to reduce emissions and improve energy efficiency. In this context, the production, storage, and utilization of hydrogen have gained increasing importance in the global energy transition, providing a clean and viable alternative to conventional transportation system. This study focuses on the technical and economic evaluation of a hydrogen-fueled transportation system within a university campus, serving as a case study for urban transit applications. The analysis examines key performance metrics, including operational cost and infrastructure requirements, providing insights into the feasibility of hydrogen-based public transportation in controlled urban environments. The findings contribute to a broader understanding of how hydrogen mobility solutions can be effectively integrated into sustainable urban transport networks.

Keywords: Public transport, Hydrogen, Hydrogen Buses, transportation

1. INTRODUCTION

A logical and sustainable approach in the energy sector involves the increased adoption of renewable energy sources to reduce dependence on fossil fuels and mitigate environmental impacts. However, the pursuit of sustainability should not be confined solely to energy production but must extend to other high-emission industries, particularly transportation, which remains a major contributor to air pollution and greenhouse gas (GHG) emissions. A critical green solution in transportation is the replacement of conventional diesel- and petrol-powered vehicles with electric or hydrogen-powered alternatives. The transition to zero-emission transport technologies presents significant environmental and economic benefits. Advancing clean transportation technologies alongside renewable energy integration is essential for building a sustainable, low-carbon economy, ensuring energy security, and fostering long-term environmental resilience[1,2]. One of the most promising applications is hydrogen usage as a fuel for vehicles, offering an environmentally friendly transportation solution that supports the transition to low-emission mobility systems. Hydrogen-powered transportation not only contributes to carbon footprint reduction but also enhances energy security and efficiency [3]. The advantages of hydrogen energy position it as a highly viable option for urban transportation, particularly in areas where environmental noise pollution and traffic congestion are significant concerns. Given these, hydrogen-based transportation solutions can play a crucial role in developing cleaner, quieter, and more efficient urban mobility systems, aligning with sustainable city initiatives and climate action goals.

As transportation remains a major contributor to greenhouse gas (GHG) emissions, transitioning to clean mobility solutions is essential for achieving global sustainability targets. Numerous studies explore and analyze the concept of ecological and sustainable transportation, emphasizing its role in reducing carbon emissions, improving air quality, and enhancing energy efficiency. The transition toward sustainable mobility solutions is driven by the need to mitigate environmental impacts caused by conventional fossil-fuel-based transport systems [4–8]. In addition to technical, economic, and feasibility studies, research is also being conducted on the environmental sustainability of green ammonia production and utilization [9]. In contrast to the extensive body of research focused on electric-powered vehicles, the literature on hydrogen-powered vehicles remains relatively limited. Despite this, interest in hydrogen-powered buses has been steadily growing driven by advancements in hydrogen production, fuel cell technology, and policy incentives promoting low-emission public transportation. The identified research gap is the lack of a thorough techno-economic analysis regarding the investment in hydrogen-powered buses, especially within the context of a specific campus area. This gap encompasses critical aspects such as infrastructure requirements, investment and operational costs, and optimal bus routes that maximize the utilization of locally produced hydrogen. To analyze the prospects and key challenges associated with the increased adoption of hydrogen powered buses. The study places special emphasis on economic and technical performance, along with the environmental impact of these buses.

2. MATERIALS AND METHODS

Road transport accounts for the largest share of energy consumption within the transport sector, representing approximately 75% of global transport energy demand. Consequently, it is a major contributor to greenhouse gas (GHG) emissions, with road vehicles alone responsible for 15–20% of total global CO_2 emissions. This translates to an estimated 3 gigatonnes (Gt) of CO_2 emissions annually from passenger vehicles worldwide, significantly impacting climate change and air quality. [10]. The graph in Figure 1 illustrates the global changes in energy consumption and carbon dioxide (CO_2)

emissions based on different transportation technologies.

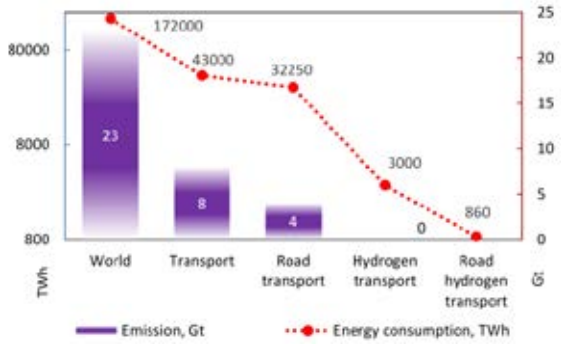

Fig. 1. Energy consumption and carbon emission values for different transportation technologies

This comparison underscores the environmental impact and efficiency of different vehicle technologies, emphasizing the need for sustainable alternatives in the transport sector. As illustrated in Fig. 1, hydrogen-based transportation technologies achieve the most favorable results in terms of both carbon emissions reduction and energy efficiency on a global scale. These findings highlight hydrogen's pivotal role in driving the transition toward a clean and sustainable transportation system. [10]. Furthermore, hydrogen-based transport systems have the potential to enhance energy security by reducing dependence on oil imports and leveraging locally produced green hydrogen from renewable energy sources such as solar and wind power. By integrating hydrogen refueling infrastructure with existing energy grids and mobility networks, the long-term scalability and feasibility of hydrogen-powered mobility solutions can be further optimized.

Although hydrogen and fuel cell technologies have a wide range of applications, they are increasingly emerging as a viable alternative to both conventional and battery-electric large vehicles, particularly for those requiring an extended driving range, such as buses. One of the key advantages of hydrogen-powered buses is their operational efficiency in urban transit systems. Since these buses regularly return to a central depot, their deployment can be achieved with minimal refueling infrastructure, making them a practical and scalable solution for public transportation networks. Additionally, they produce low or zero emissions, significantly improving their competitiveness compared to diesel-powered counterparts. By eliminating harmful pollutants, they help mitigate urban air pollution, contributing to healthier and more sustainable cities. Hydrogen-powered buses can be classified into three main configurations, each utilizing hydrogen as an energy source in different ways: Hydrogen-Powered Internal Combustion Engine (H2-ICE) Buses, Fuel Cell Buses, Hybrid Fuel Cell Buses. Fig. 2 illustrates the three primary configurations of hydrogen-powered buses.

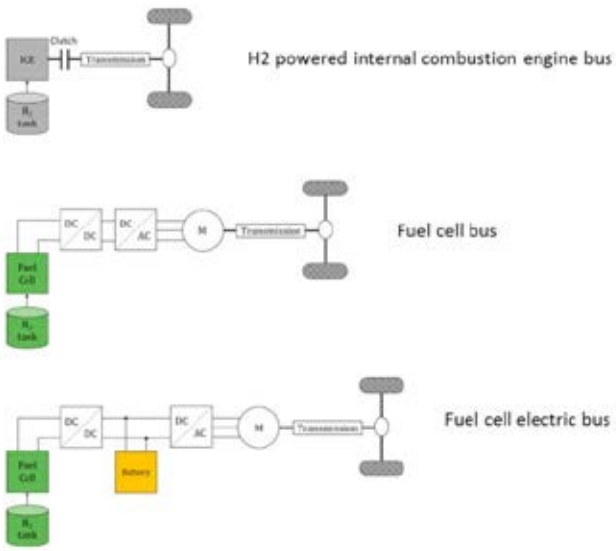

Fig. 2. Three configurations of hydrogen buses

Hydrogen-Powered Internal Combustion Engine (H_2-ICE) buses operate using modified internal combustion engines that burn hydrogen instead of conventional fossil fuels. While they still produce some NO_x emissions, they eliminate CO_2 emissions, making them a cleaner alternative to diesel buses.Unlike conventional battery-electric vehicles (BEVs), which

store energy solely in lithium-ion batteries, fuel cell electric vehicles (FCEVs) generate electricity on demand by converting hydrogen and oxygen into electricity through an electrochemical process [1]. Hybrid Fuel Cell Buses are a type of vehicle that utilize a fuel cell either as a standalone power source or conjunction with a battery or supercapacitor to power an onboard electric motor. Hybrid buses are particularly promising for urban and long-range applications, as they enhance fuel efficiency, reduce hydrogen consumption, and extend battery life, making them a sustainable and cost-effective solution for public transportation. Fig. 3 illustrates the process of producing hydrogen fuel to supply the buses.

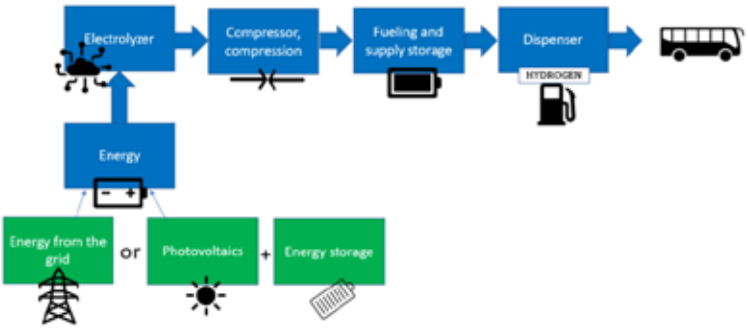

Fig. 3. Hydrogen fuel configuration supply

The integration of hydrogen technology with renewable energy sources (RES) enhances energy resilience and adaptability, ensuring the efficient utilization of renewable energy in both transportation and stationary applications. By coupling hydrogen production with RES, such as solar, wind, and hydropower, it is possible to store excess renewable energy and deploy it on demand, addressing the intermittency challenges of renewable generation [3]**.** In this study, the station infrastructure includes an electrolyzer, compressor, fueling supply and storage units, and dispensers, together forming a comprehensive hydrogen production and distribution system [11]. By combining hydrogen refueling and electric infrastructure, these hybrid stations can optimize energy distribution, improve grid stability, and support the decarbonization of mobility

3. RESULTS AND DISCUSSION

The high initial costs of Hybrid Fuel Cell Buses (HFCBs) compared to conventional diesel buses remain a major barrier to their widespread adoption. The total cost of mobility for buses is determined by evaluating investment costs (IC), annual distance traveled (d), energy costs (CE), and operating and maintenance costs (CO&M). The total cost per kilometer (TCK) is given by the following equation:

$$TCK = \frac{IC_{i,a}}{d}(C_{ei}) + \frac{CO\&Mi}{d} \text{ [\$/km]]} \quad (1)$$

where $IC_{i,a}$ represents the annualized investment costs, C_{ei} denotes the energy costs, and $CO\&Mi$ accounts for operating and maintenance expenses. The capital recovery factor (α) is calculated based on the discount rate (r) over the analysis period (n) using the formula:

$$\alpha = \frac{(1+r)^n \times r}{(1+r)^n - 1} \qquad C_{ei} = E_i \times P_{ei} \; [\$/km] \quad (2)$$

The energy cost (C_{ei}) depends on the average energy consumption of the buses (E_i) and the price of the corresponding energy source (P_{ei}) The cost analysis includes key financial factors such as investment costs (IC), annual driven distance (d), energy costs (CE), and operation and maintenance expenses (CO&M). The breakdown provides a comparative assessment of different bus technologies. It is evident that the investment costs of HFCBs remain significantly higher than those of diesel buses and battery electric buses (BEBs), making them less competitive in the current market. In addition to the high initial capital costs, HFCBs also face elevated fuel costs due to the high price of hydrogen, further impacting their overall economic feasibility. The departure and arrival routes of the hydrogen-powered bus operating within Fırat University's campus in Elazığ are illustrated in Fig. 4.

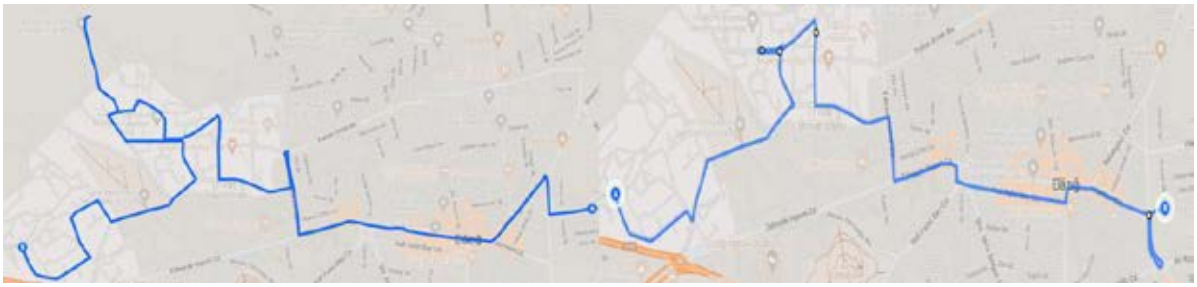

Fig. 4. The departure and arrival routes of the proposed study

The strategic location of the campus area, particularly in terms of existing energy infrastructure and accessibility to renewable energy sources, presents significant advantages for the implementation of hydrogen-fueled vehicles. A fuel station possibility integrated with both renewable energy sources and the electric grid further supports the feasibility of this clean transportation solution. The bus route spans approximately 10 kilometers, with most of the journey occurring within the university's campus boundaries. The two transportation routes include the number of stops, service frequency, and geographic positioning etc. These variations make them ideal for conducting a comparative analysis of vehicle performance under different real-world operating conditions. This controlled environment allows for optimized operational efficiency, making it an ideal case study for assessing the technical and economic feasibility of hydrogen-powered public transportation.

4. CONCLUSIONS

Public bus transportation is currently dominated by diesel-powered buses. Although these vehicles have seen considerable improvements over the years, they should ultimately be replaced by more environmentally friendly alternatives, such as hydrogen-powered buses and battery electric buses to reduce environmental impacts and support sustainable urban mobility. This study focuses on the technical and economic evaluation of a hydrogen-fueled transportation system within a university campus, serving as a case study for urban transit applications. By analyzing the feasibility, cost-effectiveness, and operational efficiency of hydrogen-powered public transportation, the research aims to provide insights into the potential advantages and challenges of integrating zero-emission vehicles into similar institutional and urban settings. As production methods improve, economies of scale and advancements in electrolysis and hydrogen storage are expected to lower hydrogen costs, making this technology more economically viable in the long term. The integration of renewable energy sources, particularly in hydrogen production, is also expected to have a catalytic effect in further reducing operational costs. Studies suggest that vehicles refueled from stations incorporating both electricity and hydrogen infrastructure will create even greater cost reductions over time. By utilizing green hydrogen, the transition toward low-carbon mobility can be accelerated while also supporting economic growth and energy security.

REFERENCES

1. Stecuła K, Olczak P, Kamiński P, Matuszewska D, Duong Duc H. 2022. Towards Sustainable Transport: Techno-Economic Analysis of Investing in Hydrogen Buses in Public Transport in the Selected City of Poland. Energies 15:9456.
2. Cevallos-Escandón A, Barragan-Escandón EA, Zalamea-León E, Serrano-Guerrero X, Terrados-Cepeda J. 2023.Assessing the Feasibility of Hydrogen and Electric Buses for Urban Public Transportation using Rooftop Integrated Photovoltaic Energy in Cuenca Ecuador. Energies 16:5569.
3. Ajanovic A, Glatt A, Haas R. 2021. Prospects and impediments for hydrogen fuel cell buses. Energy 235:121340.
4. Basma H, Haddad M, Mansour C, Nemer M, Stabat P. 2022. Evaluation of the techno-economic performance of battery electric buses: Case study of a bus line in paris. Res Transp Econ 95:101207.
5. Al-Ogaili AS, Al-Shetwi AQ, Al-Masri HMK, Babu TS, Hoon Y, Alzaareer K, et al. 2021. Review of the Estimation Methods of Energy Consumption for Battery Electric Buses. Energies 14:7578.
6. Logan KG, Nelson JD, Hastings A. 2020. Electric and hydrogen buses: Shifting from conventionally fuelled cars in the UK. Transp Res Part Transp Environ 85:102350.
7. Hensher DA, Wei E, Balbontin C. 2022. Comparative assessment of zero emission electric and hydrogen buses in Australia. Transp Res Part Transp Environ 102:103130.
8. Pyza D, Gołda P, Sendek-Matysiak E. 2022. Use of hydrogen in public transport systems. J Clean Prod 335:130247.
9. Pederzoli DW, Carnevali C, Genova R, Mazzucchelli M, Del Borghi A, Gallo M, et al. Life cycle assessment of hydrogen-powered city buses in the High V. 2022. LO-City project: integrating vehicle operation and refuelling infrastructure. SN Appl Sci 4:57.
10 Vodovozov V, Raud Z, Petlenkov E. 2022. Review of Energy Challenges and Horizons of Hydrogen City Buses. Energies 15:6945.
11 Caliskan A, Percin HB. 2025 An optimization approach to hybrid stations for hydrogen and electric vehicles. Int J Hydrog Energy.

PREPARATION OF ZINC AND COBALT WITH BORON DOPED NICKEL ELECTRODES FOR ALKALINE ELECTRO-CATALYTIC HYDROGEN PRODUCTION ACTIVITIES

[1]Aysu Doğa TÜMER,[1]Ceyda DEMİR, [1,2] Bilge COŞKUNER FİLİZ*
[1] Yıldız Technical University, Metallurgical and Materials Engineering Department, Istanbul, Turkey
[2] Yıldız Technical University, Clean Energy Technology Institute, Istanbul, Turkey

e-mail: aysudoga.tumer@gmail.com

ABSTRACT

This research investigates the preparation of Ni-B, Ni-Co and Ni-Zn doped electrodes and the evaluation of their hydrogen production activity under alkaline conditions. The electrolyte compositions included nickel, cobalt, and zinc sulfates (10 wt.%) and chlorides (3 wt.%), with a constant boric acid concentration (1 wt.%). Electrode preparation was conducted under controlled conditions, maintaining an applied voltage of 4.5 V and a bath temperature of 60°C. The impact of doping agents on electrode efficiency and hydrogen evolution was systematically evaluated in a 20 wt.% KOH alkaline solution at an applied potential of 2.3 V. The findings indicated that Ni-Co doped electrodes exhibited the highest hydrogen evolution rate, achieving 0.08 mL/s at room temperature. The analysis revealed that electrodes doped with cobalt (Co) and zinc (Zn) demonstrated significantly enhanced hydrogen production activity compared to those doped solely with Ni. The results underscore the potential of doped electrode systems in enhancing membraneless alkaline electrolysis, offering a promising strategy for improving hydrogen generation in sustainable energy applications.

Keywords: Doping Agent; Nickel Electrodes; Hydrogen Production; Alkaline Electrolysis; Electrolyte Composition

1.INTRODUCTION

The global energy demand has become a critical issue in constructing a sustainable future. In this context, Green Deal policies play a pivotal role in transitioning towards clean energy sources, forming the cornerstone of climate change mitigation strategies [1]. The significance of the transition to green energy extends beyond merely reducing fossil fuel dependency; it also contributes significantly to mitigating environmental pollution. Within this framework, hydrogen energy emerges as one of the most promising components of the green energy transformation. In particular, alkaline water electrolysis (AWE) has gained considerable attention due to its potential to utilize electrical energy to dissociate water molecules, sustainably generating hydrogen gas. This process offers a revolutionary approach to energy storage and transportation, particularly when powered by renewable energy sources. Currently, hydrogen production holds a crucial position among sustainable energy solutions, serving as a cornerstone for environmentally friendly fuel alternatives. In this regard, intensive research is being conducted on both alkaline electrolysis and electrocatalyst development strategies to enhance efficiency and scalability. Alkaline water electrolysis involves the decomposition of water (H_2O) into hydrogen (H_2) and oxygen (O_2) through an applied electric current, making it a well-established and cost-effective method [2]. However, optimizing electrocatalysts is of paramount importance to improve electrolyzer performance, reduce energy consumption, and enhance reaction kinetics [3]. Advances in electrocatalyst materials, particularly those based on transition metal oxides, perovskites, and nanostructured alloys, have demonstrated significant potential in lowering overpotentials and increasing hydrogen production efficiency.

The focus of this research is to enhance the efficiency of the alkaline water electrolysis (AWE) by delving into the interplay between alkaline electrolysis and electrocatalyst engineering. By investigating the latest developments in catalyst design, electrode structures, and reaction mechanisms, this study aims to pave the way for advanced electrolyzers capable of significantly improving hydrogen production efficiency. Nickel, zinc, and cobalt were chosen for their unique properties that make them excellent candidates for nanostructured alloys in enhancing the efficiency of hydrogen production by water splitting [4]. These elements have shown promise in lowering overpotentials and increasing AWE efficiency, making them ideal for electrocatalyst engineering in alkaline electrolysis. By exploring the interplay between these materials and electrode structures, this research aims to advance the development of electrolyzers with improved hydrogen production efficiency. Ultimately, these advancements will play a crucial role in accelerating the transition toward a more sustainable and scalable hydrogen-based energy economy.

The ”election of nickel (Ni), zinc (Zn), and cobalt (Co) for electrochemical deposition In the fabrication of electrocatalysts for alkaline water electrolysis is based on their distinct electrochemical properties, catalytic performance, and environmental considerations. Nickel (Ni), zinc (Zn), and cobalt (Co) coatings are transition metals commonly used in electrocatalytic hydrogen production processes, each offering different electrochemical advantages. The selection of these metals has been made under the principles of electrocatalytic performance, chemical stability, and sustainability. Nickel is widely used in alkaline electrolysis systems due to its high electrical conductivity and effectiveness in alkaline

water electrolysis (AWE). Additionally, nickel coatings provide corrosion resistance, extending the lifespan of the electrocatalyst [5]. Zinc is an abundant and recyclable metal found in nature, and it is considered one of the environmentally friendly alternatives in electrochemical coatings [5]. Zinc coatings can improve the reaction mechanism by optimizing the binding energy of hydrogen on the electrocatalyst surface and stand out as a sustainable choice due to their low cost. Cobalt has high electrocatalytic activity for AWE and is preferred in electrocatalysis applications due to its electrochemical stability and ability to operate over a wide pH range [7]. However, its environmental impact can be reduced by using cyanide-free plating solutions. From the perspective of green electroplating, these three metals can be coated with cyanide-free solutions to minimize the formation of toxic waste, thereby producing sustainable and environmentally friendly electrocatalysts. The individual coating of nickel, zinc, and cobalt allows for the optimization of each metal's specific electrochemical properties compared to alloys. This choice has been made in line with the goals of developing low-cost, high-efficiency, and environmentally friendly electrocatalysts.

Table 1. Evaluation of Three Different Metals in Terms of Green Electroplating

Metal	Advantages	Disadvantages	Suitability for Green Electroplating
Ni	- Excellent electrical conductivity and catalytic efficiency. - Corrosion-resistant and widely used in industry[7].	- Potential health risks and allergenic properties. - May require advanced waste treatment due to toxicity concerns.	**Moderate to Low** (Sustainability can be improved using cyanide-free nickel sulfate or chloride-based solutions.)
Zn	- High corrosion resistance. - Abundant, cost-effective, and recyclable [5]. - Non-toxic and environmentally friendly. - Can optimize hydrogen binding energy in AWE.	- Requires specific electrolyte conditions for stable deposition. - May dissolve in acidic or neutral environments.	**High** (Eco-friendly sulfate or chloride electrolytes can be used for non-toxic deposition.)
Co	-High electrocatalytic activity for AWE.[6][8] - Strong electrochemical stability. - Capable of working in both acidic and alkaline media.	-Environmental and ethical concerns related to mining. -Requires non-toxic electrolytes for sustainable deposition.	**Moderate** (Sustainable cobalt sources and cyanide-free electroplating are required to align with green principles.)

2. MATERIALS AND METHODS

The experimental studies were conducted in two stages: (I) the preparation of separate Co and Zn doped and undoped nickel electrodes for alkaline electrolysis, and (ii) the evaluation of their hydrogen production performance. Ni-B doped electrodes were fabricated using Watts Nickel bath, a widely used industrial electrodeposition solution, composed of $NiCl_2 \cdot H_2O$ (15 g/L), $NiSO_4 \cdot H_2O$ (5 g/L), and H_3BO_3 (2 g/L) maintained at temperature of 60°C. Ni-Zn and Ni-Co electrodes were prepared based on Watts Nickel solution, with doping agents introduced via their respective sulfate and chloride salts while maintaining the overall composition. For electrode preparation, 316L stainless steel plates were utilized as the substrate, while 99% pure nickel strips served as the cathode during the electroplating processes. Prior to electroplating at 4.5V, the substrate underwent pre-treatment with hydrochloric acid in an ultrasonic bath acid to ensure surface cleanliness, surface activity and adhesion. To investigate the impact of different dopants on hydrogen evolution efficiency, electrolyte solutions of potassium hydroxide (KOH) were prepared. The experiments were conducted in a 20 wt.% KOH solution at 2.3V and room temperature (25°C). The hydrogen evolution rate of the electrodes was quantified in milliliters per second (mL/s) and measured using a graduated cylinder.

3. RESULTS AND DISCUSSION

The electrochemical hydrogen evolution performance of Ni-based electrodes doped with boron (Ni-B), cobalt (Ni-Co-B), and zinc (Ni-Zn-B) was evaluated by measuring the volume of hydrogen produced over time and calculating the hydrogen production rate. The results are presented in Figure (1a) and Figure (1b), illustrating the cumulative hydrogen volume as a function of time and the corresponding hydrogen production rates for each electrode composition. Figure (a) presents the cumulative hydrogen volume (mL) generated over time (minutes) for the three doped nickel electrodes. The trend shows a nearly linear increase in hydrogen production, indicating a stable electrochemical process throughout the duration of the experiment. Among the three samples, Ni-Co exhibited the highest hydrogen evolution, producing the greatest volume of hydrogen. Ni-Zn demonstrated a moderate performance, with slightly lower hydrogen evolution compared to Ni-Co but higher than Ni-B. The Ni-B electrode displayed the lowest hydrogen production, suggesting a lower catalytic activity for the alkaline water electrolysis (AEW). The improved performance of Ni-Co may be attributed

to the enhanced electrochemical conductivity and optimized hydrogen adsorption energy introduced by cobalt doping. Figure (b) compares the hydrogen production rate (mL/s) of the three electrode materials. The Ni-Co electrode exhibited the highest hydrogen production rate, surpassing both Ni-Zn and Ni-B. The enhanced catalytic activity of Ni-Co is consistent with previous findings, where cobalt incorporation in Ni-based electrocatalysts improves electron transfer kinetics and reduces activation energy for AEW. The Ni-Zn electrode also showed a significant enhancement in hydrogen production compared to Ni-B, likely due to the favorable impact of zinc on surface reactivity and charge distribution. However, slightly lower efficiency compared to Ni-Co suggests that cobalt doping provides superior active sites for AEW, contributing to a more efficient hydrogen evolution process. The observed trend aligns with existing literature, indicating that transition metal doping significantly influences the catalytic activity of Ni-based electrodes. Cobalt doping, in particular, enhances the electronic structure, surface area, and electrochemical stability, resulting in improved hydrogen evolution kinetics. On the other hand, zinc doping appears to provide moderate benefits, possibly by modifying the hydrogen adsorption energy and surface interactions without significantly altering the electronic conductivity. These variations highlight the crucial role of transition metal selection in optimizing the performance of Ni-based electrocatalysts. These results suggest that Ni-Co is the most efficient doped electrode for hydrogen evolution applications, making it a promising candidate for electrochemical water-splitting and green hydrogen production. Further investigations on electrode stability, overpotential, and Tafel slope analysis will provide deeper insights into the long-term performance and mechanistic understanding of these materials.

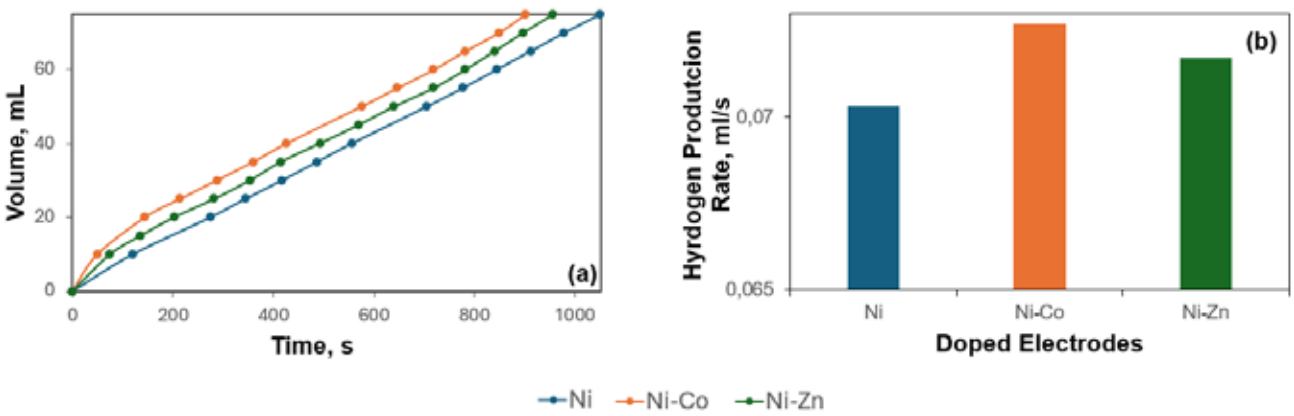

Fig. 1. (a) Time-Dependent Hydrogen Evolution Performance of Doped Stainless Steel Electrodes (b) Comparison of Hydrogen Production Rates for Different Doped Stainless Steel Electrodes

4. CONCLUSIONS

The results of this study highlight the significance of material selection and doping strategies in optimizing hydrogen evolution performance. While all three Ni-based electrodes demonstrated electrochemical activity, their effectiveness varied depending on the dopant introduced. Among the tested materials, certain modifications exhibited enhanced catalytic properties, suggesting that careful surface engineering and composition tuning play a critical role in electrochemical efficiency. Furthermore, the study aligns with the principles of green electroplating, emphasizing the potential of sustainable electrode fabrication techniques. By utilizing environmentally friendly deposition methods and avoiding hazardous chemicals, this approach contributes to the advancement of eco-conscious electrochemical systems. The findings suggest that strategic metal incorporation can lead to improved efficiency without compromising sustainability. Overall, these insights pave the way for further exploration of alternative doping elements and deposition strategies to develop efficient and environmentally responsible hydrogen evolution catalysts. Future work should focus on long-term stability, mechanistic studies, and large-scale applicability to bridge the gap between laboratory research and industrial implementation in green hydrogen production.

ACKNOWLEDGEMENT

The authors express their gratitude to the TÜBİTAK 2209 program for its support in the realization of this study.

REFERENCES

1. M.Saleh, Hosam & I.Hassan, Amal. (2024). The challenges of sustainable energy transition: A focus on renewable energy. Applied Chemical Engineering. 7. 2084. 10.59429/ace.v7i2.2084.
2. Tüysüz, H. (2024). Alkaline water electrolysis for green hydrogen production. Accounts of Chemical Research. https://doi.org/10.1021/acs.accounts.3c00709

3. Irshad, H., Zia, M., Al-Hajri, R., Khattak, Z. A. K., Al-Abri, M., Ahmad, N., & Younus, H. A. (2025). Electrocatalysts for hydrogen and oxygen evolution reactions under neutral/near-neutral conditions: Summary and challenges. In Ibrahim Dincer (Ed.), International Journal of Hydrogen Energy. https://doi.org/10.1016/j.ijhydene.2025.02.246
4. Lupi, Carla & Dell'Era, Alessandro & Pasquali, Mauro. (2009). Nickel–cobalt electrodeposited alloys for hydrogen evolution in alkaline media. International Journal of Hydrogen Energy. 34. 2101-2106. 10.1016/j.ijhydene.2009.01.015.
5. Lee, J., & Park, H. (2019). Sustainable zinc electroplating: An alternative approach. Green Chemistry, 21(8), 1568-1580.
6. Jin, C., et al. (2021). Cyanide-free cobalt electroplating: A green alternative for sustainable manufacturing. Materials Science and Engineering B, 268, 115134.
7. García, M. E., et al. (2021). Sustainable electroplating: Advances and challenges. Surface and Coatings Technology, 419, 127365.
8. Kim, S., et al. (2021). Advances in cobalt-based electrocatalysts for hydrogen evolution reaction. Electrochimica Acta, 390, 139853.

DESIGN OF A FUTURE HYDROGEN SUPPLY CHAIN UNDER CARBON EMISSION CONSTRAINTS: THE CASE STUDY OF CENTRAL ANATOLIA

[1]*Tuba Ulusoy*, [2*]*Alper Döyen*, [3]*Mehmet Güray Güler*
[1] Necmettin Erbakan University, Faculty of Engineering, Konya,42140, Turkey
[2] Konya Technical University,Faculty of Engineering and Natural Sciences,Department of Industrial Engineering,Konya,42250,Turkey
[3] İstanbul Technical University, Management Faculty, Data Science and Analytics, İstanbul, 34367, Turkey
*Corresponding author e-mail: alperdoyen@ktun.edu.tr

ABSTRACT
Clean energy sources like hydrogen, solar, and wind are essential in combating global warming, but solar and wind energy face challenges due to weather dependency and grid integration. On the other hand, hydrogen offers a stable and reliable energy supply. The economic and environmental benefits of hydrogen fuel cell vehicles (HFCVs) make them a viable substitute for fossil fuel vehicles, particularly considering the transportation sector's impact on global warming. However, widespread use of these vehicles is possible through developing a well-designed hydrogen supply chain (HSC). Therefore, this study aims to design the HSC of the Central Anatolia Region of Turkey, which has huge hydrogen energy production advantages due to its flat terrain and renewable energy sources. The problem is modelled using mixed integer linear programming (MILP) to minimize the costs related to production, storage and distribution under carbon emission constraints. Obtained results can help policymakers proactively specify the most efficient configurations for hydrogen production, storage, and transportation systems, taking carbon emissions into account.

Keywords: Hydrogen Supply Chain, Carbon Emission, Mixed Integer Linear Programming, Central Anatolia

1. INTRODUCTION

Since various effects of global warming began to threaten the world, some policymakers and governments have taken several actions to mitigate its impact. For instance, one of the European Union's environmental and climate-related goals is to be climate-neutral by 2050, establishing an economy with net-zero greenhouse gas emissions defined as minimizing greenhouse gas emissions as much as possible [1]**.** Another significant action is the Paris Agreement which aims to limit global temperature rise, focusing on limiting the increase under 1.5°C to minimize climate change risks and impacts. After this agreement came into force in 2016, countries, including the Netherlands, Spain, Norway, France, the UK, Sweden, Denmark, and Ireland, declared that they plan to gradually terminate the sales of fossil fuel vehicles [2]. This commitment is crucial, since the transportation sector, one of the major causes of global warming, consumes 65% of the world's oil products, accounts for 28% of global energy consumption, and contributes to approximately 25% of greenhouse gas emissions [3]. In addition, the European Union's Carbon Border Adjustment Mechanism (CBAM) aims to put a fair price on the greenhouse gases (GHG) emitted during the production of certain GHG-intensive goods, including hydrogen, entering the EU, and by 2025, importers will be required to report emissions data and obtain "authorized CBAM declarant" status for customs clearance by 2026. Thus, the EU's climate objectives will not be violated and cleaner industrial production in non-EU countries will be encouraged [4].

All these measures and actions against global warming rely on clean energy resources, such as hydrogen, solar, and wind, which have lower carbon emissions [5,6,7]. However solar and wind energy generation depends on weather conditions and the time of day, also their integration into a grid is challenging. On the other hand, hydrogen production technology stands out by offering stable and reliable energy supply and storage options [8].

Considering the transportation sector's impact on global warming, it is inevitable to prefer vehicles that use clean resources rather than fossil fuel vehicles that are not sustainable [9]. Therefore, HFCVs powered purely by hydrogen gas are promising alternatives for carbon emission reduction targets. HFCVs are also more environmentally and economical than Battery Electric Vehicles [10]. Many countries already recognized the promising features of hydrogen energy, and they mapped their hydrogen energy strategies [11]. Turkey is one of the countries that reported its hydrogen technology strategy and roadmap [12]. It has nearly all forms of renewable energy and abundant water resources. Moreover, it is bordered by seas on three sides. These factors can make Turkey a potential leader in global hydrogen exports if these resources are utilized in hydrogen energy generation. Furthermore, not only coastal cities but also the cities in Central Anatolia have a high potential for hydrogen energy production [13].

Considering Turkey's hydrogen production potential, several studies [14,15,16] were conducted to handle Turkey's future HSC using mathematical optimization problems. Furthermore, optimal locations of hydrogen fuel stations in Istanbul, the most crowded city in Turkey, were determined in the studies [17,18] employing different approaches.
In this study, we aim to design the HSC of the Central Anatolia region of Turkey in 2050, minimizing production, storage and distribution-related costs, considering carbon emissions. According to the best knowledge of the authors, this is the

first study that considers specifically Central Anatolia which has a high potential for hydrogen production according to the report [13] conducted in 2021.

2. METHOD

In this study, we address the HSC design problem of Central Anatolia employing a MILP model formulated by Almansoori and Shah [19]. The model aims to minimize the total daily cost of the HSC considering capital and operating costs. In addition to that, we consider the total daily carbon emissions ($TDCO_2$) produced in the HSC. The HSC model obtains the optimal number and location of production plants and storage facilities to be established in each city, the necessary transportation links in the network, and the production rates and flows of hydrogen. The model includes demand, transportation, production, storage facilities, and carbon emission constraints. This single-period model differs from the previously developed models since it handles HSC integrating production, storage, and distribution.

The total daily carbon emissions ($TDCO_2$) produced in the HSC stem from production, storage, and transportation. It is calculated according to Eq. (1).

$$TDCO2 = PRCO2 + STCO2 + TRCO2 \quad (1)$$

We adapt the model for 2050, which is the earliest projected year, utilizing Turkey's energy potential [20]. Table 1 shows the forecasted number of automobiles and large vehicles in each city of Central Anatolia in 2050 and presents a projection for hydrogen energy demand based on the estimated number of vehicles. Since Ankara has the largest population among these cities, it also has the highest number of cars and large vehicles. As a result, it has the highest hydrogen energy demand. Whereas Çankırı is the least populated city in Central Anatolia, accordingly, the demand for hydrogen energy is the lowest among the cities in the region.

Table 1. A projection for the number of automobiles and large vehicles, and hydrogen energy demand

City	Forecasted Number of Automobiles	Forecasted Number of Large Vehicles	Forecasted Hydrogen Energy Demand (kg/day)
Ankara	4,056,964	953,003	4,347,471
Konya	901,915	370,675	1,641,481
Kayseri	604,580	191,497	858,164
Eskişehir	416,268	128,784	577,836
Aksaray	165,186	57,113	254,836
Sivas	211,438	72,791	324,858
Nevşehir	135,452	64,952	285,978
Niğde	118,934	57,113	251,451
Yozgat	115,630	40,315	179,813
Kırıkkale	93,426	24,737	112,486
Kırşehir	92,504	24,633	111,580
Karaman	89,200	33,596	149,320
Çankırı	52,860	22,397	99,063

The MILP model is solved using the Gurobi solver in Python on a computer with an M1 chip and an 8-core CPU. The optimum solution of the model is provided in the following section.

3. RESULTS AND DISCUSSION

According to Fig.1, as the total daily carbon emissions ($TDCO_2$) are decreased, the unit production cost increases. In the optimal scenario, where $TDCO_2$ is minimized, the unit production cost is 6.21 ($ kg^{-1} day^{-1}). On the other hand, when there is no restriction on carbon emissions, the unit production cost decreases to 4.65 ($ kg^{-1} day^{-1}).

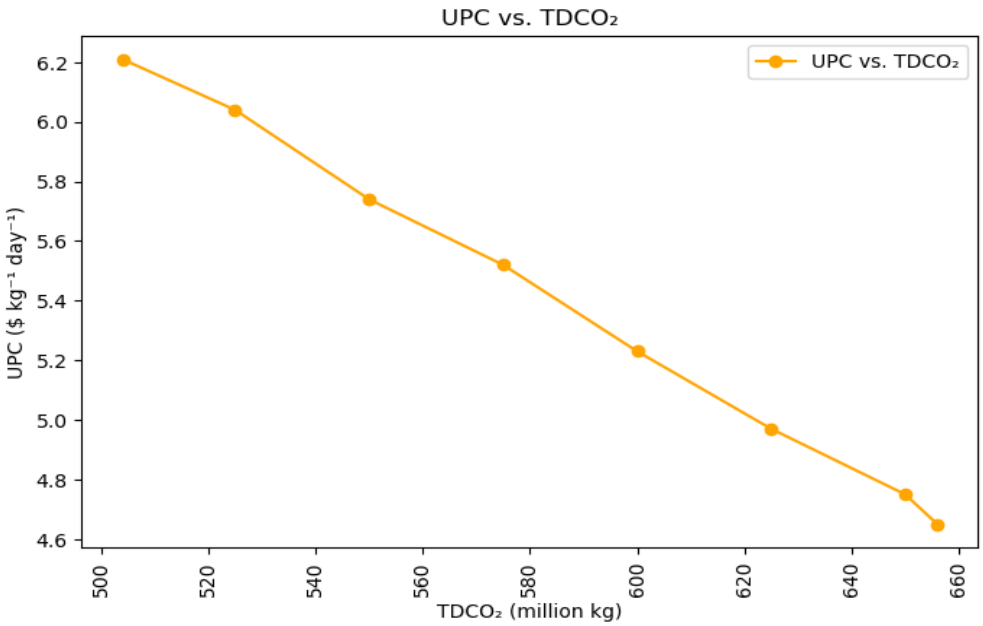

Fig. 1. Unit production cost vs. total daily carbon emission

Fig. 2 shows the number of plant types, sizes and unit production costs in the future HSC under various $TDCO_2$ levels.

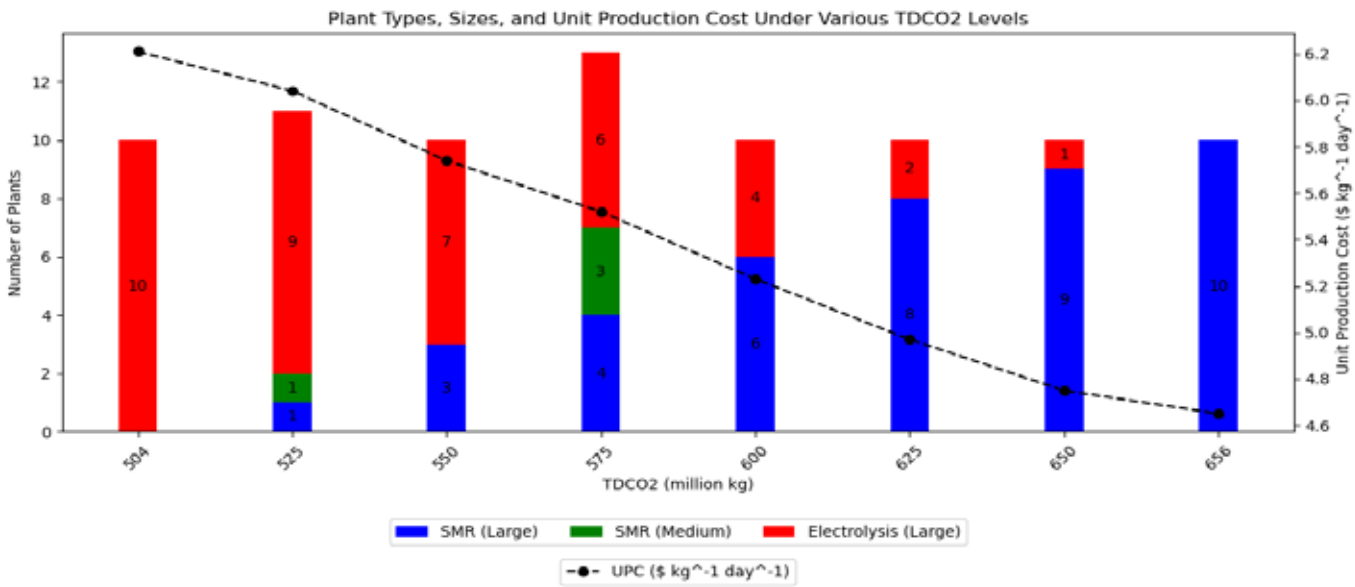

Fig. 2. Number of plant types, sizes and unit production costs under various $TDCO_2$ levels

Given that ELE technology has the lowest carbon emissions compared to the other technologies, it is reasonable to establish only Large ELE production plants in the Minimum Total Daily Carbon Emission case ($TDCO_2$ = 504 million kg). On the other hand, in the Minimum Total Daily Cost case ($TDCO_2$ = 656 million kg), it makes sense to build only the Large SMR production plant which has the lowest unit production cost among the other types. Furthermore, Large SMR production plants have the lowest Facility Capital Cost when compared to other Large-scale plant types.

4. CONCLUSIONS

Utilizing an optimization approach for the HSC_design can help determine the necessary investments to establish new production facilities and distribution networks. In other words, the results obtained by solving mathematical models can provide insights that could be crucial for both governments and policymakers while making strategic decisions [19]. Therefore, in this study, we use a MILP model to find an HSC configuration of Central Anatolia in 2050, with a particular focus on carbon emissions that contribute to global warming. From this perspective, this study provides valuable results

regarding the trade-off between carbon emissions and production costs. In future studies, Turkey's HSC can be handled with different objectives and approaches.

REFERENCES

1. Lotfi R, Khanbaba A, Ali SS, Afshar M, Mehrjardi MS and Omidi S. 2024. Net-zero, resilience, and agile closed-loop supply chain network design considering robustness and renewable energy. Environmental Science and Pollution Research, 1-19.
2. https://www.transportenvironment.org/articles/end-fossil-fuel-car-eu-agenda. Accessed on January 17, 2025.
3. Asgarian F, Hejazi SR, Khosroshahi H. 2023. Investigating the impact of government policies to develop sustainable transportation and promote electric cars, considering fossil fuel subsidies elimination: A case of Norway. Applied Energy 347:121434.
4. https://taxation-customs.ec.europa.eu/carbon-border-adjustment-mechanism_en#cbam. Accessed on January 16, 2025.
5. Cooper J, Dubey L, Bakkaloglu S, Hawkes A. 2022. Hydrogen emissions from the hydrogen value chain-emissions profile and impact to global warming. Science of The Total Environment 830:154624.
6. Güney T, Üstündağ E. 2022. Wind energy and CO2 emissions: AMG estimations for selected countries. Environmental Science and Pollution Research 1-11.
7. Kou G, Yüksel S, Dinçer H. 2022. Inventive problem-solving map of innovative carbon emission strategies for solar energy-based transportation investment projects. Applied Energy 311:118680.
8. Bade SO, Tomomewo OS. 2024. A review of governance strategies, policy measures, and regulatory framework for hydrogen energy in the United States. International Journal of Hydrogen Energy 78:1363-1381.
9. Brey JJ, Carazo AF, Brey R. 2018. Exploring the marketability of fuel cell electric vehicles in terms of infrastructure and hydrogen costs in Spain. Renewable and Sustainable Energy Reviews 82:2893-2899.
10. Habib ARR, Butler K. 2022. Environmental and economic comparison of hydrogen fuel cell and battery electric vehicles. Future Technology 1(2):25-33.
11. Alam SN, Khalid Z, Singh B, Guldhe A. 2024. Integration of government policies on the global level for green hydrogen production. In Green Hydrogen Economy for Environmental Sustainability, Vol. 1. Edited by Kothari R, Pathania D. American Chemical Society.
12. https://enerji.gov.tr/Media/Dizin/SGB/tr/Kurumsal_Politikalar/HSP/ETKB_Hidrojen_Stratejik_Plan2023.pdf. Acc. on Jan 19, 2025.
13. Dinçer İ, Javani N, Karayel GK. 2021. Türkiye için Hidrojen Çiftliği Konsepti Raporu. Report, İstanbul.
14. Erdoğan A, Geçici E, Güler MG. 2023. Design of a future hydrogen supply chain: A multi-objective model for Turkey. International Journal of Hydrogen Energy 48(31):11775-11789.
15. Erdoğan A, Güler MG. 2023. Optimization and analysis of a hydrogen supply chain in terms of cost, CO2 emissions, and risk: the case of Turkey. International Journal of Hydrogen Energy 48(60):22752-22765.
16. Özbek BT, Güler MG. 2024. A multi period and multi objective stochastic hydrogen supply chain for Turkey. International Journal of Hydrogen Energy.
17. Geçici E, Güler MG, Bilgiç T. 2022. Multi-period planning of hydrogen refuelling stations using flow data: a case study for Istanbul. International Journal of Hydrogen Energy 47(95):40138-40155.
18. Gündüz SB, Geçici E, Güler MG. 2024. Locating hydrogen fuel stations: A comparative study for Istanbul. International Journal of Hydrogen Energy 52:1234-1246.
19. Almansoori A, Shah N. 2006. Design and operation of a future hydrogen supply chain: snapshot model. Chemical Engineering Research and Design 84(6):423-438.
20. Özbek BT, Erdoğan A, Güler MG. 2024. Leveraging Renewable Energy for Turkey's Future Hydrogen Supply Chain: A Stochastic Programming Model. 8th International Hydrogen Technologies Congress.

SYNTHESIS AND CHARACTERIZATION OF (Gd,Nd) – Doped $CeO_2/SrTiO_3$ HETEROSTRUCTURES FOR LT-SOFC

Nurvet KIRKGEÇİT AKSOY[1], Derya KARA[2], Süleyman KERLİ[3], Merivan ŞAŞMAZ GÜLDAL[4], Orhan TÜRKOĞLU[5], Handan ÖZLÜ TORUN[3]*

[1]Kahramanmaraş Sütçü İmam University, Institute of Science, Department of Physics, Kahramanmaraş, 46000 Turkey
[2] Ka hramanmaraş Sütçü İmam University, Institute of Science, Department of Chemistry, Kahramanmaraş, 46000 Turkey
[3]Kahramanmaraş İstiklal University, Energy Systems Engineering, Elbistan Faculty of Engineering, Kahramanmaraş, 46000 Turkey
[4]Adiyaman University, Faculty of Engineering, Department of Electrical and Electronics Engineering, Adiyaman 02040, Turkey
[5]Erciyes University, Faculty of Science, Department of Chemistry , Kayseri,38030, Turkey
* nurvetkrkgct@gmail.com

ABSTRACT

In this study, we focused on the development of ion conducting/semiconducting ceramic electrolytes that can be used in low temperature solid oxide fuel cells. $Ce_{0.9}Gd_{0.05}Nd_{0.05}O_2$ (CeO2:0,05Gd0,05Nd) was synthesised using the combustion technique with glycine. Composites with SrTiO3 were made by solid-state method. Conductivities were calculated at different temperatures. Conductivity value for 475 oC is 73,47 ohm.cm^{-1} and 575 ^{o}C is 12,24 ohm.cm^{-1}.

Keywords: heterostructure, composite electrolyte, solid oxide fuel cell

1. INTRODUCTION

Cerium oxide (CeO_2) is one of the most reactive rare earth metal oxides with a wide range of applications in various fields[1]. In recent years, cerium (IV) oxide (CeO_2, also known as ceria) nanoparticles have attracted much attention due to their many interesting properties, such as unique UV absorption ability, high stability at high temperature, high hardness and reactivity [2,3]. Therefore, CeO_2 and CeO_2-based materials have been widely used in a variety of applications, such as solid oxide fuel cells (SOFCs) [4], catalysis [5], luminescent materials [6], gas sensors [7], polishing materials [8] and ferromagnetic oxides [9]. Each Ce^{4+} cation (formally 4f0) is coordinated by eight equivalent O^{2-} anions at the corners of a cube, and each O^{2-} is in turn coordinated by a tetrahedral Ce^{4+} ion [10].
This research aims to develop ceramic electrolytes that have the potential to provide a sustainable and innovative solution for low-temperature operation of solid oxide fuel cells. Semiconductor/ion conductor heterostructures were used to develop this innovative ceramic electrolyte proposal. Gd, Nd-doped CeO_2 has been selected as the ion conductor in this heterostructure system to be developed. $SrTiO_3$ was selected as the semiconductor. $SrTiO_3$ is expected to prevent the formation of short circuits by not allowing electronic transitions in the cell and to contribute to the increase in ionic conductivity [11].

2. MATERIALS AND METHODS

Gd^{3+} and Nd^{3+} were doped into CeO2 using the burning technique with glycine. . According to Fig1, The starting compounds were dissolved in 100 ml water. The combustion process was carried out at 300 ^{o}C on a heated magnetic plate. After combustion, the final product was sintered at 650 ^{o}C for 4 hours. The composites were ground in agate mortar with a ratio of 60:40. The composite was calcined at 700 ^{o}C for 2 hours. XRD and empedance spectroscopy were used to determine the physical and chemical structures of the synthesised compounds

Fig. 1.(a) The Moment When the Experiment Started to Boil (b) The Burning State of the Experiment c) Before the Oven (d) After the Oven

3. RESULTS AND DISCUSSION

X-ray diffraction patterns of $Ce_{0.9}Gd_{0.05}Nd_{0.05}O_2$ and 60:40 composite structures are given in Fig. 2. In the evaluations made with the Expert High Score program, it was determined that $Ce_{0.9}Gd_{0.05}Nd_{0.05}O_2$ and $SrTiO_3$ retained their crystal structure and there were no phase changes.

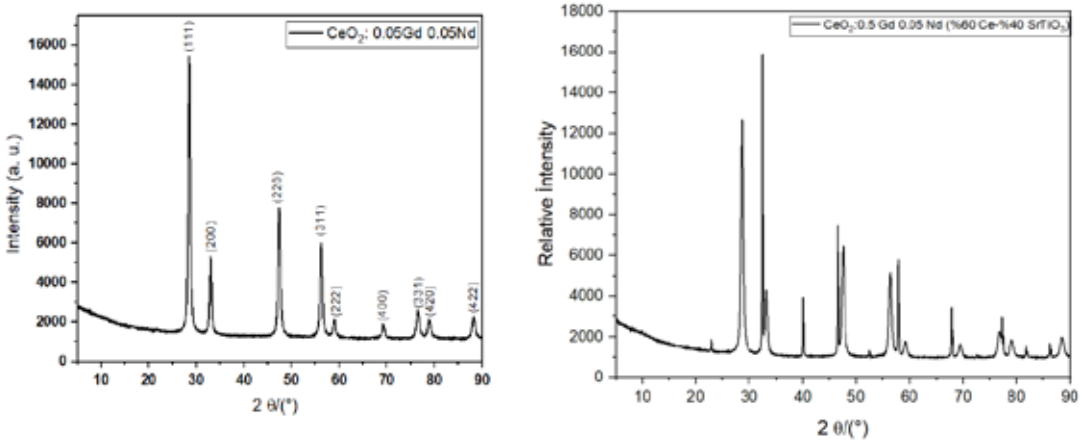

Fig. 2. X-ray diffraction patterns of $Ce_{0.9}Gd_{0.05}Nd_{0.05}O_2$ and 60:40 composite structures.

Fig.3. shows the conductivities of samples tested at different temperatures. 60:40 composite structures's total conductivity is determined as follows:

$$\sigma = t/RA$$

Where σ is the conductivity, t is the thickness of the electrolyte discs, A is the surface area of the electrolyte, and R is the resistance value obtained by fitting at different temperatures. Conductivity value for 475 oC is 73,47 ohm.cm^{-1} and 575 ^{o}C is 12,24 ohm.cm^{-1}.

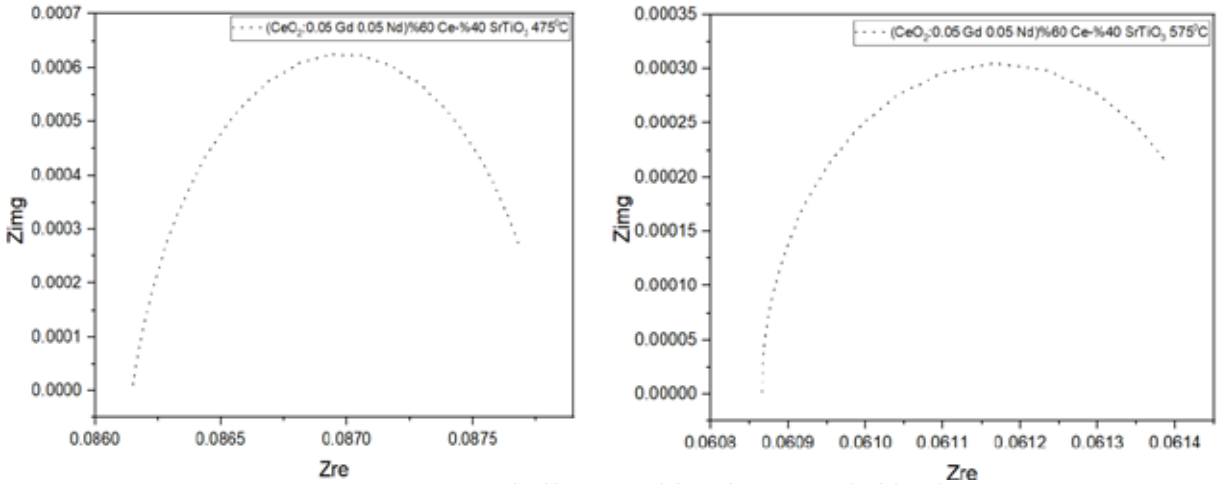

Fig. 3. Electrochemical impedance spectra (EIS) curves of $Ce_{0.9}Gd_{0.05}Nd_{0.05}O_2$ / $SrTiO_3$ composite samples 475-575 ^{o}C.

4. CONCLUSIONS

In this paper, $Ce_{0.9}Gd_{0.05}Nd_{0.05}O_2$ / $SrTiO_3$ was prepared by solid-state method for obtaining high ionic conductivity. The crystal structure and electrochemical performance of the materials $Ce_{0.9}Gd_{0.05}Nd_{0.05}O_2$ / $SrTiO_3$ electrolyte were investigated. The ionic conductivity reached ? cm-1.

ACKNOWLEDGEMENT

This study was supported by The Scientific and Technological Research Council of Turkey (TUBITAK) Project 223M571.

REFERENCES

[1] J. Fang, X. Bi, D. Si, Z. Jiang, and W. Huang, “Spectroscopic studies of interfacial structures of CeO 2 -TiO 2 mixed oxides,” *Appl Surf Sci*, vol. 253, no. 22, pp. 8952–8961, Sep. 2007, doi: 10.1016/j.apsusc.2007.05.013.

[2] S. Tsunekawa, R. Sahara, Y. Kawazoe, A. Kasuya, Mater. Trans. JIM 41 (2000) 1104.

[3] A. Trovarelli, C. de Leitenburg, M. Boaro, G. Dolcetti, Catal. Today 50 (1999) 353.

[4] H. Yahiro, Y. Baba, K. Eguchi, H. Arai, J. Electrochem. Soc. 135 (1988) 2077.

[5] E. Bekyarova, P. Fornasiero, J. Kaspar, M. Graziani, Catal. Today 45 (1998) 179

[6] X.J. Yu, P.B. Xie, Q.D. Su, Phys. Chem. Chem. Phys. 3 (2001) 5266.

[7] N. Izu, W. Shin, N. Murayama, S. Kanzaki, Sens. Actuator B: Chem. 87 (2002) 95.

[8] S.H. Lee, Z.Y. Lu, S.V. Babu, E. Matijevic, J. Mater. Res. 17 (2002) 2744.

[9] Y. Liu, Z. Lockman, A. Aziz, D.J. MacManus, J. Phys. Condens. Mater. 20 (2008) 765201

[10] K. Ackland and J. M. D. Coey, “Room temperature magnetism in CeO2—A review,” Jul. 10, 2018, *Elsevier B.V.* doi: 10.1016/j.physrep.2018.04.002.

[11] Shi, Q., Chen, J., Xing, Y., Zhu, B., & Wu, Y. (2019). Semiconductor heterostructure SrTiO3/CeO2 electrolyte membrane fuel cells. *Journal of The Electrochemical Society*, *167*(5), 054504]

SCALE UP TECHNIQUES FOR PEMFC: FLUID MECHANICS APPROACH

[1*]*Güneyhan Tol*, [1,2]*Anıl Can Türkmen,* [1]*Cenk Celik,* [3]*Fatma Gül Boyacı San*
[1] Kocaeli University Faculty of Engineering, Department of Mechanical Engineering, Kocaeli 41380, Turkey
[2] ACT Scientific Ltd., Budotek Teknopark, Istanbul, 34776, Turkey
[3] Düzce University Faculty of Arts and Science, Department of Chemistry, Düzce, 81100, Türkiye

*Corresponding author e-mail: guneyhan.tol@kocaeli.edu.tr

ABSTRACT

In this study, A fluid mechanics model based on the finite element method has been developed to evaluate the effect of scaling up on the performance of a PEM fuel cell. Three different sizes of bipolar plates were designed with areas of 50 cm², 100 cm², and 225 cm². The aim was to ensure that hydrogen flows at the same velocity in channels with equal depths. Flow rate calculations were determined based on the current density obtained from the active area size, pressure drop, and velocity calculations were performed for different stoichiometries. The designed flow fields were analyzed using the finite element method, and similar flow velocities were obtained.

Keywords: Hydrogen, PEMFC, Scale-up, Flow Channel

1. INTRODUCTION

The demand for the energy we need is increasing day by day with the growing world population, developing economies, and emerging technologies in our lives. It is widely known that fossil fuel reserves are depleting and causing environmental pollution. This pollution not only endangers living organisms but also harms the global ecosystem. The use of clean energy has become a necessity for a sustainable future. Scientists are conducting research to develop and promote the use of new energy sources such as solar-based energy, wind-based energy, biomass-based energy, and hydrogen-based energy [1].

Fuel cells stand out among renewable energy sources because they can directly convert the chemical energy in various fuels into electrical energy through electrochemical reactions. Additionally, since fuel cells do not operate based on the heat engine principle, they are not limited by Carnot efficiency. The limitation is defined by the second law of thermodynamics [2].

Among fuel cells, PEM fuel cells have many advantages, such as ease of implementation, long lifespan, low operating temperature, high power density, rapid startup, low emissions, durability, stable power generation, and suitability for portable applications. Therefore, many industries are considering integrating PEMFC technology into their respective fields [3].

The development of PEM fuel cells can be categorized into two main areas. The first involves advancements in material science and the testing of materials in small-scale single cell. The second focuses on scaling up. Since electrochemical reactions occur in fuel cells, challenges such as irregular flow distribution, unpredictable pressure drops, water management issues, non-uniform heat distribution, and weak flow field designs are among the primary obstacles to scaling up. The goal of this study is to provide solutions to the challenges of scaling up using the finite element method [4].

2. MODELING

In a PEMFC, the theoretical hydrogen flow rate required for the reaction is calculated based on the desired current density. The necessary feed flow rate is determined considering the stoichiometric ratio. Although the flow rates of the fuel cells with three different active areas examined in the scaling-up study are proportional to their active areas, it is desired that the hydrogen flow per unit area remains equal. To achieve this, the hydrogen must have the same velocity within the channels of the three different fuel cells. To maintain equal velocities at different flow rates, the cross-sectional area needs to be increased. To preserve the cross-section of a single channel, the number of channels has been increased in proportion to the growth rate of the active area. Since the active area is square and the inlet and outlet are positioned diagonally. During this calculation, the ratio of the flow field to active area was also considered. This ratio has been kept close to each other across different active areas. The fuel cell designs with different active areas were modeled using finite element analysis, achieving nearly identical flow velocities.

In the studies, dry H_2 gas was selected as the working fluid, heat transfer equations were excluded from the modeling scope, the flow was assumed to be laminar, and an isothermal model was developed at 60°C. No material deformation was considered, and solid surfaces were assumed to be smooth.

3. RESULTS AND DISCUSSION

The flow distribution is shown in Fig. 1. In dual and quadruple serpentine channels manifolds are designed to ensure that the flow reaches the channels with equal flow rates. The radius added to the channel corners has been effective in achieving a homogeneous flow distribution. It has been observed that the flow velocity yields very similar results across different active areas.

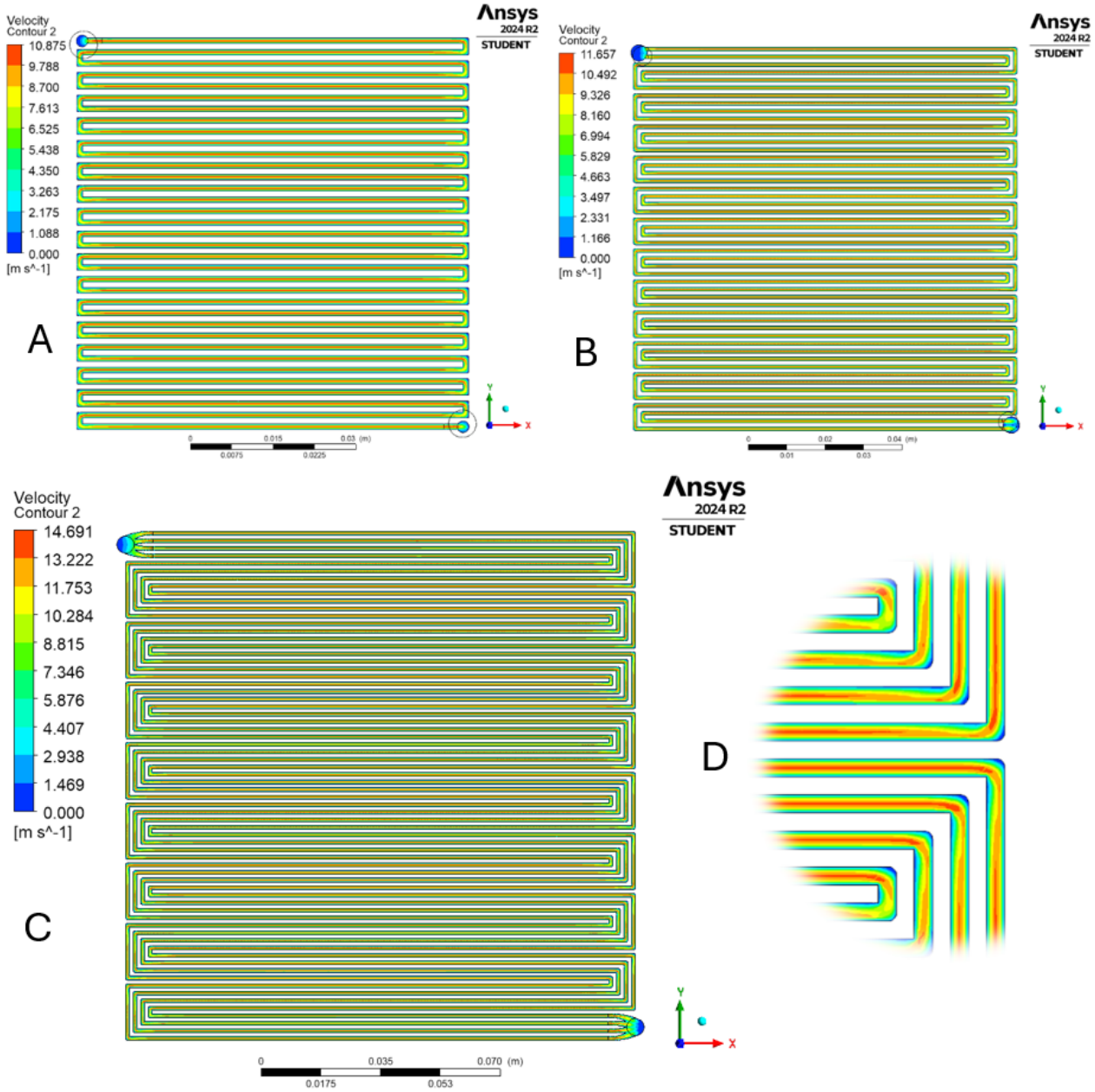

Fig. 1. Flow Distribution of the Cells (A: Single Channel Serpentine, B: Dual Channel Serpantine, C: Quadruple Channel Serpantine, D: Detail of the corners of the channels)

In Fig. 2, the relation of the required hydrogen flow rates for the desired current density and active area are shown for different stoichiometries. As stoichiometry and active area increase, the feed flow rate also increases linearly.

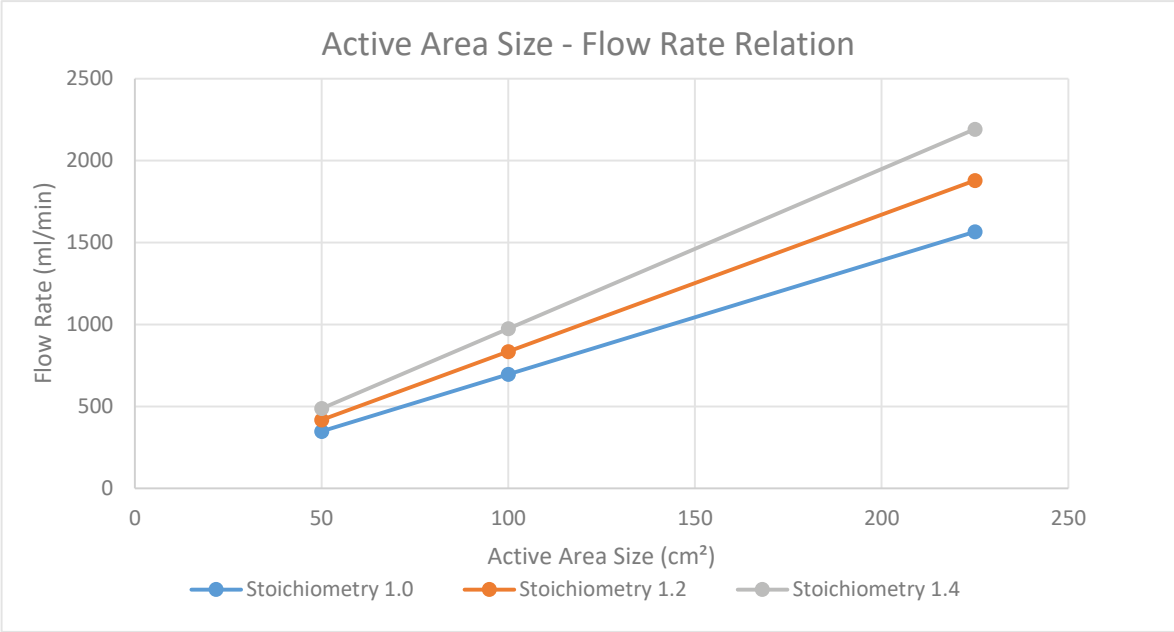

Fig. 2. Active Area Size – Flow Rate Relation

In Fig. 3, the pressure drop of the channel at different stoichiometry values for various active area sizes are shown.

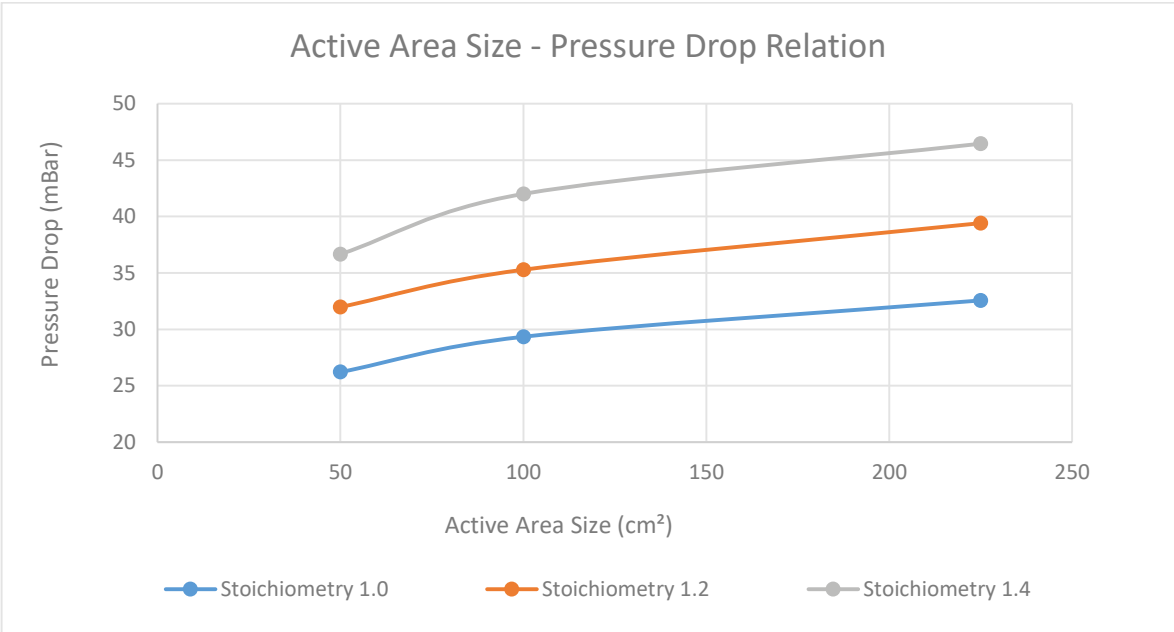

Fig. 3. Active Area Size – Pressure Drop Relation

In Fig. 4, the average velocity is shown for different active area sizes according to different stoichiometric values.

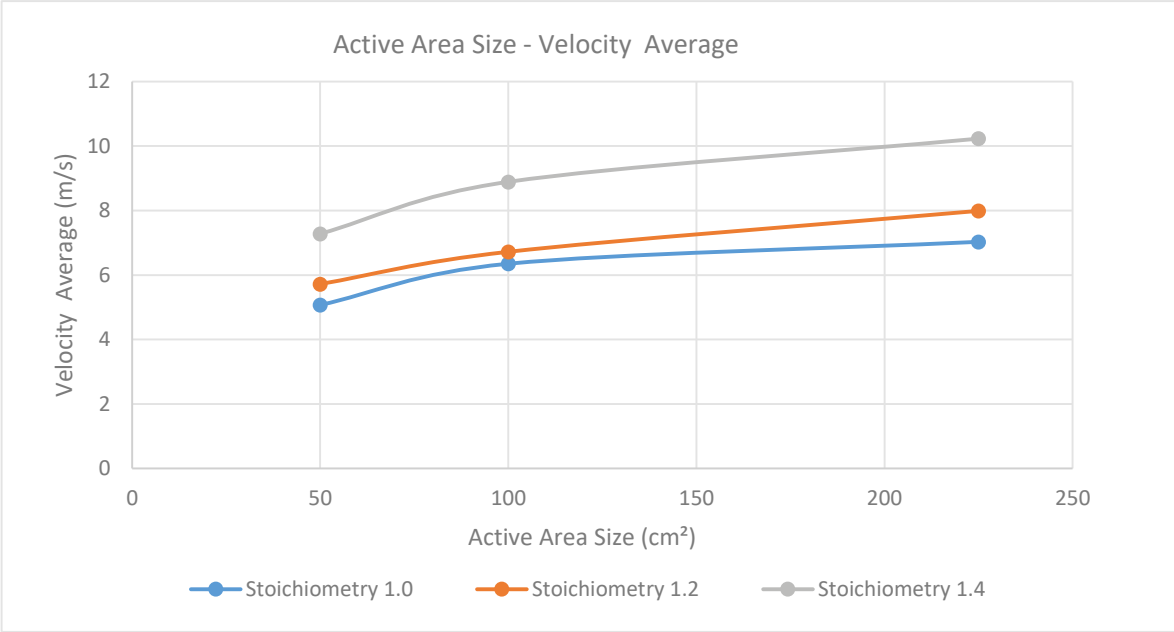

Fig. 4. Active Area Size – Velocity Average Curves

4. CONCLUSIONS

In this study, as part of the scale-up process of the PEM fuel cell, the first step, channel design, was evaluated using a fluid mechanics approach. Hydrogen supply was provided at three different stoichiometries for three active areas of different sizes. While calculating hydrogen flow rates, it was assumed that the current density of the cells was the same. Accordingly, the design was created to equalize the flow velocity in the channels within a single cell.

Modeling results showed that an increase in stoichiometry led to an increase in average velocity, pressure drop, and flow rate. While the increase in flow rate occurred linearly, the pressure drop and average velocity exhibited a nonlinear increase. In the next stage, the effect of the designed channels on performance will be experimentally examined. The relationship between performance variations and flow characteristics will be investigated.

REFERENCES

1. Ding, R., Lİ, Y., Liu, J., Ke, Z., Jiang, X., Wang, Z., . . . Ji, V. (2025). Recent progress in the preparation and performance of protective coatings on metal bipolar plates of proton exchange membrane fuel cells-A review. Applied Materials today /42, 102556.
2. E. Lutz, A., S. Larson, R., & O. Keller, J. (2002). Thermodynamic comparison of fuel cells to the Carnot cycle. International Journal of Hydrogen Energy / 27, 1103-1111.
3. BARBIR, F. (2013). PEM FUEL CELLS THEORY AND PRACTICE. Academic Press is an imprint of Elsevier.
4. Wang, J. (2015). Barriers of scaling-up fuel cells: Cost, durability and reliability. Energy / 80, 509-521

OPTIMIZATION OF ASSEMBLY TORQUE AND LUBRICATION AMOUNT FOR HYDROGEN TANK VALVES

[1*]*Olcay Özkan*
[1] Bosch Sanayi ve Ticaret A.Ş., Bursa, 16140, Türkiye
*Corresponding author e-mail: olcay.ozkan@tr.bosch.com

ABSTRACT
As the world aims to reduce carbon emissions, hydrogen-powered internal combustion engines and fuel cells are emerging as an innovative technology. However, high pressures in hydrogen storage systems can cause hydrogen leakage due to small atomic size of hydrogen and plastic deformations in the Hydrogen Tank Valve (HTV) body.

In this study, prototype-phase research was conducted to determine the optimal assembly torque values and lubricant amount to assemble hydrogen tank valve. It was observed that even if same torque is used to assemble the sub-components to valve body, resulting axial force distribution was excessively high, causing uncontrollable deformations on the body and hydrogen leakage, preventing the achievement of mass production targets. Based on these findings, this research focuses on optimizing the bolting process of devices mounted on hydrogen tank valves. The study aims to enhance assembly efficiency by optimizing lubricant application, preventing overuse or underuse of lubricants, and controlling torque application and bolting techniques that could lead to hydrogen leakage.

Assembly trials are made using prototype valve body and sub-components. Axial loads are measured after applying various torque and optimum pre-assembly bolting cycle is tried to be achieved. Furthermore, to reduce testing costs, numerical models were developed using Computational Fluid Dynamics and Finite Element Method. These models were used to determine optimal lubricant application positions, angles, and speeds, as well as to validate the axial loads exerted on the components.

Keywords: Hydrogen storage, Hydrogen tank valves, Torque optimization, Axial load, Lubrication analysis

1. INTRODUCTION

Hydrogen-powered internal combustion engines have become a key technology in reducing carbon emissions. [1] Compared to fossil fuels, hydrogen offers higher thermal efficiency, significantly lower exhaust emissions, and releases water vapor as a byproduct of combustion. One crucial component for these engines is the Hydrogen Tank Valve (HTV), which connects the fuel tank to various independent components and devices. The HTV has several threaded connection points, one for the fuel tank and many others are for mounting additional components like pressure sensor, temperature sensor, service valves, safety valve, fueling port etc. Since those connections use a threaded assembly (female on the HTV side, male on the device side), a lubricant is applied to the male threads during installation. The type, quantity, application method, and temperature of the lubricant significantly affect the assembly quality.

The primary criteria for assembly quality include (i) ensuring no hydrogen leakage through the connection points and (ii) preventing excessive wear on the threads. Considering the internal tank pressure of approximately 700 bar and hydrogen atoms are too small, maintaining a leak-proof connection is a significant challenge. Moreover, minimizing thread wear is critical since it directly affects sealing integrity and the durability of components like service valves that may require repeated installation and removal.

Among those threaded connections, two critical components are the Manual Valve (MV) and Bleed Valve (BV). The BV ensures safety by releasing hydrogen once opened before the disassembly of tank valve from the tank. The MV allows for manual isolation of the hydrogen tank from the fuel injection or fuel cell system at service condition, ensuring a secure shutoff. Proper installation of these components is essential for operational reliability.

Initial assembly tests at BOSCH have revealed several challenges:

- The physical properties of the lubricant (viscosity, density, surface tension) influence both thread filling and wear resistance.
- The application temperature of the lubricant affects its flow characteristics and coverage between threads.
- The amount of lubricant used is crucial; excessive application leads to contamination, while insufficient amounts can result in increased friction and wear.
- Manual application of the lubricant often results in inconsistent distribution, leading to potential assembly failures.
- The maximum tightening torque influence wear and overall sealing effectiveness.

- Changing tank conditions like pressure and temperature effects the axial load on seal surfaces.
- Final axial load varies too much from assembly-to-assembly even though same torque is used.

Any combination of these factors can negatively impact the performance of the BV and MV, potentially leading to hydrogen leakage. To address these issues, the study aims to establish optimized assembly parameters to ensure precise and repeatable installations for service valves.

This research will develop an assembly method to control key parameters, including: (i) Lubricant type selection (ii) Lubricant application temperature (iii) Lubricant distribution method onto male threads (iv) Lubricant quantity control (v) Applied torque characteristics.

By implementing this method assembly system, the study seeks to achieve high-quality, leak-proof connections while minimizing wear and ensuring long-term durability of the HTV components. This initiative is a crucial step toward localizing advanced hydrogen fuel component manufacturing at BOSCH, supporting the transition to a sustainable hydrogen-powered future.

2. MATERIALS AND METHODS

To achieve the objectives of this research, both simulation and assembly tests were conducted to validate the optimized parameters for hydrogen tank valve assembly. The methodology includes the following key aspects:

2.1 Development of a Modular Assembly Station:

- A modular assembly system was designed to regulate the application of lubricant, control tightening speed, and monitor torque values and derived axial loads.
- The system ensures repeatable and precise installation of components to prevent hydrogen leakage and minimize thread wear.

2.2 Simulation Studies:

- Finite Element Method (FEM) was used to model the impact of different torque values and lubricant quantities on the mechanical integrity of the threaded connections.
- Computational Fluid Dynamics (CFD) simulations were conducted to analyze lubricant distribution between male and female threads under various application methods.

2.3 Assembly Testing:

- Prototype assembly tests were performed under controlled conditions to determine the optimal torque values for BV and MV components.
- Lubricant application experiments were conducted to evaluate viscosity, temperature, and distribution efficiency.
- Real-time monitoring of hydrogen leakage levels was carried out using pressure differential measurements.

2.4 Key Performance Metrics:

- Ensuring torque and axial load values remain within requested interval for BV and MV.
- Hydrogen leakage levels not exceeding the value coming from standards.
- Improvement in component service life up to 100 installation cycles.

By integrating both experimental and computational approaches, this study establishes a robust framework for optimizing the assembly of hydrogen tank valve components, enhancing efficiency, and ensuring long-term operational safety.

3. RESULTS AND DISCUSSION

[2] It is known that axial load occurs on the threaded connections after applying torque and is increased with the torque and decreases with the effective thread diameter and friction effected by thread angles, material, lubrication amount and distribution. Our experimental study shows that among those parameters, friction coefficient is the one that has major impact on the distribution of axial load after assembly. Considering geometrical factors and applied torque is constant,

machining imperfections and torque application has negligible tolerances, lubrication amount and distribution is the driving factor of friction coefficient and causing wide range of distribution at the resulting axial load.

It is also seen that at different temperatures and tank pressures, resulting axial force on metal-to-metal sealing contact of service valves to valve body are changing. Varying torque values are used to check final axial load. Combining these effects with atomic size of hydrogen, leakage can be observed above the accepted limits.

On Fig.1, different pressures with bar unit and temperatures with Celsius unit are introduced. Different colors state different initial assembly torques that result in different axial contact forces on seal surface. When HTV goes under different boundary conditions, at the end most of contact force on seal surfaces are lost due to contraction and deformation on the valve body.

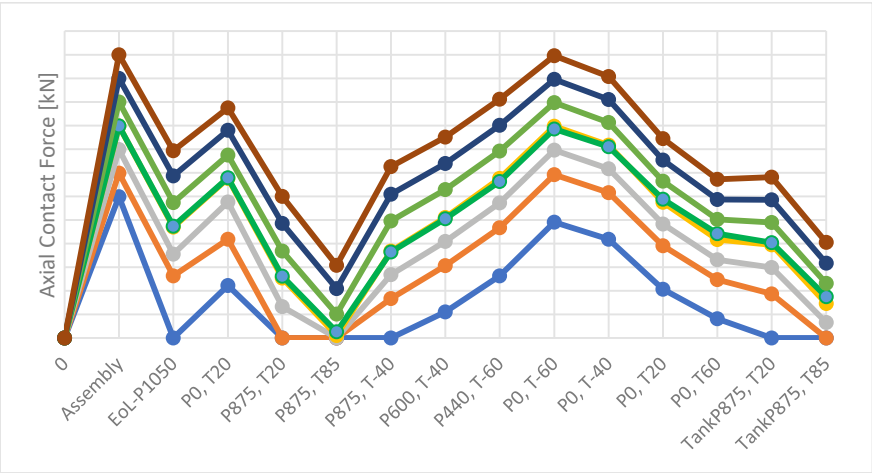

Fig. 1. Axial load of service valves for different conditions

This result is used as a good practice to choose what should be the best initial assembly torque for sealing elements to valve body. As final axial loads are decreased, ratio of initial loads and final loads are derived, and it is used to choose best assembly torques for each sealing component.

After deciding on what initial load should be, fixed amount of torque is applied to components to assemble them on the valve body. It is realized that same amount of torque does not always result in same amount of axial load and distribution of final load is too wide to obtain desired axial load for seal-proof surfaces at each assembly.

To overcome this challenge, service valves are repeatedly assembled and disassembled several times, until they plastically deform the sealing surface and create the best contact for leakage prevention. Before the assembly, lubricant is applied at a measured rate and made sure it was distributed to thread surface equally using special tooling. After specific cycle number is achieved, axial load passed necessary limit to ensure leak-proof seal.

On Fig. 2, axial forces are increasing after repeated cycles of pre-assembly. Red line represents desired axial load limit for the best sealing performance. Even though, some samples can already give necessary axial load from the first cycles, some are failing to do so. After many repetitions, it can be observed that axial loads are converging to specific values and distribution between results is getting smaller.

Furthermore, there is a visible difference between each sample caused by amount of lubrication and application method of lubrication to threads. Therefore, this assembly-trial method became a key indicator to distinguish between the best lubricant application method and amount among other methods where some of the axial load is lost due to non-homogenious distribution of grease and additional frictions introduced to the system.

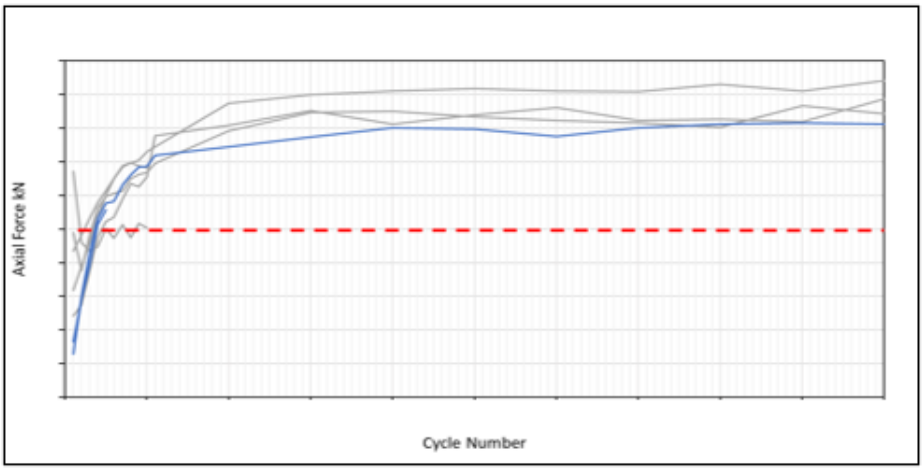

Fig. 2. Axial load of service valves after repeated assembly cycles

The results of this study confirm that optimizing lubricant application, torque control, and repeated assembly significantly improves the performance of hydrogen tank valve assemblies. Key findings include:

- Varying tank pressures and temperatures effects the axial load on seal surfaces; hence, initial assembly torque must be chosen accordingly.
- The optimized lubricant distribution method resulted in reaching desired axial loads with less cycles.
- Repeated assembly cycles before final assembly plastically deforms the seal surfaces and provide better sealing performance by keeping more axial load on the contact surface.

These findings support the importance of lubricant application on thread surfaces, as non-equal distribution of lubricant shows poorer performance to reach desired axial loads after repeated operations.

4. CONCLUSIONS

This study highlights the critical role of optimizing assembly torque and lubrication amount in ensuring the reliability and leak-proof performance of hydrogen tank valves. The findings demonstrate that friction coefficient, largely influenced by lubrication distribution, has a major impact on axial load variation.

By implementing a controlled lubrication method and repeated pre-assembly cycles, the study achieved a more uniform axial load distribution, enhancing sealing integrity and reducing the risk of hydrogen leakage. These insights contribute to the development of a standardized assembly process that enhances efficiency, extends component service life, and supports the large-scale production of hydrogen storage systems.

REFERENCES

1. Yip, H. L., Srna, A., Yuen, A. C. Y., Kook, S., Taylor, R. A., Yeoh, G. H., ... & Chan, Q. N. (2019). A review of hydrogen direct injection for internal combustion engines: towards carbon-free combustion. *applied sciences*, *9*(22), 4842.
2. Zhang, D., Wang, G., Huang, F., & Zhang, K. (2020). Load-transferring mechanism and calculation theory along engaged threads of high-strength bolts under axial tension. *Journal of Constructional Steel Research*, *172*, 106153.

SEAWATER ELECTROLYSIS FOR AN ADVANCED H_2 PRODUCTION

*Fausta Giacobello, Stefania Siracusano, Alessandra Muscolino, Veronica Cicciò, Maria Aurora Mancuso, Vincenzo Antonucci
CNR-ITAE, Salita Santa Lucia sopra Contesse, 5, 98126, Messina
* E-mail: fausta.giacobello@itae.cnr.it

ABSTRACT
Water electrolysis (WE) powered by renewable energy is the leading technology for producing "green" hydrogen. Given that freshwater is a limited resource, the concept is to use desalinated seawater for the electrolysis process. The goal of the project is to develop water electrolysers with proton and anion exchange membranes (PEM-WE and AEM-WE). New solutions are being explored for the materials and individual cell components in PEM-WE to improve performance and durability while minimizing energy consumption. The focus is on reducing the noble metal content in the oxygen evolution reaction (OER) by developing core-shell structures with Ru oxide in the core and IrO_2 on the outer layers. For the hydrogen evolution reaction (HER), the main objective is to enhance the Pt/C cathode by increasing the electrochemically active metal surface area and achieving good Pt dispersion on carbon nanofibers to address mass transport issues. In contrast, AEM-WE-based electrolysis can operate with non-precious group metal (PGM-free) catalysts and non-critical raw materials (CRM) for both OER and HER, significantly lowering the capital cost of the device. Efforts are directed toward developing non-CRM nanostructured Ni-Fe and Ni-Mo-based electrocatalysts, such as spinel and layered oxides, hydroxides, or (oxy)hydroxides, for OER and HER to improve performance and minimize material loading. The synthesis methods for the cathode catalysts involve scalable, sustainable, and low-temperature techniques (such as colloidal, sol-gel, and complexation processes). The physical-chemical properties of the developed electrocatalysts are analyzed using various characterization methods, including XRD, XRF, and TEM. A Reverse Osmosis desalination unit will be fully integrated with multiple other treatments to achieve optimal water recovery, minimal waste discharge, and the lowest energy consumption and cost, by coupling with renewable energy sources.
Keywords: green hydrogen, nanocatalysts, sustainable energy supply

1. INTRODUCTION
Water electrolysis (WE) supplied by renewable energy is the foremost technology for producing "green" hydrogen. Since freshwater is a limited resource, the idea is to use desalinated sea water for the electrolysis. The project aims to develop Water Electrolysers (PEM and AEM) specifically suited for use with renewable energies and a wide range of water salinity (i.e., from UPW up to seawater). The CNR activity is to develop low-cost electrocatalysts for oxygen and hydrogen evolution reactions with low-noble metal loading for PEM electrolysis and non-noble metal loading for the AEM.

2. MATERIALS AND METHODS
2.1. Catalysts and electrodes preparation
For the AEM electrolyser, non-CRM Ni-Fe and Ni-Mo electrocatalysts were developed for OER and HER, respectively, while IrRuOx and Pt/C were used for the PEM electrolyser. Several physico-chemical and morphological studies were carried out by XRF, XRD, SEM-EDX, TEM and BET analysis to characterize the composition, surface and morphology of the catalysts. Special attention was paid to the electrochemical characterization in a single cell with in house test station by using Ti and Ni plates, as current collector, for PEM and AEM device respectively in a temperature range of 30-90°C (PEM) and 30-60°C (AEM) and under atmospheric pressure. The tests were conducted using water, with a resistivity of 18.2 MΩ·cm (≈ 0.05 μS/cm) at 25 °C, for PEM and 1M KOH for AEM, respectively.

3. RESULTS AND DISCUSSION
Polarization, impedance spectroscopy, and durability tests were carried on to evaluate electrochemical performance.
For AEM cell, the BoT polarization curves have shown that supported NiMo (orange curve) has reached 0.6 A/cm², while unsupported NiMo (green curve) has achieved 1 A/cm² at a potential of 2.2 V. At the EoT, after a durability test of 100 hours, supported NiMo has reached 1 A/cm², while unsupported NiMo has reached 3 A/cm² at 2.2 V. EIS measurements, at the EoT, confirmed a better performance for unsupported NiMo compared to supported one with a lower polarization resistance (109 mΩ·cm² vs. 325 mΩ·cm²).
For PEM cell, the developed anode catalyst IrRuOx has shown a current of 3 A /cm² at a potential of 1.96 V. These performances are in line with the state of the art of PEM technology.

4. CONCLUSIONS
The electrochemical performance for AEM has shown better performance for unsupported NiMo compared to supported one. Good performance was observed for PEM electrolyser cell based on IrRuOx developed by CNR.

ACKNOWLEDGEMENT
This work was funded by the Ministry of University and Research (Italy) (MUR), PRIN 2022, within the project "Sustainable low cost seawater Electrolyser for Advanced "green" H2 production (SEA-H2)", Nr. 2022CX89Y9

NASICON ($Na_3NiCo_2(PO_4)(SO_4)_2$) DOPED POLYANILINE AS A NEW CANDIDATE ELECTROCATALYST IN HYDROGEN EVOLUTION REACTION

[1*]*Sıla Melahat Yılmaz*, [1,2]*Aysel Kantürk Figen*,
[1] Yıldız Technical University, Clean Energy Technologies Institute, Istanbul, 34220, Türkiye
[2] Yildiz Technical University, Chemical Engineering, Istanbul 34220, Türkiye

*Corresponding author e-mail: sila.alp@gmail.com

ABSTRACT

Electrocatalysts with a synergistic combination of reliable and cost-effective are often used in hydrogen evolution reactions (HERs) in place of noble or toxic metals. In this study, a nanostructured $Na_3NiCo_2(PO_4)(SO_4)_2$ [NCPS(Ni)] composite was synthesized by doping NASICON structure with Nickel (Ni) and polyaniline (PANI) by chemical oxidative polymerization. The composite was found to exhibit an overpotential of 145 mV at -10 mA·cm^{-2} current density against a reversible hydrogen electrode (RHE) and a Tafel slope of 67 mV·dec^{-1}, which is a promising candidate as a polymer-based composite HER catalyst compared to SS (stainless steel). The results of this study propose an efficient and original electrocatalyst with potential applications in the development of electrocatalytic systems for HER.

Keywords: Electrocatalyst, Nasicon, PANI, Stainless steel, HER

1. INTRODUCTION

Hydrogen energy is used for many applications due to its advantages such as high energy density, energy conversion and storage. In particular, water splitting photocatalysis and electrocatalysis processes are the most popular candidates for green hydrogen production [1]. The process of hydrogen production from electrolysis processes consists of two half-reactions (hydrogen evolution reaction (HER)) in which an oxidation reaction takes place at the anode to produce oxygen (oxygen evolution reaction (OER)) and a reduction reaction takes place at the cathode to produce hydrogen gas [2]. Normally, since the two main processes on the electrocatalyst surface are in competition, an electrode designed as an electrocatalyst for HER should have a good balance between the two successive processes (adsorption and desorption) occurring on its surface.

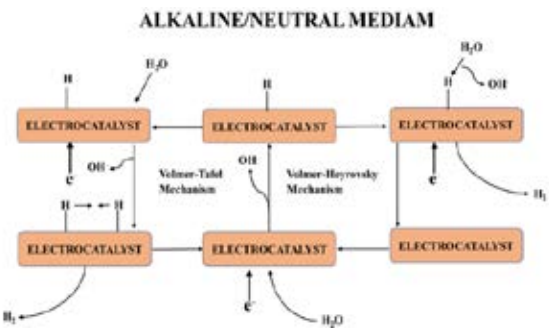

Fig. 1. HER mechanisms in alkaline media [3].

Conducting polymers are used in HER studies due to their advantages such as environmental friendliness, low cost and non-toxicity. When we look at the literature, especially conductive polymers such as polyaniline [4-6], polythiophene [7], polypyrrole [8,9] and their derivatives [10] are included.
In this work, the PANI/ NCPS(Ni) composite was synthesized via in situ chemical oxidative polymerization by incorporating NCPS(Ni) into polyaniline at the monomeric level.

2. MATERIALS AND METHODS

In the present work, PANI@NCPS(Ni) composites were synthesized by in situ chemical oxidative polymerization. Firstly, $(NH_4)_2[Co(SO_4)_2].6H_2O$ is prepared by reacting $CoSO_4.7H_2O$ with $(NH_4)_2SO_4$. After then it dissolved in 100 mL of DI water and stirred it for 1 h at temprature 80 °C. Then, 1 M NaH_2PO_3 was added to the above solution and stirred for 2 h for proper mixing. After that, 0.5 M $NiSO_4.7H_2O$ was added and Na_2CO_3 was mixed into the solution mixture, causing spontaneous CO_2 evolution. The pH of the reaction mixture was maintained basic by adding ammonia solution to precipitate, followed by calcination of as-prepared dried powder at 500 °C for 12 h in a muffle furnace (heating rate was maintained 5 °C per min) to get the final crystalline NCPS(Ni). The in situ chemical oxidation method was used to synthesise PANI/NCPS(Ni) composites. A predetermined amount of ANI monomer (0.1 M) was first mixed with 70 mL ice-cold 0.5 M hydrochloric acid (HCl) under continuous stirring. Previously synthesized nano-NCPS(Ni) was then added

to the above reaction mixture. The reaction mixture was stirred for 2 h to confirm adequate dispersion and interaction of the ANI monomer and NCPS(Ni). Next, 30 mL of 100 mM APS solution was slowly dropped into the reaction mixture for polymerization under stirring conditions. After the addition of APS, the reaction mixture was stirred for another 2 h. The mixture was then left overnight to complete polymerization. The next day, the formed composite was washed and filtered several times with DI water and ethanol to remove any residual contaminants and unreacted monomers. The materials were then oven dried at 50°C for 24 h before being used as active electrode materials. After the synthesis process was completed, coatings were deposited on the 304-type stainless steel surface selected as the substrate using the speed coating method. PANI@NCPS(Ni)/SS, PANI/SS and SS electrodes were analysed by EIS, LSV and Tafel techniques in 0.5 M KOH solution at room temperature using the three-electrode method.

3. RESULTS AND DISCUSSION

The electrocatalytic activity of the synthesized catalysts on SS was analyzed by linear sweep voltammetry at 5 $mV \cdot s^{-1}$ in 0.5 M KOH solution. The LSVs of all catalysts are shown in Fig.2a According to Fig.2b shows that the PANI@NCPS(Ni)/SS and PANI/SS catalysts exhibit activity trends with matching onset potential for HER and overpotential values of 145 and 232 mV at -10 $mA \cdot cm^{-2}$ respectively, compared to 304SS (391 mV). The higher electrocatalytic activity of PANI@NCPS(Ni)/SS compared to PANI/SS and bare SS can be attributed to its highly rough surface and the formation of a structure with a large number of protrusions [11]. This characteristic allows a greater number of active sites to be created on the surface of the catalyst, allowing increased adsorption of H_3O^+ and facilitating the desorption of H_2. The LSV curve was used to determine the Tafel slope of the catalytic materials. The determined Tafel slope of 145 $mV \cdot dec^{-1}$ (Fig.2c) suggest that the Volmer step is the rate determining step [12]. A summary of the comparative performance of HER on PANI-based catalysts from the literature in alkaline solutions is given in Table 1. The data show that the overpotential at j= - 10 $mAcm^{-2}$ is in the range of 40 to 400 mV, which means that the present PANI@NCPS(Ni)/SS represents has a potentially efficiency.

Table 1. Comparison of the performance of recently reported PANI-based HER electrocatalysts.

Metarial	Electrolyte	Tafel Slope (mV dec^{-1})	η (mV vs. RHE)	References
$FeAlO_3$/PANI	1.0 M KOH	62	165 mV	[13]
CeO_2-MoS_2 /PANI	1.0 M NaOH	62	44 mV	[14]
FeNi-LDH@Ni/SS	6 M KOH	109.1	399 mV	[15]
NiCo/ PANI	1.0 M KOH	79	220 mV	[12]
Nb_2C/$MoTe_2$(PANI)	2.0 M KOH	60.4	148.72 mV	[16]
V_2O_5/MnO_2/ PANI	1.0 M KOH	56.4	130 mV	[17]
PANI@NCPS(Ni)/SS	0.5 M KOH	67	145 mV	present work

The charging behaviour of the catalytic material was analysed using the EIS method. Nyquist plots are shown in Fig.2d using a three-electrode system in 0.5 M KOH as electrolyte, where the electrode is 304 stainless steel and Ag/AgCl and Pt are used as reference and counter electrodes respectively. The EIS measurement was performed for each electrode material at its respective onset potential between 10^5 and 10^{-2} Hz. It allows the charge transfer resistance (R_{ct}) on the surface of catalysts to be estimated. To obtain the R_{ct}, the spectra were fitted with the one-time constant that its electronic equivalent circuit is composed of a resistor (R_s) that represents the solution resistance in series connection with a resistor and a constant phase element (C_{CPE}) that are connected in parallel. C_{CPE} is used instead of ideal capacitor (C) because of deviation from ideal capacitive behaviour due to surface roughness and inhomogeneity. According to Fig.2d, it can be concluded that the PANI@NCPS(Ni)/SS (16.11 Ω) catalyst exhibits smaller charge transfer resistance (R_{ct}) compared to PANI/SS (19.35 Ω) and SS (253.28Ω).

Table 2. EIS data of PANI@NCPS(Ni)/SS composite in 0.1 M KOH

Material	R_s (Ω)	R_{ct} (Ω)	C_{CPE} (F)	n	X^2 (10^{-3})
PANI@NCPS(Ni)/SS	1.45	16.11	2.15×10^{-04}	0.91	1.19
PANI/SS	2.84	19.35	1.85×10^{-04}	0.84	6.97
SS	3.08	253.28	9.53×10^{-05}	0.89	7.69

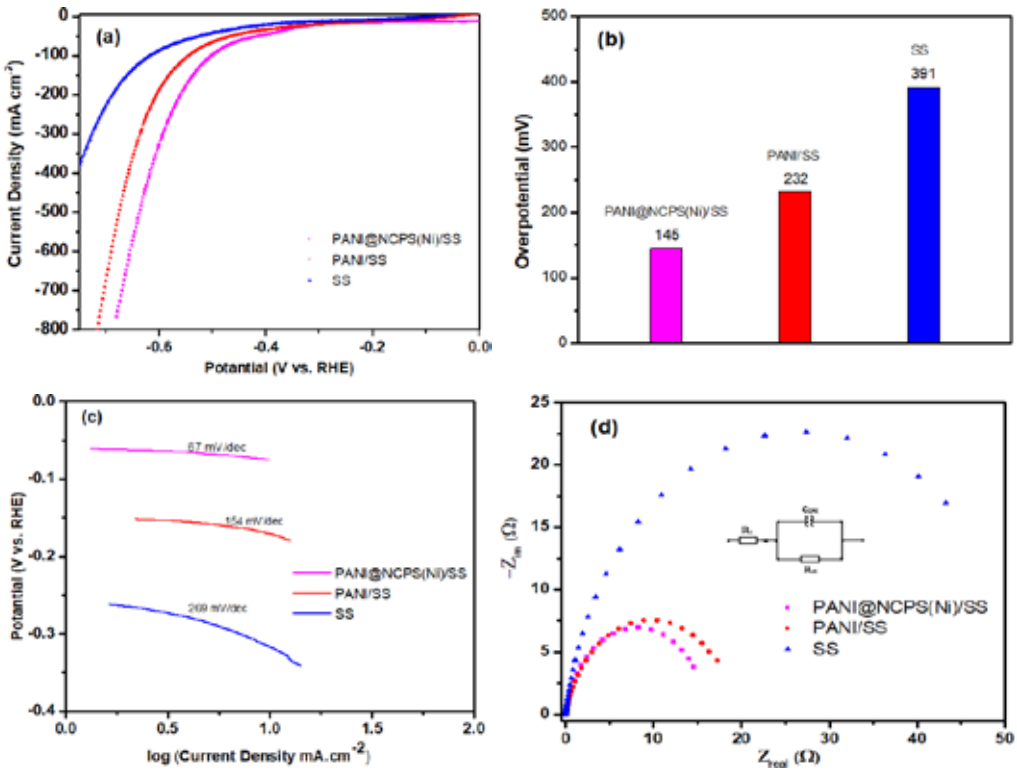

Fig. 2. For PANI@NCPS(Ni)/SS, PANI/SS and bare SS (a) LSV curves (b) overpotential comparison (c) Tafel plots and (d) EIS spectra (inset of Fig.2d shows the equivalent circuit).

4. CONCLUSIONS

A new material composition [PANI@NCPS(Ni)] for hydrogen evolution reaction (HER) catalyst was prepared by in situ polymerization method. The electrochemical tests showed that the hydrogen evolution reaction (HER) efficiency of stainless stell was significantly improved by the prepared catalysts. Higher value of current density and lower polarisation resistance was obtained with this electrode. The composite was exhibited an overpotential of 145 mV and a Tafel slope of 67 mV·dec^{-1} at a current density of -10 mA·cm^{-2} against a reversible hydrogen electrode (RHE) and was found to be a promising candidate as a polymer-based composite HER catalyst.

REFERENCES

[1] Cogal S, Mičušík , Kotlár M. and Omastová M, 2025 Incorporation of polyaniline and cobalt deposition to tune electrochemical performances of MoSe2 catalysts for overall electrochemical water splitting. Materials Chemistry and Physics. 333-130354.
[2] Sharma V, Dhiman R, Samanta S, Karwal S, and Mahajan A. 2025. PANI/MXene/MnO2 ternary heterostructure with multi-redox active sites and enhanced interfacial charge transfer for efficient hydrogen production via electro/photocatalytic water splitting. International Journal of Hydrogen Energy. 97:532–548.
[3] Ramohlola KE, Modibane KD, Ndipingwi M M and. Iwuoha EI. 2024. Polyaniline-based electrocatalysts for electrochemical hydrogen evolution reaction, European Polymer Journal. 213- 113125.
[4] Iqbal MF, Yang Y, Hassan MU, Zhang X, Li G, Hui KN, Esmat M and Zhang M. 2022. Polyaniline grafted mesoporous zinc sulfide nanoparticles for hydrogen evolution reaction International Journal of Hydrogen Energy. 47: 6067–6077.
[5] Khoshsang H and Ghaffarinejad A. 2022. Electrochemical synthesis of polyaniline silver-palladium composite coated nickel foam as an electrocatalyst for the hydrogen evolution reaction, Inorganic Chemistry Communications. 142-109631.
[6] Torres C, Moreno B, Chinarro E and De Fraga Malfatti C. 2017. Nickel-polyaniline composite electrodes for hydrogen evolution reaction in alkaline media. International Journal of Hydrogen Energy, 42: 20410–20419.
[7] Niedbała J. 2009. Electroevolution of hydrogen on the polytiophene-modified Ni–Mo composite layers, Materials Chemistry and Physics. 118:46–50.
[8] Li X, Li Q, Yan W, Fan B and WangZ. 2024. In-situ controllable electrodeposition of NiSx nanostructures coupled with polypyrrole for enhanced hydrogen evolution reaction. International Journal of Hydrogen Energy. 51:443–451.
[9] Yang Y, Wng H, Quın W, Gua Y, Yao H, Li J, Shi K and Ma S. 2020. MoS2/Au^0/N-CNT derived from Au(III) extraction by polypyrrole/MoS4 as an electrocatalyst for hydrogen evolution reaction. Journal of Colloid and Interface Science, 561: 298–306.
[10] Geng Y, Zhang C, Zhu Y, Wang H, Bai J, Huang J and Zhao Z. 2024. Catalytic Properties of PEDOT-Co3O4@Mn3O4/Mn2O3 Nanomaterials in HER Reactions and Their Application in Capacitors., International Journal of Electrochemical Science. 19:100846.
[11] Alharbi AF, Hassan N, El-Deeb H, Wazeer W, Abahussain AA and Ahmed Amine Nassr AB. 2025. Porous CoP coating on stainless

steel: Application as an electrocatalyst for acidic hydrogen evolution reaction. International Journal of Hydrogen Energy. 109:1197–1208.
[12] Djara R. Masquelez N, Lacour MA, Merzouki A, Cambedouzou J, Cornu D, Tingry S, Holade Y. 2020. Self-Supported Electrocatalysts Derived from Nickel-Cobalt Modified Polyaniline Polymer for H2-Evolution and O2-Evolution Reactions, ChemCatChem.12:5789–5796.
[13] Zahra R, Drissi and Kumar A. 2025. Enhanced HER activity through FeAlO3 perovskite oxide incorporated with conducting polymer PANI. Inorganic Chemistry Communications. 172:113609.
[14] Krishnan A., Malavika, Prasannan A and Yoosuf M. 2025. Tailoring of a novel high conductive, hydrophilic cum aerophobic CeO2-MoS2/PANI core-shell composite for enhancing the catalytic property of Ni-P electrode for hydrogen production Journal of Alloys and Compounds. 1010:178307.
[15] Jia X, Wang Y, Tang J, Song K. Zhang H, Lin B and Zheng H. 2023. FeNi-LDH@Ni film modified stainless-steel as self-supported electrodes for efficient and stable overall water splitting in alkaline environments. Surface and Coatings Technology. 464: 129502.
[16] Al-Hadeethi Y, Iqbal MW, Raffah BM and Umar E. 2024. Synergistic advancements in battery-grade energy storage: Nb2C/MoTe2(PANI) hybrid electrode material as a enhanced electrocatalyst for hydrogen reduction reaction. Electrochimical Acta. 508:145205.
[17] Varghese A, Devi KRD, Pinheiro D and Mohan MK, 2023. Molecular architecture of PANI/V2O5/MnO2 composite designed for hydrogen evolution reaction. Surfaces and Interfaces. 41: 103221.

GREEN SYNTHESIS OF MnVS AND CO-DOPED MnVS NANOPARTICLES: APPLICATIONS IN PHOTOCATALYSIS AND HYDROGEN PRODUCTION VIA METHANOLYSIS

[1]*Mine Çokyaşa*, [2]*Ömer Şahin*, [3]*Arzu Ekinci*, [1]*Orhan Baytar*
[1] Siirt University, Faculty of Engineering, Department of Chemical Engineering, , Siirt, 56100, Turkey
[2]Istanbul Technical University, Faculty of Chemical and Metallurgical Engineering, Department of Chemical Engineering, İstanbul, 34467, Turkey
[3] Siirt University, Faculty of Health Sciences, Department of Occupational Health and Safety, Siirt, 56100, Turkey

*Corresponding author e-mail: baytarorhan@siirt.edu.tr

ABSTRACT
This study presents the green synthesis of MnVS and Co-doped MnVS nanoparticles using an extract derived from fresh almond bark. The synthesized nanoparticles were evaluated as photocatalysts for the photocatalytic reduction of methylene blue and as catalysts for hydrogen generation via $NaBH_4$ methanolysis. Structural and morphological properties were characterized through XRD, SEM-EDX, TEM, and XPS analyses. The influence of $NaBH_4$ concentration, methylene blue concentration, and catalyst dosage on the photocatalytic reduction process was systematically investigated. The catalytic performance of MnVS and Co-doped MnVS was assessed at different catalyst amounts (5 mg, 7 mg, and 10 mg). Kinetic analysis yielded rate constants (k) of 1.027, 1.2679, and 1.2273 min^{-1} for MnVS and 0.6868, 0.6865, and 0.3663 min^{-1} for Co-doped MnVS, indicating optimal catalyst amounts of 7 mg and 5 mg, respectively. Reaction kinetics were modeled using the nth-order and Langmuir-Hinshelwood models, with high R^2 values confirming their applicability. The activation energies (Ea) were determined as 28.09 kJ mol^{-1} for MnVS and 21.99 kJ mol^{-1} for Co-doped MnVS. This study highlights the potential of eco-friendly nanoparticle synthesis for efficient hydrogen production and organic pollutant removal, demonstrating its significance in sustainable catalytic applications.

Keywords: Green synthesis, Photocatalytic reduction, Methylene blue, Hydrogen production, $NaBH_4$ methanolysis

1. INTRODUCTION
In contemporary times, the excessive consumption of non-renewable resources such as natural gas, crude oil, and coal to meet global energy demands has significantly increased greenhouse gas concentrations in the atmosphere, leading to global warming [1]. This phenomenon has contributed to the escalation of natural disasters, either directly or indirectly, due to climate change. Consequently, the development of clean, renewable, and economically viable energy systems has become a major priority [2]. Hydrogen has emerged as an environmentally friendly and sustainable energy carrier. With an energy density up to three times that of petroleum, hydrogen holds significant potential as an alternative to fossil fuels. However, for hydrogen to be truly considered a "green" fuel, it must be produced from non-fossil fuel feedstocks [3]. Locally produced hydrogen facilitates the integration of renewable energy into the transportation sector, offering substantial economic and energy security advantages [4]. Among hydrogen storage technologies, chemical hydrides are particularly promising. Sodium borohydride ($NaBH_4$) is one of the most widely used hydrogen storage materials due to its non-flammability, air stability, and controllable hydrogen release [5]. The methanolysis reaction of $NaBH_4$ offers lower operating temperatures and faster hydrogen production rates compared to hydrolysis [6]. However, efficient catalysts are required to enhance the performance of this reaction [7]. Metal nanoparticles and metal composites are widely preferred as catalysts for $NaBH_4$ methanolysis [8]. On the other hand, one of the most critical global challenges of the 21st century is the provision of clean and safe water [9]. The expansion of modern industries, including the textile and energy sectors, has led to significant water pollution, posing severe environmental threats [10]. The textile industry, utilizing approximately 36,000 tons of dye annually, has become a primary contributor to global water contamination [11]. Methylene blue (MB) is a commonly used dye in the textile industry, exhibiting high resistance to biological degradation [12]. Various techniques, such as adsorption, ozonation, and photocatalytic degradation, have been employed for MB removal [10]. However, the $NaBH_4$ reduction method stands out as a more advantageous option due to its rapid and efficient results [13]. This reduction reaction can occur swiftly only in the presence of nanoparticle catalysts [14]. Nanoparticles (NPs) are generally insoluble materials with sizes below 100 nm and possess a large surface area, resulting in unique physical, chemical, optical, thermal, and mechanical properties compared to conventional bulk materials [15]. Although chemical synthesis methods are cost-effective for large-scale production, their reliance on toxic chemicals and the generation of harmful by-products pose significant environmental concerns [17]. Thus, plant-based green synthesis methods have gained attention as more eco-friendly alternatives [18]. Plant extracts can serve as both reducing and stabilizing agents in nanoparticle synthesis [19]. Recent studies have demonstrated that metal sulfide nanoparticles exhibit narrower band gaps than metal oxide, making them more efficient in the visible region of the electromagnetic spectrum. As a result, sulfide-based nanoparticles have emerged as promising alternatives to conventional metal oxide-based photocatalysts [20,21].
This study aims to utilize an extract prepared from fresh almond bark as a reducing agent in the green synthesis of MnVS and Co-doped MnVS nanoparticles. The synthesized nanoparticles were evaluated as photocatalysts for the

photocatalytic reduction of methylene blue and as catalysts for hydrogen production via $NaBH_4$ methanolysis. Structural and morphological properties of the synthesized catalysts were characterized using XRD, SEM-EDX, TEM, and XPS, analyses.

2. MATERIALS AND METHODS

$Co(NO_3)_2.6H_2O$, $MnCl_2.4H_2O$ and $Na_2S.H_2O$ were obtained from Sigma-Aldrich. $C_{10}H_{14}O_5V$ was obtained from Fluka company. Almond wet peel was obtained from Siirt market.

2.1. Preparation of plant extract extract

Extract from almond wet peels was prepared by hydrothermal method. To prepare the extract, 35 g of almond wet peels and 350 mL of pure water were placed in a 500 mL autoclave, then kept in an oven at 180 °C for 12 hours and cooled to room temperature. The extract was filtered and stored at 4 °C for use in the synthesis of MnVS nanoparticles.

2.2. Synthesis of MnVS and MnVS-Co nanoparticles

MnVS nanoparticles were synthesized by green synthesis method; 100 mL of almond wet peel extract and $MnCl_2.4H_2O$, $C_{10}H_{14}O_5V$, $Na_2S.H_2O$ in amounts determined as mole ratios (Mn:V:S=0.5:0.5:1) were mixed and the pH of the solution was adjusted to 10 with 1M NaOH. The resulting mixture was stirred at room temperature for 24 hours, then filtered through 0.22 mm membrane filter paper and the solid obtained was dried at 120 °C for 3 hours.
Co doped MnVS nanoparticles were synthesized by chemical reduction method; enough $Co(NO_3)_2.6H_2O$ and 1 g MnVS NPs were mixed in 50 mL water. After heating and turning into sludge, a certain amount of $NaBH_4$ was dissolved in 50 mL of water and added dropwise. It was then filtered with filter paper and the obtained material was dried at 120 °C for 2 hours. The synthesized nanoparticles were stored in a sealed container for use in methanolysis and photocatalytic reduction of methylene blue. The synthesized nanoparticles were characterized by XRD, SEM, EDX, TEM and XPS.

2.3. Hydrogen Production

Hydrogen production in $NaBH_4$ hydrolysis was carried out using a solution containing 10 mg of catalyst, 2.5% $NaBH_4$, 2.5% NaOH and 10 mL methanol.

2.4. Photocatalytic reduction of methylene blue

Photocatalytic reduction of methylene blue with NaBH4, 0.5 mL of NaBH4 at different molarities (15 mM, 20 mM, 25 mM and 50 mM) and 3 mL of methylene blue at different concentrations (15 ppm, 20 ppm, 25 ppm and 50 ppm) were dropped into a quartz container and exposed to UV spectroscopy. The concentration of methylene blue in the medium was determined by UV spectroscopy (wavelength=664 nm). The decolorization efficiency and pseudo-first order kinetics of methylene blue were determined.

3. RESULTS AND DISCUSSION

3.1. Characterization of Nanoparticles

The nanoparticles synthesized by green synthesis method were characterized by XRD, SEM, EDX, TEM and XPS. it was determined from the characterization results that the nanoparticles were synthesized in pure and nanoscale.

3.2. Catalytic Activity

The activity of sodium borohydride was first assessed at varying concentrations in the methanolysis application of MnVS and Co-doped MnVS catalysts. It was observed that an increase in $NaBH_4$ concentration generally resulted in an elevated reaction rate. The efficiency of catalyst quantity was also evaluated alongside the concentration efficiency of sodium borohydride. The volume of hydrogen produced was shown to rise with the quantity of catalyst used. The rise in the methanolysis rate with a higher catalyst quantity is attributed to the augmented number of catalytic sites available. The impact of temperature on methanolysis was also examined. To examine the influence of temperature on the methanolysis process, tests were conducted at several temperatures (30-60 °C) using 2.5% $NaBH_4$ and 10 mg of catalyst, and the resulting graph is shown in Figure 1.

Fig. 1 illustrates that the duration of methanolysis diminishes as temperature rises. The rate of hydrogen synthesis escalates with rising temperature. This occurs because an increase in temperature leads to a rise in the frequency of intermolecular collisions and an elevation in the kinetic energy of the molecules. Kinetic studies elucidate the characterization of reaction processes. The rates of H_2 generation from $NaBH_4$ hydrolysis were assessed using nth order and Langmuir-Hinshelwood kinetic models using experimental data collected at various temperatures. The activation energy (Ea) was ascertained by the Arrhenius Equation utilizing k values derived from the nth order and Langmuir-Hinshelwood kinetic models at various temperatures. Arrhenius plots of ln (k) versus 1/T for nth order and Langmuir-Hinshelwood kinetic models are shown in Figure 2. It can be seen that both models have high R^2 values. The activation energy (Ea) values for the nth order and Langmuir-Hinshelwood kinetic models were found to be 28.10 $kJmol^{-1}$ for MnVS

and 21.99 kJmol^{-1} for Co doped MnVS. The Langmuir-Hinshelwood model is widely used to better understand the changes in n and Ea values of chemical reactions.

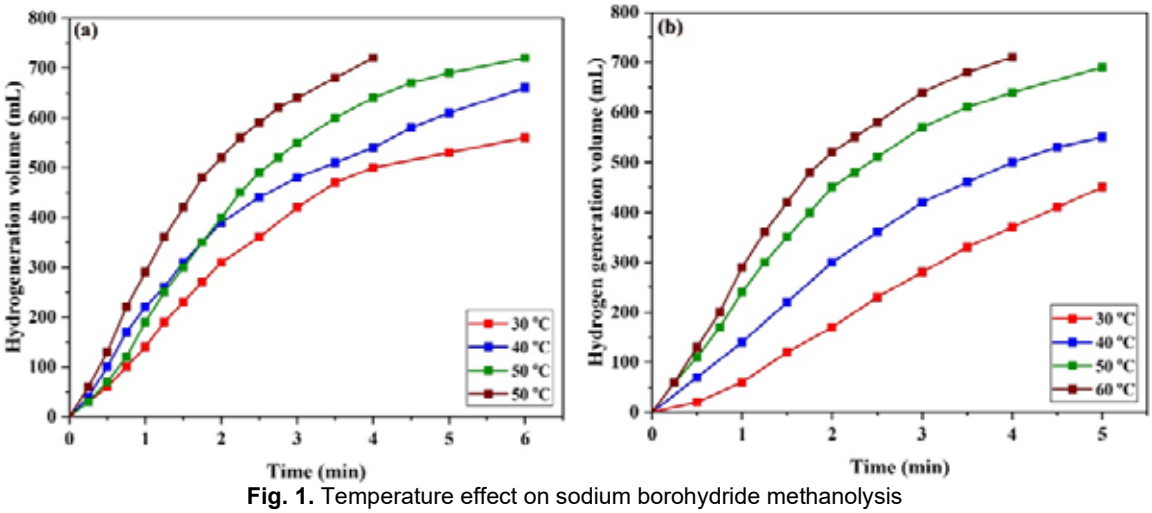

Fig. 1. Temperature effect on sodium borohydride methanolysis

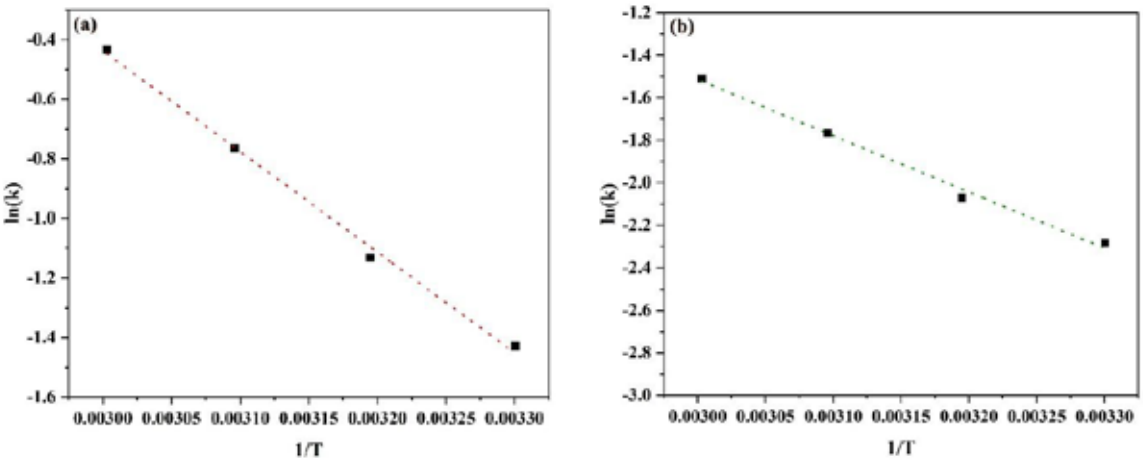

Fig. 2. Plot of ln(k) against 1/T

3.3.Photocatalytic Reduction

The factors influencing the photocatalytic reduction of methylene blue using NaBH4, including NaBH4 concentration, methylene blue concentration, and catalyst quantity, were examined. The impact of varying catalyst quantities on the photocatalytic reduction of MnVS and Co-doped MnVS catalysts was examined, and the kinetics were assessed based on these findings. This assessment revealed k values of 1.027, 1.2679, and 1.2273 min-1 for the MnVS catalyst at varying catalytic concentrations of 5 mg, 7 mg, and 10 mg, respectively. For the Co-doped MnVS catalyst at identical catalytic quantities (5 mg, 7 mg, and 10 mg), the k values were 0.6868, 0.6865, and 0.3663 min^{-1}, respectively. The optimal catalyst quantity for MnVS was 7 mg, but the ideal quantity for Co-doped MnVS was 5 mg.

4. CONCLUSIONS

In this study, the effects of MnVS and Co-doped MnVS nanoparticles produced by green synthesis method on hydrogen production and photocatalytic reduction of methylene blue were investigated. Kinetic analyses revealed that MnVS showed higher activity in the photocatalytic reduction process and the optimum amount of catalyst was 7 mg. The activation energy values determined according to the Langmuir-Hinshelwood kinetic model showed that Co-doped MnVS has a lower energy barrier. The results obtained reveal that environmentally friendly nanoparticles offer an effective alternative for energy production and water treatment.

ACKNOWLEDGEMENT

The authors like to acknowledge the Research Foundation of Siirt University for their financial support via project 2024-SİÜSBF-050.

REFERENCES

1. Wu Y, Altuner EE, el Houda Tiri RN, Bekmezci M, Gulbagca F, Aygun A, et al. Hydrogen generation from methanolysis of sodium borohydride using waste coffee oil modified zinc oxide nanoparticles and their photocatalytic activities. Int J Hydrogen Energy 2023;48:6613e23. https://doi.org/10.1016/ J.IJHYDENE.2022.04.177.
2. F. Dellano-Paz, A. Calvo-Silvosa, S. Iglesias Antelo, I. Soares, The European low carbon mix for 2030: The role of renewable energy sources in an environmentally and socially efficient approach, Renew.Sustain. Energy Rev. 48 (2015) 49–61.
3. L. Zhou, Progress and problems in hydrogen storage methods, Renew. Sustain. Energy Rev. 9 (2005) 395–408.
4. Muradov, Z. and Veziroğlu, T.N., 2005. From hydrocarbon to hydrogen–carbon to hydrogen economy, *International Journal of Hydrogen Energy,* 30 (3), 225-237.
5. Rusman NAA, Dahari M. A review on the current progress of metal hydrides material for solid-state hydrogen storage applications. Int J Hydrogen Energy 2016;41:12108e26. https://doi.org/10.1016/J.IJHYDENE.2016.05.244.
6. Wang T, Jiang T, Zhang H, Zhao Y. Advances in catalysts for hydrogen production by methanolysis of sodium borohydride. Int J Hydrogen Energy 2022;47:14589e610. https://doi.org/10.1016/J.IJHYDENE.2022.02.173.
7. H. Zhong, L. Ouyang, M. Zeng, J. Liu, H. Wang, H. Shao, M. Felderhoff, M. Zhu, Realizing facile regeneration of spent NaBH4 with Mg-Al alloy, J. Mater. Chem. A Mater. Energy Sustain. 7 (2019) 10723–10728.
8. Sahiner N, Sengel SB. Various amine functionalized halloysite nanotube as efficient metal free catalysts for H2 generation from sodium borohydride methanolysis. Appl Clay Sci 2017;146:517e25. https://doi.org/10.1016/ J.CLAY.2017.07.008.
9. Vasiljevic, Z.Z., Dojcinovic, M.P., Vujancevic, J.D., Jankovic-Castvan, I., Ognjanovic, M., Tadic, N.B.,Nikolic, M.V., 2020. Photocatalytic degradation of methylene blue under natural sunlight using iron titanate nanoparticles prepared by a modified sol–gel method, *Royal Society open science*, 7(9), 200708
10. Kitchamsetti, N., Ramteke, M.S., Rondiya, S.R., Mulani, S.R., Patil, M.S., Cross, R.W., Dzade, N.Y. Devan, R.S., 2021. DFT and experimental investigations on the photocatalytic activities of NiO nanobelts for removal of organic pollutants, *Journal of Alloys and Compounds*, 855.
11. Siregar, R.A.N., Sanjaya, A., Lucy, J., Pinontoan, R., 2020. Methylene blue decolorizing bacteria isolated from water sewage in Yogyakarta, *Indonesia. Biodiversitas Journal of Biological Diversity,* 21(3).
12. Pathania, D., Sharma, S. Singh, P., 2017. Removal of methylene blue by adsorption onto activated carbon developed from Ficus carica bast, *Arabian Journal of Chemistry*, 10, 1445-1451.
13. Moeinian, K. and Mehdinia, S.M., 2019. Removing methylene blue from Aqueous solutions using rice husk silica adsorbent, *Polish Journal of Environmental Studies*, 28(4), 2281–2287.
14. Liu, X., Li, M. and Singh, S.K., 2021. Manganese-modified lignin biochar as adsorbent for removal of methylene blue. *Journal of Materials Research and Technology*, 12, 1434-1445.
15. Pan C, Yang G, Yang H, Wu F, Wang L, Jiang J, Zhang Y, Yuan J. 2022. Facile construction of iron/nickel phosphide nanocrystals anchored on NB-doped carbon-based composites with advanced catalytic capacity for 4-nitrophenol and methylene blue. Int J Mol Sci. 23(15):8408. doi: 10.3390/ijms23158408.
16. Baytar O, Ekinci A, Şahin Ö, Akdag A. The Use of NiFe2O4 and CoFe2O4 Nanoparticles Produced by Green Synthesis as Electrode Material for Supercapacitors. ChemistrySelect. 2024;9:e202304491.
17. Gupta, R.; Xie, H. Nanoparticles in daily life: Applications, toxicity and regulations. J. Environ. Pathol. Toxicol. Oncol. 2018, 37, 209–230.
18. Ekinci A, Genli N, Şahin Ö, Baytar O. Facile “Green” synthesis of a novel Co–W–B catalyst from Rheum ribes shell extract and its effect on sodium borohydride hydrolysis: Kinetic mechanism. International Journal of Hydrogen Energy. 2024;51:796-808.
19. Ullah, H., Mushtaq, L., Ullah, Z., Bangesh, M.A., Nawaz, M., 2019. Cost effective green synthesis of NiO nanostructures as highly efficient photocatalysts for degradation of organic dyes, *Micro & Nano Letters,* 14(1), 103-106.
20. Castro, L.; Blazquez, M.L.; Munoz, J.A.; Gonzalez, F.; Garcıa-Balboa, C.; Ballester, A. Biosynthesis of gold nanowires using sugar beet pulp. *Process Biochem.* 2011, *46*, 1076–1082.
21. Mittal, A.K.; Chisti, Y.; Banerjee, U.C. Synthesis of metallic nanoparticles using plants. *Biotechnol. Adv.* 2013, *31*, 346–356.

A STUDY ON Fe-Zr/Al_2O_3 CATALYST FOR HYDROGEN PRODUCTION VIA SODIUM BOROHYDRIDE METHANOLYSIS

[1]*Ömer Şahin*, 2*Ercan Ertun
[1] Istanbul Technical University, Department of Chemical Engineering, ITU Ayazaga Campus, Maslak, Istanbul, 34469, Turkey
[2] Istanbul Technical University, Department of Chemical Engineering, ITU Ayazaga Campus, Maslak, Istanbul, 34469, Turkey

*Corresponding author e-mail: ertun23@gmail.com

ABSTRACT
This study focuses on hydrogen production via sodium borohydride methanolysis using Fe-Zr as a catalyst supported on Al_2O_3 and examines the hydrogen generation rate performance (HGR) concerning different Al_2O_3 quantities and different temperatures. Results have obtained within the temperature range from 20 to 50 ºC and Fe-Zr / Al_2O_3 (wt%) range from 5% to 15%. Characterisation of the catalyst was performed by XRD and SEM. The hydrogen generation rate for 5% Fe-Zr/ Al_2O_3 was obtained at 30 ºC was 7003.4 $L.min^{-1}$. g cat^{-1}. The power law model is used in order to calculate a reaction order of 0,824 and the Arrhenius equation for an activation energy of $kJ.mol^{-1}$. This study shows that 5% Fe-Zr over Al_2O_3 (wt%) is the most effective. Higher Fe-Zr ratio has been observed to result in lower performance, which can be attributed to the formation of multilayer adsorbtions. These findings underscore the potential of Fe-Zr/ Al_2O_3 catalyst for efficient hydrogen production with optimal performance achieved at lower Fe-Zr ratios, offering valuable insights for the design of cost-effective and alternative, sustainable hydrogen generation systems.

Keywords: Hydrogen generation, Sodium borohydride, Methanolysis, Support material, catalysis

1. INTRODUCTION
Hydrogen has a promising potential as an alternative energy source in the global transition and industry. Its high energy density, zero-emission combustion, and promising application potential make it a key player for the challenges of climate change and energy security.[1] In addition hydrogen can be used in fuel cells which has a potential of reducing greenhouse gas emissions to the nature. However, in the industry, efficient and sustainable production of hydrogen and storage of hydrogen is still a critical challenge. Sodium borohydride is one of the most studied hydrogen studied material because of its ability of delivering high purity H_2 at room temperature wih controllable kinetics. But efficient and cost-efficient catalysts and its regeneration has been challenging [2].
Among many methods of hydrogen generation, methanolysis of sodium borohydride has gained significant attention due to the spontaneous nature of the reaction, mild reaction conditions and environmentally benign by-products [3]. In this study according to the reaction showed below, methanolysis of $NaBH_4$ with Fe-Zr catalyst on a $Al2O_3$ support material is examined and effect of Fe-Zr ratio over Al_2O_3 and temperature is investigated.

2. MATERIALS AND METHODS
Hydrogen from sodium borohydride ($NaBH_4$ ≥98 %, Merck) is generated at athmospheric pressure through methanolysis reaction with Fe-Zr/Al_2O_3. Fe-Zr/Al_2O_3 is obtained from reduction of ferric chloride hexaydrate (≥97%, SRL) and Zirconium (IV) oxynitrate hydrate (≥99%, Sigma-Aldrich) by using sodium borohydrate ($NaBH_4$ ≥98, SRL) as reducing agent. Reduction reaction were carried out in a 200 mL glass beaker at room temperature. Ferric chloride hexaydrate and Zirconium (IV) oxynitrate hydrate was first added to the beaker with 50 mL of water then stirred with the magnetic stirrer for 3-5 minutes to obtain transparent solution. Afterwards Al_2O_3 is added and stirred for 2 hours in order to obtain uniformly distributed suspension. Afterwards sodium borohydrate diluted with 30 mL of water has been added to the beaker drop by drop for the reduction then stirred for 3 more hours. To ensure complete reduction 50% excess $NaBH_4$ is used. Upon the completion of the reaction, a dark orange colour should be observed. After confirming the completion of the reaction, the mixture is filtered using a membrane filter via a funnel and then dried in oven at 80 ºC for 4 hours. Finally, the catalyst was transferred to an Ependorf tube.

The experimental in order to measure HGR is illustrated in Fig. 1 [4]. The cylinder is filled with water (500 mL) was placed upside down in a contained with filled with water. Then certain amount of catalyst and methanol was added to an Erlenmayer flask and put into the water bath. Then by using the control unit rpm and temperature has been set. Flask was shaken by a device with rpm set from the control unit. Then flask is connected with the measuring cylinder by a plastic pipe in which the end of the pipe is placed into the cylinder. Later certain amount of $NaBH_4$ had added to the Erlenmayer flask and reaction began. The volume of hydrogen gas produced by the methanolysis of $NaBH_4$ is measured by water-gas displacement technique [5]. As the time progressed, the amount of hydrogen gas increased, resulting in a decrease of the water level in the cylinder. Therefore, the difference between the final and initial volume of the water in the cylinder indicates the volume of hydrogen gas produced.

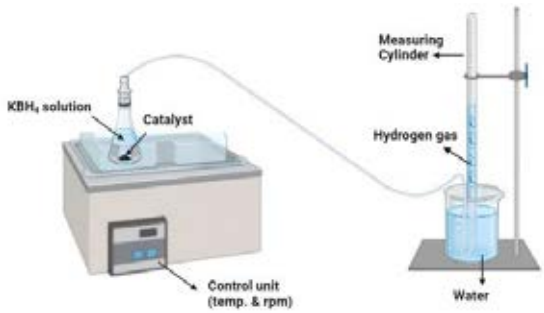

Fig. 1. Reaction setup of methanolysis process. [4]

3. RESULTS AND DISCUSSION

3.1. Characterization of the Catalyst

The SEM and EDX images and SEM EDX spectrum of 5% Fe-Ze/Al_2O_3 catalyst are given in Fig. 2. Also, smart quaf results are shown in Table 1. The images taken from the 5% Fe-Zr/Al_2O_3 catalyst sample shows an agglomerated, smooth surface structure and no phase separation between the catalyst and the support material. The images taken and spectrums given in Fig. 2. Prove the presence of Fe, Zr, Al and O and it can be seen that Fe and Zr are distributed over the support material, forming a smooth structure.

The XRD pattern shown in Fig. 3. shows that metallic Fe [6] and Zr [7] were observed in catalyst material. Also peaks at 37.4º, 45.7º, 67.05º corresponds to Al_2O_3 [8]. It can also be seen on the Fig.3. that at the 45.7º peak Fe and Al_2O_3peaks are overlapped. In conclusion, those results are proving that the metals are loaded on support material successfully.

3.2. Effect of Fe-Zr / Al_2O_3 Ratio and Temperature

Fig. 4a. shows the impact of Fe-Zr / Al_2O_3 (wt%) ratio on HGR. For the experiment $NaBH_4$ concentration, methanol volume and temperature were kept constant at 0.264 M, 10 mL and 30 ºC respectively. Catalysts with Fe-Zr / Al_2O_3 (wt%) ratio of 5-10-15% have been obtained as 7003.4, 5840.0, 5522.8 $L.min^{-1}$. g cat^{-1} respectively. Results have shown that increasing Fe-Zr / Al_2O_3 ratio decreases the hydrogen generation rate.

Fig. 4b. shows the effect of temperature on HGR. Results show that HGR increases with temperature. The HGR values obtained for 20,30,40,50 ºC are 3506.1, 7003.4, 9253.5, 14219.0 $L.min^{-1}$. g cat^{-1} respectively. Higher temperatures accelerate the methanolysis reaction by increasing the frequency of essential frequencies between reactant molecules. Therefore, as shown in Fig. 4b., HGR is increased with the temperature.

3.3. nth Order Reaction Kinetics

In order to analyze the kinetic behaviour of the catalysts and reactants, the kinetics of the methanolysis reaction of the $NaBH_4$ is mathematically analyzed with the nth order reaction kinetic model. The equations used are as below;

$$-r_{NaBH_4} = \frac{dC_{NaBH_4}}{dt} = kC_{NaBH_4}^{n} \quad (1)$$

In the equation above $-r_{NaBH4}$ represents the reaction rate of $NaBH_4$ methanolysis. C_{NaBH4} represents the concentration of $NaBH_4$ and t represents time. dC_{NaBH4} represents the rate of change of sodium borohydride concentration over time. k is for reaction rate constant and it depends on some certain parameters such as temperature and catalyst presence. n is for the reaction order. Integrating equation (1) From t=0 to t=t gives a linear equation including relationship between the reaction rate and sodium borohydrate concentration over time which is shown below;

$$\frac{1}{C_A^{n-1}} - \frac{1}{C_{A0}^{n-1}} = (1-n)kt \quad (2)$$

For for 5% Fe-Zr / Al_2O_3, by using the equation (2) a graph is created with the data calculated (drom the left side of the equation) against time. Then, by setting n values R^2 values are evaluated. The n value that gives the nearest R^2 value to 1 indicates the correct order of the reaction. According to the calculations n value of 0,824 is obtained. Later, activation energy is calculated by using the Arrhenius equation as 42.34 kJ mol^{-1}.

$$k = A \exp\left(-\frac{E_A}{RT}\right) \quad (3)$$

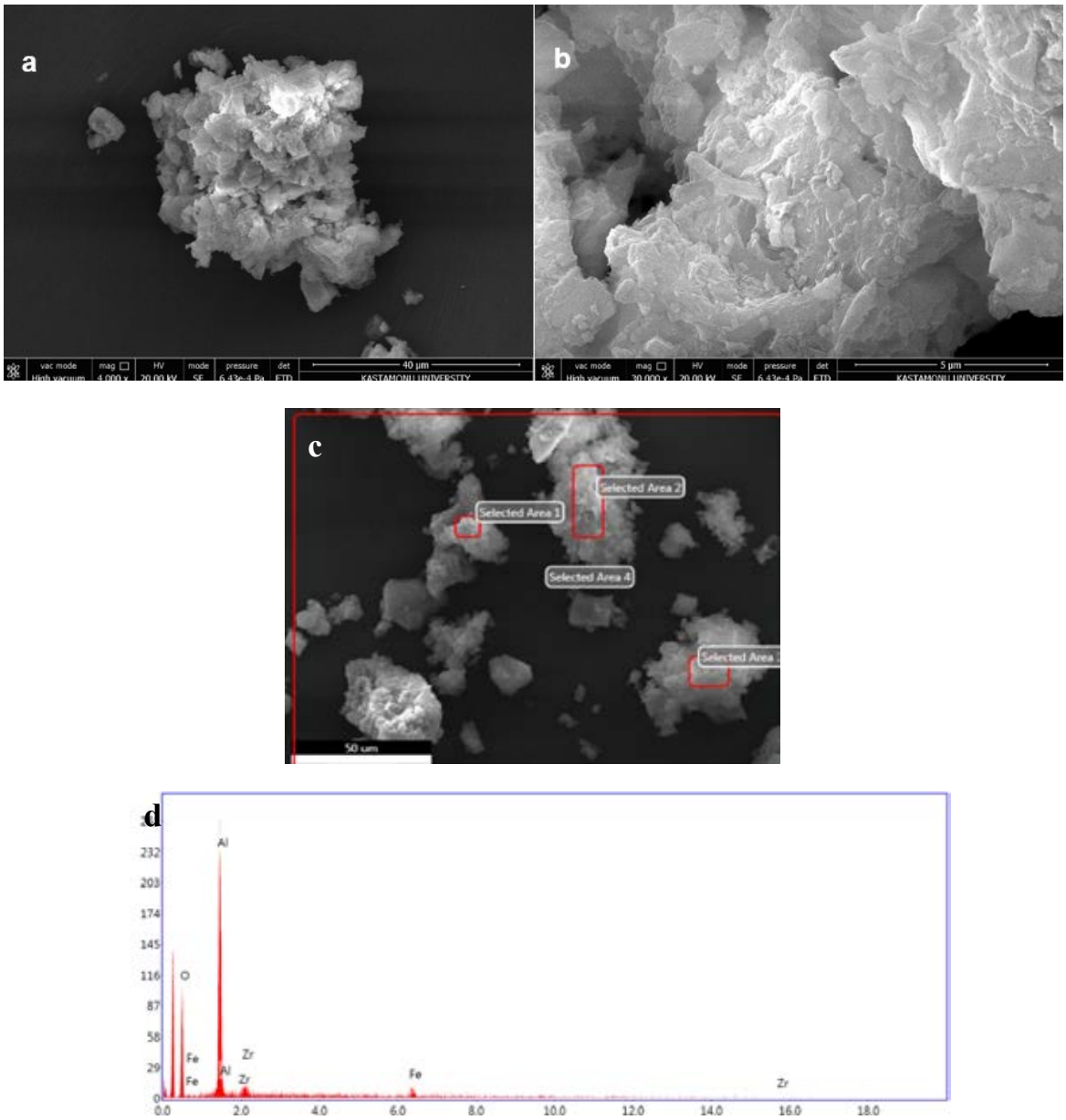

Fig. 2. SEM EDX image (a,b,c) and SEM EDX spectrum of Fe-Zr/Al_2O_3 (d, from selected area 4)

Table 1. Smart Quant Results (from selected area 4)

Element	Weight %	Atomic %
O	52.79	66.56
Al	43.11	32.23
Fe	2.19	0.79
Zr	1.91	0.42

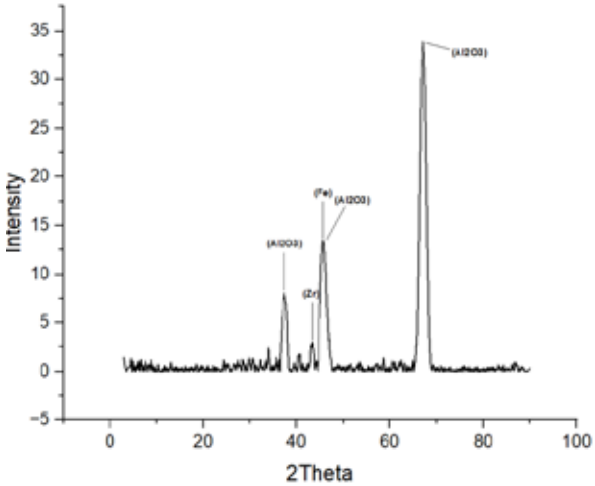

Fig 3. XRD pattern of Fe-Zr/Al2O3 catalyst

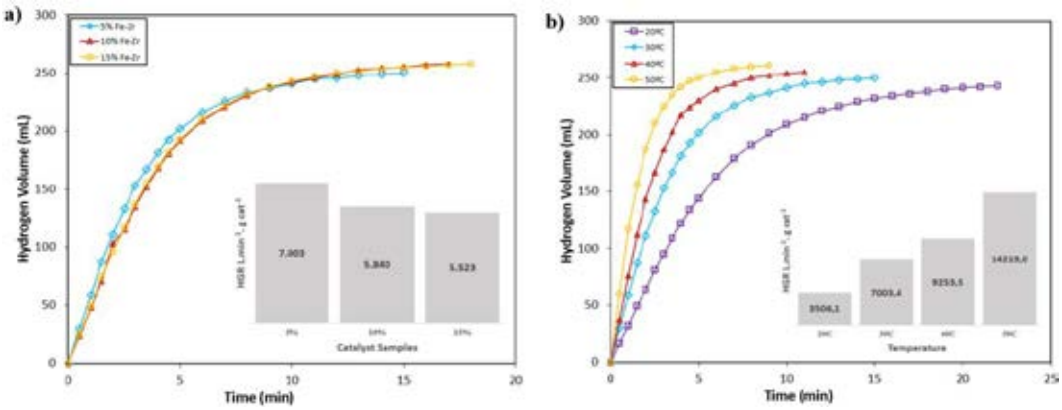

Fig. 4. Effect of Fe-Zr ratio (a) and temperature (b) on HGR

4. CONCLUSIONS

This paper studies the temperature and Fe-Zr ratio effects on hydrogen production via methanolysis of $NaBH_4$ with Fe-Zr catalyst on a Al_2O_3 support material.

This research obtained a HGR of 7003.4 $L.min^{-1}$. g cat^{-1} at 30 ºC with the reaction order of 0,824 and activation energy of 42,34 kJ mol^{-1}. Also, it is shown that increasing Fe-Zr ratio over Al_2O_3 negatively affects the performance. On the other hand, increased temperature notably boosts HGR.

This study indicates that with the lower ratios of Fe-Zr over Al_2O_3 optimal hydrogen generation efficiency can be maximized. That outcome may be promising approach to hydrogen production applications when using Fe-Zr and Al_2O_3 as an alternative catalyst and support material.

REFERENCES

1. Demirci U.B., Akdim O., Andrieux J., Hannauer J., Chamoun R., Miele P. 2010. Sodium borohydride hydrolysis as hydrogen generator: Issues, state of the art and applicability upstream from a fuel cell. Fuel Cells 10:335-350.
2. Zhu Y., Ouyang L., Zhong H., Liu J., Wang H., Shao H., Huang Z. Zhu M. 2020. Closing the loop for hydrogen storage: Facile regeneration of $NaBH_4$ from its hydrolytic product. Angewandte Chemie 132:8701-8707 .
3. Wang T., Jiang T., Zhang H., Zhao Y. 2022. Advances in catalysts for hydrogen production by methanolysis of sodium borohydride. International Journal of Hydrogen Energy 47:14589-14610.
4. Şahin Ö., Keleş G.L., Büyükkanber K. 2024. Cobalt-doped carbon spheres: Impact on potassium borohydride hydrolysis. International Journal of Hydrogen Energy 90:1227-1236.
5. Şahin Ö., Ekinci A., Büyükkanber K. 2024. High catalytic activity of cobalt nanoparticles synthesized by ultrasonic spray method in sodium borohydride hydrolysis. International Journal of Hydrogen Energy 79:335-345.
6. Hirano Y., Kasai Y., Sagata K. 2016. Unique approach for transforming glucose to C3 platform chemicals using metallic iron and Pd/C catalyst in water. Bulletin of the Chemical Society of Japan 89(9):1026-1033.
7.Devi K.R.S., Jayashree S. 2013. Eco friendly nitration of toluene using modified zirconia. Engineering & Catalysis 7(3):205-214.
8. Hossein-Zadeh M., Razavi M., Mirzaee O., Ghaderi R. 2013. Characterization of properties of Al-Al2O3 nano-composite synthesized via milling and subsequent casting. Journal of King Saud University-Engineering Sciences 25:75-80.

SIMULATION-BASED PERFORMANCE AND COST OPTIMIZATION OF ALKALINE ELECTROLYSERS

[1*] *Sami Şaban DEMİREZEN*, [2] *Hasan ÖZCAN*, [3] *Selahattin ÇELİK*
[1] Ankara Yıldırım Beyazıt University, Graduate School of Natural and Applied Sciences, Ankara/Türkiye
[2] Ankara Yıldırım Beyazıt University, Faculty of Engineering and Natural Sciences, Department of Mechanical Engineering, Ankara,Türkiye
[3] Ankara Yıldırım Beyazıt University, Faculty of Engineering and Natural Sciences, Department of Mechanical Engineering, Ankara,Türkiye
*Corresponding author e-mail: samidmrzn@gmail.com

ABSTRACT

This paper presents a simulation-based study on the performance and cost optimization of alkaline water electrolysers. COMSOL Multiphysics was used for electrochemical modeling, while the Engineering Equation Solver (EES) was employed for cost analysis. The key parameters investigated include temperature, electrolyte concentration, electrode-separator distance, and separator porosity. The study demonstrates that optimizing these parameters enhances efficiency and significantly reduces the levelized cost of hydrogen (LCOH), particularly in large-scale applications.
Keywords: Alkaline water electrolysis, cost optimization, performance optimization, LCOH, LCOE.

1.INTRODUCTION

The increasing global energy demand and the limitations of fossil fuels necessitate alternative energy sources. Hydrogen, with its high energy content (39.42 kWh/kg), is a promising clean energy carrier. Alkaline water electrolysis is one of the most commercially mature hydrogen production methods, offering cost-effectiveness and durability compared to other technologies like proton exchange membrane (PEM) or solid oxide electrolysis (SOE) [1–4].
Electrolysis involves splitting water into hydrogen and oxygen using an electrical current. The fundamental electrochemical reaction is expressed as:

$$H_2O_{(l)} + Electricity + Heat \rightarrow H_{2(g)} + {}^{1}/_{2}\, O_{2(g)} \quad (1)$$

A typical alkaline electrolysis cell consists of nickel-based electrodes in a KOH solution, operating at 60-90°C and below 30 bar pressure [5]. The minimum potential required for electrolysis is determined by the Nernst equation, with the standard reversible voltage being 1.229 V at 25°C [6].

2. ELECTROCHEMICAL MODELING AND SIMULATION APPROACHES

Electrochemical modeling is essential for understanding the reaction mechanisms, kinetics, and mass transport phenomena in alkaline water electrolysers. The cell voltage is expressed as the sum of the reversible voltage and the overpotentials due to ohmic resistance, activation, and mass transfer limitations:

$$U = U_{rev} + U_{ohm} + U_{act} + U_{conc} \quad (2)$$

where U_{rev} is the reversible voltage, and the remaining terms represent ohmic, activation, and concentration overpotentials. A widely used form of the current–voltage relationship, originally proposed by Ulleberg, is given by:

$$U = U_{rev} + r \cdot i + s \cdot \log(t \cdot i + 1) \quad (3)$$

2.1. COMSOL Modelling and Simulation Approaches

COMSOL Multiphysics 6.1 is used to simulate a 2D electrolyser cell where the geometry is simplified to clearly define the boundaries for the electrodes, separator, and gas compartments. The modeling framework incorporates the Nernst equation for equilibrium potential, Butler–Volmer kinetics for electrode reactions, and Ohm's law to describe ion transport. In the CFD modeling process, 20 different analysis utilized for determining the effects of different parameters. The parameters used in the simulation are provided in here. For the both cathode and anode side electrode-separator distance range used 2 and 4 mm. Seperator width is 1 mm and cell height is 10 mm. Temperature range used in the analysis are 25 and 75 C and separator porosity is in here 0.3-0.4. Two different electrolyte solution and concentration is used: KOH and NaOH, 6 and 10 M, respectively.

2.2. Cost Optimization Modelling

This study utilizes the EES program to calculate and optimize costs associated with alkaline water electrolyzers. The cost of alkaline water electrolyzers was determined based on real-world market data at the end of 2024, as provided in Table 2.3 for the 25 kW, the stack, mod and systems costs is 25,000, 90,000 and 160,000 $ respectively. For 250 kW system, these prices is 150,000, 350,000 and 450,000 $, respectively. Using these data, the cost per square meter of active area was calculated. This calculation yielded a single-cell cost of $19,200 per m², incorporating factors such as material costs, labor, and other project-related expenses.

In addition to the 20 analyses mentioned above, an independent analysis was conducted for the cost optimization. This analysis considered operational parameters such as a temperature of 75°C, a 6M KOH solution concentration, a separator porosity of 0.8, and a separator-electrode distance of 2 mm. The calculations were performed for a voltage range of 1.8 V to 2.5 V, and the output data obtained from analysis used in the EES program for cost optimization.

The I-U curve data were used to derive a I-U function for total system power calculations, which was subsequently implemented in the EES program using Eq.(4). The current values obtained from the function correspond to a per-square-meter basis. To determine the total area for achieving the desired system power, Eq. (5) was employed.

$$\mathrm{V}_{cell} = -0{,}000000000293 * \mathrm{I}_{cell}{}^{2} + 0{,}0000627 * \mathrm{I}_{cell} + 1{,}816 \quad (4)$$

$$\mathrm{A}_{total} = (\dot{W}_{total}/(\mathrm{V}_{cell} * \mathrm{I}_{cell})) * 1000 \quad (5)$$

Market prices for 25 kW and 250 kW systems were obtained from current sources, including manufacturer quotes, industry-specific market reports. For larger systems, these costs were interpolated using available unit prices. Based on the interpolated data, two critical factors were derived: The system factor (F_s) represents the costs associated with auxiliary systems (e.g., power sources, piping, control systems) surrounding the electrolyzer module. This factor incorporates the costs of infrastructure and integration requirements. The module factor (F_m) relates to the scale of the electrolyzer module or its capacity. Smaller systems typically have higher unit costs due to limited economies of scale, reflecting the higher installation and production expenses for smaller modules. LCOH calculations were performed using Eq. (6), dividing the total cost by the total hydrogen production.

$$LCOH = (CapEx + OpEx)/\ H_{2,total} \quad (6)$$

3. RESULTS AND DISCUSSIONS

3.1. COMSOL Analysis Results

For Effect of Temperature on Average Cell Current Density, temperature has been identified as one of the most significant factors influencing the average cell current density in the electrolysis process. This is primarily because temperature affects both the electrochemical reaction kinetics and the ionic conductivity of the electrolyte. Temperature is a critical factor influencing current density, with significant improvements observed across different electrolytes and separator porosity values, highlighting its key role in optimizing electrolysis performance.
For the Effects of Electrode-Seperator Dist. on Avg. Cell Current Density, Increasing the electrode-separator distance significantly reduces current density, with the magnitude of the decrease slightly influenced by temperature and separator porosity, while the choice of electrolyte has negligible impact.
For the Effect of Concentration on Average Cell Current Density, Increasing the electrolyte concentration from 6 M to 10 M generally reduces current density, with the magnitude of the reduction being more pronounced at lower temperatures and smaller electrode-separator distances.
For Effect of Separator Porosity on Average Cell Current Density, Increasing separator porosity significantly enhances current density, with the effect being more pronounced at lower temperatures. The trend is consistent across both KOH and NaOH, with NaOH showing a slightly higher sensitivity to porosity changes.
For the Effect of Electrolyte Solution on Average Cell Current Density, Used in here two different solution and the efficiency difference between KOH and NaOH decreases with increasing temperature, KOH is more efficient than NaOH for optimal temperatures especially at lower temperatures.

The figure above summarizing the aforementioned results. This figure focus on the parameters that most significantly affect current density, and the combined effects of these parameters are presented in graphical form. Fig.1 illustrates the impact of temperature and separator porosity on current density for KOH solution. The effects of four different temperature values on current density at porosity levels of 0.3 and 0.4 are shown in Fig.1.

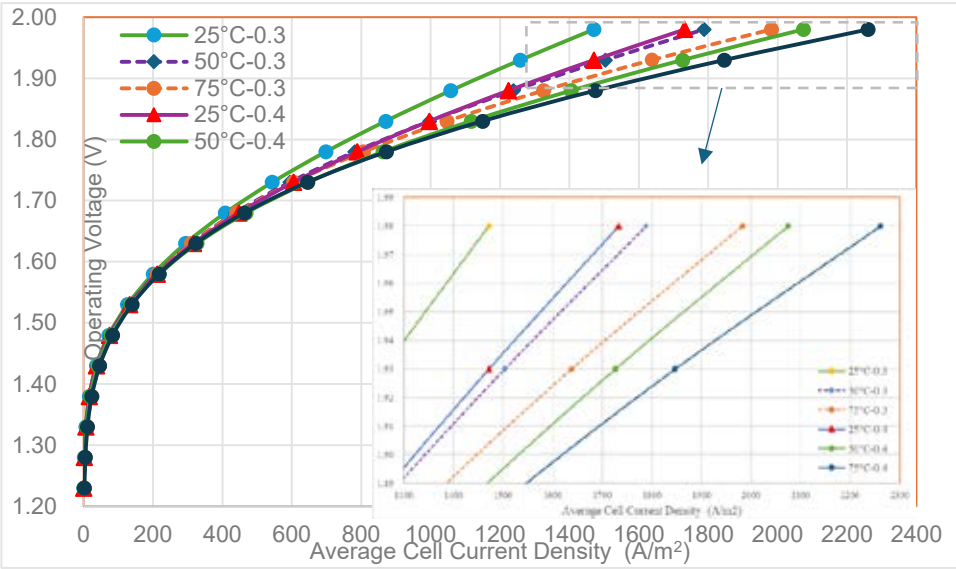

Fig.1. I-U Curve for Effect of Temperature and Separator Porosity

3.2. EES Analysis Results

In this study, cost optimization was performed using 1D modelling in COMSOL Multiphysics, providing a simplified yet effective approach to analyze the electrochemical performance and economic implications of alkaline water electrolyzers. The 1D model enabled the evaluation of key operational parameters, such as current density, voltage, and efficiency, which were subsequently integrated into the cost analysis framework to calculate the Levelized Cost of Hydrogen (LCOH).

The results from COMSOL modelling were transferred into the engineering equation solver (EES) environment to extend the analysis and systematically explore the impact of technical parameters on economic outcomes. This hybrid approach ensured that the cost optimization process combined accurate simulation data with flexible economic modeling, enabling the identification of operating conditions that minimize LCOH. By utilizing this methodology, the study demonstrates the practicality of 1D modelling-based analysis as a foundation for cost-effective hydrogen production and future design improvements.

Using the current-voltage formula derived from COMSOL data, calculations were performed in the EES program for systems with capacities of 25 kW, 100 kW, 1,000 kW, 5,000 kW and 10,000 kW. For these calculations, LCOE values of $ 0.05/kWh and $ 0.1/kWh were considered, and analyses were conducted for current densities of 10,000 A/m^2 and 20,000 A/m^2. The analysis focused on determining CapEx and OpEx values for cost optimization, while simultaneously calculating the total hydrogen produced by the system and deriving the LCOH values. A total of 20 analyses were conducted, incorporating these parameters.

As a result of the calculations, a LCOH value of $3.97 was obtained for a 10,000 kW system with an LCOE value of $0.05/kWh.

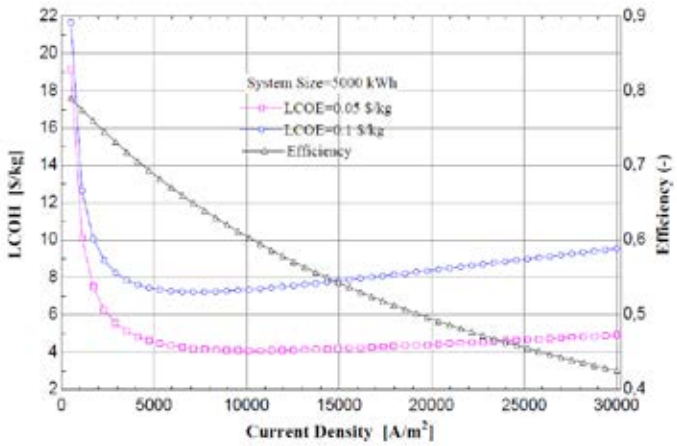

Fig. 2. LCOH and Efficiency vs. Current Density Curve for Fixed System Size

The presented graph highlights the relationship between cell current density I_{cell}, Levelized Cost of Hydrogen (LCOH), and hydrogen production efficiency. As the current density increases, LCOH initially decreases due to improved utilization of system capacity and reduced relative fixed costs. However, beyond a certain point, the efficiency starts to decline significantly because of increased energy losses, such as ohmic resistance and overpotentials, leading to diminishing returns in cost reduction. The optimal operating range for the system appears to be between 8000-12000 A/m², where a balance between low LCOH and reasonable efficiency is achieved. In this range, LCOH values for low LCOE value are around 4$/kg. The analysis further demonstrates that electricity cost (LCOE) plays a critical role in determining the overall hydrogen production cost. For instance, systems operating with a lower LCOE of 0.05 $/kWh achieve significantly reduced LCOH compared to those with a higher LCOE of 0.1 $/kWh. This underscores the importance of optimizing both current density and electricity costs to ensure economically viable and energy-efficient hydrogen production.

4. CONCLUSIONS

This study integrates electrochemical modeling in COMSOL Multiphysics with cost optimization in the Engineering Equation Solver (EES) to comprehensively evaluate the performance and cost-effectiveness of alkaline water electrolyzers. Through systematic analysis, 20 different simulations were conducted in COMSOL by varying key parameters such as temperature, electrode-separator distance, separator porosity, and electrolyte concentration and solution. The results of these simulations were used to generate current-voltage (I-V) curves, providing a detailed understanding of how each parameter influences system performance.

Among the analyzed parameters, temperature and porosity were identified as having the most significant impact on system performance. For instance, increased temperature enhanced reaction rates and reduced energy consumption, while higher porosity improved ion flow and minimized ohmic resistance. These findings emphasize the critical role of these parameters in optimizing electrolyzer efficiency.

The simulation results from COMSOL were subsequently used as inputs for cost optimization calculations in EES. Real-world market data were utilized to calculate model and system factors, which served as a foundation for system scaling studies. Additionally, analyses were conducted for two different current densities and two distinct Levelized Cost of Electricity (LCOE) values across varying system capacities. These analyses provided the necessary data to calculate the Levelized Cost of Hydrogen (LCOH). The findings demonstrated that optimizing these parameters is essential for improving both performance and economic feasibility.

Key findings of this study include the Impact of Temperature and Porosity, LCOE Sensitivity and System Scaling and Optimization. For the impact of temperature and porosity, among all parameters, temperature and porosity exhibited the most significant influence on system performance, with direct effects on energy efficiency and current density. For the LCOE sensitivity, the analyses revealed that LCOE is the dominant factor affecting LCOH, with lower electricity costs (e.g., $0.05/kWh) significantly reducing hydrogen production costs, particularly in large-scale systems. For the last finding system scaling and optimization, scaling studies based on real market data highlighted the trade-offs between capital and operational expenditures, emphasizing the need for system-specific designs to minimize overall costs.

This study provides a robust framework for evaluating alkaline water electrolyzers, offering valuable insights for system selection and optimization during the project development phase. By combining advanced electrochemical modeling with economic analyses, it establishes a pathway for designing systems that achieve the lowest possible LCOH under realistic market conditions.

REFERENCES

[1] Megía, PJ, Vizcaíno, AJ, Calles, JA, and Carrero A. 2021. From hydrogen production technologies: from fossil fuels toward renewable sources. Energy & Fuels, 35(20):16403-16415.

[2] Ursúa A, Gandía LM, Sanchis P. 2012. From hydrogen production from water electrolysis: current status and future trends. Proc. IEEE 100:410–426.

[3] Rashid MM, Mesfer MK Al, Naseem H, Danish M. 2015. From hydrogen production by water electrolysis: a review of alkaline water electrolysis, pem water electrolysis and high temperature water electrolysis. International Journal of Engineering and Advanced Technology 3: 2249.

[4] El-Emam RS and Özcan H. 2019. From Comprehensive Review on the Techno-Economics of Sustainable Large-Scale Clean Hydrogen Production. Journal of Cleaner Production.

[5] Gambou F, Guilbert D, Zasadzinski M, Rafaralahy H. 2022. From a comprehensive survey of alkaline electrolyzer modeling: electrical domain and specific electrolyte conductivity. MDPI.

[6] Zoulias E, Varkaraki E, Lymberopoulos N, Christodoulou CN, Karagiorgis GN. 2004. From a review on water electrolysis.Tcjst 4(2):41-71.

EFFECT OF TEMPERATURE AND CATHODE FLOW RATE ON PERFORMANCE OF HYDROGEN-BROMINE REDOX FLOW BATTERY

[1,2*]*Anil Can Turkmen*, [1]*Cenk Celik*, [3]*Fatma Gul Boyaci San*
[1] Kocaeli University Faculty of Engineering, Department of Mechanical Engineering, Kocaeli 41380, Turkey
[2] ACT Scientific Ltd., Budotek Teknopark, Istanbul, 34776, Turkey
[3] Biasis Enerji Ltd., Mutlukent, Ankara, 06800, Türkiye

*Corresponding author e-mail: anilcan.turkmen@hotmail.com

ABSTRACT
In the present research, the performances of a uniquely designed Hydrogen$_2$/Bromine redox flow battery with fixed cathode feed composition and fixed anode feed at different temperatures and cathode feed flow rates were investigated. The highest power density obtained was 0.33 W/cm^2. The hydrogen consumption acted in accordance with the polarization curve.

Keywords: Hydrogen, Bromine, Redox flow battery

1. INTRODUCTION

Electric Energy Storage (EES) is a set of technologies that allows the produced electrical energy to be used at times other than when it is generated [1, 2, 3]. At the core of this technology, energy is stored when supply exceeds demand and the unit cost of energy is low, and then used when demand rises or when production cannot directly supply the system [1, 2, 3, 4, 5]. Energy storage systems have a wide range of applications, as they can be used in mobile, transportation, and stationary applications [3, 6, 7, 8].

Redox flow batteries are considered within electrochemical energy storage technologies and are a highly promising technology for the future [9, 10]. Redox flow batteries (RFB) attract attention due to their ability to meet varying power and energy demands, operate independently of the grid, support a high number of charge-discharge cycles, allow for deep discharge, and be quickly deployed [11]. All of these features have highlighted the use of redox flow batteries when coupled with intermittent renewable energy sources, emphasizing their potential for continuous energy storage and supply.

There are many types of redox flow batteries. In addition to the all-vanadium redox flow batteries, which have received the most research and commercialization efforts, redox flow batteries are also being developed using iron-chromium, sodium-polysulfide, and Zn/Br_2 pairs. In addition to these, H_2/Br_2 RFBs are also a rosy type [10, 11, 12]. H_2/Br_2 RFBs are a rosy technology due to their high reaction kinetics and the use of cheap reactants [13, 14].

Cho et al. (2013) found that the composition of the solution, including HBr/Br_2, affects the area-specific resistance, hence impacting on the performance of the redox flow battery. Reach the effect of ASR led to a reduction in thickness of the membrane, achieving a 1.46 W/cm² power density and power density of 0.64 W/cm² at 80% charge-discharge efficiency [15].

Kreutzer an others tested a MEA which include electrodes with 0.55 mg Pt/cm² catalyst loading and N212 membrane under H_2-H_2, H_2-Br_2, and H_2-O_2 pairs at room temperature and evaluated their performance. The current density for the Br^-/Br_2 reactions on catalyst was 0.3 mA/cm², while for H_2-O_2 reactions, this value was 1.2 mA/cm² [16].

Peled et al. (2000) chose a high platinum loading of 1.5 mg/cm² when constructing the electrodes. After experimenting with various parameters, they reported achieving the highest power density of 1.5 W/cm² [17].

This study also investigates the performance of a uniquely designed a cell H_2/Br_2 RFB in discharge mode, under different temperatures and cathode feed flow rates.

2. EXPERIMENTAL

In this study, a redox flow battery with 10 cm^2 active area was designed and manufactured. A fixed hydrogen feed rate was used in the anode section. The anode electrode consists of a 0.75 mg/cm^2 Pt/C coated SGL 29 BC gas diffusion layer. N115 was used as the membrane. LT1200 carbon fabric was used as a three-layer in the cathode section. Cell feeds were provided via Teflon connections, a peristaltic pump in the cathode section, and a pressure tube in the anode side. Tests were conducted at 2 different temperatures as 30 and 35 °C. Cell heating was provided via a PID controller via the cathode end plate. The cathode composition was used as 1 M HBr/0.9 M Br_2. Hydrogen was provided with a dry flow rate of 60 ml/min. The gasket material was Teflon filled glass fibre material and the tightening torque was 1.5 Nm.

At 22 °C, this type of redox flow batteries OCV is 1.098 V. (Eq. (1) [18]

$$2HBr_{(aq)} \xleftrightarrow{Charge/discharge} H_2 + Br_{2(aq)},\ E_{0,cell} = 1.098\ V \quad (1)$$

3. RESULTS AND DISCUSSION

The experiments are numbered for easier understanding. Numbering details are given in Table 1.

Table 1. Parameters of the experiments

Parameter	1	2	3	4	5	6
Temperature (°C)	30			35		
Cathode flow rate (ml/min)	10	15	20	10	15	20

In Fig. 1, the polarization curves, which are the most definitive feature of the redox flow battery, are given. As can be understood from the curves, the value of 0.6 V can be determined as the limit value at which this type of battery can operate. After this value, the polarization curve reversed. The increase in temperature generally increased the performance as a result of increasing the catalytic effect. In addition, the increase in cathode flow rate also provided an increase in performance at constant temperature.

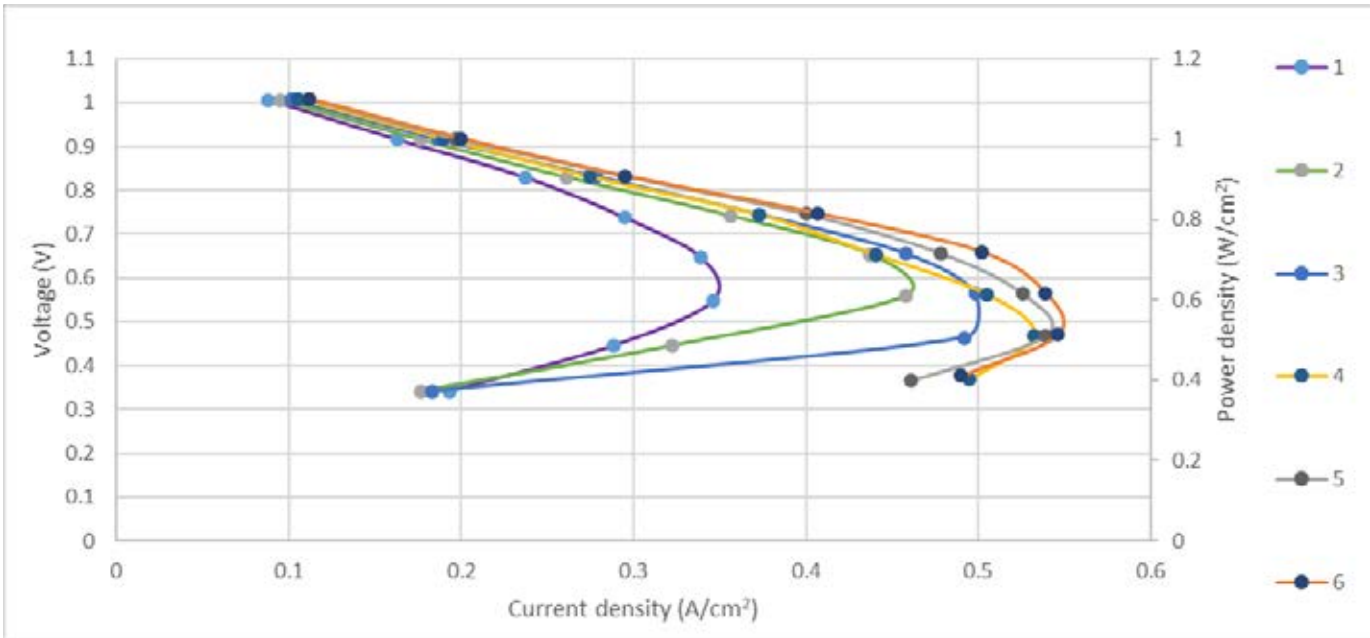

Fig. 1. Polarization curves

When looking at the power curves (Fig. 2), the highest power value obtained within the parameters used in this study was 0.33 W/cm^2.

Hydrogen consumption curves are given in Fig. 3. Hydrogen consumption follows the trend of the performance curves. There was no hydrogen flow rate limiting the cell performance. Based on this, it was determined that the reaction rate of the cathode part was the determining part of the performance.

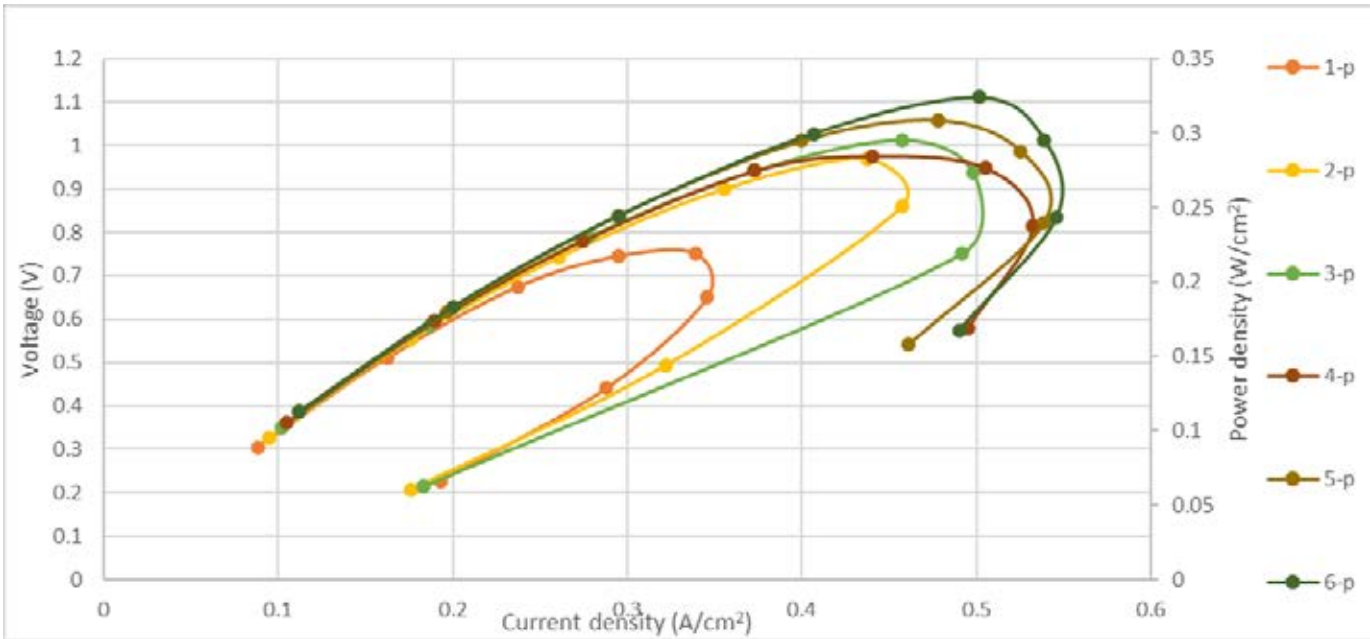

Fig. 2. Power curves

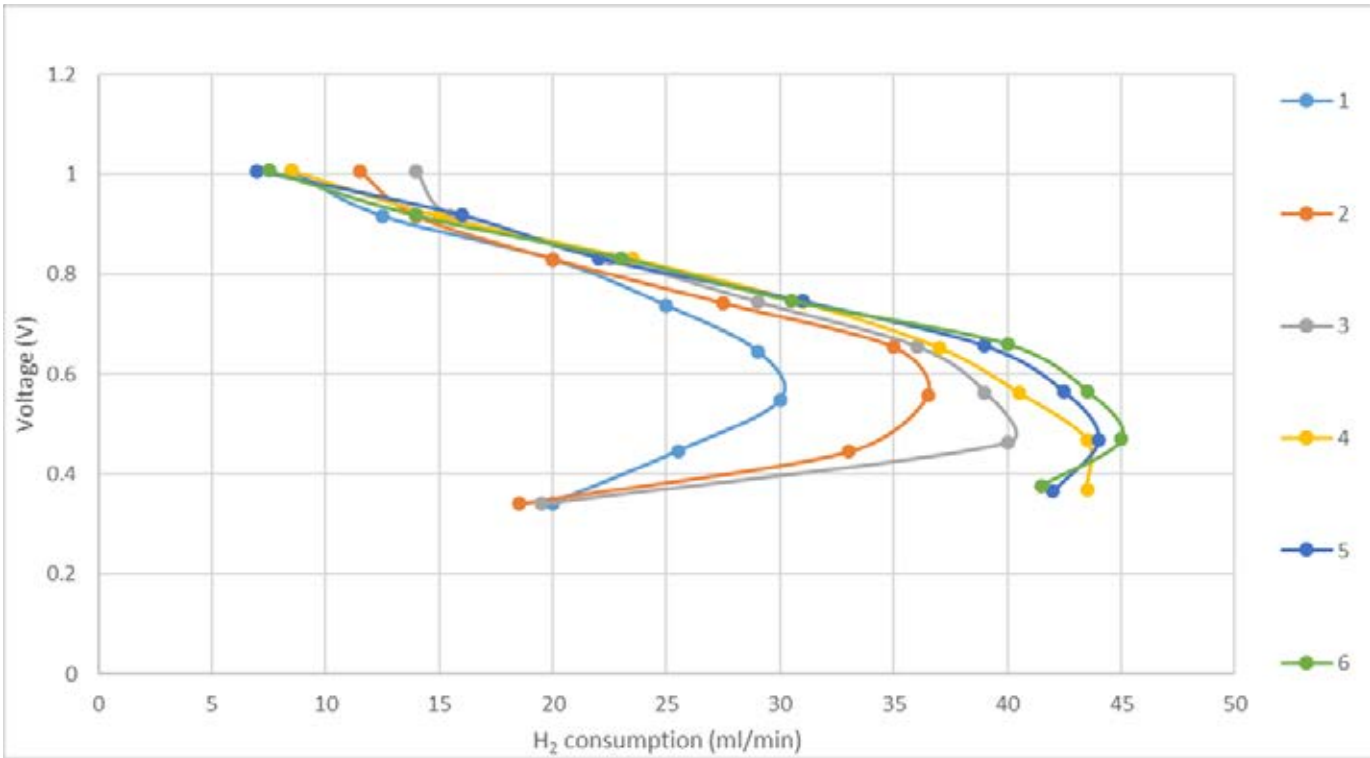

Fig. 3. Hydrogen consumption

4. CONCLUSIONS

In this study, the performance of the originally designed H_2/Br_2 redox flow battery was studied at cathode flow rates and different temperatures. It was observed that the increase in temperature and flow rate positively affected on the performance of the cell. The operating voltage of this type of redox flow battery was limited to 0.6 V levels. After this value, since the polarization is reversed, the minimum voltage that can be operated can be determined as 0.6 V. The point to be noted is that low temperature, high flow rate usage and high temperature, low flow rate usage gave similar performances. It is understood from this that when a system design is made, the operating parameter can be selected according to the importance of temperature and flow rate.

REFERENCES

1. Mclarnon F and Cairns E. 1989. Energy storage. Ann Rev Energy, 14, 241-271.
2. Baker JN and Collinson A. 1999. Electrical energy storage at the turn of the millennium. Power Eng J, s. 107-112.
3. DTI Report. 2004. Review of electrical energy storage technologies and systems and of their potential for the UK. UK Department of Trade and Industry.
4. Australian Greenhouse Office. (2005). Advanced electricity storage Technologies programme. Australian Greenhouse Office.
5. Walawalkar R, Apt J, and Mancini, R. 2007. Economics of electric energy storage for energy arbitrage and regulation. Energy Policy 2007, 5, s. 2558-2568.
6. Dobie CW. 1998. Electrical energy storage. Power Eng J, 12, 177-181.
7. Koot M, Kessels J, and Jager B. 2005. Energy management strategies for vehicular electric power systems. IEEE Transactions on Vehicular Technology, 54, 771-782.
8. Weinstock IB. 2002. Recent advances in the US Department of Energy's energy storage technology research and development programs for hybrid electric and electric vehicles. Journal of Power Sources, 110, 471-474.
9. Shigematsu T. 2011. Redox flow batteries for energy storage. SEI Technical Review, 73, 4-13.
10. Ponce de León C, Frías-Ferrer A, González-García J, Szánto DA, and Walsh FC. 2006. Redox flow cells for energy conversions. Journal of Power Sources, 160, 716-732.
11. Weber Z, Mench MM, Meyers JP, Ross PN, Gostick JT and Liu Q. 2011. Redox flow batteries: a review. Journal of Applied Electrochemistry, 41, 1137-1164.
12. Soloveichik G. 2011. Battery technologies for large-scale stationary energy storage. Annu. Rev. Chem. Biomol. Eng., 2(2), 503-527.
13. Kreutzer HM. 2012. Characterization of the hydrogen-bromine flow battery for electrical energy storage. University of Kansas.
14. Cho K, Ridgway P, Weber A, Haussener S, Battaglia V and Srinivasan V. 2012. High performance hydrogen/bromine redox flow battery for grid-scale energy storage. J. Electrochem. Soc., 159, 1806-1815.
15. Cho K, Albertus P, Battaglia V, Kojic A, Srinivasan V, and Weber A. 2013. Optimization and Analysis of High-Power Hydrogen/Bromine-Flow Batteries for Grid-Scale Energy Storage. Energy Technol, 1, 596-608.
16. Kreutzer H, Yarlagadda V and Trung Van N. 2012. Performance evaluation of a regenerative hydrogen-bromine fuel cell. J. Electrochem. Soc., 159, 331-337.
17. Peled E, Duvdevani T, Aharon A and Melman AA. 2000. Direct Methanol Fuel Cell Based on a Novel Low-Cost Nanoporous Proton-Conducting Membrane. Electrochemical and Solid-State Letters, 3(12), 525-528.
18. Yeo R and Chin D. 1980. A Hydrogen-Bromine Cell for Energy Storage Applications. J. Electrochem. Soc., 127, 549-555.

COMPARISON OF IrO_2-FeVS AND IrO_2-FeVS-Co CATALYSTS IN PEM ELECTROLYSIS AT DIFFERENT TEMPERATURES

[1]*Mine Çokyaşa*, [2]*Arzu Ekinci*, [3]*Ömer Şahin*, [1]*Orhan Baytar*
[1] Siirt University, Faculty of Engineering, Department of Chemical Engineering, , Siirt, 56100, Turkey
[2] Siirt University, , Faculty of Health Sciences, Department of Occupational Health and Safety, Siirt, 56100, Turkey
[3] Istanbul Technical University, Faculty of Chemical and Metallurgical Engineering, Department of Chemical Engineering, İstanbul, 34467, Turkey

*Corresponding author e-mail: aekinci@siirt.edu.tr

ABSTRACT
This work examined the efficacy of IrO_2-FeVS and IrO_2-FeVS-Co catalysts, produced at varying calcination temperatures (500-800 ºC), as anode catalysts in a PEM electrolyzer cell (PEMEC). The electrochemical activity of the catalyst calcined at 500ºC was assessed at various cell operating temperatures (20-70ºC). The findings indicate that the operating temperature directly influences the performance of PEMEC. At 20ºC, the voltage readings were elevated; nonetheless, the electrolysis process was inefficient owing to limited ionic conductivity and sluggish reaction kinetics. With the rise in operational temperature, proton conductivity enhanced, the reaction expedited, and the system functioned at reduced voltage levels. The optimal electrochemical performance was attained at 70°C. The catalysts calcined at 500-600ºC demonstrated optimal activity by yielding the lowest voltage values when assessed based on calcination temperature. At 700ºC, activity diminishes, although at 800ºC, the maximum voltage values were recorded owing to particle development and a decrease in active surface area. The ideal parameters for performance in PEMEC were identified as a calcination temperature of 500-600ºC and an operating temperature of 70ºC. The elevated working temperature has enhanced the catalyst's efficiency, yielding high current density at reduced voltage.

Keywords: PEM electrolysis cell (PEMEC), Anode catalyst, Calcination temperature, Electrochemical performance

1. INTRODUCTION

The global need for energy is rising due to technological advancements, population expansion, and enhanced societal wellbeing. This predicament has prompted individuals to strategically use non-renewable energy resources to fulfill demand while simultaneously enhancing and diversifying the application of renewable energy resources [1]. Among various methods for hydrogen production, electrolysis is the most environmentally sustainable technique, which utilizes electricity to separate water into high-purity hydrogen and oxygen [2]. Proton exchange membrane electrolyzer cells (PEMECs) have garnered significant attention for electrolysis owing to their small design, high-purity hydrogen generation, broad operational current density, and rapid system response [3]. The architecture of a proton exchange membrane electrolysis cell resembles that of a proton exchange membrane fuel cell, differing only in certain components, with both exhibiting symmetric structures. The typical PEMEC architecture has two bipolar plates, two gas diffusion layers, and a membrane electrode assembly (MEA), typically arranged in a symmetrical configuration with flow channels integrated into the bipolar plates. Electrochemical reforming, which consists of electrocatalytic oxidation of hydrogen-containing compounds on the anodic side of the PEMEC, can produce very pure gaseous hydrogen on the cathodic side by reducing protons passing through the membrane. Importantly, this process can take place under moderate conditions such as ambient temperature and pressure. Noble metals such as platinum and iridium-based materials have been widely selected as electrochemical catalysts for PEMECs due to their high electrochemical performance [4]. A multitude of researchers has focused on developing alternative, cost-effective electrocatalysts to substitute these metals. Consequently, a range of non-precious materials, including transition metal-based nitrides [5], carbides [6], phosphides [7], selenides [8], and sulfides [9], have been employed in PEMEC applications. Transition metal dicalcogenide materials, particularly disulfides and diselenides, are promising candidates for PEMECs owing to their affordability, remarkable stability, elevated catalytic activity, and abundant availability. Sulfur and selenium-based catalysts can offer extensive active surface area or centers to facilitate swift proton/electron adsorption and enhance overall kinetics [10]. Certain investigations demonstrated the synthesis of electrocatalysts derived from sulfur-based dichalcogenides using inexpensive and readily available transition metal elements, including molybdenum sulfide, tungsten sulfide, cobalt sulfide, and iron sulfides. The manufacture of nanoparticles used as electrocatalysts in the PEMEC system by green methods enhances their significance due to their simplicity, cost-effectiveness, and environmental sustainability. The green synthesis approach emphasizes the use of bacteria, fungus, algae, yeast, and plant extracts as reducing agents for nanoparticle production. The production of nanoparticles using natural plant extracts is an eco-friendly and cost-effective method that eliminates the need for intermediary base groups. The process may be accomplished within a few hours at ambient temperature by amalgamating plant extract and metal salt. Numerous variables affect the formation of nanoparticles from plant extract [11]. Plant extracts include many chemical elements, including flavonoids, alkaloids, steroids, tannins, saponins, cardiac glycosides, and phenolic chemicals, which are generated and stored in specific or all portions of plants [12-15]. In this study, extract was prepared from sunflower seed hulls using green synthesis method

and FeVS and Co-doped FeVS nanoparticles were produced by using this extract as reducing agent. By combining the obtained nanoparticles with IrO_2 as a support material, IrO_2-FeVS and IrO_2-FeVS-Co catalysts were synthesized to be used as anode catalyst of PEM electrolysis cell. The structural and morphological properties of the synthesized catalysts were characterized by XRD, SEM-EDX, TEM, XPS and Raman analysis. Cyclic voltammetry (CV) and impedance spectroscopy measurements were also performed to determine their electrochemical properties.

2. MATERIALS AND METHODS

2.1. Preparation of plant extract extract

Hydrothermal method was used to produce extracts from sunflower seed shells. To prepare the extract, 35 g of sunflower seed hulls were taken. 350 ml of distilled water was added to a 500 ml autoclave. It was then kept in an oven at 180 °C for 12 hours and then cooled to room temperature.

2.2. *Synthesis of FeVS and FeVS-Co nanoparticles*

For the synthesis of FeVS, 100 ml of almond green shell extract and the amounts of Fe $(NO_3)_3$ $9H_2O$, $C_{10}H_{14}O_5V$, Na_2S H_2O were mixed in molar ratios (Fe:V:S=0.5:0.5:1), and the pH of the solution was adjusted to 10 with 6M NaOH. The obtained mixture was stirred at room temperature for 24 hours, then filtered with 0.22 mm membrane filter paper, and the resulting solid was dried at 120 °C for 3 hours. Synthesize 10% Co-doped FeVS NPs, the calculated amount of $Co(NO_3)_2$ $6H_2O$ and 1 g of CoVS NPs were mixed in 50 ml of water. After being heated and turning into a paste, a certain amount of $NaBH_4$ was dissolved in 50 ml of water and then added dropwise onto it. Then, it was filtered with filter paper, and the obtained substance was dried at 120 °C for 2 hours. The synthesized nanoparticles were calcined at 500, 600, 700 and 800 ºC in nitrogen gas environment.

2.3. Synthesis of IrO_2-doped catalysts

IrO_2-FeVS and IrO_2-FeVS-Co nanoparticles were synthesized to be used as anode catalyst in the MEA of PEM electrolysis cell. 2 ml $IrCl_2$ and a certain amount of NaNO3 were mixed and then 0.2 mg FeVS nanoparticles were added and stirring was continued for 6 hours. It was then dried at 50 C in a stirring medium. The produced catalyst was calcined at 400 ºC in air. After calcination, it was washed and dried again. IrO_2-FeVS-Co nanoparticles were synthesized by the same method. The PEM electrolysis cell cathode catalyst, Pt/C catalyst containing 40 wt.% Pt, was stirred on a magnetic stirrer for 2 hours. Then, the solution was stirred at 80 ºC solution temperature for 1 hour and the solution was cooled, filtered and dried in an oven at 80 ºC for 6 hours. In order to create the MEA of the PEM electrolysis cell with 1x1 cm^2 active area, the synthesized catalysts were made into sludge, applied on carbon fabric with the help of a brush and nafion 117 membrane was used between the electrodes.

3. RESULTS AND DISCUSSION

3.1. Characterization of Nanoparticles

The nanoparticles synthesized by green synthesis method were characterized by XRD, SEM, EDX, TEM and XPS. it was determined from the characterization results that the nanoparticles were synthesized in pure and nanoscale.

3.2. PEM Electrolysis Cell Applications

In this study, FeVS and FeVS-Co nanoparticles synthesized at different calcination temperatures using the green synthesis method were tested as anode catalysts in proton exchange membrane (PEM) electrolysis cell using IrO_2 as support material and IrO_2-FeVS and IrO_2-FVS-Co catalysts. The electrochemical performances of the catalysts were evaluated at different calcination temperatures and the effect of these temperatures on the catalytic activity was investigated. In Figure 1, the electrochemical properties of the catalysts calcined at different temperatures are presented comparatively. The results obtained provide important data to determine the role of calcination temperature on the oxygen evolution reaction (OER) activity of the catalysts.

Fig. 1 illustrates the voltage-current density (V-J) curves of IrO_2-FeVS catalysts synthesized at various calcination temperatures. The catalysts' performance was assessed regarding the influence of calcination temperature on electrochemical activity. Catalysts calcined at 500 ºC and 600 °C exhibited comparable trends, however calcination at 600 ºC demonstrated superior performance with reduced voltage levels. The catalyst calcined at 700ºC exhibited effective performance at low current densities; however, the voltage escalated swiftly at elevated current densities. Calcination at 800ºC yielded the lowest performance with the greatest voltage levels. The optimal calcination temperature was shown to be between 500 and 600 °C. At 800 °C, the catalytic activity decreased markedly owing to crystal growth, reduction in surface area, and phase transitions. This suggests that high-temperature calcination negatively impacts the catalyst structure and diminishes electrochemical performance. Fig. 2 displays the performance curves of the IrO_2-FeVS catalyst calcined at 500 ºC across various cell temperatures (20, 40, 50, 60, and 70ºC). The changes in the electrochemical activity of the catalyst with rising cell temperature were examined.

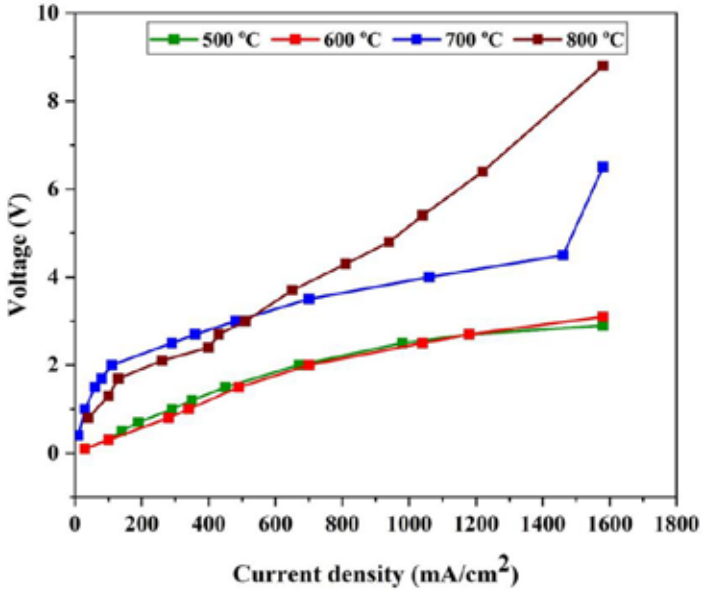

Fig. 1. Effect of different calcining temperatures on the activity of IrO_2-FeVS catalyst.

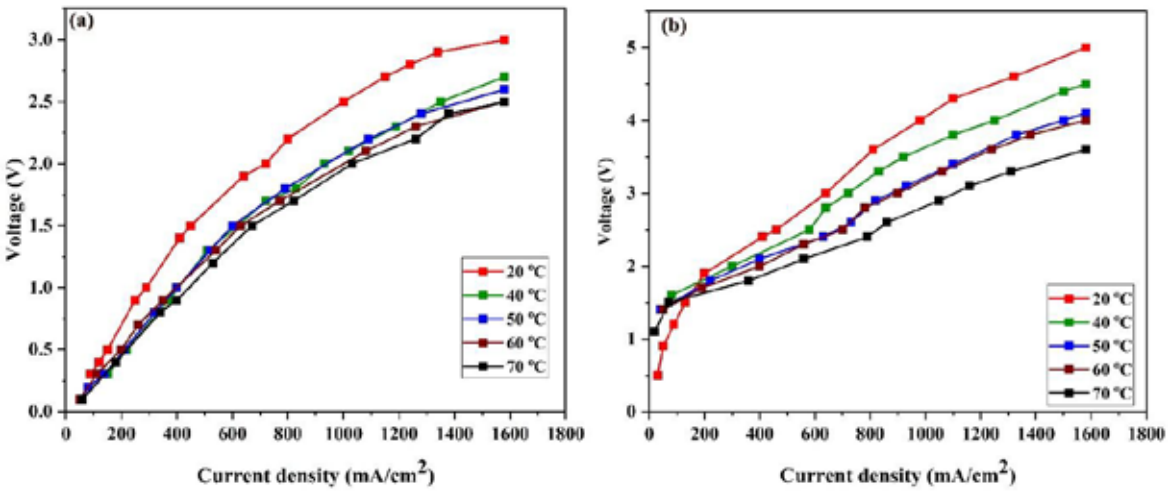

Fig. 2. Activity of IrO_2-FeVS and IrO_2-FeVS-Co catalysts at different cell temperatures

In proton exchange membrane electrolysis cells (PEMEC), the response of the anode catalyst to temperature variation is of great importance for the overall efficiency of the system. In this study, the electrochemical performance of IrO_2-FeVS and IrO_2-FeVS -Co catalysts calcined at 500 ºC at different cell temperatures (20-70 °C) were compared. The results obtained show that the voltage values of both catalysts decrease with increasing cell temperature and the efficiency of the system increases. Lower voltage levels imply that there is less energy loss in the electrolysis process and the catalyst works efficiently. In general, the IrO_2-FeVS catalyst provided lower voltages and performed better than the IrO_2-FeVS -Co catalyst at all temperatures. Especially at 20 °C and 40 °C the IrO_2-FeVS -Co catalyst showed higher voltages, indicating more energy loss. However, at 60 °C and 70 °C the performance of the IrO_2-FeVS -Co catalyst approached that of IrO_2-FeVS, but still remained slightly higher in terms of voltage. This can be explained by the fact that the Co element reduces the active surface area by oxidation in the catalyst structure and causes some limitations in terms of ion conductivity. The increase in cell temperature has accelerated the reaction kinetics, increased ion conductivity, and reduced the resistances at the electrode/electrolyte interface. Therefore, both catalysts exhibited the best performance at 70 °C. However, the IrO_2-FeVS catalyst provided significantly lower voltage at low temperatures (20-40 °C) compared to the IrO_2-FeVS -Co catalyst, making it a more efficient option under low-temperature conditions. On the other hand, the IrO_2-FeVS -Co catalyst has increased energy consumption, particularly due to the high voltage requirement at low temperatures. The addition of Co has increased the catalyst stability and improved performance at high temperatures, but it has negatively affected the reaction kinetics at low temperatures. As a result of the comparisons, the IrO_2-FeVS catalyst generally exhibited better electrochemical performance by operating at lower voltage levels. Although the IrO_2-FeVS -Co catalyst exhibited performance approaching that of IrO_2-FeVS at high temperatures (60-70

°C), it was disadvantageous in terms of efficiency at low temperatures due to energy losses. The best performance for both catalysts was achieved at 70 °C. The IrO_2-FeVS catalyst operated more efficiently at lower temperatures, consuming less energy. Although the IrO_2-FeVS -Co catalyst shows stability at high temperatures, it causes a loss of performance at low temperatures. If it is planned to operate at low temperatures in PEMEC systems, the use of the IrO_2-FeVS catalyst is more advantageous. In conclusion, while the IrO_2-FeVS catalyst offers better electrochemical efficiency at lower temperatures, the IrO_2-FeVS -Co catalyst has shown more stable performance at higher temperatures.

4. CONCLUSIONS

In this study, the electrochemical performance of IrO_2-FeVS and IrO_2-FeVS-Co catalysts, calcined at 500 °C, was compared at different cell temperatures (20-70 °C). The obtained data show that with the increase in cell temperature, the voltage values of both catalysts decreased and the electrolysis process became more efficient. Overall, the IrO_2-FeVS catalyst provided lower voltage levels and exhibited better electrochemical performance compared to the IrO_2-FeVS -Co catalyst at all temperatures. At low temperatures (20-40 °C), the IrO_2-FeVS -Co catalyst exhibited higher voltage values, indicating greater energy loss. However, at high temperatures (60-70 °C), the performance of both catalysts approached each other, but IrO_2-FeVS still provided a lower voltage, making it advantageous. The addition of cobalt to the IrO_2-FeVS -Co catalyst increased stability at high temperatures, but caused a loss of performance at low temperatures. As a result, in terms of energy efficiency at low temperatures, the IrO_2-FeVS catalyst stands out as a better option, while at high temperatures, both catalysts exhibit similar performance.

ACKNOWLEDGEMENT

The authors like to acknowledge the Research Foundation of Siirt University for their financial support via project 2024-SİÜSBF-050.

REFERENCES

1. A. Kazim, T.N. Veziroglu, Utilization of solar hydrogen energy in the UAE to maintain its share in the world energy market for the 21st century, Renewable Energy 24 (2001) 259–274.
2. Jun Chi, Yu. Hongmei, Water electrolysis based on renewable energy for hydrogen production, Chin. J. Catal. 39 (2018) 390–394.
3. Chisholm G, Kitson PJ, Kirkaldy ND, Bloor LG, Cronin L. 3D printed flow plates for the electrolysis of water: an economic and adaptable approach to device manufacture. Energy Environ Sci 2014;7(9):3026–32. https://doi.org/10.1039/ c4ee01426j.
4. Corrales-S´anchez T, Ampurdan´es J, Urakawa A. MoS2-based materials as alternative cathode catalyst for PEM electrolysis. Int J Hydrogen Energy 2014;39 (35):20837–43. https://doi.org/10.1016/j.ijhydene.2014.08.078.
5. Chakrapani V, Thangala J, Sunkara MK. WO3 and W2N nanowire arrays for photoelectrochemical hydrogen production. Int J Hydrogen Energy 2009;34(22): 9050–9. https://doi.org/10.1016/j.ijhydene.2009.09.031.
6. Levy RB, Boudart M. Platinum-like behavior of tungsten carbide in surface catalysis. Science 1973;181(4099):547–9. https://doi.org/10.1126/ science.181.4099.547.
7. Pu Z, Liu T, Amiinu IS, Cheng R, Wang P, Zhang C, et al. Transition-metal phosphides: activity origin, energy-related electrocatalysis applications, and synthetic strategies. Adv Funct Mater 2020;30(45):1–23. https://doi.org/10.1002/ adfm.202004009.
8. Ramakrishnan P, Jo S, Pitipuech N, Sohn JI. Bifunctionality behavior of phase controlled nickel selenides in alkaline water electrolysis application. Electrochim Acta 2020;354:136742. https://doi.org/10.1016/j.electacta.2020.136742.
9. Di Giovanni C, Reyes-Carmona ´A, Coursier A, Nowak S, Gren`eche JM, Lecoq H, et al. Low-cost nanostructured iron sulfide electrocatalysts for PEM water electrolysis. ACS Catal 2016;6(4):2626–31. https://doi.org/10.1021/ acscatal.5b02443.
10. Wang F, Li Y, Shifa TA, Liu K, Wang F, Wang Z, He J. Selenium-enriched nickel selenide nanosheets as a robust electrocatalyst for hydrogen generation. Angew Chem – Int Ed 2016;55(24):6919–24. https://doi.org/10.1002/anie.201602802.
11. Akintelu, S. A. Folorunso, A. S. Folorunso, F. A. Oyebamiji, A. K. 2020. Green synthesis of copper oxide nanoparticles for biomedical application and environmental remediation. Heliyon, 6(7), e04508.
12. Parekh, J. Jadeja, D. Chanda, S.V. 2005. Efficacy of aqueous and methanol extracts of some medicinal plants for antibacterial activity, Turk. J. Biol. 29: 203-210.)
13. Kaur, G.J. Arora, D.S. 2009. Antibacterial and phytochemical screening of Anethum graveolens, Foeniculum vulgare and Trachyspermum ammi. BioMed Central Complementary and Alternative Medicine, Vol. 9, Num 30.
14. Baytar O, Ekinci A, Şahin Ö, Kutluay S. Green synthesis of NiO from watermelon seed shell extract for the evaluation of H2 production from NaBH4 hydrolysis and photocatalytic reduction of methylene blue. Materials Science and Engineering: B. 2023;296:116704.
15. Ekinci A, Genli N, Şahin Ö, Baytar O. Facile “Green” synthesis of a novel Co–W–B catalyst from Rheum ribes shell extract and its effect on sodium borohydride hydrolysis: Kinetic mechanism. International Journal of Hydrogen Energy. 2024;51:796-808.

CONTRIBUTION OF SM-DOPED CeO_2 NANOPARTICLES TO HYDROGEN PRODUCTION

[1*]*Ayşe Kirkgeçit*, [2]*Handan Özlü Torun*, [3]*Nurvet Kirkgeçit Aksoy,* [4,5,6]*Murat Kisti,* [4,5,6]*Gamze Özkirar,* [5,6]*Mehmet Fatih Kaya*
[1] Kahramanmaraş İstiklal University, Institute of Science, Department of Materials Science and Engineering, Kahramanmaraş, 46000 Turkiye
[2] Kahramanmaraş İstiklal University, Energy Systems Engineering, Elbistan Faculty of Engineering, Kahramanmaraş, 46000 Turkey
[3] Kahramanmaraş Sütçü İmam University, Institute of Science, Department of Materials Science and Engineering, Kahramanmaraş, 46000 Turkiye
[4] Erciyes University, Graduate School of Natural and Applied Sciences, Energy Systems Engineering Department, 38039 Kayseri, Turkiye
[5] Erciyes University H2FC Hydrogen Energy Research Group, 38039, Kayseri, Turkiye
[6] Erciyes University, Energy Systems Engineering Department, 38039, Kayseri, Turkiye
* aysekirkgecit46@gmail.com

ABSTRACT
Today's increasing energy demand and the environmental effects of fossil fuels have increased the importance of sustainable energy sources. In this context, green hydrogen production draws attention as an environmentally friendly and renewable energy source. The characteristics and efficiency of the materials used in hydrogen production directly affect the success of the production process. In this study, the performance of CeO_2 Sm 4%, 6% and 8% doping in hydrogen evolution reaction (HER) was investigated.
Keywords: H_2 Evolution, CeO_2, Sm

1. INTRODUCTION

Hydrogen, as an environmentally friendly energy carrier, has an increasing importance in modern energy systems. It seems that hydrogen plays a critical role in the energy sector's transition away from fossil fuels and towards a more sustainable structure. Hydrogen, which is used in both power generation and industrial processes, is widely evaluated especially in sectors such as steel production, chemical industry and aviation. However, rapid developments in electric vehicles and battery technologies are increasing the role of hydrogen obtained from renewable energy sources in energy storage and transportation systems. Hydrogen, which has a wide usage area, can be produced by different reactions. This reaction is generally called the electrocatalytic reaction. The reaction occurs with two half-reactions. These are hydrogen reduction (hydrogen evolution reaction, HER) at the cathode and H_2O oxidation (oxygen evolution reaction, OER) at the anode. [1] The efficiency of these reactions is highly dependent on the properties of the electrocatalysts used.

The effectiveness of electrocatalysts is critical to make hydrogen production economical and efficient by reducing the energy requirements of the reactions. An ideal electrocatalyst is expected to have a large surface area, maintain chemical stability and exhibit high catalytic activity with low overpotential. In this context, developments in the field of materials science in recent years have revealed new strategies to increase the performance of electrocatalysts used for hydrogen production. TiO_2, Fe_2O_3, La_2O_3, CeO_2 are metal oxide compounds that can be used as electrocatalysts. [2, 3.] A good HER electrode is expected to have a porous, chemically stable and conductive structure. [4]. CeO_2, metal oxide, high surface active area, high catalytic activity, long-term durability in reactions and low overpotential enable the use of CeO_2-based electrodes in hydrogen production. [5-7]. Sun et al. investigated various electrocatalyst properties of CeO_2 compound prepared with graphene. They observed that it can be used for both OER and HER.[8]. By comparing the H_2 production made by changing the surface structure of CeO_2, it has been reported that the efficiency increases as the surface area of the nanoparticles increases. [9]

In previous CeO_2 studies, the results of limited studies on rare earth element-doped compounds have been reported. In this study, the hydrogen evolution reaction of CeO_2 compound doped with Sm at different rates was investigated comparatively. Glycine combustion [10] technique, which is used to produce nanoparticles with large surface areas, was used in the syntheses.

2. MATERIALS AND METHODS

Pure water, Cerium (III (nitrate hexahydrate, 99.9%, Alfa Aesar), Samarium [Samarium (III) nitrate hexahydrate, 99.9%, Acros Organics] and Glycine (Merck) are the materials used.

The glycine combustion method was used in the synthesis of doped CeO_2 compounds. For this method, Sm ($^{+3}$) cations were doped into the CeO_2 structure at 4,6,8 mole ratios. After the chemicals were weighed, they were dissolved in 40 ml of pure water. Glycine was added to the solution and the solution temperature was increased to 300^0 C on a heated magnetic stirrer and the combustion process was expected to take place. After the combustion process took place, the compound was burned on a heated table at 300^0 C for another hour. After the combustion process, the powder samples were taken into alumina crucibles and annealed at 700^0 C for 4 hours.

To determine the crystal structure properties, X-ray powder diffractometer scanning was performed between 0 and 90^0. HER evolution measurements were used CV analyzer.

3. RESULTS AND DISCUSSION

The powder XRD results of Sm doped nanoparticles taken between 0-90^0 are shown in Figure 1. The obtained graphics are consistent with the cubic structure with space group Fm-3m in the literature [11]. The peak of Sm was not observed. This indicates that Sm^{+3} ions have been successfully incorporated into the crystal lattice of CeO_2 by replacing Ce^{+4} ions. Using Scherrer's equation, the average crystallite size was determined using all peaks. When the size of the crystallites is examined in detail in terms of additives, it is seen at what level the Sm doped compounds are.

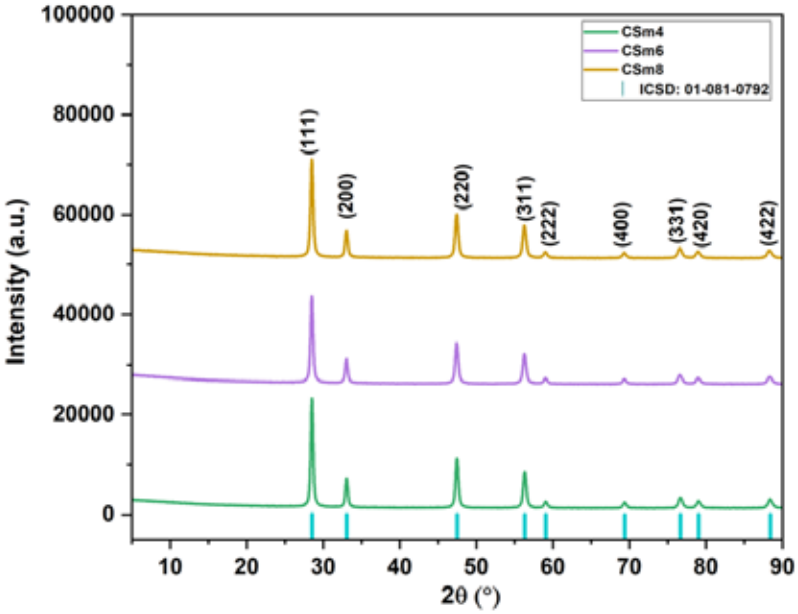

Fig. 1. X-ray pattern of Sm-doped CeO_2 samples

To investigate the crystal lattice structure and microstructure of Sm^{+3} doped CeO_2 powders, Rietveld analysis was performed using Highscore Plus software (Figure 1). The pseudo-Voigt function was used in fitting the diffraction peaks. The effects of Sm^{+3} addition to the crystal lattice sites of CeO_2 were reflected in the values of the unit cell parameters. The increase in the amount of Sm doping changes the unit cell parameter linearly. The main reason for this is the difference in the ionic radii of Ce^{+4} (0.97 Å) and Sm^{+3} (1.08 Å) ions.[12]

4. CONCLUSIONS

Glycine combustion technique was used to synthesize nanopowders of CeO_2 doped with 4,6,8 mol% Sm^{+3}, respectively. It was determined that all compounds had a cubic crystal lattice. Nanostructured compounds were obtained. The values of the obtained compounds for HER were compared. The best result in hydrogen production was observed as 19.54 minutes per 1 ml in CSm8.

ACKNOWLEDGEMENT

Kahramanmaraş İstiklal University was supported by the project number 2024/6-4 LTP

REFERENCES

1. Verma, J., & Goel, S. (2022). Cost-effective electrocatalysts for hydrogen evolution reacti-ons (HER): challenges and prospects. International Journal of Hydrogen Energy, 47(92), 38964-38982.
2. Zhang, L., Zhao, H., Xu, S., Liu, Q., Li, T., Luo, Y., ... & Sun, X. (2021). Recent advances in 1D electrospun nanocatalysts for electrochemical water splitting. Small Structures, 2(2), 2000048.,
3. Eftekhari, A. (2017). Electrocatalysts for hydrogen evolution reaction. International Journal of Hydrogen Energy, 42(16), 11053-11077
4. Yang, W., & Chen, S. (2020). Recent progress in electrode fabrication for electrocatalytic hydrogen evolution reaction: A mini review. Chemical Engineering Journal, 393, 124726.
5. Sung, M. C., Lee, G. H., & Kim, D. W. (2019). CeO2/Co (OH) 2 hybrid electrocatalysts for efficient hydrogen and oxygen evolution reaction. Journal of Alloys and Compounds, 800, 450-455.
6. Song, X. Z., Zhu, W. Y., Wang, X. F., & Tan, Z. (2021). Recent advances of CeO2 - based electrocatalysts for oxygen and hydrogen evolution as well as nitrogen reduction. ChemElectroChem, 8(6), 996-1020.
7. Lu, G., Zheng, H., Lv, J., Wang, G., & Huang, X. (2020). Review of recent research work on CeO2-based electrocatalysts in liquid-phase electrolytes. Journal of Power Sources, 480, 229091.
8. Sun, L., Zhou, L., Yang, C., & Yuan, Y. (2017). CeO2 nanoparticle-decorated reduced graphene oxide as an efficient bifunctional electrocatalyst for oxygen reduction and evolution reactions. International Journal of Hydrogen Energy, 42(22), 15140-15148.

9. Ai, C., Shi, J., Hu, S., Li, J., Luo, B., & Jing, D. (2022). Morphologies dependence of hydrogen evolution over CeO2 via ultrasonic triggering. International Journal of Hydrogen Energy, 47(34), 15149-15159.
10. Lin, S. Y., Chiu, T. W., & Dong, C. (2017). Preparation and characterization of CuCrO2-CeO2 composite nanopowder by a self-combustion glycine nitrate process. Ceramics International, 43, S639-S642.
11. Magdalane, C. M., Kaviyarasu, K., Siddhardha, B., & Ramalingam, G. (2021). Synthesis and characterization of CeO2 nanoparticles by hydrothermal method. Materials Today: Proceedings, 36, 130-132
12. Pal, A. K., Som, S., & Lu, C. H. (2018). Synthesis and spectroscopic analysis of Sm3+ doped CeO2 ceramic powders for the application of white LEDs. Ceramics International, 44(15), 18256-18263.

TECHNO-ECONOMIC ANALYSIS OF MoS_2/CARBON COMPOSITES AS SUSTAINABLE PLATINUM ALTERNATIVES IN PEM ELECTROLYZER CATHODES

Huseyin Sarıaltın
Izmir Institute of Technology, Engineering Faculty, Department of Mechanical Engineering, Gülbahçe 35430 Urla / İzmir Türkiye

Corresponding author e-mail: huseyinsarialtin@iyte.edu.tr

ABSTRACT

Proton exchange membrane (PEM) electrolysis is a key technology for sustainable hydrogen production, but its reliance on expensive platinum-group metal (PGM) catalysts poses a significant cost challenge. This study evaluates the techno-economic feasibility of replacing conventional Pt/C cathodes with molybdenum disulfide (MoS_2)-based alternatives. Two different MoS_2-based catalysts, MoS_2/Vulcan and MoS_2/RGO, were investigated. The analysis considered various electricity price scenarios and compared each system's Levelized Cost of Hydrogen (LCOH). The results indicate that the MoS_2/Vulcan system produced hydrogen at a lower LCOH than the MoS_2/RGO system. Specifically, the LCOH for MoS_2/Vulcan ranged from $6.27 to $8.05 per kg, while for MoS_2/RGO, it ranged from $6.72 to $8.62 per kg. These findings suggest that MoS_2/Vulcan is a more economically viable alternative to traditional Pt/C catalysts, approaching the lower end of the LCOH range reported for conventional systems.

Keywords: Green Hydrogen Production, PEM Electrolyzers, Techno-Economic Analysis

1. INTRODUCTION

Hydrogen, as a clean energy carrier, plays a pivotal role in the transition towards a low-carbon economy, offering a promising solution for reducing greenhouse gas emissions and mitigating climate change [1]. Proton exchange membrane electrolysis is a promising technology for sustainable hydrogen production, offering high efficiency and potential integration with renewable energy sources[2]. The widespread adoption of PEM electrolyzers is crucial for achieving a sustainable hydrogen economy, but it is hindered by the high cost of platinum-group metal (PGM) catalysts, which are commonly used in both anode and cathode electrodes [3]. Among them, platinum supported on Vulcan carbon remains the industry standard due to its high surface area and electrical conductivity.

The reliance on expensive PGMs increases the overall cost of hydrogen production and raises concerns about the sustainability and availability of these materials. Therefore, there is a growing interest in developing alternative catalysts that can provide similar or improved performance at a lower cost. MoS_2 has emerged as a promising candidate due to its excellent catalytic properties, abundance, and lower price than PGMs[4].

This study evaluates the techno-economic feasibility of replacing conventional Pt/C cathode with MoS_2-based alternatives, specifically MoS_2/Vulcan and MoS_2/RGO in the PEM electrolyzer system. By comparing the LCOH for these alternative catalysts under various electricity price scenarios, this research seeks to determine the economic viability of MoS_2-based catalysts and their potential to reduce the cost of hydrogen production. The analysis considers the impact of system efficiency, operational expenditures (OPEX), and capital expenditures (CAPEX) on the overall cost, providing a comprehensive assessment of the economic performance of these alternative cathode catalysts.

2. MATERIALS AND METHODS

Using a standardized analytical framework, the techno-economic performance of a PEM electrolyzer system is evaluated by comparing two MoS_2-based catalysts, MoS_2/Vulcan and MoS_2/RGO. A 100 kW system is chosen as the representative scenario, selected for its relevance in scalable hydrogen production applications. The catalysts are analyzed based on experimental data obtained from a reference study [4].

The annual operating hours were estimated at 4,000 hours with an expected lifespan of 10 years, and the efficiency values for MoS_2/Vulcan and MoS_2/RGO were assumed to be 75% and 70%, respectively, based on current densities of 0.35 A/cm² and 0.25 A/cm² reported in the reference study[4].

The cost analysis for the MoS_2-based catalysts was conducted by considering various parameters, including catalyst loading, current density, and surface area. These parameters were derived from experimental data and market prices to ensure accuracy and relevance. The detailed cost breakdown is presented in Table 1.

Consequently, the CAPEX for the entire PEM system was calculated by first determining the cost of the system without

the Pt/C electrode, which is assumed to constitute 20% of the total stack price in conventional systems. By subtracting the Pt/C electrode cost of $12,386 from the total system cost of $260,000, we obtained the CAPEX for the system without the electrode [5]. We then added the costs of our alternative MoS_2-based electrodes to this amount to determine the total CAPEX.

Table 1. Cost Analysis Parameters for MoS_2/Vulcan and MoS_2/RGO Catalysts

Parameter	MoS_2/Vulcan	MoS_2/RGO
Loading (mg/cm²)	5 mg/cm²; (47 wt% MoS_2)	3 mg/cm²; (43.8 wt% MoS_2)
Current Density (A/cm²)	0.35 A/cm²	0.25 A/cm²
Surface Area Assumption (m²)	15.87	22.22
Total Cost (USD)	363	756

LCOH is a measure of the cost per unit of hydrogen produced over the lifetime of the production facility[6]. This formula takes into account CAPEX, OPEX, the fixed annual cost rate (FCR), and annual hydrogen production (eq 1) [7].

$$\mathrm{LCOH} = \frac{CAPEX \cdot FCR + OPEX}{Annual\ Hydrogen\ Production}$$

FCR includes depreciation and capital costs. For a 5% interest rate and a 10-year lifespan, the FCR is calculated to be 0.1295. ($FCR = r(1+r)^n / ((1+r)^n - 1)$). The OPEX was assumed as 5% of the CAPEX, and the annual hydrogen production was determined using the lower heating value (LHV) of hydrogen. The electricity prices of $0.03, $0.05, and $0.07 per kWh (representing low, medium, and high renewable energy cost scenarios) were used for both electrodes in all three scenarios.

3. RESULTS AND DISCUSSION

Fig. 1 presents the LCOH values for both MoS_2/Vulcan and MoS_2/RGO systems under various electricity price scenarios. This visual representation emphasizes the substantial influence of system efficiency and electricity costs on the overall economic performance of hydrogen production technologies.

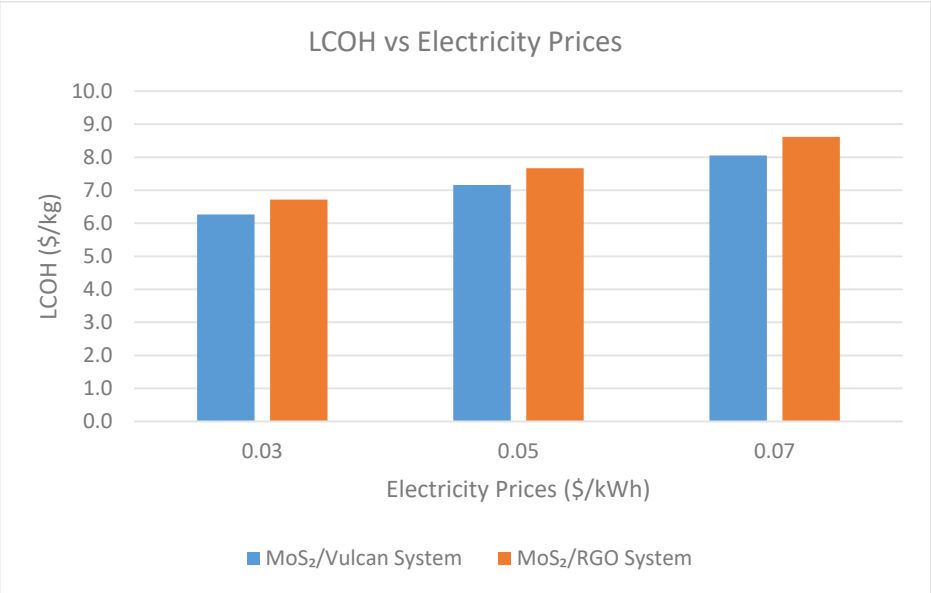

Fig. 1. LCOH values of the PEM electrolyzer with MoS_2/Vulcan and MoS_2/RGO electrodes under different electricity price scenarios

The MoS_2/Vulcan system, with an efficiency of 75%, produced 3,000 kg of hydrogen per year, while the MoS_2/RGO system, with an efficiency of 70%, produced 2,800 kg of hydrogen per year. The LCOH values for MoS_2/Vulcan were found to be $6.27/kg, $7.16/kg, and $8.05/kg for electricity prices of $0.03, $0.05, and $0.07 per kWh, respectively. For MoS_2/RGO, the LCOH values were $6.72/kg, $7.67/kg, and $8.62/kg for the same electricity prices.

The results indicate that the MoS_2/Vulcan system is more cost-effective than the MoS_2/RGO system across all electricity price scenarios. The higher efficiency of the MoS_2/Vulcan system contributes to its lower LCOH, making it a more economically viable option for hydrogen production.

Compared to traditional hydrogen production systems, which have LCOH values ranging from $5 to $7 per kg according to the Department of Energy (DOE) report [8], both alternative systems show competitive potential. However, the MoS_2/Vulcan system, in particular, approaches the lower end of this range, suggesting its feasibility as a viable alternative for cost-effective hydrogen production.

4. CONCLUSIONS

The techno-economic analysis demonstrates that MoS_2-based cathode catalysts can potentially lower hydrogen production costs in PEM electrolyzers. Among the alternatives examined, MoS_2/Vulcan exhibited a lower LCOH than MoS_2/RGO across all electricity price scenarios, making it the more economically viable. However, MoS_2/RGO remains a competitive candidate, and further optimization could enhance its cost-effectiveness. While both catalysts offer significant cost advantages over Pt/C electrodes, future studies should focus on improving long-term stability and assessing large-scale implementation to realize their commercial potential fully.

REFERENCES

[1] IEA. Global Hydrogen Review 2024. https://www.iea.org/reports/global-hydrogen-review-2024 (accessed March 1, 2025).
[2] Shiva Kumar S, Himabindu V. Hydrogen production by PEM water electrolysis – A review. Mater Sci Energy Technol 2019;2:442–54. https://doi.org/10.1016/J.MSET.2019.03.002.
[3] IRENA. Green Hydrogen Cost Reduction: Scaling up Electrolysers to Meet the 1.5^{0}C Climate Goal. International Renewable Energy Agency 2020:105.
[4] Corrales-Sánchez T, Ampurdanés J, Urakawa A. MoS2-based materials as alternative cathode catalyst for PEM electrolysis. Int J Hydrogen Energy 2014;39:20837–43. https://doi.org/10.1016/J.IJHYDENE.2014.08.078.
[5] Electrolyser cost | European Hydrogen Observatory n.d. https://observatory.clean-hydrogen.europa.eu/hydrogen-landscape/production-trade-and-cost/electrolyser-cost (accessed March 1, 2025).
[6] European Hydrogen Observatory. Levelised Cost of Hydrogen (LCOH) Calculator Manual 2024.
[7] Agora Industry. Levelised cost of hydrogen 2023. www.agora-industry.org (accessed February 11, 2025).
[8] Hubert M, Peterson D, Miller E, Vickers J, Mow DOE R, Klembara M, et al. DOE Hydrogen Program Record 24005: Clean Hydrogen Production Cost Scenarios with PEM Electrolyzer Technology. 2024.

IMPACT OF TRANSPORTATION CONSTRAINTS ON HYDROGEN SUPPLY CHAIN PERFORMANCE OF TÜRKIYE

[1*]*Busenur Türkali-Özbek*, [2]*Ahmet-Erdoğan*, [3]*Mehmet Güray Güler*
[1]Işık University, Faculty of Engineering and Natural Sciences, Department of Industrial Engineering, İstanbul, 34980, Turkey
[1]Yıldız Technical University, Faculty of Mechanical Engineering, Department of Industrial Engineering, Istanbul, 34353, Turkey
[2]Kayseri University, Faculty of Engineering, Architecture and Design, Department of Industrial Engineering, Kayseri, 38280, Turkey
[3]İstanbul Technical University, Faculty of Management, Department of Data Science and Analytics, İstanbul,34367, Turkey

*Corresponding author e-mail: busenur.turkali@isikun.edu.tr

ABSTRACT

This study proposes a hydrogen supply chain (HSC) design that consider Türkiye's renewable energy targets for the transportation sector. Two models were created within the scope of the study: Model 1, which offers an unrestricted structure, and Model 2, which limits the transfer of primary energy sources by restricting the distance to hydrogen transportation. The results show that Model 2 reduces the total cost by approximately 8.4% but increases carbon emissions by 2.3 times. In Model 2, local production is provided by importing natural gas in regions where local renewable energy resources are insufficient, which increases carbon emissions. In contrast, risk levels are reduced by 58.9% in Model 2, and a more secure and predictable supply chain is created. In addition, the establishment of small and medium-sized SMR facilities at a higher rate in Model 2 encourages the local production and consumption of hydrogen. These findings reveal that HSC can be optimized in terms of cost and risk, but that renewable energy capacity should be increased to improve environmental impacts.

Keywords: Hydrogen Supply Chain, Stochastic Programming, Transportation, Renewable Energy,

1. INTRODUCTION

Global energy demand is escalating swiftly due to population increase, urbanization, and technological advancements. This scenario results in heightened fossil fuel consumption and exacerbation of environmental issues. The transportation industry is a major contributor to global carbon emissions, accounting for roughly one-fourth of the total emissions. The usage of fossil fuels in passenger and freight transportation constitutes a significant share of these emissions [1]. Consequently, the decarbonization of the transportation sector has emerged as a critical element of the sustainable energy transition. Battery electric vehicles (BEVs) markedly diminish carbon emissions in comparison to fossil fuel vehicles. Nonetheless, range constraints and prolonged charge durations are primary problems hindering the extensive adoption of BEVs. Hydrogen fuel cell vehicles (FCEVs) seek to address these issues through their extended range and rapid refueling benefits.

For FCEVs to achieve widespread adoption, a dependable and sustainable HSC must be developed. The processes of production, transportation, and distribution are crucial in HSC design. In HSC design for the transportation sector, the primary objectives include the efficient conveyance of hydrogen from production sites to end users, while minimizing costs and reducing environmental effect. Research in this domain is expanding, and diverse hydrogen strategies are being executed across numerous nations. The European Union intends to substantially integrate hydrogen into the transportation sector by 2050, while nations like Japan and South Korea are swiftly advancing their hydrogen infrastructure [2, 3].

Türkiye also engages in numerous investigations about the HSC. Güler et al. [4] formulated a multi-period HSC model for Türkiye, which was subsequently adapted by Erdoğan et al. [5] into a single-period and multi-objective framework. Subsequently, these two studies were amalgamated to establish a multi-objective and multi-period HSC design. Subsequently, Özbek et al. [6] introduced a multi-period, multi-objective, and stochastic HSC planning framework for Türkiye to mitigate demand uncertainty by leveraging these findings. Nevertheless, these studies predominantly rely on the current energy infrastructure and inadequately address green hydrogen production and the incorporation of renewable energy sources.

While conventional hydrogen production methods include reforming natural gas or biomass gasification, the focus is increasingly shifting towards green hydrogen production to meet carbon emission reduction goals. Green hydrogen is generated through renewable energy sources like wind, solar, hydroelectric, and geothermal, and is recognized as a carbon-neutral energy carrier. Recent studies indicate that sourcing a significant amount of hydrogen for transportation from green sources is essential for achieving net zero emission targets [7, 8]. Furthermore, the use of surplus renewable energy for hydrogen production enhances energy supply security while simultaneously lowering hydrogen costs [9]. Consequently, Özbek et al. [10] performed a multi-objective and stochastic HSC analysis for 2050, informed by the

findings of Dinçer et al. [11] , which identified the hydrogen potential for Türkiye.

This study proposes an HSC design for the transportation industry, considering Türkiye's actual renewable energy infrastructure and its targeted renewable energy capacity. Türkiye's existing renewable energy capacity is insufficient; yet it possesses significant potential for solar and wind energy, as indicated by the Ministry of Energy's published reports outlining the country's renewable energy targets [12]. In this context, it will be evaluated how hydrogen production and distribution strategies can be optimized by integrating them with renewable energy sources and analysis will be made on how this will change the network in the event of some restrictions in the HSC network.

2. MATERIALS AND METHODS

Özbek et al. [6] have introduced a multi-period, multi-objective, and stochastic HSC network for the years 2025-2055, addressing the uncertainty in hydrogen consumption. In this HSC network, only Türkiye's existing resources were evaluated, disregarding the objectives for enhancing renewable energy. Özbek et al. [10] incorporated CO_2 emissions from primary energy sources (PES) into this model and produced a plan exclusively for 2050. This study integrates two previous studies and proposes a multi-period, multi-objective, and stochastic HSC network plan to address the timeframe of 2035-2065, aligned with Türkiye's actual renewable energy purposes. The demand for Türkiye throughout the three 10-year intervals from 2035 to 2065 is forecasted, with the assumption that FCEVs will constitute 4.5% of BEVs. These forecasts define scenarios based on low and moderate demand levels, where each scenario is represented as a sequence of demand states (e.g., low-medium-low), resulting in a total of eight scenarios across three periods, which then serve as inputs for the scenario-based stochastic model. It is assumed that both renewable and non-renewable energy sources will be utilized for hydrogen production. In the model, renewable energy sources are considered solely as indigenous resources of Türkiye, whilst non-renewable energy sources like natural gas and coal are presumed to be imported. The assessment of these energy sources relies on Türkiye's current power plants and future forecasts [12].

In an effort to quantify demand uncertainty, a scenario-based stochastic programming methodology with two phases is implemented. There are two types of variables in stochastic programming. The values of discrete control (i.e., here-and-now) variables will remain unchanged, regardless of any alterations in the scenario. They illustrate the decisions that must be made at the outset of the issue. An example of this is the decision to establish a plant within a grid. Another option is the quantity of hydrogen that will be transported or produced at this facility. Their values are contingent upon the circumstances. These types of decisions are demonstrated by continuous dispatch variables, which are also known as "wait-and-see" variables. The timeframe from 2035 to 2065 is segmented into three decadal intervals, resulting in the formulation of eight scenarios based on varying demand levels during these times. Furthermore, the Epsilon Constraint Method is utilized to determine the best model that minimizes both cost and CO_2 emissions [13].

Two new constraints have been added to the model to perform sensitivity analysis. The first is the constraint in Eq. (1) that prevents the flow of hydrogen between the grids if there is more than 300 km between the two grids. Since the model aims to minimize cost and CO_2, if the establishment of the hydrogen production plant is not profitable in these respects, it gives results that hydrogen is taken from another grid, even from a considerable distance. The aim of this constraint is to encourage the model to establish production plant by using its own renewable energy resources. The second is the constraint in Eq. (2) that prevents the flow of PES between the grids. The current model permits the transit of power between the grids for use in electrolysis producing facilities. This constraint has been implemented to assess the impact of grids utilizing their own resources on the model. It is important to highlight that if the grid does not have enough renewable PES to produce hydrogen, it will either open coal or natural gas-fired facilities or buy hydrogen from other grids.

$$if\ L^{R}_{lgg'} \geq 300\ , then\ Q_{lgg'ts} = 0 \quad \forall l, g, g', t, s: g \neq g' \tag{1}$$

$$QE_{egg'ts} = 0 \quad \forall\ e, g, g', t, s: g \neq g' \tag{2}$$

3. RESULTS AND DISCUSSION

The model was executed without the aforementioned constraints (Model 1) and with the constraints incorporated (Model 2). The objective function values of the most effective outcomes are displayed in Table 1.

Table 1. Results of Model 1 and Model 2

	Total Cost ($/day)	Total CO_2 (kg/day)	Total Risk (unit)
Model 1	123,133,797	448,439,969	323,722
Model 2	112,728,602	1,025,561,041	133,122

The main difference between Model 1 and Model 2 is that Model 2 imposes a distance restriction on hydrogen transportation and prevents the transfer of PES between different networks. When the results are examined, it is observed that Model 2 reduces the total cost by approximately 8.4% but increases carbon emissions by 2.3 times. This is due to the increase in fossil fuel use in grids where renewable energy sources are insufficient in hydrogen production. Due to the restrictions, the transportation of hydrogen from long distances has been prevented and local production has become mandatory. Although this reduces transportation costs, it has negatively affected the environmental impact by increasing the use of carbon-intensive energy sources such as natural gas in some grids. On the other hand, Model 2 has reduced the total risk by 58.9%, making the HSC more secure and predictable. This is due to the decrease in the risk arising from transportation.

In order to support these results, the numbers of SMR facilities opened under Model 1 and Model 2 are given in Table 2. The percentages in the table show the ratio of SMR facilities opened in a certain size in the relevant period to the total number of facilities opened in that size in that period. For example, in first period, there are 10 large SMR facilities and the total number of facilities opened in that period is 32, so the percentage for large SMR facilities is calculated as 31%. It is important to note that the number of facilities is not changed according to scenarios. Additionally, Table 3 shows the inter-grid hydrogen flows in Model 1 and Model 2 for all scenarios. This table presents a comparative analysis of the effects of constraints on these flows.

Table 2. Numbers and Distribution of SMR Facilities Opened under Model 1 and Model 2

Facility Type	t=1			t=2			t=3		
	Small	Medium	Large	Small	Medium	Large	Small	Medium	Large
Model 1	0	0	10 (31%)	0	0	10 (10%)	0	0	10 (6%)
Model 2	0	1 (100%)	14 (47%)	2 (1%)	3 (38%)	25 (27%)	2 (1%)	3 (33%)	31 (23%)

Table 3. Hydrogen flows (10^6 million liters) between grids under Model 1 and Model 2

	Scenario /Time	1	2	3	4	5	6	7	8
Model 1	1	2	2	2	2	3.3	3.3	3.3	3.3
	2	12.8	12.8	12.8	12.8	10.4	10.4	13.8	13.8
	3	7.7	12.4	12.4	17.5	9.8	15.6	15.6	17.9
	Scenario /Time	1	2	3	4	5	6	7	8
Model 2	1	2.3	2.3	2.3	2.3	3.5	3.5	3.5	3.5
	2	7	7	7	7	5.7	5.7	8.9	8.9
	3	6.5	10.2	10.2	10.5	8.	11.7	11.7	12

As seen in Table 2, since Model 1 has an unrestricted structure, SMR facilities are established on a large scale only in grids with high demand, and the needs of other regions are met by transporting hydrogen from these facilities. This situation shows that a centralized structure prevails, and long-distance transportation increases as demand is met from a single point. On the other hand, in Model 2, due to distance and energy constraints, local production of hydrogen is encouraged, which leads to the establishment of small and medium-sized facilities. In addition, it is noteworthy that the rate of SMR facilities of all sizes is generally higher in Model 2 compared to Model 1. This increase shows that Model 2 enables hydrogen to be produced and consumed regionally by providing more local production. However, in cases where local renewable energy resources are insufficient, natural gas had to be imported to operate these facilities. As seen in Table 1, this situation causes a significant increase in carbon emissions in Model 2. When looking at Table 3, it is seen that thanks to the unrestricted structure of Model 1, hydrogen can be transported to long distances and the total flow rate is higher, but this increases transportation risk. In Model 2, hydrogen flow is limited, local production is encouraged and thus risk levels are reduced. However, the increase in fossil fuel use in cases where renewable energy sources are insufficient has negatively affected environmental impacts. In general, while Model 2 provides some advantages in terms of economy and operation, it is necessary to increase renewable energy capacity and strengthen its integration in order to reduce carbon emissions.

4. CONCLUSIONS

This study evaluated the economic, environmental and operational impacts of constraints in the design of the HSC for the transportation sector in Türkiye. Model 1, with its unrestricted structure, allowed hydrogen to be transported over long distances and increased the total flow rate. However, this situation led to higher costs and risks. On the other hand, Model 2 reduced risks and costs by encouraging local production. However, the increase in fossil fuel use in regions where local renewable energy resources are insufficient has significantly increased carbon emissions. The findings of the study reveal that cost and risk optimization can be achieved in the HSC, but renewable energy integration is a critical requirement to reduce environmental impacts. In the future, the development of renewable energy infrastructure and the promotion of low-carbon production methods will be key elements for the establishment of a sustainable HSC.

NOMENCLATURE

g	grid squares
g'	grid squares such that $g' \neq g$
l	type of transportation modes
s	demand scenarios
t	time periods of the planning horizon
e	primary energy sources
$L^R_{gg'}$	regional delivery distance between grids g and g' (km)
$Q_{lgg'ts}$	flow rate by transportation mode l between grids g and g' during time period t under scenario s (kg/d)
$QE_{egg'ts}$	flow rate of primary energy source e between grids g and g' during time period t under scenario s (kg/d)

REFERENCES

[1] IEA, "CO2 Emissions in 2023," IEA, Paris, 2024.

[2] E. Commission, "A hydrogen strategy for a climate-neutral Europe," EUROPEAN COMMISSION, Brussels, 2020.

[3] T. a. I. Japan Ministry of Economy, "Basic Hydrogen Strategy," 2023.

[4] M. G. Güler, E. Geçici and A. Erdoğan, "Design of a future hydrogen supply chain: A multi period model for Turkey," *International Journal of Hydrogen Energy,* vol. 46, no. 30, pp. 6789-6801, 2021.

[5] A. Erdoğan, E. Geçici and M. G. Güler, "Design of a future hydrogen supply chain: A multi-objective model for Turkey," *International Journal of Hydrogen Energy,* vol. 48, no. 31, pp. 11775-11789, 2023.

[6] B. Türkali Özbek and M. G. Güler, "A multi period and multi objective stochastic hydrogen supply chain for Turkey," *International Journal of Hydrogen Energy,* 2024.

[7] L. Sens, U. Neuling, K. Wilbrand and M. Kaltschmitt, "Conditioned hydrogen for a green hydrogen supply for heavy duty-vehicles in 2030 and 2050 – A techno-economic well-to-tank assessment of various supply chains," *International Journal of Hydrogen Energy,* vol. 52, pp. 1185-1207, 2024.

[8] S. Kim, J. Park, W. Chung, D. Adams and J. H. Lee, "Techno-economic analysis for design and management of international green hydrogen supply chain under uncertainty: An integrated temporal planning approach," *Energy Conversion and Management,* vol. 301, p. 118010, 2024.

[9] C. Zhang, P. Song, J. Hou, L. Xiao, X. Wang, F. Yang and X. Wang, "Technical and economic analysis of hydrogen production, storage and transportation by offshore wind power in different scenarios: A Guangdong case study," *International Journal of Hydrogen Energy,* vol. 94, pp. 829-837, 2024.

[10] B. Türkali-Özbek, A. Erdoğan and M. G. Güler, "Leveraging Renewable Energy for Turkey's Future Hydrogen Supply Chain: A Stochastic," in *8th International Hydrogen Technologies Conference, IHTEC2024*, Diyarbakır, 2024.

[11] İ. Dinçer, N. Javani and G. K. Karayel, "Türkiye için Hidrojen Çiftliği Konsepti Raporu," İstanbul, 2021.

[12] "Türkiye Ulusal Enerji Planı," T.C. Enerji ve Tabii Kaynaklar Bakanlığı, 2022.

[13] G. Mavrotas, "Effective implementation of the ε-constraint method in Multi-Objective Mathematical Programming problems," *Applied Mathematics and Computation,* vol. 213, no. 2, pp. 455-465, July 2009.

MATHEMATICAL MODELING AND GROUND TESTS OF A FUEL CELL HYBRID UNMANNED AERIAL VEHICLE IN CRUISE PHASE

[1*]*Mustafa Azer*, [2,3]*Mustafa Umut Karaoglan*, [2, 3]*C. Ozgur Colpan*, [1]*T. Hikmet Karakoc*
[1] Eskisehir Technical University, Faculty of Aeronautics and Astronautics, Airframe and Powerplant Maintenance Department, Eskisehir, 26005, Turkiye
[2] Dokuz Eylul University, Faculty of Engineering, Mechanical Engineering Department, Izmir, 35160, Turkiye
[3] Dokuz Eylul University, Energy Application and Research Center, Izmir, 35160, Turkiye

*Corresponding author e-mail: mazer@eskisehir.edu.tr

ABSTRACT
Recent advancements in battery and electric motor technologies have facilitated the widespread adoption of Unmanned Aerial Vehicles (UAVs). Although electric UAVs offer advantages such as low emissions and ease of use, the limited energy density of batteries poses a significant disadvantage in terms of short flight durations. This study proposes a hybrid propulsion system that integrates hydrogen fuel cells with batteries to address this limitation. Hydrogen-based systems provide longer flight endurance than battery-only systems, achieving this in an environmentally friendly and low-emission manner. Within this scope, a relatively simple and accessible hybrid propulsion system was designed to enhance flight endurance in UAVs in a sustainable manner. Static power tests and tests based on cruise flight profiles were conducted to validate the system's performance. The results demonstrated the potential of the proposed system to significantly and sustainably extend the flight endurance of UAVs.

Keywords: Unmanned Aerial Vehicle (UAV), Hybrid Propulsion System, PEM Fuel Cell, Extended Range

1. INTRODUCTION

Unmanned Aerial Vehicles (UAVs) have become indispensable in both military and civilian applications due to their versatility and efficiency. Electric UAVs, powered by lithium-based batteries, are widely preferred in civilian applications because of their low emissions and operational simplicity. However, the low energy density of batteries poses a significant challenge for applications requiring extended flight durations.

Polymer Electrolyte Membrane (PEM) fuel cells offer a promising solution by providing high power density and generating electricity without emissions. PEM fuel cells generate electricity through an electrochemical reaction between hydrogen and oxygen, producing water and heat as byproducts. With these properties, hydrogen fuel cells emerge as a sustainable energy carrier and a practical way to extend UAV flight endurance [1].

In the open literature, there are existing studies on fuel cell-powered UAVs. Most of these studies have preferred using hybrid systems, with batteries as the secondary power source [2,3]. Typically, passive power distribution systems have been employed, and hydrogen has been stored in tanks (though systems that produce hydrogen on demand also exist) [4,5]. A notable aspect of the reviewed studies is that the designed system architectures are complex and costly [6,7].

This study focuses on developing a simple and accessible hybrid propulsion system utilizing PEM fuel cells as the primary power source and Li-Po (Lithium Polymer) batteries as the secondary power source. A hybrid system architecture was designed within this scope, and a power distribution board was developed. The mathematical model of the system was created in the MATLAB/Simulink platform, and simulation tests were conducted on the model. Subsequently, a static cruise flight power test was performed on the hybrid system, and the results were compared with the simulation outcomes. This study aims to create a system capable of extending the flight durations of electric UAVs while maintaining environmental sustainability.

2. MODELING AND EXPERIMENTAL METHODOLOGY

2.1. System Architecture

The proposed hybrid propulsion system includes PEM fuel cells and Li-Po batteries as power sources. The system architecture is designed to utilize the fuel cell as the primary power source during cruise flight. At the same time, the battery provides secondary support during high-power-demand flight phases, such as takeoff and climb. The goal of this architecture is to utilize the high energy density of the hydrogen to achieve long-range flight during the cruise phase, while the high-power density of the Li-Po battery supports power-intensive phases. The system architecture is illustrated in Figure 1.

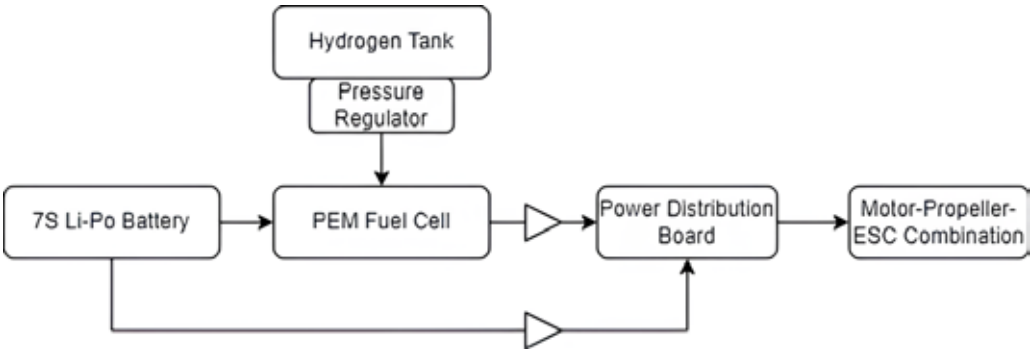

Fig. 1. System Architecture

The fuel cell used in the system is specifically designed for aviation applications and is suitable for hybrid operation. It features an integrated circuit board that enables hybrid operation with a battery. This configuration allows the battery to supplement power demands instantaneously when high power is required within the operational limits of the fuel cell. However, since the circuit board's capacity does not meet the maximum power demand of the motor selected for the system, a power distribution board has been added to the architecture. This board enables the fuel cell to be bypassed, allowing the battery to supply all the required power. The design of the board prioritizes simplicity and accessibility. It operates manually and is controlled via a UAV remote controller switch.

A composite tank with an energy storage capacity of 705 Wh has been selected for hydrogen storage. This tank stores hydrogen as compressed gas and features an ultra-lightweight internal pressure regulator that effectively reduces the hydrogen pressure to 0.5-0.6 bar, supplying the fuel cell. The tank produced by H3 Dynamics has a capacity of 2 liters and operates at pressures of up to 300 bar. The Aerostak A250 PEM fuel cell, manufactured by H3 Dynamics, with a nominal power of 250 W has been selected. A 7-cell Li-Po battery with a capacity of 2200 mAh and a discharge rate of 45C has been used.

2.2. Hybrid System Modeling

To evaluate the performance of the system and simulate its behavior under different scenarios, a system model was developed in the MATLAB/Simulink environment [8]. During the model development process, the components within the architecture were individually modeled and tested to ensure realistic results. The models were refined until the data obtained from the tests matched the results of real-world tests. Once validated, the individual models were integrated to create the overall power system model.

A load model was created based on static motor test data obtained from the motor-propeller combination selected for the architecture to enable realistic simulation tests on the power system. This load model was incorporated into the system model. Simulation tests were then conducted using the complete model, and the flight time achievable at different throttle values was observed. With the simulations, it was decided at which power value the system would operate, and the operating time obtained was compared with the operating time that could be achieved with a only Li-Po battery with the same weight.

2.3. Experimental Studies

To observe the performance of the fuel cell and analyze its behavior under load, both static and dynamic load tests were conducted [9]. A conditioning process allowed the device to reach its optimal performance, ensuring that the power values specified in the manufacturer's documentation were achieved.

Subsequently, the hybrid system was assembled, and tests were conducted under motor load to observe its response to instantaneous load variations. After determining that the observations and results were sufficient, preparations were made for the final test: the cruise flight test, which aimed to evaluate power consumption during cruise flight. The cruise flight test was conducted, and the maximum range achievable with a single hydrogen tank was observed. The cruise flight power test setup is provided in Fig. 2.

Fig. 2. Cruise flight power test setup

3. RESULTS AND DISCUSSION

3.1. Extended Flight Endurance

The hybrid propulsion system has significantly increased flight duration by up to 30% compared to conventional battery-only systems, which is a remarkable achievement. This increase in flight time was achieved without compromising the operational capabilities of the UAV. The PEM fuel cell, used as the primary power source during cruise flight, provides a sustainable solution for long-range operations. At the same time, the Li-Po battery efficiently supports high-power phases, such as takeoff and climb. As a result, the UAV could sustain longer flight times, which is critical for many applications, especially remote monitoring, surveillance, and search-and-rescue missions. The integration of both power sources, optimized for different flight phases, has enabled the system to operate efficiently and effectively, ensuring that the UAV can meet the demands of various mission profiles. This improvement enhances the practical usability of UAVs and presents a strong argument for the broader adoption of hybrid power systems in the aerospace industry, particularly for missions that require extended flight durations. Results of the cruise flight power test are provided in Fig. 3.

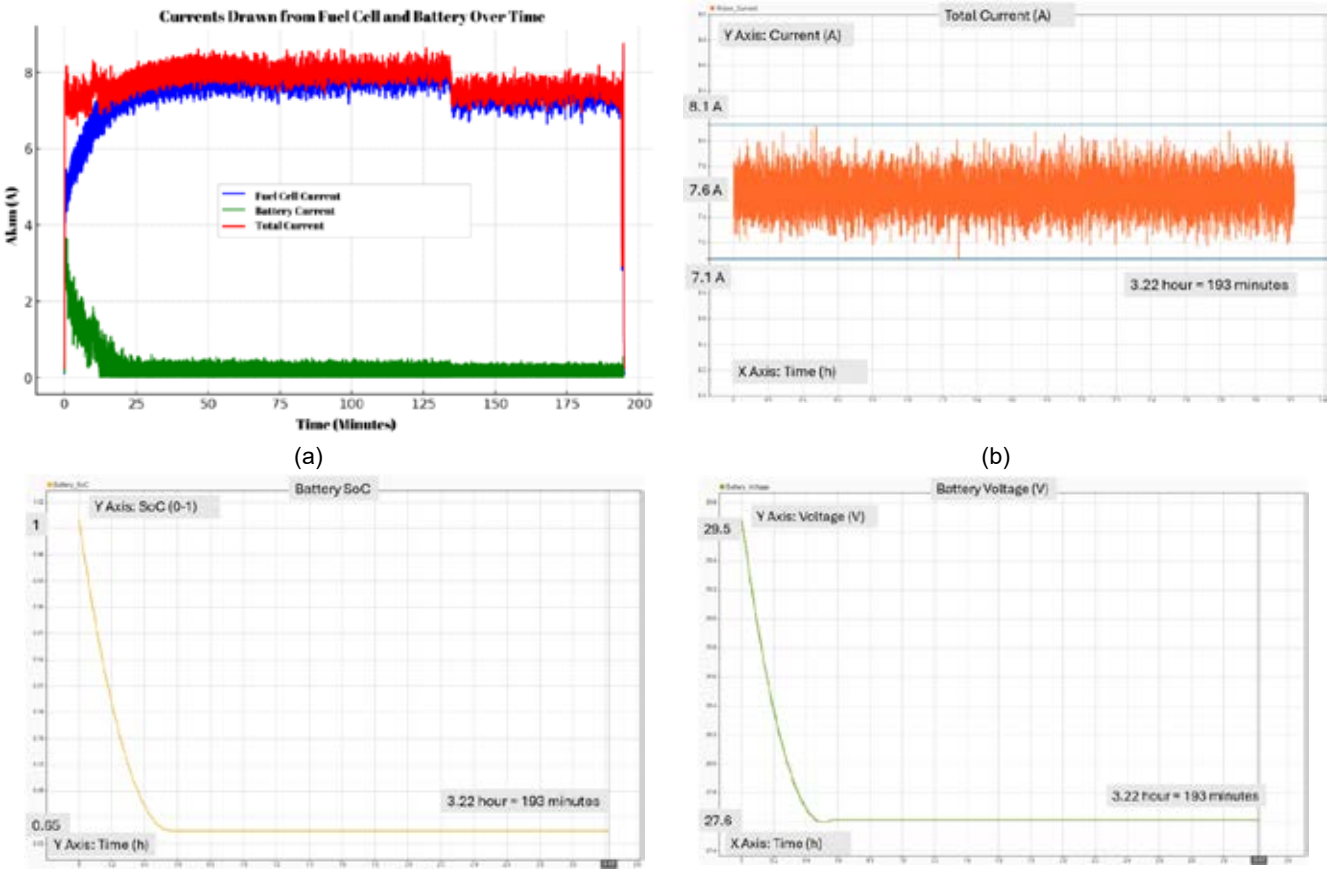

Fig. 3. Cruise flight power test results (a) and simulation results depending on operating time, (b) total current, (c) battery SoC, (d) battery voltage.

3.3. MATLAB/Simulink Simulations

The results obtained from simulations conducted on the hybrid power system model created in the Simulink platform were compared with real-world test results, and it was found that the model provided highly accurate results. In the simulation test, the system was predicted to operate for 193 minutes, while the real-world test showed that the system ran for 195 minutes. Thus, the accuracy rate of the model was determined as 98.9%.The high accuracy of the developed model demonstrates its potential as a solid foundation for future research and development. This accuracy enables further work to investigate how system boundaries may change after modifications are made to the system and its components. By conducting further simulations and adjustments to the model, it will be possible to observe the impact of these changes on the overall system performance. As a result, tests can be performed on the model with high accuracy without the need for real tests, and thus more efficient work can be done in terms of time and computational cost.

4. CONCLUSIONS

In this study, a relatively simple and accessible hybrid power system architecture consisting of a PEM fuel cell and a Li-Po battery has been successfully designed, developed, and implemented. To thoroughly evaluate the system's performance and ensure that the study is grounded in solid mathematical principles, a system model was created using MATLAB/Simulink. After the accuracy of the model was ensured by tests, simulations were performed to see how long the hybrid power system can operate with one tank of hydrogen. As a result of the simulations, it was decided to operate the system at an average value of 220 W. The system was able to operate for 193 minutes at 220 W power value. For comparison, simulations were performed with a only Li-Po battery equal to the weight of the hybrid system and it was observed that the system could operate for 150 minutes.

Following the simulation phase, real-world tests of the hybrid power system were conducted to validate the results obtained through the simulations. During these tests, the conditioning of the fuel cell was completed, and the system was subjected to a final cruise flight power test. In this crucial step, a possible flight profile for a fuel cell-powered UAV was developed, and the behavior of the UAV was carefully simulated during flight. A significant portion of this profile was dedicated to cruise flight, which allowed for extracting the corresponding power profile that was subsequently applied to the hybrid propulsion system.

The test results indicated that the system performed as expected, showcasing the reliability and accuracy of the simulated results. Additionally, the system demonstrated an extended flight duration compared to conventional battery-only systems while maintaining its operational capabilities. This increase in flight time contributes to environmental sustainability, as it helps to reduce the overall energy consumption and emissions of the UAV. The extended flight duration, in particular, addresses one of the primary challenges modern electric aircraft faces: the relatively limited flight time compared to combustion engine-powered aircraft. This study, therefore, presents a significant advancement in hybrid propulsion systems and lays the foundation for future research and improvements in the field, particularly in the context of long-endurance, environmentally friendly UAVs.

REFERENCES

[1] McConnell VP. 2007. Military UAVs claiming the skies with fuel cell power. Fuel Cells Bulletin 2007(12), 12-15
[2] Donateo T., Ficarella A., Spedicato L., Arista A., Ferraro M. 2017. A new approach to calculating endurance in electric flight and comparing fuel cells and batteries. Applied energy, 187, 807-819.
[3] Yang C., Moon S., Kim Y. 2016. A fuel cell/battery hybrid power system for an unmanned aerial vehicle. Journal of Mechanical Science and Technology, 30, 2379-2385.
[4] Herwerth C., Chiang C., Ko A., Matsuyama S., Choi S. B., Mirmirani M., Jin P. 2007. Development of a small long endurance hybrid PEM fuel cell powered UAV (No. 2007-01-3930). SAE Technical Paper.
[5] Kim K., Kim T., Lee K., Kwon S. 2011. Fuel cell system with sodium borohydride as hydrogen source for unmanned aerial vehicles. Journal of power sources, 196(21), 9069-9075.
[6] Verstraete D., Gong A., Lu D. D. C., Palmer J. L. 2015. Experimental investigation of the role of the battery in the AeroStack hybrid, fuel-cell-based propulsion system for small unmanned aircraft systems. International Journal of Hydrogen Energy, 40(3), 1598-1606.
[7] Jenal N., Kuntjoro W., Ward T. A., Aziz M. R., David N. V. 2012. A study on propeller performance of a fuel cell powered propulsion system. In 2012 IEEE International Conference on Control System, Computing and Engineering (pp. 557-561). IEEE.
[8] Khan M. J., Iqbal M. T. 2005. Dynamic modeling and simulation of a small wind–fuel cell hybrid energy system. Renewable energy, 30(3), 421-439.,
[9] Ozbek E., Yalin G., Ekici S., Karakoc T. H. 2020. Evaluation of design methodology, limitations, and iterations of a hydrogen fuelled hybrid fuel cell mini UAV. Energy, 213, 118757.

DEVELOPMENT OF ALKALINE ELECTROLYSIS CATALYST USING WASTE ZINC-CARBON BATTERIES

[1]*Hatice HANÇER*, [2*]*Murat FARSAK*
[1]Kahramnmaraş İstiklal University, Turkoglu Vocational School, Electricity and Energy, Alternative Energy Sources Technology, Kahramanmaraş, Turkey
[2]Osmaniye Korkut Ata University, Institute of Natural and Applied Science, Department of Battery Systems and Hydrogen Technologies, Osmaniye, Turkey

*Corresponding author e-mail: muratfarsak@osmaniye.edu.tr

ABSTRACT
Hydrogen is a synthetic fuel. There are many methods of producing hydrogen. The most important of these is electrolysis systems that provide green hydrogen production. It is important to produce accessible electrocatalysts in electrolysis systems and to ensure that the use of hydrogen energy becomes widespread. The biggest factor in the necessity of switching to renewable energy in energy production is the damage caused by fossil fuels to the environment. The reusability of materials that are harmful to the environment due to their production and waste, the reduction of damage to the environment and their contribution to energy efficiency also meet the criteria in the definition of renewable energy. There are many products that can be recycled and used as waste. Recycling of waste zinc-carbon batteries prevents the damage to the environment caused by the heavy chemicals they contain, while also providing economic contribution. For this reason, the catalytic effects of graphite rods obtained from waste zinc-carbon batteries on hydrogen evolution were investigated. Electrochemical Impedance Spectroscopy, Linear Scanning Voltammetry and Cyclic Voltammetry techniques were used to evaluate the electrodes obtained from waste zinc-carbon batteries. The hydrogen efficiency of graphite rods obtained from waste batteries of different trademarks was examined.

Keywords: *Energy, Hydrogen, Catalyst, Waste Battery, Recycling*

1. INTRODUCTION

Energy is one of the indispensable components of life today. The use of fossil fuels in energy production has some negative effects such as greenhouse gas effect, smog effect, acid rain and external dependency[1] Due to these negative effects of fossil fuels, it is important to turn to sustainable and environmentally harmless renewable energy sources in energy production[2]. The use of renewable energy sources means a cleaner environment. However, the use of storage systems has become necessary due to reasons such as the energy obtained from renewable energy sources changing according to climate conditions and the fact that the systems in the facility are not operated due to the full power grid when electricity supply is low and electricity can be produced in energy facilities[3, 4]. Hydrogen systems are leading in energy storage [5]. There are many methods of hydrogen production. The most environmentally friendly of these is electrolysis systems, which enable the production of green hydrogen[6]. Electrocatalyst production is important for widespread use of electrolysis systems.
Waste materials that have completed their lifespan after consumption are recycled to reduce the damage to nature and to contribute to the economy by saving energy. One of the materials that is important to recycle is waste batteries. In addition to the damage that batteries cause to the environment due to their chemical structure, the recovery of the precious metals used contributes to the economy[7]. Batteries are classified in many ways. They are divided into two groups according to their chemical properties: primary (non-rechargeable) and secondary (rechargeable). Secondary batteries (rechargeable) can be used by recharging. However, primary batteries are waste because they cannot be used again after their lifespan is over[8]. Primary batteries are harmful to the environment because their chemical components contain heavy metals. Preventing the environmental damage of waste primary batteries can be possible through recycling processes. In many publications in the literature, recycling is done by applying pyrometallurgical and hydrometallurgical techniques[7, 9-11]. In recycling using pyrometallurgical and hydrometallurgical techniques, mostly metals such as zinc and manganese are obtained. The structure of zinc-carbon batteries includes a zinc plate as the anode, a manganese dioxide-coated graphite rod as the cathode, and ammonium chloride or zinc chloride as the electrolyte. In our study; the waste zinc-carbon battery will be physically broken down, the graphite rod inside will be removed and tested as cathode material in alkaline electrolyzer systems. Electrochemical Impedance Spectroscopy (EIS), Linear Scanning Voltammetry (LSV), Cyclic Voltammetry (CV) Techniques were used to examine the catalytic activity.

2. MATERIALS AND METHODS

Graphite rods were removed from zinc-carbon batteries obtained from recycled battery boxes. Many different rademarks of zinc carbon batteries were examined and this study presents data for the three best commercial trademarks.Potentiostat-galvanostat analyzer was used for electrochemical characterizations. All experiments and

measurements were carried out in a 1.00 M KOH solution at room temperature using a three-electrode method. The platinum, which has a surface area of 2 cm^2, and Ag/AgCl (3.0M KCl) electrodes were used as counter and reference electrodes, respectively. The EIS measurements made using the method were taken by applying 10 mV amplitude in the frequency range of 10^5 -10^{-2} Hz. The LSV graphs were obtained from -1.0 V to -1.8 V at 1 mVs^{-1} scan rate. The CV has been carried out at 100 mVs^{-1} scan rate from -1 V to +0.8 V. All experiments were done in a 1.00 M KOH solution at room temperature.

3. RESULTS AND DISCUSSION

EIS measurements were taken by applying a potential of -1.5 V in the frequency range of 10^5 -10^{-2} Hz and are shown in Figure 1. As seen in the Nyquist curves in Figure 1, the resistance of the graphite rod obtained from the C trademark battery is higher than the others. The resistance of the graphite rod obtained from A trademark, B trademark, C trademark was 13.2, 14.7 and 15.5 $\Omega.cm^{-2}$, respectively.

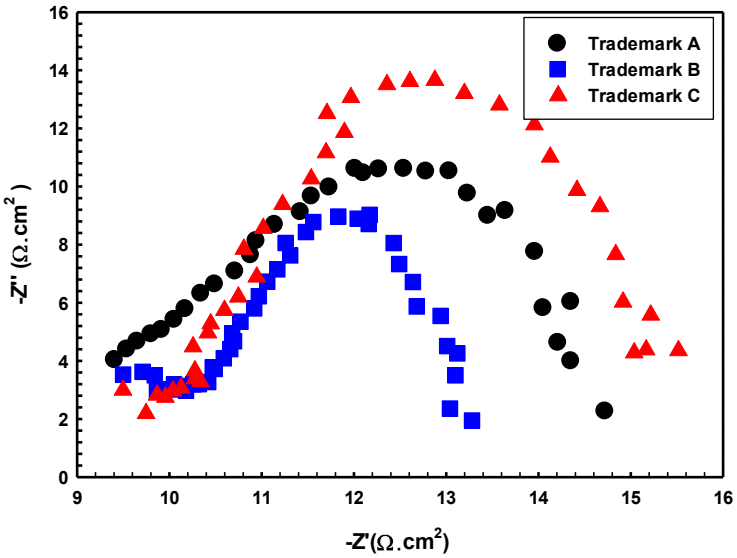

Fig. 1. Nyquist plots Trademark A, Trademark B and Trademark C at in 1 M KOH solution at 298 K

The LSV curves obtained from waste zinc carbon batteries were performed in 1.0 M KOH solution at room temperature of 25°C and are shown in Figure 2. According to the LSV results, the graphite rod obtained from Trademark A exhibited lower onset potential and higher current density for hydrogen evolution than the others.

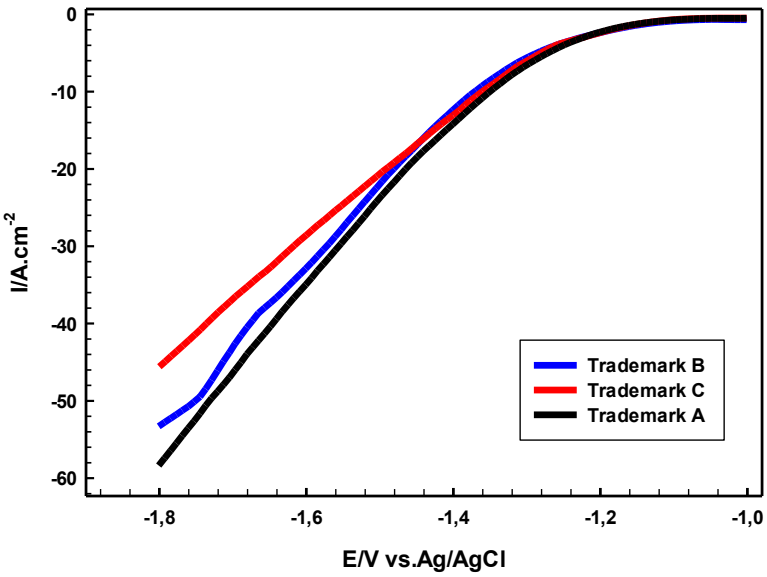

Fig. 2..LSV curves at for Trademark A, Trademark B and Trademark C in 1 M KOH solution at 298 K

The CV curves of graphite rods obtained from waste zinc-carbon batteries were obtained in 1.0 M KOH solution at room

temperature of 25° C and are shown in Figure 3. When the CV results of Trademark A and Trademark B were examined, it was seen that they had peaks at the same potential, which led to the idea that the structure of Trademark A - Trademark B may be the same but the amount of substance in Trademark A is higher. In Figure 3, it is seen that the peaks of Trademark C have peaks at different potentials than the other trademarks. Our characterization studies are continuing.

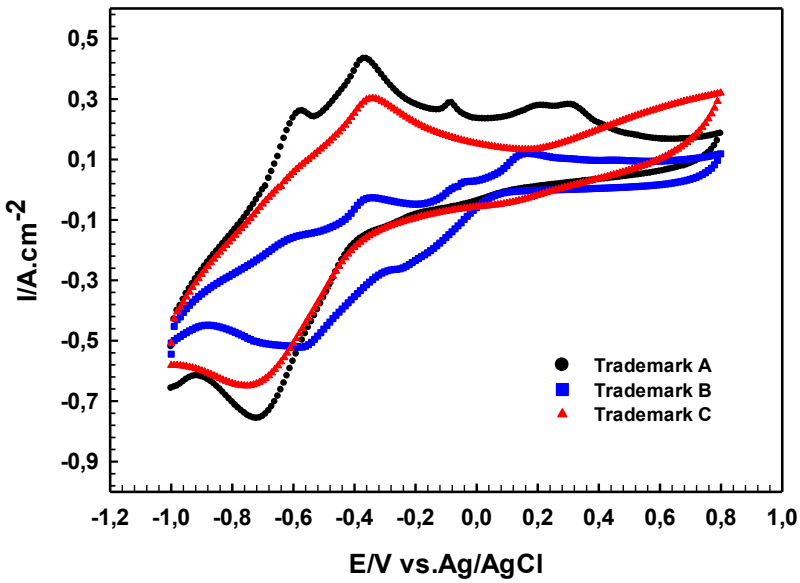

Fig. 3. CV curves at for Trademark A, Trademark B and Trademark C in 1 M KOH solution at 298 K

4. CONCLUSIONS

The catalytic activity of graphite rods obtained from waste zinc-carbon batteries was investigated for hydrogen evolution process.

- EIS shows that graphite rod obtained from Trademark B has less resistance to hydrogen evolution reaction.
- From LSV findings, it was determined that graphite rod obtained from Trademark A has the lowest initial potential and the highest current density.
- According to CV results, led to the idea that the composition of Trademark A and Trademark B may be the same, but the amount of ingredients in Trademark A is greater. Graphite rod obtained from Trademark A has the largest current increase and the highest peak.

We think that graphite rod obtained from waste zinc-carbon batteries can be used as cathode material and contribute to Hydrogen Evolution Reaction. We suggest that among the graphite rods obtained from waste batteries, graphite rod belonging to Trademark A can be used as an effective electrocatalyst for hydrogen production.

REFERENCES

1. Zhao, S. and Y. Pan, *Coordination structures design of single-atom catalysts for enhanced hydrogen evolution reaction.* Sustainable Chemistry for Energy Materials, 2025: p. 100003.
2. Cao, D., et al., *Research progress of Ce-based electrocatalysts in hydrogen evolution reaction.* Journal of Rare Earths, 2025.
3. Çakmak, R. and İ. Altaş, *Türkiye'deki Müşterilerin Akıllı Şebekelerde Yük Kaydırmaya Dayalı Talep Tarafı Yönetimine Tepkileri.* Karadeniz Fen Bilimleri Dergisi, 2020. **10**(2): p. 395-416.
4. Huhtinen, S., E. Tsupari, and M. Rämä, *Electrical Energy Storage Combined with Renewable Hydrogen Production.* e-Prime - Advances in Electrical Engineering, Electronics and Energy, 2025: p. 100922.
5. Gulraiz, A., et al., *Energy Advancements and Integration Strategies in Hydrogen and Battery Storage for Renewable Energy Systems.* iScience, 2025: p. 111945.
6. Razmi, A.R., A.R. Hanifi, and M. Shahbakhti, *A comparative techno-economic assessment between solar-based hydrogen production by methane pyrolysis and water electrolysis methods.* Renewable Energy, 2025. **242**: p. 122504.
7. Yeşiltepe, S. and M.K. Şeşen, Sinop Üniversitesi Fen Bilimleri Dergisi, 2016. **1**(1): p. 33-38.
8. Eröztürk, B., *Cep telefonu pillerinin asidik ortamda çözündürülerek metal miktarlarının tespiti ve hidroksitleri şeklinde çöktürülmesi.* 2005.
9. Yeşiltepe, S., *Atık Alkali Pillerden Pirometalurjik Yöntem İle Ferromangan Ve Çinko Üretimi*. 2015, Fen Bilimleri Enstitüsü.
10. Andak, B., *Atık çinko-karbon ve alkalin pil karışımının hidrometalurjik geri kazanım prosesinin oluşturulması.*
11. Sayılgan, E., *Kullanılmış pillerden çinko ve mangan metallerinin geri kazanımı-ekonomik analiz ve matematik modelleme*. 2009, SDÜ Fen Bilimleri Enstitüsü.

NON-PREMIXED HYDROGEN COMBUSTION FOR AN INDUSTRIAL CERAMIC FURNACE: A NUMERICAL ANALYSIS

[1*]*Semih Yilmaz*, [2]*Tolga Bayramoğlu*, [3]*Kubilay Bayramoğlu*, [4]*Ahmet Özarslan,* [5]*Bünyamin Kılıç,* [5]*Atamer Akbay*
[1] Dokuz Eylul University, Maritime Faculty, Department of Marine Engineering, İzmir, 35390, Türkiye
[2]Zonguldak Bulent Ecevit University, Alapli Vocational High School, Department of Motor Vehicles and Transportation Technologies, Zonguldak, 67850, Türkiye
[3] Zonguldak Bulent Ecevit University, Engineering Faculty, Department of Mechanical Engineering, Zonguldak, 67100, Türkiye
[4] Zonguldak Bulent Ecevit University, Engineering Faculty, Department of Mining Engineering, Zonguldak, 67100, Türkiye
[5]Canakcılar Ceramic Industry and Trade Company, Department of Research and Development, Zonguldak, 67670, Türkiye

*Corresponding author e-mail: semih.yilmaz@deu.edu.tr

ABSTRACT
Clean fuels must be used in high-temperature manufacturing processes to make the transition to sustainable energy systems. The possibility of using non-premixed hydrogen combustion as a substitute for traditional hydrocarbon fuels is examined in this study through numerical investigation in an industrial ceramic furnace. A two-dimensional numerical domain of the furnace was created using a discrete ordinates approach for radiative heat transfer, finite-rate chemistry for combustion, and turbulent flow dynamics through the k-ε model using computational fluid dynamics simulations. The analysis focuses on flame configuration, temperature distribution, heat transfer and mitigation of CO_2 emissions under different hydrogen mixing ratios such as H5, H10 and H15. Air-fuel ratios and burner configuration are held constant to understand the effects of the hydrogen addition. The results reveal key insight into the stability of non-premixed hydrogen flames mixing with methane, temperature distribution on the combustion domain, homogeneous heating of the ceramic material and lower CO_2 emissions. Comparative analysis with pure methane reveals approximately 5 K enhancement in average furnace temperatures and a 7% reduction in CO_2 emissions. The use of hydrogen in industrial ceramic furnaces will be very beneficial in terms of efficiency, environment, and decarbonization. Future studies can be performed for different furnace geometries and boundary conditions.

Keywords: Non-premixed combustion, hydrogen, ceramic furnace, CFD, CO_2 emissions, decarbonization

1. INTRODUCTION

In recent years, various alternative fuel technologies have been developed to reduce the use of fossil fuels and transition to sustainable energy sources. The use of fossil fuels causes the emissions of carbon dioxide (CO_2), nitrogen oxides (NO_x) and other harmful pollutants into the atmosphere, leading to problems such as global climate change and air pollution. As a solution to these problems, hydrogen is considered as an alternative fuel with its high energy density, clean combustion products and zero carbon emission potential. Drying, sintering and even cooling are essential process steps in producing ceramic products in industry [1]. Industrial-type furnaces are mainly used for firing and heating ceramics. Using hydrogen as an alternative fuel in these furnaces is seen as an innovative approach that can significantly reduce environmental impacts.

There are many studies on industrial-type industrial furnaces in the literature. Balli et al. conducted a numerical and experimental study on energy efficiency, fuel consumption and CO_2 emissions reduction on an industrial prototype furnace used in ceramic production [1]. Schüttensack et al. analyzed the furnace system with a mixture of hydrogen and natural gas fuel, which causes less emissions instead of electric furnaces used in steel production industries. This study found that it causes less CO_2 emissions than electric furnaces [2]. Mayrhofer et al. investigated the application of natural gas/hydrogen mixtures as an alternative fuel in industrial heat treatment furnaces and the economic potential for reducing CO_2 emissions in this application area [3]. Daurer et al. numerically modeled a semi-industrial furnace in an oxy-fuel combustion chamber. In their study, the effect of hydrogen on flame temperature and combustion characteristics was investigated [4].

There are few studies on analyzing systems using hydrogen as a fuel for ceramic production. In this study, unlike the others, the effect of the hydrogen-methane mixture on the ceramic product and combustion characteristics was investigated. It aims to explore the impact of alternative fuels on heat dissipation and emission reduction by examining the thermal behavior of an industrial prototype gas furnace for ceramic production. In this study, the flue gas outlet temperatures, temperature distributions and emissions were investigated using hydrogen with methane gas at different molar ratios in industrial-type furnaces.

2. MATERIALS AND METHODS

A 2D numerical model was established to evaluate the combustion performance of alternative fuels in industrial furnaces.

The model is mainly based on the traditional natural gas and hydrogen co-combustion model. A CFD numerical simulation study was carried out in the numerical model using ANSYS Fluent software [5,6] with a non-premixed combustion model. The computational domain is given in Fig. 1.

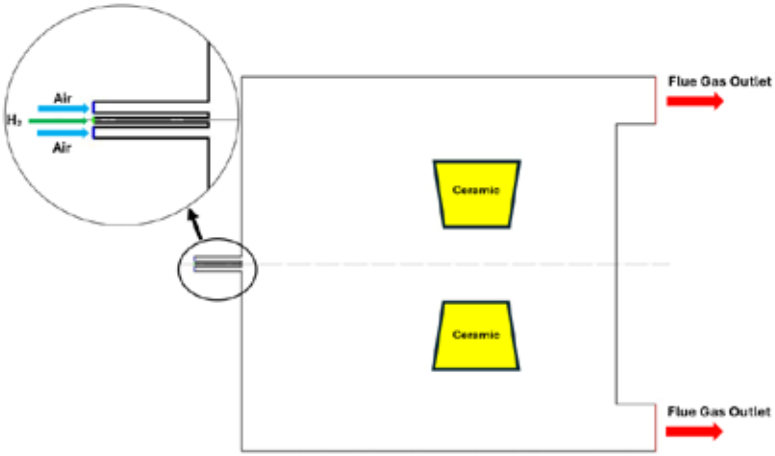

Fig. 1. Computational domain with inlets and outlets

The numerical model evaluated the effect of hydrogen natural gas co-combustion on the temperature in the combustion chamber, ceramic temperature change, and CO_2 emissions. The main boundary conditions used in the study are mass fuel mass flow inlet, air mass flow inlet, adiabatic wall, and pressure outlet boundary conditions. A pressure-based solver is used as the general solver, and a RANS-based *k*-ϵ turbulence model is used [7]. The primary combustion statement is expressed by Eq. (1) [8].

$$xCH_4 + yH_2 + \frac{a_s}{\phi}(O_2 + 3.76N_2) \rightarrow Products \quad (1)$$

Equations *x* and *y* are the methane and hydrogen molar ratios, respectively. The a_s and The ϕ are the F/A stoichiometry and equivalence rate, respectively. The boundary conditions and combustion parameters used in the study are given in Table 1.

Table 1. Boundary conditions and combustion parameters

Boundary conditions	Unit	Value and condition
Fuel and air Inlets	kg/s	Mass flow inlet
Outlet		Pressure outlet
Inner wall	-	Non-slip boundary, DO radiation model [9]
Outer wall	-	Adiabatic wall
Ambient temperature	K	300
Furnace dimensions (L x D)	mm	440 x 400
Fuel blends	vol%	D100 D95-H5 D90-H10 D85-H15

3. RESULTS AND DISCUSSION

In this study, combustion temperature and CO_2 emissions were calculated numerically according to different hydrogen blends in industrial furnaces. In the results of the study, it was observed that hydrogen addition increased the furnace temperature and decreased CO_2 emissions. Reduced CO_2 emissions are due to the non-existence of carbon atoms in hydrogen fuel. CO_2 decreases from 0.0585 (H0) to 0.0560 (H15), indicating that higher hydrogen ratios correlate with reduced CO_2 emissions. This aligns with expectations, as hydrogen combustion produces no CO_2 emissions. Due to the low ignition temperature and high calorific value of hydrogen, the temperatures in the furnace increased with hydrogen addition. Fig. 2. shows the furnace outlet temperature, ceramic surface average temperature and CO_2 emissions for different ratios of hydrogen addition to natural gas.

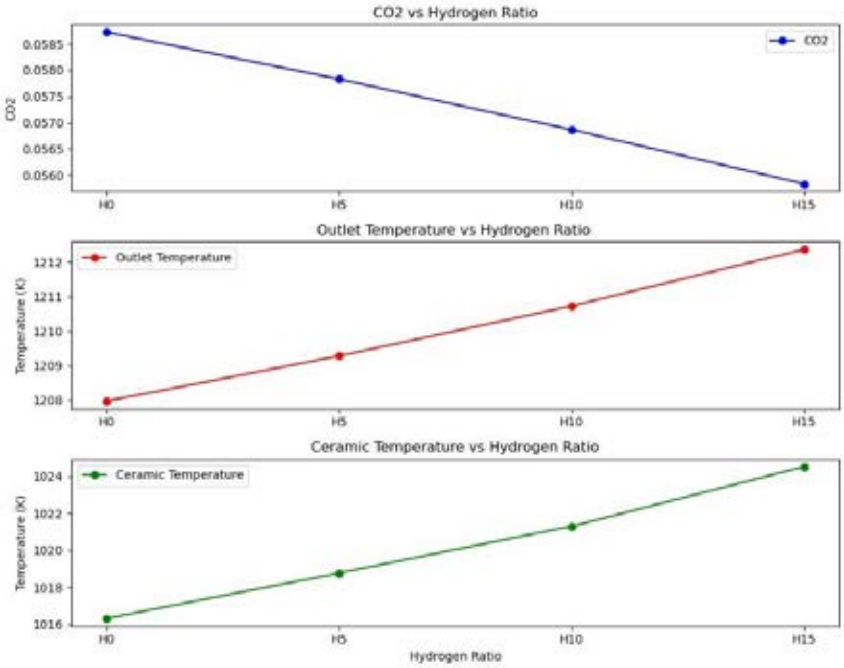

Fig. 2. Variation of temperature and emissions for hydrogen ratio

Fig. 3 shows the furnace's temperature distribution for the co-combustion of hydrogen and natural gas at different hydrogen ratios.

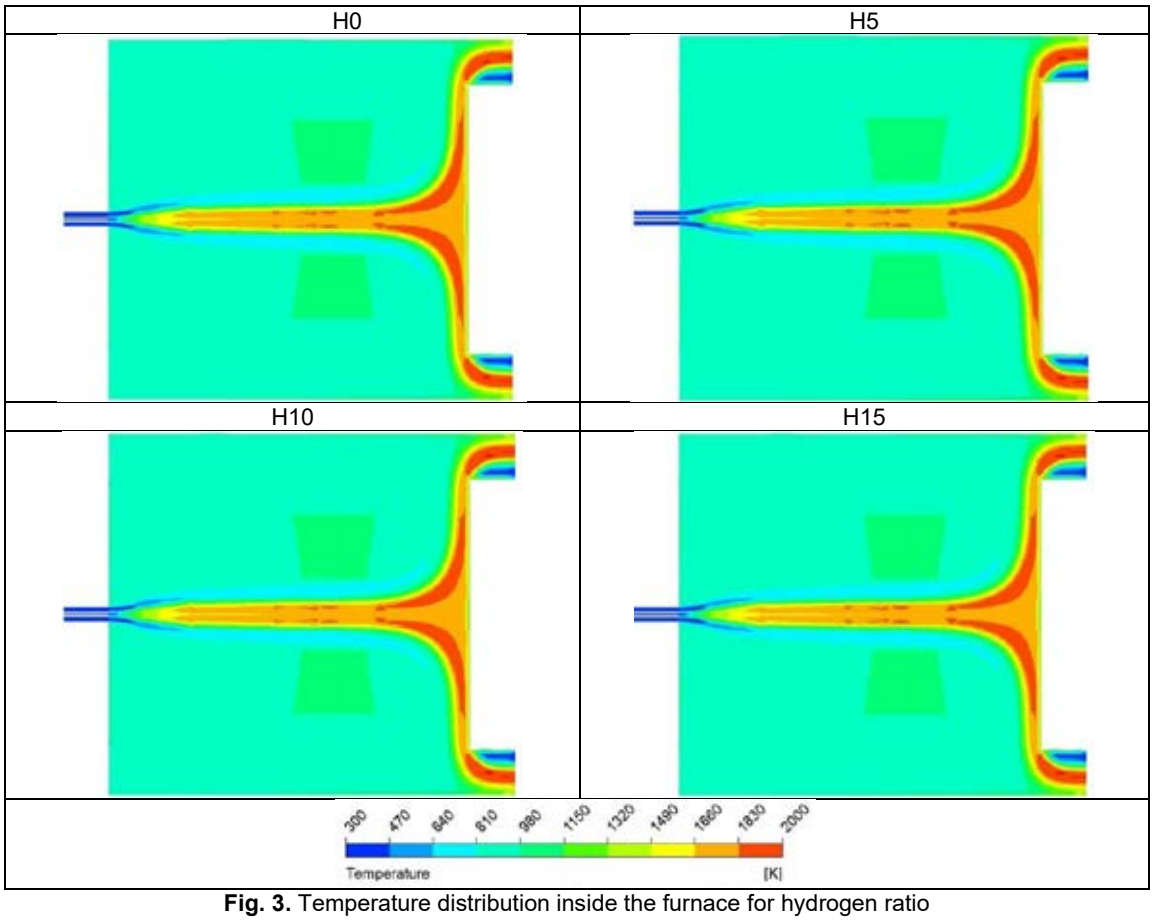

Fig. 3. Temperature distribution inside the furnace for hydrogen ratio

Due to the furnace's geometrical structure, the temperature distribution is in the same direction as the blower velocity gradient. The temperatures inside the furnace reach up to 2015 K values, while the average furnace and ceramic material temperatures are around 1000 K levels.

4. CONCLUSIONS

In this study, the temperature and emission parameters of industrial furnaces with different hydrogen additives were investigated numerically. The main findings of the study are as follows.

- Within the scope of the study, a non-premix combustion numerical combustion model was created.
- It was determined that CO_2 emissions decreased by approximately 7% with increasing hydrogen addition.
- Increasing hydrogen addition elevates temperatures inside the combustion chamber and on the ceramic surface. This is due to hydrogen's high ignition and thermal value.
- Approximately 5 K enhancement was observed in average furnace temperatures

Hydrogen is a carbon-free energy vector with high thermal potential. Therefore, system performance studies can be examined using different burner and geometric structures. In addition, with the emission restrictions imposed, hydrogen obtained from clean energy sources has a high potential for future use.

REFERENCES

[1] Balli L, Hlimi M, Achenani Y, Atifi A, Hamri B. Experimental study and numerical modeling of the thermal behavior of an industrial prototype ceramic furnace: Energy and environmental optimization. Energy Built Environ 2024;5:244–54. https://doi.org/10.1016/j.enbenv.2022.10.001.
[2] Schüttensack L, Reinicke A, Echterhof T. Application of hydrogen operated burners in the electric arc furnace. IOP Conf Ser Mater Sci Eng 2024;1309:012011. https://doi.org/10.1088/1757-899x/1309/1/012011.
[3] Mayrhofer M, Koller M, Seemann P, Prieler R, Hochenauer C. Assessment of natural gas/hydrogen blends as an alternative fuel for industrial heat treatment furnaces. Int J Hydrogen Energy 2021;46:21672–86. https://doi.org/10.1016/j.ijhydene.2021.03.228.
[4] Daurer G, Schwarz S, Demuth M, Gaber C, Hochenauer C. Evaluation of numerical modeling and combustion characteristics of hydrogen oxy-fuel combustion in a semi-industrial furnace. Fuel 2024;369:131690. https://doi.org/10.1016/j.fuel.2024.131690.
[5] Ansys Inc. ANSYS Fluent 2020 R1 User's Guide. 2021.
[6] Bayramoğlu K, Yılmaz S. Emission and performance estimation in hydrogen injection strategies on diesel engines. Int J Hydrogen Energy 2021;46:29732–44. https://doi.org/10.1016/j.ijhydene.2020.08.135.
[7] Fan H, Zhang H, Zhang X, Luo Z, Tu Y, Zhang S. Experimental and numerical modeling of co-combustion of biomass gasification gas and natural gas in a non-premixed burner. Energy 2024;313:133798. https://doi.org/https://doi.org/10.1016/j.energy.2024.133798.
[8] Bayramoğlu K. The effects of alternative fuels, cruising duration and variable generators combination on exhaust emissions, energy efficiency existing ship index (EEXI) and carbon intensity rating (CII). Ocean Eng 2024;302. https://doi.org/10.1016/j.oceaneng.2024.117723.
[9] Zhang Y, Yang Y, Weng J, Lu Q, Fan B, Jiang C, et al. Numerical investigation on the combustion characteristics and NOx emission of non-premixed H2/NH3/air in vase-shaped micro combustor. Int J Hydrogen Energy 2024;91:539–47. https://doi.org/https://doi.org/10.1016/j.ijhydene.2024.10.111.

NUMERICAL INVESTIGATION OF THE EFFECT OF THE CO-COMBUSTION OF HYDROGEN AND NATURAL GAS ON TEMPERATURE AND CARBON EMISSIONS IN CERAMIC FURNACE

[1*]*Kubilay Bayramoğlu* [2]*Semih Yılmaz*, [3]*Tolga Bayramoğlu,* [4]*Ahmet Özarslan,* [5]*Bünyamin Kılıç,* [5]*Atamer Akbay*
[1]Zonguldak Bulent Ecevit University, Engineering Faculty, Department of Mechanical Engineering, Zonguldak, 67100, Türkiye
[2] Dokuz Eylul University, Maritime Faculty, Department of Marine Engineering, İzmir, 35390, Türkiye
[3]Zonguldak Bulent Ecevit University, Alapli Vocational High School, Department of Motor Vehicles and Transportation Technologies, Zonguldak, 67850, Türkiye
[4] Zonguldak Bulent Ecevit University, Engineering Faculty, Department of Mining Engineering, Zonguldak, 67100, Türkiye
[5]Canakcılar Ceramic Industry and Trade Company-Creavit, Department of Research and Development, Zonguldak, 67670, Türkiye

*Corresponding author e-mail: kubilay.bayramoglu@beun.edu.tr

ABSTRACT
Using hydrogen as an energy vector is one of the key drivers of the shift away from fossil fuels. This study numerically investigated the effect of a hydrogen and natural gas blend on furnace temperature and emissions. It analyzed D100 pure natural gas and H100 pure hydrogen combustion with 5%, 10%, and 15% hydrogen addition. In addition, parametric studies were carried out for different equivalence ratios. The study determined that increasing hydrogen addition increases the combustion chamber temperature and decreases CO_2 emissions. Approximately 1% temperature increase was observed between D100 fuel and H100 fuel. CO_2 mole fractions were found to be approximately 5.1%, 5.0%, 4.9% and 4.8% for D100, H5, H10 and H15 fuel blends. With the study, the combustion performance of the use of hydrogen, an energy vector, in ceramic furnaces

Keywords: Hydrogen, combustion, CO_2 reduction, furnace, sustainability

1. INTRODUCTION
The development of low-carbon or zero-carbon combustion technology is crucial for the energy sector, given the swift implementation of carbon-neutral policies and technologies. Hydrogen is thought to be a superior alternative fuel among several renewable fuels. In addition to absorbing excess renewable energy from sources like wind and solar power and reducing grid instability, hydrogen also has the benefit of having a high calorific value per mass, which allows it to be burned directly and used in internal engines, boilers, and gas turbines [1,2]. Cofiring natural gas with hydrogen, however, lowers carbon emissions while aggravating the production of nitrogen oxide, another air pollutant, particularly at high hydrogen-blending concentrations. Advanced hydrogen-enriched methane combustion technologies must be developed to effectively and economically limit source NO_X production to comply with the strict NO_X emission requirements [3].

Sintered materials can be heated in conventional natural gas furnaces up to 2000 K, although greater temperatures are frequently needed to produce dense refractory ceramics. Therefore, correct combustion and fuel selection are essential in the firing process of ceramics. Using hydrogen as an alternative to natural gas fuel is one crucial step for sustainable systems [4]. Different studies have been carried out on the combustion processes of furnaces in the literature. Kang et al. [5] experimentally and numerically investigated the heat transfer performance of a ceramic honeycomb regenerator in oxy-fuel combustion. Daurer et al. [6] tested the high pulse oxy-fuel combustion of pure H_2 in an industrial environment based on experiments, theoretical calculations and RANS simulations. Li et al. [7] modeled the effect of hydrogen-rich fuel injection on combustion characteristics, thermo-chemical behavior, and coke dynamics in a three-dimensional blast furnace duct at the particle level using the computational fluid dynamics-discrete element method (CFD-DEM). Ren et al.[8] numerically investigated the effects of hydrogen content in the co-injection gas on the combustion characteristics in the duct.

Studies in the literature have generally examined low-temperature combustion and oxyfuel combustion processes. However, the combustion conditions of hydrogen with natural gas at different ratios and 100% hydrogen combustion conditions have been studied very little. In addition, the combustion conditions of hydrogen with air density are also among the main issues to be examined in the literature. In this study, 100% diesel and 100% hydrogen combustion conditions were numerically investigated and the flame appearance in the furnace was investigated. The effect of 5%, 10% and 15% hydrogen natural gas mixture on combustion chamber temperature and emissions were determined. The effect of 15% hydrogen natural gas mixture on combustion and emissions at different air excess coefficients was evaluated parametrically. The study was conducted under a computational fluid dynamics model using non-premix combustion conditions. Thus, it is expected to make significant contributions to the literature by reducing CO_2 emissions against global warming and enabling the modeling of sustainable combustion processes.

2. MATERIALS AND METHODS

A two-dimensional numerical model was developed to assess the performance of hydrogen natural gas combustion in industrial furnaces. The conventional natural gas and hydrogen co-combustion model is the primary foundation. Using ANSYS Fluent software [9,10] and non-premix combustion model, a CFD numerical simulation investigation was conducted using the numerical model. Fig. 1 shows the computational domain. The study was carried out for the test furnace and ceramics in the Çanakcılar Ceramic Industry and Trade Co. factory.

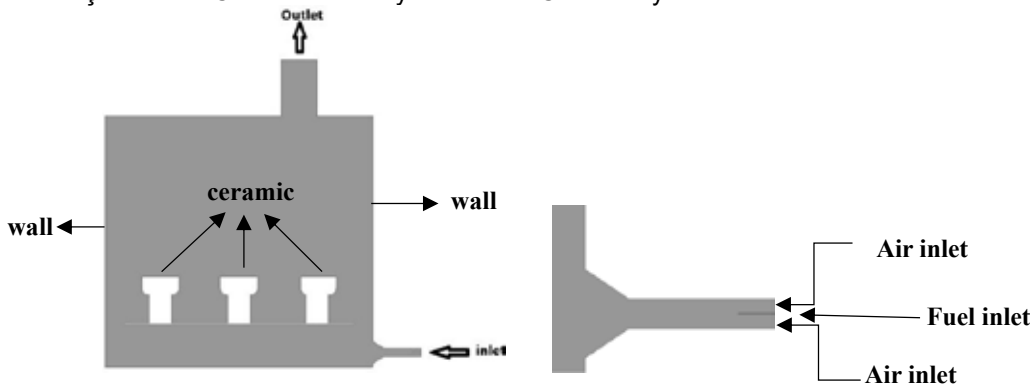

Fig. 1. Computational domain

The numerical model assessed how the co-combustion of hydrogen and natural gas affected the combustion chamber's temperature, the change in ceramic temperature, and CO_2 emissions. The study's primary boundary conditions are the adiabatic wall, pressure outlet, air mass flow intake, and mass fuel mass flow inlet. The general solver is pressure-based, while the k-ϵ turbulence model is based on RANS [9]. Eq. (1) expresses the primary combustion statement. [11].

$$xCH_4 + yH_2 + \frac{a_s}{\phi}(O_2 + 3.76N_2) \rightarrow Products \quad (1)$$

Equations *x* and *y* are the methane and hydrogen molar ratios, respectively. The a_s and the ϕ are the F/A stoichiometry and equivalence rate, respectively. Table 1 gives the boundary conditions and combustion parameters used in the study. The study used the ϕ equivalence ratio with variables x and y.

Table 1. Boundary and initial conditions

Boundary conditions	Unit	Value and condition
Inlets	kg/s	Mass flow inlet
Outlet		Pressure outlet
Inner wall	-	Non-slip boundary, DO radiation model [12]
Outer wall	-	Adiabatic vall
Ambient temperature	K	300
Furnace dimensions (L x D)	mm	1430 x 1340
Case studies	vol%	D100 H5 H10 H15 H100
ϕ	-	0.6 0.8 1.0

3. RESULTS AND DISCUSSION

Fig. 2 shows the flame temperature distribution for 100% natural gas (D100) and 100% hydrogen (H100) combustion. The flame distribution formed by hydrogen combustion spreads over more expansive areas compared to natural gas. In addition, combustion chamber temperatures are higher in hydrogen combustion than in natural gas combustion. In addition, the adiabatic flame temperature increases in the combustion process with hydrogen fuel. This is one of the main reasons for the temperature increase.

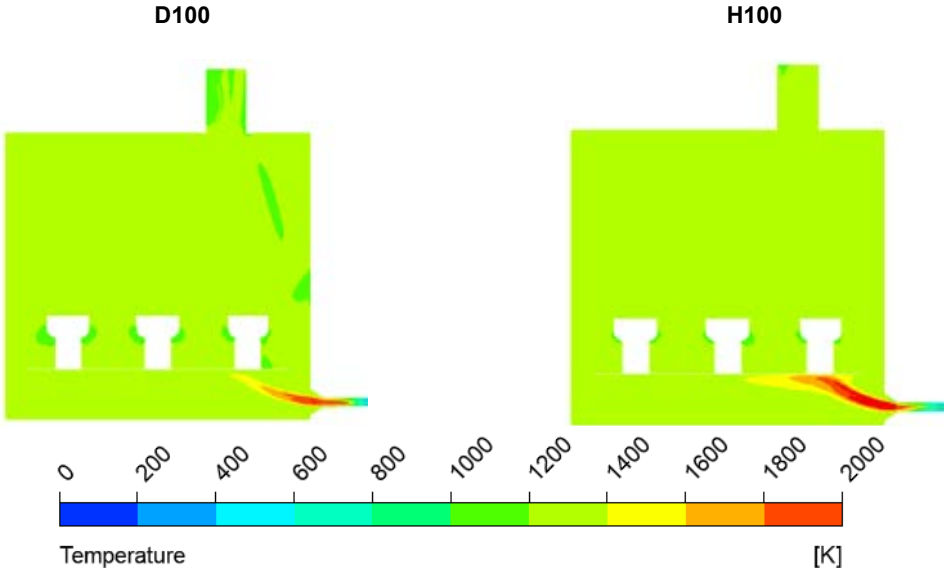

Fig. 2 Flame distribution of hydrogen and natural gas

Fig. 3 shows the distribution of combustion chamber temperature with hydrogen addition for different hydrogen ratios and equivalence ratios. It was determined that increasing hydrogen addition increased the combustion chamber's average temperature. In addition, the decrease in the equivalence ratio decreases the combustion chamber temperatures. The decrease in the equivalence ratio leads to an increase in the air-fuel ratio.

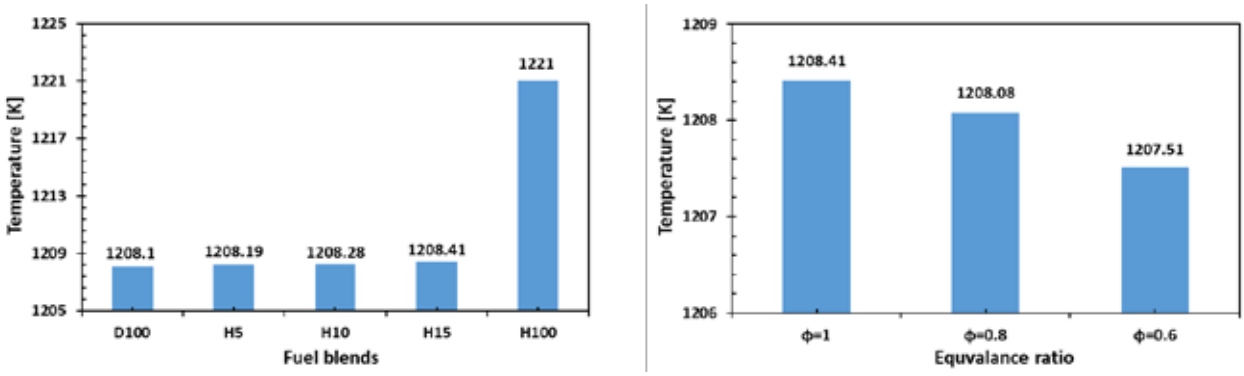

Fig. 3 Temperature of the combustion chamber for variable fuel blends and equivalence ratio

Fig. 4 shows CO_2 emissions for different hydrogen addition and equivalence ratios. It was determined that CO_2 emissions decreased with increasing hydrogen addition. In addition, the reduction in the equivalence ratio also reduces the hydrogen ratio. This is mainly because hydrogen is a carbon-free fuel.

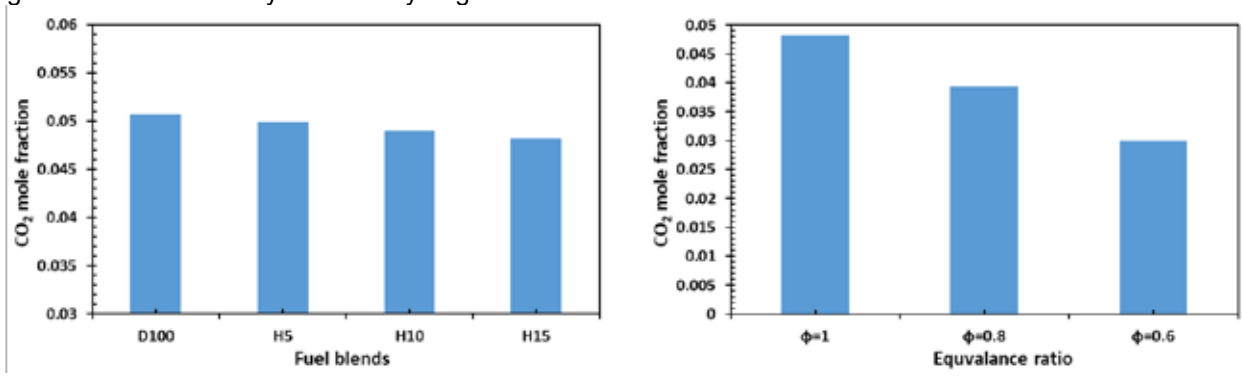

Fig. 4 CO_2 mole fraction of variable fuel blends and equivalence ratio

4. CONCLUSIONS

The fact that hydrogen is a carbon-free fuel with high energy efficiency will bring about its widespread use in energy systems. Within the scope of the study, the ceramic ceramic combustion process for different hydrogen addition and equivalence ratios was carried out parametrically. The results of the study are briefly as follows.

- With increasing hydrogen addition, combustion chamber flame and temperature values increase. The combustion temperature was approximately 1208 K for D100 fuel and 1221 K for H100, respectively.
- Combustion chamber temperature and emission values increase with increasing equivalence ratio.
- The fact that hydrogen does not contain carbon atoms is the main reason for reducing CO_2 emissions in combustion processes.

REFERENCES

[1] Tao C, Wang Y, Sun Z, Sun R, Zhou H, Duan L. Numerical simulation study on the combustion and emission characteristics of a gas-fired boiler using hydrogen-ammonia binary fuel. Therm Sci Eng Prog 2025;59:103356. https://doi.org/https://doi.org/10.1016/j.tsep.2025.103356.

[2] Bayramoğlu K. Energy and Exergy Analysis of Diesel-Hydrogen and Diesel-Ammonia Fuel Blends in Diesel Engine. J Eta Marit Sci 2024;12:128–35. https://doi.org/10.4274/jems.2024.46503.

[3] Xu S, Dou C, Tian Z, Chen Y, Li W, Liu H. Experimental and numerical study on formation and NO emission of hydrogen-enriched methane combustion in swirl flame and MILD modes. Int J Hydrogen Energy 2025;101:848–62. https://doi.org/https://doi.org/10.1016/j.ijhydene.2024.12.439.

[4] Kirdyashkin A, Gabbasov R, Kitler V, Maznoy A. Ceramic sintering furnace based on combustion of premixed natural gas in porous inert media. Fuel 2022;309:122098. https://doi.org/https://doi.org/10.1016/j.fuel.2021.122098.

[5] Kang K, Hong S-K, Noh D-S, Ryou H-S. Heat transfer characteristics of a ceramic honeycomb regenerator for an oxy-fuel combustion furnace. Appl Therm Eng 2014;70:494–500. https://doi.org/https://doi.org/10.1016/j.applthermaleng.2014.05.053.

[6] Daurer G, Schwarz S, Demuth M, Gaber C, Hochenauer C. Evaluation of numerical modeling and combustion characteristics of hydrogen oxy-fuel combustion in a semi-industrial furnace. Fuel 2024;369:131690. https://doi.org/10.1016/j.fuel.2024.131690.

[7] Li M, Li Z, Li C, Wu G, An X, Zhang H, et al. Numerical insights on the combustion characteristics in the low-carbon blast furnace raceway with hydrogen-rich gas injections. Int J Hydrogen Energy 2025;100:341–54. https://doi.org/https://doi.org/10.1016/j.ijhydene.2024.12.305.

[8] Ren M, Liu W, Zhao J, Zou C, Ren L, Wu H, et al. Effects of hydrogen fraction in co-injection gas on combustion characteristics of the raceway in low carbon emission blast furnace. Int J Hydrogen Energy 2023;48:11530–40. https://doi.org/https://doi.org/10.1016/j.ijhydene.2022.06.106.

[9] Ansys Inc. ANSYS Fluent 2020 R1 User's Guide. 2021.

[10] Bayramoğlu K, Yılmaz S. Emission and performance estimation in hydrogen injection strategies on diesel engines. Int J Hydrogen Energy 2021;46:29732–44. https://doi.org/10.1016/j.ijhydene.2020.08.135.

[11] Bayramoğlu K. The effects of alternative fuels, cruising duration and variable generators combination on exhaust emissions, energy efficiency existing ship index (EEXI) and carbon intensity rating (CII). Ocean Eng 2024;302. https://doi.org/10.1016/j.oceaneng.2024.117723.

[12] Zhang Y, Yang Y, Weng J, Lu Q, Fan B, Jiang C, et al. Numerical investigation on the combustion characteristics and NOx emission of non-premixed H2/NH3/air in vase-shaped micro combustor. Int J Hydrogen Energy 2024;91:539–47. https://doi.org/https://doi.org/10.1016/j.ijhydene.2024.10.111.

STRUCTURAL AND CATALYTIC INSIGHTS INTO Sr-MODIFIED $LaNi_{0.5}Mg_{0.5}O_3$ PEROVSKITES

[1]*Parisa Ebrahimi*, [1*]*Anand Kumar*, [1,2*]*Mohammed Al-Marri*
[1] Department of Chemical Engineering, College of Engineering, Qatar University, Doha, P O Box 2713, Qatar
[2] Gas Processing Center, College of Engineering, Qatar University, Doha, P O Box 2713, Qatar

*Corresponding authors e-mails: akumar@qu.edu.qa, m.almarri@qu.edu.qa

ABSTRACT
Enhancing the efficiency of catalysts for dry reforming of methane (DRM) requires optimizing their structural and electronic properties to maximize activity and minimize coke formation. This study investigates the effect of substituting Sr for La in $La_ySr_{1-y}Ni_{0.5}Mg_{0.5}O_3$ perovskites (y=0, 0.5 and 1) to enhance catalytic performance. Structural analysis confirms high crystallinity, with Sr incorporation optimizing oxygen mobility, CO_2 adsorption, and carbon resistance. The interplay between La and Sr influences Ni reducibility, with Sr-induced oxygen vacancies delaying low-temperature reduction and La enhancing Ni accessibility. Catalytic testing reveals that La-rich samples (y = 1) achieve the highest CO_2 and CH_4 conversion (85% and 75% at 750 °C), whereas Sr-rich samples (y = 0) exhibit relatively lower conversions at higher temperature but greater oxygen vacancy formation. Overall, $La_{0.5}Sr_{0.5}Ni_{0.5}Mg_{0.5}O_3$ achieves the best balance of oxygen mobility and catalytic efficiency, providing insights into perovskite catalyst design for syngas production.

Keywords: Dry Reforming of Methane, Perovskite Catalysts, Strontium Substitution, Oxygen Mobility

1. INTRODUCTION

The growing global demand for energy, driven by rapid industrialization, calls for sustainable alternatives that reduce environmental impact while remaining economically viable [1]. The heavy reliance on fossil fuels has significantly contributed to greenhouse gas emissions, intensifying climate change and highlighting the urgent need for cleaner energy solutions [2]. Among various methane reforming processes, DRM,Eq.(1) has gained attention due to its ability to convert both CO_2 and CH_4 and into syngas [3]. Compared to partial oxidation (POM) and steam reforming (SRM), DRM is more sustainable as it utilizes CO_2 instead of water, promoting carbon capture and utilization [4]. However, challenges such as catalyst deactivation due to sintering and carbon deposition hinder its large-scale implementation [5].

$$CO_2 + CH_4 = 2CO + 2H_2 \qquad \Delta H^o = +247.3\ kJ.mol^{-1} \qquad (1)$$

Catalysts play a crucial role in DRM by lowering activation energy, enhancing reaction rates, and improving selectivity [6]. Perovskite-based catalysts have attracted significant interest due to their structural flexibility, high thermal stability, and ability to accommodate multiple metal elements [7]. Perovskites containing transition metals at the B-site, along with La, Sr, or Ce at the A-site, have shown promising results in methane reforming applications [8]. These materials act as precursors to highly dispersed active metal species, improving catalytic efficiency and resistance to deactivation.
Strontium (Sr) substitution in perovskites has been explored for its ability to modify catalyst properties, influencing activity and stability [9]. Sr incorporation can enhance CO_2 adsorption, promote oxygen mobility, and mitigate coke formation by facilitating carbon oxidation [10]. Additionally, Sr can improve Ni dispersion on the catalyst surface, increasing the number of active sites and boosting overall performance [11]. Previous studies have demonstrated that Sr interacts synergistically with other components, such as La and Ni, to create more effective catalytic sites [12].
Building upon our previous findings, where $LaNi_{0.5}Mg_{0.5}O_3$ exhibited the highest DRM performance [13], this study investigates the effect of Sr substitution for La in the perovskite structure. We explore $La_ySr_{1-y}Ni_{0.5}Mg_{0.5}O_3$ catalysts (y=0, 0.5 and 1) with varying Sr content to evaluate its influence on structural properties, methane and CO_2 conversion, syngas production, and coke resistance. By analyzing the impact of Sr incorporation, we aim to develop highly efficient and stable catalysts for DRM, contributing to more sustainable energy solutions.

2. MATERIALS AND METHODS

$La_ySr_{1-y}Ni_{0.5}Mg_{0.5}O_3$ perovskite catalysts were synthesized using the solution combustion method (SCS) with glycine as the fuel, ensuring homogeneous mixing and controlled composition. The precursors were calcined at 700 °C to achieve the desired perovskite phase, followed by reduction in a hydrogen-containing atmosphere to activate the catalytic sites. Various characterization techniques were employed to analyze the structural properties, elemental composition, surface chemistry, and reducibility of the catalysts before and after the reaction.
The catalytic performance was evaluated in a tubular flow reactor under atmospheric pressure, using a 1:1 CO_2/CH_4 feed at a flow rate of 50 sccm. The reaction was conducted across a temperature range of 100–750 °C, and the gaseous products were analyzed via gas chromatography to determine CO_2 and CH_4 conversion, as well as syngas yield. The impact of Sr substitution on catalytic activity and stability was assessed by correlating structural and reduction properties with reaction performance.

$$CO_2 Conversion = (CO_{2,in} - CO_{2,out})/CO_{2,in} \quad (2)$$
$$CH_4 Conversion = (CH_{4,in} - CH_{4,out})/CH_{4,in} \quad (3)$$

3. RESULTS AND DISCUSSION

Fig. 1 illustrates the catalytic performance of $La_ySr_{1-y}Ni_{0.5}Mg_{0.5}O_3$ perovskites in terms of CH_4 and CO_2 conversion across different temperatures. The results show a general increase in conversion with temperature, consistent with the endothermic nature of DRM. Among the catalysts, the y=1 sample exhibited the highest CO_2 conversion, reaching approximately 85% at 750 °C. Similarly, CH_4 conversion was most efficient for the y=1 sample, exceeding 75% at the same temperature, highlighting the role of La in enhancing methane activation. The superior activity of the y=0 catalyst at lower temperatures is attributed to its higher Sr content, which enhances oxygen vacancy formation and mobility, facilitating CO_2 and CH_4 activation.

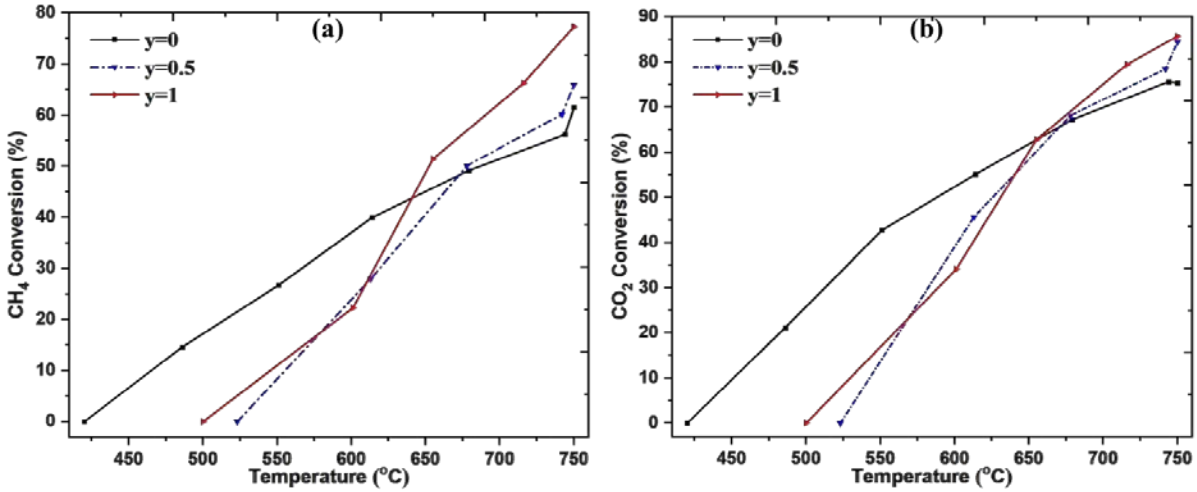

Fig. 1. $La_ySr_{1-y}Ni_{0.5}Mg_{0.5}O_3$ perovskites activity (a) CH_4 and (b) CO_2

Fig. 2a exhibits the TPR profiles of the perovskites, highlighting the influence of the La/Sr ratio on reduction behavior. A broad peak above 800 °C is attributed to lattice oxygen reduction, influenced by Sr and La substitution [14]. Increasing Sr content weakens the low- and mid-temperature peaks, indicating reduced Ni reducibility due to enhanced oxygen vacancy formation and stronger lattice oxygen binding [15, 16]. In contrast, higher La content stabilizes Ni in higher oxidation states, promoting easier reduction at lower temperatures [17].

The XRD patterns of $La_ySr_{1-y}Ni_{0.5}Mg_{0.5}O_3$ perovskites (Fig. 2b) reveal insights into phase composition, crystallinity, and structural evolution. $SrNiO_3$ is the dominant crystalline phase, with characteristic peaks in all samples except for y = 1. Additional peaks indicate secondary phases influenced by La incorporation and Mg substitution. Sharp diffraction peaks at 29°, 32°, 38°, 44°, 43°, and 63°confirm high crystallinity, matching the perovskite-type $SrNiO_3$ (PDF#28-1242) [18]. La^{3+} substitution alters the structure, with SrO peaks appearing in lower y samples and increasing with Sr^{2+} content, indicating phase segregation. At higher y values, La^{3+} stabilizes the perovskite structure. NiO (ICSD 24018) is also present, with cubic phase reflections confirming crystallinity [19]. The $Sr_9Ni_7O_{21}$ phase forms due to incomplete Sr^{2+} and Ni^{2+} incorporation, typically appearing at 19°, 57°, and 68° [20]. Its presence affects active site distribution and catalytic stability [21], influenced by synthesis conditions. Strontium segregation occurs via moisture absorption, leading to $Sr(OH)_2{\cdot}8H_2O$ formation, which reacts with CO_2 to produce $SrCO_3$. Peaks at 26.1°, 46.8°, and 50° correspond to $SrCO_3$ (JCPDS card no. 01-0556) [22], with a 2θ = 26° peak overlapping with carbon species [23]. In Sr-rich samples, increased $SrCO_3$ intensity suggests CO_2 interaction with SrO [24].

Fig. 3 presents FESEM images of some selected perovskite before and after the DRM reaction. Fresh $SrNiO_3$ has a rod-like structure, which sinters post-DRM, likely due to Sr-based perovskites' lower thermal stability [25]. Mg incorporation (Fig. 4a) disrupts this structure, forming a porous, granular morphology. Post-DRM (Fig. 3c), filamentous carbon appears, suggesting Mg improves stability but does not prevent carbon accumulation.La substitution (Fig. 3b) creates a porous-clustered morphology, enhancing stability and reducing carbon deposits post-DRM (Fig. 3d) due to improved oxygen mobility [26]. These findings highlight the need for an optimal La/Sr ratio to balance stability and carbon resistance during DRM.

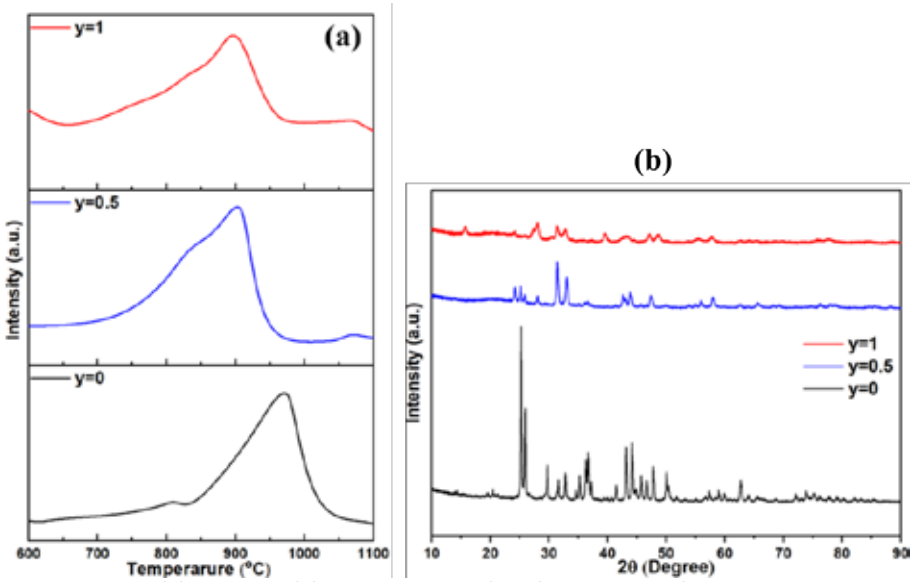

Fig. 2. (a) TPR and (b) XRD patterns of $La_ySr_{1-y}Ni_{0.5}Mg_{0.5}O_3$ perovskites

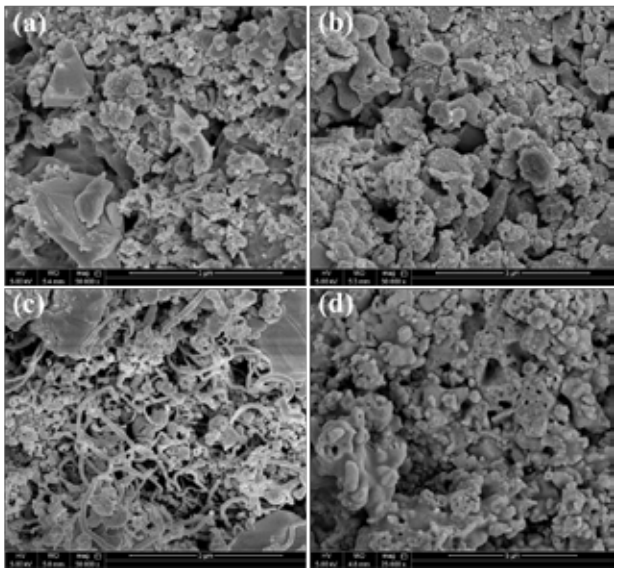

Fig. 3. FESEM images of (a,e) $SrNi_{0.5}Mg_{0.5}O_3$, and (b,f) $La_{0.5}Sr_{0.5}Ni_{0.5}Mg_{0.5}O_3$; (a,b) before and (e,f) after DRM reaction

CHN analysis aligns with FESEM results, showing increased carbon content post-DRM for $SrNi_{0.5}Mg_{0.5}O_3$ from 1.17 to 4.05, indicating higher carbon deposition. In contrast, $La_{0.5}Sr_{0.5}Ni_{0.5}Mg_{0.5}O_3$ exhibits reduced carbon content (1.71% vs. 1.93% fresh), suggesting enhanced carbon removal via oxygen mobility [27]. Carbon in fresh samples likely stems from precursor residues, with La-containing catalysts showing slightly higher values due to carbonate species formation during synthesis [28].

4. CONCLUSIONS

Sr incorporation improved catalytic activity at high temperatures, with the $La_{0.8}Sr_{0.2}Ni_{0.5}Mg_{0.5}O_3$ catalyst achieving the highest CO_2 and CH_4 conversion rates of 88% and 75%, respectively, at 750 °C. In contrast, Sr-only catalysts exhibited much lower activity, with 27% CO_2 and 20% CH_4 conversion at 500 °C. Sr substitution hindered the reducibility of Ni species by promoting oxygen vacancy formation, which stabilized the lattice and delayed reduction. XPS analysis confirmed that $La_{0.8}Sr_{0.2}Ni_{0.5}Mg_{0.5}O_3$ had the highest Ni^0 content post-DRM, correlating with its superior catalytic performance. While $SrCO_3$ formation in Sr-rich catalysts reduced catalytic activity by altering the active phase, the presence of Mg stabilized the active phase, promoting CO_2 adsorption and improving performance. Mg also modified the catalyst morphology, increasing surface area and active sites but potentially encouraging methane cracking and carbon deposition at high temperatures. Overall, $La_{0.5}Sr_{0.5}Ni_{0.5}Mg_{0.5}O_3$ exhibited the best balance of oxygen mobility and active surface oxygen, making it the most efficient catalyst.

REFERENCES

1. Omer, A.M. 2008. *Energy, environment and sustainable development.* Renewable and sustainable energy reviews12(9):2265-2300.
2. Bilgen, S. 2014. *Structure and environmental impact of global energy consumption.* Renewable and SustainableEnergy Reviews 38:890-902.
3. Aramouni, N.A.K., et al. 2018. *Catalyst design for dry reforming of methane: Analysis review.* Renewable and sustainable energy reviews 82:2570-2585.
4. Ahmad, K., K. 2022. Polychronopoulou, and M. Abi Jaoude, *CH_4 valorisation reactions: A comparative thermodynamic analysis and their limitations.* Fuel 320:123877.
5. García, L. 2015. *Hydrogen production by steam reforming of natural gas and other nonrenewable feedstocks*, in *Compendium of hydrogen energy* 83-107.
6. Abdulrasheed, A., et al. 2019. *A review on catalyst development for dry reforming of methane to syngas: Recent advances.* Renewable and Sustainable Energy Reviews 108:175-193.
7. Bian, Z., et al. 2020 *A review on perovskite catalysts for reforming of methane to hydrogen production.* Renewable and Sustainable Energy Reviews 134:110291.
8. Zhang, Q., et al. 2017. *An intelligent oxygen carrier of $La_{2-x}Sr_xNiO_{4-\lambda}$ for hydrogen production by chemical looping reforming of ethanol.* international journal of hydrogen energy 42(27):17102-17111.
9. Xu, J., et al. 2022. *Design of strontium stannate perovskites with different fine structures for the oxidative coupling of methane (OCM): Interpreting the functions of surface oxygen anions, basic sites and the structure–reactivity relationship.* Journal of Catalysis 408:465-477.
10. Mukai, D., et al. 2013. *Role of support lattice oxygen on steam reforming of toluene for hydrogen production over $Ni/La_{0.7}Sr_{0.3}AlO_{3-\delta}$ catalyst.* Applied Catalysis A: General 453:60-70.
11. Rynkowski, J., P. Samulkiewicz, A. Ladavos, and P. Pomonis. 2004. *Catalytic performance of reduced $La_{2-x}Sr_xNiO_4$ perovskite-like oxides for CO_2 reforming of CH_4.* Applied Catalysis A: General 263(1):1-9.
12. Yang, E.-h., Y.S. Noh, G.H. Hong, and D.J. Moon. 2018. *Combined steam and CO_2 reforming of methane over $La_{1-x}Sr_xNiO_3$ perovskite oxides.* Catalysis Today 299:242-250.
13. Ebrahimi, P., A. Kumar, and M. Al-Marri. 2024. *Impact of magnesium substitution on the structural stability and catalytic performance of $LaNiO_3$ perovskites for methane dry reforming.* Gas Science and Engineering 205530.
14. Valderrama, G., A. Kiennemann, and M.R. Goldwasser. 2008. *Dry reforming of CH_4 over solid solutions of $LaNi_{1-x}Co_xO_3$.* Catalysis Today 133:142-148.
15. Zhang, Y., D.R. Mullins, and A. Savara. 2019. *Effect of Sr substitution in $LaMnO_3$ (100) on catalytic conversion of acetic acid to ketene and combustion-like products.* The Journal of Physical Chemistry C 123(7):4148-4157.
16. Abhirami, S. and S.S. Basha. 2020. *Phase stabilization and effect of trivalent lanthanide substitution on Dy2FeMnO6 double perovskite compounds.* Vacuum 177:109412.
17. Liu, H., et al. 2016. *La-promoted Ni-hydrotalcite-derived catalysts for dry reforming of methane at low temperatures.* Fuel 182:8-16.
18. Zinkevich, M. 2018. *Constitution of the Sr–Ni–O system.* Journal of Solid State Chemistry 178(9):2818-2824.
19. Oliveira, A.A., et al. 2018. *One-step synthesis of $LaNiO_3$ with chitosan for dry reforming of methane.* International Journal of Hydrogen Energy 43(20):9696-9704.
20. Hong, J., et al. 2019. *H_2O absorption assisted Sr-segregation in strontium nickel oxide based chromium getter and encapsulation with $SrCO_3$.* Journal of the Electrochemical Society 166(2):F59.
21. Hong, J., S.J. Heo, and P. Singh. 2021. *Water mediated growth of oriented single crystalline $SrCO_3$ nanorod arrays on strontium compounds.* Scientific reports 11(1):3368.
22. Beglaryan, H., et al. 2018. *Preparation of hydrated strontium silicates from silica hydrogel isolated from serpentines and their thermal transformations.* Russian Journal of Inorganic Chemistry 63:1395-1402.
23. MSP, S., M.M. Hossain, G. Gnanasekaran, and Y.S. Mok. 2019. *Dry reforming of propane over γ-Al_2O_3 and nickel foam supported novel $SrNiO_3$ perovskite catalyst.* Catalysts 9(1):68.
24. Hu, B., et al. 2014. *Effect of CO_2 on the stability of strontium doped lanthanum manganite cathode.* Journal of Power Sources 268:404-413.
25. Abahussain, A.A., et al. 2024. *Impact of Sr Addition on Zirconia–Alumina-Supported Ni Catalyst for CO_x-Free CH_4 Production via CO_2 Methanation.* ACS omega 9(8):9309-9320.
26. Greluk, M., M. Rotko, and S. 2020. Turczyniak-Surdacka, *Enhanced catalytic performance of La_2O_3 promoted Co/CeO_2 and Ni/CeO_2 catalysts for effective hydrogen production by ethanol steam reforming.* Renewable Energy 155:378-395.
27. Chen, M. and L. Wang.2024. *Performance of Ni-Based Catalysts with La Promoter for the Reforming of Methane in Gasification Process.* Catalysts 14(6):355.
28. Colon, G., J. Navio, R. Monaci, and I. 2000. Ferino, *CeO_2–La_2O_3 catalytic system Part I. Preparation and characterisation of catalysts.* Physical Chemistry Chemical Physics 2(19): 4453-4459.

PERFORMANCE ASSESSMENT OF A HYBRID COMPRESSED AIR ENERGY STORAGESYSTEM FED BY HYDRIGEN FROM RES

*Vittorio Tola, Roberto Caria
University of Cagliari, Department of Mechanical and Chemical Engineering, Via Marengo 2, Cagliari, 09123, Sardinia, Italy

*Corresponding author e-mail: vittorio.tola@unica.it

ABSTRACT
To mitigate the intermittency and unpredictability of renewable energy sources (RES) energy storage systems are becoming increasingly essential. This paper analyzes a hybrid energy storage system H_2-CAES, based on the integration of two storage subsystems: a hydrogen production-storage-use one and a diabatic compressed air energy storage (CAES) plant fed by hydrogen. The proposed hybrid system aims to meet the energy demand of a medium-sized municipality, maximizing the self consumption of the energy produced by a PV plant. The H_2-CAES system utilizes RES excess energy production to store energy through both compressed air and hydrogen and then releases it during periods of low production to minimize reliance on the electrical grid. The results confirm the great potential of the H_2-CAES system and the validity of integrating these storage technologies. The hybrid system exhibits good performance, high flexibility, no pollutant emissions, and allows successfully balancing RES seasonal storage. However, some issues with hydrogen storage and use are present, and energy losses are significant.

Keywords: Hydrogen, Compressed Air Energy Storage, Renewables, Hybrid Systems

1. INTRODUCTION
The increasing share of electricity production from RES has led to a significant reduction of pollutant emissions, but has introduced considerable technical challenges. The intermittency and unpredictability of RES make the development of adequate energy storage systems a priority [1]. These systems, by providing ancillary services and applications, stabilize the electrical grid and enable a further growth of renewable energy production. There are various storage technologies, divided into categories, depending on the physical principle of exploitation: mechanical (pumped hydro, compressed air energy storage (CAES), flywheels), electrochemical (batteries), electrical (supercapacitors), thermal and hydrogen [1].
In this paper a hybrid storage system based on the integration between a CAES plant and hydrogen technologies is proposed. CAES plant is a mechanical storage technology that used excess energy to compress air and store it in a natural or artificial reservoir [2]. During peak demand periods, the compressed air is expanded in a gas turbine to generate electricity. CAES plants can be classified into two categories: Diabatic CAES (equipped with a combustion chamber to heat compressed air) and Adiabatic CAES (equipped with a thermal energy storage system to accumulate the compression heat). CAES plant offer large storage capacities, flexibility, reliability, and low maintenance costs. However, overall efficiency is relatively low, and its spread is limited by the need for suitable air storage unit. Two large diabatic CAES plant were in operation since last century: the Huntorf one (Germany) and the McIntosh one (Alabama, US). Hydrogen is an energy carrier that can be used as an alternative to fossil fuels, since it shows a great calorific value and does not produce polluting emissions. Hydrogen has large applications, ranging from the transport sector to energy production, though some issues remain [3]. Though hydrogen is currently produced mainly from fossil fuels, via methane steam reforming, coal gasification, partial oxidation, or biomass pyrolysis, “Green Hydrogen” can be produced through water electrolysis exploiting renewable energy sources.
Hybrid systems integrating CAES and hydrogen have recently been evaluated. Most analyses focus on the use of hybrid H_2-CAES systems to balance the intermittency and instability of RES [4-6]. However, also the integration of these hybrid systems with thermoelectric generation and power-to-X [7-8], has also been discussed. The main function of such hybrid systems is time shifting/peak shaving or the seasonal storage of large amounts of energy. The hybridization of the two systems makes feasible and advantageous to consider a medium to small-sized CAES plant [4]. The presence of a hydrogen-based storage system would still allow for substantial storage capacities, and the hydrogen produced could be used both for electricity generation via a fuel cell and to power the combustion chamber of the CAES.

2. RES PRODUCTION AND USER DEMAND
The proposed hybrid system was studied supposing to feed a medium town of about 40000 inhabitants, with an industrial area. The total annual energy consumptions of the user are slightly lower than 270 GWh and are partially satisfied by a large photovoltaic (PV) plant. The PV plant was sized imposing an annual production equal to the user requirements. A simulation model was developed through the commercial software SAM to evaluate the PV production curve using meteorological data obtained from the NREL database.
Fig. 1 shows both the typical load profile of the user for a week (continuous line) and a weekend day (dashed line), and the typical hourly power PV production for a summer (continuous line) and winter day (dashed line). Fig. 2 shows the monthly PV energy production, user energy demand, and PV energy production directly sent to the user. .

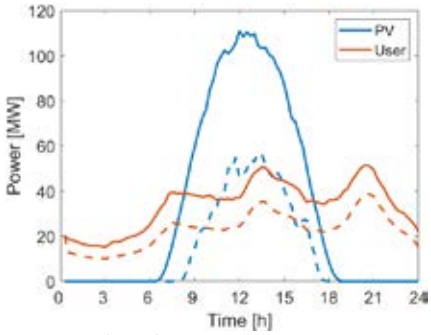

Fig 1. User load profile of a week day and a weekend day and hourly PV production for a summer and winter day

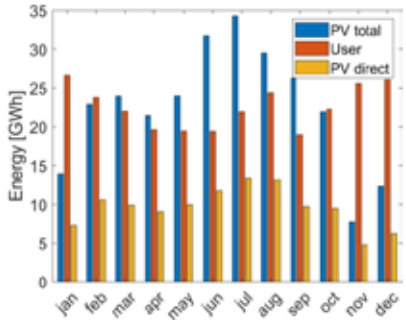

Fig 2. Monthly PV production, user demand and PV directly sent to the user

From Fig. 1 emerges as the user demand is higher during the weekday showing a peak of about 50 MW in both the afternoon and the evening. The PV production exceeds the user demand around noon, especially in summer. Fig. 2 shows that the monthly PV production is higher on summer and ranges between 7.6 and 34.3 GWh. The user demand is slightly higher in winter ranging between 19.0 and 26.6 GWh. Without any storage system, the PV plant can meet just 42.7% of the yearly user demand (115.4 of 270.0 GWh), with the grid demands being particularly high during the winter months. This situation calls for the introduction of an adequate storage system.

3. SYSTEM CONFIGURATION

The proposed energy storage system is a H_2-CAES hybrid system composed of two subsystems: a) a diabatic CAES subsystem fed by hydrogen, b) a hydrogen production, storage and use subsystem. The main objective of the storage system is to increase the share of the user energy demand directly or indirectly satisfied by the PV plant. The storage system accumulates the excess production from the PV and releases it during periods of low production to minimize the contribution of the electrical grid. The hydrogen is produced on-site by using a proton exchange membrane (PEM) electrolyzer. The H_2 subsystem also handles hydrogen storage and is equipped with a PEM Fuel Cell (PEMFC) capable of generating additional electricity. The general layout of the hybrid system H_2-CAES is shown in Fig. 3.

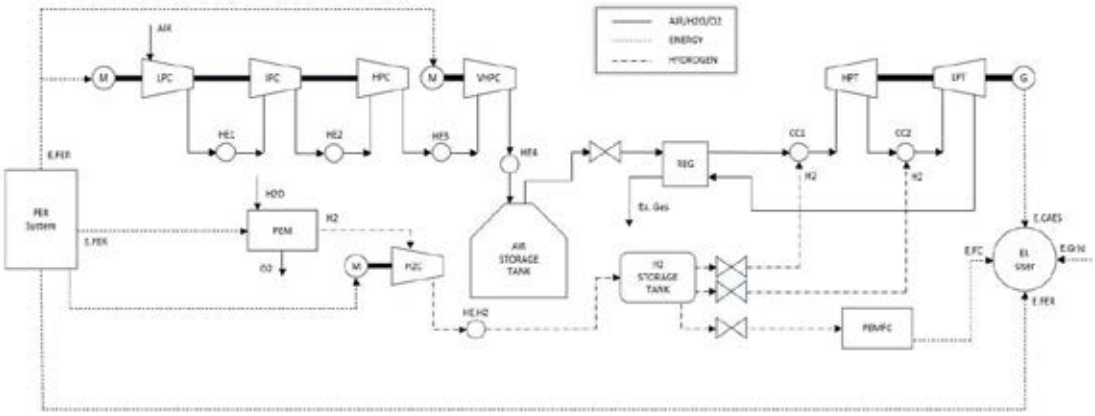

Fig. 3. Functional scheme of the H2-CAES energy storage system

3.1. The CAES subsystem

In the charge phase the CAES is fed by ambient air that is pressurized by four compressors in series: a low- (LPC), a intermediate- (IPC, a high- (HPC), and a very high- pressure (VHPC) ones. The compressed air is stored in a dedicated reservoir at a pressure ranging from 70 to 100 bar, depending on the reservoir charge level, and at a constant temperature of 35°C. The first three compressors operate at a constant pressure ratio β with an isoentropic efficiency of 0.86, while the VHPC regulates the pressure inside the reservoir by varying its rotational speed. During the discharge phase the compressed air is processed by the turbines producing electrical energy. The turbine section consists of two axial turbines on the same shaft, operating at a constant β: a high-pressure (HPT) and a low-pressure (LPT) one. The isentropic efficiency of both turbines was set equal to 0.9, while the mechanical efficiency of the plant was assumed equal to 0.97. To assure a constant operating pressure to the turbines, the air exiting the storage tank is throttled by a valve, ensuring an operating pressure of 70 bar, corresponding to the minimum pressure of the reservoir. Firstly, the airflow is preheated in a regenerative heat exchanger (REG), exploiting the residual heat from the LPT exhausts, and

then reaches 1200 °C in a combustion chamber (CC1), that is fed by hydrogen. Then the hot gas expands in the HPT and is sent to the CC2 combustion chamber, where is reheated to 1200 °C. Finally, the hot gas expands in the LPT.

3.2. The H_2 subsystem

The H_2 subsystem consists of three subsections for the production, storage, and direct use of hydrogen. The hydrogen is produced through the PEM at a pressure of 35 bar and a temperature of 25°C. The hydrogen, compressed up to 250 bar and cooled, is stored in a dedicated tank (H_2 Storage Tank) for feeding the hybrid system, while the oxygen is supposed to be released. Assuming a PEM efficiency of 0.60, the hydrogen energy density of 33.3 kWh/kg allows to produce 18.2 kg of hydrogen for each MWh absorbed. Despite the high storage pressure inside the tank, the compressor shows a quite low energy consumption, about 2% of the PEM requirements. A volume of the H_2 Storage Tank of 4920 m³ was set, imposing a maximum storage capacity of 100 tons of hydrogen. PEM fuel cells operate at relatively low temperatures, around 60-80 °C, allowing a faster start-up than other high-temperature fuel cell technologies. PEM also offers numerous advantages, including high power density, low pollutant emissions and quiet operation. A PEMFC efficiency of 0.55 was assumed in this study. Given the energy density of hydrogen, a hydrogen consumption of 0.054 kg/kWh was estimated. The role of the PEMFC in the hybrid system is to support the CAES discharge phase. The fuel cell operates to covered user energy deficits too low to be satisfied by the CAES or in case the deficit is sufficiently high to require the operation of both the subsystems. As a consequence, the size of the PEMFC is closely related to the minimum power deliverable by the CAES.

3.3. Cases studied

Three cases characterized by a different size of the main components have been analyzed. In particular, a parametric analysis of the size of the PEM electrolyzer was carried out. Table 1 summarizes the three selected cases:

Table 1. Cases analyzed

		Case 1	Case 2	Case 3
$P_{CAES,ch}$	MW	11.5-12.3	19.2-20.6	20.7-28.6
$P_{CAES,dis}$	MW	15.0	25.0	35.0
P_{PEMFC}	MW	7.5	12.5	17.5
P_{PEM}	MW	30.0-90.0	30.0-90.0	30.0-90.0

Each set was designed starting from the distribution of the residual energy expressed as the difference between the PV production and the user demand. Several sizes of the CAES subsystem were analyzed ranging from a minimum discharge power of 15 MW to a maximum of 35 MW. Since the PEMFC covers the user demand values lower than the activation threshold of the CAES turbines, (set to 50% of the nominal power) a PEMFC power equal to 50% of the CAES discharge power was selected. The variation of the size of the CAES during discharge also affects the size of the compressor unit. The PEM was finally be evaluated over a wide range of power in all cases.

4. RESULTS AND DISCUSSION

4.1. Performance Indices

To evaluate the performance of the H_2-CAES hybrid system, several performance indexes has been defined.
The Self Consumption (SC) index assesses the amount of energy produced by the PV plant E_{PV} consumed by hybrid system $E_{C,CAES} + E_{PEM}$ or directly by the user $E_{PV,dir}$ without being sent into the electrical grid. The closer this index is to 1, the more effective the storage system is in utilizing the PV energy.

$$SC = \frac{E_{C,CAES}+E_{PEM}+E_{PV,dir}}{E_{PV}} \quad (1)$$

The Self Support (SS) index evaluates the degree of satisfaction of the load demand. This index relates the energy provided directly by the PV plant $E_{PV,dir}$ and the by hybrid system components $E_{T,CAES} + E_{PEMFC}$ to the energy required by the user E_{User}.

$$SS = \frac{E_{T,CAES}+E_{PEMFC}+E_{PV,dir}}{E_{User}} \quad (2)$$

4.2. Cases studied

The operation of the H_2-CAES hybrid system strictly depends on the hourly behavior of the PV production and user request. The operation hours of the CAES charge phase range between 600 and 1600 per year. The value increases with the PEM size thanks to a greater hydrogen availability and decreases with the CAES size. Higher values of the operating hours (2500-3000) can be noticed for the PEM, with a reduction strictly related to its size. In the discharge phase both the CAES and the PEMFC increase operation hours with PEM size due to a greater availability of hydrogen and decreases with the hybrid system size do to the activation thresholds. The CAES discharge phase shows value of the operating hours ranging between 1200 and 3100, whereas the PEMFC shows lower values (550-2650 h).
Fig. 4 and Fig. 5 show the yearly energy consumption during the charge phase and the yearly energy production during the discharge phase in function of the electrolyzer size for the three different cases considered. Fig. 6 shows both the

self-consumption and the self support index as a function of the PEM size for the three cases.

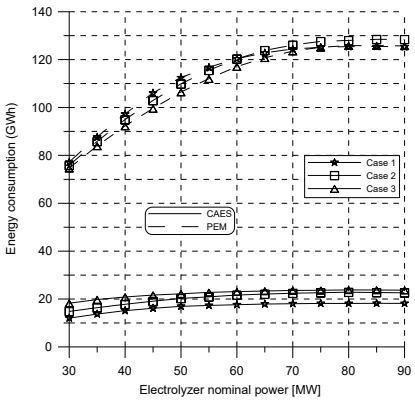

Fig. 4. Energy consumption in the charge phase as a function of PEM size

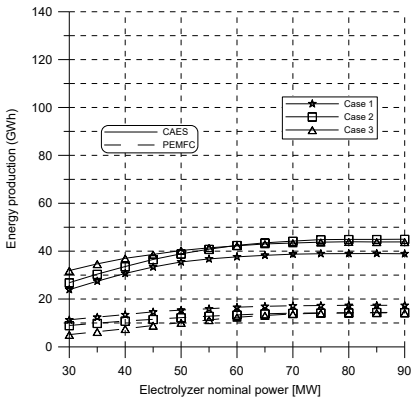

Fig. 5. Energy production in the discharge phase as a function of PEM size

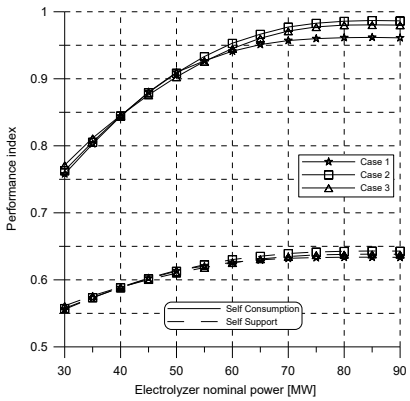

Fig. 6. Self consumption and self support indexes as a function of PEM size

Both energy consumption and energy production increase with the PEM size, due to the greater production and availability of hydrogen. For the CAES a greater size leads to a higher energy production and consumption despite a lower operating hours, but difference between case 2 and case 3 are negligible, especially at the highest PEM sizes. Small-size PEMFC assures a greater contribution to energy production thanks to a higher operation period. Globally, the H_2-CAES hybrid system contributes to satisfy the user requirements from a minimum value of about 35 MW (P_{PEM} = 30 MW) to a maximum value slightly lower than 60 MW (P_{PEM} = 90 MW).

SC index notably increases as the PEM size increases. A larger electrolyzer enhances the absorption of PV excess energy producing more hydrogen. The increase of the SC index peaks with a 80 MW PEM. Negligible differences are noticed among the three cases except for the highest PEM sizes, with case 2 showing best performance. Lowest H_2-CAES sizes do not allow to accurately exploit PV excess energy, whereas largest H_2-CAES size causes many energy deficit lower than the activation threshold. The SS index increases with the PEM size from 0.55 to 0.64. No significantly difference are noticed with the cases, with a slightly higher SS index for the case 2.

5. CONCLUSIONS

The ever increasing use of renewable energy sources makes the role of energy storage systems deeply significant as these systems overcome the limits of intermittency and non-programmability of RES. A hybrid storage system based on the integration of a CAES plant and a hydrogen production, storage, and use system was proposed. The system was integrated with a medium size city allowing to increase the self support index up to 10-20 percentage points, depending on the H_2-CAES size, starting from a reference value of 42.7%. Three different cases were analyzes in function of the H_2-CAES size with the intermediate one showing best performance. To better analyze the hybrid system behavior and identify the system size that guarantee the best performance an economic analysis is planned to be performed.

REFERENCES

1. Mitali J, Dhinakaran S, MAhamad AA. 2022. Energy storage systems: a review. Energy Storage and Saving 1:116-216.
2. Tola V, Meloni V, Spadaccini F, Cau G. 2017. Performance assessment of Adiabatic Compressed Air Energy Storage (A-CAES) power plants integrated with packed-bed thermocline storage systems. Energy 13812-18.
3. Ge L, Zhang B, Huang W, Li Y, Hou L, Xiaa J, Mao Z, Li X. 2024. A review of hydrogen generation, storage, and applications in power system. Journal of Energy Storage 75:109307.
4. Migliari L, Micheletto D, Cocco D. 2024. A hydrogen-fuelled compressed air energy storage system for flexibility reinforcement and variable renewable energy integration in grids with high generation curtailment. Energy Conversion and Management 306:118308.
5. Assareh E, Ghafouri A. 2023. An innovative compressed air energy storage (CAES) using hydrogen energy integrated with geothermal and solar energy technologies: A comprehensive techno-economic analysis - different climate areas- using artificial intelligent (AI). International Journal of Hydrogen Energy 48:12600-12621.
6. Cao R, Wang Y, Li W, Ni H, Duan Y. 2023. Thermodynamics analysis of a hybrid system based on a combination of hydrogen fueled compressed air energy storage system and water electrolysis hydrogen generator. International Journal of Hydrogen Energy 63:24492–24503.
7. Bartela L. 2020. A hybrid energy storage system using compressed air and hydrogen as the energy carrier. Energy
8. Zhao P, Xu W, Liu A, Wu W, Wang J, Wang X. 20XX. Assessment the hydrogen-electric coupled energy storage system based on hydrogen-fueled CAES and power-to-gas-to-power device considering multiple time-scale effect and actual operation constraints. Int J Hydrogen Energy 25:9198–9218.

DEVELOPMENT OF Ce-PROMOTED Ni-BASED METHANATION CATALYSTS FOR ENHANCED CH_4 PRODUCTION

[1,2]*Burcu Acar* , [2,3]*Burcu Selen Çağlayan,* [1,2*]*A. Erhan Aksoylu*
[1] Boğaziçi University, Department of Chemical Engineering, Bebek, Istanbul 34342, Turkey
[2] Boğaziçi University, SNG&HydTec Lab, Science and Technology Building, Kandilli, Istanbul 34684, Turkey
[3] Boğaziçi University, Advanced Technologies R&D Center, Bebek, Istanbul 34342, Turkey
*Corresponding author e-mail: aksoylu@bogazici.edu.tr

ABSTRACT
This study focuses on the development of Ni-based methanation catalysts with enhanced CO conversion, CH_4 selectivity, and stability under unconventional feed conditions (H_2/CO<3) by integrating methanation and WGS reactions. Various Ni-based catalysts were synthesized and evaluated to understand the effects of promoters, supports, and metal-support interactions (MSI) on catalytic performance. Among the synthesized catalysts, 5%Ce-10%Ni/γ-Al_2O_3 demonstrated the highest performance, maintaining CO conversion above 95% while minimizing carbon deposition. XPS, XRD, SEM, HR-STEM, and Raman analyses revealed that Ce incorporation enhanced Ni reducibility, improved MSI, and suppressed carbon accumulation at higher temperatures (673 K), while lower temperatures (523 K) promoted deactivation due to carbon buildup. Despite a slight reduction in metal dispersion, Ce addition improved catalyst stability and activity over prolonged operation. SBA-15-supported catalysts exhibited balanced MSI and favorable dispersion, while 5%Ce-10%Ni/ZrO_2, despite its high TOF values, exhibited lower CO conversion and CH_4 selectivity, along with stability issues at 400 °C, underscoring the complex role of MSI in catalytic performance. Stability tests confirmed that 5%Ce-10%Ni/γ-Al_2O_3 was the most durable formulation, maintaining high activity over time. Overall, these findings highlight the importance of promoter selection and MSI tuning in designing efficient and stable Ni-based methanation catalysts.

Keywords: CO Methanation, Synthetic Natural Gas, Ce-Promoted Catalysts, Ni-Based Catalysts

1. INTRODUCTION

The growing global demand for cleaner energy sources has driven extensive research into alternative fuels, like synthetic natural gas (SNG). While natural gas (primarily CH_4) is considered an efficient and environmentally friendly fossil fuel due to its high energy density and clean combustion profile, its uneven distribution and finite reserves have led to an increasing focus on SNG production via syngas methanation [1].

The conventional SNG production process begins with the gasification of coal or biomass to produce syngas (a mixture of H_2, CO, CO_2, CH_4 and minor hydrocarbons), followed by purification and methanation reactions [2]. Both methanation reactions (CO and CO_2 methanation) are exothermic, making temperature control crucial to avoid catalyst deactivation via sintering or carbon deposition. The TREMP (Topsoe Recycle Energy-efficient Methanation Process) developed by Haldor Topsøe is a widely used industrial system that employs adiabatic reactors operating at progressively lower temperatures to optimize CH_4 yield [3]. However, conventional processes typically require an H_2/CO ratio of ~3, limiting their flexibility with feedstocks exhibiting lower ratios [4].

Recent research efforts have focused on developing novel methanation catalysts capable of operating efficiently under lower H_2/CO ratios and varied reaction conditions. Ni-based catalysts are widely studied for their high activity, cost-effectiveness, and stability. However, issues like carbon accumulation, sintering, and limited high-temperature stability require further improvements [1,4]. To overcome these challenges, recent studies have investigated Ni catalysts modified with promoters such as Ce, La, Mg, and Mn, which aim to improve metal-support interactions, catalyst dispersion, and overall performance [5-10]. Si et al. [5] showed that La_2O_3 improves the catalytic activity of Ni/ZrO_2 by limiting NiO particle growth and enhancing Ni dispersion. Similarly, Hu et al. [6] demonstrated that MgO, when used as a promoter in Ni/Al_2O_3 catalysts, significantly enhances stability. Researchers have also investigated Mn-promoted Ni/Al_2O_3 catalysts, which exhibit superior CO methanation performance compared to unmodified catalysts [7,8]. Furthermore, CeO_2 has been recognized as an effective support and promoter in methanation reactions, particularly in improving CO conversion and CH_4 selectivity [9,10].

This study focuses on design and development of Ni-based methanation catalysts that integrate water-gas shift (WGS) and methanation reactions to achieve efficient methane production even under unconventional feed conditions (H_2/CO<3). By exploring a range of promoters and supports, this work seeks to maximize catalytic activity, selectivity, and stability.

2. MATERIALS AND METHODS

2.1 Catalyst Preparation

Sixteen Ni-based catalysts were synthesized via the incipient wetness impregnation, incorporating Ce, La, Mg, and Mn

as promoters and using γ-Al_2O_3, SBA-15, and ZrO_2 supports. Commercial γ-Al_2O_3 and ZrO_2 were used directly, while SBA-15 was synthesized hydrothermally with Pluronic P-123 and TEOS. For bimetallic catalysts, sequential impregnation was applied, with the promoter introduced prior to Ni loading. The samples were dried overnight at 383 K and subsequently calcined at various temperatures.

2.2 Performance Evaluation

Catalyst performance was evaluated in a fixed-bed quartz microreactor for 6 hours under H_2/CO ratios of 3, 2, and 1 at temperatures ranging from 473 to 673 K. The feed gas composition and flow rates were controlled using mass flow controllers (Brooks 5850E), and products were analyzed by gas chromatography (Agilent 6850, TCD, HayeSep D column). Stability tests were conducted for 72 hours to assess long-term performance.

2.3 Catalyst Characterization

Catalysts were analyzed using H_2-chemisorption (Micromeritics 3Flex) for dispersion and TOF, SEM (Philips XL 30 ESEM-FEG) and HR-STEM (Hitachi HF5000 200kV) for morphology and dispersion, XRD (Bruker D8 Discover) for crystalline phases, XPS (Phi 5000 VersaProbe III) for oxidation states and electronic interactions, and Raman spectroscopy (Renishaw inVia, 514 nm laser) for coke formation on spent catalysts.

3. RESULTS AND DISCUSSION

3.1 Effect of H_2/CO Ratio

CO methanation reactions were conducted at 673 K for H_2/CO ratios of 3, 2, and 1. At H_2/CO = 3, most catalysts exhibited high CO conversion values (93–99%), except for 5%Ce-10%Ni/ZrO_2 (86.5%). The highest CH_4 selectivity (76.2%) was observed for 5%Ce-10%Ni/SBA-15-550. Reducing the H_2/CO ratio to 2 led to a drop in CO conversion for 1%Mg-10%Ni/γ-Al_2O_3 (92.9%→84.2%) and 15%Ni/SBA-15-750 (92.7%→72.6%), while other catalysts showed little change in performance. At H_2/CO = 1, both CO conversion and CH_4 selectivity declined for all catalysts. The highest CO conversion (84.6%) was observed for 1.7%Mn-15%Ni/γ-A_2O_3 (Fig.1).

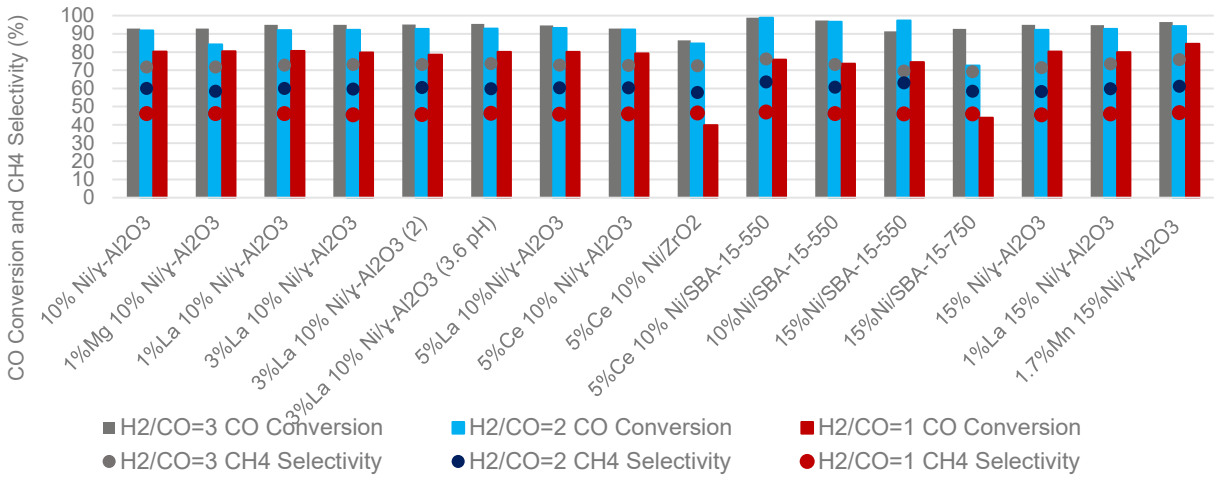

Fig. 1. Average CO conversion and CH_4 Selectivity values for 6-hour experiments conducted at 673 K for three H_2/CO ratios of 3, 2, and 1.

To evaluate the effect of temperature, six-hour performance tests were conducted with an H_2/CO ratio of 3 at five different temperatures: 473 K, 523 K, 573 K, 623 K, and 673 K. As discussed, the CO conversion value was highest for 5%Ce-10%Ni/SBA-15-550 at 673 K. When the temperature was reduced to 623 K, the CO conversion of 15% Ni/SBA-15-750 catalyst decreased significantly, from 92.7% to 45.2%. In contrast, the performance of other catalysts remained stable, maintaining high CO conversion values. At 573 K, both 10% Ni/SBA-15 and 15%Ni/SBA-15-750 exhibited the lowest performance, with CO conversion dropping to 36.6% and 7%, respectively. Other catalysts showed moderate declines in activity but maintained acceptable performance levels. At 523 K, only six catalysts demonstrated measurable CO conversion (Fig. 2). These catalysts were further tested at 523 K with an H_2/CO ratio of 2, confirming the superior performance of the 5%Ce-10%Ni/γ-Al_2O_3 catalyst (Fig. 3).

The stability of 5%Ce-10%Ni/γ-Al_2O_3 was evaluated under different conditions. At 673 K and H_2/CO ratios of 3 and 2, the catalyst maintained stable CO conversion (94% and 90%, respectively) over 72 hours. However, at 523 K with an H_2/CO ratio of 2, CO conversion declined from 95% to 79%, indicating activity loss due to carbon deposition.

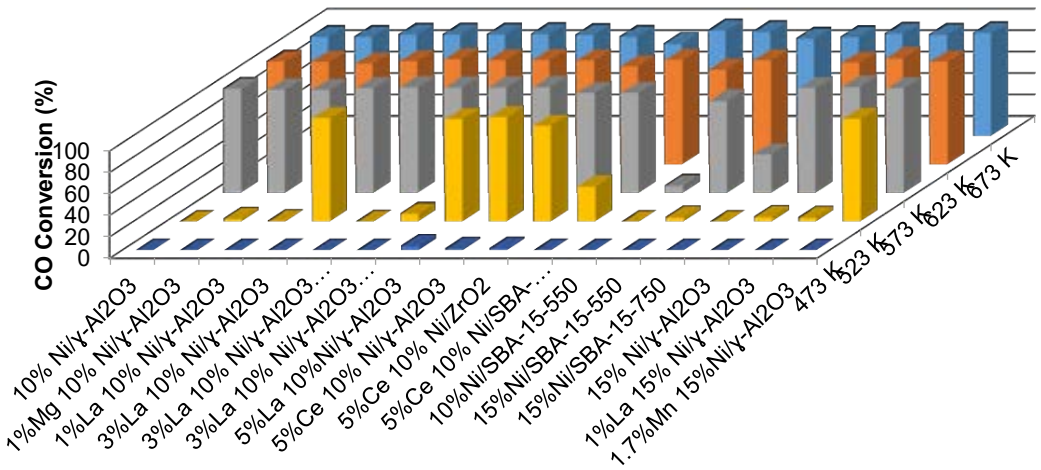

Fig. 2. Average CO conversion values for 6-hour performance tests conducted with H2/CO=3 at 5 different temperatures for all catalysts.

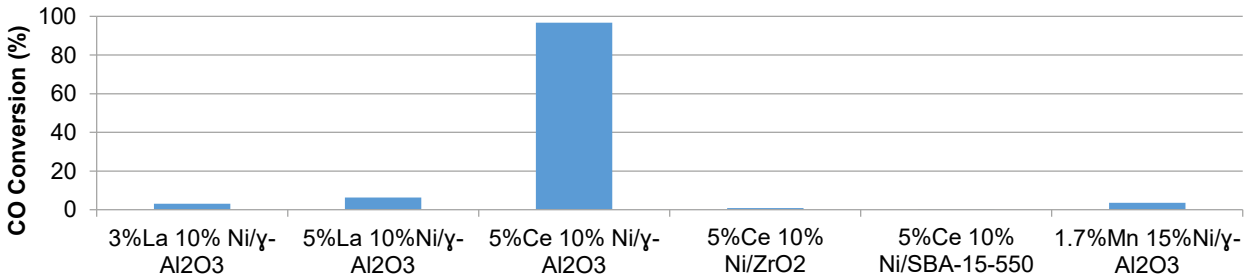

Fig. 3. Average CO conversion and CH4 yield values for 6-hour performance tests conducted with H2/CO=2 at 523 K.

3.3 Characterization

Given its superior CO methanation performance, 5%Ce-10%Ni/γ-Al_2O_3 was selected for detailed characterization alongside 5%Ce-10%Ni/SBA-15-550, 5%Ce-10%Ni/ZrO_2, and 10%Ni/γ-Al_2O_3.

SEM imaging revealed that Ni dispersion and particle distribution were significantly influenced by the support type. On γ-Al_2O_3, Ni clusters were unevenly dispersed, with cracks that could facilitate reactant diffusion. Contrary to expectations, Ce incorporation decreased Ni dispersion, as confirmed by H_2 chemisorption results, with Ce-Ni interactions evidenced in high-magnification SEM images. The ZrO_2-supported catalyst displayed an irregular Ni-Ce distribution, suggesting strong MSI that may stabilize Ni but restrict its accessibility. In contrast, SBA-15 exhibited a well-defined mesoporous structure, which favored higher Ni dispersion and enhanced reactant diffusion. STEM-EDS mapping confirmed these findings, showing that Ce preferentially decorated Ni particles, particularly in Ce-promoted γ-Al_2O_3 catalysts, thereby influencing stability and electronic interactions.

XRD confirmed metallic Ni as the active phase. $NiAl_2O_4$ formation was observed in γ-Al_2O_3-supported samples, potentially impacting reducibility. XPS indicated that Ce altered Ni's electronic environment, enhancing its reducibility and oxygen mobility, thus stabilizing Ni during methanation. Raman spectroscopy revealed carbon deposition as a major deactivation factor, with higher coke formation at 523 K compared to 673 K, further supporting the role of temperature in mitigating deactivation.

3.4 TOF Analysis

TOF values were calculated at multiple temperatures to assess the intrinsic activity of Ni sites in Ce-promoted catalysts. While 10%Ni/ γ-Al_2O_3 exhibited the highest dispersion (6.99%), 5%Ce-10%Ni/ZrO_2 had the lowest (3.33%), indicating that the support material significantly influenced metal distribution. The SBA-15-supported catalyst (6.23%) achieved a balance between dispersion and activity due to its mesoporous structure. Despite the reduction in Ni dispersion with Ce addition, Ce-containing catalysts exhibited higher TOF values, highlighting the role of MSI in enhancing reaction rates, which is consistent with SEM and HR-STEM findings (Fig. 4).

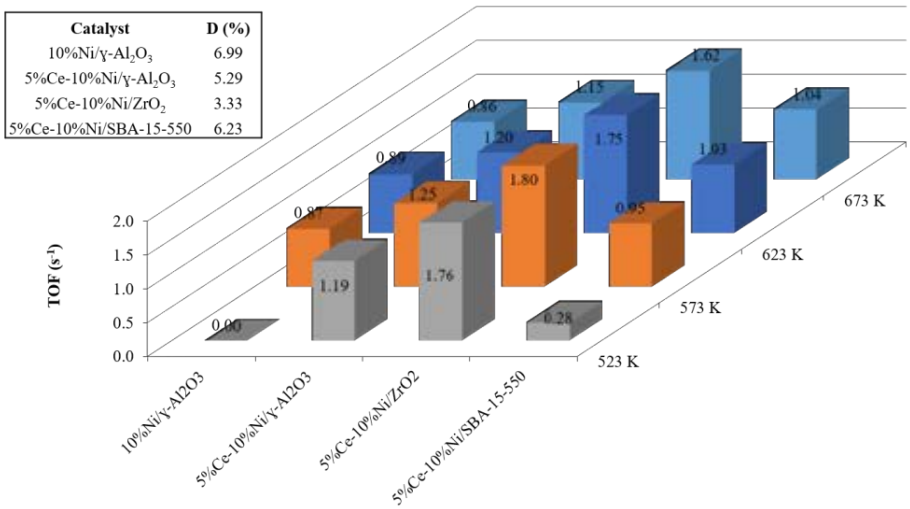

Fig. 4. TOF values for 6-hour performance tests conducted with H2/CO=3 at 4 different temperatures

4. CONCLUSIONS

This study focused on developing high-performance Ni-based methanation catalysts, enabling efficient methane production under unconventional feed gas compositions. Various catalysts were synthesized with different metal compositions, precursor types, loadings, and preparation methods. Among them, 5%Ce-10%Ni/SBA-15-550 demonstrated the highest CO conversion at 673 K for H_2/CO ratio of 3, while 5%Ce-10%Ni/ZrO_2 exhibited the lowest conversion. Additionally, at 523 K and reduced H_2/CO ratio of 2, the 5%Ce-10%Ni/ γ-Al_2O_3 catalyst demonstrated superior catalystic performances, reinforcing its stability and effectiveness under challenging reaction conditions.

Comprehensive characterization of 5%Ce-10%Ni/γ-Al_2O_3, 5%Ce-10%Ni/SBA-15-550, 5%Ce-10%Ni/ZrO_2, and 10%Ni/γ-Al_2O_3 provided key insights into structure-activity relationships. XPS analysis identified metallic Ni, NiO, and Ni^{2+} species, with Ce incorporation shifting binding energies, reducing NiO peaks, and enhancing Ni reducibility. XRD analysis revealed the presence of $NiAl_2O_4$ formation in Ce-promoted catalysts, while Raman spectroscopy confirmed that lower temperatures (523 K) accelerated carbon deposition, impacting catalyst durability. SEM and TEM demonstrated distinct Ce-Ni clustering, highlighting the role of metal-support interactions in Ni dispersion and catalytic efficiency. TOF analysis demonstrated that Ce promotion enhanced catalytic activity despite a slight decrease in Ni dispersion, underscoring the significance of MSI. While 5%Ce-10%Ni/ZrO_2 exhibited the highest TOF values, its overall CO conversion remained the lowest, indicating that strong MSI can improve reaction rates but may also limit overall catalytic efficiency depending on the support material.

REFERENCES

1. Wang H, Pei Y, Qiao M, Zong B. 2017. Advances in Methanation Catalysis. Catalysis 29:1-28.
2. Gao J, Wang Y, Ping Y, Hu D, Xu G, Gu F, Su F. 2012. A Thermodynamic Analysis of Methanation Reactions of Carbon Oxides for the Production of Synthetic Natural Gas. RSC Advances 2:2358–68.
3. Bell DA, Towler BF, Fan M. 2011. Coal Gasification and its Applications. Elsevier, Oxford.
4. Gao J, Liu Q, Gu F, Liu B, Zhong Z, Su F. 2015. Recent Advances in Methanation Catalysts for the Production of Synthetic Natural Gas. RSC Advances 5:22759–22776.
5. Si J, Liu G, Liu J, Zhao L, Li S, Guan Y, Liu Y. 2016. Ni Nanoparticles Highly Dispersed on ZrO2 and Modified with La2O3 for CO Methanation. RSC Advances 6:12699-707.
6. Hu D, Gao J, Ping Y, Jia L, Gunawan P, Zhong Z, Xu G, Gu F, Su F. 2012. Enhanced Investigation of CO Methanation over Ni/Al2O3 Catalysts for Synthetic Natural Gas Production. Industrial & Engineering Chemistry Research 51:4875-86.
7. Chang Z, Liu Z, Wang C, Li J, Zeng J, Liu Y, Zhang M, Li J, Yu F. 2021. Three-dimensional porous Mn–Ni/Al2O3 microspheres for enhanced low temperature CO hydrogenation to produce methane. International Journal of Hydrogen Energy 46:7912-25.
8. Zhao A, Ying W, Zhang H, Ma H, Fang D. 2012. Ni/Al2O3 catalysts for syngas methanation: Effect of Mn promoter. Journal of Natural Gas Chemistry 21:170-7.
9. Michalska K, Kowalik P, Próchniak WM. 2019. Methanation at Very Low COx/H2 Ratio: Effect of Ce on Ni–Ce–Al Catalyst Properties and Empirical Kinetics. Catal Lett 149:338–346.
10. Zhang W, Liu Y, Dong Y, Hao Y, Chen L, Li J, Zeng S, Wang H. 2022. Ceria engineering in nickel catalysts to improve CH4 selectivity and yield for CO methanation. Applied Surface Science 598:153802-13.

A MECHANISTIC DRIFTS-MS INVESTIGATION AND ACTIVE INTERMEDIATE DETERMINATION OF DRM AT LOW TEMPERATURE OVER Ru-La/ZrO_2 CATALYST

[1,2]*Onur Ordulu*, [2]*Ali Uzun,* [1,2]*Cihat Öztepe,* [1,2]*B. Merve Eropak,* [2,3]*Burcu Selen Çağlayan*, [1,2,3*]*Ahmet Erhan Aksoylu*
[1] Department of Chemical Engineering, Boğaziçi University, 34342 Bebek, Istanbul, Turkey
[2] SNG&HydTec Lab, Boğaziçi University, 34684 Kandilli, İstanbul, Turkey
[3] Advanced Technologies R&D Center, Boğaziçi University, 34342 Bebek, Istanbul, Turkey

*Corresponding author e-mail: aksoylu@bogazici.edu.tr

ABSTRACT
The dry reforming of methane (DRM) is a promising route for syngas production and greenhouse gas mitigation. However, its high-temperature requirement (700–1000°C) presents challenges for industrial implementation. This study investigates low-temperature DRM (≤500°C) over a Ru-La/ZrO_2 catalyst using *operando* DRIFTS-MS to elucidate reaction mechanisms and identify active intermediates. The results reveal a strong correlation between linearly adsorbed CO on Ru^0 sites (1980 cm^{-1}) and catalytic activity, suggesting CO-Ru^0 as a key active intermediate. Temperature-dependent experiments (440–480°C) indicate a mechanistic shift around 450°C, attributed to enhanced reverse water-gas shift (RWGS) reaction contributions. Deconvolution of DRIFTS spectra confirms that CO-Ru^0 peak intensities align with methane conversion trends, highlighting their role in the reaction pathway. These findings provide crucial insights into “surface group-activity” relationships and pave the way for optimizing catalyst design for efficient low-temperature DRM.

Keywords: *Operando* DRIFTS-MS, low temperature DRM, reaction mechanism, active intermediate, surface group-activity relations

1. INTRODUCTION

The dry reforming of methane (DRM) has been widely investigated due to its substantial environmental and industrial benefits. From an environmental perspective, DRM facilitates the concurrent conversion of two potent and thermodynamically stable greenhouse gases, CO_2 and CH_4, thereby mitigating their atmospheric impact. Industrially, this process is highly advantageous as it generates synthesis gas, a crucial feedstock for the production of valuable hydrocarbons via Fischer-Tropsch synthesis.

Due to its highly endothermic nature, the DRM reaction conventionally necessitates high temperatures to achieve optimal performance. Most studies on DRM catalyst development have focused on reaction temperatures ranging from 700°C to 1000°C [1]. However, the requirement for such elevated temperatures presents a considerable challenge, particularly in industrial applications, where maintaining these conditions demands substantial energy input, making the process both energy-intensive and economically less viable. This highlights the critical need to lower the operating temperature to facilitate the broader industrial adoption of DRM [2].

In response to the challenges associated with the high-temperature DRM process, there has been a growing focus on low-temperature DRM studies in recent years. These studies, typically conducted at reaction temperatures below 500°C (or 550°C), are characterized by significantly lower conversion levels, primarily due to thermodynamic and kinetic limitations. To address these issues, researchers are actively investigating methods to enhance catalyst activity at reduced temperatures while ensuring stable performance. The incorporation of noble metals, either as promoters or active metals, has become a common strategy for improving catalyst efficiency in these low-temperature DRM reactions [1,3,4].

Understanding the complex mechanisms occurring on low-temperature DRM catalysts is essential, as such insights could provide valuable information for addressing the challenges associated with slow reaction kinetics at lower temperatures. *Operando* spectroscopic techniques are particularly well-suited for probing reaction characteristics, such as surface species and active intermediates, while concurrently monitoring the catalyst's performance. This approach enables the establishment of “surface group-activity” relationships, a critical step in elucidating the catalyst properties that govern its overall performance.

Operando DRIFTS studies provide critical insights into the reaction pathway, the nature of active sites, the role of catalyst components, and reactant activation mechanisms, among other factors. While such information has been extensively explored for conventional DRM temperatures, the mechanisms at low temperatures remain largely unexplored. This study aims to systematically investigate the catalytic mechanisms and identify active intermediate species in the low-temperature DRM reaction over a bimetallic Ru-La/ZrO_2 catalyst, utilizing advanced *operando* and transient techniques with an integrated DRIFTS-MS system.

2. EXPERIMENTAL

2.1. Catalyst Preparation

The preparation procedure begins with crushing and sieving monoclinic ZrO_2 pellets (Alfa Aesar, >95%) into particles

with a size range of 125-250 µm (60-120 mesh). The support is then calcined at 800 °C for 4 hours in air using a muffle furnace. The La loading step precedes the Ru impregnation process for catalyst preparation. Initially, 5 g of the calcined support is placed in a Büchner flask, and the pores of the support are evacuated under a vacuum of 0.82 atm for 30 minutes prior to impregnation. Meanwhile, a precursor solution is prepared by dissolving 1 g of $La(NO_3)_3 \cdot 6H_2O$ (Alfa Aesar, 99.9%) in 3 ml of deionized water. Once the support pores have been adequately evacuated, the precursor solution is introduced at a rate of 0.75 ml/min. After impregnation, the sample is placed in an ultrasonic bath for 90 minutes to ensure uniform distribution. The concentration of the precursor solution is calculated to achieve a 6 wt% La loading on the freshly reduced sample. The resulting sample is then dried overnight at 110 °C, followed by calcination at 500 °C for 4 hours in air using a muffle furnace. The same procedure is repeated for Ru loading, where 2.56 ml of $Ru(NO)(NO_3)_3$ (Alfa Aesar, 15.5 g of Ru per liter of solution) precursor solution is added to 4.27 g of the La/ZrO_2 sample. This volume corresponds to a targeted Ru loading of 0.92 wt%. Finally, the bimetallic catalyst is reduced in-situ before each experiment at 500 °C with 25% H_2 in an inert atmosphere.

2.2. Deconvolution DRIFTS Spectra

The deconvolution procedure was performed using OriginPro 2023b software. Initially, baseline correction was applied to the spectrum. To address the low signal-to-noise ratio, smoothing was conducted using a 17-point Savitzky-Golay algorithm with a second-order polynomial. Peak identification was achieved through local maxima and second derivative analyses. The selected peaks for fitting were modeled as Voigt profiles. The fitting procedure was carried out using the Levenberg-Marquardt algorithm.

3. RESULTS AND DISCUSSION

3.1. Elucidating the Mechanism

Among the various *operando* DRIFTS-MS experiments conducted, linearly adsorbed CO on metallic Ru sites (observed around 1980 cm^{-1} in the DRIFTS spectra) consistently correlated with catalytic performance, similar to what has been reported in previous studies [5]. The experimental results presented thus far are sufficient to establish a qualitative correlation between MS data and the intensity of this specific peak. To investigate this relationship further, the CO-Ru^0 peak was analyzed during the initial stages of its progression under feed flow. A total of 80 spectra were recorded at a rate of 3.6 seconds per spectrum, with MS focusing exclusively on CO analysis, reducing its cycle time to 1.1 seconds. Fig. 1 displays the 80 spectra obtained using this approach.

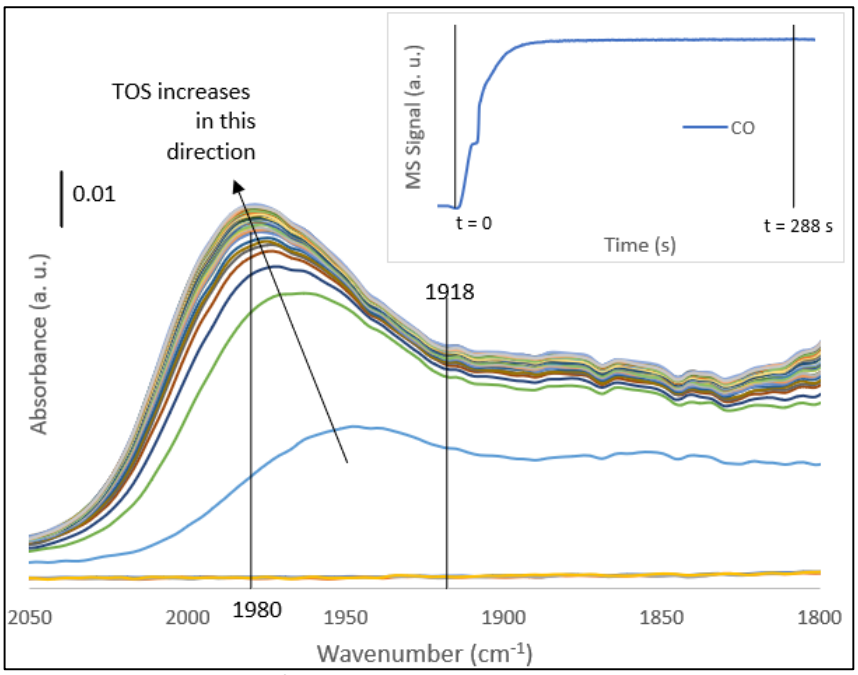

Fig. 1. Evolution of CO-Ru^0 peak within 288 seconds after initial contact with feed.

The region between 2100 cm^{-1} and 1800 cm^{-1} shown in Fig. 1 was found to be adequately represented by two distinct peaks: one at approximately 1980 cm^{-1} and a shoulder at 1918 cm^{-1}, as depicted in Fig. 1. The peak at 1980 cm^{-1} is the primary focus, as it correlates with the activity trends observed from MS measurements. The shoulder at 1918 cm^{-1} must also be considered in the analysis, as its influence needs to be differentiated from the evolution of the linearly adsorbed

CO-Ru peak. Notably, Fig. 1 demonstrates how, as the time on stream (TOS) analysis progresses, the intensity of the linearly adsorbed CO-Ru peak increases, while shifting to higher wavenumbers. To isolate the effects of these two peaks, peak deconvolution was performed on the 16 spectra that span the transient phase. Fig. 2 shows the relationship between activity and the deconvoluted peak areas.

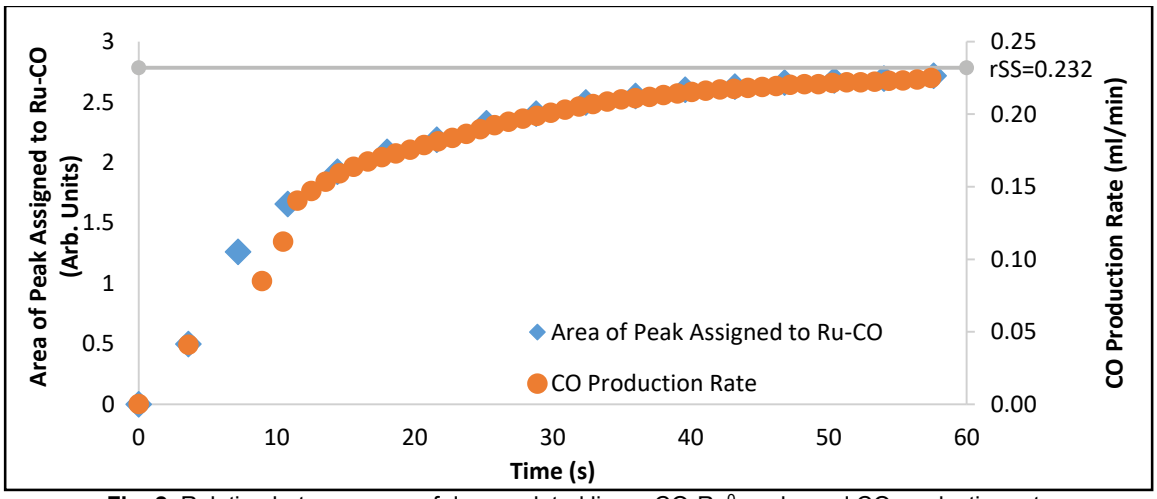

Fig. 2. Relation between area of deconvoluted linear CO-Ru^0 peaks and CO production rate

Fig. 2 confirms that the rapid *operando* measurements support the qualitative observations from earlier experiments, showing a strong correlation between the evolution of the linearly adsorbed CO-Ru peak and catalytic activity. The areas of the deconvoluted CO-Ru peaks exhibit an increase, though the rate of this increase slows over time on stream. This behavior is qualitatively reflected in Fig. 1, where the initial rapid rise in CO-Ru peak intensity for the first few spectra is followed by a more gradual and diminishing increase until the peak stabilizes at a steady-state value.
A similar methodology to that used in this study was applied to investigate Au active sites on Au/TiO_2 catalysts [6], where band fitting of carbonate, formate, and carbonyl region peaks facilitated the identification of the active intermediate. The authors argue that if a surface species is an active intermediate, its peak areas in the deconvoluted spectra over time should correlate with the observed catalytic activity. Based on this principle, the alignment between the deconvoluted areas of the linearly adsorbed CO-Ru^0 peaks and the CO production rate (as shown in Fig. 2) provides compelling evidence that CO-Ru^0 species act as active intermediates in the reaction.

3.2. Temperature Investigation

The mechanism was further investigated at temperatures ranging from 440°C to 480°C in 10°C intervals. Fig. 3 combines activity measurements (via MS) with the intensities of peaks attributed to linearly adsorbed CO on metallic Ru sites at different temperatures, illustrating the mechanism shift that occurs around 450°C.

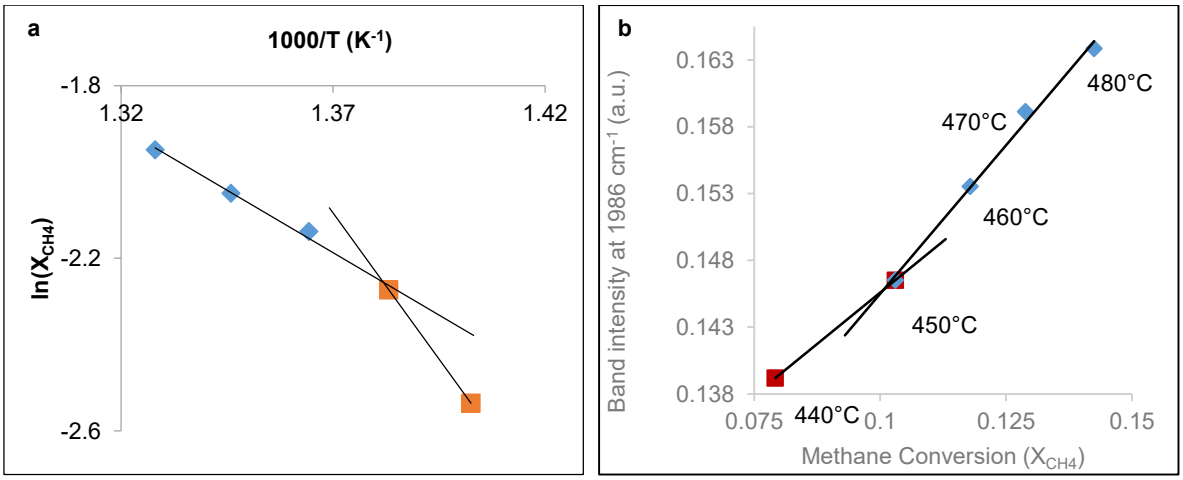

Fig. 3. Natural logarithm of observed methane conversion values versus reciprocal of temperature (in K) values (a) and CO-Ru^0 related peak intensities at observed methane conversion values (b) at 440-480°C.

Fig. 3a resembles an Arrhenius plot and demonstrates that MS readings at five different temperatures indicate a shift in activation energy near 450°C. *Operando* experimental conditions confirmed this observation through DRIFTS spectra band intensities. The strong correlation between the CO-Ru^0 peak and DRM progression (established in this study) is utilized in Fig. 3b. The results show that the behavior of CO-Ru^0 intensities in relation to methane conversion exhibits distinct patterns below and above 450°C. The change in slope around 450°C can be attributed to the increased effectiveness of the RWGS reaction at lower temperatures. CO produced via RWGS, rather than methane conversion, would result in lower band intensity for a given conversion, which is exactly what is observed in Fig. 3b at lower temperatures.

4. CONCLUSIONS

Operando FTIR-DRIFTS-MS experiments have revealed a correlation between the linearly adsorbed CO-Ru peak and measured catalytic activity. The areas of the deconvoluted peaks from FTIR-DRIFTS spectra and the CO production rate recorded by MS were integrated and analyzed comparatively to elucidate surface group-activity relationships for the bimetallic Ru-La/ZrO_2 catalyst. The strong alignment between the deconvoluted peak areas and CO production rates provides compelling evidence designating linearly adsorbed CO-Ru^0 species as the active intermediate for the low-temperature DRM reaction under the studied conditions. Temperature-variant *operando* DRIFTS-MS experiments conducted between 440°C and 480°C revealed methane conversion trends that indicated a mechanism shift around 450°C. This observation was further supported by concurrent DRIFTS spectra, which showed a change in the evolution of CO-Ru^0 related peak intensities, with a notable alteration in slope near 450°C.

ACKNOWLEDGEMENT

Financial support for this work has been provided by Presidency of the Republic of Turkey, Department of Strategy and Budget (Ministry of Development) through project 2016K12-2838.

REFERENCES

1. Soria MA, Mateos-Pedrero C, Guerrero-Ruiz A and Rodríguez-Ramos I. 2011. Thermodynamic and experimental study of combined dry and steam reforming of methane on Ru/ZrO_2-La_2O_3 catalyst at low temperature. International Journal of hydrogen energy, 36(23), 15212-15220.
2. Shen D, Li Z, Shan J, Yu G, Wang X, Zhang Y, Liu C, Lyu S, Li J, and Li L. 2022. Synergistic Pt-CeO_2 interface boosting low-temperature dry reforming of methane. Applied Catalysis B, 318, 121809.
3. Ji H, Feng D, and He Y. 2010. Low-temperature utilization of CO_2 and CH_4 by combining partial oxidation with reforming of methane over Ru-based catalysts. Journal of Natural Gas Chemistry, 19(6), 575-582.
4. Singha RK, Yadav A, Shukla A, Kumar M, and Bal R. 2017. Low-temperature dry reforming of methane over Pd-CeO_2 nanocatalyst. Catalysis Communications, 92, 19-22.
5. Androulakis A, Yentekakis IV, and Panagiotopoulou P. 2023. Dry reforming of methane over supported Rh and Ru catalysts: Effect of the support (Al_2O_3, TiO_2, ZrO_2, YSZ) on the activity and reaction pathway. *International Journal of Hydrogen Energy*, 48(63), 33886-33902.
6. Wang J, Kispersky VF, Delgass WN, and Ribeiro FH. 2012. Determination of the Au active site and surface active species via *operando* transmission FTIR and isotopic transient experiments on 2.3 wt.% Au/TiO_2 for the WGS reaction. Journal of Catalysis, 289, 171-178.

OPERANDO DRIFTS INVESTIGATION OF ACTIVE INTERMEDIATES IN CO_2 METHANATION OVER Ni-La/γ-Al_2O_3 CATALYSTS UNDER LOW H_2/CO_2 FEED RATIOS

[1,2]*Cihat Öztepe*, [1,2]*Onur Ordulu*, [2]*Ali Uzun,* [1,2]*B. Merve Eropak,* [2,3]Burcu Selen Çağlayan, [1,2]*A. Erhan Aksoylu*
[1] *Department of Chemical Engineering, Boğaziçi University, Bebek, Istanbul 34342, Turkey*
[2] *SNG&HydTec Lab, Sci. and Tech. Building, Boğaziçi University, Kandilli, Istanbul 34684, Turkey*
[3] *Advanced Technologies R&D Center, Boğaziçi University, Bebek, Istanbul 34342, Turkey*

*Corresponding author e-mail: aksoylu@bogazici.edu.tr

ABSTRACT
Operando FTIR-DRIFTS-MS was employed to elucidate the CO_2 methanation mechanism over Ni-La/γ-Al_2O_3 catalysts under conditions mimicking methane-to-hydrogen fuel processor (FP) systems, specifically focusing on low H_2/CO_2 feed ratios, such as 1:1. The study provided insights into reaction pathways and active intermediates, revealing that CO_2 methanation primarily proceeds via H-assisted CO_2 dissociation, with weakly bridged CO species identified as critical intermediates for CH_4 formation. The study quantitatively and qualitatively assessed the dynamics of surface intermediates, emphasizing the crucial role of weakly bridged CO in CH_4 production, while formate species were found to act as spectators. These results offer significant insights into the catalytic behavior of Ni-La/γ-Al_2O_3 under non-stoichiometric conditions, enhancing our understanding of the underlying mechanisms in CO_2 methanation. This work further contributes to the development of more efficient catalysts for CO_2 utilization in FP-PEMFC systems, advancing strategies for carbon capture and utilization to mitigate CO_2 emissions and support sustainable energy solutions.
Keywords: CO_2 Utilization, CO_2 Methanation at Low H_2/CO_2 Ratio, Operando DRIFTS, Active Intermediate

1. INTRODUCTION

CO_2 methanation, the catalytic conversion of CO_2 into methane, represents a promising strategy for mitigating CO_2 emissions, particularly in fuel processor (FP)-PEMFC systems. However, the characteristic low H_2/CO_2 feed ratio in these systems presents a significant challenge for achieving efficient methanation. The catalytic performance of Ni-La/γ-Al_2O_3 catalysts was rigorously assessed through both experimental investigations and computational modeling approaches tailored to these specific conditions [1]. Operando DRIFTS, a powerful technique for probing reaction mechanisms, was utilized in this study to elucidate the CO2 methanation mechanism under non-stoichiometric H_2/CO_2 feed ratios. The literature identifies two primary reaction pathways for Ni-based catalysts on Al_2O_3 supports: the H-assisted CO formation route and the direct dissociation of CO_2 into surface-bound CO, both of which subsequently undergo hydrogenation [2,3]. Furthermore, alternative mechanisms, such as the formate- and CO-routes, have been proposed to account for surface reaction dynamics under varying conditions [4,5]. In this study, operando DRIFTS, combined with FTIR and MS, was applied to investigate the CO_2 methanation mechanism over Ni-La/γ-Al_2O_3 catalysts under low H_2/CO_2 feed ratios, mimicking conditions found in FP-PEMFC systems.

2. EXPERIMENTAL

2.1. Catalyst Preparation

The high surface area γ-Al_2O_3 pellets (commercial Alfa Aesar) were used as the support material in this study. These pellets were crushed and sieved to a particle size of 0.250-0.354 mm (45-60 mesh), and the sieved γ-Al_2O_3 was directly tested as a support in preliminary experiments. To prepare the support for catalyst synthesis, the sieved γ-Al_2O_3 was calcined at 600 °C for 3 hours. For catalyst preparation, Ni was impregnated onto the support via the incipient wetness impregnation method. A $Ni(NO_3)_2{\cdot}6H_2O$ precursor was dissolved in deionized (DI) water to achieve the desired 15 wt.% Ni loading. Following impregnation, the sample was dried at 110 °C for 12 hours and subsequently calcined at 600 °C for 4 hours to obtain the Ni/γ-Al_2O_3 catalyst. In the case of promoted catalysts, La was introduced by impregnation with $La(NO_3)_3{\cdot}6H_2O$ prior to Ni addition. The wet sample was dried at 110 °C for 12 hours and calcined at 600 °C for 4 hours to obtain the La/Ni/γ-Al_2O_3 catalyst.

2.2. FTIR-DRIFTS-MS System and Operando DRIFTS Experiments

The FTIR-DRIFTS-MS system integrates feed preparation, FTIR-DRIFTS, and gas analysis components. The desired gas mixture is introduced into a Pike Technologies DRIFTS cell with a ZnSe window, and the temperature is controlled by a PIKE Technologies temperature controller. Absorbance spectra are recorded using a Bruker Vertex 70V FTIR instrument, coupled with a Mercury-Cadmium-Telluride (MCT) detector. Outlet gas analysis is conducted using a Hiden Analytical HPR-20 R&D mass spectrometer, allowing real-time tracking of gas concentration changes alongside FTIR measurements. A 4-way valve ensures flexible feed stream transitions for dynamic experimental conditions.
DRIFTS experiments were conducted on γ-Al_2O_3, La/γ-Al_2O_3, Ni/γ-Al_2O_3, and Ni-La/γ-Al_2O_3 samples in the FTIR-DRIFTS-MS system to investigate the CO_2 methanation reaction mechanism under low H_2/CO_2 feed ratios. Samples were mixed with CaF_2 powder to enable accurate FTIR spectra measurements at 350 °C, overcoming the dark color of reduced Ni catalysts. The mixture was crushed to a homogeneous consistency and placed into the ceramic sample holder of the DRIFTS cell, which is equipped with a ZnSe window to facilitate IR beam penetration.

In-situ reduction was performed from room temperature to 600 °C under H_2 flow, followed by cooling to the experimental temperature in an inert He flow. Each experiment included a 30-minute He flush at the beginning and end. FTIR spectra were recorded in the 4000-800 cm^{-1} range with a resolution of 4 cm^{-1}, using a background spectrum from the initial He flush step. Two methods were employed: the standard method, with steady-state evaluations and 128 scans recorded at intervals (1, 3, 5, 10, 20, and 30 minutes), and the quick measurement method, recording spectra every 3.6 seconds for the first 5 minutes to capture transient behavior. The product stream in these experiments was monitored using MS analysis. DRIFTS experiments with standard measurements were conducted to investigate CO, CO_2, and H_2 adsorptions, as well as low H_2/CO_2 reactions, while quick measurements were employed to study CO_2 adsorption and reactions under both low and stoichiometric H_2/CO_2 feed ratios, including specific sequential and stepwise adsorption or reaction tests. All experiments were conducted with a total flow rate of 50 ml/min and each step lasting 30 minutes to reach steady-state conditions.

2.3. Peak Deconvolution for FTIR Spectra

The carbonyl region of the spectra obtained during the reaction experiment with an H_2/CO_2 feed ratio of 1:1 was qualitatively assessed to explore a potential correlation between weakly bridged CO species and CH_4 production. Peak deconvolution was performed in the 2110-1740 cm^{-1} range, focusing on linearly bonded CO, weakly bridged CO, and strongly bridged CO species. Using OriginPro 2023b software, non-linear fitting with a Voigt function model was applied to optimize the peak locations and calculate the weakly bridged CO peak area. The MS signal for CH_4 was converted to CH_4 production rates using calibration, and a potential relationship between the surface concentration of weakly bridged CO species and CH_4 production was analyzed.

3. RESULTS AND DISCUSSION

3.1. DRIFTS Evaluation for Adsorption and Reaction Experiments

The FTIR-DRIFTS-MS system was utilized for quick measurements alongside standard experiments, particularly to examine transient phenomena in the reaction over the Ni-La/Al_2O_3 catalyst, in addition to experiments on reactant adsorptions. DRIFT spectra recorded at 350°C for the first 36 seconds in Fig. 1a revealed key surface transformations. The initial spectrum (0th) corresponded to the final He flush, while the 1st spectrum remained unchanged due to system dead-volume effects. By the 2nd spectrum, surface modifications became evident, marked by the dominance of carbonyl species (linearly bonded, weakly bridged, and strongly bridged CO species adsorbed on Ni sites as peaks at 2023 cm^{-1}, 1915 cm^{-1}, and a shoulder at 1841 cm^{-1}, respectively) in the absence of gaseous CH_4 at 3016 cm^{-1}. Additionally, carbonate species were identified at 1504 cm^{-1}, 1391 cm^{-1}, and 1655 cm^{-1}, whereas characteristic peaks of bicarbonate and formate were initially undetected. This absence suggested a rapid transformation of bicarbonate into formate and subsequently into carbonyl species, though definitive mechanistic conclusions required further evidence. By the 3rd spectrum, formate species emerged at 1590 cm^{-1} and 1382 cm^{-1}, alongside bicarbonate at 1641 cm^{-1} and 1224 cm^{-1}, indicating their presence on the catalyst surface. Notably, the gaseous CH_4 product was detected at 3016 cm^{-1} and 1305 cm^{-1} from the 3rd spectrum onward, marking its formation in the reaction pathway. A comparative DRIFTS analysis of steady-state reaction experiments on Al_2O_3, La/Al_2O_3, Ni/Al_2O_3, and Ni-La/Al_2O_3 revealed distinct surface species behavior during CO_2 methanation in Fig 1b. Gaseous CO_2 peaks (3750–3590 cm^{-1}) were present in all samples, while OH species (3562 cm^{-1}, 3523 cm^{-1}) formed over all but Al_2O_3. The CH_4 peak (3016 cm^{-1}) appeared exclusively over Ni catalysts, confirming their methanation activity. Notably, La/Al_2O_3 exhibited the most intense formate peaks (2908 cm^{-1}, 3003 cm^{-1}), whereas Ni catalysts showed overlapping formate and CH_4 peaks. In the carbonyl region, only Ni-containing samples generated adsorbed CO (2023 cm^{-1}, 1915 cm^{-1}, 1841 cm^{-1}), supporting the role of Ni active sites in facilitating formate-to-carbonyl conversion. The absence of bicarbonate species on La/Al_2O_3, Ni/Al_2O_3, and Ni-La/Al_2O_3 suggested their rapid transformation into formates, while Al_2O_3 retained bicarbonate peaks (1411 cm^{-1}, 1225 cm^{-1}) due to lower catalytic activity. The higher OH consumption over Ni catalysts, indicated by a stronger negative OH peak at 970 cm^{-1}, further corroborated their role in formate production.

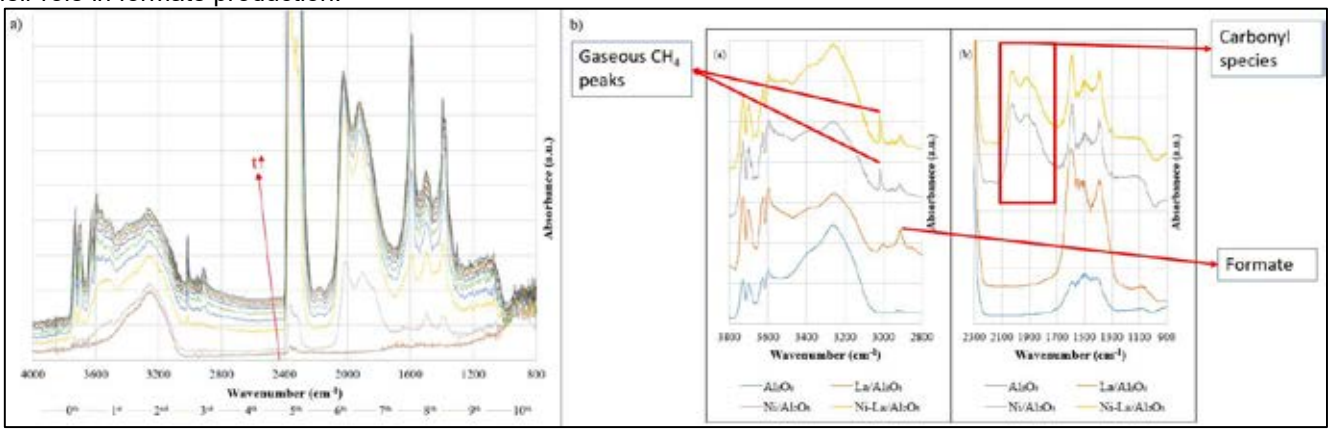

Fig. 1. DRIFT spectra of (a) reaction experiment with quick measurments (3.6 s each) and (b) catalyst and supports for comparison

3.2. Operando DRIFTS Evaluation for Consecutive Adsorption and Stepwise Removal of CO_2 and H_2

A consecutive adsorption experiment was performed over Ni-La/Al_2O_3 at 350°C using the FTIR-DRIFTS-MS system, following a sequence of He, CO_2, H_2, CO_2, and H_2 introductions with a 1:1 H_2/CO_2 feed ratio, concluding with a He flush. The first H_2 adsorption and the second CO_2 adsorption steps are illustrated in Fig. 2a and 2b, respectively. In Fig. 2a, the carbonyl region exhibited a rapid increase, reaching maximum intensity within just 7.2 seconds after which it gradually diminished. During this decline, the relative intensities of linearly bonded CO (2023 cm^{-1}) and weakly bridged CO (1920 cm^{-1}) showed different patterns in their growth and decay phases. While linearly bonded CO was the most intense during the progression phase, weakly bridged CO became dominant as the peaks diminished, suggesting its potential role in CH_4 formation in the reaction. Meanwhile, the main formate peak (1590 cm^{-1}) continued to accumulate as carbonyl species decreased, implying that formate species might act as spectators rather than direct intermediates in the reaction mechanism. In Fig. 2b, during consecutive CO_2 adsorption, the weakly bridged CO peak (initially at 1901 cm cm^{-1}, shifting to 1915 cm^{-1}) was the most intense among carbonyl species but exhibited a slower increase compared to its behavior during H_2 adsorption. Notably, it was the first to diminish, starting after 36 seconds, suggesting a direct involvement in H-related surface reactions. In contrast, the formate peak (1592 cm cm^{-1}) continued to accumulate as carbonyl species declined, reinforcing its role as a spectator spieces. Overall, the strongest quantitative correlation in methanation over Ni-La/Al_2O_3 was observed between CH_4 production and weakly bridged CO, rather than surface formate. This qualitative correlation was further substantiated by an experiment involving the stepwise elimination of reactants (not shown here).

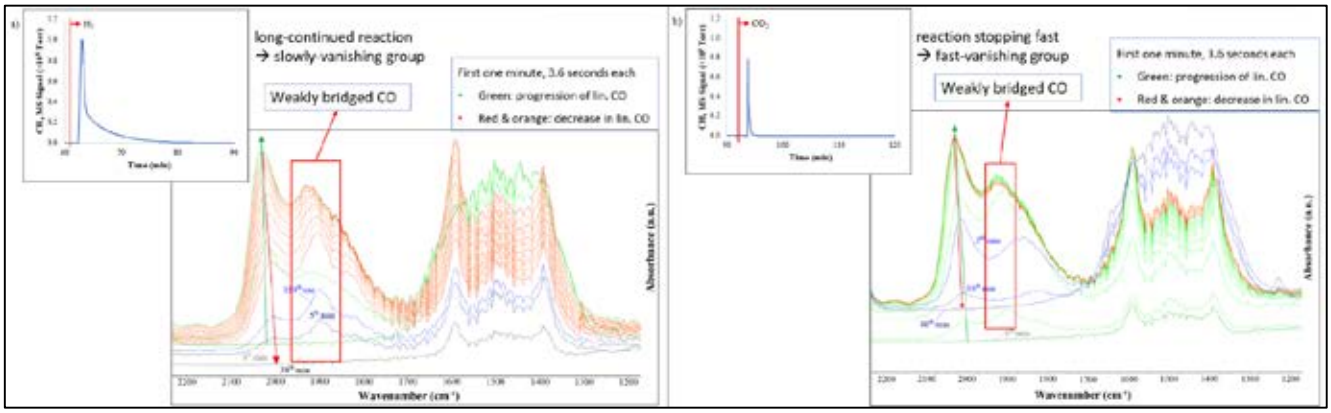

Fig. 2. DRIFT spectra of (a) the first H_2 adsorption and (b) the second CO_2 adsorption over Ni-La/Al_2O_3 at 350 °C

3.3. Quantitative Relationship between Surface Species and CH_4 Production

Building on experiments involving varying H_2/CO_2 feed ratios, consecutive reactant adsorption, and stepwise reactant removal, this section quantifies the relationship between weakly bridged CO species and CH_4 production. DRIFT spectra obtained during reaction with a 1:1 H_2/CO_2 ratio (Fig. 3a) were deconvoluted into three main peaks (Fig. 3b): linearly bonded CO (2023 cm^{-1}), weakly bridged CO (1915 cm^{-1}, shifting to 1905 cm^{-1}), and strongly bridged CO (1841 cm^{-1}). While potentially undetectable overlapping peaks may exist, the most visible peaks were analyzed to establish a quantitative correlation (Fig 3c). Simultaneous MS measurements showed that CH_4 production stabilized after approximately one minute, with the first steady-state spectrum recorded as the baseline for peak deconvolution. Ultimately, a strong correlation between weakly bridged CO and CH_4 production was identified, reinforcing its role as a key active intermediate in CO_2 methanation, while formate species were confirmed as spectators involved in secondary reaction steps.

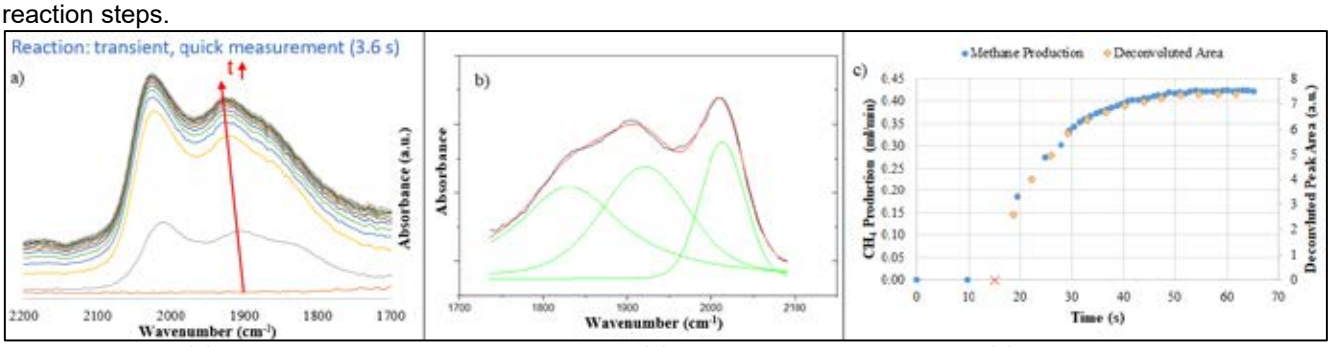

Fig. 3. (a) DRIFT spectra obtained during reaction, (b) illustrative deconvolution, and (c) quantitative correlation

4. CONCLUSIONS

In situ and operando FTIR-DRIFTS-MS reaction experiments at 350 °C with an H_2/CO_2 feed ratio of 1:1 revealed that formate and carbonyl species were stable intermediates during CO_2 methanation, leading to CH_4 production. The

transient behavior analysis, enabled by quick measurements providing spectra every 3.6 seconds, showed that carbonyl species formed before formate accumulation, indicating their role in the early stages of the reaction. Furthermore, weakly and strongly bridged CO species were identified as the most relevant to CH_4 production. The study proposed a qualitative relationship between weakly bridged CO and CH_4 production, suggesting that weakly bridged CO is the active intermediate, while formate species are spectators in the reaction. Additionally, a quantitative correlation between bridged CO species and CH_4 production was established, supporting the qualitative findings.

ACKNOWLEDGEMENT
The financial support is provided by Presidency of the Republic of Turkey, Department of Strategy and Budget (Ministry of Development) through project 2016K12-2838 (2016K121160).

REFERENCES
1. Öztepe C, Mutlu EC, Caglayan BS and Aksoylu AE. 2024. Utilizing CO_2 and rejected H_2 from FP-PEMFC system: A combined experimental and modelling study on CO_2 methanation with low H_2/CO_2 over Ni-La/Al_2O_3. International Journal of Hydrogen Energy 88:815-829.
2. Biset-Peiro M, Guilera J, Zhang T, Arbiol J and Andreu T. 2019. On the role of ceria in Ni-Al_2O_3 catalyst for CO_2 plasma methanation. Applied Catalysis A: General 575:223-229.
3. Quindimil A, Bacariza MC, González-Marcos JA, Henriques and González-Velasco JR. 2021. Enhancing the CO_2 methanation activity of γ-Al_2O_3 supported mono- and bi-metallic catalysts prepared by glycerol assisted impregnation. Applied Catalysis B: Environmental 296:120322.
4. Goncalves LPL, Mielby J, Soares OSGP, Sousa JPS, Petrovykh DY, Lebedev OI, Pereira MFR, Kegnæs S, and Kolen'ko YV. 2022. In situ investigation of the CO_2 methanation on carbon/ceria-supported Ni catalysts using modulation-excitation DRIFTS. Applied Catalysis B: Environmental 312:121376.
5. Jia X, Zhang X, Rui N, Hu X, Liu C. 2019. Structural effect of Ni/ZrO_2 catalyst on CO_2 methanation with enhanced activity. Applied Catalysis B: Environmental 244:159-169.

SIMULATION AND ANALYSIS OF METHANE THERMAL DECOMPOSITION IN AN AEROSOL FLOW REACTOR

[1] İzzet KARABAY, [2]İsmail Ekmekci
[1] EHSiM Elektronik Harp Sist. Müh. Ticaret A. Ş., ELD Director, Hacettepe Teknokent, 06800 Ankara, Türkiye
[2]İstanbul Ticaret Üniversityi, Engineering Faculty, 34840, İstanbul, Türkiye

*Corresponding author e-mail: iekmekci@ticaret.edu.tr

ABSTRACT

Methane decomposition is a key process for the production of high-purity hydrogen. Among various reactor configurations, an aerosol flow reactor utilizing concentrated solar energy is considered a highly suitable option for this process. In this study, computational fluid dynamics (CFD) methods were employed to investigate methane decomposition in an aerosol flow reactor, incorporating gas flow dynamics, chemical reaction mechanisms, heat transfer via radiation and convection, and discrete-phase interactions. Developing a generalized model that accurately describes the decomposition process and provides reliable predictive data is of critical importance. CFD modeling offers an effective approach for simulating such complex reactions, enabling faster and more precise predictions. To enhance the accuracy of the model, experimental and theoretical data from previous studies on methane decomposition in an aerosol quartz reactor were utilized. The improved CFD model accounts for methane decomposition rates and simulates the distribution of decomposition products, including hydrogen, carbon, and unreacted methane, under varying methane and carbon feed rates and temperature conditions.

Keywords: Methane decomposition, Flow Reaction, CFD Modelling

1. INTRODUCTION

Methane is a highly favorable gas for hydrogen production due to its high hydrogen density, the highest among all gases. Additionally, pure black carbon can be produced through methane decomposition methods. The methane decomposition process has been applied in industrial plants to produce both black carbon and hydrogen. Numerous studies have focused on understanding and improving the decomposition mechanism, developing stable catalysts, and enhancing reactor efficiency. The aim of this study is to analyze the reaction process, explore the aerosol reactor concept, and conduct an energy analysis. Moreover, the feasibility of solar energy conversion is closely related to the efficiency of thermochemical reactions. Various methods exist for hydrogen production, but methane decomposition is a direct process that does not involve additional reactants in its reaction mechanism. This makes it an important topic in chemical conversion, where heat and mass transfer play crucial roles. Key factors influencing heat transfer include radiation-convection mechanisms and chemical reaction kinetics. There are numerous solar-assisted methods for hydrogen production and solar energy storage as chemical energy, including steam reforming, carbon dioxide reforming, and methane cracking. Among these, the aerosol reactor is a promising candidate for methane decomposition due to its ability to directly absorb solar radiation via black carbon catalysts and gas-phase particles. The aerosol reactor, a quartz tubular reactor, allows direct absorption of solar energy by the fluid and particles, leading to a high heat transfer rate. During methane decomposition, hydrogen gas and solid carbon are produced [1,2]. As a result, the hydrogen obtained has high purity, making purification easier. Therefore, using a quartz reactor is a reasonable choice for methane decomposition to produce hydrogen. Both carbon feeding at the inlet and the carbon produced during the reaction catalyze methane decomposition. Several researchers have contributed significantly to this field. Snoeck conducted experimental and theoretical studies on the kinetic aspects of Ni-based catalysts [3]. Deutschmann investigated partial methane oxidation using finite element methods and developed computational fluid dynamics (CFD) models for both two-dimensional and three-dimensional reaction mechanisms [4]. Matowich conducted experimental research on methane decomposition in an aerosol reactor [5].

2. APPROACH AND METHODOLOGY

This study aims to provide a comprehensive understanding of the methane decomposition mechanism by examining key parameters such as chemical reactions, radiation heat transfer, and two-phase flow dynamics. Additionally, it investigates the effects of these parameters in a two-dimensional reactor model. Previous studies, such as Dahl's [1], have used one-dimensional energy balance equations to offer quick insights for engineers. While these models provide valuable approximations, reactor design engineers require a deeper understanding of how parameter distributions across the reactor cross-section influence system performance. However, ensuring mathematical consistency in simulation data remains a significant challenge. To address this, the finite element method is employed, as it allows for the simultaneous solution of multiple interacting parameters while maintaining numerical accuracy. Hydrogen production via solar-driven methane decomposition in an aerosol reactor is highly advantageous due to its efficient

production process, direct utilization of solar energy, and simplified purification requirements. Methane decomposition in an aerosol reactor involves heterogeneous chemical reactions, where complex interactions between gas-phase chemistry, discrete-phase flow, and radiation modeling play a critical role.

3. METHANE DECOMPOSITION

There are a lot of studies to explain reaction mechanism for the decomposition of hydrocarbons, especially natural gas, propane, ethylene and methane. Steinberg is one of the major proponent researchers about the thermal decomposition mechanism of CH_4 process for H_2 production [1]. Methane (CH_4) is dissociated to carbon (C) black and H_2 according to chemical mechanism below :

$$CH_4 \longrightarrow C + 2H_2 \qquad H_{298K} = 74.9 \text{ kJ/mol}$$

$$CH_4 \rightarrow C + 2H_2 \qquad \Delta H_{1000K} = 89{,}8 \text{ kJ/gmol}$$

Cantelo was the first scientist who studied theorical and experimental decomposition methane mechanism in 1927. He reported that the starting point of decomposition is 400 C and ending point is 1500 C. It is reported that methane completely is decomposed at 1500 C [10]. In another study, Holmen reported the activation energy as 370 kj/mol between 1770-2270 K [11]. Tessner determined that the activation energy of carbon nuclei formation during methane's thermal decomposition (316.8 kj/mol) is higher than activation energy of carbon crystallites growth [12]. Activation energies are reported 356- 402 kJ/mol at 2000-3000 ^oK temperature ranges for shock tubes reactors. Steinberg is reported that activation energy is 131 kJ/mol between 973- 1173 K and 28-56 atm [1]. There are a lot of studies carried out on the effects of different catalysts on the decomposition of methane. Recent studies were performed by Muradov and Wiemer co-workers. Muradov have studied carbon catalysis for methane decomposition He developed a model that describes the effect of different carbon catalysts and dimensional parameters on the methane decomposition at fluidized bed reactor according to experimental data [13,14]. Dahl and co-workers studied on a solar aerosol reactor and developed a mathematical model that describes methane decomposition [1]. Another study of them is investigating a aerosol reactor that can be used for product applications at pilot dimension [2]. In this paper, we developed a two dimensional numerical model that describes the methane decomposition process in the aerosol quartz reactor that is used by Matowich.

4. REACTOR MODEL

In this study, an aerosol reactor is used with dimension that is used by Matowich' experiments so that results could be checked via another studies results. This reactor is 0,914 m in length and has an inside diameter of 0,076 m as shown in Fig.2. Methane is fed into the top of reactor at five different amounts. Carbon particles is fed with methane so that carbon particles enhance reaction rates. The rates of CH_4 dissociation is determined by measuring the thermal conductivity of the effluent gas after filtering the carbon black particles from the sample[1,2].

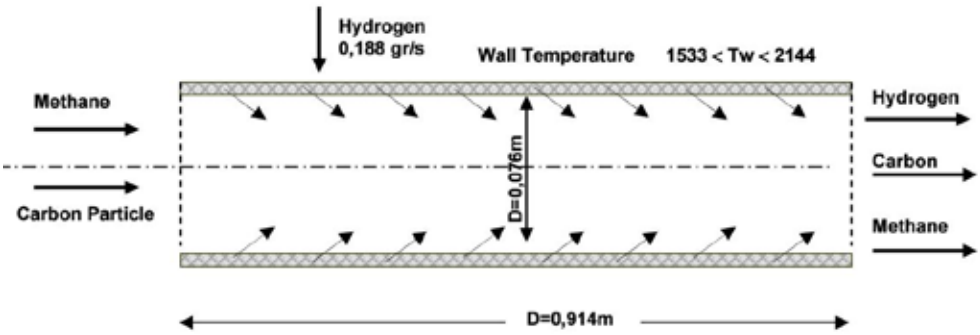

Fig. 1. Schematic representation of aerosol reactor

5. NUMERICAL MODEL

Numerical model is established CFD solutions to supply integrating mechanism elements and displaying conversion distribution in tube as two dimensional. Former studies were only based on experimental research and one-dimensional numerical solutions. We defined proper governing equations such as energy, mass and momentum conservations and species transport equations and also required boundary conditions such as radiation, diffusion and particulate movement BCs to establish numerical model of methane decomposition at the aerosol reactor. Methane decomposition mechanism includes chemical reaction, mass transfer, heat transfer, discrete phase effect,

thermophoresis effect and also lifting effect (Fig.2). On the other hand, defining of chemical conversion mechanism is very important and bringing of accompanying governing equation is one of the difficult subject. Flow in the tube is two phase flow that includes solid carbon particles and continuous methane gas flowing. Solid carbon particles enter to the tube inlet section as a mixture with methane. During the reaction of methane decomposition, carbon particles will be formed along the aerosol tube flow. Discrete phase flow is defined to model of the flow of carbon particles, methane and hydrogen gases during the conversion mechanism along the aerosol tube. Thermophoretic force and lifting effects were also added to our numerical model of aerosol reactor.

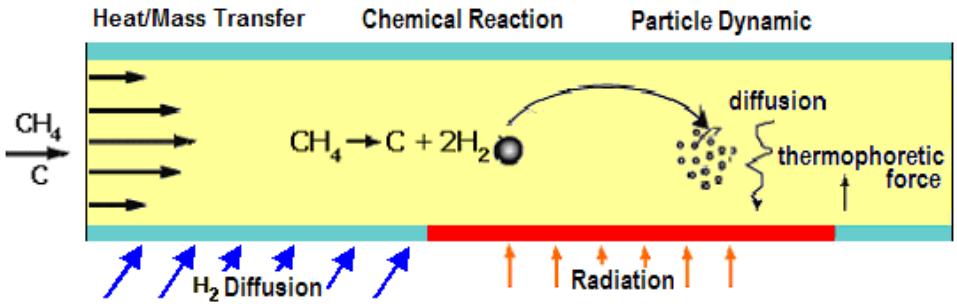

Fig. 2. Schematic representation of numerical model

6. RESULTS AND EVALUATION

Numerical model consists of mass flow, energy conversion, reaction kinetics, radiative heat transfer, discrete phase equations. Model meshing is obtained by using GAMBIT.2.1 for two-dimensional horizontal rectangle shaped reactor. This model is tried to improve the best and the most optimized solution. Using parameters for solving and simulating the reactor are indicated in table-1. These parameters are mostly closest Matovich's experiment and also Dahl and group's simulations. The numerical simulations are based on CFD codes in FLUENT 6.0.12. It solves the conservation equations that is momentum, species, energy, discrete phase and reaction by using a control volume. The methodology used for the 2-D simulations and some of the numerical issues have been explained in elsewhere. FLUENT solves the governing (momentum, species and enthalpy) equations using a control volume based finite difference method. Also the viscosity, specific heat, absorption rate, and the thermal conductivity of the mixture as well as the diffusion coefficient of species are solved simultaneously with governing equations in the mixture depending on the local composition and temperature.

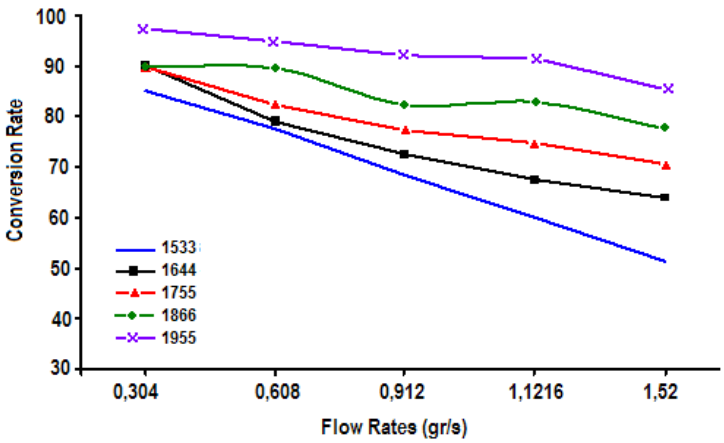

Fig. 3. Molar conversion rates for different mass flow rates and different wall temperatures

Changing of methane conversion rates through reactor related to wall temperatures and flow rates are shown in figure-4. Molar methane conversion rates are indicated for six different temperatures at five different flow rates in the figure. Methane decomposition begins at first length=3-20 cm from beginning of the reactor for all flow rates and 1533 K wall temperature. The latest starting flow rate of decomposition is 1.52 gr/s and the firstest starting flow rate is 0,304 gr/s. This condition can be explained that reaction's activation energy can not be sufficiently supplied for this wall temperatures. So, heat transfer rate is getting insufficient to complete reaction, when flow rates are increasing. Similarly, methane decomposition begins about 0-20 cm for 1644 K wall temperature. Decomposition curves resembles to 1533 K wall temperature's curves. For this reason, it can be said that all decomposition expanding characteristics are similar for these temperatures. Methane decomposition occurs at the beginning away of the reactor

for the other wall temperatures. Conversion curves inclination rises with increasing wall temperatures. As shown at Fig.4, decomposition inclination decrease with remaining flow rates.
Figures-5 indicates methane conversion rates depend on wall temperatures for three flow rates (0,304-0,912-1,52 gr/s) that are periodic difference. According to this figure, while wall temperatures are rising, conversion rate becomes considerably independent from flow rates. Methane decomposition is completing for all flow rates at 2144 K wall temperature. In conclusion, it is obvious that temperature is the most designated factor at methane decomposition mechanism for this reactor. Since carbon particles are a catalyst in the reaction, it is needed to understand the relationship between temperatures of carbon particle and gas phase. Figure-6 is a plot of comparative phase and particle temperatures. Particle temperature is bigger than phase temperature at the first 20 cm of length. After the first length of 20 cm, these temperatures approximate each other and approximately become equal values at the end of the reactor.

7. CONCLUSION

The investigated CFD model for methane decomposition mechanism includes flow-heat-chemical reaction, discrete phase flow and complex mathematical operations in detail. Different parameters' effects on flow reaction can be analysed in different aspects of engineering as well chemical, mechanical, reacting etc. CFD application by using different engineering disciplines is very useful for this type flow reacting problems. It is very useful to investigate new models and also to develop applicable reactor examining. Methane decomposition and kinetic values are another important direction that includes a lot of related intensive and extensive parameters. For example, one of these is activation energy that varies with characteristics of catalysts, particulate geometry, micro chemical structures etc. Therefore, there is not a constant value for kinetic features and chemical reaction kinetics definition is very difficult for this type heterogeneous reaction. As another conclusion from study this modelling enable characteristics of the parameters to understand and define by examining different direction application in aspect of the high way engineering. The fact is that the expanded analysis and solution also can be obtained.

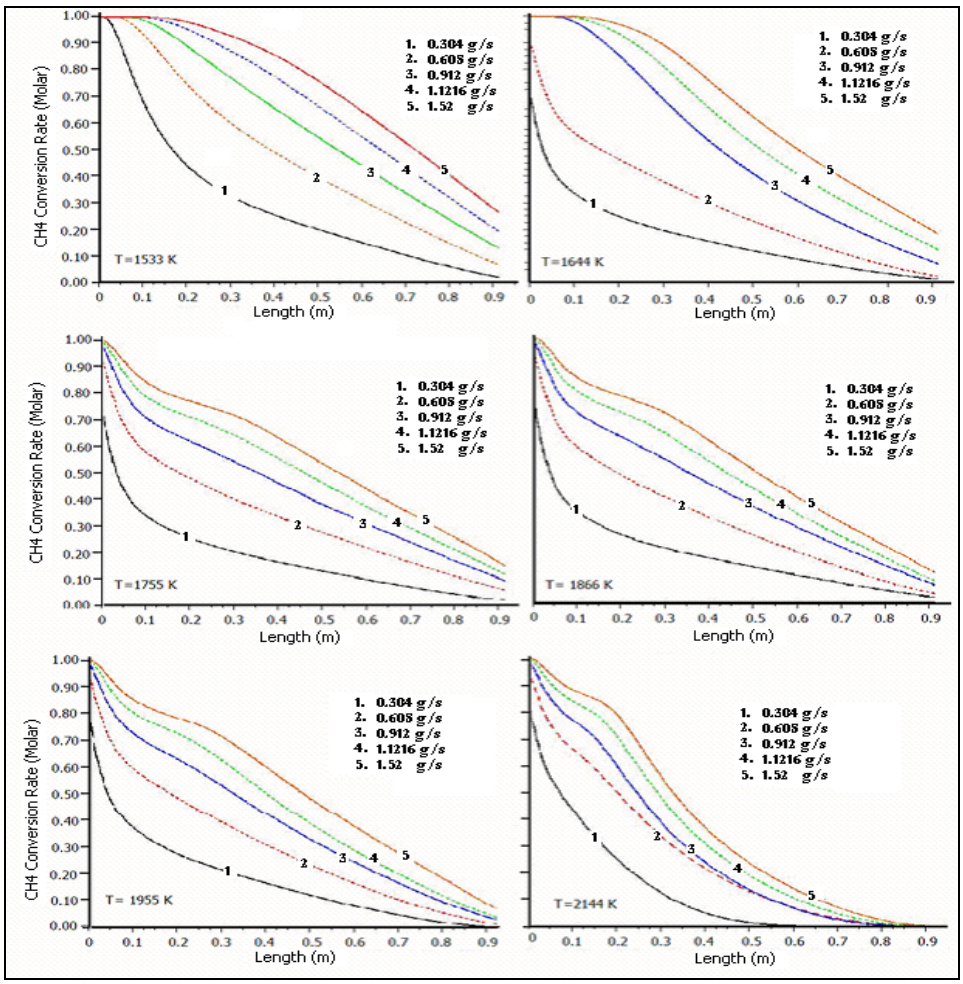

Fig. 4. Methane conversion rates through tube for 6 temperature values and 5 flow rates.

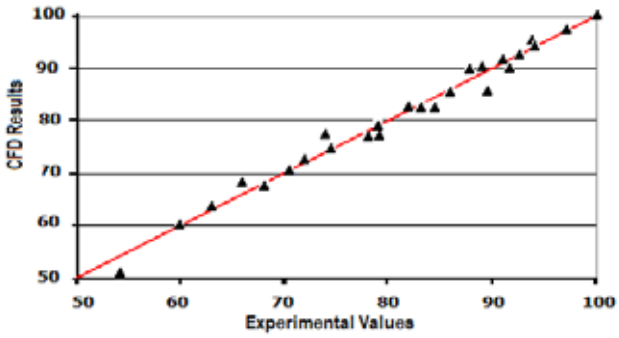

Fig. 5. Methane conversion rates through tube for 6 temperature values and 5 flow rates.

REFERENCES

1.Dahl,J.K., Barocas., Clough,D.E., and Weimer,A.V.; "Intrinsic kinetics for rapid decomposition of methane in an aerosol reactor" Intç Journal of Hydrogen Energy, 27 (2002), 377-386

2. Weimer,A.V., Dahl.J., And Buechler.K., "Thermal Dissocation of Methane Using a Solar Coupled Aerosol Flow Reactor" , Proceeding of The 2001 DOE Hydrogen Program Review,NREL/CP-570-30535

3. Snoeck.J.W., Froment.G.F., and Fowlest.M., "Kinetic Study of the Filament Formation by Methane Cracking on a Nickel Catalyst", Journal of Catalysis , V.169, p250-262, 1997.

4. Deutschmann.O., and Schmith, L.D.; "Two Dimensional Modeling of Partial Oxidation of Methane in a Short Contact Time Reactor", AIChe Journal, Vol:44 pp: 2465-2476 ,1998

5. Matowich, E., Thagard Tecnology company, United States Patent #4095974,1978

6. Hirsch, D., and Steinfeld, A., "Solar hydrogen production by thermal decomposition of natural gas using a vortex-flow reactor" International Journal of Hydrogen Energy, Volume 29, Issue 1 , January 2004, Pages 47-55

7. Trommer, D., Hirsch, D., and Steinfeld. A., "Kinetic investigation of the thermal decomposition of CH_4 by direct irradiation of a vortex-flow laden with carbon particles" International Journal of Hydrogen Energy Volume 29, Issue 6 , May 2004, Pages 627-633

8. Stephane,A., and Flamant,G., "Solar hydrogen production from the thermal splitting of methane in a high temperature solar chemical reactor", Solar Energy, accepted 14 November 2005.

9. FLUENT 6.1 User's Guide, February 2003 Fluent Inc.Centerra Resource Park 10 Cavendish Court Lebanon, NH 03766

10. GRUSE.W.A, and DONALD.R., "The Chemical Technology of Petroleum", Stevens Mc.Graw-Hill, Newyork 1942, pp:356

11. Kim, M.H., Lee, E.K., Jun,J.H., Kong.S.J., Han,G.Y., Lee, B.K., Lee, T., and Yoon, K.J., "Hydrogen production by catalytic decomposition of methane over activated carbons:kinetic study", International Journal of Hydrogen Energy, Vol.29, Issue 2, pp. 187-193, February 2004

12. Steinberg, M., and Cheng, H.C., "Modern and Prospective Technologies for Hydrogen Production From Fossil Fuels" Int. Journal of Hydrogen Energy, Vol.14, pp: 797-820, 1989.

13. Muradov, N., "Hydrogen Via Methane Decomposition: An Application For Decarbonization Of Fossil Fuels" International Journal of Hydrogen Energy, 26 (2001), 1165–1175

14. Muradov.N., "Catalysis of Methane Over Elemental Carbon", Catalysis Comunication, Vol:2, 2001, pp-89-94

15. Saffman, P.G., "The Lift on a Small Sphere in a Slow Shear Flow". J. Fluid Mech.,Vol:22, pp:385-400, 1965.

16. Chan,S.H., and Wang, H.M., "Thermodynamic Analysis of Natural-Gas Fuel Processing For Fuel Cell Applications", Int. Journal of Hydrogen Energy, Vol.25, pp: 441-449,2000.

17. Rozenman,T., "Energy transport With an Integrated Direct Solar Reactor", Journal of Solar Energy Engineering, Vol.112, pp:140-145, 1990

18. Diver, R.B., "Reciever/Reactor Concepts For Thermochemical Transport of Solar Energy", Journal of Solar Energy Engineering, Vol.109, pp:199 – 204, 1987

INVESTIGATION OF NO_x REDUCTION BY NH_3-SCR IN AFTERTREATMENT SYSTEM FOR H_2 INTERNAL COMBUSTION ENGINE

[1*]*Tarık Bercan Sarı*, [1]*Selmi Erim Bozbağ*, [2]*Deniz Şanlı Yıldız*, [1]*Can Erkey*
[1] Koç University, Engineering Faculty, Chemical and Biological Engineering, Rumeli Feneri Yolu, İstanbul, 34450, Türkiye
[2] Ford Otosan R&D Centre, Sancaktepe, İstanbul, 34885, Türkiye

* cerkey@ku.edu.tr

ABSTRACT
Synthetic gas bench data is presented related to the performance of the catalytic NOx reduction using NH_3-SCR process on Cu/zeolite washcoated monolithic reactor for the aftertreatment systems of H_2 internal combustion engine under a wide variety of feed H_2O (1-20%) and O_2(1-14%) and including inlet H_2 (500 ppm) concentrations at a wide temperature window (150-490 ℃). Data showed significant NH_3 uptake (109 g/m^3 and 66 g/m^3) at varied H_2O concentrations (1-20%) and H_2O feed concentration dependent SCR performance at low (150-250℃) and high (400-490℃) temperature ranges and N_2O by-product formation, however obtaining >99.9% deNOx performance in the 250-400 ºC range irrespective of H_2O feed at a space velocity of 60000 h^{-1}. H_2 co-feed to the main SCR feed was found to affect the deNOx slightly at higher temperatures but not significantly at 150-400 ℃ range. According to the results of the study, the well-established NH_3-SCR technology for diesel engine aftertreatment deNOx could be a promising technology for the ATS of H_2-ICE, despite the intrinsic challenges.

Keywords: hydrogen internal combustion engine, aftertreatment system, selective catalytic reduction, NOx, Cu/SSZ-13

1. INTRODUCTION

Hydrogen internal combustion engines (H_2-ICEs) are attracting increasing attention as a promising way to meet stringent Euro 7 emission regulations while addressing global carbon neutrality goals. These engines produce near-zero CO_2 emissions and represent a sustainable alternative to traditional fossil-fuel-based internal combustion engines. However, the high NOx concentrations[1], elevated water vapor content (10–20%)[2], and probable slip of unburned H_2 in the exhaust gas of H_2-ICEs[3] pose significant challenges for the effective performance and durability of selective catalytic reduction (SCR) systems. Compared to diesel aftertreatment systems, which typically operate under a feed water concentration of ~5%, H_2-ICE exhaust contains significantly higher water vapor, potentially affecting catalyst performance. Although there have been studies analyzing the performance of SCR under varying H_2O concentrations[4, 5], most of the literature have focused on the diesel engine conditions, particularly low water and oxygen concentrations in the feed stream. This study explores the performance of a commercial Cu-zeolite SCR catalyst under conditions representative of H_2-ICE exhaust. In this work, effect of water on NH_3 storage, NH_3 Oxidation, NOx conversion efficiency and N_2O formation during Standard SCR (Feed $NO_2/(NO+NO_2)$=0) and effect of H_2 at the inlet of reactor to the Standard and Fast SCR (Feed $NO_2/(NO+NO_2)$=0.5) reactions were experimentally evaluated in a wide range of conditions .

2. MATERIALS AND METHODS

The catalyst in this work was Cu/SSZ-13 washcoated onto a cordierite monolith (600 CPSI - 3 mils). The experiments were conducted on a synthetic gas bench. Cylindrical cores with 2.6 cm length and 1.8 cm diameter were wrapped with ceramic fibre paper and loaded in a quartz tube and positioned in the isothermal zone of an electric tubular furnace (Thermo Scientific Lindberg Blue M). The reaction temperature was recorded using J-type thermocouples located 0.5 cm upstream of the catalyst. H_2, NH_3, NO, NO_2, O_2 and N_2 were introduced via calibrated mass flow controllers (Brooks Instruments) whereas H_2O was delivered using a controlled evaporator mixer (CEM W202A, Bronkhorst). The lines before and after the reactor was heated to 230 °C and 190℃, respectively. Moreover, a furnace was utilized to preheat the O_2, H_2O and N_2 to 170 ℃. The species concentrations at the reactor outlet were monitored with an online FTIR spectrometer (MKS Multigas 2030) equipped with a view cell with a path length of 5.11 m and a liquid nitrogen cooled HgCdTe (MCT) detector. Detailed information on the synthetic gas bench can be found in our previous studies[6]. Hydrothermal aging was performed at 480℃ and with a feed of 20% H_2O, 14%O_2 with balance N_2 for 50h. Standard SCR reaction was conducted in 150-480℃ with a feed of 350 ppm NO, 350 ppm NH_3, 14% O_2 and various H_2O concentrations with balance N_2. For the second experiment set, O_2 concentration was varied (1-8-14%) at low temperatures (150-170-200℃).

3. RESULTS AND DISCUSSION

Investigations on impact of feed water concentration on NH_3 storage capacity of copper chabazite catalysts have revealed distinct behaviors. While NH_3 storage capacity of Cu-SAPO-34 was found to be enhanced due to increased acidity of Bronsted acid sites[7], Cu-SSZ-13 was found to encounter opposite effect[8]. In particular, due to competitive adsorption on active sites, increasing water feed concentration is known to have an inhibiting effect on NH_3 storage

capacity of the catalyst. In this study, TPD runs were conducted with water concentration ranging from 0 to 20%, after mild hydrothermal aging as described in the experimental procedure, under conditions of H_2-ICE exhaust. In Figure 1, NH_3 outlet concentration measured at the downstream of SCR catalyst was shown, during the TPD phase of the experiments, for different feed water concentrations, while keeping the other parameters unchanged. The results showed that the NH_3 storage capacity decreased from 109 molNH_3/m^3 to 66 molNH_3/m^3 due to increasing inlet H_2O concentration from 0% to 20%. NH_3 oxidation is a side reaction occurring on copper zeolite systems during Selective Catalytic Reduction, which becomes significant at temperatures higher than 300 ℃. The extent of oxidation determines the surface

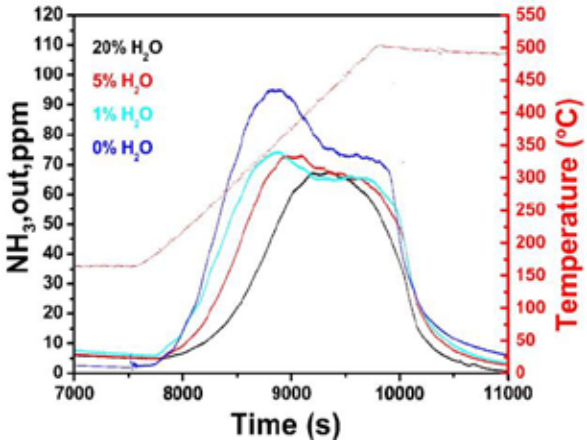

Fig. 2, NH_3 Outlet Concentrations during Temperature Programmed Desorption Phase of NH_3 Adsorption and TPD Experiments at varied H_2O feed concentrations during NH_3 adsorption step (500 ppm NH_3, 0-1-5-20% H_2O, balance N_2, 150℃, 60.000 h^{-1} space velocity).

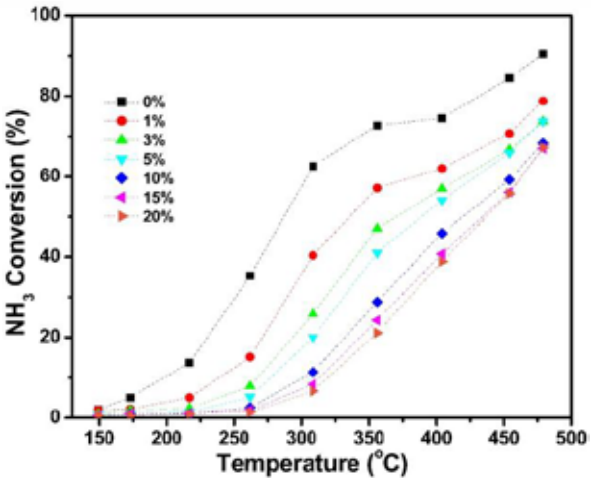

Fig. 1, Temperature vs. NH_3 Conversion via the NH_3 Oxidation Reaction with H_2O inlet ranging from 0% to 20% (Feed conditions: 500 ppm NH_3, 14% O_2, 0-20% H_2O, Balance N_2, 60.000 h^{-1} space velocity)

NH_3 availability for SCR reactions; high oxidation rate is not usually preferred due to depletion of NH_3 bounded active sites. In Figure 2, NH_3 conversion due to NH_3 oxidation at different temperatures were plotted, for inlet water concentrations ranging from 0 to 20%. Conversion of NH_3 during NH_3 Oxidation was also influenced by inlet H_2O concentration: gradually decreasing from 57% to 20% with increase of H_2O concentration from 1% to 20% at 350℃. Data for typical diesel engine outlet H_2O concentration (~5-10%) showed consistent conversion behavior with the literature [9], with minimal conversions up to 300℃, and increasing gradually to ~70% at 490℃. The results suggested that increasing the H_2O concentration to 15 and 20% decreases the NH_3 conversion for all temperatures under investigation. In particular, NH_3 conversion was about 50% at 400 ℃ with H_2O feed concentration of 10% of, and it decreased to 40% when the water concentration in the feed increased to 20%. With more significance, decreasing the inlet water concentration increased the NH_3 conversion and brought the light of to as low as 200℃ at dry conditions. These results suggested that at higher temperatures, high water feed concentrations in a H_2-ICE exhaust might have positive effects on SCR reactions due to possible presence of increased surface NH_3 sites.

Figure 3 shows the (a) steady state NO conversions and (b) N_2O formations under Standard SCR conditions (350 ppm

NO, 350 ppm NH_3, 14% O_2, Variable H_2O, balance N_2) at different temperatures. Furthermore, Figure 3a includes an inset figure which magnifies the high temperature region (T>400℃). It can be observed that NO conversion in the 150-250℃ region decreased with increasing H_2O concentration in the feed stream, whereas no significant change was observed in the 250-400℃ region, in which almost complete NO conversion was reached. However, further increase in temperature resulted in an opposite behavior than in the low temperature region: higher water concentrations promoted the NO conversion by Standard SCR. This observation is in agreement with the findings for NH_3 Oxidation in Figure 2. In Figure 3b, it can be seen that the N_2O formation during Standard SCR had a peak at around 250℃, consistent with the literature [10]. Even though the dependence of low temperature N_2O formation on water concentration was examined by several researchers, high water content as in H_2-ICE was not studied previously. The data in Figure 3b showed that as the H_2O concentration increased to typical values during operation(10-20%), the N_2O formation significantly increased at both 200 and 250 ℃, whereas no significant effect was seen for 150 and 175 ℃. After 350 ℃, the decrease in N_2O concentration was substantial and at 400 ℃ & 450 ℃, the N_2O concentration with 10 and 15% water concentration were almost identical with diesel conditions (when 3-5% water was present in the feed); however, with 20% water, the outlet concentration of N_2O was significantly higher.

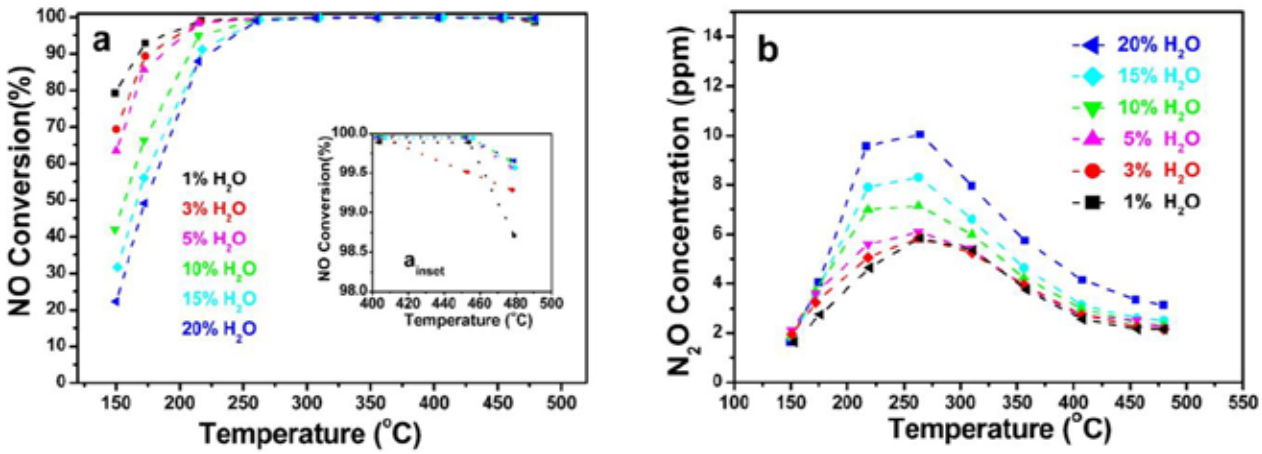

Fig. 3. (a) NO conversion and (b) N_2O Formation under Standard SCR conditions with varying water content (Feed conditions: 350 ppm NO, 350 ppm NH_3, 14% O_2, 1-20% H_2O, balance N_2, 60.000 h^{-1} space velocity).

As mentioned previously, there may be unburned hydrogen in the exhaust gas stream of the H_2-ICE that slips into the aftertreatment system. The possible effect of this H_2 on NH_3-SCR of NOx was studied experimentally, by switching a 500 ppm H_2 feed stream on and off during SCR reaction. Figure 4 shows the resulting behavior of the NO and NO_2 outlet concentrations during (a) Standard (b) Fast SCR reactions. At temperatures of 170 and 350 ℃ the feed of H_2 had no significant effect on NOx conversion, whereas at 450℃ the NOx outlet concentrations depended on the feed of H_2. Hence, the transient concentrations of NO and NO_2 for high temperature region were given in Figure 4. For Fast SCR (b) O_2 concentration were varied and the effect of H_2 inlet was found to be significant. Upon addition of 500 ppm H_2, although the total NOx conversion was not significantly changed, ~3 ppm NO_2 was detected at the outlet gas stream.

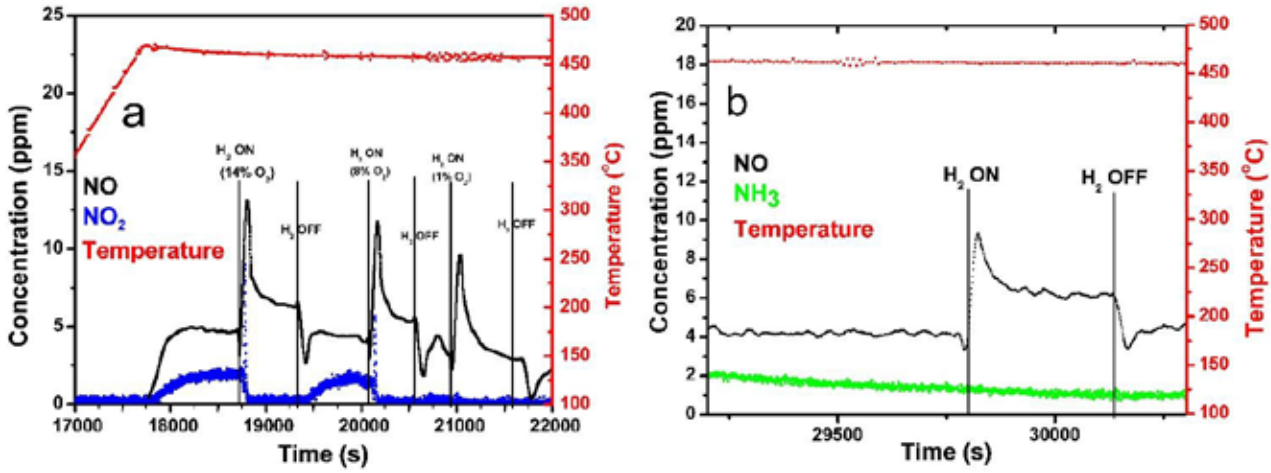

Fig. 4. NO & NO_2 outlet concentrations with H_2 Inlet for (a) Fast SCR (b) Standard SCR

4. CONCLUSIONS

This study examined the impact of water content and unburned hydrogen on NH_3-SCR performance for H_2-ICE aftertreatment. Increased H_2O concentration reduced NH_3 storage due to competitive adsorption but also suppressed NH_3 oxidation, potentially enhancing SCR reactions at higher temperatures. NOx conversion decreased at low temperatures (150–250 ℃) with rising H_2O concentration but increased above 400 ℃. N_2O formation peaked at 250 ℃, with higher water content increasing emissions at low temperatures while having minimal impact at high temperatures. Although further research in modeling and calibration is underway in our laboratory, these findings highlight key challenges and optimization opportunities for SCR systems in H_2-ICE applications, guiding catalyst design and operational strategies to meet NOx regulations efficiently.

ACKNOWLEDGEMENT

Support from Ford Otosan R&D Center and TÜBİTAK 2244 Industrial PhD program (Project No: 119C176) is gratefully acknowledged.

REFERENCES

1. Guo H, Zhou S, Zou J and Shreka M. 2020. A numerical investigation on De-NOx technology and abnormal combustion control for a hydrogen engine with EGR system. Processes. 8: 1178.
2. Srisailam SK, Patchett J, Wu R, Wang L, Shah S and Tang W. 2024. Exhaust aftertreatment solution for H_2-ICE for selective NOx removal in the presence of high amount of water content. SAE International Journal of Advances and Current Practices in Mobility. 6:8
3. Özyalcin C, Sterlepper S, Roiser S, Eichlseder H and Pischinger S. 2024. Exhaust gas aftertreatment to minimize NOx emissions from hydrogen-fueled internal combustion engines. 353: 122045.
4. Eijima W, Shibata G, Shibayama N, Kobashi Y, Ogawa H and Shimizu K. 2020. Kinetic modeling of steady-state NH_3-SCR over a monolithic Cu-CHA catalyst. 352: 237-242.
5. Ma L, Li Z, Zhao H, Zhang T, Yan N and Li J. 2022. Understanding the water effect for selective catalytic reduction of NOx with NH_3 over Cu-SSZ-13 catalysts. 2: 1684-1696.
6. Karadağ GH, Bozbağ SE, Sanli DS, Demir O, Ozener B, Hisar G, Erkey C. 2018. Mass transfer effects in SCR reactor for NOx abatement in diesel engines. In Exergetic, Energetic and Environmental Dimensions. Edited by Dincer I, Çolpan CO, Kizilkan O. Burlington, Mass.: Academic Press.
7. Yu T, Wang J, Shen M, Wang J and Li W. 2015. The influence of CO_2 and H_2O on selective catalytic reduction of no by NH_3 over Cu/sapo-34 catalyst. 264: 845-855.
8. Villamaina R, Gramigni F, Iacobone U, Liu S, Nova I, Tronconi E, Ruggeri MP, Collier J, York APE and Thompsett D. 2021. The H_2O effect on Cu speciation in Cu-CHA-catalysts for NH_3-SCR probed by NH_3 titration. 11: 759.
9. Olsson L, Wijayanti K, Leistner K, Kumar A, Joshi SY, Kamasamudram K, Currier NW and Yezerets A. 2015. A multi-site kinetic model for NH_3-SCR over Cu/SSZ-13. 174-175: 212-224.
10. Xi Y, Ottinger NA, Keturakis CJ and Liu ZG. 2021. Dynamics of low temperature N_2O formation under SCR reaction conditions over a Cu-SSZ-13 catalyst. 294: 120245.

COMPARATIVE LIFE CYCLE CARBON EMISSIONS ASSESSMENT OF UTILIZING DIESEL OIL AND HYDROGEN FUEL ON A FERRY

[1,*]*Olgun Konur*, [1,2]*Mehmet Emin Aydın*, [1,2]*Mehmet Sadık Aydın*
[1] Dokuz Eylül University, Maritime Faculty, Marine Engineering Department, Tınaztepe Campus, İzmir, 35160, Türkiye
[2] Dokuz Eylül University, The Graduate School of Natural and Applied Sciences, Tınaztepe Campus, İzmir, 35160, Türkiye

*Corresponding author e-mail: olgun.konur@deu.edu.tr

ABSTRACT
The maritime industry is under increasing pressure to adopt sustainable propulsion technologies to reduce greenhouse gas emissions and comply with stringent environmental regulations. This study conducts a comparative life cycle carbon emissions assessment of diesel and hydrogen fuel cell propulsion for a high-speed catamaran ferry operating in İzmir Bay. The results show that replacing diesel with hydrogen fuel cells can reduce life cycle carbon emissions by 87.82%, with the largest emission source in hydrogen utilization arising from the electrolysis production phase (65.88%). Notably, while hydrogen combustion itself is emission-free, the life cycle carbon emissions on renewable electricity for hydrogen production contribute to residual emissions. Additionally, the study finds that the emissions from long-distance hydrogen transportation remain only 5.17% of the hydrogen life cycle emissions. The findings underscore the critical role of green hydrogen in maritime decarbonization and provide valuable insights for policymakers, ship operators, and industry stakeholders in transitioning toward sustainable shipping solutions.

Keywords: Marine vessels, Hydrogen, Life cycle carbon emissions assessment, Decarbonization, Marine engineering

1. INTRODUCTION
This study explores hydrogen fuel cells as an alternative propulsion system for catamaran ferries in İzmir Bay to reduce emissions. It highlights the technology's efficiency, safety, and emission reduction potential. Although hydrogen-powered ferries have higher operating costs than diesel, technological advancements and renewable hydrogen production may improve cost-competitiveness by 2025–2030. Hybrid systems and green hydrogen production further enhance sustainability, though challenges in cost and infrastructure remain.

2. SYSTEM DESCRIPTION
This study examined a high-speed ferry with a capacity of 400 passengers, with characteristic features 39 meters in length and 12 meters in width, and having a gross tonnage of 486 GT, operating for 12 hours a day on the Bostanlı - Konak route. The power requirements and the daily fuel consumption of the ferry are provided in Table 1.

Table 1. The power characteristics of the examined ferry

Designated ferry particular information	Data	Unit
Working hours per day	9.67	hours/day
Installed propulsion engine power at 100% MCR (maximum continuous rating)	3,680 (1840×2)	kW
Required diesel generator (DG) power for auxiliary equipment and hoteling	55	kW
Average daily diesel fuel consumption (m_{diesel})	1,680	kg/day

The ferry operates on a steady schedule on the designated route. Fig. 1 shows the vessel's speed profile, including the daily navigation, maneuvering, and port stay periods. The vessel operates at 12 knots on navigation and 4 knots during maneuvering operations. A total of 9 hours and 40 minutes of active operation takes place with the vessel in a day.

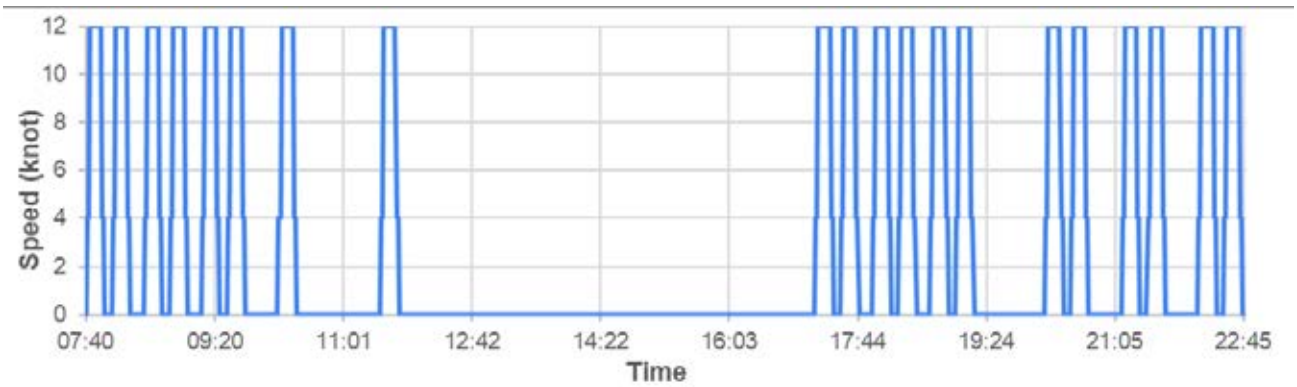

Fig. 1. Speed profile of the vessel during the one-day service period

The existing ferry operates by consuming diesel oil. A comparative life cycle carbon emissions assessment is carried out, considering that an electric motor has replaced the propulsion engine. It is assumed that the electric supply for the propulsion engine and auxiliary power requirements are provided by using hydrogen through proton exchange membrane fuel cells (PEMFCs) placed on the ferry. The specifications of the reference PEMFC are provided in Table 2.

Table 2. The specifications of the reference PEMFC to be used on the ferry [1]

Specifications	Data
Net Power (DC Supply)	200 kW_e
Gross output (rated power)	580 V / 400 A
Heat output	< 320 kW
Fuel quality	Pure hydrogen: ISO14687:2019
IP classification	IP44

The hydrogen demand for the PEMFCs was determined based on the performance curves supplied by the manufacturer, as depicted in Fig. 2. These curves provide essential insights into the relationship between power output, efficiency, and hydrogen consumption under varying operating conditions. Furthermore, an analysis was conducted to accurately estimate the power and current requirements of the PEMFC system according to the vessel's operational load profile. This analysis considers fluctuations in energy demand during different operating scenarios to ensure optimal performance and fuel efficiency.

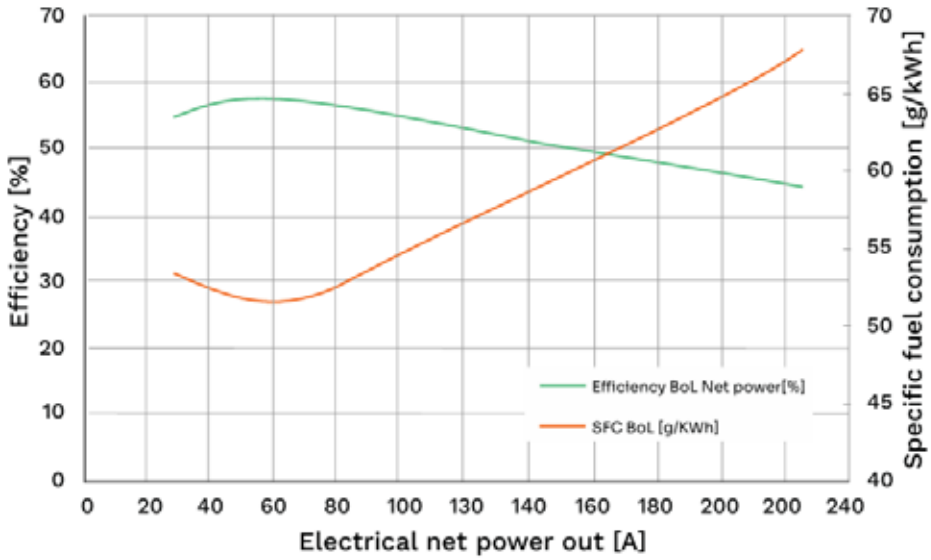

Fig. 2. Performance curve of PEMFC [1]

It is determined that the vessel operates at 35% MCR engine load during navigation while consuming 1,288 kW of power. The engine load decreases to 10% MCR during departure and docking maneuvers, which corresponds to 368 kW engine power. The engine load varies between 0% and 5% MCR while waiting at the dock according to passenger loading/unloading or standstill conditions. In all operation modes, the electric power required for the auxiliaries and hoteling needs is acquired as 55 kW.

3. METHODOLOGY

Greenhouse gas (GHG) emissions are represented as CO_2-equivalent (CO_{2eq}) by applying the 100-year global warming potential (GWP_{100}) to convert emissions of gases other than CO_2. The conversion coefficients for CO_2, CH_4, and N_2O are sourced from the IMO's 2024 LCA Guidelines [2] and IPCC's Fifth Assessment Report [3].

The emissions resulting from the ferry's daily diesel fuel consumption are calculated using the emission conversion factors from Table 3 by Eq. (1).

$$g_i = m_{diesel} \times C_{f,i} \tag{1}$$

where m_{diesel} is the mass of the diesel fuel consumed by the ferry per day, i represents CO_2, CH_4, and N_2O emissions for burning diesel oil as fuel, g_i is the emissions from the propulsion system's exhaust gas for ith emission and C_f represents the emission conversion factor.

Table 3. Initial default emission factors per fuel pathway code [2]

Properties	Marine Diesel / Gas Oil max. 10% Sulphur)	Hydrogen	Unit
Well-to-Tank (WtT) GHG intensity ($\boldsymbol{GHG_{CO_{2eq},WtT}}$)	17.7	0	gCO_{2eq} / MJ
Lower Calorific Value (LCV)	0.0427	0.12	MJ / g fuel
$\boldsymbol{C_{f,CO_2}}$	3.206	0	gCO_2 / g fuel
$\boldsymbol{C_{f,CH_4}}$	0.00005	0	gCH_4 / g fuel
$\boldsymbol{C_{f,N_2O}}$	0.00018	0	gN_2O / g fuel

$g_{CO_{2eq},TtW,diesel}$ is expressed as Tank-to-Wake (TtW) CO_{2eq} emission using GWP_{100} values to convert emissions of gases equivalent CO_2 emission basis, based on the factors provided in the IPCC's Fifth Assessment Report [3] for CO_2, CH_4, and N_2O and calculated using Eq. (2).

$$g_{CO_{2eq},TtW,diesel} = \sum(GWP_{TtW,i} \times g_i) \tag{2}$$

where GWP_{TtW} represents the Tank-to-Wake GWP_{100} values and taken as 1 gCO_{2eq} / per g of fuel burned for CO_2, 28 gCO_{2eq} / per g of fuel burned for CH_4, and 265 gCO_{2eq} / per g of fuel burned for N_2O (IMO, 2024).

The Well-to-Tank (WtT) CO_{2eq} emission from daily diesel fuel consumption is calculated using Eq. (3).

$$g_{CO_{2eq},WtT,diesel} = m_{diesel} \times LCV_{diesel} \times GHG_{CO_{2eq},WtT,diesel} \tag{3}$$

The Well-to-Wake (WtW) CO_{2eq} emission from consuming marine diesel oil in the ferry is determined by using Eq. (4).

$$g_{CO_{2eq},WtW,diesel} = g_{CO_{2eq},TtW,diesel} + g_{CO_{2eq},WtT,diesel} \tag{4}$$

The calculation methodology for the WtW CO_{2eq} emission for hydrogen fuel involves electrolysis, conditioning (liquefaction or compression), transport, and distribution stages contributing to the life cycle carbon emissions of the hydrogen fuel used in the ferry. The WtW CO_{2eq} emission for hydrogen fuel ($g_{CO_{2eq},WtW,hydrogen}$) is calculated using Eq. (5) for each stage.

$$g_{CO_{2eq},WtW,hydrogen} = m_{hydrogen} \times \sum(E_j \times EF_{electricity}) \tag{5}$$

where j represents emission production stages of electrolysis, conditioning, transport, and distribution of hydrogen. E_j is defined as the energy required for the jth stage and $EF_{electricity}$ is the emission factor for the electrical energy from renewable energy sources.

- $E_{electrolysis}$: Energy required for electrolysis - 51.2 kWh / kg H_2 [4]
- $E_{liquifaction}$: Energy required for liquefaction - 10 kWh / kg H_2 [5]
- $E_{transport}$: Distance traveled and energy consumed per kg H_2 - 32.5 g CO2 / t nm (for LNG carriers) [6]
- $E_{distribution}$: Energy required for local distribution - 0.45 kg CO_{2eq} / kg H_2 [7]
- $EF_{electricity}$: Emission factor of electricity source - 0.033 kg CO_{2eq} / kWh (for solar photovoltaics) [8]

4. RESULTS AND DISCUSSION

The total power requirement of the vessel is calculated as 1,343 kW with the addition of generator load during navigation. Considering the characteristics of the PEMFC in Fig. 2, 14 PEMFCs were selected for the vessel, each delivering 165.4 A and 580 V with ~50% efficiency and 60 g/kWh specific hydrogen fuel consumption when cruising. The specific fuel consumption is reduced to 51.5 g/kWh on maneuvering and 53 g/kWh during passenger loading/unloading phases. The calculations show that the vessel will consume 315.25 kg of hydrogen fuel per day according to the operation schedule. The comparison of emissions resulting from the use of diesel and hydrogen fuels is represented in Fig. 3.

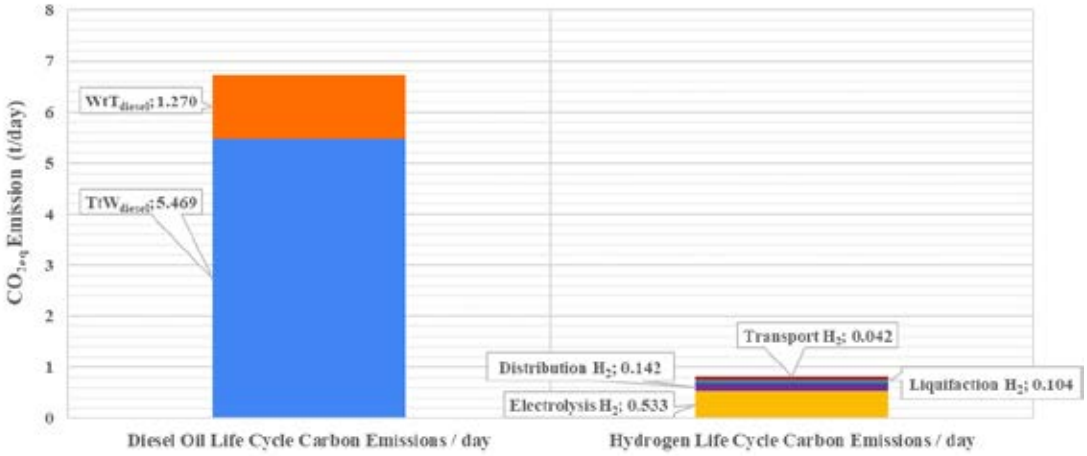

Fig. 3. Comparative life cycle carbon emissions for the diesel oil and hydrogen fuels used by the ferry

The results indicate that the utilization of hydrogen fuel instead of diesel fuel would reduce the life cycle carbon equivalent emissions impact by 87.82%. The share of H_2 production through electrolysis was obtained as the highest stage by 65.88% for the hydrogen utilization in the ferry. It is important because even though renewable electricity is used as the power source for the electrolysis of hydrogen, it is still challenging to obtain net zero emission targets unless all the stages of renewable energy production become carbon-free. Besides, when compared with the transport of H_2 from Australia to Türkiye, the transportation-based carbon equivalent emissions remain at a very low degree cause of emission production (only 5.17% of the hydrogen life cycle carbon emissions) even if the ship used for the H_2 transportation utilizes fossil fuels for navigation.

5. CONCLUSIONS

In this study, the life cycle carbon emissions assessment of diesel and hydrogen fuels were comparatively carried out. This study highlights the significant potential of hydrogen fuel cell propulsion systems in reducing the life cycle carbon emissions of maritime transportation. The comparative analysis between diesel and hydrogen fuel demonstrates an 87.82% reduction in emissions when transitioning to hydrogen-powered ferries. Despite current economic challenges, ongoing advancements in hydrogen production and infrastructure development are expected to enhance its viability as a cleaner alternative to fossil fuels. Future research should focus on optimizing hydrogen storage, distribution, and production methods to achieve net-zero emissions. Ultimately, integrating hydrogen-based solutions into the maritime sector aligns with global sustainability goals and represents a crucial step toward decarbonizing marine transportation.
In this context, hydrogen is considered a natural and clean energy source. However, to achieve the net zero emission goal, there are still gaps and challenges to be fulfilled.

REFERENCES

1. PowerCell Group. (2024). Marine System 200. Accessed on 21.12.2024 from https://powercellgroup.com/product/marine-system-200/
2. IMO. (2024). 2024 Guidelines on Life Cycle GHG Intensity of Marine Fuels (2024 LCA Guidelines). IMO, Annex-10. Resolution MEPC.391(81). London: IMO. Accessed on 20.12.2024 from https://wwwcdn.imo.org/localresources/en/KnowledgeCentre/IndexofIMOResolutions/MEPCDocuments/MEPC.391(81).pdf
3. IPCC. (2014). Climate Change 2014: Synthesis Report. Contribution of Working Groups I, II and III to the Fifth Assessment Report of the Intergovernmental Panel on Climate Change [Core Writing Team, R.K. Pachauri and L.A. Meyer (eds.)]. IPCC, Geneva, Switzerland. Accessed on 13.01.2025 from https://www.ipcc.ch/assessment-report/ar5/.
4. Parkinson, B. B. (2019). Levelized cost of CO2 mitigation from hydrogen production routes. Energy & Environmental Science, 12(1), 19-40.
5. Atilhan, S., Park, S., El-Halwagi, M., Atilhan, M., Moore, M., & Nielsen, R. (2021). Green hydrogen as an alternative fuel for the shipping industry. Current Opinion in Chemical Engineering, 31, 100668.
6. Istrate, I. R., Iribarren, D., Dufour, J., Ortiz Cebolla, R., Arrigoni, A., Moretto, P., & Dolci, F. (2022). Quantifying emissions in the European maritime sector. Publications Office of the European Union: Luxembourg.
7. Frank, E. D., Elgowainy, A., Reddi, K., & Bafana, A. (2021). Life-cycle analysis of greenhouse gas emissions from hydrogen delivery: A cost-guided analysis. International journal of hydrogen energy, 46(43), 22670-22683.
8. IEA. (2024). Life Cycle Upstream Emissions Factors 2024. Accessed on 25.02.2025 from https://www.iea.org/data-and-statistics/data-product/life-cycle-upstream-emissions-factors-2024-2#life-cycle-upstream-emission-factors

HYDROGEN PRODUCTION FROM WASTEWATER OF DOMESTIC HEAT PUMP BASED TUMBLE DRYERS: AN INNOVATIVE APPROACH FOR SUSTAINABLE ENERGY

[1*]*Anil Erdogan*, [1]*Aziz Basdemir*
[1] Vestel Home Appliances, Central R&D, Technology Development Department, Manisa, Türkiye

*Corresponding author e-mail: anil.erdogan@vestel.com.tr

ABSTRACT
Hydrogen is considered a pivotal energy carrier in the transition to a sustainable and carbon-neutral future, with applications in industry, transportation, and power generation. However, the challenge lies in producing hydrogen efficiently and sustainably. This study explores an innovative approach to hydrogen production by utilizing wastewater from domestic heat pump-based tumble dryers. As global energy demand rises and environmental concerns intensify, sustainable hydrogen production methods are gaining increasing attention. The wastewater discharged from heat pump dryers contains thermal energy that can be harnessed for electrolysis or other hydrogen generation techniques. By integrating waste heat recovery and electrochemical processes, this approach offers a novel pathway for improving energy efficiency and reducing water waste in household appliances. The feasibility, efficiency, and potential impact of this method are analyzed, highlighting its role in advancing sustainable energy solutions. The findings of this study reveal that ambient temperature and relative humidity significantly influence the performance of a heat pump-based tumble dryer as well as hydrogen production from waste water. This study highlights the critical role of environmental conditions in optimizing system efficiency and hydrogen yield, providing valuable insights for future design improvements and operational strategies.

Keywords: Hydrogen production, heat pump-based tumble dryer, thermodynamic analysis, innovative approach, sustainability

1. INTRODUCTION

Hydrogen is increasingly recognized as a key energy carrier in the global transition to sustainable energy systems. According to the IEA's 2024 report, global hydrogen production reached 97 million tonnes in 2023, with less than 1% from low-emission sources. Fossil fuel-based methods still dominate, emitting around 900 million tonnes of CO_2 annually. [1]. Green hydrogen production through Proton Exchange Membrane electrolysis (PEME) has gained attention as a clean alternative, particularly when powered by renewable energy sources. However, a major challenge in electrolysis is the dependence on high-purity water, as impurities can reduce efficiency, accelerate component degradation, and increase maintenance requirements [2]. Additionally, electrolyzers face challenges related to energy consumption, system durability, and operational costs. The efficiency of the process is influenced by factors such as electrode degradation, membrane fouling, and heat management, all of which impact long-term performance and sustainability. Nevertheless, significant progress has been made in addressing these challenges through advancements in membrane materials, electrode coatings, and system optimization. Ongoing research continues to improve efficiency, reduce costs, and enhance the viability of electrolysis for widespread hydrogen production.

Heat pump-based tumble dryers have emerged as an energy-efficient alternative to conventional vented and condenser dryers. Unlike traditional dryers, which expel hot, moist air into the surroundings, heat pump dryers recover and reuse heat, reducing energy consumption by up to 50% [3]. These systems operate by circulating refrigerant through a closed-loop system, where it absorbs heat from moist air, condenses the moisture, and reheats the air before reintroducing it into the drum. However, despite their energy efficiency, these dryers generate condensate water as a byproduct, which is typically discarded. The composition and usability of this water for other applications, such as electrolysis, remain largely unexplored.

This study introduces an innovative approach to utilizing condensate water from heat pump-based tumble dryers for decentralized hydrogen production through PEME. Unlike conventional electrolysis systems that rely on tap or purified water, this research investigates the feasibility of repurposing waste condensate, thus integrating household appliances into hydrogen energy systems. Key factors such as ambient temperature, relative humidity, coefficient of performance (COP), total exergy destruction rate, mass flow rate of condensed water and hydrogen production rate are analyzed to assess the practicality of this approach. The findings contribute to the development of sustainable water recovery strategies and open new pathways for resource-efficient hydrogen generation.

2. SYSTEM MODELING

The schematic diagram of heat pump-based tumble dryer integrated with proton exchange membrane electrolyser is given in Fig. 1.

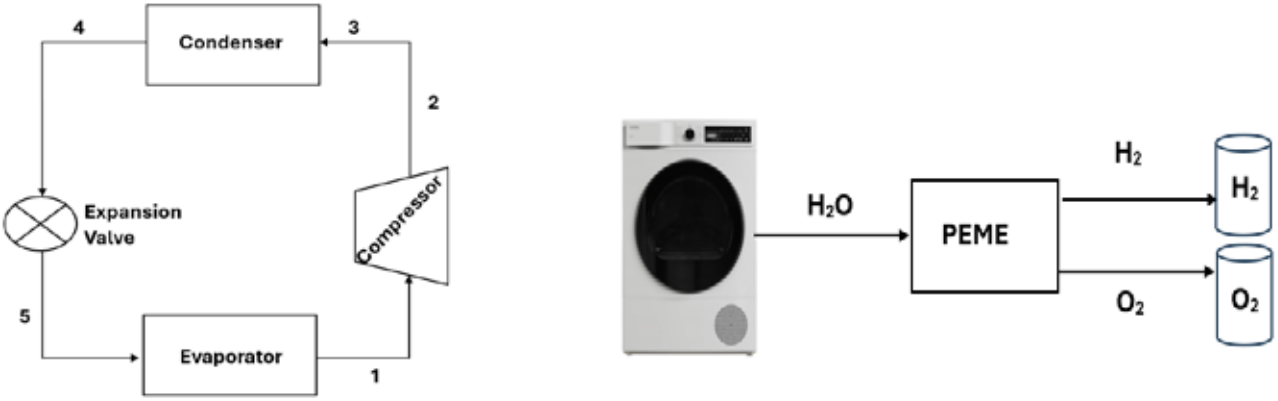

(a) (b)

Fig. 1. (a) The process flow diagram of the heat pump-based tumble dryer, (b) the overall system schematics

The proposed system integrates a heat pump-based tumble dryer with a PEME to utilize the condensed water from the drying process for hydrogen production. In the drying phase, the heat pump cycle efficiently transfers heat within the tumble dryer. The refrigerant circulates through the system, undergoing compression, condensation, expansion, and evaporation. The warm air, heated by the condenser, enters the drum to dry the wet clothes, while the evaporator cools the moist air, causing water vapor to condense into liquid form. This condensed water is collected and directed to the PEM electrolyzer, where it undergoes purification if necessary. The electrolysis process splits water molecules into hydrogen and oxygen using an electric current. Within the PEM electrolyzer, water molecules dissociate at the anode, releasing oxygen and protons. The protons migrate through the membrane to the cathode, where they combine with electrons to form hydrogen gas. The produced hydrogen can be stored or used as an energy carrier, offering a sustainable approach to utilizing waste water from heat pump-based drying systems for clean energy production.
The following assumptions have been considered in the analysis:

- The system operates under steady-state conditions.
- Pressure losses across the inlet and outlet streams, as well as heat transfer from system components to the surroundings, are neglected.
- Kinetic and potential energy effects are assumed to be negligible.
- The drum inlet air is considered to be saturated, implying a relative humidity of 100%.

The modeling approach and equations used are given as follows. These equations are solved using a software namely Engineering Equation Solver (EES). In order to ascertain the unknown properties, it is necessary to apply the open system energy balance equation for steady-state operation, which encompasses the control volume of the system's component. This equation is given in Eq. (1) [4].

$$0 = \dot{Q}_{cv} - \dot{W}_{cv} + \sum_i(\dot{m}_i \cdot h_i) - \sum_e(\dot{m}_e \cdot h_e) \quad (1)$$

Where, $\dot{Q}_{cv}$ and $\dot{W}_{cv}$ are defined as heat transfer from the components to the environment, and power, respectively. $\dot{m}$ and h are depicted as mass flow rate and specific enthalpy, respectively. The subscript i and e are inlet and exit, respectively. The condenser and evaporator capacities are calculated from Eqs. (2), and (3), respectively.

$$\dot{Q}_{cond} = \dot{m} \cdot (h_3 - h_4) \quad (2)$$

$$\dot{Q}_{evap} = \dot{m} \cdot (h_1 - h_5) \quad (3)$$

The mass flow rate of condensed water through the drying process can be calculated using Eq. (4).

$$\dot{m}_{cond,water} = \dot{m}_{air} \cdot \left(\omega_{air,drum,in} - \omega_{air,drum,out}\right) \quad (4)$$

In this equation, $\omega_{air,drum,in}$ and $\omega_{air,drum,out}$ represent the humidity ratios of the air entering and exiting the drum, respectively. The humidity ratio is determined using the Engineering Equation Solver (EES) software.

In order to produce hydrogen, PEME system has been used in the system. The main reactions occur the inside of PEME is given as follows.

Anode: $H_2O \rightarrow \frac{1}{2}O_2 + 2H^+ + 2e^-$ (5)
Cathode: $2H^+ + 2e^- \rightarrow H_2$ (6)
Total: $H_2O \rightarrow H_2 + \frac{1}{2}O_2$ (7)

The produced hydrogen, oxygen and remaining water exiting the PEME can be found using molar balance below.

$$\dot{n}_{H_2,produced} = a \quad (8)$$

$$\dot{n}_{O_2,produced} = a/2 \quad (9)$$

$$\dot{n}_{H_2O,out} = \left(\frac{\dot{m}_{cond,water}}{MW_{water}}\right) - a \quad (10)$$

In these equations, a is expressed as the reaction rate which can be found using Faraday's Law [5], and MW_{water} is defined as the molar weight of the water.

$$a = \frac{I}{n \cdot F} \quad (11)$$

In Faraday's Law equation given in Eq. (11), I is the current, n is the number of electrons and F is the Faraday's constant.

Following the energy and mass analysis, the general exergy balance equation for the open system is applied to determine the irreversibilities associated with each component of the system [4].

$$0 = \dot{Ex}_Q - \dot{Ex}_W + \sum_i(\dot{m}_i \cdot ex_{f,i}) - \sum_e(\dot{m}_e \cdot ex_{f,e}) - \dot{Ex}_D \quad (12)$$

where, $\dot{Ex}_Q$ and $\dot{Ex}_W$ are exergy transfer by heat and power, respectively. $ex_{f,i}$ is defined as specific flow exergy. This parameter can be defined using Eq. (13).

$$ex_f = (h - h_0) - T_0 \cdot (s - s_0) \quad (13)$$

Here, h_0 and s_0 are specific enthalpy and entropy at the dead state conditions (T_0=298 K, p_0=100 kPa) .

3. RESULTS AND DISCUSSIONS

The results obtained from the analysis provide valuable insights into the performance of the integrated heat pump-based tumble dryer and PEM electrolyzer system. This section discusses the key findings, including COP, exergy destruction rate of the system, and hydrogen production rates. In addition, the effect of operating conditions on system performance is evaluated. The thermodynamic properties of the system studied at the steady-state conditions and lnP-h and T-s diagrams are presented in Table 1 and Fig. 2, respectively. It is important to note that the following data were obtained from experimental studies conducted in the R&D laboratory of the tumble dryer factory at Vestel Home Appliances.

Table 1. State Properties of the System

State Number	Pressure (kPa)	Temperature (°C)	Specific Enthalpy (kJ/kg)	Specific Entropy (kJ/kg·K)	Flow Exergy (W)
1	1000	38.84	627.2	2.429	739.3
2	2200	82.47	683	2.478	991.6
3	2200	77.52	670.6	2.443	979.9
4	2200	56.07	356	1.506	764.7
5	1000	26.94	356	1.527	725.8

(a) (b)

Fig. 2. The property diagram of the system (a) lnP – h diagram, (b) T – s diagram

Fig. 3(a) illustrates the impact of ambient temperature on the coefficient of performance (COP) (left) and the total exergy destruction rate (right) under varying relative humidity conditions. As observed in the figure, the COP decreases as the ambient temperature rises from 15°C to 40°C. This trend can be attributed to several factors. An increase in ambient temperature leads to higher operating pressures in the compressor, thereby increasing its electricity consumption. Additionally, higher ambient temperatures reduce the amount of condensation, which in turn lowers the dehumidification capacity of the dryer. Conversely, as the ambient temperature increases, the total exergy destruction rate increases due to enhanced irreversibilities in both the evaporator and the condenser. On the other hand, Fig. 3(b) shows the effect of ambient temperature on the water production rate according to the different relative humidity values. The results show that as the ambient temperature increases water production rate decreases for all relative humidity values.

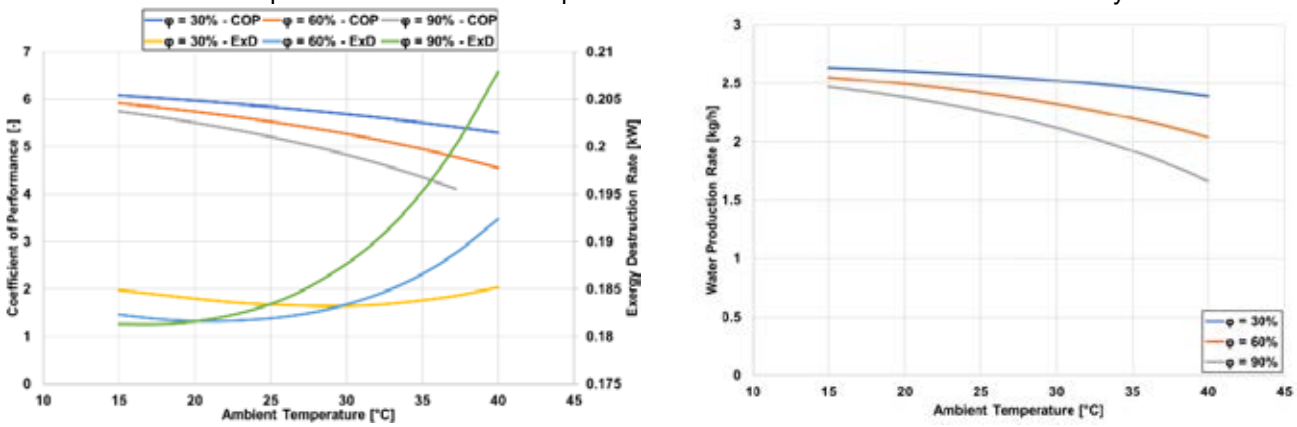

(a) (b)

Fig. 3. The effect of ambient temperature on the (a) COP and the exergy destruction rate, (b) the water production rate.

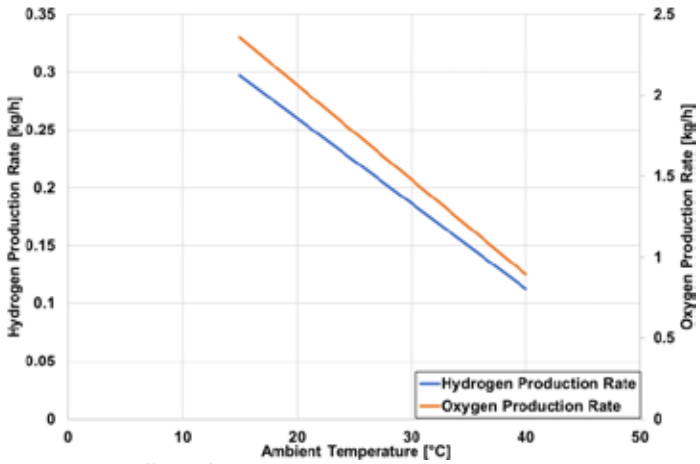

Fig. 4. The effect of ambient temperature on the production rates

Fig. 4 illustrates the effect of ambient temperature on Hydrogen (left) and oxygen (right) production rates. As the ambient temperature increases, the production rates of both gases decrease due to the reduced condensation in the tumble dryer. Moreover, the findings indicate that higher ambient temperatures have an overall negative effect on hydrogen and oxygen production rates.

4. CONCLUSIONS

In this study, a comprehensive thermodynamic analysis is performed to evaluate the feasibility of integrating a heat pump-based tumble dryer with a proton exchange membrane electrolyzer for hydrogen production. To this end, mass, energy, and exergy balance equations are applied, followed by a parametric analysis to examine the effects of ambient temperature and relative humidity on the COP, total exergy destruction, and hydrogen and oxygen production rates. The key findings derived from this study are summarized as follows.

- Increasing ambient temperature reduces the COP and hydrogen production due to decreased condensation.
- Higher relative humidity leads to lower COP and increased exergy destruction.
- At a constant ambient temperature (e.g., 25°C), an increase in relative humidity from 30% to 90% leads to a 24.07% reduction in COP, while the total exergy destruction rate increases by 8.6%.

Future research can focus on optimizing system design to enhance hydrogen production efficiency under varying

environmental conditions. Additionally, exploring alternative working fluids with lower sensitivity to temperature variations could improve energy efficiency. Lastly, experimental validation with long-term performance analysis can provide deeper insights into system reliability and operational feasibility.

REFERENCES

[1] IEA, "Global Hydrogen Review 2024," International Energy Agency, 2023. [Online]. Available: https://www.iea.org/reports/global-hydrogen-review-2024

[2] Grigoriev, S. A., Fateev, V. N., Bessarabov, D. G., & Millet, P. (2020). Current status, research trends, and challenges in water electrolysis science and technology. *International Journal of Hydrogen Energy*, *45*(49), 26036-26058.

[3] European Commission, "Energy efficient appliances" 2025. [Online]. Available: , https://energy.ec.europa.eu/news/focus-energy-efficient-appliances-2025-02-17_en

[4] Scott, K. (Ed.). (2019). *Electrochemical methods for hydrogen production* (Vol. 25). Royal Society of Chemistry.

THE SYNTHESIS OF Ni-Co-B CATALYST FOR AMMONIA BORANE DEHYDROGENATION

[1,3*]*İrem NAS*, [2]*Ragıp KIZILTAŞ*, [1]*Ahsen KOÇ*, [1,3]*Emre YILDIRIM*
[1] Türkiye Energy, Nuclear and Mining Research Agency (TENMAK), Clean Energy Research Institute (TEMEN), Dumlupınar Boulevard, No: 166, Ankara, 06510, Türkiye
[2] Türkiye Energy, Nuclear and Mining Research Agency (TENMAK) Rare Earth Elements Research Institute (NATEN), Saray District Atom Street, Ankara, 06980, Türkiye
[3] Ankara Yıldırım Beyazıt University, Institute of Science, Ayvalı Mah. 150 Street, Ankara, 06010, Türkiye

*Corresponding author e-mail: irem.nas@tenmak.gov.tr

ABSTRACT

With the depletion of fossil fuels and the validity of the Paris Climate Agreement, there is growing interest in hydrogen production and storage. Chemical storage method is an effective solution for hydrogen storage, and ammonia borane hydrogen can be stored chemically and safely. In this field, ammonia borane (AB, NH_3BH_3) stands out as a storage material due to its high hydrogen content and recoverability. The importance of the catalysts used in the dehydrogenation process to utilize the hydrogen in ammonia borane is increasing day by day. In this article, after the introduction of the subject, the synthesis of Ni-Co-B (Nickel- Cobalt- Boron) catalyst in 4 different rations (%50, %60, %70, %80 Co/Ni+Co ratio), the characterization devices used for the analysis of the synthesized catalysts and the dehydrogenation system for hydrogen production are included in the materials and methods section. The results and discussion section includes the analysis comments of the synthesized Ni-Co-B catalyst. As a result of the analysis, it was proven that the synthesized catalysts were successfully formed. In the BET analysis, it was determined that the catalyst with the highest specific surface area was found in the 80% Co/Ni+Co ratio and it was determined that the catalyst with the 80% Co/Ni+Co ratio showed the best catalyst properties in the dehydrogenation process.
Keywords: Chemical hydrogen storage, hydrogen storage, hydrogen, ammonia borane

1. INTRODUCTION

One of the most prevalent elements in the universe, hydrogen holds enormous promise for the creation of sustainable energy sources and clean energy. Hydrogen, which can be used in a wide range of applications, also plays an important role in energy storage systems. The technique of storing hydrogen in different chemical compounds so that it can be used as an energy carrier is known as chemical hydrogen storage, and it is one of the energy storage technologies. There is a lot of promise for a safer, more effective, and portable usage of hydrogen via chemical hydrogen storage. Furthermore, this storage method allows hydrogen to be easily released when needed for reuse in energy production, a critical component for sustainable energy solutions. Ammonia borane is an important type of chemical hydrogen storage system. Various catalysts can be synthesized to utilize the high hydrogen content (19.6%) of ammonia borane [1-3].
The synthesis of trimetallic catalysts enables the dehydrogenation of ammonia borane to occur more efficiently, rapidly and stably. This can be an important development, especially in hydrogen storage and transportation technologies. There are ternary catalysts synthesized for the dehydrogenation of ammonia borane in the literature. Fernandes et al. (2012) synthesized Co-Mo-B catalyst by chemical reduction method and carried out the ammonia borane dehydration process as hydrolysis and determined the maximum hydrogen production rate as 2460 ml H_2 min^{-1} (g of catalyst)$^{-1}$ [4]. Lim (2020) synthesized Ni-B-Zr catalyst by co-precipitation method and carried out the ammonia borane dehydrogenation process as hydrolysis at 45°C and the efficiency was 86.91% [5]. Fernandes et al. (2008) synthesized Co-Ni-B catalyst with Co/(Co+Ni) ratio of 0.85 by chemical reduction method and carried out the dehydration of sodium borohydride ($NaBH_4$) by hydrolysis and determined the maximum hydrogen production rate of 1175 ml/(min g) catalyst) [6].
As the originality of this study, ammonia borane compounds were subjected to dehydrogenation in the presence of different ratios of Ni-Co-B catalyst synthesized using the hydrolysis method. Dehydrogenation, i.e. the removal of hydrogen from the compound, was carried out. The ultimate goal of the study is to utilize ammonia borane as a sustainable hydrogen storage material.

2. MATERIALS AND METHODS

Cobalt (II) nitrate hexahydrate ($Co(NO_3)_2.6H_2O$), nickel (II) chloride hexahydrate ($NiCl_2.6H_2O$), sodium borohydride ($NaBH_4$), deionized water, ethanol products were used. In the drying stage, a vacuum oven with nitrogen gas and a tube oven with argon gas were used.
A brief description of the synthesis of the synthesized Ni-Co-B catalysts in different ratios, the characterization devices used for the analysis and the dehydrogenation system for hydrogen production are given below.

2.1. Synthesis of Co-Ni-B Catalysis

Cobalt (II) nitrate hexahydrate ($Co(NO_3)_2.6H_2O$) was weighed in such a way that Co/Co+Ni ratio was 50,60,70,80 % and

Nickel (II) chloride hexahydrate ($NiCl_2.6H_2O$) was weighed according to the calculations. DI water was added in the beaker. $NiCl_2.6H_2O$ was added to the beaker and allowed to dissolve completely. Then, $Co(NO_3)_2.6H_2O$ was added to the beaker and stirred. Sodium borohydride ($NaBH_4$) was added to the solution to carry out reduction and then left to stir. After a certain time, the solution was filtered by vacuum filtration. The washing with deionized water and ethanol was done to remove the impurities in the catalyst and this process was repeated 4 times.
After the filtration process was completed, the drying stage was started. It was kept in a vacuum environment under nitrogen gas. Then, the size reduction process was carried out by crushing in a mortar and pestle. Finally, the sample was dried in a tube oven under argon environment. After the final treatment, Co-Ni-B catalyst was obtained. Fig. 1 shows the experimental process schematically.

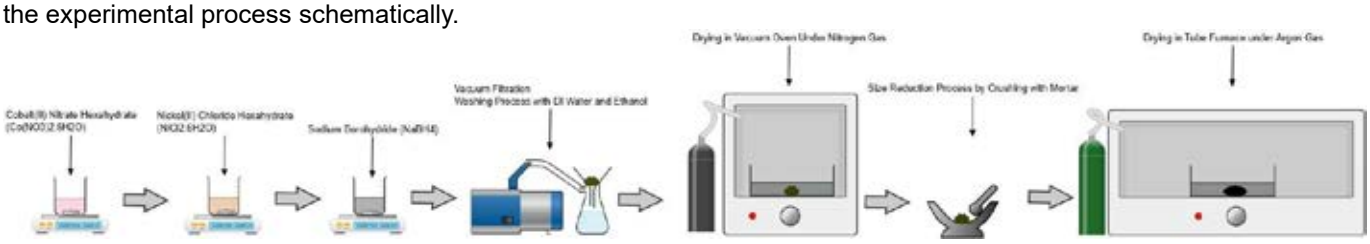

Fig. 1. Schematic illustration of the Ni-Co-B catalyst experimental process

2.2. The System of Dehydrogenation

Dehydrogenation is a type of chemical reaction in which a compound loses hydrogen atoms and hydrogen is obtained. The dehydrogenation reaction of ammonia borane is the conversion of ammonia borane (NH_3-BH_3) to hydrogen (H_2) using high temperature, low temperature, or a catalyst. In this process, ammonia borane is converted into boron (B) and hydrogen (H_2) molecules. In general, the reaction is expressed in Eq. (1) During this reaction, hydrogen is released in the form of gas and it is possible to use this hydrogen as an energy source. In this study, dehydrogenation experiments were carried out to investigate the catalytic performance of the synthesized catalysts. First, the catalyst was weighed in the calculated ratios and added to a 50 mL reactor. The temperature was set to 30°C. Then, AB was dissolved in 30 mL DI water and fed into the reactor with a syringe. The hydrogen evolution was observed as a function of time by utilizing the displacement of water.

$$NH_3BH_3 + 2H_2O = 3H_2 + NH_4BO_2 \quad (1)$$

3. RESULTS AND DISCUSSION

The synthesized catalysts were analyzed by X-ray diffraction (XRD) for structural analysis, Fourier transform infrared spectroscopy (FTIR) for bond structure, X-ray photoelectron spectroscopy (XPS) for elemental analysis, Brunauer-Emett-Teller (BET) for surface analysis and porosity.

3.1 XRD and FTIR Analyses:

The successful formation of the synthesized Co-Ni-B catalyst at different ratios was observed by XRD and FTIR analysis. XRD analysis showed that the successful doping of cobalt with nickel and the presence of boron in the structure without bonding are compatible with the literature and all four syntheses were successfully formed. In addition to the XRD analysis, FTIR analysis also showed that the peaks of the expected bond structures were found to be consistent with the literature. Related XRD and FTIR analyses are shown in Fig. 3.

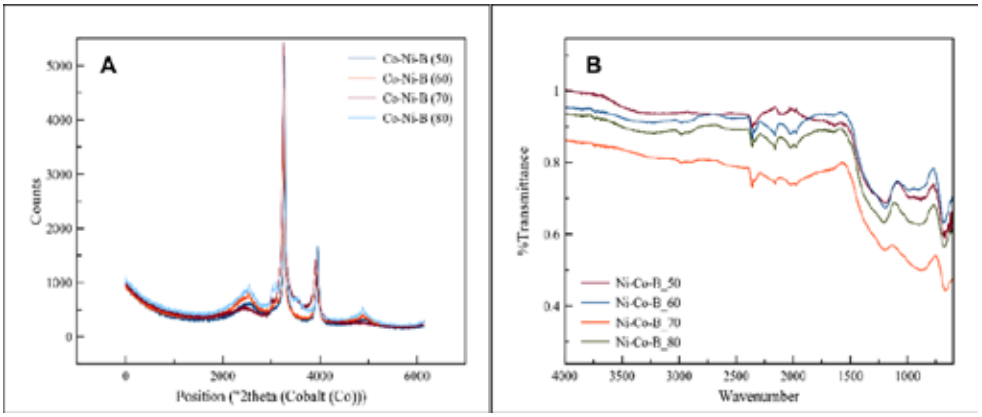

Fig. 3. XRD (A) and FTIR (B) analysis of synthesized Ni-Co-B catalysts in different ratios

3.2 XPS Analysis:

XPS analyses were performed to determine whether the synthesized Co-Ni-B catalysts at different ratios were successfully synthesized. XPS analysis is shown in Fig. 4. In the XPS analysis, it was seen that nickel, cobalt and boron were successfully formed in the structure as atomic percentages and peaks.

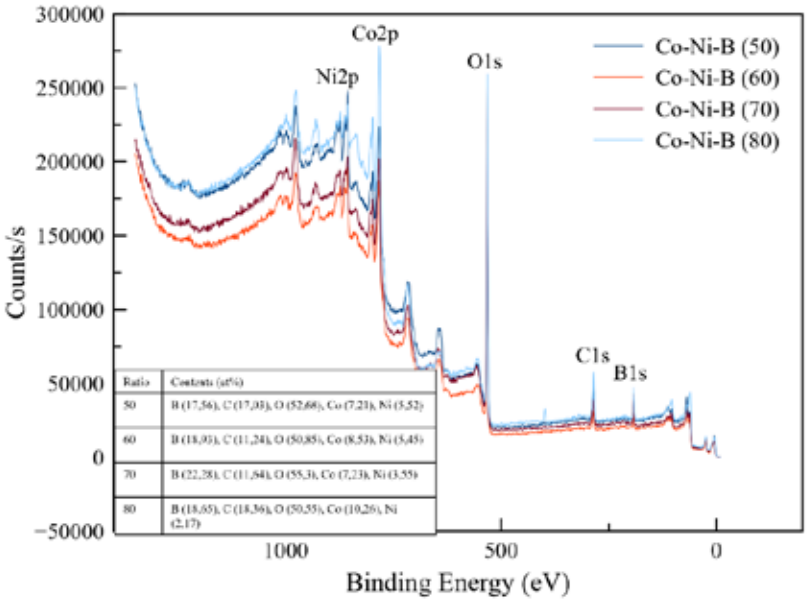

Fig. 4. XPS analysis of Ni-Co-B catalysts

3.2 BET Analysis:

Nitrogen adsorption-desorption experiment was used to characterize the surface areas of the synthesized Ni-Co-B catalysts at different ratios. BET analyses of the related catalysts are shown in Table 1. In Brunauer-Emett-Teller (BET) analysis, the specific surface areas of Ni-Co-B (50%, 60%, 70%, 80%) catalysts were measured as 81.530, 95.909, 105.998, 126.515 m^2/g, respectively. In the analysis, it was observed that Ni-Co-B (80%) had the highest specific surface area and the importance of the specific surface area in the dehydrogenation process was proven.

Table 1. BET analysis of Ni-Co-B catalysts

Catalysts	Total Surface Area (m^2)	Specific Surface Area (m^2/g)
Ni-Co-B (50%)	15.262	81.530
Ni-Co-B (60%)	19.364	95.909
Ni-Co-B (70%)	21.622	105.998
Ni-Co-B (80%)	24.304	126.515

3.2 Dehydrogenation Analysis:

As a result of the dehydrogenation experiments, the time dependence of hydrogen in mL of different ratios of Ni-Co-B catalysts was observed. It was observed that Ni-Co-B catalysts successfully catalyzed the ammonia borane dehydrogenation reaction. It was observed that the fastest hydrogen was obtained when Ni-Co-B (80%) catalyst was used in the experiment. The dehydrogenation experiment results of these catalysts are shown in Fig. 5.

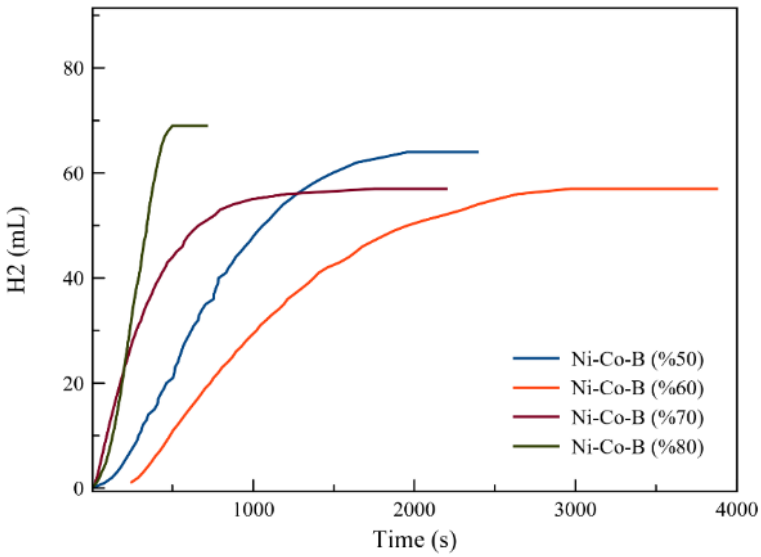

Fig. 5. Results of dehydrogenation experiment of different ratios of Ni-Co-B catalysts

4. CONCLUSIONS

Hydrogen produced with renewable energy sources offers an environmentally friendly option as a zero-emission fuel. Storage technologies are very important for the effective use of hydrogen. The successful synthesis of Ni-Co-B catalysts with different ratios synthesized for chemical hydrogen storage has been proven by characterization tests. It has been determined that the best value in the dehydrogenation process for hydrogen production is the Ni-Co-B catalyst with a Co/Ni+Co ratio of 80%. This study has proven that the catalytic properties of cobalt in the ternary catalyst system are higher than nickel. In the next process, it is aimed to complete the SEM-EDS analysis and support the XPS analysis results with SEM-EDS. At the same time, dehydrogenation experiments will be repeated and the results will be interpreted with the average of the values, and changes in the performance of the catalysts will be observed by increasing the number of cycles.

ACKNOWLEDGEMENT

This study supports chemical hydrogen storage activities carried out at the Clean Energy Research Institute (TEMEN) affiliated with the Turkish Energy, Nuclear and Mining Research Council (TENMAK).

REFERENCES

1. Manoharan Y et al (2019) Hydrogen fuel cell vehicles; Current status and future prospect. Appl Sci 9(11).
2. Midilli A, Dincer I (2008) Hydrogen as a renewable and sustainable solution in reducing global fossil fuel consumption. Int J Hydrogen Energy 33(16):4209–4222.
3. Geng S, Yang W, Yu YS (2019) Building MoS2/S-doped g-C3N4 layered heterojunction electrocatalysts for efficient hydrogen evolution reaction. J Catal 375.
4. Fernandes, R., Patel, N., Miotello, A., Jaiswal, R., & Kothari, D. C. (2012). Dehydrogenation of Ammonia Borane with transition metal-doped Co–B alloy catalysts. International Journal of Hydrogen Energy, 37(3), 2397–2406.
5. Lim D. (2020) Hydrogen Production from Sodium Boronhydride and Ammonia Borane Mixtures with Ni-B and Ni-B-Zr Catalysts. Ankara University Institute of Sciences Master's Thesis.
6. Fernandes, R., Patel, N., Miotello, A., & Filippi, M. (2009). Studies on catalytic behavior of Co–Ni–B in hydrogen production by hydrolysis of $NaBH_4$. Journal of Molecular Catalysis A: Chemical, 298(1-2), 1–6.

DEVELOPMENT of RHODIUM-BASED CATALYST for AMMONIA BORANE DEHYDROGENATION

[1*]Ahsen KOÇ, [2]Ragıp KIZILTAŞ, [1]İrem NAS, [1]Emre YILDIRIM
[1] Türkiye Energy, Nuclear and Mining Research Agency (TENMAK), Clean Energy Research Institute (TEMEN), Dumlupınar Boulevard, No: 166, Ankara, 06510, Türkiye
[2] Türkiye Energy, Nuclear and Mining Research Agency (TENMAK) Rare Earth Elements Research Institute (NATEN), Saray District Atom Street, Ankara, 06980, Türkiye

*Corresponding author e-mail: ahsen.koc@tenmak.gov.tr

ABSTRACT

The use of alternative energy sources is one of the priority areas of research today. In particular, the use and storage of clean energy sources such as hydrogen, which is considered as a potential energy source, is important in line with sustainable development goals and environmentally friendly technologies. In this context, ammonia borane (NH_3BH_3), which is one of the prominent compounds in terms of chemical storage of hydrogen with its high hydrogen content, attracts attention due to its compatibility with portable systems, its highly stable structure at room temperature and its ability to produce high purity hydrogen by dehydrogenation process. This study investigates the innovative synthesis and catalytic evaluation of rhodium (Rh) catalysts supported on hexagonal boron nitride (h-BN), graphene oxide (GO) and aluminium oxide (Al_2O_3) for the dehydrogenation of ammonia borane. The performances of the synthesised catalysts were systematically compared based on the dehydrogenation results and it was observed that Rh@GO showed the highest hydrogen release activity, with high surface area and strong interactions between Rh active species and support material contributing to this success, followed by Rh@h-BN and Rh@Al_2O_3. The structural and surface properties of the catalysts were investigated in detail by XRD, FTIR, XPS, SEM-EDS and BET analyses and the stability of the catalysts was confirmed. These investigations highlight the catalytic behaviour of Rh-based systems, emphasise the critical role of support material selection in optimising catalytic efficiency, and offer a new future-oriented approach for sustainable hydrogen production and storage systems.

Keywords: Hydrogen storage, Ammonia borane, Dehydrogenation, Supported catalysts, Rhodium catalyst

1. INTRODUCTION

Ammonia borane is used for hydrogen storage because of its high hydrogen content and chemical stability. Dehydrogenation of ammonia borane releases hydrogen gas (H_2), which can be used as a clean energy carrier. However, this process requires the use of suitable catalysts to overcome energy barriers and to be effective at low temperatures.
Chandra et al. investigated the potential of using highly active noble metal nanoparticles in the hydrolysis reaction of ammonia borane. In this study, the catalytic activities of ruthenium (Ru), rhodium (Rh), palladium (Pd), platinum (Pt) and gold (Au) nanoparticles supported on γ-Al_2O_3, carbon (C) and SiO_2 were evaluated. According to the results, Ru, Rh and Pt catalysts produced hydrogen with fast kinetics at stoichiometric ratios and showed high activity, while Pd and Au catalysts showed lower activity [1]. Dai and co-workers investigated fine Pd nanoparticles fixed and homogeneously dispersed in MIL-101 scaffold for the catalytic hydrolysis of ammonia borane. It was reported that the Pd@MIL-101 catalyst synthesised in the study exhibited the highest catalytic activity among the Pd-based nanocatalysts reported so far, with a TOF value of 45 mol H_2 min^{-1}(mol Pd)$^{-1}$ for the hydrolysis of ammonia borane [2]. Wu et al. investigated the use of hexagonal boron nitride (h-BN) supported nickel (Ni) catalyst systems in the hydrolysis of ammonia borane. Kinetic studies showed that hydrogen production depends on the amount of catalyst and the reaction temperature. The results showed that Ni@h-BN composites are promising for applications such as fuel cells [3]. Basu et al. studied the hydrolysis of dilute aqueous ammonia-borane solution over a carbon supported ruthenium catalyst. They showed that carbon supported ruthenium catalysts produced hydrogen about 13 times faster than alumina supported cobalt catalysts at 25°C [4].
Catalytic dehydrogenation of ammonia borane presents challenges such as high temperature requirements and the formation of undesired by-products. Rhodium (Rh) based catalysts are known to be suitable candidates for this reaction due to their superior activity and selectivity. However, the support material used can significantly affect the performance of the catalyst. Support materials such as hexagonal boron nitride (h-BN), graphene oxide (GO) and aluminium oxide (Al_2O_3) have physical and chemical properties that can improve catalyst stability, dispersion and activity.

This study investigates the synthesis and characterisation of Rh@h-BN, Rh@GO and Rh@Al_2O_3 catalysts for ammonia borane dehydrogenation. The synthetic method employed allows for the rapid and controlled reduction of Rh precursors and their efficient incorporation into the support material. The structural and functional properties of the catalysts have been extensively evaluated using advanced characterisation techniques such as XRD, FTIR, XPS, SEM-EDS and BET.

2. MATERIALS AND METHODS

The supported catalyst synthesis process was carried out with the use of support materials to achieve active catalytic performance and long-term stability. Hexagonal bornitride (h-BN), graphene oxide (GO) and aluminium oxide (Al_2O_3) were preferred as support materials. These materials play a critical role in increasing the surface area of the catalysts, ensuring their stability and supporting the homogeneous distribution of the active components.

2.1. Synthesis of supported catalysts:

For the synthesis process, Rhodium (III) chloride hydrate equivalent to 2% of the total catalyst weight was weighed, then deionised (DI) water was added and the solution was dissolved by stirring for 10-15 minutes. Hydrochloric acid (HCl) was added to adjust the pH of the solution to 2-3. As a support material, h-BN, GO or Al_2O_3 was added to the solution and stirred at 1000 rpm for 5 hours. Sodium hydroxide (NaOH) solution was then added dropwise to adjust the pH to 7. In the final step, Sodium borohydride ($NaBH_4$) dissolved in DI water was slowly added to the prepared mixture to initiate the reduction reaction. This process was completed by stirring the solution at 1000 rpm for 16 hours. At the end of the synthesis process, the catalysts formed were filtered by vacuum filtration and washed with DI water to remove impurities. The residue obtained after filtration was dried by freeze-drying. This process was carried out to preserve the active surface area of the catalyst and to prevent structural degradation. As a result of this process using a lyophilisation apparatus, it was observed that the surface area of the catalysts increased and their catalytic performance improved.

2.2. Characterisation of supported catalysts:

X-ray diffraction (XRD) was used to obtain information on the structures of the catalysts synthesised with the support material at 40 mA and 40 kV between 10 and 90 degrees and using cobalt (Co) as X-ray source. The bond structures of the catalysts synthesised with the support material were determined by Fourier Transform Infrared (FTIR) spectroscopy using a Tensor 37 brand FTIR instrument. Analyses were performed in the 640-4000 cm-1 region. The elemental analysis of the catalysts synthesised with the support material was determined by X-ray photoelectron spectroscopy (XPS) using a Thermo Scientific / K-Alpha brand XPS instrument. SEM-EDS imaging and elemental analysis of the catalysts synthesised with the support material were carried out using HITACHI SU5000 brand FE-SEM and Oxford X-MaxN 80 model EDS detector with 80 mm^2 detector area. Surface analysis and porosity characteristics of the catalysts synthesised using Brunauer-Emett-Teller (BET) instrument and Anton Paar Autosorb v2.01 brand and model by performing multi-point analysis (45 points).

2.3. Dehydrogenation process:

Dehydrogenation is the process of removing or separating hydrogen atoms from a chemical compound. During this process there is a loss of hydrogen in the structure of the compound and usually a double bond is formed or an unsaturated compound is obtained.
Ammonia borane dehydrogenation is the reaction of an ammonia borane (NH_3BH_3) molecule to hydrogen (H_2) by removing hydrogen atoms from its chemical structure using high temperature, low temperature or a catalyst.

In general, a theoretical total of 3 moles of H_2 is produced from 1 mole of ammonia borane in the presence of the catalyst, as shown in equation 1.

$$NH_3BH_3 + 2H_2O \longrightarrow NH_4BO_2 + 3H_2 \quad (1)$$

In this process, hydrogen is released in the gas phase and this hydrogen can be used as an energy source.

In this study, the catalytic performance of the synthesised catalysts was evaluated by performing dehydrogenation experiments. During the experiment, the catalyst was first weighed and added to the reactor. The reaction temperature was set at 30°C. Ammonia borane dissolved in DI water was then injected into the reactor using a syringe. Hydrogen gas was obtained by the water displacement method and observed in terms of hydrogen obtained (mL) versus time (s). The dehydrogenation processes of all the catalysts synthesised were carried out under the same experimental conditions.

3. RESULTS AND DISCUSSION

3.1. XRD and FTIR analysis results:

XRD and FTIR analyses were performed on the synthesised Rh@h-BN, Rh@Al_2O_3 and Rh@GO catalysts. The analyses showed that there was no change or degradation in the crystal structures and bond structures of h-BN (hexagonal boron nitride), Al_2O_3 (aluminium oxide) and GO (graphene oxide), which are the support materials of Rh@h-BN, Rh@Al_2O_3 and Rh@GO catalysts, thus preserving the characteristic properties of the support materials. The results obtained confirmed that Rh@h-BN, Rh@Al_2O_3 and Rh@GO catalysts physically coexist and there is no chemical interaction between them.

3.2. XPS ve SEM-EDS analysis results:

XPS and SEM-EDS analyses were carried out to confirm the successful synthesis of Rh@h-BN, Rh@Al_2O_3 and Rh@GO catalysts. XPS analyses clearly showed the successful binding of rhodium to the catalyst surface through atomic percentages and peaks. SEM-EDS analyses clearly demonstrated the effective adhesion of rhodium to the support materials through microscopic images and elemental mapping.

3.3. BET analysis results:

The nitrogen adsorption-desorption test was used to determine the surface area of rhodium catalysts formed on different support materials. The BET analysis results of the support materials and the synthesised Rh@h-BN, Rh@Al_2O_3 and Rh@GO catalysts are presented in Table 1. According to the results of Brunauer-Emett-Teller (BET) analysis, the specific surface areas of h-BN, Rh@h-BN, Rh@h-BN, Al_2O_3, Rh@Al_2O_3, GO and Rh@GO were measured to be 49.938, 58.883, 152.066, 165.021, 270.415 and 249.212 m²/g, respectively. According to the results of the analyses, it was observed that Rh@h-BN and Rh@Al_2O_3 catalysts showed an increase in surface area compared to the support materials, while Rh@GO catalyst showed a decrease.

Table 1. BET analysis results of h-BN, Al_2O_3 and GO supports and synthesised Rh@h-BN, Rh@Al_2O_3 and Rh@GO catalysts

Sample Name	**Total Surface Area** (m^2)	**Specific Surface Area** (m^2/g)
h-BN	9.194	49.938
Rh@h-BN	11.270	58.883
Al_2O_3	15.039	152.066
Rh@Al_2O_3	61.668	165.021
GO	49.432	270.415
Rh@GO	47.350	249.212

3.4. Dehydrogenation Results:

As a result of dehydrogenation experiments, Rh@h-BN, Rh@Al_2O_3 and Rh@GO catalysts were found to provide time-dependent release of hydrogen (H_2) in mL. Supported rhodium catalysts were found to be effective in catalysing the dehydrogenation reaction of ammonia borane. The fastest hydrogen production was obtained in the experiment using Rh@GO catalyst. The dehydrogenation experiment results of these catalysts are shown in Figure 1.

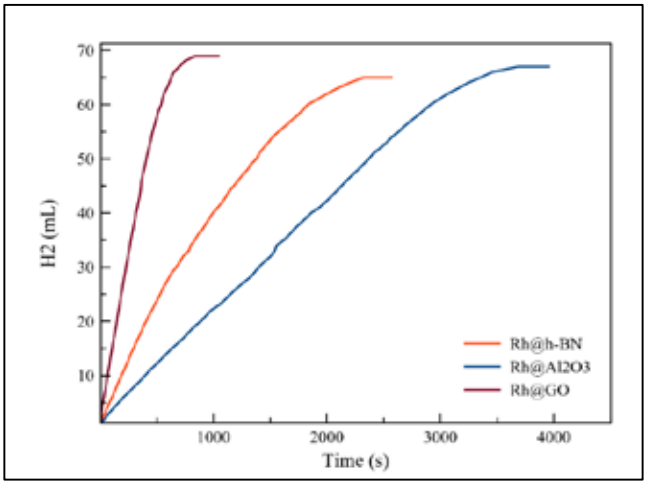

Figure 1. Results of the dehydrogenation experiment on Rh@h-BN, Rh@Al_2O_3 and Rh@GO catalysts.

4. CONCLUSIONS

In this study, the dehydrogenation performances of rhodium (Rh) catalysts supported on hexagonal boron nitride (h-BN), graphene oxide (GO) and aluminium oxide (Al_2O_3) for the dehydrogenation of ammonia borane (NH_3BH_3) were compared. The characterisation analyses and catalytic performances of Rh@Al_2O_3, Rh@GO and Rh@h-BN catalysts, the effect of the structural properties of the support materials and Rh nanoparticles on the loading and catalyst behaviour were investigated. XRD analyses showed that Rh was present in the metallic phase in all catalysts and that the structural integrity of the support materials was preserved. SEM and EDS analyses confirmed that the Rh nanoparticles were homogeneously dispersed in all catalysts and that the active centres were equally accessible. FTIR and XPS results revealed the chemical interactions between the support material and Rh and the formation of active surfaces. BET analysis showed that the Rh loading had different effects on the support materials. In Rh@Al_2O_3 and Rh@h-BN catalysts, Rh loading increased the surface area and contributed to the formation of active centres. In contrast, the initially high surface area of Rh@GO decreased after Rh loading. Rh@GO provided the fastest reaction kinetics and the highest hydrogen production capacity due to its high surface area and layered structure. Rh@h-BN showed efficient performance after Rh@GO catalyst due to its layered structure with thermal and chemical stability and homogeneous distribution of Rh nanoparticles. Rh@Al_2O_3, on the other hand, while providing long-term stability with its porous structure, achieved the lowest hydrogen production capacity due to its lower surface area and slower initial kinetics. In terms of catalytic performance, Rh@GO stood out with its fast kinetics, high hydrogen production and large surface area, while Rh@h-BN stood out as an effective alternative with its stable structure, fast reaction kinetics and high production capacity. Rh@Al_2O_3 had a lower reaction rate and the catalyst did not show sufficient effect. The results provide innovative approaches for the development of sustainable technologies for hydrogen production and storage and shed light on future applications.

ACKNOWLEDGEMENTS

This study supports the chemical hydrogen storage activities of the Clean Energy Research Institute (TEMEN), which is part of the Turkish Energy, Nuclear and Mining Research Council (TENMAK).

REFERENCES

1. Chandra, M. and Xu, Q. 2007. Room temperature hydrogen generation from aqueous ammonia-borane using noble metal nano-clusters as highly active catalysts. Journal of Power Sources 168:135–142.
2. Dai, H., Su, J., Hu, K., Luo, W., Cheng, G. 2014. Pd nanoparticles supported on MIL-101 as high-performance catalysts for catalytic hydrolysis of ammonia borane. International Journal of Hydrogen Energy 39(10):4947-4953.
3. Wu, Y., Wu, X., Liu, Q., Huang, C. and Qiu, X. 2017. Magnetically recyclable Ni@h-BN composites for efficient hydrolysis of ammonia borane. International Journal of Hydrogen Energy 42(25):16003–16011.
4. Basu, S., Brockman, A., Gagare, P., Zheng, Y., Ramachandran, P. V., Delgass, W. N. and Gore, J. P. 2009. Chemical kinetics of Ru-catalyzed ammonia borane hydrolysis. Journal of Power Sources 188(1):238–243.

PERFORMANCE ASSESSMENT OF HYDROGEN PRODUCTION FROM GEOTHERMAL-SOLAR BASED ORC SYSTEM

[1*]*Yagmur Nalbant Atak*
[1] Atilim University, Faculty of Engineering, Department of Mechanical Engineering, Ankara, Türkiye

*Corresponding author e-mail: yagmur.atak@atilim.edu.tr

ABSTRACT
Geothermal-solar hybrid systems show significant potential due to their reliance on renewable energy sources. To accurately and economically predict the performance of these systems, it is essential to develop thermal models before the construction and experimentation stages. In this study, the thermodynamic performance assessment including mass, energy, and exergy analyses of the geothermal-solar-based organic Rankine cycle system producing hydrogen and electricity is studied. This system includes geothermal-powered supercritical ORC, parabolic trough solar collector (PTSC), and proton exchange membrane electrolyzer (PEME) systems. The effects of some critical parameters (production well temperature, direct irradiation intensity, ORC fluid, PTSC fluid) on the performance of the system (electrical and energetic efficiencies), net electrical energy output, exergy destructions of components productivity lack, fuel depletion ratio, and hydrogen production rate are investigated as parametrically.

Keywords: Geotermal-solar based power system, ORC, energy, exergy, hydrogen production

1. INTRODUCTION

The transition from conventional energy systems to advanced multigenerational solutions has accelerated the exploration of sustainable energy carriers. Among these, hydrogen is gaining significant attention as a promising medium for energy storage, particularly in renewable-based power systems. Unlike conventional hydrogen production methods that heavily rely on fossil fuels, green hydrogen—produced via water electrolysis powered by renewable energy sources—offers a carbon-free alternative with substantial potential for decarbonization [1]. Solar energy, particularly through Parabolic Trough Solar Collectors (PTSC), has been widely investigated as a primary power source for Proton Exchange Membrane Water Electrolyzers (PEMWE) due to its abundant availability and capability to provide clean electricity [2]. Additionally, geothermal energy has emerged as another viable renewable source to drive PEMWE systems. Innovative approaches, such as flash-binary cycles and geothermal-driven dual-fluid Organic Rankine Cycles (ORC), have been explored to harness geothermal energy for hydrogen production [3].

In this study, the mathematical modeling of the integrated system including ORC, PTSC, geothermal, and electrolyzer systems are developed. The effects of some critical parameters on the performance of the system (electrical and energetic efficiencies), net electrical energy output, exergy destructions of components productivity lack, fuel depletion ratio, and hydrogen production rate are investigated as parametrically.

2. MATHEMATICAL MODELING

Figure 1 shows the integrated system including ORC, PTSC, and PEMEC systems. Solar heat used to raise the working fluid's temperature before it enters the turbine. Geothermal fluid heats the ORC working fluid in the heat exchanger, while solar energy heats PTSC fluid. The heated fluid enters the turbine to generate power, and part of the power is directed to a PEMWE for hydrogen production. After the turbine, the fluid enters the regenerator to increase its temperature, then moves to the air-cooled condenser, where it condenses before being pumped back into the regenerator. The cycle concludes with the working fluid entering the heat exchanger, and the geothermal fluid is returned to the injection wells. The detailed energy and exergy balance equations for all components in the integrated system, and these equations are solved using EES program. The main assumptions are the heat loss from components except for PTSC are ignored; Steady-state operation conditions are applied; pressure drops in the heat exchangers and all pipes are ignored; and kinetic and potential energy changes are ignored in the system. The main equations are given as follows:

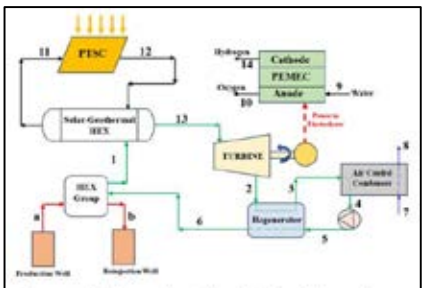

Figure 1. The schematic of integrated system including ORC, PTSC, and PEMEC systems

- A single collector's useful heat gain rate can be calculated as: $\dot{Q}_{useful} = F_R(G_b\eta_r A_a - A_r U_L(T_{11} - T_0))$ (1)

- The temperature of PTSC fluid exiting from the PTSC is found as: $T_{12} = T_{11} + \frac{\dot{Q}_{useful}}{(\dot{m}c_p)_{htf}}$ (2)

- The heat exhangers in the system are modelled using the ε-NTU (effectiveness-Number of transfer units) method. The used equations for heat exchanger are given as follows:

$$\dot{Q}_{HEX,group} = \dot{m}_{geo,fluid}(h_a - h_b) \quad (3)$$
$$\dot{Q}_{sol-geo,hex} = \varepsilon \cdot C_{min} \cdot \Delta T_{max} \quad (4)$$
$$NTU = \frac{\pi d_o L \eta_{pass} N_T U}{C_{min}} \quad (5)$$

- General mass, energy, and exergy balance equations at steady-state conditions are given for all component as follows:

$$0 = \sum_i \dot{m}_i - \sum_e \dot{m}_e \quad (6)$$
$$0 = \sum_i \dot{m}_i \left(h_i + \frac{1}{2}V_i^2 + gz_i\right) - \sum_e \dot{m}_e \left(h_e + \frac{1}{2}V_e^2 + gz_e\right) + \dot{Q}_{cv} - \dot{W}_{cv} \quad (7)$$
$$0 = \sum_j \left(1 - \frac{T_0}{T_j}\right)\dot{Q}_j - \dot{W}_{cv} + \sum_i \dot{m}_i e_{fi} - \sum_e \dot{m}_e e_{fe} - \dot{E}_d \quad (8)$$
$$\dot{W}_{net,sytem} = \dot{W}_{turbine} - \dot{W}_{pump} - \dot{W}_{fan} - \dot{W}_{electrolyzer} \quad (9)$$

- Performance assessment parameters equations are given as follows:

$$\eta_{el} = \frac{\dot{W}_{net,sytem}}{\dot{Q}_{solar} + \dot{Q}_{HEX,group}} \quad (10)$$
$$\dot{Q}_{solar} = A_a F_R S N_{PTSC} \quad (11)$$
$$\eta_{ex} = \frac{\dot{W}_{net,sytem}}{\dot{E}_{solar} + \dot{E}_{HEX,group}} \quad (12)$$
$$\delta = \frac{\dot{E}_{d,,total}}{\dot{E}_{solar} + \dot{E}_{HEX,group}} \quad (13)$$
$$P = \frac{\dot{E}_{d,,total}}{\dot{W}_{net,sytem}} \quad (14)$$

3. RESULTS AND DISCUSSION

In this study, the mathematical model of an integrated solar-geothermal-based ORC cycle system including hydrogen production from a PEM electrolyzer was developed, and the energy and exergy analyses were applied to all components. The electrolyzer data used in this model were found from a reference study [4] in the literature. The effects of the production well temperature, direct irradiation intensity, ORC fluid, and PTSC fluid on the performance of the system. Figure 2-(a) shows the effect of production well temperature on system performance. As the temperature increases, the hydrogen production rate rises significantly, while electrical efficiency remains stable, and exergy efficiency first increases and then slightly decreases. Figure 2-(b) examines exergy destruction in different components, showing that turbine exergy destruction decreases with temperature, whereas heat exchanger (HEX) exergy destruction increases significantly. Overall, higher temperatures enhance hydrogen production but also affect energy losses in various components.

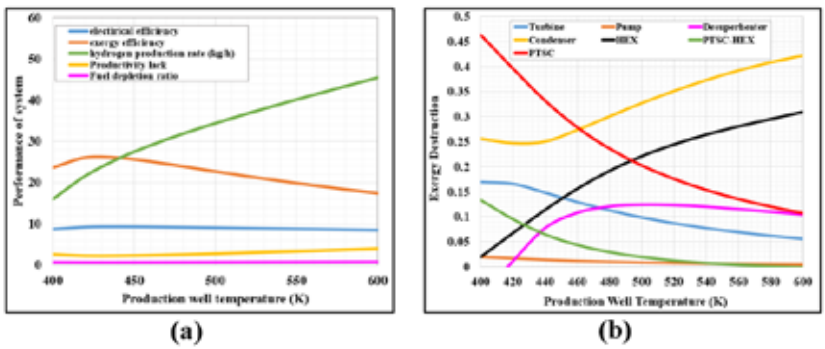

(a) (b)

Figure 2. The effects of production well temperature on (a) the system performance and (b) exergy destruction of components

Figure 3-(a) illustrates the effect of direct irradiation intensity on system performance. While electrical efficiency and hydrogen production rate remain largely stable, exergy efficiency decreases as irradiation intensity increases. Additionally, parameters such as fuel depletion ratio and productivity lack remain at low levels. Figure 3-(b) presents the monthly variation of exergy destruction in different components. The energy losses in the turbine, condenser, PTSC, heat exchanger (HEX), and desuperheater remain relatively stable throughout the year, with PTSC and HEX showing higher exergy destruction compared to other components. Overall, system performance is moderately affected by irradiation intensity, while energy losses remain consistent over time. In Table 1, the effects of different ORC and PTSC fluids on system performance are compared. Among ORC fluids, R134a shows the highest electrical efficiency (9.27%) and hydrogen production rate (29.02 kg/h), while R245fa has the lowest efficiency and production rate. For PTSC fluids, all options exhibit similar electrical efficiency (~9.42%)

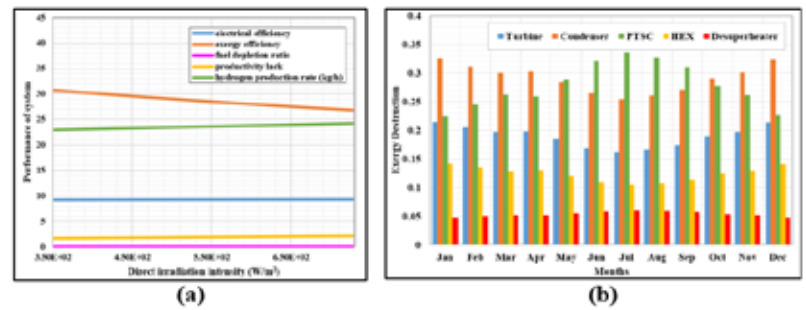

(a) (b)

Figure 3. (a) The effects of direct irradiation intensity on the system performance and (b) exergy destruction distribution of components in annual

and exergy efficiency (~26.48%), with minor variations in hydrogen production rate (~24.74-24.8 kg/h), indicating stable performance across different PTSC fluids.

Table 1. The effects of ORC and PTSC fluid on the electrical and exergetic efficiencies, fuel depletion ratio, productivity lack, and hydrogen production rate

ORC Fluid type	η_{el}**(%), electrical efficiency**	η_{ex} **(%), exergetic efficiency**	δ **(Fuel depletion ratio)**	P **(Productivity lack)**	**H_2 production rate (kg/h)**
R134a	9.27	25.13	0.59	2.376	29.02
R124	7.44	18.78	0.68	3.634	19.9
R245fa	5.56	14.87	0.72	4.849	16.93
Isobutane	6.43	18.55	0.66	3.578	22.76
PTSC Fluid	η_{el} **(%), electrical efficiency**	η_{ex} **(%), exergetic efficiency**	δ **(Fuel depletion ratio)**	P **(Productivity lack)**	**H_2 production rate (kg/h)**
Therminol VP1	9.42	26.48	0.59	2.243	24.8
Syltherm800	9.42	26.46	0.59	2.247	24.78
Dowtherm A	9.42	26.42	0.60	2.256	24.74
Xceltherm	9.42	26.48	0.59	2.244	24.8

4. CONCLUSIONS

The main findings are given as:

- The best performance is observed at 600 K, where the hydrogen production rate reaches approximately 55 kg/h, while the exergy efficiency decreases to around 18%. The worst performance occurs at 400 K, where the hydrogen production rate is the lowest (~15 kg/h). The highest exergy destruction occurs in the turbine at 400 K (~0.45), whereas the heat exchanger (HEX) has the highest exergy destruction at 600 K (~0.35). The lowest exergy destruction is observed in the desuperheater, remaining below 0.1 throughout the temperature range.
- The highest exergy efficiency is around 32% at the lowest irradiation intensity (~350 W/m²), while the hydrogen production rate remains stable at approximately 25 kg/h. The highest exergy destruction occurs in the HEX and PTSC components, reaching values close to 0.3, while the desuperheater has the lowest exergy destruction, staying below 0.05 throughout the year.
- R134a shows the best ORC performance with 9.27% efficiency and 29.02 kg/h H_2 production, while all PTSC fluids perform similarly with ~9.42% efficiency and ~24.8 kg/h H_2 production.

NOMENCLATURE

A_a	Aperture area (m^2)	$\dot{m}$	Mass flows rate (kg/s)
C_{min}	Minimum specific heat of fluids (W/K)	N_{PTSC}	Number of solar collector
d_o	Outer diameter of the tube (m)	N_T	Number of tube
e_f	The specific flow exergy (kJ/kg)	NTU	Number of transfer units
$\dot{E}_{HEX,group}$	Exergy of the geothermal water between the inlet and exit of the heat exchanger group (kW)	$\dot{Q}$	Heat transfer rate (W)
$\dot{E}_d$	Exergy destruction (kW)	$\dot{Q}_{solar}$	Heat transfer rate input from the sun (kW)
$\dot{E}_{solar}$	Exergy entering to the system by the heat transfer from sun (kW)	S	Heat absorbed by the receiver (W/m^2)
F_R	Heat removal factor	U	Overall heat transfer coefficient (W/m^{2}K)
g	Gravitational acceleration (m/s^2)	V	Velocity (m/s)
h	Enthalpy (kJ/kg)	$\dot{W}$	Power (kW)
L	Tube length per pass (m)	$\dot{W}_{net,sytem}$	Net power output of the system (kW)

REFERENCES

[1] Howarth RW, Jacobson MZ. How green is blue hydrogen? Energy Sci Eng 2021;9 (10):1676–87.
[2] L. Guo, et al., Reprint of: solar hydrogen production and its development in China, Energy 35 (11) (2010) 4421–4438.
[3] Kianfard H, Khalilarya S, Jafarmadar S. Exergy and exergoeconomic evaluation of hydrogen and distilled water production via combination of PEM electrolyzer, RO desalination unit and geothermal driven dual fluid ORC. Energ Conver Manage 2018;177:339–49.
[4] HySupply Cost Tool V1.0 Released for Stakeholder Consultation. (n.d.). Retrieved [02/03/2025], Link: https://www.globh2e.org.au/_files/ugd/8d2898_6017eabc62b748848a912d0f53c33c65.pdf

PERFORMANCE ASSESSMENT OF LOW-COST TRANSITION METAL-BASED ELECTRODE AND CATALYST FOR PHOTOELECTROCHEMICAL AND PHOTOCATALYTIC HYDROGEN GENERATION

Mohamad Ayoub, Ibrahim Dincer*
Clean Energy Research Laboratory (CERL), Faculty of Engineering and Applied Science, Ontario Tech. University, 2000 Simcoe Street North, Oshawa, Ontario L1G 0C5, Canada

*Corresponding author e-mail: mohamad.ayoub@ontariotechu.net

ABSTRACT
This paper presents low-cost and facile solutions for photoelectrochemical and photocatalytic hydrogen generation using commercial copper mesh as a photoanode and Nickel Zinc Iron Oxide catalyst (NiZnFeO), respectively. Copper mesh is first cleaned (etched) with hydrochloric acid to remove any residue material and existing oxide formations to expose a workable surface for a more uniform oxidation result, both in bulk and on the surface of the copper mesh. After cleaning the electrode, an annealing step is carried out in open air at 500°C to obtain copper oxide, which has a bandgap sensitive to both ultraviolet and visible light. Carbon paper, an Ag/AgCl reference electrode, and 0.1M Potassium Hydroxide (KOH) electrolyte are used in conjunction with the prepared photoanode for photoelectrochemical hydrogen production. Cyclic voltammetry is used to assess the performance of this photoelectrochemical assembly, and it is observed that a higher photocurrent was achieved at around -0.7V vs Ag/AgCl under light conditions. As for the photocatalytic hydrogen generation part of this study, 20mg of NiZnFeO is dispersed in 200ml of water containing 0.1M KOH and 0.1M Triethanolamine (TEOA) sacrificial agent. A maximum hydrogen concentration of 9ppm is achieved after 30 minutes, after which TEOA radicals' sedimentation hinders further hydrogen production.

Keywords: Hydrogen Production; Photoelectrochemical; Photocatalytic; Copper Mesh; Transition Metals

1. INTRODUCTION
The energy sector is facing an unprecedented need for diversifying the energy mix and establishing groundwork for reliable and independent energy sources. Renewable energy technologies are looked at as a potential replacement for conventional fossil fuel-based technologies, which have dominated the energy market supply for more than 70 years now. Some examples of these technologies are solar photovoltaics and thermal [1], wind-energy based, biomass, and geothermal energy systems. Energy reliability is considered a gray area for most of these technologies with the exception of a few, and given that an effective energy mix, requires implementing various energy sources and technologies, energy storage solutions become paramount.
Hydrogen is the most abundant element in our universe; however, it only constitutes a small percentage of the earth's atmosphere. Most of earth's hydrogen reserves exist in the form of water (H_2O), which means the in order to effectively obtain hydrogen, one must utilize water splitting techniques in order to separate the hydrogen from the oxygen. Conventionally, this requires ample amounts of energy and the use of precious metal catalysts such as platinum in a process called electrolysis. A Gibbs free energy of 237kJ/mol is required along with a potential difference of 1.23V between the electrolysis electrodes to effectively carry out a water splitting process. More advanced hydrogen production techniques that are aided with absorbed solar energy have risen within the hydrogen scene. These techniques are classified into photoelectrochemical, photocatalytic, and biophotolysis. Photoelectrochemical hydrogen generation uses a conventional electrolysis cell assembly with the difference in the anode or cathode used, which in this case would be photoresponsive. A photoanode is a semiconductor that absorbs incident light and generates an electron-hole pair, with the aid of its bandgap the electrons and holes are separated, and the electrons are transported through an external circuit to the cathode. At the cathode, the electrons are combined with water molecules, in a water reduction reaction, to produce hydrogen [2]. A photocatalytic process on the other hand, solely uses a photoresponsive catalyst, either in powder form suspended into an electrolyte, or stationary on an electrode, which splits water into hydrogen and oxygen gases. These processes allow for a passive generation of hydrogen without the need to extensive external energy input, except for that coming from incident sunlight.
The objective of this work is to test and assess the viability of low-cost solutions for photoelectrochemical hydrogen generation electrodes, as well as transition-metal-based catalysts for photocatalytic hydrogen generation.

2. MATERIALS AND METHODS
Commercial copper mesh is used as the photoanode for photoelectrochemical hydrogen generation. Hydrochloric acid (HCl) is used to initially clean copper mesh to strip the surface of any residue or any oxides that might have formed on the surface of the copper mesh preventing the following oxidation step from reaching the bulk of the copper mesh. To do so, copper mesh is immersed into concentrated HCl and sonicated for 15 minutes. Then, the copper mesh is rinsed and immersed in DI water and sonicated for another 15 minutes to remove any leftover HCl. Copper mesh is then placed on a hot plate in atmospheric air to transform the copper into copper oxide at 500°C for 30 mintues. Carbon paper is used

as a counter electrode, and Ag/AgCl is used as a reference electrode, with 0.1M KOH (Sigma Aldrich) as an electrolyte. For photocatalytic hydrogen generation, Nickel Zinc Iron Oxide (Sigma Aldrich) is used as a photocatalyst, with a loading of 10mg/100ml. Moreover, a solution of 0.1M KOH and 0.1M Triethanolamine (TEOA) are used to make up the electrolyte and the sacrificial agent in the photocatalytic hydrongen generation process. The OAI solar simulator, Gamry Reference 300 potentiostat, and DFRobot electrochemical hydrogen sensor are used for the assessment of photoelectrochemical and photocatalytic hydrogen generation. The methodology used for the preparation of the photoanode and photoelectrochemical and photocatalytic hydrogen generation and assessment is summarized in Fig 1.

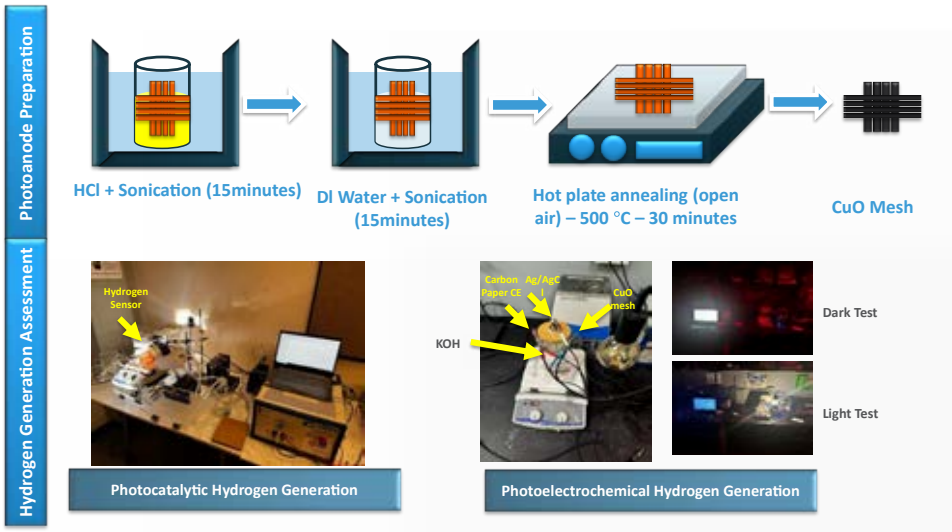

Fig. 1. Photoanode preparation and photohydrogen generation assessment methodology

3. RESULTS AND DISCUSSION

This section showcases results obtained for photoelectrochemical hydrogen generation, using CuO photoanode and carbon paper counter electrode, and photocatalytic hydrogen generation using transition metal-based catalyst.

Figure 2 shows cyclic voltammetry for photoelectrochemical hydrogen production under light and dark conditions. The scan range is chosen from -1.8V to -0.5V vs Ag/AgCl which contains the region for water reduction (hydrogen generation), with a scan rate of 10mV/s. Photoelectrochemical hydrogen generation utilizes complementing effects that increase the overall hydrogen generation in comparison to conventional electrolysis. The photoanode, CuO in this case, absorbs incident light and generates charge-carrier paris (electrons and holes). Electrons are transferred to the counter electrode through an external circuit, which are then used to reduce water into hydrogen. As seen from Fig. 2 the reduction peak at around -0.7V vs Ag/AgCl is relatively greater under light conditions than that of dark conditions, also manifested in a larger current generation which indicates higher hydrogen generation rate.

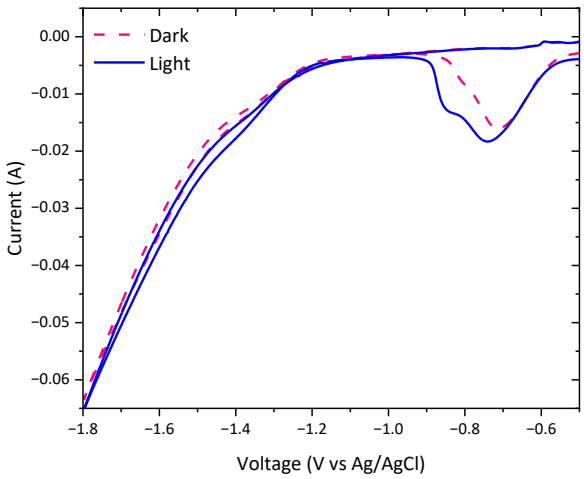

Fig. 2. Cyclic voltammetry results for photoelectorhcemcial hydrogen generation

Photocatalytic hydrogen generation, unlike photoelectrochemical counterparts, is a passive way of producing hydrogen without the need for electricity. A photocatalyst is either dispersed into the targeted solution or deposited into a stationary

electrode. Once the photocatalyst is exposed to light, individual charge carrier excitation and separation events carry out water reduction processes with the aid of a sacrificial agent that takes on the other half reaction for hydrogen generation. Moreover, there are stringent requirements when it comes to choosing a catalyst for photocatalytic hydrogen such as requiring the bottom of the conduction band of the catalyst to be higher than the standard potential for water splitting. Figure 3 showcases results for photocatalytic hydrogen production where a hydrogen concentration of 9ppm is reached after 30mintues, just before radicals from TEOA are formed and sedimented which hinder the intensity of the reactions that occur, degrading the hydrogen concentration in the process after the 30-min mark.

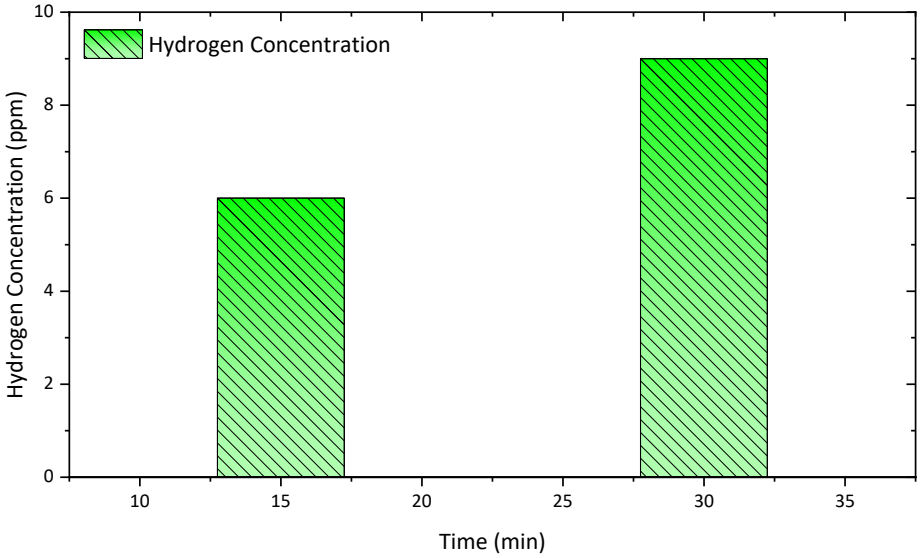

Fig. 3. Hydrogen concentration (ppm) through a 30-minute period for photocatalytic hydrogen generation

4. CONCLUSIONS

In conclusion, low-cost solutions for photoelectrochemical and photocatalytic hydrogen generation using copper mesh and Nickel Zinc Iron Oxide photocatalyst are presented, and their performance assessed. Copper mesh is cleaned with hydrochloric acid, rinsed with DI water, and annealed at 500°C to achieve a uniform formation of copper oxide in both the bulk and on the surface of the copper mesh. The photoelectrochecmial system used for hydrogen generation system comprised of copper oxide mesh photoanode, carbon paper counter electrode, Ag/AgCl reference electrode, and 0.1M KOH electrolyte. Cyclic voltammetry tests conducted under dark and light conditions show that under illumination the water reduction current produced, with a peak at around -0.7V vs Ag/AgCl, is relatively higher than that of dark conditions. Moreover, for photocatalytic hydrogen production, 20mg of NiZnFeO catalyst is dispersed in 200ml of DI water along with 0.1M KOH and 0.1M TEOA sacrificial agent, a solar simulator, and a hydrogen sensor are used to assess the concentration of the hydrogen produced throughout a 30minute period. A maximum concentration of 9ppm is achieved, after which prominent formations of TEOA radicals impede further photocatalytic reactions.

ACRONYMS

Ag/AgCl	Silver/Silver Chloride
CuO	Copper Oxide
HCl	Hydrochloric Acid
KOH	Potassium Hydroxide
NiZnFeO	Nickel Zinc Iron Oxide
ppm	part per million
TEOA	*Triethanolamine*

Acknowledgment

This publication was made possible by the NPRP grant (NPRP12S-0123-190011) from the Qatar National Research Fund (a member of Qatar Foundation). The findings achieved herein are solely the responsibility of the authors.

REFERENCES

1. I. Alsaduni and M. A. Siddiqui, “Thermodynamic and economic evaluation of a developed solar-driven system for efficient production of power and cooling,” International Journal of Exergy, vol. 45, no. 3/4, pp. 219–235, 2024, doi: 10.1504/IJEX.2024.142623.
2. C. Acar and I. Dincer, “Investigation of a novel photoelectrochemical hydrogen production system,” Chem Eng Sci, vol. 197, pp. 74–86, Apr. 2019, doi: 10.1016/J.CES.2018.12.014.

DEVELOPMENT OF MEMBRANES FOR HYDROGEN BROMIDE REDOX FLOW BATTERIES

[1*]*Kürşat Can Ata*, [1]*Anıl Can Türkmen*, [2*]*Fatma Gül Boyacı San,* [1]*Cenk Çelik*
[1] Mechanical Engineering Department, University of Kocaeli, 41380 Kocaeli, Turkey
[2] Chemistry Department, University of Düzce, 81620 Düzce, Türkiye

*Corresponding author e-mail: kursatcanata@gmail.com

ABSTRACT
Hydrogen/Bromine (H_2/Br_2) redox flow batteries (RFBs) stand out with their high energy density, efficiency, and low-cost advantages in energy storage systems. Membranes that provide ion conductivity and increase energy conversion efficiency are a critical component in these batteries. Sulfonated polyetheretherketone (SPEEK) membranes have become an increasingly popular material in H_2/Br_2 redox flow batteries. SPEEK membranes have properties such as chemical resistance, thermal stability, and high proton conductivity. SPEEK membranes increase energy conversion efficiency due to their high proton conductivity. As a solution, SPEEK can be supported by composite or blend materials or cross-linking techniques can be used. At this point, polybenzimidazole (PBI) comes to the fore. It is suggested that SPEEK be modified with hybrid structures to increase long-term stability in HBr medium. SPEEK membranes offer an efficient, durable and cost-effective solution in H_2/Br_2 redox flow batteries. However, addressing the swelling and chemical resistance issues is critical for the commercial scale applicability of these membranes. In this study, the use of PBI-SPEEK blend membranes prepared with different weight ratios of PBI in hydrogen bromine redox flow batteries, their characterization, corrosion resistance and the effects of all on performance were investigated parametrically.

Keywords: HBRB, SPEEK, PBI,

1. INTRODUCTION

Redox flow battery (RFB) is one of the emerging large-scale energy storage systems that has attracted great attention in recent years due to its high energy efficiency of about 70–80%, reasonable capital cost and economical life cycle costs without any specific site requirements [1] RFB (Redox Flow Battery) stores energy using two electrolyte solutions, which are kept in separate reservoir tanks. Electron transfer is facilitated by circulating pumps through an electrochemical cell stack made up of a series of cells connected in series or parallel. Typically, each cell consists of an anode, cathode, membrane, and flow channels, similar to fuel cells and electrolyzers [2]. The power of RFBs is determined by the number of cells in the stack and the volume of electrolyte used. This allows the system to be sized independently in terms of power and energy ratio, reducing costs for additional energy storage capacity without increasing the cost of the cell stack. Hydrogen bromide (HBr) redox flow batteries (RFBs) are a type of energy storage system that utilize a reversible electrochemical reaction to store and release electrical energy. They are part of the broader category of flow batteries, which are characterized by the use of liquid electrolytes that flow through electrochemical cells to store energy. Hydrogen bromide redox flow batteries store and release energy through the oxidation and reduction of bromine and hydrogen at two different electrodes, usually made of carbon-based materials. The two main components in these systems are involves the reduction of bromine (Br_2) to bromide ions (Br^-). On the negative side involves the oxidation of hydrogen bromide (HBr) to produce hydrogen gas (H_2) [3]. In 2006, Peled et al. started working on this technology with the aim of using it as a large-scale energy storage system and achieved a power density of more than 1.5 W/cm^2 [4]. Another study has studied HBFB systems based on long-chain perfluorosulfonic acid (LC PFSA) membranes. Cyclic performance analyses showed negligible performance degradation over 600 cycles. The commercialization of HBFB technology depends on achieving both high power density and long lifetime (with a maximum power density of 1 W/cm^2 and 20 years of operational lifetime) [5]. Although critical for the optimization and commercialization of HBFB technology, systematic studies defining fundamental structure-property relationships are still lacking. Furthermore, the availability of commercially viable membranes for HBFB applications is chemically limited, and existing commercial products may not always meet the required specifications (e.g., thickness, ion exchange capacity, water retention). Consequently, laboratory synthesis of these membranes is essential due to their unique chemistry, limitations in material processing routes, labor intensity, and the need for strict safety precautions.

In all electrochemical systems, the membrane is a vital component located in the middle of the cell. It is the electrolyte in an electrochemical cell. Its function is to complete the circuit by passing ions from the anode to the cathode or from the cathode to the anode and to separate the fuel fed to the anode from the oxidant fed to the cathode. The membrane must not have electrical conductivity and must be mechanically, thermally and chemically resistant to operating conditions. The properties of the membrane affect the entire system, especially the selection of the catalyst and the creation of the electrode. Therefore, membrane selection, development and optimization of its properties are comprehensive and important stages that are not easy. The basic properties that a good membrane must have can be summarized as having high ionic conductivity, mechanical, thermal and chemical resistance and not being permeable to the fuel and oxidant used (especially in liquid systems). These necessary properties are directly or indirectly dependent on other directly

measurable properties such as ion exchange capacity, morphology and water retention capacity. For these reasons, there is a group of characterization techniques that must be applied for an ion-conducting polymer membrane that is developed.

Membrane development studies for HBFBs are much more limited compared to Vanadium Redox Flow Batteries (VFRB). Fluorinated Nafion, which is used for VFRBs and is accepted as the industrial standard, has been used in many studies. Nafion, which is in the KDM class, is still used in many studies in HBFBs. Nafion is by far the most studied material in both VRFBs and HBFBs due to its fluorinated backbone similar to Teflon structure, which has high mechanical, thermal and chemical resistance. In this study will examine the performance parameters of SPEEKs with different sulfonation degrees in HBFBs and optimize the membrane that produces the best results.

2. MATERIALS AND METHODS

PEEK that provided by Merck, was dissolved in sulfuric acid. All membranes were prepared with the same procedure as in the study of Ata et al. [8]. The measurements were made by electrochemical impedance spectroscopy with 4-probe through-plane cell. The through-plane ionic conductivity test is commonly used to measure the ionic conductivity of a material in the direction perpendicular to its surface, which is often crucial for evaluating the performance of materials used in electrochemical applications like fuel cells, batteries, and electrolysers. The material being tested (such as a membrane or electrolyte) is cut into a suitable shape and size, typically a thin sheet, to ensure uniformity during testing. It should also be well-prepared to ensure good contact with the electrodes. A small AC signal is applied across the electrodes, and the impedance is measured. The conductivity can be extracted from the impedance spectrum by analyzing the real part of the impedance at low frequencies. The data is typically processed to obtain the ionic conductivity of the material in the through-plane direction. This gives insight into how well ions can move through the material, which is critical for applications like fuel cells, where ions need to travel from one side of the membrane to the other. All impedance measurements were made at room temperature and 100 % relative humidity (RH). Water plays a critical role in the functioning and efficiency of electrochemical cell membranes. However, the water retention capacity of the membrane is also very important, and efficiency can decrease if the correct water balance is not achieved. In a fuel cell, water interacts in a context with the passage of protons (H^+ ions) through the membrane. Water is a carrier for proton conduction in the PEM membrane. In other words, the membrane generates electricity by conducting protons through water. Therefore, it is important to have enough water in the membrane. In order for these systems to work, the membrane must be sufficiently moist. Moisture in the membrane increases the proton conductivity, thus providing more efficient energy production. Dryness of the membrane seriously reduces the proton conductivity and negatively affects the efficiency of the fuel cell. However, too much water accumulation is not desired. Excessive water retention in the membrane can cause the electrode surfaces to become wet, thus reducing the efficiency of the electrochemical reactions. Excessive water accumulation can also compromise the structural integrity of the membrane and lead to permanent damage. Water management is a critical issue in redox flow batteries. There must be sufficient water in the membrane and not too much of it. To achieve this, a water vapor transport system or humidity control mechanisms are usually used. The performance of membranes varies depending on the water content. If the membrane holds enough water, the proton conductivity is high and the battery operates more efficiently. However, excess water can cause side reactions, which reduces efficiency.

The mechanical tests of the prepared membranes were performed using the Instron 3345 desktop tensile device at a speed of 10 mm/min according to the ASTM D882 method (polymeric thin film method). Membrane samples were prepared with a length of 50 mm and a width of 10 mm. During the test, the tensile strength (MPa), Young's modulus (MPa) and tensile amount (% elongation) values were obtained from the device. Tensile test is a test performed to determine the tensile and elongation properties of the material.

Ionic conductivities were measured by electrochemical impedance spectroscopy (EIS). The resistances of the membrane samples at high frequencies were measured and these data were used with parameters such as membrane area and thickness to calculate the ionic conductivity. During the measurements, high conductivity Sigraget 34 BC carbon paper gas diffusion sheets were used to prevent short circuits. Samples and gas diffusion sheets were prepared and placed in 4 cm^2 (2x2 cm) sizes. Measurements were made at 300°C with 100% humidity and at 80°C with the same humidity.

The single cell was adapted from a 10 cm^2 active area. The cell assembly included two stainless steel current collectors and graphite bipolar plates. Carbon paper (SGL Technologies 24) was used at the positive electrode, and Teflon-treated carbon cloth (280 µm) was applied to the negative electrode. For the first experimental setup, the Pt/C anode catalyst loading was used. The Pt/C powder contained 30 wt% Pt on carbon, and the Nafion solution mixture was employed. The flow rate was controlled between 10 mL/min and 50 mL/min. The hydrogen electrode operated in single-pass mode, meaning hydrogen passed through the electrode without being recycled. Hydrogen was humidified using a humidifier bottle heated by a hot plate, with temperature controlled according to experimental conditions. Humidification was provided by the hydrogen supply. Electrochemical measurements were conducted using a potentiostat with an 80A

amplifier and open circuit voltage (OCV).

3. RESULTS AND DISCUSSION

In this section, the results of thermal, mechanical and electrochemical characterization of the produced SPEEK polymers with different sulfonations and PBI-SPEEK blend membranes are given and these data will be compared with the results of previous studies in literature. In this study, the degree of sulfonation was calculated with the help of an equation using the total number of waves of the hydrogen element (at positions A, B, C and D) and the E wave, which is the integration area of the proton, with H-NMR. SPEEK-47 with 47% DS sulfonated for 96 hours, and SPEEK-80 with 80% sulfonated for 168 hours at the same temperature (~25 C) to form SPEEK. DS from the sulfur weight percentage was assumed to be up to 100% in most of the studies. Fourier Transform Infrared Spectroscopy (FT-IR) is used for the determination of organic compounds. Most compounds, except optical isomers, have their own infrared spectrum. These spectra lie between visible light and microwaves in the electromagnetic spectrum and cover the range of 450-4000 cm^{-1}. This method determines the structure of organic samples but does not provide information about purity. The samples were examined using Perkin Elmer Spectrum 100 FT-IR device and diamond crystal. In the SPEEK spectrum, characteristic peaks are observed at 1650 cm^{-1} and 1220 cm^{-1}, while the 1080 cm^{-1} band corresponds to the symmetric stretching vibration of O=S=O. The peak at 1020 cm^{-1} is assigned to the stretching vibration of S=O, and the peak at 710 cm^{-1} is due to the symmetric stretching vibration of S-O. In the blended membranes, specifically in the SPEEK/PBI compositions with 5 wt%, 10 wt%, and 20 wt% PBI, a shift to 1710 cm^{-1} was observed. Additionally, as the PBI content increased, the intensity of the -C=N- peak in the blend membranes strengthened. This change is attributed to the enhanced ionic cross-linking between $-SO_3H$ and -C=N- groups [6,7].

When the ionic conductivity results of the SPEEK membranes with two different sulfonation degrees were examined, SPEEK-47 with a low sulfonation degree was determined as 0.047 mS/cm. SPEEK-80 with a high sulfonation degree was measured as 0.12 S/cm. Pure SPEEK at 100% RH exhibits high conductivity (0.12 S/cm). PBI-SPEEK (5-10%) blend membranes showed conductivities of 0.069 S/cm and 0.057 S/cm, respectively. For the PBI-SPEEK (20 wt%) membrane, the conductivity reached 0.042 S/cm at 80°C (Figure 1).

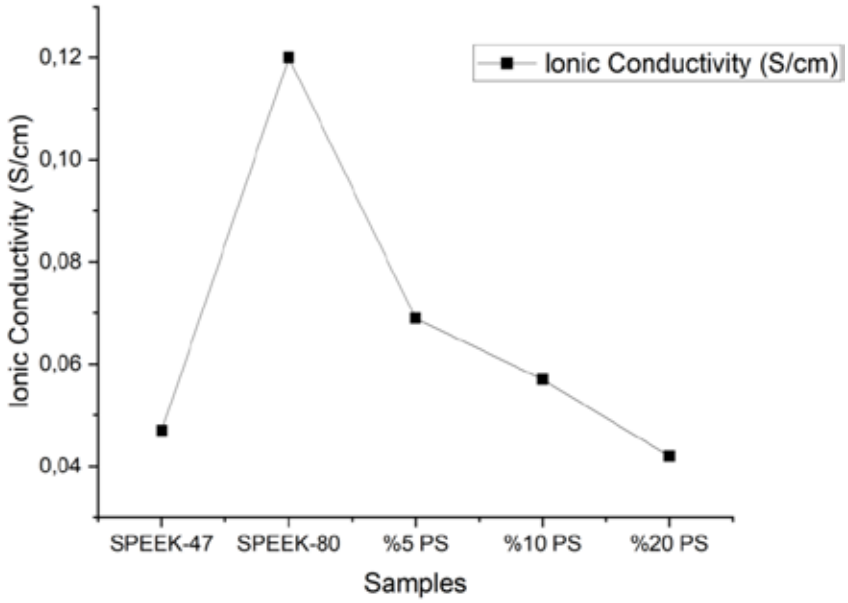

Fig. 1. Ionic Conductivity Results for All Membranes

The water uptake of the SPEEK membrane was 42.5% at 30°C and 50.9% at 60°C. For PBI-SPEEK (10 wt%) and PBI-SPEEK (20 wt%) membranes, the water uptake decreased to 12.8% and 10.7% at 30°C, while it increased to 22.4% and 20.6% at 60°C, respectively. When the PBI content was 5%, the water uptake was 29.4% at 60 C. It was observed that the swelling degree decreased with the increase of PBI content by adding PBI. [7].

In the first stage, tests were conducted using a reference setup to analyze polarization curves. A similar approach was followed here to assess the sources of losses from steady-state polarization curves. Each data point was equilibrated for 30 to 90 seconds. Polarization curves are commonly used to evaluate the performance of hydrogen-bromine redox flow batteries, as they help identify which processes contribute to overpotential at a given current. Initially, a laboratory-prepared electrode with a Nafion®117 membrane and a platinum loading of 0.75 mg/cm² was employed for each

electrode. At the positive electrode, a relatively low concentration of 0.9 M Br_2 in 1 M HBr was used. The polarization curve for this membrane-electrode assembly (MEA) is shown in Figure 2. The linear section of the polarization curve corresponds to the ohmic loss region. The starting portion of the curve indicates that kinetic losses are minimal, with the majority of the curve remaining within the linear ohmic loss region. This suggests that the discharge limiting current density of 400 mA/cm² is primarily influenced by mass transfer. Additional impedance experiments will be conducted to further elucidate this effect.

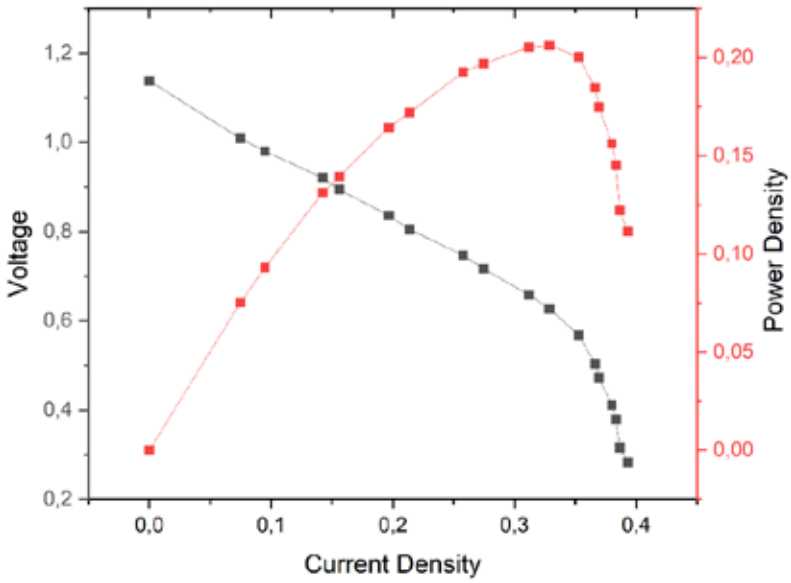

Fig. 2. Single Cell Result of Reference Setup

4. CONCLUSIONS

Hydrogen bromide redox flow battery is a promising technology in the field of energy storage, especially for large-scale applications. It offers advantages over other flow battery chemistries with its high energy density, low-cost materials and long cycle life. However, bromine handling, corrosion and membrane stability are obstacles that need to be solved. The effect of sulfonation time on the degree of sulfonation was investigated and these effects were tried to be minimized by adding PBI polymer. However, bromine handling, corrosion and membrane stability are obstacles that need to be solved. The effect of sulfonation time on the degree of sulfonation was investigated and these effects were tried to be minimized by adding PBI polymer.

REFERENCES

1. Goltsov VA and Veziroglu TN. 2001. From hydrogen economy to hydrogen civilization. International Journal of Hydrogen Energy 26:909-915.
2. Skyllas-Kazacos M, Chakrabarti M, Hajimolana S, Mjalli FS, Saleem M. 2011. Progress in flow battery research and development. Journal of Electrochemical Society 158:55–58
3. Singh N, McFarland EW, 2015. Levelized cost of energy and sensitivity analysis for the hydrogen–bromine flow battery, Journal of Power Sources 288:187–198.
4. Prifti H, Parasuraman A, Winardi S, Lim TM, Skyllas-Kazacos M. 2012 Membranes for redox flow battery applications. Membranes 2:275–306.
5. Livshits V, Ulus A, Peled E. 2006. High-power H2/Br2 fuel cell, Electrochemical Community **8:**1358–1362.
6. Feng SG, Shang YM, Wang SB, Xie XF, Wang YZ, Wang YW. 2010. Novel method for the preparation of ionically crosslinked sulfonated poly(arylene ether sulfone)/polybenzimidazole composite membranes via in situ polymerization. Journal of Membrane Science 346:105-12.
7. Wang JL, Liao JB, Yang L, Zhang SG, Huang XL, Ji JB. 2012. Highly compatible acidebase blend membranes based on sulfonated poly (ether ether ketone) and poly (ether ether ketone-alt-benzimidazole) for fuel cells application. Journal of Membrane Science 415:644-53.
8. Ata KC, Kadioglu T, Turkmen AC, Akay RG, Celik C. 2020. Investigation of the effects of SPEEK and its clay composite membranes on the performance of Direct Borohydride Fuel Cell. International Journal of Hydrogen Energy 45:5430-37.

IN SITU CHARACTERIZATION OF Pt-Re-Na/CeO_2 SYSTEM AND *OPERANDO* ANALYSIS OF WGS MECHANISM ON ITS SITES BY FTIR-DRIFTS-MS

B. M. Eropak[1,2]A. Uzun[2], B. Selen Çağlayan[2,3], A. E. Aksoylu[1,2]*
[1]Department of Chemical Engineering, Boğaziçi University, Bebek, Istanbul 34342, Turkey
[2]SNG&HydTec Lab, Science and Technology Building, Boğaziçi University, Kandilli, Istanbul 34684, Turkey
[3]Advanced Technologies R&D Center, Boğaziçi University, Bebek, Istanbul 34342, Turkey
*aksoylu@boun.edu.tr

ABSTRACT
The goal of this research study is to interpret the activity, stability, and selectivity of designed and developed alkali-promoted Pt-based catalysts via FTIR-DRIFTS-MS analysis. The WGS performances of Pt-Re-Na/CeO2 catalysts with different Na loadings and Pt-Re-Na/TiO_2 catalysts were examined under various reaction conditions previously. The freshly reduced and spent catalyst samples were characterized using SEM, XPS, XRD, and Raman spectroscopy. A combined analysis of the Na1s and Ce3d spectra of the highly active catalysts indicates that NaOx species likely play a more significant role than CeO_x species in the WGS reaction mechanism. *Operando* FTIR-DRIFTS-MS tests were conducted to examine surface formate and carbonate species under reaction conditions on Pt-Re-Na/CeO_2 catalysts. Metal dispersions of these catalysts were also evaluated via CO pulse experiments and were found to be consistent with the activity results.
Keywords: *Operando*, *in-situ*, FTIR-DRIFTS-MS, Characterization, WGS.

1. INTRODUCTION

Hydrogen is recognized as a vital clean and environmentally friendly energy carrier, offering significant advantages over traditional hydrocarbon fuels, including reduced greenhouse gas emissions, higher energy content, and enhanced economic viability.. *On-site* hydrogen production through Fuel Processors (FP) is considered the most promising and feasible alternative, addressing the challenges associated with hydrogenstorage. Conventional WGS catalysts do not meet the necessary performance criteria for fuel processor (FP) operation. These include maintaining high activity after repeated start-up and shut-down cycles, stable operation with oxygen and excess water in the feed, thermal stability, and low methanation activity—requirements that industrial WGS catalysts often fail to fulfill. Additionally, the two-step (HTS and LTS) WGS reactor configuration is unsuitable for small-scale hydrogen production due to its bulky nature, making up the largest portion of the fuel processor. Consequently, substantial research has been devoted to designing and developing active, non-pyrophoric, and durable platinum-group metal (PGM)-based catalysts supported by metal oxides with high activity at HTS-LTS transition temperatures, enabling the use of a single WGS reactor [1,2]. In this context, a detailed *in-situ* and *operando* FTIR-DRIFTS-MS study was performed in order to interpret the WGS reaction mechanism, and structure-mechanism-performance relation.

2. EXPERIMENTAL

FTIR-DRIFTS-MS analysis of the WGS reaction over sequentially impregnated 1%Pt-1%Re-1%Na/CeO_2 and 1%Pt-1%Re-3%Na/CeO_2 was conducted using a Bruker Vertex 70V equipped with a Mercury-Cadmium-Telluride (MCT) detector, combined with a Hiden Mass Spectrometer. The FTIR-DRIFTS setup included a Pike Technologies DRIFTS cell with a ZnSe window, a PIKE Technologies temperature controller, and Brooks mass flow controllers for the feed section, allowing thermal treatments in controlled atmospheres and spectral scans at temperatures between 20°C and 300°C. FTIR spectra were recorded with a resolution of 4 cm^{-1}, 128 scans, and a wavenumber range of 4000-800 cm^{-1}. For activity screening via MS, precise catalyst sample weight was essential, and it was ensured that each sample weighed 25±2 mg for every analysis. Catalyst samples were reduced *in-situ* under 15% H_2 containing inert (He) flow at 375°C for 2 hours before each FTIR-DRIFTS-MS analysis. In all tests, the total feed flow was maintained at 50 ml/min. Prior to analysis, a background spectrum was recorded under He flow at the analysis temperature (300°C). Spectra were collected every ten minutes over a 30-minute period, with the feed mixture sequence introduced over the catalyst surface as follows: (i) He flow for 30 minutes, (ii) 1% CO in He for 30 minutes, (iii) He flush following 1% CO adsorption for 30 minutes, (iv) 1.36% CO and 2.72% H_2Oin He as the WGS ideal feed, and (v) He flush after the WGS ideal feed for 30 minutes. Thirty-minute spectra were used for comparisons, as the surface did not reach equilibrium during the first 10 minutes but equilibrated after 20 minutes. SEM analysis was used to interpret the microstructure and morphology of freshly reduces and spent catalysts, along with their performance data under various realistic conditions. Crystalline phases were determined using a Rigaku X-ray diffractometer having an X-ray generator with Cu target and scan speed of 2°/min. Electronic interactions and oxidation states in the samples were examined with Thermo Scientific K-Alpha XPS. Raman spectroscopy was employed to observe coke formation on spent catalysts. Furthermore, Pt dispersion was quantified by CO chemisorption with Hiden Analytical CATLAB, utilizing 0.1 ml pulses of 5% CO to measure the metal available for reaction.

3. RESULTS AND DISCUSSION

In *operando* reaction tests, FTIR-DRIFTS spectra were employed to identify the reaction steps occurring on the surface, while MS data were used to evaluate catalytic activity and selectivity. A structure-mechanism-performance relationship for the WGS reaction over the Pt-Re-Na/CeO_2 system was tried to be established via comparative analysis of FTIR-DRIFTS and MS data obtained under *operando* conditions.

During CO adsorption over 1%Pt-1%Re-1%Na/CeO_2 at 300°C, a reduction in the wave number of 3643 cm^{-1} was observed in Fig. 1, but the significant reduction in the hydroxyl band around the 3540 cm^{-1} wave number, like in the case of CeO_2 support, attributed to the type III OH group was not observed, indicating other OH groups were used in product formation [3-5]. The absence of formate groups in C-H band suggest either the formate species do not form over Na containing catalysts or that they are generated, but consumed rapidly. The gas-phase CO_2 peak at 2350 cm^{-1} was observed under both CO adsorption and reaction conditions, with a more pronounced intensity under ideal WGS reaction conditions, consistent with the MS data for CO_2 and H_2 shown in Fig.2. Based on the literature, the 2026 cm^{-1} peak, observed alongside gas-phase CO peaks during CO adsorption, corresponds to linearly bonded CO on Pt, while the 2006 cm^{-1} peak at its crest is attributed to linearly bonded CO on Re [6,7]. The 1924 cm^{-1} peak is assigned to CO bridged to Pt, whereas the 1787 cm^{-1} peak corresponds to trifold-bonded CO. Linear and bridge bonded CO molecules were swept via He flush following CO adsorption, but the trifold bonded CO molecules remained on the surface indicating their stronger adsorption on the catalyst. An increase in peaks at 1787, 1613, 1267, 1076, 1038, and 855 cm^{-1}, attributed to carbonates, was observed. Additionally, the reduction in the hydrogen carbonate peak around 1420 cm^{-1} is believed to be specific to Na-containing catalysts and may result from interaction with Na [4,5,8,9]. The notable decrease in the hydrogen carbonate peak intensity in anhydrous conditions during CO adsorption suggests its active participation in the WGS reaction.

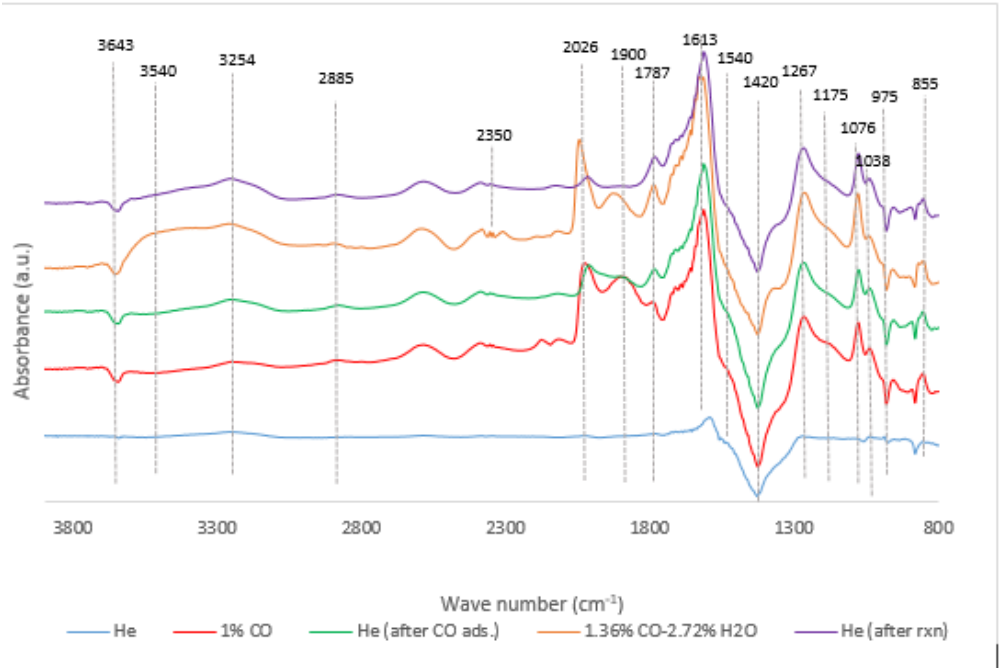

Fig. 1. FTIR-DRIFT spectra obtained over 1%Pt-1%Re-1%Na/CeO_2 at 300°C under various feed flows

After analyzing Pt-Re-Na/CeO_2 system having high WGS performance, the formulation that have shown the poorest performance, 1%Pt-1%Re-3%Na/CeO_2, was also examined under identical conditions aiming to form a comparison basis. Regarding Fig.1. and Fig. 3, while the only formate-related peak in the C-H band for 1%Pt-1%Re-1%Na/CeO_2 appeared at 2885 cm^{-1}, additional formate peaks at 2950 and 2835 cm^{-1} were detected for 1%Pt-1%Re-3%Na/CeO_2 [4,5,10]. These peaks remained unchanged throughout CO adsorption, reaction, and He flush stages. Additionally, the gas-phase CO_2 peak at 2350 cm^{-1}, which was distinctly observed for 1%Pt-1%Re-1%Na/CeO_2, was not observed in the spectrum of 1%Pt-1%Re-3%Na/CeO_2. Consistent with the WGS performance test results indicating the very low activity of 1%Pt-1%Re-3%Na/CeO_2, FTIR-DRIFTS analysis showed that the surface remained unchanged under reaction conditions. Additionally, MS data of CO_2 and H_2 signals (Fig.2.) suggest that the reaction is highly limited on the catalyst surface. The reduction of the 1420 cm^{-1} peak during the reaction over 1%Pt-1%Re-1%Na/CeO_2, in contrast to the unchanged peak under the same conditions for the essentially inactive 1%Pt-1%Re-3%Na/CeO_2, strongly suggests that these groups participate in the reaction.

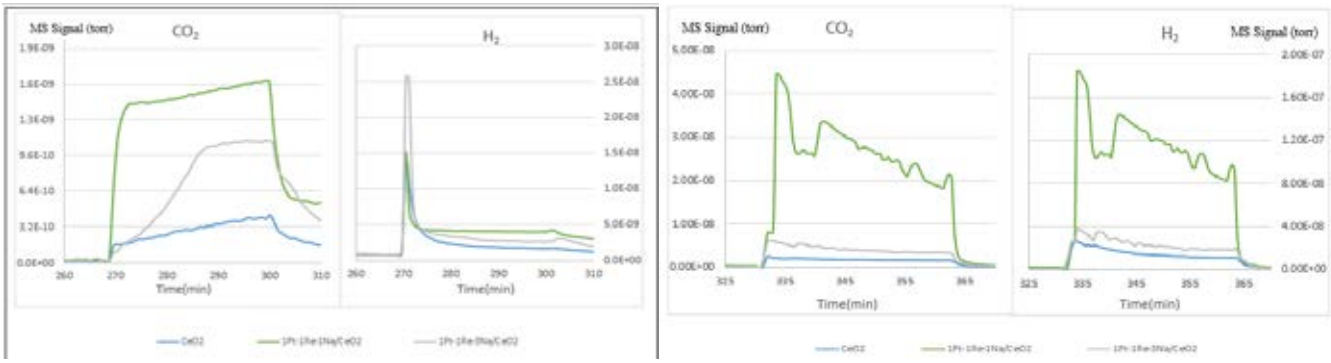

Fig. 2. MS signals of CO_2 and H_2 molecules in the exit stream of FTIR-DRIFTS system (a)during 1% CO adsorption (b) under 1.36%CO-2.72%H_2O feed flow at 300°C over in-situ reduced support and catalyst

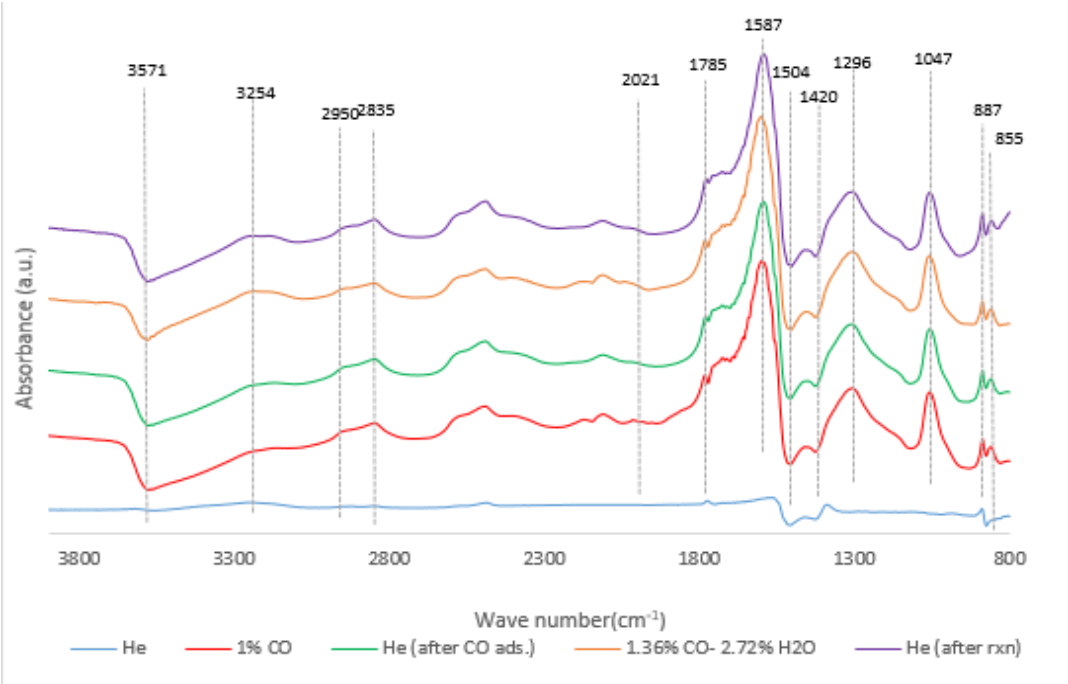

Fig. 3. FTIR-DRIFT spectra obtained over 1%Pt-1%Re-3%Na/CeO_2 at 300°C under various feed flows.

Upon examining the characterizations performed on each catalyst, homogeneous distribution of the metals were supported for Pt-1%Re-1%Na/CeO_2 sample, whereas peaks corresponding to sodium carbonate species were observed in the diftractogram of 1%Pt-1%Re-3%Na/CeO_2 catalyst. Pt4f XP spectra of the 1%Pt-1%Re-1%Na/CeO_2 and 1%Pt-1%Re-3%Na/CeO_2 confirms high WGS activity achieved over sequentially impregnated 1%Pt-1%Re-1%Na/CeO_2 and, blockage of Pt sites at higher Na loadings as in the case of 1%Pt-1%Re-3%Na/CeO_2 resulted as limited Pt^{2+} and Pt^{4+} presence and limited activity accordingly. Metal dispersion results were also correlated with the activity outcomes; specifically, the 1%Pt-1%Re-3%Na/CeO_2 sample, which showed minimal activity, exhibited nearly zero dispersion, while the sequentially impregnated 1%Pt-1%Re-1%Na/CeO_2 sample displayed quite high metal dispersion. Carbonate formation was confirmed via Raman spectroscopy analysis of spent samples.

4. CONCLUSIONS

The CeO_2 support exhibited limited WGS activity, as indicated by the barely detectable gas-phase CO_2 peak and MS data. Formate groups observed in the C-H band on CeO_2 were not present on Na-containing catalysts, which may indicate that either these groups do not form or, if formed, are consumed quickly on these catalysts. Trifold-bonded CO molecules showed stronger adsorption than linear and bridge-bonded CO, as evidenced by their persistence on the surface after a He flush. The formation of bidentate formate groups was found to be more pronounced with the addition of Na. A significant reduction in the hydrogen carbonate peak intensity during CO adsorption in anhydrous conditions suggests that these groups are actively involved in the WGS reaction. In the spectra of 1%Pt-1%Re-3%Na/CeO_2, formate

and carbonate peaks observed after CO adsorption remained unchanged during the He flush and ideal feed conditions. This result, combined with the minimal WGS activity detected via MS, suggests that formate and carbonate groups likely to play a role in the WGS reaction mechanism on Pt-Re-Na/CeO_2 catalysts.

ACKNOWLEDGEMENT
The financial support was provided by Presidency of the Republic of Turkey, Department of Strategy and Budget (Ministry of Development) through project 2016K12-2838 (2016K121160) and TÜBİTAK through project 214M170.

REFERENCES

1. Li J, Han Y, Zhu Y, and Zhou R. 2011. Purification of hydrogen from carbon monoxide for fuel cell application over modified mesoporous CuO–CeO_2 catalysts. Applied Catalysis B: Environmental 108-109:72-80.
2. Colussi S, Katta L, Amoroso F, Farrauto RJ, and Trovarelli A. 2014.Ceria-based palladium zinc catalysts as promising materials for water gas shift reaction. Catalysis Communications 47:63-66.
3. Li C, Yoshihisa S, Toru A, Domen K, Ken-ichi M, and Takaharu O. 1989. Carbon monoxide and carbon dioxide adsorption on cerium oxide studied by Fourier-Transform Infrared Spectroscopy. Journal of Chemical Society 85:929-943.
4. Holmgren A, Andersson B, and Duprez D. 1999. Interactions of CO with Pt/ceria catalysts. Applied Catalysis B: Environmental 22:215–230.
5. Jacobs G, Keogh R A, and Davis B H. 2007. Steam reforming of ethanol over Pt/ceria with CO-fed hydrogen. Journal of Catalysis 245:326-337.
6. Nguyen TS, Morfin F, Aouine M, Bosselet F, Rousset J L, and Piccolo L. 2015. Trends in the CO oxidation and PROX performances of the platinum-group metals supported on ceria. Catalysis Today 253:106–114.
7. Azzam K G, Babich I V, Seshan K, and Lefferts L. 2008. Role of Re in Pt–Re/TiO_2 catalyst for water gas shift Reaction: A mechanistic and kinetic study. Applied Catalysis B: Environmental 80:129–140.
8. Meunier FC, Reid D, Goguet A, Shekhtman S, Hardacre C, Burch R, Deng W, and Flytzani-Stephanopoulos M. 2007. Quantitative analysis of the reactivity of formate species seen by DRIFTS over a Au/Ce(La)O_2 water-gas shift catalyst: First unambiguous evidence of the minority role of formates as reaction intermediates. Journal of Catalysis 247:277-287.
9. Guerrero S, Guzmán I, Aguila G, Chornik B, and Araya P. 2012. Study of Na/Cu/TiO_2 catalysts for the storage and reduction of NO. Applied Catalysis B: Environmental 123– 124:282– 295.
10. Meunier FC, Goguet A, Hardacre C, Burch R, and Thompsett D. 2007. Quantitative DRIFTS investigation of possible reaction mechanisms for the water–gas shift reaction on high-activity Pt- and Au-based catalysts. Journal of Catalysis 252:18–22.

VARIOUS METAL OXIDE CATALYSTS SUPPORTED ON Al_2O_3 FOR HYDROGEN GENERATION FROM ALKALINE $NaBH_4$ SOLUTION

[1]*Selin Salt*, [2]*Havva Erdoğan*, [3]*Halit Eren Figen*, [2*]*Meltem Karaismailoğlu Elibol*
[1] Turkish-German University, Faculty of Science, Department of Materials Science and Technology, Şahinkaya Cad. 106, Istanbul, 34820, Türkiye
[2] Turkish-German University, Faculty of Science, Department of Energy Science and Technology, Şahinkaya Cad. 106, Istanbul, 34820, Türkiye
[3] Yıldız Technical University, Faculty of Chemistry and Metallurgy, Department of Chemical Engineering, Davutpaşa Mah. Davutpaşa Caddesi, Istanbul, 34220, Türkiye *Corresponding author e-mail: m.karaismailoglu@tau.edu.tr

ABSTRACT
The importance of green energy and energy efficiency has increased significantly. Hydrogen, as a green energy source, plays a crucial role in clean energy production. Due to its environmental benefits, hydrolysis of $NaBH_4$ is considered a useful production method.
The study's objective is to enhance the hydrogen generation from $NaBH_4$ with high-surface-area alumina pellets coated with various metal oxides, including Co, Cu, V, and Ru elements. The relevant metal oxides were deposited on pristine alumina pellets via the wash coating method, and hydrogen production was evaluated in an integrated continuous reactor. The results indicate that the $Co/CuV_2O_6/Al_2O_3$ catalyst exhibits promising catalytic activity, with Co significantly enhancing the catalytic performance of the CuV_2O_6 catalyst.
Keywords: hydrogen, sodium borohydride, catalyst, alumina

1. INTRODUCTION

In recent years, there has been a growing interest in replacing fossil fuels with renewable energy sources, primarly due to the non-renewable nature of fossil fuels and their harmful environmental emissions [1, 2]. Among renewable energy sources, hydrogen attracts significant attention. It is known for its high efficiency and status as a clean energy source [1-3].
Among various hydrogen production methods, hydrolysis of $NaBH_4$ is highly preferred. $NaBH_4$ has a very high hydrogen storage capacity (10.8 wt%), and its side product is sodium borate ($NaBO_2$), which is non-toxic to the environment [1, 2, 4]. However, the spontaneous hydrolysis of $NaBH_4$ is very slow and therefore needs to be supported by a catalyst [1, 2, 4]. Generally, catalysts used in hydrogen production from $NaBH_4$ include noble metals such as Pt, Pd, Ru, or Rh [1, 4, 5]. They show enhanced catalytic activity but have high costs [1, 5]. Therefore, using transition metals such as Co, Fe, Zn, Ni, Zr, Bi, Mo, Cu or V is essential in achieving high H_2 generation rates at a low cost [1, 3, 5-11]. Cu-based catalysts exhibit good catalytic activity alongside metals such as Fe, Co, and Zn [5, 6, 9, 12]. Recent research suggests that doping Cu element into a catalyst creates a synergistic effect, enhancing the catalytic activity [5, 7].
Shojaei et al. investigated the catalytic activity of Cu-Fe-B catalysts in the hydrolysis of $NaBH_4$ [6]. Their findings indicate that the presence of copper significantly enhances catalytic activity, provided the optimum amount is indicated into the catalyst.
Another study conducted by Deonikar et al. examined the effects of Cu and Mo elements on the catalytic activity of Co-based catalysts [5]. Among the tested catalysts, $Co_{0.9}Cu_{0.1}MoO_4$ catalyst exhibits the highest H_2 generation performance, demonstrating a synergistic effect between Cu and Co. Additionally, studies also show that the V element has a promising positive impact on the performance of catalysts [11, 13]. A study by Akkus examining the catalytic activity of NiV thin films revealed that V plays an effective role in enhancing the H_2 generation rate of the Ni element [13].
In this study, high-surface-area alumina pellets were coated with various metal oxides containing Cu, V, Co, and Ru-elements via the wash-coating method. The performance of all synthesized catalysts were evaluated in the hydrolysis reaction of an alkaline $NaBH_4$ solution at room temperature.

2. MATERIALS AND METHODS

2.1. Catalyst preparation

In the preparation process of the catalysts, the following metal salts were utilized to prepare each precursor solution: $Cu(NO_3)_2{\cdot}3H_2O$ (Carlo Erba), NH_4VO_3 (Alfa Aesar), and $RuCl_3{\cdot}xH_2O$ (Merck). Citric acid ($C_6H_8O_7{\cdot}H_2O$, Carlo Erba) was used as the chelating agent, and each precursor solution was prepared at a concentration of 1 M. The pH value of the solutions was adjusted to 7 using ammonia solution (NH_4OH, Carlo Erba). However, the pH of vanadium salts containing precursor solutions was adjusted to 1 by adding the citric acid. After the pH adjustment, alumina pellets maintained at a temperature of 50°C for 1 h, however, the Al_2O_3 pellets were wash-coated in vanadium-containing (Al_2O_3) were subjected to a wash coating process in the as-prepared precursor solutions within an ultrasonic bath precursor solution at ambient

temperature. After the coating process, the samples were oven-dried at 230°C. After oven drying, all catalysts were calcined in the air atmosphere for 2 h. Vanadium-containing catalysts were calcined at a lower temperature due to the lower evaporation temperature of vanadium. The nominal chemical structure of the synthesized catalysts, their respective sample codes, and calcination temperatures are listed in Table 1.

Table 1. The sample codes, nominal structure and calcination temperature for prepared catalysts

Sample codes	Nominal chemical structure	Calcination temperature (°C)	Maximum hydrogen generation rate ($mmols^{-1}g^{-1}$)
C-1	**V_2O_5/Al_2O_3**	500	-
C-2	**CuO/Al_2O_3**	700	0.001
C-3	**CuV_2O_6/Al_2O_3**	500	0.0008
C-4	**$RuO/CuV_2O_6/Al_2O_3$**	500	0.0009
C-5	**$Co_3O_4/CuV_2O_6/Al_2O_3$**	500	0.0019

2.2. Catalytic hydrolysis of $NaBH_4$

In this study, the hydrogen generation tests in the presence of all prepared catalysts were carried out in an integrated continuous system. An alkaline solution of $NaBH_4$ was fed to a reactor (filled with 1.7 g coated Al_2O_3-catalysts) by a peristaltic pump with a flow rate of 3 ml/min. Firstly, all catalysts were reduced in 0.075 M $NaBH_4$-solution and then tested at the ambient temperature by water displacement method to determine the hydrogen generation rate.

3. RESULTS AND DISCUSSION

In this study, a 0.5 M $NaBH_4$ solution was continuously fed into the reactor. Hydrogen generation was measured using the water displacement method. The hydrogen generation via $NaBH_4$ hydrolysis is represented by the following reaction (Equation (1)) [14]:

$$NaBH_4(aq)+2H_2O \rightarrow NaBO_2(aq)+4H_2(g) \quad (1)$$

The synthesized catalysts were tested under identical reaction conditions using a continuous flow pump, and their maximum H_2 generation rates are listed in Table 1. Among the tested catalysts, the catalyst C-1 shows no hydrogen production, indicating that the monometallic V coating does not improve the catalytic activity of alumina. Fig. 1a shows the H_2 generation rates over time for the catalysts C-2, C-3, C-4, and C-5, and Figure 1b shows the change in the H_2 generation rate over time of the C-5 catalyst. As shown in Figure 1a, the monometallic C-2 catalyst exhibited the highest initial rate of 0.001 $mmol.s^{-1}g^{-1}$, however, after about 8 minutes, its catalytic activity decreases significantly. Similarly, the catalysts C-3 and C-4 exhibit the same catalytic behavior, starting with a high initial hydrogen generation rate, which gradually declines over time. This suggests that Ru and V elements do not enhance the catalytic activity of the Cu element.

In contrast, the Co-doped C-5 catalyst demonstrated the most promising catalytic activity. Although C-5 exhibits a decelerating hydrogen generation rate at the beginning of the reaction, its activity increased significantly over time, distinguishing it from the others, as shown in Fig. 1b. The C-5 catalyst demonstrates superior performance to the C-4 catalyst, suggesting that the Co element enhances the catalytic activity of Cu and V elements higher than the Ru element. Based on these observations, it can be concluded that the C-5 catalyst shows considerable promise as a catalyst for H_2 generation from $NaBH_4$.

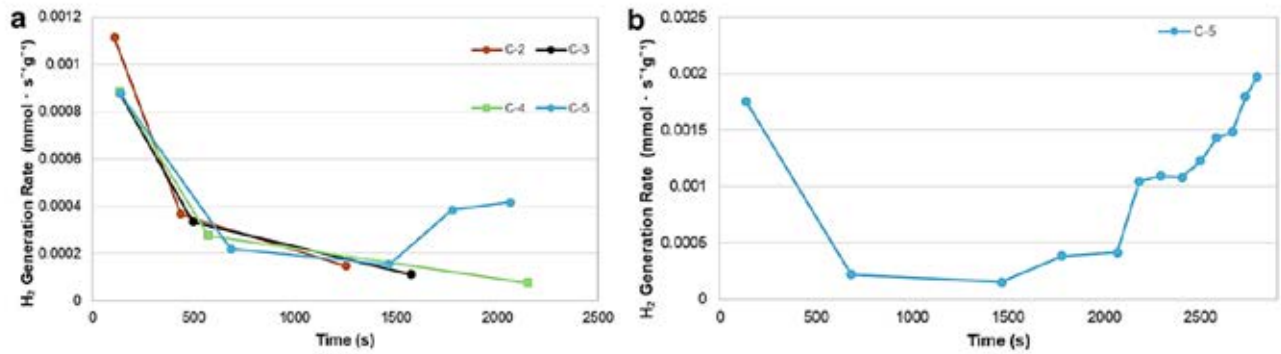

Fig. 1. (a) H_2 generation rates of the synthesized catalysts, (b) H_2 generation rate of the C-5 catalyst over time.

4. CONCLUSIONS

Alumina pellets with a high surface area are shown as effective support materials for catalysts in the hydrolysis reaction of $NaBH_4$. In this study, alumina pellets were coated with various metal oxides via the wash-coating method, and the coated pellets were tested in the hydrolysis reaction of $NaBH_4$ using the water displacement method. Among the synthesized catalysts, the vanadium oxide on the alumina sample exhibits no catalytic activity. A comparison of the initial rates of the synthesized catalysts reveals that the CuO-coated alumina catalyst (C-2) demonstrates the highest initial hydrogen generation rate among all catalysts. However, its' activity declines over time. A similar behavior is observed in CuV_2O_6 (C-3) and $RuO/CuV_2O_6/Al_2O_3$ (C-4) coated alumina catalysts. The Co-doped CuV_2O_6 (C-5) coated alumina catalyst also demonstrates a decelerating catalytic behavior. However, in the later stage of the reaction, the catalyst exhibited a significant acceleration in the hydrogen generation rate, indicating superior catalytic activity compared to the Ru-containing (C-4) catalyst. This observation suggests that the Co-doped CuV_2O_6/Al_2O_3 catalyst exhibits an enhanced catalytic activity when compared to the Ru element containing catalyst, which, despite being a noble metal, is also costly. In light of these findings, the $Co/CuV_2O_6/Al_2O_3$ catalyst emerges as a promising candidate for future studies exploring H_2 generation from $NaBH_4$, a promising option for sustainable energy research, due to its performance and cost-effectiveness.

REFERENCES

[1] Xiang, C., Jiang, D., She, Z., Zou, Y., Chu, H., Qiu, S., Zhang, H., Xu, F., Tang, C. & Sun, L. 2015. Hydrogen generation by hydrolysis of alkaline sodium borohydride using a cobalt–zinc–boron/graphene nanocomposite treated with sodium hydroxide. International Journal of Hydrogen Energy, 40(11), 4111–4118.

[2] Wang, M., Ouyang, L., Liu, J., Wang, H. & Zhu, M. 2017. Hydrogen generation from sodium borohydride hydrolysis accelerated by zinc chloride without catalyst: A kinetic study. Journal of Alloys and Compounds, 717, 48–54.

[3] Xia, Y., Pei, Y., Wang, Y., Li, F. & Li, Q. 2022. Effects of various metal doping on the structure and catalytic activity of CoB catalyst in hydrogen production from $NaBH_4$ hydrolysis. Fuel, 331, 125733.

[4] Mirshafiee, F. & Rezaei, M. 2024. Engineering of the ferrite-based support for enhanced performance of supported Pt, Pd, Ru, and Rh catalysts in hydrogen generation from $NaBH_4$ hydrolysis. Scientific Reports, 14(1).

[5] Deonikar, V. G., Rathod, P. V., Pornea, A. M., Puguan, J. M. C., Park, K. & Kim, H. (2020). Hydrogen generation from catalytic hydrolysis of sodium borohydride by a Cu and Mo promoted Co catalyst. Journal of Industrial and Engineering Chemistry, 86, 167–177.

[6] Loghmani, M. H., Shojaei, A. F. & Khakzad, M. 2017. Hydrogen generation as a clean energy through hydrolysis of sodium borohydride over Cu-Fe-B nano powders: Effect of polymers and surfactants. Energy, *126*, 830–840.

[7] Vajargah, S. G. & Gilani, N. 2024. Enhancing the activity of Ni-B catalyst via Cu doping towards hydrogen evolution from $NaBH_4$ hydrolysis. Renewable Energy, 235, 121322.

[8] Abbas, M. J. A., Caglar, A. & Kivrak, H. 2024. The synthesis and characterization of carbon nanotube-supported CuBi catalyst for H_2 production from $NaBH_4$ methanolysis. Process Safety and Environmental Protection, 185, 96–104.

[9] Patil, K. N., Prasad, D., Bhagyashree, N., Manoorkar, V. K., Nabgan, W., Nagaraja, B. M. & Jadhav, A. H. 2021. Engineered nano-foam of tri-metallic (FeCuCo) oxide catalyst for enhanced hydrogen generation via $NaBH_4$ hydrolysis. Chemosphere, 281, 130988.

[10] Wang, S., Lu, A. & Zhong, C. 2021. Hydrogen production from water electrolysis: role of catalysts. Nano Convergence, 8(1).

[11] Orłowski, P. A. & Grochala, W. 2022. Effect of Vanadium Catalysts on Hydrogen Evolution from $NaBH_4$. Solids, 3(2), 295–310.

[12] Alshammari, A. H., Alshammari, K., Alhassan, S., Alshammari, M., Alotaibi, T., Alanzy, A. O. & Taha, T. A. M. 2023. Low temperature sol-gel synthesis of copper zinc ferrite for hydrogen catalytic hydrolysis of sodium borohydride. Materials Chemistry and Physics, 308, 128287.

[13] Akkus, M. S. 2022. Examination of the catalytic effect of Ni, NiCr, and NiV catalysts prepared as thin films by magnetron sputtering process in the hydrolysis of sodium borohydride. International Journal of Hydrogen Energy, 48(60), 23055–23066.

[14] Liu, B. & Li, Z. 2008. A review: Hydrogen generation from borohydride hydrolysis reaction. Journal of Power Sources, 187(2), 527–534.

THERMODYNAMIC ANALYSIS OF SYNTHETIC FUEL PRODUCTION FROM CARBON DIOXIDE OBTAINED FROM CARBON CAPTURE FACILITY IN OIL REFINERY BY COMBINATION OF HYDROGEN PRODUCTION AND POWER CONVERSION

[1*]*Süheyl Bilal SUNGUR*, [1]*Erdem ALP* [1]*Erhan KAYABAŞI*
[1] Karabük University, Faculty of Engineering, Department of Mechanical Engineering, Karabük, 78050, Türkiye

*Corresponding author e-mail: suheylsungur@karabuk.edu.tr

ABSTRACT

This study investigates the integration of carbon dioxide obtained from a carbon capture facility in an oil refinery and hydrogen produced by electrolysis for methanol synthesis. The use of carbon dioxide and hydrogen in methanol production not only reduces environmental emissions but also optimizes the production cycle by recovering energy. The hydrogen production process by electrolysis includes the recovery of waste heat using a reheat Rankine cycle. This system maximizes both economic and environmental benefits by increasing energy efficiency. This study aims to provide an innovative solution by optimizing the energy and material flows in the hydrogen production, carbon capture and methanol synthesis cycle. In line with environmental sustainability goals, a thermodynamic analysis of this integrated system was performed, and a new perspective was presented in terms of renewable energy management and resource efficiency.

Keywords: Hydrogen production, carbon capture, rankine cycle, methanol production

1. INTRODUCTION

Our world needs sustainable energy solutions due to the increasing energy demand and environmental impacts of greenhouse gas emissions. One of the important goals of the Paris Climate Agreement is to limit the current global warming to just 2 ◦C [1], this limit was proposed to be reduced to 1.5 ◦C at the global meeting COP-26 to keep climate change much lower [2]. Therefore, there is a growing interest in carbon capture, utilization and sequestration to decarbonize the energy and industrial sectors as a measure to mitigate the ever-increasing greenhouse effect that causes climate change [3], [4]. Redirecting industrial plants, oil refinery wastes and emissions into convertible products not only increases environmental sustainability but also offers economic benefits [5].

Traditional fuels such as oil, wood, coal and natural gases are important non-renewable energy sources that have carbon and greenhouse gas emissions and are a major concern to be solved today [6]. Considering such a problem, we should look for a better alternative to fossil fuels that have the potential to change the rules of the game in the energy storage sector. Hydrogen has many unique properties that make it the best alternative to fossil fuels such as oil and natural gas [7]. Hydrogen is a clean, economical and extremely safe renewable energy source that would be ideal to replace fossil fuels because it is light, abundant and produces water as a by-product that does not harm the environment. The hydrogen economy has emerged as a promising alternative to the current hydrocarbon economy [8]. Hydrogen has been proven to be an alternative fuel that can replace fossil fuels due to its many features such as increased energy density, abundance, easy transportability and a variety of different processes from clean renewable energy fuels with zero or negligible emissions [9].

This study focuses on how carbon dioxide obtained from a carbon capture facility in an oil refinery and hydrogen produced by electrolysis are combined to produce methanol. The use of carbon dioxide and hydrogen in methanol production allows not only the reduction of environmental emissions but also the optimization of the production cycle by energy recovery. The electrolysis process used in hydrogen production involves the recovery of waste heat generated in the carbon capture and methanol production cycle by a reheated Rankine cycle. This integrated approach increases energy efficiency, allows its reuse in hydrogen production, and maximizes economic and environmental gains. Our study focuses on the thermodynamic analysis of this integrated process. In line with environmental sustainability goals, it aims to offer an innovative solution by optimizing the energy and material flows in the hydrogen production, carbon capture, and methanol production cycle.

2. MATERIALS AND METHODS

In this study, carbon capture, hydrogen production and methanol synthesis processes are discussed in detail using an integrated systems approach. Each stage of the processes is optimized to increase both environmental sustainability and energy efficiency. Figure 1 shows the flow chart of the optimization processes carried out in the facilities.

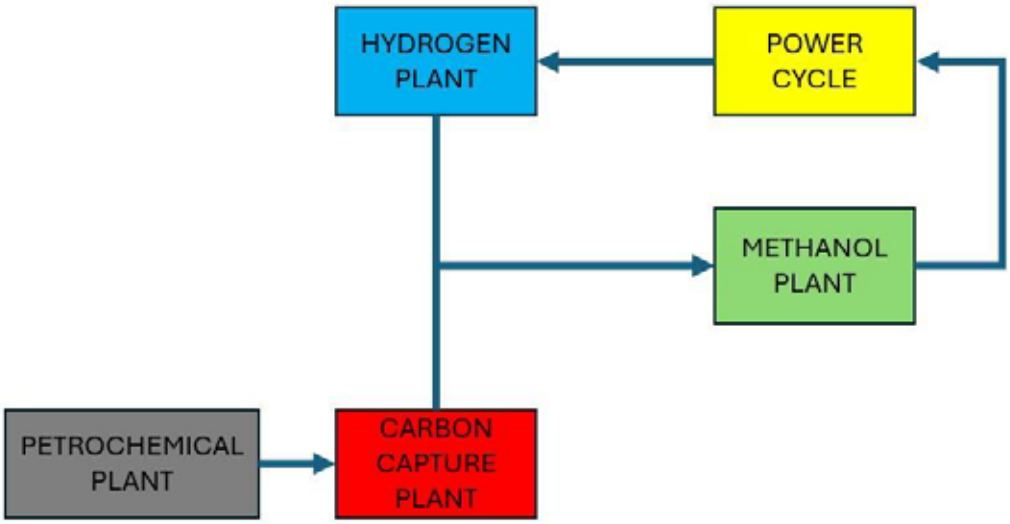

Figure 1: Flow chart of the proposed plant

The carbon capture process carried out in the Carbon Capture Facility is based on capturing carbon dioxide emissions from an oil refinery. Hydrogen production is carried out in the hydrogen facility. Electrolysis method is applied in hydrogen production. The captured carbon dioxide and the hydrogen produced by the electrolysis method are directed to the methanol facility. Methanol synthesis is carried out in this facility as a result of the chemical reaction of carbon dioxide and hydrogen. The process is optimized to provide low carbon footprint and high energy efficiency. The energy released in the methanol production process is recovered by the Rankine cycle with reheating during the power cycle phase. This energy is integrated into the system to be reused in the electrolysis process. This approach increases the total efficiency of the system by minimizing energy losses.

Thermodynamic analyses are performed to evaluate the overall performance of the system. Energy and material flows used in processes are calculated in detail and optimized. Analyses aim to increase the efficiency of the system in line with sustainable energy management goals.

3. RESULTS AND DISCUSSION

In this study, it was investigated how carbon dioxide obtained from carbon capture plants and hydrogen produced by electrolysis could be combined to produce methanol. Optimizing the energy and material flows between carbon capture, hydrogen production and methanol synthesis stages throughout the process both increased energy efficiency and contributed to the reduction of environmental emissions. The electrolysis process used for hydrogen production was supported by the energy recovered through the reheat rankine cycle. This method both recovered energy and made it possible to reuse part of the energy used in methanol production. The reuse of waste heat increased the overall energy efficiency of the system and allowed for cost reductions. This integrated approach not only saved energy but also contributed to a more sustainable design of the methanol production cycle. The use of carbon dioxide and hydrogen in methanol production has provided an effective solution for reducing environmental emissions. The use of carbon dioxide as a carbon source in this process has allowed the recycling of waste gases in energy-intensive industries. The results have shown that methanol production efficiency can be increased through the integration of energy recovery and production processes.

This study is based on the thermodynamic analysis of integrated processes between hydrogen production, carbon capture and methanol synthesis. Simulation results reveal that both economic and environmental gains can be increased by optimizing energy and material flows. In this context, this integrated approach developed in line with environmental sustainability goals stands out as an innovative solution.

4. CONCLUSIONS

Our study presents an integrated energy management model by combining carbon capture, hydrogen production and methanol synthesis processes. The results of this model show that significant gains can be achieved in terms of both energy saving and environmental sustainability. In terms of energy efficiency, the recovery of waste heat generated in the electrolysis process with the reheat Rankine cycle has significantly reduced total energy consumption. In terms of

environmental contribution, the use of carbon dioxide obtained from carbon capture facilities in methanol production has contributed to the carbon cycle and reduced emissions. In terms of economic advantages, energy recovery and integrated processes have allowed the reduction of costs and the optimization of the production cycle. This study presents an innovative production model by optimizing energy and material flows. The results show that renewable technologies such as hydrogen production and carbon capture will find a larger place in the future energy portfolio.

ACKNOWLEDGEMENT

This study was supported by the Scientific and Technological Research Council of Turkey (TÜBİTAK) Scientist Support Programs Directorate (BİDEB) within the scope of the 2224-B Program for Supporting Participation in Domestic Scientific Activities, in the 2025/2 application period, with the application number 1919B022503090.

REFERENCES

[1] G. C. Iyer et al., “The contribution of Paris to limit global warming to 2 °C,” Environmental Research Letters, vol. 10, no. 12, p. 125002, Nov. 2015, doi: 10.1088/1748-9326/10/12/125002.
[2] L. Warszawski et al., “All options, not silver bullets, needed to limit global warming to 1.5 °C: a scenario appraisal,” Environmental Research Letters, vol. 16, no. 6, p. 064037, May 2021, doi: 10.1088/1748-9326/ABFEEC.
[3] L. L. Teck Chan and J. Chen, “Economic model predictive control of an absorber-stripper CO2 capture process for improving energy cost,” IFAC-PapersOnLine, vol. 51, no. 18, pp. 109–114, Jan. 2018, doi: 10.1016/J.IFACOL.2018.09.284.
[4] A. Chakrabarti et al., “Rapid Detection of Super-Emitters Utilizing an IoT-Enabled Continuous Methane Emissions Monitoring System,” Proceedings - SPE Annual Technical Conference and Exhibition, vol. 2022-October, Sep. 2022, doi: 10.2118/210464-MS.
[5] E. G. Al-Sakkari, A. Ragab, H. Dagdougui, D. C. Boffito, and M. Amazouz, “Carbon capture, utilization and sequestration systems design and operation optimization: Assessment and perspectives of artificial intelligence opportunities,” Science of The Total Environment, vol. 917, p. 170085, Mar. 2024, doi: 10.1016/J.SCITOTENV.2024.170085.
[6] R. Poudyal, P. Loskot, R. Nepal, R. Parajuli, and S. K. Khadka, “Mitigating the current energy crisis in Nepal with renewable energy sources,” Renewable and Sustainable Energy Reviews, vol. 116, p. 109388, Dec. 2019, doi: 10.1016/J.RSER.2019.109388.
[7] Maher A.R. Sadiq Al-Baghdadi, “An Overview of Hydrogen as an Alternative Fuel,” MDPI, pp. 1–22, 2020, doi: 10.32545/ENCYCLOPEDIA202006.0003.V1.
[8] Z. Y. Yu, Y. Duan, X. Y. Feng, X. Yu, M. R. Gao, and S. H. Yu, “Clean and Affordable Hydrogen Fuel from Alkaline Water Splitting: Past, Recent Progress, and Future Prospects,” Advanced Materials, vol. 33, no. 31, p. 2007100, Aug. 2021, doi: 10.1002/ADMA.202007100.
[9] B. Paneru et al., “Techno-economic analysis of green hydrogen production, storage, and waste heat recovery plant in the context of Nepal,” Int J Hydrogen Energy, vol. 77, pp. 892–905, Aug. 2024, doi: 10.1016/J.IJHYDENE.2024.06.161.

ANALYSIS OF SYNTHETIC FUEL PRODUCTION UTILIZING THE WASTE HEAT FROM BLAST FURNACE HOT STOVES BY COMBINATION OF THERMAL ENERGY STORAGE AND POWER CYCLE

[1*]*Erdem Alp*, Süheyl [1]Bilal Sungur [1]*Erhan Kayabasi*
[1]Karabuk University, Faculty, Department of Mechanical Engineering, 78050, Karabuk, Turkey

E-mail: suheylsungur@karabuk.edu.tr

ABSTRACT

This study presents a comprehensive thermodynamic analysis of a synthetic energy plant designed to utilize waste heat from the blast furnace hot stoves of an iron and steel factory. The waste heat, ranging from 300-350°C, is harnessed to improve overall energy efficiency and reduce environmental impact. Initially, a carbon capture process is employed to capture CO2 emissions. The captured thermal energy is stored in a heat storage system comprising two distinct storage units operated sequentially. This stored energy is then converted into electricity, and water is electrolyzed to produce hydrogen (H2). In the methanol plant, the captured carbon and produced hydrogen are combined to synthesize methanol, a synthetic fuel. The analysis includes the evaluation of energy recovery potential, system efficiency, and the integration of advanced heat exchange technologies. Results indicate significant improvements in energy utilization and a reduction in greenhouse gas emissions, demonstrating the viability of waste heat recovery in industrial applications. This study provides a framework for optimizing energy use in heavy industries, contributing to sustainable industrial practices.

Keywords: Hydrogen, Methanol, Thermal Energy Storage, Carbon Capture

1. INTRODUCTION

In today's world, due to advancing technology and increasing population, the global demand for energy is continuously rising. Fossil fuels are being depleted rapidly, and countries are compelled to take necessary measures for energy independence. Consequently, research has been conducted to find new, renewable, environmentally friendly, and cost-effective energy sources and/or carriers. Hydrogen, the most abundant element in the universe, has emerged as the answer to these quests. Hydrogen is one of the cleanest energy carriers and the cleanest energy source that can potentially replace existing energy sources [1]. However, there are numerous challenges that need to be overcome for hydrogen to be used in daily life. Research continues on cost, efficiency, portability, transportation, and storage safety for daily applications. Despite being the fuel that provides the most chemical energy per unit mass, hydrogen poses significant storage challenges, especially in vehicles, due to its lightest and smallest molecular structure [2].

The global steel industry, responsible for approximately 8% of worldwide CO2 emissions, stands at a critical junction where environmental sustainability meets industrial efficiency. As nations worldwide strive to meet ambitious carbon reduction targets, the optimization of industrial waste heat presents a promising pathway toward greener steel production. Blast furnace operations, particularly their hot stoves, generate substantial thermal energy that traditionally dissipates into the atmosphere, representing both an environmental burden and a missed opportunity for energy recovery. At temperatures ranging from 300°C to 350°C, this waste heat carries significant potential for recovery and conversion into valuable products through innovative thermodynamic processes [3].

Previous studies have demonstrated the feasibility and benefits of waste heat recovery in industrial applications. For instance, researchers have explored the use of Organic Rankine Cycles (ORC) to convert low- to medium-grade waste heat into electricity, achieving notable improvements in energy efficiency. Other studies have focused on integrating waste heat recovery with carbon capture technologies, highlighting the dual benefits of reducing greenhouse gas emissions and enhancing energy utilization. In the context of steel manufacturing, investigations into advanced heat exchange systems have shown promise in capturing and repurposing waste heat for various applications, including electricity generation, district heating, and hydrogen production. Furthermore, the synthesis of methanol from captured carbon dioxide and hydrogen has been identified as a viable pathway for producing sustainable fuels, with studies emphasizing its potential to close the carbon loop in industrial processes [4].

Building on these advancements, this study presents a comprehensive thermodynamic analysis of a synthetic energy plant designed to utilize waste heat from the blast furnace hot stoves of an iron and steel factory. The proposed system integrates carbon capture, heat storage, electricity generation, hydrogen production, and methanol synthesis into a cohesive framework. By evaluating energy recovery potential, system efficiency, and the integration of advanced heat exchange technologies, this research aims to demonstrate the viability of waste heat recovery in industrial applications while contributing to the broader goals of energy sustainability and greenhouse gas reduction.

This study proposes the utilization of waste gas storage followed by power generation through a power cycle for the production of synthetic methanol. In the hydrogen plant, hydrogen produced via the Rankine cycle is combined with carbon dioxide removed from flue gas in the carbon capture facility to create synthetic methanol fuel. Additionally, the capture of carbon dioxide aims to reduce CO_2 emission levels.

2. MATERIALS AND METHODS

The recovery of waste heat generated from industrial activities holds significant potential. Despite this potential, industrial waste heat is currently underutilized. This study aims to store waste heat using the Thermal Energy Storage (TES) method for later use. Thermal energy storage systems are technologies developed to store energy derived from temperature differences and to utilize this energy when needed [5]. These systems typically store energy by utilizing heat exchanges occurring in liquid or solid media. Liquid storage systems store energy by heating or cooling liquids and recover the stored energy in this manner. Solid storage systems, on the other hand, store energy through the heating or cooling of materials under the influence of heat. Figure illustrates the stages of synthetic fuel production through the storage of waste heat from stoves in a blast furnace-operated iron factory, carbon capture, and H2 production, as depicted in the flow diagram [6,7].

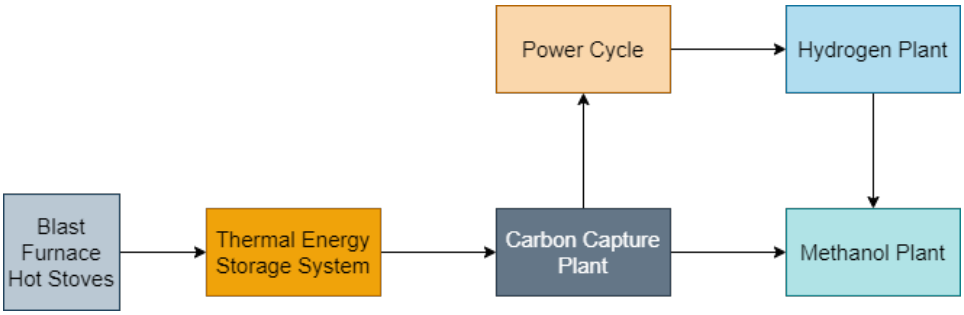

Fig. 1. General layout of the proposed plant.

The diagram represents an integrated energy system designed to enhance sustainability and efficiency by interconnecting various components. At its core, the system begins with the Blast Furnace Hot Stoves, which serve as a primary source of thermal energy. This energy is stored in a Thermal Energy Storage System, ensuring that excess heat can be utilized later to optimize energy use. The stored energy is then directed to a Power Cycle, which likely generates electricity or mechanical power, forming the central energy production hub of the system. A Carbon Capture Plant is integrated into the system to capture carbon dioxide emissions from the Power Cycle, reducing greenhouse gas emissions and promoting environmental sustainability. The captured carbon dioxide is then utilized by two downstream processes: a Hydrogen Plant and a Methanol Plant. The Hydrogen Plant likely uses carbon dioxide, along with other inputs, to produce hydrogen, a clean and versatile energy carrier. Simultaneously, the Methanol Plant synthesizes methanol, potentially using the captured carbon dioxide as a feedstock, contributing to the production of alternative fuels. This interconnected system demonstrates a closed-loop approach to energy production, carbon management, and fuel synthesis, aiming to minimize waste, reduce emissions, and promote the use of clean energy sources. By integrating thermal energy storage, carbon capture, and fuel production, the system exemplifies a forward-thinking approach to sustainable energy management [8].

3. RESULTS AND DISCUSSION

The operation of the integrated energy system depicted in the diagram yields several significant outcomes that highlight its efficiency and sustainability. By incorporating a Thermal Energy Storage System, the system effectively recovers waste heat from the Blast Furnace Hot Stoves, reducing energy losses and enhancing overall efficiency, potentially achieving energy savings of 20-30%. This stored thermal energy supports the Power Cycle, enabling stable and efficient electricity generation, with potential efficiencies reaching 50-60%, comparable to advanced combined cycle power plants. The integration of a Carbon Capture Plant further enhances the system's environmental performance by capturing 85-95% of CO_2 emissions, transforming a major pollutant into a valuable feedstock. This captured carbon dioxide is utilized downstream in the Hydrogen Plant and Methanol Plant, facilitating the production of clean hydrogen and methanol, which serve as alternative fuels and industrial feedstocks. These processes not only reduce the carbon footprint but also contribute to the circular economy by converting waste emissions into valuable products. Additionally, the system's modular design allows for scalability and integration with renewable energy sources, district heating networks, and other industrial processes, ensuring adaptability to future technological advancements and market demands. Collectively, the system exemplifies a forward-thinking approach to industrial decarbonization, achieving a balance between economic

viability, energy efficiency, and environmental sustainability.

4. CONCLUSIONS

In conclusion, this study demonstrates the significant potential of integrated energy systems in addressing contemporary industrial challenges related to energy efficiency, carbon emissions, and sustainable production. The innovative integration of Blast Furnace Hot Stoves with thermal energy storage, power generation, carbon capture, and chemical synthesis processes represents a paradigm shift in industrial process design. The results indicate that such integration can achieve substantial improvements in energy utilization while simultaneously reducing environmental impact through effective carbon capture and utilization. The system's ability to convert waste heat and captured CO_2 into valuable products, specifically hydrogen and methanol, exemplifies the practical implementation of circular economy principles in heavy industry. Furthermore, the modular nature of the system architecture ensures adaptability to future technological advances and varying industrial needs.

The findings of this study have significant implications for both industrial practitioners and policymakers. For industry, it provides a blueprint for sustainable process integration that can enhance operational efficiency while meeting increasingly stringent environmental regulations. For policymakers, it demonstrates the technical feasibility of industrial decarbonization without compromising economic viability. However, it is important to acknowledge that the successful implementation of such systems requires careful consideration of site-specific conditions, economic factors, and technological readiness levels.

Future research directions should focus on optimizing individual component efficiencies, exploring additional integration possibilities with renewable energy sources, and developing advanced control strategies for managing the complex interactions between system components. Additionally, detailed techno-economic analyses and life cycle assessments would provide valuable insights into the broader implications of implementing such systems at various scales. This study concludes that integrated energy systems represent a promising pathway toward sustainable industrial operations, though continued research and development efforts are essential to fully realize their potential.

REFERENCES

[1] Ozcan H, Kayabasi E. Thermodynamic and economic analysis of a synthetic fuel production plant via CO2 hydrogenation using waste heat from an iron-steel facility. Energy Convers Manag 2021;236:114074. https://doi.org/10.1016/j.enconman.2021.114074.
[2] Cormos AM, Dinca C, Petrescu L, Andreea Chisalita D, Szima S, Cormos CC. Carbon capture and utilisation technologies applied to energy conversion systems and other energy-intensive industrial applications. Fuel 2018;211:883–90. https://doi.org/10.1016/j.fuel.2017.09.104.
[3] Besevli B, Kayabasi E, Akroot A, Talal W, Alfaris A, Assaf YH, et al. Technoeconomic Analysis of Oxygen-Supported Combined Systems for Recovering Waste Heat in an Iron-Steel Facility 2024.
[4] Tozlu A. Techno-economic assessment of a synthetic fuel production facility by hydrogenation of CO2 captured from biogas. Int J Hydrogen Energy 2022;47:3306–15. https://doi.org/10.1016/j.ijhydene.2020.12.066.
[5] Miró L, Gasia J, Cabeza LF. Thermal energy storage (TES) for industrial waste heat (IWH) recovery : A review 2016;179:284–301. https://doi.org/10.1016/j.apenergy.2016.06.147.
[6] Akyavuz UD, Kayabasi E, Ozcan H. The effect of solar thermal energy storage on natural gas heating systems: An experimental and techno-economic investigation. Case Study Therm Eng 2024;63:105287. https://doi.org/10.1016/J.CSITE.2024.105287.
[7] Yosaf S, Ozcan H. Exergoeconomic investigation of flue gas driven ejector absorption power system integrated with PEM electrolyser for hydrogen generation. Energy 2018;163. https://doi.org/10.1016/j.energy.2018.08.033.
[8] Alsunousi M, Kayabasi E. Techno-economic assessment of a floating photovoltaic power plant assisted methanol production by hydrogenation of CO_2 captured from Zawiya oil refinery. Int J Hydrogen Energy 2024;57:589–600. https://doi.org/10.1016/j.ijhydene.2024.01.055.

ACTIVATED CHARCOAL FOR SUSTAINABLE SOLID STATE HYDROGEN STORAGE BY PHYSICAL ADSORPTION

*Ayca Capoglu and Ibrahim Dincer
[1] Clean Clean Energy Research Laboratory (CERL), Faculty of Engineering and Applied Science, Ontario Tech. University, 2000 Simcoe Street North, Oshawa, Ontario L1G 0C5, Canada

*Corresponding author e-mail: Ayca.Capoglu@ontariotechu.ca

ABSTRACT
A sectoral addiction on fossil fuels has resulted in significant energy crisis and causes greenhouse gases. Nowadays, renewable energy sources are a promising replacement for fossil fuels. Despite solar and wind energy, hydrogen is a promising energy carrier since it doesn't have limitations like place or time. In this research, solid state hydrogen storage tested with activated charcoal powder. Under a constant hydrogen flow of 2.0 L/min; 2.5 g, 3.5 g, and 5.5 g of activated charcoal were used in experiments for hydrogen storage in cylindrical cells. Results showed that the hydrogen storage was in the range of 1.95 to 4.05 wt%. Overall, considering the results it can be concluded that activated charcoal is a promising solid state energy storage material with its porous structure, surface area, and low cost.

Keywords: Hydrogen storage; Solid state storage; Activated charcoal; Renewable energy; Energy storage

1. INTRODUCTION
The number of concerns about climate change has increased over time due to energy production. Nowadays, new sustainable and green ways to produce energy have been placed such as hydrogen production. Although Hydrogen seems like a potential energy carrier for future generations, there are couple of things to consider such as storage techniques and applications. Cryogenic liquid storage systems and compressed gas tanks are the main basis for traditional hydrogen storage technologies. Although these techniques are widely used in industry, they provide some difficulties. Compressed gas storage, for example, needs high pressure around 700 bars, which causes safety issues. Liquid hydrogen storage is another way to store hydrogen. Although it's good for high-density storage, cryogenic storage requires extremely low temperatures (-253°C), hence increasing energy usage and equipment expenses [1]. Solid State hydrogen storage, on the other hand, is a promising way to store hydrogen safely [2].
In recent years, there has been an increase in the popularity of hydrogen storage in porous materials. Solid state hydrogen storage needs porous structure and extensive surface area materials, such as metal hydrides, complex hydrides, and carbon materials. These materials are a great choice for their capacity to storage physical hydrogen at reduced pressures and ambient temperatures. Carbon-based materials, including activated carbon, graphene, and carbon nanotubes, are promising materials for hydrogen storage applications due to their high surface area, tunable porosity, and chemical stability [3]. The substantial internal surface area of activated charcoal improved adsorption of hydrogen molecules, rendering it a suitable option for hydrogen storage applications.
In this regard, this study aims to hydrogen storage using activated charcoal as a sustainable and green storage material. The hydrogen storage capacity of activated charcoal is evaluated for different activated charcoal dosages (2.5, 3.5, and 5.5) by the analysis of mass differences in ambient conditions. Consequently, this study revaled that the utilization of carbon-based waste resources can be a promising option for hydrogen storage with waste minimization.

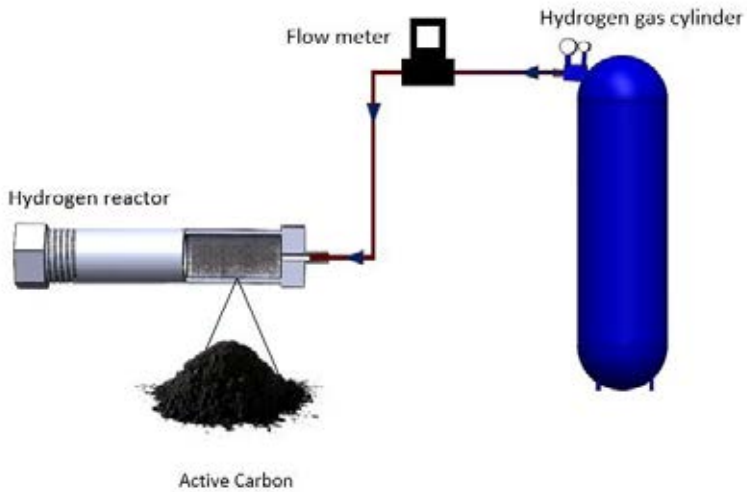

Fig. 1. Experimental setup for solid-state hydrogen storage using activated charcoal.

2. MATERIALS AND METHODS

In this paper, hydrogen storage capabilities of activated charcoal have been studied by changing the mass of the powder amount. The experimental set-up of the hydrogen storage system with its subsystems (hydrogen gas cylinder, flow meter and activated charcoal) is presented in Fig 1. Hydrogen gas has been fed into the reactor with the specified flow rate of 2.0 L/min and pressure of 400 kPa. The activated charcoal samples (2.5 g, 3.5 g, and 5.5 g) were placed into the reactor, and hydrogen gas was fed 3 times for 90 seconds for 1 h. All experiments are repeated for 3 times for each mass. Furthermore, the gravimetric analysis is used to measure the amount of stored hydrogen in activated charcoal with physosorbtion in wt%. Therefore, initial and final masses are recorded for each sample.

3. RESULTS AND DISCUSSION

The effect of activated charcoal dosage on hydrogen storage capacity is evaluated and presented in Fig. 2. As expected, the hydrogen storage capacity is increased with the increasing activated charcoal dosage. For instance, the activated charcoal dosage of 2.5 g had an average hydrogen storage efficiency of 1.95 wt%, while it was 2.85 wt% for 3.5 g and the 4.05 wt% for 5.5 g activated charcoal dosage. These results proved that the 5.5 g had the best storage rate. This indicates that the increase of mass can affect the physical hydrogen storage capacity positively most probably due to expanded surface area and improved gas diffusion.

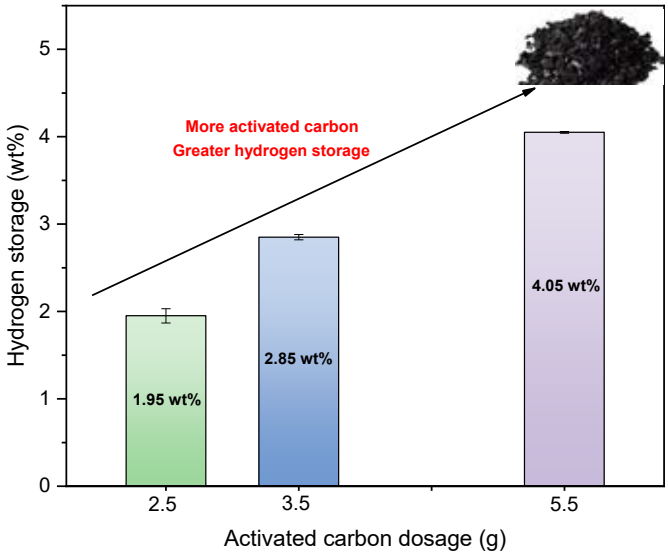

Fig. 2. Hydrogen storage capacity at different activated charcoal dosages.

Overall, these results showed that activated charcoal could be useful as an effective, affordable option for hydrogen storage applications. Future research will investigate the effects of extended exposure periods and metal-loadings on carbon-based materials to enhance storage performance.

4. CONCLUSIONS

This study experimentaly investigated the hydrogen storage performance of the activated charcoal as a sustainable material, considering waste minimization. Our results proved that activated charcoal has potential as a solid-state hydrogen storage material. The 5.5 g sample showed the highest hydrogen storage efficiency with an average of 4.05 wt%, exceeding the 2.5 and 3.5 g samples results. This indicates that the adsorption capacity of activated charcoal increases with increasing mass, likely because of an increased surface area and enhanced gas diffusion. Overall, these findings indicated that activated charcoal can serve as an efficient, economical alternative for hydrogen storage applications.

Acknowledgment

This publication was made possible by the NPRP grant (NPRP12S-0123-190011) from the Qatar National Research Fund (a member of Qatar Foundation). The findings achieved herein are solely the responsibility of the authors.

REFERENCES

1. Usman, M. R. (2022). Hydrogen storage methods: Review and current status. *Renewable and Sustainable Energy Reviews*, *167*, 112743.
2. Dincer, I., & Erdemir, D. (2023). *Introduction to energy systems*. John Wiley & Sons Inc.
3. Chen, Z., Kirlikovali, K. O., Idrees, K. B., Wasson, M. C., & Farha, O. K. (2022). Porous materials for hydrogen storage. *Chem*, *8*(3), 693-716.

HIGH-EFFICIENCY HYDROGEN STORAGE VIA POROUS GERMANENE NANOSTRUCTURES

[1]*Germán González*, [1]*Brandom J. Cid*, [1]*Marbella Calvino*, [2]*José E. Santana*, [1]*Fernando Salazar*, [1*]*Álvaro Miranda*
[1] Instituto Politécnico Nacional, ESIME Culhuacan, Av. Santa Ana 1000, Ciudad de México, 04440, México
[2] Instituto de Física, Universidad Nacional Autónoma de México, 04510, Ciudad de México, México

*Corresponding author e-mail: amirandad@ipn.mx

ABSTRACT

The growing demand for efficient hydrogen storage solutions to reduce the reliance on fossil fuels has sparked considerable interest in nanostructured materials. This study explored the hydrogen storage potential of lithium-decorated porous germanene using first-principles density functional theory (DFT) calculations. Through an analysis of the adsorption sites, binding energies, and charge transfers, the optimal Li-decorated configurations for enhanced hydrogen adsorption were identified. Results show that porous germanene functionalized with six lithium atoms (three above and three below the monolayer) achieves exceptional stability with adsorption energy of 2.39 eV and minimal structural distortion. The maximum hydrogen adsorption capacity of the three H_2 molecules per Li atom was observed with favorable adsorption energies (0.214–0.280 eV) and charge transfer values (0.710–1.113 |*e*|). This study highlights the potential of Li-decorated porous germanene for advanced hydrogen storage applications.

Keywords: Germanene, 2D materials, Hydrogen storage, Energy storage, Porous

1. INTRODUCTION

The emission of greenhouse gases such as carbon dioxide (CO_2) and nitrogen oxides (NO_X) during combustion makes fossil fuels the major contributor to environmental pollution and climate change [1,2]. Therefore, the development and study of cleaner energy sources are critical issues for the scientific community. Thus, hydrogen is a promising alternative as a clean and efficient energy source, and its use in fuel cells produces only water as a by-product [3]. However, its low density and high volatility make its practical use difficult, making its storage and transportation a great challenge.[4].
Nanostructured materials have shown great potential for addressing these challenges and offering efficient and safe hydrogen storage solutions. For instance, porous nanomaterials, carbon nanotubes, and two-dimensional (2D) materials exhibit enhanced interactions with hydrogen, making them ideal candidates for energy-storage applications [5-7]. Among these, porous materials are particularly promising owing to their high specific surface area, which can improve the adsorption and desorption of hydrogen, thereby enhancing the storage capacity and efficiency [8]. Moreover, two-dimensional (2D) materials such as graphene have attracted significant attention for hydrogen storage owing to their exceptional electronic properties, flexibility, and high surface area [9]. Particularly, germanene, a single layer of germanium atoms arranged in a honeycomb lattice, has recently emerged as a promising candidate for energy-storage applications [10]. However, despite its potential, the application of porous germanene in hydrogen storage remains largely unexplored.
In this study, we investigated the hydrogen storage capabilities of Li-decorated porous germanene using theoretical calculations. Specifically, we explored double-sided Li-porous germanene adsorption schemes to evaluate their hydrogen storage performances. Our findings not only provide a deeper understanding of the storage properties of Li-porous germanene but also offer valuable insights for the experimental development of porous 2D nanomaterials for hydrogen storage applications.

2. COMPUTATIONAL METHOD

In this study, all calculations were performed using the spin-polarized first-principles method within the framework of Density Functional Theory (DFT) [11, 12], as implemented in the SIESTA code [13, 14]. For exchange and correlation interactions, the Perdew–Burke–Ernzerhof (PBE) functional in the generalized gradient approximation (GGA) was employed [15]. Additionally, the structures of the studied systems were relaxed until the forces between the atoms reached < 0.01 eV/Å. Furthermore, the Brillouin zone was sampled using 4 × 4 × 1 and 24 × 24 × 1 Monkhorst-Pack k-point meshes [16] for geometry relaxation and electronic property calculations, respectively. To account for van der Waals interactions, long-range Grimme DFT-D2 dispersion corrections [17] were applied with double-ζ polarized basis sets alongside norm-conserving Troullier–Martins pseudopotentials [18, 19]. Subsequently, the Hirshfeld population analysis [20] was used. To ensure accuracy, the basis set superposition error (Δ_{BSSE}) was addressed using the counterpoise method [21]. Finally, the VESTA program [22] was used to visualize the electron densities and optimized geometric structures.
The binding energy (E_B) was calculated using the following equation [7]:

$$E_B = -E_{Li-PGermanene} + E_{Li} + E_{PGermanene} + \Delta_{BSSE} \quad (1)$$

where $E_{Li-PGermanene}$ is the total energy of the Li-decorated porous germanene unit cell, E_{Li} is the total energy of an

isolated Li atom, $E_{\mathrm{PGermanene}}$ is the total energy of the porous germanene, and Δ_{BSSE} is the basis set superposition error. Similarly, the adsorption energy (E_{A}) per hydrogen molecule is given by [7]

$$E_{\mathrm{A}} = \left[-E_{\mathrm{H_2-Li-PGermanene}} + nE_{\mathrm{H_2}} + E_{\mathrm{Li-PGermanene}} + \Delta_{\mathrm{BSSE}} \right] / n \quad (2)$$

where $E_{\mathrm{H_2-Li-PGermanene}}$ is the total system energy including the H_2 molecules adsorbed on the Li-decorated porous germanene, $E_{\mathrm{H_2}}$ is the total energy of an isolated hydrogen molecule, $E_{\mathrm{Li-PGermanene}}$ is the total energy of the Li-decorated porous germanene, and *n* is the total number of adsorbed hydrogen molecules. A positive sign of E_{A} indicates that the system is stable, where a larger value indicates stronger adsorption of H_2 molecules on the Li-decorated porous germanene.

3. RESULTS AND DISCUSSION

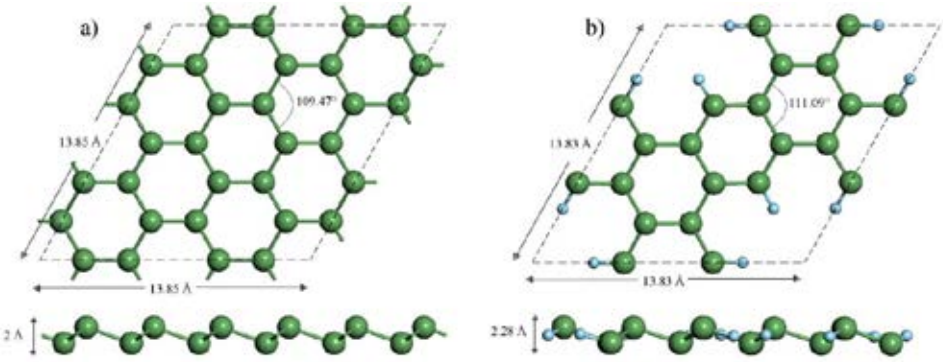

Fig. 1. Top and side view of a) pristine germanene and b) porous germanene.

As shown in the optimized structures of pristine germanene (Fig. 1a) and porous germanene (Fig. 1b), the inclusion of pores reduces the unit cell lattice size from 13.85 Å to 13.83 Å. Specifically, this structural modification introduces minor deformations in the framework of the material. Additionally, the surface roughness increases from 2.0 Å to 2.28 Å, indicating that porosity alters both the geometric and surface properties of germanene.

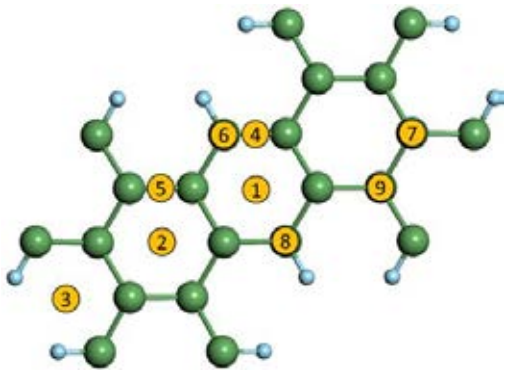

Fig. 2. All possible adsorption sites (1-9) for a Li atom onto porous germanene.

Table 1. Binding energy (E_B) and charger transfer (Q_H) values for nine proposed adsorption sites for one Li atom in porous germanene.

Initial Site	Final Site	E_B (eV)	Q_H (|e|)
1	1	2.1984	0.227
2	2	2.0544	0.219
3	3	2.3303	0.258
4	9	1.9172	0.299
5	9	1.9174	0.302
6	1	2.1978	0.232
7	1	2.1959	0.361
8	3	2.3299	0.248
9	9	2.3302	0.306

Based on the geometric arrangement of the unit cell depicted in Fig. 1b, nine potential adsorption sites (Fig. 2) were identified to determine the optimal locations for monolayer functionalization. Moreover, to analyze the best adsorption site, a Li atom was adsorbed at each site, and E_B and Hirshfeld charge transfer (Q_H) were calculated and are shown in Table 1. The binding energy (E_B) varied across the nine proposed adsorption sites for Li atoms in the porous germanene. Notably, site 3 exhibited the highest E_B value (2.33 eV, accompanied by a charge transfer (Q_H) of 0.258 |*e*|. In comparison, sites 1 and 9 show slightly lower E_B values of 2.20 eV and 2.33 eV, respectively. Based on these results, site 3 (Fig. 2) was selected as the optimal reference for Li incorporation, with Li atoms occupying equivalent positions within the unit cell to maximize stability and adsorption efficiency.

Table 2. Adsorption energy (E_A), average Ge–Li distance (β), and charge transfer (Q_H) for the porous germanene decorated with Li atoms, from 1 up to 6 Li atoms.

Metal adatom	*n*Li	E_A (eV)	β(Å)	Q_H (|e|)
Li	1	2.330	2.764	0.258
	2	2.270	2.791	0.277
	4	2.328	2.813	0.264
	6	2.390	2.788	0.252

Following the selection of the optimal adsorption site, Li atoms were systematically introduced into the identified positions to ensure uniform decoration and maximize the stability of the Li-functionalized porous germanene framework. The configuration of porous germanene functionalized with six Li atoms was selected as optimal because it exhibited the highest E_A (2.39 eV) among the tested systems (Table 2). Notably, this value surpasses those observed for lower Li-loading configurations, indicating enhanced stability of the Li-decorated framework at higher Li coverage. Furthermore, the average Ge–Li bond distance (β=2.78 Å) remains consistent across Li addition, suggesting minimal structural distortion despite increased Li incorporation. Interestingly, the charge transfer (Q_H=0.252 |*e*|) decreased slightly compared with configurations with fewer Li atoms (e.g., Q_H=0.258e for one Li atom), implying a saturation effect in electron donation from Li to the germanene substrate. These results collectively highlight that the 6 Li-atom configuration balances strong binding, structural integrity, and sufficient charge redistribution for its use in energy storage applications.

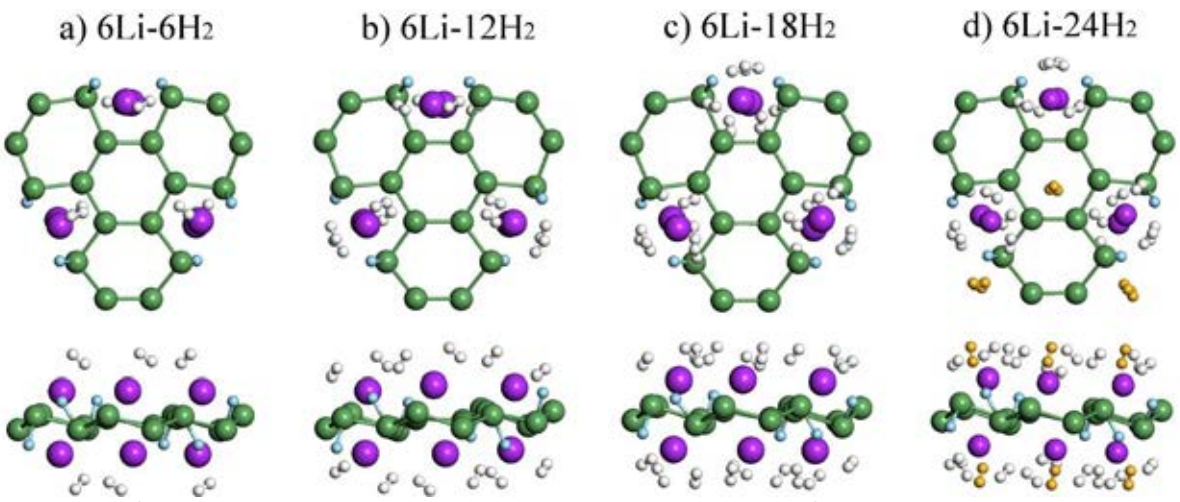

Fig. 3. Top view of the optimized porous germanene with double-sided adsorption of hydrogen molecules per Li atom. The H_2 molecules marked in yellow did not adsorb on Li atom.

Building on Li-decorated porous germanene with six Li atoms (three above and three below the monolayer), hydrogen adsorption was systematically modeled by incrementally adding 1 to 4 H_2 molecules per Li atom (Fig. 3). As shown in Table 3, E_A decreased progressively from 0.280 eV (1 H_2/Li) to 0.196 eV (4 H_2/Li), indicating reduced stability with higher H_2 loading. Notably, at 3 H_2 molecules per Li atom, the system achieved optimal adsorption parameters: E_A=0.214 eV, Q_H = 1.096 |*e*|, and average H_2–Li distance (β) of 2.03 Å. However, when a fourth H_2 molecule is introduced (Fig. 3d, highlighted in yellow), one molecule displaces with a value of β=2.57 Å, leaving only 3 molecules adsorbed per Li atom. This saturation limit aligns with the weak E_A (0.196 eV) observed in Table 3, suggesting that 3 H_2/Li represents the maximum capacity before destabilization occurs.

Table 3. Adsorption energy (E_A), charge transfer (Q_H), and average H_2–Li distance (β) in porous germanene decorated with Li atoms.

nH_2 per Li atom	E_A (eV)	Q_H (|e|)	β(Å)
1	0.280	0.710	1.96
2	0.237	0.964	2.00
3	0.214	1.096	2.03
4	0.196	1.113	2.57

4. CONCLUSIONS

This study examined the hydrogen storage capabilities of Li-decorated porous germanene using DFT calculations. The introduction of pores into the germanene structure reduces the lattice parameters and increases the surface roughness, thereby improving its adsorption properties. The optimal lithium adsorption site, Site 3, demonstrates a binding energy of 2.33 eV, with the configuration of six lithium atoms (three above and three below the monolayer) showing superior stability and consistent Ge–Li bond distances (~2.78 Å). The system can adsorb up to three hydrogen molecules per lithium atom, with stable adsorption energies ranging from 0.214 to 0.280 eV and hydrogen-lithium distances of approximately 2.03 Å. The fourth hydrogen molecule causes displacement, indicating the saturation limit of the system. Progressive charge transfer, ranging from 0.710 to 1.113 e, highlights the role of electron donation in stabilizing the hydrogen interactions. These findings suggest that Li-decorated porous germanene holds significant promise as a high-capacity material for hydrogen storage, offering key insights for future development in this field.

ACKNOWLEDGEMENT

This research was supported by UNAM-PAPIIT IN102923. Numerical calculations were performed using the Miztli supercomputer of the DGTIC-UNAM (project LANCAD-UNAM-DGTIC-180). J.E.S. acknowledges his postdoctoral scholarship from the UNAM Postdoctoral Program (POSDOC). G.R. and B.J.C acknowledge support from SECIHTI and BEIFI-IPN. We thank Luis A. Pérez for critically reading our manuscript.

REFERENCES

1. Lammel G and Graßl H. 1995. Greenhouse effect of NOX. Environmental Science and Pollution Research 2:40–45.
2. Montzka S, Dlugokencky E and Butler J. 2011. Non-CO2 greenhouse gases and climate change. Nature 476:43–50.
3. Stern AG. 2018. A new sustainable hydrogen clean energy paradigm. International Journal of Hydrogen Energy 43:4244–4255.
4. Singla MK, Nijhawan P and Oberoi AS. 2021. Hydrogen fuel and fuel cell technology for cleaner future: a review. Environmental Science and Pollution Research 28:15607–15626.
5. González I, et al. 2020. Theoretical modelling of porous silicon decorated with metal atoms for hydrogen storage. International Journal of Hydrogen Energy 45:26321–26333.
6. Zhang X, Cao D and Chen J. 2003. Hydrogen adsorption storage on single-walled carbon nanotube arrays by a combination of classical potential and density functional theory. The Journal of Physical Chemistry B 107:4942–4950.
7. Sosa AN, et al. 2021. Light metal functionalized two-dimensional siligene for high capacity hydrogen storage: DFT study. International Journal of Hydrogen Energy 46:29348–29360.
8. Chen Z, et al. 2022. Porous materials for hydrogen storage. Chem 8:693–716.
9. Momeni K, Ji Y, Wang Y, et al. 2020. Multiscale computational understanding and growth of 2D materials: a review. npj Computational Materials 6:22.
10. Sosa AN, et al. 2023. A DFT investigation: high-capacity hydrogen storage in metal-decorated doped germanene. Journal of Energy Storage 73:108913.
11. Hohenberg P and Kohn W. 1964. Inhomogeneous electron gas. Physical Review 136:B864 .
12. Kohn W and Sham LJ. 1965. Self-consistent equations including exchange and correlation effects. Physical Review 140:A1133 .
13. Artacho E, et al. 2008. The SIESTA method; developments and applicability. Journal of Physics: Condensed Matter 20:064208.
14. Soler JM, et al. 2002. The SIESTA method for ab initio order-N materials simulation. Journal of Physics: Condensed Matter 14:2745.
15. Perdew JP, Burke K and Ernzerhof M. 1996. Generalized gradient approximation made simple. Physical Review Letters 77:3865.
16. Monkhorst HJ and Pack JD. 1976. Special points for Brillouin-zone integrations. Physical Review B 13:5188.
17. Grimme S. 2006. Semiempirical GGA-type density functional constructed with a long-range dispersion correction. Journal of Computational Chemistry 27:1787–1799.
18. Junquera J, et al. 2001. Numerical atomic orbitals for linear-scaling calculations. Physical Review B 64:235111.
19. Troullier N and Martins JL. 1991. Efficient pseudopotentials for plane-wave calculations. Physical Review B 43:1993.
20. Hirshfeld FL. 1977. Bonded-atom fragments for describing molecular charge densities. Theoretica Chimica Acta 44:129–138.
21. Galano A and Alvarez-Idaboy JR. 2006. A new approach to counterpoise correction to BSSE. Journal of Computational Chemistry 27:1203–1210.
22. Momma K and Izumi F. 2011. VESTA 3 for three-dimensional visualization of crystal, volumetric and morphology data. Applied Crystallography 44:1272–1276.

THERMODYNAMICS ASSESSMENT OF A NEW THREE-STEP CYCLE FOR METHANE TO METHANOL AND HYDROGEN PRODUCTION

[1]Vinay Yadav, Ieeba Khan[1],[1*]Farrukh Khalid
[1]School of Energy Science and Engineering, Indian Institute of Technology, Guwahati, India-781039

*Corresponding author e-mail: f.khalid@iitg.ac.in

ABSTRACT

Methane, the major component of natural gas, shale gas, and combustible ice, is widely spread throughout nature. Direct conversion and efficient methane usage have emerged as a major research topic. However, two fundamental hurdles remain: activating methane and avoiding overoxidation. Recently, research in this sector has reached a critical point. This paper proposes a novel three-step cycle for direct methane to methanol conversion at comparatively lower temperatures than conventional technologies. Furthermore, based on the proposed cycle, this article reports the thermodynamic assessment of a three-step electro-thermochemical process for methane to methanol conversion. The analysis concluded that the energy and exergy efficiencies of the proposed system are 24.1-24.3% and 29.2-29.4%, respectively.

1. INTRODUCTION

Methane is abundant on earth, serving as a primary energy source and a significant element in a variety of businesses. However, it is the second-largest contributor to greenhouse gas emissions after carbon dioxide and hence plays an important role in global warming [1]. Converting methane into useful products or cleaner energy is critical for a sustainable future. Currently, two large-scale methods- methane-to-gasoline and Fischer-Tropsch synthesis-are used to produce methanol or liquid fuels from methane. However, both require a high-energy step known as steam reforming, which converts methane into synthesis gas (a mixture of carbon monoxide and hydrogen) before converting it into the desired chemicals. Methanol is an essential commodity with numerous applications, including use as a solvent in chemical industries as a fuel in the energy sector. Methanol, sometimes known as clean coal has a high-octane value of 113, making it acceptable as a fuel or gasoline additive. The need for methanol is rising, particularly in the automotive industry. The global methanol market was valued at $30.9 billion in 2023, and it is predicted to increase at a 4.2% annual pace to $38.0 billion by 2028 [2].

At present, about 90% of methanol is manufactured by converting various carbon sources into syngas, which needs extremely high temperatures (800-1000 °C). In the following step, syngas is converted to methanol at a lower temperature. This process requires a lot of energy, rapid temperature fluctuation, several processes, and a lot of carbon waste, stressing the need for a simpler and more efficient solution [3]. Direct methane to methanol conversion (DMTM) is a viable option with numerous benefits. It simplifies the process and lowers the total cost of commercial methanol production. DMTM uses an effective catalyst, which reduces temperature, prevents catalyst damage, and saves energy. Additionally, it reduces carbon waste and CO_2 emissions, making it more environmentally friendly and sustainable. However, directly converting methane to methanol is difficult. Methane is an extremely stable molecule with strong C-H bonds (438.8 kJ/mol), which makes it difficult to break. Furthermore, because methanol is more reactive than methane, controlling its overoxidation into undesirable products such as formaldehyde or formic acid remains a significant issue in DMTM conversion [4]. This study analyses and reports the thermodynamic assessment of a novel three-step cycle for direct methane to methanol production.

2. METHODOLOGY

The reactions involved in the three-step cycle are shown in Table 1. The data, such as enthalpy and change in Gibbs free energy of reactions, is obtained from HSC 10.5.3.0 chemistry software. Based on the values provided by HSC chemistry, the energy and exergy efficiencies of the proposed cycle are evaluated using equations 1 and 2, respectively. The energy and exergy required for the cycle are calculated based on the electricity required for the electrolysis process. It is assumed that the electricity is drawn from solar PV with an efficiency of around 20%.

$$\eta_{STF,\ energy} = \frac{(n_{CH_3OH} \times LHV_{CH_3OH}) + (n_{H_2} \times LHV_{H_2})}{(n_{CH_4} \times LHV_{CH_4}) + Electricity\ required} \quad (1)$$

$$\eta_{STF,\ exergy} = \frac{(n_{CH_3OH} \times ex_{CH_3OH}) + (n_{H_2} \times ex_{H_2})}{(n_{CH_4} \times ex_{CH_4}) + Electricity\ required} \quad (2)$$

Table 1. Reaction involved in the three-step cycle

Step 1 (CH_4 Bromination)	$CH_4(g) + 2H_2O(g) + 4Br_2(g) \xrightarrow{200-250\,°C} 8HBr(g) + CO_2(g)$ ΔH<0
Step 2 (Electrolysis)	$8HBr(g) \xrightarrow{200-250\,°C} 4H_2(g) + 4Br_2(g)$ ΔG>0
Step 3 (CO_2 Hydrogenation)	$CO_2(g) + 3H_2(g) \xrightarrow{200-250\,°C} CH_3OH(g) + H_2(g)$ ΔH<0
Overall	$CH_4(g) + H_2O(g) \rightarrow CH_3OH(g) + H_2(g)$

3. RESULTS AND DISCUSSION

The analysis shows that both energy and exergy efficiencies decrease with an increase in temperature. This is because the electricity required for step 2 is more at higher temperatures. The maximum energy and exergy efficiencies are found to be 24.3% and 29.4%, respectively, at 200 °C. Furthermore, the variation of energy and exergy efficiencies with different operating temperatures has been depicted in Fig. 1. Additionally, some key parameters have been found and shown in Table 2.

Table 2. Key parameters found after the analysis

Parameter	Values
Solar to fuel energy efficiency (%)	24.1-24.3
Solar to fuel exergy efficiency (%)	29.2-29.4
Temperature of the cycle (°C)	200-250
Operating voltage of the electrolyser (V)	0.7

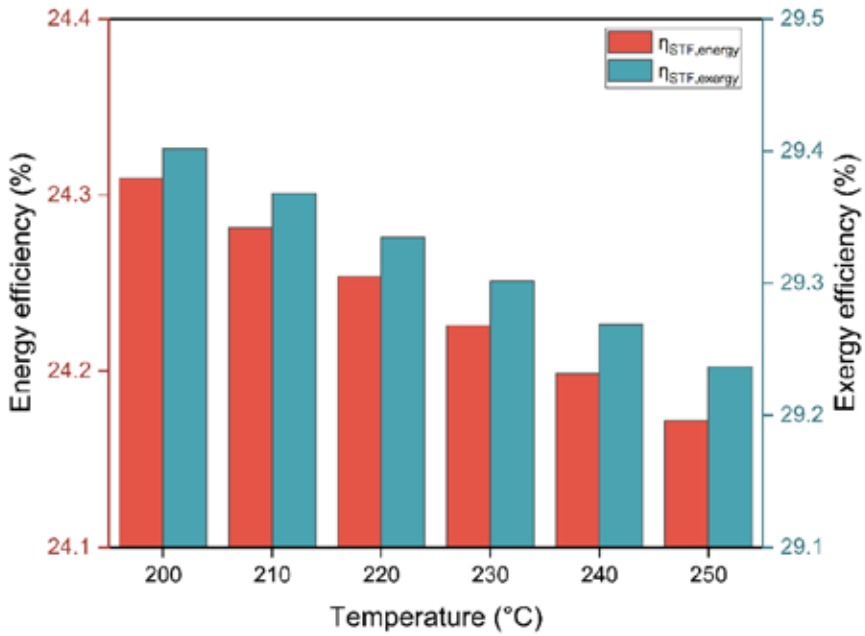

Fig. 1. Variation of energy and exergy efficiencies with different temperatures of cycle.

4. CONCLUSIONS

In this study, a novel method for producing methanol and hydrogen using methane and water as feedstock based on the three-step cycle is proposed and analysed. After doing the thermodynamic analysis, the maximum energy and exergy efficiencies of the mentioned cycle are calculated as 24.3% and 29.4%, respectively. This study can be utilised as an alternative way for producing methanol at lower temperatures and lead to the opening of new avenues for methanol production. The result shows that the proposed cycle can be efficiently integrated with renewable energy sources like concentrated solar power, waste heat, and nuclear reactors.

NOMENCLATURE

ΔG	Change in Gibbs free energy, kJ
ΔH	Change in enthalpy, kJ
ex	Specific exergy, kJ/mol
LHV	Lower heating value, kJ/mol
n	Number of moles
STF	Solar to fuel
η	Efficiency, %

REFERENCES

[1] Rocher-Ros G, Stanley EH, Loken LC, Casson NJ, Raymond PA, Liu S, et al. Global methane emissions from rivers and streams. Nature 2023;621. https://doi.org/10.1038/s41586-023-06344-6.

[2] Alvarez-Galvan MC, Mota N, Ojeda M, Rojas S, Navarro RM, Fierro JLG. Direct methane conversion routes to chemicals and fuels. Catal Today, vol. 171, 2011. https://doi.org/10.1016/j.cattod.2011.02.028.

[3] Garcia G, Arriola E, Chen WH, De Luna MD. A comprehensive review of hydrogen production from methanol thermochemical conversion for sustainability. Energy 2021;217. https://doi.org/10.1016/j.energy.2020.119384.

[4] Rajeev Anjana. Direct Methane to Methanol Conversion: An Overview of Non-Syn Gas Catalytic Strategies. The Chemical Record 2025;25. https://doi.org/10.1002/tcr.202400186

THERMODYNAMIC EVALUATION OF HYBRID THERMOCHEMICAL PROCESS FOR LIGNIN TO HYDROGEN AND METHANE CONVERSION

[1*]Shailendra Yadav, [1]Farrukh Khalid
[1]School of Energy Science and Engineering, Indian Institute of Technology, Guwahati, India-781039

*Corresponding author e-mail: y.shailendra@iitg.ac.in

ABSTRACT

A sustainable future depends on switching from fossil fuels to renewable, carbon-neutral, or decarbonized fuels. Fuels made from biomass are becoming more widely acknowledged for their ability to cut carbon emissions, pollutants, and particulates. There are numerous ways to produce value-added products using biomass through different techniques such as pyrolysis, hydrothermal liquefication, and molten salt electrolysis, etc. This study reports the energy efficiency and exergy efficiency of a novel method for hydrogen (H_2) and methane (CH_4) production using lignin through molten salt electrolysis. The analysis has been done for two different electrolysis parameters, i.e. temperature and current supplied during the electrolysis. The electrolysis temperature varies between 280 to 340°C, and the current supplied during the electrolysis ranges from 0.1 to 0.4 A. After doing the thermodynamic analysis, it has been reported that the total energy efficiency and total exergy efficiency of the mentioned method increases with increases in the current supplied. The highest total energy and exergy efficiencies of 11.2% and 11.3% have been achieved at 0.4 A current supplied.

Keywords: Lignin, Hydrogen, Methane, Molten salt electrolysis, Energy efficiency, Exergy efficiency

1. INTRODUCTION

The world's population grows, and so does the use of fossil fuels, leading to increased anthropogenic greenhouse gas emissions and global warming. Environmental problems, energy crises, and resource depletion arise from scoring 2015 World Energy Statistical Review [1]. These reserves account for around 85% of the total energy demand, and a sustainable solution is a pressing issue [2]. Scientists are researching new environmentally friendly renewable fuel sources to replace fossile fuels. Hydrogen, methane, and biodiesel represent the most potential renewable energy sources [3]. Biomass, a renewable resource, has significant application potential due to its high yields. India has the second-largest agricultural biomass supply, with an estimated 990 million metric tonnes (MMT) available yearly. India creates around 160,038.9 tons of municipal solid trash per day, providing a significant source of biomass [4]. Biomass conversion processes, including hydrothermal liquification, gasification, and pyrolysis, are energy-intensive and have limited selectivity, efficiency, and environmental sustainability [5]. The most popular method for creating hydrogen is based on natural gas or other fossil fuels, which require a lot of energy and a significant amount of carbon dioxide into the environment [6]. Innovative technology, such as biomass to hydrogen conversion, is necessary to accelerate the energy transition. Hydrogen can be produced from biomass using various biological, electrochemical, thermochemical, and hybrid processes. Utilizing biomass energy, which is regarded as a green source with nearly negligible carbon emission, is an alternative to getting hydrogen.
This paper explores an innovative approach that utilizes a thermo-electrochemical process for sustainable value-added products using lignin. H_2 and CH_4 are produced by the molten salt electrolysis of lignin at high temperatures. Furthermore, the analysis of the findings indicates the energy and exergy efficiencies of the proposed method.

2. SYSTEM DESCRIPTION AND ANALYSIS

This work evaluates the thermodynamics of a novel method for producing hydrogen and methane from lignin using molten salt electrolysis, as reported in [7]. They utilise 1 g of lignin with 17 g NaOH and 13 g KOH for performing the experiments. The analysis is done based on the different reaction temperatures and currents supplied during the electrolysis. The electrolysis temperature varies between 280 to 340°C with the step of 20°C while the current ranges between 0.1 and 0.4 A with the step of 0.1 A. Applying an electric current at a specific temperature facilitated the electrochemical reaction, producing hydrogen (H_2) and methane (CH_4), as shown in Figure 1. The heat and electricity required for the electrochemical reaction are calculated using equations 1 and 2, respectively. The energy efficiency and exergy efficiency of the method are evaluated using equations 3 and 4 based on the current supplied. Table 1 shows the amount of H_2 and CH_4 produced during the process, based on the data from [7].

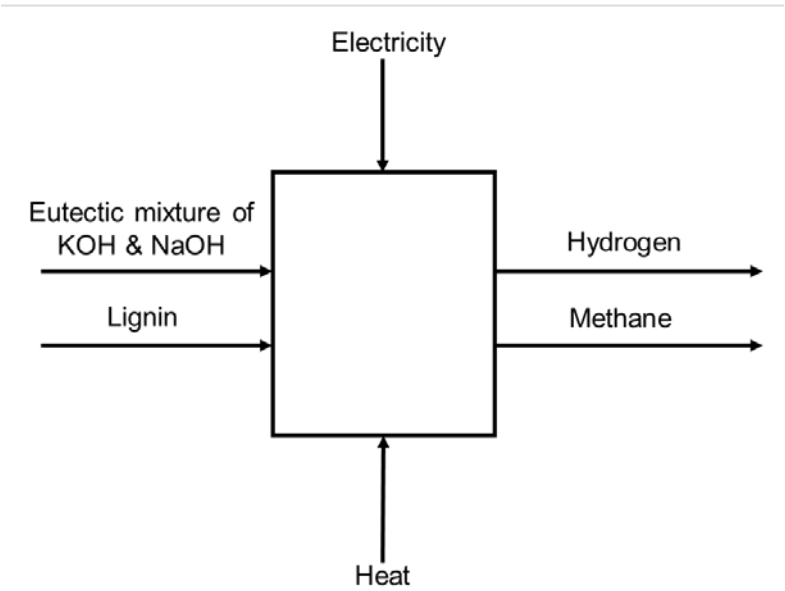

Fig. 1. Schematic diagram of high-temperature electrolysis process for lignin conversion

$$Q_{heat} = m_{Lignin} \times C_p \times \triangle T \quad (1)$$

$$W_{electricity} = I \times V \times t \quad (2)$$

$$\eta_{total\ energy} = \frac{(m_{H_2} \times LHV_{H_2}) + (m_{CH_4} \times LHV_{CH_4})}{(m_{Lignin} \times LHV_{Lignin}) + Q_{heat} + W_{electricity}} \quad (3)$$

$$\eta_{total\ exergy} = \frac{(m_{H_2} \times ex_{H_2}) + (m_{CH_4} \times ex_{CH_4})}{(m_{Lignin} \times ex_{Lignin}) + Q_{heat}\left(1 - \frac{T_0}{T_{reaction}}\right) + W_{electricity}} \quad (4)$$

where m is the mass (kg), C_p is the specific heat capacity of lignin (J/kg.K), $\triangle T$ is the temperature difference, I is the current supplied (A), V is the voltage supplied (V), t is the electrolysis time (sec), LHV is the lower heating value (J/kg), ex is specific exergy (J/kg), T_0 is the ambient temperature, and $T_{reaction}$ is the reaction temperature.

Table 1. Correlation between current (A) Hydrogen and Methane production

Current (A)	Hydrogen (mL)	Methane (mL)
0.1	67.5	13
0.2	145	14
0.3	196	14
0.4	247	14.5

3. RESULTS AND DISCUSSION

According to the investigation results, the total energy and exergy efficiencies of the mentioned method increase with increases in the current. This is because at higher currents, losses are less, resulting in improved energy and exergy efficiencies. The maximum total energy and exergy efficiency of 11.2% and 11.3% have been achieved at 0.4 A of the current supply. The energy efficiency and exergy efficiency of the current system details are illustrated in Figure 2. Furthermore, some key parameters have been calculated and reported in table 2.

Table 2. Key parameters found after the analysis

Parameter	Values
Energy efficiency of the overall process (%)	4.3-11.2
Exergy efficiency of the overall process (%)	4.4-11.3
Temperature of the process (°C)	280-340
Operating voltage of the process (V)	1 V

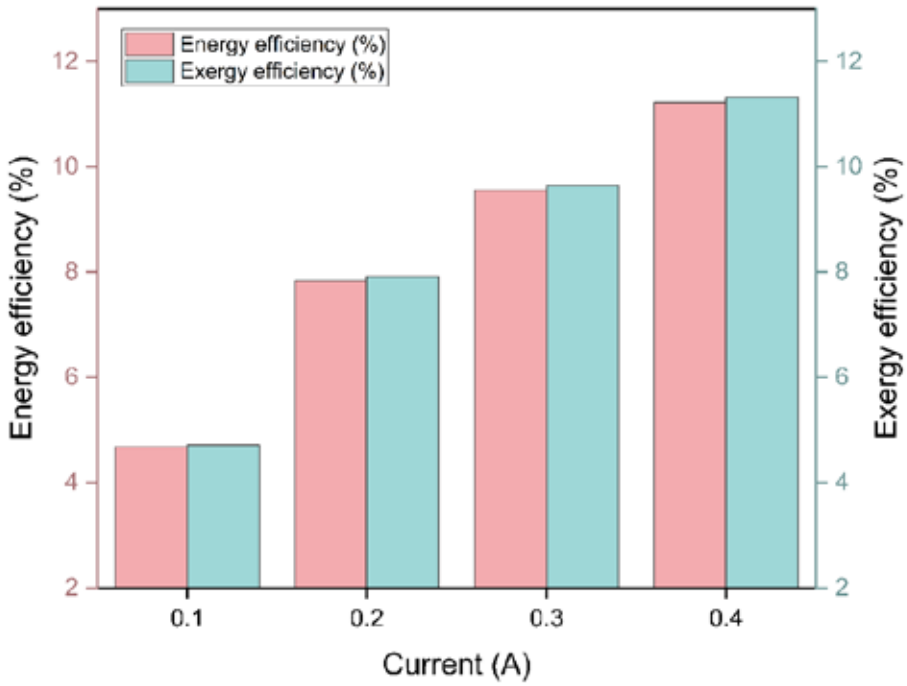

Fig. 2. Energy efficiency and exergy efficiencies variation with current

4. CONCLUSIONS

The need to produce carbon-neutral and renewable resources-based products is increasing. In this regard, biomass, which is cheap and abundant, can be the primary raw material that satisfies these requirements. It is comparatively less expensive in terms of energy. Using lignin and a thermo-electrochemical process, this study offers a novel concept for sustainable hydrogen and methane production. The result shows that the highest total energy and exergy efficiencies of 11.2% and 11.3% were achieved at 0.4 current supplied.

NOMENCLATURE

C_P	Specific heat capacity, J/kg.K
ex	Specific exergy, J/kg
LHV	Lower heating value, J/kg
m	Mass, kg
Q_{heat}	Heat required, J
$W_{electricity}$	Electricity required, J
η	Efficiency, %

REFERENCES

[1] Y. Zhang, L. Li, P. Xu, B. Liu, Y. Shuai, and B. Li, “Hydrogen production through biomass gasification in supercritical water: A review from exergy aspect,” *Int J Hydrogen Energy*, vol. 44, no. 30, 2019, doi: 10.1016/j.ijhydene.2019.01.151.
[2] H. Ishaq and I. Dincer, “Comparative assessment of renewable energy-based hydrogen production methods,” *Renewable and Sustainable Energy Reviews*, vol. 135, 2021, doi: 10.1016/j.rser.2020.110192.

[3] A. Kumar and S. N. Reddy, “Subcritical and supercritical water in-situ gasification of metal (Ni/Ru/Fe) impregnated banana pseudo-stem for hydrogen rich fuel gas mixture,” *Int J Hydrogen Energy*, vol. 45, no. 36, 2020, doi: 10.1016/j.ijhydene.2019.08.009.
[4] H. Negi, D. C. Suyal, R. Soni, K. Giri, and R. Goel, “Indian Scenario of Biomass Availability and Its Bioenergy-Conversion Potential,” 2023. doi: 10.3390/en16155805.
[5] M. I. Taipabu, K. Viswanathan, W. Wu, N. Hattu, and A. E. Atabani, “A critical review of the hydrogen production from biomass-based feedstocks: Challenge, solution, and future prospect,” 2022. doi: 10.1016/j.psep.2022.06.006.
[6] B. S. Huang, H. Y. Chen, K. H. Chuang, R. X. Yang, and M. Y. Wey, “Hydrogen production by biomass gasification in a fluidized-bed reactor promoted by an Fe/CaO catalyst,” *Int J Hydrogen Energy*, vol. 37, no. 8, 2012, doi: 10.1016/j.ijhydene.2012.01.071.
[7] W. J. Z. L. W. B. J. H. R. M. Yan Chao, “Method for electrolyzing lignin at high temperature in solar STEP process,” 2020

HIGH VOLTAGE GAIN LLC RESONANT CONVERTER DESIGN FOR ENERGY TRANSFER FROM FUEL CELL ELECTRIC VEHICLE TO ELECTRIC VEHICLE

[1*]*Murat AKKUS*, [2]*Erdem AKBOY*, [3]*Ali Rifat BOYNUEGRI*
[1,2,3] Yildiz Technical University, Faculty of Electrical and Electronics, Electrical Engineering, Davutpasa, Istanbul, 34220, Turkey

*Corresponding author e-mail: makkus@yildiz.edu.tr

ABSTRACT
The transition to sustainable energy solutions is a key requirement in the fight against climate change, while the transport sector is a major source of global carbon emissions. Fuel Cell Electric Vehicles (FCEVs) offer a promising alternative to reduce dependence on fossil fuels, but one of the technical barriers to their widespread deployment is the low output voltage of Proton Exchange Membrane (PEM) fuel cells. This paper presents the design of a high voltage gain LLC resonant converter to overcome the mismatch between the output voltage of a 160 kW PEM fuel cell and electric vehicle (EV) batteries. The converter is optimised to stabilise the variable output voltage of the fuel cell (between 227 V and 310 V) at 300-400 V DC and is designed to operate with high efficiency at a switching frequency of 100 kHz. Simulations were carried out using PLECS software and the results show that the converter provides high efficiency, stability and safe operation while meeting the isolation requirement. This study provides valuable insights into the integration of PEM fuel cells with EV batteries and lays a solid foundation for the future development of power systems of FCEVs.
Keywords: Fuel cell, electric vehicle, resonant converter, LLC converter.

1. INTRODUCTION

The rapid depletion of traditional fossil fuel resources and the environmental pollution caused by their utilization processes increase the need for sustainable energy solutions on a global scale [1,2]. Within the scope of reducing greenhouse gas emissions and combating climate change, the integration of renewable and clean energy sources is of critical importance. In this context, photovoltaic systems, wind energy, and fuel cell technologies are among the key technologies that stand out in the sustainable energy transition [3,4]. The transport sector also accounts for a significant portion of carbon emissions worldwide, and solutions to reduce fossil fuel dependency in this field are becoming increasingly important. In this regard, zero-emission FCEVs emerge as an environmentally friendly transport alternative, contributing to sustainable mobility [5]. While fuel cell vehicles attract attention with their high energy conversion efficiency and low emission profiles, they also have the potential to offer a longer range compared to EVs. These features make fuel cell vehicles an attractive option, especially for long-distance transportation and commercial vehicle applications. However, despite these advantages, fuel cell technologies face several technical challenges that must be addressed to enable their widespread adoption in electric vehicles [6-8].

One of the main challenges is that PEM fuel cells tend to produce low output voltage and high output current. This characteristic makes it difficult to directly integrate electric vehicles into DC bus systems, which usually operate at 400 V or 800 V [9,10]. Fig. 1 shows the power distribution architecture of a fuel cell vehicle. As observed in the architecture, high voltage gain DC-DC converters are utilized between the fuel cell stacks and the DC bus. Under operating conditions, the cell voltage of fuel cells tends to decrease as the output power increases. Therefore, converters must be capable of operating with high efficiency over a wide voltage gain range [11]. Among the converter topologies that provide high efficiency and a wide voltage gain range, LLC resonant converters stand out. These converters offer advantages such as high efficiency, low electromagnetic interference (EMI), and a wide operating range. Given these advantages, designing an LLC resonant converter specifically for fuel cell vehicles can significantly enhance their energy conversion performance. Their high-frequency operation reduces the size of the magnetic components and increases the overall system efficiency. These features play a critical role in improving energy conversion efficiency and optimizing system performance in fuel cell vehicles.

In this paper, a high voltage gain LLC resonant converter is designed to meet the energy conversion requirements of a 160 kW PEM fuel cell and to charge the battery of an electric vehicle from a fuel cell vehicle. The idle operating voltage of the fuel cell was determined as 310 V and 227 V under full load, and these variable voltages were converted to 400 V DC bus voltage using an isolated LLC converter. The designed LLC converter is optimized to operate with 95% efficiency at a switching frequency of 120 kHz. The design process and performance analyses are carried out in the PLECS simulation environment, verifying that the converter provides high efficiency and stability. These findings contribute to the development of more efficient and reliable power conversion solutions for fuel cell electric vehicles, paving the way for future advancements in sustainable transportation technologies.

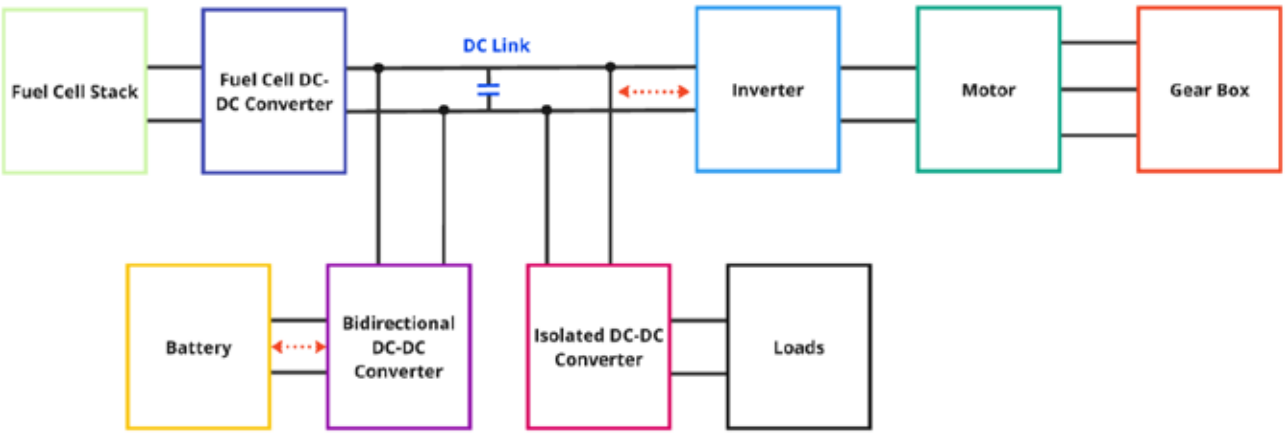

Fig. 1. Fuel cell vehicle power architecture schematic [12]

2. FUEL CELL, BATTERY and CONVERTER DESIGN

The low output voltage of PEM fuel cells is incompatible with electric vehicle (EV) battery voltage levels. To address this, a high-gain, LLC resonant DC-DC converter is designed to transfer energy from the fuel cell to the EV battery. The converter parameters are optimized based on fuel cell output characteristics and EV battery requirements, considering factors like minimum and maximum fuel cell voltages, battery voltage, and current. The design is analyzed using PLECS simulation software to verify efficiency and performance under various operating conditions.

2.1. PEM Fuel Cell and Performance Criteria

PEM fuel cell generates electricity through an electrochemical reaction, where hydrogen splits into protons and electrons at the anode. Protons pass through the membrane, while electrons flow through an external circuit, producing current. At the cathode, they react with oxygen to form water and release heat. In this study, the PEM fuel cell has a 160 kW power output, 705 A current capacity, and 227 V output voltage, with a power density of 4.4 kW/L. It uses hydrogen fuel and air (2.6 bar) as an oxidizer. The system operates between -30°C and +90°C, with a cold start at -30°C and a maximum coolant temperature of +95°C. Weighing 65 kg and measuring 572 mm, it is designed for efficient integration into EV applications [13].

2.2. Battery Specifications

Batteries are a critical component for safety, long life and high performance of EVs. Lithium Iron Phosphate (LFP) batteries are widely preferred in EV applications due to their high thermal stability, low self-discharge rate and wide operating temperature range. In addition, they offer a cycle life of 1500-4000 cycles, ensuring long-term use and minimising the risk of overheating. In this study an LFP battery with a capacity of 2.6 Ah was selected. The nominal voltage of the battery is 3.3V and the energy density varies between 90-160 Wh/kg. The charging temperature range is between 0°C and 45°C and it functions as a reliable power source against instantaneous high current demands.

2.3. LLC Converter Design and Parameters

In the design phase, the aim is to match the output voltage of the fuel cell to the voltage levels of the EV batteries. The LLC resonant converter is selected as a suitable solution based on performance criteria such as high voltage gain, high efficiency and isolation. As the energy is transferred from the FCEV to the EV, the isolation requirement is considered, the battery can not be affected in the event of a malfunction. The LLC resonant converter was selected to meet this safety requirement. The converter is designed taking into account the minimum and maximum fuel cell voltage, the battery voltage and various load conditions. The parameters used in the design are calculated according to the formulas and flowchart in [14]. The obtained results and design parameters are presented in Table 1. The circuit diagram of the design is shown in Fig. 2.

Table 1. LLC converter design parameters

Parameter	Value
Input voltage (V_{fc})	227 V - 310 V
Battery voltage (V_{bat})	300 V - 400 V
Magnetisation inductance (L_m)	81 µH
Resonant inductance (L_r)	6 µH
Resonant capacitance (C_r)	220 nF
Resonant frequency	100 kHz

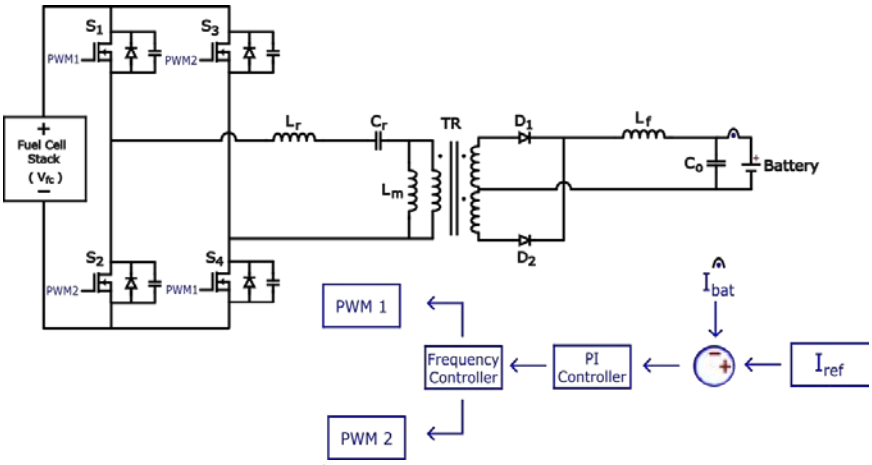

Fig. 2. LLC converter simulation schematic

3. SIMULATION AND RESULTS

Simulation of the proposed system is achieved in PLECS program under real conditions and parasitic effects (eg. capacitors) related to the design parameters. In the simulation, critical system parameters such as voltage-current levels, efficiency and transient response are analysed. Therefore, the accuracy and applicability of the design are assessed. The control signals of the switches in the LLC converter are generated using the frequency control method. The circuit diagram and control method of the converter simulated in PLECS is shown in Fig. 2. Here, the LFP type battery is chosen 2.6 Ah capacity, nominal voltage of 3.3 V. Therefore, battery pack consists of 100 series cells in one module and two modules in parallel. The results of the battery parameters considering the fuel cell at 227 V are shown in Fig. 3. Here, 2C contant current (CC) is considered for charging battery. Analysis of the waveforms shows that when the battery is charged at a constant current of 13 A, the battery voltage increases and the SoC value increases.

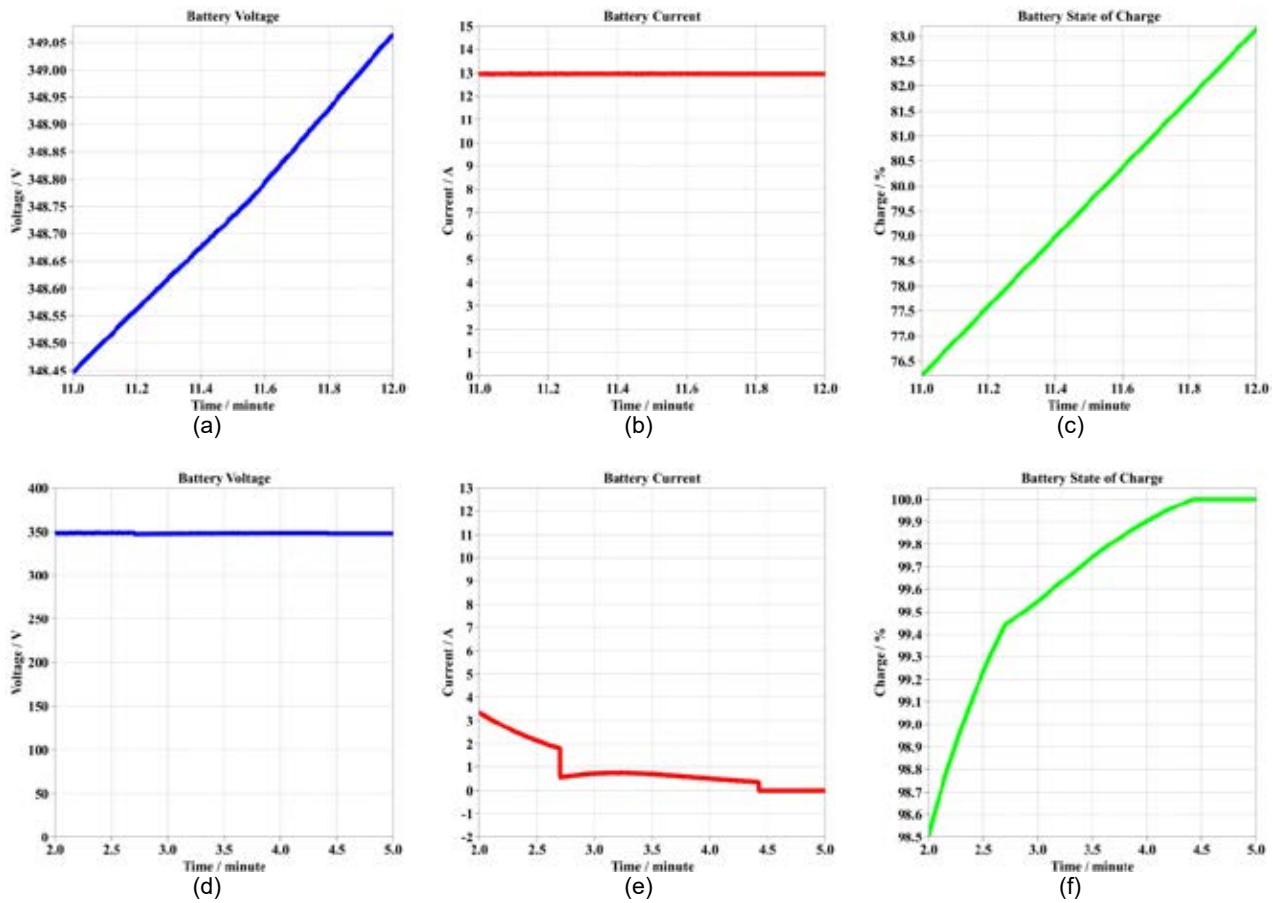

Fig. 3. (a) CC mode battery voltage, (b) CC mode battery current, (c) CC mode battery SoC, (d) CV mode battery voltage, (e) CV mode battery current and (f) CV mode battery So

4. CONCLUSIONS

The high voltage gain LLC resonant converter is designed to transfer energy from the fuel cell to the electric vehicle battery provides an efficient solution to meet the energy conversion requirements of a 160 kW PEM fuel cell. The converter is designed to operate in the fuel cell output voltage range of 227V - 310V and charge the electric vehicle battery in the range of 300V - 400V. In addition, the isolation feature of the LLC resonant converter makes the system more reliable by increasing safety under fault and arc conditions. Simulation results show that the LLC resonant converter operates with high efficiency at a switching frequency of 100 kHz and provides successful energy conversion from fuel cell to battery. The results show that LLC resonant converters provide an efficient, reliable and scalable power conversion solution for fuel cell electric vehicles. This study contributes to the development of more efficient and sustainable fuel cell electric vehicle systems by providing a solid foundation for future designs.

REFERENCES

[1] Bose BK. 2010. Global warming: Energy, environmental pollution, and the impact of power electronics. IEEE Industrial Electronics Magazine 4(1):6-17.
[2] Rudnick H. 2012. Evolution of energy: Global developments and challenges. IEEE Power and Energy Magazine 10(3):12-19.
[3] Kin T, Oh H, Kin H, and Youn BD. 2016. An online-applicable model for predicting health degradation of PEM fuel cells with root cause analysis. IEEE Transactions on Industrial Electronics 63(11):7091-7103.
[4] Vasirani M, Kota R, Cavalcante RLG, Ossowski S, and Jennings NR. 2013. An agent-based approach to virtual power plants of wind power generators and electric vehicles. IEEE Transactions on Smart Grid 4(3):1314-1322.
[5] Emadi A and Williamson SS. 2004. Fuel cell vehicles: Opportunities and challenges. IEEE Power Engineering Society General Meeting, Denver, CO, USA, June 2004, pp. 1640-1645.
[6] Tomoda K, Hoshi N, Haruna J, Cao M, Yoshizaki A, and Hirata K. 2014. Hydrolysis rate improvement in hydrogen generation system fueled by powdery sodium borohydride for fuel-cell vehicle. IEEE Transactions on Industry Applications 50(4):2741-2748.
[7] Prasanna UR, Pan X, Rathore AK, and Rajashekara K. 2015. Propulsion system architecture and power conditioning topologies for fuel cell vehicles. IEEE Transactions on Industry Applications 51(1):640-650.
[8] Zhang Y, Mou Y, and Yang Y. 2016. An energy management study on hybrid power of electric vehicle based on aluminum air fuel cell. IEEE Transactions on Applied Superconductivity 26(7):0612306.
[9] Zhang Y, Fu C, Sumner M, and Wang P. 2018. A wide input-voltage range quasi-Z source boost dc-dc converter with high voltage-gain for fuel cell vehicles. IEEE Transactions on Industrial Electronics 65(6):5201-5212.
[10] Jang M and Agelidis VG. 2014. A boost-inverter-based, battery-supported, fuel-cell sourced three-phase stand-alone power supply. IEEE Transactions on Power Electronics 29(12):6472-6480.
[11] Xiao J, Zhang X, Wen S, and Wang D. 2014. DC-DC converter based on real-time PWM control for a fuel cell system. International Conference on Advanced Mechatronic Systems, Aug. 2014, pp. 561-566.
[12] Tran HN, Le T-T, Jeong H, Kim S, and Choi S. 2022. A 300 kHz, 63 kW/L ZVT DC–DC Converter for 800-V Fuel Cell Electric Vehicles. IEEE Transactions on Power Electronics 37(3):2993-3006.
[13] Ballard. 2024. FCgen HPS specifications. Available at: https://www.ballard.com/wp-content/uploads/2024/08/Ballard_FCgen_HPS_specs.pdf. Accessed on February 10, 2024.
[14] Infineon Technologies. 2012. Resonant LLC Converter: Operation and Design. Application Note AN 2012-09 V1.0, September 2012.

$LaNiO_3$-PEROVSKITE TYPE PHOTOELECTRODE SYNTHESIS AND PHOTOELECTROCHEMICAL (PEC) PERFORMANCE FOR HYDROGEN PRODUCTION

[1]*Beyza Yıldırım,* [2]*Muhammed İberia Aydın,* [1,2]*Aysel Kantürk Figen*
[1]Yıldız Technical University, Faculty of Chemistry and Metallurgy, Department of Chemical Engineering, Istanbul, 34220, Turkey
[2]Yıldız Technical University, Clean Energy Technologies Institute, Istanbul, 34220, Turkey

E-mail: akanturk@yildiz.edu.tr

ABSTRACT
Developing energy demands and environmental concerns have increased interest in sustainable and clean energy sources. In this context, the photoelectrochemical (PEC) method for hydrogen production has become crucial in renewable energy technologies, as it directly transforms solar energy into chemical energy. The efficiency, light absorption and electrochemical stability of the electrocatalysts used in PEC systems are of great importance. Perovskite type materials provide significant advantages in this field due to their wide band gap, light absorption capacity, and excellent electrochemical stability. In this study, perovskite type $LaNiO_3$ electrocatalyst was synthesized by a sol-gel method, which provides homogeneous structure and controlled morphology. The structural, morphological and electrochemical properties of the synthesised $LaNiO_3$ perovskite were characterised by XRD, FE-SEM/EDS and electrochemical tests. XRD analyses confirmed that the synthesized catalyst features a rhombohedral hexagonal crystal structure. Additionally, FE-SEM and EDS analyses revealed uniform elemental distribution and a porous morphology. PEC tests indicate that $LaNiO_3$ possesses a capacity for sunlight absorption and shows promising electrochemical performance. These results suggest that $LaNiO_3$ perovskite-based electrocatalysts could serve as a viable alternative for sustainable and low-cost hydrogen production.

Keywords: Photoelectrochemical, Perovskite, Electrocatalyst, Sol-Gel

1. INTRODUCTION

Research on directly utilizing solar energy for hydrogen production from renewable sources has been increasing and photoelectrochemical (PEC) methods based on water splitting play a crucial role in integrating hydrogen into the hydrogen economy, contributing to advancements in production technologies. A photoelectrochemical cell fundamentally comprises a semiconductor-based photoanode (n-type) that enables the oxygen evolution reaction (OER), or a semiconductor-based photocathode (p-type) which drives the hydrogen evolution reaction (HER). Additionally, it encompasses a counter electrode where the complementary reduction and oxidation half-reactions occur [1]. The semiconductor material actively absorbs ultraviolet and visible wavelengths, accounting for 47% of the solar spectrum, and generates electron-hole pairs when excited by photons [2]. When an n-type semiconductor serves as the working electrode, water molecules interact with surface holes to generate oxygen; conversely, using a p-type semiconductor produces hydrogen. The complementary half-reaction occurs at the counter electrode. The development of PEC hydrogen production technologies, aimed at reducing production costs and improving efficiency, is particularly achievable through the synthesis of efficient photocatalysts. In traditional metal-based photocatalysts (such as TiO_2, ZnO, and Fe_2O_3), performance is limited due to the restricted mobility of charge carriers within the atomic structure, solar light absorption resulting from the wide bandgap, and rapid recombination of electron-hole pairs recombination [3]. Perovskite-type catalysts, which are widely used in fuel cells [4], supercapacitors [5], methane combustion reactions [6], and solar cells [7] offer a range of advantages for solar-based hydrogen production technologies due to their strong light absorption properties, adjustable oxide bandgaps, good stability, and low cost [8]. Perovskites consist of complex oxides with an ideal crystal structure formula of ABO_3 [9]. In this structure, the B cation can be transition metals (Cr, Mn, Fe, Co, Cu, Zn) or non-transition metals (Al, Ga, In), which are surrounded by six oxygen anions to form B-O bonds. The A cation can be lanthanides (La, Ce, Pr, Gd) or alkaline earth metals (Ba, Sr), which form A-O bonds with twelve anions. In this study, the $La_xNi_{1-x}O_3$ perovskite-type catalyst will be synthesized via the sol-gel method, which offers the advantage of low-cost synthesis of particles with different chemical compositions. Compared to high-tech hydrogen production methods, the use of direct photonic energy in the PEC process reduces energy losses, allowing for an environmentally friendly, low-operating cost approach to hydrogen production.

2. MATERIALS AND METHODS

2.1. Preparation of $La_xNi_{1-x}O_3$ Electrocatalyst by Sol-Gel Method and Characterization

The $La_xNi_{1-x}O_3$ perovskite was synthesized using the sol-gel method, which ensures homogeneity and controlled production. Lanthanum nitrate hexahydrate $La(NO_3)_3{\cdot}6H_2O$ (ABCR, 99%) and nickel nitrate hexahydrate $Ni(NO_3)_2{\cdot}6H_2O$ (Merck, 99%) were mixed with 125 mL of distilled water. Following the mixing of the precursor solution in a molar ratio of La:Ni=0.5:0.5, citric acid monohydrate ($C_6H_8O_7.H_2O$) (Merck, >99,5%) was added to induce complexation and polymerization, followed by the addition of ethylene glycol ($C_2H_6O_2$) (Merck, +99%). The pH was adjusted to 6 with 25% ammonia solution (NH_4OH) (Merck, 35%). The molar ratio of total metal ions to citric acid was set to 1.2, and the ratio of

citric acid to ethylene glycol was set to 1. The solution was then heated at 70°C until the gel formed, after which the gel was dried at 200°C for 12 hours and calcined at 1000°C for 5 hours to obtain the nano powder (Fig. 1).

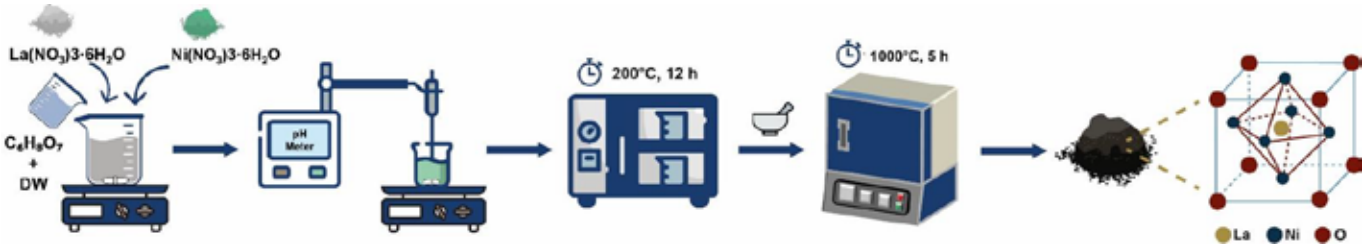

Fig. 1. Synthesis of $LaNiO_3$ Perovskite Type Electrocatalyst

XRD: The crystalline phases of the synthesized catalyst were characterized using a Philips Panalytical X'Pert Pro X-ray diffraction (XRD) instrument equipped with a copper (CuKα) tube, operating at an acceleration voltage of 45 kV and a current of 40 mA. The calcined powder samples were placed on an aluminum holder to ensure a smooth surface and were prepared for analysis. XRD measurements were carried out with a step size of 0.01° (2θ) and a scan time of 1.2 seconds.
FE-SEM: The sample's surface morphology and elemental composition were examined using field-emission scanning electron microscopy and energy-dispersive X-ray spectroscopy (FE-SEM/EDS) (Thermo Scientific Apreo 2S LoVac) images were obtained at different magnification levels under an acceleration voltage of 10 kV. The material was fixed on a sample holder and prepared for analysis by applying an Au coating to ensure conductivity.

2.2. Photoelectrode Preparation
The perovskite gel synthesized for the investigation of photoelectrochemical properties was electrode-coated using the dip-coating method. Stainless steel 306 served as the electrode substrate, and a series of sequential pre-treatment steps were conducted to enhance the catalyst's adhesion to the surface. The process includes three main steps: first, the surface was mechanically smoothed with sandpaper. Second, the electrode was cleaned sequentially with deionized water and ethanol in an ultrasonic bath, then dried under vacuum. The electrode was prepared for coating through an acid immersion process.

2.3 Performance Tests of Photoelectrochemical Systems
Electrochemical tests were carried out under a FYTRONIX solar simulator (400-1000 nm) using a three-electrode configuration in a GAMRY Reference 3000 potentiostat/galvanostat device. A graphite counter electrode, an Ag/AgCl reference electrode, and a 0.5 M KOH solution served as the electrolyte during the tests. Chronoamperometric measurements were performed to determine the photoelectrochemical response of the prepared photoelectrode under chopped light conditions at 0 V (vs. reference electrode) for 300 seconds. The experiments were conducted on a 6 cm² active surface area to investigate the stability of the photocurrent and the potential of light-induced charge carriers.

3. RESULTS AND DISCUSSION
In this study, the synthesized $LaNiO_3$ perovskite sample was initially analyzed by powder X-ray diffraction (PXRD) using a PANalytical X'Pert Pro diffractometer with CuKα radiation (λ = 1.5406 Å). Phase identification confirmed that $LaNiO_3$ has a rhombohedral hexagonal crystal structure with lattice parameters a = 5.4570 Å, b = 5.4570 Å, and c = 6.6030 Å (Fig. 2). The most intense peaks observed at 2θ = 23°, 33°, 41°, 47°, 59°, 69°, and 79° correspond to the crystal planes (101), (012), (021), (202), (122), (220), and (214), which are consistent with the standard reference data (JCPDS: 04-026-8961). These findings confirm the synthesis of $LaNiO_3$ with high crystallinity and purity, providing a foundation for further research into its photoelectrochemical performance.

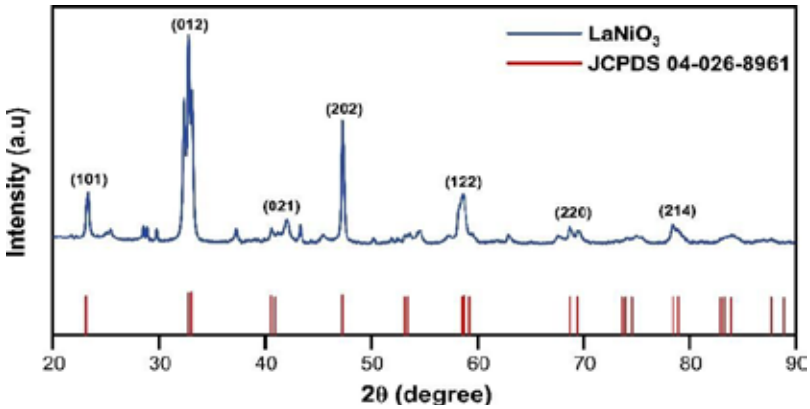

Fig. 2. XRD Pattern of $LaNiO_3$.

FE-SEM and EDS analyses assessed the morphological and chemical structure of the synthesized $LaNiO_3$ perovskite sample. The FE-SEM images indicated that the sample has a cubic, porous structure that tends to agglomerate (Fig. 3). These morphological characteristics imply that the material may have a large surface area, potentially beneficial for catalytic or electrochemical applications. EDS elemental mapping demonstrated a homogeneous distribution of La, Ni, and O elements. The elemental analysis determined the atomic percentages of the sample to be La: 20.6%, Ni: 20.1%, and O: 59.3%, which shows a composition very close to the desired molar ratio (Table 1).

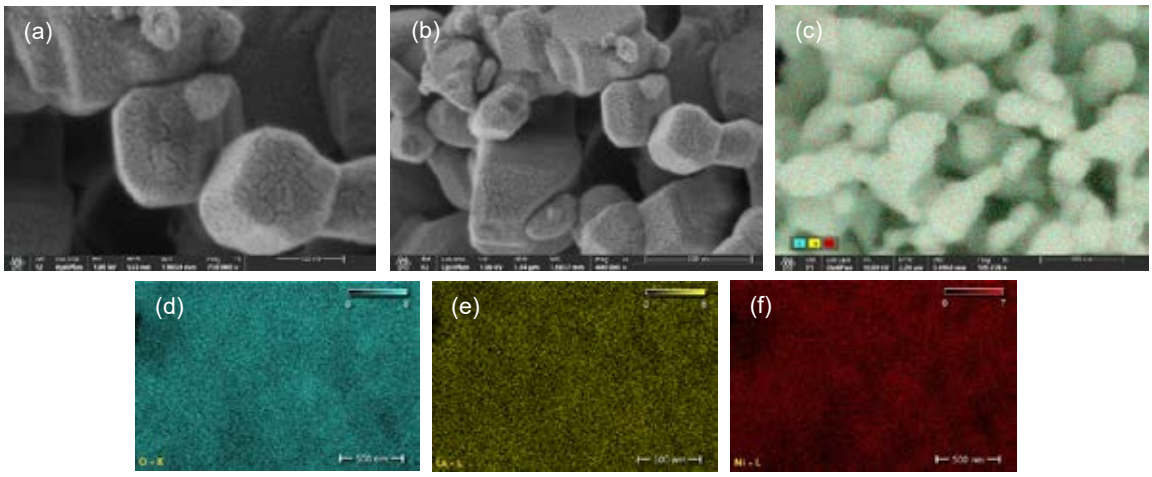

Fig. 3. SEM images of $LaNiO_3$ at a magnification scale of 100 nm (a) and 300 nm (b), along with elemental mapping at 500 nm in (c), (d), (e), and (f).

Table 1. Elemental composition of $LaNiO_3$ determined by EDS analysis.

Element	Atomic %	Atomic % Error	Weight %	Weight % Error	Net Counts
O	59.3	0.3	19.0	0.1	514 760
Ni	20.1	0.1	23.7	0.1	227 320
La	20.6	0.1	57.3	0.3	335 097

Fig. 4 shows the relationship between current density ($\mu A \cdot cm^{-2}$) and time (s) for the chronoamperometric (CA) chopping test performed at 0V for $LaNiO_3$. Periodic light on-off cycles were applied throughout the test, and a significant increase in current density was observed with each light on period. This behavior confirms the photocatalytic activity of $LaNiO_3$ and indicates the photogeneration processes under light irradiation. When the light is on, the current density quickly increases to 0.8–1.0 $\mu A \cdot cm^{-2}$, but when the light is off, it reduces to 0.2–0.4 $\mu A \cdot cm^{-2}$. It is estimated that the photoinduced current is around 0.6 $\mu A \cdot cm^{-2}$. Additionally, the material exhibits photostability over a certain period, as seen by the repeatable current density response in each light on-off cycle.

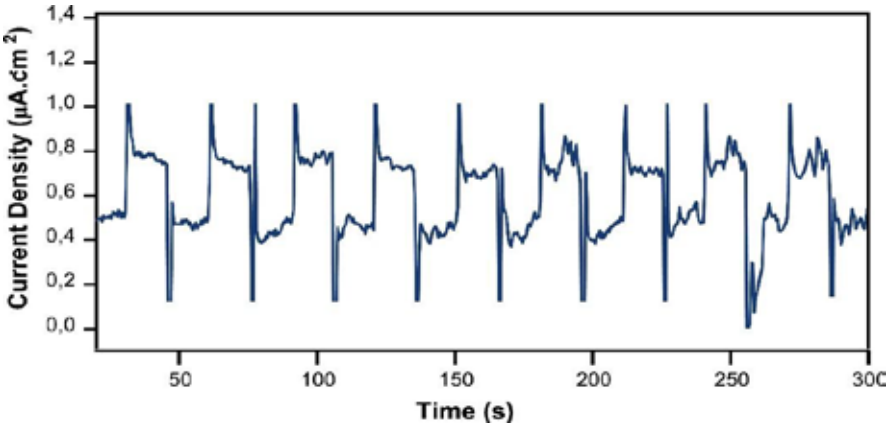

Fig. 4. Chronoamperometric chopping test of $LaNiO_3$ at 0V.

4. CONCLUSIONS

In this study, $LaNiO_3$ perovskite electrocatalyst was successfully synthesized using the sol-gel method, and its applicability for photoelectrochemical hydrogen production was investigated. XRD analysis confirmed that the synthesized catalyst has a rhombohedral hexagonal crystal structure, while FE-SEM and EDS analyses revealed homogeneous elemental distribution and porous morphology. Photoelectrochemical tests indicated that $LaNiO_3$ has sunlight absorption capacity and showed promising results in terms of electrochemical performance. These findings suggest that $LaNiO_3$ perovskite-based electrocatalysts could be a suitable alternative for sustainable and low-cost photoelectrochemical hydrogen production. Future studies will focus on exploring different synthesis conditions to improve the catalyst's efficiency and investigating the hydrogen production activities of the perovskite structure under solar light.

ACKNOWLEDGEMENT

This research was supported by Yildiz Technical University Research Foundation (Project No: FBA-2024-6145). The authors also thanks to financial support of FYTRONIX solar simulator and GAMRY Reference 3000 potentiostat/galvanostat (FBA-2023-5648).

REFERENCES

1. Marwat, M. A., Humayun, M., Afridi, M. W., Zhang, H., Abdul Karim, M. R., Ashtar, M., ... & Luo, W. (2021). Advanced catalysts for photoelectrochemical water splitting. ACS Applied Energy Materials, 4(11), 12007-12031.
2. Liu, J., Ma, N., Wu, W., & He, Q. (2020). Recent progress on photocatalytic heterostructures with full solar spectral responses. Chemical Engineering Journal, 393, 124719.
3. Han, X., Liu, P., Ran, R., Wang, W., Zhou, W., & Shao, Z. (2022). Non-metal fluorine doping in Ruddlesden–Popper perovskite oxide enables high-efficiency photocatalytic water splitting for hydrogen production. Materials Today Energy, 23, 100896.
4. Kaur, P., & Singh, K. (2020). Review of perovskite-structure related cathode materials for solid oxide fuel cells. Ceramics International, 46(5), 5521-5535.
5. Nan, H. S., Hu, X. Y., & Tian, H. W. (2019). Recent advances in perovskite oxides for anion-intercalation supercapacitor: a review. Materials Science in Semiconductor Processing, 94, 35-50.
6. Kousi, K., Neagu, D., Bekris, L., Calì, E., Kerherve, G., Papaioannou, E. I., ... & Metcalfe, I. S. (2020). Low temperature methane conversion with perovskite-supported exo/endo-particles. Journal of Materials Chemistry A, 8(25), 12406-12417.
7. Kim, J. Y., Lee, J. W., Jung, H. S., Shin, H., & Park, N. G. (2020). High-efficiency perovskite solar cells. Chemical reviews, 120(15), 7867-7918.
8. Nguyen, V. H., Do, H. H., Van Nguyen, T., Singh, P., Raizada, P., Sharma, A., ... & Van Le, Q. (2020). Perovskite oxide-based photocatalysts for solar-driven hydrogen production: Progress and perspectives. Solar Energy, 211, 584-599.
9. Wang, W., Xu, M., Xu, X., Zhou, W., & Shao, Z. (2020). Perovskite oxide based electrodes for high-performance photoelectrochemical water splitting. Angewandte Chemie International Edition, 59(1), 136-152.

UTILIZATION OF A BORON CO-DOPED ACTIVATED CARBON/STARCH BASED METAL-FREE BIOCATHODE FOR HYDROGEN PRODUCTION

[1*]*Aysegul Yagmur Goren*, [1]*Ibrahim Dincer*,
[1] Clean Energy Research Laboratory (CERL), Faculty of Engineering and Applied Science, OntarioTech University, Oshawa, Ontario, Canada

*Corresponding author e-mail: Aysegul.Kara@ontariotechu.ca

ABSTRACT
The development of cost-effective and sustainable electrocatalysts for hydrogen production is crucial for advancing clean energy technologies. In this study, a boron-doped activated carbon-starch-based (B@AC-S) bioelectrode was synthesized via a green and scalable approach and employed as a metal-free cathode for hydrogen evolution in an electrolysis system. The impact of varying boron doping concentrations (1.5–3.0 g) on electrochemical performance and hydrogen production was systematically investigated. The 2.5 g-boron-doped electrode exhibited the highest current density, demonstrating superior electron transfer capabilities, while the 3.0 g-doped electrode showed a slight decline due to potential conductivity limitations. Hydrogen evolution tests confirmed a substantial increase in H_2 production with increasing boron content, with the 3.0 g-doped electrode achieving the highest cumulative hydrogen yield of 1000 ppm in approximately 6 min. The study highlights the effectiveness of boron doping in enhancing electrochemical activity and hydrogen production efficiency, offering a promising alternative to conventional metal-based electrocatalysts.

Keywords: Hydrogen production, Green synthesis, Boron, Bioelectrode, Activated carbon

1. INTRODUCTION

Hydrogen (H_2) is a promising fuel for energy conversion and storage applications because of its high gravimetric energy density. The water splitting with electrolysis process is a well-established and eco-friendly method of producing H_2 when compared to other methods. However, traditional water electrolysis requires a large amount of external energy (> 1.8 V) and sustainable electrode materials with high electrical conductivity [1].

Mostly, precious noble metals, such as Pt-based materials for the H_2 evolution reaction (HER) at the cathode and IrO_2-based materials for the oxygen evolution reaction at the anode in the electrolysis process, have been employed as electrocatalysts, however, which increases the cost [2]. For H_2 evolution processes, Pt is the typical electrocatalyst; nevertheless, it is costly and scarce. Enhancing the electrocatalytic activity and durability of the electrodes is necessary to reduce the manufacturing cost and make the process economically viable. Therefore, it is urged to look for substitutes for Pt-based electrocatalyst. For the H_2 evolution process, alternative non-Pt-based low-cost electrocatalysts should be required. Recently, different carbons are utilized as support materials that increase the surface area and electrical conductivity to enhance H_2 production performance of the electrode [3]. Namely, high surface area, optimal porosity, high stability in an acidic environment, and strong electrical conductivity are all requirements for support material. A variety of carbons, including graphene, fullerenes, carbon nanomaterials, and carbon black, were recently identified by several studies as support materials for the H_2 evolution reaction in water electrolysis. However, because of their intrinsic properties of having few active sites on the chemically inert sp2 carbon framework for HER reaction, the performance of HER with carbon-based materials is still insufficient to reach the same level as that with Pt-based catalysts. In this regard, another potential method to improve the electrochemical ability is to dope heteroatoms with carbons to increase the number of active sites on the carbon surface and enhance the catalytic activity.

According to reports, adding the various heteroatoms (B, N, P, and S) that result from the electronic structure alteration might enhance the electrochemical performance of the cathode [4]. It has been also demonstrated that the heteroatom doping technique is an effective method to enhance the electrochemical characteristics of carbon-based materials [5]. Non-metallic elements like B, N, P, and S heteroatoms may usually be added to the carbon matrix's lattice structure to increase layer spacing, create mismatched electrons, enhance active sites, and speed up electrochemical kinetics. Overall, the carbon skeleton structure is rearranged when heterogeneous atoms are added, and the surface chemical environment of activated carbon is altered. This results in increased internal disturbance, enhanced structural stability, surface functional groups, and specific surface area. Activated carbon improves ion transit and storage, resulting in superior electrochemical qualities.

Electron-deficient boron (B) is known to be a capable component for promising chemical dopants on carbons, among other heteroatom dopants, because it only has three valence band electrons. This allows the inert sp2 carbon framework to be chemically functionalized, initiates the copious free-flowing π electrons, and functions as an electrocatalyst. Moreover, adding B could significantly increase the carbon conductivity by increasing the density of hole type charge carriers. These virtues boost the electrocatalytic activity of carbons towards the HER, therefore, the B-doped carbons have gained a growing interest in recent years. Despite the growing interest in boron-doped carbon-based electrode materials for H_2 production, several critical gaps remain in the literature. For instance, the synthesis methods for boron-doped carbon electrodes often involve costly and complex procedures, limiting their large-scale feasibility. There is also

a lack of comprehensive studies comparing the performance of boron-doped carbon materials with conventional and emerging electrode materials in terms of cost-effectiveness, sustainability, and efficiency. Moreover, in most studies on boron-doped carbon-based electrodes for H_2 production, transition metals such as nickel, cobalt, and iron have been predominantly used as base materials due to their favorable electrocatalytic properties [6]. However, considering the practical limitations of these metals, incorporating metal-free materials offers several advantages. Traditional metal-based cathodes often suffer from high costs, limited availability of precious metals, and susceptibility to degradation in harsh electrolytic environments. In contrast, metal-free cathodes, typically composed of carbon-based materials or doped polymers, provide a cost-effective and sustainable alternative with enhanced chemical stability and corrosion resistance. Moreover, these cathodes can exhibit high electrocatalytic activity for the HER when engineered with appropriate surface modifications, such as heteroatom doping or structural optimization. The absence of metal components also mitigates metal leaching and contamination concerns, ensuring long-term operational efficiency and environmental compatibility. Therefore, metal-free cathodes represent a promising path for the development of next-generation, sustainable H_2 production technologies.

To the best of our knowledge, limited studies in the literature utilize metal-free material in electrochemical H_2 production, despite its potential advantages. Therefore, this study is focused on the H_2 production performance of the B-loaded carbon/starch-based biocathode in the electrolysis process. Namely, B-loaded carbon/starch-based biocathode with various boron loading percentages have been synthesized and utilized in the electrolysis process for green H_2 production.

2. MATERIALS AND METHODS

The boron-doped activated carbon-starch-based (B@AC-S) bioelectrode is produced with green synthesis (Fig. 1). 20 mL of distilled water, 2 mL of vinegar as an acetic acid source, 10 g of starch, and 2 mL of mineral oil are mixed to synthesize the bioelectrode. Next, different quantities of boric acid (H_3BO_3, Sigma Aldrich) as a boron heteroatom source are added to the synthesized B@AC-S bioelectrode. Then, this mixture is continuously stirred at 60 °C until it becomes more concentrated and uniform. Finally, a thin layer of the B@AC-S bioelectrode mixture is put into the glass, and allowed to solidify and remove moisture for a day.

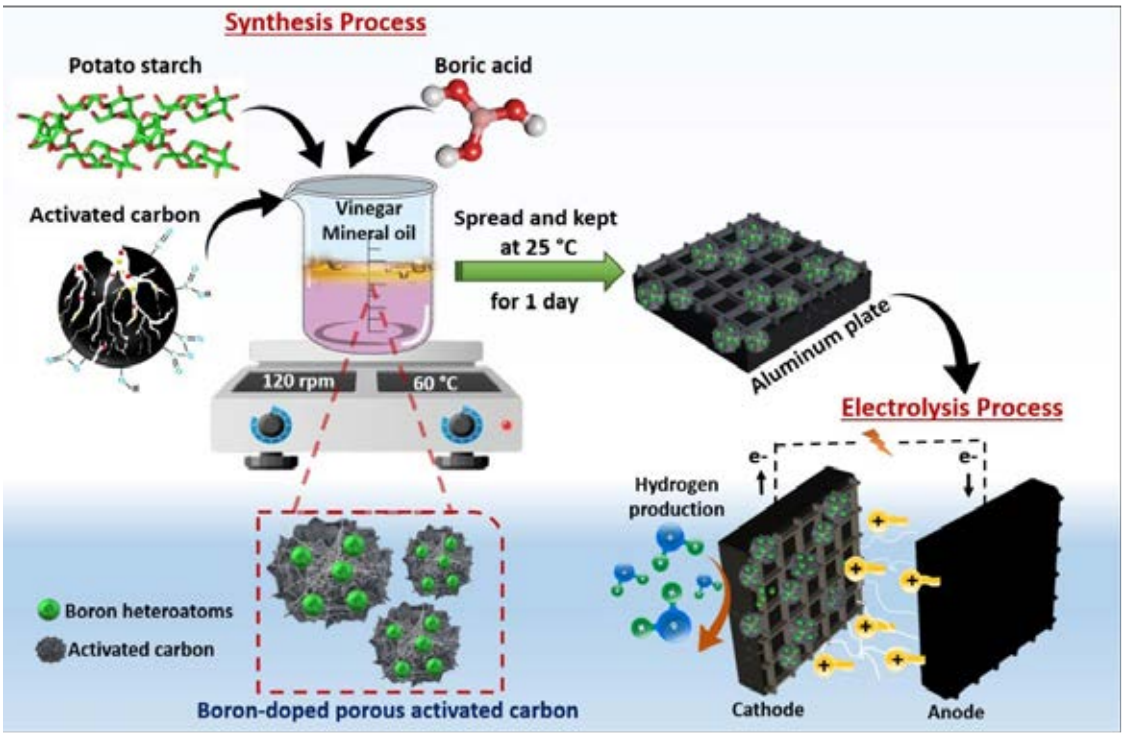

Fig. 1. Page size and margins (9 pt Arial, centered)

A laboratory-scale membraneless cylindrical electrolysis reactor is used for the H_2 production tests. A 1 M potassium hydroxide (KOH) solution is used as the electrolyte solution in the electrolysis reactor. An H_2 sensor, electrodes, electrode connection cables, and a DC power supply were among the tools and components used in the experiment. After the electrodes are first placed into the cell for the testing, the electrolysis process begins at a predetermined electrical voltage. Before and after the testing, the cell voltage and current are measured at specified intervals from the DC power supply. Furthermore, the surface morphologies and elemental content of the produced electrodes are evaluated using the scanning electron microscopy (SEM). Additionally, the electrodes are electrochemically characterized using Gamry-3000

potentiostat/galvanostat. In this analytical device, a saturated Ag/AgCl electrode acts as the reference electrode, a platinum electrode as the counter electrode, and the generated electrodes as the working electrode. Each measurement is conducted in an electrolyte solution with 1 M KOH at 24 °C. Furthermore, cyclic voltammetry measurements of the electrodes were performed in the potential range of -0.1−0.9 V at a scan rate of 50 mV/s.

3. RESULTS AND DISCUSSION

The water electrolysis tests for H_2 production are performed at different boron loadings (Fig. 2a). As expected, H_2 production performance of the B@AC-S bioelectrode is increased with the increasing boron dosage. Initially, raw activated carbon exhibits the lowest hydrogen production rate and cumulative production, indicating its limited catalytic efficiency. The introduction of boron doping significantly enhances performance, with a notable increase in hydrogen output as the doping concentration rises. Among the boron-doped samples, the 1.5 g-doped electrode shows a moderate improvement over raw activated carbon but remains suboptimal compared to higher doping levels, considering the H_2 production time. The 3 g-doped electrode further enhances hydrogen production (1000 ppm), reflecting improved catalytic activity due to increased electron transfer efficiency, and the H_2 production time considerably decreased.
Regarding the time-dependent H_2 production, all boron-doped electrodes accelerate H_2 production compared to raw activated carbon, reducing the time required to reach peak production.

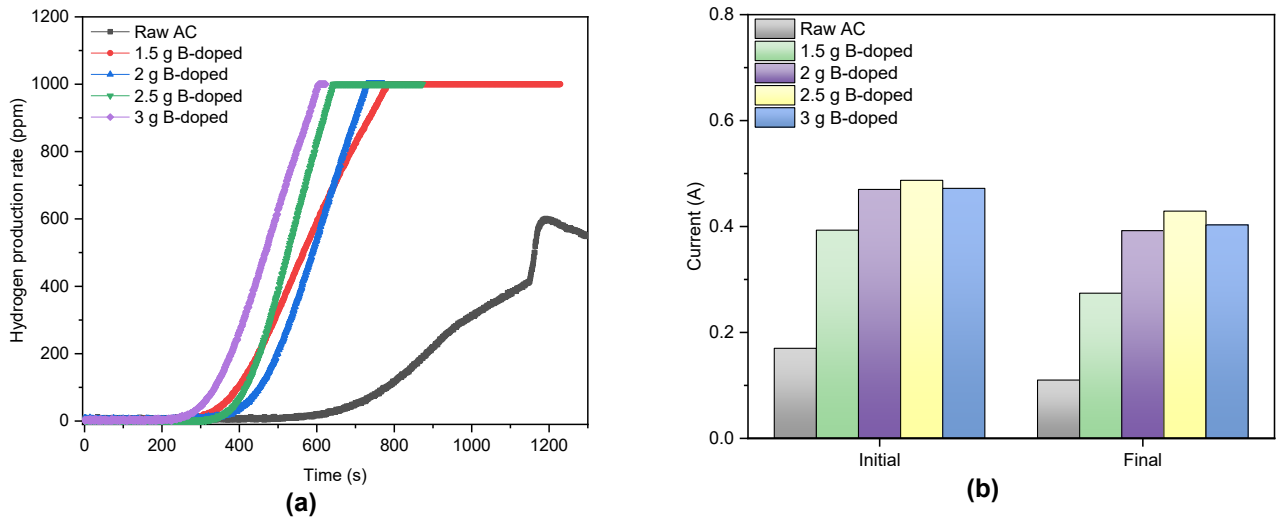

Fig. 2. The hydrogen production rate (a) at different boron loadings and (b) initial and final current values.

Moreover, the initial and final current values during the H_2 production are measured and reported in Fig. 2b. The raw activated carbon exhibits the lowest current, starting at 0.17 A and reaching a final value of 0.11 A, indicating limited conductivity and electron transfer efficiency. In contrast, boron doping significantly enhances the initial current values. The 2.5 g-doped electrode exhibits the highest current, beginning at 0.487 A and stabilizing at 0.429 A, indicating an optimal balance of boron content that maximizes electrical conductivity and minimizes charge transfer resistance.
Overall, boron doping significantly enhances both H_2 production and the electrochemical activity of the electrode by improving electrical conductivity, facilitating electron transfer, and reducing charge transfer resistance, with 2.5 g doping demonstrating the most optimal performance.

4. CONCLUSIONS

Boron-doped activated carbon-starch-based (B@AC-S) bioelectrode was successfully synthesized and utilized for the H_2 production using the electrolysis process. Boron was doped to improve the electrochemical activity of the biocathode and enhance the H_2 production performance of the bioelectrode. The highest H_2 production of 1000 ppm is obtained using 3 g-boron-doped electrodes at the end of the operating time of approximately 6 min.

Acknowledgment

This publication was made possible by the NPRP grant (NPRP12S-0123-190011) from the Qatar National Research Fund (a member of Qatar Foundation). The findings achieved herein are solely the responsibility of the authors.

REFERENCES

1. A.Y. Goren AY, Dincer I and Khalvati A. 2023. A comprehensive review on environmental and economic impacts of hydrogen production from traditional and cleaner resources. Journal of Environmental Chemical Engineering 11:111187.

2. Yang G, Yu S, Kang Z, Dohrmann Y, Bender G, Pivovar BS, Green JB, Retterer ST, Cullen DA, Zhang, FY. 2019. A novel PEMEC with 3D printed non-conductive bipolar plate for low-cost hydrogen production from water electrolysis. Energy Conversion and Management 182:108-116.
3. Fu L, Hao S, Liao H, Liu W, Zhang Y, Zhu H, Liu T, Chen B, Xie H. 2025. Efficient hydrogen production and optional power generation through coal-assisted water electrolysis, Chemical Engineering Journal 503:158668.
4. Yeh MH, Leu YA, Chiang WH, Li YS, Chen GL, Li TJ, Chang LY, Lin LY, Lin JJ, Ho KC. 2018. Boron-doped carbon nanotubes as metal-free electrocatalyst for dye-sensitized solar cells: Heteroatom doping level effect on tri-iodide reduction reaction. Journal of. Power Source 375:29-36.
5. Liu Y, Yang C, Li Y, Zheng F, Li Y, Deng Q, Zhong W, Wang G, Liu T. 2020. $FeSe_2$/nitrogen-doped carbon as anode material for potassium-ion batteries. Chemical Engineering Journal 393:124590.
6 Wang Z, Umer S, Hao L, Cheng F, Li J, Liu J. 2025. Carbon-based materials for electrocatalytic hydrogen evolution reaction. Functional Materials for Electrocatalytic Energy Conversion 103–137.

PROBATIVE ASSESSMENT OF HYDROGEN ENRICHED METHANE INDUCTION IN GASOLINE DIRECT INJECTION ENGINE FOR HOMOGENEOUS STOICHIOMETRIC LEAN MIXTURE FORMATION

[1]Jerome Stanley M, [1]Leenus Jesu Martin M, [2]Edwin Geo Varuvel*
[1]Green Vehicle Technology Research Centre, Department of Automobile Engineering,
SRM Institute of Science and Technology, Kattankulathur, Tamilnadu, 603203, India.
[2]Department of Mechanical Engineering, Faculty of Engineering and Natural Sciences,
Istinye University, Istanbul 34460, Turkey

* E-mails: vedwingeo@gmail.com

ABSTRACT
The combustion stability of the small-bore Gasoline Direct Injection (GDI) engine at homogeneous near stoichiometric and lean burn combustion is investigated experimentally. The intake manifold is slightly modified to accommodate the hydrogen induction, wherein mixture of hydrogen enriched methane (30% hydrogen enrichment-hythane30) and air is formed in the intake manifold, attaining the excess air ratio of 1.0 to 1.22. With the increment of hythane30 fraction the fuel leaning (Gasoline) is attained and achieving economical fuel consumption rate. The hydrogen fraction in the methane decreases the coefficient of variance, and it was found to be within the limit of 5%. For the lean limits it was found that the peak pressure of the lean air fuel ratio was reduced consistently. The spark timing was optimized for the lean limit with hythane30 addition to attaining the maximum brake torque and CA 50 location of the mass fraction burn. Hydrogen induction improves the combustion rate and mean effective pressure; shortens the flame propagation, maximizes the heat release rate and peak pressure attainment. On the emission side there is a consistent decrease in CO and HC emission; and an increase of NOx emission since the mean gas temperature has increased. The cycle-to-cycle variation during the lean operating condition at 1.22 shows combustion stability and effective flame propagation.

Keywords: Hythane, Small Bore, Gasoline Direct Injection, Coefficient of Variance, Lean Combustion.

1. INTRODUCTION
The utilization of small-bore engines for motorcycles and other last-mile connectivity has limited potential due to lower thermal efficiency and performance [1]. Most of these engines operate under part-load conditions due to their low compression ratio. The implications of rigorous CO2 regulations and increasing energy demand per capita highlight the need for carbon-neutral fuel gases. Since natural gases have a high-octane number and a good hydrogen-to-carbon ratio, they have higher knocking resistance [2] and can be used in spark-ignition (SI) engines that burn fuel more slowly. When used as a fuel for mobility solutions, natural gases present special problems because the amount of CO_2 in the fuel gases can change the misfiring of engines in different ways, often depending on the terrain. Using fuel gases to extend lean operation makes it harder to light the fuel-air mixture because the charge density near the spark plug is lower when the equivalence ratio is extended. Among various fuel gases, hydrogen stands out due to its physico-chemical properties, which support SI engine combustion [3-5]. However, as energy progresses toward hydrogen, its storage, and supply have limitations in implementation and continuous production for mobility solutions. Enriching existing fuel gases with hydrogen offers a midway solution to overcome these limitations in the ongoing development to meet increasing energy demand based on hydrogen [6].

The goal of this study is to find out how hythane, which is methane that is enriched with hydrogen, affects the performance of direct-injection spark-ignition engines by making smaller differences in the engine cycles. Employing gaseous fuels in these engines offers a promising solution to challenges such as wall wetting and the complexities of fuel droplet size and evaporation within the cylinder. Direct injection engines can work at higher compression ratios and quickly mix air and gaseous fuel. This makes gaseous work efficiently at a wide range of loads without engine knocking. Moreover, direct-injection engines generally achieve higher thermal efficiency compared to traditional SI engines. This technology also enables leaner engine operation, potentially leading to better fuel efficiency and lower emissions. This study builds on earlier work by looking at how well hythane30-gasoline lean burn combustion works and how much pollution it causes in small-bore GDI engines. Additionally, the study explores how adding hydrogen to methane affects combustion stability and the lean combustion limit.

2. ENGINE TEST RIG AND METHODS
The engine used in this study is a 390 cm³ small-bore single-cylinder air-cooled GDI engine. The experimental setup is illustrated in Figure 1. Initially, the engine was a carbureted model from Honda, but it was modified to a direct-injection gasoline engine. The engine head was changed to make room for a GDI injector, the throttle control was switched to an electronic actuator, and an Electronic Control Unit (ECU) was added to control the spark and injection timing. To create

a closed-loop system, CAM and crankshaft position sensors were added, along with fuel rail pressure control. The specifics of these modifications are not detailed here as they fall outside the article's scope. Engine specifications are provided in Table 1. The spark plug is located on the sides of the engine, which features a hemispherical combustion chamber. The piston head remained unmodified, retaining its original flat design. A spray-guided fuel injector was used, positioned near the spark plug.
A water-cooled eddy current dynamometer was used to load the engine under operating conditions. An HFM-type T-MAF sensor checked the amount of air coming in, and a gravimetric fuel flow system found out how much fuel was being used. A contact-type encoder attached to the crankshaft triggered the data acquisition system to record sensor data. A piezoelectric pressure transducer with a resolution of 0.1 crank angle degrees records in-cylinder pressure data. A Bosch LSU 4.9 wideband Lambda sensor monitored the air-fuel ratio, while exhaust gas temperature was measured using a K-type thermocouple. An AVL Di-gas analyzer 444 was used to record engine-out emissions.

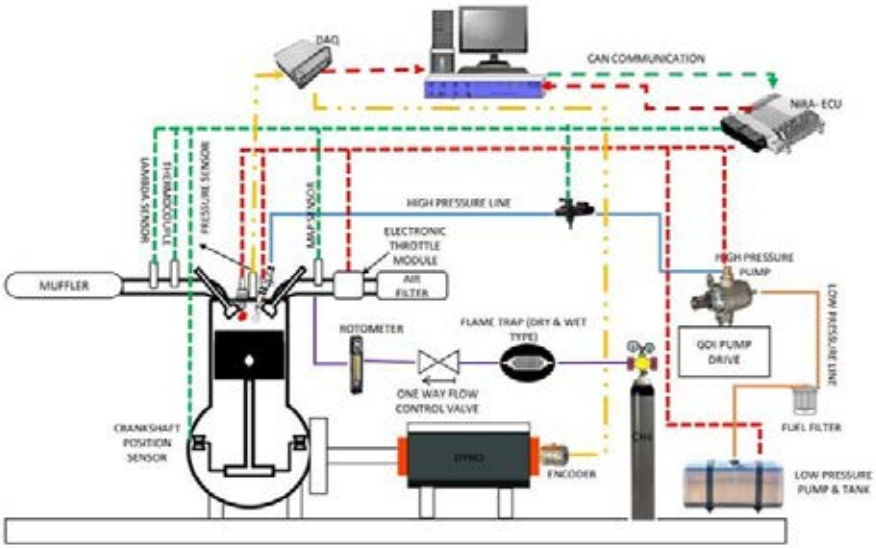

Fig. 1. Experimental Layout

2.1. Methods

The test conditions for this investigation involved operating the engine at 3000 rpm with the throttle fully open, which corresponded to the maximum brake torque achievable with the given spark timing. The specific engine operating conditions are detailed in Table 3. Hythane30 flow rates were determined based on an energy balance, ensuring that hydrogen did not exceed 30% of the total energy input. For an equivalence ratio of 1 to 1.22, the hythane30 addition fraction varied from 4.5% to 19.5%. Similarly, the equivalence ratio was increased to 1.22 wherein the gasoline injection is stratified. To maintain a consistent increase in the equivalence ratio, subsequent tests involved progressively leaning the gasoline mixture.

Table 1. Engine Details

Particulars	Details
Make	M/s. Honda
No. of Cylinders	1
No. of Valves	2
Type of CAM	Single Overhead
Ignition	Spark
Bore*Stroke (mm)	88*64
Displacement (cm^3)	390
Compression Ratio	8.2:1
Induction	Naturally Aspirated
Rated Torque	24 Nm @3000 rpm
Rated Power	8 hp @3600 rpm
Cooling system	Air

3. RESULTS AND DISCUSSION

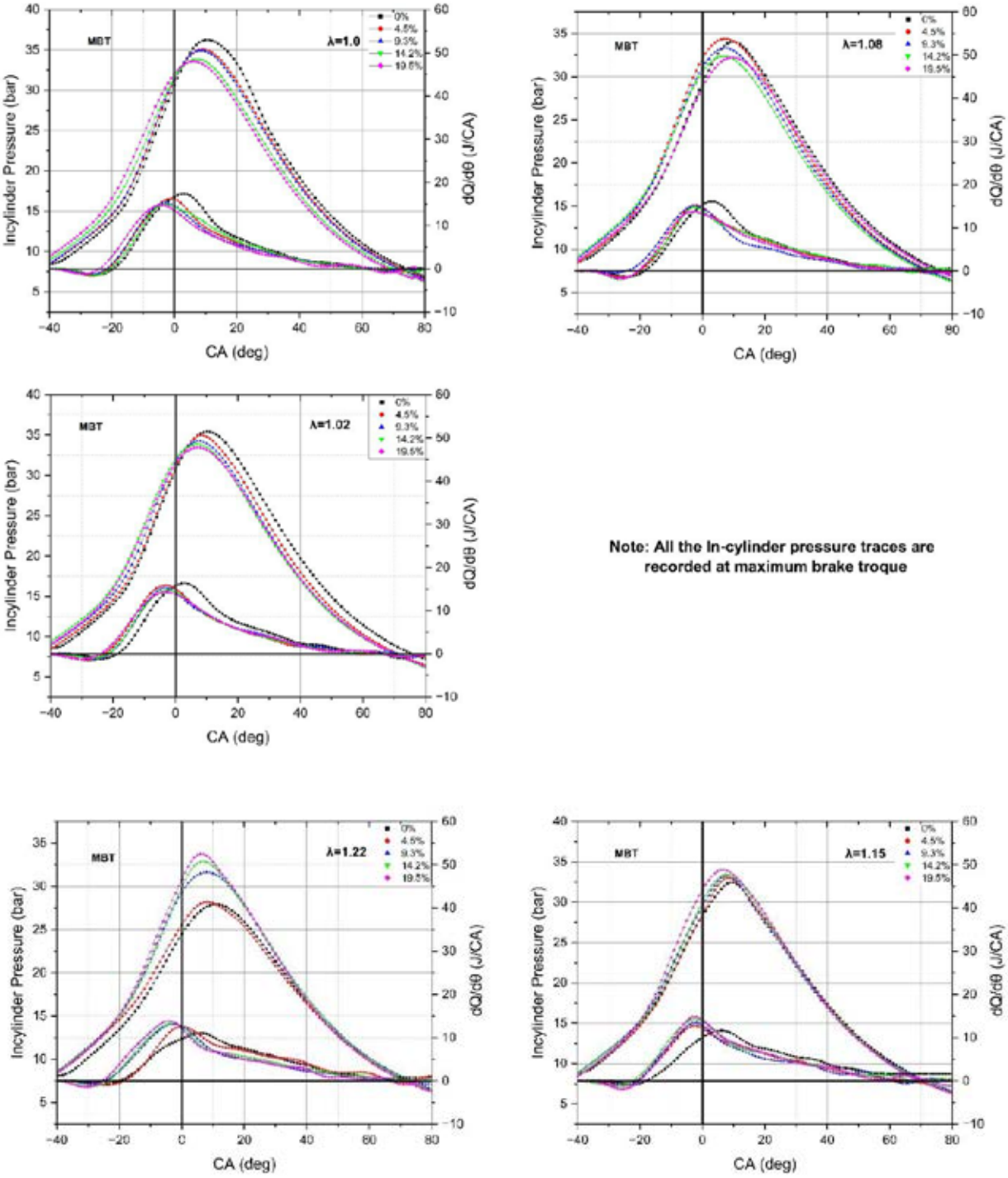

Fig. 2. Pressure Traces and Instantaneous Heat Release Rate of hythane30 for the homogeneous near stiochimetric lean mixture formation for the given equivalence ratio

4. CONCLUSIONS

1. The spark timing for the equivalence ratio for the given equivalence ratio was set as the location of CA50; the peak pressure improved by 12%. Spark advancement beyond 37°CAD causes misfire in the engine.
2. The lean limit was further increased to 1.22 for the spark timing of 30°CAD bTDC as the hydrogen addition favors the combustion stability.
3. Engine operation with 100% wide-open throttle, an equivalence ratio of 1.0, 1.02, 1.08, 1.15 & 1.22, and the varied hythane30 fraction has a significant effect on the engine performance, combustion, and emission characteristics. The thermal efficiency and indicated mean effective pressure both go up a lot as the hydrogen fraction for the equivalence ratio goes up.
4. Engine operation with 100% wide-open throttle, an equivalence ratio of 1.0, 1.02 & 1.08, and with the increase in the hythane 30 fraction, the combustion duration was shortened, leading to peak pressure attained after TDC. Keeping the hydrogen fraction constant and increasing the equivalence ratio improves the heat release rate and consistent reduction in the delay period.
5. Engine operation with 100% wide-open throttle, an equivalence ratio of 1.15 & 1.22, and with the increase in the hythane 30 fraction, CO and HC emissions decrease, and there is an increment in NO_x emissions. If you keep the Hythane30 fraction the same and raise the equivalence ratio, CO emissions go down a lot, and HC emissions go down at first and then up later. The increase in hydrogen fractions adversely affects the NO emission.

ACKNOWLEDGEMENT

The authors wish to thank the Directorate of Research SRM IST, India; under the Selective Excellence Research Initiative 2021-24 (SERI-2021-24) scheme for the financial support extended in carrying out this research

REFERENCES

1. Du Y, Yu X, Wang J, Wu H, Dong W, Gu J. (2016) Research on combustion and emission characteristics of a lean burn gasoline engine with hydrogen direct-injection. *International Journal of Hydrogen Energy*, 41(4):3240-8.
2. Eichhorn A, Lejsek D, Hettinger A, and Kufferath, A., (2013) From Challenge Determining a Combustion System Concept for Downsized SI-Engines - Comparison and Evaluation of Several Options for a Boosted 2-Cylinder SI-Engine, *SAE Technical Paper*. 2013-01-1730.
3. Gong C, Huang K, Jia J, Gao Q, Liu X., (2011) From Improvement of fuel economy of a direct-injection spark-ignition methanol engine under light loads, *Fuel*. 90:1826 to 1832.
4. Liu Y, Pei Y, Peng Z, Qin J., From Spray Development and Droplet Characteristics of High Temperature Single Hole Gasoline Spray, (2017) *Fuel*. 191:97-105.
5. Reitz R.D, Ogawa H, Payri R and Fansler T., (2019) From IJER Editorial: The Future of the Internal Combustion Engine, *International Journal of Engine Research*. 21:3-10.
6. WANG J, HUANG Z, TANG C, ZHENG J.,(2010) FROM EFFECT OF HYDROGEN ADDITION ON EARLY FLAME GROWTH OF LEAN BURN NATURAL GAS-AIR MIXTURES, INTERNATIONAL JOURNAL OF HYDROGEN ENERGY. 35:7246 TO7252

THERMODYNAMIC MODELING OF AN INNOVATIVE INTEGRATED POLYGENERATION SYSTEM USING SUSTAINABLE ENERGY RESOURCES

[1*]Mohammad Ali Sabbaghi, [2]C. Ozgur Colpan, [3]Hadi Genceli
[1] Department of Mechanical Engineering, Yazd University, Yazd, Iran
[2] Dokuz Eylul University, Faculty of Engineering, Department of Mechanical Engineering, Tinaztepe Campus, 35397, Izmir, Türkiye
[3] Faculty of Mechanical Engineering, Yildiz Technical University, Besiktas, Istanbul, 34349, Turkey

*Corresponding author e-mail: m.sabbaghi@yazd.ac.ir

ABSTRACT
This study proposes a hybrid multigeneration system that combines biomass and solar energies to overcome the limitations of individual renewable energies. The system utilizes solar energy for hydrogen production through a proton exchange membrane electrolyzer powered by photovoltaic-thermal panels. The generated hydrogen is introduced into the gas turbine cycle's combustor. The system integrates a biomass-fueled gas turbine with a closed Brayton cycle and organic Rankine-vapour compression cycles (ORC-VCR). This arrangement is quite innovative for an energy system. The system's configuration enhances the utilization of heat recovered from the turbine, producing 0.00699 kg/s of hydrogen, 931.8 kW of electricity, 180 kW of cooling, and 122.4 kW of heating. Moreover, the system demonstrates an exergy efficiency of 22.18%, showcasing its effectiveness in converting input energy into useful outputs. This innovative hybrid configuration demonstrates the capability to provide various clean energy outputs.

Keywords: Hybrid system, Multigeneration, Hydrogen production, Solar, Biomass

1. INTRODUCTION
The current era of industrialization heavily relies on the production and distribution of clean energy to facilitate sustainable development [1]. The detrimental air pollution and harmful emissions associated with fossil fuels have created a pressing need to transition towards renewable energy sources. To achieve improved reliability, the limitations of individual renewable energies can be overcome by utilizing hybrid energies [2]. In this context, there has been a growing focus on combining solar and biomass energies in multigeneration systems. Numerous studies have been conducted to explore various configurations of hybridizing biomass and solar energy in power generation systems. These investigations aim to assess the feasibility, performance, and potential benefits of combining these two renewable energy sources [3]. In a study by Khalid [4], a thermodynamic analysis was conducted on a multigeneration hybrid system that combines a biomass energy-driven gas turbine with an ORC activated by solar energy. The researchers found that the system exhibits higher efficiency when both renewable energy sources are integrated compared to relying on a single renewable energy source alone. According to research conducted by Dincer et al [5], multigeneration systems based on renewable energies offer advantages in terms of reduced fuel costs and decreased emissions of harmful pollutants compared to conventional systems. These studies suggest that integrating two renewable energy sources in a multigeneration system can yield significant benefits. In a study by Livshit et al [6], a solar hybrid steam injection gas turbine system was investigated. The researchers found that the combination of solar energy into the solar hybrid steam injection gas turbine (STIG) cycle leads to a significant improvement in system productivity. The efficiency of the combined system was reported to reach over 40-55%, whereas the efficiency of the STIG cycle without solar integration was only about 25-35%.
The literature review emphasizes that combining solar and biomass energy in a hybrid system can improve the system's efficiency. The present study introduces a novel hybrid biomass and solar energy-based combined cycle. This research is distinguished by an innovative energy system design, integrating a Closed Brayton Cycle (CBC), Gas Turbine (GT), and ORC in a novel configuration. Such a system has not been investigated in any previous study. This arrangement aims for synergistic operation, leveraging the strengths of each cycle to achieve enhanced energy recovery. The main objective is to minimize waste energy by effectively capturing and converting exhaust heat from the GT and CBC into useful power via the ORC-VCR, ultimately maximizing overall system efficiency and reducing environmental impact.

2. SYSTEM DESCRIPTION
The proposed system, illustrated in Fig. 1, comprises three cycles: a GT as the main cycle, a CBC as the middle cycle, and an ORC-VCR as the bottoming cycle. The system is operated using a combination of biomass and solar resources. Biomass is the primary fuel, while solar energy is used for hydrogen generation by Proton Exchange Membrane Electrolyzer (PEME). The hydrogen is then burned in a combustor to reheat the flue gas from the turbine. The utilization of hydrogen combustion in the gas turbine results in an elevated flue gas temperature from the turbine. This increased temperature is too high to be directly utilized as a heat source in an ORC-VCR, which would lead to significant exergy destruction in heat exchangers. To address this issue, a CBC is employed. The CBC efficiently recovers the waste heat and prevents excessive exergy destruction. In the CBC, helium is chosen as the operating medium. Helium offers yields a higher efficiency compared to similar gases, such as N_2 [7]. Additionally, the lower working pressure of helium, when

compared to CO_2, provides an additional advantage. To simplify the modeling of the investigated system, certain assumptions have been made [8].

- Thermal losses from the components of the system are disregarded.
- Changes in kinetic and potential energy were considered negligible and therefore excluded from the analysis.
- The system operates under a steady-state condition.

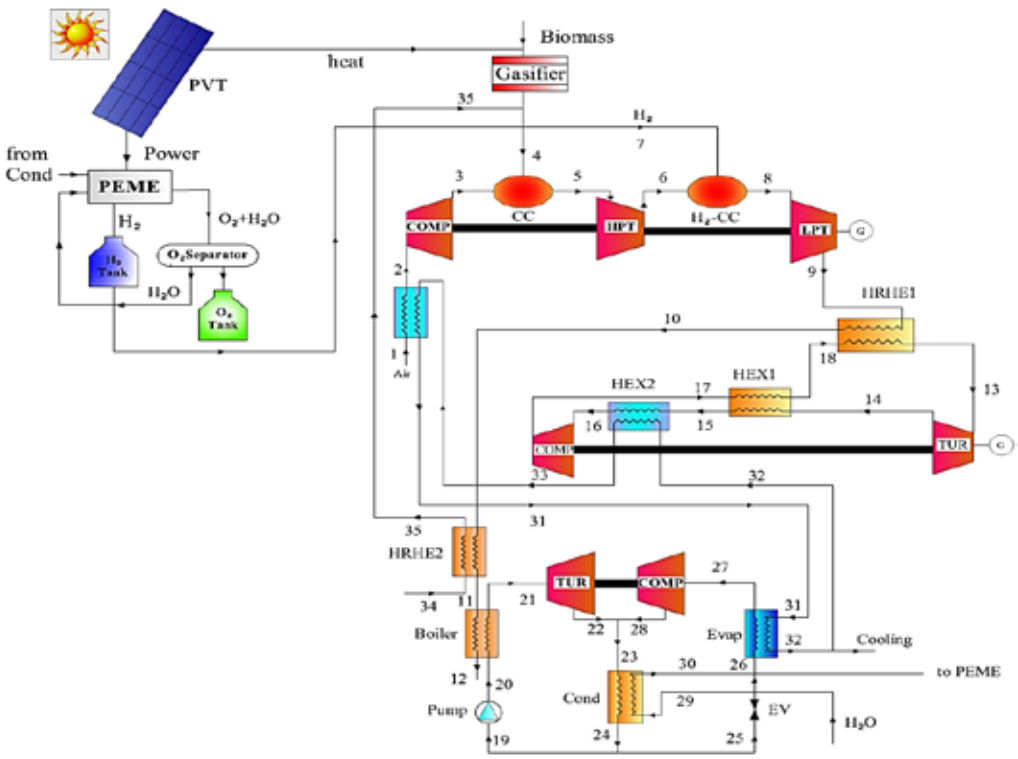

Fig. 1. Schematic of the proposed multigeneration system driven by solar and biomass energy sources

3. THERMODYNAMIC MODELING

To evaluate the feasibility of the system from both energy and exergy perspectives, the system is formulated thermodynamically. These models utilize the principles of energy conservation and exergy analysis to assess the performance of each component within the system. The Engineering Equation Solver (EES) software is used to model the system's behavior and solve the resulting system of equations [9].

$$\sum_{in} \dot{m}_i = \sum_{out} \dot{m}_e \tag{1}$$

$$\dot{Q}_{cv} + \sum_{in} \dot{m}_i h_i = \dot{W}_{cv} + \sum_{out} \dot{m}_e h_e \tag{2}$$

$$\dot{E}x_Q + \sum_{i} \dot{m}_i ex_i = \sum_{e} \dot{m}_e ex_e + \dot{E}x_W + \dot{E}x_D \tag{3}$$

$$ex_{ph} = (h - h_0) - T_0(s - s_0) \tag{4}$$

The exergy efficiency of the studied system is determined from Eq. 5.

$$\eta_{ex} = \frac{\dot{W}_{net} + \dot{m}_{31}(h_{31} - h_{32})}{\dot{E}_{Biomass} + \dot{E}_{solar}} \tag{5}$$

Chemical exergy represents the maximum useful work obtainable when a substance transitions from its initial chemical state to equilibrium with the environment. For the fluids within the investigated system, calculations of chemical exergy were performed using the equations detailed in [2-4]. The biomass properties used as well as the equations used to model the PEME, and PVT are taken from references [8-9].

4. RESULTS AND DISCUSSIONS

Figs 2 and 3 present the validation of models for the GT cycle and PEME, using previous research conducted under identical conditions. The comparisons performed in this study demonstrate a strong agreement with the findings reported in the corresponding references (less than 1.5%), indicating the reliability and consistency of the results.

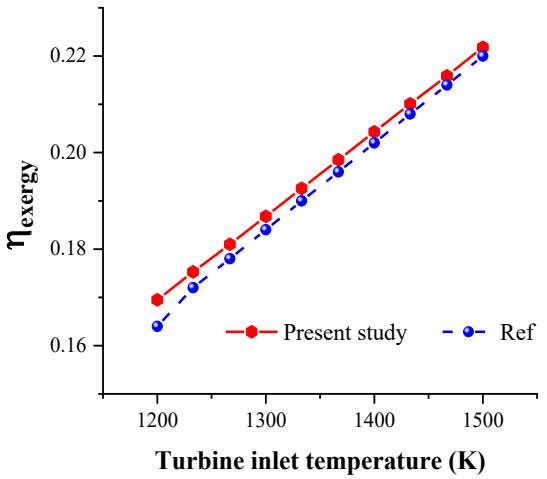

Fig. 2. Comparison of GT modeling with Ref [7]

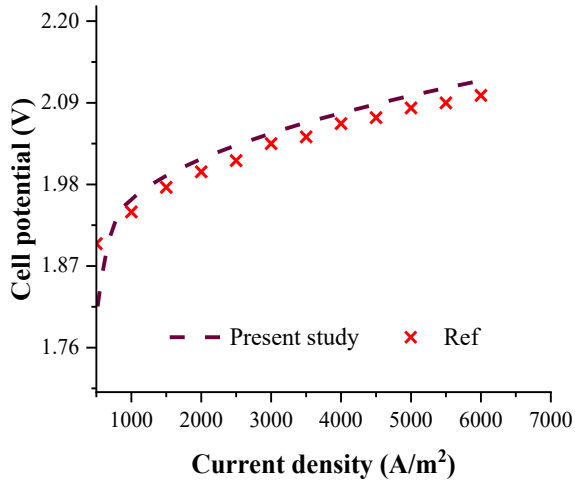

Fig. 3. Comparison of PEME modeling with Ref [10]

Fig. 4 illustrates the variations in exergy efficiency and system production power with the CBC compressor pressure ratio. As depicted in the figure, an initial increase in the compressor pressure ratio leads to a corresponding increase in both the system production power and exergy efficiency. However, beyond a certain point, these values start to decline. This indicates that the optimal values for these two parameters occur at approximately 4 for the compressor pressure ratio. This trend is because, for pressure ratios below 4, the power generated by the system surpasses the power consumed by the compressor, resulting in an overall improvement in system efficiency. Conversely, the situation is reversed for pressure ratios higher than this threshold, leading to a decrease in efficiency.

Fig. 5 illustrates the changes in exergy efficiency and system production power concerning the GT compressor pressure ratio. As clearly evident in the figure, with an increase in the compressor pressure ratio, the efficiency and production power of the system increase continuously. This finding is why, at all pressure ratios, the amount of power produced by the turbines of the GT cycle exceeds the power consumed by the compressor. It should be noted that at high-pressure ratios, the slope of the curve decreases, indicating that the increase in turbine production power compared to compressor power consumption occurs at a lower rate.

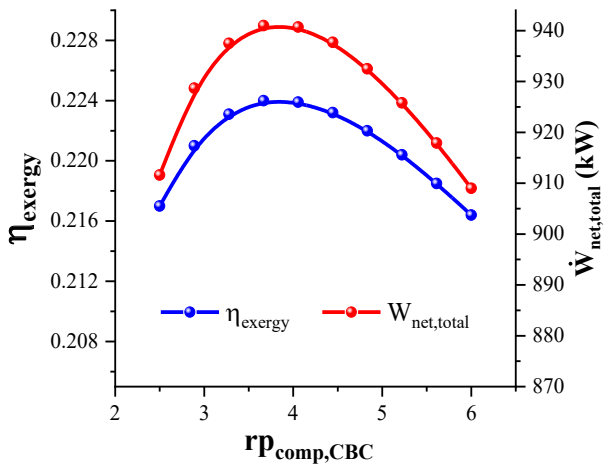

Fig. 4. Changes in $rp_{comp,CBC}$ with system performance

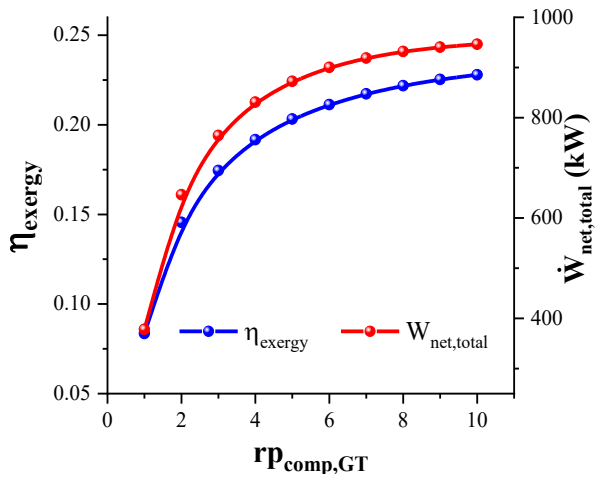

Fig. 5. Changes in $rp_{comp,GT}$ with system performance

Another parameter influencing the performance of the investigated system is the ORC-VCR turbine inlet temperature, which indicates the proportion of heat transferred to the subsystem and the portion assigned to the gasifier for recovery. Changes in T_{21} with two stated parameters are depicted in Fig. 6. According to the figure, with the increase

in T_{21}, the input energy to the subsystem rises, leading to an increase in cycle production cooling. Conversely, the amount of recovery heat to the gasifier decreases. The interaction of these two issues establishes optimal conditions for the system. Additionally, the temperature variations of T_{21} concerning the heat transferred to the subsystem and the quantity of biomass required in the gasifier are illustrated in Fig. 7. With the temperature increase, the heat input to the subsystem rises. Conversely, the amount of heat transferred to the gas turbine cycle decreases. Consequently, consuming more biomass to compensate for this heat loss becomes necessary, ensuring the required heat supply for the system through combustion.

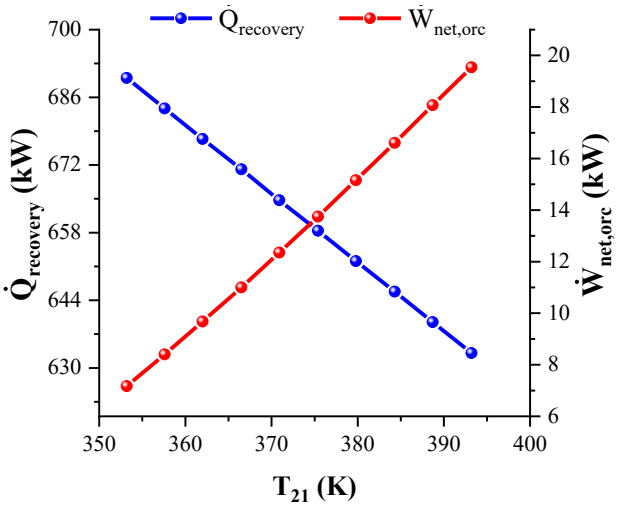

Fig. 6. Changes in T_{21} with system performance

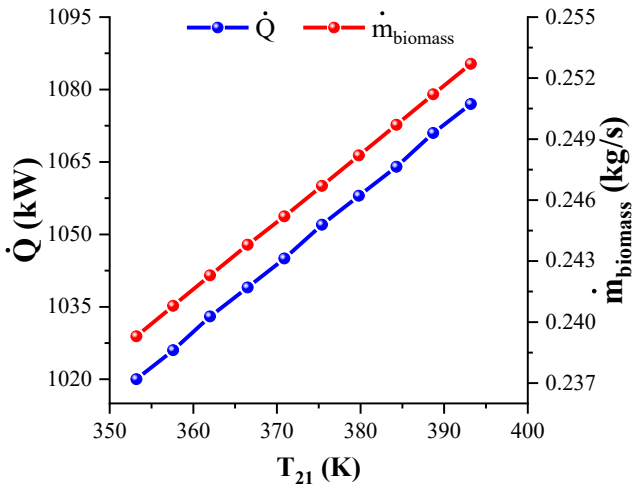

Fig. 7. Changes in T_{21} with heat and required biomass

5. CONCLUSIONS

This study presents a novel multigeneration system that integrates biomass and solar energy. The system utilizes solar energy for hydrogen production to mitigate the intermittency of solar radiation, ensuring a stable and efficient energy supply. Subsequently, the generated hydrogen is transferred to the post-firing combustor to enhance the power generation capability. The system is engineered to optimize the utilization of recycled heat from the turbine, yielding 0.00699 kg/s of hydrogen production, 931.8 kW of electricity generation, 180 kW of cooling output, and 122.4 kW of heating capacity. With these parameters, the system attains an exergy efficiency of 22.18%.

FUNDING STATEMENT

This project has received funding from the European Union's Horizon Europe research and innovation Program under the Marie Skłodowska-Curie grant agreement No 101126655. This project is also supported in part by a research grant from the Scientific and Technological Research Council of Türkiye (TÜBİTAK) under the grant number 123C459.

REFERENCES

[1] Ince AC, Colpan CO, Hagen A, and Serincan MF. 2021. Modeling and simulation of Power-to-X systems: A review. Fuel 304:121354.
[2] Arslan M and Yılmaz C. 2022. Design and optimization of multigeneration biogas power plant using waste heat recovery System: A case study with Energy, Exergy, and thermoeconomic approach of Power, cooling and heating. Fuel 324: 124779.
[3] Sabbaghi MA, Soltani M, Fraser R, and Dusseault MB. 2024. Emergy-based exergoeconomic and exergoenvironmental assessment of a novel CCHP system integrated with PEME and PEMFC for a residential building. Energy 305:132301.
[4] Khalid, F, Dincer, I, Rosen, and M. A. 2015. Energy and exergy analyses of a solar-biomass integrated cycle for multigeneration. Solar Energy 112: 290–299.
[5] Dincer I, Zamfirescu C, 2012. Renewable-energy-based multigeneration system. International Journal of Energy Research 36:1403-1415.
[6] Livshits M and Kribus A. 2012. Solar hybrid steam injection gas turbine (STIG) cycle. Solar Energy 86: 190–199.
[7] Cao Y, et al. 2021. A novel hybrid biomass-solar driven triple combined power cycle integrated with hydrogen production: Multi-objective optimization based on power cost and CO_2 emission. Energy Conversion and Management 234: 113910.
[8] Joshi AS, Tiwari A, Tiwari GN, Dincer I, and Reddy BV. 2009. Performance evaluation of a hybrid photovoltaic thermal (PV/T) (glass-to-glass) system. International Journal of Thermal Sciences 48(1): 154–64.
[9] Boyaghchi FA, Chavoshi M, and Sabeti V. 2018. Multigeneration system incorporated with PEM electrolyzer and dual ORC based on biomass gasification waste heat recovery: exergetic, economic and environmental impact optimizations. Energy 145: 38–51.
[10] Ahmadi P, Dincer I, and Rosen M. A. 2013. Performance assessment and optimization of a novel integrated multigeneration system for residential buildings. Energy and Buildings 67: 568–578.

Ga-DOPED ZnO COATED STAINLESS STEEL ELECTRODES FOR PHOTOELECTROCHEMICAL HYDROGEN PRODUCTION

*[1,2]Sumeyya Ayca and [3,2]Ibrahim Dincer
[1]Istanbul Aydin University, Faculty of Engineering, Department of Aerospace Engineering, Istanbul, Türkiye
[2] Yildiz Technical University, Department of Mechanical Engineering and Hydrogen Research Center, Istanbul, Türkiye
[3] Ontario Tech University, Clean Energy Research Laboratory, Oshawa, Ontario, Canada

*Corresponding author's e-mail: sumeyya.ayca@std.yildiz.edu.tr

ABSTRACT
This study aims to produce hydrogen using the photoelectrochemical method, which is a sustainable and reliable hydrogen production method. This study used gallium and zinc oxide due to their photocatalytic properties. Stainless steel was selected as the electrode to be coated, and the coating process was carried out using the dip coating method. Light and dark environments were created using a solar simulator, and then measurement analyses were obtained using a GAMRY device in these environments. According to the data, the photocatalytic properties of Ga-doped ZnO coating on stainless steel are highly efficient.

Keywords: Dip-coating, Hydrogen production, Ga-doped ZnO, Photoelectrochemical method, Stainless steel.

1. INTRODUCTION
Hydrogen has been playing a vital role in recent years in terms of environmental impact and sustainability as a clean and reliable energy carrier [1]. It needs to go through various processes to make hydrogen effective as a usable energy carrier. The choice of the production method of hydrogen, which must be produced safely and efficiently, is crucial in terms of the emission effect in the production process. Photoelectrochemical hydrogen production is a reliable and clean method that is very important in sustainability. Studies are being carried out on material coating methods to be used as catalysts to make hydrogen production efficient with this method. Gallium (Ga) and zinc oxide (ZnO) have been investigated recently due to their photocatalyst properties. In a study by Nuñez et al., photocatalytic hydrogen production of Ga-modified ZnO photocatalysts prepared by hydrothermal methods was investigated. Their study used Platinum (Pt) as a cocatalyst and noted that this accelerated hydrogen production as an electron scavenger [2]. Taha et al. produced Ga-doped ZnO material using a spin-coating method to be used as a sensor in a study they conducted [3]. The methods and chemicals used in their research are important for this study. In this study, hydrogen production was realized by coating Ga-doped ZnO photocatalyst on stainless steel using the dip-coating method.

2. MATERIALS AND METHOD
Figure 2 shows a schematic representation of this study. First, the solution to be used in the coating was prepared. The solution contains 2-propanol, ethanolamine, Gallium oxide, and Zinc acetate dihydrate in specific proportions. The electrolyte to be coated was determined to be stainless steel. First, the stainless-steel surface was sanded and then kept in hydrochloric acid. Then, dipping-pulling was carried out in the prepared solution, and the coating was adhered to the surface by applying heat with a heat gun. The coated material was then placed in a drying oven. A solar simulator was used for hydrogen production using the photoelectrochemical method. The necessary measurements were taken using a GAMRY device with the material coated as a photocatalyst.

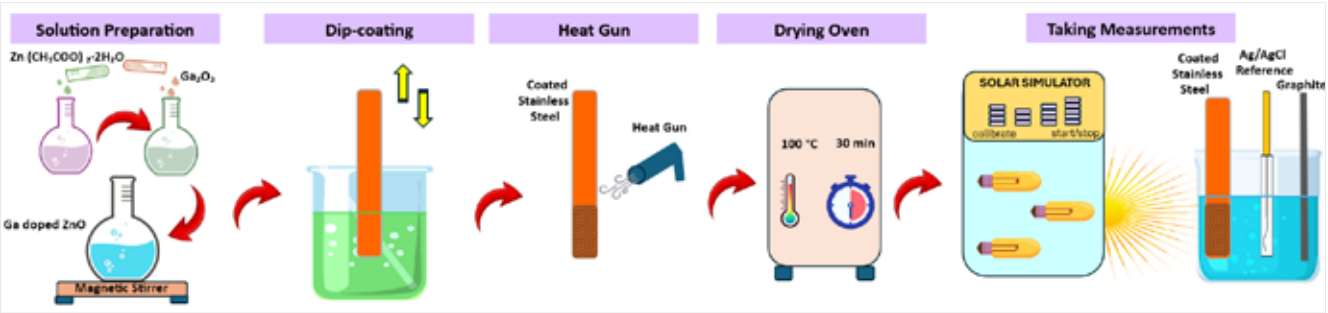

Fig. 1. Schematic representation of this study.

3. RESULTS AND DISCUSSION

Figure 2 shows the photocurrent experimental results of the coated material. The data shows the current changes under light illumination and in a dark environment. The figure shows that the coated material does not produce a photogenerated current when there is no light illumination. The increase in current value when light is applied indicates that electron-hole pairs are formed due to photogeneration; thus, photoelectrochemical reactions take place on the coated electrode. According to the graph, photogeneration of photogenerated current occurs in the coated materials when illuminated by light. This indicates that the coated materials act as photocatalysts. In addition, the fact that the photocurrent levels reached similar values in the light-on-off processes suggests that the electrode under light has a photoelectrochemically stable performance.

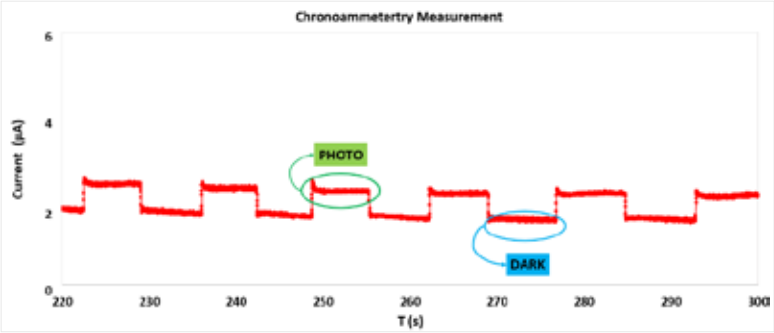

Fig. 2. Photocurrent experimental result graph of the coated material.

4. CONCLUSION

In this study, the photoelectrochemical method applied Ga-doped ZnO coating on stainless steel for hydrogen production. Dip-coating was used as the coating method, and the necessary processes were applied to ensure that the coating adhered to the surface. The GAMRY device was used to measure the photocatalytic properties of the coated material, and measurements were taken both in the dark and under light. According to the study results, the material developed as a photocatalyst shows highly efficient photocatalytic properties under light illumination. This study's innovative aspect is combining the electrode and coating method with Ga and ZnO.

ACKNOWLEDGEMENT

The research was funded by Yildiz Technical University's Scientific Research Projects Council, with the projects identified as FBA_2023_5648.

REFERENCES

1. Mesecke, L., Meyer, I., Oel, M., Lachmayer R. 2025. Challenges and potentials for additive manufacturing of hydrogen energy components: A review, International Journal of Hydrogen Energy, Volume 113,2025, Pages 198-219, doi.org/10.1016/j.ijhydene.2025.02.441.
2. Núñez, J., Fresno, F., Platero-Prats, A. E., Jana, P., Fierro, J. L. G., Coronado, J. M. de la Peña O'Shea, V. A. 2016. Ga-Promoted Photocatalytic H_2 Production over Pt/ZnO Nanostructures. ACS Applied Materials & Interfaces, 8(36), 23729-23738, doi:10.1021/acsami.6b07599.
3. Taha, I., Abdulhamid, Z.M., Straubinger, R. 2024. Ga-doped ZnO nanoparticles for enhanced CO2 gas sensing applications. Sci Rep 14, 29712. doi.org/10.1038/s41598-024-81279-0.

INVESTIGATION OF T-CLASS FUEL CELL HYBRID ELECTRIC OFF-ROAD VEHICLE

[1*]Zeynep Sude İşleyen, [1,2]Mustafa Umut Karaoğlan
[1]Dokuz Eylul University, Faculty of Engineering, Department of Mechanical Engineering, Tinaztepe, Buca, Izmir, 35390, Turkey
[2]Dokuz Eylul University, Energy Application and Research Center, Tinaztepe, Buca, Izmir, 35390, Turkey

*Corresponding author e-mail: zeynpisleyen9@gmail.com

ABSTRACT
The advancement of technology and industrialization has increased environmental pollution, prompting individuals and institutions to seek sustainable solutions. Fuel cells, offering high efficiency, an eco-friendly structure, and long range, stand out as a strong alternative to reduce dependence on fossil fuels. In this study, a T-Class Fuel Cell Hybrid Electric Off-Road Vehicle powered by an electric motor instead of an internal combustion engine was modeled in Matlab/Simulink, and drive cycle simulations were performed. In this study, electric motor power requirements were calculated and power outputs of the fuel cell and battery was compared during the simulation time. Additionally, The SOC of the battery was determined based on the battery power output. The findings highlight the potential of T-Class Fuel Cell Hybrid Electric Off-Road Vehicles for sustainable transportation and demonstrate positive improvements in range and efficiency.

Keywords: fuel cell electric vehicle, battery, Off-Road Vehicle, sustainable transportation

1. INTRODUCTION

The disruption of environmental balance has prompted people to explore alternative energy sources. Research has shown that fuel cells have the potential to solve this problem. Due to their high efficiency and minimal environmental impact, these cells have secured a significant place among the most important alternative energy sources of the future. Fuel cells are devices that produce electricity and heat by allowing a chemical reaction between a fuel, such as hydrogen, and oxygen. In this process, the energy from the fuel is directly converted into electrical energy, with minimal harmful waste released into the environment [1]. This technology offers a significant environmental advantage compared to fossil fuel-based energy production methods, as it generates less carbon emissions and pollution. Furthermore, the abundance of hydrogen makes fuel cells a sustainable energy source in the long term.

The use of fuel cells in vehicles offers important advantages, such as high energy efficiency and the ability to convert fuel directly into electrical energy, without the need for combustion, resulting in very low emission levels [2]. This technology is more environmentally friendly and ensures more efficient energy use compared to vehicles with internal combustion engines. This study aims to examine the performance of fuel cell and battery-based power systems through the design of a T-Class Fuel Cell Hybrid Electric Off-Road Vehicle powered by an electric motor instead of an internal combustion engine. The vehicle, modeled on the Matlab/Simulink platform, will be simulated using the Worldwide Harmonized Light Vehicles Test Cycle (WLTC), and a comparison of the efficiency, range, and overall effectiveness of both power sources will be made. These simulations will evaluate how the T-class fuel cell hybrid electric off-road vehicle performs in real-world conditions and highlight the advantages of both technologies.
The research results are expected to more comprehensively showcase the potential of fuel cell vehicles in contributing to sustainable transportation. Furthermore, this study will provide valuable insights into the development of FCEV technology and energy efficiency improvements, contributing to future transportation solutions. Fuel cells, compared to batteries, are expected to make significant contributions to industry developments as a more efficient and environmentally friendly option. This research aims to accelerate innovations in the sector and contribute to the development of sustainable transportation solutions.

2. MODELING AND SIMULATION

2.1 Vehicle Models

Calculating the vehicle's traction power is essential for determining the energy required by the electric motor during driving. This calculation requires knowledge of the total forces acting on the vehicle during its motion. These forces are fundamental physical factors that influence the vehicle's movement and stability and play a crucial role in optimizing its dynamic performance. Rolling resistance (F_R) represents the force caused by shape deformation during the contact of the wheels with the road surface. Aerodynamic drag resistance (F_L) is the resistance generated by air flow during the vehicle's movement. Acceleration resistance (F_a) refers to the resistance encountered by the vehicle during acceleration or deceleration. Regenerative braking force (F_a-) functions by recovering energy during braking to recharge the battery. Accurate calculation of these forces ensures a better understanding of the vehicle's energy consumption and performance. The corresponding equations are shown in (1-4).

$$F_R = m \cdot g \cdot f_R \quad (1)$$

$$F_L = \frac{1}{2} \cdot c_W \cdot A \cdot \rho_L \cdot V^2 \quad (2)$$

$$F_a = m \cdot a \quad (3)$$

$$F_a^- = m \cdot a^- \quad (4)$$

The vehicle parameters of the fuel cell hybrid electric vehicle examined in this study are presented in Table 1. These parameters were integrated into the mathematical model created in the Matlab/Simulink environment, and the desired output results were calculated. The obtained results are presented as graphs in the findings section.

Table 1. Vehicle parameters

Symbol	Parameter	Value	Unit	Symbol	Parameter	Value	Unit
m	Mass	1270	kg	SoC	State of charges	%85	-
A_f	Frontal area	2.86	m^2	P_{FC}	Fuel cell power	1	kW
F_r	Rolling resistance force	0.03	-	A_{FC}	Active area of fuel cell	500	cm^2
ρ	Density of air	1.225	kg/m^3	n_{FC}	Fuel cell cell number	48	1
C_w	Aerodynamic drag coefficient	0.7	-	i_d	Differential gear ratio	2	-
r_w	Wheel radius	0.335	m	i_t	Transmission gear ratio	2.4	-
V	Electric motor voltage	400	V	i_{em}	Electirc motor gear ratio	1	-

2.2. Powertrain Component Models

The power output of the electric motor is calculated by multiplying the total motion resistance forces, as specified above, by time as a function of vehicle speed. The power output formula is given in Equation (5). In the equation, η_m represents mechanical efficiency.

$$P_{EM} = \frac{(F_R + F_L + F_a + F_a^-)}{\eta_M} \cdot V \quad (5)$$

The torque of the electric motor represents the force applied by the motor during rotation and the rotational force in vehicles. After calculating the power requirements, the torque [Nm] produced in the model is determined using Equation (6) and Equation (7). In these equations, *ig* represents the overall gear ratio between the wheel and the electric motor, while *rdyn* represents the dynamic wheel radius [mm] [3].

$$T_{EM} = \frac{(P_{EM} \cdot 9549)}{\eta_{EM}} \quad (6)$$

$$\eta_{EM} = \frac{V}{3.6} \cdot \frac{60}{2\pi} \cdot \frac{i_g}{r_{dyn}} \quad (7)$$

SOC defines the remaining energy in the battery and is commonly expressed as a percentage. That is, when the battery is fully charged, the SOC is considered to be 100% of its nominal capacity, and when it is completely discharged, the SOC is considered to be 0% [4]. The SOC at a specific time can be found using Equation (8).
The main difference between the battery and the fuel cell is that fuel cells generate electricity, while batteries store electricity. As is well known, batteries contain energy-donating chemicals within the system. When the battery's circuit is closed and energy is used, the battery's potential starts to deplete, and eventually, the battery is drained [5].

$$SOC(t) = SOC(0) - \frac{1}{C_{bat}} \cdot \int_o^t P_{bat} \cdot dt \quad (8)$$

In this study, PEM (Proton Exchange Membrane) fuel cell type has been preferred. The PEM fuel cell model has been developed in the Matlab/Simulink environment. Using current (A) as input, the values for voltage (V), power (W), hydrogen consumption (L/min), oxygen consumption (L/min), and water production (L/min) are obtained as outputs.
The cell voltage (V_{cell}) is determined using Equation (9). When a cell supplies power to a load, the Nernst voltage (E_{Nernst}), activation loss (V_{act}), ohmic loss (V_{ohm}), and concentration loss (V_{conc}) reduce the voltage. Hydrogen consumption is influenced by electrochemical reactions and the current demand. The power required by the motor, which is converted into current (I_{motor}, [A]), is provided to the fuel cell model based on the energy management strategy, enabling precise dynamic response modeling under changing conditions [5].

$$V = E_{Nerst} - V_{act} - V_{ohmic} - V_{conc} \quad (9)$$

2.3. Simulation Model

This study presents the model of a T-class fuel cell hybrid electric off-road vehicle developed in the Matlab/Simulink environment for vehicle performance and range evaluation. The structure of the model is shown in Figure 1. The model consists of key subsystems, including vehicle dynamics, powertrain components, fuel cell, and battery. In this hybrid system, the fuel cell is used to charge the battery and supply power to the electric motor, while the battery stores energy to propel the vehicle. The electric motor utilizes the power from both energy sources to drive the vehicle. The simulation uses the Worldwide Harmonized Light Vehicles Test Cycle (WLTC) as a reference. This section presents the mathematical model of the vehicle and the underlying equations in detail.

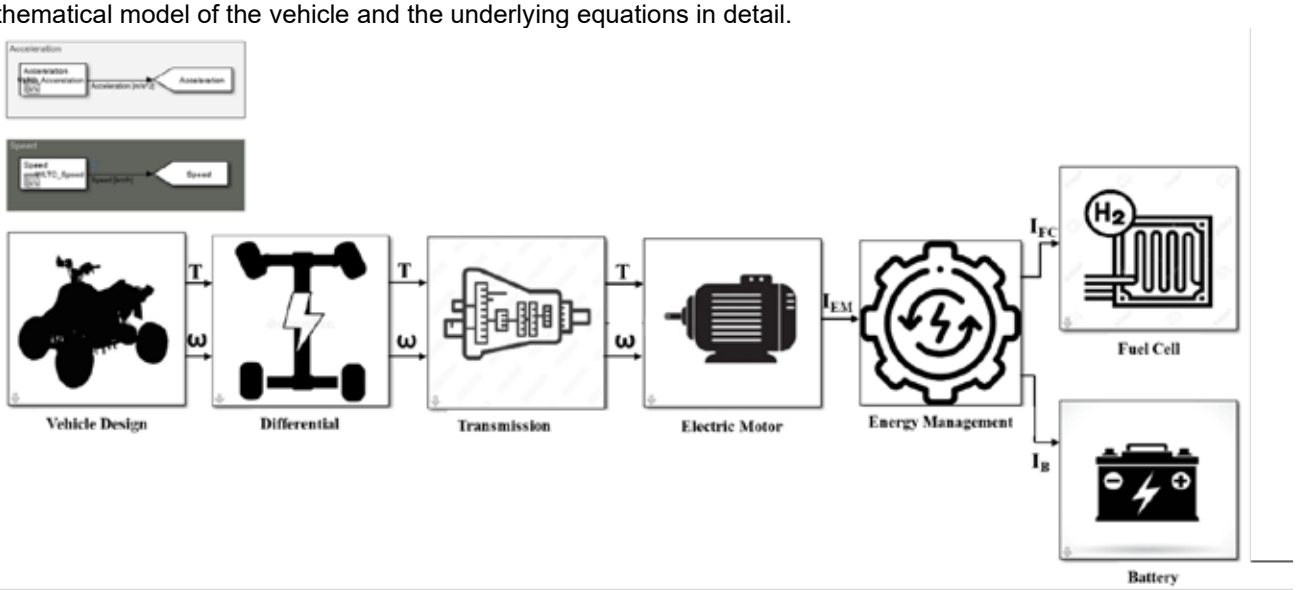

Fig. 1. Matlab/Simulink model for T class fuel cell hybrid electric off-road vehicle (T: Torque, ω: Angular velocity, I: Current)

The Max. SOC-of-FC control strategy is designed to enhance the efficiency of the fuel cell and maintain the SOC at high levels. The fuel cell can stop operating under certain conditions. In this case, the SOC comes into play to meet the vehicle's power demand. When the fuel cell stops operating, and the vehicle's SOC reaches a predetermined upper limit, the energy needs are met solely by the SOC. This prevents overloading the fuel cell, thereby increasing efficiency. Conversely, when the SOC reaches its lower limit, the fuel cell is reactivated to recharge the SOC, ensuring that the powertrain operates continuously and efficiently. This control strategy allows for the separate management of the fuel cell and SOC, ensuring that both systems operate within their optimal efficiency regions, leading to energy savings and improved performance. This control strategy is illustrated in Figure 2.

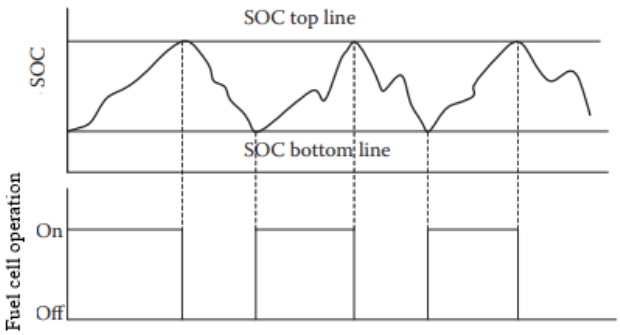

Fig. 2. Illustration of The Maximum SOC-of-FC Control Strategy

3.RESULTS AND DISCUSSION

In the vehicle model developed for the T-Class Fuel Cell Hybrid Electric Off-Road Vehicle, which utilizes a PEM fuel cell and is classified as an off-road vehicle, the vehicle parameters provided in Table 1 have been used. Based on the time-dependent driving cycle speed inputs, the required electric motor power, vehicle speed, hydrogen consumption, and fuel cell power have been calculated for the vehicle components.

As seen in Fig. 3a, the vehicle speed reaches a maximum of 65 km/h and a minimum of 18 km/h. As seen in Fig. 3b, the electric motor power varies between 19000 W and -3000 W. The Fig. 3d, shows that the electric motor torque (Nm)

varies over time and engages periodically. Sudden spikes are related to fluctuations in power demand. In Fig. 3d, the battery current exhibits constant fluctuations, occasionally reaching negative values, indicating regenerative braking. Meanwhile, the fuel cell current is generally positive and follows an irregular pattern, dynamically responding to varying load demands. In Fig. 3e, the battery's state of charge initially remains around 85% and generally maintains this level. However, occasional drops indicate an increase in energy drawn from the battery. The overall stability of the SoC level suggests that the energy management strategy is functioning effectively. In Fig. 3f, hydrogen consumption varies over time, with a noticeable increase observed after the 500th time step. This rise indicates a higher energy demand and greater power drawn from the fuel cell. Between the 600-800 time steps, hydrogen consumption reaches its peak, suggesting that the system relies more on the fuel cell during this period.

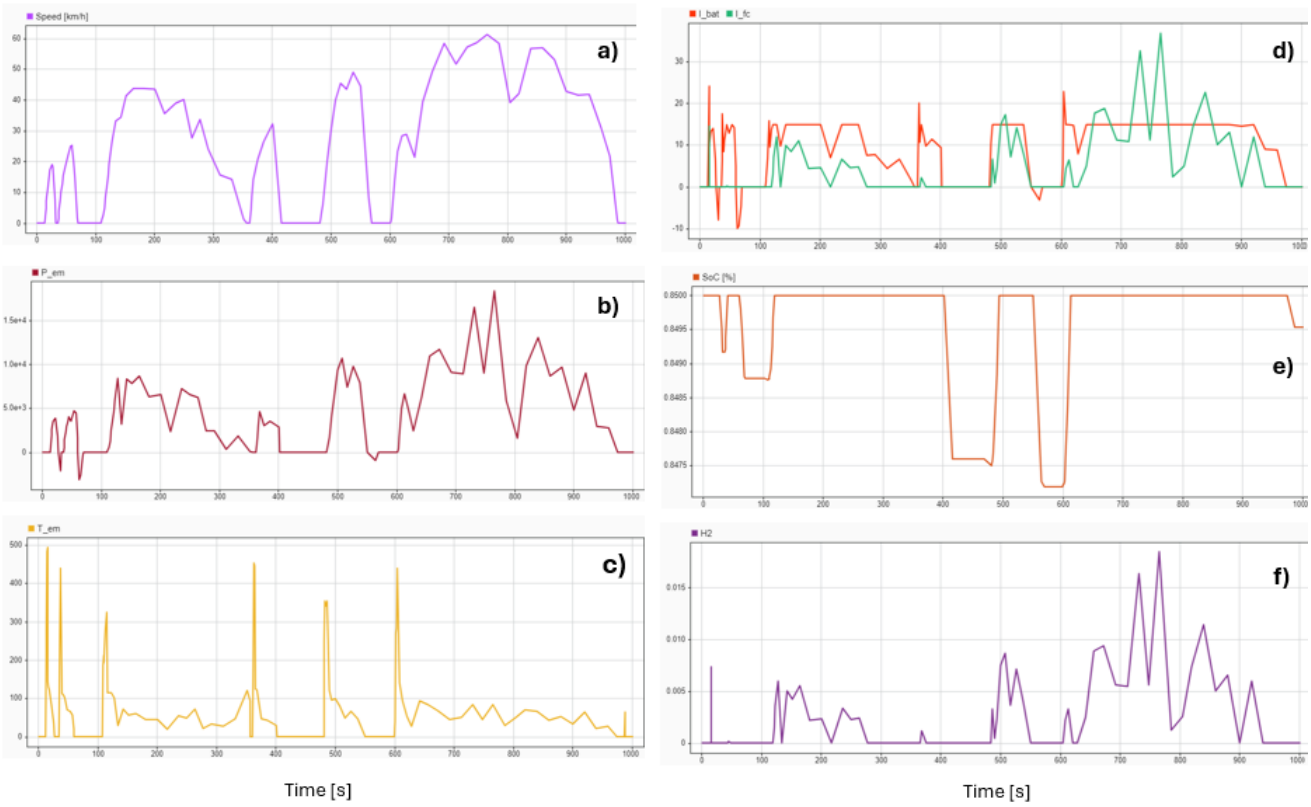

Fig. 3. Simulation results of fuel cell off-road vehicles depending on vehicle speed (a) for electric motor power (b), electric motor torque (c), battery and fuel cell current (d), state of charge (SoC) (e), H_2 consumption (f)

4. CONCLUSIONS

In this study, the performance of a T-Class Fuel Cell Hybrid Electric Off-Road Vehicle was analyzed in the Matlab/Simulink environment. The results demonstrate that fuel cell hybrid powertrains offer advantages in terms of energy efficiency, extended range, and environmental sustainability. The integration of the fuel cell and battery enabled balanced energy management, optimizing power distribution and enhancing vehicle performance. Analyzing vehicle performance plays a critical role in future studies for system optimization and component selection. Different energy management strategies can alter power distribution, leading to various choices in fuel cell and battery sizing. For instance, a larger battery can meet short-term high power demands, while a smaller fuel cell can improve system efficiency. The findings support the feasibility of fuel cell systems in off-road vehicles. Future studies can focus on system optimization and real-world testing to further improve this technology. The widespread adoption of fuel cell vehicles will contribute to reducing carbon emissions and promoting greener transportation alternatives.

REFERENCES

[1] Çavuşoğlu, A. (2006). Fuel Cells and Their Applications (Master's thesis, Bursa Uludag University, Turkey).
[2] Karaoğlan, M. U., Kuralay, N. S., & Topaç, M. M. (Year). Design Principles of Fuel Cell (PEM) Vehicles and Simulation Based on Urban Test Cycle.
[3] Karaoğlan, M. (2021). Investigation of the Effect of Gearbox Position on Vehicle Performance and Component Efficiency in Parallel

Hybrid Vehicles with Driving Cycle Simulation. *Journal of the Faculty of Engineering and Science, Dokuz Eylul University*, 25(74), 381-393.
[4] E. İ., & Okumuş, H. İ. (2018). Battery Models and State of Charge (SoC) Determination. *EMO Scientific Journal*, 8(1), 21-25.
[5] Tavman, A. (2004). Bor-Based Fuel Cells and Batteries. *Sigma*, 2.
[6] Larminie J and Dicks A. 2003. Fuel cell systems explained. Chichester, John Wiley & Sons.

IMPACT OF CURRENT DENSITY ON TEMPERATURE AND WATER CONTENT DISTRIBUTION IN A PEM FUEL CELL USING A COUPLED HEAT AND MASS TRANSFER MODEL

[1,2]*Mohammadreza Jahanbakhsh*, [1,2]*Erdal Aydın*, [1,2]*Can Erkey**
[1] Koç University, Chemical and Biological Engineering Department, Rumelifeneri Yolu, Istanbul, 34450, Türkiye
[2] Koç University, KUHyTech, Rumelifeneri Yolu, Istanbul, 34450, Türkiye
*Corresponding author e-mail cerkey@ku.edu.tr

ABSTRACT
Proton exchange membrane fuel cells (PEMFCs) offer a clean energy solution but face challenges in thermal and water management that impact performance and durability. A 1D coupled heat and mass transfer model was developed to examine the interactions between temperature distribution and membrane water content under varying conditions. Results indicate that increasing the current density leads to a higher overall temperature, with the most significant temperature gradient observed near the membrane. In other words, the temperature distribution shows a steep rise in temperature in the vicinity of the membrane. Simultaneously, the water distribution is not uniform; instead, water content progressively increases toward the cathode. Maintaining uniform water distribution is crucial for optimal proton conductivity. Imbalances can reduce performance or cause flooding. These findings emphasize the importance of managing both thermal and water profiles to enhance PEMFC efficiency and longevity.
Keywords: PEMFC, temperature distribution, water content, current density, thermal management.

1. INTRODUCTION
Proton exchange membrane fuel cells (PEMFCs) are attracting increased attention due to their high efficiency and zero emissions, with a wide variety of applications including hybrid power systems, electric vehicles, and space missions. They are considered as potential replacements for internal combustion engines due to their high efficiency and quiet operation. However, commercialization is hindered by cost and durability issues, in part caused by inadequate thermal management[1-4].
Temperature distribution in a PEMFC affects key processes, with uneven distribution reducing membrane hydration and proton conductivity, ultimately decreasing cell performance[5]. Secondly, reaction kinetics are directly affected by temperature. Furthermore, temperature gradients impact water management, leading to issues such as membrane dehydration or flooding, both of which can severely affect cell performance and durability[3]. Consequently, maintaining a uniform temperature distribution is vital to avoid performance losses and degradation[4].
Thermal modeling in PEMFCs has advanced from simple models to integrated approaches, recognizing the critical interplay of heat, water transport, and electrochemical reactions for accurate predictions[4, 6]. 1D models remain advantageous for certain applications[2], which can provide a fundamental understanding of the system. Despite progress in PEMFC thermal modeling, gaps remain in understanding the coupled effects of temperature distribution and water content[4].
This work aims to develop a 1D coupled heat and mass transfer model for PEMFCs to explore the relationship between current density, water content, and temperature profiles, accounting for operating conditions and faults to optimize thermal management and improve system performance.

2. MATERIALS AND METHODS

2.1 Model Overview

A model was developed to analyze coupled heat and mass transfer in a PEMFC, incorporating thermal, electrical, and mass transport mechanisms across multiple layers. Model equations were solved to determine temperature distribution, water content distribution, and species concentration under varying operating conditions.

2.2 Assumptions and Parameters

Steady-state conditions were assumed for thermal and mass transport. The thermal and electrical conductivity of the membrane was isotropic. The reaction kinetics were described by classical electrochemical relationships. Water transport in the membrane was described using empirical correlations based on relative humidity. The heat sources included ohmic heating, entropic contributions, and heat generated by water phase change.

Table 1. Input values for PEMFC model

Parameter Category	Component	Value	Unit
Physical Properties	Membrane thickness	51	μm
Relative Humidity	Anode	0.2	-
	Cathode	1.0	-
Thermal Conductivity	Membrane	0.21	W/(m·K)
	Catalyst layers	0.11	W/(m·K)
	Gas diffusion layers	0.6	W/(m·K)

2.3. GOVERNING EQUATIONS

2.3.1 Heat Transfer Model

The total heat generation in the PEMFC comprises multiple interconnected components that are distributed across different functional layers. The primary heat sources include ohmic heating, electrochemical reactions, and mass transport effects. The rate of ohmic heat generation through the membrane, q_{ohm} is given by:

$$q_{ohm} = r_{ohm} . j^2 \qquad (\mathrm{W/m^2}) \tag{1}$$

where j is the current density and r_{ohm} is a function of both the membrane thickness and its effective conductivity (σ_{mem}) given by:

$$\sigma_{mem} = (0.5139\lambda - 0.326).exp(1268 . (\frac{1}{303} - \frac{1}{T})) \tag{2}$$

Effective proton conductivity is computed by averaging the local conductivity profile across the membrane [7, 8]
The rate of electrochemical heat generation includes both reversible and irreversible components. In the catalyst layers, this is expressed as:

$$q_s = \frac{-j .T .\Delta S}{n_e.F} . f \qquad (\mathrm{W/m^2}) \tag{3}$$

where ΔS is the entropy change (-158 J/mol·K), F is Faraday's constant, n_e is the number of electrons transferred, and f is the distribution factor which is 0.8 for anode and 0.2 for cathode.
The rate of heat generation due to latent heat effects, q_{latent}, is computed by tracking water phase changes:

$$q_{latent} = L_v(T). \dot{m}_{evap} \qquad (\mathrm{W/m^2}) \tag{4}$$

where $L_v(T)$ represents the temperature-dependent latent heat of vaporization, and $\dot{m}_{evap}$ is determined from a material balance for water.
Heat flux due to conduction through each layer follows Fourier's law with distinct thermal resistances:

$$q_{cond} = -k. \left(\frac{dT}{dx}\right) \qquad (\mathrm{W/m^2}) \tag{5}$$

where k varies for each layer (membrane, catalyst layers, GDL, bipolar plates) based on material properties and local conditions.

2.3.2 Mass Transport Model

Species transport was modeled using modified diffusion equations that include reaction terms:

$$D_{eff}. \left(\frac{d^2C}{dx^2}\right) = \frac{j}{nF} \tag{6}$$

where D_{eff} represents the effective diffusion coefficient for either oxygen or hydrogen, adjusted for porosity and tortuosity effects in the GDL and catalyst layers.
The molar flux of species, $n"_{water}$,given by Equation (7) is governed by a complex balance between electro-osmotic drag and back diffusion [8]:

$$n"_{water} = n_{drag}. \left(\frac{j}{F}\right) . (\frac{\lambda}{22}) - \left(\frac{\rho_{dry}}{M_m}\right) . D_\lambda . (\frac{d\lambda}{dx}) \tag{7}$$

where n_{drag} is the electro-osmotic drag coefficient (normalized by $(\frac{\lambda}{22})$), λ is the water content, D_λ is the water diffusion coefficient which is a function of both temperature and water content given by[8]:

$$D_\lambda = D_{base} . (2.563 - 0.33\lambda + 0.0264\lambda^2 - 0.000671\lambda^3) \tag{8}$$

The boundary conditions were determined by the water activity at both interfaces, calculated from local temperature and relative humidity conditions, the proton conductivity of the membrane can be evaluated by[8, 9] :

$$\lambda_{eq} = (0.043 + 17.81a - 39.85a^2 + 36.0a^3) . exp((1268). (\frac{1}{T_{ref}} - \frac{1}{T})) \tag{9}$$

where a is water activity and $\boldsymbol{T_{ref}}$ is 303°C.

2.4 Numerical Implementation

The numerical model employs an explicit finite difference scheme for transients and an implicit iteration for steady-state solutions, using Newton-Raphson for nonlinear equations. It defines boundary conditions, computes water content, membrane conductivity, and heat sources, iterating until the temperature profile stabilizes within 0.01 K.

3. RESULTS AND DISCUSSION

3.1 Temperature Distribution Across PEMFC: Effect of Current Density on Temperature Profile

Fig. 1 illustrates the effect of current density (ranging from 0.32 A/cm² to 2.00 A/cm²) on temperature distribution across PEM fuel cell layers, including the Anode GDL, Anode CL, Membrane, Cathode CL, and Cathode GDL. As current density increases, so does the temperature in all layers, particularly near the membrane due to higher electrochemical activity. At the highest current density (2.00 A/cm²), the temperature reaches about 90°C, compared to 75°C at the lowest current density. This gradient is steeper near the membrane, highlighting increased heat generation from higher reaction rates. The results emphasize the importance of effective thermal management, as higher temperatures may lead to

thermal degradation, water evaporation, and reduced proton conductivity in the membrane, ultimately affecting fuel cell performance [10].

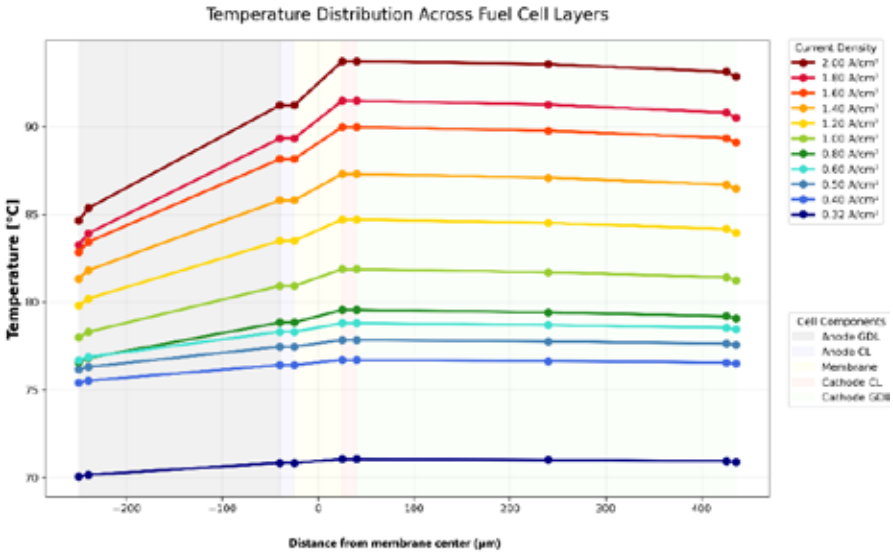

Fig. 1. Temperature distribution across PEMFC

3.2 Membrane Water Content Profile: Influence of Current Density and Humidity Conditions

Fig. 2. shows the water content profile within the PEMFC membrane, which significantly affects its conductivity and performance. At 80°C and 1.00 A/cm² current density, with relative humidity at the anode and cathode set to 0.20 and 1.00, respectively, water content increases towards the cathode (λ ≈ 6.96), while the anode region exhibits lower water content (λ ≈ 1.14), with an average of λ ≈ 4.46. This gradient arises from the water management for the PEMFC which sets the relative humidity of anode to 20% and cathode humidity to 100%. Electrochemical reaction at the cathode produces water, while higher evaporation rates at the anode contribute to dehydration[11]. Maintaining balanced water content is crucial for proton conductivity and fuel cell performance. This study examines near-dry anode conditions to assess boundary conditions and humidification effects, as imbalances can cause dehydration or flooding, reducing efficiency and increasing resistance. Figure 3 illustrates how membrane drying at high current densities creates a persistent temperature gradient, showing the operational malfunction.

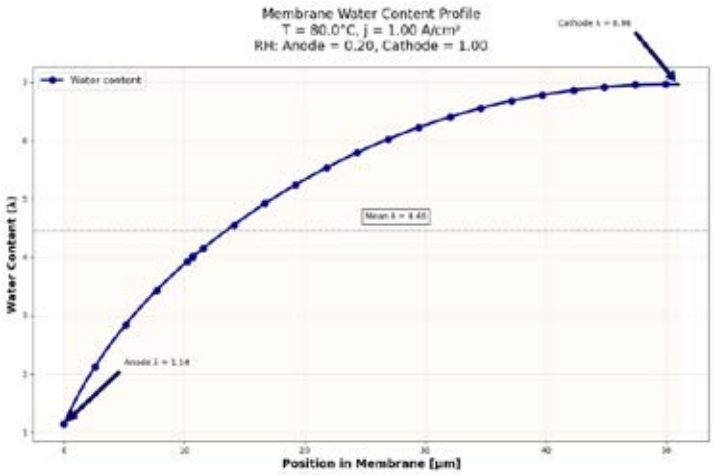

Fig. 2. Membrane water content across PEM

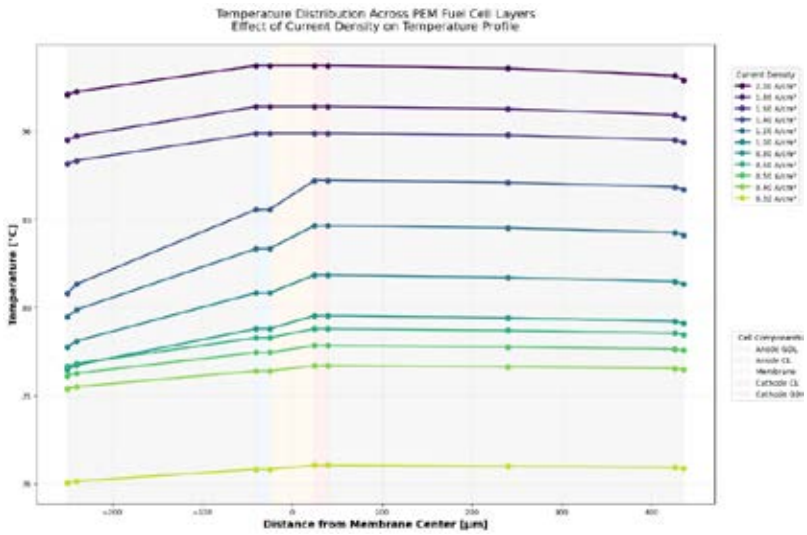

Fig. 3. Temperature distribution across PEMFC

4. CONCLUSIONS

A coupled heat and mass transfer model was developed for analyzing the temperature and water content distribution within PEMFCs. By simulating varying current densities and humidity conditions, the results provide valuable insights into the factors that influence PEMFC performance. The model demonstrates that higher current densities lead to increased temperatures, particularly in the membrane region, which can impact proton conductivity and water retention. Additionally, the water content profile varies across the membrane, with higher values at the cathode, crucial for maintaining membrane hydration and conductivity. These findings emphasize the importance of effective thermal and water management to ensure optimal fuel cell performance and longevity. The study paves the way for future optimization of PEMFC designs, with a focus on addressing the challenges of heat dissipation and water management. Further investigations are recommended to validate these results under more diverse operational conditions and to refine the models for practical applications.

ACKNOWLEDGMENTS

The authors acknowledge the support of the ProSafe project in advancing research on process safety and optimization.

REFERENCES

1. Liu, J.X., et al., *Two-dimensional analytical model of a proton exchange membrane fuel cell.* Energy, 2017. **119**: p. 299-308.
2. Bharath, K.V.S., et al., *Model-Based Data Driven Approach for Fault Identification in Proton Exchange Membrane Fuel Cell.* Energies, 2020. **13**(12): p. 3144.
3. Gao, W., et al., *Water flooding diagnosis of proton exchange membrane fuel cell based on current density scanning.* Journal of Electroanalytical Chemistry, 2024. **952**: p. 117929.
4. Wang, Y., et al., *A systematic review of system modeling and control strategy of proton exchange membrane fuel cell.* Energy Reviews, 2024. **3**(1): p. 100054.
5. Nishimura, A., et al., *Numerical Simulation on Impacts of Thickness of Nafion Series Membranes and Relative Humidity on PEMFC Operated at 363 K and 373 K.* Energies, 2021. **14**: p. 8256.
6. O'hayre, R., et al., *Fuel cell fundamentals*. 2016: John Wiley & Sons.
7. Abdol Rahim, A.H., et al., *An overview of polymer electrolyte membrane electrolyzer for hydrogen production: Modeling and mass transport.* Journal of Power Sources, 2016. **309**: p. 56-65.
8. Springer, T.E., T. Zawodzinski, and S. Gottesfeld, *Polymer electrolyte fuel cell model.* Journal of the electrochemical society, 1991. **138**(8): p. 2334.
9. Rahman, M.A., et al., *Development of 1-D multiphysics PEMFC model with dry limiting current experimental validation.* Electrochimica Acta, 2019. **320**: p. 134601.
10. Binyamin, B. and O. Lim, *Analyzing Temperature Distribution, Mass Transport, and Cell Performance in PEM Fuel Cells with Emphasis on GDL Face Permeability and Thermal Contact Resistance Parameters.* ACS Omega, 2024. **9**(1): p. 1516-1534.
11. Jiang, H., et al., *Modeling of Fuel Cell Cold Start and Dimension Reduction Simplification Method.* Journal of The Electrochemical Society, 2020. **167**(4): p. 044501.

TYPE-2 FUZZY MPPT CONTROL OF FUEL CELLS USING A HYBRID GENETIC-GREY WOLF OPTIMIZER

[1*]Ömer Faruk Özcan
[1] Dicle University, Department of Electric Power and Energy System, Sur, Diyarbakır, 21280, Turkey

* E-mail: omerfaruk.ozcan@dicle.edu.tr

ABSTRACT
This research introduces a hybrid maximum power point tracking (MPPT) technique for proton exchange membrane fuel cells (PEMFC). The suggested system employs a Type-2 Takagi–Sugeno–Kang (TSK) fuzzy logic controller, with the membership function parameters optimized using the GGWO algorithm, which integrates Genetic Algorithm (GA) and Gray Wolf Optimization (GWO). Integrating the robust global search capabilities of the Genetic Algorithm with the rapid convergence proficiency of the Gray Wolf algorithm yields a more balanced and successful optimization process. Type-2 fuzzy logic offers enhanced stability in control performance amidst environmental unpredictability and model ambiguity, while the GGWO algorithm enables systematic and adaptive adjustment of controller parameters. Simulation experiments conducted in the MATLAB/Simulink environment demonstrated that the suggested GGWO-TSK Type-2 FLS structure yields reduced power ripple, diminished settling time, and enhanced tracking accuracy relative to traditional MPPT approaches. The findings indicate that Type-2 fuzzy systems, enhanced by sophisticated intelligence algorithms, offer a viable solution for maximum power point tracking in fuel cell applications.
Keywords: PEMFC Mppt, ggwo-tsk

1. INTRODUCTION

Currently, the swiftly diminishing fossil-based non-renewable energy sources are unable to satisfy the ever-growing global energy demand, alongside their detrimental environmental impact. This predicament has heightened the significance of efficient, sustainable, and eco-friendly renewable energy sources. The production capacity of renewable energy sources, such as solar and wind systems, which are contingent upon weather conditions, have expedited scientific study and investments in this domain. Nevertheless, owing to the substantial expense and intricacy of storing surplus energy generated from renewable energy systems, fuel cells emerge as a prominent alternative clean energy source. Fuel cells possess the capability to deliver continuous electricity irrespective of environmental conditions and seasonal variations, excluding fuel availability. Proton Exchange Membrane Fuel Cells (PEMFC), utilizing hydrogen as fuel, are garnering heightened academic and industrial interest owing to their applicability across diverse sectors. The incapacity of fuel cells to deliver a consistent and stable output power is a notable drawback. The fuel cell's performance exhibits variability based on several operational parameters, including fuel flow rate, operating temperature, gas pressure, and humidity level within the cell. Consequently, maximum power point tracking (MPPT) algorithms are extensively employed to enhance the energy conversion efficiency of PEMFC systems and to identify the greatest power point at the system output.

Various MPPT approaches have been suggested in the conducted investigations. Karami and colleagues [1] evaluated the Perturb and Observe (P&O) and Incremental Conductance (IC) approaches, observing that the IC method had a more steady and rapid reaction. Ahmadi and colleagues [2] devised a PID controller utilizing particle swarm optimization (PSO), resulting in enhanced stability relative to the traditional P&O method. Derbeli and colleagues [3] accomplished rapid and precise MPP tracking across various situations utilizing the backstepping technique. Avanaki and Sarvi [4] devised a WCA-based methodology, attaining superior accuracy and adaptability relative to traditional techniques. Venkateshkumar and associates [5] have enhanced PEMFC efficiency with a fuzzy logic-based control system. Rezk and Fathy [6] attained superior monitoring performance with the VSS-INR approach, which utilizes solely voltage and current sensors. Harrag and Messalti [7] documented a reduced response time and diminished fluctuation with the neuro-fuzzy IC controller in comparison to the conventional IC. Reddy and Sudhakar [8] enhanced maximum power point tracking (MPPT) efficacy with the application of a radial basis function network (RBFN). Mallick and Mukherjee [9] enhanced voltage regulation with a DVR system utilizing artificial neural networks and Type-2 fuzzy logic. Dogan and colleagues [10] established a type-2 fuzzy logic-based MPPT framework, exhibiting a swifter response time, less power fluctuation, and enhanced efficiency relative to the P&O algorithm. Conventional MPPT techniques often face limitations when applied to fuel cell systems, particularly due to nonlinear dynamics and transient fluctuations. Classical methods such as P&O, Type-1 fuzzy logic, and genetic algorithms have shown limited success in accurately tracking the maximum power point under such conditions. As a result, recent research has increasingly focused on hybrid optimization approaches that combine global search and local exploitation capabilities with advanced fuzzy inference systems capable of handling uncertainty, such as Type-2 fuzzy logic.

In this study, a novel GGWO-TSK Type-2 fuzzy logic MPPT controller is proposed for Proton Exchange Membrane Fuel Cell (PEMFC) systems. The controller integrates Genetic Algorithm (GA) and Grey Wolf Optimizer (GWO) within a Type-

2 Takagi–Sugeno–Kang (TSK) fuzzy inference structure to regulate the duty cycle of a boost converter and maximize power output. The proposed algorithm is implemented in MATLAB/Simulink and benchmarked against several conventional and intelligent MPPT strategies.

Simulation results demonstrate that the proposed approach enables the output power to reach the target level quickly and consistently, with a short settling time, limited overshoot, and low ripple. These findings confirm that the GGWO-TSK Type-2 controller offers superior transient and steady-state performance compared to existing MPPT methods in the literature.

2. SYSTEM COMPONENT AND MODELLING

This study employs a comprehensive Proton Exchange Membrane Fuel Cell (PEMFC) model developed in MATLAB/Simulink. The model delivers a power output of 1.26 kW and a nominal voltage of 24 Vdc. A schematic, depicted in Figure 1, was constructed to examine the impact of various control schemes on fuel cell performance. This configuration facilitates an extensive examination of diverse control strategies and their influence on the efficiency and performance of the PEMFC system.

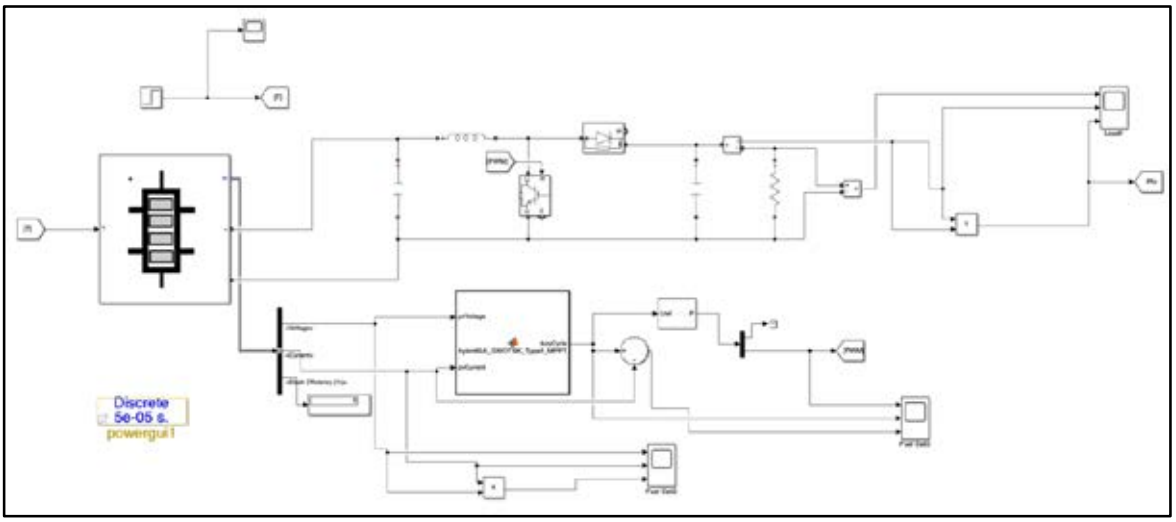

Fig.1. The Configuration of a PEMFC MPPT System

3. GGWO-TSK TYPE-2 FUZZY LOGIC MPPT ALGORITHM FOR FUEL CELL SYSTEM

The pseudocode summary for this control algorithm is shown below. The proposed GGWO-TSK Type-2 Fuzzy Logic MPPT algorithm aims to achieve accurate and robust tracking of the maximum power point (MPPT) in Proton Exchange Membrane Fuel Cell (PEMFC) systems under nonlinear and uncertain operating conditions. This hybrid approach integrates the global search capability of the Genetic Algorithm (GA) with the fast convergence and exploitation strength of the Grey Wolf Optimizer (GWO), while employing a Type-2 Takagi–Sugeno–Kang (TSK) fuzzy inference system to manage the inherent uncertainties in the system.

The algorithm begins with the initialization of a population based on the parameters of Type-2 fuzzy membership functions. Each individual in the population represents a candidate fuzzy system configuration, particularly the antecedent membership function parameters.

At each iteration, the following steps are performed:

1.Fitness Evaluation: The fitness of each individual is calculated based on the squared error and power ripple relative to a predefined reference power value (*P_ref*). This ensures both precision and stability in MPPT performance.

2.Selection, Crossover, and Mutation: Parents are selected using tournament selection, followed by crossover and mutation operations to generate a new offspring population. The best individuals among parents and offspring are retained to form the next generation.

3.Grey Wolf Optimization (GWO): The best-performing individuals from the GA phase are used to initialize the wolf population in GWO. Wolves' positions are updated using the GWO update rules, which involve computing control coefficients (*a*, *A*, *C*) and updating positions relative to the alpha wolf (the best solution).

4.Fuzzy Inference and Duty Cycle Calculation: After GWO convergence, the final alpha wolf's parameters are fed into a Type-2 TSK fuzzy inference system, which takes the fuel cell voltage (*fcVoltage*) and current (*fcCurrent*) as inputs. The system performs Sugeno-style inference to output an optimized duty cycle that drives the boost converter. This iterative procedure continues until a predefined number of generations is reached. The resulting controller not only tracks the

maximum power point with high precision but also demonstrates improved transient performance and robustness compared to conventional and non-hybrid fuzzy MPPT strategies.

Data: *Initialize parameters: maxIterations, wolfCount, populationSize, crossoverRate, mutationRate, P_ref*
Result: *Optimized duty cycle for MPPT control of the fuel cell*

```
Initialization: Randomly initialize a population of size populationSize based on Type-2 fuzzy membership functions
t ← 0
while t < maxIterations do
    Step 1: Evaluate the fitness of each individual in the population
      (based on the squared error and ripple from the reference power P_ref)
    Step 2: Select parents using tournament selection
    Step 3: Perform crossover and mutation to create new offspring
    Step 4: Evaluate the fitness of the offspring
    Step 5: Update the population with the best individuals (from parents and offspring)
    Step 6: Initialize GWO with the best individuals from GA as wolves' positions
    while gwoIteration < maxIterations do
        Step 7: Evaluate the fitness of each wolf
        Step 8: Find the alpha wolf (the best performing individual)
        foreach wolf i in wolfCount do
            Step 9: Update the position of each wolf using the GWO update formula
            Compute a, r1, r2, A1, C1, then calculate D_alpha, X1
            Update the wolf's position accordingly
        end
    end
    Step 10: Perform Type-2 TSK fuzzy inference using the alpha wolf's parameters
      Inputs: fcVoltage and fcCurrent
      Output: fuzzy-inferred duty cycle using Sugeno rules
    t ← t + 1
end
return optimized duty cycle
```

4. RESULTS AND DISCUSSIONS

The performance of the proposed GGWO-TSK Type-2 Fuzzy Logic MPPT algorithm was validated through MATLAB/Simulink simulations under dynamic load and environmental conditions. Comparative results among different MPPT strategies, including classical P&O, Type-1 and Type-2 fuzzy controllers, GA-optimized fuzzy controllers, and the proposed GGWO-TSK structure, are presented.

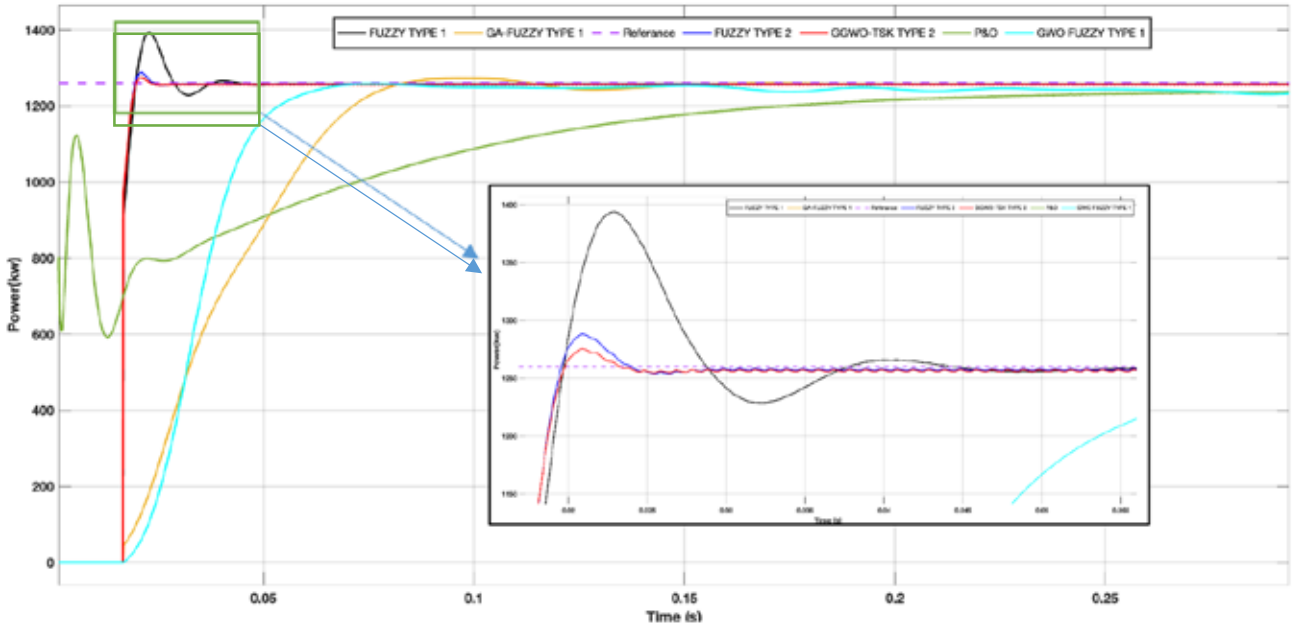

Fig.2. PEMFC MPPT output graph

Table 1. Performance Comparison of Different MPPT Methods for Fuel Cell Applications

	GWO-FUZZY TYPE 1	GGWO-TSK TYPE 2	FUZZY TYPE 2	GA-FUZZY TYPE 1	FUZZY TYPE 1	P&O
Peak Power (W)	1264.4	1275.5	1288.2	1272.7	1393.7	1121.86
Steady-State Power (W)	1243.1	1256.4	1257.3	1258.1	1257.8	1241
Overshoot (%)	1.7161	1.5152	2.4581	1.1627	10.804	0
Rise Time (s)	0.023314	0.0013832	0.0013832	0.043923	0.0018332	0.2
Settling Time (s)	0.05665	0.019115	0.0218	0.07615	0.03355	0.25
Tracking Efficiency (%)	98.658	99.717	99.782	99.846	99.825	98.49

In Table 1, numerical comparisons of key MPPT performance metrics are presented. Although all methods achieved acceptable tracking performance, classical approaches showed significant deficiencies compared to modern optimization-based techniques. The classical P&O algorithm, despite having no overshoot, reached the reference power value slowly and exhibited the lowest steady-state efficiency at 98.49%. Similarly, FUZZY TYPE 1, GWO-FUZZY TYPE 1, and FUZZY TYPE 2 methods exhibited higher overshoot and longer settling times. In contrast, the hybrid GGWO-TSK Type-2 fuzzy logic-based MPPT method demonstrated the best performance, achieving 99.72% tracking efficiency, minimal overshoot, and extremely fast dynamic response. This superior outcome is attributed to the effective combination of the global search ability of the Genetic Algorithm (GA) and the local exploitation strength of the Grey Wolf Optimizer (GWO), alongside the enhanced uncertainty handling capability of the Type-2 Sugeno fuzzy logic structure. Overall, the proposed hybrid GGWO-TSK Type-2 MPPT strategy provides the most efficient and reliable solution for maximum power tracking in fuel cell applications.

V. CONCLUSIONS

This study introduced a hybrid intelligent MPPT control strategy for Proton Exchange Membrane Fuel Cell (PEMFC) systems by combining Genetic Algorithm (GA) and Grey Wolf Optimizer (GWO) within a Type-2 TSK Fuzzy Logic framework. By integrating the global search capabilities of GA with the local exploitation strengths of GWO, the proposed controller effectively optimized the fuzzy membership functions and rule outputs.

The results revealed that the hybrid GGWO-TSK Type-2 fuzzy logic-based MPPT method provided faster dynamic response, lower overshoot, shorter settling time, and higher tracking efficiency compared to all other methods. The hybrid GGWO approach, which combines the global search capabilities of the Genetic Algorithm (GA) with the local fine-tuning abilities of the Grey Wolf Optimizer (GWO), effectively balanced solution accuracy and convergence speed. Additionally, the use of the Type-2 Sugeno fuzzy logic structure allowed for a more accurate modeling of uncertainties compared to classical Type-1 systems, thereby enhancing the system's stability and flexibility. Overall, the proposed hybrid GGWO-TSK Type-2 MPPT strategy stands out as the most effective and reliable solution for maximum power tracking in fuel cell applications.

REFERENCES

1. Karami N, El Khoury L, Khoury G and Moubayed N. 2014. Comparative study between P&O and incremental conductance for fuel cell MPPT. International Conference on Renewable Energies for Developing Countries, IEEE, pp. 17–22.
2. Ahmadi S, Abdi S and Kakavand M. 2017. Maximum power point tracking of a proton exchange membrane fuel cell system using PSO-PID controller. International Journal of Hydrogen Energy 42:20430–20443.
3. Derbeli M, Barambones O and Sbita L. 2018. A robust maximum power point tracking control method for a PEM fuel cell power system. Applied Sciences 8:2449.
4. Avanaki IN and Sarvi M. 2016. A new maximum power point tracking method for PEM fuel cells based on water cycle algorithm. Journal of Renewable Energy and Environment 3:35–42.
5. Venkateshkumar M, Sarathkumar G and Britto S. 2013. Intelligent control based MPPT method for fuel cell power system. International Conference on Renewable Energy and Sustainable Energy, IEEE, pp. 253–257.
6. Rezk H and Fathy A. 2020. Performance improvement of PEM fuel cell using variable step-size incremental resistance MPPT technique. Sustainability 12:5601.
7. Harrag A and Messalti S. 2019. IC-based variable step size neuro-fuzzy MPPT improving PV system performances. Energy Procedia 157:362–374.
8. Reddy KJ and Sudhakar N. 2018. A new RBFN based MPPT controller for grid-connected PEMFC system with high step-up three-phase IBC. International Journal of Hydrogen Energy 43:17835–17848.
9. Mallick N and Mukherjee V. 2020. Maximum power point tracking supported proton exchange membrane fuel cell based intelligent dynamic voltage restorer. International Journal of Hydrogen Energy 45:29271–29287.
10. Dogan S, Haydaroglu C and Gumus B. 2024. A new controller design for fuel cells. 8th International Hydrogen Technologies Congress (IHTEC 2024), Diyarbakır, Türkiye, 12–15 May.

HYBRID OPTIMIZED TAKAGI SUGENO TYPE 2 FUZZY-BASED VOLTAGE–FREQUENCY CONTROLLER FOR FUEL CELL INTEGRATED ISOLATED MİCROGRİD

[1*]Ömer Faruk Özcan, [2]Heybet Kılıç, [3]Ömerül Faruk Özgüven
[1] Dicle University, Department of Electric Power and Energy System, Sur, Diyarbakır, 21280, Turkey
[2] Dicle University, Department of Electric Power and Energy System, Sur, Diyarbakır, 21280, Turkey
[3] İnönü University, Engineering Faculty, Electric and Electrical, Battalgazi, Malatya, 44280, Turkey

* E-mail: omerfaruk.ozcan@dicle.edu.tr

ABSTRACT
Island microgrids encounter considerable technical and regulatory challenges in sustaining system frequency and voltage stability owing to high swings and uncertainties in energy supply and demand. The intermittent characteristics of renewable energy sources, especially the erratic output patterns of photovoltaic (PV) systems, hinder stability and demand rapid and efficient control strategies for independent operation from the main grid. This research seeks to develop and enhance a hybrid Takagi-Sugeno Type 2 fuzzy logic controller (TS-T2F) for voltage and frequency regulation in an isolated microgrid incorporating photovoltaic systems, batteries, and fuel cells, utilizing the genetic grey wolf optimization method (GGWO). The battery enhances system reliability by mitigating production discrepancies, while the fuel cell ensures energy continuity by delivering consistent power during periods of low photovoltaic output. The system has implemented a load shedding and reconnection technique based on voltage levels for three distinct loads. The GGWO-TS-T2F approach has shown enhanced frequency stability relative to the Droop V/F and GGWO-TS-T1F methods, and it has also yielded beneficial outcomes in voltage regulation and load shedding/restoration procedures. This research introduces a novel control methodology for autonomous microgrids.
Keywords: Voltage-frequency control, ggwo-tsk type 2

1. INTRODUCTION
Island microgrids face serious technical and regulatory challenges in maintaining system frequency and voltage stability due to significant fluctuations and uncertainties in energy supply and demand [1]. The intermittent nature of renewable energy sources such as photovoltaic (PV) systems leads to unpredictable production profiles, while dynamic load changes further complicate system stability [2]. Operating independently of the main grid, these microgrids need fast and robust control strategies for reliability and operational safety, as they lack a support to buffer such disorders. Conventional control methods, such as droop control, are often insufficient to provide the quick response required to manage these challenges, resulting in frequency and voltage deviations that can compromise system performance.
The literature categorizes the methods for voltage and frequency management in islanded microgrids into three groups: classical methods, fuzzy logic-based methods, and optimization-based methods. Among the traditional methodologies, droop control and PI/PID-based controllers are prominent. Droop control enables load sharing; nevertheless, it is inadequate in mitigating frequency variations caused by the variability of renewable energy sources. Furthermore, it has been noted that PI/PID controllers are employed for frequency management in islanded microgrids; however, their ability to adapt to dynamic changes is constrained [3]. Conversely, fuzzy logic-based approaches offer benefits in representing system uncertainty and nonlinear dynamics. Takagi-Sugeno (TS) fuzzy logic models, particularly those with Type 2 (T2F) configurations, are often favored in microgrid control due to their superior capacity to manage uncertainty [3]. A T2F-based controller enhances voltage management in photovoltaic and fuel cell systems. The efficacy of fuzzy logic controllers is significantly contingent upon parameter optimization [4]. At this juncture, optimization-based methodologies are employed. Genetic algorithms (GA), particle swarm optimization (PSO), and grey wolf optimization (GWO) are meta-heuristic methods that have been successfully employed to optimize control settings [5]. For instance, it has been documented that PSO yields superior outcomes by optimizing the parameters of fuzzy controllers in frequency regulation [6]. Nonetheless, a singular optimization strategy typically struggles to deliver equitable performance in both exploration and exploitation phases.
Hybrid optimization techniques have yielded substantial progress in addressing these constraints. Hybrid methodologies such as Genetic Grey Wolf Optimization (GGWO) integrate the social hierarchy and hunting tactics of Grey Wolf Optimization (GWO) with the mutation and crossover processes of genetic algorithms, resulting in accelerated convergence and enhanced capacities for identifying global optima. This benefit facilitates the precise modification of control settings, particularly in intricate systems characterized by uncertainty [7]. This paper seeks to address this deficiency by providing a hybrid TS-T2F controller optimized using GGWO for voltage and frequency regulation in an isolated microgrid incorporating photovoltaic systems, batteries, and fuel cells. The controller improves the system's dynamic performance and ensures dependability by compensating for battery output deficits; the fuel cell maintains energy continuity by delivering consistent power during periods of low photovoltaic production. A load shedding and reconnection approach predicated on voltage levels has been instituted to preserve system stability during critical circumstances. The proposed method will be evaluated against Droop V/F and GGWO-TS-T1F techniques to illustrate

the superiority of the hybrid approach in voltage and frequency regulation.

2. SYSTEM COMPONENT AND MODELLING

The proposed microgrid configuration, as illustrated in Fig.1, is designed to operate entirely in islanded mode, independently from the main utility grid. The system comprises renewable energy generation units, an energy storage system, measurement devices, and an intelligent load management mechanism. On the generation side, the microgrid integrates photovoltaic (PV) panels, a fuel cell, and a battery energy storage system (BESS). While the PV system provides intermittent power depending on environmental conditions, the fuel cell offers stable and continuous power generation. The battery system plays a crucial role in maintaining system balance by supplying or absorbing power during rapid load changes. All power sources are connected to the microgrid through DC/AC power electronic converters (inverters).

Voltage and frequency measurements are continuously monitored via dedicated sensors, and the data is processed by a Type-2 Fuzzy Logic Controller. This controller determines the operating status of loads based on optimized voltage and frequency thresholds. The load management unit then actuates three switching elements (SW1, SW2, SW3), enabling selective load shedding or reconnection according to system conditions. Through this coordinated operation, the microgrid maintains supply-demand balance, ensures voltage and frequency stability, and operates reliably in standalone mode using only its local energy resources.

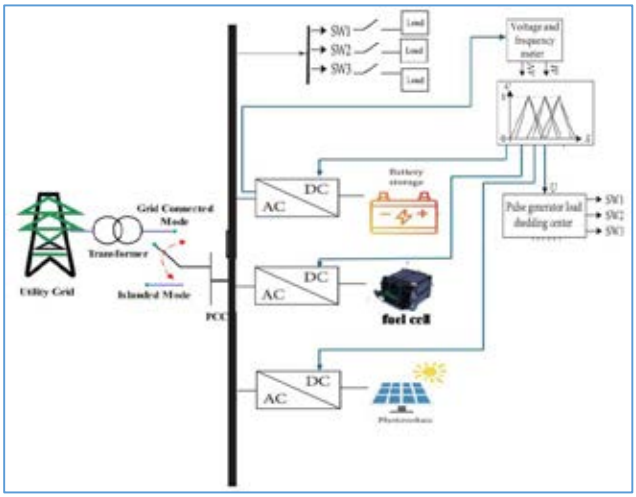

Fig.1. The Configuration of an Islanded Microgrid System

3. GGWO-TSK TYPE-2 FUZZY LOGIC ALGORITHM FOR V/F CONTROL

The control structure executes the operation of the TS-T2F controller designed for voltage and frequency control in an islanded microgrid in a step-by-step manner. Initially, voltage deviation (ΔV) and frequency deviation (ΔF) are taken as inputs. These inputs are processed by the TS-T2F controller using optimized parameters, and a fuzzy inference is performed to calculate a duty cycle. This duty cycle then regulates PV generation. Next, the generation deficit is determined by comparing the total load with the PV generation. If the duty cycle is below a certain threshold, the fuel cell activates, providing constant power; otherwise, the fuel cell remains inactive. The remaining deficit is balanced by the battery, which either discharges or charges, with the state of charge being updated accordingly. Finally, ΔV and ΔF are compared against fixed thresholds to decide on load shedding or reconnection. The system outputs the duty cycle, load states, battery power, fuel cell power, and state of charge.

Data: Parameters: maxIterations, wolfCount, populationSize, crossoverRate, mutationRate, DeltaV, DeltaF
Constants: voltageThresholds, freqThresholds, voltageReconnect, freqReconnect, Pload, maxPpv, K_SOC
Result: Outputs: U, loadStates, Pbatt, Pfc, SOC

% Step 1: Optimize TS-T2F parameters using GGWO
Initialize: Randomly create a population of size populationSize (centers, sigmaU_V, sigmaL_V, sigmaU_F, sigmaL_F, ci)
t ← 0
while t < maxIterations do
Step 2: Evaluate fitness of population (minimize DeltaV and DeltaF deviations)

```
    Step 3: Select parents via tournament selection, perform crossover and mutation
    Step 4: Update population with best individuals
    Step 5: Initialize GWO with best individuals as wolf positions
    while gwoIteration < maxIterations do
        Step 6: Identify alpha wolf, update each wolf's position using GWO formula
        gwoIteration ← gwoIteration + 1
    end
    t ← t + 1
end
Optimization result: Best parameters (centers, sigmaU_V, sigmaL_V, sigmaU_F, sigmaL_F, ci)

% Step 2: System control using TS-T2F controller
Initialize: prevLoadStates ← [1, 1, 1], soc ← 1.0
Step 7: Perform TS-T2F fuzzy inference
    for i ← 1 to 5 do
        muU_V(i), muL_V(i), muU_F(i), muL_F(i) ← Gaussian functions
    end
    W_upper ← muU_V' * muU_F, W_lower ← muL_V' * muL_F
    Normalize W_upper, W_lower
    y ← (sum(W_upper .* ci) + sum(W_lower .* ci)) / 2
Step 8: Calculate PV generation: Ppv ← y * maxPpv
Step 9: Compute generation deficit: Pgap ← Pload - Ppv
Step 10: Fuel cell control
    if y < 0.4 then
        Pfc ← 5
    else
        Pfc ← 0
    end
Step 11: Battery control
    if Pgap - Pfc > 0 and soc > 0.2 then
        Pbatt ← min(Pgap - Pfc, 2)
    elseif Pgap - Pfc < 0 and soc < 0.95 then
        Pbatt ← max(Pgap - Pfc, -1)
    else
        Pbatt ← 0
    end
    soc ← soc - 0.1 * K_SOC * Pbatt
    soc ← max(0, min(1, soc))
    SOC ← soc
Step 12: Load shedding/reconnection
    for i ← 1 to 3 do
        if DeltaV <= voltageThresholds(i) or DeltaF <= freqThresholds(i) then
            loadStates(i) ← 0
        else
            loadStates(i) ← prevLoadStates(i)
        end
    end
    if DeltaV >= voltageReconnect and DeltaF >= freqReconnect then
        loadStates ← [1, 1, 1]
    elseif DeltaV >= voltageReconnectHyst and DeltaF >= 0 then
        loadStates ← max(loadStates, prevLoadStates)
    end
    prevLoadStates ← loadStates
return y, loadStates, Pbatt, Pfc, SOC
```

4. RESULTS AND DISCUSSIONS

Simulation results are presented in Figures 2a, 2b, and 2c, illustrating the system's dynamic behavior under load shedding and reconnection scenarios. Figure 2a shows the voltage response, Figure 2b depicts the frequency response, and Figure 2c illustrates the load shedding and reconnection events. The proposed GGWO–Type 2 Fuzzy controller

successfully maintains system stability by limiting voltage and frequency deviations and ensuring rapid recovery. Specifically, during the load shedding events at 0.7 s, 1.0 s, and 1.3 s, and the load reconnection at 1.6 s, the controller minimizes transient fluctuations and restores system parameters to nominal levels. The GGWO–Type 2 Fuzzy controller limits frequency deviations within ±0.25 Hz, outperforming both the GGWO–Type 1 Fuzzy and the Droop V/F methods, which exhibit larger deviations of up to ±0.35 Hz and ±0.4 Hz, respectively, along with longer settling times. In terms of voltage response, the proposed method demonstrates lower overshoot and faster stabilization compared to alternative approaches. Furthermore, the load management strategy effectively preserves critical loads while shedding non-essential loads, ensuring system stability without unnecessary disruptions. Overall, the results confirm that the GGWO–Type 2 Fuzzy control approach provides superior dynamic performance, achieving faster frequency and voltage recovery, lower deviations, and more stable system operation compared to conventional methods.

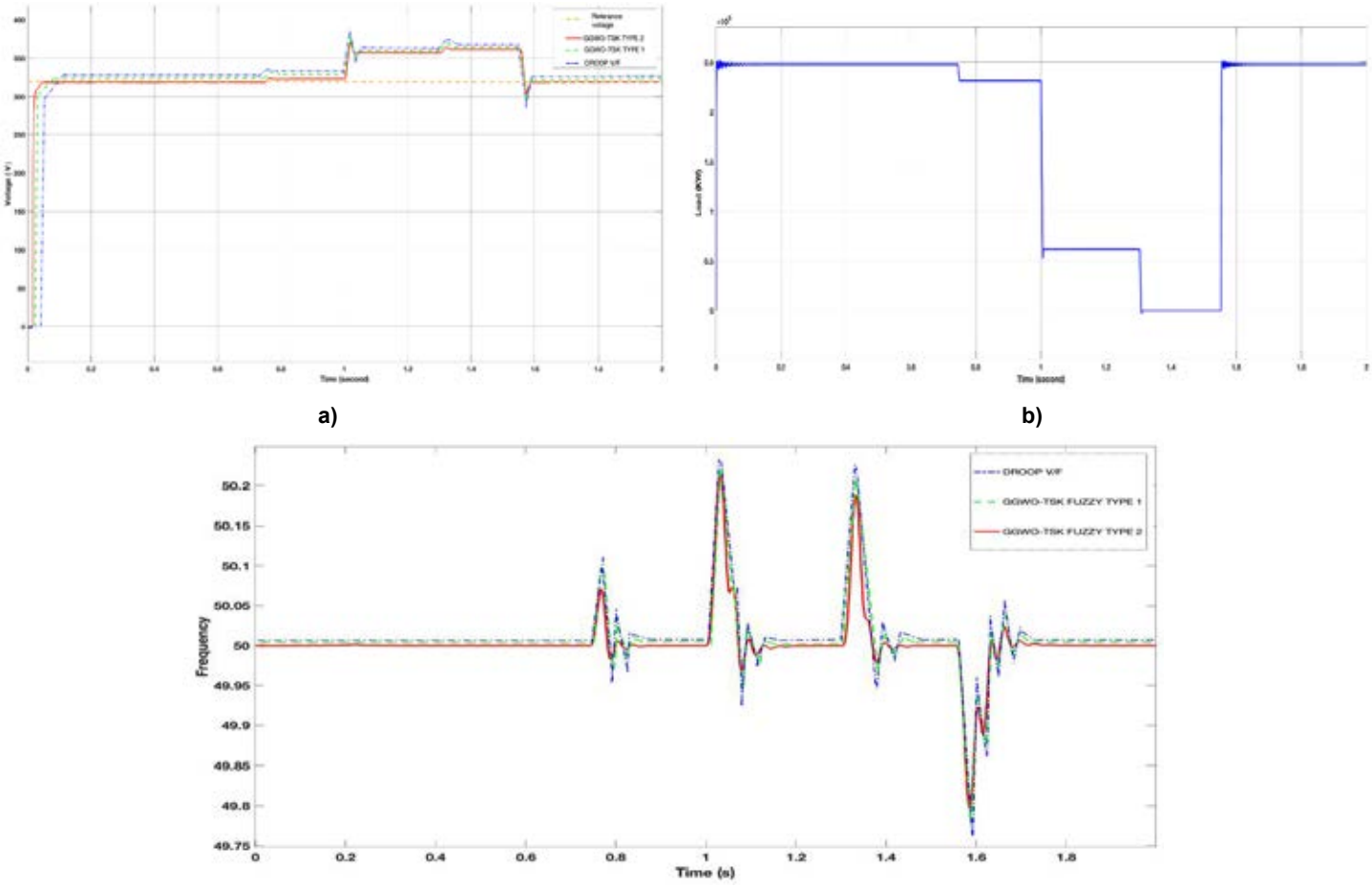

Fig.2. a) Voltage changes b) Load change c) frequency changes graph

5. CONCLUSIONS

This study proposed a voltage-frequency regulation method for an islanded microgrid based on a Takagi-Sugeno Type 2 fuzzy logic controller (TS-T2F) optimized by Genetic Grey Wolf Optimization (GGWO). In the system, the battery mitigates production discrepancies, while the fuel cell ensures continuous power supply during periods of low PV generation. The voltage-based load shedding and reconnection strategy preserves system stability by managing three distinct loads under disturbance scenarios. Simulation results demonstrate that the GGWO-TS-T2F controller maintains frequency deviations within ±0.25 Hz, outperforming the Droop V/F and GGWO-TS-T1F methods. Moreover, the proposed controller achieves lower voltage overshoot and faster recovery times. Overall, the GGWO-TS-T2F approach provides an effective, fast, and reliable solution for voltage and frequency regulation in islanded microgrids.

REFERENCES

1. Zhao H., Hong M., Lin W., and Loparo K.A. 2019. Voltage and frequency regulation of microgrid with battery energy storage systems. *IEEE Transactions on Smart Grid*, 10(1):414–424. https://doi.org/10.1109/TSG.2017.2741668
2. Özcan Ö.F., Kılıç H. and Özgüven Ö.F. 2024. A novel hybrid GGWO–Takagi Sugeno Kang fuzzy type 2 based maximum power point tracking for photovoltaic systems operating under partial shading conditions. *Proceedings of the 2024 Global Energy Conference (GEC)*, Batman, Türkiye, pp. 1–4. https://doi.org/10.1109/GEC61857.2024.10881517
3. Dashtdar, M., Flah, A., Hosseinimoghadam, S. M. S., & others. (2022). Frequency control of the islanded microgrid including energy storage using soft computing. Scientific Reports, 12, Article 20409. https://doi.org/10.1038/s41598-022-24758-6
4. Zibandeh, H., Ghafouri, A., & Nouri, T. (2024). Innovative Type II fuzzy-based voltage–frequency controller for isolated microgrid considering load shedding and uncertainties. International Journal of Energy Research, 2024, Article 8718931, 16 pages.
5. Özcan, Ö. F., Kiliç, H., & Özgüven, Ö. F. (2024, August). Energy management in microgrids with hybrid energy storage systems utilizing batteries and proton exchange membrane/fuel cells. Paper presented at the 8th International Hydrogen Technologies Congress, 12–15 May 2024, Diyarbakır, Türkiye.
6. Mishra, D., Nayak, P. C., & Prusty, R. C. (2020). PSO optimized PIDF controller for load-frequency control of AC multi-islanded microgrid system. In *2020 International Conference on Renewable Energy Integration into Smart Grids: A Multidisciplinary Approach to Technology Modelling and Simulation (ICREISG)* (pp. 116–121).
7. Ozcan, O. F., Kilic, H., & Ozguven, O. F. (2025). A unified robust hybrid optimized Takagi–Sugeno fuzzy control for hydrogen fuel cell-integrated microgrids. International Journal of Hydrogen Energy.

TRANSFER LEARNING FROM STEAM AND DRY REFORMING OF METHANE TO TRI-REFORMING OF BIOGAS FOR SYNGAS PRODUCTION

[1]Ahmet Coşgun, [2]M. Erdem Günay, [1*]Ramazan Yıldırım
[1] Boğaziçi University, Engineering Faculty, Department of Chemical Engineering, Istanbul, 34342, Turkey
[2] İstanbul Bilgi University, Engineering Faculty, Department of Energy Systems Engineering, Istanbul, 34060, Turkey

*Corresponding author e-mail: yildirra@boun.edu.tr

ABSTRACT
In this study, the predictive machine learning models were developed for tri-reforming of biogas with the help of steam and dry reforming of methane data and compared with a model developed using only the tri-reforming of bigas data to test the applicability of transfer learning approach for the new energy production systems with limited data availability. CH_4 conversion for tri-reforming process was predicted by transferring knowledge from steam and dry reforming by using 58 descriptors including catalyst properties and reaction conditions; the results showed that high predictive powers can be maintained by transfer learning when using limited number of data points in the original dataset.

Keywords: biogas reforming, tri-reforming, machine learning, transfer learning, CH4 conversion

1. INTRODUCTION
Currently, although the majority of hydrogen is produced from fossil fuels, green hydrogen production through renewable sources and biogas valorization offers significant benefits [1]. In recent years, tri-reforming of methane (TRM) has gained considerable attention as a promising yet challenging method for sustainable hydrogen production. TRM combines steam reforming (SRM), partial oxidation (POX), and dry reforming (DRM), leveraging the economic benefits of SRM, the energy efficiency of POX, and the environmental advantages of DRM [2]. Together with these advantages TRM has also advantage for producing syngas in customizable H_2/CO ratio depending on the desired final product. The process feed can be varied to get a low H_2/CO ratio around unity for dimethyl ether production, or H_2/CO ratio of around 2 for methanol production, or a high H_2/CO ratio of 3 for ammonia synthesis [3-5].
Machine learning (ML) has become a valuable tool for analyzing large datasets and identifying trends. ML models have demonstrated high accuracy in given tasks; however, they require substantial amounts of data. However, data scarcity and the high cost of data acquisition especially from laboratory experiments, often limit their predictive power and generalizability of models developed using traditional supervised learning methods [6]. ML models for predictive purposes on chemical reactions, need extensive labelled datasets to avoid overfitting or underfitting, which can result in low accuracy and transferability [7]. Transfer learning (TL) enables the development of data-driven models for tasks with limited data by sharing information from a related task. This approach is beneficial when (i) data for a particular target task is limited, (ii) there are one or more related tasks with well correlated (though not identical) domains or distributions, and (iii) a substantial amount of data is available for these related tasks. By transferring features, model structure, or parameters from related tasks, the performance of ML models for the target task can be enhanced [6]. To illustrate the approach, the following analogy can be used [8]: Two individuals learning to play the piano: one with no prior musical experience and the other with extensive guitar-playing knowledge. The individual with a music background will learn piano more efficiently by transferring their existing musical knowledge to this new task [8]. Similarly, TL operates on the principle of leveraging knowledge from related tasks to improve learning efficiency on the target task. TL process involves pre-training a model with sufficient data in a related task. In ANN models, the underlying features are learned in the first few layers. To transfer knowledge, structure and the corresponding parameters of these initial layers are transferred to the new model. The parameters are either frozen or fine-tuned. Afterwards, a few additional layers are added, and the model is trained with the limited data of the target task. This way, the number of parameters that need to be tuned for the target model is minimized [6]. Previously TL is utilized in chemical engineering in applications as; prediction and knowledge extraction of cyanobacterial bloom growth characteristics [9], prediction of temperature-dependent reaction rate constants [10], prediction of molecular properties [6].
In this work, we present a model that uses TL to predict the CH_4 conversion in TRM using the model developed for steam and dry reforming data.

2. METHOD
For TL studies, datasets are adopted from previous works done by our research group. Source datasets are adapted from DRM [11], and SRM [12] processes. Detailed explanation of data curation methods and processes are explained in the corresponding articles. TRM dataset, constructed by reviewing scientific papers sourced from “Web of Science” database, has a total of 938 data points, originating from 116 experiments across 29 articles. SRM dataset has a total of 1249 data points, originating from 175 experiments across 41 articles. DRM dataset has a total of 3301 data points, originating from 593 experiments across 101 articles. Input variables (descriptors) are chosen as the type of catalyst, catalyst preparation conditions and method, reaction conditions and feed gas compositions, while CH_4 conversion (%)

was designated as output (target) variable. All datasets are completed to 58 descriptor variables by adding the missing variables in the corresponding datasets as O_2 and H_2O in the reactant medium for DRM, and CO_2 and O_2 for SRM as 0. The variables in the dataset are presented in Table 1.

Table 1. Variables available in dataset and used in models

Category	Variables
active metal	Ni, Co, Pt, Rh, Mo, Fe, Ru, Cu, B
support type	ZnO, La_2O_3, Al_2O_3, $MgAl_2O_4$, MgO, CeO_2, ZrO_2, SrO_2, β-SiC, cordierite, SBA-15, Y_2O_3, KNO_3, Sm_2O_3, Nb_2O_5, MWCNT, TiO_2, hydrotalcite (Mg-Al-C), SiO_2, Gd_2O_3
catalyst preparation conditions	calcination time (h), calcination temperature (°C), H_2% in reduction medium, reduction time (h), reduction temperature (°C)
reaction conditions	time on stream (TOS) (min), W/F, reaction temperature (°C)
feed composition	CH_4%, CO_2% (0 in SRM), H_2O% (0 in DRM), O_2% (0 in DRM and SRM), H_2%, inert %

DRM and SRM models are used as source models, while TRM dataset serving as the target model for TL. Afterwards, we systematically applied ANN models to extract detailed insights for predicting outcomes under unstudied conditions. Fig. 1 illustrates the overall scheme followed in the study.

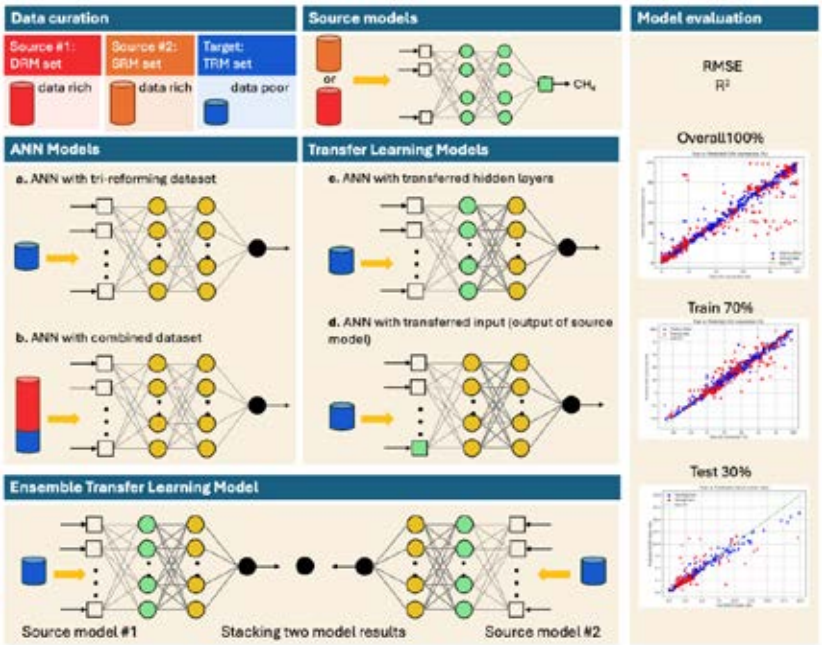

Fig.1. Structure of the study for TL approach with ANN

3. RESULTS AND DISCUSSION

ANN models were developed using the Python programming language and the Keras package. The study is divided into three main parts. In the first part, four ANN models were constructed to investigate the effect of transferring different layers for predicting CH_4 conversion. A model developed exclusively from TRM data served as the base model. Subsequently, a model using DRM data was developed as the source model. TL algorithms were then applied by transferring various layers from the source model to predict CH_4 conversion in TRM. Additionally, a general model was created by combining both datasets. In the second part of the study, TRM dataset was reduced to 75%, 50%, and 25% of its original number of datapoints. Models were developed to assess the impact of smaller datasets on the performance of both the base model and the TL models. In the last part, SRM data was also incorporated as a second source model to develop TL model. TL models of SRM and DRM datasets are combined with different merging methods and double sourced TL models are developed to enhance model performance of CH_4 conversion in TRM.

3.1. Comparison of CH_4 conversion models

For model optimization and tuning, parameters such as activation functions, learning rates, batch sizes, number of neurons per layer, and the number of layers were investigated. Activation functions (tanh, sigmoid, relu, softmax) and learning rates (0.0001, 0.001, 0.005) were tested The "relu" function with a learning rate of 0.0001 and a batch size of 80 was found to be the most robust and effective across all datasets. Data was split at a ratio of 70:30 for training and testing, except for source model development (80:20). Each layer in all models contained 70 neurons. The base model (using only TRM data) was optimized with 3 hidden layers and 180 epochs. DRM model used 5 hidden layers and 100 epochs. The combined dataset model had 3 hidden layers and 180 epochs. TL models were also optimized with 180 epochs. Various combinations of hidden layers and transferred layers were analyzed for optimum TL model. Optimal TL

configurations identified were: (1) 3 new layers with the last layer transferred (3 hidden layers total), (2) the first layer transferred and 3 new layers added (3 hidden layers total), and (3) the first and second layers transferred with 4 new layers added (5 hidden layers total). The models and their R^2 values are presented in Fig. 2. Data points from the training set are depicted in blue, while those from the test set are shown in red.

Base model developed by using solely TRM dataset demonstrated the highest predictive power. TL models varied based on which layer was transferred, with the most successful being the model where the last layer was transferred. Although in ML models the initial layers typically contain the most information and are therefore crucial, transferring these initial layers resulted in decreased overall model accuracy. It can be concluded that the TRM dataset alone was sufficient to predict the general behavior of CH_4 conversion in TRM. Additionally, model developed using the combined dataset also exhibited good predictive power, but requiring higher computational resources.

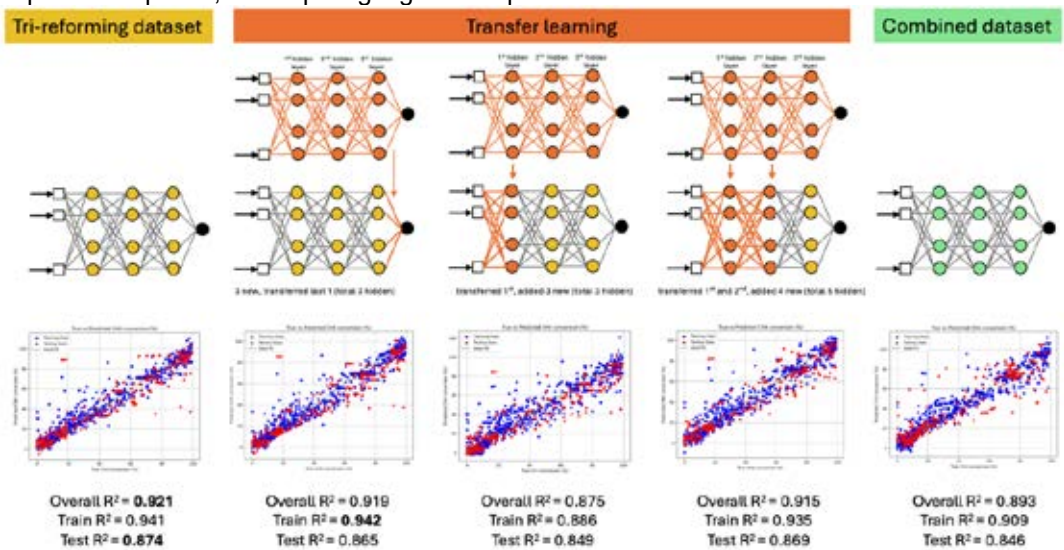

Fig. 2. Results of CH_4 models

3.2. Effect of number of datapoints in the target model

To evaluate the effectiveness of TL, the number of datapoints in the TRM dataset was reduced during model training. ANN and TL models were developed using 75%, 50%, and 25% of the TRM dataset. The results indicated that while TL may not be essential for the full dataset (with minor improvements observed when transferring only the last layer), its predictive power becomes significantly higher than only modeling with target model when fewer datapoints are available. Although transferring the last layer was the most effective TL approach for the complete dataset, this method proved less successful with reduced datasets, as it closely resembled the original model. When data is limited, leveraging knowledge from a source model becomes crucial. As presented in Fig. 3, the highest accuracy for a reduced dataset (25% of the original size) was achieved by transferring the first two layers from the source model.

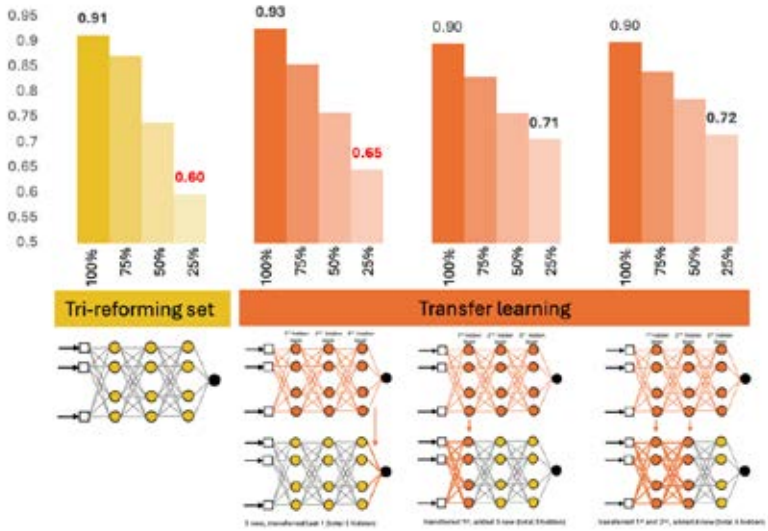

Fig. 3. Results of CH_4 TL models

3.3. Transfer learning with two source models

Merging machine learning models can be accomplished through various methods, with the most common being bagging, boosting, and stacking. In this study, stacking was utilized as a double sourced learning technique. Stacking was performed by applying regression models to the final output predictions of the two models. The results are presented in Table 2. The base model is built with 3 layers and 70 neurons each. Single and double source TL models are built by transferring first 2 layers from source model and training 3 additional layers.

The results indicate that employing a second source model did not significantly improve the overall accuracy of the CH_4 conversion predictions for TRM reaction if linear regression is used as stacking method. Although this lack of improvement can likely be attributed to many factors, and can only be guessed, most probably reasons are discussed. First, the low number of datapoints in the second source dataset (similar to the target set) may result in favoring this dataset in regression. Additionally, the physical conditions of the target model exhibit more DRM characteristics than SRM, as most studies were conducted in low H_2O and high CO_2 environments. However, an important result is achieved in gradient boosting regression (GBR), and random forest regression (RFR). The predictive power of the model is significantly improved, and even the 25% data is used from the TRM dataset, R^2 values were around 0.8 in total dataset.

Table 2. Results of CH_4 single and double sourced TL models

Data used from TRM set	Benchmark model	Single Source TL Model	Double Source TL Models		
	(only TRM dataset)	(source model: DRM)	(with LR merging)	(with GBR merging)	(with RFR merging)
100%	0.914	0.882	0.882	0.913	**0.934**
75%	0.872	0.856	0.864	0.892	**0.891**
50%	0.740	0.825	0.844	0.848	**0.871**
25%	0.598	0.737	0.729	0.796	**0.804**

4. CONCLUSIONS

In this study, the effectiveness of TL in predicting CH_4 conversion for TRM was demonstrated, utilizing DRM and SRM datasets as sources. While a model trained solely on TRM data showed high predictive accuracy, TL proved particularly valuable when data availability was limited. The most effective TL strategy involved transferring the final layers from a pre-trained model, preserving relevant features while adapting to the target dataset. Additionally, ensemble techniques such as gradient boosting and random forest regression improved predictive performance, especially with reduced datasets. These findings highlight the potential of TL in optimizing catalytic reaction modeling, reducing the need for extensive experimental data, and enhancing predictive capabilities for sustainable syngas production.

REFERENCES

1. Pham Minh, D., et al., Hydrogen Production From Biogas Reforming: An Overview of Steam Reforming, Dry Reforming, Dual Reforming, and Tri-Reforming of Methane, in Hydrogen Supply Chains. 2018, Elsevier. p. 111-166.
2. Hernandez, B. and M. Martin, Optimization for biogas to chemicals via tri-reforming. Analysis of Fischer-Tropsch fuels from biogas. Energy Conversion and Management, 2018. 174: p. 998-1013.
3. Han, D., et al., Effect of Oxidants on Syngas Synthesis from Biogas over 3 wt % Ni-Ce-MgO-ZrO2/Al2O3 Catalyst. Energies, 2020. 13(2): p. 297.
4. Osat, M. and F. Shojaati, Techno-economic-environmental evaluation of a combined tri and dry reforming of methane for methanol synthesis with a high efficiency CO2 utilization. International Journal of Hydrogen Energy, 2022. 47(14): p. 9058-9070.
5. Yin, W., N. Guilhaume, and Y. Schuurman, Model biogas reforming over Ni-Rh/MgAl2O4 catalyst. Effect of gas impurities. Chemical Engineering Journal, 2020. 398: p. 125534.
6. Li, B. and S. Rangarajan, A conceptual study of transfer learning with linear models for data-driven property prediction. Computers & Chemical Engineering, 2022. 157: p. 107599.
7. Wen, M., et al., Improving machine learning performance on small chemical reaction data with unsupervised contrastive pretraining. Chemical Science, 2022. 13(5): p. 1446-1458.
8. Weiss, K., T.M. Khoshgoftaar, and D. Wang, A survey of transfer learning. Journal of Big Data, 2016. 3(1): p. 9.
9. Ni, J., et al., An Improved Transfer Learning Model for Cyanobacterial Bloom Concentration Prediction. Water, 2022. 14(8): p. 1300.
10. Al Ibrahim, E. and A. Farooq, Transfer Learning Approach to Multitarget Temperature-Dependent Reaction Rate Prediction. The Journal of Physical Chemistry A, 2022. 126(28): p. 4617-4629.
11. Şener, A.N., et al., Statistical review of dry reforming of methane literature using decision tree and artificial neural network analysis. Catalysis Today, 2018. 299: p. 289-302.
12. Baysal, M., M.E. Günay, and R. Yıldırım, Decision tree analysis of past publications on catalytic steam reforming to develop heuristics for high performance: A statistical review. International Journal of Hydrogen Energy, 2017. 42(1): p. 243-254.

INVESTIGATION OF THE ACTIVITY OF COMPOSITE NANOFIBER CATALYSTS SYNTHESIZED BY ELECTROSPINNING TECHNIQUE FOR HYDROGEN PRODUCTION FROM BORON FUELS

[1]*Berfin Ekin Ülgen*, [2,3]*Bilge Coşkuner Filiz*, [1,3*]*Aysel Kantürk Figen*
[1] Yıldız Technical University, Faculty of Chemistry-Metallurgy, Department of Chemical Engineering, Istanbul, 34220, Türkiye
[2] Yıldız Technical University, Faculty of Chemistry-Metallurgy, Department of Metallurgy and Materials Engineering, Istanbul, 34220, Türkiye
[3] Yıldız Technical University, Clean Energy Technologies Institute, Istanbul, 34220, Türkiye

*Corresponding author e-mail: akanturk@yildiz.edu.tr

ABSTRACT
Hydrogen is a promising energy carrier due to its high energy density and low harmful emissions. Consequently, the production and storage of hydrogen have significant potential in the energy sector. Boron fuels such as sodium borohydride ($NaBH_4$) and ammonium borane (NH_3BH_3) have high hydrogen content and release hydrogen at mild conditions. Due to their abilities, they are widely used for hydrogen storage and transportation. However, efficient catalyst development is crucial to achieving controlled hydrogen release at the desired time and location. The electrospinning method is an advanced technique for synthesizing catalysts in nanofiber structures and is based on the application of controlled electric field force to the polymer solution. The electrospinning method provides enhanced or altered high surface area, porous structure, nano-sized morphology, surface area-to-volume ratio, and superior catalytic properties for catalyst production. Also, this technique demonstrates low cost and high efficiency. In this study, the impact on the efficiency of hydrogen production from boron fuels in batch and continuous flow systems was assessed via hydrolysis of $NaBH_4$ and NH_3BH_3 over synthesized Co-based carbon nanofiber catalysts (Co@CNF, Co@GCNF, CoRu@CNF, CoRh@CNF, CoRu@GCNF, and CoRh@GCNF). It is observed that CoRh@GCNF shows the best activity towards hydrogen production in the batch system (5.68 and 6.26 L/min·gcat, respectively) for $NaBH_4$ and NH_3BH_3.

Keywords: Electrospinning, Nanofiber catalysts, Hydrogen production, Boron fuels

1. INTRODUCTION
Global environmental pollution, climate change, and increasing energy crises prompt research and commercial sectors to develop clean energy materials. With this purpose, studies have focused on the development of materials consisting of catalysts, storage media, electrode membranes, separators, collectors, supercapacitors, etc. A safe and effective solution for hydrogen storage and release is essential to reduce the cost of hydrogen in industrial applications. Boron fuels have advantages in the storage of hydrogen and the release of stored hydrogen [1, 2]. Various boron-based hydrogen storage compounds with their high hydrogen content are used especially in mobile power generation systems such as fuel cells, military, and space applications. The first study on $NaBH_4$'s capacity to store and transport molecular hydrogen (10.8 wt.%) was published by H.I. Schlesinger in 1973. Research on the synthesis of novel boron-based compounds continued in the late 1990s. The US Department of Energy emphasized in 2007 that $NaBH_4$ is a significant hydrogen storage medium for vehicle applications and that research on NH_3BH_3, another possible hydrogen storage material for direct fuel cells, is also essential. Nowadays, NH_3BH_3 is still a strong candidate for in-vehicle applications because of its advantages such as high hydrogen storage capacity (19.6wt.%), low molecular weight (30.9 g mol^{-1}), high stability in air and water, and controllable reaction conditions [3]. A hydrogen storage system needs to release hydrogen in sufficient quantities and at a proper rate to power a fuel cell. Depending on the intended application, two methods are applied to release the hydrogen stored in boron fuels: hydrolysis and thermolysis (Table 1).

Table 1. Hydrogen production methods for potential applications of $NaBH_4$ and NH_3BH_3 [3].

Application	$NaBH_4$		NH_3BH_3	
	Thermolysis	Hydrolysis	Thermolysis	Hydrolysis
Mobile	✗	✓	✓	✓
Automotive	✗	✗	✓	✗
Stationary	✓	✗	✓	✗

Cost-effective and active catalysts are crucial for producing hydrogen at the desired location and time. For this purpose, metal, metal oxides, nanoalloys, and nanocomposite catalysts have been investigated [4, 5]. Electrospinning has gained significant attention in hydrogen energy systems. Electrospun fiber catalysts with smaller pores and higher surface area have been successfully applied to provide pure hydrogen gas for hydrolysis reactions of metal hydrides. Since the early

2000s, hydrolysis reactions have extensive attention, especially focusing on catalytic materials. Chemical reduction, wet impregnation, sol-gel, and precipitation techniques are used to synthesize catalytic noble and non-noble metals, metal oxides, bimetal nanoparticles, and porous powders. These materials are particularly attractive for hydrogen applications due to their large surface areas and high catalytic activities. In addition, metal oxides are more stable against atmospheric degradation and moisture than metallic forms. Metals in their oxide forms, their deposition on various supports, or their doping in polymeric environments provide high catalytic activity. Moreover, elemental boron is capable of being integrated into metal oxides to improve their activity [6]. In this study, Co-based carbon nanofiber catalysts doped with/without Rh and Ru were synthesized using the electrospinning technique, and their hydrogen production from boron fuels was investigated under batch and continuous operating conditions.

2. MATERIALS AND METHODS

Within the scope of the experimental study, the following studies were carried out to synthesize composite nanofiber catalysts using the electrospinning technique and hydrogen production and investigate their hydrogen production rate (Fig. 1).

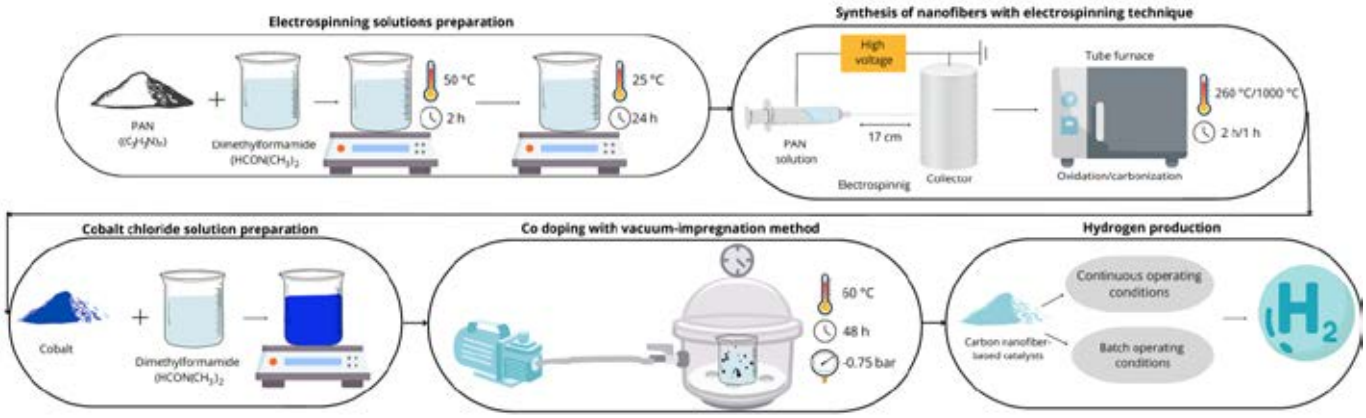

Fig. 1. Experimental methodology nanofiber catalysts synthesize and hydrogen production operations.

2.1. Synthesis of Co-Based Carbon Nanofiber Catalysts with Electrospinning Technique

In the experimental studies, two different electrospinning solutions were prepared to obtain composite nanofibers: containing PAN ($(C_3H_3N)_n$, Sigma-Aldrich, 99.995% purity) and containing graphene-doped PAN. Dimethylformamide ($HCON(CH_3)_2$, Merck) was employed as a solvent to dissolve 9wt.% PAN. The mixture was stirred continuously at 50 °C for 2 hours and at room temperature for 24 hours to obtain a homogeneous solution. Graphene-doped PAN electrospinning solution with 1 wt% graphene (Nanografi, 99.9% nanoplatelet) was prepared following a similar procedure. The electrospinning device sets the voltage (0–40 kV), the distance between the plate and the needle (1–30 cm), and the solution flow rate (0.01–1000 mL/h) automatically. Initially, electrospinning parameters such as voltage, solution flow rate, and needle-to-collector distance were optimized to obtain homogeneous and continuous fibers. PAN and graphene-doped PAN solutions were exposed to an electric field in the electrospinning device (Basic System-Nanospinner), and the formed PAN (P) and graphene-doped PAN (GP) fibers were collected on the collector. The optimal electrospinning conditions for fiber production were determined as 17 kV voltage, 2.2 mL/h solution flow rate, and 17 cm needle-to-collector distance. P and GP fibers were pre-dried under atmospheric conditions and then subjected to oxidation (2° C/min heating rate, 260 °C, 2 hours) and carbonization (5 °C/min heating rate, 1000 °C, 1 hour) processes for stabilization and activation in a furnace, respectively. After oxidation and carbonization, the Oxidized PAN (PO) and Oxidized graphene-doped PAN (GPO) fibers were transformed into electrospun carbon nanofibers (CNF) and graphene-supported carbon nanofibers (GCNF). CNFs and GCNFs were stored in a desiccator to be employed as catalytic support. Cobalt loading was performed on the synthesized CNFs and GCNFs structures using the vacuum-impregnation method. Initially, a 10 mL cobalt chloride solution was prepared to contain 15 wt.% Co and doped to CNFs and GCNFs. Subsequently, they were kept under vacuum (-0.75 bar) at 60 °C for 48 hours. The doped fibers (Co@CNFs and Co@GCNFs) were activated at 450 °C for 1 hour under a nitrogen atmosphere.

2.2. Hydrogen Production

The H_2 production performance tests of the nanofiber catalysts were carried out under batch and continuous operating conditions and with catalytic hydrolysis reactions from $NaBH_4$ and NH_3BH_3 solution ($NH_3BH_3 + 2H_2O \rightarrow NH_4(BO_2) + 3H_2$ and $NaBH_4 + 4H_2O \rightarrow NaBO_2 + 4H_2$). Firstly, a batch hydrogen production system was established for hydrolysis reactions. The reactions were performed at 60 °C in a temperature-controlled (±2 °C) glass reactor with an internal volume of 20 mL, under continuous stirring at 500 rpm using a magnetic stirrer. The volume of produced H_2 was monitored based on the principle of water displacement with an equal volume and recorded over time to generate a

batch reaction rate profile. Subsequently, a continuous-flow system was designed for continuous operation. The system included a peristaltic pump (Cole Parmer MasterFlex L/S 7518-40, ±0.1), silicone tubing, a packed-bed reactor, a specially designed liquid-gas separation unit, a heat exchanger, and a gas measuring cylinder. The reaction was carried out under conditions equivalent to batch operation conditions.

3. RESULTS AND DISCUSSION

3.1. Morphological properties of fibers

SEM analysis was performed to determine the fiber formation in the samples and to examine the morphologies. The samples were coated with gold-palladium under a high vacuum for analysis. It was observed that white PAN fibers were formed successfully when the PAN solution was electrospun. Additionally, GP maintained its homogeneous white color distribution that indicating the nanolayered graphene was distributed homogeneously in the PAN solution. It was determined that both the P and GP samples turned brown after the oxidation and after carbonization, black fibers specific to carbon fiber were obtained.

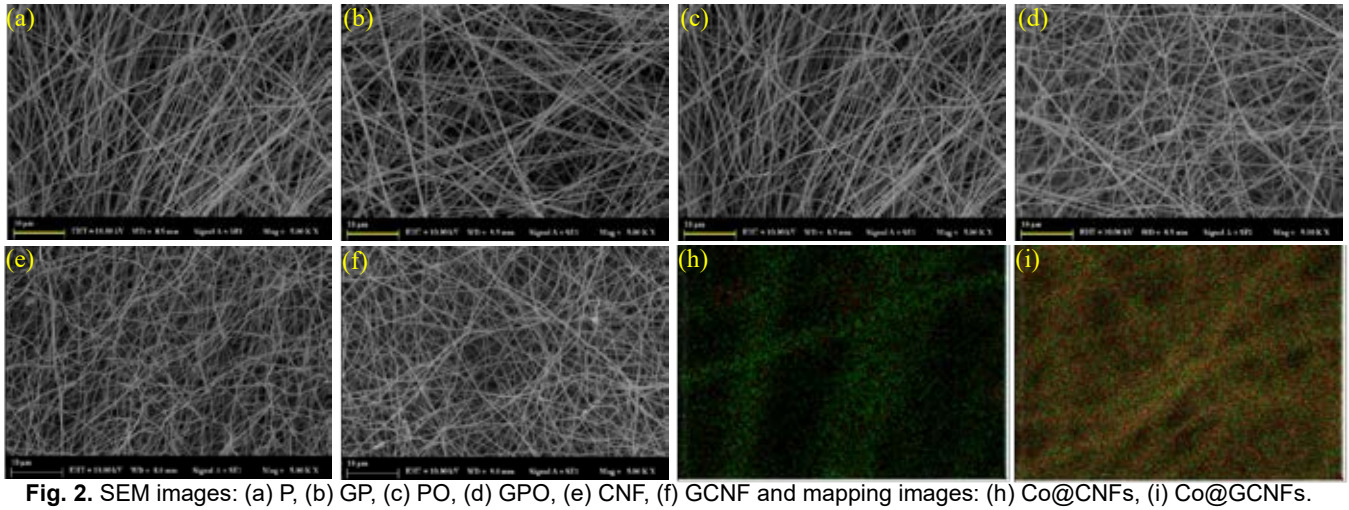

Fig. 2. SEM images: (a) P, (b) GP, (c) PO, (d) GPO, (e) CNF, (f) GCNF and mapping images: (h) Co@CNFs, (i) Co@GCNFs.

SEM and mapping images of samples at 5000x magnifications are given in Fig. 2. SEM and mapping images show that fibers with a homogeneous, spun, continuous, interwoven network structure and three-dimensional morphology are successfully synthesized. Notably, the network structure remained intact and was preserved after stabilization and activation. Furthermore, it was determined that the homogeneous, curved, continuous, interwoven network structure of fibers was not damaged after the Co doping on the fibers. However, the mapping-SEM analysis performed to determine the distribution of impregnated Co in the fiber structure reveals clustered regions. This suggests that the Co was distributed homogeneously on the fiber surface after doping. The dimensions of the fiber diameters were measured from the SEM images. Under the applied electrospinning parameters, PAN fibers were synthesized at <400 nm. The average diameter of the electrospun PAN-based carbon nanofibers obtained after stabilization and activation was measured at 177 nm. The decrease in diameters is attributed to insufficient oxidation. It was found that the addition of graphene led to the development of carbon fibers with a thicker diameter. This can be explained by graphene doping increasing the electrospinning solution's viscosity. Also, it was noted that the diameters did not significantly change after Co doping.

3.2. Batch and Continuous Hydrogen Production Profiles

Firstly, hydrogen production was carried out based on $NaBH_4$ and NH_3BH_3 hydrolysis in the presence of Co@CNFs and Co@GCNFs catalysts under batch production conditions. The reaction rates were calculated by plotting batch hydrogen production rate profiles. The hydrogen production rates for NH_3BH_3 and $NaBH_4$ hydrolysis with Co@GCNFs catalyst were calculated to be 3.50 and 2.96 L/min·gcat, respectively. These values are approximately 3.6 and 2.4 times higher than hydrogen production rates with the catalyst without graphene doping. It shows that graphene-doped carbon nanofibers synthesized as catalyst support material are effective for accumulating a sufficient amount of cobalt particles [7]. Subsequently, Co@GCNFs and Co@CNFs were utilized for Ru and Rh doping and hydrogen production rates were calculated using batch hydrogen production profiles (Table 2).

Ru and Rh doping were found to enhance the hydrogen production rate. Co@GCNF doped with Rh doped the lowest reaction time and the highest H_2 production rate. The H_2 production rate was determined as Rh>Ru>Co. It concluded that Rh doping into the carbon nanofiber structure significantly improves the catalytic properties of the nanoparticles for the hydrolysis of $NaBH_4$ and NH_3BH_3.

Table 2. Hydrogen production rates of catalysts with $NaBH_4$ and NH_3BH_3 hydrolysis.

Catalyst	H_2 Production Rate, L/min·gcat	
	NH_3BH_3 Hydrolysis	$NaBH_4$ Hydrolysis
Co@CNF	0.97	1.26
Co@GCNF	3.50	2.96
CoRu@CNF	4.39	3.86
CoRh@CNF	5.07	6.41
CoRu@GCNF	4.11	3.81
CoRh@GCNF	5.68	6.26

Hydrogen production from boron fuels under continuous operating conditions was conducted with the most active catalyst (CoRh@GCNF) from batch operation conditions and obtained a similar H_2 production rate. When the system is operated in a continuous flow, the active sites of the catalysts are emptied with the flow. Additionally, the continuous flow removes the reaction byproducts such as sodium metaborate ($NaBO_2$), diammonium borane hydrate ($H_4B_4O_9{\cdot}2(H_4N){\cdot}1.4(H_2O)$, and ammonium boron oxide hydroxide hydrate ($(NH_4)(B_5O_6(OH)_4)(H_2O)_2$) from the reaction environment and improves the interaction between the reactants.

4. CONCLUSIONS

In this study, the hydrolysis reaction of Co, Rh, and Ru doped carbon nanofiber catalysts synthesized using an electrospinning technique with $NaBH_4$ and NH_3BH_3 under batch and continuous operating conditions was investigated and the effect of the synthesized catalysts on hydrogen production efficiency from boron fuels was evaluated. The results of this study represent a significant step forward in the field of hydrogen energy. The findings indicate that Co, Rh, and Ru-doped carbon nanofiber catalysts synthesized by electrospinning are effective in hydrogen production from boron fuels. Moreover, it was determined that the Rh-doped catalyst with an H_2 production rate for $NaBH_4$ is 6.26 L/min·gcat and NH_3BH_3 is 5.68 L/min·gcat had the most effective performance. These experimental results confirm that carbon nanofiber-based catalysts suitable for continuous and batch operating conditions were successfully synthesized.

ACKNOWLEDGEMENT

The authors gratefully acknowledge the support of the Turkish Academy of Sciences (TÜBA) through the Outstanding Young Scientists Award (GEBİP/2020).

REFERENCES

1. Schlesinger HI, Brown HC, Finholt AE, Gilbreath JR, Hoekstra HR, Hyde EK. Sodium Borohydride, Its Hydrolysis and its Use as a Reducing Agent and in the Generation of Hydrogen. J Am Chem Soc. 1953;75(1):215-219.
2. Fakioğlu E, Yürüm Y, Veziroğlu TN. A review of hydrogen storage systems originated on boron and its compounds. Int J Hydrog Energy. 2004;29(13):1371-1376.
3. Demirci UB, Miele P. Sodium borohydride versus ammonia borane, in hydrogen storage and direct fuel cell applications. Energy Environ Sci. 2009;2(6):627-637.
4. Figen AK. Improved catalytic performance of metal oxide catalysts fabricated with electrospinning in ammonia borane methanolysis for hydrogen production. Int J Hydrog Energy. 2019;44(53):28451-28462.
5. Figen AK. Semi-continuous regime for continuous hydrogen production from sodium borohydride methanolytic dehydrogenation. Polyhedron. 2021;194:114920.
6. Coşkuner BF, Figen AK. Fabrication of electrospun nanofiber catalysts and ammonia borane hydrogen release efficiency. Int J Hydrog Energy. 2016;41:2016.
7. Chinthaginjala JK, Seshan K, Lefferts L. Hydrogenation of sodium borohydride and ammonia borane. Ind Eng Chem Res. 2007;46(12):3968-3978.

DESIGN AND ANALYSIS OF A BIOMASS-BASED INTEGRATED PLANT FOR GREEN HYDROGEN GENERATION AND BENEFICIAL COMMODITIES

[1*]Fatih YILMAZ, [2]Murat OZTURK, [1]Resat SELBAS
[1] Isparta University of Applied Sciences, Mechanical Engineering, Isparta/Turkiye
[2] Isparta University of Applied Sciences, Mechatronics Engineering, Isparta/Turkiye

*Corresponding authors: fatiyilmaz7@gmail.com

ABSTRACT

This study is about the thermodynamic analysis of an integrated combined system supported by biomass energy for clean electricity, heating, and hydrogen production. This system consists of an olive pit biomass-sourced Brayton cycle, a Rankine cycle, and high-temperature steam electrolysis. To produce clean and sustainable hydrogen, a comprehensive thermodynamic analysis of this renewable energy-supported system is considered, and also parametric studies are carried out. The analysis findings determined that the energy efficiency of the entire system was 53.61%. In addition, 0.00546 kg/s of green hydrogen can be produced with this system. It can be thought that the combination of integrated systems with renewable energy sources in the fight against environmental problems gives good results in terms of efficiency.

Keywords: Biomass, HTSE, exergy, Rankine cycle, hydrogen

1. INTRODUCTION

With increasing population and economic development, energy consumption around the world is also increasing, which has serious effects on the environment. In particular, the use of fossil fuels, which is still effective today, releases large amounts of greenhouse gases, especially carbon dioxide. As a result of greenhouse gas emissions, many environmental problems have emerged, such as global warming, acid rain, and melting glaciers [1]. Renewable energy sources are an important option to overcome and reduce these environmental problems. Renewable energy sources are natural and have no negative impact on the environment, such as solar, wind, geothermal, wave, tidal, and biomass. Biomass is also a biological renewable energy source [2]. Moreover, this energy source can generally be used for many purposes such as heating, cooling, and electricity generation, and can be integrated with multi-energy conversion systems.
A multigeneration system is used to produce more than three useful products with a single energy input. Therefore, these systems have an important place in energy efficiency. There are numerous studies in the literature on this subject, especially on the thermodynamic, economic, and environmental impact analysis of biomass-supported multigeneration systems. There are also comparative analyses of different biomass types to achieve higher efficiency. In general, products such as electricity, heating, cooling, clean water, hydrogen, and ammonia can be obtained with these systems. Some of the studies on the analysis of biomass-supported integrated systems conducted in 2024 and 2025 are presented here [3-6].
In this study, the thermodynamic performance analysis of heating, electricity, and hydrogen production with a combined system supported by olive pit biomass is investigated. High-temperature steam electrolysis (HTSE) was used for hydrogen production. System performance is determined by applying a detailed energy and exergy analysis method.

2. SYSTEM DESCRIPTION AND ANALYSIS

In this study, a combined system with biomass support is considered, as given in Fig. 1. The system basically consists of a Brayton cycle with intercooled and reheated supported by biomass, a Rankine cycle, and HTSE units. Electricity production is obtained from the gas turbines 1 and 2 (GT-1 and GT-2) in the Brayton cycle and the steam turbines (ST) in the Rankine cycle. Water in the vapor phase at point 21 enters the HTSE, where hydrogen and oxygen production take place. In this study, olive pits are preferred as a biomass source, and the chemical properties are also given in Table 1.

Table 1. Chemical properties of olive pits [7]

Fuel type	Value
C	48.81
H	6.23
O	43.48
N	0.36
S	0.02
HHV	21390
Moisture	-

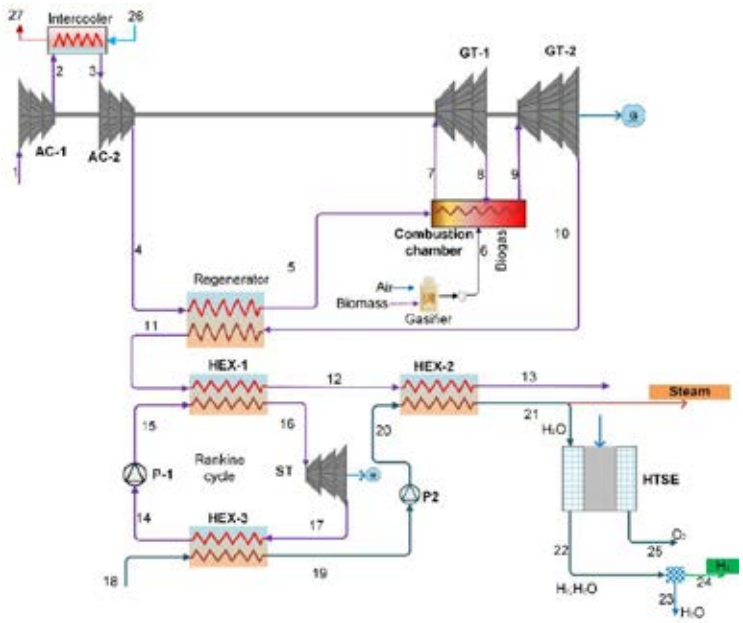

Fig.1. Schematic flow chart of the combined system

For detailed thermodynamic analysis, refer to the articles in the references [8-9]. The basic energy and exergy efficiency of the system can be formulated as follows;

$$\eta_{sys} = \frac{\dot{W}_{net} + \dot{Q}_{heating} + \dot{m}_{H_2} LHV_{H_2}}{\dot{m}_{biomas} LHV_{biomass}} \quad (1)$$

$$\psi_{sys} = \frac{\dot{W}_{net} + \dot{E}x_{Q,heating} + \dot{m}_{H_2} ex_{H_2}}{\dot{m}_{biomas} ex_{biomass}} \quad (2)$$

The net power can be written as;

$$\dot{W}_{net} = \dot{W}_{GT-1} + \dot{W}_{GT-2} + \dot{W}_{ST} - (\dot{W}_{AC-1} + \dot{W}_{AC-2} + \dot{W}_{P1}) \quad (3)$$

3. RESULTS AND DISCUSSION

A comprehensive thermodynamic analysis is performed for the developed biomass-supported integrated system's power, heating, and hydrogen production. The analysis result is illustrated in Fig. 2. Here, this system's energy and exergy efficiencies are calculated as 53.61% and 23.97%, respectively. In addition, this system can produce 3233 kW net electricity at these efficiencies.

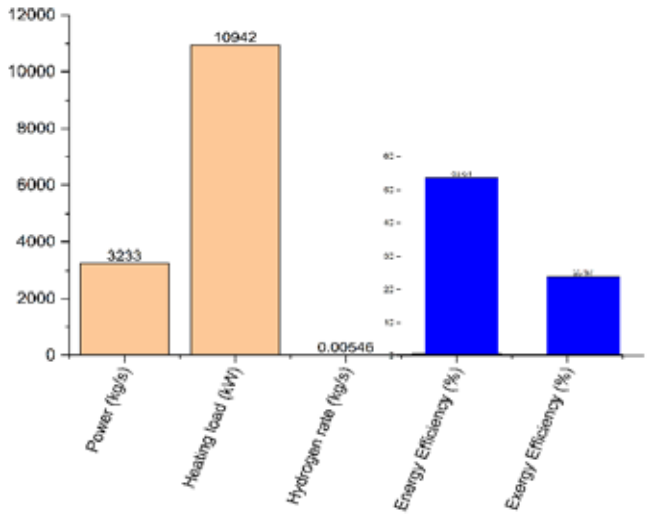

Fig. 2. Analysis results of the developed system

To examine the changes in efficiency and useful outputs in this system, the biomass mass change is examined parametrically and is presented in Fig. 3 (a-b). While the increase in biomass mass increased the useful outputs, it negatively affected the system efficiency.

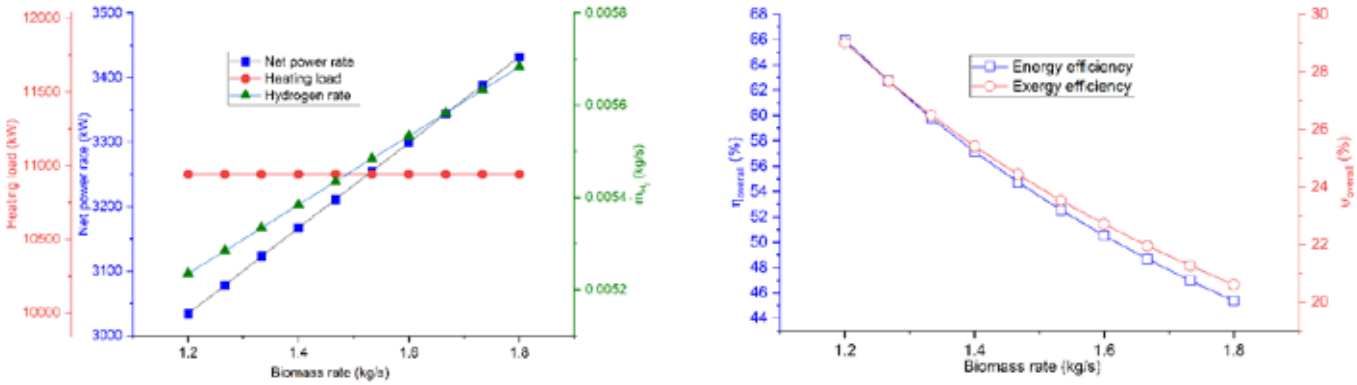

(a) (b)

Fig. 3. Impact of the biomass mass flow rate on the system products(a) and system's efficiency(b)

Fig. 4 (a and b) shows the increase in both the useful outputs produced in the system and the system efficiency by increasing the compressor compression ratio (r_p). There is a linear increase until the r_p value reaches approximately 4-4.5, then this increase rate decreases. The main reason for this situation can be interpreted as the compressors consuming more energy as the r_p value increases.

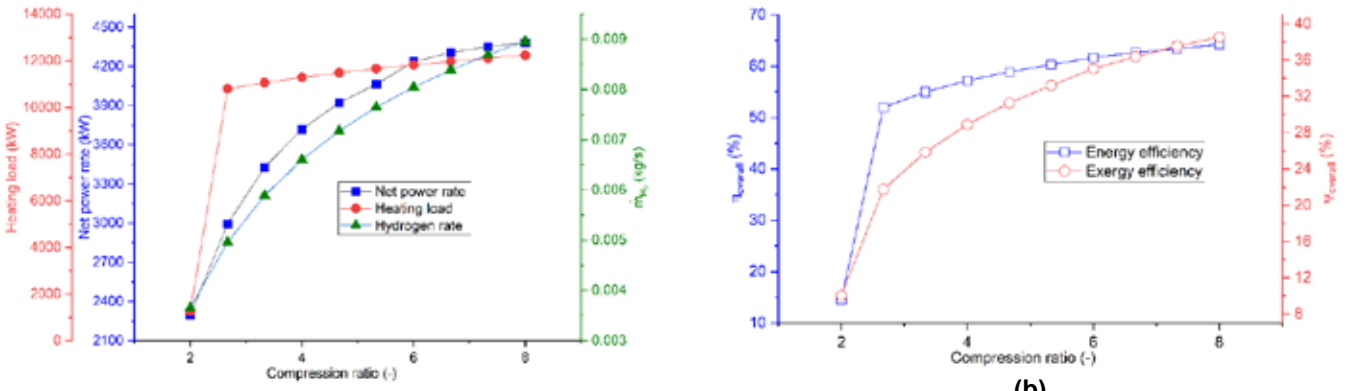

(a) (b)

Fig.4. Relationship between r_p and system variables

Finally, the effect of the combustion chamber outlet temperature (T_7), namely the turbine inlet point, on the system efficiency is analyzed and presented in Fig. 5. As the T_7 temperature increased between 900 and 1200 ℃, the energy efficiency of the whole system increased from approximately 50% to 58%, while the exergy efficiency increased from approximately 20% to 27%. It is known that increasing the turbine inlet generally increases the efficiency of power generation systems.

4. CONCLUSION

In this study, thermodynamic analysis of a new biomass-supported integrated system to produce clean and sustainable hydrogen, power, and heating is performed according to energy and exergy efficiency.

- As a result of the analysis, it is indicated that the system produced 3233 kW of net electricity. In addition, it can produce 10942 kW net heat load and 0.00546 kg/s green hydrogen. Moreover, the energy efficiency of the whole system was calculated as 53.61% and the exergy efficiency as 23.97%.
- The highest irreversibility is seen in the combustion chamber.

Renewable energy sources such as biomass are used to overcome environmental problems. These systems will be indispensable for the future, especially for sustainable energy.

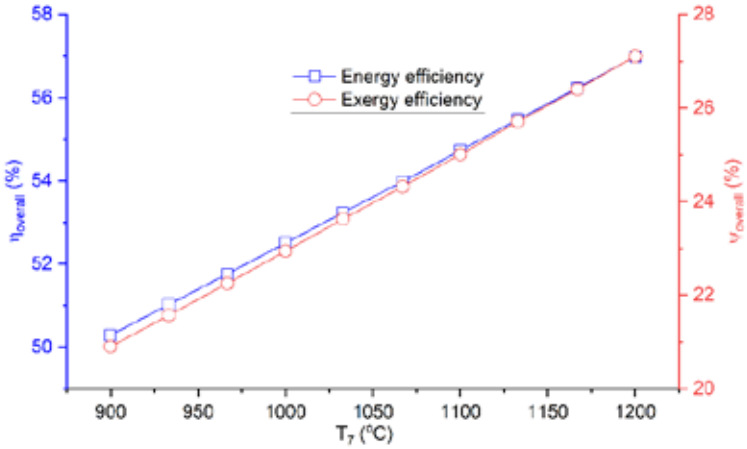

Fig. 5. Effect of turbine inlet temperature on system performance criteria

REFERENCES

1. Ahmadi, P., Dincer, I., & Rosen, M. A. (2013). Development and assessment of an integrated biomass-based multi-generation energy system. *Energy*, *56*, 155-166.
2. Cohce, M. K., Dincer, I., & Rosen, M. A. (2011). Energy and exergy analyses of a biomass-based hydrogen production system. *Bioresource technology*, *102*(18), 8466-8474.
3. Yilmaz, F., Ozturk, M., & Selbas, R. (2024). Design and performance evaluation of a biomass-based multigeneration plant with supercritical CO2 brayton cycle for sustainable communities. *International Journal of Hydrogen Energy*, *59*, 1540-1554.
4. Abedinia, O., Shakibi, H., Shokri, A., Sobhani, B., Sobhani, B., Yari, M., & Bagheri, M. (2024). Optimization of a syngas-fueled SOFC-based multigeneration system: Enhanced performance with biomass and gasification agent selection. *Renewable and Sustainable Energy Reviews*, *199*, 114460.
5. Yuksel, Y. E., Ozturk, M., & Dincer, I. (2025). Development and assessment of a biomass-gasification based multigenerational plant for production of hydrogen and ammonia fuels. *Fuel*, *380*, 133187.
6. Sharifishourabi, M., Dincer, I., & Mohany, A. (2025). Development of a Novel Biomass-Wind Energy System for Clean Hydrogen Production along with Other Useful Products for a Residential Community. *Energy and Built Environment*.
7. Sami, M., Annamalai, K., & Wooldridge, M. (2001). Co-firing of coal and biomass fuel blends. *Progress in energy and combustion science*, *27*(2), 171-214.
8. Ahmadi, P., Dincer, I., & Rosen, M. A. (2013). Development and assessment of an integrated biomass-based multi-generation energy system. *Energy*, *56*, 155-166.
9. Safari, F., & Dincer, I. (2019). Development and analysis of a novel biomass-based integrated system for multigeneration with hydrogen production. *International Journal of Hydrogen Energy*, *44*(7), 3511-3526.

DEVELOPMENT AND ASSESSMENT OF A SOLAR ENERGY-BASED MULTIGENERATION PLANT INTEGRATED WITH A HYDROGEN GENERATION UNIT FOR CLEAN PRODUCTS

[1]*Yunus Emre YUKSEL* [2*]*Fatih YILMAZ,* [3]*Murat OZTURK,*
[1] Isparta University of Applied Sciences, Department of Basic Sciences, Isparta/Turkiye
[2] Isparta University of Applied Sciences, Department of Mechanical Engineering, Isparta/Turkiye
[3] Isparta University of Applied Sciences, Department of Mechatronics Engineering, Isparta/Turkiye

*Corresponding authors: fatiyilmaz7@gmail.com

ABSTRACT
The effective use of renewable energy resources is one of the indispensable methods for overcoming environmental problems. For this reason, this study focuses on a comprehensive thermodynamic analysis of power, heating, cooling, hydrogen, and clean water production with an integrated system supported by a solar tower. The system is driven thermally by a solar tower system. Parametric analyses are performed to examine the energy and exergy efficiency changes in the system. According to the findings of the research, this system has 51.83% energy efficiency and 48.41% exergy efficiency while producing 5135 kW of net electricity and 0.0079 kg/s of green hydrogen**.**

Keywords: Energy, exergy, green hydrogen, solar tower, multigeneration.

1. INTRODUCTION

Global warming and environmental problems are among the most important threats to societies in the world's future. The main source of these problems is the efficient and widespread use of carbon-based fossil fuels in energy production and consumption. As a result of this use, global temperature increases are occurring worldwide, and limiting this increase to a maximum of 1.5 ℃ by 2100 is vital for sustainability. At this point, the renewable energy sources have gained much more importance. Among renewable energy systems, solar and wind-based systems have attracted significant attention, and significant cost reductions have been achieved through research and development activities [1]. Furthermore, another important way to struggle with the environmental problem is through energy efficiency methods, like the multigeneration energy conversion plants. Multigeneration plants present more than three beneficial products by using the same energy input. In recent years, many researchers have been focused on the renewable energy-based multigeneration plant.

Özlü and Dincer [2] have addressed the performance evaluation of a new solar energy-based multi-generation system and examined it from a thermodynamic perspective. The energy and exergy efficiency of the whole system were calculated as 36% and 44%. In 2024, the thermodynamic evaluation of combined cooling, heating, hydrogen, and power multi-generation systems for full-spectrum solar energy utilization was studied by Fang et al [3]. Moreover, Yilmaz et al. [4] presented a proposal for an advanced hybrid multigeneration power plant using solar energy for sustainable hydrogen production: They presented a thermodynamic and environmental analysis. Some of the studies on integrated solar energy-supported systems carried out in 2025 are collected here [5-7].

This study focuses on the investigation of a comprehensive thermodynamic performance analysis of an integrated solar tower-supported system. For this reason, detailed energy and exergy analyses are conducted to determine the system performance criteria and beneficial products. Furthermore, the system aims to produce clean and sustainable products as well as green hydrogen.

2. MATERIALS AND METHODS

In this study, a solar tower-supported multigeneration energy conversion system is proposed and investigated for the production of beneficial products (see Fig. 1). The system consists of 6 subsystems: solar tower cycle, Rankine cycle with two turbines, organic Rankine cycle, multi-effect desalination unit, absorption cooling unit, and hydrogen generation and compression unit.

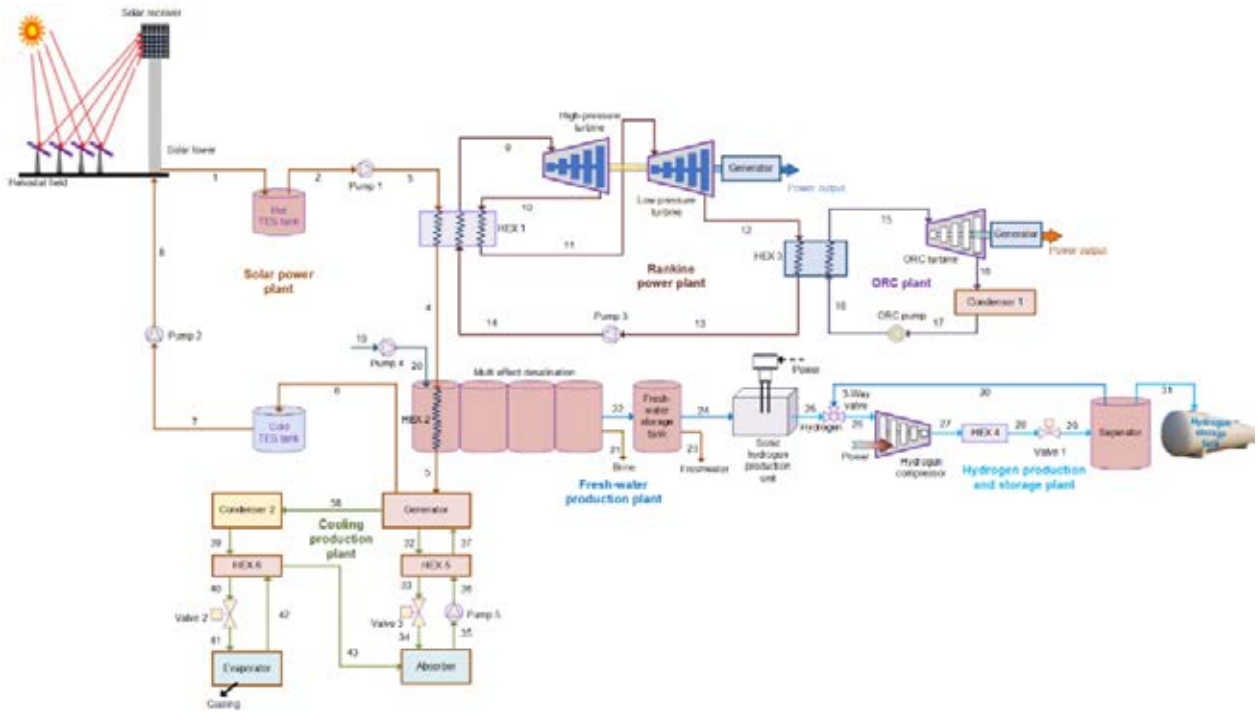

Fig. 1. A schematic diagram of the renewable energy-based integrated plant.

Here, a detailed thermodynamic analysis method is discussed. For this analysis method, it is assumed that the entire system is a steady-state flow condition. In addition, kinetic and potential energy changes are not taken into account, pumps and turbines have isentropic efficiency, and pressure loss between system elements is neglected. Following these assumptions, the general mass, energy, entropy, and exergy balance equations can be formulated as follows [8-9];

$$\dot{m}_{in} = \dot{m}_{out} \tag{1}$$

$$\dot{Q}_{in} + \dot{W}_{in} + \sum \dot{m}_{in} h_{in} = \dot{Q}_{out} + \dot{W}_{out} + \sum \dot{m}_{out} h_{out} \tag{2}$$

$$\sum \dot{m}_{in}\, s_{in} + \sum \left(\frac{\dot{Q}_{in}}{T_s}\right) + \dot{S}_{gen} = \sum \dot{m}_{out}\, s_{out} + \sum \left(\frac{\dot{Q}_{out}}{T_s}\right) \tag{3}$$

$$\dot{Ex}^{\dot{Q}_{in}} + \dot{Ex}^{\dot{W}_{in}} + \sum \dot{m}_{in} ex_{in} = \dot{Ex}^{\dot{Q}_{out}} + \dot{Ex}^{\dot{W}_{out}} + \sum \dot{m}_{out} ex_{out} + \dot{Ex}_D \tag{4}$$

Overall system;

$$\eta_{sys} = \frac{\dot{W}_{net} + (\dot{m}_{H_2} LHV_{H_2}) + (\dot{Q}_{heating}) + (\dot{Q}_{cooling})}{\dot{Q}_{solar}} \tag{5}$$

$$\psi_{sys} = \frac{\dot{W}_{net} + (\dot{m}_{H_2} ex_{H_2}) + (\dot{Ex}_{Q,heating}) + (\dot{Ex}_{Q,cooling})}{\dot{Ex}_{Q,solar}} \tag{6}$$

3. RESULTS AND DISCUSSION

The results of the thermodynamic analysis performed in this designed study are presented in Table 1. The net electricity production capacity of this system is calculated as 5135 kW. In addition, the amount of hydrogen and clean water obtained in the system is 0.0079 kg/s and 0.3319 kg/s.

Table 1. The generation capacities of the proposed integrated plant.

Productions	Quantity	Unit
Power	5135	kW
Heating	2173	kW
Cooling	1338	kW
Hydrogen	0.0079	kg/s
Freshwater	0.3319	kg/s

In parametric analysis, the effects of the reference temperature change are included to determine the effects of the change in the ambient temperature on the system. The changes in the energy efficiency, exergy efficiency, and exergy destruction of the reference temperature change on the subsystems and the entire system are shown in Fig. 2. It has been observed that it positively affects both energy and exergy efficiency.

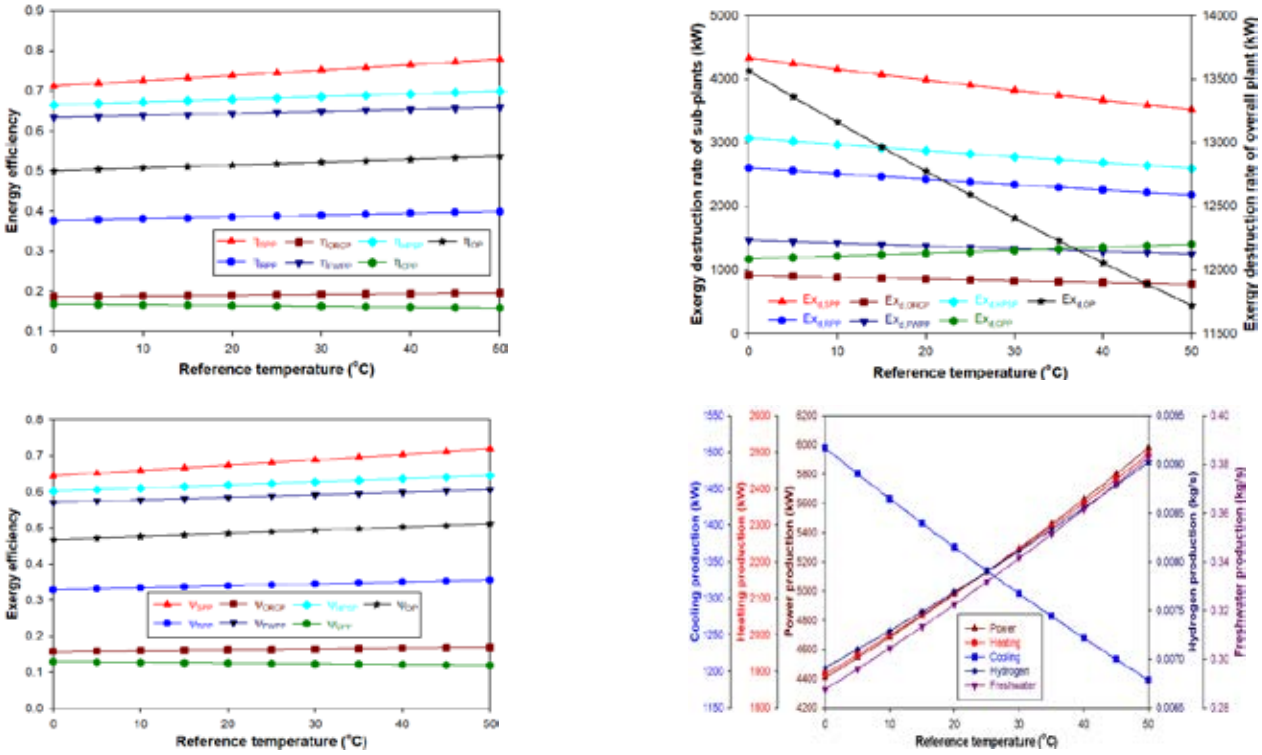

Fig. 2. Effect of the reference temperature on the system efficiency, beneficial products, and exergy destruction rates

The effect of the change in the solar radiation value on the energy and exergy efficiencies of the system as well as the total irreversibility and useful outputs produced by the system is presented parametrically in Fig. 3. The increase in the solar DNI value is the positive effect on the developed system. With these increment ratios, the net power generation rate is increased by about 4000 to 6500 kW.

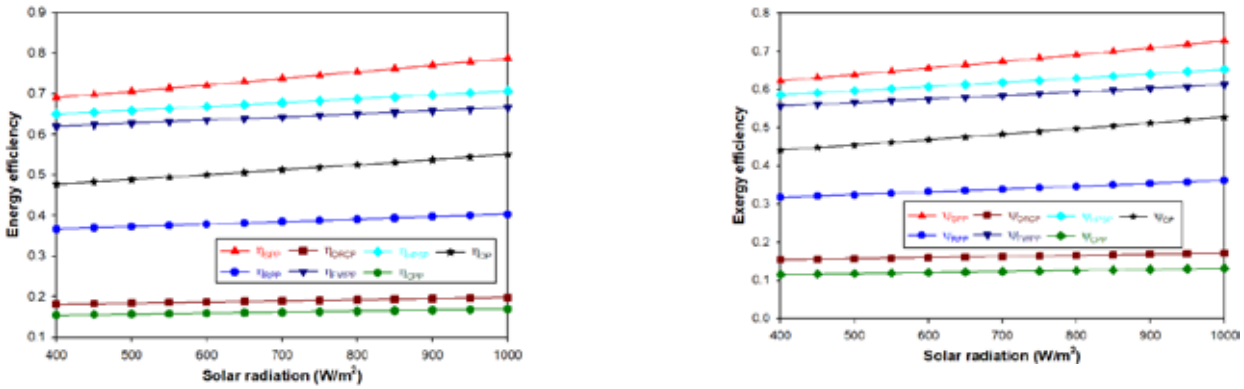

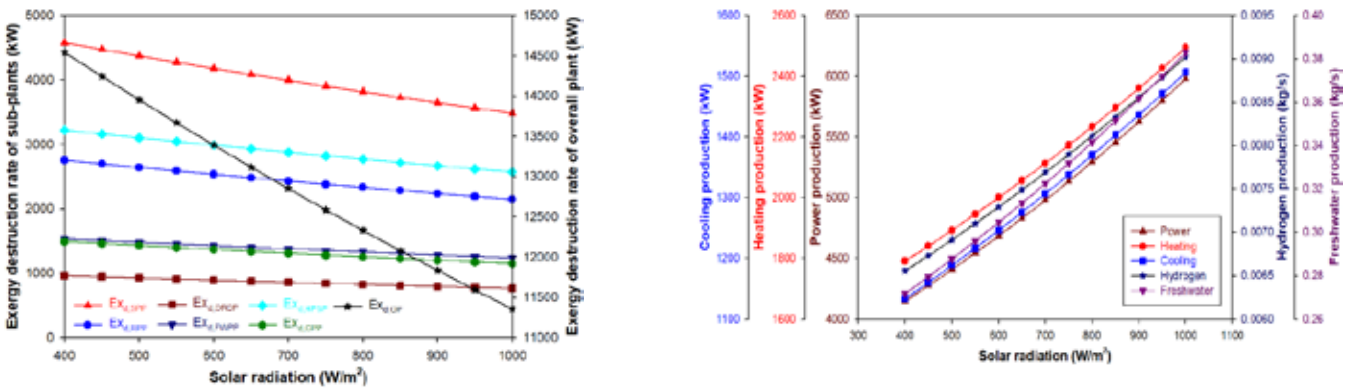

Fig. 3. Effect of solar radiation on the system efficiency, beneficial products, and exergy destruction rates

4. CONCLUSION

It is important to obtain more than one product with renewable energy-supported combined systems because it is both more efficient and has lower emissions. In this study, a new solar tower-supported integrated system is designed, and detailed parametric analyses are performed in terms of thermodynamic methods. The results obtained can be summarized as follows:

- The net electricity, heating, cooling, and hydrogen production capacity of the integrated system is 5135 kW, 2173 kW, 1338 kW, and 0.0079 kg/s.
- This system can also produce 0.3319 kg/s of drinkable clean water.
- The energy efficiency of the entire system was calculated as 51.83% and 48.94%. The total exergy destruction rate is 12591 kW and the highest value was observed in the solar tower.

REFERENCES

1. Temiz, M., & Dincer, I. (2023). Design and assessment of a solar energy based integrated system with hydrogen production and storage for sustainable buildings. *International Journal of Hydrogen Energy*, *48*(42), 15817-15830.
2. Ozlu, S., & Dincer, I. (2016). Performance assessment of a new solar energy-based multigeneration system. *Energy*, *112*, 164-178.
3. Fang, J., Yang, M., Fan, Y., Luo, T., Li, H., Liu, T., ... & Zhao, K. (2024). Thermodynamic evaluation of a combined cooling, heating, hydrogen, and power multi-generation system for full-spectrum solar energy utilization. *Energy Conversion and Management*, *300*, 118019.
4. Yilmaz, F., Ozturk, M., & Selbas, R. (2025). Proposal of an advanced hybrid multigeneration plant using solar energy for sustainable hydrogen generation: A thermodynamic and environmental analysis. *Renewable Energy*, 122621.
5. Hussein Obaid Ajam, A., Mirzaee, I., Jafarmadar, S., & Abbasalizadeh, M. A. J. I. D. (2025). Thermodynamic and Thermoeconomic Analysis of a Multigeneration System Based on Solar Energy Using Nanofluid for Power, Fresh Water, Hydrogen, Heating and Cooling Production. *Iranica Journal of Energy & Environment*, *16*(3), 389-399.
6. Goren, A. Y., Dincer, I., & Khalvati, A. (2025). A new electro-biomembrane integrated renewable-based system to produce power, fresh water and hydrogen for sustainable communities. *Sustainable Cities and Society*, 106156.
7. Ishaq, M., & Dincer, I. (2025). Process development and simulation of a Novel Solar Energy Plant Integrated with Solid Oxide Fuel Cell, Hydrogen, Heat Recovery and Carbon Capture Systems. *International Journal of Thermofluids*, 101122.
8. Cengel, Y. A., Boles, M. A., & Kanoğlu, M. (2011). *Thermodynamics: an engineering approach* (Vol. 5, p. 445). New York: McGraw-hill.
9. Dincer, İ. (2020). *Thermodynamics: a smart approach*. John Wiley & Sons.

CHALLENGES AND LIMITATIONS OF DARK FERMENTATIVE HYDROGEN PRODUCTION

Şefik Arıcı, Günnur Koçar
Ege University, Biomass Energy Systems and Technologies Application and Research Center (BESTMER)
Bornova, Izmir, 35100, Türkiye

Corresponding author e-mail: sefik.arici@ege.edu.tr

ABSTRACT

Hydrogen has emerged as a critical industrial and energy resource with increasing importance in various production technologies. From an astrobiological perspective, hydrogen dominated the early universe and played a pivotal role in the evolution of life as early microorganisms such as methanogens and sulfate reducers used hydrogen as an electron donor. Geological theories, like the hydrothermal reactor hypothesis suggest that early life forms utilized hydrogen and CO_2 in primitive metabolic pathways. Today, biohydrogen production especially through dark fermentation, has attracted significant interest due to its similarity to anaerobic digestion systems. Despite over 3,000 studies on dark fermentation in the past 20 years no commercial-scale system has been realized mainly due to low yields, substrate requirements and operational challenges. Furthermore, geopolitical factors, such as Europe's reliance on Russian natural gas, have accelerated the shift toward green hydrogen, especially in Germany. Electrolyzers, using water and electricity to produce pure hydrogen are now favored for large-scale deployment. However, biological hydrogen production remains limited by microbial metabolism especially hydrogenase enzyme dynamics and hydrogen-consuming species like methanogens. Although pretreatment methods aim to suppress these species they introduce additional technical and economic burdens. Thus, hydrogen's biological production faces both ancient and modern challenges in reaching industrial viability.

Keywords: Dark Fermentation, Limitation, Biohydrogen, Inoculum, Low-yield

1. INTRODUCTION

Hydrogen is an industrial and energetic tool that is increasingly with different methods and technologies day by day. When the formation of the universe is considered from an astrobiological perspective, it is thought that there was around 75% hydrogen in the universe when the Big Bang first began [1]. Considering the age of the world, which is 4.6 G years, it is also known that there was no atmospheric oxygen for half of this period. The first microorganisms that formed until this period were extremophiles that remained alive anaerobically (methanogen, sulphate reducer, etc.). In this period (Great Oxidation event), in which oxygen did not form for about 1 G year, it is thought that the first autotrophs/lithotrophs that used inorganic compounds such as CO and H_2 and CO_2 as electron acceptors could begin using the Wood-Ljungdahl pathway, according to the "isotopic partition model" [2].

Another geological study, under the name of hydrothermal reactor hypothesis (serpentization), argues that CO_2 formed by volcanic leakage in the seas and hydrothermal H_2, metal-catalysed reactions and the synthesis of Acetyl-CoA from inorganic metabolites and then acetate, ethanol, etc. are realised. It is also thought that this reaction was first chemical and then biochemical enzyme-catalyzed 3.8 G years ago [3]. These strict anaerobes called homoacetogens formed the first carbon building blocks using CO_2 and H_2. Another strict anaerobe, hydrogenotropic methanogens are archaitic microorganisms that produce methane with the same substrates. Similarly, groups such as sulfate reducers, nitrate reducers and syntropic propionate reducers are H_2-dependent and use H_2 as an electron donor. In this point, there is stong affinity of the usage of hydrogen by microorganism since the orign of life. Hydrogen is widely used in anaerobic environments which produced by suppressing or disabling consumer species has been an exciting topic for the last 30 years. Especially biohydrogen production via dark fermentation has been studied extensively due to its similarity to existing biogas systems [4]. In a one of the bibliometric study, it was observed that approximately 3071 dark fermentation studies were conducted in the last 20 years and almost all of them were lab-scale (max TRL 3-4-). There is no commercially operating dark fermentative pilot plant yet and some of the published trials have some techno-economic question marks that have been methodologically ignored [5,6]. In addition, the necessity of purify impurities in the obtained biohydrogen (carbon dioxide), suitable organic raw materials demads with high sugar content and operational difficulties still continue to prevent commercial biohydrogen production.

On the other hand, political and other energy-related developments in the world encourage hydrogen production in different ways. In the war that Russia started with to annex Ukraine in 2021, Europe's dependence on Russian natural gas was seriously revealed. Approximately 40% of the natural gas used in Europe is imported from Russia [7]. A series of measures have been taken within the scope of the Green agreement (10-point plan) to prevent this dependence and the gas which imported is planned to be gradually reduced by 2030 [8]. Russia's aggression against Ukraine has forced Europe to accelerate its energy transition which means that Russia has unintentionally encouraged European climate policy [9]. Reasons such as unreliability of Russia, hydrogen production based on natural gas in the industrial sector, the need to store energy critically in line with geopolitical energy security and climate goals that accelerated green hydrogen

studies both socially and academically and it has been publicly accepted, especially in Germany [10]. Because the war revealed the economic fragility of the Germans who were largely dependent on Russian gas. That's why Germany is trying to prevent this by switching to green hydrogen instead of natural gas in energy production. For this reason, encouragement for the use of electrolyzers has increased which is so simple of installation, use of water as raw material, high efficiency pure hydrogen production capacity and operation only with electricity. Therefore, electrolysers have begun to be preferred over dark fermentation as a source of green hydrogen production.
As the political and static energy security trends in the world change, the difficulties of hydrogen production by fermentation are also becoming apparent again. The theoretical maximum yield that can be achieved by dark fermentation is 4 moles H_2 per 1 mole of glucose, given as the Thauer limit [11]. This yield was increased up to 6.1 and 11.6 moles in some manipulated (by changing enzyme syntheses or metabolic pathways through genetic means) combined pure culture medium and a single species, respectively [11,12]. Apart from these special efforts (fully controlled microbial environment), the yields obtained using mixed inoculum culture (anaerobic sludge, biogas digestate etc.) have always remained below the limit. Many factors play a role in this inefficient process, where a very small portion of the substrate used energetically is converted into gas. Hydrogenase enzymes play the most important role in this process because they can catalyze hydrogen formation, consumption and sensing bidirectionally. In genomic and metagenomic studies (51 bacterial and archeal phylum hydrogenases were found), it is known that molecular hydrogen is an important electron donor for respiration in both anoxic and oxic ecosystems and therefore the main energy source for respiration in many ecosystems (geothermal, atmospheric, biological) [12]. This process could have been crucial for the emergence of autotrophic life forms, which can synthesize their own organic compounds from inorganic sources. One of the difficulties is due to the fact that H_2 output represents an energy loss for the cell and that microbial metabolic network has evolved for rationalization of energy use and optimization of specific growth rate and uptake hydrogenase [13].
The most important of that preparation phase of the inoculum culture. As it is known, some pre-treatments must be carried out to prepare the inoculum and substrate for microbial activity to start and adapt. Pre-treatments like thermal, chemical, pH, aeration etc. applied to the inoculum that are based on the principle of deactivating the species that consume hydrogen in the inoculum and activating the producers. These pre-treatments have many technical, economic and energetic handicaps. Nevertheless, these methods cannot prevent the consumption of hydrogen, especially by methanogens, homoacetogens and other species.

The Importance of Microbial H_2 metabolism

H_2 metabolism plays a crucial role in soil, sludge, aquatic systems, animal guts, and hydrothermal vents. Specific hydrogenases dominate different ecosystems:

- Aerobic soils: High abundance of oxygen-tolerant uptake hydrogenases.
- Anoxic environments (sediments, guts, bogs): More fermentative and respiratory hydrogenases.

The primordial role of H_2 as an energy source supports the theory that H_2 was one of the first electron donors for life. The great diversification of hydrogenases over time allowed microbes to adapt to different energy and environmental conditions. There types of Hydrogenases take a serious role in microbial hydrogen metabolism [13]. Those are listed below.

[NiFe]-Hydrogenases (22 subgroups)

- The most diverse and widespread type, primarily involved in H_2 oxidation for respiration.
- Subdivided into:
  - **Group 1 & 2:** Respiratory hydrogenases, involved in aerobic and anaerobic H_2 uptake.
  - **Group 3:** Bidirectional hydrogenases, capable of both H_2 production and consumption.
  - **Group 4:** H_2-evolving enzymes, essential in fermentation and energy transduction.

[FeFe]-Hydrogenases (6 subtypes)

- Primarily found in anaerobic bacteria, archaea, and unicellular eukaryotes.
- Often linked to fermentation and electron bifurcation (simultaneously directing electrons to multiple pathways).
- Includes bifurcating hydrogenases, which split electron flow to enhance metabolic efficiency.

[Fe]-Hydrogenases

- A less diverse and functionally constrained class, found only in methanogens.
- Plays a key role in CO_2 reduction and hydrogen cycling in archaea to produce methane.

2. RESULTS AND DISCUSSION

Thermodynamic and other barriers are limiting the maximize of dark fermentative hydrogen production. Some of these factors are given in below.

- **Inoculum preperation:** Inoclums are have to be pre-treated to kill or suppress hydrogen consumer microorganism such as methanogens. However most of the technics are utilizing huge amount of energy and chemicals then eventually they are not efficiently success for microbial hydrogen consumption [14,15]. In batch culture, it can be managed somehow but when new substrate adding to the reactor brings their own consumer and later becoming dominant and changing the balance of the media.
- **pH and Temperature:** Maintaining pH in optimal conditions (5.5-6.5) is always challenging during fermentation because of the alkalinity of the medium which requires chemicals continuously and mostly causing a foam formation too. Temperature is an other issue to keep reactor in same level need energy depending operation degree (themophilic etc.).
- **Sensing and Analysis:** Regular analysis of the fermentation metabolites like volatile fatty acid and other related metabolic product also curial to maintain hydrogen yield which can be perfomed well only in equipt laboratories.
- **Gibbs Free Energy:** Hydrogen production during dark fermentation is only thermodynamically favorable when the Gibbs free energy change is negative. This requires specific conditions, including a low hydrogen partial pressure. As hydrogen accumulates, the $^{o}\Delta G$ becomes less negative eventually reaching a point where further hydrogen production becomes thermodynamically unfavorable. Also process shift that stimulates butrate production is related with partial hydrogen production that allow only 2 mols of hydrogen per mol of glucose consumption.
- **Metabolic Pathways:** The specific metabolic pathways employed by fermentative microorganisms influence the amount of hydrogen that can be produced from a given substrate. Some pathways (Wood-Ljungdahl, Direct Interspices Hydrogen Transfer, Syntropic Acetate/Propionate Oxidation, Sulphate Reduction etc.) lead to the formation of by-products like acetate, butyrate, H_2S or ethanol which compete with hydrogen production for electrons and reduce the overall hydrogen yield
- **Hydrogenase Enzyme Activity:** Hydrogenases the enzymes that responsible for catalyzing hydrogen production are sensitive to environmental conditions like pH and temperature. Optimal hydrogenase activity is essential for efficient hydrogen production and deviations from these optimal conditions can hinder the process.
- **Substrate Concentration and Type:** Increasing the easy degradable carbohydrates content allows high substrate concentrations (high sugar-shock loading) which is necessary to perform hydrogen production but it may also lead to product inhibition too. On the other side, complex substrates may require additional processing steps (pre-treatment) before they can be utilized by fermentative microorganisms. Less substrate concentration also can shift the metabolism to microbial growth instead of hydrogen production. It has to be maintained well balance.
- **Gas heterogenity:** During dark fermentative hydrogen production, hydrogen is not the major gas that ocur in reactor. Besides hydrogen, considerable amount of carbondioxide can be formed during process. Stoichiometrically, each moles of glucose fermentation can produce 2 moles of CO_2 and in mixture it can be formed up to 50%. This situation has to be solved by further downstream processes like gas filtration and purification if the gas mixture wont be used in internal combustion engines.

3. CONCLUSIONS

Hydrogen production by dark fermentation is still promising renewable green hydrogen production way but some of serious operational, microbial and process modifications has to be solved.

Diversifying the substrate sources and using easily degradable sugars or performing pre-treatments to reveal potential carbohydrates in some raw materials is necessary. In addition, since it is known that hydrogen production occurs only form at high carbohydrate concentrations, the integration of remaining sugars into other processes such as anaerobic biogas, microbial fuel cells and photofermentation which can increase total energy efficiency of the process. Innovative reactor designs, such as continuous stirred-tank reactors, immobilezed, sequencing batch or packed-bed reactors can improve hydrogen production by optimizing substrate utilization, mass transfer and hydrogen of removal. Two-phase combine hydrogen-methane (biohytane) system is an another alternative way to perform energy efficiency too. In situ hydrogen removal like continuously removing hydrogen from the fermentation broth can alleviate product inhibition and shift the thermodynamic equilibrium towards further hydrogen production. Methods like gas sparging or membrane separation can be employed for in situ hydrogen removal. Microbial community composition of the fermenter plays a crucial role in hydrogen production. A diverse community with a balance of hydrogen-producing and hydrogen-consuming microorganisms can lead to more efficient hydrogen production. Furthermore, combining some pure strains or genetically modified microorganism cultivation to maintain high hydrogen yield like above Thaur limit is an another microbial modification. Maintainig the temperature and pH at optimum levels for ideal hydrogen production is a very critical process which has to be considered under energy efficiency and less chemical usage for sustainability. Checking of the fermentation process to avoid unfavarouble pathways like butyrate/ethanol production which cause a low hydrogen yield has to be monitored regularly by automation and regular analysis (feed back inhibition by H_2 build up and inhibitors etc).

As a results, over the decades, there was a serius academic studies was carried out to produce sustainable hydrogen production by dark fermentation. However, as we mentioned during the whole paper that researcher need to overcome serious technical, microbial and political bariers to use hydrogen in commercial systems as green hydrogen sources.

REFERENCES

1. Reid, D. D., Kittell, D. W., Arsznov, E. E., & Thompson, G. B. (2002). The picture of our universe: A view from modern cosmology. *Astrophysics.*
2. Ragsdale, S. W., & Pierce, E. (2008). Acetogenesis and the Wood-Ljungdahl pathway of CO2 fixation. In Biochimica et Biophysica Acta - Proteins and Proteomics (Vol. 1784, Issue 12, pp. 1873–1898).
3. Martin, W., & Russell, M. J. (2007). On the origin of biochemistry at an alkaline hydrothermal vent. In Philosophical Transactions of the Royal Society B: Biological Sciences (Vol. 362, Issue 1486, pp. 1887–1926). Royal Society.
4. Umunnawuike, C., Mahat, S. Q. A., Nwaichi, P. I., Money, B., & Agi, A. (2024). Biohydrogen production for sustainable energy transition: A bibliometric and systematic review of the reaction mechanisms, challenges, knowledge gaps and emerging trends. *Biomass and Bioenergy*, *188*, 107345.
5. Vatsala, T. M., Raj, S. M., & Manimaran, A. (2008). A pilot-scale study of biohydrogen production from distillery effluent using defined bacterial co-culture. *International Journal of Hydrogen Energy*, *33*(20), 5404–5415.
6. Balachandar, G., Varanasi, J. L., Singh, V., Singh, H., & Das, D. (2020). Biological hydrogen production via dark fermentation: A holistic approach from lab-scale to pilot-scale. *International Journal of Hydrogen Energy*, *45*(8), 5202–5215
7. https://www.iea.org/reports/a-10-point-plan-to-reduce-the-european-unions-reliance-on-russian-natural-gas Accessed on March 2, 2025.
8. Geletukha, G., Zheliezna, T., Drahniev, S., & Haidai, O. (2022). Analysis of actions for ukraine to replace Russian natural gas. Ecological Engineering &Amp; Environmental Technology, 23(4), 1-9.
9. Schreurs, M. A. (2023). Implications of the Russian war on Ukraine for climate policy and the geopolitics of energy. Canadian Journal of European and Russian Studies, 16(2), 90-113.
10. Loewe, M., Quittkat, C., Knodt, M., & Ott, I. (2024). The impact of the Russian war against Ukraine on the German hydrogen discourse. Sustainability, 16(2), 773.
11. Thauer, R. K., Jungermann, K., & Decker, K. (1977). Energy Conservation in Chemotrophic Anaerobic Bacteria (Vol. 41, Issue 1).
12. Ergal, İ., Zech, E., Hanišáková, N., Kushkevych, I., Fuchs, W., Vítěz, T., Vítězová, M., Bochmann, G., & Rittmann, S. K. M. R. (2022). Scale-Up of Dark Fermentative Biohydrogen Production by Artificial Microbial Co-Cultures. Applied Microbiology, 2(1), 215–226. https://doi.org/10.3390/applmicrobiol2010015
13. Singh, R., White, D., Demirel, Y., Kelly, R., Noll, K., & Blum, P. (2018). Uncoupling fermentative synthesis of molecular hydrogen from biomass formation in Thermotoga maritima. Applied and Environmental Microbiology, 84(17).
14. Greening, C., Biswas, A., Carere, C. R., Jackson, C. J., Taylor, M. C., Stott, M. B., Cook, G. M., & Morales, S. E. (2016). Genomic and metagenomic surveys of hydrogenase distribution indicate H 2 is a widely utilised energy source for microbial growth and survival. *ISME Journal*, *10*(3), 761–777.
15. Vignais, P. M., & Billoud, B. (2007). Occurrence, classification, and biological function of hydrogenases: An overview. In *Chemical Reviews* (Vol. 107, Issue 10, pp. 4206–4272).
16. Arıcı, Ş and Koçar G. (2014). Thermophilic Dark Fermentative Biohydrogen Production from Anaerobically Digested Cattle Manure, 1 st International Biogas and Compost Workshop, 5-6 December, Antalya, Turkey
17. Arıcı Ş and Koçar G. (2013) Preparing a Hydrogen-Producing Microflora from Anaerobic Digested Cattle Manure for Two-Phase Combine H_2 and CH_4 Production Systems, Proceedings of the Second International Conference on Water, Energy and the Environment (ICWEE'2013), Kuşadası-Turkey, September 21-24,2013

INTEGRATION OF DARK FERMENTATION AND MICROBIAL ELECTROLYSIS CELLS FOR HYDROGEN PRODUCTION FROM WHEAT STRAW

İdilay KONAR, Raushan Kunayeva, İrem Bulat, Rayaan Harb, *Yasemin Dilsad Yilmazel**
Middle East Technical University, Faculty of Engineering, Department of Environmental Engineering, Çankaya, Ankara, 06800, TÜRKİYE
*Corresponding author e-mail: dilsad@metu.edu.tr

ABSTRACT

Renewable hydrogen production offers a clean and sustainable alternative to fossil fuels. This study investigates the potential of *Thermotoga maritima* to produce biohydrogen from wheat straw, a low-cost and abundant agricultural residue. Batch experiments were conducted at concentrations ranging from 2.5 to 35 g VS/L, demonstrating successful substrate degradation without pretreatment. The bacterium achieved net biohydrogen production reaching its highest at 14.6 ± 2.6 mL at 25 g VS/L. The dark fermentation effluent, rich in acetic acid, was further processed in a microbial electrolysis cell (MEC) using *Geoglobus acetivorans*. Initial MEC tests confirmed the utilization of effluent acetate for current production. These findings highlight the potential of coupling dark fermentation with MEC technology to improve biohydrogen yields from agricultural waste.

Keywords: Dark fermentation, Biohydrogen, *Thermotoga maritima*, Bioelectrochemical systems

1. INTRODUCTION

The amount of energy derived from fossil fuels make up 80% of the world energy consumption. Heavy reliance on fossil fuels accelerates their depletion, increases energy costs, and contributes to environmental issues such as air pollution and greenhouse gas emissions [1]. To ensure energy security and address environmental concerns, attention has turned to renewable energy sources. Hydrogen is a promising clean energy alternative due to its lack of CO_2 emissions during combustion and its high theoretical energy output [2]. While the hydrogen market is rapidly expanding, with a 10% annual increase in usage, current production methods rely on energy-intensive processes [3,4]. In biological hydrogen production methods like dark fermentation (DF), various types of waste can be used to achieve high biohydrogen yields, enabling both energy production and waste management [5]. Despite its potential, the rate and yield of biohydrogen production through DF remain low. In order to develop economically viable and sustainable H_2 producing bioprocess, production rate and yield should be increased.

To make the DF process practical, abundant and low-cost feedstocks like agricultural wastes may be used as raw material. Wheat straw (WS), a byproduct of wheat production offers high biodegradability and high carbon content, making it an economical and renewable raw material for biohydrogen production. In 2020, Turkey's wheat production reached 20.5 million tons; indicating a high potential to the use of WS as a feed to DF process [6].

Thermotoga maritima is a hyperthermophilic microorganism (≥70°C) with a wide range of thermostable hydrolytic enzymes essential for breaking down complex carbohydrates. Its high growth temperature provides several advantages, including faster hydrolysis of complex substrates, higher H_2 production rates, and reduced contamination risk from H_2-consuming microorganisms [7]. The fermentation process produces CO_2, acetate, lactic acid, and H_2, approaching the theoretical maximum yield of 4 mol H_2 per mol of glucose [8]. Under optimum conditions, fermentation results in 2 mol acetate/ mol glucose Eq. (1), that the bacteria are unable to further convert to H_2. Thus, during the fermentative production of H_2, conversion efficiency is 33% and remaining organic matter is wasted as acetic acid, despite a theoretical stoichiometric potential of 12 mol H_2/mol glucose Eq. (1) [9].

Bioelectrochemical systems (BES), such as Microbial Electrolysis Cells (MECs), utilize electro-active microorganisms to produce H_2. The electrons in MEC are involved in the H_2 evolution reaction at the cathode, and the exoelectrogens that are present as a biofilm on the anode are oxidizing organics and using this electrode as an electron acceptor Eq. (2) and Eq. (3) [10]. This process, known as electrohydrogenesis, extracts H_2 from the chemical energy stored in various substrates, including organic acids, complex organic compounds, and DF effluents. However, conversion of acetate to H_2 is not spontaneous and requires an external voltage of at least 0.14 V [11]. Yet, compared to other common H_2 production methods such as water electrolysis, energy requirement is significantly lower in electrohydrogenesis [12].

$$C_6H_{12}O_6 + 2H_2O \rightarrow 4H_2 + 2CO_2 + 2C_2H_4O_2 \quad (1)$$
$$CH_3COO^- + 4H_2O \rightarrow 2HCO^- + 9H^+ + 8e^- \quad (2)$$
$$8H^+ + 8e^- \rightarrow 4H_2 \quad (3)$$

This study focuses on biohydrogen production through the DF of wheat straw using *Thermotoga maritima*. To improve

overall H_2 yields, the DF effluent, which contains residual acetate, will be further processed in an MEC via electrohydrogenesis. This integrated strategy aims to use abundant and cheap lignocellulosic substrate to maximize biohydrogen production.

2. MATERIALS AND METHODS

2.1. Microorganisms and culture conditions

T. maritima DSM 3109 and *Geoglobus acetivorans* (DSM 21716) were purchased from the German Collection of Microorganisms and Cell Cultures (DSMZ), Braunschweig, Germany. *T. maritima* culture was grown in a medium from [13] with the following modifications: increasing the reducing agent to 1 g/L L-cysteine and adjusting the overall pH to 6.8. The growth medium included 5 g/L cellobiose as pure substrate, which is a repeating unit in lignocellulosic biomass. *G. acetivorans* was initially grown with 10 mM acetate as an electron donor, and 56 mM ferric citrate as an electron acceptor. Hyperthermophile archaea growth medium was prepared as given elsewhere to grow *G. acetivorans* culture [10]. The mediums were prepared anaerobically under N_2: CO_2 (80%:20%) atmosphere.

2.2. Experimental design and sets

To determine biohydrogen production potential, batch operations were set up using serum bottles with a total volume of 110 mL (active volume of 60 mL). The reactors included (i) pure substrate (PS), (ii) seed control (SC), (iii) waste test (WT), and (iv) negative controls (NC). The PS reactors, containing 5 g/L cellobiose as the substrate, were set up to evaluate the activity of the microbial culture. SC reactors were prepared without any carbon source (C-source) to determine background gas and metabolite production. WT reactors were supplied with WS as the C-source in two concentration sets: low dose (LD) and high dose (HD). LD concentrations were 2.5, 5, and 7.5 g VS/L, while HD concentrations were 15, 25, and 35 g VS/L, designed to assess the degradability of WS by *T. maritima*. NC reactors were designed to verify that hydrogen production resulted specifically from the activity of *T. maritima* rather than native microorganisms in WS. These reactors contained the same C-source concentrations as WT reactors but lacked *T. maritima* inoculum. All reactors were set up in triplicate, the pH adjusted to 6.8, and incubation maintained at 80°C. The experimental design is given in Table 1.

Table 1. The experimental design of Wheat Straw Set

Reactors	Inoculum	C-source	C- Source Dose
Pure Substrate (PS)	*T. maritima*	Cellobiose	5 g/L
Seed Control (SC)	*T. maritima*	-	-
Wheat Straw Test (WS)	*T. maritima*	Wheat Straw (WS)	2.5, 5 ,7.5 g VS/L and 15, 25 ,35 g VS/L
Negative Control (NC)	-	Wheat Straw (WS)	2.5, 5 ,7.5 g VS/L and 15, 25 ,35 g VS/L

G. acetivorans was tested in 5 mL active volume reactors using two different acetate sources: pure acetate and dark fermentation (DF) effluent. The two media used contained a total of 10 mM acetate. In the reactors, a graphite plate (GM-10 grade, dimensions: 1.5 cm x 1.0 cm x 0.3 cm) was used as the anode and a stainless-steel mesh (Type 304, mesh size 50, dimensions: 1.5 cm x 1.0 cm) as the cathode material. The experimental design is detailed in Table 2. The objective of this study was to evaluate the ability of *G. acetivorans* to utilize acetate from different sources. The DF effluent used in the experiments was obtained from *T. maritima* pure substrate fermentation. The initial phase of the experiment assessed whether *G. acetivorans* could use the acetate present in the DF effluent as an electron donor. Reactors (PA_DF) were first operated with pure acetate and then transitioned to DF effluent acetate in subsequent cycles to determine if biofilm formation occurred prior to the introduction of DF effluent. Current density was monitored throughout the experiment to evaluate reactor performance.

Table 2. The experimental design of G. acetivorans Mini MEC Set

Reactors	Inoculum	Cycle 1 to 3 electron donor	Other Cycles Electron Donor	Applied voltage (V)
Pure Acetate Dark Fermentation acetate (PA_DF)	*G. acetivorans*	10 mM Pure Acetate	10 mM DF Acetate	0.7
Dark Fermentation acetate (DF)	*G. acetivorans*	10 mM DF Acetate	10 mM DF Acetate	0.7

2.3. Analysis

The Wheat Straw (WS) was sourced from a local farmer, the sample was blended for 15 minutes to make it homogenous, and no other treatment was applied. The Standard Methods (APHA et al., 2005) were followed for the TS (Section 2540B), VS (Section 2540E), and chemical oxygen demand (COD) (Section 5220D). Neutral detergent fiber (NDF), acid

detergent fiber (ADF), and acid detergent lignin (ADL) are three major components of the fiber content of the wheat straw. WS samples were sent to NutriLab (Konya, Turkey) to determine fiber composition via a fiber analyzer (ANKOM Technology, USA).

Total gas production was measured using a liquid displacement device. The compositions (H_2, CH_4, CO_2, and N_2) of the headspace gas samples were determined via a gas chromatograph (Shimadzu 2010-Pro) equipped with a thermal conductivity detector (TCD). Volatile fatty acids (VFAs) were analyzed using a gas chromatograph (Shimadzu 2010-Pro) with a flame ionization detector (FID).

Solubilization was performed at the end of the experiment for each reactor. This is a common gravimetric method for solubilization of plant biomass; this study used it to analyze WS degradability in the test reactors. The solubilization assay for fermentation of selected waste was implemented according to [14] with minor modifications.

The contents of the reactor were filtered by vacuum filtration through coarse filter paper and washed twice with DI water. The coarse filter was dried in an oven at 75^{0}C, and its mass was measured. Given the initial mass in the reactor, an extra reactor was prepared under the same conditions (T_0) and the same solubilization protocol was followed before the reactor was operated. The degree of solubilization in the reactor was then determined from the difference between the initial mass (T_0) and the mass at the end of the process.

3. RESULTS AND DISCUSSION

The low dose WS set was operated for 31 days while the high dose set was operated for 18 days. During the operation, hydrogen production was observed, and the net H_2 production was determined by subtracting the H_2 produced in the SC reactors from that in the test reactors. The net H_2 production in the low concentration of WS did not reach the lowest net H_2 production in the high WS concentration even though they were operated for an additional 13 days, as shown in Figure 1.A. The average net hydrogen production at high dose reactors (≥ 15 g VS/L), was around 60% higher compared to the low dose reactors (≤ 7.5 g VS/L) indicating suitability of the selected feedstock for this process.

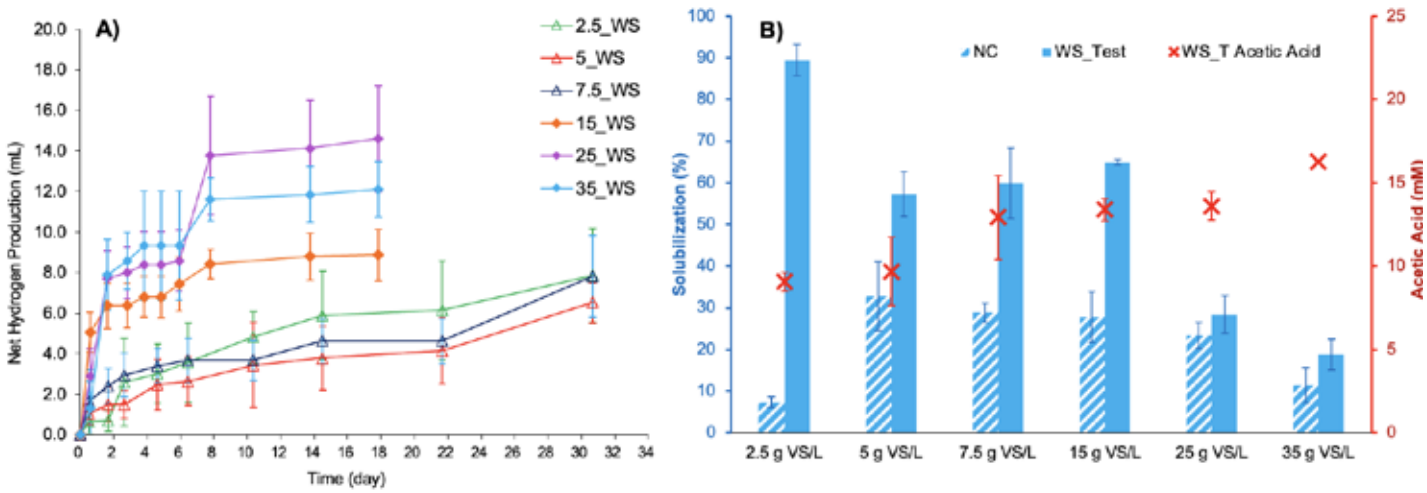

Fig.1. A) Net hydrogen production of WS set, **B)** WS set solubilization degree (%) and acetic acid concentration (mM)

At the end of the experiment, solubilization and acetic acid measurement are done (Figure 1.B). The results show that solubilization percentages tend to decrease as the concentration increases, possibly due to substrate saturation or resource limitations, where essential nutrients become insufficient for further degradation. The solubilization obtained in the NC reactors at each VS concentration is due to other processes unrelated to *T. maritima* activity such as thermal degradation of the waste. As the concentration of the feed increases the negative control solubilization rate is decreasing which may imply that there is only a certain degree of solubility achieved due to abiotic processes. The acetic acid production increases as concentration increases, test reactors average acetic acid production was relatively similar with an average of 12.5 ± 2.7 mM. The acetic acid was only detected at NCs of higher VS concentration reactors, with the maximum around 4 mM. The net acetic acid production on 35 g VS/L reactor was three times higher than respective NC.

G. acetivorans was inoculated into Mini MEC reactors containing 10 mM pure acetate and DF effluent derived from the pure substrate, cellobiose. As shown in Figure 3, the peak current densities observed were 1.64 ± 0.11 A/m² for DF_DF and 1.32 ± 0.58 A/m² for PA_DF. In the final cycle, the acetate source for the PA_DF reactors was switched to DF effluent, resulting in current densities of approximately 0.4 A/m² for both reactors. These results demonstrate that *G.*

acetivorans can utilize acetic acid present in DF effluent as an electron donor.

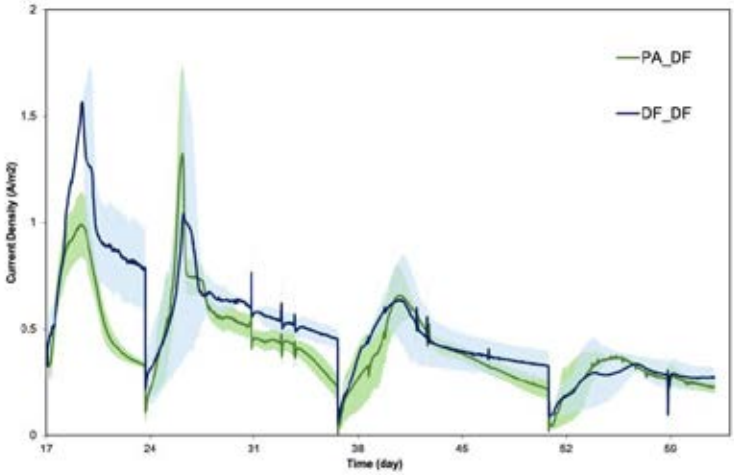

Fig.3. Current Density of Mini-MEC

4. CONCLUSIONS

The hyperthermophilic bacterium *T. maritima* effectively degraded WS without any pretreatment, even at high concentrations of up to 35 g VS/L. The highest net biohydrogen production, 14.6 ± 2.6 mL, was achieved at a concentration of 25 g VS/L, with a production rate of 4.35 mL/day. The DF effluent from these reactors was analyzed for acetic acid, which was then used as a feed in MECs. Initial tests with the MEC setup demonstrated that *G. acetivorans* could utilize the DF effluent from *T. maritima* reactors. Future stages of this study will focus on using WS DF effluent in MECs to further enhance biohydrogen production.

ACKNOWLEDGMENT

This study was supported by the Scientific and Technological Research Council of Turkey (TUBITAK) Centre of Excellence Support Program under grant number 122Y088, and the Academy of Science Award through BAGEP.

REFERENCES

[1] B. Gopalakrishnan, N. Khanna, and D. Das, “Dark-Fermentative Biohydrogen Production,” in *Biomass, Biofuels, Biochemicals: Biohydrogen, Second Edition*, Elsevier, 2019, pp. 79–122. doi: 10.1016/B978-0-444-64203-5.00004-6.
[2] I. K. Kapdan and F. Kargi, “Bio-hydrogen production from waste materials,” Mar. 02, 2006. doi: 10.1016/j.enzmictec.2005.09.015.
[3] R. Saidi *et al.*, “Biohydrogen production from hyperthermophilic anaerobic digestion of fruit and vegetable wastes in seawater: Simplification of the culture medium of Thermotoga maritima,” *Waste Management*, vol. 71, pp. 474–484, 2018, doi: 10.1016/j.wasman.2017.09.042ï.
[4] A. D. Frock, J. S. Notey, and R. M. Kelly, “The genus Thermotoga: Recent developments,” 2010, *Taylor and Francis Ltd.* doi: 10.1080/09593330.2010.484076.
[5] M. Cappelletti *et al.*, “Biohydrogen production from glucose, molasses and cheese whey by suspended and attached cells of four hyperthermophilic Thermotoga strains,” *Journal of Chemical Technology and Biotechnology*, vol. 87, no. 9, pp. 1291–1301, Sep. 2012, doi: 10.1002/jctb.3782.
[6] TÜİK Kurumsal. (n.d.). https://data.tuik.gov.tr/Bulten/Index?p=Bitkisel-Uretim-Istatistikleri-2020-33737
[7] N. Sekar, C.-H. Wu, M. W. W. Adams, and R. P. Ramasamy, “Electricity Generation by Pyrococcus furiosus in Microbial Fuel Cells Operated at 90 C,” *Biotechnol. Bioeng*, vol. 114, pp. 1419–1427, 2017, doi: 10.1002/bit.26271/abstract.
[8] C. Sehr6der, M. Selig, and P. Seh6nheit, “Glucose fermentation to acetate, CO2 and H 2 in the anaerobic hyperthermophilic eubacterium Thermotoga maritima: involvement of the Embden-Meyerhof pathway,” 1994.
[9] Liu, H., Grot, S., & Logan, B. E. (2005). Electrochemically Assisted Microbial Production of Hydrogen from Acetate. Environmental Science & Technology, 39(11), 4317–4320. https://doi.org/10.1021/es050244p
[10] Logan, B. E., Call, D., Cheng, S., Hamelers, H. V., Sleutels, T. H., Jeremiasse, A. W., & Rozendal, R. A. (2008). Microbial electrolysis cells for high yield hydrogen gas production from organic matter. Environmental science & technology, 42(23), 8630-8640.
[11] Kas, A., & Yilmazel, Y. D. (2022). High current density via direct electron transfer by hyperthermophilic archaeon, Geoglobus acetivorans, in microbial electrolysis cells operated at 80 °C. Bioelectrochemistry, 145, 108072. https://doi.org/10.1016/j.bioelechem.2022.108072
[12] Rozendal, R., Hamelers, H., Euverink, G., Metz, S., & Buisman, C. (2006). Principle and perspectives of hydrogen production through biocatalyzed electrolysis. International Journal of Hydrogen Energy, 31(12), 1632–1640. https://doi.org/10.1016/j.ijhydene.2005.12.006
[13] Boileau, C., Auria, R., Davidson, S., Casalot, L., Christen, P., Liebgott, P., & Combet-Blanc, Y. (2016). Hydrogen production by the hyperthermophilic bacterium Thermotoga maritima part I: effects of sulfured nutriments, with thiosulfate as model, on hydrogen production and growth. Biotechnology for Biofuels, 9(1). https://doi.org/10.1186/s13068-016-0678-8
[14] Zurawski, J. V., Conway, J. M., Lee, L. L., Simpson, H. J., Izquierdo, J. A., Blumer-Schuette, S., Nookaew, I., Adams, M. W. W., & Kelly, R. M. (2015). Comparative analysis of extremely thermophilic caldicellulosiruptor species reveals common and unique cellular strategies for plant biomass utilization. Applied and Environmental Microbiology, 81(20), 7159–7170. https://doi.org/10.1128/aem.01622-15

PERFORMANCE ANALYSIS OF A SMALL HYBRID VEHICLE ON INCLINED ROADS UNDER WLTP CLASS 2 DRIVE CYCLE

[1*]*Bugra Yilmaz*, [2]*C. Ozgur Colpan*
[1]Fırat University, School of Civil Aviation, Department of Aviation Electrical Electronics, Elazig, Turkey
[2]Dokuz Eylul University, Faculty of Engineering, Mechanical Engineering Department, Izmir, Turkey

*Corresponding author e-mail: b.yilmaz@firat.edu.tr

ABSTRACT

Integrating renewable energy sources into the transportation sector is essential to achieving targeted reductions in greenhouse gas emissions. While electric vehicles are promoted as an environmentally sustainable solution, the increasing battery weight associated with extended range highlights a key limitation. This challenge has driven the development of fuel cell-based hybrid electric vehicles as a viable alternative. In recent years, the simulation of powertrain systems in electric, hybrid, and fuel cell hybrid vehicles has become increasingly popular for assessing vehicle performance and powertrain efficiency. Studies on fuel cell hybrid vehicles typically focus on improving a specific powertrain component or a particular hybrid configuration, often assuming a flat road profile. In this study, a powertrain system model incorporating a battery and a fuel cell was developed and simulated in the Matlab/Simulink environment under the WLTP Class 2 driving cycle on an inclined road. The simulations provided key performance metrics, including the power output of powertrain components, battery state of charge (SoC), and hydrogen consumption. This study aims to offer a realistic simulation approach that closely reflects real-world driving conditions, achieving the desired performance in hybrid vehicles.

Keywords: Fuel cell hybrid vehicle, Battery, Hydrogen, Drive cycle simulation, Matlab/Simulink

1. INTRODUCTION

Electric vehicles (EVs) have gained significant attention as a sustainable alternative to conventional internal combustion engine vehicles due to their zero-emission operation and high energy efficiency. They utilize electric motors powered by batteries or hybrid energy sources, reducing reliance on fossil fuels and contributing to lower greenhouse gas emissions. However, range limitations and insufficient charging infrastructure remain major challenges for the widespread adoption of EVs. In this context, hydrogen-based Fuel Cell Electric Vehicles (FCEVs) have emerged as a viable solution, offering longer driving ranges and shorter refueling times than Battery Electric Vehicles (BEVs). FCEVs generate electricity through a Proton Exchange Membrane (PEM) fuel cell by converting hydrogen into electrical energy to power the motor. Despite their advantages, issues related to hydrogen production , storage, safety, and refueling infrastructure hinder their large-scale deployment. Recent advancements in fuel cell technology, such as improved catalyst materials and system integration, have significantly enhanced the efficiency and durability of FCEVs. Moreover, integrating renewable energy sources for hydrogen production improves the environmental benefits of these vehicles. EVs and FCEVs represent crucial innovations in sustainable transportation, each addressing different energy consumption and emissions challenges. Alpaslan et al. [1] investigated the driving cycle simulation performance of electric, hybrid and fuel cell powertrains of a small vehicle. Different combinations of energy sources, such as batteries, supercapacitors, and fuel cells were evaluated, and their effects on component efficiencies and vehicle range were analyzed . Dhanalakshmi et al. [2] have discussed the modeling and simulation of the electric powertrain of a hybrid electric vehicle. In the study, an effective electric powertrain design for hybrid electric vehicles is presented using permanent magnet synchronous motor (PMSM) and space vector pulse width modulation (SVPWM) techniques . Ancuta and Danciu [3] consider the modeling and simulation of an electric propulsion system equipped with a fuel cell. The model was developed using the MATLAB Simulink software and was based on the structure of the Toyota MIRAI. The simulation results include the evolution of the fuel cell and the important parameters of the vehicle over time . Wu et al. [4] developed optimal energy management strategies for hybrid electric vehicles using reinforcement learning. The proposed method was integrated with FASTSim, an open-source vehicle simulation tool, and was shown to be effective in improving energy efficiency under different vehicle models and driving cycles . Shubham and Ganguly [5] discuss a series-parallel hybrid electric vehicle's architecture and different operating modes. A standard series-parallel HEV is simulated using Matlab Simulink and its fuel consumption is estimated for different driving cycles. The results show that hybrid electric vehicles are a viable intermediate solution for the transition to full electric vehicles in developing countries . This study analyzed the performance of a hybrid electric vehicle powered by a fuel cell and a battery on a road with a different slope angle throughout the driving cycle. When the vehicle speed exceeded 30 km/h, the fuel cell was activated and speed control was performed with adaptive PID.

2. MODELING OF HYBRID ELECTRIC VEHICLE

Several forces act on an EV during its operation, influencing its dynamic behavior, energy consumption, and overall performance. A comprehensive understanding of these forces is essential for accurately modeling, controlling, and optimizing EV systems. The main forces acting on an EV include aerodynamic drag, rolling resistance, gravitational force, and inertial force. Each of these forces is described below with the corresponding mathematical expressions.

2.1. Aerodynamic Drag Force

Aerodynamic drag is the resistance exerted by air on the vehicle as it moves. It increases quadratically with vehicle speed and depends on vehicle shape and frontal area.

$$F_{aero} = {}^{1}/_{2}\, \rho C_d A_f v^2 \quad (1)$$

where F_{aero} is the aerodynamic drag force (N); ρ is the air density (kg/m³); C_d is the drag coefficient; A_f is the frontal area of the vehicle (m²); v is the vehicle speed (m/s).

2.2. Rolling Resistance Force

Rolling resistance arises due to the deformation of the tires and road surface. It is generally proportional to the vehicle's weight.

$$F_{roll} = m.g.C_r \cos\theta \quad (2)$$

where F_{roll} is the rolling resistance force (N); C_r is the rolling resistance coefficient; m is the vehicle mass (kg); g is the gravitational acceleration (9.81 m/s²); θ is the road incline angle (rad).

2.3. Gravitational Resistance Force

This force results from driving on an inclined road and depends on the slope angle. It increases the load on the powertrain during uphill motion and reduces it during downhill motion.

$$F_{grade} = m.g.\sin\theta \quad (3)$$

where F_{grade} is the grade resistance force (N)

2.4. Inertial Force

This force is associated with the acceleration or deceleration of the vehicle. It represents the force required to change the velocity of the vehicle mass.

$$F_{inertia} = m.a \quad (4)$$

where $F_{inertia}$ is the inertial force (N); a is the vehicle acceleration (m/s²)

2.5. Total Tractive Force

The total tractive force required at the wheels is the sum of all the aforementioned resistive forces. This force determines the power demand from the electric powertrain.

$$F_{tractive} = F_{aero} + F_{roll} + F_{grade} + F_{inertia} \quad (5)$$

Once the total tractive force is determined, it is possible to calculate the required torque on the wheels. Through the transmission system, this torque must be delivered by the electric drivetrain, ultimately by the Brushless DC (BLDC) motor. The wheel torque required to overcome the total resistive forces is calculated in Eq. 6.

$$T_{wheel} = F_{tractive}.R \quad (6)$$

where T_{wheel} is the required torque at the wheel (Nm); $F_{tractive}$ is the total tractive force (N); R is the effective wheel radius (m)

In most EVs, the torque generated by the BLDC motor is transmitted to the wheels via a gear reduction system. Therefore, the required motor torque can be derived from the wheel torque, considering the gear ratio.

$$T_{motor} = {}^{T_{wheel}}/_{\eta_{drivetrain}.G} \quad (7)$$

where T_{motor} is the motor torque (Nm); G, is the gear ratio; $\eta_{drivetrain}$ is the drivetrain efficiency

In this study, simulations were performed by calculating the total force and required engine torque for the WLTP Class 2 driving cycle Low part on an inclined road. Driving Cycle and slope angles are shown in Fig. 1(a). The vehicle and

simulation parameters are also given in Table 1. The model that calculates the forces acting instantly on the vehicle and the required engine torque according to the driving cycle was created in Matlab/Simulink according to the parameters in Table 1. The schematic diagram of the model is given in Fig 1(b). The primary energy source of the vehicle was determined as the battery. When the speed exceeds 30 km/h, the Perturb and Observe (P&O) algorithm controls the PEM fuel cell and supports the battery at maximum power.

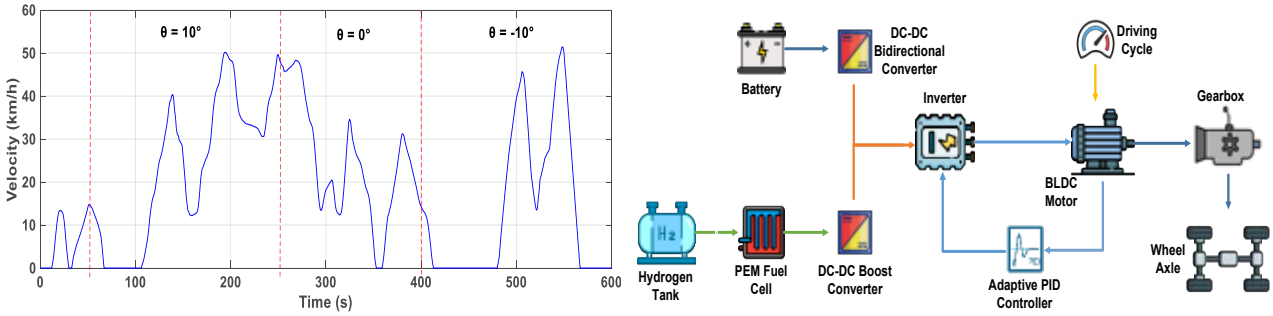

Fig. 1. (a) WLTP Class 2 low part and slope angle change **b)** The schematic diagram of the hybrid electric vehicle model

Table 1. The vehicle and simulation parameters

Definition	Parameter	Value	Unit
Vehicle Mass	m	500	kg
Rolling Resistance Coefficient	C_r	0.0015	-
Aerodynamic Resistance Coefficient	C_d	0.4	-
Vehicle Projection Area	A_f	2	m^2
Battery Capacity	Q_{Bat}	6	kWh
Initial Battery Charge	SoC_i	80	%
Maximum Fuel Cell Power	P_{FCmax}	3.48	kW
Mechanic Efficiency	$\eta_{drivetrain}$	90	%

3. RESULTS AND DISCUSSION

In this study, a Matlab/Simulink model was developed to analyze energy and vehicle performances of hybrid electric vehicles under slope change. In the simulations performed for the first flat road, the maximum battery power consumption during the driving cycle was 7 kW, while this value dropped below 6 kW in the hybrid system. Then, the vehicle performance was analyzed using battery power as the only energy source. Fig. 2(a) illustrates the battery power profile, whereas Fig. 2(b) presents the variations in the reference and the actual vehicle velocity. The change of SoC value throughout the cycle is given in Figure 2(c).

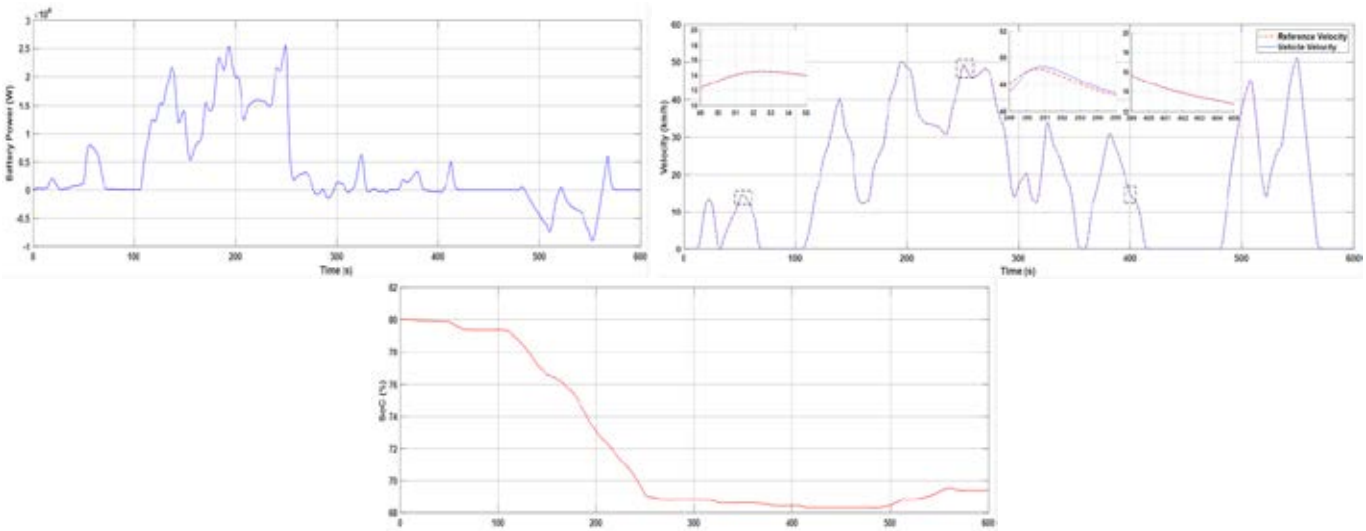

Fig. 2. (a) Battery power, **(b)** Reference and vehicle velocity, and **c)** SoC of the battery

The battery power and the reference velocity and actual vehicle velocity graphs for the vehicle operating under the hybrid power drive system are presented in Figures 3(a) and 3(b), respectively. The SoC value of the battery and the fuel cell power are also shown in Fig. 3(c) and (d).

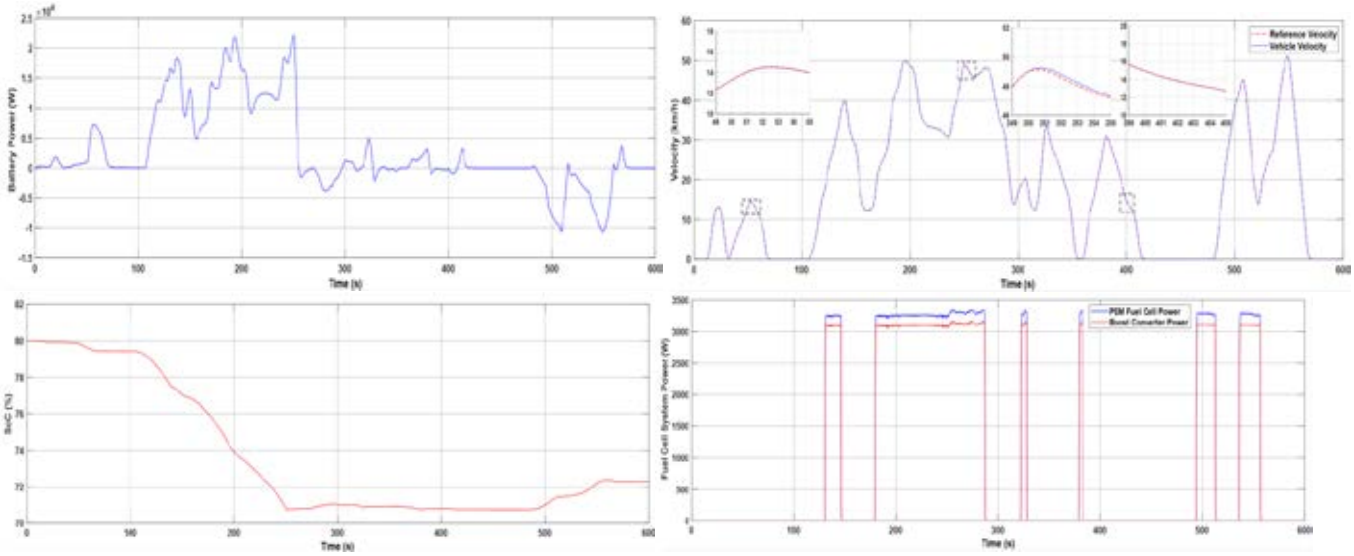

Fig. 3. (a) Battery power **(b)** Reference and vehicle velocity **c)** SoC of the battery, and **d)** PEM fuel cell power

As seen in Fig. 2(a), when the vehicle has only the battery, there is a power consumption of 25 kW according to the speed, while in Fig. 3(a) this consumption remains at a maximum of about 22 kW thanks to the fuel cell. While the slope change at low speeds caused minimal deviations from the reference speed thanks to the adaptive PID, the slope change at the 400th second, which occurred at a relatively higher speed, caused a departure from the reference speed for a few seconds. This situation is seen in Fig. 2(b) and Fig. 3(b). While the SoC value was below 70 in Fig. 2(c), it was completed above 72 due to the decrease in battery discharge when the fuel cell was activated, as in Fig. 3(c). Especially after the 500th second, the increase in the battery SoC value is because the energy generated as a result of regenerative braking due to the road slope angle being -10° charges the battery via the bidirectional converter.

4. CONCLUSIONS

In the proposed study, the WLTP Class 2 low section—representing approximately 3 km of driving for a hybrid electric vehicle—was simulated to analyze two powertrain configurations: one powered solely by a battery and the other combining a battery with a PEM fuel cell.To enhance the ability of the vehicle to accurately track the reference velocity, an adaptive PID controller was developed, in which the control parameters dynamically vary based on the instantaneous operating conditions. As can be seen from the results, the powertrain system using the fuel cell and battery together ensures that the battery capacity is used less and sudden discharges are prevented when higher velocities higher than 30 km/h are required. During hybrid operation, the fuel cell consumed approximately 210 L/min of air and 125 L/min of hydrogen to provide the required maximum power. Although the simulated inclined road model generally shows that power consumption increases compared to the case where the road is not sloped, it provides an analysis of a situation similar to real-world conditions.

REFERENCES

[1] Alpaslan E, Karaoğlan MU, Colpan CO. Investigation of drive cycle simulation performance for electric, hybrid, and fuel cell powertrains of a small-sized vehicle. Int J Hydrogen Energy 2023;48:39497–513. https://doi.org/10.1016/j.ijhydene.2023.08.358.
[2] Dhanalakshmi K V., Venkateswarlu AN, Syed MS, Tulasi Ram SS. Modelling and Simulation of a Hybrid Electric Vehicle with the Electric Power Train, 2023, p. 645–54. https://doi.org/10.1007/978-981-99-1588-0_57.
[3] Ancuţa AA, Danciu G. Modeling and simulation of an electric propulsion system equipped with Fuel Cell. IOP Conf Ser Mater Sci Eng 2022;1220:012011. https://doi.org/10.1088/1757-899X/1220/1/012011.
[4] Wu X, Wedernikow E, Nitsche C, Huber MF. Towards Optimal Energy Management Strategy for Hybrid Electric Vehicle with Reinforcement Learning. 2023 IEEE Intell. Veh. Symp., IEEE; 2023, p. 1–7. https://doi.org/10.1109/IV55152.2023.10186787.
[5] Shubham P, Ganguly A. Modelling and Simulation of Series Parallel Hybrid Electric Vehicle. IOP Conf Ser Mater Sci Eng 2021;1080:012001. https://doi.org/10.1088/1757-899X/1080/1/012001.

ENERGY MANAGEMENT IN A HYBRID SYSTEM INTEGRATING PV PANELS, PEM FUEL CELLS, AND BATTERIES

[1*]*Bugra Yilmaz*, [2]*C. Ozgur Colpan*
[1]Fırat University, School of Civil Aviation, Department of Aviation Electrical Electronics, Elazig, Turkey
[2]Dokuz Eylul University, Faculty of Engineering, Mechanical Engineering Department, Izmir, Turkey

*Corresponding author e-mail: b.yilmaz@firat.edu.tr

ABSTRACT

The growing global energy demand, when met by fossil fuels, propels the planet toward an irreversible climate crisis. Transitioning to renewable energy sources is essential to mitigate this trend. Due to the intermittent nature of renewable resources, an energy carrier that can be utilized on demand is required. Recently, environmentally friendly hydrogen has increasingly filled this gap. Hydrogen energy is becoming more popular for electricity generation through fuel cells without causing greenhouse gas emissions. This study models and evaluates a hybrid system consisting of a Proton Exchange Membrane (PEM) fuel cell, a photovoltaic (PV) panel array, and a battery to meet energy demand. For this purpose, a 1.26 kW PEM fuel cell, a 1.1 kW PV panel array, and a 12 kWh battery were integrated on a 48 V DC bus via appropriate converters in the Matlab/Simulink. The Perturb and Observe (P&O) algorithm controlled the PV panel array to achieve maximum power under varying solar irradiance and temperature conditions. Additionally, another Perturb and Observe (P&O) algorithm was employed to reduce the power output of the PEM fuel cell intentionally. This approach aims to decrease the hydrogen consumption of the fuel cell in response to specific solar radiation levels.

Keywords: Hybrid renewable energy system, Energy management, PEM fuel cell, Matlab/Simulink

1. INTRODUCTION

Fossil fuels, including coal, oil, and natural gas, have been the dominant global energy sources, but their extensive use in the 20th century has caused severe environmental damage. A global shift towards renewable energy is underway to address climate change and growing energy demand, aiming to eliminate greenhouse gas emissions. Solar energy emerges as a key alternative due to its abundance, environmental advantages, and applicability in off-grid systems. Nevertheless, the intermittent nature of solar energy necessitates integrating effective energy storage systems to ensure a consistent energy supply [1]. In this context, hydrogen stands out as a groundbreaking energy carrier. Hybrid solar and hydrogen systems, in particular, present a transformative solution for addressing energy poverty, mitigating climate change, and fostering sustainable development [2]. Integrating solar and hydrogen improves off-grid power stability by managing energy fluctuations and offers a scalable alternative to conventional batteries, addressing capacity and degradation issues. Recent studies have focused on ensuring uninterrupted electricity supply in off-grid applications. Ismail et al. [3] focused on developing a mathematical model to estimate and predict global solar radiation intensity in Egypt where solar energy is abundant year-round. Due to insufficient measurement stations, the model is validated against published solar radiation data. The results demonstrate accurate predictions of solar radiation intensity, improved system efficiency, and increased hydrogen production. The simulation outcomes align well with experimental data, validating the model . Doumbia et al. [4] introduce a dynamic simulation model developed in Matlab/Simulink to analyze the behavior of renewable energy systems with hydrogen storage. The system integrates sub-models for PV arrays, wind turbines, batteries, electrolyzers, fuel cells, and power conditioning units, suitable for both transient and steady-state analysis based on voltage, current, and temperature. The global model facilitates optimal system sizing and effective control design. Validation was performed using a state-of-charge (SoC) control method, and the simulation results aligned well with previous experimental test bench measurements . Raj and Rajasree [5] explored a hybrid energy system combining fuel cells and solar energy for electricity generation, which was modeled and simulated in Matlab/Simulink. Solar panels serve as the primary energy source, but due to their intermittency during nighttime or rainy conditions, fuel cells are utilized as an auxiliary source to ensure system reliability. Simulation results confirm the capability of the system to meet both electrical and heat demands under dynamic conditions . Yılmaz and Gençoğlu [6] focused on a hybrid system integrating solar and hydrogen energy, modeled using Matlab/Simulink. Mathematical models for a 200 W PV panel and a 100 W PEM fuel cell were developed. DC-DC boost converter models were designed for both energy sources connected in parallel to power a resistive load. The hybrid system delivered 500 W, with 3.795 A from the fuel cell and 6.205 A from the PV panel . In this work, the current study aims to meet the electrical needs of a DC load by adding a more powerful panel array, fuel cell, and battery to the system. The energy management algorithm was developed to accomplish this objective by monitoring the electricity generated from solar and hydrogen energy sources.

2. SYSTEM DESCRIPTION AND MODELING

The PV panel, which generates electricity based on changes in solar radiation and temperature, along with the fuel cell,

powers a 48 V DC bus in coordination with the battery. The variable output voltages of the PV panel and the fuel cell were regulated through boost converters, while the battery was integrated using the bidirectional converter. The energy management system (EMS) controlled the switching signals for all converters. The panel and the fuel cell were managed using the P&O algorithm to achieve their maximum power point (MPP). During periods when the power of the panel array exceeds 400 W, the duty cycle in the algorithm was reduced to decrease hydrogen consumption by the fuel cell. The control of the battery converter was implemented using a PI controller. A 1.5 Ω resistor was selected as the DC load. The characteristics of the PV array, PEM fuel cell, and battery used in the system are provided in Table 1. The design parameters for the boost converters of the PV panel and fuel cell, as well as the bidirectional converter for the battery, were calculated based on the parameters of the sources listed in the table. In the simulation, energy management was performed according to solar radiation and temperature for 9 hours between 10:00 and 19:00. Fig. 1 (a) illustrates the schematic representation of the system consisting of the PEM fuel cell, the PV panel array, and the battery. The flow chart of the P&O energy management algorithm is given in Fig. 1 (b). Solar irradiance and temperature curves are given in Fig. 2.

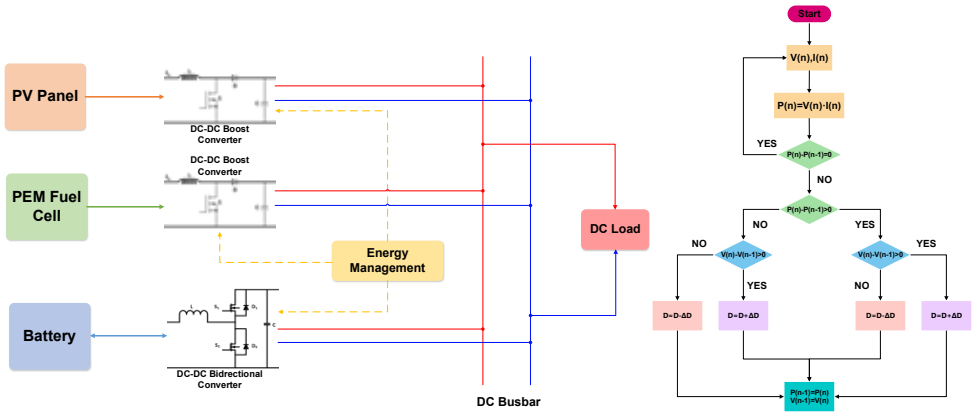

Fig. 1. (a) Schematic of the hybrid energy system **(b)** P&O MPPT algorithm

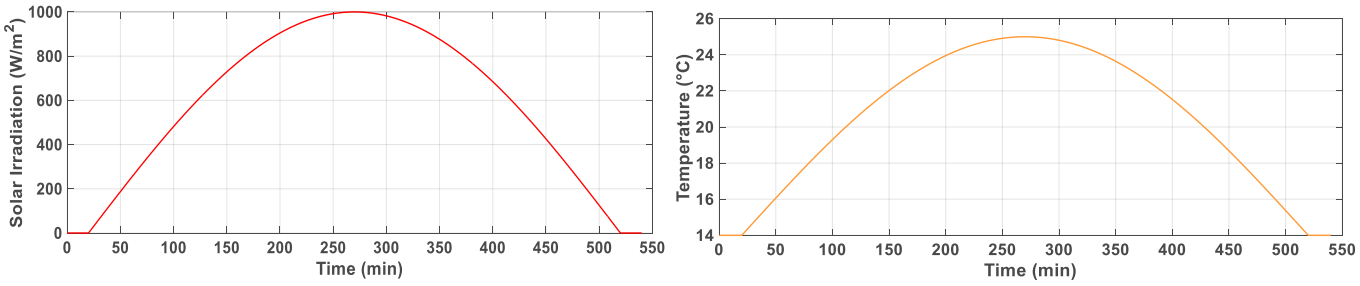

Fig. 2. (a) Solar irradiance profile **(b)** Ambient temperature profile

Table 1. PV panel, PEM fuel cell and battery specifications [7]

	Definition	Unit	Value
PV Panel Array	Maximum Power (P_{max})	W	213.5
	Open Circuit Voltage (V_{oc})	V	36.3
	Short-Circuit Current (I_{sc})	A	7.84
	Voltage at Maximum Power Point (V_{mp})	V	29
	Current at Maximum Power Point (I_{mp})	A	7.35
PEM Fuel Cell	Maximum Power (P_{max})	kW	2
	Nominal Power (P_{nom})	kW	1.26
	Nominal Current	A	52
	Nominal Voltage	V	24.23
	Maximum Current	A	100
	Maximum Voltage	V	20
	Nominal Stack Efficiency	%	46

	Operating Temperature	°C	55
Battery	Type	-	Lead-Acid
	Nominal Voltage	V	24
	Rated Capacity	Ah	500
	Nominal Discharge Current	A	100

3. RESULTS AND DISCUSSION

This study realized the energy management of a hybrid renewable energy system consisting of a PV panel, a PEM fuel cell and a battery. For this purpose, a model developed in Matlab/Simulink was used to obtain the voltage, current, and power waveforms of the sources connected to a DC load under varying solar radiation and temperature conditions based on the EMS algorithm. The power curves of the PEM fuel cell and the PV array are given in Figs. 3(a) and (b). As seen in these graphs, when the power of the PV panel exceeds 400 W, the duty cycle of the boost converter is reset to zero to reduce the amount of hydrogen consumed. In addition, Fig. 3 (c) shows the hydrogen and air consumption in the fuel cell, and Fig. 3(d) shows the DC bus voltage.

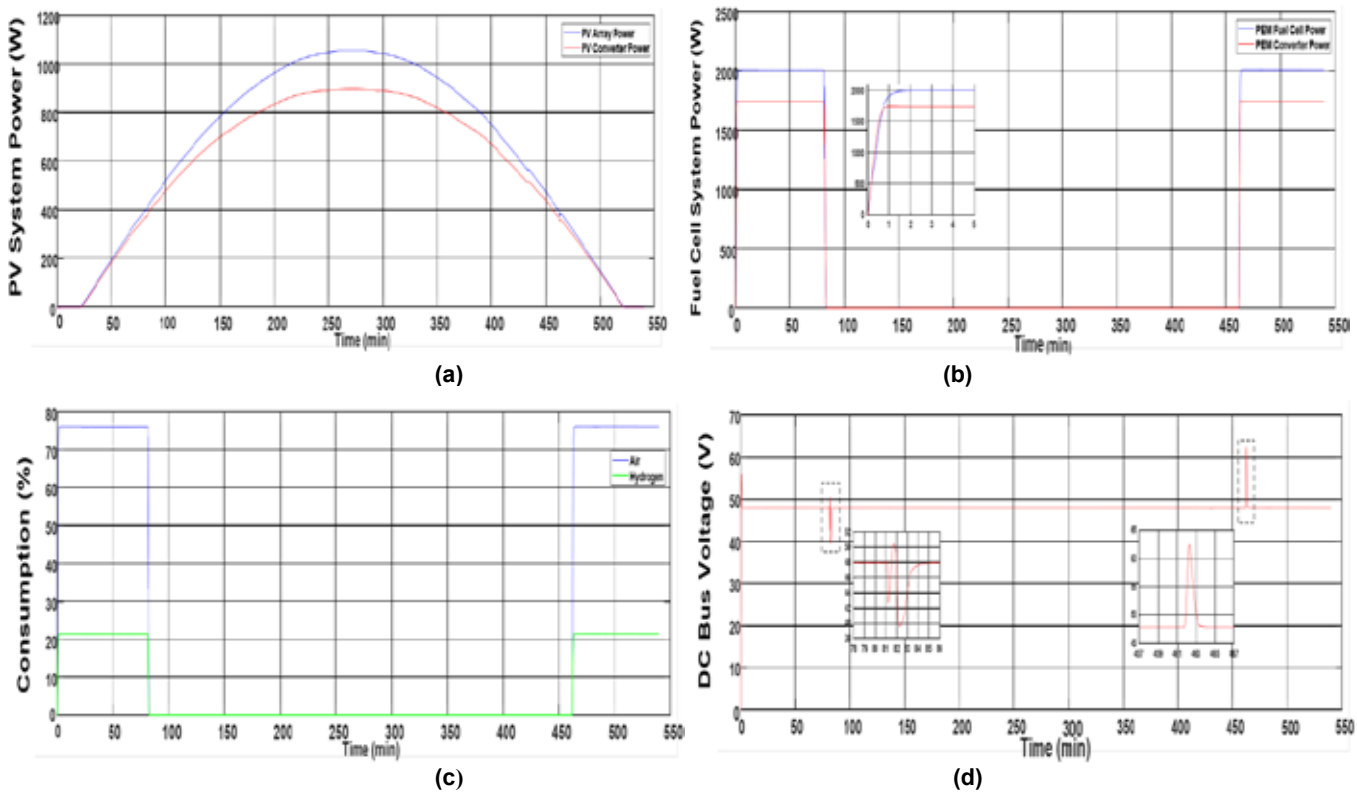

Fig. 3. (a) PV system output power curves **(b)** PEM fuel cell system output power curves **c)** Hydrogen and air consumption, and **(d)** DC bus voltage

Fig. 4(a) presents the power curves of the battery system, while Fig. 4(b) illustrates the SoC values. Figs 4(c) and 4(d) show the load current and power. The graphs show that both boost converters regulate the voltage at 48 V. Moreover, the load power, voltage, and current were maintained at stable levels, except during transient periods, by controlling energy sources. In this scenario, the bidirectional converter charged and discharged the battery.

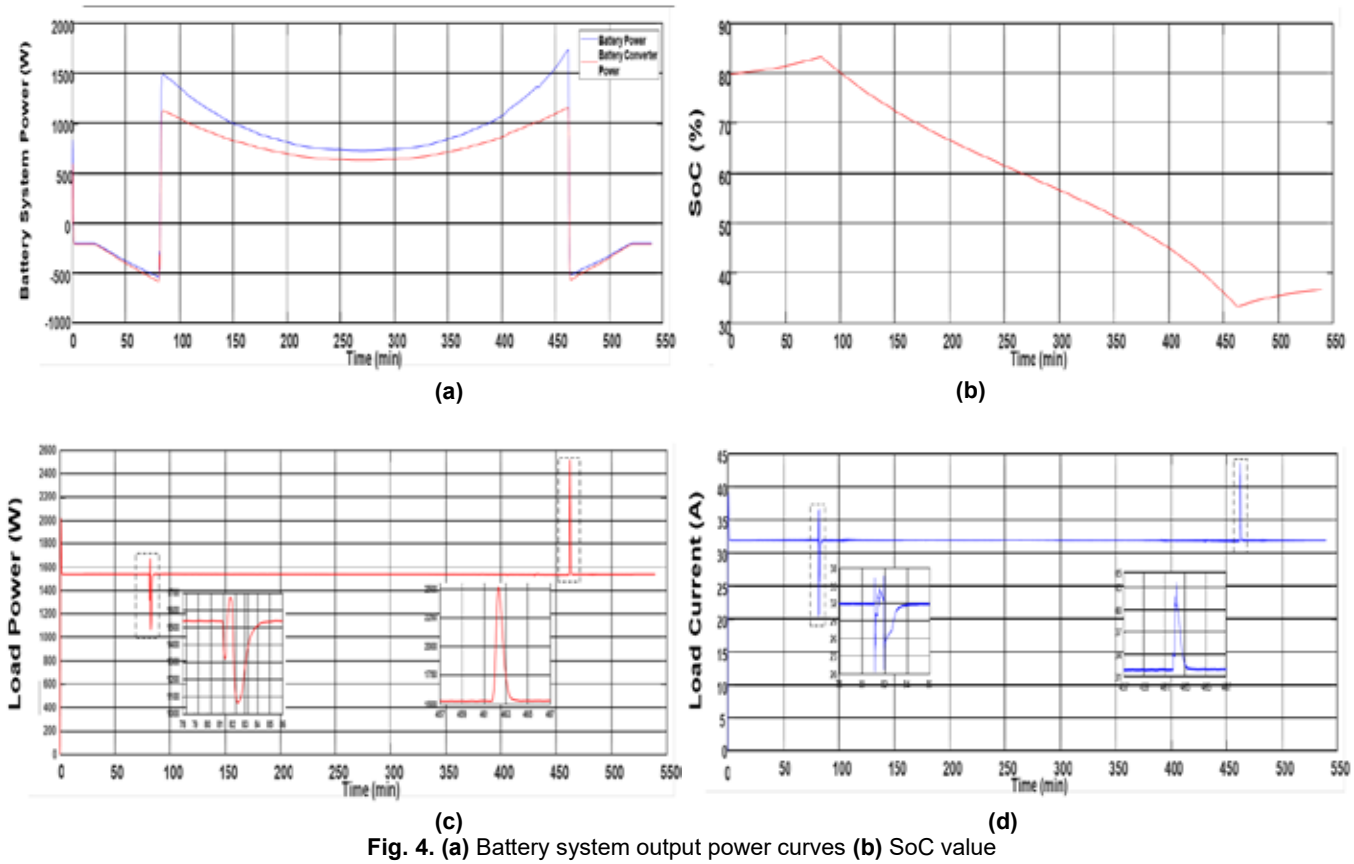

Fig. 4. (a) Battery system output power curves **(b)** SoC value
c) Load power, and **d))** Load current

4. CONCLUSIONS

This study examines a hybrid renewable energy system integrating solar energy, hydrogen energy, and a battery to meet the load demand via a DC bus. To maximize power extraction from both hydrogen and solar sources, the switching of the MOSFETs in the converter is controlled using the P&O algorithm. The P&O algorithm implemented in the Matlab/Simulink model is modified to facilitate energy management. Consequently, hydrogen consumption is significantly reduced when sufficient solar energy is available, while the fuel cell and battery continue to supply the load during periods of insufficient solar energy.

ACKNOWLEDGEMENT

The authors would like to thank The Scientific and Technological Research Council of Turkey (TUBITAK) for support with the number 123E704.

REFERENCES

[1] Ozden E, Tari I. Energy–exergy and economic analyses of a hybrid solar–hydrogen renewable energy system in Ankara, Turkey. Appl Therm Eng 2016;99:169–78. https://doi.org/10.1016/j.applthermaleng.2016.01.042.
[2] Kalinci Y, Dincer I, Hepbasli A. Energy and exergy analyses of a hybrid hydrogen energy system: A case study for Bozcaada. Int J Hydrogen Energy 2017;42:2492–503. https://doi.org/10.1016/j.ijhydene.2016.02.048.
[3] Ismail TM, Ramzy K, Elnaghi BE, Abelwhab MN, El-Salam MA. Using MATLAB to model and simulate a photovoltaic system to produce hydrogen. Energy Convers Manag 2019;185:101–29. https://doi.org/10.1016/j.enconman.2019.01.108.
[4] Doumbia ML, Agbossou K, Granger E. Simulink Modelling and Simulation of a Hydrogen Based Photovoltaic/Wind Energy System. EUROCON 2007 - Int. Conf. “Computer as a Tool,” IEEE; 2007, p. 2067–72. https://doi.org/10.1109/EURCON.2007.4400370.
[5] Raj J, Rajasree SR. A Microgrid with Hybrid Solar - Fuel Cell System With CHP Application. 2022 IEEE 2nd Int. Conf. Sustain. Energy Futur. Electr. Transp., IEEE; 2022, p. 1–6. https://doi.org/10.1109/SeFeT55524.2022.9908904.
[6] Yılmaz B, Gençoğlu MT. PV Panel ve PEM Yakıt Pilinden Oluşan Küçük Ölçekli Hibrid Sistemin Matematiksel Modeli. Fırat Üniversitesi Mühendislik Bilim Derg 2024;36:677–93. https://doi.org/10.35234/fumbd.1417251.
[7] The MathWorks Inc., MATLAB Version: 23.2.0.2365128 (R2023b) Natick, Massachusetts. 2023.

BOROHYDRIDES FOR HIGHLY SELECTIVE CATALYTIC METHANOL PRODUCTION: INSIDE INTO PEROVSKITE-TYPE CATALYST

[1]*Gizem Özdemir*, [2,4] *Bilge Coşkuner Filiz,* [3] *Fatma Noyan Tekeli,* [1,4*]*Aysel Kantürk Figen*
[1] Yıldız Technical University, Faculty of Chemistry-Metallurgy, Department of Chemical Engineering, Istanbul, 34220, Türkiye
[2] Yıldız Technical University, Faculty of Chemistry-Metallurgy, Department of Metallurgy and Materials Engineering, Istanbul, 34220, Türkiye
[3] Yıldız Technical University, Faculty of Arts and Sciences, Department of Statistics, Istanbul, 34220, Türkiye
[4] Yıldız Technical University, Clean Energy Technologies Institute, Istanbul, 34220, Türkiye
*Corresponding author e-mail: akanturk@yildiz.edu.tr

ABSTRACT
Excessive use of fossil fuels increases the concentration of carbon dioxide (CO_2) in the atmosphere, leading to major environmental problems such as global warming and climate change. In this context, the conversion of CO_2 into valuable chemicals is of great importance in terms of reducing carbon emissions and promoting a sustainable chemical industry. International agreements such as the Paris Agreement and the European Green Deal mandate the reduction of carbon emissions in order to achieve the goal of creating a carbon-neutral economy [1, 2]. In particular, the industrial sector needs to turn to innovative technologies and adopt low-carbon production processes. In this study, a highly selective catalyst system for the conversion of CO_2 to methanol using borohydride as a reducing agent to facilitate catalyst activation and hydrogenation steps was investigated in detail. Within the scope of this review, the effects of different perovskite catalyst structures, synthesis methods, activation techniques, and reaction conditions on methanol yield and selectivity were examined in detail.

Keywords: Sustainability**,** Borohydrides, CO_2 emission reduction, Methanol synthesis in liquid phase, Perovskite nanocatalysts

1. INTRODUCTION
The Paris Agreement, which was signed in 2015 to reduce the effects of global warming, was approved by the 196 countries party. Based on the limited analysis of the Intergovernmental Panel on Climate Change (IPCC), the scientific community agrees that the 1.5°C scenario will significantly reduce the negative effects on poverty and sustainable development, including food security, compared to the 2°C global warming scenario. For example, at a temperature increase of 1.5°C, the number of people expected to be exposed to extreme heat waves (which occur once every at least 20 years) is about 700 million, which accounts for 9.0% of the global population. In contrast, an increase of 2°C in temperature is expected to cause more than 2 billion people, i.e. 28.2% of the world's population, to be exposed to similar heat waves. The Paris Agreement aims to limit the global temperature increase to 1.5°C by 2050 and reduce greenhouse gas emissions to net zero. In addition, in this direction, the European Green Agreement announced by the European Union (EU) in 2019 reveals its goal of being a carbon-neutral continent by 2050. A carbon limit tax on the EU industry will require the replacement of high-emission production processes with low-carbon and innovative manufacturing technologies. In this context, industrial methanol production is becoming a critical sector [1-3].
These accepted global agreements require a strict reduction in CO_2 emissions and the creation of a closed-loop carbon economy. While CO_2 capture and storage (CCS) continues to be an important emissions reduction strategy, the conversion of CO_2 into valuable chemicals such as methanol is extremely important for a sustainable chemical processing industry. Perovskite nanocatalysts offer a promising approach to sustainable methanol production in CO_2 conversion thanks to their adjustable structural properties and high catalytic activities. Borohydrides, especially sodium borohydride ($NaBH_4$), have been widely studied as effective reducing agents in catalytic processes, due to their ability to donate hydride ions and facilitate the formation of active metal species. While the use of borohydrides has positive effects on reaction kinetics and selectivity, it has the potential to increase energy efficiency and provide more sustainable reaction conditions in the transformation of CO_2 into methanol thanks to its synergistic interactions with perovskite nanocatalysts [4]. In this context, a detailed study of reduction mechanisms and their interactions with perovskite nanocatalysts is of great importance.
In this study, the effectiveness of perovskite-type nanocatalysts in the production of methanol by conversion of CO_2 will be discussed in detail. Catalyst synthesis and characterization process, determination of active regions and borohydride-based reduction mechanism will be examined comprehensively; parameters and optimization strategies affecting catalytic performance will be evaluated. Thus, the potential of perovskite-type catalysts for high-yield methanol production processes with low carbon footprint will be revealed.

2. REACTION MECHANISM
The synthesis of methanol via the conversion of CO_2 represents a crucial process in the valorization of CO_2 into valuable chemicals. This is primarily because methanol serves not only as an alternative fuel but also as a key intermediate in the production of long-chain hydrocarbons and various high-value chemicals. The utilization of CO_2 as a feedstock enables

the conversion of large amounts of greenhouse gases, thereby contributing to environmental sustainability.
The conversion of CO_2 to methanol is a complex process that involves multiple reaction pathways and intermediate species. The reaction mechanism is highly dependent on the nature of the catalyst, reaction conditions, and the solvent environment. The overall reaction for CO_2 conversion can be expressed as follows:

$$CO_2+3H_2 \rightleftharpoons CH_3OH+H_2O \text{ , } \Delta H^o=-50 \text{ kJ mol}^{-1} \quad (1)$$

However, in addition to this overall equation, the process consists of the following intermediate reaction steps:

$$CO_2+H_2 \rightleftharpoons CO+H_2O \text{ , } \Delta H^o=-39 \text{ kJ mol}^{-1} \quad (2)$$

$$CO+2H_2 \rightleftharpoons CH_3OH \text{ , } \Delta H^o=-91 \text{ kJ mol}^{-1} \quad (3)$$

Methanol synthesis is an exothermic reaction and releases heat [5]. Compared to the realization of CO_2 conversion in the gas phase and the realization in the liquid phase, the liquid phase is more advantageous for various reasons such as thermodynamic advantages, reaction efficiency, heat transfer, and CO_2 capture/activation. The low temperature and high-pressure conditions of the liquid phase are more conducive to the formation of methanol due to the exothermic nature of the reaction, and the reaction balance progresses towards the formation of the product. On the contrary, unreacted gas in the gas phase needs to be recovered, which increases energy consumption. In addition, while the liquid phase process provides a more stable environment, the capture and activation of liquid phase CO_2 provides a more efficient conversion process. When all these factors are evaluated, CO_2 conversion in the liquid phase is more advantageous than in the gas phase [6].
Given the complex nature of CO_2 conversion to methanol, the selection of the catalyst and the method of catalyst activation play a decisive role in the reaction's efficiency and selectivity. In recent years, borohydrides—particularly sodium borohydride ($NaBH_4$)—have attracted considerable attention as strong reducing agents in catalytic processes. Rather than serving directly as a hydrogen source, $NaBH_4$ is primarily used to reduce metal precursors during catalyst preparation or activation, leading to the formation of highly dispersed and active metal nanoparticles. This enhanced dispersion significantly improves catalytic activity and selectivity in the conversion of CO_2 to methanol. Additionally, borohydride-induced reduction can alter the electronic and surface properties of catalysts, thereby influencing reaction intermediates and kinetics [4].

When the reaction temperature exceeds 240 °C in CO_2 conversion, the formation of various hydrocarbons by-products with carbon monoxide (CO) is also observed. It is of great importance to develop appropriate catalysts to ensure that the reaction progresses with high selectivity by minimizing the formation of by-products. In addition, the CO_2 molecule is kinetically inert due to its high stability, which requires the use of an effective catalyst for the reaction to progress. In recent years, it has been reported that perovskite-type nanocatalysts exhibit high activity and selectivity in the CO_2 conversion reaction. These catalysts stand out as promising materials for sustainable methanol production thanks to their adjustable structural properties and high thermal stability [7]. In our study, their catalytic performance in synthesis, characterization, and CO_2 conversion of perovskite-type catalysts will be examined in detail.

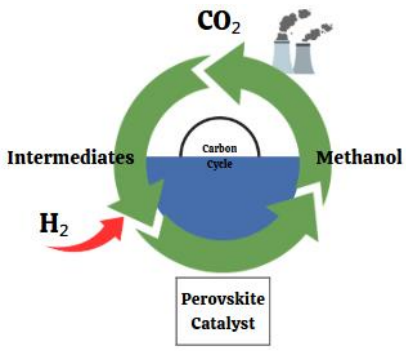

Fig. 1. Schematic representation of the reaction mechanism

3. PEROVSKİTE NANOCATALYST

The term perovskite is a general name used for oxides with ABO_3 and/or A_2BO_4 structure. In the unit cell of the ideal cubic perovskite crystal (Fig. 2.), the larger A cation is located at the corner points of the structure, while the smaller B cation is located in the center of the octahedron. O represents the anion that binds both cations together [8].

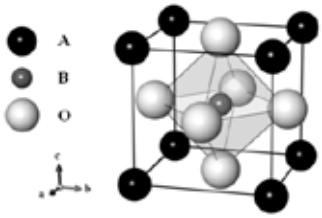

Fig. 2. Ideal crystal structure of perovskite oxides with ABO_3 composition [8]

Synthesis methods used in the synthesis of perovskite nanocatalysts directly affect the properties of the obtained materials, such as morphology, particle size, surface area, and active site distribution. Therefore, the selection of the appropriate method for the synthesis of catalysts with desired properties is critical.

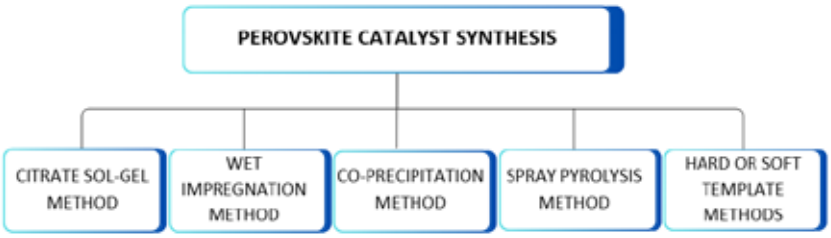

Fig. 3. Perovskite catalyst synthesis methods

In the citrate sol-gel method, which is one of the synthesis methods, after the formation of metal-citrate complexes, polymerization is carried out with a polymerization agent such as ethyl alcohol. The resulting gel structure is converted into a perovskite structure by drying and calcination processes. This method is less preferred than other methods due to its long process time and negative environmental effects. In the wet impregnation method, metal salts are impregnated into the perovskite precursor and the perovskite structure is obtained by applying calcination and reduction process. In this method, which is widely used due to its low cost, difficulties are encountered in ensuring homogeneous distribution of metal particles and preventing agglomeration. In the co-precipitation method, which is another synthesis method, cation salts A and B are dissolved in a suitable solvent and a precipitating agent (e.g. hydroxide) is added to precipitate to form perovskite. The resulting precipitate is then subjected to washing, drying, and calcination to obtain the final perovskite catalyst structure. By carefully adjusting the precipitation conditions, a homogeneous catalyst with the desired particle size can be obtained. In the spray pyrolysis method, which is also one of the synthesis methods, a homogeneous solution is prepared by dissolving the salts of metal cations in a suitable solvent, and this solution is sprayed onto a hot surface. The sprayed droplets evaporate rapidly, and the metal salts thermally decompose to form metal oxides. These oxides combine at high temperatures to form the perovskite crystal structure. High temperature and equipment costs are disadvantages of this synthesis method. In hard and soft template methods, porous materials or organic molecules are used as templates. Perovskite precursors are filled into the pores of the templates and then the perovskite structure is shaped by removing the templates. This method provides precise control of pore size and distribution but requires additional synthesis and removal steps [7,9,10].

Various analysis methods should be applied to analyze the structural and chemical properties of the synthesized perovskite catalysts to understand and optimize the basic mechanisms of their catalytic performance. In line with this purpose, various characterization techniques such as transmission electron microscopy (TEM) are applied to analyze the shape, size, and distribution of the nanoparticles of the catalyst, X-ray diffraction (XRD) to determine the crystal structure and phase composition, nitrogen adsorption (BET) to evaluate the surface area and pore structure, X-ray photoelectron spectroscopy (XPS) to determine surface chemical states and concentrations, temperature programmed reduction (TPR) to evaluate the reduction properties of metal oxides and metal-support interactions [9, 10].

The catalytic performance of perovskite nanocatalysts in the CO_2 conversion reaction is affected by various factors and these can be divided into internal and external factors. Internal factors include the composition, structure, surface area, porosity, metal distribution, and surface basicity of the catalyst. The type and distribution of metal ions in regions A and B of the perovskite structure determines the electronic structure of the catalyst and therefore the catalytic activity. The high surface area and porous structure facilitate reactant access and increase the number of active zones, which facilitates reactant diffusion and increases catalytic performance [9, 10]. LaCuZnX and La-M-Cu-Zn-O perovskite-like catalysts are produced by citrate sol-gel and co-precipitation methods and are used for methanol synthesis by CO_2 conversion in the liquid phase [7,11]. In this context, nano-sized metal particles offer high surface area and active zone density. Well-dispersed and nano-sized metal particles also provide high catalytic activity. Surface basicity and strength

also affect CO_2 adsorption and activation. Within the scope of external factors, there are factors such as the reactor type used and the temperature, pressure, flow rate, and H_2/CO_2 feed ratio of the reaction [7,9]. The optimum reaction conditions determined in these contexts maximize the activity and selectivity of the catalyst. In this study, multi-criteria decision analysis (MCDA) was used to select the appropriate perovskite-type catalyst for methanol production via CO_2 conversion [12].

4. CONCLUSIONS

It has been concluded that the use of $NaBH_4$ as a reducing agent facilitates the formation of active metal phases during catalyst preparation and enhances methanol selectivity by promoting metal dispersion and preventing agglomeration due to the reduction of methanol production reaction of CO_2 in the liquid phase due to thermodynamic advantages, reaction efficiency, and energy saving; preventing the growth of Cu particles in the liquid phase by reducing method using $NaBH_4$ and achieving high Cu distribution; It has been concluded that the use of perovskite-type catalysts as a catalyst for the reasons of high activity and selectivity is appropriate due to its more sustainable advantage.

REFERENCES

1. European Commission. European Green Deal. Available at: https://climate.ec.europa.eu/eu-action/european-green-deal_en. Accessed on March 13, 2025.
2. UNFCCC. The Paris Agreement. Available at: https://unfccc.int/process-and-meetings/the-paris-agreement. Accessed on March 13, 2025.
3. IPCC. Special Report on Global Warming of 1.5°C – Chapter 5. Available at: https://www.ipcc.ch/sr15/chapter/chapter-5/. Accessed on March 13, 2025.
4. Sabet-Sarvestani H, Eshghi H, Izadyar M, Noroozi-Shad N, Bakavoli M, and Ziaee F. 2016. Borohydride salts as high efficiency reducing reagents for carbon dioxide transformation to methanol: Theoretical approach. International Journal of Hydrogen Energy 41(26):11131-11140.
5. Bowker M. 2019. Methanol synthesis from CO_2 hydrogenation. ChemCatChem 11(17):4238-4246.
6. Wang D, Du Y, Liao Z, Hong X, and Zhang S. 2024. Liquid-phase CO_2 hydrogenation to methanol synthesis: Solvent screening, process design and techno-economic evaluation. Journal of CO_2 Utilization 90:102976.
7. Kuang ZQ, Feng LI, Jing LUO, Wang YX, Yuan DP, Qin WANG, et al. 2020. LaCuZnX (X= Al, Zr, Al+Zr) perovskite-like catalysts treated by $NaBH_4$ and their catalytic performance for CO_2 hydrogenation to methanol. Journal of Fuel Chemistry and Technology 48(3):293-301.
8. Onrubia-Calvo JA, Pereda-Ayo B, and González-Velasco JR. 2020. Perovskite-based catalysts as efficient, durable, and economical NO_x storage and reduction systems. Catalysts 10(2):208.
9. Zhu J, Li H, Zhong L, Xiao P, Xu X, Yang X, et al. 2014. Perovskite oxides: preparation, characterizations, and applications in heterogeneous catalysis. ACS Catalysis 4(9):2917-2940.
10. Goldwasser MR, Rivas ME, Pietri E, Pérez-Zurita MJ, Cubeiro ML, Grivobal-Constant A, and Leclercq G. 2005. Perovskites as catalysts precursors: synthesis and characterization. Journal of Molecular Catalysis A: Chemical 228(1-2):325-331.
11. Zhan H, Li F, Gao P, Zhao N, Xiao F, Wei W, et al. 2014. Methanol synthesis from CO_2 hydrogenation over La–M–Cu–Zn–O (M= Y, Ce, Mg, Zr) catalysts derived from perovskite-type precursors. Journal of Power Sources 251:113-121.
12. Tekeli FN, Filiz BC, Yörüklü HC, and Figen AK. 2024. Multi-criteria decision framework for catalyst selection: Production of formic acid as a circular liquid organic hydrogen carrier in the hydrogen economy. Journal of Cleaner Production 452:142125.

ENHANCEMENT OF IONIC CONDUCTIVITY IN ANION EXCHANGE MEMBRANES: EFFECT OF MODIFIED MOF STRUCTURES IN PBI MEMBRANES

[1,2]*Hasan Altınışık,* [2]*Yılser Devrim*
[1] Atılım University, Department of Energy Systems Engineering, Incek Golbasi Ankara, 06830, Turkey
[2] Atılım University, Graduate School of Natural and Applied Sciences, Department of Mechanical Engineering, Incek Golbasi Ankara, 06830, Turkey

* E-mail: yilser.devrim@atilim.edu.tr

Abstract
Anion exchange membrane water electrolyzers (AEMWE) are an emerging and focused technology in the production of hydrogen from water by electrolysis. One of the most important advantages of AEMWE technology is the use of low-cost transition metal catalysts instead of noble metal catalysts and cheaper membranes. However, AEMWEs have some limitations such as low ionic conductivity and stability of the membrane due to the harsh alkaline environment. This study aims to develop polybenzimidazole (PBI)-based zeolitic imidazolate framework (ZIF8) and modified ZIF8 AEMs with high ionic conductivity and durability for green hydrogen production. Structural and electrochemical properties of membranes were investigated by FTIR, XRD, mechanical testing and EIS method. Synergistic effects between polymer and MOF structures combined the advantages of the materials and enabled the development of anion exchange composite membranes with high hydrogen production potential.

Keywords: Anion exchange membrane water electrolysis, composite anion exchange membrane, Metal-organic frameworks, hydrogen production

1. INTRODUCTION

Global warming, climate change and environmental pollution are the most critical issues of the 21st century that are primarily driven by greenhouse gas emissions from fossil fuels [1,2]. Therefore, renewable energy sources are gaining importance in achieving net zero emission targets. Among renewable sources, hydrogen energy stands out with high energy density and zero emissions. Hydrogen energy also can be considered a sustainable source that can replace fossil fuels. There are various methods to produce hydrogen, such as hydrocarbon reforming, pyrolysis, biomass processes, and water electrolysis. Among these methods, water electrolysis has the major advantages of high efficiency, zero emissions and high purity production. Additionally, using the electricity generated from renewable energy sources during electrolysis positively affects sustainability.

Four main water electrolysis systems are used to produce hydrogen: alkaline water electrolysis (AWE), proton exchange membrane water electrolysis (PEMWE), solid oxide water electrolysis (SOWE) and anion exchange membrane water electrolysis (AEMWE) (Park et al., 2019). Among them, AWEs work with liquid alkaline electrolytes and are low-cost (David et al., 2019). PEMWEs can produce high-purity hydrogen with high efficiency. However, PEMWEs need high-cost noble metal catalysts for operation and the acidic electrolyte causes corrosion of catalyst layers and other components (Feng et al., 2021). SOWEs allow the use of high-temperature electrolyzers with high efficiency and good stability but have limitations in large-scale applications, such as bulky system design, and safety issues with electrodes and sealing (Sebbahi et al., 2022).

Over the past decade, AEMWEs have been developed as alternative water electrolysis systems. AEM water electrolysis holds important advantages of water electrolysis technology such as low-cost catalysts, low operating temperature and the presence of a solid membrane. The solid membrane in AEMWE inhibits the gas migration and allows high purity in products. However, the high pH of alkaline media leads to a reduction in electrochemical performance and stability. To overcome these challenges, research and development of new membranes are ongoing. Polymers with benzimidazole groups as repeating units in their backbone are referred to as PBIs. PBIs have a tight chain structure based on strong hydrogen bonds and π-π interactions between polymer chains. With these bonds and interactions, PBIs offer superior thermo-mechanical properties. Their favorable properties render them suitable for AEM applications in AEMWE systems [3]. In pristine form, PBI shows low ionic conductivity for electrolysis applications and low mechanical stability in highly alkaline media. Composite membranes are being produced to overcome these limiting factors. MOF structures are interesting as polymer fillers due to their large surface area, porosity, high conductivity and easy processability. Furthermore, with chemical modifications, the properties of MOFs can be improved. In this study, the PBI/ZIF8 and PBI/mZIF8 composite membranes were prepared and their characteristics were investigated for AEMWE applications.

2. EXPERIMENTAL PROCEDURE

a. ZIF-8 Preparation: In the synthesis of ZIF8, firstly, the solution of $Zn(NO_3)_2.6H_2O$ and methanol was added to the

solution of 2-methyl imidazole and methanol and stirred at room temperature for 1 hour. The white crystals formed were separated by centrifugation with methanol and dried.

b. **Modified ZIF-8 (mZIF-8) Preparation**: In the synthesis of mZIF8, ZIF8 crystals and NBu_4OH (tetrabutylammonium hydroxide) solution were prepared and stirred at 70 °C for 24 hours. At the end of the reaction, mZIF8 was separated from the solution and dried.
c. **Composite Membrane Preparation:** PBI-based composite membranes were prepared by solution casting method with PBI polymer and different weight ratios of MOF (0, 2.5, 5.0 and 7.5 wt. %) contents.

3. ANALYSIS

The structural characterization of the polymer, ZIF8 and mZIF8 and composite membranes was performed by, Fourier transform infrared spectroscopy (FTIR), X-ray Diffraction (XRD) methods and mechanical test. The electrochemical characterization was conducted by Electrochemical Impedance Spectroscopy (EIS).

4. RESULTS AND DISCUSSIONS

Fig. 1a shows FTIR spectra of synthesized ZIF-8 and mZIF-8 particles. Both MOF structures have four characteristic peaks at 2926, 1600, 1145, and 995 cm^{-1}, assigned to vibrations of C−H, C=N, and C−N in the imidazole ring, respectively [4]. Fig. 1b shows the FTIR spectra of the PBI polymer. The polymer exhibited characteristic adsorption bands at approximately 795 and 850 cm^{-1} due to the ring vibration of C-H groups, C=C/C/N stretching between 1500-1650 cm^{-1}. Additionally, the polymer exhibited characteristic bands at 2000 and 3050 cm^{-1} due to the C-H and C-H vibrations respectively [5,6].

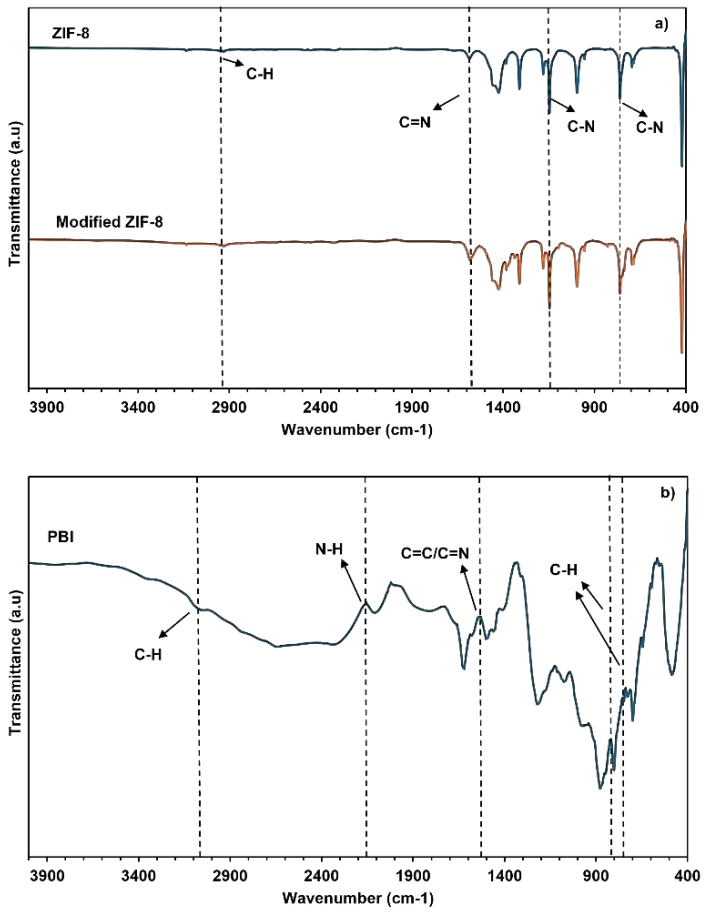

Fig 1. FTIR of a) ZIF8 and mZIF8 particles, b) PBI polymer

The XRD analysis was performed to determine the crystal structure of ZIF8 and mZIF8 (Fig 2.a). The strong peaks of ZIF8 show good agreement with the literature. The peaks at 2θ= 7.3°, 10.35°, 12.70°, 14.80°, 16.40° and 18.00° correspond to the planes (110), (200), (211), (220), (310), and (222) respectively [7]. The diffraction patterns of the modified ZIF-8 structure do not show a significant difference from the unmodified sample. This proves that the MOF

structure does not decompose in a highly alkaline environment (pH > 14) and shows high chemical stability. The decrease in the intensities of the peaks indicates that the atomic arrangement of ZIF8 was modified by tetrabutylammonium hydroxide, but the crystal structure was preserved during the process [8]. Fig 2.b shows X-ray diffraction patterns of PBI, PBI/ZIF8 and PBI/mZIF8 composite membranes. The amorphous PBI membrane exhibits a broad peak at 2θ=23.4°. In PBI/ZIF8/2.5 and PBI/mZIF8/2.5 composite membranes exhibit 2θ= 7.4°, 12.8° and 22.1° which confirm the presence of ZIF8 particles in the polymer matrix.

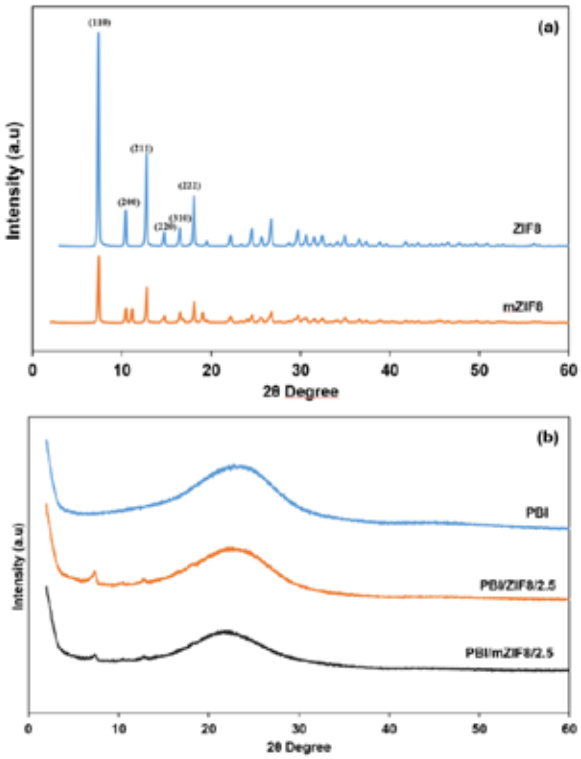

Fig 2. XRD patterns of a) ZIF-8 and mZIF-8 particles, b) PBI and composite membranes

Ionic conductivity is an important parameter for high hydrogen production in AEMs. Figure 3 shows the OH- conductivities of 1 M KOH doped PBI, PBI/mZIF8/2.5 and PBI/mZIF8/2.5 composite membranes for different temperatures. The ionic conductivity of pure PBI membrane was determined as 55.02 mS/cm. Upon the addition of ZIF8 and mZIF8 to the membrane, the ionic conductivity increased to 146.4 and 474.1 mS/cm for PBI/mZIF8/2.5 and PBI/mZIF8/2.5 membranes, respectively.

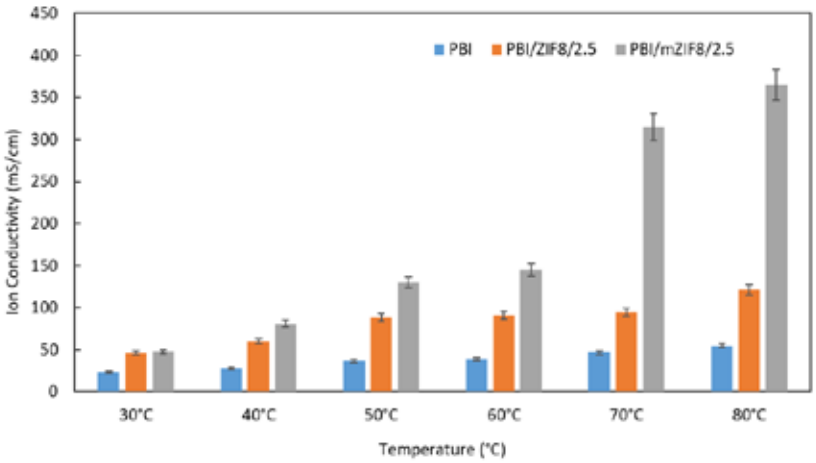

Fig. 3. Ionic conductivities of 1M KOH doped pristine PBI and composite membranes.

Mechanical properties of AEMs play important roles in AEMWE applications. AEMs need to be durable and stable in harsh alkaline conditions. Doping with alkaline solutions decreases the mechanical strength of PBI membranes due to

partial disintegration of hydrogen bonding networks [9]. Therefore, it is important to investigate the effect of alkaline aging on the mechanical properties of membranes. The aging of membranes was performed in 2 M KOH at 80 °C for 200 hours. Fig. 4a. and Fig. 4b. present the tensile strength and elongation of membranes before and after aging treatment. Before the aging test, the tensile strengths of PBI, PBI/ZIF8/2.5 and PBI/mZIF8/2.5 membranes were reported as 69.7, 87.4, 83.03, 65.6 and 61.1 MPa respectively. After the aging test, while PBI membrane preserved its 43.4% tensile strength, PBI/ ZIF8/2.5, and PBI/mZIF8/2.5 membranes preserved their tensile strength of 35.5%, and 52.2% respectively. Additionally, elongation of membranes increased with aging treatment due to the plasticizing effect [10]. The results showed that the membranes containing mZIF8, have improved mechanical stability and durability because metal-containing units of modified ZIF8 formed strong bonds between the PBI matrix and ZIF8 nanoparticles [11].

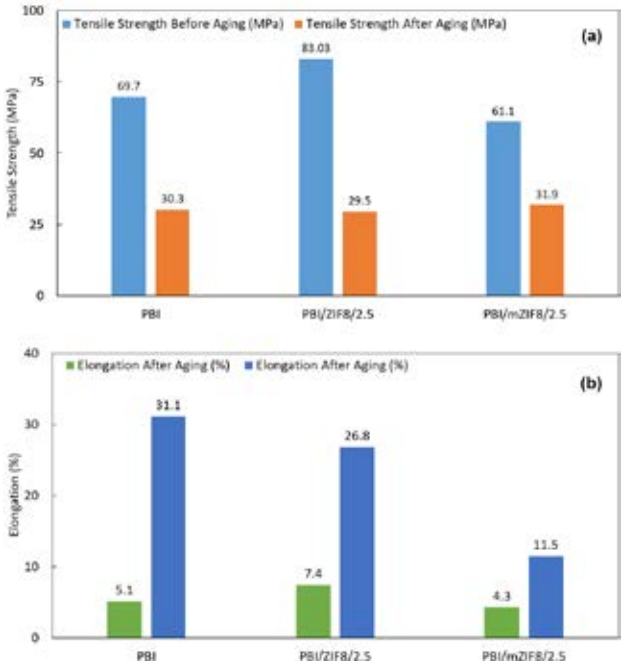

Fig. 4. Mechanical properties of pristine PBI and composite membranes before and after aging test.

5. CONCLUSIONS

In this study, PBI/ZIF8 and PBI/mZIF8 composite membranes were successfully prepared and physically and electrochemically characterized for AEMWE application. The obtained characterization results showed that the PBI-based composite membranes were suitable for the AEMWE system for hydrogen production.

Acknowledgments

The Scientific and Technological Research Council of Turkey (TUBITAK) supported this study under grant number 123M878.

REFERENCES

[1] Shang Y, Han D, Gozgor G, Mahalik MK, Sahoo BK. The impact of climate policy uncertainty on renewable and non-renewable energy demand in the United States. Renew Energy 2022;197:654–67. https://doi.org/10.1016/j.renene.2022.07.159.

[2] Wang J, Azam W. Natural resource scarcity, fossil fuel energy consumption, and total greenhouse gas emissions in top emitting countries. Geoscience Frontiers 2024;15. https://doi.org/10.1016/j.gsf.2023.101757.

[3] Cong S, Wang J, Wang Z, Liu X. Polybenzimidazole (PBI) and benzimidazole-linked polymer (BILP) membranes. Green Chemical Engineering 2021;2:44–56. https://doi.org/10.1016/j.gce.2020.11.007.

[4] Wu C, Liu Q, Chen R, Liu J, Zhang H, Li R, et al. Fabrication of ZIF-8@SiO2 Micro/Nano Hierarchical Superhydrophobic Surface on AZ31 Magnesium Alloy with Impressive Corrosion Resistance and Abrasion Resistance. ACS Appl Mater Interfaces 2017;9:11106–15. https://doi.org/10.1021/acsami.6b16848.

[5] Musto P, Karaszt FE, Macknight WJ. Fourier transform infra-red spectroscopy on the thermo-oxidative degradation of polybenzimidazole and of a polybenzimidazole / polyetherimide blend. 1993.

[6] Ngamsantivongsa P, Lin HL, Yu TL. Properties and fuel cell applications of polybenzimidazole and ethyl phosphoric acid grafted polybenzimidazole blend membranes. J Memb Sci 2015;491:10–21. https://doi.org/10.1016/j.memsci.2015.04.045.

[7] Teknologi J, Hadi NA, Nordin M, Fauzi Ismail A, Yahya N, Bahru J. ZEOLITIC IMIDAZOLE FRAMEWORK 8 DECORATED GRAPHENE OXIDE (ZIF-8/GO) MIXED MATRIX MEMBRANE (MMM) FOR CO2/CH4 SEPARATION. vol. 79. 2017.
[8] Sadakiyo M, Kasai H, Kato K, Takata M, Yamauchi M. Design and synthesis of hydroxide ion-conductive metal-organic frameworks based on salt inclusion. J Am Chem Soc 2014;136:1702–5. https://doi.org/10.1021/ja410368j.
[9] Park JH, Park JS. KOH-doped Porous Polybenzimidazole Membranes for Solid Alkaline Fuel Cells. Energies (Basel) 2020;13. https://doi.org/10.3390/en13030525.
[10] Zeng L, Zhao TS, An L, Zhao G, Yan XH. Physicochemical properties of alkaline doped polybenzimidazole membranes for anion exchange membrane fuel cells. J Memb Sci 2015;493:340–8. https://doi.org/10.1016/J.MEMSCI.2015.06.013.
[11] Escorihuela J, Sahuquillo Ó, García-Bernabé A, Giménez E, Compañ V. Phosphoric acid doped polybenzimidazole (PBI)/Zeolitic imidazolate framework composite membranes with significantly enhanced proton conductivity under low humidity conditions. Nanomaterials 2018;8. https://doi.org/10.3390/nano8100775.

UNINTERRUPTED COMMUNICATION WITH PEMFC-ENHANCED UAVs IN DISASTER SCENARIOS

[1*]*Murat KAYAOGLU*, [1]*Sencer UNAL*, [1]*Bircan CALISIR*
[1]Fırat University, Engineering Faculty, Electrical Electronics Engineering, Enstitute of Science, Elazığ, 23000, Türkiye

*Corresponding author e-mail: mkayaoglu@firat.edu.tr

ABSTRACT

Natural disasters often lead to significant disruptions in communication infrastructure, hindering search and rescue operations. In such situations, rapidly deployable and autonomous communication solutions are critical for effective intervention. Unmanned Aerial Vehicles (UAVs) have emerged as a promising technology for establishing temporary communication networks in disaster-stricken areas. Unlike fixed-wing UAVs, rotary-wing UAVs, with their hovering capability and Vertical Takeoff and Landing (VTOL) features, are well-suited to establish stable communication nodes in disaster zones. However, rotary-wing UAVs powered by conventional batteries face challenges in maintaining uninterrupted communication due to limited flight time. This study explores the integration of Proton Exchange Membrane Fuel Cell (PEMFC) technology with rotary-wing UAVs to enhance flight duration and operational efficiency. PEMFC hybrid energy systems significantly extend the flight times of UAVs, ensuring continuous connectivity between first responders, affected populations, and command centers. The proposed system is evaluated through simulation-based performance analysis, considering factors such as energy efficiency, coverage, and communication reliability. The results demonstrate that PEMFC-supported UAVs outperform traditional battery-powered UAVs in terms of flight duration and network reliability. These findings highlight the revolutionary potential of fuel cell-integrated UAV networks for post-disaster communication and search-and-rescue operations.

Keywords: UAV, communication, disaster management, fuel cell, hybrid system

1. INTRODUCTION

Natural disasters are unforeseen and destructive events that pose significant threats to human life, critical infrastructure, and economic stability [1]. Disasters such as earthquakes, hurricanes, floods, and wildfires can severely damage existing telecommunications infrastructure, thereby significantly disrupting search and rescue operations as well as emergency response efforts. In scenarios where traditional communication networks are either damaged or completely disabled, the demand for mobile and rapidly deployable alternative communication systems has been increasing [2]. In this context, UAVs have gained increasing prominence in disaster management and emergency communication in recent years. UAVs, particularly those with extensive coverage capabilities and extended flight endurance, play a crucial role in establishing temporary communication infrastructures, thereby enhancing coordination among field teams and significantly improving the efficiency of rescue operations [3]. However, conventional battery-based energy systems remain a major limiting factor for the prolonged operation of UAVs. Therefore, enhancing UAV operational efficiency through innovative energy solutions has become a critical research area. A lot of studies in the literature have explored the potential of UAVs in maintaining communication networks in disaster scenarios.

Kobayashi et al. developed a "Flying Communication Server" to ensure communication during large-scale disasters. This system enables users to share videos and engage in text-based conversations using their smart devices. Even in the event of a communication infrastructure collapse, this system facilitates information exchange, making it a critical communication tool during disasters [4]. Moreover, research on the ability of UAVs to establish communication networks in emergency situations has demonstrated that multiple UAVs can collaborate to form a communication network. Shibata et al. showed that a large number of UAVs, equipped with wireless communication units, could create an aerial wireless mesh network. This system is specifically designed to facilitate information transmission in isolated areas, playing a crucial role in mitigating communication disruptions during natural disasters [2]. Such a structure is essential in addressing communication breakdowns in disaster scenarios. Another study examined how UAV flight paths can be optimized to improve communication with individuals on the ground. The research highlighted that UAV movement strategies are a significant parameter in enhancing the efficiency of communication networks [5]. This underscores the necessity of optimizing UAV movement for effective communication during natural disasters. The communication capacity of UAVs is particularly vital in emergency situations. Mylin investigated the reliability of small-scale UAV communication links, emphasizing the impact of link quality on UAV operational reliability and mission success [6]. Additionally, Tuna et al. explored how UAVs could establish a communication network in cases where the communication infrastructure collapses during natural disasters. Their study addressed the potential applications of UAVs in emergency communication and the challenges encountered in such scenarios [7]. The communication capabilities of UAVs are not only critical in emergencies but also play a significant role in post-disaster recovery efforts. Abdu Saif et al. assessed the advantages of using UAVs as wireless service providers during post-disaster phases. Their research shows that it can provide rapid information flow [8]. Chen et al. proposed a framework outlining how UAVs could be structured within

emergency communication systems. Their study emphasized the necessity of optimizing UAV energy management strategies to ensure continuous data transmission [9].

Effective communication among UAVs is crucial for the success of search and rescue operations following natural disasters. Since such disasters often destroy existing communication infrastructure, alternative solutions are necessary. UAV-based systems encompass a variety of platforms with different operational advantages [10]. Fixed-wing UAVs are suitable for communication relays due to their wide coverage area and long flight duration. In contrast, rotary-wing UAVs provide local communication support with their Vertical Take-Off and Landing (VTOL) capabilities and ability to hover [1]. While fixed-wing UAVs may be insufficient for creating a stable communication area, rotary-wing UAVs can establish a continuous communication network in challenging terrains. However, the short flight time of rotary-wing UAVs remains the biggest limitation [11].

This study analyzes the effectiveness of PEMFC-supported rotary-wing UAVs in disaster communication systems. Suitable communication protocols for multi-UAV systems operating in disaster areas were examined, and Mobile Ad-Hoc Networks (MANET) was determined to be the most effective and appropriate communication system. Additionally, the impact of fuel cell integration on energy efficiency was evaluated. System performance was tested through simulations conducted under various scenarios. As a result, the collapse of communication infrastructure during natural disasters negatively impacts rescue efforts. PEMFC-enhanced rotary-wing UAVs offer a significant solution to this issue with their long flight times and potential for continuous communication. The use of this proposed system as an effective communication tool in disasters will significantly enhance the success of operations.

2. MATERIALS AND METHODS

The use of UAVs for post-disaster situation assessment and rescue operations is becoming increasingly widespread. In particular, the ability of UAVs to collect and transmit information in emergency situations enhances the effectiveness of rescue teams. The capability of UAVs to autonomously fly, scan specific areas, and perform designated tasks during disaster scenarios accelerates post-disaster data collection processes, enabling rescue teams to respond more rapidly [12]. The advantages of rotary-wing UAVs, such as their ability to hover, flexible maneuverability, wide communication coverage, and extended flight duration with PEMFC technology, make them ideal for use as communication servers in natural disaster scenarios. This system can significantly enhance the success of search and rescue operations by providing uninterrupted communication and facilitating the prompt delivery of aid to victims. Figure 1 illustrates how rotary-wing UAVs can establish communication in a potential natural disaster scenario.

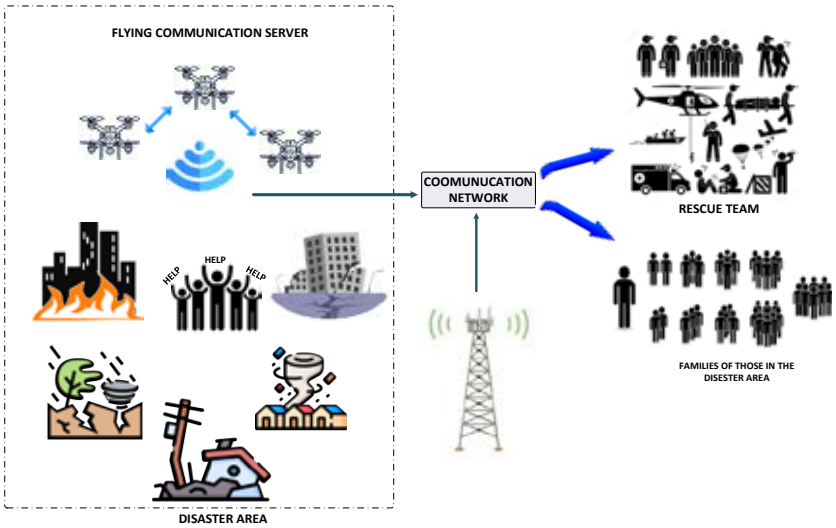

Fig 1. Uninterrupted Communication with Flying Communication Servers in Disaster Scenarios

The visual shows rotary-wing UAVs providing continuous communication between rescue teams and the families of disaster victims in affected areas. Rotary-wing UAVs, utilizing MANET technology, establish a dynamic and flexible communication network without the need for a central infrastructure. This is of critical importance, especially in situations where infrastructure has collapsed or access is restricted. Through MANET, rotary-wing UAVs enable rapid and reliable data transfer, supporting disaster management and emergency response processes.

2.1. Importance of PEMFC/Hybrid UAV Design

In natural disaster situations, communication infrastructure is often severely damaged, making continuous communication critical for the effectiveness of rescue operations [9]. In this context, the use of hybrid UAVs powered by PEMFC plays a significant role in the reconstruction of communication infrastructure post-disaster. The energy efficiency and extended flight durations provided by hybrid systems are crucial for rebuilding communication infrastructure after a disaster. As a critical component of the proposed system, rotary-wing UAVs enhanced with PEMFC technology can stay airborne for longer durations compared to traditional battery-powered systems, thereby ensuring continuous communication. This enables the seamless flow of information between rescue teams, victims' families, and other relevant organizations, strengthening post-disaster coordination. By restoring collapsed communication infrastructure through flying communication servers in the form of rotary-wing UAVs, victims in disaster areas can transmit their help requests, and rescue teams can manage operations more effectively.

2.2. UAV-Supported Mesh Network Technologies for Uninterrupted Communication

The communication techniques used in UAVs vary depending on the mission type and operational requirements. The primary methods include Radio Frequency (RF), Satellite Communication (SatCom), 4G/5G, Line-of-Sight (LOS), Beyond-Line-of-Sight (BLOS), Mesh Networks, and Optical Communication. In disaster-stricken areas where infrastructure is damaged, UAVs can maintain communication through different techniques. Mesh networks establish direct links between UAVs, ensuring uninterrupted communication. Additionally, UAVs can act as aerial base stations to restore mobile network connectivity. UAVs primarily utilize two communication methods: UAV-to-UAV communication enables direct or indirect data transfer between UAVs. In BLOS scenarios, other UAVs serve as relays for data transmission [13]. UAV-to-Ground Station communication involves UAVs establishing connections with ground stations or mobile control points. Mesh networks are classified into three main types: MANET feature dynamic and self-organizing structures. Flying Ad-Hoc Networks (FANET) are specifically designed for UAVs, accommodating high speeds and variable distances. LoRa-Mesh offers long-range communication with low power consumption. MANET-based UAV networks provide flexible and autonomous communication, particularly in infrastructure-less environments. In these systems, where UAVs function as nodes, their mobility and dynamic nature make them critical components in large-scale operations [14]. Consequently, UAVs operating as MANET nodes present significant potential for dynamic, flexible, and infrastructure-independent communication, especially in remote or rapidly changing scenarios.

3. RESULTS AND DISCUSSION

In this study, a MANET-based communication model has been developed to ensure continuous communication among multiple rotary-wing UAVs in natural disaster scenarios. Within the scope of the simulation, the long-term operational capabilities of PEMFC-powered rotary-wing UAVs were examined, and the continuity of network connectivity was analyzed.

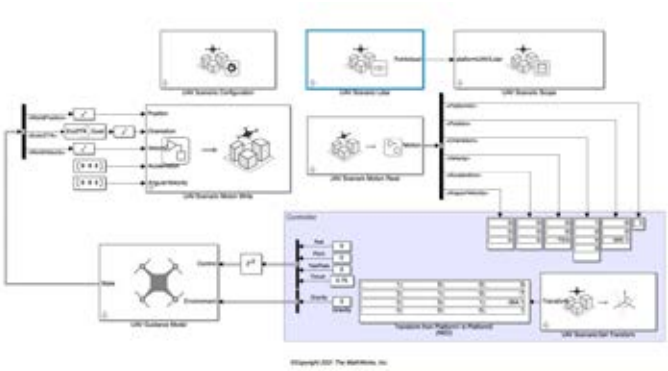

Fig 1. UAV Scenerio model

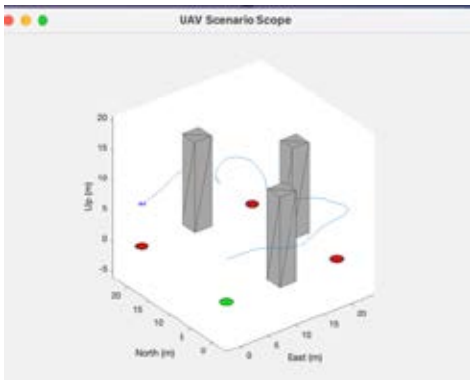

Fig 2. UAV Scenerio Scope

Figure 1 illustrates the rotary-wing UAV control model created in the Simulink environment. The model defines the rotary-wing UAVs' motion dynamics, routing algorithms, and communication protocols. Specifically, a dynamic network topology has been designed to adapt to varying environmental conditions. Figure 2 demonstrates that the rotary-wing UAVs maintain uninterrupted communication between designated points while maneuvering through obstacles in three-dimensional space. The simulation results reveal that the continuity of the connection between nodes is ensured through the MANET protocol.

Table 1 shows the advantages provided by PEMFC-powered rotary-wing UAVs in terms of flight time and energy efficiency. Compared to rotary-wing UAVs powered by traditional battery systems, PEMFC-supported systems achieve longer flight durations. For example, the hybrid quadcopter designed in the previous study, equipped with a 1000 W PEMFC and a 119 Wh Li-Po battery, achieved a flight time of 165 minutes. This enables continuous communication in a

potential disaster scenario and allows for more effective operation in areas without infrastructure. Additionally, the low hydrogen consumption enhances energy efficiency, strengthening operational sustainability.

Table 1. Performance Comparison of PEMFC-Enabled rotary-wing UAVs

Number of Rotating Propellers	PEMFC Rated Power (W)	BatteryType	Battery Power (Wh)	Total Weight (kg)	Flight Endurance (minute)	Hydrogen Consumption (g/m)	Reference
6	1500	Li-po Battery	100	11.5	90	0.644	[15]
4	30	Li-po Battery	77	3.152	11	0.0067	[16]
4	1900	Li-po Battery	55	5.16	121.2	2.37	[17]
4	1000	Li-po Battery	119	6.536	165	0.418	Designed hybrid UAV

4. CONCLUSIONS

Natural disasters cause significant damage to existing communication infrastructure, greatly disrupting search and rescue operations. To address this issue, UAV-based aerial communication networks have emerged as a critical solution for ensuring continuous connectivity in disaster areas. However, the limited flight time of UAVs powered by traditional batteries remains a significant constraint. This study aims to provide uninterrupted communication by utilizing PEMFC-supported rotary-wing UAVs, offering longer flight times and enhanced energy efficiency for disaster communication networks. Additionally, UAV-supported mesh networks, particularly those based on MANET architectures, offer a robust and flexible solution for maintaining connectivity in infrastructureless environments. The proposed PEMFC-supported rotary-wing UAV system presents a promising approach to reducing communication disruptions in disaster scenarios, aiming to enhance the effectiveness of emergency response and recovery efforts.

REFERENCES

[1] F. Wan, M. Bilal, M. Bilal, A. Shafiq, A. Thakur, and O. Rahman, “Results in Engineering Advancements and challenges in UAV-based communication networks : A comprehensive scholarly analysis,” *Results Eng.*, vol. 24, no. July, p. 103271, 2024, doi: 10.1016/j.rineng.2024.103271.

[2] Y. Shibata, N. Takana, and N. Uchida, “Information communication system consisted of multiple unmanned aerial vehicles on disaster,” *Proc. - 31st IEEE Int. Conf. Adv. Inf. Netw. Appl. Work. WAINA 2017*, pp. 627–632, 2017, doi: 10.1109/WAINA.2017.73.

[3] N. Uchida, “Evaluation of Wireless Network Communication by Autonomous Flight Wireless Nodes for Resilient Networks,” *2014 17th Int. Conf. Network-Based Inf. Syst.*, pp. 180–185, 2014, doi: 10.1109/NBiS.2014.71.

[4] T. Kobayashi, H. Matsuoka, and S. Betsumiya, “Flying Communication Server in case of a Large-scale Disaster,” *Proc. - Int. Comput. Softw. Appl. Conf.*, vol. 2, pp. 571–576, 2016, doi: 10.1109/COMPSAC.2016.117.

[5] A. Bevins and B. A. Duncan, “Aerial Flight Paths for Communication,” *Front. Robot. AI*, vol. 8, no. December, pp. 1–20, 2021, doi: 10.3389/frobt.2021.719154.

[6] A. K. Mylin, “A Communication Link Reliability Study for Small Unmanned Aerial Vehicles,” 2007.

[7] G. Tuna, T. V. Mumcu, and K. Gulez, “Design strategies of unmanned aerial vehicle-aided communication for disaster recovery,” *2012 9th Int. Conf. High Capacit. Opt. Networks Enabling Technol. HONET 2012*, pp. 115–119, 2012, doi: 10.1109/HONET.2012.6421446.

[8] A. Saif, K. Dimyati, K. A. Noordin, N. S. Mohd Shah, Q. Abdullah, and F. Mukhlif, “Unmanned aerial vehicles for post-disaster communication networks,” *2020 IEEE 10th Int. Conf. Syst. Eng. Technol. ICSET 2020 - Proc.*, no. November, pp. 273–277, 2020, doi: 10.1109/ICSET51301.2020.9265369.

[9] T. Chen, J. He, H. Zhu, L. Cai, P. Yue, and J. Wang, “Resource allocation in drone-assisted emergency communication systems,” *IEEE INFOCOM 2020 - IEEE Conf. Comput. Commun. Work. INFOCOM WKSHPS 2020*, pp. 132–137, 2020, doi: 10.1109/INFOCOMWKSHPS50562.2020.9162742.

[10] M. Yang, W. Chen, A. Tsai, and S. Cheng, “Coverage Extension with UAV Based on Constrained Uplink and Downlink Phases for Disaster-Resilient Communication Networks,” *2019 IEEE VTS Asia Pacific Wirel. Commun. Symp.*, pp. 1–5, doi: 10.1109/VTS-APWCS.2019.8851680.

[11] J. Wang, R. Jia, J. Liang, C. She, and Y. P. Xu, “Evaluation of a small drone performance using fuel cell and battery; Constraint and mission analyzes,” *Energy Reports*, vol. 7, pp. 9108–9121, 2021, doi: 10.1016/j.egyr.2021.11.225.

[12] L. Apvrille, T. Tanzi, and J. L. Dugelay, “Autonomous drones for assisting rescue services within the context of natural disasters,” *2014 31th URSI Gen. Assem. Sci. Symp. URSI GASS 2014*, pp. 1–4, 2014, doi: 10.1109/URSIGASS.2014.6929384.

[13] R. Rukaiya, S. Ahmed, M. U. Farooq, and I. Matloob, “Ad Hoc Networks Communication architecture and operations for SDR-enabled UAVs network in disaster-stressed areas,” vol. 160, no. November 2023, 2024.

[14] “Mohamed, F. (2015). Efficient data communication in unmanned aerial vehicles.,” 2015.

[15] C. Xiao, B. Wang, C. Wang, and Y. Yan, “Design of a novel fully-active PEMFC-Lithium battery hybrid power system based on two automatic ON/OFF switches for unmanned aerial vehicle applications,” *Energy Convers. Manag.*, vol. 292, no. April, p. 117417, 2023, doi: 10.1016/j.enconman.2023.117417.

[16] H. T. Arat and M. G. Sürer, “Experimental investigation of fuel cell usage on an air Vehicle’s hybrid propulsion system,” *Int. J. Hydrogen Energy*, vol. 45, no. 49, pp. 26370–26378, 2020, doi: 10.1016/j.ijhydene.2019.09.242.

[17] H. Liu, Y. Yao, J. Wang, T. Yang, and T. Li, “Energy management and system design for fuel cell hybrid unmanned aerial vehicles,” *Energy Sci. Eng.*, vol. 10, no. 10, pp. 3987–4006, 2022, doi: 10.1002/ese3.1262.

THE ROLE OF HYDROGEN ENERGY IN NET ZERO CITY STRATEGIES

[1]*Münevver Özge Balta*, [2*]*Mustafa Tolga Balta*
[1] Usak University, Architecture and Design Faculty, City and Regional Planning Department, 64200, Usak, Türkiye
[2] Usak University, Faculty of Engineering and Natural Science, Mechanical Engineering Department, 64200, Usak, Türkiye

*Corresponding author e-mail: mustafa.balta@usak.edu.tr

ABSTRACT
CO2 emissions comes from the energy and transport sectors released into the atmosphere are mostly city-based that causes environmental problems. Decarbonization is one of the main issues to be addressed in preventing environmental problems. In this context, it is necessary to determine the net zero energy city strategies. This study presents the the role of hydrogen energy in net zero city strategies.

Keywords: Net zero cities, Hydrogen, Sustainable urban planning

1. INTRODUCTION

In recent years, cities around the world have been rapidly modernizing and urbanizing, and are also facing several environmental problems. Many issues that affects urban environmental areas such as;

- increase in population,
- increase in energy demand,
- increase in transportation problems.

Urban energy demand increases with rapid population growth, urbanization and industrialization which is responsible for a significant portion of urban energy utilization and greenhouse gas emissions, and is mostly met by non-renewable energy sources. Non-renewable energy sources are still used as primary energy sources in many areas, from industrial activities to transportation, from electricity generation to heating and cooling applications. Also, inefficient use of energy is among the effects of environmental problems. Inefficient use of fossil fuels causes an increase in GHG emissions releases to the environment due to more fossil fuel consumption.

Nowadays, it has become more important than ever to combat various environmental issues such as global warming and climate change. It is stated that total energy-related greenhouse gas emissions released into the atmosphere reached 41.5 billion tons of equivalent carbon dioxide in 2022 [1,2]. In this context, the transition from non-renewable energy economies to renewable energy economies with high sustainability and decarbonization potential comes to the fore. In this regard, the use of renewable energy has become one of the key factors in meeting urban energy demand towards achieving sustainable urban areas. Meeting the ever-increasing energy demand of cities from renewable energy sources is a critical issue for the green and sustainable transformation of cities. Meanwhile, the transition from fossil-based economy to renewable energy economy for achieving carbon-free cities, it is necessary to increase energy efficiency and change energy production and consumption.

The net zero energy city concept has recently been promoted globally [3,4]. The concept of a net zero energy city is that city generates as much as energy as it demands from renewable energy sources [4-6]. Many researchers have published several reports and articles related to net zero energy systems such as at residential buildings, at commercial buildings, for electric mobility, on a community level, on a district level, and on a city-scale level [4,6-15]. The objective of the study is to presents the importance of hydrogen energy in net zero energy city strategies considering the transportation, waste management and energy systems associated with sustainable urban energy planning.

2. NET ZERO CITIES KEY STRATEGIES

Net zero cities key strategies are given below[16,17];
- Sustainable Urban Planning
  - mixed use zoning
  - density control
  - green infrastucture
  - green areas/corridors/roofs/walls

- Energy Systems
  - Transition to renewable energy sources (hydrogen based solar and wind)
  - Decreasing to use fossil fuels and greenhouse gas emissions

- Energy-efficient building and design

- Transportation
  - Promotion of public transportation
  - Creating accessible urban areas
  - Development of cycling and pedestrian zones
  - Renewable transportation

- Waste Management
  - Reduction of using plastics
  - Development of recycling infrastucture
  - Exploration of waste to energy Technologies

2.1. Sustainable Urban Planning

- Hydrogen Infrastructure Integration:
  - Planning hydrogen refueling stations for vehicles.
  - Planning regional energy systems that use hydrogen for heating and cooling in buildings.
  - Creating hydrogen production centers near renewable energy sources and transportation hubs.
- Mixed-Use Development: Designing to encourage low-carbon transportation, such as hydrogen-powered public transportation between residential and commercial areas
- Energy Efficient Buildings: Encouraging new buildings to integrate hydrogen-ready systems for future use.

2.2. Transportation

- Hydrogen-Powered Vehicles: Transition to hydrogen fuel cell vehicles (FCVs) for public transport.
- Use of hydrogen-powered buses, trains, and ferries in public transportation systems.
- Hydrogen Refueling Infrastructure: Establishment of a comprehensive citywide network of hydrogen refueling stations for hydrogen-powered vehicles.

2.3. Energy Systems

- Green Hydrogen Production: Production of green hydrogen using renewable energy sources (solar, wind, hydroelectric) through electrolysis
- Hydrogen for Power Generation: Hydrogen can be stored and used as fuel for power plants or backup generators
- District Heating Systems: Integrating hydrogen into district heating systems to provide low-emission heat to residential and commercial buildings, replacing natural gas or coal.
- Smart Grids and Energy Storage: Use hydrogen as part of an energy storage solution to balance supply and demand in a smart grid.

2.4. Waste Management

- Waste-to-Hydrogen Technologies: Convert organic waste (for example, food waste, agricultural by products, or municipal solid waste) into hydrogen through processes such as gasification, electrolysis, pyrolysis, or biogas conversion.
- Carbon Capture and Utilization (CCU): Combine waste-to-hydrogen processes with carbon capture to ensure that all carbon emissions generated during hydrogen production are captured and stored, further reducing the city's overall carbon footprint.
- Hydrogen in Recycling and Industrial Waste: Hydrogen can also be used in some industrial processes that recycle materials or convert waste into usable products.

4. CONCLUSIONS

Hydrogen can play a critical role in decarbonizing various sectors, including urban planning, transportion, energy systems and waste management.

REFERENCES

1. REN21. 2023. Renewables 2023 Global Status Report Collection, Global Overview https://www.ren21.net/gsr-2023/modules/global_overview/ Accessed on March 11, 2025.
2. Luo D, Liu J, Wu H, Zhang G, Pan Z, Huang J. 2025, Advancing smart net-zero energy buildings with renewable energy and electrical energy storage, Journal of Energy Storage, Vol. 114., Part B, 115850.
3. Edenhofer O, Pichs-Madruga R, Sokona Y, Farahani E, Kadner S, Seyboth K, Adler A, Baum I, Brunner S, Eickemeier P, Kriemann B, Savolainen J, Schlömer S, von Stechow C, Zwickel T, Minx J. 2014, Summary for policymakers. In: Climate change 2014: Mitigation of climate change. Contribution of working group III to the fifth assessment report of the intergovernmental panel on climate change. Cambridge, United Kingdom and New York, NY, USA: Cambridge University Press, IPCC, URL: https://www.ipcc.ch/site/assets/uploads/2018/02/ipcc_wg3_ar5_summary-for-policymakers.pdf/ Accessed on March 13, 2025.

4. Fachrizal R, Qian K, Lindberg O, Shepero M, Adam R, Widén J, Munkhammar J. 2024, Urban-scale energy matching optimization with smart EV charging and V2G in a net-zero energy city powered by wind and solar energy, eTransportation, 20, 100314.
5. Koutra S, Becue V, Gallas M, Ioakimidis CS. 2018, Towards the development of a net zero energy district evaluation approach : A review of sustainable approaches and assessment tools. Sustainable Cities and Society;39:784–800. http://dx.doi.org/10.1016/j.scs.2018.03.011.
6. Komninos N. 2022, Net zero energy districts : Connected intelligence for carbon-neutral cities. Land.
7. Bistline JET, Blanford GJ. The role of the power sector in net-zero energy systems. Energy Clim Change 2021;2(May):100045. http://dx.doi.org/10.1016/ j.egycc.2021.100045.
8. Luthander R, Nilsson AM, Widén J, Åberg M. 2019, Graphical analysis of photovoltaic generation and load matching in buildings: A novel way of studying self-consumption and self-sufficiency. Appl Energy;250:748–59. http://dx.doi.org/10.1016/j.apenergy.2019.05.058.
9. Doroudchi E, Alanne K, Okur O, Kyyrä J, Lehtonen M. 2018, Approaching net zero energy housing through integrated EV. Sustainable Cities and Society;38:534–42. http://dx.doi.org/10.1016/j.scs.2018.01.042.
10. Liu J, Zhou Y, Yang H, Wu H. 2022, Net-zero energy management and optimization of commercial building sectors with hybrid renewable energy systems integrated with energy storage of pumped hydro and hydrogen taxis. Appl Energy, 321:119312. http://dx.doi.org/10.1016/j.apenergy. 2022.119312.
11. Stamatellos G, Zogou O, Stamatelos A. 2022, Energy analysis of a NZEB office building with rooftop pv installation: Exploitation of the employees ' electric vehicles battery storage. Energies, 15:6206.
12. Ren H, Ma Z, Ming A, Fong L, Sun Y. 2022, Optimal deployment of distributed rooftop photovoltaic systems and batteries for achieving net-zero energy of electric bus transportation in high-density cities. Appl Energy, 319:119274. http://dx.doi.org/10.1016/j.apenergy.2022.119274.
13. Lopes RA, Martins J, Aelenei D, Lima CP. 2016, A cooperative net zero energy community to improve load matching. Renew Energy, 93. http://dx.doi. org/10.1016/j.renene.2016.02.044.
14. Liu J, Zhou Y, Yang H, Wu H. 2022, Uncertainty energy planning of net-zero energy communities with peer-to-peer energy trading and green vehicle storage considering climate changes by 2050 with machine learning methods. Appl Energy, 321:119394. http://dx.doi.org/10.1016/j.apenergy
15. Amado M, Poggi F, Amado AR, Breu S. 2017, A cellular approach to net-zero energy cities. Energies, 10:1826. http://dx.doi.org/10.3390/en10111826.
16. Wang P.,Priyadarshi R. 2025. Policy Framework for Realizing Net-Zero Emission in Smart Cities. Archives of Computational Methods in Engineering, 32(1), 63-82.
17. Adams S, Adedoyin F, Olaniran E, Bekun FV. 2020, Energy consumption, economic policy uncertainty and carbon emissions; causality evidence from resource rich economies. Econ Anal Policy 68.

ENHANCING LONGEVITY OF HYDROGEN-POWERED ELECTRIC VEHICLES, AN ADAPTIVE NEURO FUZZY CONTROL-BASED HIGH-GAIN, LOW-STRESS POWER CONVERTER

[1,2*]*Davut Ertekin*, [3]*Mustafa Özden*, [1]*Kübra Baltacı*
[1] Power Electronics Center of Electrical and Electronics Engineering Research Laboratories, Bursa Technical University, 16310, Yıldırım, Bursa, Turkey
[2] School of Engineering, Electrical, Electronic and Computer Engineering, The University of Western Australia, Perth, Australia
[3] Electrical and Electronics Engineering Department, Bursa Technical University, 16310, Yıldırım, Bursa, Turkey
*Corresponding author e-mail: davut.ertekin@btu.edu.tr

ABSTRACT
DC-DC converters are critical power conversion systems that regulate voltage and current levels for battery packs in electric vehicles (EVs) powered by fuel cells (FCs). The longevity of fuel cells is heavily influenced by the current drawn by the DC-DC converter. Additionally, the converter topology must be cost-effective, minimize voltage and current stresses on semiconductor devices, offer ease of control, and provide flexible voltage outputs to meet the dynamic demands of the battery pack. This study introduces a single-switch DC-DC power converter designed specifically for fuel cell-based electric vehicles (FCEVs), controlled by an innovative adaptive neuro fuzzy controller (ANFC). The proposed controller ensures no overshot and no oscillations on output, extremely small settling time and steady-state error. Simulation and experimental results for proposed power converter are presented, validating the theoretical findings.

Keywords: Hydrogen Energy, Electric Vehicle, DC-DC Converter, Artificial Intelligent, Adaptive neuro fuzzy controller

1. INTRODUCTION

Fuel cell electric vehicles (FCEVs) have garnered increasing attention in the automotive sector due to their low carbon emissions, reduced air pollution, and the mitigation of risks associated with fossil fuel leakage. However, integrating fuel cells (FCs) directly with a vehicle's battery pack necessitates several modifications. The ability to provide a controllable high charging voltage for the battery pack, maintain low alternating current, and extend the operating life by minimizing the current fluctuations drawn from the fuel cells (FCs) are the basic requirements of the DC/DC converter used in FCEVs. Many electric vehicle (EV) manufacturers still use traditional converter topologies, and these systems often fail to fully meet the above requirements. In addition, the efficiency of the converter is of critical importance on the battery's state of charge and the vehicle's driving range. In addition, cost effectiveness, extending the life of the components by reducing the voltage and current stress on the semiconductor circuit components, and implementing a simpler control mechanism are also very important. In recent years, studies have been conducted on Adaptive Neuro-Fuzzy Inference System (ANFIS) applications for energy management and efficiency optimization in electric vehicles. When these studies are examined, it is seen that they mostly focus on improving DC/DC converters and increasing the overall EV performance. For example, in the study of Thangavel and Kumar, a fuzzy-based interleaved boost converter was designed to meet the energy storage needs of high-capacity batteries for electric vehicle applications and to optimize torque and speed control [1]. In addition, studies have been conducted on ANFIS algorithms in the context of PEM fuel cells. In this context, Khanafari et al. developed an adaptive neuro-fuzzy controller to provide water management in a three-cell PEM fuel cell [2]. Singh et al. investigated the effect of optimized DC/DC converters to maximize power draw through maximum power point tracking (MPPT) in photovoltaic-assisted BLDC motor-based water pumping systems. In their study, they evaluated different DC/DC converter topologies and revealed how these structures contribute to increasing efficiency [3]. In addition, Ibrahim et al. proposed a fuzzy-Ant Colony Optimization (ACO) based control system to provide voltage regulation in EV energy storage systems and used a Cuk converter to integrate energy storage components with the drive system [4]. It is seen that ANFIS based control strategies and MPPT applications are popular in electric vehicles integrated with renewable energy. For example, Touti et al. proposed an innovative control approach to increase energy efficiency by integrating a PEM fuel cell system with a boost DC/DC converter [5]. Such studies provide significant contributions to the development of more efficient energy management systems for electric vehicle charging infrastructures [6-8]. Literature studies show that ANFIS based research in electric vehicle technology has made significant progress in DC/DC converter control. As a result, it is evaluated that these studies play a critical role in the development of advanced energy management strategies to increase the efficiency and performance of electric vehicles.

This study presents a high-gain topology utilizing a single power switch with adaptive neuro fuzzy controller system. The high voltage gain enables the integration of low-voltage, high-power fuel cells, which must be stepped up to 800 VDC or even higher or lower, depending on the electrical specifications of the EV, such as battery pack voltage and auxiliary loads like lighting. The use of a single switch simplifies control implementation and allows for flexible voltage generation to meet the real-time demands of the battery pack. An Adaptive Neuro-Fuzzy-based controller with three inputs and one output effectively regulates the output voltage, achieving the desired setpoint in a very short time without overshoot. The system maintains the desired output voltage with high stability, even in the presence of input voltage fluctuations and output load variations.

2. THE PROPOSED CONVERTER TOPOLOGY AND ADAPTIVE NEURO FUZZY CONTROLLER

2.1. Gain calculation

In the initial stage, the proposed converter circuit and its various operational states are introduced. To analyze the converter effectively, it is essential to evaluate the topology in two distinct modes: the intervals when the power switch is activated (ON state) and deactivated (OFF state). Figure 1 illustrates the design of the power converter. As shown in the figure, the proposed converter features a single power switch, which simplifies the controller design and ensures flexibility in generating the required voltages for the battery pack. The topology of the proposed converter indicates that totally three inductors are used. When the switch is turned on, the current from the input source flows through two parallel branches including the inductors L1 and diode D1 and inductor L2 and diode D3. The voltage on the capacitor C3 strarts to charge the inductor L3 and load is feed through the voltage on capacitor Cbat. For the next time interval, diode D2 is activated and input inductors L1 and L2 strsrt to discharged and capacitor C2 is charged again. Input current passes throughinductor L3 to charge the capacitor Cbat. Brcause of internal feature of an inductor in switching converters, the input current faces to pass in series through all the inductors that makes the current smooth with lowest possible ripple and this specification are crucial since enhances the relability of the system and help to longer longevity of the FC stack. Furthermore, the SL cell boosts the FC voltage and stores it in capacitor C1. In the subsequent stage, a soft-switching voltage enhancer cell is cascaded with the SL cell to reduce voltage stresses on the power switch (S) and further increase the voltage across capacitor C1, which is then transferred to the battery pack. The inclusion of inductor L3 ensures the generation of a smooth, low-ripple current for the battery pack, a critical feature for extending its lifespan. This characteristic is a vital consideration in designing a professional and efficient converter topology.

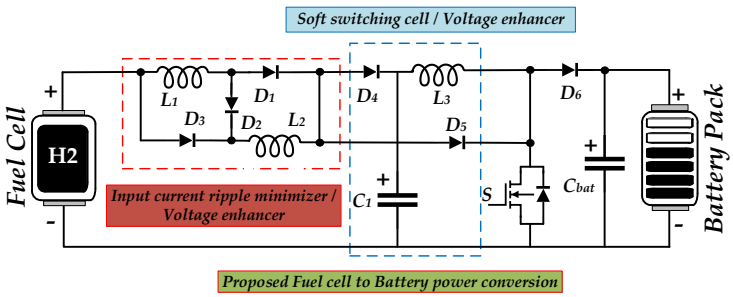

Fig. 1. The proposed FCEV converter topology and its integration with FC stack and battery pack

The operational states of the converter during the time intervals when switch S is activated (ON state) and deactivated (OFF state) are depicted in Figure 2a and Figure 2b, respectively. The current directions are illustrated using distinct colors in these figures. Referring to Figure 2a, the voltages and currents for the inductors and capacitors can be expressed as follows:

$$V_{L1} = L_1.\frac{di_{L1}}{dt} = V_{L2} = L_2.\frac{di_{L2}}{dt} = V_{FC} \quad (1)$$

$$V_{L3} = L_3.\frac{di_{L3}}{dt} = V_{C1} \quad (2)$$

$$V_{Cbat} = V_O \quad (3)$$

In these equations, V_{L1}, V_{L2}, and V_{L3} represent the voltages across the inductors L_1, L_2, and L_3 respectively. V_{Cbat} denotes the voltage across the output capacitor C_{bat}, and V_O represents the voltage across the battery pack.

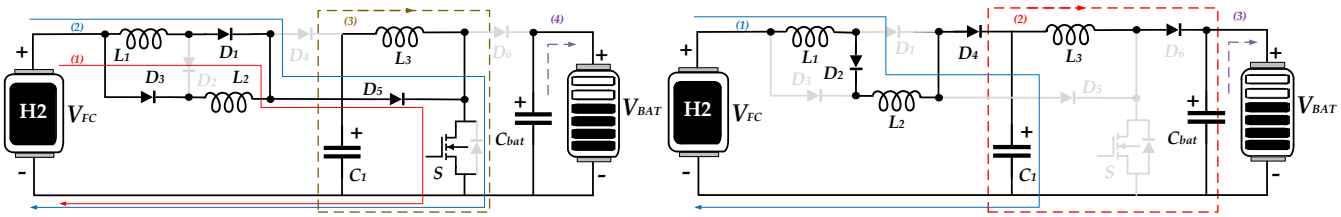

Fig. 2. The state of the circuits components when the switch is (a) activated and (b) deactivated

$$V_{L1} + V_{L2} = L_1.\frac{di_{L1}}{dt} + L_2\frac{di_{L2}}{dt} = V_{FC} - V_{C1} \xrightarrow{L_1=L_2=L_x} L_x\frac{di_{Lx}}{dt} = \frac{V_{FC}-V_{C1}}{2} \quad (4)$$

$$V_{L3} = L_3.\frac{di_{L3}}{dt} = V_{C1} - V_{bat} \rightarrow \frac{di_{L3}}{dt} = \frac{V_{C1}-V_{bat}}{L_3} \quad (5)$$

The gain of the proposed converter can be obtained by second balance rule for inductors. For inductors L_1 and L_2 which are eqaul, one can write $L_1 = L_2 = L_x$ and then:

$$V_{Lx}D + V_{Lx}(1-D) = 0 \rightarrow V_{FC}D + \frac{V_{FC}-V_{C1}}{2}(1-D) = 0 \rightarrow V_{C1} = V_{FC}(\frac{1+D}{1-D}) \quad (6)$$

For inductor L_3:

$$V_{L3}D + V_{L3}(1-D) = 0 \rightarrow V_{C1}D + (V_{C1} - V_O)(1-D) = 0 \rightarrow V_O = \frac{V_{C1}}{1-D} \quad (7)$$

The voltage gain M, can be obtained:

$$M = \frac{V_O}{V_{FC}} = \frac{1+D}{(1-D)^2} \quad (8)$$

2.2. Adaptive Neuro Fuzzy Controller

The proposed Adaptive Neuro-Fuzzy-based controller features three inputs Vin (input voltage), Vset (reference voltage), and Error (voltage error signal) and one output, ∆duty (duty cycle adjustment). Figures 3a and 3b present the combined structure of the converter and the controller, illustrating their integration within the system and the generated pulse width modulation (PWM) switching pulses for power switch in practice based on the propsed ANF controller.

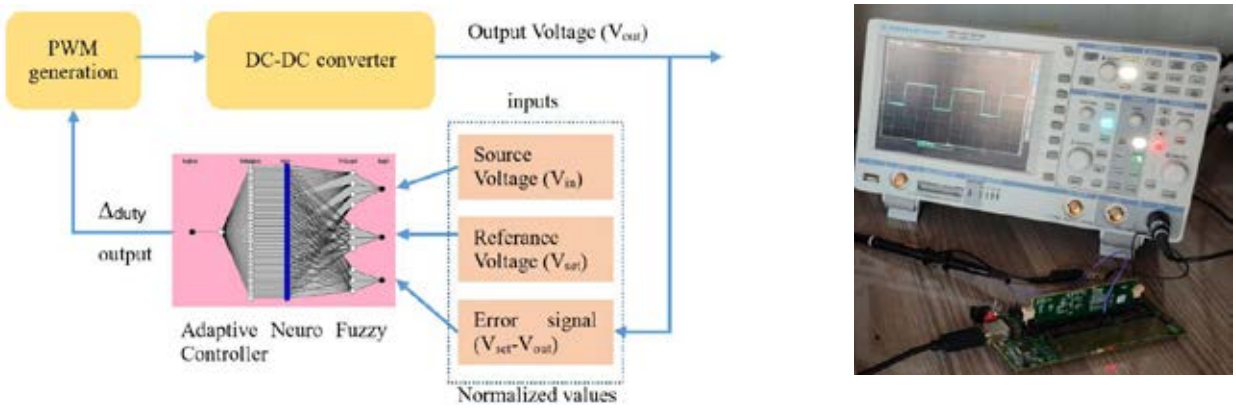

a) b)

Figure 3. (a) Proposed Adaptive Neuro-Fuzzy Controller System and DC-DC Converter and (b) generated switches PWM pulse by the DSP-based controller

The proposed Adaptive Neuro-Fuzzy Controller (ANFC) computes the required ∆duty values to achieve the desired output corresponding to the given input parameters. In the PWM block, the computed duty cycle values are used to generate the corresponding PWM signals. For the controller design, 100,000 random values were generated for Vin, V_{set}, and V_{out}. Using (8), both the required duty cycle value for the desired V_{set} and the actual duty cycle corresponding to Vo were calculated. The difference between these two values was used to determine ∆duty. To define the ANFC input membership functions, V_{in} was normalized within the range [0-1] for 22–24 V, while Vset and Vo were normalized within [0-1] for 250–350 V. This process resulted in a total of 400,000 training data points, which were utilized for training a Sugeno-type fuzzy controller. The training of the controller which has 36 rule was conducted in MATLAB 2023b using the grid partition method and a hybrid optimization approach. The Adaptive Neuro-Fuzzy System (ANFS) automatically determined the number and range of membership functions for the input signals. Consequently, the input membership function layer was structured as 4-3-3, consisting of Gaussian membership functions. The training performance achieved an MSE (Mean Squared Error) of 0.0038 after 100 epochs. The resulting model was implemented in Simulink, where it demonstrated high accuracy within the specified operating ranges.

3. RESULTS AND DISCUSSION

The results for the voltages and currents of the proposed converter, obtained using a MATLAB program, are presented in this section. As illustrated in Figure 4a, with a duty ratio of approximately 0.64, the converter is capable of boosting the input voltage from 24 VDC to around 300 VDC, achieving a voltage gain of about 12.65 times. This result validates the

accuracy of the theoretical analysis for the voltage gain calculations and the operational states of the converter depicted in Figure 2. Figure 4b displays the input current from the FC and the current stress on the switch S as sample waveforms. Figure 4c illustrates how the ANFC adjusts the duty cycle as the output voltage (V_O) reaches the 300 V setpoint. As observed, the proposed controller achieves a very short settling time (0.016 sec) with zero overshoot, zero oscillation, and an extremely small steady-state error (0.7 V). This figure also highlights the minimized current fluctuations in the FC input source, as claimed by the proposed converter design. As calculated and observed, for an output power of around 200 W and an input voltage of 24 VDC, the average current drawn from the FC is approximately 8.33 A, which aligns with the theoretical predictions. Additionally, the figure demonstrates that the converter achieves the lowest possible current ripples, ensuring an extended lifespan for the FC, a critical feature for reliable and efficient operation.

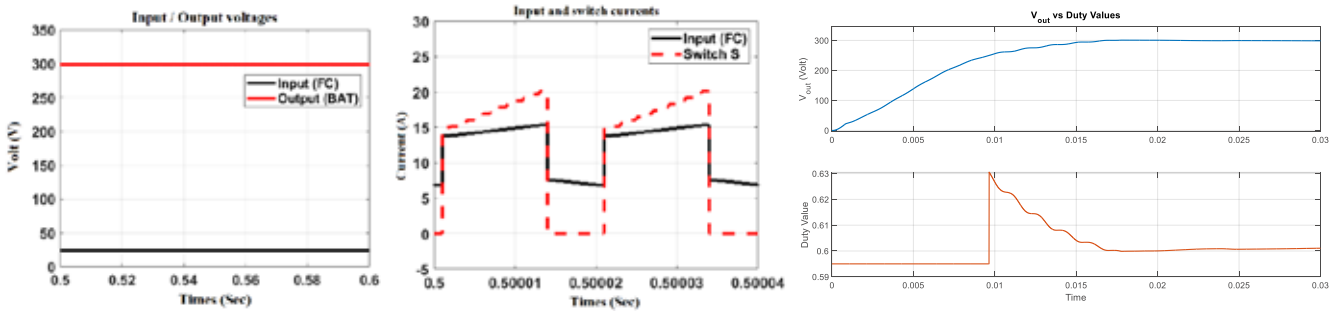

a) b) c)

Fig. 4. (a) Input and output voltages and (b) current stresses for the FC source and switch S (c) Vo vs Duty values

4. CONCLUSIONS

In this study, an adaptive neuro fuzzy-based high voltage gain, low input current dc/dc boost converter for hydrogen-powered electric vehicles is proposed. In the design of the controller, the training dataset was generated based on data obtained from the characteristic equation of the system. This dataset was used to train the Adaptive Neuro-Fuzzy System (ANFS), which enables the controller to dynamically adjust its response to varying operating conditions. The ANFS-based approach offers a significant advantage over conventional methods, as it automatically determines the membership functions and rule sets, eliminating the need for extensive manual tuning and reducing the overall design complexity. Unlike traditional PID controllers, which often suffer from dead time, overshoot, and oscillations, the proposed AI-driven controller effectively mitigates these issues. By leveraging adaptive learning and fuzzy inference mechanisms, it achieves a highly stable response with zero overshoot, minimal steady-state error, and an exceptionally short settling time. This ensures not only fast and accurate regulation of the output voltage but also improved robustness against input voltage fluctuations and load variations. The integration of an intelligent control mechanism enhances the overall system performance, efficiency, and reliability, making the proposed controller a highly effective solution for precise and adaptive DC-DC converter regulation.

REFERENCES

1. Thangavel S and Kumar R. 2023. Fuzzy-based interleaved step-up converter for electric vehicle. Intelligent Automation & Soft Computing 35(1):1103-1118. https://doi.org/10.32604/iasc.2023.025511
2. Khanafari, A. Alasty, A. Kermani, M.J. Asghari, S. 2024. Experimental study of water management of a three-cell PEM fuel cell stack using adaptive neuro-fuzzy approximation and fuzzy control, International Journal of Hydrogen Energy, Volume 50, Part C, 2024, Pages 931-944, ISSN 0360-3199,
3. Singh O, David P, Balachandran P, and Mihet-Popa L. 2022. Analysis of grid-interactive PV-fed BLDC pump using optimized MPPT in DC–DC converters. Sustainability 14(12):7205. https://doi.org/10.3390/su14127205
4. Ibrahim M, Ibrahim M, and Khather S. 2023. Design of fuzzy-ACO based controller for Cuk converter in electric vehicles. Journal Européen Des Systèmes Automatisés 56(3):425-430. https://doi.org/10.18280/jesa.560309
5. Touti E, Aoudia M, Basha C, and Alrougy I. 2024. A novel design and analysis adaptive hybrid ANFIS MPPT controller for PEMFC-fed EV systems. International Transactions on Electrical Energy Systems 2024:1-17. https://doi.org/10.1155/2024/5541124
6. Rao S, Kumar Y, Amir M, and Ahmad F. 2022. An adaptive neuro-fuzzy control strategy for improved power quality in multi-microgrid clusters. IEEE Access 10:128007-128021. https://doi.org/10.1109/access.2022.3226670
7. Zotov, L.G. Kuratov, K.A. Bolshakov, I.M. 2024, Hydrogen fuel cell energy regulators based on Boost DC-DC converters with switched capacitors, International Journal of Hydrogen Energy, Volume 95, Pages 982-992, ISSN 0360-3199,
8. Sahin, H., Çetin, M.S., Gençoğlu, M.T., Erdinç, O. 2025. Fuel cell and battery powered light electric vehicle simulation, International Journal of Hydrogen Energy, https://doi.org/10.1016/j.ijhydene.2024.12.499.

DESIGN AND IMPLEMENTATION OF PSEUDO LEVENBERG-MARQUARDT LEARNING ARTIFICIAL NEURAL NETWORK CONTROLLER FOR POWER CONVERSION IN FUEL CELL TO BATTERY CHARGING SYSTEMS, IMPROVING POWER EFFICIENCY AND RELIABILITY

[1]*Mustafa Özden*, [2,3*]*Davut Ertekin*, [2]*Kübra Baltacı*
[1] Electrical and Electronics Engineering Department, Bursa Technical University, 16310, Yıldırım, Bursa, Turkey
[2] Power Electronics Center of Electrical and Electronics Engineering Research Laboratories, Bursa Technical University, 16310, Yıldırım, Bursa, Turkey
[3] School of Engineering, Electrical, Electronic and Computer Engineering, The University of Western Australia, Perth, Australia
*Corresponding author e-mail: davut.ertekin@btu.edu.tr

ABSTRACT

The integration of artificial intelligence into the control and optimization of DC-DC converters presents promising opportunities in improving energy management and efficiency in electric vehicle (EV) sector. This study presents a low-input current and low voltage stress topology for application in fuel cell (FC) to battery charging systems in EVs. A current filter by forming a switched inductor at the input side of the converter quarantees a small ripple for input osurces that enhances the longevity and longlife of the FC stacks. The application of the switched capacitor at the end side of the converter decreases the voltage stress on the main power switch and enhances the mean time to failure rate of the converter that is between the most important featres of a converter. The converter design incorporates a three-layer, three-input artificial neural network structure. The regression values were 0.982 for training, 0.983 for testing, and 0.9827 overall, indicating minimal prediction error and confirming the effective training of the neural network model. The laboratoty test results confirm the correctness of the proposed algorithm and application of the proposed converter.

Keywords: Fuel Cell, Electric Vehicle, DC-DC Converter, Artificial Neural Network Controller, Reliability

1. INTRODUCTION

The increasing utilization of hydrogen energy and its production through environmentally sustainable approaches have gained significant attention in recent years as part of efforts to mitigate the greenhouse effect and reduce the carbon footprint. Reaserchers intensively have focused on application of FC and hydrogen energy in Evs. These techniques bring many of advantages like the green and cheap energy, abundance due to presence in the air and helping to stop global warming, and ease and spread of EVs quickly [1,2]. For instance, [3] presents an implementation of a microbial FC. On the other hand, the application of power electronic-based converters and their control mechanisms are inevitable to convert the generated voltage of the FC stack for battery pack chargings in EVs. for fast charging issues, since FC generates a DC voltage, DC-DC converters widely are used to enhance the limited generated voltage by the FC to a high voltage or high current DC voltage for EV battery pack. In recent years, the battery voltage pack has reached up to 800 VDC that is much more than generated voltage by a FC cell. Besides, the control mechanism is another significant issue that should be considered. Controllers which are based on the minimum complexity and being simply implemented are in focal point of attentions. Liu et al. implemented a control method based on genetic algorithms and artificial neural networks to enhance the efficiency of converters [4]. Since maximum power point tracking (MPPT) techniques play a critical role in optimizing the utilization of renewable energy sources, advanced control strategies have also been applied in this domain. For instance, Bharathi et al. introduced an artificial neural network-based approach to optimize power utilization in a solar-powered electric vehicle [5]. Additionally, a neural network-based MPPT technique was proposed to improve the efficiency of photovoltaic power systems, which are highly sensitive to environmental factors [6].
DC-DC converters play a pivotal role in maintaining the optimal energy balance between power sources and the energy storage system of electric vehicles. A comprehensive study on the role of such converters in energy management was presented by Gorji et al. [7]. Akyazı presented a step-up converter controlled through a PI-Fuzzy Logic Controller. The controller parameters were optimized using a Genetic Algorithm to enhance system efficiency [8]. Furthermore, Dhimish and Schofield conducted research on the industrial application of AI-based buck-boost DC-DC converters, demonstrating their potential in enhancing adaptive energy management systems [9]. These findings reinforce the notion that AI-powered control strategies can revolutionize the way power electronics systems are designed, monitored, and optimized. In this study, a DC-DC converter topology is proposed for charging of EVs purposes via a fuel cell based energy system. A 3-layer 3-input artificial neural network structure is used in the design of the DC-DC converter. Theoretical evaluations, simulation results and switching PWM pulses generated via digital signal processors (DSP) microcontroller in a laboratory environment are presented in this study.

2. THE PROPOSED CONVERTER TOPOLOGY AND AI CONTROLLER

2.1. Gain calculation

The proposed converter is presented in figure 1. This figure simply shows that the suggested converter has the capability of conecction of the FC stacks or PV arrays to the battery charging packs of EVs. The illustrated converter includes a switched-inductor-capacitor cell (SL-SC) at the input side and a switched-capacitor (SC) cell at its end side. The application of SL-SC minimizes the current ripple of the input source since both inductors are charging in parallel and discharging in series and capacitor C1 presesnts a fixed voltage to easily can be enhanced by the SC cell. The application of SC cell at the next side cause a significant decrease in voltage stresses across the main power switch and simply enhances the voltage on capacitors C1 and C2. The proposed converter has a significant voltage gain that fits its application to high voltage charging systems.

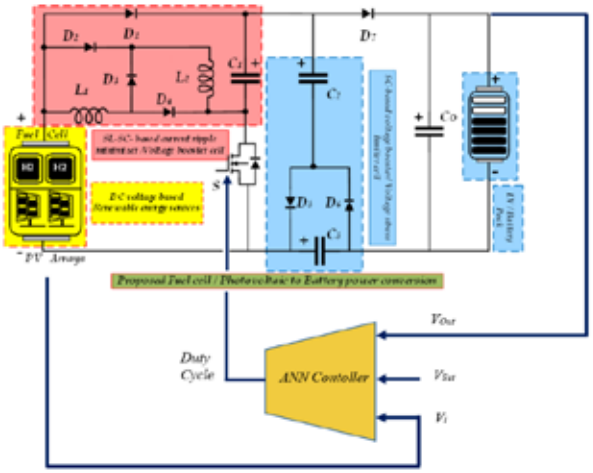

Fig. 1. The proposed FCEV converter topology and its suggested Pseudo AI controller

Figures 2a and 2b present the state of the components in the suggested power converter topology for times intervals that the switch S is turned on and off respectively. For the time duration that the main switch is activated, both inductors and capacitor C1 chrged in parallel with input voltage source. The below equations can be written for this state:

$$V_{L1} = L_1.\frac{di_{L1}}{dt} = V_{L2} = L_2.\frac{di_{L2}}{dt} = V_{in} \quad (1)$$

$$V_{C1} = V_{in} \quad (2)$$

$$V_{C2} - V_{C3} = V_{in} \quad (3)$$

$$V_{CO} = V_O \quad (4)$$

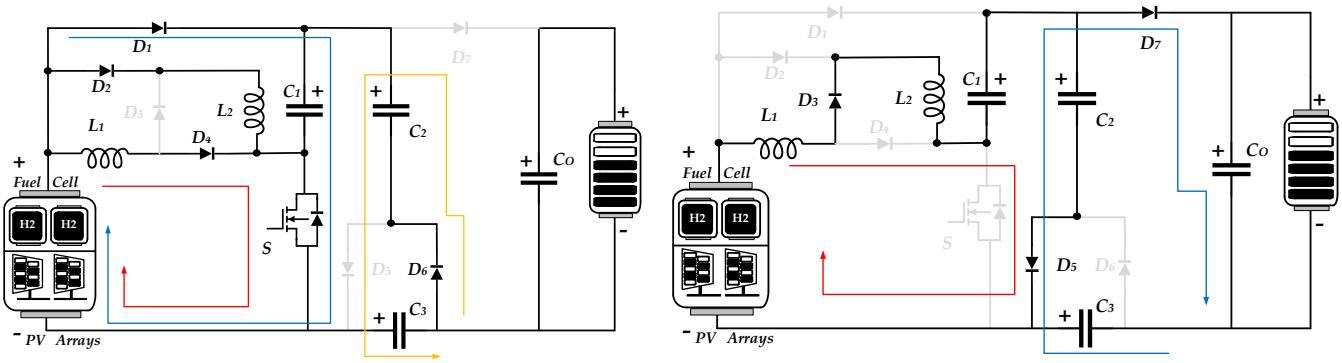

(a) (b)

Fig. 2. The state of the circuits components when the switch is (a) activated and (b) deactivated

When the switch is deactivated, the inductors begin discharging into the output capacitor and battery pack. Capacitor C2, which was discharged in the previous time interval, is now recharged, activating diode D5 to charge capacitor C3. As the voltages across capacitors C2 and C3 increase, the output voltage also rises. The following equations can be derived for this operational mode:

$$V_{L1} + V_{L2} - V_{C1} + V_{C2} = V_{in}, \xrightarrow{L_1=L_2=L_x} V_{Lx} = L_x \frac{di_{Lx}}{dt} = \frac{V_{in}+V_{C1}-V_{C2}}{2} \quad (5)$$

$$V_{C2} = V_{CO} - V_{C3} \quad (6)$$

The gain of the proposed converter can be obtained by second balance rule for inductors. For inductors L_1 and L_2 which are eqaul, one can write $L_1 = L_2 = L_x$ and then:

$$V_{Lx}D + V_{Lx}(1-D) = 0 \rightarrow V_{in}D + (\frac{V_{in}+V_{C1}-V_{C2}}{2})(1-D) = 0 \xrightarrow{V_{C1}=V_{in}} V_{C2} = \frac{2.V_{in}}{1-D} \quad (7)$$

From equation (3):

$$V_{C3} = V_{C2} - V_{in} = \frac{2.V_{in}}{1-D} - V_{in} = \frac{1+D}{1-D}V_{in} \quad (8)$$

Based on equations (6,7 and 9), the voltage gain M, can be obtained as below:

$$V_{CO} = V_{C2} + V_{C3} = \frac{2.V_{in}}{1-D} + \frac{1+D}{1-D}V_{in} \rightarrow M = \frac{V_O}{V_{in}} = \frac{3+D}{1-D}V_{in} \quad (9)$$

2.2. Controller features and Designings

In this study, a neural network-based controller is proposed for the control of a DC-DC converter. The proposed controller is designed with 3 inputs, 1 output, and 3 layers. The number of neurons in the layers is determined to be 20:40:10. The input parameters of the controller are V_{in}, V_{set}, and Error signals, while the duty cycle value forms the output parameter. The structure of the controller is shown in Figure 3.

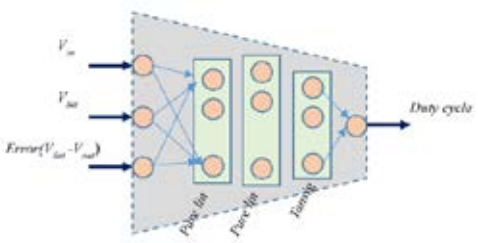

Fig.3. ANN based controller

```
1. inputs=zeros(362103,3); targets=zeros(362103,1);
2. k=1;

3. Vi=22 → 24
     VSet=200 → 350
          Vo=150 → 350
               Target_Duty=-(-VSet+3*Vi)/(VSet+Vi);
               Actual_Duty=-(-Vo+3*Vi)/(Vo+Vi);
               Err_duty=Target_Duty-Actual_Duty;
               Error=normalize(VSet-Vo);
               train_data_input(k)=[Vi,   VSet Error];
               train_data_output(k)=Err_duty;
               k=k+1;
          end
     end
end
4. Shuffle train data
5. net = newff(inp,targets',[20 40 10]);
6. net = train(net,inp,targets');
```

a)

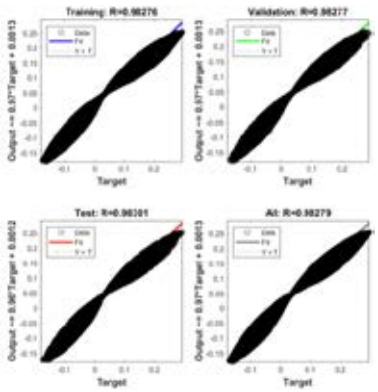

b)

Fig.4. a) Pseudo code of the algorithm developed for creating the training data, b) regression values at the end of the training phase

2.2.1.Training and Testing of the Controller

To train the controller, a training dataset consisting of input-output, set value, and duty cycle values needs to be obtained. Unlike previous studies, the training values are not generated randomly but cyclically to include all intermediate values. The data is obtained according to Equation 9. The pseudo-code of the algorithm used to create the dataset is shown in Figure 4a. The V_{in} value is produced between 22 and 24 V, the V_{set} value between 200 and 350 V, and the V_o value between 150 and 350 V. Using these values, the required and instantaneous duty values are calculated, and the difference between them, Err_duty, is obtained. This value is the output of the ANN.

As a result, 1,448,412 data points were generated, consisting of 3×362,103 input values and 362,103 target values. This dataset was shuffled and presented to the artificial neural network, and the training and testing processes were completed in 4 epochs by using Levenberg-Mardquart learning algorithm. The training performance was obtained as 29×10^{-5}. The regression values at the end of the training phase reflect the model's performance in fitting the data. These values indicate the degree of correlation between the predicted outputs and the actual target values. The regression values are shown in Figure 4b.

3. RESULTS AND DISCUSSION

A simulation study was conducted in the MATLAB Simulink environment to test the performance of the controller. The output voltage and corresponding duty cycle variation obtained for a 350 V set value are graphically presented in Figure 5a. As seen, a settling time of 0.05 seconds, low overshoot voltage, very low oscillation, and a very smooth duty cycle variation are achieved. As can be seen from this result, the proposed ANN controller successfully controls the DC-DC converter within the specified ranges. Figure 5b presents the interaction of matlab-compatible digital signal processors (DSP) and proposed AI algorithm to generate the pulse width modulation (PWM) signals to drive the power switch S in practice.

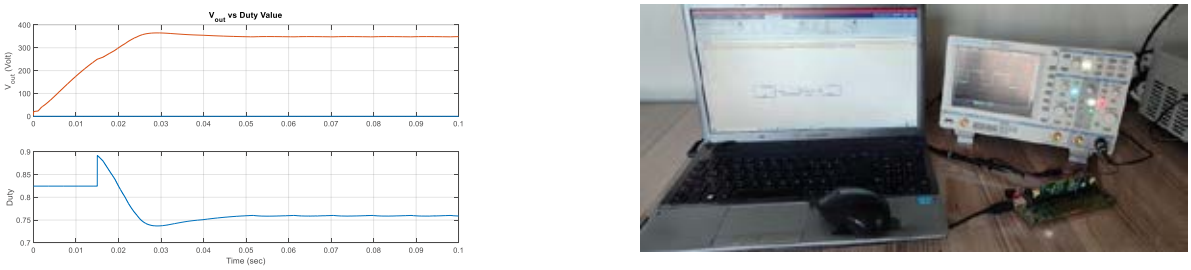

a) b)

Fig.5. (a) Simulated DC voltage output for the battery pack and (b) experimentally generated PWM driving pulses for the switch using the ANN algorithm.

4. CONCLUSIONS

This study introduces a high voltage gain DC-DC boost converter designed to increase the voltage of the fuel cell (FC) stack for battery charging in EVs. Since EVs require high voltage levels, often up to 800 VDC, a high-gain converter is essential to meet load demands. The proposed converter features a single power switch, simplifying both the control process and the complexity of the controller circuit. A DSP microcontroller, compatible with MATLAB, is utilized for implementation. On the control side, an AI-based controller is developed using pseudo codes and the Levenberg-Marquardt learning algorithm. The regression values obtained were 0.982 for training, 0.983 for testing, and 0.9827 overall, indicating minimal prediction error and confirming the effective training of the neural network model.

REFERENCES

[1] Habib M, Arefin P. 2022. Adoption of hydrogen fuel cell vehicles and its prospects for the future (a review). Oriental Journal of Chemistry 38(3):621-631. https://doi.org/10.13005/ojc/380311
[2] Khzouz M, Gkanas E, Girella A, Statheros T, Milanese C. 2020. Sustainable hydrogen production via LiH hydrolysis for unmanned air vehicle (UAV) applications. International Journal of Hydrogen Energy 45(8):5384-5394. https://doi.org/10.1016/j.ijhydene.2019.05.189
[3] Santoro C, Arbizzani C, Erable B, Ieropoulos I. 2017. Microbial fuel cells: from fundamentals to applications. A review. Journal of Power Sources 356:225-244. https://doi.org/10.1016/j.jpowsour.2017.03.109
[4] Liu H, Cheng Y, Zhao Y, Shurafa M, Wu J, Liu C, et al. 2021. A novel PID control strategy based on improved GA-BP neural network for phase-shifted full-bridge current-doubler synchronous rectifying converter. Mathematical Problems in Engineering 2021:1-14. https://doi.org/10.1155/2021/6654997
[5] Bharathi G, Rishitha B, Lakshmi D, Valli A, Durga B. 2024. Artificial neural network MPPT method of solar PV system for electric vehicles using MATLAB Simulink. IOP Conference Series Earth and Environmental Science 1375(1):012004. https://doi.org/10.1088/1755-1315/1375/1/012004
[6] Carrasco M, Mancilla-David F, Fulginei F, Laudani A, Salvini A. 2013. A neural networks-based maximum power point tracker with improved dynamics for variable DC-link grid-connected photovoltaic power plants. International Journal of Applied Electromagnetics and Mechanics 43(1-2):127-135. https://doi.org/10.3233/jae-131716
[7] Gorji S, Sahebi H, Ektesabi M, Rad A. 2019. Topologies and control schemes of bidirectional DC–DC power converters: an overview. IEEE Access 7:117997-118019. https://doi.org/10.1109/access.2019.2937239
[8] Akyazı Ö. 2018. GA-based fuzzy logic controller with booster type DC-DC converter. NWSA Academic Journals 13(1):34-43. https://doi.org/10.12739/nwsa.2018.13.1.2a0134
[9] Dhimish M, Schofield N. 2022. Single-switch boost-buck DC-DC converter for industrial fuel cell and photovoltaics applications. International Journal of Hydrogen Energy 47(2):1241-1255. https://doi.org/10.1016/j.ijhydene.2021.10.097

ELECTRODEPOSITION OF HIGHLY-EFFICIENT IRON-RUTHENIUM ALLOY CATHODES FOR HYDROGEN EVOLUTION REACTION IN ALKALINE SOLUTIONS

[1*]*Dawid Kutyła*,
[1] AGH University of Krakow, Mickiewicza Avenue 21, Kraków, 30-059, Poland

*Corresponding author e-mail: kutyla@agh.edu.pl

ABSTRACT
In this study, Fe-Ru alloys have been prepared by electrodeposition process. Cyclic voltammetry measurements confirm the possibility of co-deposition of iron with ruthenium from single bath. Formation of alloy is possible by applying the potential below the reduction value for Fe^{2+}/Fe process. Modification of electrodeposition conditions allows to obtain different composition of electrodeposited thin films. Maximal amount of iron in alloy were close to 30% mass. Morphological study and structural analysis for obtained Fe-Ru alloys were carried. Comparative analysis of catalytic activity in hydrogen evolution reaction in 1 M NaOH were conducted. All of the obtained Fe-Ru coatings are more active materials for water splitting process than electrodeposited Ru thin film. Low overpotential value can be affected by presence of RuFe and Ru_4Fe phases, homogenously distributed in ruthenium metal matrix.
Keywords: Iron, Ruthenium, electrodeposition, hydrogen evolution reaction, noble metals alloys

1. INTRODUCTION

One of the most exciting areas in materials science and electrocatalysis is designing alloys for water splitting. In particular, the synthesis of alloys containing highly active noble metals has become a major research focus. While binary alloys of platinum, palladium, and rhodium are well documented, another platinum group metal—ruthenium remains relatively underexplored. Ru-based alloys most commonly investigated for electrocatalysis include Co–Ru[1-2] and Ni–Ru.[3] Nickel–ruthenium alloys can be electrodeposited from chloride solutions at −0.5 to −1.0 V vs. SCE, with electrochemical tests confirming codeposition below the nickel reduction potential. These high-quality Ni–Ru coatings vary in phase composition (NiRu (100) and (101)) and electroactive surface area as Ni content increases, exhibiting strong water-splitting activity—likely due to their well-developed active surface and NiRu phases [4]. Similarly, Ru–Co alloys are deposited from a 0.75 M Co^{2+} + 0.025 M Ru^{3+} solution at −0.5 to −1.2 V vs. SCE. Deposition of Ru quickly becomes diffusion-controlled (−0.7 V), while Co deposition is enhanced by Ru, leading to Ru–Co films with globular morphology and increasing Co content (22.1/7.4 to 70.2/86.1 wt%) as the potential shifts from −0.6 to −1.0 V. These coatings show superior hydrogen evolution reaction (HER) performance and stability in alkaline media, with Ru–Co@Ti_2AlC formed at −0.6 V requiring an overpotential of just −95 mV to reach −100 mA cm^{-2} in 1 M KOH.[5] Although binary alloys of ruthenium with Ni and Co have been studied, Fe–Ru systems remain unexplored. This gap in the literature serves as the primary motivation for the present study on synthesizing and evaluating Fe–Ru alloys for electrocatalytic applications.

2. MATERIALS AND METHODS

Iron-Ruthenium alloys were electrodeposited from acidic chloride electrolytes. The experiments were conducted at room temperature using reagents of analytical purity. Electrochemical tests were performed with a BioLogic SP-200 potentiostat and EC-LAB software. Cyclic voltammetry and stripping analysis utilized a standard three-electrode measurement cell, with a 0.196 cm^2 carbon-glass working electrode and a platinum coil counter-electrode. The potential was measured against a saturated calomel electrode. The potentiostatic deposition system was similar. Deposition took place on 2.8 cm^2 etched copper plates, with a parallel platinum sheet counter-electrode. A custom-designed electrolytic cell (300 ml volume, 6 cm electrode distance) was used for electrodeposition, with the electrolyte replaced for each experiment. Post-deposition, the alloys were cleaned in deionized water and air-dried. Elemental composition was determined via XRF (Rigaku Rimini) with a Palladium lamp, and phase composition was analyzed by XRD (Rigaku MiniFlex II) using a copper tube (λ = 1.54059), comparing diffractograms to ICDD database cards. SEM images were captured using a Hitachi Su-70 scanning microscope. The water-splitting ability of the Fe-Ru coatings was assessed by chronopotentiometry in a 1 M NaOH solution and Tafel slope estimation in linear range.

3. RESULTS AND DISCUSSION

All the results the electrochemical synthesis of Fe-Ru alloys was preceded by cyclic voltammetry studies. Chloride electrolytes with a Cl- ion concentration of 3 M and pH = 1 were used for research. Due to the significant difference in the reduction potentials of the Ru/Ru^{3+} and Fe/Fe^{2+} redox potentials, electrolytes with a higher concentration of Fe^{2+} ions relative to Ru^{3+} ions (0.5 M Fe^{2+} + 0.01 M Ru^{3+}) were used. The obtained curves for the solution containing only Fe^{2+} ions are shown in Figure 1a).

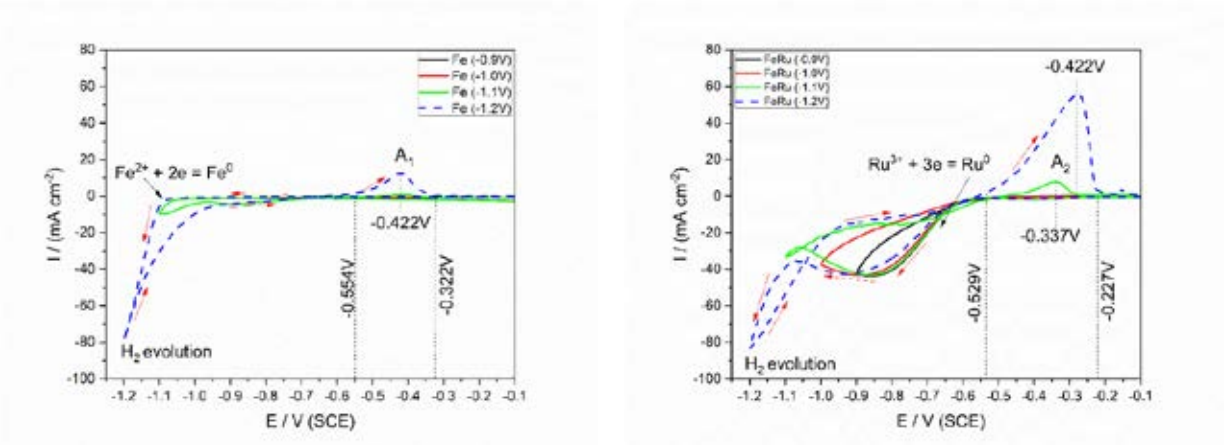

Fig. 1. Cyclic voltammetry registered on GC disc electrode at 40 mVs^{-1} scan rate for electrolytes containing: a) 1 M Fe^{2+}, Cl^- = 3 M, pH = 1 and b) 1 M Fe^{2+} , 0.01 M Ru^{3+}, Cl^- = 3 M, pH = 1 for different vertex potentials.

The use of a glassy carbon electrode was motivated by its ability to determine the reduction potential of Fe^{2+} ions while avoiding hydrogen evolution on the working electrode's surface. An increase in current density and the appearance of hydrogen bubbles were observed only when the glassy carbon surface was covered with a metallic iron deposit. During the cathodic scan, from the OCP potential range to -1.1 V, no change in current density was observed. Only after exceeding -1.15 V did the current density increase, indicating the onset of Fe^{2+} ion reduction to the metallic form. During the scan from -1.1 to -1.2 V, gas bubbles were observed on the electrode surface, likely related to hydrogen ion reduction and water splitting process. Iron, like nickel and cobalt, has relatively high catalytic activity for hydrogen evolution. After exceeding the potential of -0.55 V, further anodic scanning shows a peak corresponding to the dissolution of the metallic phase, with a maximum at -0.42 V. The next step was to compare the cyclic voltammetry curves obtained for the solution containing Fe^{2+}, Ru^{3+} ions, and their mixture at the same ion concentrations. The results are shown in Figure 1b).
As previously discussed in Figure 1a), the reduction reaction of Fe^{2+} ions starts after exceeding a potential of -1.1 V, resulting in the formation of a metallic phase on the electrode surface. This is confirmed by the presence of an anodic peak (A1) in the range of -0.55 V to -0.32 V. The voltammogram for the solution containing only Ru3+ ions showed two cathodic peaks. The first is due to the reduction of ruthenium ions to the metallic form (K1), leading to the appearance of peak K2 at -0.7 V, related to hydrogen ion reduction on the electrode surface. The increase in current density recorded from -1.1 V is due to water decomposition reaction. In the studied system, the anodic scan did not show peaks corresponding to the dissolution of the metallic ruthenium phase. The scan obtained for the solution containing both metals' ions is significantly different from the combined curves for iron and ruthenium. The first noticeable difference is the disappearance of cathodic peak K1 and the shift of the reduction process towards more negative potentials. The first cathodic process starts at -0.64 V and reaches a maximum at about -0.9 V. The recorded current density in this range is much higher than that for the ruthenium or iron only solution. After exceeding -1.1 V, an increase in current density related to water splitting is observed. The anodic scan shows a distinct peak (A2), shifted towards more positive potential values compared to the electrolyte containing only Fe^{2+} ions. The intensity of this peak is much higher in the Fe2+ + Ru3+ system. It is suspected that the presence of metallic Ru on the electrode surface during the scan may decrease the concentration of hydrogen ions in the electrode vicinity, affecting the Fe^{2+} ion reduction potential. Such a potential shift could intensify the alloy deposition process. These findings indicate that there is a possibility to electrodeposit the Fe-Ru alloys from acidic chloride solutions. For this study the different deposition potentials were applied to obtain the Fe-Ru alloys with different chemical composition. The chemical and phase composition of alloys were verified by XRF (left side of the spectra) and XRD analysis, which were presented on Figure 2.

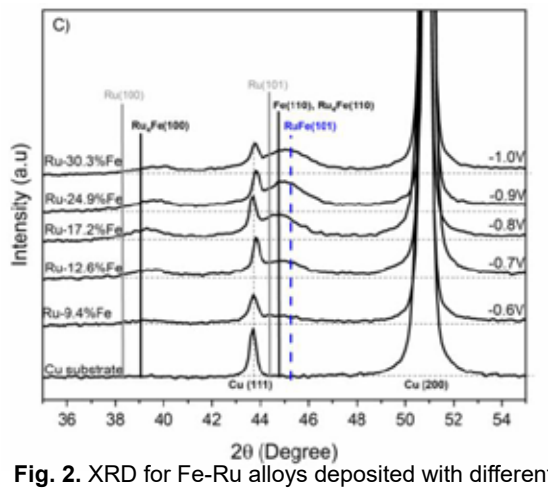

Fig. 2. XRD for Fe-Ru alloys deposited with different deposition potentials: from -0.6V to -1.0V vs SCE. Electrolyte composition: 1.0 M Fe^{2+} + 0.01 M Ru^{3+}.

The XRD patterns for Fe–Ru coatings prepared at different potentials can be explained based on the standard reference data provided by the ICDD database cards. The most prominent reflections at around 43° and 51° (2θ) belong to the copper substrate, in line with ICDD card 00-004-0836 (FCC Cu). These peaks remain unchanged in all samples, which can be taken as a convenient reference point for evolution of the diffractions obtained under different deposition potentials. At more positive deposition potentials (e.g., −0.6 V), the dominant peaks in the 36°–46° 2θ range correspond to ruthenium's HCP structure (ICDD card 00-006-0663), evident from Ru(100) and Ru(101) reflections. The relative intensity of these Ru peaks confirms that the as-deposited films are predominantly Ru-rich (according to XRF measurements). As the potential becomes more negative the alloy incorporates progressively more Fe, which manifests in the slight shift of the peaks or growth of additional reflections. Some samples begin to show weak signals that match ICDD card 00-006-0696 (BCC Fe), especially as the Fe content surpasses about 20 wt % at −0.9 V to −1.0 V. However, the formation of Fe-rich intermetallics is often more apparent than pure BCC Fe. Two HCP intermetallic compounds, RuFe (ICDD card 01-071-8378) and Ru_4Fe (ICDD card 00-040-1147), appear as new or more intense reflections around the same 2θ range occupied by Ru. Their presence indicates that the Fe does not merely substitute into the Ru lattice at random; instead, under certain alloying conditions, it can form ordered phases such as Ru_4Fe or RuFe. RuFe(101) becomes increasingly evident as the alloy shifts from predominantly Ru toward more balanced or even Fe-rich compositions. The morphology of obtained Fe-Ru alloys were also investigated by SEM observations, which are shown in Fig.3.

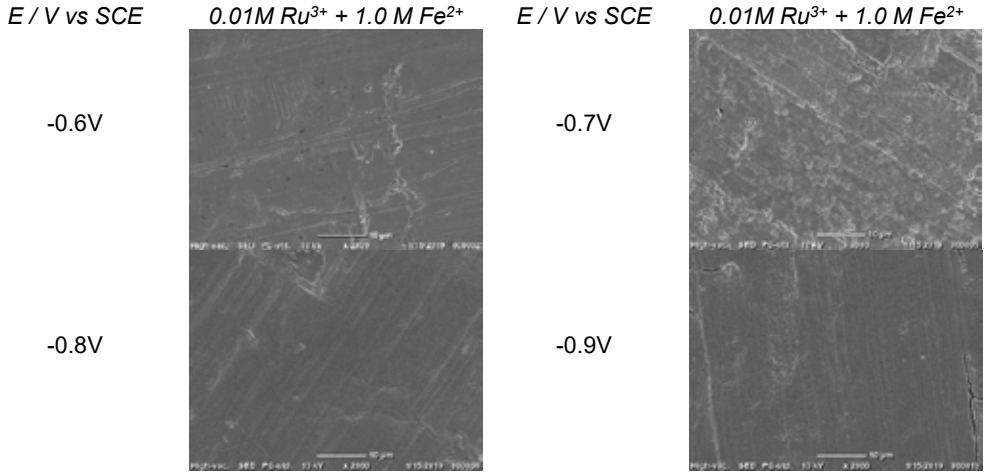

Fig. 3. Scanning Electron Microscopy images for Fe-Ru alloys deposited under different deposition potentials and electrolyte composition.

The SEM images reveal the morphological evolution of the alloys with application of different potentials. It should be noted that the irregularity of the grains is growing with the more negative potential, what can be attributed to significant hydrogen evolution reaction during the synthesis. Moreover, some cracks or voids can be seen for the potential -0.9V. In case of other samples, the surface is free of defects and the scratches from the substrate can be seen. From macroscopical point of view, the alloys are metallic-bright and very uniform, without any visible cracks, defects or discontinuity of the metallic coating. The catalytic activity of the Fe-Ru alloys were tested by two different approaches: by application of the constant current density (-10 mA cm^{-2}) for a time 600 s, to preliminary check of the potential value of hydrogen evolution reaction (Fig 4a) and application different values of the current density in a range between 0.1 and 200 mA cm^{-2}, which allows to determine the linear range of the Tafel slope. Obtained results shows that the alloy $Ru_{86}Fe_{14}$ exhibit the lowest overpotential for hydrogen evolution reaction among Fe-Ru alloys, and almost identical to pure Ru coating. It should be noted that the addition of the Fe into Ru is modifying the mechanism of HER in alkaline solutions, which can be seen as the increasing the value of Tafel slope as a function of the iron concentration in alloy.

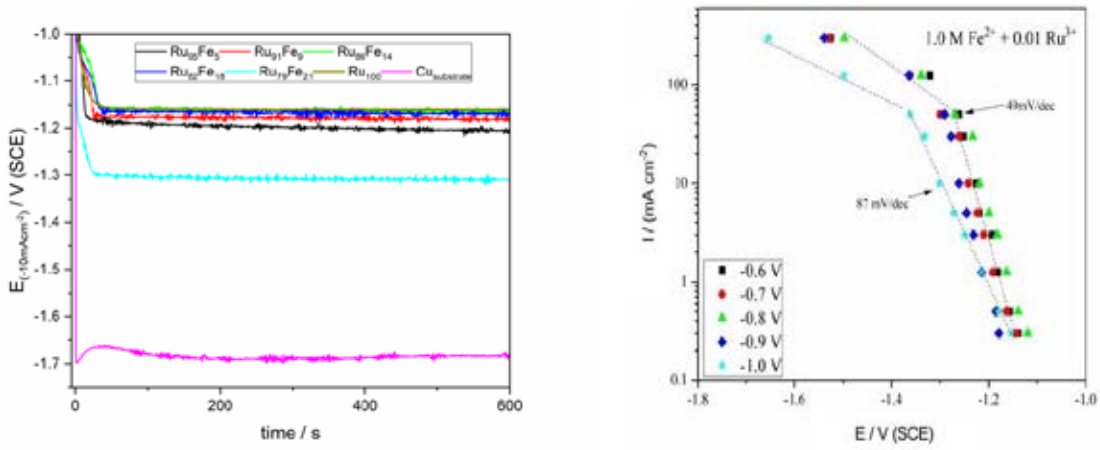

Fig. 6. a) Chronopotentiometric curves registered in 1 M NaOH after application of constant current density: -10 mAcm^{-2} for Fe-Ru alloys deposited with different deposition potentials: from -0.6V to -1.0V vs SCE with used electrolyte 1.0 M Fe^{2+} + 0.01 M Ru^{3+} and b) registered Tafel slopes.

4. CONCLUSIONS

The Fe-Ru binary alloys can be prepared in electrochemical way and successfully used as a cathode material for alkaline water splitting. The chemical composition can be tuned by modification of deposition parameters, and it significantly affect the crystalline structure of alloys. Incorporation of iron into hexagonal structure of Ru led to formation of mixture of Ru and Fe-Ru phases, visible as the shifted peaks on the XRD spectra. Morphology of alloys is uniform and free of voids and defects. Catalytic activity of alloys shows that the alloys with small addition of Fe into Ru (less than 20%) can be as active as pure Ru coatings. The incorporation of iron into alloy is modifying the HER mechanism, what was confirmed by Tafel slope measurements.

ACKNOWLEDGEMENT

This work was partially funded under the program “Excellence Initiative – research University” for the University of Krakow. Grant number: 8803.

REFERENCES

1. Jafari Fesharaki M, Nabiyouni GR, Dégi J, et al. 2012. Anomalous codeposition of cobalt and ruthenium from chloride–sulfate baths. Journal of Solid State Electrochemistry 16:715–722.
2. Mech K, Mech J, Zabinski P, Kowalik R, Wojnicki M. 2015. Electrochemical deposition of alloys in Ru^{3+}–Co^{2+}–Cl^{-}–H_2O system. Journal of Electroanalytical Chemistry 748:76–81.
3. Palowska R, Marzec MM, Sokołowski K, Yu Z, Liu L, Sulka GD, Brzózka A. 2024. Ni–Ru Electrodeposition from Ethaline Deep Eutectic Solvent: Material Preparation and Thermal Selenization. The Journal of Physical Chemistry C 128(39):16320–16333.
4. Kutyła D, Kołczyk-Siedlecka K, Kwiecińska A, et al. 2019. Preparation and characterization of electrodeposited Ni-Ru alloys: morphological and catalytic study. Journal of Solid State Electrochemistry 23:3089–3097.
5. Kutyła D, Krstajić Pajić MN, Lačnjevac UC, Marzec MM, Elezović NR, Żabiński P. 2024. Ru–Co alloy coatings electrodeposited on a MAX phase substrate as efficient catalysts for the hydrogen evolution reaction. International Journal of Hydrogen Energy 56:28–40.

DESIGNING A MULTIPLE PRODUCTION SYSTEM BASED ON CO_2 CAPTURE AND UTILIZATION IN GLASS INDUSTRY

[1*]Ibrahim Akgun and [2,1]Ibrahim Dincer
[1] Mechanical Engineering Department, Yildiz Technical University, Istanbul, 34349, Turkey
[2] Clean Energy Research Laboratory, Ontario Tech. University, Oshawa, Ontario, L1G 0C5, Canada
*Corresponding author e-mail: iakgun@yildiz.edu.tr

ABSTRACT
This research presents a pioneering, state-of-the-art multigeneration system that is specifically designed to tackle carbon dioxide emissions in glass production plants. This innovative system utilizes monoethanolamine absorption to extract carbon dioxide from glass production processes. The hydrogen gas used in the system is created through alkaline electrolysis and is supported by wind power. A portion of the hydrogen produced is used to react with carbon dioxide, producing methanol, while the remaining amount is stored in a storage tank. The system also produces valuable outputs such as electricity, district heating, and hot water. The design of the system incorporates other renewable resources, such as solar energy, to optimize its overall functionality. The system achieved a hydrogen production rate of 0.04491 kg/s and a methanol production rate of 0.1582 kg/s. Additionally, the system boasted an energy efficiency of 75.73% and an exergy efficiency of 36.59%, respectively.

Keywords: Glass industry, Hydrogen, Methanol, Exergy, Carbon Capture.

1. INTRODUCTION
Scientists and engineers work hard to come up with innovative and ground-breaking solutions to the urgent problems of climate change and rising global energy consumption [1]. Glass is used in everything from windows and dinnerware to the flat screens of smartphones. The expansion of infrastructure and the population are driving up demand. But glass is heated to incredibly high temperatures in furnaces. Its production results in 95 million tonnes of CO_2 annually worldwide and 22 million tons in Europe [2]. Sand and energy are requisite components in the production of glass. Historically, energy has been supplied through the combustion of natural gas with air to achieve temperatures sufficient for the transformation of sand into molten glass suitable for molding. However, this process is characterized by high energy consumption and significant pollutant emissions [3]. The predominant source of carbon emissions in glass production is the process of heating the melting furnace to temperatures exceeding 1,000 degrees Celsius, which constitutes an energy-intensive operation [4]. Therefore, carbon capture technology, such as monoethanolamine (MEA) absorption, can be implemented in glass production facilities to mitigate the increase in global CO_2 emissions. The utilization of concentrated CO_2 subsequent to carbon capture is directed towards the synthesis of novel materials and fuels. Through the process of hydrogenation, CO_2 from the atmosphere can be utilized to produce methanol, dimethyl ether, and formic acid. Upon combustion of these fuels, carbon dioxide is released into the atmosphere. This CO_2 can subsequently be absorbed and converted back into fuels, establishing a carbon-neutral cycle.
The primary objective of this research is to address the essential requirements of a modest residential community in Kırklareli, Turkey, by proposing an innovative multigeneration system that produces five beneficial outputs. In addition to providing district heating, hot water, and electricity, the system will also generate critical energy carriers, including hydrogen and methanol. The community's increased energy demands will be met using renewable resources, and the methanol will be synthesized using CO_2 captured from a glass production plant's monoethanolamine absorption technology to enhance sustainability. The study's evaluation encompasses comprehensive energy and exergy analyses, which assess the system's performance in its designated environment.

2. ANALYSIS
The proposed system is analysed thermodynamically to identify the mass flow rates, enthalpies, pressures, and temperatures of flows entering and exiting the system. The exergy destruction rate is determined to locate irreversible losses within each component of the system. The modelling is done using the EES software under specific assumptions, along with the balance equations written for mass, energy, entropy and exergy. The chemical reaction taking place in the methanol reactor is $CO_2 + 3H_2 \rightarrow CH_3OH + H_2O$.
The overall energetic and exergetic efficiencies of the system are defines as

$$\eta_{en,ovr} = \frac{\dot{W}_{net}+\dot{Q}_{HW}+\dot{Q}_{DH}+\dot{m}_{H2}LHV_{H2}+\dot{m}_{CH3OH}LHV_{CH3OH}}{\dot{m}_{flue}h_{flue}+W_{WT}+\dot{Q}_{Solar}} \text{ and } \eta_{ex,ovr} = \frac{\dot{W}_{net}+\dot{Q}_{HW}\left(1-\frac{T_0}{T_S}\right)+\dot{Q}_{DH}\left(1-\frac{T_0}{T_S}\right)+\dot{m}_{H2}ex_{H2}+\dot{m}_{CH3OH}ex_{CH3OH}}{\dot{m}_{flue}ex_{flue}+W_{WT}+\dot{E}x^{Q_{Solar}}}$$

where $\dot{W}_{net}$ is net power produced by the proposed system and is calculated as

$$\dot{W}_{net} = \dot{W}_{HPT} + \dot{W}_{LPT} + \dot{W}_{Exp} + \dot{W}_{GT} - \dot{W}_{Pump1} - \dot{W}_{Pump2} - \dot{W}_{Pump3} - \dot{W}_{Pump4}. - \dot{W}_{Comp1}. - \dot{W}_{Comp2}. - \dot{W}_{Comp3}. - \dot{W}_{BComp}$$

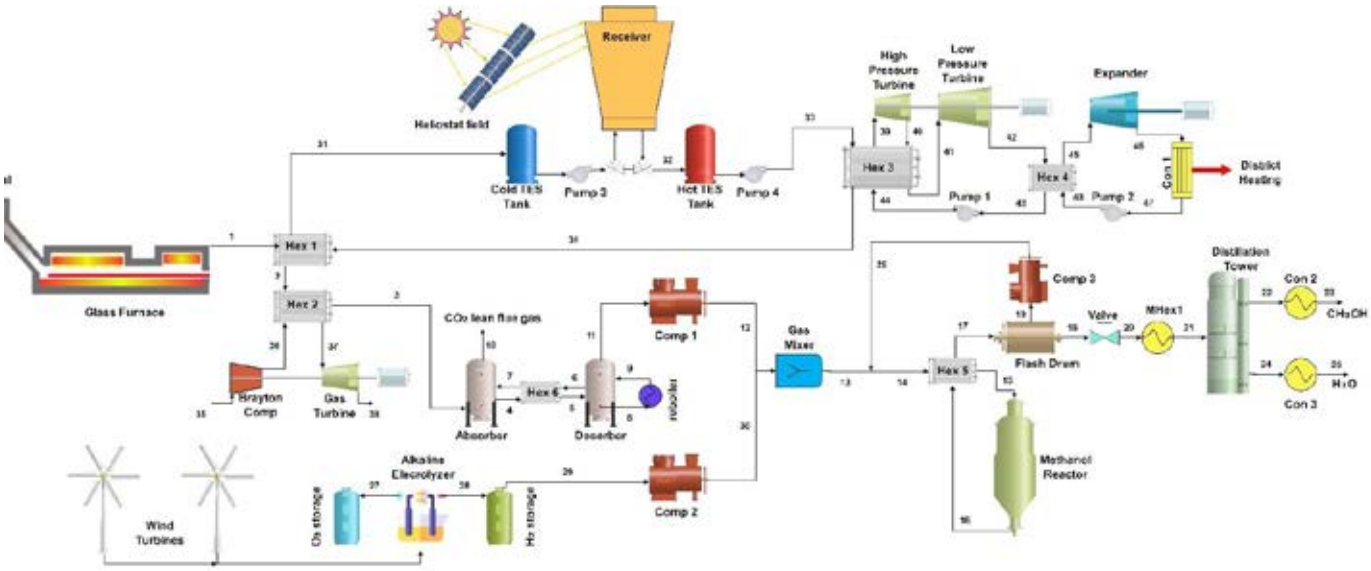

Fig. 1. Schematic view of the integrated system proposed for glass production plants.

3. RESULTS AND DISCUSSION

Consequently, the heat exchanger 3 (Hex 3) exhibits a significant exergy destruction of 1087.8 kW, while the solar thermal system (STS) demonstrates the highest exergy destruction at 1632.2 kW. The exergy destructions of the condenser 1 (Con 1), methanol reactor (Mreac), low-pressure turbine (LPT), and expander (Exp) subsystems are determined to be 738.6, 121.02, 120.72, and 11.34 kW, respectively. It is evident that the STS exhibits the highest exergy destruction, whereas the Exp demonstrates the lowest exergy destruction.

A parametric study was conducted to evaluate the performance of the integrated system, taking into account the first and second laws of thermodynamics. In the study, the change of methanol and hydrogen production rate depending on wind speed in the integrated system and the change of system performance depending on ambient temperature were investigated. Fig. 2 demonstrates that energy efficiency exhibits a slight increase as ambient temperature rises. Conversely, during heating, the overall exergetic efficiency exhibits a downward trend as the ambient temperature increases. This phenomenon is anticipated, considering that a heating system's efficacy diminishes in warmer months when a reduced heating load is required. As the temperature increases from 273 to 303 K, the energy efficiency improves from 75.28 to 75.82%, exergy efficiency increases from 36.59 to 36.56%.

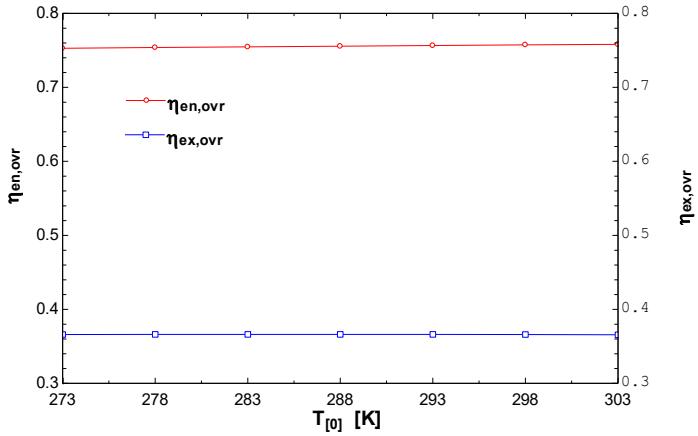

Fig 2. Variation of the ambient temperature with overall efficiencies.

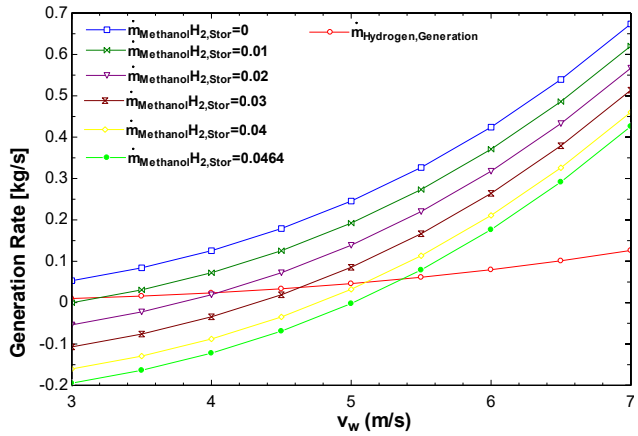

Fig 3. Exchange of supplied wind speed with CH_3OH and H_2.

Fig. 3 depicts the impact of varying wind speed input on methanol and hydrogen production. The wind speed for the selected target region varies between 3 and 7 m/s. The mean annual wind velocity is 5.87 m/s at an elevation of 100 meters. A portion of the produced hydrogen is utilized in methanol production, while the remaining portion is stored in the storage tank. In Fig. 3, parametric studies were conducted for various scenarios, including the utilization of all produced hydrogen in methanol production, as well as scenarios where 0.01, 0.02, 0.03, 0.04, and 0.0464 kg/s of hydrogen are stored in the storage tank, with the remaining portion used in methanol production. The results demonstrate that both the hydrogen production rate and the methanol production rate increase with increasing wind speed.

Furthermore, as the stored hydrogen production rate increases, the amount of hydrogen allocated to methanol production decreases, resulting in a corresponding decrease in the methanol production rate.

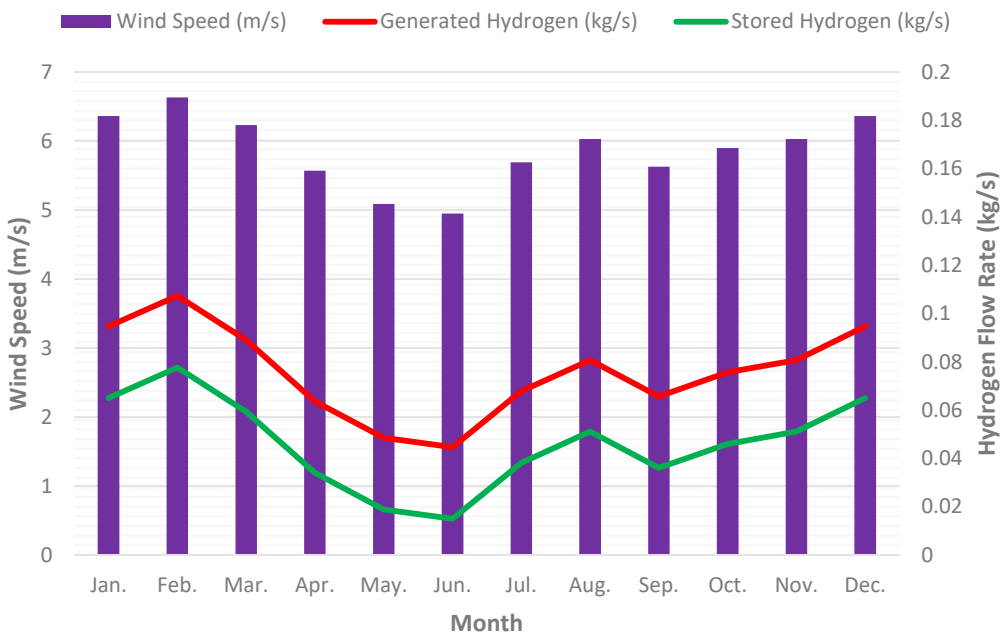

Fig. 4. Variation of wind speed and production rate of produced and stored hydrogen throughout the year.

Fig. 4 demonstrates that the maximum wind speed was observed in February, while the minimum occurred in June. Consequently, the highest rate of hydrogen production, corresponding to the wind speed, was 0.1073 kg/s in February, and the lowest rate was 0.044 kg/s in June. The quantity of hydrogen generated throughout the year is adequate for methanol production in the glass production facility, with excess hydrogen stored in storage tanks.

4. CONCLUSIONS

The primary outcomes derived from the integrated system proposed for glass production facilities are as follows. Firstly, the net power generated under the specified conditions, methanol flow rate, and hydrogen flow rate are calculated as 9541 kW, 0.1582 kg/s, and 0.045 kg/s, respectively. Additionally, the generated hot water flow rate and heating effect are calculated as 0.089 kg/s and 8898 kW. Secondly, the energy efficiency and exergy efficiency of the system are calculated as 75.73% and 36.59%, respectively. These results demonstrate the efficacy of the integrated system proposed for glass production facilities in terms of power generation and energy efficiency.

REFERENCES

[1] I. Dincer, A. Midilli, A. Hepbasli, and T. H. Karakoc, *Global Warming: Engineering Solutions*. Springer, 2009.
[2] I. and E. E. A. European Climate, “How LIFE is reducing emissions from glass production,” *European Commission*, 2022. https://cinea.ec.europa.eu/news-events/news/how-life-reducing-emissions-glass-production-2022-03-16_en (accessed Dec. 09, 2024).
[3] S. Colangelo, “Reducing the environmental footprint of glass manufacturing,” *Int. J. Appl. Glas. Sci.*, vol. 15, no. 4, pp. 350–366, 2024, doi: 10.1111/ijag.16674.
[4] M. Zier, P. Stenzel, L. Kotzur, and D. Stolten, “A review of decarbonization options for the glass industry,” *Energy Convers. Manag. X*, vol. 10, no. May, p. 100083, 2021, doi: 10.1016/j.ecmx.2021.100083.

INVESTIGATION OF CARBON FELT FABRIC AS A GAS DIFFUSION LAYER IN PEM FUEL CELLS: STABILITY AND COATING CAPABILITY

[1]Ayşegül Şirin, [1]Jülide Hazal Özdemir, [1*]Oğuz Kaan Özdemir, [2]Nurgül Alp, [2]Merve Alp, [2]Emel Akarsu
[1] Yıldız Technical University, Faculty of Chemistry and Metallurgy, Metallurgical and Materials Engineering, Çifte Havuzlar, 34220 Esenler/İstanbul, Turkiye
[2] Oba Perdesan Technical Textile, Hamzafakıhlı mah. OSB Yasar Tetiker Bulvarı No:15 Kdz.Eregli/Zonguldak, Turkiye

*Corresponding author e-mail: aysegul.sirin@std.yildiz.edu.tr

ABSTRACT
Water management in proton exchange membrane (PEM) fuel cells is crucial for the efficient operation of the system, and the materials used in gas diffusion layers (GDL) play a decisive role in this process. In this study, the use of carbon fabric as an alternative to traditionally preferred carbon paper in GDLs was evaluated. However, precipitation issues were encountered during the preparation of carbon-based coating solutions due to the instability of polytetrafluoroethylene (PTFE) in an alcohol medium. To address this issue, the non-ionic surfactant Tween 40 (TW40) was used at different concentrations (1.5%, 4.5%, 8%, and 16%), and the stability of these solutions was tested. The analysis results showed that the solutions containing 16% TW40 provided the highest stability.
Keywords: PEM Fuel Cells, Carbon Fabric Gas Diffusion Layer, Polytetrafluoroethylene (PTFE) Stabilization

1. INTRODUCTION

Proton exchange membrane (PEM) fuel cells have emerged as a strong alternative for automotive and stationary applications. Their ability to respond to rapid load changes with high power densities has increased interest in their use. However, water management is a critical factor for the efficient operation of the system. Insufficient water reduces ion conductivity in the membrane and catalyst layer (CL) while increasing membrane-CL contact resistance. On the other hand, excessive water accumulation in the membrane-electrode assembly (MEA) limits catalytic areas and hinders reactant transport. In this context, the selection and processing of materials used in gas diffusion layers (GDL) are of great importance[1].

Today, carbon paper is commonly used in GDLs. However, in this study, the use of carbon fabric as an alternative to carbon paper was investigated. The potential advantages of carbon fabric include higher mechanical durability, better gas distribution, and greater flexibility. Therefore, carbon facric is seen as having high potential for enhancing the performance of PEM fuel cells. To evaluate the feasibility of using carbon cloth as a GDL, the stability of carbon-based coating solutions was also examined.

2. MATERIALS AND METHODS

The coating solution was prepared according to the literature [2]. A total of 0.5 g of Vulcan XC-72 carbon was dispersed in 80 mL of isopropyl alcohol solution containing 120 mg of SDS and 30 wt% PEG by sonication for 30 minutes, followed by stirring for 60 minutes. A 34 wt% Teflon emulsion was added dropwise to the mixture and stirred for 15 minutes. However, precipitation occurred upon the addition of PTFE, preventing successful coating. The agglomerated solution is shown in Fig. 1a.

A carbon-free solution was prepared according to the formulation: a solution containing 34 wt% PTFE, 40 mL of isopropyl alcohol, 120 mg of SDS, and 30 wt% PEG was mixed in an ultrasonic bath for 30 minutes. Precipitation occurred in the solution (Fig. 1b). Experimental results indicated that this phenomenon was due to the dispersion conditions of PTFE and its interaction with surfactants.

Fig. 1. a) Aglomerer solutıon

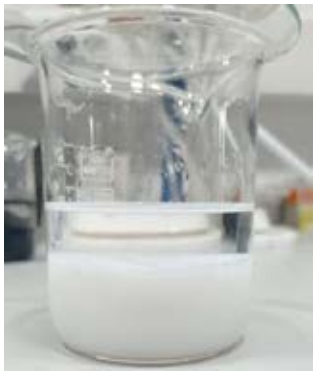

Fig. 1. b) Carbon -free solution

The cause of agglomeration was investigated, and the stability of PTFE in different solvents was examined. PTFE was dispersed in water and alcohol separately and left to stand. After one day, almost no agglomeration was observed in water, whereas in alcohol, PTFE agglomerated and precipitated within hours. It was determined that the PTFE dispersion was stabilized in water using a non-ionic surfactant. To better understand the precipitation issue observed in the alcohol medium and to analyze the composition of the dispersion, Thermogravimetric Analysis (TGA) was performed. This provided a more detailed understanding of the thermal behavior of the PTFE dispersion.

As a result, the type and amount of the non-ionic surfactant could not be precisely determined. Additionally, it was concluded that the precipitation issue arises from the instability of PTFE in alcohol and is related to the fact that the dispersion is stabilized in water.

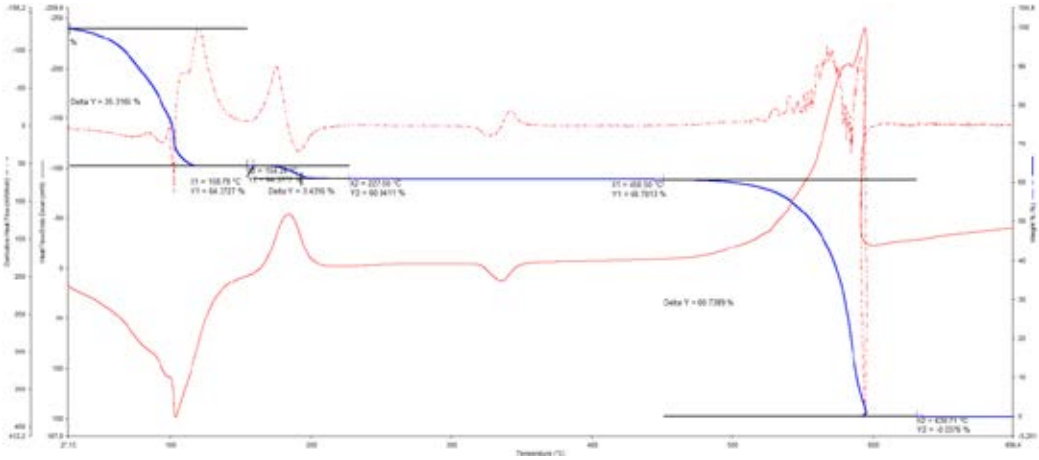

Fig. 2. PTFE's TGA and DTA analysis curve

The literature review on non-ionic surfactants examined their effects on the stabilization of PTFE dispersions and concluded that molecular structure and topology are key determining factors.[3] It was observed that the saturation level of the hydrophobic chain also influences stability, with TW80, which contains an unsaturated hydrophobic chain, providing better stabilization than TW60, which has a saturated hydrophobic chain. Additionally, surfactants with a lower critical micelle concentration (CMC) were found to enhance dispersion stability by forming a higher micelle density.
Based on these findings, Tween 40 was selected due to its suitable hydration balance and stabilization properties. Solutions containing 25 mL of water and 5 mL of PTFE were prepared with Tween 40 at volume ratios of 1.5%, 4.5%, 8%, and 16%. The mixtures were stirred on a magnetic stirrer for 40 minutes and then left to stand overnight. After the resting period, the most distinct phase separation was observed in the solution containing 4.5% TW40, while the most stable structure was exhibited by the solutions containing 8% TW40 and 16% TW40. The visual appearances of the solutions are presented in Fig. 3.

Fig. 3. a) 1,5% TW40

Fig. 3. b) 4,5% TW40

Fig. 3. c) 8% TW40

Fig. 3. d) 16% TW40

Ethanol (5 mL) was added to the solutions, stirred on a magnetic stirrer for 30 minutes, and then left to stand for 1 hour. Observations revealed that no agglomeration occurred in the solutions. This process was repeated twice, with no changes observed in the results. The solutions, with a total of 15 mL of ethanol added, were left to stand overnight, but no morphological changes or phase separation were detected. Subsequently, an additional 10 mL of ethanol was introduced, stirred for 20 minutes on a magnetic stirrer, and allowed to stand for 2 hours. At this stage, no changes were observed in the solutions.

Next, 50 mg of Vulcan XC-72 activated carbon was added to the solutions, which were then subjected to ultrasonic bath mixing for 1 hour. Upon removal from the ultrasonic bath, precipitation was observed in the solution containing 1.5% TW40. The solutions were left to stand overnight, and no phase separation was detected in those containing 4.5% and 8% TW40. The conditions of the carbon-added solutions are presented in Fig. 4.

Fig. 4. a) 1,5% TW40

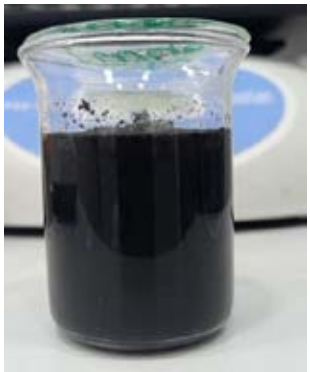

Fig. 4. b) 4,5% TW40

Fig. 4. c) 8% TW40

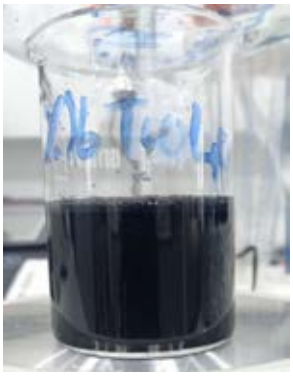

Fig. 4. d) 16% TW40

The coating was also applied to the carbon fabric by spraying and left to dry overnight in an oven at 105°C. The dried fabrics were then sintered at 350°C for 30 minutes. After sintering, the fabrics exhibited hydrophobic behavior, repelling water from their surface. The water interaction behavior of the fabrics is shown in Fig. 5.

Fig. 5. a) 4,5% TW40

Fig. 5. b) 8% TW40

Fig. 5. c) 34% PTFE 16% TW40

34 wt% PTFE, 16 wt% TW40, and 25 mL of distilled water were mixed on a magnetic stirrer for 15 minutes. Ethanol (a total of 25 mL) was then added gradually over 30 minutes while stirring. Subsequently, 50 mg of carbon was slowly introduced and mixed in an ultrasonic bath for 1 hour. A 2 mL coating was applied to the carbon fabric, which was then sintered at 350°C for 30 minutes, resulting in a coating mass of 124.35 mg. This confirmed that a stable solution was achieved. However, the dip-coating method did not yield the desired results, as a homogeneous and sufficient coating amount was not obtained.

CONCLUSION

In this study, the feasibility of using carbon fabric as a gas diffusion layer (GDL) in PEM fuel cells was investigated. It was determined that carbon fabric provides superior mechanical strength, gas distribution, and flexibility compared to carbon paper. However, to be used as a GDL, carbon fabric must be rendered hydrophobic. To achieve this, carbon-based coating solutions were prepared, and their stability was examined.

Due to the instability of PTFE in an alcohol medium, precipitation issues were encountered. To address this, TW40 was employed. The stability of solutions containing different TW40 concentrations was assessed, and solutions with 8% and 16% TW40 exhibited the highest stability. These solutions were used to coat carbon fabric, which was subsequently sintered at 350°C. The sintered fabrics demonstrated hydrophobic properties, repelling water from their surface.

In conclusion, the use of carbon fabric as a GDL is feasible, and TW40 has proven effective in stabilizing PTFE dispersion. This study offers a new perspective on the development and commercialization of PEM fuel cells. However, further research is needed to enhance the application of carbon fabric as a GDL. In particular, exploring different coating techniques and materials may further improve the performance of carbon fabric in fuel cell applications.

ACKNOWLEDGEMENT
This research study is supported with Project number 7230819 by 1507 TUBITAK SME R&D Start-up Support Program's 1507-2023-2 calls.

REFERENCES

[1] H. Guo et al., "Gas Diffusion Layer for Proton Exchange Membrane Fuel Cells: A Review," Dec. 01, 2022, MDPI. doi: 10.3390/ma15248800.
[2] G. Athanasaki, N. Chauhan, R. Ahmad, and A. M. Kannan, "Accelerated stress testing of PUREBLACK® carbon-based gas diffusion layers with pore forming agent for proton exchange membrane fuel cells," Int J Hydrogen Energy, vol. 46, no. 62, pp. 31754–31763, Sep. 2021, doi: 10.1016/j.ijhydene.2021.07.052.
[3] G. Zhang, Y. Chen, X. Sui, M. Kang, Y. Feng, and H. Yin, "Nonionic surfactant stabilized polytetrafluoroethylene dispersion: Effect of molecular structure and topology," J Mol Liq, vol. 345, Jan. 2022, doi: 10.1016/j.molliq.2021.116988.

INVESTIGATION OF FUEL CELL PERFORMANCES BY RECYCLING USED MEMBRANES

[1*]*Barış Aktaş*, [1]*Oğuz Kaan Özdemir*, [1]*Jülide Hazal Özdemir*
[1] Yıldız Technical University, Faculty of Chemistry and Metallurgy, Metallurgical and Materials Engineering, Çifte Havuzlar, 34220 Esenler/İstanbul, Turkiye

*Corresponding author e-mail: baris.aktas@std.yildiz.edu.tr

ABSTRACT
This study aims to recover and characterize Nafion membrane from used MEAs in PEMFCs through ethanol-based Soxhlet extraction. Recycling Nafion membranes is an economic necessity given their high cost and valuable structure. The recycling potential of ethanol as an environmentally friendly solvent has been evaluated, and the chemical and thermal structure of the recovered material has been examined using ATR-FTIR, UV-Vis spectroscopy, and Thermal Analysis methods. The results reveal that the recycled Nafion exhibits chemical and thermal properties similar to commercial Nafion and may have the potential for reuse in fuel cells. The ethanol-based recycling method presents an economically viable and environmentally friendly alternative for Nafion membranes.

Keywords: Proton exchange membrane, Nafion, Recycling, Soxhlet extraction

1. INTRODUCTION

Fuel cells hold strategic importance among clean energy technologies. Nafion is a fluorinated polymer that plays a central role as a proton exchange membrane (PEM), providing proton conductivity in hydrogen fuel cells [1]. Its chemical structure consists of a combination of a hydrophobic perfluorinated polymer backbone and side chains containing hydrophilic sulfonic acid groups. While Nafion membranes, a critical component of Proton Exchange Membrane Fuel Cells (PEMFCs), offer high performance, their production costs and used membrane waste pose significant problems in terms of economic and environmental sustainability. The high cost of new Nafion membranes makes recycling more economically attractive, while the waste of Nafion, a valuable material, is unacceptable in terms of resource efficiency. In this context, the recovery of used Nafion membranes has the potential to prevent both economic losses and reduce environmental impact. In the literature, it has been shown that Nafion membranes can be recycled by solvent-based methods [2]. In this study, the recovery and characterization of Nafion membranes using ethanol, an environmentally friendly solvent, were experimentally investigated. The aim is to evaluate the economic and environmental suitability of ethanol for Nafion recycling and the reuse potential of the recovered material.

2. MATERIALS AND METHODS

2.1. Materials

Used PEMFC MEA (Fig. 1.), commercial Nafion membrane reference, analytical grade ethanol, cellulose extraction cartridge were used. The extraction process was carried out with a Soxhlet apparatus (Fig. 2.), and a rotary evaporator and centrifuge were used for the separation process. Characterization analyses were performed by ATR-FTIR, UV-Vis spectroscopy, and Thermal Analysis.

Fig. 1. Used Membrane Electrode Assemblies (MEA)

Fig. 2. Soxhlet extractor

Fig. 3. Weighed membranes for efficiency calculation

2.2. Experimental Procedure

Soxhlet extraction method was used to recover the Nafion membrane from the used MEA sample. A weighed MEA sample of 3.6375 grams (Fig. 3.), was placed in a cellulose extraction cartridge and transferred to the Soxhlet apparatus.

270 ml of ethanol was added to the collection flask, and extraction was performed for 14 days. The obtained Nafion-ethanol solution was concentrated with a rotary evaporator and then catalyst separation was performed by centrifugation. The chemical structure of the recovered Nafion sample was analyzed by ATR-FTIR and UV-Vis spectroscopy, and its thermal stability was analyzed by TGA and DSC compared with commercial Nafion reference. In addition, the hydrophobicity of the recovered Nafion solution was evaluated by coating it on a glass slide using an airbrush method.

3. RESULTS AND DISCUSSION

ATR-FTIR spectra (Fig. 4.) (Fig. 5.) revealed that the recycled Nafion sample showed a high degree of similarity to commercial Nafion (Table 1.). The peaks at 1433 cm^{-1}, 1203 cm^{-1}, 1142 cm^{-1}, 1058 cm^{-1}, and 980 cm^{-1} were observed at similar positions and intensities in both samples [3]. This supports that the ethanol-based recycling method provides recovery while preserving the Nafion polymer structure. The Nafion sample coated with airbrush gave the closest results to the commercial reference. Hydrophobicity tests (Fig. 6.) showed that the surface properties of the recovered material were similar to Nafion [4]. Studies with Thermogravimetric Analysis (TGA) and Differential Scanning Calorimetry (DSC) showed that the thermal behavior of the recycled Nafion sample (Fig. 7.) significantly matched the Nafion TGA and DSC graphs in the literature [5]. This compatibility supports that the sample can be reused as a proton conductive membrane material. A Nafion solution dissolved in ethanol was analyzed using UV-Vis spectroscopy, with baseline measurements taken using ethanol as the reference. In the obtained spectrum (Fig. 8.), characteristic peaks corresponding to the recycled Nafion were observed, and these peaks were found to be consistent with the UV-Vis spectra reported in the literature. [6]

Table 1. Comparison of FTIR peak values

Peak Position (cm^{-1})	Nafion	Recycled Nafion	Functional Group
~ 3400-3200	-	3390	O-H Stretching (Ethanol/Water)
~1650 -1630	-	1651	H-O-H Bending (Adsorbed Water)
~ 1430-1440	1438	1433	S=O, SOH group
~ 1200 -1215	1198	1203	Symmetric CF_2 Stretching
~ 1130-1150	1136	1142	Asymmetric CF_2 Stretching
~ 1050 -1060	1058	1058	S-O Stretching (SO_3^- Group)
~ 980	980	980	C-O-C Stretching

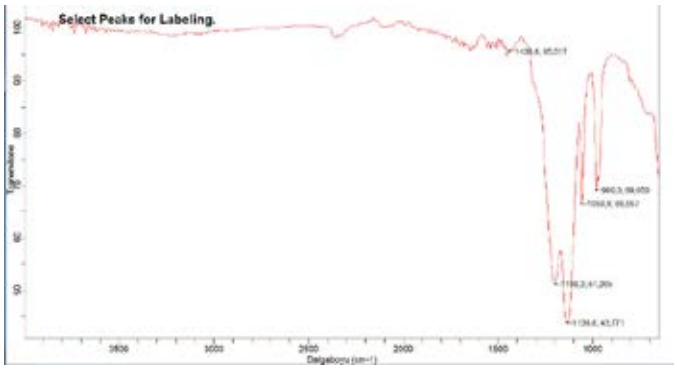

Fig. 4. Nafion ® FTIR peaks

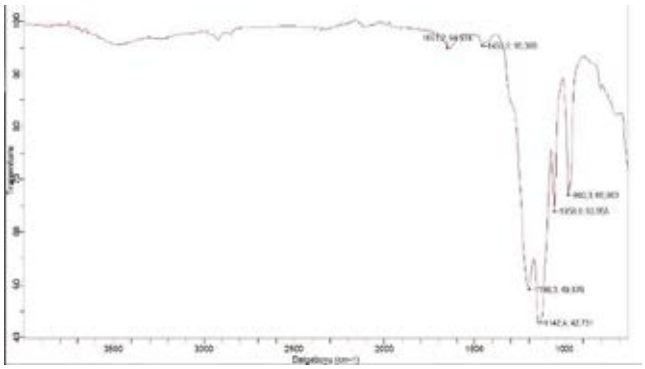

Fig. 5. Recycled nafion FTIR peaks

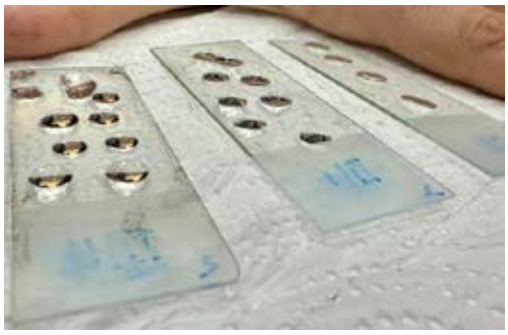

Fig. 6. On the left with 5 ml of Nafion solution, in the middle with 2.5 ml of solution, on the right with an uncoated glass coverslip, greater hydrophobicity is observed on Nafion-coated surfaces

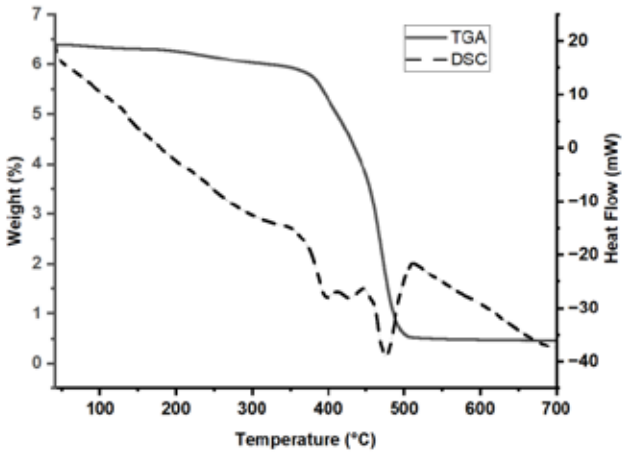

Fig. 7. TGA and DSC Curves of recycled nafion membranes

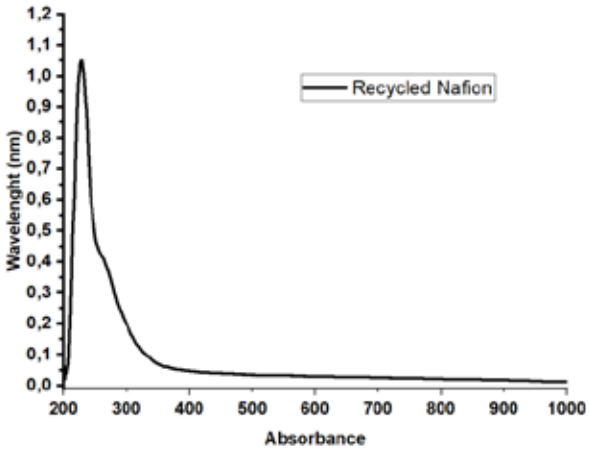

Fig. 8. UV-Vis Spectrum Graphs of Recycled Nafion membranes

4. CONCLUSIONS

This study has shown that the ethanol-based Soxhlet extraction method can be an effective alternative for the economic and environmentally friendly recovery of Nafion membrane from used PEMFC MEAs. The recovered Nafion exhibits similar chemical and thermal properties to commercial Nafion and has the potential for reuse in fuel cells. The use of ethanol as a solvent provides a safer and more environmentally sensitive recycling process, while the recovery of a valuable polymer such as Nafion provides significant advantages in terms of economic and resource efficiency. In future studies, the reuse potential of recycled Nafion membranes should be evaluated more comprehensively with detailed characterization analyses such as proton conductivity, mechanical properties, and fuel cell performance tests.

REFERENCES

1. Zhu LY, Li YC, Liu J, He J, Wang LY, Lei J. 2022. Recent developments in high-performance Nafion membranes for hydrogen fuel cells applications. In Petroleum Science, Vol. 19, Issue 3, pp. 1371–1381. China University of Petroleum Beijing. https://doi.org/10.1016/j.petsci.2021.11.004
2. Alipour Moghaddam J, Parnian MJ, Rowshanzamir S. 2018. Preparation, characterization, and electrochemical properties investigation of recycled proton exchange membrane for fuel cell applications. Energy, 161:699–709. https://doi.org/10.1016/j.energy.2018.07.123
3. Agarwal T, Prasad AK, Advani SG, Babu SK, Borup RL. 2024. Infrared spectroscopy for understanding the structure of Nafion and its associated properties. In Journal of Materials Chemistry A, Vol. 12, Issue 24, pp. 14229–14244. Royal Society of Chemistry. https://doi.org/10.1039/d3ta05653h
4. Barique MA, Tsuchida E, Ohira A, Tashiro K. 2017. Effect of Elevated Temperatures on the States of Water and Their Correlation with the Proton Conductivity of Nafion. ACS Omega, 3(1):349–360. https://doi.org/10.1021/acsomega.7b01765
5. Mayadevi TS, Goo BH, Paek SY, Choi O, Kim Y, Kwon OJ, Lee SY, Kim HJ, Kim TH. 2022. Nafion Composite Membranes Impregnated with Polydopamine and Poly(Sulfonated Dopamine) for High-Performance Proton Exchange Membranes. ACS Omega, 7(15):12956-12970. https://doi.org/10.1021/acsomega.2c00263
6. 1. Helena S, Almeida' DE, and Kawan02 Y. 1997. Ultraviolet-visible spectra of Nafion membrane. *European Polymer Journal* 33(8).

ELECTROOXIDATION OF METHANOL AND SODIUM BOROHYDRIDE ON NANO-SILVER ELECTRODE FOR ALKALINE FUEL CELLS

*Aylin Aytaç and F. Özge Gökmen
[1] Gazi University, Faculty, Science Faculty, Department of Chemistry, Yenimahalle, Ankara, 06500, Turkiye

*Corresponding author e-mail: aytaca@gazi.edu.tr; aylin.aytac@gmail.com

ABSTRACT
In this study, a silver-deposited carbon fiber electrode (Ag/AC) prepared by the electroless deposition method was investigated for its redox processes and electrocatalytic activities during the oxidation of methanol and sodium borohydride in alkaline solutions. The Ag/AC catalyst was characterized by X-ray diffraction (XRD), energy dispersive X-ray analysis (EDAX), scanning transmission electron microscopy (SEM and TEM), and electrochemical voltammetry. The electrocatalytic performance of the Ag/AC catalyst for the oxidation of methanol and sodium borohydride was evaluated by cyclic voltammetry. The anodic peak current density for sodium borohydride oxidation on the Ag/AC catalyst was found to be three times higher than that for methanol. The peak current density of methanol oxidation decreased with increasing methanol concentration, but the current density of sodium borohydride increased with increasing borohydride concentration. The maximum current density was reached at 10 M sodium borohydride concentration and remained stable. Sodium borohydride oxidation shows the highest activity on Ag/AC electrode in alkaline medium.

Keywords: Methanol and sodium borohydride, silver, alkaline fuel cells

1. INTRODUCTION
Recently, there has been renewed interest in alkaline fuel cells due to the use of non-noble metal catalysts and the potential for low-cost mass production, in contrast to other types of fuel cells [1,2]. In an alkaline fuel cell, the chemical energy of fuels (such as hydrogen, hydrazine, or alcohols) and oxidants (such as oxygen) can be converted directly and efficiently into electricity. This flexibility in fuel choice makes alkaline fuel cells a promising power source for a variety of portable electronic devices [3,4]. A key advantage of alkaline fuel cells is the replacement of platinum or platinum-based electrocatalysts with non-platinum alternatives, positioning alkaline fuel cells as a potentially more affordable technology compared to PEMFCs and DMFCs. It is widely accepted that the oxygen reduction reaction (ORR) is more straightforward in alkaline environments than in acidic conditions, supporting the viability of using less expensive catalysts instead of platinum. Among these non-platinum catalysts, silver nanoparticles stand out as a promising substitute for platinum due to their high catalytic activity for ORR in alkaline media. Silver is known to have the highest electrical conductivity of any element and is about 100 times more affordable than platinum [1]. Various methods, including electroless plating [5,6], chemical reduction [3-9], electrochemical deposition [10], and ion beam assisted deposition [11], have been developed to fabricate silver nanostructures. However, only a few studies have focused on the facile synthesis of silver nanoparticles on carbon substrates, and a more comprehensive understanding of their electrochemical performance in alkaline electrolytes is still needed. The objective of this study is to compare the electrochemical oxidation of methanol and sodium borohydride over Ag/AC catalyst in alkaline solution.

2. MATERIALS AND METHODS
2.1. Synthesis of Vucan XC-72 supported nano-Ag catalyst (Ag/AC)
The potassium hydroxide, methanol and sodium borohydride that are used in this work were analytical grade of Merck origin and were used without further purification. Vulcan XC-72 carbon (S_{BET} = 230 m^2 g^{-1}). was procured from Cabot Corp. All other reagents used were of analytical grade. For the classical preparation method, 1.573 g $AgNO_3$ (MW: 169,88 $g.mol^{-1}$,99.9% purity, Alfa Aesar) were dissolved in 100 mL of ethylene glycol (puriss. p.a.,≥99.5% Fluka). Then, pH of the solution was adjusted to 11 by adding dropwise solution of 1M NaOH in ethylene glycol. Carbon Vulcan XC-72 was thermally treated for 4 h at 600 ^oC under nitrogen and then it was added to the solution (1000 mg) and the mixture was ultrasonically homogenized for 5min and heated until 120 ^oC, then 4 mmol $NaBH_4$ was slowly added to the mixture. The mixture was mixed mechanically for 16h and then suddenly cooled until room temperature. After preparation, catalytic powders were washed with acetone, abundantly rinsed with ultra pure water, and centrifuged with 5000 rpm and then they were dried in a vacuum oven at room temperature.
2.2. Preparation of the working electrode
The catalyst inks were first homogenized within 1-2 hours using a homogenizer. Then the sample of 20µL catalyst ink (16gAg/cm2) was deposited on the glassy carbon surface to ensure the smooth thin film catalyst coating. To fix the catalyst on the glassy carbon surface, 20 µL of diluted 0.01 wt% Nafion solution was deposited on the surface of the catalyst layer.
2.3. Electrochemical measurements
The cyclic voltammetry experiments were conducted in a conventional three-electrode system, with a saturated calomel electrode (SCE) in a Luggin capillary compartment and platinum wire as the reference electrode and the counter

electrode, respectively. The working electrode was prepared by coating the catalyst ink on disk-type graphite, surface area of 1 cm^2. All the potential in this manuscript was relative to that of the SCE reference electrode. All electrochemical experiments were carried out using a CHI 660C potentiostat at room temperature (24±3 °C). Nitrogen was bubbled for 5 min in 30 ml solution before the measurements. The cell was cycled between −1.2 and 1.1V at a 100 mV/s sweep rate.

2.4. Catalyst surface characterization

X-ray diffraction (XRD) analysis was carried out with the use of a Theta–Theta Scintag powder diffractometer equipped with aCuK α source (λ = 1.5406 °A). High-resolution scanning electron microscope (SEM) micrographs of the catalyst powders were recorded with a JEOL JSM 6700F. Catalyst compositions were determined by energy dispersive X-ray spectroscopy (EDS) elemental analysis by means of an X-ray LINK detector with a Pentafet window coupled to a scanning electron microscope (JEOL JSM-6300). Unless otherwise specified, all catalyst compositions presented in the text were those resolved by EDS analysis were performed with a Philips UHV-5600 apparatus with an Al K α emission source.

3. RESULTS AND DISCUSSION

3.1. SEM, EDX and XRD Characterizations of Ag/AC

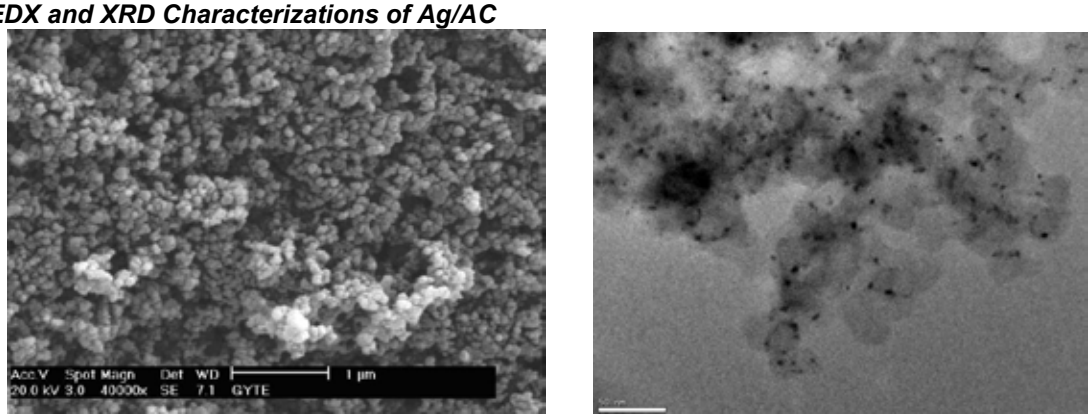

Fig.1. (a) SEM (b) TEM images of Ag/AC

The micrographs presented in Fig. 1 (a) and (b) display the morphology of the electrodeposited Ag obtained by SEM and TEM. It is observed from the Fig 1(b) that the carbon surface was deposited by Ag particles which are highly dispersed, have high multiplicity and they are regular in shape. In Fig. 2a displays the EDX analysis that has confirmed the presence of Ag with intensity. The appearance of the carbon peak was a result of the activated carbon on which Ag nanoparticles were deposited. The gold peak at around 2 keV results from the grid used for the analysis. The EDX analysis has shown strong evidence of homogeneously dispersed Ag nanocrystals at the optimum condition.

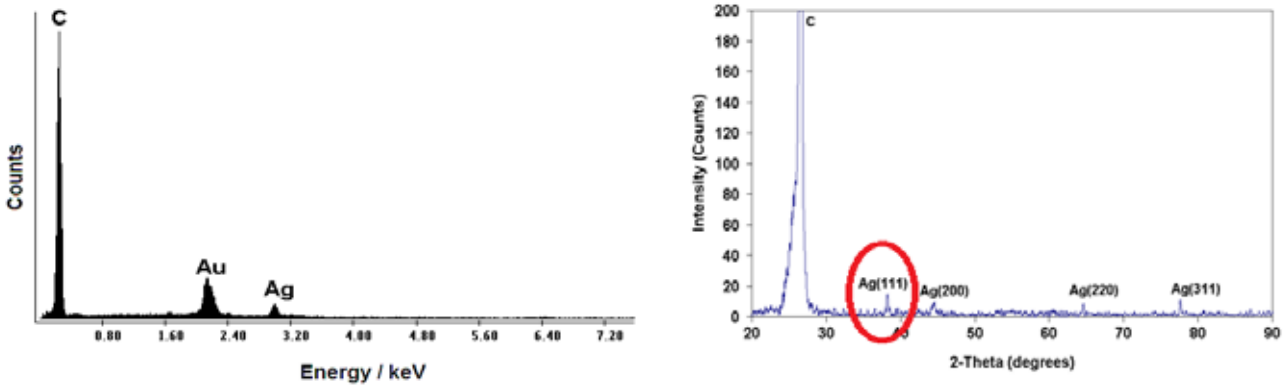

(a) (b)

Fig. 2. (a) The EDX analysis (b) The XRD pattern of Ni/CF catalyst at the optimum condition

X-ray diffraction patterns of the anode catalysts employed in this study were shown in Fig. 2b. fcc Ag have distinctive diffractions and hence can be differentiated. The major diffraction peaks of Ag nanoparticles were observed. The VulcanXC-72 show a typical peak of (002) reflection of graphiteat 26.34° . The peaks at 38.18°, 44.52°, 63.08° and 77.58° can be assigned to (111), (200), (220), (311) reflection of fcc phase of Ag. The average particle size of the catalyst was calculated from XRD diffraction peaks using Scherer's equation [46]. Ag particle sizes are calculated according to the diffraction peak of Ag (111) that was found to be in the range of 3.2 nm.

3.2. Electrochemical measurements of VulcanXC supported Ag electrode in 2M KOH

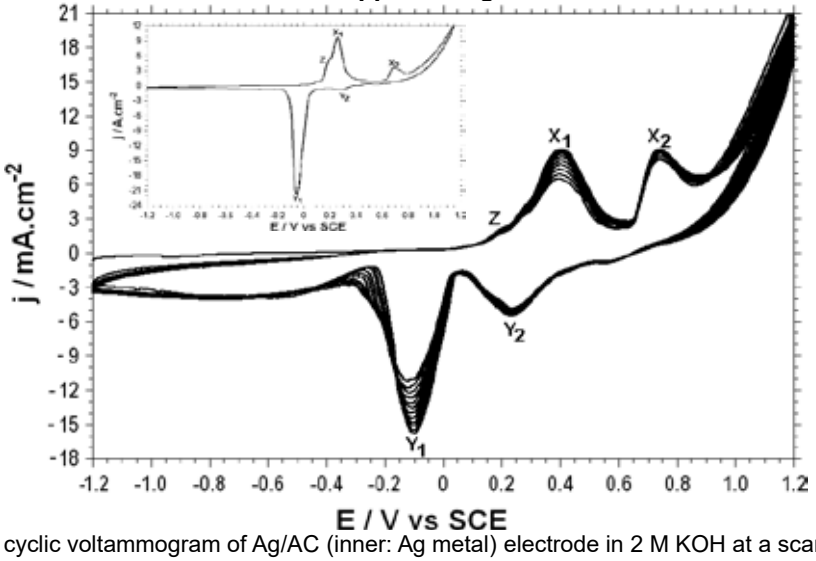

Fig 3. Consecutive cyclic voltammogram of Ag/AC (inner: Ag metal) electrode in 2 M KOH at a scan rate of 100 mVs^{-1}

The overall oxidation process involves a successive formation of Ag_2O and AgO according to the reactions:

$$2Ag + 2OH^- \leftrightarrow Ag_2O + H_2O + 2e^- \quad (1)$$

$$Ag_2O + 2OH^- \leftrightarrow 2AgO + H_2O + 2e^- \quad (2)$$

A competing process to Ag_2O formation is a Ag dissolution according to the reaction

$$Ag + 2OH^- \rightarrow [Ag(OH)_2]^- + e^- \quad (3)$$

The characteristic anodic/cathodic peaks X_1/Y_1 and X_2/Y_2 correspond to the formation/reduction of the Ag_2O and AgO phases. The observed increase of current peaks of the cyclic voltammogram for the latter cycle is caused by the increase of the surface roughness during the first oxidation–reduction cycle. In this case at the potential of prepeak Z several monolayers of Ag(I) hydroxide are formed, and above them a thicker and more porous layer of Ag_2O grows. In inner figure, in the first cycle a pair of redox peaks appearing at 0.4 and -0.11 mV/SCE was assigned to Ag/Ag^+ redox couple and a pair of redox peaks appearing at 0.74 and 0.23 mV/SCE was also assigned Ag^+/Ag^{2+} redox couple, respectively, in alkaline media recorded at a potential sweep rate of 100mVs^{-1}.

3.3. Electrocatalytic Oxidation of Methanol and Sodium Borohydride on VulcanXC supported Ag electrode

Effect of methanol and sodium borohydride concentrations on CVs of Ag/AC with the potential sweep rate of 100 mV/s was investigated and results are presented in Fig. 5 and 6. Methanol concentrations were changed from 1mmol to 10 mmol. It is shown in this figure that the methanol oxidation peak current density decreased with increasing methanol concentration. Thus, the adsorption of the oxidation products at the electrode surface causes the hindrance of further oxidation. Either anodic or cathodic currents decreased with the methanol concentrations between -1.2 to 1.2V vs SCE.

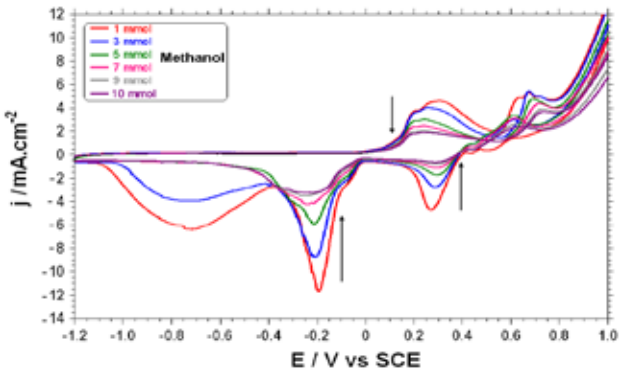

Fig.5. Cyclic voltammogram of methanol oxidation on Ag/AC catalyst in 2M KOH (at 100mVs^{-1} , 298 K)

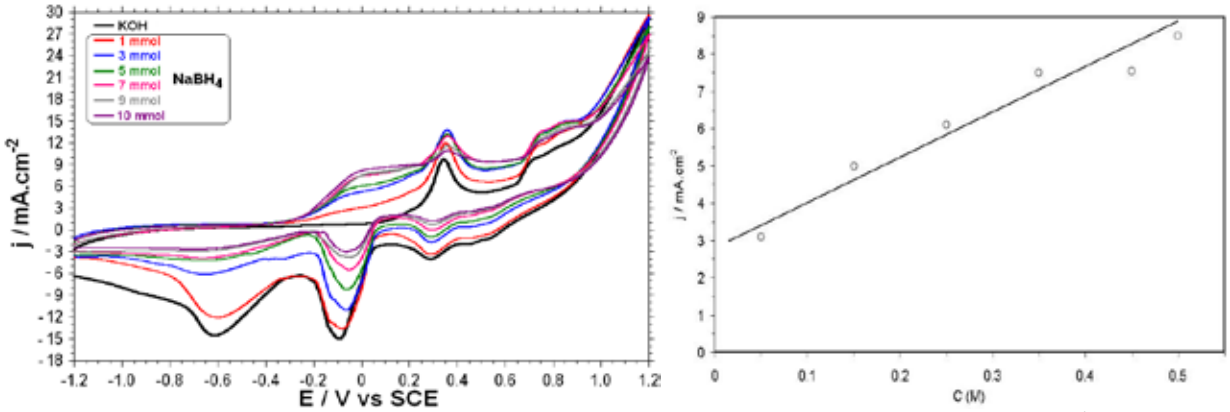

Fig.6. **(a)** Cyclic voltammogram of borohydride oxidation on Ag/AC catalyst in 2M KOH at 100mVs^{-1}, 298 K.
(b) Dependency of the anodic peak current of $NaBH_4$ concentrations

But as seen in Fig.6 the anodic current at 0.4 V in the positive sweep was proportional to the amounts of $NaBH_4$ and any increase in the amounts of $NaBH_4$ caused an almost proportional linear enhancement of the anodic current (inner line). So, electrooxidation of $NaBH_4$ on Ag/AC seems to be certain.

4. CONCLUSIONS

The oxidation reactions for sodium borohydride and methanol are given below

Borohydride $BH_4^- + 8OH^- \rightarrow BO_2^- + 6H_2O + 8e^-$

Methanol $CH_3OH + 2OH^- \rightarrow HCHO + 2H_2O + 2e^-$

$HCHO + 2OH^- \rightarrow HCOOH + H_2O + 2e^-$

$HCOOH + 2OH^- \rightarrow CO_2 + 2H_2O + 2e^-$

The current density of methanol decreased with increasing concentration to 1M and 10M. This result can be attributed to formation of the carbonate at the surface of catalyst [12-13].
The current density of sodium borohydride increased with increasing of borohydride concentrations. Maximum current density was achieved at 10M of the sodium borohydride concentration and remained stable.
The sodium borohydride oxidation shows the highest activity on Ag/AC electrode in alkaline medium.

REFERENCES

1. Ramli, ZAC, Pasupuleti, J. Zaiman, NFHN, Saharuddin, TST, Samidin, S, Isahak, WNRW, Sofiah, AGN, Kamarudin, SK, Tiong, SK., 2025.Evaluating electrocatalytic activities of Pt, Pd, Au and Ag-based catalyst on PEMFC performance: A review. International Journal of Hydrogen Energy 104:463-486.
2. Antolini E., Gonzalez E.R. 2010. Alkaline direct alcohol fuel cells. J. Power Sources 195:3431–3450.
3. Linge, JM, Erikson, H, Mooste, M, Piirsoo, H M, Kaljuvee, T, Kikas, A , Aruvali, J , Kisand, V , Tamm, A, Kannan, AM ,Tammeveski, K. 2024. Ag nanoparticles on mesoporous carbon support as cathode catalyst for anion exchange membrane fuel cell. International Journal of Hydrogen Energy 48: 11058-11070.
4. Park, JS , Seo, BG , Koo, J , Lim, JH , Lee, YS , Han, GD , Shim, JH., 2023. High-Performance Hydroxide Exchange Membrane Fuel Cell Comprising an Atomic Layer-Deposited Silver Cathode. Nano Letters 23: 7825-7830.
5. Chien-Te Hsieh, Ching Pan, Wei-Yu Chen, 2011. Synthesis of silver nanoparticles on carbon papers for electrochemical catalysts. Journal of Power Sources 196:6055-6051.
6. Kostowskyj M.A., Kirk D.W., Thorpe S.J., 2010. Ag and Ag–Mn nanowire catalysts for alkaline fuel cells. International Journal of Hydrogen Energy 35:5666–5672.
7. Figueiredo J. L., R. Pereira M. F., 2009. The role of surface chemistry in catalysis with carbons. Catalysis Today 150:2-7.
8. Spendelow J. S. and Wieckowski A.,2007. Electrocatalysis of oxygen reduction and small alcohol oxidation in alkaline media. Physical Chemistry Chemical Physics 9:2654-2675
9. Demarconnay L., Coutanceau C., Léger J.M., 2004. Electroreduction of dioxygen (ORR) in alkaline medium on Ag/C and Pt/C nanostructured catalysts—effect of the presence of methanol. Electrochim. Acta 49:4513–4521.
10. Tang Z., Liu S., Dong S., Wang E., 2001. Electrochemical synthesis of Ag nanoparticles on functional carbon surfaces. J. Electroanal. Chem. 502:146–151.
11. Kauler J., Schaefer H.J., 1982. Oxidation of alcohols by electrochemically regenerated nickel oxide hydroxide. Selective oxidation of hydroxysteroids. Tetrahedron 38:3299.
12. Q.F. Yi, J.J. Zhang, W. Huang, X.P. Liu, 2007. Selectivity in Electrochemical Reactions. Catal. Commun. 8: 1017.
13. Y. Kunugi, T. Nonaka, Y.B. Chong, 1992. Electroorganic reactions on organic electrodes—part 15: Electrolysis using composite-plated electrodes. Polarization study on a hydrophobic Ni/PTFE composite-plated nickel electrode Electrochim. Acta 37: 353-355.

THE EVALUATION OF RENEWABLE ENERGY ALTERNATIVES IN HYDROGEN SUPPLY CHAIN IN TURKEY USING HYBRID FERMATEAN FUZZY AHP- WPM APPROACH

[1*]*Hande KIRIŞ*, [2]*Özge Nalan BİLİŞİK*
[1] Yıldız Technical University, Faculty of Mechanical Engineering, Department of Industrial Engineering, Istanbul, 34353, Türkiye
[2] Yıldız Technical University, Faculty of Mechanical Engineering, Department of Industrial Engineering, Istanbul, 34353, Türkiye

*Corresponding author e-mail: hande.kiris@std.yildiz.edu.tr

ABSTRACT

Due to many factors such as increasing industrialization, technological developments and population growth, the world's energy demand is constantly increasing and existing resources are no longer sufficient to meet this need. For this reason, the search for alternative energy sources has accelerated especially in recent years and this has directed countries towards alternative renewable energy sources. Nowadays, countries are forming their strategies, policies and goals regarding the energy sector with a focus on renewable energy and are making serious investments in this field. Due to the current importance of the subject, this study attempts to determine which alternative renewable energy source would be appropriate for certain regions in the hydrogen energy supply chain in Turkey. Six renewable energy alternatives are considered: wind, solar, geothermal, biomass, wave and hydroelectric energy. First of all, the weights of the criteria and sub-criteria used in determining renewable alternative energy sources are calculated using the Fermatean Fuzzy Analytical Hierarchy Process (FF-AHP) method. Then, optimal alternatives among renewable alternative energy sources are determined with the Fermatean Fuzzy Weighted Product Method (FF-WPM). When the results of the study aref analyzed, it is clearly seen that Turkey should focus on hydroelectric and wind energy for Istanbul in its renewable energy investments.

Keywords: Renewable Energy, Hydrogen Supply Chain, Multi-Criteria Decision Making, Fermatean Fuzzy AHP, Fermatean Fuzzy WPM

1. INTRODUCTION

Recently, the rapid increase in the world population causes a constant increase in the amount of energy needed. However, traditional energy sources such as coal, oil and natural gas are limited in nature and are insufficient to meet this increasing energy need. For this reason, countries are turning to renewable alternative energy sources. Today, the three main factors that lead countries to seek alternative energy sources and thus make renewable energy so popular can be defined as follows; Energy security, Economic effects, CO_2 emission reductions [1]. This study aims to determine which energy source would be more appropriate to invest in certain regions in the renewable energy sector in Turkey, based on the increasing importance of renewable energy in the world. Dumrul vd. [2], emphasized that ensuring environmental improvement at national and global levels is a critical issue in order to create an effective energy policy, and they used the (IF-EDAS) method to find the best renewable energy alternative for Turkey and concluded that the best alternative renewable energy source for Turkey is solar energy. According to Özkale vd. [3] examined the total performance scores of renewable energy types obtained through PROMETHEE, one of the Multi-Criteria Decision Making (MCDM) methods for Turkey. As a result, they showed that each type of energy has its own advantages and disadvantages. All criteria are obtained using the PROMETHEE method and according to the general results, hydroelectricity ranked first, followed by solar, wind, biomass and finally geothermal energy. Deveci vd. [4] proposed a new performance metric to eliminate the disadvantages of the existing IVIF-CODAS methods in the literature and applied a multi-criteria decision-making method to rank renewable energy alternatives. As a result, they showed that wind and solar energy stand out with higher evaluation scores than other sources. The main contribution of the study, which is different from the literature where there are similar studies in the literature, is to make a suggestion that enables more reliable investment decisions to be made in the field of renewable energy for each of the determined regions separately. In this study, alternative renewable energy sources are applied separately for the regions and the basis for making investment decisions is strengthened. The important thing for the renewable energy source selection problem is to determine the relevant decision criteria and sub-criteria [5]. FF-AHP is used to weight the criteria and sub-criteria determined for renewable energy alternatives, and FF-WPM method is applied to determine the most suitable alternative energy source for the regions by ranking the renewable energy alternatives. Although there are studies using various methods in determining alternative sources in the field of renewable energy, this study has tried to strengthen the basis for making investment decisions by finding the most suitable alternative energy sources for specific regions.

2. MATERIALS AND METHODS

Fermatean Fuzzy Sets (FFS) can more easily handle uncertain information in the decision-making process [7]. It provides a more flexible solution in determining the uncertainty of information since it covers membership and non-membership

degrees in a wider area compared to intuitionistic and Pythagorean fuzzy sets [6]. In this study, results are obtained in the Fermatean fuzzy environment, which is less used compared to the literature. Using FF-WPM, which is a relatively new approach in the literature for selecting alternative renewable energy sources, Fermatean Fuzzy Set is used as a fuzzy set. FF-AHP solution method is presented to determine the weights of the criteria and sub-criteria.

2.1. FF-AHP Method

Step 1: A hierarchical structure is established by determining the criteria and alternatives.
Step 2: The comparison matrix $P = (p_{ij})_{mxm}$ is created by using expert opinions according to the language terms in Table 1.

$$P = \begin{bmatrix} 1 & p_{12} & \cdots & p_{1m} \\ p_{21} & 1 & \cdots & p_{2m} \\ \vdots & \vdots & \ddots & \vdots \\ p_{m1} & p_{m2} & \cdots & 1 \end{bmatrix} \tag{1}$$

Step 3: The expert opinions are verified to be consistent in each pair of comparison matrices (P). The net numbers are compared with the FFNs given in Table 1 using the Saaty scale. Then, Saaty's classical consistency formula is applied.

Step 4: The FFWG aggregation operator is applied to the aggregated opinions of each expert in accordance with the created comparison matrix.

Table 1. Linguistic scale for FF-AHP.

SI	*Definition*	*FFN*	*SI*	*FFN*
9	Absolutely more importance (AMI)	(0.970, 0.233)	8	(0.929, 0.121)
7	Very high importance (VHI)	(0.900, 0.307)	6	(0.844, 0.107)
5	High importance (HI)	(0.794, 0.083)	4	(0.737, 0.068)
3	Slightly high importance (SHI)	(0.670, 0.091)	2	(0.585, 0.059)
1	Equal importance (EI)	(0.465, 0.082)	1/2	(0.369, 0.062)
1/3	Slightly low importance (SLI)	(0.322, 0.038)	1/4	(0.293, 0.054)
1/5	Low importance (LI)	(0.272, 0.050)	1/6	(0.256,0.048)
1/7	Very low importance (VLI)	(0.243, 0.040)	1/8	(0.233, 0.053)
1/9	Absolutely low importance (ALI)	(0.224, 0.050)		

Step 5: The FFN weights of the criteria and sub-criteria are estimated. The sum of each criterion weight (w) is equal to one.

2.2. FF-WPM Method

For an MCDM problem specified in the Fermatean fuzzy environment, suppose that there are m alternatives, S_i $(i = 1,2,\dots,m)$ and n criteria C_j $(j = 1,2,\dots,n)$ and the criterion weight vector is $w = (w_1, w_2, \dots, w_n)^T$ and $0 \le W_j \le 1$, $j = 1,2,\dots,n$ and $\sum_{j=1}^{n} W_j = 1$.

Step 1: Fermatean fuzzy decision matrix is created.

$$R = (X_{ij})_{mxn} = \begin{pmatrix} u_{11}, v_{11} & u_{12}, v_{12} & \cdots & u_{1n}, v_{1n} \\ u_{21}, v_{21} & u_{22}, v_{22} & \cdots & u_{2n}, v_{2n} \\ \vdots & \vdots & \ddots & \vdots \\ u_{m1}, v_{m1} & u_{m2}, v_{m2} & \cdots & u_{mn}, v_{mn} \end{pmatrix} \tag{2}$$

Here each of the elements $X_{ij} = u_{ij}, v_{ij}$ is an FFN, which means that if the alternative S_i satisfies the attributes C_j the degree will be the value u_{ij} and if the alternative S_i does not satisfy the attributes C_j the degree will be the value v_{ij}.
Step 2: It is to normalize the matrix $\mathrm{R} = (X_{ij})_{mxn}$ by a linear method. The decision matrix R, normalize matris is transformed into the normalized matrix $\bar{R}$. The criteria are classified into a subset of benefit criteria, B and a subset of cost criteria, C. The linear normalization for any $j \in \boldsymbol{B}$ and the linear normalization for any $j \in \boldsymbol{C}$ are defined as follows, respectively:

$$\bar{X}_{ij} = \frac{X_{ij}}{max_i X_{ij}}\ , \tag{3}$$

$$\bar{X}_{ij} = \frac{min_i X_{ij}}{X_{ij}}, \tag{4}$$

Step 3: The total relative importance of alternative *i* according to WPM is denoted as Q_i and is defined as:

$$\bar{Q}_i = \prod_{J=1}^{n} X_{ij}{}^{w_j} \tag{5}$$

Step 4: In the last step, the score functions (SF) for $\bar{Q}_i$ $(i = 1,2, \dots, m)$ are calculated and the final rankings of the alternatives are determined according to the decreasing order of $\bar{Q}_i$ $(i = 1,2, \dots, m)$.

$$SF = (\mu_T^3 - \mathrm{v}_T^3\ ) \tag{6}$$

Table 2. Linguistic terms and FF numbers.

Linguistic terms		FF numbers
E	Extremely Important (E)	0.975 0.10
V	Very Important (V)	0.85 0.20
I	Important (I)	0.70 0.35
M	Moderately Imported (M)	0.55 0.50
S	Slightly Important (S)	0.35 0.70
N	Not Important (N)	0.20 0.85
U	Extremely Unimportant (U)	0.10 0.975

3. RESULTS AND DISCUSSION

In this study, renewable energy alternatives in Turkey's grid-based hydrogen supply chain are investigated in order to evaluate the applicability and effectiveness of the proposed method. For the evaluation, there is a decision-making group consisting of two academics who have been working in the field of energy for many years and an expert working in the energy sector. There are five main criteria and 21 sub-criteria from the literature for the decision-making group to choose renewable energy types. The weight of each criterion in a decision problem is not equal. The importance of the criteria varies depending on the decision maker. As a result, the values assigned to the criteria by each decision maker should be aggregated. At this point, the weights of the 21 criteria are calculated. Each expert evaluates the criteria using the linguistic terms listed in Table 1. The criterion weights are calculated according to the evaluation results. Then, the weighted combined decision matrix is obtained. The normalized decision matrix is created according to Equations 3 and 4. Exponent calculations are made according to Equation 5 and the score function, the results of which are given in Table 4, is calculated according to Equation 6. The results in Table 4 are given for the province of Istanbul in Turkey. In the continuation of the study, results will be obtained according to expert evaluations for Izmir and Ankara.

Table 4. Numerical results obtained by FF-WPM.

Alternatives	FF-WPM		Score	Rank
S_1	0.71222	0.79774	-0.14641	3
S_2	0.71334	0.79833	-0.1458197	2
S_3	0.68802	0.80226	-0.19065	6
S_4	0.70592	0.79883	-0.1579816	5
S_5	0.71119	0.80084	-0.1538957	4
S_6	0.72344	0.79588	-0.125498	1

According to the results, the renewable energy alternatives with the highest score function according to the values in Table 4 are hydroelectric energy in the first place. Then, respectively, solar energy, wind energy, wave, biomass energy and geothermal energy are in the sixth place. It is concluded that the best renewable energy alternative that will affect Turkey's sustainable development is "hydroelectric energy" for Istanbul.

4. CONCLUSIONS

In this study, a hybrid model is proposed to determine which renewable energy sources should be used on a grid basis in Turkey. Renewable energy sources will be integrated into the HSC design in the transportation sector in 2050, which is considered the earliest year in which this potential can be achieved. In the proposed hybrid model, the FF-AHP method is used to calculate the criteria weights and the FF-WPM method is used in energy selection since it can take into account many time-varying criteria such as renewable energy types and priorities. According to the results, the main criterion with the highest importance level is Environmental (0.656 0.108) from Technical, Economic, Social, Environmental and Political main criteria. Among the sub-criteria, Pollutant Emission (C16) sub-criterion has the highest importance with the weight of 0.124. Calculations will be made by increasing the number of experts for other regions of Turkey, and it is of great importance for Turkey to turn to more renewable energy sources and determine suitable resources.

REFERENCES

1. Karatop, B., Taşkan, B., Adar, E. & Kubat, C. 2021. Decision analysis related to the renewable energy investments in Turkey based on a Fuzzy AHP-EDAS-Fuzzy FMEA approach. Computers & Industrial Engineering 151.
2. Dumrul, C., Bilgili, F., Zarali, F., Dumrul, Y. & Kiliçarslan, C. 2024. The evaluation of renewable energy alternatives in Turkey using intuitionistic-fuzzy EDAS methodology. Environmental Science and Pollution Research.
3. Özkale, C., Celik, C., Türkman A.C. & Cakmaz, E.S. 2017. Decision analysis application intended for selection of a power plant running on renewable energy sources. Renewable & Sustainable Energy Reviews 70: 1011-1021.
4. Deveci, K., R. Cin, & A. Kagizman 2020. A modified interval valued intuitionistic fuzzy CODAS method and its application to multi-criteria selection among renewable energy alternatives in Turkey. Applied Soft Computing 96.
5. Büyüközkan, G. and S. Güleryüz 2016. An integrated DEMATEL-ANP approach for renewable energy resources selection in Turkey. International Journal of Production Economics 182:435-448.
6. Ayvaz, B., Tatar, B., Sağır, Z. & Pamucar, D. 2024.An integrated Fine-Kinney risk assessment model utilizing Fermatean fuzzy AHP-WASPAS for occupational hazards in the aquaculture sector. Process Safety and Environmental Protection 186: 232-251.
7. Senapati T. & Yager, R.R. 2018. Some New Operations Over Fermatean Fuzzy Numbers and Application of Fermatean Fuzzy WPM in Multiple Criteria Decision Making. Informatica 30(2): 391-412.

ELECTRODEPOSITION OF NANOCONE-SHAPED NI–PT ALLOYS FOR ENHANCED ELECTROCATALYTIC ACTIVITY IN ALKALINE SOLUTIONS

[1*]*Dawid Kutyła*,
[1] AGH University of Krakow, Mickiewicza Avenue 21, Kraków, 30-059, Poland
*Corresponding author e-mail: kutyla@agh.edu.pl

ABSTRACT
This work presents an in-depth investigation of nanocone-shaped Ni–Pt alloy coatings, produced via galvanostatic electrodeposition from chloride-based baths with varying Pt ion concentrations (0.5, 1, 2, 5, and 10 mM). By including NH_4Cl as a crystal growth modifier, lateral growth was selectively inhibited, leading to the formation of sharply defined conical structures. X-ray diffraction (XRD) revealed predominantly Ni(200) reflections, with no distinct Pt-specific peaks, suggesting that Pt is either incorporated into the Ni lattice substitutionally or dispersed as nanoclusters below the detection limit. Energy-dispersive X-ray spectroscopy (EDS) and X-ray fluorescence (XRF) analyses confirmed the uniform distribution of Pt within the cones, while scanning electron microscopy (SEM) imaging showed that all samples exhibited a high density of cone-like structures; however, the addition of Pt slightly changed the cone dimensions by making them marginally shorter and more rounded at higher Pt loadings. The electrocatalytic performance of these Ni–Pt nanocones for hydrogen evolution was assessed by chronopotentiometry and registered overpotentials progressively decreased as Pt content increased: pure Ni coatings stabilized near −1.50 V after 1800 s, while the highest Pt loading (10 mM) achieved a value around −1.05 V, corresponding to an improvement of approximately 450 mV. These findings highlight that the strategic introduction of Pt into Ni nanocones, combined with a tailored electrodeposition process, produces robust alloys with significantly improved HER activity. As a result, Ni–Pt nanoconical electrodes stand out as promising candidates for advanced water-splitting applications in alkaline media.

Keywords: Ni–Pt alloys, electrodeposition, nanocones, catalytic activity, hydrogen evolution reaction

1. INTRODUCTION

Electrochemical synthesis of nanostructured materials has become increasingly important in electrocatalysis due to their high surface area and enhanced catalytic properties. One particularly promising approach involves electrodepositing transition metal nanocones, offering a combination of high surface-to-volume ratio, mechanical stability, and catalytic effectiveness. Various strategies exist for synthesizing nanocones, including template-assisted deposition and direct electrodeposition methods employing crystal modifiers to control crystal growth direction [1].

In electrodeposition, precise optimization of bath parameters is crucial to achieving directional crystallite growth, which favors the formation of conical nanostructures [2]. Nickel-based nanocones, in particular, have attracted significant attention due to their good catalytic activity and corrosion resistance in alkaline media. Modifying these structures with noble metals such as rhodium or platinum can further enhance their electrocatalytic performance .Recent studies demonstrated that decorating Ni cones with a thin Rh layer significantly improved catalytic activity for hydrogen evolution [3] . Similarly, porous Ni–Pt alloys produced via molten salt electrodeposition exhibited high catalytic performance in alkaline HER/OER processes due to the uniform distribution of Pt [4]. Inspired by these findings, we propose synthesizing Ni–Pt alloy nanocones through electrodeposition from aqueous chloride solutions. This approach ensures Pt dispersion throughout the volume, preventing catalytic deactivation due to surface degradation.

2. MATERIALS AND METHODS

Nickel cones were galvanostatically electrodeposited on chemically polished copper substrates (2.8 cm² area). The electrolyte consisted of 200 g/L $NiCl_2$, 100 g/L H_3BO_3, and 40 g/L NH_4Cl as a crystal modifier. Pt ions were introduced into the bath at concentrations of 0.5, 1, 2, 5, and 10 mM as aqueous solutions. Electrodeposition was conducted at 50°C for 20 min at a current density of 20 mA/cm². Platinum foil served as the anode, while copper substrates were used as cathodes.The synthesis were performed with a BioLogic SP-200 potentiostat and EC-LAB software. Post-deposition, the alloys were cleaned in deionized water and air-dried. Elemental composition was determined via XRF (Rigaku Rimini) with a Palladium lamp, and phase composition was analyzed by XRD (Rigaku MiniFlex II) using a copper tube (λ = 1.54059), comparing diffractograms to ICDD database cards. SEM images were captured using a Hitachi Su-70 scanning microscope. The water-splitting ability of the nanoconical Ni-Pt coatings was tested by chronopotentiometry in a 1 M NaOH solution and Tafel slope estimation in linear range.

3. RESULTS AND DISCUSSION

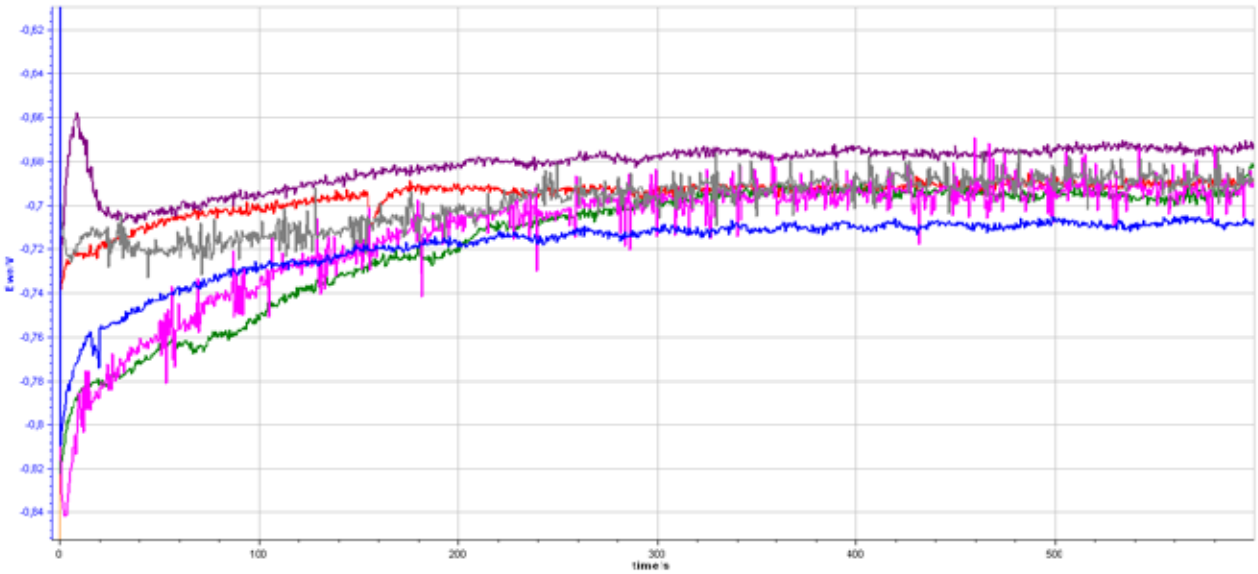

Fig.1. a) Chronopotentiometric curves registered in Ni and Ni-Pt solutions after application of constant current density: -10 mAcm^{-2}.

It can be seen that the addition of the Pt into Ni electrolyte is not significantly modyfing the registered potential value of deposition of alloy. The blank Ni solution (blue line) reach the stable potential value of -0,73 V after 200 seconds. Each addition of Pt ions (0.5, 1, 2, 5, and 10 mM) were slightly decreasing the registered value to – 0.68 V, which is related to the lower deposition overpotential. It can be also noted that, based on the previously performed research, the selected system is able to provide highly-structured nanoconical morphology, which is significantly increasing the surface area of sample, and it can also shift the registered potential value towards more positive regime. Samples after deposition were cleaned, dried and measured their mass, which allow to determine the average thickness of obtained layers, which oscillated between 2-5 um. The crystallographical analysis of obtained Ni and Ni-Pt nanoconical layers were presented on Figure 2.

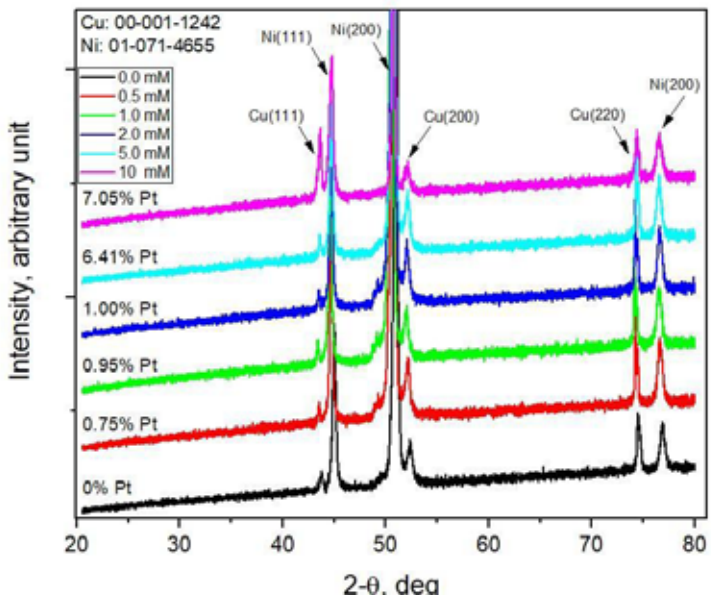

Fig. 2. XRD spectra obtained for Ni nanoconical structures with different addition of the Pt ions in electrolyte. Scan range: 20-80 degrees, scan speed: 0.5 deg/min.

The presented X-ray diffraction (XRD) patterns, the predominant reflections originate from nickel, with the Ni(200) peak standing out as the most intense and well-defined feature, suggesting a strong out-of-plane crystallographic orientation in the deposited Ni-based films. The relatively weaker Ni(111) reflection is also discernible, but the intensity ratio indicates that the film growth conditions favor the (200) texture. Notably, the copper substrate contributes characteristic Cu(111) and Cu(200) peaks, which remain visible through the thin Ni–Pt alloy layers, underscoring the nanometric thickness of these coatings. Although platinum was added to the electrodeposition bath, its concentration in the resulting Ni–Pt alloy films appears to be minimal—so low that no additional diffraction peaks attributable to distinct Pt-rich phases are discernible within this diffractogram. X-ray fluorescence (XRF) and energy-dispersive X-ray spectroscopy (EDS) measurements confirm the presence of Pt at varying concentrations that parallel the nominal bath compositions, yet the crystallographic signatures remain overwhelmingly dominated by Ni reflections. These findings collectively suggest that Pt, while incorporated in small amounts, does not disrupt the

primary fcc Ni lattice to the extent of generating new detectable Bragg peaks, nor does it significantly shift the existing nickel reflections. Instead, the Pt likely enters substitutional sites within the Ni matrix or resides in highly dispersed clusters below the detection threshold for this diffractogram. Morphology of layers are presented on Table 1.

Table 1. Nickel nanostructures obtained by electrodeposition with different addition of Pt ions in electrolyte. Magnification: 4000X

Nickel Nanoconical structures

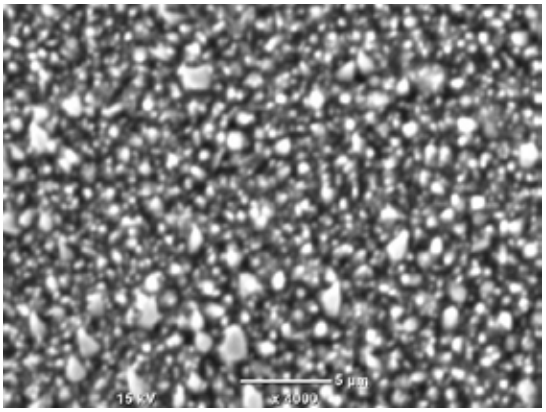

Ni - Pt Nanoconical structures – 0.95% Pt

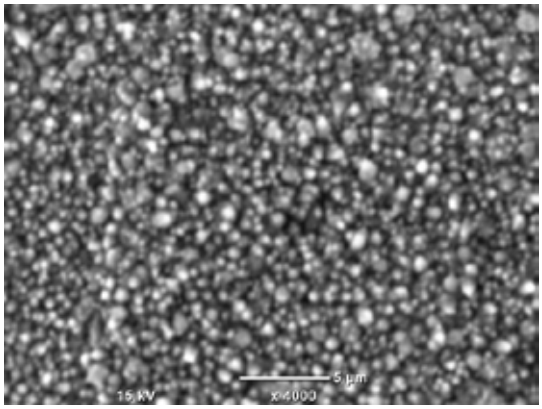

Ni - Pt Nanoconical structures – 6.41 % Pt

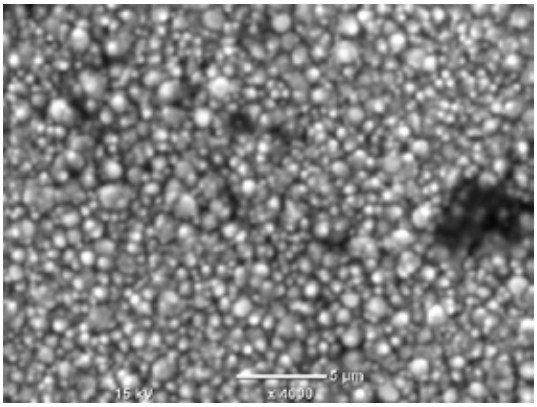

Ni - Pt Nanoconical structures – 7.05% Pt

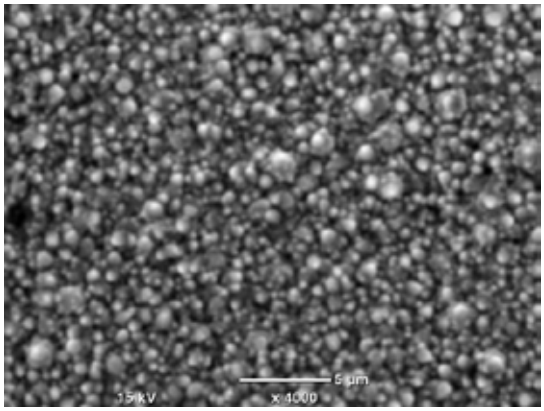

In the SEM images, all samples show a high density of tiny, cone-like structures that cover the surface. This distinctive “nanoconic” shape arises partly because a crystal growth modifier (NH_4Cl) is added to the plating solution, which selectively slows down growth in the horizontal direction. As a result, the material tends to build upward more readily, creating the pointed structures. In the pure nickel sample, these cones have fairly uniform heights and diameters and are spread evenly across the surface. When a small amount of platinum (around 0.95 wt%) is introduced, the general conical appearance is still there, but there is a slight increase in variation of cone size, indicating that even a minor Pt addition can alter local growth conditions. As more platinum is added (6.41 wt% and 7.05 wt%), you still see a dense layer of cones, yet some changes are noticeable: the cones look a bit shorter, and their tips appear more rounded. This is a sign that higher Pt content—and the way it interacts with the nickel—affects how the surface layers form, likely by changing the balance of surface energies and growth rates. These chemical and surface modification should led to modification of the catalytic activity of layers in hydrogen evolution reaction.

In the chronopotentiometric tests for hydrogen evolution in 1 M NaOH at a constant current density of −10 mA cm^{-2}, the overpotential is clearly reduced with increasing platinum content in the Ni–Pt nanoconical electrodes. For example, the pure Ni sample (blue curve) stabilizes at approximately −1.50 V after 1800 s, whereas the electrode containing 0.5 mM Pt (green) reaches around −1.40 V. Progressively higher Pt concentrations shift the potential to even less negative values: the 1 mM Pt sample (red) plateaus near −1.35 V, the 2 mM Pt sample (purple) around −1.30 V, and the 5 mM Pt sample (pink) roughly −1.20 V. Notably, the 10 mM Pt electrode (silver) exhibits a final potential close to −1.05 V, representing nearly a 450 mV improvement compared to pure Ni. This progressive decrease in overpotential confirms the beneficial role of Pt alloying in enhancing the catalytic activity of Ni-based nanostructures for the hydrogen evolution reaction.

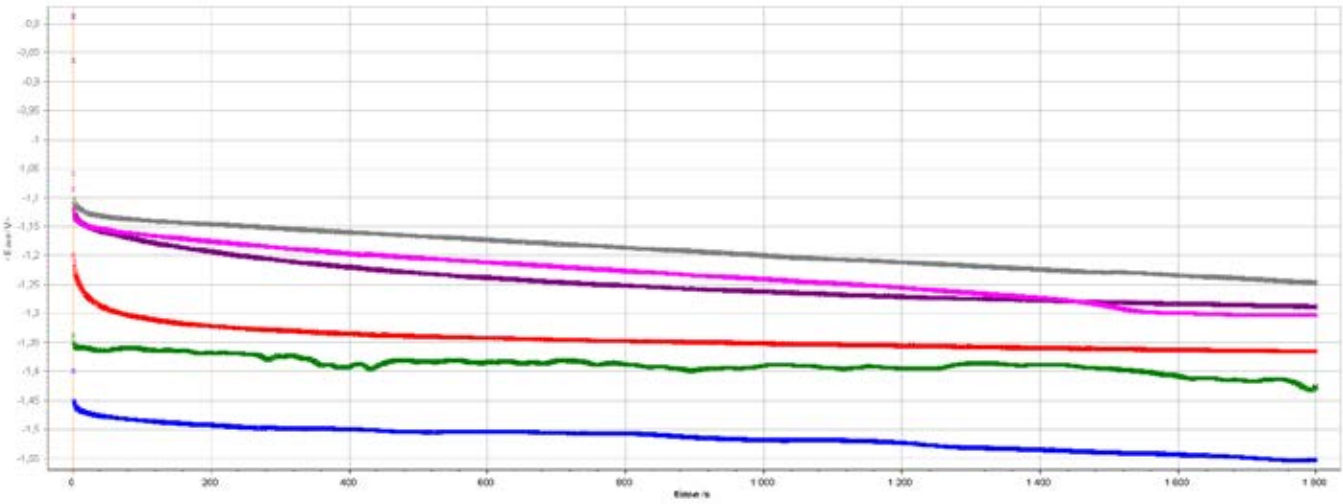

Fig. 3. Chronopotentiometric curves registered in 1 M NaOH after application of constant current density: -10 $mAcm^{-2}$ for Ni-Pt nanoconical alloys deposited with different chemical composition of electrolyte. Polarization time: 1800s.

4. CONCLUSIONS

In summary, this work demonstrates that even small amounts of platinum introduced into nickel during electrodeposition can produce nanocone-shaped Ni–Pt alloys with substantially enhanced electrocatalytic performance toward the hydrogen evolution reaction (HER). Detailed SEM analysis showed that these nanoconic structures—facilitated by the use of NH_4Cl as a crystal growth modifier—were consistently formed across all samples, with minor variations in cone height and apex sharpness correlating with Pt concentration. XRD measurements confirmed that no additional Pt-specific peaks emerged, suggesting that platinum either occupies substitutional sites in the Ni lattice or forms very fine clusters below the detection threshold.

Electrochemical evaluation in 1 M NaOH revealed a clear trend of decreasing overpotential as the platinum content increased. Pure Ni nanocones (blue curve) stabilized near −1.50 V after 1800 s, whereas the 0.5 mM Pt sample (green) improved to around −1.40 V. Increasing Pt loadings further reduced the overpotential, with the 1 mM Pt deposit reaching approximately −1.35 V, the 2 mM Pt deposit −1.30 V, and the 5 mM Pt deposit −1.20 V. Most notably, the electrode containing 10 mM Pt (silver curve) stabilized around −1.05 V, representing a significant 450 mV enhancement compared to pure Ni. These findings highlight how uniform Pt incorporation into the Ni matrix can substantially lower the activation energy for the HER, while preserving the high-surface-area benefits of the nanoconic morphology. Consequently, Ni–Pt nanoconical alloys appear to be promising electrocatalyst candidates for water-splitting technologies, owing to their improved activity and structural stability in alkaline conditions.

ACKNOWLEDGEMENT

This work was partially funded under the program “Excellence Initiative – research University” for the University of Krakow. Grant number: 8803.

REFERENCES

1. Skibińska K, Żabiński P. 2024. Nanocones: A Compressive Review of Their Electrochemical Synthesis and Applications. Materials 17(13):3089.
2. Skibinska K, Kolczyk-Siedlecka K, Kutyla D, Jedraczka A, Leszczyńska-Madej B, Marzec MM, Zabinski P. 2021. Electrocatalytic properties of Co nanoconical structured electrodes produced by a one-step or two-step method†. Catalysts 11(5):544.
3. Skibińska K, Kutyła D, Yang X, Krause L, Marzec MM, Żabiński P. 2022. Rhodium-decorated nanoconical nickel electrode synthesis and characterization as an electrochemical active cathodic material for hydrogen production. Applied Surface Science 592:153326.
4. Fukumoto M, Takahashi H, Kutyła D, Wojnicki M, Żabiński P. 2024. Morphological investigation and electrochemical performance evaluation of novel porous Ni–Pt produced by Al-deposition/dissolution in molten salts for hydrogen and oxygen evolution reaction. International Journal of Hydrogen Energy 49:754–765.

INNOVATIVE BLUE HYDROGEN PRODUCTION FROM GAS HYDRATE – METHANE

[1*]*Serdar S. Çelebi*, [1, 2, 3]*Günay Çifçi,* [1]*Salih Obut*, [1]*Ersel Ercek*,
[1] Armelsan Enerji A.Ş., Teknopark İstanbul, Sanayi Mah. Teknopark Bul. Teknopark 4A No:1/4A İç Kapı No:408 Pendik, İstanbul, 34906, Türkiye
[2] Institute of Marine Sciences and Technology, Dokuz Eylül Üniversity, İzmir,35390, Türkiye
[3] GazHidrATek, Teknopark İzmir, İzmir Institute of Technology, İzmir, Türkiye
*Corresponding author e-mail: serdar.celebi@armelsanenerji.com

ABSTRACT

This article presents a novel method for producing blue hydrogen by extracting methane from gas hydrate deposits through CO_2 injection and converting it into hydrogen via steam methane reforming (SMR). Gas hydrates, which store methane in crystalline water structures, hold immense unused energy potential but carry environmental risks due to methane leakage that can naturally happen. The proposed CO_2 injection technique to gas hydrate deposits provides controlled methane extraction while simultaneously using CO_2 formed by SMR process, reducing overall greenhouse gas emission.

Once extracted, methane undergoes SMR to generate hydrogen, with CO_2 as a byproduct. Instead of releasing into the atmosphere, CO_2 is captured and injected into hydrate formations, creating a circular process that lowers overall emissions. Economic analysis indicates that this approach could be cost-competitive with current hydrogen production methods. Additionally, environmental assessments suggest a significantly reduced carbon footprint compared to conventional techniques, though challenges such as potential methane leaks and hydrate stability require attention.

Field trials, including projects in Japan, demonstrate the viability of CO_2 injection for methane recovery. This integrated approach offers a scalable and sustainable solution for blue hydrogen production, supporting energy security and climate goals, particularly in gas-hydrate-rich regions like the Black Sea.

1. INTRODUCTION

Natural gas hydrates offer a promising pathway for producing low-carbon hydrogen. This study explores an innovative approach to blue hydrogen production by extracting methane from gas hydrate reservoirs using CO_2 injection and then converting the recovered methane into hydrogen and CO_2 through steam methane reforming (SMR). The feasibility of this integrated method is assessed using modeling and simulation, with a particular focus on Asia's gas hydrate reserves [1].

Gas hydrates are crystalline compounds that trap methane molecules within a water-based lattice structure. These deposits, found in vast quantities worldwide, represent a substantial untapped energy resource [2]. However, methane leakage from these reservoirs significantly contributes to greenhouse gas emissions. Since methane has a global warming potential approximately 25 times greater than CO_2 over a 100-year period [3], uncontrolled release could intensify climate change. The proposed CO_2 injection method not only enables efficient methane extraction but also mitigates environmental risks by preventing uncontrolled methane emissions [4]. Studies have shown that CO_2 can replace methane within hydrate structures, making this a viable method for sustainable energy production. Japan's pilot projects in the Nankai Trough have validated this technique, encouraging further research into its application for large-scale blue hydrogen production.

2. MATERIALS AND METHODS

2.1. Gas Hydrate Reservoirs: Characteristics and Extraction Methods

Gas hydrates form in high-pressure, low-temperature environments, such as deep-sea sediments and permafrost regions. It is estimated that global methane reserves trapped within these hydrates range from 500 to 10,000 gigatons of carbon, surpassing the combined known fossil fuel reserves [2]. In terms of energy potential, methane hydrates hold approximately 100 times more energy than all existing oil and gas reserves, positioning them as a crucial resource for future energy security [5].

The extraction of methane from hydrate formations can be achieved through several methods:

- *Depressurization:* Lowering the reservoir pressure to trigger methane dissociation from the hydrate structure.
- *Thermal Stimulation:* Injecting heated fluids, such as steam or warm water, to destabilize the hydrates and release methane gas.
- *Chemical Injection:* Using substances like methanol or glycol to modify reservoir conditions and induce methane release, although this method is costly.
- *CO_2 Injection:* Replacing methane with CO_2 within the hydrate lattice, allowing for controlled methane extraction and the simultaneous formation of more stable CO_2 hydrates [4].

Pilot studies indicate that CO_2 injection is particularly effective for methane displacement in gas hydrate structures within deep-sea environments, where maintaining stability is critical. This dual-purpose approach enhances methane recovery

while reducing overall greenhouse gas emissions. Gas hydrate-containing sediments are complex systems in which methane production is influenced by pressure and temperature changes [6]. Advanced numerical models confirm that CO_2 injection enhances methane recovery while minimizing environmental risks [1]. These insights are crucial for developing sustainable extraction techniques.

2.2. Steam Methane Reforming (SMR) for Hydrogen Production

The extracted methane undergoes SMR, which is the most commonly used process for large-scale hydrogen production. SMR involves two key reactions [7]:

Primary Reforming Reaction (Endothermic):

$$CH_4 + H_2O \rightarrow CO + 3H_2 \ \Delta\mathrm{H} = +206\ \mathrm{kJ/mol} \quad (1)$$

Water-Gas Shift Reaction (Exothermic):

$$CO + H_2O \rightarrow CO_2 + H_2 \ \Delta\mathrm{H} = -41\ \mathrm{kJ/mol} \quad (2)$$

Overall Net Reaction (Endothermic):

$$CH_4 + 2H_2O \rightarrow CO_2 + 4H_2 \ \Delta\mathrm{H} = +165\ \mathrm{kJ/mol} \quad (3)$$

This process occurs in a reformer unit, where methane reacts with steam at 700–1000°C over a nickel-based catalyst. The reaction produces a synthesis gas (syngas) containing hydrogen, carbon monoxide, and carbon dioxide [4]. The water-gas shift reaction further increases hydrogen yield by converting CO into CO_2 and additional hydrogen. The produced hydrogen is separated from carbon dioxide using physical methods such as Pressure Swing Adsorption (PSA) or membrane separation techniques.

2.3. Integration of SMR and CO_2 Injection

By integrating methane recovery with SMR, a closed-loop process is established, where CO_2 from hydrogen production is captured and injected into hydrate reservoirs, reducing net carbon emissions as shown in Fig. 1. This closed-loop approach offers a promising pathway to sustainable blue hydrogen production while addressing key challenges in methane extraction from abundant natural resources and effective carbon management [8].
The key advantages of this combined system include:

- *On-site Hydrogen Production:* Reducing transportation costs and emissions by converting methane to hydrogen at extraction sites.
- *Carbon Sequestration:* Capturing and storing CO_2 within hydrate reservoirs mitigates climate impact.
- *Energy Optimization:* Waste heat from the SMR process can be repurposed to facilitate hydrate dissociation, improving overall efficiency.

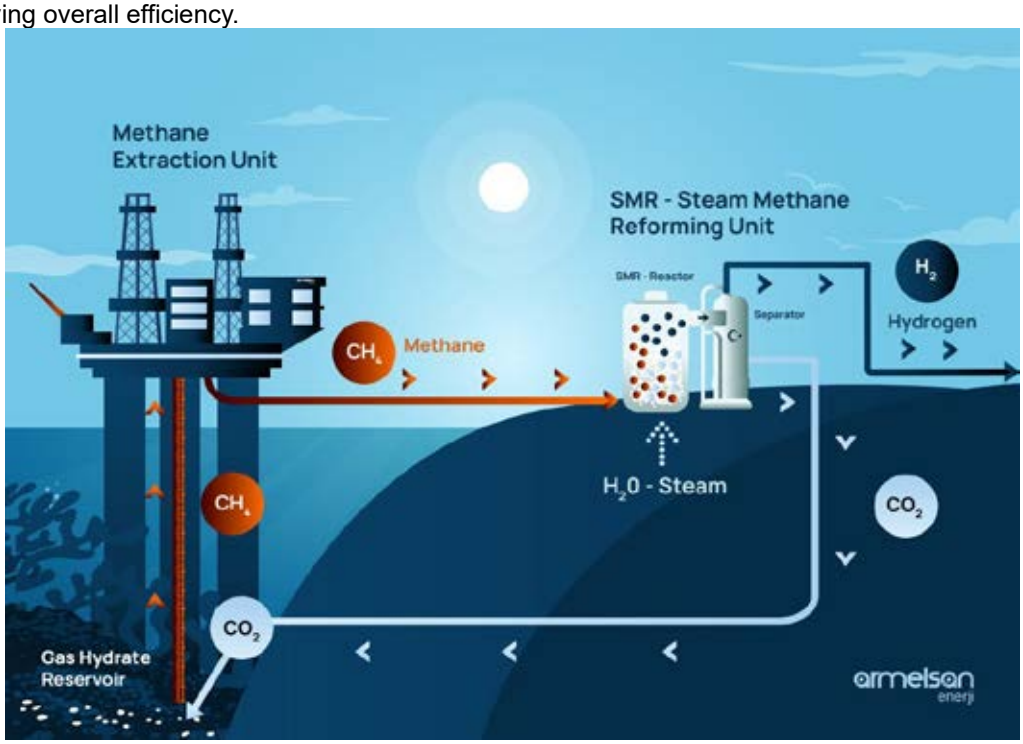

Fig.1. Schematic illustration of integrated system of SMR process with CO_2 injection

3. RESULTS AND DISCUSSION

3.1. Environmental Impact Assessment

Utilizing methane hydrates for hydrogen production presents a viable solution for reducing the greenhouse effect of methane emissions. Life-cycle assessments indicate that blue hydrogen derived from gas hydrates has a significantly lower carbon footprint compared to conventional hydrogen production methods [8]. However, certain environmental challenges must be addressed, including:

- *Potential Methane Leakage:* Advanced monitoring systems are necessary to detect and prevent unintended methane emissions.
- *Hydrate Stability Concerns:* Ensuring that CO_2 injection maintains reservoir integrity is crucial.
- *Marine Ecosystem Impact:* Minimizing disruption to marine environments remains a key focus for sustainable deployment.

3.2. Economic Viability and Market Potential

Economic models suggest that blue hydrogen from gas hydrates could be cost-competitive with existing hydrogen production methods [9]. The estimated breakeven price of $2.016 per kg hydrogen indicates that this approach can be a viable alternative, particularly in regions rich in hydrate deposits. With increasing global demand for low-carbon hydrogen in industries such as transportation and steel production, this method holds significant commercial potential.

3.3. Case Studies and Field Trials

Countries such as Japan, South Korea, and Canada have conducted successful pilot projects demonstrating methane extraction via CO_2 injection [5]. Japan's Nankai Trough experiment showcased the feasibility of replacing methane with CO_2 in hydrate structures, providing valuable data for future large-scale implementation. Ongoing trials aim to refine CO_2 injection strategies and improve the methane-to-hydrogen conversion efficiency.

3.4. Future Research Directions

Advancements in methane extraction through CO_2 injection and hydrogen production technologies such as plasma-assisted methane conversion and advanced catalysts continue to enhance overall process efficiency. Research areas include:

- *Cost Reduction:* Developing more efficient catalysts for the SMR process and refining extraction techniques using CO_2 injection.
- *Environmental Safety Measures:* Strengthening monitoring and control technologies to mitigate methane leaks.
- *Renewable Energy Integration:* Combining hydrogen production with offshore wind or solar power to improve sustainability.

4. CONCLUSIONS

The integration of methane extraction via CO_2 injection and SMR represents a groundbreaking approach to sustainable hydrogen production. By leveraging gas hydrate reserves, this method not only provides an alternative energy source but also significantly reduces uncontrolled methane emissions that could contribute to global warming, with the captured CO_2 from hydrogen production being injected into gas hydrate formations, thereby creating a circular carbon management system.

This closed-loop approach minimizes environmental impact, optimizes energy efficiency, and offers a scalable solution for future blue hydrogen production. As global efforts to transition toward low-carbon energy intensify, continued research and development will be critical in refining this method and unlocking its full potential. The adoption of this innovative process could play a crucial role in achieving long-term energy security and climate resilience. With its gas hydrate deposits in the Black Sea, Türkiye has significant potential to prevent methane emissions that contribute to global warming and produce blue hydrogen through this new integrated process.

REFERENCES

1. Wang, M., Wang, X., Deng, C., Liu, B., Sun, C., Chen, G., & El-Halwagi, M. M. (2019). Process modeling and energy efficiency analysis of natural gas hydrate production by CH4-CO2/H2 replacement coupling steam methane reforming. In *Computer Aided Chemical Engineering* (Vol. 47, pp. 131-136). Elsevier.
2. Gaddipati M, Nyayapathi L, and Anderson BJ. 2010. Comparison of gas production from gas hydrate reservoirs using vertical and horizontal wells. Paper presented at the AIChE Annual Meeting, Salt Lake City, UT, November 10.

3. . Masson-Delmotte V, Zhai P, Pirani A, Connors SL, Péan C, Berger S, Caud N, et al., editors. 2021. Climate Change 2021: The Physical Science Basis. Contribution of Working Group I to the Sixth Assessment Report of the Intergovernmental Panel on Climate Change. Cambridge: Cambridge University Press.
4. Zhang, Z., Li, Y., Xu, T., Li, S., Li, X., Lu, C., & Qin, X. (2024). Optimizing Carbon Dioxide Injection for Methane Hydrate Development and Carbon Sequestration: A Long-Term Numerical Simulation Study. *Energy & Fuels*, *38*(21), 20629-20643.
5. Jang J. 2011. Gas production from hydrate-bearing sediments. PhD diss., Georgia Institute of Technology.
6. Khan, C., Amin, R., & Madden, G. (2013). Effects of CO 2 and acid gas injection on enhanced gas recovery and storage. *Journal of Petroleum Exploration and Production Technology*, *3*, 55-60.
7. Hou, K., & Hughes, R. (2001). The kinetics of methane steam reforming over a Ni/α-Al2O catalyst. *Chemical Engineering Journal*, *82*(1-3), 311-328.
8. Jadhawar, P., Yang, J., Chapoy, A., & Tohidi, B. (2021). Subsurface Carbon Dioxide Sequestration and Storage in Methane Hydrate Reservoirs Combined With clean Methane Energy Recovery. *Energy & Fuels*, *35*(2), 1567–1579.
9. Massarweh, O., Al-khuzaei, M., Al-Shafi, M., Bicer, Y., & Abushaikha, A. S. (2023). Blue hydrogen production from natural gas reservoirs: A review of application and feasibility. *Journal of CO2 Utilization*, *70*, 102438.

FLY ASH-DERIVED SUPPORTED IRON CATALYSTS FOR EFFICIENT AMMONIA DECOMPOSITION: A SUSTAINABLE APPROACH FOR CO_x-FREE HYDROGEN STORAGE

*Büşra Sekizkardeş[1,2,3], Samira F. Kurtoğlu-Öztulum[1,2,3]**
[1]Department of Chemical and Biological Engineering, Koç University, Rumelifeneri Yolu, Sariyer, 34450 Istanbul, Turkey
[2]Koç University Hydrogen Technologies Center (KUHyTech), 34450, Istanbul, Türkiye
[3]Department of Materials Science and Technology, Faculty of Science, Turkish-German University, Sahinkaya Cad., Beykoz, 34820 Istanbul, Turkey
* samira.kurtoglu@tau.edu.tr

ABSTRACT
Fly ash (FA), a by-product of coal combustion in power plants, poses a significant global environmental challenge due to its large-scale production. Rich in metal oxides such as SiO_2, Al_2O_3, and Fe_2O_3, FA offers potential as a catalyst for ammonia decomposition to produce CO_x-free hydrogen. However, its low surface area (< 1 m^2 g^{-1}) limits catalytic performance. In this study, FA was modified by calcination at various temperatures (550, 700, and 1000 °C), HCl treatment, and HCl treatment followed by calcination at 500 °C. The most active catalyst, obtained by HCl treatment followed by calcination at 500 °C achieved 86.0% ammonia conversion at a reaction temperature of 700 °C and a space velocity of 30,000 mL NH_3 h^{-1} g_{cat}^{-1}, exhibiting significantly higher performance compared to the other FA-based catalysts. The enhanced performance on this catalyst was attributed to its enhanced surface area (18.5 m^2 g^{-1}), effective removal of Cl and S impurities, and the formation of relatively small Fe crystallites (23.8 nm). This study demonstrates an environment-friendly and efficient approach to store CO_x-free hydrogen in ammonia.

Keywords: Heterogenous Catalysis, Hydrogen Storage, Ammonia Decomposition, Waste-derived Catalysts, Fly Ash

1. INTRODUCTION
Hydrogen stands out as an energy carrier due to its exceptionally high gravimetric energy density. However, its practical application is hindered by its low volumetric energy density, which poses challenges for storage, transport, and utilization. A promising option for hydrogen storage is its chemical storage in compounds such as methane, methanol, formic acid, or ammonia, which helps mitigate the challenges associated with its low volumetric energy density. Among hydrogen carriers, ammonia stands out because of its carbon-free nature, high hydrogen density both gravimetrically and volumetrically, nonflammability, and compatibility with existing infrastructure [1]. These advantages make ammonia an excellent candidate for CO_x-free hydrogen storage and transportation.
The thermal decomposition of ammonia has been widely studied using Ru-, Ni-, Co-, and Fe-based catalysts [2]. Among them, Ru-based catalysts exhibit the highest activity, however, their practical application is hindered by the high cost and scarcity of ruthenium. Additionally, many high-performance ammonia decomposition catalysts require complex synthesis procedures, leading to increased costs and reproducibility challenges. Therefore, the development of a low-cost, stable, and efficient catalyst that can be synthesized through simple and scalable methods is essential for hydrogen production from ammonia.
In this context, coal fly ash (FA), an abundant industrial waste, represents a significant opportunity as an iron-based catalyst for ammonia decomposition to produce hydrogen [3]. FA is a readily available and cost-free, containing considerable quantities of catalytically active Fe_2O_3 (between 5-15 wt%) [4]. Furthermore, the SiO_2 and Al_2O_3 present in FA can serve as effective support materials, while trace elements such as K, Ba, and Ca can serve as promoters, potentially further enhancing catalytic performance [3]. Despite these advantages, the direct catalytic application of FA is hindered by its significantly low surface area (< 1 m^2 g^{-1}), requiring modification strategies such as acid treatment or thermal calcination to enhance its textural properties and catalytic activity.
This study is the first to systematically evaluate FA as an ammonia decomposition catalyst. Here, FA was modified via acid treatment and calcination at different temperatures to significantly enhance its catalytic performance for ammonia decomposition. This research not only provides an innovative approach to hydrogen storage and utilization but also presents substantial environmental and economic advantages through the valorization of a globally abundant waste material.

2. MATERIALS AND METHODS
FA from Tuncbilek Power Plant (Kutahya, Turkey) was calcined at 550, 700, and 1000 °C for 3 hours with a ramp rate of 10 °C min^{-1}, yielding FA-C550, FA-C700, and FA-C1000. For modified fly ash (MFA) synthesis, FA was treated with 6 M HCl, digested in a Milestone Microwave Digestion System (SK-10) at 220 °C, and precipitated with aqueous ammonia to pH ~8. The product was washed, dried, and calcined at 500 °C with a ramp rate of 10 °C min^{-1}, producing MFA-C500. Samples were thoroughly characterized using X-ray diffraction (XRD), X-ray fluorescence spectroscopy (XRF), Fourier transform infrared (FTIR) spectroscopy, thermogravimetric analysis (TGA), temperature-programmed reduction (TPR), and scanning electron microscopy coupled with energy-dispersive X-ray spectroscopy (SEM/EDX), Brunauer-Emmett-

Teller (BET) pore volume and surface area analysis, transmission electron microcopy (TEM), temperature programmed reduction (TPR), and X-ray photoelectron spectroscopy (XPS).
Catalytic performance was evaluated in a ½-inch quartz tube once-through flow reactor, using 200 mg of catalyst for each run. Before catalytic testing, catalysts were reduced in pure hydrogen (H_2, 99.99%, Air Liquide) at 700 °C. Ammonia (NH_3, 99.99%, Linde) was introduced at a gas hourly space velocity (GHSV) of 30,000 mL NH_3 h^{-1} g_{cat}^{-1}, for an induction period of approximately 30 h at 700 °C. Following the induction, the reaction temperature was varied between 480 and 510 °C under differential conversion conditions (not exceeding 8.0%) to obtain the Arrhenius plots. The outlet gas composition was monitored using a Hiden QGA quadrupole gas analyzer pre-calibrated for H_2, N_2, and NH_3.

3. RESULTS AND DISCUSSION

The composition of the as-received FA was determined by XRF analysis, revealing that the primary constituents of FA are SiO_2 (56.8 wt%), Al_2O_3 (21.1 wt%), and Fe_2O_3 (9.9 wt%). XRD analysis confirmed the presence of a mixture of crystalline phases in FA, with peaks corresponding mainly to quartz (SiO_2), mullite ($3Al_2O_3{\cdot}2SiO_2$), hematite (α-Fe_2O_3), and a lower amount of FeO(OH). Calcination at various temperatures (550, 700, and 1000 °C) did not cause significant changes in the crystalline structure compared to untreated FA. However, the XRD pattern of acid modified samples, MFA and MFCA-C500, presented an increase in amorphous character upon modification. Furthermore, acid modification significantly increased the surface area of FA (<1 m^2 g^{-1}) to 37.7 m^2 g^{-1} (in MFA), but it also introduced typical catalyst poison such as Cl. Subsequent calcination at 500 °C (MFA-C500) effectively eliminated these impurities, as confirmed by EDX analysis, although this was accompanied by a decrease in the surface area to 18.5 m^2 g^{-1}.
Next, calcined and HCl-modified FA samples were reduced in pure H_2 flow to convert the Fe_2O_3 content into the active metallic Fe phase. XRD and XPS analysis of reduced catalysts and H_2-TPR analysis of fresh samples confirmed that Fe_2O_3 present in FA, calcined FA samples, and MFA is successfully reduced to metallic Fe at 700 °C in pure H_2 [3]. The average Fe crystallite sizes determined from the XRD patterns of the reduced catalysts using the Scherrer equation were 32.2, 29.0, 25.2, 24.4, 37.6, and 23.8 nm, for FA-R, FA-C550-R, FA-C700-R, FA-C1000-R, MFA-R, and MFA-C500-R, respectively. Noncalcined reduced catalysts (FA-R and MFA-R) exhibited larger crystallites, while the acid-modified, calcined, and reduced catalyst (MFA-C500-R) showed the smallest crystallite size of 23.8 nm. The surface-averaged nanoparticle size from TEM images was 24.0 nm, consistent with the Scherrer equation result.
When testing the ammonia decomposition performances of these reduced catalysts, the apparent activation energies for FA-R, FA-C550-R, FA-C700-R, FA-C1000-R, MFA-R, and MFA-C500-R were determined as 93.9, 95.8, 93.2, 73.6, 103.7, and 104.7 kJ mol^{-1}, respectively (Figure 1). While calcination at 550, 700, and 1000 °C resulted in comparable catalytic performance, acid modification followed by calcination (MFA-C500-R) significantly enhanced NH_3 decomposition activity (Figure 1 and 2).

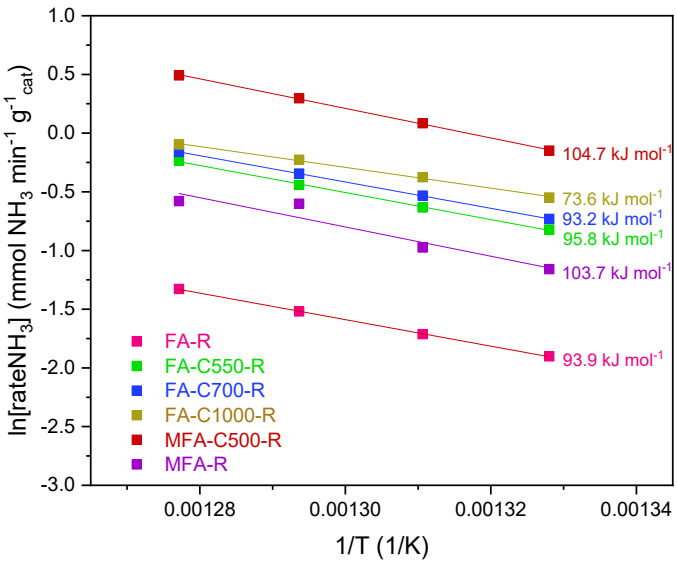

Fig. 1. Arrhenius plots for FA-based catalysts.

At a space velocity of 30,000 mL NH_3 h^{-1} g_{cat}^{-1} and a reaction temperature of 700 °C, the ammonia conversions of FA-R, FA-C550-R, FA-C700-R, FA-C1000-R, MFA-R, and MFA-C500-R were measured as 50.9, 70.4, 73.6, 71.0, 56.1, and 86.0 %, respectively (Figure 2). These results demonstrate that the HCl-modified and calcined fly ash catalyst (MFA-C500-R) exhibited the highest activity, followed by FA-C1000-R, FA-C700-R, and FA-C500-R, which showed similar performances. The non-calcined and directly reduced catalysts (MFA-R and FA-R) provided the lowest activity (Figure 2). This performance trend aligns with the Fe crystallite sizes of each catalyst: the highest-performing catalyst possessed

the smallest Fe crystallites, while the least-performing catalysts exhibited larger Fe crystallites. Data clearly indicate the crucial role of calcination, as catalysts prepared from non-calcined FA exhibited larger Fe crystallites and thus lower catalytic activities. Characterization results revealed that directly reducing FA and MFA without calcination left behind sintering agents (S and Cl impurities), which contributed to increased Fe crystallite sizes and lower catalytic performance. Overall, the highest catalytic performance in our sample pool was achieved with the HCl-modified, calcined, and reduced catalyst (MFA-C500-R), which provided 86.0% NH_3 conversion at 700 °C with a space velocity of 30,000 mL NH_3 h^{-1} g_{cat}^{-1} [3]. This performance was comparable to, or even superior to, that of several conventionally prepared Fe-based ammonia decomposition catalysts reported in the literature.

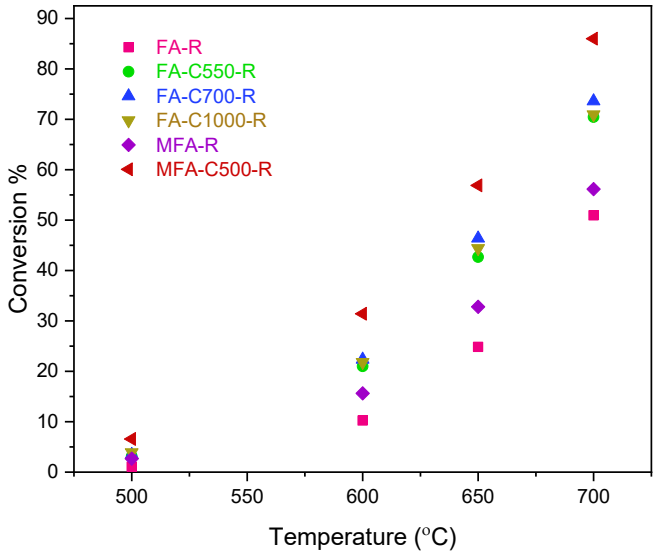

Fig. 2. The catalytic activity measured at different temperatures at a space velocity of 30,000 mL NH_3 h^{-1} g_{cat}^{-1} for FA-based catalysts.

Further investigations on MFA-C500-R were conducted at varying temperatures (400–700 °C) and space velocities (3,000–75,000 mL NH_3 h^{-1} g_{cat}^{-1}). (Figure 3). Its stability was tested for 140 hours on stream, demonstrating excellent long-term performance after an initial 30-hour induction period (Figure 4). XRD analysis of spent catalysts indicated the nitridation of Fe sites, leading to the formation of iron nitride (Fe_xN_y) species, which was also confirmed by XPS analysis. SEM images showed that spent MFA-R contained the largest Fe_xN_y moieties, explaining its low catalytic performance. In contrast, both XRD and SEM analyses of the spent MFA-C500-R catalyst revealed that the calcination step performed on the modified catalyst resulted in smaller Fe_xN_y crystallite sizes. This enhanced dispersion is attributed to the significantly increased surface area of MFA-C500 (18.5 m^2 g^{-1}), approximately 23 times higher than untreated FA, and the removal of sintering agents such as sulfur and chlorine impurities [3].

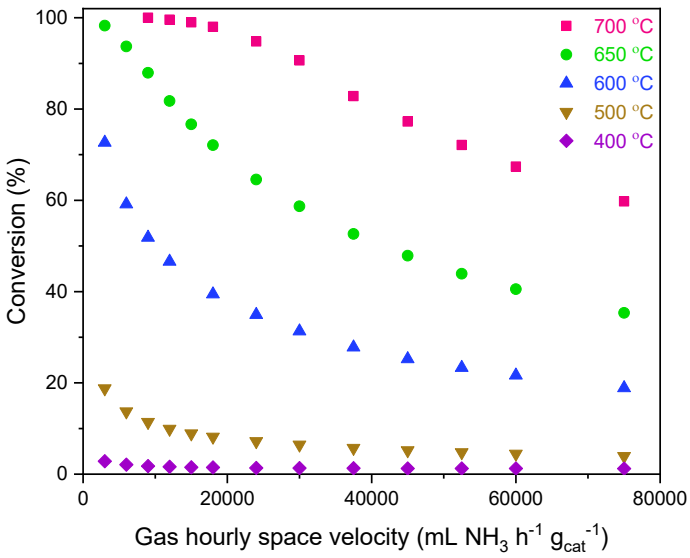

Fig. 3. The catalytic activity of MFA-C500-R at different reaction conditions.

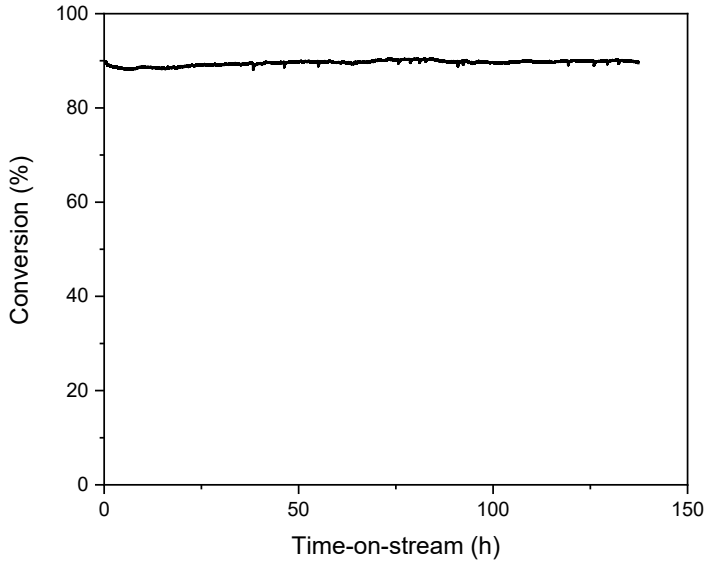

Fig. 4. The catalytic stability test of MFA-C500-R conducted at 700 °C with a space velocity of 30,000 mL NH_3 h^{-1} g_{cat}^{-1}, excluding the initial 30-hour induction period from the graph.

4. CONCLUSIONS

This study demonstrates the successful transformation of FA into an efficient alumina- and silica-supported iron-based catalyst for ammonia decomposition. The combined acid modification and calcination treatments significantly improved the surface area of FA, removed catalyst poisons such as chlorine and sulfur, and reduced Fe crystallite sizes, ultimately enhancing the catalytic performance. Among the prepared catalysts, the HCl-modified, calcined, and reduced sample (MFA-C500-R) exhibited the highest activity, achieving 86.0% ammonia conversion at 700 °C and at a space velocity of 30,000 mL NH_3 h^{-1} g_{cat}^{-1} with remarkable stability over a 140-hour operation period. Detailed characterization of the spent catalysts confirmed the formation of highly dispersed Fe_xN_y species, which contributed notably to the catalyst's excellent performance. These findings highlight the sustainable potential of utilizing low-cost, abundant FA as an efficient catalyst for hydrogen production, demonstrating a promising approach to transforming industrial waste into value-added materials.

ACKNOWLEDGEMENT

The authors gratefully acknowledge Prof. Dr. Alper Uzun for his valuable mentorship and Assoc. Prof. Uğur Ünal from Koç University for acquiring TEM images. The use of TEM facilities at Koç University Nanofabrication and Nanocharacterization Center for Scientific and Technological Advanced Research (n2STAR) is gratefully acknowledged. The authors also thank Dr. Barış Yağcı from Koç University Surface Science and Technology Center (KUYTAM) for his support with SEM/EDX and XPS measurements. This work is supported by Koç University Tüpraş Energy Center (KUTEM). The authors express their gratitude to Tunçbilek Power Plant in Kütahya, Türkiye for providing the FA sample.

REFERENCES

1. Schüth F., Palkovits R., Schlögl R., Su D.S. Ammonia as a possible element in an energy infrastructure: catalysts for ammonia decomposition. Energy & Environmental Science 2012; 5(4):6278-6289.
2. Kurtoğlu SF, Uzun A. Red Mud as an Efficient, Stable and Cost-Free Catalyst for COx-Free Hydrogen Production from Ammonia. Sci Rep 2016;6:32279.
3. Sekizkardeş B, Kurtoğlu-Öztulum SF. Modified Fly Ash: An Eco-Friendly, Cost-Free, and Efficient Iron-Based Catalyst for Ammonia Decomposition to COx-Free Hydrogen. ChemCatChem 2024:e202401666.
4. Khairul Nizar I, Al Bakri AMM, Rafiza AR, Kamarudin H, Abdullah A, Yahya Z. Study on Physical and Chemical Properties of Fly Ash from Different Area in Malaysia. Key Eng Mater 2013;594–595:985–9.

DEVELOPMENT OF A NEW GENERATION HYBRID SYSTEM FOR THE ELECTRIC VEHICLE

[1*]*Orhan Yılmaz*, [1,2]*Aylin Aytaç*
[1] Gazi University, Instute of Science, Department of Chemistry, Teknik Okullar, Ankara, 06560, Türkiye
[2] Institute of Energy and Climate Research (IEK-3), Forschungszentrum Juelich, 52425 Juelich, Germany

*Corresponding author e-mail: orhanyilmaz37@gmail.com

ABSTRACT
Today, both environmental concerns and the necessity to find solutions to the world's ever-increasing energy needs force people to find new and clean energy sources and develop environmentally friendly energy conversion systems. In this respect, the 21st century is the period in which 'hydrogen' is used as 'New Energy Technologies' and 'fuel cell' systems are adopted. For this purpose, the change in hydrogen and oxygen consumption in the fuel cell against time was ınvestigated, ranging from 0.86 V to 2.44 V, with the model being repeated each time. The results show that the optimum configuration was found to 2.44 V and 6.88 W of power with the hydrogen flow rate of 0.2 ml/min and the oxygen flow rate of 0.4 ml/min in the polymer electrolyte membrane fuel cell (PEMFC). Our future research in this area will focus on separation of water according to the volume of hydrogen and oxygen gases, as well as determining the efficiency of the solar module and PEM electrolizor.

Keywords: Photovoltaic-electrolyser-fuel cell-battery hybrid system, Optimal configuration, Electric vehicle

1. INTRODUCTION
The process of global urbanization has brought about the rapid economic expansion of all countries in the world. With the continuous the world's energy consumption, and the rapid economic development entailes serious emissions of carbon dioxide [1]. The problem of planet heats up caused by the ongoing emission of greenhouse gases has become a threat to survival and development of humanity, which become a global concern. From the 1960s, environmental degradation have pushed up worldwide, governments aim has been to achieve sustainable economic growth with low-carbon emissions and less energy consumption. The renewable energy generation technologies have shaped the future power grid. Amongst these technologies, wind energy, photovoltaic (PV) power generation technologies, which offer advantages such as superior natural resource endowment, constantly increasing development and readily available, are more mature and more productive than other renewable energy generation generation technologies [2]. According to statistics, the world's renewable energy capacity additions expanded with almost 50% in 2023, reaching almost 510 gigawatts (GW), with photovoltaic capacity accounted for three-quarters of renewable energy added globally. China commissioned more solar PV in 2023 as the entire world did a year before, while China’s wind additions also grew by 66% year-on-year. Alongside China's extraordinary acceleration, the USA, EU, and Brazil also hit all-time highs increases in their renewable energy capacity [3]. To become prevalent PV power generation, which is expected to become the largest source of global electricity production, two major problems have to be solved. One of the problems is the instability of PV power generation which will a massively affect electrical grid. In order to prevent this impact, the grid will not accept unstable electricity, which will cause a waste of power. The second problem is the energy storage challenges. Physical energy storage, electrochemical energy storage, and electromagnetic energy storage technologies, which used in energy storage, will not be able to meet the needs of large energy storage and the empowerment of clean energy in the future. Therefore, many energy storage options, such as pumped hydropower storage, hydrogen storage, compressed air, and batteries, etc. are still at the development stage. Compared with them, hydrogen storage has the characteristics of high energy density, large and easy storage capacity, lower conversion efficiency, and transmission [4]. Hydrogen gas (H_2) produced through water electrolysis using renewable energy sources such as solar, wind or hydroelectric energy can be used in areas such as transport as well as electricity supply for fuel cell vehicles.
The purpose of this work is to develop a model of a hybrid system using PV, Electrolyser, Fuel Cell and Battery for transport applications. The first step is to construct the circuit simulator and then adding all the elements that is necessary for this system such as a PV system, Electrolyser, Fuel Cell and Battery. Next, the complete model will be simulated to ensure the circuit will operate as expected. Our goal is to find the optimum design of a new photovoltaic-electrolyser-fuel cell-battery hybrid system that we model for vehicles.

2. MATERIALS AND METHODS
2.1. Photovoltaic Panel
Photovoltaic solar panels (Figure 3. (a)) are made of semiconductor materials and convert sunlight falling on them directly into electrical energy. Increasing the efficiency of photovoltaic systems is a critical step to maximize the amount of electricity obtained from solar energy. Hybrid energy systems have been developed to increase the efficiency of photovoltaic systems. These systems are integrated with photovoltaic cells along with other renewable energy sources or energy storage systems, achieving higher efficiency.

2.2. Electrolyser

Electrolyzers play a critical role in the production of hydrogen from renewable energy sources. The working principle of electrolyzers is based on the process of separating water into hydrogen (H_2) and oxygen (O_2) gases by applying an electric current between the electrodes. Proton Exchange Membrane (PEM) electrolyzers (Figure 3. (b)) separate water into hydrogen and oxygen using a proton exchange membrane, which is an acidic electrolyte. These electrolyzers are more compact, fast-responding and efficient systems. Increasing the efficiency of electrolyzers is of critical importance in reducing energy consumption, reducing costs and increasing hydrogen production capacity.

2.3. Fuel Cell

The function of a fuel cell is to convert the energy of the fuel reaction into electrical energy. A fuel cell can be modeled as a controlled current source. In this study, the H_2/O_2/Air fuel cell (Fig. 3 (c)) was used. The Fuel Cell is a single cell Proton Exchange Membrane Fuel Cell (PEMFC) for H_2/O_2, hydrogen and oxygen operation. By operating the fuel cell with pure Oxygen instead of Atmospheric Oxygen (Air), it has achieved much higher performance with better results. This Proton Exchange Membrane (PEM) fuel cell produces electricity using hydrogen and oxygen gas. Its by-products are water and heat. When using Fuel Cell H_2/O_2/Air, you also hav the option of operating the cell in air-breathing mode simply by removing the stopper. When operating with atmospheric oxygen, the power of the cell is somewhat lower than when operating with pure oxygen.

(a) (b) (c)

Fig. 3. (a) Photovoltaic Panel **(b)** Electrolyser **(c)** H_2/O_2/Air fuel cell

2.4. Electrochemical measurements

For electrochemical tests, a PEM electrolyzer was used for hydrogen and oxygen production. This cell with a surface area of 3.0 cm^2 was used in electrolyzer mode for hydrogen production. Water reacts in the electrolyzer under the influence of electrical energy according to the following formula:

$$2H_2O \text{ <---> } 2H_2 + O_2 \quad (1)$$

This process takes place in the MEA (membrane electrode assembly). The MEA consists of a cathode, an anode, and a special polymer membrane (PEM) that is permeable to protons but a barrier to electrons. Electrolyzer works according to the PEM principle. The produced gases were stored in storage tanks. The energy stored in the gases in chemical form was converted back into electrical energy in the fuel cell.

Fuel Cell H_2/O_2/Air is a single-cell Proton Exchange Membrane Fuel Cell (PEMFC) for hydrogen and oxygen operation. This Proton Exchange Membrane (PEM) fuel cell produces electricity by using hydrogen and oxygen gas. This cell with a surface area of 3.0 cm^2 was used in fuel cell mode for electric production.

3. RESULTS AND DISCUSSION

General view of the studied system is shown in Figure 4.

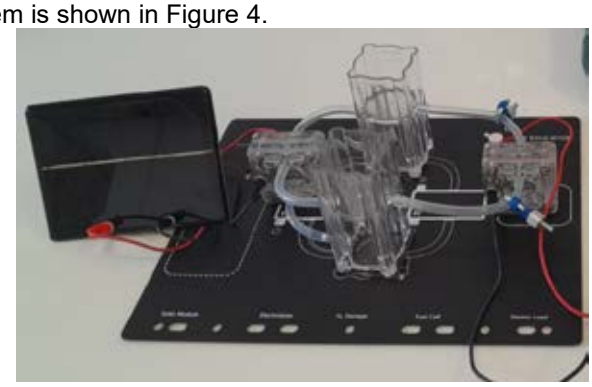

Fig.4. General view of studied system.

We oparete the PEMFC system approximately 10 minutes until the system reaches a stable state, after that *hydrogen and* oxygen *fed into* the *system* and the energy parameters of the system are investigated. The load is applied in steps of 2.82 A. Both hydrogen and oxygen flow rates have been allowed to vary from 0.1-1.0 mL·min⁻¹ gradually increased. In this context, a load-following control strategy is used. Additionally, the time evolution of hydrogen and oxygen consumption rates over a range of currents drawn through the cell has been examined.

Table 1. Hydrogen and oxygen flow rates

Component	H_2 Flow Rate (mL.min^{-1})	O_2 Flow Rate (mL.min^{-1})	Voltage of a Cell (V)
PEMFC	0,2	0,4	2,44
PEMFC	0,4	0,6	2,33
PEMFC	0,6	0,8	1,82
PEMFC	0,8	1,0	0,86

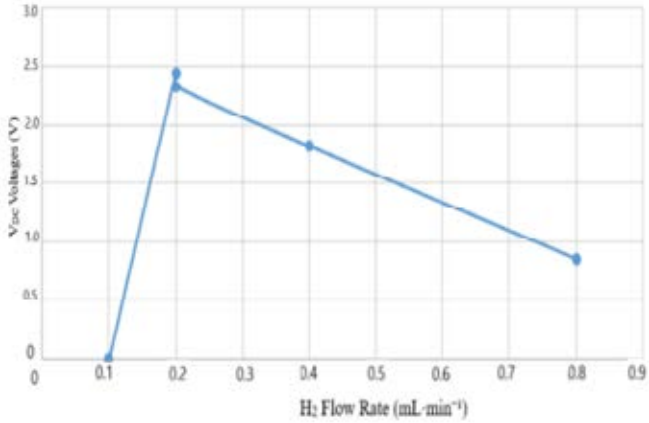

Fig. 5. Voltage versus hydrogen flow rate.

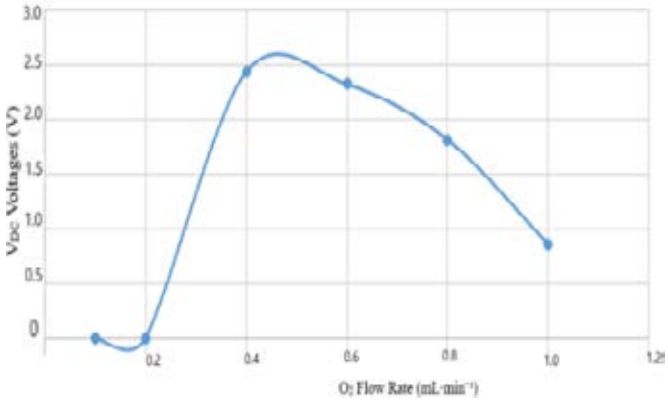

Fig. 6. Voltage versus oxygen flow rate.

As shown in Figure 5, with increase in hydrogen flow rate from 0.1 mL·min⁻¹ to 1.0 mL·min⁻¹, the voltage increases and then rapidly decreases from 0.2 mL·min⁻¹ flow rate. Figure 6 shows that with increase in oxygen flow rate from 0.2 mL·min⁻¹ to 1.2 mL·min⁻¹, the voltage increases rapidly for up to 0.4 mL·min⁻¹, then decreases rapidly. Figure 11 also presents the voltage depending on the flow rate of oxygen and hydrogen.

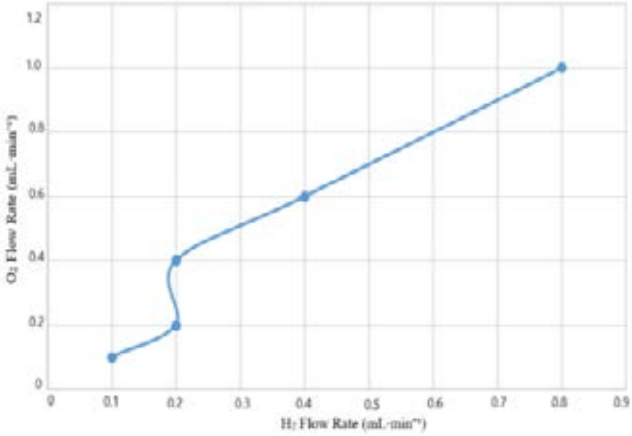

Fig.7. H_2 and O_2 flow rates against time

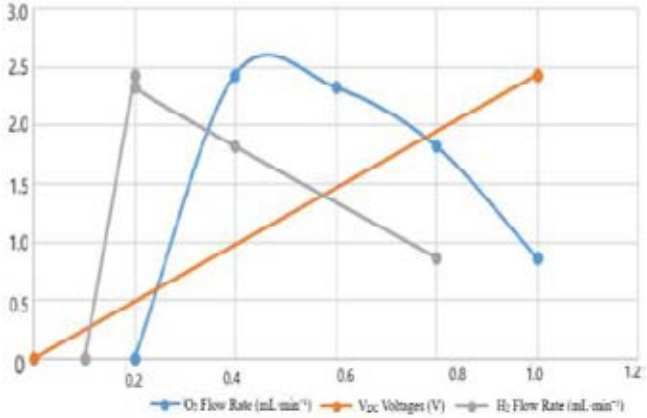

Fig.8. Voltage versus hydrogen and oxygen flow rates.

From Figure 7, it can be seen that there was no electricity production below the flow rate of 0.2 mL·min⁻¹ for hydrogen gas and 0.4 mL·min⁻¹ for oxygen gas. The fuel flow variation profile is shown in Table 1 to note the variation of the parameters of interest within the PEMFC and battery.

The available voltage and power from the fuel cell is a main limiting factor in the development of the system. Figure 8 shows the characteristic curve of the power and voltage relationship. When Figure 9 is examined, it is seen that the fuel cell power density increases with increasing voltage density. Figure shows the cell output range from 2.40 W and 6.88 W. The most efficient voltage and cell output are 2.44 V and 6.88 W, respectively, when the hydrogen flow rate is fixed at 0.2 mL·min⁻¹, and the oxygen flow rate is fixed at mL·min⁻¹ of PEMFC cell.

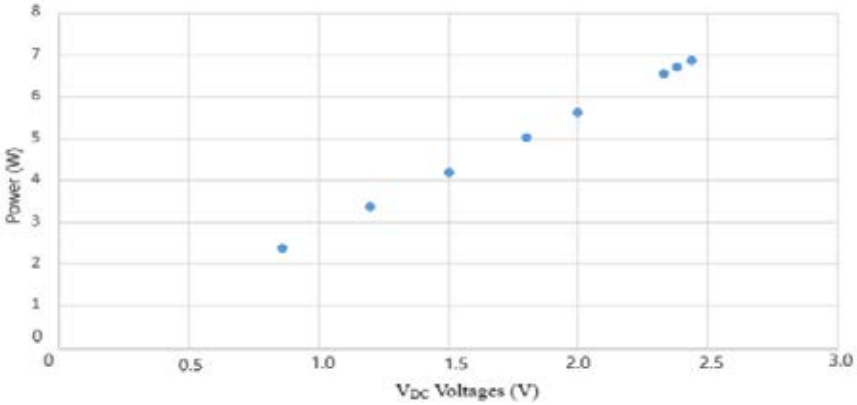

Fig.9. Experimental W-V characteristic of PEMFC cell.

4. CONCLUSIONS

This paper presents the optimum power configuration in a new generation hybrid system for fuel cell electric vehicles. The obtained results show that H2 and O2 gases were the only products from the electrolyzer with their volume ratio close to 2:1, and the efficiency was determined to be nearly 100% during water electrolysis. For this purpose, the change in hydrogen and oxygen consumption in the fuel cell against time was ınvestigated, ranging from 0.86 V to 2.44 V, with the model being repeated each time. The results show that the optimum configuration was found to 2.44 V and 6.88 W of power with the hydrogen flow rate of 0.2 ml/min and the oxygen flow rate of 0.4 ml/min in the polymer electrolyte membrane fuel cell (PEMFC).

This paper demonstrates also the effectiveness of the proposed hybrid PV/Fuel cell system. By installing this system the total cost of the installed system showed that the system can deliver energy with an acceptable cost.

Our future research in this area will focus on separation of water according to the volume of hydrogen and oxygen gases, as well as determining the efficiency of the solar module and PEM electrolizor.

A new product will be developed that will compete with the hybrid system, which is one of the elements of electric vehicle technology.

ACKNOWLEDGEMENT

I would like to thank the Department of Chemistry, Institute of Science, Gazi University for their contributions to my work.

REFERENCES

1. Zou, S and Zhang, T. 2020. CO_2 Emissions, Energy Consumption, and Economic Growth Nexus: Evidence from 30 Provinces in China, Mathematical Problems in Engineering (1) pp.1-21,
2. Li, N., and Song, Y. 2021. Hybrid Energy Systems for Combined Cooling, Heating, and Power and Hydrogen Production Based on Solar Energy: A Techno-Economic Analysis", in Li, Y., H. Phoumin, and S. Kimura (eds.), Hydrogen Sourced from Renewables and Clean Energy: A Feasibility Study of Achieving Large-scale Demonstration. ERIA Research Project Report FY2021 No. 19, Jakarta: ERIA, (Dec.2021) pp. 51-93.
3. https://www.iea.org/news/massive-expansion-of-renewable-power-opens-door-to-achieving-global-tripling-goal-set-at-cop28. Accessed on December 16, 2024.
4. Yue, M., Lambert, H., Pahon, E., Robin, R., Jemei, S., Hissel, D. 2021. Hydrogen energy systems: A critical review of technologies, applications, trends and challenges", Renewable and Sustainable Energy Reviews, 146 (C) pp. 111180-111201.
5. Wang, H. Ouyang, M. 2007. Energy Policy 35:2312-2319
6. Douglas, B. 1997. The essence way renewable energy system. Solar Today, (May/June) pp. 16-19, 1997.
7. Felix, A. F. and Simoes, M.G. 2020. Integration of Alternative Sources of Energy" John Wiley & Sons, Inc (Feb. 2006).
8. Azami M.N.M. 2020. Modelling of Photovoltaic, Fuel Cell and Battery Hybrid System Connected to Non-Linear Load. International Journal of Advanced Trends in Computer Science and Engineering 9 (1.4) pp. 495-502.
9. Scott, K., Xu, C., Wu, X. 2014. Intermediate temperature proton-conducting membrane electrolytes for fuel cells. WIREs Energy Environ. 3 (1), pp. 24–41.
10. Dupis, A.C. 2011. Proton exchange membranes for fuel cells operated at medium temperatures: Materials and experimental techniques. Prog. Mater. Sci. 56 (3), pp. 289–327.
11. Park, C.H. Lee, C.H. Guiver, M.D. Lee, Y.M. 2011. Sulfonated hydrocarbon membranes for medium-temperature and low-humidity proton exchange membrane fuel cells (PEMFCs), Prog. Polym. Sci. 36 (11) pp. 1443–1498.
12. Sun, X., Simonsen, S.C., Norby, T., Chatzitakis, A. 2019. Composite membranes for high temperature PEM fuel cells and electrolysers: A critical review. Membranes, 9 (7), pp. 83.
13. Lee, K.S., Maurya, S., Kim, Y.S., Kreller, C.R., Wilson, M.S., Larsen, D., Elangovan, S.E., Mukundan, R. 2018. Intermediate temperature fuel cells via an ion-pair coordinated polymer electrolyte, Energy Environ. Sci.11, pp. 979–987.

MACHINE LEARNING-BASED MODELING AND PERFORMANCE ANALYSIS OF SOLID OXIDE ELECTROLYSIS CELLS (SOECs)

Muhammed Talha Durmaz, Meryem Sena Akkuş
Ankara Yıldırım Beyazıt University, Department of Energy Systems Engineering, Kecioren, 06010, Ankara, Türkiye
Ankara Yıldırım Beyazıt University, Department of Energy Systems Engineering, Kecioren, 06010, Ankara, Türkiye

Corresponding author e-mail: tlhdrmz@gmail.com

ABSTRACT

Addressing climate change demands a shift from fossil-based energy to sustainable alternatives, with solid oxide electrolysis cells (SOECs) emerging as a critical technology in this transition. Functioning at elevated temperatures, SOECs transform H_2O and CO_2 into hydrogen and syngas, delivering exceptional efficiency in converting renewable energy into chemical energy carriers. Nevertheless, challenges at the nanoscale and material deterioration hinder the performance of traditional techniques. Machine learning (ML) offers a powerful approach to overcome these obstacles by forecasting SOEC efficiency, simulating degradation processes, and refining operational parameters. This research outlines the core principles of SOEC systems and explores the incorporation of ML, specifically examining the contributions of Extreme Learning Machine (ELM) and Extreme Gradient Boosting (XGBoost) to performance estimation and system enhancement. The results indicate that ML significantly boosts the practical viability of SOECs for industrial use, though it also reveals limitations such as insufficient data availability and difficulties in interpreting model outcomes.

Keywords: Solid Oxide Electrolysis Cells, Machine Learning, Hydrogen Generation, Efficiency Enhancement

1.INTRODUCTION

Mitigating the devastating impacts of climate change has rendered the transition of our energy systems from fossil fuels to renewable resources an urgent imperative. Although wind and solar power possess the capacity to meet global energy demands, their intermittent nature necessitates advanced energy storage and conversion technologies.SOECs, operating within a temperature range of 600–1000°C, efficiently convert H_2O and CO_2 into hydrogen and synthesis gas. Over the past 15 years, advancements have yielded a 2.5-fold increase in efficiency, a 100-fold extension in operational lifespan, and a 100-fold expansion in gas production. However, challenges such as nanoscale intricacies, electrode wear, and material degradation continue to render conventional physical modeling approaches—such as finite element analysis—inadequate and impede commercial scalability [1,2]. While the literature includes efforts to enhance SOEC performance, the comparative analysis of advanced machine ML techniques, such as ELM and XGBoost, alongside their integration with Genetic Algorithms (GA), remains underexplored. Traditional methods are hampered by high computational demands and limited generalizability, whereas this study addresses this gap by systematically comparing ELM and XGBoost, proposing an innovative approach integrated with GA. Using ELM, the current-voltage relationship was modeled with an accuracy of 0.999, underscoring ML's capability to unravel complex processes. This data-driven framework analyzes hydrogen production, temperature variations, and electrode resilience in SOECs, unveiling their potential for optimization at an industrial scale. Consequently, we propose a roadmap to enhance the efficiency and durability of SOEC technology in the realms of performance forecasting and system improvement [3].

2.SOEC AND ML LEARNING

2.1. Fundamentals of SOEC Technology

Modeling approaches for SOECs are categorized into two main types: physical models and ML-based methods. Physical models rely on electrochemical equations and material properties, yet their effectiveness is constrained by a lack of data for novel materials. In contrast, ML-driven techniques such as ELM and XGBoost leverage experimental data to deliver adaptable predictions. In this study, these methods were evaluated using a dataset of 322 current-voltage I-V measurements collected at 800°C, provided by Zhang et al. (2017), supplemented by an additional experimental dataset of 355 data points (encompassing ohmic resistance, current density, and hydrogen production rate measurements). A k-fold cross-validation experimental design was employed, with models trained using Python-based scikit-learn and XGBoost libraries to compare the performance of ELM and XGBoost [1,3,4,6]. Comparative results revealed that XGBoost outperformed ELM (Rcc > 0.999), Random Forest (RF), and Support Vector Regression (SVR) in terms of accuracy ($R^2 > 0.95$). While physical models excel when parameters are well-defined, ELM's single-stage training offers superior speed compared to XGBoost's iterative processes, the computational burden of RF and SVR, and the demands of physical simulations. However, ELM's generalization capacity is limited, whereas XGBoost excels with large datasets and intricate relationships, enhanced by hyperparameter optimization. In terms of interpretability, XGBoost's SHAP and PDP analyses provide an edge over ELM's less transparent structure and the limitations of other methods. Regarding

scalability, ML models readily adapt to new data, while physical models require recalibration. In predictive applications, XGBoost combined with Genetic Algorithms identifies optimal operating conditions (e.g., 1.174 L/(h·cm²) H_2 production at 1.61 A/cm²), guiding performance improvements. PDP analysis indicates increased hydrogen production under conditions of 850°C and 1.5 V, while ML predicts wear trends, aiding the development of robust electrode designs. Additionally, ELM and XGBoost forecast SOEC behavior under varying gas compositions, enhancing compatibility with renewable energy grids. At an industrial scale, these models can improve energy efficiency and reduce degradation rates, thereby extending the commercial lifespan of SOECs [1,4].

2.2. Machine Learning and Modeling Techniques

ML is integrated into SOEC technology due to its ability to predict the behavior of complex systems by learning from data, offering an advantage over physical models by analyzing system performance without requiring extensive material data or computationally intensive processes. In this study, two primary ML approaches—ELM and XGBoost stand out for modeling SOECs. ELM excels in rapidly modeling the current-voltage (I-V) relationships of SOECs; Zhang and colleagues (2017) trained ELM using 322 I-V data points collected at 800°C, achieving a fit exceeding 0.999, which enabled the prediction of system efficiency based on gas mixture ratios (H_2O, CO_2) and demonstrated the superiority of co-electrolysis over other processes. Conversely, XGBoost proves more effective in predicting SOEC performance with complex datasets; a model trained on a 355-point dataset (including measurements of ohmic resistance, current density, and hydrogen production rate) using the XGBoost library in Python delivered high accuracy for parameters such as ohmic resistance (R^2 = 0.9620), current density (R^2 = 0.9536), and hydrogen production rate (R^2 = 0.9677). SHAP analysis identified the dominant influences of active surface area, voltage, and temperature on performance, and when coupled with GA, the model achieved an optimal hydrogen production rate of 1.174 L/(h·cm²). Model training was conducted using a k-fold cross-validation experimental design implemented through the scikit-learn and XGBoost libraries [4-7].

2.3. Comparison of ML Methods and Predictive Applications

ML methods employed to predict SOEC performance offer distinct strengths: ELM is effective with small datasets due to its rapid learning and low computational demand, though its generalization ability is constrained, whereas XGBoost excels in analyzing large datasets and intricate relationships, achieving higher accuracy through hyperparameter tuning. In contrast, alternative methods such as RF and SVR yield lower R^2 values compared to XGBoost. In this study, a comparison of ELM and XGBoost was conducted using the Zhang et al. (2017) dataset (322 I-V points) and an additional 355-point dataset, implemented in Python with the scikit-learn and XGBoost libraries, and validated through k-fold cross-validation. In predictive applications, ML-based models guide the identification of optimal operating conditions for SOECs; for instance, XGBoost combined with PDP analysis demonstrated an increase in hydrogen production under conditions exceeding 850°C and 1.5 V. At an industrial scale, these models can enhance energy efficiency and reduce wear rates, thereby extending the commercial lifespan of SOECs [4-7].

3. DISCUSSION AND RESULT

Although SOEC technology holds the potential to revolutionize renewable energy conversion, challenges such as long-term durability and cost-effectiveness persist. The integration of ML offers solutions to these issues while simultaneously raising new questions. ELM's streamlined architecture provides an advantage in rapid prototyping, whereas XGBoost's complexity is essential for in-depth analyses. The success of these models hinges on the quality and volume of data, underscoring the importance of experimental studies. Kamkeng and Wang (2022) emphasized the role of dynamic simulations in modeling the structural degradation of SOECs, yet the combination of such approaches with ML remains underexplored. In this study, ELM and XGBoost models were trained using the Zhang et al. (2017) dataset (322 I-V points) and an additional 355-point dataset, tested with k-fold cross-validation in Python using the scikit-learn and XGBoost libraries, revealing their potential for performance prediction and optimization [1,2,4,5]. Looking ahead, a hybrid integration of ML and physical models could pave the way for breakthroughs in durability and performance enhancement. Innovative designs, such as proton-conducting SOECs (H-SOECs), promise high efficiency at lower temperatures when supported by ML.Solid oxide electrolysis cells stand out as a critical technology in achieving a carbon-neutral energy future by converting renewable energy into chemical fuels. ML plays a transformative role in advancing these systems, serving as a powerful tool to maximize their potential. ML methods such as ELM and XGBoost provide effective solutions for predicting SOEC performance, modeling degradation, and enhancing efficiency through optimization. Building on insights from works like Hauch et al. (2020), Zhang et al. (2017), and Kamkeng and Wang (2022), the synergy of ML with SOECs demonstrates the capacity to shape the future of renewable energy systems. In this study, ELM and XGBoost models, trained on the 322 I-V data points from Zhang et al. (2017) and an additional 355-point dataset using Python's scikit-learn and XGBoost libraries with k-fold cross-validation, showcased distinct strengths: ELM excelled with fast, straightforward predictions on smaller datasets, while XGBoost outperformed in unraveling complex relationships and improving industrial applicability [1,4,6]. These approaches pushed the boundaries of SOEC technology in areas such as performance forecasting and material resilience. Future research could focus on integrating ML with physical models

to align them with real-world conditions, bolster data infrastructure, and support novel material designs, thereby reinforcing the role of SOECs in sustainable energy systems.

4. CONCLUSION

This study highlights the revolutionary potential of ML in elevating SOECs as a key enabler of renewable energy conversion, tackling persistent challenges like long-term durability and cost-effectiveness while laying the groundwork for a carbon-neutral energy landscape. The incorporation of ELM and XGBoost has proven vital in surpassing the constraints of conventional physical modeling, delivering swift, data-driven insights into SOEC performance and degradation patterns. ELM's proficiency in capturing current-voltage relationships with exceptional precision (Rcc > 0.999) and XGBoost's adeptness at navigating complex datasets ($R^2 > 0.95$) showcase their synergistic advantages—speed and simplicity versus robustness and scalability—outperforming alternatives such as Random Forest and Support Vector Regression. Predictive applications, including achieving an optimal hydrogen production rate of 1.174 L/(h·cm²) at 1.61 A/cm² and confirming enhanced yields at 850°C and 1.5 V through PDP analysis, underline ML's ability to refine industrial-scale operations. Nonetheless, hurdles remain: the models' dependence on high-quality data underscores the value of robust experimental frameworks, and while interpretability is improved by tools like SHAP, it still requires refinement. Moving forward, blending ML with physical models and investigating cutting-edge designs like proton-conducting SOECs (H-SOECs) present compelling opportunities to boost efficiency at reduced temperatures and prolong operational longevity. By addressing these gaps, this research establishes a stepping stone for SOECs to realize their transformative promise, steering sustainable energy systems toward greater resilience and feasibility.

REFERENCES

1. Hauch, A., Küngas, R., Blennow, P., Hansen, A. B., Hansen, J. B., Mathiesen, B. V., & Mogensen, M. B. (2020). Recent advances in solid oxide cell technology for electrolysis. *Science*, *370*(6513), eaba6118.
2. Wang, Y., Li, W., Ma, L., Li, W., & Liu, X. (2020). Degradation of solid oxide electrolysis cells: Phenomena, mechanisms, and emerging mitigation strategies—A review. *Journal of Materials Science & Technology*, *55*, 35-55.
3. Yang, Q., Zhao, L., Xiao, J., Wen, R., Zhang, F., & Zhang, D. (2024). Machine learning-assisted prediction and optimization of solid oxide electrolysis cell for green hydrogen production. *Green Chemical Engineering*.
4. Zhang, C., Liu, Q., Wu, Q., Zheng, Y., Zhou, J., Tu, Z., & Chan, S. H. (2017). Modelling of solid oxide electrolyser cell using extreme learning machine. *Electrochimica Acta*, *251*, 137-144.
5. Wang, C., Deng, C., & Wang, S. (2020). Imbalance-XGBoost: leveraging weighted and focal losses for binary label-imbalanced classification with XGBoost. *Pattern recognition letters*, *136*, 190-197.
6. Liu, Y., Esan, O. C., Pan, Z., & An, L. (2021). Machine learning for advanced energy materials. *Energy and AI*, *3*, 100049.
7. Kamkeng, A. D., & Wang, M. (2022). Long-term performance prediction of solid oxide electrolysis cell (SOEC) for CO2/H2O co-electrolysis considering structural degradation through modelling and simulation. Chemical Engineering Journal, 429, 132158.

OPTIMAL DESIGN OF A NEW PHOTOVOLTAIC-ELECTROLYSER-FUEL CELL-BATTERY HYBRID SYSTEM

[1*]*Orhan Yılmaz*, [1,2]*Aylin Aytaç*
[1] Gazi University, Instute of Science, Department of Chemistry, Teknik Okullar, Ankara, 06560, Türkiye
[2] Institute of Energy and Climate Research (IEK-3), Forschungszentrum Juelich, 52425 Juelich, Germany
*Corresponding author e-mail: orhanyilmaz37@gmail.com

ABSTRACT
Today, both developed and developing countries are transitioning to 'new energy technologies', which are clean energy systems like solar-powered, electric and fuel cell (FC) vehicles for future transport planning. In our country, significant studies have been conducted in this direction and the goverment is working to encourage the use of electric vehicles. The aim of this study is to develop a new photovoltaic-fuel cell hybrid battery system as an alternative to existing hybrid battery systems. It is planned to produce twice as much electricity as other fuel cells thorough electrolysis reactions.
In this study, the fuel cell current and voltage produced with the best electrolyte solution concentration to produce hydrogen discharge were tested and the effect of temperature on fuel cell performance was investigated. In the PV-Electrolyzer-Fuel Cell test based on the change of the concentration of the KOH solution, it was determined that the output power increased with the increase of the concentration. The efficiency also increased slightly as the output power increased. It was observed that the cell voltage increased with the increase of the temperature. At the same time, the power density also increased. The optimum result was determined as 1.5 M concentration and 60 °C temperature.

Keywords: Photovoltaic-electrolyser-fuel cell-battery hybrid system, Optimal configuration, Power output

1. INTRODUCTION
Globally, the solar hydrogen and fuel cell attracted more attention as alternative energy sources in 1990s. Solar energy is the most promising source, since the fabrication with a lowercost photovoltaic (PV) devices becomes a reality [1]. However, a solar energy generation does not promise permanent output power due to intermittent weather conditions. PV plant is integrated with other power sources such as hydrogen generator, fuel cell (FC), or battery back-up [2]. The widespread use of hydrogen fuel cell is due to its high-efficiency, faster and more flexible loadresponse, modular production characteristics e.g. change in tone. Unlike batteries, FCs also do not require any special charging. Several types of fuel cells exist, but they all are composed of an anode, cathode and electrolyte membrane that enables the movement of the hydrogen ion (Proton) between the two sides in fuel cells. At the anode (fuel electrode), a catalyst separates the hydrogen molecules into protons and electrons. The ions migrate from the anode to the cathode through the electrolyte. At the same time, electrons move from the anode to the cathode through an external electric circuit, creating direct current (DC) electricity. In cathode another catalyst causes ions, electrons and oxygen (O_2) that reacts to produce water [3]. Proton exchange membrane fuel cells (PEMFC) seem to be the most commonly used type for vehicles, being characterized by low-temperature conditions, high power density, fast start-up process, and rapid response to load changes [4-8]. Our goal is to find the optimum design of a new photovoltaic-electrolyser-fuel cell-battery hybrid system that we model for vehicles.

2. MATERIALS AND METHODS
2.1. Solar Power
Solar panel is used as the primary energy source, fuel cell is used as a backup source in order to meet the electrical load. PV solar panels (Fig. 3. (c)) are composed of by semiconductor materials and they directly convert the sunlight falls onto them to electrical energy. To extract maximum power from solar panel depends on the amount of incident solar radiation on its top. So, a panel needs to be tilted in such an angle that maximum sunlight fall above surface vertically. In this study, the light source is mounted at a perpendicular angle (90° angle) to the solar panel. After turning on the lamp, we wait at least one minute to prevent errors caused due to fluctuations in temperature. An open circuit voltage ($r = \infty$) is used and generated lower resistance sequentially.
2.2. Electronic Control Components
The electrical control componentst of a fuel cell such as inverter, pump and motors, electrical connectors etc. are critical components to ensure the reliable and efficient operation of the fuel cell. In this study, an Electronic Control Interface (ECI) is designed to provide gradual increase in flow rates and to control the power flow.
2.2.1. Design of signal conditioner: To develop this system, Microchip 32mx series has been chosen to construct the electronic control system. It has a 32mx795f512l series mcu 80MHz 32-bit processor, 16 ch Analog-to-Digital Converter (ADC) and 4 Pulse-Width-Modulation (PWM) channels. The signal conditioner can be connected to the PC by USB via a serial port bluetooth. Thus, during the development of the control algorithm, all types software updates, debugging and data exchange can be done through this channel. The signal conditioner will also provide electrical isolation (galvanic) between the processor and the PC by the wireless connection (Fig. 1. (a)).
2.2.2. Motor Drive Circuit: The PFC-3phMotor card operates using the 6PWM channels. DC motor driver circuit (Fig. 1.

(b)) consists of three MOSFETs forming an H-bridge (Fig.1. (c)) as shown in fig.4. MOSFET technology ensures simpler and more efficient drive circuits with significant economic benefits compared to bipolar devices. This MOSFETs circuit can withstandup to 500V with a switch current of 8A.

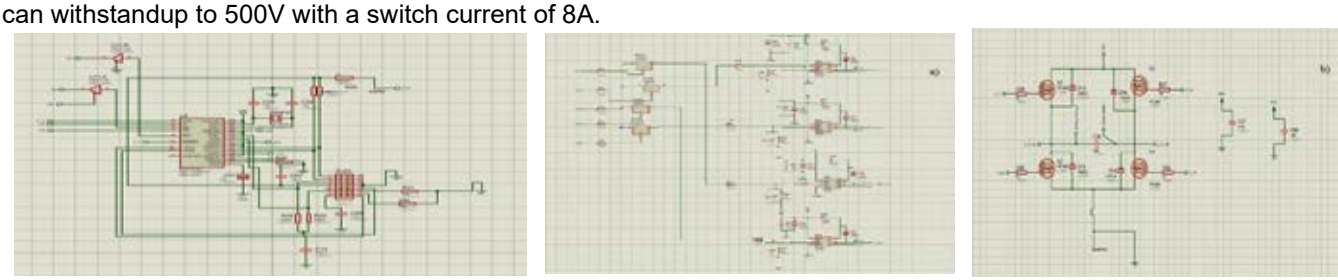

(a) (b) (c)

Fig. 1. (a) Ethernet connection circuit. (b) Motor drive circuit, (c) H-Bridge

2.2.3. Electronic Control Interface (ECI): Electronic control interface optimizes the power durability and energy efficiency of the system. ECI includes concentration/humidity/temperature sensors, semiconductor switches, output devices and other electronic units. In this study, the fuel and oxidant flow is recorded sensors with different temperature and concentration and sampled with Analog Digital Converters (ADC) in the digital signal processors (DSP). A new type of computer motherboard has also been developed. System operating characteristics are logged to an SD card using a real-time clock (RTC) module. The motherboard as shown in Figure 5 mainly consists of two modbus/485 communication terminals, one rs232 communication port, and a voice allert system. This motherboard can be connected a touch screen up to 15.1 inches and enable connection to future integrated circuits via ethernet connection.

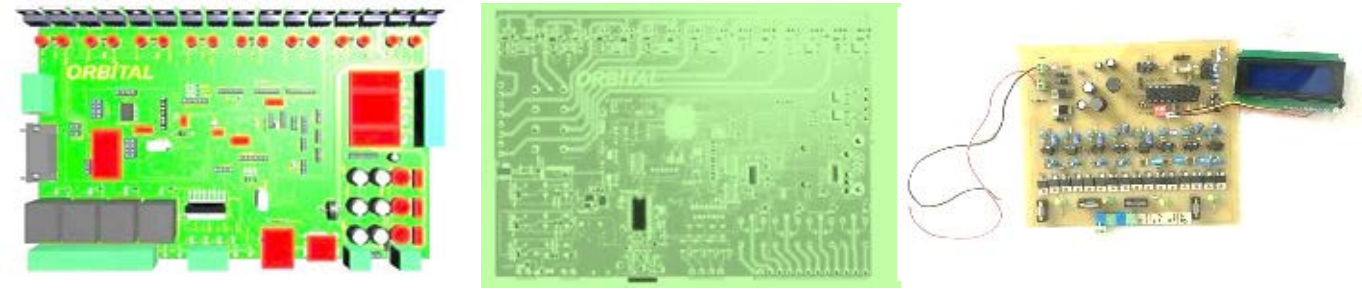

(a) ***(b)*** ***(c)***

Fig. 2. Sketches of working setup of motherboard a) top-view, b) bottom view, c) design.

2.3. Electrolyser and Fuel Cell

The function of a fuel cell is to convert the energy of the fuel reaction into electrical energy. A fuel cell can be modeled as a controlled current source. In this study, the electrolyser (Fig. 3. (a)) and the H_2/O_2/Air fuel cell (Fig. 3 (b)) was used. The Fuel Cell is a single cell Proton Exchange Membrane Fuel Cell (PEMFC) for H_2/O_2, hydrogen and oxygen operation. By operating the fuel cell with pure Oxygen instead of Atmospheric Oxygen (Air), it has achieved much higher performance with better results. This Proton Exchange Membrane (PEM) fuel cell produces electricity using hydrogen and oxygen gas. Its by-products are water and heat.

(a) (b) (c)

Fig. 3. (a) Electrolyser (b) H_2/O_2/Air fuel cell (c) Solar power.

2.4. Electrochemical measurements

For electrochemical tests, a PEM electrolyzer was used for hydrogen and oxygen production. This cell with a surface area of 3.0 cm^2 was used in electrolyzer mode for hydrogen production. Water reacts in the electrolyzer under the influence of electrical energy according to the following formula:

$$2H_2O \text{ <---> } 2H_2 + O_2 \quad (1)$$

This process takes place in the MEA (membrane electrode assembly). The MEA consists of a cathode, an anode, and a special polymer membrane (PEM) that is permeable to protons but a barrier to electrons. Electrolyzer works according to the PEM principle. The produced gases were stored in storage tanks. The energy stored in the gases in chemical form was converted back into electrical energy in the fuel cell.

3. RESULTS AND DISCUSSION

The model of Photovoltaic-Electrolyser-Fuel Cell and Battery hybrid system and circuit diagram of the studied system is shown in Figure 4.

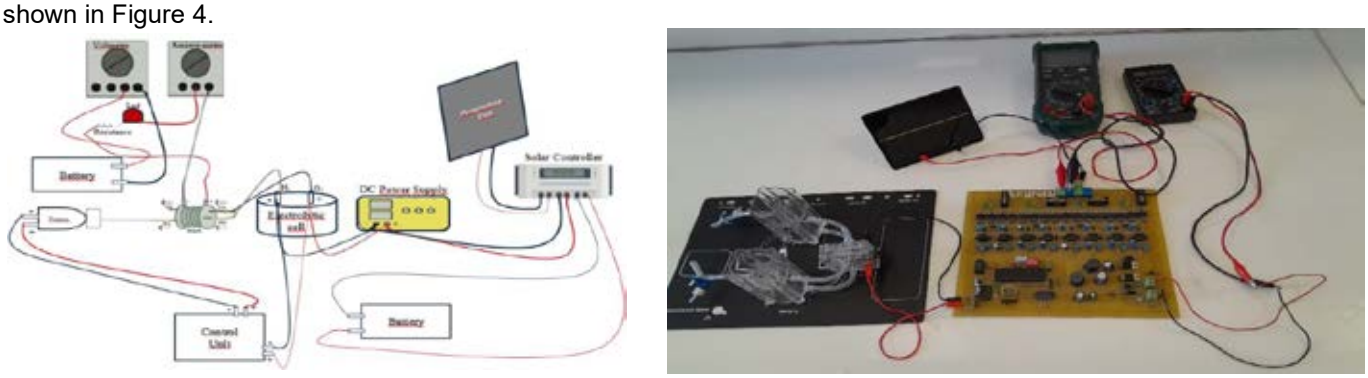

(a) (b)

Fig.4. (a) Modeling of photovoltaic-electrolyser-fuel cell-battery hybrid system. (b)Circuit diagram of the studied system**.**

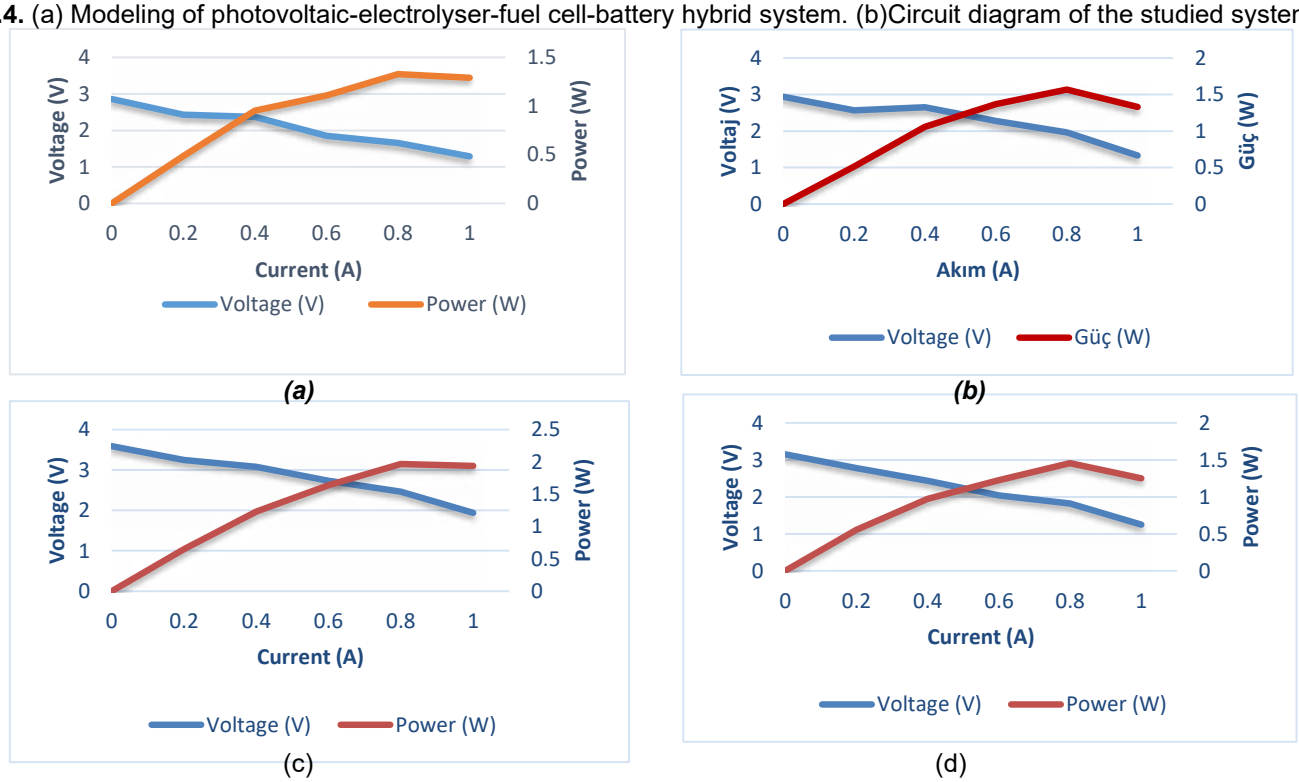

Fig 5. Relationship between current, voltage and output power of PV-electrolyzer-fuel cell and battery hybrid system at (a) 0.50 M, (b) 1,00 M, (c) 1,50 M and (d) 2,00 M KOH solution concentration

In Fig 5. (a), the highest output power of 1.66 V and 1.3280 W at a current of 0.80 A in 0.50 M KOH solution concentration was obtained. In Figure 5. **(b),** the highest output power of 1.96 V and 1.5680 W at a current of 0.80 A in 1.00 M KOH solution concentration was obtained. In Figure 5. (c), the highest output power of 2.46 V and 1.9680 W at a current of 0.80 A in 1.50 M KOH solution concentration was obtained. In Figure 5. (d), the highest output power of 1.82 V and 1.4560 W at a current of 0.80 A in 2.00 M KOH solution concentration was obtained.

In Fig. 6, the relationship between the output power and efficiency of the PV-Electrolyzer-Fuel Cell system was analyzed for a variation of KOH solution concentrations. Here, it is expected that the output power and system efficiency will increase proportionally with increasing current load. The output power is 1.3280 W at 0.5 M KOH solution concentration, 1.5680 W at 1.0 M KOH solution concentration, 1.9680W at 1.5 M KOH solution concentration and 1.9586 W at 2 M KOH solution concentration. The system efficiency is highest at 1.968 W output power in 1.5 M KOH solution and 2.3940 W

at 1.5 M KOH solution.

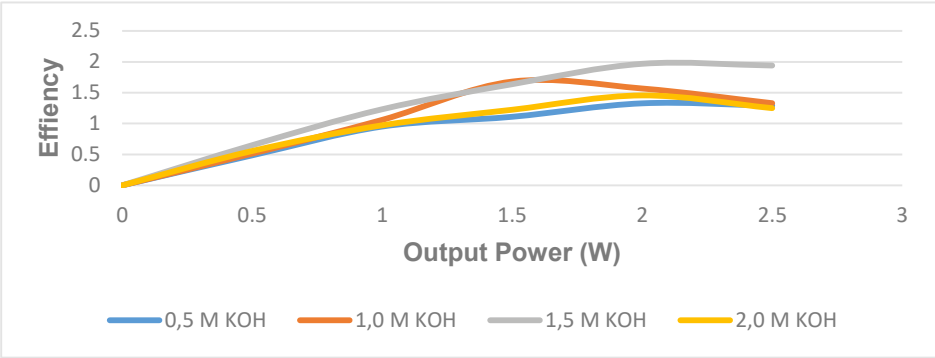

Fig. 6. Output power and efficiency of pfotvoltaic-electrolyzer-fuel cell-battery hybrid system on KOH solution concentration change

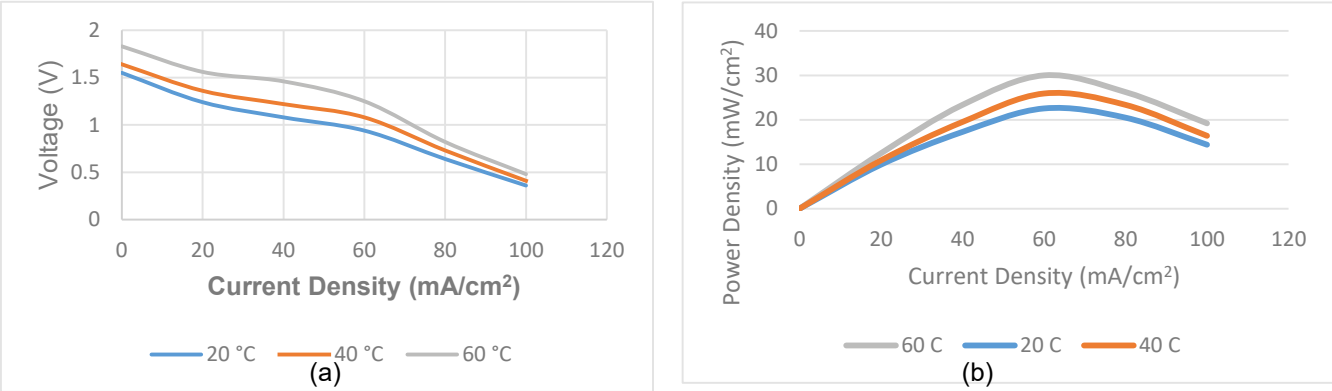

Fig 7. (a) Current density-voltage curve (b) current density-power density curve of PV-Electrolyzer-Fuel Cell system at varying temperatures

Operating temperature is an important parameter to prevent performance losses in the fuel cell. However, increasing the operating temperature is important to determine the optimum cell operating temperature. Measurements were taken at 20, 40 and 60 °C to investigate the effect of temperature on fuel cell performance. It was observed that the cell voltage increased with increasing temperature. At the same time, the power density also increased.

4. CONCLUSIONS

This paper presents the modelling of PV panel, electrolyser fuel cell and battery hybrid system. In the PV-Electrolyzer-Fuel Cell test based on the change of the concentration of the KOH solution, it was determined that the output power increased with increasing concentration. The efficiency increased slightly as the output power increased. The highest power was obtained at 1.5 M. At 2 M concentration, there was a decrease in output power and efficiency. It was observed that the cell voltage increased with increasing temperature. At the same time, the power density also increased. The best result was obtained at 60 °C. The optimum result was obtained at 1.5 M and 60 °C.

ACKNOWLEDGEMENT

I would like to thank the Department of Chemistry, Institute of Science, Gazi University for their contributions to my work.

REFERENCES

1. Douglas, B. 1997. The essence way renewable energy system. Solar Today, (May/June) pp. 16-19, 1997.
2. Felix, A. F. and Simoes, M.G. 2020. Integration of Alternative Sources of Energy" John Wiley & Sons, Inc (Feb. 2006).
3. Azami M.N.M. 2020. Modelling of Photovoltaic, Fuel Cell and Battery Hybrid System Connected to Non-Linear Load. International Journal of Advanced Trends in Computer Science and Engineering 9 (1.4) pp. 495-502.
4. Scott, K., Xu, C., Wu, X. 2014. Intermediate temperature proton-conducting membrane electrolytes for fuel cells. WIREs Energy Environ. 3 (1), pp. 24–41.
5. Dupis, A.C. 2011. Proton exchange membranes for fuel cells operated at medium temperatures: Materials and experimental techniques. Prog. Mater. Sci. 56 (3), pp. 289–327.
6. Park, C.H. Lee, C.H. Guiver, M.D. Lee, Y.M. 2011. Sulfonated hydrocarbon membranes for medium-temperature and low-humidity proton exchange membrane fuel cells (PEMFCs), Prog. Polym. Sci. 36 (11) pp. 1443–1498.
7. Sun, X., Simonsen, S.C., Norby, T., Chatzitakis, A. 2019. Composite membranes for high temperature PEM fuel cells and electrolysers: A critical review. Membranes, 9 (7), pp. 83.
8. Lee, K.S., Maurya, S., Kim, Y.S., Kreller, C.R., Wilson, M.S., Larsen, D., Elangovan, S.E., Mukundan, R. 2018. Intermediate temperature fuel cells via an ion-pair coordinated polymer electrolyte, Energy Environ. Sci.11, pp. 979–987.

EXPERIMENTAL ANALYSIS OF PROTON EXCHANGE MEMBRANES FOR WATER ELECTROLYZERS ACROSS A RANGE OF OPERATING PARAMETERS

[1,2,3] *Abdelmola Albadwi*, [1] *Saltuk Buğra Selçuklu*, [1,2,4] * *Mehmet Fatih KAYA*
[1] Erciyes University, Engineering Faculty, Department, Heat Engineering Division, Kayseri, 38039, Turkey
[2] Erciyes University H2FC Hydrogen Energy Research Group, Kayseri, 38039, Turkey
[3] Erciyes University, Graduate School of Natural and Applied Sciences, Energy Systems Engineering Department, 38039 Kayseri, Türkiye
[4] Energy Conversion Research and Application Center (ECRAC), Erciyes University, 38039, Kayseri, Turkey

* E-mail: kayamehmetfatih@erciyes.edu.tr

ABSTRACT
Proton exchange membrane water electrolyzers (PEMWE) show promise for clean hydrogen production, yet operational conditions and materials selection significantly influence their performance. This study investigates PEMWE performance across various operational parameters. Nafion 115 and Aquivion membranes were evaluated using different catalyst loadings (3-4 mg/cm² IrO_2 anode, 0.4 mg/cm² Pt cathode), various temperatures (50-80°C), and water flow rates (50-100 ml/min). Electrochemical analysis demonstrated substantial performance differences under varying conditions. The test results revealed that at 80°C with a 100 ml/min flow rate, Aquivion membrane-based cells generated approximately 280.26 mA·cm⁻² current density, substantially exceeding the 111.12 mA·cm⁻² achieved with Nafion 115 under identical conditions. Higher catalyst loading further improved system performance. These results highlight the importance of membrane type, operating temperature, flow rate, and catalyst configuration for maximizing PEMWE performance in electrochemical hydrogen production applications.
Keywords: PEM water electrolyzer, Catalyst loading, Performance, Operating parameters

1. INTRODUCTION

In response to escalating global energy demands and environmental concerns, renewable energy sources integrated with hydrogen technology offer promising sustainable alternatives to fossil fuels. Water electrolysis powered by renewable energy represents an environmentally sustainable approach to green hydrogen production without CO_2 emissions [1]. Among modern electrolyzer technologies, PEMWEs have gained industrial significance due to their ability to handle fluctuating power inputs [2]. PEMWEs function within modest thermal regimes (30-80°C) yet sustain significant current densities (2 $A.cm^{-2}$), yielding gases of exceptional purity (99.99%), and utilize solid polymer electrolyte membranes designed explicitly for proton conduction, making them well-suited for applications ranging from hydrogen refueling stations to renewable energy storage systems [3].

Performance optimization in PEMWEs remains a critical research frontier. Recent research has established vital benchmarks for catalyst integration and performance optimization. Studies have identified optimal Ir loading ranges of 0.204-0.304 mgIr/cm² in PEMWEs, minimizing voltage losses while enhancing conductivity [4]. Other studies have demonstrated that optimal PEMWE performance can be achieved at high working voltages with reduced catalyst loading (0.5 $mg.cm^{-2}$) with 10 wt% ionomer content [5]. Additionally, simplified electrode fabrication methods have achieved high performance (2.39 $A.cm^{-2}$ at 1.9 V) with minimal cathode loading (18.4 µg/cm²), though durability tests indicated a need for further optimization [6]. On the other hand, temperature effects on PEMWE performance were investigated [7]. They operated PEMWEs at 75, 80, and 85°C, demonstrating increased current density with rising temperature under identical membrane electrode assembly (MEA) conditions. Electrochemical analysis confirmed that enhanced ionic conductivity significantly contributed to this performance improvement. Additionally, higher operating temperatures decreased activation potential, exponentially improving performance through increased exchange current density [8].

In this study, PEMWE performance was investigated across multiple operational parameters. The effects of temperature, water flow rate, membrane type, and catalyst loading were examined using Nafion 115 and Aquivion membranes. Electrochemical measurements were performed to determine the relationship between these variables and system performance.

2. MATERIALS AND METHODS

In this study, electrodes were fabricated individually, with the anode catalyst ink air-sprayed onto a gas diffusion layer (GDL) maintained at 60°C. Two different IrO_2 loadings were prepared: i) a 3 $mg.cm^{-2}$ loading using an ink composition of 18 mg IrO_2, 60 µL Nafion solution (ASP-Nafion 10 wt%), 1.2 mL ethanol, and 240 mL deionized water (18 µS conductivity), and ii) a 4 $mg.cm^{-2}$ loading using 24 mg IrO_2, 80 µL Nafion solution, 1.2 mL ethanol, and 240 mL deionized water. For cathode preparation, loading 0.4 $mg.cm^{-2}$ Pt (20% Pt on Vulcan XC-72R, Fuel cell store) was utilized, with the spraying process also conducted at 60°C. All ink formulations underwent sonication for 15 minutes to ensure proper dispersion; experimental parameter values can be seen in 0.

Table 1. Experimental parameters

Parameter	Unit	Min.	Max.
Anode loading	*mg.cm^{-2}*	*3.0*	*4.0*
Cathode loading	*mg.cm^{-2}*	*0.4*	*0.4*
Flow rate	*mL.min^{-1}*	*50*	*100*
Temperature	*℃*	*50*	*80*
Torque	*N.m*	*2.0*	*2.0*

The electrodes were integrated with Nafion 115 and Aquivion E98-09S membranes. Furthermore, the membrane pre-treatment process was customized for the membrane. For Nafion 115, membranes were cut to 5 cm² active area and subjected to a sequential treatment protocol [9]. The entire Nafion pre-treatment process spanned 6 hours. The Aquivion membrane underwent an identical sequence with extended treatment durations of 1.5 hours per step to ensure thorough cleaning. Following pre-treatment, the anode and cathode catalyst inks were sprayed onto the membranes (Airbrush kit, Timbertech store). The MEA hot-pressing parameters were optimized for each membrane type: Nafion 115 was pressed at 2 bar and 120°C for 2 min. At the same time, Aquivion required more aggressive conditions of 5 MPa at 155°C for 2 min to ensure optimal MEA contact and integration.

The PEMWE cell was designed with an integrated MEA. Two titanium (Ti) mesh gas diffusion layers coated with Pt, measuring 2 mil and 10 mil in thickness, were employed as anode GDLs along with carbon paper (Toray Paper 120) to optimize water distribution across the active area. A serpentine flow field was machined into the graphite bipolar plate at the cathode side, while copper current collectors facilitated electrical contact. Teflon gaskets were used throughout the assembly to ensure leak-free operation. The complete setup was fastened between two end plates using screw connections tightened to 2.5 N·m torque. The electrochemical assessment was conducted utilizing an Autolab potentiostat-galvanostat fitted with 10A current booster.. Figure 1 shows the PEMWE single-cell test setup.

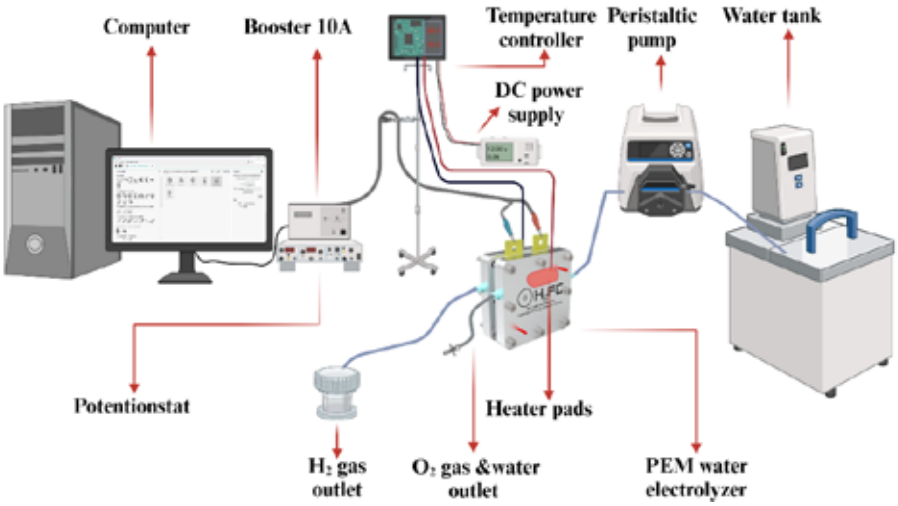

Fig. 1. Experimental setup of PEMWE single cell

The linear sweep voltammetry (LSV) was performed utilizing a scan rate of 1 mV with step increments of 2.44 mV. Each measurement step lasted 5 seconds, and a 10A high stability booster was activated throughout the procedure [10].

3. RESULTS AND DISCUSSION

Figure 2 demonstrates the performance of an electrochemical cell employing the Nafion 115 membrane under varying operational conditions. With a 3 mg/cm² IrO_2 anode and 0.4 mg/cm² cathode catalyst loading. Figure 2. a shows that maximum current density (111.12 mA.cm^{-2} at 2V) was achieved at 80°C with 100 ml/min water flow. The 100 ml/min flow rate at 80°C delivered superior performance compared to lower flow rates (75 ml/min yielded 95.45 mA cm^{-2} and 50 ml/min produced 91.75 mA.cm^{-2}) at the same temperature. Furthermore, this configuration dramatically outperformed the system when operated at a lower temperature of 50°C with 50 ml/min flow, which generated only 51.92 mA.cm^{-2}. As seen in Figure 2.b, increasing the IrO_2 anode loading to 4 mg/cm² significantly enhanced performance, yielding 184.68 mA.cm^{-2} at 80°C with 100 ml/min flow, demonstrating the critical impact of catalyst loading and operational parameters on electrochemical cell efficiency.

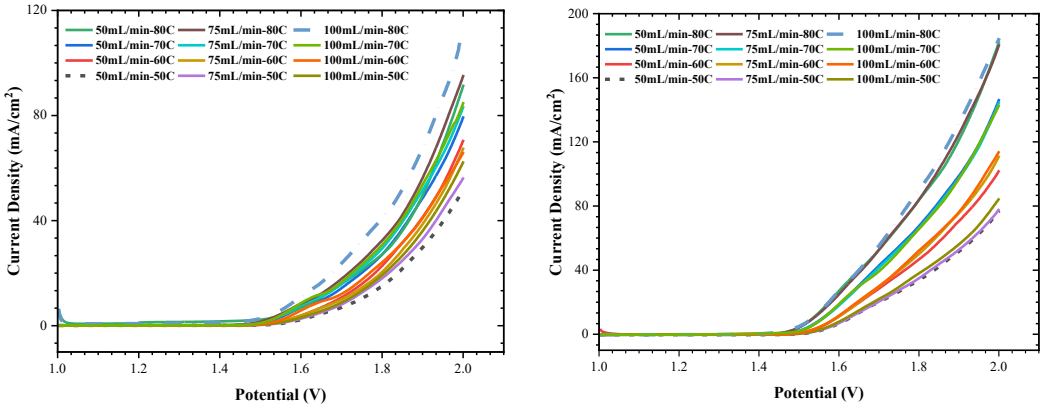

(a) (b)

Fig. 2. LSV of Nafion 115 with 0.4mg$_{Pt}$ cathode, and Anode loadings (a) 3 mg$_{IrO2}$/cm^2,(b) 4 mg$_{IrO2}$/cm^2

The electrochemical performance of Aquivion membrane-based cells, as seen in Figure 3. Figure 3.a shows that with 3 mg/cm² IrO_2 anode loading and 0.4 mg/cm² cathode catalyst, the PEMWE system achieved a maximum current density of 103.43 mA cm⁻² at 80°C with 50 ml/min flow rate. However, when operated at a lower temperature (50°C) with 75 ml/min flow, performance declined significantly to approximately 57.63 mA/cm² at 2V. Furthermore, Figure 3.b reveals that under conditions of 80°C with a 100 ml/min flow rate, same catalyst configuration produced higher current density around 280.26 mA cm⁻². In contrast, operation at reduced temperature and flow rate (50°C, 50 ml/min) resulted in a substantially lower performance of around 143.59 mA/cm² at 2V.

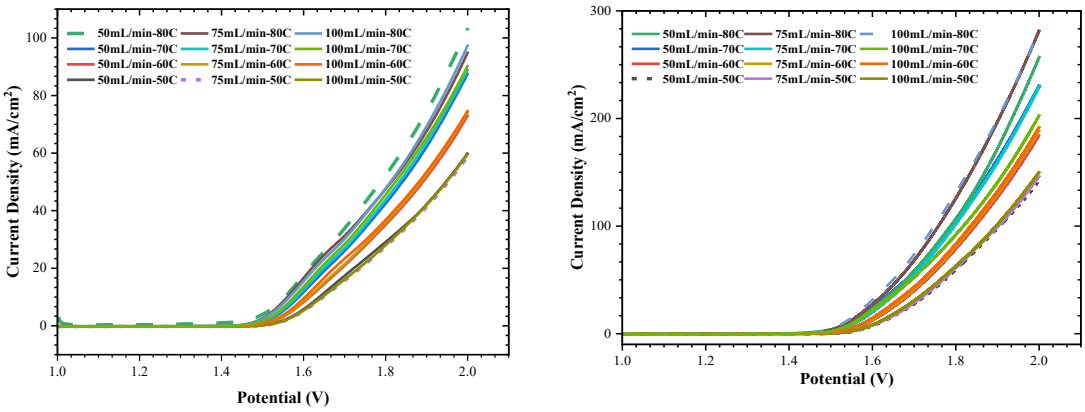

(a) (b)

Fig. 3. LSV of Nafion 115 with 0.4mg$_{Pt}$ cathode, and Anode loadings (a) 3 mg$_{IrO2}$/cm^2,(b) 4 mg$_{IrO2}$/cm^2

4. CONCLUSIONS

PEMWE experimental analysis demonstrated that optimal performance occurs at 80°C with 100 ml/min flow rate, with Aquivion membranes around 280.26 mA·cm⁻² outperforming Nafion 115 around 111.12 mA·cm⁻². Increasing IrO_2 anode loading from 3 to 4 mg/cm² further enhanced performance, confirming that membrane selection, temperature, and catalyst loading significantly impact PEMWE performance.

ACKNOWLEDGEMENT

The authors thank Erciyes University Dean of Research for providing access to essential infrastructure and laboratory facilities at the ArGe Park research building. Additionally, Abdelmola Albadwi sincerely thanks to the Scientific Research Projects Unit of Erciyes University BAP for their financial support (grant number FYL-2024-13769) and Presidency for Turks abroad and related communities' scholarship program YTB (grant number 21SD016376).

REFERENCES

[1] Li, G., L. Wu, Y. Qin, X. Du and G. Liu (2024). "Gradient catalyst layer design towards current density homogenization in PEM water electrolyzer with serpentine flow field." Energy Conversion and Management 314: 118659.

[2] Javed, A., N. L. Wolf, F. Meyer, L. Treutlein, H. Kungl, A. Karl, E. Jodat and R. Eichel (2025). "Exploring the state-of-operation of Proton Exchange Membrane Electrolyzers." International Journal of Hydrogen Energy 98: 280-294.

[3] Kong, S., A. Li, J. Long, K. Adachi, D. Hashizume, Q. Jiang, K. Fushimi, H. Ooka, J. Xiao and R. Nakamura (2024). "Acid-stable

manganese oxides for proton exchange membrane water electrolysis." Nature Catalysis 7(3): 252-261.
[4] Huang, P., X. Xu, Y. Hao, H. Zhao, X. Liang, Z. Yang, J. Yun and J. Zhang (2024). "Preparation of Ir/TiO2 Composite Oxygen Evolution Catalyst and Load Analysis as Anode Catalyst Layer of Proton Exchange Membrane Water Electrolyzer." ACS omega 9(32): 34482-34492.
[5] Jang, Y., C. Seol, S. M. Kim and S. Jang (2022). "Investigation of the correlation effects of catalyst loading and ionomer content in an anode electrode on the performance of polymer electrode membrane water electrolysis." International Journal of Hydrogen Energy 47(42): 18229-18239.
[6] Choi, K. J. and S.-K. Kim (2023). "A Pt cathode with high mass activity for proton exchange membrane water electrolysis." International Journal of Hydrogen Energy 48(3): 849-863.
[7] Choi, Y., W. Lee and Y. Na (2021). "Effect of gravity and various operating conditions on proton exchange membrane water electrolysis cell performance." Membranes 11(11): 822.
[8] Huang, J., Y. Zhou, J. Li, L. Zhang, Q. Fu, J. Song, G. Xu, X. Zhu and Q. Liao (2024). "Spatiotemporal distribution and variation of temperature in PEMWEs: Driving factors and its implication." International Journal of Hydrogen Energy 110: 74-82.
[9] Kaya, M. F., N. Demir, N. V. Rees and A. El-Kharouf (2021). "Magnetically modified electrocatalysts for oxygen evolution reaction in proton exchange membrane (PEM) water electrolyzers." international journal of hydrogen energy 46(40): 20825-20834.
[10] Ereli, N. C., M. Kıstı, T. Eşiyok, E. Özdoğan, B. Hüner, N. Demir and M. F. Kaya (2024). "First pulsed control system design for enhanced hydrogen production performance in proton exchange membrane water electrolyzers." Fuel 371: 132027.

COBALT DOPED PLATINUM-CELLULOSE-CARBON AEROGEL PREPARED BY SUPERCRITICAL DEPOSITION AS ELECTROCATALYST FOR HYDROGEN EVOLUTION REACTION

[1,3]*Ala Alsuhile,* [2]*Philip S. Pein,* [2]*Baldur Schroeter,* [2]*Irina Smirnova,* [1,3]*Can Erkey*
[1]Koç University, College of Engineering, Department of Chemical and Biological Engineering, Rumeli Feneri Yolu, Sariyer, 34450, Istanbul, Turkey
[2]Hamburg University of Technology, Institute of Thermal Separation Processes, Eißendorfer Str. 38, Hamburg, 21073, Germany
[3]Koç University Hydrogen Technology Center, 34450, Istanbul, Turkey

ABSTRACT
Green hydrogen production via water electrolysis is emerging as a key technology for reaching net zero CO2 emissions targets due to its ability to generate high-purity hydrogen with minimal environmental impact. In this study, the effect of Co doping on Pt-based electrocatalysts supported on biopolymer-based carbon aerogels (cellulose-CA) using supercritical deposition (SCD) on HER activity and stability was investigated. Pt and Co precursors were deposited onto cellulose-CA via SCD and subsequently reduced via two distinct routes (ex-situ thermal and chemical) under N_2 and H_2 flow at 1 bar and 200°C. Physical characterizations, including ICP-MS, TEM, XRD, XPS, and Raman spectroscopy, confirmed the successful incorporation of Co and Pt via SCD on cellulose-CA. The Co-doped electrocatalysts had similar overpotentials at 20 mA/cm² compared to the non-Co-doped electrocatalysts, despite having half the Pt loading. In particular, Pt-Co-Cellulose-CA reduced thermally had the lowest overpotential (64 mV). Moreover, it had the lowest potential shift (4 mV) after the stress test (1000 cycles at a scan rate of 100 mV/s). These results highlighted the potential of Co doping to enhance the activity and stability of low-Pt electrocatalysts, thereby advancing green hydrogen production via water electrolysis.

Keywords: Hydrogen evolution reaction, Low Pt-loading electrocatalysts, Co doping, Supercritical deposition, Carbon aerogels

1. INTRODUCTION

Green hydrogen is a promising energy carrier due to its remarkable gravimetric energy density (142 MJ/kg, upper heating value) and zero carbon dioxide emissions. Among different types of electrolyzers, alkaline electrolyzers and proton exchange membrane (PEM) electrolyzers have the highest technology readiness level (TRL) with PEM electrolyzers showing the important advantage of a fast response to changing power levels, rendering them the optimal choice to be coupled with dynamic energy sources like renewables [1]. Hydrogen is produced in the cathode part via hydrogen evolution reaction (HER). Platinum (Pt) is the main state-art catalyst for HER due to its optimal Gibbs free energy for adsorbed hydrogen molecules on its active sites [2]. The high costs and limited availability of Pt have motivated researchers to explore various strategies for the development of electrocatalysts with reduced Pt content. The catalyst support plays a crucial role in enhancing the dispersion, utilization and stability of Pt nanoparticles (PtNps). Carbon black, the commercial support, offers advantages due to its electrical conductivity, chemical inertness, and low cost [3]. However, it suffers from stability concerns due to detachment, dissolution, and agglomeration of PtNps [4]. Carbon aerogels (CAs) as catalyst supports have recently gained attention due to their multiscale porosity and high specific surface area. Additionally, their multiscale porosity provides anchoring sites for PtNps and facilitates efficient transport of reactants and products [5]. Various CAs with multiscale pore structures derived from biopolymer sources (e.g., cellulose, alginate, and chitosan) have been reported. Alongside their multiscale porosity and high surface area, they are considered a green alternative due to their recyclability [6]. Supercritical deposition (SCD) is particularly attractive deposition method because it avoids using additional agents that could block Pt active sites and reduce their activity. SCD is especially suitable for impregnating Pt into CAs, as it minimizes the risk of collapsing mesopores and micropores [7]. Furthermore, SCD allows precise control over Pt loading and particle size without requiring additional organic solvents. SCD can be done in different routes (in-situ/ex-situe thermal/chemical) [8]. Each route leads to PtNPs with different physicochemical properties that may affect the HER activity and stability. Another effective method to improve the HER activity and stability of PtNps is doping with other metals such as Ni, Cu, Co and P [9]. For example, it has been reported that doping Co affected the electronic structure of Pt in such a way that enhanced the HER activity and stability [10]. In this study, the aim is to investigate the effect of doping Co on Pt-biopolymer-based CA via two routes of SCD on HER activity and stability. The biopolymer-based aerogels (cellulose-CA) was employed as support. Two SCD despotion methods (ex-situ chemical and thermal routes) were used to investigate the effect of reduction method on the physical and chamical properties of PtNps. Improving PtNps activity and stability aligns with the primary goal of reducing noble metal loading in PEM electrolyzers.

2. MATERIALS AND METHODS

2.1. Materials

Microcrystalline cellulose type II was purchased from JRS Pharma GmbH & Co. KG and abcr GmbH Ger & INT. (1,5-

Cyclooctadiene) dimethyl platinum (II) (Pt(cod)Me_2) and cobalt (III) acetylacetonate, with purities of 97% and 98%, respectively, were purchased from Sigma-Aldrich. All gases used in this work (N_2, H_2, and CO_2) had a purity of 99.998% and were purchased from Ali Gaz. Nafion® 117 solution, with a 5% concentration, was sourced from Ion Solutions Inc. Sulfuric acid (95-98% concentration) was used as required. Sodium hydroxide was purchased from Merck KGaA. Ethanol (EtOH) with ≥99.8% purity and acetic acid with ≥99% purity were purchased from Carl Roth GmbH & Co. KG.All chemicals were used without further purification. Deionized water with a resistance of 18.2 MΩ was used in all experiments.

2.2. Aerogel and Electrocatalyst Preparation

Hydrogel particles were formed using a dripping method in an aqueous solution to synthesize cellulose aerogels, followed by thorough washing. Subsequently, a solvent exchange from water to ethanol (EtOH) was carried out to obtain alcogel particles. These alcogel particles were then subjected to supercritical drying to produce aerogel particles. The aerogel particles were carbonized under N_2 flow at 800°C for one hour to form carbon aerogel particles. A total of 20 mg of Pt(cod)Me_2 and Co(acac)$_3$, either separately or together (10 mg of each), was placed inside a custom-made high-pressure stainless-steel vessel (57 mL volume) along with 200 mg of cellulose-CA and pressurized with CO_2 to 20 MPa at 70°C for 24 hours. After deposition, the adsorbed precursors were thermally and chemically reduced under N_2 and H_2 flow (100 cm³ min⁻¹) for 4 hours at 200°C, respectively.

2.3. Pyhisicochemical Charaterizations

Several characterization techniques were employed to examine the properties of the synthesized electrocatalysts. Pt loadings for all samples were quantified using an Agilent 7700x ICP-MS instrument. X-ray diffraction (XRD) analysis was conducted using a Bruker D8 Advance Diffractometer equipped with a Cu Kα source, covering a 2θ range of 10° to 90°. X-ray photoelectron spectroscopy (XPS) was utilized for surface chemistry analysis, employing a Thermo-Scientific K-Alpha spectrometer with an Al anode (Al Kα = 1468.3 eV). A Renishaw InVia Raman Microscope with a 532 nm laser was used to analyze the structural characteristics of both the unloaded and Pt-loaded supports. Scanning transmission electron microscopy (STEM) was employed to investigate morphology, Pt particle size (based on a count of 100 particles), and dispersion.

2.3. Electrochemical Charaterizations

Electrochemical characterization of the samples was performed using a conventional three-electrode electrochemical cell connected to a potentiostat (Pine Instrument Company Model AFCBP1). The working electrode, provided by Pine Instruments, was a glassy carbon disk with an internal diameter of 0.1963 cm². An Ag/AgCl reference electrode was filled with a saturated KCl solution and a Pt wire counter electrode. The chosen electrolyte was a 0.5 M H_2SO_4 solution. An electrocatalyst ink was prepared by dispersing 8 mg of the electrocatalyst in 1 mL of isopropanol, 3 mL of distilled water, and 50 µL of a 5 wt% Nafion solution from Ion Solutions Inc. The mixture was sonicated in an ultrasonic water bath (Ultra-Turrax® T25) for one hour before deposition. Subsequently, 10 µL of the prepared ink was deposited onto the glassy carbon disk and allowed to air dry at ambient temperature and pressure overnight. Linear sweeping voltammetry (LSV) was conducted at a scan rate of 2 mV/s, and all reported potentials were corrected using Eq. 1.

$$E_{RHE} = E_{Ag/AgCl} + E^{\theta}_{Ag/AgCl} + 0.059pH \quad (1)$$

3. RESULTS AND DISCUSSION

3.1. Physical characterizations

The physical characterization of the synthesized electrocatalysts revealed significant effects of both the reduction method and Co doping. During the SCD process, the solubility of the Co(acac)$_3$ precursor was confirmed through the color change of the supercritical solution to green within the first 1–2 hours (Fig. 1a). After 24 hours, scCO_2 became colorless, indicating that Co(acac)$_3$ had been successfully adsorbed onto the cellulose-CA substrate, as shown in Fig. 1b. The effective deposition of both Pt and Co was subsequently confirmed by ICP-MS analysis (Table 1), which showed a Pt loading of approximately 5.5 wt% for the Pt-Cellulose-CA electrocatalysts, while the Co-doped electrocatalysts contained around 2.5 wt% Pt along with 0.6 wt% Co. Furthermore, Raman spectroscopy analysis of the cellulose-CA structure, assessed by the ID/IG ratio (indicative of defects relative to graphitic content), remained consistent at approximately 1.24 across all synthesized electrocatalysts, demonstrating that metal deposition did not significantly alter the structure of the cellulose-CA support.

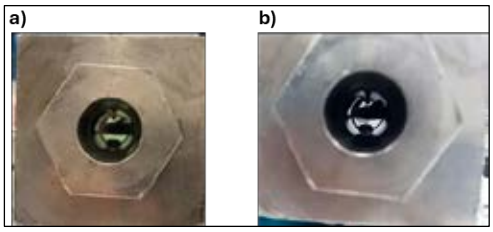

Fig. 1. Deposition of Pt and Co on cellulose-CA via SCD (a) after 1-2 hours and (b) 24 hours

.

The size of PtNPs was found to be influenced by the reduction route. Although the low Pt loading and small particle size hindered the detection of clear Pt peaks in XRD analysis, a more pronounced peak at 2θ = 39.1°, corresponding to Pt [111], was observed in the Pt-Cellulose-CA H_2 compared to Pt-Cellulose-CA N_2, as shown in Fig. 2a. TEM analysis (Fig. 2b-c) corroborated these findings, revealing that the average Pt nanoparticle sizes were 1.1 nm for Pt-Cellulose-CA N_2 and 2.2 nm for Pt-Cellulose-CA H_2, with a notably improved nanoparticle distribution in the thermally reduced electrocatalyst. Additionally, XPS results indicated that both Pt^0 and Pt^{2+} peaks shifted to higher binding energies in the N_2-reduced electroctalyst, as shown in Fig. 2d. This shift was consistent with the small nanoparticle size effect, where smaller Pt nanoparticles exhibit higher binding energies.

Table 1. summary of the physical characterizations of the synthesized electrocatalysts

Electrocatalyts	ICP-MS Pt loading [wt%]	ICP-MS Co loading [wt%]	TEM Np size [nm]	XPS Pt^0 bind energy [eV]	XPS Pt^0 fraction [atomic %]	Raman ID/IG [-]
Co-Cellulose-CA N2	-	1.5 ± 0.1	-	-	-	1.24
Co-Cellulose-CA H2	-	1.5 ± 0.1	-	-	-	1.26
Pt-Cellulose-CA N2	5.5 ± 0.2	-	1.1 ± 0.3	72.28	80	1.24
Pt-Cellulose-CA H2	5.5 ± 0.2	-	2.2 ± 0.6	71.58	82	1.22
Pt-Co-Cellulose-CA N2	2.8 ± 0.3	0.6 ± 0.07	1.3 ± 0.3	72.18	59	1.22
Pt-Co-Cellulose-CA H2	2.8 ± 0.3	0.6 ± 0.07	2.2 ± 0.6	71.58	66	1.24

Regarding the effect of Co doping, the successful incorporation of Co was confirmed by both XPS and EDX mapping, with the latter showing a clear overlap between Pt and Co signals (Fig. 2e and Fig. 2h). XPS analysis further revealed that upon Co doping, the atomic percentage of metallic Pt (Pt^0) decreased from 80% to 60% in the N_2-reduced electrocatalyst and from 82% to 65% in the H_2-reduced electrocatalyst. A slight shift in the binding energy of Pt^0 and Pt^{2+} was observed in the thermally reduced electrocatalyst, whereas no shift was detected in the chemically reduced sample. This indicates that Co doping had a slightly higher effect on the Pt electronic structure in the thermally reduced electrocatalyst compared to the chemically reduced one. Additionally, TEM analysis (Fig. 2f–g) showed that the average nanoparticle sizes for Pt-Co-Cellulose-CA N_2 and Pt-Co-Cellulose-CA H_2 were 1.3 nm and 2.2 nm, respectively. Despite containing only half the Pt loading compared to the non-Co-doped electrocatalysts, the nanoparticle sizes remained nearly unchanged. This suggests that nanoparticle growth on the cellulose-CA support was independent of Pt loading. The slight increase in nanoparticle size observed in the Co-doped electrocatalysts is likely due to the incorporation (merging) of approximately 0.6 wt% Co with Pt.

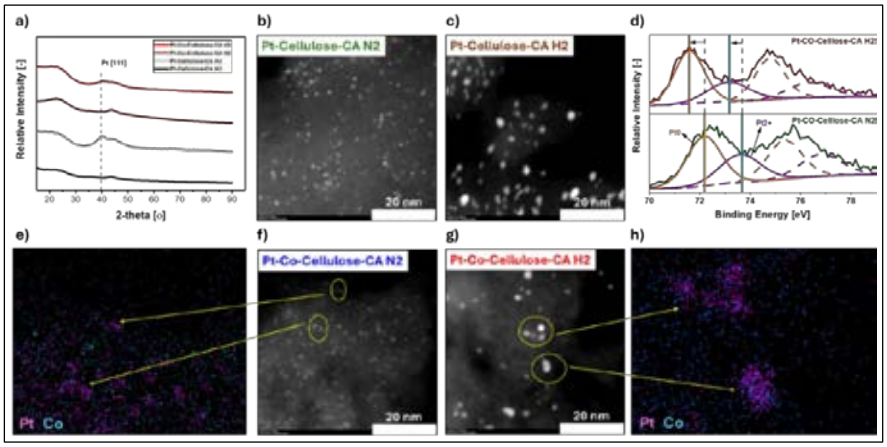

Fig. 2. Physical characterization of the synthesized electrocatalysts, including (a) XRD analysis and (b, c, f, g) STEM images of Co-doped and non-doped electrocatalysts. (d) XPS analysis and (e, h) EDX mapping of Co-doped electrocatalysts reduced via thermal and chemical reduction routes.

3.1. Electrochemical characterizations

HER activity was evaluated by conducting LSV for all electrocatalysts over a potential range of -153 to 20 mV vs. RHE at a scan rate of 2 mV/s and the data are shown in Fig. 3a. Co-Cellulose-CA electrocatalysts exhibited almost no HER activity. The overpotentials measured from the LSV at a current density of 20 mA/cm² were 63.8 ± 1.6, 67.9 ± 2.3, 64.1 ± 0.4, and 65.5 ± 0.8 mV for Pt-Co-Cellulose-CA N_2, Pt-Co-Cellulose-CA H_2, Pt-Cellulose-CA N_2, and Pt-Cellulose-CA H_2, respectively. Moreover, Tafel slopes for these electrocatalysts were found to be within the range of 29–32 mV/dec. Notably, for the non-Co-doped electrocatalysts, the reduction route did not significantly affect HER activity. However, the

Co-doped catalyst reduced under N_2 exhibited a slightly lower overpotential at 20 mA/cm². Although the intrinsic kinetic mass activity cannot be accurately measured due to mass transfer limitations for HER in acidic media [11], the beneficial effect of Co doping cannot be neglected. The Co-doped electrocatalysts achieved current densities comparable to the non-Co-doped ones, despite having nearly half the Pt loading. Co doping is known to improve PtNP dispersion and modify the electronic structure of Pt, thereby enhancing HER activity [10, 12]. Furthermore, stress test involving 1000 cycles between -153 and 20 mV vs. RHE at 100 mV/s, followed by LSV measurements, revealed that the Co-doped electrocatalyst prepared via the thermal reduction route exhibited the highest stability, with a potential shift of only ~4 mV as can be seen in Fig. 3b. This minimal shift indicates that the Co-doped catalyst maintains its electrochemical performance better over prolonged cycling, reinforcing the positive impact of Co incorporation on electrocatalyst stability.

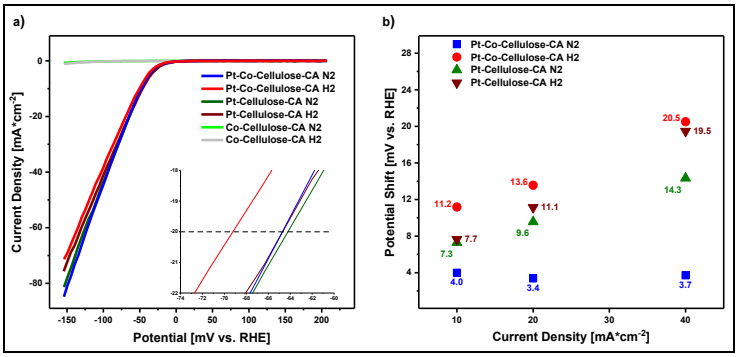

Fig. 3. (a) LSV test for all synthesized electrocatalysts and (b) potential shift after the stress test.

4. CONCLUSIONS

This study demonstrated that Co doping in Pt-based electrocatalysts supported on cellulose-derived carbon aerogels positively affected HER activity and stability. Successfull deposition of Co and Pt by SCD were confirmed through multiple characterization techniques. Among the tested electrocatalysts, the thermally reduced Pt-Co-Cellulose-CA exhibited the lowest overpotential (64 mV) at 20 mA/cm^2 and the highest stability (4 mV potential shift after 1000 cycles). These findings highlight Co doping as a promising strategy to enhance the efficiency and durability of low-Pt electrocatalysts, contributing to the advancement of green hydrogen production via water electrolysis.

ACKNOWLEDGEMENT

We are grateful for the financial support of TÜBİTAK with grant number 221N284. We also acknowledge the support of Koç University Surface Science and Technologies Center (KUYTAM), Koç University TÜPRAŞ Energy Center (KUTEM), and Koç University Nanofabrication and Nanocharacterization Center for Scientific and Technological Advanced Research (n2STAR). We are also grateful for the financial support of the Federal Ministry for Economic Affairs and Climate Action (BMWK), grant number KK5440301ZG1.

REFERENCES

1. Zhao G, et al. 2018. Heterostructures for electrochemical hydrogen evolution reaction: a review. Advanced Functional Materials 28:1803291.
2. Conway B and Jerkiewicz G. 2000. Relation of energies and coverages of underpotential and overpotential deposited H at Pt and other metals to the 'volcano curve' for cathodic H_2 evolution kinetics. Electrochimica Acta 45:4075-4083.
3. Sui S, et al. 2017. A comprehensive review of Pt electrocatalysts for the oxygen reduction reaction: nanostructure, activity, mechanism and carbon support in PEM fuel cells. Journal of Materials Chemistry A 5:1808-1825.
4. Meier JC, et al. 2014. Design criteria for stable Pt/C fuel cell catalysts. Beilstein Journal of Nanotechnology 5:44-67.
5. Arenillas A, et al. 2019. Organic and carbon gels. In Advances in Sol-Gel Derived Materials and Technologies. Edited by Aegerter M, Prassas M. Cham, Switzerland: Springer Nature Switzerland.
6. Hu Y, et al. 2016. 3D hierarchical porous N-doped carbon aerogel from renewable cellulose: an attractive carbon for high-performance supercapacitor electrodes and CO_2 adsorption. RSC Advances 6:15788-15795.
7. Barim SB, et al. 2020. Supercritical deposition: a powerful technique for synthesis of functional materials for electrochemical energy conversion and storage. Journal of The Electrochemical Society 167:054510.
8. Bozbağ SE, et al. 2015. Electrochemical performance of fuel cell catalysts prepared by supercritical deposition: effect of different precursor conversion routes. The Journal of Supercritical Fluids 97:154-164.
9. Shah SSA, et al. 2023. Recent advances in transition metal tellurides (TMTs) and phosphides (TMPs) for hydrogen evolution electrocatalysis. Membranes 13:113.
10. Guo F, et al. 2021. Confined sub-nanometer PtCo clusters as a highly efficient and robust electrocatalyst for the hydrogen evolution reaction. Journal of Materials Chemistry A 9:5468-5474.
11. Hansen JN, et al. 2021. Is there anything better than Pt for HER? ACS Energy Letters 6:1175-1180.
12. Cao Z, et al. 2022. Heteroatomic platinum–cobalt synergetic active centers with charge polarization enable superior hydrogen evolution performance in both acid and base media. ACS Applied Energy Materials 5:1496-1504.

HYDROGEN PRODUCTION VIA METHANOLYSIS OF SODIUM BOROHYDRIDE USING La_2O_3 AND $La_2O_2CO_3$ NANOWIRE CATALYSTS

[1,2*]Emel Engintepe, [3]Sibel Duman, [1,2]Ayşe Nilgün Akın
[1] Kocaeli University, Department of Chemical Engineering, Kocaeli, 41380, Turkey
[2] AYARGEM, Alternative Fuels R&D Center, Kocaeli University, Kocaeli, 41380, Turkey
[3] Bingöl University, Department of Chemistry, Bingöl, 12000, Turkey

* emel.engintepe@kocaeli.edu.tr

ABSTRACT

Hydrogen is a pivotal energy carrier in the transition toward sustainable energy systems, necessitating the development of efficient and scalable production methods. In this study, hydrogen generation is investigated via the methanolysis of sodium borohydride ($NaBH_4$) using lanthanum-based nanowire catalysts, La_2O_3 and $La_2O_2CO_3$. A comprehensive analysis of reaction kinetics, hydrogen yield, and catalyst stability is conducted to elucidate the role of these catalysts in optimizing the methanolysis process. The findings demonstrate that La_2O_3 and $La_2O_2CO_3$ nanowire catalysts significantly enhance hydrogen production efficiency, highlighting their potential for practical applications in clean energy and hydrogen storage technologies.

Keywords: Hydrogen production, sodium borohydride, methanolysis, nanowire catalysts.

1.INTRODUCTION

Hydrogen has emerged as a promising energy carrier due to its high energy density and environmentally friendly nature, making it a key component in the transition to sustainable energy systems. Among various hydrogen production methods, the methanolysis of sodium borohydride ($NaBH_4$) has attracted significant attention due to its ability to generate hydrogen efficiently under mild conditions. $NaBH_4$ is a well-known chemical hydrogen storage material with a high hydrogen content and stability, enabling hydrogen release through catalytic decomposition.

Recent studies have focused on developing efficient catalysts to enhance hydrogen production via $NaBH_4$ methanolysis. Various transition metal-based catalysts, including noble metals such as Pt, Ru, and Pd, have demonstrated high catalytic activity [1]. However, the high cost and scarcity of these metals have driven research toward alternative catalyst materials. Lanthanum-based oxides, such as lanthanum oxide (La_2O_3) and lanthanum oxycarbonate ($La_2O_2CO_3$), have shown promising catalytic properties due to their high surface activity, stability, and tunable electronic structures.

Despite extensive research on $NaBH_4$ methanolysis, no studies in the literature have specifically investigated the catalytic behavior of La_2O_3 and $La_2O_2CO_3$ in nanowire form. This study aims to address this gap by synthesizing and characterizing La_2O_3 and $La_2O_2CO_3$ nanowire catalysts for hydrogen production via $NaBH_4$ methanolysis. The catalytic performance of these materials is systematically evaluated in terms of hydrogen yield, reaction kinetics, and stability under various operating conditions. The findings of this study provide valuable insights into the design of cost-effective and efficient catalysts for hydrogen generation, contributing to the advancement of clean energy technologies.

2. MATERIALS AND METHODS

2.1. Catalyst preparation

The catalysts were synthesized via the hydrothermal method. Initially, 2 mmol of $La(NO_3)_3{\bullet}6H_2O$ was dissolved in deionized water, and the pH was adjusted using an ammonia solution. The solution was stirred at room temperature for 1 hour before being transferred to a hydrothermal reactor, where it underwent aging at 200°C for 24 hours in an oven. Following cooling to room temperature, the resulting $La(OH)_3$ precipitate was filtered, washed with deionized water and ethanol, and subsequently dried at 70°C for 12 hours. To obtain nanowire-structured La_2O_3 catalysts, the dried sample was calcined at 700°C for 2 hours in a muffle furnace. Likewise, nanowire-structured $La_2O_2CO_3$ catalysts were produced by calcining the dried sample at 500°C for 2 hours.

Figure 1. Schematic representation of catalyst preparation by hydrothermal method.

2.2. Catalyst Characterization

The catalysts were characterized using XRD for phase identification, BET for surface area analysis, FE-SEM for morphological examination and TGA for thermal stability assessment. These techniques confirmed the structural and textural properties of the synthesized La_2O_3 and $La_2O_2CO_3$ nanowire catalysts.

2.3. Catalyst Testing

The experimental setup for $NaBH_4$ methanolysis and hydrogen gas measurement comprised a 50 mL jacketed reaction flask equipped with a Teflon-coated stir bar and placed on a magnetic stirrer (Heidolph MR-301, operating within a temperature range of 10–90°C). Temperature regulation was maintained by circulating water through the reactor jacket from a constant-temperature bath (PolyScience water bath). The evolved hydrogen gas was quantified using a graduated glass tube (50 cm in height, 2.5 cm in diameter) filled with water, which was connected to the reaction flask. Additionally, a thermocouple inserted into the reactor ensured precise temperature monitoring [2].

2.4. Determination of activation parameters in the $NaBH_4$ methanolysis

Activation energy was determined by using the catalytic activity of nanowire-structured $La_2O_2CO_3$ catalyst through $NaBH_4$ methanolysis. In order to investigate the effect of temperature and to determine the activation parameters (activation energy (E_a), activation entalphy (ΔH) and activation entrophy (ΔS)), temperature experiments were performed for the 2.0 mmol $NaBH_4$ methanolysis catalyzed by 4.06 mM nanowire catalyst in the range of 20-40°C.

3. RESULTS AND DISCUSSION

3.1.Characterizations of Nanowire Catalysts

The thermal decomposition of the sample at elevated temperatures, as illustrated in Figure 2, progresses through four distinct stages.

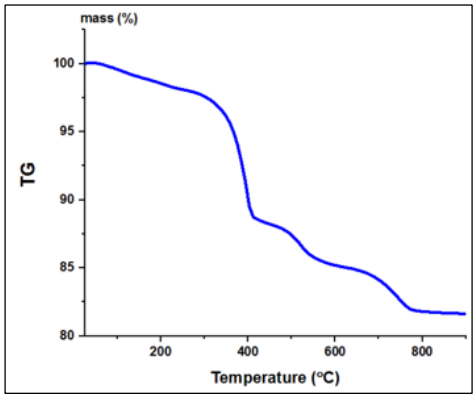

Figure 2. TG curves of synthesized $La(OH)_3$ samples.

The first stage occurs between room temperature and approximately 200°C, followed by the second stage from 200°C to 400°C, both of which correspond to the release of adsorbed and structural water. Thermogravimetric analysis (TG) confirms that water is the only volatile species released during these initial stages, whereas CO_2 evolution is observed exclusively in the third and fourth stages. Between 400°C and 600°C, the formation of $La_2O_2CO_3$ is observed, likely due to interaction with atmospheric CO_2. Finally, above 600°C, $La_2O_2CO_3$ decomposes completely, yielding La_2O_3 as the final product.

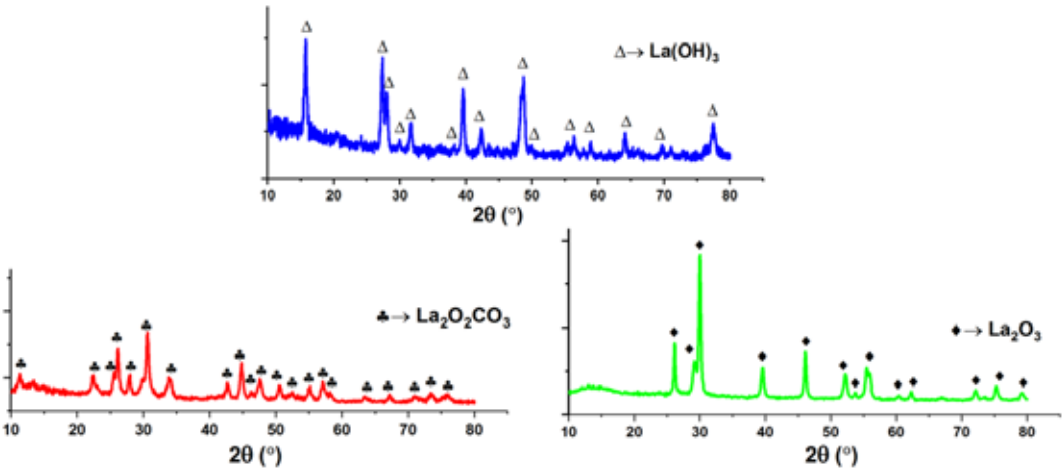

Figure 3. XRD patterns of $La(OH)_3$, $La_2O_2CO_3$ and La_2O_3 nanowire catalysts

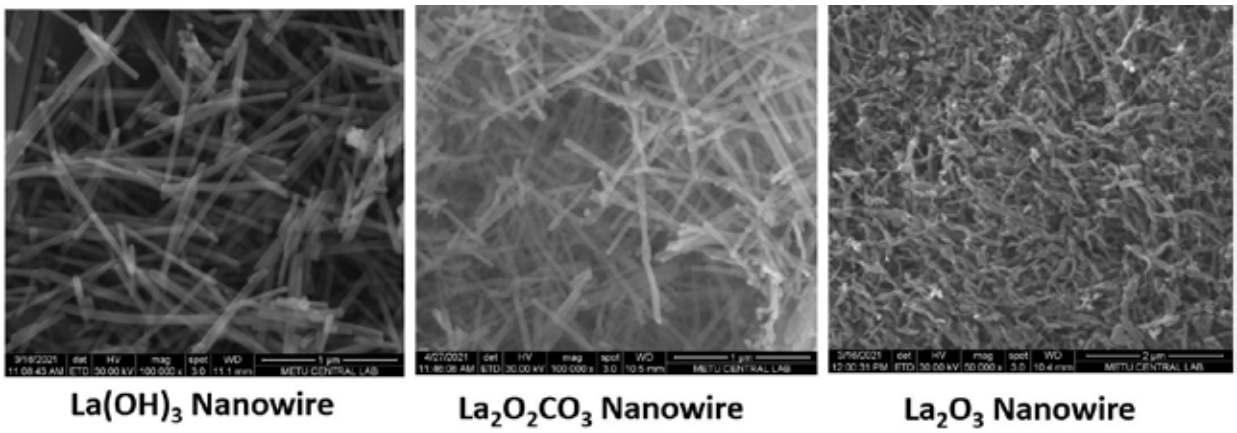

Figure 4. FE-SEM images of nanowire samples

The structural and morphological properties of the synthesized nanowire catalysts were analyzed using XRD, FE-SEM, and BET techniques. Figure 3 presents the XRD patterns, confirming the crystalline phases of $La(OH)_3$, $La_2O_2CO_3$, and La_2O_3. The nanowire morphology is observed in the FE-SEM images (Figure 4), while the textural properties are summarized in Table 1.

Table 1. BET Surface Area

Sample	Specific Surface Area (m^2/g)
$La(OH)_3$	23.5
$La_2O_2CO_3$	21.6
La_2O_3	17.9

3.2. Kinetics study for $NaBH_4$ methanolysis

Nanowire-structured La_2O_3 and $La_2O_2CO_3$ catalysts were firstly tested during both hydrolysis and the methanolysis of $NaBH_4$ at 25.0±0.1°C (Figure 5a). It was observed that Nanowire-structured La_2O_3 and $La_2O_2CO_3$ catalysts showed high activity and stability during the methanolysis of $NaBH_4$, but was rather unstable in its hydrolysis (Figure 5a). This behavior may be due to better dissolution of nanowire-structured catalyst in methanol. In order to investigate the effect of temperature and to determine the activation energy, temperature experiments were performed for the 400 mM $NaBH_4$ methanolysis catalyzed by nanowire-structured $La_2O_2CO_3$ catalysts in the range of 20-40°C (Figure 5b). The rate constant (k) values were obtained from the linear region of the plots and utilized to calculate the activation parameters for catalytic $NaBH_4$ methanolysis using the Arrhenius (Figure 5c) and Eyring (Figure 5d) equations. The activation parameters (Ea, ΔH and ΔS) are found to be E_a=32±2 $kJmol^{-1}$, 35±2 $kJmol^{-1}$ and -106±5 $JK^{-1}mol^{-1}$, respectively. These values can be compared with other catalysts under similar reaction conditions in the literature

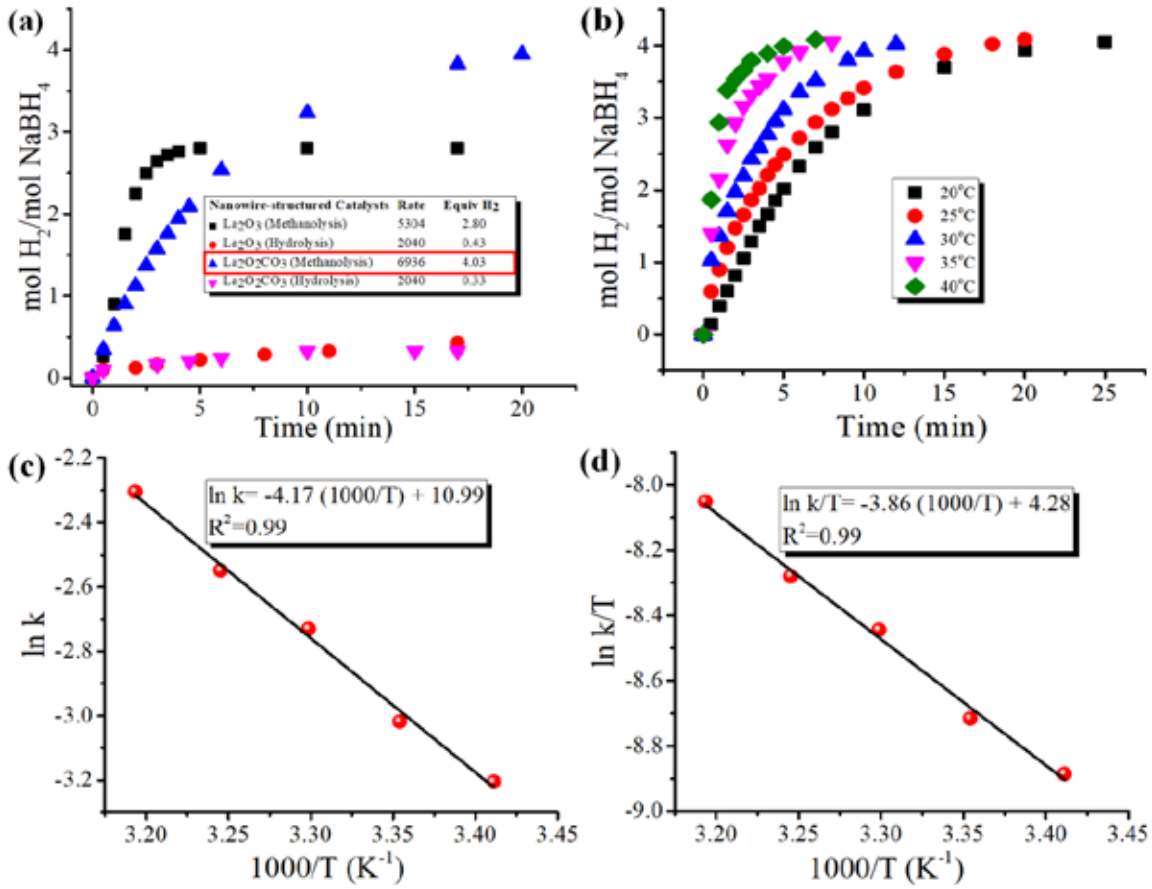

Figure 5. Plots of mol H_2 per mol $NaBH_4$ versus time (min) for (a) hydrolysis and methanolysis reactions (b) The methanolysis of SB in the presence of various temperature ([$La_2O_2CO_3$]=. 4.06 mM, [$NaBH_4$]=400 mM) (c) The Arrhenius plot; ln k versus 1000/T. (d) The Eyring plot, lnk/T versus 1000/T.

4. CONCLUSIONS

In this work, highly active nanowire-structured catalysts were used for the $NaBH_4$ methanolysis at 25.0±0.1ºC. $La_2O_2CO_3$ catalysts exhibited significantly higher catalytic activity compared to La_2O_3. The effect of temperature on the hydrogen generation rate in $NaBH_4$ methanolysis catalyzed by $La_2O_2CO_3$ was investigated by conducting reactions at varying temperatures. The activation energy for the nanowire-structured $La_2O_2CO_3$ catalyst was determined to be Ea = 32± 2 kJ mol^{-1}. All samples were characterized using XRD, FE-SEM, and BET analyses.

ACKNOWLEDGEMENTS

This work was supported by Kocaeli University Research Fund with Project Numbers: FAA-2025-4323.

REFERENCES

1. Wang T., Jiang T., Zhang H., Zhao Y. 2022. Advances in catalysts for hydrogen production by methanolysis of sodium borohydride. International Journal of Hydrogen Energy 47:14589-14610.
2. Zahmakiran M., Ozkar S. 2009. Zeolite-confined ruthenium(0) nanoclusters catalyst: Record catalytic activity, reusability, and lifetime in hydrogen generation from the hydrolysis of sodium borohydride. Langmuir 25:2667-2678.

A SIMULATION STUDY FOR HYDROGEN PRODUCTION FROM LOW RANK TURKISH LIGNITE THROUGH GASIFICATION IN TRIJEN PILOT PLANT IN SOMA

[1]*Ömer Orçun Er,* [2]*Gökhan Kavas,* [1]*Mehmet Ünsal,* [1]*Aslı Sayar Kartay,* [1]*Namık Ünlü* [2]*Emel Muşdu* [1*]*Özlem Ataç*,
[1] TÜBİTAK Marmara Research Center, Energy Technologies, Kocaeli, 41470, Türkiye
[2] Turkish Coal Enterprises, Department of R&D and New Technologies, Ankara, 06560, Türkiye

*Corresponding author e-mail: ozlem.atac@tubitak.gov.tr

ABSTRACT
Hydrogen, being an energy source, is considered as one of the most important solutions that will enable countries to achieve their carbon neutralization goals. Conversion of low rank Turkish lignite into valuable chemicals and energy, namely hydrogen, through gasification has a strategic importance for Türkiye. TRIJEN is a project, leaded by TÜBİTAK incorporation with TKİ that aims to convert Turkish lignite into valuable liquid fuel and energy. “Hydrogen Production from Coal Gasification” project is a follow-up project of TRIJEN project, aims produce hydrogen in TRIJEN Soma pilot plant after required modifications. In this phase of the project, the main goal is to produce H_2 from low rank Turkish lignite, Tufanbeyli coal, via gasification and obtain pure hydrogen. In this paper, Aspen Hysys simulation of hydrogen production process from low rank lignite studied in the project were presented. It was found that thermal efficiency of overall process for hydrogen production from Tufanbeyli coal is 50.6% and 60.5% Nm^3 hydrogen is produced per 100 kg coal feed. Final product H_2 is 99.999% after PSA process.
Keywords: Low rank coal, gasification, hydrogen production, process simulation

1. INTRODUCTION

Coal, a fossil fuel has continued to serve as the dominant energy source worldwide over the past century, mainly for use in the cement industry, iron and steel production and electricity generation. In addition, the combustion of coal in these industries causes significant emissions of greenhouse gases, nitrogen oxides, sulphur oxides and particulate matter, resulting in environmental problems such as global warming, acid rain, sudden climate change, ozone depletion, and air pollution [1]. Clean and efficient use of coal is important in the fight against global climate change in line with the net zero targets of countries and in limiting the temperature increase in the world to no more than 1.5 °C compared to pre-industrial levels [2, 3].

Thanks to coal gasification technology, which is one of the methods of using coal in a clean and efficient way, coal-based chemical synthesis (ammonia, methanol, acetic acid, olefin, etc.), synthetic liquid fuels (dimethyl ether, gasoline, diesel, etc.), electricity generation and hydrogen production can be achieved as a result of converting the fuel into synthesis gas (syngas) under high temperatures in aerobic environment using gasification agents such as O_2, H_2O and CO_2 [1, 4].

Hydrogen energy, a clean, efficient, safe and sustainable source that can also be produced through gasification, is poised to play an important role in the decarbonization of various industries, including transport, heavy industry and power generation, and is seen as one of the most promising energy sources of the 21st century [5, 6]. According to the IEA's Global Hydrogen Review 2024 Report, 20% of the approximately 97 Mt of Hydrogen produced in 2023 was produced by coal gasification [7]. On the other hand, according to the Net Zero Emission Scenario (NZE Scenario) published by the IEA, 38% of the 530 Mt of hydrogen estimated to be produced in 2050 is foreseen to be produced by gasification of CCUS-integrated fossil fuels (natural gas, oil, coal, etc.), and it is important to integrate carbon capture and storage technologies into the hydrogen production process from fossil fuels in terms of low carbon hydrogen energy production [6, 8].

Countries consider their domestic resources in terms of energy cost, energy security and supply chain in hydrogen production [9]. Establishing facilities for gasification technology of coal, which is a domestic resource in Turkey, is considered as a strategic investment [10]. Lignite, one of Turkey's most important domestic energy sources with 16.3 billion tons of reserves, have low calorific value due to their high moisture, mineral matter and organic oxygen content, and can also have high ash content [11,12]. The type of reactor used varies according to coal properties and fixed bed, entrained flow and fluidized bed gasifiers are widely used in the industry. For gasification of coals with high ash content, fluidized bed gasifiers with various advantages such as fuel flexibility, better gas/solids mixture, high heat/mass transfer rates and uniform bed temperature are preferred [12].

According to the literature, although most of the industrial gasifiers used in the world are designed according to high quality coal characteristics, technological development studies continues for gasifier designs suitable for low rank and high ash content coals. Conversion of low rank Turkish lignite into valuable chemicals and energy through gasification has a strategic importance for Türkiye. With this vision the “Liquid Fuel Production from Biomass and Coal Mixtures - TRIJEN” Project, in corporation of TÜBİTAK and Turkish Coal Enterprises (TKİ) started in 2009 aiming to produce liquid fuel from lignite through gasification, gas cleaning, gas conditioning and liquid fuel production (Fischer Tropsch) Technologies. A pilot plant with a thermal capacity of 1.1 MW was designed, constructed and operated in Soma and the Project was completed in 2020. Thus, a great deal of experience has been gained in the design, manufacturing, commissioning, operation and techno-economic feasibility required for establishment of industrial plants for such

applications.
Hydrogen stands out as one of the most important solutions that will enable countries to achieve their carbon neutralization goals without reducing economic development and welfare. TKİ aimed to produce hydrogen from low rank lignite, which are of great commercial and strategic importance for Türkiye, in corporation with TÜBİTAK. In this study, it is aimed to develop technology for hydrogen production from coal with low calorific value, high ash and volatile matter content.

2. MATERIALS AND METHODS

Tufanbeyli coal was selected as the design coal in simulation studies to produce hydrogen. After physical and chemical properties of coal were determined the project team made a technology evaluation for hydrogen production from low rank lignite, made the optimum process determinations and prepared the process flow diagram of the plant. At the end of the project, it is aimed to produce hydrogen from Tufanbeyli lignite through gasification followed by gas cleaning and conditioning units and a PSA unit to purify the hydrogen. In this paper simulation studies of the process of hydrogen production from low rank Turkish lignite will be presented.

2.1. Materials and Feedstock analysis

Ultimate and proximate analysis were carried out to characterize Tufanbeyli coal. Coal properties are given in Table 1.

Table 1 Proximate and Heating value analysis results of Tufanbeyli lignite

	As Received	Air Dried	Dried
Moisture (%)	47.87	7.23	-
Ash (%)	22.40	39.87	42.97
Volatile Matter (%)	22.10	39.33	42.39
Fixed Carbon (%)	7.63	13.58	14.64
Total Sulphur (%)	3.16	5.63	6.07
Heating Value (kcal/kg)			
-Lower Heating Value (LHV)	1313	2766	3024
-Higher Heating Value (HHV)	1669	2970	3202

The as-received moisture content of original coal was found to be quite high with a value of 47.87%. The high ash content of approx. 40% in dried coal requires a detailed and careful reconsideration of ash removal systems in the gasification process. The high volatile matter content of 42% on dry basis provides a positive feature for hydrogen production in gasification. The low fixed carbon content of around 13% on dry basis requires the selection of appropriate coal feeding point and coal size. Total Sulphur content was measured between 4.5% and 6% (Sulfur in ash 2%, Burning Sulfur >2.5%). The high sulfur ratios are important for designing of desulfurization process after gasification. The heating value was found to be low with the measured Higher Heating Value being 3000 kcal/kg (12.36 MJ/kg) and the Lower Heating Value being 2900 kcal/kg (12.1 MJ/kg). Low ash melting temperatures make it important to control the bed temperature so that it does not exceed 900°C.

2.3. Overall Process Simulation

In the first stage of conceptual design, hydrogen production processes from coal was modelled buy using a software program, ASPEN HYSYS. The flowsheet screen of the whole process is given in Figure 1. The hydrogen production process from coal consists of 4 sub-processes: (1) Gasification, (2) Gas Cleaning and Sour Water Gas Shift (SWGS), (3) H_2S and CO_2 Removal, (4) Pressure Swing Adsorption.

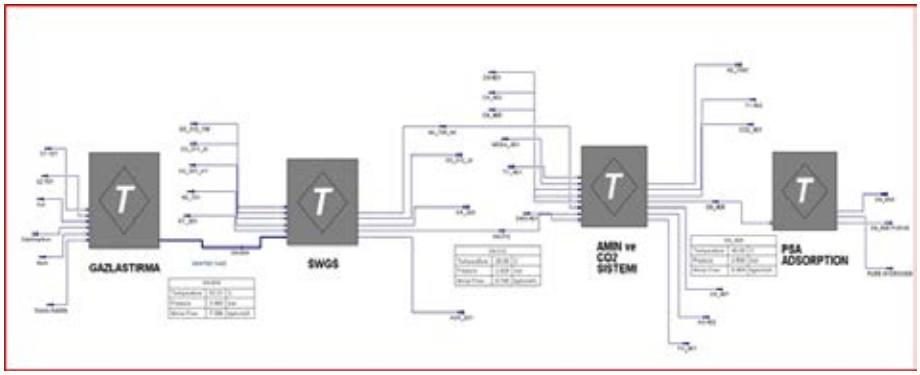

Figure 1. ASPEN HYSYS flowsheet screen of whole system

The main results obtained from the modeling are given in Table 2. As can be seen form Table 2, the thermal efficiency of the process is found as 50.62% and 7.5 kg pure hydrogen can be obtained from 140 kg of Tufanbeyli lignite.

The modeling scheme showing the “Amine Absorption System” for H_2S removal created in ASPEN HYSYS is given in Figure 2. The synthesis gas enters the absorption column at 20°C where the H_2S (hydrogen sulfide) gas will be absorbed. The rich amine solution taken from the bottom of the absorption column is sent to the desorption column for regeneration at 99°C. After the rich amine solution is regenerated, acid gas (H_2S) is taken from the top of the column, cooled to 40°C and after gas/liquid separation, the gas stream is directed to the “Flare”.

Table 2. Results obtained from ASPEN HYSYS modelling

Coal Feed Flow Rate	140	kg/hr
Coal LHV	3024	kcal/kg
Produced Hydrogen Mass Flow Rate	7.5	kg/hr
Produced Hydrogen Volumetric Flow Rate	84.8	Nm^3/hr
Hydrogen Heating Value	120	MJ/kg
Hydrogen Heating Value	28,571.43	kcal/kg
Thermal Efficiency	**50.62%**	
Produced Hydrogen per 100 kg Coal Feed	**5.36**	**kg**
Produced Hydrogen per 100 kg Coal Feed	**60.57**	**Nm^3**

After acid gas removal, synthesis gas, free of H_2S, leaves absorption column. The synthesis is then sent to the “Sulfur Adsorbent Bed” where the H_2S concentration is reduced to <1.0 ppmv.

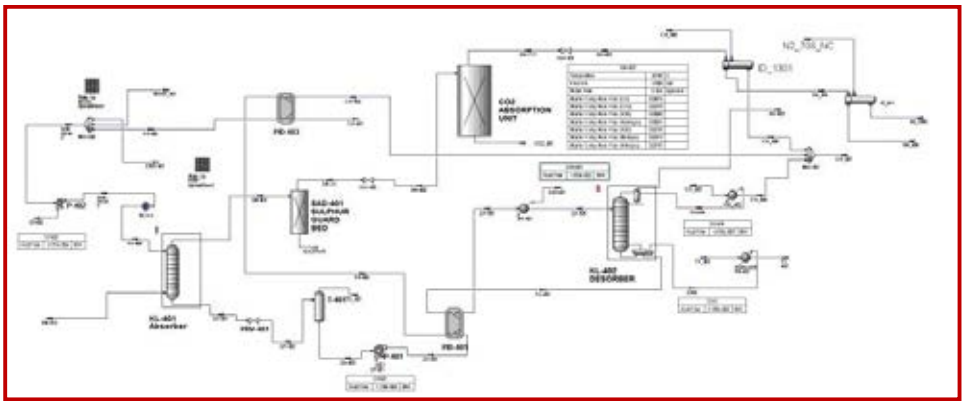

Figure 2. ASPEN HYSYS flowsheet screen of “Amine Absorption Process”

2.4. Design of sub-processes

For the design of sub-systems, the main design parameters (length, diameter, surface area vb.) of the equipment’s (columns, heat exchangers, reactors vb.) is determined.
Using kinetics taken from literature, the required catalyst amounts and reactor dimensions depending on the catalyst amount were determined for the three WGS reactors in SWGS system. The determined dimensions of the reactors were compared with the dimensions given by the catalyst manufacturer from which the SWGS catalyst was supplied. Main parameters of the system are given in Table 3.

Table 3. SWGS system main parameters

Inlet Syngas Mass Flow Rate, kg/hr	158.1
Temperature, °C and Pressure, bara	321 / 3.22
Inlet Syngas CO Concentration, %	22.19
Outlet Syngas CO Concentration, %	0.35
Reactor Number	3
1. Reactor Catalyst Volume, L	319
2. Reactor Catalyst Volume, L	801
3. Reactor Catalyst Volume, L	943

The designs of the absorption and desorption columns in the “Amine Absorption Process” used for H_2S removal were performed by using the ASPEN HYSYS program. Column dimensions (length, diameter), column packing type and flow rate of amine solution and H_2S concentration of the syngas leaving the absorption column were optimized and main properties of the system are given in Table 4. The amine absorption system can be able to reduce the H_2S amount from 12100 ppmv input value to 300 ppmv output value.

In order to reduce the H_2S concentration in the syngas coming from the “Amine Absorption Process” to <1 ppmv, it was decided to use an iron oxide based adsorbent operating at ambient temperature. An offer was received from a commercial company for this purpose. Adsorbent bed system properties are given in Table 5.

Table 4. "Amine Absorption Process" main properties

Inlet Syngas Mass Flow Rate, kg/hr	206.4
Temperature, °C and Pressure, bara	20.0 / 2.99
Inlet Syngas H_2S Concentration, ppmv	12100
Outlet Syngas H_2S Concentration, ppmv	300
Amine Flow Rate, kg/hr	1.571
Amine Concentration, % MDEA	45
Absorption Column Diameter, cm	21
Absorption Packed Height, cm	400
Desorption Column Diameter, cm	20
Desorption Packed Height, cm	400
Packing Type	MELLAPAK 250Y

Table 5. Adsorbent Bed Process properties

Syngas Flow Rate	161.1	kg/hr
H_2S concentration in syngas	**300**	**ppmv**
Adsorbent Amount Needed Adsorbent	1907	kg
Adsorbent Type	FerroSorp S (5-25 mm) FerroSorp S (2-4 mm)	
Total Bed Volume	1.6	m^3
Bed Diameter	1.2	m
Bed Height	1.5	m

PSA process will be used for H_2 purification. Syngas leaving the CO_2 removal system is sent to the PSA unit where active carbon and Zeolits will be used as adsorbent for H_2 purification. According to the simulation result H_2 concentration the final product is %99,999.

3. RESULTS AND DISCUSSION

A study of modifying TRIJEN pilot plant for hydrogen production instead of liquid fuel is being carried out. The study includes every single detail of a plant design e.g., conceptual design, process simulation, detailed design, P&ID, sizing, material and equipment selection, control and automation, HAZOP and LOPA analysis and etc..

The characterization of selected design coal, Tufanbeyli coal, showed the characteristics of this coal are far too different from the design coal, Dereköy coal, of existing TRIJEN pilot plant. Tufanbeyli coal has a low calorific value (HHV=2970 kcal/kg), high ash (39,9) %) and volatile matter content (39,3 %). This high ash content requires a modification in bottom ash removal system. The low fixed carbon content of around 13% on dry basis requires the selection of an appropriate coal feeding point and coal size, whereas the high volatile matter content of 42% on dry basis provides a positive feature for hydrogen production in gasification. The high sulfur content requires design of a new desulfurization process after gasification. After a process evaluation it was decided that some modifications in gasification system and new units for H_2S removal, SWGS and PSA system are required. Design studies are being carried out accordingly.

Aspen Hysys simulation results showed that low rank Turkish lignite can be used in production of hydrogen with a thermal efficiency of 50,62%. It was simulated that 60.57 Nm^3 hydrogen of 99,999% purity is produced per 100 kg coal feed. The high H_2S concentration, which is 12100 ppmv at the gasifier outlet according to the simulation studies, is reduced down to 300 ppmv with the new acid gas removal unit. After a final process of sulfur adsorbent bed the H_2S concentration is reduced to <1.0 ppmv.

4. CONCLUSIONS

This study gives brief information on the project "Hydrogen Production from Coal Gasification" in TRIJEN Pilot Plant, with a 1.1 MW thermal capacity, located in Soma/Manisa. The plant, which was operated between 2016-2020 for experimental purpose, was constructed to produce liquid fuel from biomass and coal mixtures. It is aimed to produce hydrogen in the same pilot plant with low rank lignite. Detailed design of the units is planned to be completed in July 2025 and after construction and installation studies, pilot plant test results are due December 2026.

ACKNOWLEDGEMENT

The authors would like to thank all the team members and partners of TRIJEN project for their grate effort to do such a work, first and only plant of its kind in Türkiye, TKİ and TÜBİTAK for supporting the project.

REFERENCES

1. T., Iglauer, S., & Keshavarz, A. (2022). A progress insight of the formation of hydrogen rich syngas from coal gasification. *Journal of the Energy Institute*.
2. Zhu, S., Jin, H., Meng, X., Wei, W., Ou, Z., Song, M., & Guo, L. (2023). Hydrogen production from low-rank coal by a two-step method combined subcritical depolymerization with supercritical gasification. Fuel.
3. Li, J., Han, W., Song, X., Li, P., Wang, Z., & Jin, H. (2024). Near-zero carbon emission power generation system enabled by staged coal gasification and chemical recuperation. Energy.

4. Shi, J., Wan, N., Li, L., Li, Z., & Han, H. (2022). Review on treatment technologies of coal gasification wastewater in China. ournal of Cleaner Production.
5. Zhou, B., Chang, J., Li, J., Hong, J., Wang, T., Zhu, Z., . . . Ma, C. (2023). Two-stage gasification process simulation and optimization of pulverized coal for hydrogen-rich production using Aspen plus. İnternational Journal of Hydrogen Energy.
6. Hosseini, T., Tabatabaei-Zavareh, M., Smart, S., & Ashman, P. J. (2024). Low-emission hydrogen production from gasification of Australian coals Process simulation and technoeconomic assessment. İnternational Journal of Hydrogen Energy.
7. International Energy Agency. (2024). Global Hydrogen Review 2024.
8. International Energy Agency. (2021). Net Zero By 2050 A Roadmap for the Global Energy Sector. International Energy Agency.
9. International Centre For Sustainable Carbon. (2022). The Role Of Emission Coal Technologies In A Net Zero Asian Future.
10. Aktan, M. (2020). Kömür Gazlaştırma Ürünlerinin Gerçek Opsiyonlar Yöntemi ile Değerlendirilmesi. Doctoral thesis .
11. Hasanoğlu, A., Faki, E., Seçer, A., & Üzden, Ş. T. (2023). Co–solvent effects on hydrothermal co–gasification of coal/biomass mixtures for hydrogen production. Fuel.
12. Gupta, S., & De, S. (2022). An experimental investigation of high-ash coal gasification in a pilot-scale bubbling fluidized bed reactor. Energy.

DESIGN OF A STANDALONE ELECTRIC VEHICLE DC FAST CHARGING STATION BASED ON A HYBRID ENERGY SYSTEM WITH FUEL CELL AND PV FOR A TOURIST RESORT

[1*]*Merve Yildirim* and [2]*Sencer Unal*
[1,2]Firat University, Engineering Faculty, Electrical and Electronics Engineering Department, Elazig, 23200, Turkey
*e-mail: merveyildirim@firat.edu.tr

ABSTRACT
The growing demand for clean and efficient Electric Vehicle (EV) charging solutions has led to the development of hybrid energy-based charging stations. This study presents the design of a standalone DC fast charging station powered by a hybrid energy system combining Photovoltaic (PV) panels and Fuel Cells (FCs) for a holiday resort. The proposed system is designed to enhance energy efficiency and sustainability while reducing dependency on the grid. A detailed system model is developed and simulated using MATLAB/Simulink, analyzing energy production, hydrogen production and consumption, and power management strategies. It is obtained from the results that integrating PV and FC systems improves charging station reliability. The findings highlight that hybrid charging stations can provide an eco-friendly and efficient alternative to conventional charging infrastructures, making them convenient for remote and off-grid locations.

Keywords: DC Charging Station, Fuel Cell, Photovoltaic, Electric Vehicle, Hybrid Energy System.

1. INTRODUCTION

Nowadays, the increasing demand for clean and sustainable energy solutions has led to the development of hybrid charging stations that combine renewable energy sources, such as solar power, with advanced energy storage technologies like the FCs. These hybrid systems aim to address the limitations of traditional charging infrastructure by offering an eco-friendlier, efficient, and reliable energy supply [1, 2]. Solar energy, with its abundance and zero-emission characteristics, provides a promising source for electricity generation, while the FCs offer a flexible and reliable means of energy storage, ensuring continuous power supply even when solar generation is low or unavailable [3].

Hybrid solar and FC charging stations are especially significant in the context of an EV charging infrastructure, where the need for sustainable energy solutions is becoming more critical. Integrating these two technologies can not only reduce the dependency on grid-based electricity but also mitigate environmental impacts associated with fossil fuels [4, 5]. These systems can also operate in remote or off-grid locations, providing energy independence and enhanced resilience.

In recent literature, various aspects of hybrid solar and FC charging stations, including system design, energy management strategies, performance optimization, and economic feasibility have been explored [6]. Researchers have focused on developing models and algorithms for effective integration, aiming to balance energy generation, storage, and consumption. Additionally, the environmental and economic benefits of these hybrid systems have been widely discussed, emphasizing their potential to contribute to global efforts for reducing greenhouse gas emissions and promoting sustainable energy transitions. Firstly, a hybrid renewable energy-based EV charging station that combines solar power, wind turbines, and FCs is proposed [7]. A control strategy is implemented to efficiently manage power distribution across multiple charging ports while reducing grid dependency by exporting excess energy. The effectiveness of the system is validated by the MATLAB/Simulink simulations, demonstrating its ability to simultaneously charge an electric car, an electric bike, and an electric auto using a three-input, three-output port structure. [8], In the context of standalone hybrid energy systems combining the FCs and PV, component costs play a crucial role in overall economic feasibility. In the study, the specifications and costs of system components, including PV panels, FCs, hydrogen tanks, and electrolyzers are examined. The findings suggest that the FCs presents more economic solution than PV panels.

A 100-kW standalone DC fast charging station in Alamein, Egypt which is powered by PV and battery energy storage is designed and controlled by [9]. Using HOMER software for sizing and MATLAB Simulink for performance verification under real weather conditions, the station demonstrates the capability to meet various load conditions effectively. The size of the charging station for Alamein, Egypt is determined as a real load profile by analyzing with HOMER software. Furthermore, MATLAB Simulink simulations are performed to assess the performance of the station under real-world weather conditions and solar irradiance levels. The results confirm that the proposed station can reliably accommodate different load demands. A novel standalone charging station powered by PV and FC is proposed for charging of the EVs [10]. Besides, a new MPPT method is used for obtaining maximally electric power from the PV in the designed system. In the system, a FC stack, an electrolyzer, two hydrogen tanks, and a FC controller are placed. In the case of the greater charge demand than PV output power, the remaining of the demand is provided by the FC. Conversely, when the PV power exceeds the charging demand, the electrolyzer utilizes the surplus energy to produce hydrogen by splitting water. The experimental results and recorded data from the normal operation of the developed charging station are presented. It is observed that the proposed system has a permanent lifetime and lower costs than conventional battery banks that have a limited lifespan. Another study [11] presents a techno-economic evaluation of an innovative standalone hybrid PV-hydrogen energy-based charging station located in Jamshoro, Sindh, Pakistan for plug-in EVs. The simulations of

the presented system are realized by using HOMER software. It is seen from the results that the hybrid PV-hydrogen-battery system is more cost-effective than the PV-hydrogen system. Total electricity generation in the system is primarily sourced from the solar PV and in addition, the FCs also provides the contribution to it. As a result, a cost-effective hybrid EV charging station is designed for the proposed location. In [12], an off-grid solar powered charging station consisting of the FC and hydrogen storage is proposed for the electric and hydrogen vehicles. In the charging station powered by the solar panels, some of the solar power is used for charging the EVs and the rest of it is converted to the hydrogen by working the electrolyzer. The stored hydrogen is utilized for charging the hydrogen vehicles. The consumed power by the EVs and hydrogen vehicles and energy are modeled in the charging station. In the system, an electrical energy is produced for supplying to the electrical loading by the FC. The diesel generator is also used in the system, and the investment and operational costs of solar and diesel systems are reduced by the solar system and diesel generator. The cost, footprint, and reliability effects of deploying hydrogen in off-grid EV charging stations are examined by using a geographic information system for the city of Riyadh, Saudi Arabia [13]. The PV, wind, battery, and hydrogen FC are used in the designed model. The capacity of the charging station which has two level charging is 11 kW and the microgrid is desired without carbon. While a microgrid inluding the PV/Battery/Wind has low cost, the PV/Battery/Wind/Hydrogen configuration has the least footprint. By using the hydrogen, the required footprint of off-grid charging station is reduced by 25% at a small incremental cost. However, in the following years, both the footprint and cost are decreased based on learning-curve assumptions. [14] presents an optimal design of a charging station using solar energy and FC to charge both EV and hydrogen-powered vehicles. In the system, solar panels, a FC, a water electrolyzer, hydrogen storage, and dual-mode vehicles operating on either electricity or hydrogen are placed. The optimal power capacities for the solar system, FC, and hydrogen storage are determined by the mathematical modeling. The simulation results show that the system predominantly depends on solar energy and the FC, while excess energy is directed to a diesel generator. Then, the FC and diesel generator are operated in low solar energy availability and energy distribution analysis is realized. It is observed that 20%, 50%, and 30% of the solar energy are utilized for electrical loads, production, and diesel generator, respectively.

Once examining the studies in the literature, hybrid solar-FC charging stations emerge as a sustainable and cost-effective solution for the EV infrastructure by integrating renewable energy sources and energy storage. Studies show that combining PV systems with the FCs enhances energy efficiency, reduces grid dependence, and ensures reliable power supply, especially in off-grid and remote locations. Besides, it is observed that optimized hybrid systems have lower operational costs, extend system lifetime, and improve overall performance compared to conventional charging methods. Hence, in this study, a DC fast charging station is designed for a standalone EV using a hybrid energy sources which are the FC and PV in tourist destinations. The proposed system is modeled using MATLAB/Simulink and energy production, hydrogen production and consumption, and power management strategies are examined by the simulations. As a result, it is seen that a reliable and robust charging station is developed by this work.

2. MATERIALS AND METHODS

The model of designed system is illustrated in Fig. 1. In the diagram, the electricity generation including the solar PV, battery, and hydrogen FC is shown in blue color. The hydrogen production including the electrolyzer and hydrogen storage is shown in green color. In the charging station powered by the PVs, while some of the solar power is utilized for charging the EVs, the remaining energy is converted into hydrogen through an electrolyzer. The produced hydrogen can either be utilized directly by the FC or stored in a hydrogen tank for using later. Therefore, a charge station model is designed for realizing an optimal energy management by modeling the hydrogen power production and consumption of the EVs.

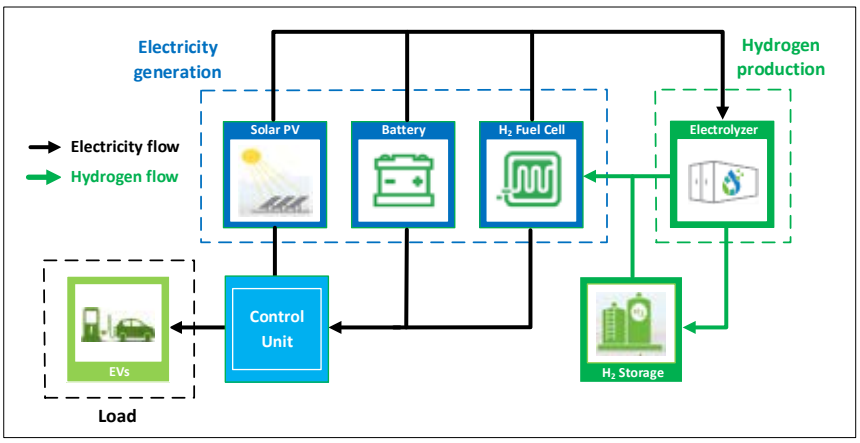

Fig. 1. The designed DC charge station model

2.1. Solar Panel System

In this study, a solar PV system with a total installation capacity of 100 kW consisting of 455 W PVs is designed. The maximum power of the PV is 455 W, optimum operating voltage and current are 43.65 V and 10.43 A, respectively. The open circuit voltage is 52.08 V and short circuit current is 10.74 A. The module efficiency is 20.90% and maximum system voltage is 1500 V DC.

2.2. Fuel Cell System

A HFC-130 model of the Horizon company is chosen as the FC pack in this work. The rated output voltage range of this FC is 500-730 V DC and maximum rated output power is 130 kW. Expected life of the FC stack is max.>25000 h. H_2 purity is >99.97% and the system efficiency at maximum rated output power is ≥42.5%. Hydrogen pressure is also 12-14 barg.

3. RESULTS AND DISCUSSION

In this study, a fast EV DC charging station based on a hybrid energy system with FC and PV is modeled by using Matlab/Simulink. Accordingly, the results are obtained. In Fig. 2, fuel tank pressure, hydrogen consumption, and energy production results are given versus the time. A steady decline in fuel tank pressure suggests continuous hydrogen depletion, while energy output increases proportionally to hydrogen consumption. This behavior corresponds to literature findings that energy efficiency in the hydrogen production depends on the method used, with electrolytic hydrogen requiring between 154% to 614% of its chemical energy equivalent for production [15]. The energy optimization strategies, such as combining hydrogen production with metallurgical processes, could improve overall efficiency.

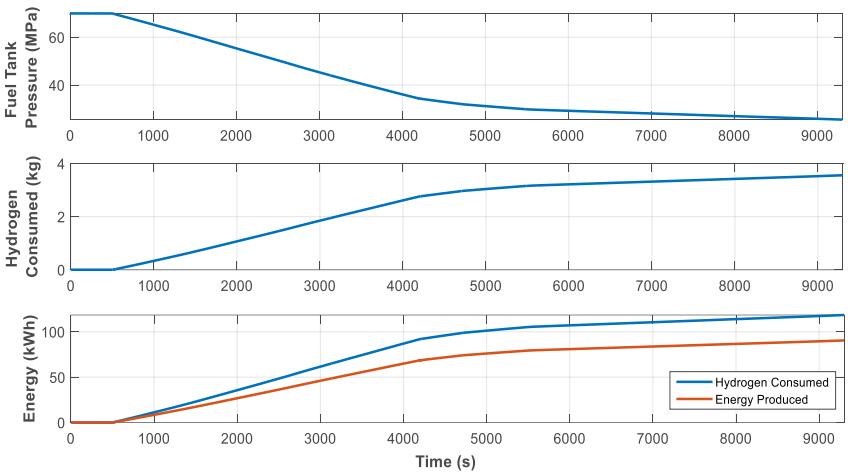

Fig. 2. The curves of the fuel tank pressure, hydrogen consumption, and energy production

As seen in the Fig. 2, the pressure drop in the fuel tank is directly related to the amount of hydrogen consumed. The decrease in tank pressure and the increase in energy production are among the factors that determine the consumption efficiency of the system. According to literature reviews, the energy efficiency of the hydrogen production process can reach 60-70%, while the total system efficiency including the FC can reach up to 90%.

The mass and energy of the hydrogen produced and power of the solar system are illustrated in Fig. 3.(a) and (b), respectively. The cumulative hydrogen production graph shows a sharp increase in mass over time, correlating with energy generation. This aligns with studies highlighting that hydrogen FCs can achieve the efficiencies exceeding 60%, with ongoing research targeting improvements beyond 70% [16].

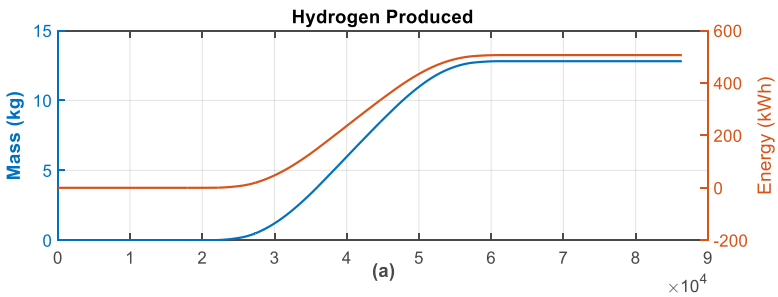

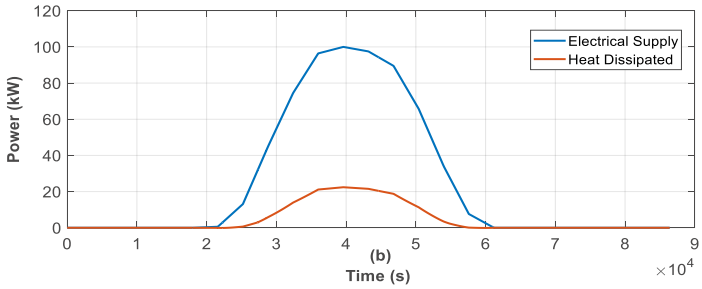

Fig. 3. (a) The mass and energy of the hydrogen produced **(b)** Power of the solar system

In Fig. 3, as the electricity supply increases, hydrogen production also rises, indicating that the system effectively utilizes excess energy for hydrogen storage. Heat dissipation, while present, remains relatively low compared to total energy production, suggesting a reasonably efficient energy conversion process. This system consisting of the combination of the PV and FC provides a balanced solution for an EV fast-charging station, ensuring both instant power supply and hydrogen storage. It can be considered a hybrid energy solution that maximizes solar energy utilization. During peak sunlight hours, excess energy is stored as hydrogen, allowing the FCs to generate power during nighttime or low solar radiation periods. Thus, with this study, a reliable EV DC fast charging station with hybrid energy system is designed for tourism resorts.

4. CONCLUSIONS

This study presents the design and analysis of a standalone DC fast charging station utilizing a hybrid PV and FC system by Matlab/Simulink. In the designed system, the fuel tank pressure, hydrogen prediction and consumption, energy production, and the mass and energy of the hydrogen produced and power of the solar system are examined. The simulation results show that the integration of PV and FC technologies effectively balances energy demand and supply, optimizing hydrogen utilization while maintaining energy efficiency. The proposed system ensures a reliable and sustainable energy supply for EV charging, making it suitable for remote locations. The findings confirm that hybrid energy-based charging stations can significantly reduce reliance on the conventional grid, lower carbon emissions, and improve economic feasibility.

REFERENCES

1. Gulzar MM, Iqbal A, Sibtain D and Khalid M. 2023. An innovative converterless solar PV control strategy for a grid connected hybrid PV/wind/fuel-cell system coupled with battery energy storage. IEEE Access 11:23245-23259.
2. Soomro AM, Rathi MK, Shaikh A, Kumar L, Assad MEH and Ehyaei MA. 2024. Techno-economic analysis of stand-alone hybrid PV-hydrogen-based plug-in electric vehicle charging station. Energy Reports, 12:3279-3290.
3. Ishaq H, Dincer I and Crawford C. 2022. A review on hydrogen production and utilization: Challenges and opportunities. International Journal of Hydrogen Energy 47:26238-26264.
4. Yap KY, Chin HH and Klemeš JJ. 2022. Solar energy-powered battery electric vehicle charging stations: current development and future prospect review. Renewable and Sustainable Energy Reviews 169:112862.
5. Sánchez-Sáinz H, García-Vázquez CA, Llorens F and Fernández LM. 2019. Methodology for the optimal design of a hybrid charging station of electric and fuel cell vehicles supplied by renewable energies and an energy storage system. Sustainability 11:5743.
6. Rafi MAH and Bauman J. 2020. A comprehensive review of DC fast-charging stations with energy storage: Architectures, power converters, and analysis. IEEE Transactions on Transportation Electrification 7:345-368.
7. Madhumitha R, Priya P and Saravanan S. 2022. Hybrid renewable energy based electric vehicles charging station. IEEE 2022 2nd International Conference on Advance Computing and Innovative Technologies in Engineering (ICACITE) 2348-2352.
8. Singh S, Chauhan P, Aftab MA, Ali I, Hussain SS and Ustun TS. 2020. Cost optimization of a stand-alone hybrid energy system with fuel cell and PV. Energies, 13:1295.
9. Selmy MS, Soliman AN, Mansour HA and Hussien AM. 2024. Design and control of standalone DC fast charging station based on photovoltaic and battery energy storage, case study: Alamein Egypt. Engineering Research Journal 53:1-9.
10. He F and Fathabadi H. 2020. Novel standalone plug-in hybrid electric vehicle charging station fed by solar energy in presence of a fuel cell system used as supporting power source. Renewable Energy 156:964-974.
11. Shaikh A, Soomro AM, Kumar M and Shaikh H. 2022. Assessment of a stand-alone hybrid PV-hydrogen based electric vehicle charging station model using HOMER. Journal of Applied Engineering & Technology (JAET) 6:11-20.
12. Mehrjerdi H. 2019. Off-grid solar powered charging station for electric and hydrogen vehicles including fuel cell and hydrogen storage. International journal of hydrogen Energy 44:11574-11583.
13. Elshurafa AM, Muhsen AR and Felder FA. 2022. Cost, footprint, and reliability implications of deploying hydrogen in off-grid electric vehicle charging stations: A GIS-assisted study for Riyadh, Saudi Arabia. International Journal of Hydrogen Energy, 47:32641-32654.
14. Nayantara C, Ambika K, Aishwarya S and Saravanan D. 2023. Charging electric vehicles at fuel stations using solar energy and fuel cell technology. IEEE 2023 Intelligent Computing and Control for Engineering and Business Systems (ICCEBS) 1-6.
15. Hemmes K. 2020. Coproduction of hydrogen and power from NG in an internal reforming fuel cell. Elsevier Current Trends and Future Developments on (Bio-) Membranes 209-223.
16. Shabani B and Andrews J. 2015. Hydrogen and fuel cells. Energy Sustainability Through Green Energy 201:453-491.

SYNTHESIS AND CHARACTERIZATION OF NANOSTRUCTURED La_2O_3-BASED CATALYSTS FOR HYDROGEN PRODUCTION VIA $NABH_4$ METHANOLYSIS

[1,2*]Emel Engintepe, [3]Sibel Duman, [1,2]Ayşe Nilgün Akın
[1] Kocaeli University, Department of Chemical Engineering, Kocaeli, 41380, Turkey
[2] AYARGEM, Alternative Fuels R&D Center, Kocaeli University, Kocaeli, 41380, Turkey
[3] Bingöl University, Department of Chemistry, Bingöl, 12000, Turkey
* emel.engintepe@kocaeli.edu.tr

ABSTRACT

In this study, nanostructured La_2O_3-based catalysts were synthesized using the hydrothermal method and characterized by X-ray diffraction (XRD), Brunauer-Emmett-Teller (BET) surface area analysis, and Field Emission Scanning Electron Microscopy (FE-SEM) to examine their structural, textural, and morphological properties. The catalytic activity of the synthesized nanomaterials was evaluated in $NaBH_4$ methanolysis for hydrogen production. The results demonstrated that the nanostructured La_2O_3 catalyst exhibited superior performance, achieving a high hydrogen generation rate. These findings highlight the potential of nanostructured La_2O_3-based catalysts for efficient hydrogen production, contributing to the advancement of sustainable energy technologies.

Keywords: lanthanum oxide, hydrothermal synthesis, $NaBH_4$ methanolysis, hydrogen production

1. INTRODUCTION

Hydrogen is considered a promising clean energy carrier due to its high energy density and environmental sustainability. Among various hydrogen production methods, sodium borohydride ($NaBH_4$) methanolysis has gained significant attention as an efficient and safe approach [1]. In this reaction, $NaBH_4$ reacts with methanol (CH_3OH) to produce hydrogen gas (H_2) and sodium tetramethoxyborate ($NaB(OCH_3)_4$), as shown in the balanced chemical equation:

$$NaBH_4 + 4CH_3OH \rightarrow NaB(OCH_3)_4 + 4H_2 \quad (1)$$

This method offers several advantages, including the high hydrogen yield per unit mass of $NaBH_4$, rapid reaction kinetics, and the use of readily available, cost-effective reactants. Additionally, $NaBH_4$ is a non-toxic and non-flammable compound, making it a safer alternative for hydrogen generation and storage. These characteristics make $NaBH_4$ methanolysis particularly attractive for portable and on-demand hydrogen production applications [1].

The efficiency of this reaction is highly dependent on the choice of catalyst. While various catalysts have been explored for $NaBH_4$ methanolysis, to the best of our knowledge, there are no reported studies on the use of La_2O_3 for this reaction. Given its promising properties in other catalytic applications, investigating La_2O_3 for $NaBH_4$ methanolysis could provide valuable insights into catalyst design for hydrogen production. In this study, La_2O_3 nanostructures were synthesized using the hydrothermal method and evaluated for their catalytic performance. The findings aim to introduce La_2O_3 as a potential catalyst for $NaBH_4$ methanolysis and contribute to the development of novel materials for sustainable hydrogen generation.

2. MATERIALS AND METHODS

2.1. Catalyst Preparation and Characterization

The catalysts were synthesized via a hydrothermal approach. For the preparation of nanorod-structured La_2O_3 (NR), 2 mmol of $La(NO_3)_3 \cdot 6H_2O$ was dissolved in 40 mL of deionized water, and the pH of the solution was adjusted to 9 using a 10 wt% ammonia solution. The mixture was stirred at room temperature for 1 hour before being transferred to a 50 mL hydrothermal reactor, where it was aged at 160°C for 16 hours. After cooling, the precipitate was filtered, washed with deionized water and ethanol, and dried at 70°C for 12 hours. The final catalyst was obtained by calcination at 700°C for 2 hours. The synthesis of nanowire-structured La_2O_3 (NW) followed the same procedure, with the only modification being an increase in the aging temperature to 220°C.

The structural and textural characteristics of the synthesized La_2O_3 nanostructured catalysts were thoroughly analyzed using multiple characterization techniques. X-ray diffraction (XRD) was employed to determine the crystalline phase composition, while Brunauer-Emmett-Teller (BET) analysis was conducted to evaluate the surface area. Additionally, Field Emission Scanning Electron Microscopy (FE-SEM) was utilized to examine the morphological features of the catalysts. These analytical techniques provided comprehensive and systematic insights into the physicochemical properties of the synthesized materials.

2.2. Catalyst Testing

The experimental setup for $NaBH_4$ methanolysis and hydrogen gas measurement comprised a 50 mL jacketed reaction flask equipped with a Teflon-coated stir bar and placed on a magnetic stirrer (Heidolph MR-301, operating within a temperature range of 10–90°C). Temperature regulation was maintained by circulating water through the reactor jacket from a constant-temperature bath (PolyScience water bath). The evolved hydrogen gas was quantified using a graduated glass tube (50 cm in height, 2.5 cm in diameter) filled with water, which was connected to the reaction flask. Additionally, a thermocouple inserted into the reactor ensured precise temperature monitoring [2].

2.3. Determination of Effect of Nanostructured La_2O_3-Based Catalysts Amount in the $NaBH_4$ Methanolysis

In order to investigate the effect of catalyst amount and to determine its high active amount, catalyst amount experiments were performed for the $NaBH_4$ methanolysis (400 mM) catalyzed by *La_2O_3-based catalysts* in the range of 2.5-10 mg.

3. RESULTS AND DISCUSSION

3.1. Characterizations of Catalysts

The morphology of the synthesized catalysts was examined using Field Emission Scanning Electron Microscopy (FE-SEM). As shown in Figure 1, The sample aged hydrothermally at 160°C for 16 hours exhibited a nanorod structure, while the sample aged at 220°C for 16 hours resulted in a nanowire structure. This shift from nanorods to nanowires indicates a change in the growth mechanism or crystal structure. The increase in temperature accelerates the chemical reactions, causing ammonium hydroxide to decompose rapidly and release OH^- ions, promoting axial growth and resulting in longer nanowires. These results suggest that the hydrothermal conditions significantly influenced the shape and size of the La_2O_3 particles.

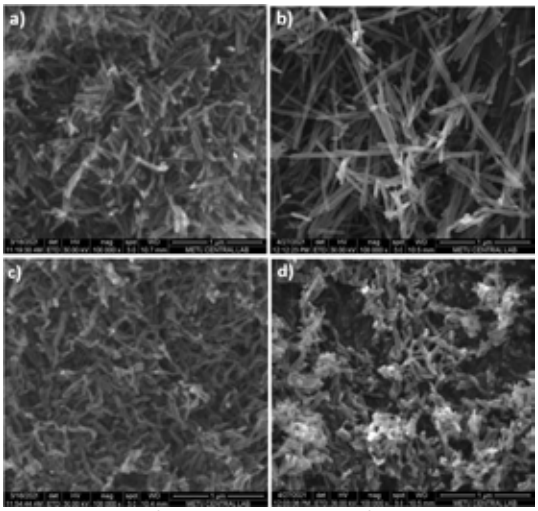

Figure 1.FE-SEM images of MR and NW catalysts. a) uncalcinated NR, b) uncalcinated NW, c) calcinated NR, and d) calcinated NW

The crystalline structure of the catalysts was analyzed by X-ray diffraction (XRD), and the patterns are presented in Figure 2. Both NR and NW catalysts show characteristic peaks of La_2O_3, confirming the successful synthesis of the desired phase.

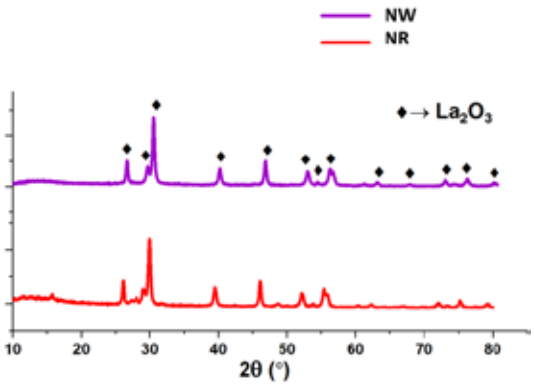

Figure 2. XRD patterns of La_2O_3 catalysts

The surface area of the catalysts was assessed using the Brunauer–Emmett–Teller (BET) technique, and the findings are presented in Table 1. The BET surface area of NR was observed to be greater than that of NW, suggesting that NR provides a higher number of active sites for catalytic reactions.

Table 1. BET Surface Area

Catalysts	BET surface area (m^2/g)
NR	22.9
NW	12.2

3.2. Effect of La_2O_3-based catalysts amount in the $NaBH_4$ methanolysis

NR-La_2O_3 and NW-La_2O_3 catalysts were firstly tested during both hydrolysis and the methanolysis of $NaBH_4$ at 25.0±0.1°C (Figure 3a). It was observed that NR-La_2O_3 catalyst showed high activity and stability during the methanolysis of $NaBH_4$, but was rather unstable in its hydrolysis (Figure 3a). This behavior may be due to better dissolution of NR-La_2O_3 catalyst in methanol. To investigate the effect of the amount of NR-La_2O_3 and to determine the amount of most active NR-La_2O_3, a series of experiments were performed for methanolysis of 400 mM $NaBH_4$ catalyzed by NR-La_2O_3 taken in the range of 2.5-10 mg (Figure 3b). Hydrogen generation rate (HGR) values were determined by taking the highest value of the graphs at 0.5 minutes ($HGR_{0.5}$) and used to determine the most active amount of NR-La_2O_3 for the catalytic methanolysis of $NaBH_4$ using the HGR graph (Figure 3c). Accordingly, the most active amount of NR-La_2O_3 that catalyzes the catalytic methanolysis of $NaBH_4$ was found to be 7.5 mg (4.05 mM). This value will be used as a constant in the following stages of the study.

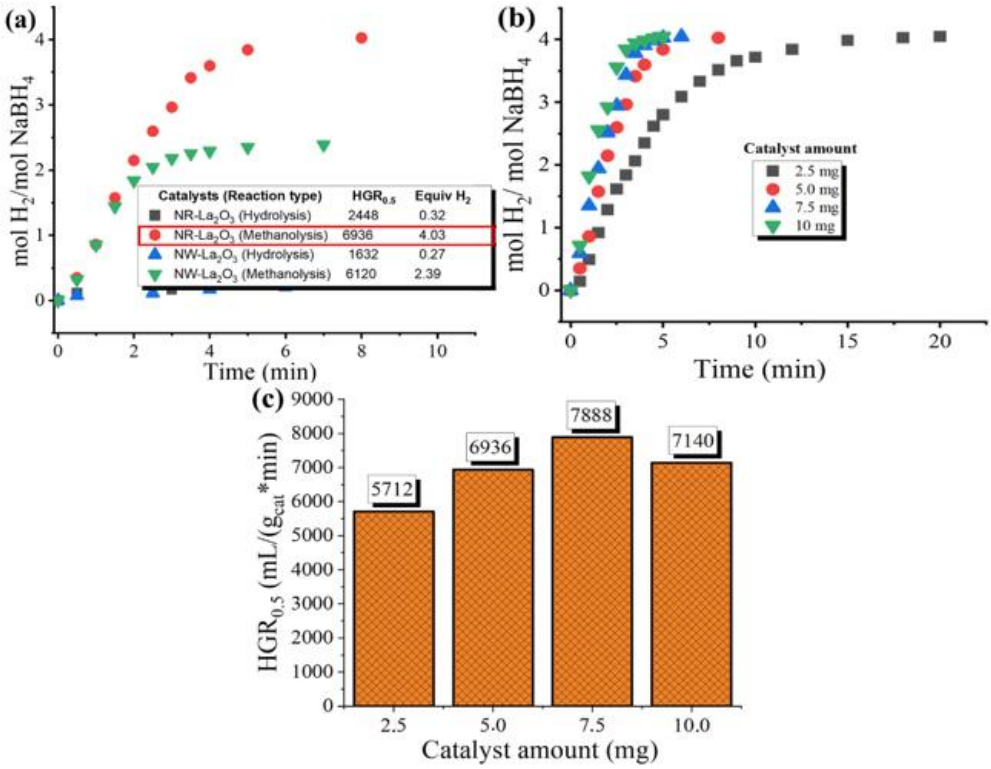

Figure 3. Plots of mole H_2 per mole of $NaBH_4$ versus time (min) for (a) hydrolysis and methanolysis of $NaBH_4$ (400 mM) in the presence of La_2O_3-based catalysts (5 mg) at 25.0 ± 0.1°C. (b) The $NaBH_4$ methanolysis starting with 400 mM SB in the presence of various NR-La_2O_3 amount at 25.0 ± 0.1°C. (c) Plot of $HGR_{0.5}$ versus NR-La_2O_3 amount.

4. CONCLUSIONS

This study is the first to explore the use of nanostructured La_2O_3-based catalysts for facilitating both the hydrolysis and methanolysis of $NaBH_4$ under controlled conditions at 25.0±0.1°C.. Due to the higher solubility of NR-La_2O_3 in methanol than in water, it was found that $NaBH_4$ has much higher catalytic activity and stability in methanolysis than in its hydrolysis. The dependence of the rate of hydrogen production from NR-La_2O_3 catalyzed $NaBH_4$ methanolysis on the amount of

NR-La_2O_3 was investigated by performing a series of catalytic reactions using different amounts of NR-La_2O_3. It was determined that the amount providing the highest activity of catalyst was 7.5 mg. In addition, the chemical structure of NR-La_2O_3 was characterized by XRD, BET surface area analysis, and FE-SEM analysis

ACKNOWLEDGEMENTS

This work was supported by Kocaeli University Research Fund with Project Numbers: FAA-2025-4323.

REFERENCES

1. Taha T.A.M., Abouhaswa A.S., Mohamed W.S. 2025. Enhanced catalytic performance of magnetic zinc-doped cobalt ferrite nanoparticles. International Journal of Hydrogen Energy 112:133-143.
2. Durap F., Zahmakiran M., Ozkar S. 2009. Water soluble laurate-stabilized rhodium(0) nanoclusters catalyst with unprecedented catalytic lifetime in the hydrolytic dehydrogenation of ammonia-borane. Applied Catalysis A: General 369: 53-59.

CRITICAL PATH ANALYSIS FOR A FUTURE HYDROGEN SUPPLY CHAIN: A CASE STUDY FOR CENTRAL ANATOLIA

[1]*Tuba Ulusoy*, [2*]*Alper Döyen*, [3]*Fuat Kosanoğlu,* [4]*Mehmet Güray Güler*
[1] Necmettin Erbakan University, Faculty of Engineering, Konya,42140, Turkey
[2] Konya Technical University, Faculty of Engineering and Natural Sciences, Dept. of Industrial Engineering, Konya,42250,Turkey
[3] İstanbul Technical University, Management Faculty, Dept. of Management Engineering, İstanbul, 34367, Turkey
[4] İstanbul Technical University, Management Faculty, Dept. of Data Science and Analytics, İstanbul, 34367, Turkey

*Corresponding author e-mail: alperdoyen@ktun.edu.tr

ABSTRACT
The growing global energy demand has intensified the need for alternative energy sources to reduce dependence on fossil fuels and mitigate climate change. Hydrogen energy is a promising solution, thanks to its stable energy supply and efficient storage capabilities, overcoming the variability and intermittency issues related to solar and wind energy. However, taking advantage of the opportunities offered by hydrogen energy depends on developing a well-designed hydrogen supply chain (HSC). One key aspect of such a supply chain is its resilience. In this study, we are taking the first step to design such an HSC. In particular, we design the HSC of the Central Anatolia Region of Turkey using Mixed Integer Linear programming (MILP) to minimize the total daily cost related to production, storage and distribution. Then we identify the critical paths in the HSC by calculating costs related to each path when it's not active. The results show that the total transportation cost can increase up to 11.57%.

Keywords: Hydrogen Supply Chain, Mixed Integer Linear Programming, Critical Path Analysis

1. INTRODUCTION

Global energy demand has been steadily increasing due to population growth, industrialization, and urbanization [1]. To meet this rising demand, the use of fossil energy sources such as coal, oil, and natural gas has also increased. However, burning these fuels for energy production releases higher levels of greenhouse gases into the atmosphere. As a result, global temperature continues to rise, emphasizing the urgency of taking immediate action [2]. This has led to an increasing focus on alternative energy sources, such as hydrogen, solar, and wind energy, to reduce reliance on fossil fuels and mitigate the effects of climate change. On the other hand, the variability and unpredictability of solar and wind energy makes their widespread adaptation unpractical on a large scale. At this point, hydrogen energy could be a reasonable solution, as hydrogen production technology stands out by offering a stable and reliable energy supply along with efficient storage options [3,4]. Therefore, hydrogen has been gaining increasing attention, especially as countries like the Netherlands, Spain, Norway, France, the UK, Sweden, Denmark, and Ireland have announced plans to gradually phase out the sale of fossil fuel vehicles [5]. Similarly, Turkey, which has nearly all forms of renewable energy and abundant water resources, outlined its hydrogen technology strategy and roadmap [6]. These advantages position Turkey as a strong candidate for global hydrogen exports if its resources are effectively utilized for hydrogen production. Additionally, not only coastal regions but also Central Anatolian cities have significant potential for hydrogen energy production [7].

Taking Turkey's hydrogen production potential into account, several studies [8, 9,10,11] were conducted to design Turkey's HSC through mathematical optimization problems. Additionally, some studies [12,13] have explored the optimal locations for hydrogen fuel stations in Istanbul, Turkey's most populated city, using various methodological approaches.

One of the important issues that should be considered in supply chain design is resilience. A resilient supply chain is one that can anticipate, adapt to, and recover quickly from disruptions while maintaining the flow of goods and services. In the energy supply chain, resilience is particularly critical due to the sector's reliance on complex infrastructure, global raw material sourcing, and fluctuating demand. Energy supply chains must withstand disruptions such as geopolitical conflicts, natural disasters, and market volatility to ensure continuous energy availability. Identifying critical paths within a supply chain is essential for resilience, as it helps pinpoint the most vulnerable points where disruptions could have the greatest impact. In this study, we aim to investigate the critical paths of the HSC network of the Central Anatolia region of Turkey in 2050. By identifying these critical paths, it becomes possible to implement preventive measures, develop alternative supply sources, and create risk management strategies to increase resilience.

2. METHOD

At the scope of this study, we handle the HSC design problem of Central Anatolia, utilizing a MILP model developed by Almansoori and Shah [14]. This model aims to minimize the Total Daily Cost (TDC) of the HSC. We, then, identify critical paths to gain deeper insights into the network cost. We adapt the model for 2050, which is the earliest year this potential can be realized, by utilizing Turkey's energy potential [15]. Table 1 presents the forecasted number of automobiles and

large vehicles in each city of Central Anatolia in 2050, along with a projection of hydrogen energy demand based on this forecast. Among the cities in Central Anatolia, Ankara, with the largest population, also accounts for the highest number of cars and large vehicles, leading to the highest hydrogen energy demand. Unlike Ankara, Çankırı, as the least populated city in the region, has the lowest demand for hydrogen energy.

Table 1. A projection for the number of automobiles and large vehicles, and hydrogen energy demand in 2050

City	Forecasted Number of Automobiles	Forecasted Number of Large Vehicles	Forecasted Hydrogen Energy Demand (kg/day)
Ankara	4,056,964	953,003	4,347,471
Konya	901,915	370,675	1,641,481
Kayseri	604,580	191,497	858,164
Eskişehir	416,268	128,784	577,836
Aksaray	165,186	57,113	254,836
Sivas	211,438	72,791	324,858
Nevşehir	135,452	64,952	285,978
Niğde	118,934	57,113	251,451
Yozgat	115,630	40,315	179,813
Kırıkkale	93,426	24,737	112,486
Kırşehir	92,504	24,633	111,580
Karaman	89,200	33,596	149,320
Çankırı	52,860	22,397	99,063

The MILP model is solved using the Gurobi solver in Python on a computer with an M1 chip and an 8-core CPU.

3. RESULTS AND DISCUSSION

In the optimal solution of the model, the total demand of the cities—Aksaray, Çankırı, Karaman, Kırıkkale, Kırşehir, Niğde, Sivas, and Yozgat—cannot be satisfied locally, these cities need to import hydrogen from Ankara, Kayseri, Konya, and Nevşehir, where production facilities are to be established. Although a production facility is to be established in Eskişehir, there is no need for hydrogen exports, as the produced amount is sufficient to meet local demand. Furthermore, it can be concluded that to minimize transportation costs, hydrogen flows should occur between cities that are as close to each other as possible.

We then examine the critical paths in this HSC network by sequentially closing each path in the optimal solution and optimizing the resulting problem independently. The paths are closed in descending order of hydrogen flow. Totally 12 optimization problems are solved and summarized in Table 2 which shows the impacts of closing a path on the total cost. It represents the percentage change in TCC (Transportation Capital Cost), and TOC (Transportation Operating Cost), resulting from various path shutdowns, as well as, nominal value of Total Transportation Cost (TTC), change in TTC, and optimum amount of hydrogen flow in a given path.

It can be observed that the cost resulting from path failure can range from almost zero up to more than 11%. This shows that paths are not equal in terms of their critical levels. Therefore, some paths are really costly if they stop working whereas others almost have no effect on the total cost. Another result is that the change in the total transportation cost is not the same as the magnitude of the flow in that path. It turns out that the cost is not affected only by the flow, but it's also affected by other criteria like distance and available alternatives. Therefore, the identification of critical paths needs independent optimization of each scenario.

Table 2. The percentage changes in the HSC network costs (%)

Closed Path	Change in TCC (%)	Change in TOC (%)	TTC ($ / day)	Change in TTC (%)	The optimum amount of hydrogen flow (kg/day)
Konya-Karaman	15.385	7.102	294,481	11,573	149,320
Nevşehir-Niğde	7.692	12.380	289,933	9.850	251,451
Ankara-Çankırı	12.821	1.242	283,710	7.492	99,063
Ankara-Kırıkkale	12.180	0.255	281,598	6.692	111,485
Nevşehir-Aksaray	1.282	9.030	276,732	4.848	146,278
Kayseri-Sivas	9.616	-3.147	273,812	3.742	101,836

Konya-Aksaray	3.847	2.920	272,963	3.420	108,558
Nevşehir-Kırşehir	-0.641	6.722	271,188	2.748	111,485
Ankara-Sivas	-1.923	4.460	266,614	1.015	58,212
Ankara-Yozgat	10.257	-10.426	265,883	0.738	179,813
Nevşehir-Sivas	10.897	-11.426	265,582	0.624	164,809

4. CONCLUSIONS

In this study, we aim to explore the critical paths in HSC of Central Anatolia in 2050. This analysis is the starting point of designing a resilient HSC which is robust to disruptions in the infrastructure. The results show that in order to identify the critical paths in an HSC, one needs to account for different criteria of each path. Hence optimization of several different alternative scenarios is needed, which may be very time consuming in large problem instances. Future studies could investigate further steps for designing resilient HSC and make it in a more efficient way to be able to cope with large problems like HSC of Turkey as a whole.

REFERENCES

1. Zakari A, Khan I, Tan D, Alvarado R, Dagar V. 2022. Energy efficiency and sustainable development goals (SDGs). Energy 239:122365.
2. Swagatika Priyadarshini LA, Kaushik V, Kataria R. 2025. The role of anthropogenic activities, energy demand, and global climate change. In: The intersection of global energy politics and climate change: A comprehensive analysis of energy markets and economics. Singh P, Ao B, editors. Singapore: Springer Nature.
3. Shu K, Guan B, Zhuang Z, Chen J, Zhu L, Ma Z, Hu X, Zhu C, Zhao S, Dang H, Zhu T, Huang Z. 2025. Reshaping the energy landscape: Explorations and strategic perspectives on hydrogen energy preparation, efficient storage, safe transportation and wide applications. International Journal of Hydrogen Energy 97:160–213.
4. Bade SO, Tomomewo OS. 2024. A review of governance strategies, policy measures, and regulatory framework for hydrogen energy in the United States. International Journal of Hydrogen Energy 78:1363-1381.
5. https://www.transportenvironment.org/articles/end-fossil-fuel-car-eu-agenda. Accessed on January 17, 2025.
6. https://enerji.gov.tr/Media/Dizin/SGB/tr/Kurumsal_Politikalar/HSP/ETKB_Hidrojen_Stratejik_Plan2023.pdf. Accessed on January 19, 2025.
7. Dinçer İ, Javani N, Karayel GK. 2021. Türkiye için Hidrojen Çiftliği Konsepti Raporu. Report, İstanbul.
8. Güler MG, Geçici E, Erdoğan A. 2021. Design of a future hydrogen supply chain: A multi-period model for Turkey. International Journal of Hydrogen Energy 46(30):16279–16298.
9. Erdoğan A, Geçici E, Güler MG. 2023. Design of a future hydrogen supply chain: A multi-objective model for Turkey. International Journal of Hydrogen Energy 48(31):11775-11789.
10. Erdoğan A, Güler MG. 2023. Optimization and analysis of a hydrogen supply chain in terms of cost, CO2 emissions, and risk: the case of Turkey. International Journal of Hydrogen Energy 48(60):22752-22765.
11. Özbek BT, Güler MG. 2024. A multi period and multi objective stochastic hydrogen supply chain for Turkey. International Journal of Hydrogen Energy.
12. Geçici E, Güler MG, Bilgiç T. 2022. Multi-period planning of hydrogen refuelling stations using flow data: a case study for Istanbul. International Journal of Hydrogen Energy 47(95):40138-40155.
13. Gündüz SB, Geçici E, Güler MG. 2024. Locating hydrogen fuel stations: A comparative study for Istanbul. International Journal of Hydrogen Energy 52:1234-1246.
14. Almansoori A, Shah N. 2006. Design and operation of a future hydrogen supply chain: snapshot model. Chemical Engineering Research and Design 84(6):423-438.
15. Özbek BT, Erdoğan A, Güler MG. 2024. Leveraging Renewable Energy for Turkey's Future Hydrogen Supply Chain: A Stochastic Programming Model. 8th International Hydrogen Technologies Congress.

INVESTIGATION OF THE EFFECT OF TWEEN SURFACTANT ON CATALYTIC PERFORMANCE AND STRUCTURAL PROPERTIES IN THE ELECTROCHEMICAL DEPOSITION OF PLATINUM

[1*]*Jülide Hazal ÖZDEMİR*, [2]*Aysel KANTÜRK FİGEN*, [1]*Oğuz Kaan ÖZDEMİR*
[1] Yıldız Technical University, Faculty of Chemistry and Metallurgy, Department of Metallurgy and Materials Engineering, Davutpaşa Campus, Esenler, İstanbul, 34220, Türkiye
[2] Yıldız Technical University, Faculty of Chemistry and Metallurgy, Department of Chemical Engineering, Davutpaşa Campus, Esenler, İstanbul, 34220, Türkiye

*Corresponding author e-mail: jhazal@yildiz.edu.tr

ABSTRACT

This study explores a novel method to enhance the performance of proton-exchange membrane fuel cells (PEMFCs) by electrochemically depositing platinum (Pt) catalysts on carbon paper using a non-ionic surface-active agent, Tween 80. PEMFCs have significant potential in renewable energy systems and portable applications, but their efficiency is limited by the slow kinetics of the oxygen reduction reaction (ORR). Pt-based catalysts are commonly used to accelerate the ORR and improve performance. Recently, electrochemical deposition of Pt has gained attention due to its simplicity, high purity, and cost-effectiveness. Among various deposition techniques, cyclic voltammetry (CV) stands out for its ability to control deposition quality, uniformity, and electrochemically active surface area. The applied potential range in CV governs the nucleation and growth of Pt on the substrate. However, challenges such as poor uniformity and weak adhesion of Pt to substrate can lead to catalyst degradation. This study investigates the use of Tween 80 to promote uniform distribution of Pt nanoparticles, enhance adhesion, and improve catalyst stability. The proposed approach optimizes Pt usage, increases the active surface area, and increases the efficiency and lifespan of PEMFCs. Preliminary results show that Tween 80 significantly eliminates the mentioned challenges, providing a promising solution to Pt electrodeposition.

Keywords: Catalysts, Platinum, Carbon Paper, Electrodeposition, Tween 80

1. INTRODUCTION

Proton-Exchange Membrane fuel cells (PEMFCs) represent a promising technology for clean energy production, offering significant potential for integration into sustainable energy solutions and mobile technologies. The performance of PEMFCs is directly related to the efficiency of the catalysts used at the electrodes, particularly in enhancing the oxygen reduction reaction (ORR), which exhibits slow kinetic rates [1]. Noble-metal platinum (Pt) catalysts are widely utilized to enhance the rate of this reaction, leading to improved performance in PEMFCs. Nowadays, one of the Pt synthesis methods electrodeposition, has emerged as a preferred technique for Pt deposition on substrate material. It is gaining attention for its benefits such as simplicity, high purity, alloying flexibility, and efficiency in both time and cost [2]. Electrodeposition can be performed by the applied current or potential, as well as whether the process is conducted continuously or pulsed manner [3]. This technique is primarily classified into potentiostatic, galvanostatic, and cyclic voltammetry (CV) depositions. Among these routes, CV provides notable advantages in electrochemical deposition, particularly in controlling coating quality, uniformity, and electrochemically active surface area. By monitoring current responses to potential variations on the electrode surface, CV enables a detailed examination of reaction dynamics [4].

Carbon paper is widely utilized as a substrate for Pt catalyst deposition due to its favorable properties such as high electrical conductivity, chemical stability, high-temperature resistance, low cost, availability, and allowing uniform and homogeneous distribution of catalyst particles. Electrochemical deposition of Pt catalysts on carbon paper minimizes Pt usage while simultaneously increasing the active surface area, thus optimizing the catalyst's performance [2]. In the case of platinum (Pt) deposition on carbon paper using CV, the applied potential range from -0.283 V to 1 V (versus the Ag/AgCl electrode) plays a crucial role in governing nucleation and growth mechanisms. When the potential approaches negative values (e.g.-0.283 V), $[PtCl6]^{2-}$ ions undergo reduction at the electrode surface, leading to the formation of Pt atoms. At more negative potentials, the reduction reaction proceeds more rapidly, thereby enhancing the nucleation rate. As the potential shifts toward positive values, the initially formed Pt nuclei begin to grow, with ion diffusion playing a key role in determining the growth rate [5]. Although the electrochemical deposition of Pt catalysts on carbon paper via the CV technique has yielded positive results, certain challenges may arise, including a reduction in the electrochemically active surface area due to inhomogeneous Pt deposition or catalyst degradation resulting from incomplete adhesion of Pt to the carbon paper surface.

Surface-active agents offer an effective solution to achieve a more uniform distribution of Pt nanoparticles during electrochemical deposition. These agents enhance the active surface area of Pt by promoting the even adsorption and accumulation of Pt ions on the substrate. Furthermore, surface-active agents can improve the catalyst's stability and

reduce Pt loss by ensuring stronger adhesion of Pt to the electrode surface. This ultimately contributes to a longer catalyst lifespan and improves the overall efficiency of the PEM fuel cell [6]. This study aims to investigate a new strategy that uses Tween 80 as the non-ionic surface-active agent to enhance the efficiency of PEMFCs by employing electrochemical deposition techniques for the application of Pt catalysts on carbon paper, thereby offering a solution to improve the performance of PEMFCs.

2. MATERIALS AND METHODS

2.1 Preparation of Carbon Paper Substrates

For the electrochemical deposition process, commercially available Freudenberg carbon papers were utilized as the substrate material. The carbon papers, each with an area of 5 cm², were precisely cut using a 31-mm punch and subjected to a cleaning procedure before deposition. Following this process, the carbon papers were dried in an oven and subsequently weighed to determine their initial mass before platinum deposition. The average weight was then calculated to establish a baseline for deposition efficiency.

2.2 Preparation of the Electrochemical Deposition Solution

The electrolyte solution, serving as the coating bath, was prepared by dissolving 0.5 M H_2SO_4 (150 mL) and the required amount of platinum precursor solution (Chloroplatinic acid hexahydrate, Sigma-Aldrich, 37%, 0.05 M). The pH of the solution was carefully adjusted to 2 using NaOH to ensure a controlled acidic environment. Maintaining a stable pH is crucial, as it directly influences the deposition mechanism, surface morphology, and coating properties. To achieve a uniform and well-controlled platinum deposition on carbon paper, a pH 2 environment was selected for this study.

2.3 Electrochemical Deposition of Platinum

The cyclic voltammetry (CV) technique was employed for platinum electrodeposition. The carbon paper substrates were placed in a Teflon sample holder, and their electrical conductivity was verified before each deposition using a multimeter (Tt Technic, 9808). The electrochemical deposition system comprised a Pt plate as the counter electrode and an Ag/AgCl electrode as the reference electrode, in addition to the working electrode.

Following the completion of the designated number of CV cycles at the specified scan rate, a post-deposition cleaning procedure was conducted in 0.5 M H_2SO_4, with a scanning rate of 100 mV/s for 50 cycles, to remove any residual impurities. After both the electrochemical deposition and subsequent cleaning steps, the obtained Pt/C catalyst samples underwent a final washing and drying process. Finally, the deposited samples were weighed, and the average value was determined to quantify the platinum loading on the carbon paper substrates. After determination of Pt deposition parameters on carbon paper with CV, the effect of the addition of different amounts of Tween 80 will be comparatively investigated.

3. RESULTS AND DISCUSSION

The platinum catalysts were coated using a 3-electrode system with cyclic voltammetry. Carbon paper (Fraudenberg) was used as the working electrode, platinum wire as the counter electrode and Ag/AgCl electrode as the reference electrode. The open circuit potential of the electrodes placed in the immersion solution was first measured and cathodic polarization was performed starting from the open circuit potential to -1V. After -1V, anodic polarization was performed again to the open circuit potential and this cycle was performed 10 times. The polarization curves where the coating process was performed are given in Figure 1.

As given in Figure 1, the reduction reaction of platinum begins with the application of cathodic overvoltages. The limiting current value was reached at approximately -0,8V (vs. Ag/AgCl). The platinum particles reduced during the first cathodic scan form the hydrogen desorption peak during anodic oxidation. In the second cathodic scan, the reduction potential of platinum shifted to more negative potential values compared to the first scan. On the other hand, the current value of the hydrogen evolution reaction increases with the number of cycles. After coating, the electrodes were removed from the coating electrolyte and immersed in 0.5 M H_2SO_4 solution for cleaning. 50 cycles were performed between -0.283 V and 1 V with a scan rate of 100 mV/s in acid. The electrochemical active surface area of the catalysts was calculated by calculating the area under the absorption and desorption peaks of hydrogen from the cyclic voltammetry curve obtained.

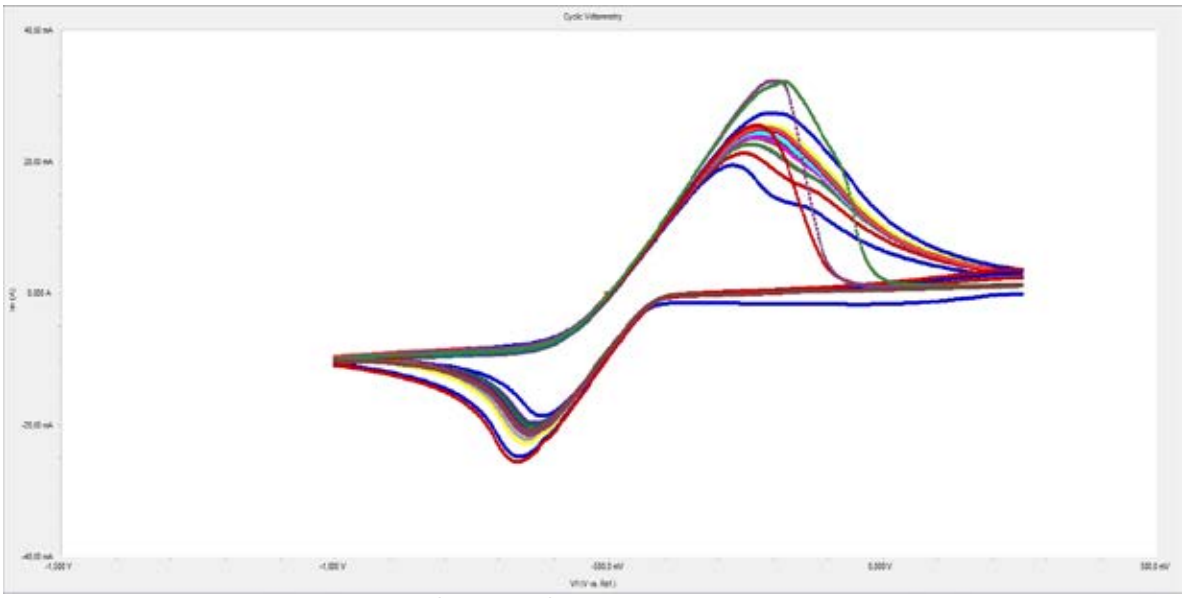

Figure 1. CV curves for catalysts electrodeposition.

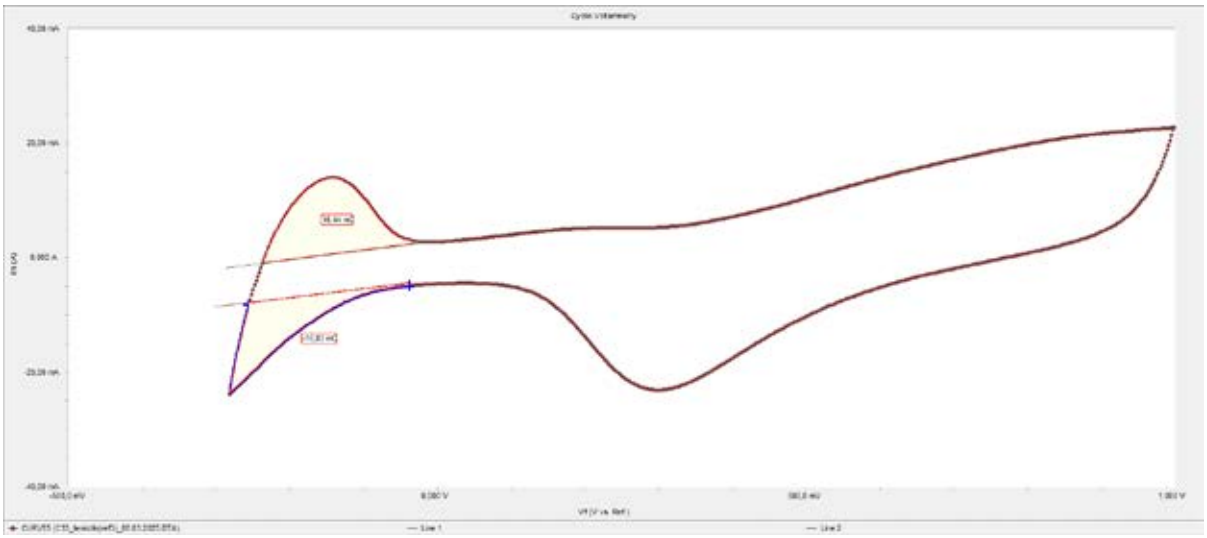

Figure 2. CV curve of electrodeposited Pt catalyst.

As shown in Figure 2, the cyclic voltammetry curve, which is well known in the literature to belong to platinum, was obtained. Surface roughness of the catalysts was calculated by calculating the areas under the peaks. The reduction reaction of oxygen is also clearly visible in the polarization curve. After coating, the open circuit potential was taken as a function of time and the open circuit potential, which was positive before coating, shifted to a negative potential value after coating. Figure 3 shows SEM images and EDS results of platinum catalysts coated on carbon paper by the electrochemical method.

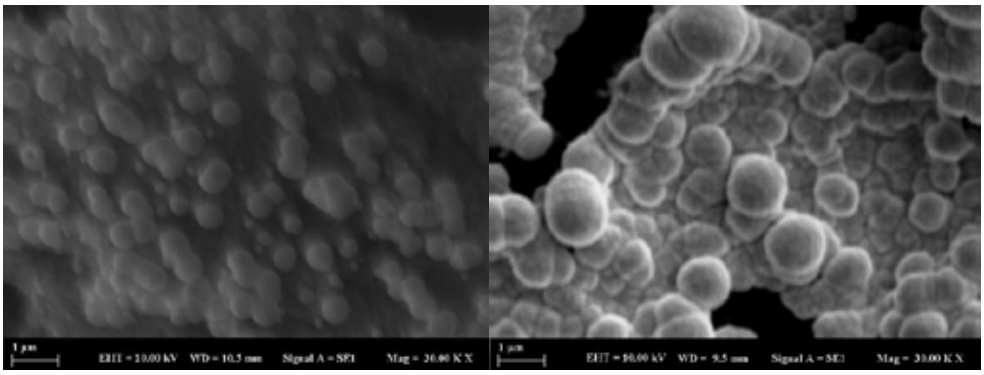

Element	Weight (%)	Atomic (%)	Net Int.	Error (%)	K (Ratio)	Z	A	F
C K	75.73	98.06	706.10	5.11	0.6266	1.1313	0.7314	1.0000
PtM	24.27	1.94	62.44	9.32	0.1614	0.5671	1.1736	0.9992

Figure 3. SEM images at different magnifications.

As can be seen from SEM images, Pt catalysts are reduced in spherical form on the carbon support. However, the particle size of Pt catalysts is quite high. EDS analysis confirms the presence of Platinum and carbon on the coating surface.

4. CONCLUSIONS

This study suggests that the use of Tween 80 as a non-ionic surfactant in the electrochemical deposition of Pt catalysts is expected to enhance the performance and stability of PEMFCs. By incorporating Tween 80 during cyclic voltammetry-based Pt deposition, a more uniform nanoparticle distribution and improved adhesion to the carbon paper substrate are expected. These improvements are predicted to increase the electrochemically active surface area, optimize Pt utilization, and enhance oxygen reduction reaction kinetics. Furthermore, the proposed method is likely to address common challenges such as poor uniformity and weak adhesion, ultimately contributing to the long-term durability of the catalyst layer. This approach is considered a cost-effective and enhanced strategy for improving PEMFC catalyst performance, making it a promising solution for future fuel cell applications.

REFERENCES

1. Jithul, K., B. Tamilarasi, and J. Pandey, *Electrocatalyst for the oxygen reduction reaction (ORR): Towards an active and stable electrocatalyst for low-temperature PEM fuel cell.* Ionics, 2024: p. 1-31.
2. Zhang, W., et al., *Electrodeposited platinum with various morphologies on carbon paper as efficient and durable self-supporting electrode for methanol and ammonia oxidation reactions.* International Journal of Hydrogen Energy, 2023. 48(7): p. 2617-2627.
3. Eiler, K., et al., *Oxygen reduction reaction and proton exchange membrane fuel cell performance of pulse electrodeposited Pt–Ni and Pt–Ni–Mo (O) nanoparticles.* Materials today energy, 2022. 27: p. 101023.
4. Song, Q., et al., *Electrodeposition of Se on carbon-supported Pt nanoparticles by cyclic voltammetry.* Journal of Solid State Electrochemistry, 2021. 25: p. 2471-2478.
5. Ko, D.H., A. Partridge, and A. Hosseini, *A mechanistic study of Pt particle electrodeposition and growth on a self-assembled monolayer as an active template.* Journal of Electroanalytical Chemistry, 2022. 920: p. 116638.
6. Özdemir, J.H., et al., *Production of Highly Efficient Pt/C for PEM Fuel Cell Applications.* Electrocatalysis, 2025: p. 1-12.

HYDROGEN VALUE CHAINS IN POSITIVE ENERGY DISTRICTS: A MULTI-LEVEL ANALYSIS ON THE DYNAMICS BETWEEN ENERGY TRANSITION PLANS AND INTEGRATED SPATIAL PLANNING

[1*]*Ahu Gürler Akdeniz*, [1] *Ebru Gürler*, [2] *Yavuz Ateş,* [1, 2] *Ali Rıfat Boynueğri*
[1] Yıldız Technical University, Clean Energy Technologies (CET) Institute, Davutpaşa Campus, Istanbul, 34200, Türkiye
[2] Yıldız Technical University, Faculty of Electrics and Electronics, Department of Electrical Engineering, Davutpaşa Campus, Istanbul, 34220, Türkiye
*Corresponding author e-mail: ahugurler@gmail.com

ABSTRACT
This research paper focuses on hydrogen value chain (HVC) in positive energy districts (PEDs) with emphasis on the dynamics between energy transition plan and integrated spatial planning. The aim is to resolve the strategic frameworks on trajectories towards 2030 and 2050 by modelling through a multi-level analysis on the dynamics of 'infrastructural' and 'inter-operational' dimensions in order to reveal the path towards integrated energy planning and management (IEPM) for systemic resilience. The role of hydrogen in sustainable and integrated development is explained with reference to scaling-up clean energy technologies that target a decarbonized resilient future through energy transition by cyber-physical systems. The multi-level performance character of coopetitive models is evaluated by multi-criteria decision analysis/analytic hierarchy process (MCDA/AHP) method with a multi-scalar parametric framework on IEPM for systemic resilience. The research framework designed from global to macro-regional and micro-regional levels is built by 30 key performance indicators ('m') and 4 key performance values ('n'). The research revealed that HVC is the common denominator for developing PEDs. The findings demonstrate that challenges and innovations for integrating advanced energy technologies into urban regions to achieve energy-based systemic resilience can be fulfilled through multi-level dynamics between 'system-based clean energy frameworks' and 'strategy-based multi-scalar operations'.

Keywords: Positive Energy Districts, Hydrogen Value Chain, Energy Transition Plan, Integrated Spatial Planning, Integrated Energy Planning and Management.

1. INTRODUCTION
Throughout the history of sustainable development, energy crises that puts energy sovereignty in a conjunctural gridlock have been overcome by either a change in production methods or an innovation in operational models. Radical transition from conventional energy resources to renewable energy alternatives had denoted a paradigm shift diffused in every aspect of the relationship between human and environment. Radical innovations in the frameworks of advanced energy technologies and accelerated progress in clean energy mechanisms has triggered coopetitive processes to be regulated by multi- and trans-disciplinary collaborations on the issues of integrated and sustainable development. Both of the radicals converged on Positive Energy Districts (PEDs) which are developed as both a localized response to the global strategy for energy transition [1] and a coopetitive instrument in the energy transition mechanism for achieving systemic resilience. Because, PEDs are defined through their annually energy balance characteristics that indicate surplus energy due to a mix of integrated renewable systems within a value chain [2], wherein energy flows between actors (consumers, producers, prosumers and storage systems) get optimized in order to improve energy efficiency among the district [3]. Moreover, Energy Transition Plan (ETP) refers to a strategic framework aimed at shifting energy systems from fossil fuel reliance to sustainable and renewable energy sources for facilitating the establishment of Hydrogen Value Chains (HVCs)[4] in PEDs, while Integrated Spatial Planning (ISP) involves a coordinated design and management of land use and infrastructure for optimizing energy efficiency and encouraging the development of self-sustaining urban areas [5] that align with the targets in Strategic Energy Technology (SET) Plans [6] synchronized with Sustainable Development Goals [7]. The joint need for HVC in PEDs arises from ongoing global energy crisis, fueled by factors such as energy bottlenecks stemmed from regional conflicts and the climate mitigation targets of decarbonization outlined in the Paris Agreement. As urban populations are expected to reach two-thirds of the total by 2050 [8], it is essential to integrate ETPs with ISPs to develop sustainable energy systems that are both resilient and self-sufficient. Furthermore, the emphasis on hydrogen as a key element of the clean energy policy on global agenda highlights the importance of developing effective infrastructure to meet urban energy demands and foster competition in clean hydrogen technologies. Due to extensive technological advances and innovations in clean energy research, deploying hydrogen infrastructure and shaping HVCs, which are structured by generation, transmission, distribution and either utilization or storage of hydrogen energy, have become at the forefront of achieving carbon-neutral future and empowering energy sovereignty[9]. Therefore, HVCs integrated into PEDs make an innovative contribution to the catalyzing effect for building mechanism-instrument relationship on the multi-dimensional dynamics of clean energy-oriented integrated and sustainable development. Moreover, ETPs bridged with ISPs make a transformative contribution to authorize the coopetitive framework and strategic tools necessary to effectively plan and implement hydrogen-based energy policies and spatial strategies. The novelty of this research is modelling of the 2030 and 2050 scenarios that include HVC for and/or PEDs from a holistic perspective by a multi-level analysis and integrated synthesis on systemic resilience.

2. MODELING AND METHODS

The scope of the research is to resolve the multi-dimensional dynamics of clean energy-driven integrated and sustainable development modelled by a qualitative-quantitative mixed research method. The research hypothesis is that 'dynamics of the inter-operational dimension, which comprised of ETP and ISP, designate an exclusive type of operative performance character of integrated energy strategy for designing, planning and managing the infrastructural dimension, which involves HVC in PEDs. In conformity with the research hypothesis, 'research-based strategic agendas' (KPIs, 'm') and 'practice-based systemic frameworks' (KPVs, 'n') in the last five years are selected for addressing the question of hydrogen energy, especially the HVC in PEDs, for resolving holistic models on systemic resilience to unveil the encoded 2030 and 2050 scenarios. Then models are configured on excel by the theory-based principles of multi-criteria decision making (MCDM) that is employed under the frameworks of soft systems methodology without any special software [10]. The parametric framework of this research is structured by the KPIs (Figure 1.a) and the KPVs (Figure 1.b) by a holistic approach on systemic resilience. The KPVs ('n') of multi-criteria set is structured by interlocking systemic layers in practice for PEDs and HVC on the (infra)structural dimension as well as for ETP and ISP on the inter-operational dimension. The KPIs ('m') of multi-criteria set is structured by dynamically strategic levels of multi-scalar interconnectivity in holistic approach ranging from global level at macro scale to regional level at meso scale and local level at micro scale. The modelling is executed by the integrated approach on "MCDA/AHP method" [11], which is a qualitative-quantitative mixed research method in multi-criteria decision-making approach on modelling and simulation for resolving real-world problems and/or testing the scenario-based hypothesis.

multi-level operations #	top-criteria	multi-level category #	criteria	HVC in PEDS: The dynamics between ETP and ISP #	sub-criteria	KPIs m #
1	Global Operations GlOp.s	1.1	Macro / Global SDGs Sustainable Development Goals	1.1.1	Goal 7 – Affordable and Clean Energy	1
				1.1.2	Goal 9 – Industry, Innovation and Infrastructure	2
				1.1.3	Goal 11 – Sustainable Cities and Communities	3
				1.1.4	Goal 12 – Responsible Consumption and Production	4
				1.1.5	Goal 13 – Climate Action	5
				1.1.6	Goal 17 – Partnership for the Goals	6
2	Macro-Regional Operations MaRegOp.s	2.1	Macro-Meso / Geopolitical IGMs Intergovernmental Mechanisms	2.1.1	Renewable Energy Road Map	7
				2.1.2	Regulatory Frameworks	8
				2.1.3	Financial Incentives	9
				2.1.4	Commitment	10
				2.1.5	Cooperation	11
				2.1.6	Participation of Political and Economic Initiatives/Unions	12
		2.2	Meso / Regional EnergyPol National Mechanism	2.2.1	(Inter)National Energy Agencies	13
				2.2.2	National Energy Policy / Strategy & Action Plan	14
				2.2.3	National Renewable Energy Policy / Strategy & Action Plan	15
				2.2.4	Competitive Advantage of the HVC	16
				2.2.5	Coopetitive Advantage of the HVC	17
				2.2.6	Multilateral Collaboration	18
3	Micro-Regional Operations MiRegOp.s	3.1	Meso-Micro / Geostrategic EnergySys Regional Mechanism	3.1.1	Integrated Regional Energy Systems	19
				3.1.2	Regional Energy Transition Frameworks	20
				3.1.3	P/C/IEDs – Positive (Clean) Energy Districts	21
				3.1.4	Power Grid Typology	22
				3.1.5	Power Grid Resilience and Security	23
				3.1.6	Institutional Collaboration	24
		3.2	Micro / Local Energy(Re)Dev Local Mechanism	3.2.1	Local Renewable Energy Strategies/Schemes	25
				3.2.2	Integrated and Sustainable Urban Development	26
				3.2.3	(Renewable) Energy Value Chain	27
				3.2.4	Energy Hubs and Data Centers	28
				3.2.5	Local Renewable Energy Communities	29
				3.2.6	Energy Market characteristics	30
macro level global scale		meso level systemic scale		micro level strategic scale		

-a- categorized interconnectivity for modelling performance (the multi-level operational spectrum by 30 KPIs (m))

research study main goal	clean energy factor #	category	HVC in PEDS: The Dynamics between ETP and ISP #	sub-criteria	KPVs n #
IEP for SR Integrated Energy Planning for Systemic Resilience	1	IF infrastructure	1.1	PEDs – Positive Clean Energy Districts	1
			1.2	HVCs – Hydrogen Value Chains	2
	2	IOP interoperation	2.1	ETP – Energy Transition Plan	3
			2.2	ISP – Integrated Spatial Planning	4
macro level global scale		meso level systemic scale		micro level strategic level	

-b- parametric framework for modelling performance scenarios (the multi-level operational spectrum of 4 KPIs (n))

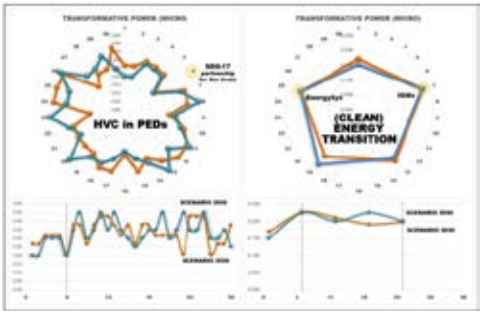

-c- Comparison of transformative power of performance in the models

Figure 1: Key Performance Values (KPVs) and Key Performance Approaches (KPAs) of the performance modelling framework

Information is quantified into data by the rule of three-tiered fuzzy logic principle (1). Then, quantified data is systematized on basis of the rule of value distribution (2) to formulate the characteristic function of the models. The characteristic performance of the model(s) is evaluated regarding the ratio between infrastructural to inter-operational dimensions on the "5-point-characterization scale" [10] from coopetitive (48/52; collaborative leadership), competitive (49/51; strategic collaboration), neutral (50/50), competitive (51/49; strategic partnership), and coopetitive (52/48; sovereign leadership).

$$criteria \rightarrow non-existing: 0 \quad uncertain: 0.5 \quad existing: 1 \tag{1}$$

$$\sum_{i=1}^{n} w_i = 1 \tag{2}$$

The integrated performance is calculated through weighted value measurement in a mxn matrix format (3) whereas the comparative performance is calculated through pairwise comparison of parametric framework in a m/m matrix format (4).

$$\sum_{j=1}^{n} a_{ij}\, w_j \quad (for\ i = 1, 2, 3 \ldots m) \rightarrow A_m, C_n(W_n) = a_{ij\ (m\ x\ n)} \tag{3}$$

$$C_i(W_i), C_j(W_j) = C_{ij}(W_{i/j}) \rightarrow C_{ij_{(m/m)}} \tag{4}$$

Evaluating the comparative performance of the model(s) is achieved by attributing relative weights to criteria from 1-9 with reference to the Saaty scale. Pairwise comparison scores under 1.000 are treated as bias, thus excluded [10]. All of the performance measurements are evaluated through the ranking rule on score and order of importance by not only the max-min strategy (5 and 6) but also the min-max strategy. Overlapping the max-min and min-max strategies provides deciphering the control code(s) of scenario(s) out the models [11].

$$A_{max.1} \geq A_{max.2} \geq A_{max.3} \dots \geq A_{max.m} \quad (5)$$
$$C_{max.1} \geq C_{max.2} \geq C_{max.3} \dots \geq C_{max.m} \quad (6)$$

Checking the consistency ratio of the models' performance (7) is excluded from the holistic modelling approach, because evaluating the reliability and validity measure of preferences limited to 10 alternatives and/or criteria by Saaty in the decision-making process [11].

$$CI = \frac{\lambda_{max} - n}{n-1}, \text{ where } \det(\sum_{model} - \lambda I) = 0 \leftarrow CR = \frac{CI}{RI} \quad (7)$$

Calculating the Yearly Energy Balance [2] in PEDs (8) is also excluded from the models as a result of hypothetical nature of the research in which practice-based strategic frameworks are employed instead of district-specific case studies in order to reveal the holistic character of the models.

$$[Onsite\ Renewable\ Energy_{generation}] + [Climate\ neutral\ Energy_{import}] - [Energy_{export}] = [PED\ Energy_{consumption}] \quad (8)$$

3. RESULTS AND DISCUSSION

The characteristic performance of the models is compatible with the targeted agenda of the SDGs for 2030 and 2050: Scenario 2030 has a "coopetitive" character (IF: 52 > IOP: 48) with 'escalating spiral shield' effect that accelerates 'clean energy frameworks' on infrastructure of HVCs in PEDs for carbon-neutral economy (Figure 2.a). Whereas, Scenario 2050 has a "coopetitive" character (IF: 48 < IOP: 52) with 'clean energy trajectory' effect that innovates interoperability of 'green hydrogen mechanism' for HVCs in PEDs for hydrogen economy (Figure 3.a).

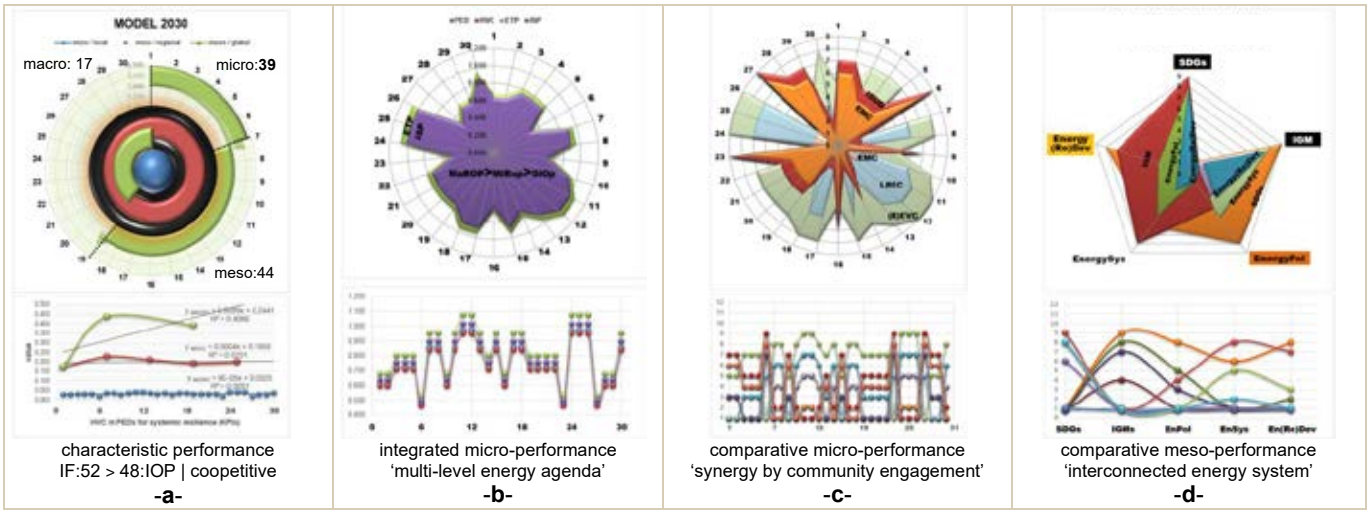

characteristic performance IF:52 > 48:IOP | coopetitive -a-
integrated micro-performance 'multi-level energy agenda' -b-
comparative micro-performance 'synergy by community engagement' -c-
comparative meso-performance 'interconnected energy system' -d-

Figure 2: Existing framework model of Scenario 2030 – hydrogen in carbon- and climate-neutral future | (green) HVC for PEDs

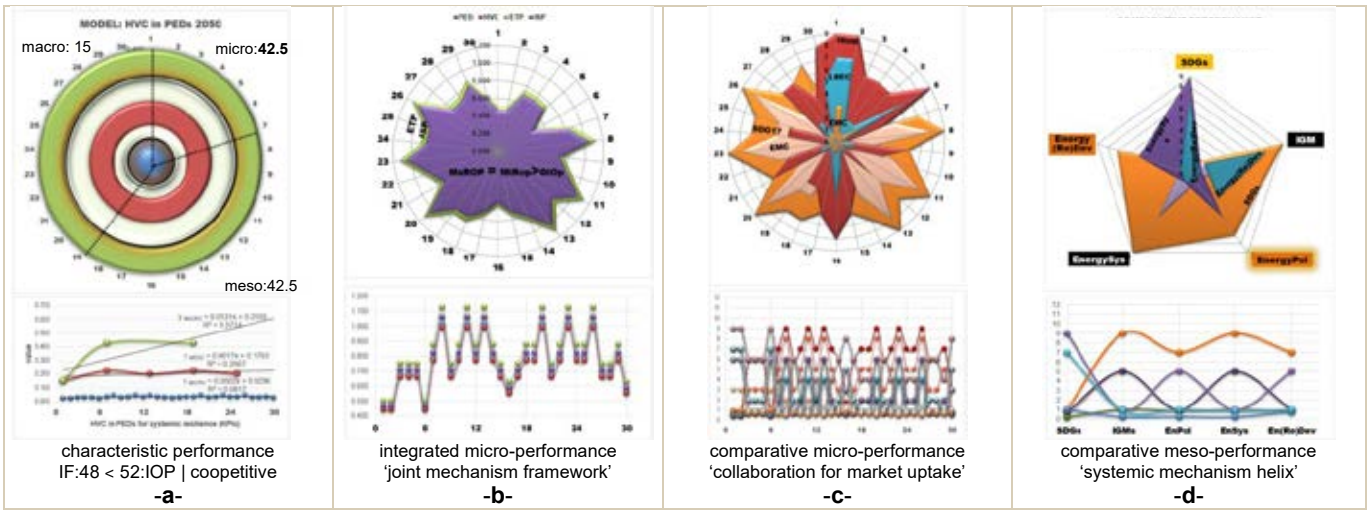

characteristic performance IF:48 < 52:IOP | coopetitive -a-
integrated micro-performance 'joint mechanism framework' -b-
comparative micro-performance 'collaboration for market uptake' -c-
comparative meso-performance 'systemic mechanism helix' -d-

Figure 3: Projected framework model of Scenario 2030 – hydrogen in low-carbon and climate-resilient future | (clean) HVC in PEDs

The integrated micro-performance converges on ETP-driven ISP approach for empowering HVC in PEDs: Although Scenario 2030 is controlled by ISP at local level, it is managed from regional level by energy market characteristics in ETPs by strategies of cooperation and participation in IGMs, i.e.: PEDs, Hydrogen Valleys, Hydrogen Hubs, etc. (Figure 2.b). Scenario 2050 is not only controlled by ISP through policy and redevelopment triggered multi-scalar interconnectivity but also managed by joint mechanism framework of regional IGMs and local ETPs, i.e.: Regional Hydrogen Unions/Cooperations/Initiatives, higher readiness levels for technology, market and community engagement, deployment of cyber-physical systems for HVC in PEDs, etc. (Figure 3.b).
The comparative micro-performance converges on multi-scalar inter-operability of integrated energy framework even if it diverges from the route for clean energy mechanism frameworks for systemic resilience: Scenario 2030 is managed by enhancing global partnership on power grid resilience, security in energy systems and local renewable energy value chain besides ensuring cooperation and participation in IGMs from global to regional level, therefore it is controlled by financial incentives defined in IGMs from regional to local level fostering competitive advantage of the HVC targeted in policy-based national energy mechanism in line with SDG 7 and 9. (Figure 2.c). Although Scenario 2050 is controlled by not only scaling-up the national renewable energy strategies with action plans and regional coopetitive advantage of the HVC targeted in policy-based national energy mechanism but also (re)developing by local renewable energy strategies with hydrogen energy schemes, it is managed by triadic cooperation of SDG 7, 9 and 17 transmitted into policy-based regional energy mechanism via IGMs on nationally determined contributions (Figure 3.c).
The comparative meso-performance not only converges on Energy(Re)Dev mechanism at local level but also diverges from each other in EnergySys strategies on clean energy mechanism frameworks for systemic resilience: In Scenario 2030, integrated mechanism framework is not only employed to manage strategic IGMs interconnecting with systemic Energy(Re)Dev on the basis of global targets in the SDGs but also exploited to control (re)development of local energy systems as well as formulating regional energy policies (Figure 2.d). Whereas in Scenario 2050, cross-relational mechanism frameworks on IGMs integrated with regional energy systems are employed not only to manage the holistic approach on energy management but also to control sustainability-led local energy policies synchronized with policy-led regional energy (re)developments (Figure 3.d).

4. CONCLUSIONS

PEDs, which not only embody principles of resilience, sustainability and innovation but also promote community welfare and environmental governance, represent a shift towards more sustainable type of urban development having energy sovereignty as a result of harnessing local resources to meet energy needs of local communities. The main findings of research indicates that HVCs provide inter-operational coopetitiveness for PEDs, if 'integrated energy planning and management approach for systemic resilience' is authorized by ETPs and controlled by ISPs. Because, the infrastructural and inter-operational dimensions of clean energy-based frameworks converge and interlock with the diverse mechanisms diffusing through multi-level dynamics. Therefore, these findings verify the hypothesis of this research (Figure 3.c). Consequently, 'value engineering' through the methods of techno-economic assessment emerges as one of the advanced research areas aimed at structuring and enhancing HVC in PEDs in further research studies. Integrating clean energy technologies within urban environments poses both challenges and innovations. Fostering dynamic interactions between 'system-based clean energy frameworks' and 'strategy-based multi-scalar operations' have potential to strengthen the connection between cyber and physical environments. As a concluding remark, trajectory on more sustainable and resilient urban future pull towards successful implementation of clean and green energy transition, which have been already addressed as complexities on the global agenda, by innovative framework of cyber-physical systems.

ACKNOWLEDGEMENT

The authors acknowledge that this study was conducted within the scope of a doctoral thesis study at The Clean Energy Technologies Institute of Yıldız Technical University. The corresponding author also declares that modelling method was also used in her MSc. thesis completed in 2013.

REFERENCES

1. Krangsås S, Steemers K, Konstantinou T, Soutullo S, Liu M, Giancola E, Prebreza B, Ashrafian T, Murauskaitė L and Maas N. 2021. Positive energy districts: Identifying challenges and interdependencies Sustainability 13(19): 10551.
2. Rampinelli C and Hofer G. 2022. D4.1 Criteria catalogue for Positive-Energy-Districts. Stockholm: Sustainable Innovation Initiative.
3. Toffler A. 1980. The third waive. London: William Collins Sons & Co., Ltd.
4. IRENA. 2024. International co-operation to accelerate green hydrogen deployment. Abu Dhabi: IRENA.
5. InforMEA. No Date. Spatial Planning. Definition. United Nation's Information Portal on Multilateral Environmental Agreements.
6 SETIS – SET Plan Information System. No Date. Positive Energy Districts. Website managed by Joint Research Center.
7. Cellura M, Fichera A, Guarino F and Volpe R. 2025. Leveraging PEDs Surplus for the Achievement of the SDGs. Energies 18:506.
8. Ritchie H, Samborska V and Rosen M. 2018. Urbanization. On Our World in Data Portal.
9. Kardaś S. 2024. Energy Sovereignty Index: Gains, gaps, and the road ahead. European Council on Foreign Relations
10. Gürler A. 2013. A comparative study on the yacht building industry: The role of design strategy and management in development of the yacht building industry in the World and Turkey (MSc. Diss.). Istanbul Technical University.
11. Belton V and Stewart TJ. 2002. Multiple criteria decision analysis: An integrated approach. Dordrecht, NL: Kluwer.

A COMPARISON OF SYSTEMIC PERFORMANCE: THE FRAMEWORK MODELS OF HYDROGEN STRATEGIES IN (INTER)NATIONAL ENERGY POLICIES FOR CLEAN ENERGY TRANSITION

[1*] *Ebru Gürler*, [1] *Ahu Gürler Akdeniz*, [2] *Yavuz Ateş*, [1,2] *Ali Rıfat Boynueğri*
[2] Yıldız Technical University, Clean Energy Technologies (CET) Institute, Davutpaşa Campus, Istanbul, 34200, Türkiye.
[3] Yıldız Technical University, Faculty of Electric and Electronics, Department of Electrical Engineering, Davutpaşa Campus, Istanbul, 34220, Türkiye.
*Corresponding author e-mail: ebrugurler@gmail.com

ABSTRACT
This research paper focuses on comparing the systemic performance with emphasis on the framework models of hydrogen strategies in (inter)national energy policies for clean energy transition. The aim is to resolve not only the existing scenario2030 but also the projected scenario2050 by modelling through a multi-scalar (re)programming on the dynamics of 'regulatory' and 'operative' dimensions in order to reveal the path towards integrated policy planning and management (IPPM) for resilient development. The role of hydrogen energy in resilient development is explained with reference to accelerated energy transition that targets green energy in 2030 and clean energy in 2050 through (inter)national energy policies by holistic approaches from geographies of the World. The strategic performance character of cooperative models is evaluated by the multi-criteria decision analysis/analytic hierarchy process (MCDA/AHP) method with a multi-scalar parametric framework on (clean) energy transition for resilient development. The research framework designed from global to region-specific multi-national and country-specific national levels is built by 41 key performance approaches ('m') and 24 key performance indicators ('n'). The research revealed that energy policies have innovative power for structuring and accelerating clean energy transition. The findings demonstrate the need for political impact assessment for 'transformative mechanism design' through policy-based performance (re)programming.

Keywords: Hydrogen Energy Policies, Clean Energy Transition, Political Impact Assessment, Scenario (Re)Programming, Integrated Policy Planning and Management.

1. INTRODUCTION
Energy transition, which is also called as energy system transformation by International Energy Agency (IEA), is defined as a paradigm shift in supply-demand models and consumption patterns of the prevailing energy system either responding to energy crises or resolving anthropocentric problems by major structural changes in energy technologies and policies [1]. Even though energy transition was not specifically identified at the 6th Assessment Report of the UN-IPCC in 2021, "transition" is defined as "the process of changing from one state or condition to another in a given period of time. Transition can occur in individuals, firms, cities, regions and nations, and can be based on incremental or transformative change" [2]. The process of energy transition has stemmed from three-tiered challenge on the issues of resource management, energy and climate, and addressed questions of energy justice, energy sovereignty and energy diplomacy on the global agenda [3]. Therefore, the performance of energy systems has been measured with reference to the trilemma dimensions of energy security, energy equity and environmental sustainability by World Energy Council since 2010. Moreover, the progress and preparedness of different geographical regions and countries for equitable, secure and sustainable energy future through energy transition has been tracked under the title of Energy Transition Index by World Economic Forum since 2018. Although, the performance of framework models on (inter)national energy policies for clean energy transition has never been holistically put under Political Impact Assessment in order to resolve the transformative performance power of policy-based planning and sustainability-based management. The novelty of this research is modelling of the 2030 and 2050 scenarios by a Hydrogen Strategy-based Political Assessment (H2-SPA) from a holistic perspective by a multi-level analysis and integrated synthesis on resilient development.

2. MODELING AND METHODS
The scope of the research is to resolve the framework models of hydrogen strategies in (inter)national energy policies for clean energy transition modelled by a qualitative-quantitative mixed research method. The research hypothesis is that interconnections between 'policy planning that encompasses technology, policy and agency on regulatory dimension' and 'sustainability management that deals with environment, social and governance (ESG) issues on operative dimension' both designates transformative performance character for clean energy transition and delineates an outline for transformative mechanism framework on clean energy transition that can be (re)programmed by integrated policy planning and management for resilient development. In conformity with the research hypothesis, 'practice-based strategic approaches (KPAs, 'm') and 'research-based systemic frameworks' (KPVs, 'n') in the last five years are selected for addressing the question of hydrogen energy, especially the international energy policy for clean energy transition ((I)NEP for CET), for resolving holistic models on resilient development to unveil the encoded existing scenario2030 and projected scenario2050. Then models are configured on excel by the theory-based principles of multi-criteria decision making (MCDM) that is employed under the frameworks of soft systems methodology without any special software [4].

The parametric framework of this research is structured by the KPAs (Figure 1.a) and the KPIs (Figure 1.b) by a holistic approach on resilient development. The KPIs ('n') of multi-criteria set is structured by interlocking systemic layers in practice for technology, policy and agency (TPA) coordinated for policy planning on the regulatory dimension as well as for environment, social and governance (ESG) cooperated for sustainability management on the operative dimension. The KPAs ('m') of multi-criteria set is structured by dynamically strategic levels of multi-scalar interconnectivity in holistic approach ranging from global level at macro-scale to regional level at meso-scale and local level at micro-scale. The KPAs represented as the selected case studies in the form of multi-level geo-political spectrum of this research obtained from open source platforms and/or information portals of the global institutional organizations, i.e.: UN and UNDP, the EU, the OECD, IPCC, WEC, WEF, McKinsey, as well as IEA, IRENA, European Hydrogen Observatory, Clean Hydrogen Partnership and Hydrogen Europe Research, etc.. The modelling is executed by the integrated approach on "MCDA/AHP method" [5], which is a qualitative-quantitative mixed research method in multi-criteria decision-making approach on modelling and simulation for resolving real-world problems and/or testing the scenario-based hypothesis.

research study main goal	geo-political factor #	category	Hydrogen Strategies in (Inter)National Energy Policies for CET #	sub-criteria	Cases m #
CET scenario(s) for Clean Energy Transition	1	AMERICAS	1.1	North American Approach: USA; Canada	1-2
			1.2	South American Approach (Latin American -LATAM- States): Colombia; Uruguay; Brazil; Mexico; Panama; Chile; Argentina	3-9
	2	EUROPE (European Union)	2.1	Anglo-Saxon Approach (Ex-EU Member State): UK	10
			2.2	European Approach (EU Member States): Denmark; Sweden; Finland; Germany; France; Italy; Spain; Ireland; Luxembourg; Netherlands; Belgium; Austria	11-22
			2.3	Euro-Region Approach (Non-EU Member States): Norway; Iceland; Switzerland	23-25
			2.4	Eurasian Approach (EU Candidate State): Türkiye	26
	3	MENA Region (AE/SD Prog.)	3.1	Middle Eastern Approach: Saudi Arabia; United Arab Emirates	27-28
			3.2	North African Approach: Morocco; Egypt; Jordan	29-31
	4	AFRICA (African Union)	4.1	South African Approach: South Africa	32
			4.2	Sub-Saharan Approach: Kenya; Zambia	33-34
	5	ASIA (Econ. Coop. & SD Prog.s)	5.1	South East Asian Approach: China; Japan; South Korea	35-37
			5.2	South Asian Approach: India	38
			5.3	North Asian Approach: Russia	39
	6	OCEANIA	6.1	Indo-Pacific Island Approach: Australia	40
			6.2	Polynesian Island Approach: New Zealand	41
macro scale global level	meso scale systemic level		micro scale strategic level		

selected cases for modelling performance scenarios
(multi-level geo-political spectrum by 41 KPAs (m))

-a-

systemic performance #	top-criteria	strategic category #	criteria	Hydrogen Strategies in (Inter)National Energy Policies for CET #	sub-criteria	KPIs n #
1	Regulatory Dimension REG. (Policy Planning Performance)	1.1	Technology TECH	1.1.1	funding and collaboration for FDI	1
				1.1.2	investment into energy technologies infrastructure	2
				1.1.3	deployment of clean energy technologies	3
				1.1.4	technology development plan (TDP)	4
		1.2	Policy POL	1.2.1	integrated management by energy frameworks	5
				1.2.2	intergovernmental cooperation	6
				1.2.3	hydrogen strategy in energy transition scenarios	7
				1.2.4	market development scenarios for twin transition	8
		1.3	Agency AGE	1.1.1	public sector-led program management	9
				1.3.2	private sector-led project management	10
				1.3.3	institutional sector-led hybrid management	11
				1.3.4	local community-led participatory action	12
2	Operative Dimension OP. (Sustainability Management Performance)	2.1	Environmental ENV	2.1.1	resource management by Env. Impact Assessment (EnvIA)	13
				2.1.2	climate change policies	14
				2.1.3	renewable energy strategies	15
				2.1.4	hydrogen (H2) in circular economy	16
		2.2	Social SOC	2.2.1	community management by Soc. Impact Assessment (SIA)	17
				2.2.2	community engagement by bottom-up participation model	18
				2.2.3	hydrogen strategy for developing value chains	19
				2.2.4	hydrogen (H2) in carbon-neutral economy	20
		2.3	Governance GOV	2.3.1	risk management by Economic Impact Assessment (EconIA)	21
				2.3.2	multilateral engagement by multi-level governance model	22
				2.3.3	energy transition instruments	23
				2.4.4	hydrogen (H2) in hydrogen economy	24
macro scale global level		meso scale systemic level		micro scale strategic level		

parametric framework for modelling performance scenarios
(multi-attribute criteria set of 24 KPIs (n))

-b-

Figure 1: Key Performance Indicators (KPIs) and Key Performance Approaches (KPAs) of the performance modelling framework

Information is quantified into data by the rule of three-tiered fuzzy logic principle (1). Then, quantified data is systematized on basis of the rule of value distribution (2) to formulate the characteristic function of the models. The characteristic performance of the model(s) is evaluated regarding the ratio between infrastructural to inter-operational dimensions on the "5-point-characterization scale" [4] from coopetitive (47/53; collaborative leadership on operations), strategic (49/51; multilateral collaboration for regulatory operations), neutral (50/50; balanced engagement by participatory commitment), strategic (51/49; unilateral partnership for operational policies) and coopetitive (53/47; sovereign leadership on policies).

$$criteria \ \rightarrow non-existing: 0 \quad uncertain: 0.5 \quad existing: 1 \tag{1}$$

$$\sum_{i=1}^{n} w_i = 1 \tag{2}$$

The integrated performance is calculated through weighted value measurement in a mxn matrix format (3) whereas the comparative performance is calculated through pairwise comparison of parametric framework in a n/n matrix format (4).

$$\sum_{j=1}^{n} a_{ij}\, w_j \quad (for\ i = 1, 2, 3 \ldots m) \ \rightarrow \ A_m, C_n(W_n) = \ a_{ij\ (m\ x\ n)} \tag{3}$$

$$C_i(W_i), C_j(W_j) = \ C_{ij}(W_{i/j}) \rightarrow \ C_{ij_{(n/n)}} \tag{4}$$

Evaluating the comparative performance of the model(s) is achieved by attributing relative weights to criteria from 1-9 with reference to the Saaty scale. Pairwise comparison scores under 1.000 are treated as bias, thus excluded [4]. All the performance measurements are evaluated through the ranking rule on score and order of importance by not only the max-min strategy (5 and 6) but also the min-max strategy. Overlapping the max-min and min-max strategies provides deciphering the control code(s) of scenario(s) out the models [5].

$$A_{max.1} \geq A_{max.2} \geq A_{max.3} \ldots \geq A_{max.m} \tag{5}$$

$$C_{max.1} \geq C_{max.2} \geq C_{max.3} \ldots \geq C_{max.m} \tag{6}$$

Checking the consistency ratio of the models' performance (7) is excluded from the holistic modelling approach, because evaluating the reliability and validity measure of preferences limited to 10 alternatives and/or criteria by Saaty in the decision-making process [4].

$$CI = \frac{\lambda_{max} - n}{n-1}, \text{ where } \det(\textstyle\sum_{model} - \lambda I) = 0 \ \leftarrow CR = \frac{CI}{RI} \tag{7}$$

3. RESULTS AND DISCUSSION

The characteristic performance of the models is compatible with the targeted agenda of the SDGs for 2030 and 2050: Scenario 2030 has an operationally 'strategic' character (REG: 49 < OP: 51) with 'integrated framework' for scaling-up the electrolyzer-driven hydrogen production systems in carbon-neutral economy (Figure 2.a). Whereas, Scenario 2050 has a legislatively 'strategic' character (REG: 51 > OP: 49) with 'relational mechanism' for proliferating hydride-based hydrogen storage systems and critical minerals value chain in carbon-free economy (Figure 3.a). Therefore, the former is a 'Greenprint Model' of hydrogen as energy carrier for net-zero and climate-resilient future whereas the latter is a 'Greenstar Model' of hydride as hydrogen carrier for nature-positive resilient development. In both models, the top-three best practices are situated in 1.China; 2.Canada; 3.USA, Norway and Japan.

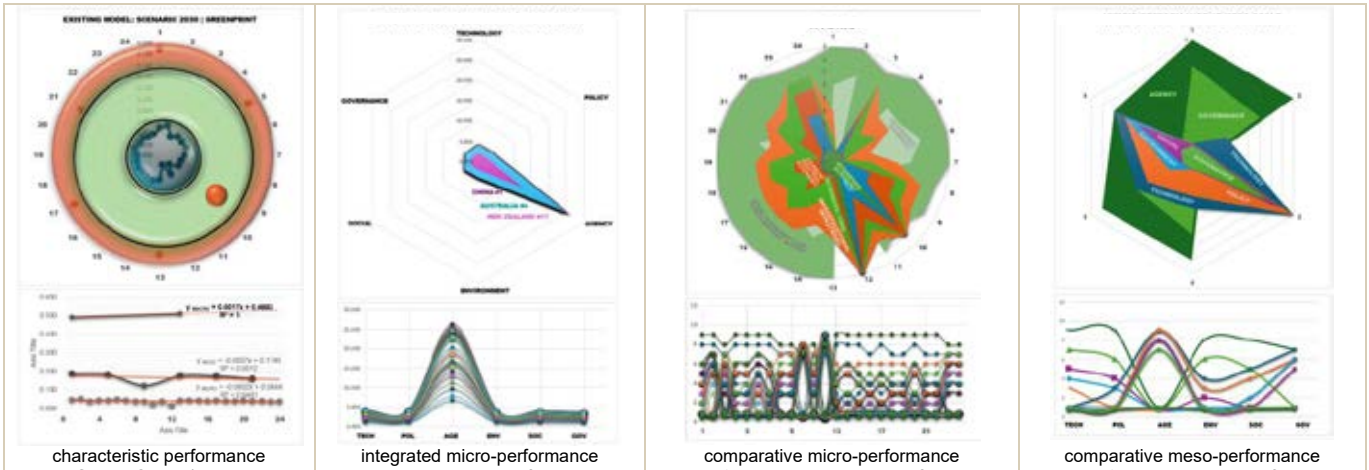

characteristic performance REG:49 < OP:51 | strategic 'integrated framework'	integrated micro-performance instrument of '(sustainability) index'	comparative micro-performance 'multi-level governance' for infrastructural energy policies	comparative meso-performance 'compass strategy of regulatory framework'
-a-	-b-	-c-	-d-

Figure 2: Existing framework model of Scenario 2030 – H2 production technologies in carbon-neutral economy | 'Greenprint Model'

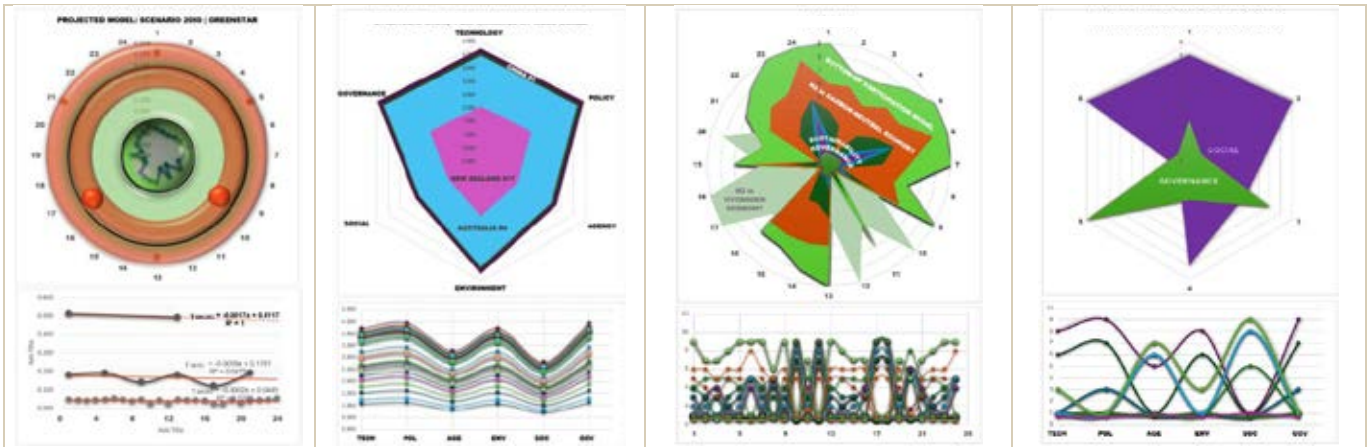

characteristic performance REG:51 > OP:49 | strategic 'relational mechanism'	integrated micro-performance mechanism of 'resilience shield'	comparative micro-performance 'sustainability governance' by operational energy policies	comparative meso-performance 'ESG strategy of operative mechanism'
-a-	-b-	-c-	-d-

Figure 3: Projected framework model of scenario 2050 – H2 storage technologies in hydrogen economy | 'Greenstar Model'

The integrated micro-performance shifts from technology policy to policy governance for achieving CET: In Scenario 2030, (H2) strategies in (I)NEPs are employed as a 'sustainability index instrument' for energy transition in which operational regulation for environmental governance is controlled by not only macro-regional policy-based intergovernmental cooperation for H2 in carbon-neutral economy but also multi-level governance of H2 strategy for developing value chains (Figure 2.b). Whereas in Scenario 2050, the H2 strategies are employed as 'regional resilience shield' in energy transition in which regulatory operations for twin transition are controlled by not only intergovernmental cooperation for deploying clean energy technologies in H2 economy but also managed by intergovernmental mechanisms for hydrogen economy (Figure 3.b).

The comparative micro-performance converges on local community-led bottom-up participation even if it diverges from the route for clean energy mechanism frameworks for resilient development: In Scenario 2030, multi-level governance

for infrastructural energy policies is managed through socio-environmental IA on renewable energy strategies for carbon-neutral economy (Figure 2.c) whereas in Scenario 2050 sustainability governance is managed through integrated management of energy framework on energy transition instruments for hydrogen economy (Figure 3.c).
The comparative meso-performance is differentiated due to the shift from project to portfolio and program management by sustainability-based technologies and policy governance for nature-positive resilient development: In Scenario 2030, regulatory CET mechanism is accelerated by policy-based strategy for sustainability management , i.e: OECD Science Tech. and Innovation (STIP) Compass strategy [6] (Figure 2.d) whereas in Scenario 2050, operative CET mechanism scaled-up by nature-based strategy of social governance by technology-based policy governance system. (Figure 3.d).
The energy transition from scenario 2030 to 2050, There are two geographies as agents of change for controlling the degree of transformative change: Brazil's path for environmental governance and Türkiye's path for policy governance.
The transformative power of the models' performance converges on nature positive policies at the intersection of technology policy and environmental operations on regional level and multi-scalar interconnectivity for integrated policy planning and management at local level (Figure 4).

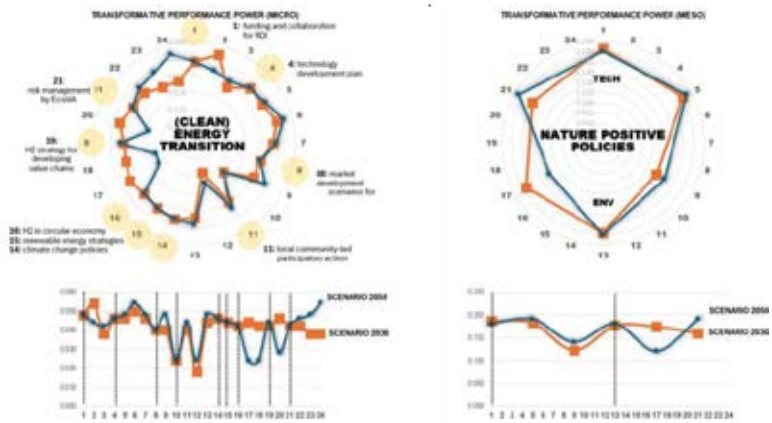

Figure 4: Comparison of transformative power of performance in the existing Scenario 2030 and projected Scenario 2050.

4. CONCLUSIONS

The main findings of research indicates that 'integrated policy planning and management approach [3] for resilient development', provide (re)programming the transformative mechanism framework, if it is authorized by (inter)national energy policies and controlled during the process of clean energy transition [7]. Therefore, these findings verify the hypothesis of this research (Figure 4). Consequently, 'value engineering' bridged with 'systems engineering' and 'transition engineering' through the methods of policy and sustainability impact assessment are advanced research areas in order not only to (re)structure and (re)program transformative mechanism framework for "clean energy transition" [8] but also to shape and accelerate "clean energy transition process" [9]. As a concluding remark, H2-SPA provides multi-dimensional simulation on systemic interaction between performance (re)programming and resilient development by the transformative power of performance by policy-based planning and sustainability-based management.

ACKNOWLEDGEMENT

The authors acknowledge that this study was conducted within the scope of a doctoral thesis study at the Clean Energy Technologies Institute of Yıldız Technical University. The corresponding author also declares that modelling method was also used in her PhD thesis completed in 2013.

REFERENCES

1. International Renewable Energy Agency. 2022. Geopolitics of the energy transformation: The hydrogen factor. Abu Dhabi: IRENA.
2. Adelekan OA, Ilugbusi BS, Adisa O, Obi OC, Awonuga KF, Asuzu OF and Ndudisi. 2024. Energy transition policies: A global review of shifts towards renewable sources. Engineering Science and Technology Journal 5 (2): 272-287.
3. UNDP. 2023. Strengthening energy governance systems. New York: UNDP-Sustainable Energy Hub.
4. Gürler E. 2013. Analytic planning and strategic management of integrated urban regeneration process: Performance measurement-evaluation-programming model (PhD Diss., Scientific Research Project no: 33438). Istanbul Technical University.
5. Belton V and Stewart TJ. 2002. Multiple criteria decision analysis: An integrated approach. Dordrecht, NL: Kluwer.
6. https://stip.oecd.org/s tip/. Accessed on 25 January 2025.
7. Lentschig H, Patonia A and Qitzow R. 2025. Multilateral governance in a global hydrogen economy: An overview of main actors and institutions, key challenges and future pathways. International Journal of Hydrogen Energy 97: 76-87.
8. Corbeau AS and Nassif L. 2025. National hydrogen strategies and roadmap tracker. New York, NY: Center on Global Energy Policy (CGEP), School of International and Public Affairs (SIPA), Columbia University.
9. www.mckinsey.com/industries/energy-en-materials/our-insights/global-energy-perspective#/. Accessed on 19 February 2025.

GREEN SYNTHESIS OF FUEL BIOADDITIVE SOLKETAL LEVULINATE BY FUNCTIONAL CATALYTIC MEMBRANE

[1]*Nazlı Yenihan Yüzer,* [1]*Güler Hasırcı,* [2]*Ahmet Oğuz Hoşöz,* [1]*Emine Emel Çakırca,* [2]*Ertan Alptekin,* [1]*Oğuzhan İlgen,* [2]*Mustafa Çanakçı,* [1*]*Nilüfer Hilmioğlu*
[1] Kocaeli University, Engineering Faculty, Chemical Engineering Department, Kocaeli 41001, TURKEY
[2] Kocaeli University, Tehcnology Faculty, Automotive Engineering Department, Kocaeli 41001, TURKEY
*Corresponding author e-mail: niluferh@kocaeli.edu.tr

ABSTRACT
Increasing energy demand due to technological developments in the world puts fossil fuels, which have limited reserves, in danger of depletion. Fossil fuel use leads to uncontrolled carbon emissions and negatively affects the ecosystem. In order to improve the conditions, research on environmentally friendly and clean green/biodegradable fuels and fuel additives has gained importance. Solketal levulinate has an environmentally friendly and green fuel additive and alternative to traditional fuel additives. Solketal levulinate (SoLE) is produced by esterification of solketal and levulinic acid in the presence of an acid catalyst. Removal of water, which is a by-product, increases the reaction conversion. Producing catalytic membranes by blending with suitable polymer solutions is an excellent alternative to converting catalysts used in the reaction from homogeneous to heterogeneous form and increasing conversion by removing the unwanted by-product. In addition, clays used to convert homogeneous catalysts to heterogeneous form was also quite suitable for use as support materials due to their cheapness and easy availability.
In this study; bentonite was functionalized with sulfuric-acid and added to poly(vinylalcohol)(PVA) solution to prepare catalytic membranes. SoLE; T=105°C; M=6 and catalytic membrane with 3mmol H_2SO_4 catalyst loading at the end of 6h, highest reaction conversion obtained as 96%.

Keywords: Esterification, Fuel Additive, Catalytic Membrane, Solketal Levulinate.

1. INTRODUCTION

The need for energy resources in the world continues day by day in line with the increasing number of people. The fact that fossil fuel reserves are in danger of depletion has also increased the search for alternative fuels to meet energy needs. Among the many studies conducted in this direction, interest in the development of bio-based fuels has increased, as they are both environmentally friendly and renewable resources. The biggest problem of bio-based fuels, which are frequently studied in the literature, is related to combustion events. The production of new generation fuel additives to improve the combustion properties of both fossil fuels and bio-based fuels is an important step towards solving this problem.
Toxic emissions resulting from the combustion of fuels are being reduced for engine-based uses by optimizing the engines and equipment used, using catalytic converters, expanding the use of NOx reducers and particulate filters, and also by revisions in the chemical composition of the fuels used. However, these regulations alone are not sufficient. For this reason, efforts to achieve low emission values and the use of fuels blended with new generation fuel additives with high oxygen numbers for better combustion performance are among the environmentally friendly alternatives [1].
In addition to traditional methods (isomerization, catalytic cracking, reforming-dehydrocyclization) to increase the octane number of gasoline and the cetane number of diesel, oxygen-rich fuel additives (oxygenates) can be added. The octane number of gasoline or the cetane number of diesel is increased by adding oxygen-rich oxygenates (such as alcohol and ether) after the refining process of crude oil [2].
Bio-ethanol, which is one of the leading bio-based fuel additives, is obtained by chemical means as well as fermentation. However, in both cases, long-term production processes cause both carbon emissions and system costs to increase. This makes the production process less environmentally friendly.
Levulinate-based oxygenates frequently encountered in the literature are solketal levulinate, glycerol levulinate, ethyl levulinate, methyl levulinate, and the like. However, the production of these levulinate-based fuel additives is basically produced by the reaction of alcohols or ketals with oxo-carboxylic acid anions (methyl levulinate, ethyl levulinate, etc.). In such reactions, alcohol is released as a by-product, and these alcohols (except ethyl alcohol) are highly toxic and ecologically dangerous.
Almost all chemical reactions carried out on an industrial or laboratory scale are carried out in the presence of a homogeneous or heterogeneous catalyst. However, it is quite difficult and costly to separate the catalysts used in the reaction (regardless of whether they are homogeneous or heterogeneous) from the reaction medium. For this reason, the use of catalytically active catalytic membranes is increasing day by day.
In chemical reactions carried out by means of catalytic membranes; separation, purification and product production can be carried out simultaneously in a single unit. Thus, the desired or undesired product/by-product of the relevant reaction could be easily selected from the reaction medium. While catalytic membranes can be used as green and environmentally friendly catalysts in chemical reactions, their catalytic properties improved with homogeneous or heterogeneous catalysts added to their structures. In addition, it is quite possible to easily separate catalytic membranes from the reaction medium and reuse them. In the literature, the production of solketal levulinate has generally been achieved by transesterification

and is very limited in number and also, no previous solketal levulinate sorption enhanced reaction study from solketal and levulinic acid has been found with catalytic membranes. In this context, it is thought that the original value and contribution of our study to the literature will be quite high.
Studies on the synthesis of solketal levulinate in the literature are very limited and were carried out by transesterification reaction using base catalyst. Mariam et al., 2022; Solketal levulinate as a potential fuel additive for palm biodiesel; with solketal and methyl levulinate has produced with the highest yield of 74.83% at the end of 6 hours of reaction with T=140°C; Molar Ratio (Methyl levulinate: Solketal)=1:4 and 1.5% catalyst loading [3]. Another limited study was conducted by MARIAM et al. in 2024: MARIAM et al., investigated the effects of Solketal levulinate (SoLE) on improving the cold flow properties of palm biodiesel by adding SoLE, which they produced by transesterification, to palm biodiesel at certain rates, while determining the density, kinematic viscosity, pour point, cloud point and cold flow plugging point values of the new fuel blend. As a result of their analysis, they concluded that the SoLE they produced has the potential to improve the cold flow properties of palm biodiesel [4]. In another study has; Chang et al., 2024; produced Methyl levulinate glycerol ketal from methyl levulinate and glycerol. The effects of different factors on the yield of Methyl levulinate glycerol ketal and glycerol conversion were investigated and the optimum reaction conditions were determined as reaction temperature T = 140 °C, catalyst loading (HZSM-5) = 0.50 g, ML/GLY molar ratio 4:1. Under these conditions, glycerol conversion were found to be 97% and Methyl levulinate glycerol ketal yield was found to be 94.7% [5].
In this study, solketal levulinate was synthesized from solketal and levulinic acid by the developed catalytic membrane.

2. MATERIALS AND METHODS

2.1. Materials

The chemicals used in this study were Solketal (2,2-Dimethyl-1,3-dioxolan-4-yl)methanol was supplied by BLDpharm, PVA (poly vinylalcohol) (Mw~125,000) polymer , Levulinic Acid and Sulfuric Acid (98%) were supplied by Merck and finally Bentonite Clay was supplied by SAMAŞ Mining in Türkiye.Method.

2.2. Preparation of Sulfonated Bentonite Clay

A certain amount of bentonite clay mineral has had left to dry overnight at 100 °C. The dried bentonite clay impregnated with 3 mmol H2SO4 was weighed to be 10% according to the PVA polymer solution and left to dry again at room temperature. As the last step, the bentonite clay, which was impregnated with acid and dried, was mechanically ground until it reached the finest mesh size and was made ready for used.

2.3. Preparation of Catalytic Membrane

Catalytic membranes were prepared based on poly(vinyl alcohol) (PVA). 6% PVA solution was prepared in a magnetic stirrer at a constant temperature of 85°C and a stirring speed of 400 rpm. The systems were supported with a reflux condenser to prevent any solvent loss during dissolution. Catalytic membrane was formed by adding 10% by weight of Sulfonated Bentonite clay to the prepared polymeric membrane solution.

2.4. Batch Reaction System

The batch reactor system is given in Figure 1. The prepared catalytic membranes were cut into small pieces and added to the system with the reactants.

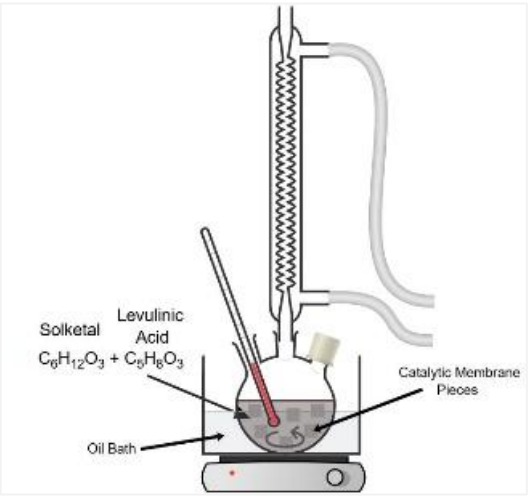

Fig. 1. Batch Reractor System

Solketal levulinate production reaction was carried out in a batch reactor at 105 °C with a molar ratio (Levulinic acid: Solketal) M = 1:6 and a catalyst loading of 3 mmol H2SO4 to 10% bentonite clay relative to PVA for 6 hours.

3. RESULTS AND DISCUSSION

3.1. Chacterizations of the Catalytic Membrane

3.1.1. FT-IR &TGA Analysis

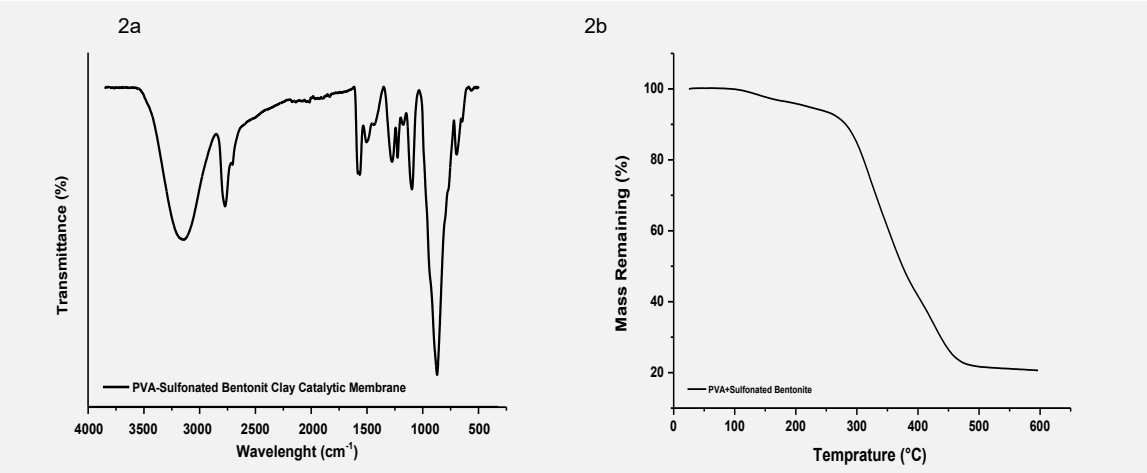

Fig. 2. (a) FT-IR Analysis of PVA-Sulfonated Bentonite Clay Catalytic Membrane; (b) TGA Analysis of PVA-Sulfonated Bentonite Clay Catalytic Membrane

FT-IR characterizations of the prepared PVA- Sulfonated Bentonite Clay catalytic membranes are given in Figure 2a. According to the FT-IR characterization, the broad peak around 3550–3200 cm^{-1} can be explained as -OH stretching vibration from intermolecular hydrogen bonds. The vibration band between 2980 and 2800 cm^{-1} represents the C–H group. The frequent peaks around 1000-1100 cm^{-1} show the strong S=O stretching and the placement of sulfo groups.
PVA-Sulfonated Bentonite Clay Catalytic Membrane is given in Figure 2b. Thermal decomposition curves of the prepared PVA-sulfonated Bentonite clay catalytic membrane were investigated in the range of 25 °C to 600 °C with a Mettler Toledo brand thermal gravimetric analysis (TGA) device.
The solvent of the PVA polymeric membrane used in this study is water and water exists in different states inside the PVA blend membranes; solvent water; forms the polymeric solution in two different ways: first, as water molecules held by weak bonds on the outer or inner surface without interacting with the chemical matrix forming the polymer, and second, as water molecules strongly bonded to hydroxyl groups.
The primary region between 50-150 °C is the loss of water molecules in the polymer solution forming the membrane, while the secondary region between 150-300 °C is related to the loss of water due to the polymer matrix.
The weight loss in the tertiary region occurred between approximately 300-450 °C due to the loss of organic components. The weight loss in the quaternary region is due to the dissociation of the sulfo group member bonds in the structure of the sulfonated bentonite clay between 450-600 °C, and the stable appearance of the graph explains that only bentonite clay residues remain.

3.2. Swelling Testing of PVA-Sulfonated Bentonite Clay Catalytic Membrane

Swelling tests are performed to determine the affinity of a material to its solvent or to the reactants present in the medium to be applied or to the products produced by the input reactants in the reaction to be used. The water sorption results of PVA-Sulfonated Bentonite Clay Catalytic Membrane used in the reaction are given in Fig. 3. Sorption % values were calculated with Eq. 1

$$Swelling\ (\%) = \frac{W_{wet} - W_{dry}}{W_{dry}} x100 \quad (1)$$

As a result of weighings made at 30-minute intervals for 6 hours, the swelling value of the membrane was determined as 139.65%. The swelling percentage did not change as a result of 24-hour weighing.

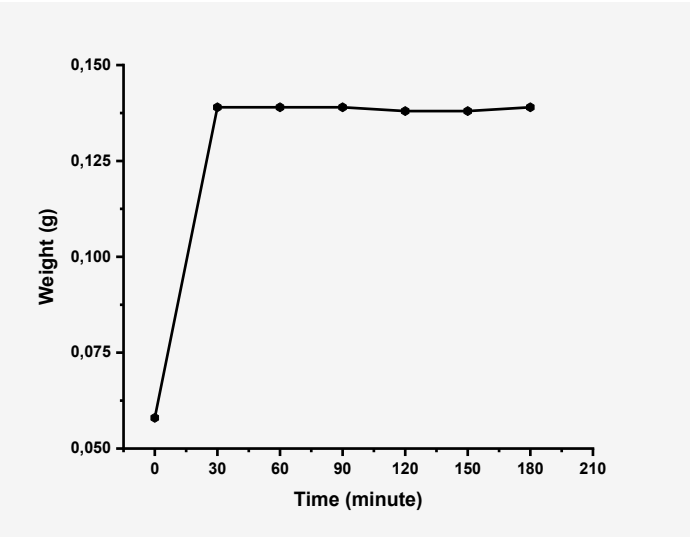

Fig. 3. Swelling testing of PVA-Sulfonated Bentonite Clay Catalytic Membrane

4. CONCLUSIONS

Oxygen-rich fuel additives are chemical substances traditionally used to increase engine performance by improving the physicochemical properties of fuels during the combustion process (reducing the number of knocks, preventing gum formation, increasing the octane or cetane number, etc.). In this context, it is aimed that the fuel additives to be used are also environmentally friendly. These substances are intended to reduce carbon emissions and make the fuel environmentally friendly by being added to fuels.

In this study; bentonite clay mineral used as support material; sulfuric acid functionalized; poly(vinylalcohol)(PVA) blended and catalytic membranes were prepared. Solketal levulinate, ambient conditions; T=105°C; M=6 and catalyst loading ratio of 3mmol H_2SO_4 with catalytic membrane at the end of 6 hours reaction time, the highest reaction conversion was obtained as 96%. In addition, the investigation of the physicochemical properties of the produced SoLE fuel additive is still ongoing.

ACKNOWLEDGEMENT

This study was supported by the scientific research projects unit of Kocaeli University. Project No FAPP- 2024/3950.

REFERENCES

1. Çakmak A and Özcan H. 2018. Benzin için Oksijenli Yakıt Katkıları. Politeknik Dergisi 21(4):831-840.
2. Demirbas A, Balubaid MA, Basahel AM, Ahmad W, Sheikh MH. 2015. Octane Rating of Gasoline and Octane Booster Additives. Petroleum Science and Technology 3(11):1190-1197.
3. Mariam NNS, Hoong SS, Arniza MZ, Adnan S, Ismail TNMT, Yeong SK, Yusop MR. 2022. Optimisation of Reaction Parameters for the Synthesis of Solketal Levulinate as Potential Biodiesel Additive. Journal of Oil Palm Research 34(3):524-534.
4. Mariam NNS, Hoong SS, Arniza MZ, Adnan S, Ismail TNMT, Yeong SK, Yusop MR. 2024. Solketal Levulinate Ester as a Potential Fuel Additive for Palm Biodiesel. Journal of Oil Palm Research 36(1):104-114.
5. Liu H, Ma Z, Liu X, Wu Y, Zhang W, Zhao S, Chen W, Chang C. 2024. Green synthesis of biobased glycerol levulinate ketal in a continuous flow reactor: Optimization, kinetics and simulation. Applied Energy 361:122910

DEVELOPMENT OF ENVIRONMENTALLY FRIENDLY CATALYTIC MEMBRANE AS A CATALYST FOR SYNTHESIS OF GREEN FUEL BIOADDITIVE GLYCERIN CARBONATE

[1]*Güler Hasırcı,* [1]*Nazlı Yenihan Yüzer* [2]*Ahmet Oğuz Hoşöz,* [1]*Emine Emel Çakırca,* [2]*Ertan Alptekin,* [1]*Oğuzhan İlgen,* [2]*Mustafa Çanakçı,* [1*]*Nilüfer Hilmioğlu*
[1] Kocaeli University, Engineering Faculty, Chemical Engineering Department, Kocaeli 41001, TURKEY
[2] Kocaeli University, Tehcnology Faculty, Automotive Engineering Department, Kocaeli 41001, TURKEY
*Corresponding author e-mail: niluferh@kocaeli.edu.tr

ABSTRACT
Green fuel additives that can be added to fuels to mitigate the adverse effects of fossil fuel use on the environment have become an attractive research topic. Green glycerin carbonate, which can be used as a fuel additive for efficient and safe fossil fuel use, was synthesized from dimethyl carbonate and glycerin via transesterification under mild conditions. The catalyst used in the reaction is a catalytic membrane obtained by loading KOH/Clinoptilolite into a polyvinyl alcohol-sodium alginate blend matrix. The polymer structure of the catalytic membrane provided sorption support, while the KOH/Clinoptilolite side catalyzed the reaction. Catalytic membrane was characterized by FTIR for chemical structure analysis, SEM and EDX analysis to observe the distribution of the catalyst in the polymer matrix, and swelling test in methanol to determine the affinity for methanol, a by-product in the reaction. Batch reaction was carried out under certain conditions (%7.9 catalyst amount, 85°C, DMC/glycerin:3/1, 4 hours). A glycerin carbonate yield of 24.5% was obtained at the end of 4 hours. Reaction parameters will be analyzed in the next steps. Methanol swelling tests showed that the catalytic membrane has an affinity for methanol. It was found that the catalytic membrane produced was suitable for the reaction.

Keywords: Transesterification, Fuel Additive, Glycerol carbonate, Functional membrane

1. INTRODUCTION

Today, dependence on fossil fuels prevents efficient and secure energy use. In particular, the environmental problems associated with the use of fossil fuels are due to the poor efficiency and safety of these fuels. To make fossil fuel use more environmentally friendly, new generation green fuel additives can be added to fuels to improve fuel properties. Glycerin carbonate, one of the new generation fuel additives, is an important candidate in this field with its high oxygen content (59%) [1]. Glycerin carbonate is produced under mild conditions (no toxic solvents, atmospheric pressure) by glycerin and green reagent dimethyl carbonate (DMC) via a base catalyst. Methanol emerged as a by-product in the reaction [2]. As shown in Fig. 1, glycerin carbonate, a five-membered cyclic carbonate, is an environmentally friendly molecule with a wide range of uses, such as polymers, cosmetics, solvents, and battery electrolytes [3]. In glycerin carbonate synthesis using homogeneous and heterogeneous catalysts, the ease of recovery and reusability of heterogeneous catalysts have increased the interest in heterogeneous catalysts. However, some heterogeneous catalysts have disadvantages, such as poor thermal stability, deactivation, and low surface area [4]. Catalytic membranes, which can be recovered from the reaction and reused, are prepared by adding catalysts to polymeric matrices. Environmentally friendly and heterogeneous catalytic membranes can increase the reaction yield by simultaneously removing the by-product from the reaction medium while catalyzing the reaction [5]. Polyvinyl alcohol (PVA) used as a polymeric matrix in the preparation of catalytic membranes is a non-toxic, biocompatible, high hydrophilic polymer [6]. Sodium alginate from brown algae is a non-toxic biopolymer with high hydrophilicity that can be blended with PVA [7]. Highly hydrophilic matrices in the catalytic membrane can sorb polar by-products in reactions, shifting the reaction equilibrium to the product side [8]. Zeolites can play an active role in catalytic reactions as catalyst supports with their high surface area, adjustable acidity, and basicity properties [9]. Clinoptilolite, a common natural zeolite, has been used as a catalyst in reactions with acidic and basic modifications [10,11]. Mahdi et al. 2016 produced glycerin carbonate from glycerin and sodium bicarbonate in a batch reactor with a modified clinoptilolite catalyst. They obtained the maximum glycerin conversion (29%) at 100°C and 9% catalyst concentration for 10 min reaction time.[12]. There are a limited number of studies in the literature on the production of glycerin carbonate from DMC with a catalytic membrane. Hasirci and Hilmioglu, 2024 produced glycerin carbonate from DMC and glycerin with the catalytic membrane produced by adding NaOH to PVA. A yield of 93.03% glycerin carbonate was obtained under the optimum conditions (75°C, 7.5% catalyst amount, DMC/glycerin:3/1, 2h) [8].

This study aimed to synthesize sorption-assisted glycerin carbonate with PVA/SA-KOH/clinoptilolite composite catalytic membrane under mild conditions. There is no synthesis of glycerin carbonate with KOH-modified clinoptilolite loaded catalytic membrane in the literature.

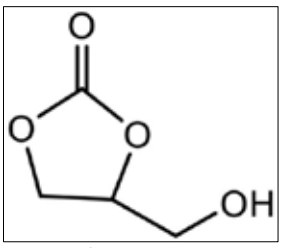

Fig. 1. Glycerin carbonate

2. MATERIALS AND METHODS

2.1. Materials

PVA (poly vinylalcohol) (Mw~125,000) polymer and glutaraldehyde (25% solution in water) used in catalytic membrane preparation were obtained from Sigma Aldrich, and sodium alginate was purchased from Isolab. KOH used in catalyst preparation was obtained from Sigma Aldrich, and clinoptilolite was obtained from ROTA mining in Türkiye. Glycerin and DMC used as reactants in the reaction were purchased from Sigma Aldrich.

2.2. Preparation of KOH/Clinoptilolite catalyst

KOH/clinoptilolite catalyst was prepared by the wet impregnation method. 2M KOH impregnated with clinoptilolite was dried at 110°C for 3 hours and finally calcined at 400°C for 5 hours. KOH/clinoptilolite ratio was prepared as 1/2.

2.3. Preparation of KOH/Clinoptilolite catalyst loaded PVA/SA blend

10 wt% PVA and 5 wt% SA were dissolved in water. The obtained PVA and SA solutions were blended at a ratio of 90/10 and mixed at 700 rpm for 1 hour. After 1 hour, KOH/clinoptilolite catalyst was added to the PVA/SA blend. Then, 0.030 g glutaraldehyde was added to the PVA/SA-KOH/Klinoptilolite mixture as a crosslinking agent and stirred for one hour. Finally, the polymer-catalyst mixture was poured onto Teflon plates and left to dry.

2.4. *Batch reactor system*

In the batch reactor system shown in Fig. 2, the catalytic membrane was cut into small pieces and added to the reactor.

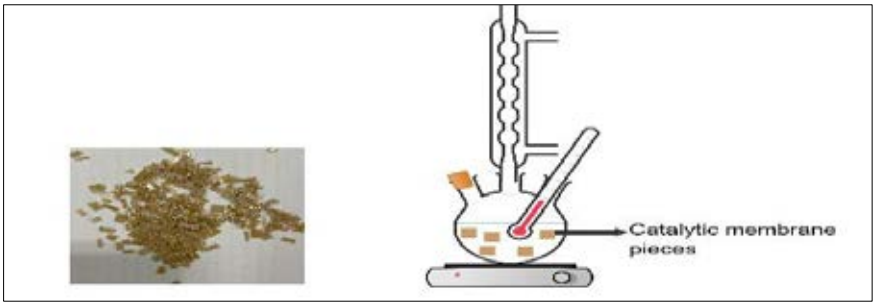

Fig. 2. Catalytic membrane and batch reactor system

2.5. Analysis of Glycerol carbonate

The amount of glycerin carbonate produced by the reaction was analyzed by gas chromatography. The formula used in the calculations is shown in Eq. (1) [5]

$$Glycerin\ carbonate\ yield\ (\%) = \frac{Produced\ \ glycerol\ carbonate\ amount\ (mol)}{initial\ amount\ of\ glycerin\ (mol)} x100 \quad (1)$$

3. RESULTS AND DISCUSSION

3.1. FTIR charactherization of PVA/SA-KOH/Clinoptilolite Catalytic membrane

FTIR analysis of PVA/SA-KOH/Klinoptilolite catalytic membrane is shown in Fig.3. Peaks at 3294.60 cm^{-1}, 2919.55 cm^{-1}, and 1088 cm^{-1} are due to O-H, C-O, and C-H groups of PVA, respectively [13]. The peak at 1424.7 cm^{-1} is associated with the COO group in the structure of SA [14]. The peak at 1712.12 cm^{-1} belongs to C=O groups originating from glutaraldehyde crosslinking agent [15].

3.2. SEM analysis of PVA/SA-KOH/Clinoptilolite Catalytic membrane

The surface morphology of the produced PVA/SA-KOH/Clinoptilolite catalytic membrane is shown in Fig. 4 by SEM and EDX analysis. KOH/Clinoptilolite catalyst agglomerated on PVA/SA matrix [16]. The high Si content in the EDX results indicates the presence of clinoptilolite in the structure [17].

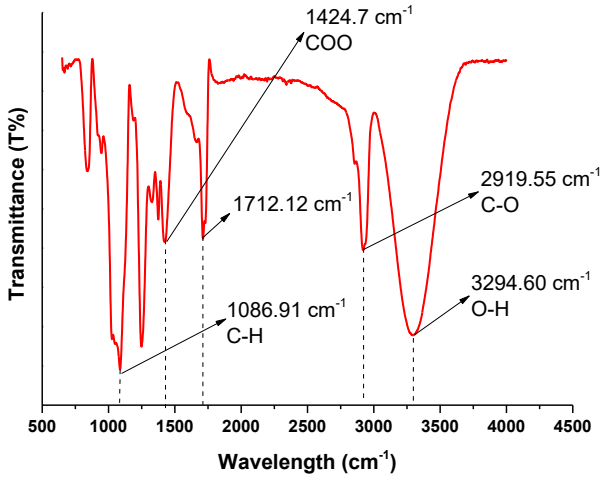

Fig. 3. FTIR spectra of PVA/SA-KOH/Clinoptilolite Catalytic membrane

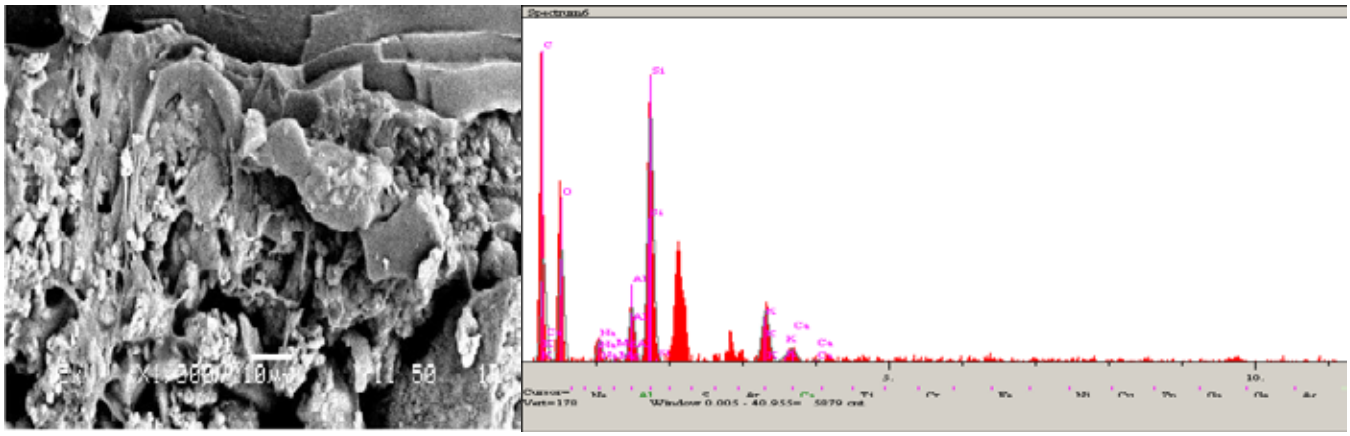

Fig. 4. SEM photo and EDX of PVA/SA-KOH/Clinoptilolite Catalytic membrane

3.3. Swelling tests of PVA/SA-KOH/Clinoptilolite Catalytic membrane

The swelling test results of the catalytic membrane in methanol are shown in Fig. 5. The Swelling test was carried out in 100% methanol for 4 hours. The percentage swelling was stabilized at 150 minutes. The maximum swelling degree was obtained as 30.8%.

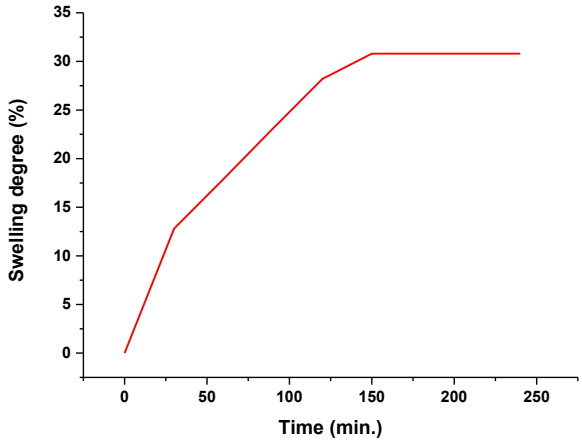

Fig. 5. Swelling of PVA/SA-KOH/Clinoptilolite Catalytic membrane

4. CONCLUSIONS

Glycerin carbonate with added value and high oxygen content offers the potential to improve fuel properties when used as a fuel additive. In this study, KOH/Klinoptilolite loaded PVA/SA catalytic membrane was preliminarily tested in a batch reactor for 4 hours reaction time at 85°C, M:3/1 with 7.9% catalyst amount. Functional group analysis and morphological distribution of the catalyst in the polymer matrix were investigated by FTIR and SEM characterizations. Methanol affinity was determined by swelling tests to contribute to the reaction yield by by-product sorption. In the batch reactor trial, a 24.5% glycerin carbonate yield was obtained. However, it is aimed to increase this ratio in the following experiments. SEM analysis showed that the catalyst agglomerated in the membrane matrix. By swelling tests in methanol, it was determined that the catalytic membrane has an affinity for methanol, and a maximum swelling degree of 30.8% was reached in 150 minutes.

ACKNOWLEDGEMENT
This study was supported by the scientific research projects unit of Kocaeli University. Project No FAPP- 2024/3950.

REFERENCES
1. Szőri M, Giri BR., Wang Z., Dawood AE., Viskolcz B., Farooq A. 2018. Glycerol carbonate as a fuel additive for a sustainable future. Sustainable Energy Fuels 2: 2171-2178.
2. De Caro P., Bandres M., Urrutigoïty M., Cecutti C., Thiebaud-Roux S. (2019). Recent Progress in Synthesis of Glycerol Carbonate and Evaluation of Its Plasticizing Properties.Front. Chem.7:308.
3. Souza Júnior, Eira LC. Detoni C., Souza MMVM. 2024. Glycerol Carbonate Production via Transesterification: The Effect of Support Porosity and Catalyst Basicity. Processes 12:2256.
4. Koranian P., Huang Q., Dalai AK., Sammynaiken R. (2022). Chemicals Production from Glycerol through Heterogeneous Catalysis: A Review.Catalysts *12*: 897.
5. Hasirci G and Hilmioglu N. (2025). Green Synthesis of Glycerin Carbonate by Functional, Environmentally Friendly Catalytic Membrane Polyvinyl Alcohol/Polyvinylpyrrolidone/Sodium Methoxide. ChemistrySelect 10:1-10.
6. Peng Q., Bao F., Tang M., Zhong F., Li W., Deng J., Lin Q., Yan M., Zuberi Z. 2024. Advances in dual-functional packaging: Visual monitoring of food freshness using plant essential oils and pH-sensitive natural pigments. Food Control 160: 110307.
7. Yan P., Lan W., Xie J. 2024.Modification on sodium alginate for food preservation: A review. Trends in Food Science & Technology 143:104217.
8. Hasirci G and Hilmioglu N. (2024). Development of a functional catalytic membrane by alkalization of PVA and green synthesis of fuel additive glycerin carbonate with high oxygen content. Energy Sources, Part A: Recovery, Utilization, and Environmental Effects 46:6816–6829.
9. Sun Q., Wang N., Yu J. 2021. Advances in Catalytic Applications of Zeolite-Supported Metal Catalysts. Advanced materials 33: 2104442.
10. Szymaszek-Wawryca A., Summa P., Duraczy ´nska D., Díaz U., Motak M. 2022. Hydrotalcite-Modified Clinoptilolite as the Catalyst for Selective Catalytic Reduction of NO with Ammonia (NH3-SCR). Materials, 15: 7884.
11. Helmi M., Hemmati A., Tahvildari K. 2022. Production of biodiesel from salvia mirzayanii oil via electrolysis using KOH/Clinoptilolite as catalyst. Journal of Environmental Health Science and Engineering 20:187–204.
12Mahdi HI., Irawan E., Nuryoto N., Jayanudin J., Sulistyo H., Sediawan WB., Muraza O. 2016. Glycerol Carbonate Production from Biodiesel Waste Over Modified Natural Clinoptilolite.Waste Biomass Valor 7:1349–1356.
13.Gomaa MM., Hugenschmidt C., Dickmann M., Abdel-Hady EE., Mohamed HFM., Abdel-Hamed MO. 2018. Crosslinked PVA/SSA proton exchange membranes: Correlation between physiochemical properties and free volume determined by positron annihilation spectroscopy. Phys. Chem. Chem. Phys. 20:28287–28299.
14. Pereira R., Tojeira A., Vaz DC., Mendes A., Ba´rtolo P. 2011. Preparation And Characterization of Films Based on Alginate And Aloe Vera. International Journal of Polymer Anal. Charact.16: 449–464.
15. Blanco-Covián L., Campello-García JR., Blanco-López MC., Miranda-Martínez M. 2020. Synthesis, Characterization and Evaluation of the Antibiofouling Potential of Some Metal and Metal. Applied Science 10:5864.
16. Unlu D., İlgen O., Hilmioglu N. 2016.Biodiesel additive ethyl levulinate synthesis by catalytic membrane: SO4-2/ZrO2 loaded hydroxyethyl cellulose. Chemical Engineering Journal 302:260-268.
17. Shiferaw K.A., Mathews JM. Yu E, Choi EY. Tarte NH. 2022. Sodium Methoxide/Zeolite-Supported Catalyst for Transesterification of Soybean Waste Cooking Oil for Biodiesel Production. Inorganics 11:163.

INTEGRATION AND STORAGE OF HYDROGEN-BASED FUEL CELLS FOR UNMANNED AERIAL VEHICLES

[1*]*Muhammet Furkan Özbek*, [2]*Ruşin Ak*, [3]*Elanur Telci*, [4]*Enes Çelik*, [5]*Hiranur Settaşı*, [6]*Salih Sezer*, [1]*Vahid Alizada*, [1]*Emir Can Duğan*, [4]*Simay Ayşe Angin*, [3]*Ramiz Gültekin Akay*, [4]*Cenk Çelik*
[1]Kocaeli University, Faculty of Engineering, Department of Electronics and Telecommunications Engineering, Kocaeli, Türkiye
[2]Kocaeli University, Faculty of Engineering, Department of Metallurgy and Materials Engineering, Kocaeli, Türkiye
[3]Kocaeli University, Faculty of Engineering, Department of Chemical Engineering, Kocaeli, Türkiye
[4]Kocaeli University, Faculty of Engineering, Department of Mechanical Engineering, Kocaeli, Türkiye
[5]Kocaeli University, Faculty of Engineering, Department of Computer Engineering, Kocaeli, Türkiye
[6]Kocaeli University, Faculty of Engineering, Department of Mechatronics Engineering, Kocaeli, Türkiye

ABSTRACT
This study explores the integration of hydrogen-based fuel cells into unmanned aerial vehicles (UAVs), focusing on integration factors, the advantages of hybrid fuel cell systems over lithium polymer batteries, and necessary safety precautions. Lithium polymer batteries, Proton Exchange Membrane Fuel Cells (PEMFCs), Direct Methanol Fuel Cells (DMFCs), and hydrogen storage systems are analyzed.
The research utilizes data from lithium polymer-based UAVs we developed, UAVs produced by other companies, hydrogen fuel cell data, and academic articles. Various hydrogen-based fuel and storage systems are examined in detail.
Findings show that lithium polymer-based UAVs are the most cost-effective to produce. However, PEMFCs in hybrid systems are more efficient in flight when operating costs are considered, offering longer flight durations despite comparable weights. In contrast, DMFCs are not yet suitable for UAVs in the 20-25 kg range due to limited industrial development. Hybrid systems require stricter safety measures than lithium polymer battery systems.
Overall, the study highlights the superior efficiency of hydrogen-based fuel cells for UAVs, particularly in flight duration, and outlines critical considerations for hybrid integration.

Keywords: Proton Exchange Membrane Fuel Cells (PEMFCs), Unmanned Aerial Vehicles (UAVs), Lithium Polymer Batteries, Hybrid System, Hydrogen Storage

1. INTRODUCTION

A fuel cell, also known as a fuel cell system, is an electrochemical device that converts the chemical energy contained in a fuel and its oxidizing agent directly into electrical energy without combustion. This conversion is achieved through a fixed electrode–electrolyte system. Fuel cells operate with high efficiency and produce emissions that are significantly lower than the limits specified by current standards. Although their operation is analogous to that of a battery, fuel cells require a continuous supply of fuel to maintain the energy conversion process [1].

Fuel cells continuously convert chemical energy into electrical energy through an electrochemical process, operating like batteries but without recharging. They require a hydrogen–oxygen or hydrogen–air system to function. A fuel cell consists of an electrolyte between two electrodes. Hydrogen at the anode undergoes oxidation, releasing electrons that travel through an external circuit to the cathode. Meanwhile, hydrogen ions pass through the electrolyte and react with oxygen at the cathode, forming water and generating electricity. Due to their high efficiency, fuel cells produce mainly heat, water vapor, and electricity. Unlike conventional combustion, they prevent energy losses and pollution by directly converting fuel into power without burning [2].

PEMFCs use hydrogen and oxygen (from air) as fuel and oxidizer, respectively. They employ carbon-based electrodes and a thin, proton-selective polymer membrane. At the anode, hydrogen atoms ionize, releasing protons that pass through the membrane while electrons flow out, generating electricity. At the cathode, protons, electrons, and oxygen react to form water, with water vapor as the only byproduct. A thin layer of platinum on the electrodes acts as a catalyst. PEMFCs convert the chemical energy of hydrogen into electricity, producing only water and heat as byproducts, achieving an efficiency of 40-50% under optimal conditions [3].
Anode Reaction: Hydrogen gas (H_2) is oxidized at the anode, resulting in the formation of two hydrogen ions ($2H^+$) and two electrons ($2e^-$):

$$H_2 \rightarrow 2H^+ + 2e^-$$

Cathode Reaction: At the cathode, molecular oxygen (O_2) reacts with four hydrogen ions ($4H^+$) and four electrons ($4e^-$) to produce two molecules of water ($2H_2O$):

$$O_2 + 4H^+ + 4e^- \rightarrow 2H_2O$$

Overall Reaction: When the anode and cathode reactions are combined, the overall reaction for the fuel cell is:

$$2H_2 + O_2 \rightarrow 2H_2O + \text{heat} + \text{electrical energy}$$

This overall reaction shows that the fuel cell converts the chemical energy of hydrogen and oxygen into water, releasing heat and generating electrical energy in the process.

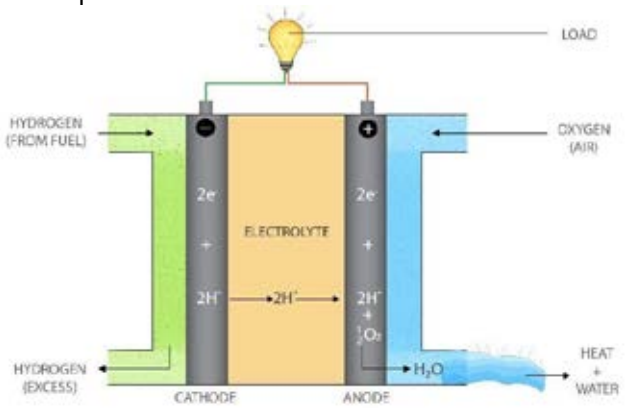

Fig. 1. Polymer Electrolyte Membrane Fuel Cell (PEMFC) [4]

Fuel cells release about 45% of hydrogen energy as heat, requiring efficient cooling to maintain stable operation. Cooling systems are categorized as water-cooled and air-cooled. Water-cooled systems circulate liquid, typically water, to dissipate heat, while air-cooled systems use airflow and are further classified into area air-cooled, edge air-cooled, and open-cathode types. The open-cathode proton exchange membrane fuel cell (PEMFC) system is efficient for a wide power range. It consists of a fuel cell stack, fan, hydrogen cylinder and regulator, lithium battery, and control module. The fan provides both oxygen and cooling, while the battery stabilizes power fluctuations. With high energy density, low noise, and minimal emissions, open-cathode PEMFCs are ideal for multirotor UAVs, where lightweight and effective cooling are essential [5]

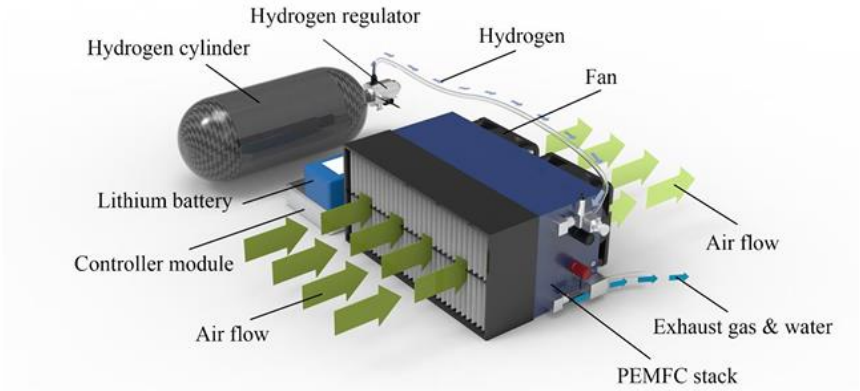

Fig. 2. Typical configuration of an open-cathode PEMFC power system [5]

2. DRONE INTEGRATION

When integrating the hybrid system into the drone, a connection diagram similar to that shown in Figure 11 can be used. The hybrid system can be incorporated into the drone through the use of a battery management system (BMS) and DC-DC converters. It is crucial that all components are securely fastened, particularly the hydrogen tank and the PEM fuel cell—to ensure that they remain undamaged during any impact and to help prevent potential accidents. A critical aspect of this integration involves the calculations for both the electronic requirements and the necessary hydrogen quantity. First, an average drone weight is determined based on the components to be used. Following that, the required thrust, power, voltage, and current values are calculated. Once these calculations are completed, the necessary amount of hydrogen is determined; subsequently, an appropriate hydrogen storage tank is selected based on this required amount. In choosing the tank, both the tank type and its cost are taken into consideration. The various tank types and their associated calculations are discussed in detail in the subsequent section. Our system has a mass of 20 kg. Based on this mass, the current drawn by an individual motor was measured to be approximately 18.72 A, leading to a total current draw of about 150 A for all eight motors. Of this total current, 80 A is supplied by the PEM fuel cell, which means that the remaining 70 A (150 A − 80 A) must be provided by the LiPo battery. Given a LiPo battery capacity of 50 Ah, the estimated flight duration under these conditions is calculated as follows:
50 Ah / 70 A ≈ 0.714 hours, which is approximately 42 minutes.

Furthermore, considering the instantaneous current draw of 150 A, when three batteries rated at 22,000 mAh (22 Ah) are configured appropriately (resulting in an effective capacity of 66 Ah) with a total battery mass of 7.5 kg, the flight duration becomes:
66 Ah / 150 A ≈ 0.44 hours, which is about 26.4 minutes.
In contrast, when using an equivalent mass of hydrogen fuel and a PEM fuel cell, the flight duration can be extended up to 42 minutes.

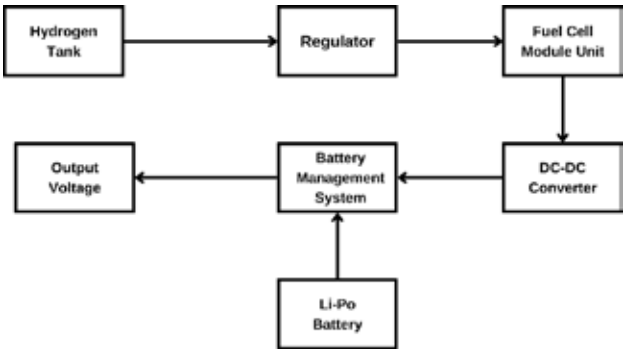

Fig. 3. Example Connection Diagram

3. DRONE DESIGNED FOR THE HYBRID SYSTEM

Initially, the motor configuration was chosen based on the components' weights and thrust requirements. Calculations indicated that an eight-motor configuration would provide sufficient thrust, leading to its selection. Subsequently, decisions were made regarding the placement of the PEM fuel cell, the hydrogen storage tank, and the LiPo battery. The hydrogen storage tank was positioned at the top to facilitate easy removal during refueling. The PEM fuel cell was placed at the bottom to ensure that, considering the operating temperature ranges of the PEM fuel cell and the LiPo battery, these critical components remain isolated from other parts and from each other. This placement also minimizes the risk of water vapor, produced by the PEM fuel cell, adversely affecting other components. The LiPo battery was located in the middle section.
The three most critical elements—the PEM fuel cell, the LiPo battery, and the hydrogen storage tank—are distinctly separated by plates to prevent any intermixing of systems. A crucial aspect of this design is the assembly of these components. To ensure secure installation, specialized mounting elements were designed. For example, two clamps were engineered to secure the hydrogen storage tank. In the design of these clamps as well as all other mounting components, careful consideration was given to weight constraints, aiming for the lightest yet most durable configuration possible.

Fig. 4. Hybrid System Drone Design

REFERENCES

1. Çavuşoğlu, A. 2006. Yakıt Pilleri ve Kullanım Alanları. Bursa Uludağ University (Turkey). ProQuest Dissertations & Theses, 28739900.
2. https://acikders.ankara.edu.tr/pluginfile.php/43602/mod_resource/content/0/Hafta5-Yak%C4%B1t%20pilleri%20-%202.pdf. Accessed on March 15, 2025.
3. 1st International Conference on Engineering, Natural and Social Sciences. Yakıt Pillerinin Tarihsel Gelişimi, Çalışma Prensipleri ve Çeşitleri İncelenmesi.
4. https://www.biolinscientific.com/blog/what-are-proton-exchange-membrane-fuel-cells-and-how-do-they-work. Accessed on March 15, 2025.
5. Shen, Z., Liu, S., Zhu, W., Ren, D., Xu, Q., & Feng, Y. 2024. A Review on Key Technologies and Developments of Hydrogen Fuel Cell Multi-Rotor Drones. Energies, 17(16), 4193.

THERMAL MODELLING OF AUTOTHERMAL, STEAM, AND PARTIAL OXIDATION SOLID OXIDE FUEL CELL REFORMERS

[1]*M. Turhan ÇOBAN*, [2]*Hadi Genceli*, [3]*Mustafa Asker,*[4]*Oguz Emrah Turgut,* [5*]*Mert Sinan Turgut*
[1] Piri Reis University, Faculty of Engineering, Department of Mechanical Engineering, Tuzla, Istanbul, 34940, Türkiye
[2]Yıldız Technical University, Faculty of Mechanical Engineering, Besiktas, Istanbul, 34349, Türkiye
[3]Aydın Adnan Menderes University, Faculty of Engineering, Department of Mechanical Engineering, Efeler, *Aydın*, 09010, Türkiye
[4]İzmir Bakircay University, Faculty of Engineering, Department of Industrial Engineering, Menemen, Izmir, 35665, Türkiye
[5]İzmir Democracy University, Faculty of Engineering, Department of Mechanical Engineering, Karabaglar, Izmir, 35110, Türkiye

*Corresponding author e-mail: mertsinan.turgut@idu.edu.tr

ABSTRACT
Fuel reformers are among the most critical components of fuel cell systems. Their essential thermodynamic performance can be analyzed using Gibbs free energy minimization. The models investigated in this article will utilize this method to calculate energy balances and exit gas formation from the reformer. The simulation models are prepared using the Java programming language. This study will investigate Autothermal, partial oxidation, and steam reformers. Four different case studies concerning various types of steam reformer applications are comparatively analyzed, and reactive products obtained from these devices have been investigated.

Keywords: Fuel Cell, Gibbs Free Energy, Reformer

1. INTRODUCTION

Solid oxide fuel cells convert chemical energy directly to electrical energy. The basic building blocks of the fuel cells are electrodes and electrolytes. The electrolyte layer of the solid oxide fuel cells are made of yttrium stabilized zirconia (For example 0.08 Y_2O_3 0.92 ZrO_2), Strontium doped lanthanum manganite ($LaSrMnO_3$ ..) and nickel zirconia cermets ($Ni - ZrO_3$) as anode, cathode and electrolyte respectively.
Wang et al. [1] presented a deatailed investigation of catalyst metal support interaction to enhance the hydrohgen production from steam reformer. Szablowski et al. [2] conducted comprehensive research on steam methane reforming to obtain hydrogen. Their research includes technological directions, mathematical representation, and various methods to overcome the energy demand of the stean reforming operations. Besides, Zhang et al. [3] investigated the different types of catalysts utilized in methanol steam reformers. Li et al. [4] used the free energy minimization method to evaluate the performance of an air-blown circulating fluidized bed gasifier. Tang and Kitagawa [5] have implemented the Gibbs free energy minimization approach to calculate the gasification product. Ezgi et al. [6] analyzed to examine diesel-fueled SOFC as a supporting engine for naval ship application.
Air is ionized in the cathode by using electrons coming through the electrical connections from anode site.

$$O_2 + 4e^- \rightarrow 2O^{2-} \quad (1)$$

Where O^{2-} ions pass through the electrolyte to the anode site. In the anode site fuel reacts with ionized air, combustion products and electrons resulted.

$$CO + O^{2-} \rightarrow CO_2 + 2e^- \quad (2)$$
$$H_2 + O^{2-} \rightarrow H_2O + 2e^- \quad (3)$$
$$CH_4 + O^{2-} \rightarrow 2H_2O + CO_2 + 8e^- \quad (4)$$

Electrons are sent through the external wires to the cathode and are used as electrical energy. The optimum operation Temperature of this device is approximately 900 °C at atmospheric pressure. Temperatures as low as 700 °C have been achieved in recent developments. The enthalpy of the exhaust gases is very high due to high operating temperatures. Some of this available energy is utilized to heat incoming air and fuel streams. Fuel is not utilized fully in fuel cells. Approximately 85% can be converted through these reactions. The rest is exhausted from the fuel cells together with the exhaust gases. These mixtures can be combusted using an exhaust air stream and additional air if required. If the mixture is combustible, the combustion process is used. For the poor mixtures, catalytic reactors can make the combustion process.

Hydrogen is an ideal fuel for fuel cells. Unfortunately, it is not a natural fuel, and storing it is incredibly challenging. Other fuels are generally converted to hydrogen, carbon, monoxide, and methane for solid oxide fuel cells. Several methods are used for this conversion (fuel reforming) process. The most common reactions are as follows [7]:

1-Water shift reaction:

$C_nH_{2n+2} + 2nH_2O \rightarrow nCO_2 + (3n+1)H_2$ (5)
$C_nH_{2n+2} + nH_2O \rightarrow nCO + (2n+1)H_2$ (6)
2- Partial oxidation reaction:
$C_nH_{2n+2} + n(O_2 + 79/21N_2) \rightarrow nCO_2 + (n+1)H_2 + 79/21N_2$ (7)

The water shift reaction is endothermic, which requires a significant amount of heat input. Heat input can be supplied with a heat exchanger before entering the reactor. This will cause the temperature to drop during the water shift reaction. This type of water shift reactor is called an adiabatic reactor. The heat exchanger can be integrated into the reactor body so that the response occurs isothermally. However, the reactor design is much more complicated in this case. Water shift reactions can be combined with partial oxidation reactions. This type of reactor is called an autothermal reactor.

2. MODELING OF REFORMERS

To model fuel cells, it will be assumed that reactors will reach a chemical equilibrium state at the exit of the reactors. Gibbs free energy minimization methods will be used to compute chemical equilibrium. The reactive species' state equation uses the NASA ideal gas equation of state.

A rich data collection is presented to calculate ideal gas thermodynamic properties [8]. The equations below outline the procedure for calculating the specific heat, enthalpy, and entropies of reacting gas components at a constant operating pressure.

$\frac{C_p^0(T)}{R} = a_1T^{-2} + a_2T^{-1} + a_3 + a_4T + a_5T^2 + a_6T^3 + a_7T^4$ (8)
$\frac{H^0(T)}{RT} = -a_1T^{-2} + a_2\frac{ln(T)}{T} + a_3 + a_4\frac{T}{2} + a_5\frac{T^2}{3} + a_6\frac{T^3}{4} + a_7\frac{T^4}{5} + b_1T$ (9)
$\frac{S^0(T)}{R} = -a_1\frac{T^{-2}}{2} - a_2T^{-1} + a_3ln\,(T) + a_4T + a_5\frac{T^2}{2} + a_6\frac{T^3}{3} + a_7\frac{T^4}{4} + b_2$ (10)
b_1 and b_2 is integral constant for the equations.

$S(T,P)=S^0(T)-Rln\left(\frac{P}{P_0}\right)$ (11)
Chemical enthalpy:
$H_T(T)=H(T)-H(298.15)+\Delta h_f(298.15)$ (12)
Chemical entropy:
$S_T(T,P) = S(T,P) - S(298.15, P0)$ (13)
where P_0=101.325 kPa
$G^0(T) = H^0(T) - T * S^0(T)$ (14)
Gibbs energy:
$G(T,P)=h(T)-S(T,P)=G^0(T)-RTln\left(\frac{P}{P_0}\right)$ (15)
Chemical Gibbs energy:
$G_T(T,P) = H_T(T) - TS_T(T,P)$ (16)

The Gibbs energy minimization process also uses methods to linearize and solve the nonlinear equation system. Definition of Gibbs energy for the reaction [9]:
$g = \sum_{j=1}^{NG} \mu_j n_j$ (17)
In equation (17) μ_j represts the chemical potential which is defined as follows
$\mu_j = \frac{\partial g}{\partial n_j}$ (18)
We should minimize the Gibbs free energy, but at the same time, the mass balance of the species should hold in the equations. The mass balance of the species can be written as follows.

$\sum_{j=1}^{NS} A_{ij}n_j - b_i^0 = 0$ (19)

So, both sides of the equations can be solved together. The mass balance equation is added to the Gibbs equation as a restriction criterion. As a result, the Gibbs free energy equation that we will minimize can be written as:

$G = \sum_{j=1}^{NG} \mu_j n_j + \sum_{i=1}^{na} \lambda_i\,(b_i - b_i^0) = \sum_{j=1}^{NG} \mu_j n_j + \sum_{i=1}^{na} \lambda_i\left(\sum_{j=1}^{NS} A_{ij}n_j - b_i^0\right)$ (20)

Where λ_i represents Lagrangian multipliers, equations (20) will be solved using Gibbs energy minimization using the NASA method. The minimum value of the equation will give the solution, but this equation is entirely non-linear and

relatively challenging to solve. We would like to introduce the NASA method for solving the equation here. The condition for equilibrium becomes:

$$\delta G = \sum_{j=1}^{NG}\left(\mu_j + \sum_{i=1}^{na} \lambda_i A_{ij}\right) \delta n_j \quad (21)$$

Treating the variations δn_j and $\delta\lambda_i$ as independent variables give the following equations

$$\left(\mu_j + \sum_{i=1}^{na} \lambda_i A_{ij}\right) = 0 \quad (22)$$

$$(b_i - b_i^0) = 0 \quad (23)$$

To carry out the computation, computer codes in Java language are developed

3. RESULTS AND DISCUSSION

Hydrocarbon converters (reformers) of various types are modeled using equations of state and Gibbs energy minimization programs written in Java. It should be noted that the purpose of these specific fuel converters is to prepare fuel for solid oxide fuel cells that can process fuels such as methane, carbon monoxide, and hydrogen. These outputs are unsuitable for other fuel cells, such as the Polymer electrolyte membrane (PEM). When the performances are compared, isothermal steam reformers are integrated devices that facilitate both mass and heat transfer. The results are listed in Table 1-Table 4, respectively.

Table 1. Adiabatic steam reformer of natural gas

Reactive components	Inlet kmol	Outlet kmol
H_2	0	1.20051
H_2O	3.3	2.60953
N_2	0	0
CO_2	0	0.33543
CO	0	0.01958
CH_4	0.82	0.82496
C_2H_6	0.12	3.78180E-6
C_3H_8	0.04	6.65340E-11
O_2	0	0
Temperature inlet	973.15	degree K
Temperature outlet	717.41	degree K
Pressure	101.325	kPa
Reaction Enthalpy	0	kJ/kmol natural gas

Table 2. Isothermal (integrated with heat exchanger) steam reformer of natural gas

Reactive components	Inlet kmol	Outlet kmol
H_2	0	3.69628
H_2O	3.3	1.68350
N_2	0	0
CO_2	0	0.47660
CO	0	0.66329
CH_4	0.82	0.04010
C_2H_6	0.12	6.70244E-8
C_3H_8	0.04	3.09825E-13
O_2	0	0
Temperature inlet	973.15	degree K
Temperature outlet	973.15	degree K
Pressure	101.325	kPa
Reaction Enthalpy	225453.50468	kJ/kmol natural gas

Table 3. Partial oxidation reformer of natural gas

Reactive components	Inlet kmol	Outlet kmol
H_2	0	1.59888
H_2O	3.3	3.05495E-4
N_2	1.61590	1.61590
CO_2	0	1.23028E-4
CO	0	0.89944
CH_4	0.82	0.28034
C_2H_6	0.12	4.27938E-5
C_3H_8	0.04	1.53808E-8
O_2	0.45	1.72896E-173
Temperature inlet	973.15	degree K
Temperature outlet	973.15	degree K
Pressure	101.325	kPa
Reaction Enthalpy	225453.50468	kJ/kmol natural gas

Table 4. Autothermal reformer of natural gas

Reactive components	Inlet kmol	Outlet kmol
H_2	0	3.05028
H_2O	3.3	2.39425
N_2	1.72119	1.72119
CO_2	0	0.64854
CO	0	0.52372
CH_4	0.82	0.00773
C_2H_6	0.12	3.02E-09
C_3H_8	0.04	3.26E-15
O_2	0.45753	1.55E-192
Temperature inlet	973.15	degree K
Temperature outlet	973.15	degree K
Pressure	101.325	kPa
Reaction Enthalpy	72.43841	kJ/kmol natural gas

REFERENCES

1. Wang C, Ren X, Cao H, and Zhang D. 2025. Insights into metal-support interaction in steam reforming reactions for hydrogen production: A recent review. *International Journal of Hydrogen Energy* 111:808-832.
2. Szablowski L, Wojcik M, and Dybinski O. 2025. Review of steam methane reforming as a method of hydrogen production. *Energy* 134540.
3. Zhang M, Liu D, Wang Y, Zhao L, Xu G, Yu Y, and He H. 2025. Recent advances in methanol steam reforming catalysts for hydrogen production. *Catalysts* 15(1):36.
4. Li X, Zhong K, and Feng L. 2023. Machine learning-based metaheuristic optimization of an integrated biomass gasification cycle for fuel and cooling production. *Fuel* 332:125969.
5. Tang H and Kitagawa K. 2005. Supercritical water gasification of biomass: thermodynamic analysis with direct Gibbs free energy minimization. *Chemical Engineering Journal* 106(3):261-267.
6. Ezgi C, Turhan Çoban M, and Selvi Ö. 2013. Design and thermodynamic analysis of an SOFC system for naval surface ship application. *Journal of Fuel Cell Science and Technology* 10(3):031006.
7. Smith WR. 1982. *Chemical Reaction Equilibrium Analysis: Theory and Algorithms.*
8. McBride BJ. 2002. *NASA Glenn Coefficients for Calculating Thermodynamic Properties of Individual Species.* National Aeronautics and Space Administration, John H. Glenn Research Center at Lewis Field.
9. Bamikole JO and Narasigadu C. 2023. Application of Pathfinder, Honey Badger, Red Fox, and Horse Herd algorithms to phase equilibria and stability problems. *Fluid Phase Equilibria* 566:113682. https://doi.org/10.1016/j.fluid.2022.113682

DETERMINING THE HYDROGEN PIPELINE ROUTE IN TÜRKIYE FOR SUSTAINABLE ENERGY TRANSITION BETWEEN ASIA AND EUROPE USING HYBRID OPTIMIZATION

[1]*Soner ÇELİKDEMİR*, [2*]*Mahmut Temel ÖZDEMİR*
[1] Bitlis Eren University, Adilcevaz Vocational School, Electric and Energy, Bitlis, 13000, Türkiye
[2] Firat University, Engineering Faculty, Electrical and Electronics Engineering, Elazig, 23000, Türkiye

E-mail: temelozdemir@gmail.com

ABSTRACT
This study investigates the foundational steps for establishing a Hydrogen Pipeline Corridor (HPC) traversing Türkiye, intended to connect European countries with growing energy demand to Asian countries with substantial energy potential. Türkiye, leveraging its strategic position as an energy bridge between Asia and Europe, applies a hybrid optimization approach and Monte Carlo simulation to determine the hydrogen pipeline route. The study considers multiple criteria, including energy demand, energy potential, geographical suitability, and cost, to optimize the route. During the optimization process, the Particle Swarm Optimization (PSO) algorithm is employed to identify the most suitable route under predefined constraints. These constraints include ensuring that the total cost does not exceed the budget limit, meeting minimum energy demand and potential requirements, and selecting a specific range of provinces. Monte Carlo simulation is utilized to analyze the impact of uncertainties in the criteria and evaluate the likelihood of route selection under different scenarios. During the simulation, random variations are introduced to the cost, energy demand, energy potential, and geographical suitability values, and the selection frequency of each province is calculated.

Keywords: Hydrogen pipeline corridor, Optimization, Energy corridor estimation

1. INTRODUCTION

The rapid increase in global energy demand and the growing environmental impacts of fossil fuels have made renewable energy sources more critical than ever. Issues such as global warming, carbon emissions, and environmental sustainability necessitate a transition to renewable energy in production. Renewable energy sources such as solar, wind, biomass, and hydroelectric power are less harmful to the environment compared to fossil fuels and enhance energy security. However, the intermittent nature of these sources and challenges in energy storage and transmission processes require the development of innovative solutions for energy transformation. In this context, hydrogen emerges as the energy carrier of the future. With its high energy density, environmentally friendly characteristics, and compatibility with various energy production methods, hydrogen holds revolutionary potential in the energy sector. [1,2]. "Green hydrogen," produced from renewable energy sources, is becoming one of the cornerstones of sustainable energy systems by reducing carbon emissions to zero. Hydrogen has a wide range of applications in energy production, transportation, and industry, which has led to a steadily increasing demand for hydrogen over time. [3]. The increasing demand for hydrogen in the future highlights its critical role in energy systems, not only in production processes but also in transmission and distribution.

The safe, efficient, and economical transportation of hydrogen from production sites to consumption centers is of great importance for the sustainability of energy infrastructure. Various methods are available for hydrogen transportation, including liquefied hydrogen transport, compressed hydrogen transport in pressurized cylinders, and chemical carriers. However, these methods are often costly and have limited capacity. Therefore, the most suitable method for transporting large quantities of hydrogen at low cost and with minimal environmental impact is pipeline transportation. Pipelines are considered one of the most efficient and reliable methods for transporting hydrogen over long distances. This method offers significant advantages over other transportation methods, both economically and environmentally. Pipelines enable the continuous and uninterrupted transport of large volumes of hydrogen while minimizing carbon emissions. In particular, in countries like Türkiye, which serves as a strategic energy bridge between Asia and Europe, the development of hydrogen pipeline infrastructure can contribute to both regional and global energy transitions. Türkiye's geographical location, renewable energy potential, and proximity to energy demand centers provide a significant advantage for hydrogen pipeline projects.

In this study, a hybrid optimization approach and Monte Carlo simulation were applied to determine the hydrogen pipeline route among Türkiye's 81 provinces. The study considers multiple criteria such as energy demand, energy potential, geographical suitability, and cost, aiming to ensure the safe and efficient transportation of hydrogen. In this context, determining the hydrogen pipeline route is considered a significant step toward enhancing the sustainability of Türkiye's energy infrastructure and contributing to the global energy transition.

2. SYSTEM DESCRIPTION AND PROCEDURE

In this study, a hybrid optimization approach and Monte Carlo simulation were applied to determine the hydrogen pipeline route among Türkiye's 81 provinces. The study aimed to identify the most optimal route under defined constraints by considering multiple criteria such as energy demand, energy potential, geographical suitability, and cost. This section

provides a detailed explanation of the methods, algorithms, variables, and procedures used in the study.

2.1. Particle Swarm Optimization (PSO)

Optimization methods in the literature are generally designed to find the most suitable solution to a given problem. Numerous optimization algorithms have been developed, each with unique approaches. Among the commonly used algorithms are the bee algorithm, genetic algorithm, and Particle Swarm Optimization (PSO). Of these, PSO is one of the most widely preferred methods. Introduced in 1995 [4], PSO is inspired by the collective behavior of certain animals that live and move in groups. These behaviors include finding food sources and protecting themselves from external threats, achieved through communication within the group. In PSO, the group, or "swarm," consists of N particles moving in an n-dimensional space. The position of a particle at iteration t is represented as $x_i(t)$, which is used to evaluate the particle's state. To solve problems, PSO relies on information sharing among the particles in the swarm. Each particle updates its position by moving toward the best position in the swarm to avoid danger and locate resources. Additionally, particles use their own past experiences to guide their movements. Each particle maintains its personal best position (X_{pbest} and is also influenced by the global best position X_{gbest} of the entire swarm. The velocity and position of each particle in the next iteration are calculated using the following equations [5,6].

$$v_i(t+1) = wv_{i,j}(t) + c_1 r_1(t)\left(X_{pbest} - x_{i,j}(t)\right) + c_2 r_2(t)\left(X_{gbest} - x_{i,j}(t)\right) \quad (1)$$

$$x_i(t+1) = x_i(t) + v_i(t+1) \quad (2)$$

In this study, the PSO algorithm is used to optimize the hydrogen pipeline route. The algorithm works to select the most suitable provinces under the specified constraints.

2.2. Monte Carlo Simulation

Monte Carlo simulation is a method used to analyze the effects of uncertainties and evaluate the system's behavior under different scenarios. In this study, uncertainties in criteria such as cost, energy demand, energy potential, and geographical suitability were modeled by introducing random variations. During each simulation cycle, the values of these criteria were perturbed as follows:

$$M_{i+1} = M_i * (1 + \Gamma * \mathrm{W}) \quad (3)$$

Here M_i represents the original value, M_{i+1} denotes the new value, Γ is the standard deviation representing the level of uncertainty, and W refers to the noise. The Monte Carlo simulation was conducted in a 100-iteration loop, and in each simulation, the PSO algorithm was executed to calculate the selection frequency of the provinces. The constraints applied in the study are as follows:

Cost Constraint;

$$\sum_{i=1}^{n} x_i.cost_i \leq budget \quad (4)$$

Minimum Energy Demand Constraint:

$$\sum_{i=1}^{n} x_i.demand_i \geq minimum_demand \quad (5)$$

Minimum Energy Potential Constraint:

$$\sum_{i=1}^{n} x_i.potantial_i \geq minimum_potential \quad (6)$$

Number of Selected Provinces:

$$minimum\ number\ of\ cities \leq \sum_{i=1}^{n} x_i \leq maximum\ number\ of\ cities \quad (7)$$

Objective Function in the Study:

$$Objective_func. = 0.4 * potential + 0.3 * demand + 0.3 * geo_suitability \quad (8)$$

This system design and procedure offer a comprehensive approach to determining the hydrogen pipeline route by analyzing uncertainties and optimizing multiple criteria.

3. RESULTS AND DISCUSSION

The results obtained in this study for determining the hydrogen pipeline route have enabled a detailed analysis of both the optimization process and the effects of uncertainties. Using the PSO algorithm, baseline optimization was performed, and provinces were selected. These provinces were chosen from among those with the highest values in terms of energy potential, energy demand, and geographical suitability. The selected provinces did not exceed the budget constraint, which utilized 85% of the total cost, and met 25% of the total energy demand.

Monte Carlo simulation was conducted under 100 different scenarios by applying 10% random variations to the criteria. Based on the simulation results, the selection frequencies of the provinces were calculated and classified into three different ranges:
Very High Frequency Provinces (≥0.75): Ankara, Antalya, Diyarbakır, Elazığ, Gaziantep, Istanbul, Izmir, Kayseri, and Van.
Medium Frequency Provinces (0.55-0.75): Balıkesir, Erzurum, Eskişehir, Mersin, Kocaeli, Konya, Malatya, Manisa, Kahramanmaraş, Muğla, Sakarya, Samsun, Trabzon, and Şanlıurfa.
Low Frequency Provinces (0.30-0.55): Adana, Adıyaman, Artvin, Aydın, Bilecik, Çanakkale, Rize, Sivas, and Düzce.

This classification highlights the strategic importance of the provinces for the hydrogen pipeline route. The results obtained based on the calculated criteria are presented in Figure 1.

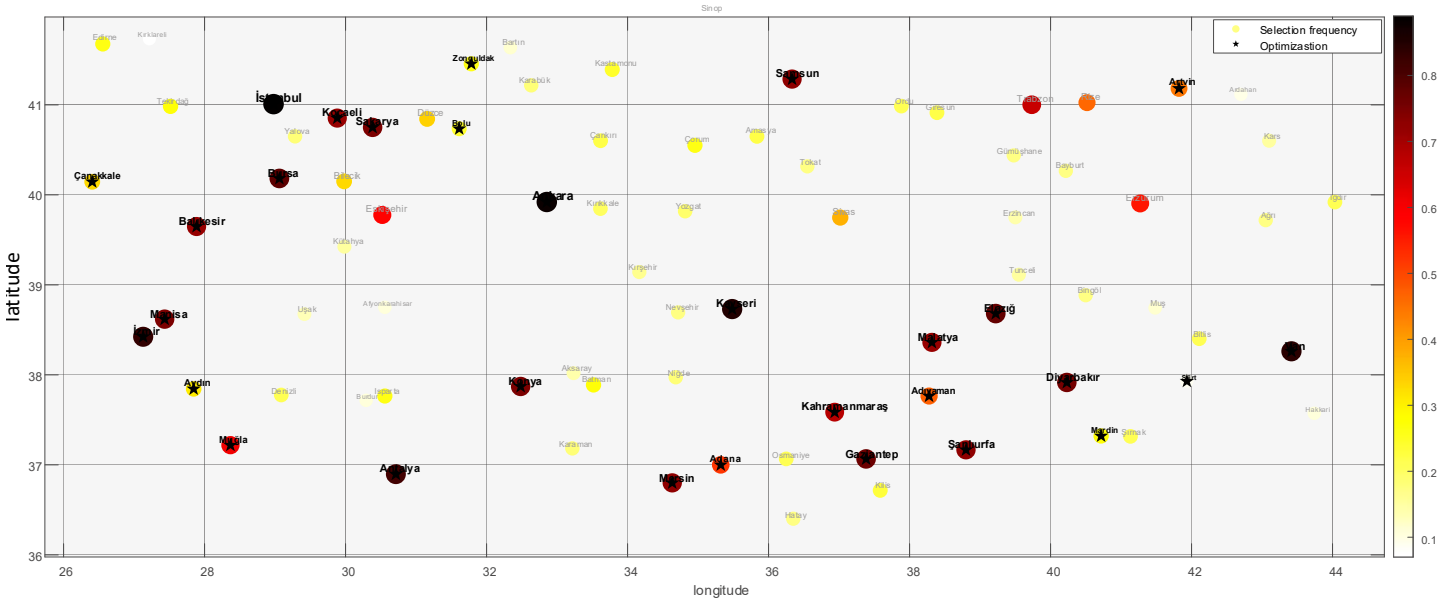

Fig. 1. Hydrogen Pipeline Route Optimization and Monte Carlo Simulation Results

Fig. 1 illustrates the results of hydrogen pipeline route optimization and Monte Carlo simulation for Türkiye's 81 provinces. The map visualizes the selection frequencies of the provinces and the provinces selected as a result of the optimization process. These results enable a detailed analysis of both the optimization process and the effects of uncertainties. The colors used on the map represent the selection frequencies of the provinces during the Monte Carlo simulation. The transition from white to black indicates the selection frequency of the provinces. Similarly, the black star symbol represents the provinces selected as a result of the optimization process. These provinces were chosen to form the most optimal route under the specified criteria (cost, energy demand, energy potential, and geographical suitability) and constraints (budget, minimum demand, and minimum potential). Provinces without a star symbol were not selected in the optimization process but may have been selected with a certain frequency during the Monte Carlo simulation. As a result, the proposed hydrogen pipeline corridor for Türkiye is presented in Fig. 2.

Fig. 2. Türkiye's hydrogen pipeline route between Asia and Europe.

As a result, some provinces, despite not being selected in the optimization process, exhibit high selection frequencies during the Monte Carlo simulation. This indicates that these provinces become more advantageous in certain scenarios due to the effects of uncertainties.

4. CONCLUSION

This study was conducted to determine the hydrogen pipeline route for Türkiye's 81 provinces using a hybrid optimization approach and Monte Carlo simulation. The study aimed to identify the most optimal route under specified constraints by considering multiple criteria such as energy demand, energy potential, geographical suitability, and cost. The results obtained allowed for a detailed analysis of both the optimization process and the effects of uncertainties. The uniqueness of this study lies in the hybrid use of Particle Swarm Optimization (PSO) and Monte Carlo simulation for hydrogen pipeline route planning. Unlike traditional methods in the literature, this approach analyzes the resilience of the route by taking uncertainties into account. The study provides decision-makers in energy infrastructure planning with the following contributions:

- Integrated evaluation of multiple criteria,
- Analysis and visualization of the effects of uncertainties,
- Numerical and visual presentation of the selection frequencies of provinces.

The optimization and simulation results reveal the selection frequencies and strategic importance of the provinces. The provinces selected as a result of the optimization process were determined based on their high values in terms of energy potential, energy demand, and geographical suitability. The selected provinces are Monte Carlo simulation was conducted under 100 different scenarios by applying a 10% random variation to the criteria. According to the simulation results, the three provinces with the highest selection frequencies are Istanbul (89%), Ankara (88%), and Kayseri (87%). As a result, a hydrogen pipeline route for Türkiye has been proposed to ensure a sustainable energy transition between Asia and Europe.

Future studies could further develop this method by incorporating additional criteria. Moreover, dynamic factors such as population growth and regional economic development could be included to enhance the model. However, as a pioneering study in this field, the current work provides a framework that can guide decision-makers in energy infrastructure planning.

References

[1] I. Dincer, Covid-19 coronavirus: Closing carbon age, but opening hydrogen age, Int. J. Energy Res. 44 (2020) 6093–6097. https://doi.org/10.1002/er.5569.

[2] S. Çelikdemir, M.T. Özdemir, Türkiye’s Offshore Hybrid Energy Potential and Cost Estimation in the Eastern Mediterranean, Türk Doğa ve Fen Derg. (2023). https://doi.org/10.46810/tdfd.1186573.

[3] I. Dincer, N. Javani, G.K. Karayel, Sustainable city concept based on green hydrogen energy, Sustain. Cities Soc. 87 (2022) 104154. https://doi.org/10.1016/j.scs.2022.104154.

[4] A.H. Elbatran, O.B. Yaakob, Y.M. Ahmed, H.M. Shabara, Operation, performance and economic analysis of low head micro-hydropower turbines for rural and remote areas: A review, Renew. Sustain. Energy Rev. (2015). https://doi.org/10.1016/j.rser.2014.11.045.

[5] B. Alatas, E. Akin, A.B. Ozer, Chaos embedded particle swarm optimization algorithms, Chaos, Solitons & Fractals. 40 (2009) 1715–1734. https://doi.org/10.1016/j.chaos.2007.09.063.
[6] M.T. Özdemir, Optimal parameter estimation of polymer electrolyte membrane fuel cells model with chaos embedded particle swarm optimization, Int. J. Hydrogen Energy. 46 (2021) 16465–16480. https://doi.org/10.1016/j.ijhydene.2020.12.203.

SUSTAINABLE ENERGY BASED ON OPTIMIZING LOAD FREQUENCY CONTROL IN MILITARY MICROGRID

[1]Soner ÇELİKDEMİR, [2]Burak YILDIRIM, [3*]Mahmut Temel ÖZDEMİR
[1] Bitlis Eren University, Adilcevaz Vocational School, Electric and Energy, Bitlis, 13000, Türkiye
[2] Bingöl University, Vocational and Tech. High School, Bingol, 12000, Türkiye
[3]Firat University, Engineering Faculty, Electrical and Electronics Engineering, Elazig, 23000, Türkiye

E-mail: temelozdemir@gmail.com

ABSTRACT
The use of military microgrids plays a crucial role in ensuring energy security, achieving sustainability objectives, and providing operational independence in military operations. This study introduces a Load Frequency Controlled (LFC) stable power system to enhance the efficiency and robustness of microgrids used in military bases. In this paper, the Whale Optimization Algorithm (WOA) is employed to optimize the load frequency model of a military microgrid. The WOA, as a novel advanced control approach, is compared with traditional Proportional-Integral-Derivative (PID) controllers through simulations, employing an innovative two-degree-of-freedom proportional-integral-derivative (2DOF-PID) controller. The comparative analysis demonstrates that the WOA-optimized 2DOF-PID controller exhibits rapid response and precise targeting capability with an average square error of 0.00001. The results show that the microgrid frequency optimized by WOA is effectively controlled. Simulation results under low Renewable Energy Sources (RES) conditions reveal that the 2DOF-PID controller, optimized by WOA, reduces the ITAE and ISE values to 2.065 and 6.478, respectively, while maintaining system stability. This research enhances the resilience of microgrid systems, ensuring reliable performance, particularly when controlling frequency during military and emergency situations.

Keywords: Load Frequency Controlled, Whale Optimization Algorithm, Military Microgrids

1. INTRODUCTION
Military bases and emergency response centers are increasingly adopting microgrids due to their energy security and uninterrupted power requirements. These systems are designed to enhance the energy independence of military bases, ensure resilience against external grid outages, and improve operational efficiency. The ability to operate sustainably off-grid, provide uninterrupted power supply, and function silently offers critical advantages, such as reducing the risk of detection. Additionally, mobile microgrid systems enable rapid deployment and flexible usage, allowing them to quickly adapt to operational requirements.
Energy management in military microgrids is a critical factor for ensuring efficient and stable system operation. In this context, the integration of renewable energy sources (RES) emerges as a key strategy to enhance the sustainability of microgrids. However, the inherently variable nature of renewable energy sources can directly impact system stability and energy quality. Specifically, fluctuations in renewable energy generation and changes in consumption demand can lead to imbalances in system frequency, negatively affecting power quality. Therefore, the development of frequency regulation strategies in microgrids is of great importance.
Continuous fluctuations in the power output of renewable energy sources increase the imbalance between energy generation and consumption, causing oscillations in system frequency [1]. Frequency deviations from the nominal value reduce energy quality and system reliability. As a result, various control methods have been developed to ensure frequency regulation in microgrids [2-3]. Achieving this control in standalone microgrids requires a more complex process. In this regard, secondary controllers play a critical role in maintaining system stability and preventing frequency deviations [4].
In this study, a military microgrid consisting of diesel generators, wind turbines, solar panels, biomass energy systems, data monitoring and communication infrastructures, energy storage batteries, electric vehicles, fuel cells, electrolyzers, and unmanned aerial vehicles was modeled in MATLAB/SMILUNIK. To ensure energy security, maintain system stability, and achieve operational independence, an appropriate Load Frequency Control (LFC) is required. For this purpose, two different controllers were designed: Proportional Integral Derivative (PID) and Two-Degree-of-Freedom PID (2DOF-PID). The Whale Optimization Algorithm (WOA) was proposed to optimize the load frequency model of the microgrid. This allowed for fine-tuning the controllers' parameters more efficiently and accurately. The main contributions of this study are listed below:

- A Proposes a stable power system to ensure load frequency control in military microgrids.
- Tests and compares the use of the WOA algorithm with traditional PID controllers to optimize the load frequency model of microgrid systems.
- Introduces an innovative solution by employing the 2DOF-PID controller, differing from traditional PID controllers.
- Demonstrates that optimizing WOA and 2DOF-PID controllers for load frequency control can enhance the efficiency and reliability of military microgrids.
- Ensures more stable and consistent operation of microgrids against fluctuations in energy generation.

- Presents a model that improves microgrid performance even under low renewable energy conditions, contributing to energy security and sustainability goals.
- Highlights the importance of load frequency control in microgrids to ensure energy independence and security in military operations.
- Prevents energy losses caused by imbalances in generation and consumption, improving energy quality and increasing efficiency.

2. MATERIALS AND METHODS

Military Microgrid

The mathematical and dynamic model of a military-type microgrid (MMG) for load frequency control is presented in Fig. 1. The model consists of an integrated structure that includes diesel generators, wind turbines, solar panels, biomass energy systems, data monitoring and communication infrastructures, energy storage batteries, electric vehicles, fuel cells, electrolyzers, and unmanned aerial vehicles.

Fig. 1. Military microgrid model

Whale Optimization Algorithm

The Whale Optimization Algorithm (WOA) is an optimization algorithm inspired by the behavior of whales in nature. Specifically, it is designed based on observations of whales' hunting and social interaction behaviors. This algorithm mimics behaviors such as the "bubble-net" hunting technique and group movements of whales. WOA is an evolutionary algorithm that performs exploration and exploitation phases in parallel while searching the solution space.

Mathematical Model;

The mathematical model of WOA is derived by expressing the aforementioned behaviors through mathematical equations. Essentially, each whale represents a solution point, and the search process is shaped by the social and individual movements of the whales. The fundamental mathematical equations modeling whale behaviors are presented below as Equations (1)–(3).

1. Exploration Behavior (Bubble-Net):

The position of the whale is updated to find a new solution. The general form of this equation is as follows:

$$Xt + 1 = Xt + A \cdot | C \cdot Xg - Xt | \quad (1)$$

where: X_t represents the current solution, X_g represents the global best solution, A and C are algorithm parameters.

2. Exploitation Behavior (Targeted Swimming):

The swimming behavior allows the whale to reach the target in smaller steps within the solution space. This is mathematically expressed as:

$$Xt + 1 = Xt + B \cdot | D | \cdot Xg \quad (2)$$

where: B is a control parameter, D is the distance between two whales.

3. Position Update:
Whales approach each other in the solution space to discover new solutions. This process is modeled as:

$$Xt + 1 = Xt + (rand) \cdot (Xbest - Xt) \quad (3)$$

where: X_t is the current solution, *rand* is a random factor.
WOA performs exploration (global search) and exploitation (local search) phases sequentially in the solution space. In each iteration, the positions of the whales are updated, and the process continues until the best solution is found. This process progresses to minimize the objective functions that need to be optimized.

3. DOF PID CONTROLLER
The degree of freedom of a controller is defined as the number of closed-loop transfer functions that can be independently adjusted [5]. Studies have demonstrated the applicability of a two-degree-of-freedom PID (2DOF-PID) controller in load frequency control systems to improve system efficiency and stability [6-7]. 2DOF-PID controllers are widely used to detect and control disturbances and rapid shocks in electric power systems without symbolic setpoint tracking overshoot [8]. The control architecture of the 2DOF-PID controller is shown in Fig. 2.

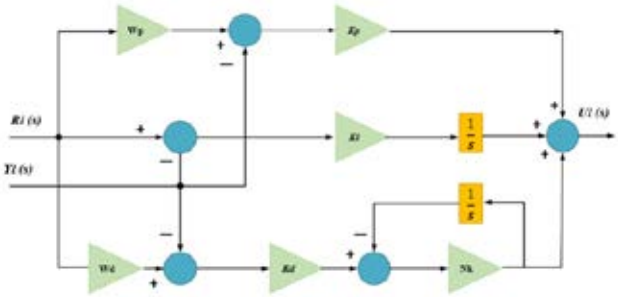

Fig. 2. 2DOF-PID control architecture

The transfer function of a 2-DOF PID controller can generally be expressed as follows:

$$C(s)= K_p+K_i/s+K_dNs/1+Ns \quad (4)$$

where: K_p Proportional gain, K_i Integral gain, K_d Derivative gain, N Derivative filter coefficient. The key difference from a classical PID controller lies in the two distinct weighting parameters (W_p and W_d) that determine the response to the reference input. The mathematical model used for the 2-DOF PID controller is shown in Equation (5):

$$U(s)=K_p[W_pR(s)-Y(s)]+K_i1/s\ [R(s)-Y(s)]+ K_d*Ns/1+Ns[W_dR(s)-Y(s)] \quad (5)$$

where: R(s) Reference input signal, Y(s) Output signal, Wp and Wd Weighting coefficients applied to the reference input. These equations are used to make the controller's behavior more flexible in response to reference changes and disturbances. Based on this model, the 2-DOF PID controller can provide superior performance compared to the conventional PID controller, enhancing system stability.

3. RESULTS AND DISCUSSIONS
Military microgrids are designed to provide uninterrupted energy without relying on external grids. These systems consist of various components, including diesel generators, wind turbines, solar panels, biomass energy systems, data monitoring and communication infrastructures, energy storage batteries, electric vehicles, fuel cells, electrolyzers, and unmanned aerial vehicles. In this study, the performance of a proposed controller for military microgrid systems was analyzed, particularly in terms of its load frequency control (LFC) capability. Accordingly, both proportional-integral-derivative (PID) and two-degree-of-freedom PID (2DOF-PID) controllers were integrated into the microgrid system. Subsequently, the specified controllers were optimized using the WOA model to evaluate system performance.

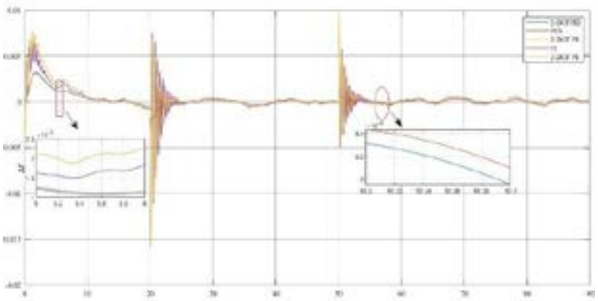

Fig. 3. The Frequency Response of the System

Implementing a robust controller to reduce oscillations and ensure stability in military microgrids is essential. For the two evaluated algorithms, the controller parameter limits were set between 0 and 10, with a maximum of 50 iterations and an initial population size of 50. Notably, the WOA model, proposed for the first time in this study, demonstrated superior performance compared to other algorithms under the same conditions. It was then compared with the designed PID and 2DOF-PID controllers. The oscillatory behavior of the PID controller, characterized by a long response time, is shown in Fig. 3. The 2DOF-PID controller exhibited the most optimal performance under load variations.

Table 1. Performance metrics

Controller	ITSE x 10^{-3}	ISE x 10^{-3}	IAE	ITAE
PID	0.26	3.32	0.027	0.0556
2DOF-PID	0.25	3.30	0.026	0.555

A more detailed comparison of the controllers optimized using the WOA model is provided in Table 1, which lists performance indices such as ITAE, ITSE, IAE, and ISE.

4. CONCLUSIONS

This study demonstrated that optimizing load frequency control systems can reduce the imbalance between energy generation and consumption, preventing oscillations in system frequency. In this context, it was shown that the proposed approach could enhance the energy quality and reliability of the system. The continuous fluctuations in the power output of renewable energy sources were mitigated by the proposed controller, which played a critical role in maintaining system stability and preventing frequency deviations. This study evaluated the performance of PID and 2DOF-PID controllers for load frequency control (LFC) in a military microgrid system. Simulation results proved that the proposed control scheme outperformed classical PID and 2DOF-PID controllers tuned using the WOA model in terms of performance metrics (ITAE, ISE, IAE, and ITSE). Among the tested controllers, the 2DOF-PID controller achieved the best results across all performance criteria. The proposed 2DOF-PID controller recorded the lowest values for ITSE (0.25×10^{-3}), ITAE (0.555), ISE (3.30×10^{-5}) and IAE (0.026), demonstrating its ability to provide precise and stable frequency regulation with minimal error and energy loss. It was the most consistent and effective controller.

In conclusion, the findings highlight the robustness and adaptability of advanced optimization techniques and controller designs in achieving efficient and reliable load frequency control for military microgrids. The 2DOF-PID controller combined with the WOA model, which outperformed all other controllers in terms of performance metrics, was identified as the best controller. This study serves as a reference point for advancing adaptive control strategies for enhanced energy infrastructures.

References

[1] Gbadega, Peter Anuoluwapo, and Akshay Kumar Saha. 2021. “Load Frequency Control of a Two-Area Power System With a Stand-Alone Microgrid Based on Adaptive Model Predictive Control.” *IEEE Journal of Emerging and Selected Topics in Power Electronics* 9 (6): 7253–63. https://doi.org/10.1109/JESTPE.2020.3012659.

[2] Irfan, Muhammad, Sara Deilami, Shujuan Huang, Tayyab Tahir, and Binesh Puthen Veettil. 2024. “Optimizing Load Frequency Control in Microgrid with Vehicle-to-Grid Integration in Australia: Based on an Enhanced Control Approach.” *Applied Energy* 366 (July): 123317. https://doi.org/10.1016/j.apenergy.2024.123317.

[3] Mishra, Sonalika, Ramesh Chandra Prusty, and Sidhartha Panda. 2020. “Design and Analysis of 2dof-PID Controller for Frequency Regulation of Multi-Microgrid Using Hybrid Dragonfly and Pattern Search Algorithm.” *Journal of Control, Automation and Electrical Systems* 31 (3): 813–27. https://doi.org/10.1007/s40313-019-00562-y.

[4] Jena, Narendra Kumar, Subhadra Sahoo, Kumari Kasturi, and Binod Kumar Sahu. 2024. “Design of a Fractional Order 2-DoF-PID Controller for Frequency Control in a Multi-Area Stand Alone Micro-Grid.” In *2024 3rd Odisha International Conference on Electrical Power Engineering, Communication and Computing Technology (ODICON)*, 1–6. IEEE. https://doi.org/10.1109/ODICON62106.2024.10797481.

[5] Wang, Xinxin, Xiaoqiang Yan, Donghai Li, and Li Sun. 2018. “An Approach for Setting Parameters for Two-Degree-of-Freedom PID

Controllers." Algorithms 11 (4): 48. https://doi.org/10.3390/a11040048.
[6] Buranaaudsawakul, Techatat, Kittipong Ardhan, Sitthisak Audomsi, Worawat Sa-ngiamvibool, and Rattapon Dulyala. 2025. "Optimal Turning of a 2-DOF Proportional-Integral-Derivative Controller Based on a Chess Algorithm for Load Frequency Control." International Journal of Electrical and Computer Engineering (IJECE) 15 (1): 146. https://doi.org/10.11591/ijece.v15i1.pp146-155.
[7] Shahi, Md. Nazmush Shakib, Nabil Anan Orka, and Ashik Ahmed. 2024. "2DOF-PID-TD: A New Hybrid Control Approach of Load Frequency Control in an Interconnected Thermal-Hydro Power System." Heliyon 10 (17): e36753. https://doi.org/10.1016/j.heliyon.2024.e36753.
[8] Tripathy, Debasis, N.B. Dev Choudhury, and B.K. Sahu. 2020. "Comparative Performance Assessment of Several Fractional Order - Two Degree Freedom Controllers Tuned Using GOA for LFC." *Procedia Computer Science* 167: 2022–32. https://doi.org/10.1016/j.procs.2020.03.239.

PARAMETRIC ESTIMATION AND PERFORMANCE ANALYSIS OF DIRECT ETHANOL FUEL CELLS AND LITHIUM BATTERIES FOR HYBRID ENERGY SYSTEMS

Meltem YAVUZ ÇELİKDEMİR
Bitlis Eren University, Tatvan Vocational School, Electronic and Automation, Bitlis, 13000, Türkiye

E-mail: meltem.ycd@gmail.com

ABSTRACT
Fuel cells and energy storage systems have become widely used in significant engineering applications today. However, one of the challenges faced in these applications is determining the exact values of unknown parameters. In this context, the use of Direct Ethanol Fuel Cells (DEFC) and lithium batteries in hybrid systems enhances the efficiency, sustainability, and longevity of energy storage and conversion systems, owing to the complementary characteristics of both technologies. This study aims to accurately estimate the parameters of the mathematical model of the DEFC and lithium battery hybrid system. For this purpose, the Starfish Optimization Algorithm, a contemporary algorithm with certain advantages in the literature, is applied for the first time. Additionally, a voltage-power-based objective function, recently proposed by researchers, is utilized. This approach ensures that the hybrid system operates within the maximum power region, thereby increasing its efficiency and operational lifespan. As a result, the absolute error sum for the DEFC is calculated as 4.2457, and the average absolute error sum for the lithium battery is 0.0469. Consequently, the parameters of the DEFC-lithium battery hybrid model are estimated with high accuracy. Furthermore, experimental data for the DEFC and lithium battery are used to improve the accuracy of the predictions.
Keywords: DEFC, The Starfish Optimization Algorithm, Objective Function

1. INTRODUCTION

In recent years, electrical power systems have undergone significant advancements. Parallel to these developments, the application areas of fuel cells have also expanded. Fuel cells offer several advantages in practical applications, such as low noise, low operating temperatures, high electrical efficiency, high current density, rapid start-up, excellent transient response, and high modularity [1-2]. These advantages have led to an increased focus in the literature on the development and optimization of fuel cells. Fuel cells are electrochemical devices that convert chemical energy into electrical energy using hydrogen gas as the fuel and oxygen/air as the oxidizer, while also producing heat as a byproduct. Among the various types of fuel cells, one of the most commonly used is the DEFC. DEFCs have been applied in numerous fields, including mobile devices, vehicles, transportation systems, industrial applications, and distributed residential energy production systems [3]. Due to their widespread use, the modeling and optimization of DEFCs have garnered significant attention in the literature. Another topic attracting significant attention in the literature is energy storage systems. These systems are developed to address the imbalance between energy production and consumption and to ensure the continuity of energy supply. By facilitating the integration of renewable energy sources, energy storage systems enhance energy efficiency and ensure energy security. Among energy storage technologies, lithium-ion batteries receive the most attention. They stand out as one of the most widely used and effective solutions due to their high energy density, long cycle life, and low self-discharge rate. These superior characteristics make lithium-ion batteries suitable for a wide range of applications, from portable electronic devices to electric vehicles and grid-scale energy storage systems. They play a critical role in accommodating the variable generation profiles of renewable energy sources. Furthermore, the decreasing costs and improving performance of lithium-ion batteries are driving their adoption on a larger scale.

Mathematical modeling and parameter estimation play a crucial role in the design and development of these two highly researched topics. In this study, for DEFCs: The literature provides various methods for modeling DEFCs, which can be broadly categorized into two groups. The first category, known as mechanistic modeling, focuses on describing the electrochemical processes occurring within fuel cells, as well as heat and mass transfer phenomena. The second category, empirical modeling, involves semi-empirical and non-linear equations to predict the effects of various parameters on the current-voltage relationship. Parameter estimation is crucial for optimizing the performance and extending the lifespan of lithium-ion batteries. Accurate parameter estimation enhances the effectiveness of battery management systems by preventing harmful conditions such as overcharging or overdischarging. Moreover, it enables the monitoring of performance metrics, such as energy density and power capacity, ensuring the safe and efficient operation of the battery.

In this study, the suitability of objective functions proposed in previous research was evaluated and compared. Unlike previous studies, the Starfish Optimization Algorithm (SFOA) is employed to optimize the proposed objective function. The results obtained were rigorously compared with a verifiable reference, and the performance of the proposed algorithm was thoroughly tested. The proposed objective function was applied to the same scenarios as previous studies, and the results are presented, demonstrating its effectiveness and potential for improving DEFC parameter estimation and performance. This study not only highlights the importance of accurate modeling and optimization of DEFCs but also introduces a new approach that could pave the way for further advancements in fuel cell technology.

2. MATHEMATICAL MODEL

Direct alcohol fuel cells convert the chemical energy of alcohol into electrical energy, heat, and other by-products. Direct ethanol fuel cells (DEFCs) have been studied in recent years due to ethanol being a non-toxic, renewable fuel that can be easily produced through the fermentation of sugar-containing raw materials. The electrochemical reaction equations of DEFCs are given below [3-4].

$$CH_3CH_2OH + 3H_2O \Leftrightarrow 2CO_2 + 12H^+ + 12e^- \quad (1)$$

$$3O_2 + 12H^+ + 12e^- \Leftrightarrow 6H_2O \quad (2)$$

$$CH_3CH_2OH + 3O_2 \Leftrightarrow 2CO_2 + 3H_2O \quad (3)$$

The mathematical model of DEFCs is given in Equation 4.

$$E_{cell} = E_{0_{cell}} - R_e j - \frac{RT}{F}\left(\frac{1}{\alpha_a} + \frac{1}{\alpha_c}\right) x \left[ln \frac{C_0^{ref}}{j_{0c}(C_0)^{N_0}} - N_0 ln\left(1 - \frac{j}{nFk_0C_0}\right)\right] - \frac{RT}{\alpha_a F} x \left[ln \frac{C_{Met}^{ref}}{j_{0a}(C_{Met})^N} - N ln\left(1 - \frac{j}{nFk_{eff}C_{Met}}\right)\right] \quad (4)$$

Here $E_{0_{cell}}$ is the standard potential for the DMFC overall reaction, which theoretically is given by the Nernst equation, j_{0a}, j_{0c} are the exchange current at reference concentration in the anode and cathode, α_a, α_c are the electronic transfer coefficients at the anode and cathode catalyst surfaces, respectively. C_{Met} is the methanol concentration, C_{Met}^{ref} is the reference methanol concentration, N and N_0 are the orders of reactions, k_0, k_{eff} are the mass transport coefficients for the cathode and anode, respectively [4]

Equivalent circuit models are a method frequently used in battery management systems to monitor and control lithium-ion batteries. For this purpose, the equations of the Thevenin model of lithium-ion batteries are given below.

$$V_t = V_{OC} - V_{Ri} - V_{RC} \quad (5)$$

$$V_{Ri} = I \; x \; R_i \quad (6)$$

$$\frac{dV_{RC}}{dt} = \frac{I}{C} - \frac{V_{RC}}{V_{RC}C} \quad (7)$$

Here V_t represents the terminal voltage, V_{OC} denotes the open-circuit voltage, V_{Ri} refers to the voltage drop across the internal resistance, and V_{RC} indicates the voltage drop across the capacitor. Additionally, I represents the battery current, and R_i denotes the internal resistance. The equation related to the state of charge (SOC) is given in Equation 8.

$$SOC(t) = SOC(0) - \frac{1}{C_n}\int_0^t I(\mathrm{r})d\mathrm{r} \quad (8)$$

Here $SOC(0)$ represents the initial state of charge, C_n denotes the nominal capacity, and $I(\mathrm{r})$ represents the current function. The open-circuit voltage is provided in Equation 9.

$$V_{OC} = f(SOC) \quad (9)$$

The expression for the effect of temperature is given in Equation 10.

$$V_t = V_t + k_T(T - T_{reff}) \quad (10)$$

Here k_T represents the temperature coefficient, T denotes the instantaneous temperature, and T_{reff} indicates the reference temperature. As a result, the mathematical model calculates the parameters V_r, R_i, C, R_{CH}, the time constant (r) and temperature-related variables.

3. THE STARFISH OPTIMIZATION ALGORITHM

Swarm-based algorithms are developed by drawing inspiration from the behavior of living organisms in nature. One such algorithm is the Starfish Optimization Algorithm (SOA). SOA is a novel bio-inspired metaheuristic method designed to solve optimization problems by simulating the behaviors of starfish, including exploration, foraging, and regeneration. It consists of two main phases: exploration and exploitation. The exploration phase mimics the exploratory behavior of starfish through a hybrid search pattern that combines five-dimensional and one-dimensional search strategies to enhance computational efficiency and search capacity. The exploitation phase simulates the foraging and regeneration behaviors of starfish using a bidirectional search strategy and specialized movements to ensure convergence during exploitation.

During the initialization phase of SFOA, the positions of the starfish are randomly generated within the boundaries of the design variables, which can be represented as a matrix. This process is provided in Equation 11 [5].

$$X = \begin{bmatrix} X_{11}X_{12} \dots X_{1D} \\ X_{21}X_{22} \dots X_{2D} \\ . \; . \; \dots \; . \\ . \; . \; \dots \; . \\ X_{N1}X_{N2} \dots X_{ND} \end{bmatrix}_{NxD} \quad (11)$$

To model the exploratory behavior of starfish, a new search pattern combining a five-dimensional search pattern for D>5 and a one-dimensional search pattern for D≤5 has been proposed. The dimensional threshold is determined based on the five arms (or eyes) of the starfish. The mathematical expressions are provided in Equations 12 and 13 [5].

$$Y_{i,p}^T = X_{i,p}^T + a_1\left(X_{best,p}^T - X_{i,p}^T\right) cos\emptyset, r \leq 0.5 \quad (12)$$

$$Y_{i,p}^{T} = X_{i,p}^{T} + a_1\left(X_{best,p}^{T} - X_{i,p}^{T}\right) sin\emptyset, r \geq 0.5 \quad (13)$$

4. RESULTS AND DISCUSSIONS

In this study, the model parameters are optimized using SOA to match the actual DEFC outputs. To achieve this, the parameters E_0, b, R_e, C_1 and C_2 must be determined to calculate the PEMFC outputs. Once these parameters are identified, the output voltage can be predicted for a given input current. Several objective functions, also known as cost functions, are used to determine the DEFC parameters. All of these cost functions are defined based on voltage. In the optimization processes using these cost functions, errors in the high-voltage regions are given priority. Specifically, the activation voltage drop region holds the highest priority, the ohmic voltage drop region is given lower priority, and the concentration voltage drop region is considered non-prioritized. Considering the power curve of fuel cells, it is more appropriate for these regions to have opposite priorities. This approach aligns with real operating conditions. In this study, the current literature uses voltage- and power-based cost functions to determine DEFC parameters [6]. The objective function used for this purpose is provided below.

$$J = \sum_{i=1}^{N}\left(\left[V_{exp.} - V_{est.}\right]^2 + \left|P_{exp.} - P_{est.}\right|\right) \quad (15)$$

In this study, only data that can be definitively validated were used. For this purpose, the experimental data employed in the works of Blanco-Cocom et al. have been provided numerically [3]. The results of these studies were examined as reference works for objective comparison. The unknown parameters of the DEFCs examined in this study, determined as a result of SOA, are presented in Table 1.

Table 1. Values of unknown parameters of the DEFC model

E_0	b_i	R_e	C_1	C_2
0.136038	0.028099	0.72525	0.285649	6.868614

Experimental data, literature study results and suggested objective function results are given in Table 2. As a result of the calculations, the proposed objective function values and experimental study data are given in Fig. 1.

Table 2. PEMFC empirical and calculation results

Empirical Results		(Blanco-Cocom et al. 2023)		(Celikdemir 2024)	
j	V	V	Error	V	Error
0.0327	0.0024	0.6756	0.6365	0.6739	0.4289
0.0276	0.0391	0.6975	0.6218	0.6883	0.4036
0.0240	0.0757	0.7202	0.6079	0.6998	0.3745
0.0211	0.1123	0.7432	0.5943	0.7102	0.3448
0.0185	0.1489	0.7667	0.5811	0.7206	0.3163
0.0162	0.1856	0.7914	0.5692	0.7308	0.2884
0.0142	0.2222	0.8179	0.5591	0.7408	0.2616
0.0123	0.2588	0.8457	0.5503	0.7511	0.2363
0.0105	0.2954	0.8750	0.5429	0.7627	0.2134
0.0088	0.3320	0.9064	0.5377	0.7753	0.1926
0.0073	0.3687	0.9412	0.5359	0.7884	0.1732
0.0060	0.4053	0.9789	0.5370	0.8030	0.1558
0.0047	0.4419	1.0201	0.5416	0.8195	0.1408
0.0035	0.4785	1.0687	0.5535	0.8403	0.1296
0.0024	0.5151	1.1293	0.5775	0.8652	0.1217
0.0015	0.5518	1.2157	0.6273	0.8967	0.1185
0.0007	0.5884	1.3893	0.7643	0.9440	0.1262
0.0001	0.6250	0.6589	0.6565	1.0935	0.2195
$\left[V_{exp.} - V_{est.}\right]^2$			10.5944		5.6469
$\left[V_{exp.} - V_{est.}\right]^2 + \left\|P_{exp.} - P_{est.}\right\|$			6.1658		4.2457

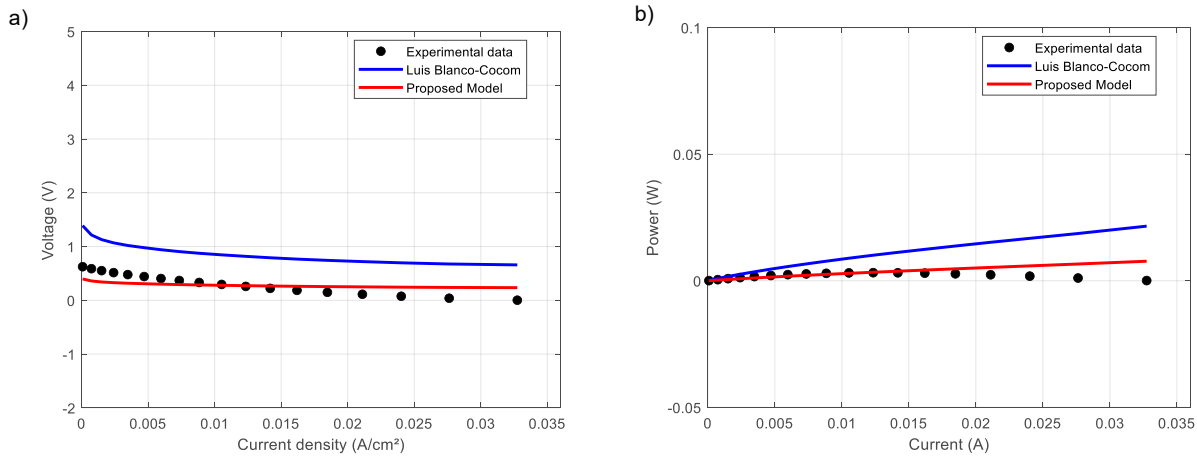

Fig. 1. Comparative results

As a result; the error value calculated according to the SAE model used in the literature is 5.64. This shows the superiority of the algorithm used. However, according to the proposed equation model, the error value is 4.24. This shows the superiority of the proposed equation model. In this study, only data that can be definitively validated were used. For this purpose, the experimental data employed in the works of Edoardo C. et al. have been provided numerically [7]. The results of these studies were examined as reference works for objective comparison. The unknown parameters of the lithium-ion batteries examined in this study, determined as a result of SOA, are presented in Table 1.

Table 3. Values of unknown parameters of the lithium-ion batteries

V_r	R_i	C	R_{CH}	r	T
5.793845	0.081007	-2.32256	-0.04777	3.891309	0.132567

The graph showing the actual voltage values and estimated voltage values of the lithium battery model is given in Fig. 2.

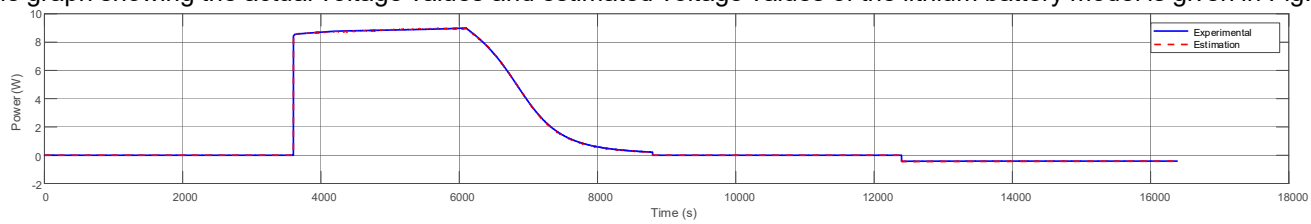

Fig. 2. Comparative results

Here, the data of the experimental study are shown in blue and the estimated voltage values are shown in red. 16384 current-voltage data were used in the experimental study. As a result, the mean absolute error sum was calculated as 0.0469 using the voltage and power based objective function.

5. CONCLUSIONS

In this study, the parameters of the DEFC and lithium battery hybrid model were determined. For this purpose, the Starfish Optimization Algorithm was applied for the first time as a novel algorithm for estimating the unknown parameters of DEFC. This demonstrated that predictions were made with high convergence, as observed in the literature. Unlike voltage-based objective functions recommended by most researchers, a hybrid objective function was used. This resulted in an absolute error sum of 4.24 for the DEFC model. Additionally, the average absolute error sum for the lithium battery model was calculated as 0.0469. This indicates that predictions with high convergence were achieved using the hybrid objective function, as demonstrated by the literature. Furthermore, the use of the proposed hybrid objective function led to a reduction in the total power error for PEMFCs, thereby ensuring more efficient operation of the fuel cells. The use of experimental data in such studies is crucial for objective evaluation.

REFERENCES

[1] Yang, Shipin, Ryad Chellali, Xiaohua Lu, Lijuan Li, and Cuimei Bo. 2016. “Modeling and Optimization for Proton Exchange Membrane Fuel Cell Stack Using Aging and Challenging P Systems Based Optimization Algorithm.” *Energy* 109 (August): 569–77. https://doi.org/10.1016/j.energy.2016.04.093.

[2] Ijaodola, O.S., Zaki El- Hassan, E. Ogungbemi, F.N. Khatib, Tabbi Wilberforce, James Thompson, and A.G. Olabi. 2019. “Energy Efficiency Improvements by Investigating the Water Flooding Management on Proton Exchange Membrane Fuel Cell (PEMFC).” *Energy* 179 (July): 246–67. https://doi.org/10.1016/j.energy.2019.04.074.

[3] Blanco-Cocom, Luis, Salvador Botello-Rionda, L.C. Ordoñez, and S. Ivvan Valdez. 2023. "Parameter Estimation for Empirical and Semi-Empirical Models in a Direct Ethanol Fuel Cell." *Energy Reports* 10 (November): 451–59. https://doi.org/10.1016/j.egyr.2023.07.002.
[4] Scott, K., C. Jackson, and P. Argyropoulos. 2006. "A Semi Empirical Model of the Direct Methanol Fuel Cell. Part II. Parametric Analysis." *Journal of Power Sources* 161 (2): 885–92. https://doi.org/10.1016/j.jpowsour.2006.04.147.
[5] Zhong, Changting, Gang Li, Zeng Meng, Haijiang Li, Ali Riza Yildiz, and Seyedali Mirjalili. 2025. "Starfish Optimization Algorithm (SFOA): A Bio-Inspired Metaheuristic Algorithm for Global Optimization Compared with 100 Optimizers." *Neural Computing and Applications* 37 (5): 3641–83. https://doi.org/10.1007/s00521-024-10694-1.
[6] Celikdemir, Soner. 2024. "A New Voltage-Power Based Approach for Identifying the Optimal Parameters of PEM Fuel Cells." International Journal of Hydrogen Energy 75 (July): 592–603. https://doi.org/10.1016/j.ijhydene.2024.04.020.
[7] Catenaro, Edoardo, and Simona Onori. 2021. "Experimental Data of Lithium-Ion Batteries under Galvanostatic Discharge Tests at Different Rates and Temperatures of Operation." *Data in Brief* 35 (April): 106894. https://doi.org/10.1016/j.dib.2021.106894.

AN INNOVATIVE APPROACH TO DETERMINE EFFECTIVE VARIABLES ON FAULT DETECTION OF PEMFCS

[1]Soner ÇELİKDEMİR, [2*]Meltem YAVUZ ÇELİKDEMİR
[1] Bitlis Eren University, Adilcevaz Vocational School, Electric and Energy, Bitlis, 13000, Türkiye
[2] Bitlis Eren University, Tatvan Vocational School, Electric and Energy, Bitlis, 13000, Türkiye

E-mail: meltem.ycd@gmail.com

ABSTRACT
The primary objective of this study is to identify the key variables influencing voltage prediction in Polymer Electrolyte Membrane Fuel Cells (PEMFC). For this purpose, 22 variables from an 80 W PEMFC dataset containing 33,899 recorded entries were analyzed using 25 different regression models through machine learning techniques. Among these models, the Bagged Trees method was selected as the most suitable model due to its lowest RMSE value. Using this model, the five most influential variables (voltage, current, temperature, time, cell temperature) were identified. These variables were then re-applied as input features in the Bagged Trees model to perform voltage prediction, achieving a minimum RMSE value of 4.131×10^{-3}. Another aim of this study was to investigate the impact of these variables on voltage. For this purpose, 4,000 external test data points were used, where four variables were kept constant while the value of the remaining variable was incrementally increased to observe its effect on voltage. The results revealed that an increase in power, temperature (3), and cell temperature variables led to an increase in voltage, whereas an increase in current and time variables caused a decrease in voltage. These findings provide significant insights into optimizing PEMFC performance and understanding the system dynamics.
Keywords: PEMFC, Voltage Estimation, Bagged Trees, Regression, Identified Variables

1. INTRODUCTION

In recent years, the use of fuel cells has become increasingly widespread due to their numerous advantages, such as high energy efficiency, fast startup, low operating temperature, and minimal noise. These features have made them a focus of research in the literature [1]. The importance of parameter tuning for the design and performance improvement of Polymer Electrolyte Membrane Fuel Cell (PEMFC) models has been emphasized to expand their use in clean energy applications [2]. For instance, variants of the Grey Wolf Optimization (GWO) algorithm have been applied to evaluate unknown parameters of PEMFCs [3]. However, one of the disadvantages of PEMFCs, which are alternative energy sources that generate electricity without causing adverse effects, is their short lifespan and the non-linear relationship between load current and voltage. To address this, a novel method based on a semi-empirical model using a transient search optimization algorithm has been proposed to predict PEMFC voltage under varying ambient conditions [4].
Operational faults such as water flooding and membrane drying during PEMFC operation can lead to performance degradation and reduced lifespan. Studies have been conducted to examine various fault indicators for PEMFC fault diagnosis, including stack voltage, pressure drops, membrane resistance, flow rate, stack temperature, oxygen excess ratio, compressor speed, hydrogen mass, and oxygen mass [5].
In this study, regression learning algorithm models were used to determine the importance ranking of parameters affecting the voltage value, which is a critical criterion for PEMFC fault diagnosis. The algorithms used gaussian process, support vector machines, neural networks, decision trees, linear regression, ensemble methods, and GLM. The dataset used in this study contains 22 variables and 33,899 recorded entries from an 80 W PEMFC. Of these, 33,799 entries were used for model training, while 4,000 entries were reserved for external testing. Additionally, internal testing was performed during model training, and the performance metrics were compared.

2. SYSTEM DESCRIPTION AND PROCEDURE

This study utilized experimental data from an 80 W PEMFC. The experimental data included 22 different PEMFC variables, including voltage information. A voltage drop of 5% in PEMFC output voltage is considered water flooding [6]. To observe PEMFC voltage drops, the feasibility of voltage prediction was first evaluated. For this purpose, 25 different regression models were trained. Among these models, the Bagged Trees model was identified as the most suitable based on the RMSE performance metric. The five variables that caused the most significant changes in voltage were determined through testing on this model. The variable importance ranking and graph for the Bagged Trees model are shown in Fig. 1. These results help identify which variables the model assigns more "importance" to and which variables contribute less to the model's accuracy. The importance ranking of the identified variables is as follows:

- Power: 3.9×10^{-5}
  This is the most critical variable contributing to the model's prediction performance.
- Current: 1.9×10^{-5}
  The second most important variable, significantly contributing to the model's accuracy.
- Temperature (3) and Time: 2×10^{-6}
  These two variables contribute minimally to the model's accuracy but have a non-zero importance level.

- Cell temperature: 1×10^{-6}
  This variable has a very low contribution to the model's accuracy.
- Other variables (e.g., hydrogen inlet temperature, air supply pressure, etc.): 0×10^{-6}
  These variables do not contribute to the model's accuracy.

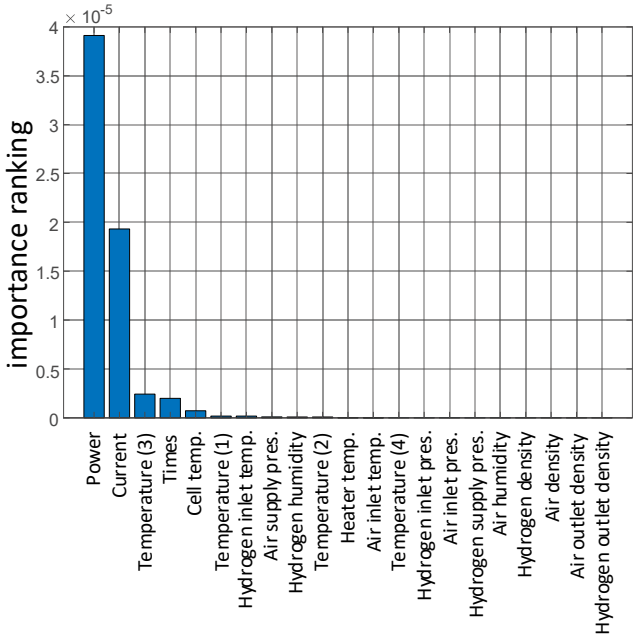

Fig. 1. Importance ranking of variables

Fig. 1 illustrates the variable importance ranking. The variables 'power' and 'current' have significantly higher importance levels compared to all other variables. This indicates that these two variables play a dominant role in the model's prediction performance. Other variables have importance levels close to zero, indicating that they do not contribute meaningfully to the model's prediction performance. Consequently, the critical variables power, current, time, temperature (3) and cell temperature are essential for the model's prediction performance and are observed to define the system's fundamental dynamics. Therefore, by focusing on these variables and excluding variables with zero importance (e.g., hydrogen inlet temperature, air supply pressure etc.), a simpler and faster model was obtained. The Bagged Trees model was retrained with the new variable set, achieving a high-performance voltage prediction with an RMSE value of 5.7368×10^{-3}. The model's accuracy, based on this variable importance ranking, explains the system's fundamental dynamics.

3. MODEL EVALUATION

Supervised machine learning algorithm models were trained on the available data. Supervised learning teaches the algorithm to memorize the expected outcomes. In the dataset, the voltage variable was evaluated as the output. The supervised machine learning algorithm models used in this study are shown in Fig. 2.

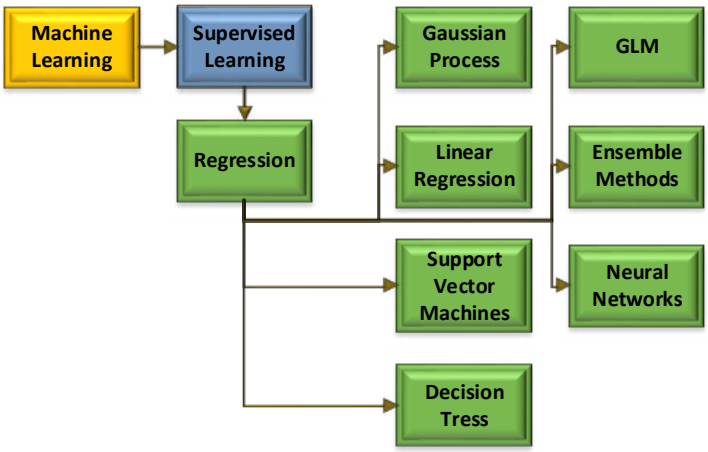

Fig. 2. Regression algorithm models

The dataset, containing 22 variables and 33,899 recorded entries, was trained using 25 different regression learning models, and the results were compared. Ten percent of the dataset was reserved for testing. The RMSE error values and training times for different algorithms are shown in Fig. 3.

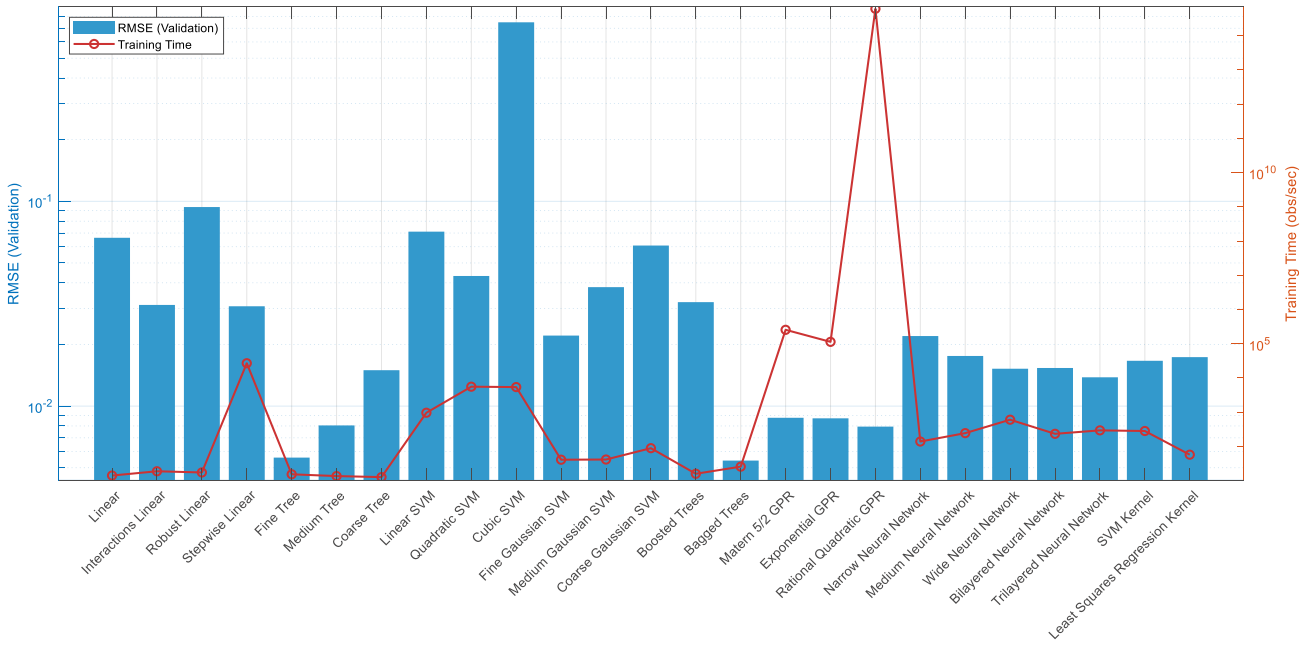

Fig. 3. RMSE error values and training times for 25 algorithm models

According to the results, the Bagged Trees regression learning model had the lowest RMSE value. The RMSE validation value for this model was 5.421×10^{-3}, with a training time of 25.59759 seconds. To improve the best-performing Bagged Trees model, the 22 input variables were ranked by importance, and five key variables were identified. When the model was trained with these five variables, the RMSE validation value was 4.131×10^{-3}, and the training time was 5.342 seconds. The voltage prediction and error graph for the 4,000 external test data points are shown in Fig. 4-a. Additionally, the graph in Fig. 4-b shows the results of the analysis conducted to determine the effects of the identified variables on voltage.

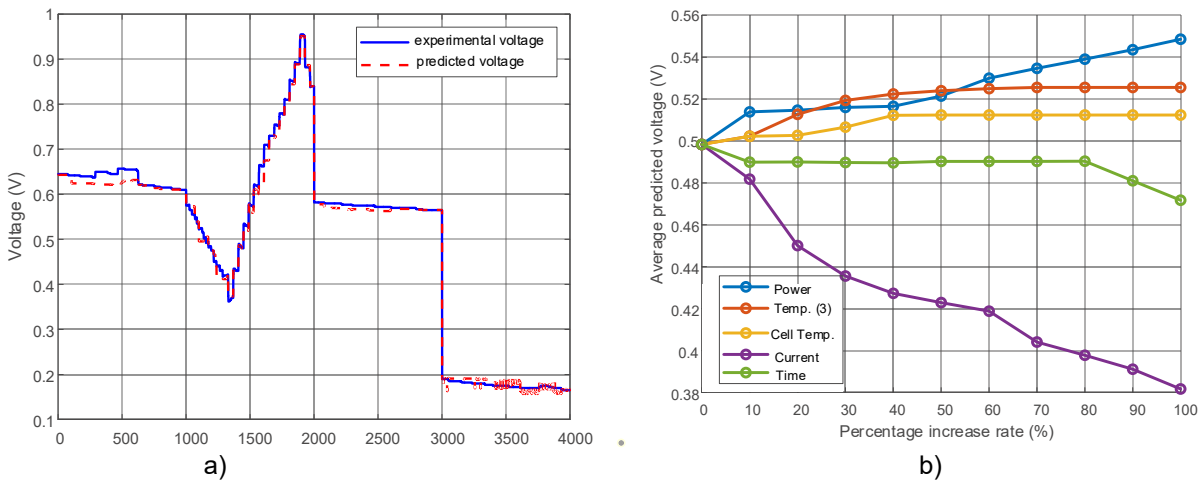

Fig. 4. a) Voltage prediction b) Identified variables

According to the results, based on the graph showing the 10% changes in the variables, the parameters affecting the voltage are ranked in the following order: current, power, temperature (3), cell temperature, and time information. Since a 5% change in voltage is considered a fault condition, it is anticipated that the importance ranking of these variables will contribute to the literature in this regard.

4. CONCLUSIONS

In this study, 22 variables from an 80 W PEMFC dataset containing 33,899 recorded entries were trained using regression models. To improve the model with the lowest RMSE value, variable importance ranking was performed. A new dataset with five variables was created, and the model was retrained. The results showed better performance metrics. The variables affecting PEMFC voltage were supported by both quantitative and qualitative graphical results. The proposed algorithm's performance was tested, and the Bagged Trees regression model achieved the lowest RMSE validation value of 4.131×10^{-3} and an RMSE test value of 5.7368×10^{-3}. The training time for this model was 5.342 seconds. Changes in the values of the variables were shown to affect PEMFC voltage, which is critical for fault evaluation and ensuring the continuous and efficient operation of fuel cells.

REFERENCES

[1] Razi, Faran, and Ibrahim Dincer. 2022. "Challenges, Opportunities and Future Directions in Hydrogen Sector Development in Canada." *International Journal of Hydrogen Energy* 47 (15): 9083–9102. https://doi.org/10.1016/j.ijhydene.2022.01.014.

[2] Jangir, Pradeep, Absalom E. Ezugwu, Arpita, Sunilkumar P. Agrawal, Sundaram B. Pandya, Anil Parmar, G. Gulothungan, and Laith Abualigah. 2024. "Precision Parameter Estimation in Proton Exchange Membrane Fuel Cells Using Depth Information Enhanced Differential Evolution." Scientific Reports 14 (1): 29591. https://doi.org/10.1038/s41598-024-81160-0.

[3] Diab, Ahmed A. Zaki, Hussien I. Abdul-Ghaffar, Abdelsalam A. Ahmed, and Husam A. Ramadan. 2022. "An Effective Model Parameter Estimation of PEMFCs Using GWO Algorithm and Its Variants." *IET Renewable Power Generation* 16 (7): 1380–1400. https://doi.org/10.1049/rpg2.12359.

[4] Abbou, Amine, and Abdennebi El Hassnaoui. 2022. "A Novel Approach for Predicting PEMFC in Varying Ambient Conditions by Using a Transient Search Optimization Algorithm Based on a Semi-Empirical Model." *AIMS Energy* 10 (2): 254–72. https://doi.org/10.3934/energy.2022014.

[5] Sani, Mukhtar, Maxime Piffard, and Vincent Heiries. 2023. "Fault Detection for PEM Fuel Cells via Analytical Redundancy: A Critical Review and Prospects." Energies 16 (14): 5446. https://doi.org/10.3390/en16145446

[6] Mao, Lei, Lisa Jackson, Weiguo Huang, Zhinong Li, and Ben Davies. 2020. "Polymer Electrolyte Membrane Fuel Cell Fault Diagnosis and Sensor Abnormality Identification Using Sensor Selection Method." Journal of Power Sources 447 (January): 227394. https://doi.org/10.1016/j.jpowsour.2019.227394.

.

Sc- AND Ti-FUNCTIONALIZED DOPED SnC NANOSHEETS FOR HYDROGEN STORAGE

[1]*Ángel R. Montoya-García*, [1*]*Dinorah Romero*, [1]*Lucia G. Arellano*, [2]*María I. Iturrios*, [3]*Luis A. Pérez,* [1]*Miguel Cruz-Irisson*
[1] Instituto Politécnico Nacional, ESIME Culhuacan, Av. Santa Ana 1000, Ciudad de México, 04440, México
[2]CECyT 8 – Narciso Bassols, Instituto Politécnico Nacional, Av. De las Granjas 618, Ciudad de México, 02020, México
[3] Instituto de Física, Universidad Nacional Autónoma de México, CP 04510, Ciudad de México, México
*Corresponding author e-mail: dromerop2300@alumno.ipn.mx

ABSTRACT
A theoretical investigation, based on density-functional calculations, was carried out to evaluate the feasibility of storing hydrogen molecules in doped and functionalized two-dimensional tin carbide (2D-SnC) nanostructures. The monolayer with substitutional doping X (X = B, Al Ga) is more stable when the X atom replaces the Sn one. The doped monolayer is also functionalized with transition metal atoms such as Sc, Ti, Ni, Pd, and Pt, where six adsorption sites for the metal atoms were tested , finding that these metal atoms have adsorption energies between 3.60 eV and 6.9 eV. The formation energy results indicate that the structures functionalized with Ni, Pd, and Pt atoms are unstable, whereas those decorated with Sc, and Ti, are stable and also they can adsorb hydrogen molecules. In particular, boron-doped 2D-SnC decorated with Sc and Ti atoms may be suitable as solid-state hydrogen storage materials.

Keywords: Hydrogen storage, DFT, Energy, 2D materials, doping – functionalization.

1. INTRODUCTION

Hydrogen is a sustainable energy source capable of replacing fossil fuels and reducing carbon dioxide (CO_2) emissions, thereby mitigating global warming [1]. It can be used as a fuel in nearly all applications that currently rely on fossil fuels. When produced from renewable resources, hydrogen offers immediate advantages over conventional fuels [2]. Despite its potential, hydrogen storage remains a challenge. Nanostructured materials, with their unique surface properties, are promising candidates for hydrogen storage due to their ability to adsorb hydrogen on their surfaces, form inter- and intragrain boundaries, and absorb significant amounts of hydrogen [3]. Additionally, they enable the development of lightweight hydrogen storage systems with enhanced capacity. Considerable research has focused on utilizing 2D materials for hydrogen storage, as they exhibit exceptionally large surface areas, high carrier mobility, and stability. Several effective 2D materials have been identified, including transition metal dichalcogenides (TMDs), lithium-modified $B_3C_2P_3$ monolayers, carbide monolayers, MXenes, and 2D boron. Doping plays a crucial role in modifying the electronic structure, introducing defects, and enhancing hydrogen adsorption and retention, thereby increasing storage capacity [4,5]. Furthermore, the adsorption of transition metals on 2D materials can significantly improve their ability to capture and release hydrogen. This study explores the impact of transition metal functionalization on doped 2D-SnC (with B, Al, and Ga) for hydrogen storage. To date, no studies have investigated the functionalization of doped 2D-SnC with transition metals such as Sc and Ti for this purpose. Here, we assess the feasibility of decorating doped 2D-SnC with transition metals (Sc, Ti, Ni, Pd, Pt) based on stability criteria, finding that only Sc and Ti form stable configurations. Additionally, we analyze the hydrogen adsorption properties of TM_XSnC systems (TM = Sc, Ti; X = B, Al, Ga) and their storage capacities. The results reveal that Sc- and Ti-decorated 2D-SnC can store up to three and four hydrogen molecules per adsorption site, respectively.

2. METHODOLOGY

In this study, the SIESTA code [6] based on Density Functional Theory (DFT) was used and a 50-atom SnC supercell was considered, where a dopant atom substitutes an atom of the former pristine lattice and a metal atom was added. To optimize the structures of the SnC-based materials and to address their energetic and electronic properties, the Perdew–Burke–Ernzerhof (PBE) exchange-correlation functional [7] was employed in conjuction with norm-conserving Troullier-Martins pseudopotentials and doubly-ζ polarized basis sets. The van der Waals interactions were accounted for through the semi-empirical Grimme DFT-D2 method [8], and the cutoff energy that defines the real-space grid for numerical integration was set at 320 Ry. Also, the Monkhorst-Pack scheme [9] was used with a 5×5×1 k-point grid to sample the Brillouin zone for geometric optimization and a 24×24×1 k-point grid for electronic calculations. After geometric optimization, it was obtained that the primitive lattice constant of the honeycomb SnC nanosheet is 3.64 Å with a C-Sn distance β=2.1 Å, and the calculations indicate that the distance between the dopant atom and the neighboring C is lower than the former Sn-C distance, as illustrated in **Fig. 1**. Also, the calculations indicate that two-dimensional SnC is an indirect bandgap semiconductor with a GGA bandgap of 0.81 eV [10], and by doping with B, Al and Ga, the SnC nanosheet becomes a p-type semiconductor. The binding energy (E_b) of a transition metal atom bound to the X-doped SnC nanosheet (X= B, Al, and Ga) is given by:

$$E_b = E_{X_2DSnC} + E_{TM} - E_{X_2DSnC+TM} \quad (1)$$

where E_{X_2DSnC} is the energy of SnC doped with B, Al, or Ga; E_{TM} is the energy of an isolated transition metal atom (TM = Sc, Ti, Ni, Pd, Pt); and $E_{X_2DSnC+TM}$ is the total energy of the optimized system of 2DSnC doped and functionalized with transition metal atoms. These binding energies were compared with the theoretical cohesion energies of metals (E_{coh}) to

determine whether metals can bind better to X_2DSnC instead of forming clusters. The cohesion energy of the metals was obtained from:

$$E_{coh} = \frac{n_{Bulk}E_{TM} - E_{Bulk}}{n_{Bulk}} \quad (2)$$

where n_{Bulk} is the number of metal atoms in the bulk unit cell, and E_{Bulk} is the energy of the bulk unit cell. Likewise, the formation energy (E_f) of the system was evaluated to determine the stability of the X_2DSnC+TM systems (X=B, Al, Ga; MT= Sc, Ti, Ni, Pd, Pt), and it is given by [11]

$$E_f = E_{X_2DSnC+TM} - (E_{X_2DSnC} + \mu_{TM}) \quad (3)$$

Here, $E_{X_2DSnC+TM}$ represents the energy of the TM-functionalized X-doped 2DSnC supercell, E_{X_2DSnC} is the energy of the doped 2DSnC supercell, and μ_{TM} is the chemical potential of the transition metal. A more negative the formation energy indicates a more stable system.
The interactions of hydrogen molecules on doped and functionalized SnC monolayers were analyzed through the adsorption energies of the H_2 molecules (E_{ads}) [10] given by:

$$E_{ads} = \frac{(E_{X_2DSnC+TM} + n\mu_{H_2}) - E_{MT_XSnC+H_2}}{n} \quad (4)$$

Here μ_{H_2} and $E_{MT_XSnC+H_2}$ are the chemical potential of the hydrogen molecule and the total energy of the doped-functionalized 2DSnC supercell with *n* hydrogen molecules adsorbed, respectively.

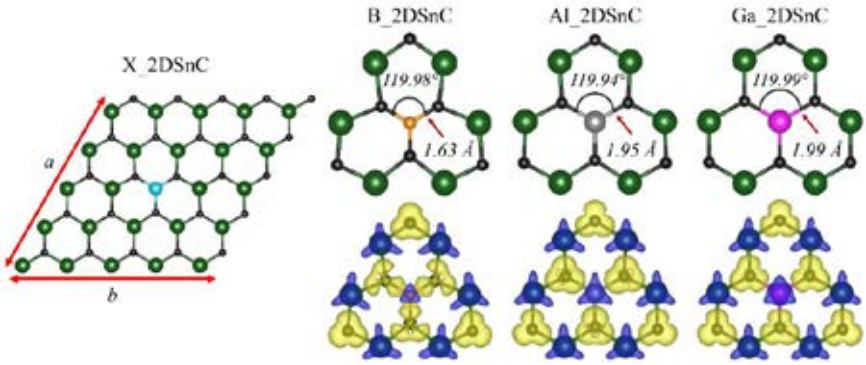

Fig. 1. Geometrical structure of a 50-atom SnC supercell with a dopant atom (left panel). Optimized structures of doped 2DSnC and their respective charge densities (right panel). Orange, gray, magenta, black and green spheres symbolize B, Al, Ga, C and Sn atoms, respectively. The accumulation (depletion) of electron charge density is represented in yellow (blue).

3. RESULTS AND DISCUSSION

The analysis of the results is divided in two parts. The first part analyzes the results regarding the functionalization of doped 2DSnC with transition metal atoms (Sc, Ti, Ni, Pd, and Pt), while in the second part, their capacities to store molecular hydrogen are discussed.

3.1. TRANSITION ADSORPTION ON DOPED 2DSnC

After optimizing the geometries of the doped nanosheets, they are decorated with transition metal atoms in six different sites, above a C atom, above a Sn atom, above the dopant X atom (X=B,Al,Ga), at the Sn-C bond, at the dopant-C bond and at the middle of a lattice hexagon. After relaxing each decorated doped monolayer, the configuration with the highest binding energy (E_b) between each metal atom and the doped nanosheet was chosen. The results indicate that the 5 metal atoms have a large binding energy, which makes them difficult to be removed from the system, being Sc, Ti and Pt the metal atoms with a more strong bond. The cohesion energy (E_{coh}) was calculated to evaluate the tendency of the added metal atoms to form clusters rather than maintaining individual bonds with the nanosheet. To ensure that the metals remain uniformly dispersed and bonded to the nanosheet, it is essential that the cohesion energy be lower than the binding energy. This condition prevents the aggregation of metal atoms into clusters and promotes stable, isolated metal adsorption on the nanosheet surface. Another criterion that determine the stability of these metal-decorated monolayers is their formation energy (E_f) given by Eq. 3. The more viable metal adatoms are Sc and Ti (see **Table 1**).

Table 1. Binding energy (E_b) of the metal atom in doped 2DSnC, formation energy of the X_2DSnC+TM system, calculated cohesion energy (E_{coh}) and distance from the adatom to the nanosheet ($d_{X_2DSnC-MT}$).

Doping	Transition Metal	E_b (eV)	E_f (eV)	E_{coh} (eV)	$d_{X_2DSnC-MT}$ (Å)
	Sc	6.79	-2.65	4.13	2.18
	Ti	6.62	-2.04	4.57	2.07
B	Ni	4.59	0.41	5.01	2.70
	Pd	3.96	0.11	4.07	2.77
	Pt	5.23	0.58	5.81	2.72
	Sc	6.88	-2.74	4.13	2.18
	Ti	6.69	-2.11	4.57	2.08
Al	Ni	4.61	0.39	5.01	2.01
	Pd	3.59	0.48	4.07	2.08
	Pt	5.10	0.71	5.81	2.05
	Sc	6.90	-2.76	4.13	2.18
	Ti	6.71	-2.13	4.57	2.07
Ga	Ni	4.66	0.34	5.01	2.01
	Pd	3.61	0.46	4.07	2.07
	Pt	5.34	0.47	5.81	2.10

3.1. HYDROGEN ADSORPTION ON DOPED AND DECORATED 2DSnC

To investigate the adsorption of molecular hydrogen on the doped and functionalized 2DSnC, hydrogen molecules were systematically located, one by one, close to the metal adatom and the system was further relaxed until no more hydrogen molecules were adsorbed. The average adsorption distance between the adsorbed hydrogen molecules and the metal adatom and the charge excesses on the hydrogen molecules were also calculated (see **Table 2**).

As shown in **Fig. 2** and **Table 2**, a maximum of three H_2 molecules per adsorption site can be adsorbed by the 2DSnC doped with Al and Ga and functionalized with Sc Sc and Ti, while the B-doped 2DSnC decorated with Ti can adsorb four hydrogen molecules per adsorption site. Also, this system has an average adsorption energy of 0.26eV, which is suitable for reversible hydrogen storage.

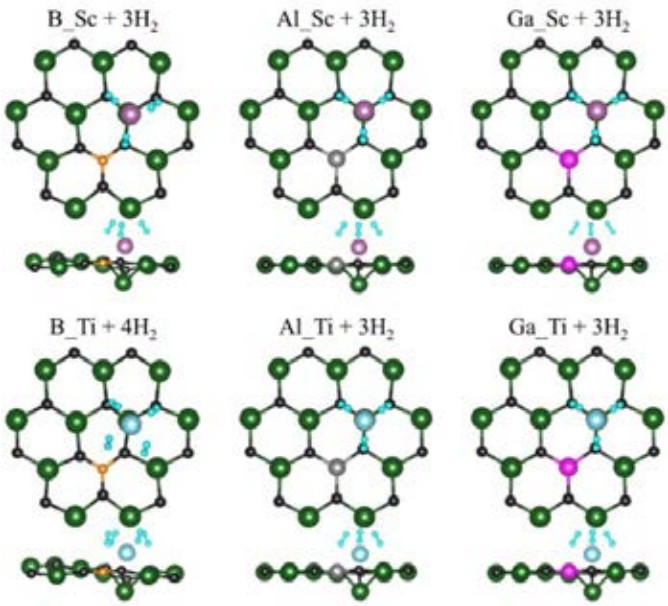

Fig. 2. Optimized structures of X-doped 2DSnC decorated with TM atoms (X=B, Al, Ga; TM=Sc, Ti) with the highest amount of H_2 molecules adsorbed. Cyan, Light Blue and Purple spheres represent H, Ti and Sc atoms respectively.

Table 2. Maximum amount of adsorbed hydrogen molecules (n_{H_2}), average adsorption energy (E_{ads}) and Hirshfeld charge excess on hydrogen molecules (δQ_H)

Doping	Transition metal	n_{H_2}	E_{ads} (eV)	$d_{MT_BSnC-H_2}$ (Å)	δQ_H (|e|)
B	Sc	3	0.34	2.32	0.067
	Ti	4	0.26	2.05	0.017
Al	Sc	3	0.41	2.14	0.070
	Ti	3	0.31	1.98	0.020
Ga	Sc	3	0.41	2.13	0.061
	Ti	3	0.31	1.98	0.012

4. CONCLUSIONS

DFT calculations were performed to study hydrogen storage in transition-metal-decorated doped SnC nanosheets. Sc and Ti, the lightest metals, have a very strong bond with 2DSnC doped with B, Al and Ga atoms. This confirms that Sc and Ti adatoms do not tend to form clusters on the doped nanosheet because their binding energies are higher than their cohesion ones. Likewise, formation energies indicate that 2DSnC decorated with Ni, Pd, and Pt atoms are not as stable as those monolayers decorated with Sc and Ti. Adsorption energy results indicate that hydrogen molecules are physisorbed on Sc- and Ti-functionalized doped 2DSnC. In particular, doped nanosheets decorated with Ti atoms show adsorption energies suitable for reversible hydrogen storage and also have the largest hydrogen storage capacity among the studied which are estimated to reach a hydrogen-storage capacity of 5.5 wt%, as required by the US Department of Energy (DOE), when the coverage of Ti reaches 68%. These results suggest that B-, Al-, and Ga-doped SnC nanosheets decorated with Ti are potential solid-state materials for hydrogen storage.

ACKNOWLEDGEMENTS

This work was partially funded by the multidisciplinary projects IPN-SIP 2023-22274 and -2279, and UNAM-PAPIIT IN102923. Computations were performed using the Miztli supercomputer of DGTIC-UNAM (Projects LANCAD-UNAM-DGTIC-180 and -381). A.R.M.G. and K.J.C.G. acknowledge support from SECIHTI and BEIFI-IPN.

REFERENCES

1. Sazali N. 2020. Emerging technologies by hydrogen: A review. International Journal of Hydrogen Energy 45: 18753-18771.
2. Abdin Z, Zafaranloo A, Rafiee A, Mérida W, Lipiński W and Khalilpour KR. 2020. Hydrogen as an energy vector. Renewable and sustainable energy reviews 120: 109620.
3. Abe JO, Popoola API, Ajenifuja E and Popoola OM. 2019. Hydrogen energy, economy and storage: Review and recommendation. International Journal of Hydrogen Energy 44: 15072-15086.
4. Chakraborty B, Ray P, Garg N and Banerjee S. 2021. High capacity reversible hydrogen storage in titanium doped 2D carbon allotrope Ψ-graphene: Density Functional Theory investigations. International Journal of Hydrogen Energy 46: 4154-4167.
5. Gupta N, Kumari A, Bhardwaj A and Sharma A. 2024. Doped Nano-Materials for Storage of Hydrogen. Green Hydrogen Economy for Environmental Sustainability 2: Applications, Challenges, and Policies. American Chemical Society, 211-230.
6. Soler JM, Artacho E, Gale JD, García A, Junquera J, Ordejón P and Sánchez-Portal D. 2002. The SIESTA method forab initioorder-Nmaterials simulation. Journal of Physics: Condensed Matter 14: 2745-2779.
7. Perdew JP, Burke K and Ernzerhof M. 1996. Generalized Gradient Approximation Made Simple. Physical Review Letters 77: 3865-3868.
8. Grimme S. 2006. Semiempirical GGA-type density functional constructed with a long-range dispersion correction. Journal of Computational Chemistry 27: 1787-1799.
9. Monkhorst HJ and Pack JD. 1976. Special points for Brillouin-zone integrations. Physical review B 13: 5188.
10. Marcos-Viquez AL, Miranda A, Cruz-Irisson M, Pérez LA. 2021. Tin carbide monolayers as potential gas sensors. Materials Letters 294: 129751.
11. De Santiago F, Arellano LG, Hernández-Hernández IJ, Heredia AR, Miranda Á, Trejo A, Pérez LA and Cruz-Irisson M. 2024. First principles study of hydrogen storage on B-doped SiC monolayers through light transition metal atoms. International Journal of Hydrogen Energy 63: 668-676.

OPTIMIZING HYDROGEN REFUELING INFRASTRUCTURE IN QATAR: A MAXIMUM COVERAGE LOCATION MODEL APPROACH

[1,2*]Carlos Méndez, [3]Roberto Baldacci, [2]Marcello Contestabile, [1]Yusuf Bicer,
[1]Division of Sustainable Development, College of Science and Engineering, Hamad Bin Khalifa University, Qatar Foundation, Education City, Doha, Qatar
[2]Qatar Environment and Energy Research Institute, Doha, Qatar
[3]Engineering Management & Decision Sciences, College of Science and Engineering, Hamad Bin Khalifa University, Qatar Foundation, Education City, Doha, Qatar
*Corresponding author e-mail: CDelgado@hbku.edu.qa

ABSTRACT
A shift towards sustainable transportation is necessary to reduce the sector's environmental footprint, particularly in countries like Qatar that rely heavily on personal hydrocarbon-based vehicles. While the country has battery electric vehicle goals, the dependence on natural gas power plants translates into emissions; hence, the deployment of hydrogen fuel cell vehicles (HFCVs) can be considered as an alternative. However, one of the major issues with this technology is the lack of infrastructure; for this reason, the present study deploys a maximum coverage location model (MCLM) to determine the required number and location of hydrogen refueling stations (HRSs) to meet a potential HFCV demand. Population density and vehicle registration data are used to develop the model alongside 107 potential HRS sites and a 10% fleet penetration assumption. As a result, 49 HRSs with a capacity of 1200 kgH_2/day are required to meet the demand; moreover, these stations are mainly located in the east, where the nation presents the highest population density and infrastructure development.

Keywords: Hydrogen Mobility, Maximum Coverage Location Problem, Hydrogen Refueling Station

1. INTRODUCTION
Increased awareness of environmental impacts originating from using conventional fuels has enhanced the necessity to seek solutions to decrease their dependency. Although the power sector is widely targeted in this regard, the transport sector is not being overlooked, and for a good reason, considering that it is the third highest CO_2 emitter after industry and power [1]. More so, road transport attracts attention since it represents up to 74% of the sector's emissions; a value that presents higher relevance in Qatar and the rest of the GCC countries since private cars represent 67% of the modal split and taxis add an additional 5%, making car use 72% of the share [2] For this reason, countries and regions have set targets and established strategies to transition away from conventional hydrocarbon-based vehicles. Qatar, in particular, has its green car initiative, which aims to have electric vehicles (EVs) representing 10% of the nation's vehicle fleet; however, with this approach, one issue remains, which is the dependency on natural gas-based power plants that supply roughly 96% of the nation's electricity [3]. Due to this, other alternatives like hydrogen fuel cell vehicles (HFCVs) must be considered.
From a vehicle technology perspective, HFCVs are not new since they were first commercialized in 2014 [4]; however, one issue remains in the form of infrastructure readiness. Qatar, in particular, has the H2 production know-how since it consumes roughly 1.3% of the globe's hydrogen demand for oil refining, as well as ammonia, methanol, and steel production [5–7]. Conversely, the country's refueling infrastructure is non-existent and it should be developed to enable HFCV adoption. For this reason, the present study develops a maximum coverage location model (MCLM) to determine the optimum location for hydrogen refueling stations (HRSs).

2. CASE STUDY
Accounting for Qatar's H_2 know-how and EV strategy, Qatar can target the deployment of HFCVs fueled by blue hydrogen obtained by steam methane reforming with carbon capture to complement the use of battery electric vehicles (BEVs). However, the potential H_2 demand must be estimated to determine the refueling station requirements. To do so, this study assumes that the HFCVs will represent 10% of the total vehicle stock and combines population density and registered vehicles to determine the projected demand for each of the country's eight municipalities (see Table 1).

Table 1. HFCV allocation based on population distribution

Municipality	Population Eligible to Drive	Distribution (%)	HFCV allocation based on population distribution
Al Daayen	58,337	2.17%	2,639
Al Khor	246,387	9.15%	11,146
Al Rayyan	617,465	22.92%	27,933
Al Shamal	9,472	0.35%	429
Al Shahaniya	232,295	8.62%	10,508

Al Wakra	349,940	12.99%	15,830
Doha	1,084,129	40.24%	49,043
Umm Salal	96,049	3.57%	4,345
Total	**2,694,076**	**100%**	**121,873**

Given that personal gasoline-fueled vehicles is Qatar's main mean of transport, existing gasoline fuel stations are used as a benchmark for potential HRS locations. With this approach, a total of 107 potential locations are obtained, while the demand points per municipality is placed based on the population's dencity as shown in Fig. 1.

Fig. 1. Potential HRS locations

3. MATHEMATICAL FORMULATION

The present study seeks to select the minimum number of locations to solve a maximum coverage location problem. Todo so, equations (1) to (5) are used; (1) represents the objective function, (2) and (3) are constraints that ensure that the demand is met and that it does not exceed the capacity, while (4) and (5) represent decision variables that enable refueling stations selection per region.

$$minimize \sum_{r \in R} \sum_{f \in F} d_{rf}\, x_{rf} \tag{1}$$

Subject to:

$$\sum_{f \in F} x_{rf} = Dem_r \; ; \; \forall r \in R \tag{2}$$

$$\sum_{r \in R} x_{rf} \leq capy_f \; ; \; \forall f \in F \tag{3}$$

$$x_{rf} \geq 0; \; \forall f \in F \tag{4}$$

$$y_f = (0,1); \; \forall f \in F \tag{5}$$

Where:
R = Region
F = Refueling station
d_{rf} = Distance between the refueling station and the demand point
Dem = Demand
Cap = Refueling station capacity in kg
x_{rf} = Decision variable based on demand availability per refueling station.

y_f = Binary decision variable set to 1 if refueling station is available and 0 otherwise.

Moreover, the refueling stations' capacities are set at 1200kgH_2/day, and d_{rf} is determined by applying the Haversine Formula.

4. RESULTS AND DISCUSSION

Table 2 shows how out of the 107 potential locations, 49 are chosen to install HRSs to meet the demand, meaning that roughly 46% of the possible locations are selected. Moreover, the results reflect how the regions with the highest density require the most HRSs.

Table 2. Maximum Coverage Location Problem Results

#	Municipality's Name	Required HRSs
1	Al Daayen	3
2	Al Khor	3
3	Al Rayyan	14
4	Al Shamal	1
5	Al Shahaniya	3
6	Al Wakra	6
7	Doha	17
8	Umm Salal	2

From a geographical perspective, Fig. 2 shows how most of the selected refueling stations are located in the east of the country, aligning with its current infrastructure development. However, since Al Rayyan's municipality extends from the country's south-west region to the east and its demand point, due to the population and infrastructure density is located closer to the east, not all of the country's surface is covered, and to ensure it, considerations must be done; like locating an additional station in the south-west region of the country. Similarly, for Dukhan (east Qatar), where no refueling station is selected, however, in this case, the distance between the city and the closest HRS does not require, initially, the deployment of a forced refueling station in that sector.

Fig. 2. Selected Hydrogen Refueling Stations

It is imperative to indicate that the development of the refueling station infrastructure must be linked with the HFCV adoption rate to align the necessary investment with the actual size of an evolving market. Especially considering that,

with the current approach, a total of eight refueling stations are underused; specifically, the results reflect a 7% overestimation.

5. CONCLUSIONS

The present study carries out a maximum coverage location model to determine the number of HRSs required to meet the potential HFCV demand, which is estimated to be the equivalent of Qatar's vehicle stock. Based on this approach, 49 HRSs of 1200 kgH_2/day must be deployed, most of which are located in the eastern part of the country, aligning with its population density and infrastructure development.

ACKNOWLEDGEMENT

The authors acknowledge the support provided by the Hamad Bin Khalifa University, Qatar Foundation (210008390).

NOMENCLATURE

BEV	Battery Electic Vehicle
EV	Electric Vehicle
H_2	Hydrogen
HFCV	Hydrogen Fuel Cell Vehicle
HRS	Hydrogen Refueling Station
MCLM	Maximum Coverage Location Model

REFERENCES

[1] International Energy Agency. CO2 Emissions in 2022. 2022.
[2] International Association of Public Transport (UITP). MENA Transport Report 2020/2021. 2021.
[3] KAHRAMAA. Annual Statistics Report 2023. 2024.
[4] Toyota Motor Corporation. Toyota Ushers in the Future with Launch of "Mirai" Fuel Cell Sedan 2014. https://global.toyota/en/detail/4198334 (accessed February 15, 2025).
[5] Qatar Steel. Sustainability Report 2022. Doha: 2023.
[6] QatarEnergy. 2022 Sustainability Report. Doha: 2023.
[7] QAFCO. Sustainability Report - 2021. Doha: 2021.

MLP HYPERPARAMETER OPTIMIZATION AND PRICE PREDICTION MODELS ON FUELCELL STOCK DATA: STABILITY AND PERFORMANCE ANALYSIS

[1]*Sıtkı Akkaya*, [2*]*Şekip Esat Hayber*
[1] Sivas University of Science and Technology, Department of Electrical-Electronic Engineering, Sivas, 58140, Turkey
[2] Bursa Uludağ University, Department of Electrical-Electronic Engineering, Bursa, 16059, Turkey
*Corresponding author e-mail: sehayber@uludag.edu.tr

ABSTRACT
This study involves optimizing the parameters of a multi-layer perceptron (MLP) to predict fuel cell stock prices over the last five years. This aims for better stability and aligns with recent trends. The model is trained under different conditions, and the best model is chosen based on the lowest root mean squared error (RMSE). The forecasting is performed for varying time spans (5, 7, 30, 180, and 360 days) and separately for specific predictions on a given day (1:1:360, 5:5:360, and 30:30:360 days). The RMSE values are also scaled and represented in a format that is better understood. Secondly, since this is an under-resourced segment, the comparison has been drawn from lithium-ion battery and pack information over the last 15 years, highlighting where this study can be related to other analogous technologies. The results offer insightful conclusions regarding fuel cell price forecasts for the next days. When the minimum batch size is 64 and the maximum epoch size is 200, the best RMSE value is 0.004987. It is recommended that future work be conducted to extend the optimization process to include deeper models of learning for longer and more detailed forecasting. This research adds to achieving accurate stock forecasting models with innovative machine learning methods.

Keywords: Fuel cell stock data, Stability, MLP hyperparameter optimization

1. INTRODUCTION

Fuel cells are the most promising technological advances in the renewable energy sector, providing a clean and efficient method of producing electricity [1]. In contrast to conventional energy sources, fuel cells operate based on converting chemical energy directly into electrical energy, resulting in negligible emissions, and thus are a perfect option for lowering the carbon footprint in most industries [2]. Fuel cell technology has the potential to become a valuable key to a sustainable energy system in the future, particularly in applications such as transportation, power generation, and industry [3]. As we increasingly use variable renewable energy sources such as sun and wind, fuel cells offer a stable way of storing energy and backup power, thus enabling the efficient incorporation of variable renewable energy into the power grid. One of the key drivers of the extensive use of fuel cells is their cost factor [4]. Fuel cell technology is relatively expensive, mainly due to the exorbitant price of materials like platinum and the intricacy of production processes [5]. Nevertheless, these expenses are bound to decrease with technological improvement over the years. Effective forecasting of fuel cell cost can yield extremely valuable information on market forces, thereby assisting investors and producers in making informed decisions [6]. A drop in the price of fuel cells will probably stimulate more investments in the field, causing more research and development activities [7]. This development will likely continue improving fuel cell technologies' performance and efficiency. Therefore, analyzing fuel cell stock data makes price prediction possible and can be used as a pointer to more investments and technological development in the field. This study aims to tune MLP hyperparameters to predict fuel cell stock prices using the latest data to increase stability and performance and provide insights for future investments and fuel cell technology advancement.

2. MATERIALS AND METHODS

In the study, the prediction of fuel cell stock prices using the optimization of MLP hyperparameters from current data is considered, and the prediction is made for different time horizons to obtain better prediction stability and accuracy.

2.1. Data Used in the Study

The data used in this research is historical fuel cell stock price data for 30 years [8], emphasizing the last 5 years for more recent and similar results. The data consists of daily stock prices processed to find patterns and trends. This research also uses MLP models to optimize hyperparameters and forecast stock prices. A comparison with lithium-ion battery statistics for the last 15 years is also provided to contextualize fuel cell technology in energy storage developments.

2.2. MLP

MLP is one of the feed-forwards artificial neural network types and is considered one of the most widely used deep learning models. MLP is a fully connected neural network model with at least one hidden layer and has a wide range of uses due to its ability to learn nonlinear complex functions.

2.3. MLP Structure

The MLP model usually consists of three essential components:
1. Input Layer: Represents the data received by the model. The number of neurons in the input layer equals the number of features used.

2. Hidden Layers: These are the layers that determine the essential learning capacity of the MLP. The neurons in each hidden layer learn complex relationships from the input data. Activation functions (ReLU, Sigmoid, Tanh, etc.) enable the model to make non-linear transformations.
3. Output Layer: This is the section where the model makes predictions or classifications. The number of neurons in the output layer is determined depending on the type of problem (for example, there may be a single neuron for regression and multiple neurons for multi-class classification).

2.4. MLP Mathematical Model

The essential mathematical components of MLP are:

• Weights and Bias Values: MLP learns by multiplying the inputs of neurons in each layer with weights and bias values added.

• Activation Function: The output of each neuron is passed through a specific activation function, applying a nonlinear transformation as in Eq. (1):

$$h = f(Wx + b)h = f(Wx + b)h = f(Wx + b) \quad (1)$$

where *W* represents the weight matrix, *x* represents the input vector, *b* represents the bias value, and *f*(.) represents the activation function (ReLU, Sigmoid, etc.).

• Forward Propagation: Forward propagation is performed by multiplying the input data with weights and passing them through activation functions.

• Backpropagation and Weight Update: The error function is calculated, and the weights are updated with the Gradient Descent method.

2.5. Error Function and Performance Measurement Metrics

RMSE is calculated by taking the square root of the mean of the squared differences between the model predicted values $(\hat{y}_i)$ and the actual values (y_i) as given in Eq. (2):

$$RMSE = \sqrt{\frac{1}{N}\sum_{i=1}^{N}(y_i - \hat{y}_i)^2} \quad (2)$$

Where, y_i represents the real values, $\hat{y}_i$ represents the values predicted by the model. The closer the RMSE value is to zero, the higher the model's prediction accuracy.

Loss function determines how the weights will be updated during the training process of the model. Since this study is a regression problem, the mean squared error (MSE) loss function is defined in Eq. (3):

$$Loss = \frac{1}{N}\sum_{i=1}^{N}(y_i - \hat{y}_i)^2 \quad (3)$$

MSE penalizes significant errors more by squaring the errors, therefore allowing the model to learn better.

3. RESULTS AND DISCUSSION

Future predictions are obtained using the MLP model, and the Adam optimizer is used. The best results in the scanned space were obtained for the following hyperparameters; MLP-based models obtained different prediction results for [5 7 30 180 360] days and [1 7 30] days intervals. The analysis shows the minimum batch size is 64, and the maximum epoch size is 200. In the study, space scanning was performed for different hyperparameters of MLP, as given in Table 1, and the best model was created by determining the best hyperparameters depending on the RMS values, as seen in Table 1. For the selected model, the best RMSE = 0.004987 was obtained. The visual of this training process is given in Fig. 1. As can be understood from Fig. 1, RMSE and loss functions converge to 0, which shows that the model is robust.

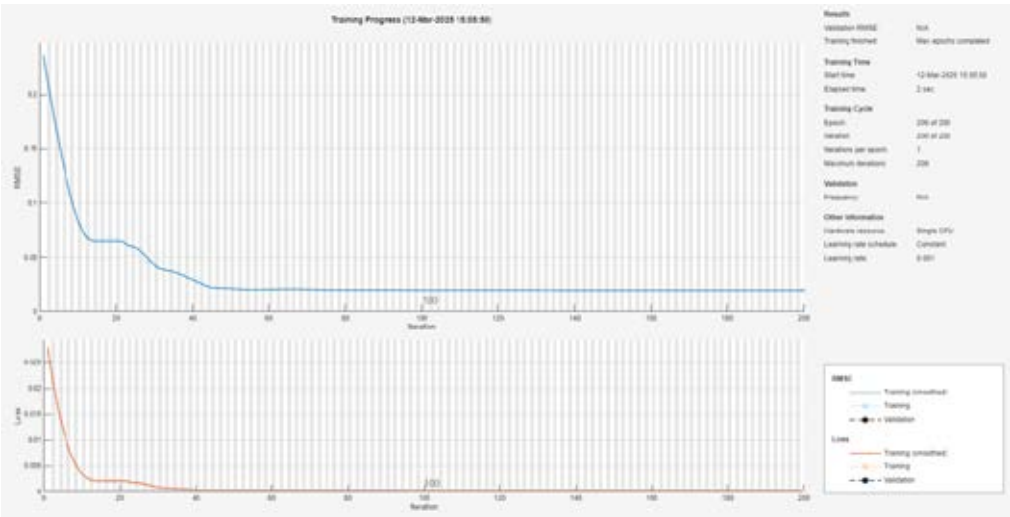

Fig. 1. Training Progress for MLP

It was then used to estimate different time intervals. This model based on MLP yielded different estimation results for [5

7 30 180 360] days later and [1 7 30] days later. The numerical results obtained for these other areas are given in Table 2 below. In addition, visual results are shown in Fig. 3.

Table 1. Hyperparameters search space, and best hyperparameters

Hyperparameters	Space	Best Hyperparameters
Optimizers	{'adam', 'sgdm', 'rmsprop'}	'adam'
MiniBatchSizes	[8, 16, 32, 64, 128]	64
MaxEpochsList	[50, 100, 150, 200]	200

Table 2. Future forecasts

Time Points	Forecast Values
5 days later	0.0134 ± 0.0001
7 days later	0.0214 ± 0.0001
30 days later	0.0143 ± 0.0001
180 days later	0.0201 ± 0.0002
365 days later	0.0194 ± 0.0013

The results obtained for the forecasts made with different day intervals, such as [1:1:360], [5:5:360], and [30:30:360], are given in Figs. 3a, b, and c, respectively.

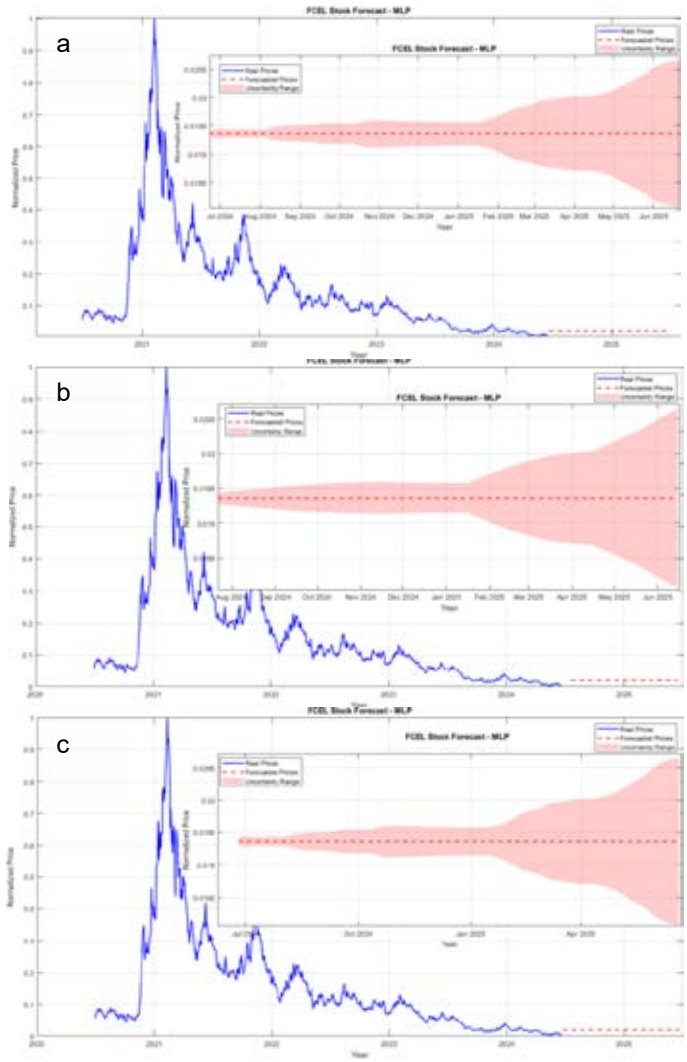

Fig. 2. Results obtained for different time intervals a) 1:1:360 b) 30:30:360 c) 5:5:360

Fig. 3 shows lithium-ion battery pack prices hit a record low of $139/kWh [9]. It is emphasized that lithium-ion batteries,

which have widespread and efficient use in terms of environment, economy, and energy, are available at very low prices.

Fig. 3. Volume-weighted average lithium-ion battery pack and cell price split, 2013-2023 [9]

The visuals obtained from the stock market dataset in Figs. 2a, b, and c, along with the estimates made for different time intervals, show that this fact given in Fig. 3 for lithium-ion can also be compatible with fuel cells.

4. CONCLUSIONS

Both fuel cell technology and lithium-ion batteries exhibit a clear downward price trend over time. The lithium-ion battery market has been experiencing a steady price decline, primarily driven by economies of scale, advances in material technology, and increasing demand for electric vehicles and energy storage devices. Fuel cell prices have been less predictable, with a peak followed by a gradual decline. This uncertainty stems from the yet-to-be-established hydrogen infrastructure and relatively smaller production scale. While lithium-ion batteries have already achieved the mass market, fuel cell technology will continue to decrease in price as mass production scales up and hydrogen infrastructure is established. Both technologies will likely be significant parts of hybrid energy systems in the future, playing different roles in various applications. In future studies, a detailed optimization study will be conducted for the fuel cell stock market data with the best deep learning model by scanning a broader space to obtain the best model for LSTM, Deeper LSTM, 1D CNN, and transformer models. In addition to this data set and related estimations, a study that includes energy and environmental effects will be conducted.

REFERENCES

1. Singla MK, Nijhawan P and Oberoi AS. 2021. Hydrogen fuel and fuel cell technology for cleaner future: a review. Environmental Science and Pollution Research 28:13:15607-15626.
2. Abdelkaree MA, Elsaid K, Wilberforce T, Kamil M, Sayed ET, Olabi A. 2021. Environmental aspects of fuel cells: A review. Science of The Total Environment 752:141803.
3. Cigolotti V, Genovese M and Fragiacomo P. 2021. Comprehensive review on fuel cell technology for stationary applications as sustainable and efficient poly-generation energy systems. Energies 14:16:4963.
4. Mohideen MM, Subramanian B, Sun J, Ge J, Guo H, Radhamani AV, ... Liu Y. 2023. Techno-economic analysis of different shades of renewable and non-renewable energy-based hydrogen for fuel cell electric vehicles. Renewable and Sustainable Energy Reviews 174:113153.
5. Zhang S, He X, Ding Y, Shi Z, Wu B. 2024. Supply and demand of platinum group metals and strategies for sustainable management. Renewable and Sustainable Energy Reviews 204, 114821.
6. İnci M. 2022. Future vision of hydrogen fuel cells: A statistical review and research on applications, socio-economic impacts and forecasting prospects. Sustainable Energy Technologies and Assessments 53:102739.
7. Jamal T, Shafiullah GM, Dawood F, Kaur A, Arif MT, Pugazhendhi R, ... Ahmed SF. 2023. Fuelling the future: An in-depth review of recent trends, challenges and opportunities of hydrogen fuel cell for a sustainable hydrogen economy. Energy reports 10:2103-2127.
8. https://www.kaggle.com/datasets/nitirajkulkarni/fcel-stock-performance. Kaggle, Accessed on March 14, 2025.
9. https://about.bnef.com/blog/lithium-ion-battery-pack-prices-hit-record-low-of-139-kwh/. BloombergNEF, Accessed on March 14, 2025.

DESIGN AND PERFORMANCE ANALYSIS OF HYBRID RENEWABLE ENERGY SYSTEM WITH HYDROGEN STORAGE: A CASE STUDY IN İZMİR

[1]*Yağmur Arıkan Yıldız*, [2*]*Şekip Esat Hayber*
[1] Sivas University of Science and Technology, Department of Electrical-Electronic Engineering, Sivas, 58140, Turkey
[2] Bursa Uludağ University, Department of Electrical-Electronic Engineering, Bursa, 16059, Turkey
*Corresponding author e-mail: sehayber@uludag.edu.tr

ABSTRACT
This study analyzes the wind and solar energy potential in the İzmir region and designs a hybrid energy system supported by hydrogen production and utilization. One-year hourly wind speed, solar radiation, and temperature data estimate renewable energy generation. The annual average wind speed in the region is 5.7 m/s, and the average solar radiation is 210 W/m². Using 600 kW solar panels with 18% efficiency and a 600-kW wind turbine with a 30% capacity factor, the total annual renewable energy generation is approximately 3.2 GWh. While wind energy production exceeds demand in winter, solar energy production increases significantly in summer. Excess energy is utilized for hydrogen production via electrolysis, while hydrogen fuel cells compensate for energy deficits. The system produces approximately 42,000 kg of hydrogen annually, requiring 2.1 GWh of electricity for electrolysis with 65% efficiency. When converted back into electricity via fuel cells with 50% efficiency, hydrogen contributes around 1.05 GWh to the system. Hydrogen storage requirements for both liquid and gaseous storage methods are also analyzed. The results indicate that integrating renewable energy with hydrogen storage ensures energy continuity. Future studies will focus on cost analysis, hydrogen production optimization, and storage strategy efficiency.

Keywords: Hybrid energy system, wind energy, solar energy, hydrogen production, electrolysis, fuel-cell

1. INTRODUCTION
The increasing global energy demand and environmental concerns have accelerated the shift towards renewable energy sources. Wind and solar power have gained significant attention due to their sustainability and minimal environmental impact. However, the intermittent nature of these energy sources poses a challenge to maintaining a stable and continuous power supply. The variability in wind speed and solar radiation throughout different seasons affects energy generation, leading to periods of excess production and energy deficits. To overcome this challenge, energy storage technologies are crucial in ensuring grid stability and reliable energy supply [1-2].
Hydrogen storage has emerged as a promising solution for integrating renewable energy sources into the energy system. By utilizing excess wind and solar power for hydrogen production through electrolysis, surplus energy can be stored and later converted back into electricity using hydrogen fuel cells during peak demand periods. This approach enhances energy security and contributes to developing a sustainable hydrogen economy. Compared to conventional battery storage, hydrogen offers a high energy density and long-term storage capabilities, making it an ideal choice for large-scale energy management [1-2].
This study examines the feasibility and efficiency of a hybrid wind-solar-hydrogen energy system in the İzmir region. The region is well known for its high wind potential and solar radiation, making it a suitable location for renewable energy integration. The research focuses on energy generation patterns, hydrogen storage requirements, and the role of hydrogen fuel cells in balancing seasonal variations. The findings provide insights into the potential of hydrogen-based energy storage in hybrid systems and contribute to the ongoing efforts to develop sustainable and resilient energy solutions.

2. MATERIALS AND METHODS
The İzmir region, favorable for wind and solar energy, has been selected as the application region. One year of hourly wind speed, solar radiation, and temperature data for İzmir province have been used [3].

2.1. The Analysis of Solar Generation of the Paper
Solar radiation and temperature data for the region are required to calculate solar energy. Using this information, the amount of power generated from a PV panel is given in Eq (1) [4].

$$P_{pv} = N_{pv} * P_r * \eta_{pv} * \left(\frac{G}{G_{ref}}\right) * \left[1 + \beta(T - T_{ref})\right] \quad (1)$$

$P_{pv} = N_{pv} * P_r *$Solar power (P_{pv}) depends on the number of panels (N_{pv}), rated power (P_r), efficiency (η_{pv}), radiation (G), and reference radiation (Gref, 1000 W/m²). The reference temperature (T_{ref}) is 25°C, with a temperature coefficient (β) of -3.7×10⁻³/°C for monocrystalline and polycrystalline silicon. Panel temperature (T) is calculated using Eq. (2). Here, T_a and T_{NOC} are the ambient and normal operating cell temperatures, respectively [4].

$$T = T_a + \left(\frac{T_{Noc} - 20}{1000}\right) * G \quad (2)$$

2.2. The Analysis of Wind Energy Potential

Equation 3 calculates the power obtained from the wind turbine [4].

$$P_{wt} = N_{WT} * \begin{cases} v(t) \prec v_{cutin} or v(t) \geq v_{cutoff} \Rightarrow 0 \\ v_{cutin} \leq v(t) \prec v_{cutoff} \Rightarrow v(t)^3 \left(\frac{P_r}{v_r^3 - v_{in}^3}\right) - P_r \left(\frac{v_{in}^3}{v_r^3 - v_{in}^3}\right) \\ v_r \leq v(t) \prec v_{cutout} \Rightarrow Pr \end{cases} \quad (3)$$

2.3. The Analysis of Hydrogen Energy

Hydrogen production is achieved by separating water into hydrogen and oxygen through electrolysis, as in Eq.(4). The electrical energy required for this process is calculated with Eq. (5) [5].

$$2H_2O \rightarrow 2H_2(g) + O_2(g) \quad (4)$$

$$H_p = \frac{P_E * t * \eta_e}{E_H} \quad (5)$$

The energy required for hydrogen production is calculated with Eq. (6), and electricity production in the hydrogen fuel cell is calculated with Eq. (7). To produce 1 kg of hydrogen, approximately 50 kWh of electricity is required. This efficiency is usually between 60-80%. When 1 kg of hydrogen is burned, it can produce approximately 33 kWh of electricity. The efficiency of this conversion is usually between 45-55% [5].

$$E_{H_2} = \frac{m_{H_2} * 50}{\eta_{electrolysis}} \quad (6)$$

$$E_{H_2,fuelcell} = m_{H_2} * 33 * \eta_{fuelcell} \quad (7)$$

3. RESULTS AND DISCUSSION

Monthly averages of wind speed, solar radiation, and temperature data obtained from NASA for Izmir province are given in Table 1.

Table 1. Monthly wind speed, solar radiation, and temperature data

Months	Wind Speed (m/sec)	Solar Radiation (Wh/m2)	Temperature (C°)
January	5.80	96.20	10.26
February	6.81	140.96	7.77
March	6.10	171.39	12.03
April	5.41	209.59	14.54
May	4.94	235.68	18.40
June	5.11	294.96	23.59
July	6.48	337.74	28.56
August	5.21	290.75	28.64
September	6.15	233.99	25.24
October	4.93	168.79	20.31
November	6.41	93.95	16.70
December	5.28	80.08	13.05

According to various studies, a house's average daily energy consumption is 20 kWh. Especially in the morning between 07.00-09.00 and in the evening between 18.00-22.00, higher consumption occurs. Accordingly, the daily load information of an average house is given in Fig. 1.

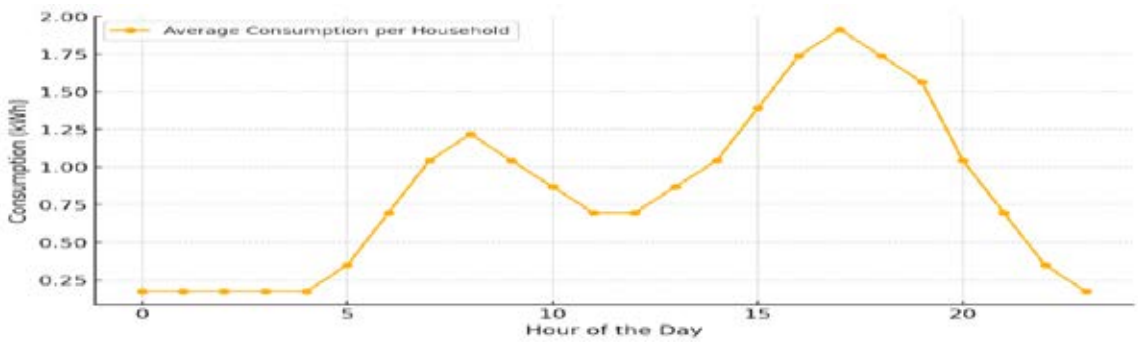

Fig.1. Hourly load profile

The energy consumption data for a site with 1,000 residences, covering 12 months, is presented in Fig. 2. While calculating the monthly consumption, the relevant values are determined based on the assumption that the region requires more energy during the summer months due to air conditioning.

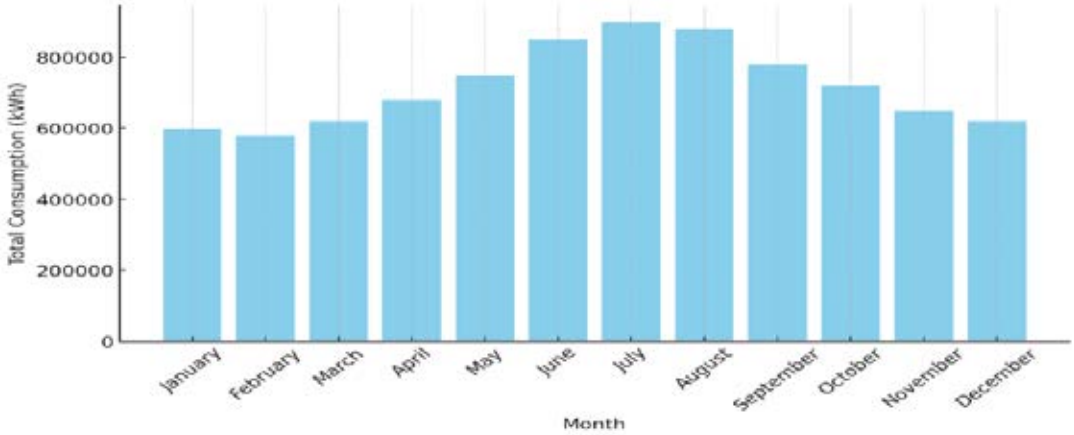

Fig. 2. Monthly electric load profile

The monthly solar energy obtainable using the region's data is presented in Fig. 3a. In contrast, wind energy is shown in Fig. 3b. The wind turbine and solar panel installed capacity is 600 kW. The efficiency of the solar panel is 18%, and the capacity factor of the wind turbine is taken as 30%.

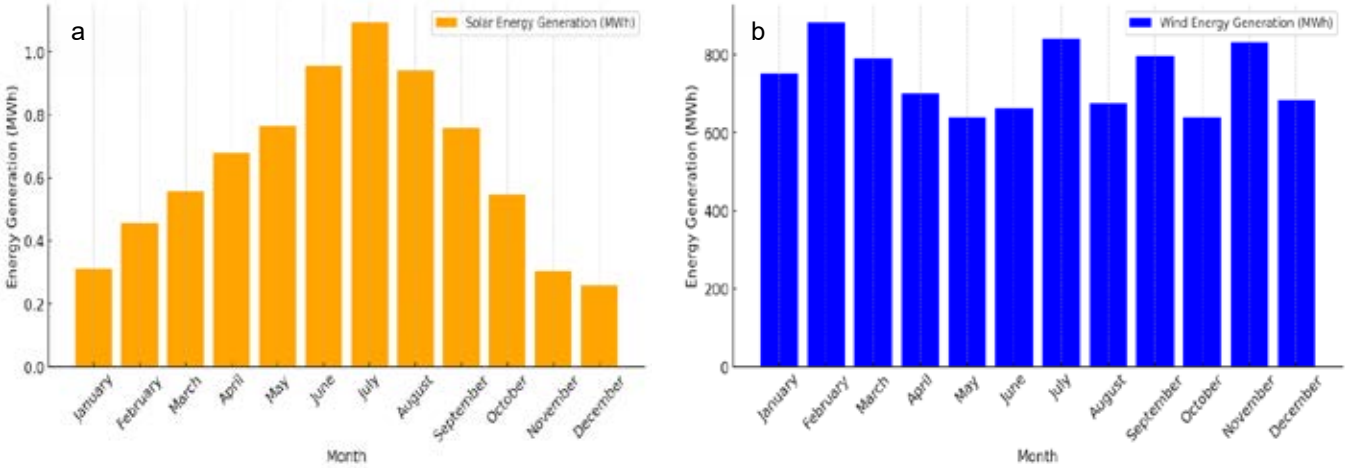

Fig.3. Monthly a) solar, b) wind energy generation

The aim is to supply the electrical load using the hybrid system. If wind and solar energy production exceeds the load, the surplus energy will be used for hydrogen production. Conversely, if the generated energy is insufficient, the deficit will be compensated by hydrogen fuel energy. In this context, the cases where excess and deficient energy occur, based on the monthly loads, are illustrated in Fig. 4. Fig 4. illustrates the balance between a 600-kW solar and 600 kW wind energy capacity and the total energy demand, highlighting seasonal variations in renewable energy production and the resulting surplus and deficit energy levels throughout the year.

Fig. 4. Monthly excess and deficit energy balance

During the winter months (January–March), there is a surplus of energy production, primarily due to higher wind speeds, which enhance wind turbine output. In spring and early summer (April–June), energy deficits emerge, particularly in May, when increased energy consumption coincides with a decline in renewable generation. This shortfall necessitates using hydrogen fuel cells to compensate for the energy deficit. In autumn (September–November), energy production and consumption become more balanced, although excess energy levels rise again in certain months. Based on these variations, Fig. 5a presents the monthly hydrogen production derived from excess energy and the hydrogen demand that must be met using fuel cells during energy shortages. Additionally, in response to these values, the required number of hydrogen storage tanks, both in liquid and gas form, has been calculated, and these values are displayed in Fig. 5b.

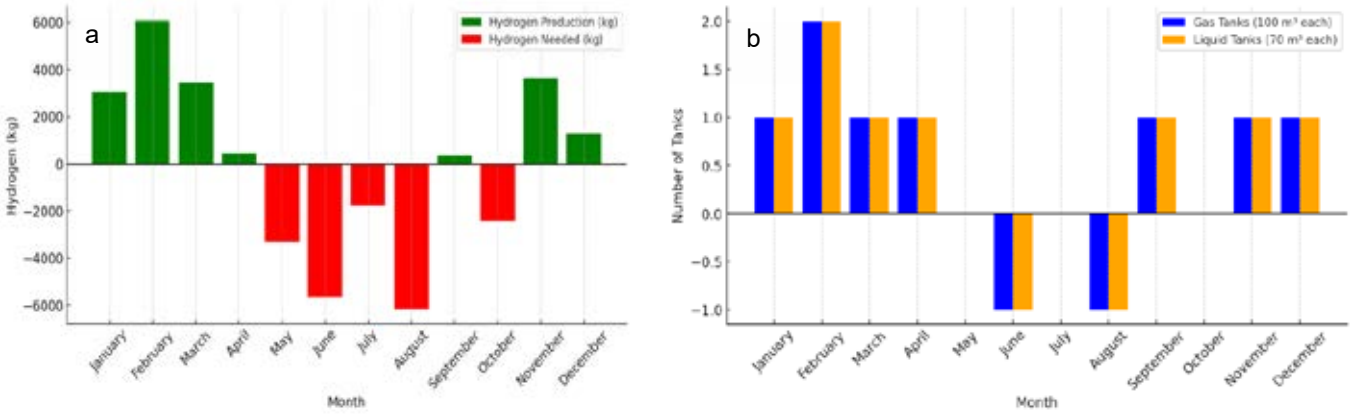

Fig. 5. Monthly a) hydrogen production and utilization, b) required hydrogen tanks

4. CONCLUSIONS

This study evaluates the efficiency of a hybrid energy system for the İzmir region and the effectiveness of hydrogen storage in ensuring energy continuity. The results show that wind energy production is high during the winter months, leading to excess energy generation, while in the summer months, increased energy demand requires hydrogen fuel cells. Hydrogen storage emerges as a critical solution for addressing seasonal imbalances. The data indicate that maintaining a balance between hydrogen production and consumption enables sustainable energy management. Future studies focus on the effectiveness of different storage methods and the development of the hydrogen economy.

REFERENCES

1. Razi F and Dinçer I. 2020. A critical evaluation of potential routes of solar hydrogen production for sustainable development. Journal of Cleaner Production, 264:121582.
2. Liu L, Zhai R, and Hu Y. 2023. Performance evaluation of wind-solar-hydrogen system for renewable energy generation and green hydrogen generation and storage: Energy, exergy, economic, and enviroeconomic. Energy, 276:127386.
3. https://power.larc.nasa.gov/data-access-viewer/. NASA POWER, Accessed on March 14, 2025.
4. Ngouleu CAW, Kohole YW, Cyrille F, Fogagui V, and Tchuen G. 2023. Techno-economic analysis and optimal sizing of a battery-based and hydrogen-based standalone photovoltaic/wind hybrid system for rural electrification in Cameroon based on meta-heuristic techniques. Energy Conversion and Management, 280:116794.
5. Ishaq H and Dinçer I. 2020. Comparative assessment of renewable energy-based hydrogen production methods. Renewable and Sustainable Energy Reviews, 135:110192.

THEORETICAL INSIGHTS INTO ZIF-71: ADSORPTION POTENTIAL FOR H_2 AND H_2S AS WELL AS ITS RESPONSE TO EXTERNAL ELECTRIC FIELD

[1]*Omer Sahin Sarisoy*, [1*]*Yeliz Gurdal*
[1] Adana Alparslan Turkes Science and Technology University, Faculty of Engineering, Bioengineering Department, Balcali Mah. Guney Kampus 10 Sokak No:1U,Saricam/ADANA, 01250, Turkiye
*Corresponding author e-mail: ygurdal@atu.edu.tr

ABSTRACT
Molecular hydrogen (H_2) is a renewable energy carrier, however, its practical applications are limited due to the challenges of developing safe and efficient H_2 storage devices. Hydrogen sulfide (H_2S), on the other hand, is a highly toxic chemical commonly found in petroleum, natural gas, and biomass synthesis gas. Even at low concentrations, it causes severe corrosion in pipelines and equipment. H_2S is also present in synthesis gases used for H_2 production and it deactivates catalysts as well as electrode catalysts in fuel cells. For these reasons, we theoretically investigated H_2 and H_2S adsorption capacities of the Zeolitic Imidazolate Framework, namely ZIF-71, applying Grand Canonical Monte Carlo (GCMC). We also examine the response of ZIF-71 to various electric field strengths to evaluate its behavior under electric field stimuli using ab initio Molecular Dynamics simulations.

Keywords: Physisorption, H_2 adsorption, H_2S adsorption, Grand Canonical Monte Carlo, ab initio Molecular Dynamics

1. INTRODUCTION

Metal-organic frameworks (MOFs), which consist of metal atoms and organic ligands linking these metal atoms, were introduced into the literature by Yaghi et al. [1]. MOFs are highly porous coordination compounds containing transition metal ions such as Co, Cu, and Zn. Zeolitic imidazolate frameworks (ZIFs) are a sub-class of MOFs named for their structural similarity to zeolites. By functionalizing imidazole (IM) linkers, ZIFs with a wide range of structural properties can be synthesized. ZIF-71 material, shown in Fig. 1, was synthesized by linking Zn metals using 4,5-dichloroimidazolate ligands and was introduced into the literature by Banerjee et al. [2].ZIF-71 ($Zn(dcIM)_2$) has surface area of 1004.7 m²/g and void fraction of 0.5. The smallest pore size is measured at 5.41 Å, while the largest pore size is 17 Å. The performance of ZIF-71 has been investigated in various applications, including CO_2 storage [3], biofuel purification [4], xylene diffusion [5], and ethanol and water adsorption [6]. ZIF-71 can potentially be used as gas storage system.

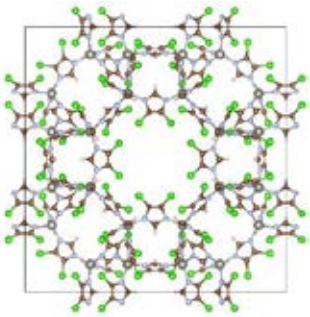

Fig. 1. ZIF-71: Zn metals are connected to each other through 4,5-dichloroimidazolate ligands.
H: white, N: blue, Cl: green, C: brown.

In the literature, modified ZIF-71 nanorods have been used for the adsorption of certain gases, and in one study, modified ZIF-71 exhibited high selectivity for H_2 [7]. Department of Energy (DOE) aims for hydrogen storage systems to achieve a volumetric capacity of 40 g H_2/L under conditions of 233 to 333 K and 5 to 12 bar pressure [8].Considering these findings and the high adsorption capacity of ZIF-71, research has been conducted on its H_2 adsorption properties.Hydrogen sulfide (H_2S) is highly toxic chemical commonly reside in petroleum, natural gas, and biomass synthesis gas [9]. Since H_2S is also present in synthesis gases used for hydrogen production, it deactivates catalysts and electrode catalysts in fuel cells [10]. For these reasons, the separation of H_2S is important for safe production and environmental protection. Zhou et al. [11] modeled MOFs with different ligands and topologies for H_2S adsorption and demonstrated that ZIF-71, ZIF-69, and ZIF-97 exhibited the best performance, adsorbing H_2S from an air mixture at room temperature and atmospheric pressure at a rate of 0.01 mmol/g. Apart from gas storage potentials, recent theoretical and experimental studies have shown that controlled and reversible structural changes occur in MOFs under externally applied electric field stimuli. Ligand rotation within the MOF structure, as well as pore opening/closing mechanisms in the presence of an electric field, have been investigated. ZIF-71, containing dichloroimidazolate ligands, is predicted that the H atoms in H_2S and H_2 could potentially adsorb onto the Cl groups. Additionally, Cl

halogens attached to the imidazolate ligands in ZIF-71 may trigger ligand rotation under an electric field.

This study aims to theoretically examine the controlled and reversible structural transformations, such as ligand rotation, that may take place in the ZIF-71 framework when subjected to external stimuli like electric fields and chemical agents. To achieve this, *ab-initio* Molecular Dynamics (AIMD), Density Functional Theory (DFT), and Grand Canonical Monte Carlo (GCMC) will be utilized. The primary goal is to determine whether the structural properties of materials can be manipulated under these external influences and to assess whether this control remains effective in the presence of industrially relevant gases, providing a foundation for smart material design research.

2. MATERIALS AND METHODS

The adsorption of H_2S and H_2 in ZIF-71 has been modeled using GCMC simulations at temperatures of 193 K, 233 K, 273 K, and 298 K for H_2S, 193 K, 233 K, and 298 K for H_2, with pressures ranging from 0.1 bar to 50 bar for H_2S and 0.1 bar to 100 bar for H_2. Adsorption isotherms of the materials have been obtained. The GCMC method is widely used in the literature to predict the gas adsorption capacities of nanoporous materials. GCMC simulations conducted using the open-source RASPA simulation package [8]. During these simulations, the MOF structures were kept fixed, and their initial configurations have been obtained from geometry optimizations using DFT. Gas-gas and gas-MOF dispersion interactions modeled using Lennard-Jones (LJ) interactions. The adsorption of H_2S and H_2 molecules into MOF pores calculated by considering both dispersion and electrostatic interactions.The force field parameters for H_2 utilized from previous studies [12]. For sulfur representation, a single Lennard-Jones (LJ) site was used, while partial charges placed at the centers of hydrogen and sulfur atoms were employed to account for electrostatic interactions. We applied the H_2S potential which was successfully used by Hamon et al. [13] to predict the H_2S adsorption capacities of MIL-53 and MIL-47. DFT simulations conducted to calculate the electronic density, and the atomic charges of the ZIF-71 were determined using the DDEC6 method [14]. An external electric field was applied in the x-direction to the cubic-symmetric ZIF-71 at strengths of 1 and 2 V/nm for a simulation duration of 40 ps using AIMD.

3. RESULTS

H_2 adsorption capacity of ZIF-71 was evaluated under various temperature and pressure conditions. Fig.3 presents the adsorption capacities at 298 K, 233 K, and 193 K as a function of pressure(bar) The results demonstrate a significant increase in adsorption capacity with decreasing temperature and increasing pressure. At 298 K, the adsorption capacity ranged from 0.0214 g/L at 0.1 bar to 11.63 g/L at 100 bar. A similar trend was observed at 233 K, where the adsorption capacity increased from 0.0714 g/L at 0.1 bar to 20.4057 g/L at 100 bar. The highest adsorption capacity was recorded at 193 K, where the values covered a range from 0.24 g/L at 0.1 bar to 29.33 g/L at 100 bar. Compared to DOE, which specifies a volumetric capacity of 40 gH_2/L under conditions of 233–333K and 5–12 bar, ZIF-71 exhibits promising adsorption behavior. Particularly at 233 K and elevated pressures, the material approaches the DOE target range, suggesting its potential applicability for hydrogen storage under optimized conditions.[8]

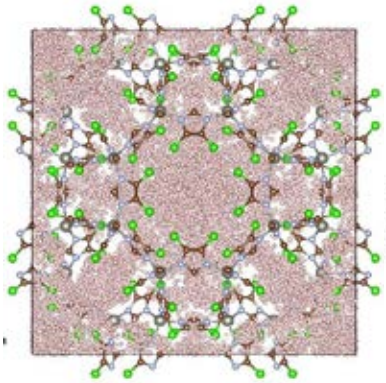

Fig. 2. ZIF-71 with adsorbed H_2 molecules, H: white, N: blue, Cl: green, C: brown.

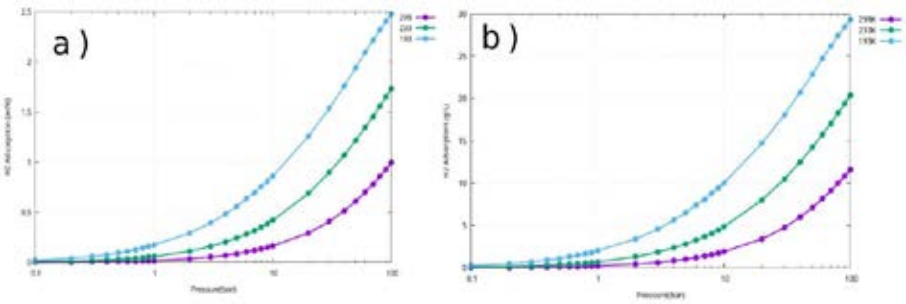

Fig. 3. H_2 adsorption values of ZIF-71 a) in g/L, b) in wt% unit.

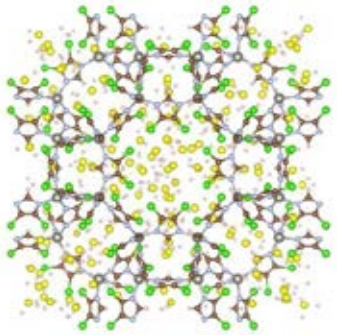

Fig. 4 . ZIF-71 with adsorbed H_2S molecules, H: white, N: blue, Cl: green, C: brown, S: yellow

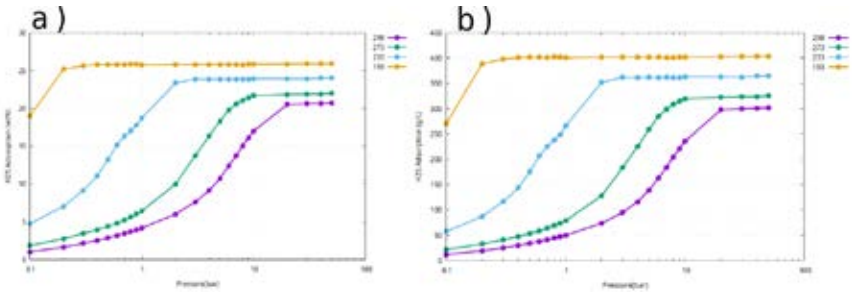

Fig. 5 . H_2S adsorption values of ZIF-71 a) in wt%, b) in g/L unit.

H_2S adsorption capacity of ZIF-71 was analyzed at different temperatures (298 K, 273 K, 233 K, and 193 K) as a function of pressure (bar). The results, summarized in Fig.5, indicate a strong dependence on both temperature and pressure.At 298 K, the adsorption capacity values covered a range of from 0.98 mg/g at 0.1 bar to 20.71 mg/g at 50 bar. As the temperature decreased to 273 K, adsorption capacity increased, reaching 21.98 mg/g at the highest recorded pressure. A more pronounced increase was observed at 233 K, where the adsorption values covered a range of from 4.75 mg/g at 0.1bar to 23.99 mg/g at 50 bar. The highest adsorption capacity was recorded at 193 K, where the values ranged from 18.97 mg/g at 0.1 bar to 25.88 mg/g at 50 bar. When compared to previous studies, such as the work of Zhou et al. [11], which demonstrated H_2S adsorption in ZIFs at 0.01 mmol/g(0.34 mg/g) under ambient conditions, the adsorption capacity of ZIF-71 under the examined conditions appears significantly higher. Furthermore, the results suggest that ZIF-71 could be a promising candidate for gas adsorption applications, particularly at lower temperatures and elevated pressures. These findings highlight the strong dependence of adsorption capacity on both temperature and pressure. The adsorption capacity significantly improves as the temperature decreases, which can be attributed to the enhanced van der Waals interactions at lower thermal energy levels. Additionally, increasing the pressure promotes higher adsorption, as more gas molecules interact with the porous structure of ZIF-71.

In Fig.6 simulations revealed that under a 1V/nm electric field, the ligand dihedral angles exhibited a slight increase, suggesting that moderate electric fields induce minor adjustments in ligand orientation. However, when the electric field strength was increased to 2V/nm, a moderate shift in ligand dihedral angles was observed. These findings indicate that the structural response of the MOF can be modulated by varying the electric field strength, which should be further investigated.

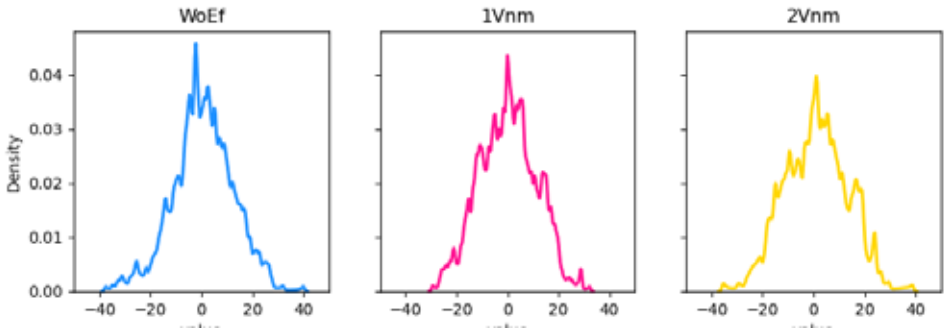

Fig. 6. The distribution of dihedral angles in the ZIF-71 exposed to an electric field strengths of 1 and 2 V/nm in the x-direction.

4. CONCLUSIONS

In this study, the adsorption performance of ZIF-71 was evaluated for both hydrogen (H_2) and hydrogen sulfide (H_2S) under various temperature and pressure conditions. The results demonstrated that adsorption capacity significantly increased with decreasing temperature and increasing pressure.For H_2 adsorption, ZIF-71 exhibited a maximum volumetric adsorption capacity showing its potential for hydrogen storage applications. ZIF-71 approaches the required performance under optimized conditions but may require further structural modifications to fully meet required specifications. Regarding H_2S adsorption, ZIF-71 showed a significantly higher capacity under ambient conditions. The highest recorded adsorptions indicate that ZIF-71 is a highly effective sorbent for hydrogen sulfide capture, especially under low-temperature conditions. Results confirm that ZIF-71 is promising material for gas storage and separation applications, particularly for H_2S removal and potential hydrogen storage. However, further studies are needed to optimize its structural properties, enhance adsorption capacity at ambient conditions, and evaluate its long-term

stability in practical applications. Electric field simulations conducted on ZIF-71 demonstrated that ligand rotations have a potential to obtain controlled behavior under external stimuli. This suggests that external fields may serve as a tunable mechanism for influencing the structural properties of the MOFs.

ACKNOWLEDGEMENT
Y.G. sincerely appreciates the support provided by the Scientific and Technological Research Council of Türkiye (TÜBİTAK) within the TÜBİTAK-1001 Research Program (Project No: 124Z002). In this work, TRUBA HPC resources were utilized.

REFERENCES

1. Yaghi, O., Li, G., & Li, H. (1995). Selective binding and removal of guests in a microporous metal-organic framework. *Nature, 378*(6558), 703–706.
2. Banerjee, R., Phan, A., Wang, B., Knobler, C., Furukawa, H., O'Keeffe, M., & Yaghi, O. M. (2008). High-throughput synthesis of zeolitic imidazolate frameworks and application to CO_2 capture. *Science, 319*(5865), 939–943.
3. Gao, W., Wang, S., Zheng, W., Sun, W., & Zhao, L. (2023). Computational evaluation of RHO-ZIFs for CO_2 capture: From adsorption mechanism to swing adsorption separation. *Separation and Purification Technology, 313*, 123469.
4. Tiempos-Flores, N., Hernández-Fernández, E., Rico-Barragan, A., Álvarez, J. R., Juárez-Ramírez, I., Garza-Navarro, M., Rodríguez-Hernández, J., Fonseca-García, A., Michaelis, D. J., & Davila-Guzman, N. E. (2022). Enhanced hydrophobicity of modified ZIF-71 metal-organic framework for biofuel purification. *Polyhedron, 217*, 115736.
5. Baniani, A., Rivera, M. P., Lively, R. P., & Vasenkov, S. (2022). Self-diffusion of mixed xylene isomers in ZIF-71 crystals dispersed in a polymer to form a hybrid membrane. *Microporous and Mesoporous Materials, 338*, 111960.
6. Lively, R. P., Dose, M. E., Thompson, J. A., McCool, B. A., Chance, R. R., & Koros, W. J. (2011). Ethanol and water adsorption in methanol-derived ZIF-71. *Chemical Communications, 47*, 8667–8669.
7. Ma, C., Zhou, T., Yang, H., Su, H., Wang, X., Wu, Q., Guo, X., & Zeng, D. (2023). High selectivity and response H_2 sensors based on ZnO@ZIF-71@Ag nanorod arrays. *Ceramics International, 49*(12), 19728–19736. https://doi.org/10.1016/j.ceramint.2023.03.090
8. U.S. Department of Energy. *DOE technical targets for onboard hydrogen storage for light-duty vehicles*. [Cited 2025 Mar 15]. Available from: https://www.energy.gov/eere/fuelcells/doe-technical-targets-onboard-hydrogen-storage-light-dutyvehicles.
9. DeCoste, J. B., & Peterson, G. W. (2014). Metal–organic frameworks for air purification of toxic chemicals. *Chemical Reviews, 114*(11), 5695–5727.
10. Peng, C., Luo, J., Sanger, A. R., & Chuang, K. T. (2010). Sulfur-tolerant anode catalyst for solid oxide fuel cells operating on H_2S-containing syngas. *Chemistry of Materials, 22*(3), 1032–1037.
11. Zhou, X., Yu, Y., Chen, H., Yang, L., Qin, Y., Wang, T., Sun, W., & Wang, C. (2020). Porous material screening and evaluation for deep desulfurization of dry air. *Langmuir, 36*(11), 2775–2785.
12. Gökdemir, T., & Gurdal, Y. (2024). Theoretical investigation of mixed-metal metal-organic frameworks as H_2 adsorbents: insights from GCMC and DFT simulations. *Molecular Simulation*, *50*(15), 1233–1245. https://doi.org/10.1080/08927022.2024.2395569
13. Hamon, L., Leclerc, H., Ghoufi, A., Oliviero, L., Travert, A., Lavalley, J.-C., Devic, T., Serre, C., Férey, G., De Weireld, G., Vimont, A., & Maurin, G. (2011). Molecular insight into the adsorption of H_2S in the flexible MIL-53(Cr) and rigid MIL-47(V) MOFs: Infrared spectroscopy combined with molecular simulations. *The Journal of Physical Chemistry C, 115*(5), 2047–2056.
14. Cui, K., Bhattacharyya, S., Nair, S., & Schmidt, J. R. (2021). Origins of acid-gas stability behavior in zeolitic imidazolate frameworks: The unique high stability of ZIF-71. *Journal of the American Chemical Society, 143*(43), 18061–18072.

KINETIC MODELLING ON TRANSIENT PHOTOCURRENT RESPONSES OF WO_3 PHOTOANODES

[1,2,3]*Ela Ayral,* [3,4]*Fatih Uçar,* [3,5]*Eğin Hznedar,* [1,3]*Esra Altuntaş,* [1,3]*Sarp Kaya*
[1]Department of Chemistry, Koç University, 34450 Istanbul, Türkiye
[2]Tüpraş R&D Center, 41780 Kocaeli, Türkiye
[3]Koç University Hydrogen Technologies Center (KUHyTech), 34450 Istanbul, Türkiye
[4]Department of Material Science & Engineering, Koç University, 34450 Istanbul, Türkiye
[5]Department of Chemical & Biological Engineering, Koç University, 34450 Istanbul, Türkiye
*Corresponding author e-mail: sarpkaya@ku.edu.tr

ABSTRACT

Photoelectrochemical (PEC) water splitting is a highly promising approach for sustainable hydrogen production, utilizing on semiconductor materials as photoanodes. Among semiconductors, tungsten oxide (WO_3) stands out for its chemical stability in acidic environments, resistance to photocorrosion, and effective charge transport properties. Despite these advantages, the wide bandgap of WO_3 limits its ability to absorb visible light, reducing its overall efficiency. This study presents kinetic modeling of transient photocurrent (TPC) behaviors in WO_3 photoanodes, aiming to understand the dynamics of electron-hole generation, separation, recombination, and charge transfer processes. TPC experiments at various applied potentials revealed significant variations in charge carrier behavior. The developed kinetic model accurately matches these experimental observations. These insights provide valuable insights for optimizing PEC systems and can be extended for further research and improve other semiconductor systems for efficient hydrogen production.

Keywords: Photoelectrochemical water splitting, Tungsten oxide (WO_3), Semiconductor, Transient photocurrent, Kinetic modeling

1. INTRODUCTION

Photoelectrochemical (PEC) water splitting is a sustainable and promising technology for producing hydrogen through light-driven water splitting. PEC water splitting produces hydrogen and oxygen without any undesired pollutants. It relies on semiconductor materials as photoelectrodes that absorb sunlight, generating electron-hole pairs, which then drive chemical reactions to split water molecules into oxygen and hydrogen. Semiconductors suitable for this process must demonstrate high chemical stability, suitable electronic properties for efficient charge transport, and robust resistance against corrosion under operational conditions. Typically, PEC systems use an n-type semiconductor as a photoanode, which captures photons to generate those crucial electron-hole pairs. Electrons move towards the external circuit, while holes move to the photoanode surface, helping to drive the oxygen evolution reaction (OER). However, the recombination of these generated charges can significantly limit efficiency.

Among various semiconductor types, tungsten oxide (WO_3) is significant due to its high stability under acidic conditions, resistance to photocorrosion, good charge carrier mobility, and cost-effectiveness. However, WO_3 possesses a relatively wide bandgap, which limits absorption light range thus its efficiency under the visible light illumination. the photo response under visible light can be enhanced by optimizing annealing conditions or doping by means of extending the light absorption range and the formation of oxygen vacancies which are acting as active sites for redox reactions. WO_3 with elements like carbon, sulfur, and nitrogen can significantly boost its performance under visible light. Among these, nitrogen (N) doping using NH_3 is the most promising, as it effectively reduces the band gap.

Kinetic modeling is a way to describe the dynamic behavior of chemical systems. It focuses on the rates of the reactions, providing insights into how various factors such as temperature, concentration, pressure affects the mechanism of a reaction to understand and enhance semiconductor performance.

The goal of this research is to optimize the conditions for high-performance PEC cells for hydrogen production by utilizing a kinetic model of WO_3 photoanodes that provide insights into charge carrier dynamics and photo response behavior.

2. REACTION KINETICS IN PEC WATER SPLITTING

When WO_3 is exposed to light, it absorbs photons that have energies greater than its band gap energy. This absorption occurs within the bulk of the semiconductor. Photon absorption creates electron-hole pairs. The electric field within the

space charge region at the semiconductor-electrolyte interface helps to separate these electron-hole pairs efficiently. Holes move toward the photoanode surface, while electrons move towards the cathode via an external circuit. The photogenerated holes that migrate to the surface of WO_3 interact with water molecules, driving the Oxygen Evolution Reaction (OER). At the same time, electrons moved to the cathode reduce protons (H^+) in the electrolyte, forming hydrogen gas.

The concentration of holes at the photoanode surface is influenced by how quickly they are generated and how fast they are removed through recombination and oxidation reactions. The surface hole concentration reaches steady state when generation and removal rates balance. The hole current density represents the generation of holes within the semiconductor due to photon absorption. This current density is always considered positive because it indicates the generation and initial movement of holes toward the semiconductor surface, initiating the water oxidation reaction. The charge transfer current density relates to how effectively the photogenerated holes are used at the semiconductor/electrolyte interface for the OER Specifically, this current describes how holes at the WO_3 surface oxidize water molecules. As holes are consumed for oxidizing water, this process contributes positively to the measurable photocurrent, indicating a productive use of created charges. The recombination current density describes losses that occur due to the recombination of electrons and holes within the semiconductor material or at its surface. Electron-hole recombination hinders the effective use of charge carriers for water splitting, thus reducing overall system efficiency. High recombination rates suggest lower overall PEC performance, as fewer holes remain available for water oxidation. The total photocurrent density at any moment is the sum of holes generated and losses due to electrons recombining with holes before they can participate in chemical reactions. The kinetics of PEC water splitting reactions are governed by the rates of electron-hole pair generation, separation, transfer, and recombination which will simulate the transient photocurrent response under different experimental conditions.

3. KINETIC MODELLING OF WO_3 PHOTOANODES

TPC measurements on WO_3 photoanodes annealed at different temperatures such as 500°C, 600°C, and N-doped WO_3 at 425°C were conducted. These measurements revealed differences in photocurrent behavior associated with crystallinity changes depending on annealing and doping conditions. It is possible to show these measurements in the kinetic model by changing certain parameters.

(a) (b)

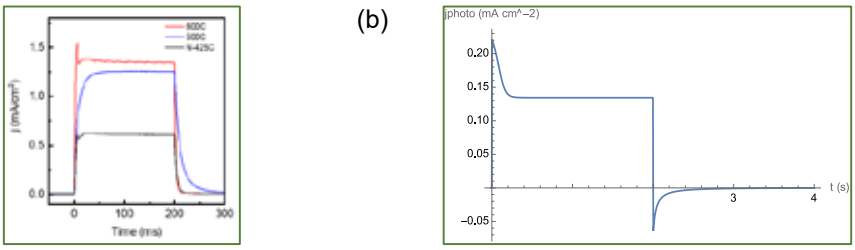

Fig. 1 (a) TPC of WO_3 photoanodes annealed at different temperatures , (b) Kinetic model of photocurrent transient behavior.

For WO_3 photoanode, potential dependence of total photocurrent response has been modeled. The results and the kinetic model are matching in showing significant variations in photocurrent dynamics at different potentials. The model of WO_3 photoanode needs to be developed to explain all the behaviors such as the instantaneous decay right after the hole accumulation. The kinetic model for N-doped WO3 photoanode will be further modeled. It will be helpful to make comparisons with N-doped WO_3 (N-WO_3) photoanodes since they revealed significantly different transient behaviors due to newly introduced surface states and enhanced oxygen vacancy concentrations.

(a) (b)

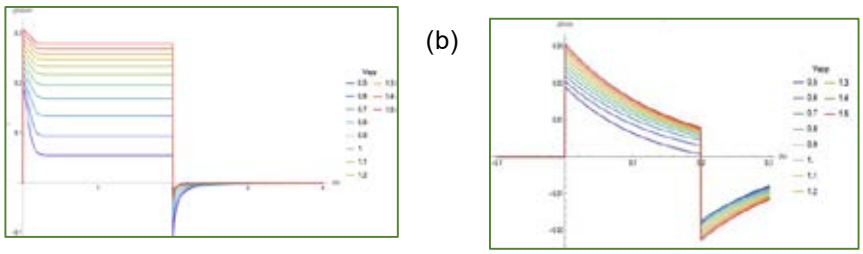

Fig. 2 (a) Kinetic model of total photocurrent transients at different applied potentials, (b) Kinetic model of total photocurrent transients at different applied potentials including charge carrier trapping.

It is possible to observe not only the total photocurrent response but also multiple behaviors such as the time-dependent surface hole concentrations of photoanodes and the variations in charge transfer and recombination rate constants with different applied potential.

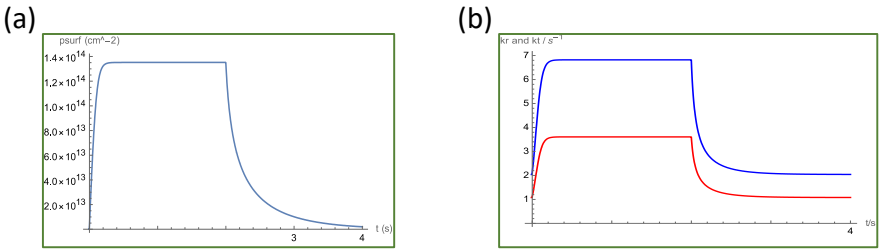

Fig. 3 (a) Kinetic model of surface hole concentration, (b) Kinetic model of charge transfer and recombination rate constants at different applied potentials

4. DISCUSSION

The annealing temperature significantly affects PEC performance by changing WO_3 crystallinity. Usually, solution-based methods yield hydrated WO_3 requiring annealing to get rid of water and enhance crystallinity. Annealing around 400°C forms stable monoclinic WO_3 with improved crystallinity, while further increasing the temperature to 600°C reduces PEC activity.

For the total photocurrent transient behavior, upon illumination, a rapid initial spike results from electron-hole separation within the space-charge region. Holes move toward the electrolyte interface, charging the space-charge capacitance, while electrons travel. Subsequent photocurrent decay arises from accumulated holes at the interface, causing increased recombination. A steady state is eventually reached when hole arrival equals their consumption by recombination and charge transfer. Turning off illumination interrupts hole flow, causing a negative current overshoot due to recombination with residual surface holes.

WO_3 photoanode results showed significant differences in photocurrent dynamics at different potentials. The total photocurrent increases with the applied potential due to enhanced charge separation facilitated by increased band bending and expansion of the space charge layer.

For N-doped WO_3, transient photocurrent behavior has been experimentally observed but is not yet fully modeled. Additional work is needed to account for N-induced surface states and oxygen vacancies, which influence charge transport and recombination dynamics.

5.CONCLUSION

The developed kinetic model successfully described the transient photocurrent behaviors observed in WO_3 photoanodes, enhancing understanding of the fundamental kinetics behind PEC water splitting. Further studies should extend this approach to other semiconductor systems. These studies will contribute significantly toward developing efficient PEC technologies for sustainable hydrogen production.

REFERENCES

1. Van de Kroll, Roel, and Michael Gretel. *Photoelectrochemical Hydrogen Production*, 2012. https://doi.org/10.1007/978-1-4614-1380-6.
2. Salvador, P. “Kinetic Approach to the Photocurrent Transients in Water Photo electrolysis at N-Titanium Dioxide Electrodes. 1. Analysis of the Ratio of the Instantaneous to Steady-State Photocurrent.” *The Journal of Physical Chemistry* 89, no. 18 (August 1, 1985): 3863–69. https://doi.org/10.1021/j100264a019.
3. Liu, Yu yang, Yaa Li, Wenchang Li, Song Han, and Cajun Liu. “Photoelectrochemical Properties and Photocatalytic Activity of Nitrogen-Doped Nano porous WO3 Photoelectrodes under Visible Light.” *Applied Surface Science* 258, no. 12 (April 1, 2012): 5038–45. https://doi.org/10.1016/j.apsusc.2012.01.080.
4. Liu, Xian, Fancying Wang, and Qing Wang. “Nanostructure-Based WO3 Photoanodes for Photoelectrochemical Water Splitting.” *Physical Chemistry Chemical Physics* 14, no. 22 (2012): 7894–7911. https://doi.org/10.1039/C2CP40976C.

5. Gurdial, Laurence M. Peter, Lydia H. Wong, and Fatwa F. Abdi. “Revealing the Influence of Doping and Surface Treatment on the Surface Carrier Dynamics in Hematite Nanorod Photoanodes.” *ACS Applied Materials & Interfaces* 9, no. 47 (November 29, 2017): 41265–72. https://doi.org/10.1021/acsami.7b13263.
6. Kim, Sangma, Nguyen the Nguyen, and Chung Wing Bark. 2018. "Ferroelectric Materials: A Novel Pathway for Efficient Solar Water Splitting" *Applied Sciences* 8, no. 9: 1526. https://doi.org/10.3390/app8091526
7. Shaban, Yorkin, Aimful Makabayan, Nourlan Baranov, and Nusrat Niraj. 2020. "Photoactive Tungsten-Oxide Nanomaterials for Water-Splitting" *Nanomaterials* 10, no. 9: 1871. https://doi.org/10.3390/nano1009187

FUZZY LOGIC-CONTROLLED LOAD MANAGEMENT IN A HYBRID MICROGRID WITH FUEL CELL, WAVE, SOLAR, AND WIND POWER INTEGRATION

[1]*Şule ATAÇ*, [2*]*Mehmet GÜÇYETMEZ*
[1] Sivas University of Science and Technology, Institute of Graduate Education, Sivas, 58140, Turkey
[2] Sivas University of Science and Technology, Department of Electrical-Electronic Engineering, Sivas, 58140, Turkey
*Corresponding author e-mail: mehmetgcy@sivas.edu.tr

ABSTRACT
Integrating renewable energy sources into hybrid microgrid (MG) systems presents a sustainable solution for meeting modern energy demands. This study investigates the performance of a hybrid energy system designed to supply uninterrupted and environmentally friendly electricity to a sample town. The system operates in island mode and incorporates four primary renewable energy sources: a 50-kW hydrogen fuel cell stack, a 100-kW photovoltaic (PV) system, a 6-kW wind turbine, and a 6-kW wave energy system. A fuzzy logic (FL)-based load management (LM) algorithm is proposed to optimize energy distribution and prevent wastage by dynamically adjusting to the system's production capacity. The PV system generates substantial energy during daylight hours, while the wind turbine complements energy production during low-light conditions. The fuel cell ensures high efficiency and reliability, particularly when renewable generation is insufficient. Wave energy also supports the system with the energy that is produced. By combining these components, the system achieves enhanced flexibility and sustainability. Furthermore, an energy storage system (ESS) is integrated to improve reliability and balance supply-demand dynamics. This study highlights the importance of intelligent load management strategies in achieving optimal energy utilization. The proposed model demonstrates the potential of hybrid MGs to provide continuous and sustainable energy, addressing the challenges of rural and urban electrification.

Keywords: Hybrid microgrid, Load management, Fuzzy logic control, Renewable energy, Wave energy

1. INTRODUCTION

The increasing demand for sustainable energy has made conventional energy sources a critical issue worldwide. Traditional energy production, primarily reliant on fossil fuels such as coal, oil, and natural gas, leads to significant environmental concerns, including carbon dioxide emissions, global warming, and climate change [8,9-14]. The depletion of fossil fuel reserves also poses challenges for energy security, driving the necessity for alternative energy solutions [4]. As a response, renewable energy sources such as solar, wind, and biomass have gained prominence due to their sustainability and lower environmental impact. These energy sources provide a viable solution for reducing dependence on fossil fuels while enhancing energy security and economic stability. In Türkiye, renewable energy has been integrated into national energy policies to decrease reliance on fossil fuels [13]. Hybrid MG systems, which integrate multiple renewable sources with ESSs, offer a promising approach to ensuring a continuous and stable energy supply. These systems can function in grid-connected and island modes, improving energy management through advanced control strategies. This study proposes a hybrid MG model incorporating solar, wave energy, wind, and hydrogen fuel cell technologies to address the energy needs of a specific town in Türkiye. The proposed system enhances energy resilience by integrating multiple renewable sources and storage solutions, making it viable for addressing energy access challenges in remote areas.

2. MATERIALS AND METHODS

An efficient MG has been designed to supply loads in the circuit and support battery storage systems. The system integrates fuel cells, wave, wind, and PV systems. An ESS has been implemented to store excess power generated within the MG. This design considers the flexibility between energy supply and demand and the connection with the ESS. After determining the total power generated, a fuzzy logic controller has been developed to optimize the operating mode of the MG. In the proposed system, loads are managed based on their priority, allowing unnecessary loads to be deactivated when not needed using fuzzy logic. The schematic diagram of the designed MG is shown in Fig. 1.

2.1. The Structure of The Wave Energy System

Wave energy will also be present in the system, unlike many MG structures. Wave energy is the energy obtained from wind waves formed by water movement in oceans and seas. A machine that can collect wave energy is called a Wave Energy Converter (WEC). The purpose of WECs is to convert the kinetic energy of incoming waves into electrical energy [10]. In this way, it can be one of the structures included in the total energy produced in the system. This study included a coastal oscillating water column system called land installed marine powered energy transformer in the simulation [2]. The " column " structure in these systems has seawater at the bottom and air at the top. The movement of the waves changes the water level inside the column and compresses the air above. The compressed air rotates a turbine and produces electrical energy [6]. Sea waves have a sinusoidal structure; therefore, the sine wave curve was used in simulation studies. While creating the sine wave, it was assumed that the waves came regularly. The wave height and period were constant. While designing the wave energy system, a place on the Aegean Sea coast in Türkiye was taken

as the basis for the input information. These values were used to calculate the total energy that was contained in wave (ΔP) in Eq. (1) [5], speed of the air (v_{air}) in Eq. (2), and the torque (T_{Nm}) Eq. (3), that rotates the turbine wheel.

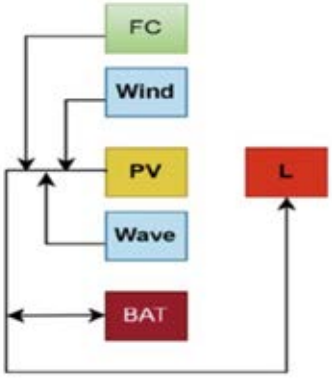

Fig. 1. Island MG diagram

This system can produce 6-kW of energy. System parameters can be seen in Table 1.

$$\Delta P = \frac{1}{8} \times p_{water} \times g \times H^2 \times \sin\left(\frac{2\pi}{T} \times t\right) \quad (1)$$

$$v_{air} = \frac{((\Delta P / p_{air}))}{A_{turb}} \quad (2)$$

$$T_{Nm} = C_t \times p_{air} \times A_{turb} \times {v_{air}}^2 \times R_t \quad (3)$$

Table 1. Parameters of The Proposed Energy System

Wave Energy Parameters	**Value**	**Units**	**PV Energy Parameters**	**Value**	**Units**
Density of water (p_{water})	1025	kg/m^3	Maximum Power, Pmax	250.205	W
Gravitational acceleration (g)	9.81	m/s^2	Open Circuit Voltage, Voc	37.3	V
Wave height (H)	1	m	Short-circuit current, Isc	8.66	A
Mean Wave Period (T)	6	s	Voltage at maximum power-point, Vmpp	30.7	V
Density of air (p_{air})	1.225	kg/m^3	Current at maximum power-point, Impp	8.15	A
Radius of Turbine (R_t)	5	m	Temperature coefficient of Voc	-0.36901	V per °C
Air exit area of turbine (A_{turb})	79	m^2	Temperature coefficient of Isc	0.086998	A per °C
			Number of cells per module	60	-
Fuel cell Parameters			**Wind Turbine Parameters**		
V_{OC}	900.8	V	Cut-in wind speed	2.5	m/s
Stack efficiency	55	%	Rated wind speed	12	m/s
Airflow rate	2100	IPM	Rotor diameter	5.5	m
Fuel cell resistance	0.66404	Ω	Stator resistance, R_s	0.0918	Ω
Load resistance (R_{load})	5	Ω	Rated power	6.5	kW
One cell voltage	1.1342	V	Number of pole pairs	4	-
H_2	99.25	%	Rated speed	2300	rpm
O_2	70.4	%	Stator Inductance L_s	0.000975	H
Number of cells	900	-	System inertia	0.003945	kg/m^2
			Viscous damping	0.0004924	Nms

2.2. The Structure of PV System

Solar panels are components that capture solar energy and convert it into electricity [3]. These panels consist of solar cells. Solar cells are usually made of silicon-based semiconductor materials. Electrons are activated when sunlight hits these cells, and an electric current is created. When cells are connected sequentially in solar panels, the voltage (tension) increases. When cells are connected in parallel, the current capacity increases. This collected energy is transmitted to consumers (homes, businesses, factories, etc.) and made available with devices such as inverters (DC-AC converters).

In this way, the light energy from the sun is directly converted into electrical energy and becomes usable for people. This system is the main energy source of the MG system. 100-kW of energy can be produced by this system. The parameters of the PV system used in Simulink design can be seen in Table 1.

2.3. The Structure of the Fuel Cell Energy System

Proton Exchange Membrane Fuel Cells (PEMFCs) are critical among environmentally friendly energy solutions [12]. They provide efficient energy conversion by directly converting the chemical energy of hydrogen into electricity. In traditional methods, fuel and oxidizer react in the same environment, while in fuel cells, these components are kept in different compartments. In this way, their direct mixing is prevented, and energy production occurs by ions and electrons moving in a controlled manner [11].

The hydrogen fuel electrochemical equation is defined in Eq. (4) [1].

$$2H_2 + O_2 = 2H_2O + electricitiy + heat \quad (4)$$

The output voltage of a PEMFC can be calculated with Eq. (5).

$$V_{FC} = n_{cell}(V_{nernst} - V_{con} - V_{act} - V_{ohm}) \quad (5)$$

Here, V_{nernst} represents the unprocessed electrical potential generated by the chemical reaction. Meanwhile, V_{act} denotes the activation overvoltage, while V_{con} and V_{ohm} indicate voltage drops due to resistance and concentration losses. The Nernst voltage is detailed in Eq. (6).

$$V_{nernst} = V_o - (0.85 \times 10^{-3})(T - 298.15) - (4.3085 \times 10^{-5})Tln(P_{H_2}{P_{O_2}}^{1/2}) \quad (6)$$

The proton exchange membrane fuel cell (PEM) system, including the buck converter, is modeled in MATLAB/Simulink. A simplified PEM model parameter is given in Table 1.

2.4. The Structure of the Wind Energy System

The input to a wind turbine is the wind, while its output is the mechanical power that drives the generator rotor. In a variable-speed wind turbine, the mechanical output power obtained from the turbine can be expressed by Eq. (7) [7].

$$P_m = \frac{1}{2}pAC_p(\lambda, \beta){V_w}^3 \quad (7)$$

Here, p represents the air density, and A represents the area swept by the turbine blades. V_w is the wind speed (m/s), C_p is called the power coefficient and is expressed as a nonlinear function of the tip speed ratio (TSR) λ. This function is defined as Eq. (8).

$$\lambda = \frac{w_r r}{V_w} \quad (8)$$

The wind turbine, including its PMSG (Permanent Magnet Synchronous Generator), boost converter, and control system, was modeled in MATLAB/Simulink. The MG system was simulated based on a 6.5 kW small wind turbine, with its parameters provided in Table 1.

2.5. The Structure of the Load Management System

The loads are prioritized according to their importance and integrated into the system accordingly. The main purpose is to feed critical loads by using the available power most efficiently and include other loads in the system if the energy status allows. Loads are divided into four different categories according to their importance. Tertiary load is of minor importance and is connected to the system whenever there is excess energy. It needs 30 kW of power and is disconnected first during a lack of energy. It can be commercial appliances or comfort equipment. The quarterly load has the lowest priority in the system. It needs 50 kW of power. It operates only if there is enough power. It shuts down as soon as there is low energy. Examples include large lighting systems or non-essential appliances. The FL-based load management system takes the total generated power as an input and calculates how to switch the loads on and off. It has a single input (total power input) and three outputs, which control load connections based on priority. These outputs ensure critical loads are connected while others are adjusted according to the available power.

3. RESULTS AND DISCUSSION

The proposed system is designed to generate high efficiency and quality line voltage. Operating in island mode, the system manages variable loads based on fuzzy logic outputs. Loads are dynamically added or removed depending on the available power, directly influencing the system's voltage and current. Furthermore, power generation has been analyzed under various operating conditions to evaluate system performance. The battery charge decreases rapidly when the system is operated without load management. This is because the loads in the system are constant even if the power generated decreases. In the system without load management, the battery is separated from the charging mode to provide sufficient energy, and its charge begins to decrease rapidly. This situation is seen in Fig. 2a.

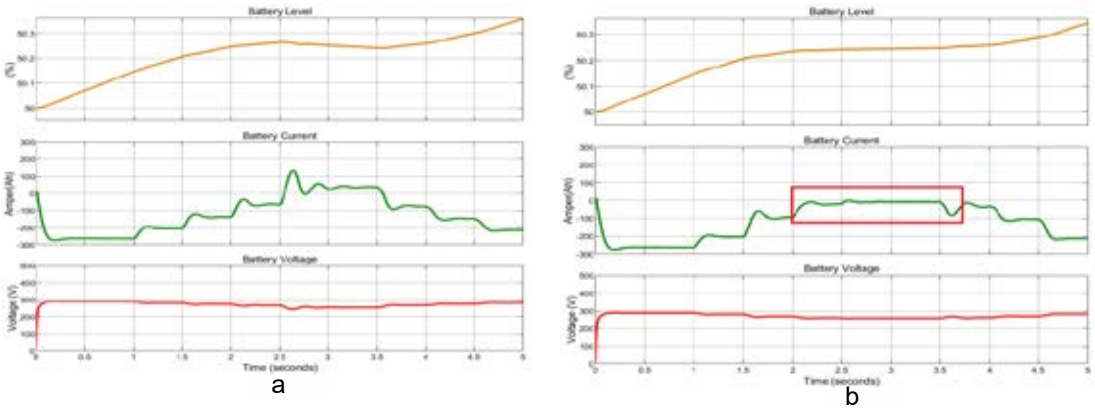

Fig. 2. a) Change of charge level without load management, b) Change in charge level after load management is applied.

When load management based on the fuzzy logic method is applied in the system, the insensitive secondary loads are separated from the system if there is not enough power. In this case, since the power drawn from the system will decrease, the battery charge level will decrease less or will switch to the charging state. In this way, the MG will continue to operate in a controlled manner. The load-shifting process ensures that there is less charge loss in the system. Fig. 2b shows the changes in battery charge levels after the load management is applied to the system.

4. CONCLUSIONS

This study presents an innovative energy solution for remote areas with renewable energy resources but struggles to utilize them efficiently. The proposed system has been introduced and thoroughly examined for the first time in this research. It has been evaluated under two different scenarios: with and without load management (LM), and the battery status has been analyzed in detail. The performance of critical, non-critical, and secondary loads has been tested under various conditions using load management and FL control. Additionally, the system has been adapted for a sample region and is supported by a storage infrastructure that provides uninterrupted energy for 24 hours. This study aims to enhance energy supply in remote areas by making it more sustainable and efficient while serving as a foundation for future innovations. In future research, load classification methods and the battery management system could be further expanded, incorporating a wider range of energy sources. Additionally, ESSs could be scaled up to support more extensive and complex power systems. These advancements would play a crucial role in improving the efficiency and sustainability of global energy infrastructure.

REFERENCES

1. Alharbi AG, Olabi AG, Rezk H, Fathy A, and Abdelkareem MA. 2024. Optimized energy management and control strategy of photovoltaic/PEM fuel cell/batteries/supercapacitors DC microgrid system. Energy, 290:130121.
2. Clément A, McCullen P, Falcão A, Fiorentino A, Gardner F, Hammarlund, K, ... and Thorpe T. 2002. Wave energy in Europe: current status and perspectives. Renewable and Sustainable Energy Reviews, 6:5:405-431.
3. Crabtree GW, and Lewis NS. 2007. Solar energy conversion. Physics Today, 60:3:37-42.
4. Dorić B. 2024. Economic perspective of renewable energy sources: Security of supply, innovations, and challenges. Croat. Reg. Dev. J, 5:59-74.
5. Fernandez de Valderrama L. 2020. Preliminary Design and Analysis of a Wave Energy Converter with Electromagnetic Induction.
6. Hong Y, Waters R, Boström C, Eriksson M, Engström J, and Leijon M. 2014. Review on electrical control strategies for wave energy converting systems. Renewable and Sustainable Energy Reviews, 31:329-342.
7. Hossain E, Hossain J, Sakib N, and Bayindir R. 2017. Modeling and simulation of permanent magnet synchronous generator wind turbine: A step to microgrid technology. International Journal of Renewable Energy Research, 7:1:443-450.
8. Kavya A, and Yadav S. 2023. A comprehensive evaluation of the environmental footprint across energy sources: Toward sustainable solutions. Preprints.
9. Lak SZ, Rezaei J, and Rahimpour MR. 2024). Health and pollution challenges of fossil fuels utilization. Encyclopedia of Renewable Energy, Sustainability and the Environment, 8:155.
10. Ozkop E, and Altas IH. 2017. Control, power and electrical components in wave energy conversion systems: A review of the technologies. Renewable and Sustainable Energy Reviews, 67:106-115.
11. Samal S, and Hota PK. 2017. Design and analysis of solar PV-fuel cell and wind energy-based microgrid systems for power quality improvement. Cogent Engineering, 4:1:1402453.
12. Tariq AH, Kazmi SAA, Hassan M, Ali SM, and Anwar M. 2024. Analysis of fuel cell integration with hybrid microgrid systems for clean energy: A comparative review. International Journal of Hydrogen Energy, 52:1005-1034.
13. https://enerji.gov.tr/bilgi-merkezi-enerji-elektrik. T.C. Enerji ve Tabii Kaynaklar Bakanlığı, Accessed on March 12, 2025.
14. Yılmaz F, Balta MT, Selbaş R, and Demiral D. 2016. Environmental Impact Assessment of Electricity Production, A Case Study of Turkey. Energy, Transportation, and Global Warming, 463-474.

SIC SCHOTTKY DIODES: ELECTRICAL CHARACTERIZATION AND GAS SENSOR APPLICATIONS

[1*]Lutfi Uğur KENDİRLİ, [2]Lütfi Bilal TAŞYÜREK, [1]Necmettin KILINÇ
[1]İnönü University, Department of Physics, 44280, Malatya, Türkiye
[2] Malatya Turgut Ozal University, Depertment of Opticians, 44700, Malatya, Türkiye
*Corresponding author e-mail: ugurkndrl@gmail.com

ABSTRACT

In this study, SiC Schottky barrier diode production was carried out by DC sputtering method. Different types of Schottky barrier diodes were produced by coating Al on the one side of the 4H-SiC wafer and Ti or Ni or Pt on the other side. The DC and AC electrical properties of the Al/4H-SiC/Metal Schottky barrier diodes were measured depending on the temperature. Inferences were made on the character of the metal-semiconductor SiC Schottky barrier diode in the I-V graphs obtained as a result of the measurements. In addition, gas measurements of SiC Schottky diodes were made and the obtained data were discussed. Al/4H-SiC/Ti and Al/4H-SiC/Ni device showed Schottky behavior but Al/4H-SiC/Pt device showed memristive behavior.

Keywords: SiC, Schottky barrier diode, Gas sensors, Metal-semiconductor contacts

1.INTRODUCTION

Since the 19th century, the interest of mankind in electronics has become an inseparable part of life today, with the development of the field of electrical and electronics. The electrical industry is currently one of the largest industries in the world. The differentiation of human needs every passing day further develops technology. In these studies, the investigation of the electrical properties of solids and the findings obtained have made great contributions to electronics. The first systematic research on metal-semiconductor rectifier systems was made by Braun in 1874. Point contact rectifiers in various forms found practical applications. In 1931, Wilson formulated the transport theory of semiconductors. This theory, based on the band theory of solids, was later applied to metal-semiconductors. In 1938, Schottky suggested that there could be a potential barrier. He stated that the chemical layer was caused only by stable space charges in the semiconductor without the existence of an entity. The model resulting from this evaluation is known as the Schottky barrier [1]. In 1938, Mott also designed a more suitable theoretical model for the swept-away ones. This model, known as the Mott barrier, takes place in metal-semiconductor contacts. These models were further developed by Bethe in 1942 and became the thermionic emission model [2]. When a metal comes into contact with a semiconductor, a barrier is formed in the metal-semiconductor. This barrier is responsible for controlling the current conduction. The energy band diagrams that lead to the formation of the barrier height and some effects can change the value of this barrier. The energy band diagrams of metal-semiconductor contacts before and after the contact are given in Figure 1 [2] (Sze et al., 2021). The work function is the energy difference between the vacuum level and the Fermi level. Here, the work function is denoted by $q\phi_m$ for a metal and is equal to $q(\chi + \phi_n)$ for a semiconductor. The $q\chi$ given for a semiconductor is the electron affinity measured from the bottom of the conduction band (E_C) to the vacuum level. Here $q\phi_n$ is the energy difference between the E_C and the Fermi level [2].

Since the realization of high-performance power devices provides high energy saving, conservation of fossil fuels and less environmental pollution, interest in devices using semiconductors is increasing. Currently, the technology of Si power devices used in most fields is experiencing difficulties in innovative breakthroughs in applications. Silicon carbide (SiC), one of the newly emerging semiconductors, has attracted considerable attention due to its superior physical properties. SiC is an extremely wide bandgap semiconductor, and its use is increasing day by day. Due to the significant development of SiC wafer quality and advancement in device technology, high voltage SiC Schottky barrier diodes (SBDs) and field effect transistors (FETs) have been proven to perform significantly better than their Si counterparts. Components that provide significant reduction of power loss will be used in various power converters in the future, indicating that SiC power devices will become the key [3].

SiC is a material that shows polytypism. Polytypism expresses different crystal structures in one-dimensional variation while preserving the same chemical structure. The change of occupied sites along the c-axis gives more than 200 SiC polytypes different crystal structures. While expressing polytypes, the number of layers in the unit cell and the crystal system (cubic for C, H for hexagonal and R for rhombic) are taken into consideration. 3C-SiC, 4H-SiC and 6H-SiC are the most common and also the most technologically important ones . In general, 3C-SiC shows a stable structure at low temperatures, while 4H-SiC and 6H-SiC are known as high-temperature resistant polytypes [3].

SiC is resistant to high-energy radiation compared to semiconductors such as GaAs and Si, which allows it to be used in space technologies. SiC is used in high voltage, high frequency, and high temperature resistant devices. SiC is found in UV photodiodes, blue light emitting diodes, and detector diodes [4].

SiC Schottky diodes were used in microwaves, radio, and radar detectors in the past, but today they are used in many areas in the semiconductor industry due to their unique properties. The main areas of these areas are MESFET elements, solar cells, varactors, high-energy detectors, switching circuits, etc. Since it is a type of diode that is open to development, it is foreseen that it will be used in many more areas in the future [5].

One of the needs of the increasing world population is undoubtedly the need for energy. In today's world where fossil resources are rapidly depleting, the demand for renewable energy is rapidly increasing. There has been an increase in the studies carried out to meet this demand from hydrogen in recent years. In the face of the challenges faced by the world in producing clean energy, it has become generally accepted that hydrogen will be a sustainable resource. In addition, the fact that hydrogen is used in many areas of space studies and industry also contributes greatly to scientific studies [6].

2.METHOD

2.1. SiC Schottky Barrier Diode Fabrication

SBD production was performed using commercially produced and ready-made 4H-SiC wafers. The ohmic and Schottky contacts of the SBDs to be created were made by coating Al, Ti, Ni, and Pt metals. In Figure 1, the upper part of the 4H-SiC was coated with Ti or Ni or Pt metals and the other side with Al metal to obtain a SBD.

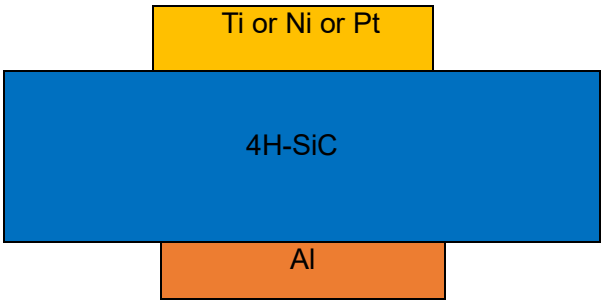

Fig. 1. Al/4H-SiC/metal SBD schematic diagram

2.2. Electrical characterization

The DC and AC electrical behaviors of the different Schottky diodes obtained were measured with the Source Measure Unit and LCR meter. The electrical characteristics of these diodes were measured depending on the temperature, frequency and ambient conditions. During the measurement, the temperature were changed between 25 - 200 ^{0}C and electrical measurements will be made in different gas environments.

2.3. Gas sensor tests

Within the scope of this study, the sensor devices produced by our group were measured in the sensor test system located in the sensor laboratory. The measurement system includes a measurement cell where the temperature of the sensor devices can be changed, a gas flow control device to obtain the desired concentration of gas mixture, a temperature control device to precisely control the temperature of the sensor device, a multimeter to measure the resistance of the sensor device, and a computer to control these devices, collect and record data from the devices. Sensor tests were performed against hydrogen gas on the produced sensor devices. The sensors were tested between room temperature and 200 ^{o}C. In order to check the repeatability of the measurements, same sensor device were taken at different times under the same conditions and their comparisons were made.

3. RESULTS AND DISCUSSION

Figure 2a and b shows the I-V and semi-logarithmic I-V graphs of the SBD we produced from Ti metal at room temperature and Al/4H-SiC/Ti device has seen Schottky behavior. The semi-logarithmic I-V graphs of the Al/4H-SiC/Ni device at different temperatures is given in Figure 2c. It is seen that the Al/4H-SiC/Ni device behaves like a diode at low temperatures and exhibits ohmic behavior at high temperatures. Figure 2d shows the semi-logarithmic I-V graph of the Al/4H-SiC/Pt device that measured in the range of -/+5V at room temperature in a dry air environment for three cycles. It is seen that Al/4H-SiC/Pt device exhibits memristive behavior in the forward bias. The I-V graph of the Al/4H-SiC/Ni device in dry air and 1% hydrogen environment at room temperature was given in Figure 2e. It is seen that the current decreases in the hydrogen environment. The semi-logarithmic I-V graph of the Al/4H-SiC/Ni device in dry air and 1% hydrogen environment at room temperature was given in Figure 2f. While the difference in current was seen clearly in dry air and 1% hydrogen environments in the forward bias, almost the same current values were seen in the reverse bias.

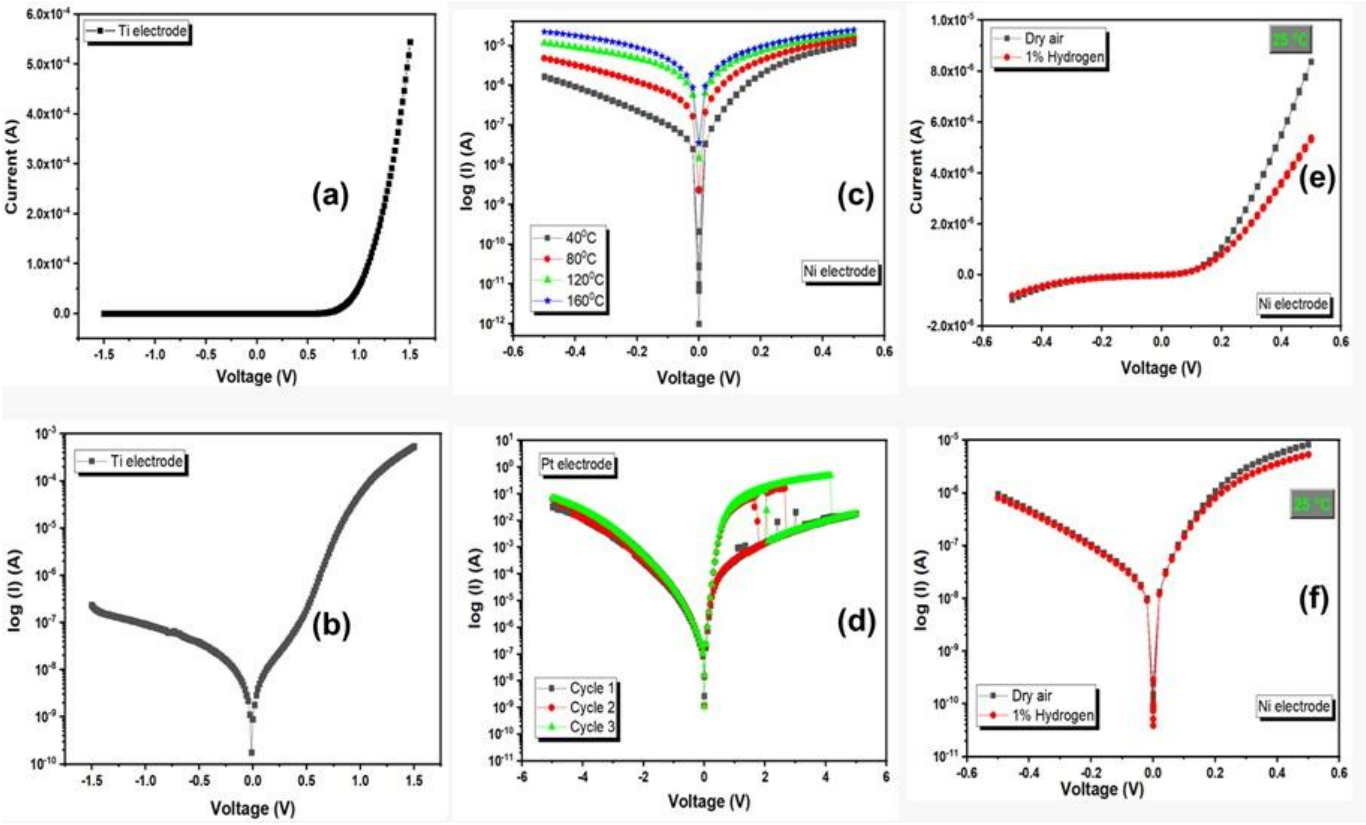

Fig. 2. (a) Al/4H-SiC/Ti I-V graph and **(b)** Al/4H-SiC/Ti semi-logarithmic I-V graph. **(c)** Al/4H-SiC/Ni semi-logarithmic I-V graph and **(d)** Al/4H-SiC/Pt semi-logarithmic I-V graph. **(e)** Al/4H-SiC/Ni I-V graph and **(f)** Al/4H-SiC/Ni semi-logarithmic I-V graph.

4. CONCLUSIONS

As a result, DC sputtering method was used to produce Al/4H-SiC/Metal Schottky barrier diodes. Different types of Schottky barrier diodes were produced by coating Al on one side of 4H-SiC wafer and Ti or Ni or Pt on the other side. DC and AC electrical properties of Al/4H-SiC/Metal Schottky barrier diodes were measured depending on temperature and I-V characteristics were investigated. In addition, hydrogen gas sensor tests of SiC Schottky diodes were performed. Al/4H-SiC/Ti and Al/4H-SiC/Ni devices showed Schottky behavior, while Al/4H-SiC/Pt devices showed memristive behavior.

ACKNOWLEDGEMENT

This study was funded by Inonu University BAP, Project Number: FOA-2023-3156 and FYL-2023-3378

REFERENCES

[1] Mönch, W. (1994). Metal-semiconductor contacts: electronic properties. Surface Science, 299, 928–944.
[2] Sze, S. M., Li, Y., & Ng, K. K. (2021). Physics of semiconductor devices. John wiley & sons.
[3] La Via, F., Camarda, M., & La Magna, A. (2014). Mechanisms of growth and defect properties of epitaxial SiC. Applied Physics Reviews, 1(3).
[4] Pizzagalli, L., Cicero, G., & Catellani, A. (2003). Theoretical investigations of a highly mismatched interface: SiC/Si (001). Physical Review B, 68(19), 195302.
[5] Pezoldt, J., Förster, C., Weih, P., & Masri, P. (2001). Electrical characterization of SiC/Si heterostructures with Ge-modified interfaces. Applied Surface Science, 184(1–4), 79–83.
[6] Trinchi, A., Kandasamy, S., & Wlodarski, W. (2008). High temperature field effect hydrogen and hydrocarbon gas sensors based on SiC MOS devices. Sensors and Actuators B: Chemical, 133(2), 705–716. https://doi.org/https://doi.org/10.1016/j.snb.2008.03.011

H_2 SORPTION POTENTIAL OF ZIFs REVEALED THROUGH GRAND CANONICAL MONTE CARLO SIMULATIONS

[1]*Güllüsüm TUNÇ*, [1*]*Yeliz GURDAL*
[1] Adana Alparslan Türkeş Science and Technology University, Faculty of Engineering, Department of Bioengineering, Sarıçam, Adana, 01250, Türkiye
*Corresponding author e-mail: ygurdal@atu.edu.tr

ABSTRACT
Zeolitic Imidazolate Frameworks (ZIFs), as a subclass of Metal-Organic Frameworks (MOFs), have gained significant attention for their potential in hydrogen storage and separation applications. This study investigates the adsorption properties and structural characteristics of ZIF-3 and ZIF-90, which exhibit high thermal and chemical stability, thus they are potential candidates for hydrogen-related technologies. The hydrogen adsorption capacities of these materials have been computed using Grand Canonical Monte Carlo (GCMC) simulations, allowing for an in-depth evaluation of adsorption, interaction energies, and pore structures under different pressure and temperature conditions. The results highlight the impact of pore size distribution, functional groups, and framework topology on hydrogen adsorption efficiency. The results add to the current research on ZIFs as potential sustainable hydrogen storage solutions and provide fresh insights into the development of advanced porous materials for clean energy purposes.

Keywords: Hydrogen storage, ZIFs, Adsorption, Grand Canonical Monte Carlo (GCMC)

1. INTRODUCTION

As a subtype of Metal-Organic Frameworks (MOFs), Zeolitic Imidazolate Frameworks (ZIFs) have significant potential in hydrogen storage and separation applications due to their high porosity and chemical resilience, which has garnered considerable interest. ZIFs are characterized by their strong porosity, large surface area, and exceptional thermal and chemical stability, which makes them highly promising for hydrogen storage applications. [1]

ZIFs are promising materials for use as adsorbents and membranes in the separation of noble gas mixtures. Due to their high porosity and selective gas adsorption properties, ZIFs can effectively separate gases such as carbon dioxide (CO_2) and methane (CH_4), as well as noble gases like neon (Ne) and argon (Ar). The structural flexibility and pore size of ZIFs allow for selective gas capture and release. Additionally, ZIFs have potential applications in membrane technology, where their properties can enhance the efficiency of noble gas separation processes. Moreover, ZIFs hold great potential for environmentally friendly gas separation and energy production applications. Specifically, the separation of methane and other gases from natural gas can contribute to reducing the carbon footprint. ZIFs are highly promising materials for adsorption and separation technologies, and their potential can be more efficiently harnessed through further exploration. [2]

Among the various ZIF structures, ZIF-3 and ZIF-90 have been extensively studied for their unique properties. ZIF-3, for instance, exhibits a sodalite (SOD) topology, which contributes to its high porosity and stability [1]. ZIF-90 is notable for its aldehyde functional groups, rendering it hydrophilic and allowing for post-synthetic modifications to enhance gas adsorption properties [3].

The hydrogen storage capabilities of these ZIFs are influenced by factors such as pore size, surface area, and functionalization. Studies have shown that ZIF-8, a structurally similar framework, can adsorb hydrogen molecules up to 4.2 wt% at high loading concentrations [4]. This suggests that ZIF-3 and ZIF-90 may also exhibit comparable hydrogen storage capacities, contingent upon their structural attributes and functional groups.

To accurately assess the hydrogen adsorption performance of these materials, computational methods such as Grand Canonical Monte Carlo (GCMC) simulations were employed. GCMC simulations enable the evaluation of adsorption isotherms, pore size distributions, and the impact of functional groups on gas uptake under various conditions. In this study, we have analyzed the hydrogen adsorption behavior of ZIF-3 and ZIF-90 under different temperature and pressure conditions using GCMC simulations. By investigating the relationship between their structural features and hydrogen storage capacities, this work aims to provide guidance for the development of advanced porous materials for clean energy applications. Theoretical insights gained from this study are crucial for optimizing the design and synthesis of ZIFs tailored for efficient hydrogen storage applications.

2. COMPUTATIONAL DETAILS

The Grand Canonical Monte Carlo (GCMC) simulation is a method based on statistical mechanics, designed to model adsorption processes at the molecular level. This method is commonly employed to study adsorption equilibrium because it has the ability to directly calculate the number of moles of molecules within the pore. [5]

The grand canonical ensemble is defined by thermodynamic variables such as chemical potential (μ) and absolute temperature (T). Additionally, it depends on mechanical parameters like volume (V), which determine the system's internal states. Since these three quantities remain constant in this ensemble, it is commonly referred to as the μVT ensemble.

2.2. Simulation Details

Grand Canonical Monte Carlo (GCMC) simulations were performed to compute the H_2 adsorption isotherms of the selected ZIF materials, namely ZIF-3 and ZIF-90, under varying temperature and pressure conditions. The open-source RASPA simulation package [6] was used to obtain H_2 adsorption isotherms at 193 K, 233 K, and 273 K with pressures ranging from 1 bar to 40 bar.

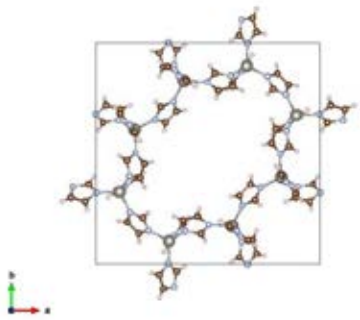

Fig. 1. Image of ZIF-3

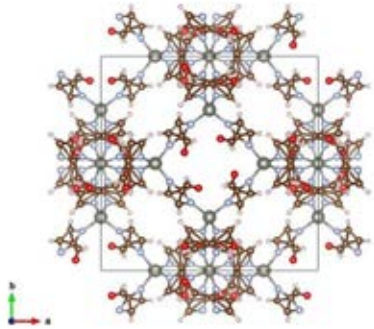

Fig. 2. Image of ZIF-90

The frameworks were kept rigid throughout the GCMC simulations.The Lennard-Jones potential was used to calculate dispersive interactions, and the force field parameters of the ZIF atoms were taken from the Universal Force Field (UFF) [7]. Lorentz–Berthelot mixing rules were applied to determine the force field parameters between different atomic pairs [8]. We applied the five-site Belof-Stern-Space (BSS) model to simulate the H_2 molecule. Table 1 displays the parameters of the BSS model, where q denotes charge and ε and σ denote Lennard-Jones force field parameters of energy and size.

Simulation cells are sufficiently replicated and a Van der Waals cut-off distance of 12 Å was employed in simulations. The Coulomb cut-off was set to 18 Å. Various Monte Carlo moves, including translation, reinsertion, and rotation, were incorporated during the simulations. The GCMC simulations consisted of a total of 500,000 cycles, including 10,000 initialization cycles, followed by 490,000 production cycles.

Following the GCMC simulations, the adsorption capacities of ZIF-3 and ZIF-90 were analyzed to determine their efficiency in hydrogen storage applications. The results provide insights into the relationship between the structural properties of ZIFs and their hydrogen adsorption performance under different temperature and pressure conditions.

Table 1. Parameters of the BSS model applied in this work.

Site Name	x (Å)	y (Å)	z (Å)	Mass (amu)	q (e)	ε (K)	σ (Å)
H2G	0	0	0	0	−0.74640	8.8516	3.2293
H2E	-0.37100	0	0	1.00800	0.37320	0	0
H2E	0.37100	0	0	1.00800	0.37320	0	0
H2N	0.32900	0	0	0	0	4.06590	2.34060
H2N	-0.32900	0	0	0	0	4.06590	2.34060

3. RESULTS AND DISCUSSION

In this study, ZIF-3 and ZIF-90 materials were used to evaluate hydrogen adsorption performance, and these materials were thoroughly examined due to their structural stability and potential in hydrogen storage capacity. Grand Canonical

Monte Carlo (GCMC) simulations were carried out at temperatures of 193 K, 233 K, and 273 K, with pressures ranging from 1 bar to 40 bar.

The adsorption results indicate that ZIF-3 exhibited the highest hydrogen uptake across all investigated temperatures. As shown in Fig. 3, the highest performance was observed at 193 K, followed by 233 K and 273 K. In both ZIF-3 and ZIF-90, an increase in pressure led to an enhancement in adsorption, confirming the pressure-dependent nature of hydrogen storage in porous materials. This trend is clearly observed in Fig. 3. The highest adsorption capacities were recorded at 193 K, where ZIF-3 showed the best performance.

A comparative analysis of ZIF-3 and ZIF-90 revealed an average difference of approximately 0.3 in adsorption capacity across all conditions, with ZIF-3 consistently outperforming ZIF-90. This difference was particularly noticeable in Fig. 3, where ZIF-3 exhibited the highest adsorption capacity at 193 K. These findings suggest that ZIF-3's structural properties are more favorable for hydrogen adsorption, making it a stronger candidate for storage applications under cryogenic conditions.

The structural stability and high hydrogen storage capacity of ZIF-3 make it a key material for efficient energy storage and transport systems. While ZIF-90 shows lower performance than ZIF-3, it still demonstrates significant hydrogen storage capacity under certain conditions, highlighting its potential for optimization in specific applications. ZIF-3's high performance is especially prominent in low-temperature environments, while ZIF-90 may be more suited for high-pressure conditions.

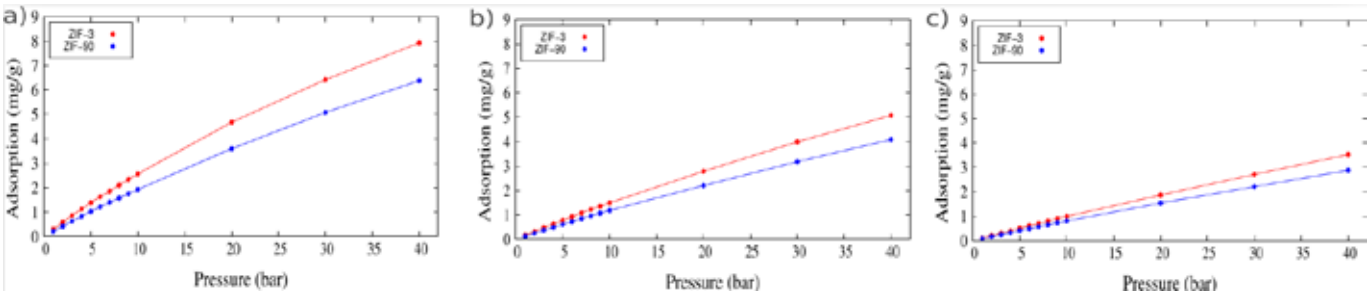

Fig. 3. H2 adsorption isotherms of ZIFs calculated at (a) 193 K, (b) 233 K and (b) 273 K

The ZIF structures remained rigid throughout the geometry optimization process. The geometry-optimized structures of the H_2/ZIF systems for ZIF-3 and ZIF-90 are presented in Fig. 4(a–d), respectively. H_2 molecules predominantly adsorb near the metal ions, and the measured distances are highly comparable. The adsorption distances observed for ZIF-3 are significantly shorter than those measured for ZIF-90. This finding further supports the higher adsorption capacity of ZIF-3, as demonstrated in Fig. 3.

4. CONCLUSIONS

This study investigated the hydrogen adsorption performance of ZIF-3 and ZIF-90 under varying temperature and pressure conditions using GCMC simulations. The results demonstrated that adsorption is significantly influenced by both pressure and temperature. The highest adsorption capacities were observed at 193 K, as shown in Fig. 3**,** confirming the superior hydrogen storage potential of these materials at low temperatures. Additionally, the pressure-dependent nature of hydrogen uptake was confirmed, as adsorption increased with rising pressure.

Among the two studied frameworks, ZIF-3 consistently outperformed ZIF-90, with an average adsorption capacity difference of 0.3 across all conditions. These findings highlight ZIF-3 as a more effective material for hydrogen storage applications, particularly in low-temperature environments. Future work could explore structural modifications, functionalization strategies, and optimization for higher temperatures to further enhance adsorption capacities and make these materials more suitable for practical hydrogen storage applications.

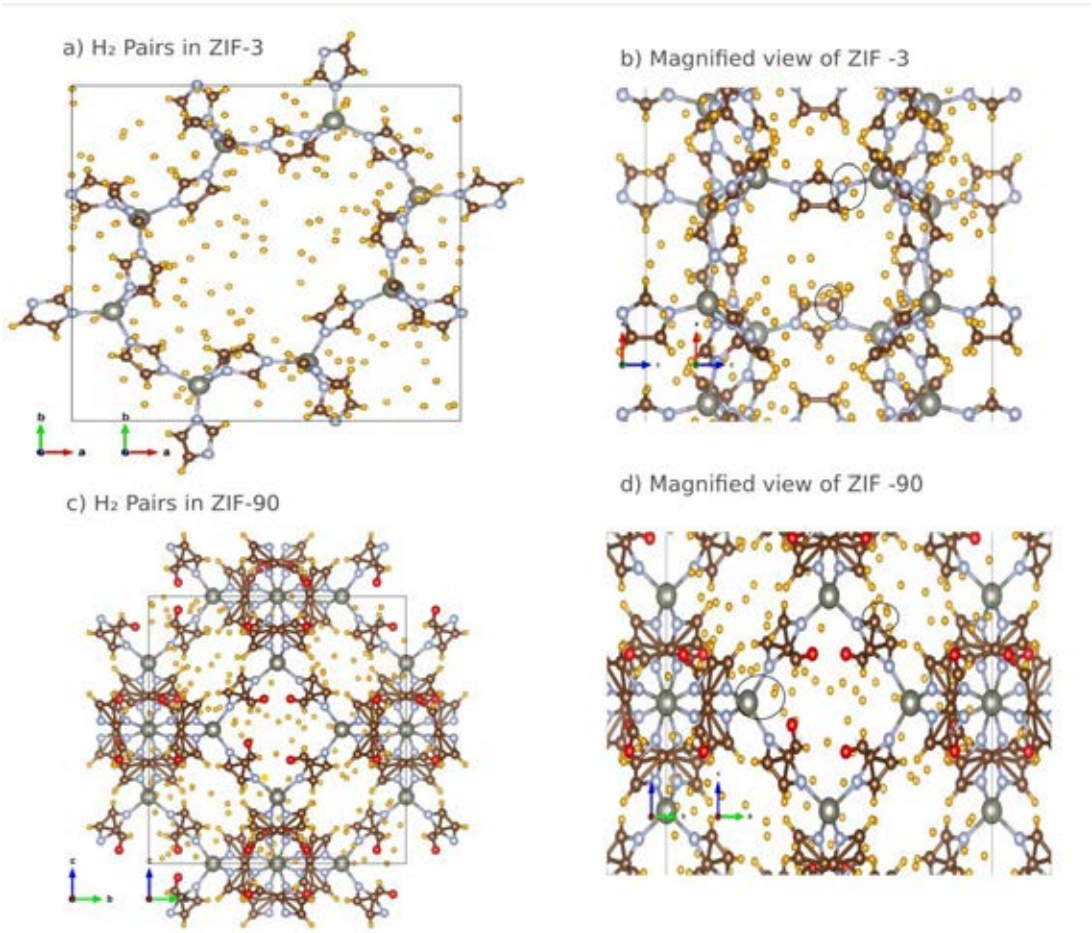

Fig. 4. (Colour online) Geometry-optimized configurations and observed interactions between metal sites and H_2 pairs for (a) ZIF-3 and (b) ZIF-90. Color code: Zn: Gray, C: Brown, O: Red, H: Orange, N: Ice blue.

ACKNOWLEDGEMENT

Y.G. thanks to the Scientific and Technological Research Council of Türkiye (TÜBİTAK) for their support within the TÜBİTAK-1001 Research Program (Grant No. 124Z002). TRUBA HPC sources have been used for the computational work presented in this paper.

REFERENCES

1. Zheng Z, Rong Z, Nguyen HL, and Yaghi OM. 2023. Structural Chemistry of Zeolitic Imidazolate Frameworks. Inorganic Chemistry 62 (51) 20861-20873.
2. Gurdal Y. 2021. Theoretical investigation of ZIFs as adsorbents or membranes for separating noble gas mixtures: applying a newer method for predicting performances. Journal of Porous Materials 28:905–917.
3. Timofeeva MN, Panchenko VN, Jhung SH. 2023. Insights into the Structure-Property-Activity Relationship of Zeolitic Imidazolate Frameworks for Acid-Base Catalysis. International Journal of Molecular Sciences 22;24(5):4370.
4. Wu H, Zhou W, and Yildirim T. 2007. Hydrogen Storage in a Prototypical Zeolitic Imidazolate Framework-8. Journal of the American Chemical Society 129, 17, 5314–5315.
5. Yun JH, He Y, Otero M, Düren T, and Seaton NA. 2002. Adsorption Equilibrium of Polar/Non-polar Mixtures on MCM-41: Experiments and Monte Carlo Simulation. Studies in Surface Science and Catalysis, 685–692.
6. Dubbeldam D, Calero S, Ellis DE, et al. 2016. Raspa: molecular simulation software for adsorption and diffusion in flexible nanoporous materials. Molecular Simulation 42(2):81–101.
7. Rappé AK, Casewit CJ, Colwell KS, Goddard WA, and Skiff WM. 1992. UFF, a full periodic table force field for molecular mechanics and molecular dynamics simulations. Journal of the American Chemical Society 114(25), 10024-10035.
8. Allen MP, and Tildesley DJ. 1987. Brooks CL. Computer simulation of liquids. 0470-20812-0.

EVALUATION OF GREEN HYDROGEN PRODUCTION USING WEIBULL AND GAMMA DISTRIBUTIONS: TECHNICAL, ECONOMIC, AND ENVIRONMENTAL PERSPECTIVES

[1]*Yağmur Arıkan Yıldız*, [2*]*Mehmet Güçyetmez*
[1,2] Sivas University of Science and Technology, Department of Electrical-Electronic Engineering, Sivas, 58140, Turkey
*Corresponding author e-mail: mehmetgcy@sivas.edu.tr

ABSTRACT
Hydrogen energy is a sustainable carrier that enables fossil fuel replacement and long-term storage for renewable energy. This study evaluates the annual hydrogen production capacity of the Sivas region using its wind and solar potential. For a realistic model, one year of hourly data is analyzed using the Weibull and Gamma distributions for wind and solar energy, respectively. Based on these analyses, wind turbines and solar panels (300 kW–450 kW) are selected, and monthly/annual energy production potential is calculated. A PEM electrolyzer is then used to estimate hydrogen production. For a comprehensive evaluation, five scenarios assessed wind and solar energy in individual and hybrid configurations. In contrast, the sixth and seventh scenarios analyzed hydrogen production using grid electricity from fossil fuels and renewables. The levelized cost of hydrogen (LCOH) is determined, showing that hydrogen costs $4.15–7.77/kg with renewables and $8.59–10.3/kg with grid power, highlighting the economic benefits of local resources. Besides, the effects of CAPEX, government incentives, and hydrogen production on LCOH are investigated. Hydrogen production is found to reduce CO_2 emissions by 1,357–1,727 tons annually, generating $19.25–25.91 million in carbon revenue, making it both an economical and sustainable energy solution.
Keywords: Hydrogen production, renewable energy, Weibull& Gama statistical method, Economic feasibility, Carbon reduction

1. INTRODUCTION

Hydrogen, abundantly available in nature, is a key energy carrier with high energy density and eco-friendly properties. It reduces carbon emissions, enhances energy security, and stabilizes energy systems by balancing fluctuations in renewable sources. Since hydrogen does not exist freely, it must be produced and is classified as grey, blue, or green based on its energy source. Grey hydrogen comes from fossil fuels, blue hydrogen captures emissions, and green hydrogen—produced via renewable-powered electrolysis—is the most sustainable. The global adoption of hydrogen energy is accelerating, making it a key part of energy policies worldwide. The EU, Japan, South Korea, and China lead the hydrogen economy with national strategies. Germany is investing €9 billion in hydrogen infrastructure, while Japan focuses on hydrogen-based transportation. Research on hydrogen energy is growing in Turkey, especially in renewable-based production. However, large-scale production, storage, and distribution costs remain significant challenges. Research on integrating hydrogen into sustainable energy systems is advancing rapidly. Some notable studies are outlined: Aziz et al. examined biomass and organic waste conversion into hydrogen, assessing economic feasibility [1]. Berrada and Laasmi analyzed green hydrogen costs in Morocco, finding prices between $3.49–5.96/kg, with variations across regions [2]. Razi and Dinçer compared solar hydrogen production methods, concluding that high-temperature processes are more efficient but environmentally harmful, while photonic and biochemical methods are greener but less efficient [3]. Ayodele et al. assessed a wind-powered hydrogen refueling station in South Africa, with costs ranging from $6.34–8.97/kg, making it globally competitive [4]. Rezai et al. evaluated offshore wind-based hydrogen production in Australia, showing that input power significantly affects electrolysis energy consumption [5]. This study evaluates Sivas's hydrogen production potential using wind and solar energy. A realistic modeling approach assesses renewable capacity, estimates energy output, and compares hydrogen production feasibility with grid-based alternatives. Economic and environmental impacts are also examined.

2. MATERIALS AND METHODS

Sivas's province is selected as the study area, located between 35° 50'–38° 14' E longitude and 38° 32'–40° 16' N latitude. Hourly wind speed, solar radiation, and temperature data from 2023–2024 NASA datasets are used. [6].

2.1. The evaluation of Wind Potential

Accurate wind energy assessment relies on analyzing wind speed distribution. For this, the two-parameterWeibull distribution defined in the Eq. (1) is widely used.

$$f(v) = \frac{k}{c}\left(\frac{v}{c}\right)^{k-1} e^{-\left(\frac{v}{c}\right)^{k}} \tag{1}$$

Here, *e* represents the Euler function, k (shape parameter) defines wind speed variability, and c (scale parameter) indicates its overall magnitude. k and c are determined using Eqs. (2) and (3), respectively [7].

$$k = \left(\frac{\sigma v}{\bar{v}}\right)^{-1.086} \tag{2}$$

$$c = \frac{\bar{v}}{\Gamma\left(1+\frac{1}{k}\right)} \tag{3}$$

Here, σ represents the standard deviation, $\bar{v}$ is the mean wind speed, and Γ denotes the gamma function. The average

power generated by the wind turbine using the Weibull distribution is calculated with Eq. (4) [7].

$$P_{avgw} = \frac{1}{2}\rho A C_P \int_{v_{cut-in}}^{cut-out} v^3 f(v) dv \quad (4)$$

Here, P_{avgw} represents average wind power, ρ is air density, C_p is the turbine's power coefficient, and A is the rotor swept area. v_{cut-in} is the minimum wind speed required for turbine operation (m/s), while $v_{cut-out}$ is the maximum wind speed at which the turbine shuts down (m/s).

2.2. The evaluation of Solar Potential

The gamma statistical method models the variability of solar radiation, with its probability density function given in Eq. (5) [8].

$$f(G) = \frac{G^{\alpha-1} e^{-G/\beta}}{\beta^{\alpha}\Gamma(\alpha)} \quad (5)$$

where G is the solar radiation. α and β denote shape and scale parameters. Using solar radiation data modeled with the gamma distribution, the average power output of a pv panel can be estimated using Eq. (6) [8]:

$$P_{avgs} = \eta A \int_0^{\infty} G f(G) dG \quad (6)$$

where η represents efficiency of pv panel. A denotes the surface area of the solar panel (m²).

2.3. The evaluation of Hydrogen Production

Hydrogen is produced via water electrolysis (Eq.7) using renewable energy [9].

$$2H_2O \rightarrow 2H_2(g) + O_2(g) \quad (7)$$

Eq. (8) is used to calculate the amount of hydrogen production.

$$H_p = \frac{P_E * t * \eta_e}{E_H} \quad (8)$$

where H_p and E_H represent the mass of hydrogen produced and energy required to produce one gram of hydrogen, respectively. P_E is the total electric power, t is the time of operation. η_e denotes efficiency of the electrolyzer [9].

2.4 Economic Analysis and Cost Evaluation of Hydrogen Production

The two most important basic formulae for the economic analysis of hydrogen production are the total cost and the levelised cost of hydrogen (LCOH). The main components that constitute the total cost of hydrogen production (C_{TOTAL}) are capital cost (C_{CAPEX}), operating cost (C_{OPEX}), and energy cost (C_{ENERGY}):

$$C_{TOTAL} = C_{CAPEX} + C_{OPEX} + C_{ENERGY} \quad (9)$$

The unit cost of hydrogen (LCOH) is found using Eq. (10):

$$LCOH = \frac{C_{TOTAL}}{H_P} \quad (10)$$

2.5. Carbon Quota and Emission Analysis of Hydrogen Energy

Hydrogen's emissions depend on its energy source; renewables produce **zero-emission green hydrogen**, while fossil fuels generate CO_2. In this study, wind and solar energy are used, and emission reduction is calculated via Eq. (11) [10]

$$\Delta_{E_{CO_2}} = \left(C_E^{fossil} - C_E^{renewable}\right) * E_{TOTAL} \quad (11)$$

Here, $\Delta_{E_{CO_2}}$ represents the reduced CO_2 amount, C_E^{fossil} while and $C_E^{renewable}$ are the carbon emission factors for electricity from fossil fuels and renewable energy, respectively. E_{TOTAL} denotes the total energy produced. In carbon markets, systems that reduce emissions earn carbon credits, which can be traded for revenue. Carbon revenue is calculated using Eq. (12). Here, R_{Carbon} , p_c represents the total revenue from carbon credits and unit price of carbon credit

$$R_{Carbon} = \Delta_{E_{CO_2}} * p_c \quad (12)$$

3. RESULTS AND DISCUSSION

This study evaluates Sivas' wind potential using the Weibull distribution. Monthly k and c values are calculated, with annual k = 2.1429 and c = 5.8577, validated by R² = 0.9821 and MAE = 0.001234 (Fig. 1). Two optimal wind turbines, Enercon E-30 (300 kW) and Vestas V27 (450 kW), are identified. The Enercon E-30 produces 900 MWh/year (34.24% capacity factor), while the Vestas V27 generates 1,487.4 MWh/year (37.27% capacity factor) (Table 1).

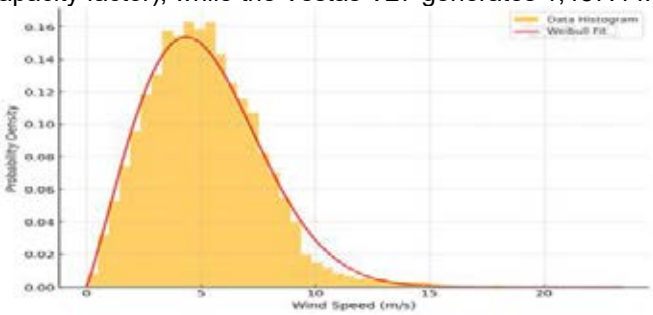

Fig.1. Weibull probability density function

Table 1. The results of wind energy analysis

k	2.1429
c	5.8527
R2	0.9821
MAE	0.001234
Energy generation (E30)	900 MWh
Capacity factor (E30)	%34.24
Energy generation (V27)	1,487.400 MWh
Capacity factor (V27)	%37.27

The Gamma distribution is applied to model solar energy data, with shape and scale parameters of 4.86 and 0.86,

respectively. The goodness of fit is evaluated using the Kolmogorov-Smirnov (KS) test and Pseudo R^2, yielding a *p*-value of 0.95 and a Pseudo R^2 of 0.85. These results confirm the Gamma distribution's suitability for representing the region's solar energy potential, though alternative distributions may also be applicable. The Gamma probability density function is shown in Figure 2. Annual energy production for PV panels with 300 kW capacity and 21% efficiency is 482.481 MWh, while 450 kW panels produce 723.722 MWh. The related results are summarized in Table 2.

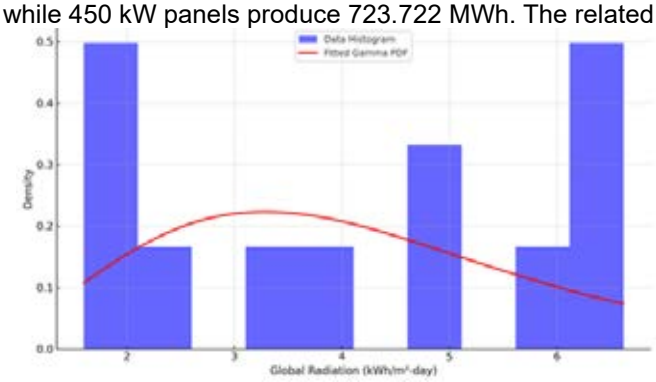

Fig.2. Gama probability density function

Table 2. The results of solar energy analysis

α	4.86
β	0.87
KS	0.27
p	0.95
Pseudo R^2	0.85
Energy production/year (300 kW-PV panel)	482.481 MWh
Energy production/year (450 kW-panel)	723.722 MWh

The monthly hydrogen production obtained using a PEM electrolyzer with 75% efficiency from wind turbines and solar panels of varying capacities is presented in Figure 3. The results indicate that wind turbines produce more hydrogen, particularly during winter, while solar energy reaches peak hydrogen production in May and June. The Vestas V27 (450 kW wind turbine) achieves the highest hydrogen output, whereas the 450 kW solar PV system approaches wind turbine performance during summer.

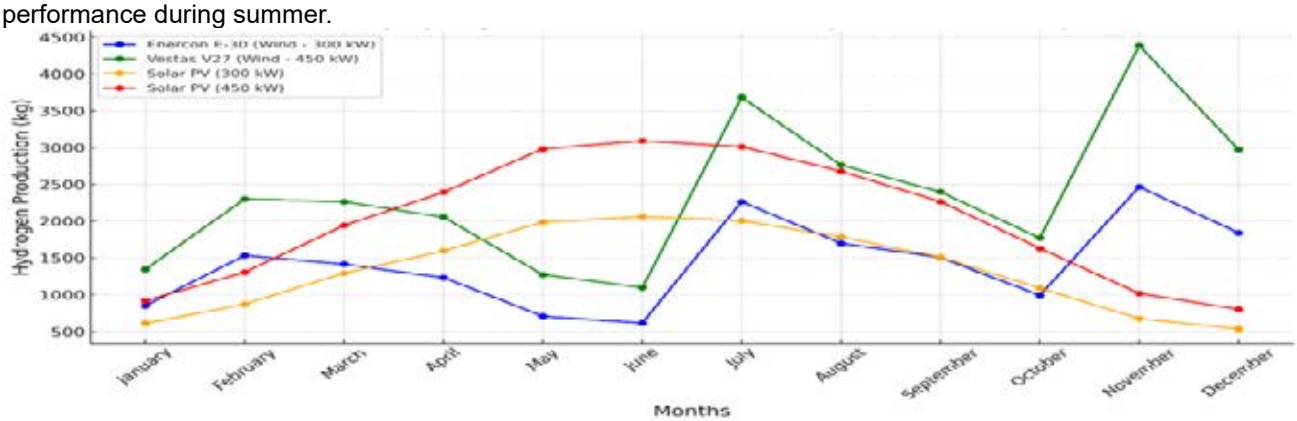

Figure 3. The monthly hydrogen production amount

Eight scenarios for hydrogen production are set up for real-world practical applicability. Scenarios one to five are based on regional solar and wind energy, either individually or as a hybrid mix. Scenario six uses grid electricity obtained from fossil fuels, and scenario seven uses only renewable grid electricity. Hydrogen production, cost, CO_2 savings, and carbon revenue are calculated for the scenarios. CAPEX for wind turbines and solar PV is $1,300/kW and $1,044/kW, respectively, while the OPEX is $16/kW-year for wind and $20/kW-year for solar. The 1 MW electrolyzer is used with CAPEX of $1,280,000/year and OPEX of $39,680/year. The emission factor is 0.6261 tons CO_2 avoided per each 1 MWh, and the carbon credit value is $15 per ton CO_2 equivalent.

Table 3. The results of economic and environmental analysis determined different scenarios

Scenarios	Contents	The amount of hydrogen production (kg)	LCOH ($/kg)	Reduced carbon emission (ton $C0_2$/year)	Carbon credit value ($/year)
1	%100 wind	54534	4.15	1727660	25914905
2	%50 wind-%50 solar	41044	5.37	1357447	20361711
3	%40 wind-%60 solar	38346	5.71	1283405	19251072
4	%60 wind-%40 solar	43742	5.06	1431490	21472440
5	%100 solar	27567	7.77	987234	14808517
6	Purchase from grid (Fossil sources)	41044	10.30	1357447	20361711
7	Purchase from grid (renewable sources)	41044	8.59	1357447	20361711

Finally, the effects of CAPEX and OPEX values and hydrogen production on the LCOH value are investigated in the

study. The graphs related to this are given in Fig. 4. An increase in CAPEX increases LCOH, while a decrease reduces costs; the effect of OPEX is more limited. Higher incentive levels reduce LCOH, increasing the competitiveness of hydrogen.

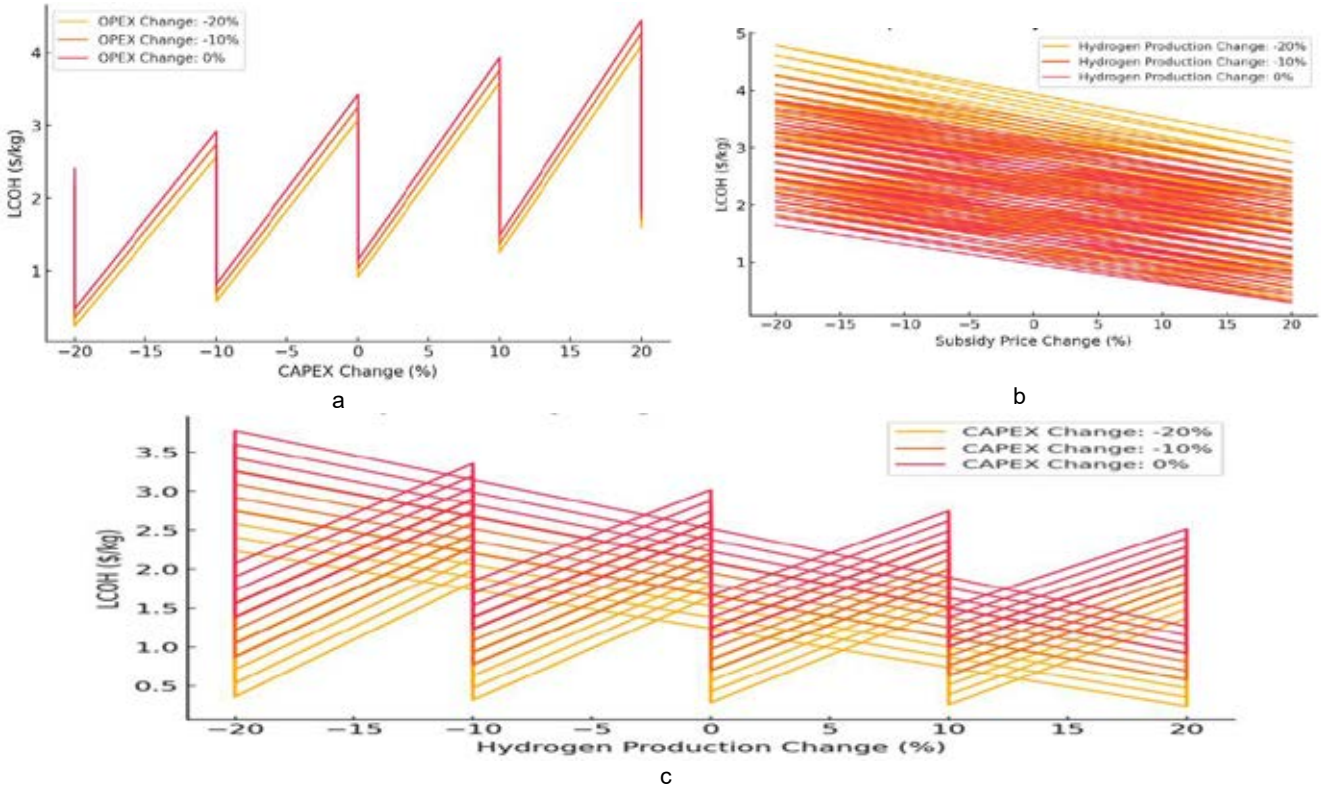

Fig.4. The effects of a) CAPEX, b) subsidy price, c) hydrogen production on LCOH

4. CONCLUSIONS

Utilizing the Sivas region's wind and solar potential for hydrogen production is more economical than purchasing on-grid electricity, reducing LCOH from $8.59–10.3/kg to $4.15–7.77/kg. Local renewable resources not only lower costs but also cut CO_2 emissions by 1,357–1,727 tons annually, generating $19.25–25.91 million in carbon revenue. This highlights regional renewable energy integration's economic and environmental advantages for sustainable hydrogen production.

REFERENCES

1. Aziz, M., Darmawan, A. and Juangsa, F.B. (2021). Hydrogen production from biomasses and wastes: A technological review. International Journal of Hydrogen Energy, 46,68:33756-33781.
2. Berrada, A. and Laasmi, M. A. 2021. Technical-economic and socio-political assessment of hydrogen production from solar energy. Journal of Energy Storage, 44, 103448
3. Razi, F. and Dinçer, I. 2020. A critical evaluation of potential routes of solar hydrogen production for sustainable development. Journal of Cleaner Production, 264,121582.
4. Ayodele, T.R., Mosetlhe, T.C., Yusuf, A.A. and Ntombela, M. 2021. Optimal design of wind-powered hydrogen refuelling station for some selected cities of South Africa. International Journal of Hdyrogen Energy. 46,49, 24919-24930.
5. Rezaei, M., Akimov, A. and Gray, E. M. 2024. Techno-economics of offshore wind-based dynamic hydrogen production. 374,124030.
6. NASA POWER. (2025). https://power.larc.nasa.gov/data-access-viewer/.
7. Teimourian, H., Abubakar, M., Yıldız, M. and Teimourian, A. 2022. A comparative study on wind energy assessment distribution models: A case study on Weibull Distribution. Energies, 15,15,5684.
8. Lopez-Meraz, R., Callejo, L.H., Jamed-Boza,L., Alonso-Gomez. (2021). Determination of photvoltaic power by modeling solar radiation with Gamma distribuition in the CEDER microgrid. Revista Facultad de Ingeniería, 99,32-43.
9. Ishaq, H. and Dinçer, I. (2021). Comparative assessment of renewable energy-based hydrogen production methods. Renewable and Sustainable Energy Reviews, 135,110192.
10. Ministry of Energy and Natural Resources of Turkiye. 2025. https://enerji.gov.tr/evced-cevre-ve-iklim-turkiye-ulusal-elektrik-sebekesi-emisyon-faktoru

UNDERSTANDING OF THE ACTIVITY OF NIFE OXIDE BASED OER CATALYSTS TOWARD MESOPOROUS NIFE OXIDE THIN FILMS

[1,2]*Alp Eren Başaran*, [1,2]*Cüneyt Karakaya*, [2]*Navid Solati,* [1,2,*]*Sarp Kaya*
[1]Department of Chemistry, Koç University, 34450 Istanbul, Türkiye
[2]Koç University Hydrogen Technologies Center (KUHyTech), 34450, Istanbul, Türkiye

*Corresponding author e-mail: sarpkaya@ku.edu.tr

ABSTRACT
Recent studies have been focusing focused on the mixed transition metal-based oxide electrocatalysts such as (CoFe, NiFe, MnNi, or FeCoNi) and layered double hydroxides (LDH) due to better performance and stability rather than pure forms for oxygen evolution reaction. Most NiFe-based electrocatalysts undergo structural and compositional self reconstruction under applied anodic potential; usually result in a dynamic activity in OER. In this study the catalytic properties of mesoporous thin film $NiFeO_x$ compounds are shown through cyclic voltammetry, and they were characterized through Raman, TEM/STEM, and XPS.
Keywords: NiFe oxides, OER, water splitting, LDH

1. INTRODUCTION

Developing abundant and cheap electrocatalysts for the electrolysis of water that minimize overpotential and Tafel slope is a challenge standing over against the efficient electrolyzers. Recent studies have focused on the mixed transition metal-based oxide electrocatalysts such as (CoFe, NiFe, MnNi, or FeCoNi) and layered double hydroxides (LDH) due to better performance and stability rather than pure forms [1]–[4]. Among them, NiFe oxide electrocatalysts have come into prominence owing to superior long-standing activity [5]. An enhanced OER activity obtained by incorporating Fe at even very low concentrations into nickel oxide had been demonstrated [6].

NiFe-based electrocatalysts with several structures, various morphologies, adjustable stoichiometries, modified electronic structures, abundant active sites, and long-range order can be synthesized in many synthesis protocols [7], [8], [9]–[12]. Mesoporous metal oxide thin film electrodes can satisfy many requirements for the next generation electrolyzer technology and the understanding of triangle among the structure-stability-activity relations. In addition, creating more surface area with interconnecting conductive networks increases the number of active sites and improves charge transfer kinetics and reagent/product diffusion as their mesoporous analogues [13], [14]–[16], [12]. Herein, we applied the liquid crystal templating method to produce mesoporous more durable flat NiFe oxide thin film electrodes. The mesoporous $NiFeO_x$, $NiFe_2O_4$, and Fe_2O_3 thin film electrodes on FTO having tunable compositions and a high surface area were successfully synthesized and comprehensively characterized. OER activities and stabilities of the electrodes were compared by numerous electrochemical tests in both Fe-free and non-purified electrolytes. Uniform and highly porous nano-sized metal oxide framework allowed the understanding of the OER mechanism of NiFe based electrocatalysts in which insertion of an infinitesimal number of Fe atoms in NiO lattice boosts the OER activity of Ni sites by altering its electronic structure.

2. MATERIALS AND METHODS

2.1. Preparation of Solutions of Nickel and Iron Precursors and Surfactants for Mesoporous NiFe Oxide Thin Films

In a typical solution preparation, CTAB, $C_{12}EO_{10}$, nickel nitrate hexahydrate, and iron nitrate nonahydrate are mixed in a 25 ml vial with deionized water. The solution is stirred for one day in order to make sure that it is homogenous and clear. Deionized water was kept constant in all solutions, 5 g. As CTAB/$C_{12}EO_{10}$ mole ratio was kept being 1.0 and total transition metal (iron and nickel nitrate)/CTAB mole ratio was kept being 9.0 for all solutions, nickel/iron salt mole ratios were altered. The nickel to iron salt mole ratios were used for labeling the solution.

2.2. Preparation of Lyotropic Liquid Crystalline (LLC) Mesophase for Mesoporous NiFe Oxide Thin Films

Spin coating was applied to prepare LLC and further mesoporous NiFe oxide thin films. An adequate amount of the solution was placed on the FTO or glass lamels and it was spun for 20 s at 1000 rpm by a spin coater. To obtain thicker mesophase, drop-cast coating on the microscopic slides was also applied. Drop-casting was applied by placing solution and aged for evaporation of deionized water. The spin-coated samples were used for XRD analysis.

2.3. Synthesis of Mesoporous NiFe Oxides

Mesoporous NiFe oxide thin films were prepared via calcination of LLC prepared by spin coating or drop-casting coating. The calcination procedure was carried out starting from room temperature up to 300 ℃ with a ramp of 2℃/min and keeping at 300 ℃ for 2 hours. The samples were annotated as mesoporous Ni_x/Fe_y, where x and y are the mole ratios

of nickel nitrate and iron nitrate to CTAB, respectively.

3. RESULTS AND DISCUSSION

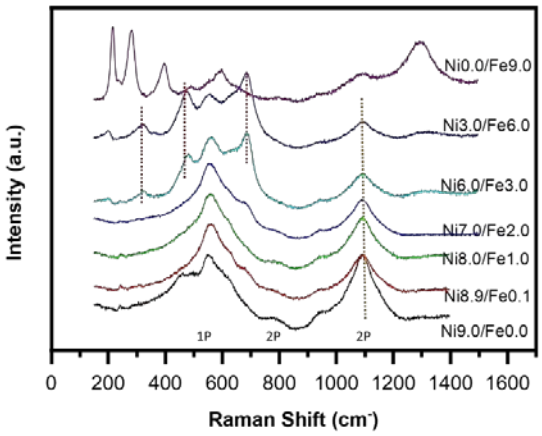

Fig. 1. Raman spectrum of the calcined samples of various Ni/Fe salt mole ratio mesophases

Raman spectroscopy analysis was conducted to figure out the oxide phases present in critical synthesized mesoporous samples, (Fig. 1). When the sample content becomes Ni6.0/Fe3.0, three new peaks appear at 320, 467, and 688 cm^{-1}, belonging to spinel structured $NiFe_2O_4$. At Ni3.0/Fe6.0, the NiO peak at 1100 cm^{-1} has low intensity compared to other peaks. The sample of pure Fe directly matches with α-Fe_2O_3. In conclusion, Up to Ni/Fe ratio, 7/2, iron atom are mixed in the rock salt type NiO, and then the formation of spinel $NiFe_2O_4$ structures starts at higher iron contents until the main oxide phase becomes spinel mixed oxide structure at Ni3.0/Fe6.0.

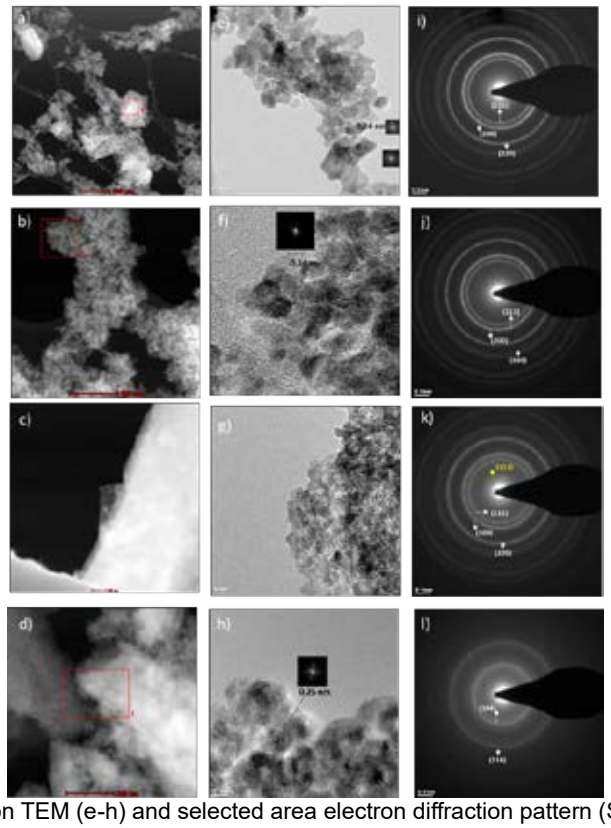

Fig. 2. STEM (a-d), high resolution TEM (e-h) and selected area electron diffraction pattern (SAED) (i-l) of calcined samples of Ni9.0/Fe0.0, Ni8.9/Fe0.1, Ni60/Fe3.0 and Ni0.0/Fe9.0, respectively

TEM/STEM experiments were performed to examine the more detailed structural and morphological analysis in selected samples at the nanoscale, (Fig. 2). Pure and mixed samples show a sponge-like mesoporous framework as seen in STEM images. High-resolution TEM images and selected area electron diffraction patterns (SAED) of Ni9.0/Fe0.0 and

Ni8.9/Fe0.1 samples are consistent with Raman analysis. Iron atoms substitute with nickel atoms in cubic NiO crystalline structure with particle sizes around 5-10 nm. At Ni6.0/Fe3.0 sample, electron diffraction pattern differs from other mixed oxide phases with the circle indexed as (111) lattice plane of spinel $NiFe_2O_4$ with a yellow arrow as detected in Raman analysis. The pure iron sample displays an α-Fe_2O_3 nanocrystalline structure, having a particle size smaller than 5 nm.

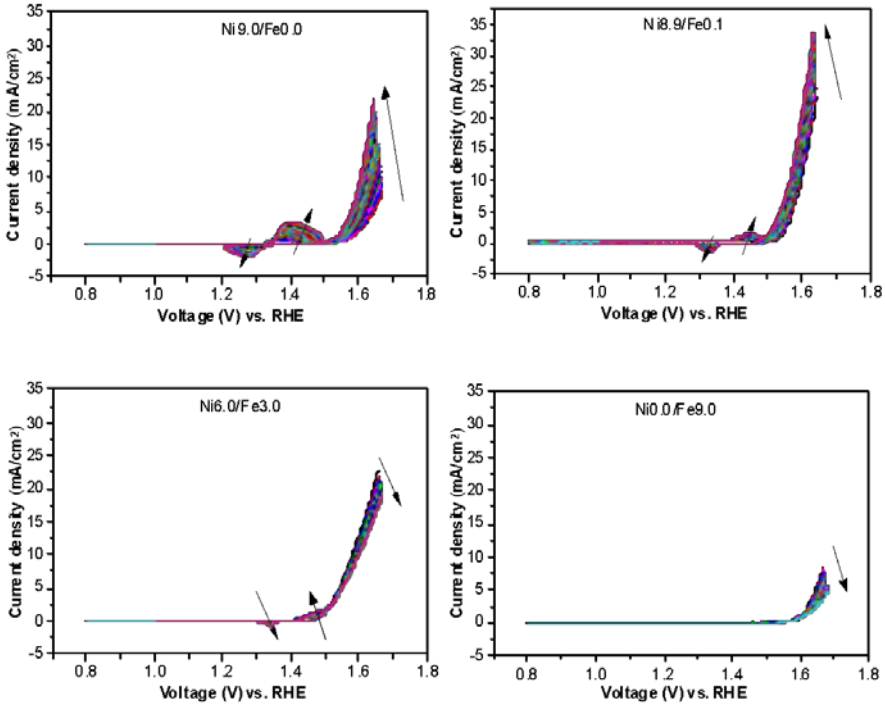

Fig. 3. Consecutive CV plots for mesoporous NiFe oxide electrodes having various compositions in alkaline electrolyte, 1.0 M KOH.

In order to verify the compositional change which is responsible for $Ni(OH)_2$/NiOOH and Fe impurities in KOH, cyclic voltammetry plots were recorded for selected electrodes in Fig.3. The observed oxidative peak is reversible due to appearing opposite reductive peak at lower potentials in the reverse cycle, evidence for the change of $Ni(OH)_2$/NiOOH. Interestingly, the OER activity of mesoporous pure nickel electrode increases with CV scans intenser than the observations in LSV measurements. Another abnormality is that the steady activities in LSV measurements of mesoporous NiFe oxide electrodes present the enhancing or diminishing trends with CV cycles accompanying alterations of oxidation/reduction potentials nickel in even pure NiO. CA tests of selected electrodes display mild changes as their LSV tests. In order to reveal the activity-structure relations regarding composition, the electrochemical tests should be conducted in Fe-free KOH electrolyte.

Fig.4 shows the XPS results of the samples before and after electrochemical measurements in the clean electrolyte. Studying the Fe 2p and Ni 2p spectra of these samples reveals no significant difference between them and the samples measured after immersing inside electrolyte. The observations for the Br/Ni content, and the nickel hydroxide/oxide peaks in the Ni 2p spectra can be observed here too. It is important to point out that the Br 3d peak intensity decreases for all of the samples and it has a shift towards lower binding energies.

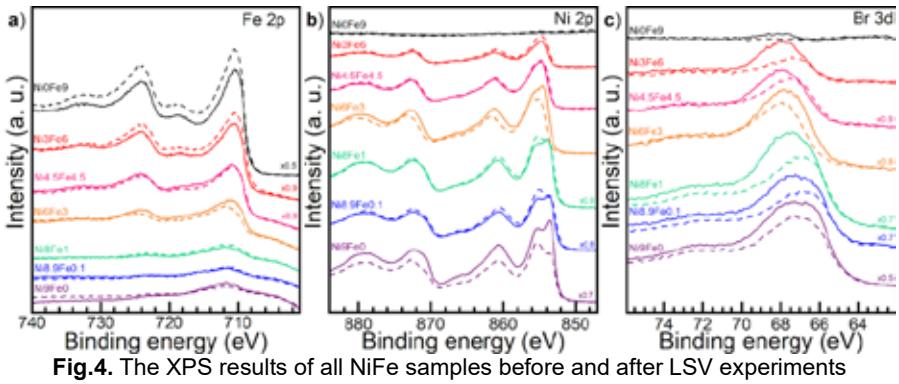

Fig.4. The XPS results of all NiFe samples before and after LSV experiments

4. CONCLUSIONS

We applied the lyotropic liquid crystalline strategy to fabricate mesoporous iron nickel oxide thin films for OER. We tuned the phase, composition, crystallinity of mesoporous iron nickel oxide. The trace content of iron yields mesoporous Fe-doped NiO and higher content of Fe promotes the formation $NiFe_2O_4$. We examined the OER activities of various phase and composition of mesoporous iron nickel oxide, including neat NiO and Fe_2O_3. The OER activity trend follows NiFeOx > $NiFe_2O_4$ > NiO > Fe_2O_3

REFERENCES

[1] M. S. Burke, M. G. Kast, L. Trotochaud, A. M. Smith, and S. W. Boettcher, "Cobalt–Iron (Oxy)hydroxide Oxygen Evolution Electrocatalysts: The Role of Structure and Composition on Activity, Stability, and Mechanism," J. Am. Chem. Soc., vol. 137, no. 10, pp. 3638–3648, Mar. 2015, doi: 10.1021/jacs.5b00281.
[2] C. C. L. McCrory, S. Jung, I. M. Ferrer, S. M. Chatman, J. C. Peters, and T. F. Jaramillo, "Benchmarking Hydrogen Evolving Reaction and Oxygen Evolving Reaction Electrocatalysts for Solar Water Splitting Devices," J. Am. Chem. Soc., vol. 137, no. 13, pp. 4347–4357, Apr. 2015, doi: 10.1021/ja510442p.
[3] D. Friebel et al., "Identification of Highly Active Fe Sites in (Ni,Fe)OOH for Electrocatalytic Water Splitting," J. Am. Chem. Soc., vol. 137, no. 3, pp. 1305–1313, Jan. 2015, doi: 10.1021/ja511559d.
[4] J. Kibsgaard and I. Chorkendorff, "Considerations for the scaling-up of water splitting catalysts," Nat Energy, vol. 4, no. 6, pp. 430–433, Jun. 2019, doi: 10.1038/s41560-019-0407-1.
[5] J. Zhao, J.-J. Zhang, Z.-Y. Li, and X.-H. Bu, "Recent Progress on NiFe-Based Electrocatalysts for the Oxygen Evolution Reaction," Small, vol. 16, no. 51, p. 2003916, 2020, doi: 10.1002/smll.202003916.
[6] D. A. Corrigan, "The Catalysis of the Oxygen Evolution Reaction by Iron Impurities in Thin Film Nickel Oxide Electrodes," J. Electrochem. Soc., vol. 134, no. 2, p. 377, Feb. 1987, doi: 10.1149/1.2100463.
[7] L. Trotochaud, J. K. Ranney, K. N. Williams, and S. W. Boettcher, "Solution-Cast Metal Oxide Thin Film Electrocatalysts for Oxygen Evolution," J. Am. Chem. Soc., vol. 134, no. 41, pp. 17253–17261, Oct. 2012, doi: 10.1021/ja307507a.
[8] K. Fominykh et al., "Iron-Doped Nickel Oxide Nanocrystals as Highly Efficient Electrocatalysts for Alkaline Water Splitting," ACS Nano, vol. 9, no. 5, pp. 5180– 5188, May 2015, doi: 10.1021/acsnano.5b00520.
[9] W. Ma et al., "A Superlattice of Alternately Stacked Ni–Fe Hydroxide Nanosheets and Graphene for Efficient Splitting of Water," ACS Nano, vol. 9, no. 2, pp. 1977– 1984, Feb. 2015, doi: 10.1021/nn5069836.
[10] X. Lu and C. Zhao, "Electrodeposition of hierarchically structured threedimensional nickel–iron electrodes for efficient oxygen evolution at high current densities," Nat Commun, vol. 6, no. 1, p. 6616, Mar. 2015, doi:10.1038/ncomms7616.
[11] G. Zhang, Y. Li, Y. Zhou, and F. Yang, "NiFe Layered-Double-HydroxideDerived NiO-NiFe2O4/Reduced Graphene Oxide Architectures for Enhanced Electrocatalysis of Alkaline Water Splitting," ChemElectroChem, vol. 3, no. 11, pp. 1927–1936, 2016, doi: 10.1002/celc.201600301.
[12] C. Dong, T. Kou, H. Gao, Z. Peng, and Z. Zhang, "Eutectic-Derived Mesoporous Ni-Fe-O Nanowire Network Catalyzing Oxygen Evolution and Overall Water Splitting," Advanced Energy Materials, vol. 8, no. 5, p. 1701347, 2018, doi:10.1002/aenm.201701347.
[13] C. Karakaya et al., "Mesoporous Thin-Film NiS2 as an Idealized PreElectrocatalyst for a Hydrogen Evolution Reaction," ACS Catal., vol. 10, no. 24, pp. 15114–15122, Dec. 2020, doi: 10.1021/acscatal.0c03094.
[14] A. Amirzhanova et al., "Synthesis and water oxidation electrocatalytic and electrochromic behaviours of mesoporous nickel oxide thin film electrodes," Journal of Materials Chemistry A, vol. 7, no. 38, pp. 22012–22020, 2019, doi:10.1039/C9TA07693J.
[15] A. Amirzhanova, N. Akmanşen, I. Karakaya, and Ö. Dag, "Mesoporous MnCo2O4, NiCo2O4, and ZnCo2O4 Thin-Film Electrodes as Electrocatalysts for the Oxygen Evolution Reaction in Alkaline Solutions," ACS Appl. Energy Mater., vol. 4, no. 3, pp. 2769–2785, Mar. 2021, doi: 10.1021/acsaem.1c00064.
[16] F. Mert Balci et al., "Synthesis of mesoporous LiMn 2 O 4 and LiMn 2−x Co x O 4 thin films using the MASA approach as efficient water oxidation electrocatalysts," Journal of Materials Chemistry A, vol. 6, no. 28, pp. 13925–13933, 2018, doi: 10.1039/C8TA04138E.

PREPARATION OF PYRIDINE POLYBENZIMIDAZOLE/ AMINE FUNCTIONALIZED BORON NITRIDE COMPOSITE MEMBRANE

[1]*Ali Hassen Ali*, [2]*Hande Nur Arkalı*, [2]*Gizem Aktaş*, [2]*Zübeyde Pekdemir*, [2]*Ebru Erünal*, [1]*R. Gültekin Akay*
[1] Kocaeli University, Engineering Faculty, Department of Chemical Engineering, Umuttepe, Kocaeli, 41000, Türkiye
[2] Gebze Technical University, Engineering Faculty, Department of Chemical Engineering, Gebze, Kocaeli 41400, Türkiye
*Corresponding author e-mail: gultekin.akay@gmail.com and ali.hassen@kocaeli.edu.tr

ABSTRACT
The importance of development of fuel cell technologies is well understood in the recent years. One of the most critical components in fuel cells is the polymer electrolyte membrane (PEM). For a long time perfluorinated Nafion^{TR} membranes and their derivatives have been used as an industry standard. But since they are not suited for all types of fuel cells, costly and environmentally not friendly, alternative PEMs especially from non*fluorinated hydrocarbon-based polymers have been studied in the recent years widely. Also, the approach of developing novel composite membranes developed by the incorporation of a functional inorganic material filler having properties such as being hygroscopic, proton conductive, decreasing fuel permeability etc is a promising and preferred method. Among the polymer side, polybenzimidazole (PBI) and its derivatives are also promising materials for further development. Therefore, in this study pyridine PBI was synthesized first and characterized as the host matrix of a novel composite membrane. Then from the inorganic filler alternatives hexagonal boron nitride (hBN) was selected because of its very good intrinsic properties (having no electronic conductivity but some intrinsic protonic conductivity) suitable for a fuel cell operation. Further this hBN was also functionalized by adding functional group for increasing the synergistic effect of the composite membrane and its compatibility. In this study both the synthesis of the polymer and its characterizations, and also the synthesis of functionalized hBN and its characterization were explained. py-PBI and amine functionalized hBN were successfully prepared according to FTIR and XRD results. Then filler was used at a fixed amount to produce the composite PEM by solvent casting method and a homogeneous well-formed film was obtained. Its most important property for a potential PEM to be used in a fuel cell, which is the proton conductivity, was measured by electrochemical impedance spectroscopy.

Keywords: polymer electrolyte membrane, composite membrane, py-PBI, hexagonal boron nitride, amine functionalization

1. INTRODUCTION

The areas of use of PEM (Proton Exchange Membrane) cells are especially in hydrogen fuel cells for energy production.[1][2] PEM fuel cells stand out as devices that directly convert chemical energy into electrical energy.[3] They are used in energy storage and conversion applications due to their advantages such as high-power density, environmentally friendly features, silent operation and fast start up speeds. The purpose of using functionalized boron nitride (BN) in proton exchange membranes is to increase the performance of PEM fuel cells and reduce material costs.[4], [5] The superior thermal and mechanical stability and high proton conductivity of boron nitride play an important role in improving the poor thermal and mechanical properties of Polybenzimidazole (PBI) membranes. In this context, the addition of BN provides a lower cost and environmentally friendly alternative compared to existing perfluorinated membranes, providing a wider potential for use in energy applications.

The unique properties of hexagonal boron nitride (h-BN) have made it a focal point in fields like electronics, energy storage, and biotechnology. Its combination of high thermal conductivity and electrical insensitivity renders it suitable for thermal management and dielectric applications. Functionalization further enhances h-BN's utility by modifying its surface properties[5] Techniques such as hydroxylation, silanization, and amination are employed to boost attributes like hydrophilicity, thermal stability, and dispersibility. These enhancements improve h-BN's integration into various matrices and broaden its potential applications, particularly in proton exchange membranes (PEMs) used in fuel cells. In PEMs, h-BN serves as a reinforcing agent, improving proton conductivity and thermal stability while addressing water retention and mechanical robustness under hydrated conditions. This makes h-BN an invaluable material for advancing the performance and longevity of PEM-based fuel cells, as well as composites and catalytic systems.[6]

In this study, h-BN was functionalized with amine groups (NH_2-) through sonication method and used to obtain a composite membrane with pyridine polybenzimidazole (Py-PBI) polymer to be utilized in a proton exchange membrane.

2. MATERIALS AND METHODS

2.1. Materials

Monomers, Polyphosphoric acid (PPA,115%), 2.5-Pyridinecarboxylic acid (PCA,98%), Sodium carbonate,99.7%,3,3'-Diaminobenzidine (DAB,98%), N, N-Dimethylacetamide (DMAc), were purchased from Sigma-Aldrich and used for polymerization. H-BN was purchased from Nanografi (99.7%) and urea (99.1%) purchased from Sigma Aldrich.

2.2. Synthesis of pyridine Polybenzimidazole

Pyridine polybenzimidazole (Py-PBI) was successfully synthesized via condensation polymerization in polyphosphoric

acid (PPA) at a temperature range of 150–230°C. The process involved dissolving 3,3'-Diaminobenzidine (DAB,98%) in PPA, followed by the addition of 2,5-pyridinedicarboxylic acid in a 2000-mL Pyrex® resin reaction vessel. The polymerization proceeded under a nitrogen atmosphere with continuous mechanical stirring. The resulting polymer was precipitated in cold water and purified through sequential washing with distilled water and a sodium bicarbonate solution [6-9]. Then, the polymer is dried between 150 °C for 4 h on a hot plate. PBI poweder was obtained after grinding the dried polymer and then PBI solution was formed with DMAc. Lastly, solution casting was conducted in vacuum overn at 80°C for 14 h. The whole procedure is given on Fig.1.

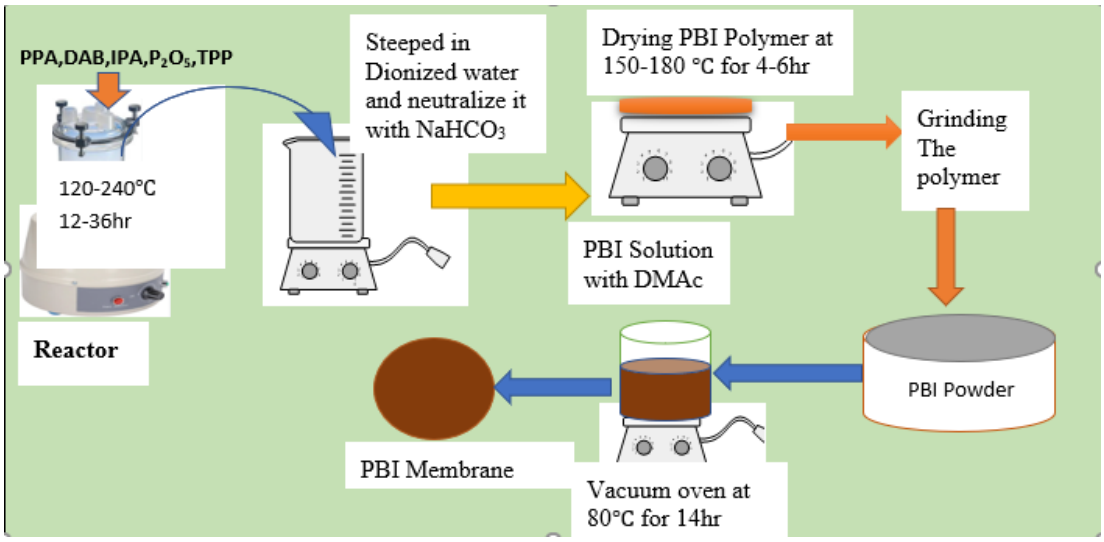

Fig. 1. A simple PBI synthesis flow diagram on a laboratory scale

2.3. NH_2-Functionalization of h-BN

The functionalization of hexagonal boron nitride (h-BN) with amine groups (NH_2) was carried out to enhance its chemical properties and compatibility with various applications. The process involved dispersing 1 g of h-BN in 100 mL of deionized water along with 60 g of urea. This mixture was subjected to ultrasonication for 1 hour to promote exfoliation and interaction between urea and h-BN. Following sonication, the BN(NH_2) suspension was centrifuged five times at 3000 rpm for 10 minutes to remove un-exfoliated h-BN. The supernatant, containing highly concentrated exfoliated BN(NH_2) nanosheets, was carefully decanted. The concentrated suspension was then filtered and thoroughly washed with ethanol and reverse osmosis (RO) water to eliminate any unreacted urea. Finally, the obtained material was dried in an oven at 60°C to obtain NH_2-functionalized h-BN.

2.4. Composite membrane of Py-PBI/h-BN

The boron nitride (BN) was functionalized, and the Py-PBI composite membrane was successfully prepared. The composite membrane was fabricated using the solvent casting method. First, 1 wt% Py-PBI polymer and functionalized h-BN were separately dissolved in 20 mL of DMAc at 150°C and 200°C for 24 hours, respectively. After dissolution, the two solutions were combined and stirred on a magnetic stirrer at 80°C for 24 hours. To ensure uniform dispersion, the mixture was then subjected to ultrasonic mixing at 60°C for 1 hour. After homogenization, 10 mL of the solution was cast onto a Petri dish. The solvent (DMAc) was gradually evaporated in a ventilated oven at 80°C for 24 hours. Finally, the dried composite membrane was carefully peeled off from the Petri dish.[6]

3. RESULTS AND DISCUSSION

The characterization of py-PBI polymer involved viscosity, thermal stability, proton conductivity, and structural analysis. The polymer exhibited an intrinsic viscosity of 1.51 dL/g and an average molecular weight of 70,999 Da.[7] Thermal analysis indicated moderate stability, with py-PBI powder retaining 76.17% residual weight at 600°C, while the undoped membrane showed lower stability at 63.72%.[8] Electrochemical impedance spectroscopy (EIS) was performed using a Gamry Instrument 3000 over a frequency range of 1 MHz to 1 Hz. Proton conductivity reached 0.26 S/cm at 120°C, making py-PBI suitable for moderate-temperature applications, though its performance declined at higher temperatures due to dehydration and structural changes.[8] FTIR analysis confirmed key structural modifications. The N-H stretching peak shifted from 3309.46 cm^{-1} to 3228.83 cm^{-1} after immersion, indicating reduced hydrogen bonding. The C=O stretching vibration at 1735.79 cm^{-1} shifted slightly, suggesting structural rearrangement, while the C-N stretching peak

(1347.9 cm^{-1}) remained stable, preserving the polymer backbone.[8][7]. In another case, the FTIR and XRD results confirm the successful functionalization of h-BN.

4. CONCLUSIONS

The successful functionalization of h-BN with amine groups (NH_2) and its integration into the py-PBI composite membrane demonstrated significant improvements in material properties. the solvent casting method enabled the uniform dispersion of functionalized h-BN within the py-PBI matrix, contributing to enhanced structural and thermal stability. Characterization results confirmed the polymer's high thermal resistance, electrochemical impedance spectroscopy (EIS) indicated a proton conductivity of 0.26 s/cm at 120°C for py-BI, making it suitable for high-temperature applications. FTIR analysis further validated the structural modifications and successful functionalization of h-BN and py-PBI. These findings highlight the potential of py-PBI/BN-11 composite membranes for advanced fuel cell and high-performance applications.

ACKNOWLEDGEMENT

This work was supported by Research Fund of the Kocaeli University project no. FKA-2024-3862

REFERENCES

[1] M. A. Haque, A. B. Sulong, K. S. Loh, E. H. Majlan, T. Husaini, and R. E. Rosli, “Acid doped polybenzimidazoles based membrane electrode assembly for high temperature proton exchange membrane fuel cell: A review,” Int J Hydrogen Energy, vol. 42, no. 14, pp. 9156–9179, 2017

[2] S. S. Araya et al., “A comprehensive review of PBI-based high temperature PEM fuel cells,” Int J Hydrogen Energy, vol. 41, no. 46, pp. 21310–21344, 2016

[3] R. M. Nauman Javed, A. Al-Othman, M. Tawalbeh, and A. G. Olabi, “Recent developments in graphene and graphene oxide materials for polymer electrolyte membrane fuel cells applications,” Renewable and Sustainable Energy Reviews, vol. 168, no. August, p. 112836, 2022

[4] G. R. Bhimanapati, N. R. Glavin, and J. A. Robinson, “2D Boron Nitride: Synthesis and Applications,” in Semiconductors and Semimetals, vol. 95, Academic Press Inc., 2016, pp. 101–147.

[5] C. G. Yin et al., “Multifunctional boron nitride nanosheet/polymer composite nanofiber membranes,” Polymer (Guildf), vol. 162, pp. 100–107, Jan. 2019

[6] D. E. Hussin, Y. Budak, and Y. Devrim, “Development and performance analysis of polybenzimidazole/boron nitride composite membranes for high-temperature PEM fuel cells,” Int J Energy Res, vol. 46, no. 4, pp. 4174–4186, Mar. 2022

[7] M. R. Berber and N. Nakashima, “Bipyridine-based polybenzimidazole membranes with outstanding hydrogen fuel cell performance at high temperature and non-humidifying conditions,” J Memb Sci, vol. 591, no. August, p. 117354, 2019

[8] Harilal, A. Shukla, P. C. Ghosh, and T. Jana, “Pyridine-Bridged Polybenzimidazole for Use in High-Temperature PEM Fuel Cells,” ACS Appl Energy Mater, vol. 4, no. 2, pp. 1644–1656, Feb. 2021

UNDERSTANDING THE KINETIC MECHANISM OF WO_3 PHOTOANODES FOR PEC APPLICATIONS

[1,2*]*Fatih Uçar*, [2,3]*Eğin İrem Haznedar*, [2,4]*Emir Ardalı*, [2,4]*Esra Altuntaş*, [2,4*]*Sarp Kaya*
[1]Materials Science and Engineering, Koç University, 34450 Istanbul, Türkiye
[2]Koç University Hydrogen Technologies Center (KUHyTech), 34450, Istanbul, Türkiye
[3]Department of Chemical and Biological Engineering, Koç University, 34450 Istanbul, Türkiye
[4]Department of Chemistry, Koç University, 34450 Istanbul, Türkiye

*Corresponding author e-mail: sarpkaya@ku.edu.tr

ABSTRACT
This study aims to elucidate the kinetics and reaction mechanisms of WO_3 photoanodes in water splitting reactions through structural and photo-electrochemical (PEC) characterization techniques.
In this study, we focused on the charge carrier dynamics behaviors that occur at the millisecond time regime such as charge accumulation, trapping, recombination and charge transfer. The effect of these kinetic events on the oxygen evolution reaction (OER) mechanism occurring on the WO_3 surface was investigated in different environmental and surface conditions. In this context, the different performance of nitrogen-doped WO_3 compared to plain WO_3 was investigated. Subsequently, nickel oxide (NiO), which is known to directly affect PEC performance, was deposited on the surface as a cocatalyst and its structural and photoelectrochemical tests were completed and compared with bare WO_3. Charge trapping occurring on the W sites is a critical bottleneck and can be circumvented by the cocatalyst layer.

Keywords: photoanode, WO_3, OER, charge carrier,

1. INTRODUCTION
Green hydrogen is essential for renewable energy and lowering CO_2 emissions. Using semiconductor materials, photoelectrochemical (PEC) water splitting effectively transforms solar energy into hydrogen. The goal of research is to create stable, affordable, and scalable photoelectrodes for various settings. A photoanode, a photocathode, and an electrolyte make up the PEC system. The photoanode undergoes the oxygen evolution reaction (OER), whereas the photocathode undergoes the hydrogen evolution reaction (HER)[1].
The choice of an appropriate semiconductor photoanode is essential for the advancement of PEC technology. It needs to be stable over a range of pH values, have an acceptable band gap, and absorb light efficiently. Though it has issues including sluggish charge transport and fast recombination that lower OER efficiency, tungsten trioxide (WO_3), an n-type semiconductor, is a promising candidate. Because of its complexity and energy-demanding nature, OER is the step that determines the rate in PEC applications[2].
Numerous techniques, including the introduction of co-catalysts, doping, surface passivation, and nanostructuring, are employed to increase OER efficiency. Although nanostructuring can create trap sites that result in recombination, it also improves surface area and charge separation. Although nitrogen doping increases photocurrent and light absorption, it can also result in structural disorder that alters surface states and OER efficiency. Charge utilization is still a major obstacle despite advancements in OER development[3].
It is essential to understand charge dynamics and utilizations in order to improve OER performance. It is important to examine charge behaviors such as charge accumulation, trapping, recombination, and transfer over time and at different potentials. Particularly in the millisecond-to-second time range, PEC characterization techniques are crucial for studying charge transport, recombination, and surface reactions.

2. MATERIALS AND METHODS
Experimental materials, including ammonium metatungstate hydrate, hydrochloric acid, methanol, and sodium sulfate, were obtained from Merck. FTO-coated glasses were used as substrates. For the preparation of WO_3 photoanodes, a solution of deionized water, HCl and ammonium metatungstate hydrate was mixed, transferred to an autoclave and subjected to hydrothermal synthesis at 180°C for 6 hours. The FTO substrates were cleaned and the coated films were annealed at 600°C to evaluate their properties.
For nitrogen doping, ammonia and nitrogen gases were introduced into a three-zone furnace at 425°C for 1 hour after the annealing part. NiO deposition as cocatalyst using $NiCl_2$ solution was done by using the drop-casting method under 250°C. PEC measurements were performed using a VSP-300 potentiostat with a three-electrode setup, including an Ag/AgCl reference electrode and a platinum wire counter electrode. A solar simulator with a 100 W Xe lamp was used to simulate sunlight at an intensity of 100 mW-cm^{-2}. Electrolyte solutions of Na_2SO_4 and H_2SO_4 were used for the PEC tests. The Nernst equation was used to convert the potential data to values relative to the reversible hydrogen electrode (RHE).

3. RESULTS AND DISCUSSION

Structural characterizations of the synthesized samples were conducted to investigate the material's crystal structure, absorption characteristics, defect analyses, and binding energy. A subsequent review of the results revealed that the nitrogen atom in the structure and the NiO catalyst had an impact on the material. Subsequent analysis was undertaken using PEC tests to gain deeper insights into the observed phenomena.

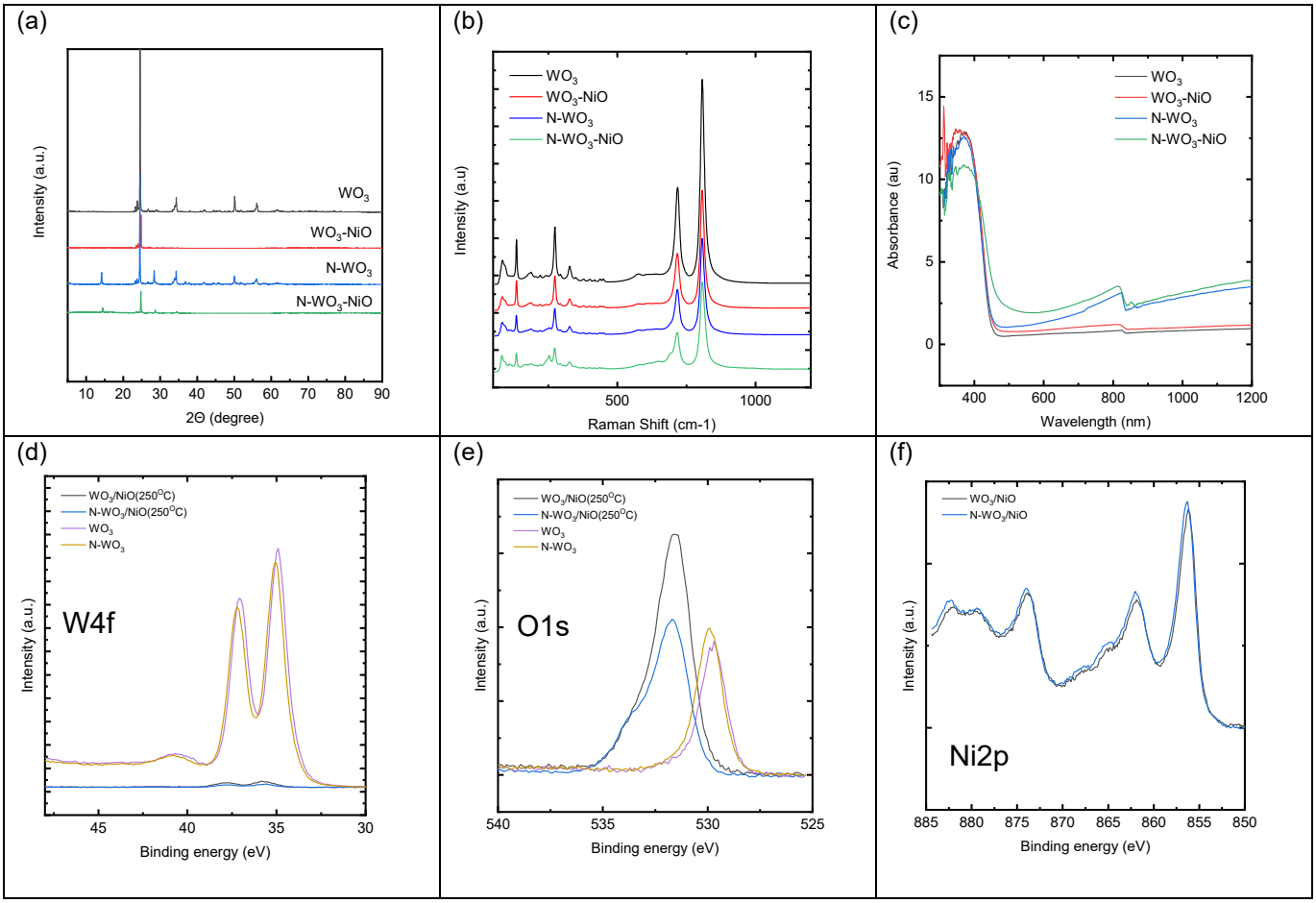

Fig.1. Structural characterizations of WO_3, WO_3-NiO, N-WO_3 and N-WO_3-NiO, (a) XRD, (b) Raman spectroscopy, (c) UV-Vis spectroscopy, (d) W 4f, (e) O 1s, (f) Ni 2p XPS

XRD and Raman spectroscopy investigations reveal that N-doping does not influence the crystal structure of WO_3. However, a small shift to higher wavelengths is observed in in UV-vis measurements, indicating that N-doping can induce a smaller bandgap. Impact of the N-doping is apparent in W 4f and O 1s XPS spectra. The absence of new XRD peaks after the cocatalyst deposition indicates that NiO overlayer is disordered. Both Raman and XPS spectral features confirm the NiO cocatalyst layer has a similar chemical composition and thickness on both WO_3 and N-WO_3.

Subsequently, all samples were subjected to a series of PEC tests. The alterations induced by the deposited cocatalyst on both bare WO_3 and N-WO_3 surfaces were investigated, leading to several conclusions. In general, the FTO-WO_3-NiO hierarchy caused an increase in thickness, resulting in weak performance in terms of charge diffusion and lower performance compared to bare WO_3. The current–voltage behavior of the photoanodes for water oxidation is shown in Fig. 2a. Linear sweep voltammograms (LSVs) show that the photocurrent density of NiO-WO_3 is significantly larger at potentials lower than 0.9 V. In addition, photocurrent onsets below 0.3 V in NiO-WO_3. A lower onset potential indicates that a smaller external driving force is required for the water oxidation reaction on NiO-WO_3 and higher photocurrent density at low potentials can be generated from the increased charge transfer rate at the interface of the photoanode/electrolyte, or reduced recombination of the charge carriers at the photoanode surface in NiO-WO_3. Howevet, the incident photon conversion efficiency (IPCE) of the NiO-WO_3 is not the highest. We investigated the charge transfer resistance at the interface of the WO_3/electrolyte using electrochemical impedance spectroscopy (EIS). Fig. 2c shows the Nyquist plots of the photoanodes under illumination. The lowest charge transfer resistance (R_{ct}) can be attributed to

an improvement in charge transfer kinetics and reduced charge recombination. NiO on both WO_3 and N- WO_3 leads to reduced R_{ct}. Electrochemical surface areas (ECSA) of the photoanodes appear to be lower after deposition of NiO cocatalyst layers.

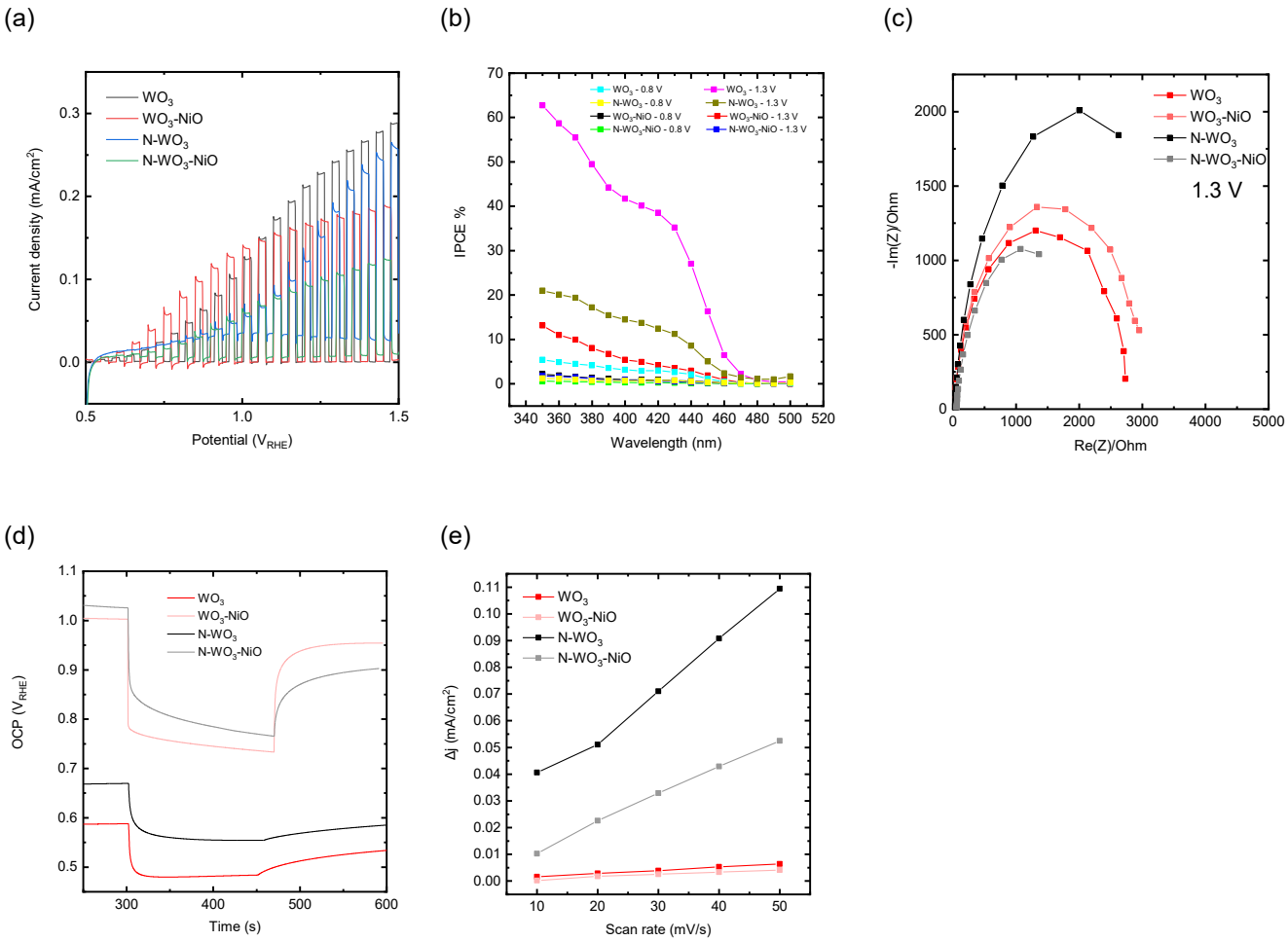

Fig.2. PEC tests, (a) LSV, (b) IPCE, (c) PEIS, (d) OCP, (e) ECSA

To better understand the effect of N-doping and NiO on the activity of WO_3, we performed transient photocurrent (TPC) measurements using a short-pulsed LED light and illuminated the photoanodes for 200 ms under different applied potentials. TPC results obtained demonstrated an increase in photocurrent with increasing potential, observed in both cases. When the light is turned on, charge accumulation was clearly evident in the bare WO_3 sample, however, this phenomenon was not observed in the N-WO_3, owing to the sluggish kinetics at the surface. This can be attributed to low mobility of charges introduced by defects and high recombination rate of N-WO_3. When the light was turned off, a negative peak was observed at low potentials, which was attributed to electron-hole recombination. Since the rate of recombination is lower at high potentials, negative peaks vanish. Furthermore, time-dependent TPC experiments were conducted in both scavenger and non-scavenger environments, thereby demonstrating the positive effect of hole scavengers on PEC performance. The hole scavenger, which has been shown to inhibit recombination events, was found to improve the charge transfer of the photoanode and increase the photocurrent.

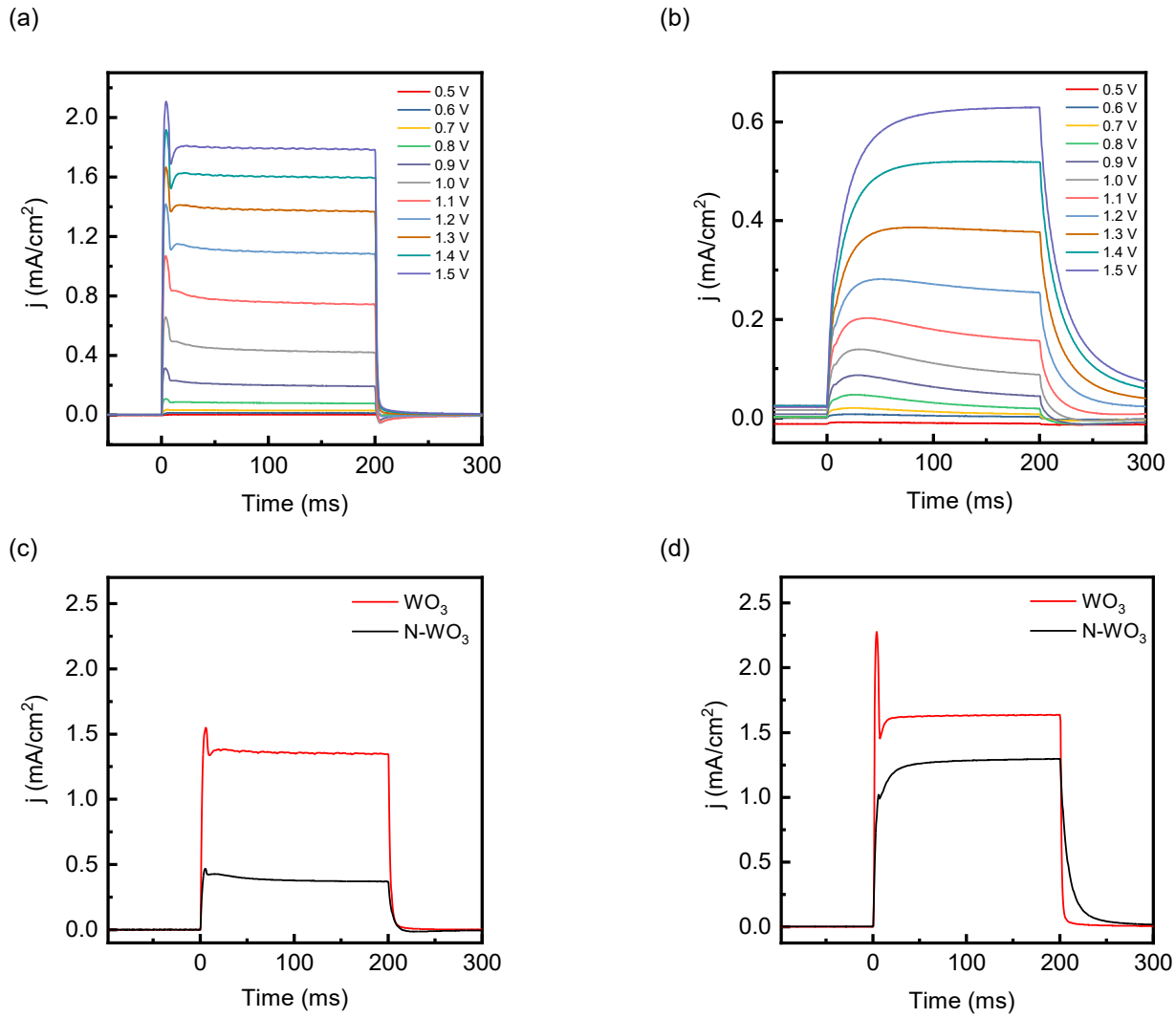

Fig.3. TPC experiments of WO_3 and N-WO_3, (a) potential-dependent TPC of WO_3 in Na_2SO_4 electrolyte, (b) potential-dependent TPC of N-WO_3 in Na_2SO_4 electrolyte, (c) TPC of WO_3 and N-WO_3 in Na_2SO_4 electrolyte, (d) TPC of WO_3 and N-WO_3 in Na_2SO_4 electrolyte with hole scavenger.

4. CONCLUSIONS

To sum up, the structural characterizations of the produced WO_3, WO_3-NiO, N-WO_3, and N-WO_3-NiO samples provide important information about their binding energies, crystal structure, absorption characteristics, and defect features. The effects of these alterations were further clarified by PEC testing, which showed that the nitrogen doping and NiO catalyst had a considerable impact on the material's characteristics. Under certain circumstances, nitrogen doping improved the photocurrent response, and NiO caused the onset potential to shift negatively, indicating better electrochemical performance for OER at lower potentials. All things considered, the results show how crucial cocatalyst alterations are for increasing photocatalytic efficiency, opening the door for more developments in material design for energy applications.

REFERENCES

1. Hellman, A.; Wang, B. First-Principles View on Photoelectrochemistry: Water-Splitting as Case Study. *Inorganics* **2017**, *5* (2), 37. https://doi.org/10.3390/inorganics5020037.
2. Rajaitha, P. M.; Hajra, S.; Mistewicz, K.; Panda, S.; Sahu, M.; Dubal, D.; Yamauchi, Y.; Kim, H. J. Multifunctional Materials for Photo-Electrochemical Water Splitting. *J. Mater. Chem. A* **2022**, *10* (30), 15906–15931. https://doi.org/10.1039/D2TA01869A.
3. Hu, J.; Zhao, S.; Zhao, X.; Chen, Z. Strategies of Anode Materials Design towards Improved Photoelectrochemical Water Splitting Efficiency. *Coatings* **2019**, *9* (5), 309. https://doi.org/10.3390/coatings9050309.

H_2 EVOLUTION REACTION PATHWAYS OF COBALT BASED MOLECULAR CATALYSTS INVESTIGATED BY *ab-initio* SIMULATIONS

[1*]*Yeliz Gurdal*
[1] Adana Alparslan Türkeş Science and Technology University, Faculty of Engineering, Department of Bioengineering, Sarıçam, Adana, 01250, Türkiye
*Corresponding author e-mail: ygurdal@atu.edu.tr

ABSTRACT
Cobalt-based molecular catalysts with polypyridyl and bis-bipyridyl ligands have been extensively studied for photocatalytic hydrogen evolution reactions (HER). While distorted ligand geometries enhance H_2 production, catalysts with ideal octahedral coordination exhibit lower efficiency. To elucidate the role of ligand structure in HER, we employed *ab initio* molecular dynamics (AIMD), density functional theory (DFT), and free energy perturbation theory to examine the reaction mechanisms of Co-based catalysts. For the pentapyridyl $CoPy_5$ complex, we simulated each intermediate of the ECEC mechanism, determining spin states and solvent responses. Although $CoPy_5$ maintains similar spin states as its distorted counterparts, its compact structure hinders H_2 diffusion, limiting catalytic turnover. Similarly, in the case of the cobalt bis-bipyridyl planar catalyst, the reaction follows two successive reductions before protonation due to an energy barrier preventing direct cobalt-proton interactions. These findings highlight the critical influence of ligand geometry on HER efficiency and provide insights for designing next-generation cobalt-based catalysts.

Keywords: Density Functional Theory, Ab-initio Molecular Dynamics, Metadynamics, bis-bipyridyl ligand, polypyridyl ligand

1. INTRODUCTION

Hydrogen (H_2) production via photocatalytic water splitting represents a promising approach to sustainable energy, utilizing solar radiation to drive the bond break in water molecules and form into hydrogen and oxygen. Unlike traditional electrolysis, which relies on electricity primarily sourced from fossil fuels, photocatalytic water reduction offers a renewable and cost-effective alternative. The core mechanism involves the excitation of a photosensitizer by photon absorption, electron transfer to a catalyst, which facilitates the reduction of water molecules into hydrogen. The electron donor present in reaction solution refreshes the photosensitizer, ensuring continuous catalytic cycles.

A key focus of recent research has been on molecular catalysts having transition metals for the hydrogen evolution reaction (HER) in solution. While noble metals such as platinum (Pt) and ruthenium (Ru) exhibit excellent catalytic efficiency, their high costs hinder large-scale application. Consequently, cobalt (Co)-based catalysts have emerged as a viable alternative due to their abundance and relatively lower cost. Polypyridyl cobalt complexes have gained significant attention for long-term stability and activity. The coordination environment of the cobalt center, determined by ligand symmetry and steric effects, plays an important role in determining effective HER activity.

HER mechanisms of a cobalt-based pentapyridyl molecular catalyst ($CoPy_5$) were studied using advanced computational methodologies, including Ab-initio Molecular Dynamics (AIMD) and Density Functional Theory (DFT) [1,2]. Previous experimental studies have demonstrated the stability and hydrogen generation efficiency of $CoPy_5$, achieving turnover numbers (TON) exceeding 1200 H_2/Co under specific reaction conditions [3]. Our theoretical approach provides critical insights into the stepwise electron transfer and protonation events (ECEC), elucidating the influence of ligand geometry on catalytic efficiency [1]. Furthermore, our study explores the EECC (electron-electron-proton-proton) mechanism of HER for the $CoPy_5$, assessing how variations in spin multiplicity and ligand coordination impact the reaction pathway [2]. Our findings reveal that the proton transfer dynamics are significantly influenced by the steric arrangement of pyridyl ligands, with an ideal octahedral coordination leading to a comparatively lower hydrogen production rate than its distorted counterparts. We also analyze the role of solvent interactions, particularly the diffusion behavior of hydroxide (OH^-) ions, in advancing the proton transfer in the close vicinity of the Co.

Furthermore, in our previous work, we explored the EECC (electron-electron-proton-proton) mechanism of HER for a catalyst having Co as reaction center and bis-bipyridyl ligands, $Co(bPy)_2CO$, assessing how variations in spin multiplicity and ligand coordination in this catalyst impact the reaction pathway [4]. Notably, the $Co(bPy)_2CO$ complex exhibits a distinct preference for the EECC mechanism which was verified using Metadynamics simulations. We also analyze the role of solvent interactions, particularly the diffusion behavior of hydroxide (OH^-) ions, in advancing proton transfer in the close vicinity of the Co.

Overall, our research contributes to the broader understanding of photocatalytic water splitting by shedding light on the mechanistic aspects of cobalt-based catalysts. By bridging theoretical and experimental insights, we aim to advance efficient and cheaper design of photocatalysts for sustainable hydrogen production.

2. MATERIALS AND METHODS

AIMD simulations were conducted to model the intermediate states of both ECEC and EECC mechanisms for the H_2 production through water splitting for the $CoPy_5$ catalyst. All simulations were performed using the open-source CP2K simulation package [5]. The PBE density functional in the generalized gradient approximation (GGA) formalism was applied for the AIMD simulations [6]. GTH pseudo-potentials [7] were used and only valence electrons were explicitly modeled. The DZVP-MOLOPT basis set [8] was employed and a cutoff of 400 Ry was utilized in all simulations. Dispersion interactions were accounted for using the rVV10 density functional [9]. Simulation cells were always extended in x-y-z directions and spin polarization were always taken into account.

We analyzed HER mechanisms for the $Co(bPy)_2CO$ catalyst, namely ECEC and EECC. The initial protonation step of the ECEC was modeled using metadynamics (MTD) simulations, a well-established technique for simulating rare events over shorter timescales. The catalysts were immersed in a cubic simulation box containing 215 water molecules. The simulation box volumes were optimized applying AIMD-NPT simulations. Following, each reaction step was simulated using AIMD-NVT simulations. AIMD time step was set to 0.5 fs. The simulation temperature was kept fluctuate around 300 K using the CSVR thermostat [10]. For more details on our computational approach, see Refs. [1-2, 4].

3. RESULTS AND DISCUSSION

We first start with the results obtained for the $CoPy_5$ catalyst. The first step of the ECEC reaction mechanism involves the first electron injection. This step was simulated by injecting one electron into the system while modeling both singlet and triplet spin states of the Co center. In the triplet spin, a stable coordination between a water molecule and the Co center is maintained throughout the simulation, with minimal conformational changes. In contrast, for the singlet spin, the closest water molecule undergoes a conformational change, forming a Co-H+ bond, and a second water molecule interacts with the reaction center which is a necessary step for the first protonation. The second of the ECEC mechanism is the first protonation, where a proton from the closest water molecule binds to the Co center, forming a stable Co-H hydride. This process is accompanied by the formation of an H_3O+ ion, and the proton remains stable at the Co center throughout the simulation. The third step, the second electron injection, was modeled for both doublet and quartet spin. In the doublet state, only one proton coordinates with the Co-H hydride, while in the quartet state, both protons from surrounding water molecules interact with the Co center. This suggests that the H_2 production reaction proceeds more favorably in the quartet spin due to the increased availability of protons. The final step is the second protonation, leading to H_2 molecule formation. The H_2 molecule remains stable at around 0.8 Å in bond distance, but struggles to diffuse away from the Co center due to the tight coordination and surrounding water molecules in the $CoPy_5$ catalyst. This reduced diffusion of the H_2 molecule explains the lower activity observed for $CoPy_5$ compared to more distorted catalysts, which are summarized in [1]. Our analysis for the EECC mechanism of the $CoPy_5$ catalyst also reveals the similar restricted diffusion of the produced H_2 molecule, for more details, see [2].

The Co center of the $Co(bPy)_2CO$ complex exhibited a doublet spin multiplicity and a +2 charge, maintaining a planar structure with Co–N distances around 1.90 Å. After geometry optimization, the catalyst was placed in water, where two water molecules coordinated with the Co center, maintaining stable Co–O_{wat} distances of ~2.25 Å during AIMD simulations. Electron injection was simulated for both singlet and triplet spin, with no conformational changes observed in the water molecules near Co [4]. However, an energy barrier prevented water molecules from changing conformation, hindering the protonation step in the ECEC mechanism. The second intermediate step of the ECEC meshanism, protonation, did not lead to Co-proton coordination, which hinders protonation reaction. Thus, an energy barrier has to be overcome in order for the water molecule to change its conformation and to exemplify the system in which the Co-H^+ bond is established. Thus, we modeled direct coordination of Co and the protons of the water molecules applying independent metadynamics (MTD) simulations having different collective variables (CVs). For the first MTD simulations the coordination numbers between Co and the nearest two proton were chosen as collective variables, see Fig. 1-(a). When the H is close to Co, the coordination number (CV1) is 1, and when they are farther away, the coordination number is 0. Snapshots taken from the MTD simulations carried out for the singlet spin are depicted in Fig. 1-(a) and Fig. 1-(b). At the starting of the MTD, oxygens have direct coordination with the Co center. As MTD simulations prolong, water molecules changes their coordinations allowing proton-Co coordination. However, H_{wat1} and H_{wat2} periodically approach and move away from the Co center, see Fig. 1-(c). At 0.3 ps, Co-H_{wat1} and Co-H_{wat2} decrease to 1.5 Å, while at 0.6 ps corresponding distances increase to 3.5 Å. The hydrogens spend more time away from the Co atom and they change their conformation again as soon as their distance with Co decreases to 1.5 Å. The snapshots taken from the MTD trajectory of the triplet spin are provided in Fig.2-(a) and Fig. 2-(b). As in the case of singlet spin, the distances between Co-H_{wat3} and Co-H_{wat4} oscillates between 1.5 Å and around 3 Å, as depicted in Fig.2-(c). Throughout the simulation, H_{wat3} and H_{wat4} simultaneously approach and move away from the Co center periodically and show the same fluctuating behavior as in the singlet spin case. At around 0.3 ps, the Co-H_{wat3} and Co-H_{wat4} distances decrease to 1.5 Å, while at 0.6 ps the distances again increase to 3 Å. Similarly, it is seen that the distances decrease to 1.5 Å at 0.9 ps. The reason for the increase in the Co-H_{wat3} and Co-H_{wat4} distances is the establishment of direct coordination between the O_{wat3} (O_{wat4}) and the Co center. The other protons in the solvent do not reach to the Co center.

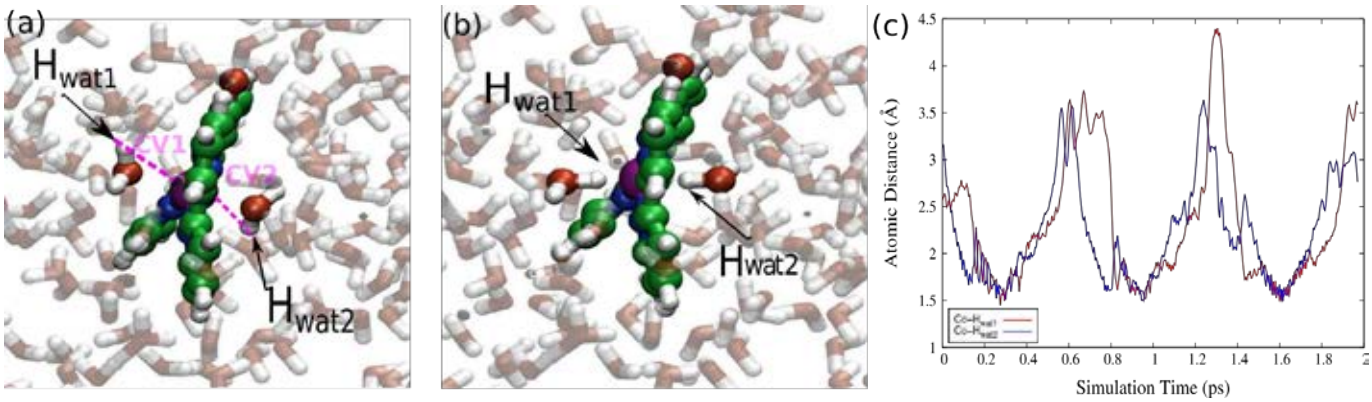

Fig. 1. Snapshots taken from the MTD trajectory of the singlet spin state of $Co(bPy)_2CO$ (a) obtained at the 0.1 ps simulation time and (b) 0.27 ps simulation time. The coordination number between Co and H_{wat1} is labeled as CV1, and coordination number between Co and H_{wat2} is labeled as CV2 in (a). (c) Interatomic distances between Co-H_{wat1} and Co-H_{wat2} are shown with red and blue lines, respectively.

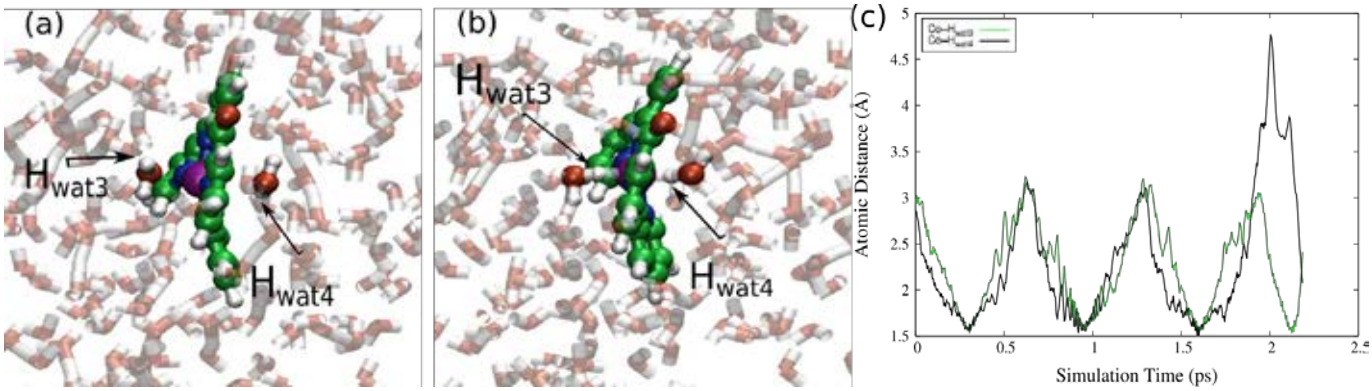

Fig. 2. Snapshots taken from the MTD trajectory of the triplet spin state of the $Co(bPy)_2CO$ (a) obtained at the 0.1 ps simulation time and (b) 0.3 ps simulation time. (c) Interatomic distances between Co-H_{wat3} and Co-H_{wat4} are shown with green and black lines, respectively.

Further MTD simulations for the singlet spin were conducted with modified collective variables (CVs). The goal was to maintain a stable Co-H coordination, so we defined the first CV (CV1) as the coordination number between Co and the proton of the closest water molecule (H_{wat1}). For the second CV (CV2), we chose the coordination number between the oxygen atom of H_{wat1} and the proton of a neighboring water molecule in the solvent. This new set of CVs was designed to better capture the stability of the Co-H coordination during the simulation. Energy barrier for establishing Co-H^+ direct coordination was calculated as 0.3 eV. The energy barrier hindered protonation in the ECEC mechanism, but protonation occurred more readily in the EECC mechanism, especially for the doublet spin. For the EECC mechanism of the Co(bPy)2CO, after a second electron injection into the Co center, we obtained steady Co-H^+ direct coordination followed by protonation of the Co center. The last step involved the protonation and the successful formation of an H_2 molecule, with Co–H_2 distances fluctuating around 4.5 Å. This contrasts with the results obtained for $CoPy_5$, which showed restricted H_2 diffusion due to compact ligand structure. For more details on the results, see Ref. [4].

4. CONCLUSIONS

We investigated the H_2 production mechanism of the $CoPy_5$ catalyst with a penta-pyridyl ligand in an octahedral arrangement, using AIMD and DFT simulations in water. The singlet spin favored proton bonding with Co due to a positional change in the closest water molecule, unlike the triplet state. During protonation, Co received a proton from the solvation shell water molecule, forming an OH^- anion that hydrogen bonds with the solvent. For the reduction step, the reaction proceeded with the quartet spin due to proton coordination. The final step showed H_2 formation, but steric hindrance from the compact structure of $CoPy_5$ limited H_2 diffusion, potentially acting as the rate-limiting step [1]. The EECC mechanism also revealed the similar restricted diffusion for the produced H_2 [2]. Investigation of the H_2 evolution mechanism of the $Co(bPy)_2CO$ catalyst, featuring a planar structure, in explicit water revealed that after the first reduction, energy barriers in the singlet and triplet spin prevent water molecules from changing conformation and coordinating with Co. MTD simulations showed a 0.3 eV barrier for direct Co-proton coordination, essential for the first protonation (ECEC). In the EECC pathway, Co-H^+ coordination was established following the second reduction, allowing proton coupling for the first protonation in the doublet spin. Following the last protonation, H_2 formed and diffused into the solvent, as

summarized in [4]. The planar catalyst follows the EECC mechanism, forming H_2 and enabling its diffusion. The study highlights how ligand type and coordination influence reaction mechanisms, aiding the design of efficient H_2 production catalysts for sustainable energy.

ACKNOWLEDGEMENT
Y.G. sincerely appreciates the support provided by the Scientific and Technological Research Council of Türkiye (TÜBİTAK) within the TÜBİTAK-1001 Research Program (Project No: 124Z002). In this work, TRUBA HPC resources were utilized.

REFERENCES

[1] A. Kiser and Y. Gurdal. 2024. Why the perfectly symmetric cobalt-pentapyridyl loses the H2 production challenge: Theoretical insight into reaction mechanism and reduction free energies. ChemCatChem, 16 (1), e202300901.
[2] A. Kiser and Y. Gurdal. 2025. Ideal octahedral geometry leads to poor H2 evolution performance: Theoretical insights on reaction intermediates of cobalt–pentapyridyl molecular catalyst. International Journal of Hydrogen Energy 106, 864-873.
[3] C. Bachmann, M. Guttentag, B. Spingler, R. Alberto. 2013. 3d Element Complexes of Pentadentate Bipyridine-Pyridine-Based Ligand Scaffolds: Structures and Photocatalytic Activities. *Inorganic Chemistry*, 52, 6055.
[4] I. Guclu, A. Kiser, Y. Gurdal. 2024. H_2 evolution reaction pathway of a cobalt bis-bipyridyl planar catalyst revealed by Ab initio simulations. Journal of Physical Chemistry C, 128 (48), 20537-20548
[5] T. D. Kühne, M. Iannuzzi, M. Del Ben, V. V. Rybkin, P. Seewald, F. Stein, T. Laino, R. Z. Khaliullin, O. Schütt, F. Schiffmann, et al.,2020. CP2K: An electronic structure and molecular dynamics software package - Quickstep: Efficient and accurate electronic structure calculations. *Journal of Chemical Physics*, 152, 194103.
[6] J. P. Perdew, K. Burke, M. Ernzerhof. 1996. Generalized Gradient Approximation Made Simple. *Physical Review Letters*, 77, 3865.
[7] S. Goedecker, M. Teter, J. Hutter. 1996. Separable dual-space Gaussian pseudopotentials. *Physical Review B,* 54, 1703.
[8] J. VandeVondele, J. Hutter. 2007. *Journal of Chemical Physics,* Gaussian basis sets for accurate calculations on molecular systems in gas and condensed phases, 127, 114105.
[9] R. Sabatini, T. Gorni, S. de Gironcoli. 2013. Nonlocal van der Waals density functional made simple and efficient *Physical Review B*, 87, 41108.
[10] G. Bussi, D. Donadio, M. Parrinello. 2007. Canonical sampling through velocity rescaling. *Journal of Chemical Physics*, 126, 014101.

FEATURE AND LSTM-BASED CAPACITY PREDICTION FOR LITHIUM-ION BATTERIES: APPLICATION OF LINEAR REGRESSION AND LSTM MODELS, WITH FUTURE EXPANSION TO FUEL CELL DATASETS AND OPTIMIZATION

[1]*Sıtkı Akkaya*, [2*]*Murat Uyar*
[1] Sivas University of Science and Technology, Department of Electrical-Electronic Engineering, Sivas, 58140, Turkey
[2] Bursa Uludağ University, Department of Electrical-Electronic Engineering, Bursa, 16059, Turkey
*Corresponding author e-mail: muratuyar@uludag.edu.tr

ABSTRACT
Lithium-ion battery capacity forecasting is critical to optimizing energy storage devices, and equivalent forecasts for fuel cells are needed to attain power generation efficiency and extended system lives. The current research used discharge data with lithium-ion battery capacity values to create four single time-series data sets, of which 10 features per series were created, resulting in 40 feature matrices. Both linear regression and Long Short-Term Memory (LSTM) models were used to predict battery capacity. The linear regression model worked with an RMSE of 0.0058, and the LSTM-based model was compared based on RMSE and loss function metrics. The results indicate the possibility of applying these methods to predict capacity accurately. The proposed approach sets a foundation for subsequent optimization and adjustment toward fuel cell data for more stable prediction and better control over the energy system in future work.

Keywords: Capacity prediction, Linear regression, LSTM model, Fuel cell data

1. INTRODUCTION
Lithium-ion batteries (Li-ion) are widely used in various applications, from electric vehicles to renewable energy storage systems, due to their high energy density and long cycle life [1]. One key element of maximizing such batteries' performance and longevity is accurately forecasting their capacity over time [2]. A battery's ability, i.e., its energy storage and delivery capacity, decreases over usage. Hence, capacity prediction becomes critical for effective energy management and battery life extension [3]. Capacity forecasting can assist in planning maintenance, reducing battery lifespan, and improving system reliability by preventing sudden failures [4].

The same capacity prediction methods can be used for fuel cells, which are increasingly considered a sustainable energy alternative to traditional sources [5]. Fuel cell technologies like lithium-ion batteries utilize future performance prediction to optimize power output and manage energy storage systems. The data and feature extraction techniques used in battery capacity prediction [6] can also be applied to fuel cell data, giving more accurate energy storage and fuel efficiency models.

Linear regression and long short-term memory (LSTM) models have been used in the current research for capacity estimation. Linear regression is used where the dataset size is small, not intricate, and needs quick outputs with minimal computation [7]. However, with more extensive and complex datasets, LSTM models are helpful [8] since they can learn and discover latent temporal patterns of time-series data. Applying these models, this study examines how capacity forecasting can be improved, not only for lithium-ion batteries but also potentially for fuel cell usage in the future.

2. MATERIALS AND METHODS
The study aims at predicting the lithium-ion battery capacity using time-series discharge data. The approaches employed are extracting features from the data and applying Linear Regression for small data sets [9] and LSTM models for big, complex data sets to improve the accuracy of capacity prediction.

2.1. Data and Feature Extraction
The capacity values of the discharge data were extracted from the.mat file. Four time-series datasets were prepared differently, and 10 features were extracted from each of the four datasets, resulting in 40 feature matrices. The matrix form to extract the voltage feature is presented below:

[mean(Discharge_voltage),std(Discharge_voltage),min(Discharge_voltage),max(Discharge_voltage), rms(Discharge_voltage),var(Discharge_voltage),skewness(Discharge_voltage),kurtosis(Discharge_voltage), abs(var(Discharge_voltage)), geomean(abs(Discharge_voltage))]

Other features were similarly extracted for current, voltage load, and current load. Ultimately, the final feature matrix was constructed as follows:

features = [voltage_features, current_features, voltage_load_features, current_load_features] labels_for_regression = capacity

2.2. Linear Regression

Linear regression is a statistical modeling technique that aims to make predictions by relating a dependent variable (Y) to one or more independent variables (X). The model learns the linear relationship between the data and makes predictions using these relationships.

Basic Concepts:

• Independent Variable (X): Variables used for the model to make predictions. These variables are considered input data in the model.

• Dependent Variable (Y): The predicted or modeled output. In other words, the variable that the linear regression model tries to predict.

The general model of the method is given as follows. Here, $\beta 0$ represents the constant term (intercept), $\beta 1, \beta 2, \ldots, \beta n$, the regression coefficients (the parameters that the model is trying to learn), and ϵ represents the error term (the model's estimation error).

$$Y = \beta 0 + \beta 1 X1 + \beta 2 X2 + \cdots + \beta n Xn + \epsilon \quad (1)$$

Linear regression uses the least squares method to minimize the squares of the error terms in the data. The goal is to find the linear model that best represents the relationship between independent and dependent variables. It is frequently used in economic forecasting, biomedical research, and machine learning applications. The benefits of linear regression are that it is simple and easy to comprehend, rendering it a suitable model for many uses. It is also computationally efficient, thus enabling fast predictions when working with small datasets. Another plus is that it offers interpretable outcomes since the relation between the input variables and the output is understandable and easy to grasp. These characteristics make linear regression an attractive option for applications where model interpretability and computational efficiency are important.

2.3. Long Short-Term Memory (LSTM)

LSTM is a member of the deep learning and recurrent neural networks (RNN) family and is used especially in predictions made with time series data and sequence data. LSTM can learn long-term dependencies based on past information, which makes it extremely effective on sequential (ordered) data. LSTM is a powerful tool for time series analysis. If changes in data over time and past events are critical for future predictions, the LSTM model can be used. LSTM allows for more accurate forecasts by capturing long-term dependencies in time series data. LSTM will be effective in cases where predictions will be made based on the past performance of some systems. LSTM is an RNN architecture optimized to handle time-series data and efficiently learn long-range dependencies. The fundamental structure of LSTM includes memory cells, which retain information over time and affect future predictions by remembering past information for long periods. LSTM cells possess three main gates: the Forget Gate, which determines what information from the past must be forgotten; the Input Gate, which determines if new information is to be included in the memory; and the Output Gate, which determines how much of the previous information will be included in the model's output. The main advantage of LSTM over other RNNs is the ability to learn long-term dependencies using these gates, resulting in more stable and long-term learning. This is extremely helpful for time-series data, where historical data points are essential to make accurate future predictions. LSTM is applied in various contexts, from time-series prediction like financial market predictions and weather forecasting, natural language processing like text generation and language translation, healthcare for patient monitoring and biomedical data analysis, and gaming or simulation for sequence-based data analysis. Although it has some advantages—e.g., it can capture long-term dependencies, provide strong performance with sequential data, and learn effectively—LSTM also has disadvantages, e.g., longer training time, increased computational requirements, and potential interpretability problems due to its complexity. The study divided the dataset into 80% training and 20% testing. The hyperparameters used for the created model are given in Table 1.

Table 1. Hyperparameters for the model

Hyperparameters	Space	The best hyperparameters
numHiddenUnits	[50 100 200 500]	100
optimizer	["sgdm" | "rmsprop" | "adam" | "lbfgs"]	"adam"
'MaxEpochs'	[100 200 500 1000]	Justification: justified 1000
'MiniBatchSize'	[8 16 32 64 128]	128

3. RESULTS AND DISCUSSION

According to the results obtained from linear regression, the actual and estimated capacity results are obtained as in Fig. 1. RMSE for linear regression was obtained as 0.0058.

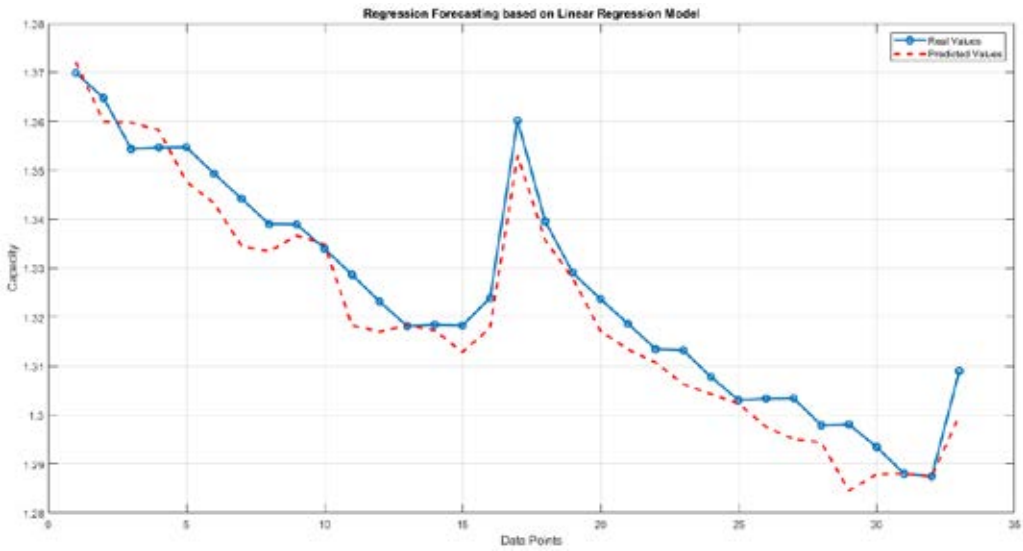

Fig. 1. Estimation of linear regression model

The model created based on LSTM was evaluated using RMSE and Loss function metrics. The graph showing the training process of this model is given in Fig. 2.

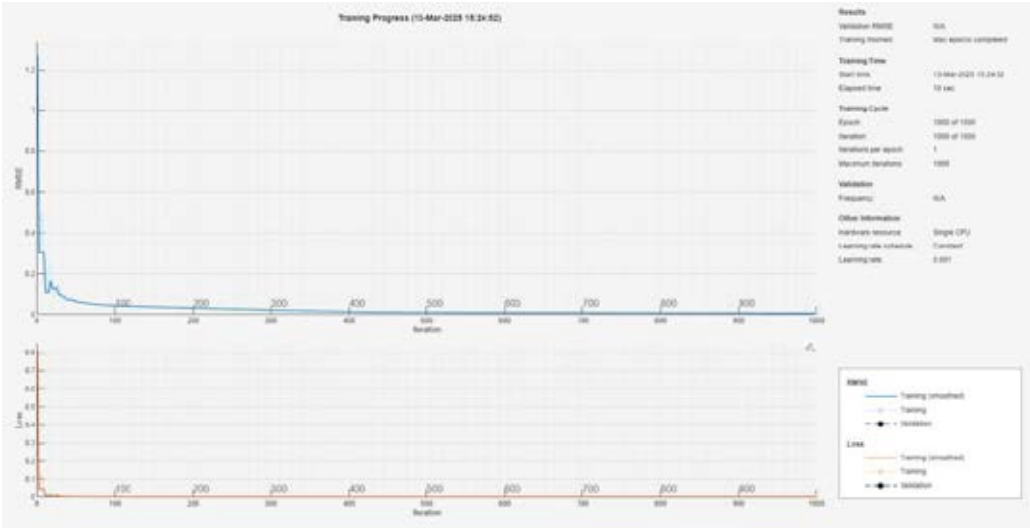

Fig. 2. Training process of LSTM method

According to the results obtained from LSTM regression, the actual and estimated capacity results are given in Fig.3. RMSE for LSTM Regression was obtained as 0.01.

Fig. 3 shows that, albeit slightly, LSTM is obtained with a higher RMSE between the two methods. The effective factors here are as follows: optimization based on these will improve the result. There are many reasons why LSTM has a larger RMSE (Root Mean Squared Error) than linear regression. Data inadequacy is one of the main reasons, as LSTM models need large volumes of data to learn and generalize well. When there is limited data, the learning ability of the model is hindered, thus tending to overfit, i.e., concentrating too much on the noise in the training data, which causes it to perform poorly on test data. Also, the complexity of LSTM models, with numerous parameters, can be troublesome when working with small datasets because the model may not use its capacity and may learn spurious patterns or noise.

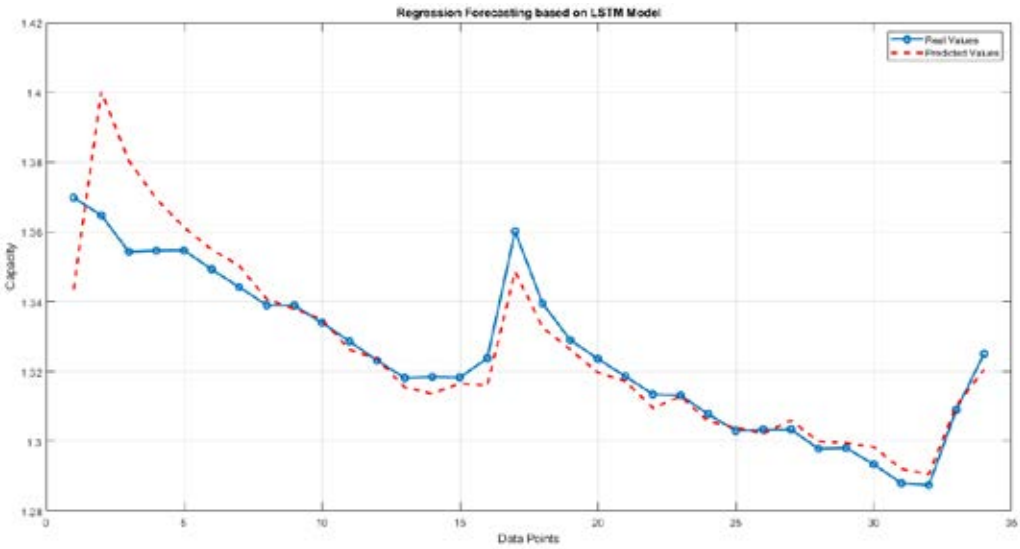

Fig. 3. The actual and estimated capacity results of the LSTM method

The training process and hyperparameters, such as learning rate and training time, can also influence performance. If the learning rate is too high, the model will overshoot the optimal values, and too little training can prevent the model from adequately learning, increasing the error. Conversely, linear regression, a simpler model with fewer parameters, will do better on smaller datasets as it will not overfit and is very well suited to learning linear relationships. Also, when the data does not have strong temporal relations, LSTM's advantage does not get very far, while linear regression might still do better in such cases. Finally, erroneous hyperparameter tuning like batch size, epochs, and dropout can disrupt LSTM's learning. In the case of small datasets, it would be more rewarding to use simple models like decision trees or linear regression instead of complex models like LSTM.

4. CONCLUSIONS

This study created features for lithium-ion batteries and capacity prediction using linear regression and the LSTM model. The findings were that while linear regression performed slightly better with low datasets, LSTM's intricate framework could potentially use more extensive and complicated datasets. The difference in performance between the two models can be attributed to LSTM's ability to capture long-term dependencies in time-series data but inefficiency with small datasets because it is susceptible to overfitting and needs more data. The presented method will be extended in the future to use a fuel cell dataset and optimization methods toward better prediction accuracy. This could potentially render the model more usable, solid, and realistic in form for application in energy storage systems. Through the development of these methods, the research hopes to make a positive impact toward even more efficient and accurate predictive models of energy systems, paving the way for further innovations in energy management and technology.

REFERENCES

1. Xu J, Cai X, Cai S, Shao Y, Hu C, Lu S, Ding S. 2023. High-energy lithium-ion batteries: recent progress and a promising future in applications. Energy & Environmental Materials, 6:5:e12450.
2. Sharma P and Bora BJ. 2022. A review of modern machine learning techniques in the prediction of remaining useful life of lithium-ion batteries. Batteries 9:1:13.
3. Nyamathulla S and Dhanamjayulu C. 2024. A review of battery energy storage systems and advanced battery management system for different applications: Challenges and recommendations. Journal of Energy Storage 86:111179.
4. Reza MS, Mannan M, Mansor M, Ker PJ, Mahlia TI, Hannan MA. 2024. Recent advancement of remaining useful life prediction of lithium-ion battery in electric vehicle applications: A review of modelling mechanisms, network configurations, factors, and outstanding issues. Energy Reports, 11:4824-4848.
5. Singla MK, Nijhawan P and Oberoi AS. 2021. Hydrogen fuel and fuel cell technology for cleaner future: a review. Environmental Science and Pollution Research, 28:13:15607-15626.
6. Tang T and Yuan H. 2021. The capacity prediction of Li-ion batteries based on a new feature extraction technique and an improved extreme learning machine algorithm. Journal of Power Sources, 514:230572.
7. Maulud D and Abdulazeez AM. 2020. A review on linear regression comprehensive in machine learning. Journal of applied science and technology trends 1:2:140-147.
8. Behera RK, Jena M, Rath SK, Misra S. 2021. Co-LSTM: Convolutional LSTM model for sentiment analysis in social big data. Information Processing & Management, 58:1:102435.
9. https://www.kaggle.com/datasets/ranitsarkar01/hydrogen-fuel-cell-anomoly-detection. Kaggle, 2025. Accessed on March 14, 2025.

INVESTIGATION ON PERFORMANCE OF ANION EXCHANGE MEMBRANE ELECTROLYZER WITH DIFFERENT FLOW FIELD CONFIGURATIONS

[1*]*Ugur Ergin*, [1]*A.B.A.Ibrahim*, [1]*Sergen Tumse,* [1]*Gokturk Memduh Ozkan,* [2]*Gulfeza Kardas,* [1]*Huseyin Akilli*
[1] Cukurova University, Faculty of Engineering, Mechanical Engineering Department, Saricam, Adana, 01330, Turkey
[1] Cukurova University, Faculty of Arts and Sciences, Chemistry Department, Saricam, Adana, 01330, Turkey
*Corresponding author e-mail: uergin@cu.edu.tr

ABSTRACT
Anion exchange membrane electrolyzers (AEMEs) are gaining attention for their potential to enable cost-effective and sustainable hydrogen production by combining the benefits of alkaline water electrolyzers (AWEs) and proton exchange membrane electrolyzers (PEMEs). However, optimizing their efficiency requires an in-depth understanding of two-phase flow characteristics and thermal effects. This study presents a numerical analysis of how different flow channel geometries influence mass transport and electrochemical performance in a non-isothermal AEM electrolyzer. A computational model was developed using COMSOL, incorporating electrochemical kinetics, gas-liquid phase interactions, and heat transfer. Various serpentine flow fields were examined to assess their impact on gas removal, ion conductivity, and temperature distribution. The findings demonstrate that multi-serpentine counter-flow configurations promote uniform temperature distribution and improved ionic conductivity, whereas single serpentine designs enhance gas bubble detachment. The polarization curve obtained from the simulations closely corresponds with experimental results from the literature, validating the model's accuracy in predicting electrolyzer behavior. These insights contribute to optimizing AEM electrolyzer designs, advancing their practical implementation in hydrogen production technologies.

Keywords: Anion exchange membrane electrolyzer, two-phase flow, flow channel configurations

1. INTRODUCTION

Anion exchange membrane electrolyzer (AEME), a modern technology that combines the advantages of alkaline water (AWE) and proton exchange membrane (PEME) electrolyzers, is the vital solution for the mentioned issue regarding the mentioned electrolyzers. Although AEME offers low-cost and sustainable H_2 production, studies of these types are still limited and impossible in commercial production. From open literature, most studies aimed to improve the performance and efficiency of AEME. This objective is achieved by minimizing component-based overpotential losses, which focuses on catalyst and membrane development and relies laboriously on experimental methods. Regarding catalyst influencing, the studies specifically focused on the oxygen evolution reaction (OER) catalyst layer, revealing the impact of critical properties such as catalyst conductivity, morphology, and catalyst layer resistance on performance [1]. These studies emphasize the importance of anode design using commercial ($NiFe_2O_4$) and custom-synthesized (Ni_8Fe aerogel) catalysts. For advanced membranes, the studies highlight the importance of membrane properties, such as ionic conductivity, physicochemical stability, mechanical durability, and compatibility with non-precious metal catalysts in improving the performance and sustainability of AEME [2]. Furthermore, the studies employed commercial catalysts in AEME to reduce the structure cost [3]. The other key parameters that play a vital role in current density and efficiency, especially in optimizing mass transport processes, are the design and properties of gas diffusion layers (GDL). The material composition, porosity, thickness, and manufacturing method are the parameters used to explore the GDL performance [4].

In addition to experimental studies, modeling is a powerful tool for analyzing complex interactions of phenomena in electrolyzers, especially when investigating the effects of electrochemical reactions, dual-phase interactions, and changing operating conditions on performance. This method provides a better understanding of physicochemical phenomena occurring within the system and provides a basis for system analysis, control, and optimization. Furthermore, simulation of the electrolyzer decreases the time-consuming, costly nature of experimental processes and recreates a critical role in determining the optimum design and operating conditions. Although these simulation studies provide valuable information in understanding the electrochemical nature of electrolyzers, experimental studies are also required to ensure the accuracy and reliability of the simulation results. Recently, researchers have shown increasing interest in parallel conducting experimental studies and modeling analyses [5]. The significance of these kinds of studies is associated with exploring the AEME optimum flow channel design. The design of flow channels directly affects water and gas flows to the reaction zones and efficiently removes formed products, including O_2 and H_2 gases, from the system. Extensive research has been conducted on the design of electrolyzer flow field structures, particularly for AWE and PEME [6]. The parameters are explored to understand their influence on the electrolyzer performance and durability, including the distribution of flow, velocity, temperature, pressure, and separation phenomena bubbles [5, 6]. On the other hand, the study of the flow structure of AEME is yet in the premature stage and is not ready for commercial utilization. Therefore, further studies on the design flow structure of AEME are an urgent necessity to address a reliable unified conclusion on the effect of flow field structure on the performance of AEME and to support selecting the best one from different criteria. This study contributes to the AEME field by investigating the effects of different flow channel geometries on two-phase flow dynamics in a non-isothermal AEM electrolyzer cell. Through modeling, it seeks to understand how variations in

channel design influence gas bubble behavior, mass transport, and overall cell performance under realistic operating conditions. Furthermore, this research will provide valuable insights into optimizing flow channel configurations to enhance the efficiency and effectiveness of AEM electrolyzers. By integrating these findings, efficient and cost-effective AEM electrolyzers can be developed, thereby advancing the practical implementation of hydrogen as a clean energy carrier.

2. MATERIALS AND METHODS

This study presents a comprehensive numerical model developed in COMSOL to analyze two-phase flow effects in a non-isothermal AEM electrolyzer. The model incorporates electrochemical reactions, gas-liquid interactions, heat transfer, and varying flow channel geometries to assess hydrogen production performance. As shown in Fig 1, the 3D electrolyzer cell consists of porous gas diffusion electrodes (GDEs) facilitating electrochemical reactions and gas transport, an anion exchange membrane (AEM) ensuring ion conduction, and different flow channel configurations directing electrolyte flow and gas removal.

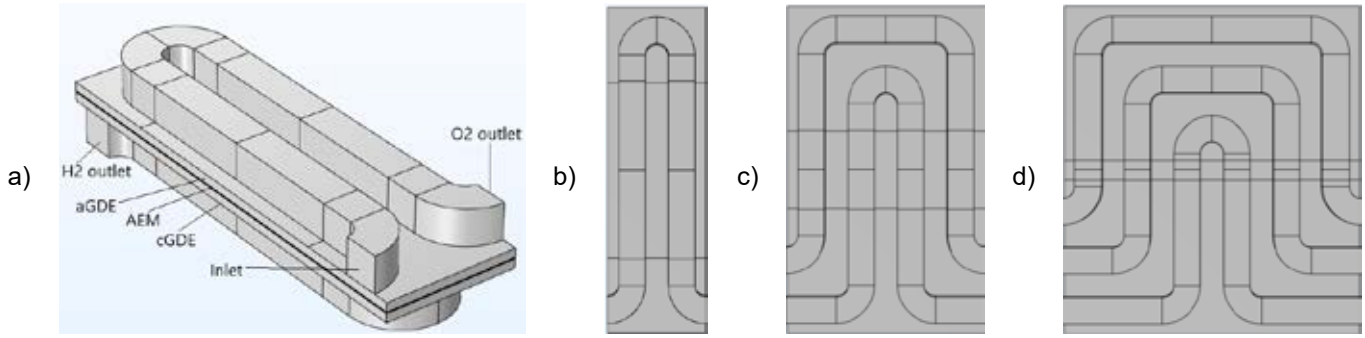

Fig. 1. a) 3D representive model b) 1-path serpentine channel c) 2-path serpentine channel d) 3-path serpentine channel

The mixture model in COMSOL was employed to simulate the two-phase gas-liquid interactions within the electrolyzer. This approach treats the gas phase as a dispersed component within the liquid electrolyte, allowing for the prediction of gas bubble distribution, volume fraction, and transport dynamics. The model effectively captures the influence of different flow channel geometries on gas removal efficiency and overall cell performance. To simplify the model, the following assumptions were made: (1) steady state condition, (2) ideal gas, (3) laminar flow in the channels, and (4) porous media flow in GDEs.

Table 1 shows the modelling parameters, and Table 2 presents the governing equations used in the current modelling simulations.

Table 1. Modelling parameters used in COMSOL simulations

Parameters	Value
GDEs thickness	0.2mm
GDEs width	10mm
AEM thickness	70µm
Channel width	0.7mm
Channel height	0.8mm
Anode and cathode exchange current densities	$i_{0,an}$=0.256 A/m^2, $i_{0,cat}$=8.885 A/m^2
Anode and cathode transfer coefficient	α_{an}= 0.5, α_{cat}=0.5
GDE porosity	0.7
GDE permeability	1e-10m^2
Inlet flow velocity	0.01m/s
Outlet pressure	25atm
Electrolyte concentration	1M
Electrical conductivity of GDE	1E5 S/m
Applied cell voltage	1.5-2.1V

Table 2. Governing equations solved by COMSOL modeling

Physics	Equations	Reference
Electrochemical reactions	Butler-Volmer, Ohmic Loss	[7, 8]
Two-phase flow	Continuity, Momentum, Darcy's Law	[9, 10]
Heat transfer in the cell	Conservation of Energy	[8]

3. RESULTS AND DISCUSSION

In the current study, the obtained polarization curve is in strong agreement with the experimental data published by Liu et al. [7]. In particular, the effects of critical factors such as gas bubble transport and ion conductivity on cell performance exhibit similar trends. These results support the reliability and accuracy of the current model and provide valuable information for the optimum structure of flow channel geometries and the improvement of electrolyzer design.
All the results obtained should be discussed in detail.

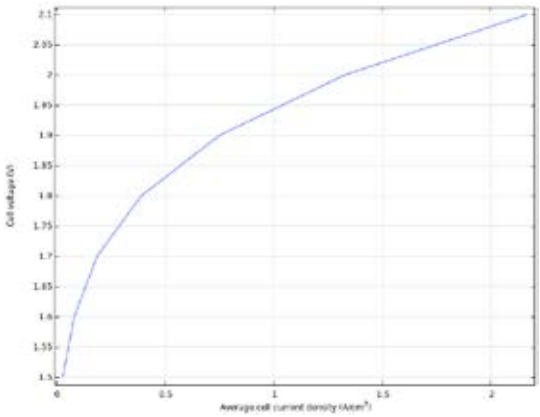

Fig. 2. Polarization curve of current modelling

a) b) c)

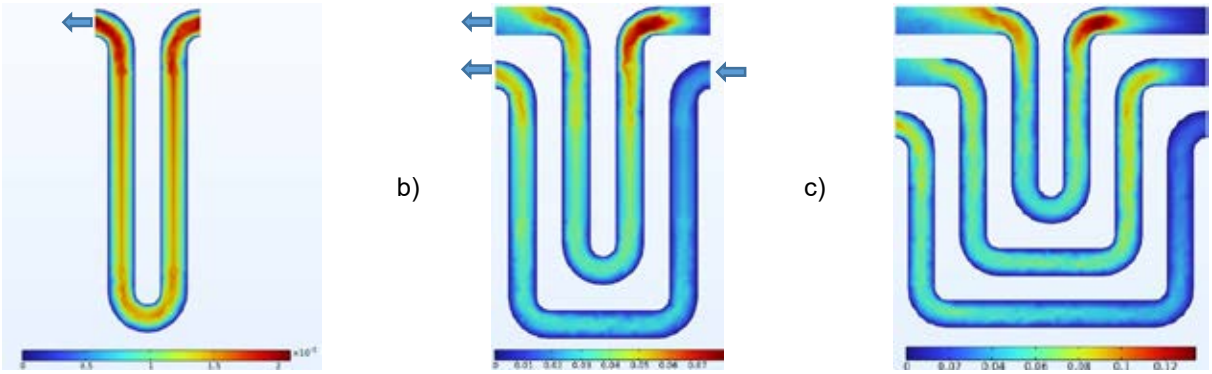

Fig. 3. Velocity magnitude (m/s) over cathode channels

a) b) c)

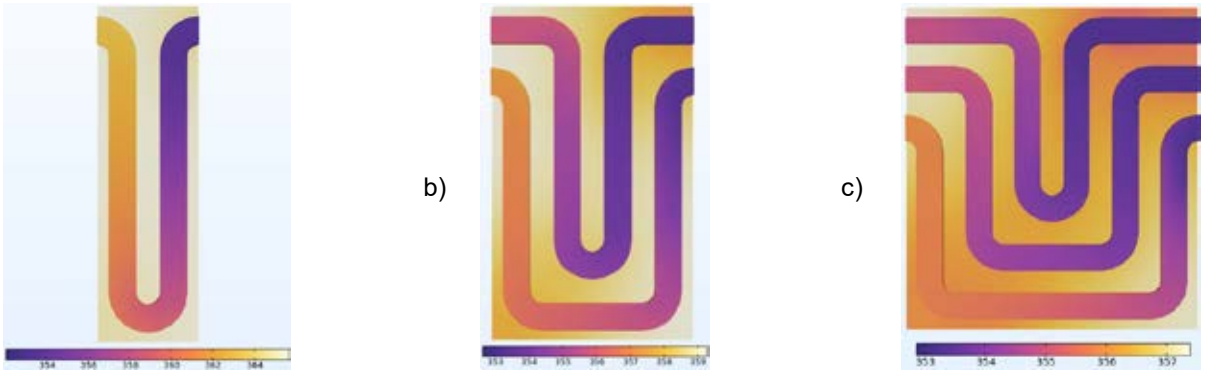

Fig. 4. Temperature distribution (K) over cathode side domains

Fig.3 indicates that increasing the number of serpentine channels (from single to double and triple) resulted in diminished performance. This decline is likely due to the division of electrolyte flow among multiple channels, reducing the flow rate in each and impairing the efficient removal of gas bubbles. Consequently, gas accumulation occurs, leading to increased ohmic resistance and reduced active electrode area. This phenomenon aligns with the findings of Ponce de León et al[11]., who observed that higher numbers of serpentine channels can lead to reduced mass flow rates, thereby affecting bubble removal efficiency and overall cell performance.
Concerning the temperature distribution, Fig.4 reveals that the multiple serpentine configurations (b and c) exhibit a more uniform temperature distribution compared to the single serpentine channel (a). This contrasts with typical co-flow

designs where local heating tends to occur near the outlet. In the single serpentine configuration (Figure 4a), a distinct temperature gradient develops along the flow path, with higher temperatures concentrated near the outlet region. This is due to the continuous flow path where heat accumulates as the electrolyte progresses through the channel. For the double and triple serpentine designs (Figures 4b, 4c), the counter-flow mechanism allows for more effective heat exchange between the anode and cathode sides, leading to a more uniform thermal distribution throughout the electrolyzer. The heat generated in one section is partially dissipated by the cooler flow from the opposite side, preventing excessive local heating. These findings are consistent with studies such as Kim et al.[12] who have shown that counter-flow configurations improve temperature regulation, reduce membrane degradation risks, and increase long-term operational stability

4. CONCLUSIONS

In the current study modeling of AEM electrolyzer was successfully aligned well with the experimental data reported in the literature. The result analysis shows the critical role of flow channel design in the performance of AEM electrolyzers. The single serpentine configuration emerges as the most effective design, offering uniform flow distribution and efficient gas bubble removal. the multi-serpentine counter-flow configurations result in more uniform temperature distribution, compared to single serpentine designs, which exhibit localized heating near the outlet. This counter-flow effect enhances heat dissipation, improves ion conductivity, and stabilizes electrochemical reactions, ultimately leading to higher efficiency and longer durability of AEM electrolyzers.

ACKNOWLEDGEMENT

This study was supported by the Çukurova University, Turkey under grant FBA202517320

REFERENCES

[1] M.E. Kreider, H. Yu, L. Osmieri, M.R. Parimuha, K.S. Reeves, D.H. Marin, R.T. Hannagan, E.K. Volk, T.F. Jaramillo, J.L. Young, P. Zelenay, S.M. Alia, Understanding the Effects of Anode Catalyst Conductivity and Loading on Catalyst Layer Utilization and Performance for Anion Exchange Membrane Water Electrolysis, ACS Catalysis 14 (2024) 10806-10819.
[2] G.H.A. Wijaya, K.S. Im, S.Y. Nam, Advancements in commercial anion exchange membranes: A review of membrane properties in water electrolysis applications, Desalination and Water Treatment 320 (2024) 100605.
[3] X. Tongwen, Y. Weihua, Fundamental studies of a new series of anion exchange membranes: membrane preparation and characterization, Journal of Membrane Science 190 (2001) 159-166.
[4] N.U. Hassan, E. Motyka, J. Kweder, P. Ganesan, B. Brechin, B. Zulevi, H.R. Colón-Mercado, P.A. Kohl, W.E. Mustain, Effect of porous transport layer properties on the anode electrode in anion exchange membrane electrolyzers, Journal of Power Sources 555 (2023) 232371.
[5] Q. Xu, L. Zhang, J. Zhang, J. Wang, Y. Hu, H. Jiang, C. Li, Anion Exchange Membrane Water Electrolyzer: Electrode Design, Lab-Scaled Testing System and Performance Evaluation, EnergyChem 4 (2022) 100087.
[6] A. Arsad, M. Hannan, A.Q. Al-Shetwi, R. Begum, M. Hossain, P.J. Ker, T.I. Mahlia, Hydrogen electrolyser technologies and their modelling for sustainable energy production: A comprehensive review and suggestions, International Journal of Hydrogen Energy 48 (2023) 27841-27871.
[7] J. Liu, Z. Kang, D. Li, M. Pak, S.M. Alia, C. Fujimoto, G. Bender, Y.S. Kim, A.Z. Weber, Elucidating the role of hydroxide electrolyte on anion-exchange-membrane water electrolyzer performance, Journal of the electrochemical society 168 (2021) 054522.
[8] F.M. Nafchi, E. Afshari, E. Baniasadi, Anion exchange membrane water electrolysis: Numerical modeling and electrochemical performance analysis, International Journal of Hydrogen Energy 52 (2024) 306-321.
[9] D. Lee, M. Kim, J. Kim, I. Moon, J. Kim, Advanced CFD simulation of two-phase anion exchange membrane water electrolysis, International Journal of Hydrogen Energy 88 (2024) 322-332.
[10] S.-C. Chang, R.-E. Gu, Y.-H. Chan, Parameter Analysis of Anion Exchange Membrane Water Electrolysis System by Numerical Simulation, Energies 17 (2024) 5682.
[11] Loh, A.; Li, X.; Sluijter, S.; Shirvanian, P.; Lai, Q.; Liang, Y. Design and Scale-Up of Zero-Gap AEM Water Electrolysers for Hydrogen Production. Hydrogen 2023, 4, 257-271.
[12] Wang, Wenjun, et al. "Three-dimensional numerical simulation of bubble dynamics and design optimization of microchannel in proton exchange membrane water electrolyzers." International Journal of Hydrogen Energy 48.93 (2023): 36240-36253.

THEORETICAL INVESTIGATION OF USING OF HYDROGEN AND NATURAL GAS BLENDING IN SLAB TUNDISH HEATING SYSTEMS FOR GREEN STEEL REVOLUTION

[1]*Mustafa Kaan BALTACIOGLU*, [2*]*Seyit Mustafa HAS*, [3]*Hüseyin Turan ARAT*
[1] Iskenderun Technical University, Faculty of Engineering, Mechatronics Engineering, İskenderun, Hatay, 31200, Turkey
[2] Iskenderun Technical University, Faculty of Engineering, Mechanical Engineering, İskenderun, Hatay, 31200, Turkey
[3] Sinop University, Faculty of Engineering, Mechanical Engineering, Korucuk, Sinop, 57000, Turkey
shas.lee23@iste.edu.tr

ABSTRACT
The increasing demand for energy, driven by population growth and technological advancements, is guiding the modern world toward addressing the issue of global warming. Especially in the past 20 years, this awareness has gained significant momentum compared to earlier periods. It is universally accepted that emissions of CO, CO2, SO2, and NOX are the primary causes of glacier loss. The iron and steel industry is responsible for 7-9% of these emissions. All countries associated with the European Union must comply with the European Green Deal, in line with the goal of achieving zero carbon emissions by 2050. One of the common production methods in the iron and steel sector is continuous casting. One of the sections where hydrocarbon fuels are most commonly used in continuous casting facilities is the tundish heating system. There are no studies in the literature regarding the use of a natural gas and hydrogen mixture in tundish heating systems. This thesis aims to conduct a theoretical study on the use of a natural gas and hydrogen mixture in tundish heating systems of slab casting. Mixture rates will be determined and compared to 0 %to 10 %.
Keywords: Green Deal, Tundish Heating, Continuous Casting, Natural Gas and Hydrogen Mixture, Green Steel

1. INTRODUCTION
The increasing demand for energy, driven by population growth and technological advancements, is pushing the modern world to address the issue of global warming. Especially in the past 20 years, this awareness has gained significant momentum compared to earlier periods. The International Energy Agency (IEA) World Energy Outlook 2024 report highlights that the time remaining to limit global warming to 1.5°C is rapidly decreasing. This report from the IEA once again strongly emphasizes the need to accelerate the global energy transition and for governments to take immediate action and support one another. In 2023, the world achieved record growth by adding more than 560 GW of new renewable energy capacity to the global energy system. However, the distribution of this growth worldwide is far from being equal across technologies and countries. This situation shows that the measures taken against global warming are not sufficient. [1]

Emissions of CO, CO2, SO2, and NOX are globally recognized as the primary contributors to glacier losses. The steel industry accounts for 7-9% of these emissions. In addition, the sector emitted 1.91 tons of CO2 per ton of crude steel produced in 2022. Furthermore, the energy intensity in the industry was 20.99 GJ per ton of crude steel in 2022. Steel plays a critical role in virtually all aspects of modern life, from the computers used for this research to the vehicles we drive. The steel industry has been fundamental in building the modern world, and as the sector evolves, it has become indispensable. Total 1 763 Mt crude steel were used by sectors on 2023 as showed Fig 2. However, this indispensability has also made it a major driver of global warming. In 2024, global crude steel production totaled 1,892 Mt, with approximately 2% of the world's steel produced in Turkey.[2]

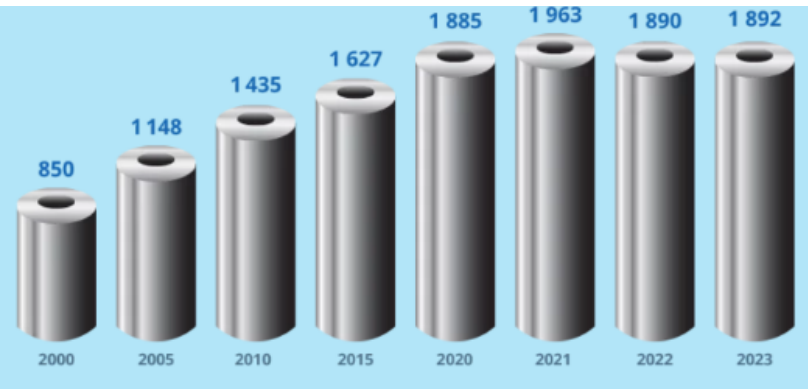

Fig. 1. Crude steel production 2000 – 2023.[2]

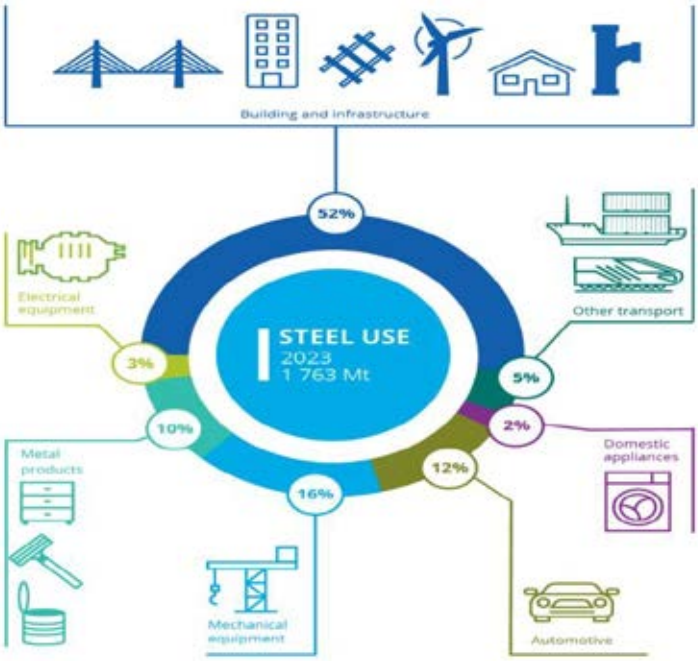

Fig. 2. Steel use by sectors on 2023.[2]

Since March 2020, the COVID-19 pandemic, which has affected the entire world and negatively impacted the economies of many countries, led numerous nations to prioritize pandemic response and economic recovery, causing the issue of global warming to fall lower on the agenda. However, in 2021, natural disasters, fires, and floods in various parts of the world brought the importance of climate change back into focus. Europe has found a solution in the form of establishing a new and lasting agreement. All countries associated with the European Union are required to adhere to the Green Deal in alignment with the zero-carbon target for 2050. This agreement aims to gradually reduce the emissions of the steel industry to zero by utilizing renewable energy sources. [3] (Ucak & Villi, 2021)

The process that began in October 2023 primarily covers heavy industries such as steel, fertilizer, energy production, and cement. Within the transition period, which will continue until January 2026, emissions from the production of products imported into the EU from these sectors, as well as the indirect emissions from the electricity used in their production processes, will be reported. As part of this compliance framework, the steel industry has increased its investments in emission reduction and energy efficiency measures by shifting towards alternative energy sources. The most critical factor in the industry's adaptation to the new regulations is undoubtedly the use of hydrogen as a fuel, produced using renewable energy sources. The global adoption of this approach is driven by the fact that hydrogen energy is considered an ideal fuel and energy carrier. It is easy to produce, a suitable fuel for all sectors, allows energy to be efficiently converted into other forms, provides high efficiency, and is environmentally harmless.[4]

2. MATERIALS AND METHODS

One of the most common production methods in the steel industry is continuous casting. The continuous casting process involves passing liquid metal through a copper mold, which has open ends and is cooled by water, to solidify it as showed in Fig.3. One of the sections of a continuous casting plant that consumes the most hydrocarbon fuel is the tundish heating system. The tundish is defined as an intermediate vessel used for the removal of inclusions from steel and for temperature control. Tundishes consist of refractory bricks and mortar applied over a steel structure. To prevent the refractory from melting and to ensure the quality of the liquid steel, the tundish must be preheated according to the steel quality before casting. Typically, it is heated to approximately 1100°C using natural gas. This process is usually performed with burners powered by coke gas or natural gas. One of the key advantages of using hydrogen either as a substitute for or in combination with natural gas is that it can be used with existing combustion turbines. However, when designing the systems, the differences between hydrogen fuel and natural gas will be significant. Firstly, the chemical formulas of the two substances differ. While the combustion of hydrogen does not result in carbon emissions, methane combustion does produce carbon emissions. [5] No studies have been found in the literature regarding the use of a natural gas and hydrogen mixture in tundish heating systems. This thesis intends to conduct a theoretical study on the application of a natural gas and hydrogen mixture in tundish heating systems.

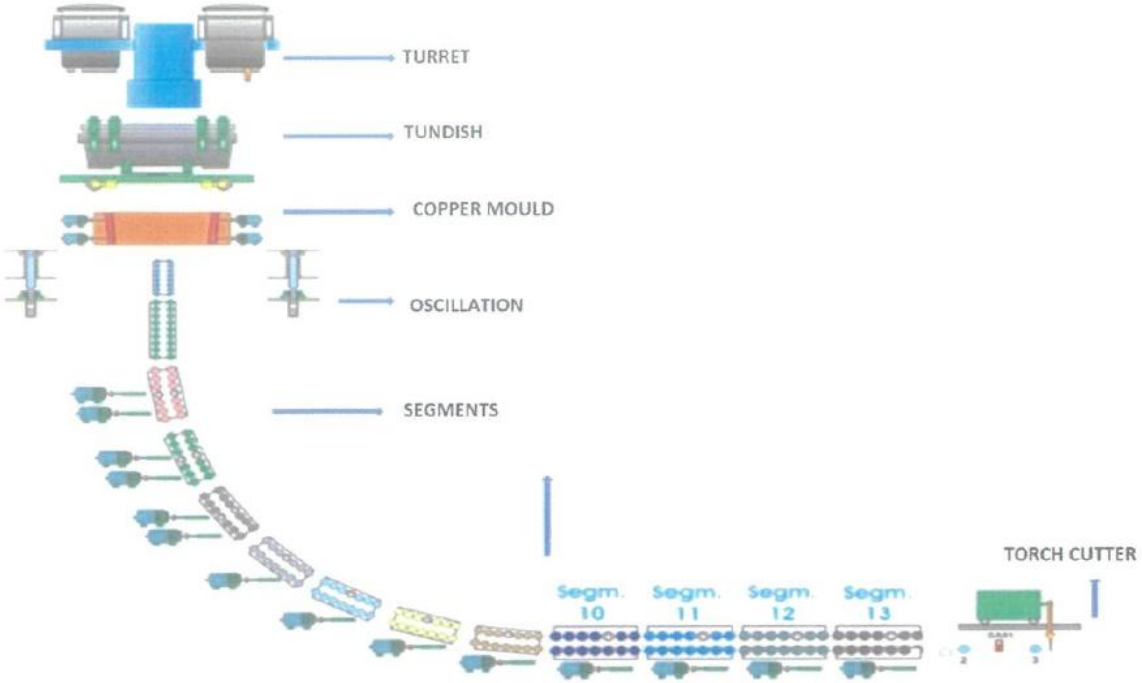

Fig. 3. Slab Casting Chart

In steel plants, due to the high consumption of natural gas, it is stored in tanks, allowing the facilities to continue operating for a period of time even if the central grid is disconnected. For this reason, hydrogen injection into the tundish heating system of the continuous casting plant cannot be performed through the main tank. The relevant injection can be made through the pipeline before the tundish heating system. Research studies are investigating the changes in emulsion values and temperature control resulting from the combustion of a natural gas-hydrogen mixture with different ratios in heaters equipped with combustion chambers and burner systems. Additionally, the hydrogen production methods required for this mixture are being explored. As is well known, according to the Green Deal, hydrogen production methods must be green. Depending on the location of the steel plant, energy required for electrolysis will be provided by utilizing wind, solar, and geothermal resources.

The prediction results obtained from the numerical simulation will be compared with the results from the literature. The differences in the flame region will be monitored in composite fuels containing varying amounts of hydrogen. Additionally, temperature control in hydrogen-rich composite fuels will be simulated and tested.

3. RESULTS AND DISCUSSION

Research studies generally indicate that in hydrogen-rich fuel mixtures, the emulsion values decrease and the temperature curve rises. The potential damage to tundish refractories due to this temperature increase or the ability to control the temperature is being investigated. The renewable energy sources to be utilized for hydrogen production will be determined based on the geopolitical situation of the regions where the research is conducted. The cost of green hydrogen will also be calculated throughout these processes. Furthermore, the percentage of total green steel production resulting from the steel produced after the tundish heating activity using green hydrogen will be calculated.

CO and CO2 values decreased in emulsions as a result of the reduction of the methane ratio in the theoretical examinations and increasing the amount of hydrogen. Mixture rates are 0 %H2- 100 %CH4, 3 %H2- 97 %CH4, 5 H2- 95 %CH4, 10 %H2- 90 %CH4, respectively, respectively. The amount of CO and C02 after the reaskiyon, which was performed by using these rates, decreased by 7-12 %.[6] (Tur & Buyukkaya, 2024)

4. CONCLUSIONS

The comparison and Ansys analyses to be conducted after this study may contribute to green steel production and the literature. Additionally, once sufficient equipment is acquired, its application will be tested in the field. The results will help for next researches.

REFERENCES

1. https://temizenerji.org/ Accessed on March 2, 2025.
2. https://worldsteel.org/ Accessed on February 19, 2025.
3. Ucak S and Villi B. 2021. From Possible Effects Of The European Green Deal On The Steel Industry. Journal of Empirical Economics and Social Sciences 2:94-113.
4. https://ticaret.gov.tr/ Accessed on March 10, 2025.
5. https://www.hidrojenhaber.com/ February 3, 2025
6. Tur V and Buyukkaya E. 2024. From Hidrojen Takviyeli Doğalgaz Kullaniminin Yoğuşmali Kazanlara Etkilerinin İncelenmesi, Mühendislikte Yakitlar, Yangin Ve Yanma Dergisi 12 (1):15-27, 2024

SYNERGISTIC EFFECTS OF TEMPERATURE, GAS FLOW, AND CLAMPING FORCE ON FUEL CELL PERFORMANCE

[1*] *Busra Yilgin*, [2] *Fatma Gul Boyaci San,*, [3] *Cenk Celik*
[1] Kocaeli University, Engineering Faculty, Mechanical Engineering Department, Kocaeli, 41380, Türkiye
[2] Düzce University, Arts and Science Faculty, Chemistry Department, Düzce, 81620 Türkiye
[3] Kocaeli University, Engineering Faculty, Mechanical Engineering Department, Kocaeli, 41380, Türkiye
*Corresponding author e-mail: busra_ylgn@hotmail.com

ABSTRACT

The performance of fuel cells is significantly influenced by operating parameters and the mechanical design of components. This study investigates the effects of operating conditions, including cell temperature, anode and cathode flow rates, and torque, on fuel cell performance using Response Surface Methodology (RSM). A stainless-steel end plate and a centered bolt arrangement configuration were employed to ensure homogeneous pressure distribution. The analysis included 27 experiments to evaluate current density, power density, and internal resistance under varying operating conditions. The findings highlight that cell temperature and cathode flow rate are critical factors influencing performance. Optimal cell temperature enhances reaction kinetics and proton conductivity, leading to increased current and power density while minimizing resistance. Cathode flow rate also plays a vital role on the fuel cell performance. The torque applied to the end plate was found to have minimal impact within the tested range, confirming the effectiveness of the closure design. Maintaining the cell temperature at an optimal level in a fuel cell has enhanced the impact of gas flow rates on performance. These results emphasize that in fuel cell design and operation, optimizing individual parameters alone is insufficient; the interactions and synergistic effects between parameters must also be considered.

Keywords: Fuel cell, Operating Conditions, Performance, Response Surface Methodology.

1. INTRODUCTION

Fuel cells stand out among environmentally friendly energy production systems due to their high efficiency and low emission characteristics. Technologies such as Proton Exchange Membrane Fuel Cells (PEMFC) meet a wide range of energy demands, from portable devices to transportation applications. However, the performance of fuel cells is directly linked not only to the efficiency of electrochemical reactions but also to the design of mechanical components and operating parameters. In this context, the force applied to the end plate and the bolt distribution have a critical impact on the operating parameters of fuel cells.

The literature includes numerous studies examining the effects of clamping force and bolt distribution on fuel cell performance. For instance, experimental studies demonstrate that excessive clamping force reduces the permeability of gas diffusion layers, leading to performance losses in the cell. Simulation-based studies model the effects of various bolt arrangements on pressure distribution, providing valuable contributions to the design process.

Dey et al. [1] examined the impact of end plate design on fuel cell performance. The study used the finite element method to analyze parameters such as cell geometry, bolt configuration, gasket thickness, and material properties on contact pressure. Experimental validation showed that the number and distribution of bolts significantly affected contact pressure, with a configuration of 10 bolts achieving a uniform distribution.

In the study by Liu et al. [2], a novel compression mechanism was proposed to optimize the contact pressure distribution and deformation of the MEA and improve the electrochemical performance of fuel cells. Using the finite element method, models of PEMFCs with traditional bolt mechanisms and a new pneumatic compression mechanism were developed. The new mechanism increased maximum power density by 10%.

Zhao et al. [3] examined the effects of bolt distribution, end plate thickness, end plate material, geometry, and clamping force on the performance of a single-cell fuel cell with a 50 cm² active area. The study found an optimal GDL compression ratio of approximately 75% as a function of clamping force and end plate thickness.

Barzegari et al. [4] analyzed the parameters of pneumatic compression systems in fuel cells using response surface methodology and finite element methods. The study concluded that pneumatic compression systems with end plates were more efficient than traditional systems.

This study aims to examine the effects and interactions of operating parameters under the conditions identified in our previous research [5], where homogeneous pressure was achieved using a stainless-steel end plate and a centered bolt arrangement (8b configuration). The objective is to analyze how these specified conditions influence the performance of the fuel cell under various operating conditions. Additionally, this study highlights the interactions between design and operating parameters that impact fuel cell performance, offering valuable recommendations to guide design engineers. A comprehensive investigation into this topic is essential to ensure that fuel cell systems operate more efficiently and sustainably.

2. EXPERIMENTAL

Selecting the appropriate end plate, configuration, and clamping force for a fuel cell is crucial to minimize ohmic resistance and identify the optimal configuration. However, the impact of operating conditions on fuel cell performance must also be examined under this configuration. In the study by Yılgın et al. [5], a configuration using stainless steel and an centered bolt arrangement (8b configuration) (Fig. 1a) with a clamping force of 9 Nm was determined. In this study, the effect of operating conditions identified through the response surface methodology on fuel cell performance was investigated using the stainless steel and centered bolt arrangement.
In the conducted research, a 50 cm² (7.071 cm x 7.071 cm) active area was selected for the fuel cell, and the MEA was prepared accordingly. The MEA was placed within the designed end plate, and the fuel cell assembly was completed. This cell is shown in Fig. 1b.

(a) (b)

Fig. 1. Centered Bolt Arrangement (8b) (a) and Test Cell (b)

The effects of operating temperature, flow rate, and torque on fuel cell performance were investigated using the fuel cell test system (Figs. 2 and 3). The test system primarily consists of gas supply/flow control modules, anode and cathode humidifiers, temperature controllers, an electronic load, and other components.

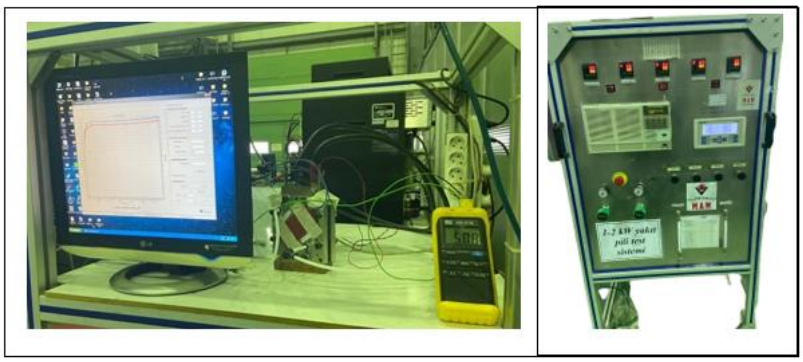

Fig. 2. Fuel Cell Test System

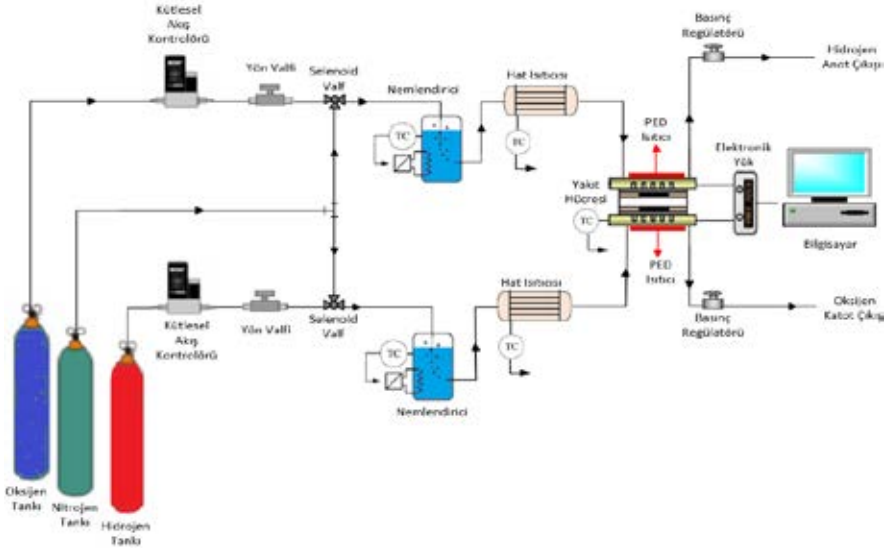

Fig. 3. Schematic Representation of the Test System

3. ANALYSIS

In this study, a total of 27 experiments were conducted, with the experimental design and analysis performed using the Design-Expert software. The experimental plan and levels of independent variables are temperatures of 35, 50, and 65 °C; anode flow rates of 0.3, 0.6, and 0.9 L/min; cathode flow rates of 0.01, 0.05, and 0.1 L/min; and torque values of 1, 5, and 9 Nm. The current density, power density, and resistance values were derived from polarization data obtained from the test system at an operating voltage of 0.6V.

4. RESULT AND DISCUSSIONS

The effect of parameters such as temperature, anode flow rate, cathode flow rate, and torque on the current density, power density and resistance of the test cell was analyzed using the response surface methodology. Fig. 4 presents 3D views of the effects of parameters such as cell temperature, anode flow rate, cathode flow rate, and torque on current density, modeled using the response surface methodology (RSM). According to RSM, the interaction between cell temperature and cathode flow rate has a more significant influence on current density than the other parameters. Cell temperature is a fundamental parameter that affects the electrochemical reaction rate of the fuel cell. Higher temperatures accelerate reaction kinetics, increase proton conductivity, and reduce membrane resistance. However, excessively high temperatures can cause membrane dehydration and performance loss. The graph indicates that within the studied range, cell temperature increases current density to an optimal point, after which it begins to decrease. As observed in the graphs, increasing the cathode flow rate enhances cell performance, even at the lowest torque levels. In other words, a higher cathode flow rate improves performance, indicating that higher oxygen flow rates are preferable for this model. In this study, at a cell temperature of 65°C, an anode flow rate of 0.3 L/min, a cathode flow rate of 0.1 L/min, and 1 Nm torque applied to the stainless-steel closure plate, the cell achieved its optimal current density. According to the RSM results, the maximum current density was found to be 513.93 A/cm².

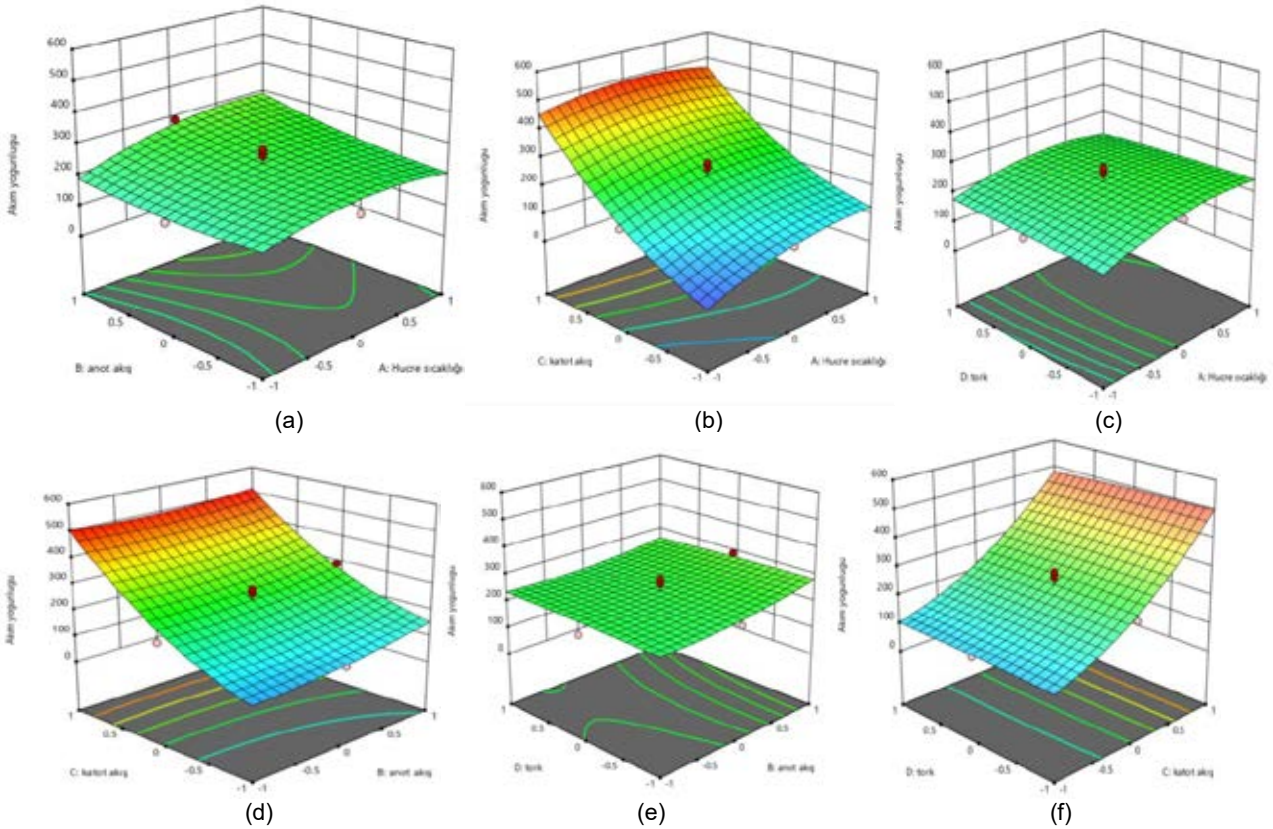

Fig. 4. 3D View of Current Density According to RSM

As shown in Fig. 5, increasing the cathode flow rate enhances cell performance, even at the lowest torque. In this study, when the cell temperature was 65°C, the anode flow rate was 0.3 L/min, and the cathode flow rate was 0.1 L/min, applying 1 Nm torque to the stainless-steel end plate resulted in the optimal power density for the cell. The RSM analysis determined the maximum power density to be 307.20 W/cm².

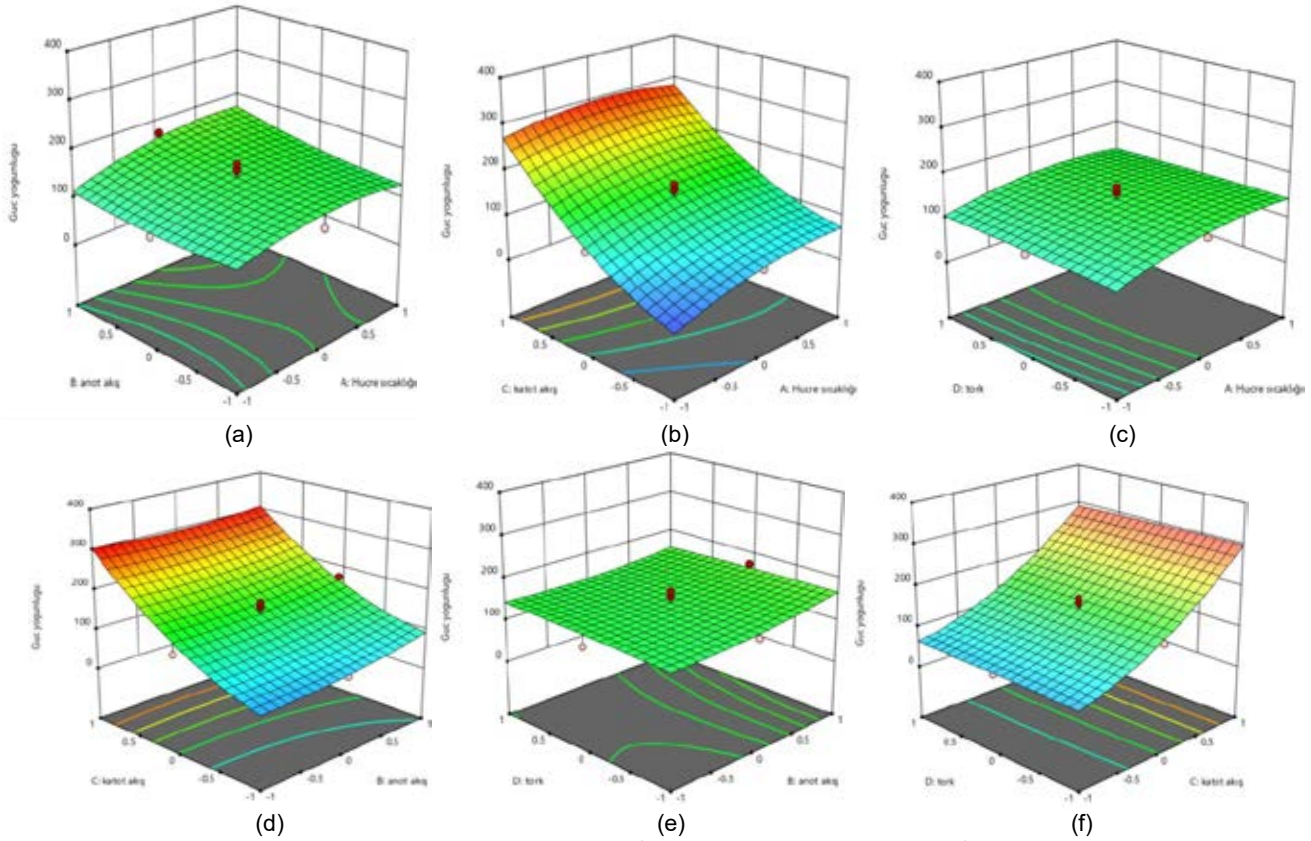

Fig. 5. 3D Visualization of Power Density According to RSM

Fig. 6 presents 3D views modeled by the RSM method, showing the effects of parameters such as temperature, anode flow rate, cathode flow rate, and torque on resistance. As observed in the resistance graph, increasing the torque value reduces cell resistance. At the lowest torque value, resistance is at its highest. However, even when torque increases from 1 Nm to 9 Nm, the difference in resistance is minimal. This outcome confirms the suitability of the cell design parameters established by Yılgın et al. (2024) and demonstrates that internal resistance varies with operating conditions. Increasing the clamping force homogeneously leads to proper compression of the membrane and gas diffusion layers, reducing internal resistance. However, excessive clamping force may cause membrane deformation, block gas flow channels, and complicate water management, resulting in increased resistance. At low temperatures, the decrease in proton conductivity within the membrane and its reduced water retention capacity, along with reduced gas diffusion on the electrode and slower electrochemical reactions, contribute to an increase in internal cell resistance. A slight reduction in resistance is observed with higher anode and cathode flow rates. This reduction is due to improved reaction efficiency and water formation, which decreases resistance when sufficient fuel and oxidant are supplied. However, excessively high flow rates may lead to membrane drying and disrupt energy balance within the cell.

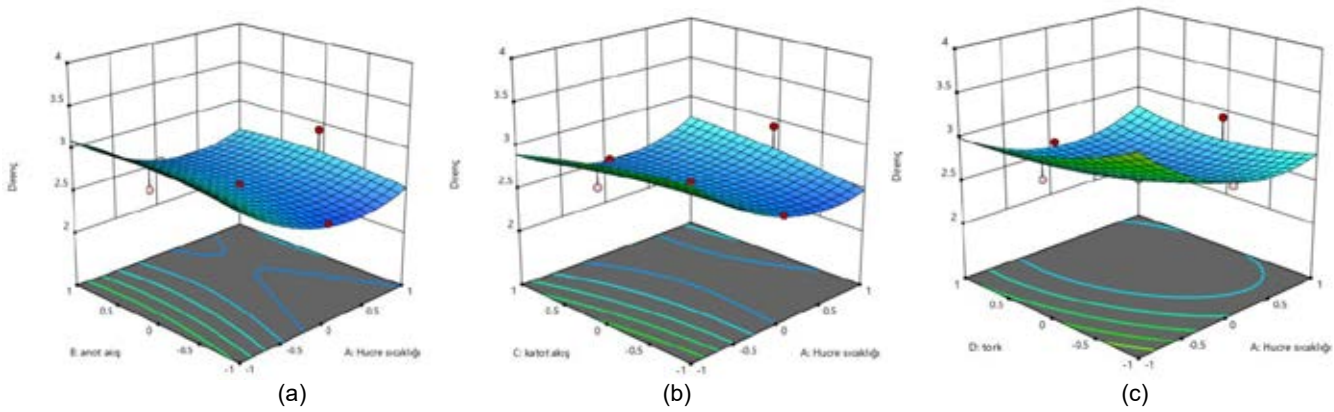

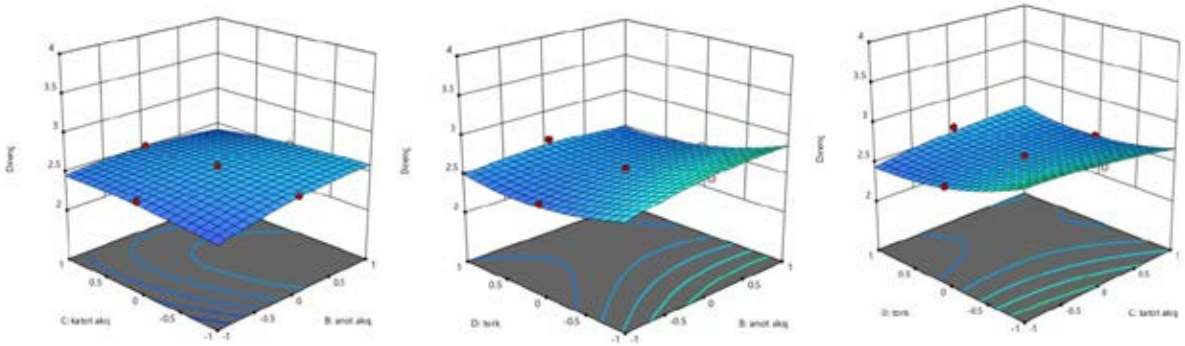

(d) (e) (f)

Fig. 6. 3D View of Resistance According to RSM

4. CONCLUSIONS

In this study, the effects of operating temperature, anode and cathode flow rates, and torque on cell performance in a fuel cell were investigated using the RSM experimental design method, employing stainless steel end plates and a previously determined closure configuration. According to the ANOVA analysis, 27 experiments were conducted to evaluate fuel cell performance, and the results of these experiments were analyzed in terms of current density, power density, and internal cell resistance. The findings obtained from the graphs highlight the critical importance of optimizing these parameters in fuel cell systems. It has been demonstrated that the increase in current and power density and the reduction of internal cell resistance are directly dependent on operating conditions. This study is significant in demonstrating the interactive relationship between parameters such as cell temperature, anode and cathode flow rates, and torque. For example, maintaining the cell temperature at an optimum level in the fuel cell increases the effect of gas flow rates on performance. These results indicate that fuel cell design and operation require not only the optimization of individual parameters but also consideration of the interactions and synergistic effects between parameters. The results obtained are summarized below:

Cell Temperature: Cell temperature is one of the most critical variables affecting the fundamental performance parameters of the fuel cell. The graphs obtained during the study indicate that temperature has a direct impact on both current and power density as well as resistance. An increase in cell temperature improves reaction kinetics while also enhancing proton conductivity within the membrane, resulting in greater current density and lower resistance. However, excessive temperatures can cause membrane drying, which limits performance.

Anode Flow Rate: An increase in anode flow rate was observed to slightly enhance current and power density. This is primarily due to the sufficient supply of reactants supporting electrochemical reactions. However, excessively high anode flow rates can disrupt water management within the cell and result in energy losses, necessitating optimization within an optimal range.

Cathode Flow Rate: The findings reveal that low cathode flow rates limit current and power density and increase resistance. This is due to insufficient oxygen transfer, which negatively affects reaction kinetics. While higher cathode flow rates improve performance up to a certain point, excessively high flow rates can cause energy losses and disrupt the membrane's moisture balance. The cathode flow rate should be optimized in harmony with other operating parameters.

*End Plate Clamping Force:*The torque applied to the end plate is a parameter used to ensure the mechanical stability of the fuel cell stack, prevent gas leakage, and optimize reactant flow. While the material, force, and configuration of the end plate were examined in our previous study, this study focused on observing the interaction of operating conditions with end plate force. As expected, no significant impact on performance was observed within the investigated range. However, a minimal effect on internal cell resistance was observed depending on the operating parameters.

REFERENCES

1. Dey, T., Deshpande, J., Singdeo, D., Ghosh, P. C. (2019). Study of PEM Fuel Cell End Plate Design By Structural Analysis Based On Contact Pressure. Journal of energy, 2019.
2. Liu, J., Tan, J., Yang, W., Li, Y., Wang, C. (2021). Better Electrochemical Performance of PEMFC Under A Novel Pneumatic Clamping Mechanism. Energy, 229, 120796.
3. Zhao, C., Xing, S., Liu, W., Chen, M., Wang, Y., Wang, H. (2020). An Experimental Study On Pressure Distribution and Performance Of End-plate With Different Optimization Parameters For Air-cooled Open-Cathode LT-PEMFC. International Journal of Hydrogen Energy, 45(35), 17902-17915.
4. Barzegari, M. M., Ghadimi, M., Momenifar, M. (2020). Investigation of Contact Pressure Distribution On Gas Diffusion Layer Of Fuel Cell With Pneumatic Endplate. Applied Energy, 263, 114663.
5. Yilgin B, Celik C And San Boyacı FB (2024) Clamping effects on the performance of proton exchange membrane fuel cell. *International Journal of Hydrogen Energy*.

MANTA RAY FORAGING OPTIMIZATION FOR ACCURATE PARAMETER ESTIMATION OF PROTON EXCHANGE MEMBRANE (PEM) FUEL CELL MODEL

[1,2]*Damla YAĞCI*, [1]*Hadi GENCELİ*, [3]*Oğuz Emrah TURGUT*
[1]Yildiz Technical University, Department of Mechanical Engineering, Istanbul, Türkiye
[2]İstanbul Gelişim University, Department of Hybrid and Electric Vehicle Technologies, Istanbul, Türkiye
[3]İzmir Bakırçay University, Department of Industrial Engineering, İzmir, Türkiye

e-mail: damla.yagci@std.yildiz.edu.tr

ABSTRACT
Proton Exchange Membrane Fuel Cell (PEMFC) systems' complex and non-linear characteristics necessitate precise modeling for design and optimization purposes. The mathematical representation of fuel cells is typically constructed using empirical equations, as the output voltage is influenced by various losses, including activation, ohmic, and concentration losses. These losses depend on specific parametric coefficients; thus, optimizing these parameters is crucial for minimizing losses and enhancing fuel cell performance.
In this study, a novel heuristic optimization approach—the Manta Ray Foraging Optimization (MRFO) algorithm—is employed to determine the optimal parameters of PEMFC models. The MRFO algorithm is also applied to optimize the parameters of various fuel cell types for which experimental data are available. Based on the resulting parameter selections, error calculations are conducted. Furthermore, the proposed validation technique validates the voltage-current (V-I) curve against experimental data.

Keywords: Manta ray foraging optimization, Fuel cell, Optimization

1. INTRODUCTION

The growing environmental concerns have accelerated the transition to renewable energy sources. As a result, the demand for hydrogen, a clean and sustainable energy carrier, has been steadily increasing. Moreover, hydrogen can be utilized for electricity generation through electrochemical processes. Among various hydrogen-based energy conversion technologies, Proton Exchange Membrane (PEM) fuel cells stand out as one of the most widely adopted systems for efficiently converting chemical energy into electrical energy.

Owing to their high efficiency, high power density, short start-up times, and environmentally friendly characteristics, Proton Exchange Membrane (PEM) fuel cells have been increasingly utilized in various applications. Consequently, improving the performance of fuel cells has become a critical area of research. In general, the performance of a PEM fuel cell is influenced by key operational parameters, including pressure, relative humidity, and reactant gas flow rate [1]Although experimental studies play a crucial role in achieving an improved design process, they are often constrained by their complexity, time-consuming nature, and high costs. As a result, such studies are typically conducted within specific operational parameter ranges. Therefore, developing mathematical models to efficiently and accurately predict the performance of Proton Exchange Membrane Fuel Cells (PEMFCs) under varying operating conditions has become essential. In recent years, numerous models have been proposed, and various metaheuristic and bio-inspired algorithms have been explored to estimate PEMFC model parameters. This study, the Manta Ray Foraging Optimization Algorithm is proposed for this purpose.

This method, which is a metaheuristic algorithm, was employed to evaluate the parameters, and the validity of the model was verified by testing the simulated values against experimental data through a polarization curve The predictive accuracy of the optimized models was quantitatively assessed using statistical metrics—R-squared (R^2), Mean Absolute Error (MAE), and Root Mean Square Error (RMSE)—by comparing simulated voltage values with experimentally measured data.

2. MODELLING OF PEMFC

While mathematical modeling can predict fuel cell performance, a parametric model allows for a rapid analysis of operational parameters such as temperature and pressure [1]. Some challenges arise in this context, including the complexity of equations and the uncertainty of model parameters. Semi-empirical methods can be employed to address these issues [2]. To mitigate certain limitations, voltage losses such as ohmic, concentration, and activation losses must be carefully evaluated, and the physical background should be thoroughly analyzed. The voltage for a single cell of a PEMFC steady-state conditions is given by Eq. 1 [3].

$$V_{cell} = E_{Nernst} - \eta_{act} - \eta_{ohm} - \eta_{con} \quad (1)$$

E_{Nernst} is the thermodynamic potential of the cell, η_{Act} is the activation overvoltage, η_{Ohm} is the ohmic overvoltage, and η_{con} is the activation overvoltage.

The activation overpotential can be expressed in a parametric form as follows. [4]

$$\eta_{act} = \xi_1 + \xi_2 T + \xi_3 T \ln(C_{O2}) + \xi_4 T \ln(I)$$

where T is the cell operating temperature (K), I is the cell current (A), and ξ are semi-empirical coefficients. These coefficients have clear physical significance and are determined through mechanistic equations based on PEMFC thermodynamics, electrochemistry, and kinetics.

3. RESULTS AND DISCUSSION

As previously described, these seven parameters ξ_1, ξ_2, ξ_3, ξ_4, λ, B, and R_c must be determined. The selection of appropriate initial search bounds for each parameter is crucial when employing numerical optimization algorithms for parameter estimation, as it significantly influences the accuracy and efficiency of the optimization process.

Table 1. The lower and upper bounds of PEMFC model parameters.[5]

Parameter	ξ_1	ξ_2	ξ_3	ξ_4	λ	R_c	B
U_b	−0.8532	5×10^{-3}	9.8×10^{-5}	-0.954×10^{-4}	24	8×10^{-4}	0.5
L_b	−1.19969	1×10^{-3}	3.6×10^{-5}	-2.6×10^{-4}	10	1×10^{-4}	0.136

Table 2. The structural and operational parameters of the test cases.[6]

Stack	N	A(cm²)	l(μm)	$T(K)$	P_{H_2}(bar)	P_{O_2}(bar)	J_{max}(A·cm⁻²)
SR12	48	62.5	25	323	1	0.2095	0.672
Horizon500W	36	52	25	≤338.15	0.55	0.2075	0.469
BCW500W	32	64	178	333	1	0.2095	0.469

Table 3. Seven model parameters (ξ_1, ξ_2, ξ_3, ξ_4, λ, R_c, B) are optimized with Manta Ray Foraging Optimization. Statistical analysis is reported in Table 3.

Model Parameter	ξ_1	ξ_2	ξ_3	ξ_4	λ	R_C	B	RMSE	R²	MAE
SR-12	-0,9658	0,003405	0,0000697	-0,000091	21,19397	0,000713	0,173287	0,24244	0,9983	0,179934
Horizon500W	-0,8532	0,003	0,000088	-0,00017	9,066667	0,000825	0,0176	0,15413	0,997603	0,139687
BCW500W	-1,09687	0,003851	0,000088	-0,0002	12	0,00085	0,01975	0,0446	0,99976	0,036903

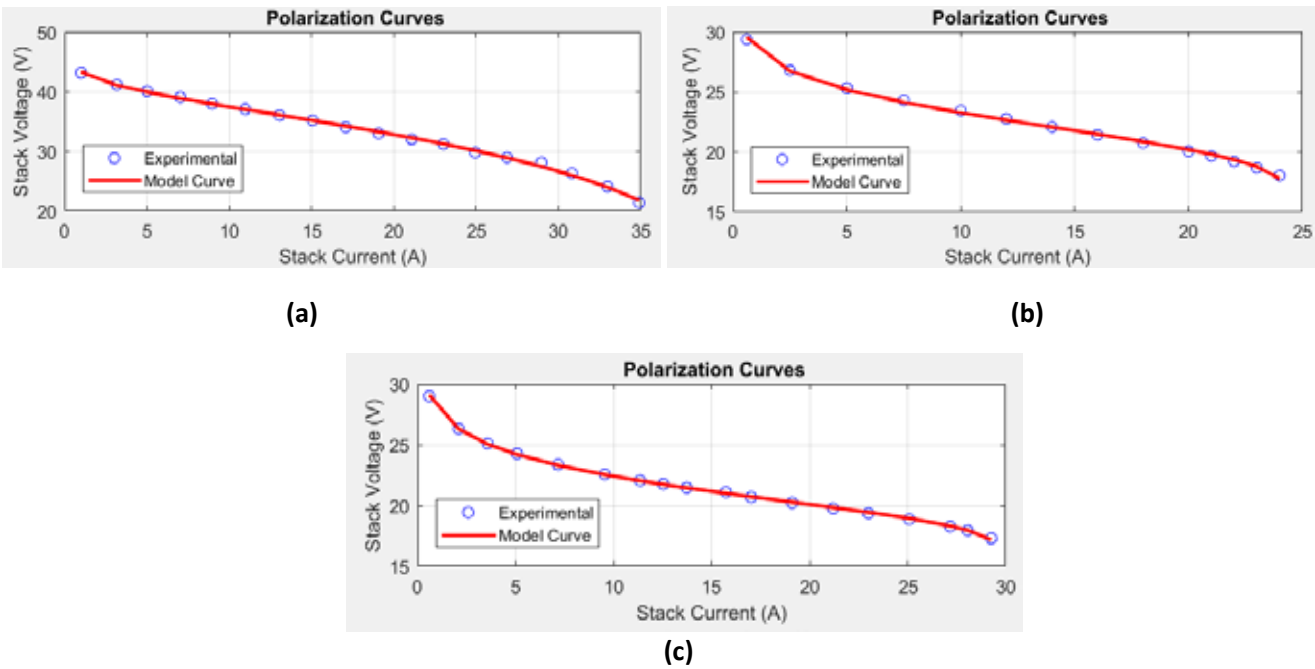

Fig. 1. Comparison of PEM fuel cell model predictions with experimental data (a) SR-12 PEMFC stack, (b) HORIZON 500 PEMFC stack, and (c) BCW 500 PEMFC stack.

4. CONCLUSIONS

The error rates for three models with experimental studies in the literature were calculated using the manta ray foraging algorithm, and the suitability of the proposed model was tested. As observed in the polarization curves, it is evident that the model exhibits an acceptable curve fit.

It is also evident that, alongside other powerful algorithms such as PSO, it is an advanced algorithmic method.

REFERENCES

[1] Zhang J. PEM fuel cell electrocatalysts and catalyst layers: fundamentals and applications. Springer Science & Business Media; 2008.

[2] Mann RF, Amphlett JC, Hooper MA, Jensen HM, Peppley BA, Roberge PR. Development and application of a generalized steady-state electrochemical model for a PEM fuel cell. J Power Sources 2000;86(1–2):173–80.

[3] J.M. Corrêa, F.A. Farret, L.N. Canha, M.G. Simões, An Electrochemical-Based Fuel-Cell Model Suitable for Electrical Engineering Automation Approach, IEEE T Ind Electron, 51 (2004), pp. 1103-1112.

[4] Amphlett JC, Baumert RM, Mann RF, Peppley BA, Roberge PR, Harris TJ. Performance modeling of the ballard mark iv solid polymer electrolyte fuel cell i. mechanistic model development. J Electrochem Soc 1995;142(1):1–8.

[5] Ayyarao, T. S. L. V., Polumahanthi, N., & Khan, B. An Accurate Parameter Estimation of PEM Fuel Cell Using War Strategy Optimization. Energy, (2024). 290, 130235.

[6] Mo Z-J, Zhu X-J, Wei L-Y, Cao G-Y. Parameter optimization for a PEMFC model with a hybrid genetic algorithm. Int J Energy Res 2006;30(8):585–97.

A DATA-DRIVEN DA-LSTM APPROACH FOR PREDICTING PEMFC DEGRADATION TRENDS IN DYNAMIC LOAD CONDITIONS

[1,2]*Nurşah Kübra EKMEKÇİ*, [3]*Murat Uyar
[1]Bursa Uludağ University, Graduate School of Natural and Sciences, Bursa, 16059, Türkiye
[2]Sirena Marine R&D Department, Bursa, 16800, Türkiye
[3] Bursa Uludağ University, Department of Electrical-Electronic Engineering, Bursa, 16059, Türkiye
*Corresponding author e-mail: muratuyar@uludag.edu.tr

ABSTRACT
This study proposes a data-driven dual attention long short-term memory (DA-LSTM) approach for predicting the degradation trends of proton exchange membrane fuel cells (PEMFCs) under dynamic load conditions. Addressing key challenges in fuel cell durability and reliability, the proposed model is compared against traditional long short-term memory (LSTM) architectures to assess its effectiveness in capturing complex degradation patterns. The predictive performance of each model is evaluated using root mean squared error (RMSE), mean absolute error (MAE), and the coefficient of determination (R^2). The results demonstrate that DA-LSTM outperforms the conventional LSTM model, offering enhanced feature selection and improved long-term prediction accuracy through its dual-stage attention mechanism. These findings highlight the potential of DA-LSTM for fuel cell prognostics, providing a robust framework for prognostics and health management (PHM) systems and advancing the development of sustainable energy technologies.

Keywords: PEMFC, Dual attention LSTM, Remaining useful life, Voltage degradation prediction

1. INTRODUCTION

Global reliance on fossil fuels has been a driving force behind industrial and economic progress for centuries; however, this dependency has come at a significant environmental cost, necessitating an urgent transition to cleaner and more sustainable energy sources to mitigate the effects of climate change [1]. Among the promising alternatives, proton exchange membrane fuel cells (PEMFCs) stand out due to their high efficiency, zero emissions, and versatility in applications such as power generation, energy storage, and various transportation sectors, including automotive and marine industries, where they are increasingly adopted for sustainable mobility solutions [2, 3].

Despite their potential, PEMFC systems face significant challenges, including performance degradation due to operational factors such as temperature, humidity, and load variations [4]. Accurate prediction of PEMFC degradation behavior is essential for enhancing system durability, reducing maintenance costs, and ensuring reliable operation. Prognostics and Health Management (PHM) frameworks are widely employed to monitor the state of health (SOH) and estimate the remaining useful life (RUL) of PEMFCs, enabling a proactive transition from a “fail to fix” strategy to a “predict to prevent” approach [3].

Existing methods for PEMFC performance prediction can be categorized into model-based and data-driven approaches. Model-based methods rely on physical principles, such as electrochemical reactions and state equations, to predict degradation, but they often struggle with the inherent complexity of PEMFC systems. On the other hand, data-driven methods leverage large experimental datasets to establish nonlinear mapping relationships between operating conditions and degradation patterns. Specifically, recurrent neural networks (RNNs), long short-term memory networks (LSTMs), and their attention-enhanced variants have demonstrated success in capturing long-term dependencies in PEMFC degradation data [4]. This success is primarily due to the ability of RNN-based approaches to model sequential dependencies in time-series data and their high capacity for learning long-term patterns. While traditional artificial neural networks (ANNs) primarily focus on static data, RNN and LSTM models retain past information, making the decision-making process more dynamic and particularly well-suited for predicting the degradation of time-evolving systems such as PEMFCs. The LSTM model, with its forget gate and cell state mechanisms, selectively retains only relevant information, filtering out unnecessary noise and effectively learning long-range dependencies [3, 4].

The proposed approach aims to improve prediction accuracy and provide interpretable insights into the degradation process. By leveraging the success of RNN- and LSTM-based methods, this study aims to establish a foundation that can be integrated with more advanced predictive models in future research. Integrating LSTM with attention mechanisms enhances the model’s ability to focus on critical time steps and essential features, improving accuracy and interpretability. Thus, rather than merely repeating existing methods, this study builds upon an adaptable framework that can be further refined with more complex hybrid approaches in future advancements.

2. MATERIALS AND METHODS

2.1. Dataset

The dataset utilized in this study originates from a long-term dynamic durability test conducted on a single PEMFC. The durability assessment was carried out using a Greenlight G20 test station, which provides precise control over load variations, gas supply conditions, and thermal management. This study follows the European Harmonized Test Protocol, which is based on ECE R15, a widely recognized test procedure for evaluating vehicle emissions and fuel efficiency

under standardized conditions [5].
Like real-world driving profiles, the ECE R15 driving cycle incorporates acceleration, deceleration, and steady-speed phases, making it a realistic benchmark for simulating fuel cell operating conditions. This protocol includes a combination of urban and extra-urban driving scenarios, ensuring that load fluctuations and transient behaviors experienced by fuel cells in automotive applications are accurately reflected. As illustrated in Figure 1(a), the urban driving cycle consists of four repetitions totaling 780 seconds, followed by a 400-second highway driving cycle, resulting in a total cycle duration of 1180 seconds, and the complete output voltage data of the PEMFC was processed and presented in Fig. 1(b) [6].

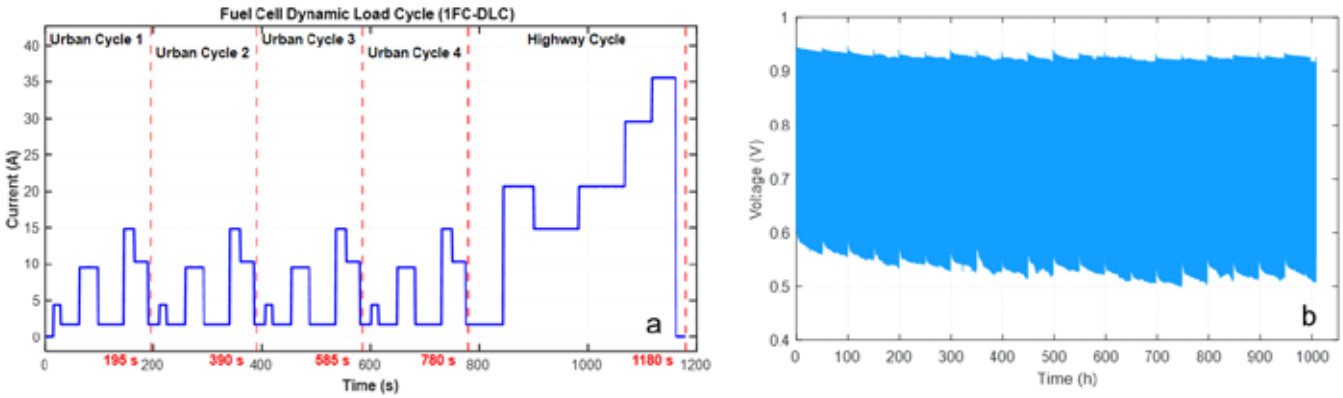

Fig. 1. (a) Current variation for one period of FC-DLC, (b) voltage change for 1008 hours of operation

In this study, the fuel cell dynamic load cycle (FC-DLC) was designed to replicate the fluctuating electrical demands observed in automotive fuel cells. This approach objectively evaluates fuel cell degradation patterns under long-term operating conditions. The FC-DLC protocol closely mimics the varying electrical requirements of automotive fuel cells, providing highly valuable degradation data for prognostics and health management (PHM) strategies [3]. The durability test consists of 3,076 FC-DLC cycles, covering approximately 1008 hours of operation. The test procedure involves applying cyclic current loads to the PEMFC while continuously monitoring electrical, thermal, and fluidic parameters, as presented in Table 1, at a sampling frequency of 1 Hz. These parameters are crucial for analyzing degradation phenomena, where the voltage drop trend is the primary indicator. At the same time, variations in temperature, pressure, and humidity offer insights into catalyst degradation and water management issues. Each test session comprises 152 FC-DLC cycles (~50 hours) and a characterization assessment. Additionally, after every 100 hours of operation, the system undergoes a 12-hour shutdown rest period. This process simulates real-world vehicle stop-start cycles, allowing for the evaluation of transient recovery effects on fuel cell degradation [5].

Table 1. Aging parameters gathered during the long-term durability test

Index	**Physical meaning**
Time	Aging time (s)
Current, voltage, power	The operating load (A), output voltage (V), and power (W) of PEMFC
Pressure anode inlet; Pressure anode outlet	Inlet and outlet pressure of H_2 (KPa)
Pressure cathode inlet; Pressure cathode outlet	Inlet and outlet pressure of air (KPa)
Temp anode inlet; Temp anode outlet	Inlet and outlet temperature of H_2 (°C)
Temp cathode inlet; Temp cathode outlet	Inlet and outlet temperature of air (°C)
Temp anode dewpoint water	Dewpoint water temperature of H_2 (°C)
Temp cathode dewpoint water	Dewpoint water temperature of air (°C)
Total anode stack flow	Total stack flow of H_2 (NLPM)
Total cathode stack flow	Total stack flow of air (NLPM)
Temp anode endplate	Operating temperature of PEMFC (°C)

These parameters are essential for understanding the multi-faceted degradation phenomena in PEMFCs. The voltage drop trend over time serves as the primary degradation indicator, while temperature, pressure, and humidity variations provide valuable insights into catalyst degradation, membrane thinning, and water management issues.

2.2. Data Preprocessing

Several preprocessing steps were implemented to enhance data quality and maintain consistency before model training. The raw dataset, collected from a fuel cell endurance test, underwent an abnormal value check to detect irregularities in the recorded parameters. Additionally, a cycle integrity verification was performed to ensure that each dynamic load cycle

contained the expected number of steps without missing or extra values. Only complete and validated cycles were retained for further processing. Furthermore, unnecessary columns were removed to streamline the dataset [3, 4]. Any rows containing NaN values were filtered out to handle missing values, ensuring that only complete data points were used [3]. The dataset was also downsampled from its original recording frequency of 1 Hz to 1/60 Hz, reducing the computational load while retaining essential degradation patterns [4].
A key step in preprocessing was applying a moving average smoothing technique, which helped reduce high-frequency noise and transient fluctuations in the voltage readings. This method ensured that the extracted features better represented the overall degradation trend rather than short-term variations [3, 4]. In alignment with prior studies, voltage was selected as the target variable for degradation prediction. The dataset was divided into training and testing subsets, with 60% allocated for training and 40% for testing. This time-based split maintained the chronological order of degradation, ensuring that the model was trained on earlier data and evaluated on later, unseen degradation trends. These preprocessing steps helped create a structured and noise-reduced dataset, optimizing the predictive model's performance in capturing long-term fuel cell degradation behavior.

2.3. Model Architecture and Training Strategy

This study utilizes RNN-based architectures to predict degradation patterns in PEMFC systems. While RNNs capture temporal dependencies effectively, they suffer from vanishing and exploding gradients, limiting their performance in long-term modeling [3]. To overcome these challenges, LSTM networks were integrated. LSTM uses memory cells with gating mechanisms to control information retention. Key components include forgetting, input, and output gates, facilitating long-range dependency learning while mitigating gradient issues [3, 4].
The computations in an LSTM cell are as given in Eqs. (1)-(6).

$$i_t = \sigma(W_{xi}x_t + W_{hi}h_{t-1} + b_i) \quad (1)$$
$$f_t = \sigma(W_{xf}x_t + W_{hf}h_{t-1} + b_f) \quad (2)$$
$$o_t = \sigma(W_{xo}x_t + W_{ho}h_{t-1} + b_o) \quad (3)$$
$$c_t^{\sim} = tanh(W_{xc}x_t + W_{hc}h_{t-1} + b_c) \quad (4)$$
$$c_t = f_t \odot c_{t-1} + i_t \odot c_t^{\sim} \quad (5)$$
$$h_t = o_t \odot tanh(c_t) \quad (6)$$

Where i_t,f_t,o_t are the input, forget, and output gates, respectively, c_t is the cell state, and h_t is the hidden state. The weight matrices W and b biases are trainable parameters, and σ denotes the sigmoid activation function. The model predicts voltage as the output variable based on input features related to fuel cell performance. An attention mechanism was added to enhance learning efficiency by focusing on key time steps. Assigning varying importance to different time steps improves feature extraction and prediction accuracy, making it valuable in fuel cell degradation modeling [3,4]. For further accuracy, a data-augmented LSTM (DA-LSTM) framework was implemented. This model uses a dual-stage attention mechanism within an encoder-decoder structure. While LSTM captures temporal dependencies, the attention mechanism enhances feature selection and temporal weighting for better long-term predictions [4]. The encoder extracts key features, and the decoder integrates them over time to refine predictions. This approach dynamically adjusts attention weights to improve understanding of degradation trends [4].
The model was trained using the Adam optimizer with mean squared error (MSE) as the loss function. Hyperparameter optimization was performed via grid search, adjusting hidden layers, dropout rate, and batch size for optimal accuracy. To prevent overfitting, a 30% dropout was applied to the LSTM layer [4]. The model was trained with dynamically loaded PEMFC degradation data and evaluated using RMSE, R^2, and MAE metrics to ensure robustness [3, 4].

3. RESULTS AND DISCUSSION

This section presents the predictive performance of the proposed DA-LSTM model in estimating PEMFC degradation trends. The results regarding prediction accuracy, model robustness, and comparative evaluation against conventional time-series prediction architectures such as standard LSTM are analyzed. The model’s effectiveness is demonstrated through time-series prediction plots, parity plots, and quantitative error metrics, including RMSE, MAE, and R^2.

3.1. Time-Series Prediction Analysis

The DA-LSTM model was evaluated using the test dataset, where predicted voltage values were compared against actual recorded values from the long-term durability test. As illustrated in Figure 2, the time-series prediction plot highlights the model's ability to track the observed degradation patterns closely. The red line represents DA-LSTM predictions, while the blue line represents the voltage values. The proposed model effectively captures the nonlinear degradation behavior of the PEMFC system, aligning well with the measured data over time. Notably, the model maintains high accuracy even in later operational stages, where voltage degradation accelerates due to cumulative aging effects.

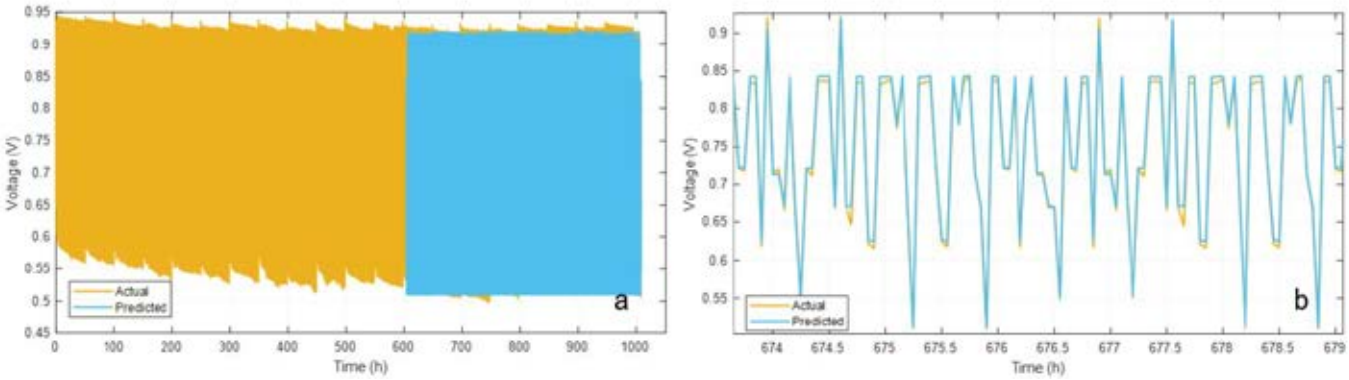

Fig. 2. (a) Time series prediction of PEMFC degradation using DA-LSTM, (b) corresponding zoomed-in view.

3.2. Comparative Performance Evaluation

The DA-LSTM model was compared with the conventional LSTM model using standard performance metrics to assess the predictive performance further. Table 2 presents the results.

Table 2. Performance comparison of DA-LSTM, LSTM, and RNN models

Model	RMSE	MAE	R^2
LSTM	0.0186	0.0143	0.9640
DA-LSTM (Proposed)	0.0135	0.0100	0.9805

The results indicate that DA-LSTM outperforms LSTM in predicting PEMFC voltage degradation, achieving the lowest RMSE and MAE values while maintaining the highest R^2 score. The DA-LSTM model's dual-stage attention mechanism enhances feature selection and temporal weighting, leading to better long-term prediction performance.

4. CONCLUSIONS

This research contributes to the growing work on PEMFC durability by developing a data-driven framework for performance degradation prediction. Leveraging deep learning techniques, including LSTM and DA-LSTM, this study provides accurate and interpretable predictions, facilitating better maintenance strategies and operational planning for PEMFC systems. Preliminary results indicate that attention-based models outperform conventional architectures, with DA-LSTM achieving the lowest RMSE of 0.0135, MAE of 0.0100, and highest R^2 of 0.9805, demonstrating its effectiveness in capturing degradation trends. The comparative analysis confirms that deep learning models can effectively model PEMFC degradation behavior under dynamic load conditions, making them suitable for real-world prognostics applications. Future work will focus on integrating experimental results, refining models based on real-world conditions, exploring new architectures to enhance predictive accuracy, and optimizing computational efficiency to ensure robust and practical implementation in PEMFC health monitoring and predictive maintenance systems.

REFERENCES

1. Sharifishourabi M, Dincer I, and Mohany A. 2025. Development of a Novel Biomass-Wind Energy System for Clean Hydrogen Production along with Other Useful Products for a Residential Community. Energy and Built Environment.
2. Sürer M, G, and Arat HT. 2022. Advancements and current technologies on hydrogen fuel cell applications for marine vehicles. International Journal of Hydrogen Energy, 47:45:19865-19875.
3. Zuo J, Lv H, Zhou D, Xue Q, Jin L, Zhou W, ... and Zhang C. 2021. Deep learning based prognostic framework towards proton exchange membrane fuel cell for automotive application. Applied Energy, 281:115937.
4. Yu Y, Yu Q, Luo R, Chen S, Yang J, and Yan F. 2024. Deep learning with dual-stage attention mechanism for interpretable prediction of proton exchange membrane fuel cell performance degradation. International Journal of Hydrogen Energy, 58:902-911.
5. Zuo J, Lv H, Zhou D, Xue Q, Jin L, Zhou W, ... and Zhang C. 2021. Long-term dynamic durability test datasets for single proton exchange membrane fuel cell. Data in Brief, 35:106775.
6. Zuo J. 2022. Development of Joint Deterioration and Energy Management Strategies for a Multi-stack PEM Fuel Cell System (Doctoral dissertation, Université Grenoble Alpes [2020]).
7. Yang Y, Yang Y, Zhou S, Li H, Zhu W, Liu Y, ... and Zhang R. 2024. Degradation prediction of proton exchange membrane fuel cell based on mixed gated units under multiple operating conditions. International Journal of Hydrogen Energy, 67:268-281.

APPLICATIONS OF MWCNTs IN HHO DRY CELL TECHNOLOGY

[1*]*Mustafa Kaan BALTACIOĞLU*, [2]*Onur BULUT*, [1]*Çağlar Conker*
[1] İskenderun Technical University, Faculty of Engineering and Natural Science, Mechatronics Engineering Department, Hatay, 31200, Turkey
[2] İskenderun Technical University, Faculty of Engineering and Natural Science, Mechanical Engineering Department, Hatay, 31200, Turkey
*Corresponding author e-mail: mkaan.baltacioglu@iste.edu.tr

ABSTRACT
This study uses alkaline water electrolysis. Several factors influence electrolysis efficiency, including electrode arrangement, cell spacing, applied voltage and current, temperature, processing time, and electrolyte type. This research focuses on optimizing the electrolyte solution, which enhances the conductivity of pure water and facilitates the electrolysis process. For this purpose, NaOH-containing solutions were used to promote the ionization of pure water. Nanomaterials, which provide high conductivity at low voltages, can improve water dissociation efficiency. In this context, multi-walled carbon nanotubes (MWCNTs) were incorporated into the electrolyte solution of the HHO dry cell to enhance hydrogen production efficiency. The effects of this approach on electrolysis efficiency were evaluated.

Keywords: Hydrogen, HHO, nanomaterial, electrolyte

1. INTRODUCTION
Among renewable energy sources, hydrogen energy stands out as a sustainable and alternative energy [1]. Hydrogen can be produced from various energy sources, stored and used as an energy carrier, making it a more efficient option compared to fossil fuels. In addition, it has the potential to reduce carbon emissions and poses a lower risk of explosion [2]. However, the transition to large-scale hydrogen use requires significant infrastructure investments [3].

In this study, alkaline water electrolysis was used to produce hydrogen in a HHO dry cell targeting renewable and green hydrogen production. Various factors, including electrode arrangement, cell gap, applied voltage and current, temperature, process time and electrolyte type, affect the electrolysis efficiency [4]. This research focuses specifically on the optimization of the electrolyte solution, which plays an important role in increasing the conductivity of pure water and facilitating the electrolysis process. For this purpose, NaOH-containing solutions were used to promote the ionization of pure water. Studies show that nanomaterials that provide high conductivity at low voltages increase water splitting efficiency [5]. However, the use of nanomaterials in the electrolyte solution of HHO dry cell has not yet been extensively investigated.

2. MATERIALS AND METHODS
The HHO dry cell is a system that operates based on the principle of electrolysis. Electrolysis is the process in which water is separated into its components through a chemical reaction using electrical energy. In this study, 316L stainless steel plates with dimensions of 14 cm × 14 cm were used as electrodes, and a total of 12 plates were used for the experiments. Rubber seals were used to ensure insulation between the plates.

For the electrolyte solution, mixtures containing pure water, NaOH, and multi-walled carbon nanotubes (MWCNTs) were selected. The properties of the multi-walled carbon nanotube are provided in Table 1. Additionally, experimental test equipment was set up as shown in Figure 1.

Table1. Multi-walled Carbon Nanotubs (MWCNTs) Properties

Purity	*> 90%*
(-COOH) Functionality	*0.55%*
Color	*Black*
Outer Diameter	*50 – 80 nm*
Inner Diameter	*5 – 15 nm*
Length	*10 – 30 µm*
Bulk Density	*0.15 g/cm³*
True Density	*2.2 g/cm³*
Specific Surface Area	*50 m²/g*
Ash Content	*9%*
Electrical Conductivity	*98 S/cm*
Production Method	*CVD (Chemical Vapor Deposition)*

The experiments were conducted under constant NaOH ratios and constant current conditions, and the effect of the

nanomaterials in the electrolyte solution was investigated. The electrolyte was tested in four different mixtures.900 gram purewater and 100 gram NaOH were mixed (10:1 w/w) separately with 0.5 g, 1 g, 2 g, and 5 g concentrations of MWCNTs, and each mixture was stirred with a magnetic stirrer at 500 rpm for 30 minutes.

All tests were conducted under the same conditions using CCPWM (Constant Current Pulse Width Modulation) with a constant voltage (22V) at 3A, 6A and 9A. The HHO production rate of the solutions was measured over time and considered in the experimental study. Finally, the effects on production results were presented graphically.

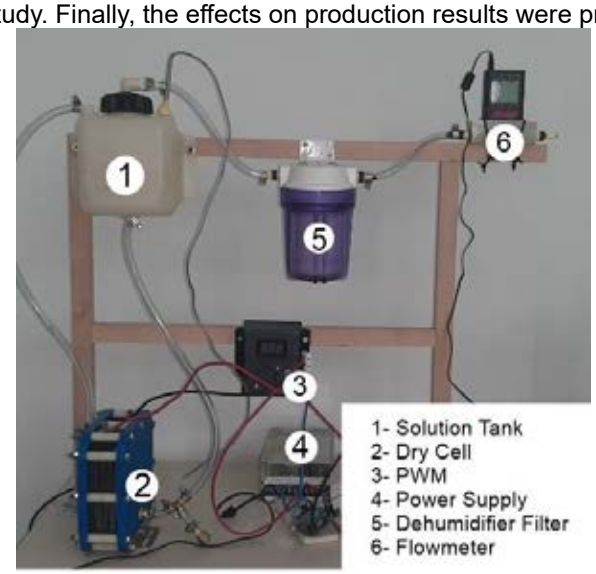

Fig.1. HHO dry cell setup

3. RESULTS AND DISCUSSION

Based on the graph below, it is observed that the HHO production rate increases as the current increases in HHO (Hydrogen-Hydrogen-Oxygen) dry cells. This trend indicates that higher current values lead to more electrical energy being supplied to the electrolysis process, thus contributing to more efficient hydrogen gas production. The increase in current accelerates the electrolysis reaction by facilitating the disintegration of water molecules into hydrogen and oxygen gases. However, it is important to note that the HHO production rate starts to decrease after certain current thresholds are reached. This phenomenon may indicate several fundamental issues, such as the onset of efficiency losses, possible overheating of the system, or a shift in the electrolysis reaction dynamics leading to diminishing returns.

Further analysis shows that the use of 3A and 0.5 grams of MWCNTs results in approximately 115% more HHO production compared to the use of 0 g of MWCNTs. This significant increase in production highlights the positive impact of MWCNTs on the electrolysis process, which is probably due to their ability to increase the surface area of the electrodes and thus increase the hydrogen production rate.

Additionally, the study observed efficiency losses at higher amperages, particularly at 6A and 9A. This suggests that, beyond a certain point, increasing current does not linearly translate into higher production rates. Rather, the system may experience energy losses due to factors such as increased resistance, heat generation, or less efficient electrolysis conditions at higher currents.

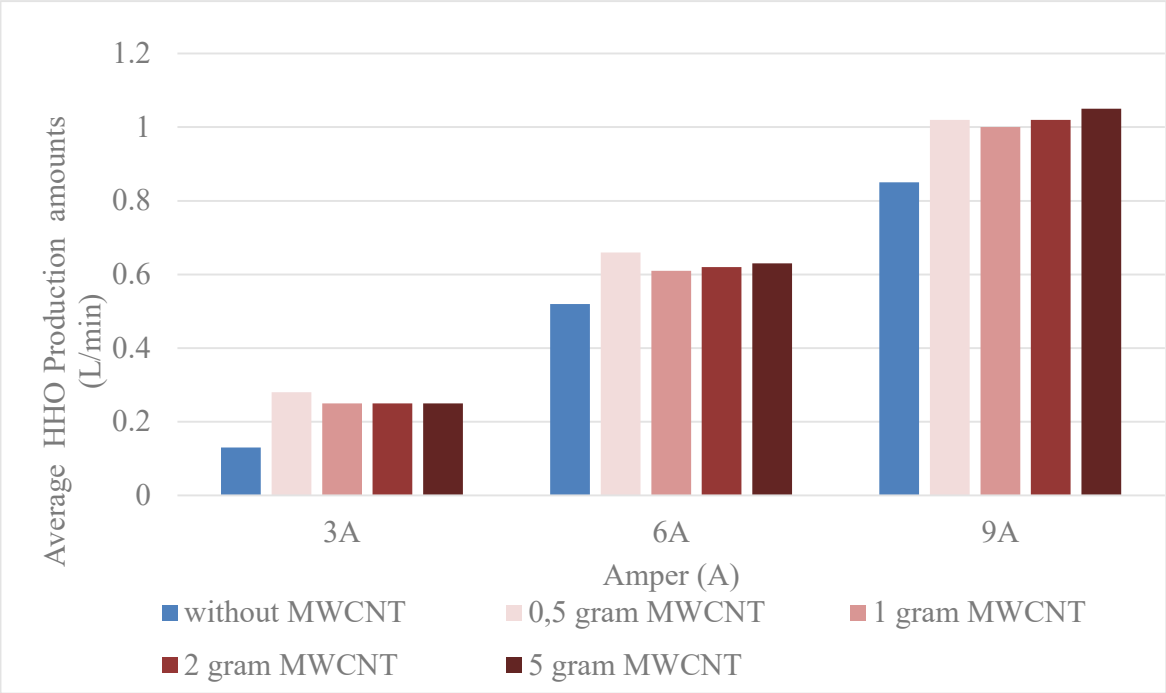

Fig.2. Impact of Current on HHO Production with MWCNT

4. CONCLUSIONS

Further research on the effects of MWCNTs in this system and optimization with experimental data will be crucial to increase efficiency. The potential of MWCNTs to enhance electrolysis performance is promising, but further studies are needed to fully understand the underlying mechanisms and determine the most effective concentrations and operational parameters. Detailed studies focusing on the interaction between MWCNTs and the electrolysis process will help fine-tune the system to achieve optimum hydrogen production rates.

Considering the cost of MWCNTs, the use of 3A with 0.5 g MWCNTs is considered a more efficient and cost-effective option compared to higher concentrations. Although 3A with 5 g MWCNTs shows significant improvements in production rates, the associated cost may not justify the marginal increase in hydrogen output. Therefore, using 0.5 MWCNT at 3A offers a balance between performance improvement and material cost, making it a more practical approach for large-scale applications. Moreover, this approach may provide a more sustainable solution, especially when cost reduction is an important factor.

In the next study, experiments will be conducted with currents ranging from 3 to 6 A and MWCNT quantities ranging from 0.1 g to 0.5 g. This range will allow for a more detailed examination of the optimum current and MWCNT concentration for maximum hydrogen production. Preliminary results indicate that increasing the current and MWCNT content can lead to higher production rates, although the rate of increase tends to be more pronounced at lower currents (3 A–6 A). Therefore, further optimization studies will focus on determining the current and MWCNT combination that leads to the most efficient production process. To maximize efficiency, adding 0.1 g to 0.5 g of MWCNT appears to be the most reasonable option, as it provides a good balance between improved production and material cost.

ACKNOWLEDGEMENT

This study was supported by Scientific and Technological Research Council of Türkiye (TUBITAK) under the Grant Number 224M476. The authors thank to TUBITAK for their supports.

REFERENCES

1. Ural, T., & Karaca, G. (2016). Hydrogen economy. Journal of Global Engineering Studies, 3(2), 145-154.
2. Mutlubaş, H., & Özdemir, Z. Ö. (2023) Hydrogen Usage Areas and Hydrogen Economy. Yekarum, 8(1), 20-31.
3. Ersoy, G. (2022). Energy Source of the Future: Green energy economy. KAYES-2022, 84.
4. El Kady, M. A., Farrag, A. E. F., Gad, M. S., El Soly, A. K., & Hashish, H. A. (2020). Parametric study and experimental investigation of hydroxy (HHO) production using dry cell. Fuel, 282, 118825.
5. Uddin, M. N., Nageshkar, V. V., & Asmatulu, R. (2020). Improving water-splitting efficiency of water electrolysis process via highly conductive nanomaterials at lower voltages. Energy, Ecology and Environment, 5, 108-117.

ENHANCING HHO DRY CELL EFFICIENCY WITH GRAPHENE-SUPPORTED ELECTROLYTES

[1*]*Mustafa Kaan BALTACIOĞLU*, [2]*Onur BULUT*
[1] İskenderun Technical University, Faculty of Engineering and Natural Science, Mechatronics Engineering Department, Hatay, 31200, Turkey
[2] İskenderun Technical University, Faculty of Engineering and Natural Science, Mechanical Engineering Department, Hatay, 31200, Turkey
*Corresponding author e-mail: mkaan.baltacioglu@iste.edu.tr

ABSTRACT
Hydrogen, with its environmentally friendly, renewable, and highly efficient properties, emerges as an alternative solution in the face of fossil fuel depletion and rising prices. When produced through electrolysis using renewable energy sources, hydrogen offers a sustainable option. HHO gas, produced via water electrolysis, has the potential to improve fuel efficiency and combustion performance, particularly when added to traditional diesel and Otto engines. It reduces fuel consumption and emissions. HHO gas production is influenced by parameters such as electrode configuration, voltage, current, and temperature. In recent years, the use of nanomaterials has improved the efficiency of water electrolysis. The aim of this study is to investigate the effects of graphene additives in the electrolyte solution on hydrogen production. The study will examine how graphene improves electrolysis efficiency by enhancing electrical conductivity and is expected to contribute to the development of new approaches for using nanomaterials in hydrogen production processes.

Keywords: Hydrogen, HHO, nanomaterial, electrolyte, graphene

1. INTRODUCTION
Hydrogen stands out as an alternative solution in the face of fossil fuel depletion and rising prices due to its lightness, high efficiency, environmentally friendly nature, and renewability. When blended with fuels such as gasoline, natural gas, and biogas, hydrogen enhances engine performance. Additionally, when produced through electrolysis using renewable energy sources, it offers a sustainable option [1,2]. By 2050, hydrogen is expected to reach a level where it can compete with fossil fuels and become more widespread [3].

HHO gas, also known as hydroxy gas or Brown's gas, is produced through water electrolysis and is preferred particularly for its potential to improve fuel efficiency and combustion performance. When introduced into conventional diesel and Otto engines, HHO gas enhances engine performance, reduces fuel consumption, and lowers emissions [4].

Several parameters influence HHO gas production, including electrode configuration, the number of plates, applied voltage, current, time, temperature, and the type of electrolyte used [5]. In recent years, the use of nanomaterials in water electrolysis has become a significant trend [6]. Research has shown that nanomaterials, which provide high conductivity at low voltage, improve water-splitting efficiency [7]. However, there is a limited number of studies in the literature regarding the effects of nanomaterial additives on HHO gas production processes.

This study aims to investigate the effects of graphene additives in the electrolyte solution of an HHO dry cell on hydrogen production. Specifically, the study will evaluate how graphene enhances electrolysis efficiency by improving electrical conductivity. The findings obtained from this research are expected to contribute to the development of new approaches for using nanomaterials in hydrogen production processes.

2. MATERIALS AND METHODS
The HHO dry cell is a system based on the electrolysis process, where water is decomposed into hydrogen and oxygen gases using electrical energy. In this study, 14 cm × 14 cm plates made of 316L stainless steel were used as electrodes, and a setup consisting of 12 plates was assembled. Rubber gaskets were used to ensure electrical insulation between the electrodes.

For the electrolyte solution, a mixture of pure water, NaOH, and graphene was used. The properties of graphene are provided in Table 1. To measure the system's performance and conduct the experiments, a dehumidifier, Alicat flow meter, and PWM were incorporated into the experimental setup (Figure 1).

The experiments were conducted under constant NaOH concentration and fixed current conditions to investigate the effect of graphene addition on the electrolysis process. The electrolyte solution was prepared with four different graphene concentrations. 900 g of pure water and 100 g of NaOH were separately mixed with 0.5 g, 1 g, 2 g, and 5 g of graphene (10:1 w/w ratio).

Table1. Graphene Properties

Purity	99,9%
Width	3 nm
Diameter	1.5 µm
Specific Surface Area	800 m²/g
Electrical Conductivity	1500 – 1980 S/m
Color	Black

All experiments were performed using fixed current (22 V) at 3A, 6A, and 9A, applying CCPWM (Constant Current Pulse Width Modulation) method. During electrolysis, HHO production rates were measured at specific time intervals, and the experimental data were thoroughly analyzed. Finally, the effect of graphene addition on hydrogen production was evaluated through graphical and comparative analyses.

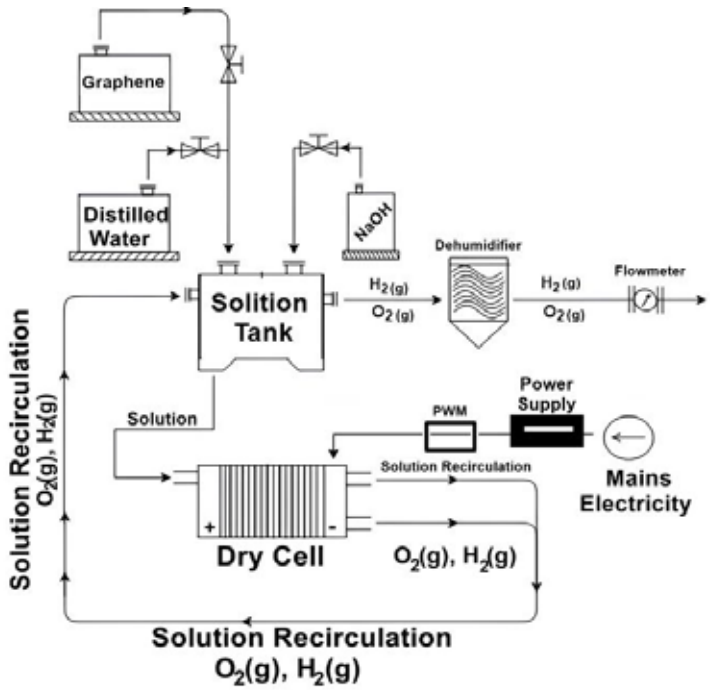

Fig.1. HHO dry cell setup

3. RESULTS AND DISCUSSION

The graph (Figure 2) shows a significant increase in the HHO production rate as current increases in HHO (oxyhydrogen) dry cells. This indicates that higher current provides more energy to the electrolysis process, thus increasing hydrogen gas production efficiency. Increasing current increases the rate at which water decomposes into hydrogen and oxygen gases, leading to a faster electrolysis reaction. However, once current reaches a certain level, the increase in HHO production rate begins to slow. This suggests that efficiency losses may have begun, possibly due to overheating or changes in the electrolysis reaction dynamics.

Detailed analysis showed that the tests conducted using 3A and 0.5 g of graphene resulted in twice as much HHO production compared to experiments without graphene. This significant increase highlights the positive effect of graphene on the electrolysis process.

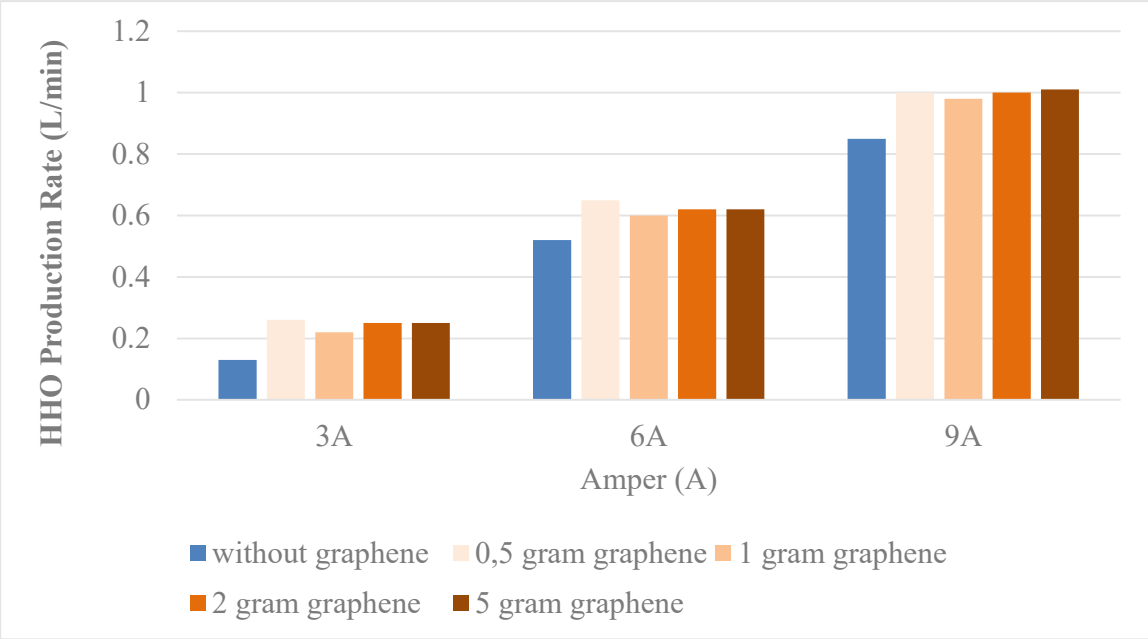

Fig. 2. Impact of Current on HHO Production with Graphene

4. CONCLUSIONS

Extensive research on the effects of graphene on the electrolysis process and optimization based on experimental data plays an important role in increasing efficiency. The potential of graphene to improve electrolysis performance is promising; however, further research is needed to fully understand this effect and to determine the most effective concentrations and operational parameters. In-depth studies on the interactions between graphene and electrolysis will contribute significantly to optimizing the system to maximize hydrogen production rates. These studies will help us better understand the impact of graphene's electrochemical properties on the hydrogen production process.

In the next stage, experiments will be conducted with currents ranging from 3A to 5A and graphene amounts ranging from 0.1 g to 0.5. This range will allow for a more detailed study of the optimum current and graphene concentration for hydrogen production.

In conclusion, ongoing studies on the effects of graphene offer significant opportunities to increase hydrogen production efficiency. However, it should be noted that further research is needed to determine the correct concentrations and parameters for the most effective results.

ACKNOWLEDGEMENT

This study was supported by Scientific and Technological Research Council of Türkiye (TUBITAK) under the Grant Number 224M476. The authors thank to TUBITAK for their supports.

REFERENCES

1. Mutlubaş, H., & Özdemir, Z. Ö. (2019). Hydrogen as an energy carrier and hydrogen production methods. Bartın University International Journal of Natural and Applied Sciences, 2(1), 16-34.
2. Momirlan, M., & Veziroglu, T. N. (2005). The properties of hydrogen as fuel tomorrow in sustainable energy system for a cleaner planet. International journal of hydrogen energy, 30(7), 795-802.
3. Incer-Valverde, J., Korayem, A., Tsatsaronis, G., & Morosuk, T. (2023). "Colors" of hydrogen: Definitions and carbon intensity. Energy conversion and management, 291, 117294.
4. Sudarmanta, B., Darsopuspito, S., & Sungkono, D. (2016). Application of dry cell HHO gas generator with pulse width modulation on sinjai spark ignition engine performance. International Journal of Research in Engineering and Technology, 5(2), 105-112.
5. El Kady, M. A., Farrag, A. E. F., Gad, M. S., El Soly, A. K., & Hashish, H. A. (2020). Parametric study and experimental investigation of hydroxy (HHO) production using dry cell. Fuel, 282, 118825.
6. Li, C., & Baek, J. B. (2019). Recent advances in noble metal (Pt, Ru, and Ir)-based electrocatalysts for efficient hydrogen evolution reaction. ACS omega, 5(1), 31-40.
7. Uddin, M. N., Nageshkar, V. V., & Asmatulu, R. (2020). Improving water-splitting efficiency of water electrolysis process via highly conductive nanomaterials at lower voltages. Energy, Ecology and Environment, 5, 108-117.

METAHEURISTIC OPTIMIZATION OF PID CONTROLLERS FOR TEMPERATURE REGULATION IN HHO DRY CELLS

[1]Caglar Conker, [1*]Mustafa Kaan Baltacioglu
[1] Iskenderun Technical University, Department of Mechatronics Engineering, Hatay, 31200, Turkey

* E-mail: mkaan.baltacioglu@iste.edu.tr

Abstract
This study explores the optimization of PID controller parameters for an HHO dry cell system utilizing metaheuristic algorithms. A reactor with 13 stainless steel plates (14×14 cm) was employed, and an electrolyte solution was prepared according to established methodologies. The primary objective was to regulate temperature effectively, leveraging Genetic Algorithm (GA) and Artificial Bee Colony (ABC) techniques to enhance system performance. The optimized control parameters were benchmarked against conventional On-Off and Fuzzy-PID controllers. Performance evaluation was conducted using key metrics, including Integral Square Error (ISE), Integral Absolute Error (IAE), Integral Time Absolute Error (ITAE), and Mean Square Error (MSE). Experimental and theoretical analyses revealed that metaheuristic-based PID controllers exhibited superior stability, minimized overshoot, and improved response time, highlighting their potential as effective solutions for temperature management in HHO systems.

Keywords: Artificial Bee Colony, Electrochemistry, Genetic Algorithm, HHO Dry Cell, Optimization

1. INTRODUCTION

Commercial application of electrolyzers commenced in the 1920s with alkaline variants but experienced economic downturn circa the 1970s with the advent of hydrogen production from natural gas and steam methane. In this investigation, the primary aim revolves around maintaining the temperature within the HHO reactor below 60°C through the modulation of Pulse Width Modulation (PWM) settings during hydrogen generation operations. Absent the utilization of PWM techniques, conventional HHO gas generator systems typically operate at full load, resulting in an elevation of the generator temperature to approximately 90°C [1]. Such elevated temperatures may precipitate critical damage to the tube material within the HHO generators. Furthermore, it is recognized that elevated temperatures within the reactor yield several adverse consequences. Firstly, heightened temperature levels contribute to increased water evaporation, consequently elevating the moisture content within the produced gas, thereby compromising the quality of the resultant hydrogen gas. Secondly, elevated temperature levels within the reactor curtail the operational lifespan of the system. Literature suggests that optimal temperature levels for HHO gas generators reside below 70°C [2-3]. The temperature control of HHO reactors emerges as a complex optimization problem. In this context, the necessity of utilizing modern artificial intelligence techniques alongside traditional control methods becomes apparent. Meta-heuristic optimization techniques inspired by natural intelligence, such as genetic algorithms and artificial bee colony, could play a significant role in managing the temperature of HHO reactors. These techniques offer potential in effectively navigating through multiple variables in complex systems, thereby potentially yielding optimized and energy-efficient solutions for temperature control in HHO reactors. Therefore, artificial intelligence-based methods such as genetic algorithms and artificial bee colony present themselves as significant tools in managing the temperature of HHO reactors.

2. EXPERIMENTAL AND NUMERICAL SET-UP

The regulation of temperature in a dry cell HHO reactor is a fundamental challenge within temperature control systems. This process can be mathematically represented through a first-order system transfer function, formulated as follows:

$$G(s) = \frac{K}{Ts+1} e^{-\tau s} = \frac{56.8}{1780s+1} e^{-50s} \tag{1}$$

where K denotes the static gain of the controlled process, represents the system's pure lag time, and T is the time constant defining the system dynamics. Consequently, the mathematical representation of the dry cell HHO reactor system's behavior is articulated through Equation 1.

The On-Off controller is widely recognized as the simplest form of feedback control. Its implementation requires minimal parameter tuning, typically involving only the determination of the on-value, off-value, and threshold level of the controller output. However, On-Off controllers often induce oscillatory behavior and generally exhibit a non-zero steady-state error. The governing equation for an On-Off controller is expressed as:

$$u(t)_{on-off} = \begin{cases} u_{on} \ for \ e(t) > 0 \\ u_{off} \ for \ e(t) < 0 \end{cases} \tag{2}$$

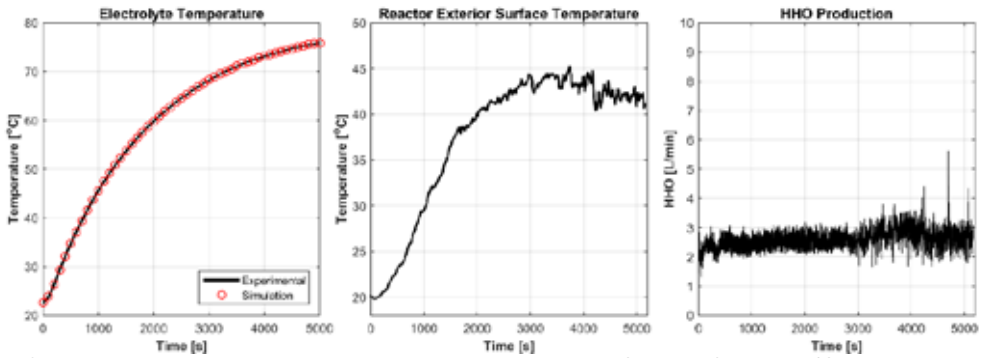

Fig. 1. Surface & electrolyte temperatures and hydroxy production rates of the HHO dry cell (Conker ve Baltacıoglu, 2020)

In this context, the output signal from the controller is denoted by *u(t)*, while the actuating error signal is presented by *e(t).*

A PID (Proportional-Integral-Derivative) controller is a ubiquitous feedback control mechanism extensively utilized in industrial control systems due to its favorable attributes, such as high reliability, stability, and computational simplicity. The PID controller aims to minimize the discrepancy between a measured process variable and a desired set point by computing and implementing corrective actions promptly to regulate the process effectively and minimize errors. The conventional transfer function of a PID controller can be expressed as follows:

$$u(t)_{PID} = K_p e(t) + K_i \int_0^t e(t)dt + K_d \frac{d(e(t))}{dt} \tag{3}$$

The suitability of a PID (Proportional-Integral-Derivative) controller is primarily limited to linear systems with well-defined mathematical models. However, the regulation of temperature in an HHO (Hydrogen-Hydrogen-Oxygen) reactor poses a distinct challenge due to its inherently non-linear, time-delayed, and time-varying characteristics.

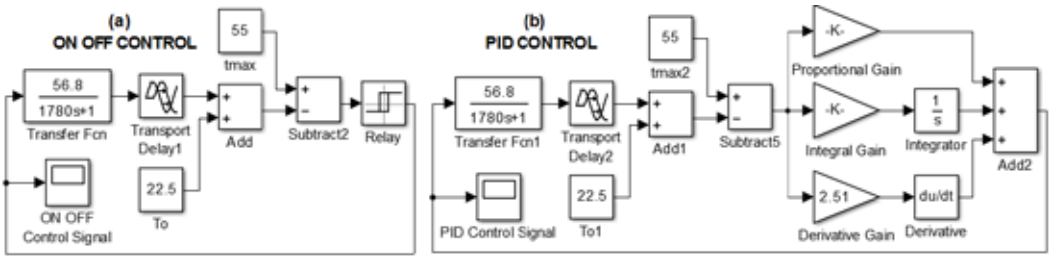

Fig. 2. Flow chart of on-off (a) and fuzzy PID (b) structures

3. ANALYSIS

Genetic Algorithm (GA)

The Genetic Algorithm (GA) begins by generating an initial population of chromosomes randomly. These chromosomes evolve iteratively through genetic operations, including selection, crossover, and mutation, with fitness evaluation guiding the optimization process. The algorithm continues until termination criteria are satisfied or a predefined number of iterations is reached. Key parameters such as population size, crossover rate, and mutation rate significantly influence the algorithm's convergence and efficiency. The evolutionary process of GA is illustrated in Fig. 3a.

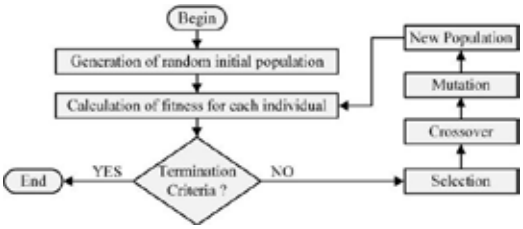

Fig. 3a. Genetic Algorithm Flowchart

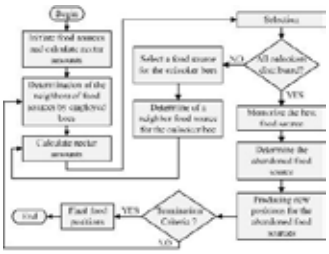

Fig. 3b. Artificial Bee Colony Algorithm Flowchart

Artificial Bee Colony (ABC) Algorithm

The ABC algorithm is inspired by the foraging behavior of honeybee colonies and comprises three distinct types of bees: employed bees, onlooker bees, and scout bees. Employed bees collect nectar from known sources and communicate information to onlooker bees, which select the most promising sources based on shared data. When nectar is depleted, bees transition into scout mode, exploring new sources randomly. The ABC algorithm seeks to locate the most optimal solution within the search space through iterative exploration and exploitation mechanisms. The operational structure of the ABC algorithm is depicted in Fig. 3b.

Fitting Functions

This section elaborates on the tuning methods utilized for various performance metrics, including Integral Square Error (ISE), Integral Absolute Error (IAE), Integral Time Absolute Error (ITAE), and Mean Square Error (MSE); Eq.4 to 7 respectively [4].

$$IAE = \int_0^t |e(t)|\,dt \tag{4}$$

$$ISE = \int_0^t e^2(t)dt \tag{5}$$

$$ITAE = \int_0^t t\,|e(t)|\,dt \tag{6}$$

$$MSE = \frac{1}{N}\sum_{k=1}^{N} e^2(k) \tag{7}$$

The primary control objective is to maintain various performance specifications, including rise time, settling time, maximum overshoot, and steady-state error, within desirable limits. To further validate the proposed technique and demonstrate its practical effectiveness compared to conventional methods, a series of experiments are conducted.

4. RESULTS AND DISCUSSIONS

The system, controller and optimization process are presented in Fig. 4. Besides, optimization results of GA and ABC due to ISE, IAE, ITAE, MSE are presented in Table 1 in numerical form. Graphical resresentation of them are shown in Figs. 5 and 6, respectively.

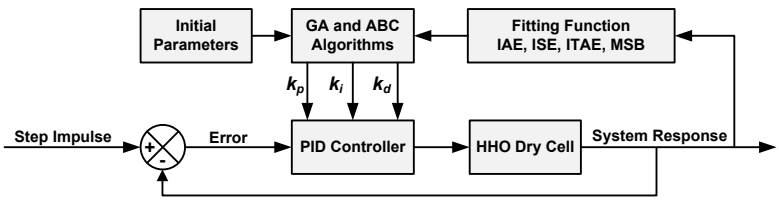

Fig. 4. Optimization and Controller Structure

Figs. 7a and 7b present system respons graphs of GA and ABC, respectively. The results indicate that, in comparison to the On-Off, PID, and Fuzzy controllers, the metaheuristic-based PID controller displays notable advantages. These include the absence of overshoot, a shorter adjustment time, improved dynamic response, and enhanced steady-state characteristics.

Table 1. Optimization results for GA and ABC algorithms

		Population Size 20		Population Size 30		Population Size 40		Population Size 50	
		GA	ABC	GA	ABC	GA	ABC	GA	ABC
ISE	*Kp*	3.1702	10	9.993619	9.645	4.2184	7.818	4.2184	7.9998
	Kd	0.0960	9.8621	9.91224	0.0815	9.9078	9.856	9.9078	9.867
	N	77.380	50	109.033	50	140.241	51.81	140.24	52.02
	Time	458.46	637.79	568.6452	928.84	825.994	1847.03	825.99	1705.67
IAE	*Kp*	6.1228	8.782	0.6606	10	4.14549	1.3937	9.2162	4.820
	Kd	1.06741	9.8737	-1.3782	0.080	9.90487	0.081	9.0375	0.0813
	N	70.878	52.32	109.986	93.301	117.85	50	92.490	50
	Time	328.731	648.23	470.243	928.48	667.71	1573.86	845.22	1655.34
ITAE	*Kp*	2.5397	0.800	1.2700	1.1698	3.9232	1.2524	0.2372	4.2993
	Kd	-1.260	0.943	-1.6050	1.1655	-1.9868	3.4279	0.2119	1.8568
	N	124.472	92.17	108.576	50	111.321	69.23	110.06	50
	Time	329.22	604.33	554.559	900.26	693.62	1206.21	864.04	1.5820
MSE	*Kp*	2.1797	3.5124	0.9048	10	5.1772	9.608	1.7123	6.3524
	Kd	0.0248	2.8795	0.0922	4.244	0.5145	1.0468	0.9368	0.8492
	N	111.14	105.13	110.911	81.979	111.28	150	106.97	50.855
	Time	362.073	607.98	514.818	941.87	716.18	1243.54	900.47	1658.78

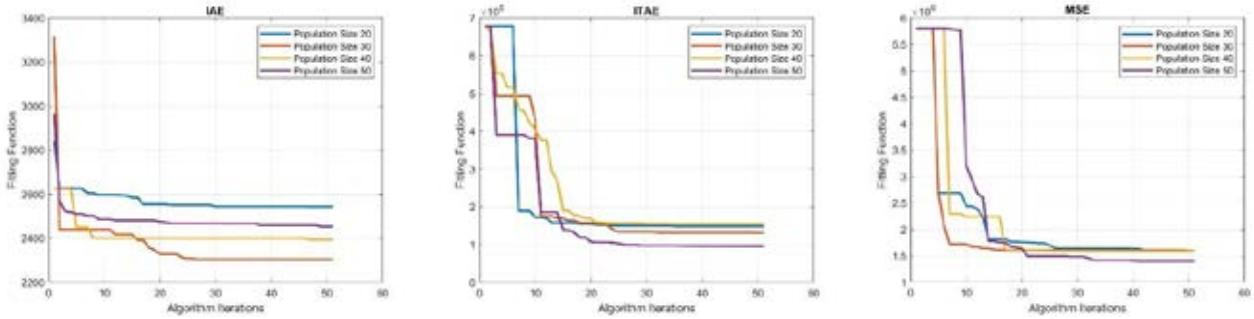

Fig. 5. Convergence histories of the GA for different values of population size for IAE, ITAE and MSE

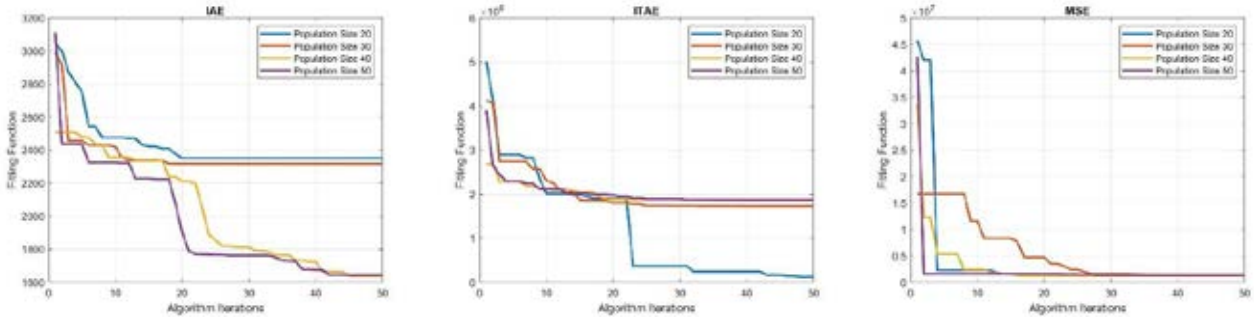

Fig. 6. Convergence histories of the ABC for different values of population size for IAE, ITAE and MSE

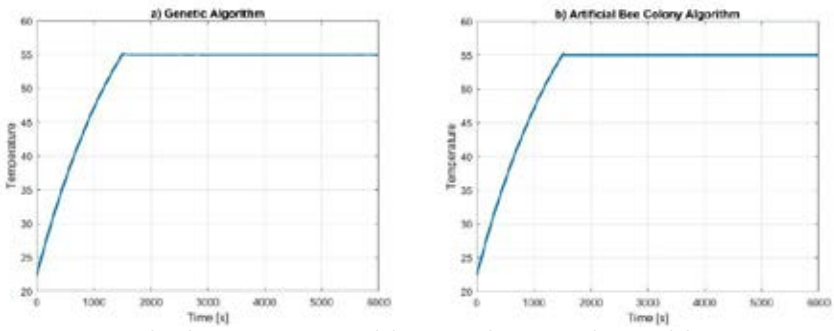

Fig. 7. HHO Dry Cell sytem response for Genetic Algorithm (a) and Artificial Bee Colony (b) based proportional-integral-derivative (PID) controller

5. CONCLUSIONS

This study presents an optimized control strategy for HHO dry cell temperature regulation by leveraging Genetic Algorithm (GA) and Artificial Bee Colony (ABC) optimization techniques. The proposed approach effectively minimizes commonly used performance indices such as ISE, IAE, ITAE, and MSE, leading to optimal controller gain selection. The obtained results confirm the viability and efficiency of metaheuristic-based PID controllers in addressing temperature regulation challenges in HHO reactors. Future research should extend the analysis by incorporating alternative optimization methodologies to further enhance control system performance.

References

[1] Baltacıoğlu, M. K. (2019). A novel application of pulse width modulation technique on hydroxy gas production. International Journal of Hydrogen Energy, 44(20), 9726-9734.
[2] Conker, Ç. (2019). A novel fuzzy logic based safe operation oriented control technique for driving HHO dry cell systems based on PWM duty cycle. International Journal of Hydrogen Energy, 44(20), 9718-9725.
[3] Conker, C., & Baltacioglu, M. K. (2020). Fuzzy self-adaptive PID control technique for driving HHO dry cell systems. International Journal of Hydrogen Energy, 45(49), 26059-26069.
[4] Furat, M., & Eker, I. (2014). Second-order integral sliding-mode control with experimental application. ISA transactions, 53(5), 1661-1669.

DEVELOPMENT OF DOPAMINE MODIFIED GRAPHENE OXIDE DOPED COMPOSITE ANION EXCHANGE MEMBRANES

[1]*Nisa Gökçen Önel*, [2*]*Yılser Devrim*
[1] Atılım University, Engineering Faculty, Chemical Engineering Department, Incek, Ankara, 06830, Turkey
[2] Atılım University, Engineering Faculty, Energy System Engineering Department, Incek, Ankara, 06830, Turkey
* E-mail: yilser.devrim@atilim.edu.tr

ABSTRACT
In light of growing concerns regarding climate change, there has been a significant increase in interest in hydrogen energy and related technologies, particularly those focused on clean hydrogen production through water electrolysis. This study explores the utilization of graphene oxide (GO) and dopamine-functionalized graphene oxide (DGO) as filler materials to enhance the performance of anion exchange membranes (AEMs) employed in water electrolysis. A comprehensive synthesis and characterization approach was undertaken to examine the structural, thermal, and conductive properties of these materials. The synthesis methodologies, including the Hummer method and the development of composite materials, are elaborated upon, alongside their influence on the properties of the membranes. The incorporation of DGO was found to improve KOH retention, conductivity, ion transport, and membrane stability. This investigation highlights the potential of these fillers in advancing AEM technology and offers valuable insights into their contribution to addressing climate change and promoting sustainable energy solutions.

Keywords: Graphene, graphene oxide, dopamine graphene oxide, anion exchange membrane

1. INTRODUCTION

Hydrogen is widely regarded as one of the most promising alternative energy carriers capable of addressing contemporary challenges related to energy security and environmental sustainability. It can be produced through various methods, including natural gas reforming, water electrolysis, and direct solar water splitting. Among these, water electrolysis stands out as a particularly advantageous technology for energy conversion, as it enables the utilization of intermittent renewable energy sources such as wind, tidal, and solar power to generate hydrogen from water. Water electrolyzers are highly efficient, capable of accommodating high current densities per unit surface area, operating in dynamic conditions, and responding rapidly to fluctuations. These characteristics make them well-suited for integrating with and storing energy from intermittent renewable sources, thereby supporting the transition to sustainable energy systems [1].

In addition to the widely utilized commercial alkaline electrolyzers (AEL) and proton exchange membrane electrolyzers (PEMEL), anion exchange membrane water electrolyzers (AEMWEL) offer a unique combination of the advantages associated with both technologies, enabling a compact and optimized system design similar to PEMELs while utilizing transition metals as catalysts instead of the noble metals required in PEMEL systems. Unlike AEL systems, which rely on concentrated potassium hydroxide (KOH) solutions, AEMWEL systems can operate using distilled water or low-concentration alkaline electrolytes. Furthermore, the membranes used in AEMWEL, which incorporate anion exchange groups, are more cost-effective compared to Nafion-based membranes utilized in PEMELs. Additionally, AEMWEL systems exhibit minimal interaction between CO2 and the membrane due to the absence of metal ions. This technology also offers several other benefits, including the elimination of corrosive liquid electrolytes, prevention of leakage, enhanced volumetric stability, ease of operation, and a reduction in the overall size and weight of the electrolyzer. These features collectively position AEMWEL as a promising and efficient alternative for hydrogen production [2,3].

The anion exchange membrane (AEM), a critical component in anion exchange membrane water electrolyzer (AEMWEL) systems, facilitates the transport of hydroxide ions (OH^-) from the cathode to the anode while preventing gas crossover and electron transfer during electrochemical processes. For effective application in electrolysis, AEMs must demonstrate high ion permeability, excellent ionic conductivity, robust thermal and mechanical stability, and superior chemical stability. Thus, both the cationic functional groups and the stability of the polymer backbone are crucial factors in ensuring the durability of AEMs. The incorporation of various filler materials has been explored to improve the mechanical properties of AEMs. Over the past decade, numerous strategies have been investigated to address the degradation of AEMs at elevated temperatures and to enhance their ionic conductivity, aiming to optimize their performance in demanding operational environments [4]. Graphene oxide (GO) has attracted significant attention as a nanomaterial filler owing to its exceptional thermal stability and high specific surface area. The synthesis of GO is commonly achieved through Hummer's method, which is preferred for its high efficiency and favorable safety characteristics. Additionally, composite GO materials integrated with phosphates and sulfates have been engineered to further enhance the properties of GO, thereby improving membrane performance [5,6]. To achieve this, extensive research and development have been conducted on advanced synthesis methodologies. Dopamine-functionalized graphene oxide (DGO) exhibits exceptional properties, including higher water uptake, enhanced tensile strength, greater elongation at break, and improved stability

in alkaline solutions. These characteristics make DGO an ideal filler for reinforcing anion exchange membranes (AEMs), ensuring superior mechanical durability, flexibility, and long-term performance in demanding applications such as water electrolysis [7].
This study is centered on the preparation of anion exchange membranes (AEMs) incorporating GO and DGO as fillers, along with a comprehensive characterization of the synthesized membranes. The findings demonstrate the successful synthesis of the targeted GO structures and reveal a significant enhancement in KOH retention, a critical factor influencing the performance of the AEMs.

2. EXPERIMENTAL SET-UP AND PROCEDURE

2.1. GO and Modified GO Preparation: The synthesis of GO was carried out using the Hummer method. Initially, 3.0 grams of graphite powder were mixed with 70 ml of sulfuric acid in a Teflon beaker, which was then placed in an ice bath and stirred continuously. Following this, 9.0 grams of potassium permanganate were gradually added to the mixture under constant stirring. The temperature of the mixture was increased to 40°C and maintained for 30 minutes with continuous stirring. Subsequently, 150 ml of distilled water was slowly added, and the temperature was raised to 95°C. After 15 minutes of stirring, an additional 500 ml of distilled water was introduced, followed by 15 ml of 30% hydrogen peroxide. At this stage, the mixture's color changed from dark brown to yellow. The solution was then allowed to settle for 24 hours. Finally, the mixture was centrifuged and washed three times with 250 ml of a 1:10 HCl solution and distilled water, after which it was dried in an oven at 60°C [6]. Additionally, DGO was synthesized for application in AEMWELs following established literature procedures [7], as illustrated in Figure 1.

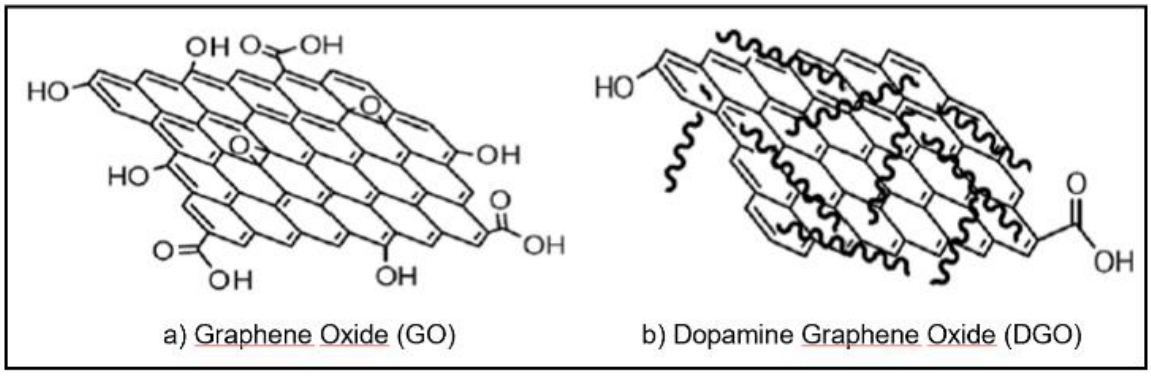

Fig.1. a) GO and b) Dopamine GO

2.2. Composite AEM Preparation: In this study, composite membranes were fabricated using a Fumion® solution as the base material. GO and DGO were incorporated into the Fumion® solution by the predetermined additive concentrations. The resulting mixture was stirred until a homogeneous solution was achieved, which was then cast onto a glass surface. Subsequently, the membranes were dried in a vacuum oven at 80°C for 12 hours to ensure complete solvent removal and proper formation of the membrane structure.

3. ANALYSIS

The crystalline structure of GO and its modified form was characterized using X-ray diffraction (XRD) (Rigaku Ultima-IV, Cu Kα radiation, λ = 1.54056 Å). The chemical composition and bonding states were analyzed via X-ray photoelectron spectroscopy (XPS) using a PHI 5000 VersaProbe instrument with Al Kα radiation under vacuum conditions (energy range: 0–900 eV, X-ray spot size: 100 µm). Fourier-transform infrared (FT-IR) spectra were acquired using a Bruker IFS 66/S spectrometer to investigate functional groups. Additionally, the membranes' suitability for AEM applications was assessed through measurements of KOH uptake and ionic conductivity.The electrochemical characterization was conducted by Electrochemical Impedance Spectroscopy (EIS).

4. RESULTS AND DISCUSSIONS

Figure 2a presents the XRD patterns of GO and its modified forms, with a sharp peak at 12.57° corresponding to the (002) planar reflection of GO layers, indicating a d-spacing of 0.703 nm. XPS analysis of dopamine-modified GO revealed new peaks at C=C (285.0 eV), C-C (282.0 eV), and C-P (288.0 eV), confirming functional group incorporation [8–10]. Figure 2b shows FTIR spectra of GO and dGO, with characteristic peaks for C-O-C (~1033 cm^{-1}), C-O (~1227 cm^{-1}), C=C (~1617 cm^{-1}), and C=O (1710–1720 cm^{-1}). The dGO spectrum exhibited N-H bending at 1512 cm^{-1}, while the absence of a CH_2 bending peak at 1345 cm^{-1} confirmed dopamine self-polymerization [5,10–12]. These results validate the successful synthesis and functionalization of GO for AEM applications.

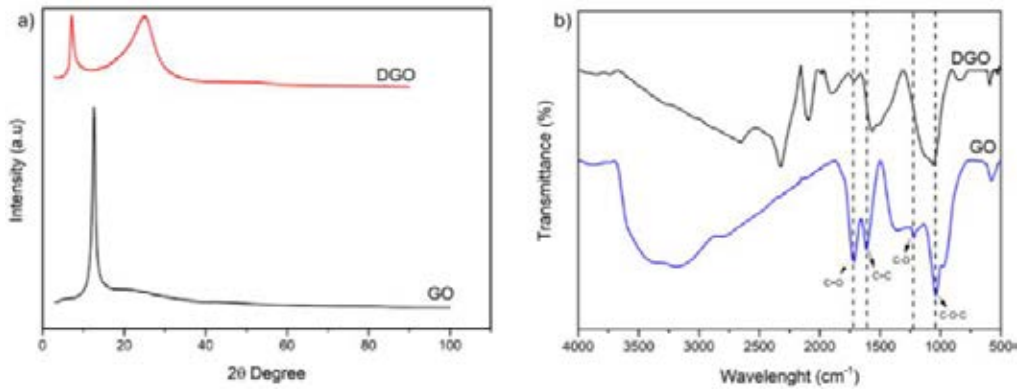

Fig. 2. a) XRD Patterns of GO, and DGO and b) FTIR Patterns of GO and DGO

Figure 3a shows the XPS survey and C1s spectra of graphene oxide (GO), highlighting high-intensity O1s peaks that confirm the presence of oxygen-containing functional groups. Quantitative analysis indicates a composition of 67.8% carbon and 31.4% oxygen, with C1s deconvolution revealing peaks for C-C (283.9 eV), C-O (285.8 eV), C-O-C (287.4 eV), and C=O (288.3 eV) [6,8]. In contrast, Figure 3b displays the C1s spectrum of dopamine-functionalized graphene oxide (DGO), deconvoluted into C=C (285.0 eV), C-C (282.0 eV), and C-P (288.0 eV), confirming successful dopamine modification [10]. These results demonstrate the structural and compositional differences between GO and DGO.

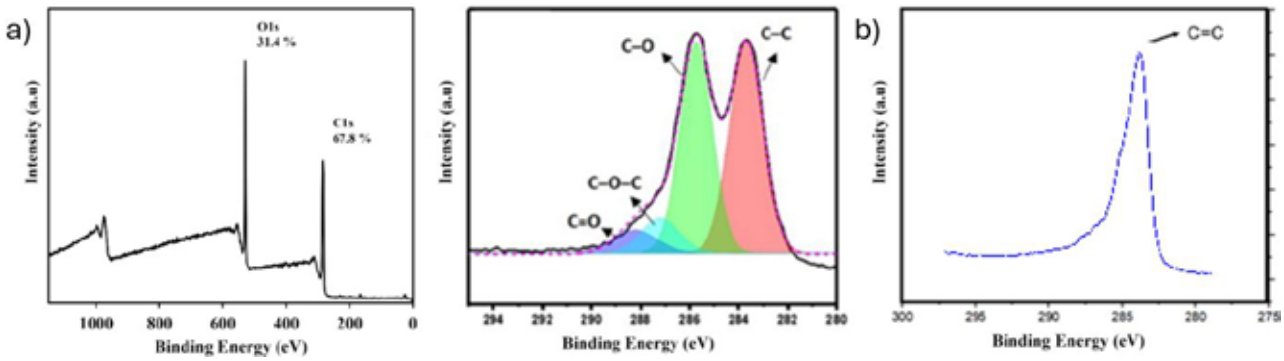

Fig. 3. XPS Patterns of a) GO and b) DGO

The ability of membranes to absorb KOH is a critical factor influencing their electrochemical performance for AEMWE applications. In this study, KOH uptake experiments were conducted on the synthesized composite membranes using a 0.1 M KOH solution. The KOH uptake rates for the commercial Fumasep, F/GO, and F/DGO membranes were measured at 30.6%, 47.6%, and 51%, respectively. The F/GO and F/DGO membranes demonstrated significantly higher KOH and water uptake capacities compared to the reference Fumasep membrane, indicating enhanced suitability for AEMWE applications. Table 1 shows the conductivity analyses, performed at temperatures between 30-80°C with 1M and 2M KOH doping, as well as after aging in 2M KOH, showed average increases of 31%, 46%, and 51% for GO and DGO-based membranes, respectively. These findings collectively highlight the superior performance of GO and DGO-based composite membranes in AEMWE applications, emphasizing their potential for advancing sustainable energy technologies.

Table 1. Ion Conductivity Analysis Results of Membranes

Temperature	Membrane					
	F/GO (1M KOH)	F/GO (2M KOH)	F/GO (2M KOH Ageing)	F/DGO (1M KOH)	F/DGO (2M KOH)	F/DGO (2M KOH Ageing)
30º C	40.5	46.5	32.5	79.0	83.5	90.0
40º C	49.0	53.5	46.0	82.5	110.5	90.0
50º C	74.0	70.5	51.5	85.0	114.5	89.5
60º C	85.0	83.5	78.5	94.5	117.0	90.5
70º C	88.5	90,5	86.0	102.0	118.5	93.5
80º C	103.0	113.5	108.5	116.0	121.0	97.5

5. CONCLUSIONS

In this study, composite anion exchange membranes (AEMs) incorporating graphene oxide (GO) and its modified forms were developed for application in anion exchange membrane water electrolyzers (AEMWEs), with their structural properties and performance systematically investigated. The results demonstrate that the GO-based composite membranes exhibit enhanced properties, making them highly suitable for AEMWE applications. This research provides valuable insights into the potential use of these synthesized fillers in advancing AEM technology, underscoring their role in enabling sustainable energy solutions and supporting global efforts to mitigate climate change. Continued research and development in this field hold significant promise for driving progress in the hydrogen economy and fostering environmental sustainability.

ACKNOWLEDGMENTS

The Scientific and Technological Research Council of Turkey (TUBITAK) supported this study under grant number 123N342.

REFERENCES

[1] Chisholm G, Zhao T, Cronin L. Hydrogen from water electrolysis. Storing Energy: with Special Reference to Renewable Energy Sources, Elsevier; 2022, p. 559–91. https://doi.org/10.1016/B978-0-12-824510-1.00015-5.

[2] Du N, Roy C, Peach R, Turnbull M, Thiele S, Bock C. Anion-Exchange Membrane Water Electrolyzers. Chem Rev 2022;122:11830–95. https://doi.org/10.1021/ACS.CHEMREV.1C00854/ASSET/IMAGES/MEDIUM/CR1C00854_0037.GIF.

[3] Vinodh R, Kalanur SS, Natarajan SK, Pollet BG. Recent Advancements of Polymeric Membranes in Anion Exchange Membrane Water Electrolyzer (AEMWE): A Critical Review. Polymers (Basel) 2023;15. https://doi.org/10.3390/polym15092144.

[4] Ion-Ebrasu D, Pollet BG, Caprarescu S, Chitu A, Trusca R, Niculescu V, et al. Graphene inclusion effect on anion-exchange membranes properties for alkaline water electrolyzers. Int J Hydrogen Energy 2020;45. https://doi.org/10.1016/j.ijhydene.2020.04.195.

[5] Chen X, Wang X, Fang D. A review on C1s XPS-spectra for some kinds of carbon materials. Fullerenes Nanotubes and Carbon Nanostructures 2020:1048–58. https://doi.org/10.1080/1536383X.2020.1794851.

[6] Chen J, Yao B, Li C, Shi G. An improved Hummers method for eco-friendly synthesis of graphene oxide. Carbon N Y 2013;64:225–9. https://doi.org/10.1016/j.carbon.2013.07.055.

[7] Luo Z, Gong Y, Liao X, Pan Y, Zhang H. Nanocomposite membranes modified by graphene-based materials for anion exchange membrane fuel cells. RSC Adv 2016;6:13618–25. https://doi.org/10.1039/c5ra21104b.

[8] Altınışık H, Getiren B, Çıplak Z, Soysal F, Yıldız N. Energy Storage Performance of Nitrogen Doped Reduced Graphene Oxide/Co-Doped Polyaniline Nanocomposites. J Inorg Organomet Polym Mater 2023;33:353–67. https://doi.org/10.1007/s10904-022-02456-0.

[9] Jiang F, Qi L, Li SC, Song G, Ge B, Yu HZ. UV/Ozone-Assisted Covalent Bioconjugation on Graphene Tapes. Langmuir 2025. https://doi.org/10.1021/acs.langmuir.4c03901.

[10] Ma J, He Y, Zeng G, Li F, Li Y, Xiao J, et al. Bio-inspired method to fabricate poly-dopamine/reduced graphene oxide composite membranes for dyes and heavy metal ion removal. Polym Adv Technol 2018;29:941–50. https://doi.org/10.1002/pat.4205.

[11] Li C, Shi G. Three-dimensional graphene architectures. Nanoscale 2012;4:5549–63. https://doi.org/10.1039/c2nr31467c.

[12] Lee W, Lee JU, Jung BM, Byun JH, Yi JW, Lee SB, et al. Simultaneous enhancement of mechanical, electrical and thermal properties of graphene oxide paper by embedding dopamine. Carbon N Y 2013;65:296–304. https://doi.org/10.1016/j.carbon.2013.08.029.

SYSTEMATIC RISK ANALYSIS FOR HYDROGEN FUEL CELL VEHICLES AND SAFETY MANAGEMENT IN FUEL CELLS

[1]Nevzat Özaslan, [2]Bahattin Tanç
[1]Iskenderun Technical University, Faculty of Engineering and Natural Sciences, Department of Mechanical Engineering, Iskenderun Technical University Rectorate, Central Campus, Iskenderun/Hatay, 31200 Turkey
[2]Iskenderun Technical University, Faculty of Engineering and Natural Sciences, Department of Mechanical Engineering, Iskenderun Technical University Rectorate, Central Campus, Iskenderun/Hatay, 31200 Turkey
Corresponding author e-mail: nevzatozaslan9@gmail.com

ABSTRACT
Hydrogen fuel cell vehicles stand out as technologies promising zero emissions and high efficiency. However, hydrogen's low density, high flammability, and pressurized storage requirements bring risks such as leakage, explosion, and system failures. This article evaluates the main risks observed in hydrogen fuel cell vehicles, including hydrogen leakage, high-pressure storage, fuel cell failures, accident scenarios, infrastructure, and operational risks within the framework of systematic risk analysis methodologies (MADS/MOSAR, FMEA, FTA). In the conclusion, strategies to minimize these risks are presented.
Keywords: Hydrogen Fuel Cell, Risk Analysis, Fuel Cell, Safety Management, High Pressure

1. INTRODUCTION
With the increasing focus on environmental sustainability in the automotive industry, hydrogen fuel cell vehicles are gaining significant attention. While hydrogen offers high energy content and zero-emission advantages, it also poses risks such as leakage, explosion, and material incompatibility due to its low density and rapid ascent properties [1,2]. This article examines the critical risk factors in the safety management of hydrogen fuel cell vehicles using systematic risk assessment methods and emphasizes applicable control strategies.

2. RISK CATEGORIES AND ASSESSMENT
2.1. Hydrogen Leakage and Explosion Risk
Definition: Hydrogen rises rapidly due to its low molecular weight. This property leads to severe explosion and fire hazards if even small amounts of hydrogen leakage combine with oxygen [1,2]. Hydrogen has a wide ignition range in air, between 4% and 75% [3].
Probability and Impact:
- Probability: High-pressure operation and mechanical connection errors can increase the risk of leakage.
- Impact: Sudden explosion, fire, and environmental damage.

Control Measures:
- Hydrogen leakage sensors monitor changes in thermal conductivity with concentration, enabling early detection.
- Development of leak-proof connection and sealing technologies.
- Emergency shut-off and evacuation mechanisms.

2.2. High-Pressure Storage and Material Compatibility Issues
Definition: Storing hydrogen under high pressure can cause mechanical stress in tanks and problems such as "hydrogen embrittlement" (material weakening) [4].
Probability and Impact:
- Probability: Mechanical fatigue and material incompatibilities can be observed in long-term use.
- Impact: Cracking, leakage, and sudden failures in storage tanks.

Control Measures:
- Special composite storage tank designs with a gravimetric capacity between 2.4% - 4.4%.
- Regular periodic maintenance and testing.

2.3. Fuel Cell Failures and Systemic Errors
Definition: Although fuel cell systems offer high efficiency, they can be subject to failures and performance degradation due to their technological complexity [5].
Probability and Impact:
- Probability: The probability of error increases with technological complexity and long-term operation.

- Impact: Decrease in fuel cell performance, need for emergency intervention.

Control Measures:

- Advanced diagnostic and remote monitoring systems.
- Regular maintenance, testing, and failure management plans.

2.4. Collision and Accident Situations

Definition: During vehicle accidents or collisions, damage to hydrogen storage tanks can trigger leakage and explosion risks [1].

Probability and Impact:

- Probability: Traffic conditions, operator errors, and external factors can increase this risk.
- Impact: Serious safety risks for passengers, structural damage, and emergency response.

Control Measures:

- Collision-resistant design, energy-absorbing materials, and configurations.
- Implementation of emergency stop systems and crash tests.

2.5. Infrastructure and Logistics Risks

Definition: Lack of compliance with international standards or technical errors at hydrogen refueling stations can lead to leakage and environmental risks [5].

Probability and Impact:

- Probability: Can increase due to regional infrastructure practices and operator inexperience.
- Impact: Leakage from refueling errors, explosion risk, and decreased user confidence.

Control Measures:

- Infrastructure compliant with international standards such as ISO and SAE.
- Employment of certified and trained operators.
- Regular inspections and systematic testing.

2.6. Operational and Usage Risks

Definition: Insufficient training of vehicle users and maintenance teams, procedural errors, and incorrect practices can increase operational risks [6].

Probability and Impact:

- Probability: Error rate increases due to lack of training.
- Impact: System failures, performance loss, and increased maintenance costs.

Control Measures:

- Comprehensive user and maintenance personnel training.
- Implementation of detailed user manuals and emergency procedures.
- Continuous updating of operational standards and maintenance plans.

3. METHODOLOGY

To systematically conduct risk analysis in hydrogen fuel cell vehicles, methodologies such as MADS/MOSAR, FMEA, and FTA were used. The study steps can be summarized as follows:

1. Risk Identification: Hydrogen leakage, high-pressure storage, fuel cell failures, collision, infrastructure, and operational risks were identified.
2. Risk Analysis: A risk matrix was created by evaluating the probability and impact of each risk.
3. Risk Assessment: Risk levels were calculated and prioritized.
4. Risk Reduction: Applicable control measures and strategies were developed.
5. Monitoring and Review: The sustainability of risk management was ensured through systematic monitoring.

Table 1. FMEA example

Failure Mode	Potential Causes	Effects	S (Severity)	O (Occurrence)	D (Detectability)	RPN	Preventive / Corrective Actions
Hydrogen Leakage	Faulty seal, connection failure, mechanical damage	Explosion risk, fire, environmental damage	9	7	5	315	Installation of leak sensors and alarm systems, periodic maintenance, connection improvements
Fuel Cell Failure	Insufficient cooling, control system malfunction	Reduced energy production, performance loss, need for emergency intervention	7	5	4	140	Advanced diagnostic systems, regular maintenance, optimization of cooling systems
High-Pressure Storage Issue	Material fatigue, use of weak alloy	Tank cracking, leakage, performance loss	8	6	6	288	Dual-layer tank design, material testing and regular inspection, selection of high-quality materials
Electronic Control Failure	Software error, faulty sensor	Incorrect data, situations requiring intervention, performance drop	6	4	7	168	Software updates, sensor calibrations, improvement of error monitoring systems
Material Damage Due to Collision	Accident, impact, or mechanical damage in a crash	Loss of structural integrity, leakage, need for emergency response	9	5	6	270	Impact-resistant design, structural tests, crash simulations, and accident scenario analyses

4. DISCUSSION

The potential advantages offered by hydrogen technologies must be balanced with the risks they bring. Academic studies [4,5] and international standards [2,6] offer suggestions for minimizing risks; however, in practical applications, the integration of regular maintenance, continuous training, and advanced technology monitoring systems comes to the forefront. Reducing operational and usage risks can be achieved, especially through user training and systematic failure management [7].

5. CONCLUSION

This article systematically examines the risks observed in hydrogen fuel cell vehicles, including hydrogen leakage, high-pressure storage, fuel cell failures, collision, infrastructure, and operational factors. Through appropriate control strategies and continuous monitoring practices, the aim is to safely utilize the advantages provided by hydrogen technology. Future technological developments and continuously updated academic research will further improve the safe use of hydrogen.

REFERENCES

1. U.S. Department of Energy. (n.d.). *Hydrogen Safety Best Practices*. Erişim: https://www.energy.gov
2. International Organization for Standardization. (2018). *ISO 19880-1:2018 – Gaseous Hydrogen – Fueling Stations – Part 1: General Concepts*.

3. Kahraman, N., & Albayrak, B. (2007). İçten yanmalı motorlarda alternatif yakıt olarak hidrojen kullanılması. Mühendis ve Makine, Cilt:48, Sayı:569.
4. Schlapbach, L., & Züttel, A. (2001). Hydrogen-storage materials for mobile applications. *Nature, 414*, 353–358.
5. SAE International. (n.d.). *SAE J2601 – Fueling Protocols for Hydrogen Fuel Cell Vehicles*.
6. International Energy Agency. (2019). *The Future of Hydrogen: Seizing Today's Opportunities*. IEA Publications.
7. Dincer, I., & Acar, C. (2015). Review and evaluation of hydrogen production methods for better sustainability. International Journal of Hydrogen Energy, Volume 40 Issue 34, Pages 11094-11111.

EXPERIMENTAL AND THEORETICAL STUDY; OF AN ACTIVE NI NANOCATALYST FOR THE HYDROLYSIS OF SODIUM BORHYDRIDE AND DIMETHYLAMINE BORANE

[1*]*Mehmet Sait İzgi*, [2]*Erhan ONAT*, [3]*Sultan Faal, Fatih Ahmet Çelik, Ömer Şahin, Ezman Karabulut**
[1] Department of Chemical Engineering, Faculty of Engineering, Siirt University, 56100 Siirt, Turkey
[2] Vocational School of Organised Industrial Zone, Department of Electrical and Energy, Bitlis Eren University, 13000 Bitlis, Turkey
[1] Department of Chemical Engineering, Faculty of Engineering, Siirt University, 56100 Siirt, Turkey
[3]Faculty of Arts & Sciences, Physics Department, Bitlis Eren University, 13000 Bitlis, Turkey
[4]Department of Chemical Engineering, Faculty of Chemical and Metallurgical Engineering, Istanbul Technical University, 34469 Istanbul, Turkey
[5]Vocational School of Health Services, Bitlis Eren University, 13000 Bitlis, Turkey

*Corresponding author e-mail: saitizgi@gmail.com

ABSTRACT
In this study, for the first time, carbon quantum dots supported nickel-based (Ni (0), Ni@Urea, Ni@DOT and Ni@CQD-MOF) catalysts were synthesized from urea by solvothermal method and inexpensive and highly catalytic catalysts for the dehydrogenation of dimethylamine borane (DMAB) and sodium boron hydride (SBH) were prepared. The catalysts synthesized herein were synthesized by different methods and their hydrolysis of both DMAB and SBH was investigated. The characterization of the synthesized catalysts was supported by some analytical methods. The catalysts were investigated at room temperature, catalyst effect, different substrates and different temperatures in DMAB and SBH. The kinetic parameters of the catalyst were found as activation energy 50.12 kj/mol for SBH and 50.86 kj/mol for DMAB. The other activation parameters were ΔH# = 48.20 kj/mol and ΔS# = -112.4 J/mol*K for SBH and ΔH# = 48.28 kj/mol and ΔS# = -48.48 J/mol*K for DMAB. However, the reproducibility of the catalyst was tested 6 times in the presence of both hydrogen sources. In addition, calculations were performed using DFT to investigate the activity of the catalyst. It was found that the calculations were in good agreement with the experimental data.

Keywords: DMAB, SBH, Hydrogen, Solvotermal, DFT

1. INTRODUCTION

Today, the trend towards renewable energy sources is increasing due to increasing environmental problems and the scarcity of fossil fuels. Since hydrogen, one of the renewable energy sources, has storage and transportation problems, borohydrides that will overcome these problems come to the fore [1-3]. Borhydrides, such as sodium borohydride (SBH) 10.9%, potassium borohydride (PBH) 7.9%, ammonia borane (AB) 19.6%, dimethyl aminborane (DMAB), are used due to some advantages such as high hydrogen content, ease of use and non-flammability. Among the available hydrogen sources, ammonia borane derivatives are attracting increasing interest due to their high hydrogen content, availability, stability, ease of use and non-flammability. The prominent ones are usually SBH and DMAB. DMAB is used because it remains in a stable form in air, is very cheap, and has a crystalline structure. However, they cannot be used as hydrogen sources without a suitable catalyst [4-7]. Both hydrogen sources are hydrolyzed at room conditions in the presence of suitable catalysts. Especially for the hydrolysis of DMAB, Pd, Ru and Ro based catalysts were used, or different heterogeneous catalysts were used. The hydrolysis reactions for both hydrogen sources (DMAB and SBH) are shown below.

$$NaBH_4 + 2\,H_2O \xrightarrow{Ni@CQDs\ Catalyst} NaBO_2 + 4H_2\uparrow \quad (1)$$

According to Equation (1), hydrolysis of 1 mole of $NaBH_4$ yields 4 moles of H_2. of this, 2 moles come from H_2O.

$$(CH_3)_2NHBH_3 + 2\,H_2O \xrightarrow{Ni@CQDs\ Catalyst} (CH_3)_2NH_2BO_2 + 3H_2\uparrow \quad (2)$$

According to Equation (2), theoretically, 3 mol H2 is obtained from the hydrolysis of 1 mol $(CH_3)_2NHBH_3$

Since the two hydrogen sources here are self-hydrolyzing, suitable catalysts with high catalytic activity are needed to control the reaction. As mentioned above, although studies with expensive catalysts are generally carried out, studies on cheap and active catalysts are limited. For this purpose, catalysts such as (Co, Cr, Fe, Cu, Mo and Ni), which are abundant in nature for hydrogen production in aqueous solutions of DMAB and SBH, are used and support materials are used to prevent their agglomeration and homogeneous dispersion. Support materials include carbon nanotubes (CNT), activated carbon (AC), metal organic framework (MOF), aluminum oxide (Al_2O_3) and carbon quantum dots (CQD). Among them, CQDs are notable for their potential catalytic applications due to factors such as their nanometer size (<5nm), surface properties, electron transfer and chemical functional groups of the materials, and green synthesis[8-9].

In this study, 4 different catalysts were synthesized by solvothermal method with 4 different synthesis models and their hydrogen activities in both DMAB and SB were compared. In addition, the 4 synthesized catalysts were characterized by analytical methods; XRD, BET, UV-PL, IR, TEM and XPS analysis. The H2 yield obtained as a result of hydrolysis of the synthesized catalyst in both DMAB and SBH, different Ni loading types on CQD support, different DMAB, SBH concentrations, different catalyst amounts and detailed kinetic studies of both hydrogen sources are presented. Here, hydrogen production rates for DMAB and SBH at 25o C for Ni@CQD in aqueous media were calculated as 862 and 1542 mL.min-1.g.cat-1, respectively. In addition, the activation parameters of the catalyst were calculated for each hydrogen source individually and the reusability of the catalyst was tested 6 times[10-11]. In addition, calculations were performed using DFT to investigate the activity of the catalyst. It was observed that the calculations were in agreement with the experimental data.

2. MATERIALS AND METHODS

2.1. Experimental procedure

Dimetil formamid (C_3H_7NO), Sodium borohydride ($NaBH_4$), Dimethylamine borane ($(CH_3)_2NHBH_3$) Nickel chloride hexahydrate ($NiCl_2.6H_20$) urea, and sodium hydroxide (NaOH) were purchased from Sigma-Aldrich and used in catalyst synthesis and hydrolysis. Ultra-distilled water was used for sample preparation.

2.2. Hydrogen generation measurement

The measurement of the hydrogen gas produced during the methanolysis reaction was carried out using the water displacement technique. The experiment involved combining predetermined quantities of catalyst with quantities of SB and DMAB within a reaction flask. Subsequently, the reaction flask was placed in a water bath maintained at a temperature of 30 °C. Subsequently, the bottle was linked to the conical container housing water. Following the introduction of 10 mL of methanol into the reaction flask, the methanolysis of SB and DMAB occurs, resulting in the generation of H_2. Subsequently, the produced H_2 migrates to the conical flask that contains water. The reduction in water volume over a given period of time serves as an indicator of the quantity of hydrogen gas (H_2) generated during this chemical reaction. No mixing occurred during the course of this reaction. The hydrogen generation rate (HGR) was defined as mL min^{-1} g^{-1}.

2.3 Ni@CQD-MOF nano-catalyst characterization

A combination of techniques was employed to comprehensively analyze the structural, chemical, and physical properties of the Ni nanocatalyst. X-ray photoelectron spectroscopy (XPS, PHI 5000 VersaProbe) was used to examine the surface chemistry, oxidation states of elements, and their binding energies. Transmission electron microscopy (TEM, JEOL JEM 1220), ideal for high-resolution analysis, was applied to study the internal structure, particle sizes, and arrangement of the nanocatalyst. Energy-dispersive X-ray spectroscopy (EDX, HITACHI TM 3030 Plus) provided information on the elemental distribution, while X-ray diffraction (XRD, Rigaku Ultima-IV) patterns revealed the crystal dimensions and structural regularity of the material. Additionally, BET (Quantachrome Corporation, Autosorb-6) and FT-IR (Shimadzu IRTracer™-100) analyses were also carried out to determine the characteristics of the catalyst surface and the presence of functional groups on it.

3. RESULTS AND DISCUSSION

In this study, the catalysts were characterized and the hydrogen efficiency of both hydrogen sources in the presence of the catalyst was studied at different temperatures for different loading type, different NaOH effect, different subtract amount and activation parameters of the catalyst. The plots of hydrogen activity versus time for 4 different catalysts in both DMAB and SBH are given below in Fig. 1(a-b). Fig. 1a shows that Ni@DOT-MOF catalyst obtained by solvothermal method has higher catalytic performance than Ni(0) and Ni@Urea catalysts synthesized by impregnation method. Likewise, if we look at the 1-b graph, it is seen that the Ni@DOT-MOF catalyst completes the hydrolysis in a shorter time and the hydrogen production rate is about 3 times faster than Ni@Urea.

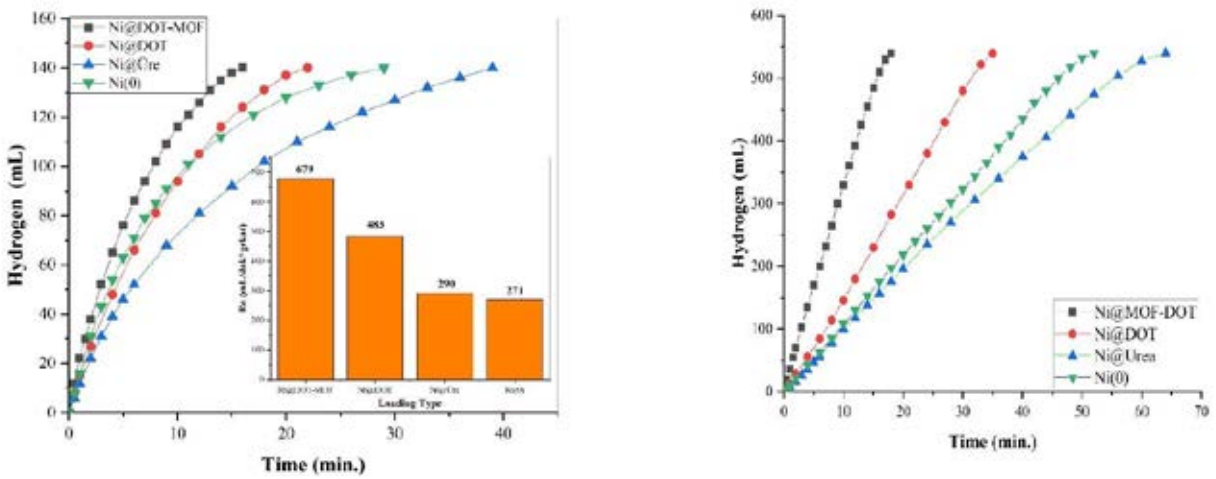

(a) (b)

Fig. 1. Different loading types of catalysts obtained by solvothermal method according to different hydrogen sources a) in the presence of DMAB (40 mg catalyst 25^{0}C, 2 mmol DMAB, 1% NaOH), b) in the presence of SBH (40 mg catalyst 25^{0}C, 0.2 g SBH, 5% NaOH).

Fig. 2 shows the hydrogen production on both DMAB and SB at different temperatures in the presence of Ni@DOT-MOF catalyst. As seen in both figures, as the temperature increases, the catalytic activity of the catalyst increases and the hydrolysis time shortens.

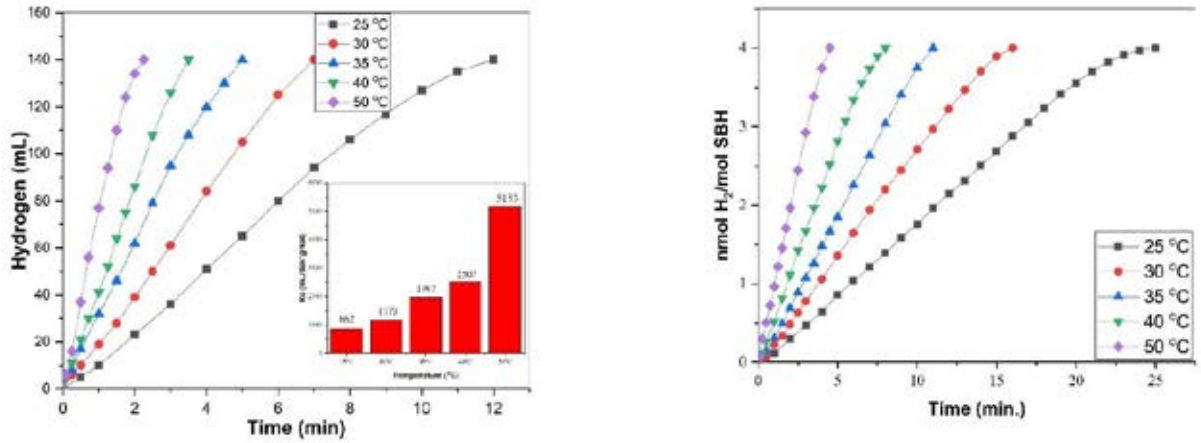

(a) (b)

Fig. 2. Temperature effect of catalysts obtained by solvothermal method according to different hydrogen sources a) in the presence of DMAB, b) in the presence of SBH

4. CONCLUSIONS

At the end of the experimental studies of the obtained Ni@DOT-MOF catalyst with respect to both SBH and DMAB concentrations, it was observed that SBH and DMAB hydrolysis reactions proceeded at the zeroth order. This shows us that the reaction rate is independent of the concentration of the reactant. However, the hydrogen production rates in both DMAB and SBH in the presence of Ni@DOT-MOF catalyst at 25 0C were calculated as 862 and 1542 mL.min-1.g.cat-1, respectively, and the activation energies were calculated as 50.86 and 50.12 kj/mol. However, the usable performance of the Ni@DOT-MOF catalyst for both hydrogen sources was performed exactly 6 times and it was observed that the catalyst retained its catalytic activity even after 6 times of usability.

ACKNOWLEDGEMENT
This study was supported by the scientific research unit of Siirt University (No: 2023-SIUFEB-003). That is why the

REFERENCES

1. Abdelhamid h n. A review on hydrogen generation from the hydrolysis of sodium borohydride. International journal of hydrogen energy 2021; 46(1): 726-765.
2. Schlesinger H I, Brown H C, Finholt A E, Gilbreath J R, Hoekstra H R, Hyde E K. Sodium borohydride, its hydrolysis and its use as a reducing agent and in the generation of hydrogen. Journal of the american chemical society 1953; 75(1): 215-219.
3. Şahin Ö, Kaya M, Izgi M S, Saka C, the effect of microwave irradiation on a co-b-based catalyst for hydrogen generation by hydrolysis of $nabh_4$ solution. Energy sources, part a: recovery, utilization, and environmental effects, 2015. 37(5), 462-467.
4. IZGI, M.S. Effect of microwave irritated Co-b-Cr catalyst on the hydrolysis of sodium borohydride. Energy sources, part a: recovery, utilization, and environmental effects 2016; 38(17): 2590-2597.
5. Gómez-Coma L, Silva D L, Ortiz A, Rangel C M, Ortiz-Martínez V M, Pinto A M, et al. Sustainable additives for the production of hydrogen via sodium borohydride hydrolysis. Applied sciences 2023; 13(12): 6995.
6. Çelik Kazici, H., Salman, F., Izgi, M. S., & Şahin, Ö. Synthesis of metal-oxide-supported triple nano catalysts and application to h_2 production and h_2o_2 oxidation. Journal of electronic materials, 2020. 49, 3634-3644.
7. Netskina O V, Kochubey D I, Prosvirin I P, Malykhin S E, Komova O V, Kanazhevskiy V. V.et al. Cobalt-boron catalyst for nabh4 hydrolysis: the state of the active component forming from cobalt chloride in a reaction medium. Molecular catalysis 2017; 441: 100-108.
8. Shen x, wang q, wu q, guo s, zhang z, sun z, et al. Cob supported on ag-activated tio2 as a highly active catalyst for hydrolysis of alkaline nabh4 solution. Energy 2015; 90: 464-474.
9. Onat E, Çevik S, Şahin Ö, Horoz S, Izgi M S. Investigation of high catalytic activity catalyst for high hydrogen production rate: co-ru@ mof. Journal of the australian ceramic society 2021; 57: 1389-1395.
10. Akbayrak s, Ozkar s. Magnetically isolable pt0/co3o4 nanocatalysts: outstanding catalytic activity and high reusability in hydrolytic dehydrogenation of ammonia borane. Acs applied materials & interfaces 2021; 13(29): 34341-34348.
11. Izgi M S, Onat E, ŞahiN Ö, Saka C. Green and active hydrogen production from hydrolysis of ammonia borane by using caffeine carbon quantum dot-supported ruthenium catalyst in methanol solvent by hydrothermal. International journal of hydrogen energy 2024; 51 (b): 180-192.

PERFORMANCE ASSESSMENT OF A HYDROGEN LIQUEFACTION CYCLE UTILIZING LIQUEFIED NATURAL GAS REGASIFICATION AND PHOTOVOLTAIC PANEL-BASED POWER GENERATION UNIT

[1,2,*]*Masoud Taghavi*, [1,2]*C. Ozgur Colpan*
[1] Department of Mechanical Engineering, Dokuz Eylul University, Izmir 35397, Türkiye
[2] Energy Application and Research Center (EUAM), Dokuz Eylul University, Izmir 35397, Türkiye
*Corresponding author e-mail: masoudtaghavi67@gmail.com

ABSTRACT
This research proposes an advanced hydrogen (H_2) liquefaction process that optimizes energy consumption by integrating liquefied natural gas regasification for the pre-cooling stage. The structure is powered by 23.45 MW of renewable solar energy, supplied through photovoltaic (PV) panels, while an absorption refrigeration unit utilizes surplus heat within the facility. Process simulations were conducted using Aspen HYSYS V12.1, and the PV system was designed with PVsyst 7.3.1, considering Izmir's meteorological conditions. This innovative approach enhances energy efficiency and promotes sustainability through renewable energy integration. To supply the cycle's power demand, 18 Swiss Solar IBEX-60M-320 PV modules and 37 Hyundai HPC-500HL-EU inverters were utilized. The energy performance analysis of the system indicates that the maximum performance ratio (PR) was achieved in July at 91.2%, whereas the lowest PR was recorded in December at 80.5%. Additionally, the maximum available energy was recorded in July, reaching 3,726.8 MWh, while the lowest value was recorded in February at 3,304.6 MWh. Furthermore, mismatch losses peaked at 95.87 MWh in July and dropped to their lowest level in December at 42.95 MWh.

Keywords: Hydrogen liquefaction process, regasification of liquefied natural gas, energy saving, photovoltaic panels (PV), sustainability energy.

1. INTRODUCTION

Over the past decades, the rapid growth of Industrial sectors and the world market has significantly intensified energy demands and environmental challenges. Climate change and ozone layer depletion have raised serious concerns among environmentalists, as they pose significant threats to the long-term sustainability of the global ecosystem. Among various energy sectors, liquefied natural gas (LNG) transportation has emerged as a crucial method for natural gas distribution, accounting for 32% of global natural gas imports in 2012, offering an alternative to conventional pipeline transmission [1]. The market feasibility of LNG projects is primarily affected by the efficiency of the liquefaction process, as this stage requires considerable energy input.

Due to the substantial energy requirement involved in the liquefaction and deep cooling of natural gas (NG) to temperatures lower than -160 °C, improving energy efficiency in LNG plants remains a top priority. A significant portion of this energy demand arises from the operation of compression refrigeration cycles (CRCs) [2]. The mixed fluid cascade (MFC) cycle is widely adopted in large-scale LNG facilities, where the Linde and Statoil MFC configurations utilize three refrigeration processes with refrigerant mixtures of methane (CH_4), ethane (C_2H_6), propane (C_3H_8), and nitrogen (N_2). These cycles are responsible for the pre-cooling (-25 °C), liquefaction (-86 °C), and subcooling (-160 °C) stages in the NG manufacturing chain [3].

This study introduces an innovative LNG process configuration that integrates an MFC system powered by solar energy and PV and an absorption-refrigeration unit. The proposed cycle is modeled employing Aspen HYSYS V12.1 with the Peng-Robinson equation of state, whereas the PV system is analyzed through PVsyst 7.3.1 software. Many studies have focused on H_2 liquefaction using LNG regasification, such as reference [4–6], but the novelty of this research is supplying the required cycle power through PV considering Izmir's climatic conditions.

2. SYSTEM DESCRIPTION

This study introduces an innovative integrated H_2 liquefaction cycle that effectively combines LNG regasification and solid oxide fuel cell (SOFC) operations. The designed framework leverages the cold energy from LNG, a 6-stage Joule-Brayton (J-B) process, an organic Rankine cycle (ORC) includes the working fluids H_2O and Refrigerant-290, CO_2-based power cycles, and PV to enhance overall efficiency. CO_2 serves as an optimal working fluid for supercritical cycles in power generation by utilizing heat recovery.

As a case study, it is considered that a PV system installed in Izmir, Türkiye, supplies approximately 23,455 kW of electricity to power the integrated process. In addition, Figs. 1 and 2 indicate the block flow and the process flow diagrams employed in the developed system, respectively. According to the process flow diagram (Fig. 2), H_2 initially enters heat exchanger HX1 through State 1 at a temperature of 25 °C, a pressure of 2100 kPa, and a mass flow rate of 1033 kmol/h.

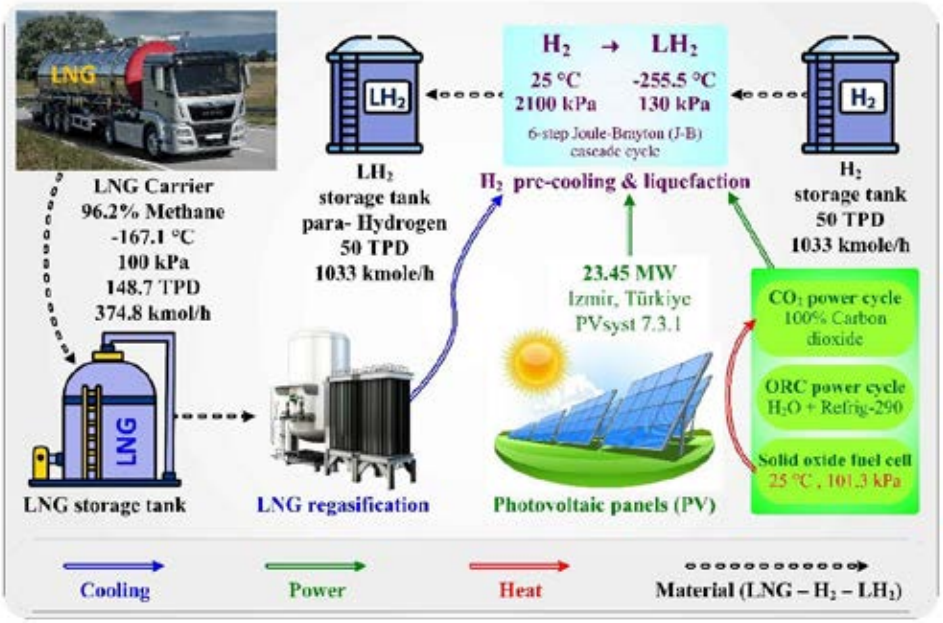

Fig. 1. The block flow diagram of the developed system.

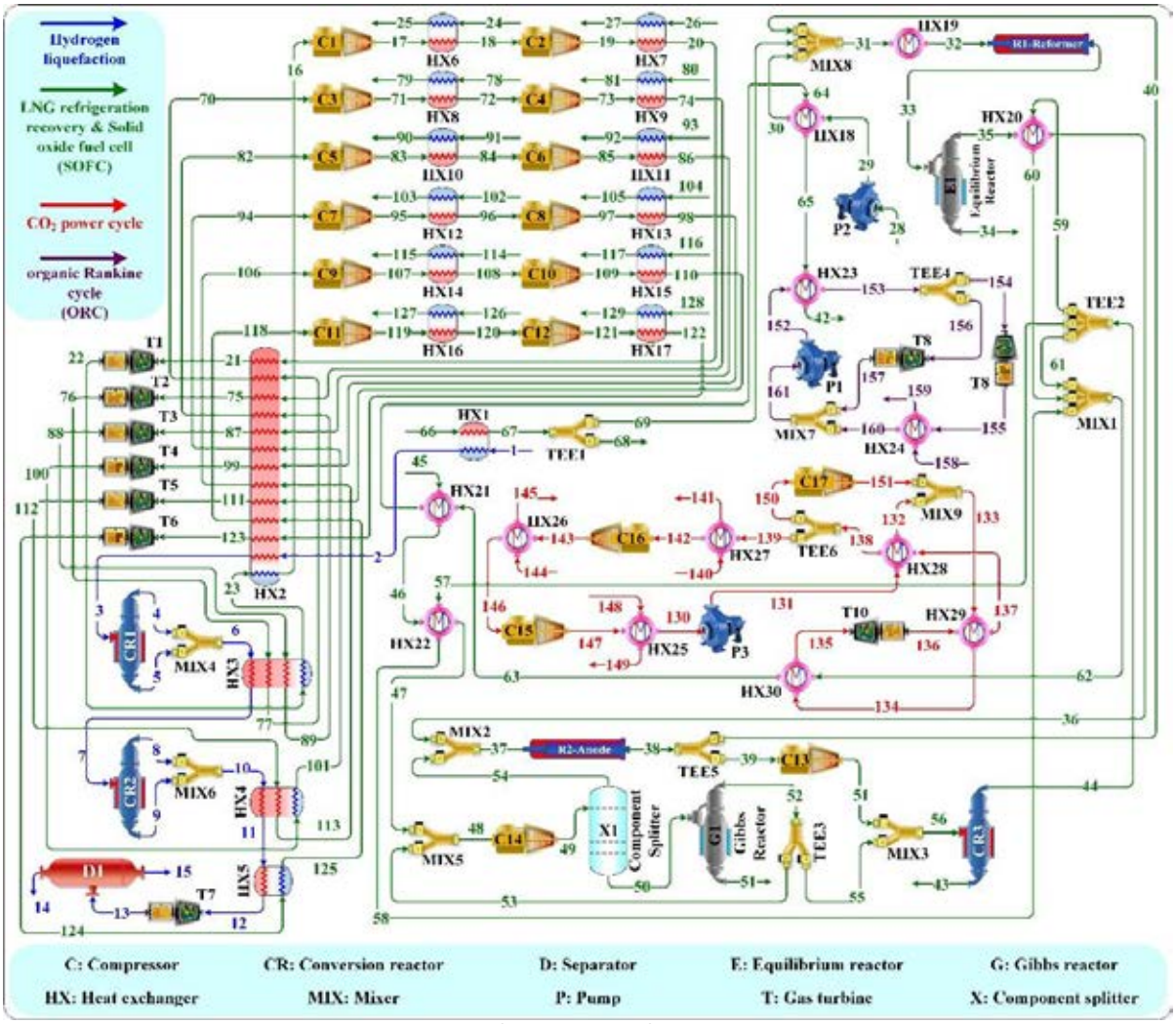

Fig. 2. The process flow diagram of the developed system.

In the final stage, liquefied hydrogen (LH_2) is released from the lower section of the D1 flash drum via state 15 at -255.5 °C and 130 kPa, maintaining a steady flow rate of 1033 kmol/h. The H_2 liquefaction process encompasses states 1 to 15, while states 16 to 129 correspond to SOFC and regasification of LNG operations. Furthermore, states 130 to 151 and 152 to 161 are linked to the CO_2 power unit and the ORC subsystem.

3. MODELING AND SIMULATION

With growing energy demand worldwide, solar power, particularly photovoltaic cells, plays a key role in converting renewable energy using the PV effect [2]. The International Energy Agency (IEA) defines essential efficiency metrics for evaluating on-grid PV systems [8]. Eq. 1 shown the final system yield (YF) is a key measure of on-grid energy output over time, calculated by the ratio of AC energy output to the peak power capacity of the PV unit's maximum power under standard test conditions (STC).

Eq. 2 shown the PV structure's efficiency is assessed using critical Indicators: final yield (YF) in kWh/kWp, energy yield (E_{AC}) in kWh/kWp, peak power output (P_{PV}) under STC, and reference yield (YR). under STC, Eq. 5 shown the total energy loss and the YA denotes DC energy output per kWh of nominal capacity per kWp. PR compares final yield to reference yield. Array absorber loss, determined by Eq. 6, represents the difference among yield of reference and yield of array, while efficiency of inverter, calculated using Eq. 7, is the ratio of AC power output to the array's of PV for DC power, and overall PV structure performance, derived from Eq. 8, is the combined efficiency of the PV inverter and the PV module [2].

$$Y_F = E_{AC}/P_{PV} \quad (1)$$
$$Y_R = H_t(kWh\ m^{-2})/G_o(kW\ m^{-2}) \quad (2)$$
$$Y_A = E_{DC}/P_O \quad (3)$$
$$PR = Y_F/Y_R \quad (4)$$
$$L = Y_R - Y_F \quad (5)$$
$$L_C = Y_R - Y_F \quad (6)$$
$$\eta_{inv} = P_{AC}/P_{DC} \quad (7)$$
$$\eta_{system} = \eta_{PV} \times \eta_{inv} \quad (8)$$

Based on PV simulations, the monthly average global radiation in Izmir varies between 55.9 kWh/m² in December and 242.9 kWh/m² in July. The hottest month in Izmir is July, with a temperature of 29.5 °C, while January is the coldest month, with a temperature of 9.5 °C.

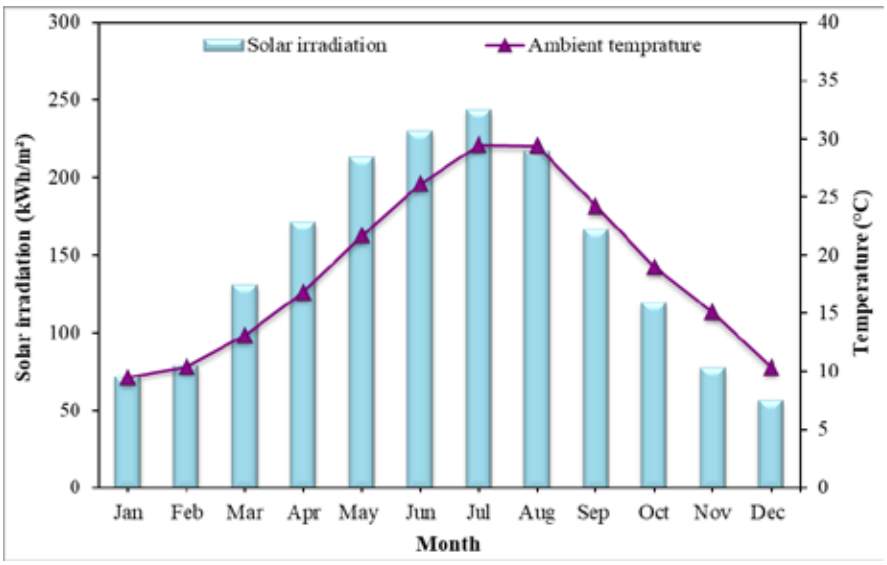

Fig. 3. Solar Irradiation and ambient temperature of Izmir.

4. RESULT AND DISCUSSION

In this research, PVsyst 7.3.1 software was used to model PV for Izmir, Türkiye (latitude 38.4237, longitude 27.1428), considering local weather conditions. This city is located on the western coast of Türkiye, bordering Balıkesir and Manisa to the north, Manisa to the east, Aydın to the south, and the Aegean Sea to the west.

Table 1 presents the specifications of the analyzed PV system. The research employed fixed-tilt PV with a 34º inclination angle in the PV structure.

Table 1. The specifications of the investigated PV system (a: module; b: inverter).

(a) PV module characteristics	
Length × Width × Thickness (mm)	1658 × 996 × 35
Weight (kg)	19.5
Number of Module	18
Manufacturer	Swiss Solar
Description and details	IBEX-60M-320

(b) PV inverter characteristics	
Width × Depth × Height (mm)	2600 × 800 × 2080
Weight (kg)	155
Number of Inverter	37
Manufacturer	Hyundai
Description and details	HPC-500HL-EU

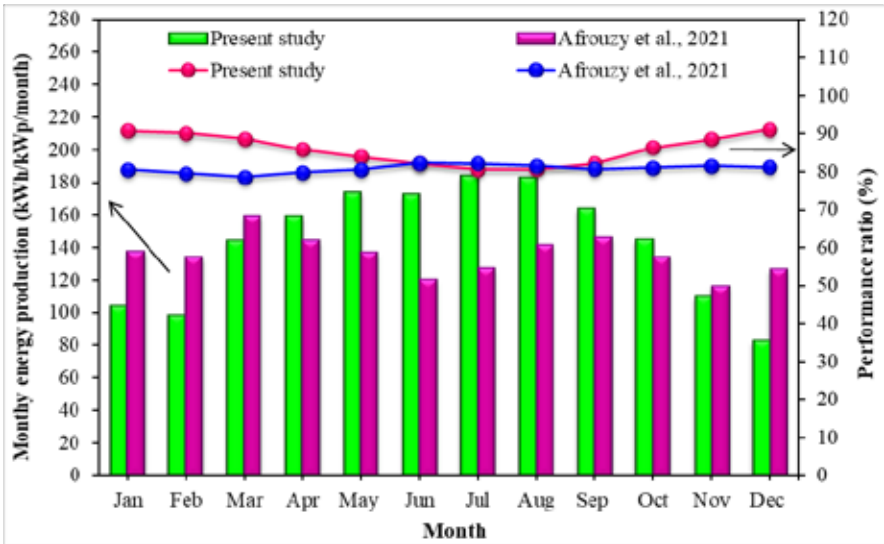

Fig. 4. Monthly energy production and yield for the proposed system and the reference model [8].

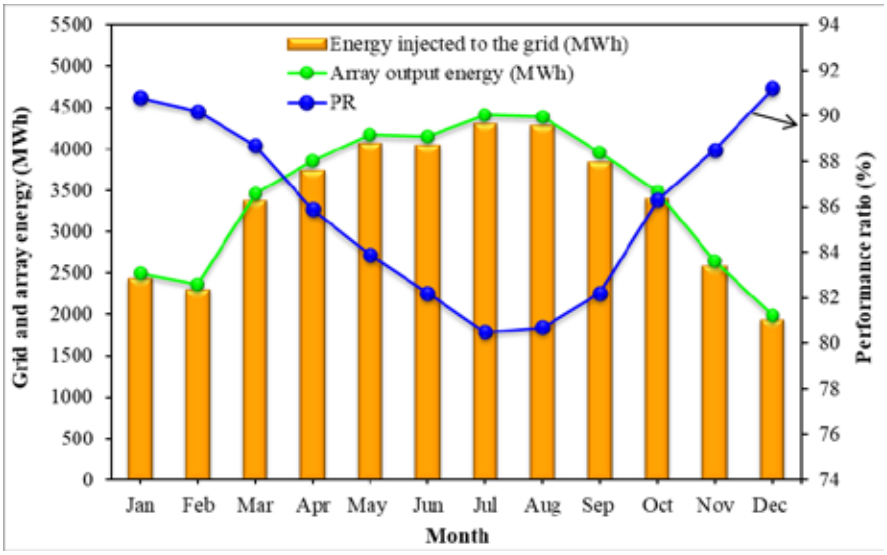

Fig. 5. Monthly PR, energy injected into the grid, and array energy production.

Fig. 4 compares the monthly yield of energy and output among the model of reference [8] and the suggested system. Fig. 5 depicts the PR, array of energy output, and the amount of energy injected into the grid. Also, illustrates the monthly solar energy injection across various structures throughout the year. The lowest PR was recorded in December at 80.5 %, while the highest value was observed in July, reaching 91.2 %.

Fig. 6 presents the simulated annual losses of the PV system. The mismatch loss was at its lowest in December, measuring 42.95 MWh, while it peaked in July at 95.87 MWh. Based on the results of the normalized annual energy in Izmir, the values of produced useful energy (YF), system loss (LS), and collection loss (LC) are 4.71, 0.11, and 0.72 kWh/kWp/year, respectively.

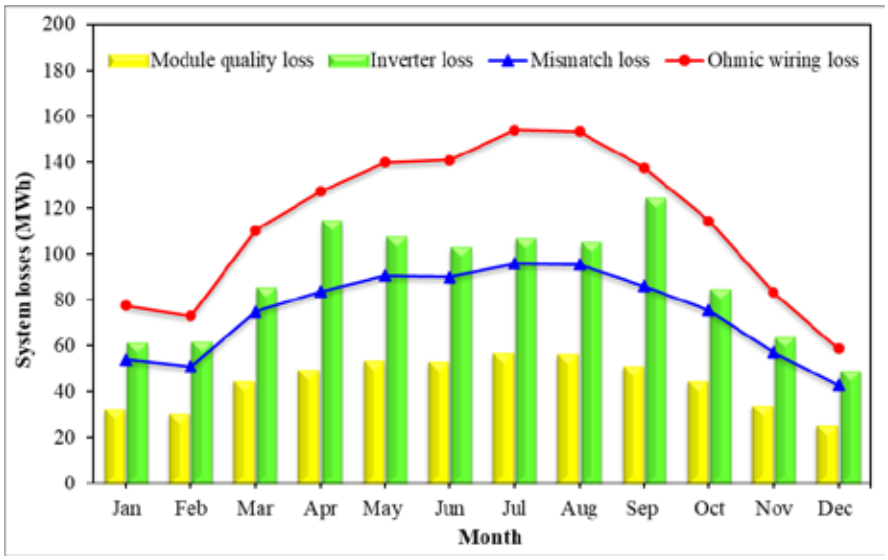

Fig. 6. The schematic represents annual system losses.

5. CONCLUSIONS

This study incorporates LNG regasification as a refrigeration source while utilizing solar energy to cover the system's power demand. The PV system with a capacity of 23.45 MW was integrated to provide the required power under the environmental conditions of Izmir. The main outcomes of the system assessment are described below:

- The proposed system successfully generates 50 TPD of LH_2.
- The LNG and NG flow rates amount to 374.70 kmol/h and 297.70 kmol/h.
- The monthly average global solar radiation in Izmir fluctuates between 55.9 kWh/m^2 in December and 242.9 kWh/m^2 in July. The PR reached its lowest level in December at 80.5%, while its peak value was recorded in July at 91.2%.
- Future research is encouraged to focus on advanced exergoeconomic assessments, detailed risk evaluations, and comprehensive environmental impact analyses to further optimize system performance and sustainability.

ACKNOWLEDGEMENT

This project has received funding from the European Union's Horizon Europe Research and Innovation Program under the Marie Skłodowska-Curie grant agreement No 101126655 (ECO-SPHERE Program). This project is also supported in part by a research grant from the Scientific and Technological Research Council of Türkiye (TÜBİTAK) under the grant number 123C459.

REFERENCES

[1] Mehrpooya M, Omidi M, Vatani A. Novel mixed fluid cascade natural gas liquefaction process configuration using absorption refrigeration system. Appl Therm Eng 2016;98:591–604.
[2] Taghavi M, Yoon H-J, Choi J-U, Lee C-J. Innovative structure of a liquefied natural gas (LNG) process by mixed fluid cascade using solar renewable energy, photovoltaic panels (PV), and absorption refrigeration system. Comput. Aided Chem. Eng. 53, 2024, p. 2071–6.
[3] Ghorbani B, Mehrpooya M, Shirmohammadi R, Hamedi M-H. A comprehensive approach toward utilizing mixed refrigerant and absorption refrigeration systems in an integrated cryogenic refrigeration process. J Clean Prod 2018;179:495–514.
[4] Taghavi M, Lee C-J. Development of a novel hydrogen liquefaction structure based on liquefied natural gas regasification operations and solid oxide fuel cell: Exergy and economic analyses. Fuel 2025;384:133826.
[5] Riaz A, Qyyum MA, Min S, Lee S, Lee M. Performance improvement potential of harnessing LNG regasification for hydrogen liquefaction process: Energy and exergy perspectives. Appl Energy 2021;301:117471.
[6] Yang J, Li Y, Tan H. Integrated hydrogen liquefaction process with a dual-pressure organic Rankine cycle-assisted LNG regasification system: Design, comparison, and analysis. Appl Energy 2023;347:121372.
[7] Taghavi M, Salarian H, Ghorbani B. Thermodynamic and exergy evaluation of a novel integrated hydrogen liquefaction structure using liquid air cold energy recovery, solid oxide fuel cell and photovoltaic panels. J Clean Prod 2021;320:128821.
[8] Afrouzy ZA, Taghavi M. Thermo-economic analysis of a novel integrated structure for liquefied natural gas production using photovoltaic panels. J Therm Anal Calorim 2021;145:1509–36.

HYDROGEN AND VOLATILE FATTY ACID PRODUCTION FROM *POSIDONIA OCEANICA* SEAGRASS BY DARK FERMENTATION

[1]*Damla Kurtdemir**, [2]*Ebru Taylan*, [3]*Şefik Arıcı*,
[1] American Collegiate Institute, High School, Göztepe, Izmir, 35290, Türkiye
[2]Young Scientist Academy, Bornova, Izmir, 35100, Türkiye
[3]Ege University Biomass Energy Systems and Technologies Application and Research Center (BESTMER)
Bornova, Izmir, 35100, Türkiye
*Corresponding author e-mail: dkurtdemir27@my.aci.k12.tr

ABSTRACT
Posidonia oceanica (PO) can accumulate up to 125 kg/m^2 in Mediterranean coasts every year. This abundant biomass resource holds a great potential for biofuels and green chemicals. In this study, the first attempt of using PO is examined as a substrate for dark fermentative biohydrogen and volatile fatty acid (VFA) production. The impact of chemical (H_2SO_4), physical (ultrasound) and biological (cellulase) pretreatment methods was examined. The highest hydrogen production (10.8 L H_2/ kgVS) was obtained by acid pretreated PO, while enzymatic pretreatment showed the maximum VFA production as a 5140 mg/L. This is the first study in the literature to produce H_2 and VFA from pretreated PO and it showed promising results for further investigations.

Keywords: Posidonia Oceanica, Biohydrogen, Volatile Fatty Acid, Pre-treatment, Dark Fermentation

1. INTRODUCTION

The world's energy demand has steadily risen in recent decades due to population growth, urbanization, and industrialization. According to the International Energy Outlook 2017, global energy consumption is projected to increase by 28% from 2015 to 2040. Similarly, the International Energy Agency forecasts a 35% rise in energy demand between 2010 and 2035 [1]. Therefore, the global energy demand and environmental concerns associated with fossil fuels have intensified research into sustainable alternatives. Hydrogen, a clean energy carrier with high energy density and zero carbon emissions, is a promising solution. Hydrogen possesses a high energy density of 120 MJ/kg, making it a strong contender as a fossil fuel alternative. Large-scale implementation has the potential to reduce global CO_2 emissions by approximately 830 million tonnes per year [2]. Posidonia oceanica (PO) is an endemic marine seagrass species widely distributed across the Mediterranean Sea, forms extensive underwater meadows that play a crucial ecological role including carbon sequestration, sediment stabilization, oxygen production and serving as habitats for numerous marine organisms. It is the most abundant seagrass species in the Mediterranean Basin covering approximately 40,000 km^2 of the seabed [3,4]. However, significant seasonal accumulations of PO residues on coastal beaches pose both environmental and economic challenges due to their decomposition resulting in odors, aesthetic issues and high costs associated with their removal. A moderately wide (1 km) seagrass belt can produce more than 125 kg of dry seagrass litter per meter of coastline each year. Annually, these residues accumulate substantially highlighting the importance of finding efficient utilization methods. Utilizing PO for bioenergy production could effectively address these waste management challenges and contribute to renewable energy generation [4,5,6].

Lignocellulosic biomass is composed of three fundamental compounds which are cellulose (30-60% of dry matter), hemicellulose (14-40% of dry matter) and lignin (7-25% of dry matter). An essential step in biomass processing is pretreatment which plays a key role in breaking down the complex structure of lignocellulosic materials making them more accessible during fermentation. Since the composition of lignocellulosic biomass varies across species, selecting an appropriate pretreatment method is critical for optimizing bioenergy production [7]. In the case of PO, it's rigid lignocellulosic structure presents challenges for direct conversion into biofuels necessitating effective pretreatment strategies such as ultrasonic disruption (physical), enzymatic hydrolysis or chemical treatments to enhance its biodegradability and fermentable sugar release. Ultrasonic pretreatment employs disruption of the crystalline highly ordered structures of cellulose and lignin by using mechanical waves [8]. Enzymatic pretreatment depends on biological catalysts with cellulase hydrolysis efficiency influenced by biomass composition including cellulose crystallinity and the structural barriers of lignin and hemicellulose [9]. Chemical (Acid) pretreatment hydrolyzes hemicellulose and partially cellulose disrupting the lignocellulosic structure and making the biomass more porous [10].

Marine biomass, including PO residues, offers promising renewable energy potential through anaerobic digestion processes like dark fermentation. Dark fermentation is an anaerobic process of organic compound degradation carried out by strict or facultative anaerobic microorganisms in the absence of light resulting in biohydrogen production through proton reduction to dissipate excess electrons from organic matter oxidation in the culture medium. As primary byproducts of fermentation compounds such as alcohols, CO_2, and organic acids are also obtained [11]. Simultaneously it generates volatile fatty acids (VFAs) such as acetic, propionic, and butyric acids. These VFAs possess substantial

industrial value in biofuel production, bioplastics, and chemical synthesis, highlighting their economic and environmental relevance. The growing demand for VFAs have diverted the scientific focus to now co-produce these with biohydrogen [12].

This study aimed to evaluate the potential of PO residues for hydrogen and VFA production via optimized pretreatment methods and anaerobic dark fermentation. Analytical methods including spectrophotometry for sugar quantification and advance techniques for hydrogen and VFA measurements were employed. Ultimately, the study seeked to demonstrate the sustainable and economically viable valorization of PO residues, contributing to effective marine biomass management and renewable energy solutions in the Mediterranean region.

2. MATERIALS AND METHODS

Posidonia Oceanica was collected from the coast of Akçakaya Area, Çeşme, İzmir, Türkiye. Prior use of these material, it was soaked in tap water for 5 min to remove salt content. After that it was rinsed with distilled water, filtered and kept in owen at 40 ºC for drying. Dried materials were scaled (1 g VS) according to their proximate analysis (Table 1), then pre-treatments were applied according to Table 2. These contiditios were selected by the previous study of Pilavtepe et al. [3] to optimize sugar recovery for bioethanol production.

Table 1. Raw material and Inoculum Characteristics

Parameters	Unit	*Posidonia Oceanica*	Inoculum
Total Solid (TS)	(%)	14.339 ± 0.755	2.038 ±0,013
Volatile Solid (VS)	TS basis (%)	90.458 ± 0.435	56.371 ±1.511
pH			8.612
Fos/Tac			0.137

Table 2. Pre-treatments

Application	Conditions	Homogenisation
Acid	% H_2SO_4 (v/v), 120 Cº , 1 h, 100 ml dH_2O	Ultra-turrax 10000 rpm 3 min
Enzymatic	30 FPU (cellulase), 50 Cº, 96 h, 100 ml 0.1 M Citrate Buffer (pH=4,8)	
Ultrasound	800 W, 25 kHz, 2 h, 100 ml dH_2O, 20 Cº	

After pretreatment methods that applied to the raw material, supernatants were separatedby centrifugation (10000 rpm, 10 min, 4 Cº). Dark fermentation experiments were conducted in 130 ml in serum bottles with 50 ml working volume. Each reactor was filled with 10 ml of supernatant and 40 ml of mix inoculum which was obtained from various biogas plants. Inoculum was kept in dry owen for 1 h at 100 ºC to suppress methanogens and activate hydrogen producer. pH of all the reactors was adjusted to 6.5 by 2 M HCl solution. Before sealing the reactors with rubber butyl stoppers, headspace was flushed with nitrogen gas for 3 minutes to maintain anaerobic conditions. All reactors were kept in incubator with orbital shaker 37 ºC and 150 rpm, respectively. All reactors including controls were carried out in triplicates. Volumetric gas measurements were carried out with water displacement device. Gas concentrations were measured by Gas Chromatograph (TCD, Agilent, USA). VFA samples were collected from reactors 0,1,3,5 and 7th day then measured in gas chromatography prior methyl tert-butyl ether extraction (FID, Scion, Netherlands). Carbohydrate fractions were measured by HPLC (RID, Agilent, USA). Structural changes of the of the pretreated solid samples were carried out with FTIR (600 and 4000 cm^{-1} with the spectral resolution of 0.5 cm^{-1},Shimadzu, Japan).

3. RESULTS AND DISCUSSION

All the reactors were monitored for gas production and VFA production for 7 days. Biohydrogen production was occurred in all reactors except control within the first 24 hours. Biohydrogen yields of the PO are given in Figure 1. Maximum biohydrogen production was obtained from acid pretreated PO as 10.8 L H_2/ kgVS. According to the carbohydrate analysis of the supernatant, acid pretreatment also resulted in the highest sugar release. Enzymatically pretreated PO showed the second highest biohydrogen and sugar production. Ultrasound pretreatment produced the lowest amount of hydrogen and sugar, respectively. Lignocellulosic structure of raw PO consist on cellulose, hemicellulose and lignin. This pretreatment conditions are selected for loosen the lignin structure for to degrade other polymers for obtaining sugars [13]. In this case, acidic pretreatment is seemed to be promising way to stimulate sugar releasing from PO. On the other side, inoculum pretreatment to suppress methanogens was not entirely successful because methane production was detected in 4th day which means hydrogenotrophic methanoges survived and consumed H_2 and CO_2.

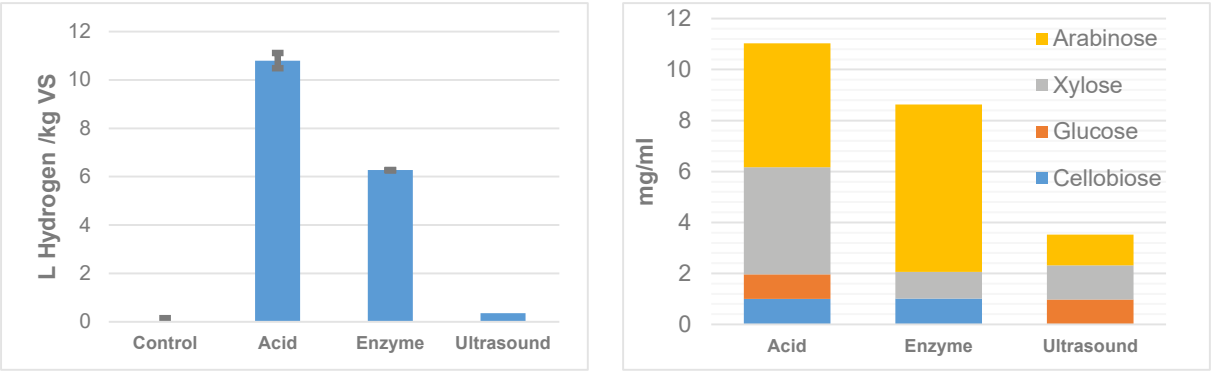

Fig. 1. Biohydrogen and sugar yields of pretreated *Posidonia Oceanica*

Figure 2 presents the VFA profiles that obtained from the dark fermention tests carried out under different pretreatment conditions. The dominant VFAs were acetic, propionic, butyric, isobutyric and isovaleric acid. The enyzmatic pretreated PO resulted in the highest VFA accumulation with the concentration peaking 5140 mg/L on day 7. The second-best performing VFA accumulation observed in the same pretreatment on day 3 as 5042 mg/L. The ultrasound pretreatment had little effect on VFA production as seen by the almost similar profile with the control without PO added.

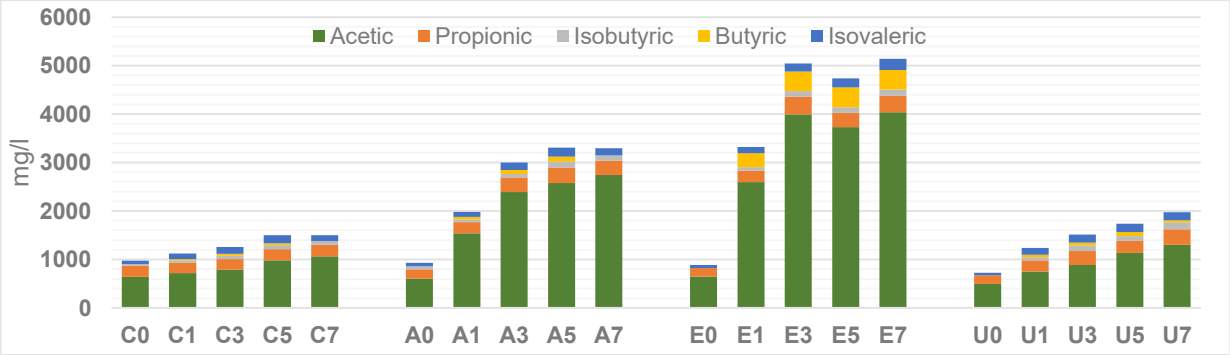

Fig. 2. Volatile fatty acid profiles during the dark fermentation of control, acid, ultrasound and enzyme pretreated Posidonia Oceanica residues (C: Control, A: Acid, E: Enzyme, U: Ultrasound).

FTIR spectral characterization of raw, acid, enzyme and ultrasound pretreated lignocellulosic PO was carried out in the region range of 600–4000 cm−1. Figure 3 showed the IR spectra of raw and pretreated dried samples.

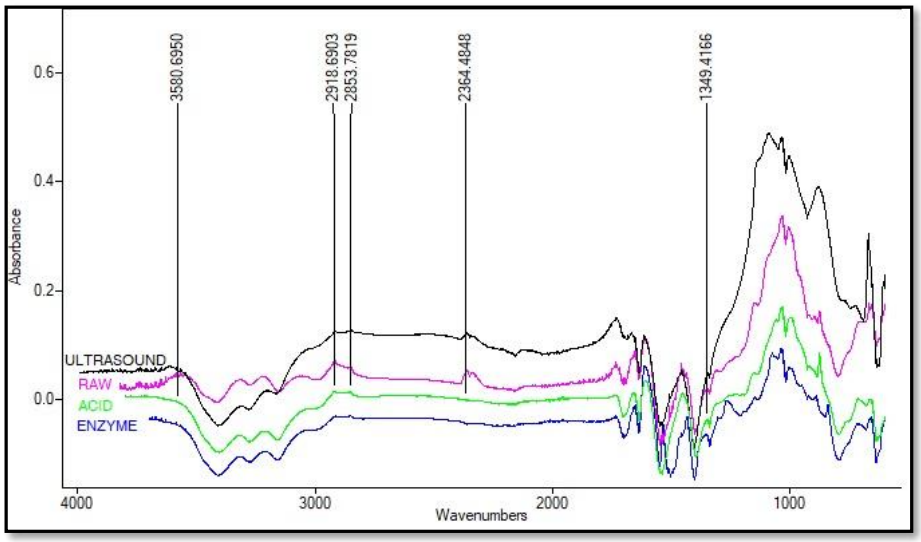

Fig. 3. FTIR spectra of Posidonia Oceanica (raw, acid, enzyme and ultrasound pretreated)

The peak around 1035 cm−1 corresponds to aromatic C–H deformation (present in lignin), C–O deformation in primary alcohol and stretching of non conjugated C=O bond (lignin and hemicellulose). The band around 2363 cm−1 corresponds to C–H stretching of lignin polymer. The band around 3318 and 3815 cm−1 corresponds to O–H stretching of lignin and hemicelluloses polymer [14]. The result showed that again the effectiveness of pre-treatment of PO by the spectrum profiles.

4. CONCLUSIONS

In this study, different physical, chemical and biological pretreatment methods that applied to seagrass Posidonia Oceanica to produce dark fermentative hydrogen and production. The highest hydrogen production (10.8 L H_2/ kgVS) was obtained from acidic pretreated PO. Besides, enzymatically pretreated PO showed maximum VFA production potential and mainly consisted of acetic, propionic and butyric acid. This is the first study in the literature to investigate H_2 and VFA from PO. Future optimization strategies, such as different pretreatment conditions and inoculum modifications, may enhance PO's potential as a sustainable biomass source for green hydrogen and chemical production.

NOMENCLATURE

TCD	Thermal conductivity dedector
FID	Flame ionisation dedector
FTIR	Fourier transform infrared spectroscopy
FPU	Filter paper unit (1 µmol of glucose equivalent per min)
Fos/Tac	Fos (such as acetic acid, propionic acid, and butyric acid) to Tac (total alkalinity or total bicarbonate alkalinity)
HPLC	High performance liquid Chromatography
RID	Refractive index dedector

REFERENCES

1. Sanctis M. Chimienti S. Pastore C. Piergrossi V. Iaconi C. 2019. Energy efficiency improvement of thermal hydrolysis and anaerobic digestion of posidonia oceanica residues. Applied Energy 252:113457.
2. Sadeq A.M. Homod, RZ. Hussein AK. Togun H. Mahmoodi, A. Isleem H.F. Moghaddam AH. 2024. Hydrogen energy systems: technologies, trends, and future prospects. Science of the Total Environment 939:173622.
3. Pilavtepe M. Çeliktaş MS. Sargın S. Yeşil-Çeliktaş Ö. 2013. Transformation of posidonia oceanica residues to bioethanol. Industrial Crops and Products 51:348-354.
4. Cocozza C. Parente A. Zaccone C. Mininni C. Santamaria P. Miano T. 2011. Chemical, physical and spectroscopic characterization of posidonia oceanica (l.) del. residues and their possible recycle. Biomass and Bioenergy 2:799-807.
5. Souii A. Cherif A, Neifar M. 2023. Biovalorization of Posidonia Oceanica waste biomass as a green approach toward a sustainable bioeconomy. Biometrics & Biom Biostat International Journal 12(5):127–134.
6. Voca N. Grubor M. Peter A. Krička T. 2019. Evaluation of Posidonia Oceanica waste as a biomass source for energy generation. Bioenerging Research 12:1104–1112.
7. Galbe M. Zacchi G. 2012. Pretreatment: The key to efficient utilization of lignocellulosic materials. Biomass and Bioenergy 46:70-78.
8. Sul'man E.M. Sul'man, M.G. Prutenskaya E.A. 2011. Effect of ultrasonic pretreatment on the composition of lignocellulosic material in biotechnological processes. Catalysis in Industry 3:28–33.
9. Wu W. Li P. Huang L. Wei Y. Li J. Zhang L. Jin Y. 2023. The Role of Lignin Structure on Cellulase Adsorption and Enzymatic Hydrolysis. Biomass 3(1):96-107
10. Chen J. Ma X. Liang M. Guo Z. Cai Y. Zhu C. Wang Z. Wang S. Xu J. Ying H. 2024. Physical–Chemical–Biological Pretreatment for Biomass Degradation and Industrial Applications: A Review. Waste, 2(4): 451-473.
11. Albuquerque MM. Sartor GdB. Martinez-Burgos W J. Scapini T. Edwiges T. Socco CR. Medeiros ABP. 2024. Biohydrogen Produced via Dark Fermentation: A Review. Methane, 3(3): 500-532.
12. Dahiya S. Lingam Y. Mohan SV. 2023. Understanding acidogenesis towards green hydrogen and volatile fatty acid production – Critical analysis and circular economy perspective. Chemical Engineering Journal 464: 141550.
13. Essien D. Richard TL. 2018. Ensiled wet storage accelerates pretreatment for bioconversion of corn stover. Frontiers in Bioengineering and Biotechnology.6.
14. Sharma V. Kuila A. 2016. Cellulase production using natural medium and its application on enzymatic hydrolysis of thermo chemically pretreated biomass. 3 Biotech, 6:2.

SUSTAINABLE HYDROGEN PRODUCTION THROUGH HYBRID NANOFLUID INTEGRATED EVACUATED TUBE SOLAR COLLECTORS WITH ORGANIC RANKINE CYCLE

[1*]*Sercan Gülce Güngör*
[1] Fırat University, Faculty of Technology, Department of Energy Systems Engineering, Elazig, 23200, Türkiye
*Corresponding author e-mail: sggungor@firat.edu.tr

ABSTRACT
In this study, sustainable hydrogen production using solar energy was carried out. An Evacuated Tube Solar Collector (ETSC) was utilized as the collector. Graphene – Al_2O_3 hybrid nanofuild was selected as the heat transfer fluid in the collector. The electricity was produced using Organic Rankine Cycle (ORC). The hydrogen production was performed by a Proton Exchange Membrane (PEM) electrolyzer. As a result of the study, the efficiencies of ETSC, ORC and PEM were investigated, and the values were found 82%, 16%, and 59% respectively. The hydrogen production rate in the PEM electrolyzer was determined as 0.0216 kg/h, 0.1296 kg/day and 3.88 kg/month. The effect of hybrid nanofluid usage on hydrogen production was investigated.

Keywords: Hydrogen production, Proton exchange membrane, Evacuated tube solar collector, Hybrid nanofluid, Organic Rankine Cycle

1. INTRODUCTION

In recent years, energy consumption has increased, and environmental problems such as global worming and the climate crisis have been observed. The main cause of these issues is the use of fossil fuels [1]. To reduce the consumption of fossil fuels and conventional energy sources, the utilize of renewable energy has been promoted. Solar energy is an abundant, economical, and renewable energy source. Hydrogen is the another fuel with high energy conversion efficiency, higher heating value, and no carbon emissions during combustion. Additionally, hydrogen is used for energy transportation and as an environmentally friendly fuel for vehicles, electricity production [2].

In the literature, solar energy has been investigated for green and sustainable hydrogen production. Atiz et al. [3] studied hydrogen production using solar energy, spesifically with an evacuated tube solar collector (ETSC). This system includes an evacuated tube solar collector (ETSC), a solar pond, an Organic Rankine Cycle (ORC), and a Proton Exchange Memebrane (PEM) electrolysis system. The system was analyzed utilizing Engineering Equation Solver (EES) software. The energy and exergy efficiencies were 5.92% and 18.21%, respectively. The daily hydrogen production was 3204 g. Karabuga et al. [4] studied solar energy-driven hydrogen production. An evacuated tube solar collector was selected as the collector. The thermal energy obtained from solar radiation was converted into electrical energy using an ORC. A PEM electrolyzer was utilized for hydrogen production. The thermodynamic analysis results showed energy and exergy efficiencies of 51.28% and 16.30%, respectively. Ghasem Khani et al., [5] designed hydrogen production system base on a solar-powered ORC and a PEM electrolyzer. Energy and exergy analyses of the system were carried out using EES software. The results of the research showed that energy and exergy variations in a double-pressure ORC system. Li et al., [6] studied a system consisting of a solar pond, an Abrobed Power Cycle (APC), an ORC, a PEM electrolyzer. The results of APC and ORC systems were compared. Additionally, an economic assessment of the system was conducted. The optimum energy and exergy efficiencies were found to be 42.44% and 27.54 respectively. Rejeb et al., [7] designed multi-generation sytems focusing on novel electricity, heat, and green hydrogen production. The system design includes a solar photovoltaic thermal collector, an ORC, a PEM electrolyzer, and liquefied natural gas (LNG). Thermodynamic analysis was performed using EES software. The research results showed that the system's exergy efficiency was 16.24%.

Furthermore, the usage of nanofluid in the solar collector enhanced the heat transfer rate and hydrogen production. Sathish et al. [8] designed a hydrogen production system that includes solar energy. This system consisted of an evacuated tube solar collector, a hybrid nanofluid (Al_2O_3 - SiO_2 - water), an Organic Rankine Cycle, and a PEM electrolyzer. The use of hybrid nanofluid with different volume concentrations (0.5%, 1%, 1.5%, and 2%) in the evacuated tube collector increased energy gains by 13.22%, 21.37%, 30.38%, and 48.52%, respectively, compared to water. ORC efficiency improved with increasing nanofluid concentrations 12.29% (0.5% vol.), 23.10% (1% vol.), 34.15% (1.5% vol.), and 48.40% (2% vol.). Hydrogen production in the PEM electrolyzer reached 2156.7 g at %2 vol. concentration, and overall system efficiency was 71.3%. In another similar study, Sathish et al. [9] designed a hydrogen production system using different hybrid nanofluids in an evacuated tube solar collector, ORC, and PEM electrolyzer. The researches selected magnesium oxide (MgO) and multi-walled carbon nanotubes (MWCNT) as nanoparticles, and thermal oil as the base fluid in the hybrid nanofluid. The nanoparticle concentration of the hybrid nanofluid was set 0.1% vol., each nanoparticle contributing 0.05% vol. The research results demonstrated the benefits of hybrid nanofluid usage in the solar system. While collector efficiency increased by 80.5% with hybrid nanofluid integration, exergy efficiency improved from 12.4% to 36.8%. The PEM electrolyzer's energy and exergy efficiencies were recorded 44.4% and 10.5%,

respectively.

In the solar-based electrical production system's the Organic Rankine Cycle (ORC) is used. The selection of a refrigerant for the ORC is an important factor affecting system efficiency. Kajurek et al. [10] studied the selection of refrigerants for the ORC. A low-temperature heat source in the range of 30 - 100 °C was designed for a 1kW electric power output ORC system. Ten different refrigerant (R134a, R152a, R227ea, R236fa, R245 fa, R290, R600a, R717, R1234yf, and R1234ze) were selected in the study. As a result of the analysis, ammonia was found to be the best refrigerant, achieving 5.68% efficiency. Another study was conducted by Ndame Ngangue et al. [11], focusing on the selection of a working fluid for the ORC system. Seven different refrigerants were examined in the ORC. The refrigerants were selected based on their Global Warming Potential (GWP) and Ozone Depletion Potential(ODP). Thermodynamic analysis results showed that R717 was the most suitable working fluid.

The literature review indicates that the solar energy-based hydrogen production process is enhanced by hybrid nanofluid. An evacuated tube solar collector is used to obtain heat from solar energy. The selection of the ORC system refrigerant is crucial for efficiency. The research gap in the literature focuses on the impact of graphene – Al_2O_3 hybrid nanofluid and R717 refrigerant usage on hydrogen production. For this purposes, a solar energy-based hydrogen production system was designed in this study. Solar energy was collected using an evacuated tube solar collector. Graphene - Al_2O_3 hybrid nanofluid was selected as the heat transfer fluid. The heat obtained solar energy was converted into electrical energy using a Organic Rankine Cycle (ORC) with ammonia as the refrigerant. A proton exchange membrane (PEM) electrolyzer was used for hydrogen production. This solar energy-based hydrogen production system was analyzed thermodynamically. The thermodynamic performance of the system was investigated utilized by Engineering Equation Solver (EES) from F-Chart Software [12].

2. SYSTEM DESCRIPTION

A solar energy-based hydrogen production system was designed. The system includes an evacuated tube solar collector, an Organic Rankine Cycle, and a PEM electrolyzer. The system design was shown in Fig. 1.

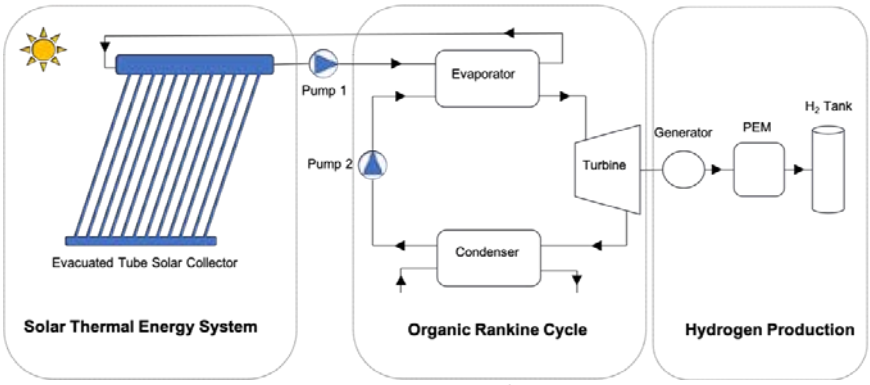

Fig. 1. Energy system design of hydrogen production

2.1. Evacuated Tube Solar Collector (ETSC)

An evacuated tube solar collector (ETSC) was selected as the solar collector. The heat transfer fluid in the collector is a hybrid nanofluid. Solar radiation was determined to be 850 W/m^2, which represents the average solar radiation during summer in the southern region of Türkiye [13,14]. The properties of the ETSC are as follows: a area of 11.92 m^2, 120 tubes, transmissivity of glass is 0.92, absorptivity is 0.91, and glass emissivity is 0.8 [9]. The heat obtained from solar energy and the collector efficiency [9] were calculated using equation (1) and equation (2).

$$Q_u = A_c F_R [I_T(\tau\alpha) - U_L(T_i - T_0)] \quad (1)$$

$$\eta = \frac{Q_u}{A_c I_T} \quad (2)$$

2.2. Nanofluid

Graphene - Al_2O_3 hybrid nanofluid was selected. The concentration of the hybrid nanofluid was determined by the proportion of graphene – Al_2O_3 nanoparticles (0.25% - 0.75%), totaling 1%. The material properties of water, graphene, and Al_2O_3 in the are presented in Table 1.

Table 1. Properties of water [15], graphene [16] and Al_2O_3 [17]

Parameters	Water	Graphene	Al_2O_3
Particle size (nm)	-	5 - 10	30 - 40
Specific heat capacity (J/kg·K)	4180	0.7	0.8
Density (kg/m^3)	997	2200	3790
Thermal conductivity (W/m·K)	0.617	4000 - 5000	765

The concentration, density, and specific heat capacity of the hybrid nanofluid [18] were calculated using equations (3), (4), and (5).

$$\emptyset_T = \emptyset_{np1} + \emptyset_{np2} \tag{3}$$

$$\rho_{hnf} = \emptyset_{np1}\rho_{np1} + \emptyset_{np2}\rho_{np2} + (1 - \emptyset_T)\rho_{bf} \tag{4}$$

$$c_{hnf} = \frac{\emptyset_{np1}\rho_{np1}c_{p,np1} + \emptyset_{np2}\rho_{np2}c_{p,np2} + (1-\emptyset_T)\rho_{bf}c_{p,bf}}{\rho_{hnf}} \tag{5}$$

2.3. Organic Rankine Cycle (ORC)

The heat energy obtained from the solar collector was converted into electrical energy in the Organic Rankine Cycle. The refrigerant of the ORC, R717 (ammonia), was selected due to its high performance. The heat obtained in the evaporator, net work, and energy efficiency of the ORC was determined using equations (6), (7), and (8) [8].

$$\dot{Q}_E = \dot{m}_R\left(h_{E,out} - h_{E,in}\right) \tag{6}$$

$$\dot{W}_{net} = \dot{W}_T - \dot{W}_P \tag{7}$$

$$\eta = \frac{\dot{W}_{net}}{\dot{Q}_E} \tag{8}$$

2.4. Hydrogen Production

Hydrogen was produced using a Proton Exchange Membrane (PEM) electrolyzer. The PEM electrolyzer generated hydrogen from water using an electrical input 1.2 kW. The hydrogen production rate was determined by measuring the flow rate and mass of the produced hydrogen. Hydrogen was generated over a 6-hour operational period per day and stored in compressed gas cylinders. The efficiency of the PEM electrolyzer was determined using equation (9) [19].

$$\eta_{PEM} = \frac{\dot{m}_{H_2}LHV_{H_2}}{\dot{W}_{PEM}} \tag{9}$$

3. RESULTS AND DISCUSSION

This study investigated hydrogen production in a solar energy system combining ETSC and ORC. A graphene - Al_2O_3 hybrid nanofluid was utilized to enhance heat transfer. The ORC was used to generate of electricity for the PEM electrolyzer. R717 (ammonia) was selected as the refrigerant in the ORC. The hybrid nanofluid properties were measured as 1025 kg/m^3 for density and 4063 J/kgK for specific heat capacity. The heat obtained from solar energy in the collector was 8.4 kW, and the efficiency of the evacuated tube solar collector was calculated to be 82%. The results of the ORC components are presented in Table 2, where the energy values of the evaporator, turbine, condenser, and pump are displayed. The energy efficiency of the ORC was calculated as 16%.

Table 2. Energy values of ORC equipment

System equipments	Energy (kW)
Evaporator	7.214
Turbine	1.216
Condenser	6.010
Pump	0.012

Hydrogen production in the PEM electrolyzer was determined to be 0.0216 kg/h hydrogen produced. The efficiency of PEMe was calculated as %59. The total daily and monthy hydrogen production was 0.1296 kg and 3.88 kg, respectively. For comparison, the literature data on solar based hydrogen production and the results of the this study are presented in Table 3. The efficiencies of the ETSC and PEM in this study were higher than those reported in previous studies. The use of a hybrid nanofluid in the ETSC proved to be effective in achieving high thermal efficiency.

Table 3. Comparison of the previous studies with current investigation

Component efficiency	Present study	Atiz et al. [3]	Karabuga et al. [4]	Sathish et al. [9]
ETSC (%)	82	n.a.	56.82	72.1
ORC (%)	16	25.4	21.48	n.a.
PEM (%)	59	n.a.	50.49	51.4

4. CONCLUSIONS

In this study, a thermal energy system was designed for green and sustainable hydrogen production. Solar energy was utilized trough an evacuated tube solar collector (ETSC). A graphene – Al_2O_3 hybrid nanofluid was used as the heat transfer fluid in the collector. Electiricity was generated using an Organic Rankine Cycle (ORC), and a PEM electrolyzer was employed for hydrogen production. As a result of this study, the efficiencies of the ETSC, ORC, and PEM were 82%, 16%, and 59%, respectively. The hourly, daily and monthly hydrogen production values were 0.0216 kg/h, 0.1296 kg/day, and 3.88 kg/month. The integration of a hybrid nanofluid in the ETSC for hydrogen production enhanced heat trasnfer performance. Hence, the use of a hybrid nanofluid in the ETSC, in conjuction with the ORC and PEM electrolyzer, proved to be an optimal choice for hydrogen productions.

REFERENCES

[1] Atiz A, Erden M, Karakilcik M. Hydrogen production of flat plate solar collectors integrated with photovoltaic thermal panels. Int J Hydrog Energy 2024;52:1408–24. https://doi.org/10.1016/j.ijhydene.2023.08.302.

[2] Sahmerdan O, Cimsit C, Arici M, Colpan CO. Thermodynamic performance assessment of solar-based hydrogen production systems in Turkey: A detailed review. Renew Sustain Energy Rev 2025;208:115034. https://doi.org/10.1016/j.rser.2024.115034.

[3] Atiz A, Karakilcik H, Erden M, Karakilcik M. Assessment of electricity and hydrogen production performance of evacuated tube solar collectors. Int J Hydrog Energy 2019;44:14137–44. https://doi.org/10.1016/j.ijhydene.2018.09.100.

[4] Karabuga A, Yakut MZ, Utlu Z. Evaluation of the thermodynamic analysis of hydrogen production from a middle-temperature intensity solar collector, a case study. Int J Hydrog Energy 2022;47:31821–32. https://doi.org/10.1016/j.ijhydene.2021.11.246.

[5] Ghasem Khani H, Nikian M, Ghazi M. Energetic and exergoeconomic analysis of different configurations of power and hydrogen generation systems using solar based organic Rankine cycle and PEM electrolyzer. Renew Energy 2024;231:121001. https://doi.org/10.1016/j.renene.2024.121001.

[6] Li J, Dhahad HA, Anqi AE, Rajhi AA. Thermo-economic investigation on the hydrogen production through the stored solar energy in a salinity gradient solar pond: A comparative study by employing APC and ORC with zeotropic mixture. Int J Hydrog Energy 2022;47:7600–23. https://doi.org/10.1016/j.ijhydene.2021.12.102.

[7] Rejeb O, Alirahmi SM, Assareh E, El Haj Assad M, Jemni A, Bettayeb M, et al. Innovative integrated solar powered polygeneration system for green Hydrogen, Oxygen, electricity and heat production. Energy Convers Manag 2022;269:116073. https://doi.org/10.1016/j.enconman.2022.116073.

[8] Sathish T, Saravanan R, Arunachalam SJ, Giri J, Al-lehaibi M, Lalvani JIJ. Enhancement of Hydrogen Production Using an Integrated Evacuated Tube Solar Collector and PEM Electrolyzer With AL_2O_3 and SiO_2 Hybrid Nanofluids. Eng Rep 2025;7:e13103. https://doi.org/10.1002/eng2.13103.

[9] Sathish T, Giri J, Ağbulut Ü. Hydrogen cultivation through an integrated ranking cycle and proton exchange membrane with an evacuated tube collector powered by hybrid nanofluids. Energy 2025;314:133941. https://doi.org/10.1016/j.energy.2024.133941.

[10] Kajurek J, Rusowicz A, Grzebielec A, Bujalski W, Futyma K, Rudowicz Z. Selection of refrigerants for a modified organic Rankine cycle. Energy 2019;168:1–8. https://doi.org/10.1016/j.energy.2018.11.024.

[11] Ndamé Ngangué M, Nguefack Lekané N, Njock JP, Sosso OT, Stouffs P. Working fluid selection for a high efficiency integrated power/cooling system combining an organic Rankine cycle and vapor compression-absorption cycles. Energy 2023;277:127709. https://doi.org/10.1016/j.energy.2023.127709.

[12] EES: Engineering Equation Solver | F-Chart Software : Engineering Software n.d. https://fchartsoftware.com/ees/ (accessed March 18, 2025).

[13] Meteoroloji Genel Müdürlüğü n.d. https://www.mgm.gov.tr/kurumici/turkiye-guneslenme-suresi.aspx (accessed March 18, 2025).

[14] Global Güneş Radyasyonu - Meteoroloji Genel Müdürlüğü n.d. https://www.mgm.gov.tr/kurumici/radyasyon_iller.aspx (accessed March 18, 2025).

[15] Kumar V, Singh SKr, Kumar V, Jamshed W, Nisar KS. Thermal and thermo-hydraulic behaviour of alumina-graphene hybrid nanofluid in minichannel heat sink: An experimental study. Int J Energy Res 2021;45:20700–14. https://doi.org/10.1002/er.7134.

[16] Natividade PSG, De Moraes Moura G, Avallone E, Bandarra Filho EP, Gelamo RV, Gonçalves JCDSI. Experimental analysis applied to an evacuated tube solar collector equipped with parabolic concentrator using multilayer graphene-based nanofluids. Renew Energy 2019;138:152–60. https://doi.org/10.1016/j.renene.2019.01.091.

[17] Vijayan G, Shantharaman PP, Senthil R, Karunakaran R. Thermal performance analysis of a low volume fraction Al2O3 and deionized water nanofluid on solar parabolic trough collector. J Therm Anal Calorim 2022;147:753–62. https://doi.org/10.1007/s10973-020-10313-w.

[18] Rasih RA, Sidik NAC, Samion S. Recent progress on concentrating direct absorption solar collector using nanofluids: A review. J Therm Anal Calorim 2019;137:903–22. https://doi.org/10.1007/s10973-018-7964-6.

[19] Sathish T. Sustainable hydrogen production by integrating solar PV electrolyser and solar evacuated tube collector with hybrid nanoparticles enhanced PCM. Appl Therm Eng 2024;257:124317. https://doi.org/10.1016/j.applthermaleng.2024.124317.

THERMODYNAMIC ANALYSIS OF CLAUDE CYCLE FOR HYDROGEN LIQUEFACTION

[1*]*Yagmur Kumlutas*, [2]*Can Ozgur Colpan*
[1] Dokuz Eylul University, Faculty of Engineering, Department of Mechanical Engineering, Tinaztepe Campus, Izmir, 35390, Türkiye
*Corresponding author e-mail: yagmur.kumlutas@ogr.deu.edu.tr

ABSTRACT
The growing energy demand and depletion of fossil fuels have increased interest in clean hydrogen production. This study focuses on the thermodynamic analysis of the Claude cycle for hydrogen liquefaction. A mathematical model was developed to evaluate the system's performance under varying operating conditions. Using energy and exergy analyses, the study examines the effects of split ratio on second-law and exergy efficiencies considering different operating parameters. The results showed that the highest exergy efficiency of 30% was observed at a split ratio of 0.5. These findings contribute to the improvement of the performance of the Claude cycle for hydrogen liquefaction.

Keywords: Hydrogen liquefaction, Claude cycle, mathematical modeling, liquid hydrogen

1. INTRODUCTION

A large share of global energy consumption relies on fossil fuels, including coal, gasoline, and oil; thus, advancing and integrating zero-emission alternatives like green hydrogen is essential for sustainability. Hydrogen is emerging as a key energy carrier due to its potential for achieving net-zero emissions, as water splitting does not produce harmful byproducts. Its advantages, such as ease of storage and transportation, make it a promising solution for various industrial and energy applications. However, the large-scale adoption of green hydrogen requires the development of efficient production and storage technologies. Hydrogen is typically stored as either liquefied hydrogen (LH_2) or compressed hydrogen (CH_2), both of which significantly reduce its volume, enhancing portability and making it suitable for various storage environments Bian et al. [1]. Among these methods, liquefaction remains a crucial technology for hydrogen storage and transportation due to its high energy density and compatibility with large-scale applications.

Several studies have focused on improving hydrogen liquefaction efficiency by optimizing thermodynamic cycles. For instance Baker and Shaner [2], examined the pre-cooled dual-pressure Claude cycle and reported an energy consumption of 10.85 kWh/kgH_2 with an exergy efficiency of 36%. Similarly, Yang et al. [3] investigated the Joule-Brayton refrigeration cycle, achieving an energy consumption of 11.05 kWh/kgH_2 for large-scale production of 300 tons/day, whereas Krasae-In [4] analyzed a mixed refrigerant Brayton cycle, demonstrating improved efficiency with an energy consumption of 5.91 kWh/kgH_2. These studies highlight the ongoing efforts to enhance hydrogen liquefaction performance through different cycle configurations and operational strategies.

This study aims to conduct a thermodynamic analysis of the Claude cycle in the hydrogen liquefaction process. By evaluating the performance of various cycle components, this study assesses both the second law and exergy efficiencies under different operating parameters. These findings are expected to contribute to the performance improvement of hydrogen liquefaction technologies.

2. MATERIALS AND METHODS

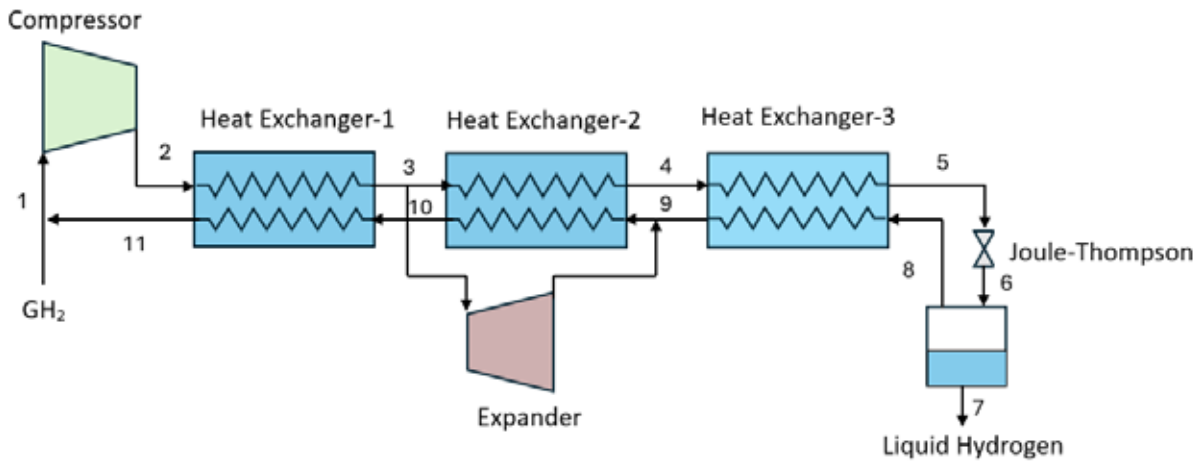

Fig. 1. Schematic of the Claude cycle

The hydrogen liquefaction system described in this study using the Claude cycle is shown in Fig.1. as a process flow diagram. The system's working principle is as follows: The first step involves compressing gaseous hydrogen (GH_2) with a compressor to raise its temperature and pressure. The high-pressure hydrogen leaving the compressor enters the heat exchanger-1, where it exchanges heat with cooling streams that are flowing counter-flowing, lowering the temperature. The hydrogen is further cooled in heat exchanger-2 as part of the cooling process. This step involves expanding a part of the high-pressure hydrogen through an expander, drastically reducing the hydrogen's temperature. This hydrogen stream is transferred to the Joule-Thomson valve after passing through heat exchanger-3, where it is further cooled. As the hydrogen expands via this valve, some of it performs a phase change and collects in the liquid hydrogen storage tank. Redirecting the remaining gaseous hydrogen to the heat exchangers, which precools the incoming hydrogen, improves the system efficiency.

The main assumptions of the thermodynamic models are as follows.

- The system operates under steady-state conditions.
- Kinetic and potential energy effects are neglected.
- Pressure drops across heat exchangers and separator are ignored.
- Heat losses from the turbine, heat exchanger, tank, and valve are neglected.

Table 1. Input Parameter

Input parameter	Symbol	Value
Pressure at the compressor inlet	P_1	100 kPa
Temperature at the compressor inlet	T_1	278 K
Pressure at the compressor outlet	P_2	10000 kPa
Temperature at the heat exchanger-1 outlet	T_3	160 K
Temperature at the heat exchanger-2 outlet	T_{10}	125 K
Isentropic efficiency of the turbine	η_t	0.80
Split ratio	x_s	0.5
Compressor efficiency	$\eta_{compressor}$	0.7

Mass and energy rate balances

The mass flow rate of the makeup hydrogen is equal to the liquefied hydrogen mass flow rate, expressed as:

$$\dot{m}_{makeup} = \dot{m}_{liq}$$

The mass flow rate at State 11 is obtained by applying the mass balance around CV1:

$$\dot{m}_{11} = \dot{m}_2 - \dot{m}_{liq}$$

From the definition of split ratio, the flow through the turbine is given by:

$$\dot{m}_{turbine} = \dot{m}_2 \cdot x_s$$

where x_s represents the split ratio, indicating the proportion of hydrogen that undergoes expansion through the turbine. By applying the first law of thermodynamics to Heat Exchanger 1, the following energy balance equation is derived:

$$\dot{m}_2 \cdot (h_2 - h_3) = \dot{m}_{11} \cdot (h_{11} - h_{10})$$

The ideal compressor work per kilogram of hydrogen is given by:

$$\dot{W}_{comp,ideal} = \dot{m}_2 \cdot (T_2 \cdot (s_2 - s_1) - (h_2 - h_1))$$

The work produced by the turbine per kilogram of H_2 is given by:

$$\dot{W}_{turbine} = \dot{m}_{turbine} \cdot (h_3 - h_9)$$

The actual compressor work per unit mass of hydrogen is calculated as:

$$\dot{W}_{comp,actual} = \frac{\dot{W}_{comp,ideal}}{0.7}$$

Total work required to produce liquid per kg of H_2 is given by the compressor-turbine work:

$$\dot{W}_{net} = \dot{W}_{comp,actual} + \dot{W}_{turbine}$$

The heat input required for compression per kg of H_2 is then:
$\dot{Q}_{comp} = \dot{W}_{comp,actual} - \dot{m}_2 \cdot (h_2 - h_1)$

The actual enthalpy at state h_9 is given by:
$h_9 = h_3 - \eta_{turbine} \cdot (h_3 - h_{9isentropic})$

Where η_t is the turbine efficiency, and $h_{9isentropic}$ represents the isentropic enthalpy at state 9.

Table 2. Exergy Rate Balance

Component	Exergy rate balance
Compressor	$0 = \dot{Q}_{comp} \cdot \frac{(1-T_0)}{T_1} - \dot{W}_{comp,actual} + \dot{m}_2 \cdot \left((h_1 - h_2) - T_0 \cdot (s_1 - s_2)\right) - \dot{E}x_{D,comp}$
Heat Exchanger-1	$\dot{E}x_{D,HX1} = \dot{m}_2 \cdot \left((h_2 - h_3) - T_0 \cdot (s_2 - s_3)\right) + \dot{m}_{11} \cdot \left((h_{10} - h_{11}) - T_0 \cdot (s_{10} - s_{11})\right)$
Heat Exchanger-2	$\dot{E}x_{D,HX2} = \dot{m}_2 \cdot (1 - x_s) \cdot ((h_3 - h_4) - T_0 \cdot (s_3 - s_4) + \dot{m}_{11} \cdot \left((h_9 - h_{10}) - T_0 \cdot (s_9 - s_{10})\right)$
Heat Exchanger-3	$\dot{E}x_{D,HX3} = \dot{m}_2 \cdot (1 - x_s) \cdot \left((h_4 - h_5) - T_0 \cdot (s_4 - s_5)\right) + (\dot{m}_2 \cdot (1 - x_s) - \dot{m}_{liq}) \cdot \left((h_8 - h_9) - T_0 \cdot (s_8 - s_9)\right)$
Valve	$\dot{E}x_{D,valve} = \dot{m}_2 \cdot (1 - x_s) \cdot \left((h_5 - h_6) - T_0 \cdot (s_5 - s_6)\right)$
Separator	$\dot{E}x_{D,sep} = \dot{m}_2 \cdot (1 - x_s) \cdot \left((h_6 - h_0) - T_0 \cdot (s_6 - s_0)\right) - \dot{m}_{liq} \cdot ((h_7 - h_0) - T_0 \cdot (s_7 - s_0)) - (\dot{m}_2 \cdot (1 - x_s) - \dot{m}_{liq}) \cdot \left((h_8 - h_0) - T_0 \cdot (s_8 - s_0)\right)$
Turbine	$\dot{E}x_{D,turbine} = \dot{m}_{turbine} \cdot \left((h_3 - h_9) - T_0 \cdot (s_3 - s_9)\right) - \dot{W}_{turbine}$

Performance assesment parameters
The second-law efficiency of the cycle is defined as:
$$\eta_{2.law} = -\frac{((h_7 - h_1) - T_1 \cdot (s_7 - s_1))}{\dot{W}_{net}}$$

The total exergy destruction ($\dot{E}x_{D,Total}$) in the system is given by:
$$\dot{E}x_{D,Total} = \dot{E}x_{D,comp} + \dot{E}x_{D,HX1} + \dot{E}x_{D,HX2} + \dot{E}x_{D,HX3} + \dot{E}x_{D,valve} + \dot{E}x_{D,sep} + \dot{E}x_{D,turbine}$$

This equation represents the summation of exergy destruction across all components of the system, including the compressor, heat exchangers, valve, separator, and turbine.

Exergy flow into the system ($\dot{E}x_F$) is expressed as the net work multiplied by -1. This indicates that the work is being supplied to the system as part of the energy balance.

Finally, the overall exergy efficiency of the system is determined as:
$$\varepsilon = 1 - \left(\frac{\dot{E}x_{D,Total}}{\dot{E}x_F}\right)$$

3. RESULTS AND DISCUSSION

Second-law efficiency ($\eta_{2.law}$) and exergy efficiency (ε), both of which are examined as functions of the parameter x_s, are used in this study to analyze the Claude cycle's performance. The effect of x_s on these efficiencies is shown graphically in Fig.2a illustrates how second-law efficiency ($\eta_{2.law}$) varies with respect to x_s. The findings show that as x_s grows, $\eta_{2.law}$ increases linearly. At x_s =0, the efficiency is roughly 0.232 at first. $\eta_{2.law}$ improves to about 0.252 as x_s approaches 0.5. Fig. 2b shows how exergy efficiency (ε) changes with x_s.The exergy efficiency begins at about 0.278 at x_s =0 and rises to about 0.305 at x_s =0.5. According to this enhancement, raising x_s results in better use of the energy resources that are accessible reducing the overall exergy destruction in the process.

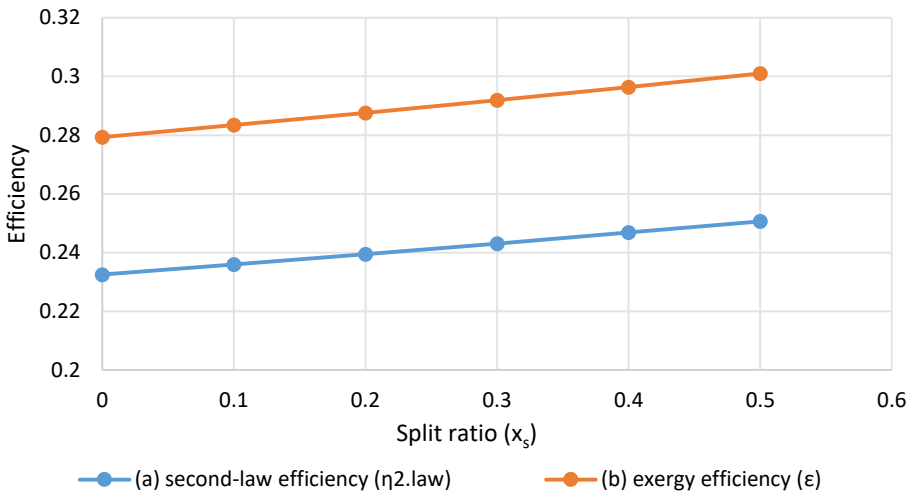

Fig. 2. The effect of x_s on (a) second-law efficiency ($\eta_{2.law}$) and (b) exergy efficiency (ε).

4. CONCLUSIONS

The damage caused by fossil fuels to the world and the increasing demand for green energy have led to a growing interest in hydrogen production. This study illustrates the thermodynamic analysis of the Claude cycle in relation to hydrogen liquefaction. Energy and exergy balances were solved and the effect of split ratio on second law efficiency and exergy efficiency was studied. A thermodynamic model was developed using Engineering Equation Solver (EES), and detailed parametric analyses were performed to explore the system's performance under various conditions. The results provide valuable insights into optimizing the hydrogen liquefaction process, offering a pathway toward more efficient and sustainable energy solutions. The main findings of this study is as follows:

- Second-law efficiency($\eta_{2.law}$) increases with the parameter x_s, showing a steady rise from approximately 0.23 to 0.252 as x_s increases.
- Exergy efficiency (ε) improves similarly, increasing from 0.275 to 0.305 with rising x_s, indicating better system performance.

REFERENCES

[1] J. Bian, J. Yang, Y. Li, Z. Chen, F. Liang, and X. Cao, “Thermodynamic and economic analysis of a novel hydrogen liquefaction process with LNG precooling and dual-pressure Brayton cycle,” Energy Convers Manag, vol. 250, no. October, p. 114904, 2021, doi: 10.1016/j.enconman.2021.114904.

[2] C. R. Baker and R. L. Shaner, “A study of the efficiency of hydrogen liquefaction,” *Int J Hydrogen Energy*, vol. 3, no. 3, pp. 321–334, 1978, doi: 10.1016/0360-3199(78)90037-X.

[3] J. H. Yang, Y. Yoon, M. Ryu, S. K. An, J. Shin, and C. J. Lee, “Integrated hydrogen liquefaction process with steam methane reforming by using liquefied natural gas cooling system,” *Appl Energy*, vol. 255, no. February, p. 113840, 2019, doi: 10.1016/j.apenergy.2019.113840.

[4] S. Krasae-In, “Optimal operation of a large-scale liquid hydrogen plant utilizing mixed fluid refrigeration system,” *Int J Hydrogen Energy*, vol. 39, no. 13, pp. 7015–7029, 2014, doi: 10.1016/j.ijhydene.2014.02.046.

Advancements and Challenges in Liquid Hydrogen Storage Tank Design for Maritime Applications: A Comprehensive Review

[1*]*Sera Ayten Çetinkaya*, [2]*S. Aykut Korkmaz*, [3]*Nuno Bimbo*, [1]*Sheida Afshan*
[1] Faculty of Engineering and Physical Sciences, University of Southampton, SO16 7QF, United Kingdom
[2] Maritime Engineering, University of Southampton, Southampton, SO16 7QF, United Kingdom
[3] School of Chemistry and Chemical Engineering, University of Southampton, Highfield Campus, Southampton, SO17 1BJ, United Kingdom
*e-mail: s.a.cetinkaya@soton.ac.uk

ABSTRACT

The maritime sector is accelerating its transition toward sustainable energy solutions in response to international regulations targeting net-zero greenhouse gas (GHG) emissions by 2050. Hydrogen has emerged as a promising clean energy carrier, particularly in liquid form, due to its high gravimetric energy density. In maritime applications, hydrogen can be used both as a fuel for ship propulsion and as cargo transported in bulk. However, the cryogenic nature of liquid hydrogen (LH_2) introduces complex storage challenges, especially in harsh maritime environments. This study presents an investigation into material selection for the design of liquefied hydrogen tanks used in maritime applications. Insulation methods, which play a critical role in LH_2 storage tanks, are examined from both passive and active perspectives. Also, other key considerations such as tank geometry, and structural integrity under extreme temperature fluctuations are examined. By addressing these factors, the study aims to support the development of safe, efficient, and scalable hydrogen storage systems that are in line with the maritime sector's decarbonisation goals by providing a comprehensive review.

Keywords: Hydrogen Storage, Liquified Hydrogen Storage, Material Selection, Maritime Applications, Insulation Methods

1. INTRODUCTION

As the maritime industry seeks to decarbonize in line with international goals, hydrogen has emerged as a key alternative fuel due to its clean combustion and high energy content on a gravimetric basis. Among its various storage forms, liquid hydrogen (LH_2) is particularly promising for long-range and large-scale marine applications because of its high volumetric density [1]. However, the cryogenic nature of LH_2, typically stored at -253°C, poses serious engineering challenges, especially in terms of insulation [2]. Maintaining hydrogen in its liquid state under dynamic marine conditions requires highly efficient thermal protection systems to mitigate boil-off gas (BoG) generation and ensure safety and efficiency [3].

The design of LH_2 containment systems must therefore integrate advanced insulation strategies that minimize heat ingress from the ambient environment. Passive insulation methods can be classified as solid-state thermal insulation and radiative thermal insulation methods, are widely used due to their effectiveness and lack of reliance on external power [3,4]. For example, Yu et al. [5] demonstrated that multi-layer insulation (MLI) combined with vapor-cooled shields (VCS) and liquid nitrogen-cooled shields (LH_2CS) can reduce heat leakage by over 80%, achieving daily evaporation rates as low as 0.002% in a 4000 m³ LH_2 tank. Similarly, Liu et al. [6] showed that forced-evaporation VCS combined with rigid polyurethane foam can reduce insulation layer thickness by nearly 60%, highlighting the potential for space-efficient and thermally effective designs in marine LH_2 transport tanks. These technical advancements are increasingly important given that insulation materials and tank designs must not only be efficient but also be compliant with international maritime safety regulations. The International Maritime Organization (IMO) , particularly through the International Code for the Construction and Equipment of Ships Carrying Liquefied Gases in Bulk (IGC Code- MSC.370(93)) and the International Code of Safety for Ships using Gases or other Low-flashpoint Fuels (IGF Code- MSC.391(95)), establishes broad safety frameworks, but these are primarily centered on LNG rather than hydrogen [7,8].

Despite these advancements, regulatory guidance tailored to LH_2 insulation in maritime environments remains limited compared to LNG. Interim guidelines such as MSC.420(97) and MSC.565(108) provide a framework for bulk carriage of LH_2 and the safety amendments of ships using fuel cell power installations released as MSC.1/Circ.1647, yet comprehensive standards for insulation systems are still evolving [9–11]. In the absence of fully mature codes, studies like those of Park et al. [12], which investigate novel vacuum insulation membranes capable of withstanding cryogenic deformation and maintaining structural integrity, offer valuable insights. Consequently, this study aims to critically examine insulation strategies for LH_2 tanks in maritime applications, with an emphasis on material selection, structural integration, and performance under harsh operational conditions.

2. MATERIAL AND METHOD

The use of LH_2 either in bunkering or in bulk transportation in maritime vessels introduces several potential hazards. Due to its colourless, odourless, and highly flammable nature, hydrogen poses unique challenges when combined with the harsh and dynamic marine environment conditions. These hazards can generally be categorised into physical, chemical, and physiological [13]. A detailed classification of these hazard types is presented in [13]. Therefore, when designing hydrogen storage tanks for maritime applications, it is essential to consider these risk factors. IMO has specified different types of tanks to ensure safety and efficiency in the storage of LNG gases used in maritime applications for bulk transportation or bunkering (Fig. 1). According to IMO's IGC, tank types can be categorized as independent tanks (type-A, type-B, type-C), membrane tanks, integral tanks, semi-membrane tanks [8]. In the IGF Code, tank types can be categorized as independent (type-A, type-B, type-C) and membrane tanks [7].

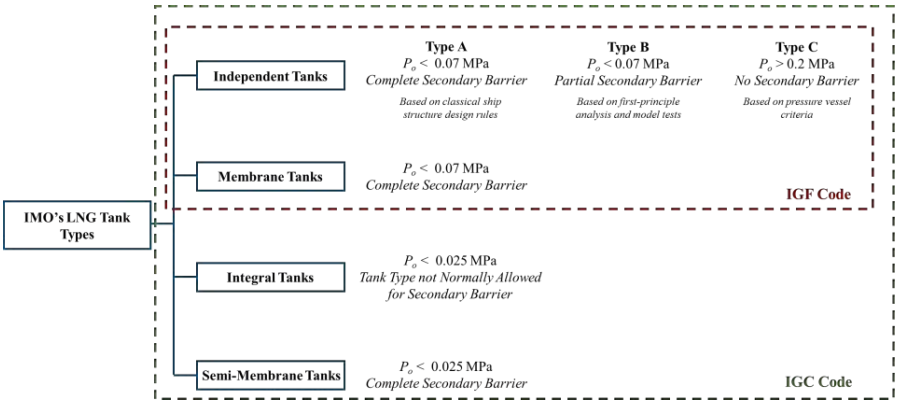

Fig. 1. Classification of the IMO's Tank Types [7,8]

To maintain cryogenic temperatures, LH_2 tanks are typically composed of three main layers: the primary barrier, vacuum space, and a secondary barrier. The primary barrier directly contains the liquid hydrogen, while the vacuum layer minimizes heat transfer by conduction, convection, and radiation. The secondary barrier, required in certain containment systems, serves to temporarily hold leaks and protect the ship's structure from extreme cold [6,12]. This multilayered configuration is standard in both spherical and cylindrical LH_2 tank designs (Fig. 2).

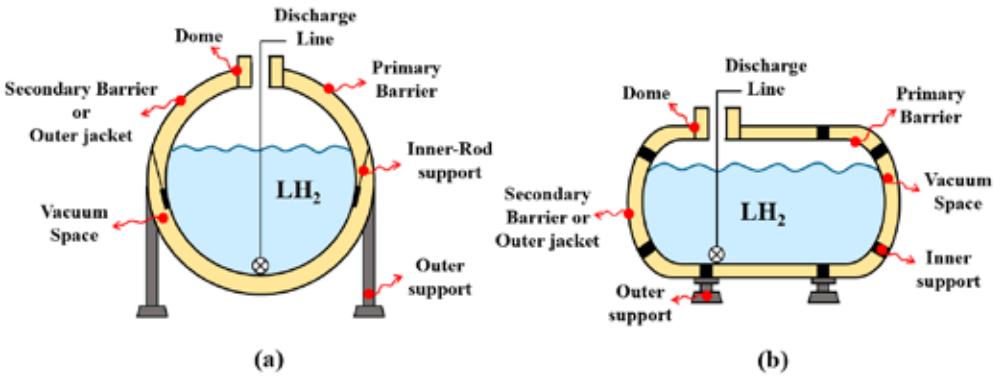

Fig. 2. Schematic of the (a) spherical, (b) cylindrical tanks

A secondary barrier is generally required when the primary barrier is not structurally integrated into the ship's hull. However, if leakage risk is low and the tank is positioned outside enclosed hull spaces, a full secondary barrier may not be necessary, partial barriers can offer localized protection. As outlined in MSC.565(108), revised interim guidelines propose a configuration where insulation is applied outside the primary barrier and inside the secondary barrier, with a dedicated gap in between to prevent condensation or solidification of hydrogen gas on the cold inner shell (Fig. 3).

Despite the improvements suggested in the IMO regulations, several studies in literature still employ type-C tanks for LH_2 storage applications. In the study by Alkhaledi et al. [14], the design focused on a large-scale LH_2 carrier named JAMILA, equipped with four massive type-C tanks (each ~70,600 m^3), yielding a total cargo capacity of 282,400 m^3 and carrying 20,000 tonnes of hydrogen at 0.5 MPa. The tanks were mechanically designed with a significant wall thickness (0.434 m aluminium with 4.4% Cu) to ensure structural integrity under pressure, while a 1 m thick polyurethane foam insulation layer limited boil-off to just 0.1% per day. The design aimed to eliminate onboard refrigeration, using boil-off

hydrogen to power the ship's propulsion system via a 50 MW combined-cycle gas turbine. The concept achieved good stability characteristics and energy efficiency, demonstrating the feasibility of large LH_2 marine transport.

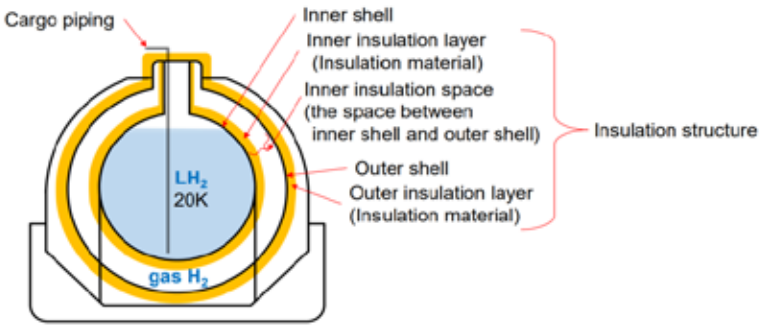

Fig. 3. Illustration of cargo containment system for hydrogen gas [10]

2.1. Insulation Methods and Material Selection in the LH_2 Tanks

Insulation methods can be classified fundamentally as passive and active insulation methods. Passive insulation methods (PIMs) can be implemented by either creating a vacuum layer on the outer surface of the LH_2 tank or by using high-performance materials, to minimise heat loss caused by thermal transfer. The most common PIM is to create a vacuum area outside the tank. The main aim of the vacuum area is minimising heat transfer resulting from convection. To support that and solid-state thermal insulation materials can be added into the vacuum area to minimise the conduction heat transfer. Solid-state thermal insulation methods can be classified as powder, foam, and fibre insulation [3]. These insulations describe the different physical forms of the insulation materials. In the absence of air or gas, conductive and convective heat transfer is minimal, and radiative heat transfer becomes predominant. To reduce the radiative heat transfer, MLI can be added in the vacuum area with or without solid-state thermal insulations methods [4].

Material selection for LH_2 tanks is a crucial part of system design, as these materials must operate reliably at very low temperatures and in direct contact with hydrogen. In addition to general cryogenic requirements, such as maintaining mechanical strength, toughness, and flexibility below -253°C, materials must also withstand specific challenges caused by hydrogen exposure such as hydrogen permeability, corrosion, thermal expansion, and most notably hydrogen embrittlement. Under this challenges, stainless steel is the most used cryogenic material [13]. Various stainless-steel alloys are developed by combining it with different elements to enhance properties such as strength, ductility, and corrosion resistance in LH_2 applications [15].

Thermal insulation material selection for LH_2 tanks in maritime environment must prioritize low thermal conductivity, cryogenic stability, and compatibility with the harsh marine environment. For powder insulation, chemical inertness, resistance to pressure and vibration, and low outgassing are key. Foam insulation should have a closed-cell structure, retain strength at cryogenic temperatures, and resist moisture and hydrogen degradation. Fibre insulation requires low density, mechanical flexibility, and vacuum compatibility. In MLI systems, reflective materials must offer high reflectivity, low emissions, and cryogenic stability, while spacer materials should minimize conduction and be lightweight, strong, and chemically compatible. Hybrid approaches, such as combining MLI with HGMs or glass fibers, show promise in reducing boil-off rates significantly [3,4]. In Table 1, several studies from literature are given for maritime vessels.

Table 3. Specification of the components in marine vessels using liquid hydrogen storage tanks

Authors	Tank Type	Insulation Method	Insulation Material	Primary Barrier Material	Secondary Barrier Material	Aim of H_2 Usage	Boil of Gas Rate
Tamura et al. [16]	Type-B (Prismatic)	N/A	N/A	N/A	Partial secondary barrier	Cargo	N/A
Moreno-Blanco et al. [17]	Cryo-compressed vessel	MLI	Metalized plastic	Aluminum lined composite	Metallic jacket	Fuel	N/A
Lee et al. [18]	C-Type	Foam	Polyurethane	N/A	N/A	Cargo	N/A
Park et al. [12]	N/A	Foam	Polyurethane	N/A	Flexible vacuum membrane	Cargo	N/A
Liu et al. [6]	Type-C	Foam, VCS	Polyurethane	AISI 316L Stainless Steel	N/A	Fuel	Heat ingress reduced by 85.86%
Li et al. [19]	N/A	MLI, VCS, VDMLI	Mylar, Dacron	N/A	N/A	N/A	Reduction by up to 50.43% (HLF)

3. CONCLUSION

This study examined the design criteria for LH_2 storage tanks in maritime applications, aiming to address gaps in the literature regarding their use onboard ships. Key focus areas included bunkering and bulk transport scenarios, insulation methods, and material selection. IMO's codes and related amendments were reviewed to identify applicable regulatory requirements, while insulation strategies were categorized as solid-state or radiative based on current literature. Although IMO does not mandate a specific tank type for LH_2, studies show that type-C tanks are commonly favored due to their effectiveness in minimizing BoG rates. As a next step, the study will explore current innovations and emerging trends in LH_2 technologies for maritime use.

REFERENCES

[1] Usman MR. Hydrogen storage methods: Review and current status. Renewable and Sustainable Energy Reviews 2022; 167:112743. https://doi.org/10.1016/j.rser.2022.112743.

[2] Shi Y. Reducing greenhouse gas emissions from international shipping: Is it time to consider market-based measures? Mar Policy 2016; 64:123–34. https://doi.org/10.1016/j.marpol.2015.11.013.

[3] Ratnakar RR, Sun Z, Balakotaiah V. Effective thermal conductivity of insulation materials for cryogenic LH2 storage tanks: A review. Int J Hydrogen Energy 2023; 48:7770–93. https://doi.org/10.1016/j.ijhydene.2022.11.130.

[4] Yin L, Yang H, Ju Y. Review on the key technologies and future development of insulation structure for liquid hydrogen storage tanks. Int J Hydrogen Energy 2024; 57:1302–15. https://doi.org/10.1016/j.ijhydene.2024.01.093.

[5] Yu Y, Xie F, Zhu M, Yu S, Li Y. Design and Optimization of the Insulation Performance of a 4000 m3 Liquid Hydrogen Spherical Tank. Processes 2023;11. https://doi.org/10.3390/pr11061778.

[6] Liu Y, Zhou P, Jeong B, Wang H. Design and optimization of a type-C tank for liquid hydrogen marine transport. Int J Hydrogen Energy 2023; 48:34885–96. https://doi.org/10.1016/j.ijhydene.2023.05.102.

[7] Maritime Organization I. Resolution MSC.391(95) (adopted on 11 June 2015) Adoption of the International Code of Safety for Ships Using Gases or Other Low-Flashpoint Fuels (IGF CODE). 2016.

[8] Maritime Organization I. Resolution MSC.370(93) (adopted on 22 May 2014) Amendments to The International Code for the Construction and Equipment of Ships Carrying Liquefied Gases in Bulk (IGC CODE). 2015.

[9] Maritime Organization I. Resolution MSC.420(97) (adopted on 25 November 2016) Interim Recommendations for Carriage of Liquefied Hydrogen in Bulk. n.d.

[10] Annex 20 Resolution MSC.565(108) (adopted on 24 May 2024) Revised Interim Recommendations for Carriage of Liquefied Hydrogen in Bulk. n.d.

[11] Annex Interim Guidelines for the Safety of Ships Using Fuel Cell Power Installations. N.d.

[12] Park H, Kim J, Bergan PG, Chang D. Structural design of flexible vacuum insulation system for large-scale LH2 storage. Int J Hydrogen Energy 2022; 47:39179–92. https://doi.org/10.1016/j.ijhydene.2022.09.063.

[13] Wang Z, Wang Y, Afshan S, Hjalmarsson J. A review of metallic tanks for H2 storage with a view to application in future green shipping. Int J Hydrogen Energy 2021; 46:6151–79. https://doi.org/10.1016/j.ijhydene.2020.11.168.

[14] Alkhaledi AN, Sampath S, Pilidis P. A hydrogen fuelled LH2 tanker ship design. Ships and Offshore Structures 2022; 17:1555–64. https://doi.org/10.1080/17445302.2021.1935626.

[15] Kim M-S, Chun KW. A Comprehensive Review on Material Compatibility and Safety Standards for Liquid Hydrogen Cargo and Fuel Containment Systems in Marine Applications. J Mar Sci Eng 2023; 11:1927. https://doi.org/10.3390/jmse11101927.

[16] Tamura H, Otsuka H, Ishida T, Miyazaki S. New LPG Carrier Adopting Highly Reliable Cargo Tank-IMO Tank Type B. vol. 50. 2013.

[17] Moreno-Blanco JC, Elizalde-Blancas F, Gallegos-Muñoz A, Aceves SM. The potential for avoiding hydrogen release from cryogenic pressure vessels after vacuum insulation failure. Int J Hydrogen Energy 2018; 43:8170–8. https://doi.org/10.1016/j.ijhydene.2018.02.150.

[18] Lee J-H, Hwang S-Y, Lee S-J, Lee JH. Numerical Study of Heat Flux and BOG in C-Type Liquefied Hydrogen Tank under Sloshing Excitation at the Saturated State. Journal of the Computational Structural Engineering Institute of Korea 2022; 35:299–308. https://doi.org/10.7734/coseik.2022.35.5.299.

[19] Li K, Wen J, Xin B. Optimization investigation on variable-density multi-layer insulation coupled with vapor-cooled shield for liquid hydrogen tank based on sequential quadratic programming. Appl Therm Eng 2024;252. https://doi.org/10.1016/j.applthermaleng.2024.123666.

AN ALTERNATIVE FUEL FOR AFTERBURNER: ENERGY AND ECONOMIC COMPARISON FOR NH3/H2 AND JP-8

[1]Emine OĞUR, [2]Ali KOÇ, [3*]Hüseyin YAĞLI, [4]Özkan KÖSE, [5]Yıldız KOÇ
[1] Iskenderun Technical University, Institute of Graduate Studies, Department of Mechanical Engineering 31200 Iskenderun, Hatay, Türkiye
[2] Iskenderun Technical University, Engineering Faculty, Department of Mechanical Engineering 31200 Iskenderun, Hatay, Türkiye
[3*] Gaziantep University, Engineering Faculty, Department of Mechanical Engineering 27310 Şehitkamil, Gaziantep, Turkiye
[4] Iskenderun Technical University, Engineering Faculty, Department of Mechanical Engineering 31200 Iskenderun, Hatay, Türkiye
[5] Iskenderun Technical University, Engineering Faculty, Department of Mechanical Engineering 31200 Iskenderun, Hatay, Türkiye
*Corresponding author e-mail: yagli@gantep.edu.tr

ABSTRACT
In this article, the F110-GE129 afterburning turbofan engine was modelled, and its thermodynamic performance was examined by considering that NH_3/H_2 and JP8 fuels perform under identical operating conditions. The thrust force was calculated as 129 kN in JP8 fuel and 116 kN in NH_3/H_2 fuel. The energy efficiency and thrust efficiency of the afterburning turbofan engine were calculated as 27.03% and 29.70%, respectively, when using JP8 fuel and 26.54% and 28.98%, respectively, when using NH_3/H_2 fuel.

1. INTRODUCTION
The bypass turbofan engine is widely used in civil and military aviation. These engines' working system produces high thrust/power by passing the air fluid drawn from the fan through the fan channel designed around the engine at a certain bypass ratio at high speed. Thus, the turbofan engine produces high thrust force with low fuel consumption. Turbofan engines used in the military field need high and fast thrust force in short distances and it is desired to do this with high thermodynamic performance. However, values below the desired engine performance can be obtained. Increasing the thrust force and power in a turbofan engine is difficult and complex. Because in military aircraft, it is desired to increase the speed to supersonic speeds. In this case, high bypass ratios are not used in these engines because they will create friction [1]. However, engineers and airline companies have done many studies to increase this data. One of these is to add an afterburner to a turbofan engine.

This paper aims to investigate both the thermodynamic performance of the afterburning turbofan engine and the thermodynamic feasibility of a new fuel formed by blending environmentally friendly fuels such as ammonia and hydrogen fuels to reduce emissions.

2. SYSTEM DESCRIPTION
The GE-F110 afterburning turbofan engine is a low bypass, two shaft, and mixed flow fighter jet engine. The turbofan engine consists of a 3-stage fan, a 9-stage high-pressure compressor, The schematic diagram of the afterburning turbofan engine used in military aircraft is presented in Fig. 1.

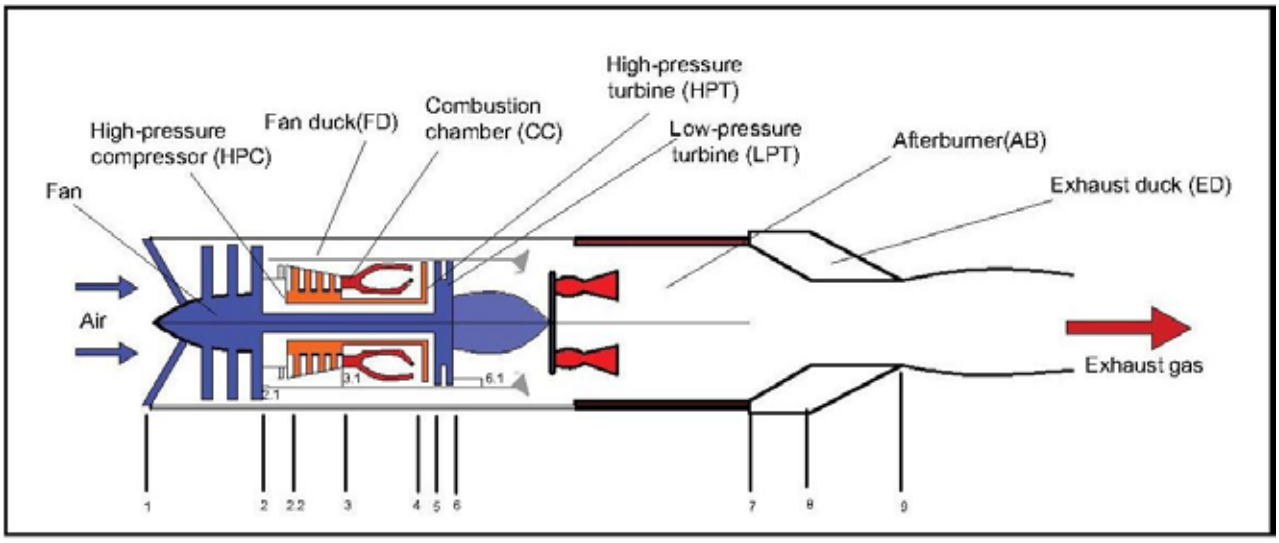

Fig. 1. Simplified version of the F110-GE-129 turbofan engine.

3. PARAMETRIC EQUATIONS FOR AN AFTERBURNING TURBOFAN ENGINE

In this section, a mathematical model has been developed to determine the performance parameters of the afterburning turbofan engine, including specific fuel consumption, thrust, thrust efficiency, thermal energy, and thermal efficiency. These equations are expressed as follows.

Thrust of an afterburning turbofan engine [3,4];

$$ET = [(\dot{m}_9 V_9) + (A_{ED} P_9)] - [(\dot{m}_1 V_1) + (A_{fan} P_1)] \quad (1)$$

Afterburning turbofan engine thrust power [5];

$$\dot{W}_p = ETV_1 \quad (2)$$

Thrust efficiency of afterburning turbofan engine [2,6];

$$\eta_{ET} = \frac{\dot{W}_p}{\frac{V_9^2}{2}\dot{m}_9 - \frac{V_1^2}{2}\dot{m}_1} \quad (3)$$

Thermal efficiency of afterburning turbofan engine [2, 6];

$$\eta_{th} = \frac{\frac{V_9^2}{2}\dot{m}_9 - \frac{V_1^2}{2}\dot{m}_1}{\dot{Q}_{in}} \quad (4)$$

3.1. Hydrogen-Ammonia Mixture Fuel

For this reason, the ammonia/hydrogen mixture has been investigated in numerous studies as an alternative fuel. The applicability of ammonia/hydrogen mixture as a fuel to eliminate the properties of ammonia gas such as its high autoignition temperature, low laminar burning speed and the presence of nitrogen that is harmful to the environment is supported by studies obtained from the literature.

4. RESULTS AND DISCUSSIONS

In this study, performance analysis is compared using different fuels in the afterburning turbofan engine. Operating conditions are assumed to be the same in the analyses. The calculated thrust force and specific fuel consumption of an afterburning turbofan engine using different fuels are shown in Fig. 2.

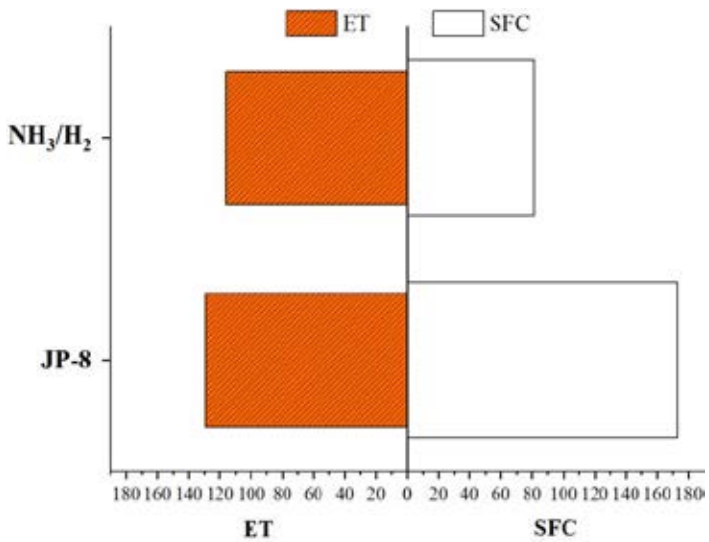

Fig. 2. Thrust force and specific fuel consumption values of afterburning turbofan engine.

Thrust is an important performance parameter in afterburning turbofan engines. As given in Figure 2, the thrust of the afterburning turbofan engine studied in this paper is 129 kN. However, to produce this thrust force, the SFC value is high with 173.37 kg/kN.h. In this study, the thrust force and SFC value are calculated assuming that the NH_3/H_2 mixture fuel, as an alternative fuel to reduce high fuel consumption, operates under the same conditions. Accordingly, the thrust force is obtained as 116 kN and the SFC value as 81.64 kg/kN.h. The thrust force is 10.1% lower compared to JP8 fuel.

5. CONCLUSION

In this essay, the results of the thermodynamic performance analysis made with the data obtained from the literature of the F110-GE129 turbofan engine are compared with the analysis results of the NH_3/H_2 fuel. The inferences from the analysis data are as follows:

- While the thrust of the afterburning turbofan engine using JP8 fuel is 129 kN, this value is obtained as 116 kN when NH_3/H_2 fuel is used.
- The SFC value of the afterburning turbofan engine is 173.37 kg/kN.h when using JP8 fuel, while this value decreased to 81.64 kg/kN.h when using NH_3/H_2 fuel.
- The thrust efficiency and thrust power of the afterburning turbofan engine are worked out as 17458.55 kW and 27.03% in JP8 fuel, and 15646.18 kW and 26.53% in using NH_3/H_2 fuel, respectively.

REFERENCES

1. Yin, Feijia & Gangoli Rao, Arvind. (2017). Off-Design Performance of an Interstage Turbine Burner Turbofan Engine. *Journal of Engineering for Gas Turbines and Power. 139. 10.1115/1.4035821.*
2. 5 Haider, BA & Davidovic, Nikola & Durrani, Naveed. (2011). Parametric Analysis of Expendable type Single-Spool Turbojet Engine with a Short Afterburner. 10.2514/6.2011-574.
3. 9 Balli, Ozgur. (2017). Exergetic, Exergoeconomic, Sustainability and Environmental Damage Cost Analyses of J85 Turbojet Engine with Afterburner. *International Journal of Turbo & Jet-Engines. 37. 10.1515/tjj-2017-0019.*
4. 20 Akdeniz, H. Yalcin & Balli, Ozgur. (2021). Impact of different fuel usages on thermodynamic performances of a high bypass turbofan engine used in commercial aircraft. *Energy. 238. 121745. 10.1016/j.energy.2021.121745.*
5. 21 Balli, Ozgur. (2017). Exergy modeling for evaluating sustainability level of a high by-pass turbofan engine used on commercial aircrafts. Applied Thermal Engineering. 123. 10.1016/j.applthermaleng.2017.05.068.
6. 22 Aydın H. Ticari uçakların ekserjetik sürdürülebilirlik indikatörlerinin geliştirilmesi. Anadolu University Institute of Science Department of Civil Aviation. April 2012.

DEVELOPMENT AND ASSESSMENT OF A UNIQUE HYDROGEN GENERATOR WITH ZnS PHOTOCATALYST

[1*] *Mehmet Gursoy, Ibrahim Dincer.*
[1]*Clean Energy Research Laboratory (CERL), FEAS, Ontario Tech University, Oshawa, Ontario, L1H 7K4, Canada*

E-mail: mehmet.gursoy@ontariotechu.net

ABSTRACT
Solar-powered water splitting offers various benefits for sustainable energy consumption. This study focuses on developing a new photo-catalytic-conventional hybrid electrolysis reactor to produce sustainable hydrogen and improve system efficiency. ZnS is commonly utilized in photocatalytic water breakdown for hydrogen production due to its quick electron-hole pair creation and inexpensive cost. ZnS catalyst concentration is 1% (w/v). At 800 W/m^2 and 25-55 °C, the maximum hydrogen generation rate from ZnS suspension was 0.24 µg/s at 40 °C, indicating potential photo-corrosion or oxidation in aqueous environments at high temperatures. Measured Cl_2 gas production on the anode side was found to be 2.95 g/h. The overall hydrogen generation rate for the hybrid reactor was obtained to be 0.74 µg/s.

Keywords: Solar energy, hydrogen, hybridized water electrolysis, photocatalytic water splitting

1. INTRODUCTION

As the worldwide energy sector undergoes rapid transformation in response to climate change and the demand for sustainability, hydrogen has emerged as an important factor in the transition away from fossil fuels. In contrast to conventional energy sources, hydrogen may serve as a clean, efficient, and adaptable energy carrier that offers a path to decarbonizing sectors that are challenging to electrify directly, including heavy industrial, aircraft, and long-haul transportation.

Photocatalytic water splitting is a promising sustainable hydrogen generation technology. However, it remains in its early stages of development. A photocatalytic system harnesses solar energy to divide water in an individual semiconductor cell. The photo-catalyst in the solution should have excellent stability and cost-effectiveness for large-scale use. Zinc sulphide (ZnS) and cadmium sulphide are examples of efficient and cost-effective photo-catalysts [1]. This research focuses on the performance of a solar reactor for splitting heterogeneous water. The photochemical/electrocatalytic-conventional hybridized reactor combines solar technology with electrolysis to produce hydrogen more efficiently.

Fig.1. A schematic of the proposed system's layout

A study by Baniasadi (2012) [2] conducted a study on an experimental apparatus designed and built to simulate processes in photo-catalytic and electro-catalytic water-splitting systems. The study utilized ZnS and CdS photo-catalysts to simultaneously enhance quantum yield and exergy efficiency. The production rate has increased by nearly 30% relative to the performance of ZnS. Han et al. (2025) [3] developed spherical ZnS@ZnO heterojunctions in situ by a simple one-step hydrothermal growing procedure. The impact of ZnO content on the H_2 generation rate of the composite was examined. ZOS-4, the composite formed after 4 hours of reaction, has the greatest photocatalytic hydrogen generation rate of 18.81 mmol $h^{-1}g^{-1}$.

ZnS is a semiconductor with a wide bandgap (~3.6 eV) that is renowned for its robust photocatalytic activity when exposed to ultraviolet (UV) radiation. When dispersed in an aqueous solution, ZnS particulates can effectively absorb UV light to generate electron-hole pairs, thereby triggering the redox reactions required for hydrogen evolution when used in suspension form. The holes oxidize water or sacrificial agents (e.g., methanol or sodium sulphide) to maintain charge neutrality, while the photogenerated electrons reduce water or protons (H^+) to produce hydrogen gas (H_2). Nevertheless, the rapid recombination of charge carriers and the reliance on UV light, which accounts for a mere fraction of the solar spectrum, restrict the potential of ZnS.

The photocatalytic suspension system can be incorporated with a conventional electrolysis cell to resolve these challenges and improve overall efficiency, resulting in a hybrid configuration. The electrolyzer's external voltage is partially reduced by the photocatalytic activity of ZnS in this configuration. This reduces the total energy input and enables the system to continue hydrogen production in low-light or non-illuminated conditions, as the conventional cell can continue operation using electrical energy from renewable or grid sources. The hybrid approach is a promising solution for scalable and continuous green hydrogen production, as it also provides extended functionality throughout the day, enhanced hydrogen yield, and greater operational flexibility.

2. SYSTEM DESCRIPTION

The hybrid hydrogen reactor is depicted in Figure 1 in operation, illuminated by the solar simulator with ZnS suspension. The process of photocatalytic hydrogen production involves the illumination of ZnS, which is suspended in basic solutions containing sulphide ions under a solar irradiation level (800 W/m^2).

The reactor is composed of two distinct electrolysis cells: the conventional cell and the photocatalytic cell. The primary components of the PC are an anode, a cation exchange membrane, and a photocathode. The common anode for both cells is the critical component of the investigation. The bipolar plate was selected as the anode electrode type due to the presence of two active surfaces during the electrolysis process. Three distinct electrolytes are employed: $NaCl_{sat}$, ZnS suspension, and KOH. Furthermore, the membrane facilitates the selective passage of Na^+ ions from the anode to the cathode partition, thereby neutralizing the presence of OH^- ions in the cathode compartment. To facilitate the irradiation of the photocathode, the reactor is equipped with transparent windows made of acrylic glass. The following equation may characterize the chemical process of hydrogen production in the hybrid electrolyzer:

For the Photocatalytic cell:

$$Overall\ reaction = 2H_2O + 2Cl^- \xrightarrow{hv} 2H_2 + 2OH^- + Cl_2 \quad (1)$$

$$Anode = 2Cl^- \rightarrow Cl_2 + 2e^- \quad (2)$$

$$Photocathode = 2H_2O + 2e^- \rightarrow H_2 + 2OH^- \quad (3)$$

For the conventional cell:

$$Overall\ reaction = 2H_2O \rightarrow 2H_2 + O_2 \quad (4)$$

$$Anode = 2H_2O \rightarrow O_2 + 4OH^-_{aq} + 4e^- \quad (5)$$

$$Cathode = 4OH^-_{aq} + 4e^- \rightarrow 2H_2 + 2H_2O \quad (6)$$

The following equations are used to compute comprehensive energy and exergy efficiencies of the hybrid system:

$$\eta_{overall} = \frac{\dot{m}_{Cl_2} h_{Cl_2} + \dot{m}_{PC} LHV_{H_2} + \dot{m}_{Con} LHV_{H_2}}{\dot{Q}_{in} + \dot{W}_{in,total}} \quad (7)$$

and

$$\Psi_{overall} = \frac{\dot{m}_{Cl_2} ex_{Cl_2} + \dot{m}_{PC}\left(ex_{PC} + ex^{ch}_{H_2}\right) + \dot{m}_{Con}(ex_{Con} + ex^{ch}_{H_2})}{Ex^{\dot{Q}}{}_{in} + W_{in,total}} \quad (8)$$

3. RESULTS AND DISCUSSIONS

The catalyst concentration is determined to be 1% (w/v) of ZnS. An increased electron concentration and improved performance under elevated solar radiation conditions are the result of a greater number of photons within the band gap energy of ZnS being accessible per unit of time. The impact of ZnS inclusion on hydrogen production in the PEC cell under high solar intensity at various operational temperatures is illustrated in Figure 2. An average standard deviation of 0.001 µg/s for the PEC cell is achieved by conducting each experimental trial three times at three distinct operating temperatures (25, 40, and 55 °C) under an 800 W/m^2 solar radiation intensity and a mass flow rate of 35 mL/min.

Operating at a temperature of 40°C, the maximum hydrogen generation rate was 0.24 µg/s. The quantity of active electrons available for hydrogen generation is reduced as a result of the faster recombination of electron-hole pairs at higher temperatures. Nevertheless, ZnS may be subjected to photo-corrosion or oxidation in an aqueous

environment at elevated temperatures, resulting in a decrease in active sites. The dissolution of sulphur or the formation of Zn $(OH)^{-2}$ layers may obstruct active sites, thereby reducing the catalytic effectiveness. The quantity of hydrogen produced at 55°C is less than that at 40°C. As a result, the efficiency of the system experiences a significant decrease as the operational temperature exceeds 50°C because of the synergistic effects of recombination, catalyst degradation, and bubble formation.

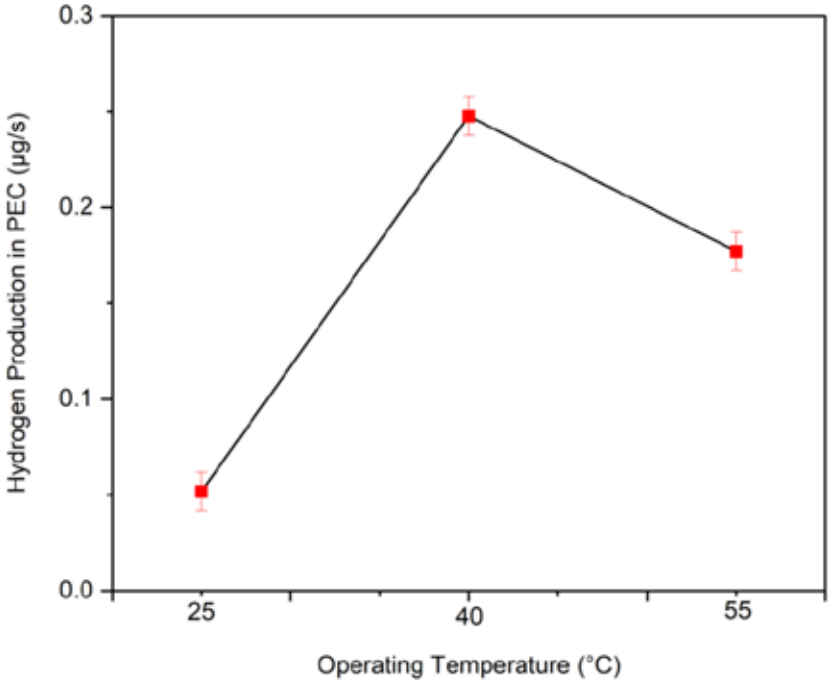

Fig. 2. The impact of ZnS suspension on hydrogen production in the PEC cell under high solar intensity at various operational temperatures.

The Cl_2 gas generation rate measured using a U-manometer was 2.95 g/h, whereas the hydrogen synthesis rate was determined to be 0.52 µg/s at 40°C. So, the overall hydrogen production rate in the hybrid reactor was found to be 0.74 µg/s.

4. CONCLUSIONS

The hybrid system offers several benefits, including generating significantly more hydrogen and operating without solar radiation. The maximal hydrogen generation rate was 0.24 µg/s when the PEC cell was operated at a temperature of 40°C and under 800 W/m^2. The hydrogen was produced using a 1% (w/v) ZnS suspension. The hydrogen synthesis rate was determined to be 0.52 µg/s at 40°C, while the Cl_2 gas generation rate was 2.95 g/h as measured by a U-manometer. Therefore, the overall hydrogen production rate of the hybrid reactor was determined to be 0.74 µg/s.

ACKNOWLEDGMENT

This publication was made possible by the NPRP grant (NPRP12S-0123-190011) from the Qatar National Research Fund (a member of Qatar Foundation). The findings achieved herein are solely the responsibility of the authors.

REFERENCES

[1] Reber, Jean Francois, and Kurt Meier. 1984. “Photochemical Production of Hydrogen with Zinc Sulfide Suspensions.” The Journal of Physical Chemistry 88 (24): 5903–13. https://doi.org/10.1021/j150668a032.

[2] Baniasadi, Ehsan. 2012. “Development of a New Hybrid Photochemical/Electrocatalytic Water Splitting Reactor for Hydrogen Production: Design, Analysis and Experiments.” Dincer, Ibrahim.

[3]Han, Shanshan, Qiyun Mao, Meijing Guo, Jinxu Feng, Yanyan Xu, and Yaqiu Sun. 2025. “One-Step Construction of ZnS@ZnO Photocatalysts with Improved Photocatalytic Hydrogen Generation Performance.” Ceramics International 51 (5): 6422–29. https://doi.org/10.1016/j.ceramint.2024.12.086.

NOVEL CYLINDRICAL ELECTROLYSIS SYSTEM WITH COPPER-COATED ELECTRODES FOR ENHANCED HYDROGEN PRODUCTION

*Esin Karatas Oguz and Ibrahim Dincer.
Clean Energy Research Laboratory (CERL), FEAS, Ontario Tech University, Oshawa, Ontario, L1H 7K4, Canada
*E-mail: esin.karatasoguz@ontariotechu.net

ABSTRACT
Electrolysis is a process that separates water into hydrogen and oxygen using an electric current. This study examines the effect of electrode surface area on hydrogen production in a cylindrical electrolysis system with copper-coated cathodes under a 3 V applied voltage. The experiments were conducted with six different electrode surface areas, and the highest hydrogen production (~42 mg) was observed at X3. After this point, production decreased, possibly due to gas accumulation or ion transfer limitations. These results highlight the importance of electrode surface optimization for improving hydrogen generation efficiency.

Keywords: Hydrogen, Coated Electrode, Electrolysis.

1. INTRODUCTION
Hydrogen generation via electrolysis occurs by applying an electric current to an electrolyte solution, causing water to split into hydrogen and oxygen gases [1]. The efficiency of this process is influenced by electrode materials, design, and operational conditions. Copper-coated electrodes are commonly used due to their excellent electrical conductivity, durability, and catalytic properties, making them beneficial for enhancing electrolysis efficiency.
A cylindrical electrode arrangement helps improve mass transfer, ensures even current distribution, and minimizes energy losses, ultimately increasing hydrogen output [2]. In electrolysis, hydrogen is generated at the cathode, where positively charged ions gain electrons, while oxygen is released at the anode. Optimizing the electrode surface area and configuration plays a key role in improving performance, offering a scalable solution for hydrogen production [3]. In this study, a new cylindrical electrolysis is developed to employ various copper-coated electrodes tested under various operating conditions for improved hydrogen production rates.

2. SYSTEM DESCRIPTION
The electrolysis reactor in this study features a cylindrical electrode design, where the outer electrode functions as the cathode and the inner electrode serves as the anode. The copper-coated cathode facilitates electron flow, improving hydrogen generation efficiency. A uniform gap between the electrodes ensures smooth ion movement within the electrolyte, reducing resistance and enhancing overall performance. When an external power source supplies direct current to the system, the electrolysis process begins. At the cathode, water molecules undergo reduction, producing hydrogen gas, while oxidation at the anode results in oxygen gas release. The cylindrical structure maximizes electrode surface utilization and supports stable gas bubble detachment, improving system stability and efficiency.

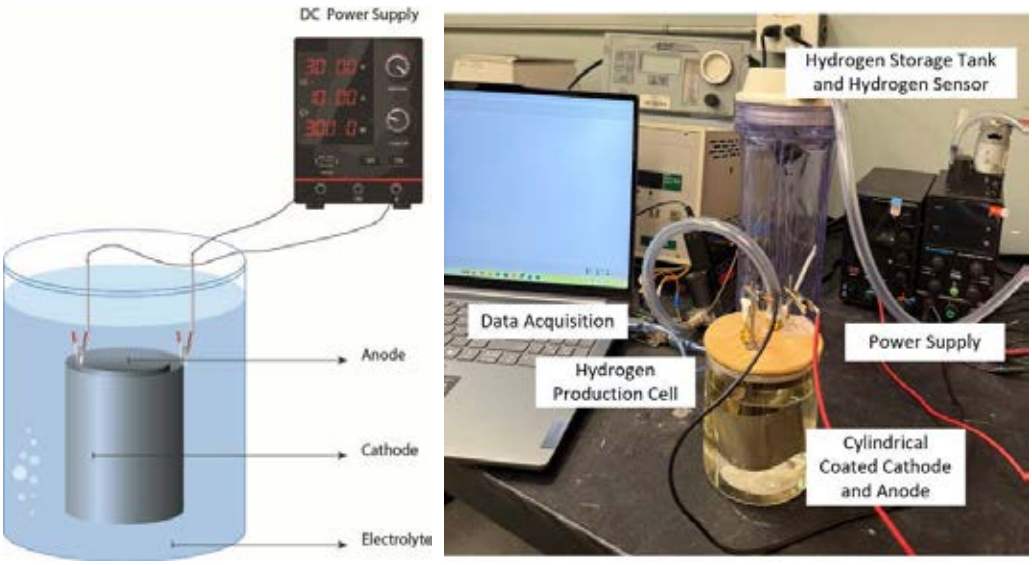

a) b)

Fig. 1. Electrolysis Reactor with Cylindrical Electrodes
a) Novel structure of the Electrolysis Reactor; b) The present Electrolysis Reactor

The electrolysis reactions occurring in the system are as follows:

Overall Reaction:
$2H_2O_{(l)} \rightarrow 2H_{2(g)} + O_{2(g)}$

Anode Reaction:
$2H_2O_{(l)} \rightarrow O_{2(g)} + 4H^+ + 4e^-$

Cathode Reaction:
$4H^+ + 4e^- \rightarrow 2H_{2(g)}$

3. RESULTS AND DISCUSSION

Fig. 2 shows the relationship between electrode surface area and hydrogen production at 3V. Initially, as the surface area increases, hydrogen production also rises, reaching its highest level (~42 mg) at X3. This suggests that a larger surface area enhances electrochemical activity. Beyond X3, production decreases at X4 and then increases slightly at X5 and X6, though it does not surpass the peak at X3. The decline after X3 may result from factors such as gas accumulation on the surface or changes in ion flow. Overall, the trend indicates that hydrogen production does not continuously increase with surface area but instead reaches an optimal level before stabilizing.

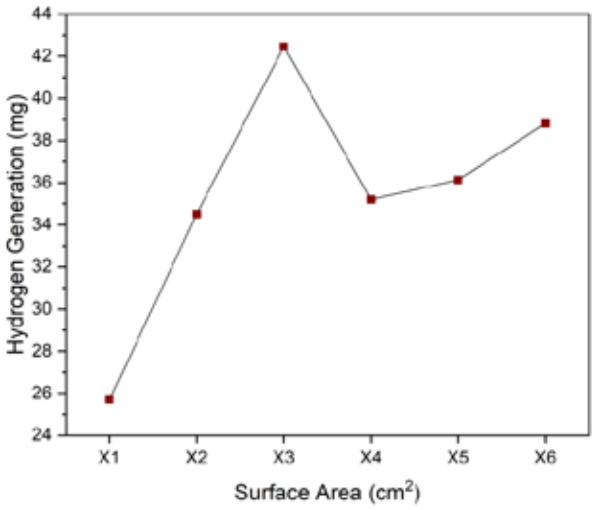

Fig. 2. Effect of Electrode Surface Area on Hydrogen Production at 3V (X1:80 cm^2, X2:130 cm^2, X3: 180 cm^2, X4: 230 cm^2, X5: 280 cm^2 and X6: 330 cm^2)

4. CONCLUSIONS

The study results show that electrode surface area plays a key role in hydrogen production. Hydrogen generation increases as surface area expands, reaching its highest level at X3 (~42 mg). After this point, production declines and varies, which may be influenced by factors such as gas buildup on the electrode, changes in ion movement, or variations in electrical resistance. These findings suggest that while a larger surface generally improves efficiency, an optimal level exists beyond which performance may decrease. Adjusting electrode design and operating conditions could help improve hydrogen generation in future applications.

ACKNOWLEDGMENT

This publication was made possible by the NPRP grant (NPRP12S-0123-190011) from the Qatar National Research Fund (a member of Qatar Foundation). The findings achieved herein are solely the responsibility of the authors.

REFERENCES

[1] Grigoriev, S. A., Fateev, V. N., Bessarabov, D. G., & Millet, P. (2020). Current status, research trends, and challenges in water electrolysis science and technology. *International Journal of Hydrogen Energy, 45*(51), 26036–26058.
[2] Dahbi, S., Aziz, A., Yahyaoui, S., Blaacha, J., & Saldine, K. (2024). The effect of the electrodes shape in water electrolysis on the production of hydrogen. *International Journal of Hydrogen Energy, 84*, 909–914.
[3] Nagai, N., Takeuchi, M., Kimura, T., & Oka, T. (2003). Existence of optimum space between electrodes on hydrogen production by water electrolysis. *International Journal of Hydrogen Energy, 28*(1), 35–41.

ELECTROLYSIS-BASED HYDROGEN PRODUCTION USING COAXIAL CYLINDRICAL ELECTRODES WITH A SCRUBBER-WIRE CATHODE

[1*] *Dogan Erdemir*, [1] *Aysegul Yagmur Goren Kara*, [1] *Ibrahim Dincer*
[1] Ontario Tech University, Clean Energy Research Laboratory, Oshawa, Ontario, L1G 0C5, Canada
* Corresponding author e-mail: dogan.erdemir@ontariotechu.ca and dogan.erdemir@yildiz.edu.tr

ABSTRACT
This study investigates the efficiency of hydrogen production via alkaline electrolysis using coaxial cylindrical electrodes with a scrubber-wire cathode. A three-dimensional (3D) cathode structure composed of 316 steel wire is utilized, with the cathode mass varied between 2g and 4g while maintaining a constant volume. The primary objective is to assess the impact of cathode mass on hydrogen production rate and energy efficiency. The experimental results indicate that while the hydrogen production rate for both configurations followed similar trends, the total hydrogen production is higher for the 2g cathode (5.02 mg) compared to the 4g cathode (2.35 mg). Furthermore, the energy efficiency for the 2g cathode reached 78.3%, significantly surpassing the 69.6% efficiency observed for the 4g cathode. The reduced efficiency of the 4g cathode is attributed to increased ohmic losses and bubble coalescence, which hinder mass transport. These findings highlight the importance of optimizing cathode mass in electrolysis systems to balance hydrogen production rate and energy consumption, ultimately enhancing the economic feasibility of hydrogen generation.

Keywords: Hydrogen; hydrogen production; alkaline electrolysis, 3D electrode

1. INTRODUCTION

Hydrogen has emerged as a promising energy carrier in the global pursuit of sustainable and clean energy solutions, offering a versatile means to decarbonize all sectors, including transportation, industrial manufacturing, power generation, and residential applications. Although hydrogen is the most abundant element in the universe, it is rarely found on Earth in its molecular form (H_2) for direct use, as it is typically bound in compounds like water or hydrocarbons, with rare exceptions such as underground hydrogen deposits. Hydrogen's potential lies in its ability to store and deliver energy with zero carbon emissions when produced using renewable resources [1]. The challenge of producing hydrogen efficiently, economically, and sustainably remains a significant obstacle to its widespread adoption.

In electrolysis processes, the cost of the cathode material, electrochemical characteristics, and specific surface area all contributed to its effective hydrogen recovery for use [2]. Due to their high electrical conductivity, biocompatibility, and hydrogen evaluation reaction potential, a variety of metal-catalyst electrodes, including Pt, stainless steel, nickel alloys, tungsten carbide, MoS_2, and iron, have been utilized for water electrolysis in the last 10 years [3]. Moreover, several geometries are used as cathode electrodes such as plates, rods, brush, felt, 3D printed electrodes, and foam [4]. Coaxial electrode configuration for water electrolysis can be a significant alternative to manage the gas evolution and electrolyte circulation inside the cell [5]. However, among these electrode types, plate and rod electrodes often suffer from limited surface area, reducing reaction efficiency. Brush and felt electrodes, while offering higher surface area, may experience structural degradation over time and exhibit non-uniform current distribution. 3D-printed electrodes, though customizable, can be costly and may have material compatibility issues in harsh electrolytic environments, while foam electrodes, despite their porous nature, often face challenges related to mechanical stability and potential clogging.

Therefore, there is a critical need for cost-effective and three-dimensional electrode materials that enhance hydrogen production efficiency while maintaining durability and scalability. In this regard, the use of a scrubber-wire cathode in electrolysis-based hydrogen production offers several potential advantages. Its high surface area-to-volume ratio enhances electrochemical activity, promoting increased hydrogen evolution reaction efficiency. The interconnected wire structure facilitates improved mass transfer, reducing diffusion limitations and ensuring uniform current distribution. Additionally, the open and porous design minimizes gas bubble accumulation, thereby decreasing ohmic resistance and improving overall system performance. Compared to conventional cathode materials, scrubber-wire electrodes are typically cost-effective, easily scalable, and mechanically robust, making them a promising alternative for sustainable and high-efficiency hydrogen production.

In closing, this paper experimentally explores the use of wire-mesh-type three-dimensional electrodes in an alkaline environment. The effect of various design and operating conditions are tested. The hydrogen production rate and energy efficiency of the electrolysis process are used for performance assessment.

2. MATERIALS AND METHODS

This study employs a concentric electrode configuration in the electrolysis cell, comprising a cylindrical anode, separator, and three-dimensional cathode. 316 anealled steel sheet is used as the anode material. The 3D electrode (cathode) is produced from 316 stainless steel pads. The amount of the cathode material is parametrically studied to be 2 and 4 g, while keeping its volume constant. Thus, the effect of the electrode porosity is investigated parametrically. A DC power supply is used for power input for the electrolysis cell. A thermocouple (Vernier stainless steel temperature probe, ±0.2°C) and conductivity sensor (Vernier conductivity sensor, ±4% µS/cm) are placed inside the electrolysis cell. To measure the

electricity current flows through the electrodes, a Vernier current probe (±0.31 mA) is included in the experimental setup. An electrochemical hydrogen sensor (±1 ppm) has been used for measuring the hydrogen production rate. A vacuum pump is installed in the setup to collect the production gases and send them to the collection vessel. A fan is used to create a uniform gas mixture to detect hydrogen. Vernier LabQuest and Arduino UNO are used for data logging. The data is recorded every second. The experiments are carried out for 30 minutes. Each experiment is repeated three times without changing the electrolyte solution. After each set of experiments, the KOH solution is replaced with a new one. The conductivity of the 2 M KOH solution varied from 320.1 to 324.2 μS/cm during the experiments. Also, no significant change in electrolyte temperature is observed.

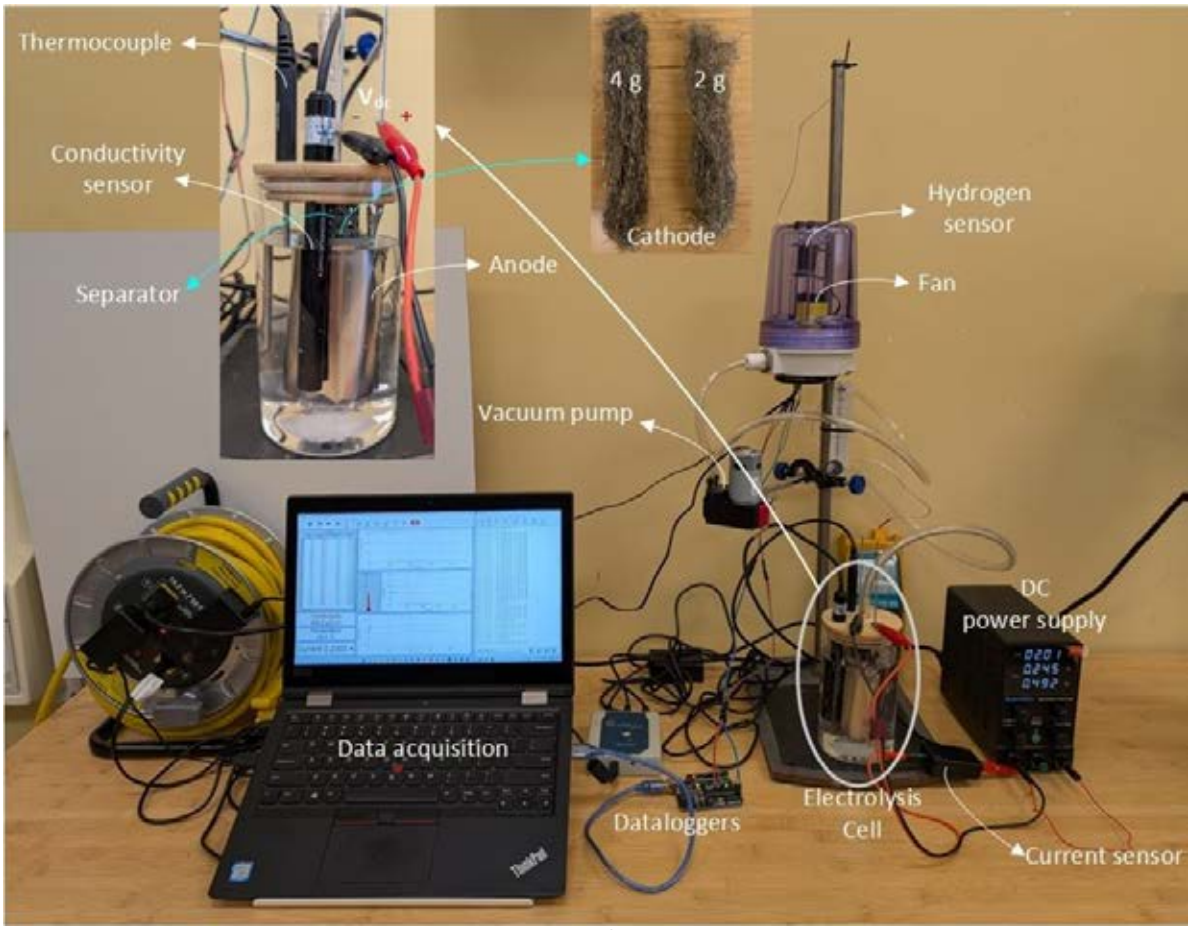

Fig. 1. The photography of the experimental setup

3. RESULTS AND DISCUSSION

The results of the present work are first assessed over the hydrogen production rate. Fig. 2 demonstrates the hydrogen production rate for 2 g and 4 g of cathode materials. Although the hydrogen production rate profiles are similar, the total hydrogen production is observed to be 2.35 and 5.02 mg for 4g and 2g of mesh mass, respectively. The average hydrogen production rate is also measured as 190 and 210 ppm concerning the mass of the cathode material. Fig. 2 illustrates the hydrogen production rate over time for the electrolysis of a 2 M KOH solution at 2 V, utilizing coaxial cylindrical electrodes with scrubber-wire cathodes of 2 g and 4 g masses. The data reveals a clear correlation between cathode mass and hydrogen production. Initially, both configurations exhibit a gradual increase in hydrogen production, likely corresponding to the establishment of electrochemical equilibrium and the activation of the electrode surface. The 2 g cathode consistently demonstrates a higher hydrogen production rate throughout the experimental period compared to the 4 g cathode. This difference is particularly pronounced in the initial stages, suggesting that a larger cathode mass provides a greater mass-to-surface area ratio for electrochemical reactions, facilitating enhanced hydrogen evolution accordingly.

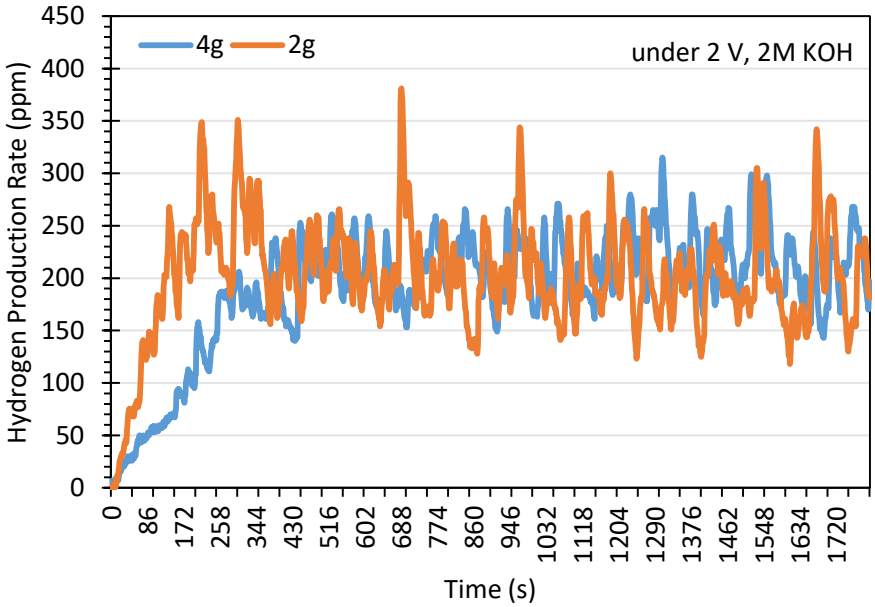

Fig. 2. Effect of the amount of cathode materials on the hydrogen production rates

Moreover, based on the total energy consumed for hydrogen production and total hydrogen production, the energy efficiency is calculated. Notably, the 2 g cathode demonstrates a significantly higher energy efficiency, reaching approximately 78.3%, compared to the 4 g cathode which exhibits an efficiency of around 69.6%. This highlights a crucial trade-off between production rate and energy efficiency in the design of electrolysis systems. While a larger cathode mass can enhance hydrogen output, it may compromise the overall energy efficiency of the process. Optimizing the electrode mass to balance production rate and energy consumption is therefore essential for achieving cost-effective and sustainable hydrogen production.

4. CONCLUSIONS

This study demonstrates that cathode mass plays a crucial role in determining the energy efficiency of hydrogen production in alkaline electrolysis. The experimental results reveal that the 2 g scrubber-wire cathode exhibits superior energy efficiency (78.3%) compared to the 4 g cathode (69.6%), despite similar hydrogen production trends. These results suggest that an optimized balance between electrode mass and effective surface area is necessary for enhancing the performance of electrolysis systems. Future research should explore the influence of additional parameters such as electrode geometry, electrolyte concentration, and operational voltage on hydrogen production efficiency.

Acknowledgment

This publication was made possible by the NPRP grant (NPRP12S-0123-190011) from the Qatar National Research Fund (a member of Qatar Foundation). The findings achieved herein are solely the responsibility of the authors.

REFERENCES

[1] Goren AY, Dincer I, Khalvati A. 2023. A comprehensive review on environmental and economic impacts of hydrogen Production from traditional and cleaner resources. Journal of Environmental Chemical Engineering 111187.
[2] Cai W, Liu W, Han J, Wang A. 2016. Enhanced hydrogen production in microbial electrolysis cell with 3D self-assembly nickel foam-graphene cathode. Biosensensors and Bioelectronics 80:118-122.
[3] Wang L, Liu W, He Z, Guo Z, Zhou A, Wang A. 2017. Cathodic hydrogen recovery and methane conversion using Pt coating 3D nickel foam instead of Pt-carbon cloth in microbial electrolysis cells. International Journal of Hydrogen Energy 42:19604-19610.
[4] Liu H, Yang Y, Liu J, Huang M, Lao K, Pan Y, Wang X, Hu T, Wen L, Xu . 2024. Constructing robust 3D ionomer networks in the catalyst layer to achieve stable water electrolysis for green hydrogen production. ACS Applied Materials and Interfaces 16:16408-16417.
[5] Ismail MM. Erdemir D., Dincer I. 2024. Hydrogen production with a novel coaxial cylindrical electrolyser: A CFD study, International Journal of Thermofluids 24, 100850.

EXPERIMENTAL INVESTIGATION FOR IMPROVED HYDROGEN PRODUCTION FROM MAGNESIUM-SEAWATER REACTION

[1*]Yasmin Hafez, [1]Ibrahim Dincer
[1] Clean Energy Research Laboratory (CERL), Faculty of Engineering and Applied Science, Ontario Tech. University, 2000 Simcoe Street North, Oshawa, Ontario L1G 0C5, Canada
* E-mail: Yasmin.hafez@ontariotechu.ca

ABSTRACT
Hydrogen is a clean and versatile energy carrier with the potential to play a crucial role in the transition to sustainable energy systems. The magnesium-seawater reaction offers a promising solution by enabling hydrogen production from an abundant and naturally available resource, providing an efficient and environmentally friendly alternative to conventional methods. Therefore, this study investigates hydrogen production through the magnesium-seawater reaction to evaluate its feasibility and potential as a sustainable energy solution. Since temperature is a crucial parameter in this process, its effect on hydrogen production performance has been examined in this study. As expected, the hydrogen production performance of the process increased with temperature (40, 60, and 70 °C), likely due to the enhanced reaction kinetics, improved magnesium corrosion rate, and accelerated hydrogen gas release in the magnesium-seawater system. The highest hydrogen production rate was achieved at 70 °C, reaching 5.78 mL/min/g Mg in 30 minutes, while the lowest rate was observed at 40 °C, yielding 4.06 mL/min/g Mg in the same duration. Overall, these results showed that the magnesium-seawater reaction is a promising method for hydrogen production, with temperature playing a key role in optimizing its efficiency and performance.

Keywords: Hydrogen production, Hydrolysis process, Magnesium-water reaction, Sustainability

1. INTRODUCTION
For the past couple of decades, hydrogen has been introduced as a fuel source in an attempt to transition from the use of fossil fuels into cleaner sources of energy. Hydrogen as a fuel source is versatile and can be used in different applications. However, the challenge is in producing hydrogen in a large-scale, efficient, and cost-effective way.
In this regard, magnesium was established as an on-demand, sustainable, and reliable source for hydrogen production. Over the years, scholars searched for different ways to control and enhance the hydrolysis reaction, whether by controlling the medium solution by adding promoters such as $AlCl_3$ or MgCl [1]. This study aimed to observe the reaction at very low temperatures from -40 °C to 0 °C with different solution promoters' percentages with ball-milled magnesium powder with no additives. It was conducted that the best production rate was at 0 °C proving that higher temperatures give better results than lower temperatures with the magnesium hydrolysis. In another study, the effect of the ball milling device, milling time, and the particle size of the magnesium powder were manipulated to improve the hydrolysis kinetics [2]. The best result was obtained with a single additive (graphite), reaching 95% yield in 5 minutes, while also investigating the effect of catalysts using metal chlorides on the hydrolysis.
Moreover, magnesium hydride hydrolysis was vastly investigated in many studies including using magnesium hydride due to its high hydrogen storage capacity [3]. The study aimed at optimizing the reaction by adjusting the flow rate of the solution and adding reactive such as graphite, solid citric acid, and aluminum sulfate obtaining a stable hydrogen production for 12 hours using a flow rate of 200 mL/min.
Different experimental setups were used in the literature such as drainage volumetric method, flow measurements, gravimetric method as well as gas chromatography. In this study, a novel setup was used for the hydrolysis reaction aiming at eliminating the waste using a distillation setup to collect the excess water byproduct, as well as collecting the magnesium hydroxide to be used in other applications such as industrial water treatment and paper industry. This study also focused on using commercially available equipment and abundant materials to make it cost-effective and accessible to all and could be done on a larger scale in the future.

2. EXPERIMENTAL PROCEDURE AND SET-UP
The proposed experimental setup used in this study is based on a distillation unit using a vigorous column, condenser, and collector for any excess water leaving the reaction (Fig. 1). The simulated seawater is first added to the flask, heated to a certain temperature using a hot plate and a temperature controller then the magnesium powder with an average particle size of 50 μm is added to the flask to start the reaction. Using a pump to supply the condenser with cold water to help with the condensation of steam byproduct. Also, there is a flow meter and a vacuum pump to make a stream for the hydrogen sensor to get the readings. All the parts used are commercially available and easy to use.

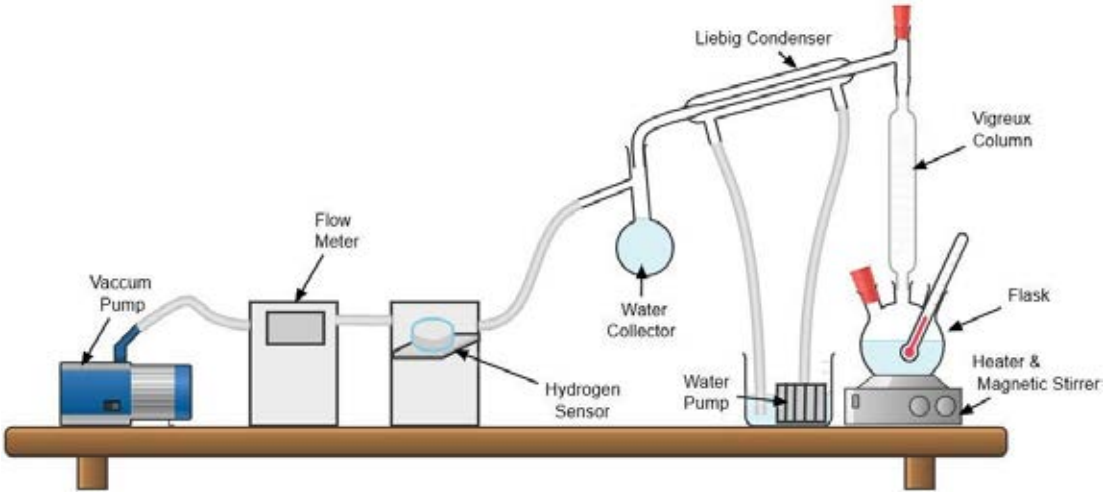

Fig. 1. Schematic illustration of the experimental set-up of the magnesium hydrolysis reaction.

3. ANALYTICAL METHODS

In this study, hydrogen measurements were conducted using the DF Robot Gravity Hydrogen Sensor (I2C&UART), which operates based on an electrochemical detection principle, providing real-time and continuous hydrogen concentration monitoring. The sensor data were continuously recorded throughout the experiments to ensure a precise evaluation of hydrogen production performance. Additionally, since temperature is a critical parameter in this process, a Digital Thermostat Temperature Controller was employed to regulate and maintain the desired experimental temperature. The temperature data were continuously monitored and recorded to ensure accuracy and reproducibility in the experimental conditions.

4. RESULTS AND DISCUSSIONS

In this study, the effect of different temperatures on hydrogen production was investigated, and the results are presented in Fig. 2. It is found that hydrogen production is highly sensitive to temperature. For example, at an operating temperature of 70 °C, it can be observed that the hydrogen production rate was the highest compared to 40 °C. The results indicate that hydrogen production increases with temperature, with the highest yield observed at 70 °C, reaching 5.78 mL/min/g Mg in 30 minutes. On the other hand, the lowest hydrogen production is recorded at 40 °C, with a yield of 4.06 mL/min/g Mg. This trend can be attributed to the fact that higher temperatures enhance the reaction kinetics, increasing the corrosion rate of magnesium in seawater and accelerating hydrogen gas release. Additionally, elevated temperatures improve the diffusion of reactants and reduce activation energy barriers, further promoting hydrogen production. However, beyond an optimal point, excessive heat may lead to increased side reactions or the formation of surface passivation layers on the magnesium, potentially limiting further improvements in hydrogen yield.

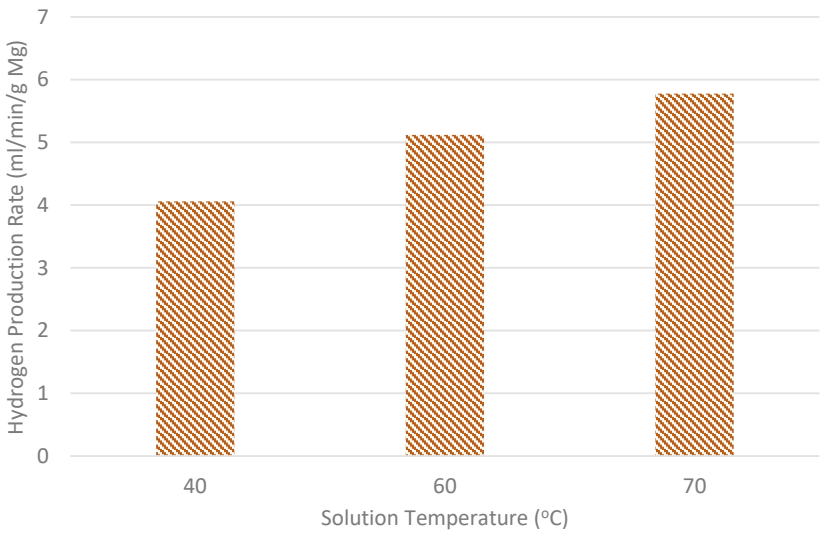

Fig. 2. Hydrogen production rate at different temperatures.

2

5. CONCLUSIONS

This study demonstrates the significant potential of the magnesium-seawater reaction for hydrogen production, highlighting the crucial role of temperature in optimizing the process. The results clearly show that hydrogen production increases with temperature, with the highest production rate of 5.78 mL/min/g Mg achieved at 70 °C. This enhancement can be attributed to improved reaction kinetics, accelerated magnesium corrosion, and increased hydrogen gas release. Overall, the findings suggest that the magnesium-seawater reaction, when carefully optimized, offers a sustainable and efficient method for hydrogen production, with temperature serving as a key parameter for maximizing performance.

Acknowledgment

This publication was made possible by the NPRP grant (NPRP12S-0123-190011) from the Qatar National Research Fund (a member of Qatar Foundation). The findings achieved herein are solely the responsibility of the authors.

REFERENCES

1. Buryakovskaya O.A, Vlaskin M.S, Ryzkova S.S. 2019. Hydrogen production properties of magnesium and magnesium-based materials at low temperatures in reaction with aqueous solutions. Journal of Alloys and Compounds 785:136-145.
2. Al Bacha S et al. 2020. Effect of ball milling strategy (milling device for scaling-up) on the hydrolysis performance of Mg alloy waste. International Journal of Hydrogen Energy 45-41:20883-20893.
3. Qin H et al. 2022. Process optimisation of controlled and continuous MgH_2 hydrolysis to produce hydrogen. Sustainable Materials and Technologies. 33: e00505.

APPLICATION OF SYNTHESIZED AMMONIUM FORMATE AS AN ELECTROLYTE IN STAINLESS STEEL-STAINLESS STEEL ELECTRODE H-CELL CONFIGURATION

*Cagri Gokhan Turk and Ibrahim Dincer.
Clean Energy Research Laboratory (CERL), FEAS, Ontario Tech University, Oshawa, Ontario, L1H 7K4, Canada
*E-mail: cagri.turk@ontariotechu.net

Abstract
This research studies the utilization of synthesized ammonium formate as an electrolyte in an H-cell setup with stainless steel electrodes. Electrochemical analyses were conducted across a range of temperatures (room temperature to 100°C). The highest stable voltage performance was recorded around 700 mV at 80°C and approximately 500 mV at 100°C, whereas significantly lower voltages (approximately 50-150 mV) were observed at lower temperatures (RT to 50°C). FTIR spectroscopy confirmed the synthesis accuracy through characteristic peaks, including NH_4^+, C=O, and C–O groups.

Keywords: Ammonium formate, Stainless stell electrode, FTIR Spectroscopy.

1. INTRODUCTION

Ammonium formate (NH_4HCO_2) is increasingly gaining attention as a promising electrolyte in electrochemical applications due to its inherent properties, such as notable ionic conductivity, high solubility, and considerable electrochemical stability under diverse operating conditions [1]. Electrolytes play a critical role in facilitating ionic transport and ensuring effective charge transfer within electrochemical systems, thus significantly impacting system efficiency and stability [2]. Stainless steel electrodes, commonly used in electrochemical experiments, offer benefits such as high corrosion resistance, durability, and economic feasibility, making them suitable candidates for wide-ranging electrochemical setups [3]. Despite various electrolyte materials available, exploring novel solutions like synthesized ammonium formate remains crucial to improving overall electrochemical performance, particularly in energy storage, electrolysis, and fuel cell technologies. In the present study study, the primary objective is to evaluate the electrochemical effectiveness, stability, and performance of ammonium formate synthesized under controlled laboratory conditions using a stainless steel-stainless steel electrode H-cell configuration across a range of operating temperatures, thereby determining its suitability and potential as an electrolyte in broader electrochemical energy systems.

2.SYSTEM DESCRIPTION

The experimental setup consisted of an H-cell with stainless steel electrodes separated by a membrane. Synthesized ammonium formate served as the electrolyte solution. Electrochemical performance, specifically voltage stability, was measured at various temperatures including RT, 30°C, 40°C, 50°C, 80°C, and 100°C. FTIR was employed to confirm the chemical and structural integrity of ammonium formate.

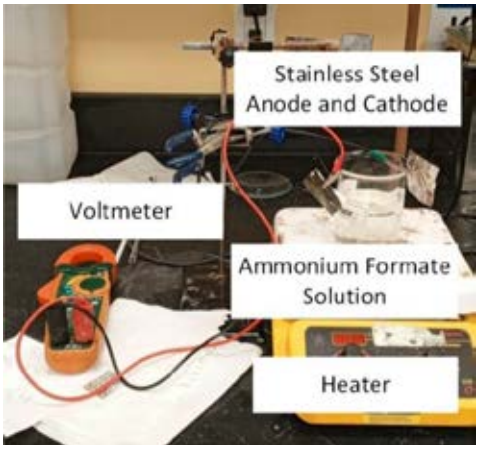

Fig. 1. Experimental Setup.

3. RESULTS AND DISCUSSION

The chemical structure and composition of the synthesized ammonium formate were examined to ensure the integrity of the electrolyte material. In Figure 2, the FTIR spectrum reveals key absorption bands that confirm the presence of characteristic functional groups. Specifically, absorption near 1400 cm^{-1} corresponds to NH_4^+ bending vibrations, the band around 1600 cm^{-1} is attributed to C=O stretching, and the signal near 1350 cm^{-1} indicates C–O stretching. These distinct peaks validate the successful synthesis and chemical stability of the ammonium formate, supporting its suitability as a robust electrolyte component.

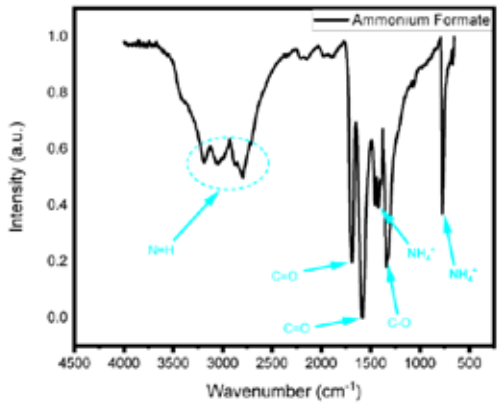

Fig. 2. The FTIR Spectroscopic Analysis of Synthesized Ammonium Formate.

Figure 3 illustrates the voltage-time profiles at different operational temperatures. Stable voltage outputs around 700 mV at 80°C and approximately 500 mV at 100°C indicate substantial electrolyte effectiveness at elevated temperatures. Conversely, lower temperature tests (RT to 50°C) demonstrated notably lower voltage outputs ranging between approximately 50-150 mV, indicating a pronounced temperature dependency in electrochemical performance.

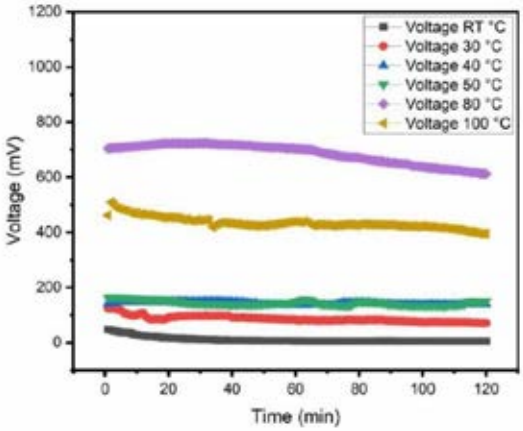

Fig. 2. The voltage-time Profiles of Ammonium Formate Electrolyte at Various Temperatures.

These observations are further supported by evidence indicating successful synthesis and preservation of the chemical structure, which is essential for stable electrolyte performance. The results strengthen the viability of ammonium formate as a potential electrolyte candidate, particularly for systems operating at elevated temperatures. The electrochemical data highlight the enhanced ionic mobility of the electrolyte at higher temperatures, directly linking temperature with improved electrochemical efficiency.

4. CONCLUSIONS

The synthesized ammonium formate demonstrated promising electrochemical stability and efficiency at higher operational temperatures within the stainless-steel H-cell configuration. Optimal voltage performances were observed at elevated temperatures (80°C and 100°C). The chemical integrity of ammonium formate was confirmed by FTIR analysis. These findings support ammonium formate's viability as an electrolyte candidate for stainless steel electrode-based electrochemical applications.

ACKNOWLEDGMENT

This publication was made possible by the NPRP grant (NPRP12S-0123-190011) from the Qatar National Research Fund (a member of Qatar Foundation). The findings achieved herein are solely the responsibility of the authors.

REFERENCES

[1] Pan, Z., Zhang, Z., Li, W., Huo, X., Liu, Y., Esan, O. C., Wu, Q., & An, L. (2023). Development of a High-Performance Ammonium Formate Fuel Cell. *ACS Energy Letters*. https://doi.org/10.1021/acsenergylett.3c01165

[2] Schiffer, Z. J., Biswas, S., & Manthiram, K. (2022). Ammonium Formate as a Safe, Energy-Dense Electrochemical Fuel Ionic Liquid. *ACS Energy Letters*, 7(10), 3260–3267. https://doi.org/10.1021/acsenergylett.2c01826

[3] Shi, L., Zhang, F., Wang, X., Li, J., Liu, Y., Fu, W., Yao, S., Wang, S., Ji, K., Ji, Y., Yang, Z., Xie, J., & Yan, Y.-M. (2025). Overcoming Interfacial Hydrogen Site-Blocking during Alkaline Formate Oxidation: Insights from Lattice-Compressed PdZr/C Catalysts. *ACS Applied Materials & Interfaces*. https://doi.org/10.1021/acsami.4c21195.

MATHEMATICAL MODELING AND SIMULATION OF AN ANION EXCHANGE MEMBRANE WATER ELECTROLYZER USING COMSOL MULTIPHYSICS

*Alperen DEMIRTAS[1, *], C. Ozgur COLPAN[2], Yilser DEVRIM[3], Yagmur NALBANT ATAK[4]*
[1]Dokuz Eylul University, The Graduate School of Natural and Applied Sciences, Mechanical Engineering Department, Tinaztepe, Buca, Izmir, 35397, Türkiye
[2]Dokuz Eylul University, Faculty of Engineering, Mechanical Engineering Department, Tinaztepe, Buca, Izmir, 35397, Türkiye
[3]Atilim University, Faculty of Engineering, Department of Energy Systems Engineering, Incek, Ankara, 06836, Türkiye
[4]Atilim University, Faculty of Engineering, Department of Mechanical Engineering, Incek, Ankara, 06836, Türkiye
*E-mail: alpdmrts@gmail.com

ABSTRACT
Anion Exchange Membrane (AEM) water electrolyzers have emerged as a promising alternative to Proton Exchange Membrane (PEM) due to their potential for cost reduction and long component life. In this study, a one-dimensional (1-D) mathematical model of an AEM water electrolyzer is developed and simulated using Electrolyzer Module in COMSOL Multiphysics. Through parametric analysis, this study investigates the effects of key operating parameters, such as KOH electrolyte concentration and membrane thickness. The primary focus is quantifying major overpotential mechanisms, particularly ohmic and activation overpotentials. The results show that the increasing membrane thickness raises ohmic losses and overall cell voltage, while higher KOH concentrations enhance performance by reducing resistance.

Keywords: AEM water electrolyzer, COMSOL Multiphysics, Modeling

1. INTRODUCTION

In today's world, where sustainability and global warming are gaining importance, the aim is to meet global energy needs with cleaner energy sources and carriers. Hydrogen is an alternative fuel with great potential to meet these demands, and it has merits such as high gravimetric energy density and high reactivity. Hydrogen must be produced using highly efficient methods and renewable energy sources to achieve this. Although there are many methods for hydrogen production, the most commonly used method without harming the environment is electrolysis. The electrolyzer technologies widely used are Proton Exchange Membrane Water Electrolyzer (PEMWE), Alkaline Water Electrolyzer (AWE), and Solid Oxide Electrolyzer Cell (SOEC). Combining the advantages of both PEMWE, which offers a fast response to load changes and high efficiency, and AWE, known for their cost-effectiveness and durability, Anion Exchange Membrane Water Electrolyzer (AEMWE) has recently emerged as a promising new type of electrolyzer [1]. As a relatively new technology, AEMWE still requires significant optimization and further development in various aspects. In this study, a 1-D mathematical model of AEMWE was developed; and parametric studies were performed to investigate the effects of membrane thickness, KOH solution concentration, and the use of NaOH or KOH as the solution on the electrolyzer performance.

2. MODEL DEVELOPMENT

Fig. 1 presents the schematic of the AEMWE used in the 1-D model. As seen in Fig. 1, electrochemical reactions occur on both the anode and cathode sides. The Oxygen Evolution Reaction (OER) occurs at the anode, where hydroxide ions (OH^-) produce oxygen gas (O_2), water (H_2O), and electrons. Simultaneously, at the cathode, the Hydrogen Evolution Reaction (HER) occurs, where water molecules use electrons to form hydrogen gas (H_2) and hydroxide ions. In this study, the boundary conditions for the 1D modeling of AEMWE are defined as follows: At x=0, the electric potential on the anode side is determined by the applied voltage (1.3–2 V). The operating temperature and pressure are set to 343 K and 101,325 Pa, respectively. At x=L, the electric potential is set to zero, serving as the system's reference (ground) potential. The model assumes a single-phase fluid, neglecting bubble effects. The experimental study [2] was tested with a single cell PBI-based membrane and Freudenberg H24C5 carbon gas diffusion layers so the modeling is based on these properties. The geometric and operating parameters used in the model are given in Table 1 [2].

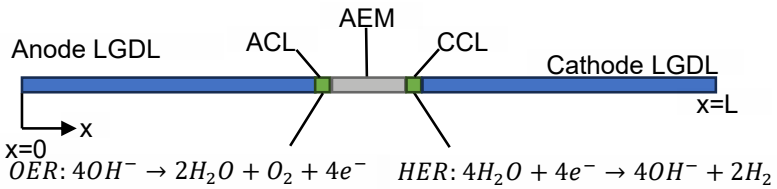

Fig. 1. Schematic diagram of the 1-D model

Table 1. Geometric and operating parameters

Parameter	Value	Unit	Parameter	Value	Unit
Membrane thickness	50	μm	Temperature	343	K
LGDL thickness	230	μm	Pressure	101325	Pa
Catalyst layer thickness	10	μm	KOH concentration	1000	mol/m^3
LGDL conductivity	100	S/m	Active Specific Surface Area	10^7	1/m
Anode exchange current density	12.2	A/m^2	Anodic transfer coefficient	0.343	-
Cathode exchange current density	13.1	A/m^2	Cathodic transfer coefficient	1.657	-

The cell voltage is defined in terms of the overpotentials as follows [3]:

$$E_{cell} = E_{eq} + \eta_{act} + \eta_{ohm} + \eta_{conc} \quad (1)$$

E_{cell} is the total voltage that must be applied (V), E_{eq} is the minimum theoretical voltage required for electrolysis to occur under ideal conditions (V), η_{act} is the activation overpotential (V), η_{ohm} is the Ohmic overpotential (V) (consisting of membrane, electrode, and electrolyte resistance losses), and η_{conc} is the concentration overpotential (V) occuring due to ion consumption or gas production.

2.1. Reversible Cell Voltage

The equilibrium potential is directly related to the change of Gibbs free energy of the reacting species, ΔG, as:

$$\mathrm{E_{eq}} = -\frac{\Delta \mathrm{G}}{\mathrm{nF}} \quad (2)$$

Since the free energy of the reacting species is concentration-dependent, the equilibrium potential also varies with concentration (activity) and is typically determined using the Nernst equation.

$$E_{eq} = E_{eq,ref} - \frac{RT}{nF} ln \prod_i \left(\frac{a_i}{a_{i,ref}}\right)^{v_i} \quad (3)$$

where $E_{eq,ref}$ (V) is the equilibrium potential, corresponds to a reference state where the activities of all species, a_i, are set to a predefined set of reference activities, $a_{i,ref}$. R, n, and F represents the universal gas constant ($\mathrm{J/mol \cdot K}$), the number of moles, and Faraday's constant (96,485.3 $\mathrm{C/mol}$), respectively.

2.2. Activation Overpotential

Activation overpotential is related to the rate of redox reactions occurring at the electrode surfaces. Butler-Volmer equation [4] gives the value of this overpotential as a function of the current density. The equation is described as:

$$i_{loc} = i_0 \left(exp\left(\frac{\alpha_a F \eta}{RT}\right) - exp\left(-\frac{\alpha_c F \eta}{RT}\right)\right) \quad (4)$$

where α_c denotes the cathodic charge transfer coefficient, α_a is the anodic charge transfer coefficient, and i_0 (A/m^2) is the exchange current density. The exchange current density is generally concentration-dependent.

2.3. Ohmic Overpotential

Ohmic overpotential refers to the potential loss due to internal resistances in ionic and electronic conductors in an electrochemical cell. This potential loss is calculated according to Ohm's Law [5]:

$$\eta_{ohm} = i\, R_{ohm} + h_m \frac{i}{\sigma_m} \quad (5)$$

where R_{ohm}, h_m and σ_m are ohmic resistance (Ωm^2), membrane thickness and conductivity of membrane, respectively. Ohmic resistance depends on the conductivity properties of both the electrolyte and electrode materials.

2.4. Continuity Equation

The continuity equation ensures mass conservation by accounting for the balance of species within the system.

$$\frac{\partial(\rho u)}{\partial x} = 0 \quad (6)$$

where u and ρ are velocity and density, respectively.

2.5. Momentum Equation

For steady, flow in the x-direction, considering only viscous and pressure forces:

$$\frac{d}{dx}\left(\mu\frac{du}{dx}\right)=\frac{dP}{dx} \tag{7}$$

where μ is the dynamic viscosity of the electrolyte. The momentum conservation equation describes the balance of forces acting on the fluid, ensuring the proper distribution of velocity and pressure within the system.

3. RESULTS AND DISCUSSIONS

In this study, the performance of an anion exchange membrane water electrolyzer was analyzed under different conditions, focusing on activation losses, membrane thickness effects, and electrolyte composition. Fig. 2 shows the relationship between the experimental data [2] and model data with cell voltage and current density. At low current densities (<0.5 A/cm²), the error rate is up to 9%. At medium current densities (0.5-2.5 A/cm²), the model and the experiment almost match. The error rates are usually around 1%, meaning the modeling is quite successful. At high current densities (>2.5 A/cm²), the model predicts a voltage slightly lower than the experimental data. Here, the error is again around 5%.This can be concluded that this difference is due to the increased formation of bubbles at higher current densities and the neglect of bubble formation in the model.

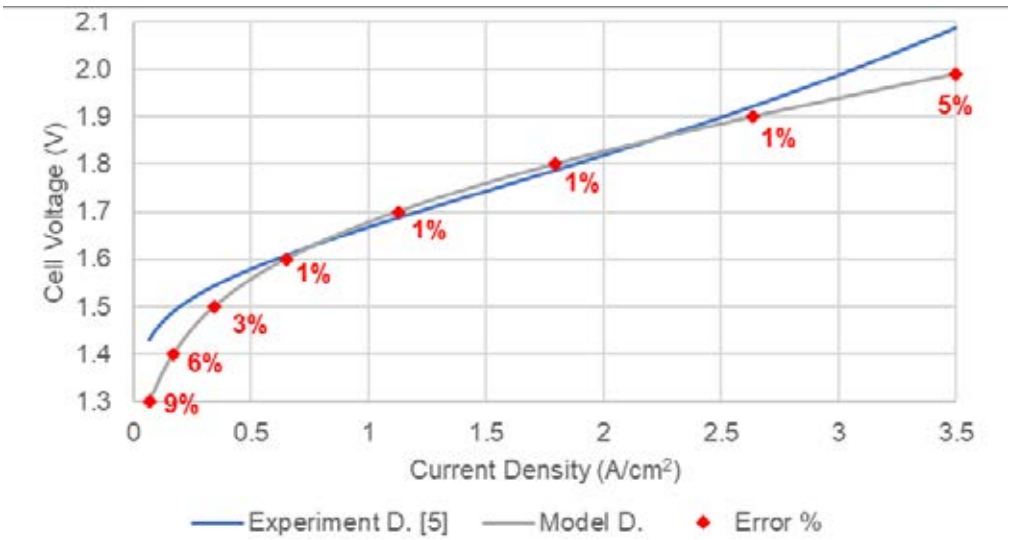

Fig. 2. Comparison of model data with experimental data [2]

In Fig. 3a, the polarization curve for a membrane thickness of 50 µm is presented, illustrating the contributions of different overpotentials to the overall cell voltage. The reversible voltage remains constant, representing the minimum theoretical voltage required for electrolysis. As the current density increases, both the ohmic and activation overpotentials contribute to a rise in the total cell voltage. The ohmic losses, which result from the resistance of the membrane and other cell components, show a linear increase with current density. Meanwhile, activation overpotentials, associated with the energy required to initiate electrochemical reactions, show a nonlinear trend at low current densities. The total cell voltage follows a rising trend as a result of these losses, emphasizing the importance of optimizing membrane properties and electrode kinetics to minimize energy consumption and improve electrolyzer efficiency. In Fig. 3b, polarization curves for different membrane thicknesses (25 µm, 50 µm, and 125 µm) are compared. In general, it is observed that the cell voltage increases as the membrane thickness increases. Thicker membranes offer more resistance to ion passage, decreasing ionic conductivity and thus increasing ohmic losses. Fig. 3c shows the polarization curves obtained when 1 M NaOH and 1 M KOH were used. As can be seen, the use of KOH at the same molarity results in lower cell potential compared to NaOH. This is due to the higher ionic conductivity of KOH. Lower cell voltage means lower energy loss and a more efficient electrolysis process. Therefore, KOH has the potential to improve electrolyzer performance compared to NaOH. Fig. 3d compares the polarization curves for different KOH concentrations (1 M, 3 M and 5 M). It is observed that the cell voltage decreases as the concentration increases. Higher electrolyte concentration reduces ohmic losses by increasing the conductivity of the solution. Especially at low current densities, the difference between different concentrations is insignificant, which becomes more significant as the current density increases.

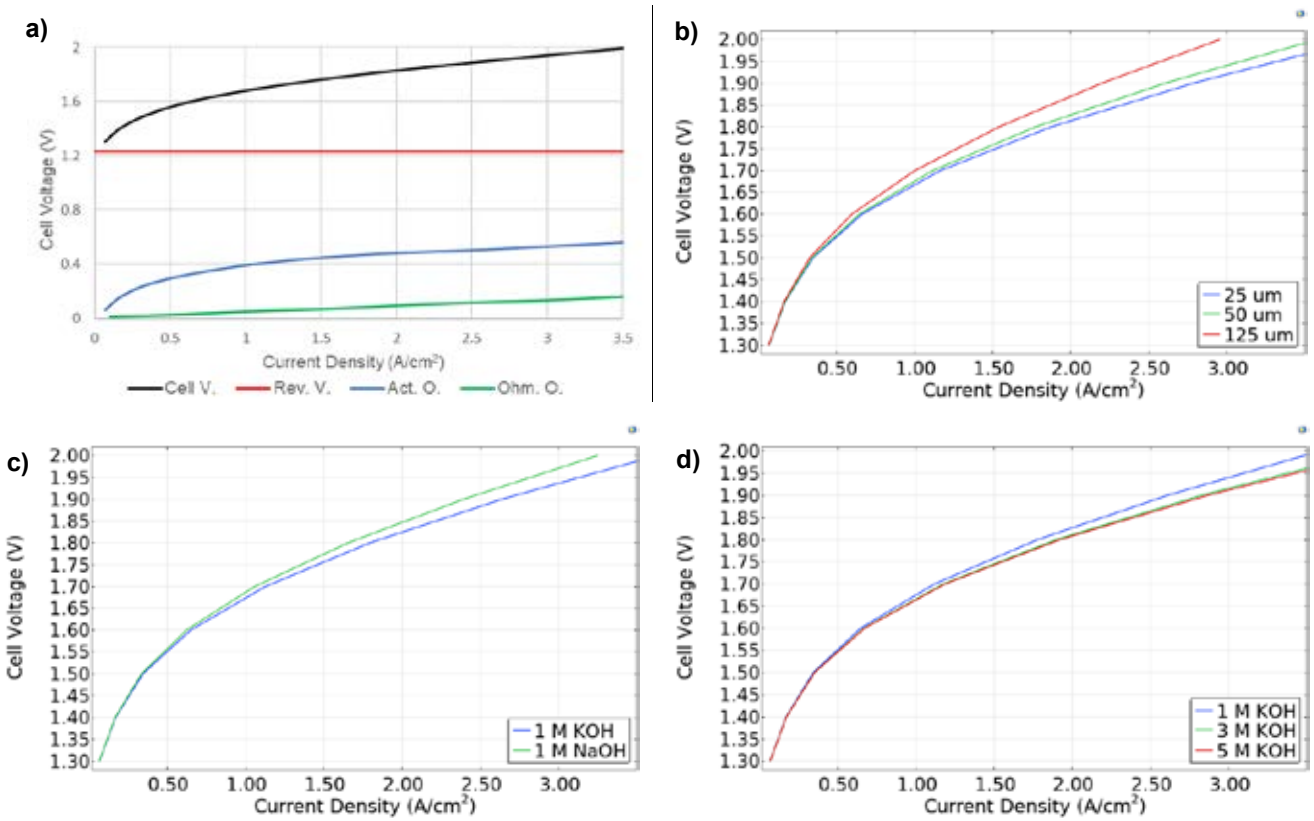

Fig. 3. a) Overpotentials effects and resulting cell voltage relative to current density, **b)** Polarization curves for different membrane thicknesses, **c)** Polarization curves for 1 M KOH and 1 M NaOH, **d)** Polarization curves for different KOH molarities.

4. CONCLUSIONS

In this study, 1-D model is developed to evaluate the performance of an AEMWE under different operating conditions. The results confirm that the model is consistent with the results observed in the literature [2]. The impact of membrane thickness on cell performance was also analyzed. The results indicated that increasing membrane thickness led to higher ohmic losses and an increase in overall cell voltage. Additionally, electrolyte composition significantly affects system performance, as seen in the comparison between NaOH and KOH solutions. Higher KOH concentrations resulted in lower cell voltage at a given current density, highlighting its higher ionic conductivity and lower resistance. These findings highlight the importance of optimizing membrane thickness to balance ionic conductivity and mechanical stability. Data obtained from this study can contribute to the optimization of AEMWE systems. However, further research is needed to improve the model by adding more detailed catalyst kinetics and additional experimental data for improved accuracy and validation.

5. ACKNOWLEDGEMENTS

The authors would like to thank The Scientific and Technological Research Council of Türkiye (TÜBİTAK) (Grant Number: 123M878) for their support and funding of the project.

6. REFERENCES

[1] Qiucheng Xu, Liyue Zhang, Jiahao Zhang, Jingyu Wang, Yanjie Hu, Hao Jiang, Chunzhong Li,Anion Exchange Membrane Water Electrolyzer: Electrode Design, Lab-Scaled Testing System and Performance Evaluation,EnergyChem,Volume4,Issue5,2022,100087 https://doi.org/10.1016/j.enchem.2022.100087

[2] Hager L, Hegelheimer M, Stonawski J, Freiberg ATS, Jaramillo-Hern´andez C, Abell´ an G, et al. Novel side chain functionalized polystyrene/O-PBI blends with high alkaline stability for anion exchange membrane water electrolysis (AEMWE). J Mater Chem A Mater 2023;11:22347–59. https://doi.org/10.1039/ d3ta02978f.

[3] Henao, C., Agbossou, K., Hammoudi, M., Dubé, Y., Cardenas, A., 2014. Simulation tool based on a physics model and an electrical analogy for an alkaline electrolyser. J. Power Sources 250, 58–67. https://doi.org/10.1016/j.jpowsour.2013.10.086

[4] Milewski, J., Guandalini, G., Campanari, S., 2014. Modeling an alkaline electrolysis cell through reduced-order and loss-estimate approaches. J. Power Sources 269, 203–211. https://doi.org/10.1016/j.jpowsour.2014.06.138

[5] Han, B., Mo, J., Kang, Z., Yang, G., Barnhill, W., Zhang, F.-Y., 2017. Modeling of two-phase transport in proton exchange mem brane electrolyzer cells for hydrogen energy. Int. J. Hydrogen Energy 42 (7), 4478–4489. https://doi.org/10.1016/j.ijhydene. 2016.12.103

TECHNO-ECONOMIC ANALYSIS OF GREEN HYDROGEN PRODUCTION: INVESTIGATING HYBRIDIZATION POTENTIAL IN İZMİR

*Engin Deniz Gülay, C. Ozgur Colpan, Mehmet Akif Ezan
Dokuz Eylül University, Engineering Faculty, Mechanical Engineering Department, 35390, Buca, İzmir, Türkiye
*Corresponding author e-mail: engindeniz.gulay@deu.edu.tr

ABSTRACT
Green hydrogen has been a trend as a key solution for the decarbonization of various sectors, offering a sustainable alternative to conventional fossil fuels. Despite its potential to drive the energy transition, green hydrogen applications are constrained by technical and economic challenges. This study aims to determine the optimal capacity values of solar and wind power plants for six districts (Çeşme, Dikili, Foça, Karaburun, Seferihisar, and Urla) in Izmir, adhering to a 200% oversizing limit based on the capacity of the electrolyzer system. While the Levelized Cost of Hydrogen (LCOH) values for the specified districts yielded similar results, Çeşme yielded the lowest value at 6.15 USD/kgH_2. Contrarily, Foça and Urla had the highest value at 6.27 USD/kgH_2. Identifying a 65 MW wind-powered 50 MW PEMWE system in Çeşme as the optimal configuration, a one-at-a-time (OAT) sensitivity analysis was conducted to investigate key cost drivers. The sensitivity analysis indicated that the scale index (SI) parameter significantly impacted LCOH. It was observed that the Scaled Purchase Cost (C_{SP}) value decreased significantly when the SI value was reduced from the baseline value of 90% to 75% and 60%. Finally, the modularity of the Proton Exchange Membrane Water Electrolyzer (PEMWE) was investigated. Increasing the number of modules led to a reduction in LCOH by 8.5%. The results offer practical insights into system sizing, cost drivers, and modularity for green hydrogen production.

Keywords: Techno-economic analysis, hybridization, modularity, sensitivity analysis, green hydrogen.

1. INTRODUCTION

As the decarbonization of the energy sector accelerates, green hydrogen produced from renewable sources is offered as an alternative to various sectors (e.g. steel industry, transportation, and heating) as a sustainable fuel. However, its production comes with a significant challenge, as it is not cost-effective compared to conventional fossil fuels. Therefore, identifying strategies to achieve a lower Levelized Cost of Hydrogen (LCOH) is essential for the future of green hydrogen. Solar and wind energy are the most commonly used renewable sources to produce green electricity [1]. Solar-wind hybrid power plants ensure a continuous energy supply by allowing them to benefit from each other. Due to the seasonal and economic variations in solar and wind energy sources, determining the optimal hybridization ratio is essential for cost-effective green hydrogen production. This study aims to analyze LCOH values by investigating the hybridization potential for six districts (Çeşme, Dikili, Foça, Karaburun, Seferihisar, and Urla) for a 50 MW Proton Exchange Membrane Water Electrolyzer (PEMWE) green hydrogen production system. Subsequently, a one-at-a-time (OAT) sensitivity analysis was performed to identify the critical input parameters of the LCOH, which was revealed to be SI. IRENA elaborated on the relationship between the manufacturing scale and the learning rate [2]. The variation of the Scaled Purchase Cost (C_{SP}) value in relation to the reduction of scale index (SI) was examined. In addition, the cost-effectiveness of the multi-module PEMWE system was investigated through a calculation that calculates the hydrogen production amount depending on the stack load by separating the specific energy consumption (SEC) of BoP and stack. This study focuses on optimizing the deployment of variable-capacity solar-wind hybrid power plants within the boundaries of İzmir. A key objective is to determine the most suitable location for these systems based on technical and economic factors. Additionally, the study aims to identify which parameter has the most influence on the LCOH. Finally, it examines how variations in the number of modules impact the LCOH. The findings of this study will provide valuable insights into determining the optimal green hydrogen production region among the considered districts, contributing to strategies for reducing green hydrogen production costs.

2. MATERIALS AND METHODS

2.1. Data Collection

The techno-economic analysis algorithm was developed in MATLAB. Reference capital cost and operational cost data were obtained from the IRENA [3], TNO Reports [4], and Khan's study [5]. The SI, the rate to predict the scaled purchase cost, was considered 90%. Annual electricity production data was collected from a website called Renewables-Ninja [6] for all districts of İzmir, excluding areas with a high degree of urbanization, and their average yearly capacity factor values are presented in Table 1. The renewable energy data are based on 2024 measurements in one-hour intervals. Reference costs for solar and wind energy and PEMWE are shown in Table 2, and the specifications of PEMWE are provided in Table 3. Crespi's industrial PEMWE's SEC curve [7] was used as a basis for the hydrogen production calculations.

Table 1. Average annual capacity factor values of the districts of İzmir.

District	Aliağa	Bayındır	Bergama	Beydağ	Çandarlı	Çeşme	Dikili	Foça	Karaburun	Kemalpaşa
Solar Ave. CF	25.71%	25.86%	24.71%	26.15%	25.71%	24.56%	25.61%	25.81%	25.92%	25.84%
Wind Ave. CF	46.63%	22.66%	37.52%	14.85%	48.24%	49.63%	48.82%	47.05%	48.38%	27.15%
	Kınık	**Kiraz**	**Menderes**	**Menemen**	**Ödemiş**	**Seferihisar**	**Selçuk**	**Tire**	**Torbalı**	**Urla**
Solar Ave. CF	25.16%	26.02%	25.94%	25.77%	25.94%	26.12%	25.95%	25.93%	25.90%	26.03%
Wind Ave. CF	39.26%	16.04%	32.89%	34.82%	18.12%	46.92%	27.59%	20.80%	28.24%	46.87%

Table 2. Input cost data for the study

	Value	Reference
Reference capital cost		
PEMWE	2000 USD/kW	[4]
Solar energy power plant	750 USD/kW	[3]
Wind energy power plant	1600 USD/kW	[3]
Reference O&M cost		
PEMWE	2.5% of total PEMWE equipment cost	[5]
Solar energy power plant	7000 USD/kW/y	[3]
Wind energy power plant	30000 USD/kW/y	[3]
PEMWE stack replacement cost	40% of the total stack equipment cost	[5]

Table 3. Technical data of the PEMWE of this study

	Value	Reference
Nominal SEC	55.5 kWh/kgH_2	[7]
Load range	20%-100% of the nominal load (stack)	(assumption)
Stack lifetime	50000 h	[2]
Degradation rate	0.19 %/1000 h	[8]

2.2. Hydrogen Production Modeling

Electricity production data of 1 kW solar and wind power plants were obtained as power plant capacity factor (CF_{pp}) and linearly scaled to calculate the electrolyzer capacity factor (CF_{el}) according to Eq. (1).

$$CF_{el} = \frac{E_{pp}}{E_{el}} \times CF_{pp} \quad (1)$$

where E refers to capacity.

Hydrogen production was calculated according to Eq. (2). This calculation is based on the SEC values that vary depending on the load, with separate consideration given to the energy use of the stack and the Balance of Plant (BoP). Stacks are assumed to degrade yearly, while BoP does not. As stack degradation progresses, SEC_{stack} increases, leading to a decline in hydrogen production performance over the years. The degradation rate changes yearly, while the SEC and CF values change hourly.

$$m_{H_{2(h,y)}} = \frac{1}{\left(1+r_{d_y}\right)\cdot SEC_{stack_{(h,y)}} + SEC_{BoP_{(h,y)}}} E_{el} CF_{el_{(h,y)}} \quad (2)$$

where $r_{d,y}$ refers to the degradation rate.

The modularity of the PEMWE system was further investigated to evaluate its impact on the LCOH. In this context, modularity divides the input electricity among multiple modules by applying a specific operational strategy: the Daisy Chain Allocation (DCA) [9]. This approach prioritizes the operation of modules sequentially. Specifically, Module 1 (M1) is supplied with electricity until it reaches its nominal load. Once M1 is fully loaded, M2 begins operating, followed by M3, M4, and so on.

2.3. Techno-economic Analysis

The techno-economic analysis conducted in this study focuses on two key cost metrics: capital expenditures (CAPEX) and operational expenditures (OPEX), which represent initial investment costs and ongoing operation and maintenance expenses, respectively. This study excludes the electrolyzer stack replacement costs from OPEX to see its impact on LCOH. The C_{SP} was calculated using Eq. (3), and the equipment cost of the asset was determined by multiplying the C_{SP} by its capacity, as shown in Eq. (4).

$$C_{SP} = C_{cap,ref}\ E_{ref}\ \left(\frac{E}{E_{ref}}\right)^{SI} \quad (3)$$

$$C_{eq} = C_{SP}E \quad (4)$$

where C refers to cost.

Land cost is another parameter representing an asset's total land procurement cost. It can be calculated as a percentage of the scaled purchase cost [5]. Finally, total capital costs are determined by summing the equipment and land procurement costs (Eq. (5)).

$$C_{CAPEX} = C_{eq} + C_{land} \quad (5)$$

OPEX is an annual cost parameter reduced due to a discount rate (r_{dis}). The total OPEX was calculated by summing these values (Eq. (6)).

$$\sum OPEX = \sum \frac{C_{op,ref}C_{eq}}{(1+r_{dis})^y} \quad (6)$$

LCOH is determined by dividing the total expenses by the total amount of hydrogen produced over the entire lifespan of the green hydrogen production facility (Eq. (7)).

$$LCOH = \sum_{y=1}^{L} \frac{CAPEX+OPEX_y}{m_{H_2 y}} \quad (7)$$

3. RESULTS AND DISCUSSION

Six districts with high solar and wind energy capacity factors were selected for this study, and they are compared for a 50 MW PEMWE system, with solar and wind power plants simulated at capacities of up to 200% of the electrolyzer's nominal capacity (i.e., up to 100 MW). Table 4 presents minimum LCOH values for considered districts. Çeşme district has the lowest, with 6.15 USD/kgH_2 for a 65 MW wind-only power plant. In contrast, Foça and Urla have the highest, with 6.27 USD/kgH_2 for 70 MW wind, combined with a 75 MW solar power plant. Çeşme's lower LCOH can be attributed to its higher wind energy CF, which ensures more consistent electricity generation, reducing the reliance on solar energy. District variations have minimal impact on minimum LCOH (≤ 0.12 USD/kgH_2). Therefore, site selection may prioritize land availability and transportation options over hydrogen production performance.

Table 4. Minimum LCOH results for each district

District	LCOH (USD/kg)	Solar - Wind Capacity (MW)
Çeşme	6.15	0 - 65
Dikili	6.16	0 - 85
Foça	6.27	75 - 70
Karaburun	6.19	70 - 70
Seferihisar	6.25	75 - 70
Urla	6.27	75 - 70

The optimal configuration for Çeşme (65 MW wind-only) was selected for further calculations. The OAT sensitivity analysis result in Figure 1 shows that the SI has the highest impact by far, with −37.35% to 68.25% impact for −20% to 20% input value variation. The SI's dominant influence indicates that manufacturing scale and technology maturity are the primary levers for LCOH. This underlines the importance of the economy of scale and the effect of the learning rate on cost-reduction strategies. In contrast, the other figure represents the C_{SP} curves that vary according to SI, referencing the wind energy power plant reference capital cost for Türkiye. Improvement in SI reflects C_{SP} as 506 USD/kW and 254 USD/kW, for 75% and 60% SI, respectively.

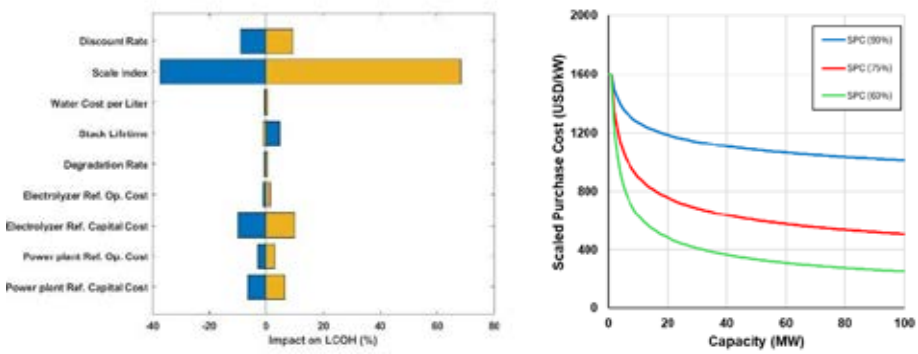

Fig. 1. Sensitivity analysis results (left) and C_{SP} curves of variable SI percentages (right)

Finally, the modularity of the PEMWE was investigated from 1 module to 400 modules. Results in Figure 2 show that using a DCA strategy for modularity can reduce the LCOH by 8.5% for the optimal configuration. The DCA strategy ensures that each module operates closer to its optimal efficiency point by leveraging the total system capacity distribution of the electrolyzer's modularity. While modularity enhances hydrogen production in this case, but its benefits may diminish in situations with lower availability of renewable energy.

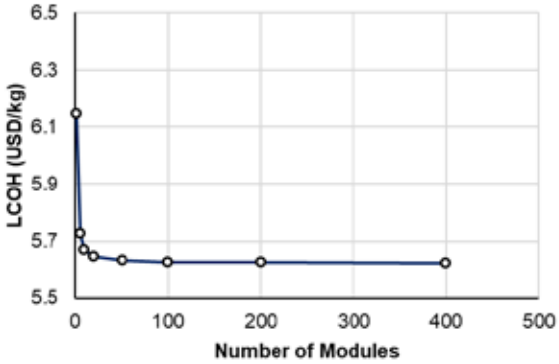

Fig. 2. The effect of changing the number of modules in the considered PEMWE system on the LCOH.

4. CONCLUSIONS

This study investigated the hybridization of solar and wind energy power plants for a PEMWE green hydrogen production system. Six districts are included, considering the solar and wind energy potential of the districts of İzmir. Minimum LCOH values for the six districts are presented for a 50 MW PEMWE system, considering zero to 200% solar and wind power plant oversizing. Results indicated that the Çeşme provides the lowest LCOH, and Foça and Urla provide the highest. LCOH is not highly varied for the six districts with high solar and wind energy potential. Therefore, different factors, such as land availability and transportation options, may be investigated for clarification to determine the most appropriate district. An OAT sensitivity analysis was conducted to determine the critical input parameters referencing the selected optimal case. This analysis presented the importance of SI. Therefore, C_{SP} curves for 60%, 75%, and 90% of SI were given, and a significant C_{SP} decrease was observed. Finally, modularization of the PEMWE system was also investigated, where the increase in the number of modules led to a reduction of LCOH. For future work, integrating a Battery Energy Storage System (BESS) will be considered to further improve the average capacity factor by storing the excess electricity. In addition, financial improvements will be considered for the techno-economic model to obtain more accurate long-term estimations.

REFERENCES

[1] IRENA, Renewable Energy Statistics 2024. 2024. [Online]. Available: www.irena.org
[2] Green Hydrogen Cost Reduction: Scaling up Electrolysers to Meet the 1.50C Climate Goal. 2020. Accessed: Oct. 30, 2024. [Online]. Available: www.irena.org/publications
[3] IRENA, Renewable Power Generation Costs In 2023. 2024. Accessed: Oct. 21, 2024. [Online]. Available: www.irena.org
[4] R. Detz and M. Weeda, “Projections of electrolyzer investment cost reduction through learning curve analysis,” 2022. [Online]. Available: www.tno.nl
[5] M. H. A. Khan, P. Heywood, A. Kuswara, R. Daiyan, I. MacGill, and R. Amal, “An integrated framework of open-source tools for designing and evaluating green hydrogen production opportunities,” Commun Earth Environ, vol. 3, no. 1, Dec. 2022, doi: 10.1038/s43247-022-00640-1.
[6] “Renewables-ninja.” Accessed: Oct. 21, 2024. [Online]. Available: https://www.renewables.ninja/
[7] E. Crespi, G. Guandalini, L. Mastropasqua, S. Campanari, and J. Brouwer, “Experimental and theoretical evaluation of a 60 kW PEM electrolysis system for flexible dynamic operation,” Energy Convers Manag, vol. 277, Feb. 2023, doi: 10.1016/j.enconman.2022.116622.
[8] Clean Hydrogen Partnership, “Clean Hydrogen JU - SRIA Key Performance Indicators (KPIs).” Accessed: Oct. 30, 2024. [Online]. Available: https://www.clean-hydrogen.europa.eu/knowledge-management/strategy-map-and-key-performance-indicators/clean-hydrogen-ju-sria-key-performance-indicators-kpis_en.
[9] X. Lu et al., “Optimization of power allocation for wind-hydrogen system multi-stack PEM water electrolyzer considering degradation conditions,” Int J Hydrogen Energy, vol. 48, no. 15, pp. 5850–5872, Feb. 2023, doi: 10.1016/j.ijhydene.2022.11.092.

CFD-BASED THERMAL AND EMISSION ANALYSIS OF A 2D HYDROGEN-FUELED COMBUSTOR USING REAL ENGINE DATA AT CRUISE ALTITUDE

[1*]*Yasin Furkan Gorgulu*, [2]*Selcuk Ekici*, [3]*T. Hikmet Karakoc*
[1] Department of Machinery and Metal Technologies, Keçiborlu Vocational School, Isparta University of Applied Sciences, Isparta, Türkiye
[2] Department of Aviation, Igdir University, Igdir, Türkiye
[3] Faculty of Aeronautics and Astronautics, Eskişehir Technical University, Eskişehir, Türkiye
*Corresponding author e-mail: yasingorgulu@isparta.edu.tr

ABSTRACT
This study presents a computational investigation of a hydrogen-fueled two-dimensional gas turbine combustor operating at cruise flight conditions (FL390). The combustor geometry was adapted from the literature and meshed with high quality (average skewness: 0.13, orthogonal quality: 0.95). Real engine-derived boundary conditions, including a hydrogen fuel mass flow of 0.3286 $kg.s^{-1}$ and an air flow rate of 13.20 $kg.s^{-1}$, were applied. Numerical simulations were performed using the RNG k–ε turbulence model and eddy dissipation combustion model in ANSYS Fluent. Temperature, velocity, pressure, turbulence kinetic energy, and species distributions were analyzed. The results revealed a maximum flame temperature of approximately 3045 K and a velocity exceeding 1000 $m.s^{-1}$ near the nozzle exit. Efficient hydrogen oxidation was confirmed by high H_2O concentrations and a sharp drop in H_2 mass fraction. NO formation was concentrated in the post-flame region, with a peak mass fraction of 0.031. The absence of CO_2 and unburned hydrocarbons highlights the clean-burning nature of hydrogen.

Keywords: CFD, cruise altitude, emission analysis, hydrogen combustion, jet engine

1. INTRODUCTION
The aviation industry faces increasing pressure to reduce environmental impact and transition toward sustainable propulsion systems [1]. Gas turbine combustors play a crucial role in determining thermal efficiency, emission levels, and operational stability. With conventional aviation fuels being associated with significant carbon-based emissions and long-term resource depletion, the exploration of alternative fuels such as hydrogen has gained notable traction [2]. Hydrogen offers several advantages including high flame speed, absence of carbon-based combustion byproducts, and a broad flammability range, rendering it a promising candidate for decarbonized aviation propulsion [3]. Nevertheless, hydrogen combustion presents several technical challenges [4]. Due to its low ignition energy and high diffusivity, hydrogen-air flames are susceptible to instabilities such as flashback and blow-off, especially under lean or premixed conditions [5–7]. This necessitates the development of advanced combustion chamber geometries and optimized mixing strategies to ensure safe and efficient operation. Various stabilization techniques, such as swirl-induced recirculation, jet-based stabilization, and micro-mixing configurations, have been employed to improve flame stability and combustion efficiency [8,9]. Recent studies have investigated the implementation of hydrogen in gas turbine combustors under diverse operating conditions. Kahraman et al. [10] demonstrate that hydrogen combustion can achieve higher pressure recovery and lower CO_2 emissions compared to Jet-A, though NO_x emissions may increase depending on excess air ratios. Lu et al. [11] explored the stability window of hydrogen-enriched fuels, highlighting the role of flue gas recirculation and inlet temperature in mitigating flashback risk. Liu et al. [12] emphasize the importance of radiative heat transfer and turbulence–radiation interaction in swirling flames, which significantly affect temperature distribution and NO_x formation. Meanwhile, Sun et al. [13] analyzed the influence of equivalence ratio on flame shape and vortex evolution in jet-stabilized combustors, identifying critical flow features that dictate flame anchoring behavior.

In the context of high-altitude flight, particularly at cruise conditions such as FL390, combustor performance becomes even more sensitive to thermal loading and pollutant formation [14]. This study aims to numerically investigate the combustion behavior of a 2D hydrogen-fueled combustor operating under cruise altitude conditions, using real jet engine boundary data. By evaluating key flow and reaction fields—such as temperature, pressure, velocity, turbulence kinetic energy, and species mass fractions—the study provides insights into hydrogen flame behavior and pollutant emissions in a representative aviation-relevant setting.

2. MATERIALS AND METHODS
In this study, a numerical investigation was conducted to evaluate the combustion characteristics of a two-dimensional hydrogen-fueled combustor operating under cruise altitude conditions. The computational domain was designed based on simplified yet representative combustor geometry with a single fuel inlet and two separate air inlets (primary and secondary). Numerical simulations were performed using validated turbulence and combustion models to capture the coupled flow, heat transfer, and chemical reaction phenomena. The modeling strategy and simulation parameters are detailed in the following subsections, including the description of the numerical model, governing equations, and boundary conditions employed in the CFD (computational fluid dynamics) analysis.

2.1. Numerical Model

The computational domain used in this study was adopted from the work of Kahraman et al. [10], who modeled a tubular combustor inspired by a Rolls-Royce Nene-type gas turbine [15,16]. The two-dimensional axisymmetric geometry features a single hydrogen fuel inlet along with two air inlets—primary and secondary. The domain dimensions are 620 mm in length and 145 mm in maximum height, as shown in Fig. 1. The simulation domain was discretized using a structured mesh, resulting in 57,166 nodes and 56,137 elements. The mesh quality metrics indicate excellent resolution, with an average skewness of 0.13299 and an orthogonal quality of 0.95328. According to ANSYS meshing criteria, skewness values below 0.25 and orthogonal qualities above 0.95 are considered excellent, ensuring reliable numerical convergence and solution stability [17]. The mesh configuration, displayed in Fig. 1. To resolve the near-wall regions and capture velocity and thermal gradients, five inflation layers were applied along all solid boundaries. The CFD simulations were performed using the ANSYS 2022 R2 Fluent software. The realizable RNG k–ε turbulence model was selected to account for the effects of turbulent flow within the combustion chamber due to its proven performance in similar geometries and reacting flow environments. Further details regarding the governing equations, chemical reaction mechanisms, and boundary conditions applied in the model are provided in the following subsection.

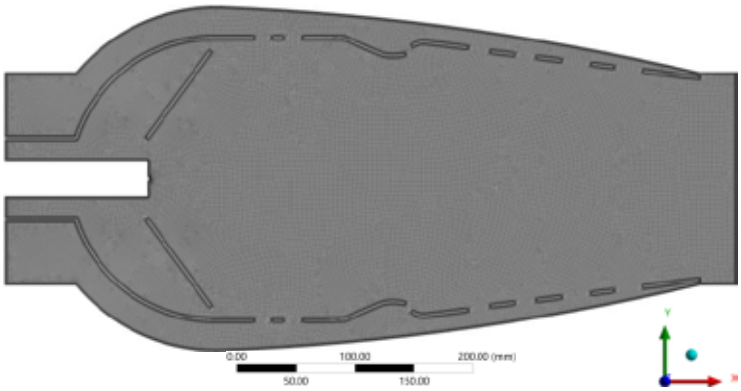

Fig. 1. Mesh structure of the hydrogen-fueled combustion chamber.

2.2. Governing Equations and Boundary Conditions

The numerical simulations were conducted by solving the steady-state, compressible Navier–Stokes equations along with species transport and energy conservation equations. The realizable RNG k–ε turbulence model and the eddy dissipation combustion model were used to capture turbulent mixing and hydrogen-air combustion behavior. The ideal gas law was used as the equation of state, with temperature-dependent material properties. Wall surfaces were assumed to be adiabatic with no-slip conditions. All boundary conditions were defined based on flight level FL390, extracted from real jet engine operational data. The ambient air enters the domain at a total temperature of 228.9 K and a density of 0.3348 $kg.m^{-3}$, while the fuel-air ratio is 0.0249. The hydrogen fuel inlet was defined with a mass flow rate of 0.3286 $kg.s^{-1}$ and the total air mass flow was 13.20 $kg.s^{-1}$. The air and fuel streams were introduced through velocity inlets with a turbulence intensity of 5%. The combustor outlet was modeled as a pressure outlet with a zero-gradient condition. A symmetry boundary condition was imposed along the central axis of the domain.

3. RESULTS AND DISCUSSION

Figure 2 presents the CFD results for the hydrogen-fueled combustor operating at FL390. The temperature distribution (Fig. 2a) indicates a peak flame temperature of approximately 3045 K, located slightly downstream of the primary air inlet. Compared to Kahraman et al. [10], where peak temperatures ranged around 2650 K at similar engine speeds, the elevated flame temperature observed here is attributed to higher hydrogen purity and reduced dilution effect under cruise-specific boundary conditions. The velocity contour (Fig. 2b) shows a maximum flow velocity exceeding 1000 $m.s^{-1}$ near the nozzle exit, which aligns with the accelerated expansion due to thermal gradients. The static pressure distribution (Fig. 2c) illustrates a gradual drop toward the outlet, consistent with combustion-induced expansion. The turbulence kinetic energy (Fig. 2d) peaks near the fuel-air mixing region, ensuring flame anchoring through recirculation effects. Species mass fraction contours reveal effective combustion. The H_2 mass fraction (Fig. 2e) drops sharply in the reaction zone, while H_2O (Fig. 2f) peaks correspondingly, validating efficient hydrogen oxidation. Similarly, O_2 (Fig. 2g) and N_2 (Fig. 2h) exhibit expected dilution patterns. Notably, NO formation (Fig. 2i) is localized in the high-temperature post-flame zone, with a peak mass fraction of ~0.031, consistent with thermal NO mechanisms. Compared to Kahraman et al. [10], where NO peaked around 0.026 under similar equivalence ratios, this slight increase is a trade-off for higher combustion efficiency.

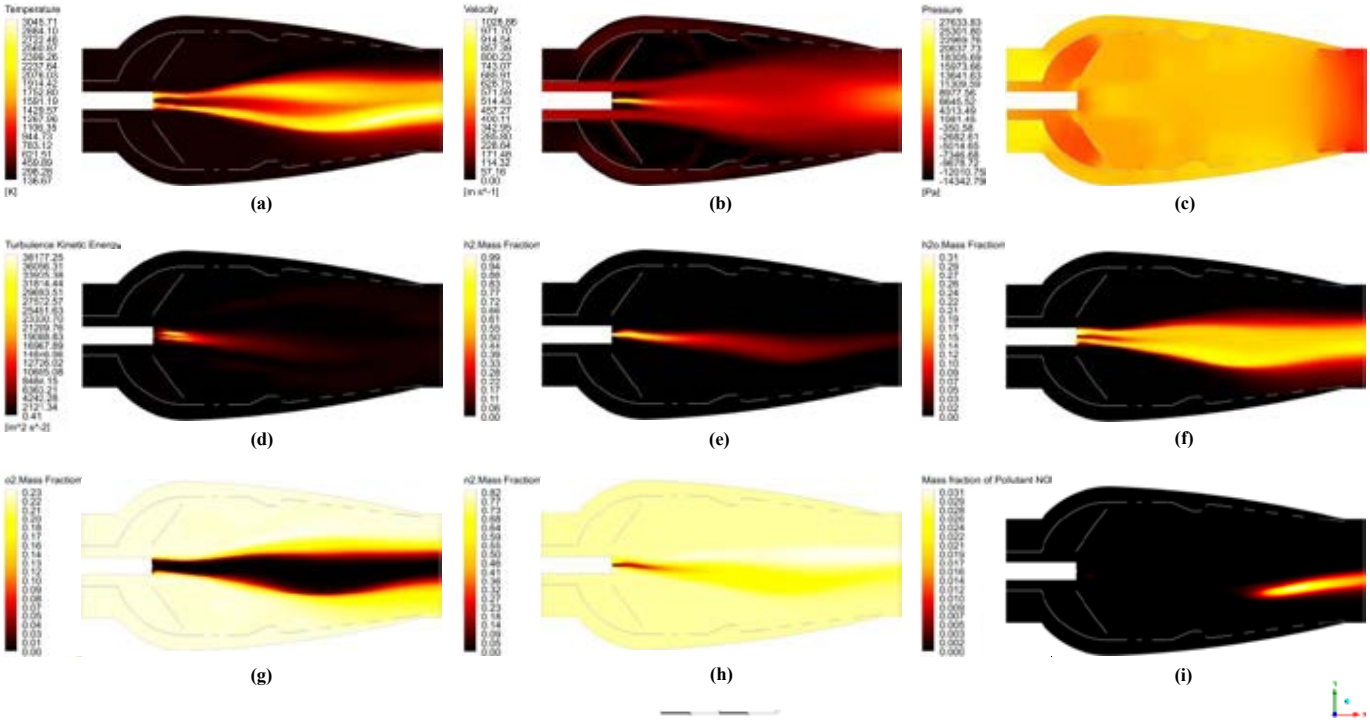

Fig. 2. CFD contours of the hydrogen-fueled 2D combustion chamber at cruise altitude: (a) Temperature distribution [K], (b) Velocity magnitude [m.s^{-1}], (c) Static pressure [Pa], (d) Turbulence kinetic energy [m^2.s^{-2}], (e) H_2 mass fraction, (f) H_2O mass fraction, (g) O_2 mass fraction, (h) N_2 mass fraction, (i) Mass fraction of pollutant NO.

4. CONCLUSIONS

- A 2D hydrogen-fueled combustor operating at FL390 was successfully simulated using real engine boundary conditions.
- Peak flame temperature reached approximately 3045 K, indicating efficient hydrogen-air combustion with complete H_2 oxidation.
- NO formation was localized and remained within acceptable limits, with a maximum mass fraction of ~0.031, comparable to previous studies.
- No CO_2 or unburned hydrocarbon emissions were observed, confirming the zero-carbon nature of hydrogen combustion.
- Mesh quality and turbulence treatment (RNG k–ε) contributed to stable and accurate CFD predictions.
- The results highlight hydrogen's strong potential for low-emission, high-efficiency aviation propulsion under cruise conditions.

ACKNOWLEDGEMENT

The authors declare that they have no conflict of interest. Also, this research did not receive any specific grant from funding agencies in the public, commercial, or not-for-profit sectors.

REFERENCES

1. Abrahamson JP, Zelina J, Andac MG, Vander Wal RL. Predictive Model Development for Aviation Black Carbon Mass Emissions from Alternative and Conventional Fuels at Ground and Cruise. Environ Sci Technol 2016;50:12048–55. https://doi.org/10.1021/acs.est.6b03749.
2. Kurzawska-Pietrowicz P, Jasiński R. A Review of Alternative Aviation Fuels. Energies 2024;17. https://doi.org/10.3390/en17163890.
3. Valera-Medina A, Marsh R, Runyon J, Pugh D, Beasley P, Hughes T, et al. Ammonia–methane combustion in tangential swirl burners for gas turbine power generation. Appl Energy 2017;185:1362–71. https://doi.org/10.1016/j.apenergy.2016.02.073.
4. Schutte JS, Payan AP, Briceno SI, Mavris DN. Hydrogen‐Powered Aircraft. Encycl Aerosp Eng 2015:1‐13. https://doi.org/10.1002/9780470686652.eae1024.
5. Marek C, Smith T, Kundu K. Low Emission Hydrogen Combustors for Gas Turbines Using Lean Direct Injection 2005:1–27. https://doi.org/10.2514/6.2005-3776.
6. Beita J, Talibi M, Sadasivuni S, Balachandran R. Thermoacoustic Instability Considerations for High Hydrogen Combustion in Lean Premixed Gas Turbine Combustors: A Review. Hydrog 2021;2:33–57. https://doi.org/10.3390/hydrogen2010003.
7. Reichel TG, Goeckeler K, Paschereit O. Investigation of lean premixed swirl-stabilized hydrogen burner with axial air injection using Oh-plif imaging. Proc ASME Turbo Expo 2015;4A:1–10. https://doi.org/10.1115/1.4031181.
8. Howarth TL, Picciani MA, Richardson ES, Day MS, Aspden AJ. Direct numerical simulation of a high-pressure hydrogen micromix combustor: Flame structure and stabilisation mechanism. Combust Flame 2024;265:113504.

https://doi.org/10.1016/j.combustflame.2024.113504.
9. Albrecht P, Bade S, Lacarelle A, Paschereit CO, Gutmark E. Instability control by premixed pilot flames. J Eng Gas Turbines Power 2010;132:1–8. https://doi.org/10.1115/1.3019293.
10. Kahraman N, Tangöz S, Akansu SO. Numerical analysis of a gas turbine combustor fueled by hydrogen in comparison with jet-A fuel. Fuel 2018;217:66–77. https://doi.org/10.1016/j.fuel.2017.12.071.
11. Lu M, Li D, Xie K, Sun G, Fu Z. Investigation of flame evolution and stability characteristics of H2-enriched natural gas fuel in an industrial gas turbine combustor. Fuel 2023;331:125938. https://doi.org/10.1016/j.fuel.2022.125938.
12. Liu G, Zhu J, Liu Y. Assessment of radiative heat transfer with/without turbulence-radiation interaction in aero-engine swirling combustors of different geometric scales. Appl Therm Eng 2025;262. https://doi.org/10.1016/j.applthermaleng.2024.125244.
13. Sun H, Yan P, Xu Y. Numerical simulation on hydrogen combustion and flow characteristics of a jet-stabilized combustor. Int J Hydrogen Energy 2020;45:12604–15. https://doi.org/10.1016/j.ijhydene.2020.02.151.
14. Baurle RA, Fuller RP, White JA, Chen TH, Gruber MR, Nejad AS. An investigation of advanced fuel injection schemes for scramjet combustion. 36th AIAA Aerosp Sci Meet Exhib 1998. https://doi.org/10.2514/6.1998-937.
15. Rolls Royce Nene - Moorabbin Air Museum 2023. https://www.aarg.com.au/nene.html (accessed March 25, 2025).
16. The Story of the Nene. J Am Rocket Soc 1947;00:12–6. https://doi.org/10.2514/8.4171.
17. Gorgulu YF. CFD-based cooling performance of gas turbine blades. Aircr Eng Aerosp Technol 2025. https://doi.org/10.1108/AEAT-01-2025-0037.

COMBUSTION AND EMISSION BEHAVIOR OF A HYBRID AMMONIA–JET-A BLEND UNDER REAL JET ENGINE OPERATING CONDITIONS

[1*]*Yasin Furkan Gorgulu*, [2]*Selcuk Ekici*, [3]*T. Hikmet Karakoc*
[1] Department of Machinery and Metal Technologies, Keçiborlu Vocational School, Isparta University of Applied Sciences, Isparta, Türkiye
[2] Department of Aviation, Igdir University, Igdir, Türkiye
[3] Faculty of Aeronautics and Astronautics, Eskişehir Technical University, Eskişehir, Türkiye
*Corresponding author e-mail: yasingorgulu@isparta.edu.tr

ABSTRACT
This study presents a numerical investigation of a gas turbine combustor fueled by a 50–50 mass fraction blend of ammonia and kerosene, evaluated under cruise flight conditions corresponding to FL390. The combustor geometry was based on a validated two-dimensional axisymmetric configuration, and real jet engine operating conditions were applied as boundary inputs. Simulations were performed using ANSYS Fluent with the RNG k–ε turbulence model and eddy dissipation combustion model. The results indicate a peak flame temperature of approximately 1934 K, with NH_3 rapidly consumed near the flame front and $C_{12}H_{23}$ persisting downstream. Velocity reached ~200 m.s^{-1}, while turbulence levels remained moderate. Species mass fraction contours showed distinct behaviors for each fuel component, with oxygen excess evident along the axial region. Emission analysis revealed a maximum NO mass fraction of ~3.8 × 10^{-7}, while NOx and CO_2 levels remained within controlled limits. These outcomes align with prior research, suggesting that NH_3–hydrocarbon blends can support stable combustion with reduced carbon emissions, albeit with thermal NO formation.

Keywords: Ammonia combustion, CFD, cruise altitude, emission, fuel blend

1. INTRODUCTION
Decarbonizing the aviation sector has become a strategic priority as emission regulations tighten and sustainability goals intensify [1–4]. Gas turbine engines, being the dominant propulsion system in commercial aircraft, are central to these efforts [5–9]. While hydrogen has gained attention for its zero-carbon emissions and high reactivity, challenges related to storage, safety, and combustion instability under practical conditions remain unresolved [10–12]. As a result, hybrid fuel strategies combining hydrogen-free alternatives with conventional fuels are gaining momentum. Ammonia (NH_3) is a carbon-free, hydrogen-rich energy carrier with high volumetric energy density and ease of liquefaction [13–15]. However, its low reactivity and high ignition temperature often result in incomplete combustion and elevated NO_x emissions when used alone. On the other hand, conventional jet fuels such as dodecane ($C_{12}H_{23}$), a surrogate for Jet-A, offer high reactivity and well-established performance in turbine systems. A balanced blend of NH_3 and $C_{12}H_{23}$ can potentially leverage the clean-burning characteristics of ammonia and the combustion stability of kerosene-based fuels. Some studies have demonstrated that ammonia–hydrocarbon blends can reduce carbon emissions while maintaining reliable flame stabilization and thermal efficiency under gas turbine conditions. Recent advancements have focused on enhancing ammonia's combustion characteristics, such as blending with more reactive fuels to improve flame propagation and stability [16]. Wei et al. [17] show that adding high-reactivity fuels to ammonia can enhance flame propagation speed, heat release rate, and overall combustion efficiency. For instance, blending ammonia with methanol has been investigated using jet ignition systems, resulting in improved flame stability and reduced emissions. Specific research on ammonia and dodecane blends has been conducted to understand their combustion mechanisms and potential as alternative fuels. A skeletal chemical kinetic mechanism for n-dodecane/ammonia combustion was developed to facilitate computational studies, providing insights into ignition characteristics and pollutant formation [18]. Despite the potential benefits, challenges remain in utilizing ammonia–hydrocarbon blends. These include optimizing combustion strategies to balance efficiency and emissions, addressing material compatibility issues due to ammonia's corrosive nature, and ensuring safe handling and storage. Some reviews have discussed these challenges and the progress made in ammonia combustion research, emphasizing the need for continued innovation to realize ammonia's potential as a sustainable fuel [19].

In this study, a numerical simulation was conducted on a two-dimensional gas turbine combustor fueled by a 50–50 mass-based blend of ammonia and Jet-A. Real engine-derived boundary conditions corresponding to flight level FL390 were applied. The objective is to assess the thermal behavior and pollutant formation characteristics of the hybrid fuel, including NO and CO_2 emissions, flame structure, and combustion efficiency under realistic cruise conditions.

2. MATERIALS AND METHODS
This study presents a numerical investigation of the combustion characteristics of a two-dimensional gas turbine combustor fueled by a hybrid blend of ammonia and dodecane. The combustor geometry and mesh structure were based on a previously validated configuration, while the operating conditions were derived from real jet engine data corresponding to cruise altitude (FL390). A 50–50 mass-based fuel mixture was introduced through a central injector,

accompanied by primary and secondary air inlets. Computational simulations were conducted using ANSYS 2022 R2 Fluent, incorporating appropriate turbulence and combustion models to capture the complex interaction between fluid flow, heat transfer, and chemical reactions. Detailed descriptions of the numerical model setup, governing equations, and applied boundary conditions are provided in the following subsections.

2.1. Numerical Model

The computational domain employed in this study was adapted from the combustor configuration introduced by Kahraman et al. [20], originally inspired by a Rolls-Royce Nene-type gas turbine. The geometry features a two-dimensional axisymmetric layout comprising a single central fuel inlet and two separate air inlets designated for primary and secondary airflow. The total length and maximum height of the domain are 620 mm and 145 mm, respectively. To resolve the domain accurately, a structured mesh was generated using ANSYS Meshing. The final mesh includes 57,166 nodes and 56,137 elements, ensuring high spatial resolution, especially in regions of steep gradients such as the flame zone and near-wall layers. A five-layer inflation zone was applied along all solid boundaries to enhance near-wall accuracy. The mesh quality metrics confirm suitability for reactive flow simulations: average skewness was 0.13299 and orthogonal quality averaged 0.95328, both classified as "excellent" based on ANSYS best practices. The mesh structure is illustrated in Fig. 1. ANSYS Fluent 2022 R2 was used to perform the simulations. The realizable RNG k–ε turbulence model was employed due to its effectiveness in predicting swirling and recirculating flows commonly encountered in combustor environments. Further modeling details, including governing equations and boundary condition specifications, are discussed in the following subsection.

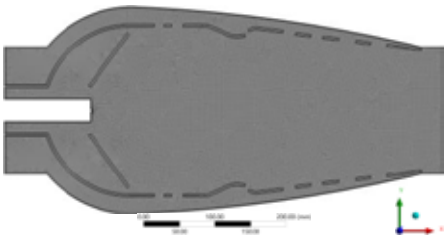

Fig. 1. Mesh structure of the hydrogen-fueled combustion chamber.

2.2. Governing Equations and Boundary Conditions

The CFD simulations were conducted by solving the steady-state, compressible form of the Navier–Stokes equations, which include the conservation of mass, momentum, energy, and species transport. The general governing equations used in the numerical model are as follows:

Continuity equation:

$$\frac{\partial \rho}{\partial t} + \nabla.\rho\vec{v} = 0 \tag{1}$$

Momentum equation:

$$\frac{\partial(\rho\vec{v})}{\partial t} + \nabla.(\rho\vec{v} \times \vec{v}) = -\nabla p + \nabla\tau + \rho\vec{g} \tag{2}$$

Energy equation:

$$\frac{\partial(\rho E)}{\partial t} + \nabla.(\vec{v}(\rho E + p)) = \nabla.(k_{eff}\nabla T) + S_E \tag{3}$$

Species transport equation:

$$\frac{\partial(\rho Y_i)}{\partial t} + \nabla.(\rho\vec{v}Y_i) = -\nabla.\vec{J_i} + R_i \tag{4}$$

Here,

ρ is the density, $\vec{v}$ is the velocity vector, p is pressure, E is the total energy, Y_i is the mass fraction of species i, $\vec{J_i}$ is the diffusion flux, and R_i represents the net rate of production due to chemical reactions. The viscous stress tensor τ, effective thermal conductivity k_{eff} and source term S_E account for viscous dissipation and heat release. Combustion was modeled using the Eddy Dissipation Model, which assumes that the reaction rate is controlled by the turbulent mixing of fuel and oxidizer. The realizable RNG k–ε turbulence model was employed to capture the effects of swirling and recirculating flows within the combustor. The working fluid was treated as a compressible ideal gas, with temperature-dependent thermophysical properties. Radiation heat transfer and soot formation were neglected due to the moderate operating temperature and low carbon content of the blend.

Real engine-derived inputs corresponding to FL390 were applied to all boundaries:

- Fuel inlet (NH_3–$C_{12}H_{23}$ mixture): 50–50 mass-based blend injected at a fixed mass flow rate of 0.3286 kg.s^{-1} and temperature of 298 K.
- Air inlets (primary + secondary): Primary air mass flow rate of 13.20 kg.s^{-1} and secondary air mass flow 6.50 kg.s^{-1} at 228.9 K, distributed between the two air ports.

- Turbulence intensity: Set to 5% at all inlets.
- Outlet: Modeled as a pressure outlet at 0 Pa gauge pressure, allowing free exit flow.
- Walls: Treated as adiabatic and no-slip.

3. RESULTS AND DISCUSSION

Figure 2 illustrates the flow, thermal, and chemical characteristics of the combustor operating with a 50–50 mass fraction NH_3–$C_{12}H_{23}$ blend at FL390 conditions. The peak flame temperature (Fig. 2a) reaches approximately 1934 K, lower than typical kerosene combustion due to the reduced reactivity of ammonia. Similar moderate temperature peaks in ammonia-based blends were reported by Valera-Medina et al. [4], emphasizing ammonia's flame-cooling effect. The velocity contour (Fig. 2b) reveals an axial acceleration of the flow, reaching a maximum velocity of approximately 200 $m.s^{-1}$ at the nozzle exit. The pressure field (Fig. 2c) indicates a steady decrease along the combustor axis, consistent with combustion-driven expansion. Figure 2d illustrates relatively low turbulence kinetic energy, particularly near the flame zone, suggesting limited shear and mixing intensity between the fuel and oxidizer streams. This is typical in partially pre-vaporized or low-reactivity fuel blends. Fuel distribution is visualized in Figures 2e and 2f. The NH_3 mass fraction drops sharply in the primary reaction region, whereas $C_{12}H_{23}$ persists longer into the chamber, indicating its slower vaporization and oxidation. The O_2 mass fraction (Fig. 2g) remains significant along the axis, implying that excess air is present, likely due to incomplete mixing or lean regions in the flow. Water vapor (Fig. 2h), primarily a product of NH_3 combustion, shows moderate levels centered along the flame front. In contrast, CO_2 concentration (Fig. 2i), originating from dodecane decomposition, is more evenly distributed across the combustion chamber. This dual-profile is a result of the chemical differences between nitrogenous and carbonaceous fuels in the blend. Pollutant formation is depicted in Figures 2j and 2k. The NO mass fraction peaks around 3.8×10^{-7} near the high-temperature post-flame region, while NO_x appears at much lower levels. These values align with findings by Li et al. [21], who noted that NO_x emissions from ammonia–hydrocarbon blends are influenced more by thermal effects than by fuel-N pathways at moderate temperatures.

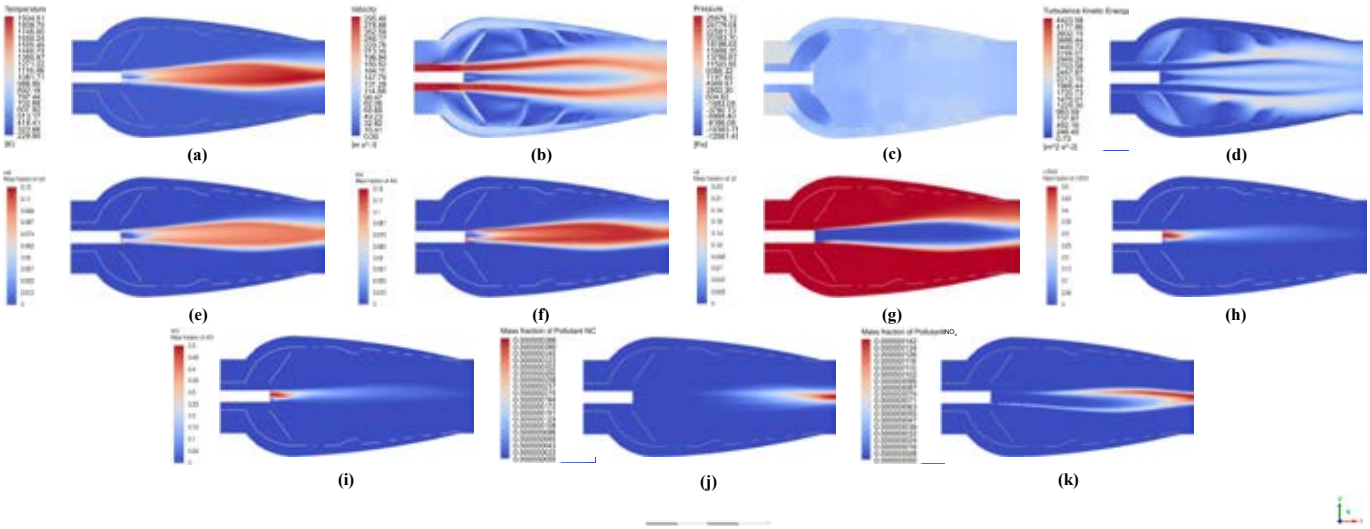

Fig. 2. Contours of the gas turbine combustor fueled by an NH_3–$C_{12}H_{23}$ blend at cruise altitude: (a) Temperature distribution [K], (b) Velocity magnitude [$m.s^{-1}$], (c) Static pressure [Pa], (d) Turbulence kinetic energy [$m^2.s^{-2}$], (e) NH_3 mass fraction, (f) $C_{12}H_{23}$ mass fraction, (g) O_2 mass fraction, (h) H_2O mass fraction, (i) CO_2 mass fraction, (j) NO mass fraction, (k) NO_x mass fraction.

4. CONCLUSIONS

- A 2D gas turbine combustor was numerically analyzed using a 50–50 mass fraction blend of NH_3 and $C_{12}H_{23}$ under FL390 cruise flight conditions.
- The simulation yielded a maximum flame temperature of ~1934 K, indicating moderate thermal intensity suitable for steady combustion.
- NH_3 was consumed rapidly near the flame front, while $C_{12}H_{23}$ remained dominant further downstream, reflecting differing combustion behaviors of the blended fuels.
- The formation of NO peaked at a mass fraction of ~3.8×10^{-7}, while NO_x levels remained relatively low, suggesting that pollutant formation was thermally driven and spatially confined.
- CO_2 distribution confirmed complete oxidation of the carbon-containing component, with no indication of unburned hydrocarbons in the post-flame region.
- The hybrid NH_3– $C_{12}H_{23}$ fuel demonstrated stable combustion, moderate emissions, and promising characteristics as a cleaner alternative to conventional jet fuels.

- Further studies are recommended to investigate variations in blending ratios, ignition behavior, and emission mitigation strategies for real engine implementation.

ACKNOWLEDGEMENT
The authors declare that they have no conflict of interest. Also, this research did not receive any specific grant from funding agencies in the public, commercial, or not-for-profit sectors.

REFERENCES

1. Li C, Wang Z, Liu H, Qin J, Wei L. Comparative study on the performance of the application of clean alternative fuels in SOFC/ICE hybrid power systems on electric aircraft. Front Energy Res 2023;11. https://doi.org/10.3389/fenrg.2023.1146587.
2. Eissele J, Lafer S, Mejía Burbano C, Schließus J, Wiedmann T, Mangold J, et al. Hydrogen-Powered Aviation—Design of a Hybrid-Electric Regional Aircraft for Entry into Service in 2040. Aerospace 2023;10:277. https://doi.org/10.3390/aerospace10030277.
3. Taylor AMKP. Science review of internal combustion engines. Energy Policy 2008;36:4657–67. https://doi.org/10.1016/j.enpol.2008.09.001.
4. Valera-Medina A, Xiao H, Owen-Jones M, David WIF, Bowen PJ. Ammonia for power. Prog Energy Combust Sci 2018;69:63–102. https://doi.org/10.1016/j.pecs.2018.07.001.
5. Bekele D, Zagorsky V, Hailu D. Exhaust Toxicity of a Gas Turbine Engine with Step-by-Step Post-Treatment: the Environmental Aspect of the Impact on Atmosphere. Ecol Eng Environ Technol 2022;23:193–8. https://doi.org/10.12912/27197050/146242.
6. Stefanizzi M, Capurso T, Filomeno G, Torresi M, Pascazio G. Recent Combustion Strategies in Gas Turbines for Propulsion and Power Generation toward a Zero-Emissions Future: Fuels, Burners, and Combustion Techniques. Energies 2021;14:6694. https://doi.org/10.3390/en14206694.
7. Takeishi K, Krewinkel R. Advanced Gas Turbine Cooling for the Carbon-Neutral Era. Int J Turbomachinery, Propuls Power 2023;8:19. https://doi.org/10.3390/ijtpp8030019.
8. Krishna VU, Mitrokhov N V. A preliminary design of a schematic evaluation of low emission turbofan combustors. J Phys Conf Ser 2021;1891:012026. https://doi.org/10.1088/1742-6596/1891/1/012026.
9. Stuttaford PJ, Oumejjoud K. Low CO2 Combustion System Retrofits for Existing Heavy Duty Gas Turbines. Vol. 3 Combust. Fuels Emiss. Parts A B, ASMEDC; 2008, p. 597–605. https://doi.org/10.1115/GT2008-50814.
10. Kurzawska-Pietrowicz P, Jasiński R. A Review of Alternative Aviation Fuels. Energies 2024;17. https://doi.org/10.3390/en17163890.
11. Oehlschlaeger MA. Grand challenges in aerospace propulsion. Front Aerosp Eng 2022;1. https://doi.org/10.3389/fpace.2022.1027943.
12. Petrescu RVV, Petrescu FIT. About Aircraft's New Power and Propulsion. Am J Eng Appl Sci 2020;13:111–23. https://doi.org/10.3844/ajeassp.2020.111.123.
13. Chai WS, Bao Y, Jin P, Tang G, Zhou L. A review on ammonia, ammonia-hydrogen and ammonia-methane fuels. Renew Sustain Energy Rev 2021;147:111254. https://doi.org/10.1016/j.rser.2021.111254.
14. Cardoso JS, Silva V, Rocha RC, Hall MJ, Costa M, Eusébio D. Ammonia as an energy vector: Current and future prospects for low-carbon fuel applications in internal combustion engines. J Clean Prod 2021;296:126562. https://doi.org/10.1016/j.jclepro.2021.126562.
15. Valera-Medina A, Amer-Hatem F, Azad AK, Dedoussi IC, de Joannon M, Fernandes RX, et al. Review on Ammonia as a Potential Fuel: From Synthesis to Economics. Energy & Fuels 2021;35:6964–7029. https://doi.org/10.1021/acs.energyfuels.0c03685.
16. Eyisse EF, Nadimi E, Wu D. Ammonia Combustion: Internal Combustion Engines and Gas Turbines. Energies 2024;18:29. https://doi.org/10.3390/en18010029.
17. Wei F, Wang P, Cao J, Long W, Dong D, Tian H, et al. Visualization investigation of jet ignition ammonia-methanol by an ignition chamber fueled H2. Fuel 2023;349:128658. https://doi.org/10.1016/j.fuel.2023.128658.
18. Kurumus AT, Bhattacharya A, Tamadonfar P, Kaario O. A skeletal mechanism for n-dodecane/ammonia combustion and an open-source reaction scheme optimization tool. Fuel 2024;373:132168. https://doi.org/10.1016/j.fuel.2024.132168.
19. Alnajideen M, Shi H, Northrop W, Emberson D, Kane S, Czyzewski P, et al. Ammonia combustion and emissions in practical applications: a review. Carbon Neutrality 2024;3. https://doi.org/10.1007/s43979-024-00088-6.
20. Kahraman N, Tangöz S, Akansu SO. Numerical analysis of a gas turbine combustor fueled by hydrogen in comparison with jet-A fuel. Fuel 2018;217:66–77. https://doi.org/10.1016/j.fuel.2017.12.071.
21. Li S, Liu Q, Zhang F, Sun J, Wang Y, Gu M. Study on Soot and NOx Formation Characteristics in Ammonia/Ethylene Laminar Co-Flow Diffusion Flame. Molecules 2024;29:4003. https://doi.org/10.3390/molecules29174003.

BOOSTING PHOTOCATALYTIC HYDROGEN PRODUCTION THROUGH $Ni_2P/g\text{-}C_3N_4/Ti_3C_2$ QUANTUM DOTS

[1*]*Duygu AKYÜZ*, [1]*Beyza Güven*, [1]*Erhan Demirbaş*
[1] Gebze Technical University, Faculty of Science, Department of Chemistry, Kocaeli, 41400, Türkiye
*Corresponding author e-mail: dakyuz@gtu.edu.tr

ABSTRACT
The growing demand for renewable energy is driven by the depletion of fossil fuels, increasing CO_2 emissions, and the rising need for energy. Hydrogen, as a clean energy carrier, plays a crucial role in future energy scenarios. Among hydrogen production technologies, photocatalytic hydrogen evolution (PCHER) remains at the research stage, with challenges such as low quantum efficiency, slow charge separation and transfer, recombination, and particle size limitations. In this study, a novel $Ni_2P/g\text{-}C_3N_4/Ti_3C_2$ quantum dot (QD) photocatalyst was synthesized to enhance photocatalytic hydrogen production. Ni_2P was obtained through the phosphorization of metal salt, $g\text{-}C_3N_4$ was synthesized via the thermal decomposition of urea, and Ti_3C_2 quantum dots were prepared using the hydrothermal method. The designed photocatalyst aims to improve visible light utilization and address key efficiency limitations in PCHER. This work contributes to the development of sustainable hydrogen production and provides a promising approach for future renewable energy applications.
Keywords: Photocatalytic Hydrogen Production, $g\text{-}C_3N_4$, Ti_3C_2 Quantum Dot, Nickel Phosphite.

1. INTRODUCTION

In a photocatalytic hydrogen production system, a semiconductor-based photocatalyst absorbs solar energy and converts it into usable energy for water splitting. Semiconductors are materials that possess a specific band gap (BG), which separates the conduction band (CB) from the valence band (VB) by a distinct energy level. Upon exposure to sunlight, electrons from the valence band of the photocatalyst are excited, jumping to the conduction band, leaving behind electron holes (h^+) in the valence band. These electron holes drive the oxidation of water (producing O_2), while the excited electrons in the conduction band promote the reduction of water (resulting in H_2 formation). This process regenerates the photocatalyst, allowing redox reactions to take place within the electrolyte.

For efficient photocatalytic hydrogen generation, the conduction band level of the semiconductor must be more negative than the standard redox potential for the H^+/H_2 reaction (0.0 V vs. SHE, not considering overpotentials). Likewise, the valence band level needs to be more positive than the standard potential for the O_2/H_2O reaction (1.23 V vs. SHE, again, without accounting for overpotentials). From a thermodynamic perspective, the semiconductor's band gap should exceed 1.23 eV to enable photocatalytic hydrogen production. However, in practical scenarios, factoring in overpotentials and energy band alignment, the band gap should ideally be above 1.8 eV. Due to the complexity and challenges of overall water splitting, most reported photocatalysts primarily focus on the half-reaction of H_2 production[1].

Since the first discovery of monolayer graphene in 2004 [2], two-dimensional (2D) materials have attracted significant interest. Due to their ability to enhance photocatalytic activity and suppress charge carrier recombination, researchers have particularly focused on materials such as $g\text{-}C_3N_4$ [3], black phosphorus[4], and transition metal dichalcogenides[5]. Among 2D carbon-based nanomaterials, $g\text{-}C_3N_4$, graphene, and carbon nanotubes exhibit unique properties, including quantum confinement effects, efficient visible light absorption, tunable energy levels, superior charge transport capabilities, large surface area, easy accessibility, and high quantum efficiency. These distinctive properties make them highly suitable for a range of photocatalytic applications. However, the practical use of $g\text{-}C_3N_4$ in photocatalytic water splitting is significantly constrained by the rapid recombination of photoexcited electrons and holes. To enhance the separation efficiency of these charge carriers, several structural modifications have been investigated, such as crystallinity improvement, heteroatom doping, heterojunction engineering, and cocatalyst incorporation [6]. Among these methods, cocatalyst incorporation is recognized as an effective means to enhance charge separation.

Various cocatalysts, including Pt, MoS_2, and graphene-based materials, assist in trapping photoinduced electrons, thereby reducing charge recombination [7]. Among these options, Pt exhibits the highest efficiency in photocatalytic hydrogen evolution. However, its widespread application is restricted by its high cost and limited availability. Consequently, the exploration of cost-effective cocatalysts is essential to support the advancement of semiconductor-based photocatalysts for industrial-scale applications.

MXenes have become one of the most intriguing two-dimensional (2D) materials, finding applications in various fields such as electromagnetic shielding, batteries, power generation, and catalysis[6]. Compared to the widely studied graphene, 2D MXenes exhibit remarkable electrical conductivity, suggesting their potential to replace conventional graphene-based materials in various applications [7]. Despite the advantages of 2D MXenes, a literature indicate that hybrid materials synthesized with zero-dimensional (0D) MXenes exhibit significantly higher photocatalytic hydrogen production rates. The superior optical and catalytic activity of 0D MXene quantum dots (QDs) has been attributed to their size-dependent properties, low Fermi level, defects, and surface functional groups.

To overcome key limitations in semiconductor-based photocatalysis, such as electron-hole recombination and short

charge carrier lifetimes, MXenes are frequently utilized as cocatalysts. Dong et al.[8] synthesized a Ti_3C_2 QD-modified 3D/2D TiO_2/g-C_3N_4 hybrid, achieving a photocatalytic hydrogen production rate of 5540.21 μmol h^{-1} g^{-1}. They also reported that Ti_3C_2 QD cocatalysts enhanced the hydrogen evolution rate of 3D/2D TiO_2/g-C_3N_4 by nearly two fold. Given these advantages, we aims to synthesize 0D Ti_3C_2 QDs as an efficient cocatalyst for photocatalytic applications.
Metal phosphides are typically formed by the combination of metal and phosphorus elements. The electronegativity of the phosphorus (P) atom in metal phosphides facilitates the conversion of positively charged hydrogen ions in the electrolyte to hydrogen gas. Transition metal phosphides (such as Ni_2P, FeP, CoP, MoP, and Cu_3P), which possess high conductivity and low overpotentials, are widely considered as promising candidates for both photocatalysis and electrocatalysis in hydrogen production reactions [9].In one study, it was reported that the nickel in Ni_2P acts as a hydride acceptor, while phosphorus serves as a proton-accepting site, synergistically accelerating H_2 formation [10].
A thorough literature review reveals that the application of 2D/0D g-C_3N_4/Ti_3C_2 QD photocatalysts in photocatalytic hydrogen production with Ni_2P cocatalysts has not been reported. Therefore, the Ni_2P/g-C_3N_4/Ti_3C_2 QD catalyst were designed as entirely novel and innovative.

2. MATERIALS AND METHODS

2.1. Synthesis of catalysts

The synthesis of g-C_3N_4 and Ti_3C_2 QDs were carried out according to Y. Li et al. method [11]The synthesis of Ni_2P was carried out according to the procedure described by K. Wang et al.[12]. Ni_2P with different weight percentages (%0.5, %1.0, %3.0, %5.0, %10.0, and %15.0) was obtained by grinding g-C_3N_4 in a mortar for 30 minutes.
A 40 mL aqueous solution of Ti_3C_2 QD at 50 mg/L concentration was mixed with 100 mg of the Ni_2P/g-C_3N_4 binary hybrid, which showed the highest hydrogen production rate, for 24 hours on a stirrer. The resulting suspension was centrifuged at 5000 rpm for 30 minutes and then dried in a vacuum oven at 60°C. Ni_2P/g-C_3N_4/Ti_3C_2 QD (%2.0 wt) was obtained. Similarly, ternary hybrid was prepared with different weight percentages (%4.0, 6.0, 8.0, and 10.0) to synthesize the optimum Ni_2P/g-C_3N_4/Ti_3C_2 QD catalyst.

2.2. Photocatalytic Performance Tests

The photocatalytic reactor was designed with a quartz glass upper part that allows UV-Vis light to pass through, equipped with gas inlet and outlet as well as water inlet and outlet. Initially, optimizations were carried out using 10 mg of catalyst to minimize the amount before determining the optimum quantity. The catalyst was transferred into the reactor with a 10% triethanolamine (TEOA) aqueous solution as the electrolyte. The temperature of the reactor was continuously controlled by water flow. During the reaction, the catalyst was mixed using a magnetic stirrer. The gas produced in the reaction was carried through a microfluidic pressure sensor connected to the system, which was used to measure the hydrogen quantity. Additionally, the gas was characterized by using gas chromatography. The light source was positioned to illuminate the entire photocatalyst, and its intensity was adjusted to 100 mW/cm² using a light meter. To prevent errors from changes in light intensity over time, the light intensity was measured before each photocatalytic reaction to ensure the stability of the light source.

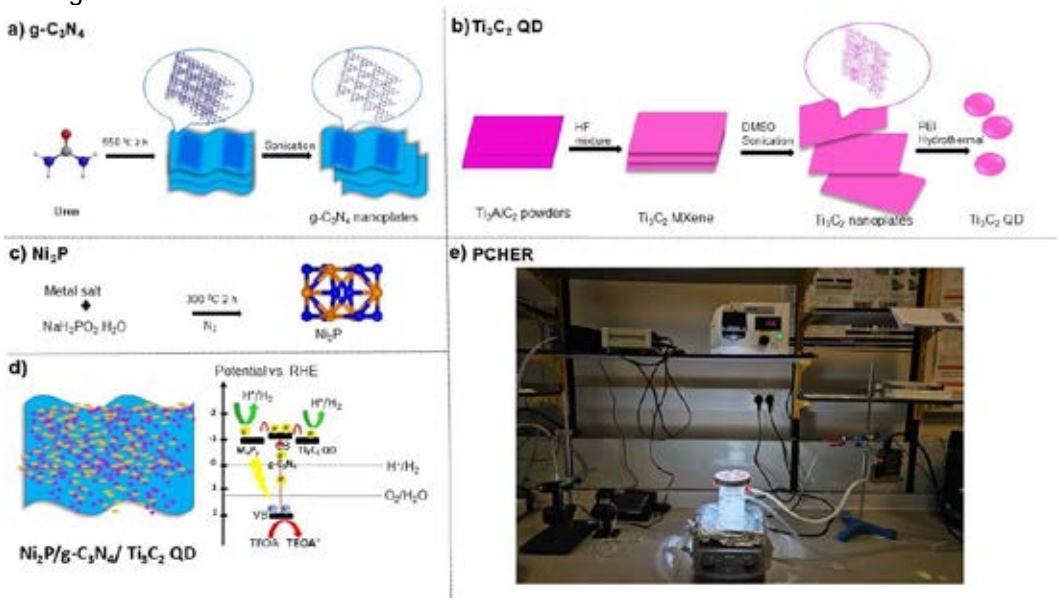

Fig. 1. a) Synthesis of g-C_3N_4, b) Synthesis of Ti_3C_2 QD, c) Synthesis of Ni_2P, d) Proposed mechanism of Ni_2P/g-C_3N_4/Ti_3C_2 QD photocatalysts, e) Design of the PCHER system.

3. RESULTS AND DISCUSSION

The characterization of the synthesized catalysts was performed prior to PCHER to verify the successful synthesis and identify any changes in the structure and morphology of the catalysts. X-ray diffraction (XRD), Fourier Transform Infrared Spectroscopy (FT-IR) and X-Ray Photoelectron Spectroscopy (XPS) analyses of the synthesized catalysts were carried out. The morphological and structural characterizations of the catalysts were performed using Scanning Electron Microscopy (SEM), Transmission Electron Microscopy (TEM), and High-Resolution Transmission Electron Microscopy (HRTEM), providing information about important parameters such as surface properties, homogeneity, and lattice spacing. Energy Dispersive X-ray Spectroscopy (EDS) was used to gather information about the elements constituting the catalyst and to determine whether the syntheses were successfully carried out. Fig. 2 shows the morphological and structural characterization of g-C_3N_4, Ni_2P, Ni_2P/g-C_3N_4, and Ni_2P/g-C_3N_4/Ti_3C_2 QDs. The SEM image of g-C_3N_4 displays the material's nanoplate structure (Fig. 2a). In Fig. 2b, the clustered rock-like structure of Ni_2P is shown. Fig. 2c displays the Ni_2P structures between graphitic nanotubes, illustrating Ni_2P/g-C_3N_4. The SEM image of Ni_2P/g-C_3N_4/Ti_3C_2 QD in Fig. 2d shows no clear MXene QD effect. Figs. 2e and 3f show the EDS spectra of Ni_2P and Ni_2P /g-C_3N_4/Ti_3C_2 QDs, respectively. The successful synthesis of Ni_2P is supported by the EDS results. The EDS spectrum of Ni_2P/g-C_3N_4/Ti_3C_2 QD shows peaks for C and N from graphitic carbon nitride and Ni and P from Ni_2P. To confirm the presence of MXene QDs, HRTEM and FFT images were recorded (Figs. 2g, f, and i). The HRTEM and FFT results show that the lattice spacing corresponding to the Ni_2P (111) crystal plane is 0.221 nm consistent with the literature[13] . Elemental mapping shows the distribution of C, N, P, Ni, and Ti elements in the Ni_2P/g-C_3N_4/Ti_3C_2 QD powder mixture (Fig. 2j).
The band gaps of the nanomaterials were determined using UV-Vis diffuse reflectance spectroscopy (DRS) analysis. The time-resolved photoluminescence spectrum (TRPL) analysis method was used to determine the lifetime of photoexcited charges. The catalyst ratios in the PCHER system were adjusted based on their hydrogen production performance. As part of the photoelectrochemical activity test, the photocurrent-time curve was recorded by switching the light on and off at specific intervals (100 s). Through photocurrent-time curves, information was obtained regarding charge transfer efficiency, photocatalytic activity, charge carrier mobility, and charge separation.

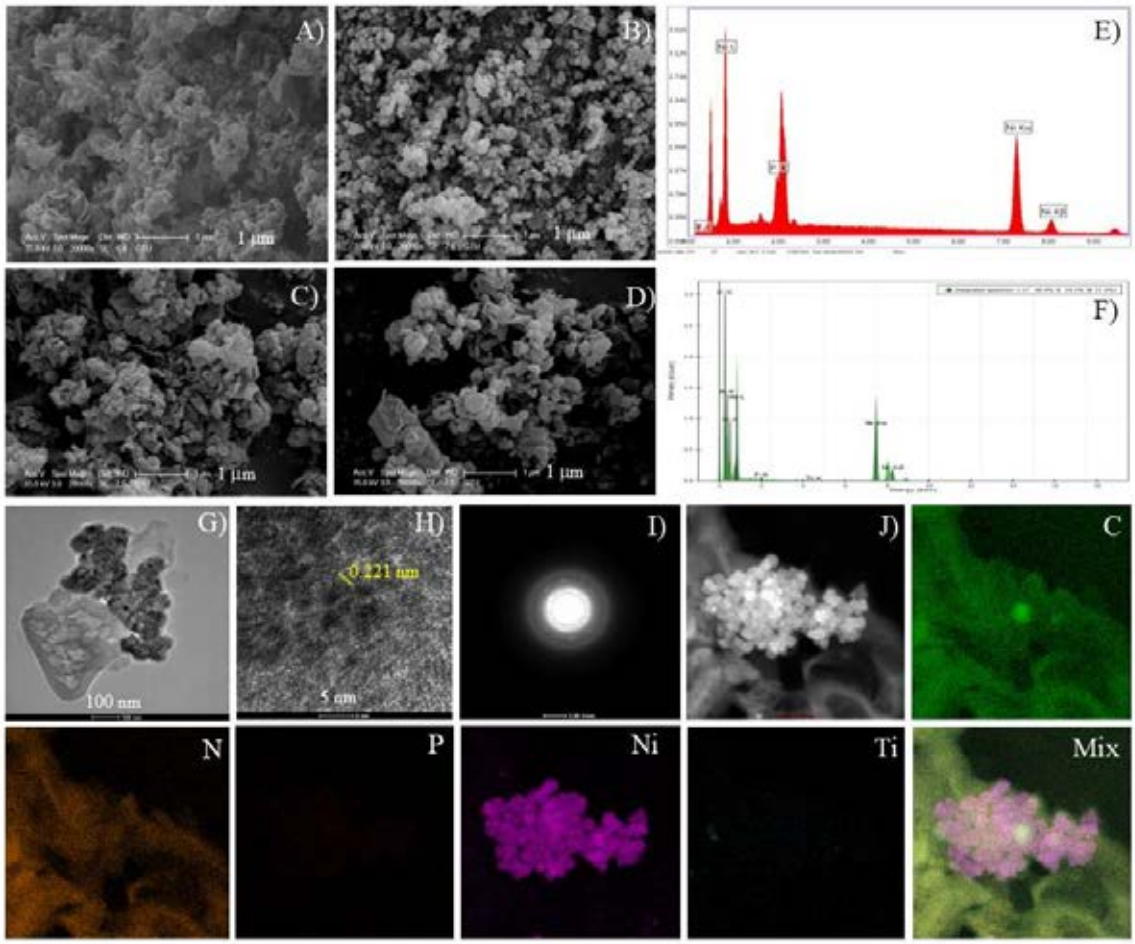

Fig. 2. SEM images of a) g-C_3N_4, b) Ni_2P, c) Ni_2P/g-C_3N_4, d) Ni_2P/g-C_3N_4/Ti_3C_2 QD. EDS spectra: e) Ni_2P, f) Ni_2P/g-C_3N_4/Ti_3C_2 QD. g-i) HRTEM images and FFT image of Ni_2P/g-C_3N_4/Ti_3C_2 QD. j) Elemental mapping of Ni_2P/g-C_3N_4/Ti_3C_2 QD.

4. CONCLUSIONS

In this study, the structural, morphological, and photoelectrochemical properties of the synthesized $Ni_2P/g\text{-}C_3N_4/Ti_3C_2$ QD nanocomposite were thoroughly investigated. SEM, HRTEM, and EDS analyses confirmed the successful synthesis of the nanocomposite and the homogeneous distribution of its components. XPS analysis verified the surface composition and the chemical bonding states of the elements. The UV-Vis DRS analysis determined the band gaps of the materials, revealing enhanced optical properties for the $Ni_2P/g\text{-}C_3N_4/Ti_3C_2$ QD composite. TRPL analysis demonstrated an extended lifetime of photoexcited charges, indicating efficient charge separation. The catalyst ratios in the PCHER system were optimized to enhance hydrogen production performance. Furthermore, photoelectrochemical activity tests, particularly photocurrent-time measurements, showed that the material exhibits high charge transfer efficiency and excellent photocatalytic activity. These findings suggest that the $Ni_2P/g\text{-}C_3N_4/Ti_3C_2$ QD nanocomposite is a promising photocatalyst for sustainable hydrogen production.

ACKNOWLEDGEMENT

This work was financially supported by The Scientific and Technological Research Council of Türkiye, TUBITAK (Project No:223Z176).

REFERENCES

1. Yan T, Liu H, Jin Z (2021) G-C3N4/α-Fe2O3Supported Zero-Dimensional Co3S4Nanoparticles Form S-Scheme Heterojunction Photocatalyst for Efficient Hydrogen Production. Energy and Fuels 35:856–867
2. Novoselov KS, Geim AK, Morozov S V., Jiang D, Zhang Y, Dubonos S V., Grigorieva I V., Firsov AA (2004) Electric field in atomically thin carbon films. Science (1979) 306:666–669
3. Kumar A, Sharma SK, Sharma G, Naushad M, Stadler FJ (2020) CeO2/g-C3N4/V2O5 ternary nano hetero-structures decorated with CQDs for enhanced photo-reduction capabilities under different light sources: Dual Z-scheme mechanism. J Alloys Compd 838:155692
4. Nakhanivej P, Yu X, Park SK, et al (2018) Revealing molecular-level surface redox sites of controllably oxidized black phosphorus nanosheets. Nature Materials 2018 18:2 18:156–162
5. Akyüz D, Koca A (2018) Photocatalytic hydrogen production with reduced graphene oxide (RGO)-CdZnS nano-composites synthesized by solvothermal decomposition of dimethyl sulfoxide as the sulfur source. J Photochem Photobiol A Chem 364:625–634
6. Li Z, Wu Y, Li Z, Wu Y (2019) 2D Early Transition Metal Carbides (MXenes) for Catalysis. Small 15:1804736
7. Huang H, Song Y, Li N, Chen D, Xu Q, Li H, He J, Lu J (2019) One-step in-situ preparation of N-doped TiO2@C derived from Ti3C2 MXene for enhanced visible-light driven photodegradation. Appl Catal B 251:154–161
8. Dong G, Zhang Y, Wang Y, Deng Q, Qin C, Hu Y, Zhou Y, Tian G (2021) Ti3C2Quantum Dots Modified 3D/2D TiO2/g-C3N4S-Scheme Heterostructures for Highly Efficient Photocatalytic Hydrogen Evolution. ACS Appl Energy Mater 4:14342–14351
9. Chung DY, Jun SW, Yoon G, et al (2017) Large-Scale Synthesis of Carbon-Shell-Coated FeP Nanoparticles for Robust Hydrogen Evolution Reaction Electrocatalyst. J Am Chem Soc 139:6669–6674
10. Zhao H, Jiang P, Cai W (2017) Graphitic C3N4 Decorated with CoP Co-catalyst: Enhanced and Stable Photocatalytic H2 Evolution Activity from Water under Visible-light Irradiation. Chem Asian J 12:361–365
11. Li Y, Ding L, Guo Y, Liang Z, Cui H, Tian J (2019) Boosting the Photocatalytic Ability of g-C3N4 for Hydrogen Production by Ti3C2 MXene Quantum Dots. ACS Appl Mater Interfaces 11:41440–41447
12. Wang K, Xie H, Li Y, Wang G, Jin Z (2022) Construction of CoP/Cu3P/Ni2P Double S-Scheme Heterojunctions for Improved Photocatalytic Hydrogen Evolution. Journal of Physical Chemistry C 126:6947–6959
13. Li T, Jin Z (2022) Unique ternary Ni-MOF-74/Ni2P/MoSx composite for efficient photocatalytic hydrogen production: Role of Ni2P for accelerating separation of photogenerated carriers. J Colloid Interface Sci 605:385–397

NUMERICAL AND EXPERIMENTAL INVESTIGATION OF ELECTRIC AND FUEL CELL HYBRID MINI UAV

[1*]İhsan Sağlam, [1]Zeynep Sude İşleyen, [1,2]Mustafa Umut Karaoğlan, [1]Şahin Yavuz
[1]Dokuz Eylul University, Faculty of Engineering, Department of Mechanical Engineering, Tinaztepe, Buca, Izmir, 35390, Turkey
[2]Dokuz Eylul University, Energy Application and Research Center, Tinaztepe, Buca, Izmir, 35390, Turkey
*Corresponding author e-mail: ihsann.sglm@gmail.com

ABSTRACT
Technological and industrial advancements have increased the need for sustainable energy solutions, leading to the widespread use of fuel cells and battery technologies in aviation applications such as unmanned aerial vehicles (UAVs). In this study, battery and fuel cell components of a fixed-wing UAV was modeled in the Matlab/Simulink environment to analyze its voltage response under variable current inputs for the comparison of the simulation results with the measurement from the flight experiment of the mini electric UAV. A 100 W fuel cell was integrated into the system with a constant current output to examine the power and flight distance contributions of both the battery and the fuel cell. Additionally, the study provides a validation of the numerical model of powertrain components of the mini electric UAV. The findings contribute to the development of energy management strategies for hybrid-powered UAVs and provide valuable insights for optimizing flight duration.

Keywords: UAV, battery, fuel cell, sustainable aviation

1. INTRODUCTION

Technological and industrial advancements, driven by the increasing concerns over environmental pollution and the growing demand for sustainable energy solutions, have facilitated the integration of innovative energy technologies across various sectors, including aviation. In particular, the aviation industry has progressively adopted fuel cell and battery systems to enhance energy efficiency and reduce the environmental impact of aerial operations, addressing the urgent need for more eco-friendly alternatives [1].

Currently, Lithium Polymer (Li-Po) batteries are widely used in unmanned aerial vehicles (UAVs). These batteries are well-suited for short-distance flights due to their high energy densities, lightweight structure, and rapid charging capabilities. Additionally, their high discharge rates provide a significant advantage in meeting the sudden power demands of UAVs. However, Li-Po batteries have limited energy capacity, which may not suffice for applications requiring extended flight durations. Furthermore, their tendency to degrade over time and the need for thermal management impose operational limitations on their efficiency. In contrast, hydrogen fuel cells offer significant advantages over Li-Po batteries by providing longer flight durations and higher energy efficiency. Fuel cells generate continuous power through the electrochemical reaction between hydrogen and oxygen, which results in longer range and operational time compared to batteries. With their low carbon emissions and environmentally friendly nature, fuel cells play a crucial role in advancing sustainable aviation solutions. Additionally, hybrid power systems, which combine both battery and fuel cell technologies, offer a more balanced and efficient energy management solution for UAVs. While fuel cells supply continuous and stable power, batteries address sudden power demands, thereby optimizing system performance. This hybrid approach enables longer flights, maximizes energy usage, and increases overall efficiency. Moreover, hybrid systems offer greater flexibility compared to systems relying solely on either batteries or fuel cells, allowing for better adaptability to diverse flight scenarios. As a result, more efficient power usage and an extended system lifespan contribute significantly to the development of sustainable aerial vehicles [2].

This study aims to explore the impact of a hybrid power system incorporating both battery and fuel cell components on UAV performance. The modeling will be conducted in the Matlab/Simulink environment, with simulation results compared to measurements obtained from flight experiments of a mini electric UAV. A 100 W fuel cell will be integrated into the system with a constant current output to analyze the power and flight distance contributions of both the battery and fuel cell. Additionally, the numerical model for the powertrain components of the mini electric UAV will be validated. The findings of this research are expected to contribute to the development of energy management strategies for hybrid-powered UAVs, offering valuable insights for optimizing flight duration.

2. NUMERICAL AND EXPERIMENTAL METHODS

2.1 Mini Electric UAV

In flight dynamics, there are four fundamental forces acting on an unmanned aerial vehicle (UAV): lift, weight, thrust, and drag. Lift is the force that keeps the aircraft airborne, which depends on the flight speed and the characteristics of the wing profile. Weight is the downward force exerted by gravity on the UAV. Thrust is the force generated by the engines that propels the aircraft forward, which varies depending on the motor and propeller configuration. Drag is the resistance

created by the airflow against the motion of the aircraft. These forces change depending on the UAV's design, weight, aerodynamic features, motor power, and flight speed [3].

In hand-launched UAVs, the thrust during takeoff is augmented by human power. In cruising flight, the ideal thrust-to-weight ratio typically ranges from 1:1 to 0.3:1, and it may vary based on the design, mission, and flight conditions [4]. In this study, calculations were made for both scenarios with the throttle at 50% in cruising flight. First, the flight time was calculated for the configuration using only a Li-Po battery. In the second case, the flight time was calculated for the hybrid system, where the integration of a fuel cell and the required body modifications were made to accommodate the increased weight, and a motor and propeller configuration capable of compensating for the additional weight was selected. The flight time formula is given in Equation (1)

$$Flight\ Time\ (hours) = \frac{Battery\ Capacity\ (mAh)}{Current\ Draw\ (A) \times 1000} \quad (1)$$

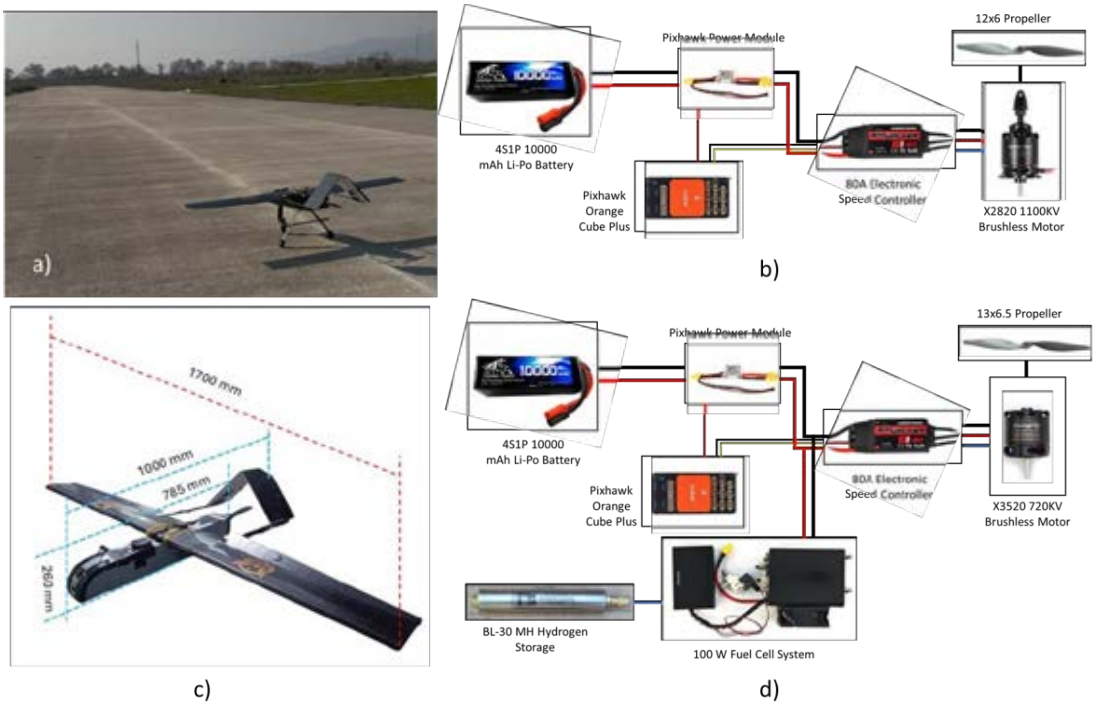

Fig. 1. Mini UAV (a) and its main dimensions (c) for electic (b) and fuel cell hybrid (d) powertrain configurations

2.2. Powertrain Components of the UAV Configurations

The Unmanned Aerial Vehicle (UAV) model examined in both cases operates with a hybrid system using only a Li-Po battery and a hydrogen fuel cell. In the developed model, the UAV parameters listed in Table 1 have been utilized.

Table 1. Parameters of the powertrain system for mini UAV

Parameter	Value	Unit	Parameter	Value	Unit
Total mass for first configuration	2700	g	Nominal power of fuel cell	100	W-
Total mass for second configuration	4000	g	Fuel cell operating voltage range	10-18	V
Wing area	28.65	dm^2	Fuel cell operating current range	0-9.6	A
Density of air	1.22	kg/m^3	Hydrogen consumption of fuel cell	1500	mL/min
Li-Po battery capacity	10000	mAh	Fuel cell weight	630	g
Li-Po battery capacity coefficient	25	C	Number of cell in fuel cell stack	20	-
Brushless motor diameter and length for first configuration	28-20	mm	Fuel cell stack size	94x78x91	mm
			Hydrogen capacity of MH tank	34	sL
Brushless motor diameter and length for second configuration	35-20	mm	MH tank cylinder diameter	28.6	mm
			MH tank mass	438	g
ESC current capacity	80	A	MH tank overall length	198	mm

In battery model, the term of OCV which represents "Open Circuit Voltage", refers to the voltage measured when an electrical circuit is not closed, meaning no load is connected. OCV indicates the maximum voltage potential of a battery or fuel cell and is an important parameter for assessing the health status and charge level of the battery.

The OCV value of a battery can be used to determine its state of charge (State of Charge - SoC) and typically varies based on factors such as the chemical composition of the battery, temperature, and current charge state. SoC describes the remaining energy in the battery as a percentage; it is considered 100% when fully charged and 0% when completely discharged. The SoC at a given time can be calculated using Equation (2) [5].

$$SOC(t) = SOC(0) - \frac{1}{C_{bat}} \cdot \int_o^t P_{bat} \cdot dt \quad (2)$$

In this study, the PEM (Proton Exchange Membrane) fuel cell type has been chosen for the fuel cell hybrid UAV. A 100 W PEM fuel cell model is also modeled in the Matlab/Simulink environment. In this model, current (A) is used as the input, and voltage (V) is observed as the output. The cell voltage (Vcell) is calculated using Equation (3), taking into account various parameters in the system.

When a fuel cell supplies power to a load, several factors contribute to reducing the voltage. These factors include Nernst voltage (E_{Nernst}), activation loss (V_{act}), ohmic loss (V_{ohm}), and concentration loss (V_{conc}). Nernst voltage represents the chemical potential difference within the cell, while activation loss refers to the energy required for the electrochemical reactions to occur. Ohmic loss is the energy loss resulting from resistance within the cell, and concentration loss is associated with the depletion of reactants reaching low concentrations within the cell. This model provides an important foundation for understanding the performance and efficiency of PEM fuel cells [6].

$$V = E_{Nerst} - V_{act} - V_{ohmic} - V_{conc} \quad (3)$$

2.3. Simulation Model

This study models the battery system of a fixed-wing UAV in the MATLAB/Simulink environment to evaluate aircraft performance and flight range. To validate the accuracy of the model, the battery's voltage response under variable current inputs was analyzed and compared with flight test measurements obtained from the mini electric UAV. Additionally, a 100 W fuel cell with a constant current output was integrated into the system to assess the contributions of both the battery and the fuel cell to power generation and flight endurance. The results confirm the validity of the numerical model for the UAV's powertrain components and provide valuable insights into the performance of hybrid power systems. Figure 2 illustrates the Simulink model of the battery.

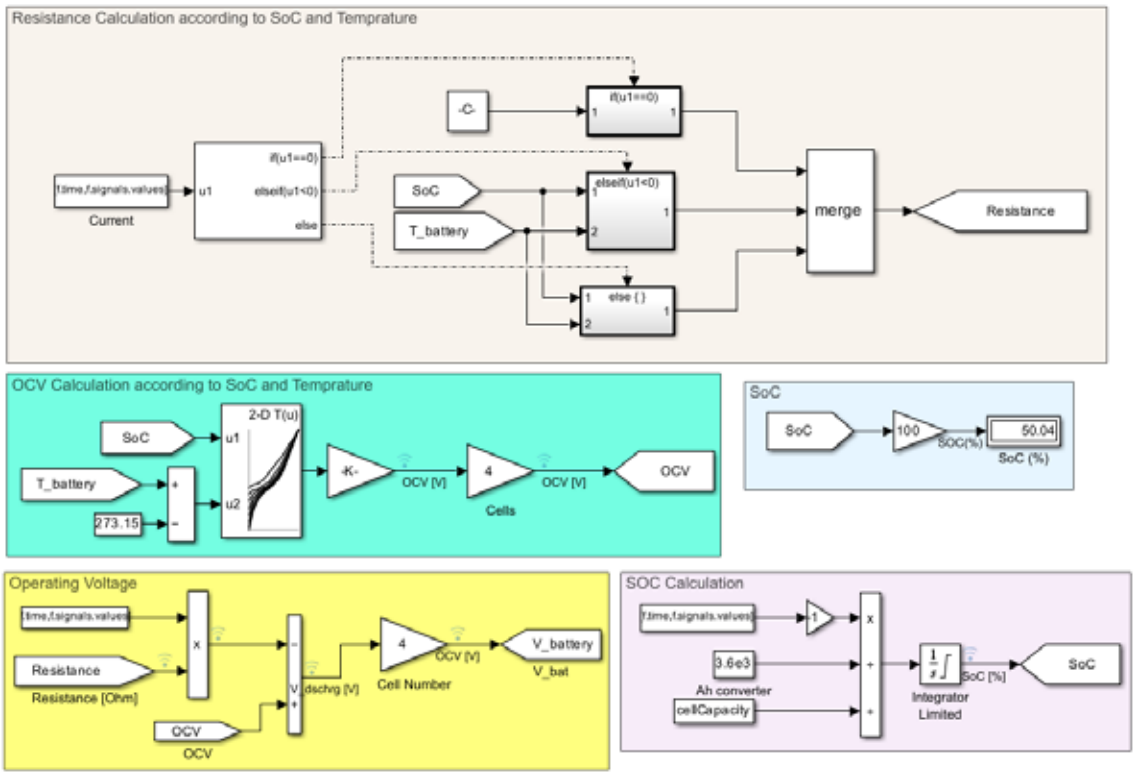

Fig. 2. Matlab/Simulink model of the battery for mini electric UAV

This Simulink model is designed to analyze the dynamic behavior of the battery system in a mini electric UAV and consists of four main components. The first component, Resistance Calculation, determines the battery's internal resistance

based on variables such as State of Charge (SoC) and battery temperature (T_battery). The second component, Open Circuit Voltage (OCV) Calculation, estimates the OCV by considering variations in SoC and temperature. The third component, SoC Calculation, computes the SoC value as a percentage based on the input current and battery capacity. Finally, the Operating Voltage Calculation determines the battery's terminal voltage by incorporating internal resistance and discharge voltage. This model serves as a critical tool for simulating battery responses under various operating conditions, providing deeper insights into its performance.

3.RESULTS AND DISCUSSION

During cruise flight, the required power demand for the UAV was observed, and the time-dependent variation in battery voltage was analyzed using both experimental and simulation data. The flight time was calculated based on the current drawn by the systems throughout the UAV's flight duration.

As shown in Fig. 3a, the decline in battery voltage over time indicates continuous battery discharge, while the similarity between experimental and numerical data confirms the accuracy of the simulation model. In Fig. 3b, the fluctuating and variable battery current demonstrates its sensitivity to load changes, whereas the fuel cell ensures a stable power supply by maintaining a constant current of 9.6 A. In Fig. 3c, the state of charge (SOC) of the battery reveals that the all-electric system depletes significantly faster compared to the fuel cell hybrid system, extending the flight duration by approximately 350 seconds (≈40% of flight time) with fuel cell support.Furthermore, the "End of the Fuel Cell" label marks the point where the fuel cell's energy is depleted, after which the battery discharges at an accelerated rate. In Fig. 3d, the battery power follows a decreasing and fluctuating trend over time, whereas the fuel cell delivers a more stable power output at 115 kW. Overall, the hybrid system offers a more balanced energy management approach, increasing flight time while reducing the load on the battery.

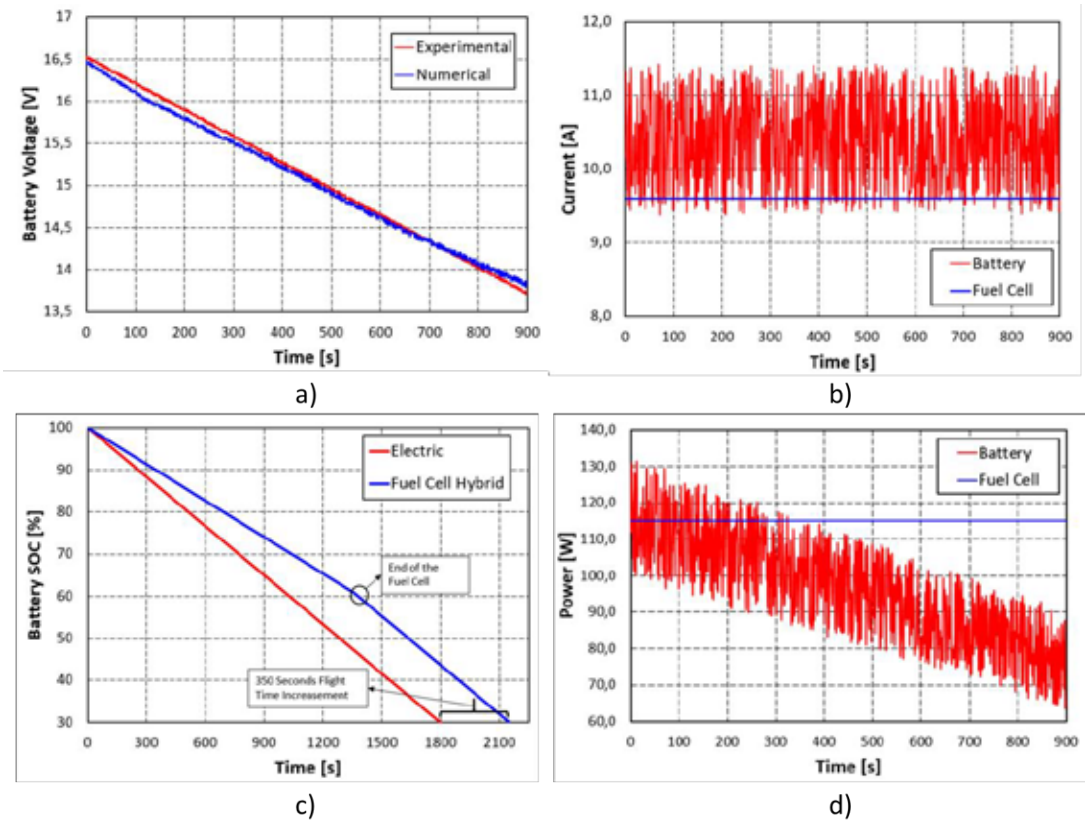

Fig. 3. Validation results for battery output voltage of electric (a) and constant fuel cell operation for hybrid UAV (b)

4. CONCLUSIONS

In this study, the performance of an Unmanned Aerial Vehicle (UAV) powered by a hybrid system, incorporating a Li-Po battery and a hydrogen fuel cell, was analyzed through both experimental and in the Matlab/Simulink environment. The results demonstrate that hybrid powertrains offer significant advantages in terms of energy efficiency, extended flight time, and environmental sustainability. The integration of the fuel cell and battery system enabled effective energy management, optimizing power distribution and enhancing UAV performance. Analyzing UAV performance is crucial for future studies aimed at system optimization and component selection. Different energy management strategies can

influence power distribution, leading to various choices in fuel cell and battery sizing. Hybrid systems, by efficiently balancing the short-term high power demands with the battery and providing long-term efficient energy use through the fuel cell, optimize power management and enhance overall performance. The findings support the feasibility of fuel cell systems for UAV applications. Future studies can focus on further system optimization and real-world testing to advance this technology. The widespread adoption of fuel cell-powered UAVs will contribute to reducing carbon emissions and promoting more sustainable aerial transportation solutions.

REFERENCES

[1] Masiol, M., & Harrison, R. M. (2014). Assessing the environmental impacts of aircraft noise and emissions. *Journal of Environmental Management.*

[2] Vargas, A., Castillo, R., & Martinez, J. (2021). Hybrid Fuel Cell - Battery System as a Main Power Unit for Small Unmanned Aerial Vehicles (UAV). Energy Procedia

[3] Anderson, J. D. (2016). Fundamentals of Aerodynamics. McGraw-Hill Education.

[4] A. Yılmaz, (2023) Taktik insansız hava aracı tasarımı ve üretimi. İstanbul, Türkiye: ABC Yayınları, 2023.

[5] E. İ., & Okumuş, H. İ. (2018). Battery Models and State of Charge (SoC) Determination. *EMO Scientific Journal*, 8(1), 21-25.

[6] Tavman, A. (2004). Bor-Based Fuel Cells and Batteries. *Sigma*, 2.

ASSESSMENT OF HYDROGEN AND METHANOL AS ALTERNATIVE FUELS IN THE SHIPPING INDUSTRY

[1*] *Evangelos - Theodoros Livanos* [1*] *S. Aykut Korkmaz* [2] Sheida Afshan
[1] Department of Civil, Maritime and Environmental Engineering, University of Southampton, UK
[2] Faculty of Engineering and Physical Sciences, University of Southampton, UK
[*]Corresponding author e-mail: aykut.korkmaz@soton.ac.uk

ABSTRACT
This study thoroughly compares hydrogen and methanol as marine fuels by implementing an analytical Life Cycle Assessment (LCA) and Return on Investment Analysis (ROI) for Kamsarmax bulk carriers. The feedstock pathways selected for each fuel consist of coal, natural gas and solar PV electricity. The effect of carbon capture technologies is applied to the natural gas pathway for feedstock processing. The life cycle inventory (LCI) model considered feedstock from Australia, processing in the Netherlands, and final bunkering in Rotterdam to simulate real-life trading environments. Software utilisation is a standard tool for most LCA studies. This study focuses on the application of combining two systematic methodologies, the Marine Environment Protection Committee (MEPC-81) well-to-wake (WtW) and the Renewable Energy Directive (RED-II), to assess the greenhouse gas (GHG) intensity of each pathway. The financial assessment is based on the International Maritime Organisation's (IMO) GHG reduction measures, which consider the global fuel intensity (GFI) of each pathway. The results will therefore help to evaluate hydrogen and methanol as plausible alternatives to heavy fuel oil and validate the effectiveness of this methodology through existing studies. The environmental results showed that the fuels with the least carbon equivalent impact, on a WtW and global warming potential (GWP) 100 basis, were "Green" Hydrogen and "Blue" Methanol, with 89.50 gCO2eq./MJ and 39.17 gCO2eq./MJ, respectively. The financial results, taken over a 20-year chartered lifetime of the vessel, showed that a "Blue" Methanol-powered Kamsarmax will generate an 8% return whilst one propelled by "Green" Hydrogen will generate a 23% return, both of which include IMO's regulatory costs. These figures shift to 14% and 11% respectively when IMO measures are included.

Keywords: Maritime Decarbonization, Alternative Marine Fuels, Hydrogen, Methanol, Life Cycle Assessment, MEPC 83

1. INTRODUCTION
Hydrogen and methanol are fuels that are being thoroughly investigated for adoption in the shipping industry [1]. hydrogen accounting for virtually zero green house gas (GHG) footprint [2] and methanol's elimination of nitrous and sulphur oxide emissions [3] form core factors which align with regulatory aims of "International Maritime Organization (IMO) 2050" for achieving net-zero GHG emissions by 2050 [4]. Implementing such fuels, however, is challenging due to the complexity of the industry and its operating environment. Therefore, with the regulatory framework posing stricter operational boundaries to industry stakeholders, emission modelling and monitoring are of the essence.
Recent literature has extensively focused on the environmental implications of various fuel production pathways as given in Table 1. For instance, Nizami [5] evaluated the techno-economic performance of renewable hydrogen production using advanced electrolyser technologies, highlighting the considerable reduction potential in life cycle emissions. Life cycle assessment (LCA) has been integral to quantifying a fuel's GHG efficiency from feedstock to end-use stages. Various studies utilise software tools, such as GREET and OpenLCA, to form their inventory, whilst others apply the ISO 14040 by specific plant data. Śliwińska et al. [6] implemented the ISO 14040 method for methanol production through coal gasification technology and found 117.5 gCO_2eq/MJ of fuel produced. The subject study applied 'system expansion' and 'avoided burdens' approaches. Sutar and Jadhav [7] applied ISO 14040 and formulated an inventory through OpenLCA for methanol production by natural gas. The papers emphasise feedstock conversion processes, a crucial pillar in LCA.

Table 1. Existing LCA studies for selected fuel pathways

Fuel Pathway	GHG Intensity (gCo_2eq/MJ)	Method	Reference	Methanol Institute GHG Intensity (gCO2eq/MJ – EWD II/GREET)
Brown Hydrogen	150.3	FUNNEL-EGY-H2-UCG	Alghool [8]	N/A
Grey Hydrogen	93.5	ReCiPe2016	Cho [9]	N/A
Blue Hydrogen	23.1	FOA	Badger [10]	N/A
Green Hydrogen	22.3	CML 2001	Alghool [8]	N/A
Brown Methanol	117.5	ISO 14040	Śliwińska [6]	300
Grey Methanol	46.2	ISO 14040	Li [11]	97
Blue Methanol	24.8	ISO 14040	Rigamonti [12]	32
Green Methanol	35.4	Ex-ante	Delikonstantis [13]	4.4

Despite this growing body of research, there remains a notable gap concerning comprehensive comparative analyses of hydrogen and methanol fuels using harmonised methodological approaches suitable for maritime applications. This study

addresses this research gap by integrating two established LCA methodologies— Marine Environment Protection Committee (MEPC) 81 [14] Well-to-Wake framework and RED-II [15]—to evaluate and compare the GHG emissions of hydrogen and methanol produced from diverse feedstocks, including coal, natural gas with carbon capture, and solar photovoltaic electricity.

Initially intended for biofuel assessment and European Union (EU) emissions reporting, RED-II is an established method of assessing different pillars of emissions from feedstock sourcing to final bunkering. Similarly, the MEPC method is based on the exact emission boundaries and applies to the maritime industry. Therefore, by combining the two systematic yet mature methodologies, the different emissions contributions can be numerically processed and ultimately form a system boundary to which emissions will be assessed individually, forming the well-to-wake impacts of each fuel pathway. Therefore, the RED II methodology is implemented to model different emissions pillars for the chosen system boundaries. The two methodologies are widely applicable in industry and form part of global environmental objectives through legislation. The return on investment (ROI) considered capital expenses (CAPEX), operational expenses (OPEX), MEPC-83 [16] regulatory effects, and annual charter revenue for a 20-year lifetime of a Kamsarmax bulk carrier utilising Methanol and Hydrogen for equivalent pathways deduced in the environmental assessment.

The novelty of this research lies in its detailed comparative analysis, employing consistent methodological boundaries and realistic geographical scenarios that mimic actual trading and operational environments. The specific objectives are: (1) to quantify and compare the GHG emissions associated with hydrogen and methanol across different production pathways, (2) to validate the applicability and robustness of integrating MEPC and RED II methodologies, 3) Perform a ROI analysis for a Kamsarmax (82,000 DWT) bulk carrier employing hydrogen and methanol and compare to conventional through OPEX, CAPEX, charter revenue and regulatory costs. 4) Quantify penalties/surpluses for the selected pathways based on the IMO's GHG reduction measures. (5) to provide clear recommendations for stakeholders in the maritime sector aiming at decarbonization.

2. METHODOLOGY

This study employs a comparative LCA framework to evaluate the environmental performance of hydrogen and methanol as alternative marine fuels. The assessment adheres to a well-to-wake (WtW) system boundary, integrating emission data derived from the RED II Directive [15] for well-to-tank (WtT) stages and the MEPC-81 [14] guidelines for tank-to-wake (TtW) calculations.

The system boundaries of this assessment consist of four different pathways. Firstly, "Brown" focuses on coal gasification whilst "Grey" focuses on natural gas reforming (SMR), two well-established processes. The former accounted for 27% and the latter for 47% of global hydrogen. "Blue" will implement the exact system boundaries as "Grey" whilst implementing the effect of Carbon Capture and Storage (CCS) technologies. "Green" considers fuel production from Solar PV electricity by PEM electrolysis. Core feedstock is assumed to be sourced in Australia, the seventh largest natural gas producer, and boasts the third largest coal reserves globally. Final vessel bunkering will occur in Rotterdam, Netherlands, the second-largest port for alternative fuel bunkering globally. Hydrogen will be assessed in liquid form to facilitate the endurance demands of the shipping industry. Tank-to-Wake calculations consider fuel combustion in a dual-cycle marine diesel engine.

As MEPC WtT emissions operate under similar boundaries and assumptions to EU methodologies, e_{fecu} (feedstock cultivation), e_p (feedstock processing), e_{td} (transportation) are deduced by the RED II Directive. In contrast, TtW is concluded using the MEPC method. Therefore, ultimate numerical processing is conducted using the MEPC method by taking input values from RED II and TtW MEPC-83.

Life Cycle Inventory Analysis (LCIA) was generated by utilising existing studies. Energy-required ratios, such as kWh/kg (grid electricity per kilogram of fuel produced) or MJ/kg (MJ of Coal/Natural Gas per kilogram of fuel produced), were extrapolated from existing studies, utilising analytical methods based on ISO 14040.

The primary equation for total WtW emissions is calculated as the sum of WtT emissions and TtW emissions, as illustrated by Equation (1):

$$GHG_{WtW} = GHG_{WtT} + GHG_{TtW} \quad (1)$$

In this equation, GHG_{WtW} indicates the total greenhouse gas emissions measured in grams of CO_2 equivalent per megajoule (gCO_2eq/MJ), while GHG_{WtT} refer to the emissions associated with fuel production and onboard combustion processes, TtW, and both are quantified similarly in gCO_2eq/MJ.

Further expanding upon the RED II directive guidelines, the WtT emissions are calculated through the aggregation and subtraction of several emission sources and sinks, shown by Equation (2):

$$GHG_{WtT} = e_{ec} + e_p + e_{td} + e_u - e_{ccr} - e_{ccs} \quad (2)$$

Here, e_{ec} represents feedstock sourcing emissions, encompassing emissions generated from extracting and harvesting fuel feedstock materials, e_p refers to feedstock processing emissions resulting from converting raw materials into usable fuels. Transportation emissions denoted as e_{td}, account for GHG emitted during feedstock, fuel transportation, and distribution stages. The emissions from direct fuel use, e_u, are considered zero in this study due to the assumption that production occurs on industrially designated land, precluding additional land-use emissions. The terms e_{ccs} and e_{ccr} represent emission reductions achieved through CCS and emissions captured for reuse in other industrial processes

(assumed zero in this study). It is important to note that e_{ccr} includes captured emissions not accounted for in the fuel processing stage itself.
For the determination of TtW emissions, calculations adhere to the MEPC-83 guidelines, defined by Equation (3):

$$GHG_{TtW} = \left(M_{CO_2} \times FC\right)/LCV \quad (3)$$

In this relationship, GHG_{TtW} quantifies the emissions released specifically during onboard fuel combustion. Here, M_{CO_2} denotes the mass of carbon dioxide emitted per kilogram of combusted fuel, measured in grams of CO_2 per kilogram (gCO_2eq/kg fuel). Fuel consumption *FC* specifies the amount of fuel combusted during the operational cycle, which is recorded in kilograms. Finally, *LCV* indicates the fuel's lower calorific value, describing the available energy content per unit mass, expressed in megajoules per kilogram.
The financial assessment considers Capital Expenses (CAPEX), Operating Expenses (OPEX), charter rates, and International Maritime Organization (IMO) Green House Gas (GHG) reduction costs. This study simulates a Kamsarmax vessel's 20-year operational lifetime, utilizing WtW intensity results (GFI) from the environmental assessment as inputs. CAPEX baselines are derived from newbuild costs, repair premiums, and steel scrap values. OPEX projections, including a 3% annual inflation, incorporate premiums for advanced machinery and specialised crew training for methanol (7%) and hydrogen (10%) vessels. Annual charter revenues are modelled using a sine wave function to simulate cyclicality and dynamic annual utilisation as shown in Equation (4):

$$Avg_{TCE(t)} = T_0 + r \cdot t + A \cdot sin\left(2\pi \cdot \frac{tmodC}{C} - \frac{\pi}{2}\right) \quad (4)$$

where Avg_{TCE} is the average time charter equivalent for a given year *t*; T_0 represents the base Panamax 5-Time charter level modelled from real data, r is the annual trend increases in the daily rate; *t* is the number of years, A is the amplitude of the earnings cycle, C represents the estimated full cycle length. IMO GHG reduction measures are based on the vessel's annual GFI. Tier-I ($150/$tCO_{eq}$) and Tier-II ($600/tCO_{eq}) targets determine compliance deficits or surpluses. The attained global fuel intensity (GFI) is calculated as given in Equation (5), and the target GFI is calculated as given in Equation (6):

$$GFI_{attained} = \frac{\sum_{j=1}^{J} EI_j \times Energy_j}{Energy_{total}} \cdot \left(1 - f_{voy}\right) \quad (5)$$

$$GFI_t = (1 - Z_T/100) \cdot GFI_{2008} \quad (6)$$

ROI is calculated as the net present value (NPV), incorporating all financial pillars, divided by the initial newbuild investment.

3. RESULTS AND DISCUSSION

The integrated environmental and financial assessment reveals critical distinctions between hydrogen and methanol pathways, underscoring the profound impact of production methods and regulatory frameworks on their viability as alternative marine fuels.
The WtW analysis, which combines RED II and MEPC methodologies, demonstrates a substantial divergence in GHG intensity across the evaluated fuel pathways (Figure 1). For hydrogen, fossil-fuel-based routes exhibit the highest emissions. "Grey" hydrogen, produced via Steam Methane Reforming (SMR) without carbon capture, is the most carbon-intensive hydrogen option, with a WtW intensity of approximately 257 gCO_2eq/MJ. "Brown" hydrogen from coal gasification follows, with an intensity of around 169 gCO_2eq/MJ. The application of Carbon Capture and Storage (CCS) in the "Blue" hydrogen pathway reduces the intensity to approximately 187 gCO_2eq/MJ. The most significant reduction is achieved with "Green" hydrogen, produced via electrolysis powered by solar PV, which registers the lowest GHG footprint among hydrogen options at approximately 90 gCO_2eq/MJ.

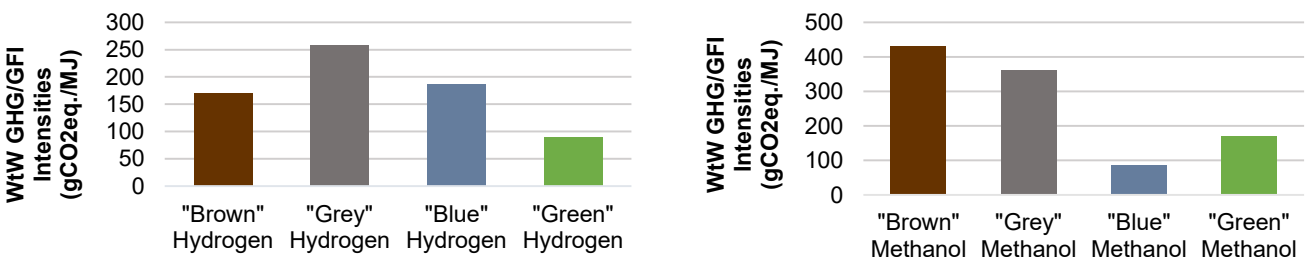

Figure 1. Well-to-Wake GHG Intensities

A similar trend is observed for methanol pathways, though with a wider range of emission intensities. "Brown" methanol from coal gasification is the highest-emitting pathway overall, exceeding 430 gCO_2eq/MJ. "Grey" methanol from SMR

follows at approximately 360 gCO_2eq/MJ. The most striking result is for "Blue" methanol, where the integration of CCS reduces the WtW emissions to approximately 86 gCO_2eq/MJ, making it the lowest-emission pathway evaluated in this study. This superior performance is attributed to the high efficiency of direct carbon capture from the methanol synthesis loop. In contrast, "Green" methanol, while a significant improvement over fossil-based routes, has a WtW intensity of about 170 gCO_2eq/MJ, which is substantially higher than both "Blue" methanol and "Green" hydrogen.

Analysis of the emission sources (Figure 1) clarifies these results. For "Brown" and "Grey" pathways, feedstock sourcing (e_{ec}) and processing (e_p) are the dominant contributors to the WtW footprint. For "Blue" pathways, the negative emission value from CCS (e_{ccs}) partially counteracts the high processing emissions, with a more pronounced effect for methanol than for hydrogen. For "Green" pathways, the lifecycle emissions associated with manufacturing the renewable energy infrastructure (solar panels and electrolysers), captured under the e_{ec} term, become the primary source of GHG impact. Furthermore, the TtW emissions are non-zero for all methanol pathways due to the carbon in the fuel molecule, whereas they are negligible for hydrogen.
The financial analysis, summarized in Table 2, reveals that regulatory costs under the IMO's GHG reduction measures are a decisive factor in determining the of each pathway. The ROI is calculated over a 20-year lifetime for a Kamsarmax vessel, both excluding and including the projected IMO-related financial penalties or surpluses.

Table 2. ROI Balance Table

Pathway	Initial CAPEX	NPV incl. IMO costs	NPV excl. IMO costs	ROI incl. IMO Costs	ROI excl. IMO Costs
Conventional	$39,100,000.00	$70,570,635.45	$5,016,933.72	-180%	13%
"Brown" Methanol	$46,920,000.00	$572,113,921.54	$6,446,106.76	-1219%	14%
"Blue" Methanol	$46,920,000.00	$3,711,768.30	$6,446,106.76	8%	14%
"Grey" Hydrogen	$58,000,000.00	$145,963,448.97	$6,256,636.77	-252%	11%
"Green" Hydrogen	$58,000,000.00	$13,330,281.92	$6,256,636.77	23%	11%

When IMO costs are excluded, the investment returns are modest and primarily dictated by CAPEX and OPEX differentials. "Blue" methanol shows the highest ROI at 14%, followed by conventional fuel (13%) and "Green" hydrogen (11%). However, the inclusion of IMO's GFI-based measures dramatically reshapes the financial landscape (Figure 2). The conventional vessel and high-emission alternatives ("Brown" methanol, "Grey" hydrogen) become financially unviable, posting large negative ROIs.

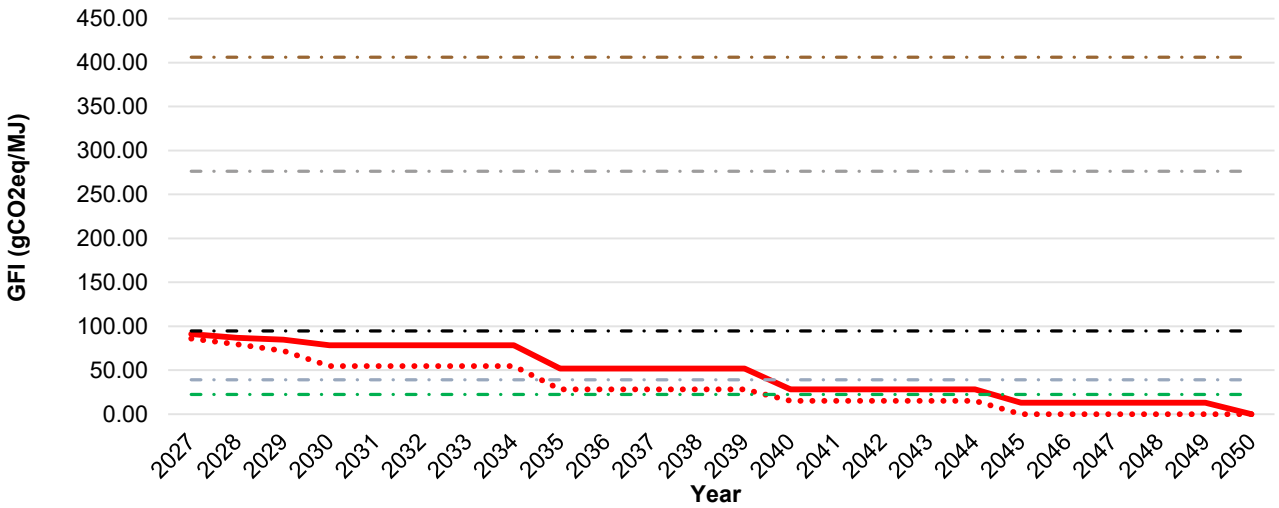

Figure 2. EU IMO GHG reduction intensities (base-strive) for Grey/Green Hydrogen and Brown/Blue Methanol

Crucially, the ranking between the two most promising low-carbon options flips. The ROI for "Blue" methanol decreases from 14% to 8%, indicating that while its WtW emissions are low, it still incurs a net cost under the regulatory scheme. In absolute contrast, the ROI for "Green" hydrogen increases significantly, from 11% to 23%. This indicates that its GFI not only meets but substantially exceeds its regulatory target, generating a financial surplus that enhances its economic attractiveness. This counterintuitive result—where the fuel with the higher WtW emissions ("Green" hydrogen at 90 gCO_2eq/MJ vs. "Blue" methanol at 86 gCO_2eq/MJ) yields a superior post-regulation ROI—highlights the specific

mechanics of the IMO GFI framework. The financial outcome is not solely dependent on the absolute GHG intensity but on the performance relative to a declining annual benchmark ($\boldsymbol{GFI_t}$).
This analysis underscores a critical insight: while CCS can dramatically reduce the WtW emissions of a fuel ("Blue" methanol), its reliance on fossil feedstocks may still place it at a disadvantage within a regulatory framework designed to progressively tighten emission standards. Conversely, a fully renewable pathway ("Green" hydrogen), despite having higher manufacturing-related lifecycle emissions in this assessment, can achieve a more favorable regulatory and financial outcome in the long term.

4. CONCLUSIONS

This study developed an analytical/numerical method of assessing hydrogen and methanol pathways in the shipping industry. By combining MEPC 83 and RED II Directive methodologies, CO_2 equivalent emissions were deduced on a GWP100 basis and compared to benchmark industry figures. LCIs from specific case studies allowed us to develop individual energy consumption ratios and extrapolate to the annual output of the Netherlands. Emissions were modelled through real-life data to simulate trading environments for Hydrogen and Methanol production infrastructure. It can be concluded that “Blue” Methanol emits the lowest WtW emissions, though its SO_x and NO_x footprint poses a considerable trade-off compared to hydrogen utilization. Nonetheless, onboard storage technology for liquid hydrogen is still premature due to the demanding pressure and temperature conditions to achieve desirable endurance.

ACKNOWLEDGEMENT

This study was supported by Lloyd’s Register and Kyla Shipping.

REFERENCES

[1] C. J. McKinlay, S. R. Turnock, and D. A. Hudson, “Route to zero emission shipping: Hydrogen, ammonia or methanol?,” *International Journal of Hydrogen Energy*, vol. 46, no. 55, pp. 28282–28297, Aug. 2021, doi: https://doi.org/10.1016/j.ijhydene.2021.06.066.
[2] “Hydrogen Fuel in Shipping | Fuel for Thought | LR,” *Lr.org*, 2024. https://www.lr.org/en/knowledge/research/fuel-for-thought/hydrogen/
[3] “Fuel For Thought: Methanol,” Lloyd’s Register, 71 Fenchurch Street, London, EC3M 4BS, 2023.
[4] T.-H. Joung, S.-G. Kang, J.-K. Lee, and J. Ahn, “The IMO initial strategy for reducing Greenhouse Gas(GHG) emissions, and its follow-up actions towards 2050,” *Journal of International Maritime Safety, Environmental Affairs, and Shipping*, vol. 4, no. 1, pp. 1–7, Jan. 2020, doi: https://doi.org/10.1080/25725084.2019.1707938.
[5] M. Nizami, Slamet, and W. W. Purwanto, “Solar PV based power-to-methanol via direct CO2 hydrogenation and H2O electrolysis: Techno-economic and environmental assessment,” *Journal of CO2 Utilization*, vol. 65, p. 102253, Nov. 2022, doi: https://doi.org/10.1016/j.jcou.2022.102253.
[6] A. Śliwińska, D. Burchart-Korol, and A. Smoliński, “Environmental life cycle assessment of methanol and electricity co-production system based on coal gasification technology,” *Science of The Total Environment*, vol. 574, pp. 1571–1579, Jan. 2017, doi: https://doi.org/10.1016/j.scitotenv.2016.08.188.
[7] D. D. Sutar and S. V. Jadhav, “Life cycle assessment of methanol production by natural gas route,” *Materials Today: Proceedings*, Jan. 2022, doi: https://doi.org/10.1016/j.matpr.2021.12.164.
[8] D. Alghool, M. Haouari, and P. Trucco, “It is not the same green: A comparative LCA study of green hydrogen supply network pathways,” *International Journal of Hydrogen Energy*, Jul. 2024, doi: https://doi.org/10.1016/j.ijhydene.2024.06.346.
[9] H. H. Cho, V. Strezov, and T. J. Evans, “Environmental Impact Assessment of Hydrogen Production Via Steam Methane Reforming Based on Emissions Data,” *SSRN Electronic Journal*, 2022, doi: https://doi.org/10.2139/ssrn.4182267.
[10] N. Badger and S. Amini, “Life cycle assessment of a novel gas switching reforming for sustainable hydrogen production with CO2 capture,” *International Journal of Hydrogen Energy*, vol. 126, pp. 308–318, Apr. 2025, doi: https://doi.org/10.1016/j.ijhydene.2025.04.063.
[11] J. Li, X. Ma, H. Liu, and X. Zhang, “Life cycle assessment and economic analysis of methanol production from coke oven gas compared with coal and natural gas routes,” *Journal of Cleaner Production*, vol. 185, pp. 299–308, Jun. 2018, doi: https://doi.org/10.1016/j.jclepro.2018.02.100.
[12] L. Rigamonti and E. Brivio, “Life cycle assessment of methanol production by a carbon capture and utilization technology applied to steel mill gases,” *International Journal of Greenhouse Gas Control*, vol. 115, p. 103616, Mar. 2022, doi: https://doi.org/10.1016/j.ijggc.2022.103616.
[13] E. Delikonstantis *et al.*, “An assessment of electrified methanol production from an environmental perspective,” *Green Chemistry*, 2021, doi: https://doi.org/10.1039/d1gc01730f.
[14] MEPC 81, 2024 GUIDELINES ON LIFE CYCLE GHG INTENSITY OF MARINE FUELS (2024 LCA GUIDELINES), vol. MEPC 81/16/Add.1, Annex 10. 2024.
[15] EUROPEAN PARLIAMENT, DIRECTIVE (EU) 2018/2001 OF THE EUROPEAN PARLIAMENT AND OF THE COUNCIL ON THE PROMOTION OF THE USE OF ENERGY FROM RENEWABLE RESOURCES, vol. L 328/82. 11AD.
[16] IMO, FURTHER CONSIDERATION OF THE DEVELOPMENT OF THE BASKET OF CANDIDATE MID-TERM GHG REDUCTION MEASURE(S), USING ANNEX 1 TO DOCUMENT MEPC 82/WP.9 AS THE BASIS, vol. ISWG-GHG 19/WP.1/Rev.1. 2025.

PRODUCING HYDROGEN AND HEAT FROM SOLAR TOWERS: A PATH TOWARD ENERGY-INDEPENDENT CITIES

[1,2]Emrullah Kocaman, [1*]Hüseyin Yağlı, [3]Hakan Tutumlu, [2]Emine Oğur, [1]Recep Yumrutaş
[1] Gaziantep University, Engineering Faculty, Mechanical Engineering Department, University Boulevard 27310 Şehitkamil - Gaziantep, TÜRKİYE
[2] Gaziantep University, Graduate School of Natural & Applied Sciences, Mechanical Engineering Department, Gaziantep, TÜRKİYE
[3] Gaziantep University, Naci Topcuoglu Vocational School, Electricity and Energy Department, Gaziantep, TÜRKİYE

* E-mail: yagli@gantep.edu.tr

ABSTRACT
This study presents the design and simulation of a hybrid solar-based energy system aimed at meeting the annual space heating demand of 8,500 households in an off-grid urban area. The proposed system integrates a solar tower, molten salt thermal energy storage, an Organic Rankine Cycle (ORC), a Proton Exchange Membrane (PEM) electrolyzer, and a district heating network. Thermal energy collected from the solar receiver is used for both electricity generation and hydrogen production. The waste heat from the ORC is utilised for district heating, enhancing the overall energy efficiency. Simulation results indicate that the system successfully meets the annual heating demand and produces approximately 722 tons of hydrogen, contributing to long-term energy storage and decarbonization goals.

Keywords: Off-grid cities, Rankine cycle, Hybrid solar-based energy system

1. INTRODUCTION

In an era marked by growing environmental concerns, energy insecurity, and increasing natural disasters, the concept of off-grid cities—urban areas that are self-sufficient and independent from centralised electricity grids has gained considerable importance. These cities are designed to produce, store, and manage their own energy by utilising locally available renewable resources, thus increasing their resilience and reducing reliance on fossil fuels [1].

Off-grid cities play a critical role in enhancing environmental sustainability by minimising carbon emissions through renewable energy integration. Technologies such as solar, wind, biomass, and small-scale hydropower are commonly deployed to meet local electricity and thermal energy demands [2]. In particular, solar-based systems have emerged as promising candidates due to their modularity, scalability, and declining cost.

Beyond environmental concerns, off-grid smart cities also contribute to social and economic sustainability by providing energy access to remote communities, improving quality of life, and enabling energy independence [3]. Moreover, the integration of digital technologies and artificial intelligence into off-grid systems enhances operational efficiency and allows for predictive energy management. This is especially relevant in the context of natural disasters, where smart data-driven systems can improve urban resilience and response strategies.

To meet the complex energy demands of future off-grid urban areas, hybrid energy systems that combine multiple technologies such as renewable electricity generation, thermal energy storage, hydrogen production, and district heating are being explored [4]. In this context, the present study proposes and simulates a hybrid solar thermal energy system that is specifically designed to support off-grid urban applications. The proposed model focuses on the integration of solar tower technology with thermal storage, power generation, and hydrogen production [5].

The detailed structure and operational principles of this integrated energy system are described in the following section.

2. SYSTEM DESCRIPTION

This study aims to develop and simulate an integrated solar-based hybrid energy system designed to meet the annual space heating demand of an off-grid urban area consisting of 8,500 households, while simultaneously producing hydrogen as a long-term energy storage medium. The system is structured to ensure energy reliability through thermal energy storage and to increase overall energy efficiency through waste heat utilisation for district heating applications.

Fig. 1 shows a schematic representation of the proposed hybrid solar-based energy system integrating thermal storage, power generation, hydrogen production, and district heating. The primary energy source of the system is a solar tower (central receiver system), where a field of heliostats concentrates solar radiation onto a central receiver located at the top of the tower. The solar radiation is absorbed by the receiver and transferred to a molten salt fluid, which serves as the thermal energy carrier. The heated molten salt is stored in a hot salt tank during sunny hours.

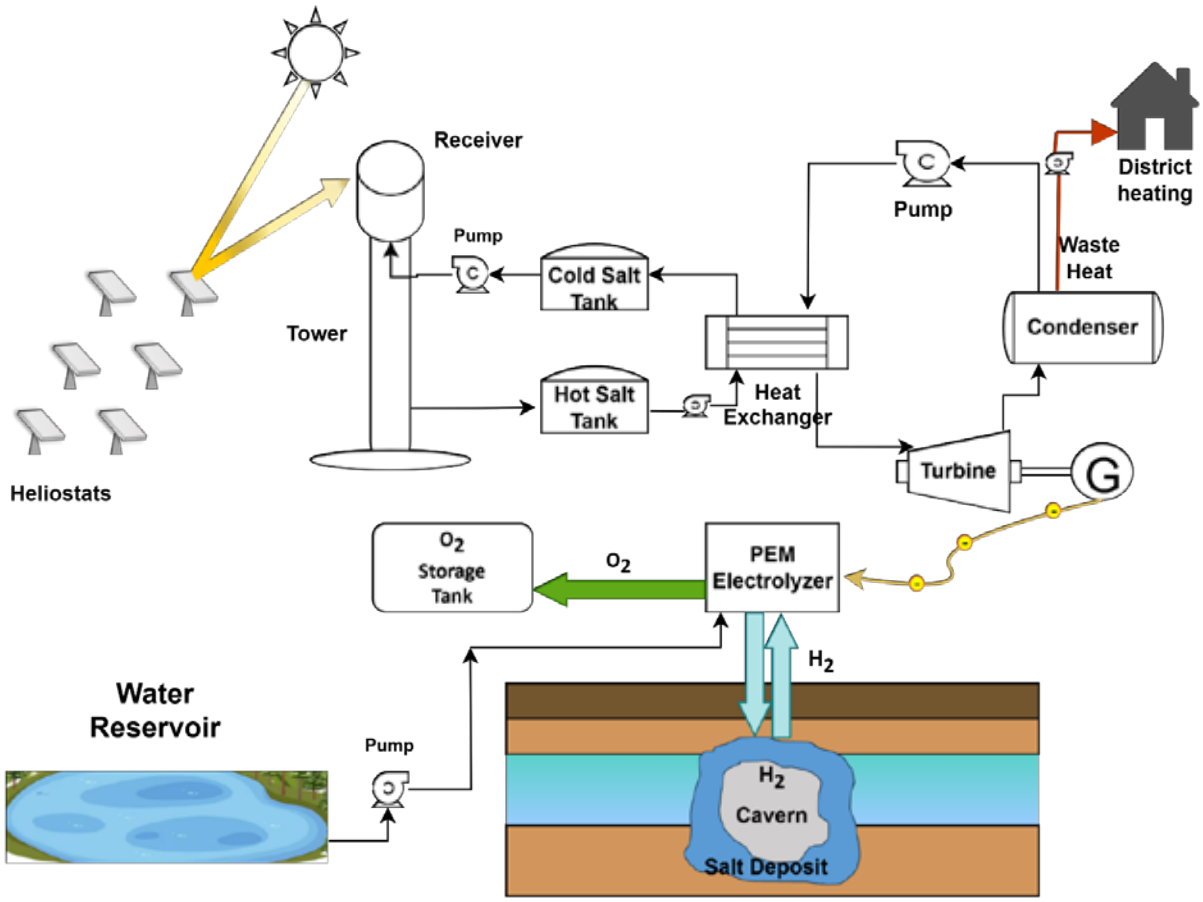

Fig. 1. Schematic representation of the hybrid solar thermal energy system.

When direct solar radiation is not available, such as at night or on cloudy days, the stored thermal energy is transferred from the hot salt tank to a heat exchanger, where it supplies heat to an Organic Rankine Cycle (ORC). The ORC is composed of a heat exchanger (evaporator), an expansion turbine, a condenser, and a feed pump. In the heat exchanger, the working fluid absorbs the heat from molten salt, evaporates, and drives the turbine to produce mechanical power, which is converted into electricity via a generator.

The electricity generated by the ORC is used to power a Proton Exchange Membrane (PEM) electrolyzer, which splits water into hydrogen and oxygen. The produced hydrogen is stored in underground reservoirs or appropriate pressurised tanks, and can later be used as an energy carrier or reconverted into electricity using fuel cells. Meanwhile, the oxygen may be released or used for industrial purposes.

An important feature of the proposed system is the utilisation of waste heat from the ORC condenser. This low-grade thermal energy is directed to a district heating network, providing space heating to residential buildings and thus increasing the overall exergy efficiency of the system.

3. RESULTS AND DISCUSSIONS

Table 1 shows the monthly distribution of heating demand, thermal energy collected from the solar tower, and hydrogen production from surplus energy. Hydrogen was produced between March and November, particularly in summer months when excess energy was available. In winter months, the system mainly relied on stored hydrogen to meet the heating demand of 8,500 households.

The simulation results demonstrate that the system is capable of supplying the required thermal energy throughout the year. Additionally, approximately 722 tons of hydrogen were produced from surplus energy, providing a promising solution for seasonal energy storage and long-term sustainability in future off-grid smart cities.

Table 1. Hydrogen production-consumption by month and the amount of energy produced by heliostats

Months	Monthly Heating Demand for 8500 houses (MWh)	Thermal Energy from Receiver (MWh)	Heating Supplied from Receiver (MWh)	Energy from H_2 Combustion (MWh)	Rankine Supplied Heating (MWh)	Rankine Heat Input (MWh)	Rankine Heat Output (MWh)	H_2 from Surplus Energy (kg)
January	19635	17280	17280	2354,298	-	-	-	-60540
February	16694	20360	15585	-	1108	4774	1491	13295
March	13744	33383	7805	-	5939	25578	7990	71219
April	9817	37425	1468	-	8349	35956	11232	100115
May	4913	48288	27129	-	4913	21158	6609	58912
June	0	51302	-	-	-	51302	16026	142843
July	0	50992	-	-	-	50992	15929	141978
August	0	44442	-	-	-	44442	13883	123741
September	1496	36292	29849	-	1496	6442	2012	17939
October	7344	27293	1310	-	6033	25983	8117	72345
November	12257	19649	10021	-	2235	9628	3008	26809
December	12274	15977	11153	-	1120	4823	1506	13431

REFERENCES

1. De Almeida, A., Moura, P., & Quaresma, N. (2020). Energy-efficient off-grid systems. Energy Efficiency, 13(2), 349-376.
2. Uddin, R., Khan, H., Arfeen, A., Shirazi, M., Rashid, A., & Khan, U. (2021). Energy storage for energy security and reliability through renewable energy technologies: a new paradigm for energy policies in Turkey and Pakistan. sustainability, 13(5), 2823. https://doi.org/10.3390/su13052823.
3. Afaneh, A., & Alshafei, I. (2023, July). The influence of smart technologies: A comparative study on developing Large to small scale smart cities and smart campuses. In IOP Conference Series: Earth and Environmental Science (Vol. 1210, No. 1, p. 012015). IOP Publishing.
4. Calado, G. and Castro, R. (2021). Hydrogen production from offshore wind parks: current situation and future perspectives. Applied Sciences, 11(12), 5561. https://doi.org/10.3390/app11125561.
5. Yamagata, Y., Murakami, D., Minami, K., Arizumi, N., Kuroda, S., Tanjo, T., & Maruyama, H. (2016). Electricity self-sufficient community clustering for energy resilience. Energies, 9(7), 543.

EFFECT OF MoP/g-C_3N_4/Ti_3C_2 QUANTUM DOTS ON PHOTOCATALYTIC HYDROGEN PRODUCTION

[1]*Elif Sude ŞAHİN,* [1]*Erhan Demirbaş,* [1*]*Duygu AKYÜZ*
[1] Gebze Technical University, Faculty of Science, Department of Chemistry, Kocaeli, 41400, Türkiye
*Corresponding author e-mail: dakyuz@gtu.edu.tr

ABSTRACT

Today, due to reasons such as the depletion of fossil fuels, the release of harmful gases by fossil fuels, and the depletion of non-renewable energy sources, people have turned to renewable energy and conducted research on renewable energy. To meet future energy requirements, hydrogen, which is among the renewable energy sources, is preferred due to its high energy density and clean burning properties. Among hydrogen production technologies, photocatalytic hydrogen evolution (PCHER) has been considered important due to its potential for sustainable and efficient hydrogen production using solar energy, and experiments have been conducted on the PCHER system.
In this study, a new MoP/g-C_3N_4/Ti_3C_2 quantum dot (QD) photocatalyst has been synthesized in order to increase photocatalytic hydrogen production. Metal phosphides, especially compounds such as molybdenum phosphide (MoP), have been obtained by passing metal salts through appropriate phosphorylation processes. In addition, g-C_3N_4 (graphitic carbon nitride) has been synthesized by controlled thermal decomposition of urea precursor. QD were prepared using a hydrothermal method. The developed photocatalyst aims to overcome the fundamental efficiency limitations in the photochemical hydrogen evolution reaction (PCHER) by improving visible light absorption. For this purpose, material design was carried out to ensure efficient separation of charge carriers, optimize surface reaction kinetics and increase catalytic activity. As a result, this new generation hybrid photocatalyst has significant potential for sustainable and efficient hydrogen production. The results showed that the synthesized photocatalyst exhibited superior photocatalytic activity and contributed to increased hydrogen production. This study provides advances in the development of efficient photocatalysts and contributes to the advancement of hydrogen production and supports future renewable energy production.
Keywords: Photocatalytic Hydrogen Production, g-C_3N_4, Quantum Dot, Molybdenum Phosphide

1. INTRODUCTION

In order to meet future energy needs and minimize environmental damage, the development of sustainable energy sources is of great importance. In this direction, photocatalytic water splitting, which is based on obtaining hydrogen from water using sunlight, stands out as a promising method in renewable energy production [1]. The success of photocatalytic hydrogen production directly depends on the properties of the photocatalysts used. g-C_3N_4 is widely used in photocatalytic applications due to its wide band gap, chemical stability and easy accessibility. In addition, although it is a remarkable material with a suitable band gap, chemical durability and low charge carrier separation efficiency, it is not effective enough alone due to its low charge carrier separation efficiency [2,3]. Therefore, it has been used with various hybrid materials in order to increase its performance. In this study, hybrid materials containing Ti_3C_2 QD and metal phosphide were developed to increase the photocatalytic activity of g-C_3N_4 [4]. The high conductivity of Ti_3C_2 QD allows charge carriers to move more efficiently, while quantum dots support photochemical processes thanks to their wide light absorption capabilities. In recent years, transition metal phosphides (TMPs), especially MoP, have emerged as remarkable materials in hydrogen production due to their high catalytic activity and low wear resistance. MoP is considered an effective hydrogen evolution reaction (HER) catalyst with its large surface area, good conductivity and strong proton adsorption ability. In addition, composite structures are formed by combining MoP with different materials to increase its photocatalytic activity [5]. It is thought that these developed hybrid structures can play an important role in the transition to clean energy. In the photocatalytic hydrogen production process, semiconductor photocatalysts absorb sunlight and trigger chemical reactions that will split water molecules [6]. In semiconductors, there is an energy gap between the valence band and the conduction band. When sunlight is absorbed, electrons in the valence band gain energy and move to the conduction band, leaving behind electron holes (h^+). These holes trigger the oxidation of water, while electrons rising to the conduction band complete the photocatalytic process by reducing hydrogen. [7]. In order to ensure effective hydrogen production, the conduction band level of the semiconductor used must be lower than the hydrogen reduction potential and the valence band level must be higher than the oxidation potential of water [8]. Although a band gap of 1.23 eV is considered thermodynamically sufficient in theory, in practical applications, values of 1.8 eV and above are preferred due to factors such as overpotentials and energy band alignment [9]. Photocatalytic hydrogen production is a complex process and studies are ongoing on methods such as photocatalyst surface modifications, improvement of light absorption properties and optimization of charge carrier separation mechanisms to increase efficiency [10].

2. MATERIALS AND METHODS

Synthesis of graphitic carbon nitride (g- C_3N_4):

The synthesis of g-C3N4 was carried out by adopting the method proposed by Y. Li and his team [11]. In this process, a certain amount of urea was subjected to thermal treatment in a tube furnace heated to 550°C with a heating rate of 5°C per minute for 4 hours. Afterwards, the product coming out of the furnace was cooled to room temperature and then ground into powder with the help of a mortar and pestle.

The synthesis of quantum dots (QD):

The synthesis of QD was adapted from the method proposed by Y. Li et al. [11]. This process was based on the method reported in the literature (C. Li et al., 2019). Firstly, 2 g of Ti_3AlC_2 powder was mixed with 240 mL of 40 percent hydrofluoric acid solution and stirred with a magnetic stirrer for 64 h. The resulting suspension was washed with pure water to remove excess HF and residues. Then, the obtained Ti_3C_2 MXene was dried at 50 °C under vacuum for 10 h. In the next step, 0.5 g of Ti_3C_2 MXene was dispersed in dimethyl sulfoxide and stirred for 24 h. This suspension was centrifuged at 4100 rpm for 20 min. After centrifugation, distilled water was added to the dispersion and sonicated in an ultrasonic bath for 3 h. Then, 3.0 mL of polyethylenimine (PEI) was added and the mixture was heated under nitrogen atmosphere for 12 h. Finally, the product was filtered through with membrane filter and purified by dialysis to obtain Ti_3C_2 QD.

The Synthesis of Molybdenum Phosphide (MoP):

The synthesis of MoP was adapted from the method proposed by Y. Li et al. [11]. 100 mg $Na_2MoO_4{\cdot}2H_2O$ and 1 g $NaH_2PO_2{\cdot}H_2O$ are measured using a precision balance. The material is mixed homogeneously in a mortar for 30 minutes. Then, the powdered mixture is placed in a closed alumina crucible. It is heated in a muffle furnace at a speed of 5°C/minute up to 700°C and kept at this temperature for 2 hours. Then, it is left to cool down to room temperature. Then, it is washed with pure water five times and then centrifuged. In the last stage, MoP is dried at 60°C for 12 hours and the MoP synthesis is completed.

2.1. Photocatalytic Performance Tests

The reactor developed for photocatalytic reactions has a quartz glass upper section that can transmit ultraviolet-visible (UV-Vis) light. The reactor was designed to have gas and liquid inlet/outlet connections. In the studies conducted to determine the most suitable level of catalyst amount, 10 mg of catalyst was used initially. Catalyst addition to the reaction medium was provided by an aqueous solution containing 10% tetraethylammonium (TEOA) as electrolyte. The temperature of the reactor was kept constant by continuous water circulation. During the reaction, the catalyst was kept in a homogeneous distribution in the solution with the help of a magnetic stirrer. The gas released as a result of the reaction was directed to a microfluidic pressure sensor with argon (Ar) carrier gas to determine the amount of hydrogen produced. The composition of the produced gas was analyzed using gas chromatography, one of the types of chromatography. The light source was positioned to provide equal distribution over the entire surface of the photocatalyst and the light intensity was adjusted to 100 mW/cm² with the help of a light meter. To prevent intensity fluctuations in the light source over time from affecting the measurement sensitivity, light stabilization was checked before each photocatalytic reaction.

A) Synthesis of g-C_3N_4

B) Synthesis of MoP

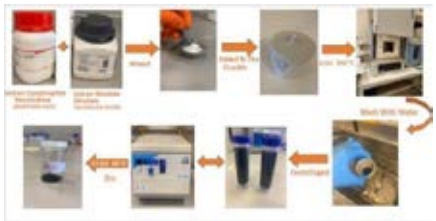

C) Synthesis of Ti_3C_2

D) Design of the PCHER system.

Fig. 1. A) Synthesis of g-C_3N_4, B) Synthesis of MoP, C) Synthesis of Ti_3C_2 QD, D) Design of the PCHER system.

3. RESULTS AND DISCUSSION

Photocatalytic hydrogen production was investigated using a composite photocatalyst composed of g-C_3N_4, Ti_3C_2 QD, and MoP. The synergistic effect of these components was analyzed using various characterization techniques and the successful synthesis of the composite and its improved photocatalytic performance were confirmed. X-ray Diffraction (XRD) technique was used for structural analysis and the characteristic peaks of MoP phase were found to be consistent with the values reported in the literature. MoP was determined to have an orthorhombic crystal structure and this structure has been reported in previous studies to show high activity in hydrogen production catalysis. When the lattice parameters of MoP were examined, it was reported in the literature that it typically has an atomic lattice spacing in the range of 0.3-0.5 nm. X-ray Photoelectron Spectroscopy analyses confirmed that the active sites on the surface of MoP were suitable for hydrogen production when evaluated in terms of surface chemistry, and especially Mo and P elements were determined to be active species in photocatalytic reactions by examining the chemical bonding status on the surface. Diffraction peaks of g-C_3N_4 were observed and new peaks related to Ti_3C_2 QD showed strong interactions between the components, while MoP changed the crystal structure and improved charge transfer Scanning electron microscope images showed the morphology of g-C_3N_4 and the uniform distribution of Ti_3C_2 QD and MoP on the surface, which further enhanced the charge transfer and caused a decrease in electron-hole recombination.The incorporation of quantum dots provided additional active sites for hydrogen production (i). HRTEM and FFT results show that the lattice spacing corresponding to the MoP (101) crystal plane is 0.210 nm, which is consistent with the literature [12-13]. UV-Vis Diffuse Reflectance Spectroscopy (DRS) was used to understand the band structure and optoelectronic properties. DRS analysis showed that the light absorption capacity of MoP/g-C_3N_4/Ti_3C_2 QD composites was broadened compared to pure g-C_3N_4 and absorbed more photons in the visible light region. This can be explained by the broad spectrum light harvesting ability of QD and the high conductivity of MXene. Fourier transform infrared spectroscopy (FTIR) spectra were used to determine the functional groups in the material. The peaks from Ti_3C_2 QD and MoP confirmed the presence of characteristic functional groups of g-C_3N_4, such as C-N and C=N stretching vibrations, and confirmed their successful integration. Photoluminescence (PL) spectroscopy showed lower fluorescence intensity in the composite, suggesting reduced charge recombination. This was supported by electrochemical impedance spectroscopy (EIS), which confirmed lower charge transfer resistance, improved electron mobility, and increased catalytic efficiency. BET surface area analysis revealed that the composite had a higher specific surface area compared to pure g-C_3N_4, and the addition of Ti_3C_2 QD created a more porous structure and provided more active sites for hydrogen production. This increased surface area facilitated mass transfer, further enhancing the photocatalytic efficiency. Photocatalytic hydrogen production experiments showed a significant enhancement in hydrogen production by the g-C_3N_4/Ti_3C_2 QD/MoP composite. Ti_3C_2 QD contributed to rapid electron transfer, quantum dots enhanced charge separation, and MoP acted as an effective water oxidation catalyst, improving the hydrogen production rate. The composite provides improvement in hydrogen production efficiency under visible light and confirms the synergistic effect between the components. The improved photocatalytic performance was attributed to the enhanced charge separation provided by Ti_3C_2 QD and the catalytic activity of MoP. As a result of g-C_3N_4 absorbing photons, electron-hole pairs are formed. Ti_3C_2QD prevents recombination by transferring photogenerated electrons to the reaction sites, while MoP facilitates effective oxidation reactions, improving the overall hydrogen production efficiency. As a result, in photocatalytic hydrogen production tests, MoP/g-C_3N_4/Ti_3C_2QD composites exhibited the highest efficiency. These results indicate that composite materials can increase photocatalytic activity with synergistic effects. In particular, it was determined that MXene accelerates electron conduction and reduces charge carrier recombination, and quantum dots make significant contributions to photochemical processes due to their broad light absorption.

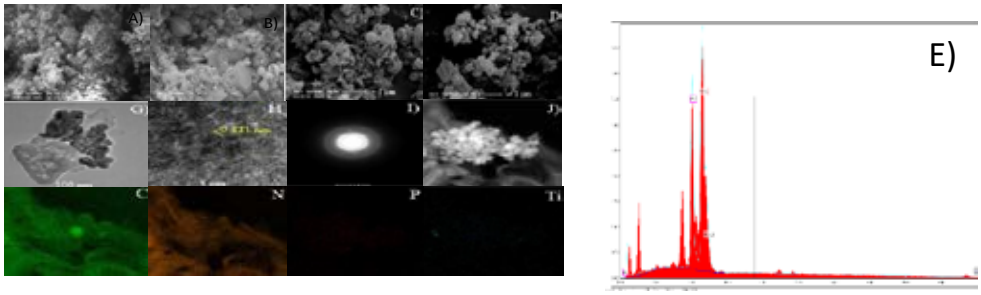

Fig. 2. SEM images of a) g-C_3N_4, b) MoP, c) MoP/g-C_3N_4, d) MoP/g-C_3N_4/Ti_3C_2 QD. EDS spectra: e) MoP, f) MoP/g-C_3N_4/Ti_3C_2 QD. g-i) HRTEM images and FFT image of MoP/g-C_3N_4/Ti_3C_2 QD. j) Elemental mapping of MoP/g-C_3N_4/Ti_3C_2 QD.

4. CONCLUSIONS

This study demonstrated the effect of synthesized MoP-based composites on photocatalytic hydrogen production. In this study, the structural, morphological and photoelectrochemical properties of the synthesized MoP/g-C_3N_4/Ti_3C_2QD nanocomposite were comprehensively investigated. SEM, HRTEM and EDS analyses confirmed that the nanocomposite was successfully synthesized and its components exhibited a homogeneous distribution. XPS analysis confirmed that the active sites on the surface of MoP were suitable for hydrogen production and proved the existence of MoP in the composite by determining the chemical bond states. UV-Vis DRS analysis examined the band gap of the material and revealed that the MoP/g-C_3N_4/Ti_3C_2QD composite had improved optical properties. In the PCHER system, catalyst ratios were optimized to increase hydrogen production efficiency. Photoelectrochemical performance evaluations, especially photocurrent versus time measurements, revealed that MoP/g-C_3N_4/Ti_3C_2QD nanocomposite exhibited high charge transfer efficiency and good photocatalytic activity. These findings indicate that MoP/g-C_3N_4/Ti_3C_2QD nanocomposite is a strong photocatalyst candidate for sustainable hydrogen production.

ACKNOWLEDGEMENT

This work was financially supported by The Scientific and Technological Research Council of Türkiye, TUBITAK (Project No:223Z176).

REFERENCES

1. Yan T, Liu H, Jin Z (2021) G-C3N4/α-Fe2O3Supported Zero-Dimensional Co3S4Nanoparticles Form S-Scheme Heterojunction Photocatalyst for Efficient Hydrogen Production. Energy and Fuels 35:856–867
2. Novoselov KS, Geim AK, Morozov S V., Jiang D, Zhang Y, Dubonos S V., Grigorieva I V., Firsov AA (2004) Electric field in atomically thin carbon films. Science (1979) 306:666–669
3. Kumar A, Sharma SK, Sharma G, Naushad M, Stadler FJ (2020) CeO2/g-C3N4/V2O5 ternary nano hetero-structures decorated with CQDs for enhanced photo-reduction capabilities under different light sources: Dual Z-scheme mechanism. J Alloys Compd 838:155692
4. Nakhanivej P, Yu X, Park SK, et al (2018) Revealing molecular-level surface redox sites of controllably oxidized black phosphorus nanosheets. Nature Materials 2018 18:2 18:156–162
5. Akyüz D, Koca A (2018) Photocatalytic hydrogen production with reduced graphene oxide (RGO)-CdZnS nano-composites synthesized by solvothermal decomposition of dimethyl sulfoxide as the sulfur source. J Photochem Photobiol A Chem 364:625–634
6. Li Z, Wu Y, Li Z, Wu Y (2019) 2D Early Transition Metal Carbides (MXenes) for Catalysis. Small 15:1804736
7. Huang H, Song Y, Li N, Chen D, Xu Q, Li H, He J, Lu J (2019) One-step in-situ preparation of N-doped TiO2@C derived from Ti3C2 MXene for enhanced visible-light driven photodegradation. Appl Catal B 251:154–161
8. Dong G, Zhang Y, Wang Y, Deng Q, Qin C, Hu Y, Zhou Y, Tian G (2021) Ti3C2Quantum Dots Modified 3D/2D TiO2/g-C3N4S-Scheme Heterostructures for Highly Efficient Photocatalytic Hydrogen Evolution. ACS Appl Energy Mater 4:14342–14351
9. Chung DY, Jun SW, Yoon G, et al (2017) Large-Scale Synthesis of Carbon-Shell-Coated FeP Nanoparticles for Robust Hydrogen Evolution Reaction Electrocatalyst. J Am Chem Soc 139:6669–6674
10. Zhao H, Jiang P, Cai W (2017) Graphitic C3N4 Decorated with CoP Co-catalyst: Enhanced and Stable Photocatalytic H2 Evolution Activity from Water under Visible-light Irradiation. Chem Asian J 12:361–365
11. Li Y, Ding L, Guo Y, Liang Z, Cui H, Tian J (2019) Boosting the Photocatalytic Ability of g-C3N4 for Hydrogen Production by Ti3C2 MXene Quantum Dots. ACS Appl Mater Interfaces 11:41440–41447
12. S.T. Oyama, T. Gott, H.Y. Zhao, Y.K. Lee, Catal. Today 143 (2009) 94–107.
13. R. Prins, M.E. Bussell, Catal. Lett. 142 (2012) 1413–1436

ENHANCEMENT OF PHOTOCATALYTIC HYDROGEN PRODUCTION WITH CoP/g-C_3N_4/Ti_3C_2 QUANTUM DOTS

[1]*Bilge CAMGÖZ**, [1]*Erhan Demirbaş**,[1*]*Duygu AKYÜZ**
[1] Gebze Technical University, Faculty of Science, Department of Chemistry, Kocaeli, 41400, Türkiye
*Corresponding author e-mail: dakyuz@gtu.edu.tr

ABSTRACT
The increasing demand for renewable energy is driven by the depletion of fossil fuel reserves and the necessity to reduce carbon emissions. In this context, hydrogen emerges as a critical energy carrier in future energy systems due to its high energy density and environmentally friendly characteristics. Among hydrogen production technologies, photocatalytic hydrogen evolution reaction (PCHER) has attracted significant attention. However, this process faces fundamental challenges, including low quantum efficiency, slow charge separation and transfer, recombination losses, and limitations in photocatalyst particle size. In this study, a novel CoP, g-C_3N_4/Ti_3C_2 quantum dot (QD) photocatalyst was synthesized to enhance photocatalytic hydrogen production efficiency. The metal phosphite (CoP) was obtained via the phosphorization of metal salts, while g-C_3N_4 was synthesized through the thermal decomposition of urea, and Ti_3C_2QD were prepared using a hydrothermal method. The designed photocatalyst aims to overcome key efficiency limitations in PCHER by improving visible light absorption. The findings of this study demonstrate a significant advancement in sustainable hydrogen production, offering a promising strategy for future renewable energy applications.
Keywords: Photocatalytic Hydrogen Production, g-C_3N_4, Ti_3C_2 Quantum Dot, Cobalt Phosphite

1. INTRODUCTION

Meeting global energy demands while minimizing environmental impacts necessitates the development of sustainable energy sources. In this context, photocatalytic hydrogen production, which relies on water splitting driven by solar energy, has emerged as a highly promising approach [1]. The efficiency of this process is intrinsically linked to the properties of the photocatalyst materials employed. Graphitic carbon nitride (g-C_3N_4) has been extensively studied in photocatalytic applications due to its suitable band gap, chemical stability, and natural abundance [2]. However, its inherently low charge carrier separation efficiency limits its standalone application [3]. Consequently, various modification strategies have been explored to enhance its photocatalytic performance. This study investigates hybrid composites incorporating Ti_3C_2QD, and cobalt phosphide (CoP) to improve the photocatalytic activity of g-C_3N_4 [4]. Ti_3C_2QD, with its high electrical conductivity and superior electron transfer capability, plays a crucial role in accelerating photocatalytic reactions. Quantum dots, owing to their broad light absorption spectrum, efficiently capture photons and optimize charge carrier dynamics. Additionally, CoP facilitates efficient water oxidation, thereby enhancing the hydrogen evolution process and contributing to the overall photocatalytic efficiency. The synergistic interaction of these materials presents significant potential for improving photocatalytic hydrogen production performance [5]. The development of such hybrid materials offers new opportunities for clean and renewable energy technologies, contributing to a more sustainable future. In photocatalytic hydrogen production, semiconductor photocatalysts absorb light energy to drive water splitting [6]. Semiconductors are characterized by a specific band gap (BG) between the valence band (VB) and conduction band (CB). Upon light absorption, electrons in the VB are excited to the CB, generating electron holes (h^+) in the VB. These charge carriers facilitate water oxidation and reduction reactions, respectively [7]. The photocatalyst also minimizes the accumulation of electrolytic intermediates through regeneration mechanisms. For efficient hydrogen production, the CB edge must be positioned at a more negative potential than the hydrogen reduction potential, while the VB edge must be at a more positive potential than the water oxidation potential, as noted by Dong et al. [8]. Although a theoretical band gap of 1.23 eV is sufficient, practical applications often require band gaps of 1.8 eV or higher due to overpotential and band alignment constraints [9]. Given the complexity of photocatalytic hydrogen production, modifications to photocatalysts are essential [10]. In this regard, strategies such as photocatalyst restructuring, surface modifications, and light absorption enhancement have emerged as key approaches for optimizing performance.

2. MATERIAS AND METHODS

2.1.1 Synthesis of graphitic carbon nitride (g- C_3N_4)

The synthesis of g-C_3N_4 was adapted from the method proposed by Y. Li et al. method [11]. In this process, a specific amount of urea was subjected to thermal treatment in a tube furnace at 550°C for 4 hours, with a of 5°C/min. The resulting product is ground into fine powder.

2.1.2 The synthesis of Quantum Dots (QD)

The synthesis of Ti_3C_2 QD was adapted from the method proposed by Y. Li et al. method [11]. In this prıcess was carried out based on the general procedure outlined in the literature (C. Li et al., 2019). In the initial stage, 2 g of Ti_3AlC_2 powder was treated with 240 mL of 40 percent hydrofluoric acid solution using a magnetic stirrer for 64 hours. The resulting

suspension was washed with pure water to remove excess HF and residues Ti_3C_2 MXene was dried under vacuum at 10 hours. Subsequently, 0.5 g of Ti_3C_2 MXene was stirred of dimethyl sulfoxide (DMSO) for 24 hours. The suspension was centrifuged at 4100 rpm for 20 minutes. After the centrifugation process, 150 mL of deionized water was added to the dispersion, and it was subjected to sonication in an ultrasonic bath for 3 hours. Following this, 3.0 mL of polyethyleneimine (PEI) was added, and the mixture was heated under a nitrogen atmosphere at 12 hours. The product was passed through a membrane filter, and Ti_3C_2 QD were purified by dialysis.

2.1.3 The synthesis of Cobalt phosphide (CoP)

The synthesis of CoP was carried out according to the procedure described by K. Wang et al.[12].Cobalt phosphide. Initially, solution of cobalt(II) nitrate hexahydrate (Co(NO3)2·6H2O) (100 mL, 0.05 M) was combined with sodium hydroxide (NaOH) solution (400 mL, 0.25 M). After 2 hours, the resulting precipitate was gathered, thoroughly washed with distilled water and ethanol, and subsequently dried under vacuum to yield the $Co(OH)_2$ precursor. Then, $Co(OH)_2$ (0.05 g) was mixed with sodium hypophosphite (NaH_2PO_2, 0.25 g) through grinding. The resulting mixture was then subjected to annealing in an argon (Ar) at 300 °C for 1 hour, with a rate of 2 °C min^{-1}. Finally, the obtained black solid was collected, repeatedly washed, and dried to obtain the final CoP product.

2.2. PHOTOCATALYTIC PERFORMANCE TEST

The reactor designed for photocatalytic reactions has an upper section made of quartz glass, which is transparent to ultraviolet-visible (UV-Vis) light. The reactor is equipped with gas inlet/outlet and liquid inlet/outlet ports. Optimization studies to determine the optimum catalyst amount were initially conducted using 10 mg of catalyst. The catalyst was introduced into the reaction medium using a 10% aqueous solution of tetraethylammonium (TEOA) as an electrolyte. The reactor temperature was controlled through continuous water circulation. During the reaction, the catalyst was maintained as a homogeneous suspension using a magnetic stirrer. The gas phase generated as a result of the reaction was carried to a microfluidic pressure sensor using an inert carrier gas (Ar) to measure the amount of hydrogen produced. The characterization of the produced gas was performed using gas chromatography (GC). The light source was positioned to ensure homogeneous illumination of the photocatalyst, and the light intensity was adjusted to 100 mW/cm² using a light meter. To minimize errors that could arise from changes in light intensity over time, the light intensity was checked before each photocatalytic reaction to ensure the stabilization of the light source.

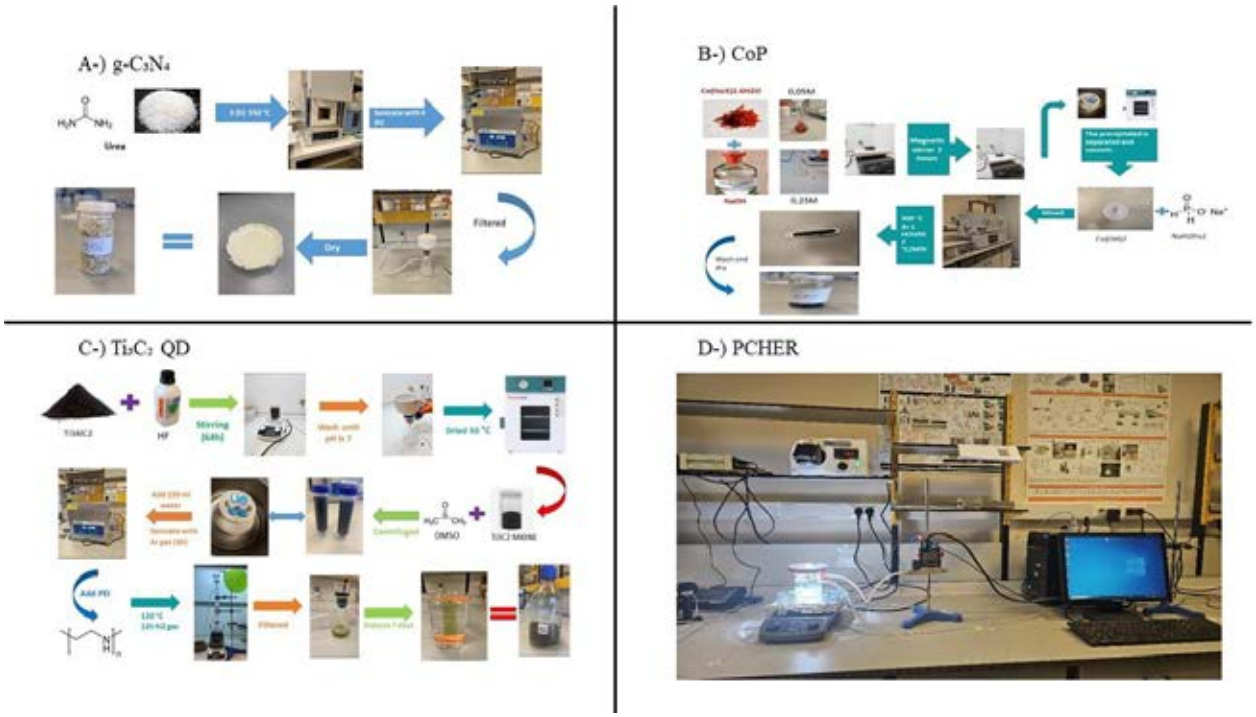

Fig. 1. A-) Synthesis of g-C_3N_4, B-) Synthesis of CoP, C-) Synthesis of Ti_3C_2QD, D-) Design of the PCHER system.

3. RESULTS AND DISCUSSION

This investigation delved into the realm of photocatalytic hydrogen generation, employing a hybrid photocatalyst formulated from graphitic carbon nitride (g-C_3N_4), Ti_3C_2QD, and cobalt phosphide (CoP). The collaborative interplay amongst these constituents was scrutinized via a suite of characterization methodologies, validating the successful fabrication of the composite and its augmented photocatalytic efficacy. X-ray diffraction (XRD) patterns elucidated the crystalline architecture of g-C_3N_4 and the seamless integration of Ti_3C_2QD and CoP. Diffraction peaks attributable to g-C_3N_4 were noted, and novel peaks associated with Ti_3C_2QD signaled robust interactions amongst the components, while CoP refined the crystalline lattice, optimizing charge transfer. Scanning electron microscopy (SEM) imagery showcased the layered morphology of g-C_3N_4 and a uniform dispersion of Ti_3C_2QD and CoP across the surface, contributing to ameliorated charge transfer and diminished electron-hole recombination. The incorporation of quantum dots furnished supplementary active sites for hydrogen evolution, thereby amplifying reaction throughput. High-resolution transmission electron microscopy (HRTEM) and fast Fourier transform (FFT) outputs corroborated that the lattice spacing congruent with the CoP (111) crystal plane was 0.221 nm, aligning with literature benchmarks [13]. UV-Vis diffuse reflectance spectroscopy (DRS) analyses revealed that the composite assimilated a broader light spectrum relative to pristine g-C_3N_4, with Ti_3C_2QD inducing a redshift in the absorption edge, thus enhancing visible light utilization. Fourier transform infrared spectroscopy (FTIR) spectra affirmed the presence of characteristic functional groups of g-C_3N_4, such as C-N and C=N stretching vibrations, alongside peaks emanating from Ti_3C_2QD and CoP, validating their successful amalgamation. Photoluminescence (PL) spectroscopy exhibited a diminished fluorescence intensity in the composite, indicative of curtailed charge recombination. This finding was buttressed by electrochemical impedance spectroscopy (EIS), which confirmed attenuated charge transfer resistance, fostering electron mobility and elevating catalytic performance. BET surface area analyses disclosed that the composite boasted an elevated specific surface area compared to pure g-C_3N_4, and the introduction of Ti_3C_2QD engendered a more porous framework, providing augmented active sites for hydrogen production. This escalated surface area facilitated mass transport, further bolstering photocatalytic efficiency. Photocatalytic hydrogen production trials manifested a pronounced surge in hydrogen yield with the g-C_3N_4/Ti_3C_2QD/CoP composite. Ti_3C_2QD contributed to expedited electron transfer, quantum dots optimized charge segregation, and CoP functioned as an efficient water oxidation catalyst, amplifying the hydrogen production rate. The composite showcased a remarkable elevation in hydrogen production under visible light, validating the synergistic interplay among the constituents. The enhanced photocatalytic performance was ascribed to the refined charge segregation afforded by Ti_3C_2QD and quantum dots, as well as the catalytic prowess of CoP. The postulated mechanism encompasses the creation of electron-hole pairs via light absorption by g-C_3N_4. Ti_3C_2QD thwarts recombination by shuttling photogenerated electrons to the reaction loci, while CoP facilitates efficacious oxidation reactions, augmenting overall hydrogen production efficiency. In summation, the amalgamation of g-C_3N_4, Ti_3C_2QD, and CoP yielded a highly competent photocatalyst for hydrogen generation. Characterization outcomes corroborated the successful integration of these components and their superior photocatalytic performance, driven by refined charge segregation, light absorption, and catalytic activity. The augmented surface area and modified electronic configuration further amplified the photocatalytic performance, underscoring the potential of MXene-based photocatalysts for sustainable hydrogen energy production.

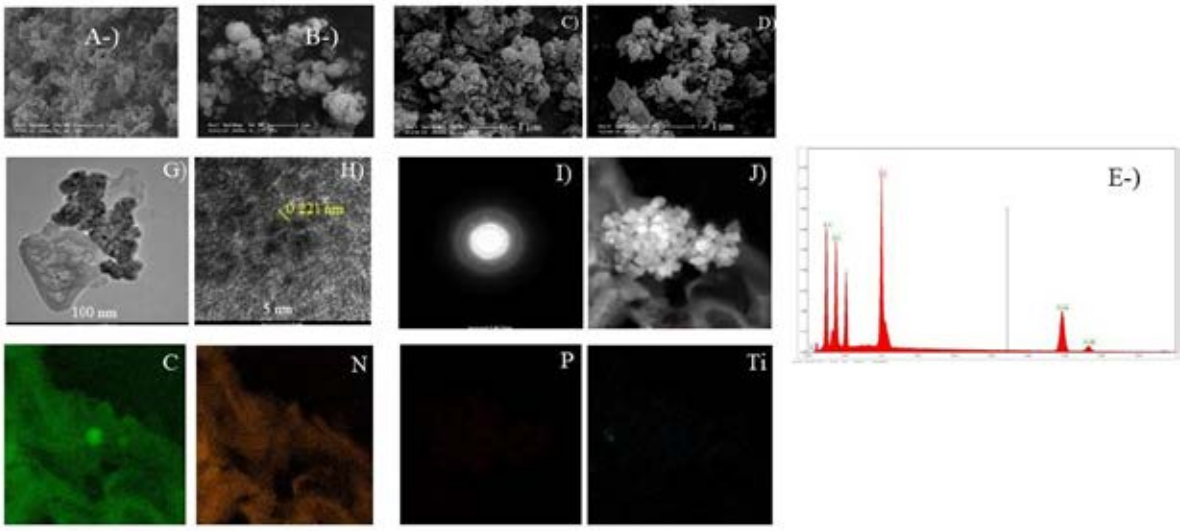

Fig. 2. SEM of a) g-C_3N_4, b) CoP, c) CoP/g-C_3N_4, d) CoP/g-C_3N_4/Ti_3C_2 QD. EDS spectra: e) COP, g-i) HRTEM images and FFT image of CoP/g-C_3N_4/Ti_3C_2 QD. j) Elemental mapping of CoP/g-C_3N_4/Ti_3C_2 QD.

4. CONCLUSIONS

Hydrogen energy serves as a clean and sustainable alternative to fossil fuels, addressing global energy challenges. The increasing demand for renewable energy has driven extensive research into efficient hydrogen production technologies. Among these, photocatalytic water splitting stands out as a promising approach, directly utilizing solar energy to generate hydrogen in an eco-friendly and sustainable manner. In this study, cobalt phosphide (CoP), graphitic carbon nitride (g-C_3N_4), Ti_3C_2 QD, and their hybrid structures were synthesized to enhance hydrogen production efficiency. These materials were chosen for their excellent light absorption, high surface area, and efficient charge separation capabilities, all of which are critical for improving photocatalytic performance. Various characterization techniques, including X-ray diffraction (XRD), scanning electron microscopy (SEM), transmission electron microscopy (TEM), UV-Vis spectroscopy, and photoluminescence (PL) analysis, were employed to assess their properties and effectiveness. The results demonstrated that hybrid nanostructures significantly improved hydrogen production compared to individual materials. The integration of these components broadens the light absorption range, enhances charge carrier transport, and minimizes recombination losses, thereby increasing photocatalytic efficiency. These advancements highlight the potential of hybrid nanomaterials in renewable energy applications. The findings contribute to the development of next-generation photocatalysts for hydrogen production, offering more efficient and cost-effective solutions. Advancing such materials is essential for the widespread adoption of hydrogen technologies, supporting the transition to a cleaner and more sustainable energy future.

ACKNOWLEDGEMENT

The Scientific and Technological Research Council of Türkiye (TÜBİTAK) provided financial support to this study with project number (223Z176).

REFERENCES

1. Yan T, Liu H, Jin Z (2021) G-C3N4/α-Fe2O3Supported Zero-Dimensional Co3S4Nanoparticles Form S-Scheme Heterojunction Photocatalyst for Efficient Hydrogen Production. Energy and Fuels 35:856–867
2. Novoselov KS, Geim AK, Morozov S V., Jiang D, Zhang Y, Dubonos S V., Grigorieva I V., Firsov AA (2004) Electric field in atomically thin carbon films. Science (1979) 306:666–669
3. Kumar A, Sharma SK, Sharma G, Naushad M, Stadler FJ (2020) CeO2/g-C3N4/V2O5 ternary nano hetero-structures decorated with CQDs for enhanced photo-reduction capabilities under different light sources: Dual Z-scheme mechanism. J Alloys Compd 838:155692
4. Nakhanivej P, Yu X, Park SK, et al (2018) Revealing molecular-level surface redox sites of controllably oxidized black phosphorus nanosheets. Nature Materials 2018 18:2 18:156–162
5. Akyüz D, Koca A (2018) Photocatalytic hydrogen production with reduced graphene oxide (RGO)-CdZnS nano-composites synthesized by solvothermal decomposition of dimethyl sulfoxide as the sulfur source. J Photochem Photobiol A Chem 364:625–634
6. Li Z, Wu Y, Li Z, Wu Y (2019) 2D Early Transition Metal Carbides (MXenes) for Catalysis. Small 15:1804736
7. Huang H, Song Y, Li N, Chen D, Xu Q, Li H, He J, Lu J (2019) One-step in-situ preparation of N-doped TiO2@C derived from Ti3C2 MXene for enhanced visible-light driven photodegradation. Appl Catal B 251:154–161
8. Dong G, Zhang Y, Wang Y, Deng Q, Qin C, Hu Y, Zhou Y, Tian G (2021) Ti3C2Quantum Dots Modified 3D/2D TiO2/g-C3N4S-Scheme Heterostructures for Highly Efficient Photocatalytic Hydrogen Evolution. ACS Appl Energy Mater 4:14342–14351
9. Chung DY, Jun SW, Yoon G, et al (2017) Large-Scale Synthesis of Carbon-Shell-Coated FeP Nanoparticles for Robust Hydrogen Evolution Reaction Electrocatalyst. J Am Chem Soc 139:6669–6674
10. Zhao H, Jiang P, Cai W (2017) Graphitic C3N4 Decorated with CoP Co-catalyst: Enhanced and Stable Photocatalytic H2 Evolution Activity from Water under Visible-light Irradiation. Chem Asian J 12:361–365
11. Li Y, Ding L, Guo Y, Liang Z, Cui H, Tian J (2019) Boosting the Photocatalytic Ability of g-C3N4 for Hydrogen Production by Ti3C2 MXene Quantum Dots. ACS Appl Mater Interfaces 11:41440–41447
12. Wang K, Xie H, Li Y, Wang G, Jin Z (2022) Construction of CoP/Cu3P/Ni2P Double S-Scheme Heterojunctions for Improved Photocatalytic Hydrogen Evolution. Journal of Physical Chemistry C 126:6947–6959
13. Li T, Jin Z (2022) Unique ternary Ni-MOF-74/Ni2P/MoSx composite for efficient photocatalytic hydrogen production: Role of Ni2P for accelerating separation of photogenerated carriers. J Colloid Interface Sci 605:385–397

PREDICTIVE MODELLING FOR ENHANCED PETROL ENGINE RELIABILITY WITH PETROLEUM AND HYDROGEN FUELS MIXTURE

[1*]*Jonas Matijošius,* [1]*Tadas Žvirblis*, [2]*Alfredas Rimkus*, [1]*Utku Kale*, [1]*Artūras Kilikevičius*
[1]Vilnius Gediminas Technical University – Vilnius Tech, Faculty of Mechanical Engineering, Institute of Mechanical Science, Saulėtekio al. 11, LT-10223 Vilnius
[2]Vilnius Gediminas Technical University – Vilnius Tech, Faculty of Transport Engineering, Department of Automobile Transport, Saulėtekio al. 11, LT-10223 Vilnius

*Corresponding author e-mail: jonas.matijosius@vilniustech.lt

ABSTRACT

Internal combustion engines that use a mixture of hydrogen and gasoline are designed to take advantage of the advantages of both fuels. These hybrid systems can reduce emissions compared to conventional gasoline-only engines. The integration of hydrogen can improve the overall efficiency and performance of the combustion process. In this research a comprehensive statistical modeling approach for ecological and energy gaining parameters was performed. Statistical models were trained using 11 input parameters such as fuel mixture level, petrol mass, petrol energy ratio, ethanol mass, ethanol energy ratio, hydrogen mass, hydrogen energy ratio, total input energy, ratio of pure carbon, oxygen, and hydrogen. Output parameters were n, CO, CO_2, lambda, O_2, HC, NOx, p_i, ISFC, and BTE. The best accuracy for the training set was achieved for n, CO_2, lambda, Pi, BTE, and ISFC with MAPE of 0.45%, 1.29%, 0.55%, 0.85%, 2.02%, and 2.48%, respectively. Developed prognostic models were also validated using test dataset and reached valuable accuracy for n, CO_2, lambda, Pi, BTE, and ISFC with MAPE of 1.67%, 0.97%, 2.66%, 2.56%, 2.61%, and 5.39%, respectively. In this study the developed predictive statistical models achieved high accuracy in predicting the ecological and energetic parameters of engine emissions generated by engines powered by a petrol-hydrogen mixture.

Keywords: hydrogen; petrol-hydrogen mixture; statistical modelling; prognostic models; MAPE.

1. INTRODUCTION

The aim of the study is to determine the effect on the energy and environmental performance of a dual fuel engine of varying concentrations of bioethanol in the liquid fuel injected into the intake manifold and the addition of hydrogen gas to the intake air. The study evaluates the changing elemental composition of dual fuel.

2. MATERIALS AND METHODS

2.1. Experimental equipment

The experimental tests were carried out using a spark ignition (SI) Opel 1.8E engine, the main technical data of which are shown in Table 1. The engine was installed on a test bench with the addition of a fuel consumption scale (xxx) with a measuring range of 0–30 kg and an accuracy of 2 g. The composition of the exhaust gases was measured with a CARTEC CET 2200 C exhaust gas analyser, which measures the emission components, their measurement limits and accuracy: CO, 0–9.99% (vol.), 0.01%; CO_2, 0–19.99% (vol.), 0.1%; HC, 0–9999% (vol.), 1 ppm; NO_x, 0–2000 ppm (vol.), 5 ppm; O_2, 0–25% (vol.), 0.01%; air excess ratio λ, 0.5–2.0%, 0.001. A schematic of the engine test is shown in Fig. 1.

Table 1. Main parameters of the tested Opel 1.8E engine.

Parameter	Specification
Engine code	18NE
Displacement V_H	1796 cm³
Engine configuration	Inline, i = 4 cylinders
Cylinder bore D	84.8 mm
Piston stroke S	79.5 mm
Compression ratio ε	8.9:1
Fuel system	Multi-port manifold injection
Engine aspiration	Naturally aspirated engine
Maximum power P_{max}	74 kW (5800 rpm.)
Maximum torque M_{max}	140 Nm (3000 rpm.)

A hydrogen-oxygen mixture produced by electrolysis from water was supplied to the engine intake manifold before the throttle body. The electrolyser was filled with a 4% mixture of distilled water and potassium hydroxide (KOH). The electrolysis produces a mixture of H_2 and O_2 gases which is labelled HHO. The device used an external energy source (12 V), the energy consumed of which was evaluated by an additional measurement of the amperage. At steady-state

operation, the electrolysis device used a current of ~35 A, which means that the electrical power used by the device is 12x35 ≈ 420 W. It is determined that the power required to generate 1 L/min of HHO gas is 190 W, and it is therefore calculated that 420/190 ≈ 2.2 L/min of hydrogen-oxygen gas mixture was generated during the engine test. 2/3 of the volume of gas generated by the electrolysis device was H_2 gas, but due to the low hydrogen density, only 0.06 g H_2 per litre of HHO gas was present [1]. The H_2 gas flow to the engine during the test was calculated to be ~0.0079 kg/h.
During the test, the engine throttle was fixed at 5% and the engine was operated at increased idle speed $n \approx 2000$ rpm. Ignition timing was fixed at 12 CAD bTDC. The engine under test does not have a lambda control system, so the air excess ratio λ varied with different fuels. The engine oil was heated to ~100° C. The test duration was 1 min, during which time the fuel consumption in B_f was measured. The test was repeated 5 times or more if there were significant differences in the measured values.

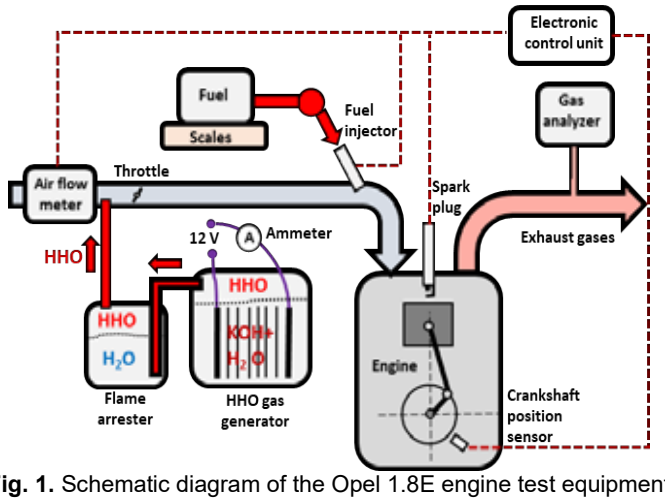

Fig. 1. Schematic diagram of the Opel 1.8E engine test equipment

2.2. Energy characteristics of the engine

The different fuels also varied the energy filling of the cylinders, resulting in different engine speed *n*. The engine was not loaded with additional braking torque and all of the indicative power generated in the cylinders was used to overcome the mechanical resistance-friction of the engine: $P_i = P_F$. Engine friction mean effective pressure, MPa:

$$FMEP = a + b \cdot v_{pist.}, \tag{1}$$

where $a = 0.5;\ b = 0.0155; v_{pist.} = S \cdot n/(30 \cdot 1000)$.
Power of mechanical losses (friction) of the engine, kW:

$$P_F = P_i = \frac{FMEP \cdot V_H \cdot n}{30 \cdot i}. \tag{2}$$

Indicated specific fuel consumption of the engine, g/kWh:

$$ISFC = \frac{(B_{f_{G100}} + B_{f_{E100}} + B_{f_{H_2100}}) \cdot 1000}{P_i}, \tag{3}$$

where: B_{f_G100}, B_{f_E100} *and* $B_{f_H_2100}$ – gasoline, bioethanol and hydrogen fuel consumption, kg/h.
Engine indicate efficiency:

$$\eta_i = \frac{P_i \cdot 3.6}{B_{f_G100} \cdot LHV_{G100} + B_{f_E100} \cdot LHV_{E100} + B_{f_H_2100} \cdot LHV_{H_2100}}, \tag{4}$$

where LHV_{G100}, LHV_{E100} *and* LHV_{H_2100} – gasoline, bioethanol and hydrogen lower heating value, MJ/kg.

2.3. Fuel Properties

The first case study used fuel blend E10, consisting of 10% pure petrol (G100) and 90% pure bioethanol (E100) by volume. The second case used fuel blend E70 consisting of 30% by volume G100 and 70% by volume E100. In the case of dual fuel, E10 or E70 is used to provide additional HHO gas to the intake air, 2/3 of the volume of which is H2. The basic physico-chemical properties of the pure fuels used are given in Table 2.
Increasing the concentration of bioethanol in the fuel increased the oxygen content and reduced the air demand to burn the same amount of fuel. Ethanol, due to its higher latent evaporation temperature, cooled the intake mixture more and increased the density and mass of air in the cylinder. In an engine without lambda control, the above factors contribute significantly to air excess, as the amount of fuel injected depends on the amount of air intake and does not take into account the oxygen concentration in the exhaust gases. With a small variation in fuel injection and a decrease in the *LHV* of the blend as the bioethanol concentration increases, the engine's indicative power decreases and the *ISFC*

increases. The performance of a dual fuel engine is affected by the addition of H_2 when both E10 or E70 fuel is injected into the cylinder and HHO gas is supplied together. Hydrogen increases the combustion speed and combustion quality. The combustion quality is also improved by a higher O_2 content in bioethanol. However, excess oxygen does not increase but even reduces the NOx concentration, due to the greater cooling effect of bioethanol and a significantly leaner mixture. Due to the reduced C/H ratio of the fuel, CO_2 emissions are also significantly reduced. Hydrogen increases the combustion speed and combustion quality. The higher O_2 content in bioethanol also improves combustion quality. However, O_2 does not increase, but even decreases NO_x concentrations, due to the higher cooling effect of bioethanol and the significantly leaner blend. The reduction in fuel C/H ratio also results in a significant reduction in CO_2 emissions.

Table 2. Basic properties of pure fuels.

Parameter		Gasoline G100	Bioethanol E100	Hydrogen $H_2$100
Density at 15°C, kg/m^3		736.0	790	0.09
Lower heating value *LHV*, MJ/kg		43.53	27.0	120.0
Elemental composition, %	C	86.42	52.14	0.0
	H	13.58	13.13	100.0
	O	-	34.73	-
C/H		6.36	3.97	-
Octane number		~95	~109	~130
Adiabatic flame temperature, °C		~2300	~2247	~2207
Laminar flame speed, cm/s		~51	~63	~270
Latent heat of evaporation, kJ/kg		364	840	~120
Stoichiometric air fuel ratio A/F, kg air/1 kg fuel		14.7	9.10	34.5

2.4. Prognostic Model Building

Multivariate linear regression models for predictions of RPM, CO, CO_2, O_2, lambda, HC, NOx, Pi, BTE, and ISFC were build. Models were trained using 11 input parameters such as fuel mixture level, petrol mass, petrol energy ratio, ethanol mass, ethanol energy ratio, hydrogen mass, hydrogen energy ratio, total input energy, ratio of pure carbon, oxygen, and hydrogen. Data set consisted of experimental data when petrol and hydrogen mixture was used. Multivariable regression models were defined as:

$$Y^E = \alpha + \beta X + \varepsilon, \tag{5}$$

where Y^E – engine outcome parameter (dependent variable), E – type of engine outcome parameter, X – prognostic factor (independent variable), ε – random error.

Accuracy between prognostic model and real data was evaluated using mean absolute percentage error (MAPE):

$$MAPE = \frac{1}{N}\sum_{i=1}^{N} \left|\frac{R_i^E - \widehat{Y_i^E}}{R_i^E}\right|, \tag{6}$$

where R_i^E – real engine outcome parameter value for i^{th} experiment, $\widehat{Y_i^E}$ – prognostic engine outcome parameter value for i^{th} experiment, E – engine outcome parameter.

3. RESULTS AND DISCUSSION

Figure 2 compares observed and forecasted (prognosis) counts (n) for four categories: E10, E10 HHO, E70, and E70 HHO. On the x-axis, we have 21 sequential points, each corresponding to specific recorded or projected data. The y-axis shows the numerical values for each category, revealing that E10 and E10 HHO have higher counts (above 2000), while E70 and E70 HHO stay closer to the 1600–1700 range. In each category, the observed and forecasted lines follow generally similar trends, but some differences and crossovers appear. Overall, the prognosis lines tend to track slightly below or above the observed values, depending on the specific data point.

Figure 3 is a correlation matrix showing pairwise relationships among ten variables: n, CO, CO_2, lamda, O_2, HC, NOx, Pi, ISFC, and BTE. In the upper-right triangle, each cell displays a numerical correlation coefficient colored from dark blue (strong positive correlation) to dark red (strong negative correlation). On the diagonal, each variable's distribution is shown by a histogram, revealing the spread of its values. In the lower-left triangle, pairwise scatter plots visualize the trend between two variables, with a smoothed line indicating their general relationship. Overall, we see several strong correlations (e.g., n with CO_2, NOx, or Pi) and strong negative correlations (e.g., lamda with NOx and Pi), suggesting important interdependencies among these variables.

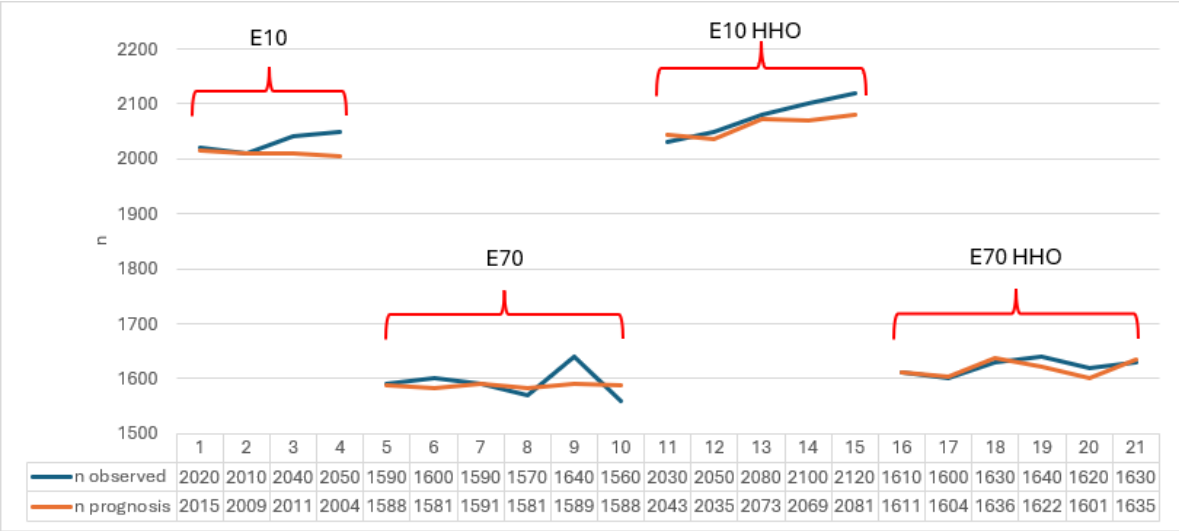

Fig. 2. Comparison of Observed and Forecasted Values for E10, E10 HHO, E70, And E70 HHO

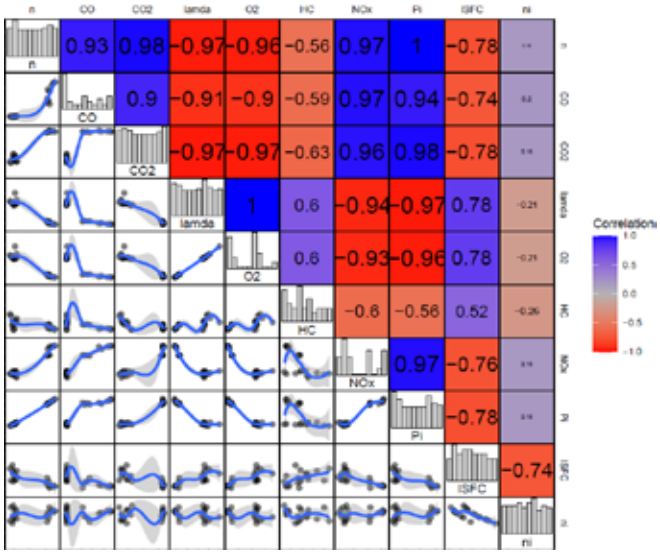

Fig. 3. Correlation Matrix and Pairwise Scatter Plots of Ten Key Variables

4. CONCLUSIONS

1. The high positive correlation between n and CO_2, NOx, Pi indicates that both exhaust gas pollution indicators and engine power increase with increasing engine speed.
2. The negative correlation between lambda and NOx, Pi indicates that a leaner fuel mixture reduces NOx emissions and engine power indicators.
3. Although the correlation between some indicators (e.g. CO and HC) is not very strong, they can be significant under certain engine operating conditions.
4. The overall picture of the correlations indicates that changes in combustion process parameters and exhaust gas composition are closely related.

ACKNOLEDGEMENT

This research work has received funding from the project „Civil Engineering Research Centre“ (agreement No S-A-UEI-23-5, ŠMSM

REFERENCES

[1] Rimkus A, Matijošius J, Bogdevičius M, Bereczky Á, Török Á. An investigation of the efficiency of using O2 and H2 (hydrooxile gas -HHO) gas additives in a ci engine operating on diesel fuel and biodiesel. Energy 2018;152:640–51. https://doi.org/10.1016/j.energy.2018.03.087.

GREEN SYNTHESIS OF FUEL ADDITIVE SOLKETAL BY A NOVEL ENVIRONMENTALLY FRIENDLY CATALYTIC MEMBRANE

[1]*Nazlı YÜZER*, [1*]*Nilüfer HİLMİOĞLU*
[1,1*] Kocaeli University, Engineering Faculty, Chemical Engineering Department, Kabaoğlu, Baki Komsuoğlu bulvarı No:515, Kocaeli 41001, TURKEY
*Corresponding author e-mail: niluferh@kocaeli.edu.tr

ABSTRACT
Polyvinyl alcohol is a water-soluble, renewable, biodegradable, bio-compatible, environmentally friendly synthetic polymer. Besides that; Solketal was produced with the hybrid material obtained by converting polyvinyl alcohol, which is called the perfect polymer in the literature, into catalytic membrane form with the addition of catalyst. Solketal; developed as a fuel additive to alleviate the negative effects of fossil fuel use, is an environmentally friendly alternative to harmful traditional fuel additives. Solketal was produced from glycerin and acetone in the presence of a functional catalytic membrane as heterogeneous catalysis under environmentally friendly and mild conditions. The catalytic membrane was prepared from polyvinyl alcohol(PVA) as a polymeric matrix and Silicomolybdicacid(SMA), a type of heteropolyacid, as a catalyst. The chemical structure and thermal resistance of the prepared hydrophilic functional catalytic membrane were investigated by FTIR and TGA analyses, respectively. The effects of reaction time, catalyst amount (1,2,3 mmol), acetone/glycerol initial molar ratio (4,5,6) and temperature parameters (40,50,60°C) on solketal yield were investigated in the batch reactions. Maximum solketal yield was obtained as 99,9% at 3 mmol SMA loading, reaction temperature at 60°C, in 1h. Moreover, the reaction parameters catalyst ratio and acetone/glycerol initial molar ratio were investigated statistically by RSM study. **Keywords:** Fuel Additive, Catalytic Membrane, Solketal.

1. INTRODUCTION

Environmental problems related to fossil fuel consumption in the world have become one of the most important problems for people. In particular, many countries, suffer from air pollution caused by toxic gas emissions resulting from the use of fossil fuels in transportations and transport. In recent years, significant increases has been observed in the biodiesel production and use as fuel in order to reduced significant harmful emissions. In fact, it is estimated that biodiesel production has been reach 41.4 billion liters in 2025, an increase of 25% compared to the production exceeding 33 billion liters in 2016 [1]. In biodiesel production, approximately 10% glycerin by weight is obtained as a by-product [2]. The industrial used of glycerin produced as a by-product and its conversion into oxygenated fuel additives has been become a very interesting subject. Oxygen fuel additives were chemical compounds that, when added to the fuel, positively affect the properties of the fuel (kinematic viscosity, density, flash point), increase the octane or cetane number, allowing more efficient combustion, reduce toxic gas emissions, and improve the cold flow properties of the fuel, which has especially important for vehicles in cold climates [3]. Converting glycerin into these compounds through various reactions has an important step both for its evaluation and for cleaner and more efficient combustion in fuels. Solketal, (2,2-dimethyl-1,3-dioxane-4-methanol), synthesized from the reaction of glycerin with acetone help of an acidic catalyst has 5-membered ring cyclic molecule; used for many purposes in the food, polymer pharmaceutical and cosmetic industries its a colorless and odorless [4,5]. Water is released as a byproduct in the synthesis of solketal. Solketal is blended with gasoline and biodiesel as a fuel additive; It improves cold flow properties, increases oxidation stability and flash point, and reduces gum formation and environmental pollution in the fuel mixture [6]. In the synthesis of solketal, traditionally hydrochloric acid (HCl) and sulfuric acid (H2SO4) has widely used as homogeneous catalysts. However, the fact that homogeneous catalysts are difficult to recover from the reaction environment and were weak in terms of reuse has shifted the studies to heterogeneous catalysts. In recent studies, Maurya et al., 2024 synthesized solketal from glycerol and acetone with solid acid SO4-2/ZrO2-Al2O3 catalyst; Under optimized conditions, 99.2% glycerol conversion was achieved at 3% catalyst loading; Acetone/glycerol: 1/10, 70 °C, 180 min [6]. Gujar and Modhera, 2024 synthesized solketal from glycerol and acetone with metal-modified (M=Fe, Co, Ni, Cu, and Zn) M-ZSM-5 catalysts. With the most effective Cu-ZSM-5 catalyst, under optimum conditions (60 °C reaction temperature, acetone /glycerin: 1/4, 0.2 g catalyst amount, 60 min), 99% glycerin conversion was achieved. [7]
Heterogeneous catalysts used as alternatives to homogeneous catalysts was heteropoly acids, zeolites, modified carbon materials, mixed metal oxides [8]. Heteropolyacids, known as green catalysts, were solid acid catalysts that has easily separated, non-corrosive, safe to use, and cause very little waste [9]. Among heteropolyacid catalysts, silicomolybdic acid (SMA) has very good catalytic properties. Silicomolybdic acid has soluble in water, it can be attached to a desired surface or used with a support material; this situation; its has important for recovery and effective use in the reaction system [10,11]. Catalytic membranes prepared by combining membranes and catalysts; it functional materials that performed reaction and sorption processes simultaneously in a single unit [12]. Membranes can be made with various materials, but catalytic membranes are generally polymer structured and can be produced by embedding or coating the catalysts to be used in the reaction in polymeric matrices, or they can be prepared as a result of the polymeric matrix itself being catalytically [13]. Polymeric based catalytic membranes; depending on the physicochemical properties of the polymer; it can be hydrophilic or hydrophobic. The polymeric matrix is used with its absorption-supported feature in

hydrophilic catalytic membranes; it removes the water molecule released as a by-product in the reaction from the environment and encourages product formation by shifting the reaction balance towards the product [14]. Polyvinyl alcohol is a water-soluble, renewable, biodegradable, biodegradable, biocompatible, environmentally friendly synthetic polymer [15, 16]. In addition, it is a good candidate for catalytic membrane production with its good film-forming properties and chemical stability. There are very limited number of solketal syntheses with catalytic membranes in the literature. Hilmioğlu, et al., 2023, synthesized solketal from glycerin and acetone with an acidic catalytic membrane they produced by blending acidic poly (2-acrylamido-2-methyl-1-propanesulfonic acid) PAMPS polymer and PVA. They observed that solketal yield increased as PAMPS content increased, and 95% yield was obtained under optimum conditions (60°C, 3 hours, M:6/1) [17]. This study aims to synthesize fuel additive solketal with acid-functionalized heterogeneous catalytic membrane under environmentally friendly conditions (atmospheric pressure, low temperature, without toxic solvents). With the heterogeneous catalytic membrane used, the recovery of homogeneous silico molybdic acid will be easy and can be used in the reaction again. With this method, homogeneous acidic catalysts can be used in a more active and environmentally friendly way. Thanks to the water sorption support provided by the high hydrophilic PVA polymer, the by-product water will be removed from the reaction medium, and product formation will be supported.

2. MATERIALS AND METHODS

2.1. Materials

PVA (polyvinyl alcohol) (MW~125,000) in solid form, and SMA (silico molibdic acid) solution were acquired from Sigma-Aldrich, while Merck Chemicals provided glycerin (≥ 99%), acetone (≥ 99.0%), and toluene (≥ 99.9%).

2.2. Preparation of Functional Catalytic Membrane

PVA pellets were dissolved in water for 3 hours at 90°C to obtain a 6% PVA solution by weight. Certain amounts of the prepared solution were taken and 1 mmol, 2 mmol, and 3 mmol of SMA acid catalyst were added to the solutions. After stirring the polymer-catalyst mixture for 1 hour, it was poured onto Teflon plates and left to dry at room temperature.

2.3. Batch Reaction System

Acetalization reactions were carried out in the batch reaction system in Figure 1 with the prepared PVA/SMA functional catalytic membrane, 1, 2, 3 mmol catalyst loading 40, 50, 60°C temperatures, and M: 4/1, 5/1, 6/1 acetone/glycerol initial molar ratios in 1 h reactions.

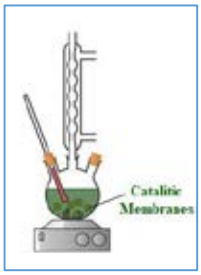

Fig. 1. Batch Reactor System

2.4. Analysis of reaction products

Solketal; was analyzed by gas chromatography (GC-FID). The detector temperature was set to 350 while the DB WAX capillary column was used as the column. Solketal yield was calculated from Equation 1; [18]

$$\textit{Solketal yield (\%)} = \frac{\textit{Mole of produced Solketal}}{\textit{Initial mole of glycerin}} x100$$

3. RESULTS AND DISCUSSION

3.1. Chacterizations of the Catalytic Membrane

3.1.1. FT-IR &TGA Analysis

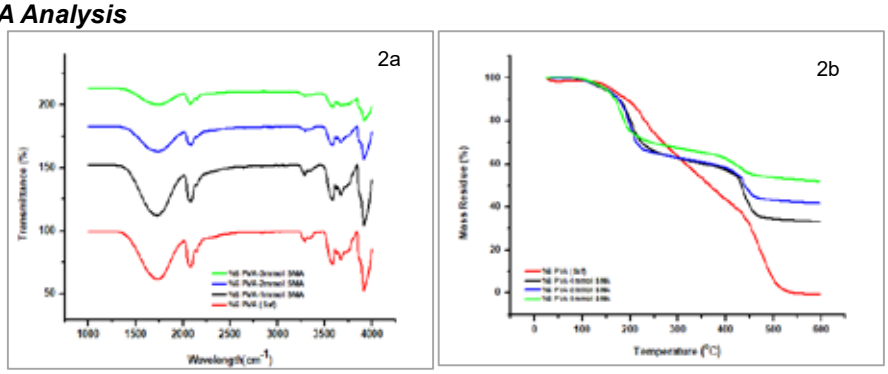

Fig. 2. (a) FT-IR Characterization of Hybrid Catalytic Membranes with SMA Catalysts; (b) TGA Characterization of Hybrid Catalytic Membranes with SMA Catalysts

FT-IR characterizations of the prepared pure PVA and PVA-SMA functional catalytic membranes are given in Fig 2a. According to the FT-IR characterization; the broad peak around 3550–3200 cm-1 can be explained as -OH stretching vibration from intermolecular hydrogen bonds [20]. The 2980 and 2800 cm-1 vibration band represent the C–H group [15, 21]. As for SMA, the peaks of Mo=O, Mo–O–Si, and Mo–O–Mo bonds, which constitute its chemical structure, are seen in the areas of 956 cm-1, 910 cm-1 and 825 cm-1, respectively. These peaks were confirmed by comparison with the literature. The peaks occurring in the band between 1700 cm-1 and 1800 cm-1 were considered cross-linking peaks thanks to the acid-active areas in the SMA catalyst [22].
Thermal degradation curves of the prepared pure PVA-SMA functional catalytic membranes were examined with a Mettler Toledo brand thermal gravimetric analysis (TGA) device between 25 °C and 600 °C. The solvent of all polymeric membranes used in this study is water, and water exists in different states within the PVA blend membranes; solvent water; It forms the polymeric solution in two different ways: firstly, it exists in the form of water molecules held by weak bonds on the outer or inner surface without interacting with the chemical matrix that forms the polymer, and secondly, in the form of water molecules strongly bonded to hydroxyl groups. TGA characterizations of the prepared PVA-SMA functional catalytic membranes are given in Figure 2b.While the primary region between 50-200 °C is the loss of water molecules in the polymer solution forming the membrane, the secondary region between 200-450 °C is related to water loss due to the polymer matrix. The first weight loss in the temperature range of 50-200 °C is due to the removal of water molecules, which are the solvent of the polymers that form polymeric membranes. Secondary weight loss occurred between 200-485 °C due to the loss of organic components. The tertiary weight loss is due to the decomposition of the bonds in the SMA structure between 485-600 °C, and the stable appearance of the graph explains that only metal oxide residues (Si-O-Mo) remain [21].

3.2. Swelling Testing of PVA-SMA Catalytic Membrane

Swelling tests; are performed to determine the affinity of a material to its solvent or to the reactants in the environment to be applied or to the products produced with the input reactants in the reaction to be used. Solketals reaction performed in this study; It is a transesterification reaction that releases water as a byproduct. The simultaneous presence of water and the product produced in the reaction environment reduces the reaction efficiency. Eliminating this situation and shifting the reaction towards the products (Le Chatelier's Principle) is possible by continuously removing water from the reaction medium. For this reason, the catalytic hybrid membrane used must be hydrophilic. Water sorption results of the catalytic hybrid membrane used in the reaction are given in Table 1. Sorption % values were calculated with Equation (2) [20]:

$$Swelling\ (\%) = \frac{W_{wet} - W_{dry}}{W_{dry}} x100 \quad (2)$$

Table 1. Investigation of Water Sorption of Hybrid Catalytic Membranes with SMA Catalyst

Membrane	Swelling (%)
Pure PVA	290.2
PVA-1mmol SMA	235.5
PVA-2mmol SMA	196.6
PVA-3mmol SMA	183.4

As a result of weighings made at 30-minute intervals for 6 hours, the swelling value of the membrane was determined as for PVA-1mmol SMA, PVA-2mmol SMA, PVA-3mmol SMA 235.5, 196.6, 183.4%. The swelling percentage did not change as a result of 24-hour weighing.

4. CONCLUSIONS

In this study, fuel additive solketal was produced under environmentally friendly and mild conditions with the prepared functional catalytic membrane. The produced functional hydrophilic catalytic membrane catalyzed the membrane reaction with SMA loading and simultaneously removed the by-product water from the reaction medium with the hydrophilicity of PVA, thus ensuring that the reaction balance was directed towards the formation of products. In addition, the produced catalytic membrane acted as a green heterogeneous catalyst and was easily recovered from the medium after the reaction. While successful loading of SMA was observed with FT-IR characterization, SMA added to the structure increased the thermal resistance of the catalytic membrane compared to pure PVA with TGA analysis. Moreover, it was observed that the thermal resistance increased even more in direct proportion to the SMA ratio. The affinity of the functional catalytic membrane to the by-product water was determined by swelling tests and interaction parameter calculations. It was observed that the membrane had a high affinity for water with swelling tests, and this ratio decreased as the SMA ratio increased. The interaction parameter of PVA/SMA catalytic membranes is closer to zero compared to pure PVA, and it can be said that SMA added to the structure increases the water affinity in the membrane. In terms of catalytic performance, the acidity of the catalytic membrane was determined by ion exchange capacity calculations. An increase in ion exchange capacity was observed as SMA loading increased. In the batch reactor studies, the maximum solketal yield was obtained as 99.9% at 3 mmol catalyst loading, M:6/1, 60°C and one hours of reaction time. Also RSM study will be conducted within the scope of this experimental study. The effects of catalyst loading and acetone/glycerin

initial molar ratio on solketal yield will be investigated statistically in the central composite design design and at constant temperature in full text.

ACKNOWLEDGEMENT
This study was supported by the scientific research projects unit of Kocaeli University. Project No: 2023-3201.

REFERENCES

1. Oyekunle DT, Gendy EA, Barasa M, Oyekunle DO, Oni B, Tiong SK. 2024. Review on utilization of rubber seed oil for biodiesel production: Oil extraction, biodiesel conversion, merits, and challenges. Cleaner Engineering and Technology 21:100773.
2. Zulaika A, Rahman H, Ningrum SS, Maulida AF. 2024. Exploring microbial lipases: Screening and identification for biocatalyst potential in bioethanol synthesis from glycerol-based biodiesel waste. Results in Engineering 23:102427.
3. Yee KF, Mohamed AR, Tan SH. 2013. A review on the evolution of ethyl tert-butyl ether (ETBE) and its future prospects. Renewable and sustainable energy reviews 22:604-620.
4. Taddeo F, Esposito R, Russo V, Di Serio M. 2021. Kinetic Modeling of Solketal Synthesis from Glycerol and Acetone Catalyzed by an Iron(III) Complex. Catalysts 11:1.
5. Zahid I, Ayoub M, Abdullah BB, Nazir MH, Zulqarnain. 2021. Glycerol Derivatives as Fuel Additive: Synthesis of Solketal From Glycerol and Acetone With Various Acid Clay Catalysts. Advances in Engineering Research 200:292.
6. Maurya S and Sharma YC. 2024. Synthesis of oxygenated additive fuels from bio-renewable glycerol using sulfated Zr-Al based heterogeneous acid catalyst. Fuel 355 129352.
7. Gujar JP and Modhera B. 2024. Green Synthesis of Solketal from Glycerol Using Metal-Modified ZSM-5 Zeolite Catalysts: Process Optimization. Environmental Science and Pollution Research 31:28353-28367.
8. Zhang Y, Feng T, Liu J, Jiao Q, Zhen B. 2023. Process intensification in the ketalization of glycerol with acetone catalyzed by NaHSO4-NaOH catalytic system. Chemical Engineering and Processing - Process Intensification 194:109576.
9. Gharib A. 2016. Application of Heteropolyacids and Nano-catalyst in Heterocycles Synthesis. Organic and Medicinal Chemistry International Journal 1:1.
10. Achary LSK, Parida R, Kumar A, Giri S, Dash P. 2022. Silicomolybdic acid intercalated graphene oxide-based solid acid: catalytic activity and investigation of structural stability by DFT analysis. Materials Chemistry and Physics 285:126096.
11. Umegaki T, Hoshino M, Watanuki Y, Kojima Y. 2016. Preparation of hollow mesoporous silica spheres with immobilized silicomolybdic acid and their catalytic activity for the hydrolytic dehydrogenation of ammonia borane. Microporous and Mesoporous Materials 223:152-156.
12. Popkov A, Malankowska M, Su Z, Pinelo M. 2023. Enhancement of biocatalytic activity in enzymatic membrane reactors: Controlled modification with novel PAH/PDA composites as a tool to optimize reactor performance. Journal of Membrane Science 688:122049.
13. Unlu D and Hilmioglu ND. 2018. Pervaporation catalytic membrane reactor application over functional chitosan membrane. JOURNAL OF MEMBRANE SCIENCE 559:138-147.
14. Li C, Song G, Lim KH, Hu F, Sunarso J, Yang N, Wong MS, Liu S, Kawi S. 2024. Transcending catalytic limits for methane decomposition: multi-functional basalt fiber-supported catalysts with membrane synergy. Advanced Composites and Hybrid Materials 7(3):99
15. Dülger ND, Samatya Yilmaz S, Uzuner H, Aytac A. 2024. Fabrication of antibacterial food packaging from polyvinyl alcohol/sodium caseinate composite films cross-linked with lactic acid. Journal of Vinyl and Additive Technology 30(6)
16. Krishnan Manthira Moorthy M, Gurusamy S, Pandiarajan B, Balasubramanian B, Pandiarajan N, Suyambulingam I, Mavinkere Rangappa S, Siengchin S. 2024. Effect of alkali-treated Putranjiva roxburghii seed shell filler on physico-chemical, thermal, mechanical, and barrier properties of polyvinyl alcohol-based biofilms. Journal of Vinyl and Additive Technology 30(6):1010.
17. Hasirci G, Ilgen O, Hilmioglu N. 2023. Synthesis of the Environmentally Friendly Fuel Bioadditive Solketal by the Green Catalytic Membrane PVA/PAMPS. WATER AIR AND SOIL POLLUTION 234:11.
18. Huang H, Mu J, Liang M, Qi R, Wu M, Xu L, Xu H, Zhao J, Zhou J, Miao Z. 2024. One-pot synthesis of MoO3-ZrO2 solid acid catalyst for solvent-free solketal production from glycerol. Molecular Catalysis 552:113682.
19. Huang H, Mu J, Liang M, Qi R, Wu M, Xu L, Xu H, Zhao J, Zhou J, Miao Z. 2024. One-pot synthesis of MoO3-ZrO2 solid acid catalyst for solvent-free solketal production from glycerol. Molecular Catalysis 552:113682.
20. Sinha A and Ullas AV. 2024. Preparation and Tensile Properties of Citric Acid Crosslinked Poly(vinyl alcohol) films reinforced with Nano-Alumina. Journal of Vinyl and Additive Technology 30(6):294.
21. Yan Z and DouQ. 2024. Preparation and characterization of poly(vinyl alcohol)/poly(lactic acid) blends containing bio-based plasticizers. Journal of Vinyl and Additive Technology 30(4):895.
22. Huong TM, Fukushima K, Ohkita H, Mizushima T, Kakuta N. 2006. Design of active molybdenum oxides: β-MoO3 and/or silicomolybdic acid supported on mesoporous MCM-41 catalysts. Catalysis Communications 7(3):127-131.

DESIGN AND ANALYSIS OF A WIND-POWERED HYDROGEN PRODUCTION SYSTEM FOR A MARITIME AUTONOMOUS SURFACE VESSEL

[1*]*S. Aykut KORKMAZ*, [1]Siddharth Balakrishnan, [1]*Panos Manias,* [1]*Stephen Turnock*
[1] University of Southampton, Faculty of Engineering and Physical Science, Department of Civil, Maritime and Environmental Engineering, Southampton, SO16 7QF, UK
*Corresponding author e-mail: aykut.korkmaz@soton.ac.uk

ABSTRACT
This paper presents the design and techno-economic analysis of an off-grid, wind-powered green hydrogen production system optimized for a Maritime Autonomous Surface Vessel (ASV). Utilizing component modelling, including Proton Exchange Membrane (PEM) electrolysis, and hourly wind resource simulations, the study demonstrates the system's capacity to meet the target vessel's annual demand of approximately 3.9 tonnes H_2. The techno-economic evaluation yielded a Levelized Cost of Hydrogen (LCOH) of approximately £2.77 per kg. This result indicates economic competitiveness and supports the technical feasibility of deploying autonomous, renewable hydrogen solutions to power specialized maritime applications, particularly in remote or off-grid scenarios.

Keywords: Green Hydrogen Production, Maritime Application, Multi-Criteria Decision Making, Techno-economic Analysis, System Design

1. INTRODUCTION

Maritime decarbonization has emerged as a global imperative, driven by commitments from numerous nations to reduce greenhouse gas emissions in alignment with international climate agreements, most notably the Paris Agreement. The International Maritime Organization (IMO) has set ambitious targets to halve greenhouse gas emissions from shipping by 2050, striving towards full decarbonization by the end of the century [1]. The inherent dependence of the shipping industry on fossil fuels, coupled with the increase in global trade, necessitates the exploration of alternative energy carriers to achieve these decarbonization goals.

Green hydrogen stands out as a viable candidate for this transformation, due to its potential to provide a zero-emission fuel alternative when produced using renewable energy sources. Several studies show that large-scale green hydrogen production can effectively decarbonise various energy sectors, including maritime applications [2, 3]. For instance, the co-development of offshore wind and hydrogen production is being explored extensively in regions like the UK [4-6], where green hydrogen can serve not only as fuel for maritime vessels but also to transport renewable energy across long distances [7]. This dual function increases hydrogen's appeal, especially given its ability to integrate with existing energy infrastructures [8].

While the literature predominantly discusses large-scale hydrogen production, there remains a critical literature gap regarding the optimization of small-scale production systems, particularly combining wind turbine technology and electrolyzers tailored for maritime uses. The application of such systems in ports is particularly promising but underexplored. The dynamics of local wind availability and fluctuating hydrogen demand profiles present unique challenges [8].

Despite these advances, existing studies rarely align system design with a real-world vessel's daily operational requirements. This work differs by integrating the hydrogen demand profile of an already manufactured, operational, autonomous surface vessel into the system sizing process. The model employs a dynamic, hourly-resolved simulation to match local wind availability to electrolyser input and utilises a TOPSIS-based multi-criteria decision-making (MCDM) framework for optimal wind turbine selection. Rated power, capacity factor and LCOE are objective criteria for identifying the configuration that best satisfies economic and technical performance targets.

By combining demand-driven system modelling, real vessel requirements, and multi-objective optimisation, this study offers a novel and practical framework for deploying scalable, cost-effective green hydrogen infrastructure at ports. This contributes to the broader goal of maritime decarbonisation through renewable energy integration.

2. MODELLING

2.1. System Overview

Figure 1 shows the general system topology. An onshore Horizontal Axis Wind Turbine (HAT) provides electrical power to a PEM electrolyser, which splits purified water (via Reverse Osmosis (RO) desalination) into hydrogen and oxygen. A hydrogen compressor then raises the pressure to 350 bar for on-site storage, ready to fuel the autonomous vessel.

2.2. Wind Resource Characterization

The Port of Plymouth (50.357°N, –4.1245°E) was selected for its favourable average wind speeds (7.8–8.7 m/s annually). The wind speed distribution for 2023 is further illustrated in Figure 1 in the form of a histogram and fitted Weibull distribution.

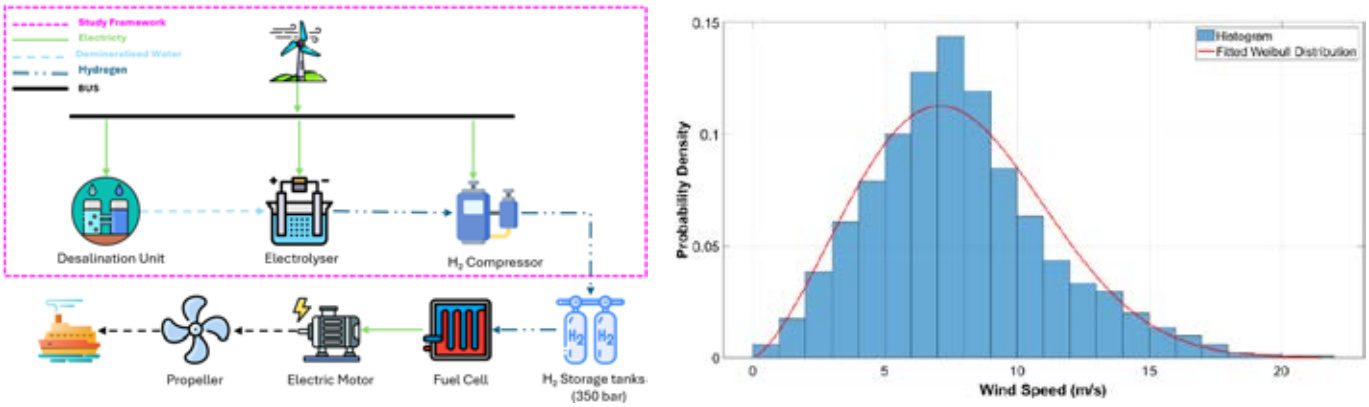

Fig. 1. Schematic of the wind-to-hydrogen production system (left) and Wind Speed Distribution for Plymouth Port (right)

Hourly wind data from the MERRA-2 database was height-adjusted to the turbine's hub (H) using the power-law equation:

$$v(h) = v_{ref}\left(h/h_{ref}\right)^{\alpha} \tag{1}$$

where v_h denotes the estimated wind speed at a specific height h, while v_{ref} indicates the measured reference wind speed at a known height. The power law exponent (α), the wind shear coefficient is a dimensionless value reflecting atmospheric stability and surface roughness. This study uses a wind shear coefficient of 0.16 as a representative value for coastal areas characterised by relatively smooth terrain [9].

2.3. Key Components

The system's key components include a wind turbine, desalination unit, electrolyser, and compressor. Detailed specifications of the key components parameters and their values are given in Table 1.

Table 1. Used parameters and values of the key components for the hydrogen system model

	Parameter	Value Range/Value	Unit	Reference
Wind Turbine	Rotor Diameter Range	20-100	m	[10]
	Hub Height Range	30-120	m	[10]
	Cut-in Wind Speeds	3, 4, 5	m/s	[10]
	Rated Wind Speeds	6-12	m/s	[10]
	Cut-out Wind Speeds	25-30	m/s	[10]
	Max Power Coefficient	0.45	-	[9]
	Mechanical Losses	3	%	[11]
	Electrical Losses	4	%	[10]
	AC-DC Converter Losses	3	%	[10]
	Reference Height (z_{ref})	50	m	[10]
	Power Law Coefficient (α)	0.16	-	[10]
	Reference Capacity	20	kW	[12]
	Reference Purchase Cost	1086	£/kW	[12]
	Scale Index	0.9	-	[12]
	Land Cost	6	% of CAPEX	[12]
	OPEX per kW per year	50	£/kW/year	[12]
Desalination Unit	Recovery Rate	0.5	kg freshwater/ kg seawater	[13]
	Inverter Losses	5	%	[14]
	Specific Energy Consumption	0.0427	kWh/kg H_2	[13]
	CAPEX Rate	1284.8	£/(m³/day)	[15]
	OPEX Percentage	3	% of CAPEX	[16]
PEM Electrolyser	Annual Hydrogen Production Target	3.9	Metric ton/year	[17]
	Initial Degradation Rate	1.0	-	-
	Stack Correction Factor	1.0	-	-
	Stack Lifetime	80000	hours	[18]
	Minimum Load	5	%	[19]
	Maximum Load	100	%	[19]
	Specific Water Consumption	17	L/kg H_2	[19]
	Specific Energy Consumption	55	kWh/kg	[19]

	Reference Capacity	10	kW	
	Reference Purchase Cost	1755	£/kW	[20]
	Scale Index	0.69 (<5 MW) 0.9 (>5 MW)	-	[21]
	Land Cost Percentage	6	%	[20]
	OPEX Percentage	2.5	% of CAPEX	[20]
	Stack Replacement Cost Rate	40	% of CAPEX	[20]
H_2 Compressor	Lifetime	10	years	[14]
	Inverter Losses	5	%	[14]
	Specific Energy Consumption	6.9	kWh/kgH2	[22]
	CAPEX Rate	1388	£/kW	[22]
	OPEX Percentage	3	% of CAPEX	[14]

2.4. Sizing Procedure

The following stepwise algorithm ensures the final system can supply the annual hydrogen target (~3.9 tonnes/year) for USV Pioneer:

Step 1: Electrolyser Rating: Determined from:

$$P_{elec}^{rated} = \left(m_{H_2,daily} \times SEC_{elec}\right)/(\eta_{stack} \times CF_{elec} \times 24) \quad (2)$$

where $m_{H_2,daily}$ is the daily H_2 target, SEC_{elec} the specific energy consumption, η_{stack} a conservative stack efficiency accounting for degradation and CF_{elec} the electrolyser capacity factor.

Step 2: Compressor and desalination unit sized proportionally based on electrolyser throughput and known energy consumption profiles.

Step 3: For each candidate wind turbine (varying rotor diameter, hub height, cut-in/rated speeds), the annual energy production (AEP) is computed using:

$$AEP = \sum_{t=1}^{8760} P_{wt,}(v_t) \times \Delta t \quad (3)$$

where v_t is the wind speed at the time step t, and Δt is the step duration from the calculated E_{annual}, the levelized cost of energy (LCOE) then follows:

$$LCOE_i = \sum_{t=0}^{n} \frac{CAPEX_i + OPEX_{i,t}}{(1+r)^t} \Bigg/ \sum_{t=0}^{n} \frac{E_{i,t}}{(1+r)^t} \quad (4)$$

where $CAPEX$ is the initial investment, $OPEX_{i,t}$ the annual operating cost at the year t, $E_{i,t}$ the energy generated in the year t, n the project lifetime, and r the discount rate. A lower LCOE implies greater cost-effectiveness.

Step 4: The TOPSIS method ranks turbines on (i) closeness to required rated power, (ii) LCOE, and (iii) capacity factor. The highest scoring turbine is selected.

2.5. Levelised Cost of Hydrogen

This study's techno-economic analysis evaluates project feasibility by estimating capital expenditure (CAPEX) and operating expenditure (OPEX). CAPEX is determined using methods like the Scale Index approach to account for system size variations. OPEX includes costs such as maintenance, parts replacement, and consumables. The primary evaluation metric is the Levelized Cost of Hydrogen (LCOH), calculated by dividing the discounted sum of total lifetime costs (CAPEX and OPEX) by the discounted total hydrogen production over the same period, as shown in Equation 5:

$$\mathrm{LCOH} = \frac{\sum_{t=0}^{T} \frac{(CAPEX_t + OPEX_t)}{(1+r)^t}}{\sum_{t=0}^{T} \frac{m_{H_2,t}}{(1+r)^t}} \quad (5)$$

LCOH represents the average production cost per unit of hydrogen, enabling comparison between different system configurations and guiding optimal design decisions for green hydrogen production systems.

3. RESULTS AND DISCUSSION

3.1. Optimal Hydrogen Production System Configuration

Since different capacity factors impact the required rated power of the electrolyser, alternative configurations were also assessed. Based on this analysis, a capacity factor of 0.9 was chosen, as it balances efficiency and system reliability while minimising the required rated power**.** Table 2 summarises the final component sizing for the hydrogen production system. This includes the selected electrolyser, compression system, desalination unit, and respective energy requirements.

Table 2. Final Hydrogen Production System Sizing Parameters

Component	Parameter	Value	Unit
Electrolyser	Rated Power	30.9	kW
	SEC @Rated Power	55	kWh/kg H_2
	Stack Lifetime	80,000	Hours
Compressor	Rated Power	**3.9**	kW
	SEC	6.9	kWh/kg H_2
Desalination Unit	Rated Power	0.0242	kW
	Recovery Rate	50	%
	SEC	0.0427	kWh/kg H_2

Applying the above method to wind data from Plymouth identified a moderate-scale turbine (approximately 43 kW rated output, hub height ~50 m, rotor diameter ~30 m) as top-ranked, as depicted in Table 3.

Table 3. Overview of MCDM outcomes for selected turbine candidates

Hub Height (m)	Rotor Diameter (m)	Cut In Speed (m/s)	Rated Speed (m/s)	Rated Power (kW)	Annual Energy (MWh)	Annual Capacity Factor (%)	CAPEX (£)	OPEX (£/y)	LCOE (£/kWh)	Rank
36	**32**	**3**	**6**	**43.25**	**312**	**82.41**	**49255**	**2162**	**0.01719**	**1**
36	32	4	6	43.25	308	81.16	49255	2162	0.01745	2
36	32	5	6	43.25	295	77.75	49255	2162	0.01822	3
33	26	3	7	45.34	296	74.57	51258	2267	0.01891	4
33	26	4	7	45.34	293	73.76	51258	22677	0.01912	5
33	26	5	7	45.34	284	71.54	51258	2267	0.01971	6
37	34	3	6	48.82	353	82.59	54570	2441	0.01696	7

3.2. Hydrogen Production Cost and Emissions

Over 8760 hourly wind resource simulations, the system produced **~3.9 tonnes H2_22/year**. The computed **Levelised Cost of Hydrogen (LCOH)** was around **£2.77 per kg**—significantly competitive for an autonomous vessel requiring ~3.9 tonnes per annum. A detailed breakdown of this LCOH, presented in Figure 2, reveals that the primary cost drivers are the capital expenditures (CAPEX) for the wind turbine and electrolyser. Operating expenditures (OPEX), particularly for electrolyser stack replacement and wind turbine maintenance, also form a significant portion of the cost. This LCOH represents the direct production cost; potential requirements for large-scale storage or distribution would incur additional expenses. H_2

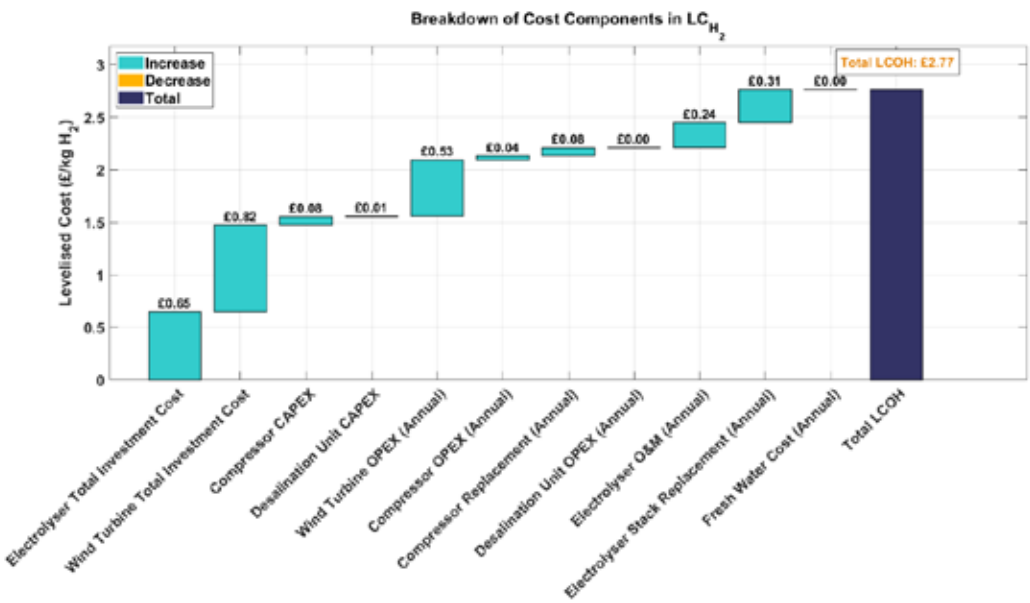

Fig. 2. Detailed LCOH Breakdown for a Wind-Powered Hydrogen Production System

4. CONCLUSIONS

This study successfully designed and evaluated a wind-powered green hydrogen production system tailored for a Maritime Autonomous Surface Vessel (ASV). Simulations confirmed the system's capacity to meet the target vessel's annual demand of approximately 3.9 tonnes H_2. The techno-economic analysis yielded an LCOH of roughly £2.77 per kg, demonstrating competitiveness for this specific off-grid application. The primary cost drivers were identified as the capital expenditures for the wind turbine and electrolyser, with operational costs also contributing significantly. These findings support the feasibility of localized, renewable hydrogen generation for niche maritime applications, providing a baseline for direct production costs.

ACKNOWLEDGEMENT

This research has been supported by the Hydrogen Innovation - Future Infrastructure & Vessel Evaluation and Demonstration (HI-FIVED) project, funded under the UK Clean Maritime Demonstration Competition Round 3 (CMDC3), Innovate UK, Project Number 10057707.

REFERENCES

1. IMO, "2024 Guidelines on Life Cycle GHG Intensity of Marine Fuels (2024 LCA Guidelines)," International Maritime Organization (IMO), London, MEPC 81/17/Add.1, Annex 10, 22 March 2024 2024. [Online]. Available: https://wwwcdn.imo.org/localresources/en/OurWork/Environment/Documents/annex/MEPC%2081/Annex%2010.pdf
2. Shi, J., Zhu, Y., Feng, Y., Yang, J., & Xia, C. (2023). A prompt decarbonization pathway for shipping: green hydrogen, ammonia, and methanol production and utilization in marine engines. *Atmosphere*, *14*(3), 584.
3. Alavi-Borazjani, S. A., Adeel, S., & Chkoniya, V. (2025). Hydrogen as a Sustainable Fuel: Transforming Maritime Logistics. *Energies*, *18*(5), 1231.
4. Giampieri, A., Ling-Chin, J., & Roskilly, A. P. (2024). Techno-economic assessment of offshore wind-to-hydrogen scenarios: A UK case study. *International Journal of Hydrogen Energy*, *52*, 589-617.
5. Davies, A. J., & Hastings, A. (2023). Lifetime greenhouse gas emissions from offshore hydrogen production. *Energy Reports*, *10*, 1538-1554.
6. Putuhena, H., White, D., Gourvenec, S., & Sturt, F. (2023). Finding space for offshore wind to support net zero: A methodology to assess spatial constraints and future scenarios, illustrated by a UK case study. *Renewable and Sustainable Energy Reviews*, *182*, 113358.
7. Dickson, R., Akhtar, M. S., Abbas, A., Park, E. D., & Liu, J. (2022). Global transportation of green hydrogen via liquid carriers: economic and environmental sustainability analysis, policy implications, and future directions. *Green Chemistry*, *24*(21), 8484-8493.
8. Rawesat, A., & Pilidis, P. (2024). 'Greening' an Oil Exporting Country: A Hydrogen, Wind and Gas Turbine Case Study. *Energies*, *17*(5), 1032. https://doi.org/10.3390/en17051032
9. J. F. Manwell, J. G. McGowan, and A. L. Rogers, *Wind energy explained: theory, design and application*. John Wiley & Sons, 2010.
10. T. Burton, N. Jenkins, D. Sharpe, and E. Bossanyi, *Wind energy handbook*. John Wiley & Sons, 2011.
11. M. Hansen, *Aerodynamics of Wind Turbines*. Routledge, 2015.
12. IRENA (2023). *Renewable Power Generation Costs in 2023*. [Online] Available: https://www.irena.org
13. A. Karabelas, C. Koutsou, M. Kostoglou, and D. Sioutopoulos, "Analysis of specific energy consumption in reverse osmosis desalination processes," *Desalination,* vol. 431, pp. 15-21, 2018.
14. A. Giampieri, J. Ling-Chin, and A. P. Roskilly, "Techno-economic assessment of offshore wind-to-hydrogen scenarios: A UK case study," *International Journal of Hydrogen Energy,* vol. 52, pp. 589-617, 2024.
15. U. Caldera and C. Breyer, "Learning curve for seawater reverse osmosis desalination plants: capital cost trend of the past, present, and future," *Water Resources Research,* vol. 53, no. 12, pp. 10523-10538, 2017.
16. R. Ragab, M. Hamdi, H. A. El Salmawy, and M. A. Ismail, "Optimized system for combined production of electricity/green hydrogen for multiple energy pathways: a case study of Egypt," *Clean Energy,* vol. 8, no. 4, pp. 219-236, 2024.
17. Zemtech, "UK Green Liquid Hydrogen Supply Chain Study.," Zemtech, 2024.
18. B. N. van Haersma Buma, M. Peretto, Z. M. Matar, and G. van de Kaa, "Towards renewable hydrogen-based electrolysis: Alkaline vs Proton Exchange Membrane," Heliyon, vol. 9, no. 7, 2023.
19. Air Liquide. "Cummins HyLYZER 250 Specification Sheet." Air Liquide Houpu Hydrogen Equipment Co., Ltd. . https://www.airliquidehoupu.com/productinfo/937892.html (accessed February 19, 2025).
20. M. H. A. Khan, P. Heywood, A. Kuswara, R. Daiyan, I. MacGill, and R. Amal, "An integrated framework of open-source tools for designing and evaluating green hydrogen production opportunities," *Communications Earth & Environment*, vol. 3, no. 1, p. 309, 2022.
21. C. T. Baumann (n.d.). "The cost-to-capacity method and scale factors." https://evcvaluation.com/the-cost-to-capacity-method-and-scale-factors/ (accessed 3 February, 2025).
22. C. Z. van Leeuwen, A., "Report on the costs involved with PtG technologies and their potentials across the EU," in "Store and GO project," April 2018 2018. Accessed: 2 February, 2025. [Online]. Available: https://erig.eu/wp-content/uploads/2023/02/20180424_STOREandGO_D8.3_RUG_accepted.pdf

PRODUCTION AND CHARACTERIZATION SULFONATED POLYPHENYL SULFONE PEM MEMBRANE FOR VANADIUM REDOX BATTERY

[1]Elif Çolak, [1]Seniyecan Kahraman, [1]Buse Çetin, [2]Derya Ünlü, [1,3]Filiz Uğur Nigiz
[1] Chemical Engineering Department, Çanakkale Onsekiz Mart University, 17020, Çanakkale, Türkiye
[2] Chemical Engineering Department, Bursa Technical University, Bursa, Türkiye
[3] Department of Energy Resources and Management, Çanakkale Onsekiz Mart University, Çanakkale, Türkiye

* E-mail: filiz.ugur@comu.edu.tr

ABSTRACT
Electricity generation from sustainable and renewable energy sources is one of the priority topics with research potential in our country. With the increase in investments in electricity generation from wind and solar energy, the development of electricity storage systems for use in smart station systems connected to electric vehicle projects, and the increase in investments in smart grid storage systems in many areas, studies in the field of electricity storage have also accelerated. Vanadium redox batteries are one of the leading technologies that can be used in smart electricity grids, providing high efficiency storage of grid electricity and advanced performance (charge-discharge efficiency, cycle life). In this study, it is aimed to produce a new membrane that is alternative to Nafion, durable, cheap and at the same time has a high proton transfer capacity. It is aimed to increase the proton transport mechanism of this membrane by increasing its hydrophilicity and bonding ability and by creating porosity. In this context, polyphenyl sulfone (PPSU), an important engineering polymer, was sulfonated and produced in the form of electrofiber and basic polymer electron membrane tests were performed. According to the test results, both ion exchange capacity and proton conductivity values were obtained as 2.1 meq/g and 1.68 x10^{-2} S/cm, respectively.

Keywords: polyphenyl sulfone, polymer electrolyte membrane, sulfonation, redox battery

1. INTRODUCTION
Today, with the increase in global energy problems and the decrease in the amount of fossil fuel resources and the increase in environmental damage, interest and investments in renewable energy resources are increasing rapidly. Renewable resources are diversified as solar energy, wind energy, geothermal energy resources and bioethanol, biodiesel, biogas, biohydrogen produced from biomass. The easiest of these sources to produce are solar, wind and geothermal energy. Turkey is a country with high potential for sustainable energy resources in many respects. Investments are accelerating especially for wind energy and the amount of investment in solar panels is increasing for solar energy. However, in both cases, the energy generated is non-continuous and uncontrollable. The electricity generated needs to be stored in order to be used in the consumption line. In addition, with the rapid increase in the number of electrically powered vehicles in recent years, the energy requirement at power stations is increasing. In order to obtain this energy from wind and sun, it must be stored and distributed under suitable conditions.

Redox flow batteries (RABs) are high-capacity electricity storage systems with high energy efficiency (>75%), feasible installation cost, high number of cycles (>20,000), long lifetime and low toxicity. Another advantage of RAB systems is that the capacity and power of the battery depend on independent factors. The capacity of the battery depends on the amount of electrolyte stored, the concentration of active species, the voltage and number of individual cells, while the power generated is related to the behavior of the active species and the electrode size. This facilitates the scalability and flexibility of technology. The simplicity of the flow battery and the reversible redox reaction realized by the presence of two soluble redox pairs allows the cycle to be theoretically unlimited. These systems can adapt well to various power applications due to their short response times of milliseconds [1]. Ultimately, this makes them suitable for integration into renewable energy generation systems such as photovoltaic (PV) systems and wind power.

The main objective of this study is to produce high performance and durable VRAB membranes as an alternative to Nafion. Accordingly, in terms of durability and cost, commercial polymeric engineering materials come to the forefront. Polyphenylsulfone (PPSU) is an engineering polymer with high chemical oxidation stability/durability, mechanical strength and relatively low price [2]. Therefore, since it can be produced in high quantities as a film with engineering production techniques, it is low cost and commercializable as an end product. VRAB membranes made with this polymer were found to have low vanadium permeability. However, the intrinsic ion conducting capacity of this polymer is very low.

Polyphenylsulfone is a fully aromatic high-performance engineering polymer known as amorphous thermoplastic materials. Its high chemical and physical properties have led to its use as a proton exchange membrane in PEM fuel cells [3]. Due to its high stability under acidic conditions due to the phenyl groups it contains and its competitive production cost, it has a high potential to be used as a redox battery membrane. Despite this, very limited research has been conducted on this subject. One of the most important features of this polymer is the permanent increase of proton

conductivity by the addition of sulfonic acid groups to the aromatic polymer backbone by chemical processes [4]. These groups also increase the hydrophilicity of the material with high hydrophobicity. The lack of detailed investigations of such a functional and durable polymer in VRAB studies and the lack of modifications that would allow its commercial use was seen as a major deficiency, and the project aimed to produce functional PPSU membranes that could be used in vanadium batteries.

2. MATERIALS AND METHODS

2.1. PPSU sulfonation

For the addition of sulfogroups, a solution containing 20% PPSU was prepared using only NMP (acetone was not added because it causes phase separation). The solution was stirred at 35°C for 24 hours. Then this solution was placed in an ice bath and chlorosulfonic acid was added dropwise (4-5 mL for 4 g PPSU). The ice bath was used to control exothermic reaction. The solution was stirred for 5 minutes and kept in the refrigerator for 1 day.The next day, the solution was poured into ice water at around 0°C with the tip of a spoon in order to form fibers from the solution. At this time, a collapsed fiber-like structure was obtained. These fibers were kept in ice water for 3-5 hours, then washed 6-7 times with distilled water to pH 5 and dried at 80°C overnight to obtain sulfated PPSU (sPPSU).

2.2. PPSU fiber membrane production

Initially, 20 different recipes were tested and the most suitable solution for electrospinning was determined to be a formulation containing 30% PPSU, 20-30% acetone and the rest NMP. This solution was stirred at 35°C for 24 hours. When the appropriate viscosity was achieved, fiber production was achieved in the electrospinning device with 20 kV voltage, 15 cm needle-collector distance and 0.015 mL/h flow rate. The fibers obtained in this way were defined as “PPSU fibers”.

2.3. Membrane characterization

After the membranes were prepared, ion exchange capacity, sulfonation degree, swelling degree, and the empirical porosity were determined according to the degree of sulfonation. The chemical bond structures of the membranes were determined by FTIR analysis. then the mechanical analysis of the prepared membranes were calculated and finally the proton conductivity values were determined. Using Versastat 3-500 electrochemistry workstation and the electrochemical impedance spectroscopy technique (EIS), the proton conductivity of membrane were determined. Platinum wires served as electrodes, and the membranes were positioned between two Teflon plates at 100% humidity. Home-made in-plane system was used for the conductivity test. For the first 24 hours, the membranes were submerged in distilled water. Then, the membranes were put in between the electrodes, which are made in a Teflon block. The membranes' impedance spectra were captured at frequencies between 0.1 Hz and 1 MHz. The conductivity measurements were done using Equation 1. Where σ is the proton conductivity (S/cm), L (cm) and A (cm^2) are the thickness and conductive area of the membrane, respectively. R is the resistance (Ω) of the membrane

$$\sigma = L/R.A \quad (1)$$

3. RESULTS AND DISCUSSION

Figure 1a shows the effect of the degree of sulfonation on the bond structures in the FTIR analysis results. In the unsulfonated and low blended membrane, both SO_3- peaks are weak and the O-H band has a narrow structure. However, as the sulfonated PPSU content increased, the intensity and width of the peak observed in these two regions increased significantly. In the graph, it is observed that the intensity of the -OH peak observed in the 3200-3400 cm^{-1} range also increases in the samples where the amount of sulfonated PPSU increases. This peak belongs to the hydroxyl (-OH) groups in the sPPSU structure and can be caused by three main reasons: Formation of free hydroxyl groups in the polymer structure during or after sulfonation, hydrophilic SO_3H groups attracting water and hydrogen bonding of sulfonic acid groups with water molecules. These observations reveal that the degree of sulfonation can be directly monitored via FTIR and the sulfonic group concentration is clearly reflected in the FTIR spectrum. In conclusion, the structural characterization demonstrated the successful production of sulfonated PPSU.

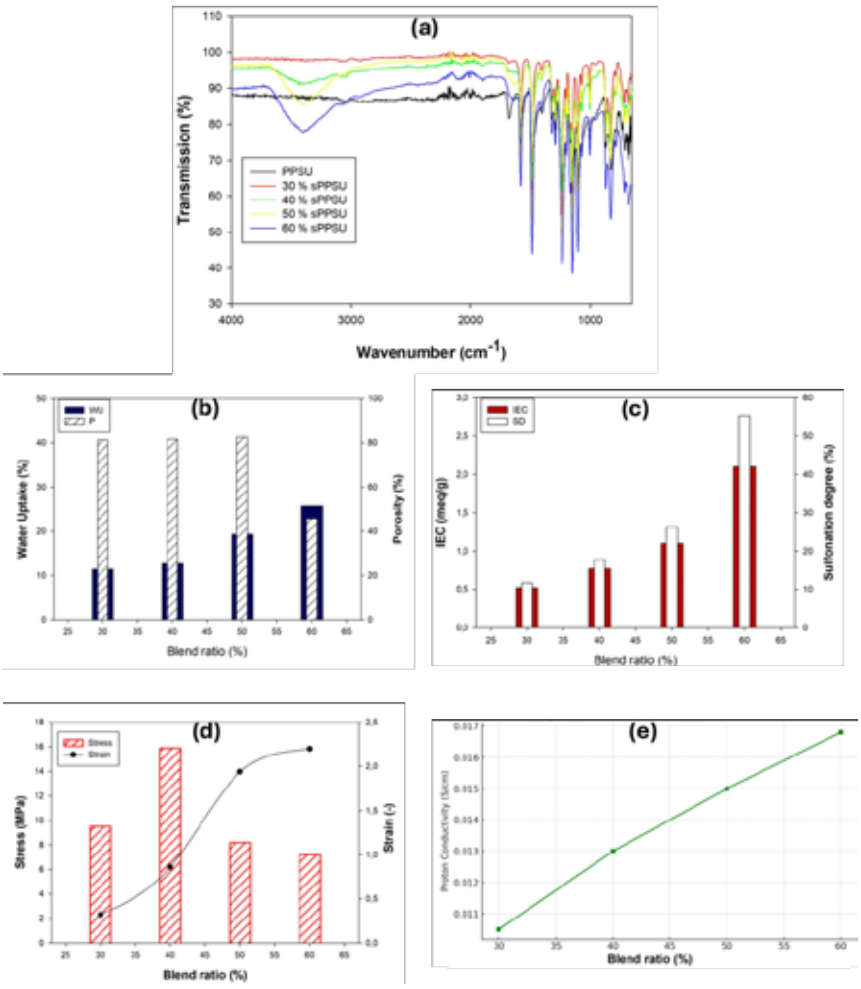

Figure 1. FTIR spectra (a), water uğtake and porosity (b), ion exchange capacity and sulfonation degree (c), mechanical results (d) and proton conductivity results (e) of membranes

Water retention studies were performed in nonporous form, while porosity calculations were performed with electrofiber films. Water retention is especially important for proton transfer. nonporous membranes are used in fuel cells and batteries, where the water retention value of the membrane is critical for proton transfer. In porous membranes, the swelling value is less important. In this study, membranes with increased hydrophilicity in addition to porosity were produced to increase both proton transport and conduction capacities. This is achieved by the degree of sulfonation of the membrane, i.e. the blending ratio of the sulfonated polymer. Figure 1b shows the water retention value and empirical porosity data. Thanks to their hydrophilic nature, sulfonic groups form strong hydrogen bonds with water molecules. These interactions increase the distance between the polymer chains, increasing the water holding capacity of the structure and thus the swelling rate. Since both sample groups contain sulfonated solution, this effect is observed in all samples. However, the main difference that determines the amount of swelling is the amount of PPSU in the formulation; membranes with more PPSU appear to exhibit higher swelling ratio [5].

Especially when used in combination with sulfonated solution, water retention is facilitated by the effect of hydrophilic groups, which increases the formation of micro and macropores. In other words, the coexistence of high PPSU content and sulfonic groups optimizes the phase separation process, resulting in higher porosity values. It is also noteworthy that there is a significant correlation between porosity ratios and swelling behavior. Especially membranes with high water retention capacity can be said to have larger or connected pore structure. This may provide advantages in terms of ion transport and proton conductivity, since high porosity allows ions to be transported more easily across the membrane, while increasing the total permeability [6]. However, this increase in porosity may not always lead to positive results. Excessively porous structures may cause negative effects, especially in terms of mechanical stability and ion selectivity. Therefore, a balance between performance and durability should be struck in membrane design, and the polymer ratio and solvent system should be carefully optimized.

IEC (Ion Exchange Capacity) analyses provide critical data to evaluate the proton conduction potential of membranes

for vanadium redox flow battery applications. IEC value refers to the number of protons that a membrane can exchange per unit mass and is one of the main parameters that determine membrane efficiency, especially in energy storage systems. As can be seen in Figure 1c, with the increase in the percentage of sulfonated polymer, i.e. the blend amount, from 25% to 60%, both the IEC value and the related sulfolization value increased significantly. Figure 1d shows the mechanical properties of the sulfonated blended membranes. The sulfonation fisrtsly increased strength then cause a decrease. The mechanical properties of membranes containing sulfonated PPSU show significant changes depending on the degree of sulfonation. As a result of tensile tests, a significant increase in both tensile strength and elasticity was observed, especially in blend membranes containing 30-40% sulfonated PPSU. The presence of sulfogroups promotes hydrogen bond formation between polymer chains, increasing chain mobility and facilitating water uptake into the structure [7, 8]. Moderate levels of sulfanation allow for the preservation of internal structural bonds with sufficient water retention capacity in the polymer network, resulting in a balanced mechanical performance. However, when the sulfation rate increases to 50% and above, the presence of a large number of hydrophilic groups increases the water uptake excessively, which increases the inter-chain distance and weakens the bond strengths, leading to loosening of the membrane structure and decreased tensile strength.

Figure 1e shows the effect of sulfonation on proton conductivity. Sulfonic groups directly affect not only swelling behavior but also important functional properties such as proton conductivity. Especially in fuel cell technologies, proton conduction is often mediated through sulfonic groups. This conduction mechanism is a process known as the Grotthuss mechanism, in which a proton hops from one water molecule to another. Therefore, as the sulfonic group content in the membrane structure increases, both the swelling rate and proton conductivity increase. Therefore, depending on the application, the optimum sulfonic group content and the amount of PPSU should be determined and a balance of both conductivity and structural strength should be achieved [9]

4. CONCLUSIONS

In this study, electrofiber membranes were produced with sulfonated PPSU and tested for their usability in vanadium redox battery. Accordingly, the swelling value increased as the degree of sulfonation increased, while the porosity first increased and then decreased. It was decided that it was structurally unsuitable because excessive swelling was observed at 60% sulfonation degree. However, sulfonation caused first an increase and then a decrease in mechanical strength. Optimally moderately sulfonated polymer was found to have a strength of 10 MPa and above. IEC value and proton conductivity increased gradually with sulfonation. 2.1 meq/g IEC was obtained at 60% sulfonation and at this point the proton conductivity showed the same value as Nafion. As a result, it was observed that a very cheap polymer exhibited results competitive with Nafion after sulfonation. In the continuation of the study, this membrane will be used in a vanadium redox battery and its charge-discharge performances will be investigated.

ACKNOWLEDGEMENT

This study was financially supported by the The Scientific and Technological Research Council of Türkiye (TÜBİTAK) (Grant Number: 124M916) and Çanakkale Onsekiz Mart University Scientific Project Units (Grant Number: FHD-2025-5097)

REFERENCES

1. Skyllas-Kazacos, M., Chakrabarti, M.H., Hajimolana, S.A., Mjalli, F.S., Saleem, M. (2011) “Progress in flow battery research and development, J. Electrochem. Soc. 158 (8) (2011) R55–R79.
2. Nor, M. Nakao N. A., Jaafar H., Kim, J. D. (2020). "Crosslinked carbon nanodots with highly sulfonated polyphenylsulfone as proton exchange membrane for fuel cell applications". International Journal of Hydrogen Energy, 45(16), 9979–9988.
3. Shang, Z., Hossain, M. M., Wycisk, R., & Pintauro, P. N. (2022). Poly (phenylene sulfonic acid)-expanded polytetrafluoroethylene composite membrane for low relative humidity operation in hydrogen fuel cells. Journal of Power Sources, 535, 231375.
4. Devrim, Y. (2014). "Fabrication and performance evaluation of hybrid membrane based on a sulfonated polyphenyl sulfone/phosphotungstic acid/silica for proton exchange membrane fuel cell at low humidity conditions". Electrochimica Acta, 146, 741–751.
5. Liu, Y., Li, N., Wang, Y., & Wang, J. (2010). Swelling behavior and water uptake of sulfonated aromatic poly(ether sulfone) proton exchange membranes. Journal of Membrane Science, 353(1-2), 50–56
6. Sengupta, S., & Smith, J. (2006). Hydrophilicity of sulfonated polysulfone membranes and their application in fuel cells. Polymer Degradation and Stability, 91(6), 1417–1424.
7. Kim, D. S., Jung, B. Y., & Kim, H. S. (2003). *Sulfonation of poly(phenyl sulfone) and characterization of proton-conducting membranes*. *Journal of Membrane Science*, 212(1–2), 263–271.
8. Lin, Y. H., Wu, Y. W., Huang, C. C., & Lai, J. Y. (2020). *Preparation and properties of sulfonated poly(arylene ether sulfone) membranes for proton exchange membrane fuel cells*. *Journal of Solid State Electrochemistry*, 24, 1223–1233.
9. Zawodzinski, T. A., Neeman, M., Sillerud, L. O., & Gottesfeld, S. (1993). Determination of water diffusion coefficients in perfluorosulfonate ionomeric membranes. Solid State Ionics, 60(3-4), 199–211

ELECTROSPUN COPPER-DOPED RECYCLED PVDF MEMBRANES FOR MICROBIAL FUEL CELL APPLICATIONS

[1]*Ayşenur Katırcı*, [2]*Özde İpsalalı*, [3]*Seniyecan Kahraman,* [4*]*Filiz Uğur Nigiz*
[1,2,3] Çanakkale Onsekiz Mart University, School of Graduate Studies Chemical Engineering Department, Çanakkale, 17100, Türkiye
[4] Çanakkale Onsekiz Mart University, Chemical Engineering Department, Çanakkale, 17100, Türkiye
*Corresponding author e-mail: filiz.ugur@comu.edu.tr

ABSTRACT
The rise of industrialization, escalating expenses, and the fast exhaustion of resources, it has become necessary to seek alternatives energy sources and evaluate waste materials. Utilizing energy from waste is considered a viable approach for sustainable energy generation and minimizing environmental concerns. In recent years, microbial fuel cell (MFC), demonstrated to be effective for the treatment of organic and inorganic pollutants in wastewater and for electricity generation, have garnered significant interest. MFC is a system that biochemically oxidizes organic molecules into electrical energy using microorganisms. Proton exchange membranes (PEM) are critical components that influence the performance and cost of MFC. PEMs facilitate electrochemical reactions that transform hydrogen into electrical energy, water, and heat. Furthermore, PEMs have been utilized in applications including biohydrogen-bioelectricity generation, biosensors, and wastewater remediation.This study involved the production of PEM doped with recycled polyvinylidene fluoride (PVDF) and copper (II) nitrate trihydrate (Cu) particles using the technique of electrospinning. The membranes were characterized by swelling, porosity, mechanical, cation exchange capacity (CEC) tests and FTIR analysis to evaluate their performance. In the cation exchange capacity (CEC) test, the increase in CEC values with increasing Cu concentration indicates that Cu-PVDF membranes can be used for MFC.

Keywords: Microbial fuel cell, Proton exchange membranes, PVDF

1. INTRODUCTION

With the developing industry and rapid population growth, the demand for energy is increasing. However, meeting this demand largely based on fossil fuels leads to both depletion of energy resources and serious environmental problems. Excessive consumption of fossil fuels increases competition for energy supply on a global scale, while extraction and utilization processes cause soil, water and air pollution. This has necessitated the development of sustainable and environmentally friendly energy sources [1, 2]. Hydrogen-based systems have significant potential in energy production as an emerging technology. Fuel cells generate electrical energy using the electrochemical conversion of hydrogen, and this process offers great advantages in terms of both energy efficiency and waste management. Hydrogen technology plays an important role in future energy systems by providing an innovative solution for sustainable and carbon-free energy production [3, 4]. The Microbial Fuel Cell (MFC) generates electricity using microorganisms that break down organic matter found in wastewater. Anaerobic microorganisms in the motherboard break down organic matter into protons, electrons and carbon dioxide. The electrons produced are transported via the external circuit to the cathode, where they react with oxygen to form water. Protons migrate through the proton exchange membrane to the cathode chamber. For the MFC to work efficiently, one proton for each electron must be transferred from the anode to the cathode through the membrane. This process enables the metabolic activities of microorganisms to extract energy from organic compounds and convert them into electricity [4].

Membranes play a critical role in MFC internal resistance, as high internal resistance leads to decreased proton transfer, resulting in reduced performance. In order to achieve better performance and lower production costs, membranes with good ionic selectivity, high proton conduction capacity, low fouling, chemical and biological stability need to be developed. Such membranes will improve the efficiency and longevity of MFC, thus providing economic benefits in large-scale applications [5]. Since membrane costs account for a large proportion of the total cost of MFCs, optimization of this factor becomes an important factor affecting the wide-scale use of MFCs. Nanofibers can be used to enhance proton transfer in MFCs as functionalized materials that can selectively transport specific ions or molecules, such as proton-selective membranes. Nanofiber membranes can reduce the internal resistance of MFCs by acting as microfiltration, especially as proton exchange membranes. Nanofibers produced by electrospinning provide flexibility in material selection and advantages in production capacity, thus becoming a popular choice in various applications. Proton exchange membranes commonly used in MFCs provide high conductivity and low internal resistance, but existing membranes such as Nafion can affect performance due to limitations such as oxygen permeability, bioaccumulation, and water loss at high temperature [2]. To solve these problems, membrane modifications are emerging as an effective method to improve the performance of MFCs.

PVDF is a thermoplastic with advantages such as low density, chemical stability and corrosion resistance. PVDF, which is more economical than Nafion membrane, can increase its water retention capacity and environmental durability with modifications. In this way, overall cost-effectiveness can be increased by improving both electricity generation and wastewater treatment efficiency in MFC systems. In a study by Fan et al. [2], PVDF-modified Nafion membranes were shown to increase the water holding capacity of MFCs and thus improve electricity generation and wastewater treatment

efficiency. In addition, acetone-modified PVDF was reported to further improve the stability of the output power of the MFC. With these modifications, the stable output voltage of the MFC increased above 0.21 V and the Chemical Oxygen Demand (COD) removal rate of molasses wastewater reached about 66.7%, which were 96.3% and 75.1% higher than those of MFCs using ordinary Nafion membrane, respectively.
Copper (Cu) modification plays an important role in enhancing the performance of Microbial Fuel Cells (MFC) systems by improving membrane properties. Cu-doped membranes offer increased ion exchange capacity (IEC), improved mechanical strength and enhanced antibacterial properties. The antimicrobial effect of copper improves the long-term stability and efficiency of the membrane by reducing biofouling, while contributing to higher power densities by increasing ion conductivity. In addition, it is reported in the literature that PVDF membranes modified with copper-based materials such as Cu-MOF increase the membrane's adaptability to temperature and humidity changes by improving its water retention capacity, thus providing a more stable and efficient electrochemical environment in MFC systems [6]. These modifications increase the energy generation capacity of MFC systems and allow them to provide a more efficient performance in wastewater treatment processes.
In this study, PEM doped with recycled polyvinylidene fluoride (PVDF) and copper (II) nitratetrihydrate (Cu) particles were fabricated using electrospinning. Characterization tests were conducted to investigate the effects of PVDF and modified PVDF on the power generation performance and water treatment effect of MFCs. The membranes were characterized by swelling, porosity, mechanical, cation exchange capacity (CEC) tests and FTIR analysis to evaluate their performance.

2. MATERIALS AND METHODS

2.1. Membrane Synthesize

A solution comprising 20% (w/w) recycled PVDF and 2.5% (w/w) PVP were dissolved in DMF and acetone. Various concentrations of 1%, 2%, and 3% (w/w) copper (II) nitrate trihydrate (Cu) were dissolved in DMF, added into the PVDF solution and stirred until get homogeneous. Approximately 10 mL of this solution was taken into a syringe, and membranes coded PVDF, PVDF-Cu1, PVDF-Cu2, and PVDF-Cu3 were produced using the electrospinning technique. The electrospinning conditions were established at 19 kV, a flow rate of 0.01 ml/min, and a plate spacing of 18 cm.

2.2. Characterization Tests

The membranes were characterized using FTIR, swelling analysis, empirical pore size measurement, mechanical strength evaluation, and cation exchange tests. The bonding structures of the membranes correspond to those observed in FTIR. Swelling is determined by the weight of the membranes, empirical pore size as described by the equation in 1 [7].

$$Pore\ size\ (\%) = \left(\frac{\frac{Ma-Mb}{\rho a}}{\frac{Ma-Mb}{\rho a} + \frac{Mb}{\rho p}} \right) x100 \quad (1)$$

Ma: Mass after to wetting, Mb: Mass before to wetting, *p*a: Density of water, *p*b: Density of polymer

Cation exchange capacity (CEC) of membranes was evaluated after immersion in NaCl solution overnight at room temperature, followed by titration with 0.1M NaOH and calculation by the equation in 2 [8].

$$CEC = (M_{NaOH} x V_{NaOH}) x W \quad (2)$$

M_{NaOH} and V_{NaOH} are the molarity and volume of NaOH and W is the weight of the membrane.

3. RESULTS AND DISCUSSION

Fig. 1 shows the SEM image of the PVDF (a) pure membrane and the microscope images of the PVDF (b), 2 wt% (c) Cu-doped fiber membranes. The fiber structure diameters are homogeneous, and no accumulation or pilling is observed, indicating that the membranes were successfully formed.

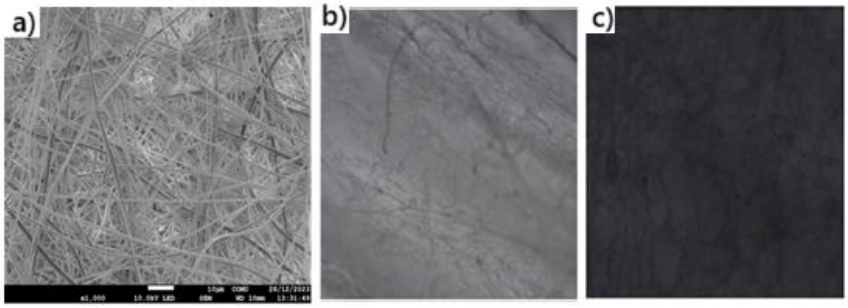

Figure 1. SEM image of PVDF (a) and microscope images of PVDF (b)PVDF-Cu2 (c).

ATR-FTIR spectra are shown in Fig. 2. The reason for the absence of different peaks depending on the doping ratio is the alpha (α) and beta (β) phases formed due to electrospinning. The spectrum around 870 cm^{-1} can be attributed to the alpha (α) phase, while the spectra around 1170 cm^{-1} and 1400 cm^{-1} can be attributed to the beta (β) phase. The spectrum at 1660 cm^{-1} can be attributed to the C=O bond, while the spectra around 1170 cm^{-1} and 1400 cm^{-1} can be attributed to the C-F bond [9-12].

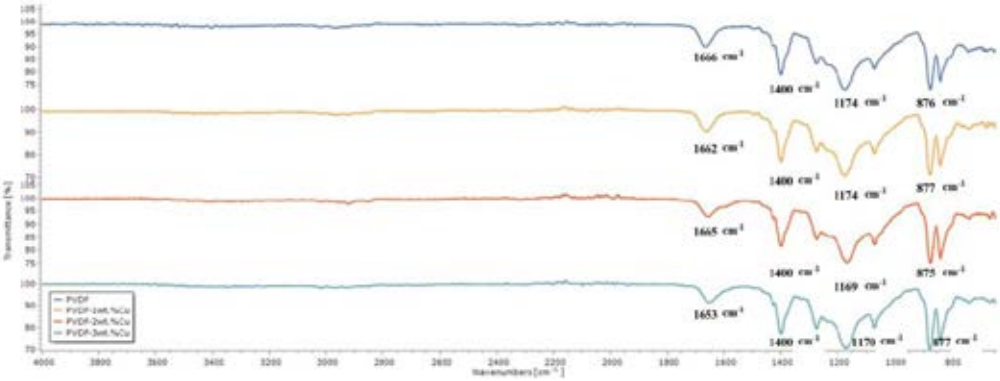

Fig. 2. ATR-FTIR spectra of PVDF and PVDF-Cu

A reduction in porosity and water retention was noted with the incorporation of Cu particles into PVDF (Fig. 3a). This occurs because copper particles tend to aggregate due to their elevated surface area and diminutive size. Coalescing particles can occupy voids and pores, resulting in reduced porosity. Similar to the literature, Cu addition decreased porosity [13-14].

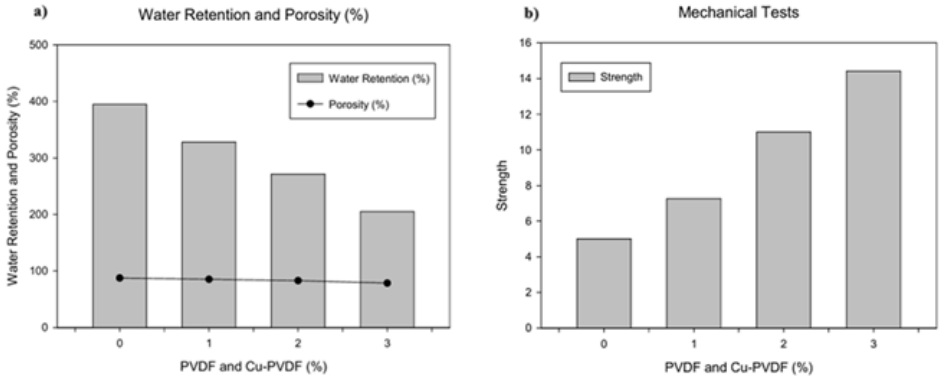

Fig. 3. Results of water retention and porosity (a) and mechanical strength (b).

The mechanical strength of pure PVDF membrane is 5 N/mm² (Fig. 3b). The tensile strength of PVDF-Cu membranes ranges from 7.26 to 14.42 N/mm². It was shown that an increase in Cu concentration improves the mechanical strength of the membranes. The maximum durability is to membranes coded as PVDF-Cu3. Merugu et al. [13] demonstrated enhanced mechanical strength with the incorporation of carbon nanofibres and copper oxide nanoparticles into electrospun PVDF-based membranes.

The cation exchange values give information about the proton carrying capacity of the membranes. The CEC value of the membranes with Cu added significantly increased (Table 1). The highest value is 2.56 mmol/g in PVDF-Cu3 membranes. A study shown that increased copper concentration in cation exchange membranes composed of polyvinyl chloride (PVC) and multi-walled carbon nanotubes enhanced ion exchange [15].

Table 1. Cation exchange values of membranes.

Membrane	Cation Exchange Values (mmol/g)
PVDF	1.96
PVDF-Cu1	2.13
PVDF-Cu2	2.32
PVDF-Cu3	2.56

4. CONCLUSIONS

In this study, Cu-doped PVDF membranes were successfully fabricated by electrospinning method to be used as PEM for use in MFC. The fiber structure of the membranes was successfully imaged with the help of a microscope. With the increase in Cu concentration, the water retention and porosity values of the membranes decreased due to the properties of Cu. However, it was found that the mechanical strength of the membranes increased with the increase in Cu concentration. Also, CEC increased with increase in Cu concentration. This shows that Cu-PVDF membranes are suitable for MFC use. In the next stage, a microbial fuel cell (MFC) system using wastewater will be established to evaluate the performance of the Cu-doped PVDF membranes within the MFC, and the membranes will be tested accordingly.

Acknowledgements

This research was supported by the Scientific Research Center of Çanakkale Onsekiz Mart University (Grant Number: FHD-2025-5097). The proton conductivity system was supplied as part of the project.

REFERENCES

1. Ravi J, Sridhar K, Ponnusami AB, Kumar PS, Rangasamy G. 2024. A recent development of low-cost membranes for microbial fuel cell applications. Desalination and Water Treatment. 8:100698.
2. Fan L, Shi J, Xi Y. 2020. PVDF-modified Nafion membrane for improved performance of MFC. Membranes.10(8):185.
3. Özyörü Zİ, Nigiz FU. 2025. Electricity production from dairy wastewater using phosphotungstic acid-Poly (vinylidene fluoride) Membrane supported microbial fuel cell. International Journal of Hydrogen Energy.
4. Fan L, Tu Z, Chan SH. 2021. Recent development of hydrogen and fuel cell technologies: A review. Energy Reports. 7:8421-46.
5. Hoang AT, Nižetić S, Ng KH, Papadopoulos AM, Le AT, Kumar S, Hadiyanto H, Pham VV. 2022. Microbial fuel cells for bioelectricity production from waste as sustainable prospect of future energy sector. Chemosphere. 287:132285.
6. Ling H, Tian B, Hu X, Wang W, Zhang J, Liu R, Lu Z, Guo Y, Zhao H. 2025. Applications of Metal–Organic Frameworks and Their Derivatives in Fuel Cells. Molecules. 30(5):981.
7. Babazadeh-Mamaqani M, Roghani-Mamaqani H, Alidaei-Sharif H, Salami-Kalajahi M. 2023. Development of pH sensing colloidal nanoparticles and oil/water separating electrospun membranes containing oxazolidine from functional polymers. J Mater Chem C. 11(2):685-97.
8. Terbish N, Popuri SR, Lee C. 2023. Improved performance of organic–inorganic nanocomposite membrane for bioelectricity generation and wastewater treatment in microbial fuel cells. Fuel. 332:126167.
9. Medeiros KAR, Rangel EQ, Sant'Anna AR, Louzada DR, Barbosa CRH, d'Almeida JRM. 2018. Evaluation of the electromechanical behavior of polyvinylidene fluoride used as a component of risers in the offshore oil industry. Oil Gas Sci Technol – Rev IFP Energies nouvelles. 73:48.
10. Wang J, Chao X, Li G, Feng L, Zhao K. 2017. Fabrication and enhanced characterization of copper powder filled copper calcium titanate/poly(vinylidene difluoride) composite. J Mater Sci: Mater Electron. 28(7):5435-9.
11. Kim K, Woo S, Lee J, Park H, Park J, Min B. 2015. Improved Permeate Flux of PVDF Ultrafiltration Membrane Containing PVDF-g-PHEA Synthesized via ATRP. Applied Sciences. 5(4):1992-2008.
12. Lopes AC, Ribeiro C, Sencadas V, Botelho G, Lanceros-Méndez S. 2014. Effect of filler content on morphology and physical–chemical characteristics of poly(vinylidene fluoride)/NaY zeolite-filled membranes. J Mater Sci. 49(9):3361-70.
13. Merugu S, Kearney LT, Keum JK, Naskar AK, Ansary J, Herbert A, et al. 2024. Investigating Permselectivity in PVDF Mixed Matrix Membranes Using Experimental Optimization, Machine Learning Segmentation, and Statistical Forecasting. ACS Omega. 9(26):28764-75.
14. Wang Q, Zhu X, Li X, Chen L, Mao H, Meng X, et al. 2024. Designing anti-fouling PVDF membranes by synergizing Cu2+ and sodium lignosulphonate additives. Separation and Purification Technology. 330:125554.
15. Zendehnam A, Mokhtari S, Hosseini S, Rabieyan M. 2014. Fabrication of novel heterogeneous cation exchange membrane by use of synthesized carbon nanotubes-co-copper nanolayer composite nanoparticles: Characterization, performance in desalination. Desalination. 347:86-93.

SOLAR SYNGAS PRODUCTION VIA A ZNO/ZN BASED CARBOTHERMAL REDUCTION AND WATER SPLITTING CYCLE

Rahul R. Bhosale
Department of Chemical Engineering, University of Tennessee, Chattanooga, 615 McCallie Ave, Chattanooga, TN 37403, USA
*Corresponding author e-mail: rahul-bhosale@utc.edu

ABSTRACT
This investigation presents a comprehensive computational thermodynamic analysis of a combined carbothermal reduction and water splitting cycle utilizing a ZnO/Zn redox system. Initially, a thermodynamic equilibrium analysis was conducted to gain insights into the temperature requirements for effective cycle operation, as well as the equilibrium compositions related to the involved redox reactions. Following this, a computational efficiency analysis was performed to quantify various process parameters, including the energy penalties associated with the reduction chamber, heating of the ZnO, and gas separation. Ultimately, the study estimates the total solar energy required for the cycle and explores the corresponding solar-to-fuel energy conversion efficiency, particularly in relation to variations in the C/ZnO molar ratio. This work advances our understanding of the potential efficacy of this innovative cycle for sustainable energy production.

Keywords: ZnO, Carbothermal Reduction, Water Splitting, Hydrogen, Syngas

1. INTRODUCTION
Concentrated solar power presents a promising approach to enhance fuel production through its ability to support chemical reactions. One notable application is in a redox cycle involving metal oxides, which facilitates thermochemical water splitting to generate hydrogen (H_2)[1]. H_2 can be directly utilized as a clean fuel source. Moreover, it can be combined with carbon monoxide (CO)—which can be produced through CO_2 splitting or the oxidation of carbon—to produce solar syngas[2], further expanding the potential for sustainable energy solutions.

The ZnO/Zn-based redox cycle has been extensively explored among the various metal oxides studied. Between 1990 and 2005, research focused on ZnO decomposition using solar thermal energy[3], the role of O_2 in Zn crystallization[4], ZnO reduction kinetics[5], economic factors of the ZnO water-splitting cycle[6], and the development of a solar chemical reactor for ZnO dissociation[7]. Since 2005, research on the ZnO/Zn thermochemical cycle has diversified. Studies included the hydrolysis of Zn in an aerosol reactor[8], analyzing ZnO decomposition in a fluid wall reactor[9], and exploring reaction kinetics for H_2 and syngas production through thermogravimetric experiments[10]. To achieve higher Zn production at 2000 K, a solar concentration ratio of 2500 is necessary[11]. A solar reactor, initially with a 10 kW capacity, was scaled up to 100 kW and tested for nearly 100 hours, resulting in the thermal decomposition of 28 kilograms of ZnO[12].

One of the key challenges associated with the ZnO/Zn cycle is the high temperature required for thermal reduction. This elevated thermal reduction temperature complicates the operational aspects of the process. To address this issue, this study explores the carbothermal reduction of ZnO to produce Zn. By employing carbothermal reduction, we can not only lower the temperature needed for the reduction of ZnO but also generate CO through the oxidation of carbon. This innovative approach combines carbothermal reduction with water splitting, yielding a valuable mixture of H_2 and CO, commonly referred to as syngas. Syngas serves as an essential precursor for the production of liquid transportation fuels. This paper aims to perform a thorough thermodynamic evaluation of the ZnO/Zn-driven carbothermal reduction and water splitting cycle, with a focus on generating solar syngas. The results of this computational thermodynamic study will provide a solid foundation for future experimental investigations.

2. THERMODYNAMIC ANALYSIS
Utilizing the HSC Chemistry Software, we conducted a comprehensive thermodynamic analysis, consisting of two pivotal sections: (a) equilibrium analysis and (b) efficiency analysis. The equilibrium analysis was essential for determining the carbothermal reduction and the water splitting temperatures pertinent to the ZnO/Zn redox cycle. Furthermore, this analysis provided valuable insights into how the C/ZnO molar ratio influences the reduction of ZnO to Zn, along with the oxidation of carbon to CO. The findings from the equilibrium analysis subsequently informed our efficiency analysis. We developed a thermodynamic model (illustrated in Fig. 1) that incorporates reduction and oxidation chambers, a separator, and multiple heat exchangers and heaters. This model served as the foundation for deriving the equations listed below, enabling a thorough efficiency analysis of the ZnO/Zn driven carbothermal and water splitting cycle.

<u>Heater-1:</u>

$$\dot{Q}_{heater-1} = \dot{n}_{C(s)} \Delta H|_{aC(s)@T_0 \rightarrow aC(s)@T_{red}} \quad (1)$$

Reduction Chamber:

$$\dot{Q}_{ZnO-red} = \dot{n}_{ZnO(s)}\Delta H|_{ZnO(s)+Ar(g)+aC(s)@T_{red} \rightarrow aZn(g)+(1-a)ZnO(s)+aCO(g)+Ar(g)@T_{red}} \quad (2)$$

Heat Exchanger-2 and Heater-2:

$$\dot{Q}_{Ar-heat} = \varepsilon_{gg}\left[\dot{Q}_{(Ar+\,aCO)-cool}\right] + \dot{Q}_{heater-2} \quad (3)$$

$$\dot{Q}_{Ar-heat} = \dot{n}_{Ar}\Delta H|_{Ar(g)@T_0 \rightarrow Ar(g)@T_{red}} \quad (4)$$

$$\dot{Q}_{(Ar+\,aCO)-cool} = \dot{n}_{Ar}\Delta H|_{Ar(g)@T_{red} \rightarrow Ar(g)@T_0} + \dot{n}_{CO}\Delta H|_{aCO(g)@T_{red} \rightarrow aCO(g)@T_0} \quad (5)$$

Separator-1:

$$\dot{Q}_{sep-1} = \dot{n}_{ZnO}\left[\frac{T_{sep-1}}{\eta_{sep-1}}(\Delta S_{mix,R_2} - \Delta S_{mix,R_1})\right] \quad (6)$$

$$\Delta S_{mix,R_1} = -R\{n_{Ar}\ln(1 - y_{CO,R_1}) + n_{CO,R_1} ln y_{CO,R_1}\} \quad (7)$$

$$\Delta S_{mix,R_2} = -R\{n_{Ar}\ln(1 - y_{CO,R_2}) + n_{CO,R_2} ln y_{CO,R_2}\} \quad (8)$$

Heat Exchanger-1 and Sensible Heat for ZnO Heating:

$$\dot{Q}_{ZnO-sens} = \dot{Q}_{ZnO-heat} - \varepsilon_{ss}[\dot{Q}_{(aZn+(1-a)ZnO)-cool}] \quad (9)$$

$$\dot{Q}_{ZnO-heat} = \dot{n}_{ZnO}\Delta H|_{ZnO(s)@T_{oxd} \rightarrow ZnO(s)@T_{red}} \quad (10)$$

$$\dot{Q}_{(aZn+(1-a)ZnO)-cool} = \dot{n}_{Zn}\Delta H|_{aZn(g)@T_{red} \rightarrow aZn(s)@T_{oxd}} + \dot{n}_{ZnO}\Delta H|_{(1-a)ZnO(s)@T_{red} \rightarrow (1-a)ZnO(s)@T_{oxd}} \quad (11)$$

Oxidation Chamber:

$$\dot{Q}_{ZnO-oxd} = -\dot{n}_{ZnO}\Delta H|_{aZn(s)+(1-a)ZnO(s)+aH_2O(g) \rightarrow ZnO(s)+aH_2(g)@T_{oxd}} \quad (12)$$

Heat Exchanger-3 and Heater-3:

$$\dot{Q}_{H_2O-heat} = \varepsilon_{gg}\left[\dot{Q}_{H_2-cool}\right] + \dot{Q}_{heater-3} \quad (13)$$

$$\dot{Q}_{H_2O-heat} = \dot{n}_{H_2O}\Delta H|_{aH_2O(l)@T_0 \rightarrow aH_2O(g)@T_{red}} \quad (14)$$

$$\dot{Q}_{H_2-cool} = \dot{n}_{H_2}\Delta H|_{aH_2(g)@T_{oxd} \rightarrow aH_2(g)@T_0} \quad (15)$$

Conductive-Convective Surface Losses:

$$\dot{Q}_{surf} = 0.2 \times \dot{Q}_{ZnO-red} \quad (16)$$

Thermochemical Energy Requirement:

$$\dot{Q}_{TC} = \dot{Q}_{heater-1} + \dot{Q}_{ZnO-red} + \dot{Q}_{heater-2} + \dot{Q}_{sep-1} + \dot{Q}_{ZnO-sens} + \dot{Q}_{heater-3} + \dot{Q}_{surf} \quad (17)$$

Solar Energy Absorption Efficiency:

$$\eta_{abs} = 1 - \left(\frac{\sigma T_{red}^4}{IC}\right) \quad (18)$$

Total Solar Energy Requirement:

$$\dot{Q}_{solar} = \frac{\dot{Q}_{TC}}{\eta_{abs}} \quad (19)$$

Re-radiation Losses:

$$\dot{Q}_{re-rad} = \eta_{abs} \times \dot{Q}_{solar} \quad (20)$$

Solar-to-Fuel Energy Conversion Efficiency:

$$\eta_{solar-to-fuel} = \frac{[\dot{n}_{CO} \times HV_{CO}] + [\dot{n}_{H_2} \times HV_{H_2}] - [\dot{n}_C \times HV_C]}{\dot{Q}_{solar}} \quad (21)$$

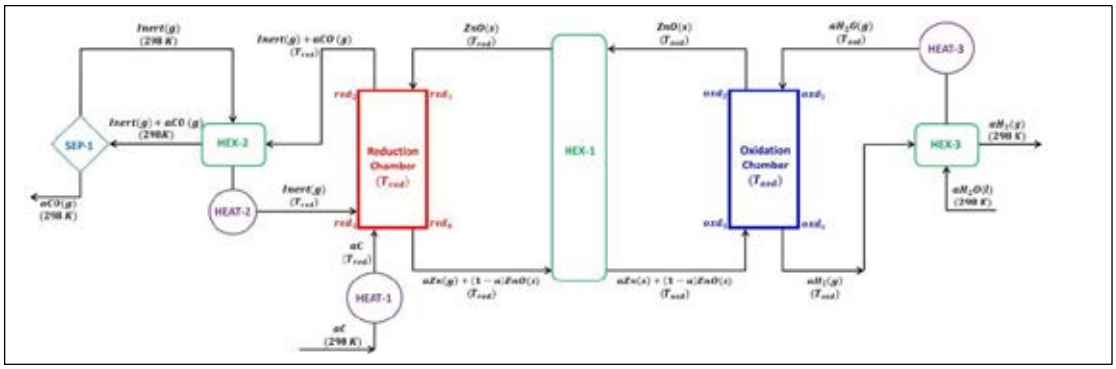

Fig. 1. Process Flow Diagram (ZnO/Zn-Carbothermal Reduction-Water Splitting Cycle).

3. RESULTS AND DISCUSSION

The impact of increasing the C/ZnO molar ratio from 0.2 to 1.0 on the equilibrium compositions related to the carbothermal reduction of ZnO is illustrated in Fig. 2. As demonstrated, a higher C/ZnO molar ratio significantly enhances the reduction of ZnO to Zn, as well as the generation of CO compared to carbon. This positive correlation highlights the importance of optimizing the C/ZnO ratio for improved efficiency in the reduction process.

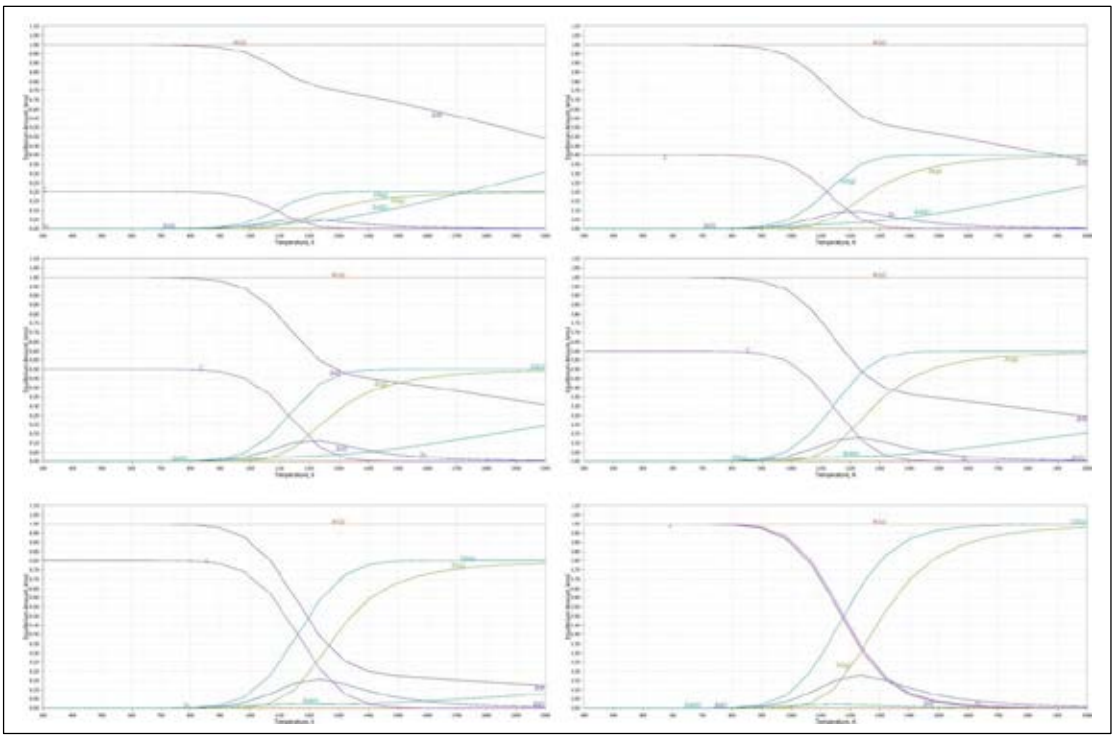

Fig. 2. Equilibrium Compositions associated with the carbothermal reduction of ZnO.

The thermodynamic efficiency analysis performed at gas-to-gas and solid-to-solid heat recuperation equal to 0.1 and 0.0 using our developed model and equations (described in the previous section) revealed insightful trends regarding energy requirements. Specifically, it was found that the energy needed to elevate the temperature of carbon (C) from 298 K to the reduction temperature of 1250 K increased significantly, from 3.48 kW to 17.39 kW, as the C/ZnO molar ratio rose from 0.2 to 1.0. This adjustment in the ratio also resulted in a notable energy penalty associated with the carbothermal reduction of ZnO, which increased by 282.88 kW.

Additionally, while heat exchanger-2 effectively recuperated energy from the cooling of the Ar + CO gas mixture for preheating inert Ar to 1250 K, it became evident that further heat energy from heater-2 was necessary. Encouragingly, this requirement was reduced by 2.41 kW as the C/ZnO molar ratio increased from 0.2 to 1.0, showcasing the potential for improved efficiency with optimized ratios.

The increase in CO production was notably influenced by the rising C/ZnO molar ratio, which escalated from 0.2 to 1.0. This adjustment necessitated an additional 13.87 kW of energy to operate separator-1. Meanwhile, the sensible heat required for preheating ZnO remained consistent at 38.13 kW, as the temperature difference between the water splitting reaction (500 K) and the carbothermal reduction reaction (1250 K) stayed the same. With an increased availability of Zn for the water splitting process, there was a corresponding rise in H_2 production, which contributed to a significant increase in exothermic heat release. For example, as the C/ZnO ratio improved from 0.2 to 1.0, the energy generated by the oxidation chamber rose by an impressive 80%. Additionally, the heightened demand for H_2O supply resulted in a fivefold increase in the heat energy requirements from heater-3.

The total thermochemical energy required for the ZnO/Zn driven carbothermal reduction and water splitting cycle increased significantly, rising from 162.64 kW to 567.74 kW. This increase in thermochemical energy demand has implications for the total solar energy needed, which in turn affects the solar-to-fuel energy conversion efficiency. For instance, with a C/ZnO ratio of 0.2, the total solar energy requirement was 170.51 kW, but this escalated to 595.21 kW when the C/ZnO ratio increased to 1.0. Interestingly, while the solar-to-fuel energy conversion efficiency was lower at 20.62% for a C/ZnO ratio of 0.2, it improved to 29.54% as the ratio rose to 1.0. This suggests a complex interplay between energy requirements and conversion efficiency that merits further exploration.

4. CONCLUSIONS

Increasing the C/ZnO ratio improved ZnO reduction to Zn and CO production from carbon. The energy needed to heat carbon from 298 K to 1250 K increased from 3.48 kW to 17.39 kW as the C/ZnO ratio rose from 0.2 to 1.0, resulting in an energy penalty of 282.88 kW. While heat exchanger-2 preheated inert argon effectively, it required less energy from heater-2, decreasing by 2.41 kW with a higher C/ZnO ratio. CO production raised the energy demand for separator-1 by 13.87 kW, and preheating ZnO energy remained constant at 38.13 kW. With more Zn, hydrogen production and exothermic heat increased, boosting energy from the oxidation chamber by 80%. Energy from heater-3 increased fivefold due to H2O supply needs. Overall, thermochemical energy for the ZnO/Zn process surged from 162.64 kW to 567.74 kW, raising solar energy needs from 170.51 kW to 595.21 kW, while solar-to-fuel energy conversion efficiency improved from 20.62% to 29.54%.

REFERENCES

1. Bhosale RR. 2019. Thermodynamic analysis of Ni-ferrite based solar thermochemical H2O splitting cycle for H2 production. International Journal of Hydrogen Energy 44:61–71.
2. Agrafiotis C, Roeb M, and Sattler C. 2015. A review on solar thermal syngas production via redox pair-based water/carbon dioxide splitting thermochemical cycles. Renewable and Sustainable Energy Reviews 42:254-285.
3. Palumbo R, Lédé J, Boutin O, Ricart E, Steinfeld A, Möller S, Weidenkaff A, Fletcher E, and Bielicki J. 1998. The production of Zn from ZnO in a high-temperature solar decomposition quench process - I. The scientific framework for the process. Chemical Engineering Science 53:2503–2517.
4. Weidenkaff A, Steinfeld A, Wokaun A, Auer P, Eichler B, and Reller A. 1999. Direct solar thermal dissociation of zinc oxide: Condensation and crystallisation of zinc in the presence of oxygen. Solar Energy 65:59–69.
5. Möller S, and Palumbo R. 2001. Solar thermal decomposition kinetics of ZnO in the temperature range 1950-2400 K. Chemical Engineering Science 56:4505–4515.
6. Steinfeld A. 2002. Solar hydrogen production via a two-step water-splitting thermochemical cycle based on Zn/ZnO redox reactions. International Journal of Hydrogen Energy 27:611–619.
7. Haueter P, Moeller S, Palumbo R, and Steinfeld A. 1999. The production of zinc by thermal dissociation of zinc oxide - Solar chemical reactor design. Solar Energy 67:161–167.
8. Funke HH, Diaz H, Liang X, Carney, CS, Weimer AW, and Li P. 2008. Hydrogen generation by hydrolysis of zinc powder aerosol. International Journal of Hydrogen Energy 33:1127–1134.
9. Perkins C, Lichty P, Weimer AW, and Bingham C. 2007. Fluid-wall effectiveness for preventing oxidation in solar-thermal ZnO reactors. AIChE Journal 53:1830–1844.
10. Ernst FO, Steinfeld A, and Pratsinis SE. 2009. Hydrolysis rate of submicron Zn particles for solar H2 synthesis. International Journal of Hydrogen Energy 34:1166–1175.
11. Charvin P, Abanades S, Neveu P, Lemont F, and Flamant G. 2008. Dynamic modeling of a volumetric solar reactor for volatile metal oxide reduction. Chemical Engineering Research Design 86:1216–1222.
12. Koepf E, Villasmil W, and Meier A. 2016. Pilot-scale solar reactor operation and characterization for fuel production via the Zn/ZnO thermochemical cycle. Aplied Energy 165:1004–1023.

SOLAR ENERGY STORAGE VIA H_2 PRODUCTION USING A THERMOCHEMICAL $MNSO_4$/MNO WATER SPLITTING CYCLE

Rahul R. Bhosale, Amya Arnold, Monia Ball, Katie Collins, Katelyn Hamilton, Nolan Heath, Jessica Hobbs, Cael Howell, Wesley Johnson, Caleb Kouvarakis, Vitaliy Kyslytsya, Caleb Latham, Gavin Prater, Maria Sanchez, Reese Self, Acelynn Sellers, Matt Serven
Department of Chemical Engineering, University of Tennessee, Chattanooga, 615 McCallie Ave, Chattanooga, TN 37403, USA
*Corresponding author e-mail: rahul-bhosale@utc.edu

ABSTRACT
The hybrid $MnSO_4$/MnO water splitting (WS) cycle that produces H_2 from the sun is carefully examined thermodynamically in this work. It seeks to calculate solar-to-fuel energy conversion efficiency by considering variations in inert sweep gas flow rates and reduction temperatures, gas separation methods, and heat recovery techniques. Teaching solar thermochemical fuel production to University of Tennessee at Chattanooga undergraduate students is another aspect of the research. Assuming total thermal reduction of MnSO4 to MnO, SO_2, and O_2, as well as re-oxidation via WS, a thermodynamic model was created. It was discovered that a 7.4% decrease in efficiency resulted from raising the inert sweep gas flow rate from 10 to 100 mol/s, which increased the solar energy requirements by 403.5 kW.

Keywords: Manganese Sulfate, Hydrogen, Solar Energy, Thermodynamics, Water Splitting

1. INTRODUCTION
The dependence on fossil fuels presents serious issues as the world's energy needs increase. In order to guarantee a sustainable energy future, efforts must be made to develop renewable energy sources. As a clean energy carrier from renewable sources, H_2 is crucial for sustainability because it only emits water vapor when used and helps lower greenhouse gas emissions, especially in industries like the transportation sector. It is a viable energy carrier since H2 can be coupled with CO to form syngas for liquid fuels and chemicals.

Because of the high heat needs and safety issues, direct water thermolysis is not a practicable method for producing H_2. As a result, studies have turned to water-splitting (WS) techniques, especially solar thermochemical WS with metal oxides (MOs). This technique can use a variety of volatile and non-volatile MOs and works at temperatures between 1700 and 2000 K, which is lower than direct thermolysis, which occurs at temperatures above 2700 K [1–10].

Alternative methods that operate between 1073 and 1473 K, closer to the temperatures utilized in methane reforming, like the sulfur-iodine and hybrid sulfur cycles [11–12], provide valuable benefits. On the other hand, sulfur trioxide (SO_3) breakdown is complicated and frequently results in sulfation poisoning, which reduces catalytic activity. Although cost is a barrier, researchers are looking into noble metal catalysts supported on metal oxides to improve SO_3 breakdown [13-15].

One possible remedy is a hybrid metal oxide-metal sulfate (MO-MS) WS cycle, in which metal sulfate (MSO4) is broken down by solar-driven thermal reduction into MO, SO_2, and O_2. The second stage creates H_2 by reoxidizing MO with SO_2 and water. To produce a trustworthy estimate of the solar-to-fuel energy conversion efficiency for the MnSO4/MnO WS cycle, our team assessed the thermodynamics of the cycle (Fig. 1), taking into account energy losses from gas separation and heat transmission.

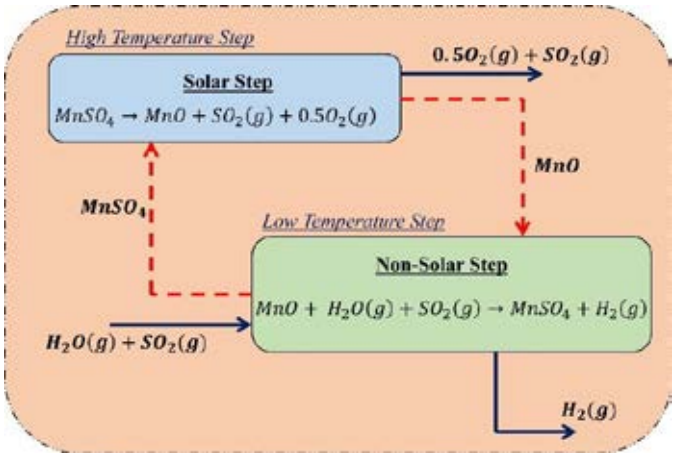

Fig. 1. $MnSO_4$/MnO WS cycle.

2. THERMODYNAMIC MODEL AND EQUATIONS

As illustrated in Fig. 2, this study employed a thermodynamic process model for efficiency analysis. The model makes the following assumptions: perfect gas behavior under equilibrium conditions, complete conversion for reactions, and constant temperatures for the reduction and oxidation reactors. It has two separators for inert/O_2/SO_2 and inert/O_2 gas combinations, with a 99.9% separation rate, and integrates an H_2/O_2 fuel cell with a maximum efficiency of 100%. All calculations were standardized to 1 mol/s, and a 20% thermal energy loss from the reduction reactor was considered.

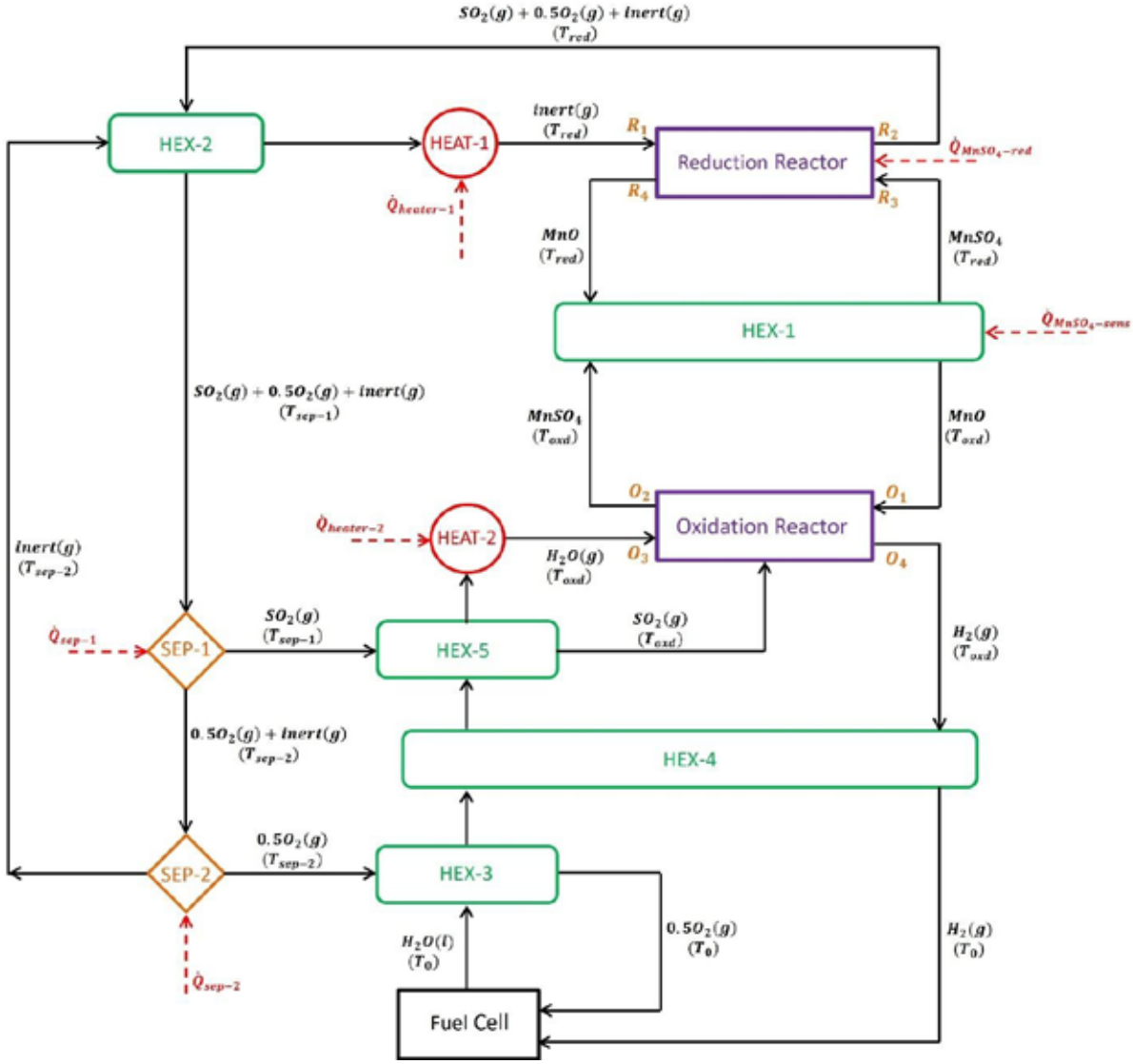

Fig. 2. Process Flow Thermodynamic Model: $MnSO_4$/MnO WS cycle.

Here is a collection of key formulas created and applied to the $MnSO_4$/MnO WS cycle efficiency analysis.

The reduction reactor's heat penalty:

$$\dot{Q}_{MnSO_4-red} = \dot{n}_{MnSO_4}\Delta H|_{MnSO_4 \rightarrow MnO+SO_2(g)+O_2(g)} \quad (1)$$

Exothermic heat produced throughout the oxidation process:

$$\dot{Q}_{MnSO_4-oxd} = -\dot{n}_{MnSO_4}\Delta H|_{MnO+SO_2(g)+H_2O(g) \rightarrow MnSO_4+H_2(g)} \quad (2)$$

Sensible heat required to heat $MnSO_4$:

$$\dot{Q}_{MnSO_4-sens} = \dot{n}_{MnSO_4}\Delta H|_{MnSO_4@T_{oxd} \rightarrow MnSO_4@T_{red}} \quad (3)$$

The energy needed for separators 1 and 2 to function:

$$\dot{Q}_{sep-1} = \dot{n}_{MnSO_4}\left[\frac{T_{sep-1}}{\eta_{sep-1}}(\Delta S_{mix,R_2} - \Delta S_{mix,R_1})\right] \quad (4)$$
$$\Delta S_{mix,R_1} = -R\{n_{mix}\ln(1 - y_{SO_2,R_1}) + n_{SO_2,R_1} ln y_{SO_2,R_1}\} \quad (5)$$
$$\Delta S_{mix,R_2} = -R\{n_{mix}\ln(1 - y_{SO_2,R_2}) + n_{SO_2,R_2} ln y_{SO_2,R_2}\} \quad (6)$$

$$\dot{Q}_{sep-2} = \dot{n}_{MnSO_4}\left[\frac{T_{sep-1}}{\eta_{sep-1}}(\Delta S_{mix,R_2} - \Delta S_{mix,R_1})\right] \quad (7)$$
$$\Delta S_{mix,R_1} = -R\{n_{inert}\ln(1 - y_{O_2,R_1}) + n_{O_2,R_1} ln y_{O_2,R_1}\} \quad (8)$$
$$\Delta S_{mix,R_2} = -R\{n_{inert}\ln(1 - y_{O_2,R_2}) + n_{O_2,R_2} ln y_{O_2,R_2}\} \quad (9)$$

The following is an estimate of the additional heat energy needed from heaters 1 and 2:
$$\dot{Q}_{inert-heat} = \varepsilon_{gg}\left[\dot{Q}_{(inert+\,O_2+SO_2)-cool}\right] + \dot{Q}_{heater-1} \quad (10)$$
$$\dot{Q}_{H_2O-heat} = \varepsilon_{gg}\left[\dot{Q}_{O_2(g)-cool} + \dot{Q}_{H_2(g)-cool} + \dot{Q}_{SO_2(g)-cool}\right] + \dot{Q}_{heater-2} \quad (11)$$

Conductive/convective heat losses from the solar reactor were calculated as:
$$\dot{Q}_{surf} = 0.2 \times \dot{Q}_{MnSO_4-red} \quad (12)$$

The total amount of thermochemical energy required to drive the cycle was calculated as follows:
$$\dot{Q}_{TC} = \dot{Q}_{MnSO_4-red} + \dot{Q}_{MnSO_4-sens} + \dot{Q}_{heater-1} + \dot{Q}_{heater-2} + \dot{Q}_{sep-1} + \dot{Q}_{sep-2} + \dot{Q}_{surf} \quad (13)$$

The solar-to-fuel energy conversion efficiency was estimated as per the following equation.
$$\eta_{solar-to-fuel} = \frac{\dot{n}_{H_2} \times HHV_{H_2}}{\dot{Q}_{solar}} \quad (14)$$

Where,
$$\dot{Q}_{solar} = \frac{\dot{Q}_{TC}}{\eta_{absorption}} \quad (15)$$

3. RESULTS AND DISCUSSION

The study analyzed the impact of Ar flow rates on the temperature required for 100% dissociation of $MnSO_4$. Complete dissociation was achieved at different temperatures depending on the Ar flow rates. Although the temperature decreased from 1488 K to 1361 K when increasing Ar flow rates up to 100 mol/s, the thermal energy needed to drive the reduction reaction increased by 3.5 kW. Equilibrium analysis indicated that the MnO re-oxidation into $MnSO_4$ via WS reaction is feasible at temperatures ≤ 500 K. Though a solid-to-solid heat exchanger was in place, all calculations assumed no heat recovery and the sensible heat required to hear the MnSO4 from oxidation to reduction temperature was higher at Ar = 10 mol/s (150.8 kW) as compared to Ar = 100 mol/s (130.4 kW). The separation of SO_2 from the $Ar/O_2/SO_2$ gas mixture was achieved using an ion transport membrane at high temperatures. The energy required for the operation of separator-1 and separator-2 was recorded to be increased by 39.5 kW and 36.2 kW with a rise in the Ar flow rate from 10 mol/s to 100 mol/s. As the Ar exiting separator-2 was at a lower temperature than the reduction reactor, HEX-2 and an auxiliary heater-1 were installed for preheating. The auxiliary heat needed to increase the temperature of Ar was supplied by heater-1, and it was recorded to be increased by a factor of 9.9 as the Ar flow rate surged by 90 mol/s. On the other hand, the energy supplied by the auxiliary heater-2 remained steady at 24.8 kW.

The total thermochemical energy required for the $MnSO_4$/MnO WS cycle was calculated, with recorded values ranging from 961.3 kW at 10 mol/s to 1368.1 kW at 100 mol/s. To calculate the solar energy required for the cycle, absorption efficiency was also considered. The absorption efficiency rose from 90.7% to 93.5% as flow rates increased from 10 to 100 mol/s. The total solar energy required surged above 1059.4 by 403.5 kW due to the rise in Ar flow rate from 10 to 100 mol/s, respectively. Solar-to-fuel energy conversion efficiency was the highest (26.7%) when the Ar flow rate was equal to 10 mol/s, and it decreased to 19.4% because of the rise in the Ar flow rate up to 100 mol/s.

4. CONCLUSIONS

Thermodynamic efficiency modeling investigated the $MnSO_4$/MnO solar-driven hybrid thermochemical WS cycle. The reduction temperature decreased by 127 K when the Ar flow rate was increased from 10 to 100 mol/s, with the lowest reduction temperature equal to 1361 K for 100 mol/s. Around 500 K, MnO re-oxidation made it possible to produce H_2 via WS. While other parameters either stayed the same or decreased, the higher Ar flow resulted in a decrease in the sensible heat needed by 20.4 kW to increase the temperature of $MnSO_4$ from oxidation to the reduction temperature. Gas separation entropy was significantly impacted by the shifting mole fractions of SO_2 and O_2, which raised the energy requirements for gas heating. Even with gas-to-gas heat exchangers installed, more energy was needed to preheat the Ar. Even though the temperature dropped, the total solar thermal energy demands increased from 1059.4 kW to 1462.9

kW. At 1488 K, the highest solar-to-fuel energy conversion efficiency was recorded (26.7%) for 10 mol/s.

REFERENCES

1. Loutzenhiser PG, Galvez ME, Hischier I, Stamatiou A, Frei A, Steinfeld A. 2009. CO_2 splitting via two-step solar thermochemical cycles with Zn/ZnO and FeO/Fe_3O_4 redox reactions II: Kinetic analysis. Energy and Fuels 23:2832–2839.
2. Bhosale RR, Kumar A, AlMomani F, Ghosh U, Sutar P, Takalkar G, et al. 2017. Effectiveness of Ni incorporation in iron oxide crystal structure towards thermochemical CO2 splitting reaction. Ceramics International 43:5150–5155.
3. Chambon M, Abanades S, Flamant G. 2011. Thermal dissociation of compressed ZnO and SnO2 powders in a moving-front solar thermochemical reactor. AIChE Journal 57:2264–2273.
4. Bhosale RR, Kumar A, Sutar P. 2017. Thermodynamic analysis of solar driven SnO2/SnO based thermochemical water splitting cycle. Energy Conversion and Management 135:226–235.
5. Scheffe JR, Steinfeld A. 2012 Thermodynamic analysis of cerium-based oxides for solar thermochemical fuel production. Energy and Fuels 26:1928–1936.
6. Chueh WC, Haile SM. 2009 Ceria as a thermochemical reaction medium for selectively generating syngas or methane from H2O and CO2. ChemSusChem 2:735–739.
7. Dey S, Rao CNR. 2016. Splitting of CO2 by Manganite Perovskites to Generate CO by Solar Isothermal Redox Cycling. ACS Energy Lett 1:237–243.
8. Kubicek M, Bork AH, Rupp JLM. 2017. Perovskite oxides-a review on a versatile material class for solar-to-fuel conversion processes. Journal of Material Chemistry A 5:11983–2000.
9. Takalkar G, Bhosale R, AlMomani F. 2019. Combustion synthesized A0.5Sr0.5MnO3-δ perovskites (where, A = La, Nd, Sm, Gd, Tb, Pr, Dy, and Y) as redox materials for thermochemical splitting of CO2. Applied Surface Science 489:80–91.
10. Cooper T, Scheffe JR, Galvez ME, Jacot R, Patzke G, Steinfeld A. 2015. Lanthanum Manganite Perovskites with Ca/Sr A-site and Al B-site Doping as Effective Oxygen Exchange Materials for Solar Thermochemical Fuel Production. Energy Technology 3:1130–1142.
11. Yang H, Zhang Y, Zhou J, Wang Z, Liu J, Cen K. 2016. Influence of calcination temperature on CuO-CeO2/SiC catalysts for SO3 decomposition in the sulfur-iodine cycle for hydrogen production. International Journal of Hydrogen Energy 41:3339–3348.
12. Vitart X, Le Duigou A, Carles P. 2006. Hydrogen production using the sulfur-iodine cycle coupled to a VHTR: An overview. Energy Conversion and Management 47:2740–2747.
13. Norman JH, Mysels KJ, Sharp R, Williamson D. 1982. Studies of the sulfur-iodine thermochemical water-splitting cycle. International Journal of Hydrogen Energy 7:545–556.
14. Onuki K, Kubo S, Terada A, Sakaba N, Hino R. 2009. Thermochemical water-splitting cycle using iodine and sulfur. Energy and environmental Science 2:491–497.
15. Chen Y, Wang Z, Zhang Y, Zhou J, Cen K. 2010. Platinum-ceria-zirconia catalysts for hydrogen production in sulfur-iodine cycle. International Journal of Hydrogen Energy 35:445–451.

MODIFICATION OF MOF-235 WITH GRAPHENE OXIDE FOR ENHANCED HYDROGEN PRODUCTION FROM SODIUM BOROHYDRIDE HYDROLYSIS

[1]*Ruveyda Ozdemir*, [1*]*Derya Unlu*
[1] Bursa Technical University, Faculty of Engineering and Natural Sciences, Department of Chemical Engineering, Bursa, 16310, Turkey
*Corresponding author e-mail: derya.unlu@btu.edu.tr

ABSTRACT
The increasing demand for clean and sustainable energy sources is driving research into alternatives due to the environmental issues associated with fossil fuels. Hydrogen energy stands out among these alternatives because of its high energy density, low environmental impact, and renewable characteristics. This study focuses on the synthesis, characterization, and application of metal-organic frameworks (MOFs) that hold the potential to enhance hydrogen energy efficiency. For this purpose, MOF-235 was synthesized to facilitate hydrogen production. Subsequently, MOF-235 was modified with graphene oxide to improve hydrogen production. Characterization of the MOFs was successfully conducted using BET, FT-IR, TGA, and SEM techniques. Additionally, the catalytic activity of the hydrolysis reaction of sodium borohydride in the presence of the efficient MOF-235 and MOF-235@GO catalysts was investigated. Both MOF-235 and MOF-235@GO were found to serve as effective catalysts in hydrogen production. This study presents promising advancements for hydrogen energy efficiency and supports ongoing research in this area.

Keywords: Graphene oxide**,** Hydrogen, Metal organic frameworks, MOF-235, Sodium borohydride

1. INTRODUCTION

The world is currently facing a climate crisis, predominantly manifested as global warming, which is driven by the increasing levels of greenhouse gases, particularly carbon dioxide (CO_2), in the atmosphere, leading to a rise in the Earth's temperature. Addressing this urgent challenge requires the reduction of non-carbon-neutral CO_2 emissions from various transportation methods and industrial sectors. This has prompted a potential transition from hydrocarbon-based fuels to a hydrogen economy as a means to tackle this global issue. As a result, extensive efforts have been undertaken over the past few decades to develop sustainable hydrogen production processes through a variety of methods.have been made over the past few decades to develop sustainable hydrogen production processes through various routes [1,2].

Metal-organic frameworks (MOFs) are a class of crystalline materials formed by the coordination of organic linkers with metal ions or clusters. They have gained significant attention in recent years due to their exceptional porosity and adaptable structures [3]. MOFs' structures can be engineered to meet specific needs by varying the metal ions and organic linkers used in their formation. This customization allows for fine-tuning of properties such as pore size and functionality. The combination of organic and inorganic components provides unique properties that can result in enhanced performance in various applications. MOFs exhibit high levels of crystallinity, which is essential for reproducibility in both synthesis and application, thus ensuring consistent performance. MOFs typically have a large surface area and significant pore volume, making them suitable for applications that require efficient gas adsorption and storage [4]. Because of these unique characteristics, MOF structures are perfect for a wide range of uses, including as gas storage, biomedicine, magnetics, sensing, separation procedures, and heterogeneous catalysis [5-8]. Due to their structural versatility, MOFs can host acidic and basic Lewis sites, enhancing their effectiveness as catalysts in hydrogen production [9-10]. Composites made of graphene oxide (GO) and metal-organic frameworks (MOFs) have attracted a lot of interest lately.

MOF-235, also known as $[Fe_3O(1,4\text{-}BDC)_3(DMF)_3]FeCl_{43}$, is a notable metal-organic framework characterized by its distinct orange powder appearance and octahedral crystal formation. MOF-235 is composed of trivalent iron atoms that are coordinated with ditopic ligands—specifically, 1,4-benzenedicarboxylic acid (BDC). This coordination creates a complex structure where the iron ions serve as nodes in a three-dimensional lattice. The structure of MOF-235 consists of repeated metal complex units, leading to a robust three-dimensional framework. This architecture is instrumental in defining the material's porosity and stability [9]. By strategically selecting different metal ions and organic ligands, the pore size and overall framework topology of MOF-235 can be customized. This tailoring capability allows for specific functional properties that cater to various applications [10].

In this study, MOF-235 was first synthesised and then modified using GO. The synthesised MOFs were characterised and structurally validated using different characterisation tests. Then, hydrogen production performances were investigated and interpreted.

2. MATERIALS AND METHODS

2.1. MOF-235 Synthesis
The terephthalic acid was dissolved in 60 mL of DMF, and the mixture was stirred for 10 minutes until a clear solution was obtained. Following this, $FeCl_3 \cdot 6H_2O$ was added to the solution, and the mixture was stirred for an additional 5 minutes to allow for the integration of the metal precursor into the solution. The reactant mixture (30 mL) and an additional 30 mL of ethanol were combined. This combined mixture was then transferred to a Teflon-lined autoclave. The autoclave was placed in a preheated oven at 80 °C for 24 hours. After the reaction period, the resulting orange powder of MOF-235 was collected using centrifugation, which separates the solid product from the liquid phase. The product was then washed with a DMF/ethanol mixture at least three times to remove any unreacted materials, excess solvent, or by-products that may interfere with the purity of the final product. The obtained MOF-235 was dried overnight at 150 °C.

2.2. Modification of MOF-235 with Graphene Oxide
The process began by dissolving the certain amount of terephthalic acid in 30 mL of DMF. The solution was stirred for 10 minutes until a clear solution was formed, ensuring that the terephthalic acid was fully dissolved to promote effective reaction conditions. Following the initial stirring, certain amount of $FeCl_3 \cdot 6H_2O$ was added to the solution, and the mixture was continually stirred for an additional 10 minutes. The graphene oxide was added to the solution, with concentrations varying between 1% and 5%. This inclusion aims to improve the structural and functional attributes of the synthesized MOF. The final solution (30 mL reaction solution plus 30 mL of ethanol) was transferred into a Teflon-coated stainless steel autoclave. The autoclave was heated at 80 °C for 24 hours. Upon completion of the heating period, the reaction vessel was allowed to cool to room temperature. The crystals were then dried at 150 °C for 15 hours to eliminate any residual solvents. After drying, the crystals were washed several times with a DMF-ethanol mixture to remove any unreacted materials or impurities, ensuring the final product's purity.

2.3. Characterization of MOF-235 and MOF-235@GO
The obtained MOF-235 and MOF-235@GO was characterized by using BET, FTIR, TGA and SEM analysis. The thermal stability of the MOF-235 is determined by using thermal gravimetric analyzer. The MOF sample heated from 25 °C to 600 °C at a rate of 10 °C/min under a nitrogen flow. A Carl Zeiss/Gemini 300 and a Bruker/XFlash 6-100 were used for SEM. A Leica/ACE600 apparatus was used to gold-coat the samples. Using a PerkinElmer Spectrum Two FT-IR spectrometer, the chemical functional groups of the MOFs were identified. Analysis was done with a resolution of 4 cm^{-1} and a scanning range of 400–4000 cm^{-1}. A Micromeritics TriStar II 3020 analyzer with nitrogen adsorption was used for the BET measurements. Before analysis, samples were degassed for 12 hours at 200 °C to eliminate any moisture or adsorbed gases. The structural, thermal, morphological, compositional, and surface properties of the MOF catalysts are all thoroughly understood thanks to these analytical methods.

2.4. Hydrogen Production from Sodium Borohydride Hydrolysis
To carry out the dehydrogenation experiments of sodium borohydride, an alkaline solution was initially prepared. This was accomplished by adjusting the pH of the medium to a range of 12-13 using sodium hydroxide (NaOH), which is the metal hydroxide linked to sodium borohydride. The solution was stirred until the sodium hydroxide completely dissolved in pure water. Subsequently, the required amount of sodium borohydride was weighed and added to prepared solution. Following this, a MOF235 and MOF-235@GO catalysts were included in the alkaline mixture, and the reactor lid was securely closed. The reaction commenced immediately after adding the catalyst to the solution. The hydrogen produced during the experiment was measured by monitoring the change in liquid level in a burette at specified intervals, employing the reverse burette method.

3. RESULTS AND DISCUSSION

3.1. SEM Analysis

SEM analysis results of the synthesised MOFs are given in Fig. 1. SEM analysis shows that MOF-235 has regular and well-defined crystal structure. Crystals are usually observed in octahedral or cubic morphology with smooth surfaces and prominent edges. This structure reflects the strong three-dimensional network structure formed by regular coordination bonds between iron ions and terephthalic acid ligands. The high resolution in SEM images allows a detailed study of the porous structure of MOF-235 and any defects in this structure [11].

3.2. BET Analysis
The surface areas of the synthesised MOF-235 and MOF-235@GO were measured and found to have surface areas of 870 and 1024 m^2/g, respectively.

3.3. Hydrogen Production
To investigate the influence of reaction time, the hydrogen generation yield was assessed over time. Fig. 2 illustrates the impact of reaction duration. The reaction was conducted using 0.25 M (25 mL) sodium hydroxide and a 0.1 g MOF

catalyst at a temperature of 50°C.

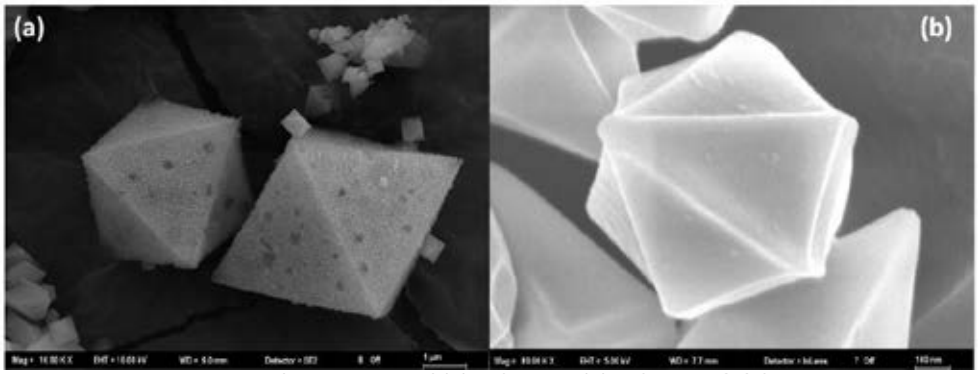

Fig. 1. SEM images of (a) MOF-235 (b) MOF-235@GO

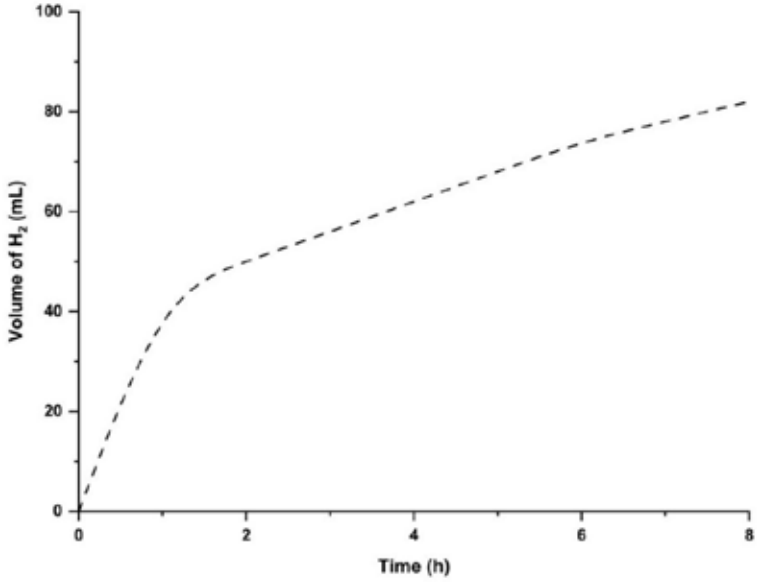

Fig. 2. Hydrogen production

Hydrogen production rate has increased over time. Hydrogen production increased rapidly for about the first 2 hours and then increased more slowly. This may be related to the fact that the MOF used as a catalyst acts as a catalyst at the beginning and stores the hydrogen produced as time progresses. At the end of 8 hours, 82 mL of hydrogen was produced.

4. CONCLUSIONS

In this study, sodium boron hydride was utilized as a source of boron and hydrogen for hydrogen production, and a heterogeneous catalyst was synthesized for the dehydrogenation experiments. The synthesized catalysts, MOF-235 and MOF-235@GO, have not been previously explored in the literature for hydrogen production from sodium boron hydride. Various analyses, including BET for surface area measurement, FTIR for chemical bond structure, TGA for thermal stability, and SEM for structural analysis, were conducted on the catalysts. The results from these analyses confirmed the successful synthesis of the metal-organic frameworks (MOFs). To evaluate the catalytic activity of the synthesized catalysts, hydrogen production from sodium borohydride was investigated, yielding a total of 82 mL of hydrogen after an 8-hour reaction period. The findings indicate that MOF-235 and MOF-235@GO exhibit potential as effective catalysts for hydrogen production from sodium borohydride.

REFERENCES

1. Goltsov VA and Veziroglu TN. 2001. From hydrogen economy to hydrogen civilization. International Journal of Hydrogen Energy 26:909-915.
1. El-Fawal EM, El Naggar AMA, Morshedy AS. 2024. Copper/cerium metal organic frame work as highly efficient structures for solar power-induced hydrogen generation through the process of water splitting. Energy Conversion and Management 320:118975.
2. Moneim MA, El Naggar AMA, El Sayed HA, Mostafa MS, Khalil NM, Hassan MED. 2018. Direct conversion of an agricultural solid waste to hydrocarbon gases via the pyrolysis technique. Egyptian Journal of Petroleum 27: 991-995.

3. Mohamed RS, Al Kahlawy AA, El Naggar AMA, Gobara HM. 2020. Innovative approach for the production of carbon nanotubes (CNTs) and carbon nanosheets through highly efficient photocatalytic water splitting into hydrogen using metal organic framework (MOF)-nano TiO 2 matrices as novel catalysts. New Journal of Chemistry 44:5097-5108.
4. Xu K, Zhang S, Zhuang X, Zhang G, Tang Y, Pang H. 2023. Recent progress of MOF-functionalized nanocomposites: from structure to properties. Advances in Colloid and Interface Science 2023;103050.
5. Haider J, Shahzadi A, Akbar MU, Hafeez I, Shahzadi I, Khalid A. 2022. A review of synthesis, fabrication, and emerging biomedical applications of metal-organic frameworks. Biomaterials Advances 140:213049
6. Xu X, Wei Q, Xi Z, Zhao D, Chen J, Wang J. 2023. Research progress of metal-organic frameworks-based materials for CO2 capture and CO2-to-alcohols conversion. Coordination Chemistry Reviews 495:215393
7. Zhu Z, Duan J, Chen S. 2024. Metal‐organic framework (MOF)‐Based clean energy conversion: recent advances in unlocking its underlying mechanisms. Small 20:2309119
8. Li Q, Li Q, Wang Z, Zheng X, Cai S, Wu J. 2024.Recent advances in hierarchical porous engineering of MOFs and their derived for catalytic and battery: methods and application. Small 20:2303473.
9. Li Y, Hou G, Yang J, Xie J, Yuan X. 2016. Facile synthesis of MOF 235 and its superior photocatalytic capability under visible light irradiation, RSC Adv. 6:16395–16403.
10. Haque E, Jun JW, Jhung SH. 2011. Adsorptive removal of methyl orange and methylene blue from aqueous solution with a metal-organic framework material, iron terephthalate (MOF-235). Journal of Hazardous Materials 185:507–511.
11. Wang C, Liu D, Lin W. 2017. Metal-Organic Frameworks as A Tunable Platform for Designing Functional Molecular Materials. Journal of the American Chemical Society 135(32):13222-13234.

GREEN HYDROGEN PRODUCTION STATION: APPLYING EXERGETIC SUSTAINABILITY PARAMETERS TO A 1 MW PEM ELECTROLYZER

[1*]Ali Eren Aluç, [1,2]Adnan Midilli
[1] Istanbul Technical University, Energy Institute, Ayazaga, Istanbul, 34469, Türkiye
[2] Istanbul Technical University, Faculty of Mechanical Engineering, Department of Mechanical Engineering, Gumussuyu, Istanbul, 34437, Türkiye
*Corresponding author e-mail: aluc23@itu.edu.tr

ABSTRACT
Due to the use of fossil fuels, the world is dealing with a series of catastrophes. In order to avoid potential future hazards, the intensive studies and efforts are ongoing to replace them with renewable and non-carbon-based energy sources. Currently, one of the most promising ways to eliminate carbon emissions caused by fossil fuels is to use hydrogen. In order to increase the level of decarbonization, which means getting the optimum benefit from the element, it needs to be produced through green production with renewable energy support. The clean energy fuel produced in this way, called green hydrogen, will play a crucial role in the fight against global carbon emissions. Under these considerations, the main aim of this paper is to apply some exergetic sustainability parameters to a 1MW electrolyzer installed in a green hydrogen production station. For the selected electrolyzer, the values of 0.647 as exergetic efficiency, 0.0415 as waste exergy ratio and 0.65 as exergetic sustainability factor were estimated.

Keywords: Decarbonization, Exergy, Green Hydrogen, Hydrogen Station, Sustainability.

1. INTRODUCTION

Because of the carbon emissions, promoting the adoption of green technologies to replace carbon in the industry is one of the primary goals. At this point, hydrogen is among the favourites in terms of sustainability. Considering its many attractions, the element hydrogen makes sense for production and usage. Oxygen can be mixed with it. Water is the reaction's product, and there are no emissions. Of all the fuels, it has the largest gravimetric energy density [1]. Its electrochemical and chemical activity is adequate [1] . This element is among the greatest candidates for decarbonization because of these benefits [1].

Compared to the previous years, global hydrogen demand increased by 2% to 54 Mt [2]. 60% of the demand was for ammonia production, 30% for methanol and 10% for Direct reduced iron process [2]. Most of the hydrogen used in these processes is produced by natural gas reforming and gasification and is called gray hydrogen. These methods have their own carbon emissions that disrupt the intended full clean life cycle of hydrogen production [2]. This implies that the life cycle of hydrogen production also needs to be decarbonized for maximum impact. The production process could be cleaner when electricity or high temperature comes from renewable sources. This is where electrolyzer technology that can produce green hydrogen comes in [2]. For hydrogen to be considered green, no GHG gases or pollutants must be released into the atmosphere during its production. Renewable energy sources such as wind, solar, hydro, wave, tidal, thermal, geothermal, ocean thermal, biomass and another clean energy sources and energy recovery systems are the pathways of the production of the green hydrogen [3]. Through these systems, we can generate electrical, thermal, biochemical and photonic energies [3]. There are currently 4 types of electrolyzer that produce green hydrogen in this clean way [4]. Alkaline and proton exchange membrane electrolyzers are currently used commercially [4]. Solid oxide and anion exchange membrane-based electrolyzers have high potential but low commercial maturity [4]. In this study, the proton exchange membrane (PEM), whose commercialization is more mature, is considered for the system.

In the literature, there are many studies on the evaluation of such green systems in terms of exergetic sustainability. In a study [5], the importance of energetic and exergetic assessment of the sustainability of renewable energy systems such as green hydrogen stations are emphasised. In another study [6], a hibrit system of hydrogen production from renewable energy and storage of the produced hydrogen was evaluated from energy, exergy, economic and environmental perspectives.

Due to the high cost, the role of electrolyzer in hydrogen production is currently limited. Nevertheless, as technology advances, the time for green hydrogen will eventually come. Therefore, it is important to investigate the exergetic indicators that give some important clues about the sustainability of a green station, which is also the aim of this study.

2. ANALYSIS

Considering a system similar to the one shown in Fig. 1, some exergetic parameters to be calculated for the electrolyzer part will have an important place for further analyses of the system. The inputs and outputs in a typical PEM electrolyzer are shown in Fig. 2. The definitions for the calculations are shown in Table 1.

Fig. 1. General View of a Green Hydrogen Station

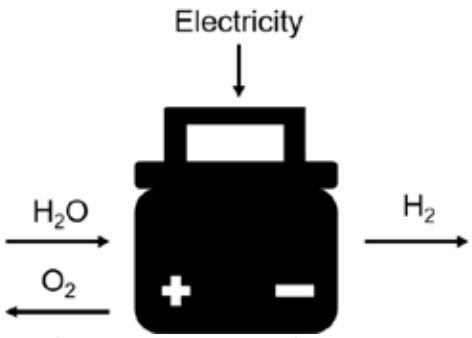

Fig. 2. Schematic Illustration of a PEM Electrolyzer

Table 1. Exergetic sustainability definitions for the electrolyzer

Parameters	Definitions	Range	Ref.
Exergetic efficiency	$\frac{\textit{Total exergy of desired output}}{\textit{Total exergy input}}$	Ranging from 0 to 1	[7]
Waste exergy ratio	$\frac{\textit{Total waste exergy output}}{\textit{Total exergy input}}$	Ranging from 0 to 1	[7]
Exergy destruction factor	$\frac{\textit{Exergy destruction}}{\textit{Total exergy input}}$	Ranging from 0 to 1	[7]
Unusable exergy ratio	$\frac{\textit{Unusable waste exergy}}{\textit{Total exergy input}}$	Ranging from 0 to 1	[7]
Reusable exergy ratio	$\frac{\textit{Reusable waste exergy}}{\textit{Total exergy input}}$	Ranging from 0 to 1	[7]
Environmental destruction coefficient	$\frac{1}{\textit{Exergetic efficiency}}$	Ranging from 1 to +∞	[7]
Environmental destruction index	$(\textit{Exergy destruction factor} + \textit{Unusable waste exergy ratio}) \times \textit{Environmental destruction coefficient}$	Ranging from 0 to +∞	[7]
Environmental benign index	$\frac{1}{\textit{Environmental destruction index}}$	Ranging from 0 to +∞	[7]
Exergetic stability factor	$\frac{\textit{Total exergy of desired output}}{(\textit{Total exergy of desired output} + \textit{Unusable waste exergy} + \textit{Exergy destruction})}$	Ranging from 0 to 1	[7]
Exergetic sustainability index	$\textit{Environmental benign index} \times \textit{Exergetic stability factor}$	Ranging from 0 to +∞	[7]
Sustainability index	$\frac{1}{1 - \textit{Exergetic efficiency of system}}$	Ranging from 1 to +∞	[6]
Improvement potential ratio	$\frac{(1 - \textit{Exergetic efficiency}) \times (\textit{Total exergy input} - \textit{Total exergy output})}{\textit{Total exergy input}}$	Ranging from 0 to 1	[8]

The data required for the calculation of exergy-based sustainability characteristics for the electrolyzer are obtained from [4, 9, 10]. Chemical exergy values are taken from [11]. The following assumptions were also made.

- The PEM electrolyzer functions under steady-state conditions.
- The water used as reactant is laminar, incompressible and steady.
- The water used is in liquid form.
- All gases are considered ideal gases.
- Kinetic and potential exergies are ignored.
- Based on the PEM operating conditions at the source, the cell temperature is assumed to be 353 K [10].
- The cell pressure is defined as 30 bar [10].
- The death state temperature is 298.15 K, while the dead state pressure is 1 atm [7].
- The physical exergy of the hydrogen in the output is assumed to be reusable.
- The physical and chemical exergies of oxygen in the output are assumed to be unusable.
- Depending on the electrolysis technique, it has been stated in the literature that the amount of electrical energy required to produce 1 kg of hydrogen (H_2) varies between 50 and 55 kWh [9]. In this study, it is assumed that 50 kWh of electrical energy is required to produce 1 kg of hydrogen.

3. RESULTS AND DISCUSSION

According to the calculations, the exergetic sustainable parameters in Table 2 were obtained by putting the data of the selected electrolyzer into the specified definitions.

Table 2. Some exergetic sustainability parameters of selected electrolyzer

Parameters	Results	Reference values [6–8]
Exergetic efficiency	0,647	Close to 1
Waste exergy ratio	0,0415	Close to 0
Exergy destruction factor	0,3115	Close to 0
Unusable waste exergy ratio	0,018	Close to 0
Reusable waste exergy ratio	0,0235	Close to 0
Environmental destruction coefficient	1,545	Close to 1
Environmental destruction index	0,509	Close to 0
Environmental benign index	1,964	>>1
Exergetic stability factor	0,65	Close to 1
Exergetic sustainability index	1,2766	>>1
Sustainability index	2,832	>>1
Improvement potential ratio	0,124	Close to 0

The identification and calculation of exergetic sustainability parameters can be the cornerstones for vital analysis prior to the establishment of such systems. By obtaining indicators for the electrolyzer part of the station, the exergy efficiency of the electrolyzer can be found, losses can be discovered and improvement possibilities for better production can be accessed. Furthermore, the station's impact on decarbonization and contribution to the environment can be measured.

4. CONCLUSIONS

Green hydrogen production with clean methods is of great importance for the decarbonization of hydrogen production, which will be a solution to global decarbonization. For this purpose, it is essential to determine and analyze the exergetic sustainability criteria of green hydrogen production stations. These findings can be used in feasibility analyses to provide information on the barriers that may be encountered during and after the establishment of the station and contribute to the sustainability of the green hydrogen economy. Considering the values obtained, the exergetic efficiency of the electrolyzer is close to the values in the literature [12, 13]. As with the value found as waste exergy ratio, it is desired to be close to 0. The exergetic stability factor was also measured as 0.65, which is an acceptable value. Improvement potential is a relative concept. If the system is already working properly, a low value can be considered positive. However, if the system is not currently performing as expected, a high value is a good sign of upgradability. A low value in the calculations indicates that the system is working efficiently.

REFERENCES

1. Scott K. 2020. Introduction to Electrolysis. Electrolysers and Hydrogen Production.
2. International Energy Agency. 2024. Global Hydrogen Review 2024.
3. Dincer I. 2012. Green methods for hydrogen production. International Journal of Hydrogen Energy. pp 1954–1971.
4. IRENA. 2020. Green Hydrogen Cost Reduction: Scaling up Electrolysers to Meet the 1.5°C Climate Goal. International Renewable Energy Agency.
5. Dincer I. 2007. Exergetic and sustainability aspects of greeen energy systems. Clean - Soil, Air, Water 35:311–322. https://doi.org/10.1002/clen.200700108.
6. Nasser M, Megahed TF, Ookawara S and Hassan H. 2022. Performance evaluation of PV panels/wind turbines hybrid system for green hydrogen generation and storage: Energy, exergy, economic, and enviroeconomic. Energy Conversion and Management 26:115870. https://doi.org/10.1016/j.enconman.2022.115870.
7. Midilli A and Dincer I. 2009. Development of some exergetic parameters for PEM fuel cells for measuring environmental impact and sustainability. International Journal of Hydrogen Energy. 34:3858–3872. https://doi.org/10.1016/j.ijhydene.2009.02.066
8. Maruf MH, Rabbani M and Ashique RH. 2021. Exergy based evaluation of power plants for sustainability and economic performance identification. Case Studies in Thermal Engineering 28:101393. https://doi.org/10.1016/j.csite.2021.101393.
9. Squadrito G, Maggio G and Nicita A. 2023. The green hydrogen revolution. Renewable Energy 216:119041. https://doi.org/10.1016/j.renene.2023.119041.
10. Bornemann L, Lange J and Kaltschmitt M. 2024. Optimizing temperature and pressure in PEM electrolyzers: A model-based approach to enhanced efficiency in integrated energy systems 325: 119338. https://doi.org/10.1016/j.enconman.2024.119338
11. Rivero R and Garfias M. 2006. Standard chemical exergy of elements updated. Energy 31:3310–3326. https://doi.org/10.1016/j.energy.2006.03.020.
12. Ni M, Leung MKH and Leung DYC. 2008. Energy and exergy analysis of hydrogen production by a proton exchange membrane (PEM) electrolyzer plant. Energy Conversion Management 49:2748–2756. https://doi.org/10.1016/j.enconman.2008.03.018.
13. Ahmadi P, Dincer I and Rosen MA. 2013. Energy and exergy analyses of hydrogen production via solar-boosted ocean thermal energy conversion and PEM electrolysis. International Journal of Hydrogen Energy 38:1795–1805. https://doi.org/10.1016/j.ijhydene.2012.11.025.

EFFECT OF THERMAL CONDITIONS ON A PV-AEMWE SYSTEM INTEGRATED WITH METAL HYDRIDE STORAGE TANKS

[1,2*]Ceren Celebi, [3]Mehmet Akif Ezan, [3]C. Ozgur Colpan, [4]Yilser Devrim
[1]Dokuz Eylul University, Maritime Faculty, Department of Maritime Engineering, Tınaztepe, Buca, Izmir, 35390, Türkiye
[2]Dokuz Eylul University, The Graduate School of Natural and Applied Sciences, Mechanical Engineering Department, Tinaztepe, Buca, Izmir, 35397, Türkiye
[3]Dokuz Eylul University, Faculty of Engineering, Mechanical Engineering Department, Tinaztepe, Buca, Izmir, 35397, Türkiye
[4]Atilim University, Faculty of Engineering, Department of Energy Systems Engineering, Incek, Ankara, 06836, Türkiye

*E-mail: ceren.celebi@deu.edu.tr

ABSTRACT
This study explores a solar-powered hydrogen production and storage system developed and simulated in MATLAB/Simulink. The system integrates photovoltaic panels (PV), anion exchange membrane water electrolyzers (AEMWE) utilizing polybenzimidazole (PBI) membranes, and metal hydride (MH) tanks. AEMWE presents a cost-effective alternative to traditional water electrolysis methods, and MH tanks provide safe, low-pressure hydrogen storage, addressing one of the main challenges in hydrogen commercialization: safe and efficient storage. Based on Izmir's average irradiation and ambient temperature in July, the simulation estimates a total hydrogen production of 0.35 kg. To illustrate the significant impact of operating temperature and thermal management on storage efficiency, the thermal behavior of MH tanks is assessed under varying convection coefficients (10–1500 $W/m^2 \cdot K$). The effects on tank temperature and hydrogen weight fraction are evaluated, with pressure and temperature limits applied to ensure a realistic depiction of system operation. Results indicate that higher convection coefficients (500 and 1500 $W/m^2 \cdot K$) facilitate efficient storage within acceptable limits, while lower values (10 and 100 $W/m^2 \cdot K$) result in up to 0.28 kg and 0.04 kg of unstored hydrogen, respectively, highlighting the crucial significance of thermal management in system performance.

Keywords: Metal Hydride, Electrolyzer, AEMWE, Thermal Effect, PV-Integrated Electrolyzer

1. INTRODUCTION
Climate change adversely affects the environment, economy, and public health, necessitating a transition to renewable energy sources (RES) like solar, wind, and hydrogen energy, which serve as cleaner alternatives to fossil fuels. Solar energy, produced by PV panels, has an edge due to its abundance and easy accessibility and is particularly promising in various regions. Hydrogen energy, on the other hand, stands out as it is not only a promising fuel but also a versatile energy carrier, offering exceptional energy storage capability with a high heating value (HHV) of approximately 142 MJ/kg. Sustainable hydrogen production through water electrolysis has been established for over two centuries, with alkaline water electrolysis (AWE) and proton exchange membrane water electrolysis (PEMWE) being the most common two methods. While AWE is a well-established technology, its design involves gaps that reduce efficiency and raise safety risks under pressure differences. With a zero-gap design, proton exchange membrane (PEM) electrolyzers improve proton transfer and high-pressure operation but require expensive noble metals for their electrodes, increasing costs. Anion exchange membrane water electrolysis (AEMWE) presents a promising alternative by combining the zero-gap structure of PEM with cheaper electrode materials, like nickel-based electrodes, and operating in near-neutral or alkaline conditions. Among various membranes used for anion exchange membrane (AEM) electrolyzers, polybenzimidazole (PBI) is favored for its mechanical strength and thermal stability, potentially enhancing the viability of green hydrogen technologies.

Challenges remain in hydrogen transport and storage, typically handled as gas or liquid. Gaseous storage needs high pressures (up to 700 bar), which raises safety and energy concerns, while liquid storage requires cryogenic temperatures around -253°C, complicating infrastructure and operational costs. Solid-state storage using metal hydride tanks is an alternative, allowing hydrogen to be stored in solid form through reversible chemical absorption with transition metals. This method supports lower pressures (10-30 bar) and moderate temperatures, enhancing safety and simplifying operations. The temperature of the metal hydride tank bed can be effectively adjusted by changing the flow rate of hydrogen gas fed into the tank, thus improving operational safety and enabling efficient thermal management. In this context, this study investigates how variations in convection coefficients, influenced by thermal management systems, affect the temperature of metal hydride tanks and the amount of hydrogen stored.

2. MODELING
The system consists of a PV panel powering a PBI-based AEM electrolyzer, enhanced by a maximum power point tracking (MPPT) unit for improved efficiency. Hydrogen is managed through a PID-controlled system that regulates pressure and flow to metal hydride (MH) storage tanks—filling switches to the next tank when one reaches its maximum temperature, resuming only after it cools to a safe level, ensuring efficient and safe hydrogen storage. A schematic of the system is shown in Fig. 1.

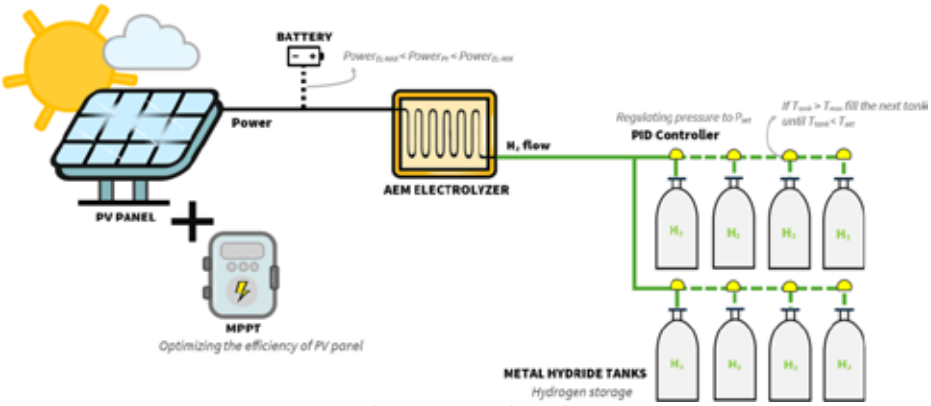

Fig. 1. Schematics of the System

An AEMWE involves complex transport and electrochemical processes. A 0D model is developed to relate cell voltage and current, focusing on deviations from ideal voltage as described in Eq. 1 [1]. This model is implemented in Simulink using a MATLAB Function block for integration with system simulation

$$V_{cell} = V_{Rev} + \eta_{act,a} + \eta_{act,c} + \eta_{ohm} + \eta_{KOH} + \eta_{Bub} \quad (1)$$

Here, V_{cell} represents the cell voltage and calculated as the sum of the reversible voltage (V_{Rev}), the anodic ($\eta_{act,a}$) and cathodic activation overpotential ($\eta_{act,c}$), the ohmic losses (η_{ohm}), the electrolyte (KOH) resistance losses (η_{KOH}), and the bubble resistance losses (η_{Bub}). PBI was employed as the membrane in the AEMWE model, where the ohmic overpotential was calculated using membrane resistance determined by Eq. 2.

$$R_{mem} = \frac{t_{AEM}}{\sigma_{AEM}} \quad (2)$$

Here, t_{AEM} is the membrane thickness (50 µm), σ_{AEM} is the OH^- conductivity, and R_{mem} is the area-specific resistance, taken as 84.4 Ω·cm² for the selected PBI membrane [2]. The resulting hydrogen mass flow rate is used to compute the hydrogen volumetric mass flow input for the metal hydride model, as shown in Eq. 3 [3].

$$\epsilon \frac{\partial \rho_g}{\partial t} = \dot{m}_{in}''' - \dot{m}''' \quad (3)$$

This equation describes the rate of change of hydrogen gas density (ρ_g) within the porous medium of the metal hydride bed. The porosity of the metal hydride bed is described by ϵ, $\dot{m}_{in}'''$ represents the volumetric mass flow rate of hydrogen entering the tank, and $\dot{m}'''$ represents the volumetric mass flow rate of hydrogen absorbed by the metal hydride.

Fig. 2 shows the overall proposed system, including the PV-electrolyzer system (Fig. 2a) and metal hydride storage units (Fig. 2b) modeled in Simulink.

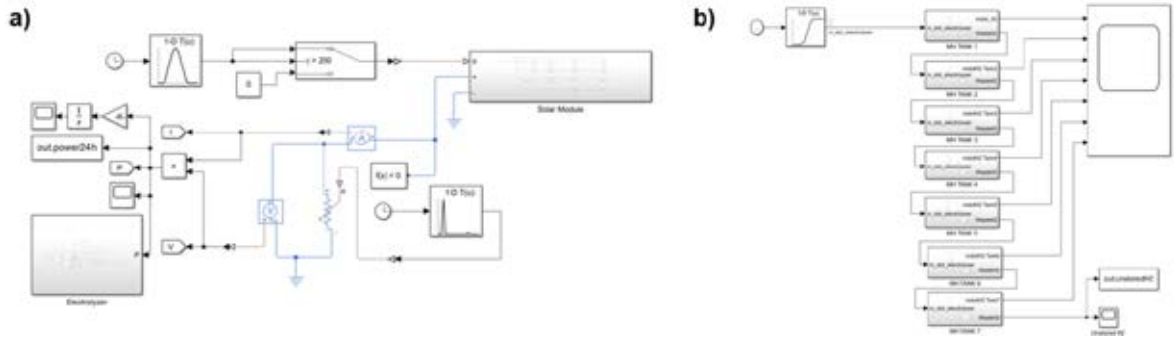

Fig. 2 (a) PV-electrolyzer **(b)** MH tank system blocks in Matlab-Simulink

3. RESULTS AND DISCUSSION

Simulations were performed considering Izmir's average irradiation and ambient temperature in July [4]. The analysis utilized 12 TrinaSolar Duomax_TSM_DEG5_60C_280W photovoltaic modules, achieving a maximum output of 2796 W at midday. Power generation begins around 5th hour peaks near midday, and ends around 15th hour. In parallel, the hydrogen mass flow rate, as shown in Fig. 3b, reached a maximum of 0.0466 kg/s at around 10th hour. The electrolyzer efficiency, depicted in Fig. 3c, was operated under conditions that allowed a minimum efficiency of 55%. Throughout the operational period, it successfully maintained an average efficiency of 60.45% (LHV). System efficiency remained consistently above this threshold, so battery integration was not required for the selected configuration. As shown in Fig. 3d, cumulative hydrogen production increased steadily, totaling 0.3527 kg by the end of the day.

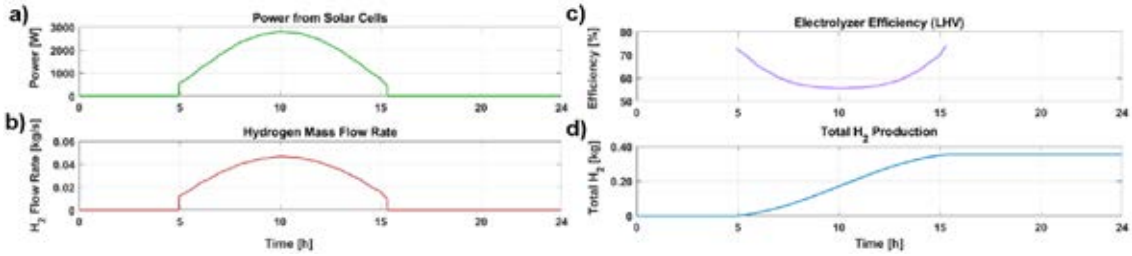

Fig. 3 (a) Power from solar cells (W) **(b)** Hydrogen mass flow rate (kg/s) **(c)** Electrolyzer LHV efficiency **(d)** Total H_2 production (kg)

Based on the total mass of hydrogen produced, the required number of MH tanks was calculated to be 6.56; therefore, 7 tanks were employed in the analyses. A PID controller managed the hydrogen flow rate and maintained pressure within a safe range, set conservatively at 25 bar, below the maximum of 30 bar specified by the MyH_2 300 tank manufacturer. The maximum operational temperature for the tanks was 60°C, pausing hydrogen filling until temperatures dropped to 40°C. The filling can co-occur in two or more tanks when temperatures are below 40°C, but the pressure is near the 25 bar threshold. Analyses were conducted using convection coefficient (*h*) values of 10, 100, 500, and 1000 W/m^2·K. Fig. 4 demonstrates the tanks' filling process when the *h* is set to 100 W/m^2·K.

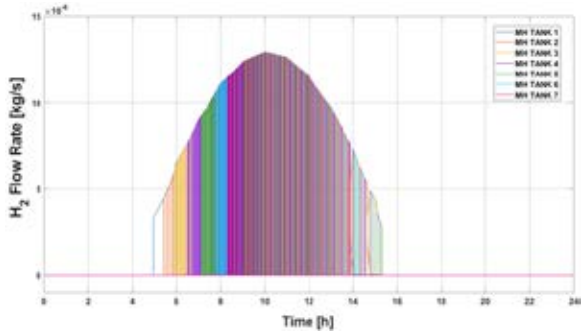

Fig. 4 Hydrogen flow rate distribution into each MH tank over time when the convection coefficient (*h*) is set to 100 W/m^2·K.

Fig. 5 highlights how different convection coefficients influence the tank temperature behavior as the ambient temperature varies.

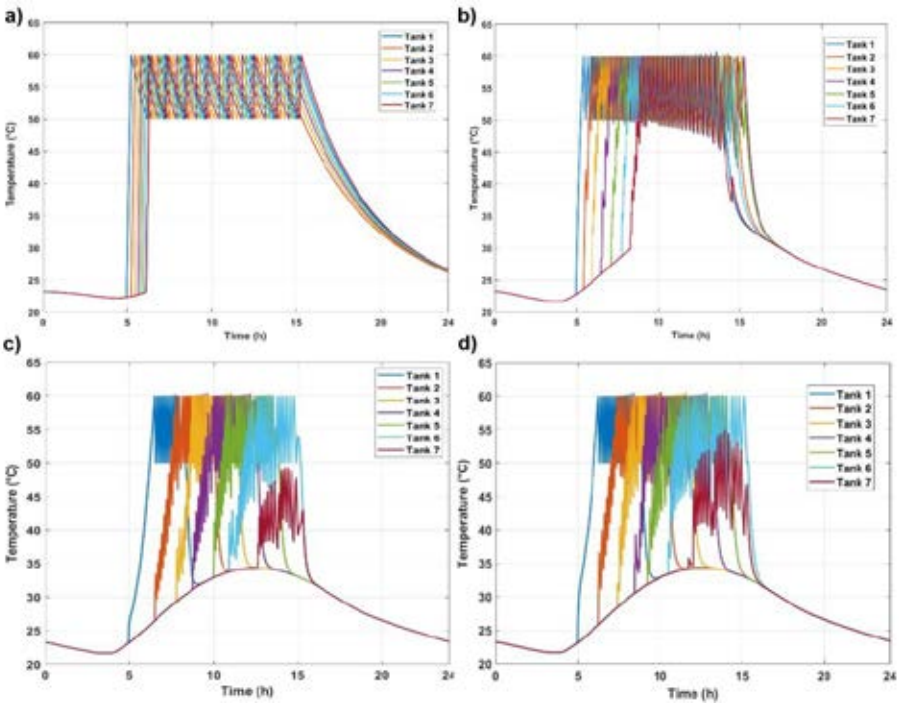

Fig. 5 Temperature profiles of metal hydride tank bed with a convection coefficient (W/m^2·K) of **(a)** *h* = 10 **(b)** *h* = 100 **(c)** *h* = 500 **(d)** *h* = 1500

As shown in Fig. 5, when the *h* is 10 and 100 W/m²·K, the slow temperature decrease prevents sufficient cooling, which in turn limits the filling process in the tanks. Consequently, most tanks cannot reach the maximum achievable weight

fraction (*wf*) of 1.3087. Finally, Fig. 6 shows the impact of convection coefficients on the hydrogen weight fraction stored in the MH tanks.

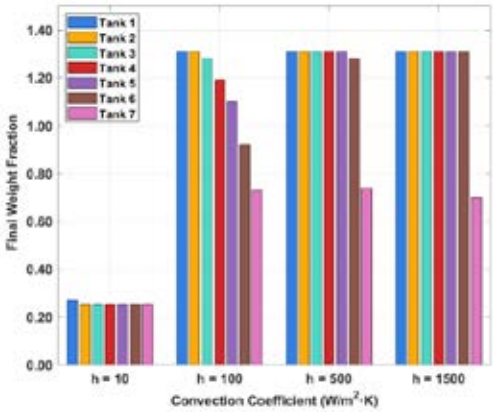

Fig. 6 Final weight fraction in metal hydride tanks at the 24th hour for different convection coefficients

As shown in Fig. 6, the maximum *wf* for one tank is approximately 0.27 by the end of the day when *h* is 10 W/m^{2}K. In contrast, the tanks reach complete filling when *h* is increased to 500 or 1500 W/m^2·K. This directly affects the amount of hydrogen that can be stored versus the amount that remains unutilized. Fig. 7 illustrates this impact by comparing the cases with *h* = 10 and *h* = 100 W/m^2·K.

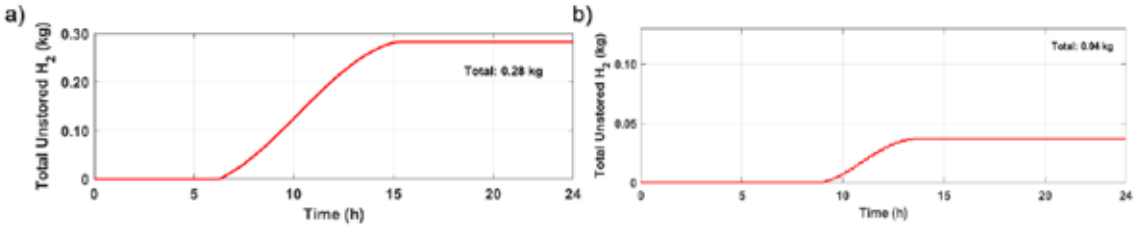

Fig. 7 Unstored H_2 mass flow rate (kg/s) and total unstored H_2 (kg) with a convection coefficient (W/m^2·K) of **(a)** *h* = 10 **(b)** *h* = 100

Fig. 7a illustrates the amount of hydrogen that remains unstored when *h* = 10 W/m^2·K, while Fig. 7b presents the case for *h* = 100 W/m^2·K. In these scenarios, 0.28 kg and 0.04 kg of hydrogen remain unstored, corresponding to 80% and 11.43% of the total 0.35 kg produced, respectively. The entire amount of hydrogen is successfully stored at higher convection coefficient values.

4. CONCLUSIONS

Simulation results indicate that under typical July conditions in Izmir, using 12 photovoltaic modules and 8 AEMWE cells, approximately 0.3527 kg of hydrogen can be produced throughout the day. Different convection coefficients were tested to highlight the importance of thermal management strategies. Metal hydride tanks achieved complete filling at 500 and 1500 W/m²·K while remaining within safe limits. In contrast, lower coefficients of 10 and 100 W/m²·K resulted in insufficient cooling, leaving 0.28 kg and 0.04 kg of hydrogen unstored, respectively. This demonstrates that effective thermal management enhances storage efficiency and overall system performance, with the convection coefficient playing a crucial role in managing operational temperature limits.

ACKNOWLEDGEMENTS

The authors thank the Scientific and Technological Research Council of Türkiye (TÜBİTAK) (Grant Number: 123M878) for supporting and funding the project.

REFERENCES

[1] Celebi, C., Colpan, C. O., & Devrim, Y. (2025). Performance assessment of anion exchange electrolyzer with PBI-BASED membrane through 0-D modeling. International Journal of Hydrogen Energy. https://doi.org/10.1016/j.ijhydene.2025.01.422

[2] Hager, L., Hegelheimer, M., Stonawski, J., Freiberg, A. T. S., Jaramillo-Hernández, C., Abellán, G., Hutzler, A., Böhm, T., Thiele, S., & Kerres, J. (2023). Novel side chain functionalized polystyrene/O-PBI blends with high alkaline stability for anion exchange membrane water electrolysis (AEMWE). Journal of Materials Chemistry A, 11(41), 22347–22359. https://doi.org/10.1039/d3ta02978f

[3] Disli, T., Çetinkaya, S. A., Ezan, M. A., & Colpan, C. O. (2024). Numerical investigations on the absorption of a metal hydride hydrogen storage tank based on various thermal management strategies. International Journal of Hydrogen Energy, 51, 504–522. https://doi.org/10.1016/j.ijhydene.2023.07.122

[4] European Commission. (n.d.). Photovoltaic Geographical Information System (PVGIS). https://re.jrc.ec.europa.eu/pvg_tools/en/

AN EFFICIENT AND SUSTAINABLE APPROACH TO GREEN HYDROGEN PRODUCTION USING PV SYSTEMS

[1,2,*]Hamdi Topcan, [1]Alper Nabi Akpolat, [3]Umut Aydemir
[1] Marmara University, Faculty of Technology, Department of Electrical-Electronics Engineering, Maltepe, Istanbul, 34854, Türkiye
[2] Bursa Uludag University, Institute of Science and Technology, Department of Electrical-Electronics Engineering, Nilufer, Bursa, 16059, Türkiye
[3] Bursa Uludag University, Faculty of Engineering, Department of Electrical-Electronics Engineering, Nilufer, Bursa, 16059, Türkiye

* E-mail: hamdi.topcan@marmara.edu.tr

ABSTRACT

Recently, the high penetration of solar photovoltaic (PV) panels has emerged as a prominent solution for hydrogen production. With the easy availability of solar energy and the high efficiency of solar energy conversion systems, these systems have been adopted to maximize solar energy use to supply local loads, such as electrolyzers. The power generated by the PV module fluctuates depending on both solar radiation and ambient temperature. This variability in solar PV energy must be minimized to ensure a steady flow of energy to the electrolyzer. To reliably power the electrolyzer and provide constant power to direct current (DC) loads, it is crucial to maintain the output voltage of the PV converter within the desired range. The primary challenge addressed in this work is managing the fluctuations in energy generated by PV panels to produce hydrogen efficiently. To achieve this, the Perturb and Observe (P&O) algorithm, a type of maximum power point tracking (MPPT) algorithm, was implemented in the model to make optimal use of the energy provided by PV panels. Consequently, a DC-DC buck converter is designed to lower the voltage to the appropriate level and supply the electrolyzer both safely and efficiently. Simulation studies were conducted in the MATLAB/Simulink environment. Our findings indicate that the design operates with high efficiency and yields satisfactory results concerning sustainability. This study confirms that the designed system operates stably under varying solar irradiance values and can contribute to advancements in related fields for future work.
Keywords: Photovoltaics (PVs), Power Electronic Converters, Hydrogen Energy, Maximum Power Point Tracking (MPPT), Electrolyzer.

1. INTRODUCTION

Nowadays, renewable energy sources such as solar, wind, hydro, geothermal, and hydropower are becoming increasingly important due to the growing energy crisis, environmental pollution, and global warming [1]. Thanks to the easy accessibility of solar energy, which is abundant among these renewable energy sources, and highly efficient solar energy conversion systems, PV panels have become a preferred energy source in many areas, such as green hydrogen production. However, the energy produced by PV modules varies depending on environmental factors such as ambient temperature and solar radiation. This variability can complicate the smooth and continuous supply of electrolysers for green hydrogen production. Therefore, it is important to ensure a stable, constant, and highly efficient transfer of the generated energy to the electrolyser. To solve this problem, the study focuses on designing a system that optimizes the energy flow by stabilizing the variable state of solar energy.

Hydrogen is seen as the most promising energy carrier of the future due to its zero emissions and high energy density. Electrolysis is essentially the process of splitting water into hydrogen and oxygen, its elements. Solid oxide electrolysis (SOE), proton exchange membrane (PEM), and alkaline electrolysis are the most widely used methods for hydrogen production, and integration with renewable energy sources can produce green hydrogen [2]. However, the variable nature of PV systems poses challenges such as integration and energy management. Since electrolyzers operate stably at certain power levels, irregular energy input can lead to system performance degradation and equipment failure. Therefore, it is crucial to employ an effective power management strategy for the safe and efficient operation of the system [3]. For this reason, a DC-DC buck converter is included in our study to adjust the voltage and current values generated by the PV system to the required level for the electrolyzer.

Among the electrolyzers prominent in the literature, PEM electrolyzers possess advantages such as high purity gas production, low power consumption, and efficiency compared to other electrolyzers [4]. M. E. Amri et al. developed a model for battery charging with PV energy and green hydrogen production using the electrolyzer. The system modeled in Simulink showed good performance under varying solar irradiation [5]. N. J. W. Chieh et al. studied the efficiency of green hydrogen production by integrating PV panels and electrolyzers in a simulation environment. The simulation results confirmed that the proposed model operates at high efficiency [6].

In this study, a model is proposed to produce green hydrogen efficiently and safely by managing the variable energy output produced by the PV system with the aid of an electrolyzer. With the proposed model, the variable output of the PV system is stabilized, and the electrolyzer that produces green hydrogen receives the current and voltage values at which it will operate at an optimum level. As for the remaining sections of the study, a general summary of the proposed

model for green hydrogen production is presented in Section II. The findings obtained in the study are presented in Section III, while the conclusions drawn from this research are summarized in Section IV.

2. GENERAL OVERVIEW SOLAR PV GREEN HYDROGEN PRODUCTION MODEL

Solar panels are renewable resources that convert sunlight into electricity. The voltage produced by solar panels and the current values transferred to the load vary depending on weather conditions. Additionally, the installation order of the panels and dust significantly affect the operation of the solar panel. The green hydrogen production model, aided by the proposed PV-based electrolyzer, consists of the PV system, electrolyzer, DC-DC Buck converter, MPPT P&O Algorithm, and hydrogen storage tube, as shown in Figure 1.

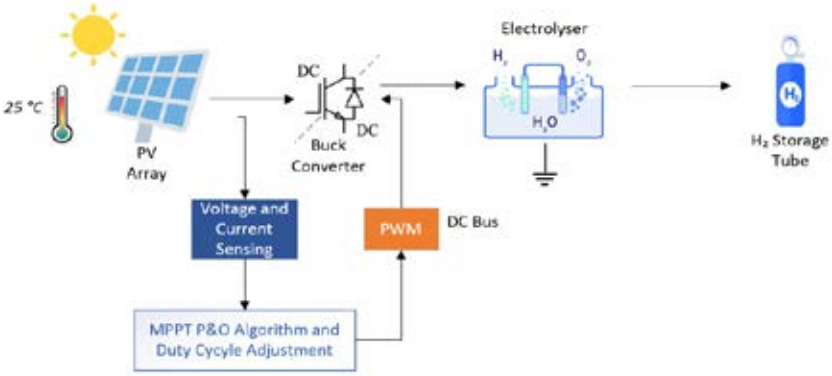

Fig. 1. Overview of proposed solar PV green hydrogen production model.

As shown in Figure 1, the energy from the solar panel is directly routed to the electrolyzer through a DC-DC buck converter managed by the P&O algorithm. The buck converter is integrated into the system to ensure a stable and safe energy supply to the electrolyzer. The Perturb & Observe (P&O) approach is chosen as the MPPT algorithm to reduce the fluctuations caused by the variable output of the PV system and to improve energy efficiency. In the simulation, ramp, trapezoidal, and staircase irradiance profiles, shown in Figure 2, are selected as PV system irradiance inputs to analyze system performance under varying real environmental conditions. The ramp irradiance profile examines the system behavior at periodically varying irradiance levels throughout the day, while the trapezoidal irradiance profile assesses the irradiance levels during the late and early hours. The staircase irradiance profile is used to analyze the system behavior during sudden changes, such as cloud cover.

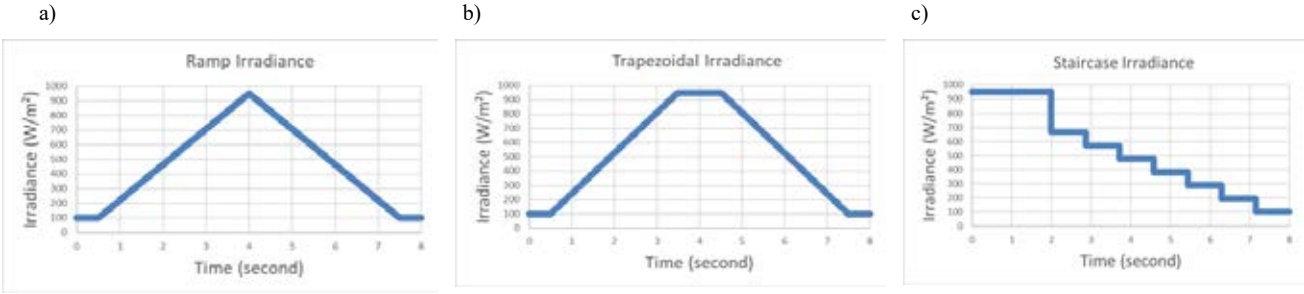

Fig. 2. a) Ramp irradiance profile, b) Trapezoidal irradiance profile, c) Staircase irradiance profile.

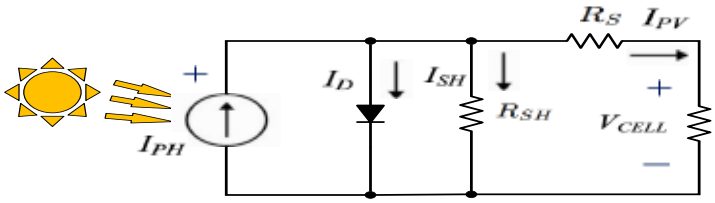

Fig. 3. Conventional PV panel equivalent circuit.

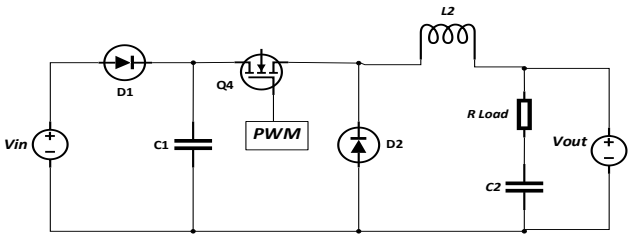

Fig. 4.DC-DC Buck Converter Circuit

The electrical equivalent circuit diagram of a conventional PV panel is shown in Figure 3. When PV cells absorb sunlight, the photons excite electrons, producing a photocurrent (*Iph*). This current depends on solar irradiance (G) and panel temperature (T). In the equivalent circuit of a conventional PV panel, Ipv is represented as (2).

$$-Iph+Id+Ish+Ipv=0, \quad (1)$$

$$Ipv=Iph-Id-Ish, \quad (2)$$

$$Vt= \frac{nk(Tstc)}{q}, \quad (3)$$

$$Vt= Iph-Id(e^{\frac{Vcell+IpvRs}{nVt}} - 1) - \frac{Vcell+IpvRs}{Rsh} \quad (4)$$

$$Iph=Isc +ki(T-Tstc) \frac{G}{Gstc} \quad (5)$$

Here, Id is the saturation current of the diode, Rs is the series resistance, and Rsh is the shunt resistance. n is the ideality factor of the diode, which affects the electrical behavior of the cell. Environmental factors cause the thermal cell voltage, known as Vt, to occur. q is the charge of the primary charge carrier, the electron, while k is the Boltzmann constant. Furthermore, Isc is the short-circuit current, Tstc is the reference temperature determined under standard test conditions, and Gstc is the solar irradiation level under the same conditions [7]. In this project, a buck converter, also called a step-down converter, is used to regulate the output voltage supplied to the electrolyzer. It operates in two states depending on the switch position: when open, energy is stored in the inductor; when closed, the stored energy is transferred to the capacitor and through the diode to the load, i.e., the electrolyzer. The capacitor meets instantaneous power demands, preventing current and voltage fluctuations in the circuits and ensuring stable operation. This cycle repeats continuously according to the duty cycle of the MOSFET, and the output voltage is lower compared to the input voltage. The following formulas can be used to calculate the inductor, duty cycle, and capacitor values in the DC-DC buck converter model schematically shown in Figure 4.

$$D = \frac{Vo}{Vin} \quad (6)$$

$$L= \frac{Vo(1-D)}{\Delta IL\ fs} \quad (7)$$

$$C= \frac{Vo(1-D)}{8\Delta Vofs^2L} \quad (8)$$

To maximize the benefits of the photovoltaic system, the MPPT P&O algorithm was employed in our study. When discussing the operational logic of the P&O algorithm, it first calculates the power output produced by the PV system using sensor data, while simultaneously introducing voltage distortion values into the algorithm to determine the direction for maximum power point tracking. These values are then compared with previous measurements, allowing adjustments in the system's output power based on the voltage distortion. This process enables the algorithm to oscillate around the maximum power point (MPP) and operates on the principle of continuously monitoring the MPP. The P&O algorithm was integrated into our proposed model, ensuring the PV system operates at peak efficiency. The electrolyzer received the appropriate energy input through a DC-DC buck converter controlled by the algorithm. Compared to other hydrogen electrolyzers, PEM electrolyzers are favored for their ease of maintenance, wide operating temperature range, and higher energy efficiency. The electric current flowing through the PEM electrolyzer is converted into a calculation for hydrogen production in accordance with Faraday's law. According to Faraday's law, the molar production rate of hydrogen gas is expressed by the following equation:

$$nH_2(t) = \frac{I(t)\eta\text{faraday}}{2\text{F}} \quad (9)$$

Here, I(t) represents the instantaneous electric current (A) of the system, η is the Faraday efficiency of the Faraday electrolyzer (taken as 95% in this project), and F is the Faraday constant (96485C/mol).

$$VH_2(t) = \frac{I(t)\eta\text{faradayVm}}{2\text{F}} \quad (10)$$

The amount of hydrogen produced is converted to volume according to the ideal gas law and is calculated using formula (10). The total amount of hydrogen produced is determined by integrating the instantaneous flow rate with respect to time.

3. RESULTS AND DISCUSSION

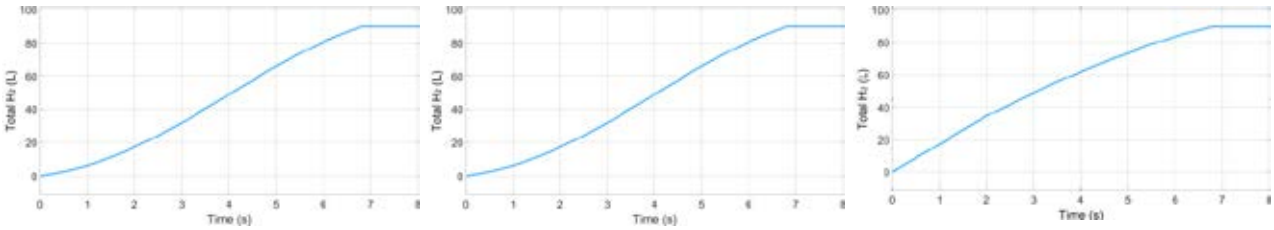

Fig. 5. a) Total hydrogen production in ramp irradiance profile, b) Total hydrogen production in trapezoidal irradiance profile, c) Total hydrogen production in staircase irradiance profile.

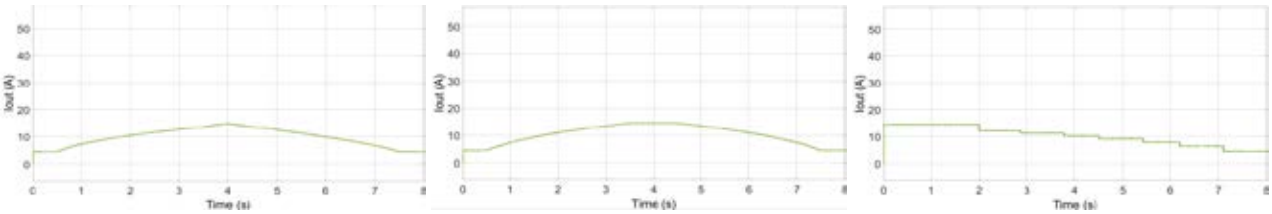

Fig. 6. Current curves for different irradiance profiles.

According to the simulation results conducted under various irradiance profiles, as can be seen in Figure 5, hydrogen production curves differ based on the temporal changes in irradiance. In the ramp irradiance scenario, where irradiance increases gradually, the hydrogen production curve initially shows a slow increase before accelerating over time, ultimately reaching the tube's capacity. In the Staircase profile, due to sudden changes in irradiance at specific steps, hydrogen production rises in parallel to these steps, leading to sharp transitions in the production curve. In the trapezoidal irradiance scenario, irradiance increases to a certain level, remains constant for a period, and then decreases again; thus, hydrogen production initially accelerates, displays a linear increase during the constant irradiance phase, and is constrained by the tube capacity as the irradiance decreases in the final segment. These results highlight the dynamic effect of solar irradiance on hydrogen production and demonstrate that the irradiance profile directly influences the production characteristics. Furthermore, the current curves for different conditions are shown in Figure 6.

4. CONCLUSION

This study introduces a system for producing green hydrogen using a PEM electrolyzer powered by variable energy from photovoltaic panels. The paper thoroughly discusses the MPPT P&O maximum power tracking algorithm and the buck converter circuit. A simulation environment was established to assess solar panel efficiency across different irradiance profiles—staircase, ramp, and trapezoidal—representing real-world conditions. With MPPT, the hydrogen production system successfully generated hydrogen in the PEM electrolyzer, even under changing irradiance levels, by optimizing power from solar panels rated at approximately 790 W. Consequently, the system effectively and safely completed the hydrogen production process, maximizing the use of solar energy despite variability in solar irradiance. This study aims to contribute to the advancement of hydrogen production systems reliant on renewable energy and to enhance performance by incorporating more advanced MPPT algorithms in future work. Notably, this system is intended to serve as a foundation for an experimental dashboard in our upcoming research.

REFERENCES

[1] S. Farhani, C. Kaddachi and F. Bacha, "Study and Simulation of Green Hydrogen Production Systems Coupled With Concentrated Photovoltaic Generators," 2024 IEEE International Conference on Artificial Intelligence & Green Energy (ICAIGE), Yasmine Hammamet, Tunisia, 2024, pp. 1-5

[2] E. O. Ogundimu and C. Graham Richards, "Enhancing Green Hydrogen Production and Sustainability," 2025 33rd Southern African Universities Power Engineering Conference (SAUPEC), Pretoria, South Africa, 2025, pp. 1-6

[3] C. Blanco, S. Díaz, I. Peláez, C. Rech and P. García, "Maximizing Green Hydrogen Production Efficiency for Hybrid Energy Storage and Solar Photovoltaic Systems: A Design Methodology," 2024 IEEE Energy Conversion Congress and Exposition (ECCE), Phoenix, AZ, USA, 2024, pp. 386-391

[4] L. Wan, W. Zhang and Z. Xu, "Overview of Key Technologies and Applications of Hydrogen Energy Storage in Integrated Energy Systems," 2020 12th IEEE PES Asia-Pacific Power and Energy Engineering Conference (APPEEC), Nanjing, China, 2020, pp. 1-5

[5] M. E. Amri and C. B. Salah, "Study of a PV/Battery System for Hydrogen production and storage," 2022 IEEE 21st international Ccnference on Sciences and Techniques of Automatic Control and Computer Engineering (STA), Sousse, Tunisia, 2022, pp. 522-527

[6] N. J. W. Chieh, H. N. Afrouzi and J. Tavalaei, "Development of Integrated Structure of Hydrogen Production Using Photovoltaic Panels and Detailed Electrical Model for Electrolyser," 2023 7th International Conference on Electronics, Materials Engineering & Nano-Technology (IEMENTech), Kolkata, India, 2023, pp. 1-5

[7] A. N. Akpolat, E. Dursun and A. E. Kuzucuoğlu, "Deep Learning-Aided Sensorless Control Approach for PV Converters in DC Nanogrids," in IEEE Access, vol. 9, pp. 106641-106654, 2021, doi: 10.1109/ACCESS.2021.3100857

HYDROGEN PRODUCTION FROM NaCl, $CaCl_2$ AND $MgCl_2$ SALTS USING CARBON RODS EXTRACTED FROM WASTE BATTERIES

[1,2*] *Serdal Damarseckin*, [2]*Mustafa Erden,* [2]*Ayhan Atiz,* [3]*Hatice Karakilcik,* [2]*Mehmet Karakilcik*
[1] Sirnak University, Faculty of Engineering, Department of Renewable Energy Systems Engineering, Sirnak, 73000, Türkiye
[2] Cukurova University, Faculty of Science and Letters, Department of Physics, Adana, 01250, Türkiye
[3] Cukurova University, Faculty of Engineering, Department of Geology, Adana, 01250, Türkiye
*Corresponding author e-mail: serdalseckin@hotmail.com

ABSTRACT
In this study, 3 different electrolytes were used as 1 M sodium chloride (NaCl), calcium chloride ($CaCl_2$) and magnesium chloride ($MgCl_2$) salts. The hydrogen production performance of these solutions was investigated using the chlor-alkali method. While the electrodes were made of carbon rods consisting of a mixture of carbon and graphite obtained from waste batteries, the main body of the reactor was manufactured from Delrin polymer material using CNC technology. Nafion 117 membrane was used to separate the anode and cathode compartments. The study was carried out at 20 ° C temperature and 5 V cell voltage. According to the experimental results, in the electrolysis process carried out using NaCl solution, 10 mL of hydrogen was produced in 5.30 minutes, 20 mL in 9.40 minutes and 30 mL in 13.20 minutes, and the average current during was measured 0.30 A. Similarly, in the experiments conducted with $CaCl_2$ solution, the same amount of hydrogen production was completed in 6.58 min, 13.54 min and 21.42 min, respectively, and the average current was measured 0.16 A. In contrast, in the experiments conducted with $MgCl_2$ solution, the hydrogen production times of 10 mL, 20 mL and 30 mL were recorded as 45.32 min, 92.04 min and 134.10 min, respectively, and the current was only 0.02 A. As a result, $MgCl_2$ solution was found to have much lower current but required more time compared to the other two solutions.

Keywords: Hydrogen production, Waste batteries, Chlor-Alkali reactor, Electrolysis,

1. INTRODUCTION

Hydrogen presents significant potential for clean energy production and is recognized as a crucial element in the shift towards sustainable energy systems, owing to its eco-friendly attributes. As an energy carrier, hydrogen can play a key role in reducing carbon emissions across various sectors, such as transportation, industry, heating, and power generation, offering sustainable alternatives. Its significance goes beyond just mitigating greenhouse gas emissions; it also enables the seamless integration of renewable energy sources and offers viable energy storage solutions. Therefore, hydrogen is a fundamental element in building a more sustainable and robust energy infrastructure. Since chlor-alkali processes consume large amounts of energy, it is obvious that processes supported by renewable energy sources will be more advantageous for hydrogen production. A significant number of studies have been undertaken to research hydrogen production via the chlor-alkali process. These studies focus on the production of a hydroxide with hydrogen and chlorine gases, which are the natural results of the chlor-alkali process. Research has been conducted on hydrogen production efficiency, usually based on reactor design, variety of electrolytes used, and temperature and cell voltage.

In one of these studies, a mini chlor-alkali reactor was constructed to compare the hydrogen production performances of aqueous solutions of NaCl, KCl and $CaCl_2$ salts. The hydrogen production rates of these salts were experimentally investigated by changing the cell voltage, operating temperature and electrolyte flow rate. In this study, since steel electrode was used, very active chlorine gas was produced in trace amounts while an effective hydrogen gas evolution was observed. It was found that KCl salt was slightly faster than NaCl salt in terms of hydrogen production rate, while $CaCl_2$ salt was far behind them [1].

The electrode surface area used in the chlor-alkali process and the distance between the electrodes and the undesirable gas accumulation on the electrodes also have significant effects on the current density, which directly affects hydrogen production. In another study conducted to investigate these effects, the effects of electrolyte temperature and flow rate on the current density were also examined in addition to these variables. It was observed that increasing the electrode surface area and operating temperature increased the current density, while increasing the distance between the electrodes significantly reduced the current density by reducing the electric field. It was noted that increasing the electrolyte flow rate increased the current density very slightly. Apart from these, it was observed that air bubbles on the electrodes caused the current density to decrease very slightly over time [2-3].

In another paper, the hydrogen generation efficiency of the aqueous solution of $ZnCl_2$ salt, which is very various from the salts commonly utilized in the chlor-alkali method, was researched. The anode and cathode sections of the reactor divided by Nafion 212 membrane were injected with $ZnCl_2$ water-based solution and clean water, respectively. The hydrogen generation ratio was 0.89 mL/min under 20°C working temperature, 0.3 g/s mass flow ratio and 5 V operating voltage. Under the working temperature of 45°C, mass flow ratio of 0.3 g/s and cell voltage of 10 V, the hydrogen generation ratio was 5 mL/min [4].

The effect of treatment with HCl, H_2SO_4, and HNO_3 on the physicochemical properties of the Nafion 117 membrane has been investigated. Water uptake capacity, crystallinity, proton conductivity, and water dynamics were evaluated for both

treated and untreated membranes [5]. The effect of acid pretreatment on the conductivity of Nafion 117 was comprehensively studied using HNO_3, HCl, H_2SO_4, and H_3PO_4 at different concentrations [6-7].
In this study, a durable N177 membrane was used to separate the pure water and brine compartments of the chlor-alkali reactor. The chlor-alkali process supported by renewable energy systems appears to be an important application for hydrogen production despite some difficulties. Therefore, the energy efficiency of the chlor-alkali system and sustainable hydrogen production are important goals. The impact of certain system components involved in achieving this will be investigated in terms of their effect on hydrogen production performance.

2. SYSTEM DESCRIPTION

The schematic diagram of the chlor-alkali reactor constructed for the experimental study and the auxiliary equipment around the reactor is shown in Fig. 1. The nafion membrane 117 was used to separate the compartments of the rector. Electrolyte feed tanks were used to feed the reactor compartments, and another tanks were used to collect the waste electrolyte from the reactor. The volume of the produced gases was measured according to the water displacement principle and graduated cylinders were used for this purpose. Additionally, a DC power supply is employed to provide energy to the reactor. Peristaltic pumps are utilized to ensure continuous and smooth circulation of the liquid, controlling the flow of the electrolyte. The entire system is equipped with electrodes made from waste batteries, which facilitate the production of hydrogen and chlorine gases during the reaction.

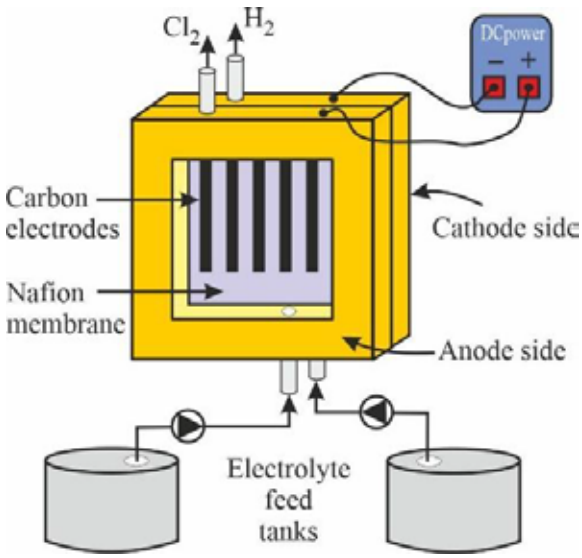

Fig. 1. The schematic representation of the experimental setup.

3. RESULTS AND DISCUSSION

In the study, hydrogen production from NaCl, $CaCl_2$ and $MgCl_2$ salts was investigated using the chlor-alkali method under conditions of 20°C temperature and 5 Volt cell voltage. The main body of the reactor was fabricated from Delrin polymer using CNC machining. A Nafion 117 membrane was used to separate the anode and cathode compartments, with carbon rod electrodes obtained from waste batteries used in both compartments.
Fig. 2 shows the outcomes achieved by placing NaCl solution in the anode compartment and pure water in the cathode compartment, maintaining a steady cell voltage of 5 V, an average current density of 0.30 A, and a temperature of 20°C. Hydrogen gas volumes of 10 cm³, 20 cm³, and 30 cm³ were generated and collected in the cathode section at time intervals of 5.30 minutes, 9.40 minutes, and 13.20 minutes, respectively.
Fig. 3 shows the outcomes achieved by placing $CaCl_2$ solution in the anode compartment and pure water in the cathode compartment, maintaining a steady cell voltage of 5 V, an average current density of 0.30 A, and a temperature of 20°C. Hydrogen gas volumes of 10 cm³, 20 cm³, and 30 cm³ were generated and collected in the cathode section at time intervals of 6.58 minutes, 13.54 minutes, and 21.42 minutes, respectively.
Fig. 4 shows the results from introducing $MgCl_2$ solution into the anode compartment and deionized water into the cathode compartment, with a stable cell voltage of 5 V, a consistent current density of 0.02 A, and a temperature of 20°C. Hydrogen gas volumes of 10 cm³, 20 cm³, and 30 cm³ were collected in the cathode section at time intervals of 45.32 minutes, 92.04 minutes, and 134.10 minutes, respectively.

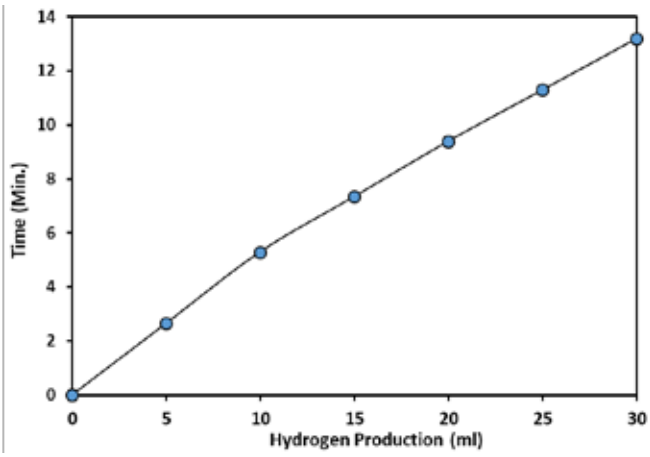

Fig. 2. Time-dependent hydrogen production (NaCl)

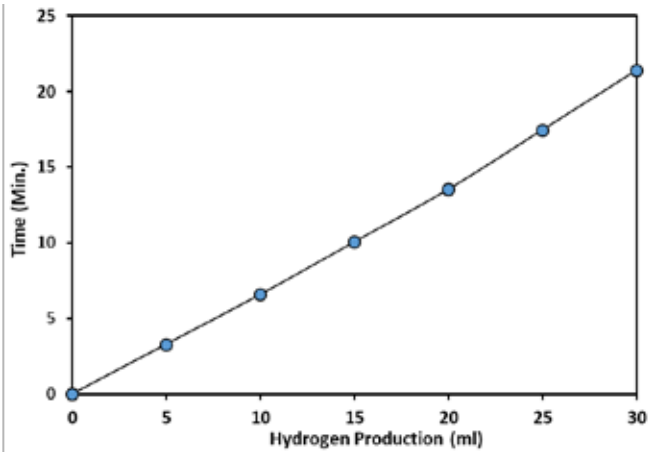

Fig. 3. Time-dependent hydrogen production ($CaCl_2$)

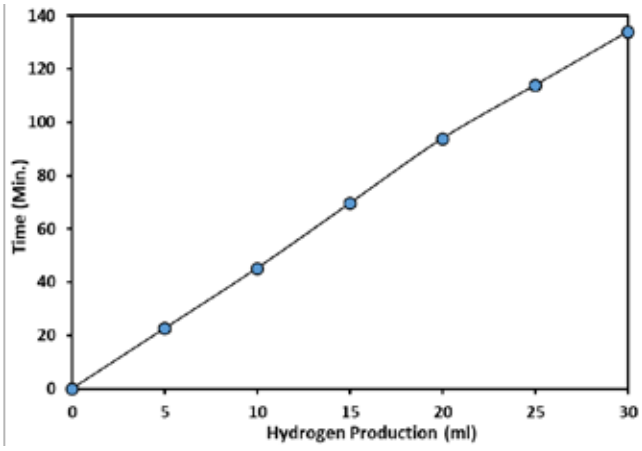

Fig. 4. Time-dependent hydrogen production ($MgCl_2$)

4. CONCLUSIONS

As a result, based on the experimental studies, when the hydrogen production performance of different electrolyte solutions was compared, 30 mL of hydrogen was produced in 13.20 minutes with an average current of 0.30 A using a 1 M NaCl solution, whereas the same amount of hydrogen was produced in 21.42 minutes with an average current of 0.16 A using a 1 M $CaCl_2$ solution. In contrast, when a 1 M $MgCl_2$ solution was used, the time required to produce 30 mL of hydrogen was significantly longer—134.10 minutes—with an average current of only 0.02 A. These results indicate that the $MgCl_2$ solution generated a much lower current during electrolysis and required considerably more time to produce

the same volume of hydrogen. Overall, it was observed that the most efficient hydrogen production, in terms of higher current and shorter duration, was achieved using the NaCl solution.

REFERENCES

1. Erden M., Karakilcik M. Experimental investigation of hydrogen production performance of various salts with a chlor-alkali method. Int J Hydrogen Energy 2023; 52:546-560.
2. Erden M., Atiz A., Karakilcik H., Karakilcik M. Investigation of some factors affecting the current density that directly governs the hydrogen production in a membrane cell chlor-alkali reactor: An experimental study., 7th International
3. Hydrogen Technologies Congress, Turkiye. Proceedings Book, Editors: Dinçer I., Çolpan CO., Özdemir MT., Gençoğlu MT., ISBN: 978-605-70717-5-0; 2023:637-640.
4. Damarseckin S. Hydrogen production from ZnCl2 salt: Application of chlor-alkali method. Int J Hydrogen Energy 2024:88: 888-897.
5. Iriarte, D., Andrada H., Ochoa SAM., Silva OF., Chávez FV., Carreras A. Effect of acid treatment on the physico-chemical properties of Nafion 117 membrane. Int J Hydrogen Energy 2022:47: 21253-21260.
6. Kuwertz R., Kirstein C., Turek T., Kunz U. Influence of acid pretreatment on ionic conductivity of Nafion membranes J Membr Sci, 500 (2016), pp. 225-235.
7. Napoli L., Franco J., Fasoli H., Sanguinetti A. Conductivity of Nafion 117 membrane used in polymer electrolyte fuel cells. Int J Hydrogen Energy, 2014: 39(16):8656-8660

EVALUATION OF THE SOCIAL DIMENSIONS OF INTEGRATING NATURAL GAS AND HYDROGEN IN ENERGY CONSUMPTION: THE CASE OF TURKIYE

1Bora Yenihan, 2 Kerem Çolak, [3]Orhan Özcan
[1]Kocaeli University, Faculty of Political Sciences, Labor Economics and Industrial Relations, Kocaeli/Türkiye
[2]Kocaeli University, Hereke Asım Kocabıyık Vocational School, Textile, Clothing, Shoes and Leather, Textile Technology Program, Kocaeli/Türkiye
[3]Kocaeli University, Faculty of Engineering, Department of Chemical Engineering, Kocaeli/Türkiye
bora.yenihan@kocaeli.edu.tr, orhan.ozcan@kocaeli.edu.tr, kerem.colak@kocaeli.edu.tr

ABSTRACT
The need for energy is as old as human history. While early humans primarily used energy for heating, the Neolithic Age marked a transition to a settled lifestyle, shifting humanity from passive consumers to active producers. Since then, energy demand has steadily increased. Initially focused on production, energy consumption evolved by the 20th century to include comfort and convenience. During this period, fossil fuel-based energy became central to modern life, while concerns about environmental impacts led to growing interest in clean energy alternatives. Hydrogen energy has emerged as a promising solution in the search for sustainable energy, attracting attention from both engineers and social scientists. This study examines the social necessity of clean energy adoption, particularly the integration of hydrogen into natural gas systems, from a social policy perspective. Using data and models from previous studies, Aspen HYSYS simulation software was employed to analyze the physical properties and flow dynamics of hydrogen, natural gas, and their mixtures. A comparative literature review was also conducted to evaluate historical and current energy trends. Findings indicate that hydrogen integration is both strategically and technically viable, offering environmental benefits, economic efficiency, improved infrastructure utilization, and enhanced household welfare through its positive macroeconomic effects.

Keywords: Energy, Natural gas, Hydrogen, Houshold consumption

1. INTRODUCTION

Energy, commonly defined as the capacity to do work or perform tasks, is an indispensable component of human life due to its fundamental role in sustaining both universal and biological processes. In the modern era, energy has become more critical than at any other point in human history. It influences not only our quality of life but also the economy, environmental sustainability, and international relations [1]. Since the Industrial Revolution, the increased diversity and production of consumer goods have contributed to a dramatic, and often unpredictable, rise in the global population. This rapid population growth has, in turn, significantly escalated the demand for energy [2].

Although today's energy needs are met by a variety of sources, discussions increasingly center on the necessity for sustainable energy alternatives. At present, the majority of global energy demand is fulfilled by non-renewable and finite resources. These non-renewable sources are primarily categorized as fossil-based, followed by nuclear-based types. Fossil-based energy sources, which account for a substantial share of global energy consumption, include coal, oil, and natural gas. In contrast, renewable energy sources include hydropower, solar, biomass, wind, geothermal, wave/tidal, and hydrogen energy [3].

In particular, to address the ongoing reliance on fossil fuel-based energy, the use of natural gas, one of the primary energy sources, is projected to increase annually and maintain this upward trend in the coming years. Natural gas is composed of more than 90% methane, along with smaller amounts of ethane, propane, butane, and carbon dioxide. It is a colorless, odorless gas that is lighter than air. An analysis indicates that natural gas accounts for over 23% of global energy consumption [4]. However, natural gas is inherently a fossil-based and finite resource. Furthermore, its uneven geographic distribution and the resulting economic dependence hinder its accessibility and widespread use in certain countries. These limitations have prompted increased attention to energy efficiency. As a result, researchers across different disciplines continue to explore ways to improve both energy production and consumption efficiency. In this context, the concepts of "hydrogen" and the "hydrogen economy" have gained prominence.

Hydrogen is primarily regarded as a promising alternative in the transition to clean energy sources. Its classification as a "clean" energy source stems from the fact that its combustion produces only water and energy [5]. Composed of a single proton and one electron, hydrogen is the most abundant element in the universe [6]. Its potential as both a fuel and an energy carrier was recognized after the Industrial Revolution. Initially, it was used as fuel in internal combustion engines, later in diesel engines that utilized carbon and hydrogen compounds [7]. While not a primary energy source, hydrogen, as an energy carrier, holds significant potential to support and enhance the use of renewable energy systems [8]. In this context, the 1974 Hydrogen Economy Miami Energy Conference (THEME) marked a pivotal moment, establishing a shared vision for integrating hydrogen into future energy systems. Since THEME, efforts and research on hydrogen energy and the hydrogen economy have intensified considerably [9].

As a form of chemical energy storage, hydrogen is notable for its minimal environmental impact. However, the high cost of hydrogen storage remains a significant concern. To avoid these costs and reduce expenses associated with natural

gas usage, the injection of hydrogen into natural gas pipelines for use as fuel has emerged as a promising solution [10]. Integrating hydrogen into natural gas networks, due to its carbon-free nature, can help mitigate environmental issues such as air pollution and global warming [11], while also reducing the cost of natural gas for end users. This approach has the potential to lower overall energy costs and, consequently, reduce consumption-related expenditures. Nonetheless, it is important to recognize that there is an upper limit to the proportion of hydrogen that can be safely injected into natural gas pipelines [12]. These limitations must be carefully considered during cost-benefit analyses. Despite such constraints, the integration of hydrogen into natural gas infrastructure offers several key advantages, which can be summarized as follows:

- Significant reduction in greenhouse gas emissions can be achieved when hydrogen is produced from renewable resources.
- A decline in fossil fuel use, such as oil, can lead to reduced air pollution and enhanced air quality.
- Utilizing a natural gas-hydrogen blend for electricity generation can support the integration of renewable energy sources into existing energy systems and infrastructure.

2. METHODOLOGY

All calculations of the properties and flow rates of hydrogen, natural gas, and their 15% hydrogen-85% natural gas (by mole) blend were performed using Aspen HYSYS simulation software. The natural gas composition, adopted from a previous study [13], is presented in Table 1 alongside the blend composition. The simulation included the following components: CH_4, C_2H_6, C_3H_8, C_4H_{10}, C_5H_{12}, C_6H_{14}, CO_2, N_2 and H_2. The Peng-Robinson (PR) property package, selected for its efficiency and reliability, was used for all calculations, as detailed in Eq. (1) [14]. As shown in Table 1, methane (CH_4) is the dominant component in both cases, with a slightly lower concentration in the hydrogen blend (82.85% by mass, 78.45% by mole) compared to pure natural gas. This decrease is expected due to the inclusion of hydrogen, as methane is the primary combustible component in conventional natural gas.

Table 1. Compositions of natural gas and the hydrogen-natural gas blend used in the simulation.

	Mass Fractions (%)		Mole Fractions (%)	
	Blend	Natural Gas	Blend	Natural Gas
CH_4	82.85	84.53	78.45	92.29
C_2H_6	5.75	5.87	2.91	3.42
C_3H_8	2.76	2.82	0.95	1.12
C_4H_{10}	1.76	1.79	0.46	0.54
C_5H_{12}	0.65	0.66	0.14	0.16
C_6H_{14}	0.19	0.20	0.03	0.04
CO_2	0.66	0.68	0.23	0.27
N_2	3.39	3.45	1.84	2.16
H_2	1.99	0.00	15.00	0.00

$$P = \frac{RT}{V-b} - \frac{a\alpha}{V(V+b)+b(V-b)} \quad (1)$$

Table 2 outlines the operating conditions and various key properties of natural gas, pure hydrogen, and the hydrogen-natural gas blend. All data were obtained from Aspen HYSYS under identical conditions (100 kPa and 15 °C), ensuring a consistent basis for comparison. Together, Tables 1 and 2 provide a comprehensive overview of how hydrogen blending alters the composition and fundamental properties of natural gas. These changes have significant implications for combustion efficiency, safety, transportation, and appliance compatibility, highlighting the importance of such analyses in evaluating hydrogen as a transitional fuel within existing gas infrastructure.

The data on hydrogen production and associated costs from Kayfeci et al., as cited in the study by Rasul and colleagues [15], are presented in Table 3. As shown, the cost information includes both operational expenses and fixed capital investment costs related to hydrogen production from fossil fuels. Assuming an average payback period of eight years for the fixed investment costs, listed under the “Capital Cost” heading in the table, the cost of hydrogen per kilogram was calculated by Kayfeci et al. [16].

Table 2. Operating conditions and properties of natural gas, hydrogen, and the blend obtained from Aspen HYSYS.

Properties	Units	Natural Gas	Hydrogen	Blend
Pressure	kPa	100.00	100.00	100.00
Temperature	°C	15.00	15.00	15.00
Molecular Weight	kg/kmol	17.52	2.02	15.19
Mass Density	kg/m^3	0.73	0.08	0.64
Mass Enthalpy	kJ/kg	-4317.51	-141.02	-4234.24
Mass Entropy	kJ/kgK	10.53	60.59	11.76
Mass Exergy	kJ/kg	-1.49	-13.77	-1.74
LHV Molar Basis (Std)	MJ/kmole	833.73	241.94	744.96
LHV Mass Basis (Std)	MJ/kg	47.60	120.01	49.04
LHV Vol. Basis (Std)	MJ/m^3	35.34	10.22	31.55
Wobbe Index	MJ/m^3	50.32	45.88	48.42

Table 3. Comparison of Hydrogen Production Costs by Different Methods

Process Energy	Source	Feedstock	Capital cost (M$)	Hydrogen cost ($/kg)
SMR with CCS	Fossil fuels	NG	226.4	2.27
SMR without CCS	Fossil fuels	NG	180.7	2.08
CC with CCS	Fossil fuels	Coal	545.6	1.63
CG without CCS	Fossil fuels	Coal	435.9	1.34
ATR of methane with CCS	Fossil fuels	NG	183.8	1.48
Methane pyrolysis	Internally generated steam	NG	–	1.59–1.70

3. RESULTS AND DISCUSSION

Based on the preceding analysis, Table 4 presents data on natural gas supplied for final household consumption in Türkiye, incorporating a 15% hydrogen blend. Monthly household consumption figures were calculated using Aspen HYSYS simulation software. Natural gas in households is primarily used for cooking, water heating, and space heating, representing a significant portion of household expenditures.

Tablo 4. Residential Natural Gas Consumption in Türkiye (2024) and NG+H_2 Simulation Values

Month	Consuption (M Sm^3)	Cost per Sm^3 ($)	Total Cost (M$)	Simulated NG (M Sm^3)	Simulated H_2 (M Sm^3)	Avarege H_2 Cost ($/Sm^3)	15% Blend for Equivalent Exergy-Total Cost (M$)	Savings Ratio (%)	Savings (M$)
December	3071.00	0.35	1089.46	2585.59	456.28	0.155	988.06	0.09	101.40
November	1569.00	0.35	554.68	1321.00	233.12	0.155	503.18	0.09	51.50
October	435.00	0.34	150.02	366.24	64.63	0.155	136.33	0.09	13.68
September	303.00	0.34	104.50	255.11	45.02	0.155	94.96	0.09	9.53
Agust	290.00	0.34	97.50	244.16	43.09	0.155	88.78	0.09	8.73
July	339.00	0.28	95.54	285.42	50.37	0.155	88.25	0.08	7.29
June	478.00	0.28	134.12	402.45	71.02	0.155	123.94	0.08	10.18
May	852.00	0.30	258.02	717.33	126.59	0.155	236.88	0.08	21.14
April	1960.00	0.28	540.27	1650.20	291.21	0.155	500.06	0.07	40.21
March	2946.00	0.27	790.21	2480.35	437.71	0.155	733.23	0.07	56.99
February	3602.00	0.29	1028.51	3032.66	535.17	0.155	948.98	0.08	79.53
January	3266.00	0.28	908.34	2749.77	485.25	0.155	840.06	0.08	68.28
Annual Total	19111.00		5751.18	16090.26	2839.46		5282.72		468.46

The data were compiled from the monthly reports of GAZBIR and EPIAŞ and were calculated by the authors.

Supplying households with a 15% hydrogen blend could reduce energy costs, allowing savings to be redirected toward other forms of consumption, potentially increasing national income through the multiplier effect [17]. In Türkiye, this shift could result in an estimated annual saving of $468.5 million, or approximately 8% of household natural gas spending, equivalent to 0.035% of the national income. With the 2024 national income projected at $1,323,255 million, reallocating these savings to other expenditures or investments could generate an additional $936.92 million in national income with an increase of 0.07%. These findings suggest that redirecting energy savings to broader household consumption can have a greater impact on economic growth than the original utility spending. Thus, blending hydrogen with natural gas to meet residential energy demand not only offers environmental benefits but also contributes to economic development. Promoting hydrogen integration is, therefore, a strategic step toward sustainability and growth.

4. CONCLUSIONS

This study examines the technical advantages of integrating hydrogen into natural gas systems, focusing on environmental sustainability and economic efficiency. Engineering analyses using Aspen HYSYS simulation software demonstrate that a natural gas mixture with 15% hydrogen is compatible with existing infrastructure, confirming its feasibility within current energy systems. This hydrogen-enriched blend enhances energy efficiency, reduces greenhouse gas emissions, and helps optimize energy costs. Hydrogen integration into natural gas pipelines significantly lowers the carbon footprint of energy systems and supports the efficient use of renewable energy resources. Engineering calculations confirm that a 15% hydrogen blend positively impacts both energy intensity and cost-efficiency. Economic modeling shows that this integration results in substantial savings on natural gas expenses, improving the cost-effectiveness of energy distribution. As a carbon-free element, hydrogen can address environmental challenges linked to fossil fuels and offers a strategic solution for enhancing long-term energy security. Additionally, incorporating hydrogen into existing infrastructure supports the economic sustainability of energy policy and fosters technological progress. In conclusion, hydrogen integration is a strategic and technically viable approach, enabling more efficient use of infrastructure, lowering costs, and promoting sustainability. It also improves household welfare at the micro level while contributing to macroeconomic growth through the multiplier effect.

REFERENCES

1. Fanchi R J, 2005. Energy in The 21st Century, World Scientific Publishing Company.
2. Yue M, Lambert H, Pahon E, Roche R, S. Jemei, and Hissel D, 2021. Hydrogen energy systems: A critical review of technologies, applications, trends and challenges, Renewable and Sustainable Energy Reviews, 146, 111-180, doi: 10.1016/J.RSER.2021.111180.
3. Koç E and Kaya K. 2015. Enerji Kaynakları–Yenilenebilir Enerji Durumu, Mühendis ve Makina, 56, 36-47
4. Aydın C, 2022. Enerji Arz Güvenliği ve Türkiye: Doğal Gaz Tedarik ve Bağımlılıkları Açısından İnceleme, Malatya Turgut Özal Üniversitesi İşletme ve Yönetim Bilimleri Dergisi, 3/2, 87-103.
5. Zhiznin S Z, Shvets N N, Timokhov V M and Gusev A L, 2023. Economics of hydrogen energy of green transition in the world and Russia, Part I, Int J Hydrogen Energy, doi: 10.1016/J.IJHYDENE.2023.03.069.
6. Johnston B, Mayo M C and Khare A, 2005. Hydrogen: the energy source for the 21st century, Technovation, 25,/6, 569-585.
7. Dixon R K, 2007. Advancing Towards a Hydrogen Energy Economy: Status, Opportunities and Barriers, Mitigation and Adaptation Strategies for Global Change, 12, 325–341.
8. Clark W W and Rifkin J, 2006. A green hydrogen economy, Energy Policy, 34/17, 2630-2639.
9. Veziroglu T N, 2000. Quarter century of hydrogen movement 1974–2000, International Journal of Hydrogen Energy, 25/12, 1143-1150.
10. Melaina M W, Antonia O and Penev M, 2013. Blending hydrogen into natural gas pipeline networks: a review of key issues (NREL/TP5600-51995). NREL. https://www.nrel.gov/docs/fy13osti/51995.pdf.
11. Sherif S A, Goswami D Y, Stefanakos E L and Steinfeld A (Eds.), 2014. Handbook of hydrogen energy, CRC Press.
12. Götz M, Lefebvre J, Mörs F, Koch A M, Graf F, Bajohr S. and Kolb T, 2016. Renewable Power-to-Gas: A technological and economic review, Renewable Energy, 85, 1371-1390.
13. Ozturk, M., Sorgulu, F., Javani, N., & Dincer, I., 2023. An experimental study on the environmental impact of hydrogen and natural gas blend burning. *Chemosphere*, *329*, 138671.
14. Özcan, M. D., Özcan O. & Akın A.N., 2020. Thermodynamic modelling and optimization of oxy-reforming and oxy-steam reforming of biogas by RSM, Environmental Technology, 41:1, 14-28, DOI: 10.1080/09593330.2019.1639828
15. Rasul, M. G., Hazrat, M. A., Sattar, M. A., Jahirul, M. I., & Shearer, M. J. (2022). The future of hydrogen: Challenges on production, storage and applications. *Energy Conversion and Management*, *272*, 116326.
16. M. Kayfeci, A. Keçebas¸, M. Bayat. Chapter 3 - Hydrogen production. in: F. Calise, M.D. D'Accadia, M. Santarelli, A. Lanzini, D. Ferrero, (Eds.), Solar Hydrogen Production. Academic Press2019. pp. 45-83.
17. Çebi, C., & Özdemir, K. A. (2021). Cyclical variation of the fiscal multiplier in Turkey. *Emerging Markets Finance and Trade*, *57*(2), 495-509.

CLEAN ENERGY DEMAND: EVALUATING THE USE OF HYDROGEN IN ELECTRICITY GENERATION FROM A CORPORATE COST PERSPECTIVE

[1]Kerem Çolak, [2]Bora Yenihan, [3]Orhan Özcan
[1]Kocaeli University, Hereke Asım Kocabıyık Vocational School, Textile, Clothing, Shoes and Leather, Textile Technology Program, Kocaeli/Türkiye
[2]Kocaeli Üniversitesi, Siyasal Bilgiler Fakültesi, Çalışma Ekonomisi ve Endüstri İlişkileri, Kocaeli/Türkiye
[3]Kocaeli University, Faculty of Engineering, Department of Chemical Engineering, Kocaeli/Türkiye
kerem.colak@kocaeli.edu.tr, bora.yenihan@kocaeli.edu.tr, orhan.ozcan@kocaeli.edu.tr

ABSTRACT
For nearly three centuries, efforts have been ongoing to meet the growing energy demand that began with the Industrial Revolution. While technological advancements continue, energy policy and research increasingly emphasize clean and renewable sources. Fossil-based energy, still widely used, is both finite and environmentally harmful, making the shift to sustainable alternatives urgent. Electricity plays a central role due to its potential for clean end-use; however, challenges in its generation and storage persist. Hydrogen has emerged as a promising solution for clean energy storage. Though not a primary energy source, its role as an energy carrier strengthens its importance in future energy systems. Environmentally responsible hydrogen production and storage also carry broader societal implications. This study employs Aspen HYSYS simulation software, using adaptations from prior research, to simulate the properties and flow rates of hydrogen, natural gas, and their blends. The natural gas composition was obtained through a literature review. Economically, hydrogen-natural gas blends could offer advantages in future regulatory contexts, such as carbon taxation, due to their lower emissions. However, current findings show that electricity generation using hydrogen-natural gas blends remains more expensive than natural gas, making it economically unviable under present electricity generation conditions.

Keywords: Energy**,** Hydrogen, Electiricity

1. INTRODUCTION

The Industrial Revolution represents a pivotal turning point in humanity's energy demands and the utilization of energy from various sources. Prior to this period, both the concept of production and the associated production relationships were relatively rudimentary, and the role of energy and its sources in human life was arguably minimal. However, the transformation in production practices brought about by the Industrial Revolution introduced new energy sources and significantly increased the demand for energy. Initially, production relied on steam power [1], but it later progressed through distinct phases with the advent of electricity [2] and internal combustion engines [3]. In the contemporary era, clean and renewable energy has become one of the most widely debated topics. The emergence of hydrogen as a potential energy source, and the concept of a hydrogen economy, gained prominence following the Hydrogen Economy Miami Energy Conference (THEME) in 1974 [4], which marked a critical milestone in discussions on renewable energy.
Hydrogen, regarded as a significant alternative among clean energy sources, consists of a single proton and electron, and is the most abundant element in the universe [5-6]. In contemporary discussions on decarbonization, hydrogen is increasingly associated with economic frameworks and is widely viewed by researchers as a promising energy carrier of the future. Although the concept of the hydrogen economy is not new, it has gained renewed attention based on the idea that future energy demands could be met through hydrogen-based systems [7]. Importantly, hydrogen is not a primary energy source but rather an energy carrier [8]. In this context, Boretti (2021) argues that a hydrogen economy on its own may lack substantial impact, but it could serve as a valuable complement to a broader electricity-based economy [9].
Electric energy plays a vital role in contemporary society. It is a critical component in sectors such as heating, cooling, and water purification, offering environmentally sustainable solutions. There is considerable potential for generating electricity from renewable sources to mitigate environmental impact. However, as in many sectors today, fossil fuels remain a dominant source in electricity generation, resulting in severe environmental consequences [10]. At this point, hydrogen is increasingly emphasized as a chemical energy storage medium for storing electricity generated from renewable sources [11]. Currently, energy production and consumption are largely based on fossil fuels, which are responsible for approximately two-thirds of global greenhouse gas emissions. Therefore, substantial transformations in the energy sector are essential to advance the global energy transition toward a carbon-neutral society. Hydrogen, in this regard, has the potential to accelerate the shift to clean and renewable energy systems while enhancing the stability and reliability of power grids [12].
Regarding the ongoing transition to green and carbon-neutral energy vectors, natural gas (NG) and hydrogen are emerging as critical components of future energy systems. By the 2030s, although green hydrogen is expected to become a competitive solution among alternative energy sources, large-scale storage remains a significant challenge. Salt caverns, while effective, are geographically limited; compressed hydrogen has very low energy density and high storage costs; and hydrogen liquefaction requires approximately 10 kWh/kg (nearly one-third of hydrogen's lower heating value (LHV)) as well as extremely low cryogenic temperatures (-253 °C). Currently, green hydrogen cannot fully replace

natural gas as a long-term energy storage solution due to the lack of economically viable and scalable storage technologies. Therefore, the transition to a green hydrogen economy will be gradual, dependent on both technological advancements and economic feasibility. In the short- to mid-term, natural gas is expected to play a pivotal role in the energy transition due to its significantly lower carbon intensity compared to coal and petroleum-based fuels [13]. Integrated natural gas and hydrogen solutions may serve as an essential step in achieving a fully decarbonized energy system.

The ever-growing global population, along with the parallel rise in individual and societal needs, has driven energy demand to unprecedented levels. Despite significant technological advancements, humanity continues to rely heavily on fossil-based energy sources, which are finite and unsustainable. This reliance confronts societies with the dual challenges of resource depletion and escalating environmental degradation, both of which are becoming increasingly evident. In this regard, the transition to renewable and clean energy has emerged as a critical priority to reduce energy costs, preserve environmental quality, and mitigate the risks associated with resource scarcity. While electricity remains central to meeting modern energy demands, the ability to generate and store it in a renewable and environmentally friendly manner is of vital importance. Hydrogen, in this regard, stands out as a promising solution. Its potential to lower energy costs and enhance both societal well-being and economic resilience is of considerable significance.

This study aims to compare the costs of electricity generated in existing natural gas power plants in Türkiye when operated using a hydrogen-natural gas mixture. In this analysis, hydrogen will be integrated into the energy cycle at blending ratios of 15% and 30% [14]. The resulting electricity generation costs will then be compared, and the economic viability of this approach for the operating firm will be evaluated.

2. METHODOLOGY

All calculations to determine the properties and flow rates of hydrogen, natural gas, and their blend (comprising 15% hydrogen and 85% natural gas and 30% hydrogen and 70% natural gas by mole) were conducted using Aspen HYSYS simulation software. The natural gas composition was adopted from a previously reported study [15] and is presented in Table 1 alongside the blend composition. The components considered in the simulation included CH_4, C_2H_6, C_3H_8, C_4H_{10}, C_5H_{12}, C_6H_{14}, CO_2, N_2 and H_2. The Peng-Robinson (PR) property package, known for its high efficiency and reliability, was employed for the calculations, as described by Eq. (1) [16].

Table 1. Compositions of natural gas and hydrogen-natural gas blends used in the simulation.

	Mass Fractions (%)			Mole Fractions (%)		
	Blend (%15)	Blend (%30)	Natural Gas	Blend (%15)	Blend (%30)	Natural Gas
CH_4	82.85	80.56	84.53	78.45	64.60	92.29
C_2H_6	5.75	5.60	5.87	2.91	2.39	3.42
C_3H_8	2.76	2.69	2.82	0.95	0.78	1.12
C_4H_{10}	1.76	1.71	1.79	0.46	0.38	0.54
C_5H_{12}	0.65	0.63	0.66	0.14	0.11	0.16
C_6H_{14}	0.19	0.19	0.20	0.03	0.03	0.04
CO_2	0.66	0.65	0.68	0.23	0.19	0.27
N_2	3.39	3.29	3.45	1.84	1.51	2.16
H_2	1.99	4.70	0.00	15.00	30.00	0.00

$$P = \frac{RT}{V-b} - \frac{a\alpha}{V(V+b)+b(V-b)} \quad (1)$$

Table 2 outlines the operating conditions and various key properties of natural gas, pure hydrogen, and the hydrogen-natural gas blend (%15 and %30). All data were obtained from Aspen HYSYS under identical conditions (100 kPa and 15 °C), ensuring a consistent basis for comparison. Together, Tables 1 and 2 provide a comprehensive overview of how hydrogen blending alters the composition and fundamental properties of natural gas. These changes have significant implications for combustion efficiency, safety, transportation, and appliance compatibility, highlighting the importance of such analyses in evaluating hydrogen as a transitional fuel within existing gas infrastructure.

In the study conducted by Rasul et al. [17], data on hydrogen production and associated costs, originally reported by Kayfeci et al., are presented in Table 3. As noted, the cost data include both operational expenses and fixed investment costs for hydrogen production from fossil fuels, particularly natural gas. Considering the average fixed investment costs (referred to as capital costs in the table) and assuming a payback period of approximately eight years for each option, the cost of hydrogen per kilogram was calculated by Kayfeci et al. [18].

Table 2. Operating conditions and properties of natural gas, hydrogen, and their blend obtained from Aspen HYSYS.

Properties	Units	Natural Gas	Hydrogen	Blend (%15)	Blend (%30)
Pressure	kPa	100.00	100.00	100.00	100.00
Temperature	℃	15.00	15.00	15.00	15.00
Molecular Weight	kg/kmol	17.52	2.02	15.19	12.87
Mass Density	kg/m^3	0.73	0.08	0.64	0.54
Mass Enthalpy	kJ/kg	-4317.51	-141.02	-4234.24	-4120.93
Mass Entropy	kJ/kgK	10.53	60.59	11.76	13.28
Mass Exergy	kJ/kg	-1.49	-13.77	-1.74	-2.07
LHV Molar Basis (Std)	MJ/kmole	833.73	241.94	744.96	656.19
LHV Mass Basis (Std)	MJ/kg	47.60	120.01	49.04	51.00
LHV Vol. Basis (Std)	MJ/m^3	35.34	10.22	31.55	27.78
Wobbe Index	MJ/m^3	50.32	45.88	48.42	46.52

Table 3. Comparison of hydrogen production costs by method.

Process Energy	Source	Feedstock	Capital cost (M$)	Hydrogen cost ($/kg)
SMR with CCS	Fossil fuels	NG	226.4	2.27
SMR without CCS	Fossil fuels	NG	180.7	2.08
ATR of methane with CCS	Fossil fuels	NG	183.8	1.48
Methane pyrolysis	Internally generated steam	NG	-	1.59-1.70

3. RESULTS AND DISCUSSION

As of December 2024, Turkey has a total installed capacity of 24,673 MW in natural gas power plants. These facilities are combined cycle power plants, capable of generating electricity not only from natural gas combustion but also through the conversion of waste heat into steam. Additionally, by incorporating a third-stage steam recovery system, these plants have the potential to produce hydrogen. In this analysis, it is assumed that all natural gas power plants operate as combined cycle systems. The economic feasibility of a new scenario has been evaluated, wherein these plants produce hydrogen, and a portion of the hydrogen is integrated into the gas turbine fuel mixture (comprising both natural gas and hydrogen) during the initial stage of electricity generation. Based on the unit cost data presented in Table 3, the total fuel costs for plants utilizing hydrogen production have been recalculated and are presented in Table 4.

Table 4: Comparison of a 30% hydrogen blend based on equal energy equivalence at the same lower heating value (LHV).

Month	NG Cost ($/m^3)	NG Volume (Mm^3)	Total NG Cost (M$)	Simulated NG Volume (Mm^3)	Simulated H_2 Volume (Mm^3)	H_2 Cost ($/m^3)	Total NG+H_2 Cost (M$)
December	0.52	1660.00	854.90	1476.38	632.74	0.16	864.03
November	0.53	1380.00	724.50	1227.36	526.01	0.16	730.57
October	0.55	1071.00	584.77	952.53	408.23	0.16	586.99
September	0.55	1231.00	681.97	1094.84	469.22	0.16	683.44
August	0.54	1703.00	916.21	1514.63	649.13	0.16	921.25
July	0.54	1553.00	843.28	1381.22	591.95	0.16	847.01
June	0.53	985.00	525.01	876.05	375.45	0.16	528.46
May	0.53	809.00	432.01	719.52	308.36	0.16	434.76
April	0.53	553.00	293.09	491.83	210.79	0.16	295.21
March	0.51	996.00	511.94	885.83	379.64	0.16	517.53
February	0.53	693.00	367.29	616.35	264.15	0.16	369.95
January	0.54	831.00	449.57	739.08	316.75	0.16	451.75
Total		13465.00	7184.54	11975.61	5132.41		7230.95

Under the specified assumptions, Table 4 compares the scenario in which natural gas power plants generate electricity using a fuel mixture of 30% hydrogen and 70% natural gas against the baseline scenario where plants operate with 100% natural gas. As observed, despite fluctuations in exchange rates, electricity production costs for plants using 100% natural gas remain more favorable than those using the hydrogen-natural gas mixture. In such a scenario, firms facing increased production costs may adopt a more rational strategy by selling the hydrogen through domestic distribution channels rather than using it for electricity generation. When the analysis is repeated for a 15% hydrogen blend, production costs are found to be approximately 50% lower compared to the 30% blend. As a result, power plants are unable to achieve the economies of scale necessary to significantly reduce costs. This inability to scale affects the anticipated economic benefits of increasing hydrogen content. Therefore, under present conditions, electricity generation using a hydrogen-natural gas mixture is not considered economically viable.

4. CONCLUSIONS

This study evaluates the use of hydrogen-natural gas blends in existing natural gas power plants in Turkey from both technical and economic perspectives. Simulations and analyses indicate that integrating 15% and 30% hydrogen blends into combined cycle plants is not economically viable under current conditions. From an economic perspective, the low carbon emission potential of hydrogen-natural gas blends may offer a competitive edge under future regulatory frameworks, such as carbon taxation. However, current analyses indicate that electricity production with H_2-natural gas blend remains costly and is not yet competitive with existing electricity generation costs based solely on natural gas. Considering capital investment payback periods and operational expenditures, hydrogen blending does not present a viable economic solution to produce electricity in the short term. In the future, increasing the cost-effectiveness of hydrogen through technological innovations and efficiency improvements may enable the achievement of economies of scale. In this regard, advancements in hydrogen production technologies, along with infrastructure investments, will be essential to facilitate a broader energy transition. It is crucial to implement both technological and economic policies that support the integration of hydrogen and natural gas in hybrid energy systems, thereby promoting more sustainable and environmentally responsible energy solutions.

REFERENCES

1. Vinitha, K., Prabhu, R. A., Bhaskar, R., & Hariharan, R. (2020). Review on industrial mathematics and materials at Industry 1.0 to Industry 4.0. Materials Today: Proceedings, 33, 3956-3960.
2. Yin, Y., Stecke, K. E., & Li, D. (2018). The evolution of production systems from Industry 2.0 through Industry 4.0. International Journal of Production Research, 56(1-2), 848-861.
3. Sharma, A., & Singh, B. J. (2020). Evolution of industrial revolutions: A review. International Journal of Innovative Technology and Exploring Engineering, 9(11), 66-73.
4. Veziroglu T N, 2000. Quarter century of hydrogen movement 1974–2000, International Journal of Hydrogen Energy, 25/12, 1143-1150.
5. Zhiznin S Z, Shvets N N, Timokhov V M and Gusev A L, 2023. Economics of hydrogen energy of green transition in the world and Russia, Part I, Int J Hydrogen Energy, doi: 10.1016/J.IJHYDENE.2023.03.069.
6. Johnston B, Mayo M C and Khare A, 2005. Hydrogen: the energy source for the 21st century, Technovation, 25,/6, 569-585.
7. Fanchi, R. John (2005); Energy in The 21st Century, World Scientific Publishing Company.
8. Clark W W and Rifkin J, 2006. A green hydrogen economy, Energy Policy, 34/17, 2630-2639.
9. Boretti A. The hydrogen economy is complementary and synergetic to the electric economy. Int J Hydrogen Energy 2021;46:38959e63. https://doi.org/10.1016/j.ijhydene.2021.09.121.
10. Stougie, L., Giustozzi, N., van der Kooi, H., & Stoppato, A. (2018). Environmental, economic and exergetic sustainability assessment of power generation from fossil and renewable energy sources. *International Journal of Energy Research*, 42(9), 2916-2926.
11. Melaina M W, Antonia O and Penev M, 2013. Blending hydrogen into natural gas pipeline networks: a review of key issues (NREL/TP5600-51995). NREL. https://www.nrel.gov/docs/fy13osti/51995.pdf.
12. Risco-Bravo A, Varela C, Bartels J and Zondervan E, 2024. From green hydrogen to electricity: A review on recent advances, challenges, and opportunities on power-to-hydrogen-to-power systems, Renewable and Sustainable Energy Reviews, 189, 113930.
13. Fioriti, D., Baccioli, A., Pasini, G., Bischi, A., Migliarini, F., Poli, D., & Ferrari, L. 2021. LNG regasification and electricity production for port energy communities: Economic profitability and thermodynamic performance. *Energy Conversion and Management*, *238*, 114128.
14. Ozturk, M., Sorgulu, F., Javani, N., & Dincer, I. 2023. An experimental study on the environmental impact of hydrogen and natural gas blend burning. *Chemosphere*, *329*, 138671.
15. Ozturk, M., Sorgulu, F., Javani, N., & Dincer, I., 2023. An experimental study on the environmental impact of hydrogen and natural gas blend burning. *Chemosphere*, *329*, 138671.
16. Özcan, M. D., Özcan O. & Akın A.N., 2020. Thermodynamic modelling and optimization of oxy-reforming and oxy-steam reforming of biogas by RSM, Environmental Technology, 41:1, 14-28, DOI: 10.1080/09593330.2019.1639828
17. Rasul, M. G., Hazrat, M. A., Sattar, M. A., Jahirul, M. I., & Shearer, M. J. (2022). The future of hydrogen: Challenges on production, storage and applications. *Energy Conversion and Management*, *272*, 116326.
18. M. Kayfeci, A. Keçebas¸, M. Bayat. Chapter 3 - Hydrogen production. in: F. Calise, M.D. D'Accadia, M. Santarelli, A. Lanzini, D. Ferrero, (Eds.), Solar Hydrogen Production. Academic Press2019. pp. 45-83.

NUMERICAL SIMULATION OF HIGH-TEMPERATURE PROTON EXCHANGE MEMBRANE FUEL CELL PERFORMANCE USING 3-D COMSOL MODEL

[1*]Murat Büyük, [1]Yagmur Nalbant Atak, [2]Yılser Devrim
[1] Atilim University, Faculty of Engineering, Department of Mechanical Engineering, Ankara, Türkiye
[1] Atilim University, Faculty of Engineering, Department of Energy Systems Engineering, Ankara, Türkiye

*Corresponding author e-mail: murat.buyuk@atilim.edu.tr

ABSTRACT
This study comprehensively investigates a High-Temperature Proton Exchange Membrane fuel cell (HT-PEMFC) using a 3-D COMSOL Multiphysics model. HT-PEMFCs are promising energy conversion devices, offering higher efficiency and durability compared to low-temperature PEM fuel cells. In this work, a 3-D model of the HT-PEMFC was developed to simulate its performance under various operating conditions. The model was validated by comparing its results with experimental data from the literature, ensuring the accuracy and reliability of the simulations. Subsequently, the effects of different operating parameters such as the operating temperature and pressure on the performance of the fuel cell were systematically examined. The results provide valuable insights into optimizing HT-PEM fuel cell design and operation, highlighting key factors that influence efficiency and longevity.
Keywords: HT-PEMFC, COMSOL Multiphysics, 3-D Model

1. INTRODUCTION

Fuel cells are electrochemical devices that convert chemical energy directly into electrical energy with high efficiency and low emissions. Especially, HTPEMFCs have emerged as a key technology, offering advantages such as improved efficiency, better tolerance to fuel impurities, and enhanced durability compared to low-temperature counterparts [1]. The modeling and simulation of fuel cell performance are critical to understanding and optimizing their operation. A 3-D model allows for a more accurate representation of the complex phenomena occurring within a fuel cell, such as multi-species transport, electrochemical reactions, and heat management. By simulating these processes in detail, engineers and researchers can gain valuable insights into performance at various operating conditions, identify potential design improvements, and optimize fuel cell efficiency. There are three-dimensional HT-PEMFC models in the literature. For example: Das and Gibson [2] studied the impact of multi-species transport on HTPEMFC performance using a 3-D model at 180°C. Their model was validated with experimental data and explored the effects of membrane thickness and conductivity on fuel cell efficiency. Xia et al. [3] studied the effects of operating temperature, membrane thickness, and catalyst layer thickness on the performance of HT-PEMFCs using a 3-D COMSOL model. Their results showed that increasing temperature improves fuel cell performance, while decreasing catalyst layer thickness and membrane thickness enhance performance as well. Losantos et al. [4] developed a methodology for characterizing electrochemical parameters in HT-PEMFCs using non-invasive data, validated with a 40-cell stack. Their approach combines genetic algorithms with 3-D simulations to analyze thermodynamic behavior efficiently. This method also paves the way for future studies on efficiency loss and degradation analysis.
In this study, a 3-D HT-PEMFC model was developed using COMSOL Multiphysics, and the results were compared and validated against data from a study [5] found in literature. Following this validation, the effects of several operating parameters, including temperature and pressure, on the performance of the fuel cell were systematically investigated. The analysis aimed to provide a deeper understanding of how these parameters influence the overall performance of the HT-PEMFC, contributing valuable insights for optimization in real-world applications.

2. MATHEMATICAL MODELING

A three-dimensional, isothermal, single-phase model is created in this study to simulate the performance of a HT-PEMFC using a polybenzimidazole (PBI) membrane. Figure 1 shows the computational domain of HT-PEMFC. The computational domain includes PBI membrane, anode and cathode gas flow channels, anode and cathode gas diffusion layers (GDLs). The catalyst layers are considered to have negligible thickness and are treated as boundary conditions between the GDL and the membrane.

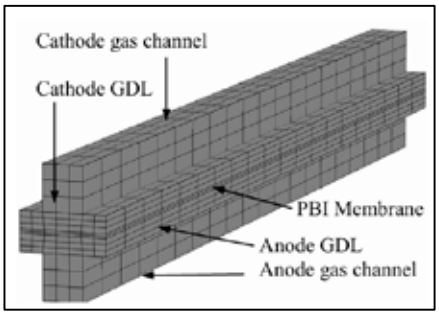

Fig 1. Computational domain of HT-PEMFC

The modeling assumptions for the HT-PEMFC include operating at temperatures above 100°C and around 2 atmospheric pressures, where water is only present in vapor form. Due to the unique properties of the PBI membrane, the water drag coefficient from the anode to the cathode is considered zero, unlike typical low-temperature PEM fuel cells with Nafion membranes. Additionally, proton transfer occurs via phosphoric acid doping in the membrane, the gas mixture is treated as ideal, the flow is incompressible and laminar, and the GDL is

assumed to be composed of isotropic and homogeneous porous materials [5]. The general governing equations (mass and momentum) used in the model are given below:

$$\nabla \cdot \boldsymbol{u} = 0 \quad (1)$$

$$\rho \boldsymbol{u} \nabla \cdot \boldsymbol{u} = \nabla[-p\boldsymbol{I} + \eta(\nabla \boldsymbol{u} + (\nabla \boldsymbol{u})^T)] \quad (2)$$

where $\boldsymbol{u}$ is the velocity vector of the gas mixture, m/s, ρ is the density of gas mixture, kg/m^3, p is the pressure, N/m^2, and η is the dynamic viscosity of the mixture, kg/m-s. The mass transport of multiple species throughout the entire computational domain, which includes both the gas channels and the gas diffusion layer, is modeled using the Maxwell-Stefan equation. This equation determines the fluxes of individual species based on their mass fractions. Below is the general expression of the Maxwell-Stefan equation [5]:

$$\nabla \cdot \left[-\rho w_i \sum_{j=1}^{N} D_{i,j} \left(\frac{M}{M_j}\left(\nabla w_j + w_j \frac{\nabla M}{M}\right) + (x_j - w_j)\frac{\nabla P}{P}\right)\right] = R_i \quad (3)$$

where $D_{i,j}$ is binary diffusion coefficient, x is the molar fraction, R_i is the reaction rate, w is the mass fraction, ρ is the density, and M is the molecular mass. In a PEM fuel cell, the total current is divided into two components: ionic current and electronic current. Protons move through the ionic conductor (membrane), creating an ionic current, while electrons flow solely through the solid electrode matrix, generating an electronic current. The equations governing current continuity are derived using Ohm's law [5].

$$\nabla \cdot (-\sigma_s \nabla \cdot \varphi_s) = 0 \quad (\textit{Electrons transport}) \quad (4)$$

$$\nabla \cdot (-\sigma_e \nabla \cdot \varphi_e) = 0 \quad (\textit{Protons transport}) \quad (5)$$

where φ is the phase potential, V; σ is the effective electric conductivity, S/m; and the subscribes s and e denote the solid phase property and electrolyte phase, respectively.

The fuel cell model described above is simulated using COMSOL Multiphysics software. The parameters for the base case utilized in the model are provided in Table 1.

Table 1. Operation and Geometric Parameters used in 3-D model [5]

Parameter	Value	Parameter	Value
Fuel Cell Temperature	100-180°C	Ionic Conductivity of membrane	7.86 S/m
Anode Stoichiometric Ratio	1.2	Membrane Thickness	100 µm
Cathode Stoichiometric Ratio	2	Electrical Conductivity of GDL	222 S/m
Open Circuit Voltage	0.93 V	Porosity of GDL	0.4
Pressure	101325 Pa	Permeability of GDL	1.18x10^{-11} m^2
Channel Patterns	Serpentine	Catalyst Layer Thickness	50 µm
Channel Cross Section Area	0.7844 mm^2	Anode exchange current density	10^5 A/m^2
Width of the shoulder	0.90932 mm	Cathode exchange current density	1 A/m^2

3. RESULTS AND DISCUSSION

In this section, the results of the 3-D modeling are first validated against the results of the reference study [5], and then the effects of operating temperature (100-180°C) and pressure (1 and 2.7 atm) are examined. Figure 2 shows the typical behavior of a fuel cell, where the cell voltage decreases as the current density increases due to activation, ohmic, and mass transport losses. In Figure 2, the polarization curves for T=180° at P=1 atm and P=2.7 atm are obtained from both numerical simulation and a reference study. The simulation results fit the reference study [5] results very well. Another key observation is that there appears to be no loss of concentration, even at elevated current densities. The reason for this can be explained by a high operational temperature where water exists in vapor form only.

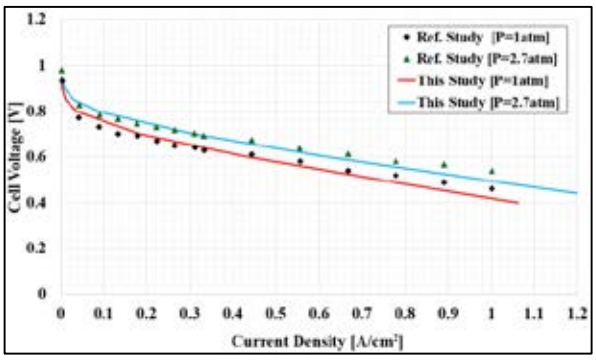

Fig. 2. Comparison of Polarization Curves with the Reference Study [5] at 180°C for 1 and 2.7 atm.

Figures 3-(a) and 3-(b) show the effects of operating temperature at 1 atm and 2.7 atm pressures, respectively. According to Figures 3-(a) and 3-(b), It is evident that increasing the operating temperature significantly improves the overall performance of the fuel cell. According to Figures, at higher temperatures, such as 180°C, the cell exhibits higher voltage values across the entire range of current densities. This enhancement is primarily due to improved reaction kinetics, increased proton conductivity of the membrane, and better water and heat management at elevated temperatures. In contrast, at lower temperatures, particularly at 100°C, the performance is notably reduced. This is attributed to slower electrochemical reaction rates and higher internal resistance, which result in greater voltage losses, especially at medium to high current densities.

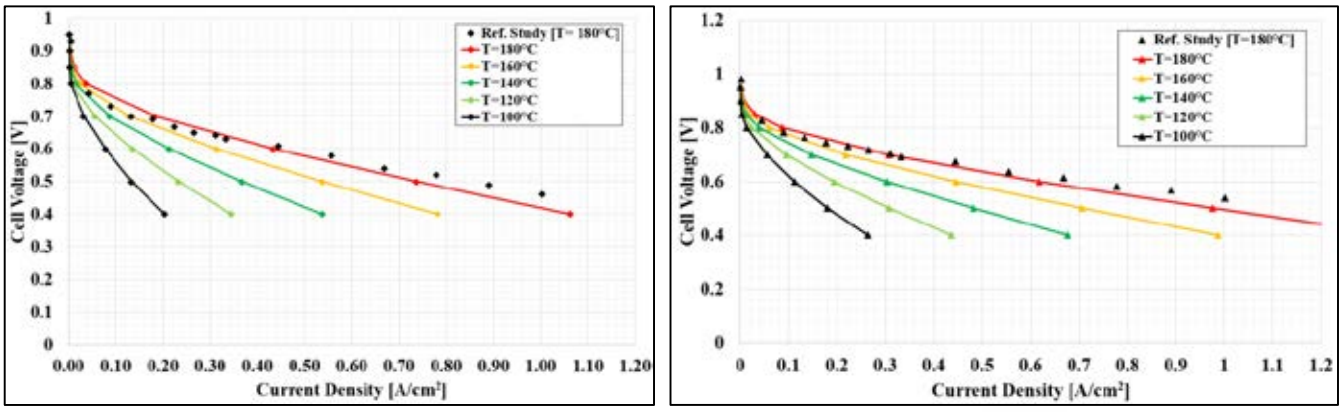

(a) (b)

Fig. 3. The effects of operating temperature on the performance of HT-PEMFC at; (a)1 atm and (b) 2.7.

According to Figure 3-(a) (P=1 atm), at a current density of 0.2 A/cm², the cell voltage at 180°C is approximately 0.72 V, while at 100°C it drops to around 0.50 V, representing a significant improvement of about 44%. Similarly, at 0.6 A/cm², the voltage at 180°C remains around 0.57 V, whereas it is only about 0.4 V at 160°C. These observations confirm that operating the HT-PEMFC at higher temperatures leads to better efficiency and overall performance. According to Figure 3-(b) (P=2.7 atm), at a current density of 0.1 A/cm², the cell voltage is approximately 0.82 V at 180°C, while it drops to around 0.68 V at 100°C. This represents a voltage loss of nearly 17% due to lower temperature operation. At 0.3 A/cm², the voltage at 180°C is around 0.72 V, compared to 0.47 V at 100°C, indicating a performance improvement of over 50%. The performance gap becomes even more pronounced at higher current densities. At 0.6 A/cm², the cell voltage at 180°C remains at about 0.62 V, whereas it falls to approximately 0.36 V at 100°C showing a difference of nearly 72%. When comparing Figures 3-(a) (P=1 atm) and Figure 3-(b) (P=2.7 atm), it is evident that increasing the operating pressure significantly improves the performance of the HT-PEMFC at all temperatures. Higher pressure enhances the partial pressure of reactant gases, which leads to better electrochemical reaction kinetics, reduced mass transport limitations, and overall higher cell voltage for the same current density. For example, at 180°C and 0.6 A/cm², the cell voltage at 1 atm is approximately 0.57 V, while at 2.7 atm it rises to around 0.62 V, indicating an improvement of about 0.05 V (nearly 9%). Similarly, at 160°C and 0.6 A/cm², the voltage increases from ~0.50 V (1 atm) to ~0.55 V (2.7 atm), which is a 10% gain. At lower temperatures, such as 100°C, the improvement is also noticeable: at 0.3 A/cm², the voltage increases from ~0.47 V at 1 atm to ~0.51 V at 2.7 atm.

Figure 4-(a), (b), and (c) illustrate the spatial distribution of mole fractions for hydrogen (H_2), oxygen (O_2), and water (H_2O), respectively, within an HT-PEMFC. In Figure 4 (a), the mole fraction of H_2 is highest at the inlet and gradually decreases along the flow path, indicating hydrogen consumption at the anode during the electrochemical reaction. Figure 4 (b) shows a similar trend for O_2, where the mole fraction decreases from the inlet to the outlet, reflecting its consumption at the cathode to form water. In contrast, Figure 4 (c) displays an increasing mole fraction of H_2O along the flow path, confirming water production due to the electrochemical reaction. The streamlines represent the total flux and visualize how each species is transported through the cell. These results demonstrate the expected behavior of reactant consumption and product formation in the HT-PEMFC, highlighting effective species transport and reaction zones within the system.

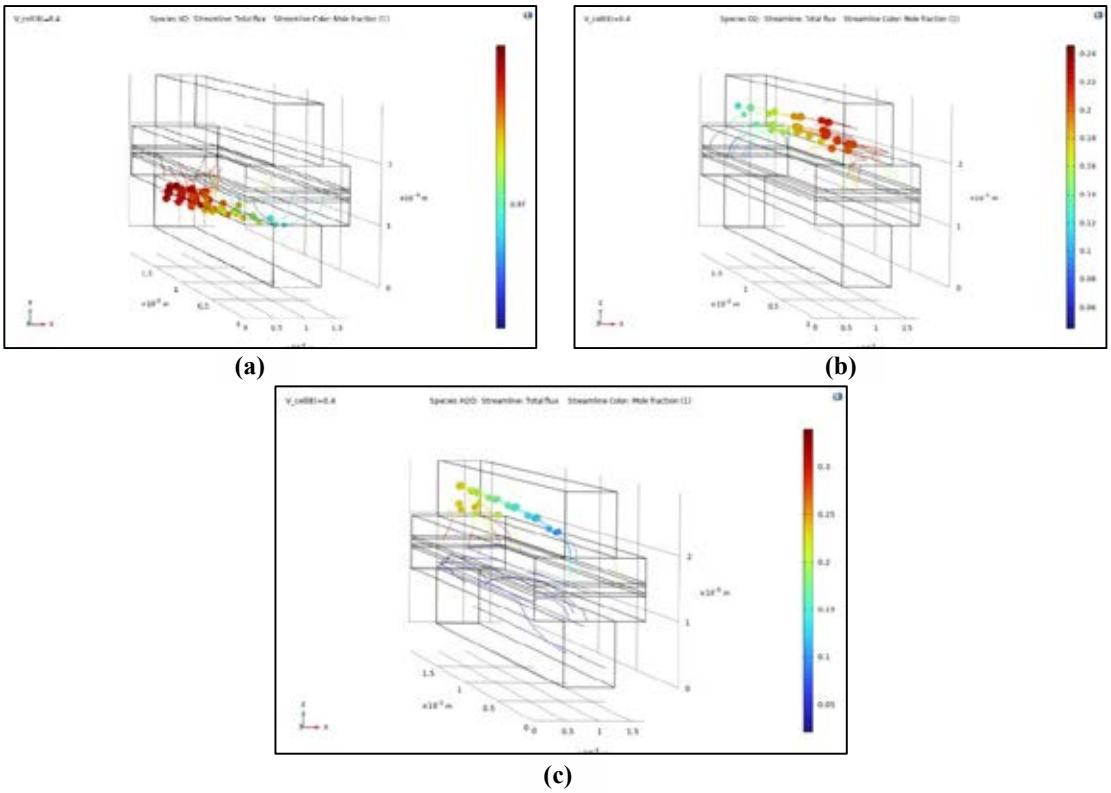

Fig. 4. Streamline representation of species transport and mole fraction distribution in an HT-PEMFC for (a) hydrogen (H_2), (b) oxygen (O_2), and (c) water (H_2O) (Streamlines indicate total flux, and colors represent local mole fractions.)

4. CONCLUSIONS

The main findings are given as:

- Higher operating temperatures (up to 180°C) significantly enhance HT-PEMFC performance by improving reaction kinetics, membrane conductivity, and water management, resulting in up to 72% higher cell voltage at high current densities compared to operation at 100°C.
- Increased operating pressure (from 1 atm to 2.7 atm) improves fuel cell performance across all temperatures by enhancing reactant partial pressures and reducing mass transport limitations, leading to up to 10% voltage gains at typical current densities.
- Mole fraction distributions confirm proper species transport within the cell: H_2 and O_2 are consumed along the flow path, while H_2O is produced and increases downstream, indicating effective electrochemical activity.

REFERENCES

[1] Rasheed, R. K. A., Liao, Q., Caizhi, Z., & Chan, S. H. (2017). A review on modelling of high temperature proton exchange membrane fuel cells (HT-PEMFCs). *International journal of hydrogen energy*, *42*(5), 3142-3165.

[2] Das, S. K., & Gibson, H. A. (2021). Three dimensional multi-physics modeling and simulation for assessment of mass transport impact on the performance of a high temperature polymer electrolyte membrane fuel cell. *Journal of Power Sources*, *499*, 229844.

[3] Xia, L., Zhang, C., Hu, M., Jiang, S., Chin, C. S., Gao, Z., & Liao, Q. (2018). Investigation of parameter effects on the performance of high-temperature PEM fuel cell. *International Journal of Hydrogen Energy*, *43*(52), 23441-23449.

[4] Losantos, R., Montiel, M., Mustata, R., Zorrilla, F., & Valiño, L. (2023). Parameter characterization of HT-PEMFC stack with a non-isothermal 3D model. *Electrochimica Acta*, *468*, 142930.

[5] Ubong, E. U., Shi, Z., & Wang, X. (2008). A-3D-modeling and experimental validation of a high temperature PBI based PEMFC. *ECS Transactions*, *16*(2), 79.

METAL-ORGANIC FRAMEWORKS FOR HYDROGEN STORAGE

Selçuk Demir
Recep Tayyip Erdoğan University, Faculty of Arts and Sciences, Department of Chemistry,
Rize, Turkey

selcuk.demir@erdogan.edu.tr

ABSTRACT

Metal-organic frameworks (MOFs) have emerged as highly promising materials for hydrogen storage, offering tunable porosity, exceptional surface areas, and tailored chemical functionality. This review highlights key advancements in MOF design strategies—including open metal sites, ligand functionalization, and lithium doping—that enable superior hydrogen adsorption capacities, with leading frameworks like NU-1501-Al and MOF-5 exceeding U.S. DOE 2025 targets (14 wt% and 51.9 g/L, respectively). Experimental and computational studies reveal critical structure-performance relationships, emphasizing the role of pore geometry (optimal 12–15 Å) and adsorption enthalpy (15–20 kJ/mol) in optimizing storage efficiency. While grand canonical Monte Carlo (GCMC) simulations and machine learning accelerate material discovery, challenges persist in stability, scalable synthesis, and system integration. Overcoming these barriers through interdisciplinary approaches will be essential for transitioning MOF-based hydrogen storage from laboratory breakthroughs to commercial reality in the clean energy landscape.

Keywords: Hydrogen storage, Metal-organic frameworks, Physisorption, Computational screening, DOE targets

1. INTRODUCTION

The growing global energy demand and climate change concerns have positioned hydrogen as a pivotal clean energy carrier. Despite its high energy density (142 MJ/kg)—three times that of fossil fuels—hydrogen's low density (0.07 g/cm³ in liquid form) and storage challenges limit practical applications. Conventional methods like high-pressure gas (700 bar) and cryogenic liquid hydrogen (-253°C) remain prevalent but pose significant safety risks and energy efficiency issues [1]. In this context, Metal-Organic Frameworks (MOFs), with their nanoporous structures and tunable chemical properties, offer a promising solution through physisorption-based storage, addressing these challenges effectively [2]. The 1292 publications obtained with searching the terms "metal-organic framework*" and "hydrogen storage" on Scopus is an indication of the interest in the subject (Figure 1). Figure 2 shows the comparison of the performances of different hydrogen storage techniques [3] with respect to the Department of Energy (DOE) targets [4].

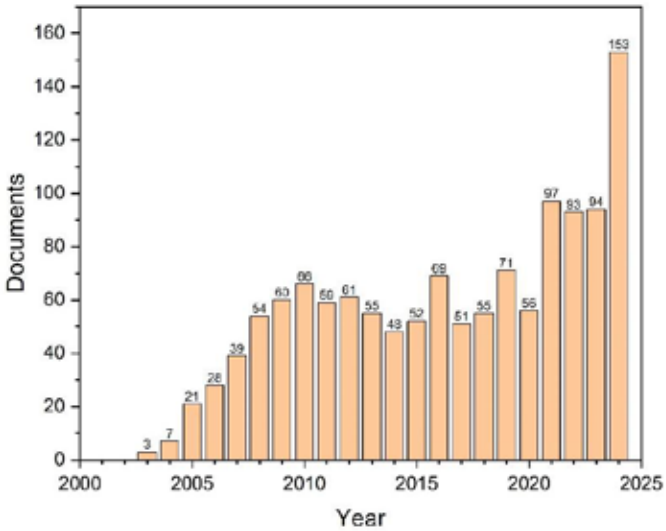

Fig. 1. Publications with topics "metal-organic framework*" and "hydrogen storage" searched in title, abstract and keywords (source: Scopus in April 2025)

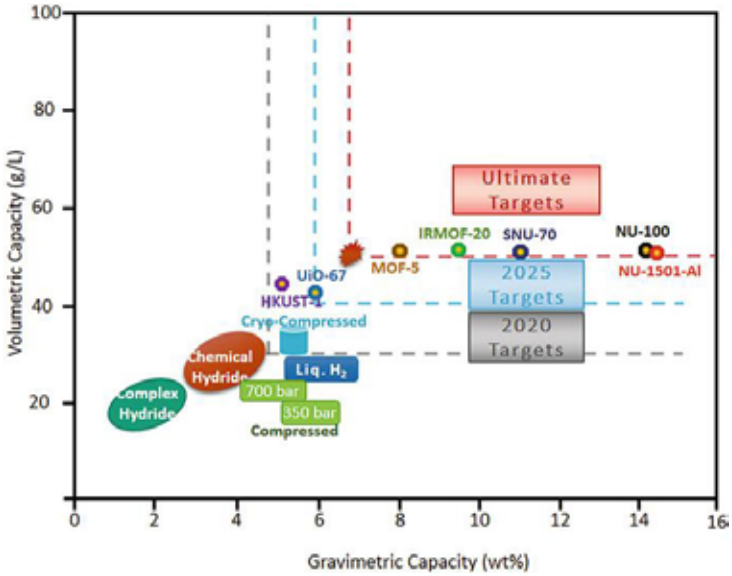

Fig. 2. Comparison of the performances of different hydrogen storage techniques with respect to the DOE targets. Hydrogen delivery capacities of the MOFs were used at material level in this figure, and when packing density at large scale is considered, a 25% decrease of capacity should be expected. (Reprinted with permission from ref. [3], Copyright 2022, Springer)

2. FUNDAMENTAL PROPERTIES AND DESIGN PRINCIPLES OF MOFS

The hydrogen storage performance of MOFs is governed by factors such as crystalline structure, pore geometry, and chemical functionality. Structurally, MOFs consist of three-dimensional networks formed by metal ions/clusters and organic linkers. Their most remarkable feature is the precise control over pore size and surface chemistry during synthesis. For instance, UiO-series MOFs exhibit surface areas exceeding 1000 m²/g with exceptional water stability, while triptycene-based frameworks like NU-1501 achieve surface areas beyond 7000 m²/g. Adsorption enthalpy (ΔH) is another critical parameter; an ideal range of 15–20 kJ/mol balances high capacity with room-temperature operability.

3. EXPERIMENTAL ADVANCES AND PERFORMANCE METRICS

Recent experimental studies have significantly enhanced MOF performance for hydrogen storage. MOFs with open metal sites (e.g., HKUST-1) or lithium doping (e.g., MFU-4l-Li) demonstrate strong interactions with hydrogen molecules, achieving capacities above 10 wt% at 77 K. Under pressure swing (100 bar → 5 bar) and temperature swing (77 K → 160 K) conditions, materials like MOF-5 and IRMOF-20 exhibit volumetric capacities exceeding 50 g/L—surpassing the U.S. DOE's 2025 targets [3]. However, industrial adoption faces difficulties such as air/moisture stability, large-scale synthesis costs, and system integration challenges. Practical considerations like packing density and thermal management in tank designs further complicate the adaptation of lab-scale performance to real-world applications.

4. COMPUTATIONAL METHODS AND MATERIAL DISCOVERY

The design possibilities of MOFs (millions of possible combinations) necessitates computational approaches. Grand Canonical Monte Carlo (GCMC) simulations are widely used to predict hydrogen adsorption behavior under varying conditions. Screening 130,000 hypothetical MOFs revealed optimal pore sizes (12–15 Å) and porosities (~90%) [5]. Machine learning models, particularly those using energy-based descriptors, can predict storage capacities with ~90% accuracy, guiding experimental efforts [6]. These tools accelerate the discovery of high-performance materials, such as MFU-4l-Li, which achieved a record deliverable capacity of 54 g/L (experimentally validated at 47 g/L).

5. FUTURE PROSPECTS AND CHALLENGES

Commercializing MOF-based hydrogen storage requires addressing material stability, production costs, and system-level optimization. Future research should focus on enhancing mechanical robustness (e.g., cross-linked structures), improving stability under ambient conditions, and standardizing large-scale synthesis protocols. Granular or pelletized MOF forms must retain porosity for practical use. Thermal management systems (e.g., phase-change materials) and performance under impure hydrogen streams also demand attention. Interdisciplinary collaborations (materials science, chemical engineering, and energy systems) will be key to unlocking MOFs' full potential in the hydrogen economy within the next decade.

REFERENCES

1. Yürüm Y., Taralp, A. and Veziroglu, T.N. 2009. Storage of Hydrogen in Nanostructured Carbon Materials. International Journal of Hydrogen Energy 34:3784-3798.
2. Yaghi O.M., Kalmutzki M.J., and Diercks C.S. 2019. Introduction to Reticular Chemistry: Metal-Organic Frameworks and Covalent Organic Frameworks, Weinheim, Wiley.
3. Demir S., Altintas C., Keskin S., Topcu Y. 2022. Metal-Organic Frameworks for Hydrogen Storage. In: Gupta, R. (eds) Handbook of Energy Materials. Springer, Singapore.
4. https://www.energy.gov/eere/fuelcells/doe-technical-targets-onboard-hydrogen-storage-light-duty-vehicles, Accessed on March 15, 2025
5. Bobbitt N.S., Chen J., Snurr R.Q. 2016. High-Throughput Screening of Metal-Organic Frameworks for Hydrogen Storage at Cryogenic Temperature. Journal of Physical Chemistry C 120:27328-27341.
6. Bucior B.J., Bobbitt N.S., Islamoglu T., Goswami S., Gopalan A., Yildirim T., Farha O.K., Bagheri N. and Snurr, R.Q. 2019. Energy-based descriptors to rapidly predict hydrogen storage in metal–organic frameworks. Molecular Systems Design & Engineering 4:162-174.

HYDROGEN STORAGE PROPERTIES OF A ZIRCONIUM METAL-ORGANIC FRAMEWORK

*Selçuk Demir, Nuray Bilgin
Recep Tayyip Erdoğan University, Faculty of Arts and Sciences, Department of Chemistry,
Rize, Turkey

selcuk.demir@erdogan.edu.tr

ABSTRACT

Metal–organic frameworks (MOFs) composed of the bridging linkers and the metal ions are an very important class of porous materials employed for custom-designed purposes. Among the MOFs composed of carboxylate linkers, Zr-based MOFs have attracted great attention due to their high thermal and chemical stability, which are important for practical applications, including hydrogen (H_2) storage. Herein, using 6,6'-dimethyl-2,2'-bipyridine-5,5'-dicarboxylic acid (H_2Me_2bipy) we prepared a Zr-based MOF [MOF-553, $Zr_6O_4(OH)_4(Me_2Bipy)_6$] with usable Lewis basic sites of the linker. Later H_2 adsorption capacity of MOF-553 were measured at atmospheric pressure.

Keywords: Hydrogen storage, Metal-organic frameworks, Zirconium

1. INTRODUCTION

The increasing global energy demand and growing concerns about climate change have established hydrogen as a critical clean energy carrier. Although hydrogen boasts a high energy density (~142 MJ/kg) its low density (0.07 g/cm³ in liquid form) and storage challenges hinder practical applications. Traditional storage techniques, like high-pressure gas (700 bar) and cryogenic liquid hydrogen (-253°C), continue to be prevalent but pose considerable safety hazards and energy efficiency limitations [1]. Physisorption-based storage addressing these challenges effectively [2]. With their microporous structures and adjustable chemical properties, metal-organic frameworks (MOFs) offer a viable solution to these risks. MOFs are a highly versatile class of porous crystalline materials composed of metal nodes connected by organic linkers. Their tunable properties make them suitable for various applications, including hydrogen and natural gas storage, atmospheric water harvesting, and carbon capture. Among MOFs, zirconium-based frameworks (Zr-MOFs) stand out due to their exceptional thermal and chemical stability, attributed to the strong Zr(IV)-carboxylate bonds. A well-known example, UiO-66, and its expanded analogs like UiO-67(bipy), feature the robust $Zr_6O_4(OH)_4(COO)_{12}$ cluster.

Herein, prepared MOF-553 ([$Zr_6O_4(OH)_4(Me_2bipy)_6$]) has a high density of Lewis-basic sites for H_2 capture while achieving superior water stability. The methyl groups not only protect the framework but may also enhance H_2 affinity through additional host-guest interactions.

2. MATERIALS AND METHODS

Synthesis of UiO-67(Me_2Bipy) (MOF-553): MOF-553 was prepared as reported before [3]. H_2Me_2bipy (43.5 mg, 0.159 mmol) was placed in a beaker with 5 mL N,N-dimethylformamide (DMF) and dissolved via sonication. After the addition of a 5 mL DMF solution of $ZrCl_4$ (37.5 mg, 0.160 mmol), the mother solution was stirred for 10 min and formic acid (2 mL) was added. The solvent mixture was incubated at 120 °C for 24 h. After cooling to room temperature, the corresponding pale yellow materials were collected by vacuum filtration, washed with DMF (3 × 10 mL), followed by soaking in acetonitrile (MeCN) for 3 days, in which the solution was exchanged with fresh MeCN (10 mL) every 24 h. After 3 days of soaking, the solids were collected via vacuum filtration and dried under vacuum at 120 °C for 24 h.

3. RESULTS AND DISCUSSION

MOF-553 was prepared via the reaction of $ZrCl_4$ with H_2Me_2bipy in DMF as reported (Fig. 1a). It consists of the hexanuclear zirconium clusters, [$Zr_6O_4(OH)_4(COO)_{12}$], that is connected by 6 Me_2bipy linkers to 3D. The crystal structure suggests that MOF-553 has pores. The porosity verified via nitrogen adsorption experiments at -196 °C. Calculated BET surface area is 2164 m^2/g and the total pore volume is 0.39 cm^3/g for MOF-553.

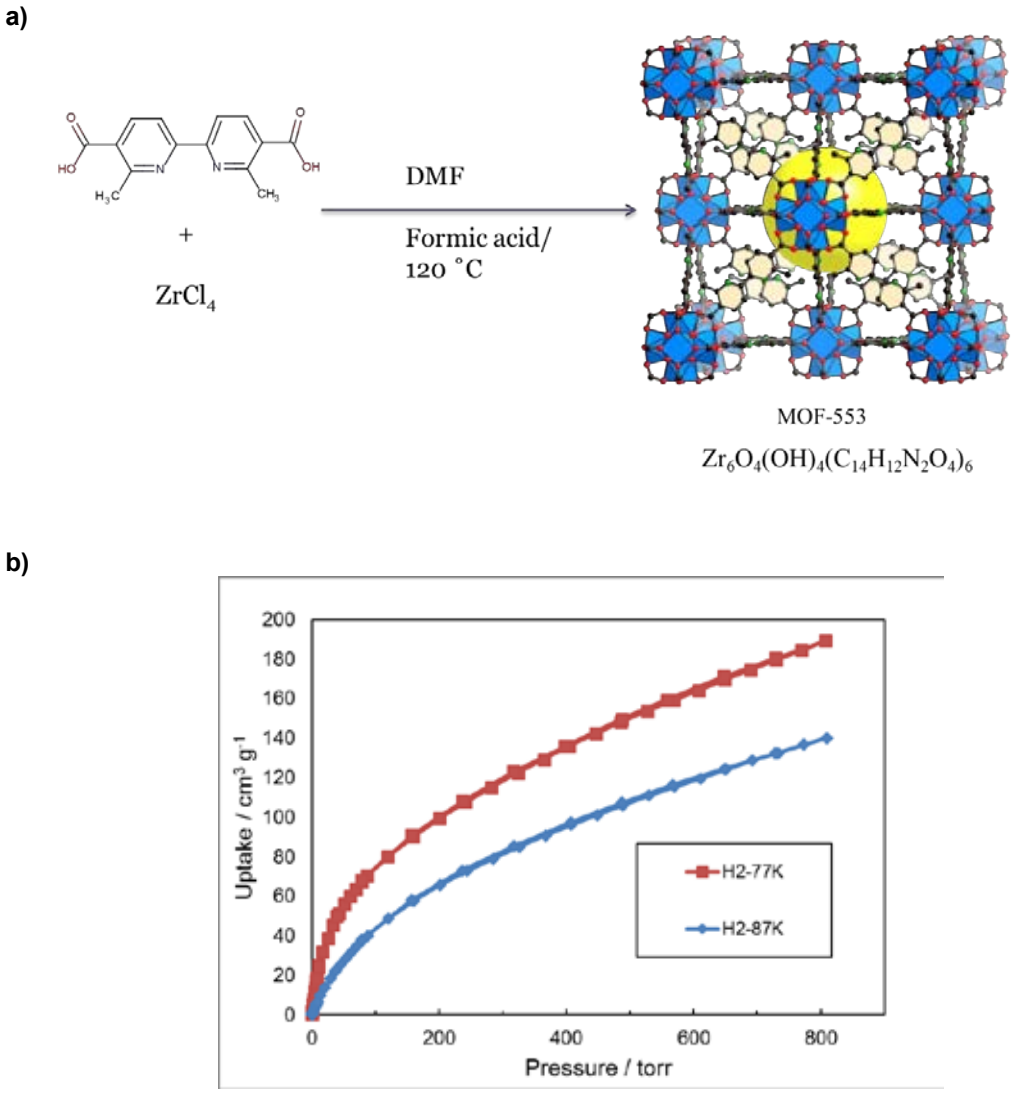

Fig. 1. Crystal structure (a) and H_2 adsorption isotherms of MOF-553 at 273 K (b)

4. CONCLUSIONS

The hydrogen uptake capacity of MOF-553 is 189.2 cm^3/g at 273 K and 807 torr pressure, and the calculated Qst value is 8.2 kJ mol^{-1}.

ACKNOWLEDGEMENT

This work was financially supported by the Scientific and Technological Research Council of Turkey, (TÜBİTAK) under Project Number 112T956.

REFERENCES

1. Yürüm Y., Taralp, A. and Veziroglu, T.N. 2009. Storage of Hydrogen in Nanostructured Carbon Materials. International Journal of Hydrogen Energy 34:3784-3798.
2. Demir S., Altintas C., Keskin S., Topcu Y. 2022. Metal-Organic Frameworks for Hydrogen Storage. In: Gupta, R. (eds) Handbook of Energy Materials. Springer, Singapore.
3. Demir S., Bilgin N., Cepni HM., Furukawa H., Yilmaz, F., Altintas, C., and Keskin S. 2021. Enhanced water stability and high CO_2 storage capacity of a Lewis basic sites-containing zirconium metal–organic framework. Dalton Transactions, 50:16587-16592.

BOOSTING THE PERFORMANCE OF LAYERED TITANATE IN PHOTOCATALYTIC WATER SPLITTING

[1,2]Tugce Ustunel, [3]José Julio Gutiérrez Moreno, [1,2,3]Sarp Kaya,[4,5,]*Esmail Doustkhah
[1]Koç University Tüpraş Energy Center (KUTEM), 34450 Sarıyer, Istanbul, Turkey
[2]Materials Science and Engineering, Koç University, 34450 Sarıyer, Istanbul, Turkey
[3]Department of Chemistry, Koç University, 34450 Sarıyer, Istanbul, Turkey
[3]Barcelona Supercomputing Center, Plaça d'Eusebi Güell, 1-3, Barcelona 08034, Spain
[4]Hydrogen plus laboratory, Istinye University, Istanbul, Turkiye
[5]Chemistry Department, Faculty of Engineering and Natural Sciences, Istinye University, Sariyer, Istanbul 34396, Türkiye
*Corresponding author e-mail: esmail.doustkhah@istinye.edu.tr.

ABSTRACT Layered titanates, although they have large bandgaps, represent a fascinating class of two-dimensional (2D) materials with highly tunable structural and electronic properties, making them attractive candidates for advanced photocatalytic applications [1]. These materials, characterized by their perovskite-like layered frameworks, exhibit unique features such as ion-exchangeable interlayers, adjustable surface chemistry, and high theoretical surface area which needs to be activated by exfoliation. The intrinsic architecture of layered titanates allows for the precise manipulation of active sites and offers abundant opportunities to overcome the longstanding limitations of bulk photocatalysts, such as poor charge separation and limited surface reaction kinetics, and the large bandgaps.
One of the most promising strategies to unlock the full photocatalytic potential of layered titanates is through exfoliation and single atom loading, which can yield ultrathin nanosheets with dramatically increased specific surface area and exposed active facets. These exfoliated nanosheets provide ideal platforms for the rational design of photocatalysts at the atomic scale, including the immobilization of single-atom catalysts (SACs) [2]. The incorporation of single atoms into the 2D titanate matrix maximizes atomic utilization and introduces well-defined active sites, thereby enhancing charge carrier dynamics and catalytic selectivity.
Furthermore, the native interlayer spaces and surface defects of layered titanates can serve as interatomic cavities for hosting guest species such as water molecules, hydrogen and oxygen to conduct the watersplitting reaction (**Figure 1**). On the other hand, this can modulate the local electronic environment, leading to the formation of a mid-gaps and further contribute to photocatalysis. These confined sites offer favorable conditions for charge accumulation, adsorption, and activation of reactants — particularly for the photocatalytic hydrogen evolution reaction (HER). When synergistically combined, exfoliation, single-atom loading, and cavity engineering enable the construction of advanced photocatalysts with superior light-harvesting ability, optimized reaction pathways, and enhanced long-term stability.

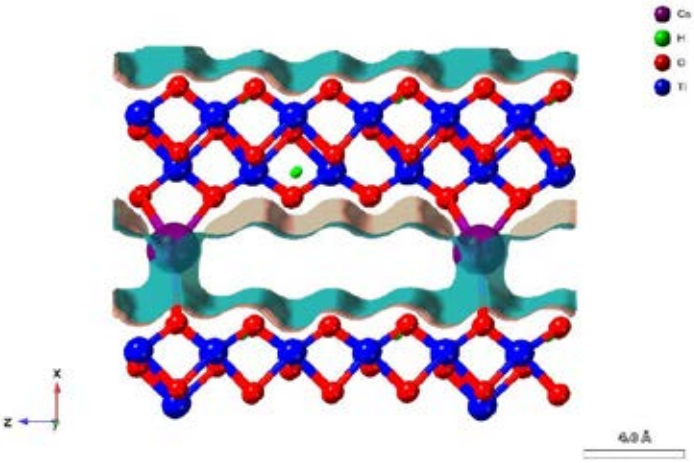

Fig. 1. Interatomic cavity in cesium layered titanate.

Keywords: Hydrogen generation, water splitting, layered titanate, photocatalysis, single atom catalysis, TiO_2.

ACKNOWLEDGEMENT
This research was supported by funding from the Japan Science and Technology Agency (JST) and TÜBİTAK (Project No. 123N224) as the EIG CONCERT-JAPAN program under the project entitled 2023-MLALH.

REFERENCES

1. E Doustkhah, MHN Assadi, K Komaguchi, N Tsunoji, M Esmat, N Fukata, Ide Y. 2021. In situ Blue titania via band shape engineering for exceptional solar H_2 production in rutile TiO_2. Applied Catalysis B: Environmental 297:120380
2. Ustunel T, Ide Y, Kaya S, Doustkhah E. 2023. Single-atom Sn-loaded exfoliated layered titanate revealing enhanced photocatalytic activity in hydrogen generation. ACS Sustainable Chemistry & Engineering 11 (8):3306-3315

ENHANCED PHOTOELECTROCHEMICAL PERFORMANCE OF CeO_2/TiO_2 HETEROSTRUCTURE FOR HYDROGEN AND OXYGEN EVOLUTION REACTIONS

*Milad Behroozi[1,2], Esmail Doustkhah[1,2]**
[1] *Hydrogen plus laboratory, Istinye University, Istanbul, Türkiye*
[2]*Chemistry Department, Faculty of Engineering and Natural Sciences, Istinye University, Sariyer, Istanbul 34396, Türkiye*
*Corresponding author e-mail: esmail.doustkhah@istinye.edu.tr

ABSTRACT Environmental pollution and the growing demand for clean, renewable energy have intensified research into photocatalysts such as titanium dioxide (TiO_2), known for its affordability, non-toxicity, and chemical stability. However, the anatase phase of TiO_2 has a wide band gap and suffers from rapid electron-hole recombination, limiting its photoactivity under sunlight. To overcome these limitations, we synthesized CeO_2-TiO_2 heterojunctions by calcination at 600°C, 700°C, 800°C, and 900°C. Cerium oxide (CeO_2), a rare-earth oxide with high UV absorption and excellent electron transport properties, was combined with TiO_2 to enhance charge separation and light harvesting. X-ray diffraction (XRD) fig1.c , analysis confirmed the formation of Ce-Ti bonds and effective integration between the two oxides. The resulting heterojunctions exhibited type-II band alignment, which promoted charge separation and suppressed recombination. Photocatalytic performance was evaluated using methylene blue (MB) as a model organic pollutant, and photoelectrochemical behavior was studied using linear sweep voltammetry (LSV) fig1.a, b. Among all synthesized samples, the CeO_2-TiO_2 composite prepared at 800°C showed the highest performance, suggesting enhanced electron transfer and improved photocatalytic activity [1]. These findings demonstrate the potential of temperature-optimized CeO_2-TiO_2 heterostructures in solar energy conversion and environmental remediation applications [2,3].

Keywords: Hydrogen generation, water splitting, layered titanate, photocatalysis, single atom catalysis, TiO_2.

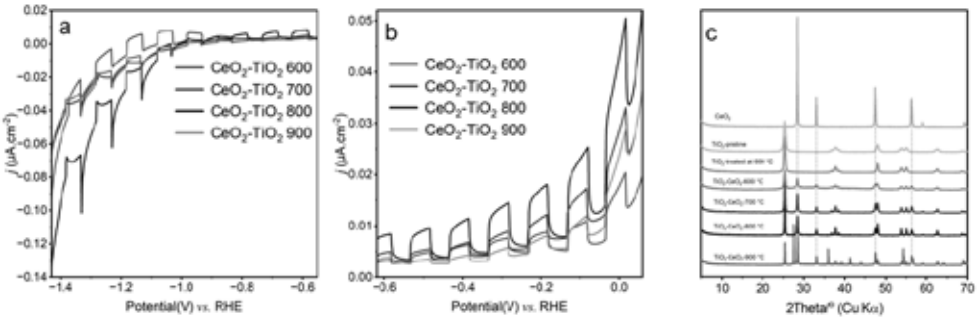

Fig. 1. Photoelectrochemical response LSV of CeO_2-TiO_2 heterostructures under light illumination: a) Hydrogen evolution reaction (HER); b) Oxygen evolution reaction (OER); c) X-ray diffraction (XRD) patterns of CeO_2-TiO_2 composites calcined at different temperatures.

ACKNOWLEDGEMENT
This research was further supported by funding from the Japan Science and Technology Agency (JST) and TÜBİTAK (Project No. 123N224) as the EIG CONCERT-JAPAN program under the project entitled 2023-MLALH.

REFERENCES

1. Doustkhah E, Luque R and Assadi MHN. 2023. ACS Sustainable Chemistry & Engineering Virtual Special Issue on Emerging Layered Nanomaterials for (Photo)(electro) catalytic Green H_2 Production. *ACS Sustainable Chemistry & Engineering* 11(18):6774–6775.
2. Fei H, Dong J, Arellano-Jiménez MJ, Ye G, Kim ND, Samuel EL, Peng Z, Zhu Z, Qin F, Bao J and Yacaman MJ. 2015. Atomic cobalt on nitrogen-doped graphene for hydrogen generation. *Nature Communications* 6(1):8668.
3. Jones TE, Teschner D and Piccinin S. 2024. Toward realistic models of the electrocatalytic oxygen evolution reaction. *Chemical Reviews* 124(15):9136–9223.

INTEGRATION OF METAL–ORGANIC FRAMEWORKS WITH THIN FILM TITANIUM DIOXIDE FOR ENHANCED PHOTOELECTROCHEMICAL HYDROGEN PRODUCTION

*Sepideh Sadighi[1,2] Esmail Doustkhah[1,2]**
[1] Hydrogen plus laboratory, Istinye University, Istanbul, Turkiye
[2]Chemistry Department, Faculty of Engineering and Natural Sciences, Istinye University, Sariyer, Istanbul 34396, Türkiye
*Corresponding author e-mail: esmail.doustkhah@istinye.edu.tr

ABSTRACT Porous and highly tunable materials such as metal–organic frameworks (MOFs) represent an appropriate platform to enhance photocatalytic and photoelectrochemical performance [1]. A well-known wide-bandgap semiconductor, titanium dioxide (TiO_2), was synthesized by the sol–gel method and employed as a photoactive substrate in the current study. Three different MOFs like Fe-MOF, Ni-MOF, and Nd-MOF were then uniformly coated onto the surface of TiO_2 to form composite photocatalysts. Photoelectrochemical activity of the resulting MOF/TiO_2 heterostructures was measured by performing linear sweep voltammetry (LSV) under chopped illumination (Figure1). Light-responsive current behavior was displayed by all composite samples, with intriguing differences in the magnitude and reversibility of the photocurrent. Among the samples, Fe-MOF/TiO_2 showed the highest photocurrent response, with Ni-MOF/TiO_2 demonstrating a similar response, indicating increased interfacial electron transfer and charge separation facilitated by the MOF coatings. Conversely, Nd-MOF/TiO_2, despite a higher baseline current, responded comparatively weaker and less clearly to light, most likely due to variations in its electronic structure or interaction with the TiO_2 substrate. These outcomes demonstrate that rational MOF–semiconductor composite design holds great promise for the creation of next-generation photoelectrocatalysts, particularly to produce sustainable hydrogen and other solar-driven energy-related conversions [2,3].
Keywords: Photocatalysis; TiO_2, Metal–Organic Frameworks (MOFs), Sol–Gel synthesis, Photoelectrochemical cells, green hydrogen, Linear Sweep Voltammetry (LSV)

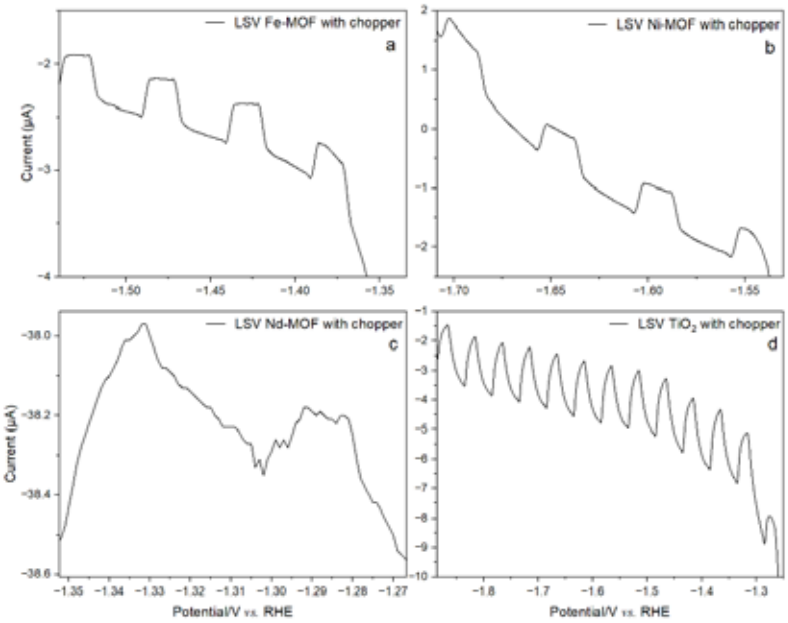

Fig. 1. Linear sweep voltammetry (LSV) curves of TiO_2 and MOF/TiO_2 composites: a) Fe-MOF/TiO_2; b) Ni-MOF/TiO_2; c) Nd-MOF/TiO_2; d) TiO_2 under chopped light illumination.

ACKNOWLEDGEMENT

This project is co-funded by TÜBİTAK and the SEA-Europe-JFS 2023 Wplast2Plast Project (project No. 224N737).

REFERENCES

1. Khan A, Le Pivert M, Ranjbari A, Dragoe D, Bahena-Uribe D, Colbeau-Justin C, Herrero C, Rutkowska-Zbik D, Deschamps J, Remita H. 2025. Cu-Based MOF/TiO2 Composite Nanomaterials for Photocatalytic Hydrogen Generation and the Role of Copper. Advanced Functional Materials 2501736.
2. Patricia DP, Solomon RV. 2025. Recent Advances in Lanthanide-based Metal-Organic Frameworks for 1 Photocatalytic Hydrogen Evolution Application. Energy Advances.
3. Musa EN, Yadav AK, Smith KT, Jung MS, Stickle WF, Eschbach P, Ji X, Stylianou KC. 2024. Boosting Photocatalytic Hydrogen Production by MOF-Derived Metal Oxide Heterojunctions with a 10.0% Apparent Quantum Yield. Angewandte Chemie International Edition. 14:63(42).

HYBRID HYDROGEN SYSTEMS FOR MITIGATING SUB SYNCHRONOUS OSCILLATIONS IN WEAK POWER GRIDS

Sulman Shahzad[1], Heybet Kilic[2]
[1]Department of Electrical Engineering, Islamia University of Bahawalpur, Bahawalpur 63100, Pakistan
[2] Department of Electric Power and Energy Systems, Dicle University, 21280 Diyarbakır, Turkey

* Corresponding authors: Heybet Kilic (heybet.kilic@dicle.edu.tr)

ABSTRACT

This study addresses the challenges of sub-synchronous (SSOs) in weak AC networks with high renewable energy penetration, focusing on the effectiveness of hybrid energy storage systems (HESS). By combining hydrogen-based energy storage with electric double-layer capacitors (EDLCs), HESS provides comprehensive damping for slow and fast oscillatory dynamics. Simulation results demonstrate the hybrid system's ability to mitigate grid instability caused by step changes in solar insolation, transmission line disconnections, and sudden load variations. The findings highlight significant improvements, including a 70% reduction in oscillation amplitude, enhanced phase stability, and quicker recovery times, underscoring HESS as a critical solution for stabilizing weak grids.

Keywords: Hydrogen energy systems, hydrogen-based grid stabilization, hybrid hydrogen energy solutions, renewable energy sources

1. INTRODUCTION

The worldwide transition to renewable energy sources (RES) has been crucial in alleviating climate change and diminishing reliance on fossil fuels. Photovoltaic power plants (PvPPs) and hydrogen-based energy storage systems (HESS) are among the most promising RES technologies. These systems have become essential to contemporary power networks owing to their efficiency, scalability, and ecological advantages. Nonetheless, their incorporation into weak alternating current (AC) networks has posed considerable hurdles, especially regarding the preservation of grid stability. Weak AC networks, defined by low short-circuit ratios (SCRs), are particularly susceptible to disturbances, rendering them prone to sub-synchronous oscillations (SSOs) [1]. If unmitigated, these oscillations can destabilize the grid, disrupt operations, and diminish the overall efficiency of power systems. The growing integration of RES in contemporary energy systems has altered conventional grid dynamics. In contrast to traditional synchronous generators that offer intrinsic inertia via mechanical coupling, RES, such as photovoltaic power plants, rely on inverter-based generation units. These inverters, albeit efficient, lack physical inertia and replicate grid dynamics through sophisticated control mechanisms. SSO, generally occurring within the frequency range of 10–60 Hz, results from intricate feedback interactions between grid dynamics and the control systems of inverters, including phase-locked loops (PLLs) and current control loops (CCLs). SSO in weak AC networks are dynamic phenomena that amplify with time, leading to significant repercussions such as equipment failure, voltage instability, and potential large-scale blackouts [2]. The principal factors leading to SSOs are inverters' dynamic properties, weak grids' low inertia, and inadequately calibrated control systems. These oscillations become crucial in weak AC networks with significant RES penetration. Traditional synchronous generators are frequently supplanted with IBRUs, eliminating the physical connection between generation units and the grid, hence exacerbating instability. Furthermore, the nonlinear behavior of inverters during grid disruptions complicates the prediction and mitigation of SSOs. The incorporation of PvPPs and HESS in weak AC networks intensifies these difficulties. Voltage and frequency instability frequently occur due to the substantial alteration of the grid's impedance profile by the presence of PvPPs [3]. This increased sensitivity to voltage and frequency fluctuations often results in oscillatory modes that are challenging to control. Furthermore, weak grids lack the intrinsic damping properties of synchronous generators, rendering them less capable of mitigating oscillations. These problems highlight the necessity of designing sophisticated mitigation measures to guarantee weak AC networks' steady and dependable functioning.This study aims to investigate the underlying causes of SSOs in weak AC networks with significant RES integration, create a hybrid energy storage system that integrates hydrogen storage with EDLCs for effective oscillation reduction, and validate the proposed solution. This research seeks to enhance the existing knowledge on RES integration and grid stability while providing practical guidance for implementing hybrid systems in weak alternating current networks.

2. METHODOLOGY

The simulation model captures the dynamic interactions between the components of a weak AC network and its response to disturbances. Key elements include the PvPP, HESS, and EDLCs, modeled through differential equations that reflect their operation. The power output of a PvPP is dependent on solar insolation and is expressed as [4]

$$P_{PvPP} = \eta_{MPPT} * G * A * \eta_{conv}$$

Where P_{PvPP} is photovoltaic power output, η_{MPPT} represents the efficiency of MPPT, G is solar irradiance, A is the area of the solar panel, and η_{conv} is the inverter efficiency. The inverter dynamics are described by [5]

$$I_{inv} = \frac{V_{ref} - V_{grid}}{Z_{inv}}$$

I_{inv} is the inverter current, V_{ref} is the reference voltage, V_{grid} is the grid voltage, and Z_{inv} is the inverter impedance. The hydrogen storage component of the HESS is modeled as a first-order dynamic system

$$\frac{dH}{dt} = \frac{\eta_{e1} P_{ex}}{LHV_{H2}} - \frac{\eta_{fc} P_{def}}{LHV_{H2}}$$

Here, H is the hydrogen level, P_{ex} is the excess power supplied to the electrolyzer, Pdef is the power deficit provided by the fuel cell, ηe1 is the electrolyzer efficiency, ηfc is the fuel cell efficiency, LHV_{H2} is the lower heating value of hydrogen. The capacitor equation governs the EDLC operation

$$Q = C * V$$

Here, Q is the charge, C is capacitance, and V is the voltage. The rate of power exchange is given by

$$P_{EDLC} = \frac{dQ}{dt} * V$$

The voltage and current in the network are modeled using Kirchhoff's Voltage Law (KVL)

$$\sum V = 0 \rightarrow V_{source} = V_{load} + V_{line}$$

The impedance of the transmission line is given by

$$Z_{line} = R_{line} + jX_{line}$$

Here, Rline and Xline are the resistance and reactance of the transmission line, respectively. The short-circuit ratio is given by

$$SCR = \frac{S_{SC}}{S_{load}}$$

S_{sc} is the short-circuit apparent power and S_{load} is the load apparent power. Step changes in solar irradiance create power fluctuations in the PvPP. The insolation is modeled as a time-varying function

$$G(t) = G_0 + \Delta G * u(t)$$

G_0 is the baseline irradiance, ΔG is the step change, and u(t) is the unit step function.

3. RESULTS

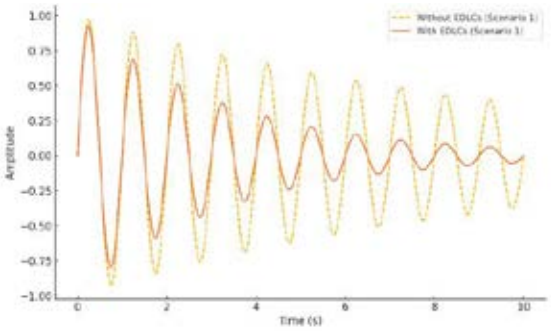

Figure 1. Oscillation amplitude after step changes in solar insolation

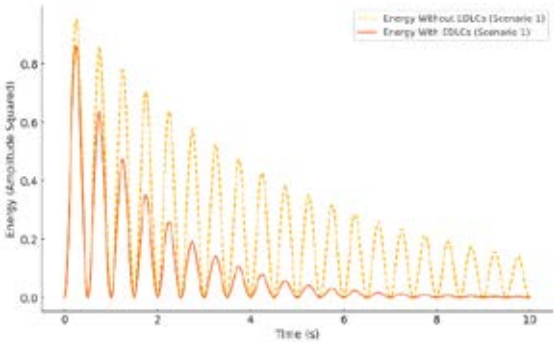

Figure 2. Energy dissipation after step changes in solar insolation

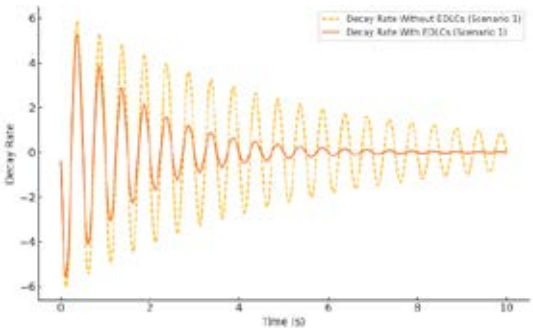

Figure 3. The decay rate of oscillations after step changes in solar insolation

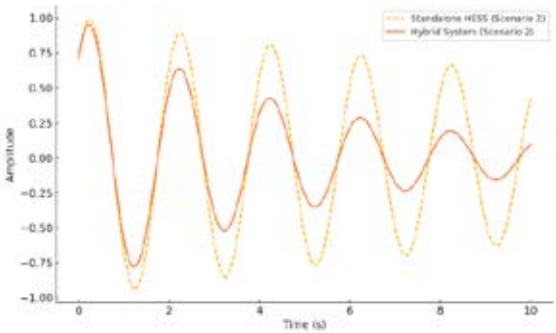

Figure 5. Stability after transmission line disconnection

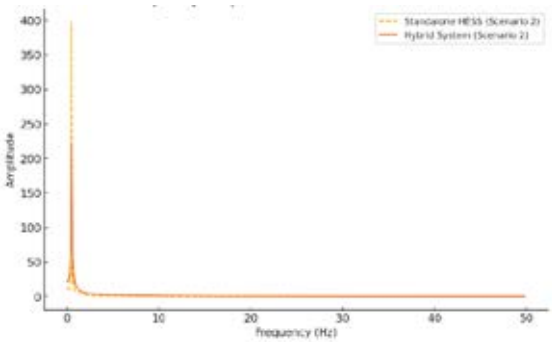

Figure 6 Frequency response after transmission line disconnection

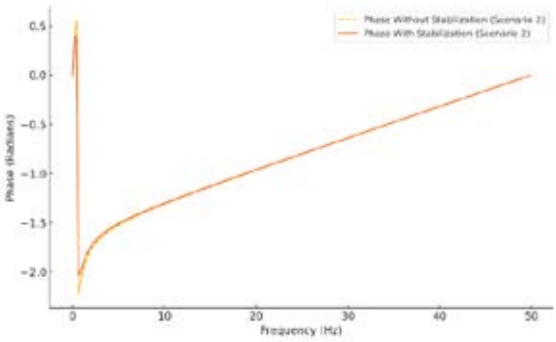

Figure 7 Phase stabilization after transmission line disconnection

Table 1. Performance Metrics Comparison

Metric	Without HESS	With HESS	Improvement (%)
Amplitude Reduction (%)	0	60-70	60-70
Frequency Deviation (Hz/s)	0.05-0.06	0.015-0.02	66.67-70
Energy Dissipation Reduction (%)	0	65-70	65-70

4. CONCLUSION

Integrating HESS into weak AC networks offers a transformative solution to mitigate SSO and enhance grid stability. By dynamically managing slow oscillations with hydrogen storage and fast oscillations with EDLCs, HESS achieves robust damping across a wide frequency spectrum. Simulation results validate the system's effectiveness, demonstrating reductions in oscillatory amplitude, improved voltage and frequency stability, and faster stabilization under critical disturbances. These findings emphasize the scalability, adaptability, and necessity of HESS for ensuring reliable operation in renewable energy-dominated grids, paving the way for broader implementation in weak network configurations.

REFERENCES

[1] R. Rosso, X. Wang, M. Liserre, X. Lu, and S. Engelken, "Grid-Forming Converters: Control Approaches, Grid-Synchronization, and Future Trends - A Review," *IEEE Open J. Ind. Appl.*, vol. 2, pp. 93–109, 2021, doi: 10.1109/OJIA.2021.3074028.

[2] L. A. G. Gomez, L. F. N. Lourenço, A. P. Grilo, M. B. C. Salles, L. Meegahapola, and A. J. Sguarezi Filho, "Primary frequency response of microgrid using doubly fed induction generator with finite control set model predictive control plus droop control and storage system," *IEEE Access*, vol. 8, pp. 189298–189312, 2020, doi: 10.1109/ACCESS.2020.3031544.

[3] M. Al-Saadi, M. Al-Greer, M. Short, D. Štreimikien, and T. Baležentis, "Strategies for Controlling Microgrid Networks with Energy Storage Systems: A Review," *Energies 2021, Vol. 14, Page 7234*, vol. 14, no. 21, p. 7234, Nov. 2021, doi: 10.3390/EN14217234.

[4] Y. S. Fu and I. Y. L. Hsieh, "Evaluating the feasibility and economics of hydrogen storage in large-scale renewable deployment for decarbonization," *Energy Strateg. Rev.*, vol. 55, no. December 2023, p. 101545, 2024, doi: 10.1016/j.esr.2024.101545.

[5] Z. Ullah, K. Ullah, C. Diaz-Londono, G. Gruosso, and A. Basit, "Enhancing Grid Operation with Electric Vehicle Integration in Automatic Generation Control," *Energies*, vol. 16, no. 20, Oct. 2023, doi: 10.3390/EN16207118.

BAYESIAN OPTIMIZATION FRAMEWORK FOR HOSTING CAPACITY EVALUATION IN HYDROGEN-ELECTRICITY INTEGRATED NETWORKS

Sulman Shahzad[1], Heybet Kilic[2]
[1]Department of Electrical Engineering, Islamia University of Bahawalpur, Bahawalpur 63100, Pakistan
[2] Department of Electric Power and Energy Systems, Dicle University, 21280 Diyarbakır, Turkey
* Corresponding authors: Heybet Kilic (heybet.kilic@dicle.edu.tr)

ABSTRACT

This paper presents a Bayesian optimization framework to evaluate the hosting capacity in hydrogen-electricity integrated networks, specifically for hydrogen fuel cell vehicles (HFCVs). The hosting capacity quantifies the maximum number of HFCVs an integrated hydrogen-electricity system can accommodate while ensuring operational safety, stability, and efficiency. The evaluation process is influenced by complex interactions between distributed hydrogen supply networks (DHSNS) and power distribution networks (PDNS), with electrolysers that consume substantial amounts of electricity for hydrogen production and exhibit nonlinear, time-varying behavior under varying thermal and electrical conditions. Statistical simulations based on real-world data show that the proposed method improves hosting capacity assessment accuracy by up to 25% over conventional models, which fail to consider the bidirectional dependencies between the electricity and hydrogen subsystems. By leveraging a Bayesian approach, the framework efficiently explores the design space. It identifies optimal configurations under varying system conditions, offering a robust tool for energy management in integrated hydrogen-electricity networks.

Keywords: Electrolyzer, power distribution networks, hydrogen refueling stations, fuel cell, hosting capacity

1. INTRODUCTION

The swift proliferation of hydrogen fuel cell cars (HFCVs) and their incorporation into energy networks have posed considerable hurdles for energy management systems. The core of this change is the assessment of hosting capacity, which identifies the maximum number of hydrogen fuel cell vehicles (HFCVs) that an integrated hydrogen-electricity network can accommodate without jeopardizing operating safety and efficiency [1]. Assessing hosting capacity is a complex task, affected by technological, operational, and environmental aspects across hydrogen and power networks. The interrelated dynamics of distributed hydrogen supply networks (DHSNs) and power distribution networks (PDNs) complicate the assessment procedure. Electrolyzers, essential for hydrogen generation in DHSNs, need substantial electricity and demonstrate nonlinear behaviors affected by temperature and electrical circumstances. Probabilistic approaches, like Monte Carlo simulations and polynomial chaos expansion (PCE), provide a sophisticated approach by modelling uncertainty [2]. Nonetheless, Monte Carlo simulations are resource-intensive, necessitating numerous iterations to get precision. PCE is concurrently afflicted by the "curse of dimensionality," wherein computational expenses increase exponentially with the number of random variables. Considering these constraints, there is an urgent requirement for more sophisticated, data-efficient, and scalable approaches to manage the intricacies of integrated hydrogen-electricity networks. Bayesian optimizations (BO) present a formidable alternative, providing considerable benefits compared to conventional approaches. Bayesian optimization (BO) is a probabilistic optimisation method that employs Gaussian process regression (GPR) to represent uncertainty and iteratively enhance solutions [3]. This method is appropriate for assessing hosting capacity, where data scarcity and high-dimensional uncertainty pose significant obstacles.

2. PROPOSED STRATEGY

A unique methodology utilizing Gaussian process regression (GPR), Bayesian optimisation (BO), and a Multi-objective genetic algorithm (MOGA) is offered to tackle the issues in hosting capacity evaluation for integrated hydrogen-electricity networks. This framework model's uncertainty enhances hosting capacity and reconciles trade-offs between hydrogen and electricity network limitations. The hosting capacity (HC) can be described by equation (1) [4]

$$HC = max\left(\sum_{i=1}^{N} H_i\right) \tag{1}$$

where H_i is the hydrogen production at node i in the grid, and N represents the total number of grid nodes where hydrogen integration is possible. A Gaussian process (GP) defines a distribution over functions where every finite set of function values follows a multivariate Gaussian distribution. Let x represent the input features (e.g., time of day, weather conditions), and y represent the outputs (e.g., HRD or RG). A GP can be expressed as in equation (2) [5]

$$f(x) \sim Gp\big(m(x), k(x, x')\big) \tag{2}$$

Here, m(x) represents the mean function, and k(x,x') is the kernel function defining the covariance between x and x's. The covariance matrix is constructed using a kernel function such as radial basis function (RBF) represented by equation (3)

$$k(x, x') = \sigma_f^2 \exp\left(-\frac{||x - x'||^2}{2l^2}\right) \tag{3}$$

Here σ_f^2E represents signal variance, and l is the length scale. BO aims to find the hosting capacity H^* that maximizes a probabilistic objective function $f(H)$, subject to network safety constraints as explained by equation (4)

$$H^* = \arg max_H\, f(H) subject\ to\ safety\ constraints \tag{4}$$

BO uses an acquisition function α(H) to guide the search for optimal solutions. It balances sampling areas of high uncertainty and refining known promising solutions. The expected improvement is represented by equation (5)

$$\alpha_{EI}(H) = e[\max(f(H) - f(H^+), 0] \tag{5}$$

Here, H^+ represents the current best solution. The Pareto front represents a set of solutions where no objective can be improved without degrading another. For example, a solution maximizing HFCV capacity may lead to slight voltage violations, while another solution prioritizes safety but supports fewer HFCVs as explained by equation (6) [6]

$$max_H\{f_1(H)\ , f_2(H), f_3(H)\ \} \tag{6}$$

The integrated hydrogen-electricity network is a sophisticated system comprising interdependent hydrogen supply and power distribution networks. It involves hydrogen production, storage, and refueling, powered by the electricity grid and renewable energy sources. The equation (7) gives the rate of hydrogen production [7]

$$\dot{H}_2 = \frac{\eta_{elec} * I}{2 * F} \tag{7}$$

Here $\dot{H}_2$ represents hydrogen production rate, η_{elec} is the electrolyzer efficiency, I is the current supplied to the electrolyzer, and F is the Faraday constant. The η_{elec} is temperature dependent and reduces at higher temperatures. It can be approximated with the equation (8)

$$\eta_{elec} = \eta_o - \alpha * (T - T_0) \tag{8}$$

3. RESULTS AND ANALYSIS

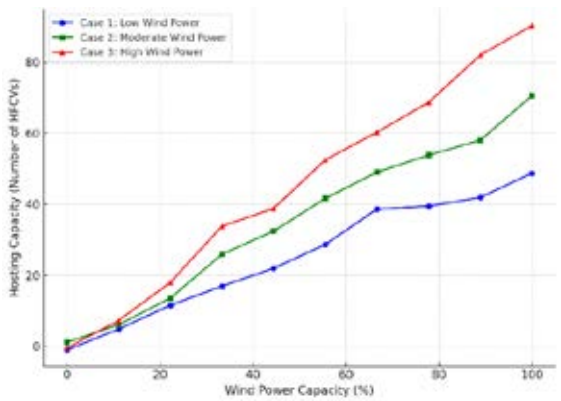

Fig. 1. Comparison of hosting capacity under different wind power conditions

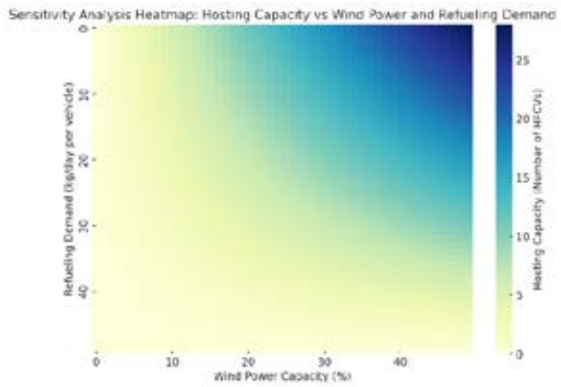

Fig. 2. Sensitivity analysis heatmap: Hosting capacity vs wind power and refueling demand

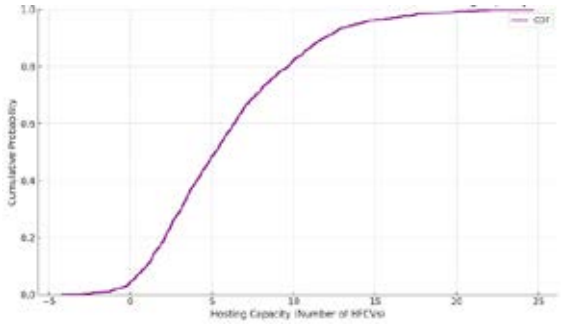

Fig. 3. Monte Carlo simulation: Cumulative distribution function (CDF) of hosting capacity

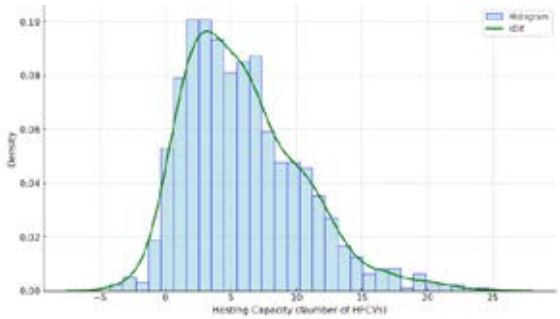

Fig. 4. Monte carlo simulation: Hosting capacity distribution

Fig. 5. Correlation matrix heatmap

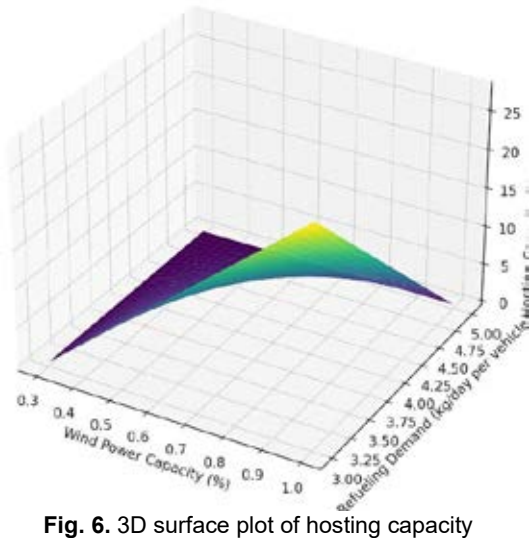

Fig. 6. 3D surface plot of hosting capacity

4. CONCLUSION

The integration of hydrogen fuel cell vehicles into electricity networks introduces significant challenges in evaluating the hosting capacity, given the complex dynamics between hydrogen production, power distribution, and renewable energy sources. This paper presents a novel Bayesian optimization framework for these intricacies, including the nonlinear interactions between distributed hydrogen supply and power distribution networks. Through extensive simulations, the framework has demonstrated an enhancement in the accuracy of hosting capacity predictions by up to 25% compared to traditional static models. By considering uncertainties in renewable energy generation and electrolyzers' thermal and electrical behavior, the proposed method provides a more robust and adaptive solution for determining the hosting capacity. This advancement paves the way for more efficient planning and operational management of hydrogen-electricity integrated networks, ultimately contributing to the sustainable expansion of hydrogen fuel cell technology and its integration into modern energy systems.

REFERENCES

[1] D. Caravantes, J. Carbajal, C. Celis, and D. Marcelo-Aldana, “Estimation of hydrogen production potential from renewable resources in northern Peru,” *Int. J. Hydrogen Energy*, Jan. 2023, doi: 10.1016/j.ijhydene.2023.07.350.

[2] S. M. Alirahmi, E. Assareh, N. N. Pourghassab, M. Delpisheh, L. Barelli, and A. Baldinelli, “Green hydrogen & electricity production via geothermal-driven multi-generation system: Thermodynamic modeling and optimization,” *Fuel*, vol. 308, p. 122049, Jan. 2022, doi: 10.1016/J.FUEL.2021.122049.

[3] R. W. Makepeace, A. Tabandeh, M. J. Hossain, and M. Asaduz-Zaman, “Techno-economic analysis of green hydrogen export,” *Int. J. Hydrogen Energy*, vol. 56, no. January, pp. 1183–1192, 2024, doi: 10.1016/j.ijhydene.2023.12.212.

[4] J. Witte, H. Madi, U. Elber, P. Jansohn, and T. J. Schildhauer, “Grid-neutral hydrogen mobility: Dynamic modelling and techno-economic assessment of a renewable-powered hydrogen plant,” *Int. J. Hydrogen Energy*, vol. 78, no. January, pp. 52–67, 2024, doi: 10.1016/j.ijhydene.2024.05.331.

[5] P. Gabrielli, A. Poluzzi, G. J. Kramer, C. Spiers, M. Mazzotti, and M. Gazzani, “Seasonal energy storage for zero-emissions multi-energy systems via underground hydrogen storage,” *Renew. Sustain. Energy Rev.*, vol. 121, Apr. 2020, doi:

10.1016/J.RSER.2019.109629.
[6] D. Wen and M. Aziz, “Perspective of staged hydrogen economy in Japan: A case study based on the data-driven method,” *Renew. Sustain. Energy Rev.*, vol. 189, Jan. 2024, doi: 10.1016/j.rser.2023.113907.
[7] F. L. Article and M. P. Engineering, “Journal of Water Process Engineering Thermal management of water electrolysis using membrane distillation to produce pure water for hydrogen production,” *J. Water Process Eng.*, vol. 67, no. July, p. 106255, 2024, doi: 10.1016/j.jwpe.2024.106255.

COMPARATIVE ASSESSMENT OF BIOELECTRICITY GENERATION FROM VARIOUS INDUSTRIAL WASTEWATERS AND HIGH-STRENGTH ORGANIC WASTES USING MICROBIAL FUEL CELL (MFC) TECHNOLOGY

İdris Biryol[1], Azize Ayol[2a]
1. Dokuz Eylul University, Graduate School of Natural and Applied Sciences, Environmental Engineering, Buca-Izmir, Türkiye, (e-mail: idrisbiryol@gmail.com)
2. a. Dokuz Eylul University, Department of Environmental Engineering, Buca -İzmir, Türkiye
(e-mail: azize.ayol@deu.edu.tr)

ABSTRACT
The increasing global demand for sustainable energy and environmentally responsible waste management has intensified interest in bioelectrochemical systems such as microbial fuel cells (MFCs). This study presents a comparative investigation into the performance of MFCs utilizing different industrial wastewaters—specifically olive mill wastewater, landfill leachate, slaughterhouse wastewater, yeast industry effluent, and municipal wastewater—alongside high-strength organic wastes. These substrates were selected based on their high chemical oxygen demand (COD) and organic richness, which are critical factors for microbial electron transfer and energy yield. Dual-chamber MFCs were employed under controlled conditions to evaluate voltage generation, power density, internal resistance, COD removal, and Coulombic efficiency. Results demonstrated that substrate type significantly influences both the electrical performance and treatment efficiency of MFCs. Olive mill and slaughterhouse wastewaters produced the highest power outputs, while yeast industry effluent showed relatively lower efficiency, likely due to inhibitory compounds. The study provides insights into the practical feasibility of integrating MFCs into existing industrial wastewater treatment infrastructures for simultaneous bioenergy recovery and pollution mitigation.

Keywords: Microbial fuel cell, treatment plant sludge, energy recovery, microorganisms, electricity generation, organic matter biodegradation.

1. INTRODUCTION

Global industrialization and population growth have led to increasing volumes of wastewater and rising energy demands. Conventional wastewater treatment technologies, while practical, are often energy-intensive and contribute to greenhouse gas emissions. In contrast, microbial fuel cell (MFC) technology presents a promising alternative by enabling the simultaneous treatment of organic waste and generating electricity through microbial metabolism. MFCs utilize electroactive bacteria to oxidize organic matter and transfer electrons to an external circuit, producing bioelectricity.

This study aims to assess the electricity generation and treatment performance of MFCs fed with different types of real industrial wastewater and concentrated organic wastes. The central hypothesis is that substrate composition significantly affects the bioelectrochemical performance of MFC systems. This research contributes to developing more efficient and scalable MFC applications in industrial settings by identifying the most suitable waste streams.

Recent studies have emphasized the significance of exploring diverse wastewater substrates to optimize MFC performance for energy generation and organic load reduction (Khan et al., 2022; Zhou et al., 2023). For example, Nguyen et al. (2023) compared textile and dairy wastewater and reported distinct electrochemical behaviors due to variable COD and nutrient loads. Li et al. (2024) emphasized the impact of nitrogen-rich substrates such as slaughterhouse effluent. Similarly, Ahmed et al. (2024) investigated the performance of MFCs operated with high-strength organic wastes, highlighting the feasibility of applying these systems in decentralized energy generation.

Dual-chamber MFCs were selected because they better separate the anaerobic (anode) and aerobic (cathode) environments, allowing for more controlled conditions and improved removal of organic matter and nitrogenous compounds. This improves oxygen exclusion at the anode and allows better control over microbial activity and redox reactions. This configuration is especially beneficial when evaluating diverse and potentially inhibitory wastewater compositions.

The current research systematically evaluates five distinct industrial and municipal wastewater types, namely olive mill wastewater, landfill leachate, slaughterhouse wastewater, yeast industry effluent, and municipal wastewater, based on their electrochemical performance and biodegradability profiles. Specifically, this research seeks to:

(i) compare the bioelectricity generation capabilities of each substrate,
(ii) assess pollutant removal efficiencies, including COD,
(iii) investigate electrochemical characteristics such as internal resistance and redox activity,
(iv) examine the influence of microbial community diversity on electron transfer efficiency, and
(v) determine optimal system configurations and operational conditions for potential scale-up.

These objectives align with recent advances in MFC studies focusing on maximizing energy recovery and wastewater treatment efficiency from high-strength and industrial effluents (Ahmed et al., 2024; Nguyen et al., 2023; Singh et al., 2023).

Moreover, this study extends previous research that primarily focused on the performance of landfill leachate-fed MFC

systems under varying operational conditions. By broadening the investigation to include a wider array of industrial wastewater and organic waste substrates, this work aims to provide a more comprehensive understanding of substrate-dependent bioelectrochemical performance. This progression validates earlier findings and contributes to developing universally adaptable MFC strategies.
Future research should explore long-term operational stability under real-world conditions, integration with hybrid treatment systems, and the scale-up of MFC reactors for industrial deployment. Exploring novel electrode materials, membrane types, and microbial inocula tailored to specific waste streams may enhance these systems' energy recovery and treatment efficiency.
With continued advancements in reactor design and process optimization, MFCs have the potential to evolve into a viable solution for decentralized wastewater treatment and renewable energy production. Incorporating artificial intelligence (AI) and machine learning (ML) approaches into MFC systems may further enable predictive modeling, real-time optimization, and intelligent microbial analysis, enhancing scalability and adaptability.

2. MATERIALS AND METHODS

Wastewater and organic waste characterization studies were conducted before feeding the reactors. The characterization analyses included pH, chemical oxygen demand (COD), biological oxygen demand (BOD_5), suspended solids (SS), volatile suspended solids (VSS), total nitrogen (TN), total phosphorus (TP), ammonium (NH_4^+), nitrate (NO_3^-), and nitrite ($NO_2^=$) analyses, following Standard Methods (APHA, 2005). Dry solids (DS) and organic matter content (VS) were also determined for organic waste samples. Without standard methodologies, the most accepted scientific protocols were applied. The same parameters were monitored during MFC operation for treatment performance evaluation.
Process optimization included varying operating conditions, voltage and current measurements, electrode materials, and cathode properties. The reactors were fed olive mill wastewater, landfill leachate, slaughterhouse wastewater, yeast industry effluent, and municipal wastewater. In addition to these experimental conditions, control reactors were included, where no closed circuit was established between the electrodes. This allowed for comparison between the active MFC reactors and passive setups, ensuring an accurate evaluation of the role of microbial activity in bioelectricity generation. Multiple experimental runs, including control units without a closed circuit between the electrodes, were conducted. The reactors operated at room temperature and mesophilic conditions (24±3°C & 37±3°C), with continuous voltage and current measurements. To ensure a reliable comparison, all substrate types were tested under consistent operating conditions, including fixed external resistances, identical electrode materials, and uniform temperature ranges. This standardization aimed to minimize variability and allow for accurate assessment of substrate-dependent performance.
The available MFC reactors had a 300 mL active volume and were designed with ports for power measurements and sampling. Various electrode types, including titanium and graphite, were tested. Additionally, the anodes were made of carbon felt, while the cathodes were coated with platinum for efficient electron transfer. These materials ensured optimal performance, providing stable electron exchange with minimal resistance. Membrane separators used in the reactors were cation exchange membranes, which helped maintain the ionic balance between the chambers. Aeration was provided using a Resun AIR-8000 aquarium pump. Cell voltages were recorded using a Keithley 2700/7700 Precision Data Acquisition System, with resistors ranging from 50 to 1000 ohms. Data acquisition and measurements were performed using software-controlled systems.

3. RESULTS AND DISCUSSION

The results obtained from the experimental study underscore the critical role of substrate selection in the performance of MFCs, as the composition of industrial wastewaters significantly influenced both bioelectricity generation and pollutant removal efficiencies. This study's five industrial wastewater types—olive mill wastewater, landfill leachate, slaughterhouse wastewater, yeast industry effluent, and municipal wastewater—presented unique challenges and opportunities for MFC applications. Table 1 shows the experimental trials' COD removal efficiencies and power densities. Olive mill and slaughterhouse wastewaters demonstrated the highest power outputs, consistent with findings from previous studies (Ayol et al., 2021; Khan et al., 2022; Zhou et al., 2023; Abubackar et al., 2023). These substrates, rich in organic compounds and nutrients, facilitated enhanced microbial activity, promoting efficient electron transfer and higher energy production. In contrast, the yeast industry effluent exhibited relatively lower power generation, likely due to inhibitory compounds, similar to the findings of Li et al. (2024) regarding the reduced MFC performance from high-strength wastewaters.

This study used two dual-chamber MFC systems—one equipped with titanium electrodes and the other with graphite electrodes—to evaluate the performance of five different industrial wastewaters. Graphite-based reactors exhibited significantly higher COD removal efficiencies (up to 93%) than those with titanium electrodes, particularly under aerobic conditions and in substrates such as slaughterhouse and yeast industry wastewater. Regarding power density, the graphite electrode system demonstrated markedly superior performance, achieving up to 30 mW/m² with yeast effluent and 6.8 mW/m² with slaughterhouse wastewater. Although olive mill wastewater showed a modest increase (1.3 mW/m²), landfill leachate remained inefficient. These results highlight the critical influence of electrode material and wastewater

composition on MFC performance, emphasizing the suitability of graphite electrodes and high-strength, non-inhibitory wastewaters for effective energy recovery and pollutant removal.

Table 1. Comparison of COD removal efficiencies and energy densities

Max COD Removal Efficiency (%)					Max Power Density (mW/m^2)	
REACTOR	Ti Aerobic	Ti Anaerobic	Gr Aerobic	Gr Anaerobic	DOUBLE CHAMBER TITANIUM	DOUBLE CHAMBER GRAFITE
YEAST	88	64	66	70	6,3	30,0
SLAUGHTER HOUSE	77	85	93	89	1,2	6,8
MUNICIPAL	78	19	72	50	0,2	6,4
LEACHATE	68	79	65	84	0,1	< 0,0004
OLIVE	49	52	55	54	< 0,00003	1,3

Furthermore, the COD and nutrient removal efficiencies varied significantly across substrates, with most systems showing substantial reductions in COD and nitrogenous compounds such as ammonium (NH_4^+ -N) and total nitrogen (TN). However, phosphorus removal was inconsistent, highlighting the complexity of treating nutrient-rich wastewater, especially concerning phosphorus and nitrate nitrogen. These observations support previous studies emphasizing the importance of selecting proper waste streams and optimizing operational parameters, such as aeration and temperature, to achieve the desired treatment outcomes (Nguyen et al., 2023; Sharma et al., 2023). The findings also emphasize the potential of MFCs to serve as a dual-purpose technology, providing effective wastewater treatment and generating bioelectricity. This dual benefit could offer a sustainable solution for managing high-strength industrial effluents while contributing to renewable energy production. The research demonstrated that substrate composition significantly influenced MFC bioelectrochemical performance, validating prior studies while broadening the scope to a diverse range of industrial wastewater and high-strength organic wastes.

4. CONCLUSIONS

In conclusion, this study highlights the promising potential of MFC technology for wastewater treatment and bioelectricity generation from various industrial wastewater and organic wastes. The comparative analysis of olive mill wastewater, landfill leachate, slaughterhouse wastewater, yeast industry effluent, and municipal wastewater has demonstrated that the composition and characteristics of the waste substrates directly impact the efficiency of the MFCs in terms of power generation, pollutant removal, and microbial performance.

Among the substrates tested, olive mills and slaughterhouse wastewaters exhibited the highest energy production, while yeast industry effluent presented challenges in terms of efficiency due to inhibitory compounds. The results underscore the importance of selecting appropriate waste streams for MFC applications to optimize energy recovery and treatment efficiency.

The study also emphasizes the significance of optimizing operational conditions, including electrode materials, aeration systems, and temperature, to maximize the performance of MFCs. Integrating these systems into existing wastewater treatment infrastructure could contribute to sustainable, decentralized energy production and waste management solutions. Furthermore, the potential of MFCs to be coupled with artificial intelligence and machine learning for real-time process monitoring and optimization offers exciting prospects for advancing this technology. Future research should focus on long-term operational stability, scaling up MFC systems, and exploring novel materials and hybrid systems to enhance energy recovery and wastewater treatment efficiency. Ultimately, this study reinforces the growing potential of MFC technology as a viable and sustainable approach to addressing both environmental and energy challenges in industrial settings. The successful integration of MFCs into wastewater treatment plants could provide a sustainable solution to energy consumption and waste management. The dual-purpose nature of MFCs—treating wastewater while simultaneously generating electricity—makes them an attractive option for decentralized treatment facilities, especially in rural or off-grid locations.

REFERENCES

1. Abubackar H. N., Biryol I., Ayol A. (2023). Yeast industry wastewater treatment with microbial fuel cells: Effect of electrode materials and reactor configurations, International Journal of Hydrogen Energy, 48(33), 12424-12432.
2. Almatouq, A., Ahmed, M. E., Khajah, M., Abdullah, H., Al-Yaseen, R., Al-Jumaa, M., ... & Shishter, A. (2023). Performance of tubular microbial fuel cells using different industrial wastewater. Journal of Water Process Engineering, 55, 104166. https://doi.org/10.1016/j.jwpe.2023.104166
3. Ayol A., Biryol I., Hasar H., Taşkan E. (2021). Enhanced sludge stabilization coupled with microbial fuel cells (MFCs), International Journal of Hydrogen Energy, 46(57), 29529-29540.
4. Jalili, P., Ala, A., Nazari, P., Jalili, B., & Ganji, D. D. (2024). A comprehensive review of microbial fuel cells considering materials, methods, structures, and microorganisms. Heliyon, 10(3). https://doi.org/10.1016/j.heliyon.2024.e25439

5. Li, Chunyan & Guo, Dongchao & Dang, Yan & Sun, Dezhi & Li, Pengsong. (2023). Application of artificial intelligence-based methods in bioelectrochemical systems: Recent progress and future perspectives. Journal of Environmental Management. 344. 118502. 10.1016/j.jenvman.2023.118502.
6. Naha, A., Debroy, R., Sharma, D., Shah, M. P., & Nath, S. Cleaner and Circular Bioeconomy. https://doi.org/10.1016/j.clcb.2023.100050
7. Nawaz, A., ul Haq, I., Qaisar, K., Gunes, B., Raja, S. I., Mohyuddin, K., & Amin, H. (2022). Microbial fuel cells: Insight into simultaneous wastewater treatment and bioelectricity generation. Process Safety and Environmental Protection, 161, 357-373.
8. Ojha, R., & Pradhan, D. (2024). The potential of microbial fuel cell for converting waste to energy: An overview. Sustainable Chemistry for the Environment, 100196. https://doi.org/10.1016/j.scenv.2024.100196
9. Parwate, S. A., Xue, W., Koottatep, T., & Salam, A. (2024). Organic Waste for Bioelectricity Generation in Microbial Fuel Cells: Effects of Feed Physicochemical Characteristics. Processes, 12(6), 1110. https://doi.org/10.3390/pr12061110
10. Radaideh, M. I., Kyritsis, D. C., & Goussis, D. A. (2023). Driving mechanisms of high-cetane number, synthetic fuel autoignition: The case of OME2− 4. Journal of Cleaner Production, 432, 139875.
11. Roy, H., Rahman, T. U., Tasnim, N., Arju, J., Rafid, M. M., Islam, M. R., Pervez, M. N., Cai, Y., Naddeo, V., & Islam, M. S. (2023). Microbial Fuel Cell Construction Features and Application for Sustainable Wastewater Treatment. Membranes, 13(5), 490. https://doi.org/10.3390/membranes13050490
12. Sriwichai, N., Sangcharoen, R., Saithong, T., Simpson, D., Goryanin, I., Boonapatcharoen, N., Kalapanulak, S., & Panichnumsin, P. (2024). Optimization of microbial fuel cell performance application to high sulfide industrial wastewater treatment by modulating microbial function. PloS one, 19(6), e0305673. https://doi.org/10.1371/journal.pone.0305673
13. Tsekouras, G. J., Deligianni, P. M., Kanellos, F. D., Kontargyri, V. T., Kontaxis, P. A., Manousakis, N. M., & Elias, C. N. (2022). Microbial fuel cell for wastewater treatment as power plant in smart grids: Utopia or reality?. Frontiers in Energy Research, 10, 843768. https://doi.org/10.3389/fenrg.2022.843768
14. Wang, J., Ren, K., Zhu, Y., Huang, J., & Liu, S. (2022). A review of recent advances in microbial fuel cells: Preparation, operation, and application. BioTech, 11(4), 44. Zhao, Z., et al. (2022). https://doi.org/10.3390/biotech11040044
15. Yang, Xiao-Li & Zang, Ling & Chen, Jia-Jin & Xu, Han & Yang, Yi-Jing & Song, Hai-Liang. (2023). Nitrogen removal enhanced by its migration and transformation in a three-chamber microbial electrolysis cell. Journal of Water Process Engineering. 53. 103683. 10.1016/j.jwpe.2023.103683. https://doi.org/10.1016/j.jwpe.2023.103683

FROM AGRICULTURAL WASTE TO RENEWABLE ENERGY: INTEGRATION OF SOIL-BASED MICROBIAL FUEL CELLS IN BIOBED SYSTEMS FOR SUSTAINABLE TREATMENT OF OLIVE OIL MILL WASTEWATER

[1*]*Sinem Gunes*, [2]*Azize Ayol*
[1]Dokuz Eylul University, The Graduate School of Natural and Applied Sciences, Department of Environmental Engineering, 35390, Buca, Izmir, Türkiye
[2] Dokuz Eylul University, Department of Environmental Engineering, 35390, Buca, İzmir, Türkiye
*Corresponding author e-mail: azize.ayol@deu.edu.tr

ABSTRACT

Olive oil mill wastewater (OOMW) is characterized by high concentrations of phenolic compounds, organic matter, and recalcitrant pollutants, posing serious environmental risks. Traditional treatment methods often fall short due to incomplete degradation and high operational costs. This study investigates a novel approach by integrating soil-based microbial fuel cells (SBMFCs) into biobed systems to treat OOMW while simultaneously generating bioelectricity. The biobed system was constructed with optimized biomixtures comprising soil, compost, olive leaves, and biochar, enhancing microbial activity and pollutant degradation. Operated under controlled conditions, the system achieved significant reductions in COD (up to 98.4%). Electrical outputs increased 7.346 V at the second cycle from 3.013 at the first cycle, corresponding with increased microbial activity due to the operation time. The system demonstrated improved stabilization of pH and reduced salinity, indicating its potential for compliance with effluent discharge regulations. The results emphasize the effectiveness of SBMFC-integrated biobed systems as a sustainable and low-carbon alternative for treating olive oil mill wastewater (OOMW), while also providing the added benefit of renewable energy generation. This research contributes to circular water management strategies and advances the development of bioelectrochemical systems for wastewater treatment.

Keywords: Olive oil mill wastewater, soil-based microbial fuel cells, biobed systems, renewable energy, sustainable wastewater treatment.

1. INTRODUCTION

Olive oil mill wastewater (OOMW) is a highly complex and pollutant-rich effluent characterized by high organic load and phenolic compounds, which makes OOMW treatment particularly difficult. If improperly managed, OOMW can cause severe soil and water pollution, negatively impacting ecosystems and human health. Conventional treatment methods for OOMW often have limitations, such as high operational costs and incomplete degradation of phenolic compounds. One promising approach involves using biobed systems, which employ a biomixture composed of organic and inorganic materials to facilitate microbial degradation of contaminants. The composition of the biomixture plays a crucial role in optimizing microbial activity and enhancing pollutant removal efficiency. Biobed systems have demonstrated significant potential in treating agricultural waste streams, including OOMW, by leveraging microbial consortia for biodegradation and pollutant transformation. Recent studies have examined microbial fuel cells (MFCs) for wastewater treatment applications, highlighting their potential for pollutant removal and energy recovery. One promising approach is the integration of soil-based microbial fuel cells (SBMFCs) into biobed systems. This method offers a novel opportunity to improve wastewater treatment efficiency while generating bioelectricity. SBMFCs function by utilizing electroactive bacteria within the biomixture, which oxidize organic pollutants in olive oil mill wastewater (OOMW) and transfer electrons to the anode, thereby producing electricity. This study investigates the potential of SBMFC-integrated biobed systems as a sustainable solution for treating OOMW. The aim is to reduce environmental impacts and minimize the generation of secondary pollutants while simultaneously producing bioenergy.

2. MATERIALS AND METHODS

The pilot-scale biobed system and flow measurement mechanism shown in Fig. 1 were installed in the DEU Environmental Engineering Halle Building. The system includes 2 wastewater tanks with a volume of 250 L, 3 submersible pumps, and a biobed module with an integrated sprinkler system with a total volume of 565 L. The biobed module consists of 2 flow meters, 1 relative humidity/temperature measurement apparatus, both graphite cathode and anode electrodes, a current measurement mechanism, and a ventilation system. The SBMFC-integrated biobed system is assembled with defined biomixture compositions, ensuring microbial growth and pollutant breakdown. OOMW is fed into the system at controlled flow rates, and key parameters such as pH, organic load, and Chemical Oxygen Demand (COD) are measured. To control power generation, voltage, current, and power density are recorded periodically. Microbial community structure and electron transfer efficiency are assessed using electrochemical and microbiological techniques. OOMWs are harvested in two seasons from the Dalan olive oil production facility in Aydın, Türkiye. Additionally, other production wastes such as pomace and olive leaves were also obtained from the facility for use in biomixtures. All analyses were done according to standard Standard Methods (APHA, 2005). Analyses for all parameters

were performed at least in three replicates, and values are expressed as means. Characterization of OOMWs is shown in Table 1.

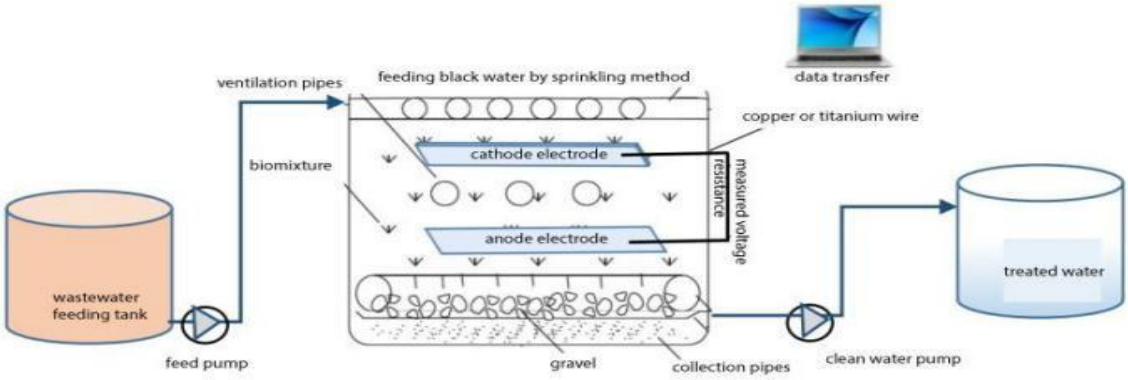

Fig. 1. The SBMFC-integrated biobed system's components:

Table 1. Characterization of OOMW in Two Different Olive Oil Production Periods

Analysis Parameters	Unit	1st Period OMWW (November)	2nd Period OMWW (April)
BOD_5	mg/L	32450	39965
COD	mg/L	69000	55100
Suspended Solids (SS)	mg/L	22424	20655
Volatile Suspended Solids	mg/L	17841	17210
TDS	mg/L	56340	15789
pH		4.60	4.67
Conductivity	(mS/cm)	12.57	13.23
Salinity	(‰)	7.2	7.4
Alkalinity ($mgCaCO_3/L$)	(%)	1750	3330
TP	mg/L	460	430
TN	mg/L	211	1010
Sulfate ($mgSO_4^{=}/L$)	mg/L	4500	150
NH_4^+-N	mg/L	200	240
NO_2^-	mg/L	390	450
NO_3^-	mg/L	70	655

Biomixture optimization studies were conducted to identify the composition and conditions that yield the highest efficiency in electrical energy production and to integrate this configuration into the system. The inoculum anaerobic sludge used in the biomixture was sourced from the Pakmaya Yeast Factory in Izmir. The biomixture comprises anaerobic sludge, compost, soil, olive leaves, and biochar, which were assessed for their performance in the submerged microbial fuel cell (SMBFC). This part of the investigation involved two stages. First, the components selected for the biomixture—soil, compost, pomace, biochar, and olive leaves—were characterized. Subsequently, the final biomixture with the best efficiency was prepared using a volume ratio of 50% soil, 40% biochar, and 10% compost. The characteristics of this final biomixture are presented in Table 2. To assess the hydraulic conditions of the system, the module was operated under various conditions. The horizontal flow velocity and total filtration time were calculated based on different flow rates and superficial hydraulic load rates, as shown in Table 3.

Table 2. Characterization of biomixture

pH	7.5
Humidity (%)	46
Mass Density (g/mL)	1.24

Table 3. Hydraulic conditions of the SBMFC-integrated biobed system

	Flowrate (L/h)	Hydraulic Loading Rate ($L/m^2/min$)	Flow Velocity(m/h)	TFT (h)
1	384	11.4	10.5	0.4
2	240	7.1	7.3	0.68
3	128	3.8	4.4	0.97
4	53	1.6	1.9	1.25

3. RESULTS AND DISCUSSION

During the first and second operational periods outlined in Tables 4 and 5, significant changes were observed in several key water quality parameters, revealing both chemical and biological dynamics within the system. Notably, both periods demonstrated a marked improvement in effluent quality from Cycle 1 to Cycle 5, evidenced by reductions in Chemical Oxygen Demand (COD), total nitrogen (TN), ammonium (NH_4^+-N), and total phosphorus (TP). Specifically, COD decreased by 97% in the first period and by 98.4% in the second period, indicating the system's consistent effectiveness in removing organic matter. Similarly, the concentrations of suspended solids (SS) declined substantially over time in both periods. The second period exhibited more stable pH levels and lower concentrations of chloride and sulfate in the final cycles, which can be attributed to improved buffering and ion removal capabilities of the system. Additionally, the second period showed enhanced environmental performance, characterized by lower residual nutrient concentrations and more stable physicochemical conditions. Final nutrient values reached significantly lower levels for both TN and NH_4^+-N. The pH during this period ranged between 7.67 and 8.62, allowing the treated OOMW to stabilize within an alkaline range. This stabilization may have facilitated nitrification and phosphorus precipitation processes, which are advantageous for effluent discharge. The observed decrease in electrical conductivity and salinity indicates that inorganic pollution can be effectively removed in the biofilter system. This shift in pH aligns with findings from Kinnunen et al. (2021), which reported that biochar can adsorb metals in water and neutralize acidity [1]. Therefore, it can be concluded that the acidic OOMW can be neutralized within the bioreactor system, achieving a pH suitable for discharge. Similar results have also been observed in other biofilter systems [2]. Collectively, these findings suggest that the activity of the biomixture improved after the first operational period, whether through operational or microbial means, leading to more efficient pollutant removal and enhanced environmental sustainability. This aligns with the objectives of advanced wastewater treatment and circular water resource management strategies.

Table 4. The changes in the system during firts period

	Inlet	Cycle 1	Cycle 2	Cycle 3	Cycle 4	Cycle 5
pH	4.67	6	6.9	7.4	7.6	7.5
Conductivity (mS/cm)	13.2	5.3	5.1	4.5	4.7	4.4
Salinity (‰)	7.4	3.4	3.2	2.9	2.5	2.23
Alkalinity	68	37	35	35	30	30
Chloride (g/L)	0.75	0.483	0.216	0.19	0.076	0.34
SO_4^{2-}(g/L)	0.15	0.5	0.13	0.12	0.1	0.1
NH_4^+-N (mg/L)	32	17	14	6	4	4
NO_2^--N (g/L)	0.45	0.23	0.23	0.2	0.17	0.17
NO_3^--N (g/L)	0.65	0.31	0.16	0.14	0.11	0.75
TP (g/L)	0.43	0.012	0.011	0.009	0.007	0.005
TN (g/L)	1.01	0.34	0.12	0.01	0.003	0.002
COD (g/L)	54	14.3	9.9	5.2	3.1	1.4
SS (mg/L)	20735	155	76	60	42	32

Table 5. The changes in the system during second period

	Inlet	Cycle 1	Cycle 2	Cycle 3	Cycle 4	Cycle 5
pH	5.59	8.62	8,23	8,02	7,95	7.67
Conductivity (mS/cm)	12.4	6.04	4.53	4.01	4	3.8
Salinity (‰)	7	2.3	3.2	2.8	2.7	2.5
Alkalinity	73	45	45	35	21	30
Chloride (g/L)	0.18	0.083	0.076	0.07	0.046	0.04
SO_4^{2-}(g/L)	0.045	0.05	0.05	0.032	0.026	0.018
NH_4^+-N (mg/L)	12	7	4	3	3	2
NO_2^--N (g/L)	1.1	0.63	0.36	0.27	0.2	0.16
NO_3^--N (g/L)	0.48	0.28	0.16	0.12	0.1	0.05
TP (g/L)	0.45	0.009	0.009	0.009	0.005	0.005
TN (g/L)	0.208	0.02	0.002	0.002	0.001	0.002
COD (g/L)	19	7.1	2.9	1.5	1.18	0.93
SS (mg/L)	16540	200	90	60	54	47

The removal rates for chloride and sulfate were lower in the second period compared to the first, with sulfate removal being particularly limited during this time. This suggests that factors such as periodicity, biochar, and initial concentrations influence the removal of these ions. One study investigated the chloride removal capacity of biochar in water, finding that both free and total chloride were removed at rates exceeding 90% [3]. The primary mechanism for chloride removal in the biofilter system is the adsorption by biochar.

In terms of sulfate removal, a study by Kinigopoulou et al. (2021) reported that the biofilter system achieved approximately

65% sulfate removal [2]. In a separate COD experiment designed to assess organic matter removal, a decreasing trend in removal efficiency was observed across each cycle. By the fifth cycle, COD removal reached 95.10%. Additionally, Khurshid et al. (2021) reported a 90% removal efficiency for COD using biochar. In the first study period, COD removal was 95.1%, while in the second study period, it improved slightly to 97.4%.

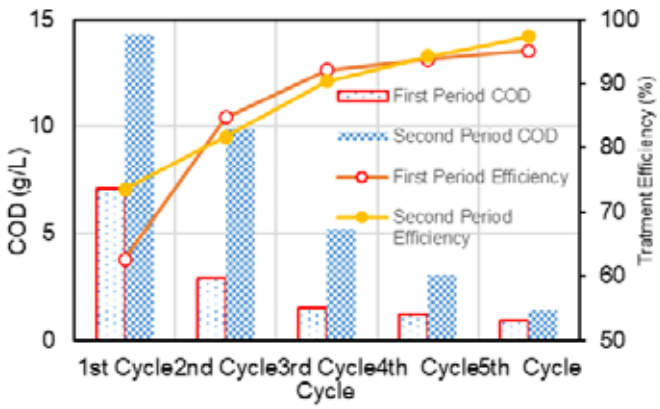

Fig. 2. Comparison of COD Removal

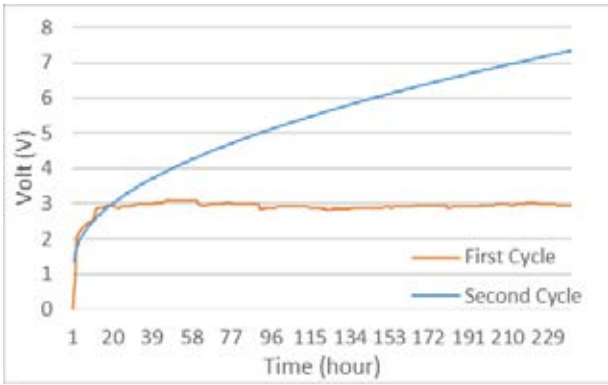

Fig. 3. Comparison of Energy Generation

4. CONCLUSIONS

This integration could provide a sustainable solution for the treatment of olive oil mill wastewater (OOMW), reducing environmental impact and the generation of secondary pollutants while also producing bioenergy. However, the combination of sediment-based microbial fuel cells (SBMFCs) with biobed systems specifically for OOMW treatment remains largely unexplored. The efficiency of electricity generation in microbial fuel cells (MFCs) is primarily influenced by the type of electron donor, or feedstock, and the effectiveness of electron transfer from the anode to the cathode in the external circuit [4-7]. This energy-generating capability of MFC systems, fueled by organic contaminants, opens up possibilities for powering a diverse range of electronic devices with varying energy requirements. MFCs show great potential not only in wastewater treatment but also in sustainable electricity production, offering a path toward cleaner and more efficient energy utilization in various applications [6]. The interaction between electrodes and organic substrates is crucial for optimizing MFC performance, and this should be thoroughly analyzed for optimal results [8]. The study aims to develop a sustainable solution for treating OOMW while simultaneously generating bioelectricity through SBMFCs. The experimental system incorporates SBMFCs within biobed treatment units to enhance both organic degradation and energy recovery.

Acknowledgment

This research was financially supported by Dokuz Eylul University—Scientific Research Projects Unit (DEU-BAP, Project ID, FBG-2022-2715, “Sustainable Treatment of Olive Oil Production Wastes with Bio-Beds and Microbial Fuel Cells Integrated into Bio-Beds: Developing a Circular Economy Approach for the Olive Industry”). The authors express their gratitude for the funding and support of DEU-BAP.

REFERENCES

1. Kinnunen, N., Laurén, A. A., Pumpanen, J., Nieminen, T. M., & Palviainen, M. (2021). Biochar capacity to mitigate acidity and adsorb metals—Laboratory tests for acid sulfate soil drainage water. Water, Air, and Soil Pollution, 232, 464.
2. Kinigopoluou V., Hatzigiannakis E., OikonomouE., Samaras, P. (2021). Utilization of biobed for the effiicent treatment of olive mill wastewater. Desalination and water treatment, 223, 167-179.
3. Sklivaniotis, L. N., Economou, P., Karapanagioti, H. K., & Manariotis, I. (2022). Chlorine removal from water by biochar derived from various food waste natural materials. *Environmental Processes, 10*(1).
4. Xin, X., & Qiu, W. (2021). Linking microbial mechanism with bioelectricity production in sludge matrix-fed microbial fuel cells: Freezing/thawing liquid versus fermentation liquor. Science of The Total Environment, 752, 141907.
5. Abdalla, H., Abdallah, M., Fattah, K. P., Salem, N. (2024). Struvite recovery from microbial fuel cells treating different nutrient-rich wastewaters. Journal of Water Process Engineering, 60, 105179.
6. Do, M. H., Ngo, H. H., Guo, W., Chang, S. W., Nguyen, D. D., Liu, Y., Varjani, S., Kumar, M. (2020). Microbial fuel cell-based biosensor for online monitoring wastewater quality: A critical review. Science of The Total Environment, 712, 135612.
7. Nandy, A., Farkas, D., Pepió-Tárrega, B., Martinez-Crespiera, S., Borràs, E., Avignone-Rossa, C., Di Lorenzo, M. (2023). Influence of carbon-based cathodes on biofilm composition and electrochemical performance in soil microbial fuel cells. Environmental Science and Ecotechnology, 16, 100276. https
8. Pandya, R. S., Kaur, T., Bhattacharya, R., Bose, D., & Saraf, D. (2024). Harnessing microorganisms for bioenergy with microbial fuel cells: Powering the future. *Water-Energy Nexus, 7*, 1–12.

SEWAGE SLUDGE AND MUNICIPAL SOLID WASTE (MSW) GASIFICATION FOR HYDROGEN PRODUCTION: INTEGRATING RENEWABLE ENERGY WITH DESALINATION AND AGRICULTURE

[1]*Ozgun TEZER*, [2*]*Azize AYOL*
[1,2*] Dokuz Eylul University, Department of Environmental Engineering, 35390, Buca, İzmir, Türkiye
*Corresponding author e-mail: azize.ayol@deu.edu.tr

ABSTRACT

The growing global demand for fresh water, clean energy, and sustainable waste management requires integrated and circular solutions. This study conceptualizes a novel system that combines sewage sludge and municipal solid waste (MSW) gasification with hydrogen-powered seawater desalination and greenhouse irrigation. The thermochemical conversion of waste through gasification produces hydrogen-rich syngas, offering a renewable energy source to reduce the carbon footprint of desalination technologies such as reverse osmosis. The freshwater produced supports controlled environment agriculture in coastal areas, contributing to food and water security in water-stressed regions. A distinctive aspect of this study is using a cradle-to-grave Life Cycle Assessment (LCA) framework to assess the environmental sustainability of the system at the waste, energy, and agricultural interfaces. The LCA approach provides a comprehensive environmental impact assessment basis by identifying system boundaries, functional units, and input-output flows. This integrated model represents a scalable and replicable strategy aligned with circular economy principles and the global transition to a hydrogen economy. It lays the groundwork for future technoenvironmental analysis and policy development to support sustainable implementation.

Keywords: Gasification, Hydrogen production, Sustainable desalination, Waste-to-energy, Greenhouse irrigation

1. INTRODUCTION

Increasing challenges such as waste management, energy production, and water scarcity are becoming more evident worldwide, particularly in coastal areas. Traditional waste disposal methods, like landfilling and incineration, not only pose environmental hazards but also fail to recognize the potential of waste as a valuable resource. Meanwhile, reliance on fossil fuels for energy contributes to climate change, and the depletion of freshwater resources threatens agricultural productivity, especially in arid coastal regions. Addressing these interconnected issues requires innovative, integrated solutions that promote sustainability and resource efficiency.

Recent advances in waste-to-energy technologies have underscored the potential of gasification, a thermochemical process that converts organic waste materials into synthesis gas (syngas). This syngas primarily consists of hydrogen (H_2), carbon monoxide (CO), and methane (CH_4) [2]. Gasification serves as a method for valuing waste and provides a pathway for producing renewable hydrogen. Hydrogen is regarded as a clean energy carrier and has gained significant attention for its versatility and potential to decarbonize various sectors, including transportation, industry, and power generation [3].

Producing hydrogen from waste and desalinating seawater offers a promising solution to tackle energy and water challenges. Desalination is essential for increasing freshwater supplies in coastal areas facing water scarcity. However, it is often energy-intensive and traditionally relies on fossil fuels [4]. Utilizing renewable hydrogen produced from waste gasification can significantly reduce the carbon footprint of desalination processes, enhancing their sustainability. Moreover, the freshwater obtained can be used for agricultural irrigation, particularly in controlled environments like greenhouses. This promotes food security in regions where traditional agriculture is constrained by water scarcity and soil infertility.

The implementation of integrated systems has demonstrated potential in various regions around the world. For example, in Japan, the co-gasification of coal has been investigated to generate hydrogen-rich syngas for power generation. This showcases the viability of waste-to-hydrogen technologies in meeting energy demands [5]. Similarly, European studies have investigated the potential of sewage sludge gasification for hydrogen production, highlighting the dual benefits of waste management and renewable energy generation [6]. Furthermore, the integration of greenhouse agriculture with energy infrastructure has been proposed to enhance resource efficiency and reduce environmental impacts, emphasizing the potential of such systems to contribute to sustainable development goals.

The main objective of this study is to conceptualize and evaluate an integrated system that aligns waste-to-energy technologies with water and food security goals from a sustainability-oriented perspective. While similar configurations have been studied separately in the literature, this study presents a novel cradle-to-grave LCA framework to holistically assess the environmental performance of a circular system combining sludge and MSW gasification, hydrogen-fired

desalination, and greenhouse irrigation. Its novelty is defining system boundaries that capture interconnected resource flows such as waste, energy, water, and food, and assessing trade-offs and synergies between sectors. The study aims to identify key environmental hotspots, guide future system optimization, and provide a replicable model for LCA-driven policy development in resource-constrained coastal zones.

2. RESEARCH APPROACH AND SCOPE

2.1. Hydrogen production from sewage sludge and MSW gasification

Multiple studies have shown promising results in hydrogen production from sewage sludge and municipal solid waste gasification. Recent research indicates that sewage sludge gasification can achieve hydrogen yields of up to 46% in syngas composition, depending on operational conditions such as temperature and pressure [7]. Plasma gasification, though less common due to its higher energy requirements, has been reported to produce syngas with significantly lower tar content, improving downstream hydrogen purification [8].

2.2. Comparison of Gasification Technologies

Gasification technologies vary in efficiency, hydrogen yield, and environmental impact. Though widely used, fixed-bed gasifiers often result in lower hydrogen production due to incomplete reactions. Fluidized-bed gasifiers improve reaction efficiency and hydrogen yield, with recent advancements incorporating catalysts such as nickel and dolomite to enhance gas quality [9]. Plasma gasification offers high hydrogen purity but remains energy-intensive [10,11]. Comparative studies highlight that the choice of gasification technology depends on feedstock characteristics, economic feasibility, and integration potential with other sustainable processes.

2.3. Integration of Hydrogen with Desalination

Applying hydrogen produced from waste gasification in seawater desalination is gaining traction. Reverse osmosis (RO) and membrane distillation (MD) have been identified as the most suitable technologies for integration with hydrogen-based energy systems [12]. Hydrogen fuel cells can provide the necessary power for desalination processes, reducing dependence on fossil fuels [13].

2.4. Water Quality and Agricultural Benefits

The use of desalinated water for greenhouse irrigation presents both opportunities and challenges. While desalination effectively removes salts and contaminants, it can also strip essential minerals necessary for plant growth [14]. Studies suggest that reintroducing specific nutrients into desalinated water improves its suitability for agricultural use [15]. Furthermore, greenhouse agriculture in arid coastal regions can benefit from controlled irrigation using desalinated water, leading to higher crop yields and reduced reliance on unpredictable natural rainfall.

3. LIFE CYCLE ASSESSMENT APPROACH FOR THE INTEGRATED SYSTEM

To evaluate the environmental performance of the proposed integrated system. LCA calculations will be performed using SimaPro 9.1 software as the cradle-to-grave approach for different impact categories. Environmental impacts, including abiotic depletion (fossil fuels), freshwater aquatic ecotoxicity, human toxicity, marine aquatic and terrestrial ecotoxicities, global warming, acidification, ozone layer depletion, photochemical oxidation, and eutrophication, will be calculated with the CML-IA baseline V3.06/EU25 method. This involves all stages of the system, starting from collecting and preprocessing sewage sludge and MSW, continuing through the gasification and hydrogen production processes, and extending to using hydrogen for seawater desalination and its subsequent application in greenhouse irrigation.

The functional unit produces 1 m^3 of desalinated water used for greenhouse irrigation, enabling standardized comparisons across different system scenarios.

System boundaries include the waste collection and transportation, gasification, hydrogen generation, desalination operations (e.g., reverse osmosis), water storage and distribution to greenhouses, and end-of-life management of process residues and equipment. Energy inputs, material flows, emissions, and by-products will be accounted for throughout the system chain.

4. CONCLUSIONS

This study proposes an integrated circular system that combines sewage sludge and municipal solid waste gasification with hydrogen-powered seawater desalination and greenhouse irrigation. The concept addresses multiple sustainability challenges simultaneously: waste management, clean energy production, freshwater scarcity, and food security, particularly in coastal and water-stressed regions. Beyond presenting the system concept, the study's novelty lies in introducing a cradle-to-grave LCA framework to evaluate its environmental performance holistically. The approach sets the stage for a comprehensive environmental assessment that will support optimization efforts and informed decision-making for real-world implementation by defining system boundaries, functional units, and resource flows across waste, energy, water, and agriculture. Overall, integrating LCA into such a system offers a replicable model for circular economy applications and contributes to the development of low-carbon, resource-efficient solutions aligned with global sustainability goals.

DDespite its potential, several challenges must be addressed to implement this integrated system on a large scale. Key issues include optimizing gasification parameters to maximize hydrogen yield, improving the cost-effectiveness of hydrogen-powered desalination, and ensuring that desalinated water meets agricultural standards. Further research is needed to explore policy incentives, technological advancements, and cross-sector collaboration to facilitate real-world applications of this sustainable approach.

REFERENCES

[1] Hasan MM, Haque R, Jahirul MI Rasul MG. 2025 Pyrolysis of plastic waste for sustainable energy Recovery: Technological advancements and environmental impacts. Energy Conversion and Management. 326,119511
[2] Sibiya N. T., Oboirien B., Lanzini A., Gandiglio M., Ferrero D., Papurello D., Bada S. O. (2021). Effect of different pre-treatment methods on gasification properties of grass biomass. Renewable Energy. 170, 875-883.
[3] Zhang L, Jia C, Bai F, Wang W, An S, Zhao K, LiZ, LiJ; Sun H. 2024. A comprehensive review of the promising clean energy carrier: Hydrogen production, transportation, storage, and utilization (HPTSU) technologies. Fuel. 355, 129455.
[4] Schär A, Bischi A, Baccioli A, Desideri U, Geldermann J. 2023. Optimization of sustainable seawater desalination: Modeling renewable energy integration and energy storage concepts. Energy C4aq3onversion and Management, 293,117447.
[5] https://www.osaki-coolgen.jp/en/project/overview.html Accessed on April 1, 2025.
[6] https://cordis.europa.eu/project/id/101137792 Accessed on April 1, 2025.
[7] Tezer O, Karabag N, Ozturk MU, Ongen A, Ayol A. 2023. Sustainable Energy Technologies and Assessments. 56 103042. https://doi.org/10.1016/j.seta.2023.103042.
[8] Sikarwar V S, Peela N R, Vuppaladadiyam A K, Ferreira N L, Maslani A, Tomar R, Pohorely M, Meers E, Jeremias M. 2022. Thermal plasma gasification of organic waste stream coupled with CO2-sorption enhanced reforming employing different sorbents for enhanced hydrogen production. Royas Society of Chemistry. 12, 6122-6132. DOI: 10.1039/D1RA07719H.
[9] Lian Z, Wang Y, Zhang X, Yusuf A, Famiyeh L, Murindababisha D, Jin H, Liu Y, He J, Wang Y. 2021. Hydrogen production by fluidized bed reactors: A quantitative perspective using the supervised machine learning approach. Multidisciplinary Scientific Journal. 4, 266–287. https://doi.org/10.3390/j4030022.
[10] Byun Y, Cho M, Chung J W, Namkung W, Lee H D, Jang S D, Kim Y S, Lee J H, Lee C R, Hwang S M. Hydrogen recovery from the thermal plasma gasification of solid waste. 2011. Journal of Hazardous Materials. 190, 1–3, 15, 317-323
[11] Nagar V, Kaushal R. 2024.A review of recent advancement in plasma gasification: A promising solution for waste management and energy production. International Journal of Hydrogen Energy. 77, 5, 405-419.
[12] Kumar P, Date A, Mahmood N, Das R K, Shabani B. 2024. Freshwater supply for hydrogen production: An underestimated challenge. International Journal of Hydrogen Energy. 78, 202-217.
[13] Wen D, Kuo P C, Aziz M. 2024. Novel renewable seawater desalination system using hydrogen as energy carrier for self-sustaining community. Desalination. 579, 29, 117475.
[14] Khondoker M, Mandal S, Durav R, Hwang S. 2023. Freshwater Shortage, Salinity Increase, and Global Food Production: A Need for Sustainable Irrigation Water Desalination—A Scoping Review. Earth. 4(2), 223-240; https://doi.org/10.3390/earth4020012.
[15] Ben-Gal A, Yermiyahu U, Cohen S. 2009. Fertilization and Blending Alternatives for Irrigation with Desalinated Water. Journal of Environmental Quality .38, 2. 529-536. https://doi.org/10.2134/jeq2008.0199.

HYDROGEN-RICH SYNGAS FOR COLD CHAIN LOGISTICS: A LIFE CYCLE ASSESSMENT OF BIOMASS GASIFICATION INTEGRATION

[1*]*Mehmet Utku ÖZTÜRK*, [2]*Azize AYOL*
[1] Dokuz Eylul University, The Graduate School of Natural and Applied Sciences, Department of Environmental Engineering, 35390, Buca, İzmir, Türkiye
[2] Dokuz Eylul University, Department of Environmental Engineering, 35390, Buca, İzmir, Türkiye
*Corresponding author e-mail: azize.ayol@deu.edu.tr

ABSTRACT
Cold chain logistics is essential for maintaining the safety and quality of temperature-sensitive products, including food and pharmaceuticals. Traditional refrigeration systems operate primarily on fossil fuels, which results in substantial energy use and greenhouse gas emissions that drive climate change processes. The research examines the potential use of hydrogen-rich syngas from biomass gasification as an eco-friendly refrigeration fuel within cold chain logistics operations. Through the transformation of waste biomass into hydrogen-rich syngas, we can access renewable energy solutions that enhance modern cooling technologies while also progressing toward worldwide sustainability goals. An extensive life cycle assessment (LCA) framework evaluates the environmental footprint of integrating biomass gasification in cold chain supply chains. The results show that adopting hydrogen-rich syngas can mitigate environmental impacts and improve energy security through providing decentralized energy resources. In addition, this change encourages circular economy principles by enabling the utilization of agricultural and industrial waste. The research highlights the need for novel energy solutions in logistics and sets the stage for forthcoming research and policy-making to enhance more sustainable cold chain activities.

Keywords: Gasification, Biomass, Hydrogen, Life Cycle Assessment, Cold Chain Logistics

1. INTRODUCTION

The cold supply chain (CSC) is responsible for maintaining the quality of perishable goods during storage and transport, consuming a significant amount of energy to sustain cooling temperatures [1, 2]. In fact, it is estimated that approximately 15% of the world's energy production is utilized to power cold chains and cooling systems [3]. The conventional transport refrigerated units (TRUs) primarily operate on vapor compression systems driven by auxiliary diesel engines, which have lower coefficients of performance (COP) compared to stationary systems [4]. Transitioning from diesel-powered TRUs to hydrogen-based systems could not only reduce carbon emissions but also improve energy efficiency, as hydrogen fuel cells can provide a cleaner and more sustainable energy source for refrigeration [4].

The integration of innovative cooling systems in cold chain logistics using biomass-derived hydrogen-rich syngas presents a promising avenue for enhancing energy efficiency and reducing carbon emissions. Conventional cooling systems predominantly rely on fossil fuels, which contribute significantly to greenhouse gas emissions and energy consumption [5].

Biomass gasification is a thermochemical conversion process that occurs at temperatures between 700°C and 1200°C, where biomass is broken down in the presence of a gasifying agent such as air, oxygen, or steam. This process generates hydrogen-rich syngas composed of hydrogen (H_2), carbon monoxide (CO), methane (CH_4), carbon dioxide (CO_2), and other trace gases [3, 4]. Feedstocks such as olive pomace, green waste, and sewage sludge are particularly suitable due to their abundance and potential for waste valorization [3, 4]. To maximize hydrogen yield, the syngas undergoes processes like the Water-Gas Shift (WGS) reaction, which converts CO and water into additional hydrogen and CO_2, and Pressure Swing Adsorption (PSA), which separates and purifies hydrogen for energy applications [3, 7]. These methods are essential for enhancing the viability of hydrogen as a clean energy source for refrigeration systems.

The application of hydrogen-rich syngas in cooling systems can be approached through two main methodologies. The first involves the use of fuel cell-assisted cooling systems, where hydrogen is utilized in proton exchange membrane fuel cells (PEMFC) or solid oxide fuel cells (SOFC) to generate electricity. This electricity can then power traditional refrigeration units, while the waste heat generated from the fuel cells can be harnessed for absorption cooling cycles, thereby enhancing the overall energy efficiency of the system [8]. The second approach employs absorption cooling systems that utilize the waste heat from hydrogen combustion or fuel cells to drive lithium bromide-water (LiBr-H_2O) or ammonia-water (NH_3-H_2O) absorption cycles. This method is particularly advantageous for mobile cold storage applications in remote areas, where traditional energy sources may be limited [9].

The environmental benefits of utilizing biomass-derived hydrogen in cold chain logistics are substantial. By replacing diesel generators with biohydrogen-based energy solutions, carbon emissions can be significantly reduced, contributing to a more sustainable energy landscape [10]. Furthermore, this approach supports energy independence in rural and developing regions, where biomass resources are often abundant and underutilized [11]. The economic viability of hydrogen-based cooling systems is also noteworthy, as they typically require lower operational costs and maintenance compared to conventional systems, making them an attractive long-term solution for cold chain logistics [12].

Life cycle assessment (LCA) is crucial for evaluating the environmental and economic feasibility of the proposed

hydrogen-rich syngas cooling systems. LCA allows for a comprehensive analysis of the environmental impacts associated with the entire lifecycle of the cold chain logistics, from biomass feedstock sourcing to the end-of-life disposal of refrigeration systems [7, 13]. The integration of renewable energy sources, such as solar and wind, into the cold chain has also been explored, indicating potential pathways for decarbonizing the refrigeration sector [14, 15]. By employing innovative technologies and sustainable practices, the cold chain can transition towards a more environmentally friendly model that aligns with global sustainability goals.

2. MATERIALS AND METHODS

2.1 Definition of the Study

This study investigates the production and utilization of hydrogen derived from biomass gasification for sustainable cold chain logistics. Biomass feedstock, including green waste, sewage sludge, and olive pomace, is gasified to generate a hydrogen-rich syngas. Produced hydrogen is then used as the sole energy source for refrigerated trucks, covering both propulsion and cooling demands. A life cycle analysis is performed to assess the environmental impacts of this integrated system. Also, to better illustrate the positive impact of the hydrogen-powered truck in cold chain logistics, a comparative life cycle assessment was also conducted under identical conditions and system parameters for a conventional diesel truck. This comparison enables a clearer understanding of the environmental advantages offered by hydrogen as a fuel alternative.

For green waste gasification, the cultivation of trees and grass, gasification of green waste, gasifier production, and gas cleaning systems have been evaluated. Moreover, for sewage sludge gasification, sewage sludge formation in wastewater treatment facilities, gasification of sewage sludge, gasifier production, and gas cleaning systems have been analyzed. Lastly, for olive pomace gasification, planting and cropping of olive, olive oil production and olive pomace formation, transportation, gasification, and gas cleaning systems have been evaluated. After stage 1 and stage 2, hydrogen use in cold chain logistics is investigated.

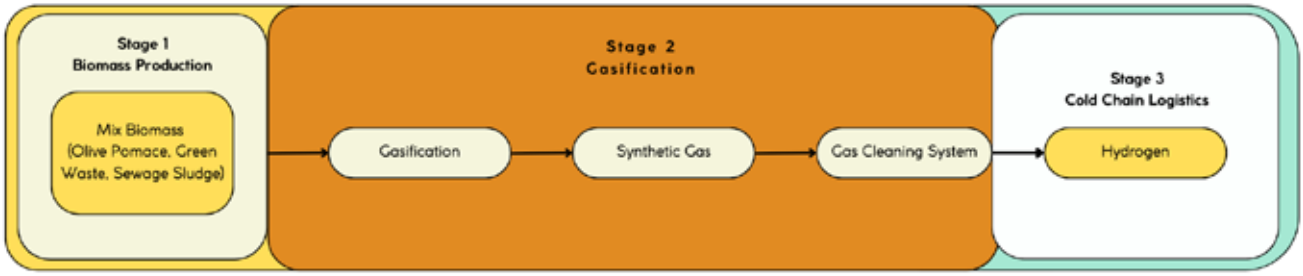

Fig. 1. System description

2.2 Functional Unit

The functional unit is a quantified definition of a product function, and it is a reference for all calculations during the impact assessment. In this study, the functional unit is defined to evaluate the environmental impact of cold chain logistics operations. Given the high variability in cold chain systems, certain parameters were standardized to ensure consistency. A medium-duty truck suitable for refrigerated transport was selected, with a curb weight of 3320 kg and a frontal surface area of 3.762 m². The logistics operation is modeled for the city of İzmir, Türkiye, during the month of July, where the average ambient temperature is approximately 28 °C and the urban speed limit for trucks is 50 km/h. The truck departs from a central storage facility carrying 1200 kg of food products maintained at 4 °C (it is a standart value for cold chain logistic guidelines in Türkiye for dairy products), travels a total of 100 km within the city, and operates for 8 hours per day at an average speed of 50 km/h. Under these specific conditions, a single distribution trip made by the truck is defined as the functional unit.

2.3 System Boundaries

The system boundaries for this study are defined as gate-to-gate, encompassing the production and utilization of hydrogen for cold chain logistics. The system includes the gasification of biomass to produce syngas, the subsequent cleaning and processing of the syngas, and the use of the resulting hydrogen as fuel in refrigerated transport. Specifically, the scope covers the energy consumption associated with a single truck's daily operation—from the moment it departs the storage facility in the morning until the completion of its delivery route after eight hours of operation. All fuel consumption, including that required for vehicle propulsion and refrigeration, is included within the system boundaries.

2.4 Calculations

$$F_{drag} = \frac{1}{2} \times \rho \times Cd \times A \times v^2 \quad , \quad E_{drag} = \frac{Fdrag \times d}{3{,}16\times10^6} \tag{1}$$

$$F_{roll} = m \times g \times Cr \quad , \quad E_{roll} = \frac{Froll \times d}{3{,}16\times10^6} \tag{2}$$

$$F_{slope} = m \times g \times sin\theta \quad , \quad E_{slope} = \frac{Fslope \times d}{3{,}16\times10^6} \tag{3}$$

$$Q = m_{load} \times Cp \times \Delta T, \quad P = \frac{Q}{t}, \quad E_{cooling} = P \times t \tag{4}$$

$$E_{total} = E_{drag} + E_{roll} + E_{slope} + E_{cooling}, \quad E_{total} = 95.313 \text{ kWh} \tag{5}$$

$$m_{H2} = \frac{E_{total}}{\eta_{SOFC} \times \text{LVH2}} = \frac{95.313}{0.55 \times 33.33} = 5.2 \text{ kg hydrogen} \tag{6a}$$

$$V_{diesel} = \frac{E_{total}}{\eta_{dizel\ motoru} \times \text{LHVdiesel}} = \frac{95.313}{0.3 \times 9.7} = 32.75 \text{ L diesel} \tag{6b}$$

Table 1. Description of parameters used in calculations

Parameter	Description	Value	Source
A	Frontal area of the truck, m^2	3.762	[16]
ρ	Air density for İzmir at 28°C, kg/m^3	1.158943	[17,18]
C_d	Coefficient of aerodynamic drag	0.7	[16]
C_r	Coefficient of aerodynamic drag	0.01	[16]
v	Average vehicle velocity, km/h	50	-
d	Distance traveled, km	100	-
t	Time duration of journey, h	8	-
g	Gravitational constant, m/s^2	9.81	-
m	Gross vehicle weight, kg	3320	[16]
m_{load}	Payload of vehicle, kg	1200	-
θ	Road gradient for İzmir, degrees	1.72 – 4.00	
C_p	Specific heat value of food carried, kJ/kg°C	3.9	
ΔT	Temperature difference between inside and outside, °C	28-4=24	-
LHV_{diesel}	Lower Heating Value of diesel fuel, kWh/L	9.7	
LHV_{H2}	Lower Heating Value of hydrogen, kWh/kg	33.33	
η_{SOFC}	Efficiency parameter for SOFC used in hydrogen powered vehicles, %	0.55	
η_{diesel}	Efficiency parameter for diesel engines, %	0.3	
Q	Thermal energy required to maintain cargo temperature inside the refrigerated truck during transport, kJ	112320	-
F_{drag}	Aerodynamic drag force, N	294.4106	-
E_{drag}	Aerodynamic drag energy required to overcome air resistance during motion, kWh	8.1781	-
F_{roll}	Rolling resistance force, N	443.4120	-
E_{roll}	Rolling resistance energy due to friction between tires and road, kWh	12.3170	-
F_{slope}	Gravitational slope resistance force, N	2212.4350	-
E_{slope}	Gravitational potential energy required to overcome road slope, kWh	61.4565	-
$E_{cooling}$	Total cooling energy required by the refrigeration unit to maintain internal temperature, kWh	31.2000	-
E_{total}	Total energy demand of the refrigerated transport operation, kWh	113.4730	-
V_{diesel}	Volume of diesel consumed, L	38.99	-
m_{H2}	Mass of hydrogen consumed, kg	6.19	-

2.5 Impact Assessment Methodology

A life cycle assessment was conducted in accordance with the ISO 14040 series to evaluate the environmental impacts of producing hydrogen through biomass gasification and its subsequent use in cold chain logistics. All LCA calculations were carried out using SimaPro 9.1 software. The “Ecoinvent 3 – allocation, cut-off by classification” has been chosen as the central database for this study, and the calculation method, Center of Environmental Science of Leiden University (CML)-IA Baseline V3.06 / EU25, has been chosen. CML-IA Baseline calculates eleven different impact categories from the environmental aspect.

3. RESULTS AND DISCUSSION

Through a series of calculations, the total energy required (5) by the truck for both driving operations (1, 2, 3) and refrigeration (4) was determined. To meet this energy demand, the amount of hydrogen needed for the hydrogen-powered vehicle was calculated using Formula (6a), while the required diesel fuel for the comparison scenario was determined using Formula (6b). As a result of these calculations, the total hydrogen demand was found to be 6.19 kg. Based on this figure, the corresponding amount of syngas required to supply the necessary hydrogen was also estimated.

Syngas produced via the gasification of mixed biomass at 900°C contains approximately 47% hydrogen by volume and has a calorific value of 11.73 MJ/m³. Assuming a gasification efficiency of 60%, 120.127 m³ of syngas must be generated to obtain 6.19 kg of hydrogen.

The required biomass input was calculated in reverse to produce 120.127 m^3 of syngas. By feeding a homogeneous blend consisting of 46.64 kg from each biomass type (green waste, olive pomace, sewage sludge) into the gasification unit, the necessary volume of syngas was successfully produced to meet the hydrogen demand.

Following all calculations, all elements within the defined system boundaries were entered into the SimaPro software, and a life cycle analysis was conducted. The results of the calculations are shown in Table 2.

Table 2. LCA results

Impact category	Unit	LCA Results
Abiotic depletion	kg Sb eq	0,002207574
Abiotic depletion (fossil fuels)	MJ	266,21189
Global warming (GWP100a)	kg CO_2 eq	64,495167
Ozone layer depletion (ODP)	kg CFC-11 eq	2,80E-06
Human toxicity	kg 1,4-DB eq	57,247487
Freshwater aquatic ecotox.	kg 1,4-DB eq	25,815102
Marine aquatic ecotoxicity	kg 1,4-DB eq	43108,447
Terrestrial ecotoxicity	kg 1,4-DB eq	0,37980334
Photochemical oxidation	kg C_2H_4 eq	-0,43073956
Acidification	kg SO_2 eq	0,8162006
Eutrophication	kg PO_4^{---} eq	0,35885198

4. CONCLUSIONS

This study demonstrated the feasibility of using hydrogen, produced via gasification of three different biomass sources (sewage sludge, olive pomace, and green waste), as a clean fuel alternative in cold chain logistics. The synthesis gas derived from each biomass showed high hydrogen content, supporting its suitability as a feedstock for hydrogen production.

LCA results indicate that the hydrogen production and its use in logistics have relatively low environmental impacts in several critical categories. The global warming potential (64.5 kg CO_2 eq) and abiotic depletion of fossil fuels (266 MJ) suggest a significant reduction compared to conventional diesel-based logistics systems. Furthermore, the negative value observed in the photochemical oxidation potential (-0.43 kg C_2H_4 eq) indicates a possible benefit in terms of reducing ground-level ozone formation. However, high values in marine aquatic ecotoxicity (43108 kg 1,4-DB eq) and human toxicity (57.2 kg 1,4-DB eq) suggest that some emissions, possibly related to the biomass feedstock or gasification process, may require mitigation strategies or process optimization in future implementations.

REFERENCES

1. Marchi B, Zanoni S and Jaber M. 2020. Energy implications of lot sizing decisions in refrigerated warehouses. Energies, 13(7), 1739.
2. James S. and James C. 2010. The food cold-chain and climate change. Food Research International, 43(7), 1944-1956. https://doi.org/10.1016/j.foodres.2010.02.001
3. Gallo A, Accorsi R, Baruffaldi G and Manzini R. 2017. Designing sustainable cold chains for long-range food distribution: energy-effective corridors on the silk road belt. Sustainability, 9(11), 2044. https://doi.org/10.3390/su9112044
4. Tezer O., Karabag N., Ongen A., Çolpan C.Ö., Ayol A. 2022. Biomass gasification for sustainable energy production: A review. International Journal of Hydrogen Energy, 47(34), 15419-15433.
5. Meneghetti A, Pagnin C and Simeoni P. 2021. Decarbonizing the cold chain: long-haul refrigerated deliveries with on-board photovoltaic energy integration. Sustainability, 13(15), 8506. https://doi.org/10.3390/su13158506
6. Matveev K and Leachman J. 2023. Rate of para-orthohydrogen conversion in cryogenic vortex tube. Journal of Fluid Flow Heat and Mass Transfer. https://doi.org/10.11159/jffhmt.2023.003
7. Kumar N, Tyagi M and Sachdeva A. 2022. A sustainable framework development and assessment for enhancing the environmental performance of cold supply chain. Management of Environmental Quality an International Journal, 34(4), 1077-1110. https://doi.org/10.1108/meq-03-2022-0046
8. Ozlu S and Dincer I. 2016. Analysis and evaluation of a new solar energy-based multigeneration system. International Journal of Energy Research, 40(10), 1339-1354. https://doi.org/10.1002/er.3516
9. Spertino F, D'Angola A, Enescu D, Leo P, Fracastoro G and Zaffina R. 2016. Thermal–electrical model for energy estimation of a water cooled photovoltaic module. Solar Energy, 133, 119-140. https://doi.org/10.1016/j.solener.2016.03.055
10. Yuksel Y. 2020. Jeotermal enerji kaynaklı multi-jenerasyon enerji sisteminin termodinamik ve performans değerlendirmesi. El-Cezeri Fen Ve Mühendislik Dergisi. https://doi.org/10.31202/ecjse.648657
11. León M, Silva J, Ortíz-Soto R and Carrasco S. 2023. A techno-economic study for off-grid green hydrogen production plants: the case of chile. Energies, 16(14), 5327. https://doi.org/10.3390/en16145327
12. Shenton M. 2024. Development of a research cryostat for direct thermoacoustic cooling and conversion of hydrogen. Iop Conference Series Materials Science and Engineering, 1301(1), 012069. https://doi.org/10.1088/1757-899x/1301/1/012069
13. Heard B. and Miller S. 2016. Critical research needed to examine the environmental impacts of expanded refrigeration on the food system. Environmental Science & Technology, 50(22), 12060-12071. https://doi.org/10.1021/acs.est.6b02740
14. Garcia J. 2024. Sustainable CO2 refrigeration system for fish cold storage facility using a renewable integrated system with solar, wind, and tidal energy for Cape Verde—analyzing scenarios. Sustainability, 16(10), 4259. https://doi.org/10.3390/su16104259
15. Khosla R, Miranda N, Trotter P, Mazzone A, Renaldi R, McElroy C and McCulloch M. 2020. Cooling for sustainable development. Nature Sustainability, 4(3), 201-208. https://doi.org/10.1038/s41893-020-00627-w
16. Lin H. J, Chen P. C, Lin H. P, Hsieh I. Y. L. 2025. Quantifying carbon emissions in cold chain transport: A real-world data-driven

approach. Transportation Research Part D: Transport and Environment, 142, 104679.
17. https://www.omnicalculator.com/physics/air-density. Accessed on March 2, 2025.
18. https://www.karabaglar.bel.tr/files/10-iklim-verileripdf_23-10-2017_11-36-54.pdf. Accessed on March 2, 2025.

DEVELOPMENT OF STABILITY AND EFFICIENCY OF $CsPbBr_3$ PEROVSKITE SOLAR CELLS

[1*]*Şeyda TÜZÜNER*, [2]*Othman Haji MAHMOOD*, [3]Şule ERTEN ELA, [4] Alberto VOMIERO
*Corresponding author e-mail: suleerten@yahoo.com

ABSTRACT

Perovskite-based solar cells have emerged as promising candidates for efficient and cost-effective solar energy conversion. In particular, $CsPbBr_3$ perovskite materials offer excellent thermal stability and suitable bandgap for integration with water-splitting systems. This project focuses on utilizing $CsPbBr_3$ perovskite solar cells to drive hydrogen production through photoelectrochemical water splitting.

The Project aims successful hydrogen production electrochemically by $CsPbBr_3$ based perovskite solar cell (PSC) was designed layers as ITO/TiO_2/Perovskite/SpiroOMeTAD/Au. $CsPbBr_3$ is the best perovskite structure that can provide the required voltage for H_2 production. However, the main criticisms related to cell stability and improved V_{oc} still exist. Also, we aimed to integrate carbon besed quatnum dots into the perovskite layer with the antisolvent applicaiton. Such nanostructures may exert an antisolvent role, increasing the crystal quality, surface defect treatments of the film, and increasing the solar cell performance. In this study, 2.5X2.5 cm scaled perovskite solar cells were produced with high Voc (>1.35 V) target by increasing efficiency and controlling stability and using them in hydrogen evolution reactions. However, the main purpose is to generate the perovskites contain high V_{oc} value resulting the highest power conversion efficiency with high stability and combine the solar energy and water splitting process to produce ~12 ml H_2 gas in 100 s by ardunio uno system. We have aimed to provide sufficient voltage for producing H_2 throughout one perovskite cell.

Keywords: Perovskite Solar Cells,

1. INTRODUCTION

Cesium lead tribromide ($CsPbBr_3$) perovskite exhibits remarkable resilience against environmental factors such as light exposure, humidity, heat, and oxygen, rendering it a promising candidate for applications in photoelectric devices, communication systems, power plants, satellites, spacecraft, and space-based solar power installations. However, the development of $CsPbBr_3$ perovskite solar cells (PSCs) has been limited compared to their organic–inorganic hybrid counterparts. This is primarily due to $CsPbBr_3$'s relatively large optical bandgap, which restricts its ability to absorb a broad spectrum of sunlight. This limitation can lead to increased recombination losses at interfaces and grain boundaries because of energy level mismatches.

Xue et al, (2016), presented that the inclusion of polar functional groups on the polymer side chains enhances the surface energy of the hole selective layers (HSLs), resulting in improved wetting with the perovskite films and higher crystallinity films. High-performance $CH_3NH_3PbI_xCl_{3x}$ perovskite solar cells with a power conversion efficiency of 16.6% (Voc: 1.07 V) and $CH_3NH_3Pb(I_{0.3}Br_{0.7})_xCl_{3x}$ cells with a PCE of 10.3% (Voc: 1.34 V) might be realized in the presence of HSLs [1].

In this project, a photoelectrochemical water electrolysis system that can separate hydrogen and oxygen gases was constructed based on the perovskite solar cell to detect photo-assisted hydrogen and oxygen synthesis in a photoelectrochemical water splitting system. Depending on the electrode characteristics, it follows distinct reaction routes. Table 1 summarizes the widely known potential reaction processes in acidic and alkaline electrolytes [2-3]

Table 1. Reaction pathways of HER in acidic and alkaline electrolytes

Overall Reaction	Intermediate Reaction Steps
$2H^+ + 2e^- \leftrightarrow H_2$ (Electrolyte; Acidic Solutions) $2H_2O + 2e^- \leftrightarrow H_2 + 2OH^-$	$M + H^+ + e^- \leftrightarrow M\text{-}H^*$ $M\text{-}H^* + H^+ + e^- \leftrightarrow M + H_2$, $2M\text{-}H^* \leftrightarrow 2M + H_2$
$2H_2O + 2e^- \leftrightarrow H_2 + 2OH^-$ (Electrolyte; Alkaline Solutions)	$M + H_2O + e^- \leftrightarrow M\text{-}H^* + OH^-$ $M\text{-}H^- + H_2O + e^- \leftrightarrow M + OH^* + H_2$

$CsPbBr_3$ is a stable orthorhombic structure at room temperature. It has higher carrier mobility, better optical properties and superior stability in humid and high temperature environments. These properties make it a suitable candidate for photovoltaic device applications. Despite its high stability, its efficiency is around 10%, making it an attractive material for many researchers to increase its efficiency. It has been reported that $CsPbBr_3$ solar cell device without any encapsulation can maintain 80% of its initial PCE after 120 days at 25 °C, 80% RH and 90% after 30 days at 85 °C, 85% RH [4].

Overall, PV-EC hybrid systems can enhance solar-to-hydrogen (STH) conversion efficiency by incorporating optimal electrocatalysts that operate at low potentials alongside stable photovoltaic cells and electrolysis units. Compared to PC and PEC systems, a key benefit of PV-EC setups is their superior STH efficiency due to the hybrid configuration.

Basically, Perovskite solar cells are placed outside the electrolysis system and can be connected to electrocatalysts that fall into two main categories, creating a photovoltaic-electrocatalytic system (PV-EC). Specifically, an electrocatalytic system can include a photoelectroactive electrode (anode or cathode), creating a subtype known as a photovoltaic-photo-electrocatalytic (PV PEC) system.

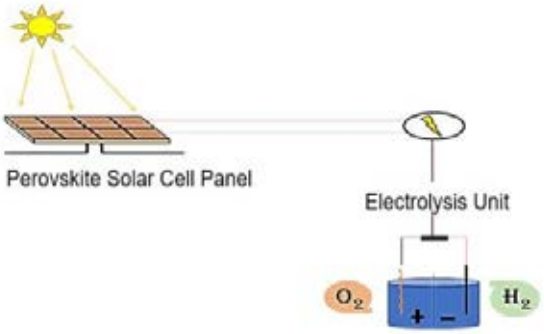

Fig. 1. Perovskite solar cell panel as an external power supply in the water splitting process

2. MATERIALS AND METHODS

- All quantum dots (QDs) was prepared by using colloidal synthesis and All QDs was fully characterized optically and structurally using UV-vis absorption, PL and TRPL spectroscopy, FTIR and NMR spectroscopy, EDX, TGA, XPS, TEM, and XRD. Thin film deposition of the QDs was performed using spin-coating. Prior to this, to enhance the coupling between the QDs in the thin film and increase the mobility, surface ligand exchange was carried out to substitute the bulky, insulating pristine ligands with small molecules or ions.
- Perovskite Solar Cells were designed as ITO/TiO_2/Perovskite/SpiroOMeTAD/Au by following the procedure steps as below;

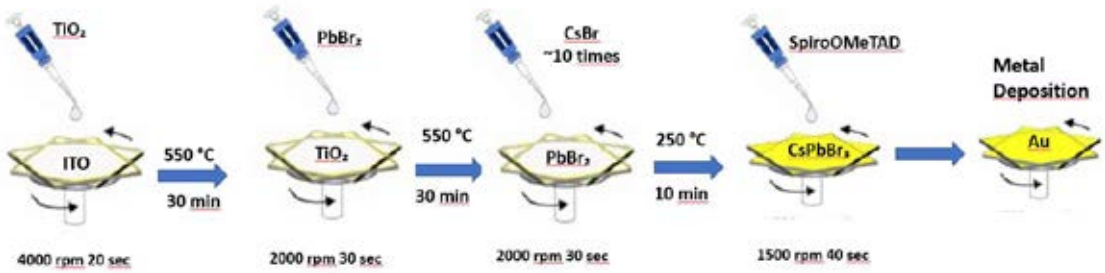

Fig. 2. Fabrication Process Steps for $CsPbBr_3$ Solar Cells.

- Characterization of synthesized perovskite solar cell components; Crystal structures, optical properties, band gaps, efficiency and stability tests

- Crystal structures was determined with the data obtained by Fourier Transform Infrared Spectroscopy (FT-IR) and X-ray diffraction (XRD) analyses. The change in the peaks belonging to functional groups was detected.

- Morphological and structural characterizations of both synthesized components and additives will be carried out with Scanning Electron Microscope (SEM), Transmission Electron Microscope (TEM), and information was obtained about important parameters such as surface properties, homogeneity, laticce gaps

- Structural characterizations was carried out with X-Ray Photoelectron Spectrometry (XPS) technique and the change in bond energies will be determined.

- Optical properties and band gaps of the synthesized materials was determined by UV-vis Spectrum and Photoluminescence Spectroscopy analysis.

- Hydrogen gas detection system was established with ardunio uno detector.

3. RESULTS AND DISCUSSION

Quantum dot structures have an important place in the development of today's technologies. Carbon based quantum dots were synthesized and used in perovskite solar cells in the project. The produced perovskite solar cells was used as an external power supply in the water splitting process for green hydrogen. Green hydrogen can be produced by electrolysis method, which uses renewable energy source as energy source and is one of the most important methods used to separate water into hydrogen and oxygen.

It is stated that several cells of both structures were connected in series, in order to obtain the minimum Gibbs free energy potential of 1.23 eV theoretically and 1.8 eV practically for electrochemical hydrogen production. This expresses the minimum amount of energy required to split water molecules into hydrogen and oxygen during water electrolysis. Theoretically, an energy of 1.23 eV is required for this process; however, in practice, this value is usually higher, up to 1.8 eV, due to losses in the system and additional resistances that must be overcome. Therefore, in order to obtain the desired potential difference and to ensure efficient separation of water, a certain number of cells are connected in series.

In this study, 2.5X2.5 cm scaled perovskite solar cells were produced with high Voc (>1.35 V) target by increasing efficiency and controlling stability and using them in hydrogen evolution reactions. However, Based on our measurements the highest Voc was found as 1,10 V as shown in table 2 and we will connect serial the two PSCs to reach 2,20 V for hydrogen evolution process.

The main purpose is to generate the perovskites contain high V_{oc} value resulting the highest power conversion efficiency with high stability and combine the solar energy and water splitting process to produce ~12 ml H_2 gas in 100 s by ardunio uno system.

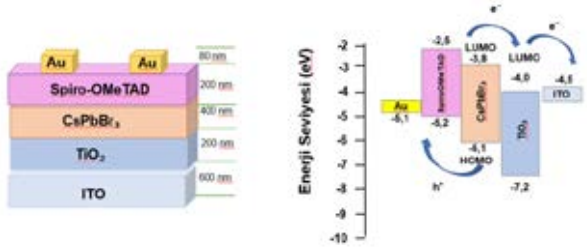

Fig. 4. Schematic Illustration of Perovkite Solar Cell Energy Band Diagram

Table 2. Perovskite Solar Cell Device Measurement.

Sample	Jsc (mA cm-2)	Voc (mV)	FF (%)	PCE (%)
TiO_2 - Spiro	1,39	1110	39,86	0,62

4. CONCLUSIONS

Green hydrogen production by producing hydrogen from green sources is very important in the next 30 years and the support in this field is gradually increasing. The study supports both perovskite solar cell production and green hydrogen production, that is, clean hydrogen production with new generation solar cells via the electrolysis system.

In this study, perovskite solar cells were fabricated to function as an external power source for hydrogen evolution reactions (HER). One of the major challenges facing perovskite solar cells is their stability. Therefore, enhancing both their efficiency and stability is crucial, and various methods have been explored in the literature to tackle this issue. This project presents a novel strategy involving the integration of quantum dots into the perovskite solar cell structure. Carbon based quantum dots, found to be energetically compatible, were utilized as substitutes for TiO_2 in the electron transport layer.

In summary, the advancement of perovskite device architecture is significantly limited by issues such as the accelerated degradation of the perovskite absorber under high temperatures or humid conditions, as well as inefficient charge

transport due to severe charge recombination at grain boundaries. To address these challenges, this study also investigated the influence of environmental and long-term stability on device performance, along with strategies to enhance open-circuit voltage by minimizing charge recombination.

ACKNOWLEDGEMENT
We would like to express our sincere gratitude to The Scientific and Technological Research Council of Türkiye (TÜBİTAK) and the Italy CNR for their invaluable support through the Bosphorus Program with the project number is 122N947. We also extend our appreciation to all individuals and institutions who contributed to the successful completion of this research.

REFERENCES

1. Xue Q, Chen G, Liu M, Xiao J, Chen Z, Hu Z, et al. Improving Film Formation and Photovoltage of Highly Efficient Inverted-Type Perovskite Solar Cells through the Incorporation of New Polymeric Hole Selective Layers. Adv Energy Mater 2016;6:1–9. https://doi.org/10.1002/aenm.201502021.
2. L. Sun, F.-Q. Bai, Z.-X. Zhao and H.-X. Zhang, Design of new benzothiadiazole-based linear and star molecules with different functional groups as solar cells materials: A theoretical approach, Solar Energy Materials and Solar Cells, 2011, 95 (7), 1800-1810, https://doi.org/10.1016/j.solmat.2011.02.003.
3. E.L. Miller, R.E. Rocheleau and X.M. Deng, Design considerations for a hybrid amorphous silicon/photoelectrochemical multijunction cell for hydrogen production, International Journal of Hydrogen Energy, 2003, 28 (6), 615-623, https://doi.org/10.1016/S0360- 3199(02)00144-1.
4. Zhou Q, Duan J, Yang X, Duan Y, Tang Q. Interfacial strain release from the WS2/CsPbBr3 van der Waals heterostructure for 1.7 V voltage all-inorganic perovskite solar cells. Angew Chem Int Ed. 2020;132(49):22181-22185. doi:10.1002/anie. 202010252

DEVELOPMENT OF STABILITY AND EFFICIENCY OF $FAPbI_3$ PEROVSKITE SOLAR CELLS FOR HYDROGEN EVOLUTION

[1]*Şeyda TÜZÜNER,* [2]*Othman Haji MAHMOOD,* [3]Şule ERTEN ELA, [4] Peter REISS
*Corresponding author e-mail: suleerten@yahoo.com

ABSTRACT

The use of renewable energy sources obtained from natural sources (wind, solar and hydroelectric) that reduce CO_2 emissions should be our common global goal. Among these sources, solar energy is an excellent option since it is based on an environmentally friendly working principle and has high accessibility. In this context, our study aims to increase the stability and efficiency of perovskit solar cells (PSCs) containing Formaamidinium Lead Triiodide ($FAPbI_3$) for photocatalyic hydrogen production.
In this study, the PV-EC system was developed by synthesized a novel HTM and ETL used in PSCs. The cell configuration system was designed with to a series and parallel connected 2.5x2.5 cm PSCs to electrolysis unit and MQ-8 gas sensor was used for the detection of H_2 gas. This system combined a photocathode made of a p-type semiconductor and/or a photoanode made of an n-type semiconductor connected in series to an external circuit. This produced H_2 at the photocathode and O_2 at the photoanode. It was observed that the system relies on the power created by the semiconductor/electrolyte interfaces to drive the process.
This multidisciplinary study will bring together scientists working in the fields of engineering, chemistry, physics and applications solar enegy in hydrogen technologies.

Keywords: Perovskite Solar Cells, Hydrogen Evoluation, Electrochemical Green Hydrogen and Oxygen Evolution, Quantum Dots

1. INTRODUCTION

Solar energy is an important source of renewable energy to reduce our reliance on fossil fuels and has crucial impact value in decarbonizing future products. Although the cost of solar energy is increasing day by day, there is a need for new technologies that cause a gradual decrease in the cost.

One of the most effective approaches for solar energy conversion is the photocatalytic splitting of water to produce hydrogen, which has been the subject of much research in the past decades. Water splitting occurs via a chemical reduction-oxidation reaction (redox reaction) involving the hydrogen evolution reaction (HER) and the oxygen evolution reaction (OER) by acting on external energy.

The energy level of carbon dot is -5.5 eV. Hydrogen energy is a promising alternative source. It is important to obtain hydrogen from renewable energy sources in a clean way. The energy obtained in this way is called green energy. Electrolysis of water is one of the important ways in energy conversion [34]. In the project, perovkite solar cells will be used as an external power supply unit in the system that provides hydrogen production by photoelectrochemical method by providing electrolysis of water. We aimed to provide sufficient voltage to produce H_2 with the several cells of perovskite in a 2.5 cmX2.5 cm size. Hydrogen evolution reactions are the simplest electrochemical system. Commonly known reactions of the hydrogen evolution in acidic and basic electrolytes are summarized in Table 1 [1–2].

Table 1. Reaction pathways of HER in acidic and alkaline electrolytes

Overall Reaction	Intermediate Reaction Steps
$2H^+ + 2e^- \leftrightarrow H_2$ (Electrolyte; Acidic Solutions) $2H_2O + 2e^- \leftrightarrow H_2 + 2OH^-$	$M + H^+ + e^- \leftrightarrow M\text{-}H^*$ $M\text{-}H^* + H^+ + e^- \leftrightarrow M + H_2$, $2M\text{-}H^* \leftrightarrow 2M + H_2$
$2H_2O + 2e^- \leftrightarrow H_2 + 2OH^-$ (Electrolyte; Alkaline Solutions)	$M + H_2O + e^- \leftrightarrow M\text{-}H^* + OH^-$ $M\text{-}H^- + H_2O + e^- \leftrightarrow M + OH^* + H_2$

In general, PV-EC hybrid systems can increase solar-to-hydrogen (STH) conversion efficiencies by using optimum electrocatalysts with low potential for stable PV cells and electrolysis units. Compared with PC and PEC systems, one of the most notable advantages of the PV-EC system is the high STH efficiency of the hybrid structure.

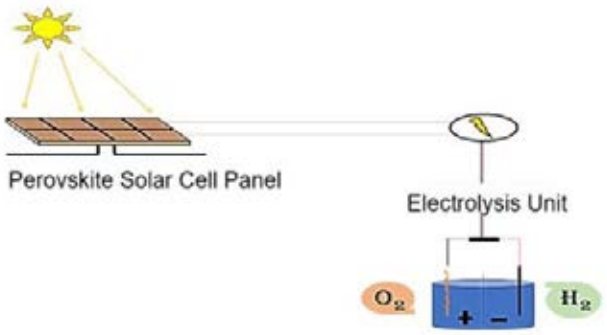

Fig. 1. Perovskite solar cell panel as an external power supply in the water splitting process

Wang et al. CsSnI3 perovskite quantum dot-based solar cells prepared with the antioxidant solvent additive triphenyl phosphite (TPPi) retained 72% of the initial PCEs after 30 days of aging. They achieved a maximum PCE of 5.03%, the highest performance for completely inorganic lead-free perovskite solar cells [3]. Li et al fabricated CsSnI3 perovskite films with low deep trap density using vapor deposition and surface passivation strategies. CsSnI3 reverse PSCs treated with the S=C-N functional group as surface passivation retained 90% of their initial PCE after 500 hours of continuous illumination. It also presented a maximum PCE of 8.2% [4].

2. MATERIALS AND METHODS

- All quantum dots (QDs) was prepared by using colloidal synthesis and all QDs was fully characterized optically and structurally using UV-vis absorption, PL and TRPL spectroscopy, FTIR and NMR spectroscopy, EDX, TGA, XPS, TEM, and XRD. Thin film deposition of the QDs was performed using spin-coating. Prior to this, to enhance the coupling between the QDs in the thin film and increase the mobility, surface ligand exchange was carried out to substitute the bulky, insulating pristine ligands with small molecules or ions.
- Perovskite Solar Cells were designed as ITO/ETL QDs/Perovskite/HTL QDs/Au by following the procedure steps as below;

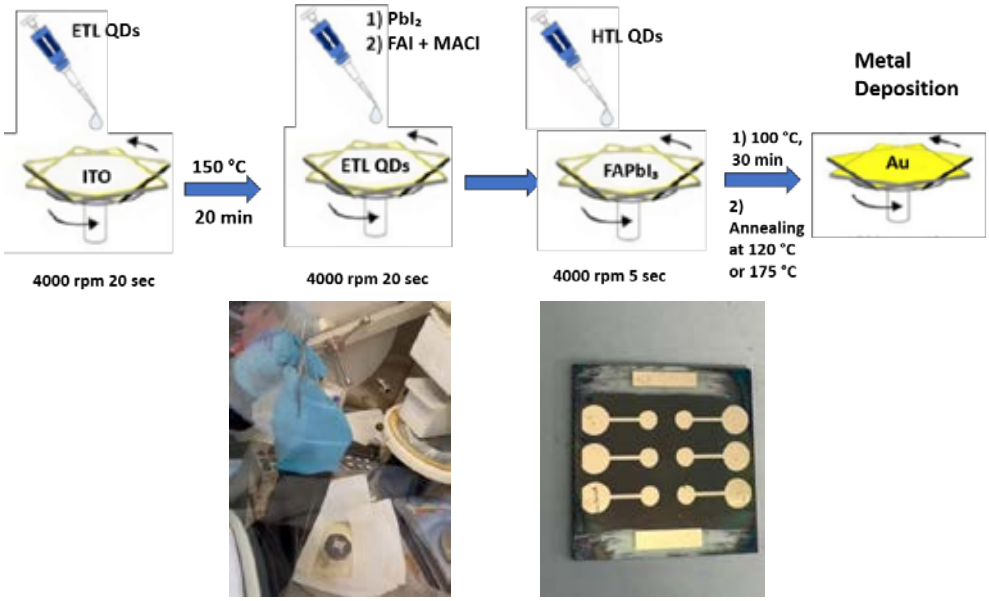

Fig. 2. Fabrication Process Steps for $FAPbI_3$ Solar Cells.

- Characterization of synthesized perovskite solar cell components; Crystal structures, optical properties, band gaps, efficiency and stability tests

- Crystal structures was determined with the data obtained by Fourier Transform Infrared Spectroscopy (FT-IR) and X-ray diffraction (XRD) analyses. The change in the peaks belonging to functional groups was detected.

- Morphological and structural characterizations of both synthesized components and additives will be carried out with Scanning Electron Microscope (SEM), Transmission Electron Microscope (TEM), and information was obtained about important parameters such as surface properties, homogeneity, laticce gaps

- Structural characterizations was carried out with X-Ray Photoelectron Spectrometry (XPS) technique and the change in bond energies will be determined.

- Optical properties and band gaps of the synthesized materials was determined by UV-vis Spectrum and Photoluminescence Spectroscopy analysis.

- Hydrogen gas detection system was established with ardunio uno detector

3. RESULTS AND DISCUSSION

Quantum dot structures have an important place in the development of today's technologies. Carbon and Cd based QDs structures were synthesized and used in perovskite solar cells in the project. The produced perovskite solar cells was used as an external power supply in the water splitting process for green hydrogen. Green hydrogen can be produced by electrolysis method, which uses renewable energy source as energy source and is one of the most important methods used to separate water into hydrogen and oxygen.

It is stated that several cells of both structures were connected in series, in order to obtain the minimum Gibbs free energy potential of 1.23 eV theoretically and 1.8 eV practically for electrochemical hydrogen production. This expresses the minimum amount of energy required to split water molecules into hydrogen and oxygen during water electrolysis. Theoretically, an energy of 1.23 eV is required for this process; however, in practice, this value is usually higher, up to 1.8 eV, due to losses in the system and additional resistances that must be overcome. Therefore, in order to obtain the desired potential difference and to ensure efficient separation of water, a certain number of cells are connected in series.

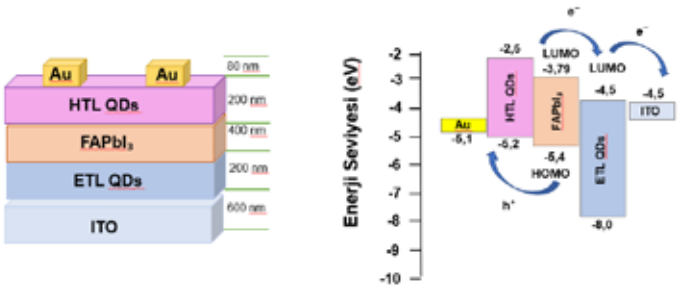

Fig. 4. Schematic Illustration of Perovkite Solar Cell Energy Band Diagram

In the project, we produced 2.5x2.5 scaled perovskite solar cells by increasing efficiency and controlling stability and using them in hydrogen evolution reactions. PSCs with high Voc (>1.20 V), and long-term stability (PCE>95% of the initial value over 1600 hours at 85 °C). Hydrogen production rate (ml s- 1) was measured over a specific time length by applying current of 1 A and generated ~10 ml H_2 and in 100 s electrolysis.

4. CONCLUSIONS

The production of clean hydrogen with the use of a renewable energy source is important and the combustion product of hydrogen produced from water is pollution-free.

In this study, perovskite solar cells was fabricated for external power supply in HER reactions. However, the most important problem in Perovskite solar cells is about stability. It is very important to improve efficiency and stability in perovskite solar cells. There are different approaches to this in the literature. With this project, a different approach was demonstrated with the use of quantum dots in perovkite solar cells. Since it has been determined that carbon and Cd based quantum dot structures are energy compatible, they can be used instead of TiO_2 in perovskite solar cells as electron transport layer. And also Cu and Ga based quantum dots was used as hole transport layer. It has also been observed that efficiency and stability are improved in studies with quantum dots.

To sum up, factors such as accelerated degradation of the perovskite absorber at high temperature or ambient humidity and insufficient charge-carrying capacity due to severe charge recombination at the perovskite grain boundary significantly hinder the development of perovskite device architecture. Therefore, the interrelated effects of environmental and long-term stability of the PSC device, the open circuit voltage increase also investigated by avoiding charge recombination.

ACKNOWLEDGEMENT
We would like to express our sincere gratitude to The Scientific and Technological Research Council of Türkiye (TÜBİTAK) and the French Ministry of Foreign Affairs for their invaluable support through the Bosphorus Program with the project number is 123N879. We also extend our appreciation to all individuals and institutions who contributed to the successful completion of this research.

REFERENCES

1. L. Sun, F.-Q. Bai, Z.-X. Zhao and H.-X. Zhang, Design of new benzothiadiazole-based linear and star molecules with different functional groups as solar cells materials: A theoretical approach, Solar Energy Materials and Solar Cells, 2011, 95 (7), 1800-1810.
2. E.L. Miller, R.E. Rocheleau and X.M. Deng, Design considerations for a hybrid amorphous silicon/photoelectrochemical multijunction cell for hydrogen production, International Journal of Hydrogen Energy, 2003, 28 (6), 615-623.
3. Y. Wang, J. Tu, T. Li, C. Tao, X. Deng and Z. Li, Convenient preparation of CsSnI3 quantum dots, excellent stability, and the highest performance of lead-free inorganic perovskite solar cells so far, J. Mater. Chem. A, 2019, 7 (13), 7683-7690.
4. B. Li, H. Di, B. Chang, R. Yin, L. Fu, Y.-N. Zhang and L. Yin, Efficient passivation strategy on Sn related defects for high performance all-inorganic CsSnI3 perovskite solar cells, Adv. Funct. Mater., 2021, 31, 2007447.

A COMPARATIVE STUDY ON THE HYDROGEN PRODUCTION EFFICIENCY OF VARIOUS MEMBRANES IN A CHLOR-ALKALI ELECTROLYZER

[1,2*] *Serdal Damarseckin,* [2]*Esra Durar,* [2]*Ayhan Atiz,* [3]*Hatice Karakilcik,* [2]*Mehmet Karakilcik*
[1] Sirnak University, Faculty of Engineering, Department of Renewable Energy Systems Engineering, Sirnak, 73000, Türkiye
[2] Cukurova University, Faculty of Science and Letters, Department of Physics, Adana, 01250, Türkiye
[3] Cukurova University, Faculty of Engineering, Department of Geology, Adana, 01250, Türkiye
*Corresponding author e-mail: serdalseckin@hotmail.com

ABSTRACT
In this study, the hydrogen production performances of two perfluorosulfonic acid (PFSA) membranes, Nafion 212 and Nafion 117, were comparatively evaluated through chlor-alkali electrolysis using a 1 M NaCl electrolyte solution. Electrochemical experiments were carried out under constant conditions of 5 V cell voltage and 20 °C. The Nafion 212 membrane, with its significantly lower thickness (~50.8 µm) compared to Nafion 117 (~183 µm), exhibited superior electrochemical performance, as evidenced by faster hydrogen generation and higher average current values (0.93 A vs. 0.30 A). Specifically, hydrogen volumes of 10, 20, and 30 mL were produced in 1.18, 2.35, and 3.59 minutes, respectively, with Nafion 212, whereas the same volumes required 5.30, 9.40, and 13.20 minutes with Nafion 117. These results are attributed to the structural properties of Nafion 212, whose thinner membrane architecture facilitates higher proton conductivity and lower ohmic resistance, enabling enhanced hydrogen production efficiency. Conversely, Nafion 117, while offering greater mechanical robustness and long-term operational stability due to its higher thickness, imposes increased ionic resistance, thereby reducing its electrochemical efficiency under identical operational parameters. Therefore, Nafion 212 is more suitable for applications prioritizing high performance and rapid hydrogen output, whereas Nafion 117 may be advantageous in scenarios demanding extended durability and structural integrity.

Keywords: Hydrogen production, Waste batteries, Chlor-Alkali reactor, Electrolysis, Nafion Membranes

1. INTRODUCTION

Nowadays, interest in hydrogen energy is increasing in line with the goals of combating climate change and reducing carbon emissions. Hydrogen, considered as one of the clean energy sources of the future, plays a strategic role in achieving climate neutrality [1]. In this context, a new energy model called the “hydrogen economy” has been developed [2,3]. In this system, hydrogen stands out as an energy carrier that minimizes environmental impacts, especially when produced using renewable energy sources [4].

In an experiment, the hydrogen generation performance of an aqueous solution of zinc chloride ($ZnCl_2$) salt, in the chlor-alkali electrolysis method, was researched. The reactor was splitted into two compartments by Nafion 212 membrane, and $ZnCl_2$ solution was supplied to the anode section, while pure water was added to the cathode section. During the experiment process, the hydrogen production rate was saved as 0.89mL/min under a temperature of 20°C, a mass flow rate of 0.3g/s, and a voltage of 5V. On the other hand, it was recorded that under the conditions where the operating temperature was increased to 45°C and the voltage was increased to 10V, the hydrogen production rate reached 5mL/min at the same flow rate [5].

In another experiment, chlor-alkali reactor was designed to compare the hydrogen generation quantities of NaCl, KCl and $CaCl_2$ salts using aqueous solutions. The hydrogen generation performances were experimentally investigated by changing the parameters such as cell voltage, temperature and electrolyte flow rate. Since steel electrodes were used for cost-effectiveness, the amount of chlorine gas produced remained very low, while a significant amount of hydrogen gas was generated. The results show that the hydrogen production rate of KCl salt is slightly higher than NaCl, while $CaCl_2$ exhibits a significantly lower efficiency in hydrogen production [6].

In this study, Nafion 212 and Nafion 117 membranes, which stand out with their durable structures, were used to separate pure water and salt water compartments in the chlor-alkali reactor system and the hydrogen production performances of these two membranes were compared. The chlor-alkali electrolysis process supported by renewable energy sources is considered a remarkable method in terms of sustainable hydrogen production despite some technical difficulties. In this context, increasing the energy efficiency of chlor-alkali systems and enabling environmentally friendly hydrogen production are among the important goals. In achieving these goals, the main purpose of this study is to examine in detail the effects of membranes, which are one of the basic components of the system, on hydrogen production.

2. SYSTEM DESCRIPTION

The schematic representation and peripheral equipment of the reactor system designed for chlor-alkali electrolysis experiments are presented in Figure 1. The anode and cathode compartments in the reactor are isolated from each other by Nafion 212 and Nafion 117 membranes used as separators. Specially designed feed tanks were used to provide the electrolyte solution to enter the reactor, and the waste electrolytes exiting the reactor were collected in separate collection tanks. In determining the gas volumes, the measurement method based on the water displacement principle was preferred and graduated cylinders were used for this process. A direct current (DC) power source was used to provide

the necessary electrical energy to the reactor. The continuity and stability of the electrolyte flow in the system was provided by peristaltic pumps. The entire system was equipped with carbon and graphite based electrodes recovered from waste batteries, which would enable the production of hydrogen and chlorine gases during the reaction period.

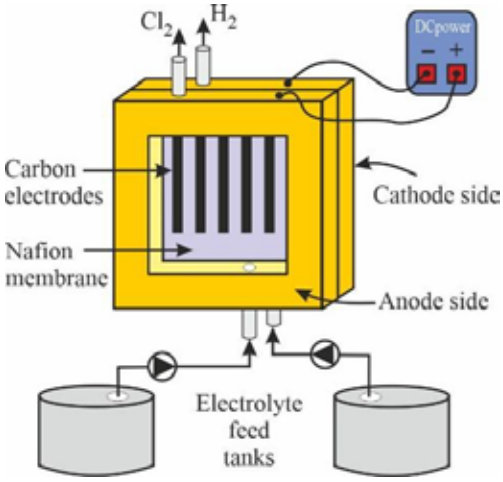

Fig. 1. The schematic representation of the experimental setup.

3. RESULTS AND DISCUSSION

In this study, chlor-alkali electrolysis method was applied using 1M NaCl solution for hydrogen production and the performances of different membrane types were evaluated. The experiments were carried out at a constant temperature of 20°C and a cell voltage of 5V. The body of the electrochemical cell was manufactured from Delrin (POM) polymer processed with CNC technology. In each experimental set, Nafion 212 and Nafion 117 membranes were used separately as separators between the anode and cathode compartments. Carbon rods recovered from waste batteries were preferred as electrodes in both compartments.

Fig. 2 presents the data of the experimental study carried out using Nafion 212 membrane. In this experiment, 1 M NaCl solution was pumped into the anode compartment and pure water into the cathode compartment so that the mass flow rate (0.3g/s) remained constant; 5V constant cell voltage, 20°C temperature and 0.93A average current value were maintained. Under these conditions, 10cm³, 20cm³ and 30cm³ of hydrogen gas were produced and collected in the cathode compartment in 1.18 minutes, 2.35 minutes and 3.59 minutes, respectively.

Fig. 3 shows the results of a similar experiment with the Nafion 117 membrane. In the experiment carried out with an average current value of 0.30A under the same temperature and cell voltage conditions, the 10cm³, 20cm³ and 30cm³ hydrogen volumes produced in the cathode compartment were obtained in 5.30 minutes, 9.40 minutes and 13.20 minutes, respectively. These findings clearly show that the Nafion 212 membrane provides hydrogen production in a shorter time and with a higher current.

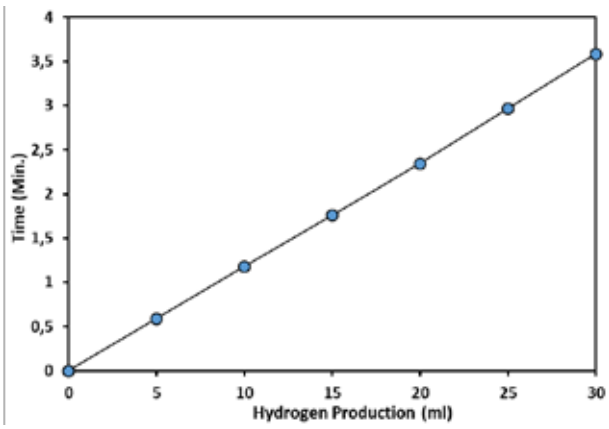

Fig. 2. Time-dependent hydrogen production for Nafion 212

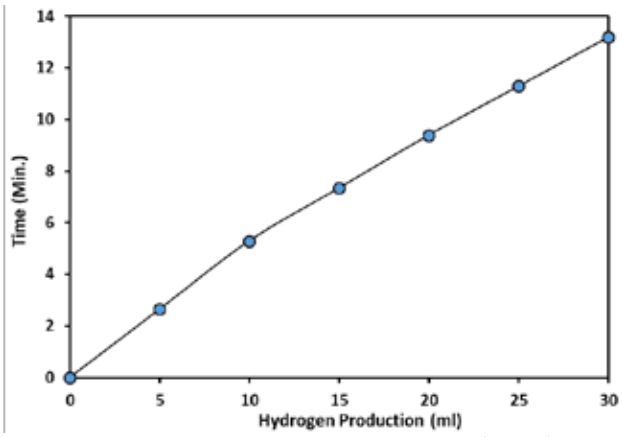

Fig. 3. Time-dependent hydrogen production for Nafion117

4. CONCLUSIONS

In this study, the hydrogen production performances of Nafion 212 and Nafion 117 membranes were evaluated using 1 M sodium chloride solution through the chlor-alkali electrolysis method. The system included carbon rod electrodes derived from spent batteries and a Delrin polymer reactor body processed via CNC machining. Each membrane was tested separately under identical conditions of 20 °C and 5 V.

Experimental data revealed that the Nafion 212 membrane enabled faster hydrogen generation, as it produced 10, 20 and 30 mL of hydrogen in 1.18, 2.35 and 3.59 minutes respectively, with an average current of 0.93 A. In contrast, the Nafion 117 membrane required significantly longer times of 5.30, 9.40 and 13.20 minutes for the same hydrogen volumes, and operated with a lower average current of 0.30 A.

These results demonstrate that Nafion 212 provides better electrochemical performance by achieving higher efficiency and shorter hydrogen production times under the same experimental conditions.

REFERENCES

1. Van Renssen S. The hydrogen solution? Nat Clim Change 2020;10(9):799–801. https://doi.org/10.1038/s41558-020-0891-0.
2. Abe JO, Popoola API, Ajenifuja E, Popoola OM. Hydrogen energy, economy and storage: review and recommendation. Int J Hydrogen Energy 2019;44(29): 15072–86. https://doi.org/10.1016/j.ijhydene.2019.04.068.
3. Bockris JOM. The hydrogen economy: its history. Int J Hydrogen Energy 2013;38 (6):2579–88. https://doi.org/10.1016/j.ijhydene.2012.12.026.
4. Nowotny J, Veziroglu TN. Impact of hydrogen on the environment. Int J Hydrogen Energy 2011;36(20):13218–24. https://doi.org/10.1016/j.ijhydene.2011.07.071.
5. Damarseckin S. Hydrogen production from ZnCl2 salt: Application of chlor-alkali method. Int J Hydrogen Energy 2024:88: 888-897.
6. Erden M., Karakilcik M. Experimental investigation of hydrogen production performance of various salts with a chlor-alkali method. Int J Hydrogen Energy 2023; 52:546-560.

PROCESS SIMULATION OF HYDROGEN GENERATION FROM BIOMASS USING ASPEN PLUS

[1,2*]*Ali Ataş*, [2]*Nader Javani*, [3]*Özgün Yücel*
[1] Istanbul Topkapi University, Department of Motor Vehicles and Transportation Technologies, 34020, Istanbul, Türkiye
[2] Yildiz Technical University, Department of Mechanical Engineering, 34210, Esenler/Istanbul, Türkiye
[3] Gebze Technical University, Department of Chemical Engineering, 41400, Gebze/Kocaeli, Türkiye
*Corresponding author e-mail: aliatas@topkapi.edu.tr

ABSTRACT

Biomass gasification integrated with Sorption-Enhanced Reforming (SER) represents a promising thermochemical pathway for producing high-purity hydrogen while lowering carbon emissions. In this study, a fixed-bed gasification model is developed and validated in Aspen Plus® using municipal solid waste (MSW) as the sole feedstock. The SER process employs calcium oxide (CaO) as a solid sorbent to capture CO_2 in-situ, thereby shifting the equilibrium of water-gas shift and reforming reactions toward enhanced hydrogen production. Simulation results indicate that hydrogen purity reaches up to 99.4% under optimal conditions of 923 K and 20 bar. For MSW, the maximum H_2 mole fraction reaches 92.8% at 1000 K. Sensitivity analyses demonstrate that gasifier temperature and air mass flow rate play critical roles in determining both the hydrogen mole fraction and mass flow rate. This study emphasizes the viability of SER-integrated MSW gasification as a scalable, efficient, and environmentally sustainable approach for clean hydrogen production, supporting the transition toward low-emission energy systems.

Keywords: Biomass gasification, Hydrogen, Sorption Enhanced Reforming

1. INTRODUCTION

Hydrogen, with its high energy density and clean combustion properties, is widely regarded as a promising energy carrier capable of replacing fossil fuels, and its production through thermochemical gasification of low-grade biomass offers a sustainable and efficient alternative to conventional fossil-based methods [1]. Sorption Enhanced Reforming (SER) of biomass is an innovative and efficient method for producing high-purity hydrogen, in which CaO is used as a CO_2 absorbent to remove CO_2 generated during gasification, thereby shifting the reaction equilibrium to favor additional hydrogen formation and enhancing both hydrogen yield and overall process efficiency [2].
The limited literature on sorption-based gasification modeling, which predominantly emphasizes kinetic approaches, lacks sufficient equilibrium-based simulations involving CaO as a CO_2 sorbent; this study addresses that gap by developing a two-stage Aspen Plus® model comprising fixed-bed gasification of municipal solid waste validated with experimental data, followed by sorption-enhanced reforming [3]. The SER system is validated using literature-based data, modeled in Aspen Plus®, and integrated downstream of the gasification unit [4].
The primary objective of this study is to simulate a Sorption Enhanced Reforming (SER) model to enhance hydrogen yield from the gasification of municipal solid waste (MSW) biomass, while simultaneously enabling CO_2 capture through CaO-based sorption, thereby increasing both the fraction and amount of hydrogen produced. Unlike previous studies in which gasification and SER models are operated separately, the novelty of this research lies in the integration of these two processes within a unified simulation framework. In this study, the effects of gasifier temperature on hydrogen fraction and air mass flow rate on hydrogen mass flow rate have been investigated. As a result, the production of nearly pure hydrogen has been made possible.

2. MATERIALS AND METHODS

This study presents the flow diagram of the sorption-enhanced staged (SER) gasification process of MSW biomass with calcium oxide (CaO) in Aspen Plus, as illustrated in Figure 1. The entire process was modeled based on mass-energy balance and chemical equilibrium principles, with the minimization of Gibbs free energy, ensuring sufficient reaction time for all chemical reactions to reach equilibrium. Biomass and ash were characterized based on ultimate and proximate analyses, while non-conventional components were defined and modeled accordingly. The Peng-Robinson equation of state was employed to calculate the physical properties of the conventional components in the simulation.The model shown in Figure 1 consists of a total of 8 unit blocks and 14 material streams. This simulation is divided into two distinct stages: gasification and Sorption-Enhanced Reforming (SER). The section up to the unit labeled 'MIX' represents the gasification stage, while the units following the 'MIX' unit represent the SER process.

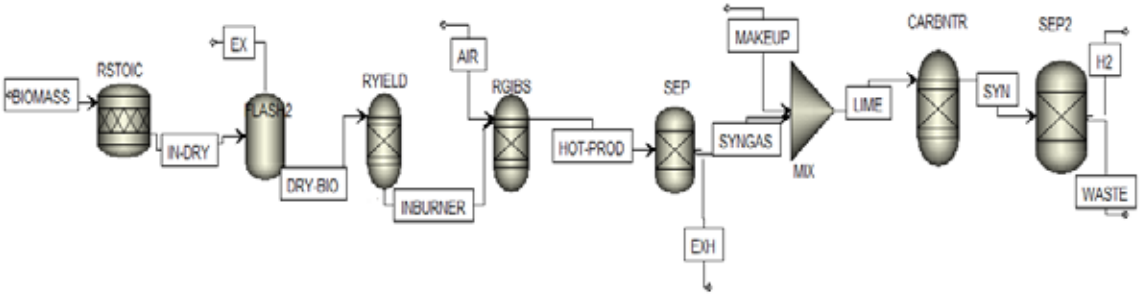

Fig. 1. Flow Diagram of the Integrated SER Process for Municipal Solid Waste (MSW) Gasification

The biomass material used in this study is municipal solid waste (MSW). The ultimate analysis of MSW is as follows: C: 36.35%, H: 4.96%, O: 10.13%, N: 1.43%, S: 0.83%, and Ash: 22.7%. The proximate analysis reveals the following composition: moisture: 50.9%, volatile matter: 18.8%, and fixed carbon: 7.6%[5].
The fixed-bed gasifier model was developed by defining the flow class and property method, identifying system components and conventional/non-conventional substances, creating the process flow diagram with connected unit operations and material/energy streams, and specifying feed streams in terms of flow rate, composition, and thermodynamic conditions. The model operates under steady-state, kinetically free, and isothermal conditions, with chemical reactions occurring at equilibrium and no pressure drop. Biomass is considered a non-conventional feedstock, and all elements except sulfur participate equally in the reactions. Gases are assumed to behave as ideal gases and volatile matter consists of carbon, H_2, and O_2. Tars are treated as non-equilibrium products to simplify hydrodynamics, and calcium oxide (CaO) is defined as a solid feed to the system [6].

3. RESULTS AND DISCUSSION

The simulation model developed in Aspen Plus consists of two stages: the first stage is the gasification process, and the second stage is the sorption-enhanced reforming (SER) process. These two stages were validated separately through relevant literature studies. The gasification model was validated based on the experimental studies conducted by Naveed et al. as part of their laboratory work[7]. The SER stage was validated using the studies carried out by Yücel and Aydın [1]. Subsequently, the SER process was integrated into the gasification stage. The model validation was carried out by comparing the obtained results with previous studies. Accuracy was assessed using the widely used metric, Root Mean Square Error (RMSE). RMSE quantitatively measures the deviation between predicted and actual values, indicating the model's performance.[8]. The syngas composition obtained from the experiments was found to be similar to the syngas content predicted by the developed Aspen Plus model, with an RMSE value of 3.90 for MSW. In the study conducted by Begum et al., the RMSE value for the MSW validation was found to be approximately 3. The RMSE value of the Sorption Enhanced Reforming unit was found to be 0.68.
In the simulation, the reaction temperature ranges from 800 K to 1500 K, while the system pressure remains constant at 1 bar. Figure 2 illustrates the H_2 mole fraction of MSW (Municipal Solid Waste) as a function of temperature after the integration of the sorption-enhanced reforming unit.

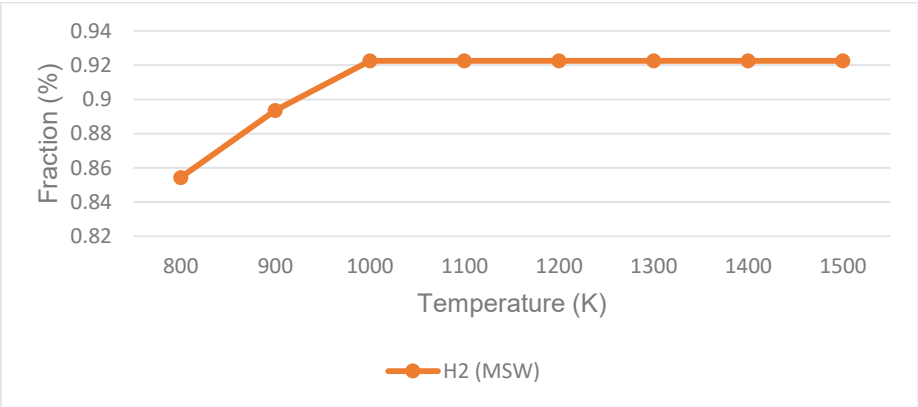

Fig. 2. Impact of Gasification Temperature on MSW Syngas Composition

The temperature variation takes place in the Rgibbs reactor during the gasification stage. The H_2 mole fraction increases

significantly from 800 K to 1000 K and remains stable beyond this point. The maximum H_2 mole fraction is observed at 92.8% at 1000K.

The Effect of Air Mass Flow Rate on H_2 Mass Flow Rate

Figure 3 presents the relationship between air mass flow rate and hydrogen mass flow rate for MSW. At an air feed rate of 3 kg/h, the equivalence ratio (ER) is calculated as 0.39. As the air mass flow increases from 1 to approximately 3 kg/h, the hydrogen production rises, reaching a peak of around 0.085 kg/h, indicating an optimal air-to-fuel ratio that maximizes H_2 yield. Beyond this point, further increases in air flow lead to a decline in hydrogen production, likely due to excess oxygen promoting complete combustion reactions that convert hydrogen into water, thereby reducing its availability. This trend highlights the importance of optimizing the air supply to enhance hydrogen yield and maintain the efficiency of the system.

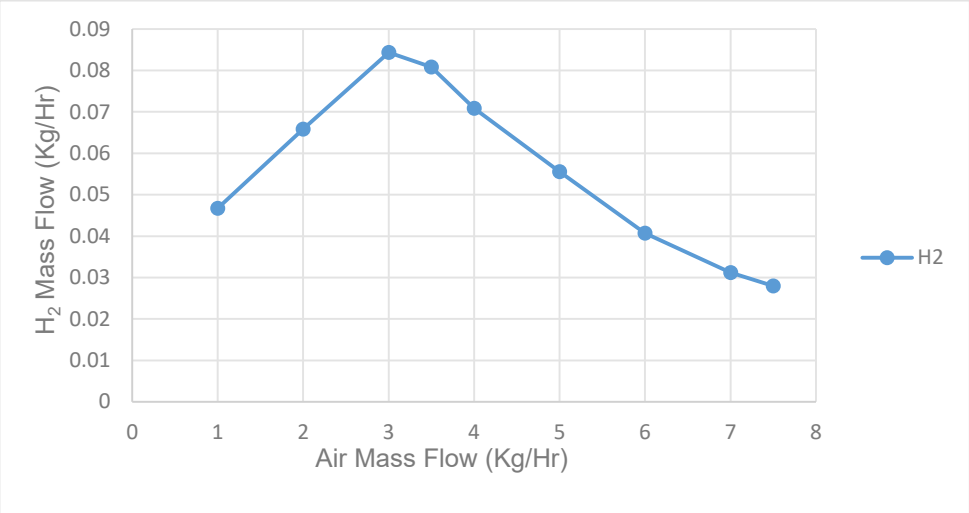

Fig. 3. Influence of Air Mass Flow on the Hydrogen Mass Flow Rate in MSW

4. CONCLUSIONS

This study demonstrates that integrating Sorption-Enhanced Reforming (SER) with fixed-bed gasification of municipal solid waste (MSW) significantly enhances hydrogen purity, achieving up to 99.4% under optimized conditions (923 K, 20 bar). The highest hydrogen mole fraction of 92.8% is observed at 1000 K, underlining the importance of gasifier temperature. Simulation results also reveal that an air mass flow rate of around 3 kg/h is optimal, as higher rates lead to reduced hydrogen output due to complete combustion. Model validation shows strong agreement with experimental and literature data, with RMSE values of 3.90 for MSW gasification and 0.68 for the SER unit. Overall, the Aspen Plus® simulation confirms the scalability and sustainability of this approach, supporting SER-based gasification as an effective low-emission hydrogen production method.

REFERENCES

[1] O. Yucel and E. S. Aydin, “Modeling of biomass-based hydrogen production via catalytic sorption-enhanced reformer integrated with a gasifier,” Journal of the Indian Chemical Society, vol. 100, no. 1, p. 100854, Jan. 2023, doi: 10.1016/J.JICS.2022.100854.
[2] L. Wei et al., “Absorption-enhanced steam gasification of biomass for hydrogen production: Effect of calcium oxide addition on steam gasification of pyrolytic volatiles,” Int J Hydrogen Energy, vol. 39, no. 28, pp. 15416–15423, Sep. 2014, doi: 10.1016/J.IJHYDENE.2014.07.064.
[3] M. Shahbaz et al., “Syngas Production from Steam Gasification of Palm Kernel Shell with Subsequent CO2 Capture Using CaO Sorbent: An Aspen Plus Modeling,” Energy and Fuels, vol. 31, no. 11, pp. 12350–12357, Nov. 2017, doi: 10.1021/acs.energyfuels.7b02670.
[4] M. H. Sedghkerdar, E. Mostafavi, and N. Mahinpey, “Investigation of the kinetics of carbonation reaction with cao-based sorbents using experiments and aspen plus simulation,” Chem Eng Commun, vol. 202, no. 6, pp. 746–755, Jun. 2015, doi: 10.1080/00986445.2013.871709.
[5] N. Ramzan, A. Ashraf, S. Naveed, and A. Malik, “Simulation of hybrid biomass gasification using Aspen plus: A comparative performance analysis for food, municipal solid and poultry waste,” Biomass Bioenergy, vol. 35, no. 9, pp. 3962–3969, Oct. 2011, doi: 10.1016/J.BIOMBIOE.2011.06.005.
[6] G. Schuster, G. Löffler, K. Weigl, and H. Hofbauer, “Biomass steam gasification – an extensive parametric modeling study,” Bioresour Technol, vol. 77, no. 1, pp. 71–79, Mar. 2001, doi: 10.1016/S0960-8524(00)00115-2.

[7] S. Naveed, A. Malik, N. Ramzan, and M. Akram, “The Nucleus A Quarterly Scientific Journal of Pakistan Atomic Energy Commission A COMPARATIVE STUDY OF GASIFICATION OF FOOD WASTE (FW), POULTRY WASTE (PW), MUNICIPAL SOLID WASTE (MSW) AND USED TIRES (UT),” 2009.
[8] H. Yaka, M. A. Insel, O. Yucel, and H. Sadikoglu, “A comparison of machine learning algorithms for estimation of higher heating values of biomass and fossil fuels from ultimate analysis,” Fuel, vol. 320, p. 123971, Jul. 2022, doi: 10.1016/J.FUEL.2022.123971.

SOLAR-BASED GREEN HYDROGEN PRODUCTION FOR DECARBONIZING NATURAL GAS: AN EMISSIONS PERSPECTIVE

[1*]*Habip Sahin*
[1] Department of Electricity and Energy, Vocational School of Technical Sciences, Fırat University, 23119, Elazığ, Türkiye

* E-mail: habipsahin@firat.edu.tr

ABSTRACT
The integration of green hydrogen into natural gas networks represents a viable strategy to reduce carbon emissions in energy systems reliant on fossil fuels. This study investigates the potential of solar-powered electrolysis for green hydrogen production and its subsequent blending with natural gas as a transitional decarbonization approach. Focusing on hydrogen volumetric ratios from 10% to 17%, the analysis evaluates changes in emissions profiles. A solar-driven alkaline electrolyzer model is developed using regional solar irradiance data, and the hydrogen output is coupled with combustion simulations to assess environmental impacts. Results indicate that substituting a fraction of natural gas with solar-derived hydrogen significantly decreases CO_2 emissions. Moreover, the integration of hydrogen into the fuel mix not only mitigates its net carbon intensity but also supports energy sustainability by either extending the usability of domestic natural gas reserves or reducing dependency on external energy sources. The findings underscore the role of solar-based hydrogen as an immediate and scalable pathway for decarbonizing existing gas infrastructure without major alterations to end-use systems.

Keywords: Electrolysis, Emission mitigation, Green hydrogen**,** Hydrogen-Enriched natural gas**,** Renewable Energy

1. INTRODUCTION

The increasing global energy demand and the adverse environmental effects of fossil fuel consumption have intensified the search for low-carbon and sustainable alternatives. Among various solutions, hydrogen has emerged as a promising energy vector due to its high energy density, zero carbon emissions at the point of use, and potential for integration with renewable energy systems. Hydrogen production through water electrolysis powered by solar energy represents a particularly attractive pathway, offering a clean and decentralized means of generating hydrogen fuel [1].

Natural gas, while cleaner than coal and oil, remains a significant source of CO_2 emissions, particularly in sectors such as residential heating and industrial processes. Recent efforts have focused on blending green hydrogen with natural gas to reduce the overall carbon footprint while utilizing existing gas infrastructure [2]. This hydrogen-enriched natural gas (HENG) can serve as a transitional fuel, helping to decarbonize energy systems without requiring immediate and large-scale infrastructure changes [3].

Studies have demonstrated that the addition of up to 20% hydrogen by volume into natural gas networks is technically feasible and can lead to measurable reductions in CO_2 emissions [4,5]. However, the emissions dynamics of such blends must be carefully assessed, as elevated flame temperatures from hydrogen combustion can lead to increased nitrogen oxide (NOx) emissions [6]. Therefore, a comprehensive analysis of emission behavior is essential when evaluating HENG as a decarbonization strategy.

This study aims to assess the emissions implications of integrating solar-based green hydrogen into natural gas systems. By modeling hydrogen production from photovoltaic-powered electrolysis and analyzing combustion outputs across different hydrogen blend ratios, the research provides insights into the trade-offs and benefits of this approach. The work builds upon existing literature while offering a focused emissions perspective, which is crucial for policy and infrastructure planning in the transition to cleaner energy sources.

2. METHOD AND SIMULATION

In this study, solar energy is selected as the renewable energy source for sustainable green hydrogen production. Electrical power generated by a 236 kW solar photovoltaic (PV) system is utilized to supply a 200 kW proton exchange membrane (PEM) electrolyzer. Additionally, a battery system is employed as an auxiliary power source.

I. Green Hydrogen Production System

The solar PV array, with a total capacity of 236 kW, was assembled using 400 panels. Eight panels were connected in series to form a string, and 50 strings were connected in parallel to complete the system. The Talesun TP7F78M(H) 590 W panel was selected for use, and its specifications are presented in Table 1.

Table 1. Specifications of The Talesun TP7F78M(H) 590 W panel.

Spesification	Unit	Value
Maximum Power	W	590
Operating Voltage	V	45.25
Operating Current	A	13.04
Open-Circuit Voltage	V	53.87
Short-Circuit Current	A	13.93
Module Efficiency	%	21.1
Cell Number		156 (26*6)
Cell Type		Monocrystalline Silicon

Province of İzmir, Türkiye, was chosen as the study location, and solar irradiation data from May 25 to May 28, 2022, were used. The solar irradiation values over the four-day period, with a 15-minute resolution, are illustrated in Fig 1. [7].

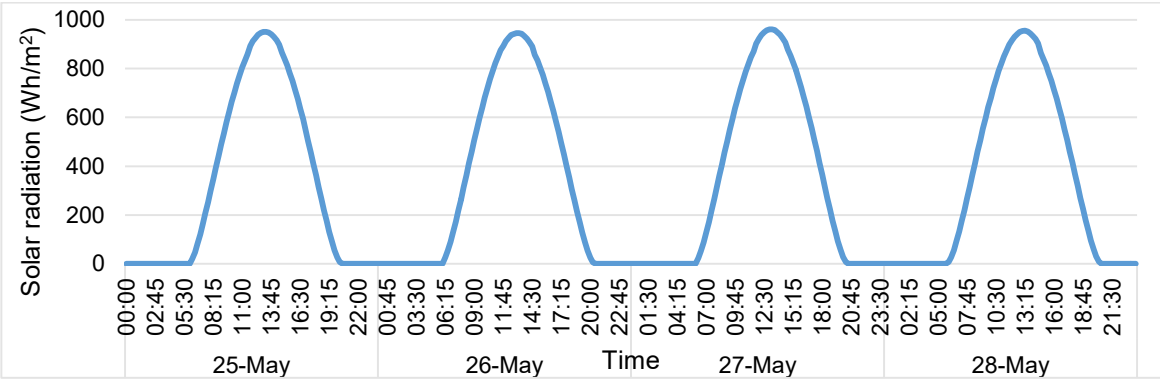

Fig. 1. Solar irradiation values for İzmir province.

Various electrolysis processes have been developed for hydrogen production from renewable sources, among which PEM electrolysis is well known for its high efficiency (80–90%), high hydrogen purity (99.99%), and oxygen as a byproduct. In addition to these advantages, PEM electrolysis is preferred due to its ability to operate at low temperatures (20–80 °C) and at high current densities (above 2 A/cm²) [8]. The battery system is 240V 100Ah and can store 24 kWh of energy.

II. Simulation

The Green Hydrogen Microgrid example from the Matlab Simscape library was taken as a basis and further developed according to the specific parameters and operating conditions of this study [9]. Throughout the four-day simulation period, the maximum recorded solar irradiance was 958 W/m², corresponding to a peak solar power generation of 206.4 kW. The battery system was employed to sustain the operation of the electrolyzer during periods of no solar irradiance, while it was intentionally disengaged when solar energy was available. Under these conditions, the electrolyzer achieved a maximum operational power of 195.8 kW. The time-dependent power variations of the electrolyzer, solar, and storage system are presented in Fig. 2. The control of the solar PV power generation was achieved using a Maximum Power Point Tracking (MPPT) technique. The instantaneous current and voltage values of the PV array were utilized to compute the corresponding power output. This output served as the input to the DC-DC converter, with the MPPT algorithm continuously providing a reference signal to optimize the duty cycle. In each iteration, the change in power due to a small adjustment in the duty cycle was evaluated. If the power increased, the duty cycle adjustment proceeded in the same direction. However, if an increase in current led to a drop in voltage, and no further power improvement was observed, the duty cycle was maintained at its most recent optimal setting.

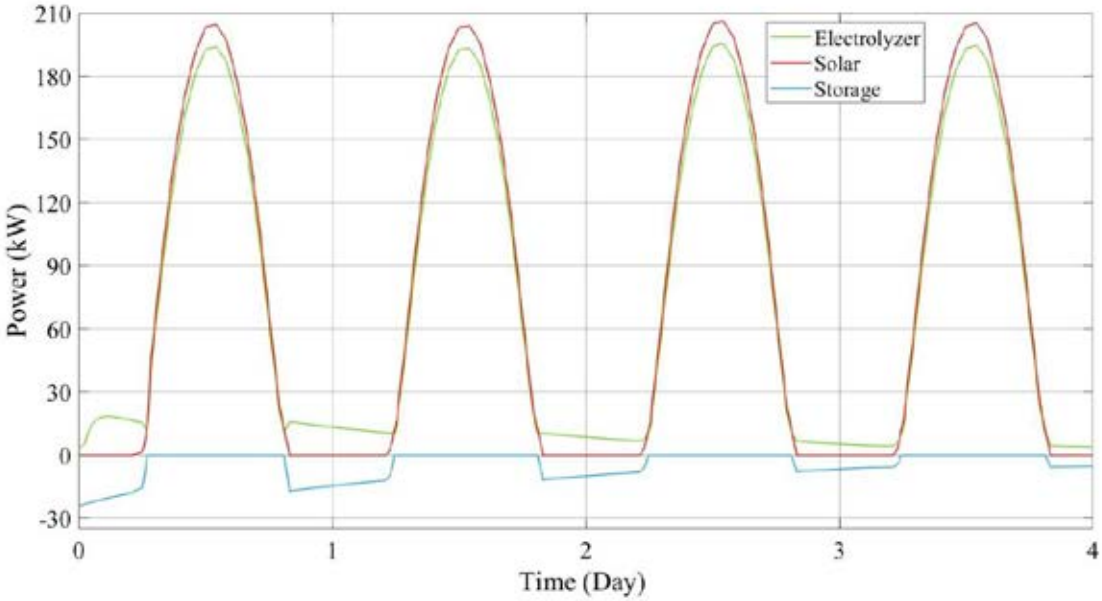

Fig. 2. Electrolyzer, solar, and storage system powers

3. RESULTS AND DISCUSSION

During the initial stage of the system operation, the electrolyzer was supplied with power sourced from both the solar PV system and the battery storage system to facilitate green hydrogen production. Following a four-day simulation, the performance outcomes—including the total solar-based electricity generation, total battery energy discharge, total electrolyzer energy consumption, and the amount of hydrogen produced—are compiled and presented in Table 2.

Table 2. Energy flow and the amount of hydrogen produced.

Spesification	Unit	Value
Solar-based electricity energy	kWh	7109
Battery energy	kWh	446
Total electricity energy	kWh	7555
Electrolyzer energy	kWh	7197
Electrical efficiency	%	95.3
Hydrogen production	kg	120.2
Energy consumption per hydrogen	kg/kWh	59.9

The energy consumption range reported in commercial and academic studies varies between 42.2 and 65.6 kWh/kg of hydrogen. For PEM technology, the average energy consumption is approximately 53 kWh/kg [10]. The deviation of the result obtained in this study from the average value can be attributed to scaling effects and various characteristics of system efficiency. The properties of the hydrogen and natural gas (NG), which will be blended together, are presented in Table 3 [11].

Table 3. Properties of the hydrogen and natural gas.

Property	Natural Gas	Hydrogen
Energy content (Lower Heating Value, LHV)	35–40 MJ/m³	120 MJ/kg
Energy content (Higher Heating Value, HHV)	39–42 MJ/m³	142 MJ/kg
Density	0.72–0.85 kg/m³	0.09 kg/m³
Energy content (per m³)	37.5 MJ/m³ (LHV)	10.8 MJ/m³ (LHV)
CO_2 emission (on combustion)	2.75 kgCO_2e/m³	0

The volume of the 120.2 kg of produced hydrogen under the blending conditions will be 1335.6 m³. The thermal performance and emission metrics of the mixtures at different blending proportions are summarized in Table 4.

Table 4. Thermal performance and emission metrics of the mixtures at different blending proportions.

Blend ratio	%5	%10	%17
Required NG amaunt (m^3)	26711.1	13355.6	7856.2
Energy content (MJ/m³)	36.2	34.8	33.0
Energy deviation from NG (%)	-3.6	-7.1	-12.1
Correction factor for isothermal value	1.037	1.077	1.138
Emission ($kgCO_2e/m^3$)	2.61	2.48	2.28
Emission for isothermal value ($kgCO_2e/m^3$)	2.71	2.66	2.6
Emission deviation from NG (%)	1.5	3.1	5.6

As the hydrogen content in the mixture increases, the energy content decreases. Simultaneously, the emission intensity also decreases with the increasing hydrogen proportion. Therefore, when comparing emissions, it is necessary to consider that a higher amount of fuel must be consumed to achieve the same calorific value. Under these conditions, emission intensity reductions of 1.5%, 3.1%, and 5.6% are observed for hydrogen blending ratios of 5%, 10%, and 15%, respectively.

4. CONCLUSIONS

In this study, a green hydrogen production system powered by a solar PV array and a battery storage unit was analyzed through a four-day simulation. The produced hydrogen was subsequently considered for blending with natural gas to assess the impact on energy content and emissions. The results indicate that as the hydrogen blending ratio increases, the overall energy content of the gas mixture decreases, necessitating higher volumetric fuel consumption to maintain equivalent calorific output. However, a notable advantage is the concurrent reduction in CO_2 emission intensity, with decreases of 1.5%, 3.1%, and 5.6% observed for hydrogen blending ratios of 5%, 10%, and 15%, respectively. These findings highlight the potential of hydrogen-enriched natural gas as a transitional strategy for lowering carbon emissions in existing natural gas infrastructure while acknowledging the need for recalibration in fuel delivery systems to accommodate the changes in energy density.

REFERENCES

[1] Dincer I, Acar C. A review on clean energy solutions for better sustainability. Int J Energy Res 2015;39:585–606. https://doi.org/10.1002/er.3329.
[2] Melaina MW, Antonia O, Penev M. Blending hydrogen into natural gas pipeline networks: A review of key issues. 2013.
[3] Kouchachvili L, Entchev E. Power to gas and H2/NG blend in SMART energy networks concept. Renew Energy 2018;125:456–64. https://doi.org/10.1016/j.renene.2018.02.088.
[4] Zhao Y, McDonell V, Samuelsen S. Influence of hydrogen addition to pipeline natural gas on the combustion performance of a cooktop burner. Int J Hydrogen Energy 2019;44:12239–53. https://doi.org/10.1016/j.ijhydene.2019.03.100.
[5] Deng Y, Dewil R, Appels L, Van Tulden F, Li S, Baeyens J. Hydrogen-enriched natural gas in a decarbonization perspective. Fuel 2022;318:123680. https://doi.org/10.1016/j.fuel.2022.123680.
[6] Sun M, Huang X, Hu Y, Lyu S. Effects on the performance of domestic gas appliances operated on natural gas mixed with hydrogen. Energy 2022;244:122557. https://doi.org/10.1016/j.energy.2021.122557.
[7] NREL. National Solar Radiation Database 2025. https://nsrdb.nrel.gov/data-viewer (accessed April 26, 2025).
[8] Shwe Sin PP, Wai SH, Ota Y, Nishioka K, Suzuki Y. Performance recovery of proton exchange membrane electrolyzer degraded by metal cations contamination. Int J Hydrogen Energy 2024;53:86–92. https://doi.org/10.1016/J.IJHYDENE.2023.12.049.
[9] MATLAB. Green Hydrogen Microgrid 2024. https://ch.mathworks.com/help/sps/ug/green-hydrogen-microgrid.html?searchHighlight=hydrogen+storage&s_tid=srchtitle_support_results_1_hydrogen+storage (accessed April 26, 2025).
[10] Aghakhani A, Haque N, Saccani C, Pellegrini M, Guzzini A. Direct carbon footprint of hydrogen generation via PEM and alkaline electrolysers using various electrical energy sources and considering cell characteristics. Int J Hydrogen Energy 2023;48:30170–90. https://doi.org/10.1016/J.IJHYDENE.2023.04.083.
[11] Deng Y, Dewil R, Appels L, Van Tulden F, Li S, Yang M, et al. Hydrogen-enriched natural gas in a decarbonization perspective. Fuel 2022;318:123680. https://doi.org/10.1016/J.FUEL.2022.123680.

THE EFFECT OF EARTHQUAKES ON UNDERGROUND HYDROGEN STORAGE CAVERNS

[1,*]Hatice Karakilcik
[1]Cukurova University, Faculty of Engineering, Department of Geology, Adana, 01250, Türkiye
*Corresponding author e-mail: hkilcik@cu.edu.tr

ABSTRACT
This study investigates the effects of earthquakes on underground hydrogen storage facilities. Salt caverns, located within large underground salt domes, are used to store significant volumes of hydrogen gas. These caverns are typically designed with large capacities, ranging from approximately 500,000 to 1,000,000 m³, and are characterized by a dome-like shape that narrows both the floor and ceiling. Similar to their impact on surface structures, earthquakes also affect subsurface structures in various ways. The severity of these effects depends on several factors, including the tectonic and geological characteristics of the region, depth, magnitude, and acceleration of the earthquake. Computational modeling studies have identified potential structural damage, the formation of cracks, and uplift, particularly at the base of the caverns. Furthermore, disruptions in gas balance and potential volumetric changes in the cushion gas are possible. Following an earthquake, the structural integrity of these underground storage facilities should be assessed using geophysical methods, and appropriate mitigation measures should be implemented.

Keywords: Hydrogen storage, Salt dome, Salt cavern, Earthquake, Geophysics

1. INTRODUCTION

An earthquake is a phenomenon in which the energy accumulated within the Earth's crust is abruptly released due to fractures, propagating as seismic waves (P, S, Love, and Rayleigh waves) that cause vibrations in both the medium they traverse and the Earth's surface. Earthquakes are classified by their depth into shallow, intermediate, and deep categories and occur at varying depths, leading to deformations and subsidence both underground and on the surface. Earthquakes not only impact surface structures but also induce a range of structural damage to underground facilities. The tremors generated during seismic events can lead to significant geotechnical issues in artificially created environments, such as underground caverns. Particularly, earthquakes of larger magnitudes are more destructive, meaning caverns may suffer considerable damage, leading to the weakening of existing cavern structures.

In the context of underground hydrogen storage (UHS), the most suitable geological formations are salt domes or salt beds. The location, size, and structural integrity of these formations are assessed using geophysical methods such as gravity, magnetic, and seismic techniques, while well logs determine the quality of the salt. Based on these findings, the suitability for cavern formation is evaluated. Furthermore, when the mineralogical properties of the salt are favorable, large-volume underground hydrogen storage caverns are constructed [1]. These salt caverns are typically located between 500 and 2000 meters below the surface [2]. From a land management perspective, UHS systems offer various advantages over traditional surface storage tanks, particularly concerning the surface area required for the same volume of gas storage [3]. Studies on UHS technology have shown a preference in many countries for creating caverns in salt domes or thick salt layers [4-5]. Another proposed alternative involves storing hydrogen-rich gas mixtures in porous underground formations, such as depleted oil and natural gas fields or deep aquifers [6-8]. Ensuring the safety of UHS facilities is of utmost importance. Necessary safety measures should be in place not only against military attacks, terrorist threats, and fires but also against natural disasters, including earthquakes. Earthquakes can lead to the following effects:

Formation of New Cracks and Fractures: Earthquakes may generate new fractures and faults within the Earth's crust. This can lead to the formation of new cracks in the roof, floor, or walls of caverns, potentially causing subsidence in certain areas, which results in changes to the cavern's volume.

Reconfiguration of Cavern Systems: Large earthquakes can alter underground water pathways. Fractures and cracks can lead to the formation of new water-filled chambers within the underground caverns.

Soil and Sediment Accumulation: The tremors can cause surrounding loose soil and materials to enter the caverns through cracks and fractures, potentially filling the cavern chambers with sediments.

Underground Pressure Changes: Following an earthquake, the balance of underground pressure may shift, potentially negatively affecting the movement of gases or liquids within the cavern and compromising storage integrity.

Gas Imbalance: In some caverns, gas accumulation may reach hazardous levels. In underground hydrogen storage, cavern deformation may result in gas leakage. Earthquakes can cause the dispersal of these gases due to underground movements, posing significant risks to both safety and the environment.

2. MATERIALS AND METHODS

Currently, hydrogen is stored in both liquid and gas forms in tanks and natural or artificial underground geological formations, such as depleted/abandoned oil and gas fields, aquifers, and salt caverns, using physical methods. Among these, underground salt caverns, artificially created in salt domes, have a very large-scale potential for gas storage. Salt caverns are constructed in highly impermeable and tight underground salt formations using solution mining methods [9].

As shown in Figure 1, salt caverns are artificially created in large volumes within underground geological salt domes [10]. Figure 2 illustrates the earthquake resulting from a fracture along a fault line near a cavern where hydrogen is stored underground, as well as the structural changes that occur in salt caverns due to the effects of the earthquake [11].

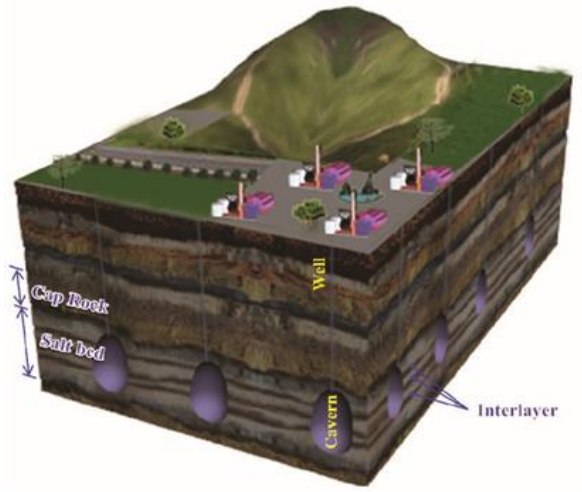

Fig. 1. The structure of the underground salt caverns [10].

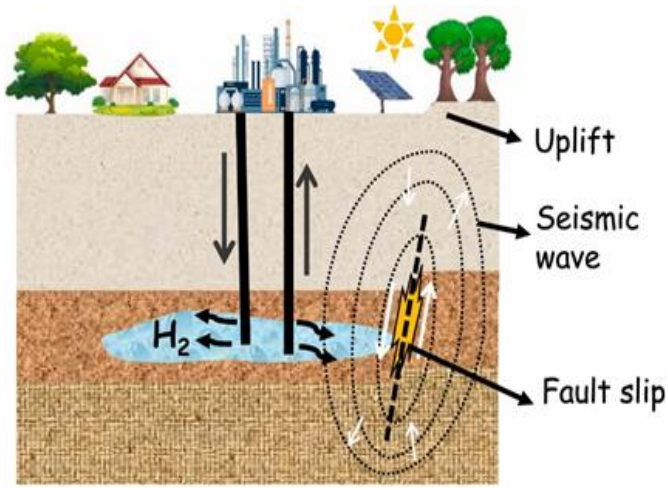

Fig. 2. The salt cavern was affected by the earthquake [11].

3. RESULTS AND DISCUSSION

The magnitude of the earthquake, its distance from the epicenter, the type of geological formation in which the cavern is located, and the condition of any potential existing underground fluids (such as oil, natural gas, water, and geothermal resources) determine the intensity of these effects.

Caverns in karst regions are more affected by earthquakes, especially because karstic rocks (particularly limestone) are rich in cracks and voids.

Seismic waves (P and S) generated during the earthquake can cause fractures or other deformations in the rocks surrounding salt domes or salt layers.

These fractures can lead to the expansion of the cavern, the formation of new voids, or the weakening of existing structures.

Earthquakes impact both the physical structure and the volume capacity of caverns. The intensity of the effect depends on the geological characteristics of the region, the magnitude of the earthquake, and the depth of the cavern.

The earthquake may act as an accelerating factor in the long-term evolution of salt caverns.

By placing seismographs at specific locations on the surface, earthquakes can be continuously monitored, and the tectonic movements underground can be tracked. Additionally, the caverns should be consistently monitored and analyzed using geophysical imaging systems.

To identify potential deformations that may occur in the caverns following large earthquakes, modeling should be done, and hazard risk analyses should be carried out.

The effect of the earthquake on underground caverns is directly proportional to the magnitude of the earthquake. Other important parameters include the cavern's proximity to the surface, its distance from the focus depth, and the lithological and structural characteristics of the underground. Based on these factors, the cavern's potential for earthquake-induced damage can be assessed.

After a potential large earthquake, maximum safety must be ensured in underground hydrogen storage facilities. To achieve this, effective monitoring and surveillance technologies should be developed to ensure that underground hydrogen storage caverns remain safe and secure until they are needed for hydrogen production and storage applications [15].

4. CONCLUSIONS

The impact of an earthquake on cavern structures depends not only on the magnitude of the earthquake but also on factors such as the distance from the epicenter, the geological structure, and the presence of underground fluids (such as water, gas, and oil). This highlights the critical importance of regional characteristics in seismic hazard analysis. Active regions can directly influence the stability of underground voids. As a result, caverns in such areas are more susceptible to seismic waves, potentially leading to the formation of cracks. Earthquakes and their aftershocks can cause these cracks to expand and new voids to form, which could result in both changes to the cavern's volume and an increased risk of collapse. This is because salt formations, being prone to plastic deformation, can experience significant fractures or shape changes around their structures during an earthquake. This poses a serious risk,

especially for flammable gases such as hydrogen stored in salt domes. In other words, an earthquake could cause deterioration in the cavern's natural process at an earlier stage. These deteriorations can be continuously monitored through seismographs and geophysical imaging systems, enabling the ongoing tracking of underground activity. These technologies should be made a mandatory safety standard, particularly for strategic structures (e.g., hydrogen storage caverns). Moreover, seismic risk modeling can help predict potential deformation scenarios, enabling structural interventions to be planned. Such caverns are both strategic and hazardous structures. After an earthquake, the following risks may arise in these structures: gas leaks, structural collapse, and explosion risks. Therefore, these facilities must:

- Be located within resilient geological formations,
- Be equipped with advanced sensors and monitoring systems,
- Undergo regular stress tests.

This ensures the safe production and storage of hydrogen. In conclusion, earthquakes pose significant threats to underground caverns, particularly those used for storing sensitive substances such as hydrogen. These risks should be minimized through continuous monitoring, modeling, and engineering solutions. A multidisciplinary approach, including geology, geophysics, civil engineering, and energy security, is essential in addressing these challenges.

REFERENCES

1. Karakilcik H. 2017. Investigation of Underground Hydrogen Storage Areas, Proceedings Book, Eds:İbrahim Dinçer, Adnan Midilli, Mehmet Karakılçık, 2nd International Hydrogen Technologies Congress, March 15-18, 223 15-18,223-228. Çukurova University, Adana, Turkey. ISBN: 978-605-66381-2-1
2. Saygin S, Karakilcik H, Karakilcik M, Erden M and Atiz A. 2023. Investigation of cushion gas/working gas ratios of underground salt caverns for hydrogen storage, Emerging Trends in Energy Storage Systems and Industrial Applications, Pages 67-78: Academic Press.
3. Crotogino F. 2022. Underground storage of hydrogen–technical challenges and new approaches. Journal of Energy Storage. 45: 103526. https://doi.org/10.1016/j.est.2022.103526
4. Lankof L. And Tarkowski R. 2020. Salt caverns as hydrogen storage facilities: Geomechanical and microbiological aspects. International Journal of Hydrogen Energy, 45(39):20175–20191. https://doi.org/10.1016/j.ijhydene.2020.05.182.
5. Caglayan DG, Weber N, Heinrichs HU, Linßen J, Robinius M and Stolten D. 2020. Technical potential of salt caverns for hydrogen storage in Europe. International Journal of Hydrogen Energy, 45(11):6793–6805. https://doi.org/10.1016/j.ijhydene.2019.12.161
6. Hassannayebi S, Allen MB., and Davies RJ. 2019. Geomechanical feasibility of hydrogen storage in depleted gas reservoirs. International Journal of Hydrogen Energy, 44(57):30240–30252. https://doi.org/10.1016/j.ijhydene.2019.09.081.
7. Heinemann N, Alcalde J, Miocic JM, Hangx SJT, Kallmeyer J, Ostertag-Henning C and Stuart FM. 2021. Enabling large-scale hydrogen storage in porous media: the scientific challenges. Energy & Environmental Science, 14(2):853–864. https://doi.org/10.1039/D0EE03536J.
8. Amid A, Mignard D, and Wilkinson M. 2016. Seasonal storage of hydrogen in a depleted natural gas reservoir. International Journal of Hydrogen Energy 41(12):5549–5558. https://doi.org/10.1016/j.ijhydene.2016.01.094.
9. Karakilcik H., Karakilcik M. (2020). Underground Large-Scale Hydrogen Storage. In: Uyar, T. (eds) Accelerating the Transition to a 100% Renewable Energy Era. Lecture Notes in Energy, vol 74. Springer, Cham. https://doi.org/10.1007/978-3-030-40738-4_17
10. Shi X, Liu W, Chen J, Yang C, Li Y, Ma H, Peng H, Tongtao H, Wang T. and Ma X. 2017. Geological Feasibility of Underground Oil Storage in Jintan Salt Mine of China. Advances in Materials Science and Engineering, 11. https://doi.org/10.1155/2017/3159152
11. Kumar RK, Honorio H, Chandr D, Lesueur M, and Hajibeygi H. 2023. Comprehensive review of geomechanics of underground hydrogen storage in depleted reservoirs and salt caverns. Journal of Energy Storage 73:108912.https://doi.org/10.1016/j.est.2023.108912
12. https://fuelcellsworks.com/news/netl-conducts-surveillance-and-monitoring-technology-research-for-underground-hydrogen-storage-as-part-of-shasta-collaboration. Accessed on April 20, 2025.

.

ASSESSING ELECTROLYTE EFFECTS IN FUEL CELL SYSTEMS

[1]Esra Durar, [1]Başak Memişoğlu Güzelgün, [1,2]Serdal Damarseckin, [1]Ayhan Atız, [1,*]Mehmet Karakılçık
[1]Cukurova University, Faculty of Science and Letters, Adana, 01250, Türkiye
[2]Sirnak University, Faculty of Engineering, Department of Renewable Energy Systems Engineering, Sirnak, 73000, Türkiye
*Corresponding author e-mail: kkilcik@cu.edu.tr

ABSTRACT
This study presents a comparative investigation into the effects of electrolytes, one of the fundamental components of fuel cells (FCs), on overall cell performance. For this purpose, the most common types of fuel cells and the electrolytes used in these systems were evaluated. Five different fuel cell types were analyzed based on their electrolyte structures. The type of electrolyte is a key determinant of several operational parameters, including operating temperature, efficiency, usability, and potential application areas. The evaluations revealed the extent to which electrolyte selection influences overall fuel cell performance. It was found that low-temperature fuel cells, such as Alkaline Fuel Cell (AFC) and Proton Exchange Membrane Fuel Cell (PEMFC), are more suitable for mobile and portable applications. In contrast, high-temperature systems, namely Phosphoric Acid Fuel Cell (PAFC), Molten Carbonate Fuel Cell (MCFC), and Solid Oxide Fuel Cell (SOFC), are better suited for industrial-scale energy production. The structural characteristics of fuel cells are among the primary factors enhancing energy efficiency. In particular, the performance of the electrolyte component plays a critical role in overall energy conversion efficiency. It was seen that the electrolytes employed in PEMFC offer superior energy efficiency compared to those used in other fuel cell types, and this efficiency has been improving over time.

Key Words: Hydrogen energy, Fuel cell, Electrolyte, Energy efficiency.

1. INTRODUCTION

Fuel cells are widely regarded as one of the most promising clean energy technologies due to their high efficiency, low environmental impact, and broad application potential. Among the various components of a fuel cell, the electrolyte plays a pivotal role in determining the electrochemical behavior and operational efficiency of the system. The type of electrolyte used in a fuel cell significantly influences the system's operating temperature, fuel compatibility, cost, and overall applicability in different contexts.

This study aims to provide a comparative assessment of the impact of different electrolyte types on the performance of fuel cells by analyzing five widely utilized fuel cell technologies: Alkaline Fuel Cell (AFC), Molten Carbonate Fuel Cell (MCFC), Phosphoric Acid Fuel Cell (PAFC), Proton Exchange Membrane Fuel Cell (PEMFC), and Solid Oxide Fuel Cell (SOFC). The performance metrics considered in this evaluation include energy efficiency, thermal stability, potential application areas, and material durability.

Fuel cells are electrochemical devices that directly convert chemical energy into electrical energy, typically utilizing hydrogen and oxygen as the primary reactants. Several critical factors influence the performance of these systems, such as efficiency, power density, response time, operating temperature, durability, and service life. These factors make fuel cells essential for advancing sustainable energy solutions, offering substantial advantages over traditional energy systems in terms of both performance and environmental impact. Notably, fuel cells exhibit far greater efficiency than internal combustion engines.

The efficiency of fuel cells varies according to the type of fuel cell and its associated electrolyte structure. The main fuel cell types based on electrolyte materials are AFC, MCFC, PAFC, PEMFC, and SOFC. Theoretical efficiency for PEMFC can reach up to 80%, and with cogeneration, it may increase to as high as 85% [1]. However, in practical applications, efficiency typically ranges between 40% and 60%. Power density, which refers to the power output per unit of volume or weight, is significant for portable and automotive applications. Due to their high power density, PEMFCs are commonly favored in these sectors [2].

Response time, another key performance parameter, refers to the fuel cell’s ability to adjust to changes in electrical demand quickly. Some fuel cell types, such as PEMFCs, respond rapidly, while others, such as SOFCs, have slower response times. Operating temperature is another differentiating factor. Low-temperature fuel cells, such as PEMFCs, start up quickly but are sensitive to the purity of the fuel. In contrast, high-temperature fuel cells like SOFCs offer greater fuel flexibility but require longer warm-up periods. While low-temperature PEMFCs are advantageous for rapid startup, high-temperature SOFCs provide the benefit of wider fuel compatibility [3].

Durability and lifespan are critical considerations for fuel cells, as electrodes and membrane materials degrade over time. Depending on the specific application, fuel cell lifespan can range from 2,000 to 40,000 hours. This lifespan is primarily determined by the materials used for the membrane and electrodes [4].

This study specifically evaluates five distinct types of fuel cells based on their electrolyte structures, highlighting the significant structural and material-related factors that influence their energy efficiency, operational characteristics, and suitability for various application areas.

2. MATERIALS AND METHODS

Fuel cells represent one of the most critical components within hydrogen technologies. These electrochemical devices are typically categorized into five distinct types based on the nature of their electrolyte structures: Alkaline Fuel Cells (AFC), Molten Carbonate Fuel Cells (MCFC), Phosphoric Acid Fuel Cells (PAFC), Proton Exchange Membrane Fuel Cells (PEMFC), and Solid Oxide Fuel Cells (SOFC) (Figs. 1–5). This study employs a qualitative comparative analysis to assess various fuel cell systems, with a specific focus on the characteristics of their electrolytes. Data for this analysis were obtained from peer-reviewed journal articles, technical manuals, and manufacturer specifications. Each fuel cell type was evaluated across several key parameters, including electrolyte composition and structure, operating temperature range, energy efficiency potential, applicability across different sectors, and technological maturity and scalability. This methodology provides a comprehensive understanding of how electrolyte properties influence the overall performance and operational behavior of fuel cell systems.

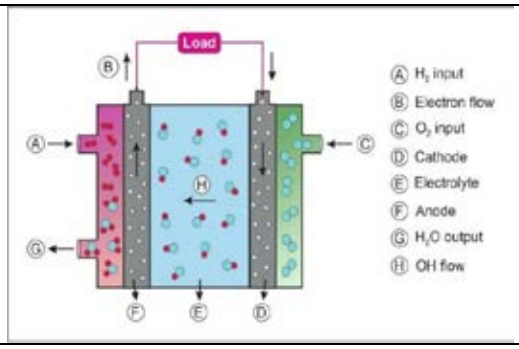

Fig. 1. Alkaline Fuel Cells (AFC)

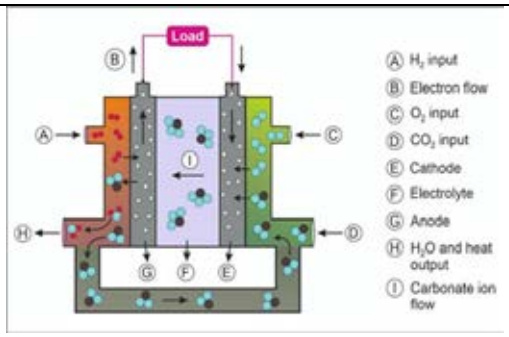

Fig. 2. Molten Carbonate Fuel Cells (MCFC)

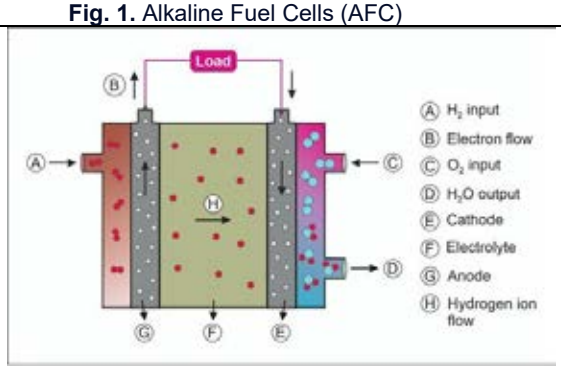

Fig. 3. Phosphoric Acid Fuel Cells (PAFC)

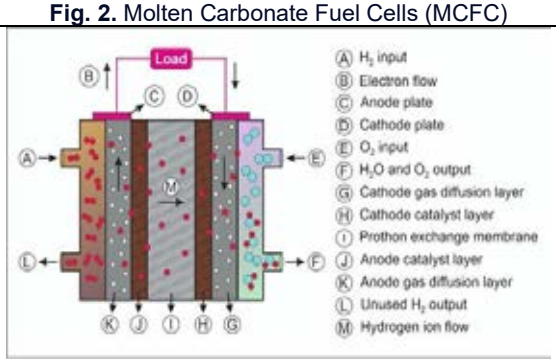

Fig. 4. Proton Exchange Membrane Fuel Cells (PEMFC)

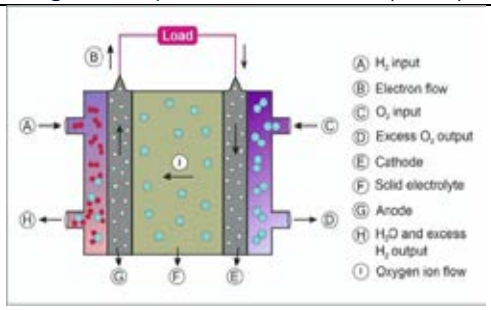

Fig. 5. Solid Oxide Fuel Cell (SOFC)

Table 1. General Chemical Reactions of Fuel Cells

Fuel Cells	Anode	Cathode	Overall Reaction	Electrolyte Types
Alkaline Fuel Cell (AFC)	$H_2 + 2OH^- \rightarrow 2H_2O + 2e^-$	$½O_2 + H_2O + 2e^- \rightarrow 2OH^-$	$H_2 + ½O_2 \rightarrow H_2O$	Potassium hydroxide (KOH) – alkaline medium
Molten Carbonate Fuel Cell (MCFC)	$H_2 + CO_3^{2-} \rightarrow H_2O + CO_2 + 2e^-$	$½O_2 + CO_2 + 2e^- \rightarrow CO_3^{2-}$	$H_2 + ½O_2 + CO_2 \rightarrow H_2O + CO_2$	Molten carbonate salts (e.g., Li_2CO_3/K_2CO_3 mix.)
Phosphoric Acid Fuel Cell (PAFC)	$H_2 \rightarrow 2H^+ + 2e^-$	$½O_2 + 2H^+ + 2e^- \rightarrow H_2O$	$H_2 + ½O_2 \rightarrow H_2O$	Phosphoric acid (H_3PO_4)
Proton Exchange Membrane Fuel Cell (PEMFC)	$H_2 \rightarrow 2H^+ + 2e^-$	$½O_2 + 2H^+ + 2e^- \rightarrow H_2O$	$H_2 + ½O_2 \rightarrow H_2O$	Proton conducting polymer membrane (e.g., Nafion)
Solid Oxide Fuel Cell (SOFC)	$H_2 + O^{2-} \rightarrow H_2O + 2e^-$	$½O_2 + 2e^- \rightarrow O^{2-}$	$H_2 + ½O_2 \rightarrow H_2O$	O^{2-} conducting ceramic (e.g., YSZ)

3. RESULTS AND DISCUSSION

The results of this study demonstrate that the electrolyte type is a pivotal factor in the design and application of fuel cells. Proton Exchange Membrane Fuel Cells (PEMFCs), which operate at low temperatures (60–80 °C), utilize polymer membrane electrolytes and are highly efficient for transportation and portable energy systems due to their compact design and rapid start-up times. Consequently, PEMFCs are ideal for vehicular applications, particularly when hydrogen is produced using green energy, resulting in zero emissions. However, the need for highly pure hydrogen increases the cost. Alkaline Fuel Cells (AFCs), which also operate at low temperatures, use aqueous potassium hydroxide as the electrolyte. While they offer high efficiency, they are sensitive to CO_2, which limits their practical deployment, despite their strong performance in controlled environments. AFCs have been used by NASA in space missions due to their high efficiency and low waste energy generation. However, their efficiency decreases in the presence of CO_2, making them unsuitable for open-air applications. Phosphoric Acid Fuel Cells (PAFCs), which operate at intermediate temperatures (150–200 °C), use phosphoric acid as the electrolyte and are particularly suited for stationary power generation and combined heat and power (CHP) systems. PAFCs are commonly deployed in buildings because of their silent operation and long lifespan, with the added benefit of waste heat recovery. However, their weight and slow start-up time present challenges in terms of portability. Molten Carbonate Fuel Cells (MCFCs) and Solid Oxide Fuel Cells (SOFCs), which operate at high temperatures (600–1000 °C), use molten carbonate salts and solid ceramic oxides, respectively, as electrolytes. These high-temperature systems offer high efficiency in industrial applications, and their ability to tolerate a wide range of fuels makes them suitable for large-scale energy production. When used in cogeneration (producing both electricity and heat) and their energy efficiency is particularly high. However, challenges include material degradation and long start-up times. SOFCs, in particular, can use various fuels, such as hydrogen, natural gas, and biogas, and even when powered by fossil fuels, they produce fewer emissions. However, their very high operating temperature leads to structural stress and prolonged warm-up times.

The analysis confirmed that electrolyte conductivity, chemical stability, and compatibility with system components are directly linked to a fuel cell's energy output and operational lifespan. PEMFCs, in particular, have experienced rapid advancements due to improvements in membrane materials, leading to an increasing trend in efficiency over time.

Fuel cells are categorized according to their electrolyte structures, with each type presenting distinct advantages and limitations. This study focuses on the five primary types of fuel cells: AFC, MCFC, PAFC, PEMFC and SOFC. These systems exhibit significant variation in terms of electrolyte composition, operating temperatures, reaction mechanisms, and potential application domains. PEMFCs operating at relatively low temperatures (60–80 °C), offer rapid start-up times and compact system designs, making them particularly well-suited for portable electronics and automotive applications. They utilize proton-conductive polymer membranes such as Nafion which provide high ionic conductivity at low temperatures, thereby enhancing overall system efficiency. However, their performance is dependent on effective humidification, and the use of expensive noble metal catalysts (e.g., platinum) introduces both economic and operational challenges. AFCs, which utilize liquid electrolytes such as potassium hydroxide, also operate at low temperatures (60–90 °C). While they offer high electrical efficiency, their vulnerability to carbon dioxide contamination limits their practical deployment, particularly in large-scale commercial applications. PAFCs use phosphoric acid as the electrolyte and operate at intermediate temperatures (150–200 °C), facilitating heat recovery and making them ideal for combined heat and power (CHP) applications.

High-temperature fuel cells, such as MCFCs (600–700 °C) and SOFCs (800–1000 °C), are capable of internally reforming a broader range of fuels, including hydrogen, methane, and carbon monoxide. MCFCs use molten carbonate salts as electrolytes, while SOFCs rely on ceramic-based oxide ion conductors, such as yttria-stabilized zirconia (YSZ). These configurations offer substantial advantages for large-scale power generation, cogeneration, and industrial applications; however, the high operating temperatures create challenges related to system durability, thermal management, and material degradation [5].

A comparative analysis of these technologies reveals that the choice of electrolyte has a significant impact not only on the internal electrochemical behavior but also on external factors such as system cost, longevity, environmental

performance, and suitability for specific applications. From an environmental standpoint, fuel cells are considered a key component of sustainable energy systems, as their electrochemical reactions yield only water as a by product resulting in much lower emissions compared to traditional fossil fuel-based technologies. When powered by pure hydrogen, fuel cells emit only water vapor and produce no CO_2 or NO_x pollutants [6].

The absence of moving mechanical components also minimizes noise pollution, making fuel cells ideal for urban and residential environments. Furthermore, their high energy efficiency reduces waste heat generation. When integrated with renewable energy sources such as solar or wind power and powered by green hydrogen, fuel cells can operate as fully carbon-neutral systems. However, the current reliance on natural gas for hydrogen production leads to indirect carbon emissions. Additionally, the use of scarce and expensive materials, particularly platinum, raises concerns regarding both environmental and economic sustainability [7-8].

In conclusion, fuel cells are classified into five primary types based on their electrolyte materials: PEMFC, SOFC, AFC, PAFC and MCFC. Each type exhibits unique characteristics that determine its performance, cost, environmental impact, and potential applications.

As seen in the table, the electrolyte type directly influences key operational parameters, including efficiency and application suitability. The continuous development of PEMFCs, particularly in membrane technology, is expected to drive further advancements in fuel cell systems, aligning with sustainability goals and expanding their potential for wider adoption in various industries. Table 1 below summarizes the key performance indicators for each fuel cell type based on their electrolyte materials.

Table 1. Key performance indicators for each fuel cell types

Fuel Cell Type	Operating Temp. (°C)	Efficiency (%)	Primary Fuel
AFC	60-130	60-70 [1, 3, 9]	Hydrogen
MCFC	600-700	45-59,5 [9-10]	Hydrogen, Natural gas
PAFC	150-220	35-49 [1, 11]	Hydrogen
PEMFC	120-160	40-69.48 [1, 2]	Pure Hydrogen
SOFC	800-1000	45-69.48 [12, 13]	Hydrogen, Methane gas, Biogas

Fuel cells exhibit distinct technological advantages based on their operating temperatures and efficiency levels. PEMFCs, operating in the range of 120–160 °C with efficiencies between 40% and 69.48% are particularly well-suited for portable power applications due to their relatively low operating temperature and rapid start-up capabilities [1-2]. Similarly, AFCs, functioning within a lower temperature range of 60–130 °C and offering efficiencies of 60–70%, demonstrate high performance; however, their susceptibility to carbon dioxide contamination restricts their use to controlled environments [3]. PAFCs operate at intermediate temperatures of 150–220 °C, achieving efficiencies of 35–49%, and are predominantly utilized in commercial stationary applications [1]. In contrast, high-temperature fuel cells such as SOFCs, operating at 800–1000 °C with efficiencies ranging from 45% to 69.48%, and MCFCs, functioning at 600–700 °C with efficiencies of 45–59.5%, are particularly advantageous for cogeneration and industrial energy systems due to their ability to utilize various fuels, including methane, biogas, and natural gas [12, 13].

Overall, an increase in operating temperature generally leads to improved system efficiency and fuel flexibility. Nevertheless, this improvement is accompanied by increased system complexity, greater material degradation risks, and higher capital and operational costs. Based on the reported efficiency values, AFCs emerge as the most efficient among low-temperature fuel cells, whereas SOFCs offer the highest efficiency among high-temperature systems.

4. CONCLUSIONS

The comparative evaluation clearly highlights the central role of electrolytes in determining the efficiency, applicability, and operational domains of fuel cell technologies. As fuel cells become increasingly integrated into both stationary and mobile energy systems, optimizing electrolyte selection becomes a critical requirement for maximizing system performance and minimizing overall costs. In this context, future research in materials science, particularly focused on the development of more durable, cost-effective, and highly ion-conductive electrolyte materials will be essential for the broader commercialization and long-term sustainability of fuel cell technologies. This study has comprehensively demonstrated the impact of electrolyte materials used in various types of fuel cells on overall system performance. The findings reveal that the structural properties of the electrolyte play a decisive role in several key parameters, including operating temperature, energy efficiency, fuel adaptability, and application scope. While low-temperature fuel cells offer notable advantages in terms of portability and mobility, high-temperature systems provide more effective solutions for industrial applications and stationary power generation.

REFERENCES

1. O'Hayre R, Cha SW, Colella W, Prinz FB. 2016. Fuel Cell Fundamentals (3rd ed.). Wiley.
2. Barbir F. 2005. PEM Fuel Cells: Theory and Practice. Elsevier.
3. Larminie, J and Dicks A. 2003. Fuel Cell Systems Explained (2nd ed.). John Wiley & Sons.
4. EG&G Technical Services. 2004. Fuel Cell Handbook (7th ed.). U.S. Department of Energy, Office of Fossil Energy, National Energy Technology Laboratory, USA.
5. Singhal SC. 2000. Advances in solid oxide fuel cell technology. Solid State Ionics, 135(1–4), 305–313.
6. Bauen A, Hart D and Fouquet R. 2003. Greenhouse gas implications of using fuel cells in transportation. Journal of Power Sources, 106;1–2:225–235.
7. Steele BCH and Heinzel A. 2001. Materials for fuel-cell technologies. Nature 414; 6861:345–352.
8. Kashem SBA. 2025. A comprehensive review of alkaline fuel cells, Future Sustainability 3;2:35-46.
9. Attada Y, Lezcano G, Velisoju VK, Trueba D, Kulkarni SR, Almofleh A, Aljama H ve Castano P. 2025. Mechanistic and kinetic effects of Ga on a Cu catalyst for CO_2 hydrogenation to methanol. Journal of CO_2 Utilization 96:103086.
10. Kousheshi N, Nouri A, Chitsaz A ve Mehr AS. 2025. Comparative study of CO_2 capture strategies in optimized MCFC-based power systems: Performance, cost, and environmental perspectives. Journal of CO_2 Utilization, 95:103085.
11. Biebl M, Roes J and Hoster H. 2024. Investigation of the technical potential of a hydrogen powered phosphoric acid fuel cell (PAFC) for CHP, Journal of Physics: Conference Series 012014.
12. Kuterbekov KA, Kabyshev AM, Bekmyrza KZ, Kubenova MM, Kabdrakhimova G, Abdullayeva I and Ayalew AT. 2025. Advancements in electrolyte materials and hybrid integration for enhanced solid oxide fuel cell performance. International Journal of Low-Carbon Technologies 20:353-367.
13. Appleby AJ and Foulkes FR. 1989. Fuel Cell Handbook. Van Nostrand Reinhold.

DEVELOPMENT AND ANALYSES OF A NUCLEAR-DRIVEN POLYGENERATION SYSTEM WITH HELIUM BRAYTON CYCLE, HYDROGEN AND AMMONIA PRODUCTION, EJECTOR COOLING, AND DESALINATION

[1*]*Onder Kizilkan*, [1]*Gamze Soyturk*
[1] Isparta University of Applied Sciences, Faculty of Technology, Department of Mechanical Engineering, 32200, Isparta, Türkiye
*Corresponding author e-mail: gamzeyildirim@isparta.edu.tr

ABSTRACT
This study presents the development and analysis of an integrated nuclear-driven polygeneration system combining a helium-cooled closed Brayton cycle with hydrogen and ammonia production, ejector-based combined cooling and power generation, and multistage desalination. The system utilizes high-temperature nuclear heat to simultaneously generate electricity, produce hydrogen via PEM electrolysis, synthesize ammonia, provide refrigeration, and deliver freshwater. A detailed thermodynamic model is established, and energy–exergy analyses are conducted to evaluate system performance. Results indicate that efficient integration of all subsystems ensures high resource utilization and supports sustainable, emission-free multi-output energy generation.

Keywords: Helium Brayton cycle, Nuclear-driven polygeneration, Hydrogen and ammonia production, Ejector refrigeration, Multistage desalination

1. INTRODUCTION
The growing demand for clean, reliable, and sustainable energy has intensified the global focus on advanced nuclear technologies. As societies seek to reduce dependency on fossil fuels and minimize carbon emissions, nuclear-based systems present a promising solution for delivering consistent and high-density energy with minimal environmental impact [1,2]. The rising need for modular, flexible, and scalable power generation has led to the development of compact nuclear systems capable of supporting both centralized and distributed applications [1,3]. Modern nuclear systems are being designed not only for electricity generation but also for cogeneration and multi-generation purposes. These systems aim to efficiently supply combined outputs such as electricity, heat, hydrogen, or freshwater using high-temperature nuclear heat sources. Compared to traditional designs, new-generation modular reactors offer advantages in deployment flexibility, operational safety, and integration with hybrid energy infrastructures [2,4]. Among the available reactor technologies, helium-cooled nuclear systems are particularly attractive due to their high outlet temperatures, chemical stability, and compatibility with closed Brayton cycles. Helium's excellent thermal conductivity and inert nature make it an ideal working fluid for direct or indirect gas-cycle integration. Despite design challenges related to compression and component scaling, helium-based systems enable compact, high-efficiency energy conversion with zero emissions during operation [5]. Recent studies have explored various hybrid configurations that integrate nuclear energy with hydrogen production to improve both operational flexibility and overall plant utility. For instance, Kowalczyk et al. investigated a cogeneration nuclear energy system coupled with power-to-gas technology and demonstrated its potential for balancing intermittent renewables through flexible hydrogen-electric output [6]. Similarly, the GTHTR300 project demonstrated the viability of helium gas turbine-driven high-temperature reactors with compact and simplified safety systems [7]. Other studies have analyzed nuclear-thermochemical cycles for hydrogen production, showing that integrating high-temperature reactors with combined Brayton–Rankine configurations can yield energy efficiencies approaching 50% [8]. Design advancements such as raising reactor outlet temperatures and applying advanced turbine materials have enabled next-generation gas-cooled reactors to surpass 50% overall efficiency without major technology shifts [8]. Previous research on nuclear-assisted hydrogen and electricity co-generation has predominantly emphasized conceptual frameworks, particularly those employing thermochemical cycles such as the iodine–sulfur (IS) process. However, detailed design studies and comprehensive thermodynamic analyses of such systems remain relatively limited. Furthermore, the majority of existing systems rely on conventional steam Rankine or combined gas–steam cycles for power generation, while the implementation of helium closed Brayton cycles—despite their thermodynamic efficiency and structural simplicity—has been relatively underexplored [9]. The helium Brayton cycle is especially well-suited for utilizing high-temperature heat from advanced nuclear systems, enabling compact configurations and improved conversion efficiency. Recognizing this research gap, the present study introduces a novel nuclear-driven polygeneration system that employs a helium Brayton cycle not only for electricity generation but also for supporting hydrogen production, ammonia synthesis, ejector refrigeration, and desalination. Unlike prior efforts limited to dual-output configurations, this work offers a more integrated solution and performs detailed energy and exergy analyses to guide system optimization and performance assessment.

2. CONCEPTUAL SYSTEM LAYOUT
The proposed polygeneration system is centered around a helium-cooled closed Brayton cycle, which utilizes high-temperature nuclear heat to drive multiple subsystems including hydrogen and ammonia production, ejector-based

refrigeration, and multistage desalination (Fig. 1). The primary energy input is supplied by a compact nuclear reactor, which delivers 60 MW of thermal power to the helium working fluid within the reactor core (RC). The helium is heated to a turbine inlet temperature of 850 °C, allowing high-efficiency expansion in the first turbine stage (T1), followed by power extraction through a generator. After expansion, the partially cooled helium enters HE1, where it transfers a portion of its residual thermal energy to the power-ejector refrigeration cycle (PERC). In this subsystem, ammonia (R717) is used as the refrigerant to deliver both refrigeration and additional shaft power via an ejector and turbine assembly (Eje and T2). The helium then continues to HE2, where it provides low-grade heat to the multistage flash (MSF) desalination unit, facilitating seawater evaporation and freshwater extraction. Subsequently, the helium passes through a recuperator (Rec1) to recover part of its thermal energy before entering the compression stages (C1 and C2). Between the compressors, an intercooler (IC) and gas cooler (GC) remove additional heat, maintaining stable cycle operation. This regenerative configuration enhances cycle efficiency and supports stable reactor outlet conditions. Beyond electricity and refrigeration, the system also integrates hydrogen and oxygen production using a proton exchange membrane electrolyzer (PEME). A portion of the electrical output is directed to PEME, where preheated water from HE3 is electrolyzed into hydrogen and oxygen. The produced oxygen is intended for use in aquaculture and industrial oxidation applications, while the hydrogen is directed to an ammonia synthesis reactor (AR). In this reactor, hydrogen reacts with nitrogen—compressed in stages (C3 and C4)—to form ammonia (NH_3), contributing to the chemical output of the system. Freshwater is generated via a three-stage MSF desalination block, where heat from HE2 is used to flash seawater (delivered by P2) in successive chambers. Freshwater is collected (stream 29), while concentrated brine is discharged (stream 30). This configuration enables efficient utilization of the helium stream's temperature gradient across multiple subsystems before its return to the reactor.

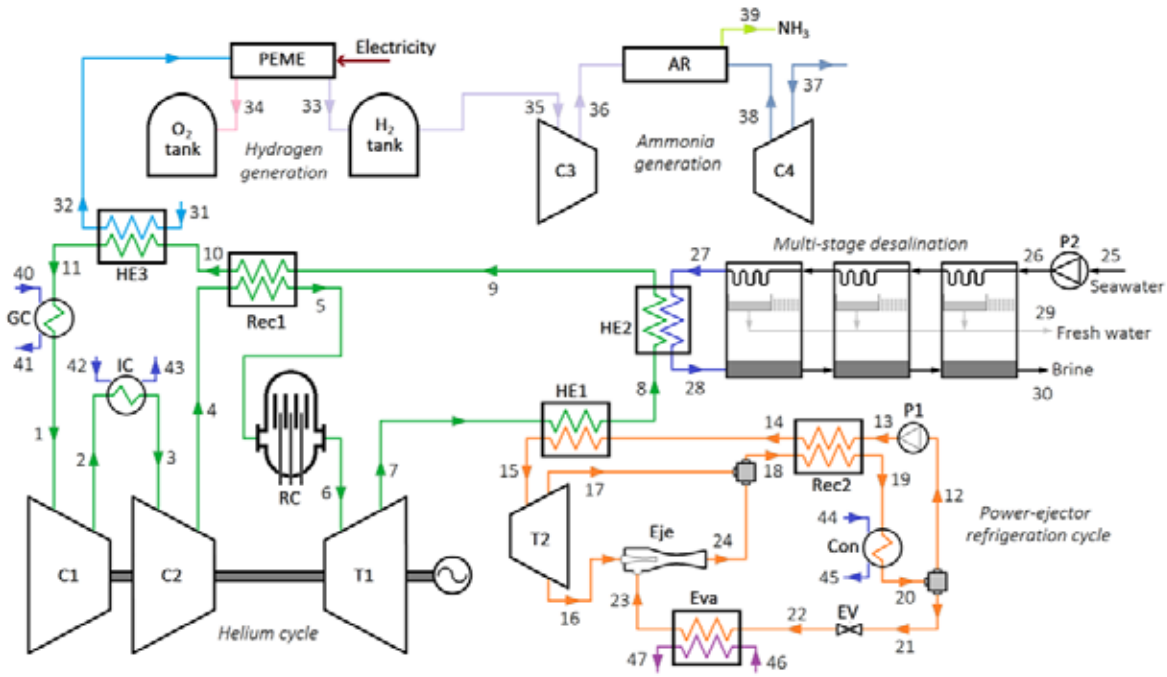

Fig.1. Schematic of the integrated nuclear-driven polygeneration system

3. RESULTS AND DISCUSSION

The proposed nuclear-driven polygeneration system demonstrates strong performance in terms of both energy conversion and multi-product generation. As illustrated in Fig. 2, the system achieves a total net electricity output of 26585 kW, the majority of which—25527 kW—is produced by the helium Brayton cycle. An additional 1335 kW of power is recovered from the power-ejector refrigeration subsystem via the organic Rankine cycle (ORC). Beyond electricity production, the ejector cycle also provides a substantial cooling capacity of 1303 kW, which can be utilized for process or environmental cooling demands. In addition to power and cooling, the system delivers valuable chemical and water products. The proton exchange membrane electrolyzer generates 4.2 kg/h of hydrogen, accompanied by 33.75 kg/h of oxygen as a byproduct. The produced hydrogen is subsequently fed into the ammonia synthesis unit, resulting in an ammonia output of 22.28 kg/h. Moreover, the multistage desalination unit—driven by waste heat recovered from the helium loop—produces 2.31 m^3/h of distilled water.

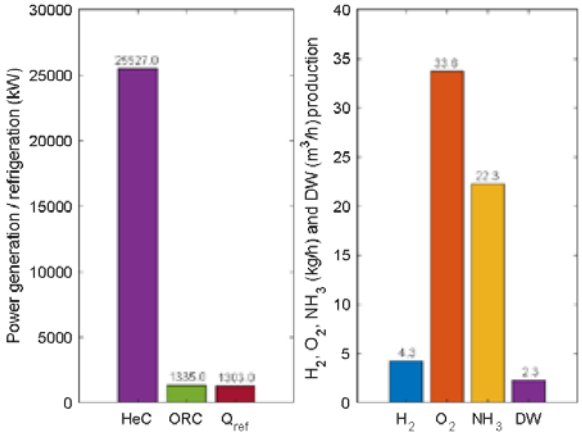

Fig. 2. Energy outputs and product yields of the integrated nuclear polygeneration system

A detailed exergy analysis was conducted to quantify the internal irreversibilities within the proposed system and identify the dominant sources of exergy destruction. As shown in Fig. 3, the total exergy destruction across the entire polygeneration configuration amounts to 19285 kW, indicating the thermodynamic cost of converting nuclear heat into useful outputs under the given design conditions. The most significant source of exergy destruction is the reactor core, which accounts for 7234 kW, corresponding to approximately 37.5% of the total irreversibility. This is primarily due to the large thermal gradients and heat transfer limitations inherent to high-temperature nuclear heat exchange. The second highest contributor is HE1, the heat exchanger that transfers residual helium heat to the power-ejector refrigeration cycle, with a destruction value of 4384 kW. This reflects the thermal mismatch between helium and the ammonia working fluid, as well as the complexity of coupling two subsystems with differing temperature requirements. Other notable sources include the gas cooler (GC) with 1674 kW, the intercooler (IC) at 1463 kW, and the high-temperature turbine T1, which contributes 1317 kW.

To further assess the thermodynamic effectiveness of the integrated polygeneration system, both energy and exergy efficiencies were evaluated across major subsystems, as shown in Fig. 4. The overall system performance reveals an energy efficiency of 46.87% and a higher exergy efficiency of 59.49%, highlighting effective utilization of high-grade nuclear heat with relatively low internal irreversibilities. The helium Brayton cycle, as the core power generation unit, operates at 42.54% energy efficiency and 54.93% exergy efficiency, aligning well with expectations for high-temperature, closed-cycle helium systems. In contrast, the power-ejector refrigeration cycle (PERC) shows more modest performance, with efficiencies of 23.25% (energy) and 31.26% (exergy), due to additional losses associated with ejector expansion and multi-stage heat recovery. For the desalination subsystem (MSF), the energy efficiency is calculated at 29.71%, while the exergy efficiency is significantly lower at 10.95%, indicating substantial exergy destruction in low-temperature heat transfer and phase-change processes typical of thermal desalination. The PEM electrolyzer, powered by TEG-generated electricity, performs with nearly identical energy and exergy efficiencies of 52.59% and 52.24%, respectively.

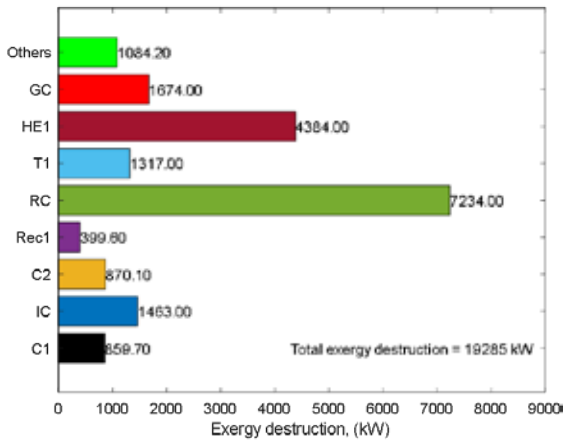

Fig. 3. Component-wise exergy destruction distribution within the integrated system

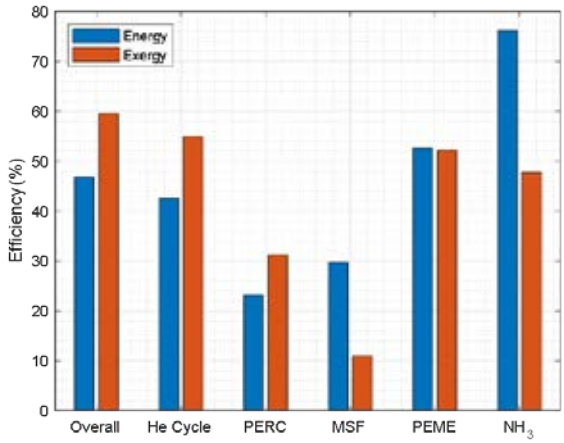

Fig. 4. Energy and exergy efficiencies of the overall system and its major subsystems

A parametric study was conducted to investigate the effect of helium turbine inlet temperature on the thermodynamic performance and subsystem outputs of the proposed polygeneration system. The analysis covers a temperature range from 700 °C to 900 °C, and the results are presented in Fig. 5. Four key performance indicators—net power generation, exergy destruction, energy efficiency, and exergy efficiency—are evaluated simultaneously. As shown in the figure, increasing the turbine inlet temperature leads to a steady rise in net power output, from 22973 kW at 700 °C to 27613 kW at 900 °C. This enhancement is attributed to the greater availability of high-grade thermal energy at the reactor outlet, which improves the expansion work within the helium Brayton cycle. Fig. 6 illustrates the impact of helium turbine inlet temperature on the performance of key secondary outputs of the proposed system, namely refrigeration capacity, distilled water production, hydrogen yield, and ammonia synthesis. Unlike power generation and efficiency trends, all these parameters exhibit a gradual decline as turbine inlet temperature increases from 700 °C to 900 °C.

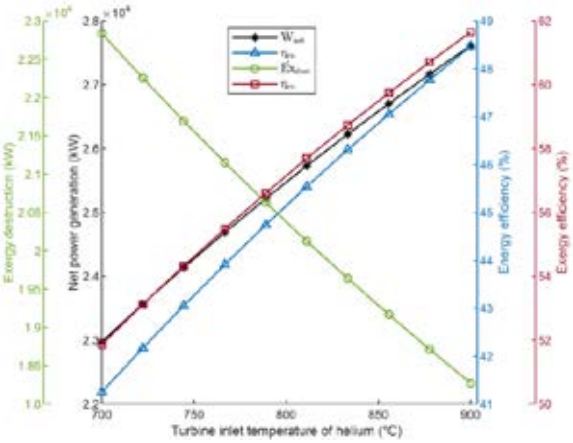

Fig. 5. Variation of net power, exergy destruction, and energy/exergy efficiencies with helium turbine inlet temperature

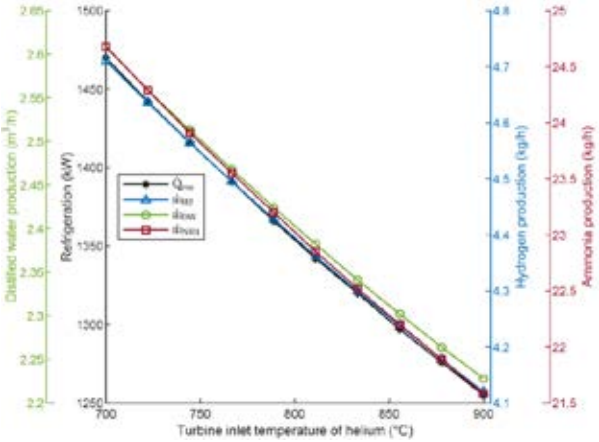

Fig. 6. Variation of refrigeration, distilled water, hydrogen, and ammonia production with helium turbine inlet temperature

4. CONCLUSIONS

This study presented a nuclear-driven polygeneration system integrating a helium Brayton cycle with hydrogen and ammonia production, ejector refrigeration, and multistage desalination. A thermodynamic model was developed, and the system was evaluated through energy and exergy analyses, along with a parametric study based on turbine inlet temperature. The system achieved a total net power output of 26.6 MW, 1.3 MW of refrigeration, and delivered multiple outputs including 4.2 kg/h hydrogen, 22.3 kg/h ammonia, 33.8 kg/h oxygen, and 2.3 m³/h of distilled water. Exergy analysis revealed that the reactor core and HE1 were the main sources of irreversibility, while overall energy and exergy efficiencies reached 46.9% and 59.5%, respectively. Parametric analysis showed that increasing helium turbine inlet temperature improved power and efficiency, but reduced secondary outputs such as cooling, freshwater, and hydrogen, due to reduced low-grade heat availability. This highlights the need to balance high efficiency with multipurpose output in system design. The results confirm that the proposed system offers a feasible and sustainable pathway for clean energy and fuel production, particularly in settings requiring high efficiency and flexible output capability.

REFERENCES

1. Guan C, Chia X, Zhang T, Liu X Y, He H. 2024. The investigation of thermo-economic performance for dry-cooled closed Brayton cycle coupled to nuclear microreactors using different coolants. Journal of Cleaner Production, 455, 142314.
2. Geng X, Wang J. 2024. Simplified Reactor Model for Microreactor Coupled with HeliumClosed Brayton Cycle. Nuclear Technology, 210, 941-957.
3. Gad-Briggs A, Pilidis P, Nikolaidis, T. 2017. Analyses of the control system strategies and methodology for part power control of the simple and intercooled recuperated Brayton helium gas turbine cycles for Generation IV nuclear power plants. ASME Journal of Nuclear Engineering and Radiation Science, 3(4), 041016.
4. Malik A, Zheng Q, Lin A. 2019. The design and performance analysis of highly loaded compressor of closed Brayton cycle HTGR power plant with helium xenon gas mixture as working fluid. Progress in Nuclear Energy, 117, 103084.
5. Qiu L, Liao S, Fa, S, Sun P, Wei, X. 2023. Dynamic modelling and control system design of micro-high-temperature gas-cooled reactor with helium Brayton cycle. Energy, 278(PB), 128030
6. Ni H, Wang X, Zhang Y. 2023. Study of two innovative hydrogen and electricity co-production systems based on very-high-temperature gas-cooled reactors. Energy, 273, 127206.
7. Kowalczyk T, Badur J, Bryk M. 2019. The cogeneration nuclear energy cycle with a power-to-gas solution. Energy, 189, 116189.
8. Kunitomi K, Katanishi S, Takada S, Takizuka T, Yan X. 2004. GTHTR300—A nuclear power plant design with 50% generating efficiency. Nuclear Engineering and Design, 275, 190–196.
9. Jaszczur M, Rosen M. A, Śliwa T, Dudek M, Pieńkowski L. 2016. Hydrogen production using high temperature nuclear reactors: Efficiency analysis of a combined cycle. International Journal of Hydrogen Energy, 41(46), 21378–21388.

DESIGN AND EVALUATION OF DUAL-FLUID GEOTHERMAL CYCLES WITH TRC TOPPING AND ORC BOTTOMING FOR ELECTRICITY, HYDROGEN, AND HDH UNIT

[1*]*Onder Kizilkan*, [1]*Gamze Soyturk*
[1] Isparta University of Applied Sciences, Faculty of Technology, Department of Mechanical Engineering, 32200, Isparta, Türkiye
*Corresponding author e-mail: gamzeyildirim@isparta.edu.tr

ABSTRACT
This study presents the conceptual design and thermodynamic analysis of a geothermal-driven dual-fluid cycle integrating a transcritical Rankine cycle (tRC) as the topping unit and an organic Rankine cycle (ORC) with pentane as the bottoming unit. The system utilizes geothermal heat to drive power generation in both cycles. Various transcritical working fluids, primarily CO_2, are comparatively assessed for the topping cycle to identify the optimal performance configuration. The generated electricity is further utilized to operate a proton exchange membrane (PEM) electrolyzer for hydrogen and oxygen production. In addition, a humidification-dehumidification (HDH) desalination unit is integrated to utilize low-grade heat for freshwater generation. Energy and exergy analyses are conducted to evaluate the performance of individual subsystems and the overall polygeneration potential. The results highlight the advantages of fluid selection in tRC, and the effective use of geothermal heat for multi-output generation with zero carbon emissions.

Keywords: Geothermal energy, Transcritical CO_2 cycle, Hydrogen and water production, Polygeneration system

1. INTRODUCTION

The increasing global demand for energy, driven by population growth and industrialization, has led to a sharp rise in fossil fuel consumption, resulting in severe environmental problems such as CO_2 emissions and global warming [1,2]. The Paris Climate Agreement highlights the urgent need to cut carbon emissions and shift towards renewable energy sources [3]. This transition is essential not only for reducing greenhouse gases but also for enhancing energy security and supporting regional economic growth [4]. However, many renewables like solar and wind are weather-dependent, which limits their reliability. Geothermal energy, on the other hand, offers stable, weather-independent supply with minimal CO_2 emissions [5,6]. Globally, geothermal energy is primarily used for electricity generation through technologies such as flash, binary, and combined flash-binary systems [7]. Among various cycles evaluated for low-temperature geothermal applications, the organic Rankine cycle (ORC) is considered the most promising [8,9]. In recent years, dual-fluid organic Rankine cycles (ORCs) have emerged as a promising configuration for enhancing geothermal energy utilization. A typical dual-fluid ORC configuration includes a thermal linkage between two distinct fluid loops, often using a shared heat exchanger like a low-pressure evaporator. The thermodynamic coordination between the working fluids is crucial—when properly selected, these fluids can operate synergistically, enhancing the overall system efficiency by optimizing heat recovery across different temperature levels. Though such systems offer potential performance benefits, they also introduce added complexity and cost due to their multi-loop architecture and integration demands [10]. Recent studies have demonstrated that dual-fluid ORCs can outperform conventional single-fluid systems in terms of both power output and thermal efficiency, primarily owing to the ability to select different fluids tailored to each cycle's temperature range [11]. This flexibility allows designers to better match the thermodynamic profiles of available heat sources and achieve improved operating conditions [11]. However, dual-fluid configurations that employ a transcritical Rankine cycle (tRC) as the topping cycle and an organic Rankine cycle (ORC) as the bottoming unit are scarcely found in the literature. This combined structure offers potential thermodynamic advantages, yet remains underexplored, particularly for geothermal applications. Despite the widespread focus on geothermal power generation, systems that simultaneously produce electricity, hydrogen, and fresh water remain largely unaddressed in the literature. Few studies have investigated the integration of dual-fluid ORCs with hydrogen production via PEM electrolyzers and desalination technologies [12]. However, to the best of the authors' knowledge, no study has yet examined a dual-fluid configuration utilizing a transcritical Rankine cycle (tRC) as the topping unit and an organic Rankine cycle (ORC) as the bottoming unit for such polygeneration purposes. In the present work, a novel geothermal-based system is proposed that combines a tRC–ORC dual-fluid structure, a proton exchange membrane (PEM) electrolyzer, a humidification–dehumidification (HDH) desalination unit, and a thermoelectric generator (TEG) for enhanced heat recovery. The system is evaluated through detailed energy and exergy analyses to assess its performance in delivering multiple outputs—namely, electricity, hydrogen, and freshwater—with high efficiency and minimal environmental impact. Furthermore, the thermodynamic performance is assessed for various topping cycle fluids, including R744 (carbon dioxide), R170 (ethane), R41 (fluoromethane), and R125 (pentafluoroethane), to identify the optimal working fluid configuration.

2. SYSTEM ARCHITECTURE AND PROCESS FLOW

As illustrated in Fig. 1, the geothermal fluid is extracted from the reservoir at a temperature of 150°C and a pressure of 1200 kPa. It first passes through heat exchanger HE1, where it transfers thermal energy to the working fluid of the transcritical Rankine cycle (tRC). Subsequently, in HE2, the supercritical fluid undergoes a preheating process before entering the high-pressure turbine (T1) and the low-pressure turbine (T2), generating mechanical power. After expansion,

the supercritical working fluid enters HE4, where it transfers residual heat to the organic Rankine cycle (ORC) loop, which uses n-pentane as the working fluid. The partially cooled tRC fluid then flows through TEG1, a thermoelectric generator that converts a portion of the remaining thermal energy—based on the temperature gradient between the working fluid and ambient conditions—into electricity. Finally, the fluid is pressurized by Pump P1 and recirculated to continue the tRC cycle. In the ORC loop, n-pentane is pressurized by Pump P2 (state 15) and preheated in HE3 using geothermal heat. It is further heated in HE4, using waste heat from the tRC cycle, and then expanded through an ORC turbine to produce power. The exhaust from the turbine enters TEG2, generating additional electrical power before the working fluid completes the cycle.

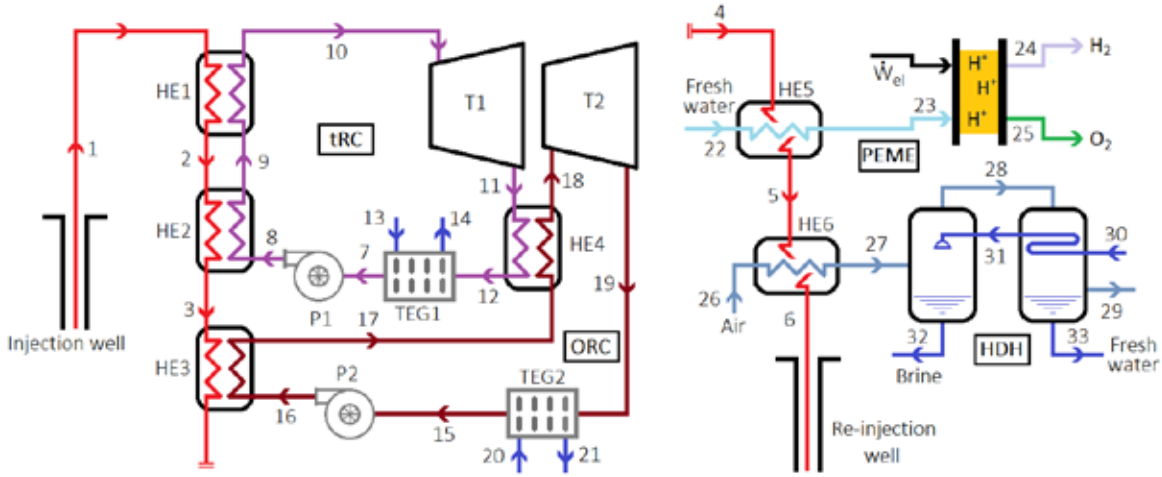

Fig.1. Schematic of the proposed geothermal-based dual-fluid polygeneration system

A portion of the residual heat from the geothermal fluid, after serving both Rankine cycles, is directed to HE5. Here, it is used to preheat deionized water (state 22), which then enters the PEME. The required electrical power for electrolysis is supplied by the TEG units. In the PEME, water is split into hydrogen (H_2) and oxygen (O_2) gases, which are extracted at states 24 and 25, respectively. Following its final heat recovery duty, the geothermal fluid is directed to the air heated HDH desalination unit before re-injection into the reservoir. In this subsystem, ambient air (state 26) is heated in HE6 to approximately 70 °C and enters the humidifier, where it comes into direct contact with a warm saline water stream. The air becomes saturated with moisture and then flows into the dehumidifier, where it transfers heat to incoming cold saline water, causing the moisture in the air to condense. The condensed water is collected as freshwater (state 33), while the remaining brine is discharged at state 32.

3. RESULTS AND DISCUSSION

Fig. 2 presents the comparison of total net power output and total exergy destruction for different topping cycle fluids: carbon dioxide (R744), ethane (R170), fluoromethane (R41), and pentafluoroethane (R125). Among the evaluated options, R170 provides the highest net power generation at 1884 kW, followed closely by R744 (1790 kW) and R41 (1770 kW). The lowest power output is obtained with R125, reaching 1710 kW. In terms of total exergy destruction, R744 exhibits the best performance with 4220.7 kW, indicating lower thermodynamic irreversibility compared to the other fluids. R125, on the other hand, results in the highest exergy destruction (4647.6 kW), which correlates with its relatively low power output. The exergy losses of R170 and R41 are found to be close to each other at approximately 4290.1 kW and 4254.1 kW, respectively. These results indicate that R170 (ethane) offers a favorable balance between high power output and moderate exergy destruction, while R744 (carbon dioxide) stands out for its superior exergy efficiency despite a slightly lower net power output. Thus, both fluids appear as promising candidates for the transcritical topping cycle in geothermal-based polygeneration systems.

Fig. 3 presents the variation in hydrogen production rate (kg/h) and total TEG power output (kW) for different supercritical fluids used in the topping cycle. Although detailed discussion of TEG performance is beyond the current scope, it is important to note that the electrical energy required for the PEM electrolyzer is supplied entirely by the thermoelectric generators, which directly influences the amount of hydrogen produced. Among the evaluated working fluids, R125 (pentafluoroethane) enables the highest hydrogen generation rate, reaching 9.64 kg/h, followed by R170 (ethane) with 8.70 kg/h. These two fluids benefit from higher TEG power outputs and thus yield greater electrolysis capacity. In contrast, R744 (CO_2) and R41 (fluoromethane) result in lower hydrogen production, at 7.60 kg/h and 7.37 kg/h, respectively. This strong correlation highlights the dependency of hydrogen output on TEG-generated power, which in turn is affected by the thermodynamic characteristics of each working fluid.

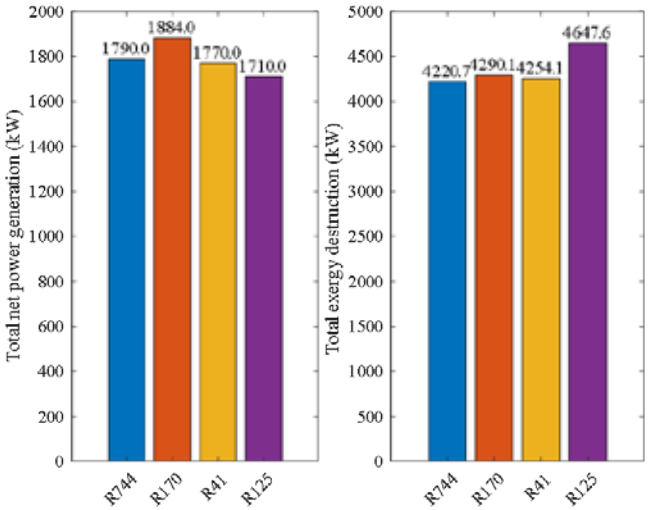

Fig. 2. Total net power output and exergy destruction for different transcritical working fluids

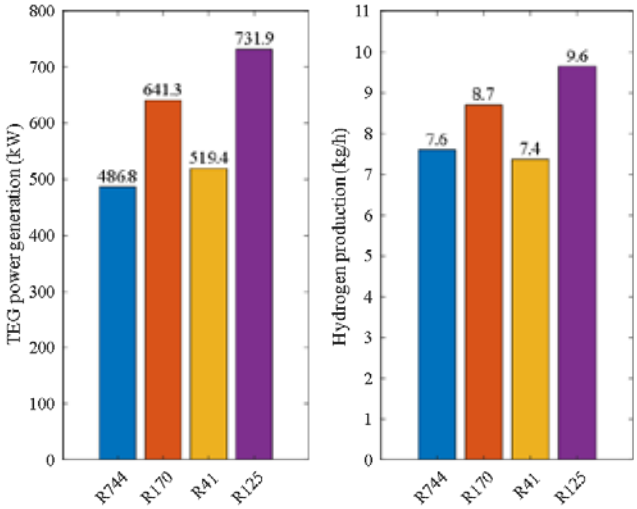

Fig. 3. TEG power generation and corresponding hydrogen production for different transcritical working fluids

Fig. 4 illustrates the total energy and exergy efficiencies of the integrated system for each transcritical working fluid. R170 (ethane) yields the highest performance in both metrics, with an energy efficiency of 12.55% and an exergy efficiency of 30.96%. R744 (carbon dioxide) follows closely, achieving 12.13% energy and 30.87% exergy efficiency. In contrast, R41 and R125 show lower overall performance, with exergy efficiencies of 27.62% and 24.82%, respectively, and energy efficiencies around 10.8%. These results reinforce the thermodynamic advantages of ethane and CO_2 as topping cycle fluids, offering better energy utilization and lower irreversibilities across the polygeneration system.

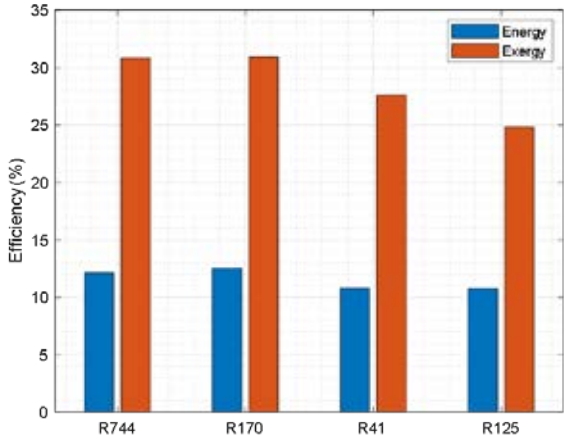

Fig. 4. Total energy and exergy efficiencies of the proposed system for different transcritical working fluids

Fig. 5 illustrates the component-wise exergy destruction distribution for each working fluid. In all cases, the highest

irreversibility occurs in HE2, the primary heat exchanger in the tRC preheating section. For instance, R125 exhibits the greatest exergy destruction in HE2 (1694 kW), followed by R41 (1573 kW), indicating substantial thermal mismatches or inefficiencies during high-temperature heat transfer. HE6, responsible for heating feedwater for the HDH and PEME subsystems, also contributes significantly across all cases (approx. 1070–1108 kW).

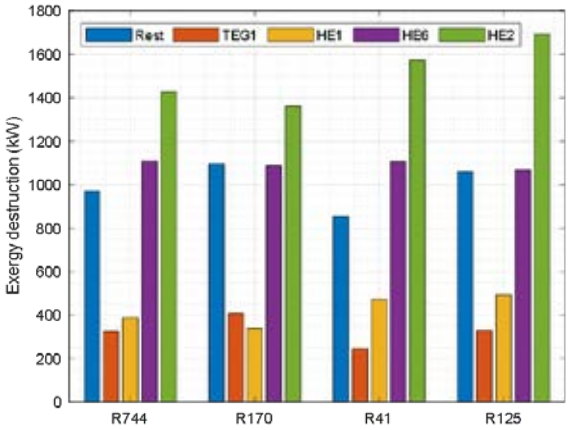

Fig. 5. Component-wise exergy destruction distribution for different transcritical working fluids

4. CONCLUSIONS

This study investigated a novel geothermal-driven polygeneration system integrating a tRC, an ORC, TEGs, a PEM electrolyzer, and an HDH desalination unit. A comparative thermodynamic analysis was conducted for different topping cycle working fluids. The key findings are summarized below:

- Ethane (R170) achieved the highest net power output (1884 kW) and overall system energy (12.55%) and exergy (30.96%) efficiencies.
- CO_2 (R744) demonstrated the lowest exergy destruction (4220.7 kW) and competitive efficiency levels, making it a strong candidate for sustainable operation.
- The highest hydrogen production was obtained with R125, reaching 9.64 kg/h, due to greater TEG power generation (731.9 kW).
- All fluids except R170 provided similar freshwater production via the HDH unit (≈ 4.1 m3/h), while R170 yielded the lowest (1.78 m^3/h) due to limited residual heat.

REFERENCES

1. Cao L, Lou J, Wang J, Dai Y. 2018. Exergy analysis and optimization of a combined cooling and power system driven by geothermal energy for ice-making and hydrogen production. Energy Conversion and Management, 174, 886-896.
2. Boyaghchi FA, Nazer S. 2017. Assessment and optimization of a new sextuple energy system incorporated with concentrated photovoltaic thermal - Geothermal using exergy, economic and environmental concepts. Journal of Cleaner Production, 164, 70-84.
3. Behzadi A, Gholamian E, Ahmadi P, Habibollahzade A, Ashjaee M. 2018. Energy, exergy and exergoeconomic (3E) analyses and multi-objective optimization of a solar and geothermal based integrated energy system. Applied Thermal Engineering, 143, 1011-1022.
4. Lee I, Tester JW, You F. 2019. Systems analysis, design, and optimization of geothermal energy systems for power production and polygeneration: State-of-the-art and future challenges. Renewable and Sustainable Energy Reviews, 109, 551-577.
5. Cheng SWY, Kurnia JC, Ghoreishi-Madiseh SA, Sasmito AP. 2019. Optimization of geothermal energy extraction from abandoned oil well with a novel well bottom curvature design utilizing Taguchi method. Energy, 188, 116098.
6. Pan SY, Gao M, Shah KJ, Zheng J, Pei SL, Chiang PC. 2019. Establishment of enhanced geothermal energy utilization plans: Barriers and strategies. Renewable Energy, 132, 19-32.
7. Cao L, Lou J, Wang J, Dai Y. 2018. Exergy analysis and optimization of a combined cooling and power system driven by geothermal energy for ice-making and hydrogen production. Energy Conversion and Management, 174, 886-896.
8. Darvish K, Ehyaei MA, Atabi F, Rosen MA. 2015. Selection of Optimum Working Fluid for Organic Rankine Cycles by Exergy and Exergy-Economic Analyses. Sustainability, 7, 15362-15383.
9. Gholamiana E, Habibollahzade A, Zare V. 2018. Development and multi-objective optimization of geothermal-based organic Rankine cycle integrated with thermoelectric generator and proton exchange membrane electrolyzer for power and hydrogen production. Energy Conversion and Management, 174, 112-125.
10. Guzovic Z, Raskovic P, Blataric Z. 2014. The comparision of a basic and a dual-pressure ORC (Organic Rankine Cycle): Geothermal Power Plant Velika Ciglena case study. Energy, 76, 175-186.
11. Nami H, Nemati A, Fard Farshad Jabbari. 2017. Conventional and advanced exergy analyses of a geothermal driven dual fluid organic Rankine cycle (ORC). Applied Thermal Engineering, 122, 59-70.
12. Kianfard H, Khalilarya S, Jafarmadar S. 2018. Exergy and exergoeconomic evaluation of hydrogen and distilled water production via combination of PEM electrolyzer, RO desalination unit and geothermal driven dual fluid ORC. Energy Conversion and Management, 177, 339-349.

DEVELOPMENT OF INNOVATIVE CATALYSTS FOR AEM ELECTROLYZERS THROUGH VARIOUS ELECTRODEPOTIONS TECHNIQUES

[1]*Emin Serhat Akyüz*, [2]*Özkan Aydın*, [3]*Bulut Hüner,*[1*]*Esra Telli,* [3]*Murat Farsak*
[1]Osmaniye Korkut Ata University, Faculty of Engineering and Natural Sciences, Department of Energy System Engineering, Osmaniye, 80000, Türkiye
[2] Osmaniye Korkut Ata University, Department of Environmental Protection and Control Technology, Osmaniye, 80000, Türkiye
[3] Osmaniye Korkut Ata University, Department of Hybrid and Electric Vehicles Technology, Osmaniye, 80000, Türkiye

*Corresponding author e-mail: esratelli@osmaniye.edu.tr

ABSTRACT
With the enhancing global energy demand, the environmental impact of carbon emissions from fossil fuels, and concerns about global warming have significantly increased interest in clean and sustainable energy technologies. This study aims to develop and optimize innovative catalyst materials to enhance the performance of Anion Exchange Membrane (AEM) electrolyzers, which hold significant potential for green hydrogen production. In this context, the low-cost transition metal nickel (Ni) was coated onto graphite-based substrates using various electrodeposition techniques, and the electrochemical performance of these electrodepositions was investigated. Electrochemical analyses, including chronoamperometry, chronopotentiometry, cyclic voltammetry (CV), and multi-step chronopotentiometry, were used to compare the effects of different electrodeposition methods on catalytic activity. The results indicate that the electrodepositions obtained via the chronoamperometry method formed more homogeneous and catalytically active surfaces, leading to lower overpotential values and higher hydrogen production performance.

Keywords: AEM Electrolyzer, Electrodeposition Methods, Catalyst, Green Hydrogen

1. INTRODUCTION

The rapidly increasing global energy demand, the environmental impact of fossil fuel dependency, and the worsening climate crisis have made the transition to sustainable and clean energy sources imperative. In this context, hydrogen has emerged as a promising energy carrier due to its high energy density, carbon-free utilization, and wide range of applications. In particular, water electrolysis technologies integrated with renewable energy sources pave the way for carbon-neutral hydrogen production and improve the economic feasibility of green hydrogen. Among electrochemical water-splitting methods, Anion Exchange Membrane (AEM) electrolyzers have attracted considerable attention by combining the advantages of both Proton Exchange Membrane (PEM) and Alkaline Water Electrolyzers (AWE). Among current electrolysis technologies, AEM electrolyzers demonstrate significant potential. However, several challenges must be overcome for their widespread adoption. These include the development of membranes with high ionic conductivity and chemical stability, the enhancement of catalyst efficiency, and the optimization of electrode structures. Operating in an alkaline environment, AEM electrolyzers eliminate the need for expensive and scarce platinum group metals (PGMs), allowing the use of more abundant and cost-effective transition metals such as nickel, iron, and cobalt [1, 2].

The high efficiency of AEM electrolyzers depends not only on membrane materials but also on the performance of electrodes, particularly the effectiveness of catalytic electrodeposition techniques. Electrodes produced using advanced electrodeposition methods with nickel-based materials exhibit high catalytic activity for both the hydrogen evolution reaction (HER) and the oxygen evolution reaction (OER), as well as good mechanical durability and chemical stability. These electrodepositions increase the active surface area of the electrodes, thereby enhancing electrochemical reaction performance [3]. Advanced electrodeposition techniques such as electrodeposition, atomic layer deposition (ALD), and spray pyrolysis have enabled the formation of uniform, nanostructured, and porous catalytic layers that provide a larger electrochemically active surface area and more accessible active sites [4]. This morphological control is critical for reducing charge transfer resistance and improving mass transport during electrolysis. For instance, CP deposition has been shown to produce conformal and homogeneously distributed nickel-based electrodepositions, resulting in electrodes that exhibit lower Tafel slopes and higher current densities at reduced overpotentials [5]. Moreover, surface modifications—such as incorporation of oxygen vacancies or heteroatom doping—can further optimize the electronic structure of catalysts, thereby enhancing their intrinsic activity. Furthermore, the mechanical robustness and chemical stability of these electrodepositions under prolonged electrolysis conditions are critical for the operational durability of AEM electrolyzers. Ni-based electrodes with optimized nanostructures have shown to maintain their structural integrity and catalytic activity over extended testing periods, making them promising candidates for long-term green hydrogen production systems [6].

In this study, the low-cost transition metal nickel (Ni) was deposited onto graphite-based substrates using various electrodeposition techniques, and the resulting electrodes' electrochemical performances were comparatively evaluated.

The electrodepositions were examined with a focus on their impact on catalytic activity, overpotential values, and long-term stability, particularly regarding hydrogen production capability. Electrochemical characterization techniques—such as chronoamperometry, chronopotentiometry, cyclic voltammetry (CV), and multi-step chronopotentiometry—were employed to explore the relationship between surface morphology generated by different electrodeposition methods and hydrogen generation efficiency. The results demonstrated that electrodepositions applied via the chronoamperometric method produced more homogeneous and active surfaces, operated at lower overpotential values, and significantly improved hydrogen production performance. In conclusion, the electrodeposition strategies developed in this study pave the way for the design of optimized electrodes capable of operating AEM electrolyzers with higher efficiency. These strategies offer a sustainable and cost-effective roadmap for green hydrogen production. This research highlights the potential of transition metals in developing low-cost, environmentally friendly, and high-performance electrodes, underscoring their crucial role in the advancement of AEM technology.

2. MATERIALS AND METHODS

For the preparation of the nickel-plating bath, three different chemical components were used: 30 grams of nickel (II) chloride hexahydrate ($NiCl_2 \cdot 6H_2O$), 1.25 grams of nickel (II) sulfate hexahydrate ($NiSO_4 \cdot 6H_2O$) and 1.25 grams of boric acid (H_3BO_3). After weighing these components with a precision balance, they were placed in a beaker and some pure water was added. The resulting mixture was stirred with a magnetic stirrer for approximately 30 minutes until complete dissolution was achieved. After the solution was prepared, it was diluted with pure water to a total volume of 100 mL with a graduated cylinder and finally transferred to a volumetric flask to make the plating bath ready for use. Before the plating process, preliminary cleaning processes were carried out to prepare electrodes suitable for surface electrodeposition. The electrode surfaces were first cleaned in an ultrasonic bath using isopropanol and pure water, and then the drying process was applied. The cleaned electrodes were made suitable for operation in a three-electrode system. In this system, Ag/AgCl was used as a reference electrode, platinum wire as an auxiliary electrode and the sample was used as an electrode. The electrodeposition processes were carried out using different electrochemical methods. Figure 1 shows the I-V curves of different electrodeposition methods.

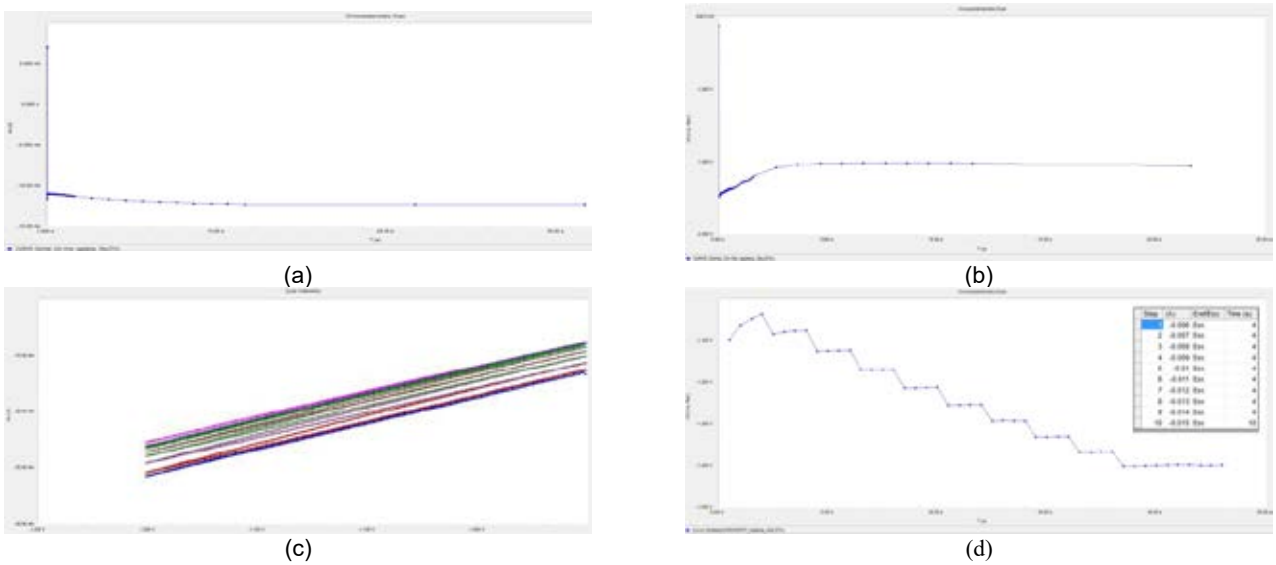

Fig. 1. Electrochemical deposition techniques a) chronoamperometry (CA) b) chronopotentiometry (CP) c) cyclic voltammetry (CV) and d) multi-step chronopotentiometry (MSCP)

With the chronoamperometry (CA) method, a current of 12.3 mA was applied at a constant -1.2 V potential and approximately 0.43 C charge transfer was achieved during this time. In the chronopotentiometry (CP) method, electrodeposition was carried out with a potential of -1.51 V under a constant 14 mA current and a total charge of 0.42 C was transferred. In the cyclic voltammetry (CV) technique, potential scans were performed in three cycles at 5 mV/s, 10 mV/s and 50 mV/s scanning speeds and the electrodeposition characteristics obtained at each speed were compared. In addition, ten steps were applied with multi-step chronopotentiometry method at current values starting from 6 mA and increasing up to 15 mA, a total of 40 seconds of electrodeposition was performed for 4 seconds at each step and approximately 0.42 C charge transfer was achieved. With this multi-step method, it was aimed to obtain a more active and homogeneous electrodeposition on the electrode surface.

3. RESULTS AND DISCUSSION

In this study, various electrochemical electrodeposition techniques were employed to deposit nickel (Ni) onto graphite-

based substrates for use in AEM electrolyzers, and their catalytic performance was evaluated with respect to hydrogen evolution reaction (HER) efficiency. The electrodeposition methods investigated included chronoamperometry (CA), chronopotentiometry (CP), cyclic voltammetry (CV), and multi-step chronopotentiometry (MSCP). Each method influenced the morphology and electrochemical activity of the resulting Ni electrodepositions, thereby affecting hydrogen production performance. Among these techniques, the CA method demonstrated the most promising results. The application of a constant current at -1.2 V produced a uniform and homogeneous Ni electrodeposition, as evidenced by lower overpotential values and higher current densities observed in subsequent electrochemical analyses. Electrodes coated using the CA method exhibited enhanced HER performance due to an increased electrochemically active surface area and improved charge transfer kinetics. Electrodepositions obtained via the CP and MSCP methods also showed moderate catalytic activity, with the MSCP method offering better homogeneity than CP. This improvement was attributed to the stepwise application of current in MSCP, which provided better control over nucleation and growth of the Ni layer. However, both methods exhibited slightly higher overpotentials and less uniform electrodepositions compared to CA. CV-based electrodeposition technique, although useful for understanding redox behavior, resulted in relatively poor catalytic performance. This was primarily due to the less controlled nature of the deposition process and the potential aggregation of Ni particles, which reduced the number of accessible active sites. The superior performance of the CA-based electrodeposition technique can be attributed to the uniform deposition of fine Ni particles, leading to enhanced catalytic activity, improved charge transfer characteristics, and better mechanical stability under operating conditions.

4. CONCLUSIONS

This study successfully demonstrated the development of Ni-based catalyst layers using various electrochemical electrodeposition methods for application in AEM electrolyzers. The CA-based electrodeposition method produced the most homogeneous and catalytically active electrodepositions, leading to lower overpotential values and higher hydrogen production efficiency. These findings highlight the critical role of the electrodeposition technique in determining catalyst morphology, electrochemical performance, and long-term durability. The use of low-cost and abundant transition metals such as nickel, in combination with optimized electrochemical deposition strategies, presents a sustainable and scalable approach to advancing green hydrogen production through AEM electrolyzers. Future research may focus on incorporating dopants or exploring alloying strategies to further enhance catalytic activity and stability.

REFERENCES

1. Lei YC, Zhou W, Zhou Y, Wang M, Zhang A, Zhang L, Wang L. 2024. Advanced development of anion-exchange membrane electrolyzers for hydrogen production: from anion-exchange membranes to membrane electrode assemblies. Chemical Communications 60:11000–11016.
2. Ha JS, Park Y, Jeong JY, Lee SH, Lee SJ, Kim IT, Park SH, Jin H, Kim SM, Choi S, Kim C, Choi SM, Kang BK, Lee HM, Park YS. 2024. Solar-powered AEM electrolyzer via PGM-free (oxy)hydroxide anode with solar to hydrogen conversion efficiency of 12.44%. Advanced Science 11:2401782.
3. Volk EK, Kreider ME, Kwon S, Alia SM. 2024. Recent progress in understanding the catalyst layer in anion exchange membrane electrolyzers – durability, utilization, and integration. EES Catalysis 2:109–137.
4. Jang Y, Kim Y, Jeong W, Ko S, Gil D, Jeong I, Lee M, Ryu S, Jang KH, Cha SW. 2024. Corrosion behavior of Ta and TiN double-layer-coated SUS316L for PEMFC bipolar plates using plasma-enhanced atomic layer deposition and magnetron sputtering. Journal of Alloys and Compounds 977:173379.
5. Ashok V, Mathi S, Sangamithirai M, Jayabharathi J. 2022. Regulated bimetal-doped polyaniline: amorphous-crumple-structured viable electrocatalyst for an efficient oxygen evolution reaction. Energy & Fuels 36:14349–14360.
6. Oni BA. 2025. A review on electrochemical water splitting electrocatalysts for green H_2 production: unveiling the fundamentals and recent advances. Langmuir. (In Press).

Main Sponsor

TENMAK
TURKISH ENERGY, NUCLEAR AND MINERAL RESEARCH AGENCY

Gold Sponsors

armelsan enerji

HABAŞ

Silver Sponsors

Anton Paar

HYDROGENIX

International Association for Hydrogen Energy

Other Sponsors

KURUKAHVECİ MEHMET EFENDİ

B PLAS

DOĞU

TRUVA BAKIR

KUHyTech

TÜBİTAK
(Supported by TÜBİTAK BİDEB 2223-B Program)

CONSAPP innovative solutions

KFC GIDA

DİMES HAYATA BAŞKA BAK

ORGANIZATION SECRETARIAT

BROS
Congress, Incentive and Events

Esentepe Mah. Sağlam Fikir Sok. Esen Palas Apt. A Blok No:2 D:9
Esentepe / Şişli - İstanbul / TURKEY
Tel: + 90 212 296 66 70 / **Fax:** + 90 212 296 66 71
hatice.cilek@brosgroup.net / www.brosgroup.net

ISBN: 978-625-95734-1-0